NGM 2016 Reykjavik

The 17th Nordic Geotechnical Meeting

Reykjavik Iceland

25th – 28th of May 2016



Conference Proceedings

Icelandic Geotechnical Society
Jarðtæknifélag Íslands

NGM 2016 Proceedings

Proceedings of the 17th Nordic Geotechnical Meeting, Reykjavík,
25-28 May 2016

© 2016 The authors and The Icelandic Geotechnical Society: All rights reserved,

Except for fair copying, no part of this publication may be reproduced, stored in a retrieval system, or transmitted in any form or by any means electronic, mechanical, photocopying, recording or otherwise without the prior written permission of the Icelandic Geotechnical Society or the author of the respective paper.

Papers or other contributions in this publications and the statements made or opinions expressed therein are published on the understanding that the author of the contribution is solely responsible for the opinions expressed in it and that its publication does not necessarily imply that such statements or opinions are or reflect the views of the Icelandic Geotechnical Society.

ISBN 978-9935-24-002-6

This proceedings are published as e-book only

The Icelandic Geotechnical Society encompasses members interested in geotechnical engineering, engineering geology and rock mechanics. The members of the Society are simultaneously members of one or more of the international societies:

- ISSMGE - International Society for Soil Mechanics and Geotechnical Engineering
- IAEG - International Association of Engineering Geology and the environment
- ISRM - International Society for Rock Mechanics

Jarðtæknifélag Íslands / Icelandic Geotechnical Society

E-mail: ngm2016@road.is

Web site: www. jtfi.net

Preface

The Icelandic Geotechnical Society welcomes you to Iceland for this 17th Nordic Geotechnical Meeting taking place at Harpa Congress Center in Reykjavík. We hope that the conference exceeds your expectations, with interesting papers, presentations and posters. The aim of the conference is to strengthen the relationship between practicing engineers, researchers and scientists in the Nordic region. The conference is a time of learning and sharing experience and knowledge with fellow colleagues about various challenges in Nordic geotechnics.

The participants are geotechnical engineers and scientists from the Nordic countries as well as other countries all over the world. Five keynote speakers have been invited to the conference; Suzanne Lacasse, Douglas F. VanDine, Jørgen S. Steenfelt, Antonio Gens and Fjóla Guðrún Sigtryggsdóttir. Altogether 137 papers have been received, covering the 12 conference topics, and majority of these will be presented with oral and poster presentation during the meeting.

All submitted papers are included in this publication. The society would like to use this opportunity to gratefully thank the authors and reviewers for making these proceedings and meeting come to life. All others that have contributed to the meeting such as presenters, chairmen and members of the Icelandic Geotechnical Society, we sincerely thank you.

Apart from the technical program, the meeting offers social occasions, with an Opening Ceremony and Reception at the City Hall, a get-together event at Fákasel and a banquet in one of our prides, Perlan, with exceptional views over the city whilst enjoying good company and entertainment.

Please do not hesitate to ask for our assistance, so we can help making your stay in Iceland pleasant and remarkable.

Finally, we would like to thank you all for coming to the bright midnight sun. We hope you have a pleasant stay in Iceland and look forward to seeing you again.

Reykjavík, May 2016

The NGM 2016 Organizing Committee
Aldís Ingimarsdóttir
Andrés Jónsson
Fjóla Guðrún Sigtryggsdóttir
Haraldur Sigursteinsson
Magnea Huld Ingólfsdóttir
Sigurður Erlingsson
Þorbjörg Sævarsdóttir
Þorri Björn Gunnarsson

COMMITTEES & SECRETARY

The local Organizing Committee

Haraldur Sigursteinsson
Fjóla Guðrún Sigtryggsdóttir
Þorri Björn Gunnarsson
Aldís Ingimarsdóttir
Andrés Jónsson
Magnea Huld Ingólfsdóttir
Sigurður Erlingsson
Þorbjörg Sævarsdóttir

Nordic Advisory Committee

Denmark: Jørgen S. Steenfelt, Anders Tovsig S. Andersen, Morten Anker Jørgensen

Finland: Tim Länsivaara, Leena Korkiala-Tanttu, Ilkka Vähäaho

Norway: Frode Oset, Rolf Sandven

Sweden: Gunilla Franzén, Ulf Possfelt, Sölve Hov

Iceland: Birgir Jónsson, Björn Jóhann Björnsson, Pálmi Ragnar Pálmason, Jón G. Skúlason

Congress Secretary

ATHYGLI
RÁÐSTEFNUR

Athygli Conferences,
Síðumúla 28, 108 Reykjavík
www.athygliradstefnur.is
Project manager Þorbjörg Þráinsdóttir
tobba@atconferences.is

Table of contents

Keynotes 15

Hazard, Reliability and Risk Assessment – Research and Practice for Increased Safety
Suzanne Lacasse 17
What is a Geotechnical Professional?
Douglas F. VanDine 43
Working abroad – Expect the unexpected
Jørgen S. Steenfelt 53
The Icelandic national lecture – Hydropower dams in the Land of Ice and Fire
Fjóla Guðrún Sigtryggsdóttir 55

Technical Paper 75

Innovation in Geotechnical Engineering

New Developments in On-line Monitoring of Geotechnical Data
Andres Thorarinsson 77
Bundle Towhead Foundation Design on Rock Berm Installed on Soft Clay
Christian Olsen 87

Investigation, testing and monitoring

Test of bored piles and the outcome of the Danish standard for designing bored piles
Morten Schousboe Rasmussen 99
Is it reasonable to reduce the shaft resistance for bored piles?
Jannie Knudsen 105
Tensile capacity of steel pipe piles drilled in the bedrock
Leena Katariina Korkiala-Tanttu 113
In-situ detection of sensitive clays
Rolf Sandven 123
In-situ detection of sensitive clays
Rolf Sandven 133
Detecting quick clay with CPTu
Sigurður Már Valsson 143
Influence of Operator Procedures on Obtained Accuracy in CPTu Testing
C. Kardan 153
Sample disturbances in block samples on low plastic soft clays
Helene Alexandra Amundsen 159

OATV for strength estimations in Copenhagen Limestone
Natasa Katic ... 169
A preliminary attempt towards soil classification chart from total sounding
Egil Haugen, *Yu Xiang* ... 177
Preliminary results from a study aiming to improve ground investigations data
Bruno di Buò ... 187
Solutions for Various Obstacles Encountered with Laboratory Piping Tests
Axel Manuel Montalvo-Bartolomei ... 199
Determination of pull-out strength and interface friction coefficient of geosynthetic reinforcement embedded in expanded clay LWA
Joanna Gorniak ... 205
Some recent developments on geophysical testing of peat
Mike Long ... 215
Installation of fully grouted piezometers
Kristoffer Kåsin ... 225
Extended interpretation basis for the vane shear test
Anders Samstad Gylland ... 233
COBRA Cable Site Investigations in the Wadden Sea, Denmark
Anna Bondo Medhus ... 241
Founding on (un)known chalk in Aalborg
Caspar Thrane Leth ... 249
Field measurements of pore water pressure in very high plasticity Palaeogene clays in connection to deep excavation and pile driving
Thomas Rye Simonsen ... 257
Freezing-Thawing Laboratory Testing of Frost Susceptible Soils
Amin Zeinali ... 267
Investigation into the effect of uncertainty of CPT-based soil type estimation on CPT-based pile bearing capacity
Omar Hamza ... 277
Oedometer tests with measurement of internal Friction between Oedometer ring and reconstituted clay specimen
Michael Rosenlund Lodahl ... 289
Correlations between shear wave velocities and geotechnical parameters in Norwegian clays
Jean-Sebastien L'Heureux ... 299
Triaxial testing of overconsolidated, low plasticity Clay Till
A. H. Augustesen ... 309
ERT and seismic refraction tomography test at Äspö Hard Rock Laboratory
Mathias Ronczka ... 321
Effects of data acquisition parameters on estimation of stiffness profiles of loose post glacial sites using MASW
Elín Ásta Ólafsdóttir ... 327

Temporary Groundwater Control for Construction of Railway Tunnels in Copenhagen
Jes Michaelsen 337
Strength and deformation properties of volcanic rocks in Iceland
Niels Nielsen Foged 347
Strength increase below an old test embankment in Finland
Marco D'Ignazio 357
Swell pressure and yield stresses in Danish, highly overconsolidated, Palaeogene clays of extreme plasticity
Nik Okkels 367
Utilisation of recycled aggregates in urban earth construction: crushed concrete, foamed glass and ashes
Taavi Dettenborn 377
The influence of grain size distribution and grain shape on the small strain shear modulus of North Sea Sand
Taisiya Biryaltseva 387
Comparison between field monitoring and calculated settlement for railway embankment built on peat
Ulrika Isacsson 397
Forensic engineering of a bored pile wall
Willem Robert De Bruin 403
Theoretical Analysis of the Relationship between Heave and Net Heat Extraction Rates Based on Freezing Experiments
Deniz Dagli 411
Monitored Preloaded Embankments for a County Road in Eastern Norway
Tseday Damtew 423
Undrained shear strength determination and correlations on Søvind Marl
Gitte Lyng Grønbech 431

Modelling, analysis and design

Analysis of a laterally loaded pile in settling soil
Fredrik Resare 441
Contributions of Janbu and Lade as applied to Reinforced Soil
Peter Hoffman 451
Laboratory study on two-dimensional image analysis as a tool to evaluate degradation of granular fill materials
Tommy Edeskar 461
Effect of pile sleeve opening and length below seabed on the bearing capacity of offshore jacket mudmats
Maria Vanberg 471
3D FE tool for time dependent settlement predictions
Hans Petter Jostad 479
Risk analyses in excavation and foundation work
B. Kalsnes 487

Reliability-based design of a monopile foundation for offshore wind turbines based on CPT data
Ida Elise Vikestad Overgård 495
Reliability analysis of pile groups based on dynamic pile testing
Jimmie Andersson 503
A Case Study of the Interaction between a Pile and Soft Soil focusing on Negative Skin Friction using Finite Element Analysis
Pablo Belinchón 513
Application of Thermal Piles in Thawing a Frozen Ground
Gowthaman Sinnathamby 523
A procedure for the assessment of undrained shear strength profile of soft clays
Vikas Thakur 533
Study on the practices for interpretation of preconsolidation stress from oedometer tests
Priscilla Paniagua 547
Physical modeling and numerical analyses of vibro-driven piles with evaluation of their applicability for offshore wind turbine support structures
Aligi Foglia 557
Influence of deviatoric stress dependent stiffness on settlement trough width in 2D and 3D finite element modelling of tunnelling
Nicolas Gilleron 567
Bearing Capacity, Comparison of Results from FEM and DS/EN 1997-1 DK NA 2013
Bjørn Staghøj Knudsen 577
Numerical Models on Anisiotropy of Rocks
Henok Mekonnen Kassa 587
Interpretation of Danish Chalk Design Parameters Applicable to Foundation Design
Lindita Kellezi 597
GeoBIM for optimal use of geotechnical data
Mats Svensson 605
Communication and dissemination, the transition from geotechnical design to construction
Einar Helgason 613
Load bearing capacity of railway embankments
Torben Thorsen 623
Modeling soft Scandinavian clay behavior using the asymptotic state
Jon Abusland Rønningen 633
A rate-dependent creep model for anisotropic soft soils
John Phillip Carter 643
Evaluation of soil parameters for creep calculation of field cases
Gustav Degago 651
Simulation of the Density-driven Groundwater Flow Using the Meshless Local Petrov-Galerkin Method
Juraj Muzik 661

Geosuite - A Modular System for Geotechnical Design
Suzanne Lacasse 667
Geo-assistance for Design Calculations
Suzanne Lacasse 675
Modelling of pile groups and implementations of the non-linear effects in structural modelling programs. -The interface between pile group and superstructure.
Søren Bjerregaard Christensen 685
Back-calculation of the Saint-Alban A test embankment with a new modelling approach in LEM
Ville Jussi Lehtonen 691
Vacuum preloading for a truck parking area in Luhtaanmäki
Monica Susanne Löfman 701
The influence of the shaft friction and pile shape on the pile tip bearing capacity
Stefan Van Baars 711
V-H-M Yield Surface describing Soil Structure Interaction of Sub-sea Structures and Wind Turbines on Caisson Foundations in Soft Clays
Madeleine Brandt 719
Numerical analysis of an upstream tailings dam
Lovisa Hassellund 727
Analysis of settlements in the project The South Marieholm Bridge
Anders Kullingsjö 737
Effects on an earthfill dam undergoing dam safety measures
Jasmina Toromanovic 747
Dynamic analysis of Offshore Wind Energy Converters supported on monopiles in the elastic domain
M .H. Aissa 765

Geotechnical structures and infrastructure

Small-displacement stiffness of static p-y curves for piles in sand
Søren Peder Hyldal Sørensen 775
Design of protective dolphins in demanding geotechnical conditions
Andrija Krivokapic 787
On the use of vertical drains and pore pressure control for soft soil stabilization with lime/cement columns
Frode Oset 797
Engineering and execution of tight sheet walls
Robert Bruin 807
Foundation of the new bridge over the Gota River in downtown Gothenburg
Kien Du-Thinh 817
The traffic junction Lindholmsmotet in Gothenburg: An example of creative geotechnical engineering in the construction phase
Torbjörn Edstam 827

Construction of the Sporðöldu Dam, Iceland
Björn Jóhann Björnsson 835
A geostatistical analysis of variations of permeability within a compacted dam core
Étienne Hébert 845
Deformation Modelling of Unbound Materials in a Flexible Pavement
Þorbjörg Sævarsdóttir 855
Theoretical and experimental investigations of Continuous Compaction Control (CCC) systems
Johannes Pistrol 865
The Experimental Pressure and Sealing Plug (EPSP) Experiment as part of the wider European DOPAS project - rock mass improvement and construction
Irena Hanusova 873
Geotechnical Engineering for a new container terminal in Lomé, Togo, west Africa.
Morten Anker Jørgensen 879
The Use of Geosynthetic Reinforced Retaining Structures Working as Bridge Abutments in Scandinavia and Europe
Marie-Therese van Keßel 887
Compressibility and deformation studies of compacted fly ash/GGBS mixtures
Anil Sharma 897
Peaty ground- made for mass stabilization
Madelene Markusson 905
Modelling of Earth Pressure from nearby Strip Footings on a Free & Anchored Sheet Pile Wall
Hans Denver 913
Geotechnical Infrastructures of New Capital Astana on Problematical Soil Ground
Askar Zhussupbekov 923
Design and construction of a reinforced soil avalanche barrier at Neskaupstaður
David J. Halifax 931
Bearing Capacity, Comparison of Results from FEM and DS/EN 1997-1 DK NA 2013
Bjørn Staghøj Knudsen 941

Foundation and deep excavations

Heave of pile-supported structures due to pile driving in heavily overconsolidated very high plasticity Palaeogene clays
Kenny Kataoka, Dedenroth & Hørlykke 951
Experience and challenges in using a new pile drilling method in highly sensitive clays
Samson Abate Degago 961
Dynamic stiffness of horizontally vibrating suction caissons
Chiara Latini 973
On the design of a deep secant pile wall
Ole Kristian Lied 983

Pore pressure reduction and settlements induced by deep supported excavations in soft clay
Jenny Langford 993
Education of drilling personnel carrying out pile and anchor drilling in Norway
– effect on work quality and new plans for education in Norway.
Ingunn Veimo 1003
Design of Retaining Walls at Metro Nordhavnen - a Case Story
Asbjørn Mathias Dam 1013
Suction caissons subjected to monotonic combined loading
Varvara Zania 1019
Time-related increase in bearing resistance of friction piles
Jussi Kinnunen 1027
Comparison of pile driveability methods based on a case study from an
offshore wind farm in North Sea
Ivana Anusic 1037
Large scale driving of concrete piles in stiff to very stiff clay
Thomas Sandene 1047
DR Koncerthuset in Copenhagen - a concert hall on three legs
Anders Bjerregaard Christensen 1057
Experimental study on axial and lateral bearing capacities of non-welded
composite piles based on pile load test results
Jae Hyun Park 1065
Deep excavation close to the iconic Havnelageret in Oslo city centre
Torbjørn Johansen 1071

Underground infrastructures

Decision-making for increased sustainability in underground construction works by use of
Analytical Decision-making for increased sustainability in underground construction works
using Analytical Hierarchy Process
Miriam S. Zetterlund 1081
Guldborgsund. Immersed tunnel
Per Beck Laursen 1089
Freezing techniques made a new tunnel possible
Jakob Hausgaard Lyngs 1097

Environmental geotechnics

Mechanical weathering effect on tailing particles
Tommy Edeskär 1107
Commercialising reclaimed materials in earthworks – guidelines for productization
and the process of appending these materials in the Finnish national code of practice
Kirsi Koivisto 1117
Multi hazards - Contaminated land vulnerable to natural hazards and climate change effects
Gunnel Göransson 1127

Geotechnical implications of climate change

Climate change and renovation of roads on peat
Henrik Lundström 1137

Geohazards and slope stability

Stress-strain behaviour of the quick clays involved in landslides
Vikas Thakur 1141
The Refne landslide, Halden, Norway: case history and use of risk assessment
Tone Fallan Smaavik 1153
Effects of extreme rainfall on geotechnical hazards in the Canadian Rocky Mountains
Emily Catherine Hunter 1163
Pore pressure response in the upper open aquifer- field investigations and modelling
Hanna Blomén 1173
Climate change induced river erosion as a trigger for landslide
Gunnel Göransson 1183
Landslide risks in a changing climate - The Nors River pilot study area
Karin Bergdahl 1193
Structural characterization of hard rock formation using wireline borehole logging techniques in Titania open pit mine in Norway
Balazs Bela Rigler 1203
Slope Stability Assessment and Evaluation of Remedial Measures Using Limit Equilibrium and Finite Element Approaches
Manuel Neves 1213
Metodik för identifiering av slänter och raviner känsliga för vegetationsförändringar till följd av skogsbruk eller exploatering
Karin Lundström 1223

Geotechnical eartquake engineering

Effects of soil-structure interaction on the excitation and response of RC buildings subjected to near- and far-field earthquake strong-motion
Jónas Þór Snæbjörnsson 1233
On the HVSR characteristics at Icelandic strong-motion stations
Benedikt Halldórsson 1243
Seismic Response of Squat Walls Founded on Gravel Cushions
Sara Rose Nodroff 1253

Geotechnical code and standards

An attempt towards harmonizing the Norwegian guidelines related to construction on sensitive clay
Kristian Aunaas 1263

Transportation geotechnics and geophysics

Experiences of integrated GPR and Laser Scanner analysis
- We should not only look down but also around
Timo Saarenketo 1273
Full scale reinforced road embankment test sections over soft peat layer, Võõby, Estonia
Juha Forsman 1279
Refraction seismic for mapping of limestone surface in a tunnel project in Copenhagen
Roger Wisén 1289
Deep excavation close to the iconic Havnelageret in Oslo city centre
Guillaume Sauvin 1297
Underwater ERT Surveys in Central Stockholm
Torleif Dahlin 1307
An integrated approach to Geotechnics and Geophysics on the Electrification Programme in Denmark
David Ross Alvin 1313
Statistical analysis of thaw index for thaw weakening design purposes
Tommy Edeskar 1321
Resistivity measurements as a tool for optimizing groundwater protection at a highway construction in Sweden
Roger Wisén 1329
Automated co-interpretation of geophysical data for site investigation
Kristofer Hellman 1335

List of authors 1339

Conference Sessions 1343

Keynotes

Plenum 1 – Suzanne Lacasse

Norwegian Geotechnical Institute (NGI)

Hazard, Reliability and Risk Assessment
- Research and Practice for Increased Safety

Plenum 2 – Douglas F. VanDine

President of the Canadian Geotechnical Society 2015-2016

What is a Geotechnical Professional?

Plenum 3 – Jørgen S. Steenfelt

Technical Director Marine & Foundation Engineering, COWI, Dk.

Working abroad – Expect the unexpected

Plenum 4 – Antonio Gens

Vice-President of the ISSMGE for Europe 2013-2017

The current status and ongoing work at ISSMGE with a special focus on the activities of the TCs

Plenum 5 – Fjóla Guðrún Sigtryggsdóttir

NTNU, Department of Hydraulic and Environmental Engineering, Trondheim, Norway

The Icelandic National Lecture
- Hydropower dams in the Land of Ice and Fire

Hazard, Reliability and Risk Assessment - Research and Practice for Increased Safety

Suzanne Lacasse
Norwegian Geotechnical Institute (NGI), Norway, suzanne.lacasse@ngi.no

ABSTRACT
Society increasingly requires the engineer to quantify and manage the risk which people, property and the environment are exposed to. The role of the geotechnical engineering profession is to reduce exposure to threats, reduce risk and protect people. Hazard, reliability and risk approaches are excellent tools to assist the geotechnical engineer in design, selection of engineering foundation solutions and parameters and decision-making. The significance of factor of safety is discussed, and basic reliability and risk concepts are briefly introduced. The importance of designing with a uniform level of reliability rather than a constant safety factor prescribed in codes and guidelines is illustrated. The paper illustrates the use of the reliability and risk concepts with "real life" case studies, in particular for situations encountered for Nordic environments. The calculation examples are taken from a wide realm of geotechnical problems, including avalanche, railroad safety, mine slopes and soil investigations. The synergy of research and practice and their complementarity for increasing safety and cost-effectiveness is illustrated. With the evolution of reliability and risk approaches in geotechnical engineering, the growing demand for hazard and risk analyses in our profession and the societal awareness of hazard and risk makes that the methods and way of thinking associated with risk need to be included in university engineering curricula and in most of our daily designs.

Keywords: Hazard, risk, risk assessment, uncertainties, factor of safety.

1 INTRODUCTION

More and more, society requires that the engineer quantify the risk to which people, property and the environment can be exposed. The geo-engineering profession should increasingly focus on reducing exposure to threats, reducing risk and protecting people. The paper shows how concepts of hazard, risk and reliability can assist with safer design and in decision-making. After an introduction of reliability concepts, the paper presents "real life" case studies where risk and reliability tools provided insight for informed decision-making. Because factor of safety remains the main indicator of safety in practice, its significance for design is also briefly discussed in terms of reliability. The tolerable and acceptable risk and risk perception are illustrated.

There is a need for increased interaction among disciplines as part of providing a soundly engineered solution. The engineer's role is not only to provide judgment on safety factor, but also to take an active part in the evaluation of hazard and risk.

Societal awareness and need for documenting the safety margin against 'known' and 'unknown' hazards require that the engineer manage risk.

The calculation examples presented in the paper are taken from a wide realm of geoscientific problems, including avalanches, hazards and risk associated with railroad traffic, mine slopes and soil investigations.

2 EXPOSURE TO GEO-RISKS

Society is exposed to both natural and human-induced risks, and while the risk can never be eliminated, the engineer's goal is to reduce the risk to levels that are acceptable or tolerable. Coordinated, international, multidisciplinary efforts are required to develop effective societal response to geo-risks. The

needs in practice are accentuated by recent events with disastrous impact:

- Recent earthquakes in El Salvador (2001), India (2001), Iran (2003), Pakistan (2005), China (2008), Haiti (2010), Japan (2011), Christchurch (2011) and Nepal (2015) caused high fatalities and made many homeless. In 2010, earthquakes ravaged Chile, China, Sumatra and Iran. Earthquakes often lead to cascading events such as landslides, avalanches, lake outburst floods and debris flows.
- Tsunamis (e.g. Indian Ocean 2004; Tōhoku 2011) cause enormous personal and societal tragedies. The Japan disaster showed the vulnerability of a strong prosperous society, and how cascading events paralyzed an entire nation, with worldwide repercussions. Since 2004, at least eight tsunamis have caused fatalities. In Norway, tsunamigenic rock slides caused the loss of 174 lives in the past 110 years.
- The Baia Mare tailings dam breach for a gold mine in Romania (2000) released cyanide fluid, killing tons of fish and poisoning the drinking water of 2 million people in Hungary. The Aznalcóllar tailings dam failure in Spain (1998) released 68 million m^3 of contaminated material into the environment. The Mount Polley tailings dam breach (2014) was Canada's largest environmental disaster ever.
- The collapse of Skjeggestad bridge in Norway and of a viaduct at Scillato in Italy, both due to landslides in early 2015, as well as unexpected failures in tunnels, cost millions of dollars for repairs. Roads and railways in Norway are increasingly exposed to landslide and avalanche hazards. Often, the fact that no lives were lost in these four examples is only due to coincidental sets of lucky circumstances.

Many lives could have been saved if more had been known about the risks associated with the hazards and if risk mitigation measures had been implemented. A proactive approach to risk management is required to reduce the loss of lives and material damage. A milestone in recognition of the need for disaster risk reduction was the approval by 164 United Nations (UN) countries of the "Hyogo Framework for Action 2005-2015: Building the Resilience of Nations and Communities to Disasters" (ISDR 2005).

Since the 80's, hazard and risk assessment of the geo-component of a system has gained increased attention. The offshore oil and gas, hydropower and mining sectors were the pioneers in applying the tools of statistics, probability and risk assessment in geotechnical engineering. Environmental concerns and natural hazards soon adopted hazard and vulnerability assessment.

Whitman (1996) offered examples of probabilistic analysis in geo-engineering. He concluded then that probabilistic methods are tools that can effectively supplement traditional methods for geotechnical engineering projects, provide better insight into the uncertainties and their effects and an improved basis for interaction between engineers and decision-makers. Nowadays, the notion of hazard and risk is a natural question in the design of most constructions

3 IMPORTANCE OF UNCERTAINTIES IN GEOTECHNICAL ENGINEERING

3.1 Uncertainty-based analyses

Accounting for the uncertainties in foundation analysis has now become a frequent requirement. Statistics, reliability and risk estimates are useful decision-making tools for geotechnical problems that can account for the uncertainties. Uncertainty-based analyses are needed because geotechnical design is not an exact science. Uncertainty in foundation performance, due to soil spatial variability, limited site exploration, limited calculation models and limited soil parameter evaluation, is unavoidable.

Uncertainty-based analysis can be done with the statistical and reliability theory tools available today (Lacasse 1999; Ang and Tang 2007; Baecher and Christian 2003).

It is important to adopt approaches that inform of and account for the uncertainties. Only by accounting for the uncertainties, can the designer get insight in the risk level.

Risk considers the probability of an event occurring and the consequences of the event should it occur. The purpose of risk analysis is to support the decision-making process, given plausible scenarios. The probabilities are the quantification of one's uncertainty.

3.2 Factor of safety and uncertainties

The factor of safety gives only a partial representation of the true margin of safety that is available. Through regulation or tradition, the same value of factor of safety is applied to conditions that involve widely varying degrees of uncertainty. That is not logical.

The factor of safety against instability is a measure of how far one may be from failure. Factors of safety are applied to compensate for uncertainties in the calculation. If there were no uncertainties, the factor of safety could be very close to 1.

There is therefore always be a finite probability that the foundation slope. Defining the level of the finite probability that is tolerable is the challenge. The geotechnical engineer should provide insight in this discussion. To select a suitable factor of safety, one therefore needs to estimate the uncertainties involved. There exists no relationship between safety factor based on limit equilibrium analysis and annual probability of failure. Any relationship would be site-specific and depends on the uncertainties in the analysis.

3.3 Factors of safety for a piled installation

As example of deterministic (conventional) and probabilistic analyses of the axial capacity of an offshore piled foundation were done. First, before pile driving (1975), with limited information and limited methods of interpretation of the soil data, and second, 20 years later, when more information had become available and a reinterpretation of the data was done with the new knowledge accumulated over the 20 years. The soil profile consisted of mainly stiff to hard clay layers, with thinner layers of dense sand in between. The profiles selected originally showed wide variability in the soil strength, with considerably higher shear strength below 20 m. No laboratory tests, other than strength index tests, were run for the 1975 analyses to quantify the soil parameters, and sampling disturbance added to the scatter in the results.

During pile installation, records were made of the blow count during driving. These records were used 20 years later to adjust the soil profile, especially the depth of the stronger bearing sand layers. New samples were also taken and triaxial tests were run. The new evaluation indicated less variability in the strength than before.

The requirement was a factor of safety of 1.50 under extreme loading and 2.0 under operation loading. The analyses used the first-order reliability method (FORM). Each of the parameters in the calculation and the calculation model were taken as random variables, with a mean and a standard deviation and a probability density function.

Figure 1 presents the results of the analyses. The newer deterministic analysis gave a safety factor (FS) of 1.4, which was below the requirement of 1.50. However, the newer information reduced the uncertainty in both soil and load parameters. The pile with a safety factor of 1.4 has significantly lower failure probability (P_f) that the pile which had a safety factor of 1.79 twenty years earlier. Taking into account the uncertainties showed that the pile, although with lower safety factor, had higher safety margin than the pile with a much higher safety factor calculated at the time of pile driving.

The implications of Figure 1 are very important. A foundation with a central factor of safety of 1.4 was safer than a foundation with a higher central factor of safety 1.8 and had a much lower annual probability of failure. Factor of safety alone is not a sufficient measure of the actual safety.

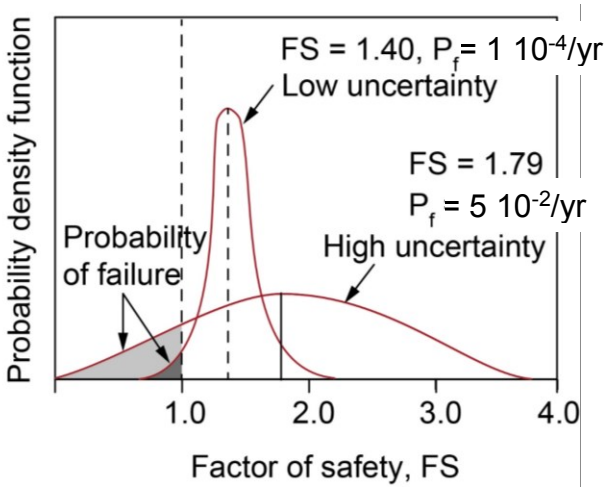


Figure 1 Factor of safety and probability of failure.

One also needs to be aware that the factor of safety is never zero. Factor of safety is not a sufficient indicator of safety margin because the uncertainties in the analysis parameters

affect probability of failure. The uncertainties do not intervene in the conventional calculation of safety factor.

Figure 1 illustrates with probability density functions the notion that the factor of safety alone is not a sufficient measure of the margin of safety. In addition, the safety factor should not be a constant deterministic value, but should be adjusted according to the level of uncertainty. Ideally, one could calibrate the required safety factor that would ensure a target annual probability of failure of for example 10^{-3} or 10^{-4}.

The essential component of the estimate of an annual probability of failure estimate is geotechnical expertise. A clear understanding of the physical aspects of the geotechnical behavior to model is needed. The experience and engineering judgement that enter into all decisions for parameter selection, choice of most realistic model and reasonableness of the results, are also absolutely essential components. The most important contribution of uncertainty-based concepts to geotechnical engineering is increasing awareness of the uncertainties and of their consequences. The methods used to evaluate uncertainties, annual probability of failure are tools, just like any other calculation model or computer program.

3.4 Comparison of two analysis approaches

Stability analyses were done with the effective stress (ESA) and the total stress (TSA) approaches. The first approach uses friction angle (ϕ'), cohesion and pore pressures (or the effective stress path), the second uses undrained shear strength and in situ effective stresses (total stress path). Factor of safety was defined as the ratio between the tangent of the friction angle at failure and the tangent of the friction angle mobilized at equilibrium for the ESA approach. For the TSA approach, the factor of safety was defined as the ratio between the undrained shear strength and the shear stress mobilized at equilibrium.

A shallow foundation on a contractive and on a dilative soil was analyzed (Nadim *et al* 1994; Lacasse 1999). The effective stress paths for each soil type are illustrated in Figure 2. The "true" safety margin for the foundation (or probability of failure, P_f) is independent of the method of analysis.

Table 1 presents the results of the calculations. Depending on soil type, the computed annual probability of failure differed significantly for the two approaches.

The results of the analyses, both deterministic (in terms of factor of safety, *FS*) and probabilistic (in terms of annual probability of failure, P_f) showed significant differences for the dilatant soil as the uncertainties in the soil parameters influenced differently the failure probability.

For the effective stress approach, the uncertainties in the cohesion and pore pressure close to failure had the most significant effect on the probability of failure. For the total stress approach, the uncertainties in undrained shear strength had the most significant effect on the probability of failure. To have the two analysis methods give consistent results at a safety factor of 1.0, a model uncertainty would have to be included. Again factor of safety gives an erroneous impression of the actual safety margin.

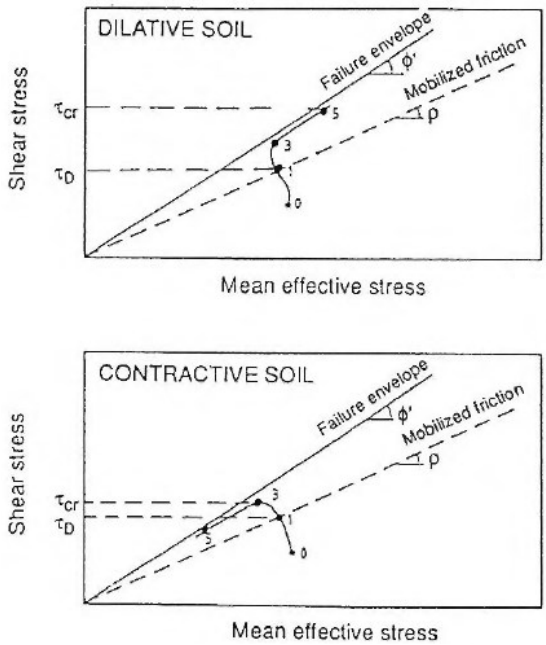


Figure 2. Mobilized friction angle and available shear strength approaches for contractive and dilative soils[1].

[1] Notation: ρ is the mobilized friction angle; numbers on stress path indicate shear strain in percent; τ_{cr} is the critical shear stress at yield; τ_D is the mobilized shear stress in design; in the ESA analysis, the material coefficient is $\tan\phi'/\tan\rho$; in the TSA analysis, the material coefficient is τ_{cr}/τ_D.

Table 1. Stability analyses with two approaches.

Analysis	Soil type	*FS*	Annual P_f
ESA	Contractive	1.9	1.7×10^{-5}
TSA	Contractive	1.4	2.5×10^{-3}
ESA	Dilative	1.4	6.7×10^{-3}
TSA	Dilative	1.5	2.3×10^{-6}

Notation
ESA Effective stress analysis
TSA Total stress analysis
FS Factor of safety
P_f Probability of failure

4 BASIC RELIABLITY CONCEPTS

4.1 Terminology

The terminology used in this paper is consistent with the recommendations of ISSMGE TC32 (2004) Glossary of Risk Assessment Terms:

Danger (Threat): Phenomenon that could lead to damage, described by geometry, mechanical and other characteristics, involving no forecasting.

Hazard: Probability that a danger (threat) occurs within a given period of time.

Exposure: The circumstances of being exposed to a threat.

Risk: Measure of the probability and severity of an adverse effect to life, health, property or environment. Risk is defined as Hazard × Potential worth of loss.

Vulnerability: The degree of loss to a given element or set of elements within the area affected by a hazard, expressed on a scale of 0 (no loss) to 1 (total loss).

Figure 3 illustrates how hazard, exposure and vulnerability contribute to risk with the so-called "risk rose".

4.2 Risk assessment and management

Risk management refers to coordinated activities to assess, direct and control the risk posed by hazards to society. Its purpose is to reduce the risk. The management process is a systematic application of management policies, procedures and practices. Risk management integrates the recognition and assessment of risk with the development of appropriate treatment strategies. Understanding the risk posed by natural events and man-made activities requires an understanding of its constituent components, namely characteristics of the danger or threat, its temporal frequency, exposure and vulnerability of the elements at risk, and the value of the elements and assets at risk. The assessment systemizes the knowledge and uncertainties, i.e. the possible hazards and threats, their causes and consequences. This knowledge provides the basis for evaluating the significance of risk and for comparing options.



Figure 3. Figure 1. Components in the "risk rose" (after IPCC 2012).

Risk assessment is specifically valuable for detecting deficiencies in complex technical systems and in improving the safety performance, e.g. of storage facilities.

Risk communication means the exchange of risk-related knowledge and information among stakeholders. Despite the maturity of many of the methods, broad consensus has not been established on fundamental concepts and principles of risk management.

The ISO 31000 (2009) risk management process (Fig. 4) is an integrated process, with risk assessment, and risk treatment (or mitigation) in continuous communication and consultation, and under continuous monitoring and review. ISO correctly defines risk as "the effect of uncertainties on objectives".

Higher uncertainty results in higher risk. With the aleatory (inherent) and epistemic (lack of knowledge) uncertainties in hazard, vulnerability and exposure, risk management is effectively decision-making under uncertainty. The risk assessment systemizes the knowledge and uncertainties, i.e. the possible hazards and threats, their causes and consequences (vulnerability, exposure and value). This knowledge provides the basis for comparing risk reduction options.

Today's risk assessment addresses the uncertainties and uses tools to evaluate losses

with probabilistic metrics, often in terms of expected annual loss and probable maximum loss, costs and benefits of risk-reduction measures and use this knowledge for selecting the appropriate risk treatment strategies.

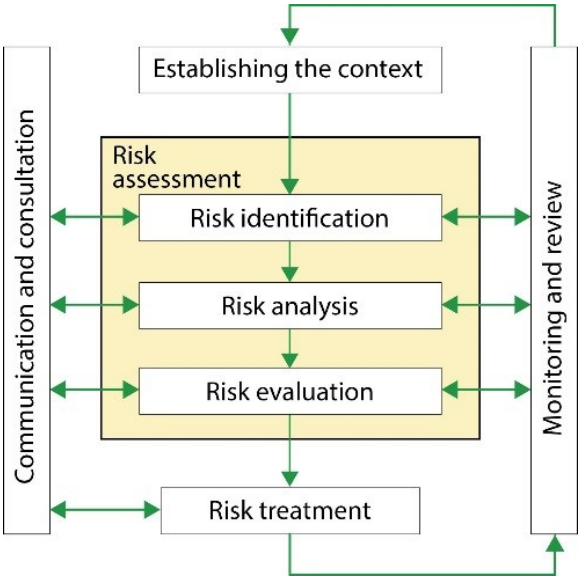


Figure 4 Risk management process (after ISO 2009).

Many factors complicate the risk picture. Urbanization and changes in demography are increasing the exposure of vulnerable population. The impact of climate change is altering the geographic distribution, frequency and intensity of hydro-meteorological hazards. the impact of climate change also threatens to undermine the resilience of poorer countries and their citizens to absorb loss and recover from disaster impacts.

4.3 Acceptable and tolerable risk

A difficult task in risk management is establishing risk acceptance criteria. There are no universally established individual or societal risk acceptance criteria for loss of life due to landslides.

For individual risk to life, AGS (2000) suggested, based on criteria adopted for Potentially Hazardous Industries, Australian National Committee on Large Dams (ANCOLD 1994; ANCOLD 2003), that the tolerable individual risk criteria shown in Table 2 "might reasonably be concluded to apply to engineered slopes". They also suggested that acceptable risks can be considered to be one order of magnitude lower than the tolerable risks.

Table 2. Suggested tolerable risk (AGS 2000).

Slope types	Tolerable risk for loss of life
Existing engineered slopes	10^{-4}/year for person most at risk 10^{-5}/year for average person at risk
New engineered slopes	10^{-5}/year for person most at risk 10^{-6}/year for average person at risk

With respect to societal risk to life, the application of life criteria reflects that society is less tolerant of events in which a large number of lives are lost in a single event, than of the same number of lives are lost in several separate events. Examples are public concern to the loss of large numbers of lives in an airline crash, compared to the many more lives lost in traffic accidents.

As guidance to what risk level a society is apparently willing to accept, one can use *'F-N* curves'. The *F-N* curves relate the annual (or any temporal) probability (*F*) of causing *N* or more fatalities to the number of fatalities. The term "*N*" can be replaced by other measures of consequences, such as costs. *F-N* curves give a good illustration for comparing calculated probabilities with, for example observed frequencies of failure of comparable facilities. The curves express societal risk and the safety levels of particular facilities.

Figures 5 and 6 present families of *F-N*-curves. GEO (2008 compared societal risks in a number of national codes and standards Figure 5 presents the comparison. Although there are differences, the risk level centers around 10^{-4}/year for ten fatalities. Figure 6 illustrates the risk for different types of structures. Man-made risks tend to be represented by a steeper curve than natural hazards in the *F-N* diagram (Proske 2004). On the *F-N* diagram in Figure 7, lines with slope equal to 1 are curves of equirisk, where the risk is the same for all points along the line. The *F-N* curves can be expressed by the equation:

$$F \cdot N^{\alpha} = k \qquad (1)$$

For a *k*-value of 0.001, α becomes unity (1). An *F-N* slope greater than 1 reflects the aforementioned risk aversion The ALARP zone represents the risk considered to be "As Low As Reasonably Practicable". Figure 7 also contains an illustration of ALARP: risk

is to be mitigated to a level as low as reasonable practical. The residual risk is marginally acceptable and any additional risk reduction requires a disproportionate mitigation cost/effort, or is impractical to implement.

Acceptable risk is the level of risk society desires to achieve. Tolerable risk refers to the risk level reached by compromise in order to gain certain benefits. A construction with a tolerable risk level requires no action nor expenditure for risk reduction, but it is desirable to control and reduce the risk if the economic and/or technological means for doing so are available.

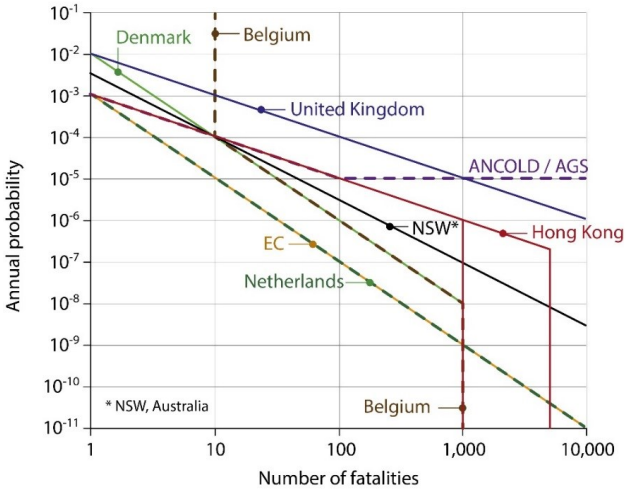


Figure 5. Comparison of risk guidelines in different countries (after GEO 2008).

Risk acceptance and tolerability have different perspectives: the individual's point of view (individual risk) and the society's point of view (societal risk). Figure 8 presents an example of accepted individual risks for different life or recreation activities. The value of 10^{-4}/year is associated with the risk of a child 5 to 9 years old dying from all causes.

The *F-N* diagrams have proven to be useful tools for describing the meaning of probabilities and risks in the context of other risks with which society is familiar.

Risk acceptability depends on factors such as voluntary vs. involuntary exposure, control or not, familiarity vs. unfamiliarity, short vs long-term effects, existence of alternatives, consequences and benefits, media coverage, personal involvement, memory, and trust in regulatory bodies. Voluntary risk tends to be higher than involuntary risk (driving a car).

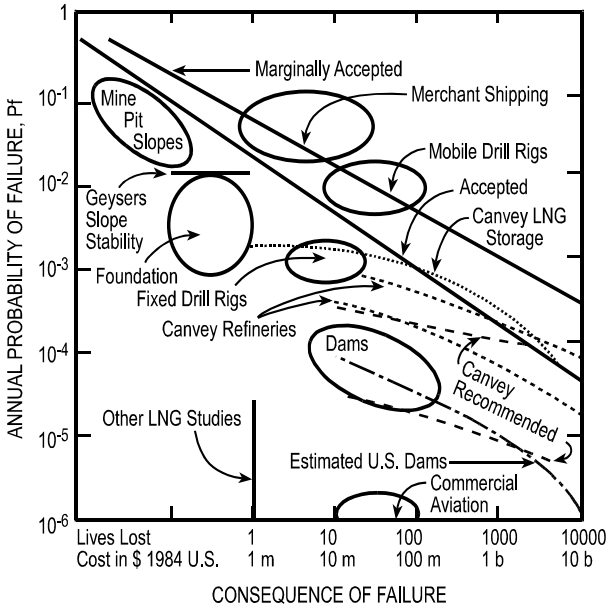


Figure 6. Examples of risk levels for different construction and activities (Whitman 1984).

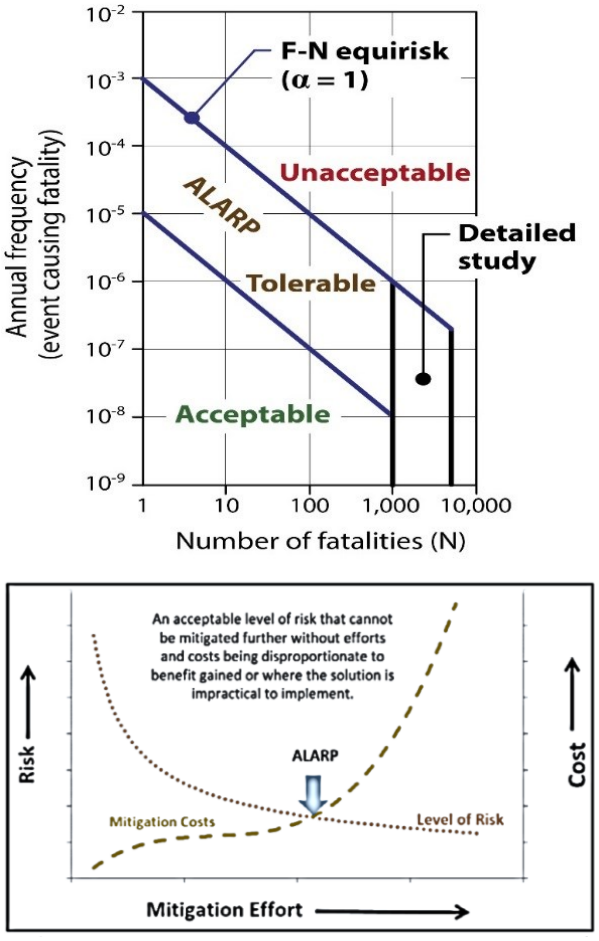


Figure 7. F-N curves, lines of equirisk and significance of ALARP (lower diagram, CAA 2016).

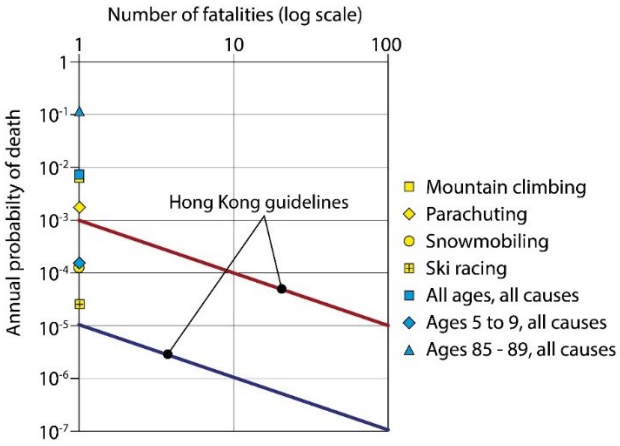


Figure 8. Accepted individual risks (Thomas and Hrudey 1997; Hutchinson2011 Personal comm..)

Figure 9 illustrates how "perceived" and "objective" risk can differ. Whereas the risk associated with flooding, food safety, fire and traffic accidents are perceived in reasonable agreement with the "objective" risk, the situation is very different with issues such as nuclear energy and sport activities.

4.4 Risk treatment (risk mitigation)

To reduce risk, one can reduce the hazard (or P_f, the probability of failure, reduce the consequence(s), or reduce both. Figure 10 illustrates this risk reduction concept on the *F-N* diagram. The United States Bureau of Reclamation 2003 guideline for dams is also shown. A mitigation strategy involves: 1) identification of possible disaster triggering scenarios, and the associated hazard level, 2) analysis of possible consequences for the different scenarios, 3) assessment of possible measures to reduce and/or eliminate the potential consequences of the danger, 4) recommendation of specific remedial measures and, if relevant, reconstruction and rehabilitation plans, and 5) transfer of knowledge and communication with authorities and society.

The strategies for risk mitigation can be classified in six categories: 1) activation of land use plans, 2) enforcement of building codes and good construction practice, 3) use of early warning systems, 4) community preparedness and public awareness campaigns, 5) measures to pool and transfer the risks and 6) physical measures and engineering works. The first five categories are "non-structural" measures, which aim to reduce the consequences. The sixth includes active interventions such as construction of physical protection barriers, which aim to reduce the frequency and severity of the threat.

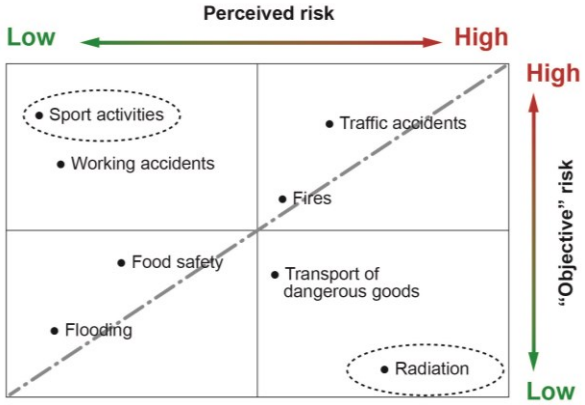


Figure 9. Perceived vs. "objective" risk (Max Geldens Stichting 2002).

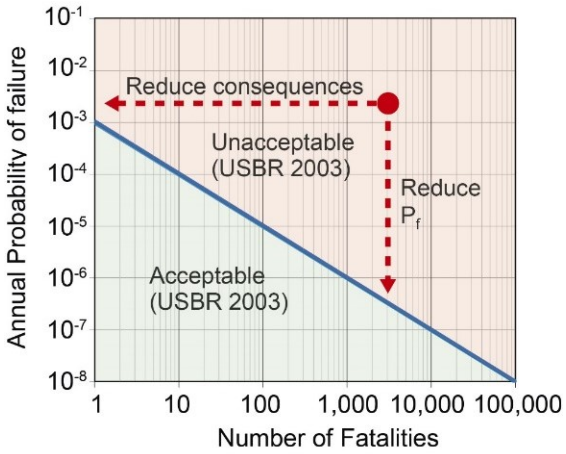


Figure 10. F-N curves and reducing risk.

In many situations, an effective risk mitigation measure can be an early warning system that gives sufficient time to move the elements at risk out of harm's way.

Early warning systems are more than just the implementation of technological solutions. The human factors, social elements, communication and decision-making authorities, the form, content and perception of warnings issued, the population response, emergency plans and their implementation and the plans for reconstruction or recovery are essential parts of the system. An early warning system without consideration of the social aspects could create a new type of emergency (e.g. evacuating a village because sensors indicate an imminent landslide, but without giving the village population any

place to go, shelter or means to live). Challenges in designing an early warning system include the reliable and effective specification of threshold values and the avoidance of false alarms. The children's story about the little shepherd boy who cried "wolf" is the classic example of how false alarms can destroy credibility in a system.

The earthquake-tsunami-nuclear contamination chain of events in Japan is a telling example of cascading hazards and multi-risk: the best solution for earthquake-resistant design (low/soft buildings) may be a less preferable solution for tsunamis (high/rigid buildings). The sea walls at Fukushima gave a false sense of security. The population would have been better prepared if told to run to evacuation routes as soon as the shaking started.

5 CASE STUDIES

5.1 Slide in mine waste dump

The risk to persons living in the houses and travelling on the road below a mine waste dump, and an assessment of whether or not the risks are acceptable was evaluated. Figure 11 presents schematically the slope layout and the elements at risk (persons, houses, road, and the damage to the mining property and facilities).

Danger (landslide) characterization

The mine waste is silty sandy gravel and gravelly silty sand coarse reject from a coal wash deposited over 50 years by end tipping. Geotechnical site investigations, hydrological and engineering analyses showed that the waste is loose, and that the lower part is saturated, and that the waste is likely to liquefy and flow liquefaction occurs for earthquakes loadings larger than 10^{-3} annual exceedance probability (AEP) or once in a 1,000 years. The culvert through the waste dump exceeds its capacity and runs full for floods greater than 0.1 AEP (once in 10 years). For larger floods, water flows over the sides of the waste dump and leaks onto the waste material through cracks in the culvert, thus increasing the pore pressures in the waste.

The factor of safety of the waste dump slope under static loading was 1.2 for the annual water table levels. If the dump slides under static loading, it is likely to flow because of its loose, saturated granular nature.

Given that a slide has occurred, the annual probability of a debris flow reaching the houses is 0.5 based on post-liquefaction shear strengths obtained in the laboratory, and empirical methods for estimating travel distance (Fell *et al* 2005). The volume of the likely landslide and resulting debris flow is about 100,000 m^3 and the debris are likely to be travelling with high velocity when they reach the road and houses.

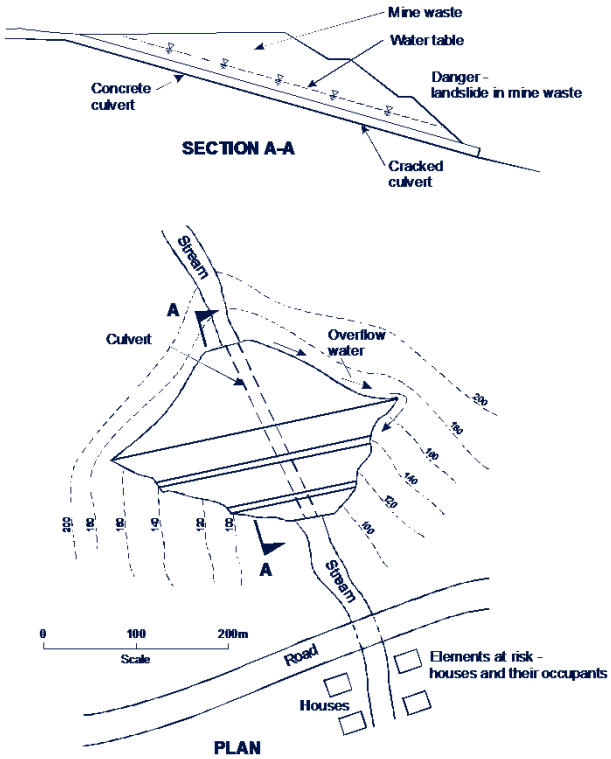


Figure 11. Slide in mine waste dump area: slope hazard and elements at risk (Fell et al 2005).

Hazard (frequency) analysis

The potential failure modes are:

- The culvert runs full, water leak, saturates the downstream toe and causes a slide.
- As above, but a smaller slide blocks or shears the culvert and causes a slide.
- The culvert collapses, flow saturates the downstream toe and causes a slide.
- A larger flood causes the culvert overflow, saturates the fill and causes a slide.
- As flood above, but the scour by the flowing water at the toe of fill initiates a slide.
- Rainfall infiltration mobilizes earlier slide.
- An earthquake causes liquefaction.

Based on the catchment hydrology, the culvert hydraulics, the stability analyses and engineering judgement, the sliding frequency of the waste for the seven potential modes of failure was estimated as 0.01/yr (or $1 \cdot 10^{-2}$/yr). An analysis of the liquefaction potential (Youd *et al* 2001) and of the post-liquefaction stability suggested that the frequency of sliding was 0.005 per yr (or $5 \cdot 10^{-3}$/yr). Hence the total annual probability of a slide, P_{slide}, was 0.015 or ($1.5 \cdot 10^{-2}$/yr). The probability of the slide reaching the elements at risk (P_{reach}) was uncertain, and was taken as at a value of 0.5 (i.e. completely uncertain, therefore 50% uncertain/certain, or "as likely as not"[2] to reach the road and houses).

Consequence analysis

The temporal spatial probability of the persons in the houses, and travelling on the road was estimated as follows. A survey of occupancy of the houses showed that the person most at risk in the houses spent on an average 18 hours/day, 365 days per year, or an annual proportion of time of 0.75. Each house was occupied by four persons for an average 10 hours/day and 325 days/year. Assuming that the persons were in the houses at the same time, the annual occupancy for the 16 persons is [10/24 · 325/365] or 0.36. Vehicles susceptible to be affected by the debris flow were assumed to travel with average velocity of 30 km/hr on the 100-m long stretch of road. For each vehicle on the road, the annual exposure was [(100/30,000) × 1/(365 × 24)], or $3.8 \cdot 10^{-7}$. If a vehicle travels 250 times a year (such as a school bus), the annual exposure probability became 9.5 x 10^{-5}.

To estimate the vulnerability (V), the velocity and the volume of the slide were considered. With the likely slide high velocity and large volume, the vulnerability of persons in the houses was estimated as 0.9, and the vulnerability of persons on a bus as 0.8.

Risk estimation

The annual probability of loss of life for the person most at risk (P_{LoL}) was obtained as follows (Eq. 2):

$$P_{LoL} = P_{slide} \times P_{reach} \times P_{most\ vulnerable\ person} \times V$$

$$P_{LOL} = 0.015 \times 0.5 \times 0.75 \times 0.9 = 5 \cdot 10^{-3}/\text{yr} \quad (3)$$

If all four houses are hit by the slide, 0.9 × 16 persons lose their lives (14 fatalities). The annual probability for 14 fatalities in houses is:

$$0.015 \times 0.5 \times 0.36 = 2.7 \cdot 10^{-7}/\text{yr} \quad (4)$$

If a 40-passenger bus is taken, 0.8 × 40 persons lose their lives (32 fatalities) The annual probability for 32 fatalities in a passing bus is:

$$0.015 \times 0.5 \times 0.5 \times 95 \cdot 10^{-5} = 7.1 \cdot 10^{-7}/\text{yr} \quad (5)$$

Ignoring loss of life in other vehicles on the road, the cumulative probabilities are (Table 3):

Table 3. Risk of fatalities, slide in mine waste dump.

Consequence	Annual frequency
≥ One fatality	$5 \cdot 10^{-3} + 2.7 \cdot 10^{-3} + 7.1 \cdot 10^{-7} = 7.7 \cdot 10^{-3}$/yr
≥ 15 fatalities	$2.7 \cdot 10^{-3} + 7.1 \cdot 10^{-7} = 2.7 \cdot 10^{-3}$/yr
≥ 33 fatalities	$7.1 \cdot 10^{-7}$/yr

Risk assessment and management

Individual risk: The risk for the person most at risk is 5 x 10^{-3}/year, which is in excess of the acceptable individual risks Shown in Table 1 and Figures 5 to 7.

Societal risk: Compared to the *F-N* charts in Figures 3 to 7, the three points in table 3 have risks that are in excess of the tolerable risk for the loss of 1 and 15 lives, but fall within in the *ALARP* range for the loss of 33 lives.

Mitigation

Risk mitigation options should be adopted and the risks recalculated. Mitigation options include reducing the probability of sliding by repairing the cracks in the culvert, controlling water overflow when the culvert capacity is exceeded, removing and replacing the outer waste well compacted so it will not flow if it fails, adding a stabilizing berm, or installing a warning system so persons in the houses can be evacuated and the road blocked to traffic when movement are detected in the waste.

5.2 Avalanches risk management

Avalanche forecasting

Avalanche forecasting uses several different spatial and temporal danger scales. Many

[2] "As likely or not" is IPCC language in extreme event report (IPCC 2012).

mountainous countries have public service forecasting programs that estimate the avalanche danger in a given region during a given time period. Avalanche forecasting services in Europe warn of the danger over a region, typically on a mountain range scale with an area of minimum 100 km^2 (Nairz 2010). They predict the hazards for one or a few days (EAWS 2010). In Europe, the level of danger uses The European Danger Scale. In the USA and Canada, the similar North American Danger Scale is used. These danger scales describe qualitatively the danger potential using a five level scale. On the local level, the benefit of a general forecast can be somewhat limited.

To help decision-making locally, one needs to state not only a qualitative danger level, but also to provide a quantitative estimate of the danger. The quantitative estimate is obtained by calculating the probability of an event in a given period of time.

Kristensen *et al* (2013) proposed a procedure to associate the probability of an avalanche reaching objects at risk within a specified time period to specific mitigation measures. The procedure is illustrated with two examples of local avalanche forecasting programs in western Norway.

Quantifying the probabilities

An object-specific forecasting program able to assess the probability of encountering the objects needs to take into account not only the general avalanche hazard but also the susceptibility of the object, the probability of encountering the object should the avalanche occur and the local conditions (weather, snow drift, slope, elevation, etc.). The probability of an avalanche reaching a given point is a function of the probability of avalanche occurrence and the distance the avalanche is able to travel downslope. Estimating frequency-magnitude relationships can also be done where historical records exist. A statistical inference can therefore be used in the forecasting. Examples of probabilistic techniques are given after the two examples.

Highway 15, Strynefjellet

Highway 15 in western Norway is one of the main arteries that connect the west coast to Highway 6, the main north-south transport corridor in Norway. Highway 15 crosses "Strynefjellet. The annual (2010) traffic is around 800 cars per day, with peaks of up to 2500 cars per day in the holiday periods.

The 922-m long unprotected stretch of road in Grasdalen on Highway 15 has a history of frequent avalanches reaching the road. The main avalanches come from the NE-facing slope of Sætreskarsfjellet and can reach and impact the road over a length of 650 m. A 200-m portion of this stretch is permanently protected by a gallery. Two rows of breaking mounds on the uphill side of the road have also been constructed, but proved to be ineffective for all but the smallest wet snow avalanches. Pro-active protection, including an avalanche control system using explosive charges in the release zone and controlled avalanche release combined with preventive road closures, were estimated to reduce the individual risk for road users by about one-fourth (Kristensen 2005).

For Highway 15, an avalanche forecasting program was developed for the period between December 1st and April 30th. The forecasting service would then provide a daily avalanche danger assessment and an estimate of the probability of an avalanche reaching the road in the next 24-hour period.

To obtain weather and snow data, several automatic weather and snow stations were used. A database of all observed avalanches having reached the road earlier was also used (database over more than 50).

The forecasting procedure relied on both traditional and statistical methods. The relationship between the three- and five-day accumulated precipitation and wind conditions and the probability of an avalanche reaching the road were estimated for one particular avalanche path (Bakkehøi, 1985).

Table 4 presents the danger scale classes and local probabilities (P) for avalanches reaching Highway 15 in the next 24 hours and the corresponding actions to be taken for each level, for both traffic and road maintenance. For ease of communication, the European "Danger Scale" terminology and colours was used. However, the probabilities of avalanches reaching Highway 15 are not in accordance with the conventional use of the European Danger Scale. In Class 4 (red), the

exposed area is under avalanche control. F0r Class 5, the road is closed.

Table 4. Probability of avalanche reaching Highway 15 in the next 24 hours, and required actions (after Kristensen et al 2013).

Danger Scale	$P_{(Hwy\ 15\ reached)}$ (%)	Required actions, Traffic	Required actions, Hwy maint'ce
1 Low	P≤1	No restrictions.	No restrictions.
2 Moderate	1<P≤5	No restrictions.	No restrictions.
3 Considerable	5<P≤20	No restrictions; Stopping not allowed	Work in area allowed during daylight only.
4 High	20<P≤50	Traffic monitoring cont'ly Road closing if dark or difficult driving cond.	Road clearing only in daylight under avalanche watch.
5 Very high	P>50	Road closed.	No activity in exposed areas.

Cont'ly: continuously
Maint'ce: maintenance

Construction site, Highway 60, Strandadalen

During the completion of a large avalanche protection along Highway 60 in Strandadalen winter 2012, three of the work and loading locations were considered exposed to avalanche danger. As part of the risk management for the safe project completion, an avalanche-forecasting program was implemented, with the possibility of using controlled avalanche release by helicopter with conventional explosives or a gas detonation system. Table 2 was prepared through a dialogue and cooperation among all involved parties in the project. The guiding criterion was that it was unacceptable that any avalanche should reach the area during active working operation.

Two of the three elements at risk were located in the same path but at different location on the slope. To arrive at a measure of susceptibility for the three sites, a frequency-magnitude relationship was established. Using the statistical/topographic model developed by Lied and Bakkehøi (1980), an index of the proximity to the slope was calculated based on the position of each of the three elements at risk relative to the Beta point (where slope angle is 10 degrees) in the avalanche path (Kristensen *et al.* 2008; Kristensen and Breien, 2012). Meteorological data and avalanche observations were available for about 30 years.

The probabilities (*P*) are presented in Table 5 together with the required actions. The probability classes have boundaries different from those for Highway 15. In this case (developed after the previous case study), the Danger Scale had been renamed Probability Classes.

Table 5. Probability of avalanche reaching elements at risk on Highway 60 under construction in the next 24 hours, and required actions (after Kristensen et al 2013).

Probability Scale	*P* (%)	Required actions, Presence in work areas
1 Low	P≤0.1	Permanent presence allowed*.
2 Moderate	0.1<P≤0.2	Limited presence under daylight & good visibility; Continuous local assessment of any change.
3 Considerable	0.2<P≤2	Only few and short, temporary presence allowed.
4 High	2<P≤50	No presence allowed; Quick passing-through allowed if good visibility.
5 Very high	P>50	No presence or passing-through allowed.

* Presence of the work force in exposed areas during normal working hours (8 hours a day).

Figure 12 illustrates the forecast for the three elements at risk (Sites 1, 2 and 3) during the Highway 60 construction between February 1st and April 30th 2012. The regional danger ratings (1 to 5) from the National Avalanche Forecasting program are shown at the top.

Observations from the two examples

Since the local and regional forecasting programs operate at different spatial and temporal resolutions, there will be differences in the danger assessment. The local forecasting was very useful and enabled a significantly increased number of hours.

Local forecasts can benefit from insight from the regional forecast. However, the probability of an avalanche reaching a specific object depends on the exposure of the object to the threat. Figure 12 showed that the regional forecasts can provide only limited insight into the avalanche probability of reaching specific objects and the actions required at the local level. The regional and

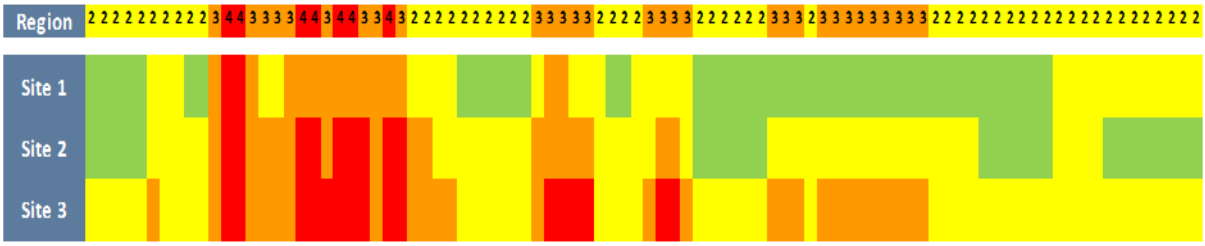


Figure 12. Forecasts for three elements at risk during Highway 60 construction (February 1st to April 30th 2012). Chart shows the daily regional danger rating 1 to 5 (top) and the probability classes for Sites 1, 2 and 3 (see Table 5 for colour codes) (Kristensen et al 2013).

local forecasts agree well in the cases of high probability of avalanche.

The probabilities reflect only a best estimate of a likelihood and not a precise value. This understanding can be "lost in the transition" from avalanche experts to the media and to the public concerned.

The local forecasting should provide decision-makers with quantified probabilities of avalanches reaching specific elements at risk. A list of actions to temporarily mitigate the impact of avalanches on exposed objects can be made, and the persons concerned can be prepared for a potential avalanche occurring.

Reliability methods for snow avalanches

Harbitz *et al* (2001) discussed several aspects of probabilistic analyses for avalanche zoning. In particular, the first order reliability method (FORM) and Monte-Carlo simulations were used to evaluate the probability of occurrence associated with avalanches. Two of the models used are described herein: a mechanistic probabilistic model and a model based on observations of avalanches.

Mechanical probabilistic model

For the standard snow slab avalanche model, the safety factor (FS) is defined as the ratio of the total resisting forces in the downslope direction to the driving shear force:

$$FS = (F_S + F_T + F_C + F_F)/T \qquad (6)$$

where

F_S is the shear force along the shear surface,
F_T is the tension force at the crown,
F_c is the compression force at the wall,
F_F is the flank force,
T is the total weight driving component,
W, of the release slab
$W = \rho gBLD + W_{ext}$ (W_{ext} external load on slab),
$T = W \sin \psi$ (ψ is the slope inclination),
$F_F = 2LDc$
$F_C = BD\sigma_c = 2BDc(1+\rho gD/c)$,
$F_T = BD\sigma_t$,
$F_s = BL\tau_s$,
ρ density of snow,
g gravity acceleration
B, L, D width, length and thickness of slab,
c shear strength of the slab,
σ_c compressive strength of the wall,
σ_c compressive strength of the wall,
σ_t tensile strength of the snow,
τ_s shear strength on the shear surface.

Equation 6 was used for both the Monte-Carlo and the FORM analyses. Details on the approaches can be found in Harbitz *et al* (2001) and many other sources quoted in this paper. A standard slab avalanche was used. Nine basic variables were defined with mean, standard deviation and the probability distributions given in Table 6.

Table 6. Probability distribution of basic random variables in the mechanical probabilistic model (after Harbitz et al 2001).

Random variable	PDF	Mean	SD
Thickness of slab, D (m)	LN	0.7	0.1
Slope angle, ψ (degree)	LN	38°	3
Cohesion-snow, c (kPa)	LN	6	1.5
Tensile strength-snow, σ_t (kPa)	LN	9	2.4
Shear strength on sliding plane, τ_s (kPa)	LN	1.05	0.32
Width of slide, W (m)	LN	50	25
Length of slide, L (m)	LN	50	25
Density of snow, ρ (kg/m³)	N	220	20
External load, W_{ext} (kN)	LN	10	2

PDF: Probability density function
N, LN: Normal, Lognormal
SD: Standard deviation

With 100,000 simulations, the Monte-Carlo analyses gave an annual probability of failure P_f of 0.051 (or $5 \cdot 10^{-2}$/yr). The FORM analyses gave an annual probability of failure of

0.063 (or $6 \cdot 10^{-2}$/yr). The difference is negligible. Both approaches gave the same "design point" (i.e. the most probable combination of parameters leading to an avalanche).

In the FORM analysis, the directional cosines of the vector of random variables are called the sensitivity factors, because they indicate the relative influence of each basic variable on the reliability index and probability of avalanche occurrence.

Figure 13 illustrates the sensitivity factors for a representative analysis. The data demonstrate that the uncertainties in the shear resistance on the sliding surface and in the snow-slab dimensions (length and width) are the most significant influencing the probability of the occurrence of an avalanche.

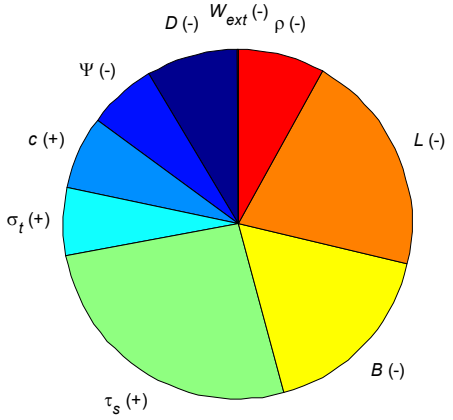


Figure 13. Sensitivity factors from the FORM analyses indicating the relative influence of each random variable on the probability of an avalanche occurring (Harbitz el al 2001).

Model based on observed events.

It is difficult to quantify the annual probability of an avalanche occurrence on the basis of mechanical models. In areas where general climatic conditions and topography are prone for avalanche activity, local wind conditions may prevent the accumulation of snow and an avalanche would rarely occur. As an alternative, Harbitz *et al* (2001) presented two easily applicable statistical approaches.

The P_f is defined as the probability of an extreme avalanche occurring in a specific path during one year, which is assumed to be small (e.g. $P_f < 0.1$). It is assumed that the probability of more than one (extreme) avalanche in one year is negligible, and that the probability in a future year is independent of avalanche activity in previous years.

The number of avalanches, r, occurring during a period of n years, conditional on P_f is then binomially distributed. The return period, $\Delta t_r \approx 1/P_f$ is the mean time period between successive avalanches. If denotes a random period between two successive avalanches, it can be approximately exponentially distributed with mean ΔT_r :

$$f(\Delta T_r) \approx (1/\Delta T_r) e^{-\Delta Tr/\Delta tr} \quad \text{for } \Delta T_r \geq 0 \qquad (7)$$

The number of avalanches occurring during any time period, Δt, can be approximated by a Poisson distribution with mean $m = \Delta t / \Delta t_r$. Two methods can be used to estimate the probability of avalanche release:

Within a "classical" statistical framework P_f is considered a constant, and the term probability has a strict frequentist interpretation. This is equivalent to saying that P_f is close to the ratio R/n for large n. For example, if $r = 1$, i.e. one avalanche has occurred during an observation period of $n = 200$ years, the estimate of P_f is 1/200. If one tries to estimate a conservative upper value, with "95% certainty" for P_f not to be exceeded, one can construct a 95% confidence interval for P_f. The upper interval limit is then found from the cumulative binomial distribution function.

In the Bayesian approach, contrary to the classical approach, the P_f is treated as a stochastic variable with an a priori probability density function called the prior. The prior can be based on subjective knowledge, historical observations or both, before (new) observations are made. Once new observations are available, the so-called posterior probability density function for P_f conditional on r can be found. The Bayesian approach is particularly useful if a good a priori knowledge exists (e.g. observations from similar paths. It can also be implemented if no a priori knowledge is available, by applying so-called non-informative, or "vague", priors. As an illustrative example, let a prior be applied before the first year of observations, which will give one or zero av-

alanches. The posterior, $f_n(p_f \mid r)$, after n years of observations with totally r avalanches observed, is then:

$$f_n(p_f \mid r) = \text{Beta}(r + 1, n + 1) \quad (8)$$

with Bayes estimate of:

$$p_f = (r + 1) / (r + n + 2) \quad (9)$$

Figure 14 presents examples of the updating procedure for one to eight years of no observations of avalanches in one location. Analogous to the classical confidence intervals, a credibility interval for P_f, can be constructed.

Figure 15 compares the "classical" and the Bayesian approaches in terms of P_f and confidence level.

Canadian guidelines on avalanche risk

The Canadian Avalanche Association (2016) recently published a useful guide on the technical aspects of snow avalanche risk management. The handbook, published online, is a detailed resource and guidelines for avalanche practitioners. The publication provides operational guidelines for:

1) Municipal, residential, commercial and industrial areas.
2) Transportation corridors.
3) Ski areas and resorts.
4) Backcountry travel and commercial activities.
5) Worksites, exploration, survey, resource roads, energy corridors and utilities, managed forest land and other resources.

The handbook describes element(s) at risk, their vulnerability, and their potential for exposure, along with tables that summarize both planning and operational risk management guidelines for specific activities or industry sectors. The helpful guideline tables include:

- Element at risk.
- Avalanche size or impact pressure.
- Return period (years).
- Risk management guidelines for planning.
- Risk management guideline for operation.

CAA (2016) illustrates the effect on uncertainty on probabilities (Fig. 16). Vulnerability in Figure 16 is defined as the probability of loss of life, for the case of snow avalanches.

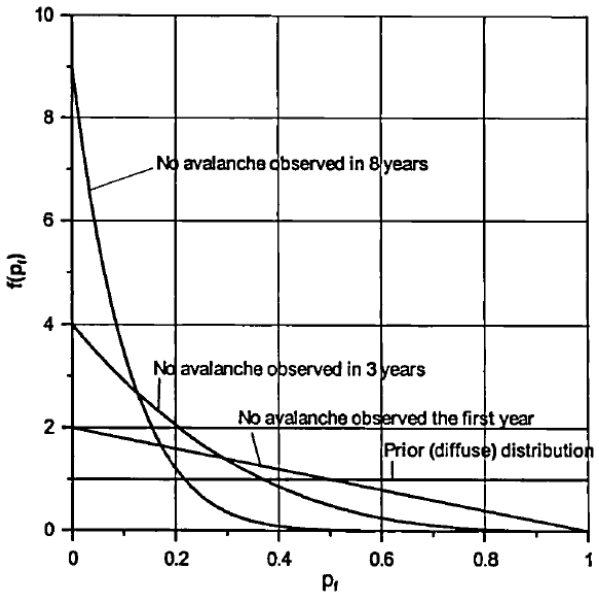


Figure 14. Probability distribution of annual avalanche cibsuderubg 0, 1, 3 and 8 years of observations of no avalanche (Harbitz et al 2001).

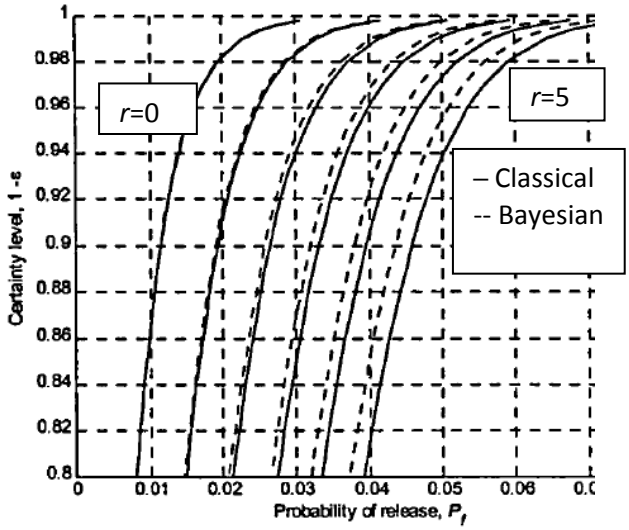


Figure 15. Annual probability of failure with confidence P_f from classical and Bayesian approaches; 0 to 5 avalanche observations (*r*) over *200 years (n) (Harbitz et al 2001).*

Statham *et al* (in prep.) suggests a model of avalanche hazards. For each avalanche type at a location, the hazard is determined by evaluating the relationship between likelihood of triggering and avalanche size. The likelihood of triggering an avalanche depends on the triggers and spatial distribution of the weaknesses in the snow mass.

5.3 Risk assessment for railways

A GIS-based methodology for regional scale assessment of hazard and risk along railway corridors was developed for the Norwegian

National Rail Administration (Hefre *et al* 2016).

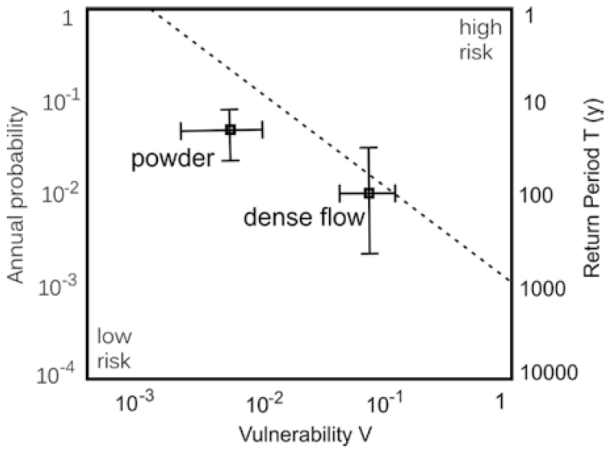


Figure 16. Risk graph showing the annual probability of occurrence and vulnerability for two hypothetical scenarios (CAA 2016).

Field investigation of hundreds of kilometres of railway would be time-consuming and expensive to conduct. The assessment of the risk along railway corridors was aided with a Geographical Information System (GIS), combining detailed Digital Elevation Models (DEM) and railway data. The GIS analyses identified risk hotspots.

A relative quantification of the hazards and consequences was done over the complete network of railway and combined to identify zones of low, medium and high-risk. The results were presented in a series of detailed maps showing the most critical areas along the railway, thus providing the stakeholders the background to make decisions on the need for further investigations and/or mitigation measures. The GIS-based methodology proved to be a time- and cost-efficient approach to conduct risk assessment over wide areas such as railway corridors.

The hazard analysis considered the average slope angle within the exposed slope, slope direction relative to railway, soil type, area of exposed slope, earlier sliding evidence, drainage capacity (expected discharge, culvert capacity and upstream slope angle) and potential erosion (distance between toe of railway and river and height difference between embankment and river).

The consequence analysis included elements at risk, accessibility for rescue, terrain conditions at time of potential derailment and impact speed.

Figure 17 presents an example of the resulting risk map. The map covers one km of railway. Such map is produced for each one km of railway analysed. On Figure 17, the hazard class, consequence class and risk class are shown graphically (with colours). The resulting risk is in the middle. A short section, close to an earlier landslide, was identified as high risk, and mitigation measures should be implemented in this area.

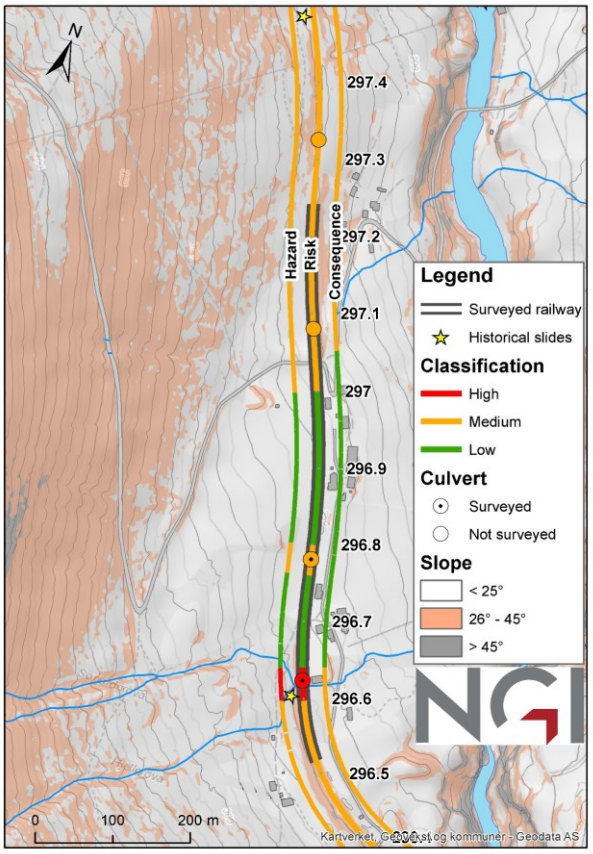


Figure 17. Risk map for 1 km of railway. The hazard, consequence and risk classes along the railway are shown continuously, in addition to risk level of culverts and location of historical slides (Hefre et al 2016).

5.4 Excavation and foundation works

Kalsnes et al (2016, this conference) present the concepts and an example of the application of risk analysis to excavation and foundation works. The proposed method is based on ISO's framework, with five stages: 1-Establish basis; 2-Risk identification; 3-Semi-quantitative risk analysis; 4-Risk Assessment; 5-Risk reduction measures. The method has been implemented in a spread-

sheet. The analysis can best be completed by a team. As the project progresses and new information becomes available, the spreadsheet can be reviewed and revised.

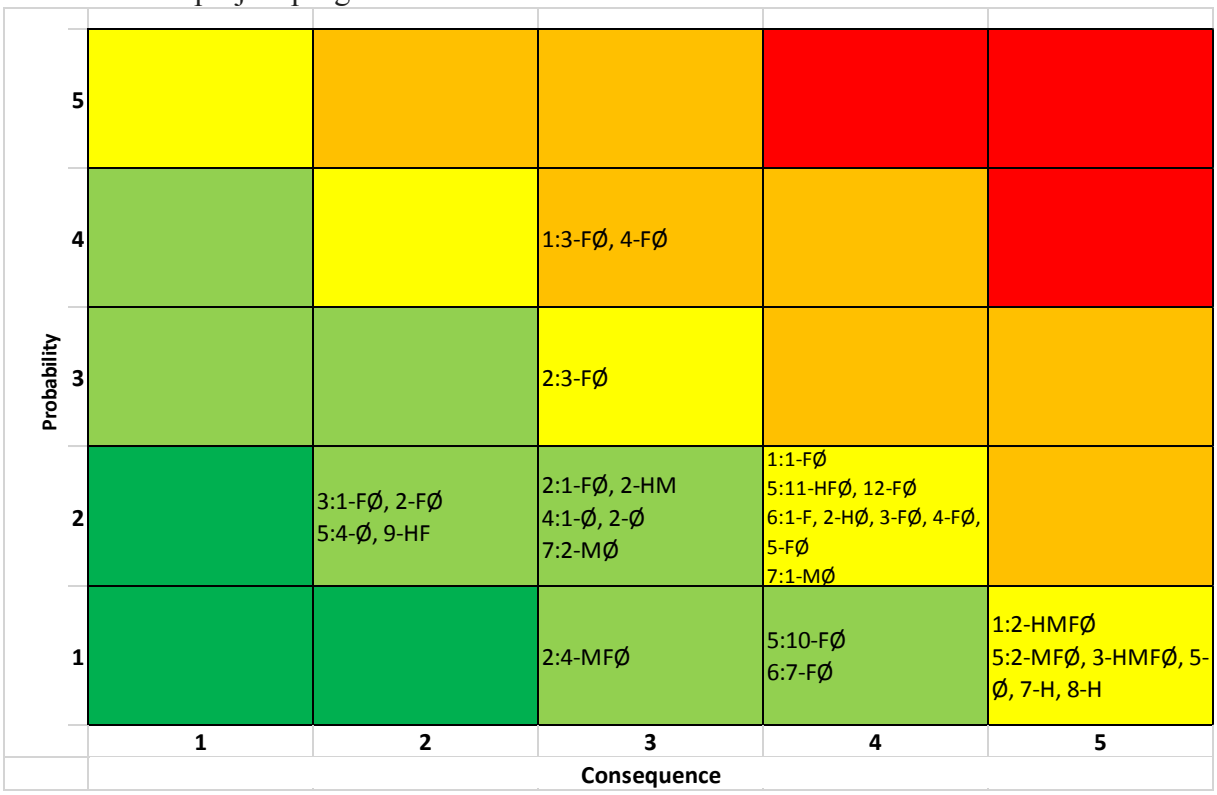


Figure 18. Risk assessment example for sheetpiling (after Kalsnes et al 2016; Vangeslten et al 2015).

Notation in each risk matrix cell: n:m-consequence = project phase:source of uncertainty-consequence

Project phases:	*1*	*Design and planning*
	2	*Preparation work*
	3	*Pre-excavation for sheetpiling*
	4	*Sheetpiling*
	5	*Excavation, construction pit*
	6	*Shoring and stiffeners*
	7	*Local conditions, environment*
Sources of uncertainty	*1*	*Material*
	2	*Design*
	3	*Execution*
	4	*Environmental loads (natural sources)*
	5	*External loads*
	6	*Extreme rainfall*
	10	*High groundwater*
	11	*Fallout on excavated slopes*
Consequences	*H*	*Health damage or fatality*
	M	*Environment*
	F	*Progress in execution*
	Ø	*Economy*

Figure 18 gives an example of the resulting risk matrix for an excavation. Kalsnes et al (2016) suggested designations for the hazard and consequence classes. Each project selects its project phases, sources of uncertainty and consequences.

For probabilities, S1 corresponds to "Extremely unlikely", S2 to "Very unlikely", S3 to "Unlikely", S4 to "Somewhat likely", and S5 to "Likely". The probabilities may range from less than 0.1%/year for Class S1 to more than 10%/year for Class S5.

For consequences, C1 would correspond to "Hazardous", C2 to "Harmful", C3 to "Critical", C4 to "Very critical" and C5 to "Catastrophic". Such classes and their meaning are to be established for each project.

The approach allows to vary the model for risk evaluation process by changing the shapes of the coloured regions in the risk

matrix in Figure 18. In Figure 18, a standard staircase colour distribution is used. In a risk aversion case, the orange and res zones in the matrix would be made much larger.

The aspects requiring actions are found in the orange and red zones in the risk matrix. In the example, the uncertainties associated with the execution of the sheetpiles and the environmental loads should be examined in more detail to establish mitigation measures. Examples are given in Kalsnes *et al* (2016).

5.5 Cost-effective soil investigations

Soil investigations represent a subconscious risk-based decision. Soil investigations, in the way they are planned, represent a risk-based decision. The complexity of a soil characterization is based on the level of risk of a project. Lacasse and Nadim (1998; 1999) illustrated this graphically (Fig. 19).

A low risk project involves few hazards and has limited consequences. Simple *in situ* and laboratory testing and empirical correlations would be selected to document geotechnical feasibility. In a moderate risk project, there are concerns for hazards, and the consequences of non-performance are more serious than in the former case. Specific *in situ* tests and good quality soil samples are generally planned. For a high-risk project involving frequent hazards and potentially risk to life or substantial material or environmental damage, high quality *in situ* and laboratory tests are required, and higher costs are involved. The decision-making process for selecting soil investigation methods, although subconscious, is risk-based. It involves consideration of requirements, consequences and costs.

In general, more extensive site investigations and laboratory testing programs reduce the uncertainties in the soil characteristics and design parameters. At a certain point however, as Wilson Tang (1987) pointed out, the benefit obtained from further site investigations and testing may not yield sufficient added value (read: increase in the reliability of the performance) to the geotechnical system, and hence may not justify the additional cost (e.g. Folayan *et al* 1970).Probabilistic concepts can also help optimize site investigations.

The uncertainty in a geotechnical calculation is often related to the possible presence of an anomaly, e.g. boulders, soft clay pockets or drainage layer. Probability approaches can be used to establish the cost-effectiveness of additional site investigations to detect anomalies. Figure 20 presents an example where the presence of a drainage layer was determinant on the resulting post-construction building settlements. A settlement of less than 50 cm would mean an important reduction in costs. With drainage layer detectability for each boring of 50% or 80% (Fig. 20), and assuming a given drainage layer extent, 3 to 6 borings were required in this case to establish whether the drainage layer was present or not.

6 THE OBSERVATIONAL METHOD AND BAYESIAN UPDATING

One recurring factor in geo-failures is that the construction does not follow the original script, or changes occur underway which effects were not checked (Lacasse 2016). Examples include the pillar collapse on Skjeggestad bridge in Norway in 2015 due to as slide in quick clay and the Aznalcóllar tailings dam failure in Spain in 1998 and the Mount Polley tailings dam failure in Canada in 2012 where the downstream slopes were steeper than originally intended. Such events reinforce the importance of and the need for the "observational method", a seminal deterministic method in geotechnics (Peck 1969). The observational method consists of:

(a) Exploration sufficient to establish at least the general nature, pattern and properties of the deposits, but not necessarily in detail.
(b) Assessment of the most probable conditions and the most unfavourable conceivable deviations from these conditions. In this assessment geology often plays a major role.
(c) Establishment of the design based on a working hypothesis of behaviour anticipated under the most probable conditions.

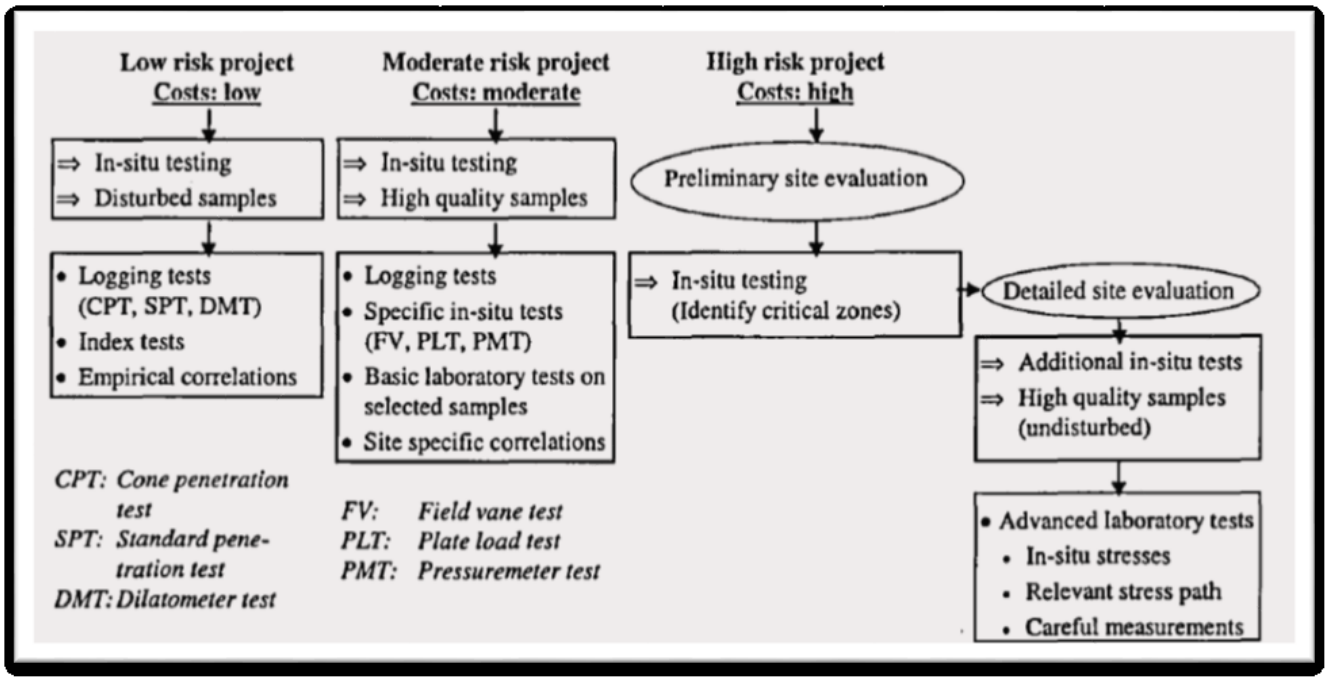


Figure 19. Site investiagtions: a subconscious risk-based decision (Lacasse and Nadim 1998).

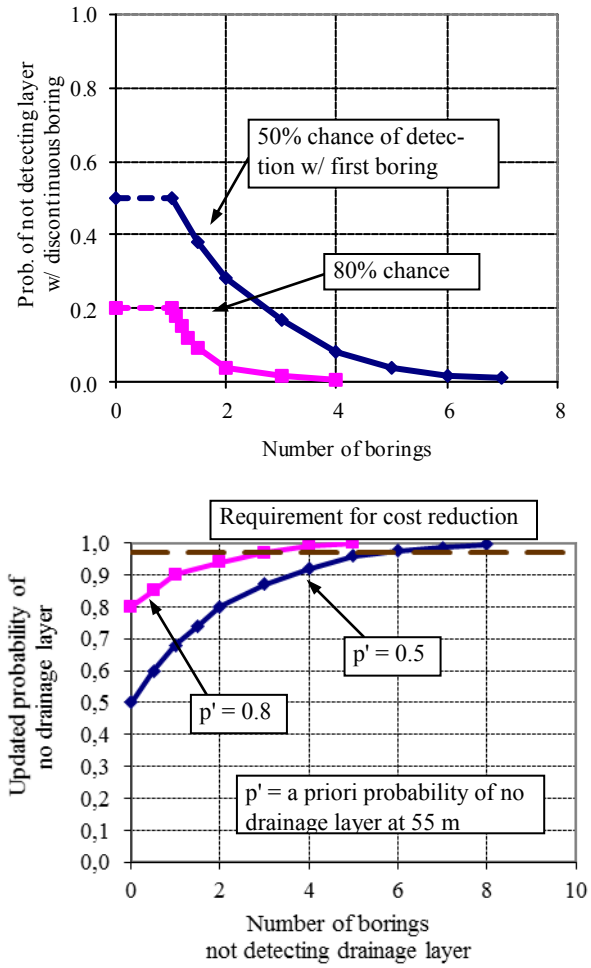


Figure 20. Cost reduction with increased number of borings (Tang 1987; Lacasse and Nadim 1998); p' is the prior probability.

(d) Selection of quantities to be observed as construction proceeds and calculation of their anticipated values on the basis of the working hypothesis.
(e) Calculation of values of the same quantities under the most unfavourable conditions compatible with the available data concerning the subsurface conditions.
(f) Selection in advance of a course of action or modification of design for each foreseeable significant deviation of the observational findings from those predicted with the working hypothesis.
(g) Measurement of quantities to be observed and evaluation of actual conditions. (h) Modification of design to suit actual conditions.

The "observational method" is closely related to the techniques of Bayesian updating (Lacasse 2015). Bayes' theorem provides a probabilistic framework to allow updating of prior estimates with new information. Bayesian updating can be in fact a mathematical continuation of the observational method.

It would be very useful to couple the observational method to risk management, with focus on dynamic updating of the risk picture on the basis of observations and prepared scenarios. The contribution of the quantitative assessment of hazard and consequences (risk) is to reveal (quantitatively) the risk-

creating factors and the need for remedial changes. It therefore encourages foresight rather than hindsight. Risk management combining the observational method and Bayesian updating will provide the preparedness with risk mitigation options selected and evaluated in advance.

7 RISK MANAGEMENT AND FORWARD STRATEGIES

7.1 Current directions and lessons

Risk management encompasses several necessary steps, including:

- Quantifying the uncertainties, and not the least, the modelling uncertainty(ies).
- Doing scenario-based risk assessments, including scenarios with future expected and climate impact.
- Applying improved technology and methods.
- Addressing national policies.
- Improving national and international cooperation and coordination.
- Enhancing communication.

Emphasis should be placed on improving warning systems, enhancing emergency preparedness and response, community resilience and recovery. For enhanced preparedness and resilience to take root, effective public education and strong government support are essential.

7.2 Extreme events

Occurrence

The U.S. National Science Foundation defines an extreme event as "a physical occurrence that with respect to some class of related occurrences, is either notable, rare, unique, profound, or otherwise significant in terms of its impacts, effects, or outcomes." The Intergovernmental Panel on Climate Change (IPCC) has the following, more quantitative definition for an extreme events "... An event that is rare at a particular place and time of year. Definitions of “rare” vary, but an extreme weather event would normally be as rare as or rarer than the 10th or 90th percentile of the observed probability density function…" (IPCC, 2012).

An example of an extreme event is the Great East Japan earthquake (Tōhoku earthquake) and tsunami of 11th March 2011. This magnitude 9.0 (Mw) earthquake was the most powerful earthquake ever recorded to have hit Japan, and the fourth most powerful earthquake in the world since modern record-keeping began in 1900. One of the catastrophic consequences of this event was the Fukushima Dai-ichi nuclear power plant accident.

Another example of a "usual" natural hazard event leading to extreme consequences was the 2010 eruptions of Eyjafjallajökull volcano in Iceland (Gudmunsson et al. 2012). These relatively small volcanic eruptions caused enormous disruption to air travel across western and northern Europe over a period of six days in April 2010. During the period 14–20 April, ash covered large areas of northern Europe when the volcano erupted. About 20 countries closed their airspace for commercial jet traffic and it affected about 10 million travellers (WENRA 2011).

The impact of extreme weather events (near-‘black swans’ events), which may be exacerbated by climate change, is considered as a major risk concern. An extreme weather event can also be a natural aleatory phenomenon within the natural and intrinsic variability of the weather system.

Stress testing

Conventional strategies for managing the risk posed by natural and/or man-made hazards rely increasingly on quantitative risk assessment. One of the challenges in the management of risk associated with extreme events is that the mechanism triggering an extreme event may be different from those triggering the more frequent events. Climate change has introduced substantial non-stationarity into risk management decisions. Non-stationarity is the realization that past experiences may no longer be a reliable predictor of the future character and frequency of events; it applies both to hazards and to the corresponding response of the systems.

The conventional design approach implicitly accepts that there is a "residual" risk, which could be "neglected" because the probability of that risk being realized is extremely small. This residual or neglected risk

can be due to "extreme events", which have a longer return period than the return period for the design load (denoted with blue stars in Fig. 21), or they could be due to the uncertainty in the prediction models and lack of knowledge of the mechanisms at work (denoted with red stars in Fig. 21).

Both types of events pose a risk. This risk which is implicitly accepted and knowingly neglected in conventional engineering design. Nevertheless, these events can occur, and when they do, they are referred to as extreme events. Therefore, the conventional engineering design is not suitable for dealing with the risks posed by extreme events.

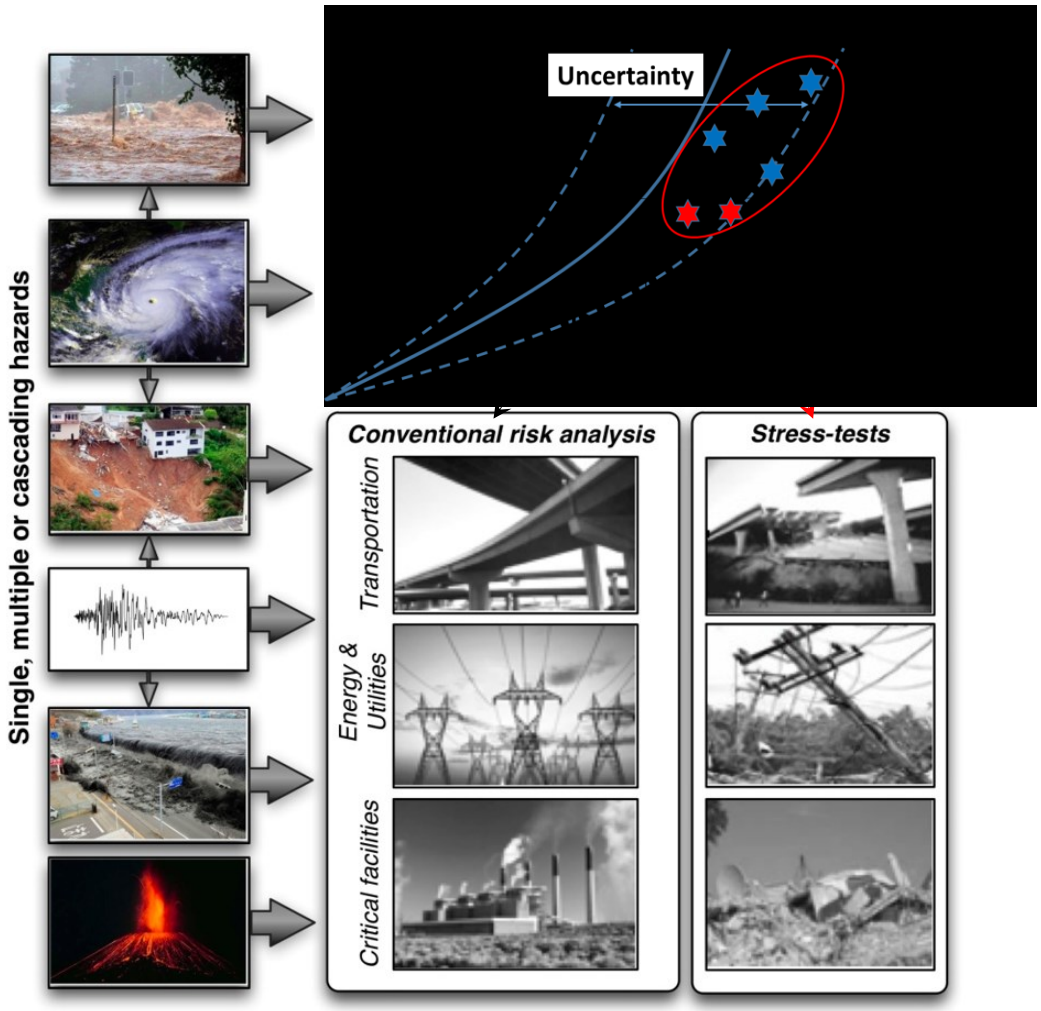


Figure 21. Residual (or neglected) risks in conventional reliability-based design approach (Nadim, 2016).

Stress testing is a procedure used to determine the stability and robustness of a system or entity. It involves testing the specific system or entity to beyond its normal operational capacity, often to a breaking point, in order to observe its performance/reaction to a pre-defined internal or external pressure or force. Stress tests have been used for many years in air traffic safety, in particular for airplanes and helicopters. In recent years, stress testing has often been associated with methodologies to assess the vulnerability of a financial system or specific components of it, such as banks. A number of analytical tools have been developed in this area and have been frequently used since the late 1990's (e.g. Borio et al. 2012).

Stress testing has been applied to the comprehensive safety and risk assessment of Nuclear Power Plants, in particular in the aftermath of the 2011 Fukushima Dai-ichi accident. In particular, the accident highlighted three areas of potential weakness in present safety approaches: (1) inadequacy of safety margins in the case of extreme external events (especially natural hazards); (2) lack

of robustness with respect to events that exceed the design basis; and (3) ineffectiveness of current emergency management under highly unfavorable conditions. These issues were the focus of the stress tests imposed on all nuclear power plants in Europe in 2011 and 2012 (WENRA, 2011).

Nadim (2016) proposed stress testing as a complement to traditional risk assessment for managing the risk posed by extreme events, focusing on the challenges faced by civil engineers in general, and geotechnical engineers in particular, in managing the risk posed to critical infrastructure by extreme natural hazard events. Most risk evaluations are based on probability estimates using historical data and consequence models that try to estimate the impact of unwanted future hazard situations. For natural hazards, historical data may in some cases be sparse or highly uncertain. Similarly, simplified models of highly complex situations may yield forecasts containing significant uncertainty. Both of these situations may therefore neglect risks that should be introduced into the evaluations.

7.3 Interaction and communication

There is much room for cross-fertilization of ideas and insights, as well as joint development of strategies and best practice within the area of risk assessment and management.

Within risk, communicating the message effectively is of paramount importance, at least at three levels: (i) on the cross-disciplinary scientific level, (ii) with the stakeholders and (iii) with the general public. Good communication is imperative to provide the insights required to shape a resilient environment prepared for future challenges.

Enhanced interaction and communication among the geo-disciplines and outside the geo-arena can be achieved through multi-disciplinary gatherings on geotechnical hazard and risk management. The discussions should preferably involve also government officials who are responsible for formulating policies.

7.4 Risk management strategy

In the context of protecting the community from the adverse consequences of geo-related disasters, the following strategies are pertinent in the management of hazards and risk (after Ho *et al* 2016):

a) Avoidance, with use of planning, warning or alert systems, and public education.
b) Prevention, such as enforcing slope investigation, design, construction, supervision and maintenance standards.
c) Mitigation, with the implementation of engineering measures to reduce the impact of hazards, e.g. retrofitting of substandard slopes or adding mitigation measures.
d) Preparedness, focusing on procedures, human resource management, emergency systems, training of the vulnerable community for a prompt response etc.
e) Response, involving search and rescue, evacuation and provision of basic humanitarian needs, relief measures, inspections for identification of any imminent danger, settlement of evacuated people etc.
f) Recovery, starting after the immediate threat to life has been dealt with, to bring the affected area back to the normal and carry out repair or mitigation works.

Items (a) to (c) are broad risk reduction or control strategies whereas items (d) to (f) relate mainly to emergency management. Items (b) to (e) reflect the ability of a system to withstand shocks and stresses whilst maintaining its essential functions (defined as resilience). Resilient systems are also more amenable to recovery.

8 RECENT RESEARCH

In terms of improved technology and methods mentioned in Section 7.1, recent work is aiming to bridge some of the knowledge gaps. Two recently completed European collaborative research studies, namely the CHANGES *(www.itc.nl/changes*) and SafeLand projects *(esdac.jrc.ec.europa.eu/projects/safeland)*.

8.1 SafeLand Project

The need to protect people and property in view of the changing pattern of landslide hazard and risk caused by climate change, human activity and changes in demography, and the need for societies in Europe to live with the risk associated with natural hazards,

formed the basis for the 2009-2012 European SafeLand project "Living with landslide risk in Europe: Assessment, effects of global change, and risk management strategies". The project involved 27 partners from 12 European countries, and had international collaborators and advisers from mainland China, Hong Kong, India, Japan and USA. SafeLand also involved 25 End-Users from 11 countries. SafeLand was coordinated by the Norwegian Geotechnical Institute's (NGI) Centre of Excellence "International Centre for Geohazards (ICG)" (http://safeland-fp7.eu/; Nadim and Kalsnes 2014).

The SafeLand conclusion was that climate change, human activity and change in land use and demography all need to be considered in the assessment of landslide risk, and that climate impact on slope safety need to be given high priority. The SafeLand project provides, among other results:

- Guidelines on landslide triggering processes and run-out modelling.
- Methods for predicting the characteristics of threshold rainfall events for triggering of precipitation-induced landslides, and for assessing the changes in landslide frequency as a function of changes in the demography and population density.
- Guidelines for landslide susceptibility, hazard and risk assessment and zoning.
- Methodologies for the assessment of physical and societal vulnerability.
- Identification of landslide hazard and risk hotspots in Europe.
- Simulation of regional and local climate change at spatial resolutions of 10 x 10 km and 2.8 x 2.8 km.
- Guidelines for the use of remote sensing, monitoring and early warning.
- Prototype web-based "toolbox" of mitigation measures, with over 60 structural and non-structural risk mitigation options.
- Case histories and "hotspots" of European landslides covering almost all types of landslide in Europe.
- Stakeholder workshops and participatory processes involving population exposed to landslide risk in the selection of the most appropriate risk mitigation measure(s).

8.2 CHANGES Project

The CHANGES Marie Curie Training Network education network (Changing Hydro-meteorological Risks – as Analyzed by a New Generation of European Scientists) aimed at developing an advanced understanding of how global changes (environmental and climate changes and socio-economical change) affect the temporal and spatial patterns of hydro-meteorological hazards and associated risks in Europe. The project focused on the assessment and modelling of the changes, and incorporating them in sustainable risk management strategies, including spatial planning, emergency preparedness and risk communication. The work was inter-disciplinary and inter-sectoral, with stakeholder participation. The main objectives of the project were to:

- Provide high-level training, teaching and research in the field of hazard and risk management in a changing environmental context to European young scientists;
- Reduce the fragmentation of research on natural processes; and
- Develop a methodological framework combined with modelling tools for probabilistic multi-hazard risk assessment taking into account changes in hazard scenarios (related to climate change) and exposed elements at risk.

The network consisted of 11 full partners from seven European countries. The network was run by ITC, Faculty of Geo-Information, Science and Earth Observation of the University of Twente in The Netherlands, and employed 17 Early Stage Researchers from all over the world.

A "Risk Change Spatial Decision Support system for the Analysis of Changing Hydro-meteorological Risk" was developed. The Spatial Decision Support System analyses the effect of risk reduction planning alternatives on reducing the risk now and in the future, and support decision makers in selecting the best alternatives. The decision support system is composed of a number of integrated modules. It is available online, and can be accessed through the URL:http://changes.itc.-utwente.nl/RiskChanges.

8.3 Other EU initiatives

Following the Great East Japan earthquake and tsunami of March 2011, leading to the Fukushima Dai-ichi nuclear accident, the European Commission initiated collaborative research projects to develop methods for stress testing of critical infrastructure and management of the risk posed by rare, extreme events and by cascading hazards or events. Key European research projects on stress testing of critical infrastructure and management of the risk posed by rare, extreme events and by cascading hazards include (see Ho et al 2016, Nadim 2016 and websites for further details):

- STREST: Harmonized approach to stress tests for critical infrastructures against natural hazards (coordinator: ETHZ, Switzerland.
- MATRIX: New Multi-Hazard and Multi-Risk Assessment Methods for Europe (Coordinator: GFZ, Germany.
- INFRARISK: Novel Indicators for Identifying Critical Infrastructure (CI) at Risk from Natural Hazards (Coordinator: Roughan & O'Donovan Limited, Ireland.
- INTACT: Impact of Extreme Weather on Critical Infrastructures (Coordinator: TNO, The Netherlands.

9 SUMMARY AND CONCLUSION

Risk and reliability in geotechnical engineering represent a shift in practice. The concepts of probabilistic risk analyses for dams, mining and offshore structures have been around for a long time.

With increasing frequency, society demands that some form of risk analysis be carried out for activities involving risks imposed on the public. At the same time, society accepts or tolerates risks in terms of human life loss, damage to the environment and financial losses in a trade-off between extra safety and enhanced quality of life.

The most effective applications of risk approaches are those involving relative probabilities of failure or illuminating the effects of uncertainties in the parameters on the risks. The continued challenge is to recognize problems where probabilistic thinking can contribute effectively to the engineering solution, while at the same time not trying to force these new approaches into problems best engineering with traditional approaches.

The tools of statistics, probability and risk can be intermixed, to obtain the most realistic and representative estimate of hazard and risk. It is possible to do reliability and risk analyses with simple tools, recognizing that the numbers obtained are relative and not absolute. It is also important to recognize that the hazard and risk numbers change with time, and as events occur or incidents are observed at a facility.

For the purpose of communication with stakeholders, the profession needs to focus on reducing the complexity of the technical explanations. The geo-engineer's role is not only to provide judgment on safety factor, but also to take an active part in the evaluation of hazard and risk. The hazard and risk models should be easy to perceive and use, without reducing the reliability, suitability and value of the models required for the assessment.

There should be increased attention on hazard- and risk-informed decision-making. Integrating deterministic and probabilistic analyses in a complementary manner will enable the user (with or without scientific background) to concentrate on the analysis results rather than the more complex underlying information.

Conventional risk assessment methodologies are not well suited for dealing with the risk posed by low probability – high impact (extreme) events.

Stress testing provides a complementary approach to conventional risk or safety assessments. The approach is used for managing the risk posed by extreme events to constructed facilities and critical infrastructure. In stress tests, the focus is on the performance of the system under consideration subject to extreme event scenarios. This is a rapidly evolving field and the new research initiatives in Europe and elsewhere. Stress testing provides valuable additional insight for extreme situations.

It is imperative to remain vigilant of geotechnical hazards under a changing climate and to be prepared to deal with extreme

events. The engineering approach needs to be supplemented by other measures involving enhanced emergency preparedness, response and recovery.

Disasters can manifest themselves as fast events, but the vulnerability for disasters is built up slowly, and can be the result of neglecting to be adequately prepared. Focus needs to shift from prevention-mitigation to building resilience and reducing risks.

Focus needs to remain on "safety". Faced with natural and man-made hazards, society's only resource is to learn to live and cope with them. One can live with a threat provided the risk associated with it is acceptable or is reduced to a tolerable level. It is important to understand that:

- Risk estimates are only approximate, and should not be taken as absolute values.
- Tolerable risk criteria are themselves not absolute boundaries. Society can show a wide range of tolerance to risk.
- One should use several measures of tolerable risk, e.g. *F-N* pairs, individual and societal risk, and costs vs and maximum justifiable cost for risk mitigation.
- The risk will change with time because of natural processes and development.
- Extreme events (Taleb's (2007) "black swans)" should be considered as part of possible triggers of a cascade of events.
- Often, it can be the smaller, more frequent, events that contribute most to risk.

With the evolution of reliability and risk approaches in geotechnical engineering, the growing demand for hazard and risk analyses in our profession and the societal awareness of hazard and risk makes that the methods and way of thinking associated with risk need to be included in university engineering curricula and in most of our daily designs.

There is a need to adopt a risk awareness and risk reduction culture

ACKNOWLEDGEMENTS

The author recognizes the useful contributions by Dr Farrokh Nadim, Dr Jenny Langford, Bjørn Kalsnes, Heidi Hefre, Kjetil Sverdrup-Thygeson, Unni Eidsvig, Krister Kristensen and Hedda Breien from NGI and that of Dr Ken Ho from GEO in Hong Kong. Part of the work presented on avalanches was carried out with the funding from the Norwegian Water Resources and Energy Directorate (NVE) and with the assistance of Mesta AS and NPRA Regions Central and East.

REFERENCES

ANCOLD 1994. *Guidelines on risk assessment.* Australian Committee on Large Dams.

ANCOLD 2003. *Guidelines on risk assessment*. Australian National Committee on Large Dams.

Australian Geomechanics Society (AGS) (2000). "*Landslide risk management concepts and guidelines"*. Australian Geomechanics Society, Sub-Committee on Landslide Risk Management, Australian Geomechanics, 35: 49-92.

Ang, A, H-S. and Tang, W.H.(2007). *Probability concepts in engineering. Emphasis on applications to civil & environmental engineering*. 2nd Ed., Wiley. 406 pp.

Baecher, G.B. and Christian, J.T. (2003). *Reliability and statistics in geotechnical engineering*. Wiley. 605 pp.

Bakkehøi, S. (1985). Oppdatering av skredkriterier for Rv. 15 på strekningen Grotli-Skåre. NGI Report 81403-2, Statens Vegvesen, Vegsjefen i Oppland.

Borio C., Drehmann M. and Tsatsaronis K. (2012). Stress-testing macro stress testing: Does it live up to expectations? BIS Working Papers, No 369, January.

Canadian Avalanche Association (CAA) (2016). Technical Aspects of Snow Avalanche Risk Management and Resources and Guidelines for Avalanche Practitioners in Canada. (C. Campbell, S. Conger, B. Gould, P. Haegeli, B. Jamieson, & G. Statham Eds.). Revelstoke, BC, Canada: Canadian Avalanche Association.

(http://c.ymcdn.com/sites/www.avalancheassociation.ca/resource/resmgr/Standards_Docs/TASARM_English.pdf.

EAWS (Europe Avalanche Warning Services). (2010)

Fell, R., Ho, K.K.S., Lacasse, S., Leroi, E. (2005). A framework for landslide risk assessment and management. State-of-the-art paper." International Conference on Landslide Risk Management. Vancouver 2005. Proc. pp. 3-25.

Folayan, J.I., Høeg, K. and Benjamin, J.R. (1970). Decision theory applied to settlement prediction," ASCE .J. *of the Soil Mechanics and foundation Division.* 96 (SM4) 1127-1141.

GEO (Geotechnical Engineering Office) (1998). "Landslides and Boulder Falls from Natural Terrain: Interim Risk Guidelines." *GEO Report 75*, Gov. of Hong Kong.

GEO (Geotechnical Engineering Office) (2008). Ken HO (personal communication).

Gudmunsson, M.T., Thordarson, T., Höskuldsson, Á., Larsen, G., Björnsson, H., Prata, F.J., Magnússon, E., Högnadóttir, T., Petersen, G.N., Hayward, C.L., Stevenson, J.A. and Jónsdóttir, I. (2012). Ash generation and distribution from the April-May 2010 eruption of Eyjafalljökull, Iceland, Scientific Reports, 2, 572, doi: 10.1038/srep00572.

Haegeli, P. and McClung, D.M. (2000). A new perspective on computer-aided avalanche forecasting:

Scale and scale issues. International Snow Science Workshop - Big Sky. Montana. Oct. 2-6, 2000: 66-73.

Harbitz, C., Harbitz, A. and Nadim, F. (2001). On probability analysis in snow avalanche hazard zoning. *Annals of Glaciology*. **32** 290-198.

Hefre, H., Sverdrup-Thygeson, K., Eidsvig, U. and Høydal, Ø.A. (2015). Efficient risk assessment of Norwegian railways combining GIS and field studies. Interpraevent 2016. Lucerne. CZ, June 2016.

Ho. K.K.S., Lacasse. S. and Picarelli, L. (2016). Preparedness for Climate Change Impact on Slope Safety. Overview paper in *Slope Safety Preparedness or Climate Change Effects*. Taylor & Francis (in prep).

IPCC (2012). Special Report on Managing the Risks of Extreme Events and Disasters to Advance Climate Change Adaptation (SREX). http://ipccwg2.-gov/SREX/report/.

ISDR (Intern. Strategy for Disaster Reduction) (2005). *Hyogo Framework for Action 2005-2015*, 21 pp.

ISO 31000:2009(E) International Standard on Risk management - Principles and guidelines, 2009-11-15. ISO/IEC 31010 (2009) Ed. 1.0, 2009-11. Risk Management-Risk Assessment Techniques.

ISSMGE TC32 (Technical Committee on Risk Assessment and Management) (2004). Technical Glossary of Risk Assessment Terms.
http://140.112.12.21/issmge/2004Glossary_Draft1.pdf

Kalsnes, B, Vangelsten, B.V. and Eidsvig, U. (2016). Risk analysis in excavation and foundation work. NGM 2016 (this conference).

Kristensen, K. (2005).

Kristensen, K. (2005). Rv. 15 i Grasdalen. Skredforhold ved Riksveg 15 gjennom Grasdalen, Strynefjellet. NGI Report 20051040-1.

Kristensen, K., Breien, H. and Lacasse, S. (2013). Avalanche forecasting and risk mitigation for specific objects at risk, Proc. International Snow Science Workshop. Grenoble – Chamonix Mont-Blanc.

Kristensen, K. and Breien, H. (2012). Fv. 60 Røyr-Herdal Snøskredvarsling, Strandadalen anlegg. Grunnlagsrapport. NGI Report 20111019-00-2-R 25.

Kristensen, K., Kronholm K. and Bjørdal, N.H. (2008). Avalanche Characterization for Regional Road Forecasting. Proc. ISSW'08. Whistler, Canada.

Lacasse, S. (1999). The importance of dealing with uncertainties in foundation analysis. 15th ECSMGE. Amsterdam. Proc. Balkema (Rotterdam). ISBN 90 5809 047 7. pp. 385-392.

Lacasse, S. (2016). The 55th Rankine Lecture (2015). Manuscript for Geotechnique (in preparation).

Lacasse, S. and Nadim, F. (1998). Risk and Reliability in Geotechnical Engineering. State-of-the-Art paper. Fourth International Conference on Case Histories in Geotechnical Engineering, St-Louis, MO, USA.

Lied, K. and Bakkehøi, S. (1980). Empirical Calculations of Snow-Avalanche Run-Out Distance Based on Topographic Parametres. *Journal of Glaciology*. 26 (94).

Nairz, P. (2010). Results. Meeting of the Working Group of the European Avalanche Warning Services (WG EAWS) Innsbruck, June 11th 2010.

Max Geldens Stichting (2002). "Als je leven je lief is".

Nadim, F. (2016). Challenges in managing the risk posed by extreme events. Keynote Paper. 6th Asian-Pacific Symposium on Structural Reliability and its Applications (APSSRA6). Shanghai. Huang *et al* (eds).

Nadim F. and Kalsnes B.G. (2014). Progress of Living with landslide risk in Europe. Plenary Lecture. World Landslide Forum 3 Beijing. Ch. in "*Landslide Science for a Safer Geoenvironment*". (IPL), ISBN 978-3-319-04999-1, 3-20.

Nadim, F, Lacasse, S, and Guttormsen, T.R. (1993). Probabilistic foundation stability analysis: Mobilized friction angle vs available shear strength approach. International Conference on Structural Safety and Reliability, 6. ICOSSAR'93. Innsbruck 1993. Proc. 3, pp. 2001-2008.

Peck, R.B. (1969). Advantages and Limitations of the Observational Method in Applied Soil Mechanics. Géotechnique. 19(1)171-187.

Proske, D. 2004. *Katalog der Risiken.* Eigenverlag Dresden. 372 p.

Statham, G., Haegeli, P., Birkeland, K., Greene, E., Israelson, C., Tremper, B., . . . Kelly, J. (In prep.). The Conceptual Model of Avalanche Hazard. In preparation for *Natural Hazards*.

Taleb, N.N. (2007). *The Black Swan: The Impact of the Highly Improbable*. Random House (USA), ISBN 978-1400063512.

Tang, W.H. (1987). Updating anomaly statistics – single anomaly case. *Structural Safety*. 4 151-163.

Thomas, S.P. and Hrudey, S. (1997). "Risk of Death in Canada: What We Know and How We Know It". University of Alberta Press, 1997. ISBN: 0888642997, 280 pp.

Vangelsten, B.V., Haugen, T. and Kalsnes, B. (2015). DP5 Verktøy for risikovurdering – Risikoveiledning. BegrensSkade Report (c/o NGI. Oslo). 31 March 2015.

WENRA (West European Nuclear Regulators Association) (2011). "Stress tests" specifications – Proposal by the WENRA Task Force, 21 April 2011. http://www.-oecd-nea.org/nsd/fukushima/documents/WENRA-20110421StressTestsSpecifications2011-04-21.pdf.

Whitman, R.V. (1984). "Evaluating calculated risk in geotechnical engineering". *Journal of Geotechnical Engineering,* ASCE, Vol. 110, No. 2; 1984.

Whitman, R.V. (1996). Organizing and Evaluation Uncertainty in Geotechnical Engineering. Uncertainty 1996. ASCE STP 58 Uncertainty in the Geologic Environment. Madison, WI, **1** (1-28).

Youd, T.L., Idriss, I.M., Andrus, R.D., Arango, I., Castro, G., Christian J.T., Dobry, R., Finn, W.D.L., Harder, L.F., Hynes, M.E., Ishihara, K., Koester, J.P., Liao, S.S.C., Marcuson, W.F., Martin, G.R., Mitchell, J.K., Moriwaki, Y., Power, MS., Robertson, P.K., Seed, R.B. and Stokoe, K.H. (2001). Liquefaction resistance of soils: summary report from the 1996 NCEER and 1998 NCEER/NSF Workshops on evaluation of liquefaction resistance of soils. J. Geotechnical and Geoenvironmental Engineering, ASCE, Vol. 127, No. 10, 817-834.

What is a Geotechnical Professional?

D.F. VanDine
VanDine, Geological Engineering Limited, Canada, vandine@islandnet.com, and
Canadian Geotechnical Society, Canada, President@cgs.ca

ABSTRACT
For the purpose of this paper, a 'geotechnical professional' is a 'geotechnical engineer' or an 'engineering geologist'. Such a professional likely has not graduated from an undergraduate or graduate degree program in 'geotechnical engineering' or 'engineering geology', and likely has not had to become registered as a 'geotechnical engineer' or 'engineering geologist' to be able to practice. The result is that geotechnical professionals are currently only self-regulated or, at best, regulated by peer opinion. In today's current global marketplace, in which many geotechnical professionals practice in a number of different jurisdictions, countries and even continents, these issues are becoming increasingly important for all stakeholders, clients and the geotechnical professionals themselves. This paper suggests two possible solutions to these issues:
1) Geotechnical professionals must come to some general world-wide consensus on the definitions of 'geotechnical engineering' and 'engineering geology'. I suggest that the ISSMGE and IAEG definitions are good starting points, but that these definitions should be revisited with input from all member countries.
2) Geotechnical professionals must come to some general world-wide consensus on the minimum standards, or competencies, required to practice 'geotechnical engineering' and 'engineering geology'. I suggest that the UK RoGEP and the draft FedIGS JTC-3's competencies are good starting points, but that they need to be adapted with input from all countries.

Keywords: geotechnical engineer, engineering geologist, competencies, professionalism

1 INTRODUCTION

'Geotechnical engineering' is a hybrid composed of soil mechanics, rock mechanics and geology, among others subjects. Most 'geotechnical engineers' have an undergraduate degree in Civil Engineering, Geological Engineering, Mining Engineering, or Petroleum Engineering. Similarly, 'engineering geology' is a hybrid of geology, geomorphology and at least an appreciation of engineering, among other subjects, and most 'engineering geologists' have an undergraduate degree in Geology, Earth Sciences, or perhaps even Physical Geography.

To my knowledge, there are no post-secondary institutions that offer undergraduate or graduate degrees in 'geotechnical engineering' or 'engineering geology'. There are specific programs, but no specific degrees. Therefore, there are no minimum standards or competencies for 'geotechnical engineers' or 'engineering geologists' (collectively referred to as 'geotechnical professionals'), and, as far as I am aware, there is nowhere in the world that requires a geotechnical professional to be registered as a 'geotechnical engineer' or 'engineering geologist' to be able to practice.

In addition, even though the phrases, 'geotechnical engineer' 'geotechnical specialist', 'geotechnical consultant' or something similar, often appear in various jurisdictional acts, regulations, bylaws, ordinances, guidelines and/or policies, the term 'geotechnical' is seldom, if ever, defined. Each jurisdiction likely has a different idea of what 'geotechnical' means and what qualifications geotechnical professionals have, or should have.

Geotechnical professionals themselves likely have different ideas of what qualifications they should have. The result is that geotechnical professionals are currently only self-regulated or, at best, regulated by peer opinion. In today's current global marketplace, in which many geotechnical professionals now practice in a number of different jurisdictions, countries and even continents, these issues are becoming increasingly important for all stakeholders, clients and the professionals themselves.

Most geotechnical professionals follow their respective professional engineering or professional geology code of ethics that states, for example, something similar to "a professional must undertake and accept responsibility for assignments only when qualified by training or experience". But how do geotechnical professionals know if they are qualified?

This paper suggests two possible solutions to these issues that, if followed, will help better protect the public, geotechnical professionals and the profession. First, there should be some general world-wide consensus on the definitions of 'geotechnical engineering' and 'engineering geology'. Second, there should be some general world-wide consensus on the minimum standards, or competencies, that geotechnical professionals should possess.

2 DEFINITIONS

2.1 Background

There is currently no world-wide consensus on the definitions of 'geotechnical engineering' and 'engineering geology'. Definitions, of course, depend on who is doing the defining and for what purpose.

The International Society of Soil Mechanics and Geotechnical Engineering (ISSMGE) defines 'geotechnical engineering' as "the story of the engineering relationship between humans and earth. The science that explores the mechanics of soils and rocks and its engineering application to the development of human kind" (ISSMGE, 2013). The International Association of Engineering Geology (IAEG) defines 'engineering geology' as "the science devoted to the investigation, study and solution of the engineering and environmental problems which may arise as the result of the interaction between geology and the works and activities of man as well as to the prediction and of the development of measures for prevention or remediation of geological hazards." (IAEG, 1992). But in the literature, and on the internet, one can find numerous other definitions, some of which vary considerably from the above.

In fact, there is not even agreement on the terms 'geotechnical engineering' and 'engineering geology'. The former is frequently referred to as 'geomechanics', 'ground engineering', and/or 'geo-engineering'[1], and the latter is frequently referred to as 'geotechnics', 'environmental geology' and/or 'applied geomorphology'.

Why are there no commonly accepted definitions of 'geotechnical engineering' and 'engineering geology'? One reason, as discussed above, is because 'geotechnical professionals' enter this profession from a wide range of educational backgrounds. Another reason could be that typical geotechnical activities and projects cover a very wide spectrum and, therefore, it's difficult to provide a 'definitive definition'.

2.2 Suggestion

It is my suggestion that geotechnical professionals must come to some general world-wide consensus on the definitions of 'geotechnical engineering' and 'engineering geology'. I suggest that the ISSMGE and IAEG definitions are good starting points, but the fact that they have not been universally adopted indicates that perhaps these definitions should be revisited, with input from all member countries.

3 COMPETENCIES

The following subsections describe a number of, at best, voluntary methods that various jurisdictions have established to help evaluate

[1] 'Geo-engineering' has relatively recently been adopted by some to mean the human intervention (at obviously a very large scale) of the Earth's climatic system to limit adverse effects of climate change.

the competencies of geotechnical professionals.

3.1 Canada

Engineers Canada is the national consortium of the country's 12 provincial and territorial professional engineering regulating bodies. Similarly, Geoscientists Canada is the national consortium of the country's nine provincial and territorial professional geosciences regulating bodies. These two organizations help to develop and maintain national standards for the engineering and geoscience undergraduate degree programs. This is done through the Canadian Engineering Accreditation Board of Engineers Canada and the Canadian Geoscience Standards Board of Geoscience Canada, respectively.

Because these boards only look at undergraduate degree programs, and as mentioned previously, there are no geotechnical-specific undergraduate degree programs in Canada, national competencies for 'geotechnical engineering' and 'engineering geology' have not been established.

However, one provincial regulating body, the Association of Professional Engineers and Geoscientists of British Columbia (APEGBC) has established ten geotechnical engineering-specific competencies, and within each competency there are between two and five 'indicators'. The competencies include the knowledge of: current and applicable acts, regulations, codes, permits, standards and guidelines; site and geotechnical characteristics; engineering principles to develop appropriate design solutions; safety; effective communication; and quality systems, and the ability to assess: that designs conform with actual site conditions; and the performance of the design solution over the design life of the project. The full document is available upon request from registrar@apeg.bc.ca.

These APEGBC competencies and indicators are intended to help new practitioners determine if they have suitable training and experience to practice 'geotechnical engineering'. Currently this is a voluntary self-evaluation process.

Therefore, in Canada, there are no nationally-defined geotechnical-specific competencies.

3.2 United States of America (US)

Within the broad discipline of Civil Engineering, the American Society of Civil Engineers (ASCE) has developed a 'Body of Knowledge' (BOK) (ASCE, 2008). Table 1[2] summarizes the BOK; the six levels of achievement and the 24 appropriate outcomes (competencies) for entry into to the practice Civil Engineering at the professional level. This BOK, however, is not geotechnical-specific.

In 2008, the (US) Academy of Geo-Professionals (AGP) was founded as an independent body, but is related to the Geo-Institute of the ASCE[3] among a number of other US geotechnical professional and trade organizations. The AGP provides a voluntary method for engineers who are already licensed to practice engineering in one or more US states (or elsewhere) to be recognized as having "a special knowledge and experience in the field of geotechnical engineering" (AGP, 2016).

The criteria for an engineer to become an AGP 'Diplomate Geotechnical Engineering' (D.GE.) are:

- have a professional engineer's US state license (or foreign equivalent)
- have a minimum of eight years of progressively increasing responsibility after obtaining a US state licence (or foreign equivalent)
- have a master's degree in Civil Engineering with an emphasis on geotechnical engineering
- have satisfactory experience in at least one of the following areas:
  - site characterization
  - laboratory testing and analysis
  - foundation design
  - slope stability
  - excavations and retaining structures
  - tunnels and underground construction

[2] All tables are at the end of the paper.

[3] The Geo-Institute is the specialty institute within the ASCE that is most closely focused on 'geotechnical engineering'.

- embankments, earth and rockfill dams
- satisfactorily orally defend his / her application to a Board of Trustees.

Although national and geotechnical-specific, the AGP has not defined any geotechnical-specific competencies.

Therefore, in the US, although there is a voluntary program to become a Diplomate Geotechnical Engineer[4], there are no nationally-defined geotechnical-specific competencies.

3.3 United Kingdom (UK)

In the UK, nationally-defined geotechnical-specific competencies do exist.

In 2011, the voluntary UK Register of Ground Engineering Professionals (RoGEP) was established with the support of the Institution of Civil Engineers (ICE), the Geological Society of London (GSL), and the Institute of Materials, Minerals and Mining (IMMM), to identify members "who are suitably qualified and competent in ground engineering" [5] (ICE, 2014)

There are three grades of RoGEP registration: 'Ground Engineering Professional'; 'Ground Engineering Specialist'; and 'Ground Engineering Advisor', and progression from 'Professional' to 'Specialist' to 'Adviser' is encouraged. The RoGEP registration requirements common to all grades are:

- be a chartered engineer or geologist with ICE, GSL or IMMM
- possess a sound knowledge and understanding of scientific / engineering / technical principles together with experience of ground engineering
- by training and experience, meet the competence requirements set out in an appendix (Table 2)
- have a commitment to continuing professional development, particularly in the area of ground engineering.

The competencies in Table 2 are grouped into six areas: innovation; technical solutions; integration; risk management; sustainability; and management.

The emphasis of the 'Professional' is the ability to carry out certain tasks, the emphasis of the 'Specialist' is to manage certain tasks, and the emphasis of the 'Advisor' is to take responsibility for certain tasks.

Registrants also need to select one to four areas of expertise from:

- coastal / marine / offshore
- contaminated land / landfill engineering
- engineering geology / hydrogeology
- foundations / retaining structures
- ground investigation
- ground treatment
- materials and earthworks
- mining / quarrying
- soil and/or rock mechanics
- slopes, soil and/or rock
- underground works
- other

Competencies, requirements and typical responsibilities of each of the three grades, 'Professional'; 'Specialist' and 'Advisor', are summarized in Table 2 and 3.

Therefore, in the UK, there is a voluntary program to become designated as a 'Ground Engineering Professional', 'Ground Engineering Specialist' and 'Ground Engineering Advisor'[6], and there has been a start to broadly nationally-define geotechnical-specific competencies.

I understand that this UK geotechnical-specific voluntary professional registry program is being currently being evaluated for use by other European countries.

3.4 International

In 2002, the ISSMGE, the IAEG and the International Society of Rock Mechanics (ISRM) jointly began to look at the question of competencies of 'geotechnical engineers' and 'engineering geologists'. In 2006, the Joint Technical Committee on Education and Training (JTC-3) was established under the umbrella of the Federation of International Geo-engineering Societies (FedIGS). Its mandate was to prepare a "state-of-the-art report on education and training of

[4] Currently there are approximately 330 AGP members who are designated 'Diplomate Geotechnical Engineering' (D.GE.)

[5] I interpret 'ground engineering' to be closely related to 'geotechnical engineering' and 'engineering geology'.

[6] It is my understanding that the UK RoGEP hopes to have 400 members by the end of 2016.

engineering geologists, geological engineers, geotechnical engineers, and rock engineers". This committee produced its progress report in 2010 (Turner and Rengers, 2010).

Turner and Rengers (2010) adapted the ASCE BOK (as discussed in Section 3.2 above) as the basis of their work. They used the same six levels of achievement as the ASCE BOK, but adapted the outcomes (competencies) that they felt were better suited to geotechnical professionals:

- foundational: mathematics; statistics, basic science, and geoscience
- technical-engineering science: statics, mechanics of materials, fluid mechanics, soil mechanics, and rock mechanics
- technical-engineering design: numerical modelling, engineering geology, hydrogeology, site investigation, foundations, and underground construction
- professional: communication, public policy, business and public administration, globalization, leadership, teamwork, attitudes, lifelong learning, and professional and ethical responsibility.

Turner and Rengers (2010) developed four conceptual competency profiles to provide examples how this approach could be used to assess education and training, one for each of 'geotechnical engineers', 'engineering geologists', 'geological engineers', and 'rock engineers'. The four conceptual competency profiles are shown in Tables 4 to 7. Because these tables are conceptual, education and training levels were not assigned, but are simply indicated with an 'X'. The common 'professional' competencies for all four sub-disciplines were taken directly from the ASCE BOK table and are shown in Table 8.

These conceptual competency profiles are useful in themselves, but are also useful to compare the relative competencies between the sub-disciplines of geotechnical professionals.

It is my understanding that since 2010, JTC-3 has not progressed further in the development of these tables.

3.5 Suggestion

It is my suggestion that geotechnical professionals must come to some general world-wide consensus on the minimum standards, or competencies, of 'geotechnical engineering' and 'engineering geology'. I suggest that the UK RoGEP and the draft FedIGS JTC-3's competencies are good starting points, but that they need to be adapted with input from all.

4 CONCLUSIONS AND SUGGESTIONS

So, what is a geotechnical professional? He or she is a professional that, as far as I know. has not graduated from an undergraduate or graduate degree program in 'geotechnical engineering' or 'engineering geology'. And as far as I know, does not have to become registered as a 'geotechnical engineer' or 'engineering geologist' to be able to practice. The result is that geotechnical professionals are currently only self-regulated or, at best, regulated by peer opinion. In today's current global marketplace, in which many geotechnical professionals now practice in a number of different jurisdictions, countries and even continents, these issues are becoming increasingly important for all stakeholders, clients and the professionals.

Most geotechnical professionals follow their respective professional engineering or professional geology code of ethics that requires them to be "qualified by training or experience". But how do geotechnical professionals know if they are qualified?

This paper suggests two possible solutions to these issues:

1) Geotechnical professionals must come to some general world-wide consensus on the definitions of 'geotechnical engineering' and 'engineering geology'.

2) Geotechnical professionals must come to some general world-wide consensus on the minimum standards, or competencies, of 'geotechnical engineering' and 'engineering geology'.

It is my opinion that, if followed, these suggestions will help better protect the public, geotechnical professionals and the profession.

5 ACKNOWLEDGEMENTS

I thank the organizers of NGM2016 for asking me to present this topic. This paper is the result of discussions with many colleagues, specifically Richard Jackson, Keith Turner and Wayne Savigny. I thank them all, and the two anonymous reviewers.

The opinions expressed herein are mine, and not necessarily those of the Canadian Geotechnical Society.

6 REFERENCES

AGP (Academy of Geo-Professionals) (2016) http://www.geoprofessionals.org/ (accessed February 2016).

ASCE (American Society of Civil Engineers) (2008) Civil Engineering Body of Knowledge for the 21st Century, preparing the Civil Engineer for the future, 2nd Edition, 181 p.

IAEG (International Association of Engineering Geology (1992) Statues, http://www.iaeg.info/about-iaeg/mission/ (accessed February 2016).

ICE (Institution of Civil Engineers) (2014) UK Register of Ground Engineering Professionals, ICE3009(4), Version 8 Revision 2, 13 p.

ISSMGE (International Society of Soil Mechanics and Geotechnical Engineering) (2013) What is Geotechnical Engineering? https://www.youtube.com/watch?v=uElPkghqoJw (accessed February 21 2016).

Turner, A.K. and Rengers, N. (2010) A Report Proposing the Adaptation of the ASCE Body of Knowledge Competency-based Approach to the Assessment of Education and Training Needs in Geo-Engineering, a progress report, FedIGS,, Joint Technical Committee (JTC-3: Education and Training), 37 p.

Table 1 The ASCE Body of Knowledge (adapted from ASCE, 2008). 'B' indicates fulfilled through a bachelor's degree; 'M' through a master's degree or equivalent; and 'E' through pre-license experience.

OUTCOME NUMBER AND TITLE	LEVEL OF ACHIEVEMENT					
	Know-ledge	Compre-hension	Appli-cation	Analy-sis	Systhe-sis	Evalu-ation
Fundamental						
1. Mathematics	B	B	B			
2. Natural sciences	B	B	B			
3. Humanities	B	B	B			
4. Social sciences	B	B	B			
Technical						
5. Materials science	B	B	B			
6. Mechanics	B	B	B	B		
7. Experiments	B	B	B	B	M	
8. Problem recognition and solving	B	B	B	M		
9. Design	B	B	B	B	B	E
10. Sustainability	B	B	B	E		
11. Contemp. issues and hist. perspectives	B	B	B	E		
12. Risk and uncertainty	B	B	B	E		
13. Project management	B	B	B	E		
14. Breadth of civil engineering areas	B	B	B	B		
15. Technical specialization	B	M	M	M	M	E
Professional						
16. Communication	B	B	B	B	E	
17. Public policy	B	B	E			
18. Business and public administration	B	B	E			
19. Globalization	B	B	B	E		
20. Leadership	B	B	B	E		
21. Teamwork	B	B	B	E		
22. Attitudes	B	B	E			
23. Lifelong learning	B	B	B	E	E	
24. Professional and ethical responsibility	B	B	B	B	E	E

Table 2 Assessment of Competence Level for UK RoGEP (adapted from UK RoGEP, 2014)

Attribute	Registered Ground Engineering Professional	Registered Ground Engineering Specialist	Registered Ground Engineering Adviser
Innovation	Ability to introduce and develop innovation in connection with ground engineering activities in respect of the challenges associated with research, design or construction	Manage the introduction and development of innovation in connection with ground engineering activities in respect of the challenges associated with research, design or construction	Take responsibility for the introduction and development of innovation in connection with ground engineering activities in respect of the challenges associated with research, design or construction
Technical Solutions	Ability to apply and implement technical solutions in connection with ground engineering activities in respect of problems associated with research, design or construction	Manage the application of technical solutions in connection with ground engineering activities in respect of problems associated with research, design or construction	Take responsibility for technical solutions in connection with ground engineering activities in respect of problems associated with research, design or construction
Integration	Ability to integrate ground engineering activities in a multidisciplinary environment associated with research, design or construction	Manage ground engineering activities in a multidisciplinary environment associated with research, design or construction	Take responsibility for ground engineering activities in a multi-disciplinary environment associated with research, design or construction
Risk Management	Ability to identify and assess risks in connection with ground engineering activities in respect of the challenges associated with research, design, construction, health, safety and welfare	Manage the identification and assessment of risks in connection with ground engineering activities in respect of the challenges associated with research, design, construction, health, safety and welfare	Take responsibility for the identification and assessment of risks in connection with ground engineering activities in respect of the challenges associated with research, design, construction, health, safety and welfare
Sustainability	Ability to investigate and promote sustainability in connection with ground engineering activities in respect of problems associated with research, design or construction	Manage the identification and promotion of sustainability in connection with ground engineering activities in respect of problems associated with research, design or construction	Take responsibility for the identification and promotion of sustainability in connection with ground engineering activities in respect of problems associated with research, design or construction
Management	Ability to plan and deliver ground engineering activities in respect of problems associated with research, design or construction	Manage the planning and delivery of ground engineering activities in respect of problems associated with research, design or construction	Take responsibility for the planning and delivery of ground engineering activities in respect of problems associated with research, design or construction

Table 3 UK RoGEP Grades (adapted from UK RoGEP, 2014)

Registered Ground Engineering Professionals will typically be competent to:
- carry out a range of routine ground engineering activities
- contribute within a team to the design and execution of a wider range of activities
- appreciate the role of their areas of ground engineering expertise within a project and in relation to other disciplines

Registered Ground Engineering Specialists will typically have eight years relevant post-graduate experience, or a relevant master's degree and six years relevant post-graduate experience, in ground engineering, and will typically be competent to:
- design and manage a range of ground engineering activities
- check the output documents from the same activities, when undertaken by others
- approve and/or authorise factual work and routine interpretative work by others

Registered Ground Engineering Adviser will typically have five years of practice as a Registered Ground Engineering Specialist, will be required to demonstrate sufficient additional post-chartership competence over and above the Specialist grade, and will typically be competent to:
- design, manage, check, approve, authorise and take responsibility for a wide range of ground engineering services
- act as a technical mentor to all other ground engineering professionals.

Tables 4-7 Four conceptual competency profiles demonstrating how the different specializations each have a distinct set of required competencies (adapted from Turner and Rengers, 2010.) 'X' indicates that the education and training levels are unassigned to either: 'B' fulfilled through a bachelor's degree; 'M' through a master's degree or equivalent; and 'E' through pre-license experience.

Table 8 is common to all four specializations, and should be attached to the bottom of each of Tables 4-7.

Table 4

GEOTECHNICAL ENGINEER

OUTCOME	LEVEL OF ACHIEVEMENT					
	Know-ledge	Compre-hension	Appli-cation	Analy-sis	Systhe-sis	Evalu-ation
Foundational						
Mathematics	X	X	X			
Statistics	X	X	X			
Basic science	X	X	X			
Geoscience	X	X				
Technical-Engineering Science						
Statics	X	X	X	X		
Mechanics of materials	X	X	X	X		
Fluid mechanics	X	X	X	X		
Soil mechanics	X	X	X	X		
Rock mechanics	X	X	X			
Technical-Engineering Design						
Numerical modelling	X	X				
Engineering geology	X					
Hydrogeology	X					
Site investigation	X	X	X			
Foundations	X	X	X	X	X	X
Underground construction	X	X				

Table 5 Refer to note above Table 4

ENGINEERING GEOLOGIST

OUTCOME	LEVEL OF ACHIEVEMENT					
	Know-ledge	Compre-hension	Appli-cation	Analy-sis	Systhe-sis	Evalu-ation
Foundational						
Mathematics	X	X				
Statistics	X	X	X			
Basic science	X	X	X			
Geoscience	X	X	X	X	X	X
Technical-Engineering Science						
Statics	X					
Mechanics of materials	X					
Fluid mechanics	X					
Soil mechanics	X	X				
Rock mechanics	X	X				
Technical-Engineering Design						
Numerical modelling	X					
Engineering geology	X	X	X	X	X	X
Hydrogeology	X	X	X	X	X	
Site investigation	X	X	X	X	X	X
Foundations	X	X				
Underground construction	X					

Table 6 Refer to note above Table 4

GEOLOGICAL ENGINEER

OUTCOME	LEVEL OF ACHIEVEMENT					
	Know-ledge	Compre-hension	Appli-cation	Analy-sis	Systhe-sis	Evalu-ation
Foundational						
Mathematics	X	X	X			
Statistics	X	X	X			
Basic science	X	X	X	X		
Geoscience	X	X	X	X	X	X
Technical-Engineering Science						
Statics	X	X	X	X		
Mechanics of materials	X	X	X	X		
Fluid mechanics	X	X	X	X		
Soil mechanics	X	X	X	X		
Rock mechanics	X	X	X	X		
Technical-Engineering Design						
Numerical modelling	X	X				
Engineering geology	X	X	X	X	X	X
Hydrogeology	X	X	X	X	X	X
Site investigation	X	X	X	X	X	X
Foundations	X	X	X			
Underground construction	X	X	X	X		

Table 7 Refer to note above Table 4

ROCK ENGINEER

OUTCOME	LEVEL OF ACHIEVEMENT					
	Know-ledge	Compre-hension	Appli-cation	Analy-sis	Systhe-sis	Evalu-ation
Foundational						
Mathematics	X	X	X			
Statistics	X	X	X			
Basic science	X	X	X			
Geoscience	X	X				
Technical-Engineering Science						
Statics	X	X	X	X		
Mechanics of materials	X	X	X	X		
Fluid mechanics	X	X	X	X		
Soil mechanics	X	X				
Rock mechanics	X	X	X	X	X	X
Technical-Engineering Design						
Numerical modelling	X	X	X	X	X	
Engineering geology	X	X	X			
Hydrogeology	X	X				
Site investigation	X	X	X			
Foundations	X	X				
Underground construction	X	X	X	X	X	X

Table 8 Common outcomes to all four specializations shown in Table 4 to 7. Refer to note above Table 4

COMMON OUTCOMES

OUTCOME	LEVEL OF ACHIEVEMENT					
	Know-ledge	Compre-hension	Appli-cation	Analy-sis	Systhe-sis	Evalu-ation
Professional						
Communication	B	B	B	B	E	
Public policy	B	B	E			
Business and Public administration	B	B	E			
Globalization	B	B	B	E		
Leadership	B	B	B	E		
Teamwork	B	B	B	E		
Attitudes	B	B	E			
Lifelong learning	B	B	B	E	E	
Professional and ethical responsibility	B	B	B	B	E	E

Working abroad – Expect the unexpected

Jørgen S. Steenfelt,
Technical Director at COWI, Denmark

ABSTRACT

The Nordic countries represent an impressive variety of soil conditions: quick clays, gyttja, peat, sands, clays, extremely strong clay till, volcanic deposits, pumis, chalk and limestone to strong rocks. However, the Nordic countries only represent a small temperate to subarctic part of the globe (with significant internal diversion) leaving out a huge area of subtropical and tropical geological settings.

Thus, working abroad presents challenges in understanding the local geology and not least the local "geo-culture". Empirical rules, preferences in terms of investigation tools, laboratory practices, interpretation rules and conceptual understanding of the geotechnical theory vary significantly as soon as you leave your home base. This leads to three rules of travelling: (i) Expect the unexpected, (ii) Respect well-winnowed local experience and (iii) Use your full "tool-kit" and present innovative solutions (as you will be "competing" with the locals).

Examples of "unexpected conditions and innovative solutions" are described by means of case histories. The overall experience is synthesized in the perceived challenges facing the geo-engineers in developed and developing countries together with the skills and necessary changes in the geo-disciplines needed to handle these challenges.

Hydropower dams in the Land of Ice and Fire

Fjóla Guðrún Sigtryggsdóttir
NTNU, Department of Hydraulic and Environmental Engineering, Norway, fjola.g.sigtryggsdottir@ntnu.no

ABSTRACT
Iceland's development from being one of Europe's poorest countries, at the onset of last century, to one with a very high standard of living is directly associated with the utilization of its renewable energy sources. In this development, dams have been indispensable in harnessing glacial rivers and mountain streams for hydropower. The dams retain storages for Iceland's melting glaciers/ice, however at the same time they may be located in the threatening settings of active tectonics and volcanism. In Iceland there are 29 large dams, as per ICOLD (International Commission on Large Dams) register of large dams. These are all built for hydropower generation and include 7 earthfill dams, 17 earth-rockfill dams, 3 rockfill dams and 2 concrete dams. The highest of these is a concrete faced rockfill dam, the Kárhnjúkar dam, about 200 m high. In addition to the 29 large dams, numerous small dams belong to the hydropower system that connects to the national power grid. In this paper Iceland's hydropower development is reviewed with focus on large dams, particularly erath-rockfill and rockfill dams. Challenges relating to: glacial, volcanic, tectonic, and seismic settings are discussed on general terms along with relevant design criteria and/or measures.

Keywords: Iceland, renewable energy, dams, geohazards.

1 INTRODUCTION

Iceland is often referred to as the Land of Ice and Fire. The former from its glaciers and ice caps. The latter, from its location as a volcanically and tectonically active island on the Mid-Atlantic Ridge. These two elements, ice and fire, are also sources for renewable energy, hydro and geothermal, currently providing 85% of the primary energy used in Iceland (see Fig. 1). The share of, hydropower and geothermal, in this is respectively; 20% and 65%.
Iceland's development from one of Europe's poorest countries, at the onset of last century, to a one with a high standard of living is directly associated with the utilization of its renewable energy sources. Geothermal energy is mainly used for district heating while hydropower is the main provider of electricity. Hydropower currently provides 73% of the total electricity production (see Table 1). Substantial amount of Iceland´s precipitation is stored in ice caps, glaciers and groundwater. This combined with extensive highlands, has enormous energy potential assessed up to 220 TWh/yr. However, considering feasibility and environmental constraints it has been estimated that 30 TWh/yr of hydropower could be produced (Bárðardóttir, 2006). This can be compared to the current energy production from hydropower of 12,9 TWh/yr. The first hydropower station (6 kW) was established in 1904. The ensuing decades, or till the 1950s, a number of small hydro were constructed. Subsequent hydropower development (see Fig. 2), with large-scale hydropower stations requiring large dams, followed in response to the establishment of energy intensive industries, such as aluminium smelters (Sigurðsson, 2002). The first large-scale station, Búrfell harnessing the Þjórsá River in South Iceland, was completed in 1969-1972 then with installed capacity of 210 MW (currently 270 MW). Enlargement of this station (100 MW) is in the construction phase.

In Iceland's utilization of renewables, dams have been indispensable in harnessing the glacial rivers and mountain streams for hydropower. The largest dams generally retain storages for Iceland's melting glaciers/ice, however at the same time they may be located in the threatening settings of active tectonics and volcanism.
In this paper the focus is on large dams in Iceland, an overview is given along with the general design criteria. Challenges relating to; glacial, volcanic, tectonic, and seismic settings are discussed.

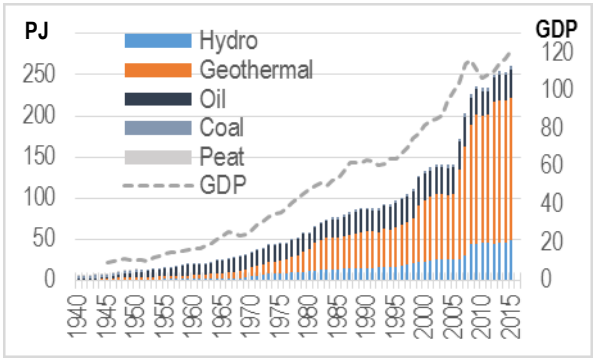


Figure 1 Primary energy use in Iceland's (PJ) 1940-2015 along with Gross Domestic Production index (GDP). (Data: Orkustofnun and Hagstofa Íslands).

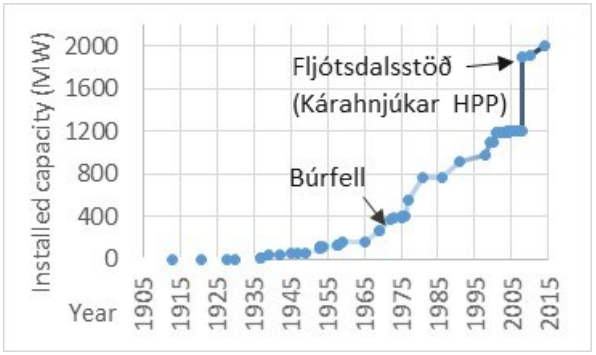


Figure 2 Installed capacity from hydroelectric power stations.

Table 1 Generation of electricity in Iceland 2015. (Orkustofnun, 2016).

	Installed		Production	
	MW	%	GWh	%
Hydro	1986	71,7	13780	**73,3**
Geothermal	665	24,0	5003	**26,6**
Fuel	117	4,2	4	**0**
Wind	3	0,1	11	**0,1**
Total	**2771**	**100**	**18798**	**100**

2 DAMS IN ICELAND

According to ICOLD (International Commission on Large Dams) register of large dams, there are 29 large dams in Iceland (ICOLD, 2016). Update of this number is required, but the discussion in this paper will comply with ICOLD registry. The National Power Company of Iceland (Landsvirkjun) is the owner of all but two of the large dams.

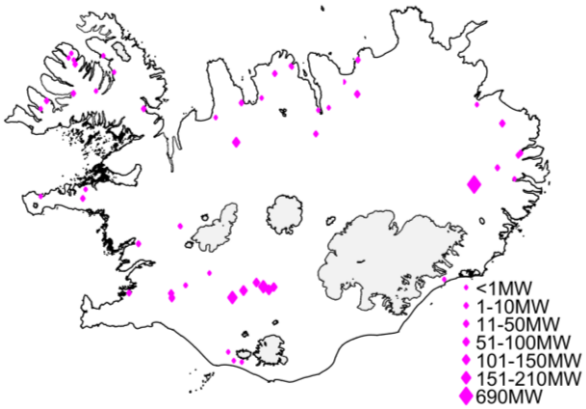


Figure 3 Hydropower plants in Iceland.

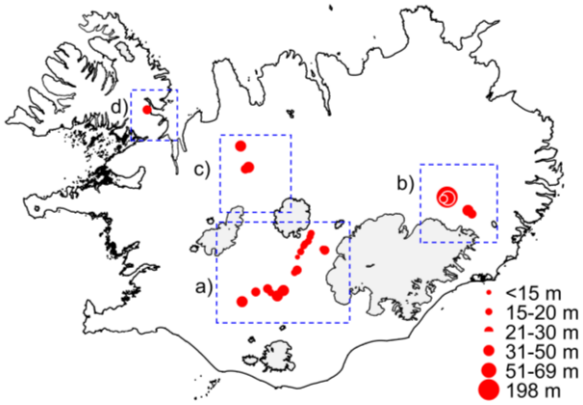


Figure 4 Large dams in Iceland : a) In South-and Mid-Iceland, in the Þjórsár-Tungnár catchment area. b) In East Iceland, in the catchment area of Jökulsá á Dal og Jökulsá á Brú. c) In North-West Iceland, in the Blanda catchment area. d) On the Vestfirðir Peninsula. Maximum dam height is indicated by marker size, see legend.

A large dam as per ICOLD definition is one which is: (a) more than 15 m in height measured from the lowest point of the general foundations to the crest of the dam, (b) more than 10 m in height provided they comply with at least one of the following conditions: (i) the crest is not 1ess than 500 m in length (ii) the capacity of the reservoir

formed by the dam is not less than 1 million m³ (iii) the maximum flood discharge dealt with by the dam is not less than 2000 m³/s, (iv) the dam is of unusual design.
The first large dam in Iceland was built in 1945, the 33 m high Skeiðsfoss concrete buttress dam in North Iceland. Second is the Búrfell dam completed in 1969. Subsequent construction of large dams followed the hydropower development shown in Fig. 2. Icelandic large dams are all built for hydropower generation and include 7 earthfill (TE) dams, 17 earth-rockfill (ER) dams, 3 rockfill (RF) dams and 2 concrete dams (ISCOLD, 2016; Pálmason, 2016). The highest of these is the Kárhnjúkar concrete faced rockfill dam, 198 m, completed 2007. In addition to the large dams, numerous small dams belong to the hydropower system of 59 stations that connect to the national power grid (Fig. 3). Official information on the small dams is not available in one place, and thus not the exact number of this. Furthermore, national regulations on dam safety do not exist.
Here the focus is on large fill dams.

2.1 Large fill dams in Iceland

The most common earth-rockfill dams in Iceland have a central impervious core, abutted by gravel filters, supporting fills and riprap for erosion and wave protection (see Fig. 5). Filter criteria has generally considered these presented by Sherard and Dunnigan (1989).
The criteria set for slope stability of the large earth-rockfill dam at the different design stages has generally been set as follows:

Construction stage, completed dam
- Empty reservoir $F_s \geq 1.4$
- Critical reservoir level $F_s \geq 1.4$

Steady stage, finished dam
- Full reservoir, $F_s \geq 1.5$
- Empty reservoir, $F_s \geq 1.5$

Rapid reservoir drawdown, finished dam
- Long term pore pressure $F_s \geq 1.3$

Earthquake
- Crest/slope displacement, <0.3 m

Example material properties for stability considerations are presented in Table 2.

In dam design and re-evaluations on flooding, the trend the past few years has been, to follow more directly the criteria set by Norwegian regulations on dam safety (Forskrift om sikkerhet ved vassdragsanlegg).

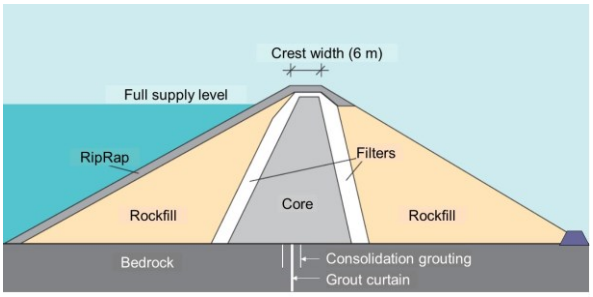


Figure 5 Typical cross section of an Icelandic Earth-rockfill dam

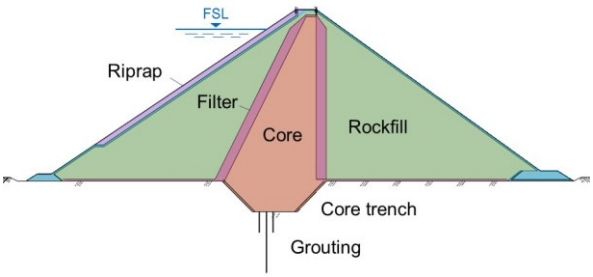


Figure 6 Example cross section of an Icelandic earth-rockfill dam with a core trench.

Table 2 Example material properties

	Density [kN/m³]		Cohesion	Friction
	Saturated	Moist	[kN/m²]	angle [°]
Core*	22		0	40-42
Shell**	20-21	19	0	>45

*Morain; **Rockfill, generally pillow lava.

The dam slopes of the Icelandic dams vary somewhat, although there is a clear relation to dam type (fill material), or as follows: Earthfill dams have generally an upstream slope (U/S slope) of 1:2.2 and downstream slope (D/S slope) of 1:2. Earth-rockfill dams built in Mid, South and North-East Iceland typically have an U/S slope of 1:1.8 and D/S slope of 1:1.6. The most recent earth-rockfill dams, built in East Iceland generally have an U/S slope of 1:1.5 and a D/S slope of 1:1.4. The rockfill dams with the impervious element on the U/S slope have somewhat steeper slopes upto U/S slope of 1:1.3 and D/S slope of 1:~1.25 (the Kárahnjúkar CFRD).
The rock, used in the Icelandic rockfill dams and the supporting zones of the earth-rockfill

dams, is generally volcanic (pillow lava, basalt), i.e. originally magma erupted from a volcano. Conversely, the material in the core of the earth-rockfill dams is generally moraine of low permeability (~10^{-7} to 10^{-8} m/s). Moraine is a glacially formed accumulation of unconsolidated glacial debris. Thus the Icelandic earth-and rockfill dams are built of material formed through the forces of ice and fire. The settings relating to these forces additionally have to be considered in the design of the dams and appurtenant structures.

3 COMPLICATIONS, CRITERIA AND/OR MEASURES RELATING TO GEOLOGICAL SETTINGS

Iceland straddles the Mid-Atlantic Ridge which marks the boundary of the North-American Plate (NAP) and the Eurasian Plate (EP). See Fig.7. These plates move continuously apart, resulting in intrusion of magma on the boundary which again leads to tectonic activity.

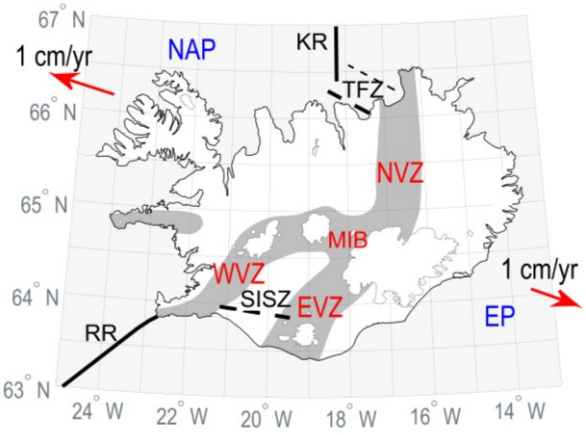


Figure 7 Volcanic zones of Iceland (grey) and tectonic settings. KR and RR are on the Mid-Atlantic Ridge. KR Kolbeinsey Ridge, RR Reykjanes Ridge, WVZ West Volcanic Zone, MIB Mid-Iceland Belt, EVZ East Volcanic Zone, NVZ North Volcanic Zone, TFZ Tjörnes Fracture Zone, SISZ South Iceland Seismic Zone.

The three main volcanic zones (VZ) of Iceland follow the Mid-Atlantic Ridge. These are also called spreading zones with the NAP moving 1 cm/yr to the north west while the EP moves 1 cm/yr to the north east. On the transformation zones (Fig. 7), the TFZ and SIZS, the largest earthquakes in Iceland originate.

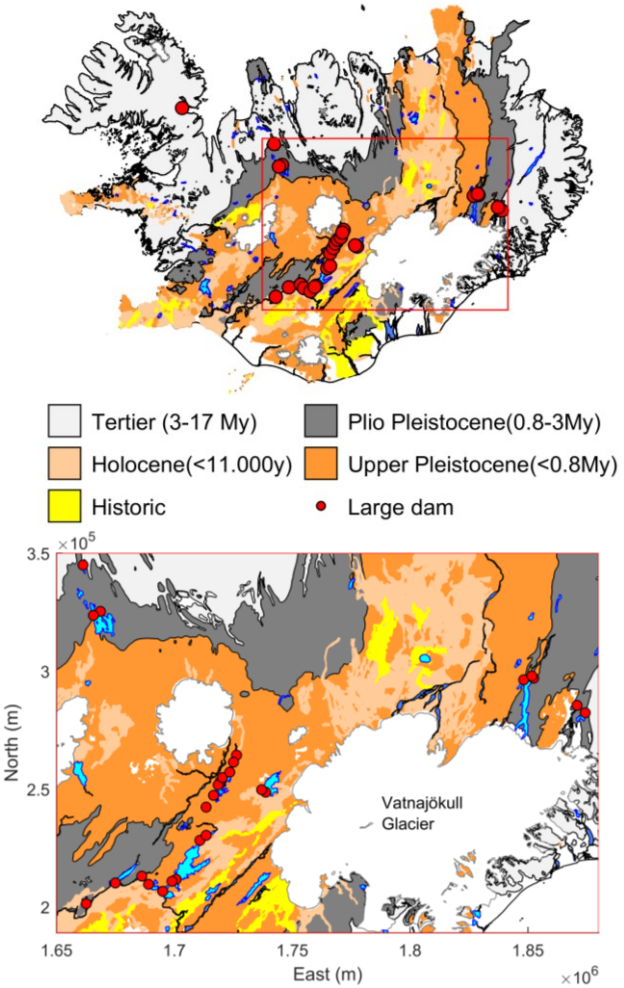


Figure 8. Bedrock geology of Iceland (Náttúrufræðistofnun Íslands) and the location of large dams. Bedrock is classified on the basis of its age. Postglacial lavas are divided into prehistoric (Holocene) and historic lavas (Historic- since Iceland's settlement in 874).

3.1 Geology and hydropower dams

The main features of Iceland's bedrock geology, is shown in Fig 8, classified by age. The distribution of the youngest bedrock (<0.8 My) is mostly confined to the active volcanic zones. This area is covered with hyaloclastites formed by subglacial volcanism during the Pleistocene, and partly by postglacial (Holocene) lava formations, including since after the settlement of Iceland (Historic, i.e. after 874 AD).

South- and Mid-Iceland. Many of the large dams (18 large dams of height from about 13 to 44 m) along with a number of smaller dams, are located in the Þjórsár-Tungnár

basin which lies within the volcanic zone of central Iceland (MIB and EVZ) highlands (Fig. 4 & 7). In this river system six hydropower plants (HP) have been built in steps during the last five decades. The latest one was brought online 2014, and the extension (100 MW) of the first station in this sequence (Búrfell) is ongoing. Additionally, three potential hydropower projects (total of 255 MW) in the lower region of the Þjórsá river are under consideration.

Holocene formations characterize the Þjórsár-Tungnár basin (Fig.8), constituting the Holocene Tungnaá lava flows of which the Great Þjórsá lava is the oldest, 8600 years, and Veiðivötn lava the youngest or 500 years old (Hjartarson, 2003). These are basaltic pillow lava originating from fissure eruptions (see Fig.10) within the Bárðarbunga-Veiðivötn volcanic system (Halldórsson et al. ,2008). A zone of highly permeable scoria usually exists at both the base and the surface of each lavaflow. These are commonly separated by sedimentary interbeds, comprising sand, volcanic ash and loess (Pálmason, 2016). Additionally, the lavas are highly porous allowing infiltration of precipitation into groundwater aquifers (Johannesson et al, 2007).

The lava flows and the foundation conditions have directly influenced the dam design in the area and measures taken to limit groundwater flow and seepage through the dam foundation. Pálmason (2016) describes in some detail the measures taken at each dam site. In this paper these measures are summarized and related to the overall geological conditions and formations in the area (see Fig. 8), the same principles have been used for earth-rockfill dams in other parts of the country, and are as follows:

(1) In the older formations (Upper Pleistocene) consolidation grouting of the dam foundation is generally sufficient. Usually the grouting is conducted on three rows. A relatively deep cement grout curtain is provided on the middle row, typically 10-20 m deep, adjoined by consolidation grouting, 3-10 m, deep on each side.

(2) In the Holocene formations (including historical formation since after the settlement of Iceland in 874 AD) trenches are typically excavated, preferably down to a more sound and less porous lava. The trenches are then refilled as may apply with fine grained alluvial gravel, moraine, a moraine-bentonite slurry mixture or similar. The trenches are typically located in the foundation of the dam core (Fig. 6) or, if outside of this, generally connected to the core with an impervious blanket. In the core trenches filter fabrics or other filters, are normally provided prior to placing the refill.

These measures have resulted in decreased groundwater flow in the foundation. Furthermore, self-sealing of the foundation by suspended sediments of the glacial rivers has also lead to decreased groundwater flow. Generally, at the design stage, the self-sealing has been roughly estimated to reduce the flow by as much as 50% over the first decade of operation (Pálmason, 2016).



Figure 9. The Hálslón Reservoir and dams.

East-Iceland. While most of the large dams are in South-and Mid Iceland, the two highest dams in Iceland are located in East Iceland, on the east border of the NVZ (Fig. 4 ,7 and 8). These are the Kárahnjúkar CFRD (198 m) (K dam) and the Desjarár dam (69 m) (D dam). The K and D dams are in the catchment area of the glacial river Jökulsá á Brú originating from under Vatnajökull Glacier, and retain the Hálslón Reservoir (2600 Gl) along with Sauðárdalur dam (S dam) (29 m high). See Fig. 9. Additionally three large earth-rockfill dams (15-32 m high) are further east in the catchment of another glacial river, also originating from the Vatnajökull glacier. These dams altogether provide storages for the 690 MW Fljótsdalur Station (of the Kárahnjúkar hydropower project).

The S dam is founded on soil layers. The other dams are founded on basalt and/or pillow lava of the Plio or Upper Pleistocene formations. The foundation conditions can vary markedly along the length of the dams, from relatively sound basalt to pillow lava. Additionally, the foundations of the D dam and the K dam are crossed with lineaments and faults. Mitigation measures and the foundation conditions are described in papers presented at NGM 2008 (Pálmason & Sigtryggsdóttir, 2008; Stefánsson & Kröyer, 2008; Skúlason, 2008). For the D dam the combined dam and foundation design is based on the same principles described above, i.e. with a core trench and underlying grout curtain through the more pervious lava layers (pillow lava) in the dam foundation, and grout curtain underlying the core on a basalt foundation.

North-West Iceland. Three large earth-rockfill dams (26 to 44 m high) are located in North-West Iceland (Fig. 4), in the basin of the rivers Blanda River originating partly in the Hofsjökull Glacier area and Kolkukvísl River, harnessed in the Blanda Power Station (150 MW). These dams are founded on Plio Pleistocene basalt, or on both basalt and sandstone. Trenches were generally excavated into the sandstone, but foundation measures in basalt foundation followed largely these described above for dams founded on the Pleistocene Formations.

Vestfirðir Peninsula. One large earth-rockfill dam, Þverárdam of 20 m height, is located in the Vestfirðir Peninsula. This dam forms the storage for a small hydro (2.3 MW). The dam is founded on Tertier basalt formations. Foundation measures largely followed these described above for dams founded on the Pleistocene Formations, however with grouting on two rows. Additional measures were required where a fault crosses the foundation, comprising placing gravel over some length of the fault upstream, aiming at reduced leakage by lengthening the leakage pathway.

3.2 Glaciovolcanism and jökulhlaups

The large dams discussed above are located within and on the border of the volcanic zones. Large dams, hydropower stations, and the volcanic systems are presented in Fig. 10a. A volcanic system consists of a central volcano, a fissure swarms or both. A central volcano is a deep-seated magma reservoir and the focal point of eruptive activity, while the fissure swarm present a shallower crustal magma chamber (see Fig. 10b,c) (Thordarson and Larsen, 2007).

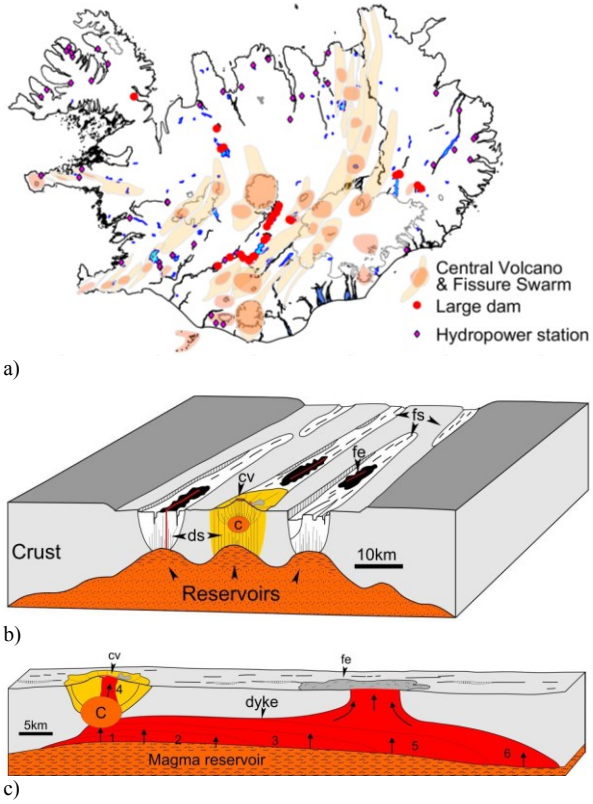


Figure 10. (a) Large dams, hydropower stations and the distribution of active volcanic systems in Iceland. (Landinformation on volcanic systems: FUTUREVOLC). b) The main structural elements of a volcanic system. Abbreviations: c, crustal magma chamber, ds, dyke swarm, cv, central volcano, fs, fissure swarm, fe fissure eruption. B) Injection and growth of a dyke feeding an eruption during a rifting episode. (fig b and c: Thordarson and Larsen, 2007)

The large dams, within or in the vicinity of the volcanic zones, retain glacial rivers fed by the nearby glaciers. All of the glaciers overlay one or more central volcano and fissure swarms. In Vatnajökull five subglacial volcanic systems have been identified. Recent eruptions, include Grímsvötn central volcano in 2011, 2004, 1998 and a fissure swarm eruption in 1996 at Gjálp (Fig. 11) midway between Grímsvötn and Bárðarbunga central volcanoes. (See Fig.

13). The 1996 eruption has been influential in defining catastrophic flood events for the design of Icelandic dams as later explained. Subglacial lakes created by subglacial eruptions, and/or, above geothermal systems, may cause jökulhlaup (glacial outburst flood) For example, injection of magma to shallow depths (see Fig.10) may bring heat up to the glacier above, continuously melting the ice and creating a subglacial lake that breaks out in jökulhlaups as the basal water pressure increases enough to lift the overlying glacier (Björnsson, 2002). In Iceland several subglacial lakes are known to exist, six such in Vatnajökull. The location of these can usually be identified from depressions in the glacier surface (see Fig.12). One such subglacial lake is Grímsvötn, associated with the central volcano Grímsvötn. Grímsvötn Lake's water level generally rises due to melting of the ice by geothermal action (see Fig.12), resulting in regular drainage of the subglacial lake usually with a period of about 10 years or less. However, the extraordinary jökulhlaups from Grímsvötn in 1996 was associated with subglacial fissure eruption in Gjálp. (Björnsson, 2002). The jökulhlaup occurred in November 1996. This was preceded and indirectly triggered by the Gjálp eruption in October 1996. Meltwater due to the eruption flowed from the eruption site to Grímsvötn subglacial lake, accumulated for a month until it drained in the catastrophic jökulhlaup. During the first four days of eruption, meltwater was created at a rate of 5000-7000 m^3/s. (Gudmundsson et al, 1997; Björnsson,2002).

Dams, fuse plugs and jökulhlaups. The jökulhlaups may pose a threat to dams and other infrastructures. Fig 13 shows areas inundated by Holocene jökulhlaups attributed to volcanic and geothermal activity. The inundated areas include the Þjórsár-Tungnár basin in Mid-and South Iceland were many of the large dams and associated storages and hydropower stations are located (Fig.4).
In design criteria for dams located on waterways susceptible to such occurrences, the jökulhlaups are considered catastrophic flood events. The general criterion set for the relevant dams is that this should not breach during the assigned catastrophic event, although limited damage may be expected.



Figure 11. Gjálp subglacial eruption (Oct 1996) (See the airplane for scale). (Oddur Sigurðsson)

Accommodating this a fuse plug is commonly included in a dam or on a reservoir. This comprises, a dam section with a lower crest than the other dams retaining the particular reservoir. In the relevant flood event overtopping will thus first occur on the fuse plug, initiating erosion and subsequent breaching of this. The fuse plug is thus designed to divert the flood to the downstream of the pertinent dam and ensure that overtopping and breaching will not occur on the main dams. (Pálmason & Sigtryggsdóttir, 2008; Pálmason, 2016). However, there is a great uncertainty in the definition of the catastrophic event. The approach taken has been to look to the extraordinary jökulhlaup event of 1996. For example, the design criteria for the three dams retaining the Hálslón Reservoir in East Iceland considered the rate of ice melting in the 1996 event. The general criteria deduced from this has been to design the fuse plug to pass an outburst flood of 6000 m^3/s lasting four days (Pálmason & Sigtryggsdóttir, 2008). Most of the dams in the Þjórsár-Tungnár basin in Mid and South Iceland are designed before 1996, and thus although jökulhlaups are considered in the design of these by incorporating a fuse plug, this particular criterion relating to the 1996 event was not used for all of the dams in this area. Assessment of the magnitude of jökulhlaup

in the relevant area should be considered. Recent volcanic activities in the nearby Bárðarbunga volcanic system urged reassessment of relevant mitigation measures in the Þjórsár-Tungnár basin.

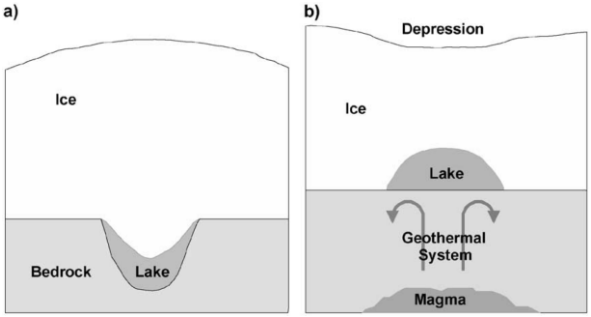


Figure 12. Schematic drawing of a) a stable subglacial lake, b) an unstable subglacial lake that drains in jökulhlaup (Björnsson, 2002).

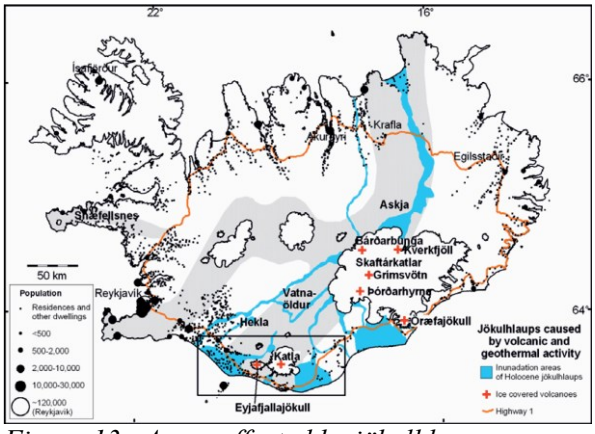


Figure 13. Areas affected by jökulhlaups attributed to volcanic activity in Iceland during the Holocene. (Volcanic zones gray shaded) (Gudmundsson et al., 2008).

3.3 Iceland's thin crust

The Icelandic crust is relatively thin (10-46 km). Post-glacial rebound uplift due to the melting of Vatnajökull is in the range of 12 mm/yr in the vicinity of the glacier. In central Iceland the uplift rates are about 25 mm/yr partly attributed to glacial isostatic adjustment. Deformations close to Vatnajökull ice cap have a peak-to-peak seasonal displacement of ~16 mm. The thin crust was a consideration for the impounding of the 57 km² Hálslón Reservoir in East Iceland (Sigtryggsdóttir et al., 2013). The effect of the reservoir on crustal movements was estimated prior to the inundation. Measured settlement after the first impounding suggested an average measured subsidence of (14±10) mm due to the reservoir filling (Ófeigsson et al 2008).

4 TECTONIC SETTINGS AND SEISMIC DESIGN CRITERIA

The largest earthquakes in Iceland occur on transform faults and fracture zones in South and North Iceland (see SISZ and TFZ on Fig. 7). Conversely, the earthquakes originating on the spreading zones/volcanic zones are relatively small. This can be observed from the earthquake hazard map of Iceland in Fig.14, presenting horizontal peak ground acceleration (PGA) with a mean return period of 475 years. Location of hydropower stations and large dams in Iceland are plotted on the hazard map (Fig. 14) along with the location of central volcanoes.
Iceland's major earthquake faults thus lie within the fracture zones. However, in general the Icelandic bedrock is crossed with lineaments and faults, although these may not be active in generating earthquakes.

4.1 Lineaments and active faults

Faults with movement in Holocene time (last 11.000 years) are by ICOLD definition (ICOLD, 1998) characterized as active and thus capable of generating earthquakes.
In general, faults and lineaments passing through a dam foundation are examples of serious deficiencies. Faults have been encountered in the foundation of some of the large dams and/or in the vicinity of these. Furthermore, such features are a major concern for proposed dams within the SISZ, where the possibility of fault movement and opening of faults in earthquakes has to be considered.
In the case of the Hálslón Reservoir in East Iceland, active faults by ICOLD definition were encountered in the foundation of the K and D dam, as well as within the reservoir area. This information resulted in foundation measures considering possible fault movement, as well as re-evaluation of the earthquake action in the area. (Sigtryggsdóttir et al, 2012; Sigtryggsdóttir et al., 2013).

4.2 Selecting seismic parameters

The hazard map on Fig. 14 indicates that the large dams in Mid, East and North-West Iceland (see Fig. 4), are located in a low seismic hazard area with a PGA of only 0.1g or less for a mean return period of 475 years. Conversely, dams and hydropower stations in the South (close to or within the SISZ) or in the North (the TFZ (see Fig.7)) are in an area of high seismic hazard with a PGA of 0.5g. The PGA values of Fig. 14 have a mean return period of 475 years. However, in the design of large dams, ICOLD (1989) recommends consideration of the Maximum Credible Earthquake (MCE). The MCE is defined as the largest conceivable earthquake that appears physically possible along a recognized active fault or within a geographically defined tectonic province. The MCE is thus based on geological evidence and little regard is given to probability of occurrence.

The approach recommended by ICOLD was adopted for the dams in East Iceland retaining the Hálslón Reservoir. The assessment of the earthquake action focused on near-field events, considering the latest information on faults and overall relevant geology. Credible earthquake scenarios were defined resulting in predicted maximum PGA of 0.3, compared to the PGA of 0.1g for the 475 year event. (Sigtryggsdóttir et al, 2012).

4.3 Seismic Analysis

Dynamic analysis of an earth dam preferably requires knowledge of the dynamic properties of the dam fill material. The maximum shear modulus has been measured for some Icelandic soils. However, neither modulus reduction behaviour of these nor damping variation has been studied. In the absence of this information, estimates based on available such from relevant literature has been used in recent analysis, and sensitivity to the selection of this investigated.

The seismic analysis of the most recent and largest Icelandic earth-rockfill dams has included both pseudo-static and dynamic analyses. This has e.g. considered the dam model response to the design earthquake motions and permanent displacement along specified slip surfaces. The pseudostatic analysis is then considered as an index of the seismic resistance further established by the dynamic analysis. Liquefaction potential has also been investigated where relevant. Sigtryggsdóttir et al (2012) describe the dynamic analysis of the D dam, which involved the use of two of GeoSlope's products one for the dynamic analysis of the dam subjected to the earthquake shaking and other for the stability of the dam slope and permanent deformation. The calculated permanent deformation along the selected slopes were compared to the deformation criteria for the crest/slope displacement.

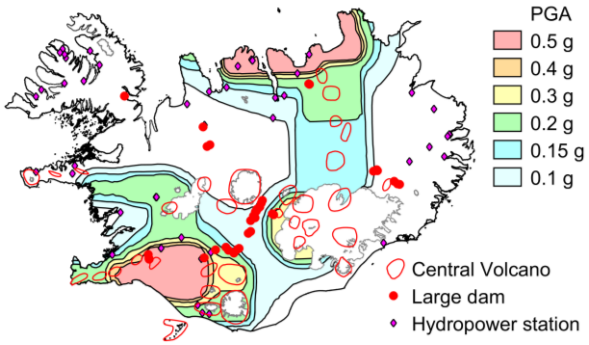


Figure 14. Location of large dams and hydropower stations in Iceland, along with central volcanoes (FUTUREVOLC), plotted on an earthquake hazard map for Iceland (ÍST EN 1998:2004/NA2010) presenting horizontal reference acceleration (PGA) for earthquakes, with a mean return period of 475 years.

5 FINAL REMARKS

A general overview of large dams in Iceland is presented in this paper. Information on small dams in Iceland are incomplete and a listing of these is required. Furthermore, information on the large dams need to be updated. As for the older large dams, update of the earthquake action with a definition of MCE and subsequent revaluation of the dams should be considered. Furthermore, a study on geodynamic properties of Icelandic soils would indeed support earthquake analysis and design of Icelandic dams and other geostructures. Additionally, geohazards such as jökulhlaup need to be assessed more systematically than hitherto for dam design applications, and with due consideration to consequences and possible mitigation measures. In this respect, monitoring of the

respective dams, with structural health assessments as well as monitoring the geohazards that pose threat to these, is a mitigation measure that enhances safety (see Sigtryggsdóttir, 2015; Sigtryggsdóttir et al, 2015a,b). It is the author's opinion that this in general requires further attention and interest by dam owners in Iceland, particularly during dam operation. The enforcement of national regulations on dam safety may be required to boost such interest, as well as to ensure minimum design requirements.
Large dams in Iceland may not be many, but their setting is challenging and have resulted in interesting dam designs. Both of which are worth studying further.

ACKNOWLEDGEMENT

The review of this paper by senior geotechnical engineer Pálmi R. Pálmason at Verkís Ltd and the designer of more than two thirds of all large dams in Iceland is gratefully acknowledged. The use of Verkís Ltd. facilities partly when writing this paper is appreciated.

6 REFERENCES

Bárðardóttir, H (Editor). Energy in Iceland. Orkustofnun/Ministies of Industry and Commerce. ISBN: 9979-68-198-5

Björnsson, H. 2002. Subglacial lakes and jökulhlaups in Iceland. Gobal and planetary change. (35) 255-272.

Gudmundsson, MT, Sigmundsson, F, Björnsson,H. 1997.Ice-Volcano interaction of 1996 Gjálp subglacial eruption, Vatnajökull, Iceland. Nature,Vol 398.

Gudmundsson, M.T., Larsen, G., Höskuldsson, Á., Gylfason, Á.G. 2008. Volcanic hazards in Iceland. Jökull No.58.

Halldorsson, S., et al 2008. Isotopic-heterogeneity of the Thjorsa lava—Implications for mantle sources and crustal processes within the Eastern Rift Zone, Iceland. Chem. Geol. 255, 305–316. doi:10.1016/j.chemgeo.2008.06.050

Hjartarson, Á. 2003. The Skagafjörður Unconformity North Iceland and its Geological History. Art. 6: Postglacial lava production in Iceland. PhD thesis, Geological Museum, University of Copenhagen.

ICOLD. 1989. Selecting Seismic Parameters for Large Dams, Committee on Seismic Aspects of Dam Design. ICOLD Bulletin; 72; Paris.

ICOLD. 2016. Web page: Number of Dams by Country Members. Accessed Feb. 2016.

ISCOLD (Iceland national committee on large dams), 2016. Data sheet on large dams in Iceland.

Jóhannesson, T., Aðalgeirsdóttir, G., Björnsson, H. Crochet, P, Elíasson, E.B., Guðmundsson, S, Jónsdóttir, J.F., Ólafsson, H., Pálsson, F., Rögnvaldsson, Ó., Sigurðsson, O., Snorrason, Á., Sveinsson, Ó.G.B., Thorsteinsson, Th.. (2007), Effect of climate change on hydrology and hydro-resources in Iceland. Report OS-2007/011.

Orkustofnun. 2016. Data Rep. OS.2016.T002.01.

Ófeigsson BG, Sigmundsson F et al (2008) Crustal movements 2005-2007 in the Kárahnjúkar area, NE Iceland, in relation to formation of the Hálslón water reservoir, Memo.

Palmason, P.R, Sigtryggsdottir, FG (2008). Some Design Aspects of the Desjararstifla Dam. NGM 2008

Pálmason, P.R. 2016. Draft manuscript on dams.

Thordarson, T., Larsen, G., 2007. Volcanism in Iceland in historical time: Volcano types, eruption styles and eruptive history. J. Geodyn. 43, 118–152. doi:10.1016/j.jog.2006.09.005

Sherard, J.L., Dunnigan, L.P..1989. Critical filters for impervious soils. Journal of Geotechnical Engineering Vol 115 No7.

Sigtryggsdóttir, F.G., Snæbjörnsson, J.T., Pálmason, P, 2012. On the seismic design history and analysis of the Desjarárstífla Dam in Iceland. 15WCEE, Lisboa.

Sigtryggsdóttir, F.G., Snæbjörnsson, J.Th., Ingólfsson, P, Sigbjornsson, R, 2013. Results from the monitoring of geohazards since the impounding of the Hálslón reservoir. Presented at the ICOLD 2013 International Symposium, Seattle

Sigtryggsdóttir F.G. 2015. Monitoring of structural health and danger state for safety and sustainability of infrastructure systems, PhD thesis. NTNU 2015:142

Sigtryggsdóttir, F.G., Snæbjörnsson, J.T, Grande L, Sigbjörnsson,R. 2015a. Methodology for geohazard assessment for hydropower projects. Nat. Hazards 79, 1299–1331. doi:10.1007/s11069-015-1906-4

Sigtryggsdóttir, F.G., Snæbjörnsson, J.T., Grande, L., Sigbjörnsson, R., 2015b. Interrelations in multi-source geohazard monitoring for safety management of infrastructure systems. Struct. Infrastruct. Eng. 1–29. doi:10.1080/15732479.2015.1015147

Sigurðsson, H.M. 2002. Vatnsaflsvirkjanir á Íslandi. Verkfræðistofa Sigurðar Thorodssen. ISBN 9979772239.

Skúlason, J., 2008. Design and performance of the Sauðárdalsstífla Dam. NGM. Norway.

Stefánsson, B., & Kröyer, J..2008. Some geotechnical challenges at the Kárahnjúkar dam. NGM, Norway.

Landinformation and digital data to produced some of the figures were obtained from:
Landmælingar Íslands (www.lmi.is)fig 3,4,8,10a,14)
FUTUREVOLC (http://futurevolc.hi.is), (fig10a,14)
Náttúrufræðistofnun Íslands (www.ni.is). (fig 8)
Orkustofnun (www.os.is), (fig. 1-3) and
Hagstofa Íslands (www.hagstofa.is) (fig.1).
Information on the contribution of individuals, e.g. on geology, is provided on the websites referred to.

Technical Papers

Topics of the Conference

1 Innovation in Geotechnical Engineering

2 Investigation, testing and monitoring

3 Modelling, analysis and design

4 Geotechnical structures and infrastructure

5 Foundation and deep excavations

6 Underground infrastructures

7 Environmental geotechnics

8 Geotechnical implications of climate change

9 Geohazards and slope stability

10 Geotechnical eartquake engineering

11 Geotechnical code and standards

12 Transportation geotechnics and geophysics

New Developments in On-line Monitoring of Geotechnical Data

A. Thorarinsson
Vista Data Vision, Iceland, andres.thorarinsson@vistadatavision.com

A. J. Simmonds
Geokon Inc., USA, tsimmonds@geokon.com

ABSTRACT

Improvements in sensor designs over the past 20 years have generally only been marginal, except in the case of those which now employ micro-electronics. On the other hand data acquisition systems, communications and data handling have changed dramatically, having passed through several generations of development in the same time frame. The net result has provided reliable and simpler monitoring systems, with more features and, due to improved manufacturing productivity, all at lower cost.

This paper focuses on recent developments in on-line monitoring systems and, in particular, the way in which the data can be handled. It follows the path set in pervious papers by the same authors who both work on the subject: How to handle, display and work with geotechnical data in a modern on-line monitoring system.

1 PHILOSOPHY

The benefits of automated data acquisition systems and data visualizations are now generally well understood (Marr, A 2005), providing, stakeholders and contractors alike, a convenient and near real-time means of assessing instrument data and, in turn, the performance of the structure. It also provides a means to verify the design of the structure, develop maintenance strategies and a means to advance the state of the art.

Essentially, the main purpose of the data acquisition system is to supervise the behavior of the structure being monitored, through a system of on line instruments and sensors. In general, various groups of sensors are connected to strategically placed dataloggers, in which the readings are processed, stored and then transmitted, quickly and securely, to a centrally located Automatic Data Acquisition System (ADAS) (Fiorini, As et al, 2007), which can, when necessary, promptly alert alarm conditions if pre-set threshold criteria are met.

The data obtained at the ADAS is typically stored in a data base where analyses and actions based on sensor specific data can be initiated, and the performance of the ADAS itself be assessed. Sensor data can be processed to determine trend lines, max. min. and mean values, accelerations, cumulative displacement, and even to output in engineering units, for example; if the Young‘s Modulus and cross sectional area of a structural member is known, readings of strain can be presented in terms of stress or load. At the same time, built in diagnostics can report the status of the data acquisition system itself,

including battery voltage, capacity, etc. and send alarms when necessary.

2 OVERVIEW OF SENSORS, DATA ACQUISITION SYSTEMS

Generally, the most important parameters required by the geotechnical engineer are Physical Parameters which include the following; deformation, strain, load, pressure, pore water pressure, earth pressure, inclination, temperature, precipitation, soil moisture and corrosion. There are hundreds of different sensors available for geotechnical monitoring, based on a wide variety of technologies, some of which have been in use for more than 80 years.

The ultimate selection of any sensor must consider that its output is directly proportional to the quantity being measured and that it is reliable and repeatable. The sensors must also be capable of providing the required accuracy and sensitivity and, where long term monitoring is required, exhibit excellent long term stability. Finally, no matter which type of technology is chosen, the sensor must be durable and capable of withstanding the environment in which it will be installed. Today, the most widely used technologies include, Wheatstone Bridge, MEMS, DCDT, Potentiometric, Vibrating Wire, 4-20mA and, most recently, fiber optic.

The past 20 years have witnessed huge advances with respect to data acquisition systems (Thorarinsson, A et al 2007). Now they are available with sophisticated processing and error checking capabilities, operate from low power supplies, and have communications devices built in to allow for remote data collection via a variety of means (hard wire, fiber optic cable, telephone, Ethernet, satellite, and wireless). They have become more affordable, even for small scale projects, and most are designed in a modular way which better facilitates housing in small, field ready, enclosures and, moreover, allows them to be easily customized (and expandable) for the type, number, and location of sensors being monitored.

The widespread availability (and relative low cost) of sensors and data acquisition systems has greatly improved the ability to retrieve data from geotechnical monitoring sites (including those in remote locations) reliably, and in a timely manner. On top of this, the Internet, as a communications tool, has provided a highly reliable and inexpensive link to show data from a sensor located anywhere in the world to a user located anywhere else, at any time.

4 ROLES IN MONITORING SYSTEMS

Important in every data monitoring system today is the need to identify certain roles that must be managed in order to ensure the integrity of the system. From a data handling point of view the main roles are those of the Designer, Maintenance Manager, On-duty Manager and Analyst. As a data monitoring system becomes bigger and more complex it is vital to identify those role, and to assign each role to an individual who is capable of handling all the requirements.

4.1 The Designer

Although data monitoring systems can be planned in a number of different ways, let's consider the data part of the monitoring system, where the designer must decide which information he needs, how it should be presented and reported and then decides on the appropriate sensors, data loggers and communications.

An important part of any design is the decision as to how alarms should be handled to allow for reasonable response time and to minimize the possibility of false alarms, (Thorarinsson, A 2015). A

typical false alarm can arise when, for some reason, the data logger returns an out-of-range (high or low) value caused by electrical noise or a voltage spike. One method to facilitate this, is to adjust the protocol such that an alarm will not be triggered unless the data logger returns at least two consecutive readings which fall outside the alarm limit(s).

This leads to another important consideration (and decision); how long after an alarm event should an alarm be made? Keep in mind that all alarms do not require rapid response, common are alarms which warn about slow moving process like low battery voltage, seepage or gradual movements (accelerations) in an active slope.

Finally, the designer should also be aware that too much data may not be helpful, it may over load the communication link, the data storage and all the data handling. To illustrate, consider a data acquisition system monitoring every 10 minutes (52.000 readings per year) versus one monitoring every 0.1 second (320 million readings per year).

4.2 The Maintenance Manager

The responsibility of the maintenance manager is to ensure that the monitoring system is operational and performing as expected. A well designed monitoring system will incorporate "health indicators" which will indicate if parts of the system need maintenance or replacement (see Thorarinsson, A et al 2011). Two important health indicators are update and power, but there may be others including those related to individual sensors or to the internal life of the sensor. Health indicators greatly simplify the task of the maintenance manager who now only needs to spend a short amount of time to check if all is well

If data is no longer being updated from a monitoring system then something is clearly wrong. It would be very time consuming to always be checking update status, better if this task is automated and to receive a notification. The main reasons why data may not be updated are no power (or power has been removed), failed communications, or there a network problem. If automated update notifications are set in a reasonable way, for example as 5 to 10 times the scheduled update, then the operator can rest assured that he will be notified if data is not updated in a timely manner

The duties of the Maintenance Manager become a lot easier when key data is organized in such a way that, in a single glance (on one screen), it can be shown all is well.

4.3 The On-duty Manager

The purpose of a monitoring system is to collect data. The role of the on-duty manager is to review the data at regular intervals to ensure correctness and to decide if it indicates a need for some action. The larger the system the more important it becomes to organize graphs and overviews such that the daily workflow of data browsing becomes as easy as possible. The tools to facilitate this include naming of sensors, trend lines, overviews, setting alarm thresholds and the creation of groups of data such that differences can be more clearly seen. It must also be possible that the layout of data be adaptable to changing situations as time passes, and areas of interest shift from one aspect to another.

On most occasions the On-duty manager is in contact with several clients, each with different needs; for example the contractor, the owner, the engineer, and the regulatory body; as such, the on-duty manager has to be able to create the various requirements by tweaking the web interface to the data. This may include automatic forwarding of data into another data system or to allow an external system to retrieve data from his, and it may well require the assistance of the maintenance manager to create the necessary views and associated data handling.

4.4 The Data analyst

Everyone who works with data becomes a data analyst. Data analysts use data to get results, whether it be the sum or average for a time period, correlation of data, comparing one period to another, identifying trends or creating reports. Originally the input for the data analyst was a series of data in which each reading had its own time stamp, and the analysis tool of choice was a spreadsheet program. This process was a major task and very time consuming to. Nowadays, however, it is expected that data monitoring systems incorporate an arsenal of d tools which makes it possible to perform a variety of analyses and to achieve deterministic results with just a few keystrokes. However the old, classic, and fundamental problem is always present; “Can I trust the result?” After all, the result is only as good as the integrity of the data being used as input. The data can be suspect to a variety of errors; incorrect units, spikes, drift, gaps and so on. And as the amount of data collected is constantly rising the role of the data analyst, to validate the results are correct, becomes increasingly important. This leads to the conclusion that an important part of the data analyst’s work is to check it for integrity and to make corrections where necessary such that the data being used for the analyses is correct.

5 DATA VISUALIZATION AND REPORTING

To see is to understand! How true it is. But what one person sees (or wants) may not the same for another. Now, however, are many tools available that can be used as quick reports and, by a few simple key-clicks, it is possible for the analyst to reveal hidden information that is not immediately obvious from the sensor data alone. Let's look at few examples.

5.1 XY graph

Let's first look at what the classical XY graph can do for us.

Figure 5.1.1 shows 6 months of data from an extensometer installed in a slope close to a main road. The graph shows some movement, the sensor returns a low of 2.7 inches and a high of 4.7 inches. The question is, of course, “Is this is true?” In this case there is a temperature sensor inside the extensometer, see figure 5.1.2.

Now, what is interesting is to plot the extensometer data as a function of the temperature on a XY plot, see figure 5.1.3.

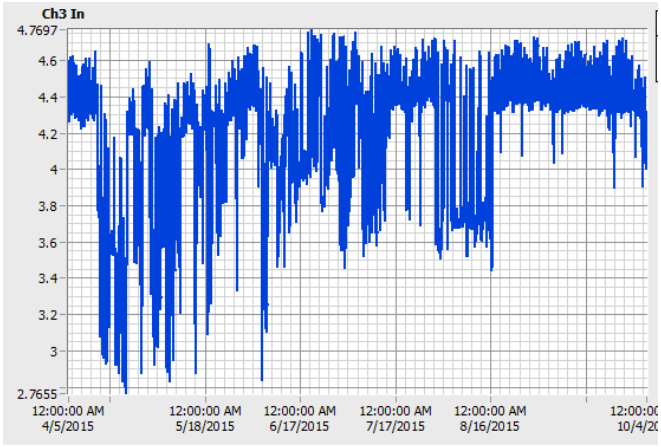


Figure 5.1.1: 6 months of extensometer data

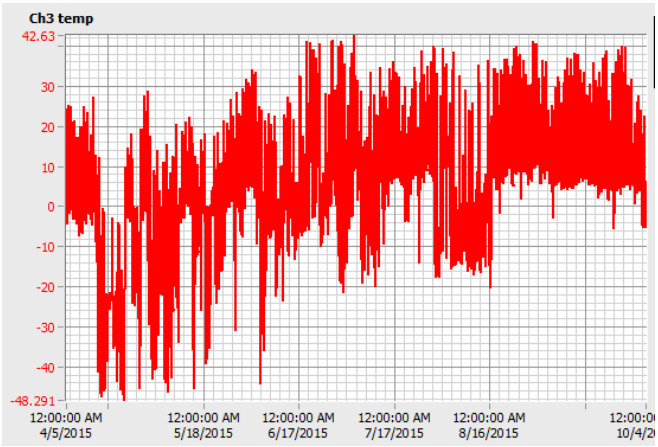


Figure 5.1.2: Temperature readings from the extensometer sensor in fig. 5.1.1

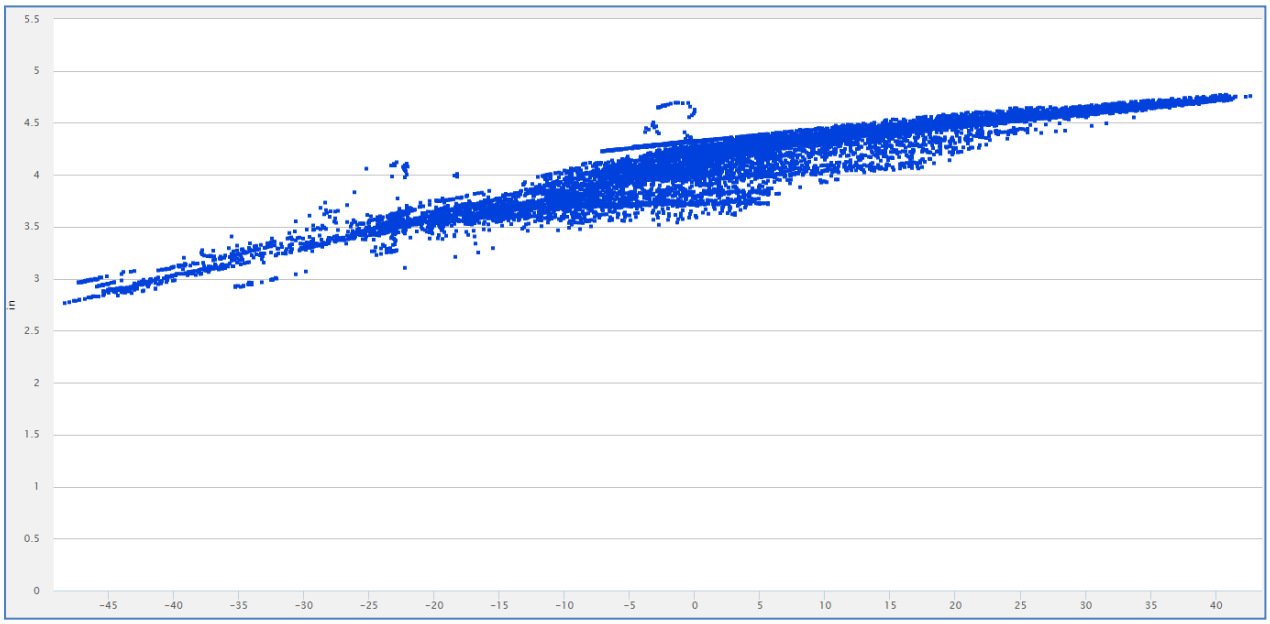


Figure 5.1.3: XY plot of 6 months of extensometer sensor data. X-axis is sensor temperature, Y-axis is extensometer sensor readings.

As it turns out, there is a linear relationship between the extensometer readings and the ambient temperature. Is it possible that there are movements at the site and that they are greater when the temperature gets higher? Or it is equally possible that the current temperature correction of the extensometer is incorrect or that the AD conversion of the data logger is temperature sensitive which, in either case, would lead us to believe that there is actually no movement at all! The final conclusion is that if such a correlation between a sensor reading and temperature is discovered the real cause must be investigated via an on-site inspection and possibly additional instruments.

5.2 Overlay graph and intensity plot

Overlay graphs and Intensity plots are great tools for investigating trends in sensor readings. If there are trends it is of utmost importance to understand if they are the result of actual changes or if there is some kind of an instrumentation error that one should be aware of. The following example shows data from a piezometer in borehole at the edge of a landfill, close to a pond and few miles from the sea.

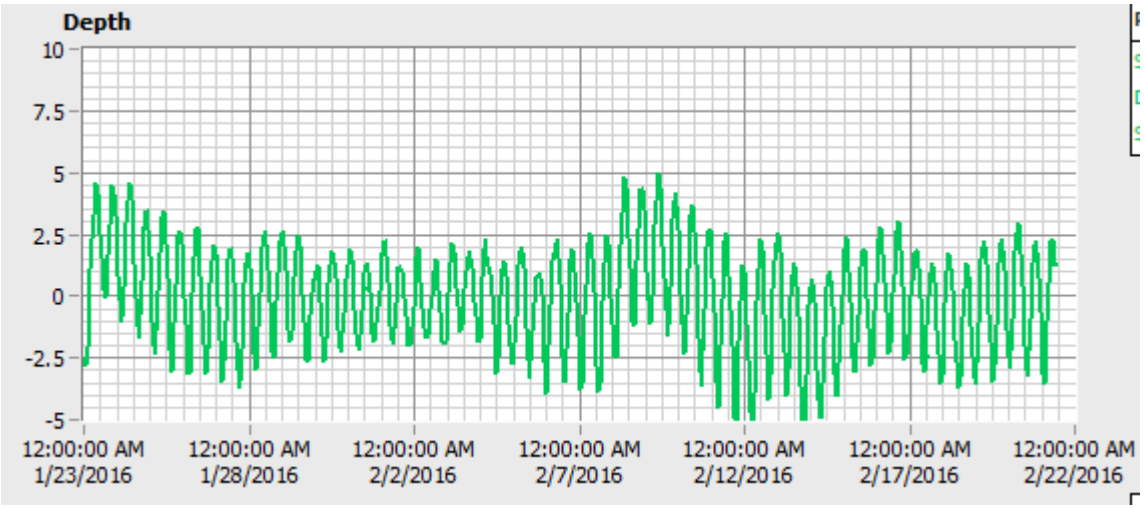


Figure 5.2.1: One month of groundwater level sensor readings

Clearly there are regular swings in the water level readings. The operator could ask if this is true and if so, why? Or is this some kind of an instrumentation error? In order to find the answer the operator could start by plotting the data on Overlay graph reporting tool.

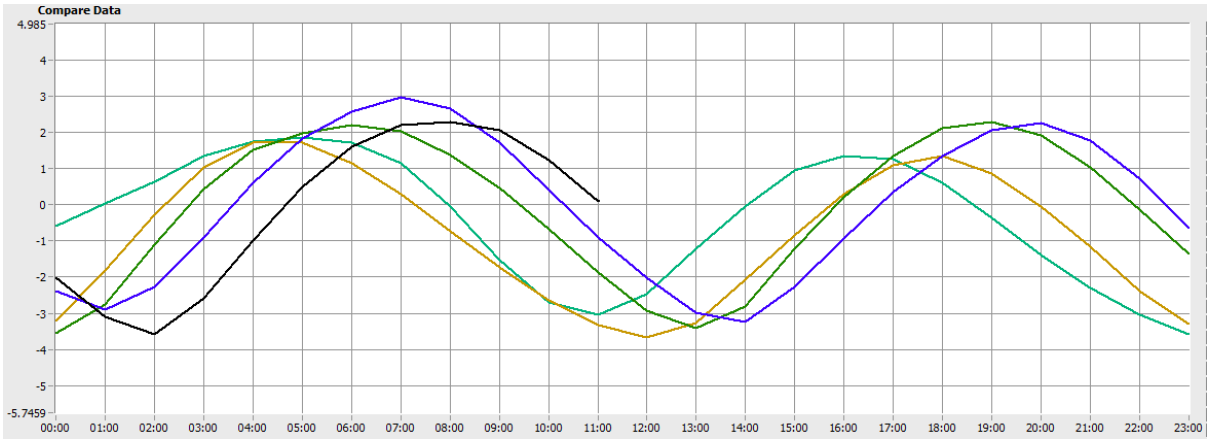


Figure 5.2.2: Overlay graph, four and a half days, of water level readings on top of each other.

The Overlay graph reveals that the maximum and minimum of the sensor readings occur almost every 12 hours but not always at the same time of day, and that they move slightly forward in time every day.

Now let's plot the same data in the Intensity plot reporting tool:

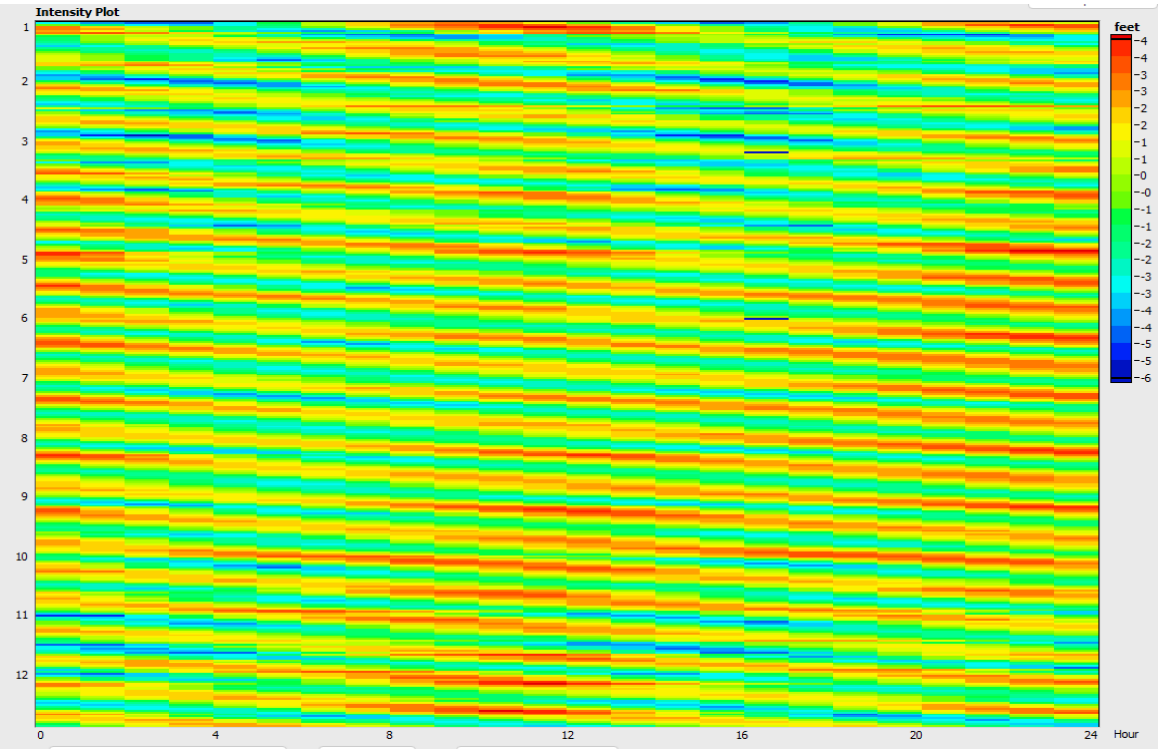


Figure 5.2.3: One year of water level sensor readings. Y-scale is the months, starting on month 1 (January) and ending on month 12 (December). X-scale is hours of the day.

The Intensity plot reveals the answer; the water level correlates with the tide, which influences the ground water even though is some miles away.

5.3 *Wind rose*

Weather data can give information which is useful when planning work at a building site, and one reporting tool that can be extremely helpful is the wind rose reporting tool. The wind rose reporting tool not only shows the wind speed as function of the wind direction but also other variables as a function of the wind direction. In the following example check from which direction the heaviest rain hits the site and from which direction the highest wind speed comes.

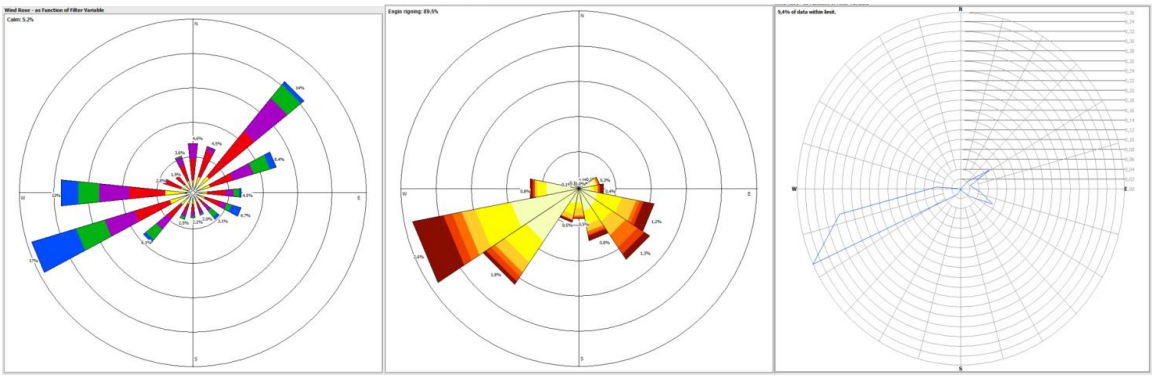


Figure 5.3.1: Three "wind" roses: a) Classic wind rose, b) Precipitation as function of wind direction, heaviest from WSW and ASA, c) Strongest wind is blowing from WSW.

5.5 *Automatic reports*

Automatic reports are just that; sent automatically to the recipient daily, weekly or monthly, or however the requirement may be. Automatic reports may include just the raw sensor data, or all the text, photos, data sets, graphs, alarms and notes for the preceding period and therefore greatly simplifies the task of providing reports to the client. Other types of reports can send data automatically from the on-line monitoring system to another system, or receive and store data from another data system.

5.6 *Dashboard*

While graphs with trend lines are the traditional method of displaying data there are other tools now available which can show a mix of latest data *and* trend lines which gives a great overview of the entire project. In this way, the operator only needs to select the work site and he then has, at his fingertips, all the information for that site, including latest readings, alarm status, trend lines and data all presented in quick reporting tools.

6 DATA FROM VARIOUS INSTRUMENTS

6.1 *Wireless instrument systems*

Wireless transmission of data from sensors connected to data acquisition systems is not particularly new, as far as data communications are concerned, but what is becoming increasingly popular of late, is the use of wireless sensor networks, where one sensor (or a small group of sensors) are connected to a wireless nodes which, in turn, transmit data to one common base station.

Communication protocols in wireless networks can be rather complex, but essentially comprise a header, identifying its source node, destination node and the data content. When multiple nodes desire to transmit, protocols are needed to avoid collisions and lost data. Similarly, in a distributed network, there may be multiple paths from the source to the destination and so message routing becomes very important. Routing can be Fixed, which dictates the destination (and so cannot take into account failed links, or congested queues) or Adaptive (which can take into account various performance measures and take into account link or node failures).

The database/data visualization software used to handle data from wireless systems must take into account all of the abovementioned and, more often than not, integrate it along with data from larger data acquisition systems, to which a larger number of sensor are connected.

6.2 *Vibration recorders*

In order to capture vibrations caused by blasting, or any other event, a vibration recorder is used. A typical vibration recorder uses three sensors in the x, y and z planes, and samples all three constantly, at high sampling rate, 500Hz or higher, even up to 5kHz, and stores these data in a buffer. If there is a vibration that is higher than a preset trigger value the vibration recorder stores a data set starting few seconds before, and up to 30 seconds, after the event. This set of data is called event data and is sent to the on-line monitoring system for handling. Sometimes a microphone is part of the vibration recorder, returning some metrics for the sound and sometimes full audio sampling for the period. In order to show the background vibration it is not uncommon that the vibration recorder to store one

sample every couple of minutes which may then be plotted on a graph.

6.3 *Automatic motorized total station (AMTS)*

Increasingly being used to detect even the smallest surface movement with high precision are automatic motorized total stations (AMTS) which uses a laser beam to measure the distance and angle to a target prism. Often the AMTS is programmed to wake up every hour, make its measurements to the group of prisms and return the readings to a central data base storage along with data from all the other sensors on the project site..

6.4 *Tunnel boring machines (TBM)*

The TBM is a major piece of equipment used for boring underground tunnels, and is loaded with various control systems and collects data from a wide variety of on-board sensors. Now, instead of using an outside system to connect and read the data, a more efficient method is to have the TBM output a set of its sensor readings into a text fil,e for other systems to read. The data being output may include forward movement, pressure on head, direction, location and much more. A special forward program forwards the data to a FTP site to be input to the on-line monitoring system and therefore the vital information about the TBM may be presented together with other data in the on-line monitoring system.

6.5 *Other systems*

With each passing year, new field devices are being developed and deployed in geotechnical projects. Common with many of these devices is their wireless capability and automatic forwarding of data to a FTP site or by sending its data to an email address. This remarkable feature means that no centralized call engine is needed for data collection. Therefore, all the on-line monitoring system needs to be able to do is to monitor a FTP site for new data and to monitor an email account for the same purpose, and to import all new data into its data base.

7. WHAT'S NEXT?

In recent years, remote sensing methods, such as Interferometric Synthetic Radar (InSAR), Automated Motorized Total Stations, 3D laser scanners, etc., have seen more widespread use and acceptance in the geotechnical community. The various techniques allow macroscopic evaluations of surface data to be made which, in turn, can be used to identify localized zones where conventional contact sensors should be used for more detailed (real time?) observations, or to correlate those surface measurements with measurements from subsurface sensors; for example settlement resulting from dewatering.

Recent interest in remote sensing techniques has not gone unnoticed by the geotechnical research community who are now starting to better assess how these technologies can be gauged against widely-accepted standards, such as extensometers and piezometers. Clearly this initiative will require more complex and sophisticated data bases and visualization platforms, and will undoubtedly require interactive 3D representations and animations to visually demonstrate how subsurface and surface measurements are related. Exciting times indeed.

8 REFERENCES

Marr, A 2005, Automated Collection of Instrumentation Data. *Boston Society of Civil Engineers, USA.*

Fiorini, As, Porto, EC, Saccarello do Santos, M & Zattoni, A, 2007, 'Automation of the Monitoring System at the Itaipu Hydroelectric Power Plant´. *Proceedings of the Seventh International Symposium on Field Measurements in Geomechanics*, American Society of Civil Engineers, Reston, Va. USA.

Thorarinsson, A 2007, 'Methods for automatic storage, visualization and reporting in datalogging applications', in J DiMaggio & P Osborn (eds), *Proceedings of the Seventh International Symposium on Field Measurements in Geomechanics*, American Society of Civil Engineers, Reston, VA, USA..

Thorarinsson, A & Simmonds, A 2008, 'A new, effective way of storing, reporting and visualizing geotechnical data on a web page', *Proceedings of the Fifteenth* Nordic Geotechnical *Conference* (NGM 2008), Norway.

Thorarinsson, A & Simmonds, A 2011, 'Real time, on-line monitoring for every project', *Proceedings of the Eigth International Symposium on Field Measurements in Geomechanics*, Technische Universität Braunschweig, Berlin.

Thorarinsson, A 2015, 'Geotechnical data handling from A to Z', *Proceedings of the Ninth International Symposium on Field Measurements in Geomechanics*, Australian Centre for Geomechanics, Australia.

Bundle Towhead Foundation Design on Rock Berm Installed on Soft Clay

C. Olsen
Subsea 7, Norway, christian.olsen@subsea7.com

M. Kahlström
Subsea 7, Norway

T. Powell
Subsea 7,UK

S.P.H. Sørensen
COWI, Denmark

ABSTRACT
As part of the BG Knarr project, a flowline bundle was installed during September 2014 including a template towhead (leading) connected by a 4.5km rigid bundle carrier pipeline to the FPSO towhead (trailing). The field is located in the norther part of the North Sea in a water depth of approximately 410 m. The two bundle towheads were landed on pre-installed rock berms. The rock berms were installed May 2013 and have an approximate size of 100 m x 50 m and a height of 2.5 m above seabed. The leading bundle towhead submerged weight is 270 t with a length of 33.5 m and width of 16 m while the tailing towhead submerged weight is 170 t with a length of 32.5 m and width of 6 m.

During production of the Knarr field, the bundle will expand longitudinally causing the towheads to displace up to 1 m on each rock berm. The geotechnical design comprised a series of bearing capacity calculations, using PLAXIS 2-D and PLAXIS 3-D. The main objective has been to validate that the towheads slide as near to the horizontal as possible on the rock berms, while maintaining an adequate level of safety against bearing failure of the rock berm and under laying very soft clay. It is believed that these towheads are the world's largest subsea sliding foundations.

Keywords: Bundle towhead foundation, rock berm on soft clay.

1 INTRODUCTION

A 4.5 km flowline bundle containing two production, one water injection and one service line and controls was installed during 2014, between the production template and the Knarr floating production storage and offloading (FPSO) vessel. The bundle has a towhead at each end which is used during installation to tow the bundle to the field and during production to connect flowlines and controls. The template towhead, during launch is shown in Figure 1-1. Reference is made to Goodlad (2013) for further information on bundle technology.



Figure 1-1: Launch of the template towhead. The bundle is seen on the shore side connected to the towhead.

During start-up of the system and also during production, temperature and pressure differences will lead to longitudinal expansion loads in the bundle, which exceeds the horizontal sliding capacity of the towhead foundations. The towheads are therefore required to slide on the seabed several times during the 20 years lifetime of the system.

In order to ensure the foundations can slide and prevent the towheads from rotating horizontal at the Knarr location, a rock berm was installed onto the very soft clay seabed 16 months prior to bundle installation. Rock berms were surveyed in November 2013 in order to identify settlements and document the consolidation and verify the strength increases in the very soft clay. Reference is made to Kahlström et al. (2015) for further details on the settlement survey.

The towhead foundation design methodology is a performance-based design where the bearing capacity is proven with an appropriate factor of safety while at the same time the towheads are allowed to slide on the rock berm. This paper outlines the experience with towhead foundation design on very soft clay.

2 BACKGROUND

2.1 Knarr Field Development

The Knarr oil and gas field is located approximately 112 km west of Florø, Norway, in the Norwegian Sector of the Northern North Sea at an average water depth of 410 m.

A subsea production template is tied back to the Knarr FPSO vessel using a pipeline bundle and flexible risers. Production oil and condensate will be exported by shuttle tanker from the Knarr FPSO whereas the gas is exported by pipeline to the St Fergus gas terminal in the UK, via the Far North Liquids and Associated Gas System (FLAGS).

The bundle carrier pipeline has a diameter of 1.01 m and is connected to a towhead structure at each end; the Template Towhead (Figure 1-1) and the FPSO towhead (Figure 2-1).



Figure 2-1: Picture of Knarr FPSO towhead during launch. The bundle is seen entering the water.

2.2 Rock Berm Structures

Due to the soft clay seabed, the towhead structures were installed on rock berm foundations. The rock berm foundations were constructed with a ramp of rock with an inclination of 1° to ensure a straight connection between the bundle and the towhead. The FPSO towhead rock berm is shown in Figure 2-2. Notably, the rock berm has a wing on each side, which is designed to support the flexible risers connected to the towhead. Reference is made to Kahlström et al. (2015) for more information on the rock berms and installation method of rock berms.

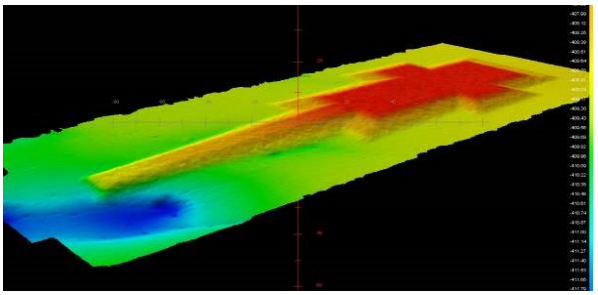


Figure 2-2: FPSO towhead rock berm with a ramp and two wings to support risers exiting the towhead.

The Template Towhead and template including spool which is covered by Glass Reinforced Plastic (GRP) covers are illustrated in Figure 2-3.

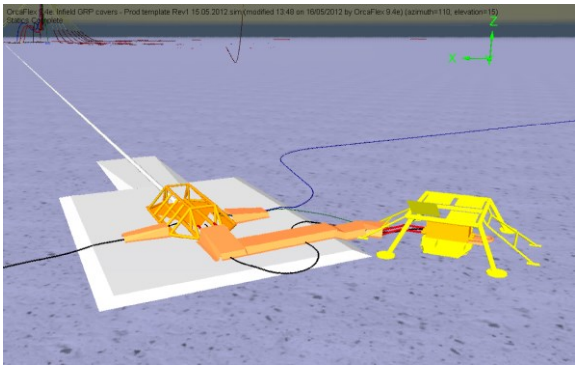


Figure 2-3: Illustration of template towhead on Rock berm in close proximity to template.

2.3 Towheads

The towheads are used to tow the bundle to the field suspended between two tugs using the controlled depth tow method. The towheads are made neutrally buoyant with use of buoyancy tanks during the tow. A survey/patrol vessel accompanies the tow, see Figure 2-4 for typical tow arrangement. The towheads also have a secondary purpose during production as the method of connection of flowlines and controls.

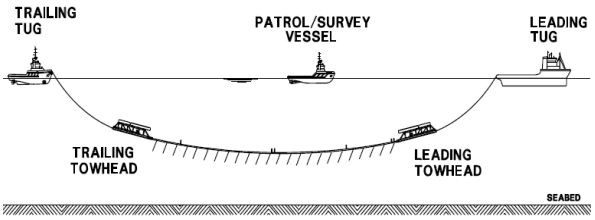


Figure 2-4: Typical bundle tow fleet arrangement.

The dimensions of the towheads and the steel mudmats are given in Table 2-1. For the template towhead, the mudmat consists of two parts with a 5.5 m gap in between. The two parts are connected at both sides of the towhead. Hence, the two mudmat parts will move as one. It should be noted that the length of the mudmats are smaller than the length of the towheads.

Table 2-1. Details of towheads and mudmats.

Structure	Submerged Weight [kN]	Length [m]	Mudmat [m x m]
Template towhead	2700	33.5	2 of 27 x 5.25, 5.5 m apart
FPSO towhead	1700	32.5	30 x 6

The Knarr towheads are designed with a free drainage cooling spools. To ensure self-drainage of the cooling spools during field life, the maximum allowable rotation in any direction of the towhead is 1.5°. This enforces strict requirements on the differential settlements.

2.4 Soil Conditions

Geotechnical core sampling was performed at the site to a depth of 30 m below the seafloor, revealing a 5-layered soil profile as described in Table 2-2. Layer I, in between 0.0 – 13.5 m, belongs to the Kleppe Senior Formation and consists of very soft to soft slightly sandy Glaciomarine clay, deposited after the last glacial peak. Layer I has a high plasticity and contain traces of organic material. Geophysical surveying revealed a flat boundary in between soil layer I and layer II. Due to the homogeneity of the soil, differential settlements are not expected.

Table 2-2. Description of soil profile.

Soil Layer	Average depth below seafloor, m	Soil description
I	0.0 - 13.5	Very soft to soft slightly sandy clay
II	13.5 - 14.8	Soft to firm slightly sandy clay
IIIa	14.8 - 17.6	Firm to stiff slightly sandy clay
IIIb	17.6 - 22.1	Loose to medium dense clayey sand
IIIc	22.1 – 30.0	Firm to stiff slightly sandy clay

Table 2-3 provides soil properties for each soil layer. In total, 6 Cone Penetration Test samples, 2 piston samples and 11 Wireline Push samples from a borehole drilled at the location of the trailing towhead rockberm were analyzed to obtain the soil data.

Table 2-3: Soil properties for each layer in the soil profile.

Soil Layer	Undrained shear strength, S_u^C, kPa	Water content, w, %	Submerged unit weight, γ', kN/m^3
I	5 - 24	61 - 87	6.0
II	24 - 53	23	10.3
IIIa	75	21	10.5
IIIb	-	17	10.5
IIIc	67 - 87	23	10.3

The soil conditions are further described in Kahlström et al. (2015).

3 LOADS

3.1 Trawl (fishing) loads

The FPSO towhead is located within a 'no fishing zone'. The template towhead is designed as an overtrawlable structure. The trawl load can either consist of trawl net friction or of trawl board over pull, given in NORSOK U-001 (2002):

- The trawl net friction consists of 2x 200 kN applied at 0-20° relative to horizontal acting in opposite corners of the structure and acting in the same direction.
- The trawl board over pull load of 300 kN applied horizontally at 0-20° relative to horizontal at the most critical point.

3.2 Hydrodynamic current loads

The towheads are exposed to hydrodynamic loading from currents. The characteristic hydrodynamic horizontal load is 43 kN for the template towhead and 20 kN for the FPSO towhead. Given that the trawl load on the template towhead exceeds the hydrodynamic load, only the FPSO towhead is designed for hydrodynamic load.

3.3 Expansion loads

During the lifetime of the BG Knarr field, a number of bundle start-up and shut-down cycles are expected to occur, in which the temperature and pressure in the bundle changes. The temperature and pressure change will lead to expansion and contraction of the bundle.

For a gravity based foundation of the towheads, it is not possible to statically resist the bundle expansion load due to the ratio between the horizontal load and the submerged weight of the towheads. Therefore, the towheads are designed to slide on top of the rock berms. The template and the FPSO towheads are expected to experience a maximum longitudinal horizontal displacement of 1 m. The force applied to the towheads will correspond to the sliding capacity of the interface between the towheads and the rock berms. The sliding capacity can theoretically be determined as the submerged weight of the towheads multiplied with $\tan(\varphi_{rock,inter})$, in which $\varphi_{rock,inter}$ denotes the rock / steel interface friction angle. The bundle expansion load acts over the lower 1.05 m of the towhead.

4 DESIGN

4.1 Introduction

As stated, the contraction and expansion forces induced through the bundle during flow shut-down and start-up cycles lead to loads on the towheads of such a magnitude that the sliding capacity of the underlying rock berm will be exceeded and cause the structure to shift. Alternatives to the rock berms were considered early in the design process. One alternative was a sliding mechanism in the towheads; however, this turned out to increase in deadweight of the towheads coursing installation problems. The second alternative was fixing the towheads with use of suction buckets. The suction bucket was found infeasible due to the expansion from the bundle.

The rock berm dimensions are determined such that an adequate safety is obtained against a failure mode occurring within the clay or rock berm.

The critical failure mode during flow shut-down and start-up cycles is sliding between the rock berms and the clay, which means that the upper 5 m of the soil profile is of principal importance to the design.

In the following sections, the performance-based design methodology and settlement assessment is described in further detail.

4.2 Performance-based design

The rock berm dimensions are designed such that the rock berms do not become unstable

during bundle expansions and such that the towhead foundations can withstand trawl loading, hydrodynamic loading and/or self-weight of the rock berms and towheads. The dimensions of the foundation are designed based on an iterative procedure ensuring an adequate level of safety in line with DNV partial factors. The design approach is similar to the combined failure approach for sand described by Cathie et al. (2008).

It is found that the load from bundle expansion is governing for the length of the rock berms, i.e. the size of the rock berms in the direction parallel to the bundle. Furthermore, the width of the rock berms, i.e. the size of the rock berms in the direction transverse to the bundle direction, also has an influence of the stability of the rock berms during bundle expansion loading due to three-dimensional distribution of stresses. The stability of the rock berms when exposed to bundle expansion loading has been assessed by means of numerical calculations in PLAXIS 2D Version 2011-2 and PLAXIS 3D 2012. The purpose of the numerical models were to investigate the safety against failure. Hence, the Mohr-Coulomb material model was considered to be sufficiently advanced.

Analytical analyses of the rock berm stability during bundle expansion loads have been conducted in order to validate the numerical models. In the analytical modelling, the capacity of three kinematic failure modes were assessed. These included; a failure mode consisting of mudmats sliding on top of rock berm (this failure mechanism is the desired failure and hence considered as controlled sliding); a failure mode consisting of the entire rock berm sliding on top of the clay, see Figure 4-1; and a failure mechanism consisting of sliding between the rock berm and the subsoil directly beneath the towhead and a passive wedge forming in the rock berm in front of the mudmats, see Figure 4-2.

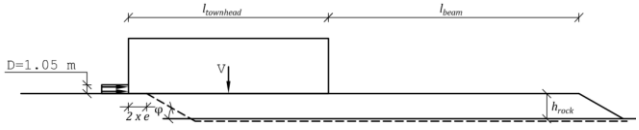


Figure 4-1: Berm failure on top of clay.

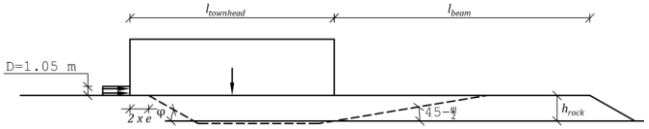


Figure 4-2: Passive failure mechanism in berm.

The undrained shear strength in the analysis was calibrated to consider the consolidation effects of the pre-installed rock berm. A conservative consolidation period of six months was chosen rather than the actual planned duration between installation of the rock berm and towhead installation of 15 months. Further, as the main direction of the slip surface is horizontal the undrained shear strength was therefore analysed as direct simple shear. The use of the direct simple shear strength accounts for strength anisotropy was in accordance with DNV (1992).

The width of the rock berms were primarily governed by trawl load, hydrodynamic load and/or self-weight of the rock berms and towheads. However, it should be noted that the bundle expansion load also affected the necessary width of the rock berms due to three-dimensional distribution of stresses. The stability of the rock berms against trawl load, hydrodynamic load and/or self-weight of the rock berms and towheads was assessed by means of PLAXIS 2D. For these design cases, three-dimensional effects were considered to be insignificant. Further, two-dimensional analyses of the rock berm stability against these design cases were considered to be conservative. In the numerical modelling, infinite failure modes were assessed. Hence, the failure modes in the numerical modelling accounted for bearing capacity failure, slope failure, and any combinations of these. An example of the two-dimensional failure mode of a towhead exposed to trawl loading acting in the direction perpendicular to the bundle axis is given in Figure 4-3.

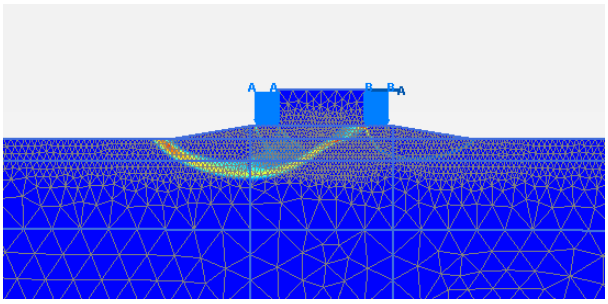


Figure 4-3. Deviatoric strains at failure. Dark blue colour indicates no or little deviatoric strains. Light blue/yellow/red colours indicate significant deviatoric strains.

4.2.1 Design methodology

The design methodology adopted was to prove that sliding was the governing failure mechanism with an acceptable margin of safety. Two methods have been considered:

1. Undrained shear strength was reduced until the failure mechanism changed from a sliding mechanism to a failure mechanism in the clay.
2. Friction in rock - structure interface friction was increased until a non-sliding failure mechanism was encountered. By increasing the rock - structure interface friction stresses were increased in the subsoil.

These two methods can be illustrated graphically in the vertical and horizontal forces (VH) stability envelope, see DNV (1992) for further details on the stability envelope. The stability envelope is a combination of the undrained stability envelope overlaid the drained stability envelope. This was also proven for the Knarr towheads with use of finite element analysis.

The undrained shear strength reduction method "shrank" the size of the undrained envelope within the VH stability envelope. This is illustrated in Figure 4-4 with the blue arrows. It was shown that the failure mechanism changed from a sliding between the towhead and the rock berm to a sliding failure in the clay with a partial factor of 2.0. The expansion load is illustrated as a yellow arrow exceeding the stability envelope.

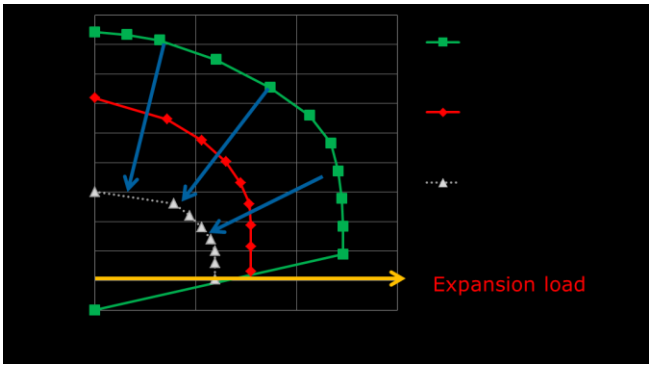


Figure 4-4: Capacity assessment, undrained shear strength reduced.

A PLAXIS 2-D illustration of the failure mechanism when it changed from sliding on the rock berm to a failure in the clay underneath is given in Figure 4-5. The failure mechanism is a result of the undrained shear strength being reduced with a partial safety factor.

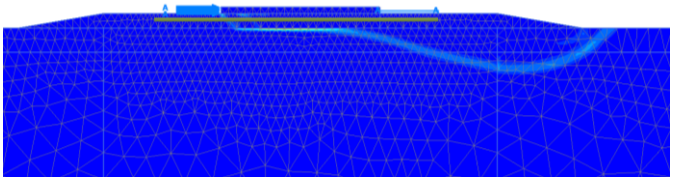


Figure 4-5: Horizontal failure mechanism developed in the clay.

It is worth noting the similarity between the failure mechanism identified by FEM in Figure 4-5 and the analytical failure mechanism defined in Figure 4-1. This supports the use of direct simple shear strength for the very soft clay model.

The increase in rock – structure friction can also be illustrated graphically in the VH stability envelope. In Figure 4-6, the change to the VH envelope caused by the increase in rock - structure friction is illustrated by the blue arrow. The expansion load is illustrated as a yellow arrow exceeding the stability envelope.

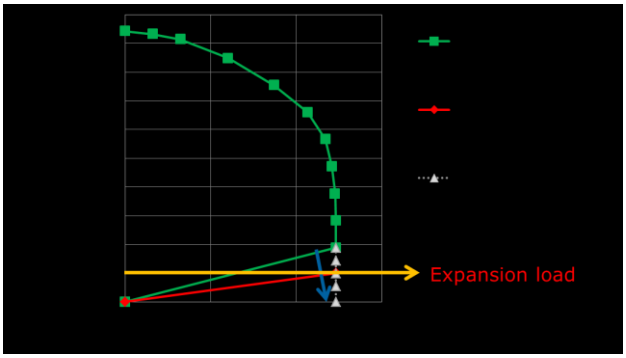


Figure 4-6: capacity assessment, friction angle increased.

From Figure 4-6, it was shown that at a certain increase in friction angle, the failure mechanism changed from sliding failure along the rock structure sliding limit to a sliding failure within the clay. The sliding limit in the clay was defined as the vertical part of the clay stability envelope, see DNV (1992).

The factor of safety was increased by increasing the towhead bearing area (the length of the rock berms) or decreasing the towhead submerged weight. As expected, both of these methods were shown to distribute less pressure onto the clay and thereby increase the factor of safety. Also note that the rock berm height is governing for the safety against failures of the type illustrated in Figure 4-2.

4.3 Settlements

The purpose of the settlement assessment was to determine the magnitude of the total and differential settlements of the Template Towhead and FPSO Towhead. The differential settlements were restricted to 1° to ensure free draining of the cooling spools. For further details on the cooling spools, see Goodlad (2013).

The settlement of the pre-installed rock berm was measured twice between rock berm installation and towhead installation, 31 months & 200 days post rock installation. The results are described in Kahlström et al. (2015).

The template towhead is connected to a series of umbilicals and flowlines, which are protected by rock dumped GRP covers. This introduced an uneven distributed load over the rock berm, see Figure 2-3 and Figure 4-7.

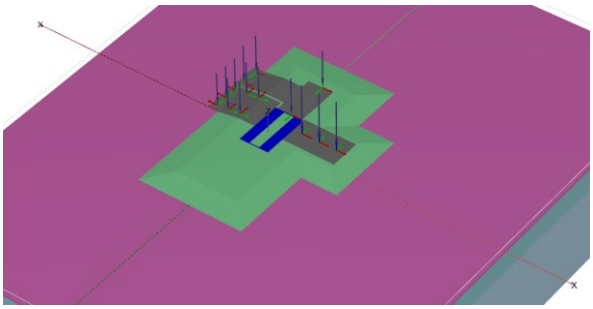


Figure 4-7: Geometry in PLAXIS 3D of the Template Towhead area.

In order to determine the differential settlements over a 20-year lifespan for the Towhead structures, the problem was considered as 3-dimensional. Analysis in PLAXIS 3D was selected to compute the differential settlements of the Towhead structures.

As described in Kahlström et al. (2015), the most accurate soil model adopted to predict settlements in PLAXIS 3D is the soft soil creep material model (SSCM). The input parameters have been validated by the on-site settlement survey.

Figure 4-7 shows the geometry of the problem as modelled in PLAXIS. In total, the geometry is 230 x 300 m^2 large and 60 m deep. The rock dumped GRP structures were modelled as a vertical surface load. The soil layers were created with reference to Table 2-2. The towheads were modelled as stiff plates with sizing equal to the mudmat area, having a distributed vertical surface load with magnitudes equal to the submerged weight of the structure.

Figure 4-8 illustrates the 20 year vertical settlement of the template towhead including creep. The rock dumped GRP covers created a differential pressure on the soil beneath. The additional pressure resulted in larger local settlements. The increase in local settlements caused differential settlements of the Template Towhead. The maximum 20-year differential rotational settlement was predicted to be 0.25° in a longitudinal

direction. The transverse rotation was found to be less than 0.25°. The predicted maximum settlement was predicted to be 85 cm.

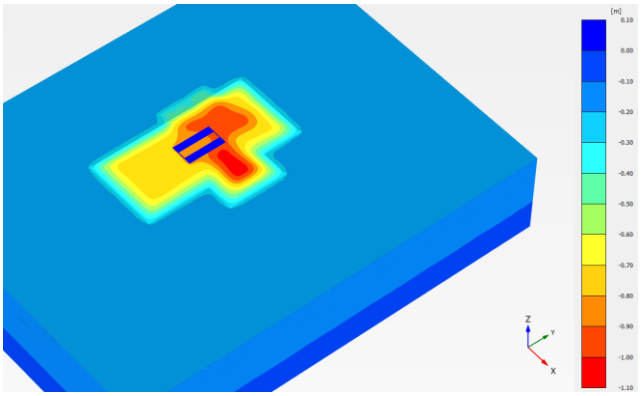


Figure 4-8: 20 year vertical settlement of Template Towhead area including creep.

In order to reduce the risk of that the rotational settlement exceeding the allowable rotation of 1°, it was decided that additional rock should be installed at the opposite end of the towhead to even out the differential pressure. Design proved that the additional rock berm would not increase the total settlements, but it would reduce the differential settlements.

5 OFFSHORE OBSERVATIONS

Following installation, a digiquartz survey was carried out to calculate the pitch and roll of the towheads approximately one week after installation. The results of the of the survey are given in Table 4-1. It is seen that the maximum recorded inclination was 0.04°.

Table 4-1: Installation inclination of the towheads.

Towhead:	Pitch (°)	Roll (°)
FPSO	-0.02	0.04
Template	0.04	-0.02

The FPSO towhead is shown in Figure 4-9 on top of the rock berm. The picture indicates a flat rock berm supporting the FPSO towhead.



Figure 4-9: Picture taken four days after installation of FPSO towhead on rock berm.

The position of the towheads have not been accurately measured after the pressurisation of the bundle. Therefore, at this time it has not been possible to quantify the actual displacement/rotation due to expansion of the bundle.

6 CONCLUSION

Rock berm foundations, situated on a subsoil consisting of very soft clay, have been designed and installed for the two towhead structures for the BG Knarr project. The subsoil consists of very soft clay. The towhead structures are connected with a bundle.

The governing load is an expansion load due to pressure and temperature changes in the bundle occurring during start-up and operation. The expansion load exceeds the weight of the towheads and therefore the rock berms have been designed to ensure that the towheads can slide on the rock berms and to prevent the towheads from rotating. The design methodology has been to prove that the sliding mechanism is the governing failure mechanism with an acceptable margin of safety.

The towhead behaviour during bundle expansions has been assessed by means of two- and three-dimensional finite element modelling using the Mohr-Coulomb model.

The settlements of the towheads have been assessed with use of three-dimensional numerical models using the soft soil creep material model. The material model was

calibrated against settlement observations of the rock berms.

7 ACKNOWLEDGEMENT

The authors would like to acknowledge Subsea 7 and BG Norge for permission to publish the results presented in the paper. The authors are grateful to Dr. Daniel Karunakaran and Project Manager Oddbjørn K. Olsen for their comments and review to this paper. It is emphasized that the conclusions put forth reflect the views of the authors alone, and not necessarily those of Subsea 7.

8 REFERENCES

Cathie, D. N., Morgan, N. and Jaeck, C. (2008). Design of Sliding Foundations for Subsea Structures. ICOF2008.

DNV (1992), ”Foundations” classification note 30.4.

Goodlad, M. (2013), Bundle Technology for the Future, SPE Offshore Europe Oil and Gas Conference and Exhibition in Aberdeen.

Kahlström, M. et al. (2015). Predicted and observed settlements or face subsea rock installation - comparison between field measurements and FE simulation of North Sea clay. ISFOG, Oslo, Norway.

NORSOK U-001 (2002). Subsea production systems, revision 3 October 2002.

Test of bored piles and the outcome of the Danish standard for designing bored piles

M.S. Rasmussen
Züblin A/S,Denmark,msrl@zueblin.dk

ABSTRACT
At a location in Copenhagen a 1.2 m circular bored pile was installed with a length of 24.6 m. The pile was installed with an Osterberg cell with a test capacity of 2x28460 kN corresponding to a design bearing capacity of at least 29000 kN. Calculated in accordance with the design methods in DE/EN1997-1 the geostatic calculated design bearing capacity for bored piles was 2930 kN. The pile was tested to its full capacity 56920 kN without reaching failure. The results of the test are evaluated in the different zones, limestone, clay till and fill for the surface bearing capacity as well as the toe resistance are evaluated and presented. An alternative method for calculating the bearing capacity are presented as well.

Keywords: Bored piles, Limestone, bearing capacity, static load test.

1 INTRODUCTION

This article is a case story with the results of a static load test of a ø1200 mm bored concrete pile. The static load test was carried out with an Osterberg cell (O-cell). The knowledge from the load test is used on a nearby site to show how the very conservative Danish design approach gives less safe structures. On the actual construction site ø900 mm bored piles were planned. Due to the very conservative calculation method for bored piles described in DS/EN 1997-1 the VC3 consultants required a full scale static load test. The costs are very high for testing a large diameter pile compared with smaller piles. As so the planned ø900 mm piles were shifted to 2xø180 mm concrete piles with 2.5 times less surface area and 12.5 times less toe area.

2 THE STATIC LOAD TEST

Thesoil conditions and the results of the static load test carried out are presented below.

2.1 Soil condition

The soil conditions on site are as listed in Table 1.

Table 1: The soil conditions

Soil type	Levels [m]
Fill – clay	+2,0 to -0,3
Fill – Sand	-0,3 to -4,3
Gravel	-4,3 to -5,1
Clay till	-5,1 to -8,9
Sand	-8,9 to -11,8
Limestone	-11,8 to

The strength parameters are show in Table 2

Table 2: The strength parameters

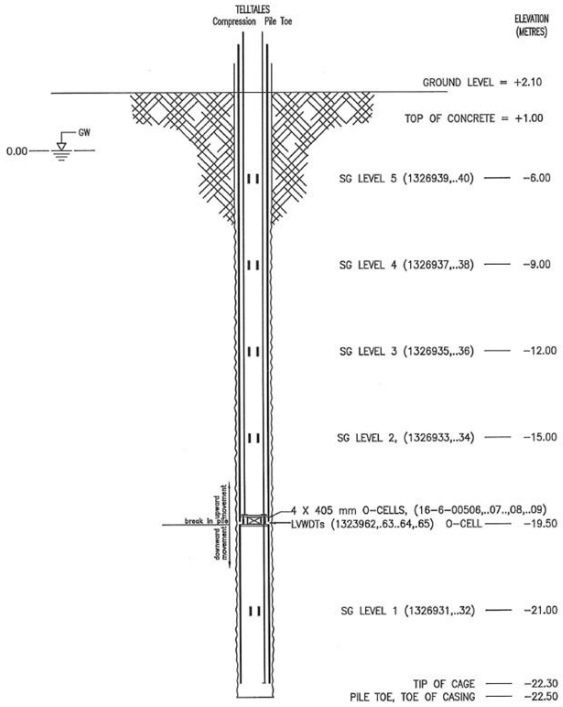
Soil type	γ/γ_m [kN/m³]	$\varphi'_{pl;k}$ [˚]	$c_{u;k}$ [kN/m²]
Fill – clay	19/19	--	50
Fill – Sand	19/19	27	--
Gravel	19/19	27	--
Clay till	22/22	--	300
Sand	22/22	37	--
Limestone	22/22	--	1500/500

2.2 Test setup

The test pile is a ø1200 mm concrete pile. The pile is drilled with casing. Top- and toe level for the pile is +1,00 m og -22,50 m. Four 405 mm Osterberg cells (O-cells) are installed 3 m above the toe level, level -19.5. Strain gauges are installed in 5 different

levels to make it possible to determine where the skin resistance is obtained. The strain gauges are installed in levels -6,0 m, -9,0 m, -12,0 m, -15,0 m and -21,0 m. The setup are shown in Figure 1.

Figure 1: The test setup

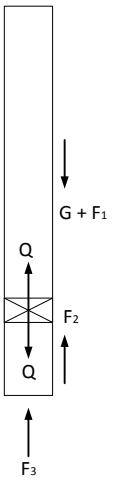


2.3 Test procedure

After breaking the weldings that keept the O-cells in the correct position during installation the test is started. The pile is loaded in 15 load steps with a maximum of 28460 kN,(Max capacity). After max load the pile is destressed in 4 steps.

Each load step is kept constant until the deformation rate is less than 0,1mm/20min. The deformations are measured after 0,1, 2, 5, 10, 30 minutes and therafter every 30 minuts.
The load cell gives loads in both directions and as so both the surface capacity above the O-cells and the surface capacity and toe bearing capacity below the O-cell are investigated at the same time. Figure 2 shows in principle the loading principle.

Figure 2: Principle of loading



2.4 Expected bearing capacity

For an ø1200 mm circular pile with a length of 23.5 m, with toe level = -22.5 the theoretical bearing capacity of a bored pile is calculated according to DS/EN 1997-1:2007 NA:2013. It is calculated as a skin bearing capacity, $R_{s,k,dril}$ and a tip bearing resistance $R_{b,k,dril}$.

The geostatic calculation method is in principle the same for both bored piles and driven piles. For bored piles a few limitations are given in DS/EN 1997-1. These are:

$$R_{s,k,dril} = 0.3 \times R_{s,k,driv} \quad (1)$$

$$R_{b,k,dril} = \min \begin{cases} R_{b,k,driv} \\ 1950 \times A_b \end{cases} \quad (2)$$

With the soil conditions near the test pile the calculated characteristic skin bearing capacity for a bored pile becomes:

$$R_{s,k,dril} = 3505\,\text{kN} \quad (3)$$

And the calculated characteristic tip bearing capacity becomes:

$$R_{b,k,dril} = 0.6^2 \cdot \pi \cdot 1950 = 2205\,\text{kN} \quad (4)$$

This gives an total bearing capacity $R_k = 3505 + 2205 = 5710$ kN for the 23,5 m long ø1200 mm drilled pile.

Based upon (1) and (2) the characteristic geostatic calculated bearing capacity for a

driven pile can be determined. For the skin friction the bearing capacity is calculated to:

$$R_{s,k,driv} = \frac{3505}{0.3} = 11675\,\text{kN} \qquad (5)$$

The tip bearing capacity is calculated by:

$$R_{b,k,driv} = 9 \cdot c_u \cdot A_b \qquad (6)$$

c_u is according to DS/EN 1997-1 limited to a maximum of c_u = 500 kN/m² even though the Limestone has a $c_u \approx 1500$ kN/m². Using c_u = 500 kN/m² in (6) the tip resistance of a driven pile would be:

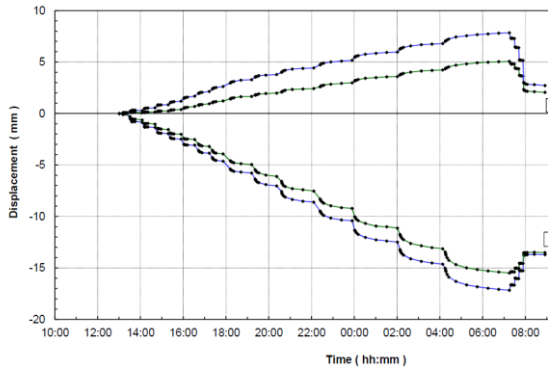
$$R_{b,k,driv} = 9 \cdot 500 \cdot 0.6^2 \cdot \pi = 5089\,\text{kN} \quad (7)$$

This gives in total an expected total bearing capacity of $R_k = 11675 + 5089 = 16764$ kN for a driven pile or approximately 3 times the bearing capacity of a similar bored pile. As so the expected measured bearing capacity of the fictive driven ø1200 mm 23.5 m long pile is 16764 kN.

2.5 Results

The displacement of the pile during the load test are shown on Figure 3.

Figure 3: The measured deformations during the test



The blue lines (The upper and lower line) are the movement of the O-cells and the green (the two middle lines) is the deformation of the top/bottom of the pile.
As shown there is a plastic deformation of approximately 2 mm for the upper part of the pile indicating that the pile has not reached failure. The deformation at the toe is approximately 13 mm, which as well indicates that the toe of the pile is not in a failure mode, while the skin friction might have reached its maximum as the deformations necessary for developing failure for the skin friction is much smaller than what is necessary for the tip failure to develop.
By looking into the stain gauge measurements it is possible to determine the skin friction measured in the different layers of the pile.

Table 3: The measured surface resistance

	Measured		Calculated	
Level	$R_{s;k;O\text{-}celle}$		$R_{s;k;dril}$	$R_{s;k;driv}$
[m]	[kPa]	[kN]	[kN]	[kN]
+1- -6	21,8	575	394	1.312
-6- -9	19,1	216	404	1.346
-9- -12	104	1.176	330	1.100
-12- -15	591	6.684	679	2.262
-15- -19.5	1.136	19.272	1.018	3.393
-19.5- -22,5	2.098	23.728	679	2.262
Total		51.651	3.505	11.675

Please note that this is for a pile not at failure. Based upon the measured results it is possible by the use of the program CEMSOLVE to estimate the failure capacity. This gives a surface capacity of approximately 53700 kN, an additional 2049 kN. As the deformation is smallest near the top of the wall it is here where the full "failure" has not yet occurred. If assumed equally divided between the 3 top layers the revised results are given in Table 4

Table 4: Revised result at expected failure

	"Failure"	Calculateded	
Level	$R_{s;k;O\text{-}cell}$	$R_{s;k;dril}$	$R_{s;k;driv}$
[m]	[kN]	[kN]	[kN]
+1- -6,0	1678	394	1.312
-6- -9,0	689	404	1.346
-9- -12	1.649	330	1.100
-12- -15,0	6.684	679	2.262
-15- -19,5	19.272	1.018	3.393
-19,5- -22,5	23.728	679	2.262
Total	53.700	3.505	11.675

The limestone is located from -12 and downwards. By comparing the measured and the calculated skin resistence in the limestone the measured is minimum 10 times larger than calculated for the drilled pile and at least 3 times the bearing capacity of the calculated capacity for a driven pile. As listed in Table 2 the undrained shear strength was acctually 1500 kN/m², and as so the results indicates a fine connection between the geostatic calculated bearing capacity if the requirement

from the Danish annex to the eurocode that a max value of 500 kN/m² is disregarded. For the layers above the limestone the measured bearing capacity at ”failure” is 4016 kN, where the calculated value for a bored pile is 1128 kN and 3758 kN for the driven pile. The results shows that the calculations carried out for a bored pile is highly conservative. It seems as if the results of a geostatic calculation as carried out for a driven pile gives reasonable results for a bored pile as well.
The test indicates that the 70% reduction of the skin bearing capacity that are used in Denmark according to the Danish annex should be neglected for this type of bored piles.

As the pile has not reached failure it is not possible to verify the tip resistance. In Table 5 the measured, the calculated for a bored pile, for a driven pile with a 500 kN/m² and with 1500 kN/m² as shear strength are shown

Table 5: The measured and calculated tip resistance

	Measured	Calculated		
Kote	$R_{b;kO-cell}$	$R_{b;k;dril}$	$R_{b;k;driv}$	$R_{s;k;1500}$
[m]	[kN]	[kN]	[kN]	[kN]
-22,5	4.740	2.205	5.089	15.260

Please note that even though the pile is not at failure the values calculated for a drilled pile in limestone is clearly underestimating the tip resistance and a value at least equal to what can be calculated for a driven pile should be used.

As for the skin resistance an estimate of the tip resistance has been made by use of CEMSOLVE. This shows a tip resistance of as high as 55000 kN, but as only 4740 kN are activated during the test the extrapolation is too large and as so are not reasonable to use in the evaluation of the results.

2.6 Conclusion of the load test

As the results shows the Danish method for calculating the skin friction capacity in both limestone and quaternary layers are very conservative. The skin friction capacity is at least as large as calculated for a driven pile.

In limestone indications shown much higher capacities. At least in limestone the results shows that the limitation from the Danish annex where the shear strength is limited to 500 kN/m² should be disregarded.

For the tip resistance it is more difficult to conclude, as failure did not occur. At least the results shows that the limitation from the Danish annex of 1950 kN/m² (1000 kN/m²) for the tip resistance is very conservative and should be disregarded at least if the tip of the pile is in limestone.

3 A STORY FROM REAL LIFE

At a nearby construction site it was planned to use 16.5 m long ø900 mm bored concrete piles, with the toe of the pile in H4 Limestone (σ_c >25 MPa) as the foundation of a part of a new building. The soil conditions was similar to the site where the test pile described above was installed.

To carry out static load tests is expensive, but with the above results from the nearby construction site we expected to be able to verify that the pile had a bearing resistance at least equal to what could be determined with a geostatic calculation of a driven pile. It was not possible to get this approved by the owners consultants. The augmentation were:

- The test pile was carried out on a location approximately 800 m from the actual construction site.
- The toe of the test pile was deeper than the planned piles and could as so not be used as documentation
- As so the tip bearing capacity could neither be used as documentation

Due to that 2 pcs 20,5 m long bored GEWI pile with a diameter of 180 mm was installed to replace the planned ø900 mm piles.

3.1 Soil profile

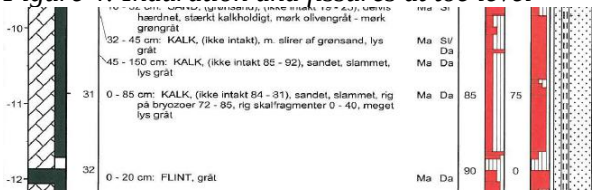
The soil profile at the construction site was

Table 6: The soil profile

Soil type	Level
Fill, clay	+5,8 - +2,1
Clay till	+2,1 - -0,5
Sand till	-0,5 - -1,0
Clay till, lower	-1,0 - -8,0
Greensand	-8,5 - -9,5
Limestone	-9,5 -

For evaluation of the strength of the soil/limestone at toe level the nearest borehole profile was evaluated. Figure 4 shows the induration and fissures at toe level. As shown the induration of the limestone is a H4 limestone (the right red column) with almost no fissures, S2 (the left red column).

Figure 4: Induration and fissures at toe level



This is even better than what was found at toe level of the test pile.

3.2 Theoretical bearing capacity

The required capacity of the ø900 mm piles was

$$F_d = 3347\,\text{kN} \qquad (8)$$

The theoretical bearing capacity was

$$R_{d,dril} = 1568\,\text{kN} \qquad (9)$$

if calculated as a bored pile.

For a driven pile, which according to the static load test carried out is a conservative assumption for a bored pile as well, the bearing capacity of the planned ø900 mm pile becomes:

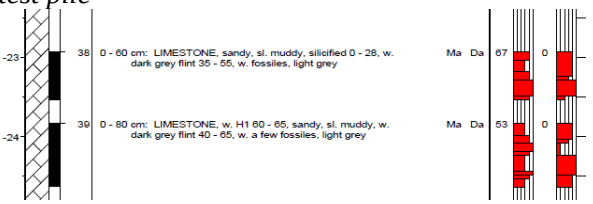
$$R_d = 7511\,\text{kN} \qquad (10)$$

As so it was expected that the ø900 mm piles could be accepted.

The acceptance of the design was supported by the fact that eventhough the distance between the sites were 800 m the soil profile was similar as shown by comparing table 1 and table 6, till above limestone. The limestone level at the construction site was even higher than at the location of the test pile.

The bearing capacity of the tip of the pile is, as indicated in (6) not depending on the depth of the pile but on the strength of the pile. Figure 5 shown the induration and fissures at the toe level of the test pile

Figure 5: Induration and fissures at toe level of test pile



As shown by comparring figure 4 and 5 the induration at the toe of the test pile was H2-H4, where at the construction site the induration is more constant H4 and as so should be stronger. At the toe level of the testpiles a large number of fissures were found S3-S5, while almost no fissures were found at the construction site, S2. This indicates that the soil at the construction site should be stronger and more homogenious at the construction site.

This documentation could not be accepted by the VC3 consultants without a full scale load test on a pile with the same dimensions and installed with the same equipment.

3.3 Result

As the number of piles on the project was limited and as we could not get the calculation of the ø900 mm approved we had to find another solution.

It was chosen to install 2 pcs ø180 mm piles instead. These piles have approximately 2,5 times less surface area and approximately 12.5 times less toe level.

The only advantage is that a test of a ø180 mm bored pile is much less expensive.

The tensile test carried out showed the same results as the static load test. Using the geostatic calculated bearing capacity without the limitations given in (1) and (2) this design

approach is still a very conservative design approach.

3.4 Conclusions

The two ø180 mm piles was as well installed as bored piles, where casing was used during the drilling work. As the much larger ø900 mm pile could not theoretically verify sufficient bearing capacity, the two much smaller piles with 2.5 times less skin area and 12.5 times less tip area have theoretic much to low bearing capacity, but in line with the static load test, the tensile test showed that the bearing capacity of the piles was much higher than what can be calculated according to Danish calculation method. The Danish calculation method is way too conservative and should be changed. In the actual case the calculation method was the main reason to switch pile type to piles with much less bearing capacity and much less stiffness and as so the Danish approach in principle have given a less safe construction.

4 REFERENCES

/1/ DS/EN 1997-1 + DK NA:2013. Eurocode 7 – Geotechnical design – Part 1: General

/2/ England, M.G. (2009) Review of methods of analysis of test results from bi-directional static load tests, Deep foundation on bored and augered piles, Ghent, sept. pp. 235-239 - CEMSOLVE

4.1 Symbols

γ : Unit weight [kN/m³]

$\varphi_{pl,k}$: characteristic plan friction angle

$c_{u,k}$: characteristic undraind shear strength

$R_{s,k,dril}$: Calculated skin bearing capacity for a bored pile

$R_{b,k,dril}$: Calculated tip bearing capacity for a bored pile

$R_{s,k,driv}$: Calculated skin bearing capacity for a driven pile

$R_{b,k,driv}$: Calculated tip bearing capacity for a driven pile

$R_{s,k,O-cell}$: Measured skin bearing capacity during O-cell test

$R_{b,k,O-cell}$: Measured tip bearing capacity during O-cell test

$R_{s,k,1500}$: Calculated skin bearing capacity for a driven pile if c_u =1500 kN/m²

$R_{b,k,1500}$: Calculated tip bearing capacity for a driven pile if c_u =1500 kN/m²

σ_c : Compressive strength

F_d : Design load

R_k : Bearing capacity

H : Induration grade (H1 to H5)

S : Fissure grade (S1 to S5)

A_b : Base area of pile

Is it reasonable to reduce the shaft resistance for bored cast-in-situ piles?

Jannie Knudsen
COWI A/S, Denmark, jahs@cowi.dk

ABSTRACT
According to the Danish National Annex to Eurocode 7, the shaft resistance for a bored cast-in-situ pile should not be assumed to be greater than 30 per cent of the shaft resistance of the corresponding driven pile. This principle has been applied in Denmark for many years due to an unsuccessful project. Today, however, it is widely recognised that this reduction is not reasonable if the bored cast-in-situ pile is established correctly.

This reduction of the shaft resistance proved problematic during the expansion of the Køge Bay motorway, which involves construction of a new bridge. The bridge is an underpass of a new railway line below the existing motorway, and the bridge shape required the establishment of a middle support. Because of the heavy load and the reduced shaft resistance, documenting the bearing capacity of the foundation of the middle support proved problematic.

As no recognised documentation allowing a larger bearing resistance was available, it was decided to establish a Ø508 mm bored cast-in-situ test pile. In order to document the bearing capacity of the test pile, in particular the shaft resistance, the test pile was re-driven and PDA measurements (a CAP-WAP analysis) were performed.

The geological conditions at the location primarily consist of limestone (H1), clay till and sand till. The expected bearing capacity of the test pile based on an analytical method and the measured capacity of the test pile were compared, showing that no reduction was necessary.

Keywords: bored cast-in-situ pile, shaft resistance, test pile, PDA measurements.

1 INTRODUCTION

According to the Danish National Annex to Eurocode 7 – part 1 (2013), Annex L (6), the shaft resistance for a bored cast-in-situ pile should not be assumed to be greater than 30 per cent of the shaft resistance of a corresponding driven pile. This principle has been applied in Denmark for many years due to an unsuccessful project.

This reduction of the shaft resistance proved problematic during the expansion of the Køge Bay motorway, and as no recognized documentation was available for comparable ground conditions, allowing a larger bearing capacity, it was decided to establish a bored cast-in-situ test pile. In order to document the bearing capacity of the test pile, in particular the shaft resistance, the test pile was re-driven and PDA measurements (a CAP-WAP analysis) were performed.

This paper contains a description of the test pile from planning and establishment to test and interpretation of the results.

2 PROJECT

The expansion of the Køge Bay motorway involves construction of a new bridge (Bridge no. 79.80). The bridge is an underpass of a new railway line below the existing motorway, and the bridge shape required the establishment of a middle support.

The middle support is a contiguous pile wall designed with 15 pieces of Ø880 mm concrete piles cast with a pile spacing of 760 mm. Consequently, the pile wall measures 0.88 m in width and 11.52 m in length. The piles above ground level are finished with a concrete cover, giving the final wall a width of 1.2 m and a length of 12.1 m.

Because of the heavy load and the reduced shaft resistance, documenting the bearing capacity of the middle support proved problematic. Therefore, it was decided to establish a Ø508 mm bored cast-in-situ test pile.

The location of Køge Bay motorway is shown in the following Figure 1.



Figure 1 Location of Køge Bay motorway.

3 GROUND CONDITIONS

For bridge no. 79.80 at Køge Bay motorway, geotechnical investigations were carried out and reported in the geotechnical investigation report by Rambøll (2014). The test pile was established near geotechnical borehole no. J102, see Figure 2.

Uppermost in the geotechnical borehole is 0.8 m of clay fill, beneath which there are glacial deposits, primarily consisting of clay till down to the top of the limestone at level -0.7 m.

Locally within the clay till, there is observed a 1.2 m deposit of sand till from level +5.4 m to +4.2 m.

Flint layers have been encountered in the limestone.

The primary groundwater level is measured at level +2.9 m in a screen positioned in the limestone.

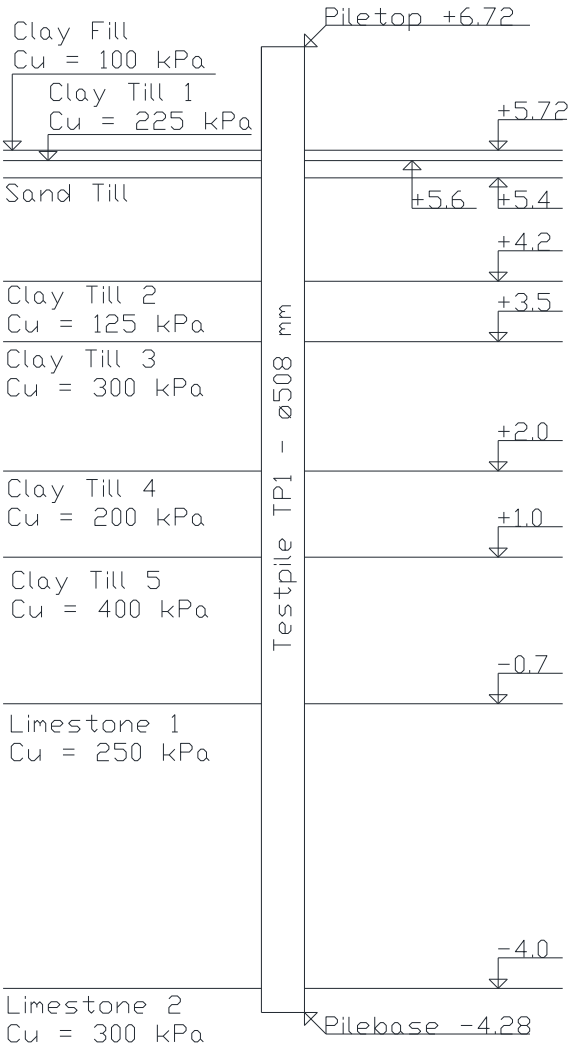


Figure 2 Geotechnical borehole no. J102.

4 ESTABLISMENT OF TEST PILE

The test pile was established as close as possible to the middle support and near a geotechnical borehole (Borehole no. J102). See Figure 3.

The test pile was established using a Ø508 mm casing, and a Ø350 mm auger for drilling inside the casing. The first 5 m of the test pile was drilled using a Ø500 mm auger to establish a stable hole for the casing, and the deepest 1 m of the test pile was drilled using a Ø400 mm hole saw in order to ensure the best clean-up possible for the bottom. Dimensions of the test pile are shown in Table 1:

Table 1 Dimensions of test pile.

Pile no.	Dim. (mm)	Top (m)	Ground (m)	Base (m)
TP1	Ø508	+6.92	+5.72	-4.28

A casing was left behind at the uppermost 3.2 m of the test pile in order to ensure casting of the test pile at a sufficient height above ground level to re-drive the test pile and perform PDA measurements (a CAP-WAP analysis).

5 TEST

The test pile was established on 14 October 2014, and it was re-driven on 10 November 2014 after 27 days of rest.

The test pile was re-driven with three blows and PDA measurements (a CAP-WAP analysis) were carried out in order to verify the shaft resistance, while this type of analysis determines the measured compressive resistance, divided into shaft resistance and base resistance.

The measured base resistance was used to check whether or not the bottom was cleaned sufficiently before casting, and whether or not the base resistance, as a minimum, corresponds to the value provided in the design.

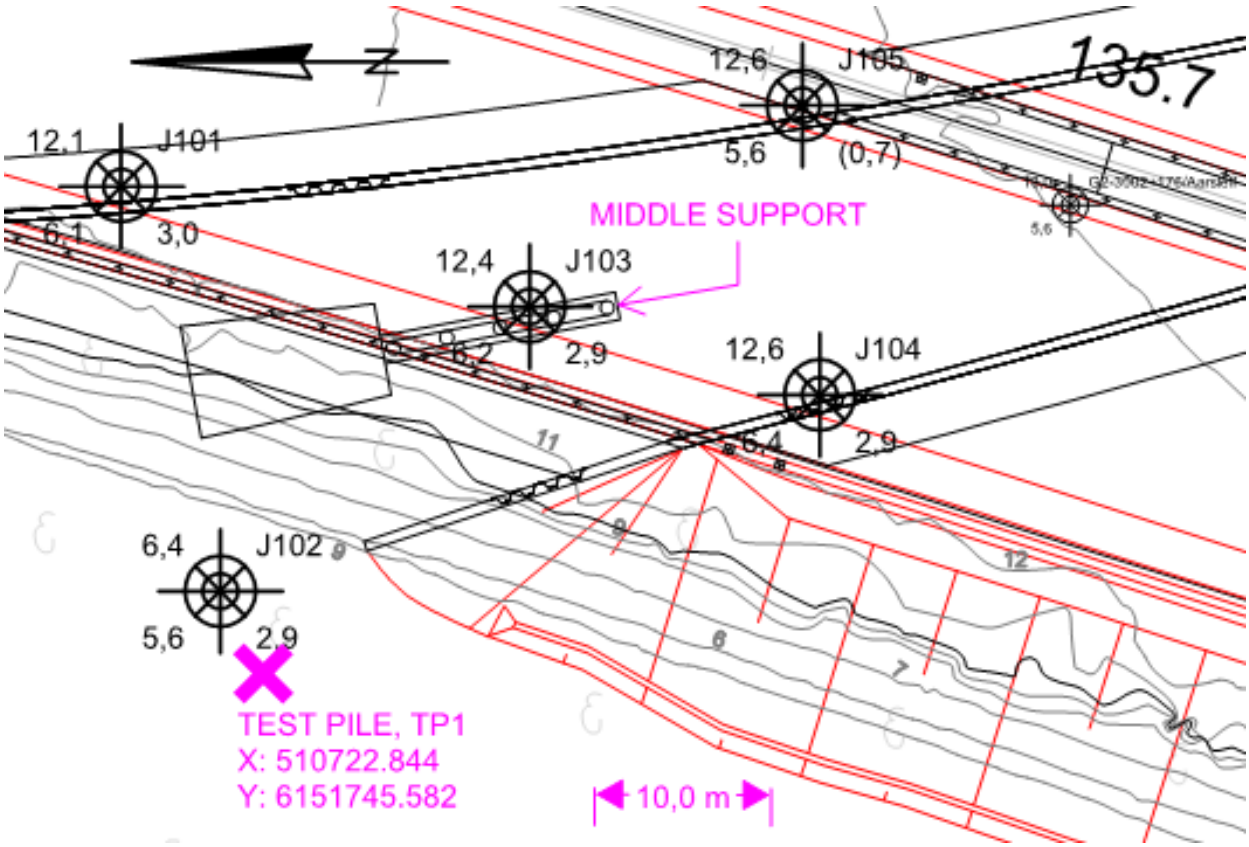


Figure 3 Illustration of middle support, test pile TP1 and geotechnical borehole no. J102.

6 RESULTS

6.1 General

An analytical method was used to determine the expected bearing capacity of the test pile to compare it with the results from the PDA measurements (a CAP-WAP analysis) in order to determine whether or not the 30-per cent reduction of the shaft resistance is reasonable.

6.2 Analytical method

An analytical method was used to determine the expected bearing capacity of the test pile based on the ground conditions described in section 3. The analytical method is based on equations according to the Danish National Annex to Eurocode 7 – part 1 (2013), Annex L (1):

$$R_{c,cal} = R_{s,cal} + R_{b,cal} \quad (1)$$

Where $R_{c,cal}$ (kN) is the expected bearing resistance for compression piles, $R_{s,cal}$ (kN) is the shaft resistance, and $R_{b,cal}$ (kN) is the base resistance.

Shaft resistance for cohesive soils:

$$R_{s,cal} = \sum m \cdot r \cdot c_u \cdot A_s \quad (2)$$

Shaft resistance for non-cohesive soils:

$$R_{s,cal} = \sum N_m \cdot q'_m \cdot A_s \quad (3)$$

Base resistance for cohesive soils:

$$R_{b,cal} = 9 \cdot c_u \cdot A_b \quad (4)$$

Where m (-) is a material factor, r (-) is a regeneration factor, c_u (kPa) is the undrained shear strength, N_m (-) is a bearing capacity factor, q'_m (kPa) is the effective overburden pressure, A_S (m²) is the shaft surface area, and A_b (m²) is the base area.

Realistic strength parameters (not design values) in the clay deposits and conservative strength parameters in the limestone due to lack of strength measurements were applied.

At the uppermost 3.2 m of the test pile, a casing was left behind, and the material factor was reduced to $m = 0.5 \cdot 0.7 = 0.35$, because the supervision considered there to be limited contact between the test pile (casing) and the soil.

The following calculation results show an expected total bearing capacity of the test pile of 1893 kN, consisting of a shaft resistance equal to 1346 kN and a base resistance equal to 547 kN. Please note that all calculations are based on measured values, which means no use of partial factors γ_s and ξ values. See Table 2 and Table 3.

Table 2 Analytical method – shaft resistance.

Layer no. I	Top (m)	Base (m)	Soil (-)	c_u (kN/m²)	t (m)	D (m)	A_s (m²)	r (-)	m (-)	$R_{s,cal,I}$ (kN)
1	**5.72**	5.6	ClayFill	100	0.1	0.508	0.19	0.4	0.35	3
2	5.6	5.4	ClayTill 1	225	0.2	0.508	0.32	0.4	0.35	10
3	5.4	4.2	SandTill	-	1.2	0.508	1.92	-	0.35	6
4	4.2	3.92	ClayTill 2	125	0.3	0.508	0.45	0.4	0.35	8
5	3.92	3.5	ClayTill 2	125	0.4	0.508	0.67	0.4	0.35	12
6	3.5	2.52	ClayTill 3	300	1.0	0.508	1.56	0.4	0.35	66
7	2.52	2.0	ClayTill 3	300	0.5	0.508	0.83	0.4	1.0	100
8	2.0	1.82	ClayTill 4	200	0.2	0.508	0.29	0.4	1.0	23
9	1.82	1.0	ClayTill 4	200	0.8	0.508	1.31	0.4	1.0	105
10	1.0	-0.18	ClayTill 5	400	1.2	0.508	1.88	0.4	1.0	301
11	-0.18	-0.7	ClayTill 5	400	0.5	0.508	0.83	0.4	1.0	133
12	-0.7	-2.28	Limestone 1	250	1.6	0.508	2.52	0.4	1.0	252
13	-2.28	-4.0	Limestone 1	250	1.7	0.508	2.74	0.4	1.0	274
14	-4.0	**-4.28**	Limestone 2	300	0.3	0.508	0.45	0.4	1.0	54
Total										**1346**

Table 3 Analytical method – base resistance.

Layer no.	Top (m)	Base (m)	Soil (-)	c_u (kN/m²)	t (m)	D (m)	A_b (m²)	r (-)	factor (-)	$R_{b,cal}$ (kN)
15	-4.28	**-4.28**	Limestone 2	300	0.0	0.508	0.20	0.4	9	**547**

6.3 PDA measurements

PDA measurements (a CAP-WAP analysis) were performed by CP test A/S (2014) on the test pile, showing a measured shaft resistance equal to 1642 kN and a measured base resistance equal to 4933 kN. See Figure 4.

The PDA measurements were performed with a permanent settlement of 1.3 mm/blow, which means that the measured resistances are mobilized bearing resistances, not ultimate bearing resistances. To achieve ultimate bearing resistance, a permanent settlement of at least 3 mm/blow is required.

CAPWAP SUMMARY RESULTS

Total CAPWAP Capacity: 6575.1; along Shaft 1642.0; at Toe 4933.1 kN

Soil Sgmnt No.	Dist. Below Gages m	Depth Below Grade m	Ru kN	Force in Pile kN	Sum of Ru kN	Unit Resist. (Depth) kN/m	Unit Resist. (Area) kPa	Smith Damping Factor s/m	Quake mm
				6575.1					
1	2.0	1.8	24.9	6550.2	24.9	13.53	8.48	0.669	0.100
2	4.1	3.9	211.9	6338.3	236.8	103.87	65.08	0.669	5.000
3	6.1	5.9	399.3	5939.0	636.1	195.74	122.64	0.669	6.000
4	8.2	8.0	452.6	5486.4	1088.7	221.86	139.01	0.669	4.500
5	10.2	10.0	553.3	4933.1	1642.0	271.23	169.94	0.669	4.000
Avg. Shaft			328.4			164.20	102.88	0.669	4.694
Toe			4933.1				24338.99	0.083	7.693

Figure 4 Results from PDA measurements.

6.4 Comparison

Table 4 illustrates a comparison between the expected bearing capacity of the test piles and the results from the PDA measurements (a CAP-WAP analysis). The table states the results as shaft resistance, base resistance and total bearing capacity, respectively.

Table 4 Comparison between the analytical method and the results from the PDA measurements.

Shaft resistance								
Layer no. I		**Top**	**Base**	**Soil**	**c_u**	**$R_{cal,I}$**		**$R_{m,I}$**
Calc.	**PDA**	**(m)**	**(m)**	**(-)**	**(kN/m²)**	**(kN)**	**(kN)**	**(kN)**
1	1	**5.72**	5.6	ClayFill	100	3		
2		5.6	5.4	ClayTill 1	225	10		
3		5.4	4.2	SandTill	-	6		
4		4.2	3.92	ClayTill 2	125	8	27	25
5	2	3.92	3.5	ClayTill 2	125	12		
6		3.5	2.52	ClayTill 3	300	66		
7		2.52	2.0	ClayTill 3	300	100		
8		2.0	1.82	ClayTill 4	200	23	200	212
9	3	1.82	1.0	ClayTill 4	200	105		
10		1.0	-0.18	ClayTill 5	400	301	406	399
11	4	-0.18	-0.7	ClayTill 5	400	133		
12		-0.7	-2.28	Limestone 1	250	252	385	453
13	5	-2.28	-4.0	Limestone 1	250	274		
14		-4.0	**-4.28**	Limestone 2	300	54	328	553
						Total	**1346**	**1642**
Base resistance								
15	6	-4.28	-4.28	Limestone 2	300	**Total**	**547**	**4933**
Total capacity								
						Total	**1893**	**6575**

In Figure 5 and Figure 6 the shaft resistance and base resistance from calculations and PDA measurements are shown in bar charts.

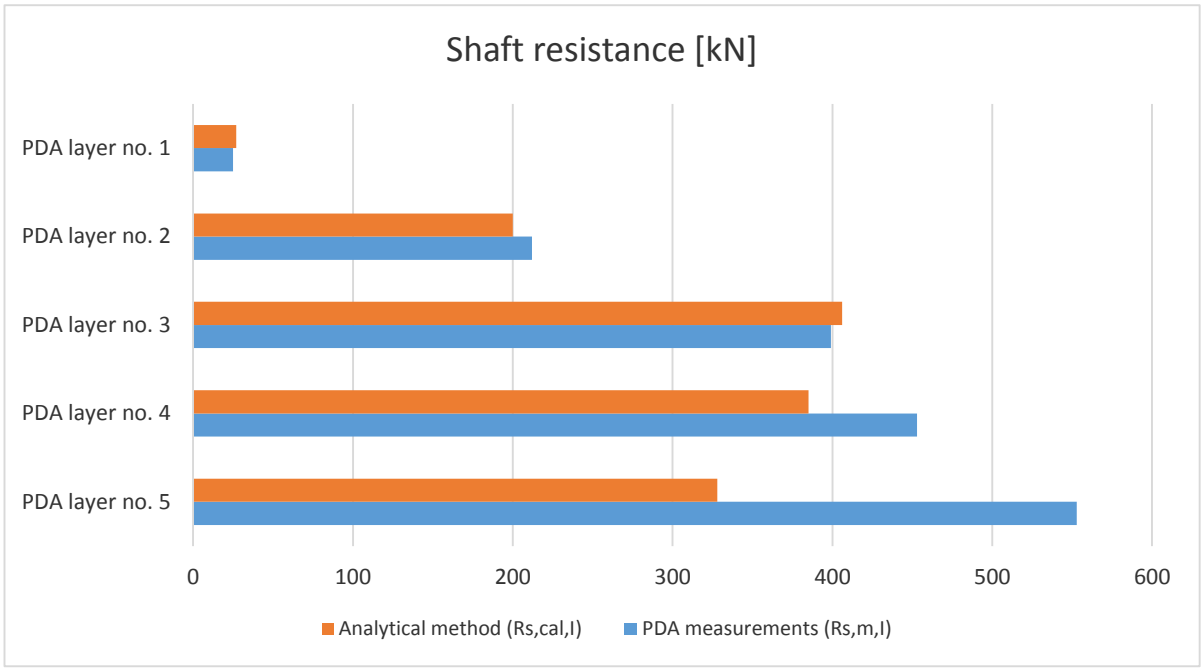


Figure 5 Bar chart showing shaft resistance from analytical method and PDA measurements, respectively.

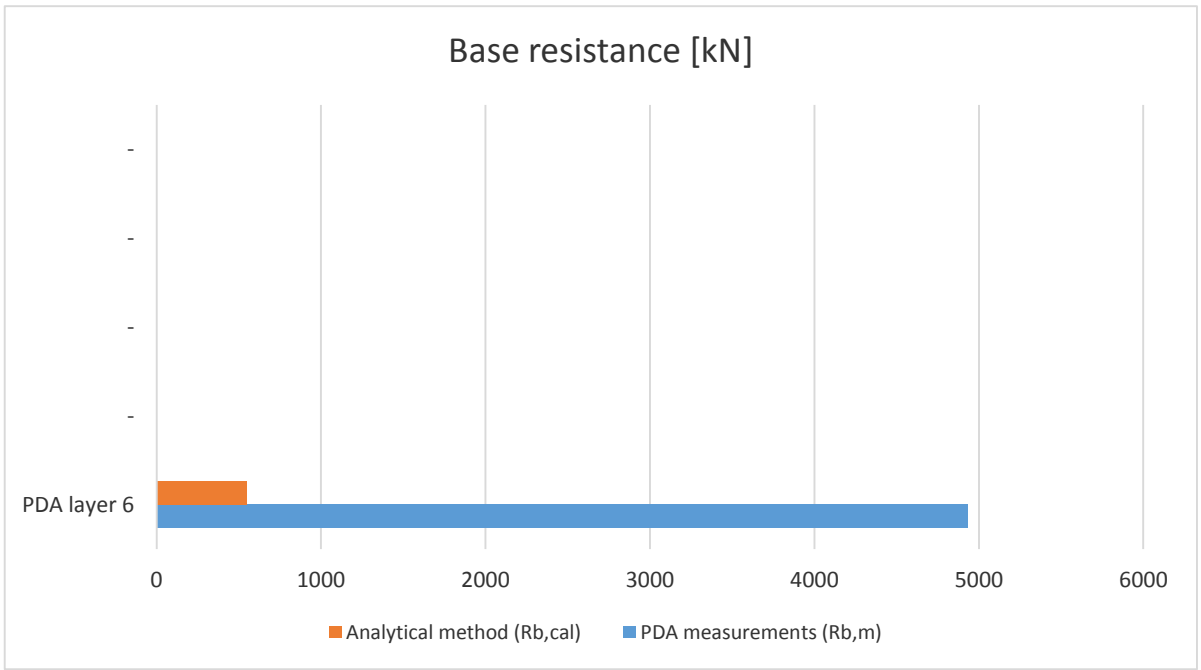


Figure 6 Bar chart showing base resistance results based on analytical method and PDA measurements, respectively.

7 CONCLUSION

The results listed in section 6 clearly shows that both the actual shaft resistance and the actual base resistance demonstrated by the PDA measurements are larger than those indicated by the representative calculation carried out for a similar driven pile based on the analytical method.

Regarding the shaft resistance, it is seen that the assumption regarding partial contact between pile and soil at the upper 3.2 m of the pile, due to the casing left behind, was correct.

The shaft resistance in the clay till from level +2.52 m to level -0.7 m shows good correlation between the analytical method and the results from the PDA measurements.

Finally, it is seen that the strength parameters in the limestone from level -0.7 m to pile base at level -4.28 m were significantly underestimated by the conservative estimate, because the actual shaft resistance demonstrated by the PDA measurements significantly exceeds the shaft resistance derived from the analytical method.

The actual base resistance in the limestone is especially higher in the results from the PDA measurements, which might be caused by locating the test pile on strong limestone/ flint layers, as the strength of the limestone may be expected to vary significantly. Nevertheless, it might be safe to conclude that there is no indication of insufficient cleaning of the bottom at the pile base.

Based on the results from the test pile, it is concluded to be safe to disregard the norm-based requirement in this particular case. Thus, the 30-per cent reduction of the shaft resistance for a bored cast-in-situ pile compared to a similar driven pile is disregarded.

Please note that conservative strength parameters (not realistic values) in the clay deposits naturally were applied in the final design.

8 PROJECT PARTNERS

Thanks to the Danish Road Directorate for permission to publish this article.

Other relevant partners for this project are listed below:

- Rambøll: Geotechnical investigation report.
- M. J. Eriksson A/S: Contractor, establishment of test pile.
- CP test A/S: Contractor, PDA measurements.
- COWI A/S: Consulting engineer, design of test pile.

9 REFERENCES

CP test A/S (2014). PDA measurements. M10, Køge Bugt, Bro 79.80. Case no. P15_001964.

DS/EN 1997-1 DK NA (2013). National Annex to Eurocode 7: Geotechnical design – Part 1: General rules.

Rambøll (2014). Geotechnical investigation report. Bro 1052-079.80, UF af bane, MV. ST. 135.7. Case no. 1100007980.

The tensile capacity of steel pipe piles drilled into the bedrock

R. M. Sirén
Aalto University School of Engineering, Finland, rosa.siren@vr.fi

L. K. Korkiala-Tanttu
Aalto University School of Engineering, Finland, leena.korkiala-tanttu@aalto.fi

ABSTRACT
The tensile forces affecting pile foundations are usually transferred to the bedrock by rock anchors. If drilled piles could transfer some of these tension forces, foundations could be lighter, execution works easier and the whole system could be more cost-efficient. The aim of the paper is to present the loading tests made for the drilled, grooved pipe piles to define their tensile capacity and to assess their ability to work as tension force transferring structure. The study includes literature review of existing research on tension piles and testing. The review covers the different methods for transferring tensile forces, the geotechnical design of tension piles and the main problems in the design. The testing part focuses on a pull-out test on pipe piles with a grooved surface.

The literature review found several reasons to update current geotechnical design practices on tension piles. It showed that the design methods are conservative and not at an optimal level of precision. In addition, several recent studies have examined the tensile resistance of piles, revealing three main factors affecting bond strength: the relation between the diameter of the drill hole and that of the pile, the roughness of the steel surface and the quality of the grouting. Furthermore, the stresses are not distributed uniformly along the length of the pile, but are highest on the top of the pile and lowest at the tip of the pile. Hence, the bond strength cannot be increased by increasing the bond length. The results of the pull-out test proved that the bond strength of the pile is significantly increased by the grooved surface. However, over half of the steel piles could not be pulled out of the bedrock as loading had to be discontinued at the yield capacity of the steel piles for safety reasons. Thus, the actual tensile capacity of the piles remained undetermined. Anyway the grooved pipe piles proved to have a great potential to be used as tensile force transferring structures.

Keywords: Steel pipe piles, drilled pile, tension pile, bond strength, grooving

1 INTRODUCTION

Large, heavy counterweight structures often transfer tensile loads. If drilled piles could transfer some of the tensile loads formed to the structure, the cost savings could be significant. For this reason it is important to investigate what options are available to improve tensile capacity and how much these methods increase the tensile capacity of drilled piles in practice?

A preliminary study about drilled pipe piles under tensile forces was done by Ahomies (2015) as his Master's thesis. The title of the study was: "The grouted and anchored drilled pile in the bedrock". The study was done in cooperation with Finnish Transport Agency and SSAB. The study contained a pull-out test for 15 steel pipe piles which were drilled and grouted into the bedrock. The results showed that the most common failure mechanism of the tension piles was the failure of the bond capacity between the steel and grouting. Based on this, the purpose of the following study (Sirén, 2015) was to investigate methods to improve the tensile capacity and especially the bond strength between grouting and steel. These were

investigated based on literature and a pull-out test. Literature was studied to identify methods to improve the tensile capacity and a pull-out test was conducted to investigate the bond capacity. To be more precise, the pull-out test examined the bond strength of drilled and grouted pipe piles that had cut grooves on the surface.

The pull-out test was arranged in Masku, Finland in the summer of 2015. In the test, 13 drilled and grouted pipe piles were tested. All piles were drilled two and a half meters into the bedrock. The purpose was to test the effect of a grooved pile surface to the bond strength and at the same time to test the total pull-out capacity. Piles were also monitored during the load test. (Sirén, 2015)

2 TENSION PILES

2.1 Literature review

Literature review studied the basic failure mechanisms of tension piles and factors that impact on the bond capacity. The failure mechanisms were bond strength between grouting and steel, bond strength between grouting and rock and the tensile strength of the bedrock. In addition, stress distribution, cracking of grouting and corrosion protection was covered.

The bond strength between grouting and steel pile depends on friction force on pile surface. Because the friction force depends on the normal force and friction factor, the friction can be increased by shaping steel surface and changing the properties of steel and grouting, which effect on normal force on pile surface when pile is under tensile stress.

Jesús Comés et al (2005) tested the bond strength for four different pile types that were grouted in footings. They observed several things from the results. First, by comparing the behavior of smooth surface casing and casing with ribs welded onto the surface they noticed that the casing with welded ribs offered greater bond capacity. Second, the behavior was more plastic with welded casing. Third, they did not find any substantial correlation between bond length and mobilized bond strength. Although bond length did not affect maximum bond strength, it seemed to decrease displacement caused by small loads. The diameter of the drilled hole had a remarkable effect on bond strength. They observed the same effect on the test made for a casing that was cast in a concrete footing. When the diameter of the drill hole was decreased, the bond strength increased. (Jesús Comés et al., 2005)

Brown (2014) addressed the very conservative approach to the failure of rock mass, from the point of view of rock mechanics. Several methods can be used to evaluate the possibility of rock cone failure, but the minority of these are satisfactory. The main problems in this rock cone assumption are the theoretical stress distribution, the failure mechanism of the rock mass uplift, ignorance of the real structure of the bedrock and the constant value for the tensile and shear strengths (Brown, 2014).

The distribution of the stresses was observed to have a high impact on the tensile capacity of the drilled pipe piles. The stresses are at highest on the top of the bond length of the pile and lowest near pile tip. Hence, if the tensile capacity of the pile is increased by increasing the pile length, the stress in the uppermost part of the bond length will increase unpredictably high and it may break the beginning of the bond length. (Sirén, 2015)

This distribution of stresses was observed in several studies. First of all, the study of Jesús Comés et al (2005) found the same behavior for tested piles and the study of Littlejohn (1997) revealed the same distribution for fully grouted rock anchor. Also a study of Charlie C. Li et al (2014) observed the same behavior for rock bolts.

2.2 Design of tension piles

The basic failure mechanisms to determine in geotechnical design of tension piles according to Eurocode are the bond strength between grouting and steel and that of between rock and grouting. Also the rock cone failure needs to be calculated. (RIL 254-2011)

The bond strength between grouting and steel is based on the compression strength of grouting and on the shape of the steel surface.

The bond strength between rock and grouting is based on compression strength of grouting (EN 1997). Hence, the design does not take into account majority of the factors that effect on the bond strength.

3 PULL-OUT TEST

3.1 Test configuration and conditions

Altogether 13 steel pipe piles, which were drilled and grouted 2.5 m into the bedrock, were load tested. The main purpose was to study the bond capacity between grouting and steel, which was improved by cutting grooves on the surface of the piles. For additional information on the test, refer to Sirén (2015).

Loading was done using hydraulic jacks through a load transfer structure. Monitoring was carried out using strain and displacement gauges, and the applied force was monitored using stress gauges. The displacements were monitored from two points on the pile surface and from two points on the rock surface. The strains were monitored from three points on the pile surface. The pile testing was made approximately twelve days after grouting. The structure of the pile is illustrated in Figure 1.

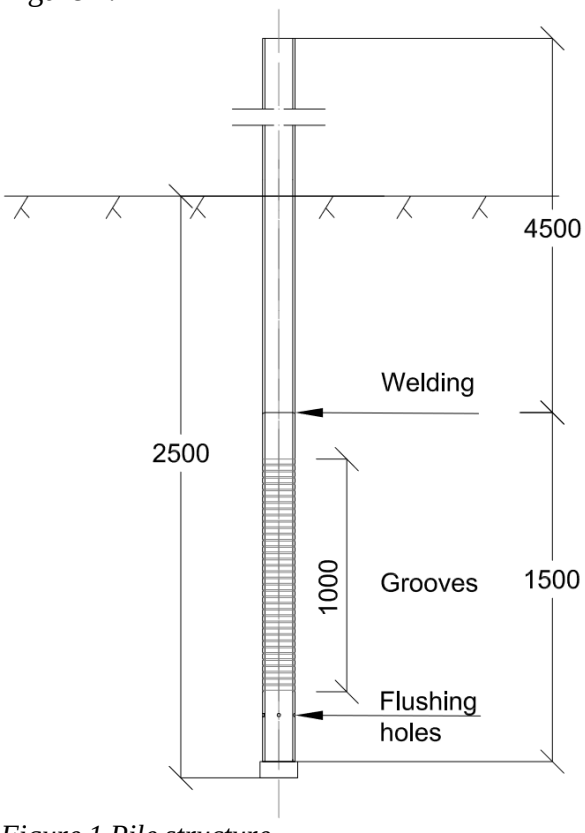


Figure 1 Pile structure

Flushing holes were made at the lower end of the pile for cleaning and grouting the pile. The purpose of the flushing holes was to ensure proper cleaning of the drill hole and even spreading of the grouting. The grouting had to be able to fill the space between the pile and rock.

The test included one pile which was monitored differently to the others. Hereafter, this pile is referred to as the instrumented pile. The purpose of the instrumented pile was to monitor how the tensile force was transmitted along the pile length.

All drilling was done in an exposed bedrock surface. The bedrock surface was close to the ground surface and the clearance of the construction site included a maximum excavation of 0.5 m. The main rock type at the construction site was mica gneiss and the rock was observed to have good quality and only few fractures.

The pile types tested were RD140/10, RDs140/10, RD220/10 and RDs220/10. The small letter "s" refers to the steel grade of S550J2H. Basic steel grade is S440J2H. The RD140/10 pile has a diameter of 139.7 mm and the RD220/10 pile a diameter of 219.1 mm. Two types of grooves were used in the test, shallow and deep. From these variables, the tested pile types are shown in Table 1.

Table 1 Tested pile types

Number of piles	Pile type	Steel grade	groove type
4	RD140/10	S440J2H	shallow
3	RD140/10	S440J2H	deep
3	RDs220/10	S550J2H	shallow
3	RD220/10	S440J2H	deep

Drilling was done using the centralized drilling method and down-the-hole hammer. In both pile sizes, the ring bit diameter was approximately 20 mm larger than the diameter of the pile. Hence, the RD140/10 piles had a relatively larger empty space around the pipe pile. This also meant cleaning and grouting was relatively easier for RD140/10 piles.

The piles were flushed with compressed air immediately after drilling and later with water. Water was conducted to the bottom of the pile pipe through a tube-á-manchette and

through the flushing holes outside the pipe. The pile was flushed with water until the water was clean or the pile had been flushed with at least 1000 liters of water.

The grouting was mixed at the construction site. The grouting used in the test was Nonset 50, a cement based dry grout made by Mapei AS. Nonset 50 consists of cement, selected sand and additives, which cause expansion, stabilizing and plasticizing of the grouting. The grouting expands 1-3% before hardening. The maximum grain size of Nonset 50 is 0.2 mm.

Grouting work was started after cleaning the piles. The tube-á-manchette was assembled near the bottom of the hole to ensure the grouting would not fall to the bottom and separate with the water in the hole.

The quality of the grouting was ensured using test samples, which were taken from the grout mass. This was done to verify the intended compression strength of the grouting. The prism samples were taken on each grouting day at the beginning of grouting and when finishing the work.

3.2 Loading and monitoring

Figure 2 shows the load transfer system. The applied force for the piles was induced using four hydraulic jacks. On the pile surface was affixed a console part by longitudinal welds and the force was transmitted from the jacks, through the console to the pile. The reaction force was directed to the bedrock.

The force was monitored using separate stress sensors, load cells. The load cells were assembled between the jacks and pile consoles. Monitoring the load between the jacks and the pile console ensured that all the jacks transferred the same size load to the pile console. Hence, the force that was transmitted through the console to the pile was axial.



Figure 2 Load transfer structure

For each pile, the maximum applied load was based on the maximum axial resistance, which was based on the yield strength of the pile material. The axial resistance was calculated based on the actual yield strength of the steel from the material certificates and the actual cross-section area. If the yield strength of the steel material had been reached, the pile could have failed suddenly. If this had been allowed to happen, the failure of the load transfer structure would have been uncontrollable. In addition, the analyzing of the results would be harder once the yield behavior of the pile is non-linear.

Pile displacements were monitored through a steel band placed around the pile surface. When pile moved in a vertical direction, the steel band also moved. The displacement gauge was attached to the stationary platform and measured the movement of the steel band, from two sides of the pile.

Displacement of the rock surface was monitored to ensure the rock did not move and affect the results. Bedrock displacement was measured from two points around each pile. The first point was at a distance of 0.5 m

and second point was 1 m away from the pile.

The strains were monitored for each pile during the pull-out test. Each pile had three strain gauges above the bedrock surface. All three strain gauges were affixed at the same level at regular intervals around the pile surface. The gauges were affixed with glue on grind and cleaned the steel surface.

The strains were investigated more closely from the instrumented pile that had nine strain gauges. The strain gauges were set at three different levels, which each had three gauges. The first level was above the bedrock surface and others were below the bedrock surface. Figure 3 shows the positions of the two lowest levels of the strain gauges. As shown in the figure, the measuring level in the middle was located between the grooved sections.

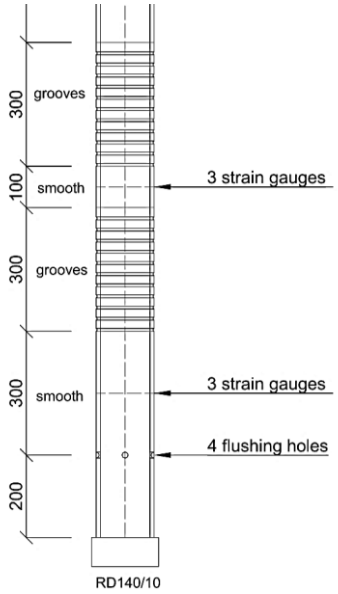


Figure 3 Instrumented pile and the positions of the strain gauges

4 RESULTS

4.1 Bond strength

Only four of test piles exhibited bond strength failure between the grouting and steel. These piles were all RD220/10 piles. With the other piles, the maximum applied load was too low to cause failure. Thus the bond strengths are calculated using the maximum applied load. Therefore also the bond strength is lower for piles with deeper grooves because the maximum applied load was smaller due to smaller cross-section area.

The maximum target load for RD140/10 piles with shallow grooves was 1.6 MN and for piles with deep grooves it was 1.3 MN. The calculated average bond strengths were 1.47 MPa for RD140/10 piles with shallow grooves and 1.20 MPa for piles with deep grooves.

Maximum target load for RD220/10 piles with shallow grooves was 3.0 MN and for piles with deep grooves 2.0 MN. The average bond strength for RDs220/10 with shallow grooves was 1.85 MPa and for RD220/10 with deep grooves it was 1.23 MPa. Three of the piles that had bond strength failure were RD220/10 piles with shallow grooves and one was a pile with deep grooves.

The observed failure point of the bond capacity in RD220/10 piles was sudden and displacement grew varying between 50 mm and 80 mm before re-attachment. Failure point was determined to be at the point where displacement grew at constant tensile force. Re-attachment was assumed to be caused by the ring bit, which was greater than the pile diameter.

Figure 4 shows the bond strengths that were calculated from the test results. Each pile has a small letter after the number which tells whether the groove type was shallow (s) or deep (d). RD140/10 piles are in blue columns and RD220/10 piles in red columns. The piles (7, 8, 9, 13) that had bond capacity failure are shown with a pattern. Pile 13, which was an RD140/10 pile, was the instrumented pile.

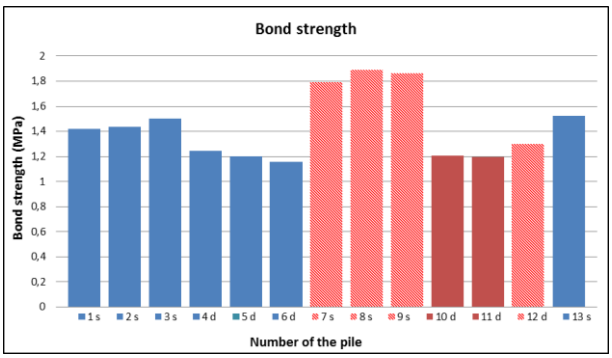


Figure 4 Bond strength between grouting and steel

4.2 Grouting

Average value for compression strength of the grouting was 41.3 MPa. This is calculated according to EN 196-1 (8). The grouting samples can be divided into four batches. Each batch comprised three samples from the mixer and three samples of the grouting that rose from the drill hole. Based on results, the quality of the uplift grout is practically the same as the quality from the mixer and that the required quality was reached.

4.3 Longitudinal strains

The average strains for RD140/10 piles are shown in Figure 5 and that of RD220/10 piles are in Figure 6. The average strains are calculated from the three gauges on the same pile and at the same cross-section. From these figures it is easy to see elastic and plastic behavior of the piles.

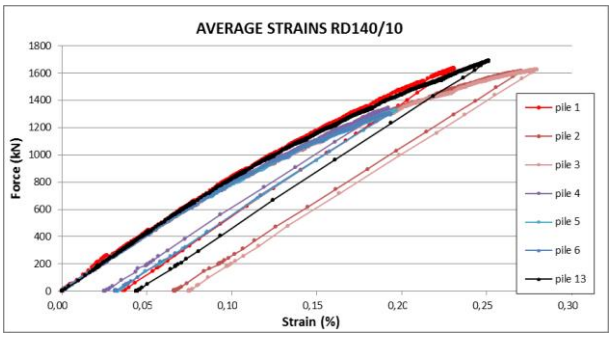


Figure 5 Average strains in RD140/10 piles

The strains are the relatively same for each RD140/10 pile. The piles are colored based on groove type; red curves are piles (1, 2 and 3) which had shallow grooves and blue curves are piles (4, 5 and 6) which had deep grooves. Pile number 13, the instrumented pile, is in black, because it had fewer grooves.

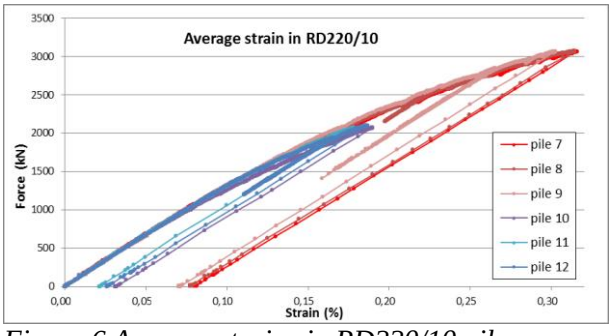


Figure 6 Average strains in RD220/10 piles

Figure 6 shows that the force-strain relation was similar in all RD220/10 piles, although a small difference can be seen between piles of a different groove depth. Piles with shallow grooves are shown in red and piles with deep grooves are in blue. The strains appear to grow with smaller force in piles that had the deep grooves. Groove depth should not affect this because strain gauges were on the smooth part of the pile. The biggest strains were measured in piles 7 and 8. Both had the maximum strain of 0.32%. These were also the piles that had the maximum loads. The behavior in load removal was the same with each pile.

In the instrumented pile, the strain gauges that were at the uppermost level on the pile are marked with U1, U2 and U3, strain gauges that were below the bedrock surface and at the lowest level are marked with L1, L2 and L3. The strain gauges M1, M2 and M3 were below the bedrock surface in between the afore-mentioned strain gauge levels. The maximum strain at the lowest strain gauge level was 0.01%, at the middle level it was 0.12% and at the uppermost level it was 0.27%. Thus, strains did not develop evenly along the pile length. Distance between the uppermost strain gauges and the middle strain gauges was about 1.7 m, and the distance between middle strain gauges and lowest strain gauges was about 0.5 m. Even so, the strains in the uppermost gauges were 2.3 times greater than the strains in middle gauges and the strains in the middle gauges were 8.7 times greater than the strains in the lowest strain gauges. Totally, the strains in the uppermost gauge were 20 times greater than strains in the lowest gauges.

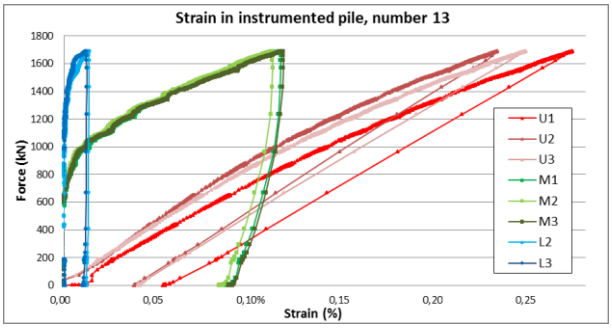


Figure 7 Strain development in instrumented pile, strain gauges at the uppermost level were U1 – U2, at the middle level M1 – M2 and at the lowest level L2-L3

4.4 Displacements

The displacement sensors of the pile were about 0.5 m above the rock surface, both at the same level and in the same cross-section. Figure 8 shows displacements for RD140/10 piles and Figure 9 displacements for RD220/10 piles. The maximum displacement of RD140/10 piles was 6.27 mm. The displacements had a greater variation than the strains between pile because the development of displacement is in relation to many factors, like grouting, voids, steel, grooves, etc. The strains above the bedrock surface mainly depend on pile size and steel properties.

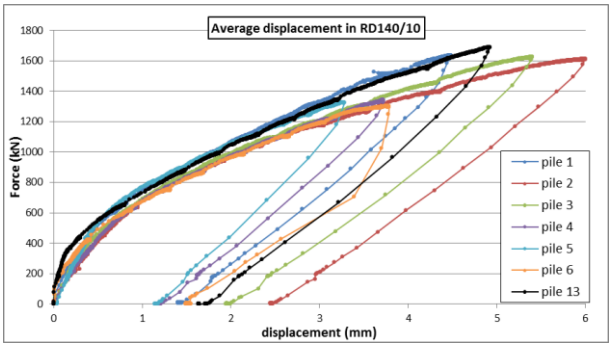


Figure 8 displacements in RD140/10 piles

For RD220/10 piles that were loaded at the failure point of bond capacity, the displacements were larger. Piles 10 and 11, which did not reach the failure load, do not show in the figure due to small displacement. Maximum displacement was 86.1 mm. It occurred at a load of about 2.1 MN. The displacement for piles 10 and 11 were less than 5 mm.

Displacements on the bedrock surface were monitored to ensure that they did not occur. Some displacements were observed near the piles, but displacement was mostly small scale.

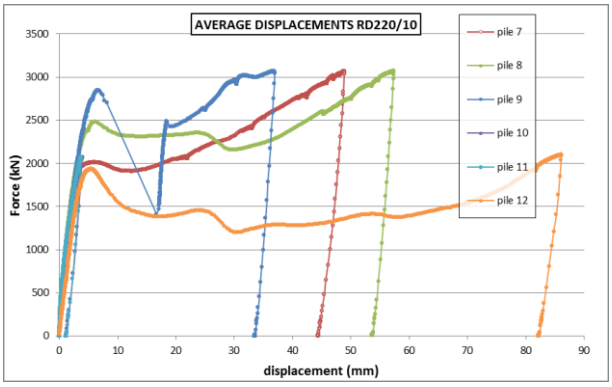


Figure 9 displacements in RD220/10 piles

5 ANALYSE OF THE RESULTS

5.1 Factors effecting on the results

The main difference was that piles were drilled straight into the rock surface. Piles are normally drilled into the surface of the ground and through a soil layer. Now the absence of the soil layer simplified several construction phases.

First of all cleaning of the drill hole was easier and more reliable because there was no soil collapsing into the drill hole. Also it was possible to see the mouth of the drill hole. This, in turn assisted flushing of the hole because it was possible to see when the hole was definitely cleaned. The drill cutting was observed to block the drill hole easily, so if there had been a soil layer, a more effective cleaning method might have been required.

The absence of the soil layers helped also grouting work. The quality of uplifted grout could be ensured because it was not mixed with the soil. On the other hand, while the soil layer may complicate the observation of quality, now piles were grouted against a purely open drill hole. Normally, soil would close the upper part of the hole and cause a little counter pressure at the beginning of grouting. This could induce better penetration of grouting to surround of the pile.

Bedrock quality was observed to be good. There were no remarkable fractures or weakness zones that could have had seriously affected to the work. The strength of the bedrock was considered high.

Piles that ended up failing in bond capacity were re-attached to the drill hole after large displacement and the load started to increase again. This re-attachment can be explained by the mechanical bonding of the ring bit. The ring bit is larger than the pipe diameter and after bond failure the ring bit no longer fits through the hole, but remains stuck in the grouting. The ring bit will start to transfer larger loads than the failure load of the bond capacity.

Flushing holes can also affect the results and especially the magnitude of the displacement after bond capacity was exceeded. The flushing holes were made 200 mm above the ring bit. It is possible that the grout did not spread downwards from the

flushing holes. Or the grout may have gone downwards, but only for a short distance. This might have caused a gap between the flushing holes and the ring bit. If there was a gap, the pile would have had a chance to move upwards until the grouting was reached. This gap is shown more closely in Figure 10.

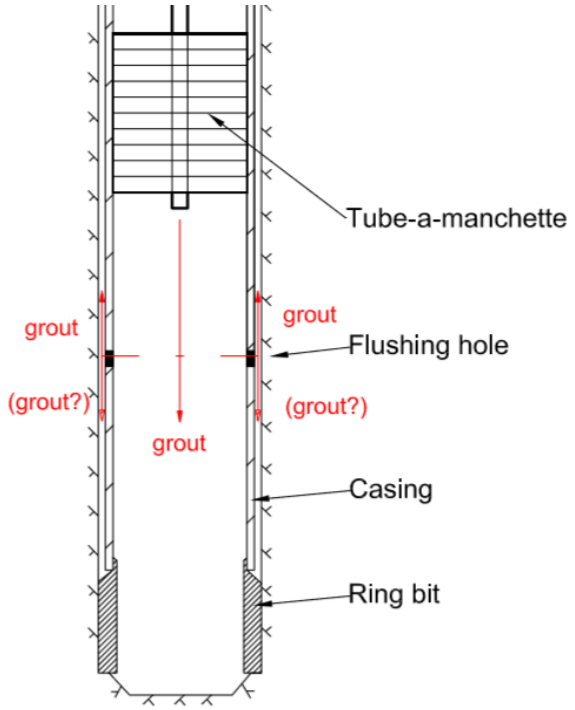


Figure 10. The spread of grouting and the gap between ring bit and flushing holes

One of the problems was that the failure mechanism could not be proved. The failure of the bond strength between the grouting and steel was assumed to be the failure mechanism based on the previous study and the fact that the failure was a brittle failure. In addition, if the failure had been between the rock and grouting, the grouting would have moved upwards with the pipe. This was not observed in the test. Furthermore, if the failure had occurred between the grouting and rock, the failure would have happened more slowly, displacement would have grown more steadily and the re-attachment would not have taken place.

In this study, the objective was to find failure mechanisms of drilled piles. A reasonable accuracy for displacement of a pile could be about 0.1 mm. The scale of displacement is comparable with a strain accuracy of 0.0025% and a force accuracy of 20 kN. The measurements were uniaxial and done in the direction assumed to have greatest deformations. The measuring devices were more accurate that was practically needed.

5.2 Discussion of the load test results

The main problem on the utilization of the results is the fact that the work was executed from a revealed rock surface, which does not correspond to an actual execution of drilled piles. This absence of a soil layer may have affected the results. The soil layer might affect the cleaning of the drill hole, which in turn may weaken the quality of grouting. The soil may remain on the pile surface or get stuck in the grooves on the pile surface. Either way, the bond strength will decrease.

While the grooved surface was detected to have a great impact on the bond strength, the groove depth was not found to affect the results. This may be due to the fact that the piles could not be pulled up with sufficient force. The results gave no reason to use deeper grooves. If the steel properties already limit the design before the bond capacity, deep grooves are not needed. When grooved piles are designed in practice, it is important to realize the influence of corrosion. While the grooves decrease the yield capacity of the steel, the sacrificial steel for corrosion protection will decrease the capacity even more.

The utility of bond length was quite obvious from the results of the instrumented pile. With loads of this size, there are no reasons to increase the bond length, because loads are transferred to the bedrock at the beginning of the bond length. Figure 11 shows the difference between applied maximum force and developed stress. The presented stresses are calculated based on measured strains so they are not exact values of stress but are exact in relation to each other and suitable for illustrating purpose.

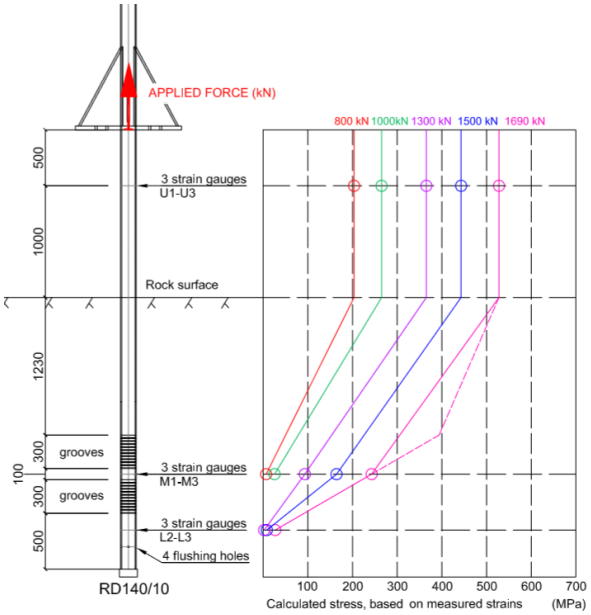


Figure 11 Stress distribution in instrumented pile

In Figure 11, each color represents a different applied force and the magnitudes of the forces are shown above the curves. Hence, the applied force is shown in upperpart of the figure and the induced stress is on the horizontal axis. In the left side of the figure is an illustration of the strain gauge locations on the pile length. The first two applied forces did not cause any stresses at the lowest measuring points, so the curves end at the middle gauge. The stress is assumed to be constant in the length of the pile, which is above the bedrock. Below the bedrock, the bond length will start to transfer loads. The stress clearly decreases faster between the lowest two gauge levels than between the highest gauge levels. The impact of the grooves cannot be separated from the figure, but it is possible, that the behavior is the same in both grooved lengths. This possibility is illustrated for the applied force of 1,690 kN, with purple dashed line.

If these piles are designed according to Eurocode, one problem to be considered is the effect of the grooves on bond capacity. Eurocode's instructs to use a different friction factor for piles that have a smooth surface and for piles that have a threaded surface. For smooth piles, the friction factor is 0.7 and for threaded piles, the friction factor is 2.0. So, the problem is to decide whether the grooved pile is smooth, threaded or something between these two.

Bond strengths for these pile types were calculated according to Eurocode and these characteristic values are shown in Table 2. The bond strength values were calculated both for smooth and threaded piles. Hence, the calculation for smooth piles was made for a bond length of 2.5 m and the calculation for threaded piles was made as a combination of a threaded and smooth pile which included 1.5 m of smooth pile and 1 m of threaded pile. When this is compared with the actual results obtained from this study, it can be observed that the actual results are closer to the smooth surface steel than the threaded steel. The bond strengths from the pull-out test are given in the same table on the right side. The "note" box contains a reference to whether the bond strength is real or based on the maximum load.

*Table 2. Designed and measured bond strengths (*no failure, **all failed, ***one failed)*

Pile no.	Designed bond strength between grouting and … (MPa)			Measured avg. bond strength (MPa)	
	Smooth steel	Threaded steel	Rock	Grooved	Note
1-3	1.54	2.68	1.13	1.47	*
4-6	1.54	2.68	1.13	1.20	*
7-9	1.26	2.20	0.91	1.85	**
10-12	1.40	2.44	0.99	1.23	***

If measured bond strength between grouting and rock are compared with the results of the Eurocode calculation, the difference is also quite big. The pull-out test clearly showed that the bond strength between grouting and rock was over 1.20 MPa.

6 CONCLUSIONS

The grooved surface of the pile improved the bond strength between the pile and grouting. In an earlier study by Ahomies (2015), the average bond strength was 0.30 MPa and in this test the average bond strength was 1.38 MPa. Hence, the average bond strength improved 460% by grooved surface. The conditions and the methods were not the

same in tests, but these results still give a reliable direction for further investigations.

The only real limiting factor of the use of the study was the absence of the soil layer and the cleaning of the drill hole can be considered as the greatest risk in the work. Drill cutting was observed to block the drill hole easily and if there was also a soil layer above, there might be a need for more effective cleaning methods. The main problem would be that the grooves would become clogged during drilling. Cleaning the grooves would be challenging, but it might be even more difficult to verify the cleanliness of the grooves. The study did not found any effect of the groove depth on the results, but cleaning of the deep grooves may be easier. The best option is to do a trial pile and test the functionality of the grooves.

The uneven stress distribution affects also pile design. In this study, the most limiting factor when using steel pipe piles for transferring tensile forces was the yield capacity of the steel. Due to the uneven stress distribution, this yield load could have been increased based on the results. The main stresses were along the smooth length of the steel pile and the strains decreased rapidly along the bond length. Thus, the stresses on the grooved part were only about 50% of the yield resistance of the steel.

The literature review revealed some weaknesses in pile design practices and concerns about the inaccuracies in design calculations. The currently used methods have not been developed in years, although the methods and knowledge have grown. These design methods should be questioned and compared with the actual conditions and properties of the construction site. Design should be based on proper site investigations and on test piles. With target specific design the designer can pay attention to the main risks in the construction and avoid overdimensioning.

7 ACKNOWLEDGEMENTS

The idea and organization for the study was by SSAB. They provided this study and did it possible and hence the greatest complement goes to them. The pull-out test was organized on the yard of Suomen Teräspaalutus Oy and it was also the used contractor. Tampere University of Technology was responsible for the monitoring during the loading. Special thanks for all participants.

8 REFERENCES

Ahomies, Marko. (2015). The grouted and anchored drilled pile in the bedrock. Master of Science Thesis. Tampere University of Technology. Civil Engineering, Tampere.

Brown, E.T. Rock engineering design of post-tensioned anchors for dams - a review. [Online]. September 18, 2014. [Accessed 11 September 2015]. Available at: http://www.sciencedirect.com/science/article/pii/S1674775514000730.

Charlie C. Li, Gisle Stjern, Arne Myrvang. A review on the performance of conventional and energy-absorbing rockbolts. [Online]. March 19, 2014. [Accessed 11 September 2015]. Available at: http://ac.els-cdn.com/S1674775514000225/1-s2.0-S1674775514000225-main.pdf?_tid=4e0c1fa6-5869-11e5-8ec9-00000aacb360&acdnat=1441964680_ec9b6b42c3aff4ea10019f8dde7abc88.

Jesús Gómez, Allan W. Cadden, Robert P. Traylor, Donald A. Bruce (2005). Connection Capacity between Micropiles and Concrete footings: Interpretation of Test Results and Design Recommendations. [Online]. 2005. [Accessed 11 September 2015]. Available at: http://www.geosystemsbruce.com/v20/biblio/215%20Connection%20Capacity%20between%20Micropiles%20and%20Concrete%20Foot.pdf

Littlejohn, G. S (1997). Uplift capacity of shallow anchorages in weak mudstone. Ground anchores and anchored structures. London : Thomas Telford, , ss. 23-33. ISBN: 0-7277-2607-2 .

Sirén, Rosa. (2015). The tensile capacity of steel pipe piles drilled into the bedrock, Master's thesis. Aalto University School of Engineering, Espoo.

Suomen Rakennusinsinöörien Liitto RIL ry, Suomen Geotekninen Yhdistys SGY ry. RIL 254-2011 Paalutusohje 2011, PO-2011. 1. Helsinki : Suomen Rakennusinsinöörien Liitto RIL ry, 2011. ISBN 978-951-758-528-6

In situ detection of sensitive clays – Part II: Results

R. Sandven
Multiconsult, Norway, rolf.sandven@multiconsult.no

A. Gylland, A. Montafia
Multiconsult, Norway

K. Kåsin, A.A. Pfaffhuber
Norwegian Geotechnical Institute, Norway

M. Long
University College Dublin, Ireland

ABSTRACT

Sensitive and quick clays are typically found in Norway, Sweden and Canada, and are characterised by a remoulded undrained shear strength considerably lower than the undisturbed shear strength. In geotechnical engineering, the presence of sensitive clays poses a major challenge. The landslides at Rissa in 1978, and more recently at the Skjeggestad bridge in Norway, are devastating reminders of the potential threats related to such soils. In a construction project it is hence important to 1) determine if there is sensitive clay present and 2) clarify the extent of the quick clay deposit. This is currently done based on interpretation of soundings and to some extent geophysical methods such as electrical resistivity measurements. However, for verification of quick clay, sampling and laboratory testing must be performed.

Here, a set of updated and new guidelines for classification of sensitive clays from in-situ measurements are presented. The aim is to provide the geotechnical engineer with a practical classification tools where all available information is utilized and combined efficiently. The classification tools are based on results from methods such as conventional soundings, CPTU with measurement of total force, electrical field vane testing in combination with geophysical methods such as R-CPTU, 2D resistivity profiles (ERT) and airborne electromagnetic measurements (AEM). The methods, and how they are utilized in investigation strategies for detection of quick and sensitive clays, have been described in another paper to this conference. An extensive database of Norwegian test sites forms the basis for the work. The results from this study show that the above mentioned site investigation methods holds information that complements each other, to form a solid basis for detection of sensitive clays. In turn, this opens for more efficient site

investigations where all available data are interpreted in a systematic manner to produce a reliable map of sensitive clay deposits.

Keywords: Quick clay, geotechnical investigations, resistivity measurements, interpretation.

1 INTRODUCTION

1.1 The NIFS project

The NIFS project is a joint venture between the Norwegian Water Resources and Energy Directorate (NVE), The Norwegian Railroad Administration (NNRA) and the Norwegian Public Roads Administration (NPRA). One of the goals of the project is to coordinate guidelines and develop better tools for geotechnical design in quick clay areas.

Work task 6 in this project focus on Quick clay, where a study on *"Detection of brittle materials"* has been carried out. The results reported herein are based on results from this study, where various new and existing criteria for detection of quick and sensitive clays have been evaluated. Reference is made to the reports NIFS report no. 2015-126 and 2015-101 for detailed results and soil data (www.naturfare.no).

1.2 Scope of work

The work tasks in this project can be summarized as follows:

- Evaluation of conventional sounding methods and their ability to detect brittle materials (rotational weight sounding DT, rotational pressure sounding DRT and total sounding TOT)
- Suggest improved CPTU-based identification charts for classification of brittle materials
- Evaluation of resistivity measurements for mapping of quick clay deposits (downhole mode (R-CPTU), surface mode (ERT) and airborne mode (AEM))
- Evaluate and compare results from electrical field vane tests (EFVT)
- Evaluate correlations between resistivity values from R-CPTU and ERT with results from index tests and salinity measurements
- Recommended site investigation strategy based on integrated geotechnical and geophysical methods for detection of quick and sensitive clays

The following methods have been included in the study:

- Rotary weight sounding (DT)
- Rotary pressure sounding (DRT)
- Total sounding (TOT)
- Cone penetration tests (CPTU)
- Piston sampling (ϕ54 mm, ϕ76 mm) (PS)
- Block sampling (ϕ250 mm Sherbrooke, ϕ160 mm NTNU) (BS)
- Electric field vane test (EFVT)
- Cone penetration tests with resistivity measurement (R-CPTU)
- Surface resistivity measurements (ERT)
- Airborne Electromagnetic Measurements (AEM)

Table 1 provides a detailed overview of the investigations carried out at the most important test sites.

Table 1 Test program on important selected test sites.

Test site	Methods
Smørgrav	DT, CPTU, R-CPTU, ERT, PS
Kløfta	TOT, CPTU, R-CPTU, ERT, AEM, PS, BS
Klett	DT, TOT, CPTU, R-CPTU, ERT, EFVT, PS, BS
Fallan	TOT, CPTU, R-CPTU, ERT, EFVT, PS
Tiller	TOT, CPTU, R-CPTU, ERT, EFVT, PS, BS
Esp, Byneset	TOT, CPTU, R-CPTU, ERT, EFVT, PS, BS
Dragvoll	CPTU, R-CPTU, ERT, BS
Tiller	CPTU, R-CPTU, ERT, PS, BS, EFVT
Rissa	TOT, DRT, CPTU, R-CPTU, PS, BS

2 SELECTED RESULTS FROM THE STUDY

2.1 Conventional sounding tests

The rod friction is often the dominating component in sensitive materials, except at

small penetration depths. It can hence be expected that a good correlation exists between the penetration force and the remoulded shear strength for the clay. This correlation is however influenced by the diameter of the drillrods, the tip design, the ratio between tip and rod diameter, the penetration principle (rotation, pressure, dynamic) and finally the penetration rate.

The detection of brittle materials by conventional sounding methods may however be influenced by features in soil composition and layering, such as:

- Laminated clays with sand- and silt lenses
- Brittle materials below a top layer with variable thickness and content of coarse materials
- Loose, water-saturated silt and sand
- Profiles with artesian pore pressure

In most soils, the increasing friction along the drillrods will result in an increasing penetration force with depth. In a sensitive or quick clay, an increase in the friction component is close to zero. Hence, no increase in penetration force will be noticed, resulting in the characteristic vertical curve in sensitive clays. In addition, the collapse behaviour of quick clays may in some cases result in a negative slope of the curve.

When drilling through a dense, thick top layer, the friction in this layer may influence the sounding profile considerably. Figure 1 shows examples of sounding profiles with and without predrilling through a 10 m thick dense top layer. The results show that the quick clay layer is identified reasonably well after predrilling through the top layer (Figure 1 right), whereas it is not revealed when the sounding is commenced at the surface (Figure 1 left). If deposits of brittle materials are expected at a site, one should hence predrill through present top layers, to better reveal possible underlying sensitive strata.

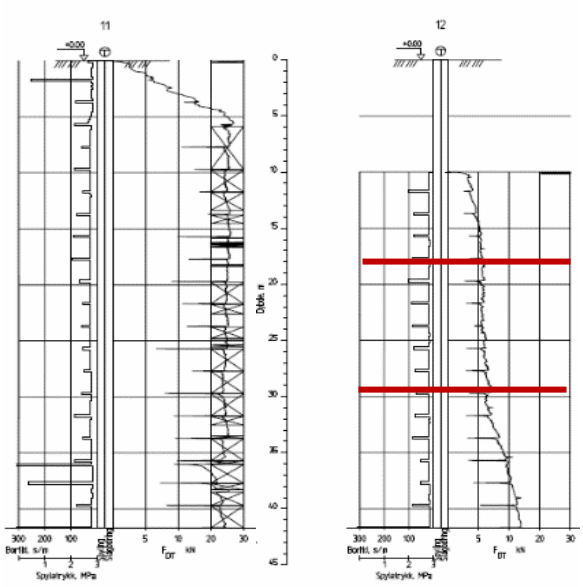


Figure 1 Total sounding profile in quick clay deposit with and without predrilling (NIFS-report 2015-126).

2.2 Cone penetration tests (CPTU)

CPTU has a great potential for detection of quick and sensitive layers through measurements of cone resistance, sleeve friction and pore pressure. Despite the obvious potential in these measurements, mixed experiences exist with CPTU for detection of brittle materials. The reason may be that the results obtained are influenced by other factors, not related to the clay being sensitive or not. As a result of the NIFS study, new and alternative interpretation CPTU data have been introduced, and some of them are elaborated in the following.

2.2.1 New identification charts

A series of soil identification charts have previously been developed, but they appear in many cases to be misleading for indication of sensitive Norwegian clays. One aim of this study has hence been to develop new classification charts for classification of sensitive clays, based on the following approaches:

- Use of revised cone resistance number N_{mc} (based on the preconsolidation stress)
- Use of revised pore pressure ratio B_{q1} (based on the estimated pore pressure at the cone face)

The cone resistance number is defined as:

$$N_m = q_n/(\sigma_{vo}' + a) \quad (1)$$

where:

σ_{vo}'= present effective overburden stress (kPa)
a= attraction (kPa)

In this definition, the present effective overburden stress σ_{vo}' is used as the reference stress. It is however more appropriate to use the preconsolidation stress σ_c' as reference, due to its influence on the material behaviour. This leads to the revised expression:

$$N_{mc} = q_n/(\sigma_A' + a) \quad (2)$$

where:

σ_A'= reference stress (see Eq.(3)) (kPa)

To introduce the preconsolidation stress and also to account for swelling effects, the expression shown in Eq.3 is used as reference stress σ'_A, similar to the approach used by Ladd & Foott (1974) in the SHANSEP-adaption. The stress exponent m account for the effect of unloading and swelling of the sediment.

$$\sigma'_A = \sigma'^{m}_c \cdot \sigma'^{(1-m)}_{vo} \quad (3)$$

where:

σ_c'= preconsolidation stress (kPa)
σ_{vo}'= effective overburden stress (kPa)
m= stress exponent for swelling effects ($0 < m < 1{,}0$) (-)

The stress exponent m is derived from experience of the active undrained shear strength in Norwegian clays, with m in the order of 0,7 - 0,8. This expression requires reliable values of the preconsolidation stress σ_c' so that a $\sigma_c' - z$ profile can be established. The preconsolidation stress should primarily be determined from oedometer test data, from known topographical information and previous terrain level, secondarily from independent interpretation of CPTU data. Empirical relations between over-consolidation ratio OCR and pore pressure distribution around the probe can also be used (see e.g. Sully et al, 1988), see Eq.4:

$$u_1 = u_2 + u_o*(OCR-0{,}66)/1{,}43 \quad (4)$$

where:

u_1= pore pressure at the conical tip (u_1 usually > u_2) (kPa)
u_2= pore pressure at reference level behind conical tip (kPa)
u_o= in situ pore pressure before penetration (kPa)
OCR= overconsolidation ratio ($=\sigma_c'/\sigma_{vo}'$) (-)

The revised expression for the pore pressure ratio B_{q1} hence becomes:

$$B_{q1} = (u_1-u_o)/(q_n) = (k*(u_2-u_o))/q_n \quad (5)$$

where:

k= experience based correction factor expressing the ratio between the pore pressure at various locations on the probe (-)

Tentative values of k in various clays are given below:

Soft NC-clay: k = 1,25
Medium soft clay, low OCR: k = 1,50
Stiff OC-clay, high OCR: k = 1,90

The combination of N_{mc} and B_{q1} is used in a simple identification chart for sensitive clays, see Figure 2. The figure includes datapoints from all sites included in the study.

The following classification criteria are suggested, based on the results in this study:

- $N_{mc} \leq 3{,}5$ and $B_{q1} \geq 0{,}75$: Possibly brittle material
- $N_{mc} \leq 2{,}5$ and $B_{q1} \geq 1{,}00$: Most likely quick clay

This approach represents some uncertainty due to the utilized empirical relationships between u_1 and u_2, and it may hence be relevant to use B_{q2} since this pore pressure ratio is based on the measured pore pressures.

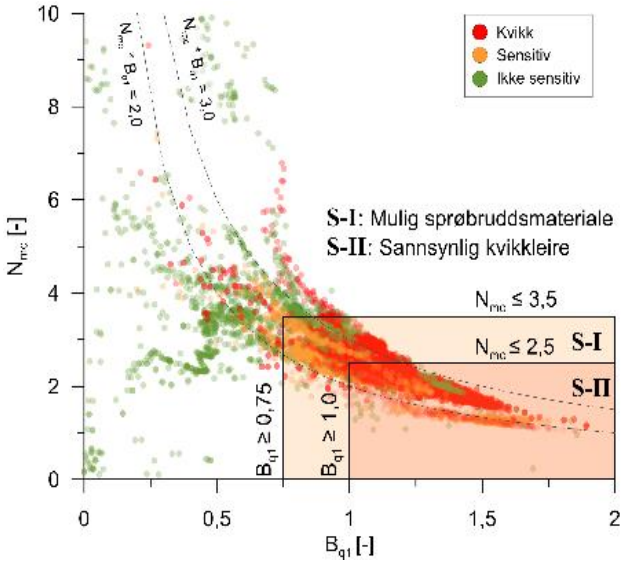


Figure 2 New identification chart for brittle materials based on N_{mc} and B_{q1} (NIFS-report 2015-126).

By plotting data from all the test sites selected in this study, a relatively clear identification of layers with quick and sensitive clays is obtained. In the data sets, there are certainly some discrepancies, but for most test sites very good agreement is obtained.

2.2.2 Interpretation of sleeve friction

In brittle materials, the pore pressure based interpretation is usually the most reliable, provided that the pore pressure recording system is sufficiently saturated. It is hence suggested to express the friction ratio in terms of the excess pore pressure u_1 (alternatively u_2) instead of the net cone resistance q_n, see Eq.6.

$$R_{fu} = f_s*100\ \% / \Delta u_1 \qquad (6)$$

where:

f_s= measured sleeve friction (kPa)
Δu_1= u_1-u_o, corrected excess pore pressure at the conical tip (kPa)
u_o= in situ pore pressure (kPa)

This formulation has the added effect that materials with distinct differences in pore pressure response becomes easier to classify and with less scatter.

This principle is used in Figure 3, where N_{mc} is plotted versus the friction ratio R_{fu} for all test sites. As previously discussed, the interpretation of sleeve shows some scatter, which is also revealed in the classification in the $N_{mc} - B_{q1(2)}$ in Figure 3. Based on this, the following classification is suggested:

- $N_{mc} \leq 3,5$ and $R_{fu} \leq 2,0\%$: Possible brittle material

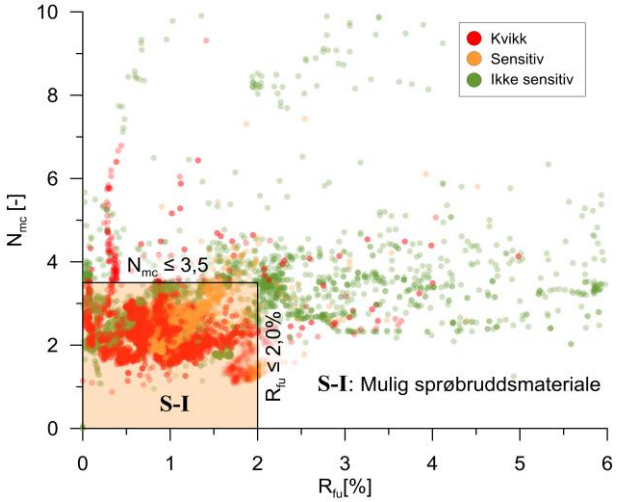


Figure 3 New identification chart based on N_{mc} and R_{fu} (NIFS-report 2015-126).

The sleeve friction is however an uncertain parameter to use for detection of quick clays due to reasons discussed earlier.

2.2.3 Interpretation of rod friction

After penetration of the CPTU-probe, the sleeve friction may not represent a fully remoulded condition. This means that the evaluation of quick clay from the sleeve friction (f_s) may be misleading. The rod friction will however represent remoulded conditions according to the continued penetration of the rods into the ground. After continuous penetration of the rods, the remoulding of the materials will gradually become more complete along the drillrods. The friction may hence be determined as the average friction along the drillrods.

In the interpretation of the rod friction, the weight of the drillrods and the tip force is subtracted from the total thrust, see Eq.7. The total rod friction Q_s can then be determined as a function of penetration depth:

$$Q_s = F + G - q_t*A_c \qquad (7)$$

where:
F = Total penetration force (kN)
G = Weight of drillrod (N)
q_t = Corrected cone resistance (kN/m^2)
Q_s = Mobilized rod friction (kN)
A_c = Cross-sectional probe area (mm^2)

The curve for the calculated friction along the rods can be determined by a theoretical line, corresponding to an evenly distributed friction of 0,5 kPa (quick clay definition) or 2,0 kPa (brittle material definition). For quick clays, the slope of the friction force Q_s should be less than the slope for the theoretical line corresponding to 0,5 kPa sleeve friction.

The detection of brittle materials from calculated rod friction has been carried out on a number of test sites in this study. The results indicate that layers of brittle materials can be detected, but there is a slight overestimation of the thickness of these layers compared to classification from laboratory tests. Similar experiences were made in the Swedish Göta älv project (Löfroth et al (2011)). It is recommended to record the total penetration force routinely in a CPTU.

2.3 Vane testing

In the interpretation of shear strength from a vane test, it is assumed that the mobilization of shear stresses is evenly distributed at the cylindrical failure surface. The shear strength can hence be determined from the following expression:

$$c_{u,rv} = 6T/7\pi D^3 \quad (8)$$

where:
T= measured torque (Nmm)
D= vane diameter (mm)

To determine the undisturbed undrained shear strength (c_{uv}), the maximum torque T_{max} is used.

By using an electric field vane, one may record the whole mobilization curve for the torque versus the rotation angle of the vane. This can give valuable information of the material behaviour, in addition to the shear strength values. To utilize this curve, the test must be run to minimum 90˚ rotation of the vane, so that a full failure circle is defined. A method for utilization of the remoulding energy of clays for landslide runout evaulations is currently developed developed, based on vane test results (Thakur et al. 2015).

For determination of the remoulded shear strength (c_{rv}), the measured residual torque after remoulding of the clay is utilized. A quick clay has by definition a remoulded shear strength of c_{rv} < 0,5 kPa.

The complete remoulding of the clay is obtained by applying 25 full rotations of the vane. When the clay in the zone around the vane is remoulded, a local excess pore pressure is generated. Since the failure zone has a very limited thickness of about 1 mm (Gylland et al, 2013), this pore pressure will dissipate relatively quickly, resulting in an increasing shear strength with time. For correct measurement of the remoulded shear strength it is hence important that the readings take place as soon as possible after remoulding, to avoid excessive pore water drainage in the failure zone.

By using vane equipment with a slip coupling, it is recommended that the torque is measured immediately after remoulding, before reading of the resistance in the slip coupling. A corresponding rotation of ca. 5^o is recommended for reading of the torque in the remoulded state.

Conventionally, the torque is applied and measured at the top of the drillrods. The transfer of the applied torque down to the vane will however be influenced by friction and deformations in the rod system, and some of the torque will be lost before it reaches the vane. This friction will typically be around 1-3 Nm, and will increase somewhat with depth. It may be reduced by proper maintenance, lubrication and suffi-cient cleaning of the vane equipment.

For a remoulded shear strength of 0,5 kPa, and a vane diameter of 65 mm, the moment contribution from the remoulded shear

strength will be about 0,5 Nm. This is lower than the friction, and hence challenges the resolution of the equipment. For determination of the undisturbed undrained shear strength, the necessary resolution is expected to be ±1 kPa. For the remoulded shear strength, a resolution about 10 times better (±0,1 kPa) will be required. This is usually not obtainable, even with modern equipment, but electric vanes are at least better than the manual. For equipment that does not allow measurement of friction, it is not recommended to carry out measurements of the remoulded shear strength in quick and sensitive clays.

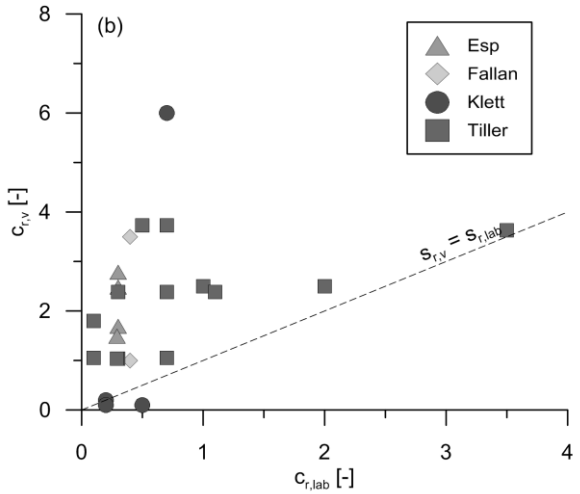


Figure 4 Comparison between remoulded shear strength obtained in field vane and fall cone tests (units in kPa) (NIFS report 2015-126).

Figure 4 shows a summary of the remoulded shear strength measured by vane tests and fall cone tests in the laboratory. The results clearly show that vane tests with measurement of the torque on top of the drillrods overestimate the remoulded shear strength in brittle materials for depths below > 10-15 m.

Measurement of the remoulded shear strength is one of the attractive features with vane testing when it comes to detection of brittle materials. At the same time, it is evident that the method has obvious limitations when it comes to measurements of this parameter, particularly if the torque is measured on top of the drillrods. For measurements of the remoulded shear strength in sensitive and quick clays, it is hence recommended to measure the torque down at the vane.

2.4 Resistivity measurements

The electric resistivity of soils is generally a function of porosity, the ion content of the pore water, salinity, clay content and content of charged minerals such as graphite and some sulfides.

For clays, it is mainly the salt content that influences the resistivity, at least for salinities higher than about 1 g/l (Montafia, 2013). The resistivity will hence be higher in brittle materials than for intact marine clays. Table 2 summarizes the resistivity in various geological materials based on Norwegian experiences. By measuring the resistivity of the soils, one may hence be able to detect potentially leached zones according to the classification values in Table 2. It is emphasized that local site specific variations from the tabulated values may occur.

Table 2 Resistivity in geological materials (after Solberg et al (2008)).

Soil type	**Resistivity** (Ωm)
Salt, marine clay	1 – 20
Leached clay	20 – 90
Dry crust, coarse materials, sand and gravel	70 – 300
Silt, saturated	50- 200
Sand, saturated	200 - 1000
Rock	Several 1000

2.4.1 Identification of leached zones

Resistivity measurements on the surface (Electrical Resistivity Tomography ERT) give an overview of the resistivity along profiles that can be several hundred meters long, with a depth range of several tens of meters. Primarily, the method can be used to get an overview of the homogeneity of the sediments. Since the resistivity of the clay primarily is determined by the salt content, a resistivity model can be established and indicate the extension of layers of leached and possibly quick clay. If the results from ERT-measurements are available before the geotechnical borings are carried out, the boring plan can be developed based on the interpreted resistivity model.

ERT can also be used in steep areas where drillrigs cannot access, for example in forests, in steep terrain, and for detection of clay beneath dense layers that cannot be penetrated by geotechnical sounding equipment. The method is also well-suited for investigation of large areas or along planned road- or railway lines in a more cost-efficient way than with borings alone.

The resistivity is however not a unique measure of a leached clay. High resistivity can be caused by a lower salt content, but may also by due to high silt content. It is hence recommended to always calibrate the resistivity model by geotechnical borings.

Using constrained inversion, one include other available information in the processing of the resistivity profile, for example location of the rock surface from total sounding or measured resistivity from R-CPTU. This will generally improve the interpretation of the resistivity models.

Resistivity measurements from airplanes or helicopters (Airborne Electromagnetic Measurements AEM) may be used for detection of brittle materials in more or less the same way as for ERT. AEM produces models for the electric resistivity in a regional scale, along profiles of almost unlimited length and several hundred meters penetration depth. Use of AEM is favourable in regional mapping at an early investigation stage, in large projects or in large-scale mapping of clay deposits.

The limitation of the method is mainly the economy in the project. AEM is very cost-effective in large projects, but it is not economically feasible to mobilize the equipment for a limited project area. AEM has somewhat poorer resolution than ERT, and the method cannot be used over urban areas or roads with dense traffic.

Modern equipment for hydrogeological mapping has given results close to the accuracy of ERT (Anschütz et al, 2015). As long as the clay layer is thick enough (some tens of meters), the AEM resolution may hence be sufficient to detect differences in the resistivities between salt and leached clays.

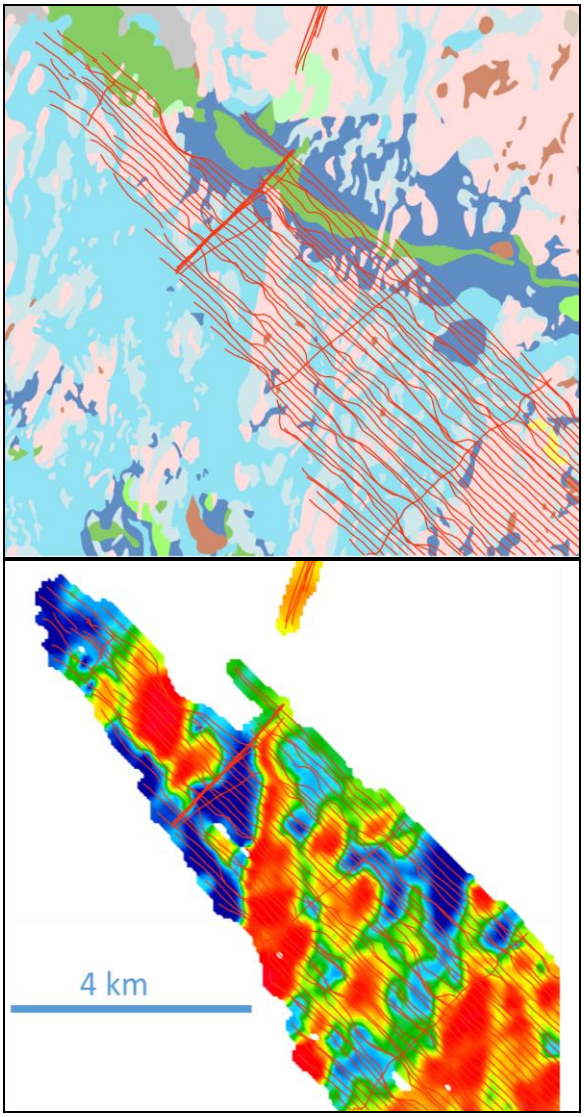


Figure 5 Example of results from AEM in a quick clay area. Upper: Quaternary soil map (NGU) and AEM flylines. Lower: AEM resistivity section from 0-15 m depth.(NIFS rep. 2015-126).
Legend geology: Blue: marine deposits, Green: moraine, Pink: rock exposures, Brown: bog. Legend resistivity: Blue 1 Ωm to Red 1.000 Ωm.

2.4.2 Comparison of R-CPTU, ERT and AEM results

The difference in resolution between the three methods for resistivity measurements is important to be aware of when comparing results obtained with these methods. The measurements are representative for a soil volume ranging from some centimeters to some tens of centimeters for R-CPTU, some meters or tens of meters for ERT and finally some tens of meter to some hundreds of

meters for AEM. For example, resistivity values measured by R-CPTU for a 3 meter thick clay layer over rock with high resistivity will be correct, whereas ERT-measurements will be influenced by the rock, even in shallow measurements. AEM will probably not be able to detect the clay layer at all. The same will be the case for thin layers that are depicted sharply by R-CPTU, but will show a gradual transition in presentation of ERT- and AEM-data. Except from these conceptual limitations, experience show that the measurements agree well where the soil conditions are favourable.

3 CONCLUSIONS AND FINAL REMARKS

A combination of geophysical and geotechnical methods have become more usual in modern ground investigations, particularly in larger projects. In such integrated measurements, geotechnical engineers and geophysicists cooperate closely, and by joint knowledge decide where geotechnical soundings, in situ tests and sampling should be located for optimal cost-efficiency.

The penetration force for different sounding methods are influenced by several features such as effect of top layers, increasing rod friction by depth and previous consolidation. In particular, thick and dominating top layers with presence of stiff and coarse materials may influence the penetration force significantly. This may conceal layers of soft and brittle materials at larger depths. Predrilling through such layers is generally recommended. Moreover, it is a general impression that conventional soundings tend to overestimate the thickness of the quick clay layers.

Existing soil identification charts for CPTU often give misleading classification of brittle materials for various reasons. It is recommended to use new identification charts for quick and sensitive clays presented herein. These charts consider the stress history of the materials, together with the estimated pore pressures in the failure zone beneath the probe (u_1).

If CPTU is combined with downhole resistivity measurements in an R-CPTU, a new physical property is introduced in addition to cone resistance, pore pressure and sleeve friction/rod friction. In this way, a wider basis for classification and interpretation of the results is obtained. The experiences from this study shows that the quick clay layer for all sites plots within the expected variation range of 10 - 100 Ωm. Measured resistivity values outside the reported range may hence with large reliability be classified as non-leached clays, even if some non-sensitive clays also show resistivities in this range.

It is recommended to measure the resistivity in a CPTU if a resistivity module is available, since this procedure only requires a marginal increase in test duration. Furthermore, local correlations between resistivity values and other soil properties may be established by relating R-CPTU results with other field or laboratory data. Such site specific relationships may be more precise than general expressions.

Use of ERT- and AEM-methods gives approximately the same resistivity values as R-CPTU, and there is generally good agreement between the three methods, particularly in homogenous soils. One major advantage obtained with these methods is the continuous information of soil layers in the ground, something that is very important in evaluation of slope stability, possible slide extension and run-out distance for the remoulded and liquefied slide debris.

A field vane test traditionally gives information about the in situ undrained shear strength (undisturbed and remoulded), and hence the sensitivity. Modern electrical systems give possibilities for measurement of the friction using an electro-mechanical unit applying the torque. For these systems it is required that the torque is measured at the vane, to avoid important sources of errors in the measurements. Such equipment is now commercially available. If the torque is measured at the top of the drillrods it is shown that the measured torque is heavily influenced, particularly for remoulded conditions. Consequently, it is <u>not</u> recommended to use the method for determination

of the remoulded shear strength of quick clay for depths exceeding 10 m.

Determination of the remoulded shear strength by fall cone tests in the laboratory will still be the most reliable method for determination of quick or sensitive clays. This method has however also some possible sources of error, such as operator dependency and non-standard correlations between intrusion and shear strength.

The resistivity correlates well with salt content down to concentrations around 1 g/l. For lower salt contents, other influence factors seem to dominate. This may be one of the reasons to the large scatter in measured resistivity in leached clays.

None of the methods reported herein are without the possibility of misleading interpretation, and the evaluation of results requires critical judgement and caution. The integrated use of geophysical and geotechnical measuring methods makes each of the approaches stronger and will be the recommended strategy in larger projects,

4 ACKNOWLEDGEMENTS

The partners in the NIFS project are greatly acknowledged for the financial support and good discussions throughout the study. The board of the Norwegian Geotechnical Society (NGF) are acknowledged for financial support for development of the summary report. The authors want to extend thanks to Rambøll, Multiconsult, NGI, Statens vegvesen (NPRA) and NGU for allowing the use of data in the study.

5 REFERENCES

Anschütz, H., Bazin, S. and Pfaffhuber, A. (2015). Towards using AEM for sensitive clay mapping – A case study from Norway. 1st European Airborne EM conference. Torino, Italia, Mo AEM 04.

Ladd, C.C. and Foott, R. 1974. New design procedure for stability of soft clays. Journal of the Geotechnical Engineering Division, ASCE, 100(7), pp.763–786.

Löfroth, H., Suer, P., Dahlin, T., Leroux, V. and Schälin, D. (2011). Quick clay mapping by resistivity - Surface resistivity, CPTU-R and chemistry to complement other geotechnical sounding and sampling. Statens Geotekniska Institut, SGI. Göta älv utredningen. GÄU. Report 30. Statens Geotekniska Institut, Linköping, Sverige.

Montafia, A. (2013). Influence of physical properties of marine clays on electric resistivity and basic geotechnical parameters. Master thesis, Department of Civil and Transport Engineering, NTNU, Trondheim.

NIFS (2015). Detection of brittle materials. Summary report with recommendations. Final report. NIFS Report no. 126/2015 (www.naturfare.no)

NIFS (2015). Detection of quick clay by R-CPTU and electrical field vane tests. Results from field study (in Norwegian). NIFS Report no.101/2015 (www.naturfare.no)

Solberg, I. L., Rønning, J. S., Dalsegg, E., Hansen, L., Rokoengen, K. and Sandven, R. (2008). Resistivity measurements as a tool for outlining quick-clay extent and valley-fill stratigraphy: A feasibility study from Buvika, central Norway. Canadian Geotechnical Journal, 45(2), pp.210-225.

Sully, J.P., Campanella, R.G. and Robertson, P.K. (1988). Overconsolidation ratio of clays from penetration pore water pressures. ASCE Journal of Geotechnical Engineering, ASCE, 114 (2), pp.209-15.

Thakur, V., Degago, S., Gylland, A.S. and Sandven, R. (2015). In-situ measurement of remolding energy of sensitive clay. GEOQuebec 2015 – Challenges from north to south, Quebec, Canada, september 2015.

In situ detection of sensitive clays – Part I: Selected test methods

R. Sandven
Multiconsult, Norway, rolf.sandven@multiconsult.no

A. Gylland, A. Montafia
Multiconsult, Norway

K. Kåsin, A.A. Pfaffhuber
Norwegian Geotechnical Institute, Norway

M. Long
University College Dublin, Ireland

ABSTRACT

Sensitive and quick clays are typically found in Norway, Sweden and Canada, and are characterized by a remoulded undrained shear strength that is considerably lower than the undisturbed shear strength. In geotechnical engineering, the presence of sensitive clays pose a major challenge. The landslides at Rissa in 1978, and more recently at the Skjeggestad bridge in Norway, are devastating reminders of the potential threats related to such soils. For a geotechnical engineering project it is hence important to 1) determine if there is sensitive clay present and 2) clarify the extent of the quick clay deposit. This is currently done based on interpretation of soundings and to some extent by geophysical methods such as electrical resistivity measurements. However, for verification of quick clay, sampling and laboratory testing must be performed. Here, a set of methods for classification of sensitive clays from in situ measurements are presented. The aim is to provide the geotechnical engineer with practical and rational methods, from which all available information is utilized and combined efficiently. The methods presented herein include conventional soundings, CPTU with measurement of total force, vane shear testing in combination with geophysical methods such as R-CPTU, 2D resistivity profiles (ERT) and airborne electromagnetic measurements (AEM). An extensive database of Norwegian test sites forms the basis for the work. This paper describes the methods utilized in this study and how they may be combined in a strategy for detecting deposits of quick and sensitive clays. The major results from the study are presented in another paper presented to this conference.

Keywords: Quick clay, geotechnical investigations, resistivity measurements.

1 INTRODUCTION

1.1 The NIFS project

The NIFS project is a joint venture between the Norwegian Water Resources and Energy Directorate (NVE), The Norwegian Railroad Administration (NNRA) and the Norwegian Public Roads Administration (NPRA). One of the main goals of the project is to coordinate guidelines and develop better tools for geotechnical design in quick clay areas.

Work task 6 in this project focus on the detection and behavior of quick clays, where a study on *"Detection of brittle materials"* has been carried out in the period 2012-2015. This report concludes this study, giving recommendations of methods and procedures for detection of brittle materials from various field and laboratory tests. Various new and existing criteria have been tested and evaluated on test results from a number of test sites. Reference is made to the reports NIFS report no. 2015-126 and 2015-101 for detailed results and soil data (www.naturfare.no).

1.2 Background

Indication of quick and sensitive clays is an important issue in many projects, since this will change the project assumptions and provide stricter guidelines for the ground investigations. It will also influence geotechnical planning and design, as well as control and documentation routines for the geotechnical work carried out.

The field methods used in Norway today give sufficient indications of brittle materials in many cases. However, sounding profiles obtained by conventional methods may give misleading indications in some situations. This may either be on the conservative side, where results indicate quick clay in the field, but where the laboratory testing show non-sensitive behaviour. More difficult is the opposite, where the sounding profiles show no signs of quick clay, but where such materials are discovered later in the project.

The great efforts undertaken for mapping of quick clay zones have led to an increasing need of quicker and more reliable identification of such materials. Today, there is an increasing tendency of using a combination of geophysical and geotechnical methods in mapping of quick and sensitive clays. In general, one may say that geophysical methods cover large areas in relatively short time, but possibly with poorer resolution and less refinement than most geotechnical tests. By combining geophysical and geotechnical methods, the outcome may hence be a more rational and cost-effective ground investigation, see e.g. Löfroth et al (2011).

1.3 Scope of work

The methods applied in mapping of brittle materials must be chosen based on a cost-benefit perspective, the applicability of the methods for the actual ground conditions and the general use of soil data in the project. In this work, it has been important to present recommendations based on the experiences and observations made with various detection methods. In particular, this is valid for the resistivity methods R-CPTU, ERT and AEM, where limited experiences exist from practical use.

The work carried out in the study can be summarized as follows:

- Evaluation of conventional sounding methods and their ability to detect brittle materials (rotational weight sounding DT, rotational pressure sounding DRT and total sounding TOT)
- Suggest improved CPTU-based identification charts for classification of brittle materials
- Evaluation of resistivity measurements for mapping of quick clay deposits (downhole mode (R-CPTU), surface mode (ERT) and airborne mode (AEM))
- Evaluate and compare results from electrical field vane tests (EFVT)
- Evaluate correlations between resistivity values from R-CPTU and ERT with results from index tests and salinity measurements

- Recommended site investigation strategy based on integrated geotechnical and geophysical methods for detection of quick and sensitive clays

1.4 Definitions and terminology

In this report, quick clay, sensitive clay and brittle materials have been defined according to NGF Guideline 2 Symbols and terminology in geotechnics and NVE Guideline 7/2014 for planning and development of quick clay areas.

Quick clay: Clay that in its remoulded state has a measured shear strength c_r less than 0,5 kPa.

Sensitive clay: Clay showing a certain level of strength loss in the remoulded state. A clay has low sensitivity if S_t < 8, medium sensitivity for 8 < S_t < 30 and very high sensitivity if S_t > 30 (S_t = sensitivity = ratio between intact, undisturbed undrained and remoulded undrained shear strength).

Brittle behaviour: Brittle materials are clays and silts that exhibits strain softening for strain levels beyond the failure strain. The NVE guideline classifies all materials with a remoulded shear strength c_r < 2,0 kPa and sensitivity S_t > 15 as brittle materials. Both criteria have to be satisfied.

2 SELECTED TEST SITES

In the NIFS-project, two new test sites were established (Klett and Fallan), which are documented in NIFS report R101-2015 (www.naturfare.no). In addition, several other well-established test sites have been included, either by research studies or in commercial projects. The following investigation methods have been included in the study:

- Rotary weight sounding (DT)
- Rotary pressure sounding (DRT)
- Total sounding (TOT)
- Cone penetration tests (CPTU)
- Piston sampling (ϕ54 mm, ϕ76 mm) (PS)
- Block sampling (ϕ250 mm Sherbrooke, ϕ160 mm NTNU) (BS)
- Electric field vane test (EFVT)
- Cone penetration tests with resistivity measurement (R-CPTU)
- Surface resistivity measurements (ERT)
- Airborne Electromagnetic Measurements (AEM)

Table 1 provides a detailed overview of the investigations carried out at the most important test sites.

Table 1. Test program on selected test sites.

Test site	Methods
Smørgrav	DT, CPTU, R-CPTU, ERT, PS
Kløfta	TOT, CPTU, R-CPTU, ERT, AEM, PS, BS
Klett	DT, TOT, CPTU, R-CPTU, ERT, EFVT, PS, BS
Fallan	TOT, CPTU, R-CPTU, ERT, EFVT, PS
Tiller	TOT, CPTU, R-CPTU, ERT, EFVT, PS, BS
Esp, Byneset	TOT, CPTU, R-CPTU, ERT, EFVT, PS, BS
Dragvoll	CPTU, R-CPTU, ERT, BS
Tiller	CPTU, R-CPTU, ERT, PS, BS, EFVT
Rissa	TOT, DRT, CPTU, R-CPTU, PS, BS

3 DETECTION METHODS

3.1 Conventional soundings

Conventional sounding methods such as rotary pressure and total sounding use, directly or indirectly, the measured total penetration force for indication of brittle materials.

3.1.1 Rotary pressure sounding (DRT)

Rotary pressure sounding is a method where the drillstring is pushed and rotated into the ground. by a drillrig. During penetration, the procedure shall satisfy the following conditions:

- Penetration rate: 3 ± 0,5 m per min.
- Rotation rate: 25 ± 5 rotations per min.

The sounding resistance corresponds to the penetration force required to obtain these normative conditions.

Rotary pressure sounding can be used in most types of soils, from clay to gravel. The results are used for interpretation of soil stratification and the depth to firm layers or bedrock. The sounding profile may also be used for an experience-based interpretation of soil type.

3.1.2 Total sounding (TOT)

Total sounding is used to determine soil stratification and depth to dense strata. The method also enables drilling through larger stones and penetration of the bedrock surface. Total sounding requires a hydraulic drillrig with a percussion hammer and flushing possibilities.

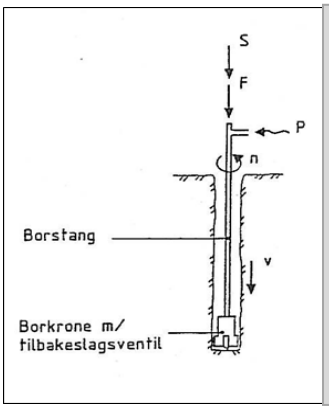


Figure 1 Test principles for total sounding.

Total sounding combines the sounding principles from rotary pressure sounding and rock control drilling, see Figure 1. In rotary pressure mode, the drill rods are penetrated into the ground with constant penetration and rotation rate. If these methods are not sufficient to advance the drillrods, it is possible to switch to rock control mode with increased rotation, then flushing and hammering.

Detection of brittle materials from rotary pressure and total soundings is mainly based on the shape of the sounding curve, to a lesser degree the magnitude of the recorded penetration force.

3.2 Cone penetration tests (CPTU)

In Norway, the Cone Penetration Test with pore pressure measurement (CPTU) is one of the most used methods nowadays. The test is performed with an instrumented cylindrical probe with conical tip that is penetrated into the ground at a constant rate of 20 mm/sec. The probe contains electronic transducers for recording of the load against the cone, the force against the friction sleeve and the pore pressure at the location of the porous filter. A location immediately above the cone tip is selected as reference level for the pore pressure measurement (u_2). In addition, the recording of the total penetration force may be used to deduct the mobilized friction along the drillrods. This information can be used to detect layers of quick and sensitive clays.

The accuracy of CPTU measurements is organized in four Application classes (1-4). Application class 1 (best class) is used for soft to very soft, homogenous soil conditions and is always required for design evaluations in quick clay areas (NVE, 7/2014).

The presence of quick or sensitive clays from CPTU may be evaluated from the following results:

- Net cone resistance (q_n) – sounding depth (z) (or effective overburden stress (σ_{vo}')).
- Sleeve friction (f_s) or friction ratio ($R_f = f_s*100\ \% /q_n$) – sounding depth (z).
- Pore pressure ratio ($B_q = \Delta u/q_n$) – sounding depth (z).
- Use of available soil identification charts

Despite the obvious potential in these approaches, mixed experiences exist with CPTU in detection of brittle materials. The reason may be that the results obtained are influenced by other factors, not related to the clay being sensitive or not. This is further elaborated in the following.

Sleeve friction f_s

A completely remoulded quick clay has a shear strength $c_{ur} < 0{,}5$ kPa. Hence, the material is close to being a liquid after full degradation of the soil structure. In CPTU, this should result in a very small mobilized sleeve friction along the sleeve, assuming that the clay becomes completely remoulded by the first penetration of the probe. However, analyses of a series of CPTU-profiles show that the sleeve friction can be high, even in quick or sensitive clays. This is often the case in silty, lean clays, where the material requires several repeated penetration cycles of the probe before full remoulding is obtained.

Pore pressure ratio B_q

The pore pressure ratio $B_{q2} = \Delta u_2/q_n$ may be an efficient indicator of quick or sensitive NC clays. In these clays, $B_q \geq 1{,}0$ is common due

to the collapsible behaviour at failure, associated with large excess pore pressures.

In stiffer, overconsolidated clays, the B_{q2} – values in quick clays are usually significantly lower, often between 0,6 and 0,9 depending on the overconsolidation ratio. Due to dilatancy effects, the measured pore pressures behind the cone are smaller than the pore pressure in the compression zone beneath the tip (u_1). Due to this influence, the pore pressure ratio B_q is not a unique identification parameter in brittle materials, and a pore pressure ratio based on u_1 (B_{q1}) might be better suited.

3.3 Vane testing

Vane testing can be used to determine the undrained shear strength in clays. Both intact (c_{uv}) and remoulded shear strength (c_{rv}) can be found. The vane test is the only in situ test method which can be used to determine the remoulded shear strength and the sensitivity ($S_t = c_{uv}/c_{rv}$) directly.

A complete set of field vane equipment consists of a lower part with the vane protection shoe, a set of inner rods with the vane mounted on the tip, outer rods and a recording instrument. The vane consists of four rectangular plates in cruciform shape.

The test is carried out in depth intervals, usually one measurement per 0,5 or 1,0 m. Before the measurement, the vane system is pushed down to the level where the measurements should take place. Here, an increasing torque is applied on the inserted vane, until the material adjacent to the vane reaches failure. The corresponding maximum torque is recorded, and enables determination of the undrained vane strength c_{uv}. The test should reach failure in 1-3 minutes with a rotation rate of about 0.2°/sec. The remoulded shear strength (c_{rv}) is determined after at least 25 full, rapid rotations of the vane.

The vane test is susceptible to heterogenities in the soil. If parts of the vane (side, top or base) is weaker or stronger, or if fragments of shells or small stones interfere with the vane, this may influence the measured values significantly. Moreover, it is important that the vane position is fixed during the measurements. If the vane is sinking or lifted during the measurements, it may result in a higher torque since parts of the vane then will rotate in an undisturbed or partially disturbed material.

3.4 Resistivity measurements

The resistivity is a measure of the ability of soils to conduct electric current. The resistivity ρ (Ωm) is defined by the electric field potential E (V/m) over the current density J ((A/m^2)m), and can be computed from the electrical current, a geometry factor and the measured potential. The resistivity gives information about the soil layers, and may in this context indicate the salt content in the ground water.

The computed resistivity from the measurements is an apparent resistivity. This will be identical to the real resistivity in the ground if the material is homogeneous. If the ground is non-homogeneous, the apparent resistivity from a weighted average of the resistivity in individual layers can be used.

Resistivity measurements seem to have a great potential for detection of brittle materials and the extent of the deposit. Resistivity profiles give a continuous image of the ground layering, where local information from geotechnical borings may be used to support the geophysical inter-pretation.

So far, the most popular geophysical method for detection of brittle materials has been 2D-resistivity measurements on the surface (Electrical Resistivity Tomography ERT). The resistivity can however also be measured locally in a borehole by R-CPTU. Recently, airborne electromagnetic measurements (AEM) have been introduced for mapping of leached clays. This method is now regarded as a very efficient method for mapping of large areas and investigations for road or railway projects.

3.4.1 Downhole measurements (R-CPTU)

The sounding equipment used for R-CPTU consists of an ordinary CPTU probe and a resistivity module mounted behind the probe,

see Figure 2. The module is powered by batteries, and it can read, store and transmit measured data acoustically through the rods, or via an electric cable to a receiver on the surface.



Figure 2 Example of R-CPTU probe (NIFS-report 2015-126).

Scandinavian manufacturers of R-CPTU equipment have chosen to manufacture their probes with four ring-electrodes. The two outer electrodes transmit electric current into the soil, whereas the two inner electrodes measures the difference in potential. The distance between the electrodes defines the configuration.
Application of current in the soil is not similar for all probe types. Some probes send short impulses of DC current into the soil, whereas others use AC current, where the intensity can be adjusted. The resistivity module is usually calibrated by brine solutions of salt and water. When the salt concentration is known and the temperature is measured, the electrical conductivity of the solution can be determined. This is used as reference for the measurements.

The additional time for R-CPTU compared to a conventional CPTU is only a few minutes. This is the time needed to mount the resistivity module on the battery package. Apart from that, the sounding procedure is similar.

3.4.2 Surface measurements (ERT)

Electrical resistivity tomography (ERT) is a geophysical method that uses DC current for measurement of the resistivity distribution in the ground, see test principle in Figure 3. The current is applied to the soil volume by using short steel electrodes. These are installed from the surface, penetrating 10-20 cm into the ground. By evaluating the differences in electric potential, a measurement of the soil resistance is obtained for all electrode locations. With the aid of an inversion algorithm, a 2D or 3D resistivity model of the ground is processed from the results, see Figure 4. By comparing the resistivity model with data from geotechnical borings, supported by the geological knowledge of the area, the resistivity can be interpreted in terms of a geological ground model. This principle rests on the assumption that the soil resistivity is determined by sediment or rock type.

The measurement profiles are organized in one or more straight lines in the terrain. Using modern multi-channel equipment, the *Gradient array* is today the most popular configuration. A general estimate of the investigation depth is a reach of about 10-20 % of the profile length, depending on the resistivity distribution in the soil.

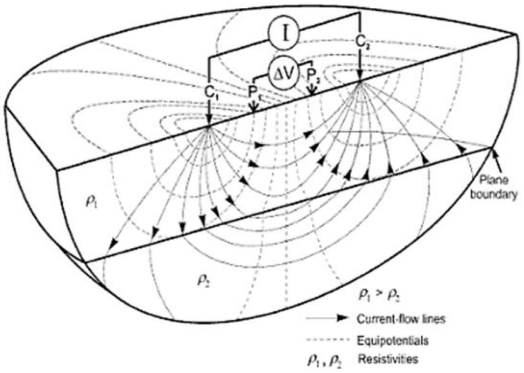


Figure 3 Test principle for ERT measurements (Knödel et al (2007)).

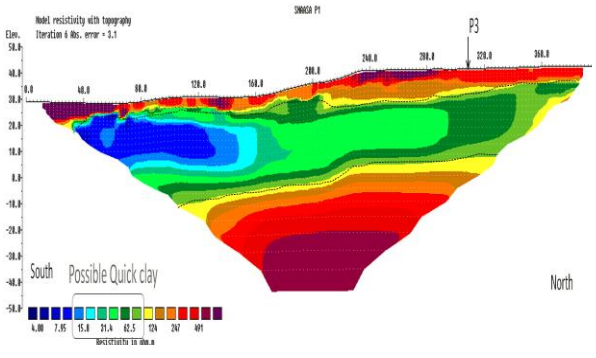


Figure 4 Resistivity profile from ERT measurements (NIFS-report 2015-126).

The obtained resolution is dependent on the electrode spacing. Near the surface, the resolution in depth and along the profile is about half the electrode spacing, but becomes poorer with depth due to the size of the influenced soil volume. It is however possible to measure a profile with several different electrode spacings to obtain a combination of high resolution and sufficient penetration depth. High resolution is particularly important if the aim is to separate the small differences in resistivity between salt and leached clay.

ERT is a robust method that give results of high quality in most cases (see e.g. Rømoen et al (2010)). The measurements are however sensitive to objects in the influenced zone. This may be issues like electrical cables, tubes and other structures influencing the resistivity model.

3.4.3 Airborne measurements (AEM)

AEM (Airborne Electromagnetic measurements) are used to map the electrical resistivity of the ground in a larger area. Modern systems may have sufficient resolution to be used in hydrological and geotechnical applications. Recent studies show that it is possible to distinguish salt from leached clays with high resolution measurements, similar to what can be done by R-CPTU and ERT-measurements (e.g. Anschütz et al (2015)).

All AEM systems have in common that a magnetic field generated by the primary antenna induces current in the ground, which distributes downward and outwards from the source. The rate of change in the electro-magnetic field these currents produce, is recorded by a secondary coil. The antenna is usually lifted by a helicopter, see Figure 5. By inversion of the measured data points, the resistivity distribution in the ground can be modelled.



Figure 5 Equipment for AEM measurements (NIFS report 2015-126).

The possible investigation depth may vary from 50 m to about 500 m, depending on the geology and type of soil in the area, the AEM system and the influence of noise from surrounding infrastructure. The vertical resolution may be as good as 3-6 m close to the surface, but gradually gets poorer with depth. The lateral resolution is determined by the size of the soil volume where current is induced.

AEM data can be collected both over land and sea areas, and may distinguish between cultivated land, forests and exposed rock. Fresh water is not an obstacle for evaluation of the ground conditions, whereas measurements above salt water are limited to a water depth of about 20 m. Up to 300 km flylines can be gathered daily, which corresponds to an area of about 30 km^2 with line spacing of 100 m. Urban areas cannot be covered by AEM-measurements, since it is not allowed to fly over human beings with a hanging object.

Table 2 Summary of investigation strategies for detection of quick and sensitive clays.

Project	Strategy
General – desk study: Introductory knowledge of brittle materials can be expected	The degree of detailing can be lower for simple projects compared to more complicated cases
Geophysical measurements: Overview of area and indication of leached clays	Geophysical measurements are placed to cover important parts of the area. **Use:** Soil stratification and planning of geotechnical borings **Note:** Methods indicate leached clays. This is not necessarily the same as brittle materials
Simple geotechnical soundings: Indication of brittle materials	Located for optimal use and verification of geophysical data. **Use:** Soil stratification, depth to bedrock and quick clay indication **Note:** With soft, sensitive clay underlying dense and thick top layer, sensitive clay layers will not always be revealed in the sounding profile
In situ methods: Indication of brittle materials, may give better interpretation than simple soundings	Located for optimal use of test results. **Use:** Determination of parameters and soil classification **Note:** These methods give a good, but not always safe, classification of brittle materials
Sampling: Failsafe detection of brittle materials	Parameter determination and soil classification. **Use:** Required in all projects according to the Eurocodes **Note:** Focus on areas where interpretation of in situ tests is uncertain.

4 STRATEGY FOR INTEGRATED SITE INVESTIGATIONS

Integration of geophysical and geotechnical methods has become more common in ground investigations nowadays, particularly in larger projects. In such integrated measurements, geotechnical engineers and geophysicists can cooperate and by joint knowledge decide where geotechnical soundings, in situ tests and sampling should be located with optimal cost efficiency. This approach may give large advantages when it comes to cost-efficient location of borings, but also more reliable interpretation of the ground conditions.

Resistivity measurements are well suited for mapping of the ground conditions in larger projects. With resistivity measurements, one may cover corridors for road or railway lines in relatively short time and with reasonable accuracy. As an outcome of this, one may detect critical areas with possible quick or sensitive clays, which need further geotechnical investigations for verification of the findings.

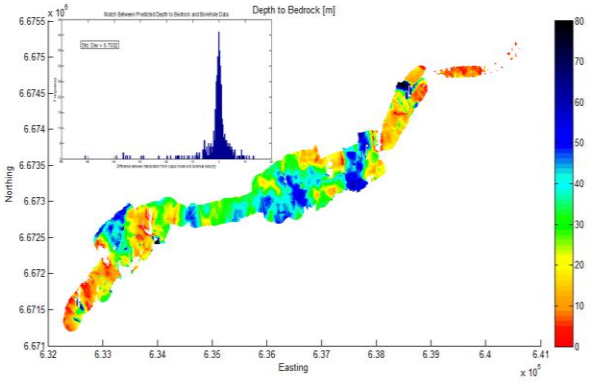


Figure 6 Map of AEM depth to rock compared to results from borings. The histogram shows a standard deviation between borings and AEM of 6 m (NIFS-report 2015-126).

Results from resistivity measurements can also be used to identify barriers of non-sensitive materials in the ground, for example rock outcrops, massive layers of sand or gravel or other continuous layers of non-sensitive material. This information is of crucial importance in stability evaluations, since it enables realistic assessment of potential slide areas and run-out distances of slide debris from a possible quick clay slide.

A desk study should always be carried out ahead of a geophysical and geotechnical survey, possibly in combination with airborne measurements (AEM). This will help develop an optimal strategy for combination of AEM, ERT and introductory geotechnical borings. AEM appears to have roughly the same potential for detection of leached clays as ERT.

In urbanized areas, it may however be difficult or impossible to carry out resistivity

measurements with sufficient quality. In this case, local downhole measurements using R-CPTU can be a practical solution in some cases, since this method is not particularly influenced by these obstructions.

5 CONCLUSIONS AND FINAL REMARKS

The conventional sounding methods (rotary weight, rotary pressure and total sounding) combined with sampling and laboratory testing will continue to be an important methodology for detection of brittle materials.

Cone penetration tests with pore pressure measurement (CPTU), alternatively with resistivity measurements (R-CPTU), has great potential for detection of brittle materials through combined recordings of cone resistance, sleeve friction and pore pressure. CPTU/R-CPTU, and possibly the electrical field vane test (EFVT), will provide natural follow-up investigations in strategically important locations, where the results will be used for supplementary classification and parameter determination.

When choosing these methods, one should have a more general perspective, based on the particular needs in each project. This may contain more than just detection of brittle materials. Both CPTU and R-CPTU enables a detailed mapping of the ground conditions with determination of soil stratification, soil type and mechanical parameters. Using R-CPTU, a new physical property is introduced in addition to cone resistance, pore pressure and sleeve friction/rod friction. In this way, a wider basis for classification and interpretation of the results is obtained.

Measurements of the total penetration force should always be carried out in a CPTU. This information can be used to detect layers of sensitive and quick clays by interpreting the variation in rod friction with depth. The measurement does not require any additional preparation time, so the added information comes for free.

There is generally good agreement between the measured resistivities from AEM, ERT and R-CPTU, particularly in homogenous soils. One major advantage of the resistivity measurements is the continuous information obtained about the soil layers. This is very important information for evaluation of stability problems, possible slide extension and run-out distance for remoulded and liquefied slide debris.

Vane test traditionally gives information about the in situ undrained shear strength (undisturbed and remoulded), and the sensitivity. The determination of the remoulded shear strength may give information about the presence of quick or sensitive clay. However, measurements with the manual vane equipment has to an unknown extent been influenced by rod friction. Modern systems, however, give possibilities for measurement of the friction, using an electro-mechanical unit for application of the torque, either at the top of the drillrods or down at the vane.

Determination of the remoulded shear strength by fall cone tests in the laboratory will still be the most reliable method for determination of quick or sensitive clays. However, this method also represents some possible sources of error, such as operator dependency and non-standard correlations between intrusion and shear strength.

The resistivity correlates well with salt content down to concentrations around 1 g/l. For lower salt contents, other influence factors seem to dominate.

It is recommended to summarize information from several boring methods for evaluating the presence of quick or sensitive clays. The results from all methods can then be evaluated at the same time. Both conventional soundings and CPTU/R-CPTU will require soil sampling and laboratory tests for verification.

None of the methods reported herein are without the possibility of erroneous interpretation, and the evaluation of results requires critical judgement and caution.

6 ACKNOWLEDGEMENTS

The partners in the NIFS project are greatly acknowledged for the financial support and good discussions throughout the study. The board of the Norwegian Geotechnical Society (NGF) are acknowledged for financial support for development of the summary report. The authors want to extend thanks to Rambøll, Multiconsult, NGI, Statens vegvesen (NPRA) and NGU for supplying test data in the study.

7 REFERENCES

Anschütz, H., Bazin, S. and Pfaffhuber, A. (2015). Towards using AEM for sensitive clay mapping – A case study from Norway. 1st European Airborne EM conference. Torino, Italia, Mo AEM 04.

Knödel, K., Lange, G. and Voigt, H.-J. (Eds.) (2007). Environmental Geology, Handbook of Field Methods and Case Studies, Springer, ISBN 978-3-540-74669-0, Berlin, Tyskland.

Löfroth, H., Suer, P., Dahlin, T., Leroux, V. and Schälin, D. (2011). Quick clay mapping by resistivity - Surface resistivity, CPTU-R and chemistry to complement other geotechnical sounding and sampling. Statens Geotekniska Institut, SGI. Göta älv utredningen. GÄU. Delrapport 30. Statens Geotekniska Institut, Linköping, Sverige.

NIFS (2015). Detection of brittle materials. Summary report with recommendations. Final report. NIFS Report no. 126/2015 (www.naturfare.no)

NIFS (2015). Detection of quick clay by R-CPTU and electrical field vane tests. Results from field study (in Norwegian). NIFS Report no.101/2015 (www.naturfare.no)

Rømoen, M., Pfaffhuber, A. A., Karlsrud, K. and Helle, T. E. (2010). Resistivity of marine sediments retrieved from R-CPTU soundings: A Norwegian case study. In Proceedings of 2nd International Symposium on Cone Penetration Testing CPT'10, pp. 9-11, Huntington beach, USA.

Detecting quick clay with CPTu

S.M. Valsson
Norway, sigurdur@meancpt.com

ABSTRACT
The cone penetration test with porepressure measurements (CPTu) is a popular in-situ test, used to investigate geotechnical properties of soils as well as layering.

In the standard test, three main variables are registered in the cone while penetrating at a fixed rate. These parameters are the cone resistance, sleeve frictional resistance and porepressure.

Many classification diagrams exist for the CPTu test, and some of these include areas meant to indicate the presence of sensitive materials. These diagrams provide very useful information for a rough evaluation of soil type and layering, but when it comes to identifying sensitive materials, they have been found to be unreliable.

In this study CPTu data from five test sites in Norway are linked with results from laboratory tests, and divided into two categories, quick clays and non-sensitive materials, for further analysis.

The objective of the study is to show that if the standard CPTu test produces results that can be used to detect sensitive materials in the soil, then the accuracy of detection can be improved by analyzing all three variables simultaneously.

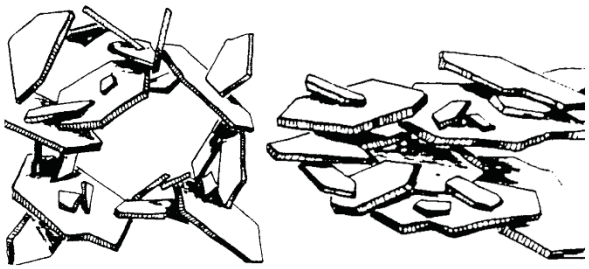
The result of the study is that this approach shows promise. A model that has an improved rate of detection as well as a reduced rate of false positives is presented.

Keywords: Quick clay, CPTu, field investigations

1 QUICK CLAY

The term quick clay describes extremely sensitive fine-grained materials. These materials were sedimented in a marine environment following the retreat of the glaciers at the end of the last ice age.

The post-glacial rebound lifted these sediments above the sea level, exposing them to fresh water that over time washed the salt out of the porewater. Such materials can be found up to the previous sea level of the last ice age. (NGI, 1982)



a) b)

Figure 1 A simplified drawing showing clay particles in materials sedimented in a) a marine environment and b) a fresh water environment. (Statens vegvesen 2010 - figure from Leirskred i Norge by Jørstad F.A., 1968).

An illustration of the marine clay "card-house" structure is shown in Figure 1 a) (Statens vegvesen 2010).

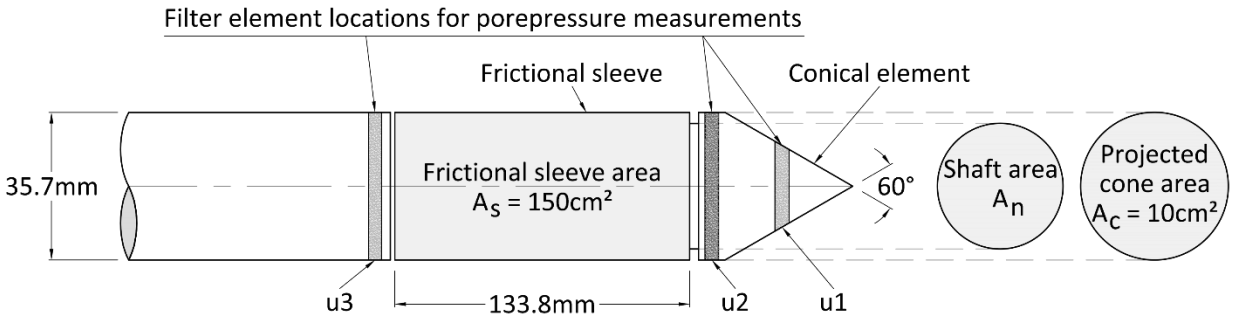


Figure 2 The standard (reference) 10cm^2 piezocone. Based on a similar figure in CEN (2012)

The edge versus face orientation of the quick clay particles allows for high water content as well as a collapsible grain structure, compared to the parallel alignment of the fresh water clay particles.

The sensitivity of soil materials is defined as

$$S_t = \frac{c_u}{c_{ur}} \quad (1)$$

where c_u is the undrained shear strength and c_{ur} is the remoulded undrained shear strength, usually determined by the fall cone test. Quick clay is defined from the remoulded undrained shear strength alone as

$$c_{ur} < 0{,}5kPa \quad (2)$$

Undisturbed quick clays can exhibit considerable strength, but their state can change to liquid so they flow in their own porewater when subjected to stresses above their capacity (*extremely sensitive*).

Because of the potential devastating consequences of even a small initial landslide in quick clay areas (NGI 1982), extensive field investigations and use of larger safety factors for geotechnical design is required in areas with sensitive soils.

2 PIEZOCONE PENETRATION TEST – CPTU

The cone penetration test is a popular soil investigation method used to evaluate the geotechnical properties of soils as well as layering.

The cone design has been standardized (CEN, 2012), and the geometry of the standard (reference) 10cm^2 piezocone is shown in Figure 2.

Using a standard reference test (*cone design and test procedure*), experience from one site can be transferred to another. This then aids in the establishment of general empirical models for evaluation of the various material properties.

2.1 Basic measurements

The test procedure consists of pushing a cone into the ground at a fixed rate of 20mm/s and taking measurements at fixed intervals. The measurements required to reach the highest Application class (CEN, 2012) are

- Cone resistance force
- Sleeve frictional resistance force
- Penetration length
- Porepressure
- Cone inclination

The cone resistance, q_c (kPa), and the sleeve friction resistance, f_s (kPa) are the basic output parameters, calculated by dividing the force measurements with the projected cone and frictional sleeve area respectively.

2.2 Porepressure measurements

Porepressures acting on the cone during a test will influence the load measurements. This is due to both the geometry of the cone, as well as porepressure variations along the cone during the test.

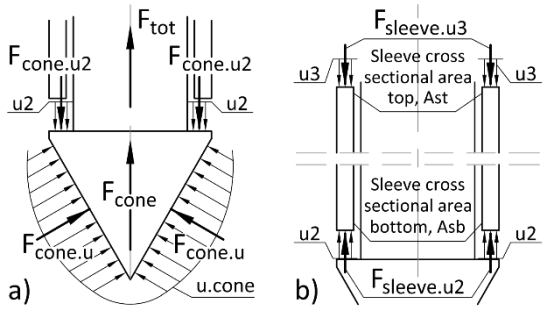


Figure 3 Porepressure influence on load measurements. Drawing created from figures and graphs in Lunne et al. (1997).

Figure 3 a) illustrates how porepressures acting on top of the conical element will result in a downward pointing force, resulting in lower registrations for the cone resistance.

Porepressures acting on the ends of the frictional sleeve will influence the frictional force measurements in a similar manner as illustrated in Figure 3 b).

These porepressure effects can be eliminated with the following equations

$$q_t = q_c + u_2 \cdot (1 - \alpha) \qquad (3)$$

$$f_t = f_s - \frac{u_2 \cdot A_{sb} - u_3 \cdot A_{st}}{A_s} \qquad (4)$$

where q_t (kPa) is the corrected cone resistance, u_2 and u_3 (kPa) are the porepressures measured just behind the conical part and friction sleeve respectively, α (-) is the cone net area ratio, f_t (kPa) is the corrected sleeve frictional resistance, A_{sb} and A_{st} (cm^2) are the sleeve cross sectional areas at the top and bottom of the friction sleeve and A_s (cm^2) the area of the friction sleeve.

All soundings used in this study are made using a standard 10cm^2 reference piezocone with porepressure measurements just behind the cone, at the u_2 location. In order to correct the sleeve frictional resistance, a measurement of u_3 is required.

As u_3 is not registered in any of the cones used in this study, f_s is used for the frictional resistance in all calculations.

3 APPLICATION OF CPTU TESTS

The CPTu test is often used in combination with other methods to provide a more detailed description of the soil conditions at selected locations and depth intervals.

Because of small logging increments, the engineer *(often)* ends up with a continuous profile of relevant data. When combined with high quality laboratory tests on samples from the project site, the cone penetration test can provide a strong basis for geotechnical design.

3.1 Classification with CPTu

When it comes to evaluating soil strength, stiffness and classification, no in-situ method replaces soil sampling and laboratory testing. Collecting and testing soil samples is both time consuming and expensive, field methods that reduce the need for- or better focus the sampling are therefore valuable.

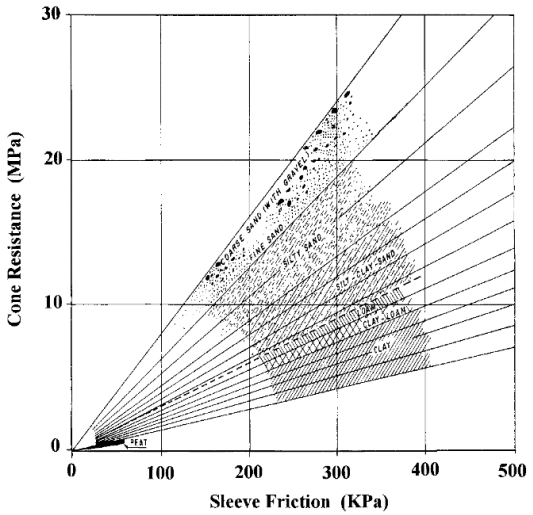


Figure 4 The first soil profiling chart for CPT, after Begemann in 1965 (from Eslami and Fellenius, 2000)

Begemann published the first soil-profiling chart in 1965, which showed that the soil type should not be evaluated as a function of the cone resistance or the sleeve friction alone, but rather as a combination of both. (Eslami et al., 2000)

Using soil-profiling charts has become popular practice for CPTu interpretation and the method is available in most software packages.

Throughout this paper, the terms *classification* and *classification diagrams* are used to describe the analysis of CPTu data. This is not the same as *soil classification*, which refers to the determination of soil type with laboratory testing.

3.2 Derived variables for classification diagrams

There are many classification diagrams available today, and some of these are covered later in this paper. To provide a foundation for these diagrams a few relations are given

$$q_n = q_t - \sigma_{v0} \quad (5)$$

$$\Delta u = u - u_0 \quad (6)$$

$$Q_t = \frac{q_n}{\sigma'_{v0}} \quad (7)$$

$$B_q = \frac{\Delta u}{q_n} \quad (8)$$

$$F_r = \frac{f_s}{q_n} \cdot 100 \quad (9)$$

$$R_f = \frac{f_s}{q_t} \cdot 100 \quad (10)$$

$$q_e = q_t - u \quad (11)$$

$$\Delta u_n = \frac{\Delta u}{\sigma'_{v0}} \quad (12)$$

where q_n (kPa) is the net cone resistance, σ_{v0} (kPa) and σ'_{v0} (kPa) are the total- and effective vertical stresses, Δu (kPa) is the excess porepressure, u (kPa) is the measured porepressure, u_0 (kPa) is the at rest in-situ porepressure, Q_t (-) is the normalized cone resistance, B_q (-) is the porepressure ratio, F_r (%) is the normalized friction ratio, R_f (%) is the friction ratio and q_e (kPa) is the effective cone resistance and Δu_n (kPa) is the normalized excess porepressure.

Any mention of the measured porepressure, u, or the excess porepressure, Δu, without an identifying number refers to the porepressure measured just behind the conical element, at the u_2 location.

Eslami et al. (2000) pointed out that many classification diagrams rely on dependent variables. Without accepting the statements made by Eslami et al. about the possible impact of such variable dependence, one starts to wonder about the true independence of the measured values in CPTu tests.

In order to study this in more detail the following variables are introduced

$$q_{tn} = \frac{q_t}{\sigma'_{v0}} \quad (13)$$

$$f_{sn} = \frac{f_s}{\sigma'_{v0}} \quad (14)$$

where q_{tn} (-) is the normalized corrected cone resistance and f_{sn} (-) is the normalized sleeve frictional resistance.

4 IN-SITU TESTS AND SENSITIVE MATERIALS

As previously stated, the consequences of small initial slides involving very sensitive materials can be devastating. This is why it is important to be able to accurately identify such materials quickly.

It is common practice in Norway to study the force needed to push a rotating probe though the soil at a fixed rate (rotary pressure sounding and total-sounding), and look for either very low push-resistance or alternatively depth intervals with constant or decreasing push resistance. Such behavior is often an indicator of sensitive materials as the remoulding caused by the probe acts to reduce rod-friction. Because the push-force in these tests is registered above terrain level, any friction between the rod and layers of compacted/coarse materials has the potential to *hide* sensitive layers.

In order to evaluate the soil sensitivity (*1*), in-situ tests need to be able to give an estimate of both the undisturbed and remoulded shear strength. Identifying quick clay only requires the test to be able to evaluate the remoulded shear strength.

The shear vane test is by definition suited to evaluate material sensitivity, as it can be used to evaluate both the undisturbed and the remoulded shear strength of the soil. As shown in the work of Gylland (2015), the test falls short because it apparently overestimates the remoulded shear strength and thereby underestimates the sensitivity.

CPTu classification diagrams often show zones indicating sensitive materials. Color-coded/patterned columns and diagrams are commonly used to present results from classification, which often provides useful information for the evaluation of layering and approximation of soil types. The application of such diagrams for the detection of quick clay is covered in chapter 6.

5 DATABASE OF CPTU DATA AND LABORATORY RESULTS

To provide a basis for this study, a database was created where CPTu data and laboratory results were linked together. The data was collected from actual projects.

The database currently consists of data from 37 positions from 5 test sites in Norway. The locations of the actual sites/municipalities are illustrated in Figure 5.

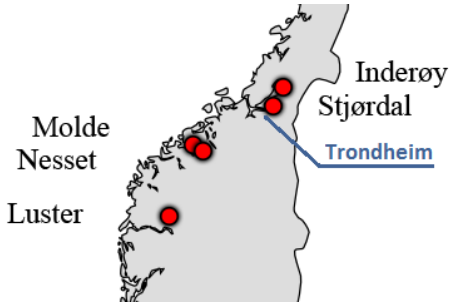


Figure 5 Test site locations currently in the database.

The CPTu tests are conducted using cones with a net area ratio $\alpha = 0{,}605 - 0{,}868$. The equipment used had the accuracy required to achieve Application class 1, but this class was not reached in all the soundings.

The laboratory data is collected from remoulded representative samples, as well as undisturbed soil samples with a diameter of 54mm. The undisturbed and remoulded shear strengths of the test samples are determined in the laboratory using the fall cone test.

The undisturbed samples are cut into 10cm long pieces, and different tests are performed on each piece. The standard setup used for most of the test cylinders has only one fall cone test. This means that for most of the samples, only a 10cm depth interval has a value registered for the remoulded shear strength.



Figure 6 an undisturbed 54mm soil sample after ejection and cutting. Each piece is approximately 10cm long.

In an effort to counteract the limited amount of data from each cylinder, the values for the remoulded shear strength are inter-/extrapolated inside test cylinders.

Where the soil conditions are homogenous, the remoulded shear strength is also interpolated between test cylinders in the same position. This increases the amount of datapoints by a factor of about 13.

Such manipulation has the obvious downside of introducing *fictional* data that may skew the results.

In addition to the relevant geotechnical parameters, it is also possible to query the database in such a way that the extrapolated data and tests with an Application class lower than a specified value are excluded from the result.
The database was queried for data where the remoulded shear strength is less than 0,5kPa (*quick clay)* and again where the remoulded shear strength is larger than 2kPa (*non-sensitive)*. Samples having a with remoulded shear strength between 0,5 and 2kPa were

excluded. Soundings with Application class 1, 2 and 3 were accepted.

A 3D presentation of the base CPTu parameters for both datasets is shown in Figure 7. This is done for all three degrees of data extrapolation.

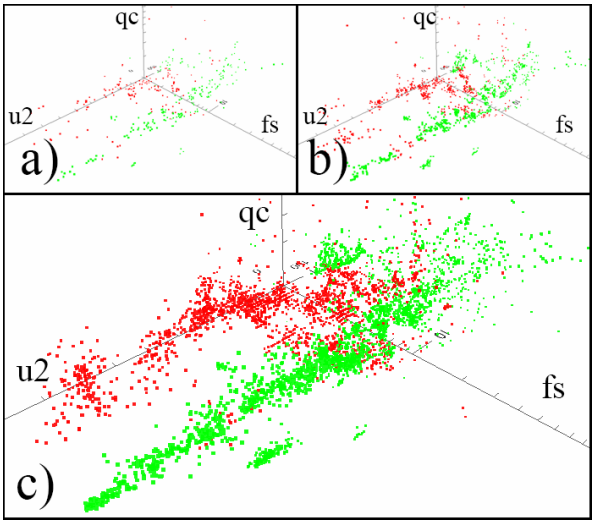


Figure 7 Quick clay (red) and non-sensitive points (green) points with and without data interpolation; a) original data, b) interpolation within the sample cylinder c) interpolation between cylinders

When the datasets in Figure 7 a) to c) are compared it can be argued that with increasing extrapolation, the general shape of the volumes defined by the point cloud becomes enlarged and more distinctive.

6 QUICK CLAY DETECTION WITH CLASSIFICATION DIAGRAMS

The database from chapter 5 can be used to evaluate how accurately classification diagrams separate the highly sensitive quick clays from non-sensitive materials.

6.1 Database results drawn on classification diagrams

In Figure 8 throughout Figure 14 points from the database are drawn on some common classification diagrams, where the data is interpolated inside each cylinder (Figure 7b). Red points indicate *quick clay* and green points indicate *non-sensitive materials*. The sensitive area in each diagram is specified.

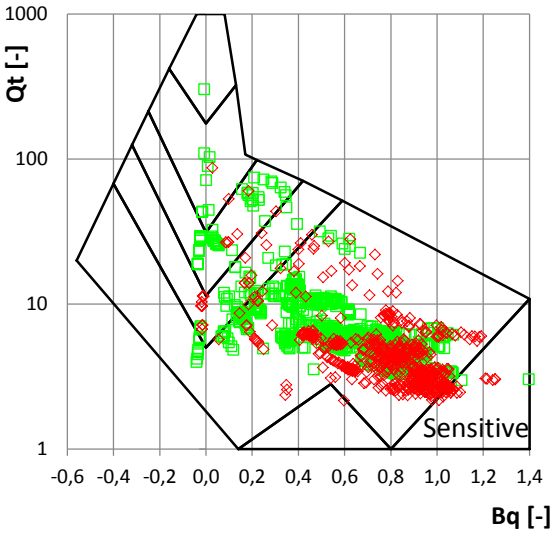


Figure 8 Datapoints on soil behaviour type chart by Robertson '90 (Lunne et al, 1997) [Rob'90-Bq]

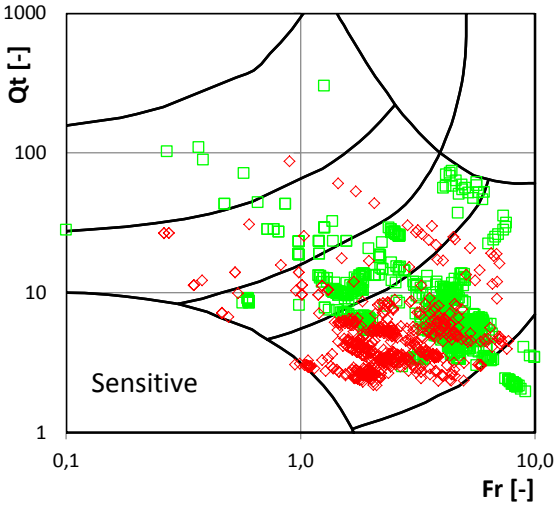


Figure 9 Datapoints on soil behaviour type chart by Robertson '90 (Lunne et al, 1997) [Rob'90-Fr]

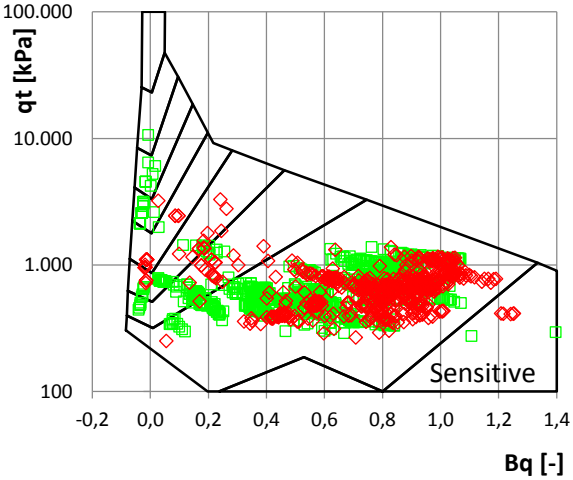


Figure 10 Datapoints on soil behaviour type chart by Robertson et al.'86 (Lunne et al, 1997) [Rob'86-Bq]

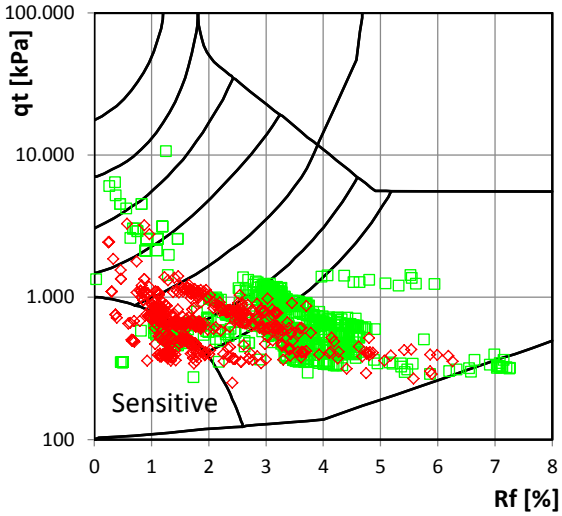


Figure 11 Datapoints on soil behaviour type chart by Robertson et al.'86 (Lunne et al, 1997) [Rob'86-Rf]

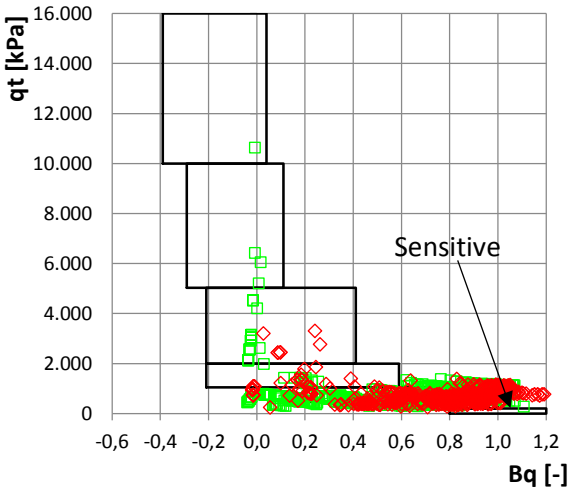


Figure 12 Datapoints on chart by Senneset et al.'89 (Eslami et al, 2000) [Sen'89]

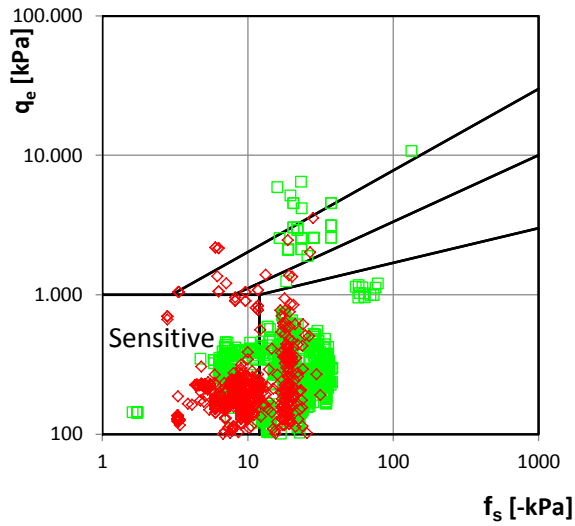


Figure 13 Datapoints on soil behaviour type chart by Eslami et al., 2000 [Esl'00]

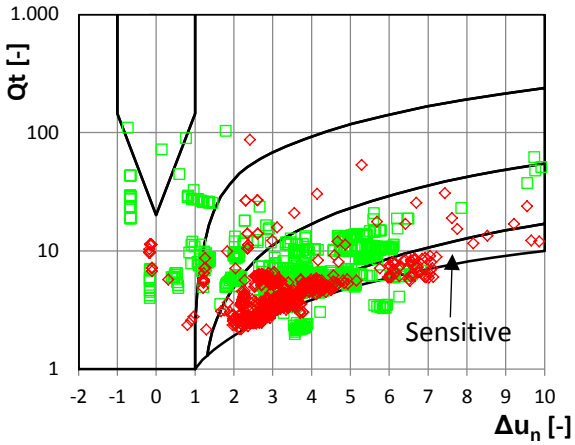


Figure 14 Datapoints on soil behaviour type chart by Schneider et al. 2008 [Sch'08]

Table 1 contains the results from the analysis with no interpolation of the data. It seems as if methods based on sleeve friction have an advantage over the others when it comes to detecting presence of sensitive materials, with the exception of Rob'90-Fr.

Table 1 Summary of classification of sensitive materials with classification diagrams for the case of no data interpolation

Diagram	Quick clay points classified as quick clay [%]	Non-sensitive points classified as quick clay [%]
Esl'00	64,9	10,3
Rob'86-Rf	38,6	8,5
Sch'08	15,2	13,0
Rob'90-Bq	0,6	0,9
Rob'86-Bq	0,6	0,9
Rob'90-Fr	0,0	0,0
Sen'89	0,0	0,0

Every method that correctly identified over 1% of the quick clay datapoints as sensitive also had a high percentage of false positives.

It should be emphasized that the points used in this study are taken from only five test sites, as shown in Figure 5. It is likely that with a larger database these results will change.

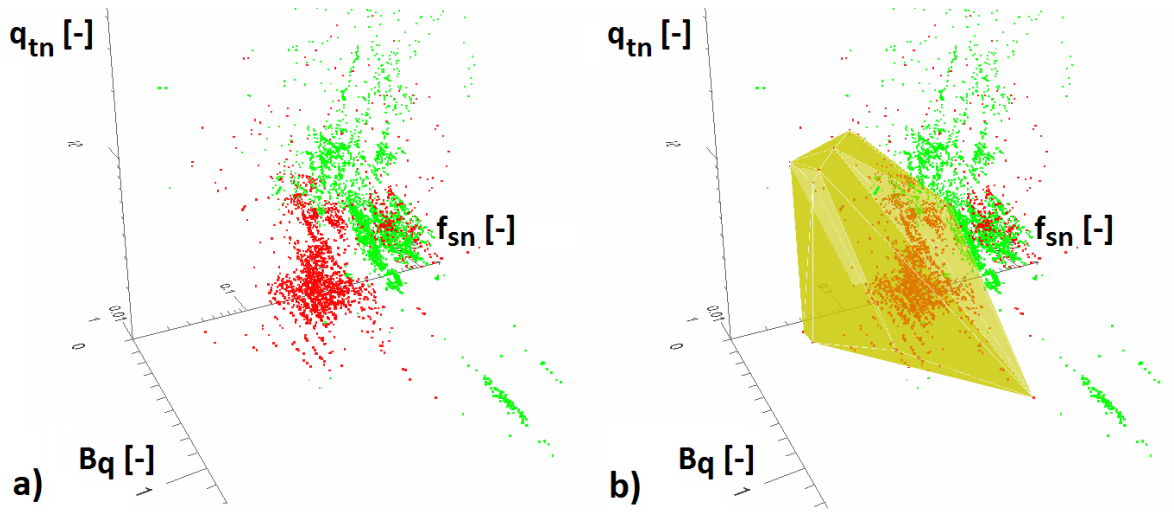


Figure 15 Datapoints with interpolation between cylinders viewed in the selected 3D space a) without- and b) with the proposed quick clay detection model. Red points represent quick clay.

7 VARIABLES FOR A NEW 3D MODEL

Choosing a set of variables for a new model was done by checking all variables shown in in chapters 2 and 3 against each axis in a 3D space and selecting the ones that best divided the datasets *(a purely visual study)*.

The result of this process was that the variables B_q (linear-), f_{sn} (logarithmic-) and q_{tn} (logarithmic scale) would give a good starting point. The datasets are shown in this 3D space in figur 15 a).

Using a logarithmic scale on the two axis helps exaggerate the area/volume in the model occupied by quick clay points.

8 PROPOSED MODEL

The datasets with the most data (*interpolation between test cylinders*) were chosen as a base for the new model.

In order to define the model, points from areas dominated by non-sensitive materials as well as from areas where quick and non-sensitive materials lie close together were removed. This task was done by hand in a CAD-program.

This process continued until the model was little more than a loosely defined volume defined by an almost entirely red point cloud. Boundary points were then removed until the expected false positives of the model, defined by the imagined bounding volume, were estimated to be at a minimum.

The proposed model is defined as a convex hull, directly from the remaining points using an automated meshing algorithm (UniPi, 2005). It is meant to be an example of what is possible to achieve with this kind of study. No attempt was made to make any predictions about areas not occupied with data.The results from the detection process for the database points are shown in Table 2.

Table 2 Summary of classification with proposed 3D model for varying degree of data interpolation

3D model	Quick clay points classified as quick clay [%]	Non-sensitive points classified as quick clay [%]
Original data	71,9	2,2
Cylinder interpolation	64,8	1,6
Int. between cylinders	71,6	0,6

When compared to the results in Table 1 it is apparent that one can expect an increased accuracy for detection of quick clay with CPTu by using more variables simultaneously. By implementing a 1 to 1 penalty for false positives the accuracy increases about 10-15%.

The database used to create this model is however not large enough to create a general model for quick clay detection.

9 CONCLUSION

The goal of this study is to show that it is possible to define a 3D model that can detect quick clay with greater precision than 2D diagrams in use today.

If the dataset used in this study is assumed to represent *the true nature* of the problem of detecting quick clay with CPTu, the classification diagram proposed by Eslami et al., in 2000 is by far the best of all the 2D diagrams tested. However, it still had over 10% of points from non-sensitive materials classified as sensitive (false positives). The other diagrams gave somewhat unreliable results, and some even had more false positives than correct answers.

These results will almost certainly change with an updated, larger database.

Out of all tested parameters, the ones chosen for the proposed model seemed to best separate quick clay points from points from non-sensitive materials.

It should be stated that other variable combinations were noted as viable candidates that could also give excellent results.

The approach shows potential and merits further exploration. Increasing the database size (*greatly)* should be a priority in future work so that a more general model can be created.

In an effort to harvest more data for such studies the laboratory setup for undisturbed samples from CPTu positions could be modified so that more tests of the remoulded shear strength are conducted. These tests should be close to both ends, as this would aid in the evaluation of remoulded shear strength variations within each sample.

The proposed model is defined by (*extrapolated*) datapoints from CPTu tests where laboratory testing has confirmed the presence of quick clay. By defining a model using three parameters the accuracy of quick clay detection is increased.

10 DEFINITION OF PROPOSED MODEL

The axis system of the proposed model is shown in Table 3.

Table 3 Axis definition of proposed model

Parameter	Axis	Scale
B_q [-]	x	Linear
f_{sn} [-]	y	Logarithmic
q_{tn} [-]	z	Logarithmic

The model is defined as a convex hull using triangular faces. Using numbered points each face can be defined with 3 point numbers.

The points in the proposed model are summed up in Table 4 and the triangles are defined with corresponding point numbers in Table 5.

Table 4 Points in proposed model

Point nr.	B_q	f_{sn}	q_{tn}
0	1,1598	0,0286	4,1096
1	1,2015	0,0322	3,5900
2	1,2131	0,0385	3,5867
3	1,2561	0,0384	3,6191
4	0,8853	0,1581	6,6850
5	0,2696	0,0363	10,1695
6	0,5446	0,1834	8,4703
7	0,6468	0,1898	8,2376
8	0,0410	0,1538	7,1121
9	-0,0159	0,1153	11,4235
10	-0,0183	0,0983	11,4499
11	-0,0159	0,1155	11,4393
12	0,0381	0,1406	6,7484
13	0,3798	0,1769	5,5348
14	0,6754	0,1868	7,2310
15	0,2139	0,2137	7,3418
16	0,3442	0,1168	4,0077
17	1,0162	0,1068	3,7540
18	1,1952	0,1201	4,1314
19	0,5736	0,1114	3,7897
20	1,1607	0,0473	3,5892
21	0,8829	0,0892	7,0795
22	0,1843	0,0537	11,7247
23	1,6032	0,0823	4,0318
24	0,6727	0,1617	8,4450
25	-0,0183	0,0984	11,4630

Table 4 (continued)

Point nr.	B_q	f_{sn}	q_{tn}
26	-0,0144	0,0332	8,9351
27	-0,0143	0,0333	8,9454
28	-0,0171	0,0988	12,0893
29	0,8012	0,0131	3,4706
30	0,3099	0,0311	9,2215
31	0,8992	0,0131	3,5481
32	-0,0145	0,0332	8,9228
33	-0,0155	0,0331	8,4898
34	0,5210	0,0461	3,2787
35	1,1487	0,0322	3,5392

Table 5 Triangle definition of proposed model

Triangle nr.	Point nr.			Triangle nr.	Point nr.		
	1	**2**	**3**		**1**	**2**	**3**
0	0	31	23	**29**	27	22	28
1	23	5	0	**30**	5	22	27
2	1	23	31	**31**	27	30	5
3	1	31	35	**32**	6	7	15
4	15	7	14	**33**	11	6	15
5	22	5	23	**34**	6	11	7
6	16	19	34	**35**	8	11	15
7	16	34	33	**36**	11	8	12
8	16	33	12	**37**	8	15	16
9	30	31	0	**38**	8	16	12
10	30	0	5	**39**	33	10	9
11	10	33	25	**40**	11	9	10
12	1	3	23	**41**	12	33	9
13	3	1	35	**42**	9	11	12
14	2	35	34	**43**	15	14	13
15	20	2	34	**44**	18	13	14
16	2	3	35	**45**	13	16	15
17	2	20	23	**46**	13	18	19
18	3	2	23	**47**	19	16	13
19	11	28	7	**48**	17	18	23
20	28	11	25	**49**	19	18	17
21	11	10	25	**50**	34	19	17
22	4	7	23	**51**	17	23	20
23	4	14	7	**52**	17	20	34
24	18	4	23	**53**	21	22	23
25	18	14	4	**54**	21	23	24
26	7	28	24	**55**	21	24	22
27	24	28	22	**56**	33	32	25
28	24	23	7	**57**	32	28	25

Table 5 (continued)

Triangle nr.	Point nr.			Triangle nr.	Point nr.		
	1	**2**	**3**		**1**	**2**	**3**
58	26	27	28	**63**	29	30	32
59	28	32	26	**64**	29	32	33
60	26	30	27	**65**	29	33	34
61	26	32	30	**66**	29	35	31
62	30	29	31	**67**	34	35	29

This volume definition is available for download as a PLY document (Valsson, 2015).

11 REFERENCES

CEN (2012). EN ISO 22476-1:2012: Geotechnical investigation and testing -- Field testing -- Part 1: Electrical cone and piezocone penetration test. Comité Européen Normalisation,

Eslami, A., Fellenius, B.H. (2000): Soil profile interpreted from CPTu data. "Year 2000 Geotechnics", Geotechnical Engineering Conference, Asian Institute of Technology, Bangkok, Thailand, November 27 - 30, 2000, 18 p.

Gylland A.S. (2015): Utvidet tolkningsgrunnlag for

Vingebor. Rapport 79/2015. Naturfareprosjektet: Delprosjekt 6 Kvikkleire (NIFS). Norges vassdrags- og energidirektorat.

Lunne, T., Robertson, P.K & Powell, J.J.M (1997). Cone Penetration Testing in Geotechnical Practice. E & FN Spon, an imprint of Routledge, ISBN 0 419 23750 X.

NGF (2010). Melding nr. 5 - Veiledning for utførelse av trykksondering. Norsk geoteknisk forening

NGI (1982): The Rissa landslide, quick clay in Norway. Video presentation of a famous landslide in Norway. (https://youtu.be/3q-qfNlEP4A). Norges Geotekniske Institutt.

Statens vegvesen (2010). Håndbok V220: Geoteknikk i vegbygging.

UniPi (2014): MeshLab. Open source program for the processing and editing of unstructured 3D triangular meshes. University of Pisa, department of computer science.

Valsson S.M. (2015): MeanCPT.com. Web application for CPTu interpretation.

Influence of operator performance on quality of CPTu results

C. Kardan
Ramböll, Sweden, caesar.kardan@ramboll.se

K. Viking
NCC, Sweden

L. Nik
Geosigma, Sweden

S. Larsson
KTH Royal Institute of Technology, Sweden

ABSTRACT
Cone penetration tests (CPT) is one of the most sophisticated geotechnical field investigations methods. As for all test methods, the CPT is associated with many uncertainties. However, there are two main sources that have an influence on the quality of CPTu measurements. One is the choice of equipment since different equipment differs in design and functionality. The other source relates to operator performance and incorrect execution of the method as well as lack of competence to analyze the results. However, in order to achieve satisfying results, the operator should be skilled, competent and well-educated. Some countries don't have any formal education and in countries were formal education do exist, the achieved quality of results does quite frequently still come out unsatisfactory. This fact is seldom mentioned, but still a well-known fact amongst practicing geotechnicians. The objective of this paper is to discuss operator performance related factors and contribute to a better knowledge of how important every single procedure contributes to the outcome as well as quality of the results.

Keywords: CPT, operator performance, undrained shear strength

1. INTRODUCTION

Ground investigations form the basis for geotechnical analyses design and decisions at various phases in sustainable building. In a report presented by Rydell & Johansson (2001), it is stated that the quality of geotechnical investigations and the documentation have gradually deteriorated. This problem is by no means new (Magnusson et al. 1989). There are fortunately few occasions of geotechnical shortcomings that have lead to any serious consequences, but the loss expenses of these occasions are obvious (Lind 2012).
The cone penetration test (CPT) is one of the most used geotechnical in-situ testing field method in Sweden. However, due to the gradual deterioration of quality of CPT test results, geotechnical engineers in Sweden have lately displayed a tendency to choose alternative method for investigations of clay. Du to this, presented study aims to discuss operator performance related factors and their influence on the accuracy of CPT results. To mention previously studies with the same subject, see Gauer et al. (2002) and Sandven (2010).
The two common piezometer CPT probes (CPTu) used by commercial actors in Sweden are either made by Envi or Geotech. The equipments can either be equipped with a porous filter or a slot filter (Larsson 1995). One of the original intention with this study, inspired by the work of Gauer et al. (2002),

was to investigate the effect of mentioned equipment factors on the results when sounding in typical Stockholm/Mälar-dalen soft sediments, i.e. post-glacial clay on top of deposits of varved glacial clay. However, presented study instead ended up in documenting and analyzing how the effects of operator performance influenced the outcome of the quality of the results. The study has been performed as a MSc thesis project at KTH Royal Institute of Technology by Kardan (2015).

2. TEST SITE AND METHODS

The CPTs were conducted over a period of six week, from April 24th 2014 to May 22th 2014, in the vicinity of a recycling facility in Hagby, 25 km northwest of Stockholm. The geotechnical condition of the test site is typical for Stockholm/Mälardalen region. A short description of the soil stratigraphy can be found Table 1. The ground water level was approximately 0.7 m below the ground surface.

Before the investigations, a written invitation was sent to a number of commercial actors in Stockholm/Mälardalen region to ask for their interest to participate in the test. Five actors reported interest to participate, named A to E in this paper. There was no secret for each actor, as in the study presented in Magnusson et al. (1989), that other actors participated. No special instructions provided, other than the desire to get as many CPTu results as possible and that they should follow the ISO standard for Electrical cone and piezocone penetration test (SS-EN 2012) and the Swedish guidance for CPT tests (SGF 1993). The actors had thus the opportunity to perform as good as possible. A description of the equipment used by the participating actors can be found in Table 2. A total of 24 CPTu-tests were performed and the relative location of the bore holes is illustrated in Figure 1.

Table 2 Equipment used by the five actor's contributing to this study.

Actor	Cone penetrometer	Drill rig
A	Envi Memocone	GM 75 GT
B	Geotech Nova	GEORIG 604
C	Envi Memocone Geotech Nova	GM 65 GT
D	Geotech Nova	GEORIG 605
E	Envi Memocone	GM 75 GT

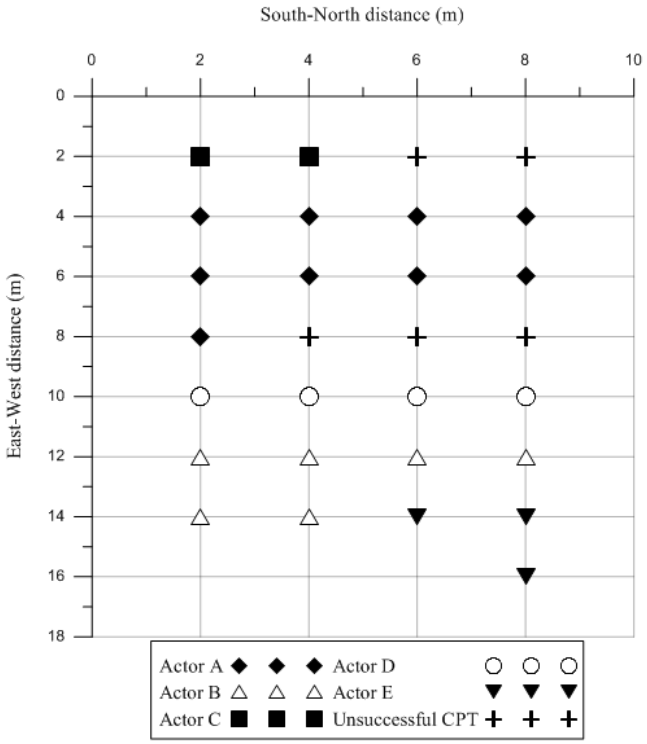


Figure 1 Relative location of the CPTs.

Table 1 Soil profile and soil properties at test site.

Layer	Depth (m)	ρ (t/m^3)	w_n (%)	w_l (%)	S_t (-)	OCR (-)	c_u (kPa)
Fill	0 – 0.3	1.75	-	45	-		
Dry crust	0.3 - 1	1.7	-	60	-		
Organic clay	1 – 2	1.4	115	110	12	(3)	14
Sulphide clay	2 – 6	1.5	65-85	50-65	18-30	1.2 – 1.3	9.5 - 12
Varved clay	6 - 12	1.65	60-75	50-65	17-25	1.0 – 1.2	11 - 19

3. PERFORMANCE RELATED FACTORS

According to the Swedish guideline (SGF 1993) and Sandven (2010), the following performance related factors are the most common to affects the results, see Figure 2:

- pre-drilling
- calibration of cone penetrometers
- saturation of pore pressure system
- control of inclination (verticality)
- reference measurements
- reading of zero values
- rate of penetration

For each mentioned factor, there is detailed instruction to be found in both the Swedish as well as International standards. If actors as well as operators followed these instructions, the impact of operator procedures on CPTu-results would decrease.
During the execution of the CPTs in this presented study, the used equipment as well as performance of each operator with respect to mentioned factors were noted and well documented.

Calibration

Three of the five cone penetrometers used in the study were not calibrated according to the standard. Due to the sensitivity of this method, use of uncalibrated equipment will affect the accuracy of the results.

Saturation

Full saturation of the pore pressure chamber and filter are required. Negligence of this process affects the result of the measured excess pore pressure (Δu). One actor used both porus stone and slot filter. Another operator used three liquids; oil, glycerin as well as water and took the initiative to perform a dissipation test.

Cleaning

Two of tree operators did not clean the probe from dirt and other particles properly using new and clean rugs. Carelessness in the cleaning process will affect the result of the recorded values.

Inclination

In the ISO standard (SS-EN 2012), there are five criteria for classification of CPTu. One of them relates to the maximal angle of inclination. However, one of the operators did not have an inclinometers installed in the cone used and it is thus not possible to classify the performed penetration.

Reference measurements

Registration of reference measurements can help the operator to check if the results are free from environmental impact such as differences in temperature. Not all of the operators were aware about it. Instead of invalidating the results and perform the penetration again when the differences where large in the reference measurements, some of them chose to consider the result as an approved result.

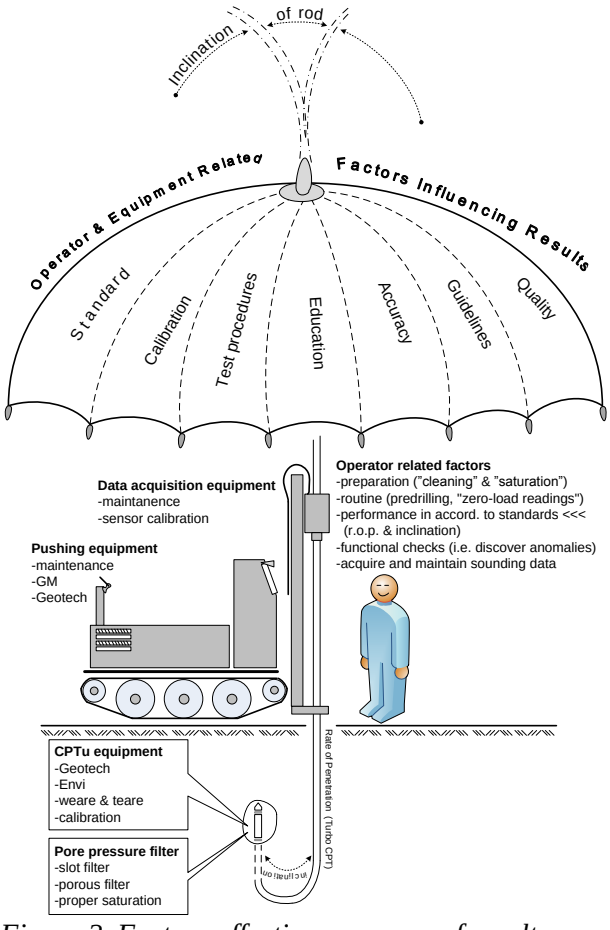


Figure 2 Factors affecting accuracy of results.

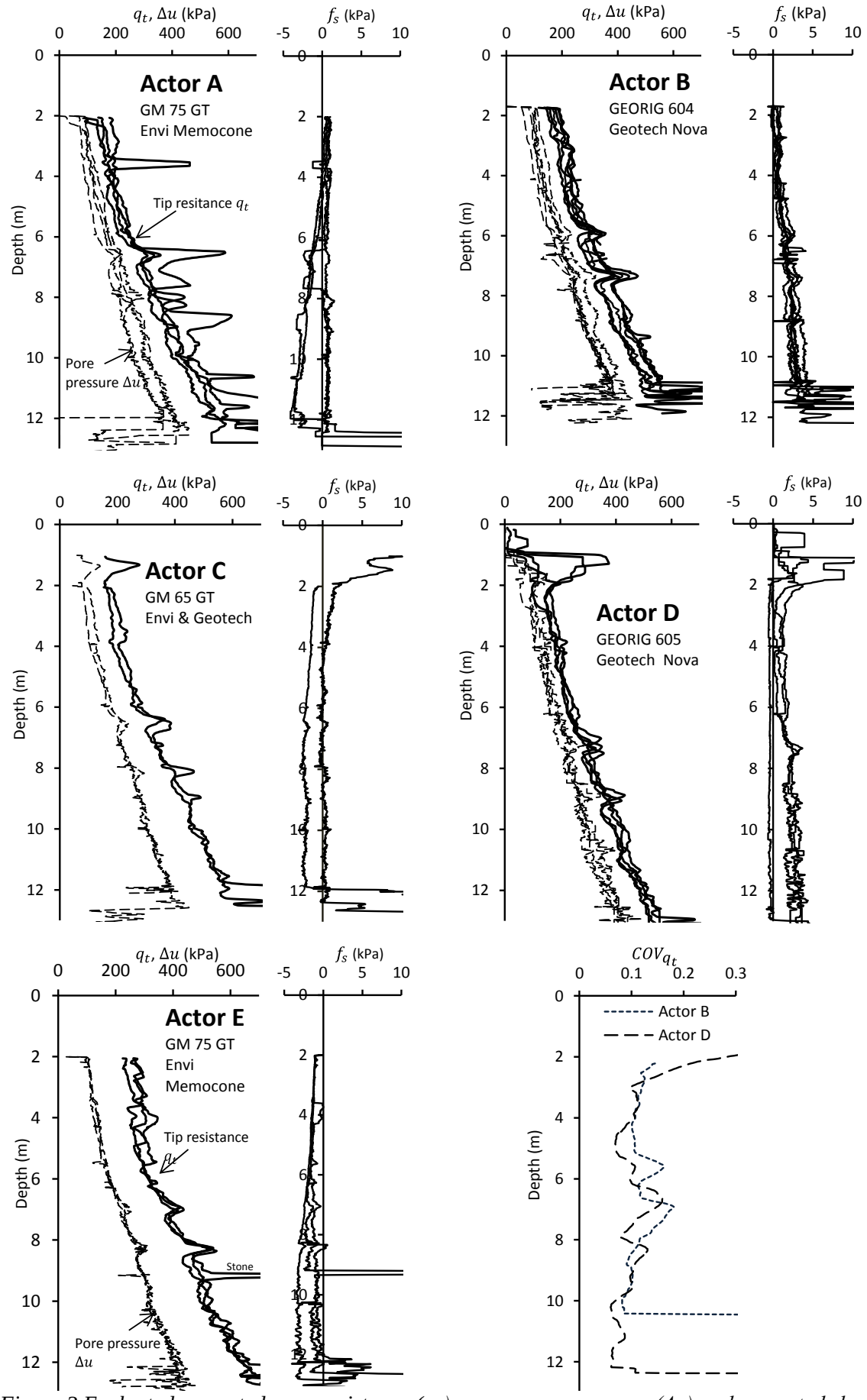


Figure 3 Evaluated corrected cone resistance (q_t), excess pore pressure (Δu) and corrected sleeve friction (f_t) for each actor A-E.

Pre-drilling

Pre-drilling of the fill and crust is normally always required in the Stockholm/Mälardalen region. However, one operator neglected to pre-drill which produced results that was obvious effected by this negligence. The most obvious affect were the negative value of recorded sleeve friction (f_s), see Figure 3.

Rate of penetration

Rate of penetration is perhaps the most important factor of performance. The rate of 20 mm/s with an allowed deviation of ±5 mm/s according to the ISO standard (SS-EN 2012). One operator neglected the rate of 20 mm/s and named these as turbo CPT. The results have for obvious reasons been omitted in this paper.

Other

Other factors observed during the conducted test that might not influence the outcome of results, but reflects the need to educate the field operators. One actor omitted to unsplice three sections of steel rods (totally 6 m) wile relocating from one spot to another (illustrated in Figure 2).

4. RESULTS

A representative part of obtained results of conducted field test by the five actors are presented Figure 3 and 4. The results are evaluated by the commercial program CONRAD (Larsson 2006). Figure 3 shows; the corrected cone resistance (q_t), the excess pore pressure (Δu), and the corrected sleeve friction (f_t), as well as evaluated coefficient of variation of q_t (COV_{q_t}) of actor B and D who performed sufficient number of tests. For reader interested of complete set of results are kindly referred to Kardan (2015). The variability expressed as COV_{q_t} is approximately 10% which can be considered relatively small for the evaluated q_t in soft clay. The variability includes both measurement errors and the natural variation in the soil. The evaluated COV_{q_t} is twice as high as the COV related to measurement errors for CPT around 5% as reported by Lunne et al. (1997). Somewhat unexpected, the variation of evaluated Δu for each actor were smaller than variation of evaluated q_t. The variation of evaluated f_s compared to q_t and Δu is much larger. Results of actors A and E displays consistently negative values of evaluated f_t, results that are obviously unreasonable.

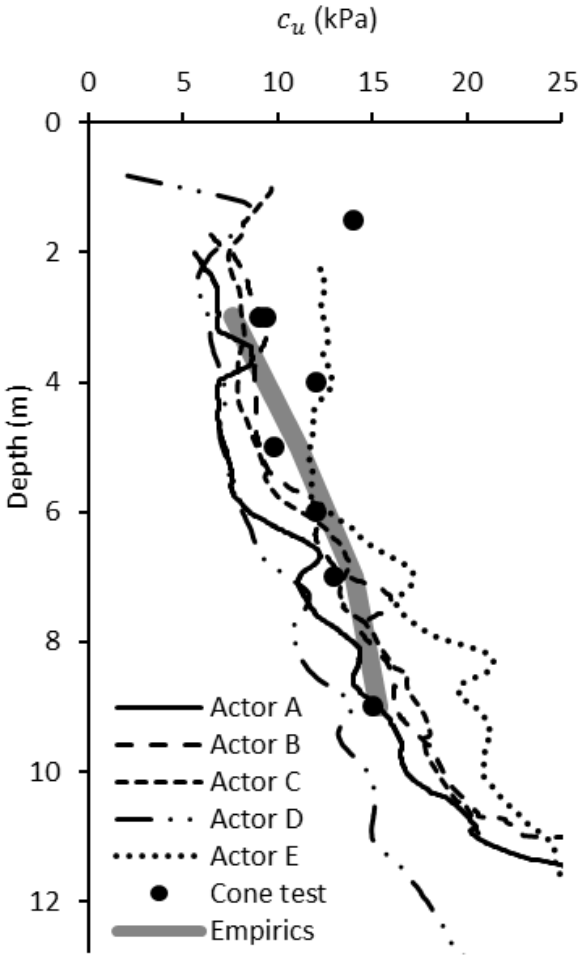


Figure 4 Evaluated undrained shear strength.

The interpretation of the undrained shear strength (c_u) in clays is probably one of the most important parameter evaluated from CPTu results. Figure 4 shows the evaluated c_u as a moving average over 1 m, for each commercial actor. The results can be compared with a simple empirical evaluation $c_u = 0.22\sigma_c'$ (Larsson 1980) based on results from CRS tests and results from fall cone tests on samples taken on the site.

Results of actor E show evaluated c_u 60 to 150% higher than results of actor E. It can also noted that results of actor E have the largest variation of evaluated c_u over the depth range analyzed. The largest difference

of evaluated c_u is found at depth level 2 to 4 m. This large variation is particularly troublesome in relation to estimates of stability of shallow excavations.
It has been possible to clarify reason related to the large variation of evaluated c_u. A probable reason is that the variation correlates to systematic errors due to the lack of calibration of the cone penetrometers. Another possible explanation could be the choice to use high-capacity CPT-probes in soft clay layers which reduces the resolution of the conducted measurements.

CONCLUSIONS

The results from the conducted study have provided valuable insight and proof of the correlation between poor quality in relation to routine performance of CPTu-tests. The poor performance correlates to operator performances as well as insufficient internal controls and lack of procedures to regularly calibrate the equipment. It´s clear that CPT results are highly operator-dependent.
And finally, it can be concluded that there is an immediate need to both increase the awareness amongst the geotechnical society as well as clients together with the need to increase the quality of CPTu tests and analysis of results. It's the authors' opinion that this is best accomplished with education of field operators, geotechnical engineers and not least clients. This will hopefully lead to improved internal controls, routines, calibrations and maintenance of equipment belonging to commercial actors.

ACKNOWLEDGMENTS

The authors would like to acknowledge their gratitude to the commercial actors for their support of presented field study: Bjerking AB, Cowi AB, Grontmij AB, Sweco AB, WSP AB.

REFERENCES

Gauer, P., Lunne, T., Mlynarek, Z., Wolynski, W. & Croll, M. (2002). Quality of CPTu -Statistical analyses of CPTu data from Onsøy. NGI Report No.: 20001099-2, Oslo.

Johannesson, L-E. (1990). CPT-sondering i finjord -olika aspekter på handhavande av utrustning och uttolkning av jordparametrar, Report TVGT-1003 Licentiate Dissertation, Lund University, Lund.

Kardan, C. (2015). Quality of CPTu -Analyses of CPTu-data from commercial actors in Stockholm/ Mälardalen, MSc thesis, KTH Royal Institute of Technology, Stockholm, Sweden.

Larsson, R. (1980). Undrained shear strength in stability calculation of embankments and foundations on soft clays. Canadian Geotechnical Journal 17(4), 591-602.

Larsson, R. (1995). Use of a thin slot as filter in piezocone tests, Proc. CPT'95, Linköping, Swedish Geotechnical Society. SGF Report 3:95.

Larsson, R. (2006) CPT-sondering utrustning – utförande – utvärdering. En in-situ metod för bestämning av jordlagerföljd och egenskaper i jord. SGI Information 15, Statens geotekniska institute, Linköping.

Lind, B. (2012). Skadekostnader i byggprocessen - En litteraturgenomgång. SGI Varia 642, Statens geotekniska institute, Linköping.

Lunne, T., Robertson, P.K., & Powell, J. (1997). Cone Penetration Testing in geotechnical practice. Blackie Academic & Professional, London.

Magnusson, O., Sällfors, G. & Larsson, R. (1989). Ödometerförsök enligt CRS-metoden, Byggforskningsrådet. Rapport R44:1989, Stockholm.

Rydell, B. & Johansson, Å. (2001). Kvalitets-värdering inom geoteknikområdet. Resultat och förslag till utvecklingsarbete. Slutrapport över verksamheten 1997-2001. SGI Varia 481, Statens geotekniska institute, Linköping.

Sandven, R. (2010). Influence of test equipment and procedures on obtained accuracy in CPTu, Proc. CPT'10, Huntington Beach, CA.

SGF(1993). Recommended standard for CPT tests, SGF Report 1:93E, Swedish geotechnical society, Linköping.

SS-EN (2012). Geotechnical investigation and testing - Field testing - Part 1: Electrical cone and piezocone penetration test. SS-EN ISO 22476-1:2012.

Sample disturbances in block samples on low plastic soft clays

H. A. Amundsen[1], V. Thakur and A. Emdal
Norwegian University of Science and Technology, Norway
[1]*helene.amundsen@ntnu.no*

ABSTRACT
The issue of sample disturbance is essential with regards to determining reliable and representative parameters for low plastic soft clays. Block sampling is considered to be the best sampling method to achieve high quality samples in soft clays. This study confirms this but also illustrates that it can be challenging to obtain excellent quality samples of low plastic soft clays even with a block sampler. The block sampler reduces sampling and handling induced disturbance to a minimum but cannot eliminate the total stress relief at sampling and the subsequent reduction of the effective stresses. This paper presents an extensive set of results from a testing programme carried out on block samples on low plastic soft clays from six different sites around central Norway. The results confirm that block sampling in general gives high quality samples in these low plastic brittle clays but they also illustrate that the quality tends to go down as the sampling depth increases. Hence there is still a challenge connected to high quality sampling at large depths, and sampling technique, sample storage and handling should be further addressed to reduce this.

Keywords: sample disturbance, sample quality, stress relief, sensitive soft clays, block sampling

1 INTRODUCTION

The applicability of engineering parameters for geotechnical design is linked to the quality of soil sampling and testing. Over the years, significant development has been made to improve sampling techniques. Despite this, sampling of low plastic soft clays remains challenging. The literature, e.g., Berre et al. (1969), La Rochelle and Lefebvre (1970), Bjerrum (1973), Leroueil et al. (1979), Lacasse et al. (1985), Nagaraj et al. (1990), Hight et al. (1992), Lunne et al. (1997), Tanaka (2000), Nagaraj et al. (2003), Ladd and DeGroot (2003), Leroueil and Hight (2003) and Karlsrud and Hernandez-Martinez (2013), Gylland et al. (2013), Amundsen et al. (2015a) and (2015b), confirms that low plastic soft clays such as Norwegian clays are prone to sample disturbance, especially when sampled using tube samplers. On the contrary, block sampling in such materials is considered to be a relatively gentle approach. In return, a more realistic soil behaviour can be captured in the laboratory, as illustrated in Figure 1 for a low plastic sensitive clay sample (Klett clay). It is believed that block sampling is among the best methods of collecting high quality samples of soft clays.

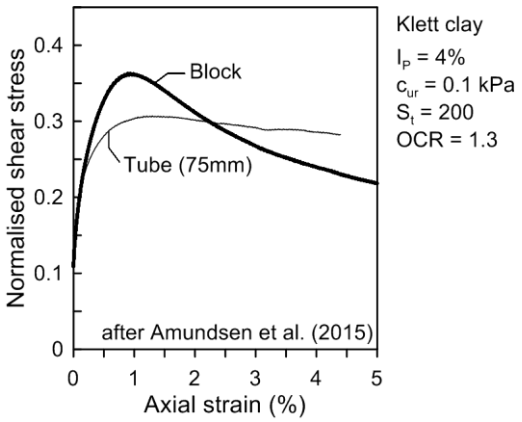


Figure 1 Illustration of sampling induced disturbances in Klett clay (Amundsen et al., 2015b). Here I_p refer to the plasticity index, c_{ur} is the remoulded shear strength measured using the Swedish fall cone, S_t is the sensitivity and OCR is the over consolidation ratio.

However, even block samples may fail to capture the true and unique response of low

plastic clays if they are not sampled and handled properly. For instance, stress relief, transportation effects, storage time and testing procedures may lead to inaccurate response, e.g., Hvorslev (1949), Skempton and Sowa (1963), Ladd and Lambe (1963), Leroueil and Vaughan (1990) and Hight et al. (1992). This is illustrated in Figure 2 where a single block sample was tested by two different laboratories with a time difference of 4.5 hours, due to transportation and delayed testing. Despite similar testing procedures, the odometer results such as the preconsolidation stress (σ_c') and the constrained modulus (M) were found to be far lower for the sample (Lab 2) stored for 4.5 hours, see Figure 2.

For low plastic soft clays, the issue of sample disturbance is yet to be fully addressed. The reason could be that block samples generally give a better response than routine tube sampling. This observation leads to some interesting questions; to what degree is block sampling free from sample disturbances regardless of soil type? What should be the correct reference to distinguish a representative soil sample from a poor quality sample?

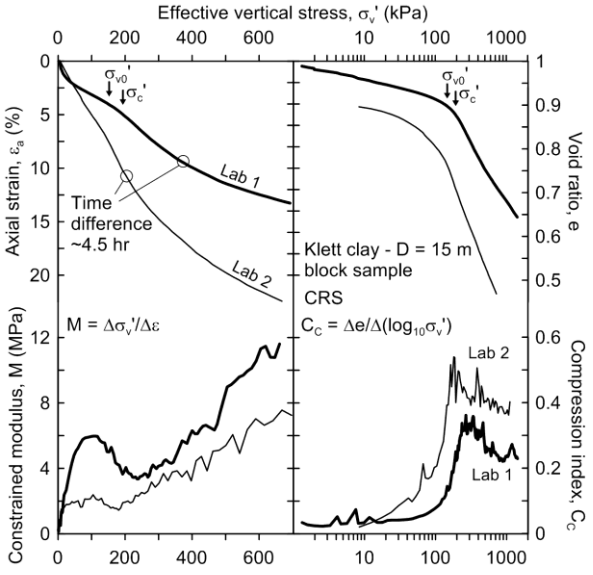


Figure 2 Non-unique response from a single block sample from Klett tested by two different laboratories (Amundsen et al., 2015a).

These questions are examined in this paper using six low plastic soft clays from six different sites in central Norway. In doing so, the paper presents data from 50 mm diameter Constant Rate of Strain (CRS) oedometer tests on specimens taken from block samples with 160 mm and 250 mm in diameter. The results are discussed in this paper in light of existing sample quality assessment methods and the factors that may influence their sample quality.

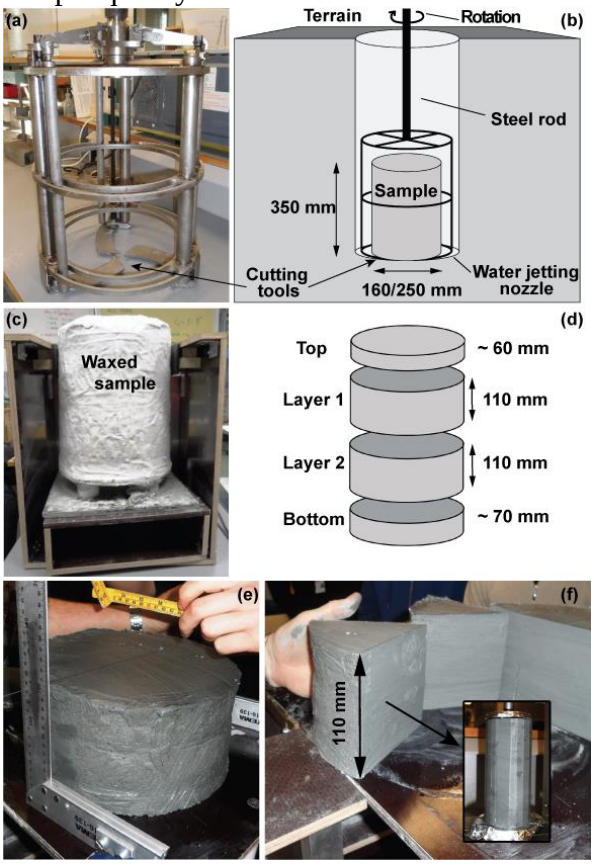


Figure 3 (a) Sherbrooke block sampler at NTNU, (b) schematic view of a block sample being carved, (c) waxed sample, (d) schematic view of a sliced sample, (e) a block sample slice and (f) a piece of clay from block sample (photo: Amundsen).

2 BLOCK SAMPLING AND SAMPLING DISTURBANCE

The samples in this study were taken by two block samplers, an original Sherbrooke (250 mm) (Lefebvre and Poulin, 1979) and a downsized Sherbrooke block sampler (160 mm) developed at NTNU.

The Sherbrooke block samplers do not use a sampling tube, but cores out an annulus around the block of soil to be sampled, Figure 3b. The cutting knives are shown in Figure 3a and b. When the sample is extracted from the ground, it may be waxed and stored or trimmed and tested directly after sampling, shown in Figure 3c, d and f.

Table 1 Indicators and methods of sample quality estimation from literature (Amundsen et al., 2015b).

Year	Method	Para-meter	"Very good to excellent" quality	"Very poor" quality
Triaxial and oedometer tests:				
1979-1988	Volumetric strain (ε_{v0}) at *in situ* effective stress (σ_{v0}') (Andresen and Kolstad, 1979), (Lacasse and Berre, 1988)	ε_{v0}	<1%	>10%
1996	Specimen Quality Designation (SQD) (Terzaghi et al., 1996)	ε_{v0}	<1%	>8%
1997	Change in void ratio ($\Delta e/e_0$) (Lunne et al., 1997), which depends on the overconsolidation ratio (OCR)	$\Delta e/e_0$	<0.04(OCR 1-2) <0.03(OCR 2-4)	>0.14 OCR 1-2) >0.10(OCR 2-4)
2013	Oedometer stiffness ratio (Karlsrud and Hernandez-Martinez, 2013)	M_0/M_L	>2.0	<1.0
Uniaxial compression tests:				
1979	Strain at failure (ε_{vf}) in an unconsolidated and undrained (UU) test on soft clay (Andresen and Kolstad, 1979)	ε_{vf} (UU)	3-5%	10%
1980	Unconsolidated and undrained shear strength, s_u (UU), measured in the laboratory (Ladd et al., 1980), (Ladd and DeGroot, 2003)	s_u (UU)	Relative assessment based on information about stress history and predicted strength using SHANSEP	
Suction and shear wave velocity measurements:				
1963-2002	Residual effective stress (σ_s') and the effective stress for a "perfect sample" (σ_{ps}') (Ladd and Lambe, 1963), (Hight et al., 1992), (Ladd and DeGroot, 2003)	σ_s'/σ_{ps}'	≈0.25-0.50 (OCR>1.5) ≈0.05-0.25 (OCR<1.5)	
1996-2000	Soil suction (u_r) (Tanaka et al., 1996), (Tanaka, 2000)	u_r/σ_{v0}'	≈ 1/5 to 1/6	
2007	Shear wave velocity (V) (Landon et al., 2007), V_{vh} is measured in the field and V_{SCPTU} is from SCPTU.	V_{vh}/V_{SCPTU}	≥0.60	<0.35
2010	Combination of normalized shear wave velocity (L_{vs}) and normalized soil suction (L_u) (Donohue and Long, 2010)	L_{vs} L_u	L_{vs} < 0.65 L_u < 0.4	L_{vs} > 0.8 L_u > 0.6
1985-2014	Radiography (Ladd and DeGroot, 2003)	Visual identification of sample disturbance.		

Soil disturbance can occur during sampling, transportation and storage, as well as during handling and preparation before testing. The mechanisms related to soil disturbance are stress changes, mechanical disturbance, changes in water content, void ratio and pore water chemistry.

DeGroot et al. (2005) pointed out that the most important effect of sample disturbance in soft clay is soil destructuring, which is accompanied by a significant reduction in the effective stress. The stress relief is unavoidable and its impact depends on the sampling depth and soil properties.

Table 1 provides an overview over different indicators that have been proposed in the literature. Of these, only two methods are used in Norway and they are briefly discussed below.

2.1 Change in the void ratio, $\Delta e/e_0$

The change in sample void ratio (Δe), caused by reapplying the in situ effective stress (σ_{v0}'), is recognized as a useful indicator of sample quality. Lunne et al. (1997) proposed this criterion for sample quality evaluation using the $\Delta e/e_0$ value, where e_0 is the in situ void ratio of a soil, as indicated in Table 2. The criterion is based on triaxial tests on a medium plastic soft clay (I_P = 14-20%) from Lierstranda with an assumption that block samples give the best sample quality compared to piston samples. This is discussed in detail by Amundsen et al. (2015a).

2.2 Oedometer stiffness ratio, M_L/M_0

The ratio M_0/M_L has been proposed as a new sample quality evaluation criterion by

Karlsrud and Hernandez-Martinez (2013). The maximum constrained modulus in the overconsolidated stress range (M_0) and the minimum constrained modulus after preconsolidation stress (M_L) show the effect of sample disturbance, as illustrated in Figure 4. The sample disturbance causes a reduction in the M_0 modulus and an increase in M_L due to a denser soil structure caused by a large volumetric change during reloading.

Table 2 Sample quality assessment on basis of $\Delta e/e_0$ (Lunne et al., 1997) and M_0/M_L (Karlsrud and Hernandez-Martinez, 2013) values from oedometer tests.

Sample quality	$\Delta e/e_0$ OCR 1-2	$\Delta e/e_0$ OCR 2-4	Ratio M_0/M_L
1 - Very good to excellent	<0.04	<0.03	>2
2 - Good to fair	0.04-0.07	0.03-0.05	1.5-2
3 - Poor	0.07-0.14	0.05-0.10	1-1.5
4 - Very poor	>0.14	>0.10	<1

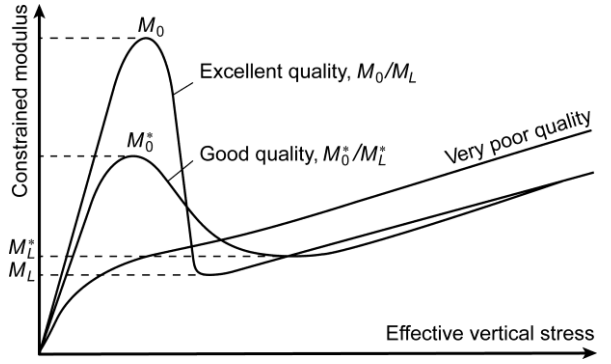


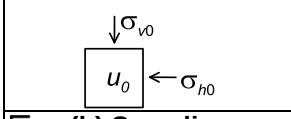
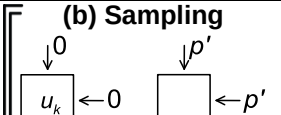
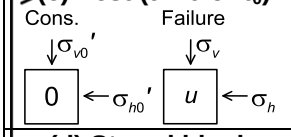
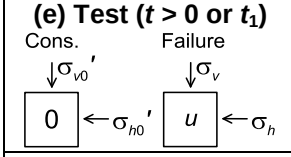
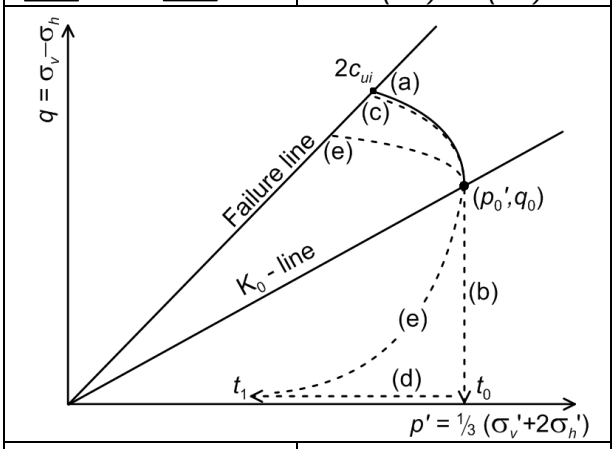
Figure 4 Definition of constrained modulus relationships from oedometer tests (Amundsen et al., 2015b).

2.3 Stress relief

Stress relief of the sample refers to the undrained removal of the in-situ stresses during sampling and extraction from its parental soil deposit. Due to stress unloading, the clay will have a tendency to swell. If the swelling is prevented, as in undrained unloading, negative pressure, or suction, (u_k) will develop in the pore water. The suction will result in additional effective stresses in the sample, which is isotropic. Therefore, the magnitude and the nature of the effective stresses in the soil samples are different from the in-situ condition. The concept of stress relief in a saturated clay block sample, with Skempton's pore pressure parameter $B=\Delta u/\Delta\sigma=1.0$, is schematically presented in Table 3.

The block sample is removed from its in-situ conditions, shown in Table 3(a), to an isotropic state, $\sigma_h=\sigma_v=0$ (b). When the sample is reconsolidated and sheared (c) to failure immediately after unloading ($t=0$, no storage time), the undrained shear strength (c_u) should be close to the in-situ strength (c_{ui}). This is illustrated in experimental results by Skempton and Sowa (1963) on a remoulded medium plastic clay, see Figure 5. A small reduction in negative pore pressure during "sampling" was observed, which had reduced the undrained shear strength by about 1.5% compared to the "ground" sample.

Table 3 Sampling induced stress changes.

(a) In situ 	$\sigma_{v0}' = \sigma_{v0} - u_0$ $\sigma_{h0}' = \sigma_{h0} - u_0 = K_0' \sigma_{v0}'$ $p_0 = 1/3(\sigma_{v0} + 2\sigma_{h0})$ $p_0' = p - u_0$
(b) Sampling 	Undrained, ΔV=0 $u_k = -1/3(\sigma_{v0}' + 2\sigma_{h0}')$ $p' = -u_k$ and $p = 0$
(c) Test (t = 0 or t_0) 	No swelling, ΔV=0 Consolidation: $\Delta V \approx 0 \rightarrow$ good quality Undrained shear: $c_u \approx c_{ui}$
(d) Stored block sample ($t > 0$ or t_1)	Sample disturbance due to the loss of suction $t_1 \rightarrow u_{k,1}$ ($\lvert u_{k,1}\rvert < \lvert u_k\rvert$) $\rightarrow$ Swelling: $\Delta V > 0$
(e) Test ($t > 0$ or t_1) 	Consolidation: $\Delta V > 0 \rightarrow$ poorer quality Undrained shear: $c_u < c_{ui}$ $u\ (t>0) > u\ (t=0)$
	
Sample quality assessment	$\frac{\Delta e}{e_0} = \frac{\Delta V}{V_0} \cdot \frac{1+e_0}{e_0}$

If the block sample is stored (t>0), the suction in the sample reduces with time and swelling occurs (ΔV>0), see Table 3(d). The swelling after sampling influences the potential change of volume during consolidation to in-situ stresses, which is used as an indicator of sample quality; the $\Delta e/e_0$-criterion. Therefore, a decrease in the suction may cause a significant reduction in sample quality as well as undrained shear strength (c_u<c_{ui}), even if the sample is consolidated back to its original stress state, shown in Table 3(e). A disturbed sample is described by a reduction of undrained shear strength and an increase of pore pressure at failure, $u\,(t>0) > u\,(t=0)$.

The effect is also illustrated in Figure 5 with tests on a low plastic quick clay from Ellingsrud. Bjerrum (1973) concluded that the internal swelling which had occurred after 3 days had reduced the undrained shear strength by 15 %.

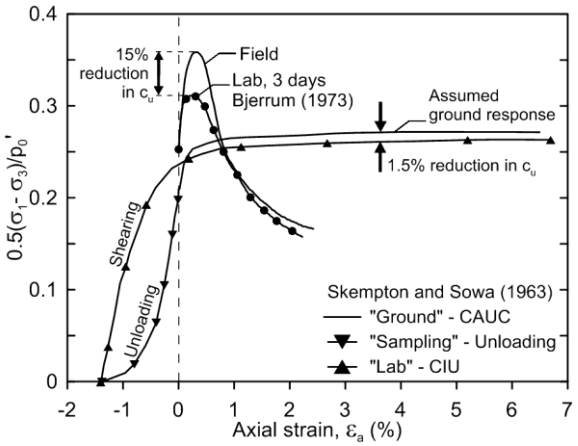


Figure 5 Stress paths for medium plastic clay (S_t=2) after Skempton and Sowa (1963) and for Ellingsrud clay (S_t=70) after Bjerrum (1973).

Adams and Radhakrishna (1971) conducted a series of tests on block samples, from deep open excavation, which showed that specimens that were allowed to take on water and lose suction experienced significant reduction in strength.

Measuring the pore pressure changes in a sample during and after sampling is key to understanding how quickly a block sample may be subjected to stress relief. This is however not a straightforward task. An attempt has been made by Schjetne (1971) to measure the pore pressure changes during sampling in a soft clay with a hypodermic needle piezometer built into a piston sampler. The results showed that sampled quick clay had lost most of the pore pressure quickly and swelled inside the tube due to free water in the remoulded material along the tube walls.

Figure 6 shows loss of suction with storage time in two reconstituted samples of kaolin and illite (Kirkpatrick and Khan, 1984). The remaining suction in a sample will not be a perfect u_k value due to non-elastic behaviour during unloading. Tanaka and Tanaka (2006) noted that the remaining suction has a tendency to decrease with decreasing plasticity index (I_p).

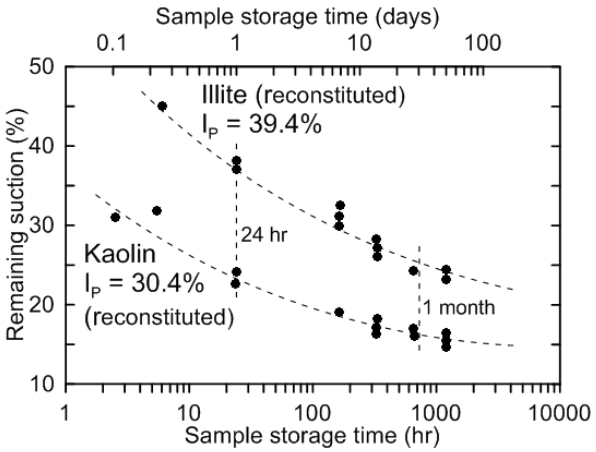


Figure 6 Normalized loss of suction versus sample storage time on reconstituted samples (Kirkpatrick and Khan, 1984).

In engineering practice it is rare that samples are tested on the same day that they are extracted. This is a problem also for block samples.

Table 4 Material properties of tested low plastic soft clays in central Norway.[1]

Sites (sample diameter)	Water content w (%)	c_{ur} (kPa)	Plast. index I_P (%)	OCR
Møllenberg (250 mm)	40.3	0.1	5.9	2.3
Rissa (250 mm)	36.1	0.7-1.5	8.5	2.1-2.2
Tiller (160 mm)	43.1	0.1-1.1	8.7	1.9-2.2
Byneset (160 mm)	37.0	0.3	6.5	1.5-2.0
Dragvoll (160 mm)	38.8	0.1	4.4	1.4-1.9
Klett (160 mm)	34.5	0.1	4.0	1.2-1.4

[1]*Here c_{ur} is the remoulded shear strength measured using the Swedish fall cone and OCR is the overconsolidation ratio.*

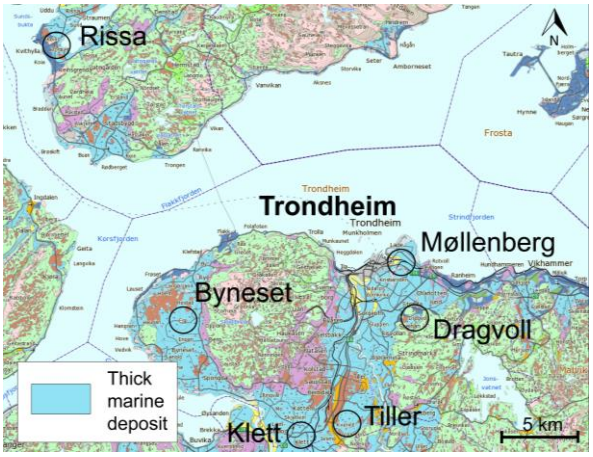


Figure 7 Sampling site locations near Trondheim, central Norway (geological map, NGU).

2.4 Testing and results

NTNU collected low plastic soft clay block samples from six different sites in central Norway. Table 4 summarises some selected geotechnical material parameters of six clays, Møllenberg (Amundsen, 2011), Rissa (Amundsen, 2012), Tiller, Byneset, Dragvoll (Bryntesen, 2014), (Helle et al., 2015) and Klett, most of which are highly sensitive in nature, with an S_t value up to 387.

Over the years, these clay deposits have been extensively tested by NTNU. The handling and testing procedures were more or less identical for all presented sites. Moreover, given the scope of this paper, only selected results are presented and discussed.

2.5 Geological history of sites

From the geological history of the marine deposits near Trondheim, no exceptional loading events are known, only normal sedimentation processes. Groundwater level is about 0-1 m below ground level at all investigated sites, but some fluctuations may have induced changes in the stress history.

Rissa and Møllenberg sites may have experienced some erosion due to their location close to a slope.

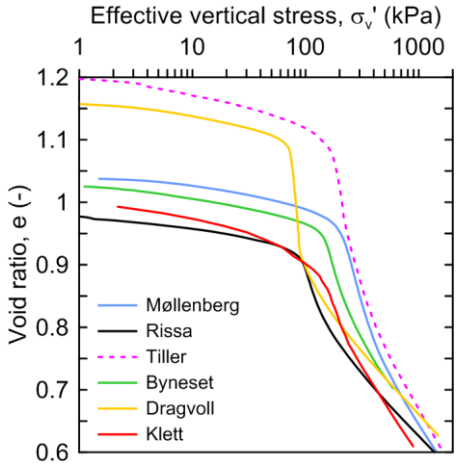


Figure 9 Typical e-logσ_v' relations for low plastic soft clays.

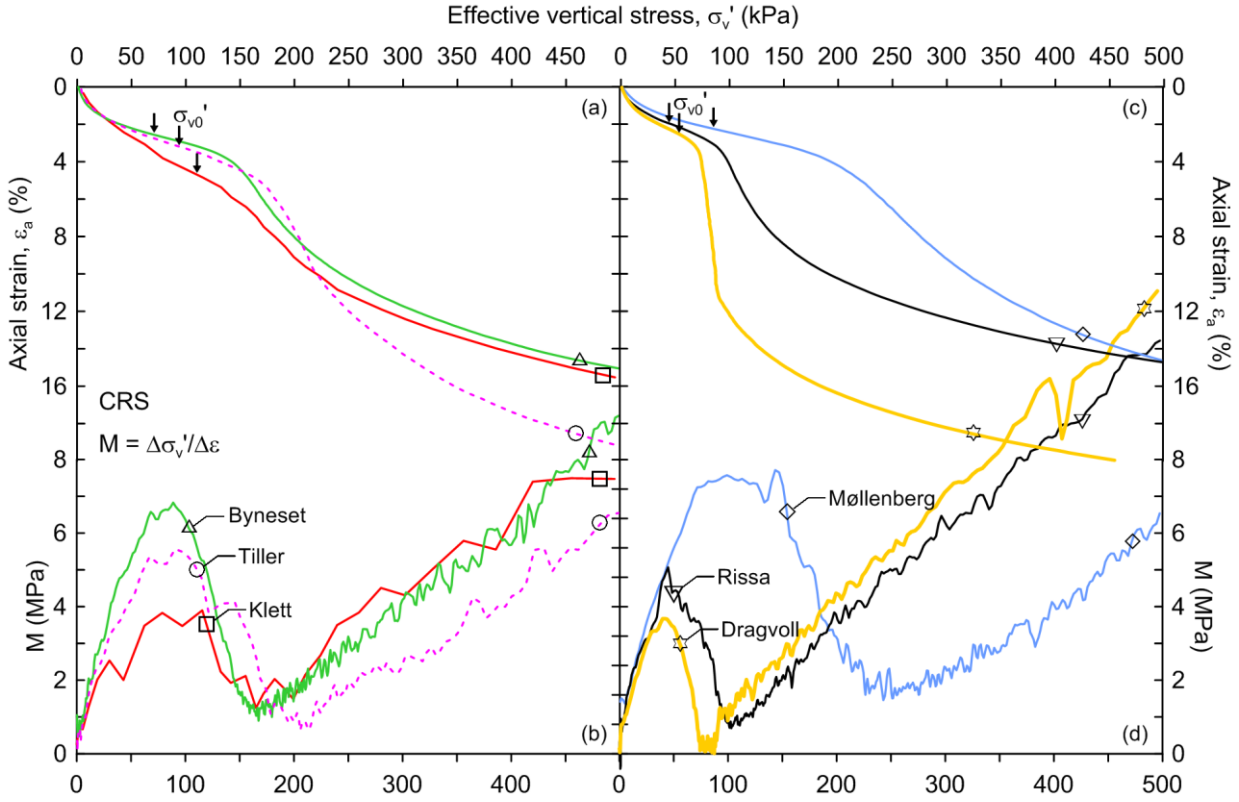


Figure 8 Typical oedometer test results on block samples from low plastic soft clays.

2.6 Oedometer tests

Figure 8 shows typical results of constant rate of strain (CRS) type oedometer tests performed on the clay samples from each of the investigated sites. All specimens, extracted using block sampling, were trimmed to a cross sectional area of 20 cm^2 and a height of 2 cm. The material properties of these specimens are given in Table 5.

Table 5 Results of CRS tests on low plastic soft clays in central Norway.

Site:	Møll.	Rissa	Tiller	Byn.	Drag.	Klett
Samp. (mm)	250	250	160	160	160	160
Depth (m)	8.66	4.02	9.83	7.95	6.23	9.99
w (%)	40.4	35.8	42.5	36.0	41.1	35.7
σ_{v0}' (kPa)	87.9	45.9	93.5	76.5	53.8	110
σ_{c0}' (kPa)	200	96	180	150	75	150
OCR	2.3	2.1	2.0	2.0	1.4	1.4
ε_{v0} (%)	2.3	2.0	3.6	2.5	2.5	4.8
$\Delta e/e_0$	0.045	0.040	0.065	0.049	0.047	0.096
M_0 (MPa)	7.3	4.1	5.1	6.6	3.4	3.5
M_0/M_L	4.4	4.9	6.1	5.7	9.2	2.8

Typical e-logσ_v' curves of the soil samples are presented in Figure 9. Their distinguishing features are the sharp bend at the preconsolidation stress (σ_c'). The approach to estimate σ_c', proposed by Janbu (1963) and adopted in Norway, is to use ε-σ_v' plots as shown in Figure 8a and Figure 8c.

The constrained modulus ($M=d\sigma'/d\varepsilon$), introduced by Janbu (1963), is shown in Figure 8b and d. For a low stress level on the loading branch, the resistance against deformation is large, with a maximum M_0. While the stresses increase, the resistance eventually decreases to M_L due to partial collapse of the grain skeleton. The diagram in Figure 4 contains the definitions of the mentioned constrained module.

2.7 Heterogeneity and loss of suction

Sampling of normally consolidated clays is challenging. When the clays are also low plastic, it makes it even more difficult. Schjetne (1971) made an attempt to measure the stress changes in a low plastic clay (I_P=3%) during sampling. He concluded that a low plastic soft clay lost most of its suction and swelled inside the cylinder before testing.

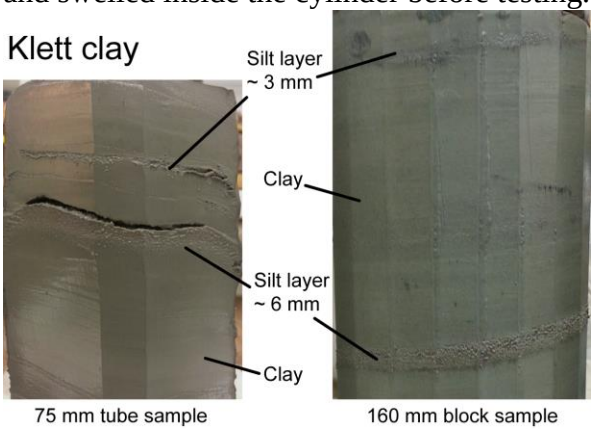


Figure 10 Example of silt layers in Klett clay.

This fact demands an understanding of how quickly the suction may be lost. The answer to this issue lies in the sizes of and the interparticle bonding between clay particles. Permeable materials have a lower tendency to exhibit suction and higher tendency to lose it during and after testing (Fredlund et al., 2012). Kirkpatrick and Khan (1984) tested kaolin which had about 30% left of its suction after three hours of storage. The permeability of kaolin is about hundred times lower than for example Dragvoll or Klett clay. In addition, clays may have layers of highly permeable material, such as silt. Internal drainage of pore water through thin silt layers can reduce the soil suction tremendously, which seems to be the case with the Klett clay. An example of silt layering in the Klett clay is illustrated in Figure 10.

Temperature changes and other chemical reactions will also influence the quality of a sample; however, this aspect is not addressed herein. A descriptive study is necessary in order to determine how this influences the quality of a block sample.

3 CONCLUDING DISCUSSION

A detailed sample quality assessment was carried out and it was found that the quality varied regardless of the type of block sampler and how careful the samples were tested.

Figure 11a compares the magnitude of $\Delta e/e_0$ for samples retrieved at six different sites with low plastic soft clays.

According to the $\Delta e/e_0$ criteria of Lunne et al. (1997), the quality of most samples in Figure 11 may be judged as "good to fair" and "poor". The "poor" quality samples have been retrieved from a depth of 7 to 15 m and the "good to fair" samples from 4 to 10 m.

The $\Delta e/e_0$-value is, at least in part, caused by stress relief followed by a loss of suction. It is clear from Figure 11a, where sampling procedure and handling were identical, that the sample disturbance increases with depth or with magnitude of stress relief, and consequent swelling, experienced by a sample. Another contributing part to the $\Delta e/e_0$-value is the disturbance induced by the sampler during extraction, transport and handling. This disturbance is dominant for tube sampling, but minimal for block sampling.

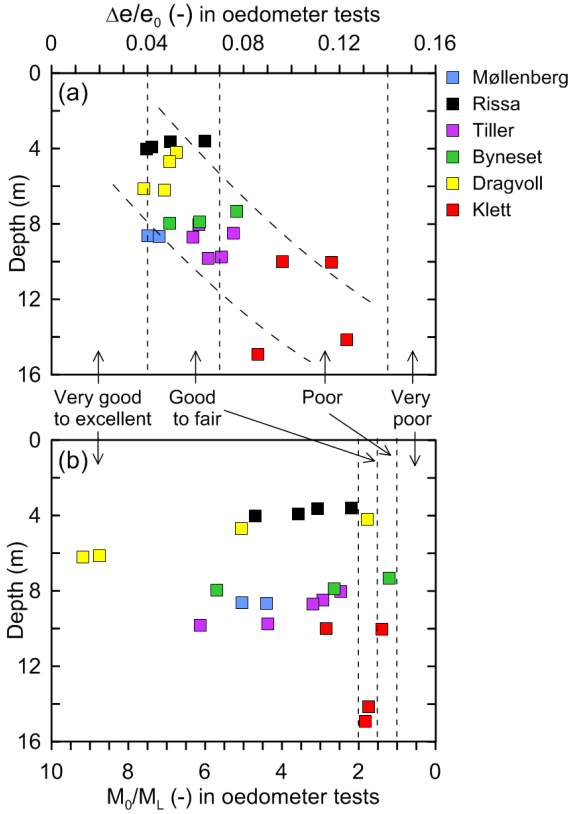


Figure 11 Profile of (a) $\Delta e/e_0$ and (b) M_0/M_L ratios for block samples in low plastic clays.

An advantage of tube samplers is that the stress relief may be delayed by the support of the tube. However, for low plastic soft clays, this effect has diminished before testing is performed (Schjetne, 1971).

If one accepts the $\Delta e/e_0$-criterion, then it is fair to say that one is not guaranteed a high quality sample by using block sampling. In order to ensure good quality sampling, stress relief should be avoided or at least reduced.

Figure 11a has been replotted according to the new M_0/M_L-criterion in Figure 11b. It shows that most of the oedometer tests in this study are classified as of highest quality according to this classification. This is discussed in detail in the following sections.

3.1 Stiffness parameters, M_0 and M_L

The behaviour of the soil changes dramatically when the vertical load exceeds the preconsolidation stress. Samples of high porosity and water content may get a low M_L-value. This may further result in a high M_0/M_L-ratio and a sample quality labelled as perfect. In other words, the M_0/M_L-ratio describes brittleness of the material.

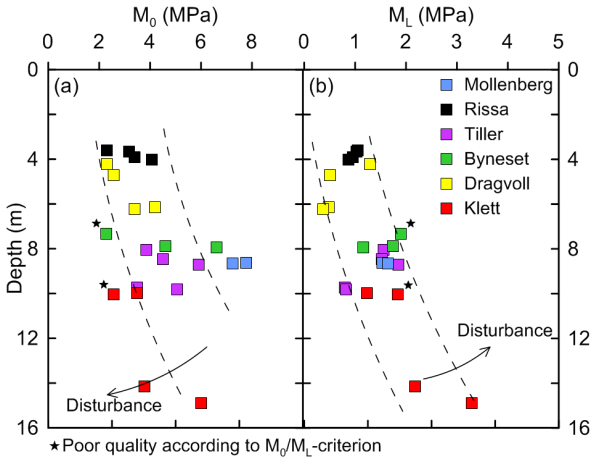


Figure 12 Profiles of (a) M_0 and (b) M_L for block samples in low plastic clays.

The soil stiffness, M_0, is naturally dependent on effective vertical stress and OCR. Soil disturbance causes a destructuring of the soil skeleton and it results in a reduction of the M_0 modulus and an increase of the M_L modulus. This is illustrated in Figure 12.

3.2 The $\Delta e/e_0$ versus M_0/M_L criteria

Figure 13 illustrates the M_0/M_L versus $\Delta e/e_0$ with some OCR values. It is clear that M_0/M_L decreases with increasing $\Delta e/e_0$ or sample disturbance. However, the criteria limits do not match well for low plastic soft clays. Clays with a higher OCR value give the best quality according to both criteria, but the scatter is much larger for clays with low OCR. The difference between Dragvoll and Klett is the sampling depth, see Figure 13.

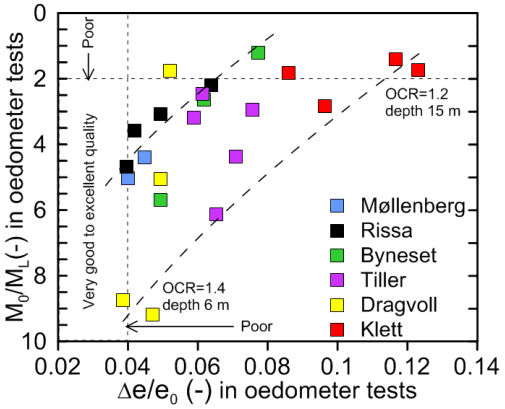


Figure 13 Change in void ratio versus stiffness ratio from oedometer tests.

One primary reason for conducting an oedometer test is to determine a reliable preconsolidation stress. The understanding is that if one does not have a good sample, it is hard to estimate σ_c'. In the results shown in Figure 8 and Figure 9 it is definitely possible to estimate σ_c' even though some of the samples are classified as of "poor" quality according to the $\Delta e/e_0$-criterion. On the other hand, the M_0/M_L-criterion labels the same samples as excellent. The M_0/M_L-criterion takes the sharp bend of the oedometer curve into account and therefore may be more suitable to assess the quality of estimated preconsolidation stress in low plastic soft clays. It however does not indicate the quality of constrained modulus M_0 and may judge a sample as excellent based on an extremely low M_L value.

3.3 Closing remarks

In this paper, an attempt has been made to highlight the challenges related to the handling of block samples. The results show that it is not given that block sampling will produce a high quality sample. Due to stress relief, loss of suction, handling and storage time one may expect poorer sample quality, especially for low plastic soft clays. The key to overcome this issue is to develop a storage procedure for the sample so that loss of suction is minimized. This is the topic of ongoing research at NTNU, and more detailed results may be expected in the future.

4 ACKNOWLEDGEMENTS

Engineers J. Jønland, G. Winther, E. Husby and P. Østensen at NTNU are gratefully acknowledged for their skills and knowledge that made the experimental work possible. The authors are also grateful for a good collaboration with Multiconsult AS and Norwegian Public Road Admin. (NPRA).

The authors wish to acknowledge support from the intergovernmental R&D program NIFS (2012-2015), funded by the NPRA, Norwegian Water Resources and Energy Dir., and Norwegian National Rail Admin. The authors gratefully acknowledge the OFFPHD, a program by the Research Council of Norway their financial support.

5 REFERENCES

Adams, J. I. and H. S. Radhakrishna (1971). Loss of Strength Due to Sampling in a Glacial Lake Deposit. Sampling of Soil and Rock, ASTM.

Amundsen, H. A. (2011). (prev. Kornbrekke) Laboratory tests on high-quality Sherbrooke block sample from Møllenberg. Project thesis, NTNU.

Amundsen, H. A. (2012). (prev. Kornbrekke) Slope stability at Rein Kirke based on results from Sherbrooke block samples (in Norwegian). MSc thesis, NTNU.

Amundsen, H. A., A. Emdal, R. Sandven and V. Thakur (2015a). On engineering characterisation of a low plastic sensitive soft clay. GeoQuebec, Quebec.

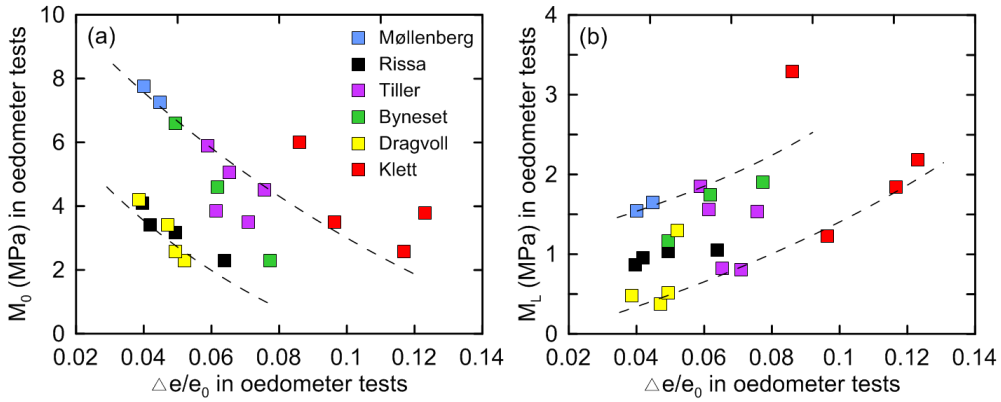


Figure 14 Stiffness M_0 and M_L from oedometer tests versus $\Delta e/e_0$-ratio.

Amundsen, H. A., V. Thakur and A. Emdal (2015b). Comparison of two sample quality assessment methods applied to oedometer test results. Proc. of the 6th Int. Symp. on Deformation Characteristics of Geomaterials, Buenos Aires.

Andresen, A. and P. Kolstad (1979). The NGI 54-mm samplers for undisturbed sampling of clays and representative sampling of coarser materials. Proc. of the Int. Symp. on Soil Sampling, Singapore.

Berre, T., K. Schjetne and S. Sollie (1969). Sampling disturbance of soft marine clays. Proc. of the 7th ICSMFE, Special Session, Mexico.

Bjerrum, L. (1973). Problems of soil mechanics and construction on soft clays. State-of-the-art report. Proc. of the 8th ICSMFE, Moscow.

Bryntesen, R. N. (2014). Block sample testing at Dragvoll. Project thesis, NTNU.

DeGroot, D. J., S. E. Poirier and M. M. Landon (2005). Sample disturbance-Soft clays. Studia Geotechnica et Mechanica 27(3-4), 91-105.

Donohue, S. and M. Long (2010). Assessment of sample quality in soft clay using shear wave velocity and suction measurements. Géotechnique 60(11), 883-889.

Fredlund, D. G., H. Rahardjo and M. D. Fredlund (2012). Solving Saturated/Unsaturated Water Flow Problems. Unsaturated Soil Mechanics in Engineering Practice, John Wiley & Sons, Inc.**,** 375-449.

Gylland, A., M. Long, A. Emdal and R. Sandven (2013). Characterisation and engineering properties of Tiller clay. Engineering Geology 164, 86-100.

Helle, T. E., R. N. Bryntesen, H. A. Amundsen, A. Emdal, S. Nordal and P. Aagaard (2015). Laboratory setup to evaluate the improvement of geotechnical properties from potassium chloride saturation of a quick clay from Dragvoll, Norway. GeoQuebec, Quebec.

Hight, D. W., R. Böese, A. P. Butcher, C. R. I. Clayton and P. R. Smith (1992). Disturbance of the Bothkennar clay prior to laboratory testing. Géotechnique 42(2), 199-217.

Hvorslev, M. J. (1949). Subsurface exploration and sampling of soils for civil engineering purposes, Report on soil sampling, U.S. waterways experiment station, Vicksburg. 521.

Janbu, N. (1963). Soil compressibility as determined by oedometer and triaxial tests. Proc. of the European Conf. on Soil Mech. and Found. Eng., Wiesbaden.

Karlsrud, K. and F. G. Hernandez-Martinez (2013). Strength and deformation properties of Norwegian clays from laboratory tests on high-quality block samples. Can. Geotech. J. 50(12), 1273-1293.

Kirkpatrick, W. M. and A. J. Khan (1984). The reaction of clays to sampling stress relief. Géotechnique 34(1), 29-42.

La Rochelle, P. and G. Lefebvre (1970). Sampling disturbance in Champlain clays. Proc. of the Symp. on Sampling of soil and rock, ASTM.

Lacasse, S. and T. Berre (1988). State-of-the-Art: Triaxial testing methods for soils. Advanced Triaxial Testing of Soil and Rock. STP 977, ASTM.

Lacasse, S., T. Berre and G. Lefevbre (1985). Block sampling of sensitive clays. Proc. of the 11th ICSMGE, San Francisco.

Ladd, C. C., A. S. Azzouz, R. T. Martin, R. W. Day and A. M. Malek (1980). Evaluation of the compositional and engineering properties of offshore Venezuelan soils. I.

Ladd, C. C. and D. J. DeGroot (2003). Recommended practice for soft ground site characterization: Arthur Casagrande Lecture. 12th PCSMGE, MIT, Cambridge, Massachusetts.

Ladd, C. C. and T. W. Lambe (1963). The strength of undisturbed clay determined from undrained tests. Symp. on Laboratory Shear Testing of Soils, ASTM.

Landon, M., D. DeGroot and T. Sheahan (2007). Nondestructive Sample Quality Assessment of a Soft Clay Using Shear Wave Velocity. J. Geotech. Geoenviron. Eng. 133(4), 424-432.

Lefebvre, G. and C. Poulin (1979). A new method of sampling in sensitive clay. Can. Geotech. J. 16(1), 226-233.

Leroueil, S. and D. W. Hight (2003). Behaviour and properties of natural soils and soft rocks. Characterisation and Engineering Properties of Natural Soils. T. S. Tan, K. K. Phoon, D. W. Hight and S. Leroueil. 1**,** 29-254.

Leroueil, S., M. Roy, P. L. Rochelle and F. A. Tavenas (1979). Behavior of Destructured Natural Clays. J. Geotech. Eng. Div. 105(6), 759-778.

Leroueil, S. and P. R. Vaughan (1990). The general and congruent effects of structure in natural soils and weak rocks. Géotechnique 40(3), 467-488.

Lunne, T., T. Berre and S. Strandvik (1997). Sample disturbance effects in soft low plastic Norwegian clay. Proc. of the Symp. on Recent Develop. in Soil and Pavement Mech., Rio de Janeiro.

Nagaraj, T. S., N. Miura, S. G. Chung and K. N. Prasad (2003). Analysis and assessment of sampling disturbance of soft sensitive clays. Géotechnique 53(7), 679-683.

Nagaraj, T. S., B. R. S. Murthy, A. Vatsala and R. C. Joshi (1990). Analysis of Compressibility of Sensitive Soils. J. Geotech. Eng. 116(1), 105-118.

Schjetne, K. (1971). The measurement of pore pressure during sampling. Proc. of the 4th Regional Asian Conf., Bankok, ISSMFE.

Skempton, A. W. and V. A. Sowa (1963). The Behaviour of Saturated Clays During Sampling and Testing. Géotechnique 13(4), 269-290.

Tanaka, H. (2000). Sample quality of cohesive soils : Lessons from three sites, Ariake, Bothkennar and Drammen. Soils and foundations 20(4), 57-74

Tanaka, H., P. Sharma, T. Tsuchida and M. Tanaka (1996). Comparative Study on Sample Quality Using Several Types of Samplers. Soils and foundations 36(1), 57-68.

Tanaka, H. and M. Tanaka (2006). Main factors governing residual effective stress for cohesive soils sampled by tube sampling. Soils and found. 46(2), 209-219.

Terzaghi, K., R. B. Peck and G. Mesri (1996). Soil Mechanics in Engineering Practice, Wiley.

OATV for strength estimations in Copenhagen Limestone

N. Katić
Geo, Denmark, nka@geo.dk

R. Chalmas & H.F. Christensen
Geo, Denmark

ABSTRACT
Copenhagen Limestone is a highly variable material. The sizes of rock constituents vary, as well as the basic classification parameters of the matrix material, such as the bulk density and the degree of induration. In the usual practice, these properties are observed at a limited number of specific locations along a core, most often discontinuous due to the intrinsic nature of material as well as the effects of coring process. Application of continuous logging techniques, such as Optical and Acoustic Televiewer (OATV), enables observation of rock properties in a continuous manner. Due to the differences in applied techniques and tested domains in situ and in the laboratory, the measurements are not necessarily interchangeable, but are able to supplement each other.
The Copenhagen Limestone OATV data considered in this work is gathered within the Copenhagen Cityring project
Previous experience shows that UCS strength and bulk density are well correlated in Copenhagen Limestone. The current work extends the framework of combined interpretation of laboratory and in situ tests presented recently, see Katic & Christensen 2014 2015.
The work investigated possibilities of making continuous estimation of UCS strength along a core. The correlations between the bulk density and the formation density are used as a basis for observing material variation, using acoustic and optical televiewer. The work shows that the logarithm of the acoustic amplitude can be used to describe the vertical variation of the material along the borehole depth. Hereafter, it is showed that a match between the acoustic amplitude and the density logs can be used for continuous estimation of UCS. Finally, the use of optical televiewer results is discussed and an interpretation method is suggested.

Keywords: Copenhagen Limestone, OATV, UCS.

1 INTRODUCTION

Copenhagen Limestone is a highly variable material. The sizes of rock constituents vary, as well as the basic classification parameters of the matrix material, such as the bulk density and the degree of induration. In the usual practice, these properties are observed at specific locations along a core, most often discontinuous due to intrinsic nature of material as well as the effects of the coring process. Application of continuous logging techniques, such as Optical and Acoustic Televiewer (OATV), enables observation of rock properties in a continuous manner; see Foged et al. (2011). Due to the differences in applied techniques and tested domains in situ and in the laboratory, the measurements are not necessarily interchangeable, but are able to supplement each other.

The Copenhagen Limestone data considered in this work is gathered within the Copenhagen Cityring project. The current work extends the framework of simultaneous interpretation of laboratory and in situ tests presented recently (Katic & Christensen 2014, 2015).

The work investigates possibilities of making continuous estimation of UCS strength along the core. A hypothesis implied herein is that if the strength measured in the laboratory correlates to the sample bulk density or one of its proxies (e.g. porosity), then a similar

correlation can be seen on the geophysical proxies of strength and density, such as the amplitude of acoustic wave measured by the acoustic televiewer, and formation density, respectively. A similar hypothesis has been made earlier by prof. Foged, suggesting that the median amplitude found by the acoustic televiewer relates to the induration of the core. However, it is understood that the correlations derived from the continuous OATV and/or geophysical logs may not be as clear as the correlations derived from the laboratory measurements. These differences may stem from the properties of the rock mass, such as fracturing, disturbance due to coring as well as other technical limitations of the field methods, such as the clarity of the fluid filling the borehole (see e.g. Williams & Johnson, 2004).

Using the correlations between the parameters assessed using OATV and laboratory measurements, UCS strength can be estimated from the established correlations between the UCS strength and bulk density. The final aim of the work is hence to assess the applicability of OATV for estimating the limestone strength.

2 SELECTED LABORATORY AND FIELD TESTING

2.1 Correlation of UCS strength and bulk density

Previous experience shows that UCS strength and the bulk density are well correlated in Copenhagen Limestone, see e.g. Hansen & Foged 2002 and Foged et al. 2007, 2011.

Figure 1 presents the measurements carried out during the additional investigation phase of the Cityring project.

The data shows a factor of 2 to 3 between the maximum and minimum UCS strength for the same bulk density. The UCS for the strongest and the weakest samples varies by a factor of nearly 40. These findings are in good agreement with aforementioned references and other available data.

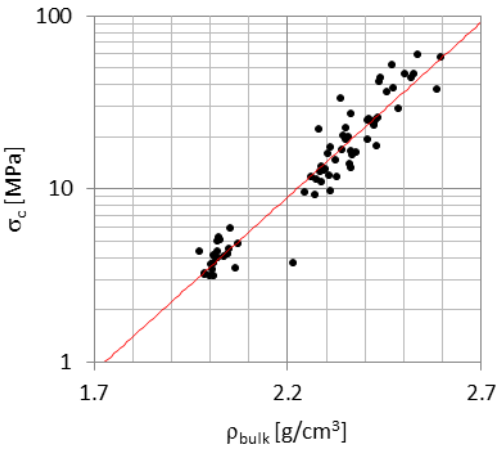


Figure 1 Correlation between UCS and bulk density of the samples on boreholes carried out in the additional investigation phase.

In terms of porosity, the semi-logarithmic plot presented in Figure 2 also shows a clear trend in agreement with previously published works (see e.g. Katić & Christensen 2015, Eberli et al. 2003).

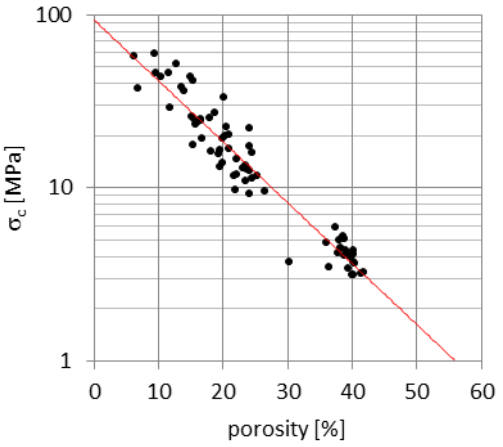


Figure 2 Correlation between UCS and porosity of the samples on boreholes carried out in additional investigation phase.

2.2 Formation density and density of laboratory samples

The formation density (compensated gamma-gamma density) is measured with a caesium source mounted on the probe that emits directional gamma radiation into the formation. The gamma radiation emitted from the source collides with the electrons in the formation and is scattered. The more electrons per volume unit (as in dense rocks), the larger the scattering of the gamma radiation, and the less gamma radiation is

received by the sensors in the probe. The electron density is related to the density of the solid material, and the extent of the reflected radiation is inversely proportional with the formation density.
Three sensors are incorporated in the probe with an increasing distance from the source.
During logging, the probe is pressed against the borehole wall by a caliper arm. In boreholes drilled with the DTH method, the borehole diameter can vary considerably. In these situations, the contact pressure between probe and sidewall is not constant and the borehole fluid influences the measured values. In the part of the borehole with steel casing, the density log can reflect cavities behind the casing and not the exact density of the formation.
In some instances, the density log cannot be carried out due to unstable boreholes. Furthermore, the passage from the top soil drilling to the 146 mm core drilling sometimes obstructs the probes to enter the core-drilled section.
The large scattering of extensive datasets caused by the nature of the site and material is often caused by variation in technical means and conditions. This is found discouraging while seeking a correlation between parameters; namely, the parameters that are expected to correlate well based on the underlying physics show very weak to no correlation.
In this particular presentation, a choice was made to demonstrate the observations from OATV and geophysical testing on an example borehole, rather than on the whole dataset. The scattering stemming from different conditions between borings, including e.g. different ratios of Upper to Middle to Lower Copenhagen limestone, variable fracturing and positions of the flint beds due to possible inclinations of the rock mass layers, variable flow conditions etc. is minimized by focusing on a single borehole.
The same example borehole has been used for all of the following illustrations.
Figure 3 presents a correlation between the formation density and the density of laboratory UCS test specimens from the example borehole. It can be seen on Figure 3 that the formation density and bulk density of laboratory samples correlate within a tolerance.

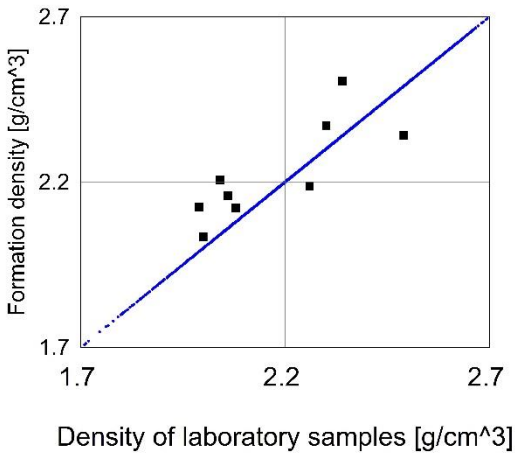


Figure 3 Correlation between the formation density and the density of UCS samples from the example borehole.

The scattering between the bulk density and the formation density stems from the difference in the way of measuring the density on laboratory samples and in situ, as well as from the difference in the volumes of material involved in a particular measurement. This is further emphasized by the fact that the values from the geophysical logs relate to a particular depth (although involving a certain volume of rock around the measurement point), whereas the bulk densities of the laboratory samples average the measurement over the height of a sample. If the formation density values are averaged over a length of the corresponding sample, the scattering can occasionally be reduced, depending on the horizontal distribution of indurations.
It is important to notice that bulk density and formation density parameters do not strictly reflect each other. While the laboratory-measured values of the bulk density reflect the core, the formation density measured in the field reflects the surrounding of the core. Given the presented variability of Copenhagen limestone, an argument can be made that these two domains are in fact as comparable as neighbouring samples and that large variations can occur. However, if the density within a core and out of the core are rather dissimilar, this information can be used

for an assessment of the horizontal variability.
In line with this, points where the density measured in the laboratory is rather dissimilar from the assessed formation density, should be excluded from the set when attempting continuous estimation of correlated parameters such as UCS strength.

2.3 UCS estimates based on formation density

Figure 4 shows a combined plot between the bulk density and UCS strength (red symbols) and formation density and UCS strength (blue symbols).

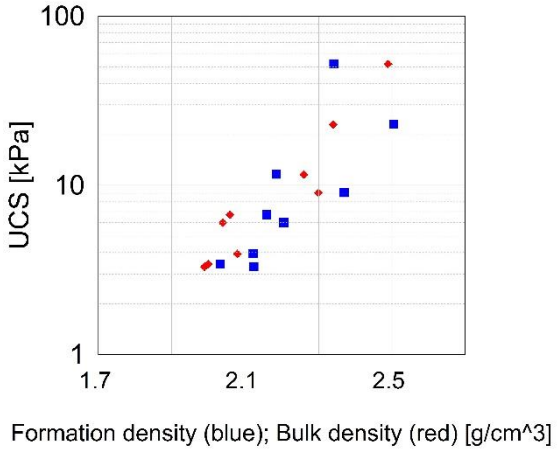


Figure 4 Correlation between the formation density and the density of UCS samples with UCS on the example borehole.

It can be seen that the trend between the UCS and density exists, whether the bulk density or formation densities are considered. This implies, although the correlation is not smooth, that an estimation of strength based solely on the formation density is possible, under condition that an appropriate pre-determined correlation between the UCS and the bulk density has been established on the samples from the same material and formation.

2.4 OATV

The Optical and Acoustic Televiewer (OATV) probes measure a continuous and orientated image (+-3 degrees) of the borehole walls. Both optical and acoustic images are oriented from the north.

The Acoustic Televiewer (ATV) probe uses a fixed acoustic transducer and a rotating acoustic mirror to scan the borehole walls with a focussed ultrasound beam. The amplitude and travel time of the reflected acoustic signal are recorded simultaneously as separate image logs. Features such as fractures reduce the reflected amplitude. Fractures appear as dark traces on the log. These traces are sinusoidal if the fractures are inclined.
The zone of passage between the top soil drilling and the 146 mm core drilling challenges the televiewer logging similarly as the density logging (see ch. 2.1).
The optical televiewer is recorded with a vertical resolution of 0.7 mm and a horizontal resolution of 720 pixels/revolution.
The acoustic televiewer is recorded with vertical resolution of 2 mm and horizontal resolution of 360 pixels/revolution.

3 CORRELATIONS OF LABORATORY TEST RESULTS AND FIELD TEST RESULTS

3.1 Amplitude of acoustic televiewer as index test

The acoustic amplitude images are believed to correlate to the degree of induration at a certain depth along the borehole. If so, the hypothesis is extended to believe that acoustic images will present a reflection of density and thereby correlate to the UCS strength.
The following analysis is carried out using statistics on the data collected around the perimeter of the example borehole. As the data is collected with different vertical raster, in the first step, the logs are statistically processed around the perimeter of the borehole at particular record depth, and thereafter reduced to the same vertical scale.
Figure 5 presents a correlation between the amplitude of acoustic televiewer (average, median, and 50% percentile), formation density, the bulk density measured on UCS samples and the UCS strength along the depth of the example borehole.
The 50% percentile of the acoustic amplitude and the density of UCS samples along the depth of the example borehole presented on

Figure 5 are isolated on Figure 6, where the presentation scale of the acoustic amplitude log is chosen to show the correlation with the density.

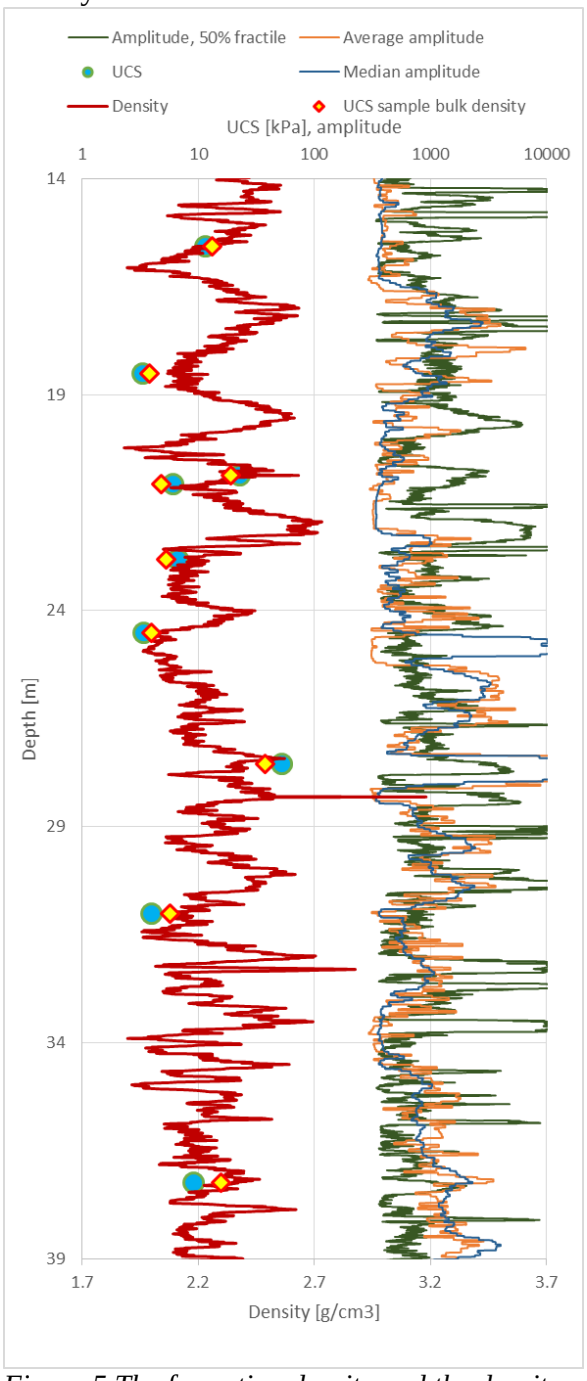


Figure 5 The formation density and the density of UCS samples with the UCS strength and the amplitude of acoustic televiewer through various statistical means along the depth of the example borehole.

Based on the results of the amplitude versus depth plot presented on Figure 6, a cross-plot of the read-out values of the logarithm of the amplitude vs. UCS, together with the plot of the bulk density vs. UCS is given on Figure 7.

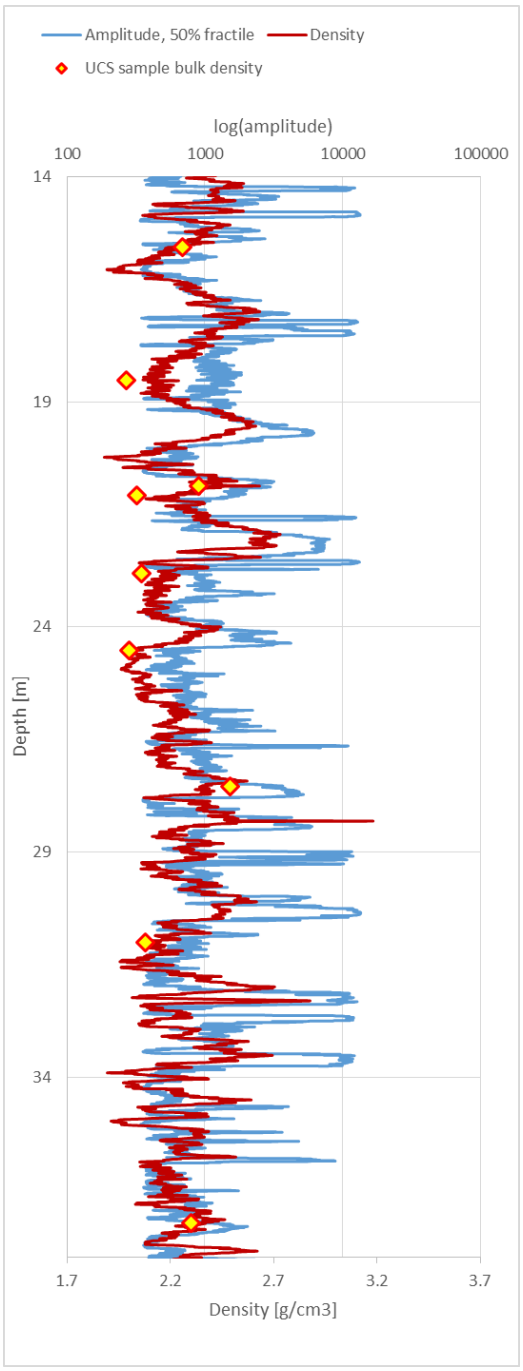


Figure 6 Correlation between the amplitude of acoustic televiewer (50% percentile), formation density and the density of UCS samples along the depth of the example borehole.

It is apparent from the presented Figure 6 & Figure 7, that a correlation between the amplitude and UCS has the trend following the correlation between the bulk density and the UCS. Discrepancies between the values seem to reflect different conditions within the core and around the borehole.

Based on the presented plots, it is concluded that a direct correlation between the UCS

strength and the amplitude of the acoustic televiewer is possible in this particular case.

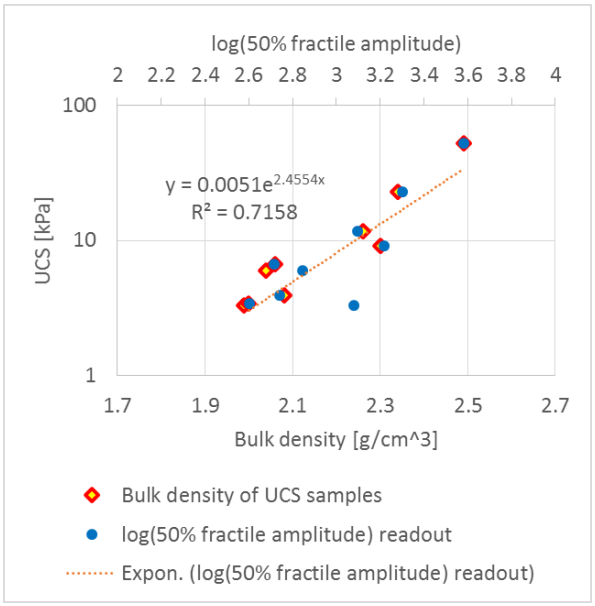


Figure 7 Cross-correlation between the amplitude of acoustic televiewer (50% percentile), formation density and the density of UCS samples on example borehole.

3.2 Linking the optical televiewer log to acoustical and mechanical measurements

In a common logging procedure, the optical televiewer log is recorded first, in order to provide a visual estimate of material prior to running the acoustic logging. This estimate is subjective and depends on the experience of the personnel doing the logging. An attempt to quantify such an estimation, and hence reduce the subjectivity by comparing the visual log with the other measurements, is carried out hereafter.

In order to compare the results of the optical televiewer with the other measurements presented, the full two dimensional visual log is reduced to a longitudinal log plotted versus the borehole depth in a similar way as the acoustic amplitude log.

The image of the optical televiewer is a matrix-sorted collection of points along the depth and perimeter, where each point is associated with a set of coordinates in a chosen colour system. The data processed on the particular example borehole have been presented in terms of RGB system, where each of the coordinates (Red, Green and Blue) is independent of the other two. The matrix representing the picture is therefore five-dimensional, out of which two dimensions (the depth and the angle along the perimeter measured from the north) are physical, and the other three are colour coordinates.

The range of the colour coordinates in the RGB system is from (0, 0, 0) depicting black colour, i.e. the darkest materials, to (255, 255, 255) depicting pure white colour, i.e. the brightest materials. In order to enable direct comparison with the density log, the results are presented in terms of an average colour, where the average is taken as a third of the sum of the component colours along the perimeter.

In comparison with the geophysical, acoustic and mechanical measurements, optical televiewer has the smallest penetration into the bulk of the material. In fact, it reflects only the surface of the borehole, hence the engaged volume described by the test is close to zero.

Averaging of the optical televiewer results in terms of colours is particularly influenced by the occurrence of flint and fractures, and more so than the other measurements mentioned within this study. Possible reasons for this are as follows.

The fractures are depicted by the optical televiewer as dark lines, which coincides with the dark flint – whether present in the fracture or not. Hence, the spikes in the optical televiewer log will coincide with mechanical properties of either flint or hollow space, which are on two opposite ends of the range of values. This is depicted on Figure 8.

More so, not all of the flint in Copenhagen Limestone is dark. For these reasons, it is understood that averaging of the optical televiewer results is not likely to correlate noticeably with the other measurements. However, as the fractures are generally very thin, it is expected that some notions of the trend may be visible.

Figure 8 shows that the average colour log weakly correlates with the formation density log, with a limitation in the depths including flint. The discrepancies between the logs, however, can partially be explained by the horizontal variability of the material, as well

as different absolute volumes of material involved in various logs.

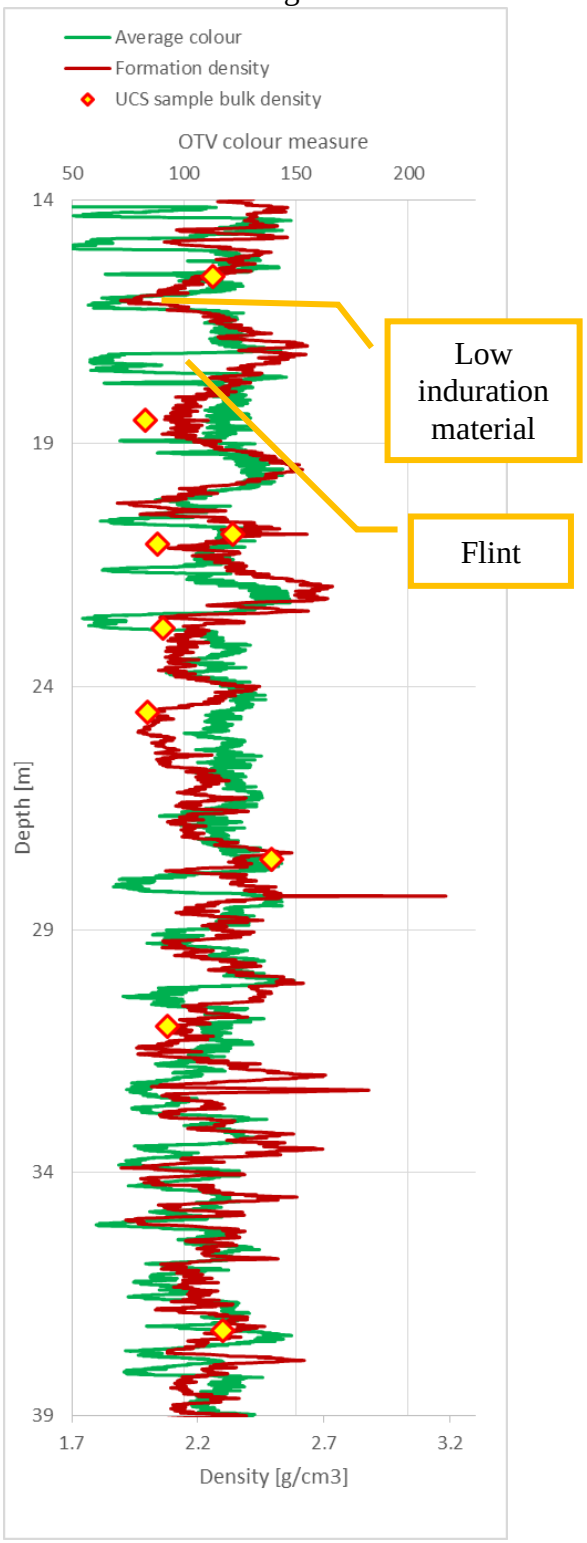


Figure 8 Formation density and UCS strength with the optical televiewer colour measure along the depth of the example borehole.

4 DISCUSSION AND CONCLUSION

The initial work presented a systematic correlation between the mechanical strength tests (UCS) carried out at certain depths along a borehole, and continuous logs of formation density. Despite the obvious difference in measuring domains, namely core material vs. the surrounding rock mass, the presented correlation is in general agreement with the previously established dependencies between UCS and the bulk density measured on the laboratory samples. Based on the observations, the differences between the formation density and the bulk density can be primarily attributed to the variation of the induration, i.e. material, within the core and in the surrounding rock mass. The differences in the actual measurement methods amplify the scattering, but seem to be secondary to the variation of material properties.

The tensorial representation of the acoustic amplitude and the colour logs makes it challenging to correlate these measurements with longitudinal logs and pointwise measurements. In order to enable a correlation, different ways of linearizing the two presented tensors are considered, including statistical measures such as percentiles, median or average.

While attempting to establish the correlation between the acoustic amplitude and density / strength measurements, average, median and 50% percentile have been visually compared. It is concluded that for this particular location the 50% percentile measure, presented herein, matches the formation density log somewhat better than the average and median values, and therefore it is presented on the Figure 6 and Figure 7. However, further investigation is needed to conclude if this is a general rule or an exclusive occurrence.

It should be noted that the scattering of the results of the acoustic amplitude is related to the scattering of the borehole radius and variable induration in the horizontal plane.

For example, if the induration close to the edge of the borehole (and possibly inside the core) is low, then the radius may be enlarged during the drilling process, by washing out some of the material. This means that the material left in the borehole, which is logged thereafter, is stronger, hence the amplitude will relate to the higher induration than what is estimated along the surface of the core, and

possibly higher than within the core. On the contrary, if the material close to the surface of the boring (and possibly inside the core) is stronger, then it is possible to have it chipped from the weaker underlying material during the coring process. Consequently, in this case, the amplitude might relate to a lower induration.

These observations indicate that only measurements relating to a stable borehole wall conditions should be taken into account for establishing general trends. When establishing the relevant correlations based on the amplitude, applicable to a wider area and including several logs, the amplitude measurements need to be filtered in such a way that all the measurements relating to radii outside of certain bounds have to be disregarded. This has not been included in the present study.

The questions stemming from the acoustic televiewer analysis, namely what are the relevant bounds of radii to be included and how do they relate to the evaluation of the existing, natural, fracturing of the limestone depicted by OATV, are not discussed herein.

Although the presented processing of the optical televiewer log is merely more than an intellectual exercise, a certain overlapping of trends depicted in Figure 8 is observed.

A major obstacle with the presented analysis of the optical televiewer results is the colour match between fractures and flint, as mentioned above. However, if the average colour is understood as a "pressure-equivalent measure" of a colour log, a question can be risen if an alternative "shear-equivalent measure" representing a distance between the darkest and the brightest pixels around a perimeter, would bring an additional insight for continuous comparison. Based on this, it is concluded that while the presented optical televiewer results cannot be independently successfully used for correlations with density, and thereby strength, a direct comparison of the longitudinal logs shows how the intensity of colours correlates to the density of the samples.

Based on the presented logs, it is concluded that a continuous estimation of the strength is possible by using formation density and the amplitude of the acoustic televiewer.

5 ACKNOWLEDGEMENTS

We are grateful to CMT and Metroselskabet for permission to publish the study.

We would also like to thank our dear colleague Sonny O. T. Kristiansen, for shearing field observations and his accurate geophysical logging reports throughout the Copenhagen Cityring project, parts of which have been used in this work.

6 REFERENCES

Eberli, G. P., Beachle T.G., Anselmetti, F.S. & Incze M.L. (2003). Factors controlling elastic properties in carbonate sediments and rocks. The Leading Edge.pp.: 654-660 July 2003.

Foged, N., Jakobsen, L., Jackson P. & Erichsen L. (2007). Rock mass characterization for tunnels in the Copenhagen limestone. In: The Second Half Century of Rock Mechanics, Three Volume Set. 11th Congress of the International Society for Rock Mechanics, Olalla, C., Grossmann, N. & Ribeiro e Sousa, L. (eds.). CRC Press; Pap/Cdr edition (July 5, 2007).

Foged N., Stabell B., Foged B. (2011). Rock mass characterization for tunnels in limestone in Copenhagen and Malmö area. In: Geotechnics of Hard Soils – Weak Rocks. Proceedings of the 15th European Conference on Soil Mechanics and Geotechnical Engineering. Anagnostopoulos A., Pachakis M., Tsatsanifos C.(Eds.) pp. 331 – 336. IOS Press

Hansen, H.K. & Foged, N.N. (2002). Kalkens bjergmekaniske egenskaber. In: Ingeniørgeologiske forhold i København. dgf-Bulletin no. 19, Frederiksen J.K. (ed.) pp. 31-34. DGF, Danish Geotechnical Society.

Katić N. & Christensen H.F. (2014). Upscaling elastic moduli in Copenhagen Limestone. In Rock Engineering and Rock Mechanics: Structures in and on Rock Masses: Proceedings of EUROCK 2014, ISRM European Regional Symposium, Vigo, Spain, 26-28 May 2014. Alejano, Perucho, Olalla & Jiménes (eds). 2014. pp. 235-240. Taylor & Francis Group, London.

Katić N. & Christensen H.F. (2015). Composite Elasticity of Copenhagen Limestone. 2015. In: Proceedings of the ISRM Regional Symposium EUROCK 2015 & 64th Geomechanics Colloquium - Future Development of Rock Mechanics, Schubert, W. & Kluckner, A. (eds), Salzburg, Austria, 7.-10. October 2015, pp. 451-456. Austrian Society for Geomechanics: Salzburg.

Williams, J.H. & Johnson, C.D. (2004). Acoustic and optical borehole-wall imaging for fractured-rock aquifer studies. Journal of Applied Geophysics, vol. 55, Issue 1-2, pp. 151-159.

A preliminary attempt towards soil classification chart from total sounding

E. Haugen
Norwegian Public Roads Administration, Norway, eigil.haugen@vegvesen.no

X. Yu, S. A. Degago, D. Nigussie, O. V. Kirkevollen
Norwegian Public Roads Administration, Norway

ABSTRACT
Total sounding is an in-situ soil investigation method that combines conventional rotary pressure sounding with rock control drilling. It is a quick method that can be used in most soil types. It is mainly used for preliminary characterization of soil layering and to identify location of bed rocks. In Norwegian geotechnical practice, total sounding is generally adopted as a standard method to start an in-situ soil investigation scheme. The main measurement in a total sounding is the penetration resistance force (in kN). The main shortcoming of this measurement is its susceptibility to the increasing rod friction by depth. As a result this measurement is only used subjectively but it still usually provides an important first time insight to the soil layering that is later verified with additional field and laboratory investigations. Thus, it would be an advantage to systematically study measurements of total sounding for a better soil characterization in a more objective way. In this work three parameters were derived from the penetration resistance force: the smoothed normalized penetration pressure, the standard deviation of penetration force, and the gradient of the smoothed normalized penetration pressure. Then the correlations among these parameters and grain size distributions are explored. Based on this an attempt is made to sketch a soil classification chart, in which four general soil types including quick clay are distinguished. Using data from selected sites the proposed chart is evaluated by comparing with two CPTU-based classification methods as well as laboratory-based classification. The paper also discusses additional potential improvements that can be incorporated to the chart and more broadly to this sounding method to asses its possible use for the current geotechnical practice.
Keywords: In-situ investigation, total sounding, soil classification chart

1 INTRODUCTION

Total sounding is a rotary pressure sounding technique which can be used in almost all soil types. The method was developed in Norway through cooperation between the Norwegian Geotechnical Institute and the Norwegian Road Research Laboratory back in 1980s, with the purpose of combining rotary pressure sounding and bedrock control sounding into one operation (NGF, 1994). It is now established as the most used sounding method in Norway. The Swedish *rock soil total sounding* (JB totalsondering) is based on the Norwegian counterpart and is increasingly used in Sweden (Wister, 2010).

In the Norwegian geotechnical practice, a total sounding is generally adopted as a standard method to start an in-situ soil investigation scheme. The main use of total sounding is for a preliminary characterization of soil layering and to identify location of bed rocks. It provides a basis for planning subsequent in-situ investigations such as CPTU (cone penetration test with pore pressure measurement), soil sampling and pore pressure measurements. The main measurement in a total sounding that is used in classifying soil layering is the penetration resistance force (in kN). This is used for a qualitative classification of soil. A main shortcoming in this measurement is its susceptibility to the influence of increasing rod friction by depth. The inaccuracy is especially remarkable in soft to medium firm soils as compared to CPTU (Sandven et al., 2012).

However, given the fact that it is used extensively as a standard method in the practice, it is appealing to attempt to get more out of its measurements in an objective way

and explore further extensions. Thus, this work is a preliminary attempt in that direction. The aim of this work is to quantitatively explore the potential of total sounding in soil classification, and evaluate its soundness against two CPTU based classification methods and grain size analysis from laboratory investigation. Laboratory data on physical and mechanical properties are used as references.

On this instance, it is worthwhile to mention that Sofia (2010) has correlated the penetration force of total sounding with tip resistance from CPTU in a simple manner, and proposed formulas for evaluating friction angle and elastic modulus out of the penetration force of total sounding in accordance with the Swedish practice.

2 CURRENT PRACTICE

2.1 Equipment and procedure

The total sounding equipment consists of a 57 mm diameter rock-drilling bit, connected to hollow 45 mm "geo-rods". The drilling bit has a hole with a spring-loaded steel ball, for flushing. The penetration rate is kept at 3 m/min and rotation rate might vary from 25 rev./minute up to 70 rev./minute (NGF, 1994). An illustration of the equipment is given in Figure 1.

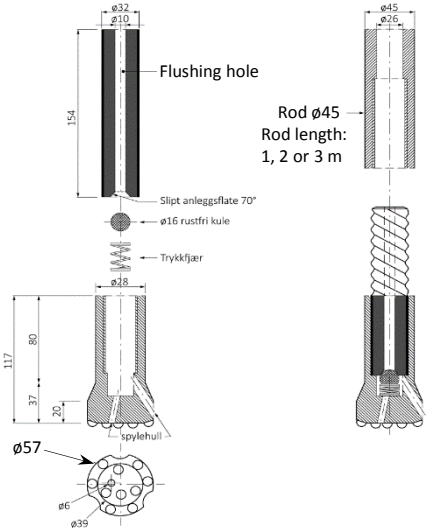


Figure 1 Total sounding drilling bit and rod (courtesy of NGF Pub. 9, 1994).

When encountering very firm layers and penetration cannot be maintained at a desired rate, the operator can increase rotation rate. If this does not penetrate further, flushing and hammering mode can be enabled in sequence to facilitate drilling through firm soil or rock (NGF, 2016).

The total sounding system records the following data: depth (m), penetration force (kN), penetration rate in rock (sec/m), rotation rate (rev./sec), hammering and flushing (binary) and flushing fluid pressure (kPa).

2.2 Interpretations of results

In Norway, the interpretations of total sounding results are done in accordance with Norwegian Geotechnical Society (Norsk Geoteknisk Forening (NGF)) guideline nr. 7 and nr. 9. However, considerable subjective judgement has to be involved. Generally, smooth curves and low resistance indicate soft clays. Increasing fluctuations of the penetration resistance indicates a larger fraction of coarse material. Also the overall trend of resistance force changing with depth gives an indication in relative stiffness. Sensitive soils have been observed to have a decreasing resistance with depth. Increased rotation rate indicates very firm soils or boulders. Enabled hammering together with recorded low resistance and constant low penetration rate imply the existence of bedrock, rather than boulders or very firm soils. Figure 2 shows a total sounding plot together with soil classifications. Information of the first four layers are obtained from laboratory tests, while glacial till is speculated considering the geological history of the site.

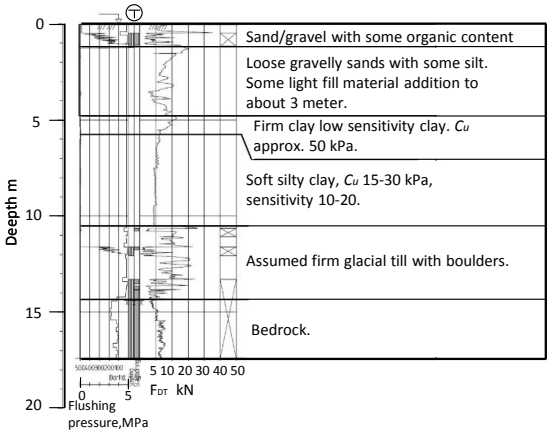


Figure 2 Example of a total sounding from a project in Drammen, Norway.

3 SOME LIMITATIONS OF TOTAL SOUNDING

In principle, the penetration force is a function of the soil firmness. This concept is adopted in total sounding for a rough interpretation of soil types and layering. The limitations in accuracy of such use arise due to certain inherent aspects of the method. The main one being the effect of friction along the rod and its significant influence on the measurement of penetration resistance. Another aspect is the lack of control on the inclination of the rod during drilling.

Resistance force is measured at the top (as opposed to CPTU's tip resistance measurement). This means that all resistance in the system is included in the measured values, such as friction along the rods and resistance in the drill tower itself.

Water flushing is used to push the rod further down in firm layers as it reduces friction along the rods and the drilling bit. It has also been observed that, when flushing is enabled to penetrate through firm layers, it disturbs relatively soft soil layers below, and gives recorded resistance much lower than in soils undisturbed by flushing. Thereafter, two similar soils may show different resistance depending on if flushing has been used or not in the above layer. It is also worthy to mention that under favourable soil condition the bore hole may not collapse and very limited friction could be expected (Fredriksen, 1997).

It is logical to assume that total sounding results could be sensitive to change in rod direction while drilling. The drill tower direction may not be identical to the rod direction. This adds a lateral force to both the rod and the drill tower; and is often seen as abruptly increased resistance near the end of each 2-meter rod. Considering the aforementioned aspects, one must take caution when interpreting results from total sounding.

It is well known by both geotechnical engineers and drilling operators that the fluctuations of the penetration force curve is descriptive of the coarseness of soil. The penetration force is indicative but could be deceiving when used alone as forces may come from other places in the system than the tip. Therefore a preliminary study is initiated by analysing some existing data aiming to (1) explore more indicative parameters from total sounding results; (2) investigate where total sounding results may be misleading or ambiguous; (3) investigate if a quantitative soil classification chart can be made, in a similar fashion as to those extensively used with CPTU (Robertson, 1998).

4 DATA SETS AND PROCESSING

4.1 Total sounding data

Total sounding data, together with laboratory investigation results, were compiled from road projects under the Norwegian Public Roads Administration (NPRA) Region South for the study in this paper. The data are gathered from 2011 to 2015 in the counties; Buskerud, Vestfold, Telemark and Aust-Agder. Figure 3 displays the geographic distribution of tests; the number in circle indicates the number of data sets obtained from that site.

Cases where there has been no use of hammering, flushing and increased rotation rate have been chosen. Besides this care was taken to include only data that are not close to rod changes, as abrupt resistance changes are often observed at those points.

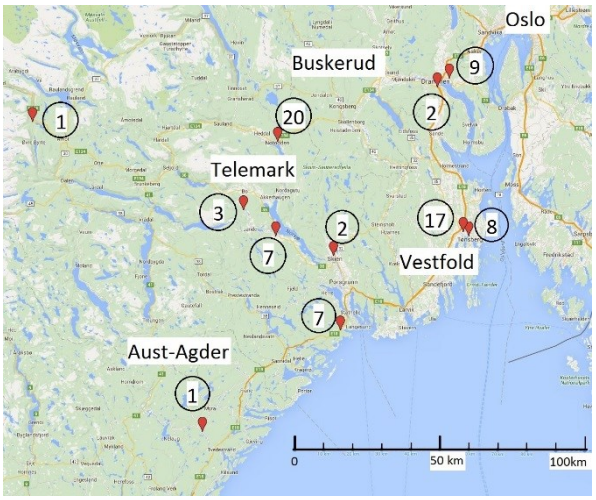


Figure 3 Geographic distribution of sites for data sets (background map courtesy of Google.com).

4.2 Total sounding data processing

Analogous to CPTU, penetration force (F_{dt}) tends to increase with depth in most layers. For CPTU various normalization methods have been proposed to account for this

influence as can be seen in work by Wroth (1984, 1988), Olsen (1984), Senneset and Janbu (1982), Douglas et al. (1985), Olsen and Farr (1986), Robertson (1989). In most of these approaches, the normalized cone resistance (Q) is computed by first subtracting overburden stress (σ_{v0}) from corrected tip resistance (q_t) and then dividing the remainder by the effective overburden stress (σ'_{v0}). Sometimes different normalization methods and iterations are applied to account for different type of soil (e.g. Robertson, 2009). In that case Q is also dependent on rod friction f_s.

In this paper, taking into account the available reading, a straightforward normalization method has been adopted. Thus, F_{dt} is first divided by σ'_{v0} and then divided by crossectional area of the drilling bit A to give the normalized penetration pressure q_n as shown in Equation 1. Moreover, as soil unit weights are only made available when laboratory investigations are performed. Besides, generally the ground water level is unknown until piezometer is installed. Therefore, a uniform effective soil weight for all layers and ground water level at terrain surface are assumed to facilitate a fast interpretation right after total sounding is finished.

$$q_n = \frac{F_{dt}}{A \cdot \sigma'_{v0}} = \frac{F_{dt}}{A \cdot \gamma' \cdot z} \qquad (1)$$

where,

q_n is the normalized penetration pressure;

F_{dt} is the penetration force measured on the top of rod;

A is the cross-area of drilling bit (i.e. $A = 2.55 \times 10^{-3}\ m^2$);

σ'_{v0} is the effective overburden stress;

γ' is the average effective unit weight of penetrated soils (a value 8 kN/m^3 is taken for simplicity);

z is depth from terrain level.

The normalized penetration pressure q_n is further smoothened by a median filter and then referred to as smoothened normalized penetration pressure and denoted as q_{ns} Besides, the gradient dq_{ns}/dz and the standard deviation of penetration force $std(F_{dt})$ within the smoothing length are also adopted. The fluctuation of penetration force F_{dt} instead of q_n or q_{ns} was found to offer better indication of soil grains composition.

A suitable length needed for smoothening q_n and calculating dq_{ns}/dz and $std(F_{dt})$ was chosen with these criteria met: (1) being small to keep resolution with depth; (2) including a reasonable amount of data in order to deliver stable results; (3) being robust for small changes of the length. In current study, 0.3 m appears to be suitable.

An example of the processed data is shown in Figure 4.

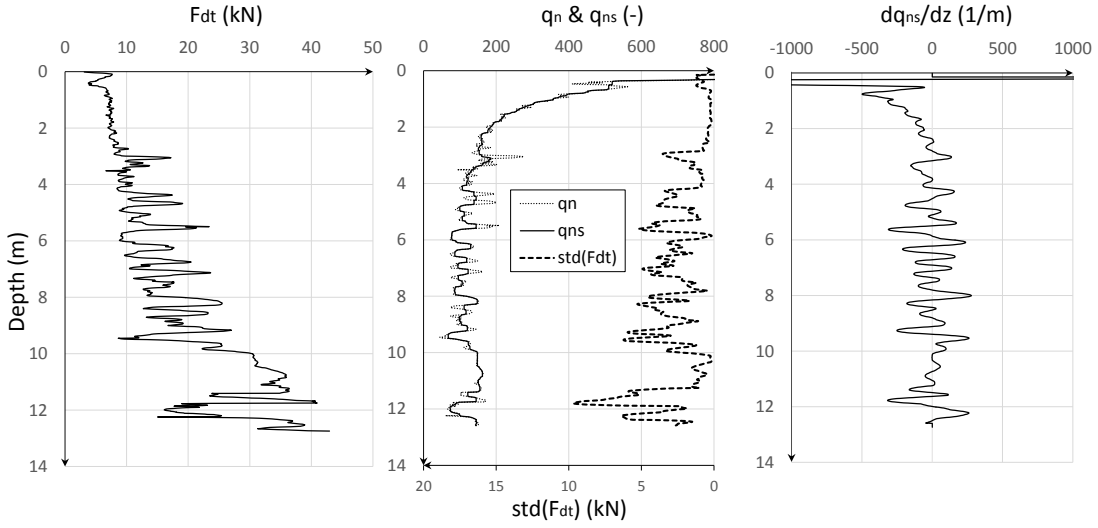


Figure 4 An example of processed sounding data (raw data taken from project Rv. 359 Kaste-Stoadalen).

4.3 Laboratory data

Grain size analysis has been performed on soil samples taken from the selected sites. This shall provide basis for soil classification. The undisturbed (c_u) and remoulded shear strengths (c_{ur}) are determined from fall cone tests. The sensitivity (S_t) is calculated as the ratio of c_u and c_{ur} (i.e. $S_t = c_u/c_{ur}$).

5 RESULTS

5.1 Possible correlations among the parameters and soil fractions

In an attempt to examine the dependence or independence of parameters q_{ns}, dq_{ns}/dz and $std(F_{dt})$ each two of them has been plotted below (Figure 5).

In all the three plots (Figure 5), most data points cluster near the origin and some others are randomly farther distributed. No simple or decisive relationships could be identified.

An attempt has also been made to correlate the parameters q_{ns}, dq_{ns}/dz and $std(F_{dt})$ to grain size distribution in terms of fractions of sand or gravel (f_s), silt (f_{si}) and clay (f_c) by weight (Figure 6). These three parameters are seen to have no role in classification of soil type in terms of fractions of specific soil grains. Nevertheless, comparatively q_{ns} and $std(F_{dt})$ tend to have better convergence of data than dq_{ns}/dz. Though considerable scattering exist, q_{ns} greater than 100 and $std(F_{dt})$ over 1.0 are likely to indicate sands or gravels.

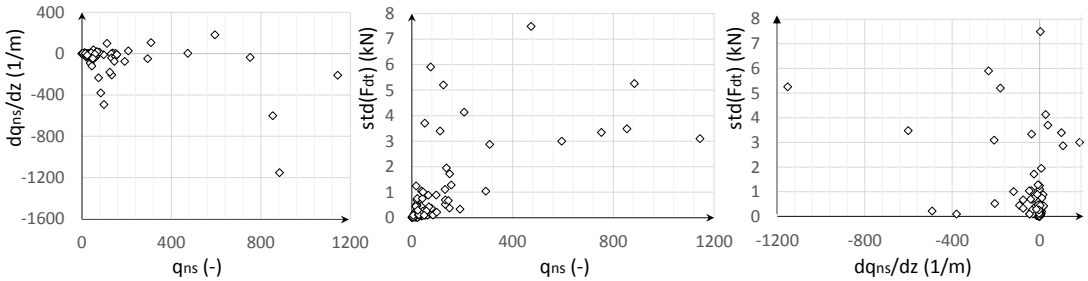


Figure 5 Correlations among q_{ns}, dq_{ns}/dz *and* $std(F_{dt})$.

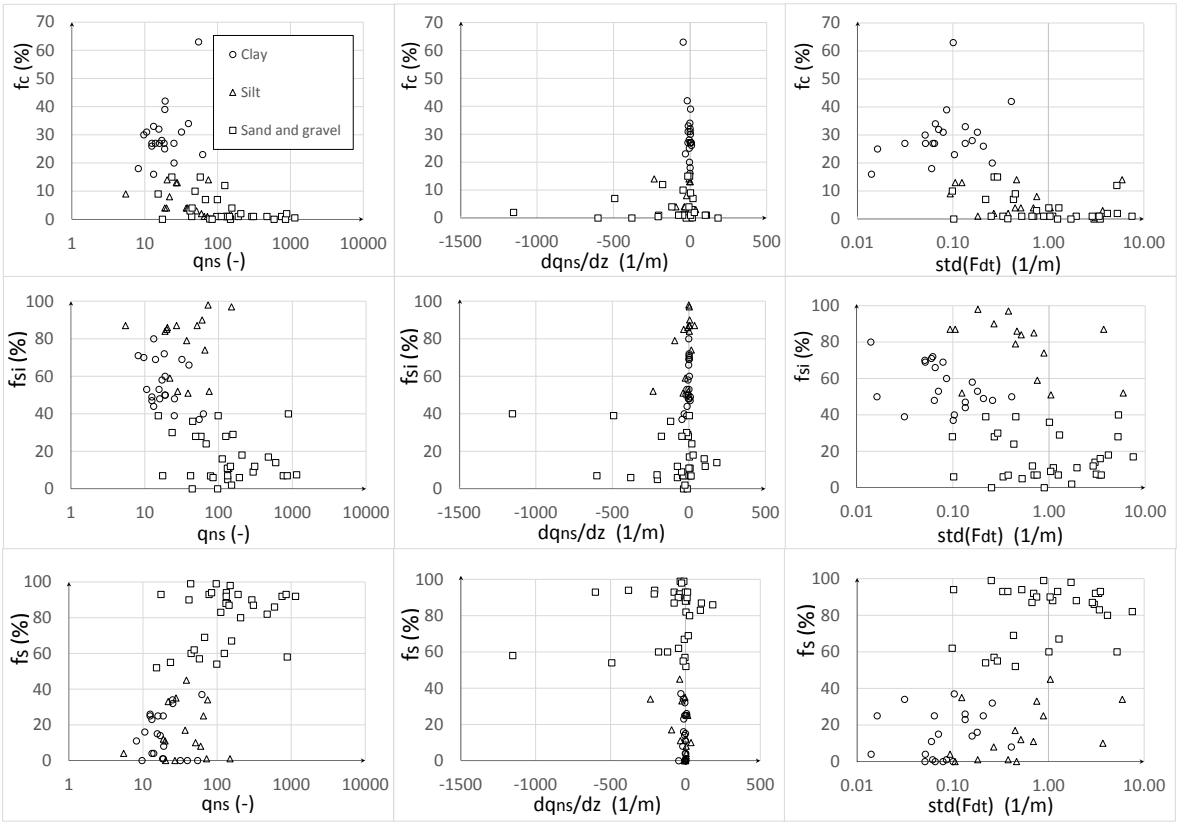


Figure 6 Correlations between parameters q_{ns}, dq_{ns}/dz *and* $std(F_{dt})$ *and grain size distribution.*

5.2 Soil classification chart

The proposed classification is based on the mechanical response of soils, in a similar fashion as CPTU soil behaviour type charts. The reference soils are classified by laboratory grain size analysis. Other mechanical properties such as friction angle, overconsolidation ratio (OCR) and physical properties like water content were disregarded. Despite this inconsistency, the current classification method, based on laboratory grain size analysis, is considered as identical to classification that incorporates comprehensive soil characteristics.

According to Figure 6, parameters q_{ns}, dq_{ns}/dz and $std(F_{dt})$ cannot be expected to deliver accurate classifications of soil based on grain size distributions but offer a guide of soil type. Besides q_{ns} and $std(F_{dt})$ have demonstrated more distinctive correlation to soil type than dq_{ns}/dz.

Having all data plotted against q_{ns} and $std(F_{dt})$ in Figure 7, the data points are found confined in a band in which $std(F_{dt})$ tends to increase with increasing q_{ns}. Within the band, three zones as separated by wide shaded transition areas could be distinguished.

In the lower-left zone, all clay-type soils are located though very few points of silt and sand can be seen near the boundary. In case of specific soil type, clays cluster closely, while silty sandy clays and silty clays distribute sparsely. In the transition area between clay and silt, a handful of all three general types of soil exist.

The zone to the upper-right is dominated by sand-type soils with one exception of silt. Manifested by gravely sand, data sets in this zone are highly scattered if plotted with linear x-axis. Another zone confined in the middle sees the majority of silts, but also has considerable number of sandy soils randomly mixed.

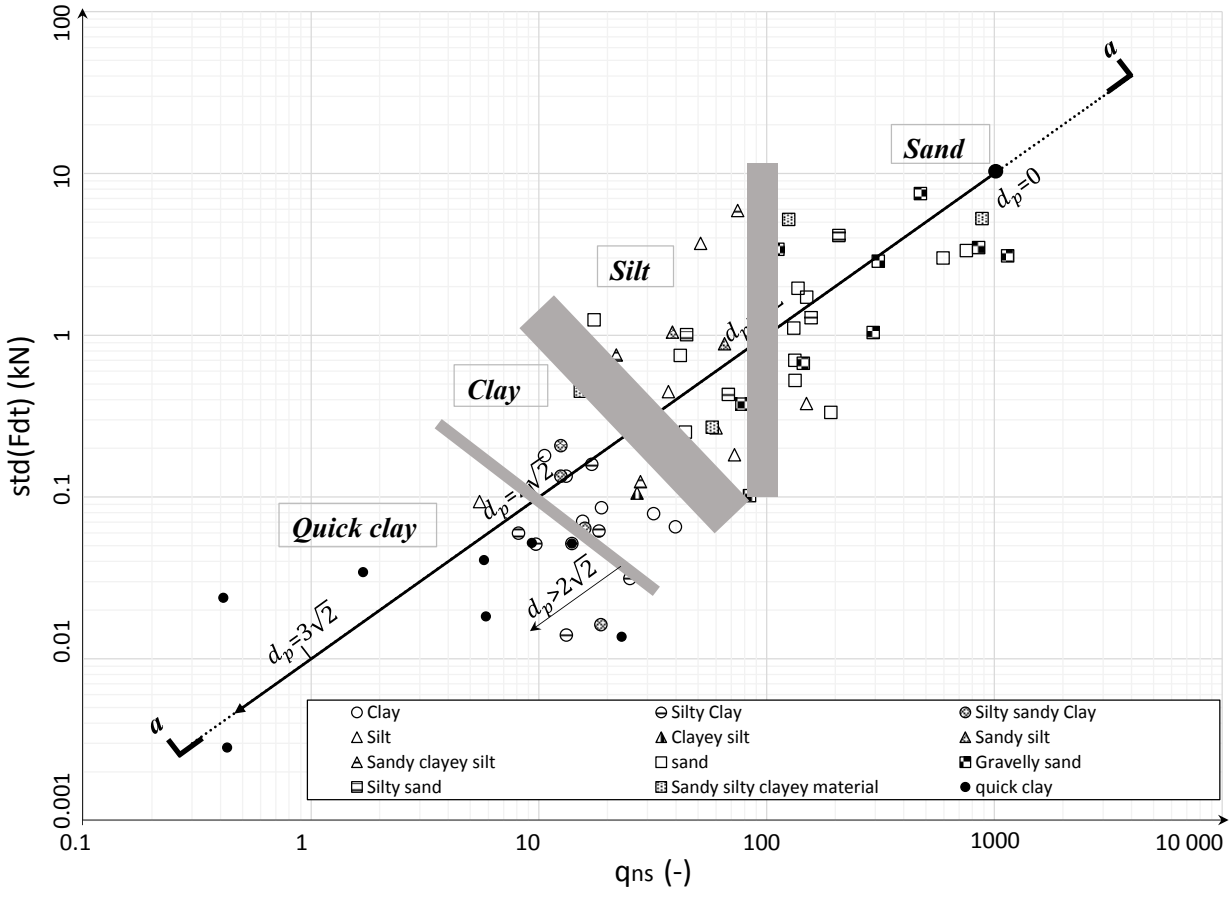


Figure 7 Soil classification chart.

One of the most important soil parameters that can be interpreted from CPTU tests is the undrained shear strength of soils (c_u) (Kjekstad et al., 1978; Lunne & Kleven, 1981; Aas et al., 1986; Senneset et al., 1982; Karlsrud et al., 2005). A common trend with these extensive studies is that there exists a correlation between c_u and excess pore pressure Δu or corrected cone resistance q_t. In the study presented in this paper, possible relations of remoulded undrained shear strength c_{ur} and sensitivity S_t to the parameters derived from total sounding (q_{ns} and $std(F_{dt})$) were also explored.

Inspired by the soil behaviour type index I_c introduced by Robertson (1998), which behaves as radius and delineates the boundaries of soil behaviour type zones, and the fact that all present data points congregate in a band, it becomes natural to study the trend of c_{ur} and S_t along the band. Therefore a line (a-a) going through the data points is chosen and defined in equation 2. Later these points are projected to line a-a, and distances are measured starting from a reference point (1000, 10) to the projected points. Then the S_t and c_{ur} information mainly of clay-type soils are plotted against their projection distance d_p (Equation 3) as shown in Figure 8.

$$\log\big(std(F_{dt})\big) = \log(q_{ns}) - 2 \qquad (2)$$

$$d_p = \sqrt{\left[\log\left(\frac{q_{ns}}{1000}\right)\right]^2 + \left[\log\left(\frac{std(F_{dt})}{10}\right)\right]^2 - 0.5\left[\log\left(\frac{q_{ns}}{100\,std(F_{dt})}\right)\right]^2} \qquad (3)$$

It can be seen that S_t increases with increased d_p while c_{ur} decreases. In spite of considerable scattering, $d_p > 2\sqrt{2}$ potentially suggests the existence of quick clay, which requires $S_t > 30$ and $c_{ur} < 0.5\ kPa$ (NVE, 2011).

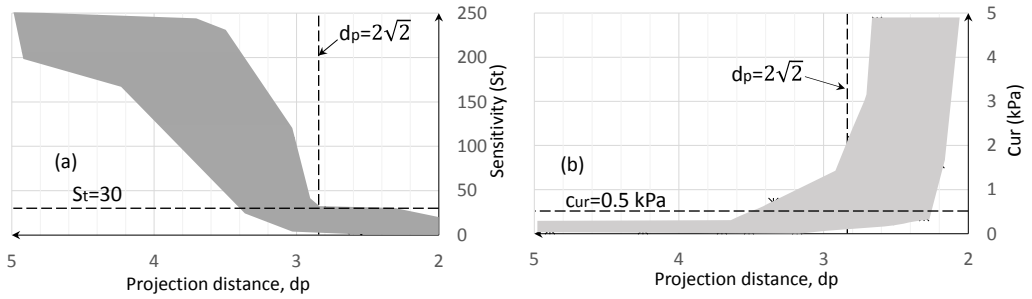


Figure 8 Sensitivity (a) and remoulded shear strength (b) on projection line a-a (in Figure 7).

6 EVALUATION AND COMPARISON

6.1 Evaluation based on employed data

Soil type zones in the proposed chart are evaluated against all data points that were employed in producing this chart in Figure 7. Results are shown in Table 1. Values in every row explain the fact that the number of data points of each soil type decided by grain size analysis is distributed over multiple zones of the chart. Underlined numbers in the table signify the dominance of good or acceptable correspondence, and thus sound predictions.

Compared with current practice of total sounding interpretation, this chart provides more objective interpretations into soil types. The major advantages are summarised as:

- Clay-type soils could be differentiated from silts, which is difficult before performing laboratory tests as only penetration force is interpreted in current practice.
- One could imply the existence of sand or gravel type soils with considerable confidence if data points lie in the upper-right zone.
- It turns out to be ambivalent when silt or mixture of silt and sand are encountered.
- When d_p exceeds $2\sqrt{2}$ the chart successfully classifies all quick clay data points correctly. However, it has been observed that some silty clays are also wrongly classified as quick clay.

Given that the analysed database is not sufficiently large, the boundaries of zones could be altered, and the specific areas for transitional soil types could be delineated after the inclusion of more data.

Table 1 Evaluation of the soundness of the proposed chart.

Results from laboratory	Predicted results by present study					
	Sand or gravelly sand	Transition sand-silt	Silt	Transition silt-clay	Clay	Quick clay
Gravelly sand	9	2				
Sand	8	1	3	1		
Silty sand	2	3	1			
Sandy silty clayey material	2	1	1	3		
Sandy silt	1	2				
Sandy clayey silt		1	1	3		
Silt	1	1	3	1	1	
Clayey silt				1	1	
Silty sandy clay				2	4	
Silty clay				1	2	5
Clay			1	1	10	
Quick clay*						8

*Silty clays that behave as quick clay are counted here.

6.2 Comparison with other classification methods

Site investigations performed in five sites, that involve both total sounding and CPTU, together with laboratory test results make it possible to evaluate the accuracy of the predictions of the present chart.

The soil behaviour type chart proposed by Robertson (1998, 2009) and the classification method developed in Swedish Geotechnical Institute (SGI) (Larsson, 2007) are adopted for comparison. In the chart by Robertson, the normalized tip resistance Q_m, the normalized friction F_r and the soil behaviour type index I_c altogether define 9 soil behaviour type zones. Using similar parameters $(q_t - \sigma_{v0})/\sigma'_{v0}$ and $f_t/(q_t - \sigma_{v0})$, SGI's chart characterizes three general soil types: clay/organic soil, silt and sand. As for silt and sand, plural subtypes are defined in light of varying firmness, which makes it distinct from Robertson's chart.

Through comparison (Table 2), some significance could be drawn as below.

- Compared with laboratory results, the proposed classification method exhibits promising consistency.
- The proposed soil classification method has another advantage over CPTU in case of firm materials, as the drilling bit is adaptive in penetrating through gravels and boulders.
- Deviation of prediction by present method is more noticeable when data points fall into the zone of silt.
- Predictions of present study seem to closely resemble the results by the soil behaviour type chart of Robertson (1998, 2009).

Table 2 Comparison with other classification methods

Site	Depth (m)	q_{ns} (-)	$std(F_{dt})$ (kN)	Soil type			
				Based on Lab. investigation	Based on total sounding	Based on CPTU	
					Present study	Robertson (1998, 2009)	SGI method
Fv32 Gimlevegen – Augestadveg en. Hovenga borehole 101	3.2-4.0	46.69	1.42	sand	silt	sand/silty sand	silt/sand
	5.2-6.0	19.73	0.31	sand	silty clay/clayey silt	silt/clayey silt	clay
	9.2-10 .0	13.18	0.41	clayey sandy silt	silty clay/clay	silt/clayey silt	silt
	16.2-17.0	6.67	1.10	clayey sandy silt (quick)	silty clay/clayey silt	sensitive soil	clay
	29.2-30.0	3.85	0.60	silty clay (quick)	clay	clay	clay
	38.2-39.0	8.73	5.08	silty clay	silt		
Fv415 Ubergsmoen borehole 1002	2.0-3.0	59.79	0.63	sand (humus)	silty sand/sandy silt	sand/silty sand	silt
	4.0-5.0	245.63	4.47	gravelly sand	sand		
	6.0-7.0	145.21	2.55	gravelly sand	sand		
Fv308 Kjelle-Barkåker borehole 1104	7.2-8.0	14.05	0.39	silty clay	clay/silty clay	clay/silty clay	clay
	8.2- 9.0	11.94	0.08	clay	clay	clay/silty clay	clay
	9.2- 10.0	12.74	0.37	clay	clay	clay/silty clay	clay
E18 Skjeggestad bru, borehole b2	5.0- 5.8	52.15	0.28	silty clay	silt	silt/clayey silt	silty clay
	7.0- 7.8	37.30	0.69	silty clay	silt	clay	clay
	10.0- 10.8	36.03	0.17	clay	silty clay/clayey silt	clay	clay
E18 Skjeggestad bru, borehole G5	2.2- 3.0	23.39	0.10	silty clay	clay	clay	clay
	5.2- 6.0	11.65	0.11	clay	clay	clay	clay
	9.2- 10.0	10.33	0.24	silty clay	clay	quick clay	clay
	11.2-12.0	9.77	0.37	quick clay	clay	quick clay	clay

7 CONCLUSIONS

In this study, a preliminary attempt towards soil classification chart from total sounding is made. In doing so, a simple normalization method to account for depth influence is introduced for measured penetration force of total sounding. Later the normalized penetration pressure (force measurement divided by the tip end area and effective overburden stress) and the standard deviation of penetration force were used to explore the possibility of classifying soils into four general soil types. This generally seems to be promising. However, noticeable ambiguity remains especially in classifying silty soils.

Sensitivity and remoulded shear strength of clays are found to demonstrate somehow a distinct trend along a projected data points band. A threshold is thus sketched to enable the detection of quick clay. Nevertheless, extensive data points are needed to improve the proposed classification chart. Through comparison with two CPTU and a laboratory based classification method, the proposed approach is seen to be in fairly consistent agreement.

In evaluation of total sounding results, factors like rod friction, inclination of rods have not been taken into considerations. And ground water level and soil unit weights have been assumed for the sake of simplicity. Additionally, the soil types referred merely express the grain size distributions; other essential information like the mechanical properties, void ratio or OCR were not incorporated.

It is vital to mention that the data adopted in this study is from selected road projects in southern part of Norway. The suitability of the proposed classification chart has to be evaluated cautiously as it is a preliminary work based on a few test sites. It will be

interesting to look at extensive sounding data from different location and ground conditions to test the applicability of the proposed approach presented in this paper.

Regarding future work, extensive studies can be foreseen. For instance, the effects of recording penetration force and torque at the rod tip rather than at the top could be explored. This is believed to reduce the effect of rod friction that has a huge effect in the current measurements resistance force from total sounding. In addition to some possible modifications to the equipment, some aspects of the test procedure (e.g. penetration rate) could be made similar to that of CPTU to explore possibility of benefiting from the existing correlations for CPTU. Another important aspect that could be considered in further development of the equipment is to explore the possibility of incorporating seismic test with total sounding. Recent developments on the use of seismic measurements with CPTU have been very promising (Mayne, 2016). Given the fact that total sounding test can be performed in any geomaterials, unlike CPTU, measuring seismic waves with total sounding seems to be appealing and one that needs to be considered. Such measurements will definitely be valuable and help significantly in better characterization of geomaterials.

8 REFERENCE

Aas, G., Lacasse, S., Lunne, T., & Hoeg, K. (1986). Use of in situ tests for foundation design on clay. Publikasjon-Norges Geotekniske Institutt, (166), 1-15.

Douglas, B. J., Strutynsky, A. I., Mahar, L. J., & Weaver, J. (1985). Soil Strength Determinations from the Cone Penetrometer Test. Civil Engineering in the Arctic Offshore (pp. 153-161). ASCE.

Fredriksen, F. (1997). P-466 Totalsondering. Statens vegvesen Intern rapport 1984.

Karlsrud, K., Lunne, T., Kort, D. A., & Strandvik, S. (2005). CPTU correlations for clays. Proceedings of the international conference on soil mechanics and geotechnical engineering (Vol. 16, No. 2, p. 693). AA Balkema Publishers.

Kjekstad, O., Lunne, T., & Clausen, C. J. (1978). Comparison between in situ cone resistance and laboratory strength for overconsolidated North Sea clays.Marine Georesources & Geotechnology, 3(1), 23-36.

Larsson, R. (2007). CPT-sondering. Swedish Geotechnical Institute, Information, (15).

Lunne, T., & Kleven, A. (1981, October). Role of CPT in North Sea foundation engineering. In Cone penetration testing and experience (pp. 76-107). ASCE.

Lunne, T., P. K. Robertson, P. K., & Powell, J. J. M. (1997). Cone penetration testing in Geotechnical Practice.

Mayne (2016). In-Situ Geocharacterization of Soils in the Year 2016 and Beyond. 15th Pan-American Conference on Soil Mechanics and Geotechnical Engineering. Geotechnical Synergy in Buenos Aires 2015 - Invited lectures, Page.139-161.

Norsk Geoteknisk Forening (1989). Veiledning for utførelse av dreietrykksondering. Melding Nr. 7.

Norsk Geoteknisk Forening (1994). Veiledning for utførelse av totalsondering. Melding Nr. 9.

Norsk Geoteknisk Forening (2016). Veiledning for utførelse av totalsondering. Melding Nr. 9, Rev. Nr. 1, 2016. (unpublished manuscript).

NVE (2011). Plan for statlig skredfarekartlegging: Delrapport kvikkleireskred. Noregs vassdrags-og energidirektorat (NVE) rapport 18/2011. Written by Wiig T., Lyche E., Helle T.E, Hansen L., Solberg I. L, L'Heureux J. S, Eilertsen R..

Olsen, R. S. (1984). Liquefaction analysis using the cone penetrometer test. InProc., 8th World Conf. on Earthquake Engineering (pp. 247-254). San Francisco: EERI.

Olsen, R. S., & Farr, J. V. (1986). Site characterization using the cone penetrometer test, Proceedings of In-situ '86, ASCE specialty Conf., Blacksburg, Virginia.

Robertson, P. K., & Campanella, R. G. (1989). Design manual for use of CPT and CPTU. The University of British Columbia, Vancouver, BC.

Robertson, P. K., & Wride, C. E. (1998). Evaluating cyclic liquefaction potential using the cone penetration test. Canadian Geotechnical Journal, 35(3), 442-459.

Robertson, P. K. (2009). Interpretation of cone penetration tests - a unified approach. Canadian Geotechnical Journal, 46(11), 1337-1355.

Sandven, R. et al. (2012). Detektering av kvikkleire fra ulike sonderingsmetoder (Rapport nr. 46/2012). Norges vassdrags og energidirektorat i et samarbeid med Statens vegvesen og Jernbaneverket.

Senneset, K., Janbu, N., & Svano, G. (1982). Strength and deformation parameters from cone penetration tests. Proceeding of the Second Eouropean Symp. on Penetration Testing, Amsterdam (pp. 24-27).

Wister, S. (2010). JB-totalsondering: Jämförande sonderingar och utvärdering av egenskaper i isälvsavlagringar kring Igelstaviken

Wroth, C. P. (1984). The interpretation of in situ soil tests. Geotechnique, 34(4), 449-489

Wroth, C. P. (1988). Penetration testing-A more rigorous approach to interpretation, Penetration Testing. ISOPT-1, 1988, 1, 303-311.

Preliminary results from a study aiming to improve ground investigation data

B. Di Buò
Tampere University of Technology, Finland, bruno.dibuo@tut.fi

M. D'Ignazio, J. Selänpää, T. Länsivaara
Tampere University of Technology, Finland

ABSTRACT
Site investigation and assessment of soil strength and deformation properties represent a crucial aspect for a safe and cost-effective design. A proper plan of laboratory and in-situ tests can provide a deep knowledge of soil behaviour. In-situ tests are becoming increasingly important in practice as, besides being cost-time effective, soil disturbance due to sampling is avoided. However, laboratory tests provide very versatile possibilities to test soil samples under various stress conditions, while in-situ testing involves more complex boundary conditions and low control over stress path.
Both field and laboratory investigations are under constant development. This paper presents some preliminary results of an ongoing study conducted at Tampere University of Technology aimed to improve the quality of ground investigation data. A new field vane has been taken into use where the rotation and torque moment are measured right above the vane. In addition, a sensitive CPTu probe is used with the possibility to connect resistivity and seismic cones into the probe. For the verification of the field investigations laboratory test are done. During the last decades many investigations have pointed out that block sampling is needed to obtain high quality undisturbed soil samples. Comparisons between results from traditional ST2 50 mm sampler and a new 132 mm Laval type piston sampler are shown. The quality of soil samples is investigated considering the strain required to reach preconsolidation pressure in oedometer test.

Keywords: soil investigation; in-situ testing; soft clay; piezocone; undrained shear strength.

1 INTRODUCTION

Site investigation plays an important role in civil engineering design. Both field and laboratory tests should be planned according to the level of knowledge required by the project. In Finland, field vane test is widely used for the determination of undrained shear strength of soft clays. Recent research studies conducted at Tampere University of Technology (Mansikkamäki 2015, D'Ignazio et. al. 2015) showed that field vane test is affected by uncertainties due to limitations of the apparatus, test procedure and some special soil conditions. The measurement of torque at the ground surface seems to be the greatest source of error, especially if casing is not used.

Unlike field vane test, piezocone test (CPTu) is not of common use in Finland. Among all the advantages, CPTu is particularly known for being an efficient and economical tool for soil investigation. Continuous (with depth) and independent information can be obtained from a single sounding. As the CPTu test is rather fast to perform, a much larger part of a site can be investigated compared to e.g. field vane test in the same time frame. Also much more versatile results can be obtained. Various correlations can be used to evaluate, for instance, the soil shear strength from the cone tip resistance, based on the soil type (e.g. Robertson and Campanella, 1983; Larsson and Mulabdic, 1991). However,

more difficulties are encountered in the determination of deformation properties based on CPTu data.

The use of piezocone can be further extended since additional sensors can be installed into the cone (Powell, 2010). Of special interest are the seismic and the resistivity modules added to an ordinary CPTu probe chassis. Such modules give the possibility to measure shear wave velocity and electric conductivity of the soil.

Due to the enormous potentiality of CPTu testing device, TUT has purchased a piezocone equipped with seismic and resistivity cone. In order to ensure accurate measurements in the very soft and sensitive Finnish clays, an extra sensitive cone with high accuracy is used. Also, a new type of vane tester has been taken into use. Its main advantage is that the rod friction is eliminated from the measurement, as the torque moment is measured right above the vane. Both equipments are integrated into a fully equipped crawler rig.

In parallel with the development of in-situ testing, a new 132 mm Laval type tube sampler has been designed by Tampere University of Technology to obtain high quality samples for laboratory testing.

The main objective of the research project is to create a database of high quality field and laboratory test results from different sites in Finland. This database will then be used to develop and verify correlations to evaluate CPTu data.

In this paper, field and laboratory data obtained from three sites is shown and discussed. Furthermore, disturbance induced by soil sampling is evaluated by comparing test results from block and piston samples.

2 EQUIPMENT AND TEST PROCEDURE

The new CPTu equipment that Tampere University of Technology has recently purchased from van den Berg consists of:

1) Pushing system installed on tracked CPT truck
2) Cone penetrometers
3) Seismic cone
4) Resistivity cone
5) Field vane apparatus
6) Data acquisition system

The penetrometer consists of a standard 60º cone, with 10 cm^2 base area and a 150 cm^2 surface area of the friction sleeve located above the cone. Excess pore pressure is measured right above the cone.

In order to get relevant information from each test site, two different cone types, with different capacities, have been used. 1) A high capacity cone with capacity of 75 MPa and 2) a lower capacity cone (hereinafter referred to as “sensitive” cone) with capacity of 7.5 MPa. As Finnish clays are very soft, the sensitive cone appears to be the most suitable for assessing tip resistance and sleeve friction. The differences between results from the two cones have so far been quite small.

Initial pre-drilling has been performed at all sites in the dry crust layer in order to avoid possible loss of saturation. The penetrometer has been then placed into the hole filled with water to ensure the temperature balancing. A successful saturation of the filter stones is very important not only for the penetration part of the test, but also for the quality of the dissipation tests. Dissipation tests are performed to evaluate the decay of pore water pressure with time at a given depth and, therefore, the equilibrium pore pressure. Results from such test are exploited to estimate the groundwater table position.

The rate of penetration of the piezocone test is 20 mm/s according to the European Standards (EN ISO 22476-1-2012). However, tests at faster and lower speed have also been performed and results are shown and discussed later.

In addition to the standard CPTu tests, resistivity and seismic tests have been also performed. The seismic cone provides additional information on shear wave velocities, thus avoiding separate downhole or cross-hole testing. Both shear and compression wave velocities can be measured and, therefore, small strain stiffness assessed.

For detailed profiling of each site, CPTu with resistivity cone has been also carried out. The conductivity method is generally used for environmental purposes, e.g. the evaluation

of contamination and corrosive potential of the soil using the electrical resistivity (see e.g. Lunne et al., 1997b). Recently, a study has been conducted to map quick clay areas using electrical resistivity measurements (Solberg et al, 2008). One important aspect to be studied in future is whether the electrical conductivity can be linked to the natural water content, which is known to correlate with deformation properties (e.g. Janbu, 1998).

Field vane test has been also performed at each test site with the new equipment. Such a test provides a continuous strength – rotation profile, revealing nicely the nature of the failure behavior. However, vane testing is often affected by uncertainties related to test procedure and disturbance caused by vane insertion and soil conditions, as also pointed out by Chandler (1988). Therefore, field vane measurements have been taken three times for all the test sites.

Results from field vane tests are later discussed and exploited to evaluate the undrained shear strength from CPTu test results.

Besides in-situ tests, laboratory tests have been performed in parallel. Sampling has been done using a new open-drive block sampler designed by the geotechnical group at TUT. At the same time, a piston sampler has been used in order to compare the quality of the test results.

Open-drive samplers consist of a tube which is open at its lower end, while in piston drive samplers the movable piston is located within the sampler tube. Piston samplers can be pushed through the soil to the desired sampling level, while open-drive samplers will admit soil as soon as they are brought into contact with, for example, the bottom of a borehole (Clayton et al. 1982).

The newly-built sampler is a small-scaled copy of the SGI type Laval open-drive block sampler (Larsson 2011). However, few changes have been made. The soil is stored in the same tube used during sampling, unlike the Swedish sampler type from which the soil is extruded in the field. This was chosen to avoid unnecessary handling of the sample and to avoid the reduction of lateral stress during sample storage.

Moreover, a cutting wire system is used prior to sampler withdrawal to isolate the soil sample. Air feeding is used to prevent suction at the cutting end.

3 DESCRIPTION OF THE TEST SITES

The investigation has been conducted so far at three different sites in the marine clay area of the South-West region of Finland. The study is mainly oriented to the evaluation of undrained shear strengh. In this section, the three test sites are described and index properties (liquid limit, *LL*, plastic limit, *PL* and natural water content, w_n), unit weight (γ) and sensitivity (S_t) are shown. Sensitivity is defined as the ratio between the intact (s_u) and the remolded undrained shear strength (s_u^{rem}), both determined from the Fall Cone test (CEN ISO/TS 17892-6 (CEN, 2004b)). From the Fall Cone test, liquid limit was also determined. Plastic limits were determined according to the standard plastic limit test (CEN ISO/TS 17892-12 (CEN, 2004c)).

3.1 Perniö test site

The Perniö test site is located on the South-West coast of Finland, near the town of Salo. A full-scale embankment failure experiment was conducted in 2009 gathering extensively amount of data which have been used for embankment stability evaluation and assessment of new soil models (Lehtonen et al., 2015).

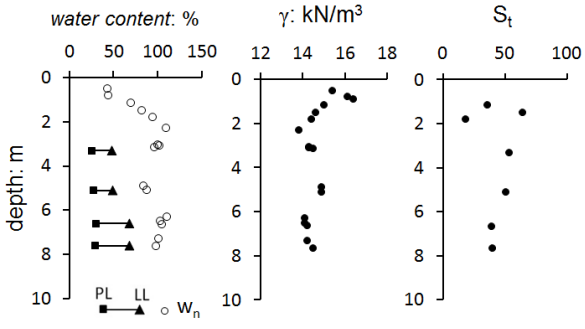


Figure 1 Properties of Perniö clay.

The site is located next to the coastal railway track connecting the cities of Helsinki and Turku. The stratigraphy consists of a 1-1.5 m thick weathered clay crust layer followed by a 8–9 m thick soft clay layer overlaying silty and stiff sandy layers located at greater

depths. Natural water content ranges from 60% to 120%, while it is lower than 50% in the dry crust. Unit weight is 15-17 kN/m^3 in the upper part and 14-15 kN/m^3 in the lower soft clay. Sensitivity (S_t) varies between 20 and 60. The piezometric level is located at 0.63 m from the ground surface according to the dissipation test. Some of the properties of Perniö clay are summarized in Figure 1.

3.2 Lempäälä test site

The site is located in the South-West region of Finland next to the railway track between Tampere and Helsinki.

The stratigraphy consists of a 1.5 m thick layer of weathered clay crust, 1–1.5 m thick layer of organic soil over a 6-7 m thick soft sensitive clay deposit. The top 4-5 m are characterized by high natural water content, between 100% and 150%, thus suggesting the presence of organic material. Below 4 m, the interval of variation of w_n is restricted to 70-80%. Measured unit weight is lower than 14 kN/m^3 in the upper part, increasing up to about 15 kN/m^3 at greater depths. Sensitivity seems to increase with depth, from 10 to 33 at about 7.5 m depth. From the dissipation test performed at 4.8 m depth, the piezometric level seems located at the ground surface, while the groundwater table is located below the dry crust layer. Properties of Lempäälä clay are shown in Figure 2.

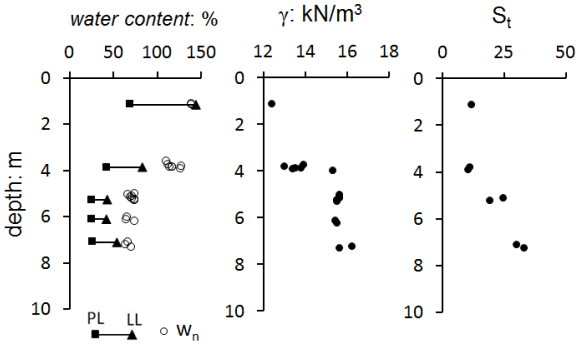


Figure 2 Properties of Lempääla clay.

3.3 Masku test site

The site is located on the South-West coast of Finland, near the city of Turku. The stratigraphy consists of 11 m thick soft clay deposit overlain by a 1.5 m thick weathered clay crust layer. Below 12 m, a stiffer clay layer is encountered. The piezometric level is located at the ground surface, according to the dissipation tests.

From a few available data points, natural water content seems to increase from 90% at 3 m depth up to about 110% at 5 m depth, decreasing to about 95% at 8 m depth. Unit weight, in accordance with the natural water content, decreases from about 15 to 14 kN/m^3 at 5 m, increasing up to about 15 kN/m^3 at 8 m depth. Only one sensitivity measurement is currently available. At 3.15 m depth S_t = 21.5. Properties of Masku clay are reported in Figure 3.

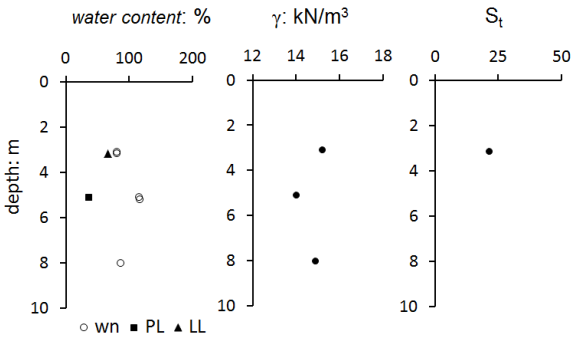


Figure 3 Properties of Masku clay.

4 PIEZOCONE TEST RESULTS

CPTu test results are available for each test site. In order to investigate the accuracy and repeatability of measurements, the tests have been repeated at different nearby points. Corrected cone resistance, friction ratio and pore pressure data are presented.

4.1 CPTu parameters

The measured cone resistance, q_c, needs to be corrected to account for "the unequal area effect" (see Lunne et al., 1997b). The area correction factor is equal to 0.75 for the piezocone used.

The corrected friction ratio is calculated from eq. (1):

$$R_f = f_t / q_T \times 100 \quad (1)$$

Where f_t is the sleeve friction corrected for pore pressure effects.

4.2 Test results

Preliminary results from Perniö, Lempäälä and Masku are shown in Figure 4, Figure 5 and Figure 6, respectively.

The piezocone was pushed up to 9 meters depth in Perniö and in Lempäälä, since the investigation was mainly focused on the soft clay layer. For Masku, measurements are available up to 15 m depth.

Consistency between measurements taken at different nearby points can be observed for all the three test sites, suggesting that good repeatibility can be obtained using CPTu test. Moreover, the high capacity cone seems to provide fairly accurate results in the soft clay layers. However, some scatter in the results can be observed in the uppermost part of the deposit both in Perniö and Lempäälä, right below the dry crust.

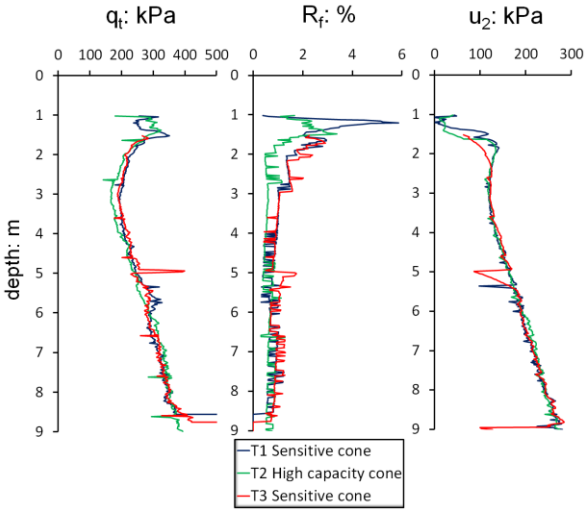


Figure 4 CPTu measurements at Perniö site.

The observable localized drops in pore water pressure in Figure 4 and Figure 5 are due to the fact that the cone penetration was stopped and a dissipation test performed.

While for cone resistance and pore pressure there seems to be a strong convergence of the measurement regardless of the cone capacity, Figure 4 and Figure 6 would suggest some discrepancy in terms of measured friction ratio. R_f estimated from the high capacity cone results lower than R_f from the sensitive cone in the top 4 m in Perniö. On the contrary, in Masku, R_f from high capacity cone is always higher than R_f from the sensitive cone. Further investigation is though needed for a better understanding of the phenomena.

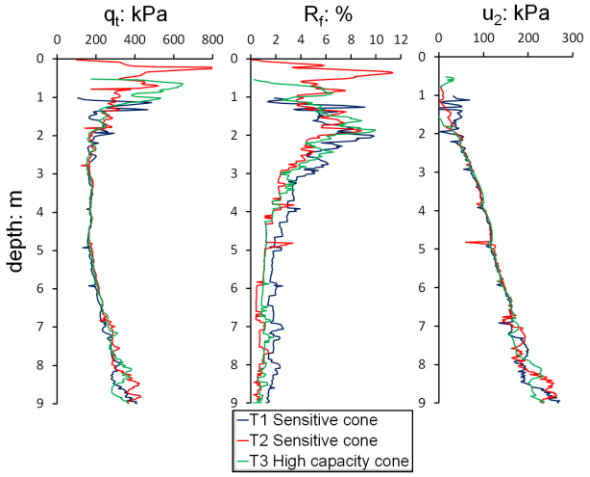


Figure 5 CPTu measurements at Lempäälä site.

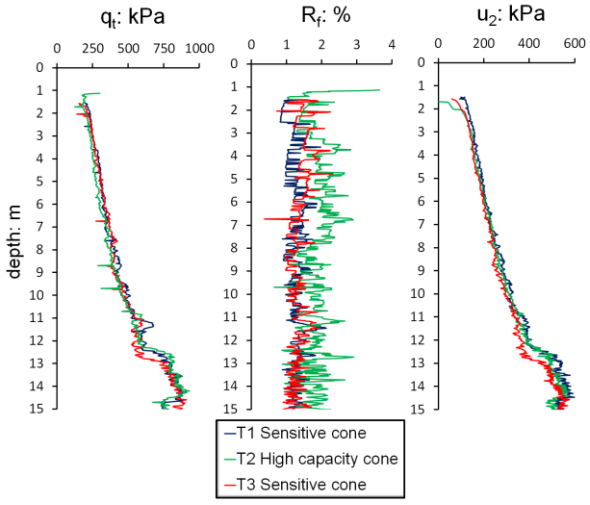


Figure 6 CPTu measurements at Masku site.

5 FIELD VANE TEST RESULTS

Field vane test results from Perniö, Lempäälä and Masku are shown in Figure 7, Figure 8 and Figure 9, respectively.

The vane used consists of four plates fixed at 90° with a length/width ratio of 2 (75 mm diameter, length of 150 mm and 2 mm thickness). Two different rotation speeds are used (EN ISO 22476-9-2014): 0.1°/sec for measuring the undisturbed peak shear strength and the residual strength (rotation of 90°), and 6°/sec for rotation >90°, to evaluate the remoulded shear strength. In particular, the remoulded strength is measured by rotating the vane 20 times at 6°/sec after reaching the 90° rotation.

The measured shear stress is plotted against the angle of rotation of the vane during shearing, up to 90°. For Masku, the vane rotation was stopped at 45°. A marked

difference between pre-peak and post peak regime is visible from the test results. The softening (post-peak) regime is initiated with a sudden and dramatic loss of shear stress at very small strain (rotation < 5°). This would suggest that the clays object of study behave like brittle materials. Moreover, in Perniö there seems to be an increase in brittleness at greater depth, as the test performed at 7 m depth shows a more noticeable strength loss after peak than at 4.80 m depth. From previous oedometer test results (Länsivaara 2012) a higher structuration was found for samples taken from 6.5 m depth than for samples from shallower depths.

Nevertheless, even when using a more sophisticated vane, some disturbance always occurs. The new field vane used in the current research project is driven into the ground protected by a steel casing. The vane is eventually pushed down when the desired depth is reached and then rotated. Disturbance mainly affects peak strength, but it can also cause higher strain at peak, as shown in Figure 9. The amount of disturbance remains though hard to evaluate, and it may not be the same for each measurement. For this reason, field vane test is repeated at least once or twice for each depth.

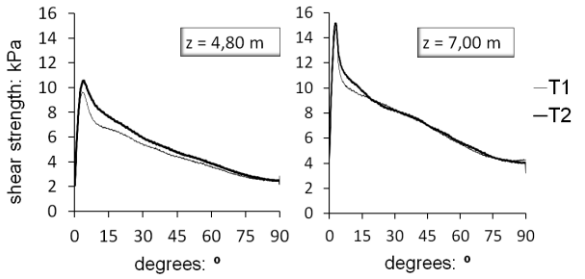


Figure 7 Field vane test in Perniö clay at different depths.

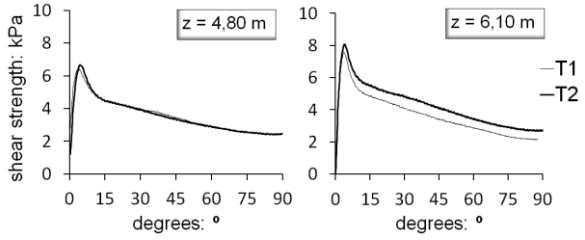


Figure 8 Field vane test in Lempäälä clay at different depths.

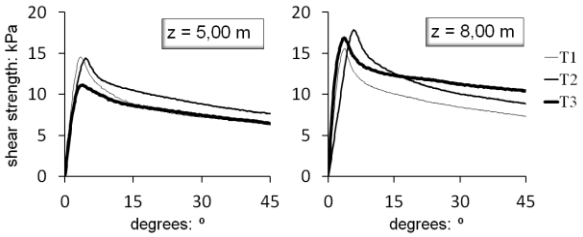


Figure 9 Field vane test in Masku clay at different depths.

6 DETERMINATION OF UNDRAINED SHEAR STRENGTH

6.1 Transformation models used

A preliminary evaluation of the undrained shear strength at the test sites is done by exploiting both piezocone and field vane measurements. Field vane data points are corrected based on plasticity according to the guidelines of Finnish Road Administration [eq. (2)]. Undrained shear strength (s_u) is evaluated from both cone tip resistance and pore pressure measurements according to the transformation models of eq. (3) and eq. (4), respectively.

$$\mu = \frac{1.5}{1+W_L} \tag{2}$$

$$s_u = \frac{q_t - \sigma_{v0}}{N_{kt}} \tag{3}$$

$$s_u = \frac{u_2 - u_0}{N_{\Delta u}} \tag{4}$$

Where W_L is the liquid limit of the clay, q_t is the corrected cone resistance, σ_{v0} the total overburden vertical stress, u_2 the measured pore pressure, u_0 the hydrostatic pore pressure, N_{KT} the cone factor for q_t and $N_{\Delta u}$ the cone factor for $\Delta u=u_2-u_0$.

To evaluate the cone factors, different equations have been tested. As non of them gave a superior fit, the cone factors presented in this study have been determined by fitting the results to undrained shear strength values obtained from the new vane test. A range of cone factors is given for each site, since a single value of N_{kt} or $N\Delta_u$, could not cover the entire variation with depth. In order to obtain the best fit to the vane results, the soil

has been divided into layers with assigned cone factors based on variability of other properties. Such variability might depend on e.g. index parameters, such as the liquid limit (Larsson and Mulabdic, 1991).

6.2 Results

As the scatter in the field vane data points is quite low, the estimation of cone factors (N_{kt} and $N_{\Delta u}$) for Perniö clay appears to be fairly reliable (Figure 10). Further investigation is though needed in the top 3 m, where field vane data disagree with the cone measurements. Such deviation may be due to soil disturbance caused by the insertion of the vane into the soil right below the dry crust layer. Above 2 m depth the soil is stiffer and more over consolidated. As suggested by Karlsrud et al. (2005), over consolidation might affect cone factor values. Therefore, using $N_{\Delta u}$ for estimation of undrained shear strength would not seem appropriate in over consolidated soils, unless dependence of $N_{\Delta u}$ on OCR is studied.

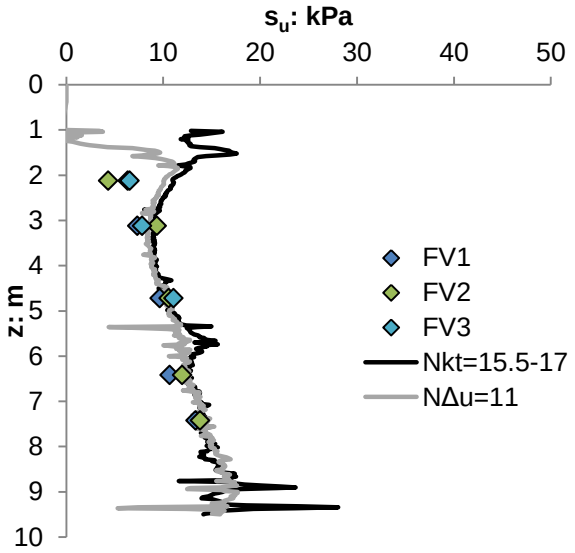


Figure 10 Undrained shear strength of Perniö clay from field test results.

The undrained shear strength at Lempäälä site can be satisfactorily assessed by using N_{kt} varying from 13 to 15 (Figure 11). However, using $N_{\Delta u}$ would lead to a severe underestimation of s_u in the top 4.5 m. One possible reason could be the presence of organic material in the upper 4-5 m (as discussed in section 3.2), besides a clearly high over consolidation, causing low excess pore pressure during cone penetration. On the other hand, N_{kt} values used seem to give a good estimate of s_u of the organic layers. These aspects need though more thorough investigation in the future.

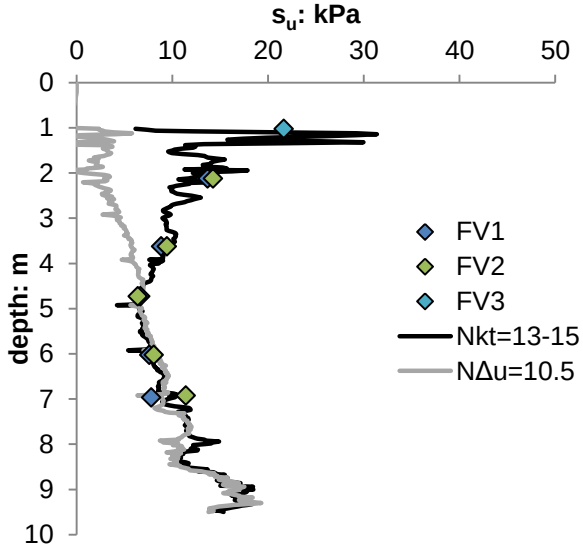


Figure 11 Undrained shear strength of Lempäälä clay from field test results.

Field vane test results from Masku show the highest scatter among the three test sites (Figure 12). In this regard, mineralogy and geological conditions at the test site may have affected the performance of the tests. As suggested by the q_t profile with depth, there seems to be noticeable layering, which may have caused variation of the peak strengths.

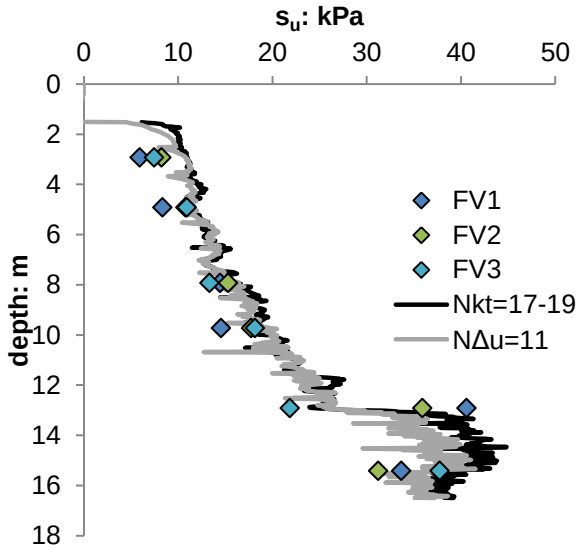


Figure 12 Undrained shear strength of Masku clay from field test results.

The cone factor N_{kt} resulted higher than in the other two test sites (N_{kt}=17-19 versus N_{kt}

ranging from 13 to 17). Nevertheless, s_u predicted by $N_{\Delta u}$ is consistent with the shear strength obtained using N_{kt}.

7 RESISTIVITY AND SEISMIC TESTS

7.1 Electrical conductivity

The resistivity module is embedded in the cone. It consists of four electrodes and a temperature sensor and it provides a measure of the electrical conductivity and temperature with depth.

Figure 13 shows the conductivity data from the three test sites. To avoid loss of saturation, 1 m pre-drilling was made. In the upper layer some fluctuations in the measurements can be observed, mainly due to the partial saturation of the upper clay. On the other hand, high data quality and repeatability is observed in the lower soft clay.

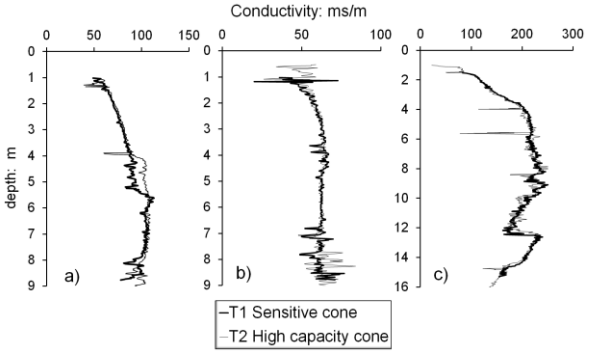


Figure 13 Electrical conductivity at a) Perniö, b) Lempäälä, c) Masku.

7.2 Seismic parameters

The shear wave velocity (V_s) profile with depth can for example be used to evaluate the maximum shear modulus (G_0 or G_{max}) as shown by eq. (5).

$$G_0 = \rho V_S^2 \tag{5}$$

Where ρ is the soil mass density.

Seismic cone consists of a piezocone unit with a receiver placed right above it. Extra equipment is needed, such as oscilloscope and impulse source. The source consists of a steel beam pressed against the ground by the weight of the CPT vehicle. The shear wave is generated by hitting the beam with the hammer in different directions in order to create compression and shear waves. The test has been repeated at 1 m intervals. During the pause in penetration, waves are generated and their intensity is measured from the time required to reach the seismometer. Seismic cone test results from the test sites are shown in Figure 14. Good repeatibility is obtained at Masku site (Figure 14c), while a moderate scatter in the data can be observed at Perniö (Figure 14a). Further investigation is required to evaluate factors affecting the measurements. In-situ bender element test has also been performed and data is compared with those obatined from the seismic test. In order to investigate the disturbance induced by transportation and storage, bender element test is repeated at different times as an indicator of sample quality. However, the study is still ongoing and results will be shown in a later publication.

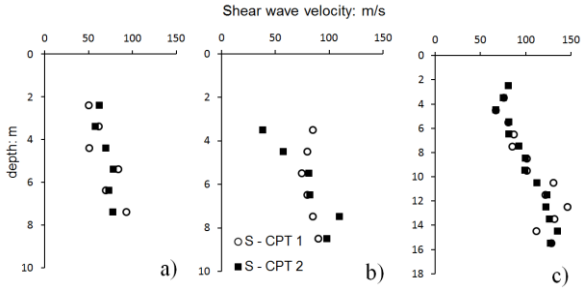


Figure 14 Shear wave velocity at a) Perniö, b) Lempäälä, c) Masku.

8 TESTS AT DIFFERENT RATES

According to the European Standard ISO 22476-1-2012, the rate of penetration for a CPT test is 20 mm/s ± 2 mm/s. A study conducted by Danziger et al. (1997) has shown that rate effects are visible when the rate of penetration deviates from the standard.

By varying the rate of penetration during a CPT test it may be possible to simulate undrained, partially drained or fully drained conditions for a particular soil, especially for intermediate soils such silts (Lunne et al., 1997b). However, since the investigation is conducted mainly in soft clay deposits, the penetration is considered fully undrained for all the different tests. Bemben and Myers (1974) conducted a study on the influence of penetration rate in a lightly overconsolidated

varved clay using speeds between 0.2 mm/s and 200 mm/s. The minimum value of cone resistance was obtained at 2 mm/s.

The influence of penetration rate has been investigated at Masku test site. Results are shown in Figure 15.

It can be noticed that an increase in cone resistance is obtained by increasing the penetration rate. Accordingly, the test performed at lower speed (0.5 cm/s) shows lower values of tip resistance. However, pore pressures do not seem to be affected by the speed of penetration. In addition, it appears difficult to detect marked differences from the measured friction ratios.

For a better understanding of the influence of penetration speed, collected data will be elaborated in the near future. Preliminary results clearly show that viscous effects and water drainage at different penetration rates may affect the measurements.

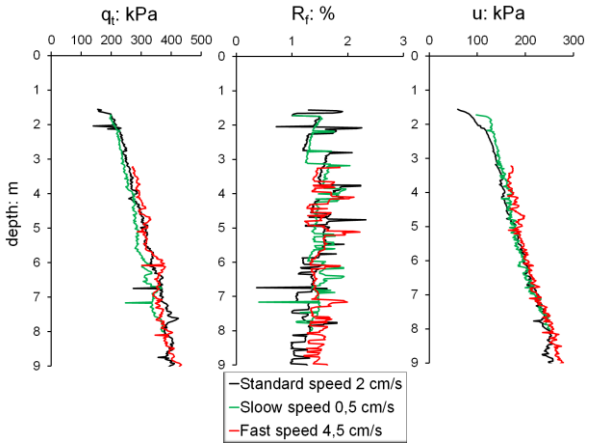


Figure 15 CPTu measurements at different penetration rates at Masku test site.

9 LABORATORY TEST RESULTS

Laboratory tests on undisturbed specimens obtained from both tube and piston samplers have been carried out. Piston samples from Masku are not available at present.

Preliminary results from CRS (constant rate of strain) oedometer tests from the test sites at different depths are shown in Figures 16-18, where the main effective vertical stress is plotted against the total vertical strain.

A standard test procedure has been adopted for sample trimming and preparation. Therefore the quality of the test results would be mainly affected by the sampling procedure.

CRS-oedometer test results from Perniö clearly show that piston samples do not provide a distinct value of preconsolidation pressure (σ'_p). On the contrary, clearer transition from the over consolidated to the normally consolidated state can be observed from the block samples. Piston and block samples from Lempääla show, instead, comparable values of σ'_p. CRS tests from Masku show a net change in stiffness beyond the preconsolidation stress.

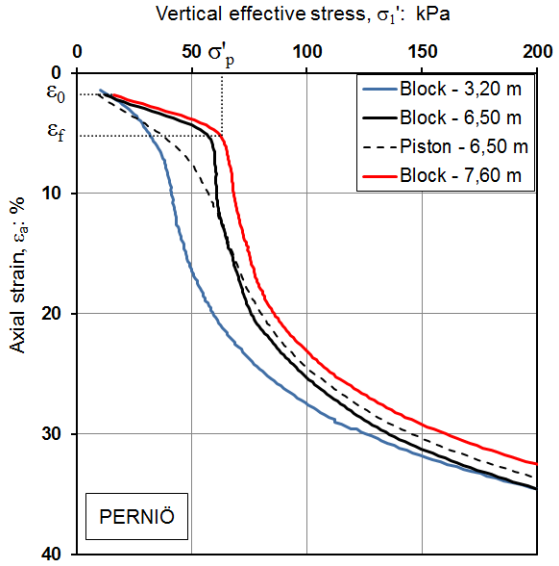


Figure 16 CRS tests on block and piston samples of Perniö clay.

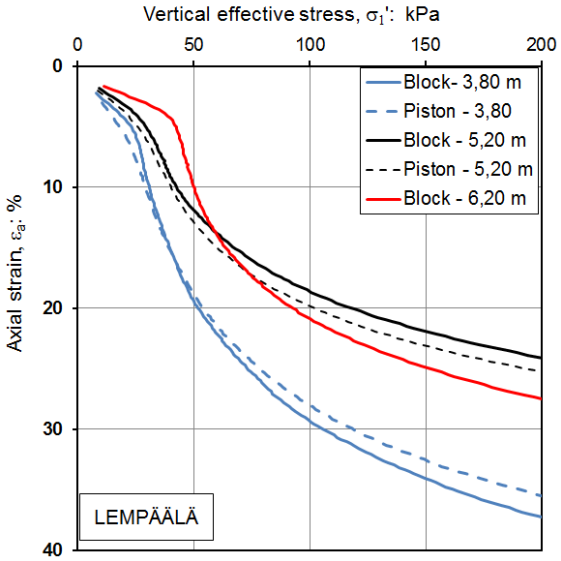


Figure 17 CRS tests on block and piston samples of Lempäälä clay.

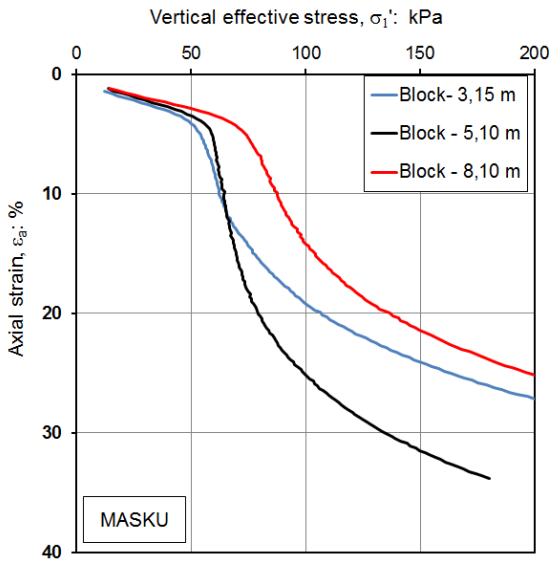


Figure 18 CRS tests on block samples of Masku clay.

The sample quality of CRS oedometer tests has been investigated using the method proposed by Lunne et al. (1997a), and results are shown in Figure 19. The increment of vertical strain (ε_p) needed to reach preconsolidation pressure is plotted against the water content. ε_p is the difference between ε_f and ε_0, as defined in Figure 16.

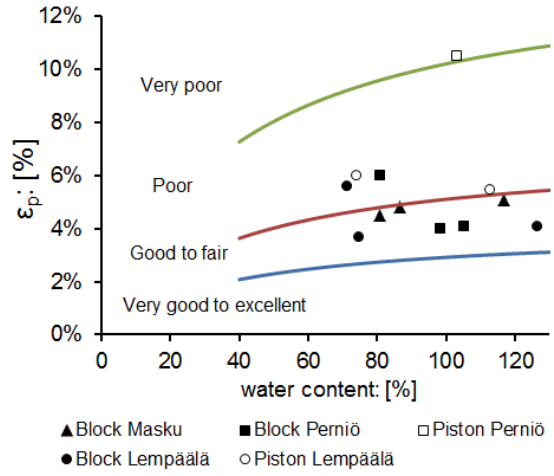


Figure 19 Vertical strain at preconsolidation pressure from CRS oedometer tests compared to the limits of disturbance categories by Lunne et al. (1997a).

According to the boundary lines suggested by Lunne et al. (1997a), the quality of the tested specimens trimmed from the block samples seems reasonably good. Conversely, those obtained from the piston sampler are generally characterised by lower quality. It must be also mentioned that preconsolidation pressure could not be observed for the majority of the piston samples. Therefore, data points could not be reported in Fig. 19. In order to evaluate the impact of sampling procedure on the quality of the test results, further investigation is though needed. The influence of soil structure and mineralogy should be also addressed in the future.

10 CONCLUSIONS

Tampere University of Technology has been carrying out a research project on the calibration of CPTu test in Finnish clays. The main goal is to create a database of clay parameters from high quality in-situ and laboratory tests and derive transformation models for strength and deformation properties.

In this study, some preliminary test results from three test sites from Finland are presented and discussed.

Piezocone test results are compared to field vane test results obtained using an innovative in-situ vane tester. Cone factors for undrained shear strength are hence evaluated.

The piezocone used includes also seismic and resistivity modules. Moreover, penetration tests performed at different rates showed a positive trend between measured cone resistance and test speed.

The quality of the specimens taken from block and piston samples is assessed based on the vertical strain needed to reach the preconsolidation pressure in oedometer tests. CRS oedometer tests on block samples from the test sites suggest that sample quality is generally higher than the quality obtainable from a piston sampler.

11 REFERENCES

Bemben, S.M. and Myers, H.J. (1974). The influence of rate of penetration on static cone resistance in Connecticut River Valley varved clay. In Proceedings of the European Symposium on Penetration Testing, ESOPT, Stockholm, Vol. 2(2), 33-43.

CEN, (2004b) ISO/TS 17892-6: Geotechnical investigation and testing. Laboratory testing of soil. Part 6: Fall cone test. Brussels, Belgium: CEN.

CEN, (2004c) ISO/TS 17892-12: Geotechnical investigation and testing. Laboratory testing of soil. Part 12: Determination of Atterberg limits. Brussels, Belgium: CEN.

Chandler, R. J. (1988). The in-situ measurement of the undrained shear strength of clays using the field vane. In Vane shear strength testing in soils: field and laboratory studies, 13-44.

Clayton, C. R., Simons, N. E., & Matthews, M. C. (1982). Site investigation.

Danziger, F. A. B., Almeida, M. S. S., & Sills, G. C. (1997). The significance of the strain path analysis in the interpretation of piezocone dissipation data. Geotechnique, 47(5), 901-914.

D'Ignazio, M., Di Buò, B., & Länsivaara, T. (2015). A study on the behaviour of the weathered crust in the Perniö failure test. In Proceedings of the XVI European Conference on Soil Mechanich and Geotechnical Engineering, XVI ECSMGE, Edinburgh, Scotland, ICE Publishing, 3639-3644.

ISO. 2012. Geotechnical investigation and testing - field testing - part 1: Electrical cone and piezocone penetration test. ISO 22476-1. 2012.

ISO. 2014. Geotechnical investigation and testing - field testing - part 9: Field vane testing. ISO 22476-9. 2014.

Janbu, N. (1998). Sediment deformation. Bulletin 35. Norwegian University of Science and Technology.

Karlsrud, K., Lunne, T., Kort, D. A., & Strandvik, S. (2005). CPTU correlations for clays. In Proceedings of the international conference on soil mechanics and geotechnical engineering, Vol. 16(2), AA Balkema.

Larsson, R. (2011). Metodbeskrivning för SGI:s 200 mm diameter 'blockprovtagare'-Ostörd provtagning i finkornig jord (In Swedish) Swedish Geotechnical Institute, SGI. Göta River Commission. GÄU. Subreport 33. Linköping.

Larsson, R., & Mulabdic, M. (1991). Piezocone tests in clay. Swedish Geotechnical Institute, Linköping, Sweden. Report No. 42

Lehtonen, V. J., Meehan, C. L., Länsivaara, T. T., & Mansikkamäki, J. N. (2015). Full-scale embankment failure test under simulated train loading. *Géotechnique*, 1-14. doi:10.1680/jgeot.14.P.100

Lunne, T., Berre, T., & Strandvik, S. (1997a). Sample disturbance effects in soft low plastic Norwegian clay. In Proceeding of the International Symposium on Recent Developments in Soil and Pavement Mechanics. Rio De Janeiro, Brazil, 81-102.

Lunne, T., Robertson, P. K., & Powell, J. J. M. (1997b). Cone Penetration Testing in Geotechnical Practice, Blackie Academic and Professional, London.

Länsivaara, T. (2012). Some aspects on creep and primary deformation properties of soft sensitive Scandinavian clays. In Proceedings of the 16th Nordic geotechnical meeting, NGM, 9-12 May 2012, Copenhagen, Denmark. pp. 397-404.

Mansikkamäki, J. (2015). Effective stress finite element stability analysis of an old railway embankment on soft clay. PhD thesis, Tampere University of Technology, Tampere.

Powell, J. J. M. (2010). Session Report 1: CPT Equipment & Procedures. In Proceeding of the 2nd International Symposium on Cone Penetration Testing, CPT'10, California 2010.

Robertson, P. K., & Campanella, R. G. (1983). Interpretation of cone penetration tests. Part II: Clay. Canadian Geotechnical Journal, 20(4), 734-745.

Solberg, Inger-Lise; Ronning, Jan Steinar; Dalsegg, Einar; Hansen, Louise; Rokoengen, Kare; Sandven, Rolf (2008). Resistivity measurements as a tool for outlining quick-clay extent and valley-fill stratigraphy: a feasibility study from Buvika, central Norway. Canadian Geotechnical Journal 45, (2), pp210-225, 2008/02

Solutions for Various Obstacles Encountered with Laboratory Piping Tests

Montalvo-Bartolomei, A.M.
U.S. Army Engineer Research and Development Center, Vicksburg, MS, United States of America
axel.m.montalvo-bartolomei@usace.army.mil

López-Soto, J.F., Stephens, I.J., Robbins, B.A.
U.S. Army Engineer Research and Development Center, Vicksburg, MS, United States of America

ABSTRACT
Backward erosion piping, historically called piping, is a form of internal erosion that refers to a process by which seepage forces gradually erode soil particles from beneath a water-retaining structure creating an open pipe from the downstream to the upstream end of the structure, such as dams and levees. Piping may lead to the failure of a structure. Different approaches have been developed to estimate the critical hydraulic gradient necessary for the initiation and continuation of piping. Laboratory tests, physical models, and empirical equations are among the approaches that researchers have used to determine critical gradients. The Engineer Research and Development Center of the U.S. Army Corps of Engineers developed a small scale, laboratory flume to measure the critical gradient of nine uniform sands. Several obstacles were encountered during the initial testing phase. Examples of these complications include entrapped air in the system, ensuring that piping occurred in the center of the sample, and problems caused by head losses. The corrective actions that were implemented for the completion of a successful test program are discussed. The solutions used to overcome these obstacles led to repeatable tests with satisfactory results. The solutions are presented to ensure future efforts can make use of the lessons learned.

Keywords: piping, flume test, backward erosion, dams, levees

1 INTRODUCTION

Erosion is considered the most common cause of incidents and failures in dams and levees due to either overtopping or internal erosion (Bonelli, 2013). Internal erosion refers to any type of erosion that occurs within or beneath an embankment. According to Foster et al. (2000), internal erosion constitutes almost half (46.1%) of dam failures around the world. There are four different types of internal erosion: concentrated leaks, suffusion, contact erosion, and backward erosion piping (USACE & USBR, 2012; ICOLD, 2015). Backward erosion piping (BEP) occurs when particles are eroded away at an unfiltered exit, and a "pipe" is formed under a more cohesive material, progressing from the downstream to the upstream end of an embankment in the opposite direction of flow. The pipe is formed in the foundation material beneath the embankment.

Laboratory tests have been performed around the world as a way to study the phenomenon of BEP. The results of laboratory tests have been used to propose theoretical or empirical models that predict BEP. Small-scale and medium-scale tests have been typically performed in box-shaped flumes filled with soil samples. BEP research is currently being conducted at the U.S. Army Engineer Research and Development Center (ERDC) in Vicksburg, MS, USA.

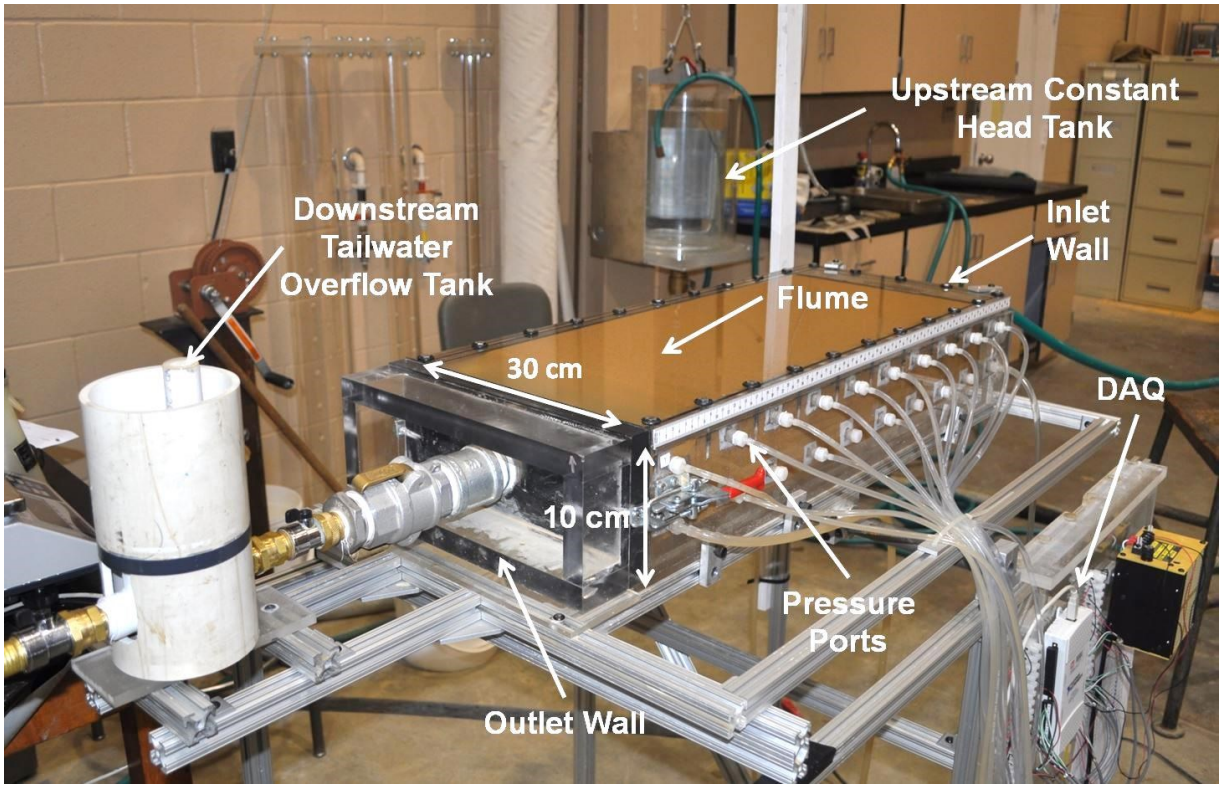


Figure 1. Overview of the small-scale flume and rest of equipment.

In the 1980s, laboratory tests to study BEP were performed by Townsend et al. (1981) and Townsend & Shiau (1986) at the University of Florida (UF) and by de Wit et al. (1981) and de Wit (1984) in the Netherlands. The research at the University of Florida was conducted by testing sands using a flume to determine the average hydraulic gradient at piping. Similarly, the studies at the Delft Soil Mechanics Laboratory in the Netherlands were performed using a flume and tested a range of sands with different particle sizes, exit conditions, and experiment scales. More recently, small-scale and medium-scale experiments have been performed by van Beek et al. (2010, 2011, 2014) at Deltares in the Netherlands. These laboratory tests were conducted to study the processes of initiation and progression of piping. These studies were performed in parallel with numerical analyses to study the local hydraulic conditions at the initiation of piping.

A similar experimental study to measure critical horizontal gradients in laboratory flumes was initiated in 2013 at ERDC. A small-scale flume was constructed to test a variety of uniform sands (Figure 1). The objective of these tests was to study the hydraulic conditions required for BEP by measuring the horizontal gradient at the moment of initiation. In these tests, flow through a soil sample would be gradually increased at discrete time intervals until BEP would initiate and progress through the entire sample. The results obtained from the tests performed in this apparatus were compared with the test results in the literature and the predicted values obtained from models such as those proposed by Sellmeijer (1988), Schmertmann (2000), and others.

The small-scale flume discussed in this paper was designed and built by taking into consideration the designs of the different laboratory flumes found in the literature. The testing program aimed at estimating the critical gradient required for BEP to initiate and progress through nine poorly-graded sands with similar coefficients of uniformity. The two principal variables of these tests were the soil grain size and density. The smallest and largest of these sands had a median grain size diameter (d_{50}) of 0.30 mm and 2.52 mm, respectively. Samples were tested either in a loose state or a dense state. To achieve a loose state, the soil was placed

carefully without any compaction effort, while the dense state was achieved by compaction of the sand in lifts. The size of the flume made it possible to rapidly construct uniform, high quality samples such that a large number of tests could be completed. The goal of the testing program at ERDC was to perform more than one test per workday. However, some issues were found that needed to be corrected to be able to run the tests smoothly and to obtain the necessary results. This paper presents a brief description of the design of the small-scale flume device, the problems and issues encountered during the testing program, and the implemented solutions that resulted in repeatable tests.

2 DESCRIPTION OF SMALL SCALE FLUME FOR BEP TESTS

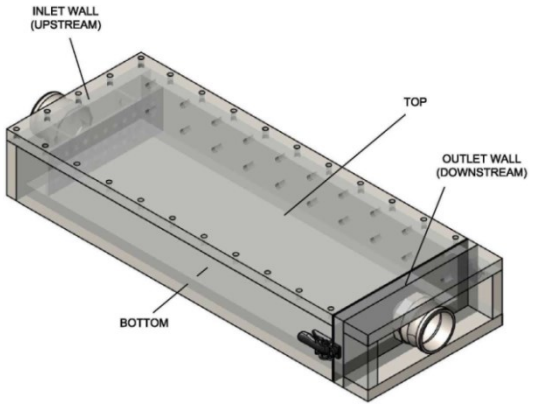


Figure 2. Schematic of small-scale flume.

The small-scale flume was designed and built as a rectangular-shaped box (Figure 2). The flume was built with 2.54-cm-thick acrylic (top, bottom, and all of its walls). The acrylic design permitted a clear view of the whole sample before, during, and after a test. Seeing through the flume would be effective not just for monitoring the initiation of piping, but also during sample preparation for visual inspection of air bubbles trapped in the system.

The top of the flume was attached along the edges of three walls by 25 bolts. The outlet wall of the box was designed to be removable and was attached to the side walls using two latches, one on each side of the flume. The leak-proof seal was obtained by O-ring gaskets and vacuum grease in shallow grooves between the removable faces and the body of the flume. Also, a closed-cell foam rubber sheet was adhered to the outlet wall, allowing a better sealing contact.

To ensure integral contact between the soil and acrylic, the flume was designed to be rotated 90° from an upright vertical position for filling (Figure 3) to a horizontal position for testing (Figure 4). This is similar to the tests performed by van Beek et al. (2011), whereas the flume used by Townsend et al. (1981) used a rubber bladder to apply pressure and ensure contact between the sand and the acrylic top. After testing, the flume could then be rotated an additional 90° to empty the flume by gravity. The flume was mounted to a custom frame designed for its rotation. This frame was built with aluminum t-slotted framing (80/20). The design of the frame took into consideration its capacity to sustain the weight of the flume, hoses, soil, water, and instrumentation. A rod and bearings made it possible to rotate the flume smoothly a full 180°.

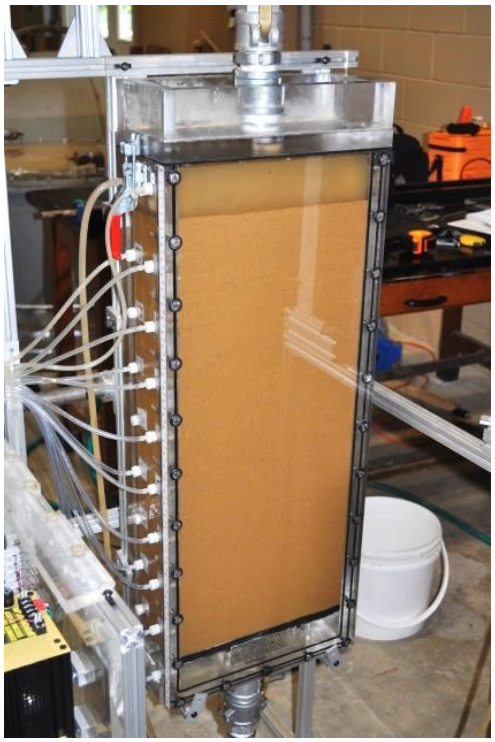


Figure 3. Small-scale flume in vertical position after sample preparation.



Figure 4. Small-scale flume in horizontal position for testing.

At the beginning of sample preparation, the outlet wall (downstream side of flume) was removed and the flume was rotated to the vertical position. Full saturation of samples was obtained by first filling the flume with water and pluviating (or "raining") the air-dry sand into the flume (Figure 5). This method was used to prevent trapped air in the soil sample. Typically, about half of the flume was filled from the inlet with water before placing sand, and this was sufficient for full saturation of the sample. For the majority of the tests, a constant head water tank was used for supplying constant flow. This tank supplied water through a hose attached to the inlet wall of the flume with a 3.81-mm NPT (National Pipe Thread) stainless steel male-female coupling connector.



Figure 5. Pluviating sand for the preparation of test sample.

The pore pressures during the test were monitored continuously to study the hydraulic conditions during the test. The flume had twenty 0.635-cm threaded holes on one side wall that were used for obtaining pore pressure data inside the sample. From the available ports, sixteen were used for testing, and the rest were plugged. Fourteen pressure transducers (Honeywall 26PC – ranges from 0.0-34.5 kPa) were connected to fittings in each hole by using clear PVC 0.3175-cm tubes. The remaining two ports were used for manometers that allowed for real-time visual readings upstream and downstream and that could be compared to the pore pressure readings. Clear PVC tubes with a diameter of 0.635 cm were used for these manometers. The average global gradient of the sample was estimated quickly by using the difference in head readings and dividing it by the shortest flow path, measured at the top of the soil sample. It was important to ensure that all of these tubes were fully saturated and that no air bubbles were present during the tests, as they could cause erroneous pressure readings. As the flume was being saturated, water was allowed to enter the PVC clear tubes, thus releasing the air from them. After all the air exited these tubes, they were connected to the pore pressure transducers, ensuring accurate readings.

Samples tested in the small-scale flume were prepared in two states: loose or dense. The flume holds approximately 30 to 40 kg of sand, and the desired density conditions were obtained through compaction during preparation. This allowed studying the effect that density had on the hydraulic critical gradient for piping. To prepare the samples in a loose state, the sand was pluviated into the water continuously while avoiding any vibrations. Dense samples were prepared by compacting with a steel rod and tapping the acrylic with a rubber mallet. Typically, the sample would be densified in lifts 10 cm thick. The highest density possible, using this densification method, was always desired when preparing dense samples. If a desired density had to be achieved, the required weight for obtaining it was calculated, and the sand would be densified accordingly.

The soil sample formed a slope between the acrylic top and a downstream filter wall. This wall, a perforated acrylic plate covered with filter fabric, held the sample in place while letting water flow through. After the samples were prepared, this plate was placed on top of the sand. Six steel springs were fixed to the plate, and they pushed against the outlet wall as the flume was closed with the latches. When rotating the flume to the horizontal position, particles roll down over this half wall and a slope is naturally formed on the sample exit. During testing, eroded soil particles fall to the bottom of the flume without interrupting the erosion process, while some others were washed away during the test.

After attaching the outlet wall and conducting a final visual inspection to ensure there was no air trapped in the flume or in the tubes, the water was raised until water came out of the downstream overflow tailwater tank attached to a 3.81-mm NPT stainless steel male-female coupling connector. The flume was then rotated to a horizontal position, the pore pressures transducers were zeroed with the tailwater head, and the test was initiated. The test procedure consisted of slowly increasing the flow at discrete time intervals until it was observed that BEP initiated at the downstream slope and progressed through the whole sample. The time of BEP initiation was recorded, and the critical gradient was obtained after processing the data.

3 PROBLEMS AND SOLUTIONS FOR SMALL-SCALE BEP TESTS

The following sections discuss the problems that occurred during the testing program of uniform sands with the small-scale flume and how these problems were effectively solved.

3.1 Head loss due to area reductions

The first problem was related to head losses due to the reductions of cross-sectional area from the water supply to the flume. The setup of the test had small modifications as the testing program progressed. The initial tests were conducted with mason sand, which had a d_{50} of 0.33 mm. The average size of the sand particles increased until finishing the testing program with a d_{50} of 2.52 mm. The larger particles required higher flow to initiate piping due to the higher sample permeability. The requirement of providing sufficient head (energy) to initiate BEP became a limiting factor to the initial soil testing procedure for coarse sands. It was found that the fittings, valves, and hoses that were used to connect the constant head tank to the flume had to be replaced because their cross-sectional area caused considerable head losses in the system. Originally, the constant head tank was connected to the flume through garden hoses, and a 1.90-cm-diameter threaded valve was connected to the inlet, which had an internal diameter of approximately 0.8 cm. Another source of head loss occurred inside a small turbine flow meter that was used for several tests. The flow meter, installed to measure the inflow just before it entered the flume, allowed continuous flow measurements. Inside this flow meter, significant head loss was caused by a drastic reduction in diameter. Also, this flow meter required the use of 0.635-cm hoses that added to the losses in the system. To solve the problems with head losses associated with the water supply, several solutions were implemented:

- The garden hose valves were replaced with 1.90-cm-diameter valves that had no significant area reduction through them.
- The turbine flow meter was replaced with an electromagnetic flow meter (FMG82 with a flow range of 0.113-11.3 L/min). This flow meter had minimal head losses through it and used 1.90-cm hoses.
- After replacing the valves, all of the hoses were replaced as well with 1.90–cm hoses. No hoses of a smaller diameter to supply water were used afterward.
- For most tests, water was inserted into the flume and controlled with a constant head water tank that could be raised or lowered with a hand winch. For a few samples with a high permeability, the flow rate necessary

to induce BEP was higher than the flow supplied by the municipal water supply, and thus, the constant head tank could not be used. For these tests, a pump capable of 300 L/min (Gould Model 316 S.S.) was used to pump water from a 1,900 L reservoir. This pump used 3.80-cm hoses and valves that allowed recirculation control.

3.2 Head loss due to low permeability of filter

Another source of head loss was identified when pressure transducer data were processed. During a test, the gradient was obtained with manual readings of manometers and was calculated as the difference in upstream and downstream heads versus the sample length. One manometer was installed upstream (behind the sample and end plate) and the other one downstream (outside the sample). Measurements were taken from the manometers while the pore pressure transducers readings were logged to a computer at one second intervals using a program coded in LabVIEW. A comparison of the two measurements revealed the drastic head loss due to the upstream filter.

Reviewing the piezometric data showed a disproportionate head loss between the pressure transducer upstream (behind the sample and the plate) of the filter and the next transducer when compared with the head loss occurring generally in the sample. This loss increased proportionally with flow. This indicated that the filter fabric and plate geometry used was much less permeable than the material tested, as it was getting clogged with fines from the tested sands and from the water supply. This considerable head loss caused an inaccurate value for the average global gradient calculated from the upstream and downstream manometer measurements. Replacing the filter fabric periodically was not enough, therefore, the solution to this problem was to determine the hydraulic gradient by a linear fit of the hydraulic heads (converted from the measured pressure from each transducer) along the sample. The slope of this plot (Figure 6 and Figure 7) determined the hydraulic gradient across the sample. The time at piping initiation was recorded, and the critical hydraulic gradient was calculated using this method. Figure 6 shows the significant head loss due to the upstream wall between pressure transducers 9 and 10. Figure 7 shows the linear fit of piezometric data points without the total head obtained from pressure transducer 10 for the calculation of a precise value of hydraulic gradient.

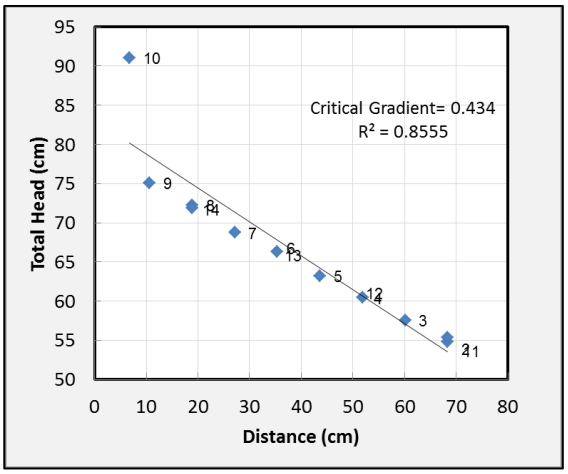


Figure 6. Piezometric data points showing head loss due to filter wall.

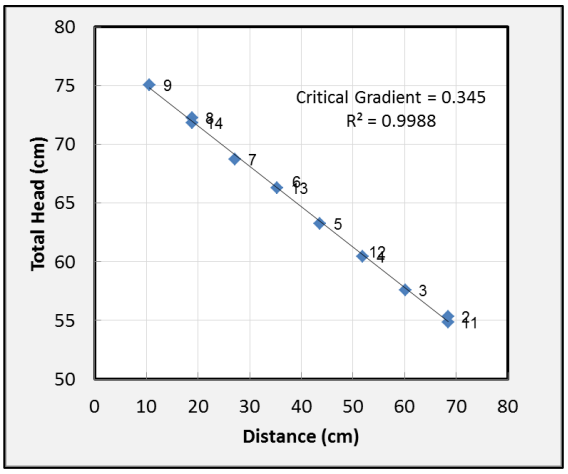


Figure 7. Piezometric data points showing linear-fit for estimating critical hydraulic gradient.

3.3 Trapped air

BEP tests were performed in fully saturated samples. It was very important to avoid any air bubbles from getting into the sample. Bubbles that were present during a test moved between the acrylic top and the sample, and they could cause movement of particles that could trigger erosion

prematurely. There were four possible ways that air bubbles could get into the sample:

- Air could get trapped behind the plate on the upstream side of the flume. Before pouring sand for preparing a sample, the flume was usually filled halfway with water. If the water level was raised slowly, the chance of air getting trapped on the filter fabric of the plate was high. To avoid this problem, the flume was filled with pressurized water rapidly while tapping with a rubber mallet. After filling with the necessary volume of water, the filter fabric was vigorously tapped to ensure air released from the filter fabric.
- It was noted that bubbles became trapped if the sand was deposited quickly, principally in loose samples. Dense samples did not usually exhibit this problem as the compaction helped to get rid of any bubbles. To avoid air bubbles in the sample, the sand was poured from the scoops slowly and evenly. Samples that were prepared carefully did not have problems of air trapped within.
- Even when the flume was completely saturated, it was found that air could still be trapped in the hoses leading to the flume. As a precautionary measure to avoid air during testing, all of the 1.90-cm garden hoses were replaced with clear 1.90-cm PVC tubing. These hoses could be saturated easily before a test by letting the water run and observing carefully that all the bubbles escape. Usually, once the clear hoses were saturated, the water supply system would be kept saturated for a series of tests by closing a series of strategically placed valves. Adding clear hoses such that air bubbles could be visually observed was a critical aspect of ensuring saturation of the water supply system and obtaining a successful testing program.
- As a last measure to avoid trapped air, three bleed valves were installed: one upstream (behind the sample, next to the inlet) and two downstream (in front of the sample, close to the outlet). Air was let out from these valves if bubbles were present prior to the test.

3.4 Piping through the center

The most important part of the procedure of these tests is being able to increase the flow carefully until erosion initiated. Piping usually starts on the weakest flow path, which most of the time is the shortest path. A problem that was observed during the first trials was that the location of erosion initiation was not consistent. For some of the small-scale experiments at Deltares (van Beek et al., 2010), an arc-shaped exit was manually formed in the sample to force piping to occur at the center of the sample.

To correct this issue and ensure the pipe developed through the center of the sample in every test (or close to the center), a shallow 1:12 v-notch was cut into the half wall where the slope is formed (Figure 8). This shape caused a natural arc to form in the exit slope due to the sand coming to equilibrium at the angle of repose (Figure 9). The deepest portion of the notch was at the sample center, which forced the shortest path length to be in the center as well. When setting the flume from the vertical to the horizontal position, the newly formed exit slope of the sample was arc-shaped with the shortest flow path in the center. The shortest path distance was measured at the beginning of every test.



Figure 8. Filter wall plate with v-notch.



Figure 9. Arc-shaped slope formed by v-notch.

4 CONCLUSIONS

The design and operation of laboratory equipment used for measuring the critical gradient of nine different uniform sands was discussed. Multiple issues were encountered during the initial testing phase and as the tests progressed. These issues and the corresponding solutions were presented to ensure future efforts can make use of the lessons learned. The three main problems encountered in these tests were: trapped air, head losses, and piping not initiating at the center of a sample. Trapped air bubbles in the sample could trigger erosion earlier than expected when they pushed soil particles. Bubbles were avoided by: pushing the air through a filter with pressurized water, pluviating the sand slowly into the water, using clear PVC hoses to connect the flume to the water supply, and adding bleed valves to the flume. The head losses due to reduction in area through fittings, hoses, and flow meters caused a significant reduction of the maximum head that could be obtained from the constant head tank that supplied the water during the tests. They were all replaced with equivalents of larger inner diameter when higher flows were required for piping initiation and progression. Also, head loss through a filter fabric resulted in inaccurate readings of gradients and therefore, the readings from behind the filter were not used in the final estimates of critical hydraulic gradient, which was obtained from the slope of a linear-fit of pressure within the sample. Finally, a v-notch was added to the downstream filter wall to naturally form an arc-shaped slope, ensuring the piping erosion would begin close to the sample center in every test. The solutions to the problems involved using all the available tools, knowledge, and some creativity to progress in the testing program and obtain satisfactory results.

5 REFERENCES

Bonelli, S. (2013). Erosion in geomechanics applied to dams and levees. John Wiley & Sons.

de Wit, J.M. (1984). Research report on sand boil model tests. Delft, Netherlands.

de Wit, J.M., Sellmeijer, J.B., & Penning, A. (1981). Laboratory testing on piping. In Soil Mechanics and Foundation Engineering. Rotterdam, pp. 517–520.

Foster, M., Fell, R., & Spannagle, M. (2000). The statistics of embankment dam failures and accidents. Canadian Geotechnical Journal, 37(10), pp.1000–1024.

ICOLD. (2015) Bulletin 164 - Internal Erosion of Existing Dams, Levees and Dikes, and Their Foundations. Volume 1: Internal Erosion Processes and Engineering Assessment. Vol. 1.

Schmertmann, J. H. (2000). The non-filter factor of safety against piping through sand. ASCE Geotechnical Special Publication No. 111, Judgment and innovation, F. Silva and E. Kavazanjian, eds., ASCE, Reston, VA, 65–132.

Sellmeijer, J.B. (1988). On the mechanism of piping under impervious structures. Delft University of Technology.

Townsend, F.C., Schmertmann, J.H., Logan, T.J., Pietrus, T.J., & Wong, Y.W. (1981). An analytical and experimental investigation of a quantitative theory for piping in sand, Gainesville, FL.

Townsend, F. & Shiau, J.-M. (1986). Analytical and experimental evaluation of piping and filter design for sands, Gainseville, FL.

USACE & USBR (2012). Internal erosion risks. In Best Practices in Risk Assessment for Dams and Levees. Denver, CO.

van Beek, V.M., Knoeff, H. & Sellmeijer, H. (2011). Observations on the process of backward erosion piping in small-, medium- and fullscale experiments. European Journal of Environmental and Civil engineering, 15(8), pp.1115–1137.

van Beek, V.M., Knoeff, J.G., Rietdijk, J., Sellmeijer, J.B. & Lopez De La Cruz, J. (2010). Influence of sand and scale on the piping process — experiments and multivariate analysis. In Physical Modeling in Geotechnics. Delft, Netherlands, pp. 1221–1226.

van Beek, V. M., Vandenboer, K., Van Essen, H. M., & Bezuijen, A. (2014). Investigation of the backward erosion mechanism in small scale experiments. In 8th international conference on Physical Modelling in Geotechnics (Vol. 2, pp. 855-861). CRC Press-Taylor and Francis Group.

Determination of pull-out strength and interface friction of geosynthetic reinforcement embedded in expanded clay LWA

Gorniak Joanna
Texinov, France, joanna.gorniak@hotmail.com

Marie Tankéré
Texinov, France

Philippe Delmas & Camille Barral
Cnam, Ecole SITI, France

Arnstein Watn
SINTEF, Norway

Oddvar Hyrve & Allan Dahl
Saint-Gobain Weber, Norway & Saint-Gobain Weber, Denmark

ABSTRACT
The determination of the interaction between geosynthetic reinforcement and granular soils is one of the key factors in the design of mechanically stabilised earth structures. Only a few experimental investigations dealing with the interaction of geosynthetics and expanded clay LWA can be found in literature. Large-scale pull-out tests were carried out in order to determine the interface coefficient of friction and the pull-out strength under low normal load in the framework of the development of a new type of geotechnical structure. The project was undertaken to design and evaluate a reinforcement product embedded in expanded clay LWA 10/20 mm. Three different geosynthetics were tested under low normal loads using an anchorage box. Geosynthetics of two meters length and one meter width were embedded between two 40 cm thick expanded clay LWA layers. The samples were instrumented with displacement transducers distributed along the sample. A force transducer enabled the measurement of the pull-out force. The tests have shown a direct relationship between the geosynthetic products of opened or closed geometry and the diameter of the expanded clay LWA grain size (10/20mm) on the obtained pull-out force. Considerably higher anchorage strength and interface coefficient of friction are obtained for geosynthetic products of opened geometry (geogrids). Also the influence of geosynthetic stiffness on the pre-peak pull-out behaviour is discussed in the paper. The observations also suggest that the obtained results on a narrow particle size distribution are not necessarily transferable to conventional soils.

Keywords: MSE structure, expanded clay LWA, geosynthetics, pull-out tests, interface coefficient of friction

1 INTRODUCTION TO TEMASI

The research project TeMaSi deals with the development of a new type of retaining wall namely a mechanically stabilized earth structure, also called MSE Structure. In the scope of the study the combination of geosynthetics and expanded clay lightweight aggregates is considered. The present well-developed technique of geosynthetic soil reinforcement and parallel development of alternative construction materials as expanded clay LWA gives good possibilities to combine these two materials in geotechnical engineering. This offers an innovative solution to classical retaining walls, as for example rigid or modular gravity walls. The new developed structure is composed of geosynthetic tubes stacked on each other and anchored with geosynthetic reinforcement in the expanded clay LWA backfill (Figure 1). The new proposed struc-

ture offers in comparison to the classical solution a number of advantages.

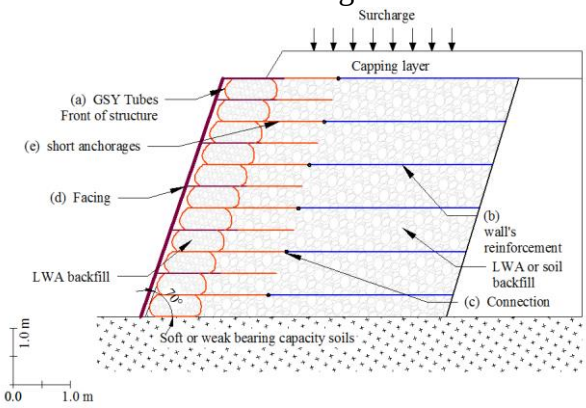


Figure 1. Cross-section of innovative geotechnical structure.

Expanded clay LWA aggregates gives the possibility for rapid construction (blow in place) and can be combined with geosynthetics to be filled into long continuous geosynthetic tubes. The unit weight of the filling material contributes to a significant reduction of the gravity weight of the entire structure. As a consequence, the construction of the new structure is interesting in areas where soft and compressible soils are considered. A significant reduction of total and differential settlements can be achieved. In the scope of the research project a new developed filling system the so called Low Pressure System is introduced to provide a uniform and continuously filled geosynthetic tube (Górniak, 2013). The control of filling density and the shape of the geosynthetic tube, enables to obtain a pre-defined facing part of the structure without the use of any scaffolding. The behaviour of the geosynthetic tubes under normal actions (Gorniak *et al.*, 2015) and combined vertical and lateral actions simulating the earth pressure effect have been studied experimentally and numerically. In the year 2010 and in year 2012 geotechnical structures had been constructed. It was demonstrated that the developed filling system is very efficient and less time consuming than other construction method of existing retaining walls. A total time of six minutes is needed to fill a thirty meters long geosynthetic tube. Moreover numerical studies of the geosynthetic tubes have provided useful results and a better comprehension of the new type of structure (Górniak, 2013).

As it was shown in Figure 1, the geosynthetic tubes are anchored in the backfill of the structure by help of long geosynthetic reinforcements. To provide an optimal design of the geosynthetic reinforcements, qualitative information about the interaction of geotextiles or geogrids and the mobilising shear strength are necessary for the optimal design of a reinforced earth structure. The study presented in this article aims with the measurement and the determination of the pull-out strength, as the interface coefficient of friction of the expanded clay LWA and three geosynthetic products (woven geotextiles and geogrids).

2 INTRODUCTION TO EXPERIMENTAL TESTING: PULL-OUT TESTING

During the last decade, the knowledge of geosynthetic - soil interaction under pull-out testing has become well known in geotechnical engineering. Numerous experimental studies large scale pull-out devices (Moraci & Recalcati, 2006; Palmeira, 2004) developed for the study of geosynthetic-soil interaction and numerical studies (Huang *et al.*, 2011; Tran *et al.*, 2013) demonstrated the importance of several factors affecting the bearing and pull-out strenght of the reinforcement. Also experimental analysis of shear interface tests between geosynthetics and LWA have shown high interface friction angles (Bakeer *et al.*, 1998b; Karri & Reis, 2009; Valsangkar & Holm, 1990). However, the application of non-classical filling soils as expanded clay LWA aggregates in interaction with geosynthetic reinforcement requires additional studies to permit a better comprehension of the interaction phenomenon. Accordingly to the properties of the filling soil (infrequent granulometry 10/20 mm and considerably lower than by classical soils bulk density 350 kg/m^2) the characterisation of the pull-out resistance and interface friction coefficient was conducted under moderate effective stresses and large size specimens. The study considered the development of an optimal reinforcement product, that could be adapted to any required reinforcement length and geometry.

2.1 Experimental studies of expanded clay LWA interaction with geogrids

During the last decade the investigation of geosynthetic properties considered as reinforcement of classical soils stayed noticeable. Numerous research works (Bakeer *et al.*, 1998a; Bakeer *et al.*, 1998b; Delmas, 1979; Moraci & Recalcati, 2006; Palmeira, 2004; 2009; Yuan *et al.*, 2002) had been performed, starting with simple pull-out apparatus and ending up with complex and well developed devices. Those principles have been also introduced into geosynthetic reinforced lightweight aggregate structures, where the soil develops considerable large anchor strength and interface friction (Jenner *et al.*, 2008; Watn *et al.*, 2008). In the literature the expanded clay LWA-GSY interaction, should be more investigated because of its infrequent grain size and grain shape. Moreover, a more particular attention should be given to the possible limited compressive strength of those materials and the crushing resistance. Nevertheless, those materials offer in comparison to classical soils numerous advantages: their high internal friction angle ϕ'=35 - 38°, resistance to oedometric loading R = 0.48 - 0.6 N/mm², low bulk density 350 kg/m^3 and fast and easy procedure of installation and compaction in the field (Watn, 2001; Wood & Høva, 2009).

Carried out pull-out tests demonstrated high anchor strength at various effective stress levels for embedded geogrids in LWA 0/10 mm (Bakeer *et al.*, 1998b; Yuan *et al.*, 2002) and in LWA 4/20 mm (Forsman & Slunga, 1994). The results of the studies of Yuan *et al.* (2002) and of Bakeer *et al.* (1998b) are set in Figure 1. Both of the authors applied various normal stresses to the specimen and both concluded, that the length of the geosynthetic influences the mobilised interface friction between the reinforcement and the LWA and the bearing resistance. This could explain, the higher resistance of the reinforcement tested by Yuan *et al.* (2002) at vertical stress equal to 31 kPa in comparison to the one tested by Bakeer *et al.* (1998b) at normal stress equal to 60.4 kPa. Note that the inclination of the force-displacement curve is very gentle. This may be an indication for the possible rolling of LWA grains along the reinforcement and considerable displacements mobilised between the geosynthetic reinforcement and the LWA.

Clear discrepancy is observed when increasing the normal load for the two various lengths. The interface friction coefficients obtained in the testing are set in Figure 3. Please note that Yuan et al. (2002) considered for his calculation the residual friction angle and cohesion of LWA, as the surface of the embedded geogrids, not the length of the embedded reinforcement as (Bakeer *et al.*, 1998b).

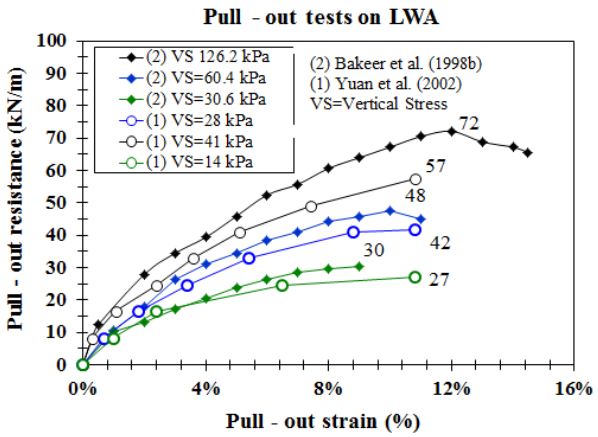


Figure 2. Pull-out strength versus pull-out strength of Bakeer et al. (1998b) et Yuan et al. (2002).

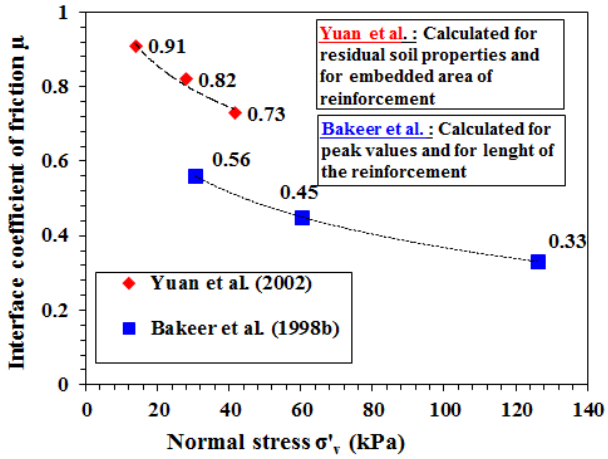


Figure 3. Results of pull-out tests: Pull-out resistance for various levels of normal stress performed by Yuan et al. (2002) and Bakeer et al. (1998b).

Also the peak values of soil properties were introduced in their calculations. Thus, the

values can't be compared directly from the chart.
Mentioned parametric and geometric factors that establish the pull-out behviour of the extensible products has to be optimised for the 10/20mm expanded clay LWA.

3 TEMASI – EXPERIMENTAL RESEARCH ON PULL-OUT STRENGTH

3.1 Testing apparatus and instrumentation

The testing apparatus, as described also in Brainçon (Briançon, 2001), is a steel framework device composed of four beams and pillars supplemented with wooden boards (plywoods). The apparatus has a length of 2.5 m, width of 1.2 m at the external sides and 2.45 m long and 1.15 m at the inside as in Figure 4.
Two meters long samples can thus be freely tested in the apparatus and be embedded at various depths in the apparatus up to 1.5m height. The pull-out load is provided by the manually operated pulley fixed to a steel and rigid frame. The frame is additionally fixed to the slab by screws. Additionally, to avoid friction between the testing material and the surface of the wood, plastic films are clamped at the sides of the box. The load application speed can be chosen between slow and fast and is controlled by the number of rotations of the pulley and equals approximately v_t = 5 mm/min.
The geotextile is hold by help of a steel clamp (Figure 4), that has the width of the fabric and enables to overlap the specimen around its circumference. At the clamp device a force transducer is installed that can provide the pull-out force. It is important to determine the displacement along the reinforcement using displacement LVDTs placed directly on the diagonal along the specimen. The obtained measurements are recorded by help of a data logger and enable the transfer of the results to a PC. The normal load is applied by help of steel plates (one package of steel plates represents a normal load of 3.69 kPa). The steel plates are placed on a transition layer a 12 mm thick wooden plate that enables the application of normal loads on the whole testing surface.

3.2 Testing materials

Tested geosynthetic products are presented in Table 1. All the products are warp knitted geotextiles produced of two various polymers: high tenacity polyester and polypropylene. The mechanical properties of these geotextiles have been tested in the laboratory in accordance to the actual standard (NF-EN-ISO-10319).
The product A is a knitted geogrid with rectangular mesh (size of the openings approx. 80x40 mm) . Its ultimate tensile strength is 130 kN/m in the direction of the pull-out force, and 60 kN/m in the transverse direction. The elongation at break of product A equals ε = 11 %. The two other products, product B and Product C, are warp knitted geotextiles.

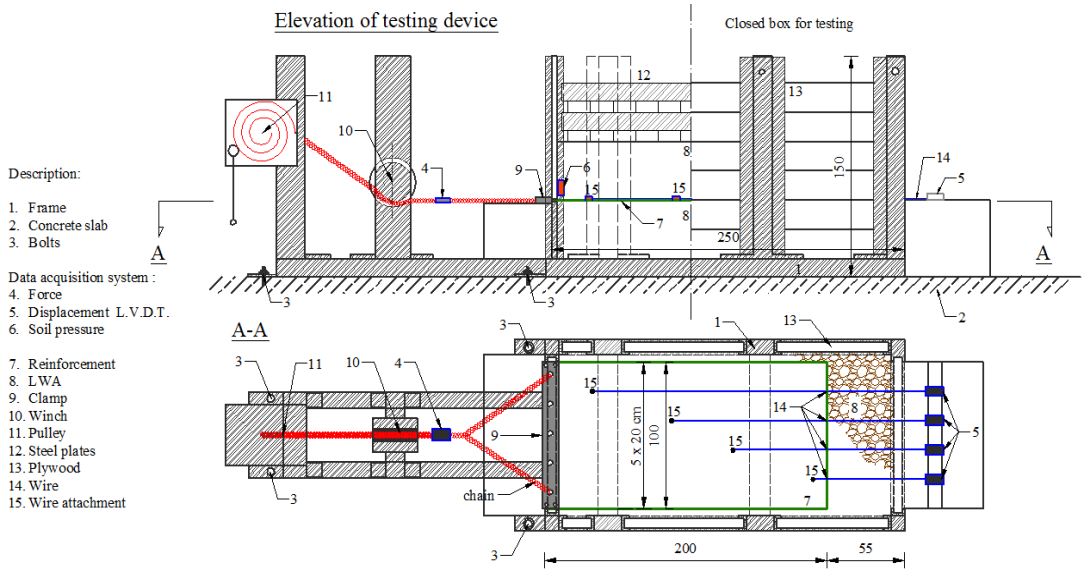


Figure 4 Testing apparatus after (Briançon et al., 2008)

Product B of tensile strength 150 kN/m in the length direction with significantly smaller opening sizes 3 x 3 mm. Product C has no openings. The properties of the other products are given in Table 1. Note, that product B and product C had the same axial strength but different stiffness, hence they are produced either from polyester or polypropylene.

Table 1 mechanical properties of tested geotextiles and geogrids

Label/ Polymer Tensile strength MD x CD	Opening size [mm]	*R* [kN/m]	*ε* [%]	*J* [kN/m]
A Polyester 130 x 130	80 x 40	130	11	1500
B Polyester 150 x 50	3 x 3	150	11	2300
C Polypropylene 150 x50	no openings	150	16	1100

Tensile strength R, elongation at break ε and stiffness J of the products are given in the Machine Direction (pull-out direction).

Properties of tested expanded clay LWA are set in Table 2. Physical and mechanical properties of expanded clay LWA have been investigated in laboratory testing in a research project (Wood & Høva, 2009). Results are based on performed laboratory analysis at Sintef in a 150 mm diameter tri - axial apparatus. Please note, that the applied confinement of the tested samples was in the range of σ_3 = 20 - 80 kPa.

Table 2 properties of tested expanded clay LWA

State	Bulk density [kg/m^3]	Shear strength	
		At peak ϕ_p'°	Residual friction angle ϕ_{pr}'°
Loose 10/20 mm	320	34	34
Compacted 10/20 mm at 10%	350	38	38

In order to insure the sustainable functions of the geosynthetic products the geochemical degradation of the polymer in the environment of the soil has to be studied. The authors have performed first geochemical analysis (immersion tests) of expanded clay LWA in tap-water. At the beginning of testing, after two days of immersion, high pH-values > 10 were measured. After seven days of immersion a decrease in pH-values > 9 was obtained. The authors are aware that the performed tests should be improved, however for pH-values grater than 9 other polymeric products than the polyolefines (polypropylen, polyethylen) cannot be considered for the further development for this project. The tested polyester products serve only as experimental basis of products with higher geosynthetic stiffness (Górniak, 2013).

3.3 Experimental plan

The defined length of the sample equalled 2.0 m and the width 1.0 m. The prepared soil is covered by large plywood, sufficiently thick to disable deformations of the box and the exerted deformations at the frontal wall. Three different normal loads are applied by help of steel plates: 5.0 kPa, 8.9 kPa and 12.4 kPa. Every product was tested twice under the same configuration, which makes 18 tests in total. The tests were performed to 20 cm displacement at clamp. The experimental plan is presented in Table 3.

Table 3 performed number of tests

Number of performed tests	Product	Applied normal load (kPa)
6	A	5.0, 8.9, 12.4
6	B	5.0, 8.9, 12.4
6	C	5.0, 8.9, 12.4

4 ANALYSIS OF TEST RESULTS

4.1 Pull-out strength

Pull-out forces, measured for the tested extensible reinforcements vary according to the applied normal loads, their stiffness and lengths. The obtained results in this study demonstrated however, that the geometry (opening size) of the geosynthetic has an in-

fluence on the obtained initial stiffness and post-peak regime of the pull-out strength. The measurements obtained from the data acquisition system are represented for the first displacement transducer D-1, placed in the front of the sample plotted versus the measured pull – out force (see Figure 8). In Figure 5 the results of testing of product A, B and C at vertical stress σ_n = 8.9 kPa are presented, while in Figure 6 the results of testing at vertical stress σ_n = 12.4 kPa are presented.

At first, two different force-displacement responses of products can be observed from the plotted results. Globally, the geogrid (Product A) in comparison to the geotextiles (Product B and Product C) show likely a displacement-softening behaviour, with a progressive decrease in the pull-out strength after reaching a peak value.

In opposite, geotextiles with 'closed' structure have the tendency to maintain the pull-out resistance when reaching the peak; no abrupt decrease of the residual strength in this case is observed.

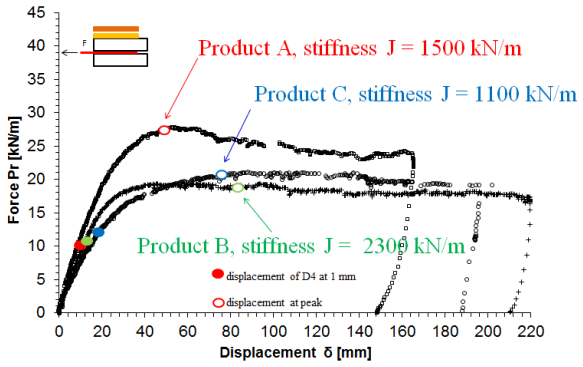


Figure 5 Pull-out force – displacement D1 tested at normal load σ_n=8.9 kPa for product A, B and C.

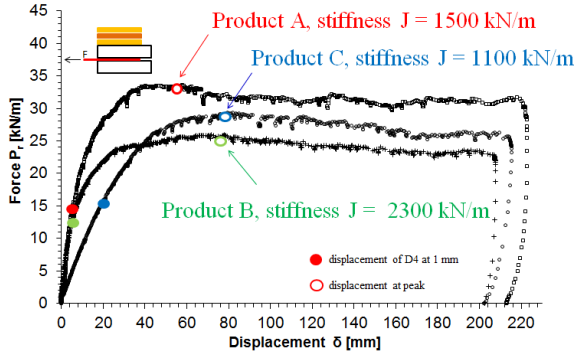


Figure 6 Pull-out force – displacement D1 tested at normal load σ_n=12.4 kPa for product A, B and C.

At the ultimate residual strength the reinforcement tend to slip between the embedded soil layers. This phenomenon is related to the aggregate – interaction in the pull-out box, where interface friction is affected by the aperture size and size of grains as demonstrated in Figure 7.

At second, the effect of product stiffness is clearly visible at the pre-peak region, so at the onset of loading (geosynthetic pulling) 20, 30 and 40 mm of displacement, where the stiffness of the product seem to play an important role.

During every test, the geotextile C has the tendency to undergo larger displacements as geotextile B. The stiffness of the pull – out force – displacement curve could be increased by a factor of two for the geotextile B for the range of two tested geotextiles (almost 1,5 bigger stiffness of geosynthetic). In case of comparable geotextile stiffness (product A and C), the stiffness of the pull-out force – displacement curve could be increased by a factor of around 1.2, for the range of two tested geotextiles.

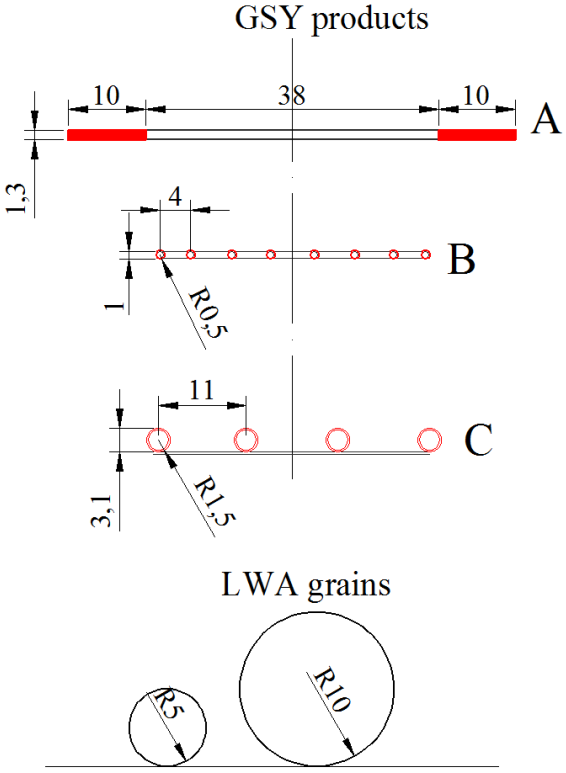


Figure 7 Geometry of tested geotextile products and size of LWA grains (min and max radius) in mm.

Please note, that also pull-out forces and displacements (see section 4.2) are mobilised differently along the whole length of the rein-

forcement showing a strong non-linear behaviour of tensile strain. The pull-out peak values under sequent normal loads of the products show similar tendencies, where pull-out resistances stay in similar ranges for geotextiles, while for "open" products, obtained peak values are 20 - 30% higher.
After reaching the peak values, the reinforcements tend to leave the box in a uniform manner (maximal clamp displacement 200 mm), maintaining the post – peak (residual) pull-out force at a constant level for product B and C. The apparent difference for product B and C despite lower stiffness of product C can be affected by the geometry of the product that enables the reinforcement sheet to achieve higher interface friction values. The steepness of the curve is developed accordingly to the stiffness of the reinforcement and the friction law. In Figure 7 the possible interaction was observed by the installation of the product on the LWA's first layer in the pull-out box. The case of product A represents packing and penetration of grains between the openings of the product, while B and C represent more a separation of the two layers than penetration. The former product can however enable better interlocking of smaller LWA grains (R_{grain} = 5 mm) between the longitudinal bars (distance = 8-10 mm) in comparison to product B. This might have been the reason why the post-peak strength of the product C exceeds the one of product B.

4.2 Pull-out displacements

The displacement transducers are located along the diagonal of the geosynthetic reinforcement at 20, 80, 120 and 180 cm distance (Figure 8).

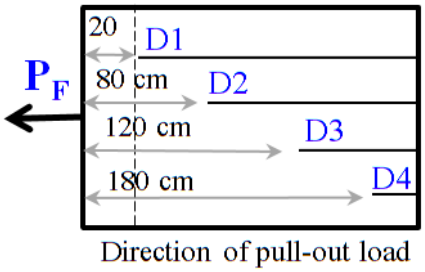
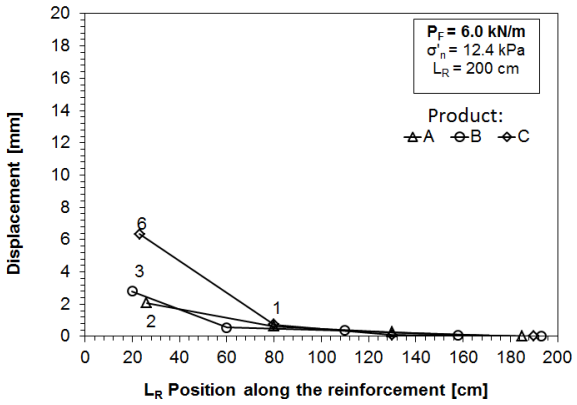
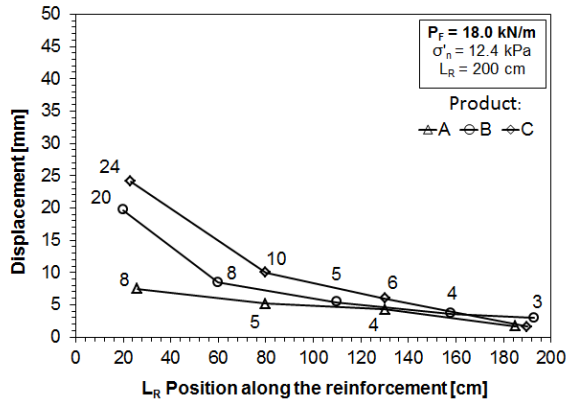


Figure 8 location of displacement transducers along the reinforcement.

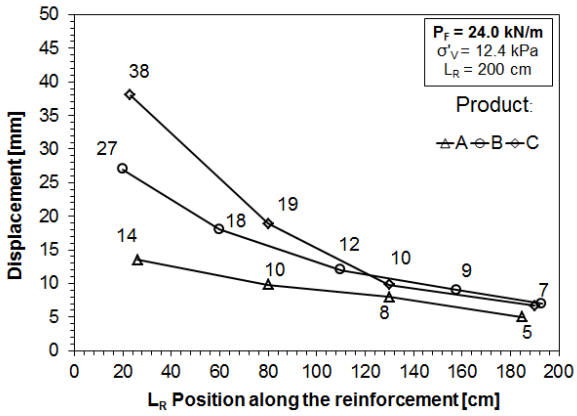
At a given pull-out force the values of displacements are represented along the 2.0 m samples for each position of the displacement transducer at normal stress σ_n = 12.4 kPa in Figure 9(a-c). The mobilisation of displacement is compared for all three products and takes place in a non-linear manner for each configuration along all marked nodes/points of the reinforcement in Figure 9(a-c).



(a)



(b)



(c)

Figure 9 Measured displacements along the geosynthetic reinforcements at (a) pull-out force 6 kN/m, (b) pull-out force 18 kN/m and (c) 24 kN/m

As can be observed from Figure 9 the less extensible product A has the tendency to reach rather simultaneously the mobilisation of displacements along its length responding

with relative small values of displacement in comparison to the products B and C.
Products represented by geotextiles, with more 'close' geometry, can be characterised by higher response to pull-out loading at the face of the apparatus and lower mobilisation in displacement at tail. At the pre-peak regime of the reinforcements, the stiffness of the products appears to play an important role before reaching its maximal value of shearing. It is even more remarkable for product C, while achieving higher pull-out forces.
Values of displacements at the onset of loading (where the displacements at tail are equal to 0 or 1 mm), confirm that the mobilisation of friction between the LWA grains and the reinforcement is reached as the tail of the reinforcement starts to displace. It can be seen as an important point of the interaction of the geogrids and geotextiles. At small values of displacements, the mobilisation of displacements becomes more favourable for product A and C, where the tail undergoes smaller displacements. As the pull-out force increases, the displacements of products B and C exceed the values recorded for product A. It can be said, that once the friction is mobilised along the whole reinforcement, geotextile grids are able to retain higher pull-out forces compared to geotextiles. In all cases in the pre-peak phase, the product C exceeds the values of product B.
Once the peak regime is reached, the embedded product continues to leave the confined zone of LWA uniformly increasing the values of displacements. In this phase, the displacements of each product become 'parallel' to each other and increase. Inversely, in comparison to the pre-peak region, the displacements at peak for product A become larger than for product B and C. At this point, the LWA - geotextile ensemble confined at three different normal stress values, where by increasing surcharge, contact forces between the grains and the reinforcement lead to uniform pull-out force. At this point the stiffness doesn't play any role in the test and the reinforcement continues to slip between the soil layers.

4.3 Interface coefficient of friction

The interface coefficient of friction is calculated on the obtained result of the pull-out force. Values of pull-out forces can be compared to shear stresses mobilised at the interface for different normal loads applied to the samples and the embedded area of the reinforcement.
The estimation is made as following in Equation 1.

$$\tan\varphi_{soil/GSY} = \frac{P_i}{2.(L_R - D_i).B_R.\sigma_v'} \qquad (1)$$

where:
P_i - measured pull-out force at displacement D_i,
B_R - width of the tested reinforcement,
L_R - the embedded length of the sample,
D_i - measured displacement of the reinforcement of transducer D-1,
σ'_v - applied normal load.
From pull-out tests the coefficient $C_{i\Phi}$ is defined as follows in Equation 2 (NF-G38-064):

$$C_{i\Phi} = \frac{\tan\varphi_{LWA/GSY}}{\tan\varphi_{LWA}} \qquad (2)$$

The interface coefficients of friction $C_{i\Phi}$ are estimated for the internal friction angle at peak of the LWA defined under triaxial compression as $tan\ \varphi_{LWA} = 0.78$ ($\varphi_{LWA} = 38°$). It is however necessary to mention, that the internal angle of friction is estimated for 10% of compaction by vibration of the soil. In the case of the anchorage tests and the field installation of the soil, the upper layers cannot be considered as compacted, thus smaller values of shear resistance should be considered.
In Table 4 the plotted values of $C_{i\Phi}$ and $tan\varphi_{LWA\text{-}GSY}$ are represented for the three products versus the displacement D_i corresponding to the measurements of the displacement transducer D1.

Table 4 Values of interface friction coefficient of three tested products

Product	Width B_R (m)	Length L_R (m)	Internal friction angle $tan\varphi_{LWA}$ (-)	Interface coefficient of friction $C_{i\Phi}$ (-)
A	1.0	2.0	0.78	0.79
B	1.0	2.0	0.78	0.61
C	1.0	2.0	0.78	0.73

It could be easily said, that the values of the coefficient of friction should be considered as the design value of the LWA-geotextile for reinforced structures at the peak strength of the anchorage measured in the test. It is however not obvious with regard to the displacements of the reinforcement in the tests. For the tested products, the mobilised friction along the reinforcement, could be properly estimated when the reinforcement stays in the box and its tail is submitted only to negligible displacements. It is because, even when the peak strength was not entirely reached, the geotextile had started already to leave the box.

5 CONCLUSION

Large-scale pull-out tests are carried out on three different geosynthetics under three normal loads, using an anchorage box. Geosynthetic reinforcements of 2 m x 1 m dimensions are embedded between two 40 cm thick LWA layers. They are instrumented with displacement transducers distributed along the length of the sample. A force transducer enables the simultaneous measurement of the pull-out force. One earth pressure transducer is installed on the frontal wall of the box and records the increments in horizontal pressure.

The main objective is to test products with different opening geometries and apparent stiffness embedded in LWA to develop a reinforcement product of the MSE wall. The tests are carried out on one geogrid that can be considered as similar to the optimal product that needs to be developed for the MSE reinforcements. The remaining two products are tested to compare the behaviour of geogrids and geotextiles embedded in LWA.

The tests have shown the importance of opening size regarding the diameter of the LWA grains (grain distribution 10/20 mm).

A good design of the opening can naturally improve the interaction coefficient soil - geosynthetic. It is shown, that the integrated LWA grains inside the opened product achieve higher anchorage strength in comparison to products of closed geometry, for the range of tested products. Nevertheless, by providing useful information on the pre-peak behaviour, it opens the possibility to optimise the product to minimise the displacements at the service state.

The gained knowledge on the testing concerns also the experience made on the implementation method of LWA and its interaction with reinforcements. The way to fill the testing box with backfill is very easy and fast, in comparison to classical soils. The light LWA can be installed by blowing or by help of big shovels. The round grains of LWA facilitate the installation of products with openings between the layers. Products of very narrow or almost no openings don't have the adaptability to interlock with the grains and will rather act by friction on both sides of the geosynthetic. It shall be noted, that in this case the local deformation created by the LWA grains pressure increases the pull-out strength similarly as in gravel materials. This observation can lead to optimisation of the implementation conditions for the future specifications of reinforcements in the LWA (low C_u ratio equal to 1.5), and is rather a positive argument for the use of products with optimised openings, where the grains can penetrate through the product. This statement also demonstrates the necessity to use products with 'open' geometry for a better optimisation of reinforcement lengths in a real structure. The statement is also confirmed by Watn *et al.* (Watn *et al.*, 2004).

Values of chosen geosynthetic stiffness appear to be adequately high to observe differences in anchorage behaviour. Additional tests should confirm these encouraging results. The choice related to the testing box (rigidity of box, testing velocity and pulling mechanism) should be reconsidered while

employing higher values of normal stresses. It should be noted that these results on a narrow particle size distribution (10/20 mm) are not necessarily transferable to conventional soils.

More generally, it should be noted that today the standards enable to evaluate the material‘s parameters at break (e.g. pull - out force at peak or residual stresses). This study in terms of reached pull-out strength can provide useful information on the design of structures in particular the approach to assessing displacements.

6 ACKNOWLEDGMENTS

The research project TeMaSi has been supported by the European Commission (Eureka label) and funded by the FFN (Norway) and Oseo (France).

7 REFERENCES

Bakeer, R. M., Abdel-Rahman, A. H. & Napolitano, P. J. (1998a). Geotextile friction mobilization during field pullout test. *Geotextiles and Geomembranes*, 16 (2): 73-85.

Bakeer, R. M., Sayed, S. M., Cates, P. & Subramanian, R. (1998b). Pullout and shear tests on geogrid reinforced lightweight aggregate. *Geotextiles and Geomembranes*, 16 (2): 119-133.

Briançon, L. (2001). Stabilité sur pentes des dispositifs géosynthétiques - Caractérisation du frottement aux interfaces et application. Université de Bordeaux I, Bordeaux, France, 200 pages p.

Briançon, L., Girard, H. & Villard, P. (2008). Geosynthetic anchorage : Experimental and numerical studies. *Proceedings of the 4th European Conference on Geosynthetics*, Vol. 103, Edinburgh, United Kingdom. pp: 8.

Delmas, P. *Sols renforcés par Géotextiles. Premières études.* 1979. Institut de Recherches Interdisciplinaires de Geologie et de la Mecanique. Grenoble, Université Scientifique et Médicale de Grenoble. Ph. D. 202.

Forsman, J. & Slunga, E. (1994). The Interface Friction and Anchor Capacity of Synthetic Georeinforcements. *Proceedings of the 5th International Conference on Geotextiles, Geomembranes and Related Products*, Vol. 1, Singapore. pp: 405-410.

Górniak, J. (2013). Geosynthetic tubes filled with lightweight aggregate in new geotechnical structures: first studies. Thèse de Docteur ès Sciences, Université Pierre et Marie Curie, Paris, France, 220 p.

Gorniak, J., Villard, P., Barral, C., Delmas, P. & Watn, A. (2015). Experimental and analytical studies of geosynthetic tubes filled with expanded clay lightweight aggregate. *Geosynthetics International*, 22 (3).

Huang, J., Bhandari, A. & Yang, X. (2011). Numerical Modeling of Geosynthetic - Reinforced Earth Structures and Geosynthetic - Soil Interaction. *Geotechnical Engineering Journal of the SEAGS & AGSSEA*, 42 (0046-5828).

Jenner, C. G., Wills, P. G., Karri, S. & Blundell, L. (2008). Modular block faced, reinforced soil bridge wingwalls, utilising lightweight expanded clay fill. *Proceedings of the 14th European Conference on Soil Mechanics and Geotechnical Engineering*, Vol. 5.3., Madrid, Spain, September 2007. pp: 1473-1479.

Karri, S. & Reis, C. (2009). Modular block reinforced earth structures using lightweight expanded clay fill to reduce bearing pressures and to protect important assets. *Proceedings of the 3rd Portuguese Seminar on Geosynthetics*, Vol. 1, Coimbra, Portugal, November 2009. pp: 12 pages.

Moraci, N. & Recalcati, P. (2006). Factors affecting the pullout behaviour of extruded geogrids enbedded in compacted granular soil. *Geotextiles and Geomembranes*, 24 (4): 220-242.

NF-EN-ISO-10319. *Géosynthetiques. Essai de traction des bandes larges.* Afnor, l'Association française de normalisation, La Plaine Saint-Denis, France.

NF-G38-064. *Murs inclinés et talus raidis en sols renforcés par nappes géosynthétiques - Justification du dimensionnement et éléments de conception.* AFNOR.

Palmeira, E. M. (2004). Bearing force mobilisation in pull-out tests on geogrids. *Geotextiles and Geomembranes*, 22 (6): 481-509.

Palmeira, E. M. (2009). Soil-geosynthetic interaction: Modelling and analysis. *Geotextiles and Geomembranes*, 27 (5): 368-390.

Tran, V. D. H., Meguid, M. A. & Chouinard, L. E. (2013). A finite–discrete element framework for the 3D modeling of geogrid–soil interaction under pullout loading conditions. *Geotextiles and Geomembranes*, 37 (1): 1-9.

Valsangkar, A. J. & Holm, T. A. (1990). Geotechnical properties of expanded shale lightweight aggregates. *Geotechnical Testing Journal*, 13 (1): 10-15.

Watn, A. (2001). Lightweight aggregate for civil engineering. Technical solutions, mechanical properties, certification and quality control. *Proceedings of Brisk Events, New Technology Seminar*, Vol. 1, Amersfoort, Netherlands. pp: 20 pages.

Watn, A., Gylland, A., Reis, C. & Hyrve, O. (2008). Expanded Lightweight Aggregates for geotechnical applications. *Proceedings of the 11th Portuguese Geotechnical Society Meeting: Congresso Nacional de Geotecnica*, Vol. 1, Coimbra, Portugal. pp: 8 pages.

Watn, A., Øiseth, E. & Aabøe, R. (2004). Reinforced slope of road embankment with light weight aggregates. *Proceedings of the 3rd European Conference on Geosynthetics*, Vol. A - 5, Munich, Germany, March 2004. pp: 175 - 179.

Wood, J. R. & Høva, M. E. (2009). Characterization of LWA for geotechnical applications. Internal report from tests conducted on lightweight expanded clay aggregate at SINTEF (Norway). Report SBF IN F09414, 76 pages.

Yuan, Z., Moore, J. K. & Swan, R. H. J., 2002. *Pullout Resistance of Geogrid in Expanded Clay Lightweight Aggregate Material*. TRB Annual Meeting CD-ROM.

Some recent developments on geophysical testing of peat

A. Trafford
APEX Geoservices Ltd., Gorey, Co. Wexford, Ireland, atrafford@apexgeoservices.ie

M. Long
University College Dublin, School of Civil Engineering, Ireland, mike.long@ucd.ie

ABSTRACT
This paper highlights recent developments in the application of geophysics to geotechnical engineering in peat. For example GPR can accurately profile peat thickness and inform on internal peat structure. Together with GPS and LiDAR imaging, GPR can be used to develop high quality 3D site images thus providing valuable information for scheme planning and for landslide studies. Despite the very low velocity values encountered work presented here shows that the shear wave velocity of peat can be reliably measured by a variety of methods. This paper describes the development of a lightweight portable sonde which has proven useful for this purpose. Work is ongoing on developing a relationship between shear wave velocity and peat undrained shear strength for the purposes of landslide stability assessments.

Keywords: Peat, geophysics, ground penetrating radar, shear wave velocity, landslides, undrained shear strength.

1 INTRODUCTION

There are many different facets of studying the engineering parameters of peat soil including the determination of the mechanical, electrical, chemical and decompositional properties. The study of many of these elements is difficult and their interrelationships are complex. As a material to be studied, peat has its own difficulties, many of them associated with the conditions required for the formation of this uniquely complex material. Access, stability, sampling and surveying each form their own challenges to site investigations.

It is out of the need to exploit, preserve or develop upon this fragile environment that much of the research and development of various testing methodologies has emerged. For example:

- the development of GPR as a technique for measuring peat thickness came about from the need to estimate the peat as a resource for exploitation in power generation,
- the need for robust peat stability assessment for upland windfarm projects has led to the development of the combined approach using GPR, Lidar and GPS,
- the latest development of geophysical research has come about due to the need to accurately determine the undrained shear strength of peat in situ.

In this paper some of these recent developments are described and examples are given of their application to the study of Irish peat. It is hoped that the techniques and approaches identifed will be of use to engineers working in similar environments elsewhere. Finally topics which require further research work are identied.

2 GROUND PENETRATING RADAR (GPR)

2.1 Introduction

Ground Penetrating Radar (GPR) techniques involve the transmission and reflection measurement of electromagnetic waves. The penetration depth achievable depends on the nature of the peat (especially its electrical conductivity), the location of the water table and on the frequency of the transmitted wave. Work at Lund University in Sweden by Ulriksen (1979), Ulriksen (1980), Ulriksen (1983), Bjelm & Ulriksen (1980) and Bjelm (1980) investigated various factors related to the technique and showed that not only could the peat thickness be estimated accurately, information can be obtained on the material beneath the peat.

These techniques have been also used successfully for many years in Sweden, e.g. Carlsten (1988) and Finland, see Saarenketo et al. (1992) for the determination of the thickness of both the road pavements and that of the underlying peat. Edil (2001), Warner et al. (1990), Francese et al. (2002) and Plado et al. (2011) have reported similar findings for work in the US, Canada, Italy and in Estonia respectively.

2.2 Peat thickness from GPR

To date most equipment has involved moving a single frequency antenna over the surface of the peat. For example Trafford (2009) reported on the use of 100 MHz and 250 MHz transmitters for the assessment of large areas of peatlands in Central Ireland, either by man-hauling the antenna or by use of all-terrain vehicle (Figures 1a and 1b).

A variety of challenging conditions can therefore be dealt with. Trafford (2009) found that the maximum depth of penetration for the 100 MHz transmitter in Irish raised bogs was typically 6 m. Transmitters with varying input frequency have also been used to achieve greater penetration depth. For example, for the equipment shown on Figure 1c, the input frequency can be altered by varying the length of the boom.



Figure 1. Investigation of peat with GPR (top) man-hauling 250 MHz equipment (middle) all-terrain vehicle with 100 MHz unit (bottom) variable frequency antennae.

In Ireland it has been found that a good compromise between depth of penetration and resolution is possible by combining results from two different frequency inputs, e.g. 80 MHz and 40 MHz.

Further details on the techniques used and on the calibration of the equipment can be found in Trafford (2009) or in Long (2015).



Figure 2. Clara raised bog in Central Ireland

2.3 Thickness & internal structure of peat

In order to investigate the effectiveness of the GPR equipment, specifically in its ability to locate the thickness of the peat and to resolve the internal structures in the peat some work was carried out at Clara raised bog in Central Ireland. The test site is shown on Figure 2.

Clara bog is one of the few large raised bogs remaining in Ireland in a relatively intact state. The bog was subject to a Irish / Dutch research study, into the hydrology and biology of the peat as well as distribution of spatial patterns within the peat and the mechanics of peat formation, in the late 1980's and early 1990's, see for example Smit (1989) or Van der Molen and Wijmstra (1994). As a result the bog was acquired by the Irish National Parks and Wildlife Service (NPWS) and together with the nearby Raheenmore bog has been the subject of the Irish Raised Bog Restoration Project funded by the EU LIFE Nature programme.

Feehan and O'Donovan (1996) report that similar to many Irish bogs, in the 18th and 19th, centuries a road was made across Clara bog. Road construction involved drainage and it is thought that as a result up to 5 m of settlement has occurred and the effects of the settlement extend up to 500 m into the bog.

The peat at Clara was sampled using a "Russian" peat corer which produces a 0.5 m long hemispherical sample of peat, similar to that shown on Figure 3. Some logs of the peat at Clara are shown on Figure 4.



Figure 3."Russian" coring of peat

The peat material has been classified according to the scheme described originally by von Post and Granlund (1926) as extended by Hobbs (1986). Both probes were taken on a GPR profile which was perpendicular and westwards from the Clara - Rahan road which bisects the bog. The probes were about 10 m north of an elevated wooden walkway (see Figure 2). P1 was located some 20 m from the road (at the 13 m mark on the GPR line) and P2 was some 80 m from the road (at 60 m on the GPR line).

P1 proved the base of the peat at about 5.65 m. The water content log shows a relatively uniform peat with average water content of some 1350%. This is on the higher end of that normally recorded in Irish peat. The peat overlies a thin layer of very soft clay / silt which overlies calcareous marl. Both have much lower water content than the peat.

Figure 5. Output for 80 and 40 MHz transmitters at Clara bog

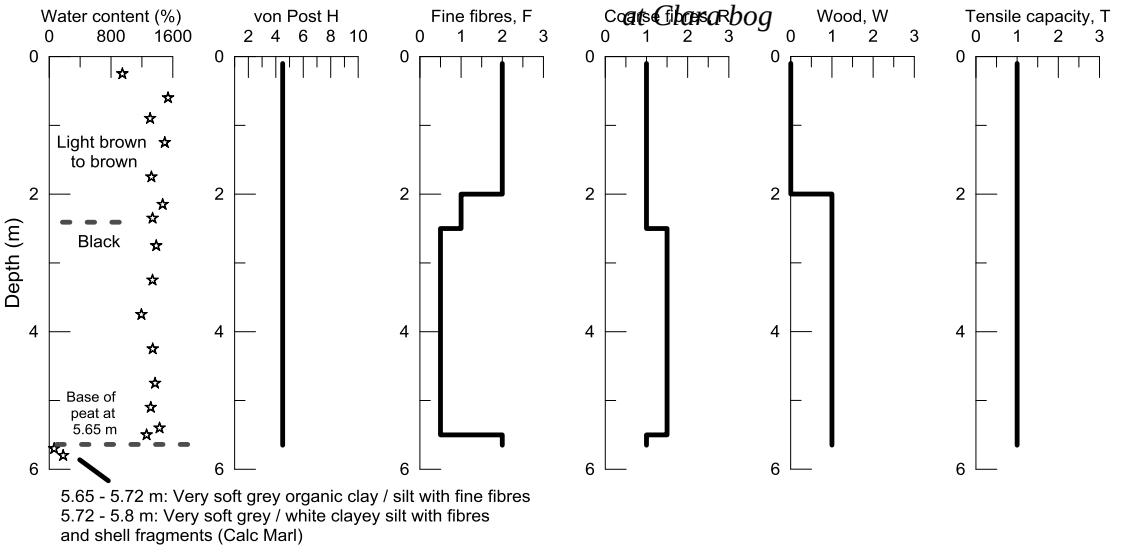
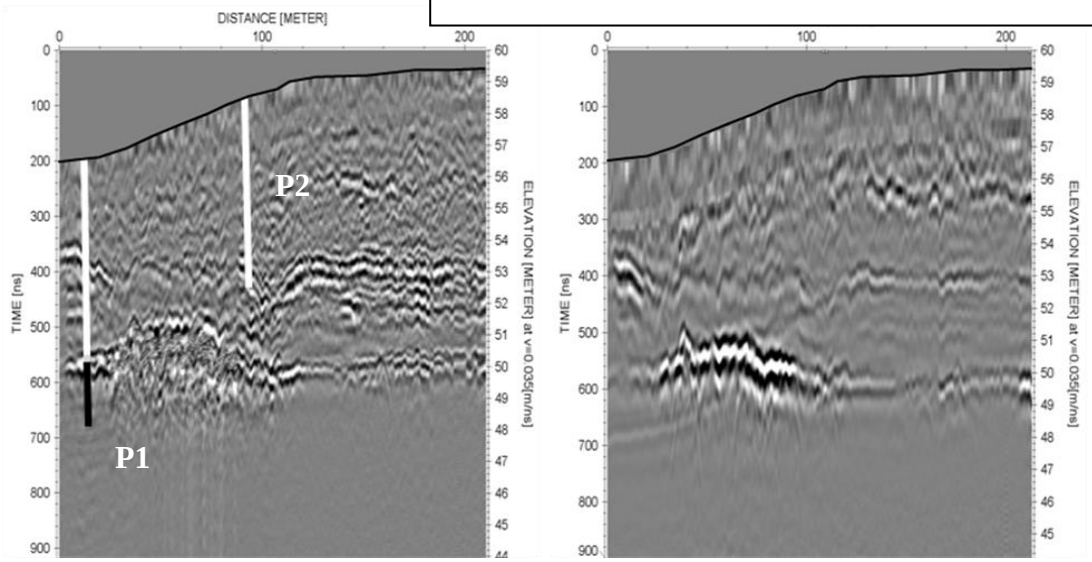


Figure 4. Peat logs from Clara bog

(H = degree of humification: 1-10, F = fine fibres: 0-3, R = coarse fibres: 0-3, W = wood: 0-3, T = tensile strength: 0-3, P = plastic: 0 or 1)



There is a clear difference in the peat above and below about 2.5 m (circa 54 mOD). Above 54 mOD the peat is light brown to brown in colour, has a relatively high fine fibre content but low coarse fibre and wood content. Below this level the colour of the material is black and there are less fine fibres but more coarse fibres and wood.

GPR traces across the probes are shown on Figure 5. Output from two different signal input frequencies is used. The base of the peat at approximately 5.6 m in P1 is clearly identified in the GPR data. In addition GPR is able to resolve some internal boundaries in the peat, for example one at about 2.5 m, which is in agreement with the physical log of the peat as described above.

The base of the peat was not proven in P2. The depth limit of the Russian corer with the available rods is 6 m. The GPR trace suggests that the peat base is actually at about 7 m depth. The water content log at P2 shows more variability than P1. The average water content of the peat is some 1420%. It is perhaps not surprising that this value is greater than P1 due the consolidation effects of the Clara – Rahan road.

In P2 the peat can be sub-divided into two zones with a border at about 2.25 m to 2.5 m (consistent in both the P2 log and in the GPR trace). There is a particularly wet zone of peat below about 2.5 m. This corresponds to a definite later of very high coarse content fibres below which the coarse fibre content drops to a low value in uniform orange brown peat.

2.4 Present day commercial application

GPR work is now usually linked to an accurate GPS system which allows spatial relocation to GPS co-ordinates as well as providing topographic information. These systems are now being used regularly in design and risk assessment for infrastructural works on peatlands. The example on Figure 6 is for a windfarm site in western Ireland where the combined GPR, LiDAR and GPS data are integrated to produce contour maps for planning and design purposes.

3 LANDSLIDE RISK ASSESSMENT

Landslides in peatland areas are relatively common in Ireland, see for example Boylan et al. (2008). Assessment of the risk of landslides is a major issue in planning and design of infrastructural projects in upland areas.

As peat slope failures for the most part resemble planar translational slides Dykes and Kirk (2001; Hendrick (1990; Long and Jennings (2006; Warburton et al. (2003), these stability assessments are generally undertaken using relatively simple infinite slope analysis approaches. According to Haefli (1948) and subsequently Skempton and DeLory (1957), the factor of safety, FOS, for a planar translation slide, if the peat is assumed to behave in an undrained manner is given by Equation 1.

$$FOS = \frac{s_u}{\gamma_b z Sin\beta Cos\beta} \quad (1)$$

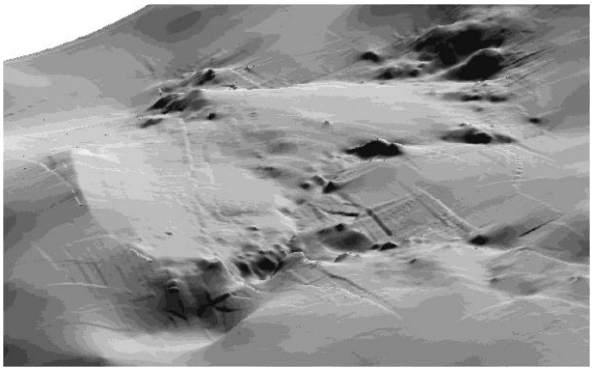
where: s_u = undrained shear strength of peat, γ_b = bulk unit weight, β = slope angle on base of sliding and z = depth of failure surface.

As the bulk unit weight of peat in Ireland is generally about 10 kN/m^3, the main unknowns are the values of β and s_u.

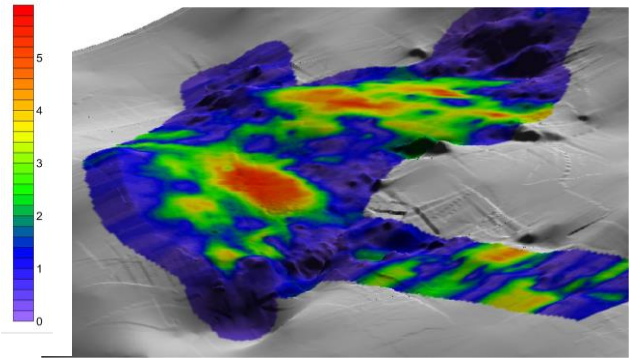
The assessment of peat slope stability often involves the use of relatively coarsely spaced physical soundings and surface slope assessments. With the provision of topographical Lidar data and the ability to collect continuous profiles of peat thickness using GPR, more detailed assessments of basal peat slopes and slope stability can be obtained.

Using the assessment of infinite slope analysis it is possible to provide potential risk maps of a site in order to predict where interaction with the ground may pose a potential hazard.

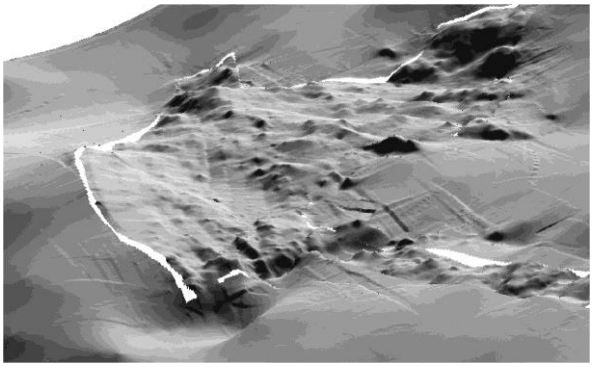
Figure 6 shows the stages employed in the production of potential risk maps for a site.



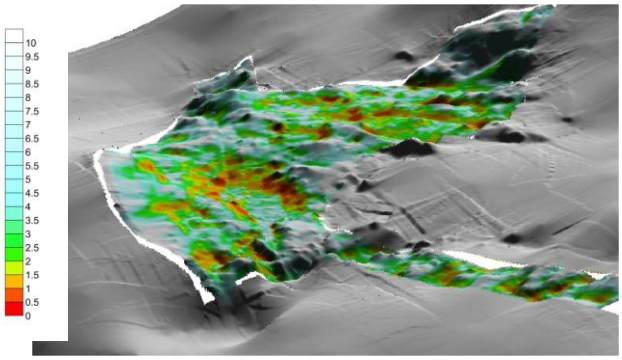
a) Surface topography from Lidar data



b) Peat Thickness (m)



c) Sub Peat topography



d) Potential Risk map showing sub peat topography with FOS

Figure 6. Results from GPR investigation of peat site in Connemara, Ireland.

By virtually stripping away the peat it is possible to accurately determine the sub peat slope and therefore produce a map of the FOS of the site. The potential risk map approach to assessing a site identifies areas where additional testing and peat sampling should be carried out,

One key element to the assessment of potential risk is s_u across a site. This is often determined from laboratory DSS testing of block samples taken from site. The need for a robust, practical methodology for the determination of s_u becomes increasingly obvious when sites are being assessed using much more detailed thickness and basal slope information. Many 'hidden slopes' would potentially fail and may have failed in the past but have now reached a relatively stable state due to being constrained by the subsequent build-up of the peat soil. In these situations it is essential to assess whether a slide is kinematically possible and how future interaction will affect slope stability.

4 IN SITU MEASURMENT OF SHEAR WAVE VELOCITY IN PEAT

4.1 Introduction

Characterisation of the stress-strain behaviour of soils is an integral part of many geotechnical design applications, including site characterization, settlement analyses, seismic hazard analyses, site response analysis and soil-structure interaction. The shear modulus (G) of geomaterials is highly dependent upon strain level. The small-strain shear modulus (G_{max} or G_0) is typically associated with strains on the order of 10^{-3}% or less. With information of G_{max}, the shear response at various level of stain can be estimated using published modulus reduction curves (i.e. G/G_{max}). According to elastic theory, G_{max} may be calculated from the shear wave velocity using the Equation 2:

$$G_{max} = \rho V_s^2 \qquad (2)$$

where G_{max} is the shear modulus (in Pa), V_s is the shear wave velocity (in m/s), and ρ is the density (in kg/m^3).

G_{max} can be measured in the laboratory using a resonant column device or bender elements. Laboratory testing requires very high-quality, undisturbed samples which is a challenging task in peat. Additionally, laboratory tests only measure G_{max} at discrete sample locations, which may not be representative of the entire soil profile.

Unlike laboratory testing, in situ geophysical tests do not require undisturbed sampling, maintain in situ stresses during testing, and measure the response of a large volume of soil. In situ measurement of V_s has become the preferred method for estimating the small strain shear properties and has been incorporated into site classifications systems and ground motion prediction equations worldwide.

In addition Eurocode 8, for seismic design, requires an earthquake risk assessment to be carried out for all important structures. Sites are classified based on the V_s of the top 30 m of the soil profile (V_{s30}).
Some important practical applications of the knowledge of V_s in peat include that for the development of high speed railways across peaty ground in Belgium and in Norway as described by Gupta et al. (2010) and Berggren et al. (2010) respectively.

4.2 Previously published V_s values in peat

V_s values in peat are very low. For example Tanaka (2014) measured V_s in the range 22 m/s to 44 m/s, with a seismic CPT, for depths of between 0.5 m and 2.5 m at a site in Hokkaido, Japan. Amaryan (1993) reported a wide scatter of values for Russian peat varying between 11 m/s and 44 m/s and he suggested: "studies are incomplete because of the scarce technology and poor techniques.....a satisfactory solution has not yet been achieved".

In view of the uncertainties involved, a study involving two different methods, namely direct shear wave transmission and down-hole shear wave transmission was undertaken at the Clara site and the results obtained are as follows.

4.3 V_s by down-hole method

A portable downhole sonde has been developed in order to take V_s readings through the vertical peat column with a view to correlating V_s to undrained shear strength.
The sonde was connected to a seismograph and recorded as single channel data at different depths within the peat. A shear wave was produced at the surface by striking a hammer against a block within the peat. An integral trigger within the source was used to start the recording of the traces. A reference geophone was also used to check the consistency of the time break. The integral trigger switch was found to be both reliable and repeatable. The down-hole field set-up is shown on Figure 7.

The down-hole sonde and shear wave source are shown in diagrammatic form on Figure 8 and in the photograph in Figure 9.

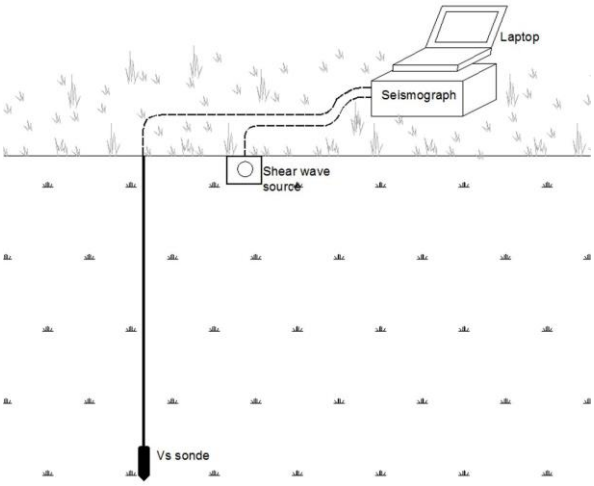


Figure 7. Downhole Field Setup

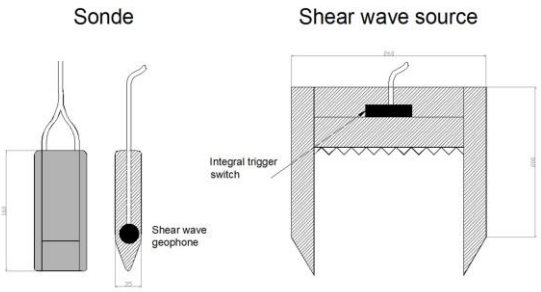


Figure 8. Downhole sonde and shear wave source



Figure 9. Downhole sonde and shear wave source

Figure 10 shows the results from the downhole Vs testing showing relatively constant Vs of c. 16 m/s. The Von Post log at this location showed a relatively consistent level of humification of the peat with H = 4.

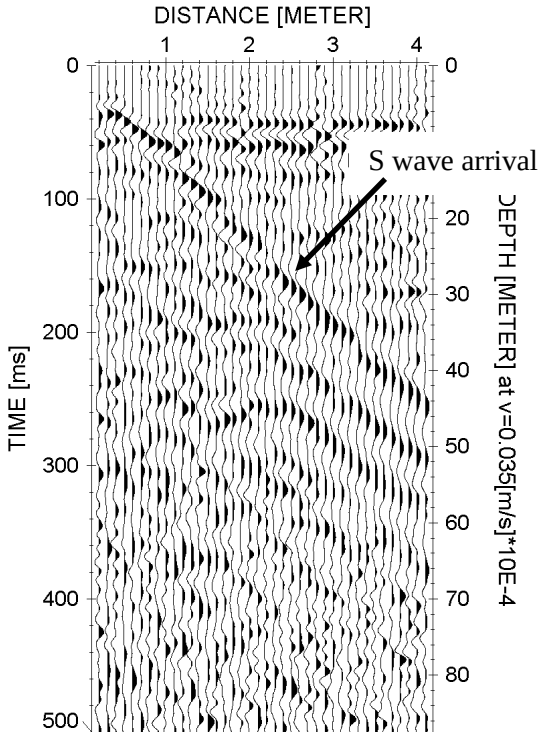


Figure 10. Downhole record showing V_s of about 16 m/s

4.4 V_s by direct shear transmission

This method involves the use of shear wave geophones on the surface at 0.5 m spacing and the generation off a shear wave at the surface in the same way as for the downhole V_s measurements. That data were collected to act as a control for the V_s downhole measurements. The method samples the upper layers of the peat and provides a bulk reading of V_s of the peat.

The results of the survey are shown on Figure 11. The shot record shows both P wave and S wave arrivals with the shear wave being dominant due to the orientation of the geophones. The V_s of about 15.7 m/s shows a good level of consistency with the readings from the downhole sonde.

4.5 Relationship between V_s and s_u

The other significant unknown in the stability assessment (Equation 1) is the value if s_u. Many techniques are available for the determination of s_u but these rely on either high quality samples or the need to bring heavy equipment onto a site in order to carry out in situ testing.

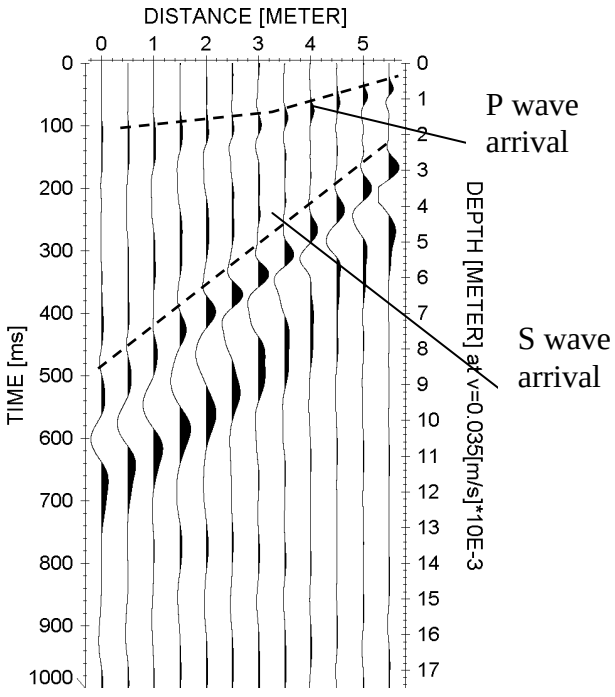


Figure 11. Direct shear wave transmission record

A review of available methods is given by Long and Boylan (2012).

If it were possible to obtain a relationship between V_s and s_u, then given the ability to measure V_s on peat bogs with light and portable equipment as described above, it might be possible to use the geophysical technique to give reliable estimates of s_u.

It is well know that laboratory derived s_u in peat is related strongly to the consolidation stress used in the test, especially if this stress exceeds the presonsolidation stress (p_c'), see for example Boylan and Long (2014).

Some work has therefore been carried out to determine the relationship between V_s and consolidation stress. This work was carried out in the laboratory using bender elements as shown on Figure 12.

The samples used were 70 mm in diameter and had an initial height of about 67 mm. Testing has shown that this approximately 1:1 ratio is the most efficient from the point of view of signal interpretation. The bender elements used were specifically designed for work in peat and had a protrusion of about 3 mm into the specimen. A sine wave pulse of frequency 2 kHz was applied and the time of first arrival determined.

A typical relationship between V_s and consolidation stress is shown on Figure 13. It is clear that there is a linear relationship between the applied consolidation stress and the resulting V_s in the peat.

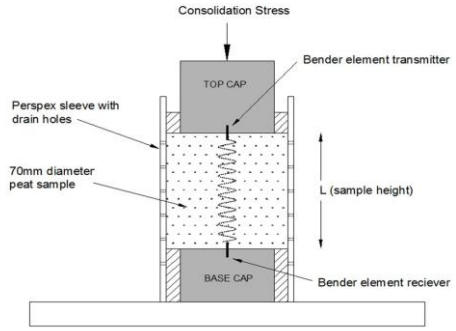


Figure 12. Laboratory bender element set-up

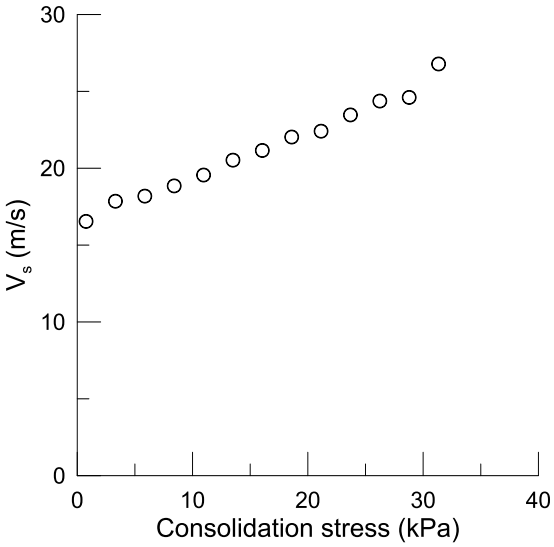


Figure 13. V_s versus consolidation stress

Although further work is required on this topic it is clear that the approach holds some promise.

5 CONCLUSIONS

This paper has provided a review and an update on some recent developments on geophysical testing of peat for civil engineering purposes. It was found that:

- GPR is a powerful tool for determination of peat thickness. Once peat thickness is obtained, the GPR data can be combined with GPS and LiDAR imaging to yield data such as the sub-bottom peat profile. The slope of the peat base can be obtained for use in landslide assessment studies.
- GPR can also give details of the internal structure of the peat and of the soils beneath the peat.
- Although the literature suggests that shear wave velocity measurements in peat are difficult due to the low values obtained, it has been shown here that it is possible to obtain consistent values with a variety of techniques.
- A lightweight down-hole sonde has been described for the purposes of measuring V_s of peat in remote environments.
- Work is ongoing on the development of a relationship between in situ V_s and the undrained shear strgth of peat for the purposes of landslide stability assessment.

REFERENCES

Amaryan, L.S. (1993) *Soft soil properties and testing methods*, Rotterdam: Balkema.

Berggren, E.G., et al. (2010) "Identification of substructure properties of railway tracks by dynamic stiffness," *Sound and Vibration*, Vol. 329, No. 19, pp 3999 - 4016.

Bjelm, L. (1980) "Geological interpretation with subsurface interface radar in peat lands," Lunds Tekniska Högskola. Teknisk Geologi, p 6p.

Bjelm, L., and P. Ulriksen (1980) "System för torvmark sundersökning med radar. Slutrapportetapp," Lunds Tekniska Högskola. Teknisk Geologi, p 104p.

Boylan, N., et al. (2008) "Peat slope failure in Ireland " *Quarterly Journal of Engineering Geology and Hydrogeology*, Vol. 41, No. 1, pp 93-108.

Boylan, N., and M. Long (2014) "Evaluation of peat strength for stability assessments," *Institution of Civil Engineers Journal of Geotechnical Engineering*, Vol. 167, No. GE5, pp 421 - 430.

Carlsten, P (1988) "Geotechnical properties of peat and up-to-date methods for design and construction," Swedish Geotechnical Institute (SGI), Varia 215.

Dykes, A. P. , and K. J. Kirk (2001) "Initiation of a multiple peat slide on Cuilcagh Mountain, Northern Ireland," *Earth Surface Processes and Landforms*, Vol. 26, pp 395-408.

Edil, T.B. (2001) "Site characterisation in peat and organic soils," *Proc. Int. Conf. on In Situ Measurement of Soil Properties and Case Histories*. Bali, Indonesia, pp 49-59.

Feehan, J. , and G O'Donovan (1996) *The bogs of Ireland – An Introduction to the Natural, Cultural and Industrial Heritage of Irish Peatands*: UCD Environmental Institute.

Francese, R., et al. (2002) "Geophysical investigation within the Zennare Basin (Venice) " In: C. Campostrini, Ed., *Scientific Research and Safeguarding of Venice (CORILA Research Program 2001-2003 - Vol. I, 2001 Results)*: Istituto Veneto di Scienze Lettere ed Arti, La Garangola, Padova, Italy, pp 229 - 239.

Gupta, S., et al. (2010) "Numerical modelling of vibrations from a Thalys high speed train in the Groen Hart tunnel," *Soil Dynamics and Earthquake Engineering - Elsevier Press*, Vol. 30, No. 3, pp 82 - 97.

Haefli, R. (1948) "The stability of slopes acted on by parallel seepages," *Proc. 2nd ICFSMFE*, pp 134-148.

Hendrick, E. (1990) "A Bog Flow at Bellacorrick Forest, Co. Mayo," *Irish Forestry*, Vol. 47, No. 1, pp 32-44.

Hobbs, N. B. (1986) "Mire morphology and the properties and behaviour of some British and foreign peats," *Quarterly Journal of Engineering Geology and Hydrogeology*, Vol. 19, pp 7-80.

Long, M. (2015) "Developments in the use of geophysics in geotechnical engineering in soft ground," *XVIth European Conference on Soil Mechanics and Geotechnical Engineering (ECSMGE)* Edinburgh, Scotland Thomas Telford Ltd., pp 129 - 150

Long, M., and N. Boylan (2012) "In situ testing of peat – a review and update on recent developments," *Geotechnical Engineering Journal of the SEAGS & AGSSEA*, Vol. 43, No. No. 4, December, pp 41 - 55.

Long, M., and P. Jennings (2006) "Analysis of the peat slide at Pollatomish, Co. Mayo, Ireland," *Landslides*, Vol. 3, No. 1, pp 51-61.

Park, C.B., et al. (1999) "Multichannel analysis of surface waves," *Geophysics*, Vol. 64, No. 3, pp 800 - 808.

Plado, J., et al. (2011) "Ground-penetrating radar study of the Rahivere peat bog, eastern Estonia," *Estonian Journal of Earth Sciences*, Vol. 60, No. 1, pp 31 - 42.

Saarenketo, T., et al. (1992) "GPR applications in geotechnical investigations of peat for road survey purposes," *Geological Survey of Finland, Special Paper 16*: Geological Survey of Finland, Special Paper 16, pp 293 - 305.

Skempton, A.W., and F.A. De Lory (1957) "Stability of natural slopes in London Clay," *Proc. 4th ICSMFE*. Rotterdam, pp 72-78.

Smit, R. (1989) "The hydrology of a hummock-hollow complex on Clara Bog in Ireland in relation to chemistry and vegetation." Internal Report 265, Hugo de Vries Laboratory, University of Amsterdam.

Tanaka, H. (2014) "Geotechnical properties of peaty ground in Hokkaido, Japan " In: Z. Mlynarek, and J. Wierzbicki, Eds., *Proceedings 5th International Workshop CPTU and DMT in soft clays and organic soils*. Poznań, Poland,: Exemplum, Poland.

Trafford, A. (2009) "Mapping thickness of raised peat bog deposits using GRP," *Proceedings EAGE Near Surface 2009, 15th Annual Meeting of Environmental and Engineering Geophysics*. Dublin: EAGE.

Ulriksen, P. (1979) "Geo-radar för torv djups bestämning," Lunds Tekniska Högskola. Teknisk Geologi, p 6p.

Ulriksen, P. (1980) "Investigation of peat thickness with radar," Lunds Tekniska Högskola. Teknisk Geologi, p 14p.

Ulriksen, P. (1983) "Computer processing of subsurface impulse radar data," *International symposium on soil and rock investigations by in-situ testing*. Paris, pp 335 - 340.

Van der Molen, P. E., and T. A. Wijmstra (1994) "The thermal regime of hummock-hollow complexes on Clara Bog, Co. Offaly " *Biology and Environment: Proceedings of the Royal Irish Academy (RIA)*, Vol. 94B (3) pp 209 - 221.

von Post, L. , and E. Granlund (1926) "Peat resources in southern Sweden," *Sveriges geologiska undersökning, Yearbook*, Vol. 335, No. 19.2 Series C, pp 1 – 127.

Warburton, J., et al. (2003) "Anatomy of a Pennine Peat Slide, Northern England," *Earth Surface Processes and Landforms*, Vol. 28, No. 5, pp 457-473.

Warner, B.G., et al. (1990) "The application of ground penetrating radar to peat stratigraphy of Ellice swamp, southwestern Ontario," *Canadian Journal of Earth Sciences*, Vol. 27, pp 932 - 938.

Installation of fully grouted piezometers

Kristoffer Kåsin
Norwegian Geotechnical Institute, Norway, krk@ngi.no
Amund Augland
Geovita AS, Norway, aau@geovita.no

ABSTRACT
In the planning and design phase of the E16 Sandvika – Wøyen road project in Bærum Municipality in Norway, NGI installed a large number of piezometers using the "Fully grouted" installation method. Because of layered soil conditions, with soft clay overlaying very hard moraine, traditional "push in place" installation method was not feasible for a large number of the planned sensors. Instead, a method that could ensure that sensors installed in both the clay and the moraine at the same locations had to be used.

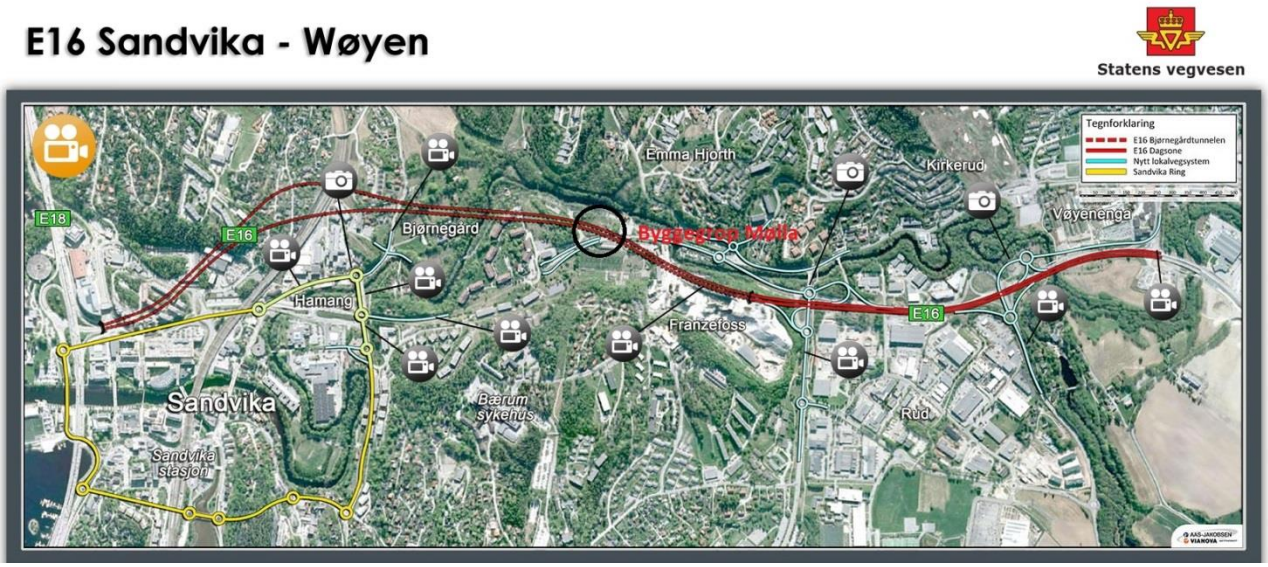
In total, 35 sensors were installed using the grout in place method, and two sensors were installed in the clay as control. The results from a pumping test performed in close proximity to the installed sensors, confirm that the installation method was successful, and that the sensors respond rapidly to changes in the in situ pore pressure.

Keywords: Piezometers, grout, groundwater, pore pressure,

1 INTRODUCTION

The Norwegian Public Road Administration is building a new 4 lane road between Sandvika and Wøyen in Bærum municipality in Norway. Aas Jackobsen AS designs the project with Geovita AS as geotechnical design engineers. NGI have performed geotechnical site investigations in the field and lab based on the specifications made by Geovita AS.

The project consists of several tunnels in rock as well as excavation and cuts in both soil and rock. At several sites in the project sheet pile walls or secant pile walls are planned. Within the project there is a building site named Mølla that is in the focus in this paper. An overview of the project is shown in Figure 1. Building site Mølla is marked by a black circle.

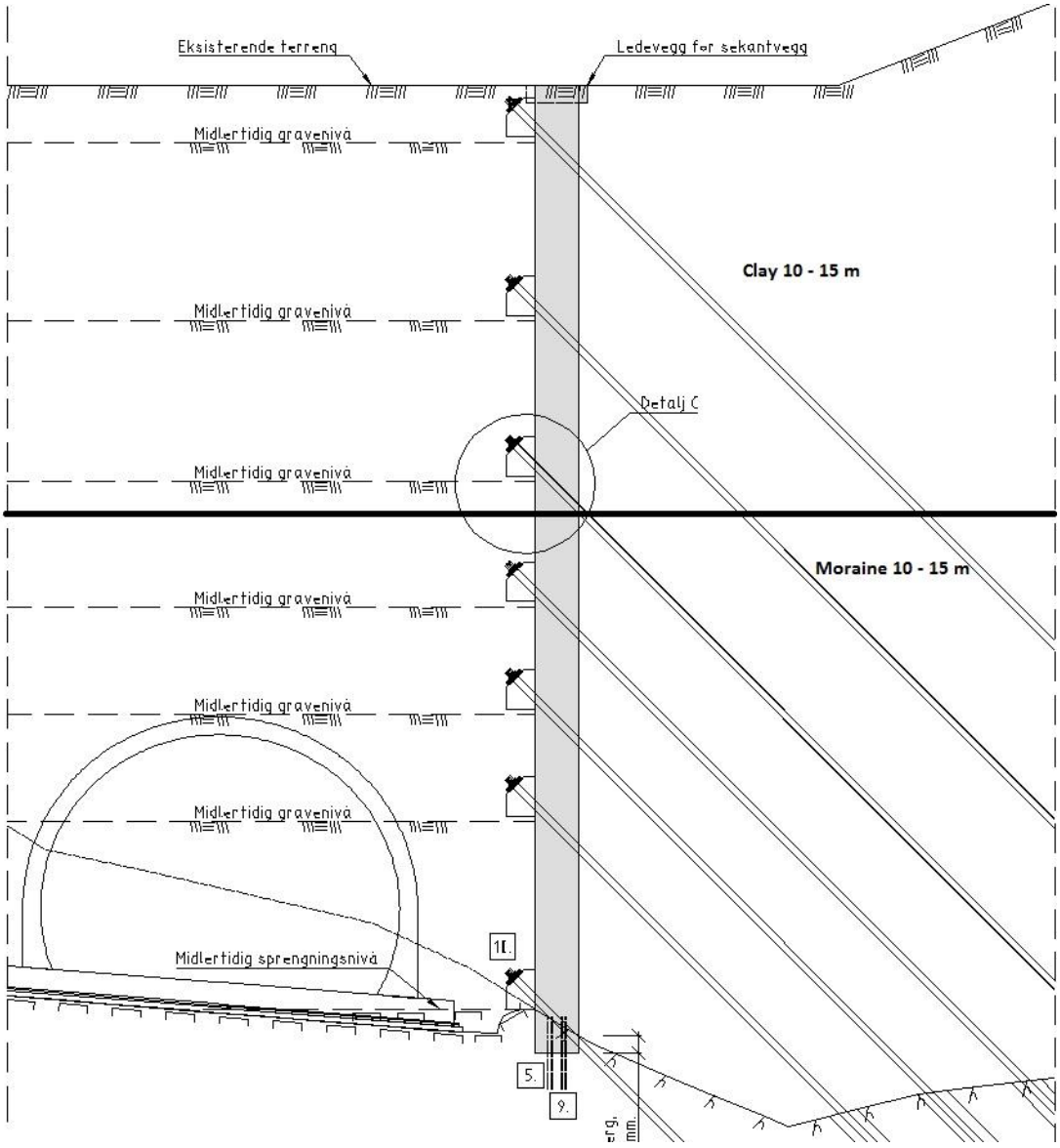


2 GROUND CONDITIONS AND CHALLENGES IN MEASURING PORE PRESSURE

At the planned site at "Mølla", a one sided construction pit is under construction. A cross section of the planned secant pile wall is shown in Figure 2. The wall is up to 25 m high at the highest point and 125 m long. The wall is retained with 5 – 7 levels of tieback rods, depending on the height of the wall. Figure 2 show a cross section through the planned secant pile wall, and the planned tunnel at the bottom.

The ground conditions consist of 10 – 15 m of soft clay on top of 10 – 15 m of very hard moraine. The thick black line in Figure 2 show the transition between clay and moraine. This level is varying in the whole area, as does the depth to bedrock. There are two separate ground water tables at the site, one in the clay and one in the lower, and more permeable moraine. The pore pressures in the moraine was known, from previously installed hydraulic piezometers, to vary with precipitation.

The design of the wall required that the pore pressures in both layers to be measured in real time, and that sensors in the moraine had rapid response to changes in the pore pressure in the surrounding soil. This was because lowering of the pore pressures in the moraine through pumping during the construction phase, would be desirable for the design of the wall.



To make sure that lowering of the pore pressure in the moraine was possible, a pumping test was performed. This pumping test had to be monitored in several locations and with several sensors in each location, to make sure that the pore pressures was lowered sufficiently during the pumping, and that the response in the pore pressure in both soil layers was as expected.

To accomplish this, a monitoring programme was designed by Geovita AS, for installation by NGI. If the program was successful, the same set of sensors was to be used to monitor the construction phase. The monitoring program consisted of a total of 35 sensors in 6 different locations. Each location had a sensor every 5 m depth, regardless of whether the type of soil was soft clay or hard moraine.

3 FULLY GROUTED PIEZOMETERS

It was decided to use the "Fully grouted" piezometer installation method, proposed by Mikkelsen & Green, 2003, to install the piezometers at Mølla, as this made it possible to install sensors in the same borehole, regardless of the soil type at the sensor location. The method uses a cement/bentonite/water grout, This grout is pumped into the annum between the sensors and the soil around the borehole, to fully enclose the sensors.

Some other options for the installation was considered:

1. Installing the piezometers in clay with the normal push in place method normally used in soft soil in Norway.
2. Installing the sensors in the moraine by predrilling with a drill bit, and hoping that the borehole in the moraine wouldn’t collapse. This would require one borehole for each sensor in the moraine.
3. Drilling casings down in the moraine, and placing sandfilters around each sensor and bentonite seals to isolate the sensor levels in the traditional way to install piezometers in hard soils.

Figure 3 show the difference between installation of fully grouted and traditional piezometers.

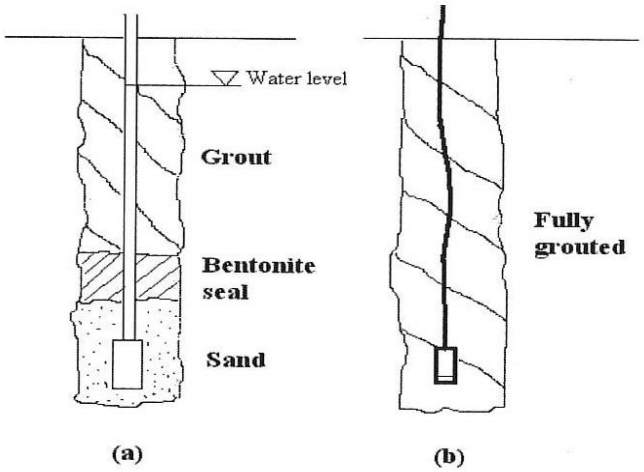


Figure 3: Traditionally piezometer and fully grouted piezometer, Mikkelsen & Green 2003

Installation of the sensors in the clay would not be an issue, but option 2 and 3 had large contained risks of vertical leakage between sensor levels and also contained a larger amount of work and number of drilled boreholes in the very hard moraine. This made the "Fully grouted" method seem attractive, as only one borehole was necessary at each sensor location, and all the sensors in the single borehole would be installed simultaneously.

As described in Mikkelsen & Green, 2003; as long as the piezometer used is of the electrical diaphragm type, the permeability of the grout can be low and the response to changes in the in situ pore pressure will still be within minutes. Figure 4 show the relationship between permeability and response time, for different type of piezometers, after Terzaghi & Peck, 1968.

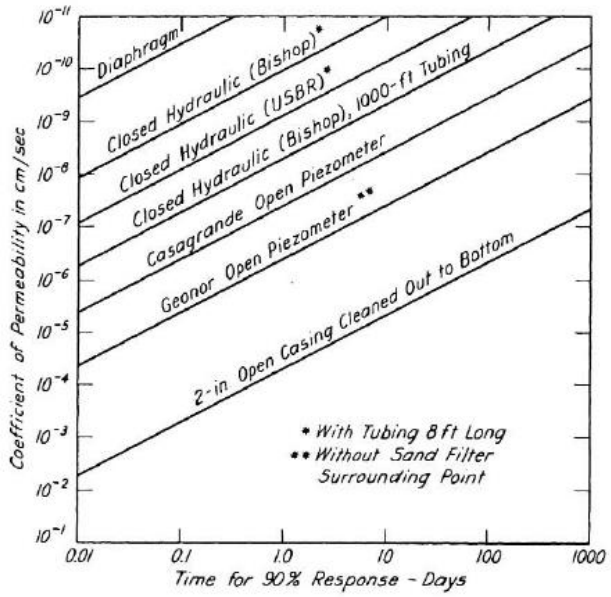


Figure 4: Response time for different piezometers

4 ADVANTAGES WITH THE FULLY GROUTED METHOD

The fully grouted method has several advantages compared to the traditional method with a filter and bentonite seal:

- The grouting can be completed quickly, as it just requires a tremie pipe into the borehole to pump in the grout.
- Several sensors can easily be installed at different depths in the same borehole.
- The filter and bentonite seals can be skipped, and this leads to lower probability of hydraulic leaks due to errors during the installation of the sand filter and bentonite seal.
- The strength/stiffness of the grout can be adjusted to mimic that of the soil at the site.
- Other measuring systems, like inclinometers, can easily be installed in the same borehole since the grout is in contact with the surrounding soil in the borehole.

As long as the soil is too hard in order to use the push in place method, the best way to install piezometers will probably be with the fully grouted method, as there is not a lot of disadvantages, as long as the correct equipment is avaliable.

5 DETAILED DESCRIPTION OF THE INSTALLATION METHOD AT E16 MØLLA

At Mølla the following steps was executed to install the sensors.

1. A cased borehole was drilled down to 50 cm below the level of the deepest sensor using ODEX drilling system. The inner diameter of the casing was either 76 mm or 92 mm.
2. The bottom of the borehole was cleaned thoroughly through water flushing.
3. The drill string and drill bit was retrieved from the casing.
4. The casing was kept full of water after retrieving the drill string to make sure that the sensors were fully saturated when installed.
5. The sensors were attached to the outside of a steel tremie pipe that was lowered down into the casing. A sensor was attached every 5 m depth, with plastic strips, the wires to the sensors was fastened every meter. Figure 5 show the sensors fastened to a central pipe.
6. During the lowering of the tremie pipe with the sensors attached, the sensors were checked continuously, to verify that the sensors were working.
7. When the tremie pipe was installed, the grout was mixed according to the ratios listed in Table 1, and pumped down to the bottom of the borehole. As the grout is heavier than water, the water in the borehole is displaced out of the top of the borehole.
8. When the borehole was completely filled with grout, the casing was pulled out of the borehole. Grout was added to the borehole to replace the volume of the casing being pulled out, to keep the borehole full of grout.
9. The real time monitoring system, developed at NGI, was installed and data was transmitted through the mobile phone network. An general description of the system shown in figure 6.

Table 1: Mixing ratios for the grout used at E16 Mølla.

Material	Ratio	Ratio by weight
Cement	1	9
Bentonite	0,1	1
Water	2,1	18,9

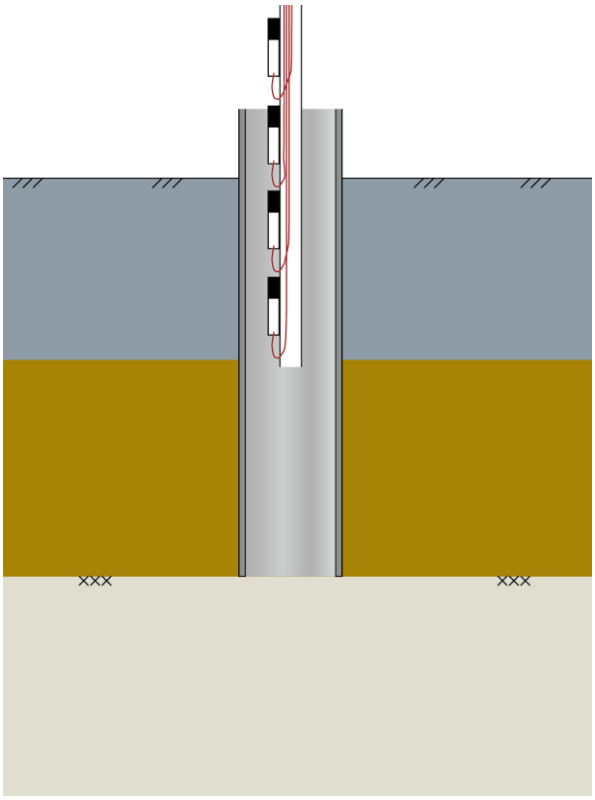


Figure 5: Sketch of cased borehole, with a pipe and several sensors under installation.

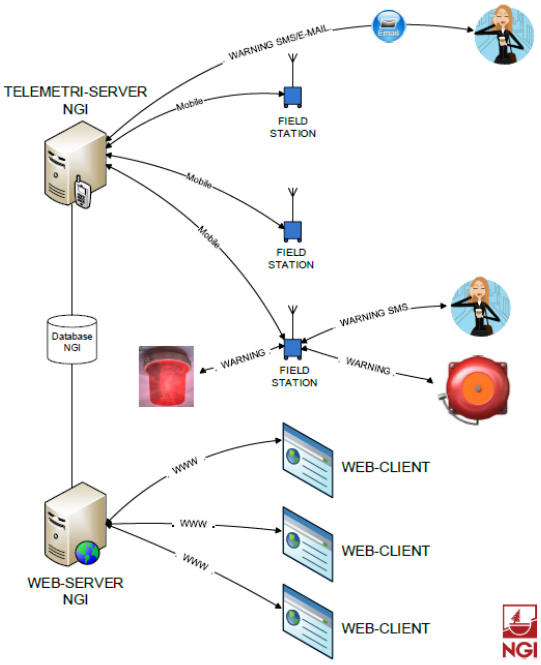


Figure 6: NGI's remote monitoring system.

6 CHALLENGES DURING THE INSTALLATION

Installation at the site was carried out by using 2 geotechnical Geomachine 100 drill rigs to install the casings. Two types of drilling systems were used, Atlas Copco Odex 76 mm, and Atlas Copco Odex 90 mm. The size of the drilling systems was chosen to make sure that the horizontal distance from the sensor out to the in situ soil was as small as possible. With these systems, the distance from the filter of the sensor to the in situ soil would nominally be 38 and 45 mm. The drill rigs were selected based on availability.

There was challenges with the drilling of the consuming a lot of time with both drilling systems when drilling in the hard moraine at the site. It was known that the moraine at the site was hard, but it was harder than expected, and in combination with the geotechnical drill rigs top hammer drives the penetration rate was not satisfactory. In retrospect, to use well drilling rigs, with down the hole hammers would probably have been more efficient, but this would probably have required an increase in the casing size to 4 1/2 ". The use of a symmetrical drilling system, with a ring bit and pilot bit, could probably have improved the penetration rate when drilling.

7 PUMPING TESTS AND RESPONSE TO THE CHANGE IN PORE PRESSURE

To verify that the pore pressure in the moraine could be lowered, two pumping wells were installed close to three of the installed sets of piezometers.

Two casings, diameter 219 mm, were drilled down to bedrock. A slotted filter with a diameter of 114 mm and 0,3 mm large slots was installed in the moraine. The length of the filter was 15 m. Through the clay layer on top, an unslotted pipe was used.

Filter sand was backfilled around the slotted filter in the borehole and the casings were

pulled up to the transition between the clay and the moraine.

A pump was installed at the bottom of each filter, and water was pumped out of the borehole at a rate of around 0,8 m^3/hour in one well, and 1,6 m^3/hour in the other. The pumps were kept running over a period of four days, and the pore pressures in all the sensors were continuously monitored in this period.

Figure 7 show the monitored pore pressures in monitoring location ST_312, where four sensors where installed in the moraine (Pink, light green, purple and blue lines), and one sensor (dark green) was installed in the clay.

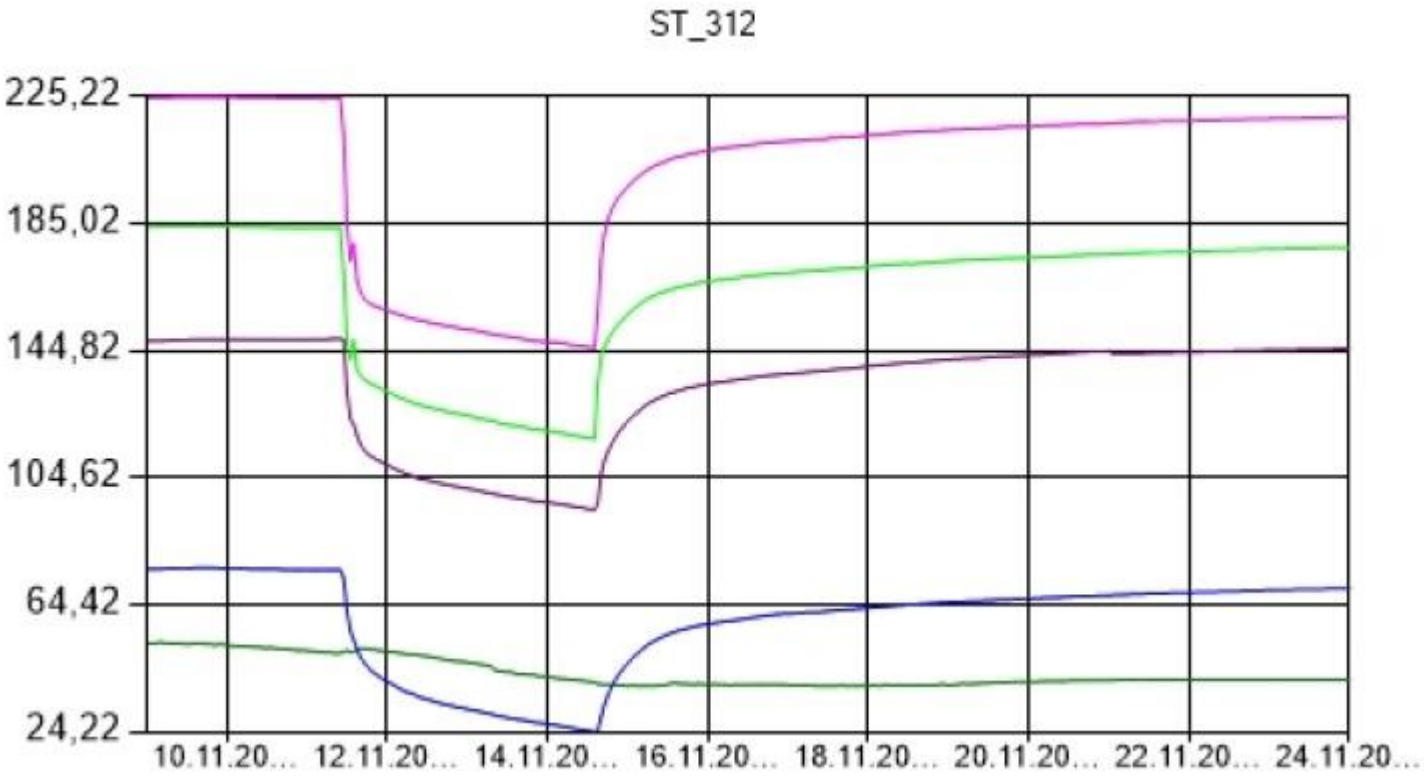


Figure 1: Logged pore pressures vs time in borehole ST_312 during the pumping test.

The logging show an immediate response to the pumping in the permeable moraine layer where the water was pumped out. One can also see that after the pumps are turned off, the pore pressure rapidly increases. The sensor installed in the clay have almost no response – and the pore pressure is actually increasing in the beginning of the pumping test – indicating that the grout has worked as a hydraulic seal between the sensors.

8 CONCLUSION

Even though the drilling of the casings proved to be time consuming in the hard moraine at Mølla, the installation of the sensors with the tremie pipe and the following grouting was a lot faster than installing several levels of sand/gravel filters, bentonite seals and grout in the same borehole.

The results show that the grout in place piezometeres worked as intended and the measured pore pressures are as expected. The response during the pumping test show that the grout has a permeability that lets the sensors measure rapid changes in pore pressure, and that there is no leakage between sensor levels.

The author would recommend the fully grouted piezometer method in all applications where electric piezometers needs to be installed in hard soil that requires drilling a borehole with casing.

9 ACKNOWLEDGEMENTS

The author want to extend thanks to Statens Vegvesen (NPRA) for allowing the data to be published and for the courage to try a new method that had not been tested in the Norwegian soils.

Geovitas AS, especially geotechnical engineer Amund Auglands, contribution, through both design of the testing programme and the idea to use the fully grouted method is greatly appreciated. Without them, the method would probably not have been proposed at all.

10 REFERENCES

Mikkelsen P. E. & Green G.E., 2003, Piezometers in fully grouted boreholes, Proceedings FMGM, p545 – p555.

Terzaghi, K.and Peck R. B., 1968, Soil Mechanics in engineering practice, 2 ed., Wiley, New York.

Extended interpretation basis for the vane shear test

A. S. Gylland
Multiconsult, Norway, anders.gylland@multiconsult.no

V. Thakur & A. Emdal
The Norwegian University of Science and Technology (NTNU), Norway

ABSTRACT
The vane shear test has been widely used as an in-situ test device in Norway from the sixties to the eighties. However, the last decades, its popularity has decreased, partly because of the increasing popularity of the CPTU-test, but also because of uncertainties related to interpretation of the vane shear test. With the aim of an improved and extended interpretation basis for the vane shear test, a database consisting of parallel vane shear tests and laboratory tests performed on high quality block samples has been compiled. The work focus on correlations between the vane shear test and active undrained shear strength and stiffness as well as factors that could improve the vane test as a "quick-clay-detector", e.g. sensitivity and remoulding energy. The latter factors are important in areas where mapping of sensitive clays is necessary and an efficient tool is needed. The work show that it is possible to establish a strong relation between the active undrained shear strength and the undrained shear strength as interpreted from the vane shear test as a function of the plasticity index. If is further seen that there is a potential for deducing OCR from the vane test. There is not a one-to-one relation between sensitivity as measured from the vane test and by the falling cone test in the laboratory. The vane appears to measure too high values for the remoulded undrained shear strength. On the other hand, work on deducing disintegration energy from the shear vane tests show promising results. In total, the shear vane holds several advantages and further research on the device is recommended to strengthen its position in the geotechnical tool case.

Keywords: In-situ testing, clays, undrained shear strength, interpretation

1 THE VANE SHEAR DEVICE

The vane shear test (VST) is mostly used in clays and clayey silts for determination of undrained intact and remoulded shear strength. The vane shear device consists of two rectangular plates forming a perpendicular cross (Figure 1). The cross is penetrated into the ground to a given depth before rotation is applied. Torque and rotation is measured.
Despite its simplicity, the VST suffers from several uncertainties related to installation-effects, equipment and interpretation. In order to shed new light on the VST, a database of test results is here presented where the potential of deducing active undrained shear strength, soil stiffness, remoulded shear strength, disintegration energy and OCR from the test is investigated.

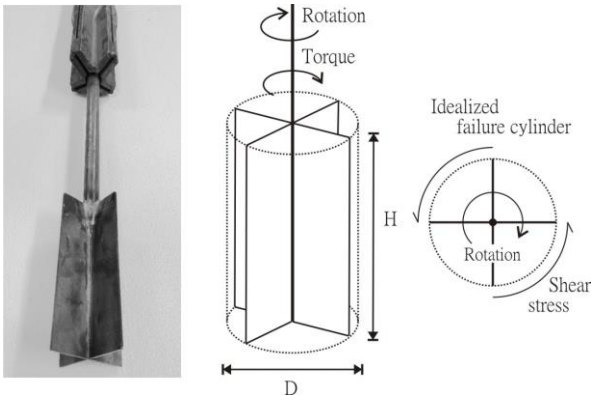


Figure 1 Vane shear blade cross

2 EQUIPMENT AND TEST SITES

2.1 The NTNU vane shear device

For the execution of the VST-experiments, a rotation device was developed at NTNU (Figure 2). It utilizes the hammer on the drill rig to apply rotation and incorporates an encoder, 1:100 gear and torque cell before

connection to the rod system. Torque and rotation is continuously logged. The vane itself is produced by Geotech and based on the protection shoe principle. A system for measuring the internal friction in the system is incorporated. The tests were performed at a rotation rate of 0,2 ˚/s using a D = 65 mm, H = 130 mm vane.

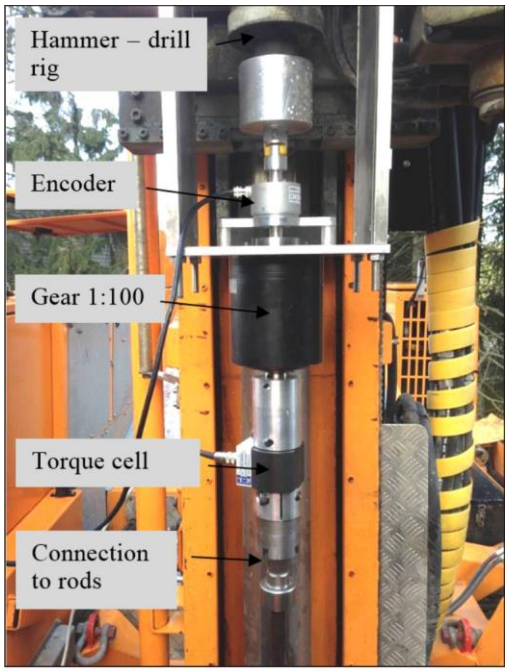


Figure 2 NTNU vane shear device

2.2 Characterization of test sites

The main data source in the work is based on data from three clay sites in Mid-Norway: Esp, Glava and Tiller. At these sites there exists high quality lab data from block samples (NTNU-Miniblock and Sherbrooke sampler). Vane tests are performed at depths equal to the block samples to allow one-to-one comparison. The database is also supplemented by two other sites: Klett and Fallan (only VST). All sites, except Glava, consists of sensitive and quick clays. Glava is a more plastic and less sensitive clay. A set of characteristic parameters is summarized in Table 1. All sites have a clay content in the range of 30-40% and an undrained shear in the range of 20-80 kPa, increasing with depth. Block sample data from Tiller is gathered from Ørbech (1999), Gylland et al. (2013) and new sampling at NTNU. Data from Glava is gathered from Sjursen (1996). Data from the other sites is gathered in relation to this study.

Table 1 Characteristic parameters of test sites

	Esp	Glava	Tiller	Klett	Fallan
w [%]	38	38	40	34	33
I_p [%]	5	18	5	7	9
S_t [-]	100	8	200	150	120
OCR [-]	1,7	4	1,7	1,5	1,6

2.3 Typical response curves and definition of parameters

A typical test result from the VST is shown in Figure 3, including definitions of peak and remoulded torque as well as peak undrained shear strength.

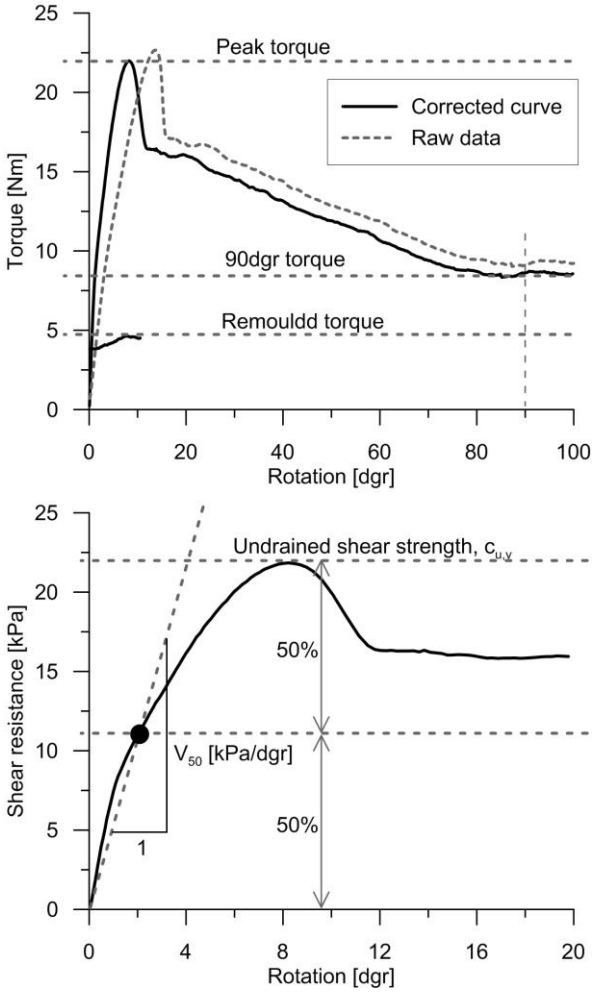


Figure 3 Definition of parameters

The corrected curve is obtained by subtracting the measured friction in the system and adjusting for rotation in the rods. A full circle is sheared in the soil at 90˚ rotation and the torque stabilizes at a constant level. The remoulded reading is done after rotating the vane 25 manual turns. The mobilized shear resistance is interpreted using $c_{u,v}=6T/(7\pi D^3)$ where T is the torque.

The parameter V_{50} [kPa/°] is defined as shown in Figure 3. This parameter gives a representative inclination of the mobilization curve and is thus a measure of stiffness.

3 CORRELATIONS

This section presents correlation between parameters deduced from the VST and relevant engineering parameters. The plasticity index (I_p) and stress state are used as the main correlation parameters as these are important factors when strength, stiffness and anisotropy are concerned.

3.1 Active undrained shear strength

Figure 4 shows a compilation of data points found in the literature where active undrained shear strength ($c_{u,a}$) from triaxial tests are reported at sites and depths parallel to vane tests. The gathered data points incorporates uncertainty regarding execution and interpretation of both vane and triaxial tests and should thus be viewed as a background for evaluating the new tests.
There is a clear trend in increasing $c_{u,a}/c_{u,v}$ ratio for reducing I_p. For low I_p, the ratio approaches 3,5. This range is mostly governed by three sites: Ellingsrud, Rissa and Esp, all being fairly silty and highly sensitive clays. The high $c_{u,a}/c_{u,v}$ ratio is mainly caused by low $c_{u,v}$ readings. For high I_p, the $c_{u,a}/c_{u,v}$ ratio approach 1,0.

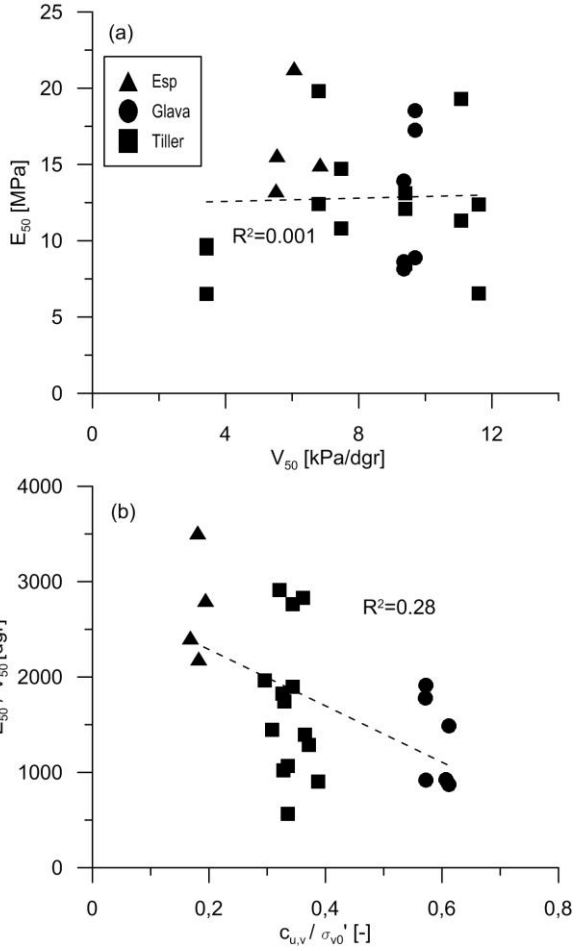


Figure 5 Stiffness

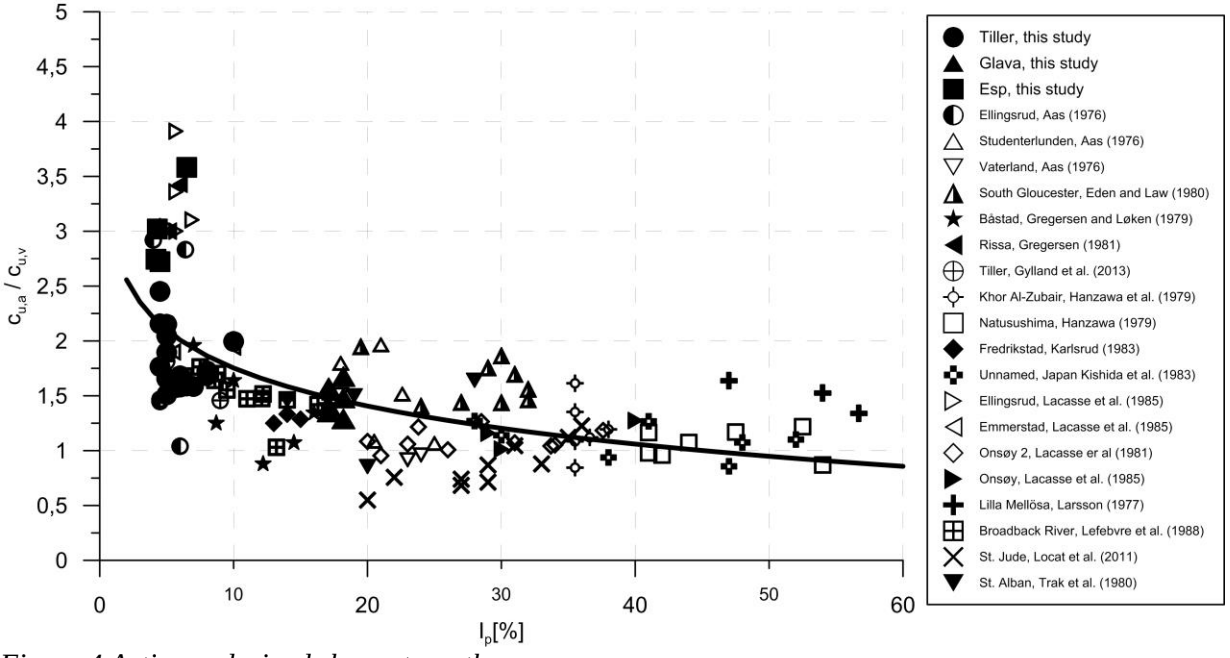


Figure 4 Active undrained shear strength

3.2 Stiffness

Two plots showing relations related to the stiffness parameters V_{50} from vane tests and E_{50} from triaxial tests are shown in Figure 5. In (a) it is clear that there is no direct relation between V_{50} and E_{50} for the sites investigated here. In (b) there is a possible trend of reducing E_{50} / V_{50} relation for increasing $c_{u,v}/\sigma_{v0}$' (vertical effective overburden stress). This suggests that the V_{50} increases for increasing strength ratio. No relation between V_{50} and σ_{v0}', OCR, I_p nor sensitivity is found.

3.3 Remoulded shear strength and sensitivity

One of the strengths of the VST is its ability to measure the soil sensitivity in situ. Often one finds a deviation when comparing values as obtained from the vane and obtained with the falling cone in the laboratory. This is investigated in Figure 6. From Figure 6a it is quite clear that the remoulded shear strength from the vane in general is higher than what is measured in the lab. Figure 6a and c suggests that the deviation between remoulded shear strength and sensitivity between vane tests and laboratory tests does not show any trend with increasing vertical effective overburden (depth). The main reason for this deviation is that for low values of the remoulded shear strength it appears that the device used is not able to measure reliably the low torques involved. Figure 6d indicates that the different in vane and laboratory measurements of the remoulded shear strength increases with increasing water content.

3.4 Overconsolidation

Work on the relation between OCR and the VST exists in the literature. One of these, Mayne and Mitchell (1988), use the SHANSEP framework (Ladd and Foott 1974)

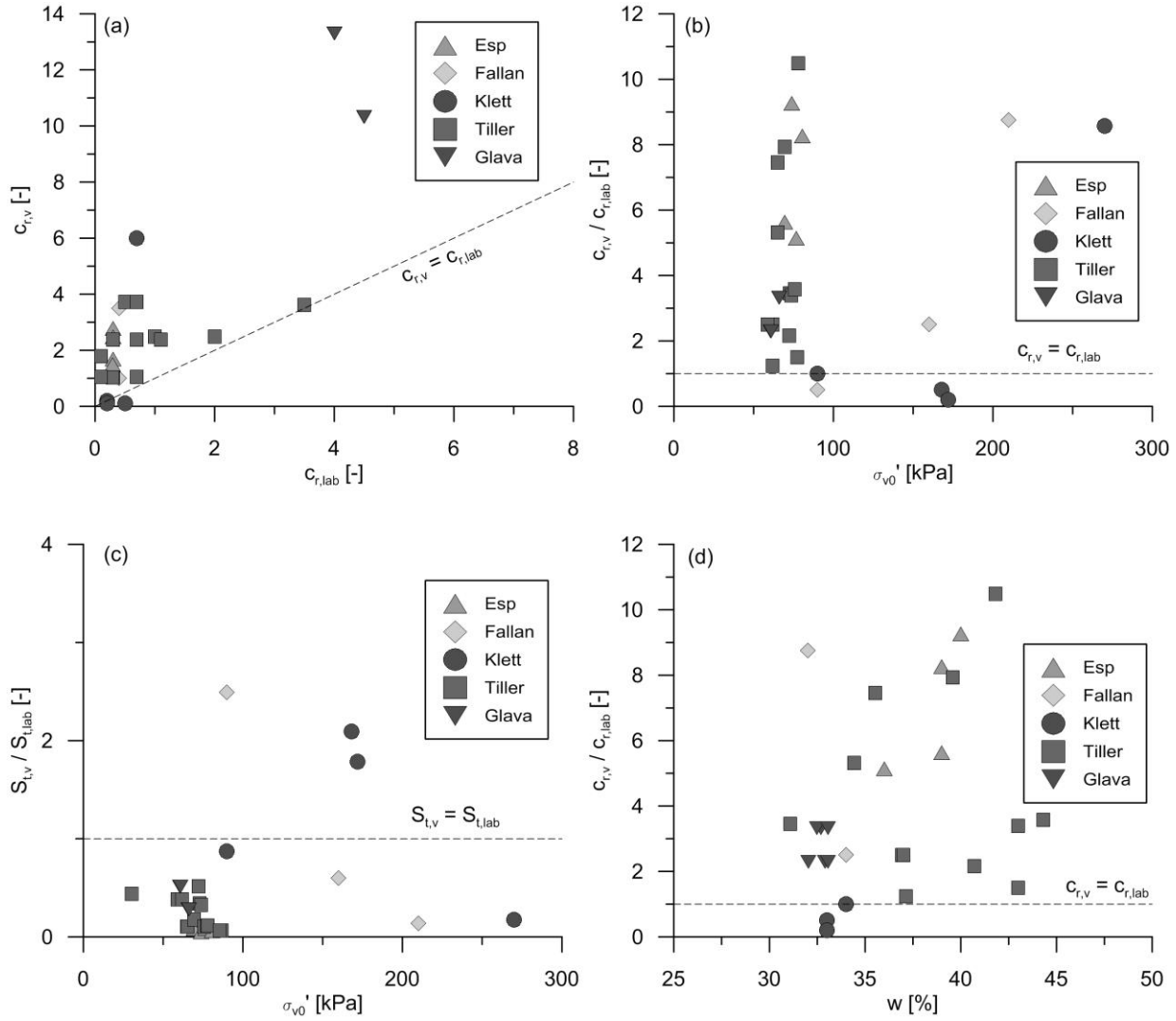


Figure 6 Sensitivity and remoulded shear strengt

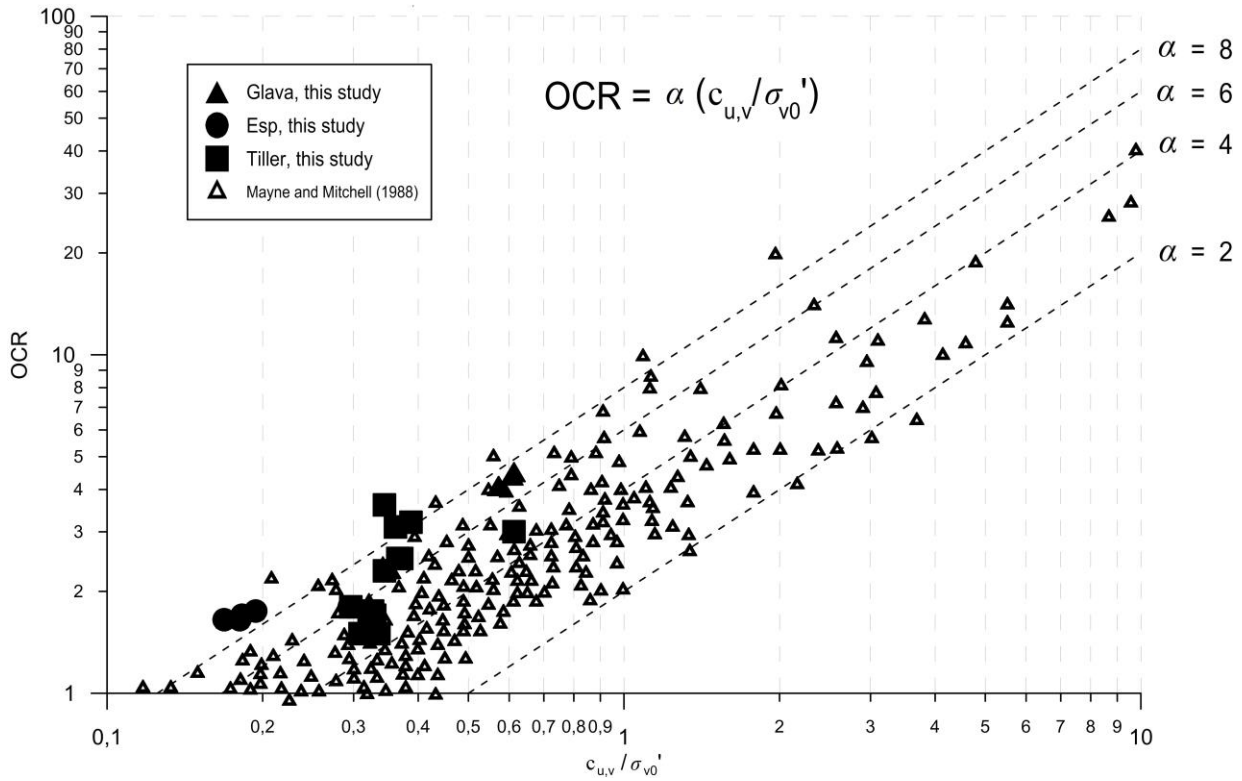


Figure 7 OCR and $c_{u,v}$ / σ_{v0}' (adapted from Mayne and Mitchell 1988)

which is based on the relation between undrained shear strength and OCR: (c_u/ σ_{v0}') = a OCR^m. By knowing the undrained shear strength from the VST together with appropriate factors (a og m), it is possible to determine OCR. A considerable dataset is gathered in Mayne and Mitchell (1988) to investigate the validity of this approach. The dataset is reproduced here in Figure 7 together with data from Glava, Esp and Tiller. The dataset of Mayne & Mitchell (1988) show a clear trend of increasing c_u/ σ_{v0}' for increasing OCR. Lines for four α-values (1/a) are included in the figure. The three Norwegian clays tested here lies within the data trend. α-values in the range of 6-8 are indicated. m = 1 is assumed in this interpretation.

3.5 Disintegration energy

The disintegration energy is a measure on how easy it is to remould a material. Some clays needs extensive remoulding to reach the fully remoulded state whereas some others can barely be touched before they collapse. This property of a clay is a useful supplement to the remoulded shear strength when the potential for retrogressive landslides is assessed. A clay that remoulds easily has a higher likelihood of fully reaching the fully remoulded shear strength during the failure process and hence flow out of the slide pit so that further retrogression can take place. Tavenas et al. (1983) investigated different approaches for determining the energy needed to remould a material; disintegration energy. The VST holds a potential to determine the disintegration energy in situ as the area under the torque rotation curve from peak to the residual state as shown in Figure 8. The normalized disintegration, W_N, is the disintegration energy divided by the area under the curve in the intact state, W_{LS}, as defined in Figure 8. Due to effects related to local drainage in the failure zone around the vane, the residual torque at 90˚ rotation does not correspond to the remoulded level after several manual turns. To overcome this issue it is possible to either draw a pragmatic curve extension of the torque reading to zero torque or to use the levels of disintegration that can be read from the graph. The latter can be handled through the remoulding index as defined by Tavenas et al. (1983). I_r (x) = (c_{ui}-c_{ux})/(c_{ui}-c_{ur}) where x is the degree of remoulding, c_{ui} is the intact strength and c_{ur} is the remoulded strength.

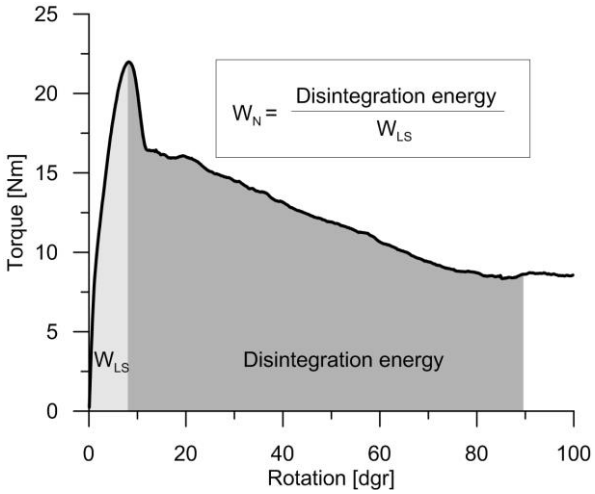


Figure 8 Definition of disintegration energy

Thakur et al. (2015) has interpreted disintegration energy from the same vane tests as included in this study (Tiller, Fallan, Klett). The results are summarized in Figure 9 and Figure 10 where a good match between disintegration energy from vane interpretations and previously reported values is seen. The reader is referred to Thakur et al. (2015) for further details.

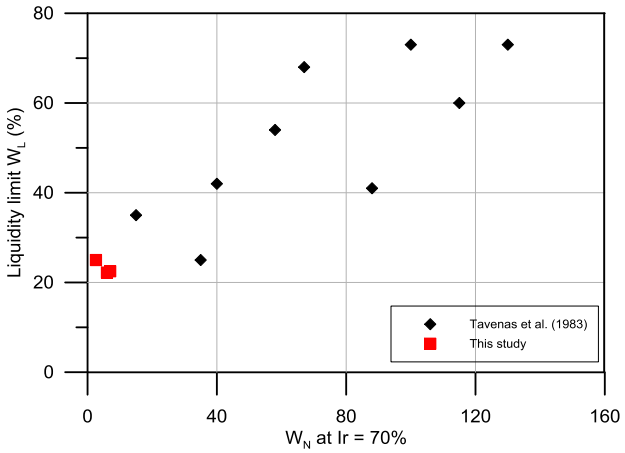


Figure 9 Disintegration energy at I_r = 70% as a function of liquid limit (from Thakur et al. 2015)

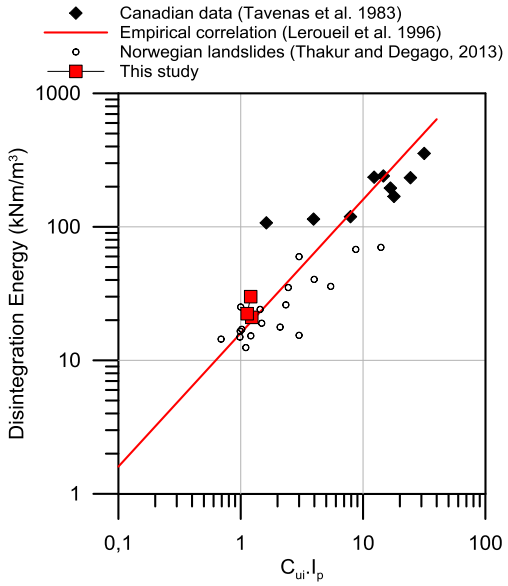


Figure 10 Disintegration energy of Norwegian and Canadian clays (from Thakur et al. 2015)

4 DISCUSSION OF RESULTS

The main strengths of the VST is its ability to give the intact and remoulded shear strength in situ and thus reduced the need for sampling in a project. The main drawbacks of the VST includes disturbance of the soil during installation, accounting for friction in the system and interpretation of a design shear strength through a correction factor. However, these factors does not all act equally strong under all circumstances.

4.1 Undrained shear strength

Disturbance effects appears to be highly relevant for low plastic and highly sensitive clays. Such clays show very low $c_{u,v}$-values compared to active triaxial tests. This introduces significant uncertainty related to the use of $c_{u,v}$-values in such clays and it is suggested that the VST is not used for this purpose in clays with I_p under 10%. For clays with higher plasticity the correspondence between $c_{u,v}$ and $c_{u,a}$ is better and use can be recommended provided that a proper correction factor is applied.

4.2 Stiffness

It is suggested by the results presented here that the interpretation of soil stiffness from the VST torque-rotation curve is not feasible.

4.3 Remoulded shear strength

With a VST device that measures torque at the top of the rod system, the influence of friction in the system appears to reduce the validity of measurements of the remoulded undrained shear strength. The friction in the system is often measured in the range of 2-5 Nm. A remoulded shear strength of 0,5 kPa corresponds to about 0,5 Nm. To separate the actual contribution from the soil resistance under such circumstances is not reliable. For measurements of remoulded shear strength in sensitive soils it is recommended that equipment where torque is measured close to the vane cross is used. For clays with higher remoulded shear strength (over 5 kPa), equipment with the torque cell at the top can be considered.

4.4 OCR

It is indicated that the approach for determination of OCR from the vane as proposed by Mayne & Mitchell (1988) is valid for the clays tested here. However, as the interpretation relates to $c_{u,v}$, care should be taken if operating in low plastic clays.

4.5 Disintegration

The disintegration energy as interpreted from the vane shear test fits well with other data reported in the literature. The disintegration energy is to a less extent influenced by friction in the system and installation effects and can thus be used also in low plastic clays. The initial investigations by Thakur et al. (2015) fit well with previous published data and further research on this particular application of the shear vane device can be recommended.

5 CONCULSIONS

The main conclusions are as follows:

- Interpretation of undrained shear strength from the VST should only be done for clays with I_p>10%. A proper correction factor must be applied
- Stiffness parameters can not be interpreted from the VST
- For measurement of remoulded shear strength (and sensitivity) it is recommended to use a VST-device with torque registration close to the vane cross
- OCR can be interpreted from the VST
- Disintegration energy can be interpreted from the VST, but more research is needed on this particular topic.
- With proper use and setup, the vane shear device has a strong potential as a reliable “quick clay detector”.

ACKNOWLEDGEMENTS

This study has been made possible by support from the National research program ‘Natural hazards: Infrastructure, Floods and Slides (NIFS)’ initiated by the Norwegian Public Roads Administration, Norwegian Water Resources and Energy Directorate and Norwegian National Railways Administration.

REFERENCES

Aas, G. (1976). Stability of slurry trench excavations in soft clay. ECSMFE 6, Vienna, 1.1, 103-110.

Eden, W.J. and Law, K.T. (1980). Comparison of undrained shear strength results obtained by different test methods in soft clays. Canadian Geotechnical Journal 17(3) 369-381.

Gregersen, O. (1981). The quick clay landslide in Rissa. ICSMFE 10, Stockholm, 3 421-426.

Gregersen, O. and Løken, T. (1979). The quick-clay slide at Baastad, Norway, 1974. Engineering Geology 14 183-196.

Gylland, A.S., Long, M., Emdal, A. And Sandven, R. (2013). Characterisation and engineering properties of Tiller clay. Engineering Geology 164, 86-100.

Hanzawa, H. (1979). Undrained Strength Characteristics of an Alluvial Marine Clay in the Tokyo Bay. Soils and foundations 19(4) 69-84.

Hanzawa, H., Matsuno, T. and Tsuji, K. (1979). Undrained shear strength and stability analysis of soft Iraqi clays. Soils and foundations 19(2) 1-14

Karlsrud, K. (1983). Analysis of a small slide in sensitive clay in Fredrikstad, Norway. SGI Report 17 175-184.

Kishida, T., Hanzawa, H. And Nakanowatari, M (1983). Stability analysis with the simple and the advanced φ=0 method for a failed dikes. Soils and foundations 23(2) 69-82.

Lacasse, S., Berre, T. and Lefebvre, G. (1985). Block sampling of sensitive clays. ICSMFE 11, San Fransisco, 2, 887-892.

Lacasse, S., Jamiolkowski, M., Lancellotta, R. and Lunne, T. (1981). In situ characterization of two Norwegian clays. ICSMFE 10, Stockholm, 2, 507-511.

Ladd, C.C. and Foott, R. (1974). New design procedure for stability of soft clays. Journal of the Geotechnical Engineering Division 100(7) 763-786.

Larsson, R. (1977). Basic behavior of Scandinavian soft clays. SGI Report 4,1-108.

Lefebvre, G., Ladd, C.C. and Paré, J-J. (1988). Comparison of field vane and laboratory undrained shear strength in soft sensitive clays. Vane shear strength testing in soils: Field and laboratory studies. ASTM STP 1014. 233-246

Leroueil S, Locat J, Vaunat J et al (1996). Geotechnical characterization of slope movements. Proceedings of the 7th International Symposium on Landslides (Senneset, K. (ed.)) 1, 53–74.

Locat, P. et al. (2011). Glissement de terrain du 10 mai 2010, Saint-Jude, Montérégie. Report MT11-01 Transports Québec

Mayne, P. & Mitchell, J. (1988). Profiling overconsolidation ratio in clays by field vane. Canadian Geotechnical Journal 25 150-157.

Sjursen, M.A. (1996). Prøveforstyrrelse i leire og silt. Masteroppgave, NTNU

Tavenas, F., Flon, P., Lerouil, S. and Lebuis, J. (1983). Disintegration energy and risk of slide retrogression in sensitive clays. Symposium on Slopes on Soft Clays, Linköping, Sweden.

Thakur, V. and Degago,S. A. (2013). Disintegration energy of sensitive clays. Géotechnique Letters 3(1) 21–25.

Thakur, V., Degago, S., Gylland, AS. & Sandven, R. (2015). In-situ measurement of disintegration energy of sensitive clay. GEOQuebec september 2015

Trak, B., La Rochelle, P., Tavenas, F., Leroueil, S. And Roy, M. (1980). A new approach to the stability analysis of embankments on sensitive clays. Canadian Geotechnical Journal 17(4) 526-544.

Ørbech, T. (1999). Prøveforstyrrelse i leire. Masteroppgave, NTNU

COBRA Cable Site Investigation in the Wadden Sea, Denmark

L. Klinkby
COWI, Denmark, lokl@cowi.dk

R. Juncher, Energinet.DK, Denmark, M. Laier, A. Rosborg, A. B. Medhus and K. Pedersen, COWI, Denmark.

ABSTRACT
Energinet.dk and TenneT plan to develop a 320-350 km long high voltage DC cable between Endrup, Denmark, and Eemshaven, the Netherlands. COWI A/S was contracted in 2014 by Energinet.dk to map the corridor in the challenging Wadden Sea environment between Esbjerg and Fanø.
The survey covered a 6.2 km long and 200 m wide cable route corridor specified by Energinet.dk. The purpose of this survey was to provide detailed geological and geographical data to support the plan for design, installation and protection of the cable.
Three surveys were carried out: a geotechnical survey at eight positions using a drill rig drilling from a barge, a geophysical survey using a small boat and an airborne survey using two drones.
The seafloor mapping was accomplished by multi beam echo sounder data (MBES) with backscatter and single beam data (SB) combined with detailed photogrammetry from the drone survey.
On the geotechnical positions, boreholes and Swedish Dynamic Probing were carried out to a maximum of 6 m below the seafloor. Samples were taken for laboratory test results. The barge could work floating in water but also be manoeuvred during high tide to land on the mud flats. Thereby data were acquired on positions otherwise not reachable. The geophysical survey included a seismic pinger survey and the results were utilized trough integrated interpretation of the seismic data and geotechnical results.
The three surveys combined have allowed mapping of the seabed and mapping of the geometry and geotechnical properties of sub-bottom layering in the corridor. The interpretation identified 12 different layer boundaries in a very active and variable geological setting of mud and tidal flats gyttjas, sandy channel fills and recent prograding sediments.

The authors wish to thank Energinet.DK for permission to publish these results.

Keywords: Boreholes, probing, seismic, drone, bathymetry

1 INTRODUCTION

In collaboration with the Dutch TSO TenneT, Energinet.dk plans to establish a 320-350 km long HVDC cable with converter stations in Endrup near Esbjerg and Eemshaven in the Netherlands. The connection is called COBRAcable (www.energinet.dk). The cable will cross the Island of Fanø. In 2014 COWI carried out a cable route survey for Energinet.DK in the Wadden Sea from Esbjerg to Fanø (Figure 1).

The survey mapped a 6.2 km long and 200 m wide corridor with vessel, barge and drone to provide coverage of seabed and the shallow sub-bottom.
The conditions in the Wadden Sea is challenging as neither onshore nor offshore standard methods will cover the entire area. Furthermore, soft mudflats and tidal schemes add complexity to the survey conditions. The tidal difference in the area during time of acquisition was up to 2 m.

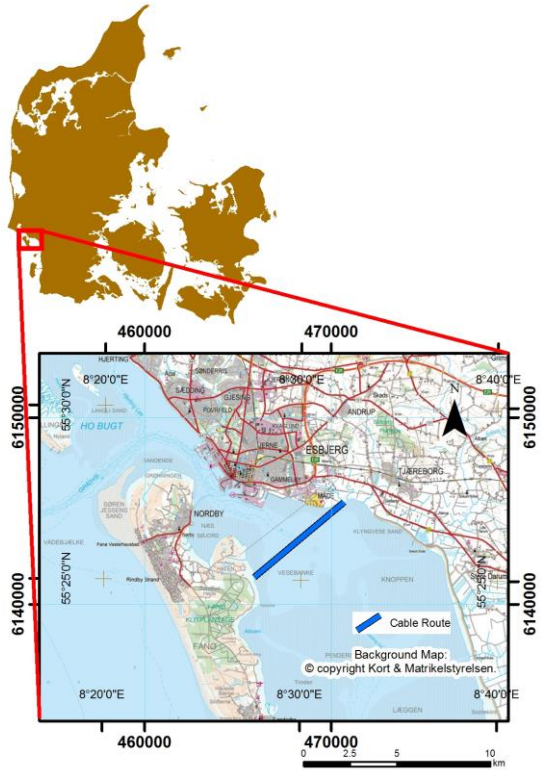


Figure 1. Overview of the survey area: A 200m corridor centred at a straight line.

2 METHODS

2.1 Mapping of seabed

In order to map the seabed a combination of vessel survey with multibeam ecco sounder (MBES) and single beam ecco sounder (SBES) along with airborne photogrammetry (Ortho-photos) was suggested. During planning it was impossible to predict precisely the coverage of each method.

In planning the tidal scheme was taken into account in order to cover the full corridor. Ortho-photo coverage utilized low tide and day light were as both MBES and SBES took advantage of high tides.

A GNSS base station was set up at the southern end of Esbjerg Harbour for the geophysical survey in order to deliver RTK corrections during the survey. The GNSS position accuracy during the geophysical survey was approximately 3 cm horizontal and vertical.

The DTM accuracy from the airborne survey is approximately 10 cm.

Vessel Survey

The 15 ft Finnspeed "Nellebjørn" (Figure 2) with draft of 0.9 m, was used for the geophysical and hydrographic survey. The following equipment was used for the bathymetric survey:

- R2 Sonic 2020 multibeam ecco sounder with TruePix back-scatter sonar output.
- Atlas Deso 15 Single beam ecco sounder
- Navisuite Software

SBES data were acquired using a 210 KHz transducer mounted over the side of the survey vessel. A GPS antenna was mounted on top to the transducer setup. SBES data and GNSS RTK data was time stamped during acquisition for post-processing purposes. The survey lines were designed with 10m spacing parallel to the survey area centre line. Data were acquired from a minimum water depth of 0.78 m LAT (0.50 m relative to MLWS).

MBES data were acquired from the three channels in the survey area. The channel locations were based on the SBES data. The survey equipment was deployed from the survey vessel's moonpool. Data were acquired using a 400 MHz transducer and the survey covered 100% of the channels. Sound velocity of the water column was measured with 2-3 hours interval and for quality control a patch test was performed during the survey.



Figure 2 Survey vessel Nellebjørn.

Airborne Survey
The airborne survey was accomplished using the following equipment:

- Leica GPS (GNSS) VivaGS12,
- Ebee UAV (COWI No.1 and 2), Drones.
- Marking material for GCP's
- 10 feet boat for transportation in the survey area.

Prior to operation, a number of ground control points (GCP) were stationed at various locations in the survey area and positioned using differential GPS. The purpose was to be able to fix the resulting terrain model and orthophoto into the project coordinate system.

The operations was performed at lowest tidal conditions possible. Two un-manned aerial vehicle (UAV) teams sampled simultaneously from Fanø and Esbjerg, resulting in full areal coverage of the project trace. During the operation, sampled imagery were quality checked.



Figure 2. Picture from establishment of GPS's

2.2 Subbottom Profiling

SBP data were acquired using an Innomar SES 2000 compact narrow-beam parametric profiler on three survey lines parallel to the centre line of the cable corridor and nine lines perpendicular to the centre line. The nine perpendicular lines focused on surveying the channels. The survey equipment was deployed from the survey vessel's moonpool.

2.3 Geotechnical Positions

The shallow waters pose a challenge for heavy gear and COWI had therefore opted to use a small barge carrying a light-weight belt-mounted rig (mini-rig) with the capability to drill to 6 m depth with a 6” drill bit using an auger with casing.

The drill rig and barge had a total weight of 2500 kg. The barge had a draft of 0.4 m and was therefore manoeuvrable in the shallow waters. The barge was equipped with an outboard engine and had two retractable legs, each with a diameter of about 3". The legs were placed in the seabed to maintain the correct position and to stabilise the barge during work.

The drill rig and barge can operate in water depths from 0.5 to 5 m. During high tide it will be possible to place the drill rig on the mudflats (Figure 3). If low tide occurs during the drilling this will not affect the equipment. A small service boat was used for transport of personnel and for safety measures.



Figure 3. Picture of Barge at mud flat

In addition to the geotechnical drilling, Swedish Dynamic Probing tests (Svensk Rammesondering) were carried out from which the strength of the soils can be

estimated with results equalling those of Soil Penetration Test (SPTs).

In total eight geotechnical boreholes including Swedish Dynamic Probing tests were undertaken. Furthermore, temperature measurements within the upper 100 mm of the soil were undertaken at each borehole location using a data logger and a thermometer. The data logger used was the model WTW Multi 3430 set F (IP67/68).

The relationship between the Swedish Dynamic Probing results, N_{20}, and cone resistance, q_c, is described in Bulletin 6, March 1976 by Borros AB, Swedish Geotechnical Institute. According to this reference, the relationship is assessed for granular soils; $qc = \frac{N20 + 4.45}{1.8}$

3 SEABED

In Figure 4 the resulting data coverage is shown. SBES data was surveyed first and covered both channels and mudflats in order to establish the positions of the deeper parts where MBES and SBP could be used. MBES was sailed using the highest tidal conditions possible, but only at depth greater than – 1.5 m LAT could MBES provide coverage. Airborne data were collected for the entire area. However, after processing it was clear that the photogrammetry could only work in depth range above 0 m LAT as the wet soils only gave the water surface. Therefore, in total 4 km of the 6.2 km corridor are covered mainly with single beam data.

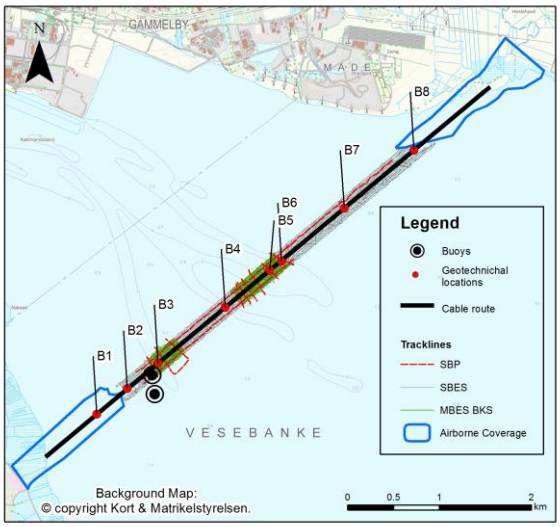


Figure 4 Data coverage.

Each method covered a part of the depth range in the area that the other methods could not reach.

Table 1. Methods used to map seabed/terrain.

Method used	Depth Range
Multibeam Ecco Sounder	-5 - -1.5 m LAT
Singlebeam Ecco Sounder	-1.5 - 0 m LAT
Airborne photogrammetry	0-4 m LAT

Each of the methods also have different resulting coverage and resolution (Table 2).

Table 2. Methods used and their resolution

Method used	Resolution horizontal/vertical to LAT
Multibeam Ecco Sounder	25x25 cm / 10 cm to LAT
Singlebeam Ecco Sounder	Lines 10 m apart / 20 cm to LAT
Airborne photogrammetry	25 x 25 cm / 10 cm to LAT

3.1 Bathymetry/DTM

Three Northwest-Southeast trending channels with water depths of more than 2 m are shown on the available nautical charts based on which the geophysical survey was planned (Figure 4). The MBES data clearly shows that one of the channels is located approximately 150 m more easterly than expected (Figure 5). The seabed in the channels have steep slopes of more than 2°

toward the centre of the channel. The deepest parts of the channels are found at -5.1 m LAT.

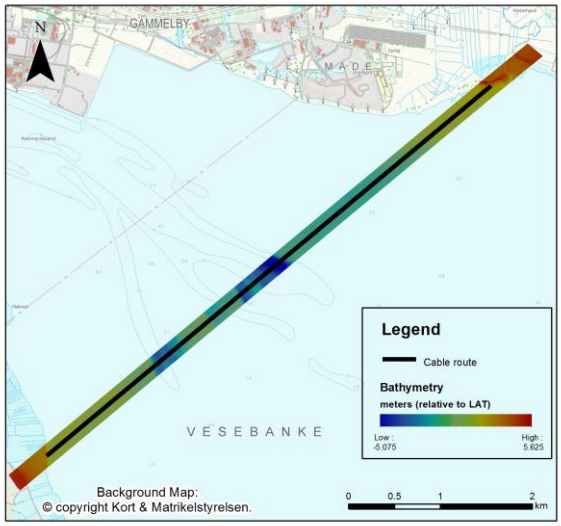


Figure 5. Bathymetry after gridding. Note that the channels marked in the nautical charts does not correspond to the channels mapped in this survey.

3.2 Seabed, texture and objects

The backscatter data acquired with the MBES data are of low to medium quality and are clearly affected by being acquired in marginal conditions. The low and varying water depth only allowed for a small beam width and have caused a lot of distortion.

In the central part of the deepest channels the data quality was reasonably good and the range large enough to allow for independent identifications of targets.

24 targets were identified in the backscatter sections. Only targets greater than 0.5 m were picked. Most of these are white spots and may have been denoted debris/boulder. The second most abundant target is parts of pipe/cable troughs or uncovered pipes.

The Airborne data were of excellent quality. Targets larger than 0.5 m were prioritized, but several targets down to 0.25 m were identified. After picking the smaller point targets, larger features e.g. oyster beds or clay outcrops were identified and digitized as polygons. 124 targets were identified from the orthophotos. Of these 30 are onshore. Offshore the most abundant target type was interpreted as boulders.

Seabed classification was established from the backscatter data and orthophotos. The outline of the beach and the intertidal zone of the shore face (Figure 6) as well as the extent of ripples was included in the classification. Seabed classification was an important part of the scope but highly challenged by lack of data coverage in the areas covered by SBES data (-1.5 – 0 m LAT). For interpretation of differences in seabed characteristics also geotechnical boreholes, bathymetric data and interpretations from the SBP data were taken into account for deciding what sediment type was expected. Six different classes were employed. These are listed in Table 3

Table 3 Summary of classification scheme

Description	Orthophoto/ Backscatter characteristic
Vegetated area/ beach	Green vegetation shows clearly on the orthophotos. Small occurrences detached from the shore are not included.
Intertidal zone	A small rise with some sand deposition. Identified on orthophotos, interpreted to represent previous land areas with present day deposition following a transgression.
Gyttja/Peat	Dark colours in orthophotos, may have some sand content. Relatively featureless in backscatter data.
Sand (small ripples)	Small ripples seen in backscatter data. Distance between crests around 0.5m.
Sand (large ripples)	Larger sand ripples observed in backscatter data and visible in the bathymetry. Distance between crests typically around 5 m.
Mixed/coarse sediments	Patches of variable backscatter intensity observed.



Figure 6 Example of seabed classification from ortho-photos showing the outline of the vegetated area/beach and intertidal zone of the shore face as black lines.

4 GEOLOGICAL MODEL

4.1 Geotechnical Data

Geological descriptions of the samples collected during the drilling campaign were carried out by a geologist according to "A guide to engineering geological soil description" by the Danish Geotechnical Society. The sediments encountered in the boreholes were postglacial sediments with the exception of two boreholes, where sediments of glacial origin were found.

A series of laboratory tests were conducted with the objective to evaluate selected properties of the sediments encountered.

Swedish dynamic probing results was used to assess the relative density of the sand deposits. The blows per 0.2 m, N_{20}, are recorded as 1 to 18, equating to very loose to medium dense soil. Based on the relationship referenced in section **Error! Reference source not found.**, this equates to a cone resistance in the order of 3-12 MPa.

Gyttja was present in all boreholes in thicknesses ranging from 0.6 m to more than 3.0 m. Peat was encountered in 2 boreholes with thicknesses of 0.3 m to an excess of 1.3 m. The peat and gyttja were deposited in marine, freshwater and brackish environments. Postglacial sand was encountered in two boreholes and described as slightly organic to very organic. The thickness of the sand layer found in the boreholes ranges from 0.2 m to 3.0 m. Clay was encountered in one borehole and described as highly plastic with organic lamina.

4.2 Subbottom Profiler Data

The SBP data were interpreted in IHS™ Kingdom® version 2015. A total of 12 different layer boundaries were identified. A very active and variable geological setting of mud and tidal flats gyttjas, sandy channel fills and recent prograding sediments was revealed.

4.3 Integrated Interpretation

The vertical scale of both the bathymetric grid and the geotechnical data were converted from depth (m) to two-way-time (TWT) (s) for interpretation. After interpretation, grids of the layer boundaries have been converted from TWT to depth. The TWT-depth relations for the conversions are given below. The interpretations are presented in alignments sheets (Figure 7).

- Seawater: 1480 m/s,
- Geological layers below seabed: 1600 m/s.

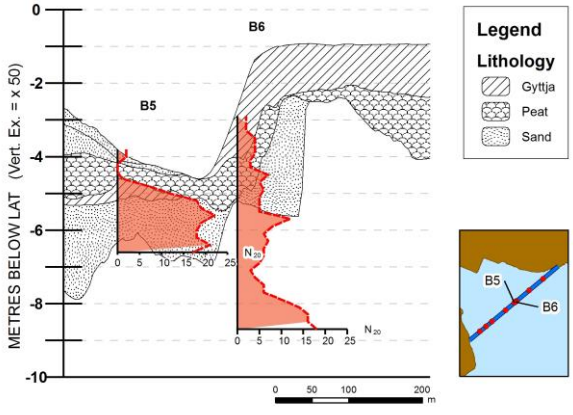


Figure 7: Snapshot from alignment sheets showing the results of the Swedish Dynamic Probing and its correlation in the integrated interpretation along the deepest channel.

Layers interpreted are all deposited in upper or lower tidal environments, with the shallower part dominated by salt marsh deposits and mud flats, while the deeper parts are good examples of an active tidal channel system (Figure 8). The varying facies of the different layers indicate that sea water level has fluctuated during deposition. The character of the upper layers indicates that the water level has been rising relative to the land (transgression). The lower boundary of the Post Glacial deposits could not be interpreted since seismic penetration did not reach the depths where borehole information have records of it in the shallowest waters (Figure 7).

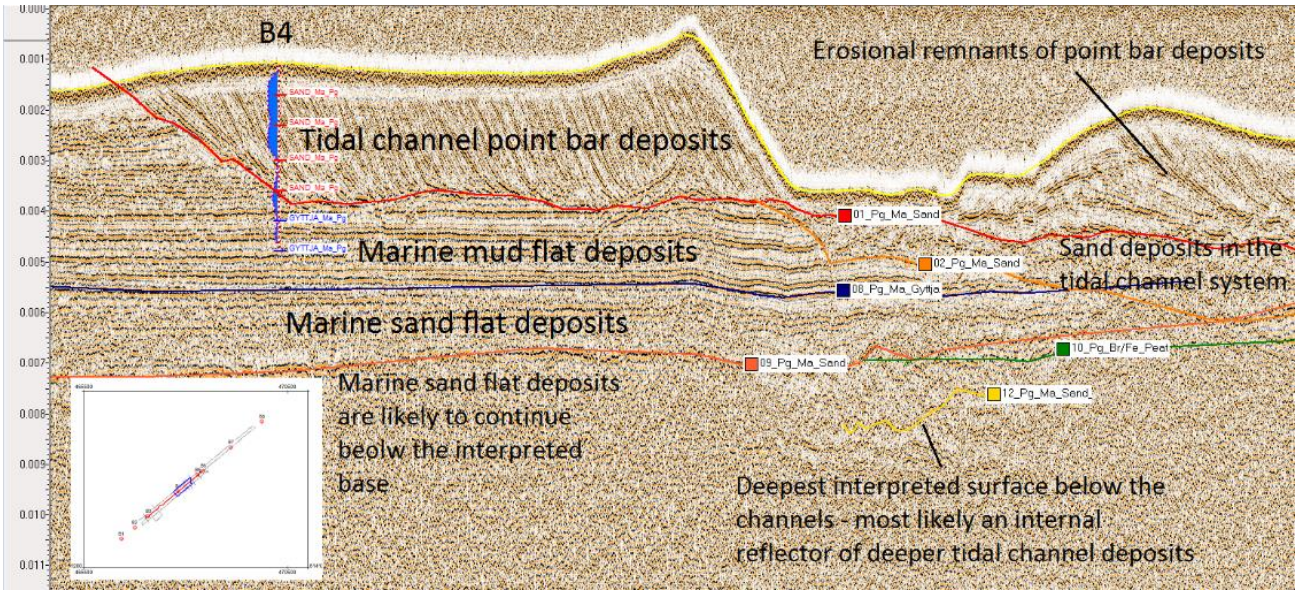


Figure 8. Arbitrary section of SBP profiles with geotechnical data. This section illustrates the stratigraphic layers within the active tidal channel around borehole B4. A series of sand and mud flat deposits is covered by the active tidal channel system with migrating point bar sand deposits.

5 REFERENCES

Bulletin 6, March 1976 by Borros AB, Swedish Geotechnical Institute

A guide to engineering geological soil description.

Founding on (un)known chalk in Aalborg

C. T. Leth
COWI A/S, Denmark, ctl@cowi.dk

J. Dannemand Andersen, T. Madsen and K. A. Larsen
Geo (Danish Geotechnical Institute), COWI A/S and COWI A/S.

The North Denmark Region wishes to build a new hospital to accommodate all hospital functions in Aalborg. At a budget of DKK 4.1 billion, the complex of buildings will cover 155,000 m². The first turf was cut in 2013 and the construction works will run from 2015 to 2020. The foundation level will vary from approximately four metres to ten metres below ground surface.
The soil at the site consists of recent deposits, top soils and fillings, and below these are late glacial clay/silt/sand and clay till on top of chalk. A large proportion of the buildings are founded on chalk. The chalk in the Aalborg area is to some degree known from other projects, and is expected to be relative soft with 'chimneys' (decomposed chalk fissures filled with loose material).
The paper focuses on describing the general characteristics of the Aalborg chalk presenting results from old projects and comparing with results from new laboratory tests specified for the current project. Results from new oedometer and triaxial tests on the chalk are presented along with observations from the geotechnical supervision during construction.

Keywords: Direct foundation, chalk, testing, supervision.

1 PROJECT

1.1 Background

In 2007 the Danish Parliament passed a reform named the Quality Fond including a DKK 25 billion investment in new modern hospital facilities to improve the effectiveness of the Danish Health System. North Denmark Region (Health Authority) was interested in developing a Greenfield area of 92 hectares in the outskirts of Aalborg to a new Health Centre of North Jutland to join together different facilities spread across the city.

In 2012 North Denmark Region received final commitment from the Quality Fond to finance a new hospital building, named Nyt Aalborg Universitetshospital (NAU), of approx. 155,000 m² with a budget of DKK 4.1 billion. North Denmark Region contracted in 2012-13 joint venture company, INDIGO, for planning and design, NIRAS for construction management and COWI for geotechnical investigations to complete NAU before 2020.



Figure 1: Illustration of Nyt Aalborg Universitetshospital (NAU).

1.2 Building

NAU consists of 3-10 story buildings with up to 3 level basements (K0-K2) on slab and pad foundations of reinforced in-situ casted concrete, in total approx. 21,700 m². Foundation of the 10-story section is a 9,000 m² slab with a thickness of 500-1500 mm in basement level K2 (3 levels below ground surface). Design load on foundations is up to 450 kPa.

Construction started end of July 2015.

1.3 Excavation

The building is constructed in an open excavation of 250 x 300 m. Existing terrain level varies between level (DVR90) +10 m to +18 m and deepest foundation (basement level K2) is level +2.95 m.

Ground water level is measured as high as +5.5 m and a temporary groundwater lowering is installed consisting of 18 dewatering wells with a yield of approx. 80 m³/h.



Figure 2: Excavation for basement level K2.

1.4 Codes and categories

The buildings are designed according to Eurocode 7 and Danish national annex, with consequence class CC3 for the 10-story section and consequence class CC2 for the remaining part of the buildings.

2 GEOLOGY

The geology in the area of the city of Aalborg is dominated by three "islands" of Cretateous deposits, upon which Quartenary deposits are present. Layers from the geological periods in between these formations are not found in Aalborg.

On the "islands" the top of the chalk is found up to level +40 m to +60 m and at shallow depths, only covered by topsoil/mull, otherwise the chalk is often covered by glacial till and meltwater deposits. In the low-lying areas between the "islands" the top of the chalk is found at levels -30 m to deeper than -60 m, and the chalk and glacial deposits are additional overlain by various deposits of late glacial and postglacial origin.

The soil at the NAU site consists of recent deposits, top soils and fillings, and below these are late glacial clay/silt/sand and clay till on top of chalk.

This article focuses solely on the Cretateous layers, which consist of Maastrichtian chalk deposited in the period 65-144 million years ago.

The chalk may be found in its original deposition and state, but a number of processes have degenerated the chalk. Tectonic disturbance may be the dominating reason for the varying topside levels. Furthermore, the chalk is often glacially disturbed, e.g. by glacier erosion of weak chalk and dislocation of lumps of chalk (dislocated chalk of a thickness of more than 30 meters is registered on the northern "island"). Glacially created fractures caused by shear stresses during passage of glaciers and/or passive earth pressure during meltdown of glaciers have also affected the chalk. Erosion may also have taken place in the late glacial period. The surface of the chalk has subsequently been exposed to weathering and drying-out.

All these processes affects potentially the geotechnical properties of the chalk, but the relevant states of the chalk are seldom fully recovered by traditionally geotechnical investigations.

In addition, dissolution pipes ('chimneys') of varying sizes are often seen in the surface of the chalk, in which case the produced cavities are filled with loose wash-down or drop-down materials from the deposits above. Hollow cavities in the chalk is seldom registered.

Aalborg has a glorious industry history for extracting chalk for production of cement, which is still produced in Aalborg as the only remaining production plant in Denmark.

3 INVESTIGATION OF CHALK

3.1 Investigation borings

Drilling in the chalk can be done by e.g. the traditionally auger method used for soils. Extracted of intact samples can normally be done by pressing traditionally Ø42 or Ø70 mm tubes into the chalk. Core drilling has occasional been used, but flushing out of soft material may lead to relatively poor core recovery.

Normally field vane tests and CPT's (Cone Penetration Test) can be performed in the chalk. In zones of hardened chalk these tests may though be rejected.

3.2 Classification

At normal investigation depths for structures, the chalk is usually seen as a purely white or light grey matrix of unhardened chalk (hardness H1) with parts of slightly hardened or hardened chalk (H2/H3). In some borings the chalk is registered as hardened and blocky. The structure of the chalk is muddy with particles predominantly corresponding to silt (0.002 – 0.06 mm) or may sometimes seem grainy/sandy in extracted samples. The chalk in Aalborg is poor of flint.

In Table 1 typical classification parameters are listed. The chalk may be categorised as low-density chalk according to CIRIA.

Table 1: Typical classification parameters

Parameter	Range
Moisture content, w (%)	24 – 39
Density, ρ (Mg/m^3)	1.71 – 2.04
Calcium carbonate content (%)	95 – 99
Specific density, ρ_s (Mg/m^3)	2.69 – 2.71
Saturation, S_r (%)	95 – 100
Dry density, ρ_d (Mg/m^3)	1.31 – 1.60
Void ratio, e (-)	0.85 – 1.01
Porosity, n (%)	46 – 50

3.3 Performance of the chalk

In geological terms the Maastrichtian chalk is often denoted limestone. This term is not descriptive for the general performance of the chalk in Aalborg, as the chalk rather performs as silt with hardened gravels of chalk.

The chalk may consequently be handled as a soil and not as a rock.

The undrained shear strength may be measured by triaxial tests (c_u) in the laboratory or by field vane tests (c_{fv}), SPT's and CPT's.

SPT's (Standard Penetration Test) is traditionally not used in Denmark for cohesive soils (e.g. unhardened chalk). SPT's may though be used to document hardened chalk, but an evaluation of the corresponding strength is uncertain.

CPT's have been used for the last 20 years in Denmark, but no comprehensive study of the evaluation of CPT-data in chalk has yet been produced. It seems though reasonable to use $c_u \approx q_c/N_k$, where q_c is the cone resistance and N_k is the cone factor. Further analyses of N_k is though necessary for a specific site.

4 PREVIOUS INVESTIGATIONS

The a-priori knowledge of the geotechnical properties of Aalborg chalk is based on advanced geotechnical investigations for relatively large structures and building projects, as minor projects seldom is subject for investigations beyond simple tests. Most of these advanced investigations are performed by the Danish Geotechnical Institute in the period from the 1950's and the decades thereafter, see e.g. references below. The essence of a number of these investigations has been made available for the current paper and is described in the following.

4.1 Undrained shear strength parameters

A number of triaxial tests have been performed to determine the undrained shear strength of the chalk. The results of undrained shear strengths from a number of these tests (made as $CU_{u=0}$) are in Figure 3 compared with corresponding field vane tests made close to the tested sample.

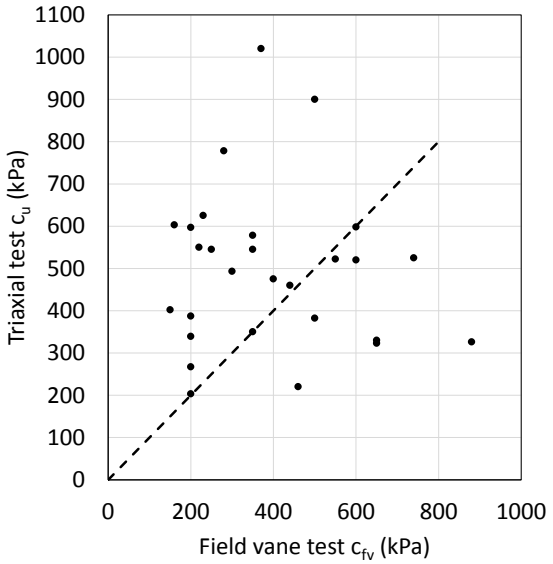


Figure 3: c_u versus c_{fv} from older tests

The comparison of triaxial tests and field vane tests shows some scatter for the factor $\mu = c_u/c_{fv} = 0.37 – 3.77$, but a linear regression through origo of the data gives $\mu = 1.0$ (equals dashed line in Figure 3). The scatter may be explained by the nature of the chalk with inhomogeneous hardening and fractures. It is noted, that $\mu \geq 1.0$ for $c_{fv} < 450$ kPa, which seems to indicate that use of $c_u = c_{fv}$ is conservative for $c_{fv} < 450$ kPa. A larger scatter of μ is observed for $c_{fv} > 450$ kPa. In 1972 (Geo, 1972), eight plate load tests were carried out on a surface of intact chalk. The plate used was Ø300 mm and the deflection during pressure was increased to respectively 4 % (slow loading) and 10 % (quick loading) of the plate diameter. A number of field vane tests was performed in the area around the plate load tests. In Table 2 the results of the tests are presented, using:

c_{fv} = field vane test
e = void ratio
$\sigma_{c,4\%}$ = stress at 4 % deflection
$\sigma_{c,10\%}$ = stress at 10 % deflection

Table 2: Results of plate load tests

No.	c_{fv} (kPa)	e (-)	$\sigma_{c,4\%}/c_{fv}$ (-)	$\sigma_{c,10\%}/c_{fv}$ (-)
101	325	0.95	6.3	-
102	325	0.94	5.6	-
103	300	0.96	5.6	-
104	300	0.95	-	8.3
201	92	0.95	6.5	11
202	>119	0.95	<7.6	<11.6
203	>117	1.00	<6.5	<9.7
204	>119	-	<8.8	<17

The ratio of $\sigma_{c,x\%}/c_{fv}$ (load/resistance) is, based on the general bearing capacity equation for undrained failure, expected to be $1.2 \cdot (\pi+2) \approx 6.2$, and it was concluded that the field vane tests may be used to estimate the undrained shear strength $c_u = \mu \cdot c_{fv}$, using $\mu = 1.0$, maybe even on the conservative side for large deflections ($\sigma_{c,10\%}$). This in compliance with the results in Figure 3 as $c_{fv} < 450$ kPa.

4.2 Drained strength parameters

The drained strength parameters have also been investigated by triaxial tests. It is often seen that the evaluation of the effective angle of friction and the effective cohesion is dependent of the stress level because of curved failure lines in a Mohr diagram. In Figure 4 and Figure 5 the results of these tests are presented, using:

σ_1' = Largest principal stress at φ'/c' read
φ' = Effective angle of friction
c' = Effective cohesion

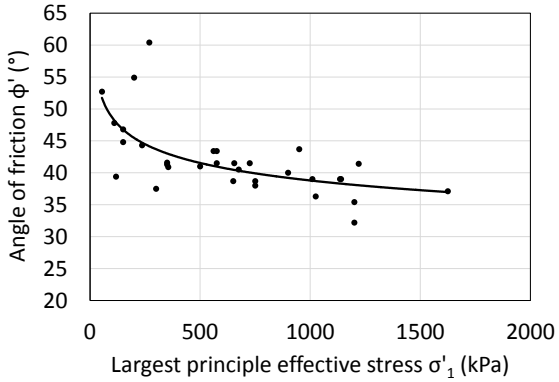


Figure 4: Angle of friction from previous triaxial tests

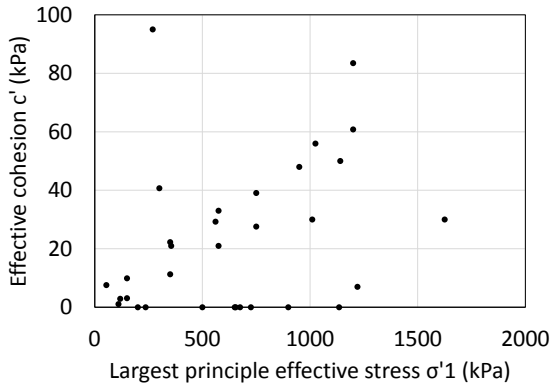


Figure 5: Effective cohesion from previous triaxial tests

The triaxial tests indicates a variability of φ' with the stress level, represented by σ_1'. For normal foundation stress levels less than 1,000 kPa it seems that an effective angle of friction φ' ≥ 38 – 40° may be applied. In some projects lower values of φ' have been used in the topside zone of chalk, where φ' for remoulded/weathered chalk may be indicated as low as 30 - 33°.

The effective cohesion varies and seems to be nearly independent of the stress level and the evaluated angle of friction, which presumably is caused by more or less random fracturing of the chalk and evaluation of parameters from individual tests. Consequently, it has often been necessary to choose a conservative value c' = 0 kPa in the design of structures.

4.3 Deformation parameters

The oedometer modulus of chalk is evaluated on the basis of 16 oedometer tests in Geo (1964 and 1965) for the Limfjordstunnel. The natural moisture content in the test samples was w = 29 – 34 % and field vane tests showed c_{fv} = 220 – 540 kPa. The following relation was determined:

$$E_{oed} = 5{,}000 \text{ kPa} + 1{,}200 \cdot \sigma'_a + 400 \cdot \Delta\sigma'$$

where:
σ'_a = effective stress before loading
$\Delta\sigma'$ = additional effective stress

5 PRESENT INVESTIGATIONS

5.1 Scope

A geotechnical investigation campaign was planned and executed based on the general knowledge of the geology in the area of the NAU. The objective of the investigation was to determine the soil conditions at the site and derive deformation and strength parameters for the slap and pad foundations utilized for the structure. The majority of the building is, as described in Section 1, build on chalk and the primary focus of the investigation campaign has been put on analysing the encountered chalk.

The geotechnical investigations consisted of:

- 49 initial borings with sampling and field vane tests carried out to a depth between 7 and 20 m below existing terrain.
- 33 supplementary borings with sampling and field vane tests carried out to a depth between 7 and 20 m below existing terrain.
- 3 oedometer and 6 triaxial tests on intact chalk samples.

The following sections summarizes the findings from the investigations with respect to the strength properties of the chalk. The investigations are further elaborated in COWI (2015).

5.2 Field vane tests

All borings include vane tests along the full depth of the borings. Ten of the supplementary borings have been carried out from an excavated level and next to initial borings, where up to 7 m has been excavated. These ten supplementary boreholes from the excavated level are used to investigate the change in undrained shear strength from unloading of the chalk during construction.

The measured strength in the chalk from the field vane tests between level +8 m and +2 m are plotted in Figure 6, where the field vane tests carried out from existing terrain has been plotted in blue where-as the latest field vane tests carried out from excavated level is plotted in red.

It is observed from Figure 6 that there is a significant variation in both horizontal and vertical direction of the measured field vane strengths prior to excavation across the site with majority of the measured values between 200 kPa and 400 kPa, though with some outliers between 80 kPa and 660 kPa.

Comparing the measured field vane strength values from before and after excavation shows a general tendency of strength reduction after excavation, where the majority of the measured values after excavation are between 100 kPa and 300 kPa, with some outliers above 300 kPa.

The variation in horizontal and vertical direction may be explained by the nature of the upper part of the chalk with variation in hardening and fractures.

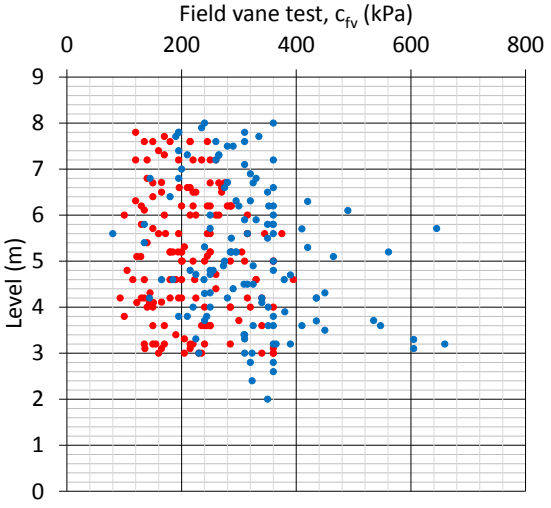


Figure 6: Field vane tests. Blue: before excavation and Red: after excavation to level +8 m.

5.3 *Oedometer tests*

A total of three oedometer tests were carried out on intact chalk samples:

- One constant rate of strain (CRS) test on a sample from level +6.3 m.
- Two incremental loading (IL) tests on samples from level -1.52 m and +3.69 m.

The maximum applied load in the CRS test was 8,800 kPa, whereas the final load step in the two IL tests was 4,800 kPa.

The yield stress of the chalk was estimated to be at least 1,500 kPa and the constrained modulus varied between 30 MPa and 500 MPa, depending on the effectives stress level in the soil.

It is assessed that the chalk behaves equivalent to an overconsolidated soil.

5.4 *Triaxial tests*

A total of six Anisotropic Consolidated Undrained triaxial tests (CAU), were for the NAU project carried out on samples taken at different levels, see Table 3.

Table 3: Samples for CAU tests

Boring and sample	Depth below existing terrain	Level for sample
B30B-3A	10.5 m	+4.4 m
B30B-11A	14.5 m	+0.4 m
B31B-15A	16.5 m	-1.6 m
B32B-3A	10.2 m	+3.5 m
B42B-P12	6.6 m	+6.4 m
B56-13	12.0 m	+1.5 m

The measured stress-strain curves from the six CAU tests are plotted in Figure 7 for comparison.

It is observed from Figure 7 that the strength generally increases with depth, and that the samples exhibit the same behaviour from 0 % to 1-1.5 % axial strain. The behaviour deviates after an axial strain of 1-1.5 %, with the three deepest samples bundled until an axial strain of 5-6 %.

The undrained shear strength is interpreted from the CAU tests, where failure is defined based on a deviator stress at 10 % axial strain.

The undrained shear strength determined from the CAU tests is plotted in Figure 8 with corresponding strength determined by field vane tests. Comparison of results from triaxial tests and field vanes gives a factor of $\mu = c_u/c_{fv} = 0.76 - 2.54$, and Figure 8 shows that a factor of $\mu = 1.0$ is applicable and reasonable conservative for the site. This complies with findings from other locations in the Aalborg area, cf. Figure 3, for $c_{fv} < 450$ kPa.

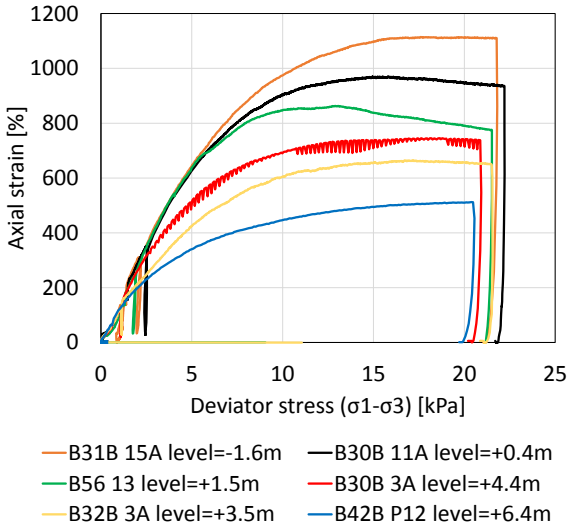


Figure 7: Stress strain curves from CAU tests

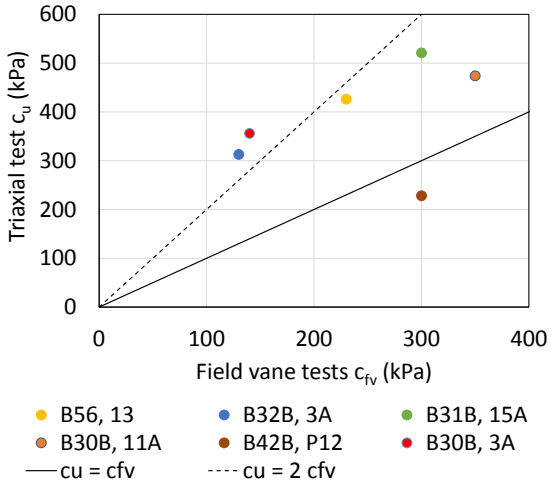


Figure 8: c_{fv} versus c_u from CAU tests

The effective stress path is for the six CAU tests plotted in Figure 9. There is a good agreement between the tests, having more or less the same inclination with a slight parallel displacement, corresponding to different effective cohesions. The two fitted dashed lines presented in Figure 9 corresponds to an effective friction angle of 40° and an effective cohesion of 20 kPa and 75 kPa. The range of effective cohesion represents an lower and upper bound value for the chalk at the NAU

site, based on the actual tests (stress levels) and limited fractures in the tested chalk.

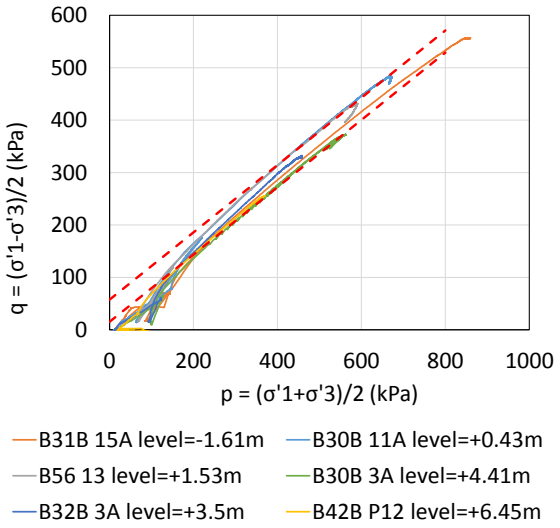


Figure 9: Effective stress path from CAU tests

6 CONSTRUCTION PHASE

Building on chalk includes a number of challenges to be handled during construction, due to the nature of the chalk and the geological processes that the chalk has been subject to:

- Variation in chalk surface
- Erosion, "chimneys"
- Variation in hardening and fractures
- Effects from the elements during construction.

6.1 Surface of chalk

The large open excavation for the NAU project made it possible to investigate the variation of the chalk surface. It was observed from the cuts, see. e.g. Figure 10, that the surface can vary significantly with slopes up to 1:1 and changes in level of 4-6 m.

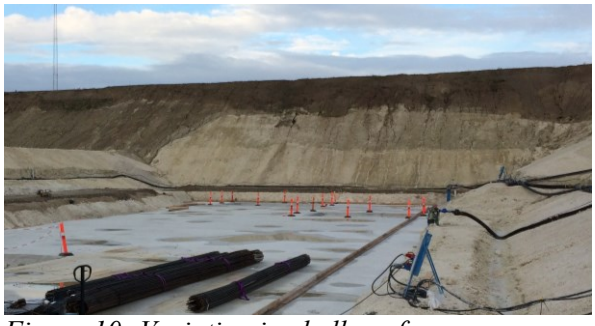


Figure 10: Variation in chalk surface.

6.2 'Chimneys'

Over the years surface water has dissolved chalk creating holes filled with loose material with very limited load bearing capacity. This karst phenomenon, also known as 'chimneys', are very frequent at the current site.

The designer requested 'chimneys' excavated and filled with concrete before casting of blinding layer and reinforced concrete.

A situation with 'chimneys' at level +6.5 m can be seen at Figure 11. The foundation area consists of a section with many 'chimneys' (right side of photo) and a section without any chimneys (left side of photo).



Figure 11: Excavations of 'chimneys'

Existing terrain level was for the area shown in Figure 11 at +12.0 m with stratigraphic sequence of 1 m topsoil, 1 m glacial meltwater sand and chalk from +10.0 m. One of the 'chimneys' was measured to 400 mm in diameter and 3.1 m in depth, equivalent to bottom level at +3.4 m or approx. 8.5 m below terrain.

In general, field vane tests indicated lower strength characteristics in areas with chimneys.

6.3 Variation in strength

All foundations are inspected by a geotechnical engineer before casting of blinding layer. A part of this inspection is field vane tests. At the deepest basement level, K2 at level +2.95 m to +3.35 m, approx. 2200 test were performed across the area.

The variation in the undrained strengths measured by use of the field vanes are shown in Figure 12. It was possible to measure up to 330 kPa. Strength requirement was set by the designers to 150 kPa.

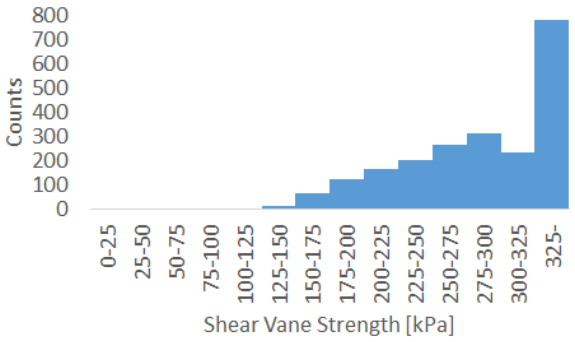


Figure 12: Variation in shear vane strength measured during inspection.

The slab at the deepest basement level has an area of 9000 m² where two small areas, in total 50 m², was replaced with concrete as geotechnical inspection showed unacceptable strength characteristics.

The entire foundation slab was excavated and closed with a blinding layer from 2015-08-10 to 2015-09-02, equal to 18 working days. The small areas with unacceptable strength was costly for the client as it interfered with this high speed and effective construction process.

6.4 Effects from the elements

The chalk is sensitive to the combination of water and mechanical processes, which combined easily results in a remoulding of the soil and a significant softening. In addition, the chalk is very sensitive to frost.

To protect the surface of the chalk a blinding layer was cast after excavation and geotechnical inspection.

Foundation work will continue through winter 2016 and therefore risk of frost induced heave will require monitoring and necessary protection of blinding layer. Methodology is measuring of soil temperature and levelling of casted blinding layer. No information is retrieved from this procedure yet.

7 SUMMARY AND LESSON LEARNED

The large excavation substantiated the existing knowledge regarding the possible variation in the surface of the chalk, and showed that slopes up to 1:1 and level variations of 4-6 m can be expected. In addition, significant variation in the distribution and density of chimneys was observed.

The present tests for the NAU project:

- showed that the stiffness of the chalk can be determined from oedometer tests, but it is necessary to be aware of the upper disturbed zone.
- substantiated that $c_u = c_{fv}$ is a reasonable conservative choice.
- showed that an unloading of the chalk results in a reduction of the undrained shear strength by approx. 15 - 35 %.
- documented that the effective friction angle of the chalk may be assessed to $\varphi' = 40°$ for the NAU project.
- substantiated that the effective cohesion can vary significant and that a value of $c' \geq 20$ kPa is representative for the NAU project. The large variation substantiated the necessity of project specific assessments of the effective cohesion.

8 REFERENCES

Berthelsen, O. (1987): Geologi i Aalborgområdet. Danmarks Geologiske Undersøgelser.

Geo (1963): Job no. 56090, Aalborg, Oliehavnen. Report 34.

Geo (1958): Job no. 58121, Aalborg, Roerdal Cementfabrik. Report 1.

Geo (1960): Job no. 58140, Aalborg. Sohngårdsholmvej. Report 1.

Geo (1959): Job no. 58189, Aalborg Sohngaardsholmvej. Report 1.

Geo (1964 and 1965): Job no. 60124, Aalborg, Limfjordstunnel. Report 11 and 18.

Geo (1965 and 1968): Job no. 65032, Aalborg, Limfjordstunnel, Report 1 and 2.

Geo (1972): Job no. Aa72062, Aalborg, Gasvaerksvej. Report 1.

COWI (2015), Region Nordjylland. Aalborg Postgårdsvej, Jordbundsundersøgelser for universitetshospital, Område 3, Sammenfattende geoteknisk undersøgelsesrapport, Rapport 11. Doc. 39108-1.6.

Lord, J. A, et al (2002). CIRIA Report C 574: Engineering in chalk.

Field measurements of pore water pressure changes in very high plasticity stiff clays adjacent to driven piles

T. R. Simonsen
Geo and Aarhus University, Department of Eng., Denmark, trs@geo.dk and thrs@eng.au.dk

K. K. Sørensen
Aarhus University, Department of Engineering, Denmark

ABSTRACT
The pore pressure distribution surrounding driven piles in heavily overconsolidated high plasticity stiff clays is a complex matter and affected by a range of factors such as soil permeability, soil strength, distance from piles and number of piles. In this paper pore pressures measured in Søvind Marl before, during and after driving of numerous HE300B steel piles at a construction site are presented and discussed. The complexity in pore pressure distribution during pile driving and subsequent dissipation is highlighted from the results and the fully grouted method for installation of piezometers is discussed.

Keywords: Pore water pressure, Field tests, Pile driving, High plasticity stiff clays, Fully grouted method

1 INTRODUCTION

When a pile penetrates into a clay deposit it will cause very large shear strains in the surrounding clay, and as a consequence induce large changes in the total stress and pore pressure regime (Karlsrud, 2012).

Driving of displacement piles into a cohesive soil generate large excess pore pressures close to the pile (Figure 1) and at the pile-soil interface – a phenomenon that have been thoroughly described in the literature. The excess pore pressures may be positive or negative dependent on soil type. In the past both field and model studies have been performed but relatively few accurate field data are available on the distribution of excess pore water pressures between driven piles. Especially for piles in highly overconsolidated clay and so far no data have been published on the distribution of pore water pressure near driven piles in highly overconsolidated Danish clay of Palaeogene origin. From the literature, it is clear that no known numerical model can predict the induced excess pore pressure regime and subsequent dissipation in highly overconsolidated clays in an operational way. Hence, additional field measurements are required for different soil types to be able to correlate a given model with full scale field conditions. Figure 1 shows a principle sketch of the influence of pile driving on the movement and pore pressure changes in the adjacent soil.

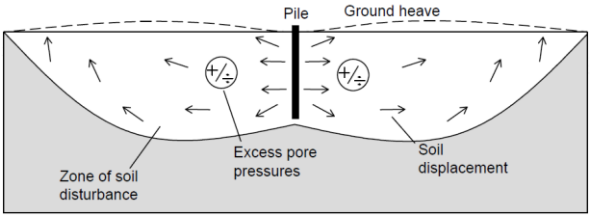


Figure 1. Influence of pile driving on the movement and pore pressure changes in the adjacent soil. Principle sketch.

In this paper, a field study of pore water pressure measurements using fully grouted vibrating wire piezometers adjacent to clusters of driven steel piles are presented. The piles are driven through made ground into a highly overconsolidated high plasticity Palaeogene clay – the so-called Søvind Marl.

Rarely have pore water pressure been measured under realistic conditions at actual construction sites during pile driving in highly overconsolidated clays. The aim of the

study is to present and highlight the complex pore pressure conditions adjacent to a cluster of HE300B steel piles at a construction site. Focus are on the pore pressure profile before, during and up to 200 days after driving in highly overconsolidated high plasticity clay.

2 PREVIOUS STUDIES

Prediction of pore pressures in relation to driven piles is not a straightforward matter. As shall be seen in the following section, the pore pressure regime around a driven pile can vary a lot and is strongly dependent on factors such as soil type, distance from the pile, stress history, degree of fissuring, time, permeability and other factors. In fact excess pore pressures measured at any position along the shaft of a pile (or a CPT cone) can be positive or negative immediately after installation (Burns and Mayne, 1999).

2.1 Pore water pressure measurements in relation to pile driving

Previous studies show that the excess pore pressure build up around a driven pile in clay soil is very much dependent on the soil type. The excess pore pressure response is quite different for soft clays and normal consolidated (NC) clays compared to highly over consolidated (OC) clays. The majority of studies have focused on NC and slightly OC clays whereas only few studies have been performed on heavily OC clays.

Poulus and Davis (1980) have presented a summary of measured excess pore pressure developed due to pile driving from 11 case histories. Their findings are shown in Figure 2 which shows that in the vicinity of the pile, very high excess pore pressures build up. The figure also shows that beyond a radial distance of 4 – 8 pile radii there is a rapid decrease in pore pressure and that beyond 30 pile radii, the excess pore pressure can be considered negligible for a single driven pile.

Randolph and Wroth (1979) conclude that attempts to measure the pore pressure distribution in the vicinity of a driven pile usually produce scattered and inconclusive results. However, for NC clays the excess pore pressure appears to decrease approximately linearly with the logarithm of the radius from the pile axis.

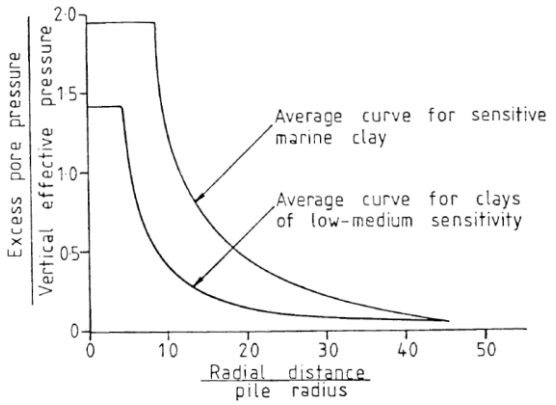


Figure 2. Typical measured excess pore pressure developed due to pile driving. Data from 11 case histories. Gue (1984) based on data from Poulus and Davis (1980)

Through numerical modelling Bergset (2015) demonstrated this trend for OC clays as well. He also showed that for OC clays negative excess pore pressures were likely to appear close to the pile due to dilation in the clay when sheared in contrast to the typical behavior.

Bond and Jardine (1991) and Coop and Wroth (1989) did field experiments using instrumented close-ended steel piles with a length of up to 6 m in heavily OC London Clay confirm this. They conclude that their results differ in several important respects from the response predicted by current theories of pile behaviour and they found among other things that negative excess pore pressures are generated at the pile surface during installation.

From the literature it has been found that pile driving can influence the pore pressures in a zone of up to approx. 100 pile radii from a driven pile dependent on the soil type. In NC clays the distance is approx. 14 – 35 pile radii (Chandra et al., 1993 and Robertson et al., 1990) while it is 30 – 90 pile radii for slightly OC clays (Lo et al., 1965 and Eigenbrod et al., 1996). For a sensitive marine clay, the influence of pile driving on the pore pressures were seen to be negligible beyond a distance of 100 pile radii from a pile group (Bozozuk et al., 1978).

The large variation in the extent of the influence zone (14 to 100 pile radii) corre-

sponds to a distance between 2 and 15 meters for a 300 mm x 300 mm precast concrete pile (which are often used at Danish construction sites). The lateral distance from the pile within which excess pore pressures are build up depends on the soil type as a likely result of differences in permeability, strength, stiffness, stress state (e.g. K_0) etc. However, no distinct pattern is found even when comparing similar soil types. Consequently, it is difficult to predict the lateral distribution of excess pore pressures around driven piles and especially in highly OC Palaeogene clays, as the available field data from this specific soil type is very sparse.

3 SITE CHARACTERIZATION

Field measurements were conducted at a construction site at the harbour of Aarhus in the central part of Denmark. This earlier industrial harbour area at the city centre, comprising more than 400000 m^2 of area, is currently undergoing a major urban re-development. Common for all building projects at Aarhus harbour are, that soil conditions necessitate deep foundations, which in Denmark normally mean pile foundations with driven piles. This field study is based on data obtained at the construction site for the building project referred to as Z-huset. A building of up to 10 storeys with a 2-storey underground parking facility is to be constructed at the site.

3.1 Previous construction activities

The construction of Z-huset, was commenced in 2008 with an approx. 7 m deep excavation (locally up to 8.5 m) followed by driving of hundreds of precast quadratic concrete piles. Due to the financial crisis, the construction ceased in 2009 after completion of only the 2-storey concrete basement structure.

3.2 Current construction activities

In 2014 the construction of the building recommenced and at that time the project had undergone significant design modifications. The modifications meant a redistribution of loads at the foundation level, which called for additional approx. 400 piles to be driven. The basement structure was demolished, apart from the outer basement walls and the pile-founded concrete bottom plate (500 mm thick), so the additional piles had to be driven through cut open sections of the bottom plate. For a principle sketch of the construction see Figure 3. Steel piles (HE300B) were chosen in favour of concrete piles due to a smaller cross-sectional area. The purpose was to minimize damage of the existing pile founded bottom plate due to soil displacement and heave from driving the new piles. Nevertheless, pile driving resulted in heave of the concrete bottom plate between zero and 27 mm (based on information from the contractor).

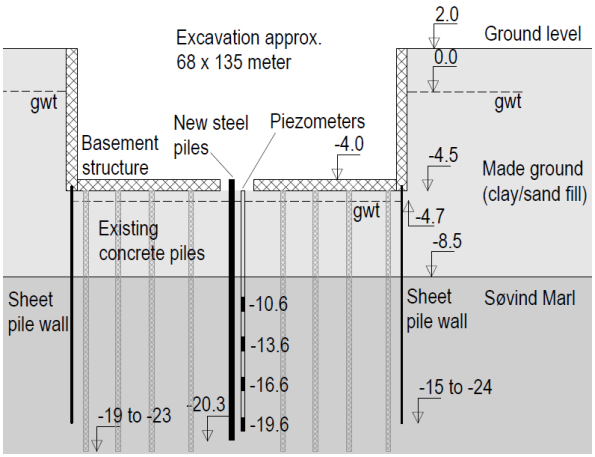


Figure 3. Principle sketch of the basement structure and piezometer installation. (gwt = groundwater table).

3.3 Ground and groundwater conditions

At this site the ground conditions are quite uniform. The site area was reclaimed 25 years ago for which reason the ground consist of approx. 8 – 10 meter of made ground (primarily sand and clay fill) and directly hereunder Søvind Marl to approx. 70 meters below sea level over similar high plasticity clays to several hundred meters depth.

The groundwater level is under influence from the water level in the adjacent sea and is normally found in level 0 ± 0.5 m. After construction of the basement, drains below the bottom plate in approx. level -4.7 govern the groundwater level.

Geotechnical investigations including several geotechnical borings and cone penetration tests (CPT) were carried out in 2007 and earlier. Previous construction activities have resulted in an assumed non-hydrostatic pore pressure profile at the site.

3.4 Geotechnical characterization of Søvind Marl

The Søvind Marl is a sedimentary marine calcareous clay of extreme plasticity deposited in an Eocene ocean covering the Danish area from around 45 to 35 million years ago. The clay is highly OC due to previous glaciations and geological erosion events. Søvind Marl is a fissured clay with slickensides and clay can be assumed to be fully saturated. Typical index properties and geotechnical parameters of the clay are given in table 2.

Table 1. Index properties and geotechnical parameters of Søvind Marl (From the archive of Geo and previous site investigations at Z-huset)

Property	Value/Range
Natural water content	35-55 [%]
Liquid Limit	80-350 [%]
Plasticity Index	50-250 [%]
Unit weight	17-19 [kN/m^3]
$CaCO_3$	0-75 [%]
Undrained shear strength	80 – 170 [kPa]
Coefficient of permeability (k_{lab})	$3\cdot10^{-12}$ – $5\cdot10^{-13}$ [m/s]
Oedometer modulus (E_{oed}) between level -10 and -30	~85 – 340 [MPa]
Coefficient of consolidation (c_v)	$2.9\cdot10^{-7}$ – $3.6\cdot10^{-9}$ [m^2/s]

4 RECENT INVESTIGATIONS

4.1 Field instrumentation and installation process

Installation of the piezometers (Geosense multilevel vibrating wire piezometers (VWP), 690 kPa HAE) took place on the 24th of January 2015. A string with piezometers in four levels was installed in a borehole that was subsequently filled with a cement-bentonite grout (Figure 3). This method, termed the fully grouted method, has been described by e.g. Vaughan (1969), McKenna (1995), Mikkelsen and Green (2003) and Simeoni et al. (2011) and its applicability in heavily OC London Clay has been illustrated by Wan and Standing (2014). The equipment was installed according to the principles described by Mikkelsen and Green (2003). Due to a fault in delivery of the bentonite, a premixed cement/bentonite mix was used instead of pure bentonite. This led to a grout with a very low bentonite content almost comparable with a neat cement grout. Grout details are given in Table 2. The mistake was not realised until after the installation was completed.

Table 2. Grout properties (w: water, c: cement, b: bentonite)

Mix proportion by mass (w: c: b)	Marsh Funnel viscosity [sec.]	Permeability (curing time 37 days) [m/s]
2: 1: 0.014	27	$9.8\cdot10^{-10}$

4.2 Grout permeability

Previous studies have shown that the grout permeability is crucial for successful measurements when using fully grouted piezometers. (Vaughan 1969, McKenna 1995, Mikkelsen and Green 2003, Contreras et al. 2008). When choosing a grout with an appropriate permeability the horizontal hydraulic gradients adjacent to the piezometer will be much higher than the vertical gradients inside the grouted borehole. Therefore, the piezometer will read the correct formation pore pressure (Mikkelsen and Green, 2003). Different studies show that the grout permeability can be some orders of magnitude greater than the permeability of the surrounding soil without introducing significant errors Vaughan 1969, Contreras et al. 2008, Marefat et al., 2014).

Recently constant head and falling head permeability tests have been performed for 5 different grout mixtures at different curing stages in connection to this study. They indicated a very low permeability for a mixture with a very low bentonite content. The grout accidently used in this study had one of the lowest permeabilities measured. At the same time however, it showed significant shrinkage during curing. McKenna (1995) describes that the shrinkage of neat cement grouts during hydration may potentially result in the grout pulling away from the borehole. Based on the field measurements it is later discussed if the very low bentonite content in the applied grout is sufficient to meet the requirements for the relevant purpose.

4.3 Permeability of Søvind Marl

The permeability of Søvind Marl is, similar to all other Palaeogene clays, very low and

the permeability of such clays are normally derived indirectly from oedometer tests. Oedometer tests in relation to previous investigations in the area have yielded a coefficient of permeability (k_{lab}) for Søvind Marl around $3 \cdot 10^{-12} – 5 \cdot 10^{-13}$ m/s.

However, Thorsen (2015) did a numerical (2D Plaxis) comparison of k_{lab} with settlements observations for a large structure over a period of years and concluded that the insitu permeability for a Palaeogene clay may be up to 30 times larger than k_{lab} derived by indirect methods.

In order to get an estimate of the coefficient of permeability without having to derive it from an oedometer test, a constant head permeability test was performed on a sample of Søvind Marl that was built into a triaxial cell. The soil sample was taken during drilling for the installation of the piezometers at level -10.6. The permeability test yielded a coefficient of permeability $k \approx 4 \cdot 10^{-11}$ m/s which is between 13 and 80 times higher than the previous indirect results from oedometer tests. The findings by Thorsen (2015) may indicate that the coefficient of permeability derived from constant head test in the lab may give a better representation of field permeability. More tests should be performed to confirm this.

5 PILE DRIVING

The 15.6 m long HE300B steel piles were driven by a Junttan PM20 pile driver with a 60 kN hammer. The tip of the piles after driving were approx. at level -20,3 i.e. approx. 0.7 meter deeper than the lowest piezometer. Driving started on the 19th of January 2015 and was completed 49 days later. In total approx. 400 steel piles were driven during that period. The sequence and number of piles driven each day after the start of pile driving is shown in Figure 4 together with existing piles. Note that the sketch is only a minor section of the construction site as only the piles within the zone around the piezometer where pore pressure response were registered during pile driving are shown.

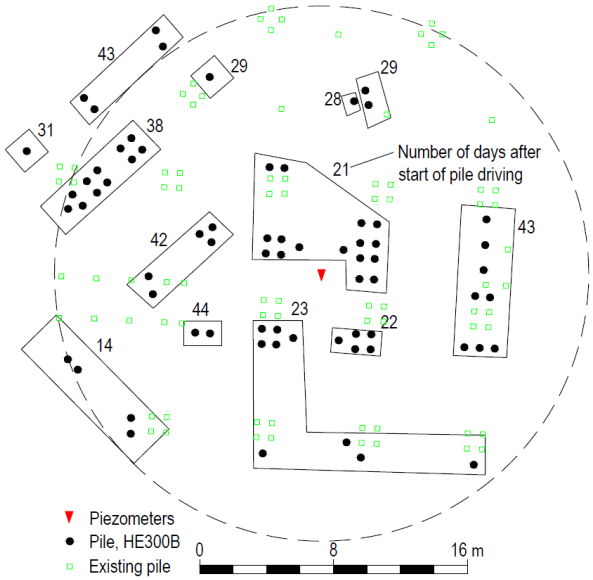


Figure 4. Location of new and existing piles and the piezometers. Numbers show the sequence of pile driving. The dashed circle indicates 100 pile radii from the piezometers. The piezometers were installed on day 5. (*equivalent radius = 160 mm for a HE300B steel pile assuming a plug at the pile tip)*

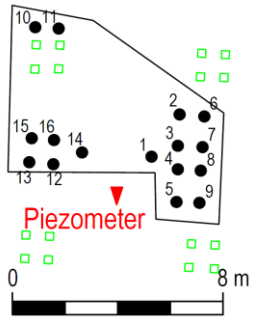


Figure 5. Piles driven at day 21. Numbers refer to the sequence of driving.

6 PORE PRESSURE MEASUREMENTS

6.1 Expected pore pressure profile before recent pile driving

In order to evaluate the pore pressures measured right after installation of the piezometers an estimation of the present pore pressure regime should be made for critically assessment of the measured data.

However, the pore pressure profile in the Søvind Marl at Z-huset has proven very difficult to predict due to several activities at the site over the years. Activities that would entail changes in pore pressure. Thus the area was reclaimed and filled up 25 years ago inducing excess pore pressures in the clay and subsequent recompression. In 2008 the

excavation for the basement was commenced inducing negative changes in the pore pressures leading to swelling in the upper zone. Subsequently hundreds of concrete piles were driven into the Søvind Marl leading to further changes in pore pressures (positive or negative).

An estimate of the pore pressures after these loading/unloading events can be derived from Terzaghi's theory of consolidation assuming one-sided drainage (Okkels and Bødker, 2008). A calculation has been conducted under the assumptions that pore pressures were hydrostatic before the loading 25 years ago and with a coefficient of permeability $k \sim 9 \cdot 10^{-11}$ m/s for Søvind Marl. The calculated deviation in pore pressures from hydrostatic conditions after the loading and unloading events (without taking the pile driving in 2008 into consideration) is in the order of -15 to -50 kPa from level -10.6 to -19.6. With present analytical models it is not possible to make a more accurate estimation of the pore pressure distribution with depth before the recent pile driving. Uncertainties mainly related to the permeability of Søvind Marl and insufficient knowledge about the influence from driving the concrete piles. However, owing to the mentioned activities the pore pressure regime prior to driving of the new piles is assumed non-hydrostatic.

6.2 Pore pressures measured before driving steel piles

The measurements of pore pressure started immediately after backfilling of the borehole with grout and connection of the piezometer string to a data logger. Figure 6 show the changes in pore pressure profile with depth after installation of the piezometers. The excess pore pressure measured at all levels right after installation is approx. 25 % higher than hydrostatic pressure due to the weight of the liquid grout. As the grout hardens, the piezometers show more or less hydrostatic conditions which is in contrast to the expected non-hydrostatic conditions. After the initial drop in pore pressure during curing a slight increase in pore pressure is observed between 21 and 36 hours after installation. This could indicate a minor effect of stress relief in the borehole or be due to ongoing curing of the grout. A similar effect, although considerably more pronounced and prolonged, have been seen for pore pressure measurements in London Clay (Wan and Standing, 2014). The authors also showed that the initial pore pressure profile was non-hydrostatic with locally induced negative excess pore pressures. The latter has not been observed in this study.

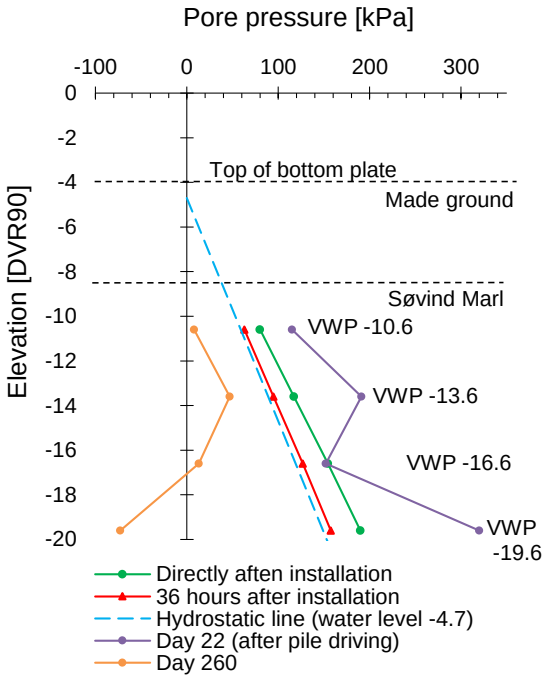


Figure 6. Pore pressure profiles.

6.3 Pore pressures measured during pile driving

The first piles to yield measurable changes in pore pressures were driven at day 14. On this day 4 piles were driven at a distance of 100 pile radii from the piezometers (Figure 4).

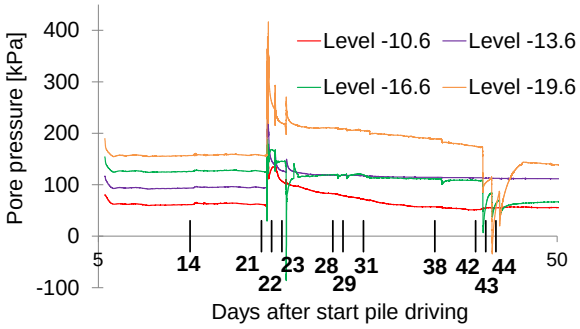


Figure 7. Pore pressure measurements in the period of pile driving. The numbers in bold refer to the days where piles near the piezometer was driven (see Figure 4)

Only minor pore pressure changes were registered from these four piles (about 2% increase) (Figure 7). The pore pressure increase

were uniform in all 4 piezometers and the excess pore pressure dissipated in around 24 hours. At day 21, 22 and 23 clusters of 16, 5 and 9 piles respectively were driven. These were the piles closest to the piezometers and the influence on the measured pore pressures was seen to be very significant. The nearest piles (day 21) were in a distance of only 1.8 meters (~11 pile radii) from the piezometers. The pore pressure measurements during day 21 – 23 are presented in Figure 9. Excess pore pressures measured were in the range of 40% – 160% of the initial value. In the minutes after completion of a pile driving sequence a quick dissipation of excess pore pressures is observed. Within hours, the dissipation seem to follow a more gradual dissipation course.

The highest excess and the most fluctuations in pore pressures were measured with the lowest piezometer in level -19,6 near pile tips. It is out of scope for this paper to go into details with every driven pile and its influence on the measured pore pressure, however the pile sequences at day 21 are shown in detail in Figure 8 for illustration of the complexity in pile driven induced pore pressures.

The figure shows how the build-up of excess pore pressure progress differently with depth. While the pore pressure build up is relatively smooth at the upper levels (-10.6 and -13.6 in particular) the pore pressure response in the lower piezometers closer to the pile tip (-16.6 and -19.6) are more irregular. Regular abrupt drops in pore pressure (level -19.6) are observed after driving of piles 4, 5, 8, 9, 12, 14 and 16. It seems to be coinciding

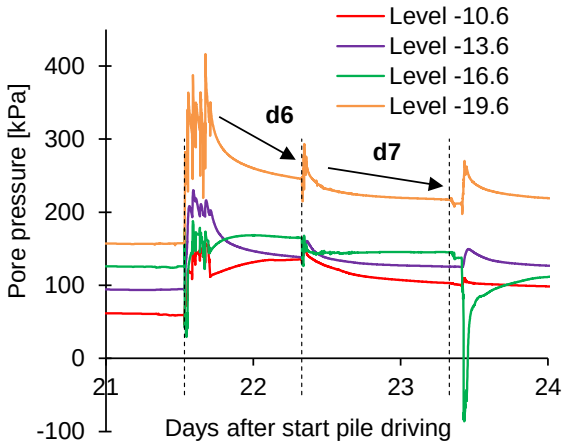


Figure 9. Pore pressure measurements day 21 - 23. (dashed lines indicate start of pile driving).

with the pile passing the piezometer and is probably due to local disturbance in the grout and clay surrounding the piezometers. The pore pressure is seen to undergo a quick reversion (within minutes).

The arrows in Figure 8 show pore pressure build-up and dissipation trends for the lowermost piezometer. It is seen how the piles near (N) the piezometers result in pore pressure build-up whereas distant piles (D) and piles experiencing a shadow effect from already driven piles (S) do not affect the pore pressures much.

A somehow atypical pore pressure response was seen at day 42 – 44 (Figure 10). Although a profound shadow effect would be expected due to the amount of already driven piles (cf. Figure 4), the pore pressure in level -16.6 and -19.6 was severely affected by the piles whereas level -10.6 and -13.6 was unaffected. The response was solely negative changes in pore pressures directly associated

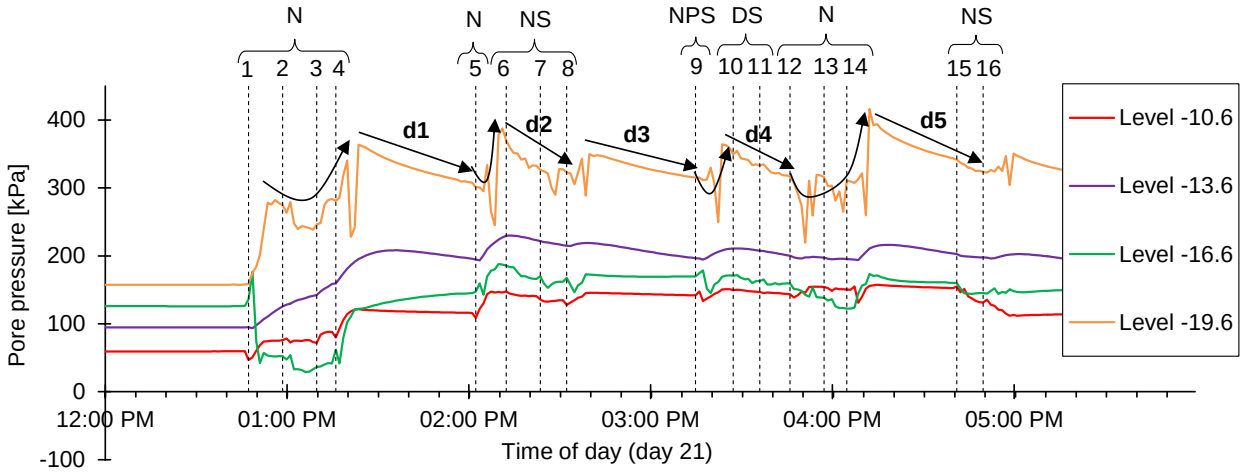


Figure 8. Pore pressures measured during day 21. Dashed lines indicate a starting point of a pile driving sequence. (Pile numbers refer to Figure 5). N = near, S = shadowed, PS = partly shadowed, D = distant.

with each pile driving.

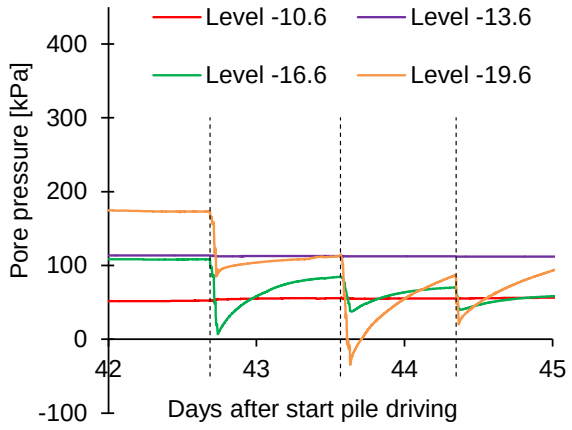


Figure 10. Pore pressure measurements day 42 – 44. (dashed lines indicate start of pile driving).

6.4 Dissipation and pore pressures measured after pile driving

As pile driving ceased, the pore pressures started to dissipate. The dissipation is clearly seen at Figure 11.

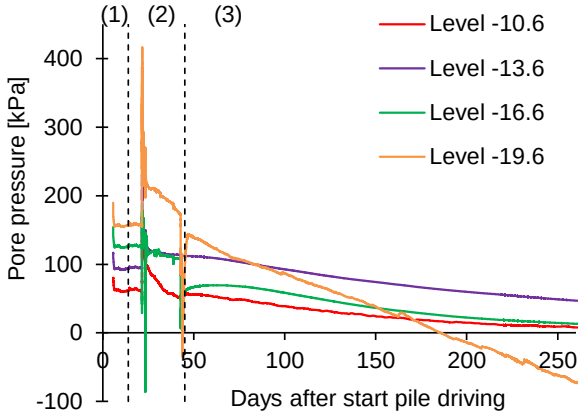


Figure 11. Pore pressure measurements over the entire period (day 250 = 25th of September 2015). Stage (1), (2) and (3) = before, during and after pile driving near piezometers.

The induced excess pore pressures are expected to dissipate towards the initial values over time. However, at this site the pore pressures in all four levels have continued to decrease for more than 200 days and have so far reached values far below the measured initial pore pressures. The pore pressure profile at day 260 after pile driving is presented at Figure 6. The pore pressure in level -19.6 is dissipating linearly over time with a constant rate and do not yet seem to move towards a steady state. The pore pressures in the other three levels display a slight decrease in dissipation rate but have not yet reached constant levels.

Different mechanisms are believed to control the dissipation and in Figure 12 dissipation events are illustrated with plot of the normalized dissipation with time where Δu is the decrease in pore pressure (dissipation) and u_0 is the pore pressure start value (peak value) before dissipation starts. d1 – d7 (cf. Figure 8 and Figure 9) illustrate the quite rapid and short-termed decrease of large excess pore pressures immediately after pile driving, whereas a long-term and more gradual dissipation trend is seen in stage (3) at Figure 11. The short-term dissipation courses are believed to be controlled by local conditions e.g. permeability of the grout around the piezometers, whereas the long-termed dissipation supposedly is governed by soil permeability.

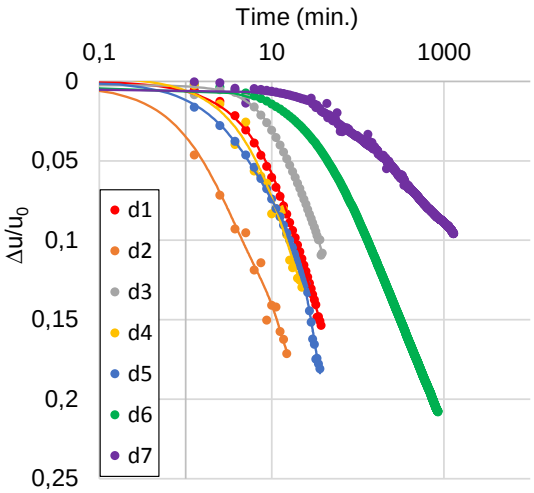


Figure 12. Dissipation d1 – d7 (cf. Figure 8 and Figure 9). From piezometer in level -19.6

7 DISCUSSION

Diverse steady-state pore water pressure profiles immediately after piezometer installation have been found between this study and the study by Wan and Standing (2014). This is likely to be a result of differences in grout and soil properties. The grout used in the present study may have experienced significant shrinkage during hydration due to a very low bentonite content, which could have led to a vertical flow path between the borehole wall and the grout column or even cracks that could have increased the macro-permeability of the grout. These factors could have caused pseudo-hydrostatic conditions in the bore-

hole, leading to an initial observed pore pressure profile which is near hydrostatic. From the continued measurements, it seems though that pile driving processes may have closed such shortcuts in the drainage paths in the grout, as the continued measurements show no signs of interconnection between piezometer levels.

During the initial stage of pile driving (day 21), large positive excess pore pressures are build up. But in the latter stage of the driving process (day 42 – 44) large negative changes in pore pressures are observed – solely in the clay near the pile tip. The pore pressures in the upper part of the clay were apparently unaffected by the piles, maybe due to shadow effects. The rapid dissipation indicate that the conditions are locally induced and hence controlled by grout properties. Dilation in the grout due to shearing can have caused the negative changes in pore pressure.

Dissipation of excess pore pressures begin immediately after pile driving. After a rather rapid dissipation in the minutes after pile driving a prolonged and gradual dissipation trend is observed in the days and monts after pile driving. The measurements show an almost linear dissipation trend continuing for more than 200 days after pile driving with pore pressures significantly lower than before pile driving and even negative values near the level of the pile tips. This tendency is not fully understood, but according to the theory, the pore pressures should dissipate over time and adjust to the initial values. However, as the initial pore pressure values are not accounted for due to presumably misleading initial pore pressure measurements, it is unknown at which stage the pore pressures will display steady state conditions. The pore pressure measurements will continue in the following years in order to shed light on this.

8 CONCLUSION

Pile driving in highly overconsolidated clay lead to the build-up of large excess pore pressures. Through pore pressure measurements with multilevel vibrating wire piezometers near clusters of piles at a construction site it has been found, that pile driving lead to a redistribution of pore pressures and that magnitude and distribution of pore pressures in relation to pile driving in highly OC clays is very complex. The interplay between grout and soil permeability and shadow effects from existing piles makes it very difficult to make a reliable estimate of the pore pressure conditions without direct measurements.

A summary of findings from this study is listed below:

- Pile driving in highly OC clays induce large excess pore pressures in the soil close to the pile. In this study pore pressures are influenced by pile driving within 100 pile radii from the pile. Beyond this distance no influence on pore pressures from pile driving has been observed. However, the distance depends on the distribution of already driven piles. Piles near a piezometer can generate a shadow effect so that no pore pressure changes are registered from piles placed behind these even though they may be within 100 pile radii from the piezometer.
- Pile driving is seen to not only induce positive pore pressure changes. Several pile driving events have caused locally negative changes in pore pressure controlled by the grout properties.
- The pore pressure response differs with depth in the soil. The most irregular pore pressure progress is seen near the pile tip where excess pore pressures of up to 160% are induced. In the remaining levels, a more smooth development is detected with excess pore pressures of 40% – 100%.
- General soil and local grout permeability conditions are believed to play a role in dissipation of long term and short term excess pore pressures respectively. The long term dissipation is observed to reach values far below the initial values.
- The importance of using a suitable grout for equipment installation with the fully grouted method has to be considered to obtain the desired properties. In this study it is likely that shrinkage of the grout has influenced the pore pressures measured before pile driving.

One of the goals with this study was to shed light on the complexity of the pore pressure distribution in heavily OC high plasticity clays during pile driving. Additional pore pressure measurements are planned at neighboring construction sites and test fields with similar ground conditions. Results from these tests will hopefully help to further shed light on the mechanisms of pore pressure development due to pile driving in heavily OC high plasticity clay. The results are to be discussed in future publications.

The significance of grout properties when using the fully grouted method in heavily OC high plasticity clays require further examination.

9 ACKNOWLEDGEMENTS

Geo and Innovation Fund Denmark has funded this work. The authors would like to acknowledge A. Enggaard A/S for permission to access the construction site and master students at Aarhus University for help with permeability testing in the lab.

10 REFERENCES

Bergset, K. H. (2015). Radial consolidation of pore pressure induced by pile driving. NTNU Trondheim, master degree thesis.

Bond, A. J. & Jardine, R. J. (1991). Effects of installing displacement piles in a high OCR clay. *Geotechnique* 41, No. 3, pp. 341-363.

Bozozuk, K., Fellenius, B. H. & Samson, L. (1978). Soil disturbance from pile driving in sensitive clay. Canadian Geotechnical Journal 15, pp. 346 – 361

Burns, S. E. & Mayne, P. W. (1999). Pore Pressure Dissipation Behavior Surrounding Driven Piles and Cone Penetrometers. Transportation research record 1675, paper no. 99-0423, pp. 17-23.

Chandra, S. & Hossain, M. I. (1993). Prediction and Observation of Pore Pressure Due to Pile Driving. Proceedings: Third International Conference on Case Histories in Geotechnical Engineering, St. Louis, Missouri, June 1-4, Paper No. 1.66.

Contreras, I. A., Grosser, A. T. & Ver Strate, R. H. (2008). The Use of the Fully-grouted Method for Piezometer Installation. Geotechnical News, Bi Tech Publishers, pp. 30 - 40, June.

Coop, M. R. & Wroth, C. P. (1989). Field studies of an instrumented model pile in clay. *Geotechnique* 39, No. 4, pp. 679-696.

Eigenbrod, K. D. & Issigonis, T. (1996). Pore water pressures in soft to firm clay during driving of piles into underlying dense sand. Canadian Geotechnical Journal, 33, pp. 209 – 218.

Gue, S. S. (1984). Ground heave around driven piles in clay. PhD Thesis, University of Oxford

Karlsrud, K. (2012). Prediction of load-displacement behaviour and capacity of axially loaded piles in clay based on analyses and interpretation of pile load test results. NTNU Trondheim. PhD Thesis.

Lo, K. Y. & Stermac, A. G. (1965). Induced pore pressures during pile-driving operations. Proc. 6th International Conference on soil mechanics and foundation engineering, Montreal, Vol. II, pp. 285-289

Marefat, V., Chapuis, R. P., Duhaime, F., 2014. Piezometric error for fully grouted piezometers Installed in clay layers. GEO Regina 2014, 67th Canadian Geotechnical Conference

Martin, R. E., Seli, J. J., Powell, G. W. & Bertoulin, M (1987). Concrete pile design in tidewater Virginia. Journal of geotechnical engineering, vol. 113, no. 6, pp. 568-585.

McKenna, G. T. (1995). Grouted-in installation of piezometers in boreholes. Can. Geotech. J. 32, pp. 355-363.

Mikkelsen, P. E. & Green, G. E. (2003). Piezometers in Fully Grouted Boreholes Symposium on Field Measurements in Geomechanics, FMGM 2003, Oslo, Norway, September.

Okkels, N. & Bødker, K. (2008). Beregning af hævninger under antagelse af retlinjet dræning. NGM 2008.

Poulus, H. G. & Davis E. H. (1980), Pile foundation analysis and design, John Wiley and Sons, New York.

Randolph, M. F. & Wroth, C. P. (1979). An analytical solution for the consolidation around a driven pile. Int. Journal for numerical and analytical methods in geomechanics, vol. 3, pp. 217-229.

Robertson, P. K., Woeller, D. J. & Gillespie, D. (1990). Evaluation of excess pore pressures and drainage conditions around driven piles using the cone penetration test with pore pressure measurements. Canadian Geotechnical Journal, JV27, N2, pp. 249 - 254, April.

Simeoni, L., De Polo, F., Caloni, G. & Pezzetti, G. (2011). Field performance of fully grouted piezometers. FMGM, Berlin.

Thorsen, T. & Okkels, N. (2015). The New Lillebælt Bridge – a settlement model. XVI European Conference on Soil Mechanics and Geotechnical Engineering, Edinburgh, September.

Vaughan, P. R. (1969). A note on sealing piezometers in boreholes. *Geotechnique* 19, No. 3, pp. 405-143.

Wan, M. S. P. & Standing, J. R. (2014). Field measurements by fully grouted vibrating piezometers. Proceedings of the Institution of Civil Engineers. Geotechnical engineering. Vol. 167, Issue 6, pp. 547-564.

Freezing-Thawing Laboratory Testing of Frost Susceptible Soils

Amin Zeinali. Corresponding / primary author
Lulea University of Technology, Sweden, amin.zeinali@ltu.se

Deniz Dagli. Co-Author
Lulea University of Technology, Sweden

Tommy Edeskär. Co-Author
Lulea University of Technology, Sweden

ABSTRACT
Frost heave and thaw weakening are two common concerns in designing and constructing roads throughout cold region areas. Cold regions can be defined in terms of air temperature and frost penetration by frozen ground engineering. Researchers have been studying frost action in soil for the past 85 years in order to design ways to reduce the costly damage to roads. Conducting the test on frost-susceptible soil must be done in order to retrieve data for frost heave and thaw weakening modeling in the soil body during a certain freezing-thawing cycle. This paper reviews and discusses the apparatuses used for this purposes. The studied apparatuses are cylindrical and provide heat through one dimension. The studied apparatuses mostly differ in the diameter and length of their cylindrical cell; likewise, temperature gradients differ from one apparatus to another. In this study the LTU's apparatus which was primarily designed to investigate the research related questions concerning freezing and thawing phenomena is presented in detail. The theory of segregation potential is applied for evaluation of the frost heave test and the thaw consolidation theory is applied for the thaw test. The main goal of the project is to conduct a series of experimental tests on various types of soil while exposing them to frost action in the apparatus to propose a classification system for the different types of soil in question with respect to their susceptibility to the frost action phenomena.

Keywords: Frost heave, Thaw weakening, Laboratory freezing test, Cold regions.

1 INTRODUCTION

Freeze-thaw action occurs in the cold regions of the world. As long as soil is frost-susceptible and temperature is cold enough to freeze the soil moisture, the freeze-thaw action is likely to happen. Large parts of northern Europe, Alaska, Canada, southern part of south America and large parts of the United States are known as cold regions. Cold region areas can be either permafrost area (where the ground is partly frozen even in summer) or seasonal frost. In these regions soil structures are subject to freezing during winter time and also thaw weakening during spring. Consequently, frost heave in pavement structures and thaw weakening occur during freeze-thaw action. Seasonal temperature decrements result in changed mechanical properties of subgrade soil. Expansion (heave) of the saturated freezing soil may be about 9% of the freezing pore water volume and if there is access to an external source of water, this water will also be drawn into the frost front thereby forming ice lenses. Ice lenses expand upwards and consequently secondary frost heaves form inside the soil. The resulting frozen soil in the subgrade increase the stiffness of the unbound layers in the winter as well as frozen soil due to ice bonding of the soil particles in the base and sub-base layers. During winter the stiffness of the pavement

structure increases which is not an issue from a structural point of view. Frost heave is not problematic as long as it does not result in an uneven pavement, yet this is highly unlikely. On the other hand during spring, thaw weakening occurs and the reduction of stiffness in the pavement structure will cause road settlement. Thawed ice trapped between the deeper frozen layers and the surface saturates the thawed part of the pavement structure and as results consolidation occurs. The excessive water can weaken the pavement materials to the point where load restrictions must be applied to prevent pavement failure. These load restrictions are a severe burden on the trucking industry and the economic vitality of the affected regions. (Miller, 1980)

The damage to pavement due to freeze-thaw action in the road costs millions of euros annually. Therefore, it is highly important for road authorities to understand the phenomena in order to reduce the costs of maintenance and/or rehabilitations, as well as costs sustained by customers. Research on freeze-thaw action has been in focus for over 85 years with numerous studies being conducted in the 1980's. Researchers have simulated freeze-thaw action in their bench-scale studies in order to understand the fundamental mechanisms associated with freeze-thaw action and susceptibility of the commonly used materials in the pavement structure. The purpose of this paper is to review some of the equipment employed in freeze-thaw tests, and also some important findings from different laboratory tests are discussed. Finally Lulea University of Technology's setup is presented and explained in detail.

2 FROST ACTION IN SOIL

Frost heave is vertical displacement of the soil surface due to freezing. It involves heave formation as a result of the freezing of the in-situ moisture of soil, followed by formation of secondary frost heave due to segregation. Freezing of the soil moisture is termed in-situ freezing. Due to the negative pore pressure at the frost front, free water (in case there is access to free water) is drawn into the frost front and forms ice lenses. Depending on how quickly the frost penetration develops, in-situ freezing will be affected accordingly. In general, the main portion of heave is primarily formed as a result of formation of ice lenses, and partly due to in-situ freezing. In the event of a quick soil freezing process, the role of in-situ freezing becomes more pronounced, however, the segregation process (formation of ice lenses) still accounts for a larger portion of the heave formed. When winter commences and the soil surface temperature starts to decrease frost front develops downwards. Ice lenses will form whenever extracted energy from soil in the frost front is equal to the energy provided by the underlying soil in the form of latent heat or the heat of crystallization released as water freezes. The growth of ice lenses depends on accessibility to free water and stability in thermal gradients.

Thawing in frozen soil can be explained in a way similar to that explained for freezing. When the air temperature is positive, thaw front starts to develop downwards as long as soil is frozen (seasonal frost conditions). However, the thawing process is hindered according to the thermal condition (permafrost condition). Thaw settlement involves a phase change, from ice to water; it also involves the outwards flow of excess water. Drainability plays an important role when it comes to excess pore pressure in thawed soil. Depending on how fine-grained the soil is, consolidation in thawed soil has a higher impact on thaw settlement. (Andersland O.B. Ladanyi B. 2012). Typical thaw settlement test result is shown in figure 1. Where e is void ratio, e_f is donates the frozen void ratio and e_{th} the thawed void ratio. When pressure increased by an amount $\Delta\boldsymbol{\sigma}$, consolidation will occur until new equilibrium void ratio e is attained at point d.

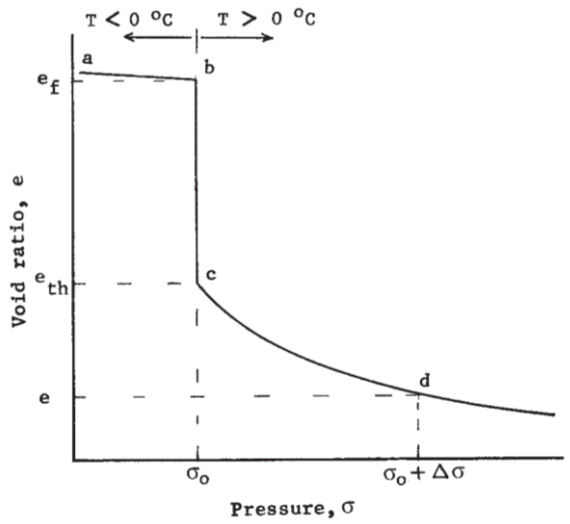


Figure 1 Typical void ratio pressure curve for frozen soil subjected to thawing. (Andersland O.B. Ladanyi B. 2012

3 PARAMETERS TO BE CONSIDERED

Temperature profile, frost heave, thaw settlement and pore pressure are common measurements during the freeze-thaw tests. Depending on the purpose of the research, one or several parameters can be measured during the freeze-thaw tests. Frost front penetration and thaw front penetration are determined using the temperature profile. The frost heave measurement during tests can be recorded applying the LVDT (linear variable differential transformer) transducer. The frost heave test will be used to verify the existing theories regarding frost heave determination. It is important to keep track of water intake in the freezing soil. Keeping track of pore pressure during the tests gives a better understanding of thaw settlement and thaw weakening. In order to understand the importance of these measurements, frost front calculations, thaw consolidation theories, and segregation potential theory will be discussed briefly.

3.1 The modified Berggren equation

This equation yields a value for frost penetration which is the product of a correction factor and the frost front penetration value calculated from the Stefan equation. The Stefan equation assumes a linear temperature distribution. Equation 1 is the Stefan equation for calculating frost front penetration (Andersland O.B. Ladanyi B. 2012).

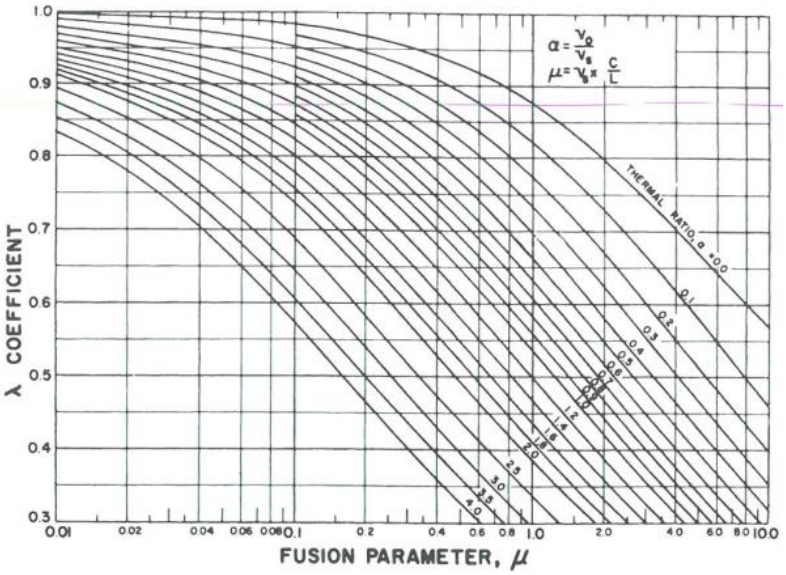
$$X = \alpha\sqrt{t} \tag{1}$$

Where X is frost depth in meters, t is time in seconds, and $\alpha\ (m/\sqrt{s})$ is a constant and α is computed using equation 2.

$$\alpha = \sqrt{\frac{2k_s T_0}{L}} \tag{2}$$

Where $k_s\ (W/m,c)$ is thermal conductivity, T_0 (^{o}C) is annual temperature, and L (J/m^3) is latent heat. The Stefan equation does not take account of the volumetric heat; therefore the values calculated for frost front penetration are overestimated in the literature when the Stefan equation is applied. The modified Berggren equation gives the ultimate frost depth reached by the frost line within the soil. .

Figure 2 Correction coefficients in the modified Berggren equation. (Andersland O.B. Ladanyi B. 2012)



The dimensionless correction coefficient, λ, is multiplied by the frost penetration depth computed from the Stefan equation.

Both α and μ in figure 2 are dimensionless. α is thermal ratio and μ is fusion parameter.

$$\alpha = \frac{v_0}{v_s} = \frac{v_0 t}{I_{sf}} \quad (3)$$

$$\mu = \frac{c_v v_s}{L} = \frac{c_v I_{sf}}{Lt} \quad (4)$$

Where c_v (kJ/m^3.^{o}C) is the soil volumetric heat capacity, L(kJ/m^3) is the volumetric latent heat,v_0 is initial surface temperature, v_s is surface temperature at the onset of the freezing period, I_{sf} is the surface freezing index and t is the duration of the freezing index.

3.2 Thaw consolidation theory

Based on the thaw consolidation theory assumptions, frozen soil is uniform, isotropic, homogeneous, and temperature is constant throughout the entire frozen fraction. Warm temperature from the top surface makes the frozen fraction start to thaw while the heat flow is assumed to be one dimensional (Andersland O.B. Ladanyi B. 2012).
Figure 3 shows the one dimensional thaw consolidation theory.

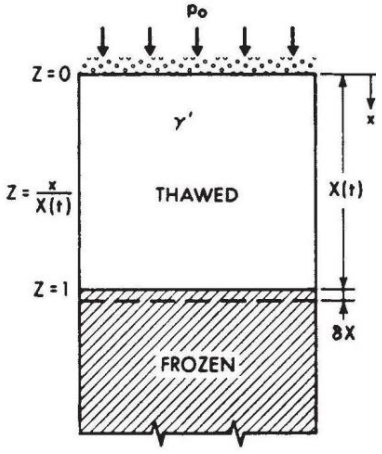


Figure 3 One-dimensional thaw consolidations. (Andersland O.B. Ladanyi B. 2012)

Thaw depth (X) is computed from equation 1. Where α is the thermal constant which depends on the initial temperature of the soil, the step temperature applied to the surface of the soil, and the thermal properties of both frozen and thawed soil. The Terzaghi consolidation theory for saturated soil is assumed to be valid for the thawed region.

3.3 Segregation potential theory

The Segregation potential theory (SP) was introduced by Konrad and Morgensten in 1980. It is defined as the ratio of water migration rate to the overall migration rate in the frozen fringe, in order to characterize a freezing soil. (Kujala, 1991).
Due to negative pore pressure at the frozen fringe, water will be drawn in and new ice lenses start to form. As long as the ice lens develops frost front does not move. Equation 5 is the segregation potential equation by Konrad and Morgensen (Konrad, 1980).

$$v(t) = SP(t) grad\ T_f(t) \quad (5)$$

Where v(t) is the flow of water to the growing ice lens at the time of the formation of the final ice lens, grad T_f (t) is the overall thermal gradient in the frozen fringe and SP(t) is a constant. This theory can be used to calculate the amount of heave as a result of freezing in the soil. Overburden load has a descending exponential impact on the segregation potential (Konrad, 1980).

4 FROST HEAVE AND THAW WEAKENING APPARATUSES

Frost and thawing problems were highlighted in 1930 by Stephen Taber. Researchers in cold regions tried to conduct laboratory scale tests in order to simulate frost action in soil and understand it. The main goal of freezing-thawing tests within these years was soil classification with respect to frost and thaw susceptibility. Several classifications have been proposed based on frost susceptibility of soil and still there is hope to improve it. In this paper we review some of the lab setups within the past 85 years. The reviewed frost heave and thaw weakening apparatuses have similarities and the principles are the same. They are all cylindrical in shape and the heat flow is one dimensional. The differences are mainly the accessibility to free water, diameter, height, temperature gradients,

overburden pressure, cooling system, and degree of saturations. According to the literature, none of the test apparatuses is 100 percent desirable. Most of them are not able to accommodate course- grained materials, for instance the base materials, because of the small diameter of the cylinder. (Chamberlain, E.J. 1981)
In other words, similarities of freezing-thawing apparatuses are:

- Specimen is cylindrical,
- Water is provided from the bottom (if applicable)
- Surface of the specimen is exposed to the freezing or thawing temperature
- Heat source is at the bottom
- Specimen is insulated

Direction of freezing is from top to bottom in most of the cases. In this study, the reviewed freezing thawing apparatuses are classified into two groups with respect to the cooling system:

1. Circulating air (top cap) and heated water (bottom cap):

In this case the entire freezing-thawing apparatus should be placed in a cold chamber. During the freezing test, circulation of the freezing air removes heat from the specimen surface while during the thawing test, the specimen surface extracts heat from the circulating air.

2. Circulating glycol/alcohol water:

In this case a cooling unit circulates a cold coolant such as a mixture of glycol/alcohol-water, through the top cap placed on the surface of the specimen. In order to provide heat at the other end, the coolant should be circulated through the bottom cap as well. Two separated cooling unites are needed for each specimen. Although the specimen is insulated, the entire freezing-thawing apparatus should be maintained at a constant temperature (cold chamber) in order to prevent heat extraction from the ambient.

Three different conditions are found in the literature regarding the water supplied to the specimen for frost heave and thaw weakening tests: Konrad (1980) used fully saturated soil before the test and tried to keep it saturated during the test by keeping the water level as high as the surface of the specimen. Some researchers used saturated specimens, but they kept the water level at the base of the specimen. In some cases unsaturated specimens were used. (Kujala 1991).

In most of the cases overburden pressure can be applied although there are few exceptions. (Kujala 1991).

Table 1 mentions some of the selected apparatuses used. In most cases the principal goal is to classify soil frost susceptibility.

Table 1 Diameter, height and temperature gradient of some apparatuses.

Research	Year	D (cm)	H (cm)	Cold end (^{o}C)	Temperature gradient (^{o}C/cm)
Taber	1930	8.4	16	-17	1.22
Alekseeva	1957	6	10	-7	0.80
USACE	1970	14	12.7	-15	1.50
Aguirre-Puente	1970	7.5	25	-5.7	0.27
Vlad	1980	10	20	-25	1.45
Brandl	1970	30	50	-24	0.56
Brandl	1980	12.5	15	-15	1.27
Henry	2001	10	15	-1.4	0.21
Kolisoja	2003	15	15	-3	0.27

5 ASTM: D5918

The American Society for Testing and Materials (ASTM) proposed a standard for frost heave and thaw weakening tests. It is standard test methods for frost heave and thaw weakening susceptibility of soils. It should be used for soils where frost-susceptibility considerations are met, meaning that particle size should exceed the limit of 3% finer than 20 mm. This test is to estimate the relative degree of frost-susceptibility of soil used in pavement systems. ASTM proposes two freeze-thaw

cycles on compacted soil specimens, 146 mm in diameter and 150 mm in height. The soil specimen is frozen and thawed by applying specified constant temperatures in steps at the top and bottom of the specimen. Water can be supplied freely or the test can be run without access to free water. A surcharge of 3.5 kPa can be applied to the top. Test procedure can be completed within five days.

Table 2 shows frost susceptibility criteria based on ASTM. It is classified in six categories from negligible frost-susceptible soil to very high frost susceptible soil.

Table 2 Frost-susceptibility criteria (American Society for Testing and Materials 2013)

Classification	8-h Heave rate mm/day	Bearing ratio after thaw, %	Symbol
Negligible	<1	>20	NFS
Very low	1 to 2	20 to 15	VL
Low	2 to 4	15 to 10	L
Medium	4 to 8	10 to 5	M
High	8 to 16	5 to 2	H
Very high	>16	<2	VH

The bearing ratio is determined after the second thawing cycle. The ASTM method can be used to determine the frost-susceptibility of soil and thaw weakening susceptibility.

This method is not applicable to permafrost conditions and is only recommended for seasonal frost conditions. The amount of frost heave or thaw weakening cannot be predicted by the ASTM method. A schematic of the ASTM apparatus is illustrated in figure 4.

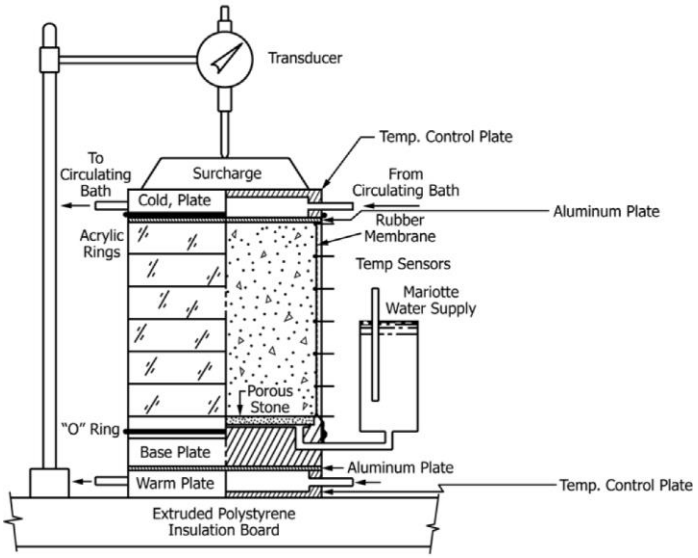


Figure 4 Specimen assembly for freezing tests by ASTM D 5918. (American Society for Testing and Materials 2013)

6 LTU APPARATUS

Lulea University of Technology (LTU) began specializing in frost action on soil during the 70s and 80s. Interest in this topic has experienced a resurgence in Sweden and LTU has seized the opportunity to continue research on frost action. The setup was further developed recently by Oulu university researchers in Finland. The new apparatus at LTU is based on the improved design and great support is received from Finnish colleagues. To begin, we reviewed the most recent progress and improvements. The principles of LTU apparatus are quite similar to the reviewed apparatuses. Heat flow is one dimensional, water is supplied from the bottom, side insulated, glycol-water coolant is supplied to both cold and warm ends, it is also possible to apply overburden load, the apparatus is cylindrical with a diameter of 10cm, and the specimen is 10cm in height. There is also a possibility to use taller specimens for the same apparatus if there is a need to do so.

A schematic of the LTU apparatus including the data logger system is shown in figure 5.

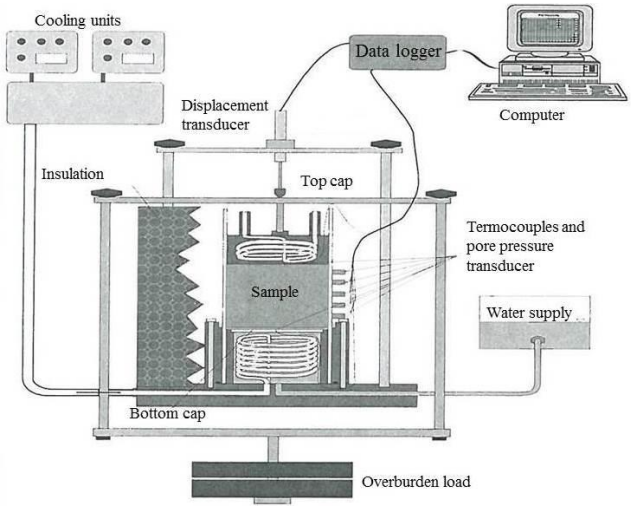


Figure 5 Sketch of LTU freezing-thawing apparatus(Kujala 1991)

Transparent cell is used and after the freezing-thawing test, there is a possibility to check out the soil profile and the formed ice lenses due to the freezing tests allows image analysis of the freezing-thawing test. In this case insulation shouldn't be used; therefore, heat flow will be three dimensional. A comparison between the images gives frost/thaw penetration as well as frost heave/thaw settlement. Frost/thaw penetration and frost heave/thaw settlement can be computed by image analysis. There is a possibility to compare the calculated frost/thaw penetration and the measured frost heave/thaw settlement to image analysis results in order to verify the functionality of the apparatus. Figure 6 the specimen it is exposed to freezing tests after 4 days.



Figure 6 Specimen during freezing test after 4 days

Friction between the top cap and cell during frost heave was one of the main concerns at LTU. The manufactured apparatus reduces friction between the top cap and cell and between the cell and frozen soil by allowing the cell to move upwards as the soil freezes. Thus preventing the soil and top cap from moving against the cell.
Figure 7 shows different parts of the freezing-thawing apparatus. Freezing units, load cells, membrane, thermocouples, and the data logger are not shown in this figure.

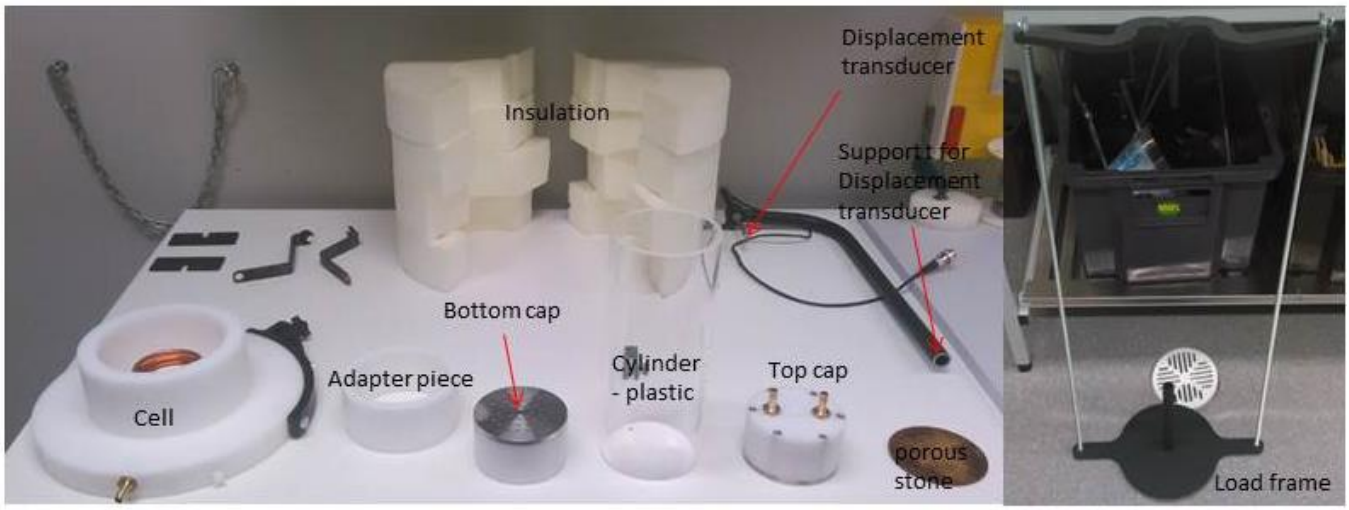


Figure 7 Freezing-thawing apparatus parts

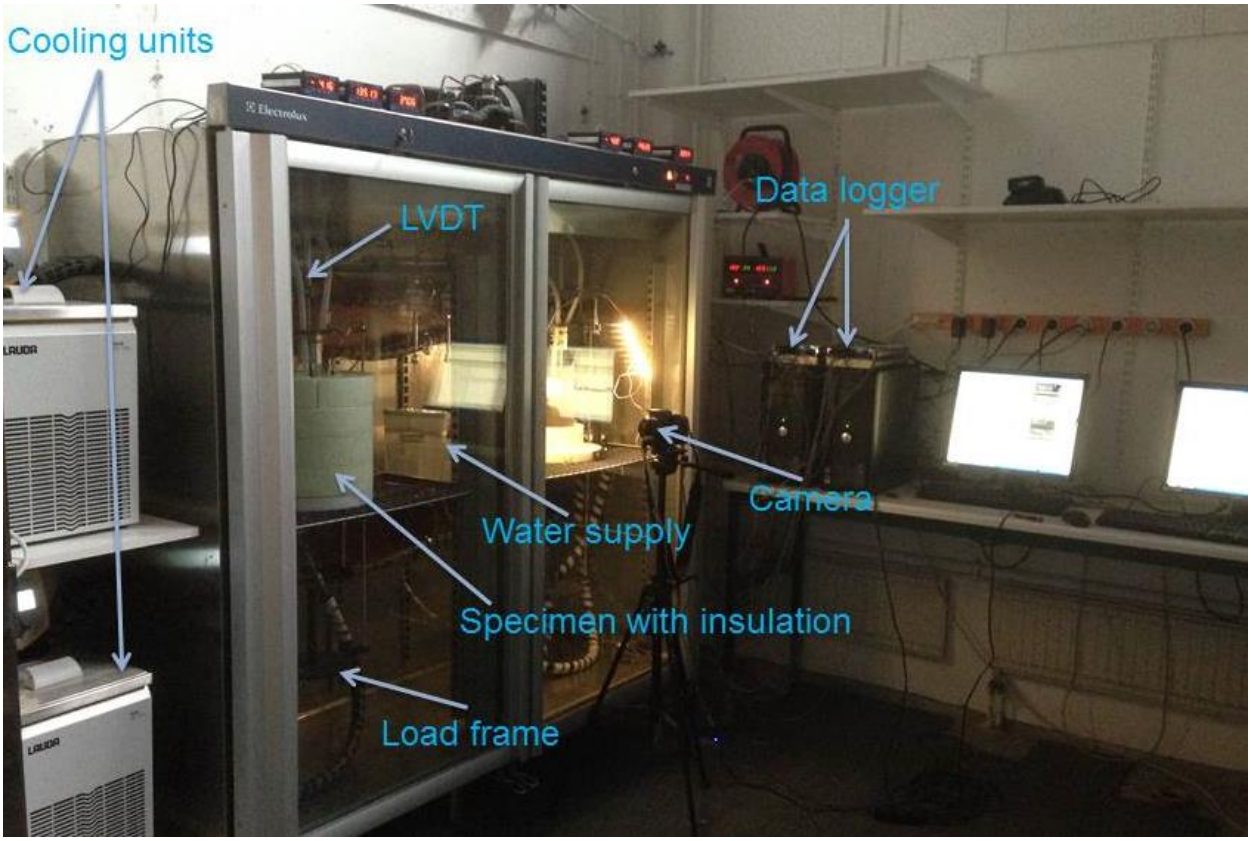


Figure 8 LTU frost lab

The specimen should be prepared and compacted to a desired degree of compaction. Compaction is done in five layers to prepare a uniform specimen in terms of density and fine particles. Prior to compaction a desired amount of water (10% water content) will be added to the soil. When conducting a freezing test on a saturated specimen, a membrane must be wrapped around the cell after placing the cell on the bottom cap. The membrane is important to keep the moisture in the specimen and to secondly fill the gap between the cell and the edge of the bottom cap, while the water level is kept at the level of the specimen surface. There is a possibility to run the test on undisturbed samples. If so, the core sample should be prepared with a diameter of 10cm (equal to that of the apparatus cylinder), then gently transferred to the freezing-thawing cylinder. Five holes are created on the cell for thermocouples, and five holes for pore pressure transducers. Two holes have been created for drainage in order to keep the water level at the bottom of the specimen during the experiment. Thermocouples should be attached gently and ASTM recommends that thermocouples be inserted 6.5 mm into the specimen. After assembling the unit and connecting it to the cooling units, thermocouples, LVDT, pore pressure transducers and load cell will be connected to the data logger. The freezing-thawing apparatus is shown in figure 8.

7 FREEZING-THAWING TEST DATA

Several pre-tests have been conducted at LTU and in this paper some topline results are presented. During the freezing test water intake has been recorded (which causes the ice lenses when the sample is saturated), frost heave and frost depth. Five thermocouples are used to measure temperature in the soil in 2 cm intervals. When the frost depth is located between two of the thermocouples interpolation method is applied to find the zero temperature location (frost front). Frost heave, water intake and frost penetration will be used for modeling and frost susceptibility classification.

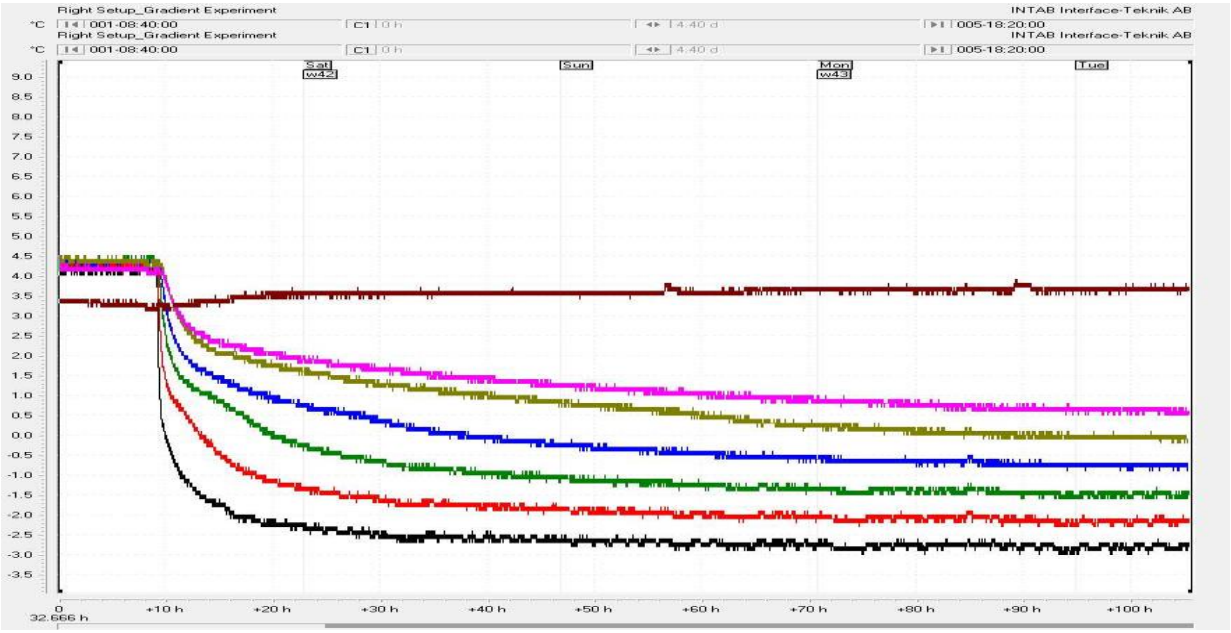


Figure 9 Thermocouples data for freezing test

Figure 9 shows the thermocouples data. Two thermocouples are attached to the cold and warm ends and the rest are inserted into the soil to represent soil profile temperature. Frost penetration depth and heave measured by LVDT from one of the pre-tests are illustrated in figure 10 and 11 respectively. Basically these are input data for further investigations.

These data has been discussed and analyzed in the other paper written by the same authors. Dagli et al. (2016) discussed the relationship between heave and net heat extraction rate based on these data.

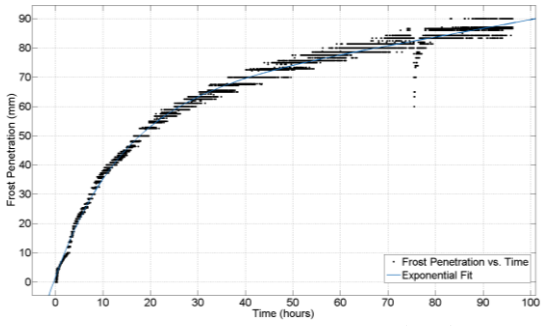


Figure 10 Frost penetration curve (mm)

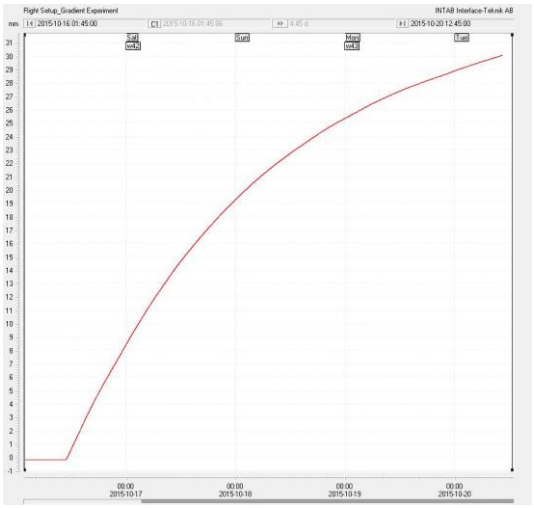


Figure 11 Frost heave (mm)LVDT readings

8 CONCLUDING REMARKS

The LTU apparatus is one of the most latest bench-scale apparatus designed for freezing and thawing tests. In terms of basic design such as dimension, heat flow, insulation etc. there are similarities to the pervious setups and thanks to more advanced data loggers and transducers, LTU apparatuses is more friendly user. Moreover, LTU apparatus is the most complete setup in terms of both frost and thaw action in the soil. In addition to modeling frost action there is a possibility

to improve soil susceptibility classification. For classification, plenty of freezing-thawing tests on various types of soil should be conducted as well as basic soil mechanic laboratory tests. Soil will be classified based on their properties and the degree of frost susceptibility will be defined.

9 ACKNOWLEDGMENT

The authors would like to acknowledge the financial support of research project by Swedish Transport Administration (Trafikverket).

10 REFERENCES

Andersland OB, Ladanyi B. (2012). FROZEN GROUND ENGINEERING. American Society Of Civil Engineering; 2012.

ASTM Standard D5918-13, (2013). "Frost Heave and Thaw Weakening Susceptibility of Soils," ASTM International, West Conshohocken, PA 19428-2959. United States

Beskow, G. (1935) soil freezing and frost heaving with special applications to roads and railroads, Swedish Geol. Survey year book 26(3), No.375.

Boyd, D.W. (1976). Normal freezing and thawing degree-days. Canadian Geotechnical Journal, vol.13. pp:176-80

Chamberlain EJ. Frost susceptibility of soil. Hanover, New Hampshire: Cold Regions Science and Engineering; 1981.

Dagli, D., Zeinali, A., Laue, J and Edeskär, T. (2016). Theoretical Analysis of the Relationship between Heave and Net Heat Extraction Rates Based on Freezing Experiments Data. The 17th Nordic Geotechnical Conference, Reykjavik, Iceland.

Darrow MM, Huang SL, Shur Y, Akagawa S. Improvements in frost heave laboratory testing of fine-grained soils. J Cold Regions Eng. 2008;22(3):65-78.

Drumm ECM, R. LTPP Data Analysis: Daily Seasonal Variations in In-situ Material Properties. Knoxville, Tennessee: National Cooperative Highway Research Program; 2003. Report No.: NCHRP Web Document 60.

Kettle MRJ, Williams RIT. (1976). Frost heave testing. Matériaux et Constructions. 1976;9(4):310.

Konrad, J.M. (1980). Frost Heave Mechanics. Ph.D. thesis, University of Alberta, Alberta.

Konrad, J.M, Morgenstern, N.R. (1981). The segregation potential of a freezing soil. Canadian Geotechnical Journal, vol.18. pp:482-91

Kujala K. (1990). Factors Affecting Frost Susceptibility And Heaving Pressure In Soils. 1st ed. Oulu University, editor. Oulu: Oulu University; 1991.

Ladanyi B. (1981). Mechanical behaviour of frozen soils. In proc.Int. symp. on Mechanical Behaviour of Structured Media, Carleton Univ. Ottawa. New York:Elsevier, vol. B, pp 205-45.

Miller RD. (1980). Freezing phenomena in soil. Application of soil physics. 1980:254-99.

Miller RD. Freezing phenomena in soil. Application of soil physics. 1980:254-99

Nixon, J. (1987). Ground freezing and frost heave review. The Northern Engineering, Vol. 19, No. 3&4, pp.8-18.

Niu, F.J. Cheng, G.D and Lai, Y.M. (1998). Laboratory study on a Duct-Ventilated Roadbed of Qinghai-Tibet International permafrost conference. Zurich, Switzerland. pp:815-820.

Taber, S. Freezing and Thawing of soils as Factors in the destruction of the Road Pavements. Public Roads, Vol. 11, March 1930-FRebruary 1931, pp. 113-132.

Saarenketo,T., Scullion, T. and Kolisoja, P. (1998). Moisture Suceptibility and Electrical Properties of Base Course Aggregates. In fifth International Conference on the Bearing Capacity of Roads and Airfields, Trondheim, Norway, 1998, pp. 1401-1410.

Zarling, J.P., Barley, W.A., and Ecsh, D. (1988). Thaw Stabilization of Roadway Embankments. 5th International Permafrost Conference, Trondheim, Norway, vol.2. pp:1352-1357.

Investigation into the effect of uncertainty of CPT-based soil type estimation on the accuracy of CPT-based pile bearing capacity analysis

O. Hamza
University of Derby, UK, o.hamza@derby.ac.uk

A. Bellis
Atkins Ltd, UK

ABSTRACT
Cone Penetration Test (CPT or CPTu) is commonly used for estimating soil types and also for the geotechnical design of pile foundation. However, the level of agreement between the CPT-based soil types and the traditional identification of soil types based on samples may vary significantly; and it is not clearly understood if this variation has any sort of relationship with the CPT-based pile design. To investigate into this area, a ground investigation trial was carried out at six different locations as part of a highway scheme in East of England. At each location the trial comprised one CPTu adjacent to one borehole (BH) with conventional sampling and laboratory testing. The soil types were estimated from the CPTs and compared with the boreholes findings, and the levels of correlation between them were established. Similarly, the ultimate bearing capacity of a typical bored pile based on the CPTs and on the BHs were calculated and compared. Despite the variable level of disagreement of the CPT-based soil type estimation with the BHs findings, the pile capacity based on CPT data was found to be generally consistent with the values obtained from the traditional BHs-based pile design.

Keywords: In situ testing, CPT, Piles, Design

1 INTRODUCTION

The cone penetration test (CPT or CPTu) has been extensively used for characterization of soils due to its specific advantages such as fast operation, relatively low cost, near-continuous profile, and stratigraphic detailing. In addition to the determination of soil stratigraphy and the identification of soil type, CPT-data can be used directly in the design of pile foundation with high reliability (Lunne et al. 1997, Robertson, P.K. & Cabal, 2012).
However, the currently available semi-empirical methods may present a significant variability in the estimation of soil type (Robertson, 2010, Robertson, P.K. & Cabal, 2012). In particular, for some mixed soils (i.e. sand-mixtures & silt-mixtures) where the CPT-based SBT (Soil Behaviour Type) may not always agree with traditional soil classification system (such as USCS and BS) which are based on samples and laboratory testing. Furthermore, it is not clearly known if the uncertainty in soil type estimation has any relationship with pile capacity based on direct application of CPT.
This paper investigates if there is any correlation between the uncertainty of CPT-based interpretation of soil type and the CPT-based pile design. This was conducted by accessing data from a CPT/Boreholes trial carried out at 6 different locations as part of a recent site investigation for a highway scheme in East of England (Atkins, 2009). The CPT-based pile design (the calculation of the ultimate vertical bearing capacity of a typical bored pile) was carried out and compared with the results of the design based on standard boreholes, where the soil parameters were conventionally obtained from Standard Penetration Test (SPT) results and laboratory testing. Figure 1 shows the

conceptual model of the aim of the study presented in this paper.

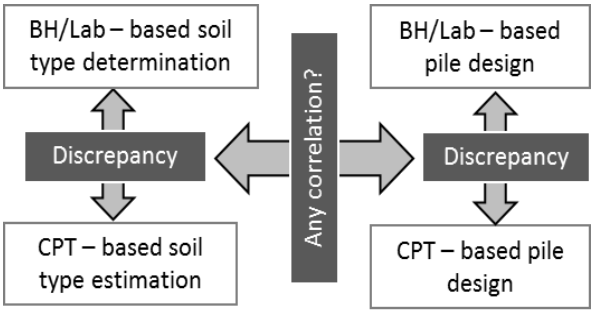


Figure 1 Conceptual model showing the aim of the study.

2 BACKGROUND ABOUT THE SITE INVESTIGATION

The geotechnical data used for this study was retrieved from a recent ground investigation (GI) which was conducted for a highway project "A14 Ellington to Fen Ditton Improvement Scheme - Section 1" (Atkins, 2009). This section bypasses the developed areas around Huntingdon (see Figure 2); it begins 1.0km west of the A1/A14 Brampton Hut interchange and runs approximately south alongside the A1.

The main GI included a total of 80 borings and 70 CPT soundings performed along the project route. In situ testing included the Cone Penetration Test (CPT) and the Standard Penetration Test (SPT). As part of the boring program, the retrieved samples were subjected to a full suite of laboratory index tests to determine water content, unit weight, specific gravity of solids, liquid limit, plastic limit, and particle size distribution by means of sieve and hydrometer.

During this ground investigation, a CPT trial was undertaken adjacent to the locations of 6 no. cable-percussion boreholes. This particular data was used within the scope of the paper.

3 BOREHOLES (BHS) AND GEOLOGY OF THE SITE

At the locations of the CPT trial, 6 no. cable-percussion boreholes have been excavated (BH2003, BH2005, BH 2015, BH 2017, BH2024 and BH2031). From the borehole findings the geology of the site comprises Glacial Till and Oxford Clay, overlain by Head deposits and River Terrace Gravels in the western quarter of site. The borehole logs of the exploratory holes are shown in Figure 3. Both the Glacial Till and Oxford Clay are heavily overconsolidated deposits. The extension of Glacial deposits revealed at BH 2005/2015 a buried channel. The depth of groundwater tends to lie at depths of between 1m and 3m bgl. More details can be found in the Ground Investigation Report (Atkins, 2009) and Factual Report (Lankelma, 2008).



Figure 2 Map showing approximate location of the site investigation

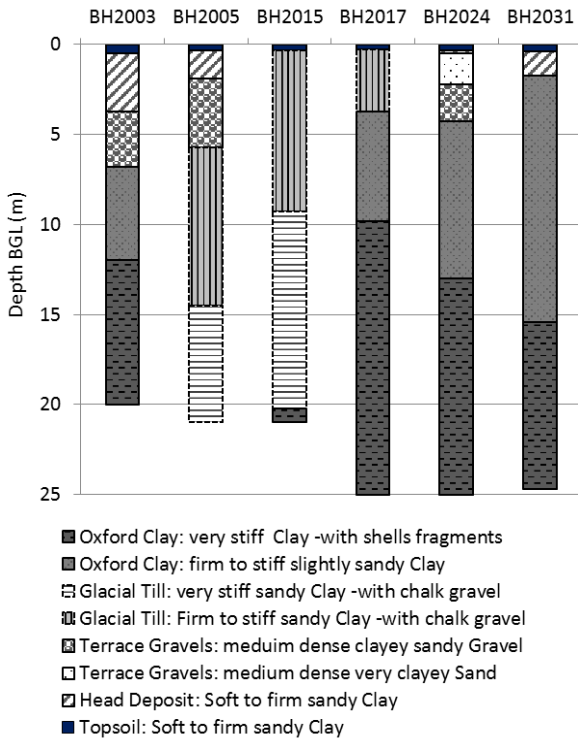


Figure 3 Borehole logs showing the geology of the site where the CPT trial has taken place.

4 SOIL TESTING AND PARAMETERS

In addition to the boreholes, in-situ tests including Standard Penetration Tests (SPT), and a selection of laboratory tests were carried out to confirm the soil type and provide data which would enable the geotechnical design. The laboratory testing included: MC, PSD, Atterberg Limits (PL, LL), Bulk density, Quick Undrained Triaxial (UU), Consolidated Undrained Triaxial (CU), and Hand Shear Vane (HSV). Table 1 summaries the soil properties and their typical values obtained from some of the tests, and considered in the study.

5 CPT TESTING AND INTERPRETATION

The investigation consisted of performing 6 electric Piezocone Penetration Tests (CPTU's) to a maximum depth of 23m or refusal. The Cone Penetration Tests were performed with a track mounted CPT unit equipped with a 20 Tonne Capacity Hydraulic ram set. A single electric piezocone conforming to the requirements of clause 3.1 of BS1377: 1990: Part 9 was used on this investigation. All tests measured the cone end resistance (qc), the local side friction (fs) and porewater pressure (u2). The test results are presented in Figure 4.
Many studies have been performed on the interpretation of the estimated soil type from the CPT test data (Robertson et. al., 1986; Meigh, 1987; Zhang & Tumay, 1999).
One of the more common CPT-based methods to estimate soil type is the chart suggested by Robertson et al (1986) based on cone resistance, qc and friction ratio, Rf. Although newer charts have been developed based on normalized parameters, the simple chart based on qc and Rf is still popular because of its simplicity (Robertson, 2010; Long, 2008). Therefore in this study the original Robertson et al (1986) chart was used for the interpretation of the CPT data (i.e. to evaluate soil type) as presented in the next section.

6 COMPARISON BETWEEN THE FINDINGS OF THE BOREHOLES (BHS) AND CPTS

The soil type information obtained from the CPT tests (based on the method proposed by Robertson et al 1986) was compared with the soils encountered within the adjacent exploratory holes, which were described according to British Classification System (BS5930).
In order to determine how far the information obtained from the exploratory holes (BHs) and the CPT reveals similar ground conditions, a system of three different categories (i.e. Good, Acceptable and Poor)

Table 1 Summary of engineering properties of soil layers found in the site investigation trial.

Parameter (Unit)		**Range (Typical value)**			
		HD	**RT**	**GT**	**OC**
Natural Moisture Content (%)		10-46 (23)	5-25	15-25 (17)	**15 – 45(24)**
Bulk Density (Mg/m^3)		1.7 - 2.1	2.0 ‡	2.1-2.2	**1.9 -2.2**
Liquid Limit (%)		23-87 (45)	20-70 ⌜	40-55 (45)	**40 – 75(57)**
Plastic Limit (%)		12-35 (18)	12-23 ⌜	12-22 (18)	**16 – 30(22)**
Plasticity index (%)		10–41(25)	5-46 ⌜	4-42 (30)	**25 – 55(35)**
Particle Size Distribution (PSD)	Clay (%)	5-56 (27)	(16)	37	**51**
	Silt (%)	10-30 (25)	(8)	38	**43**
	Sand (%)	5-40 (28)	(37)	14	**3**
	Gravel (%)	0-50 (10)	(35)	9	**3**
	Cobble (%)	0-1 (1)	(4)	1	**1**
SPT 'N'		2 - 30	10 - 35	(13+2.0Z)	**(5+1.9Z)**
Shear Strength	c' (kN/m^2)	0-5 ⊤	-	0-5 ⊤	**0-5 ⊤**
	ϕ' (degree)	26-33 ⊤	30–37 ¥	25-26.5 ⊤	**23.6-26 ⊤**
	C_u (kN/m^2)	5-129	-	(60+12Z) ¥ ⊤ ≠	**45+10Z ¥ ⊤ ≠**
Notation: ¥ : based on empirical correlation with SPT (Peck, 1974; Tomlinson, 2001); ‡ : Typical value found in literature; ⊤ : based on Traixial Test; Z: depth from top of layer; ≠ : based on HSV test; ⌜ : carried out on the cohesive content of the materials.					

was proposed by the Authors. The three levels of agreement between CPTs and BHs are explained as follow:

- Good: when the description of the soil generally agree with each other
- Acceptable: when the major class of soil

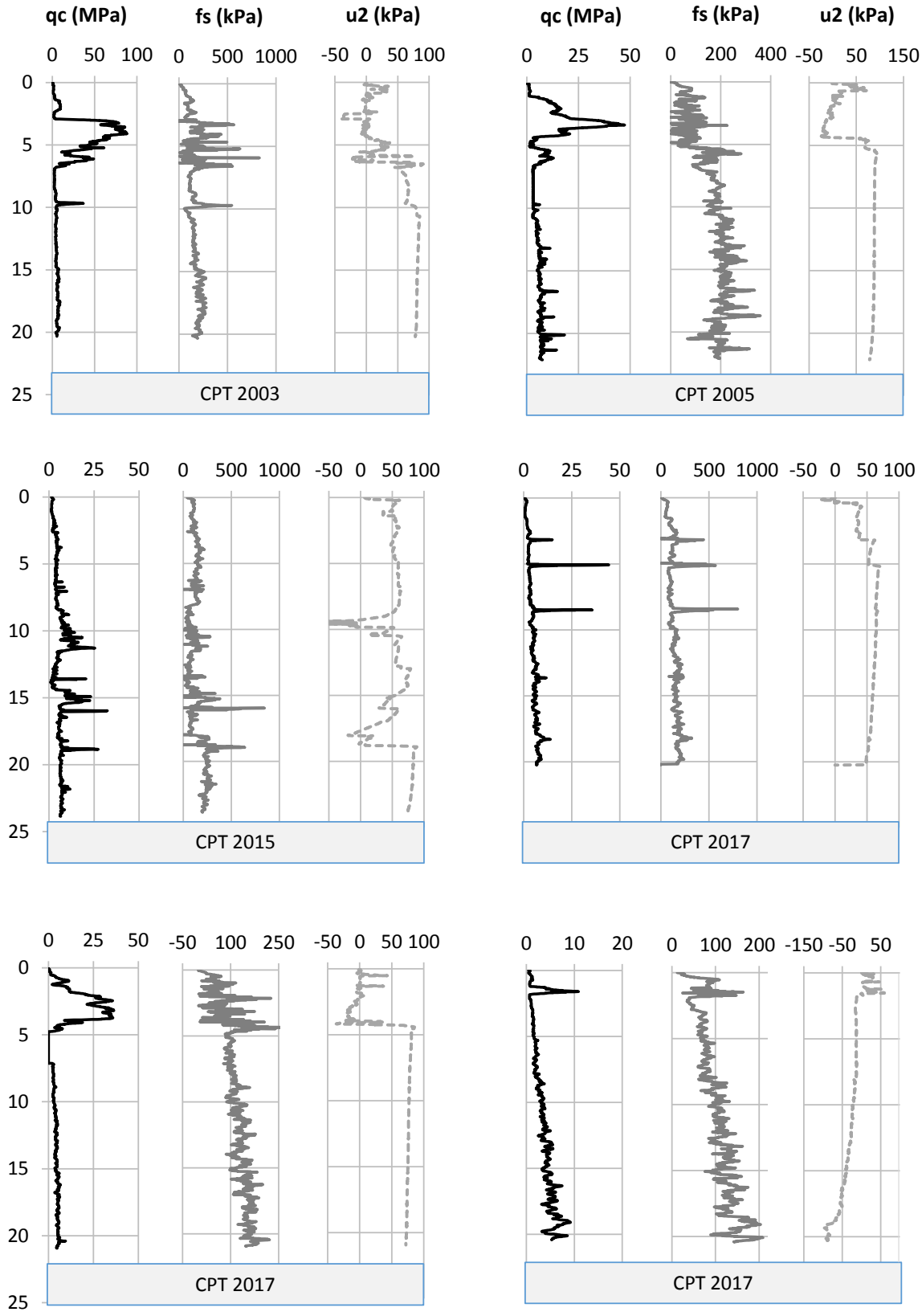


Figure 4 The measurements of CPTUs: Tip Resistance qc, Sleeve Resistance fs, and Pore Pressure u2.

agree (Coarse-grained and Fine-grained soil), but the sub-class does not agree (Clay against Silt, and Sand against Gravel)

- Poor: when the major class of soil totally disagree

The tables from 2 to 5 represents the findings from both Boreholes and CPT for each type of soil found in the site investigation trial (excluding the top soil); the correlation level was also added to the tables.

7 FINDINGS OBTIANED FROM THE COMPARISION OF BHS AND CPTS

7.1 Head Deposits

This soil type was encountered in four boreholes at shallow depth of about 0.3-0.5mbgl (see Table 2). From the four cases encountered, only 52% of the total length (see Figure 5) coincided (i.e. Good correlation level) with the description of the exploratory holes but with a slight difference in soil conditions and strength. The rest (i.e. 48%) described totally different major type of soils that the conditions described on the CPT.

7.2 Terrace Gravel (TG)

The Terrace Gravel was encountered below the Head Deposits between a minimum depth of 0.5mbgl in BH2024 to a maximum of depth of 6.80m bgl in BH2003.
The CPT-based soil descriptions appear to be similar to the soils encountered into the boreholes with slight differences in density; however two of the descriptions (Table 3) differ completely in soil class and strength. The general correlation levels for this soil were: 16% Good, 77% Acceptable, and 7% Poor as shown in Figure 5.

7.3 TG Glacial Till (GT)

Glacial Till was encountered in three boreholes between a minimum depth of 0.25mbgl in BH2017 to a maximum of depth of 20.25m bgl in BH2015 (see Table 4).
A total of 59% of the descriptions from CPT test appears to be correct, 16% was acceptable, and 26% was poor.

7.4 Oxford Clay

The Oxford Clay is encountered between a minimum depth of 2.0mbgl in BH2031 to a maximum of depth of 25.0m bgl in BH2003. There was a total run of 82m of this type soil in all boreholes; only 33% of the description was correct, 55% was acceptable but with some differences in soil material and strength, and 46% of the description was totally different (i.e. Poor).

7.5 General comment

As shown in Figure 5, the overall level of correlation for the four types of soil discussed above scored 42% as “Good”, 40% “Acceptable”, and 18% “Poor”. The lowest score (i.e. Poor correlation) was occurred in Head Deposit followed next by the Oxford Clay.
Head Deposit was described as “firm sandy clay” which falls within mixed soils region (i.e. sand mixtures) where CPT has been reported to have some difficulty predicting the soil type (Roberson, 2010).
For the case of Oxford Clay, the majority of the description of this soil was given as stiff to very stiff (slightly) sandy clay - with some gravel. The difficulty of predicting soil type by CPT may be explained in this particular case on the basis that very stiff, heavily overconsolidated fine-grained soils are more inclined to behave like a coarse-grained soil in that they tend to dilate under shear and can have high undrained shear strength compared to their drained strength and can have a CPT-based soil behavior type in a coarse grained zones (Roberson, 2010).
However, it is commonly accepted (Roberson, 2010) that the geotechnical design is more connected with in-situ soil behaviour than a classification based on grain-size distribution and plasticity carried out on disturbed samples, although knowledge of both is helpful. Therefore, the second part of this study tried to find out if the uncertainty encountered in CPT-based soil type estimation has any relationship with the CPT-based geotechnical design, taking pile foundation as an example.

Table 2 Head Deposits (HD)

CPT / BH no.	BH log		CPT log		Correlation level
	Depth bgl(m)	**Soil description**	**Depth bgl(m)**	**Soil description**	
2003	0.5 – 1.8	Firm slightly sandy clay (HD)	0.5 -0.9	Firm clay	**Good**
			0.9-1.2	Stiff clay	**Good**
			1.2- 1.5	Very stiff clay	**Good**
			1.5-1.8	Medium dense sand	**Poor**
2003	1.8 – 3.70	Firm sandy clay (HD)	1.8 – 2.5	Medium dense sand	**Poor**
			2.5 – 3.0	Stiff clayey silt to silty clay	**Good**
			3.0 – 3.7	Very dense gravelly sand	**Poor**
2005	0.35 – 1.90	Firm sandy clay (HD)	0.35 – 1.1	Firm silty clay	**Good**
			1.1 – 1.6	Medium dense silty sand	**Poor**
			1.6 – 1.9	Dense sand	**Poor**
2024	0.3 – 0.50	Firm sandy clay (HD)	0.3 – 0.5	Firm clay	**Good**
2031	0.40 – 1.20	Soft sandy clay (HD)	0.40 – 1.20	Soft to firm clay	**Good**
2031	**1.20 – 1.70**	**Firm slightly sandy clay (HD)**	**1.20 – 1.70**	**Medium dense sand**	**Poor**

Table 3 Terrace Gravel (TG)

CPT / BH no.	BH log		CPT log		Correlation level
	Depth bgl(m)	**Soil description**	**Depth bgl(m)**	**Soil description**	
2003	3.70 – 6.80	Medium dense clayey very sandy gravel (TG)	3.7 – 6.4	Very dense gravelly sand	**Acceptable**
			6.4 – 6.80	Dense silty sand	**Acceptable**
2005	1.9 – 5.7	Medium dense clayey sandy gravel (TG)	1.9 – 4.6	Dense to very dense sand	**Acceptable**
			4.6 – 5.1	Stiff clayey silt to silty clay	**Poor**
			5.1 – 5.7	Medium dense silty sand	**Acceptable**
2024	0.50 – 2.20	Medium very clayey sand (TG)	0.5 – 2.1	Medium dense sand	**Good**
			2.1 – 2.2	Very dense sand	**Good**
2024	2.20 - 4.25	Medium very sandy gravel	2.20 – 4.25	Very dense sand	**Acceptable**
2031	**1.70 – 2.00**	**Loose slightly sandy gravel**	**1.70 – 2.00**	**Soft clay**	**Poor**

Table 4 Glacial Till (GT)

CPT / BH no.	BH log		CPT log		Correlation level
	Depth bgl(m)	**Soil description**	**Depth bgl(m)**	**Soil description**	
2005	5.7 – 13.30	Stiff sandy clay (GT)	5.7 – 6.5	dense to medium dense sand	**Poor**
			6.5 – 7.6	Stiff clay	**Good**
			7.6 – 13.30	Very stiff clay	**Good**
2005	13.30 – 22.0	Stiff clay - becoming very stiff	13.30 – 13.8	Medium dense sandy silt	**Acceptable**

		from 14.50m depth. (GT)	13.8- 16.4	Very stiff clayey silt to silty clay	**Good**
			16.4 – 22.18	Medium dense sandy silt to clayey silt	**Acceptable**
2015	0.3 – 1.1	Firm slightly sandy clay with chalk gravel (GT)	0.3 – 1.1	Firm clay	**Good**
2015	1.1 – 9.25	Stiff slightly sandy clay -with chalk gravel (GT)	1.1 – 2.6	Stiff clay	**Good**
			2.6 – 6.9	Very stiff clayey silt to silty clay	**Acceptable**
			6.9 – 9.25	Medium dense sand to silty sand	**Poor**
2015	9.25 – 20.25	Very stiff slightly sandy clay/silt - with chalk gravel (GT)	9.25 – 12.5	Medium dense sand to silty sand	**Poor**
			12.5-15.0	Loose silty sand to sandy silt	**Good**
			15.0 – 18.8	Medium dense silty sand	**Poor**
			18.8 – 20.25	Very stiff clayey silt to silty clay	**Good**
2017	0.25 – 1.65	Firm slightly sandy clay -with chalk gravel (GT)	0.25 – 0.9	Firm clay	**Good**
			0.9 – 1.65	Soft clay	**Good**
2017	1.65 – 3.70	Stiff slightly sandy clay -with chalk gravel (GT)	1.65 – 3.1	Stiff clay	**Good**
			3.1 – 3.70	**Very stiff clay**	**Good**

Table 5 Oxford Clay

CPT / BH no.	**BH log**		**CPT log**		**Correlation level**
	Depth bgl(m)	**Soil description**	**Depth bgl(m)**	**Soil description**	
2003	6.80 – 25.0	Stiff slightly sandy clay - with little gravel become very stiff from 12m depth. (Oxford Clay)	6.80 – 7.2	Stiff clay	**Good**
			7.2 – 8.6	Stiff silty clay	**Good**
			8.6 – 9.6	Very stiff clayey silt	**Acceptable**
			9.6 – 10.3	Medium dense to dense silty sand	**Poor**
			10.3 – 11.1	Medium dense sandy silt	**Acceptable**
			11.1 - 15	Very stiff clayey silt to silty clay	**Good**
			15 – 16.5	Medium dense sandy clay	**Good**
			16.5 – 20.39	Alternate of very stiff clayey silt and medium dense sandy silt	**Acceptable**
2015	20.25 – 21.0	Very stiff clay (Oxford Clay)	20.25 -21.6	Very stiff clayey silt to silty clay	**Good**
			21.6 – 23.93	Medium dense sandy silt	**Acceptable**
2017	3.70 – 9.80	Stiff Slightly sandy clay (Oxford Clay)	3.70 – 6.1	Stiff clay to silty clay	**Good**
			6.1 – 7.6	Very stiff clayey silt	**Acceptable**
			7.6 – 9.80	Loose to medium dense silt	**Acceptable**

2017	9.80 - 25	Very stiff slightly sandy clay	9.8 – 20.26	Medium dense sandy silt to silty sand	**Poor**
2024	4.25 – 13.0	Stiff clay -with shells fragments (Oxford Clay)	4.25 -8.6	Stiff clay	**Good**
			8.6 – 10.5	Very stiff silt	**Acceptable**
			10.5 – 12.0	Loose to medium dense sandy silt	**Acceptable**
			12.0 – 13.0	Very stiff clayey silt to silty clay	**Good**
2024	13.0 – 25.0	Very stiff clay -with shells fragments	13.0 – 21.0	Medium dense sandy silt to clayey silt	**Acceptable**
2031	2.0 – 7.70	Firm clay -with shells and gypsum.	2.0- 7.70	Firm clay becoming stiff at 4.1	**Good**
2031	7.70 – 15.70	Stiff clay -with shells and gypsum. (Oxford Clay)	7.70 – 12.5	Stiff to Very stiff clayey silt to silty clay	**Good**
			12.50 – 15.70	Loose to medium dense sandy silt	**Acceptable**
2031	**15.70 - 25**	**Very stiff clay - with shells and gypsum**	**15.70 – 20.49**	**Medium dense silty sand.**	**Poor**

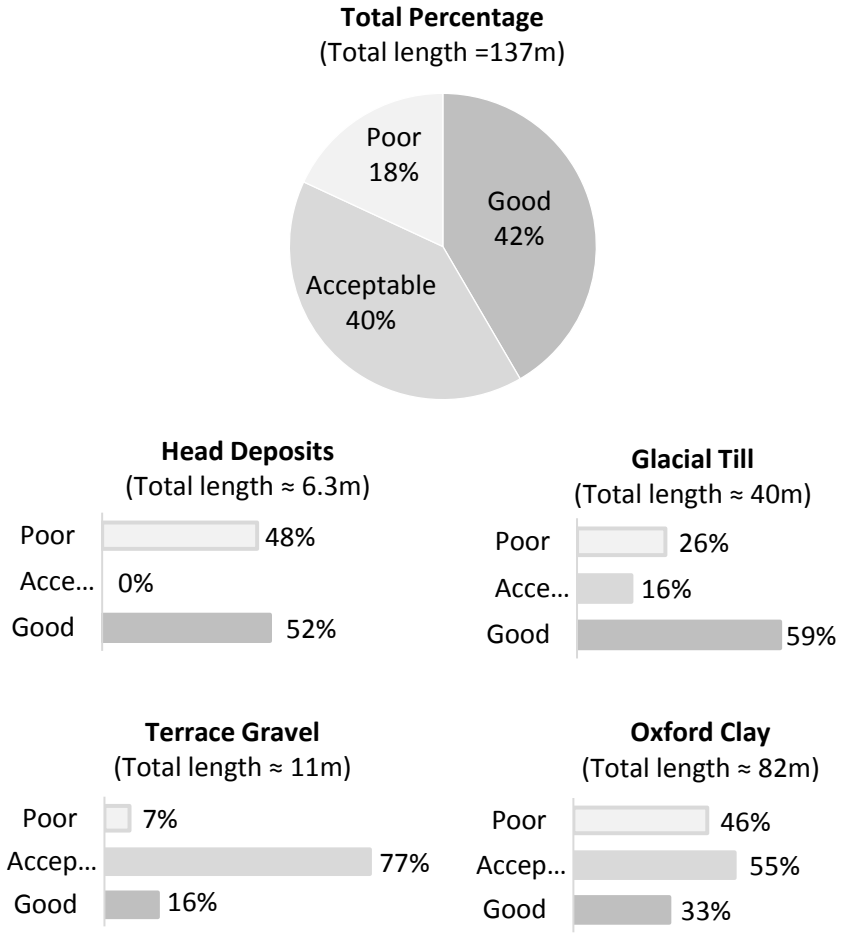


Figure 5 Percentage of the level of agreement between BH-based and CPT-based soil types.

8 PILE DESIGN ANALYSIS –METHOD

To investigate the effect of uncertainty of CPT-based soil type estimation on the geotechnical design of pile foundation (particularly the ultimate bearing capacity of a single axially loaded pile), a typical bored pile is used to evaluate this effect.
CPT results are widely used by geotechnical engineers to predict the ultimate load carrying capacity (Briaud 1988; Eslami & Fellenius, 1997; Price & Wardle, 1982; Titi & Abu-Farsakh, 1999, Tumay & Fakhroo, 1982.). Bored piles are the most common type of non-displacement piles and many design methods have been well established in literature (Poulos & Davis, 1980). The ultimate pile load carrying capacity was calculated in this study applying two analytical methods:

- The first design method was Meyerhof's method (1976) which is based on soil properties conventionally acquired from the BHs and its associated laboratory and in-situ tests.
- The second method of estimating the ultimate pile carrying capacity was based on Bustamante method (LCPC) (Bustamante & Gianeselli, 1982) which is a direct approach that utilizes data on the cone penetration test (CPT).

Both methods represent static analytical approach where the load carrying capacity of the pile consists of two components: shaft tangential resistance Q_s and base compressive resistance Q_b. Thus, the ultimate load-carrying capacity of a pile is given by equation 1.

$$Q_u = Q_b + Q_s \quad (1)$$

The ultimate pile load-carrying capacity obtained by both methods will allow the comparison between BH- based design and CPT-based design, and ultimately any discrepancy between them will be compared with the discrepancy of soil type estimation obtained from CPT and BH (see Figure 1). The assumption used in both pile design methods are summarised in Section 8.1 and 8.2. In both methods the pile was assumed of a plain bored type with circular cross section of a diameter of 0.5m (uniform along the pile length) and a total length of approximately 23m i.e. corresponding to CPTs and BHs depths.

8.1 BHs-based pile design

Using the shear strength parameters obtained from the testing associated with the boreholes (BHs) it is possible to determine the ultimate bearing capacity of a pile using Meyerhof's method (1976) (explained in Braja, 2010):
For cohesive soil:

$$Q_b = 9\, C_u\, A \quad (2)$$

$$Q_s = p\, \Sigma\Delta L\ \alpha\, C_u \quad (3)$$

For granular soil:

$$Q_b = \min\{A\, q'\, Nq;\ 0.5 P_a\, N_q \tan \phi'\} \quad (4)$$

$$Q_s = p\, \Sigma\Delta L\, K\, \sigma_0' \tan \delta' \quad (5)$$

where C_u: undrained cohesion; ϕ': effective soil friction angle of the bearing stratum; p: perimeter of the pile; L: pile length; A: cross section area of the pile; δ': soil-pile friction angle=$2/3\phi'$; K: effective earth pressure coefficient =1- sin ϕ'; σ'_0 : effective vertical stress at the depth under consideration; Nq: bearing capacity factor; its variation with soil friction angle is estimated according to Meyerhof (1976); q': effective vertical stress at the level of the pile tip; P_a: atmospheric pressure =100kN/m2; α: empirical adhesion factor estimated according to Terzaghi, Peck and Mesri (1996).
The multilayer effect on end bearing was ignored.

8.2 CPT-based pile design

According on LCPC method (Bustamante & Gianeselli, 1982), pile ultimate bearing capacity is estimated as:

$$Q_b = A\, k_c\, q_{eq} \quad (6)$$

where k_c= is an empirical end bearing factor that varies from 0.15– 0.60 depending on soil type and installation procedure.

q_{eq} = equivalent average of qc values of zone ranging from 1.5D below pile tip to 1.5D above pile tip, where D is pile diameter.

$$Q_s = p \, \Sigma \Delta L \, f_p \quad (7)$$

where f_p : unit side friction = $q_c / \alpha_S \leq max$
α_S= friction coefficient =30– 200 depending on soil type, pile type and installation procedures.

9 PILE DESIGN ANALYSIS – RESULTS & DISCUSSION

The pile design analysis was carried out using the soil profiles of the 6 boreholes and the adjacent 6 CPTs. To allow comparison between the BH-based & CPT-based design, the results are arranged in couples as presented in Figure 6. Each couple represents the variation of the ultimate bearing capacity Q_u with depth at a single location.
As shown in Figure 6, the Q_u curves exhibited similar trends and general increases with depth. However there were three exceptions (in BH/CPT2003, 2005, and 2024) of sharp increases over relatively short runs, which were found to be coincided with the existence of Terrace Gravel (TG). Granular materials (such as Terrace Gravel) tend to have a base resistance Q_b several times larger than the shaft frictional resistance Q_s.
The maximum agreement between the two sets of results (i.e. BH & CPT based analyses) were found at three locations (BH/CPT 2015, 2017, and 2031), which are referred as "Group A" in Figure 6. However, at the other three locations (BH/CPT2003, 2005, and 2024) the CPT-based pile capacity is remarkably larger than the values obtained from the BH-based analysis. These three locations are referred as "Group B" in Figure 6. It is apparent from this figure the higher divergence in Group B is more pronounced around the location of Terrace Gravel (TG) as the divergence became narrower with depth.
Figure 6 shows also that for Group A, the poor correlation between BHs-based and CPTs-based soil types varied from 0 to 45%. Despite this variation in predicting soil type, the bearing capacity results was consistent. On the contrary in Group B, where the "poor" prediction of soil type varied from 0 to 12% only, the bearing capacity results showed more discrepancy between BH-based analysis and CPT-based analysis. However the discrepancy has a consistent trend and therefore it is very likely to be caused by the different assumptions used in each method

10 CONCLUSIONS

A site investigation trial consisting of 6 boreholes (BHs) and 6 Cone Penetration tests (CPTUs) was conducted in this study to investigate if there is any relationship between the uncertainty of CPT-based soil type estimation and CPT-based pile ultimate bearing capacity estimation.
This study has shown that the soil types established from the boreholes (based on soil samples and classification tests) and from the CPT (based on the original Robertson-1986 chart) appeared to be more similar for the shallow granular geology strata: Terrace Gravel. On the contrary, the CPT-based soil descriptions along the cohesive soils (Head Deposit, Glacial Till and Oxford Clay) divided the geological units in small layers that included great variations in composition (cohesive and granular) and strength/density, this may be due to the nature of soil mixture and the present of some cobbles or shells into the ground. However, the uncertainty in soil type estimation using CPT may be reduced using other chart/ method, which will be part of future work.
This study has also found that the variation in soil type estimation did not show any particular relationship with the pile geotechnical design (ultimate bearing capacity). This finding conforms to previous findings and contributes additional evidence suggesting that the cone responds to the in-situ mechanical behavior of the soil and not directly to soil classification criteria based on grain-size distribution and soil plasticity (Roberson et al, 2012).
The findings of the paper also conform to the perceived applicability of the CPTu for pile design and bearing capacity as highly reliable

(Bond A. and Harris, 2008). However, the reliability rating decreases for settlement and other geotechnical design. Therefore, investigating the relationship between the uncertainty of CPT-based soil type determination and CPT-based pile settlement will be part of future work.

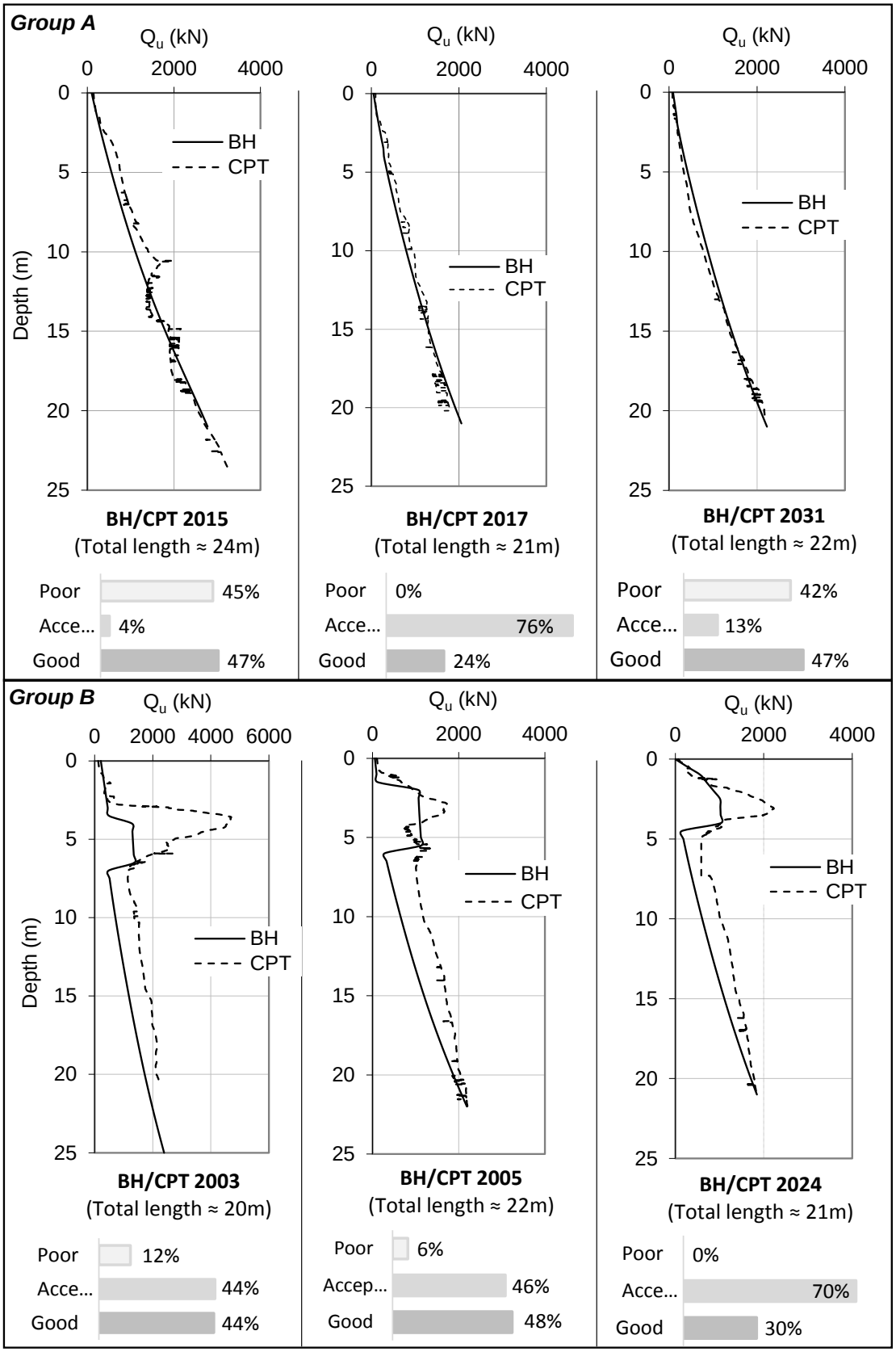


Figure 6 Variation of the predicted ultimate pile capacity (Q_u) with depth at the six locations. The level of agreement of soil type estimation is also added for comparison purposes.

11 ACKNOWLEDGEMENT

The authors gratefully acknowledge the support of the Highways England.

12 REFERENCES

Atkins Ltd, (2009). A14 Ellington to Fen Ditton-Phase 1a: Ground Investigation Report: Section 1. Document reference: 5062774-TE-DO-GEO-606.

Bond, A. & Harris, A. (2008). Decoding Eurocode 7, London: Taylor & Francis, 616pp.

Braja, M.D., (2010). Principle of Foundation Engineering, 7th edn. USA: Cengage Learning.

Briaud, J.L., & Tucker, L. M. (1988). Measured and predicted axial response of 98 piles. J. Geotech. Eng., 114(9), 984–1001.

BS 1377, (1990). Methods of Test for Soils for Civil Engineering Purposes. Part 9: In-situ tests. BSI, London, UK

BS 5930, (1999). Code of practice for site investigations. BSI, London, UK.

Bustamante, M. & Gianeeselli, L. (1982). Pile bearing capacity predictions by means of static penetrometer CPT. Proceedings of the Second European Symposium on Penetration Testing ESOPT-2, Amsterdam, May 24fi27, AA. Balkema, Vol. l.

Eslami, A., & Fellenius, B. H. (1997). Pile capacity by direct CPT and CPTU methods applied to 102 case histories. Can. Geotech. J., 34, 886–904.

Lankelma Ltd (2008). Static Cone Penetration Test. Factual Report. Report Ref Report No: 85071R001EL.

Long, M. (2008). Design parameters from in situ tests in soft ground – recent developments.

Lunne, T., Robertson, P.K. & Powell, J.J.M. (1997). Cone penetration testing in geotechnical practice. UK: Blackie Academic & Professional 1997: 16424. Mayne, PW 2001.

Meigh, A.C., (1987). Cone Penetration Testing - Methods and Interpretation. CIRIA. Butterworths.

Meyerhof, G.G. (1976). Bearing capacity and settlement of pile foundations. ASCE Journal of Geotechnical Engineering. 102(GT3)197-228.

Peck, R. B., Hanson, W. E. & Thornburn, T. H. (1974). Foundations Engineering, 2nd edn. New York, NY: John Wiley and Sons.

Poulos, H. G. & Davis, E. H. (1980). Pile Foundation Analysis and Design. New York: John Wiley.

Price, G., & Wardle, I. F. (1982). A comparison between cone penetration test results and the performance of small diameter instrumented piles in stiff clay. Proceedings of the 2nd European Symposium on Penetration Testing, Amsterdam, The Netherlands, Vol. 2, 775–780.

Proceedings of Geotechnical and Geophysical Site Characterization. Taylor & Francis Group, 89-116.

Robertson, P.K. & Cabal, K. L. (2012). Guide to Cone Penetration Testing for Geotechnical Engineering

Robertson, P.K. (2010). Soil behaviour type from the CPT: an update. 2nd International Symposium on Cone Penetration Testing, CPT'10, Huntington Beach, CA, USA.

Terzaghi, K., Peck, R. B., & Mesri, G. (1996). Soil Mechanics in Engineering Practice, 3rd Edition, Wiley.

Titi, H. H., & Abu-Farsakh, M. Y. (1999). Evaluation of bearing capacity of piles from cone penetration test data. Rep. No. FHWA/ LA.99/334, Louisiana Transportation Research Center, Baton Rouge, La.

Tomlinson, M. J. (2001). Foundation Design and Construction, 7th edn, 569 pages, Upper Saddle River, NJ : Prentice Hall.

Tumay, M. T., & Fakhroo, M. (1982). Friction pile capacity prediction in cohesive soils using electric quasi-static penetration tests. Interim Research Rep. No. 1, Louisiana Department of Transportation and Development, Research and Development Section, Baton Rouge, La.

Zhang, Z., & Tumay, M. T. (1999). Statistical to fuzzy approach toward CPT soil classification. J. Geotech. Geoenviron. Eng., 125(3), 179–186.

Oedometer tests with measurement of internal friction between oedometer ring and clay specimen

M. R. Lodahl
COWI A/S and Aarhus University, Denmark, mirl@cowi.dk / mirl@eng.au.dk

K. K. Sørensen
Aarhus University, Department of Engineering, Denmark

N. Mortensen
nmGeo, Denmark

H. Trankjær
COWI A/S, Denmark

ABSTRACT
The effects of friction in the oedometer cell have been studied in a series of tests carried out in a cell, where the load transferred to the bottom pressure head is measured, and the friction in the oedometer ring is back-calculated. In the test series, both natural and artificial specimens were tested. Based on these tests, the influence of plasticity of the specimen on the friction and the influence of friction on the stiffness parameters have been assessed. It was found that the friction has insignificant effect on the compression index, whereas swelling and recompression stiffness may be influenced. For the derived tangent stiffnesses, particular when the loading is reversed, an overestimation of up to approx. 30 % was found in the tests due to frictional stress loss.

Keywords: Oedometer test; Friction; High-plasticity clays; Deformation parameters

1 INTRODUCTION

Prediction of the future settlements of structures founded on clay is an important part of the geotechnical design. In many countries, the oedometer test is used for estimating the deformation parameters relevant for the particular design situations. An oedometer cell fulfilling the standards usually has a specific height-to-diameter-ratio to minimize the effects of friction between the oedometer ring and the soil specimen. The minimum diameter-to-height ratio required is 2.5, according to many standards, e.g. ASTM D 2435, BS 1377 - part 5 and DS/CEN ISO/TS 17892-5. Development of friction may affect the results, yielding lower compression, swelling and recompression indices, which in turn may cause unsafe settlement and heave predictions, cf. Watabe et al. (2008).

For Danish Palaeogene, high plasticity clays, a very high stiffness ($E_{oed} \geq 50$ MPa) is often reported from oedometer tests for the first load step in unloading and reloading after reversal of the loading direction; cf. (Christensen and Hansen 1959; Krogsbøll et at., 2012). The high stiffness identified may be influenced by the friction between the oedometer ring and the tested specimen. Since the direction and magnitude of the frictional stresses are changed when going from loading to unloading and vice versa, the specimen is 'held in place' by the friction, causing the mean stress change for the specimen to be lower than the stress change at top of the specimen, especially for the fixed ring oedometer setup. This effect may thus cause the high reported stiffness for the first step in un- and reloading.

The development of friction between the oedometer ring and the tested specimen may partly be reduced by using a floating ring setup. In the floating ring setup the oedometer ring is unsupported and carried by the fricti-

on. Thus, the total shear force between the specimen and the ring cannot exceed the weight of the ring. However, it should be noted that the magnitude and direction of the shear stresses may vary over the height of the specimen and the stress state is thus unknown.

To investigate the effect of friction on the compression curves obtained from the oedometer cell, a series of tests was planned and carried out. Two natural and four artificial, reconstituted, preconsolidated specimens with known contents of clay minerals were tested using a custom cell (the nmGeo cell) and a cell based on a NGI DSS-membrane, which is essentially friction free.

The overall aim of the study was to investigate the effects of plasticity on the magnitude of the friction between the specimen and the confining ring, and to investigate the effect of a difference in void ratio and hence compressibility of the tested specimen on the magnitude of developed stress loss due to friction.

2 MATERIALS AND METHODS

When a specimen is installed in an oedometer ring, very low friction is initially maintained between the specimen and the oedometer ring, especially when a polished ring coated with vacuum grease is used, which is suggested by most standards, e.g. ASTM D2435. An illustration of the stress state in an oedometer cell is presented in Figure 1 with vertical stress, σ'_v and horizontal stress, σ'_h. As seen from the figure, the frictional shear stress, $\tau_{\text{ring,}}$ acts upwards during loading and is thus directed downwards during unloading.

The total frictional shear force transferred between the ring and the specimen, F_{ring} is calculated by Eq. (1),

$$F_{\text{ring}} = \int_{A_{\text{ring}}} \tau_{\text{ring}} \qquad (1)$$

where A_{ring} denotes the area of the ring in contact with the specimen. In a fixed-ring setup, the stress loss due to friction means that the vertical load changes with depth in the specimen. The magnitude of frictional

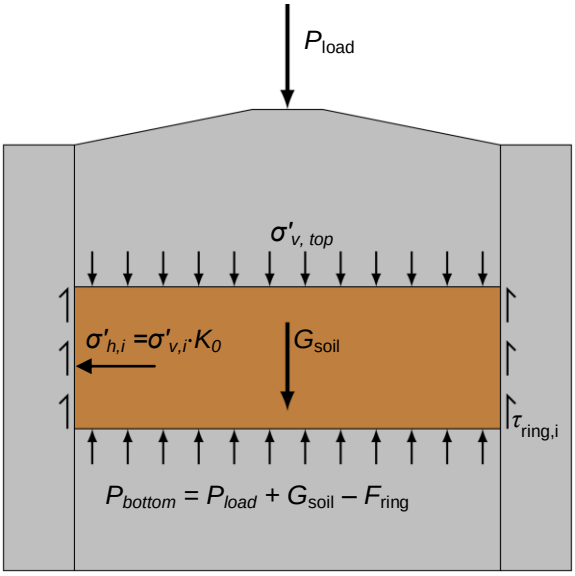


Figure 1: Illustration of stress conditions in the fixed ring oedometer cell (compression stage).

shear stress at end of primary consolidation in depth increment *i* of the height of the ring, is dependent on the horizontal stress in that depth increment, $\sigma'_{h,i}$, and the interface friction angle, $\delta'_{\text{interface}}$, as given in Eq. (2),

$$\tau_{\text{ring},i} = a + K_0 \sigma'_{v,i} \tan(\delta'_{\text{interface}}) \qquad (2)$$

where a is the adhesion. The coefficient of earth pressure at rest, K_0, of the tested specimen is typically assumed to be dependent on the angle of internal friction of the soil, φ', and the overconsolidation ratio, *OCR*, cf. Eq. (3) after Mayne and Kulhawy (1982).

$$K_0 \approx (1 - \sin(\varphi'))OCR^{\sin(\varphi')} \qquad (3)$$

The value of $\delta'_{\text{interface}}$ and adhesion may be somewhat lower than the angle of internal friction and effective cohesion of the specimen, e.g. $\delta'_{\text{interface}} = 0.5\varphi'$ and $a = c'$ was proposed by Lovisa (2014). The dependency of the K_0-value on *OCR* suggest that the effect of friction is most significant when the specimen is in an overconsolidated (OC) stress-regime. Thus, the largest values of friction are expected to occur along unloading and reloading curves in oedometer tests due to larger K_0-values. This claim is supported by the findings of Watabe et al. (2008) in tests on slightly overconsolidated, high plasticity Osaka Bay Clay.

Table 1: Selected classification parameters for the selected core of Little Belt Clay used for testing, cf. Rambøll/Arup JV (2013).

Parameter	Value
Unit weight (kN/m³)	18.1
e_0 (-)	1.23
Clay fraction (%)	~75
σ'_{pc} (kPa)	400-500*

* Values obtained at similar depth on other specimens extracted from Little Belt, cf. Banedanmark, (2013)

2.1 Natural, undisturbed specimens

The tested natural specimens consist of Little Belt Clay, sampled in Little Belt, Denmark. A borehole with full retrieval of cores were drilled approx. 50 m from the first pier on the Funen side of the Little Belt Bridge from 1935. A Geobor-S system with a triple barrel coring device was employed to retrieve the undisturbed cores which were wrapped in cling film and waxed inside a cardboard pipe before storage. Both natural specimens reported in this study origins from borehole 10.A.801, core no. 10-107904, sampled from a depth of 18.0 – 18.6 m below the seabed. The sampled Little Belt Clay is a marine sedimentary, Palaeogene clay and is described as a slightly fissured clay of very high plasticity, slightly calcareous. Selected classification parameters for the core of Little Belt Clay are presented in Table 1.

Two specimens of intact Little Belt Clay (LB001 and LB002) were hand-trimmed to fit the applied oedometer devices. Water content, w, initial void ratios, e_0 and degrees of saturation prior to testing, S_0 are presented in Table 2, along with index parameters, w_L, w_p and I_p determined from the trimmings. The diameter of the tested specimens in the special cell were 60 mm and the height approximately 20 mm, whereas the diameter of the specimens tested in the DSS-membrane cell are 66.8 mm and the specimen height approximately 20 mm.

2.2 Artificial, reconstituted specimens

To analyse the effect of the mineralogical composition of the clay on the magnitude of the developed friction, four tests were carried out using artificial, reconstituted, pre-consolidated clay specimens.

Table 2: Classification parameters and natural water content for the tested specimens.

	w_p (%)	w_L (%)	I_p (%)	w (%)	e_0 (-)	S_0 (%)
LB001	44	182	138	42	1.15	98
LB002	41	180	138	41	1.06	100
K60B40 (x2)	37	177	140	84	2.23-2.45	95-99
K100B0 (x2)	32	59	27	42	1.14-1.16	95-97

The clay specimens were prepared from bentonite and kaolinite powders, mixed in different ratios. In the present paper, the specimens are named after the convention KXXBYY, where the XX signifies the percentage of kaolinite and YY the percentage of bentonite, both determined from dry mass.

The clay powders were mixed with tap water to form a slurry with a water content $w = 1.25w_L$, cf. Burland (1990). The slurry was then installed in Ø70 mm acrylic floating ring consolidometers and preloaded incrementally to a final nominal stress of 163 kPa. The final height of the preconsolidated slurries were sufficient to allow two specimens to be trimmed; one for each oedometer cell. Frictional effects may have developed between the sample and the acrylic tube wall, which may have lowered the actual preconsolidation pressure. However, measures as applying a thin coating of vacuum grease inside the cylinder prior to installation of slurry and moving of the acrylic ring between the load steps were taken to avoid excessive build-up. The classification parameters and water contents for the specimens in the present study are presented in Table 2.

2.3 Oedometer apparatus

An oedometer cell able to measure the accumulated friction between the oedometer ring and the test specimen was developed by nmGeo. This oedometer cell, the nmGeo-cell, is a further development of the oedometer cells developed by Moust Jacobsen, cf. Jacobsen (1970). The cell consists of a very rigid steel ring, a bottom plate, a lower pressure head and an upper pressure head. A force transducer was fitted between the bottom plate and the bottom pressure head, enabling measurements of the force transferred to the bottom pressure head by the soil specimen.

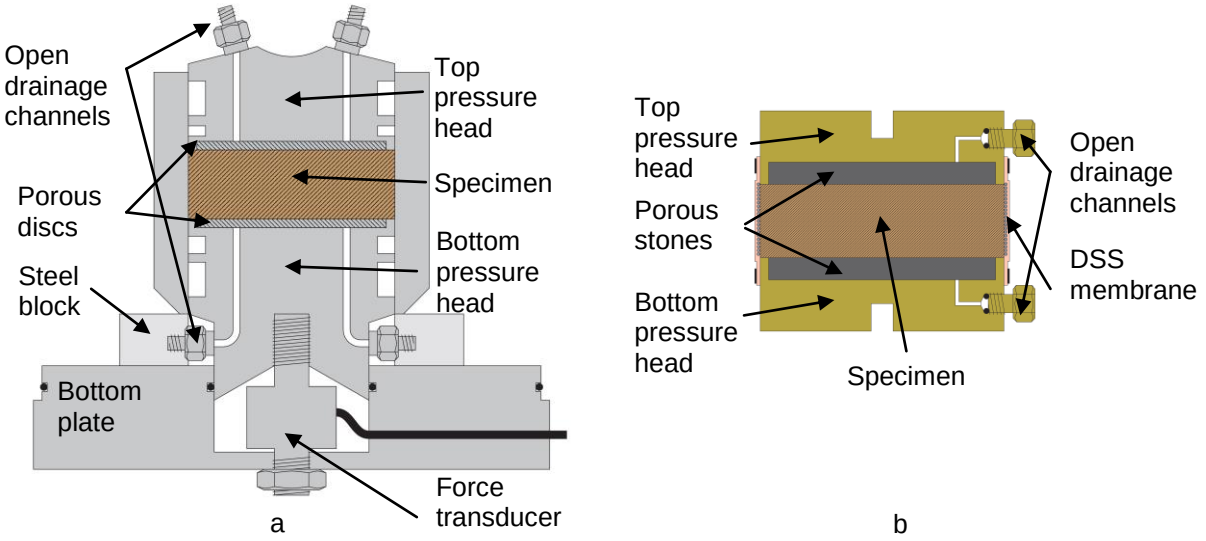


Figure 2: Illustration of the oedometer cells used in the tests presented in this paper. a) the nmGeo-cell and b) the NGI DSS-membrane cell.

Steel blocks and a yoke support the ring to prevent movement of the ring in loading and unloading, respectively, creating a fixed-ring setup. Thus, any difference in the applied total force and the force measured by the force transducer between the bottom plate and the bottom pressure head is caused by frictional loss. A sketch of the nmGeo-cell is presented in Figure 2a.

A NGI DSS membrane cell was used in parallel with the nmGeo-cell (cf. Figure 2b), to obtain results which are almost unaffected by friction between specimen and oedometer ring. In the DSS-cell setup, the 'oedometer ring' consists of a steel-reinforced rubber membrane, which prevents radial expansion of the specimen, but allows axial deformation, cf. NGI (2015). As only vertical loading was applied in the tests, porous stones without spikes were applied.

All oedometer tests were performed as incrementally loaded (IL), 1D compression tests without pore pressure measurements, using double-sided drainage. The Geocomp LoadTrac III loading frame was used during the tests, where the applied load was controlled by a stepper motor based on readings from a S-type load cell. The axial strain was measured by a potentiometric displacement transducer and was corrected for self-deflection of the loading frame measured on a rigid steel disk using the planned load steps. For the nmGeo cell, simultaneous readings of the displacement and the load transferred to the bottom pressure head were recorded during the tests.

Table 3: Concentration of the artificial pore water PC02 used for testing of natural specimens, cf. Rambøll Arup Joint Venture, (2014) and tap water used for artificial specimens, cf. Aarhus Vand A/S, (2015).

	Concentration [mg/l]	
Ion	**PC02 water**	**Tap water**
Cl^-	13500	29
SO_4^{--}	545	48
Na^+	8030	26
K^+	82	3.3
Mg^{++}	235	11
Ca^{++}	405	96

2.4 Test methods

The specimens were loaded incrementally, allowing for full consolidation prior to application of the next load step, avoiding excessively long phases of secondary consolidation. The specimens were installed in the oedometer cells and a seating pressure was applied before the cell water was added during the first load step. No volume change was allowed during the first load step. For the natural specimens the Fehmarn Belt artificial pore water PC02 was used to simulate natural pore water conditions for the specimen, whereas the artificial specimens were tested

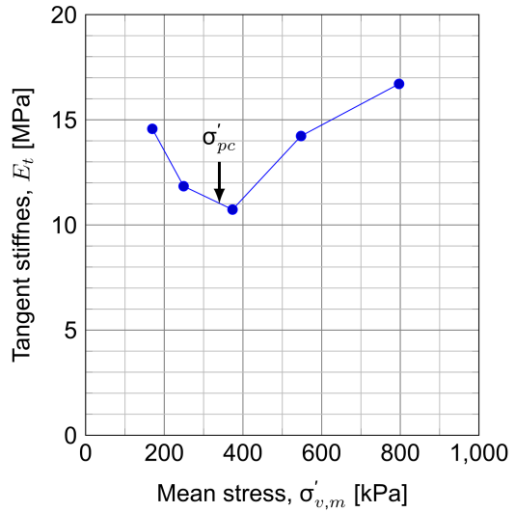


Figure 3: Janbu plot for specimen LB002 with interpreted preconsolidation pressure along the initial loading curve.

using tap water. The ion-concentration of the pore fluids is presented in Table 3.

Due to limitations in the capacity of the DSS-membrane, the maximum load applied to the specimens were limited to 1100 kPa. A load increment ratio of 1.5 was adopted to achieve a closer spacing of the load steps, meaning that the load in a new load step was increased with half of the total load from the previous load step. In unloading the same load steps were applied as in loading. However, during unloading every other load step was skipped for the sake of time as each of the load steps took up to 48 hours to achieve complete consolidation. The obtained time-settlement curves were interpreted using the Casagrandes method, Casagrande (1938). The stress-strain curves were analysed using the theory of both Casagrande (1936) and Janbu (1969) to identify the apparent preconsolidation pressure, σ'_{pc}, cf. Figure 3.

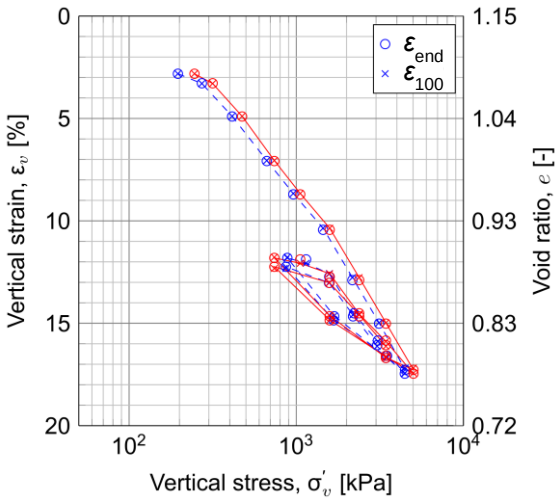


Figure 4: Stress-strain curve for specimen LB001 obtained using the nmGeo-cell. Red line denotes the stress at the top pressure head, whereas the dashed blue lines denotes the stress calculated from the force measured in the bottom plate.

3 RESULTS

The obtained results from the natural specimens are presented in section 3.1, and results from reconstituted, artificial specimens are presented in section 3.2.

3.1 Natural, undisturbed specimens

The specimens, LB001 and LB002 were tested using the nmGeo-cell and the DSS-membrane, respectively. The obtained stress-strain curves are presented in Figure 4 and Figure 5, respectively. As seen from the figures, the maximum obtained stress levels were very different, which was mainly due to the limitation of the DSS membrane. In Figure 4 two stress-strain curves are presented; one linking strains with the applied loading at the top pressure head (as usually done) and one using the measured force below the bottom pressure head. Both stress readings were plotted with the same measured axial strain. As seen from the figure, an offset is present between the two curves, illustrating the magnitude of friction developed during testing. As seen from Figure 4 the points plotted using the measured values of the stress at the bottom

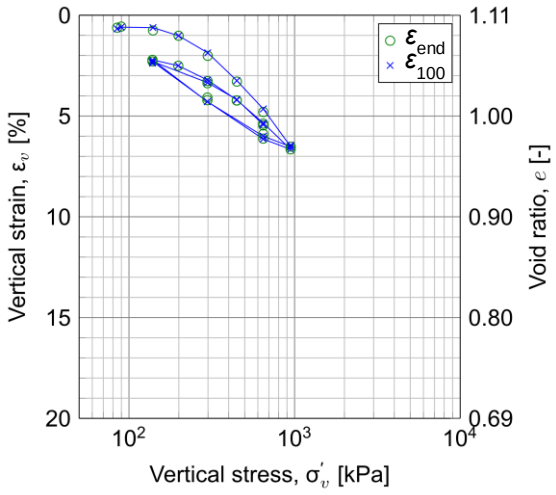


Figure 5: Stress-strain curve for specimen LB002 tested with the DSS-membrane cell.

Table 4: Stiffness parameters determined for tests on intact Little Belt Clay and on artificial mixtures.

Parameter	LB001 nmGeo	LB002 DSS	K100B0 DSS	K100B0 nmGeo*	K60B40 DSS	K60B40 nmGeo	Stress range (σ'_v)
C_C [-]	0.25	0.26	0.32	0.45	1.35	1.30	LB001: 300 – 5000 kPa LB002: 300 – 950 kPa Artificial: 150 – 1000 kPa
C_S [-]	0.15	0.14	0.05	0.08	0.33	0.25	LB001: 5000 – 750 kPa LB002: 950 – 140 kPa Artificial: 700 – 70 kPa
C_R [-]	0.18	0.16	0.07	0.09	0.47	0.29	LB001: 1050 – 5000 kPa LB002: 200 – 950 kPa Artificial: 100 – 700 kPa

* Significant soil loss observed after testing.

pressure head plotted to the left of the points plotted with the values of applied loading and vice versa when in unloading, i.e. the direction of the friction is as stated in section 2.
The stiffness parameters determined from the oedometer tests are presented in Table 4 and preconsolidation pressures in Table 5.

The obtained C_C values are in the lower range compared to values obtained by Sørensen and Okkels (2015), who suggested C_C = 0.25 – 0.65 for I_p = 140 % based on $\sigma'_v \geq$ 5000 kPa, which was expected due the lower stress levels applied in the current tests.

3.2 Artificial, reconstituted specimens

The obtained stress-strain curves for the artificial specimens are presented in Figure 6 to Figure 9. The K60B40 specimens had same plasticity index, I_p as the natural Little Belt clay, cf. Table 2. However, the obtained compression indices were larger for reconstituted specimens compared to natural specimens which may be have been due to differences in structure, pore fluid salinity, etc.

As seen from the stress-strain curves obtained with the nmGeo-cell (Figures 6 and 8), the friction acted in the opposite direction of the load change as for intact specimens, except for first step in unloading and reloading. The derived stiffness parameters are presented in Table 4 and σ'_{pc}-values in Table 5.

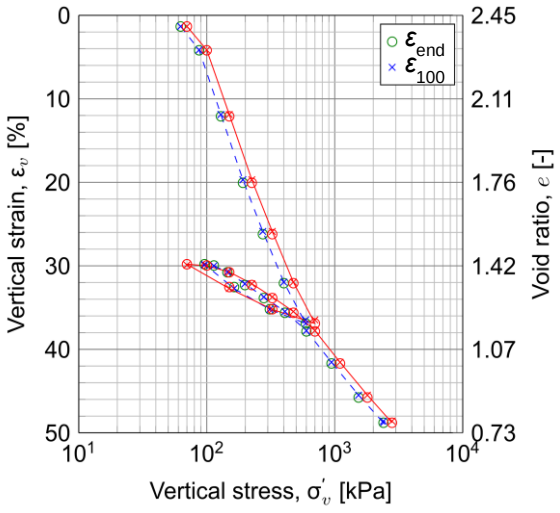


Figure 6: Stress-strain curve for a K60B40 specimen tested in the nmGeo cell. Red line denotes the stress at the top of the specimen, and dashed blue lines the stress at bottom of the specimen.

4 DISCUSSION

The friction acted in the opposite direction of the applied load increment, which is why the stress at the bottom pressure head was small when the specimen was in loading and vice versa when in unloading. In the individual tests, the difference between the top and the bottom stress (in %) was rather constant on the primary compression curve (e.g. Figure

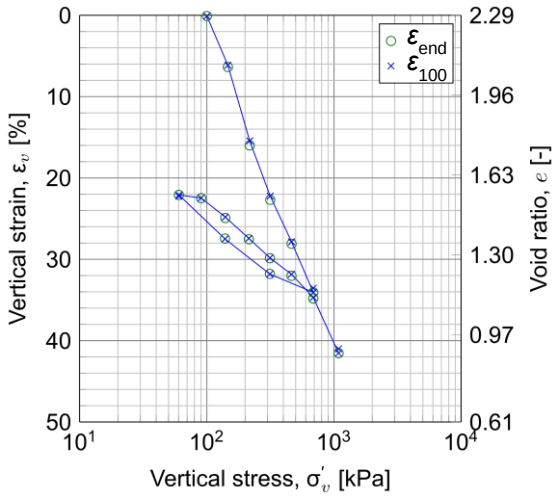


Figure 7: Stress-strain curve for a K60B40 specimen tested in the DSS-membrane cell.

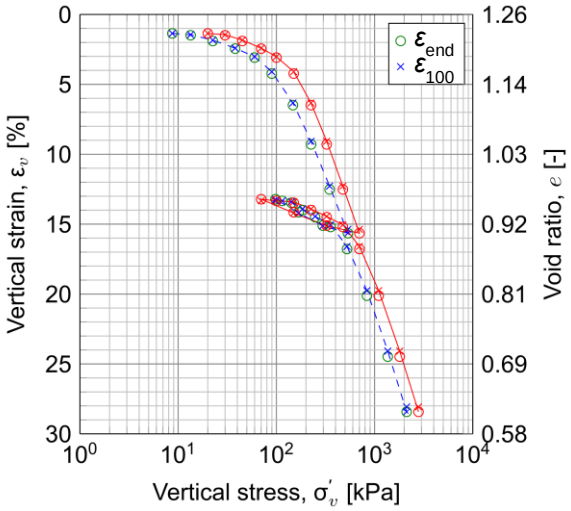


Figure 8: Stress-strain curve for a K100B0 specimen tested in the nmGeo cell. Red line denotes the stress at the top of the specimen, and dashed blue lines the stress at bottom of the specimen.

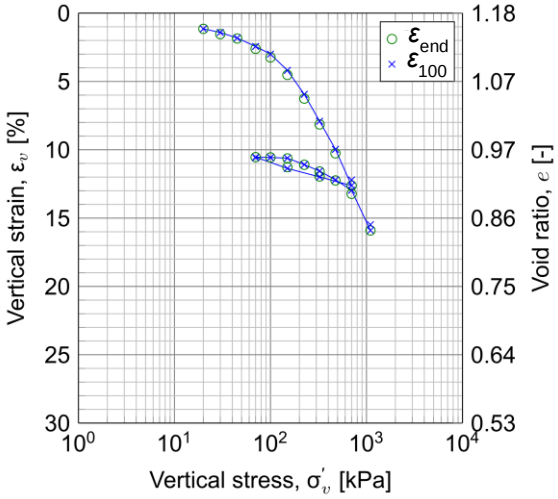


Figure 9: Stress-strain curve for a K100B0 specimen tested in the DSS-membrane cell.

8), which is why practically no influence was seen on the compression indices obtained using the nmGeo cell and the NGI DSS cell, cf. Table 4.

However, when the loading was reversed, the actual stress change was smaller than expected, which is why the swelling and recompression index identified for the first load steps when reversing the load direction may be very wrong. For all the tests performed in the nmGeo-cell, the loss (in %) of vertical stress due to friction between the specimen and the oedometer ring is plotted against the applied stress, cf. Figure 10. As seen from the figure, the stress loss due to friction was rather constant (in %) for normally consolidated (NC) load steps, as may also be inferred from the compression curves. The curve in Figure 10 for the specimen of pure kaolinite K100B0, suggests a very large friction during initial loading, which may be linked with the observed loss of soil during testing (liquefied soil residue was found on top of the upper pressure head after testing. This residue had been squeezed out between the ring and the upper pressure head). Generally, when in unloading, the friction increased and hence the stress loss increased for all specimens. As

Table 5: Apparent preconsolidation pressures σ'_{pc} determined for tests on intact Little Belt Clay and on artificial mixtures. For the nmGeo cell (T) designates measurement from top pressure head and (B) bottom presssure head.

Stage	Parameter	LB001 nmGeo	LB002 DSS	K100B0		K60B40	
				DSS	nmGeo	DSS	nmGeo
Initial loading	**σ'_{pc} [kPa]** Casagrande	*	260	150	190 (T) 130 (B)	~100	70 (T) 80 (B)
	σ'_{pc} [kPa] Janbu	*	340	140	180 (T) 110 (B)	~150	110 (T) 100 (B)
	Past σ'_{max} [kPa]	>3000 (geological)		163 (preconsolidation of slurry)			
1. reloading	**σ'_{pc} [kPa]** Casagrande	1660 (T) 1490 (B)	325	570	700 (T) 490 (B)	130	270 (T) 350 (B)
	σ'_{pc} [kPa] Janbu	1700 (T) 1550 (B)	365	280‡	670 (T) 440 (B)	130	190 (T) 160 (B)
	Past $\sigma'_{max,lab}$ [kPa]	5020 (T) 4480 (B)	946	694	700 (T) 534 (B)	688	700 (T) 593 (B)

* Not identified due to lack of load steps below σ'_{pc}.

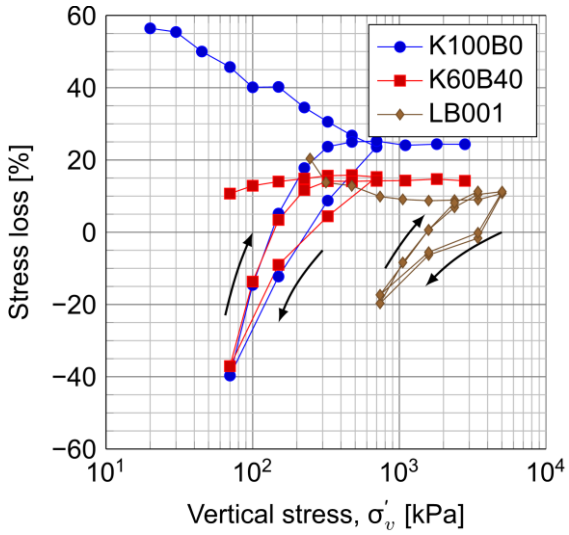


Figure 10: Illustration of stress loss during testing for all specimens tested in the nmGeo cell.

seen from Figure 10 a maximum of 20 % and 40 % stress loss was obtained for the natural and artificial specimens, respectively, for the final unloading step.

4.1 Natural vs. reconstituted specimens

Comparing the tests on natural, intact Little Belt clay with the tests on artificial, reconstituted K60B40, a large difference in compression potentials was seen, even as both specimens had the same plasticity index, I_p, cf. Figure 4 and Figure 5 versus Figure 6 and Figure 7. This was expected as the artificial specimens lacked the natural structure found in the intact clays. As seen from Table 4, the effect the natural structure on the compression index was rather significant. However, no significant difference on the magnitude of measured friction in NC range was found in the tests, when results from LB001 and K60B40 were compared, cf. Figure 10. However, it is unknown whether the difference in stress loss for the final load step in unloading was observed due to the difference in the initial structure of the specimens.

4.2 Influence of plasticity

As seen from Figure 10 the stress loss (in %) for the NC load steps in the stress-strain curves tended to be constant, yielding an unique value for the individual specimens. As seen from the figure, the specimen of pure kaolinite (K100B0) yielded higher stress loss (≈ 25 % loss in the NC regime) compared to specimens of higher plasticity (K60B04 and LB-001) where 10 – 15 % loss was identified. This effect may be explained from a lower angle of internal friction for the high plasticity specimens. Generally a decreasing angle of internal friction, φ' has been reported with increasing plasticity, e.g. by Sørensen and Okkels (2013) for Palaeogene clays of high plasticity ($I_p \geq 50$ %), incl. Little Belt Clay. From a low φ' follows a low $\delta'_{\text{interface}}$ between the oedometer ring and the soil specimen, which in turn limits the magnitude of stress transfer (even as K_0 increases). φ'_{peak} was found to be approximately 26° for kaolinite cf. Terzaghi et al. (1996), and a $\varphi'_{peak} \approx 17°$ may be calculated from Eq. 6 in Sørensen and Okkels (2013) for Little Belt clay and K60B40.

Table 5: Calculated and measured stress loss in NC and OC stress regime using a = 0 kPa.

	NC		OC*	
	Calc. †	**Meas.**	**Calc.** †	**Meas.**
K100B0	14 %	24 %	40 %	39 %
K60B40	9 %	14 %	20 %	37 %
LB001	14 %	10 %	23 %	20 %

* *OCR* = 10 for artificial specimens and *OCR* = 6.8 for Little Belt specimen.
† Actual height of the specimen during testing is used for calculating contact area of ring and soil.

From Eq. (1) - (3) the expected stress loss due to friction was calculated based on the φ' suggested above for the specimens. A comparison of the measured and the calculated stress loss due to friction is presented in Table 5. As seen from the table the calculated loss for NC conditions was much lower than what was observed in the K100B0 test, whereas the values for OC conditions were very close. For the K60B40 specimen, the calculated value for NC conditions was quite close to what was measured during the test, whereas the value for OC conditions was much below the measured value. For the Little Belt Clay both calculated values were in good correspondence with what was observed in the tests. Using the actual adhesion of the tested specimens, may introduce a better correspondence between the calculated and the observed results. However, as a was unknown for the specimens, a = 0 kPa was assumed in the presented calculations.

For $OCR \geq 1$ no plateau was identified in any tests as seen for the NC regime, cf.

Figure 10. However, it remains unknown whether the observed development of the frictional stress loss was due to the reversal of direction of the shear stresses between specimen and ring, or the change in K_0 during loading. Possibly both effects were at play.

4.3 Determination of oedometer stiffness

As the stress loss from friction influenced the obtained mean stress subjected to the tested specimens, the oedometer modulus that can be calculated from the oedometer test was affected. In Figure 11 the calculated oedometer stiffness, E_{oed} for specimen K60B40 is presented for the reloading phase. E_{oed} was calculated based on the stress at the top of the specimen, σ'_{top} and on the average value of the stress at the top and the bottom of the specimen, σ'_{avg}. σ'_{avg} was expected to be the closest representation of the actual behaviour of the tested specimen. As seen from the figure, the influence of the stress loss on the measured stiffness was most radical in the beginning of the reloading phase where a 26 % too large E_{oed} was calculated, if σ'_{top} was used as reference, whereas the error was smaller for the rest of the load steps. For the final three load steps E_{oed} increased linearly with σ'_v as known from Janbus (1969) framework. The modulus number, m, seemed not to be influenced by the frictional stress loss.

For the specimens K100B0 and LB001, the same tendencies were observed; a clear overestimation of E_{oed} (28 % for K100B0 and 10 % for LB001) in the first reloading step and a similar m calculated from σ'_{top} and σ'_{avg} for the final NC load steps. As may be observed from Figure 11, the friction affected both the stiffness and the applied stresses and hence both values should be corrected. However, from all the tests a high initial stiffness was identified for the first step in reloading.

4.4 Preconsolidation pressure in reloading

An interesting characteristic of both the Little Belt Clay and the K60B40 specimens is the low σ'_{pc} identified along the recompression curve from the test, despite having been subjected to a much higher stress level, cf. Figures 4 and 6 and Table 5. This effect has been presented as a 'lack of stress memory' of

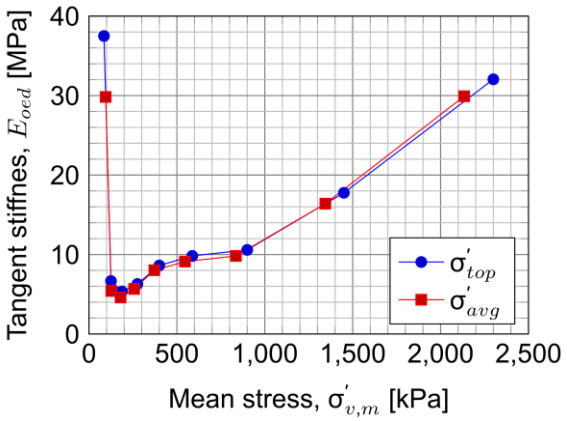


Figure 11: Calculated oedometer stiffness, E_{oed} for specimen K60B40.

the Danish Palaeogene clays cf. (Krogsbøll et al., 2012 and Mortensen, 2012). As this effect was found for the specimens with the highest content of smectite and thus the highest plasticity (Little Belt Clay and K60B40), it may be assumed that the high content of smectite in the natural Palaeogene clays is responsible for this observed behaviour. The content of smectite may thus be the cause of the gradual yield as suggested by Lodahl and Sørensen (2015).

4.5 Limitations of conducted tests

The behaviour of the tested specimen will depend on a stress level located between the applied load and measured load. However, as the distribution of the frictional forces was not known over the height of the ring, the exact value cannot be found. A simple mean value has been used in the present paper which was expected to be sufficiently accurate.

5 CONCLUSION

The tests presented in this paper focused on the development of interface friction between the oedometer ring and the test specimen for a fixed-ring setup. Three specimens were tested in the nmGeo cell, where the stress lost due to friction were measured below the lower pressure head, and three in the NGI DSS-membrane cell, which is essentially friction free due to the ability of the membrane to deform. The stress loss observed in the tests was compared with theoretical estimations for NC and OC conditions.

From the conducted oedometer tests a constant stress loss due to friction (in %) was observed for NC load steps. Thus, the effect on the deformation parameter, C_C, was small due to the logarithmic stress axis. However, when assessing the recompression index, C_R the effect of friction caused the apparent stiffness to be too large, as the unloading stress sustained by the specimen was larger than the top stress (up to 40 % loss). Calculating E_{oed} for first reloading step yielded an overestimation of 26 – 28 % for artificial specimens and 10 % for the natural specimen. Thus, the frictional effects may cause excessively high stiffness if not accounted for. However, it should be kept in mind that the applied stress was underestimated for the first load steps on the recompression branch.

An effect of the plasticity was found in the tests, where specimens of lower plasticity yielded higher frictional losses compared to the specimens of higher plasticity. This effect may be explained by the lower angle of internal friction of the high plasticity specimens. The lower angle of internal friction causes a lower $\delta'_{\text{interface}}$-value and thus lower interface friction even as K_0 increases.

6 ACKNOWLEDGEMENTS

Banedanmark is acknowledged for allowing the use of the intact samples from Little Belt.

A series of preliminary tests were performed at NGI, Oslo using both the nmGeo cell and the DSS-membrane cell. The first author is very grateful for valuable advices and the fruitful environment during his stay in the lab at NGI. The willingness of NGI to share experience, help and equipment is greatly appreciated.

The technical director of nmGeo is acknowledged for lending the nmGeo-cell to be used in the present research.

All conclusions presented in this paper is the responsibility of the authors and does not necessarily reflect the opinions of the bodies mentioned above.

7 REFERENCES

Aarhus Vand (2015). Bederværket, Udvidet control, personal correspondence.

Banedanmark (2013). Stability of the Bridge Piers of the Little Belt Bridge – Cover Report on the Work of the Geotechnical Expert Panel.

Burland, J.B. (1990). On the compressibility and shear strength of natural clays, Géotechnique 40(3), 329-378. DOI: 10.1680/geot.1990.40.3.329.

Casagrande, A. (1936). Determination of the preconsolidation load and its practical significance. 1st ICSMFE, 3(D-34), 60-64.

Casagrande, A. (1938). Notes on Soil Mechanics – First Semester" Harvard University (unpublished), Cambridge MA. As cited by (Holtz et al, 2011).

Christensen, N.H. & Hansen, B. (1959). Shear strength properties of Skive septarian clay. DGI bulletin No. 7.

Holtz, R.D., Kovacs, W.D. & Sheahan, T.C. (2011). Introduction to Geotechnical Engineering, Pearson, ISBN: 9780137011322.

Jacobsen, M. (1970). New oedometer and new triaxial apparatus for firm soils. DGI bulletin No. 27.

Janbu, N. (1969). The resistance concept applied to deformations of soils. Proc. 7th ICSMFE, 191-196.

Krogsbøll, A., Hededal, O. & Foged, N. (2012). Deformation properties of highly plastic fissured Palaeogene clay – Lack of stress memory? 16th NGM (DGF-Bulletin 27), 133-140.

Lodahl, M.R. and Sørensen, K.K. (2015). Influence of smectite content on the one-dimensional deformation behaviour of reconstituted high plasticity clays, 6th ISDCG, Argentina, 1057-1064. DOI: 10.3233/978-1-61499-601-9-1057

Lovisa, J. and Sivakugan, N. (2014). Tall Oedometer testing: Method to account for Wall Friction. International Journal of Geomechanics, 15(2), DOI: 10.1061/(ASCE)GM.1943-5622.0000359.

Mayne, P.W. and Kulhawy, F.H. (1982). K_0-OCR relationships in soil. J. Geotech. Eng. Div. ASCE, GT6, 851-872

Mortensen, N. (2012). High plasticity Palaeogene clay; A soil type with a very moderate long-term memory. 16th NGM (DGF-Bulletin 27), 413-420.

NGI (2015). Direct simple shear test – DSS. http://www.kortlink.dk/ngi/kcpk (Accessed 30.10.15)

Rambøll Arup Joint Venture (2014). Ground investigation report. Volume 1 and 2 of 2. Femern-doc GDR 00.1-001, 2013.

Sørensen, K.K. and Okkels, N. (2015). Correlations between compression index and index parameters for high plasticity Palaeogene clays. 16th ECSMGE. 3371-3376.

Sørensen, K.K. and Okkels, N. (2013). Correlations between drained shear strength and plasticity index of undisturbed overconsolidated clays. 18th ICSMGE, 423-428.

Terzaghi, K., Peck, R.B. & Mesri, G. (1996). Soil Mechanics in Engineering Practice. Third Edition. John Wiley & Sons. ISBN 9780471086581.

Watabe Y., Udaka, K., Kobayashi, M., Tabata, T. & Emura, T. (2008). Effects of friction and thickness on long-term consolidation behaviour of Osaka bay clays. Soils and Foundations, 48(4), 547-561.

Correlations between shear wave velocity and geotechnical parameters in Norwegian clays

J. S. L'Heureux
Norwegian Geotechnical Institute (NGI), Norway, jsl@ngi.no

M. Long
University College Dublin, School of Civil Engineering, Ireland

ABSTRACT
The purpose of this paper is to present guidelines and correlations to assists geotechnical engineers in estimating V_s profiles in Norwegian clays in the absence of site-specific data. For this, a database of in situ V_s measurements and standard geotechnical engineering material properties for Norwegian clays has been established. The database allowed the development of several empirical correlations between in situ V_s and basic soil properties, cone penetration parameters, undrained shear strength and 1D compression parameters. Based on the results from regression analyses, empirical functions based on cone penetrometer data to determine the best estimate in situ V_s of Norwegian clay are recommended to use when in situ measurements of V_s at the site are not available. Relationships based on undrained shear strength can also be used in practice as presented herein.

Keywords: *In situ* shear wave velocity, clay, undrained strength, compression parameters.

1 INTRODUCTION

The small-strain shear modulus of soils, G_{max}, is an important parameter for many geotechnical design applications, including site characterization, settlement analyses, seismic hazard analyses, site response analysis and soil-structure interaction. This is typically associated with strains on the order of 10^{-3}% or less. According to elastic theory, G_{max} may be calculated from the shear wave velocity (V_s) using the following equation:

$$G_{max} = \rho \cdot V_s^2 \quad (1)$$

Where G_{max} is the shear modulus (in Pa), V_s is the shear wave velocity (in m/s), and ρ is the density (in kg/m^3).

G_{max} and V_s are primarily functions of soil density, void ratio, and effective stress, with secondary influences including soil type, age, depositional environment, cementation and stress history Hardin and Drnevich (1972).

G_{max} can be measured in the laboratory using a resonant column device or bender elements. As suggested by Kramer (1996), while the void ratio and stress conditions can be recreated in a reconstituted specimen, other factors such as soil fabric and cementation cannot. Laboratory testing requires very high-quality, undisturbed samples which is often a challenging and expensive task in soft and sensitive clays. Additionally, laboratory tests only measure G_{max} at discrete sample locations, which may not be representative of the entire soil profile.

Unlike laboratory testing, in situ geophysical tests do not require undisturbed sampling, maintain *in situ* stresses during testing, and measure the response of a large volume of soil. *In situ* measurement of V_s has become the preferred method for estimating the small strain shear properties and has been incorporated into site classifications systems and

ground motion prediction equations worldwide.

In the absence of site-specific measurement, guidelines for estimating V_s profiles based on correlations with *in situ* penetration tests, soil index parameters and undrained shear strength may be used, recognizing that these indirect methods introduce greater uncertainties. The main objective of this paper is to present such guidelines for estimation of V_s in Norwegian clays.

2 DATA AND METHODS

The data used for correlation purposes originates from a total of 29 sites (Fig. 1). Out of these sites, 15 are located in south-eastern Norway while 13 are in mid Norway. The last site included in the database is the Bothkennar clay site in Scotland where much work has been carried out over the last 30 years (including testing of block samples by NGI), see for example Long et al. (2008). The reader is referred to NGI (2015) for a detailed overview of all sites in the database.

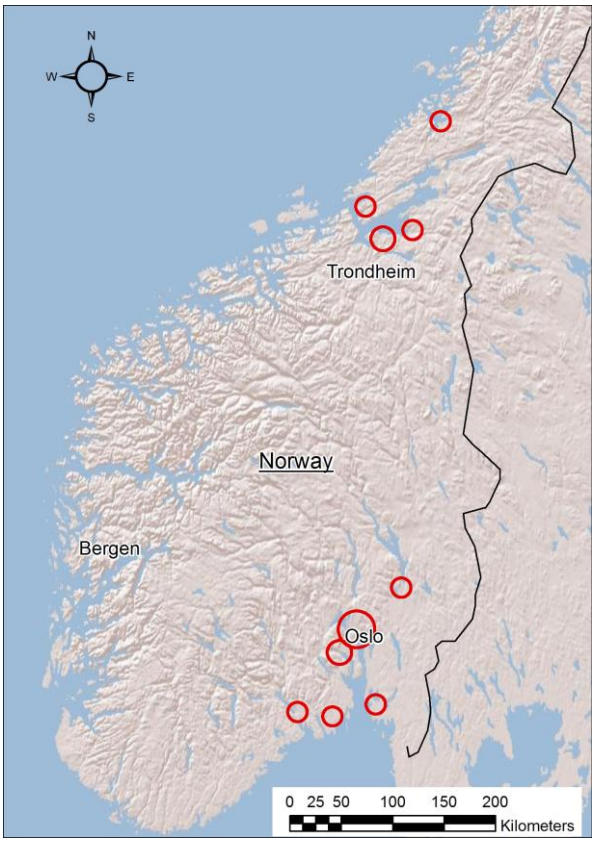


Figure 1 Overview map showing location of study sites included in database.

2.1 Measurement of in situ V_s

In situ V_s measurement was carried out at several Norwegian clay sites during the last decades for research purposes and/or as a part of construction projects. Source of existing data includes e.g. papers by Long and Donohue (2007) and Long and Donohue (2010), L'Heureux et al. (2013). In the present study previously published information was assemble with new field data. The *in situ* V_s data was acquired at most of the sites using the non-invasive method called multichannel analysis of surface wave (MASW). In addition comparative *in situ* V_s data was collected using the seismic cone penetrometer (SCPTU; 7 sites), cross-hole test (CHT; 5 sites) and spectral analysis of surface wave (SASW; 4 sites).

2.2 Available soil properties

The compiled database contains index and engineering properties obtained from classification tests, strength tests and consolidation tests. The database includes index properties such as total unit weight, water content, clay content, remoulded shear strength, sensitivity and Atterberg limits. Also, engineering properties such as undrained shear strength (s_u), net cone resistance (q_{net}), *in situ* effective vertical stress (σ'_{v0}) and 1D compression parameters were available to this study. Only data from high quality samples is used in this study (c.f. Lunne et al. 1998).

The Norwegian clays in the database are of marine or glacimarine origin. Natural water content (w) data range between 20 and 80% with most of the data in the range between 40 to 50% (Fig. 2). The plastic index (I_p) being defined as the difference between the liquid and plastic limits is presented in Fig. 3. Most of the plasticity index data vary between 5 and 20%. The clay content of the soil tested ranges from 10 to 70% with most of the data in the range between 30 to 50% (Fig. 4). The effective vertical stress in the database varies between 10 and 240 kPa with the highest number of observations at around

100 kPa corresponding to a depth of approximately 6-8 m below ground surface.

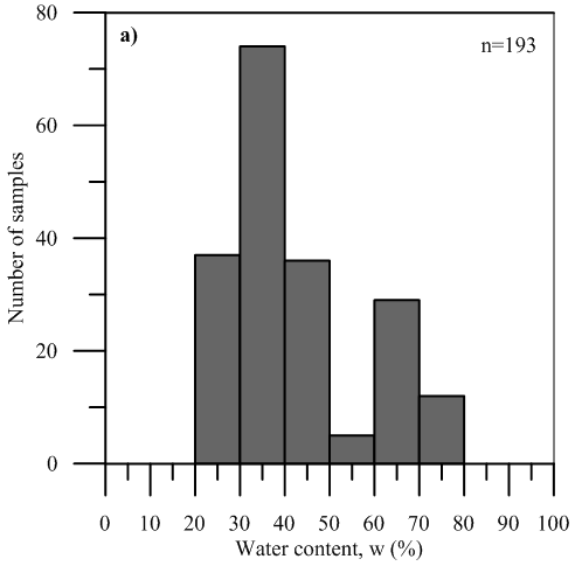


Figure 2 Range of water content in the database.

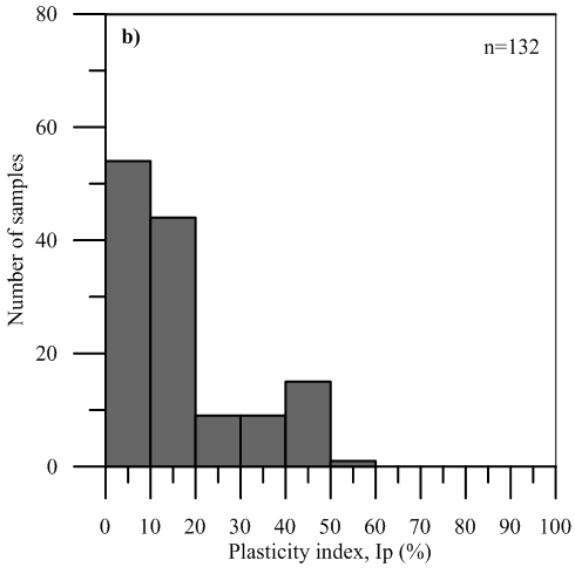


Figure 3 Range of I_p in the database.

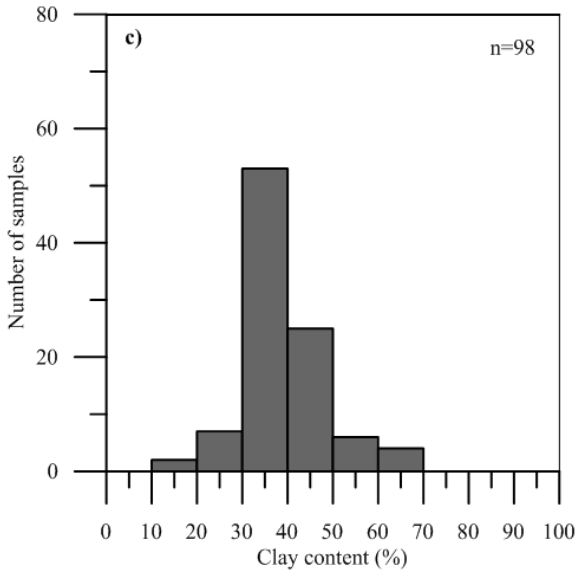


Figure 4 Range of clay content in the database.

Most of the clays in the database have developed some apparent overconsolidation due to aging. The overconsolidation ratio (OCR) data range between 1.0 and 8 with most of the OCR data falling between 1.5 and 2.0, indicating that most of the soil samples in the database are normally consolidated to lightly over-consolidated. Hence, the developed correlations below may not be valid for moderately to heavily overconsolidated clays.

The *in situ* shear wave velocity (V_s) data range between 50 and 300 m/s with the majority of the data between 120 and 250 m/s (Fig. 5). With the exception of Onsøy and Farriseidet the data follows a very similar depth pattern. V_s values are typically 120 m/s at ground level and increase to 180 m/s and 200 m/s at 10 m depth and 12 m depth respectively. The very soft high water content organic clays at Onsøy and especially Farriseidet show much lower values of V_s.

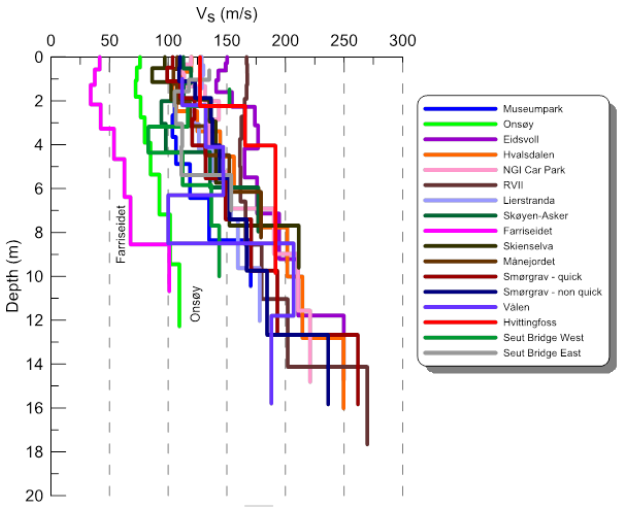


Figure 5 In situ shear wave velocity profile for sites in Southern Norway.

Shear wave velocity data for the Trondheim area in mid Norway are shown on Fig. 6. Broadly speaking the data can be divided into two groups. The main group show similar values to those from Southern Norway with V_s increasing from about 100 m/s at ground level to 200 m/s at about 12 m depth. There is a second group of sites all located in south and south-west Trondheim (comprising the Rosten, Saupstad, Okstad and Hoseith sites) with higher values. Here the V_s values reach 300 m/s at 10 m to 12 m. The very soft clay at Dragvoll show the lowest values on average. Generally it can be seen that all the Trondheim data fits with those from South Norway except for the Rosten (high OCR at the bottom of slope), Hoseith and Okstad sites.

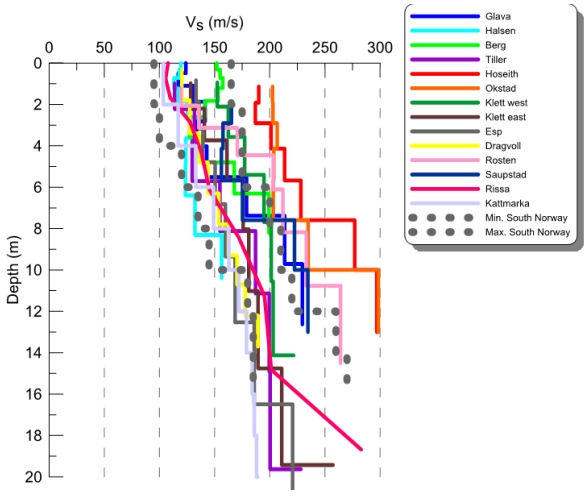


Figure 6 In situ shear wave velocity profile for sites in the Trondheim region.

3 CORRELATION WITH INDEX PROPERTIES

Correlations between index parameters and V_s or G_{max} can provide rapid estimates useful for preliminary design and for verifying *in situ* and laboratory results. Hardin (1978) suggested that G_{max} for clays depends on the *in situ* (or applied) stress (σ'), void ratio (e), and OCR. It has been shown, however, that the effects of OCR are, to a large extent, taken into account by the effect of void ratio and could be neglected, see for example (Leroueil and Hight, 2003). The empirical equation describing the influence of the controlling factors on G_{max} can then be written as follows:

$$G_{max} = SF(e)(\sigma_v' \sigma_h')^n p_a^{(1-2n)} \quad (2)$$

Where S is a dimensionless parameter characterizing the considered soil; $F(e)$ is a void ratio function; σ'_v and σ'_h are the vertical and horizontal effective stresses, respectively; n is a parameter indicating the influence of stress; and p_a is the atmospheric pressure.

Figure 7 presents the relationship between V_s and σ'_{v0} for all sites in the database. Results show a clear tendency for V_s to increase with σ'_{v0}. The best fit equation for the data gives a regression coefficient of 0.68.

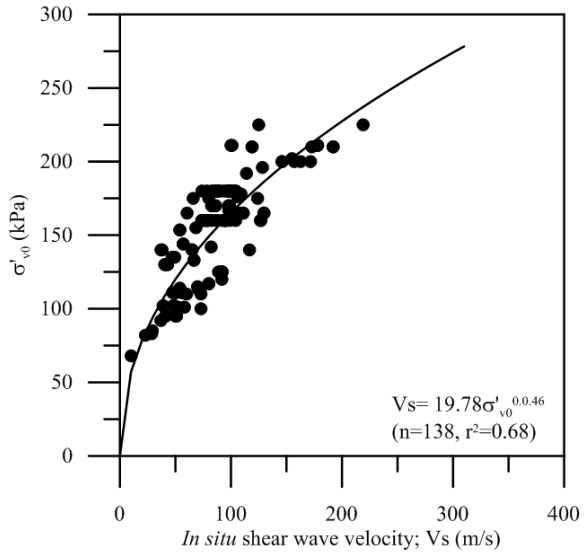


Figure 7 In situ V_s against vertical effective stress for all sites in the database.

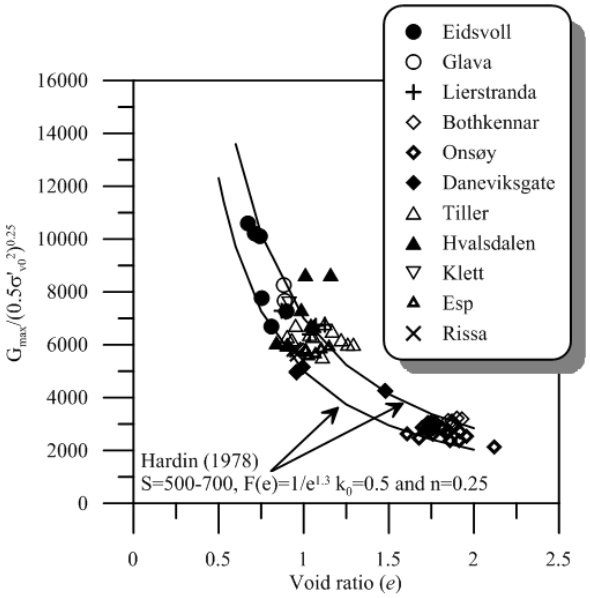


Figure 8 Relationship between G_{max} normalized according to Hardin (1978) and Hight and Leroueil (2003) and e.

The void ratio in the database was calculated using:

$$e_0 = \frac{G_s\,\gamma_{w\,(1+w)}}{\gamma_{tot}} - 1 \qquad (3)$$

Where G_s is the specific gravity of soil solids, γ_w is the unit weight of water, *w* the water content, and γ_{tot} the total unit weight of the soil. G_{max} values were normalized by the corresponding *in situ* vertical effective stress (σ'_{v0}). G_{max}/σ'_{v0} typically varies between 250 and 1000 in the database.

In Figure 8 the data have been normalized using Eq. [2]. Two lines have been added corresponding to S = 500-700, $F(e) = 1/e^{1.3}$, $K_0' = 0.5$ (where K_0' is the coefficient of earth pressure at rest), and n = 0.25. It can be seen that the fit is good and that S ranges from 500 to 700. This further confirms that G_{max} values for Norwegian clays are consistent with those from a large volume of other published experimental data.

For other correlations between index properties (e.g. Ip or w) and *in situ* Vs data from the Norwegian clay database, the reader is refered to NGI (2015) and L'Heureux and Long (submitted).

Table 1 Example of available CPTU-Vs correlations for clays.

Study/Reference	Number of data pairs	r^2	V_s (m/s) or G_{max} (kPa)
(Tanaka et al., 1994)			$G_{max} = 50 \cdot (q_t - \sigma_{v0})$
(Hegazy and Mayne, 1995)	406	0.890	$V_s = 14.13 \cdot (q_c)^{0.359} \cdot (e_0)^{-0.473}$
(Hegazy and Mayne, 1995)	229	0.780	$V_s = 3.18 \cdot (q_c)^{0.549} \cdot (f_s)^{0.025}$
(Mayne and Rix, 1995)	339	0.830	$V_s = 9.44 \cdot (q_c)^{0.435} \cdot (e_0)^{-0.532}$
(Mayne and Rix, 1995)	481	0.740	$V_s = 1.75 \cdot (q_c)^{0.627}$
(Piratheepan, 2002)	20	0.910	$V_s = 11.9 \cdot (q_c)^{0.269} \cdot (f_s)^{0.108} \cdot D^{0.127}$
(Mayne, 2006)	161	0.820	$V_s = 118.8 \cdot \log(f_s) + 18.5$
(Long and Donohue, 2010)	35	0.613	$V_s = 2.944 \cdot (q_t)^{0.613}$
(Long and Donohue, 2010)	35	0.758	$V_s = 65 \cdot (q_t)^{0.15} \cdot (e_0)^{-0.714}$
(Long and Donohue, 2010)	-	0.777	$V_s = 1.961 \cdot (q_t)^{0.579} \cdot (1 + B_q)^{1.202}$
(Taboada et al., 2013)	274	0.94	$V_s = 14.4 \cdot (q_{net})^{0.265} \cdot (\sigma'_{v0})^{0.137}$
(Taboada et al., 2013)	274	0.948	$V_s = 16.3 \cdot (q_{net})^{0.209} \cdot \left(\frac{\sigma'_{v0}}{w}\right)^{0.165}$

4 CORRELATION WITH CONE PENETRATION DATA

The piezocone penetration test (CPTU) is a common tool used for characterization of soft and sensitive clay deposits. Several studies have explored relationships between *in situ* V_s and parameters such as CPTU tip

resistance (q_c), corrected tip resistance (q_t), cone net resistance (q_{net}), sleeve friction (f_s), pore pressure parameter (B_q), normalized cone resistance (Q_t), effective stress (σ'_v) and void ratio (e).

An overview of some of the most popular V_s prediction equations found in the literature for clays is presented in Table 1. For consistency, some of the equations have been modified to use of SI units: q_c, q_t, q_{net}, f_s and (σ'_v) are in kPa. The number of points used to develop each correlation equation is presented as well as the coefficient of determination (r^2).

Following the relationships proposed by Taboada et al. (2013), multiple regression analyses were conducted on the Norwegian clay database to provide power function expressions for *in situ* V_s in terms of q_{net}. The relationship with the highest coefficient of correlation using q_{net}, and σ'_{v0} is:

$$V_s = 8.35 \cdot (q_{net})^{0.22} \cdot (\sigma'_{v0})^{0.357} \quad (4)$$

The coefficient of determination r^2 is 0.73 and a total of 115 datasets were used in the regression analysis. The trend between the *in situ* measured V_s and the prediction given by Eq. [4] is illustrated in Figure 9. The figure shows that most of the predicted values of V_s are within 20 % of the measured V_s.

The prediction given by equation [4] was improved when the water content was introduced giving rise to the following expression:

$$V_s = 71.7 \cdot (q_{net})^{0.09} \cdot \left(\frac{\sigma'_{v0}}{w}\right)^{0.33} \quad (5)$$

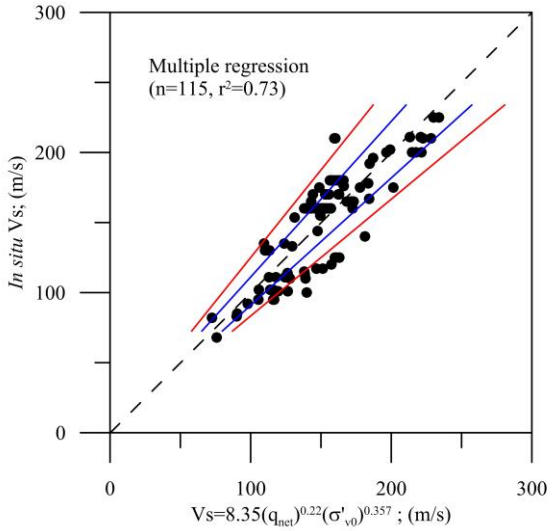


Figure 9 Comparison of measured and predicted V_s as a function of q_{net} and σ'_{v0}. Blue lines show +/-10% envelope while red lines show +/- 20%.

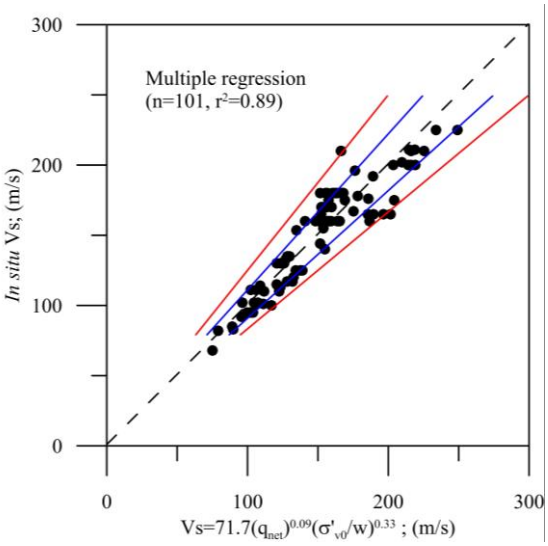


Figure 10 Comparison of measured and predicted V_s as a function of q_{net} , σ'_{v0} and w. Blue lines show +/-10% envelope while red lines show +/- 20%.

The coefficient of determination r^2 is 0.89 and a total of 101 datasets were used in the analyses. The trend between *in situ* measured V_s and the expression given in Eq. [5] is presented in Fig. 10. When using Eq. [5] most of the predicted values of V_s are within 10-15 % of the measured V_s. Equations 4 and 5 are similar to those presented by Taboada et al. (2013) for clays from the Gulf of Mexico (see Table 1). However, the empirical factors vary greatly. *In situ* V_s for Norwegian clays seem to be more strongly controlled by water content and vertical

effective stresses, and to a lesser extent by the net cone resistance.

5 CORRELATION WITH UNDRAINED SHEAR STRENGTH

Similar to CPTU penetration-based correlations, relationships between V_s and undrained shear strength (s_u) for clays can be developed since both properties depend on common parameters.

The undrained shear strength values obtained from direct simple shear tests (DSS) on Norwegian clay samples are plotted against *in situ* shear wave velocity in Fig. 11. The results show an increase in $s_{u,DSS}$ with increasing V_s. The best fit is given by Eq. 6 with a regression coefficient (r^2) of 0.91.

$$V_s = 14.87\, s_{u,DSS}^{0.69} \quad (6)$$

Equation 6 can also be used to assess undrained shear strength from V_s measurements by rewriting the relationship and solving for s_u as follow:

$$s_{u,DSS} = 0.02\, V_s^{1.45} \quad (7)$$

The data in Fig. 11 is compared to the relationships proposed by Andersen (2004) (i.e. $G_{max}/s_{u,DSS}$= 800 – 900). Note that to compare with the relationships proposed by Andersen (2004) we made use of Eq. [1] by varying the density between 1.6 and 1.9 Mg/m^3 and the empirical factor between 800 and 900. Figure 11 shows the 2 extreme lines from the Andersen (2004) relationship. The fit is good at low Vs value, but large difference arise for higher Vs results. The reason for these differences may come from the fact that the relationships proposed by Andersen (2004) are based on laboratory measurements of V_s and G_{max}, whereas *in situ* V_s data are used in this study.

Correlations between *in situ* V_s data and undrained shear strength from CAUC and CAUE triaxial tests have also been established based on data collected in this study. For more details the reader is referred to NGI (2015) and L'Heureux and Long (submitted).

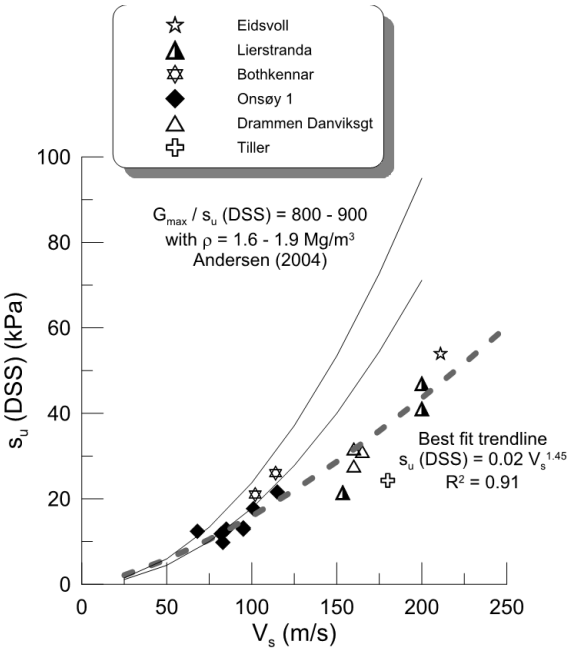


Figure 11 Results of in situ shear wave velocity against undrained shear strength from direct simple shear tests (s_{uDSS}).

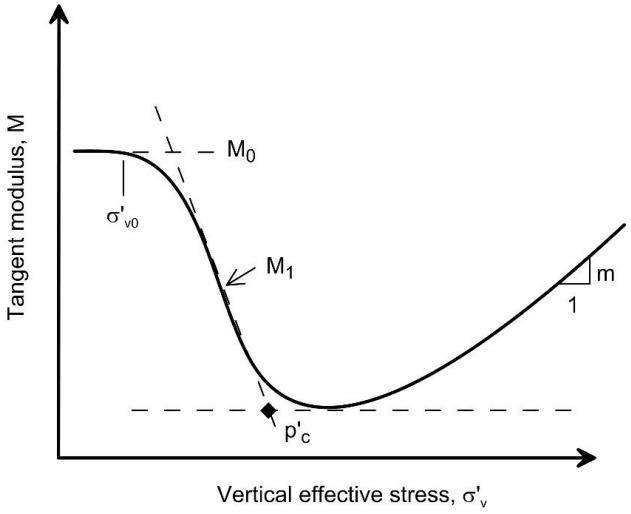


Figure 12 NGIs interpretation of the classical Janbu tangent modulus versus stress model.

6 CORRELATION WITH 1D COMPRESSION PARAMETERS

In this section the *in situ* V_s measurements in the database are compared Janbu's classical 1D compression parameters presented in Figure 12.

The relationship between M_0 and M_1 and V_s is shown on Figure 13 and 14, respectively.

Reasonable correlations would be expected here as V_s is a function of the current state of stress. Both M_0 and M_1 increase with increasing V_s as expected. The scatter in the data increases for increasing V_s and the greatest variation is for the highly overconsolidated Eidsvoll and Hvalsdalen clay. The best fit power trend lines shown give a reasonable r^2 values for both M_0 and M_1.

Values of the preconsolidation stress (p_c' as determined by the method presented in Figure 12) are plotted against V_s on Fig. 15. A good correlation is expected here as the shear wave velocity is strongly dependent on the maximum past stress experienced by the clay. The relationship between p_c' and V_s is good and the best fit power function has an r^2 value of 0.81 (Fig. 15).

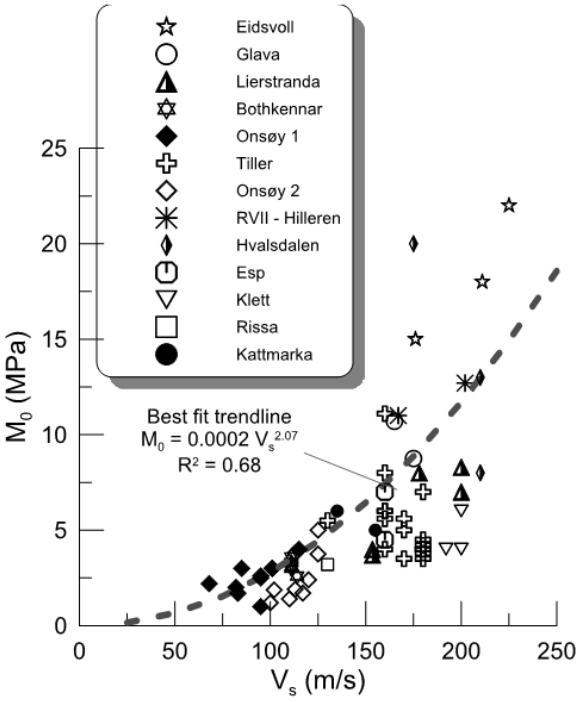


Figure 13 Results of Mo versus in situ V_s.

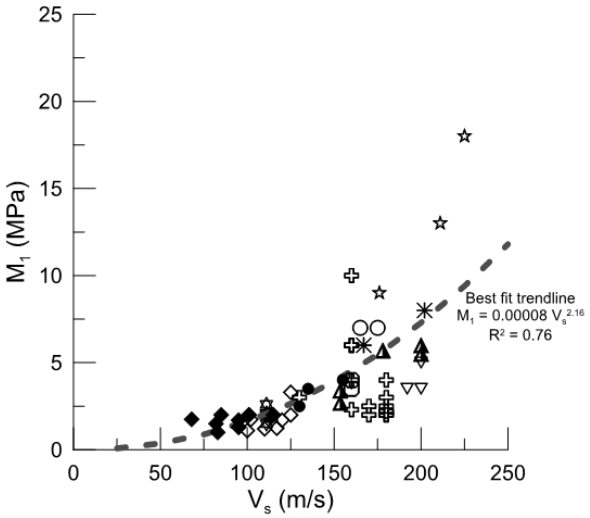


Figure 14 Results of M_1 versus in situ V_s.

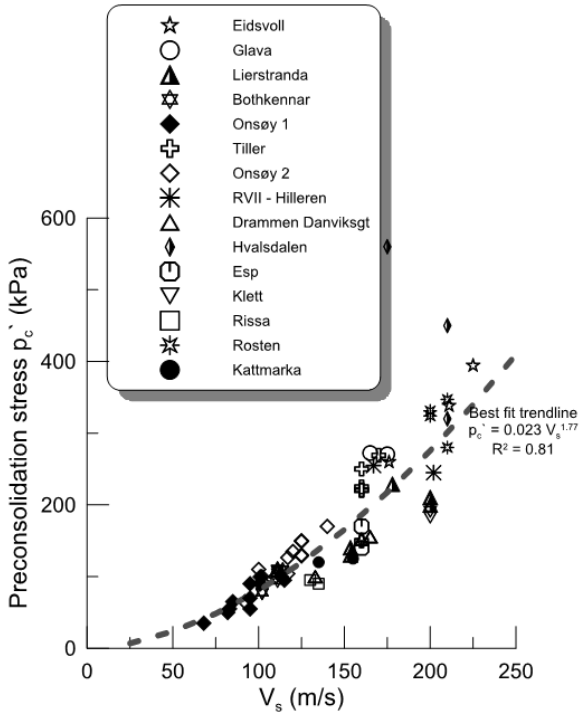


Figure 15 Results of p'_c versus in situ V_s.

The variation in the modulus number *m* versus shear wave velocity is shown on Fig. 16. There is a clear tendency for an increase in *m* with increasing V_s. However the fit is not as good for M_0, M_1 and p_c'. This is not surprising as you would expect V_s to represent the current state of stress not at some arbitrary higher stress stiffness.

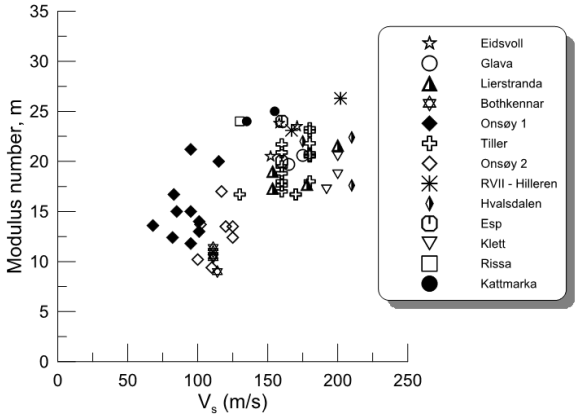


Figure 16 Modulus number versus V_s.

7 CONCLUSIONS AND RECOMMENDATIONS

The purpose of this study is to present guidelines and correlations to assist geotechnical engineers in estimating V_s profiles in Norwegian clays in the absence of site-specific data. For this, a database of *in situ* V_s measurements and standard geotechnical engineering material properties for Norwegian clays has been established. The database allowed the development of several empirical correlations between *in situ* V_s and basic soil properties, cone penetration parameters, undrained shear strength and 1D compression parameters. Based on the results from regression analyses, we recommend the use of empirical functions based on cone penetrometer data to determine the best estimate *in situ* V_s of Norwegian clay when *in situ* measurements of V_s at the site are not available. Relationships based on undrained shear strength can also be used in practice. Note that the relationships presented herein can be used either to evaluate V_s from a given soil property, or the way around to evaluate soil properties from V_s.

In general, it is recommended that engineers consider all available data including available relationships, *in situ* measured V_s profiles, and site-specific geotechnical data. The use of correlations in geotechnical engineering should be limited to the conditions for which they were developed and calibrated. The recommendations presented in this report should be used in conjunction with the engineer's own experience and engineering judgment. Site-specific correlations may be developed based on a limited number of site-specific V_s measurements and using a similar functional form.

8 ACKNOWLEDGEMENTS

This work was funded by the Norwegian Geotechnical Society (NGF) through NGF stipend 2014-2015 and through the NFR strategic research project SP8- GEODIP at NGI. The authors would like to thank the many colleagues at NGI, NTNU, Multiconsult, SVV and APEX that helped assembling the large dataset, for the help during field data acquisition and for the numerous discussions.

9 REFERENCES

Andersen, K. H., 2004, Cyclic clay data for foundation design of structures subjected to wave loading Proceedings International Conference Cyclic Behaviour of Soils and Liquefaction Phenomena Bochum, Germany, p. 31.33-32.34.

Hardin, B. O., & Drnevich, V. P. (1972). Shear modulus and damping in soils: measurement and parameter effects: Journal Soil Mechanics and Foundation Division, ASCE, no. 6, p. 603 - 624.

Hardin, B. O., 1978, The nature of stress – strain behaviour for soils, In Proceedings ASCE Speciality Conference on Earthquake Engineering and Soil Dynamics, Pasadena, California, Volume 1, p. 3 - 90.

Hegazy, Y. A., and Mayne, P. W., 1995, Statistical correlations between Vs and CPT data for different soil types, Proceedings, Symposium on Cone Penetration Testing, Volume 2, Swedish Geotechnical Society, Linköping, Sweden, p. 173 - 178.

Kramer, S., 1996, Geotechnical Earthquake Engineering, Simon & Schuster.

Leroueil, S., and Hight, D. W., 2003, Behavior and properties of natural soils and soft rocks, *in* Tan, T. S., Phoon, K. K., Hight, D. W., and Leroueil, S., eds., Proceedings International Workshop on Charaterisation and Engineering Properties of Natural Soils, Volume 1: Singapore, Balkema, Rotterdam, p. 29 - 254.

L'Heureux, J.-S., and Long, M. (Submitted) Relationship between shear wave velocity and geotechnical parameters for Norwegian clays. Submitted to Journal of Geotechnical and Geoenvironmental Engineering.

L'Heureux, J.-S., Long, M., Sauvin, G., Polom, U., Hansen, L., Lecomte, I., Vanneste, M., Dehls, J., and Janbu, N., 2013, Settlement prediction from high-resolution shear-wave reflection seismic data: the

Trondheim harbour case study, mid Norway Engineering Geology v. 167: 72 - 83.

Long, M., and Donohue, S., 2007, In situ shear wave velocity from multichannel analysis of surface waves (MASW) tests at eight Norwegian research sites: Canadian Geotechnical Journal, v. 44, no. 5 (May), p. 533-544.

Long, M., and Donohue, S., 2010, Characterisation of Norwegian marine clays with combined shear wave velocity and CPTU data Canadian Geotechnical Journal, v. 47, no. July, p. 709 - 718.

Long, M., Donohue, S., and O'Connor, P., 2008, Rapid, cost effective and accurate determination of in situ stiffness using MASW at Bothkennar: Ground Engineering, v. November, p. 43 - 46.

Mayne, P. W., 2006, In-situ test calibrations for evaluating soil parameters, Overview paper, Characterization and Engineering Properties of Natural Soils II (Proc. Singapore Workshop), Taylor & Francis Group, London, United Kingdom.

Mayne, P. W., and Rix, G. J., 1995, Correlations between cone tip resistance and shear wave velocity in natural clay: Soils and Foundations, v. 35, no. 2, p. 107 - 110.

Lunne, T., Berre, T. & Strandvik, S. (1998). Sample disturbance effects in deepwater soil investigations. Conf. Soil Invest. Found. Behav., London.

NGI 2015. SP8-GEODIP. Correlations between shear wave velocity and geotechnical parameters in Norwegian clays. Report nr. 20150030-04-R.

Piratheepan, P., 2002, Estimating shear-wave velocity from SPT and CPT aata. Master of Science Thesis, Clemson University.

Taboada, V. M., Cruz, D., and Barrera, P., 2013, Predictive equations of shear wave velocity for Bay of Campeche clay, Offshore Technology Conference (OTC), Volume Paper OTC 24068: Heuston, Texas, OTC.

Tanaka, H., Tanaka, M., and Iguchi, H., 1994, Shear modulus of soft clay measured by various kinds of tests Proceedings Symposium on Pre-Failure Deformation of Geomaterials Volume 1: Sapporo, Japan, p. 235 - 240.

Triaxial testing of overconsolidated, low plasticity clay till

A. H. Augustesen
COWI A/S, Denmark, ahau@cowi.dk

J. S. Steenfelt
COWI A/S, Denmark

J. N. Goth
Formerly COWI A/S, Denmark

ABSTRACT
In northern Europe, clay till (Boulder Clay) is very common. It is characterised by high overconsolidation ratios and low plasticity (7% to 10%). The undrained shear strength vary significantly, mostly between 50 kPa and 1500 kPa. The natural water content and the clay content are below 25% and 20%, respectively. Due to its origin the soil is well-graded and it can contain particles up to boulder size.
In accordance with Danish tradition, the clay till is tested in the triaxial apparatus employing a height equal to the diameter and smooth pressure heads. This is in contrast to standard international practice where a height-diameter ratio of two and rough pressure heads are employed. Supported by test results from a test campaign the paper discusses the impact on the stress-strain behaviour and the strength from the height-diameter ratio and the consolidation procedures, respectively.

Keywords: Triaxial testing, undrained strength parameters, clay till, consolidation procedures in triaxial testing, specimen size, height-diameter ratio.

1 INTRODUCTION

Triaxial testing is considered by far the most reliable tool for assessment of the shear strength and stiffness of clay till in the laboratory. The tests serve to provide a link (calibration) to available in situ testing methods, SPT, CPTU, plate loading tests etc. However, the shape and size of the samples and the stress path show very significant differences in-between laboratories across the world.

In the crossfires between local traditions, research efforts and commercial interests, different systems have been developed and refined (automated) by the advent of faster and cheaper computer systems.

The Danish clay tills may exhibit in situ undrained shear strength values in excess of 1500 kPa. Thus, it was early on recognised that testing in standard triaxial equipment may produce erroneous results as the defor

mations in the apparatus itself were far from negligible for the stiff to very hard clay till samples. As a result, Jacobsen (1970) developed a very rugged type of triaxial apparatus. Apart from reducing the apparatus deformations to insignificant values the new triaxial apparatus introduced a height/diameter ratio H/D = 1, a minimum sample diameter D = 70 mm and smooth pressure heads. This has subsequently formed the basis for both commercial and research triaxial testing in Denmark.

Working on international projects or projects in Denmark with international participation, the Danish triaxial testing tradition is constantly challenged. The main reason for this is that the standard (commercially available) triaxial set-ups use H/D = 2 and rough pressure heads in accordance with international standards (ASTM, AASHTO etc.).

This type of apparatus is available worldwide and often allow for testing on small diameter samples down to 33 mm.

The preparation and execution of tests in the "traditional type apparatus" is simpler, cheaper and less demanding in terms of technician skills. Thus, it is not surprising that only a small percentage of tests world-wide are carried out using what (in Denmark) is considered the superior type of apparatus.

Due to unavailability of the Danish type triaxial set-up by the successful laboratory contractor on a major Danish bridge project, a campaign of triaxial testing using the traditional and the Danish set-ups was initiated.

The purpose of the campaign was to elucidate the impact on the results from different height diameter ratios (H/D = 1 or H/D = 2), the consolidation stress path before the undrained failure phase and the specimen diameter (D = 70 mm and D = 100 mm).

The impact on the test results from the above differences is presented and discussed in the paper.

2 LITERATURE REVIEW

During the development of triaxial testing set-ups and procedures some of the main controversies (for undrained testing) are related to:

- Sample size (diameter and height/diameter ratio)
- Sample disturbance from sampling and possible re-creation of stress history in the triaxial cell
- Rough or smooth rigid end platens (a few attempts with flexible)
- Failure criterion as maximum deviator stress or maximum principal stress ratio
- Application of back pressure as a means to achieve acceptable degree of saturation

Extensive experience with testing in soft, homogeneous (marine) clays have been published in relation to some of the controversies above (e.g. Berre 1979 and 1982, Lacasse and Berre 1988, Lunne et al. 2007, Berre et al. 2007). However, it may not necessarily be transferable to testing of very stiff to hard overconsolidated glacial tills and vice versa. For the soft clays (OCR up to two) the axial strain to failure is typically of the order of 2-5% (followed by strain softening) whereas it is in excess of 10-15% for the high strength overconsolidated clay tills. However, Lacasse and Berre (1988) report on tests on Drammen clay with laboratory induced OCRs of up to 40. They conclude, that higher compressive strengths are observed for H/D = 1 (smooth pressure heads), but only at strains higher than 10 %. Furthermore, the initial part of the stress-strain curve is steeper when employing rough end platens.

From a theoretical point of view specimens with H/D = 1 and frictionless pressure heads provides a homogeneous stress-strain field in the sample and hence mimic a theoretical element test. This further implies that the principal stress directions are well-defined acting vertically (piston pressure plus cell pressure) and horizontally (cell pressure). The "smooth" end platens are ensured by high vacuum grease located in-between a number of membranes. However, the deformations in the grease and the membranes are non-linear and stress dependent, which is difficult to account for in the interpretation of the tests.

In contrast the H/D = 2 specimens with rough pressure heads produce non-uniform stress-strain fields with "dead zones" below the pressure heads and may show pronounced stress-strain peak behaviour and post failure softening. This is the reason for the requirement of use of proximity strain devices on the middle third of the sample to get representative axial and radial strain measurements (mostly applied in research).

However, the H/D = 2 samples also promote the development of shear bands (bifurcation) in particular for low-plasticity, fissured or heterogeneous soil samples, which may be the failure mechanism for many real life situations. The creation of a shear band in combination with highly dilative soils may infer that water flows into the shear band from the stiff zones surrounding it. Hence, the strength will theoretically decrease and the shear band acts as a "drainage line".

Re-creation of the stress history (by loading the samples to the insitu preconsolidation pressure followed by unloading to the insitu stress and thereafter take the specimen to failure) and thereby also reduce sample disturbance has been Danish tradition for decades. Jacobsen (1970) states the importance of do-

ing this. However, as noted by Berre (1982) it can lead to significant reduction in the water content. This may result in a too high stiffness and strength. Lately, some of the clay tills at the Fehmarn Belt have been tested without pre-loading samples. An alternative to Danish tradition has been proposed by Ladd and DeGroot (2003).

Many of the above controversies were addressed by Jacobsen (1967, 1968, 1970, 1979) in relation to the development of the new Danish triaxial apparatus and testing of clay till. His conclusions clearly advocated the use of *H/D* = 1, smooth pressure heads as well as pre-loading samples. However, the tremendous efforts to develop the apparatus, the testing technique and addressing most of the controversies simultaneously, somewhat weakens the conclusions in that the test series were not strictly carried out to allow a one-one comparison.

The test series in the new apparatus with direct comparison of height/diameter ratios (*H/D* = 0.5, *H/D* = 1 and *H/D* = 2) were carried out as UU tests (unconfined compression tests with a confining membrane but no confining pressure). Furthermore, the sample diameter was 35mm and a clear definition of failure was not provided.

To back up the theoretical considerations a series of ten CAU triaxial tests were carried on clay till in Malmö for the Citytunneln project using *H/D* = 2 and rough pressure heads. The average water content was 13% and the undrained shear strength from the field vane was 267 kPa thus comparable to the test series presented in this paper and by Jacobsen (1970).

The triaxial tests all showed a distinct barrel shape and in some cases clear bifurcation. Failure was defined as the maximum deviator stress (for the undrained shear strength) at axial strains from 10 to 15%. All tests were carried out to 15- 20% axial strain. The average undrained shear strength in the triaxial tests was 193 kPa and notably the drained triaxial friction angle was 30.5 degrees (c' = 26 kPa) kPa which is at the lower range expected based on *H/D* =1 tests on similar clay till in Denmark.

3 TEST PROGRAMME

3.1 Clay till

The clay till tested was sampled in relation to the New Storstrømmen Bridge project in Denmark. This new bridge will connect the islands of Zealand and Falster in the South-eastern part of Denmark.

Table 1 Summary of classification tests

	Depth [m]	**w [%]**	**w_L [%]**	**w_P [%]**	**I_P [%]**
B09A	9.0	12.3	21.5	12.4	9.1
B09A	9.9	11.2	20.4	12.6	7.8
B14	6.62	9.6	21.5	11.2	10.4
B34	13.9	10.4	19.7	10.2	9.5
B34	14.7	11.1	18.3	9.9	8.5

High quality core samples with *D* = 102 mm were retrieved with the Geobor S system. In some cases it was necesarry to trim down the specimen to a diameter of approximately 70 mm (laboratory capacity demands).

Due to the heterogeneity of the soil, specimens for comparison were sampled from the same core within approximately one meter distance, see Section 3.3.

The deposits are generally firm to very stiff clay till, slightly sandy to sandy and slightly gravelly to gravelly. The colour is grey to brownish grey to dark brown. Clasts of chalk and flint are found as well as a few cobbles.

Classification test values are summarized in Table 1 and Table 2. The initial water content, *w*, varies between 9.6 and 15 % with the majority around 12.5%. Plasticity index tests show I_p between 7.8% and 10.4%. The classification values are in the range normally observed for Danish clay tills east of Storebælt.

The clay till is highly overconsolidated with overconsolidation ratios *OCR* from 4.9 to 8.3.

3.2 Stress paths

In principle, all tests are carried out as anisotropically consolidated undrained triaxial compression tests with pore water measurements and constant cell pressure during the shear phase to failure.

All specimens have been pre-loaded in order to reduce the effects of sample disturbance and to partly restore the insitu stress history (Steenfelt and Foged, 1992).

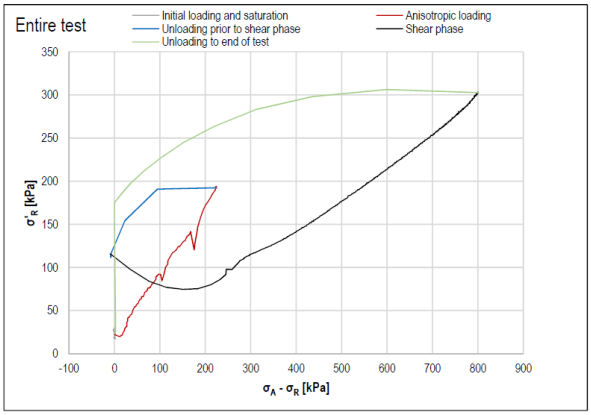


Figure 1 Stress path for a Type 1 test, B 09 (B) cf. Table 2. Red line: Anisotropic loading, blue line: unloading prior to shear phase, black line: Shear phase.

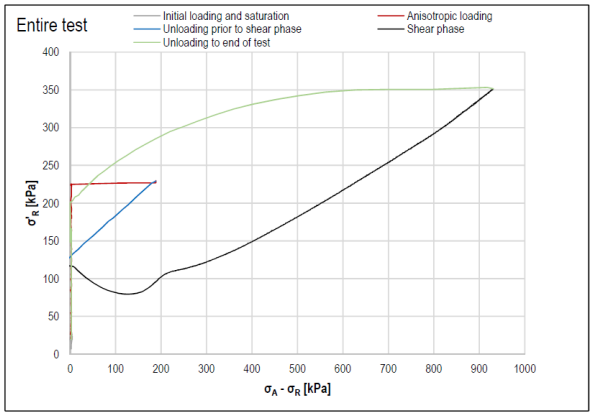


Figure 2 Stress path for a Type 3 test, B 09 (A) cf. Table 2. Grey line: Initial isotropic loading, red line: Anisotropic loading, blue line: unloading prior to shear phase, black line: Shear phase.

Two types of tests - distinguished by differences in the consolidation phases - were carried out, denoted Type 1 and Type 3 in the following.

Type 1 tests have been undertaken according to Danish Practice using *H/D* = 1 and smooth pressure heads. The stress history is "replicated" employing area-constant consolidation (loading and unloading), in which the specimen is constrained in the horizontal direction by adjusting the cell pressure. After (i) saturation, the specimen is (ii) taken to approximately 80% of the vertical preconsolidation pressure followed by (iii) unloading (also area-constant) to the in situ vertical stress, before (iv) shearing undrained to failure (at a constant strain rate and cell pressure). During the area-constant consolidation the specimen follows it's "true" K_0-path and hence the horizontal effective stresses do not need to be estimated (in contrast to the Type 3 tests). Figure 1 shows a typical stress path followed in a Type 1 tests. The red and blue lines show the stress path for the area-constant loading and unloading during the consolidation phase. The black line in Figure 1 indicates the effective stress path for the shear phase to failure, which clearly shows that the soil exhibits a dilative behaviour during the shearing.

A simplified consolidation procedure (in terms of test control and time duration) was adopted for the Type 3 tests. However, compared to Type 1 tests, the test specification requires more input from the Designer.

In the test campaign, Type 3 tests have been undertaken for specimens with *H/D* = 1 and smooth pressure heads as well as a *H/D* = 2 and rough pressure heads. The test sequence adopted for the consolidation phase was: (i) saturation, (ii) isotropic loading to 80% of the estimated horizontal effective preconsolidation pressure. (iii) Anisotropic loading to 80% of the vertical effective preconsolidation pressure with a constant cell pressure equal to the stress state described under item (ii), (iv) Unloading to a stress state representing in situ conditions. The horizontal effective stress was established based on the in situ overconsolidation ratio, *OCR*, using

$$K_{0,OC} = (1 - sin\varphi) \cdot OCR^{sin\varphi} \qquad (1)$$

where $K_{0,OC}$ is the coefficient of earth pressure at rest corresponding to the insitu conditions. *OCR* has been evaluated based on oedeometer (incremental loading and constant rate of strain tests) and piezocone penetration tests. Again, the last phase of the test involves undrained shearing to failure at a constant strain rate and constant cell pressure. Figure 2 shows a typical stress path followed in a Type 3 tests. The red and blue lines show the consolidation phases (Items (ii) and (iii) described above). The black line indicates the effective stress path for the shear phase to failure, which clearly shows that the soil exhibits a dilative behaviour during the shearing.

The rationale for the pre-consolidation to 80% of the estimated pre-consolidation pressure in both types of tests was to partly restore the stress history without destroying the initial structure of the specimen. Accidentally, the tests on B34 were taken beyond the pre-consolidation stress. However, the impact on the results and comparisons undertaken seem negligible.

3.3 Test details

11 successful tests were carried out. All tests were conducted on high quality specimens with limited sample disturbance.

Three of the tests are of Type 1 and eight are of Type 3. In seven tests *H/D* = 1 and in four *H/D* = 2. Specimens with diameters of approximately 70 mm (six tests) and 100 mm (five tests) were tested.

An overview of the test types, specimen dimensions, consolidation stresses and strength parameters are shown in Table 2. $\sigma'_A = \sigma'_1$ and $\sigma'_R = \sigma'_3$ are the axial and radial stresses, respectively, at the end of the different stages of the consolidation phase. The subscripts *loa.* and *unl.* denote loading and unloading, respectively. w_{init} is the natural water content at the start of the test whereas

$$K_0 = \frac{\sigma'_R}{\sigma'_A} = \frac{\sigma'_3}{\sigma'_1} \qquad (2)$$

is the coefficient of earth pressure at rest corresponding to the end of the loading and unloading phases. Hence, the stresses reflect the different stress paths for the consolidation parts of the Type 1 and Type 3 tests as described in Section 3.2.

The same values of the coefficient of earth pressure at rest, K_0, and the mean effective stress, $p' (=\sigma'_1 + 2\ \sigma'_3)/3)$, are specified for tests to be compared. This was achieved for all tests except B 14 (C). However, this is accounted for as described below. It should be mentioned that this test was conducted at a very early stage of the test campaign.

Due to the way the Type 1 tests are undertaken (cf. Section 3.2), the K_0-values and the mean effective stresses in the loading and unloading phases differ in some circumstances from the corresponding stresses in the comparable Type 3 tests, in which the K_0 values are a part of the test specifications.

Table 2 Test characteristics and results.

Label	Borehole no.	Depth	Test type	H	D	H/D	w_{init}	σ'_A,	σ'_R,	$\sigma'_{A,loa.}$	$\sigma'_{R,loa.}$	K_0	$\sigma'_{A,unl.}$	$\sigma'_{R,unl.}$	K_0	Strain rate	σ'_A ε_1=10%	σ'_R ε_1=10%	s_u	ε_{50}
		[m]	[-]	[mm]	[mm]	[-]	[%]	[kPa]	[kPa]	[kPa]	[kPa]	[-]	[kPa]	[kPa]	[-]	[%/hr]	[kPa]	[kPa]	[kPa]	[%]
B09 (A)	B09A-BH	9.20-9.30	3	102.6	96.1	1	13.4	229	229	418	229	0.55	105	118	1.12	0.66	911.1	242.6	334.2	3.06
B09 (B)	B09A-BH	9.90-10.10	1	100.0	100.0	1	12.6	N/A	N/A	416	192	0.46	106	114	1.08	0.66	878.5	232.3	323.1	1.18
B09 (C)	B09A-BH	10.20	3	181.4	99.0	2	15.0	227	227	416	227	0.55	104	118	1.13	0.66	879.0	246.0	316.5	1.61
B14 (A)	B14-BH	6.72-6.79	1	70.0	70.0	1	11.3	N/A	N/A	419	159	0.38	63	69	1.10	0.20	611.8	146.4	232.7	0.77
B14 (B)	B14-BH	6.81-6.88	3	70.0	70.0	1	11.4	182	182	418	182	0.44	62	90	1.45	0.20	635.5	168.1	233.7	1.05
B14 (C)	B14-BH	5.31	3	140.2	69.8	2	10.7	177	177	351	177	0.50	58	79	1.36	0.50	677.5	188.9	244.3	1.11
B14 (D)	B14-BH	5.72	3	204.8	97.4	2	11.3	184	184	416	183	0.44	59.3	89	1.50	0.20	700.8	194.9	253.0	1.75
B14 (E)	B14-BH	7.07-7.17	3	100.0	99.5	1	11.0	183	183	419	183	0.44	58	87	1.50	0.20	683.9	182.8	250.6	1.95
B34 (A)	B34-BH	13.92-13.99	1	70.0	70.0	1	12.5	N/A	N/A	584	255	0.44	121	106	0.88	0.29	646.9	163.5	241.6	0.26
B34 (B)	B34-BH	14.09-14.16	3	70.0	70.0	1	13.4	255	255	582	255	0.44	121	144	1.19	0.29	717.0	169.3	273.8	0.44
B34 (C)	B34-BH	14.70	3	140.0	70.0	2	12.3	257	257	581	257	0.44	122	145	1.19	0.29	799.1	208.8	295.1	0.25

This could ideally have been avoided if the Type 3 tests were conducted after the Type 1 tests. However, this was not possible due to time constraints in the laboratory campaign for the project.

The strengths compared in Section 4 are the undrained shear strengths, s_u, shown in Table 2 corrected for differences in loading and unloading mean stress level and thereby K_0. With the considerations presented in Steenfelt and Foged (1992) as a starting point, s_u is more rigorously corrected due to differences in mean effective stress and laboratory induced overconsolidation ratio, $R = p'_{max}/p'_{min}$. p'_{max} and p'_{min} are the mean effective maximum (= p'_{loa}) and minimum stresses (= p'_{unl}) in the consolidation phase, respectively. Based on Critical State Soil Mechanics with the modified Cam Clay conceptual soil model it appears after some manipulation that

$$\frac{s_{u,ii}}{s_{u,i}} = \left(\frac{p'_{loa,ii}}{p'_{loa,i}}\right)^{\Lambda} \cdot \left(\frac{p'_{unl,ii}}{p'_{unl,i}}\right)^{1-\Lambda} \quad (3)$$

where the indexes *ii* and *i* refer to two different stress conditions. $\Lambda = 0.85$, similar to the power in the SHANSEP relation for clay till, has been adopted, cf. Steenfelt and Foged (1992). The mean effective stress, p', in the triaxial set up is

$$p' = \frac{\sigma'_A + 2\cdot\sigma'_R}{3} = \frac{\sigma'_1 + 2\cdot\sigma'_3}{3} \quad (4)$$

As indicated in Table 2, the strain rate (=0.5%/h) applied in the shear phase to failure in B14 (C) differs from the strain rate (=0.2%/h) applied for the other B14 tests. Therefore, the undrained shear strength for B14 (C) has been corrected based on the recommendations by Lunne et al. (2006), i.e. on average the undrained shear strength increases by 9.4 % per log cycle of strain rate.

Typically, the stress-strain behaviour did not exhibit a pronounced peak in a deviator stress, q, – axial strain, ε_1, plot; hence the undrained shear strength, $s_{u,qmax}$, corresponds to an axial strain of 20% (the approximate axial strain at which the tests were terminated). In contrast, when plotting the principal stress ratio (σ'_1/σ'_3) versus the axial strains, a peak and thereby an undrained shear strength, $s_{u,max\sigma1/\sigma3}$, can be found. However, making use of this criterion to define failure in case of design, a lower bound of the undrained shear strength is estimated. Hence, in this paper the undrained shear strength, $s_{u,\varepsilon1=10\%}$, is defined according to a certain axial strain, which is chosen to be 10% according to common practice. These values are given in Table 2.

The pre-failure stress-strain behaviour is in a simple manner characterised by ε_{50}, which is the axial strain corresponding to 50% of the deviator stress q at failure. ε_{50} has not been corrected for the stress level and the overconsolidation ratio.

4 RESULTS

The clay tills tested are relative weak (uncorrected undrained shear strengths vary between 230 kPa and 350 kPa, cf. Table 2) compared to other clay tills encountered in Denmark; however comparable to those tested by Jacobsen (1968, 1970). Furthermore, the *OCR*s (vary between 4.9 and 8.3) are not particularly high. Still, in all tests the soil exhibited a highly dilative nature when approaching failure (see for example Figure 6 and Figure 12) and in the none of the tests a clear shear band (bifurcation) were detected, even for *H/D* = 2. Hence, the observations presented in the following may not be applicable for the stiffest and strongest clay tills found in Denmark and Northern Europe.

In the following sections, the effects of sample size (*H/D* = 1 versus *H/D* = 2) and stress path (Type 1 versus Type 3) on the undrained shear strength and the pre-failure stress-strain behaviour are elucidated.

For each label in the legend, the letters in parenthesis refer to Table 2 and they indicate the tests that are compared, e.g. B14 (D-E) indicates that tests B14 (D) and B14 (E) in relation to B14-BH are compared. Furthermore, the first letter in the parenthesis refers to the value of the ordinate and the second to the abscissa. This notation and methodology are employed throughout Section 4 and it implies that each data point in a graph involves two tests. Solid lines bisect the plots, i.e. data points located on these lines indicate a perfect match between the parameters compared.

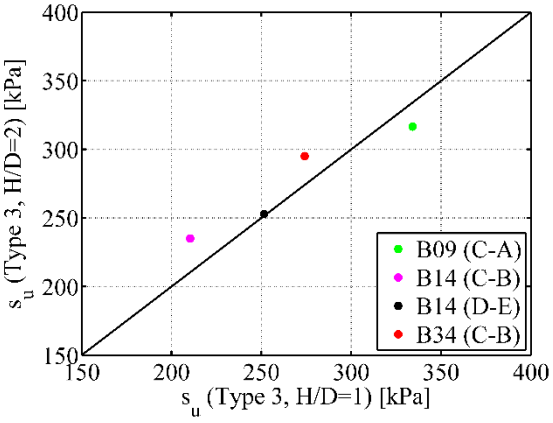


Figure 3 Comparison of undrained shear strengths based on Type 3 tests for H/D = 1 and H/D=2.

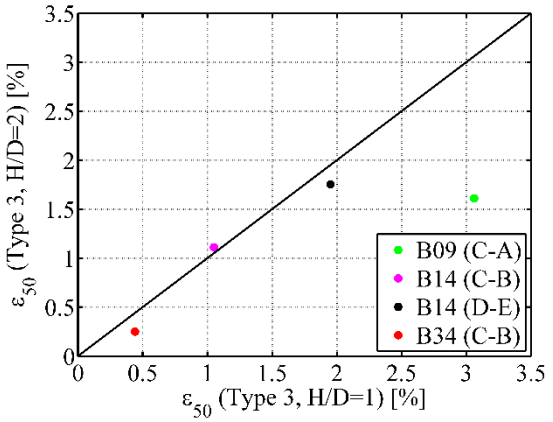


Figure 4 Comparison of uncorrected ε_{50} based on Type 3 tests for H/D = 1 and H/D=2.

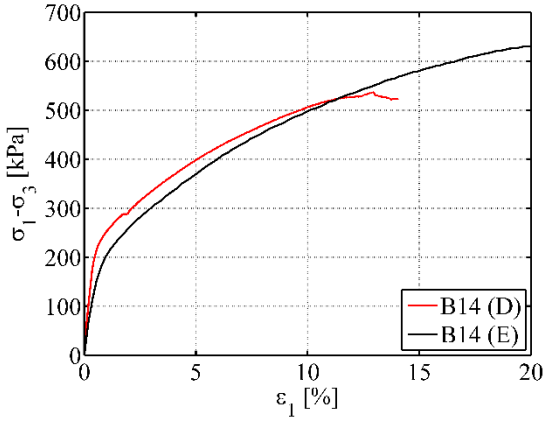


Figure 5 Deviator stress – axial strain for B14 (D) (Type 3, H/D = 2, D=100mm) and B14 (E) (Type 3, H/D=1, D = 100mm).

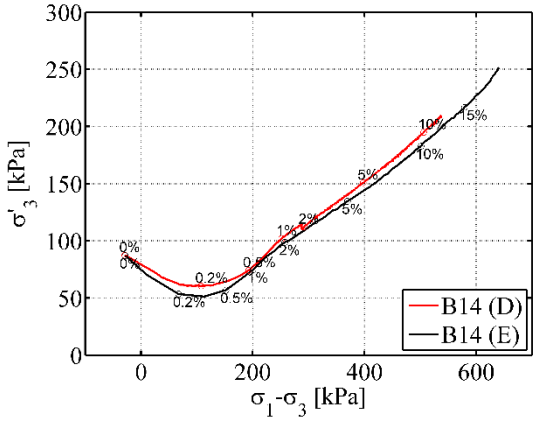


Figure 6 Effective stress paths for the shear phase for B14 (D) (Type 3, H/D = 2, D=100mm) and B14 (E) (Type 3, H/D=1, D = 100mm). 0% to 15% indicate the axial strains.

4.1 H/D ratio

The influence of height-diameter ratio, *H/D*, on the undrained shear strength, s_u, and ε_{50} is shown in Figure 3 and Figure 4, respectively. The tests compared have the same diameter and follow similar stress paths in the consolidation phase.

Figure 3 indicates, based on the limited amount of tests, that there is no significant difference in undrained shear strength (ε_1 = 10%), from a design point of view, between conducting *H/D* = 1 and *H/D* = 2. The variation is below ± 10%. There is a tendency that *H/D* = 2 gives rise to the highest strength for relatively low undrained shear strengths (<250 kPa), whereas *H/D* = 1 provides higher undrained strengths for strengths exceeding 250 kPa. Furthermore, when increasing the diameter the undrained shear strength from the *H/D* = 1 tests exceeds the strengths based on the corresponding *H/D* =2 tests.

Compared to the variation in s_u, the variation in ε_{50} is higher, as expected, cf. Figure 4. However, for the tests on B14 the variation is below ± 10%. Despite differences, the stress-strain curve shapes can be very similar as exemplified in Figure 5 for B14 (D) and B14 (E). Generally, the pre-failure stress-strain curve for *H/D* = 2 is stiffer than the corresponding curve for *H/D* = 1. Jacobsen (1968, 1970) also reported this based on unconfined compression tests.



Figure 7 Specimen shape at failure (ε_1 = 10%) for B34 (C), Type 3, H/D=2, D = 70mm.



Figure 8 Specimen shape at failure (ε_1 = 10%) for B34 (B), Type 3, H/D=1, D = 70mm.

Figure 5 indicates that for B14 (D), *H/D* = 2, a potential shear band may have started to develop at the end of the test, which is not the case for B14 (E), *H/D* = 1. However, a shear band cannot be detected from the sample photos. For other *H/D* = 2 tests (not shown here) the deviator stress-strain curves also start to flatten out after 12 – 15% axial strain indicating that a potential shear band develops, which theoretically should be the failure mechanism, see Section 2. This is not the case for the *H/D* = 1 tests. This is also reported by Berre (1982).

Exemplified by B14 (D) and B14 (E), cf. Figure 5 and Figure 6, there is a relatively good match between the effective stress paths and stress-strain curves.

The advantage of testing *H/D* = 1 and employing smooth end platens is that homogenous stress and strain conditions exist in the specimen. If such conditions prevail, the specimen keeps its cylindrical form when approaching failure. Figure 7 and Figure 8 show the shape of B34 (B) and B34 (C), respectively, for ε_1 = 10%. As expected, the *H/D* = 2 test develops this "barrel-shaped" form. But maybe more surprisingly, even though it is not to the same extent, the *H/D* = 1 test also exhibits this "barrel-shaped" form.

Generally, the influence of the definition of failure on the undrained shear strength seems higher compared to the effects of testing samples with height-diameter ratios of either unity or two.

4.2 Stress path

The influence of consolidation stress path on the undrained shear strength, s_u, and ε_{50} is shown in Figure 9 and Figure 10. The tests compared have the same height-diameter ratio and diameter.

Figure 9 indicates, based on the limited amount of tests, that there is no significant difference in undrained shear strength (ε_1 = 10%), from a design point of view, between conducting Type 1 and Type 3 tests. The variation is below ± 10%. Still, there is a tendency that Type 1 tests gives rise to the highest strength.

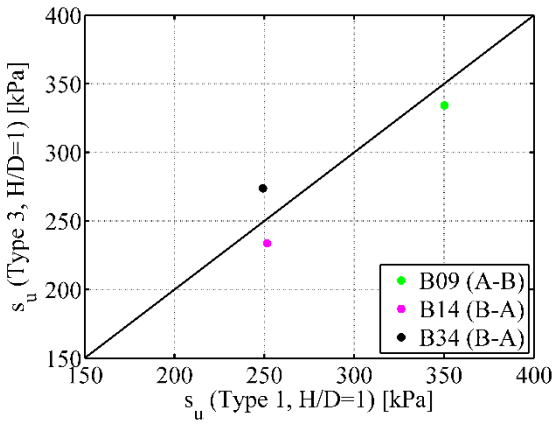


Figure 9 Comparison of undrained shear strengths based on Type 1 and Type 3 tests for H/D = 1.

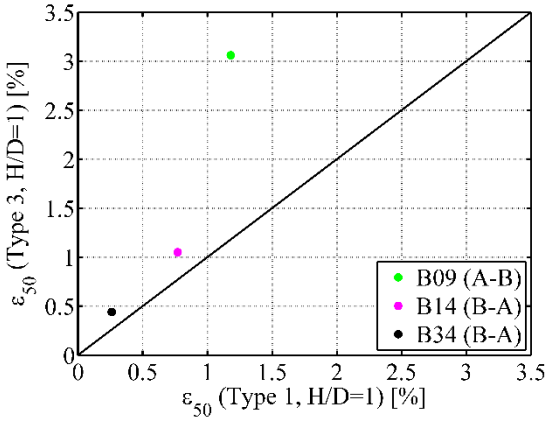


Figure 10 Comparison of uncorrected ε_{50} based on Type 1 and Type 3 tests for H/D = 1.

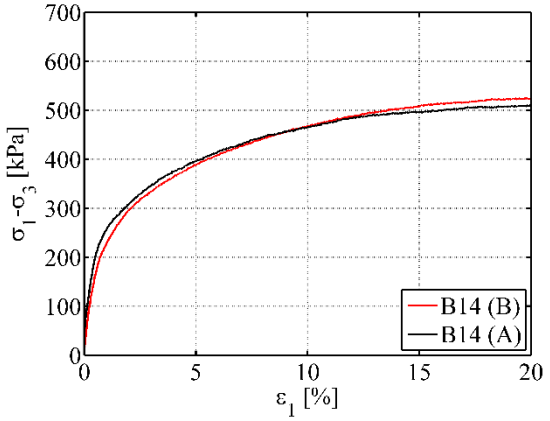


Figure 11 Deviator stress – axial strain for B14 (A) (Type 1, H/D = 1, D = 70 mm) and B14 (B) (Type 3, H/D = 1 and D = 70mm).

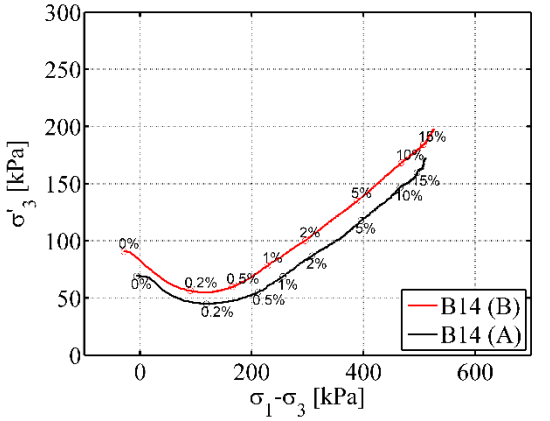


Figure 12 Effective stress path for the shear phase for B14 (B) (Type 3, H/D = 1, D = 70 mm) and B14 (A) (Type 1, H/D = 1, D = 70mm). 0% to 15% indicate the axial strains.

Figure 10 indicates, based on uncorrected ε_{50}s, that the pre-failure stress-strain curves for Type 1 tests is stiffer than the corresponding curves for Type 3 tests. Despite differences, the shape of the stress-strain curves can be very similar as seen in Figure 11 for B14 (B) and B14 (A).

Figure 12 shows the effective stress paths for B14 (A) and B14 (B). There is a relative good match between the effective stress paths. The difference may be due to the fact that the unloading stress state is not completely identical for the two tests.

Steenfelt and Foged (1992) and Jacobsen (1970) state the importance of pre-loading the clay till samples before shearing it to failure. This has been Danish tradition for decades and it is undertaken to replicate the insitu stress history. However, as noted by Berre (1982) it can lead to significant reduction in the water content. This may result in a too high stiffness and strength. Lately, some of clay tills at the Fehmarn Belt have been tested without pre-loading samples. From the authors point of view it is recommended to pre-load clay till samples, especially if the *OCR* is high, if the test campaign is limited and if prior knowledge about the subject for the tills to be tested is not available.

Results (not presented here) from the New Storstrømmen Bridge indicate that pre-loading samples yield undrained shear strengths that are higher compared to samples that have not been pre-loaded.

5 CONCLUSIONS

The basis for the Danish tradition of undertaking trixial testing on clay tills has been reviewed (Section 2). A tremendous and outstanding work has been done in the early days by Jacobsen (1967, 1968, 1970, 1979) to update and cope with shortcomings and uncertainties of testing highly overconsolidated and stiff clays. Theoretically, the proposed way of testing clay till seems plausible and correct. But the experimental documentation is weakened since the test series where *H/D* = 1 (smooth end platens) and *H/D* = 2 (rough end platens) are compared were not strictly carried out to allow a one-one comparison.

The results from a limited test campaign have been presented in this paper. The effects of conducting *H/D* = 1 and *H/D* = 2 on the undraind shear strength and prefailure stress-strain characteristics have been investigated. The results indicate, from a design point of view, that no significant differences are observed if the tests are carried out by well renowned and highly experienced companies. The same is the case if comparing results of tests in which highly sophisticated area-constant consolidation stress paths are compared with a much more simplified and faster consolidation stress paths. Furthermore, it is important to test samples with a minimum diameter of 70 mm.

Generally, the influence of the definition of failure (here ε_1 = 10%) on the undrained shear strength seems higher compared to the effects of testing samples with height-diameter ratios of either unity or two or employing different consolidation stress paths.

The clay tills tested are relative weak (undrained shear strengths between 230 kPa and 350 kPa) compared to other Danish clay tills. Furthermore, the *OCR*s (ranging between 4.9 and 8.3) are not particularly high. Hence, the observations presented may not be applicable for the stiffest and strongest clay tills found in Denmark and Northern Europe.

This paper is intended as an appetizer and more research should be undertaken before decisive conclusions can be drawn.

6 ACKNOWLEDGEMENT

The authors would like to thanks Andreas Elkjær Riis and Martin Underlien Østergaard (both COWI) for assistance in preparation of plots. Last but not least, the authors gratefully acknowledge permission by the Danish Road Directorate to publish the test results.

7 REFERENCES

Berre, T. (1979). Sources of error for undrained triaxial tests on soft sand medium stiff clay. Nordic Geotechnical Meeting NGM-79, 597-608.

Berre, T. (1982). Triaxial testing at the Norwegian Geotechnical Institute. Geotechnical Testing Journal, GTJODJ, Vol. 5, No. 1 / 2, 3-17.

Berre, T., Lunne, T., Andersen, K.H., Strandvik, S. & Sjursen, M. (2007). Potential improvements of design parameters by taking block samples of soft marine Norwegian clays. Canadian Geotechnical Journal, Vol. 44, 698-716.

Jacobsen, M. (1967). Morænelers deformationsegenskaber. Ph.D. Thesis (in Danish), Danmarks Tekniske Højskole.

Jacobsen, M. (1968). The undrained shear strength of preconsolidated boulder clay. The Danish Geotechnical Institute, Bulletin No. 26.

Jacobsen, M. (1970). New oedometer and new triaxial apparatus for firm soils. The Danish Geotechnical Institute, Bulletin No. 27.

Jacobsen, M. (1979). Triaxial Testing in the Design of shallow Foundations. In proceedings of VII ECSMFE. Brighton

Lacasse, S. & Berre, T. (1988). Triaxial testing methods for soils. Advanced Triaxial Testing of Soil and Rock, ASTM STP 977. R.T. Donaghe, R.C. Chaney & M.L. Silver (editors). American Society for Testing and Materials, 264-289.

Ladd, C.C. & DeGroot, D.J. (2003). Recommended practice for soft ground site characterization: Arthur Casagrande Lecture. 12th Panamerican Conference on Soil Mechanics and Geotechnical Engineering. MIT, Massachusetts, USA.

Lunne, T., Berre, T., Andersen, K.H., Strandvik, S. & Sjursen, M. (2006). Effects of sample disturbance and consolidation procedures on measured shear strength of soft marine Norwegian clays. Canadian Geotechnical Journal, Vol. 43, 726-750.

Steenfelt, J.S. & Foged, N. (1992). Clay till strength–SHANSEP and CSSM. Nordic Geotechnical Meeting – NGM-92, 81-86.

ERT and seismic refraction tomography test at Äspö Hard Rock Laboratory

Mathias Ronczka
Lund University, Sweden, m.ronczka@gmail.com

Roger Wisén, Kristofer Hellman, Marcus Wennermark, Torleif Dahlin
Lund University, Sweden

ABSTRACT
Tunnelling below water passages is a challenging task, as fracture zones in the underlying bedrock are often associated with these. Surveys prior to the construction phase that provide information of the subsurface can also be logistically difficult at water passages. An approach that combines refraction seismic and ERT (electrical resistivity tomography) at the Äspö Hard Rock Laboratory (HRL) is presented. The rock laboratory consists of an approximately 2 km long access tunnel and a spiral tunnel that reaches more than 450 m below ground.
The presented surveys cover a water passage along part of the access tunnel which is located around 100 m below the survey line. Seismic and ERT data with co-located sensor positions were collected. The profiles were roughly oriented in north-south direction with a length of about 780 m for ERT and 450 for the seismic survey. A sensor spacing of 5 m was used. Strong power grid noise, the geologic and the test site conditions were logistically challenging for the geophysical surveys. The large resistivity range made it difficult to fit the ERT data appropriately. The unexpected large thickness of the sediments in the southern part of the survey led to a poor signal quality of the seismic data. Nonetheless, inversion results of both data sets are promising, and show that previously unknown geological features can be found by the approach even in an unusually well documented geological environment. The joint interpretation showed that the sedimentary deposits as well as the fracture zones in the northern part could be imaged. A further quality enhancement of the inversion results is possible by including a-priori information and/or a joint inversion of both data sets.

Keywords: Refraction seismic, ERT, joint interpretation.

1 INTODUCTION

The construction of underground structures has attracted much attention recently. They are used for example in the transportation sector to challenge the growth of traffic in and around cities, for underground storage facilities, etc. Detailed subsurface information is essential for a successful completion. A critical point in order to ensure a smooth construction phase is to locate possible weak zones that might slow down the construction progress.

In Sweden, underground infrastructure is mostly built within the crystalline bedrock, where weakness zones are indicated by dry or water bearing fractures. Different methods exist for their location. For example a set of boreholes give information with a high resolution in depth. Nevertheless, these are very expensive and deliver only punctual information. For the extrapolation into 2D or even 3D geophysical surface based investigations can be used. Recently, Swedish transportation authority's started an increasing number of projects with the aim to develop a scheme of different geophysical methods to map fractures.

Seismic and ERT (electrical resistivity

tomography) surveys were conducted to locate fracture zones at the Äspö Hard Rock laboratory (HRL). In order to increase the reliability of the results, the combination of both methods will be investigated. This can be done for example by a joint interpretation and inversion of both data-sets. Äspö HRL is an underground facility for research and tests around the concept of final disposal of nuclear waste material in hard rock (Rhén et al. 1997), which provides a research opportunity in a well documented and relatively undisturbed environment also for other branches of research.

2 SITE DESCRIPTION

The Äspö Hard Rock Laboratory is located on the Baltic east coast of Sweden, about 30 km north of Oskarshamn and 400 km south of Stockholm (see Figure 1). The Swedish Nuclear Fuel and Waste Management Company (SKB) started to design a deep final disposal for nuclear fuel. From 1990 – 1995 the excavation of a 3600 m long tunnel that connects the nuclear power plant with the disposal in approximately 450 m depth was conducted. During that phase, a detailed site characterization was done that included geological, hydrogeological and geochemical investigations.



Figure 1: Location of Äspö Hard Rock Laboratory, approx. 30 km north of Oskarshamn

The Äspö bedrock is part of the Trans-Scandinavian Igneous belt (TIB), which extends from southern Sweden towards north and northwest. Mainly granitoids and volcanic rocks can be found in the TIB. Four rock types are dominating: the Äspö diorites, Ävrö granite, greenstone and fine-grained granite. Wikbert et al. 1991 found out that continuous magma-mingling and mixing processes supported the development of dikes and mafic inclusions which form an inhomogeneous rock mass. The crystalline bedrock exhibits porosities of 0.4-0.45 % for the Äspö diorite and 0.23-0.27 % for the fine-grained granite (Stanfors et al. 1999). During the pre-investigation of Äspö HRL, fracture zones were divided into major (width > 5 m) and minor (width < 5 m) ones. The majority of the fractures are oriented northwest-southeast (Berglund et. al 2003), and the most important fractures are depicted in Figure 2. Minerals that fill the fractures were extracted from drill cores and analysed. Thus, unconsolidated material that might have been additionally filling the fractures was probably washed away.

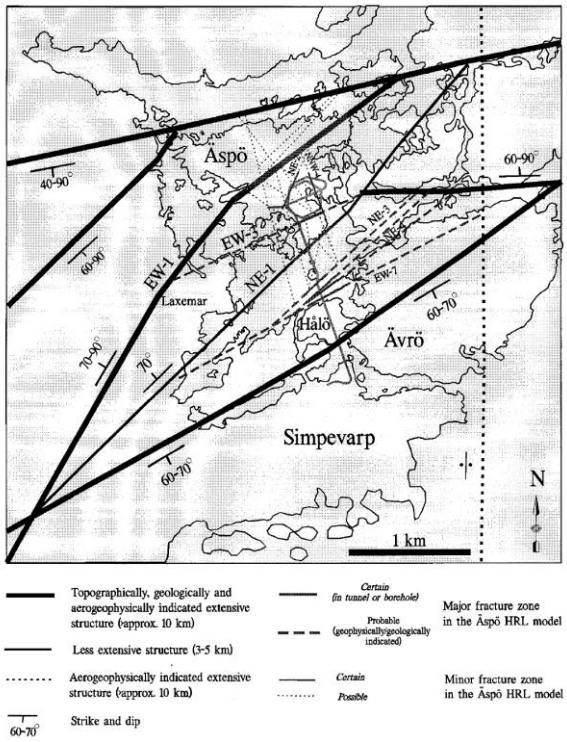


Figure 2: Fracture zones at Äspö HRL (Stanfors et al. 1999).

Quaternary sediments on top of the bedrock are scarce at the Äspö test site. Due to the deep target of the Äspö HRL within the bedrock, no detailed investigation of the Quaternary sediments were done. Vidstrand 2003 stated that the unconsolidated overburden rarely exceed 5 m thickness and consists mainly of clay, sand and gravel.

3 FIELD SURVEYS

3.1 Electrical resistivity tomography

ERT measurements were carried out along a profile in N-S direction directly above the tunnel line. The profile lies between Hålö and Äspö (see Figure 3) to the west of the tunnel line, about 10 m away from a small island. Electrodes were placed onshore and underwater, with a 5 m electrode spacing, along a profile with a length of about 780 m. Data were recorded using the ABEM Terrameter LS instrument. A multiple gradient array was employed to ensure fast progress. The ERT measurement was conducted simultaneously with the seismic survey on 20-24 April 2015.

3.2 Seismic survey

As indicated by Figure 3, seismic refraction data were collected on the sea bed. Hydrophone streamers were laid out with 91 hydrophones using 5 m spacing along a 450 m profile line. For data acquisition the instruments ABEM Terraloc and Geometrics Stratavizor were used, both with 48 channels and with a 5 channel overlap of the two streamers. Hydrophone positions were determined by a differential GNSS, while the topography of the sea bed was mapped with a multibeam echo sounder (Lasheras Maas 2015). For the excitation of seismic p-waves, small explosives were placed approximately 0.5m above the sea bed with a scheduled spacing of 20 m. Due to time constraints not all planed shots were fired and hence there are two small gaps in the data coverage in the northern part of the dataset.



Figure 3: Location of the seismic (red line) and ERT (blue line) profile at Äspö HRL (after Lasheras Maas 2015).

4 RESULTS

About 6700 data points were gathered in the ERT survey. The surveying conditions were challenging with electrodes lying in brackish water as well as on outcropping rock, leading to contact resistances ranging from around 100 Ω to over 100 kΩ. Nevertheless, data quality is generally good judging from apparent resistivity pseudosection plots, although recorded full waveform data reveals high power grid noise levels.

While processing the raw data, electrodes with apparently wrong GNNS position were identified and combinations containing these electrodes deleted. For the inversion it was assumed that data were contaminated with 3% Gaussian noise and a voltage error of 0.1 mV. Data were interpreted as models of the resistivity distribution via inverse numerical modelling (inversion) using BERT (*add reference*). A smoothness constrained inversion was done with the abort criterion $\chi^2 = \Phi_d/N = 1$, whereas Φ_d is the data misfit and N the data amount.

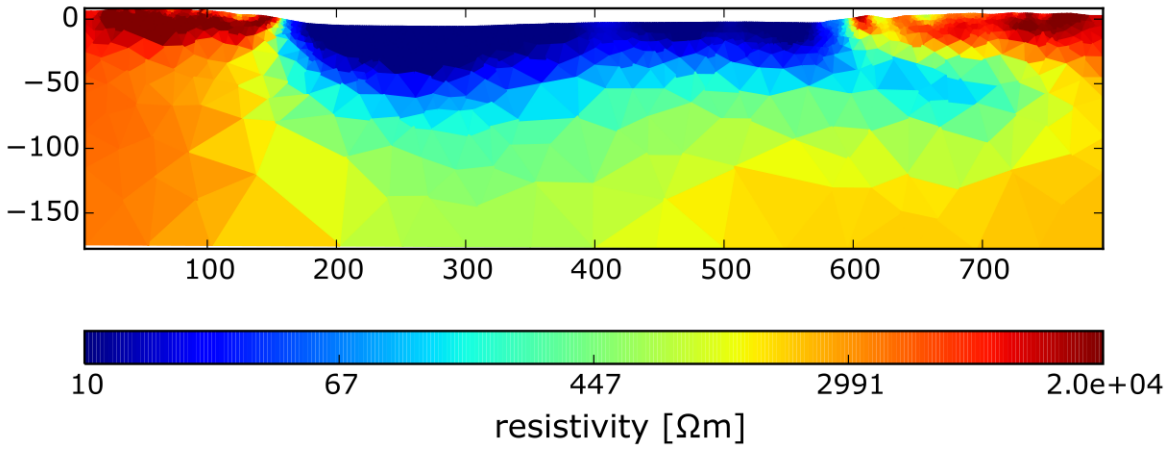


Figure 4: Inversion result of the ERT data set at Äspö HRL.

The L_1 norm (robust inversion) was used for Φ_d. Although some apparent resistivities that exhibit a high error and/or does not fit into the raw data distribution were deleted. One explanation for the difficult data fit is that the measured apparent resistivity distribution covers several orders of magnitude and that extraordinary high resistivity jumps occur, which is always a challenging task for ERT. It is also expected that 3D effects will occur due to the site characteristics, namely towards the end of the line and in the middle. The corresponding inversion result is given in Figure 4. The sea water was incorporated as a single region with a fixed resistivity of 1.4 Ωm, which is the mean fluid resistivity measurements in three different depths.

Outcrops of the bedrock lead to high resistivities of about 28000 Ωm at the northern and southern end of the profile. A low resistive zone appears at x = 200-600 m, directly below the sea, down to approximately 60-80 m depth, which could possibly be caused by a change of the geologic conditions that could be interpreted as a steep valley filled with sediments. This has not been documented previously. It might be caused by a graben structure formed between the well documented fracture zones NE3 and NE4. At the end of the sea (x = 600 m), a second low resistive zone appears that reaches down to 140 m depth, which correspond with the well-known fracture zone NE1. But is most likely possible that this is caused by 3D effects.

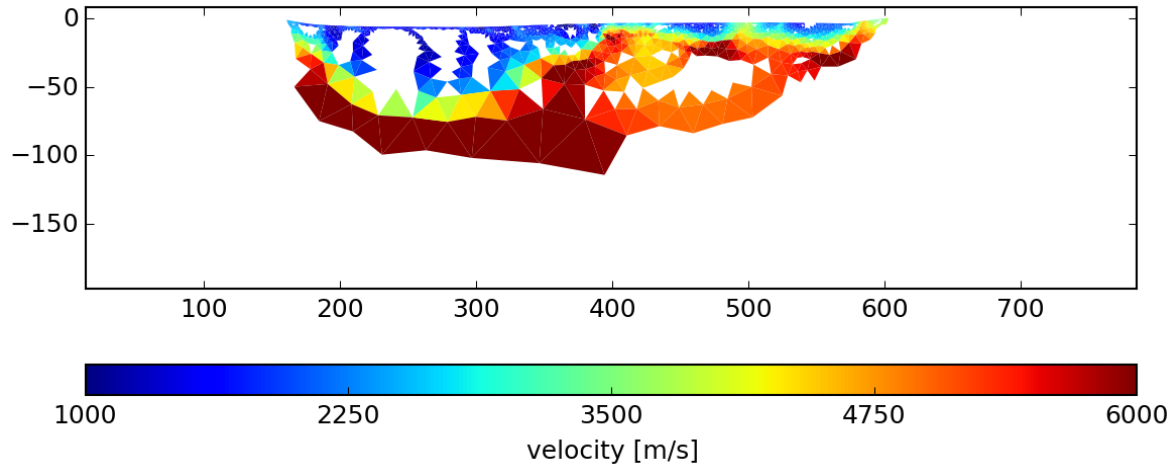


Figure 5: Inversion result of the seismic survey at Äspö HRL

A clear identification for the reason that might cause the low resistive zones can be possibly made using the results of the seismic refraction survey. As stated before, it covers the middle part of the ERT profile below the sea. Prior to the data fitting, negative travel times were deleted. For data inverse modelling, the

software GIMLi for geophysical modelling and inversion was used. The fitted p-wave velocity distribution is shown in Figure 5.
The crystalline bedrock appears as a high velocity zone of about 5600 m/s. Towards the northern part, the velocity of the bedrock decreases down to 5000 m/s. At the southern part, between x = 200-300 m, the result shows a low velocity zone down to 60 m depth, which is extended towards the north for shallow parts of the model, above 20 m depth. This finding coincides with the low resistive part in ERT result and is interpreted as sedimentary deposits that exhibit low velocities and, if water saturated, low resistivities. The sediments damp the seismic signal significantly that leads to a poor data quality below the sediments in the southern part. No further low velocity zones at larger depth appear, but at the near surface zone down to approximately 20 m depth. The fracture zone is not visible in the seismic result, due to the low data coverage in this part of the model.

5 CONCLUSION AND OUTLOOK

The inversion of the ERT data shows that the fracture zone in the northern part could be imaged as a low resistive zone. Additionally, a second low resistive anomaly in the southern part appears, which is interpreted as a previously unknown steep sediment valley. A comparison with the seismic result shows a low velocity zone in the same region, which is verification for sedimentary deposits. Due to insufficient data coverage, the fracture zone in the northern part of the profile could not be imaged by the seismic survey. An extension of the profile would be one way to ensure sufficient coverage.
In conclusion the preliminary evaluation shows that the approach has given very promising results, which illustrates that continuous information provided by geophysics can reveal previously unknown geological features even in an unusually well documented geological environment. There are possibilities for further developments of the interpretation of the data without costly additional data acquisition. For example, the reliability of the inversion results can be enhanced by implementing a-priori information, which could confine the ambiguity of the model space. Another possibility is to implement structurally coupled inversion, in which the data from the different geophysical models supports each other to reduce ambiguities.

6 ACKNOWLEDGEMENTS

Funding which made this work possible was provided by BeFo, Swedish Rock Engineering Research Foundation, (ref. 314) and SBUF, The Development Fund of the Swedish Construction Industry, (ref.12718) as part of the Geoinfra-TRUST framework (http://www.trust-geoinfra.se/). Furthermore, Formas, The Swedish Research Council, provided funding as part of the GESP project (ref no. 2009-797). NovaFOU also proved essential economic support the field campaign. Leibniz Institute for Applied Geophysics (LIAG) and Lund University (LU) provided in-kind support.

7 REFERENCES

Berglund, J. et al., 2003. Äspö Hard Rock Laboratory. Update of the geological model. SKB (Swedish Nuclear Fuel and Wast Management Company) P-03-07.

Lasheras Maas, N., 2015. Site characterisation at the Äspö Hard Rock Laboratory through seismic refraction, Bachelor Thesis, Lund University, Sweden

Rhén, I. et al., 1997. Äspö HRL-Geoscientific evaluation 1997/2 Results from pre-investigations and detailed site characterization. SKB (Swedish Nuclear Fuel and Waste Management Company) TR-97-03

Stanfors, R., Rhén, I., Tullborg, E.L. and Wikberg, P., 1999. Overview of geological and hydrogeological conditions of the Äspö hard rock laboratory site. Applied Geochemistry, 14(7), 819-834

Vidstrand, P., 2003. Äspö Hard Rock Laboratory. Update of the hydrogeological model 2002. SKB (Swedish Nuclear Fuel and Waste Management Company) IPR-03-35

Wikberg, P. et al., 1991. Äspö Hard Rock Laboratory. Evaluation and conceptual modelling based on the pre-investigations 1986-1990. SKB (Swedish Nuclear Fuel and Wast Management Company) Technical Report 91-22, (June)

Effects of measurement profile configuration on estimation of stiffness profiles of loose post glacial sites using MASW

E. Á. Ólafsdóttir
Faculty of Civil and Environmental Engineering, University of Iceland, Reykjavík, Iceland, eao4@hi.is

S. Erlingsson, B. Bessason
Faculty of Civil and Environmental Engineering, University of Iceland, Reykjavík, Iceland

ABSTRACT
Post glacial loose surface sediments are common in Iceland. Knowledge of the geotechnical properties of these sites is essential in various civil engineering projects. The shear wave velocity is a key parameter in this sense. Multichannel Analysis of Surface Waves (MASW) is a new and advanced technique to estimate shear wave velocity profiles of soil sites. The MASW method has been applied at two loose sites close to Landeyjahöfn harbour in South Iceland. The MASW field measurements were performed using twenty-four 4.5 Hz geophones as receivers spaced between 0.5 and 2 m apart. A 6.3 kg sledgehammer and jumping were used as impact sources. For each receiver setup, up to seven different source offsets were used, ranging from 5 to 50 m. Fourier analysis and phase velocity scanning was applied to evaluate dispersion curves based on data acquired with diverse receiver setups in order to assess the effects of the receiver spacing and the source offset on the quality of the surface wave records. The results indicate that the configuration of the MASW measurement profile has a substantial effect on the acquired time series and that it is beneficial to combine dispersion curves obtained from several different records which have been gathered at the same site prior to the inversion analysis.

Keywords: Multichannel Analysis of Surface Waves (MASW), field measurements, measurement profile configuration, dispersion analysis, shear wave velocity.

1 INTRODUCTION

Post glacial loose surface sediments of different nature are common in Iceland. Knowledge of the geotechnical properties of these sites is essential in various civil engineering projects. The shear wave velocity is a key parameter in this sense. The stiffness of individual soil layers is directly proportional to the square of their characteristic shear wave velocity. Furthermore, the shear wave velocity is vital in both liquefaction potential and soil amplification assessments (Kramer, 1996) and when defining site specific earthquake design loading according to Eurocode 8 (CEN, 2004).

For two decades, the seismic exploration method Spectral Analysis of Surface Waves (SASW) has been applied in Iceland to estimate the shear wave velocity and stiffness profiles of soil sites (Bessason, Baldvinsson and Þórarinsson, 1998; Bessason and Erlingsson, 2011). The Multichannel Analysis of Surface Waves (MASW) is a relatively new and more advanced technique. Implementation of the MASW method in Iceland began in 2013 (Ólafsdóttir, Bessason and Erlingsson, 2015). The first MASW measurements were carried out in South Iceland and a new set of software tools for analysis of MASW field data is under development at the Faculty of Civil and Environmental Engineering, University of Iceland (Ólafsdóttir, 2016).

The objective of the study presented in this paper is to develop and customise the new MASW method. This includes evaluation of the effects of the measurement profile configuration on the quality of the acquired surface wave records, as well as further development of the set of software tools used to carry out the analysis of the MASW field data.

2 MASW

In MASW, Rayleigh waves are generated and used to infer the shear wave velocity profile of the test site as a function of depth (Park, Miller and Xia, 1999). Compared to other available methods, surface wave analysis methods are low-cost, as well as being non-invasive and environmentally friendly since they neither require heavy machinery nor leave lasting marks on the surface of the test site.

The main advantages of the MASW method over the SASW method include a more efficient data acquisition routine in the field, faster and less labour consuming data processing procedures and improved identification and elimination of noise from recorded data (Park et al., 1999; Xia et al., 2002). Furthermore, observation of stiffness properties as a function of both depth and surface location becomes possible and economically feasible by using MASW (Xia, Miller, Park and Ivanov, 2000). Finally, it is possible to map significantly deeper shear wave velocity profiles when using the same impulsive source, i.e. a reasonably heavy sledgehammer. The observed difference between results obtained by MASW and direct borehole measurements is approximately 15% or less and random (Xia et al., 2002).

The maximum depth of investigation in a MASW survey varies with site, the natural frequency of the geophones that are used in the field measurements and the type of seismic source that is used. The investigation depth is determined by the longest Rayleigh wave wavelength that is obtained during data acquisition. A commonly adopted empirical criterion (Park and Carnevale, 2010) is that:

$$z_{max} \approx 0.5\lambda_{max} \quad (1)$$

where z_{max} (m) is the investigation depth and λ_{max} (m) is the longest wavelength.

MASW surveys can be broken down into three steps; field measurements, dispersion analysis and inversion analysis (Park et al., 1999). A general overview of the three-step procedure is provided in Fig. 1.

2.1 Field measurements

For field measurements, low frequency geophones are lined up on the surface of the test site as shown in Fig. 1a. For active MASW surveys (Park, Miller, Xia and Ivanov, 2007), which are the focus of this study, a wave is generated by an impulsive source that is applied at one end of the measurement profile. The geophones record the resulting wave propagation as a function of time (Fig. 1b). The distance from the impact load point to the first receiver in the geophone line up is referred to as the source offset and denoted by x_1 (see Fig. 1a). The receiver spacing is dx and the number of receivers is n. Hence, the length of the receiver spread is $L = (n-1)dx$ and the total length of the measurement profile is $L_T = x_1 + (n-1)dx$.

2.2 Dispersion analysis

In the dispersion analysis, Rayleigh wave dispersion curves are obtained using the recorded time series. Here, the so-called phase shift method (Park, Miller and Xia, 1998) is employed to obtain a dispersion image (a phase velocity spectrum). The dispersion image visualizes the dispersion properties of all types of waves contained in the recorded time series in the frequency – phase velocity domain. Different modes of Rayleigh waves are recognized by their frequency content and characterizing phase velocity at each frequency. Noise sources, e.g. body waves and reflected/scattered waves, are likewise recognized by their frequency content.

The phase shift method can be divided into three steps; Fourier transformation and amplitude normalization, dispersion imaging and extraction of dispersion curves (Park et al., 1998). The three main data processing steps are illustrated in Fig. 2 and briefly described below.

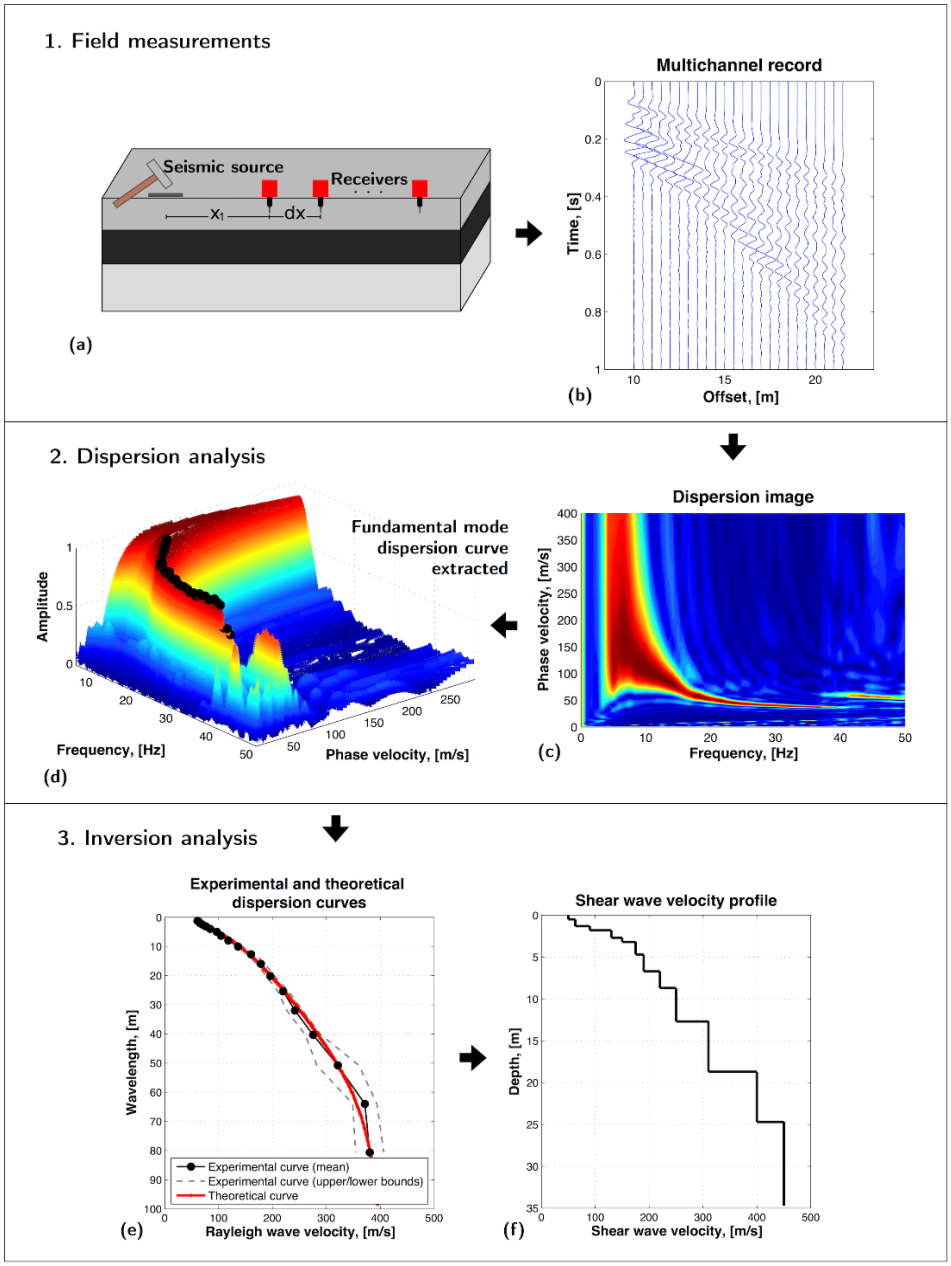


Figure 1. Overview of the MASW method. (a) Geophones are lined up on the surface of the test site. (b) A wave is generated and the wave propagation is recorded. (c) A dispersion image is obtained from the recorded surface wave data. (d) The high-amplitude bands display the dispersion characteristics and are used to construct the fundamental mode dispersion curve. (e) A theoretical dispersion curve is obtained based on assumed layer thicknesses and material parameters for each layer and compared to the experimental dispersion curve. (f) The shear wave velocity profile and the layer structure that results in an acceptable fit are taken as the results of the survey.

A Fourier transform is applied to each trace of the multichannel record. The transformed record can be expressed in terms of amplitude and phase, $\tilde{u}_j(\omega) = A_j(\omega)P_j(\omega)$. The phase term, $P_j(\omega)$, is determined by the characteristic phase velocity of each frequency component. The amplitude term, $A_j(\omega)$, preservers information regarding other properties such as the attenuation of the signal and its geometrical spreading. As all information regarding phase velocity is contained in the phase term, the amplitude of the transformed record can be normalized in both the offset and the frequency dimensions without loss of vital information (Park et al., 1998; Ryden, Park, Ulriksen and Miller, 2004).

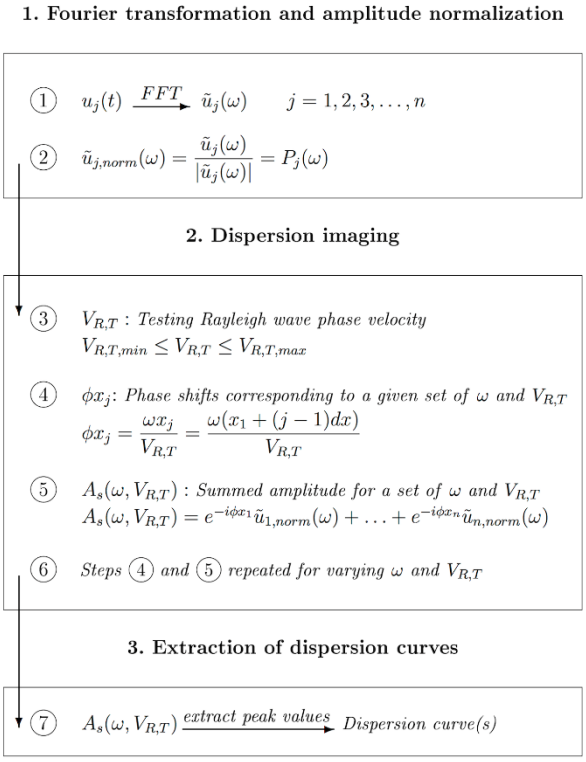


Figure 2. Overview of the phase shift method.

For a given testing phase velocity ($V_{R,T}$) and a given frequency (ω), the amount of phase shifts required to counterbalance the time delay corresponding to specific offsets are determined. The phase shifts (determined in step 4 in Fig. 2 for a given testing phase velocity) are applied to distinct traces of the transformed record that are thereafter added to obtain the slant-stacked amplitude corresponding to each pair of ω and $V_{R,T}$ (Park et al., 1998; Ryden et al., 2004). This is repeated for all the different frequency components of the transformed record in a scanning manner, changing the testing phase velocity in small increments. The dispersion image is obtained by plotting the summed amplitude in the frequency – phase velocity domain (Fig. 1c). The high-amplitude bands, which are indicated by the height of the peaks and/or a colour scale, display the dispersion characteristics of the recorded surface waves (Fig. 1d) and are used to construct the fundamental mode dispersion curve for the site (Park et al., 1998; Ryden et al., 2004). Noise is usually automatically removed in this process (Park et al., 2007).

The quality of the acquired surface wave records can be evaluated in terms of the resolution of the phase velocity spectrum, i.e. the sharpness of the amplitude peaks observed at each frequency, the extractable frequency range and the continuity of the fundamental mode high-amplitude band.

2.3 Inversion analysis

The third step of the MASW method is to obtain a shear wave velocity profile by inversion of the fundamental mode dispersion curve. Computations are based on Rayleigh wave propagation theory assuming a plane-layered elastic earth model. The last layer is assumed to be a half-space.

Inversion problems involving the dispersion of Rayleigh waves in a layered medium must be solved by iterative methods due to their non-linearity. A theoretical dispersion curve is obtained based on an assumed number and thickness of soil layers and assumed material parameters for each layer. For a layered earth model, the shear wave velocity profile has a dominant effect on the fundamental mode dispersion curve (Xia, Miller and Park, 1999). Theoretical dispersion curves are in most cases determined by matrix methods that originate in the work of Thomson (1950) and Haskell (1953). Here, the stiffness matrix method, developed by Kausel and Roësset (1981), is used for computations of theoretical dispersion curves (Fig. 1e).

A simple local search method is employed to fit observations with theoretical predictions from assumed soil models (Ólafsdóttir, 2016). A layered soil model is suggested where the thickness of the layers increases with depth. The initial value of the shear wave velocity for each layer is estimated from the measured dispersion curve. It is based on the ratio between the propagation velocities of Rayleigh waves and shear waves in a homogeneous medium, and a simple relation between Rayleigh wave wavelength and representative depth (Kramer, 1996; Park et al., 1999). Other model parameters, i.e. Poisson's ratio (or the compressional wave velocity) and the mass density of each layer, are either estimated based on independent soil investigations or on experience of similar soil types from other sites. The shear wave velocity of each layer is updated during the inversion process while all other model parameters are kept unchanged. In each iteration, the misfit between the theoretical dispersion

curve and the experimental dispersion curve is evaluated in terms of the root-mean-square (RMS) error between the theoretical and experimental Rayleigh wave phase velocities. The shear wave velocities obtained by this approach, along with the layer thicknesses, are then used to represent the soil profile at the survey site (Fig. 1f).

2.4 Measurement profile configuration

It is commonly recognised that the configuration of the MASW measurement profile can affect the quality of the surface wave records that are obtained (Park and Carnevale, 2010; Park, Miller and Miura, 2002; Park, Miller and Xia, 2001). The main parameters related to the setup of the measurement profile are the length of the receiver spread (or the receiver spacing if a fixed number of geophones is used) and the source offset.

The length of the receiver spread is related to the longest Rayleigh wave wavelength that is obtained during data acquisition and therefore also related to the maximum depth of investigation:

$$\lambda_{max} \approx L \qquad (2)$$

where λ_{max} (m) is the longest wavelength and L (m) is the length of the receiver spread.

Attempts to analyse longer wavelengths than indicated by Eq. (2) can lead to less accurate results. A recent study has shown that the fluctuating inaccuracy will although be within 5% for $L \leq \lambda_{max} \leq 2L$ (Park and Carnevale, 2010).

The minimum source offset required to avoid undesirable near-field effects, i.e. the risk of non-planar surface waves being picked up by the receivers, depends on the longest wavelength that is analysed. It is commonly regarded that plane-wave propagation of surface waves first occurs when the source offset is greater than half the longest wavelength. However, studies have shown that this criterion can be relaxed significantly for MASW surveys (Park et al., 1999; 2002).

3 MASW FIELD MEASUREMENTS

MASW field measurements were carried out in August 2014 at two test sites at Bakkafjara in South Iceland, referred to as sites B1 and B2 (see Fig. 3). The soil at Bakkafjara is mainly uniformly graded dark basalt sand. The groundwater table is estimated to be at a 4.0 m depth (Ólafsdóttir, 2016).

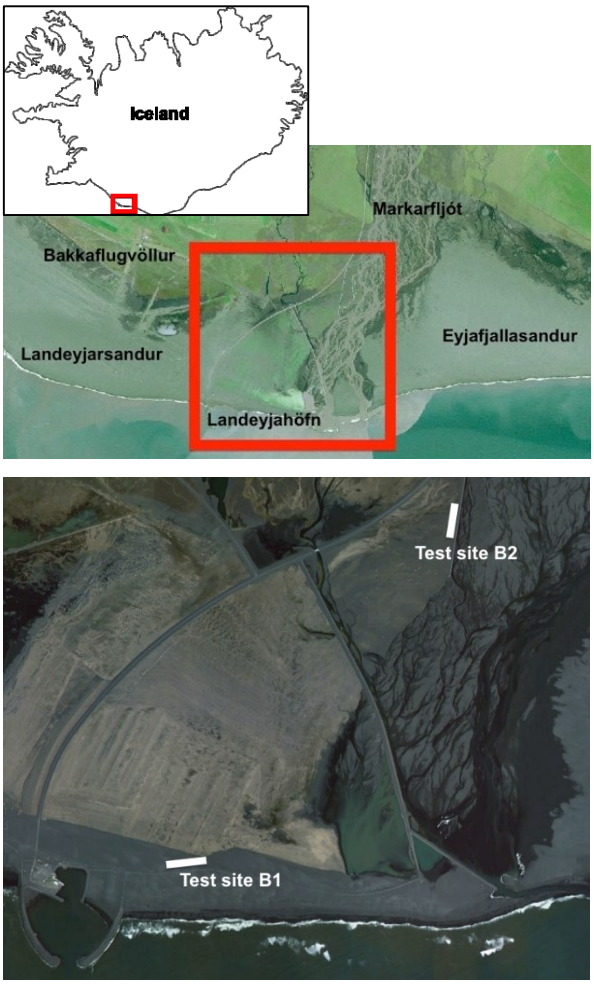
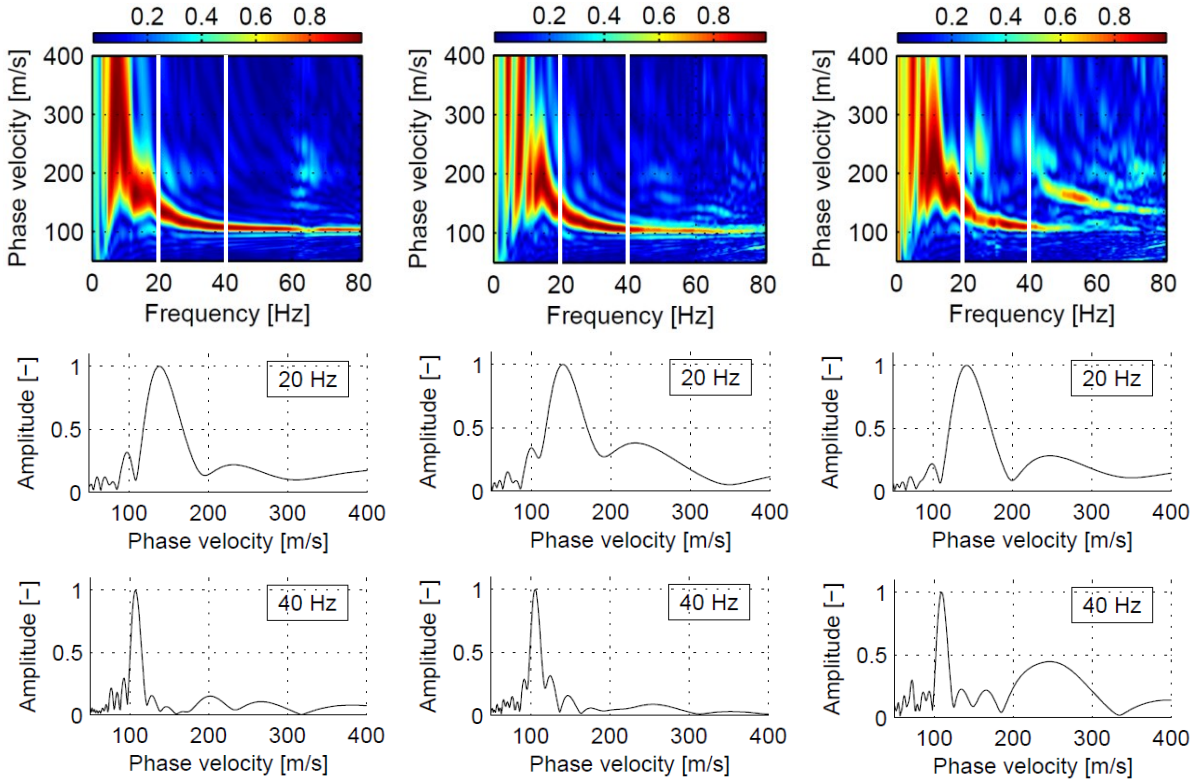


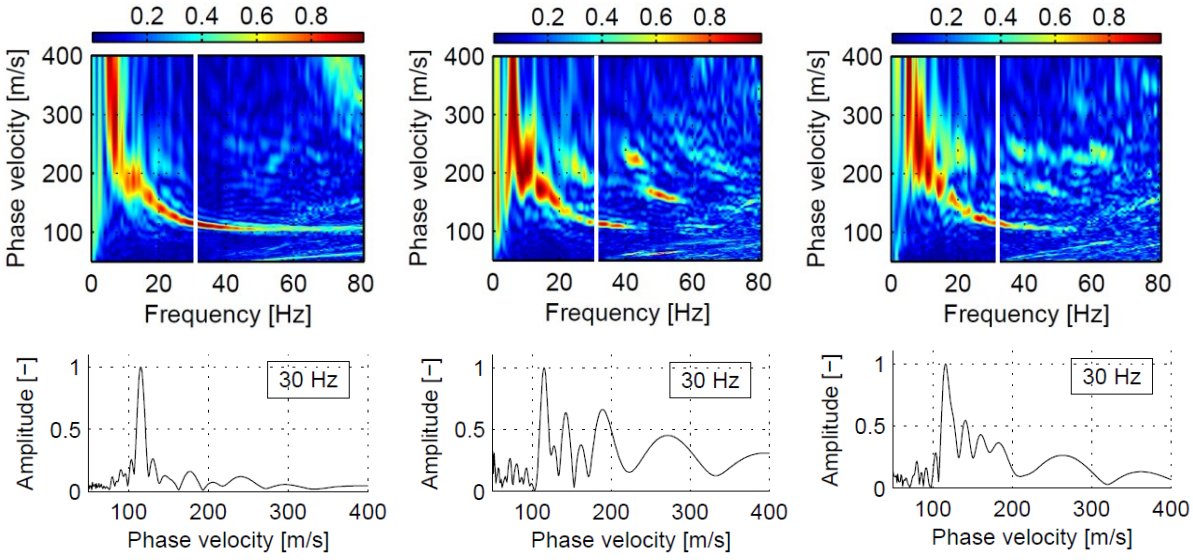
Figure 3. Location of MASW field measurements at Bakkafjara in South Iceland. Data were acquired at two test sites, referred to as test site B1 and test site B2.

The field measurements at Bakkafjara were performed using twenty-four 4.5 Hz geophones as receivers. A 6.3 kg sledgehammer and a single jump at the end of the measurement profile were used as impact sources. At each test site, three receiver spreads with the same midpoint but different receiver spacing, i.e. $dx \in \{0.5, 1.0, 2.0\}$ m, were tested.



(a) x_1 = 10.0 m. *(b) x_1 = 20.0 m.* *(c) x_1 = 30.0 m.*

Figure 4. Change in spectral resolution with length of source offset. Top. Typical dispersion images obtained at Bakkafjara test site B2 with a receiver spread of length L = 23.0 m (dx = 1.0 m) and a source offset of (a) x_1 = 10.0 m, (b) x_1 = 20.0 m and (c) x_1 = 30.0 m. A 6.3 kg sledgehammer was used as an impact source. Middle/bottom: Cross sections through the dispersion images at f = 20 Hz and f = 40 Hz. The location of the cross sections is indicated by vertical lines in Fig. 4 (top).



(a) x_1 = 10.0 m. *(b) x_1 = 20.0 m.* *(c) x_1 = 40.0 m.*

Figure 5. Change in spectral resolution with length of source offset. Top. Typical dispersion images obtained at Bakkafjara test site B2 with a receiver spread of length L = 46.0 m (dx = 2.0 m) and a source offset of (a) x_1 = 10.0 m, (b) x_1 = 20.0 m and (c) x_1 = 40.0 m. A 6.3 kg sledgehammer was used as an impact source. Bottom: Cross sections through the dispersion images at f = 30 Hz.

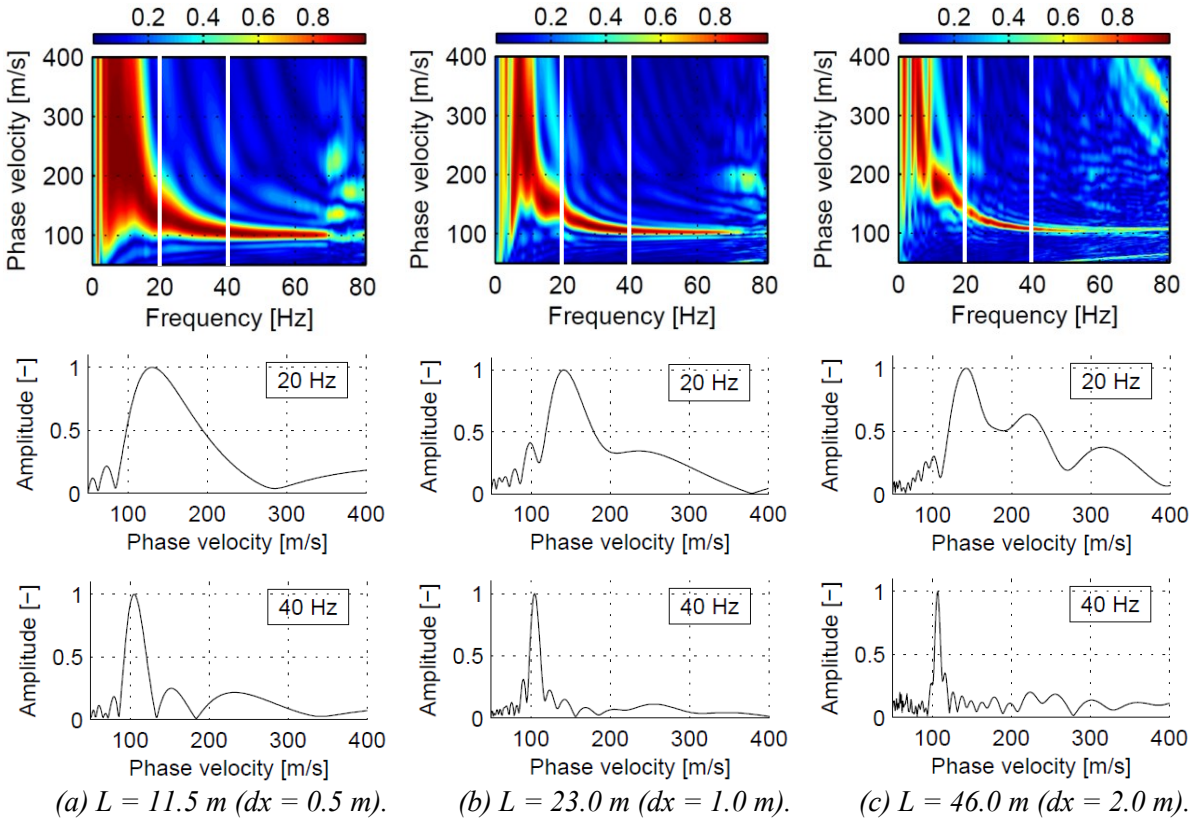


Figure 6. Change in spectral resolution with length of receiver spread. Top. Typical dispersion images obtained at Bakkafjara test site B2 with receiver spreads of length (a) L = 11.5 m, (b) L = 23.0 m and (c) L = 46.0 m. The source offset is x_1 = 5.0 m in all cases. A 6.3 kg sledgehammer was used as an impact load. Middle/bottom: Cross sections through the dispersion images at f = 20 Hz and f = 40 Hz.

For each receiver setup, up to seven source offsets in the range of 5 m to 50 m were used. No systematic difference was observed between surface wave records where the impact load was created by a sledgehammer and where it was created by a jump.

3.1 Observed effects of measurement profile configuration at Bakkafjara

Typical dispersion images of records acquired at the Bakkafjara test site B2 with receiver spreads of fixed length (23.0 m in Fig. 4 and 46.0 m in Fig. 5) but with source offsets of various lengths are shown in Figs. 4 (top) and 5 (top). A 6.3 kg sledgehammer was used as an impact source in all cases. Figures 4 and 5 (middle and bottom) show the variation of the amplitude band with Rayleigh wave phase velocity at frequencies 20 and 40 Hz (Fig. 4) and 30 Hz (Fig. 5). The amplitude band is normalized such that the maximum amplitude at each frequency is one. The highest peaks correspond in all cases to the identified fundamental mode.

The results presented in Figs. 4 and 5 indicate that the length of the source offset did not have a strong effect on the sharpness of the amplitude peaks. The same was observed based on data acquired at the Bakkafjara test site B1. However, for a given length of the receiver spread, an increased length of the source offset tended to cause increased disturbances in the spectral high-amplitude band. Moreover, the presence of overtones and/or other noise became more evident in the higher frequency range of the phase velocity spectrum with increasing source offset.

Figure 6 (top) shows typical dispersion images obtained at test site B2 with receiver spreads of length (a) 11.5 m, (b) 23.0 m and (c) 46.0 m. The source offset was 5.0 m in all cases. The impact load was created by a sledgehammer. Cross sections through the dispersion images at frequencies 20 and 40 Hz

are shown in Fig. 6 (middle and bottom). The highest peaks correspond to the fundamental mode.

Based on the results presented in Fig. 6, the length of the receiver spread had a substantial effect on the resolution of the dispersion image. In general, by lengthening the receiver spread (i.e. increasing the receiver spacing and keeping the number of geophones used for recording unchanged), the fundamental mode high-amplitude peaks appeared sharper and better separation of overtones was observed. The same was noticed by analysis of surface wave records acquired at test site B1. At the Bakkafjara test sites, records acquired with a 46.0 m long receiver spread allowed in general extraction of the fundamental mode dispersion curve at lower frequencies than records acquired with receiver spreads of length 11.5 m or 23.0 m. However, the dispersion images presented in Fig. 6 (top) indicate that increased length of the receiver spread tended to have a negative effect on the continuity of the fundamental mode high-amplitude band, especially in the higher frequency range, which counteracted to some extent the benefits of increasing the length of the receiver spread.

4 DISCUSSION

Based on the results acquired at the Bakkafjara test sites, dispersion images of records acquired with a short receiver spread and/or a short/medium-length source offset showed in most cases a relatively unbroken fundamental mode high-amplitude band and allowed identification and extraction of the fundamental mode dispersion curve in the higher frequency range. Hence, time series recorded by a relatively short measurement profile provided in general the most information about the dispersion properties of the short wavelength wave components that propagated through the topmost soil layers.

The high-amplitude band observed in a dispersion image acquired with a short receiver spread can be very wide, especially at the low- and mid-range frequencies. The low spectral resolution can cause difficulties in identification of the spectral peak values, which risks less accurate dispersion curves. In general, by lengthening the receiver spread, the observed spectral resolution increases, which facilitates the identification and the extraction of the fundamental mode dispersion curve, especially in the lower frequency range. Hence, the study found that time series recorded by long receiver spreads tended to provide the most investigation depth.

The observed effects of the data acquisition parameters suggest that an increased range in investigation depth can be obtained by combining dispersion curves acquired with measurement profiles of different lengths. Furthermore, combining several dispersion curves creates possibilities to estimate the accuracy of the extraction process, to compensate for segments of missing data in the extracted dispersion curves and to diminish the effect of poor quality surface wave records without the analyst having to selectively choose records for further analysis.

The dispersion analysis software tool that is under development includes a special algorithm to obtain an average experimental dispersion curve, along with upper and lower boundary curves (Ólafsdóttir, 2016). The average dispersion curve is obtained by grouping data points from multiple dispersion curves together within 1/3 octave wavelength intervals. All phase velocity values within each interval are added up and their mean used as an estimate of the phase velocity of Rayleigh wave components belonging to the given wavelength range. Upper and lower boundaries for the average dispersion curve are obtained using the standard deviation of the values within each wavelength band. The average dispersion curve, along with its upper and lower boundaries, is subsequently used as an input in the inversion analysis.

The average experimental dispersion curves obtained for the Bakkafjara test sites B1 and B2 by using the aforementioned methodology are shown in Figs. 7a and 8a. The upper and lower bounds correspond to plus/minus one standard deviation of the average curve. Inversion was then used to obtain the shear wave velocity profiles for the sites (see Figs. 7b and 8b).

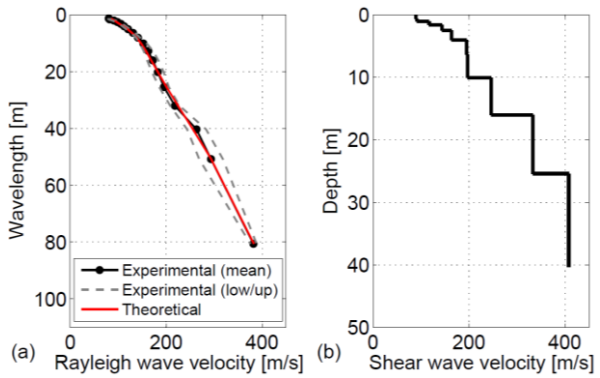


Figure 7. (a) Comparison of experimental and theoretical dispersion curve based on inversion. (b) The estimated shear wave velocity profile for the Bakkafjara test site B1.

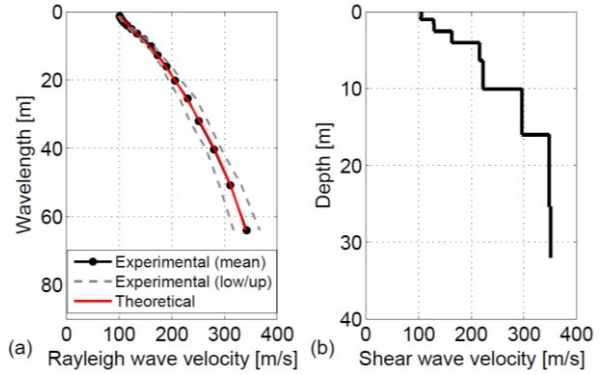


Figure 8. (a) Comparison of experimental and theoretical dispersion curve based on inversion. (b) The estimated shear wave velocity profile for the Bakkafjara test site B2.

5 CONCLUSIONS AND SUMMARY

MASW is a relatively new seismic exploration method to estimate the shear wave velocity profile of near-surface materials. MASW measurements have been carried out at two test sites at Bakkafjara in South Iceland using twenty-four 4.5 Hz geophones for recording. For each receiver setup, up to seven different source offsets were used, ranging from 5 m to 50 m. Dispersion analysis was then applied to evaluate a phase velocity spectrum and a dispersion curve based on each surface wave record that was acquired.

The results indicated that the configuration of the MASW measurement profile had a substantial effect on the acquired surface wave data. Records obtained using a relatively short measurement profile provided in general the most information about the dispersion properties of the short wavelength wave components that propagated through the top-most soil layers. However, time series recorded by long receiver spreads provided in general the most investigation depth. The observations are in accordance to existing recommendations where the obtainable investigation depth is suggested to be directly related to the length of the receiver spread.

Analysis of the dispersion images and the dispersion curves indicated that it is beneficial to combine results from several measurements which have been carried out using measurement profiles of different lengths prior to the inversion analysis. A new algorithm has been developed to compute an average experimental dispersion curve, along with upper and lower boundaries, by adding up dispersion curves obtained based on multiple surface wave registrations. The new data processing procedure has been applied to the data acquired at the Bakkafjara test sites to evaluate average dispersion curves for wavelengths up to 80 m.

Optimum values of measurement profile setup parameters for MASW surveys are to some extent documented in references. An effort is though necessary to collect more information about the optimal setup, since there are many site-specific factors that may affect the setup, for instance the depth to bedrock and the soil type. Future research topics include further and more detailed analysis of the effects of the measurement profile configuration and development of guidelines for the setup of the measurement profile(s) and the execution of the MASW measurements in the field.

6 ACKNOWLEDGEMENTS

The project is financially supported by grants from the University of Iceland Research Fund, the Icelandic Road and Costal Administration and the Energy Research Fund of the National Power Company of Iceland.

7 REFERENCES

Bessason, B., Baldvinsson, G. I., & Þórarinsson, Ó. (1998). SASW for evaluation of site-specific earthquake excitation. Proceedings of the 11th European Conference on Earthquake Engineering, CD-ROM, Paris.

Bessason, B., & Erlingsson, S. (2011). Shear wave velocity in surface sediments. Jökull, 61, 51-64.

CEN. (2004). EN1998-1:2004, Eurocode 8: Design of structures for earthquake resistance - Part 1: General rules, seismic actions and rules for buildings. Brussels: European Committee for Standardization.

Haskell, N. A. (1953). The dispersion of surface waves on multilayered media. Bulletin of Seismological Society of America, 43(1), 17-34.

Kausel, E., & Roësset, J. M. (1981). Stiffness matrices for layered soils. Bulletin of the Seismological Society of America, 71(6), 1743-1761.

Kramer, S. L. (1996). Geotechnical Earthquake Engineering. Upper Saddle River, NJ: Prentice Hall.

Ólafsdóttir, E. Á, Bessason, B. & Erlingsson S (2015). MASW for assessing liquefaction of loose sites. Proceedings of the 16th European Conference on Soil Mechancis and Geotechnical Engineering, 13-17 September 2015, Edinburgh, UK.

Ólafsdóttir, E. Á. (2016). Multichannel Analysis of Surface Waves for assessing soil stiffness. (Unpublished master's thesis). Faculty of Civil and Environmental Engineering, University of Iceland, Reykjavík, Iceland.

Park, C. B., Miller, R. D., & Xia, J. (1998). Imaging dispersion curves of surface waves on multichannel record. 68th Annual International Meeting Society of Exploration Geophysicists, Expanded Abstracts, 1377-1380.

Park, C. B., Miller, R. D., & Xia, J. (1999). Multichannel analysis of surface waves. Geophysics, 64(3), 800-808.

Park, C. B., Miller, R. D., & Xia, J. (2001). Offset and resolution of dispersion curve in multichannel analysis of surface waves (MASW). Proceedings of the Symposium on the Application of Geophysics to Engineering and Environmental Problems (SAGEEP 2001), Denver, Colorado, SSM-4.

Park, C. B., Miller, R. D., & Miura, H. (2002). Optimum field parameters of an MASW survey. Expanded Abstracts, SEG-J, Tokyo, May 22-23, 2002.

Park, C. B., Miller, R. D., Xia, J., & Ivanov, J. (2007). Multichannel analysis of surface waves (MASW) - active and passive methods. The Leading Edge, 26(1), 60-64.

Park, C. B., & Carnevale, M. (2010). Optimum MASW Survey - Revisit after a Decade of Use. In Fratta, D. O., Puppala, A. J., & Muhunthan, B. (editors), GeoFlorida 2010: Advences in Analysis, Modeling and Design,1303-1312. doi: 10.1061/41095(365)130.

Ryden, N., Park, C. B., Ulriksen, P., & Miller, R. D. (2004). Multimodal approach to seismic pavement testing. Journal of Geotechnical and Geoenvironmental Engineering, 130, 636-645.

Thomson, W. T. (1950). Transmission of elastic waves through a stratified solid medium. Journal of Applied Physics, 21(2), 89-93.

Xia, J., Miller, R. D., & Park, C. B. (1999). Estimation of near-surface shear-wave velocity by inversion of Rayleigh waves. Geophysics, 64(3), 691-700.

Xia, J., Miller, R. D., Park, C. B., & Ivanov, J. (2000). Construction of 2-D vertical shear-wave velocity field by the multichannel analysis of surface waves technique. Proceeding of the Symposium of the Application of Geophysics to Engineering Environmental Problems (SAGEEP 2000) Arlington, VA., February 20-24, 1197-1206.

Xia, J., Miller, R. D., Park, C. B., Hunter, J. A., Harris, J. B., & Ivanov, J. (2002). Comparing shear-wave velocity profiles from multichannel analysis of surface wave with borehole measurements. Soil Dynamics and Earthquake Engineering, 22(3), 181- 190.

Temporary Groundwater Control for Construction of Railway Tunnels in Copenhagen

Jes Michaelsen
Rambøll, Denmark, JSXM@ramboll.dk

Judith Wood
Rambøll, Denmark

ABSTRACT
As part of the construction of the new high-speed railway line between Copenhagen and Ringsted, two cut-and-cover tunnels are constructed in the urban zone in Copenhagen. The tunnels are each about 1000 m long and intersect a series of known contaminated sites as well, as an area used for drinking water supply.

In order to meet the construction requirements of maintaining a dry excavation, the groundwater must be lowered between 2 and 5 m to approximately level -2 m AOD and -4 m AOD respectively. The tunnels are located in strata consisting of clay till of relatively low permeability overlying limestone of high permeability.

Given the dense urbanization and the intersection of existing contaminated sites, requirements from the authorities have focused on reducing the drawdown effects in the surrounding residential areas and minimizing the movement of contaminant plumes, in order to protect existing drinking water supply wells and basement air quality.

This paper describes how these challenges are overcome by undertaking a series of detailed preliminary hydrogeological investigations. The investigations include installation of test boreholes, pumping testing, geophysical borehole logging, water quality sampling, soil-gas sampling and air quality measurements in residential basements. Subsequently, updating and calibration of a numerical 3D groundwater model, designed to assess the different strategies and provide the optimal design of the system, was undertaken.

The selected design of the groundwater control system consists of some 100 pumping wells located inside or near the excavation, some 120 injection wells located at a perimeter of up to 400 m from the excavation, and a system of 100 monitoring wells. Both abstraction and injection is from and to the limestone aquifer. During operation of the groundwater control system, up to 700 m^3/h is abstracted, treated in activated-carbon filters and injected, thereby meeting the requirements from the involved authorities.

Keywords: Groundwater lowering, Tunnels, Authority liaison, Hydrogeological investigations,

1 BACKGROUND

As part of the construction of the new high-speed railway line between Copenhagen and Ringsted, two cut-and-cover tunnels are constructed in the urban zone in Copenhagen. The tunnels intersect a dense urban area with existing well known contaminated sites (chlorinated solvents and benzene) but also an area used for groundwater abstraction,

where the main concerns relate to high nickel and chloride concentrations, that already, prior to the project, exceed the acceptable concentrations, as set by the Authorities. A stream that crosses the alignment between the two tunnels, on the border between the Municipality of Copenhagen and the Municipality of Hvidovre is classified as a protected stream.

The location of the new railway line is marked in red on Figure 1.

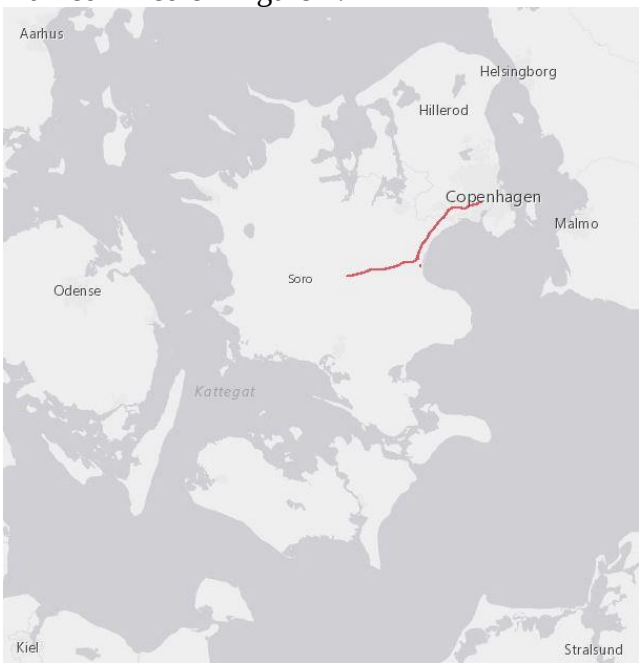


Figure 1 The new railway line Copenhagen – Ringsted.

The construction is divided into a number of tender packages of which the tender package covering two urban tunnels is the largest and most complicated.

The project owner is Banedanmark, operator of the Danish railway network.

2 THE PROJECT

The tunnels and troughs are each about 1000 m long and intersect a series of known contaminated sites, as well as an area used for drinking water supply.
Figure 2 and Figure 3 show the location of the two tunnels, investigation boreholes and existing contaminated sites.



Figure 2 Location plan showing Hvidovre Tunnel and troughs, investigation boreholes and contaminated sites in Hvidovre Municipality.

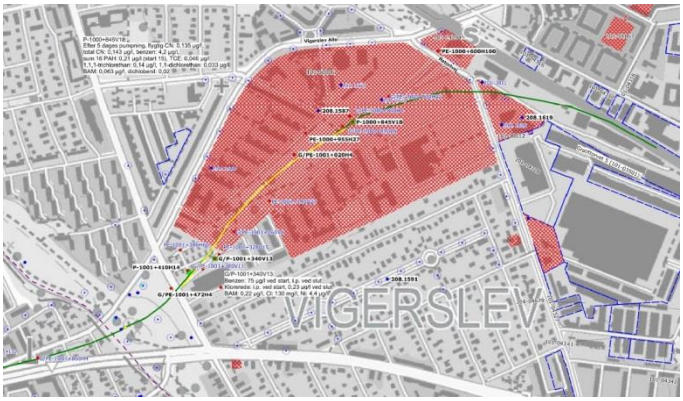


Figure 3 Location plan showing Kulbane Tunnel and troughs, investigation boreholes and contaminated sites in Copenhagen Municipality.

In order to meet the construction requirements of maintaining a dry excavation, the groundwater must be lowered between 2 and 5 m to approximately level -2 m AOD and -4 m AOD respectively. The tunnels are located in strata consisting of clay till of relatively low permeability overlying limestone of high permeability.
Given the dense urbanization and the intersection of existing contaminated sites, requirements from the authorities have focused on reducing the drawdown effects in the surrounding residential areas and minimizing the movement of contaminant plumes, in order to protect existing drinking water supply wells and air quality in neighbouring residential buildings.
This paper describes how these challenges are overcome by undertaking a series of detailed preliminary hydrogeological investigations. The investigations include installation of test boreholes, pumping testing, geophysical borehole logging, water quality sampling, soil-gas sampling and air

quality measurements in residential basements. Subsequently, updating and calibration of a numerical 3D groundwater model, designed to assess the different strategies, and provide the optimal design of the system, was undertaken.
The selected design of the groundwater control system consists of approximately 100 pumping wells located inside or near the excavation, 120 injection wells located at a perimeter of up to 400 m from the excavation, and a system of almost 100 monitoring wells. Both abstraction and injection is from and to the limestone aquifer. During operation of the groundwater control system up to 700 m^3/h is abstracted, treated in activated-carbon filters and injected, thereby meeting the requirements from the involved authorities.

3 PRELIMINARY HYDROGEOLOGICAL INVESTIGATIONS

Geological and hydrogeological investigations were carried out in order to refine the existing conceptual model of the area. The model was updated with detailed information about the borehole geology, groundwater level in the limestone aquifer, hydraulic parameters (T, S) of the geological units, and stage and flow of the Damhusåen stream where it intersects the project, between the two tunnels and on the border between the municipalities of Copenhagen and Hvidovre. The various investigations are discussed in the following sections.

3.1 Drilling investigations

A large number of geotechnical boreholes were drilled and subsequent tests conducted in the tunnel alignment area to obtain detailed design parameters for the construction of the tunnels. Where feasible, hydrogeological investigations were performed in the geotechnical boreholes. In addition, a number of wells, installed with screens targeting the primary limestone aquifer, were established outside the alignment.

The borehole-information from these preliminary investigations provided a detailed picture of the lateral variation of strata thickness: This was incorporated into a revised conceptual groundwater model.

3.2 Flow logging

Prior to completing the well installations, a geophysical flow log was performed in selected boreholes. The purpose of geophysical logging was to assess the vertical flow distribution in the limestone aquifer to optimize well design and determine the required target depth of the secant pile walls. Furthermore, flow logging results were applied in the conceptual groundwater model, and permitted separation of the limestone layer into high- and low-yielding units.

3.3 Pumping testing

Following the well completion development pumping test were carried out in order to obtain information about the hydraulic characteristics of the pumped limestone aquifer, the overlying confining clay till and the shallow aquifer, where present.

In most cases, the constant-rate pumping tests included a number of monitoring wells screened in different levels in order to assess the effects on the shallow aquifer and hence undertake an assessment on potential settlement of neighbouring buildings.

The findings of the geophysical flow logging identified two flow zones in the limestone separated by a low permeability flow zone. In order to obtain field data that would permit simulation of this in the groundwater model, 12 pumping well where installed along the alignment with an associated monitoring well about 20 m away. In each of the well-pairs, the pumping well was screened targeting the deep flow zone in the limestone, whereas the monitoring well was screened in the upper flow zone (as well as the pumped aquifer). A constant-rate pumping test was carried out in these well-pairs to obtain data for the design depth of cut-off walls.

3.4 Groundwater monitoring

In order to obtain background water levels from the project area, an online monitoring system consisting of 35 monitoring wells screened in the limestone aquifer were

established. Existing wells were used where possible, but in addition, 9 new monitoring wells were drilled to provide sufficient coverage in all directions from the excavation. The 35 monitoring wells were equipped with pressure transducers and modems that continuously send water level data to a custom-designed online supervision system. The collection of background data was completed by conducting a comprehensive monitoring round where more than 100 wells in the area were manually sounded in one single day, prior to starting the groundwater lowering.

The online supervision system has been operating throughout the project collecting data.

Detailed, baseline groundwater-quality data was obtained via the following activities: literature searches of environmental site assessment reports to find historical water quality data; extensive environmental assessments, performed in 2011, including water quality sampling at the final stage of step-drawdown tests in 11 wells and 7-day pumping tests performed in 14 wells; environmental screening for contaminants and undesirable parameters, such as nickel, which started in selected monitoring wells several months prior to start of groundwater lowering activities, and finally, prior to test of the groundwater lowering and injection system, the water quality of every fifth pumping well and infiltration well, was screened.

Furthermore, residential buildings that are neighbours to a former automobile repair shop were investigated for benzene levels under the basement floors as well as in the basement, to document background concentrations prior to start of groundwater lowering activities.

3.5 Stream flow gauging

Even though the groundwater control system is based on recharging 100 % of the abstracted groundwater back into the aquifer, the contingency plan included discharging excess groundwater to the stormwater sewer system as well as into the conveniently located Damhusåen stream that intersects the central part of the project. In order to obtain an authority permit to discharge groundwater to the stream, flow profiles were gauged at an upstream and downstream location from where the stream intersects the tunnel alignment. The flow profiles were gauged every two weeks from 6 months before the groundwater lowering commenced and continued after the project started. This allowed assessing the seasonal variation in both water quality and the stream flow, as well as quantifying the groundwater discharge to the stream or recharge from the stream to the groundwater.

4 RESULTS

4.1 Geology

The borehole information from preliminary investigations was used to update the geological model. An example of the cross section is provided in Figure 4. The conceptual model consists of a fill layer of approximately 1 m thickness overlying a clay till layer between 2 and 6 m thickness again overlying the regional limestone aquifer. A shallow sand aquifer is encountered in places within the clay till layer. These sand units are generally considered to contain only limited volumes of groundwater since they are relatively thin and of limited lateral extent.

However, it is noted that where Damhusåen stream crosses the project area, the clay till layer is thin. Instead, the sand layer is sitting directly on the limestone providing a higher degree of hydraulic contact between the limestone aquifer and the stream.

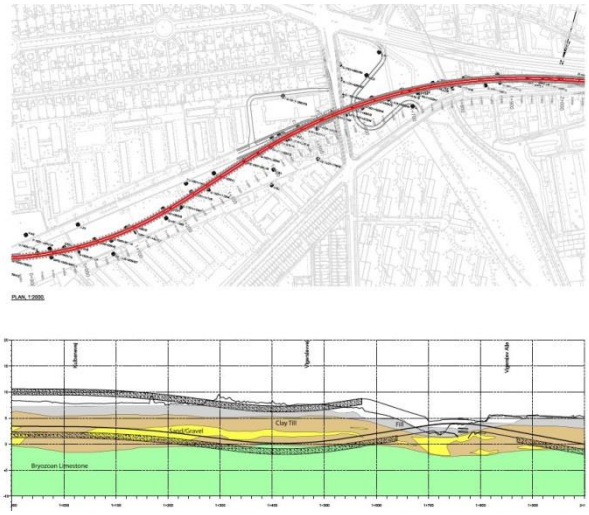
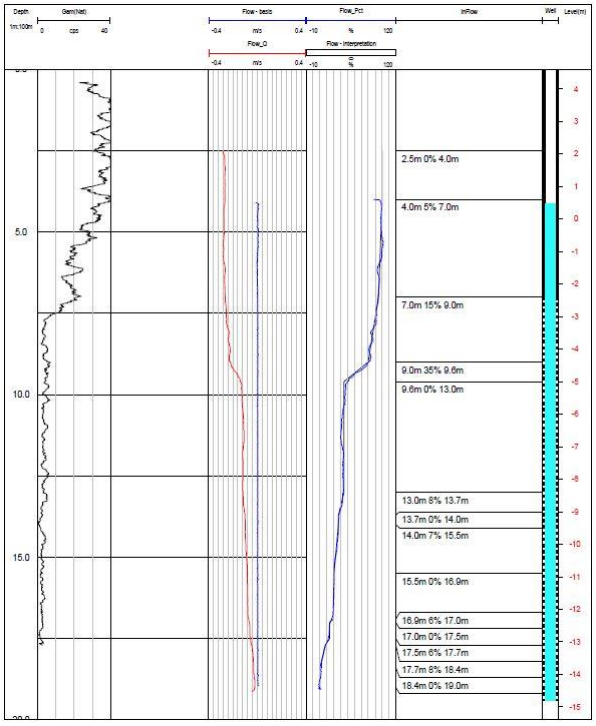


Figure 4 Example of the geological cross section.

4.2 Geophysical flow logging

The results of the geophysical flow logs indicated that the primary flow zone in the limestone is in the upper 5 m of the unit. In some of the boreholes, mainly near Damhusåen and Vigerslevparken a sand layer is encountered overlaying the limestone, making this aquifer unit high-yielding compared to the area further west in the tunnel alignment.



4.3 Pumping testing

A number of pumping tests have been performed in existing and new boreholes to assess the transmissivity of the limestone aquifer. Where the wells where considered for use as abstraction or injection, a step-drawdown pumping test followed by recovery was carried out, whereas constant-rate pumping tests followed by recovery where carried out in order to obtain information about the lateral variation of the transmissivity. Figure 5 shows an example of the density of wells used for pumping tests during the investigations.



Figure 5 Map showing location of wells used for pumping tests and flow logs around the centre of the Hvidovre Tunnel. Blue dots denote wells used for pumping tests and red dots denote wells used for flow logging.

The results show that the horizontal distribution of the transmissivity varies: the high-yielding limestone is found around the Damhusåen stream. The limestone aquifer becomes less transmissive to the west, by a factor of 5. The calculated transmissivities were used to produce a contoured map showing the transmissivity distribution of the limestone aquifer, refer to *Figure 6*. Along with the results of the geophysical flow logging, the transmissivities were applied to refine the 3D groundwater model.

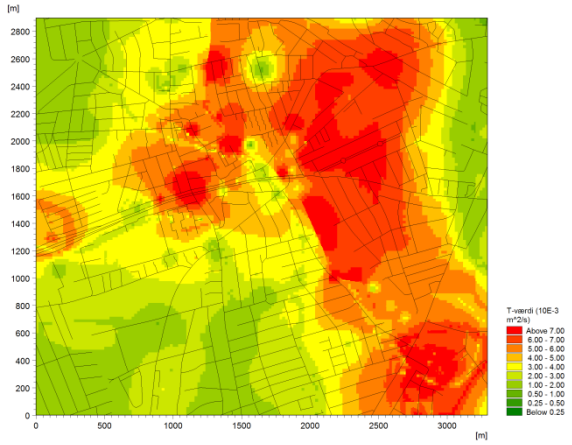


Figure 6 Transmissivity map

4.4 Monitoring

Groundwater quality
Water samples from the pumping tests in the initial investigations identified a single well with a relatively low benzene concentration.

Similarly, water samples taken from pumping and infiltration wells indicated that contamination at the former gasworks site was moderate, and that not all water would require treatment with activated charcoal. However, under the construction phase, on-going monitoring revealed increasingly high benzene-concentrations in pumping wells on site. In the end, all groundwater at the Kulbane site required treatment with activated charcoal prior to injection.
Off-site monitoring wells indicated the presence of contaminated groundwater from a former gas station in Hvidovre, as well as benzene-contamination, likely from the former gasworks site, south of the Kulbane tunnel area. Mapping of existing groundwater quality, before start and during the construction phase of the project, was crucial information in our liaison with the authorities regarding permit compliance.

Stream gauging documented extreme seasonal variation in streamflow. During the warm summer period, with little precipitation, flows as low as 30 m^3/h were measured. In contrast, flows of over 2000 m3/h were observed several times each year. Flow information provided the background data for applications for permits to discharge groundwater to Damhusåen. Futhermore, frequent analysis for nickel, ammonium and barium concentrations in the stream, documented actual background levels and resulted in discharge criteria that were higher than generally accepted.

4.5 Groundwater modelling

Updating the existing groundwater model with the information obtained from the field investigations provided a strong and powerful tool in the process of preparing the detailed design for the groundwater control system. In the end, the contractor-firm to whom the contract was awarded, could implement the design, with almost no changes and carry out the tunnel construction under dry conditions. Furthermore, the model results provided the background-information regarding water quantities and pumping rates that are required information when applying for abstraction, injection and discharge permits for groundwater. The 3D model results provided an overview and facilitated an understanding of the project and its impacts that was invaluable in liaison with the authorities.

5 AUTHORITY LIAISON

In Denmark, permits regarding groundwater activities such as dewatering, groundwater lowering and injection are granted with restrictive conditions. Firstly, groundwater-authorities generally require that 90-100 % of the groundwater abstracted during a construction project be injected into the aquifer from which it was abstracted. Secondly, the quality of the water that is injected generally must comply with the maximum acceptable concentrations for contaminants and undesirable parameters in groundwater, (e.g. nickel and chloride) as specified by the Danish Environmental Protection Agency's groundwater criteria. Typically, this condition is stipulated in permits, regardless of the existing water quality in a project area. In practice, this means that situations arise where contaminated groundwater must be treated with activated carbon prior to injection in wells that lie within a contaminant plume, for example on the south side of the Kulbane Tunnel.

Geographically, the project is divided along a north-south axis at the stream Damhusåen, which is also the border between the municipalities of Copenhagen and Hvidovre. Thus, two sets of permits for all groundwater activities were required. Furthermore, the conditions stipulated by each municipality, regarding monitoring of injection water quality, water quality in the surroundings, plus water levels reflect differences in permitting practises in the two municipalities, their drinking water supplies, and in particular, the contaminant situations in the two project areas.

Despite extensive and precise documentation of groundwater quality and contamination, prior to start of activities, groundwater contamination was strongly affected by the dynamic pumping rates, dynamic pumping strategies and by other groundwater activities in the vicinity. Here, dialog with the permitting authorities is vital to achieving the 'least poor' solution, when chemistry or water levels do not meet the conditions in a permit.

For example, in the case of the Hvidovre tunnel, injection of groundwater requires activated carbon treatment, filter-by pass for water from pumping wells that are documented clean (to improve residence times in the carbon filter system) and injection of nickel-impacted groundwater only in areas that are previously impacted (to protect an active drinking water well). This complex injection system is the pragmatic solution that addresses the following issues:

- Groundwater contaminated with heavy hydrocarbons at concentrations up to 550 µg/l;
- Costs associated with procurement, operation and maintenance of an activated carbon filter system;
- Nickel concentrations ranging up to 94 µg/l;
  Lack of satisfactory nickel-treatment solutions; and
- A groundwater injection system that was constructed prior to comprehensive mapping of nickel concentrations.

The solution meets the authorities' overall requirement that injection water within drinking water supply areas have the lowest nickel and contaminant concentrations possible. A pragmatic solution must take regard of the authorities' role and obligations, while also taking regard of what is reasonable and relevant in the 'big environmental picture'.

After documentation of benzene in the injected water, the City of Copenhagen agreed to a reduced sampling program, where 1) 'non-detect' compounds and compounds at concentrations below the EPA's maximum acceptable concentrations were omitted; 2) water samples for the priority-compound, benzene, were taken each week, at each manifold, with analysis results provided within 24 hours; and 3) non-priority compounds were analysed for only once a month.

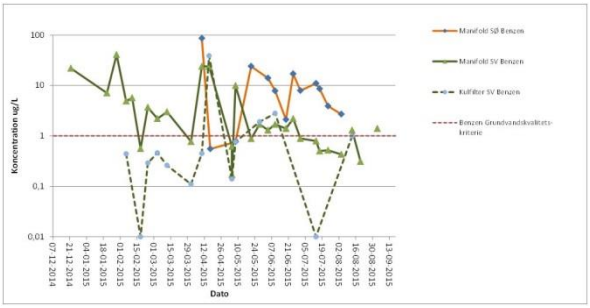


Figure 7: Benzene concentrations measured at the manifolds and after the activated carbon filter. High concentrations in April were first 'discovered' almost a month later, when the final analysis report from the extensive sampling program was released by the laboratory. The dashed line denotes the maximum concentration permitted by the authorities.

This focused and simplified sampling-program, accepted by the City of Copenhagen provides the most relevant information about the carbon filter capacity and sign of contaminant breakthrough.

Furthermore, these results are used to plan supplementary sampling at critical points, for example after each carbon filter, if there is sign of breakthrough. A rapid 24-hour analysis time facilitates a rapid response on the part of the supervising engineer and the groundwater contractor to take remedial action.

Achieving a water-sampling program that is relevant, from the consultant's point of view (can indicate when contaminate breakthrough can be anticipated, if there is contaminant spreading) and for the authorities (ensures that the water treatment system is complying with the permits) also requires an active dialogue between the supervising engineer, the contractor and the authority.

Finally, a simple and long-term groundwater quality program in offsite monitoring wells provides valuable background information regarding contaminant levels prior and during to the project. Several times these data series provided substantial evidence that groundwater activities related to the tunnel construction were not responsible for changes in groundwater chemistry.

6 LESSONS LEARNED

6.1 Detailed preliminary investigations removes a lot of the guesswork and saves money at a later stage

- The preliminary geotechnical and hydrogeological investigations and the subsequent groundwater modelling provided robust and detailed background information, which permitted alternative scenarios to be explored prior to the final project design.
- The actual groundwater lowering and injection system ultimately designed by the contractor is, with the exception of 4 supplementary pumping wells, exactly what was modelled and designed by Rambøll.
- The excellent agreement between the planned design and the actual conditions resulted in a project that is generally on-budget and on-time.
- Environmental screenings provided valuable planning information regarding groundwater treatment requirements and regarding permit applications. However, these investigations are relatively short term, and local in scope. These cannot provide an accurate picture of the contaminate conditions during a long term groundwater lowering project. Consequently, if screening results and site history indicate that activated-carbon treatment will be required, the system must be planned to be flexible and robust to allow for rapid changes in treatment strategy and even injection areas.
- A simple and long-term groundwater quality program in offsite monitoring wells provides background information regarding contaminant levels prior to and during the project. This information was invaluable in assessing unforeseen contaminant concentrations off site.

6.2 Keep it simple

One or two broad, groundwater-screening programs, performed at observations wells and on-site, provide a picture of the groundwater chemistry. Thereafter the program may be reduced, to focus on priority contaminants/compounds, that are sampled for more frequently, with rapid analysis times. A broader program can be performed once a month. A crucial link in a flexible and robust water treatment system is a frequently conducted, but simple water sampling program at critical points in the system.

6.3 Apply for authority approval as early as possible

Even though the standard processing time of applications related to groundwater lowering projects in Denmark is about 2-3 months, the experience from this project, crossing the border between two municipalities, is that it took more than one year to obtain all the required permits.

6.4 Strive for an open and inclusive dialogue with the authorities when problems arise.

Immediate and open contact to the authorities regarding the lack of compliance is the first step in achieving an agreement on a solution that considers the following:

- All possible remedial options
- Implementation timeframes
- Costs
- Technical feasibility
- The authorities' assessment of the seriousness of the situation
- Environmental ramifications
- Legal ramifications

Ideally, the groundwater contractor participates in these meetings or is in close dialog with the consulting engineer, so repercussions of any decision can be considered prior to agreement on a final solution.

6.5 Too little capacity too late

The water treatment systems and pipework must be as flexible and robust as possible. The contaminant situation, based on initial investigations, is most definitely not the situation the consulting engineer will be dealing with 1 or 2 months after start of the project.

6.6 *3-D approach to monitoring*

A tunnel alignment is basically 2D but in order to assess the effects on the environment, and meet requirements of the authorities, it is important to include borehole information from wells scattered throughout the area, at an early stage, and hence consider the project and its environmental implications in 3D.

7 CONCLUSIONS

Well-considered and thorough preliminary investigations provide geotechnical, hydrogeological and environmental information that are the cornerstone of 1) a robust project design, 2) rapid and flexible solutions to permit non-compliance and 3) in-depth assessment of project impacts.

An open and inclusive dialog with the groundwater authorities is crucial to achieving agreement on the 'least poor solution'. The bigger the project, the more likely that one, or several situations arise, where requirements stipulated in permits cannot be met.

8 Acknowledgements

This paper is prepared with the assistance of our colleague Per Beck Laursen who has been involved in the project from the very beginning and still manages to keep track of the many hydrogeological aspects of the project area.
We would also like to acknowledge the representatives of the Principal Banedanmark Martin Ipsen and Atli Runar Kristjansson for the ongoing discussions about the management of the groundwater control system throughout the tunnel construction.

Strength and deformation properties of volcanic rocks in Iceland

N. N. Foged
Department of Civil Engineering, Technical University of Denmark, nf@byg.dtu.dk

K. A. Andreassen
Department of Civil Engineering, Technical University of Denmark, kall@byg.dtu.dk

ABSTRACT
Tunnelling work and preinvestigations for road traces require knowledge of the strength and deformation properties of the rock material involved. This paper presents results related to tunnelling for Icelandic water power plants and road tunnels from a number of regions in Iceland.

The volcanic rock from Iceland has been the topic for rock mechanical studies carried out by Icelandic guest students at the Department of Civil Engineering at the Technical University of Denmark over a number of years in cooperation with University of Iceland, Vegagerðin (The Icelandic Road Directorate) and Landsvirkjun (The National Power Company of Iceland). These projects involve engineering geological properties of volcanic rock in Iceland, rock mechanical testing and parameter evaluation. Upscaling to rock mass properties and modelling using Q- or GSI-methods in combination with the finite element code Phase 2 from Rocscience have been studied by the students and are available in their MSc-theses, but will not be covered here.

The present contribution gives a short engineering geological overview of the volcanic rock formations in Iceland. Furthermore, the results of a number of unconfined, Brazilian, and a limited number of triaxial compression tests are presented and evaluated. The results are grouped according to engineering geological classification and classification properties as bulk density. We find correlations between the bulk density and the logarithm to the elasticity modulus and strength parameters.

Keywords: Volcanic rocks, Iceland, UCS test, Brazilian test, elasticity modulus.

1 INTRODUCTION

This paper presents extracts from a number of MSc-theses in Rock Mechanics carried out by Icelandic students at the Technical University of Denmark (DTU) in cooperation with University of Iceland, Icelandic Engineering Companies and Vegagerðin and Landsvirkjun representing the Icelandic Road Directorate and Power Administration.
Most of these studies have been related to ongoing tunneling projects and include engineering geology, description of selected cores from representative boreholes, laboratory classification, and strength and deformation tests. Based on this the students have evaluated element properties of the actual volcanic rock types and established an upscaling of these to rock mass parameters which then have been used for numerical analysis using international methods like GSI, RMR and Q-methods for stability, stand-up time and necessary support, i.e. shotcrete thickness and rock bolt spacing. These evaluations is not covered in any details in this contribution but can be retrieved from DTU.
During the projects valuable support and data from the engineering investigations have been provided from our cooperation partners, and the student reports are in full handed over to these authorities when the MSc-theses have been defended. In this paper we present selected results of the rock mechanical testing and give an overview on basic classification properties covering different Icelandic rock types. The studied projects cover sites from several regions of Iceland.

2 SHORT GEOLOGICAL OVERVIEW

Iceland is situated on the Mid-Atlantic ridge on the rifting plate boundary between the Eurasian and North American plates. When the plates drift apart, the gap between them fills constantly with extrusive and intrusive igneous rock. The active zone of rifting and volcanism is found across the country from the southwest Reykjanes peninsula to the northeast where it connects with the Iceland-Jan Mayen ridge. Iceland is geologically very young and all bedrock was formed within the past 25 million years. The stratigraphical succession of Iceland covers two geological periods, the Tertiary and the Quaternary. The oldest rock observed at the surface are about 15 million years old, and is late Tertiary time. It is found in the Northwest and Eastern coast of Iceland. The rock closer to the rifting plate boundary is younger.
The surface of Iceland has changed radically with time. The rocks are weathered by the frequent change of the frost and thaw, and the wind, seas and glaciers deteriorate down the land.

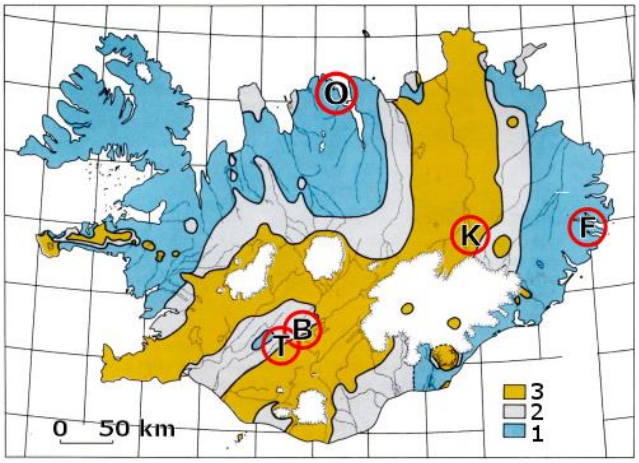


Figure 1 Extent of the Islandic geological formations. Bedrock: 1) Tertiary Basalt Formation; 2) Grey Basalt Formation, Late Pliocene and Early Pleistocene; 3) Móberg (eng. Hyaloclastite) Formation, Late Pleistocene. Site locations: Olafsfjörður (O), Núpur and Þórsá (T), Kárahnjúkar (K), Fáskrúðsfjörður (F) and Búðarhálsvirkjun (B). Based on Map from Einarsson (1994).

The studied sites are placed in regions being representative for the Tertiary Basalt Formation and volcanic features from the Quaternary period (The Grey Basalt Formation and the Móberg formation).
Figure 1 is extracted from the monograph by Thorleifur Einarsson: "Geology of Iceland. Rocks and Landscape" (Figure 24-2; Page 233) and edited to include the localization of the different tunnel sites discussed. The Icelandic bedrock consist of primary numerous, extensive but relatively thin basaltic lava flows, lying on top of each other, interbedded with subordinate acidic rock and relatively thin sedimentary beds. The bedrock's overall composition is as follows:

- 80–85% basalt lava flows,
- 10% acidic and intermediate rocks,
- 5–10% sedimentary interbeds originating from both erosion and transport of volcanic rocks. Mainly consolidated tuff and eolian soil and to some extent sandstones and conglomerates.

Each lava flow may be divided into three parts as follows:

- The top scoria, often 10–25 % of the lava flow thickness,
- The dense crystalline middle part, often 60–85 % of the lava flow thickness,
- The bottom scoria, often 5–10 % of the lava flow thickness.

The top scoria is to the uppermost portion of a lava flow, characterized by rapid cooling and expansion of gas. The matrix of scoria is highly vesicular and glassy. The structure is chaotic, with large voids of any size, some up to several meters. When the subsequent deposition of sediment occurred, these voids were infiltrated and filled with sand and silt. Palagonitisation later cemented the sediment into a sandstone or siltstone and gives the rock mass a relatively compact aspect. In cores the top scoria often has character of a matrix supported breccia with scoria fragments. The vesicles in the scoriaceous fragments are also often filled with secondary zeolites or calcite. The scoria can be recognized from its specific structure and because of its red, orange and green colour, which contrast the grey colour of the basalts.
The crystalline middle lava consists of hard, dense basalt of light to dark grey colour. The rock is usually affected by subvertical columnar jointing, resulting from the cooling of the lava. The frequency of the joints is low

for these large columnar jointed basalts with spacing between 1–2 m. Correspondingly the frequency is high for small columnar jointed basalts and between 0.1– 0.3 m, showing a sugarcube structure. The joint surfaces are usually smooth to slightly rough, undulating with gauge absent or only with thin clayey coatings or calcites.
The bottom scoria is commonly observed to be thin, well consolidated, sometimes containing sandstone fillings, originating from underlying sediments.
The basalt is classified according to Walker's classification system based on petrology and texture of the rock and is divided into the following three different petrographic types (Walker, 1959):

- Tholeiite basalt,
- Olivine basalt,
- Porphyritic basalt.

Table 1 gives a number of rock engineering properties of which UCS for fresh basalts show relatively high strengths (Jónsson, 1996).

3 ROCK MECHANICAL PROPERTIES EXTRACTED FROM MSC-THESES

3.1 Gudmundur Nikulasson (1987): "Tunneler i vulkanske bjergarter i Island"

This MSc-thesis was carried out based on project investigations in cooperation with Vegagerðin Rikisins – the Islandic Road Directorate – for a road tunnel at Olafsfjörður Muli in Northern Iceland established 1988–1990.

Table 1 Icelandic basalt classified according to rock engineering properties, Jónsson (1996).

Field mapping of Icelandic basalts[1]	**Proposed geotechnical field mapping of basalt**	**Structural and mechanical properties**		
		Scoria content	Common thichness of lava unit (m)	Common UCS strength[2] (MPa)
Tholeiite basalt	Tholeiite, thin layered (from central volcanoes)	25–35	3–8	>200 (150–300)
	Tholeiite, thick, regional	15–20	10–20	>200 (150–300)
Porphyritic basalt	Porphyritic basalt esp. massive. Phenocrysts>10% by volume	1–5	10–20	200 (100–300)
	Porphyritic basalt. Phenocrysts < 10% by volume	5–15	10–20	200 (150–300)
Olivine tholeiite	Olivine basalt			
	Compound lavas, from lava shield volcanoes	0–5	20–80	100 (80–140)

[1]According to Walker (1959)
[2]Fresh basalt

Rock samples from the Tertiary Basalt Formation were selected from boreholes OM1-4 under guidance of Hrein Haraldsson and Gunner Bjarnason from Vegagerðin Rikisins. Five different basalt types were selected (Porphyritic B1, Olivin B2, Olivinporphyritic B3, Tholeiite B4 and Tholeiiteporphyritic

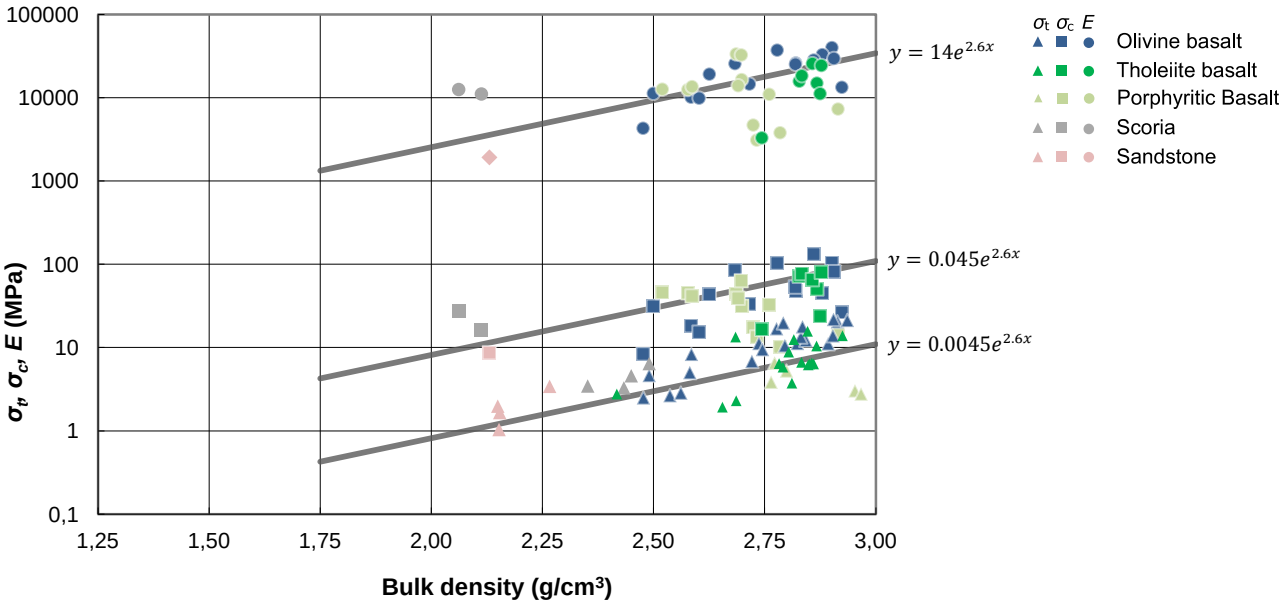


Figure 2 Rock mechanical test results from Olafsfjörður Muli (Nikulasson, 1987).

B5) together with Scoria and sedimentary samples, all from the Tertiary Basalt Formation.
The rock mechanical testing by the student at the Rock Mechanical Laboratory at the Danish Geotechnical Institute involved classification tests, 86 point load tests, 51 Brazilian tests and 41 unconfined compression tests in which 10 were performed used strain gauge techniques for Young's *E*-modulus and Poisson's ratio and the rest using external LDVT's for determination of only *E** (where the index * include bedding effect at end platens in the compression machine and we found the ratio $E/E^* = 1.80 \pm 0.57$).
Figure 2 shows the main results of the strength and deformation properties correlated with the bulk density determined on water saturated surface dry test specimens.

3.2 Karen Kristjana Ernstdottir (2003): "Rock mechanical studies for a hydroelectric power station–Near Núpur and Þórsá, Iceland"

This MSc-study was carried out in cooperation with Landsvirkjun and Almenna Consulting Ltd. with Björn Stefánsson and Jón Skulason as contacts. The project investigations related to preliminary plans for a hydroelectric powerstation at Núpur and included 12 km headrace tunnels. The main subject of this project was to obtain rock parameters for the different rock in the region based on laboratory tests on rock samples from drilling cores made available. The geology in the area around the mountain Núpur and the river Þórsá is various and complicated including the 8700 years old Þórsá lava being the most significant rock layer in the area. It overlies sedimentary layers, e.g. silt-and sandstone, volcanic sand and conglomerate being 1.64 million years old.
For the present project 12 different volcanic and sedimentary rock types were selected from 12 boreholes in the area which contributed to 48 test specimens used for 82 Brazilian tests, 46 unconfined compression tests and 5 triaxial tests.
The results in form of σ_t, σ_c and E with different signatures for the studied rock types are plotted as function of the bulk density in water saturated surface dry condition being saturated as part of the preparation of the test specimens. Figure 3 shows the main results grouped in selected rock types together with a regression analysis of the trendlines for the 3 set of results with great variation depending on bulk density and lowest values for the Móberg formations. The triaxial tests confirm the level of friction angle and cohesion for Tillite, Porphyritic Basalt, and Hyaloclastic.

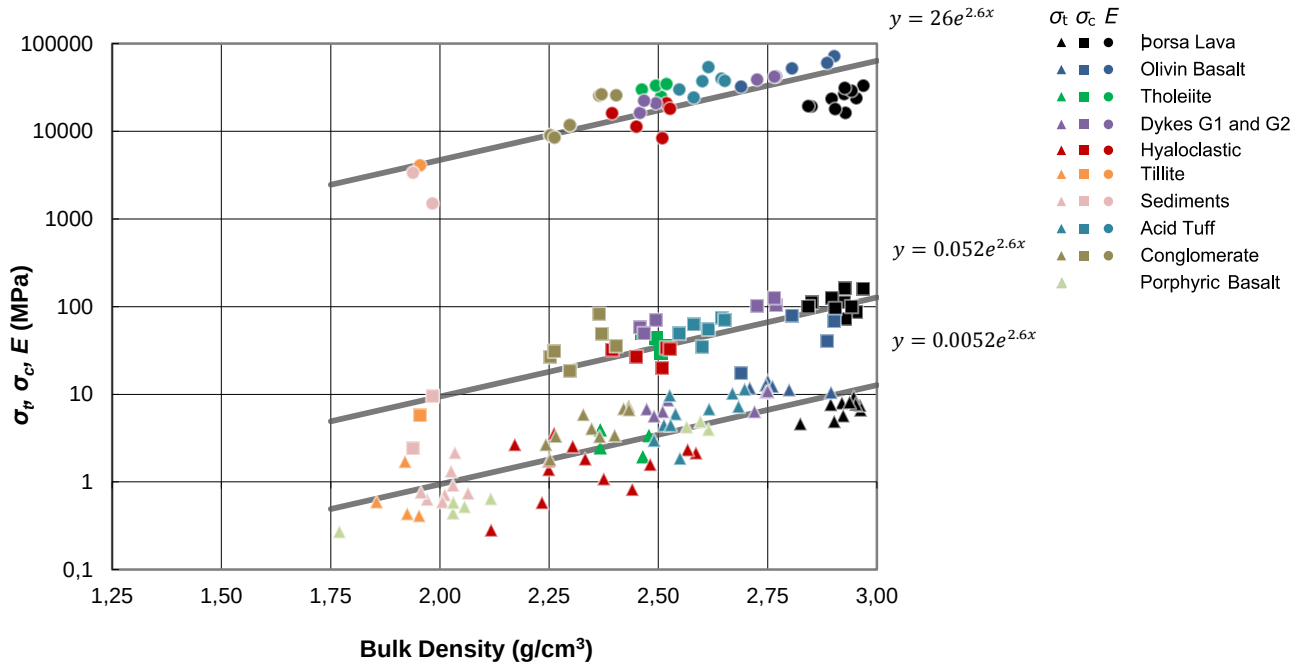


Figure 3 Rock mechanical properties from volcanic rock types in the Núpur – Þórsá region (Ernstdottir, 2003).

3.3 Hlif Isaksdottir (2004): "Rock mechanical studies of volcanic tephra for a hydroelectric power station–Near Núpur and Þórsá, Iceland"

This MSc project was carried out on one of the largest tephra layers found below the Þórsá Lava with varying thickness from a few to about 30 m and properties ranging from slightly cemented sand to sandstone. The layer is a result of a sub-glacial volcanic activity 10300 years ago followed by an outburst flood. From this tephra layer three different types of samples were available: Two buckets of variable cemented sand and a sandstone core from borehole NK-28. Generally, RQD and Q-index are very low (0–3% and 0 respectively with exemption of the core from NK-28 having RQD = 88 and Q = 3–46). The tephra particles have a vesicular nature with air trapped inside the grains, weathering may change density due to when volcanic glass alters to palagonite. Four and two subsamples from the two buckets of tephra showed low saturated bulk density of 1.74 g/cm^3 to 1.79 g/cm^3 and w_{sat} from 43% to 39% compared to natural water contents w_{nat} from 13% to 12.5%. Deformation properties in consolidation test on the tephra showed very low E_{oed}-moduli and consequently the material may be vulnerable to creep and to additional settlements under dynamic loads. The tephra sands in Bucket 1 and 2 were very friable and could not be orderly used for Brazilian tests in saturated condition. However, at natural water content the partially saturated test specimens showed $\sigma_t \approx 0.28$ MPa and 0.025 MPa, respectively. Properly conducted tensile strength tests on six cemented subsamples from the cores from NK-28 with saturated bulk density of ρ_{bulk} = 2.01 g/cm^3 showed a mean value of $\sigma_t = 0.69$ MPa. Four triaxial tests and one unconfined compression test on test specimens from NK-28 carried out in the MTS 815 rock mechanical equipment at DTU showed in combination with the Brazil tests for ρ_{bulk} = 2.02 g/cm^3 a friction angle of $\varphi = 55.4^o$ and c = 1.35 MPa for sandstone.

3.4 Gunnar Arnar Gunnarsson (2008): "Rock Mass Characterisation and Reinforcement Strategies for Tunnels in Iceland, Fáskrúðsfjörður Tunnel."

This MSc-thesis was worked out in cooperation with the University of Iceland, Faculty of Civil and Environmental Engineering (Sigurður Erlingsson) and GeoTek Ltd. (Oddur Sigurðsson) and Vegagerðin – the Islandic Road Administration. Hallgrimur Örn Arngrimsson (a fellow student) participated at GEO (The Danish Geotechnical Institute) and DTU in the rock cores classification and preparation of test specimens and the actual laboratory testing.
The project investigation for this site being established 2003–2005 was used and twelve rock cores were collected for supplementary testing mainly of scoria and sediments. A large laboratory test dataset from the headrace tunnel in the Kárahnjúkar hydroelectric project was analysed for comparison of strength properties for the Fáskrúðsfjörður tunnel having a geological age of about 6.5 and 10 mill years, respectively. Consequently, focus has been on scoria or porous basalts and sediments in the present case. Gunnar used a comparison method applied on limestone from the construction of the Citytunnel in Malmö (Foged et al., 2004) based on the semilogarithmic plot of tensile strength, unconfined compression strength and Young's modulus versus bulk density for the different rock types. The comparison is available in Figure 5 and Figure 4 and the reduced rock mechanical properties at Fáskrúðsfjörður compared to Kárahnjúkar is discussed to be due to different age, weathering and high stress conditions.

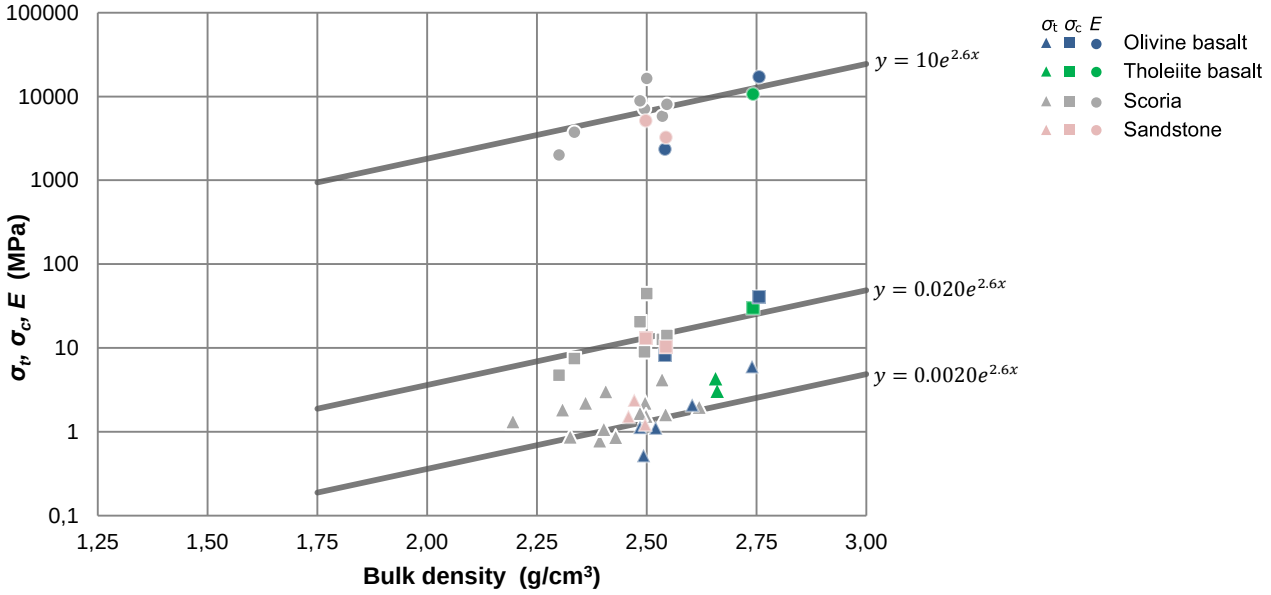


Figure 5 Rock mechanical properties for the Fáskrúðsfjörður region (Gunnarsson, 2008).

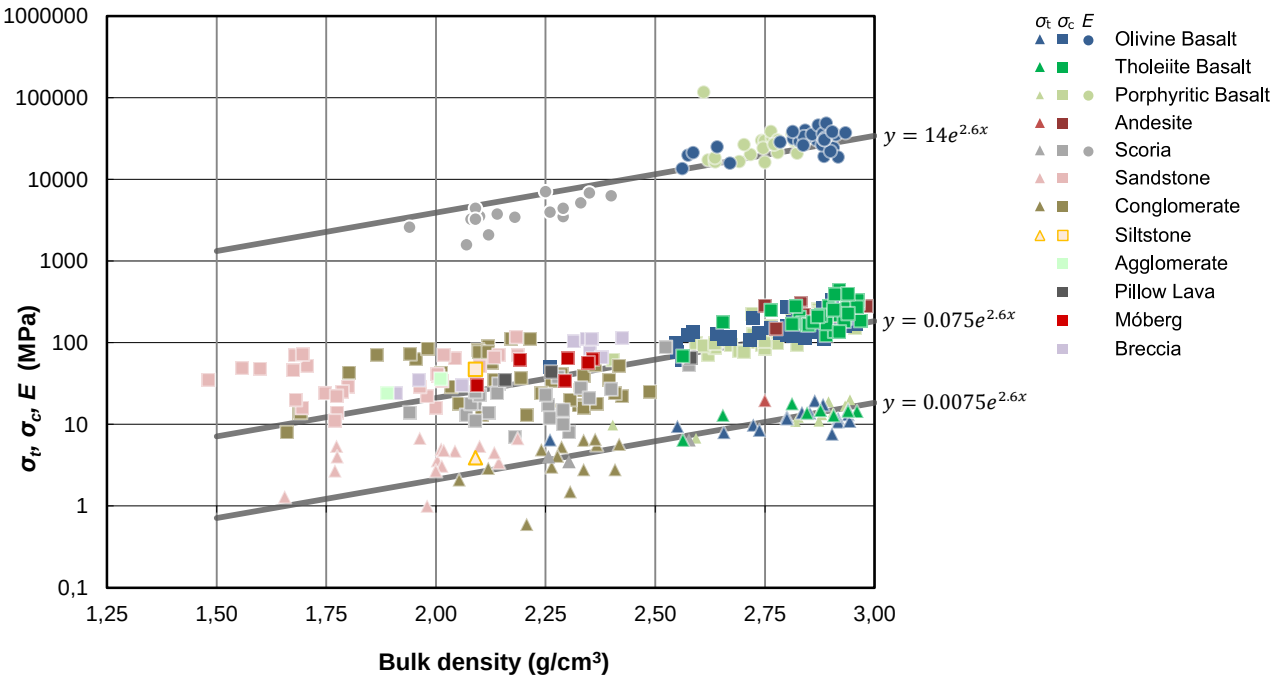


Figure 4 Rock mechanical properties for the Kárahnjúkar region (Gunnarsson, 2008). Data received from the Kárahnjúkar hydroelectric project.

3.5 Hallgrimur Ôrn Arngrímsson & Þorri Björn Gunnarsson (2009): "Tunneling in acidic, altered and sedimentary rock in Iceland, Búdarhálsvirkjun"

This MSc project was performed in cooperation with the University of Iceland, Faculty of Civil and Environmental Engineering (Sigurður Erlingsson) and Landsvirkjun (Matthias Loftsson and Jón H. Steingrimsson) and was in part funded by the Icelandic Road Administration (Vegagerðin). The focus of this thesis is tunnelling in soft rock formations like acidic, altered and sedimentary rock. The top part of Búðarháls formation is pillow lava generated by subglacial eruption during the last glacial period (hyaloclastic rock approx. 0.7 million years old). It is underlain by multiple basaltic lava flows

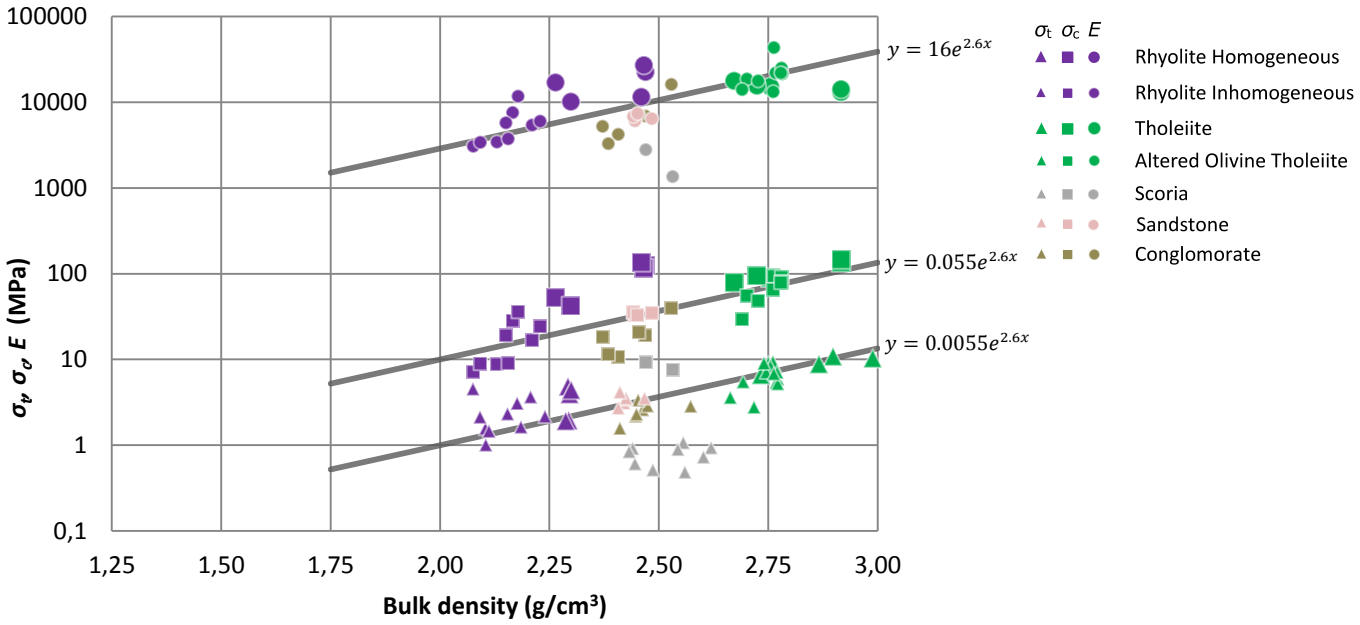


Figure 6 Rock mechanical properties for the Búðarháls region (Arngrímsson & Gunnarsson, 2009).

and sediment layers. The oldest rock is altered basalt over 2.0 million years old. At the power house location the relatively rare rhyolite was found calling for supplementary mechanical testing. Core samples were collected on eight different rock types which were used for Brazilian, unconfined compression and triaxial compression tests performed at Geo and DTU. The Geological Strength Index GSI was used to estimate rock mass properties analysed in three different tunnel cross-sections using the finite element program Phase^2 and the designed rock support classes recommended in the contract documents (Arngrímsson et al., 2010).

4 ROCK MECHANICAL TESTS AND EVALUATION

All test specimens were cut from the available cores (or recored) to the wanted dimensions *H* and *D* measured by a caliper. The cutting was done using a water-cooled diamond saw. Afterwards the test specimens were water saturated under vacuum in order to determine the water-saturated bulk density in surface dry condition. This property was used as abscissa in the preceding figures showing the obtained strength parameters σ_t and σ_c and elasticity moduli *E* as ordinates on logarithmic scale. When performing rock mechanical surveys the traditional tests are unconfined uniaxial compression tests (UCS) and Brazilian tests. The Brazilian tests are performed according to the ISRM standard for determining indirect tensile strength of rock materials (Bieniawski & Hawkes, 1978), and the setup is as seen in Figure 7 (C). The purpose of the uniaxial compressive tests is to measure the uniaxial compressive strength and to determine stress-strain curves for Young's modulus *E* and Poisson's ratio υ. Figure 7 (A) and (B) illustrate the different deformation measuring methods: Strain clips and strain belts, LVDT's and strain gauges glued upon the test specimen cylindrical surface. Most of the *E*-moduli have been determined as *E** using LDVT's which include bedding effects at end platens in the compression machine and we have found the ratio E/E* = 1.80±0.57 in comparison to strain gauges measurements.

The uniaxial compressive tests are performed according to the ISRM standard for determining the uniaxial compressive strength (Bieniawski et al., 1979). More advanced test schemes have comprised triaxial tests in the DTU MTS-815 rock testing facility according to the ISRM standard for determining the strength of rock materials in triaxial compression (ISRM 1983). The triaxial tests are

performed for obtaining the strength at higher confining pressures to determine the friction angle, φ (°), and the cohesion, c.
In the cases where triaxial tests are not performed it is possible to use the procedure described by Madland et al. (2002) to combine UCS and Brazilian test results and determine the friction angle by:

$$\sin\varphi = \frac{\sigma_c - 4\sigma_t}{\sigma_c - 2\sigma_t} = \frac{\sigma_c/\sigma_t - 4}{\sigma_c/\sigma_t - 2}, \quad (1)$$

where σ_c (MPa) is the UCS strength and σ_t (MPa) is the Brazilian strength. This procedure requires that the material is isotropic and that both the extensional and compressional failure can be described by the Mohr-Coulomb failure criteria, which is not always the case (Ramsay & Chester, 2004; Labuz & Zang, 2015).

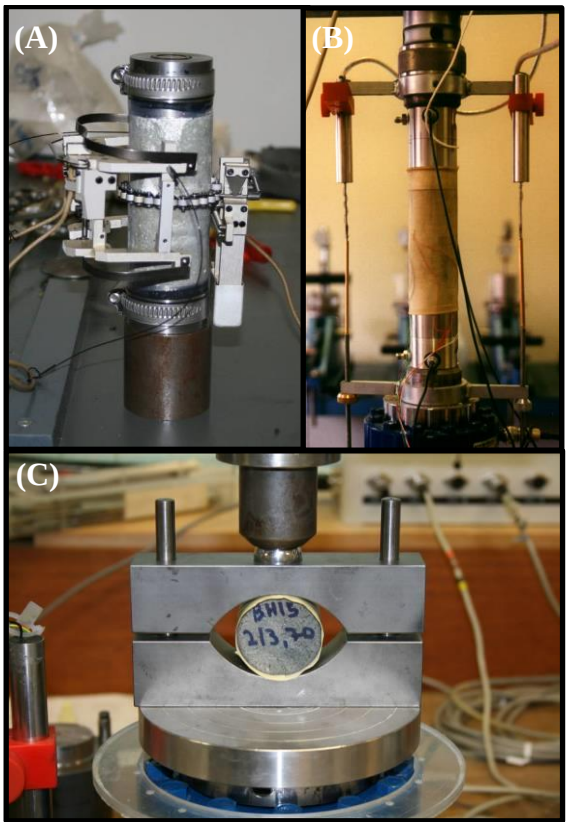


Figure 7 Test setup overview with specimens equipped for strain measurements. (A) Triaxial test. (B) UCS test. (C) Brazilian test.

5 EVALUATION AND CONCLUSION

The trends established for compression strength, tensional strength and elasticity modulus must be taken with some caution. The different rock types included and the local variability should be included in an overall evaluation.

Table 2 Parameter evaluation for the five sites presented in Section 3 taking into account that the exponential factor in the regression equations is equal as listed here: $\sigma_c = A\ exp(2.6\ \rho_b)$, $\sigma_t = B\ exp(2.6\ \rho_b)$ and $E = C\ exp(2.6\ \rho_b)$.

		Coefficients for:				
		σ_c	σ_t	E		
Locality	Type	A	B	C	A/B	C/A
Olafsfjör-ður	Tertiary Basalt	0.045	0.0045	14	10	311
Nupur Þórsá	Early Pleisto-cene/ Þórsá Lava	0.052	0.0052	26	10	500
Kárahn-júkar *	Early Pleisto-cene Moberg	0.075	0.0075	14	10	187
Fáskrúðs-fjörður	Tertiary Basalt	0.020	0.0020	10	10	500
Búðarháls virkjun	Early Pleisto-cene/ Móberg and Rhyolite	0.055	0.0055	16	10	290

* C/A influenced by low density or porous rock types.

However, the main finding that an exponential factor of 2.6 in the regression equations fit all the different plots from sites in different geological type formations seem to be well defined. Consequently, using the Madland method discussed in Section 4 the ratio for σ_c/σ_t = A/B = 10 gives a first order estimate for the friction angle

$$\varphi = \sin^{-1}\left(\frac{\sigma_c/\sigma_t - 4}{\sigma_c/\sigma_t - 2}\right) = \sin^{-1}(0.75) = 49°, \quad (2)$$

for most volcanic rock types. A lower bound value may be A/B ≈ 8, i.e. $\varphi = 41°$. As φ is difficult and costly to determine using triaxial tests on such rock formations this makes evaluations of strength parameters simpler taking into account that the internal cohesion c may be estimated from (Madland et al., 2002)

$$c = \sqrt{3}\sigma_t\ . \quad (3)$$

The design value of σ_t should be carefully estimated as a lower bound value related to the actual rock types and their classification

properties in form of saturated surface dry bulk density.

Using the constants A, B and C summarized in Table 2 the differences between sites are evident related to the different volcanic rock types like scoria and sand- and siltstone derived from tephra. Beside the influence of porosity and variable mineralogy there seems to be an effect of weathering and age of the volcanic formations. The Tertiary Basalt sites show lower strength parameters than the Þórsá Lava and especially all formations prone to weathering like scoria sedimentary interbeds of acidic tuffs show very variable strength and deformation properties depending on their position in the basaltic successions.

Most of the determination of elasticity moduli has been done with LVDT's measuring the total deformation between end platens in the compression machine. As this include bedding effects the *E*-modulus may be underestimated which may explain the relative low E/σ_c=187 to 500 where values of 500 to 1000 were expected.

In conclusion the present analysis of test results from MSc theses on well-defined formations (Einarsson, 1994; Jónsson, 1996) including provided data from Kárahnjúkar gives a frame for comparison with future rock mechanics test results. The evaluation principles may guide the use of established parameters towards an upscale to field parameters.

6 ACKNOWLEDGEMENTS

We thank the six Icelandic guest students at the Department of Civil Engineering, Technical University of Denmark for their dedicated work during the period of 1987–2009. The cooperation with and support from University of Iceland, Vegagerðin and Landsvirkjun, and from Icelandic Engineering Companies are highly appreciated. Furthermore, the Rock Mechanical Laboratory at Geo, Denmark, has kindly provided facilities for sample preparation and testing.

7 REFERENCES

Arngrímsson, H.Ö. & Gunnarsson, T.B. (2009). Tunneling in acidic, altered and sedimentary rock in Iceland – Búdarhálsvirkjun. MSc-thesis at Department of Civil Engineering, Technical University of Denmark.

Arngrímsson, H.Ô., Gunnarsson, T.B., Foged, N.N. & Erlingsson, S. (2010). Numerical Analysis of Rock Support Strategy for the Búdarháls Tunnel. Conference on Rock Mechanics in the Nordic Countries, Kongsberg, Norway.

Bieniawski, Z.T., Franklin, J.A., Bernede, M.J., Duffaut, P., Rummel, F., Horibe, T., Broch, E., Rodrigues, E., van Heerden, W.L., Vogler, U.W., Hansagi, I., Szlavin, J., Brady, B.T., Deere, D.U., Hawkes, I. and Milovanovic, D. (1979). Suggested Methods for Determining the Uniaxial Compressive Strength and Deformability of Rock Materials. International Journal of Rock Mechanics and Mining Sciences & Geomechanics Abstracts, Vol. 16, No. 2, pp. 135-140.

Bieniawski, Z.T. & Hawkes, I. (1978). Suggested Methods for Determining Tensile Strength of Rock Materials. International Journal of Rock Mechanics and Mining Sciences & Geomechanics Abstracts, Vol. 15, No.3, pp. 99-103.

Einarsson, T. (1994). Geology of Iceland. Rocks and Landscape. Published by Mál og menning, Reykjavík.

Ernstdottir, K.K. (2003). Rock mechanical studies for a hydroelectric power station – Near Núpur and Þórsá, Iceland. MSc-thesis at Department of Civil Engineering, Technical University of Denmark.

Foged, N., Hartlén, J., Jackson, P.G. & Steenfelt, J.S. (2004). Evaluation of Bryozoan limestone properties based on in-situ and laboratory element tests. Proceedings of International Conference on Site Characterisation ISC inPorto, Portugal 2004.

Gunnarsson, G.A. (2008). Rock Mass Characterisation and Reinforcement Strategies for Tunnels in Iceland – Fáskrúðsfjörður Tunnel. MSc-thesis at Department of Civil Engineering, Technical University of Denmark.

Ísaksdottir, H. (2004). Rock mechanical studies of volcanic tephra for a hydroelectric power station – Near Núpur and Þórsá, Iceland. MSc-thesis at Department of Civil Engineering, Technical University of Denmark.

Jónsson, B. (1996). Geotechnical Field Classification of Basalts in Iceland. Proceedings of NGM, Reykjavík, Iceland, 469–473.

Labuz, J.F. & Zang, A. (2015). Mohr–Coulomb Failure Criterion. In *The ISRM Suggested Methods for Rock Characterization, Testing and Monitoring: 2007–2014*, Ulusay, R. (ed), Springer, London, 227–231.

Madland, M.V., Korsnes, R.I. & Risnes, R. (2002). Temperature effects in Brazilian, uniaxial and triaxial compressive tests with high porosity chalk SPE Annual Technical Conference and Exhibition, San Antonio, Texas, 29 September–2 October 2002, 77761, 1–11.

Nikulasson, G. (1987). Tunneler i Vulkanske Bjergarter i Island – Olafsfjörður Muli Muli. MSc-thesis at Soil Mechanics Laboratory, Department of Civil Engineering, Technical University of Denmark.

Ramsey, J.M. and Chester, F.M. (2004). Hybrid fracture and the transition from extension fracture to shear fracture. Nature, Vol. 428, 63–66.

Walker, G.P.L. (1959). Geology of the Reyðarfjörður Area, Eastern Iceland. Geo. Soc. London Quart. Jour. 114, 367–393.

Strength increase below an old test embankment in Finland

M. D'Ignazio
Tampere University of Technology, Finland, marco.dignazio@tut.fi

T. Länsivaara
Tampere University of Technology, Finland, marco.dignazio@tut.fi

ABSTRACT
An instrumented test embankment was built in Murro, Western Finland, in 1993. The purpose was to monitor the long term settlement of the embankment on a silty clay deposit, and use the information for the design of Highway 18 between the cities of Jyväskylä and Vaasa.
Field vane test was performed prior to construction and after 8 years of consolidation. Test results in 2001 showed increase of undrained shear strength up to a depth of 6-7 m under the centerline of the embankment, while below 7 m depth the strength decreased compared to the initial stage.
In 2013, 20 years after construction, CPTu and field vane test were performed by Tampere University of Technology at the test site. From CPTu measurements no strength decrease could be observed. The undrained shear strength below the embankment was higher than beside the embankment up to a depth of 11 m, after which the two coincided.
In this study, a critical comparison between the old soil data and the new tests results is made. The strength distribution below the test embankment is assessed and the strength increase evaluated. Existing correlations for undrained shear strength are compared with field measurements. Finally, the long term behavior and the impact of strength increase on the stability of Murro test embankment are studied through the Finite Element software PLAXIS 2D.

Keywords: soft soil; embankment; piezocone; consolidation; finite element.

1 INTRODUCTION

In order to study the long term behavior of an embankment on a soft clay deposit, a highly instrumented test embankment was built in Murro, Western Finland, near the city of Seinäjoki, in 1993, commissioned by the Finnish Road Administration (Koskinen et al., 2002). The subsoil conditions consisted of a 23 m thick low organic silty clay deposit with presence of sulfur. The soft clay is overlain by a stiff, fissured crust layer less than 2 m thick. Settlement and pore pressures have been monitored for more than 20 years.
An important aspect to be evaluated in staged construction for both old and new embankments is how the undrained shear strength increases with time. The general assumption is that there will be an increase of strength if the preconsolidation pressure of the clay increases due to consolidation. To investigate this, field vane test was performed 8 years after construction below the embankment. Test results showed an increase in undrained strength up to 7 m depth. However, below 7 m the field vane test indicated that the strength would have decreased.
In contrast, CPTu tests performed in 2013 by Tampere University of Technology revealed strength increase up to 10-12 m depth, while no strength decrease could be observed.
In the present study, after a brief overview on the phenomenon of strength increase with time, the old soil investigation data from Murro site and the new test results are compared. The undrained shear strength distribution below the test embankment is assessed using both existing transformation models for undrained shear strength from piezocone and field vane test results. Finally,

an attempt to model the long term settlement of Murro test embankment and the strength increase is done using the Finite Element software PLAXIS 2D.

2 SHEAR STRENGTH INCREASE

Natural soft clay deposits generally show an over consolidation ratio (OCR = σ'_p/σ'_{v0}, ratio between vertical preconsolidation pressure and effective vertical stress) higher than 1 because of aging effect (Bjerrum, 1973; Hanzawa, 1995), without necessarily having previously experienced any release of overburden stress. Due to chemical bonding and secondary compression, s_u of clays subjected to aging process possesses additional strength (Suzuki and Yashuara, 2007). As shown in Figure 1, the line A-B represents the process of aging where, under a constant overburden stress, the clay gains additional strength and becomes over consolidated with $s_u = s_{uf}$, effective vertical stress equal to σ'_{v0} and preconsolidation pressure equal to σ'_p. For a given increase in consolidation stress ($\Delta\sigma_v$), s_u will increase along C-D, provided that the total effective vertical stress is higher than σ'_p. On the contrary, below σ'_p, s_u will be equal to s_{uf}.

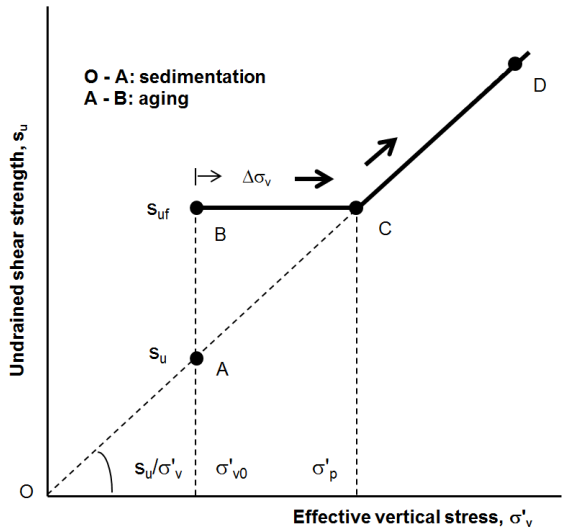


Figure 1 Relationship between s_u, σ'_v and σ'_p (modified after Suzuki and Yashuara, 2007).

The dependency of s_u on consolidation stresses is a well-known phenomenon (e.g. Mesri, 1975; Jamiolkowski et al., 1985). The shear strength of a clayey soil increases under loading due to the consolidation process, as the dissipation of excess pore water pressure will lead to a change in the stress state beneath the load, with consequent increase of effective stress. Moreover, secondary consolidation (creep) will also contribute to the long term settlement (Craig, 2004).

For geotechnical structures built on clay deposits where the ground water table is located in the proximity of the ground surface, buoyancy effects will have a significant impact on the final stress distribution.

A correct assessment of the shear strength increase would seem beneficial when improving old embankments. Indeed, the improved capacity, which is often neglected, would reduce to a minimum or exclude possible countermeasures needed to achieve the new target safety level. For instance, when such phenomenon is taken into account, the calculated factor of safety of existing embankments will result higher than at the initial stage (e.g. Tavenas et al., 1978; Slunga, 1983).

Estimating the increase in undrained shear strength becomes also important when multi stage loading for construction on soft clay is performed (e.g. Tavenas et al., 1978).

Strain rate dependency of s_u and σ'_p (e.g. Leroueil et al., 1985; Länsivaara, 1999) must be also considered when assessing such properties. s_u/σ'_v will result higher when the soil is sheared at faster strain rates than at low strain rates (Leroueil et al., 1985).

3 SITE INVESTIGATION AT MURRO

Murro test embankment is 2 m high and 30 m long (Figure 2). The top width of the embankment is 10 m. The body of the structure consists of crushed rock with a grain size of 0-65 mm.

The embankment was built on a 23 m deep normally to slightly over consolidated soft silty clay deposit, overlain by a dry crust layer 1.6 m thick. Displacements and pore water pressures have been monitored for over 20 years. The original purpose was to exploit the experimental observations for the design of Highway 18 between the cities of Jyväskylä and Vaasa.

Soil characteristics of Murro clay are shown in Figure 3. The water content (w) ranges from 65% to 100%, with sensitivity (S_t) varying between 2 and 10. The liquid limit (W_L) increases from 55% near the ground surface, up to 120% at 5 m depth. After that point, W_L shows a negative trend with depth, decreasing up to about 60% below 15 m depth. Preconsolidation pressure (σ'_p) values in Figure 3 were obtained from CRS (constant rate of strain) oedometer tests.
A detailed description of the physical and mechanical characteristics of Murro clay can be found in Koskinen et al., (2002), Karstunen et al., (2005), Karstunen and Yin, (2010).

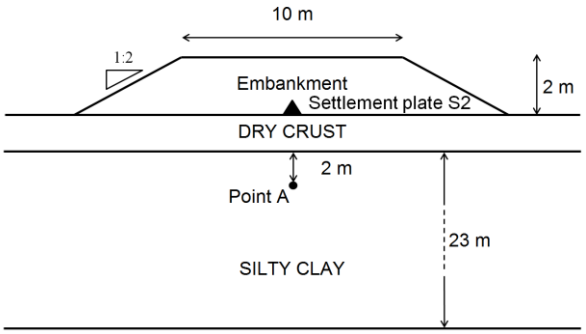


Figure 2 Murro test embankment (section).

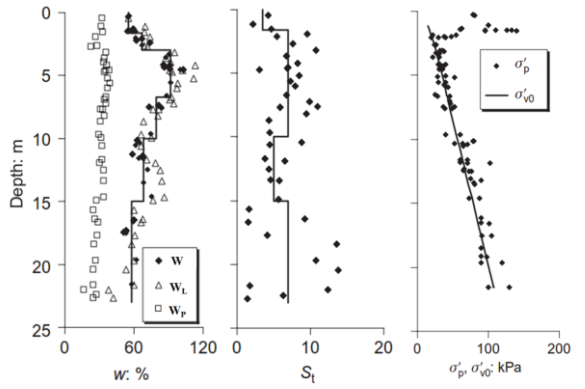


Figure 3 Characteristics of Murro clay (modified after Karstunen and Yin, 2010).

In order to assess the undrained shear strength due to consolidation of the subsoil, field vane test was performed in 2001, 8 years after construction. Corrected field vane test results showed increase of undrained shear strength up to a depth of 6-7 m below the centre-line of the embankment. However, below 7 m depth the strength seemed to have decreased compared to the initial stage (Figure 4). A possible explanation for the unexpected observed phenomenon could be the destructuration of the clay induced by the change in stress state (Karstunen et al., 2005; Karstunen and Yin, 2010).
In 2013, after 20 years of consolidation of the soft clay foundation, piezocone (CPTu) and field vane tests were performed by Tampere University of Technology at Murro test site. Field vane test was repeated also in 2015, as measurements from 2013 were available only up to 10 m depth.
Tampere University of Technology has recently bought 1) CPTu equipment with seismic and resistivity cone and, 2) a new field vane which allows for rotation and torque measurements right above the vane. The purpose is to increase the use of CPTu in Finland for the determination of soft soil properties and to improve the existing transformation models for strength and deformation characteristics of soft clays.

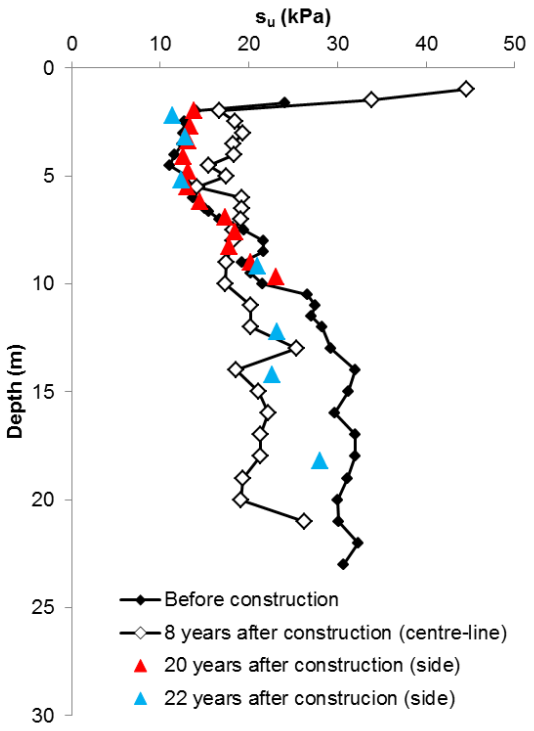


Figure 4 Corrected field vane test results at Murro test site prior to construction, 8 years, 20 years and 22 years after the construction of the embankment.

For the Murro test site, CPTu soundings are available from both the centre-line of the embankment and the East side (about 3 m off the slope). Field vane test was performed only at one side of the embankment, due to technical difficulties. Results from field vane

test are presented in Figure 4. Measured s_u agrees fairly well with s_u measured at the initial stage. Fairly good correspondence can be also observed at greater depths, except for two points at 12.2 m and 14.2 m, where s_u seems lower than at the initial stage. Furthermore, as shown in Figure 5, cone tip resistance differs significantly at the two measurement points, up to a depth of about 11 m. No strength decrease could be observed in the subsoil, thus contradicting the trend observed in Figure 4.

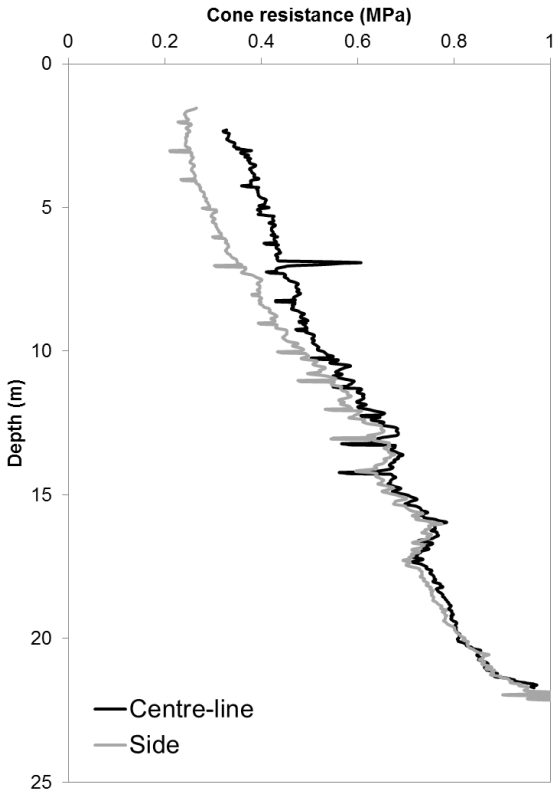


Figure 5 Cone tip resistance at the test site under the centre-line and at the East side of the embankment.

4 UNDRAINED SHEAR STRENGTH OF MURRO CLAY

Figure 6 shows the undrained shear strength profile at Murro test site. In-situ measurements obtained from piezocone and field vane test are compared. Field vane data points (s_u^{FV}) are corrected based on plasticity and converted to mobilized s_u ($s_{u(mob)} = \mu \cdot s_u^{FV}$) according to Larsson and Åhnberg (2005) [eq. (1)]. The effective cone resistance ($q_t - \sigma_{v0}$) is converted into s_u from the general transformation model of eq. (2).

$$\mu = \left(\frac{0.43}{W_L}\right)^{0.45} \quad (1)$$

$$s_u = \frac{q_t - \sigma_{v0}}{N_{kt}} \quad (2)$$

Where W_L is the liquid limit of the clay, q_t is the measured cone resistance corrected for pore pressure effects, σ_{v0} the total overburden vertical stress and N_{kt} is the cone factor. N_{kt} is firstly evaluated according to Larsson and Mulabdic (1991) and secondly estimated from field vane test results.
According to Larsson and Mulabdic (1991), N_{kt} increases linearly with increasing liquid limit, as N_{kt}=13.4+6.65W_L. Liquid limit profile with depth is shown in Figure 2 and both μ and s_u are calculated accordingly.

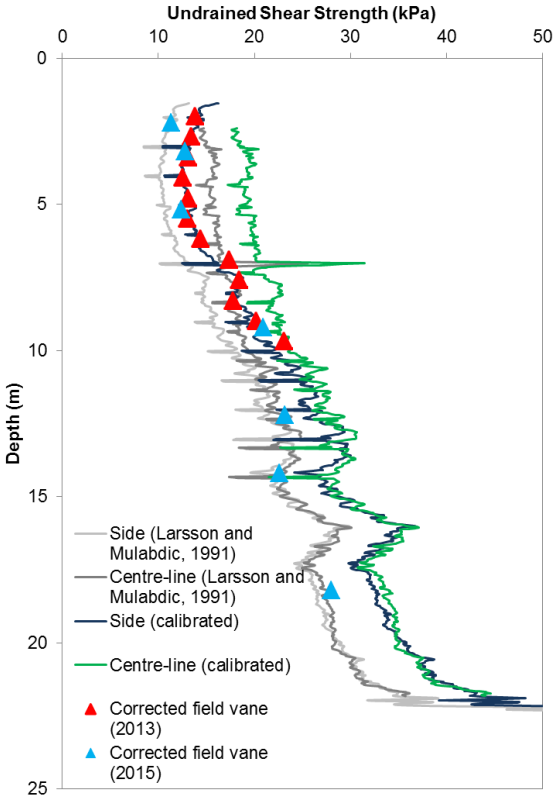


Figure 6 Undrained shear strength from piezocone and field vane test at the test site.

The stress increase below the embankment is estimated using the FE software PLAXIS 2D (see Section 5), in order to account for buoyancy effects. W_L values are assumed to be the same before and after consolidation.

According to Figure 6, Larsson and Mulabdic's model (N_{kt}=18-19) predicts lower s_u than the field vane. Therefore, such a model, which is used in Sweden, does not seem adaptable to the soil conditions at Murro test site. A calibrated average cone factor equal to N_{kt}=15 seems to provide a better description of the variation of undrained shear strength with depth. Assuming N_{kt}=15 also below the embankment, shear strength increase can be clearly observed up to a depth of 11 m. The maximum strength increase is observed at about 3.5 m depth, where s_u results about 7 kPa higher than at the side of the embankment.

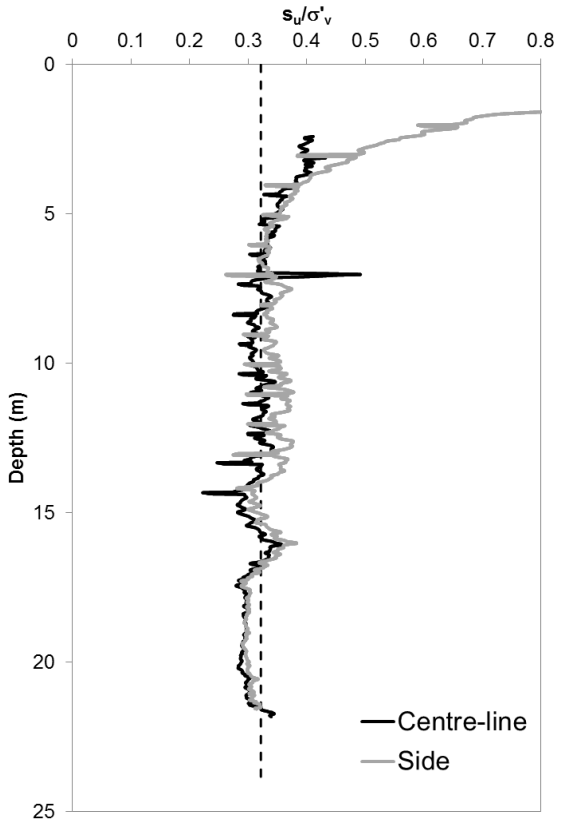


Figure 7 Variation and change in s_u/σ'_v with depth and consolidation.

As shown in Figure 7, measured values of s_u/σ'_v vary from 0.26 to 0.83 at the side of the embankment, with mean value of 0.36. Under the embankment, s_u/σ'_v ranges from 0.22 to 0.49, with mean value equal to 0.32. The ratio s_u/σ'_v is reduced due to consolidation, as also observed by Tavenas et al. (1978) from embankments built on Canadian clay deposits. Therefore, s_u/σ'_v = 0.32 would give an indication of the undrained shear strength of Murro clay for normally consolidated state. s_u/σ'_v = 0.32 would seem, in the authors' opinion, rather high for a soft normally consolidated clay. However, Murro clay is referred as silty clay or clayey silt (Karstunen et al., 2005). With respect to the latter definition, the silty component might play a key role. Laboratory tests (e.g. direct simple shear tests) are though needed in the future to verify the field observations.

5 FINITE ELEMENT ANALYSIS

5.1 Description of the soil models considered in this study

An attempt to model Murro test embankment using finite element method is done. The Soft Soil (SS) model (Plaxis, 2012) is used and the analyses are performed through the finite element software PLAXIS 2D 2012 AE.

The Soft Soil (SS) model is an isotropic effective stress soil model based on the Modified Cam Clay (MCC) model. The model assumes a logarithmic relationship between volumetric strain and mean effective stress. The model does not include rate dependency of soft clays. A special feature of the SS model is the Mohr-Coulomb failure criterion, while for MCC model failure is defined by the critical state line. In the SS model, the *M* line (see section 5.3) just defines the shape of the yield surface, thus making the model more adaptable to the actual yielding behavior of soft Finnish clays (Mansikkamäki, 2015). The principal input parameters for the SS model are the modified compression index λ^*, the modified swelling index κ^*, the OCR, the effective cohesion (c') and friction angle at critical state (ϕ'), the unloading-reloading Poisson's ratio (ν_{ur}), the lateral earth pressure coefficient for normally consolidated state K_0^{nc} (used as yield parameter, discussed in Section 5.3) and the lateral earth pressure coefficient ($K_{0\,\text{initial}}$).

The Soft Soil Creep model (Plaxis, 2012) is an extension of the Soft Soil model that takes secondary compression into account. SSC model is based on the isotache concept (Šuklje, 1957) and capable to model the time dependent creep behavior of clays. Input

parameters of the two soil models differ only for the modified creep index μ^* not included in the SS model.
However, as discussed by Mansikkamäki (2015), SSC model tends to severely overestimate the creep settlement of normally to slightly over consolidated soils. Especially for Finnish soft soil conditions, significantly reduced values of μ^* or increased OCR values have to be used to correctly simulate the creep settlement (Mansikkamäki, 2015). Mansikkamäki (2015) suggested that OCR should be at least 1.6-1.8 to achieve realistic creep strains. For this reason, SSC model does not seem suitable for modelling the creep behavior of Murro clay.

5.2 Finite element model and calculation results

The embankment and the dry crust are modelled as Mohr-Coulomb drained materials. The soft clay is divided into 5 sublayers (see Figure 8), as suggested by Koskinen et al. (2002), and modelled using Soft Soil model. Soil parameters for Mohr-Coulomb and Soft Soil models are chosen according to Koskinen et al. (2002).
Furthermore, according to Koskinen et al. (2002) the ratio λ^*/κ^* for Murro clay varies between 11 and 14 for Layers 1-4. For Layer 5, λ^*/κ^*=36.
The FE plane-strain model used for the analyses is shown in Figure 8. Due to the symmetry of the problem, only one half of the embankment is considered in the analyses. The lateral boundary is 36 m from the symmetry axis and the vertical boundary is at 23 m depth. A "very fine" type of mesh is used in order to ensure convergence of the results, consisting of 1094 15-noded triangular elements with average element size of 0.97 m. Full fixities are assigned at the base and roller conditions at the vertical sides. The ground water table is located at 0.8 m depth.
The initial stress state is generated assuming K_0 conditions and $K_{0\,\text{initial}} = 1 - \sin\phi'$. A two-day loading phase is used to reproduce the construction of the embankment. Finally, a 20-year consolidation analysis is performed.

Two parallel analyses are conducted: firstly, using the standard calculation settings (small strain analysis), and secondly, using the updated pore water pressure option (large strain analysis). The advantage of using the large strain option is that buoyancy of the fill material and dry crust material is taken into account, as they become submerged during the consolidation process.

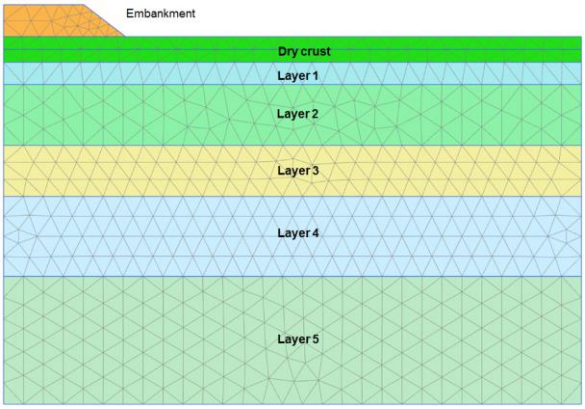


Figure 8 FE plane-strain Mesh.

Figure 9 shows a comparison between the measured settlement from Settlement Plate S2 (located at the centre-line of the embankment, as shown in Figure 2) and the results of the FE simulations. Figure 9 also illustrates the dissipation of excess pore pressures with time at Point A (see Figure 2), where the maximum strength increase was observed.

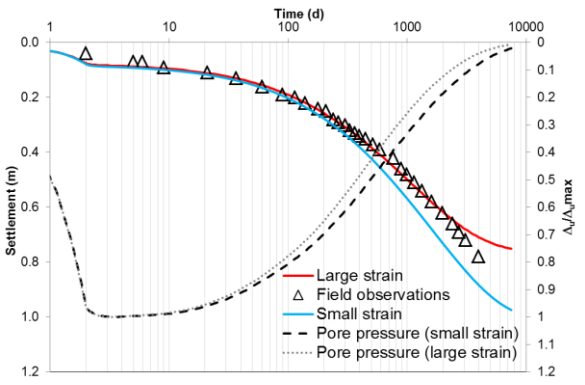


Figure 9 Long term settlement behavior of Murro test embankment and decay of excess pore pressures with time.

When using the large strain option, the settlement will result lower than in small strain analysis, as the stresses in the soil will be reduced due to buoyancy. As a

consequence, calculated pore pressures will be higher in small strain analysis. Overall, the settlement can be predicted reasonably well for the first 8 years after construction, before the calculation results deviate from measurements due to creep. Pore pressure dissipation, and therefore strength increase, mainly occurs during the first 6 years, as almost 90% of the maximum Δu seems to have dissipated at t = 2000 d.

The calculated factor of safety of the embankment, evaluated through the "safety" calculation option in PLAXIS, increases from 2.02 to 3.14.

5.3 Undrained shear strength in PLAXIS

One method to determine s_u, corresponding roughly to the vane strength, is to conduct Direct Simple Shear (DSS) tests. DSS tests can be simulated through a Soil Test tool implemented into PLAXIS. In the Soft Soil model, the shape of the initial yield surface is defined by the M parameter. M is automatically defined based on K_0^{nc} parameter, which can be set by the user. M can be approximated as in eq. (3) (from Plaxis user's manual):

$$M \approx 3.0 - 2.8K_0^{nc} \qquad (3)$$

Being K_0^{nc} calculated according to Jaky's K_0^{nc} = 1-sinϕ', the resulting M will be much higher than M based on the friction angle of the material (Mansikkamäki, 2015), as shown in Figure 10.

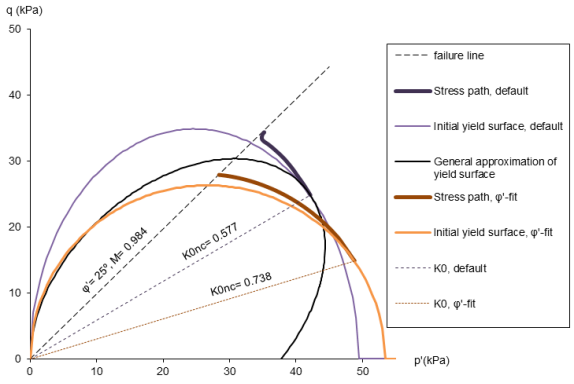


Figure 10 Yield surfaces and stress paths of Perniö clay depending on K_0^{nc}- and M-values (Mansikkamäki, 2015).

For ϕ'=37°, the average default M value for Murro clay is 1.98. The "fitted" M value, based on the friction angle would be 1.51. The main benefit of this procedure is that the excess pore pressure potential before failure can be realistically estimated, thus leading to a maximum deviatoric stress level lower than in the default case. The fitted yield surface was found to reproduce the behavior of Finnish clays better than the default yield surface (Mansikkamäki and Länsivaara, 2010). Furthermore, rate effects are not considered in this study, as the Soft Soil model is a rate independent model.

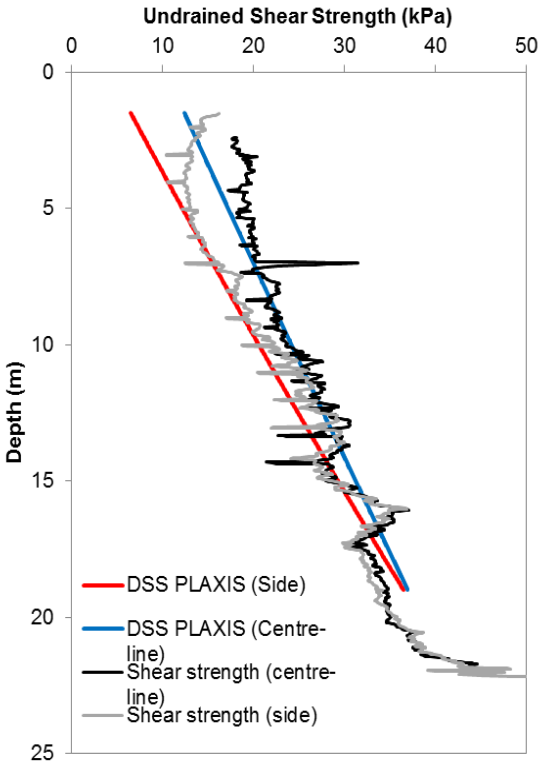


Figure 11 Undrained shear strength of Murro clay in Soil Test DSS simulations in PLAXIS using Soft Soil model.

Figure 11 shows the DSS strength modelled with PLAXIS compared to the undrained shear strength of Murro clay measured from piezocone. For OCR = 1, M = 1.51 and $K_{0\ initial}$=0.4, the predicted s_u/σ'_v is equal to 0.32, which corresponds to the average measured strength in Section 4. The predicted s_u agrees fairly well with the strength conditions at the test site up to 17 m depth. However, up to 5-7 m depth, measured s_u appears to be higher than the calculated one. From 17 to 23 m

depth, s_u values are overestimated. Nevertheless, the soil strength is highly dependent on friction angle and K_0^{nc} values assumed. For K_0^{nc}=0.4 (default value), s_u/σ'_v is equal to 0.38.

6 DISCUSSION

According to Janbu (1985), undrained shear strength is theoretically related to preconsolidation pressure (σ'_p), effective friction angle (ϕ') and attraction (a) as shown by eq. (4):

$$s_u \approx \frac{1}{2}\left(\sigma'_p + a\right)\cdot \sin\phi' \qquad (4)$$

Typically, a is taken equal to zero for normally consolidated clays. Table 1 summarizes values of s_u/σ'_v obtained using different friction angle and OCR values, based on eq. (4). By definition, σ'_p=OCR·σ'_v. For normally consolidated clays, eq. (4) for ϕ'=37° gives s_u/σ'_v equal to 0.30, against a value of 0.32 measured for Murro clay. s_u/σ'_v=0.32 can be obtained for ϕ'=30° only if a light over consolidation exists (OCR~1.3), or perhaps if a is greater than zero.

Table 1 s_u/σ'_v for different values of ϕ' and OCR assuming a=0 according to Janbu (1985).

ϕ'	OCR=1	OCR=1.1	OCR=1.3
25	0.21	0.23	0.27
30	0.25	0.28	0.33
33	0.27	0.30	0.35
37	0.30	0.33	0.39

According to the authors' experience, a friction angle of 37° (Koskinen et al., 2002) seems quite high for soft normally consolidated silty clay. In order to improve the knowledge of friction angle of Murro clay, triaxial compression and extension tests on block samples of Murro clay will be performed in the coming months at Tampere University of Technology.
Furthermore, the author's experience would suggest that OCR=1 is a too conservative assumption, as the aging effect would be neglected. Sample disturbance may have led to such a cautious hypothesis.

An attempt to evaluate the preconsolidation pressure (σ'_p) of Murro clay is done according to Larsson and Mulabdic (1991) using eq. (5).

$$\sigma'_p = \frac{q_t - \sigma_{v0}}{1.21 + 4.4\cdot W_L} \qquad (5)$$

Where $N_{kt}(\sigma'_p)$=1.21+4.4W_L is the cone factor for preconsolidation pressure. As shown in Section 4, the cone factor predicted by Larsson and Mulabdic for undrained shear strength (N_{kt}=18-19) is lower than the cone factor calibrated using the field vane test results (N_{kt}=15). Assuming that the same discrepancy exists for preconsolidation pressure, $N_{kt}(\sigma'_p)$ is then multiplied by 0.81.
The variation of OCR with depth is shown in Figure 12. The OCR under the embankment is calculated by dividing the initial σ'_p values (at the side) with the effective stress values after consolidation at the same depth.

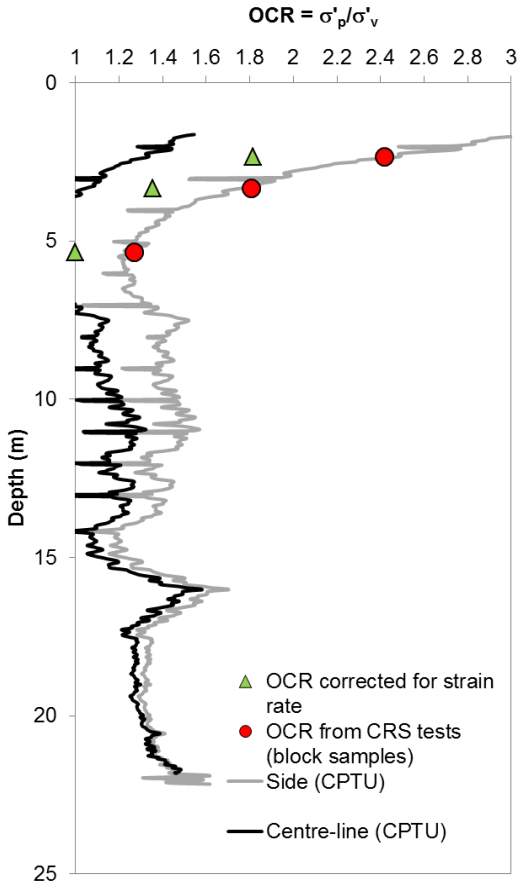


Figure 12 Hypothesis of variation and change in OCR with depth and consolidation.

According Figure 12, Murro clay seems to be slightly overconsolidated, with average OCR=1.4. OCR decreases from about 3 below the dry crust to 1.2 at about 6 m depth, while a marked fluctuation (OCR ranging from 1.1 to 1.6) is visible at depth of 14-18 m, where the soil is probably less homogeneous. This theoretical speculation is though consistent with the OCR trend with depth suggested by three OCR data points calculated from CRS oedometer tests on block samples of Murro clay. After 20 years, a reduction in the OCR is estimated (Figure 12). The normally consolidated state is only reached from 4 up to about 7 m depth. However, if σ'_p is corrected for strain rate as suggested by Leroueil (1996), the clay would seem to be normally consolidated at 5-6 m depth.

7 CONCLUSIONS

In this paper, the increase in undrained shear strength below Murro test embankment was studied by means of in-situ tests and the finite element software PLAXIS 2D. A series of conclusions can be drawn from this study:

1. Piezocone test results from the centre-line and the side of the embankment proved that the strength after 20 years of consolidation is higher than at the initial stage, prior to construction. Field vane test results from 2001 are, hence, contradicted.
2. According to the more recent field vane test results, the transformation model proposed by Larsson and Mulabdic (1991) for Swedish clays seems to overestimate the cone factor and, therefore, underestimate the undrained shear strength of Murro clay.
3. Based on this study, the average normalized undrained shear strength (s_u/σ'_v) of Murro clay is equal to 0.32, which is, in the authors' opinion, a considerably high value for a normally consolidated silty clay. Generally, s_u/σ'_p is assumed equal to 0.22 for inorganic clays (Mesri, 1975), roughly corresponding to DSS conditions. The observed elevated value might be due to the presence of silt particles and to the organic content of 2-3%. At the same time, the authors' experience would suggest that 0.22 represents a lower boundary strength value for Finnish clays.
4. Preconsolidation pressure from CRS oedometer tests (Karstunen and Yin, 2010) would suggest that Murro clay is normally consolidated. CRS tests on block samples of Murro clay done at Tampere University of Technology show OCR values higher than 1. OCR values greater than 2 are found below the dry crust. Moreover, the friction angle of 37° reported by Koskinen et al. (2002) seems excessively high according to the authors' experience with normally consolidated clays. In the near future, in order to further investigate this aspect, triaxial tests on block samples of Murro clay will be performed at Tampere University of Technology.
5. The long term settlement behavior of Murro test embankment can be satisfactorily modelled using the Soft Soil model in PLAXIS 2D. Being secondary compression not included, the observed deviation of the FE predictions from measurements was likely to be expected. According to the FE analyses, about 90% of the excess pore pressure seems to dissipate after the first 6 years.
6. For a realistic assessment of the change in stress state underneath the embankment, buoyancy should be taken into account. Neglecting the fact that the embankment and the dry crust become partly submerged during consolidation would lead to an overestimation of the effective stresses and, consequently, of the undrained shear strength.
7. The factor of safety of the embankment results magnified after consolidation (FOS=3.14 after 20 years, against FOS=2.02 after 2 days).
8. Undrained shear strength of Murro clay can be realistically modelled using the Soft Soil model in PLAXIS, provided that the initial yield surface is set based on the friction angle of the soil. When default parameters are used, s_u is severely over predicted.

8 REFERENCES

Bjerrum, L. 1973. Problems of soil mechanics and construction on soft clays. Proceedings of the 8th International Conference on Soil Mechanics and Foundation Engineering. 3: 111-159. Moscow.

Craig, R. F. (2004). Craig's soil mechanics. CRC Press.

Hanzawa, H. (1995). In Situ shear strength of marine clay related to aging effect. In Proceedings of the 11th European Conference IMFE, Vol. 1, 141-146.

Jamiolkowski, M., Ladd, C. C., Germaine, J. T., and Lancellotta, R. (1985). New developments in field and laboratory testing of soils. Theme lecture. In Proceedings of the 11th International Conference on Soil Mechanics and Foundation Engineering, San Francisco, California. A. A. Balkema, Rotterdam, The Netherlands, Vol. 1, 57-153.

Janbu, N. (1985). Soil models in offshore engineering. Géotechnique, 35(3), 241-281.

Karstunen, M., Krenn, H., Wheeler, S. J., Koskinen, M., & Zentar, R. (2005). Effect of anisotropy and destructuration on the behavior of Murro test embankment. International Journal of Geomechanics, 5(2), 87-97.

Karstunen, M., & Yin, Z. Y. (2010). Modelling time-dependent behaviour of Murro test embankment. Géotechnique, 60(10), 735-749.

Koskinen, M., Vepsälainen, P. & Lojander, M. (2002). Modelling of anisotropic behaviour of clays – Test embankment in Murro, seinäjoki, Finland, Finnra Report No. 16/2002. Helsinki, Finland: Finnish Road Administration.

Larsson, R., & Mulabdic, M. (1991). Piezocone tests in clay. Swedish Geotechnical Institute, Linköping, Sweden. Report No. 42.

Larsson, R., & Åhnberg, H. (2005). On the evaluation of undrained shear strength and preconsolidation pressure from common field tests in clay. Canadian Geotechnical Journal, 42(4), 1221-1231.

Leroueil, S. (1996). Compressibility of clays: fundamental and practical aspects. Journal of Geotechnical Engineering, 122(7), 534-543.

Leroueil, S., Kabbaj, M., Tavenas, F., & Bouchard, R. (1985). Stress–strain–strain rate relation for the compressibility of sensitive natural clays. Géotechnique, 35(2), 159-180.

Länsivaara, T. T. (1999). A study of the mechanical behavior of soft clay (Doctoral dissertation, Norwegian University of Science and Technology).

Mansikkamäki, J. (2015). Effective stress finite element stability analysis of an old railway embankment on soft clay. PhD thesis, Tampere University of Technology, Tampere.

Mansikkamaki, J., & Lansivaara, T. (2010). Analysis of a full scale failure test on old railway embankment. In Proceedings of the 7th European Conference on Numerical Methods in Geotechnical Engineering (NUMGE'10), 541-545.

Mesri, G. (1975). New design procedure for stability of soft clays. Journal of Geotechnical and Geoenvironmental Engineering, 101(Discussion).

Plaxis, B. V. (2012). User's manual of PLAXIS.

Slunga, E. (1983). On the increase in shear strength in soft clay under an old embankment. In Proc. 8th European Conference on Soil Mechanics and Foundation Engineering, Helsinki, Finland. Vol. 1, 83-89.

Šuklje, L. (1957). The analysis of the consolidation process by the isotache method. In Proceedings of the 4th International Conference on Soil Mechanics and Foundation Engineering, London, Vol. 1, 200-206.

Suzuki, K., & Yasuhara, K. (2007). Increase in undrained shear strength of clay with respect to rate of consolidation. Soils and foundations, 47(2), 303-318.

Tavenas, F., Blanchet, R., Garneau, R., & Leroueil, S. (1978). The stability of stage-constructed embankments on soft clays. Canadian Geotechnical Journal, 15(2), 283-305.

Swell pressure and yield stresses in Danish, highly over-consolidated, Palaeogene clays of extreme plasticity

Okkels, N. and Hansen, P. B.
Geo, Denmark, nio@geo.dk

ABSTRACT
Oedometer tests with highly overconsolidated clays of extreme plasticity often detect two yield stresses at very different stress levels. In the tests, the clay specimens yield first time when exposed to a rather low stress, which is only slightly - but significantly - higher than both the in situ stress and the swell pressure. The second time, the specimens yield at a much higher stress level, which can only be identified, if the specimens are exposed to stress levels beyond the typical range for conventional oedometer testing equipment. It is the widespread opinion that the geological preloading causes the high yield stress, whereas a profound physical explanation to the low yield stress has not yet been found.
The paper starts from the oedometer apparatus, which is subject to shortcomings and sources of error, such as non-control of the radial stresses and friction stresses between specimen and load cell, as well as non-control of the full range of creep processes. The paper provides consistent models on how these shortcomings and errors affect the performance curve of the test. Based on this, a physical explanation not solely to the low yield stress has been derived, but also to phenomena as swell pressure and hysteresis with its yield points that can be observed in connection with unloading and reloading processes. As expected, the performance curve of the test suffers from this, and there is potential risk for misinterpreting the stiffness parameters of the clays, unless being able to sort out, what is governed by the soil properties and what shall be referred to the test procedures and the test apparatus itself.

Keywords: Oedometer, Yield, Swell, Friction, Creep, Palaeogene clays

1 INTRODUCTION

Oedometer tests with highly overconsolidated clays of extreme plasticity exhibit some striking features and divergences, when compared with oedometer tests with more widespread clays of lower plasticity.

First and foremost, the clays exhibit swell potential. This is reflected in an oedometer test, where the clay specimen is being soaked, before being exposed to an axial load which is even distinctly larger than the vertical effective in situ stress.

Further, two yield stresses are often being identified at very different stress levels. A yield stress is defined as a point, which separates elastic from plastic behavior, but this condition is not necessarily fulfilled in both cases.

The low yield occurs, when the specimen is exposed to a stress, which is slightly, but significantly, higher than both the vertical effective in situ stress and the swell pressure.

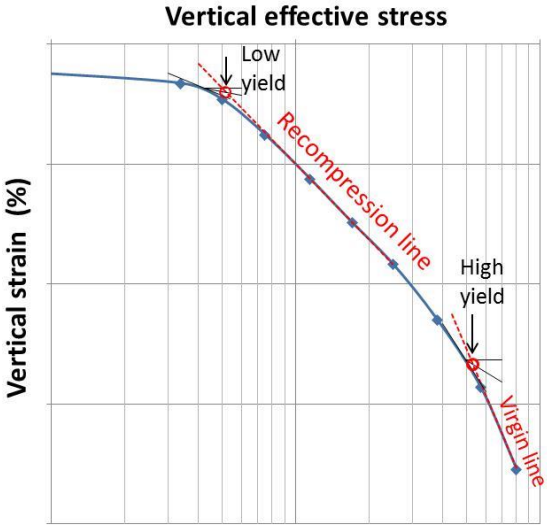


Figure 1 Example of a stress-strain curve for highly overconsolidated Palaeogene clay of extreme plasticity showing low yield and high yield.

The high yield occurs at a much higher stress, which can only be identified, if the specimens are being exposed to stresses beyond the typical range for conventional oedometer test equipment.

The low yield stress often can be detected from Casagrande's (Casagrande, A., 1936), Janbu's (Janbu, N., 1969) and Becker's (Becker, D.E., 1987) methods, but not from Akai's (Akai, K., 1960) method. The high yield stress is best detected from Akai's method, but often also the other methods are applicable.

There has not yet been found a physical explanation to the low yield stress, whereas it is widely held that the high yield stress shall be referred to the geological preloading.

Those two yield stresses separate the stress-strain curve into an initial part, representing the adaptation of the specimen to the load cell, a recompression curve, representing compression in overconsolidated state, and a virgin curve, representing normally consolidated state. A full understanding of those striking features is a prerequisite of interpreting and deriving swell pressure, stiffness parameters and yield stresses from the testing; i.e. whether the results refer to soil characteristics, or whether they are a consequence of shortcomings of conventional oedometer test equipment:

- The radial stresses in the specimen can neither be controlled nor measured in the conventional oedometer test apparatus.
- The stress-strain curves are subject to interference from frictional stresses between the specimen and the load cell.
- The creep processes affect the specimen in a way different from the in situ conditions.

These shortcomings of the oedometer test have an effect on all the phases of the test, viz. loading, unloading and reloading, as can be seen by examples in the following chapters. The changes of stress conditions throughout the whole process have been analyzed, from in situ conditions to sample recovery, to trimming of specimen and to the loadings, unloadings and reloadings during the testing. This gives rise to the understanding, what is de facto the outcome of an oedometer test.

To simplify and clarify the analyses it is a precondition that sample disturbance from the drilling work, from handling of samples and from trimming of specimens can be neglected.

2 DANISH PALAEOGENE CLAYS

Danish Palaeogene clays are high-colloidal clays of extremely high plasticity, and practically free of sand and larger particles. The index properties are summarized in Table 1.

The clays are deposited in Palaeogene oceans, and they are now heavily preconsolidated by the weight of the many glaciers and the weight of younger layers now eroded away during the Quaternary period.

Table 1 Index properties of Palaeogene Clays.

Property	**Range**
Natural water content	25-70 %
Liquid Limit	80-350%
Plasticity Index	50-290 %
Unit weight	17-19 kN/m^3
$CaCO_3$	0-60 %

The samples extracted are frequently fissured and show slickensides with shining surfaces in the fractures. Such features shall be referred to slips and failures caused by ice dynamics and/or release of ice pressure.

Usually, the clays are saturated due to the wet Danish climate, the relatively high lying ground water and the capillary rise of the clay. In the following the clay samples are considered being completely saturated, when installed into the oedometer apparatus.

3 THE RATIO BETWEEN HORIZONTAL AND VERTICAL STRESSES IN SITU

Throughout the geological periods the highly overconsolidated Palaeogene clays have undergone parts of the stress history illustrated in Figure 2.

The stress path OA represents the virgin loading (compression) as it occurs during the sedimentation – i.e. compression in the normally consolidated state. The vertical

stresses are larger than the horizontal stresses, so that the coefficient of earth pressure at rest $K_0 = K_{0,NC} < 1.0$ during this virgin loading.
During unloading (ABC) the vertical stresses reduce faster than the horizontal stresses, implying that the horizontal stresses become larger than the vertical stress at a certain unloading stress, so that $K_0 = K_{0,OC} > 1.0$. If unloading continues further, the stress path may reach the failure stress path, and then follow that path for the continued unloading.

During reloading (CDA), the original ratio between horizontal and vertical stresses will gradually restore. The coefficient of earth pressure at rest reduces again to a value below 1.0.

Thus, for highly overconsolidated clays K_0 decreases when the vertical load increases, whereas K_0 increases when the vertical load decreases (Mayne, P. W., 1982).

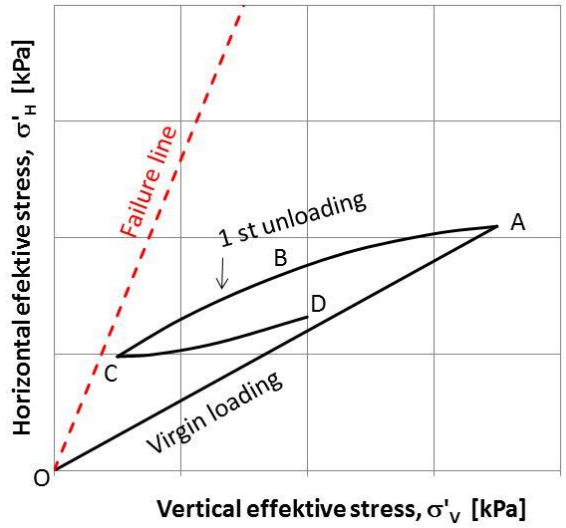


Figure 2 The ratio between the horizontal and the vertical stresses under virgin loading, unloading and reloading

For the Palaeogene clays, the geological preloading typically ranges some 4,000-6,000 kPa. For the near surface deposits the pertaining overconsolidation ratios, *OCR*, are excessive, so there is no doubt that the failure line in Figure 2 has been reached during the geological unloading, and further that this is the case for the layers to tens of meters below surface. Consequently, for the uppermost highly overconsolidated Palaeogene clays the mutual connection between *OCR* and K_0 has been broken.

4 STRESS CONDITIONS AND SWELL PRESSURE

When carrying out oedometer tests with Danish, highly overconsolidated Palaeogene clays of extreme plasticity it is observed that the specimens often exhibit swell during the minor load steps. This is due to a procedure, where the specimen is being soaked at an axial load in the oedometer test, which is too small to resist the swell pressure in the specimen.

The presence of a swell pressure is a term of an imbalance of the total water potential, defined as the potential energy per unit volume. Such imbalance occurs, when the total water potential changes in situ or if the in situ conditions are not correctly regenerated in the oedometer cell. For saturated soil, the total water potential is the sum of the pressure potential and the osmotic potential.

In this paper it is a precondition that the salinity of the pore water in the specimen equals the salinity of the water used for soaking the specimen in the apparatus, so that the osmotic potential can be neglected.

4.1 The sample under in situ conditions

Under in situ conditions the effective vertical stress is well-known. For the uppermost tens of meters it represents the minor principal stress, as often $K_0 > 1.0$, and thus the horizontal stresses represent the major principal stresses. However, these major stresses are often unknown.

4.2 The sample after recovery

When extracting and trimming a high plasticity Palaeogene clay sample to a specimen for testing, the partial vacuum pore pressure keeps the soil structure together as a monolithic specimen. Thus, the negligible compressibility of the pore water compared to the one of the soil skeleton ensures that both the void ratio (the volume) of the specimen and the effective mean stress of the specimen remain unchanged, compared to the in situ conditions.

The total water potential of the specimen after trimming is equal to the partial vacuum

pore pressure that arises during extraction of the sample.

In this specific phase the ratio between the horizontal and the vertical stresses is equal to unit, $K = 1.0$, despite the size of $K_{0,insitu}$. Even though the volume and the mean stress become unchanged compared to the in situ conditions, the change of K implies that the shape of the specimen will change. However, most likely this is a matter of secondary importance as to affecting the result.

4.3 The specimen in the oedometer cell

The void ratio and the mean stress remain unchanged, when installing the specimen in the oedometer apparatus. This is valid until the specimen is being loaded or being soaked (without loading), after which the void ratio and the mean stresses change.

The swell pressure is the same in all directions. This has been demonstrated experimentally in a constant volume test, where the swell pressure is measured in specimens, extracted in pairs from one and the same level, in both horizontal and vertical direction. As seen from Figure 3, the measured swell pressure is broadly identical in both directions.

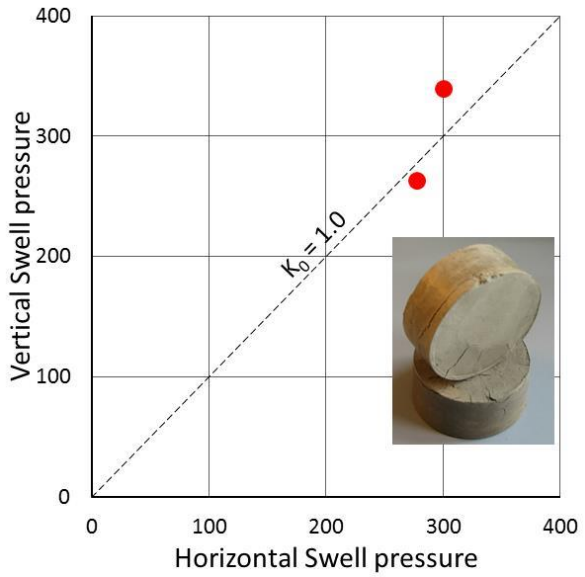


Figure 3 Measured swell pressure in specimens extracted from horizontal and vertical direction, respectively (Okkels, N. 2012).

In constant volume tests the ratio between the horizontal and vertical stresses is at unit, $K_0 = 1.0$. This is also the case, when the specimen is being soaked, under the precondition that the void ratio (the volume) is kept unchanged compared to the in situ conditions.

By keeping the void ratio (the volume) constant and unchanged until and during measuring the swell pressure, this implies that the mean stress in situ is identical with the swell pressure. This further implies that $K_{0,in\ situ}$ can be assessed from the swell pressure, σ_{swell} and the vertical effective in situ stress, $\sigma'_{v,in\ situ}$:

$$K_{0,insitu} = \frac{1}{2}\left(3\frac{\sigma_{swell}}{\sigma'_{v,insitu}} - 1\right) \quad (1)$$

5 MEASURING SWELL PRESSURE

It is of the utmost importance to measure the swell pressure at the same void ratio (volume) as is the case in situ; i.e. the measuring shall be a true constant volume test. Otherwise, the swell pressure – or rather the mean stress of the specimen – will change.

In a constant volume test, the vertical stress inside the specimen is known, as no frictional forces between specimen and load cell are present. At the same time, the horizontal stresses are known as well ($K_0 = 1.0$). The swell pressure in such a test can only be determined with an approximation, by continuously adjusting the vertical stress so that the vertical deformation maintains at mini-mum; cf. Figure 4a.

5.1 Dubious procedures for determining swell pressure

Some recognized procedures to determine the swell pressure are based on test phases with distinct deformations and thereby with effects from a changed K_0 as well as effects from side friction. Consequently, the mean stress will change. The virtual stress conditions are therefore unknown, and in reality it is not possible to derive a swell pressure that reliably represents the in situ swell pressure.

In the *Free Swell-Consolidation test method*, ref. ASTM D4546 2003 Method C, the specimen is allowed to freely swell for an exposed small load (point 0 to 1 in Figure 4b). The swell pressure is then determined as

the further exposed load that brings the specimen back to its initial void ratio (point 2 in Figure 4b).

In the *Loading-Wetting test method*, ref. ASTM D4546 2008 Method A, a number of specimens (1 – 4 in Figure 4c) are loaded under dry conditions to predetermined stress levels, after which they are being soaked and allowed to swell or consolidate for the respective stresses. The swell pressure is then determined as the stress, where these tests indicate that no strain will occur; cf. Figure 4c.

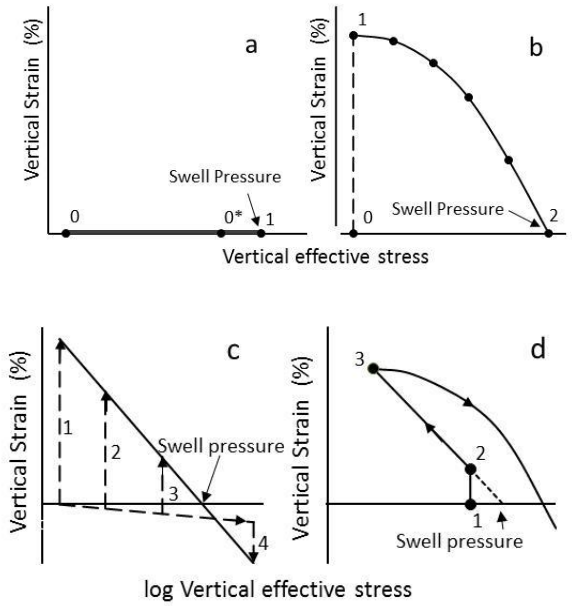


Figure 4 Determination of swell pressure. (a) Constant volume method, (b) Free Swell-Consolidation method, (c) Loading-Wetting method and (d) AASHTO Code method.

In the *AASHTO Code test method (AASHTO Standard T258-81)* the specimen is exposed to a vertical load equal to the in situ stress under dry conditions (point 1 in Figure 4d). After adding water to the specimen, it is allowed to swell for this constant in situ stress (point 2). Then the specimen is being stepwise unloaded (point 3). The swell pressure is determined as the resection of the unloading line to the 0-line.

5.2 Adjusted procedures to Constant volume tests

In practice, it is an inevitable consequence to allow for a certain deformation during the initiation of a swell test. This is due to the fact that the adaptation of the specimen to the load cell and the filters together with the potential sample disturbance gives rise to volume changes, i.e. an initial compression to restore the in situ void ratio.

In the *CEN ISO/TS 17892-5:2004* test method the following pragmatic description has been chosen. The specimen is quickly loaded under dry conditions to an estimated swell pressure (point 0 to 0* in Figure 4a), where the measuring is set to zero. Then the specimen is soaked, and the vertical stress is adjusted to hinder development of strains in excess of ±0,01mm. The swell pressure is equal to the applied stress that stabilizes accordingly. However, it cannot be excluded that the result is influenced by friction forces and change of K_0, due to deformations during initiation of the test.

6 CREEP AND CREEP PRESSURE

According to Degago S.A. (2013) the existence of creep during primary consolidation is evident. Consequently, the stress-strain curve (End Of Primary consolidation, EOP) depends on the rate of loading; the higher rate, the farther the stress-strain curve will move to the right; cf. figure 5.

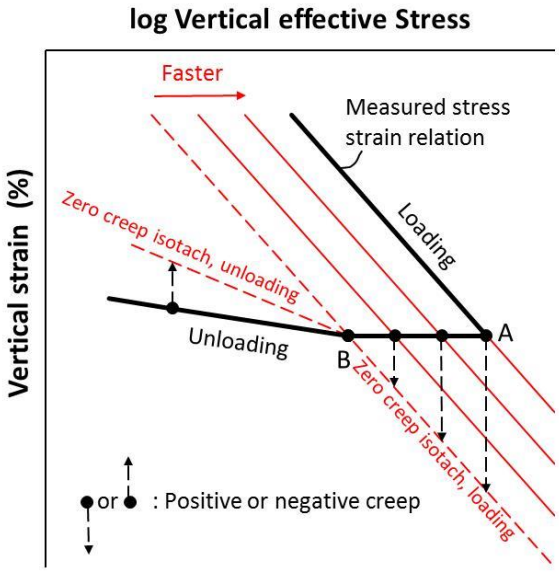


Figure 5 Illustration of stress-strain relations and creep. Unloading from A to B is performed so creep exactly is avoided (after Kawabes S., 2013).

Also the shape of the stress-strain curve is affected, when loading shifts to unloading. Immediately after such a shift the creep acts in opposite direction to the change of load (point A in Figure 5), (Kawabes S., 2013).

Not until the change of load reaches a certain size, the unloading path will intersect the zero creep isotach (point B in Figure 5), and then the creep will act in the same direction as the unloading. A creep isotach is defined as a line of equal creep strain, and the pertaining stress change necessary to reach the zero creep isotach is interpreted as a negative creep pressure.

Conversely, when unloading is shifted to loading the stresses shall be increased, if upwards creep shall be hindered. The pertaining excess stress required for totally hindering upwards creep, and thereby ensure constant volume during this stage of test, is interpreted as a positive creep pressure.

In conclusion, creep pressure at the individual load steps changes by time as creep strains develop. Creep affects the initial part of the unloading as well as the reloading paths. Therefore, the deformation parameters shall be derived with due consideration to the creep, alternatively, creep shall be incorporated in the constitutive model.

7 SIDE FRICTION

During oedometer testing shear forces develop along the cylindrical surface of the specimen, due to the relative movements of the specimen against the inflexible oedometer ring.

Therefore, during loading the specimen in reality is loaded by a vertical stress less than the applied stress, whereas during unloading the vertical stress is larger than the applied vertical stress; cf. Taylor, D.W. (1942) and Olson, R.E. (1986).

Side friction between specimen and steel surface is not present during the initial part of the test. It will not generate, till the in situ volume of the specimen changes after change of loading. The induced vertical strains in the specimen will generate shear strains, and in doing so also shear stresses will generate in the boundary surface between the specimen and the steel ring.

The side friction will generate rapidly during loading beyond the swell pressure, cf. Figure 7. When loading is shifted to unloading, the side friction will gradually decrease to zero and eventually be regenerated in the opposite direction. This process will repeat, when the unloading is shifted to loading, etc.

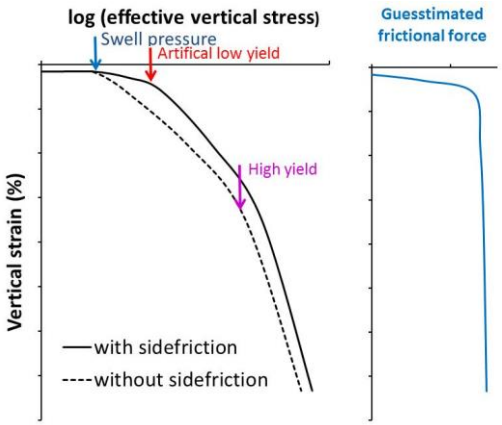


Figure 7 Illustration of the effects of side friction. The test result without friction is constructed by subtracting the guesstimated frictional force from the applied load. The generation of side friction changes the position of the yield points.

In the oedometer test, the stress-strain curve is conventionally drawn with the applied load, i.e. without any correction for side friction. This means that the generation of side friction will create an artificial yield point on the stress-strain curve as shown in Figure 7. This yield point indicates the stress, where the main part of side friction is generated during the loading. The same occurs, when the side friction turns around and regenerates during unloading and reloading. In all cases, the generation of side friction makes the specimen stiffer than it really is.

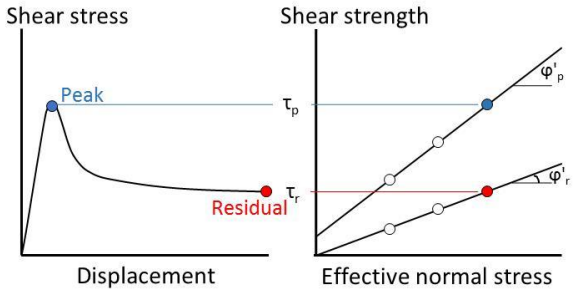


Figure 8 Shear strength tests with Palaeogene clays.

Unfortunately, it is normally not possible to compute the side friction. Partly, it depends on the radial stresses from the oedometer steel ring, which cannot be measured in conventional oedometers. Partly, it depends on the lack of knowledge to the shear stress-strain relationship in the lubricated interface between the specimen and the steel ring at the actual stress levels, cf. Figure 8.

However, we do know the displacements in the interface. In case of a fixed ring, the displacement decreases approximately linearly from a maximum value at the top of the ring, equal to the measured displacement, to zero at the bottom of the ring. In case of a floating ring, the displacement decreases approximately linearly from half of the maximum value at both ends of the ring to zero at the middle of the ring; cf. Figure 9.

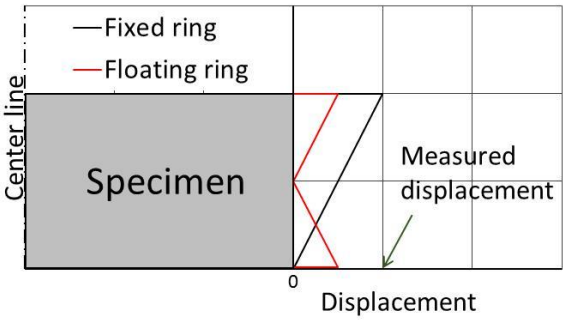


Figure 9. Simplified variation of soil-ring displacements in a fixed and floating ring oedometer

Following Figure 8 the shear stress-displacement relationship depends on the effective normal stress on the failure envelope.

The side friction can be separated into a static contribution, where no failure occurs in the interface between specimen and steel ring (pre peak friction), so that the specimen sticks to the steel ring, and a kinematic contribution, where failure appears (post peak friction) in the interface. Due to the softening behavior of the Palaeogene clay the static contribution is larger than the kinematic contribution.

Both types of friction will normally contribute to the side friction, as the displacements vary along the surface of the ring. Further, the two contributions depend on the size of displacements, where the static contribution is directly proportional to the size, whereas the kinematic contribution converges to a constant residual value.

For the Palaeogene clay with its distinct softening behavior, it cannot be concluded in beforehand, whether the side friction is the lesser in a floating ring or in a fixed ring. Most probably, this depends on the actual distribution between static and kinematic friction, and likely, the distribution will change with the increase of loading.

8 PERFORMANCE CURVE AT PRIMARY LOADING

A typical stress-strain curve for high plasticity Palaeogene clay exposed to loading is shown in Figure 10a and 10b. The strain refers to end of primary consolidation.

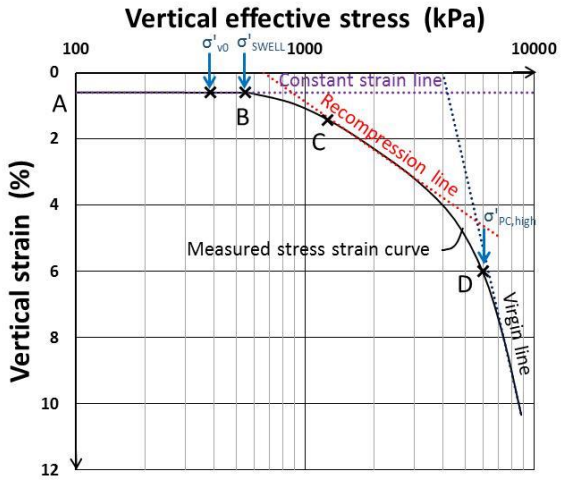


Figure 10a Logarithmic stress-strain curve, loading.

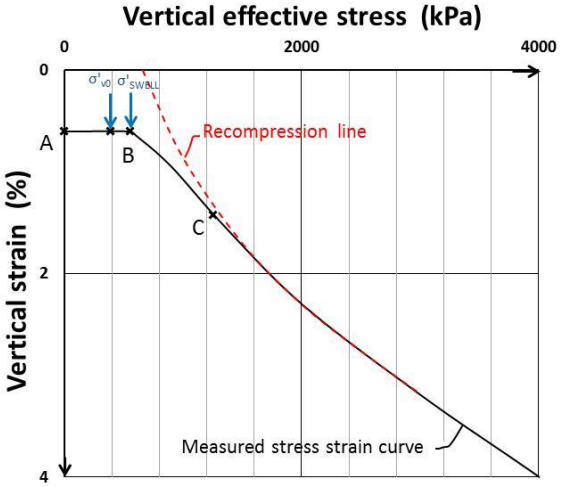


Figure 10b Arithmetic stress-strain curve, loading.

During the initial part of the primary loading, the swell pressure has been measured at constant volume (point A to B). Constant volume ensures that no frictional forces act on the sides of the specimen (the strain is zero), that the relation between the horizontal and vertical stresses is known (K = 1.0), and further that the swell pressure can be measured being equal to the vertical stress being exposed to the specimen to maintain constant volume (no strain). Thus, knowing the effective vertical stress in situ, the earth pressure at rest in situ, $K_{0,insitu}$, can be computed from equation (1).

The curvature A-B is a sort of regeneration phase, where the effective mean stress in situ is regenerated in the oedometer specimen at the in situ void ratio.

The change at point B from the regeneration phase to the virtual compression phase appears as a distinct break. This point B might be interpreted as a yield point; however, as the virtual compression starts at point B, such an interpretation is meaningless.

The curvature B to C is a transition part from the initial constant volume part to the recompression part of the curve.

In this transition phase, where the loading is increased, the vertical strains will develop, and at the same time, side friction generates in the reverse direction of the loading. Thus, the vertical stress will be less than the applied stress, and the specimen, therefore, looks stiffer than it de facto is for small stress increases in excess of swell pressure.

Without friction the recompression curve in Figure 10a and 10b would start from the swell pressure (point B), however, the effect from side friction will move the curve to the right by inserting a somewhat stiffer transition curve, point B to C; cf. Figure 7.

The curvature B – C causes that a yield point appears in this inserted transition curve, cf. Figure 1, which can be detected by the recognized methods as stated in chapter 1. From C to D the loading increases, and K decreases further. At point D the side friction is still acting upwards. The vertical stress in the specimen, therefore, is still larger than the applied stress.

At point D the stress-strain curve goes from a bending curvature to a straight curve, as it passes a yield point. At the same time, the creep index increases to a maximum value, typically around 1 %/lcs for the Palaeogene clays. This yield point represents the geological preconsolidation; cf. the high yield stress in Figure 1.

After point D the stress-strain curve enters the virgin curve, and K is reduced to its minimum value, $K_{0,NC}$.

It is the overall evaluation that the short-comings of the oedometer test apparatus influence especially the initial part of the stress-strain curve (point A to C in figure 10).

The influence upon the performance curve, obviously, will make the derivation of reliable deformation characteristic subject to uncertainties.

9 HYSTERESIS IN RELATION TO UN-LOADING AND RELOADING

Figure 11 shows a typical unloading-reloading path for Palaeogene clay of extreme plasticity, compared with the same path cleaned for stresses related to side friction. The strains refer to end of primary consolidation.

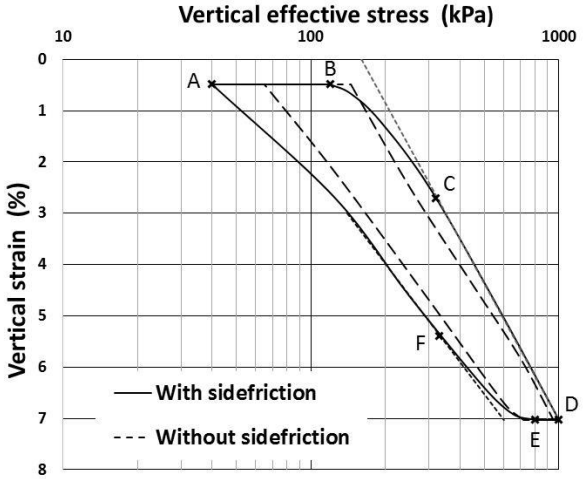


Figure 11 Hysteresis in relation to unloading and reloading with and without sidefriction.

The unloading starts from point D, where the fully soaked specimen after stepwise loading has reached end of primary consolidation. At this stage the stresses from side friction acting on the specimen are pointing upwards,

so that the true vertical effective stress in the specimen is less than the applied stress.

From point D to E the test from pedagogical reasons is being carried out, so that downwards directed creep is just hindered by reducing the applied load appropriately. During this phase the vertical strain is unchanged (constant volume), and so the side friction must be unchanged as well.

The true vertical stress in the specimen, thus, is still less than the applied stress in point E.

From point E to F the loading is being reduced. Concurrently with the change of loading the side friction will eventually and gradually change from directed upwards at point E to directed downwards at point F. The true vertical stress in the specimen now has become larger than the applied vertical stress.

The curvilinear part between point E and F might be interpreted as a yield point with a yield stress that can be determined from a Casagrande construction. However, as this yield point is caused by creep and friction stresses, it has only a marginal effect upon the conventional deformation characteristics of the clay.

The loading is being further reduced from point F to A, and concurrently with this the ratio between horizontal and vertical stresses, *K*, increases. After end of primary consolidation at point A the side friction on the specimen is still directed downwards, and its numerical value is somewhat larger than at point F. This is due to the fact that the vertical effective stresses reduce faster than the *K* increases. The true vertical stress in the specimen is still larger than the applied load. From point B to C the loading is being increased, and the side friction gradually decreases and changes direction so that it is directed upwards at point C. The true vertical stress in the specimen now is less than the applied load.

The curvilinear part between point B and C is similar to E-F and the part from C-D are similar to F-A.

10 CONCLUSIONS

The Danish Palaeogene clays are highly overconsolidated clays of extreme plasticity. For these clays in general, this implies that the horizontal in situ stresses are in excess of the vertical ones, and thereby that the earth pressure at rest $K_0 > 1.0$. However, for the near-surface layers the conventional connection between the overconsolidation ratio, *OCR* and K_0 has been broken due to passive failure, emerging during the unloading from the very high geological preconsolidation stresses.

This paper has analysed shortcomings and sources of error of conventional oedometer tests, caused by non-control of the radial stresses and friction stresses generated in the specimen from the contact to the oedometer load cell, as well as non-control of the full range of creep.

The analysis starts from the premise that a laboratory specimen of high plasticity Palaeogene clay preserves the effective in situ mean stresses and the in situ void ratio during the whole process from sampling to trimming for testing. This premise has been made, so that the analysis can focus directly upon the shortcomings and sources of error of the oedometer test equipment, without being blurred by potential effects from sample disturbance.

The analysis draws attention to the following items, the ones of which might affect the results of oedometer tests:

(i) Swell pressure shall be measured at the same void ratio (volume) as is the case in situ; i.e. the measuring shall be a true constant volume test. Otherwise, the swell pressure, or rather the mean stress of the specimen, will change and friction stresses evolve in the specimen.

(ii) Creep affects the shape of the stress-strain curve, especially when loading shifts to unloading and vice versa. Immediately after such a shift, the creep acts contrary to the change in load. This affects the initial parts of the unloading and reloading paths to an extent that these parts of the performance curve are not representative of the true stress-strain relation.

(iii) Shear forces develop along the cylindrical surface of the specimen, as vertical strains generate friction against the oedometer ring. Therefore during loading, the specimen in reality is loaded by a vertical stress less than the applied stress, whereas during unloading the vertical stress is larger than the applied vertical stress. This again affects the initial part of the unloading and reloading paths to an extent that these parts of the performance curve are not representative of the true stress-strain relation.

(iv) The mobilization of shear forces along the cylindrical surface of the specimen generates an artificial low yield point on the stress-strain curve, when the stress-strain curve conventionally is drawn with the applied load and without correction for side friction.

(v) Many of the current methods for deriving yield stresses are solely based on the curvature of the stress-strain curve, and without due consideration, whether the curvature solely is defined from characteristics of the soil, or whether the shortcomings of the oedometer apparatus affect on the curvature to a conclusive degree. Thus, when the curvature is affected from side friction and creep an artificial yield point will appear on the performance curve. Such an artificial yield point is a fine example of a spurious relationship, as no causality with a genuine yield point is detected.

(vi) Hysteresis during unloading and reloading are much more profound for high plasticity Palaeogene clays compared with more widespread clays of lower plasticity. This is due to the fact that the loops of high plasticity clays are affected from side friction and creep pressure.

It is the overall conclusion that the stiffness parameters derived from an oedometer test shall take due consideration to the short-comings and sources of error of the oedometer test apparatus, as the performance curves are affected from side friction and creep pressure.

In this respect, the stiffness parameters should be derived from an extrapolation of the lesser affected parts of the unloading and reloading paths, often being the parts that lies after the artificial yield points provoked by side friction.

The extrapolation shall extend those lesser affected parts of the performance curve to include also the specific stresses relevant for the project, and the stiffness parameters here-after shall be derived from the extrapolated curves.

11 REFERENCES

Akai, K. (1960) De strukturellen eigenschaften von schluft mittelugen, Die Technische Hochschule Aachen, Heft 22.

Becker, D, Crooks, J.H.A, Been, K. and Jefferies, M.G. (1987) Work as a criterion for determining in situ and yield stresses in clays. Can. Geotech., Journal 24. pp. 549-564.

Casagrande, A. (1936) The determination of the preconsolidation load and its practical significance. International Conf. on Soil Mech. And Found. Eng. 1936, Cambridge, Massachusetts, USA.

Degago S.A., Grimstad G., Jostad H.P. and Nordal S. (2013) Misconceptions about experimental substantiation of creep hypothesis A. Proceedings of the 18th International Conference on Soil Mechanics and Geotechnical Engineering, Paris.

Fredlund D.G. Geotechnical problems associated with swelling clays, Chapter 14 in "Vertisols and technologies for their management" edited by Ahmad, N. and Mermut, A. pp. 499-524, 1996.

Janbu, N. (1970) The Resistance Conceot Applied to Deformation of Soils, Proc. 7th International Conf. on Soil Mech. And Found. Eng. Mexico City, Vol. 1, pp 191-196.

Kawabe, S. and Tatsuoka F. (2012) Creep characteristics of clay in one-dimensional compression with unloading/reloading cykles. Proceedings of the 18th International Conference on Soil Mechanics and Geotechnical Engineering, Paris.

Mayne P.W., Kulhawy, F.H. (1982) K_0-OCR Relations in Soil. Journal of the Geotechnical Engineering, ASCE, Vol. 108, No. GT6.

Okkels, N. (2012) Determining the geological preconsolidation of Søvind Marl from Aarhus Harbour and a Model for swelling pressure and pressure at rest. PowerPoint presentation (in Danish) www.dansk geotekniskforening, Mødereferater, Møde nr. 9, 2012.

Olson R.E. (1986) State of the Art: Consolidation Testing. ASTM STP 892, pp. 7-70.

Taylor D.W. (1942) Research on Consolidation of Clays. MIT. Department of civil and sanitary Engineering, part 2 section 4, pp. 25-35.

Utilization of recycled materials in urban earth construction: crushed concrete, foamed glass and ashes

T. Dettenborn
Aalto University, Finland, taavi.dettenborn@aalto.fi

J. Forsman
Ramboll Finland Oy, Finland

M. Napari
Aalto University, Finland

J. Pekkala
Uusioaines Oy, Finland

J. Pieksemä
Rudus Oy, Finland

M. Suominen
City of Helsinki, Finland

ABSTRACT
In recent years, the utilization of recycled aggregates has expanded from traditional road pavement construction to new applications in urban earth construction (UEC). The "speciality" in UEC is the nature of roads as a place for networks of water supply and sewerage, electrical and telecommunication which means that the streets are commonly excavated because of the repairs of existing pipes or cables or installation of new ones. In the cases where "traditionally used" natural aggregates are replaced with recycled aggregates, some UEC applications bring about certain new challenges that need to be considered. The differences between natural aggregate and recycled aggregate and due to the nature of UEC, designers and contractors need more information on the recycled materials used. Information is needed e.g. about the possible effect of recycled materials to adjacent underground municipal engineering pipelines etc. To tackle this matter, Helsinki Region Environmental Services Authority (HSY) and the metropolitan cities have initiated comprehensive study to investigate the crushed concrete aggregate and foamed glass aggregate behaviour in UEC. Based on literature, field and laboratory studies, HSY released guidelines regarding the utilization of those materials in streets and pipeline trenches. The guidelines provide designers and contractors with basic information on design, utilization, maintenance and the environmental aspects of the life cycle. This article also presents some results of a study to investigate the suitability of ashes (fly ash, bottom ash and flue gas desulphurization residue) from energy production in pipeline trenches. Preliminary literature study indicates that coal ashes could be considered as a noncorrosive "aggregate" and to be used near metallic materials (excluding aluminium). However, unburned carbon content may cause major concern when in contact with electronegative metals, such as, aluminium, zinc or steel.

Keywords: recycled crushed concrete aggregate, foamed glass, ash, corrosion, guidance

1 INTRODUCTION

Vast amounts of mineral aggregates such as sand, gravel or crushed rock are required for municipal construction activities. Construction consumes over 100 million tons of rock materials in Finland annually. (Finnish Transport Agency 2014, Koivisto et al. 2015)

There is a desire to conserve nature and to minimize the consumption of mineral aggre-

gates. Other important aspect is the need to reduce the amount of waste materials and by-products generated by community activities. This process has been driven by the EU recycling and material efficiency targets, the growth of landfill taxes, as well as increased transportation distances from natural aggregate (NA) extraction areas.

Mineral aggregates and light weight aggregates can be substituted by various types of waste materials and by-products generated by industrial and other activities. The use of recovered materials in earthworks can be significantly increased by developing construction technology, planning and acquisitions. Also challenges in utilization can be general unawareness, incorrect impressions, rules and legislations.

Traditionally the construction, design and maintenance guidance of recycled materials is mainly focused to pavement engineering. The differences between natural and recycled aggregates and due to the nature of urban earth construction (UEC) projects - frequent digging up of existing street structures and possible effect to adjacent underground municipal engineering pipelines etc., designers and contractors need more information on the materials used. To tackle this matter in UEC-projects, Helsinki Region Environmental Services Authority (HSY) and the metropolitan cities had initiated comprehensive study to investigate crushed concrete aggregate (CCA) and foamed glass aggregate (FGA) behaviour in UEC.

After the release of the guide books (HSY 2014a, and Cities of Helsinki, Espoo and Vantaa 2015), the utilization of CCA and FGA has increased in metropolitan area. This article gives an overview of the main issues and findings of the literature, field and laboratory studies and lists the aspects that need to be take in account when utilizing certain RA in UEC. This paper presents three different by-products that can be used in earth construction: recycled crushed concrete aggregate, foamed glass and ashes from energy production.

2 RECYCLED CRUSHED CONCRETE AGGREGATE (CCA)

Concrete is the most commonly recycled demolition product. Approximately, one million tonnes of concrete waste is annually generated in Finland and approximately 0.5 million tonnes of the total quantity in metropolitan area. Approximately 70-80 % of concrete waste is recycled in Finland. The majority of recycling takes place in road and earth construction works. Despite this relatively high recycling percentage, there are still challenges in utilizing processed concrete waste as the CCA even though the major entrepreneurs in this field have CE-marked and high quality CCA products for road base and sub base layer construction.

2.1 Mechanical and environmental properties of CCA

Table 1 presents the classification of CCA to different categories in Finnish guidance and some technical properties. Long-term follow-up studies have proven CCA mechanical capability in road and pavement structures (Dettenborn et al. 2015a).

Table 1. Classification of crushed concrete aggregate to categories I to IV in Finnish guidance. In category I the raw material originates directly from concrete industry and in category II to IV from demolition of old concrete structures or buildings.

Category	Maximum size of the CCA particles [mm]	Self hardening properties	Frost susceptibility	E-modulus [MPa]	Max. content of bricks [weight-%]	Max. content of other materials ** [weight-%]
I	50	Hardens	No	700	0	0.5
II	50	Hardens	No	500	10	1
III	50	Uncertain	No	280	10	1
IV	Varies	No hardening	Varies	≤ 280 *	30	1

* to be considered in each case

** wood, plastic, etc. In addition of the weight-% demand there may not be harmful amounts of special light materials (such as polystyrene and other insulation materials)

Categories II-IV differs from each other by grain size distribution, self-hardening properties, frost susceptibility, E-modulus and content of other materials. Wastes resulting from demolition of various structures usually con-

tain some foreign materials. For this reason, demolition should be well supervised and materials sorted to ensure that the product obtained from waste is as clean and usable as possible. (Finnra 2000, Forsman et al. 2000).

In case CCA is used with declaration procedure without heavy case by case environmental permit process, the environmental requirements are presented in Government Decree 591/2006. The Decree presents the limit values for content and leaching of harmful substances in waste and also requirements that waste does not contain any other harmful substances in such a way that its recovery might cause a danger or hazard to health or the environment. The Government Degree 591/2006 have been updated 2009 and will be updated 2016 to contain more recycling materials and more utilization targets.

The supervisory authorities for activities are the regional environment center and the municipal environmental protection authority. The supervisory authorities can differ depending of the utilization site or/and utilized material and/or quantity.

2.2 CCA effect on corrosion behaviour and excavability in maintenance operations

HSY guidelines from 2012 prohibited the utilization of CCA in pipeline trenches because of the CCA self-sementing properties. To advance the effective utilization of CCA in UAC projects, it was necessary to carry out field investigations and literature study to research and resolve practical problems regarding the use of CCA. The research was conducted from the view of water supply network engineering perspective. As the result from field investigations and literature study CCA is now allowed to be used in pipeline trenches according to HSY (2014a) guidance. The background study is presented in the article of Dettenborn et al. 2015b. The study revealed that CCA does not increase the corrosiveness of pipeline materials and the maintenance operations in CCA structures are possible to carry out with normal excavating equipment used by HSY.

2.3 Utilization of CCA in urban earth construction projects

In metropolitan area CCA is principally utilized according to Government Decree 591/2006. HSY released guidelines regarding the utilization of CCA in streets and pipeline trenches (HSY 2014a). Complementary guidance for the utilization of CCA in metropolitan area was released by the metropolitan cities (Helsinki, Espoo and Vantaa 2015). Government Decree 591/2006 is national, but the other two guidelines give more specific guidance for utilizing CCA in urban earth construction projects. The guideline divides the utilization to three different categories and several locations. The categories and locations are:

A. CCA can be used according to the Government decree 591/2006 for the following earth construction purposes:
1) public roads, streets (Fig 1), bicycle lanes, pavements and areas directly connected to these, necessary for road maintenance or traffic, excluding noise barriers;
2) parking areas;
3) sports grounds and routes in recreational and sports areas;
4) railway yards as well as storage fields and roads in industrial areas, waste processing areas and air traffic areas.

B. Additional utilization sites in metropolitan area:
5) pipeline trenches final fills;
6) under tram service structures;
7) harbors field structures; (*)
8) backfills at leisure areas (e.g. parks); (*)
9) noise barriers; (*)
* sites need an environmental permit.

C. Utilization must be considered critically:
10) small sites (utilization volume < 500 m^3);
11) street categories 4-6 apart from bicycle lanes, parking areas and routes in recreational areas;
12) only minor part of cross-section is CCA;
13) locations where high amounts of water can migrate through CCA layer.

2.4 Crushed concrete aggregate lifecycle

Recycling and re-using the excavated CCA from another site is possible and recommended. In metropolitan area clean CCA (not mixed in other aggregates) is also possible to re-use and store trough special recycling centres. In metropolitan area these special recycling centres are arranged by cities or by CCA suppliers (like Rudus Oy). If CCA cannot be utilized in earth construction it is disposed as concrete waste.

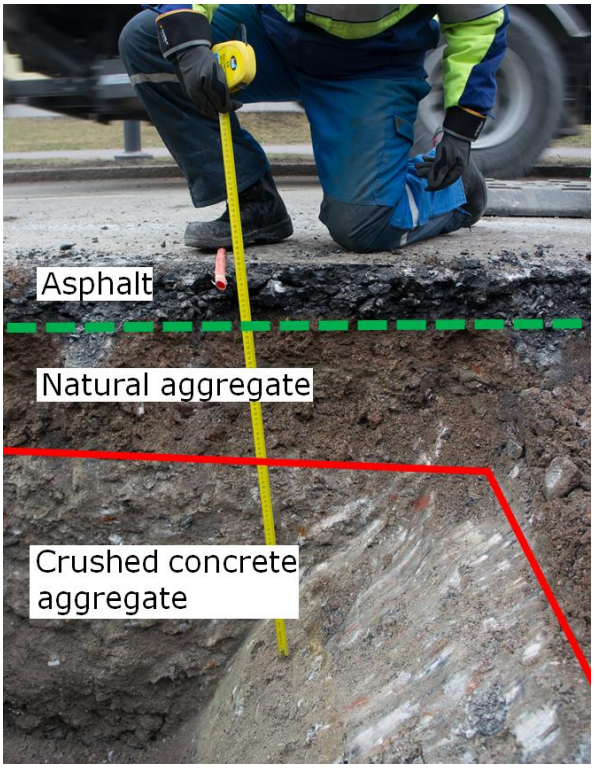


Figure 1. Utilization of crushed concrete aggregate (category II) in street area.

Primarily, when CCA structure is excavated, it must be replaced with similar CCA aggregate. If similar CCA is not available then careful compaction of good quality NA must be conduct to prevent discontinuities in structures. Discontinuities may appear because CCA has self-hardening properties compared to natural aggregates that don't have.

The new metropolitan area guideline (2015) requires contractors to document locations and quantities of the utilized CCA in constructed structures. That documentation will be transferred to a geographic information systems (GIS) of the cities later. The GIS database also includes other underground information e.g. ground improvements, wooden piles, georeinforcements, etc. The GIS information is used to foresee and design maintenance operations in urban areas.

3 FOAMED GLASS AGGREGATE (FGA)

3.1 Basic properties

Foamed glass aggregate (FGA) is produced industrially by treating cleaned glass particles. These glass particles are ground into a powder of under 0.1 mm and mixed with a foaming agent. The powdered glass is then spread onto a conveyor belt and then slowly passed through a furnace. The furnace heats the powdered glass to a temperature of 900 °C. This causes the glass mass to expand to five times its original size and it subsequently hardens into foamed glass. 92 % of foamed glass´s composition is air bubbles. As the foamed glass cools, it breaks up into pieces and forms FGA. (Auvinen et al. 2013)

Types of structures where FGA can be used are numerous. Application can be in infrastructure or building construction. The main benefits of the use of foamed glass in infrastructure construction are; reduced settlements, increased slope stability, reduced lateral earth pressures (Fig 2) and thermal insulation (Fig. 3). (Foamit 2012)

FGA is CE-marked construction product and it does not need an environmental permit. Based on the risk assessment (Ramboll 2010), utilization of FGA in road, street or field areas as lightening or insulation material does not cause significant risk for pollution in groundwater areas. Requirements of FGA are presented in the standard SFS-EN 13055-2. Recycling and re-using of FGA excavated from structure is possible and recommended.

The new guideline "*Foamed glass - Guidelines for the design, construction and maintenance"* have been published by the Helsinki Region Environmental Services Authority (HSY, 2014b). The motivation for creation of the new guideline was increasing interest of developers of cities to use FGA in metropolitan area in streets and pipe trenches. The guideline focuses on FGA utilization in water

supply and sewerage network in engineering perspective.



Figure 2. Up to 8 m high FGA embankment between sheet pile walls during bridge construction worksite at E12 highway (Auvinen et al. 2013).



Figure 3. Foamed glass being spread on a sports area worksite (Foamit 2012).

3.2 Some design properties and life cycle of foamed glass

Finnish FGA (Foamit®) has a relatively low unit weight, combined with a high angle of friction making it ideal for embankments. Technical properties from literature and actual measurements with Foamit® are presented in Table 2.

The "traditional" use of FGA in road structures is presented in the guide book of Finnish Transport Agency (2011).

The guideline of HSY (2014b) describes the working specification for utilizing FGA in pipeline trenches. FGA is suitable for initial fills beside and over the pipes and for final fills. Typical thickness of the fill is approximately 0.3-2.0 meters. FGA particles have rough edges that could damage or grind the surface of pipelines. The guideline of HSY (2014b) recommends to use an initial "natural aggregate" filling around pipelines except with following materials: PVC, PE, coated cast iron, coated steel (Polyurethane coating) and concrete.

Table 2. Technical properties of FGA (Foamit 2012).

Properties	Variations recorded in technical literature	FOAMIT ® Measured values
Granular size	10 - 50 mm 10 - 60 mm	10-60 mm
Density (dry bulk)	180 - 230 kg/m^3	210 kg/m^3 ± 15 %
Density (dry compacted)*	225 - 290 kg/m^3	220 - 280 kg/m^3
Density (long-term in a road structure)	270 - 530 kg/m^3	350 kg/m^3
Density (long-term underwater , <1 year)	-	600 kg/m^3
Density (permanently underwater)	-	1000 kg/m^3
Bulk density (in buoyancy)	-	3.5 kN/m^3
Bulk density (permanently underwater)	-	10 kN/m^3
Friction angle	36 - 45°	36 - 45°
pH-value	-	10
Compaction factor	-	1.15 - 1.25
Water absorption** Short-term (4 weeks)	30 - 60 weight-%	~60 weight-%
Water absorption** Long- term (1 year)	40 - 116 weight-%	~100 weight-% ***
Compression strength 10 % compression	-	0.3 - 0.4 MPa
Compression strength 20 % compression	0.77 - 0.92 MPa	> 0.9 MPa
Thermal conductivity (k-value)	0.11 - 0.15 W/mK	0.1 W/mK (dry) 0.15 W/mK (moist) 0.2 W/mK (saturated)

* density depends on amount of compaction
** immersed in water
*** will be verified in further long-term studies

FGA is not considered to accelerate corrosion on metals even in direct contact. However, aluminium materials should not be used in direct contact with FGA unless they are protected with coating material that tolerates the alkaline environment (pH value of FGA is ≈10).

Construction with FGA is easy because after compaction the surface of the FGA layer is trafficable for site traffic. Regardless of that it is recommended that FGA surface is covered with thin aggregate layer before site traffic. The relatively low particle strength in FGA and high traffic loading could crush the FGA particles at the surface. The FGA has a high friction angle and therefore very shallow

trench excavations (in good conditions) could be excavated with vertical slopes put all deeper excavation slopes have to be inclined or strutted. The design of pipeline trenches have to be made according to national guidelines.

3.3 Possible limitations for utilizing FGA

The guideline of HSY (2014b) presents some cases where the use of FGA (or lightening at all) is not recommended:
1) Lightening produces greatly of surplus soils (handling surplus soils in metropolitan area is very expensive),
2) Deep lightening excavations can cause stability, settlement or dislocation of adjacent structures,
3) Buoyancy in flooding areas,
4) Settlement requirements and
5) Preparation for future higher leveling.

4 ASHES

4.1 Technical properties of ashes

Energy industry produces variety of ashes as by-product or waste material. These ashes are fly ash (FA), bottom ash (BA) and flue gas desulphurization (FGD) residue. Fly ash is residue captured from flue gases. Ash that falls in the bottom of the boiler is called bottom ash. In Finland, the energy industry uses variety of solid organic fuels, such as, coal, biomass, peat and municipal waste.

In terms of geotechnical properties, fine-grained ashes are usually superior when compared to natural soil with equivalent grain size distribution, which usually varies between silt and fine sand for FA. According to numerous laboratory tests results compiled by Kiviniemi et al. (2012) FA has lower unit weight and thermal conductivity, higher friction angle and if hardened FA develops significantly higher compression strength compared to natural soil equivalent. Self-cementing fly ashes contain high amount of calcium oxide and are capable of cementation without external activator in contrast to pozzolanic fly ashes that require e.g. limestone or Portland cement. FGD residue may also serve as an activator for the cementing process.

The grain size distribution of fly ash falls essentially within the normally recognized limits for frost-susceptible soils. However, self-cementing fly ashes tend to reach lower segregation potential, which is often used to evaluate frost-susceptibility and are often classified as frost resistant. Furthermore, even small additions of commercial binder such as Portland cement allow pozzolanic FA to sustain freeze-thaw cycles and are therefore classified as frost resistant. (Kiviniemi et al. 2012)

The grain size distribution of bottom ash varies in the range of fine sand and fine gravel. Bottom ash generally has no self-hardening properties. From the geotechnical aspect, technical properties of bottom ash usually correspond to natural soils with similar grain size distribution.

Technical properties, excluding strength and self-hardening properties, of FGD residue generally corresponds to those of fly ash.

4.2 Utilizing ashes in Finland

Coal ashes have been used in earth construction for several decades. Occasional uses have been reported in the early 1960's. In the early 1980's more organised utilization has been carried out in Helsinki metropolitan area. Applications in earth works varies from street and road construction to parking lots, sport fields and outdoor routes as well as beds of pipe lines. (Havukainen 2000). Ashes have also been utilized as bulk material in massive structural layers and as a binder in layer stabilisation or in deep stabilisation (deep mixing). FGD residue and surplus ashes have mainly served as backfilling material in Tytyri Mine in Lohja. (Napari 2016)

The utilization of ashes faced strong opposition in the beginning of 1990’s. Concerns for environmental issues, such as, dusting and ashes suspected being carcinogenic, limited the utilization. In addition, fly ashes were deemed very corrosive to cast iron, steel and aluminium. However, majority of the litera-

ture references indicating metallic corrosion in ashes refer back to the survey conducted during 1979-87. After which the quality of the ashes has clearly improved for several reasons. In Finland flue gas desulphurization (FGD) was first introduced in 1987 resulting in strict pollution control and burning of low-sulphur coal. Furthermore, burning processes in coal-fired power plants have advanced significantly and the ash qualities are nowadays very consistent and controlled. (Napari 2016)

The utilization of some ashes (FA, BA) is possible without environmental permit according to Government Decree (591/2006) in defined structures and sites. With other ashes (FA, BA, FGD residue, MSWI ash) and in other structures and sites the utilization remains possible through environmental permit. (MWSI = municipal solid waste incineration)

4.3 Corrosion properties of ashes

Test field Sorsavuorenpuisto 1995: In the year 1995 an in-situ experiment was conducted in Sorsavuorenpuisto in Helsinki. The objective of the field test was to determine metallic corrosion in different types of ashes. The test specimens were left in the ash filling for six months. During this time only little corrosion took place on the cut along the cast iron pipe with zinc and bitumen coating. (Rämö 1999). Cast irons have particular corrosion mechanism in soils. The surface may corrode quickly as the iron rusts leaving brittle graphitic structure. The rust particles are then captured in the residual graphite structure forming protective layer, consequently decreasing the rate of the ongoing corrosion. (Schweitzer 2007)

The results provided in the original report of the field test by Technical Research Centre of Finland (VTT 1997) indicated that fly ash has not caused corrosion in cast iron or copper material during the six month period. However, fly ash mixed with FGD residue showed mild corrosion on copper and steel specimens. Furthermore, steel was found susceptible to corrosion not only in fly ash but also in natural soil.

The six month period surveyed in 1995 is not considered adequate for long-term evaluation of the corrosiveness of ashes. One set of test specimens were left in the ground for later inspection. However, in fall of 2015 during excavation of the testing field in Sorsavuorenpuisto turned out that the testing field had been destroyed due to lack of information and no test specimens were salvaged from the site. (Napari 2016)

Designed new test field: A new well-documented field test have been designed to be conducted in near future but the timetable and the location are not sure yet (Napari 2016). In the new field test, the most utilized and the most potential by-products across the energy production industry will be taken into account. The test materials include, but are not limited to, coal FA, coal FA mixed with FGD residue, coal BA, with FA binder stabilised sediment (properties of some stabilised sediment presented by Forsman et al. 2015), different types of MSWI bottom slag and control materials from natural aggregates.

Designed metal materials included in the new field test cover most of the commonly used piping materials i.e. SG cast, steel, different types of stainless steel, copper and aluminium. Definitive results from the test field are expected no earlier than 10–20 years from the beginning of the test.

A preliminary literature study on corrosion:
Main reasons affecting corroding properties of ashes are broad variation of chemical composition, leachate of soluble salts, low resistivity and high alkalinity of ashes. The pH of FA varies in range of 9–13 which can be favourable for some metals, such as, steel, cast iron and zinc, whereas some amphoteric metals, mainly aluminium, corrode in alkaline solutions. With CE-marked coal ashes, the chemical and mechanical properties are more consistent and corrosiveness can be better evaluated. (Napari 2016)

The preliminary literature study gave the impression that the unburned carbon could prove to be significant factor determining

resistivity of ashes. Coal is formed by amorphous carbon which is a semi-conductor with electrical resistivity of 0.003–0.005 Ωcm. However, this is measured from solid substance and does not correlate well with actual crushed coal. Naik et al. (2010) have studied the effect of high-carbon fly ash on the electrical resistivity of FA concrete containing carbon fibres. The study indicated that carbon content, measured as a loss on ignition, or LOI, could be used to evaluate the resistivity of FA.

Napari (2016) studied the effect of carbon content on resistivity of two different FA samples and, in contrast to the study by Naik et al (2010), the experiment showed no correlation between the carbon content (measured as LOI), and the resistivity of FA. However, the results of both studies indicate that FA derived from bituminous coals might exhibit smaller resistivity in general compared to fly ashes from other types of coal.

The resistivity of compacted fly ash varied in range of 3100-4500 Ωcm measured during the experiment by Napari (2016). Low-carbon FA actually exhibited smaller resistivity throughout the experiment. Both specimens were tested near optimum water content in two different densities. Measured resistance of crushed coal was approximately double that of FA.

Although unburned carbon content does not seem to affect the resistivity of FA, it may still present major issue with electronegative metals, such as, aluminium, zinc and steel. Carbon is highly electropositive substance and may cause strong galvanic cell and provide in some circumstances adequate potential difference for corrosion to occur. Combined with low resistivity the rate of corrosion is further increased. (Napari 2016)

4.4 Utilization of ashes in infra construction

Practical construction applications for utilization of ashes in civil engineering are earth works that require large volumes of back-fill material, such as embankments, road base (Fig. 4) and structural fills.

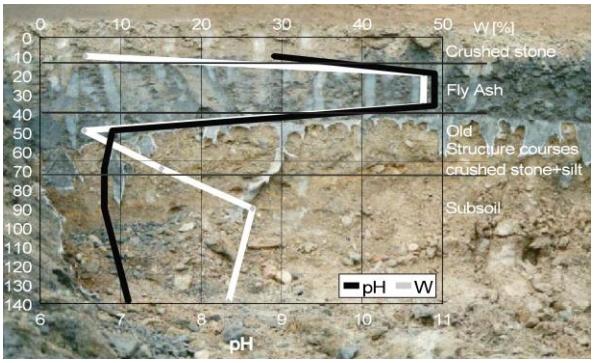


Figure 4. Utilizing fly ash as a flexible structural material for low-volume road (Lahtinen 2001).

Self-cementing FA is widely used as a cement replacement in concrete industry. However, many applications have been recognized for self-cementing FA in earth construction, including soil stabilization, asphalt filler material as well as road base and structural fill that require higher strength properties. BA is generally utilized similarly to natural soil, which has a corresponding grain size distribution. (Havukainen 2000; Kiviniemi et al. 2012)

Because of the technical properties FGD residue can be utilized in earth construction, but only mixed with other material, such as FA. FGD residue may act as an activator for pozzolanic FA. Certain proportions of FA and FGD residue mixture may develop higher strength properties than FA alone (Lahtinen 2001). However, FGD residue has high soluble salt content and can be estimated as highly corrosive and should not be used in contact with metals susceptible to corrosion. (Napari 2016)

5 CONCLUSIONS

After the release of the guidance's, the utilization of CCA and FGA has increased in metropolitan area. Designer and contractor now have more information about recycled materials behavior and have information what to take into account when utilizing recycled aggregates in urban earth construction.

According to background study conduct for the guide books, CCA and FGA does not increase the corrosion risk near metallic ma-

terials (excluding aluminum) when utilized according to guidance's ,except in exceptional cases. Aluminum materials should be treated with coating material tolerating the alkaline environment.

Main reasons affecting corroding properties of ashes are broad variation of chemical composition, leachate of soluble salts, low resistivity and high alkalinity of ashes. According to the preliminary literature study, the residual carbon in ashes may present increase in corrosion risk with electronegative metals, such as aluminium, zinc and steel. With CE-marked coal ashes, the chemical and mechanical properties are more consistent and corrosiveness could be better evaluated. According to field test conduct in 1995 FA and BA did not increase the corrosion risk in metallic materials compared to natural aggregates. However, fly ash mixed with FGD residue showed mild corrosion on copper and steel specimens.

6 ACKNOWLEDGMENTS

The research presented in this paper was supported financially by the Rudus Oy (CRH plc), the cities of Helsinki, Espoo and Vantaa, Uusioaines Oy, Environmental Geotechnics Forum (YGOFORUM), Fortum Power and Heat Ltd, Helen Ltd, Vantaan Energia Oy, Helsinki Region Environmental Services Authoritys (HSY), Aalto university and Ramboll Finland Oy

7 REFERENCES

Auvinen, T., Pekkala, J. and Forsman, J. 2013. *Covering the highway E12 in the centre of Hämeenlinna – innovative use of foamed glass as light weight material of approach embankment*. The XXVIII International Baltic Road Conference, Vilnius, Lithuania, 26-28 August 2013.

Cities of Helsinki, Espoo and Vantaa. 2015. *Utilizing crushed concrete aggregate in metropolitan area infra construction* (in Finnish). 11 p. Released 17.3.2015

Dettenborn, T., Forsman, J. and Korkiala-Tanttu, L. 2015a. *Crushed concrete in road structures – two decades of experience*. Proceedings of the Institution of Civil Engineers - Construction Materials ISSN 1747-650X. DOI: 10.1680/jcoma.15.00005.

Dettenborn, T., Forsman, J., Rämö, P., Pieksemä, J., Suominen, M. and Korkiala-Tanttu, L. 2015b. *Utilization of crushed concrete aggregate in urban earth construction: streets and pipe trenches*. XVI European Conference on Soil Mechanics and Geotechnical Engineering (ECSMGE). Edinburgh, 13.-17.September 2015. pp. 919-924. ICE Publishing, London 2015.

Eriksson L. and Hägglund, J. 2008. *Manual for Foam Glass in soil and road construction*. Information 18:1. The Swedish Geotechnical Institute (SGI). Linköping. ISSN 0281-7578

Finnish Road Administration (Finnra) 2000. *Use of Reclaimed Concrete in Pavement Structures.* Finnish Road Administration, Helsinki, Finland, pp. 1–25, Report TIEL 3200594 (in Finnish).

Finnish Transport Agency. 2011. *Design of light weight structures.* Guidelines for road foundation construction 05/2011. In Finnish. 9.3.2011. ISBN 978-952-255-638-7.

Finnish Transport Agency. 2014. *Use of waste materials in road construction "Uusiomateriaaliopas"*, draft for test use 28.2.2014. (in Finnish). Helsinki 2014.

Foamit. 2012. *Design and construction guideline. In Finnish*. 24 pages.

Forsman, J., Lindroos, N. and Korkiala-Tanttu, L. 2015. *Three mass stabilization phases in the west harbor of Helsinki, Finland – geotechnical and environmental properties of mass stabilized dredged sediments as construction material*. Deep mixing 2015 conference, 2.-5.6.2015, San Francisco.

Government Decree. 2006. Government Decree 591/2006 - *Concerning the recovery of certain wastes in earth construction*. Issued in Helsinki 28 June 2006. In Finnish.

Havukainen, J. 2000. *More than 20 years' experience of coal ash utilization in Helsinki*. XIII Nordiska Geoteknikermötet. Helsinki 5-7.6.2002. NGM-2000. p. 399-406 and 6th International Symposium on Environmental Geotechnology and Global Sustainable Development. Seoul, Korea.

HSY. 2014a. *Crushed concrete aggregate - Guidelines for the design, construction and maintenance* (in Finnish). 8 p. Released 07.10.2014.

HSY. 2014b. *Foamed glass - Guidelines for the design, construction and maintenance (in Finnish).* 21 p. Released 27.06.2014.

Kiviniemi, O., Sikiö, J., Jyrävä, H., Ollila, S., Autiola, M., Ronkainen, M., Lindroos, N., Lahtinen, P. & Forsman, J. 2012. *Ash construction manual.* (*Tuhkarakentamisen käsikirja), Energiantuotannon tuhkat väylä-, kenttä- ja maarakentamisessa*. (in Finnish), pdf 13.1.2012.

Koivisto, K., Forsman, J., Ronkainen, M., Lahtinen P., Mäkelä, H. and Korkiala-Tanttu, L. 2015. *Development of design and procurement for earthworks with recycled materials – Finnish UUMA2 programme*. XVI European Conference on Soil Mechanics and Geotechnical Engineering (ECSMGE). Edinburgh, 13.-17.September 2015. pp. 2577-2582. ICE Publishing, London 2015.

Lahtinen, P. 2001. *Fly Ash Mixtures as Flexible Structural Materials For Low-Volume Roads*. Helsinki 2001. Finnish Road Administration. Finnra Reports 70/2001. 95 p. ISSN 1457-9871, ISBN 951-726-826-2.

Napari, M. 2016. *Corrosion by ashes from energy production in metropolitan area*. Master's thesis, (in Finnish). Espoo 2016.

Ramboll. 2010. *FOAMIT foamed glass, performance in a groundwater area*, Risk assessment. In Finnish.

RIL 2014. RIL 263-2014 - *Excavation safety guideline* (in Finnish). Finnish Association of Civil Engineers, Helsinki. 2014.

Rämö, P. 1999. *Survey on Corrosiveness of Fly Ash and Flue Gas Desulphurization residue*. (in Finnish). Helsinki: the Finnish Funding Agency for Innovation (Tekes). 24 p. Technology Review 71/99. ISBN 951-53-1439-9.

Schweitzer, P. 2007. *Corrosion Engineering Handbook. Fundamentals of Metallic Corrosion*: Atmospheric and Media Corrosion of Metals. 2nd ed. Boca Raton, Florida: Taylor & Francis. 727 p. ISBN 978-0-8493-8243-7.

VTT. 1997. *Test Report No. VAL74-7075.* (in Finnish). Espoo 2.4.1997. Technical Research Centre of Finland Ltd (VTT).

The influence of grain size distribution and grain shape on the small strain shear modulus of North Sea Sand

T. Biryaltseva
Fraunhofer IWES, Germany, taisiya.biryaltseva@iwes.fraunhofer.de

D. A. Hepp, S. Kreiter
MARUM – Center for Marine Environmental Sciences, University of Bremen, Germany

R. Dyvik
NGI, Norwegian Geotechnical Institute, Norway

ABSTRACT
Small strain shear modulus of three North Sea sand samples and one onshore sand sample from the North Sea coast has been measured and the results are compared with existing empirical equations. Appreciable differences between the measured data and predictions are presented as functions of sand type, void ratio and stress level. The discrepancies are possibly influenced by amount of rounded particles in the sand composition.

Keywords: small strain shear modulus, particle shape, North Sea, sand composition.

1 INTRODUCTION

More than fifty years ago (Hardin & Richart, 1963) proposed an empirical relationship allowing estimation of the small strain shear modulus G_{max} in [kPa] from void ratio:

$$G_{max} = A\frac{(a-e)^2}{1+e}p^n \quad (1)$$

where e is the void ratio [decimal], p is the mean confining pressure in [kPa], A, a, and n are material constants.
The relationship was developed based on experiments with Ottawa and crushed quartz sands. Originally two sets of material constants for round $(A = 6900, a = 2.17, n = 0.5)$ and angular $(A = 3200, a = 2.97, n = 0.5)$ grain shape were established.
The Hardin equation therefore takes the grain shape into account and predicts an increase of the shear modulus with the mean effective stress and a decrease with the void ratio. Equation (1) has been widely used as a first estimate for the G_{max}-values for different sands.
Further modifications also include a dimension-true form by Hardin & Drnevich (1978) and a dimensionless form by Wichtmann & Triantafyllidis (2014).
Wichtmann & Triantafillydis (2009) proposed the following empirical relations to calculate the material constants A, a, and n for each sand independently as a function of coefficient of uniformity $C_u = d_{60}/d_{10}$:

$$A = 1563 + 3.13\,C_u{}^{2.98} \quad (2)$$

$$a = 1.94 \cdot exp\,(-0.066C_u) \quad (3)$$

$$n = 0.40\,C_u{}^{0.18} \quad (4)$$

These coefficients do not converge to Hardin's coefficients neither for angular nor for round grain shape. The relationships were elaborated on the basis of artificial grain size distribution (GSD) curves, which are linear in semilogarithmic scale and verified them also on gap-graded, stepwise linear and smoothly

shaped GSD curves (Wichtmann & Triantafyllidis, 2014). They found that these extended relationships predict development of G_{max} reasonably well. In this study both the original Hardin & Richart (1963) and the improved Wichtmann & Triantafyllidis (2009) relationships are applied in the form of Equation (1) on three sands from the North Sea and one onshore sand with natural grain size distributions. It was found that both empirical relationships show appreciable deviations from the measured data. This study is going to show:

- whether this deviation is statistically significant
- what kind of parameters may influence this deviation.

2 MATERIAL

2.1 Study area

In the Quaternary the southeastern North Sea and northern Germany was affected by a series of glacial, terrestrial and marine controlled depositional or erosional processes, which resulted in a complex stratigraphy of repeated glacial, fluvial and lacustrine or marine sedimentation, interrupted by phases of erosion. Meltwater discharge beneath ice margins generated several overdeepened tunnel valleys, which are filled by a typical pattern of coarse-grained meltwater sediments at the base and the flanks overlain by fine-grained, often stratified, glaciomarine and/or glaciolacustrine sediments (Lutz et al. 2009). The sand samples S1-2 were recovered along the flanks of an Elsterian tunnel valley (Hepp et al. 2012) at the depth of 43.5 and 16.4 m below seafloor (mbsf), whereas sand sample S3 was obtained from the valley surroundings (5.5 mbsf). The onshore sand sample S4 was taken from a proximal fluvial deposit near a Saalian terminal moraine complex Altenwalde, Germany (Sindowski, 1965).

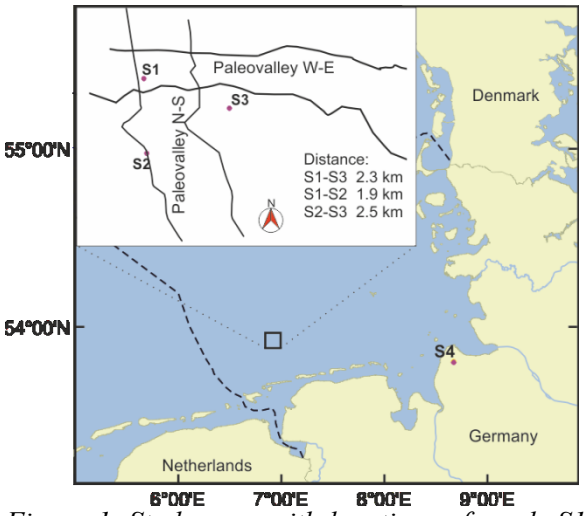


Figure 1. Study area with locations of sands S1, S2, S3 and S4 in relation to glacial tunnel valleys and the distance between them.

2.2 Classification parameters for sands tested

The sand samples are composed of almost 100% quartz, S1 and S2 reveal some cementation between its grains. Grain size distributions for each sample are shown in Figure 2.

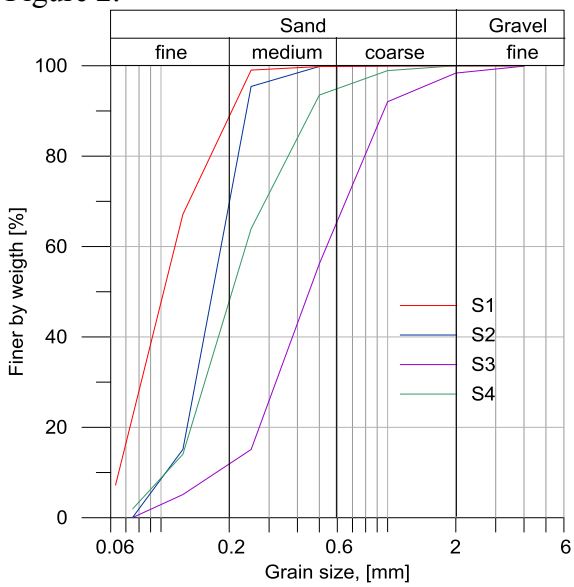


Figure 2. Grain size distributions

Mean grain size (d_{50}), coefficient of uniformity (C_u), minimum and maximum void ratios (e_{min}, e_{max}) according to NGI in-house procedure e.g. Blaker et al. (2015) as well as grain density (ρ_{grain}) measured in a helium pycnometer are shown in Table 1. For further testing the samples were separated at 2 mm by dry sieving.

Table 1. Index properties

Sand	d_{50} [mm]	C_u [/]	e_{min} [/]	e_{max} [/]	ρ_{grain} [g/cm³]
S1	0.123	2.15	0.62	0.98	2.67
S2	0.177	1.92	0.60	0.90	2.64
S3	0.453	3.55	0.39	0.69	2.67
S4	0.215	2.2	0.53	0.79	2.644

The grain size range of the sieves used is conform to the grain size classes in φ ($\varphi = -\log_2 d[mm]$). The normality of the grain size distribution (e.g. $\boldsymbol{\chi^2}$-test) and its moments calculated in the φ-space are shown in Table 2.

Table 2. Moments and the χ^2 -probability of the grain size distribution in φ units.

Sand	μ	σ	μ_3	μ_4	$F(\chi^2)$
S1	3,16	0,648	0,106	4,06	0,838
S2	2,51	0,414	0,130	6,61	0,836
S3	1,08	0,969	0,128	3,58	0,937
S4	2,12	0,835	-0,250	3,89	0,878

With μ mean, σ standard deviation, μ_3 skewness, μ_4 kurtosis of the grain size distribution. $F(\chi^2)$ is the cumulative distribution function of the χ^2 statistic.
The grain roundness was estimated visually using roundness charts after Powers (1953) as weighted average over 100 grains retained in each sieve with the mesh size w_i.

$$shape = \sum_{i<I} shape_i \cdot w_i \qquad (5)$$

Where $shape_i$ is the percentage of specific grain shape retained in the sieve with the mesh size *i*, w_i is the percentage of grains retained by weight in the sieve with the mesh size *i*. *I* is the maximal mesh size used for investigation
The grain shapes are shown in Table 3.

Table 3. Grain shape properties (A- Angular, S/A- Subangular, S/R- Subrounded, R-Rounded).

Sand	*I* mm	A [/]	S/A [/]	S/R [/]	R [/]
S1	0.25	0.327	0.277	0.288	0.108
S2	0,5	0.21	0.41	0.32	0.06
S3	1	0.29	0.36	0.21	0.14
S4	0,5	0.01	0.44	0.34	0.21

3 SMALL STRAIN STIFFNESS

The small strain stiffness was determined during 16 isotropically consolidated drained (CID) triaxial tests instrumented with bender elements at Norwegian Geotechnical Institute. Specimens were prepared in four relative densities at approximately D_r=50%, 65%, 80% and 95%. The specimens were built in in six layers using undercompaction technique (Ladd 1978) with a low water content. Initial water contents after saturation are shown in the Table 3.

Table 4. Initial water contents (%) after sample saturation

Sand	D_r=95 %	D_r=80 %	D_r=65 %	D_r=50 %
S1	24,30	26,32	28,13	30,44
S2	23,25	25,43	27,09	28,57
S3	20,77	22,64	23,83	25,26
S4	15,31	17,20	18,82	20,32

Shear waves were triggered and received using piezoceramic bender elements. Details concerning bender element technique are described in Dyvik & Madshus (1985).
v_s measurements were performed during consolidation at effective isotropic confining pressures of 100, 200 and 400 kPa. At each loading stage the specimen was first subjected to a consolidation period of at least 120 min, then v_s was measured before the next stress increment was applied.

3.1 Repeatability of G_{max}

In order to estimate the influence of the internal fabric a repeatability test was carried out. For this purpose three specimens of sand S4 were prepared with D_r=95%.The shear wave velocities were measured at three pressure stages for each specimen as described above. The results are shown in Figure 3 and Table 5.
All three specimens show an increase of the G_{max} with the mean effective stress. The gradient $\frac{\partial G_{max}}{\partial p}$ between two consequtive pressure stages is almost the same for all three specimens. The values of the test 1B agree well with the average values. The measured values deviate from the mean between 14.5%

at $p = 100\ kPa$ and 9.7% at $p = 400\ kPa$ (Table 5). The deviation appears to decrease with the stress level.

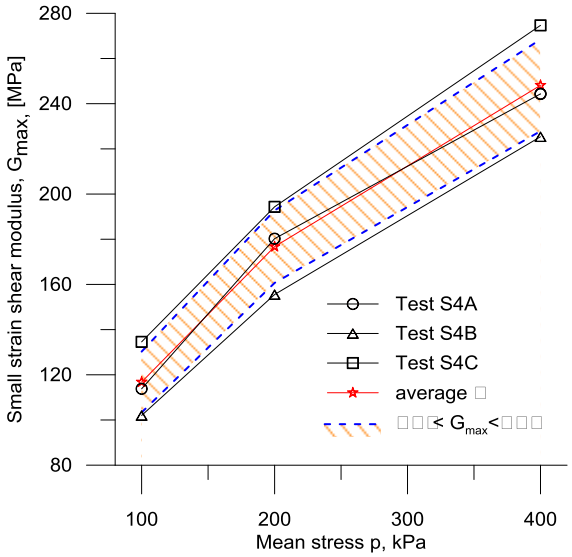


Figure 3. Value range of the repeatability test on sand S4 specimens prepared with Dr=95%. Red stars present the average values over three tests for each stress level, dashed area depicts the range of one standard deviation.

Table 5. Average (μ, [MPa]), standard deviation (σ, [MPa]) and deviation of the results from the average for S4 prepared with D_r=95% at different stress levels p[kPa].

P	μ	σ	$(G_{max}^{meas} - \mu)/G_{max}^{meas}$		
			S4A	S4B	S4C
100	117	13,47	-0,026	-0,145	0,132
200	177	16,04	0,020	-0,136	0,091
400	248	20,3	-0,015	-0,101	0,097

3.2 G_{max} for different sands

G_{max} for four investigated sands are combined with the empirical predictions in Figure 4.

As expected G_{max} decreases with void ratio and increases with rising confining pressure. The bulk of the data generally follows the Hardin empirical equation but reveal considerable scatter at comparable void ratios. The Wichtmann equations show a steeper decrease of the G_{max} with the void ratio and seems to fit the laboratory data better for p=400 kPa.

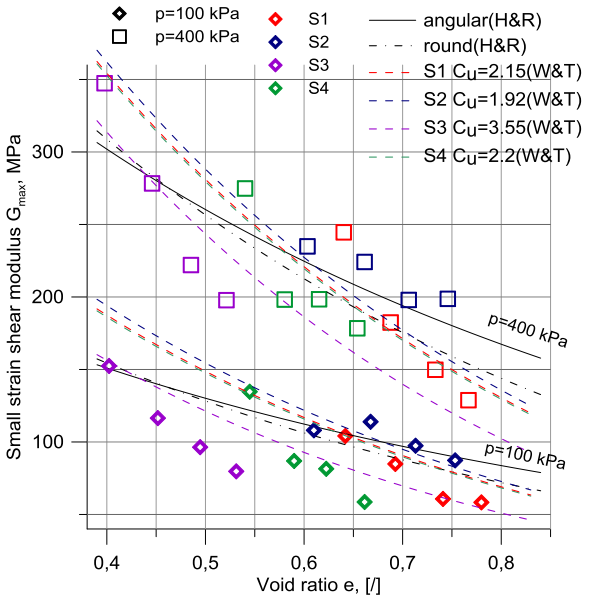


Figure 4. Test results for two stress levels. Black solid and dot-dashed lines depict empirical equations after Hardin& Richart (1963) (Marked as H&R). Coloured dashed lines depict empirical equations after Wichtmann & Triantafyllidis (2009) (Marked as W&T) for each sand with corresponding colour. The C_u-values for each sand used to calculate empirical constants after Wichtmann & Triantafyllidis (2009) are shown in brackets. In order to maintain the readability of the figure the test results and empirical predictions for the stress stages p=100 kPa and p=400 kPa are shown. The stress stage p=200 kPa is omitted.

3.3 Residual analysis

The relative residuals r_i between measured and predicted small strain shear moduli G_{max} were determined by:

$$r_i = \frac{G_{max}^{predicted}{}_i - G_{max}^{measured}{}_i}{G_{max}^{measured}{}_i} \quad (6)$$

and the root mean square error RMSE as measure of the prediction quality was calculated by:

$$RMSE = \sqrt{\sum_i r_i^2} \quad (7).$$

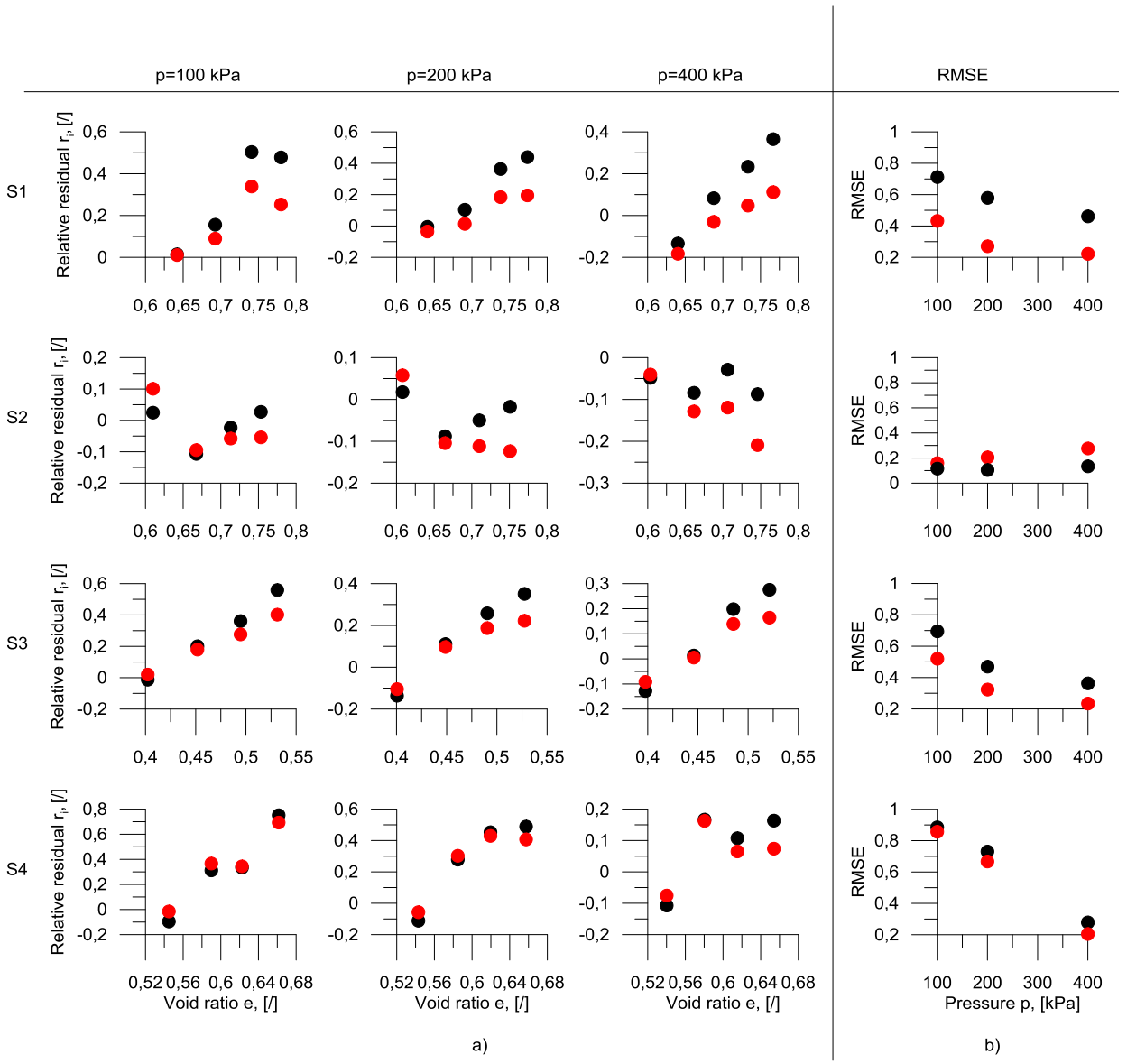


Figure 5. a) Relative errors as function of void ratio; b) RMSE as function of confining pressure. Measured data compared to predicted with Hardin constants for angular grain shape (black) and Wichtmann constants (red)

Figure 5 presents the relative residuals between the predictions of Hardin and Wichtmann and the measured data of every sand, at all three pressured and four densities S1, S3 and S4 show for both predictions an increase in relative residual with the void ratio for every stress level. In contrast S2 shows no trend in the residuals. RMSE decreases for both predictions with increasing confining pressure for samples S1, S3 and S4, while it is almost constant or even slightly increasing for S2.

For samples S1, S3 and S4 both equations overpredict measured G_{max} for specimens prepared with relative densities D_r=50-80%, while G_{max} for D_r=90-95% is predicted correctly or slightly underpredicted especially at higher confining stress. The sample S2, however, fits well with the empirical equations with slight tendency to underestimation, more so by the prediction after Wichtmann.

The residual distribution is not random; this suggests that either the equation itself may be inapplicable to describe the dependency of the G_{max} on the void ratio, or that the coefficients depend on more factors than the coefficient of uniformity.

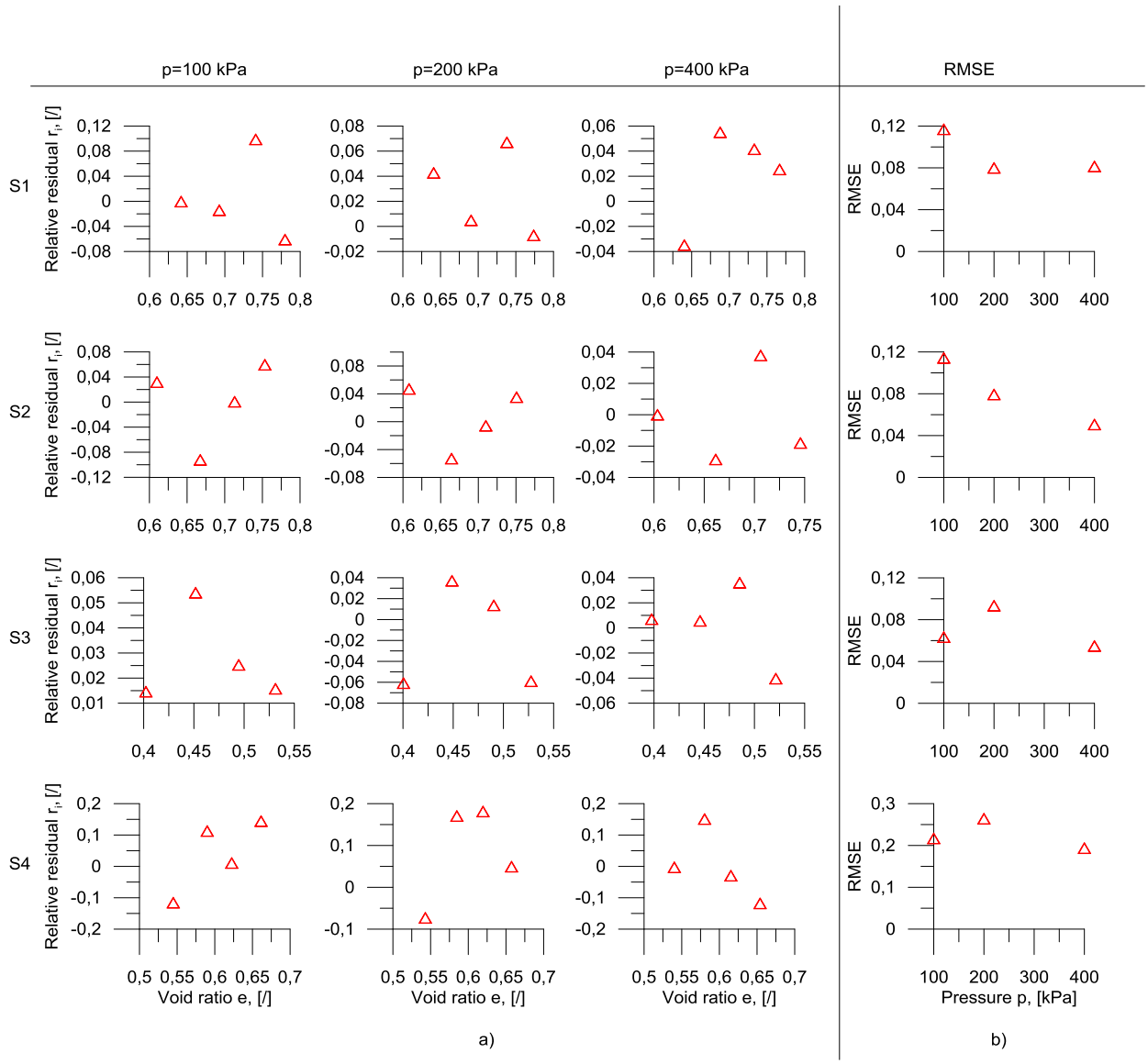


Figure 6. a) Relative errors as function of void ratio; b) RMSE as function of confining pressure. Measured data compared to predicted by Equation (1) with coefficients from Table 6

3.4 Fitting of material constants

For each sand a set of empirical coefficients was fitted to Equation (1) in order to check the general applicability of this equation type (Table 6). The 12 experimental points of four relative densities at three stress stages for each sand provide some statistical significance, the residuals and RSMEs are given in Figure 6. As expected the relative residuals are very low, however in contrast to residuals shown on Figure 5 the new residuals are distributed randomly and do not exhibit any dependency on the void ratio. Even though a slight decrease of RMSE with the stress level is still evident, the (1) type of equation seem to be applicable for the G_{max} prediction and give a good fit if the empirical coefficients A, a, and n have been adjusted for each type of sand.

Table 6. Fitted empirical coefficients

Sand	A	a	n
S1	36,215	1,206	0,586
S2	1,847	3,511	0,531
S3	55,004	0,931	0,574
S4	44,778	1,070	0,586

Influence of the grain shape on the empirical coefficients is shown in Figure .

There is no apparent dependency except for a possible increase of the coefficient A with

percentage of rounded particles and decrease of coefficient a again with percentage of rounded particles. In this case it could seem that the shear modulus depends on the percentage of rounded particles within the sample. Considering four distinct but known coefficients the number of their permutations is equal to 4!. Therefore the probability they will line up coincidently in ascending or descending order is equal to 1/24, while the probability of a monotone sequence in one trial is 1/12. Since 2 monotone sequences were obtained in 12 trials the probability that this dependency is coincidental amounts to 19.2%. This probability is high but not high enough to fully discard the presumption. To increase the statistical relevance of this statement, more samples have to be tested.

4 DISCUSSION

Empirical equations proposed by Hardin and Richart (1963) and Wichtmann & Triantafyllidis (2009) were compared with G_{max} measured at four sand samples from the North Sea and the plain of Northern Germany. In the case of prediction by Hardin & Richart (1963), 37.5% of predicted values differ by more than 20% from the measured data. Accounting for the coefficient of uniformity in the prediction after Wichtmann & Triantafyllidis (2009) improves the agreement, so only 25% of predicted values differ by more than 20% from the measured data. However, it does not achieve the quality reported in Wichtmann & Triantafyllidis (2014) where this prediction applied on various grain size distributions deviates more than 20% from the measured data in only 7% the cases.

Comparisons among S1 and S2 demonstrate that changes in the coefficient of uniformity alone cannot lead to the observed differences in the small strain stiffness. All samples were freshly pluviated in the laboratory and subjected to the same testing procedure, therefore the geological history, aging and cementation cannot appreciably affect the

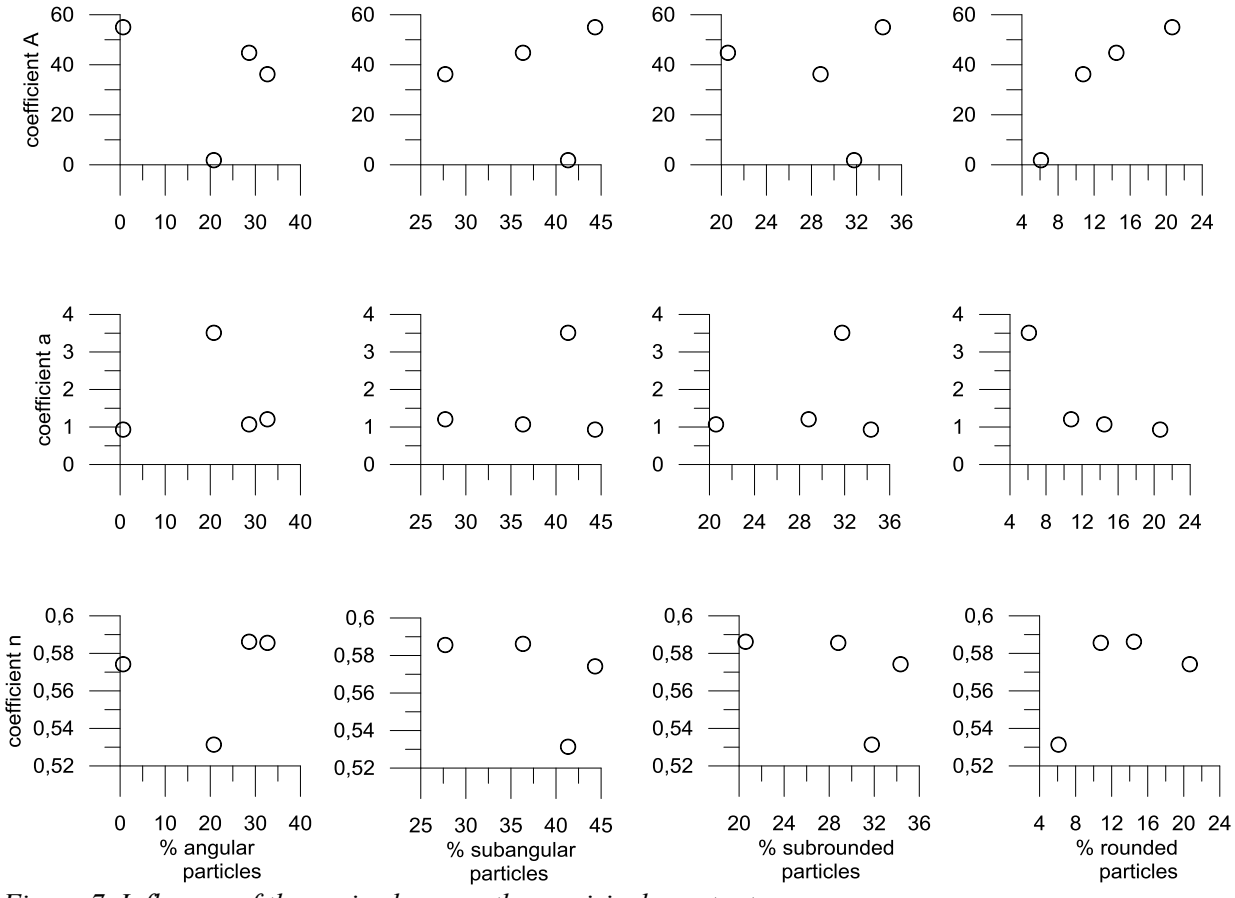


Figure 7. Influence of the grain shape on the empirical constants

results. Grain shape analysis shows that sample S2 contains the minimum percentage of rounded particles. This study seems to indicate that an increased percentage of rounded particles may lead to a decrease in the small strain stiffness for the same void ratio and isotropic confining stress.

On the one hand this observation follows the study of Shin & Santamarina (2013), who mixed rounded and angular natural and crushed sand particles at selected mass fraction and found an increase in small strain shear modulus as the mass fraction of angular particles increases. The experiments were carried out in oedometer instrumented with bender elements. On the other hand, no direct dependency on the amount of angular particles was found. Cho et al (2006), Santamarina & Cascante (1998), and Otsubo et al. (2015), however, conclude that a decrease in particle roundness or sphericity leads to a decrease in the small strain stiffness. The methods applied differs for each study: Cho et al. (2006) carried out oedometer tests on natural and crushed sands, Otsubo et al. (2015) investigated artificially roughened beads in true triaxial isotropically consolidated tests with bender elements, and Santamarina & Cascante (1998) conducted resonant column tests on rusted balls.

It was also found in this study that the deviations of the measured data from the empirical equations are more pronounced at low mean stress and low relative densities. Repeatability tests also reveal less deviation between measurements at higher stress levels. Based on Cho et al (2006) argumentation that the small strain shear stiffness deformations localize on interparticle contacts we assume that a decreasing RMSE with increasing confining stress should also be caused be the influence of the grain shape. This is in agreement with findings by Yimsiri and Soga (2000) and Otsubo et al. (2015) that the difference between rough and smooth samples gradually reduces as confining stress increases. As the confining stresses applied by Otsubo et al (2015) do not exceed 500 kPa, no or minimal grain crushing can be assumed.

Visual observation of the grain shape is somewhat subjective and operator-depended, therefore a direct comparison in terms of grain shape with other laboratories is not straightforward. Cho et al (2006) and Shin & Santamarina (2013) apply the sphericity-roundness-roughness charts for visual inspection, Otsubo et al. (2015) the optical interferometry and in this study roundness charts after Powers (1953) were applied.

The statistical relevance of the presumption is found to be of a magnitude that will neither accept nor discard it. To make a clear conclusion the number of tests, especially with soils containing higher percentage of rounded particles, has to be increased and the description of the grain shapes has to be made comparable with other studies.

As no quantity exists to describe the overall sample roughness it is possible that the combinations of subrounded and subangular particles may influence the small strain stiffness if their percentage is significant in comparison to “truly” round and angular particles. Since the empirical equations tend to overestimate the Gmax for Dr=50-80% they should be used with caution in these cases.

5 CONCLUSIONS

The empirical equations by Hardin & Richart (1963) or Wichtmann & Triantafyllidis (2009) do not always adequately describe the small strain properties of four investigated sands from the North Sea. Deviation of measured data from empirical equations was shown statistically. In case of prediction by Wichtmann & Triantafyllidis (2009), 25% of predicted values differ more than 20% from the measured data. Both Hardin& Richart and Wichtmann & Triantafyllidis empirical equations tend to overestimate the measured results up to 60% at low confining stresses and up to 40% at high confining stresses for medium and dense sands (D_r=50-80%) and underestimate for very dense sands (D_r=95%). However, the form of the void ratio function in Equation (1) has been proven to be satisfactory in describing the dependency of G_{max} on the void ratio. The coefficients of the

Equation (1) have to be adjusted to match the laboratory measurements.
It was found that the percentage of the rounded particles may influence the small strain stiffness of investigated sands, but due to the few samples tested in this study, the statistical relevance of this has not been proven. Grain shape is difficult to describe mathematically and human factors may affect the results of visual determination by charts. This must be improved in order to more closely evaluate the effect of the grain shape.

6 ACKNOWLEDGEMENTS

The research project was partly funded by German Federal Ministry for Economic Affairs and Energy as well as by DFG-Research Center / Cluster of Excellence „The Ocean in the Earth System". Many valuable discussions with Amir M. Kaynia and Ton Lunne are greatly appreciated.

7 REFERENCES

Blaker, O., Lunne, T., Vestgarden, T., Krogh, L., Thomsen, N.V., Powell, J.J.M., Wallace, C.F.(2015). Method dependency for determining maximum and minimum dry unit weights of sands. Int. Symp. On Frontiers in Offsh. Geotechnics, ISFOG, Oslo, Norway.

Cho, G-C.,Dodds, J., Santamarina, J.C., (2006). Particle shape effects on packing density, stiffness and strength:natural and crushed sands. J. Geotech. Geoinviron. Eng., ASCE, 132 (5): 591-602.

Dyvik, R. & Madshus, C. (1985). Lab measurements of Gmax using bender elements. Advances in Art of Testing: soils under cyclic conditions, ASCE Annual Convention, Detroit, Michigan, 186-196.

Hardin, B.O & Richart, F.E, Jr. (1963) Elastic wave velocities in granular soils. Journal of the Soil Mechanics and Foundation Division, ASCE, 89 (SM1):33-65.

Hepp, D.A., Hebbeln, D., Kreiter, S., Keil, H., Bathmann, C., Ehlers, J., & Mörz, T. (2012). An east-west-trending Quaternary tunnel valley in the south-eastern North Sea and its seismic-sedimentological interpretation. J. Quatern. Sci. 27, 844-853.

Ladd, R.S. (1978). Preparing test speciments using undercompaction. Geotechnical Testing Journal, GTJODJ, 1(1), 16-23.

Lutz, R., Kalka, S., Gaedicke, C., Reinhardt, L., Winsemann, J., (2009). Pleistocene tunnel valleys in the German North Sea: spatial distribution and morphology. Zeitschr. Dt. Ges. Geowiss. 160, 225-235.

Otsubo, M., O'Sullivan, C., Sim, W.W., & Ibraim, E., (2015). Quantitative assessment of the influence of surface roughness on soil stiffness. Geotechnique 65 (8): 694-700

Powers, M.C., (1953). A new roundness scale for sedimentary particles. J. Sediment. Res. 23, 117-119

Rodriguez, J.M., Johansson, J.M.A., & Edeskär, T. (2009). Particle shape determination by two-dimensional image analysis in geotechnical engineering. NGM 2012 - Proceedings of the 16th Nordic Geotechnical Meeting, Copenhagen, Denmark, May 2012.

Santamarina, J.C. & Cascante G., (1998). Effect of surface roughness on wave propagation parameters. Geotechnique 48 (1): 129-136

Shin, H. & Santamarina, J.C., (2013). The role of particle angularity on the mechanical behavior of granular mixtures. J. Geotech. Geoinviron. Eng., ASCE, 139(2);353-355

Sindowski, K.-H., (1965). Die drenthestadiale Altenwalder Stauchmoräne südlich Cuxhaven (Beitrag zum Punkt 1 Hohe Lieth der Exkursion B der Frühjahrstagung der Deutschen Geologischen Gesellschaft in Cuxhaven 1963.). Zeitschr. Dt. Ges. Geowiss. 115, 158-162.

Wichtmann, T. & Triantafylidis, Th. (2009). On the influence of the grain size distribution curve of quartz sand on the small strain shear modulus G_{max}. J. Geotech. Geoinviron. Eng., ASCE, 135 (10), 1404-1418

Wichtmann, T. & Triantafylidis, Th. (2014). Stiffness and damping of clean quartz sand with various grain size distribution curves. J. Geotech. Geoinviron. Eng., ASCE, 140 (3)

Maximum and minimum dry unit weight. NGI in-house procedure. (not published)

Yimsiri,S. & Soga, K., (2000). Micromechanics-based stress-strain behavior of soils at small strains. Geotechnique 50 (5): 559-571.

Comparison between field monitoring and calculated settlement for railway embankment built on peat

Ulrika Isacsson
WSP Sverige AB, Sweden, ulrika.isacsson@wspgroup.se

ABSTRACT
On the part Rydbo – Åkers Runö, North East of Stockholm, the narrow gauge railway Roslagsbanan have during the later years been expanded with a second track. The original railway was built during the beginning of the 20th century.
The ground at the part km 21+720 – 21+920 consists of a wood covered marsh, a.k.a. Igelkärret. The soil generally consists of an upper layer of ca 2 m medium decayed to decayed peat and mud, resting on soft clay down to at most 15 m below the ground surface. The new track is located on the south side of the existent embankment, with 4,5 m between the tracks. The height of the embankment is 3 – 5 m.
Both the old and the new tracks are reinforced with lime-cement columns and expanded clay. There are also loading berms on each side of the embankment. The settlement of the reinforced embankment, both the original embankment and the new embankment, as well as the loading berms resting directly on the peat have been monitored for a period of 1,5 years.
The settlement of the embankment situated on the lime cement columns were calculated by means of Excel. The settlement of the loading berms resting on the peat have been estimated according to the diagrams in SGF Information 6. These results have been compared to the measured settlement to determine the accuracy of the calculation methods both in terms of the resulting settlement and during which period of time it took place.

Keywords: sättning, KC-pelare, torv, järnväg

1 BAKGRUND

Järnvägen har på aktuell sträcka, xxx, byggts ut från enkelspår till dubbelspår. Ursprunglig järnvägsbank byggdes i början av 1900-talet och ny järnvägsbank färdigställdes 2014. Det nya spåret har förlagts på södra sidan utmed det befintliga spåret med 4,5 m spåravstånd. Banken är 3 – 5 m hög.
Terrängen består av ett kärr, Igelkärret, som är skogsbevuxet. Järnvägen korsar kärret i öst-västlig riktning. Marken är generellt sett plan.

2 FÖRUTSÄTTNINGAR

2.1 Jordlagerföljd

Den naturliga jorden utgörs av torv och gyttja på lera ovan friktionsjord som vilar på berg. Jorden består överst av mellan 1 – 2 m medel- till högförmultnad torv. Torven underlagras generellt av mellan 1 – 2 m gyttja. Lerans mäktighet varierar mellan 3 och 12 m. Djupet till fasta jordlager är som mest ca 15 m.

2.2 Grundvatten och portrycksförhållanden

På sträckan finns installerat en portryckstation och ett grundvattenrör.

Grundvattenröret visar på hydrostatiskt tryck i friktionsjorden under leran, med en nolltrycksnivå strax under markytan. Portrycket på 10 m djup har vid mättillfällena varierat mellan 63 och 95 kPa. På 5 m djup har portrycket uppmätts till mellan 40 och 45 kPa.

2.3 Konsolideringsförhållanden

För den jungfruliga marken bedöms leran vara normalt konsoliderad till svagt överkonsoliderad (OCR 1,2 – 1,4). Under befintlig järnvägsbank har leran konsoliderat i över 100 år. Den ökade konsolideringsgraden har bedömts enligt ”Stabilitet för befintliga järnvägar” (BVS1585.002) och visar på en ökning av σ'_c med ca 85 kPa.

2.4 Förstärkningsåtgärder

Geotekniska förstärkningsåtgärder har utförts för både ursprunglig och ny järnvägsbank.

Förekommande organisk jord ovan leran har skiftats ur och marken har förstärkts med kalkcementpelare installerade i skivor. Jordförstärkningen kombineras med 2 m lättklinkerfyllning i järnvägskroppen samt 1 m höga tryckbankar på vardera sidan av banken, se Figur 1.
I övergången mot fastmark i väster och i öster, där kalkcementpelarna blir för korta, skiftas all lös jord ut.

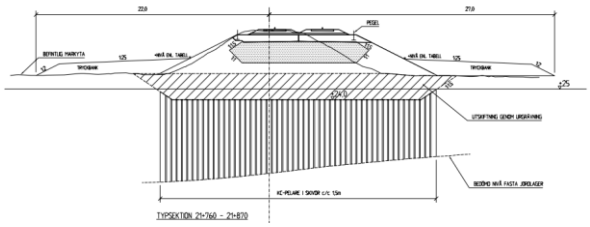


Figure 1 Typsektion för geoteknisk förstärkningsåtgärd.

3 BERÄKNADE SÄTTNINGAR

3.1 Sättningar i torv

Sättningsuppskattning för tryckbankar på torv har utförts enligt SGI Information 6, Torv – geotekniska egenskaper och byggnadsmetoder.

Då torven i området har en relativt låg vattenkvot innebär detta att den pålagda lasten om ca 20 kPa resulterar i en bedömd deformationssgrad om ca 15 – 20%. Med en torvtjocklek om 1,5 – 2 m innebär detta ca 40 cm sättning som till största delen utvecklas inom 1 – 2 månader med belastning.

3.2 Sättningar i KC-pelare

Sättningsberäkningarna och kontroll av kryplasten för den kalkcementförstärkta delen av jorden är utförda enligt SGF Rapport 2:2000 med hjälp av excel. Jorddjupet varierar längs med sträckan. Redovisad sättningsberäkning är utförd för en typsektion med bankhöjd ca 3 m samt jorddjup ca 10 m. För resultat av sättningsberäkning för bank på jungfrulig mark, se Figur 2. För resultat av sättningsberäkning för bank på tidigare belastad mark, se Figur 3.

4 OBSERVERADE SÄTTNINGAR

Det har placerats ett antal peglar på banken och tryckbanken. Peglarna har beteckningar P och OR, för planläge se Figur 4.

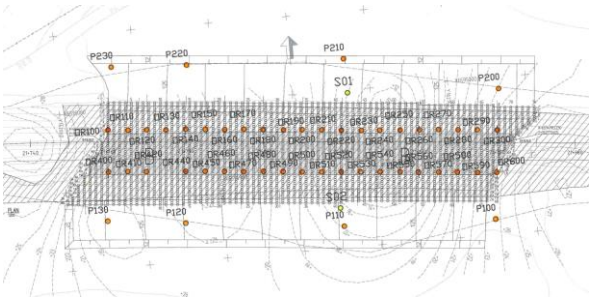


Figure 2 Peglar km 21+740 – 21+880.

Arbetet med järnvägsbanken samt den södra tryckbanken slutfördes i maj 2014. Arbetet med den norra tryckbanken slutfördes i juli 2014. Krönpeglarna på banken installerades i juni 2014 och peglarna på tryckbankarna installerades i juli 2014. Samtliga peglar har avlästs kontinuerligt, men med tidsintervall som varierat under mätperioden. Se sättningskurvor för södra bankdelen i Figur 5 samt för norra bankdelen i Figur 6.

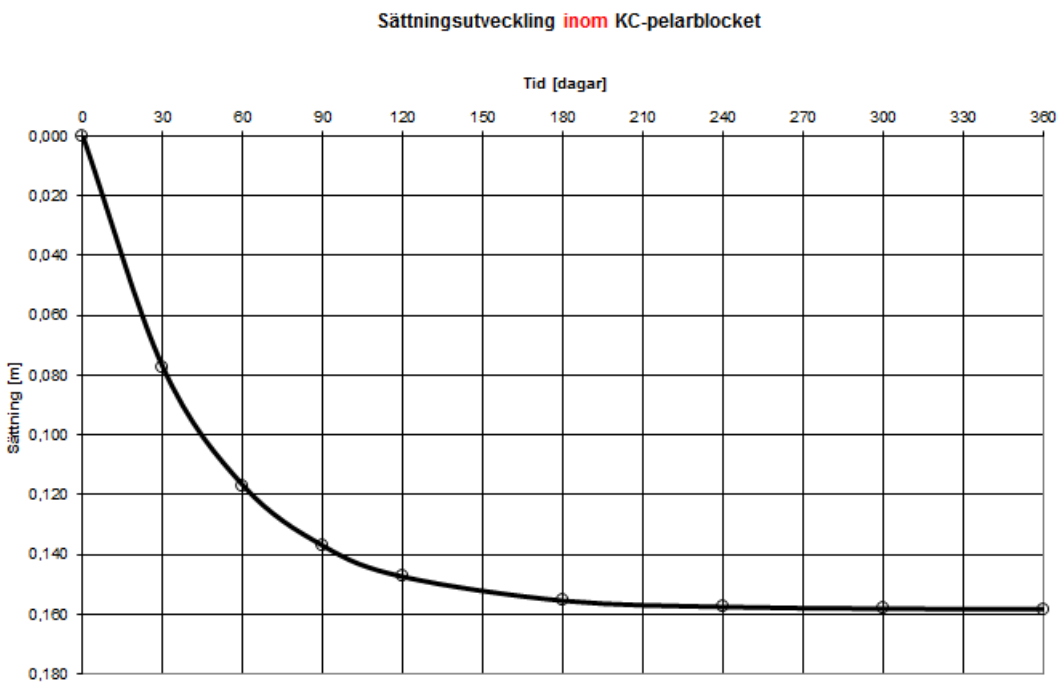


Figure 3 Beräknad sättning inom KC-pelare under ny järnväg (södra banken).

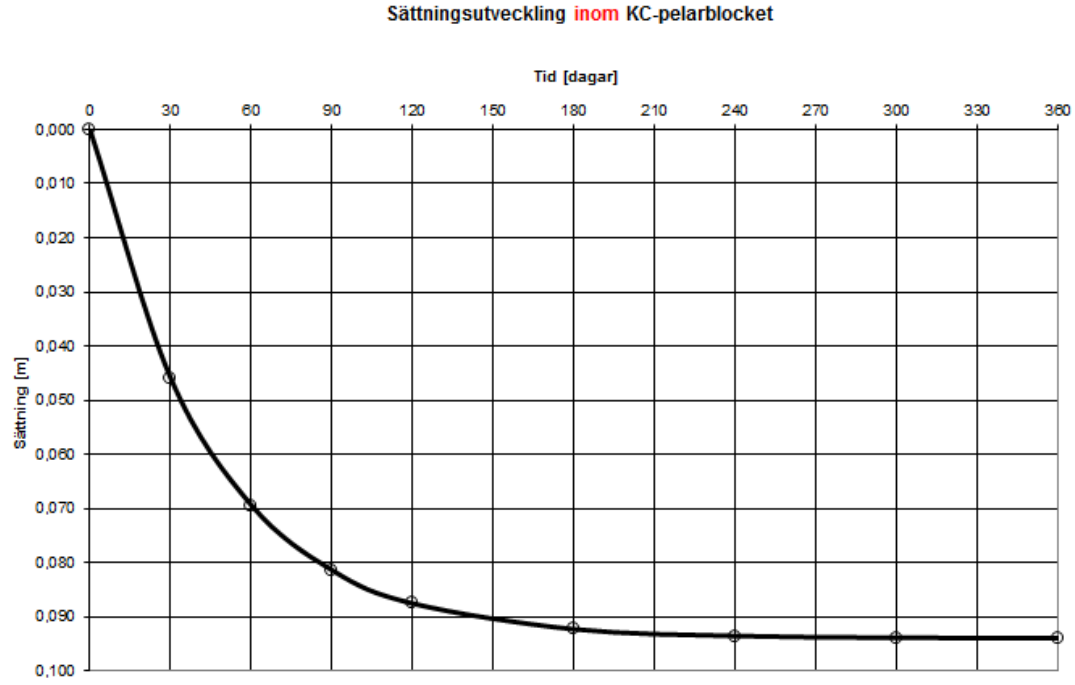


Figure 4 Beräknad sättning inom KC-pelare i tidigare belastad jord (norra banken).

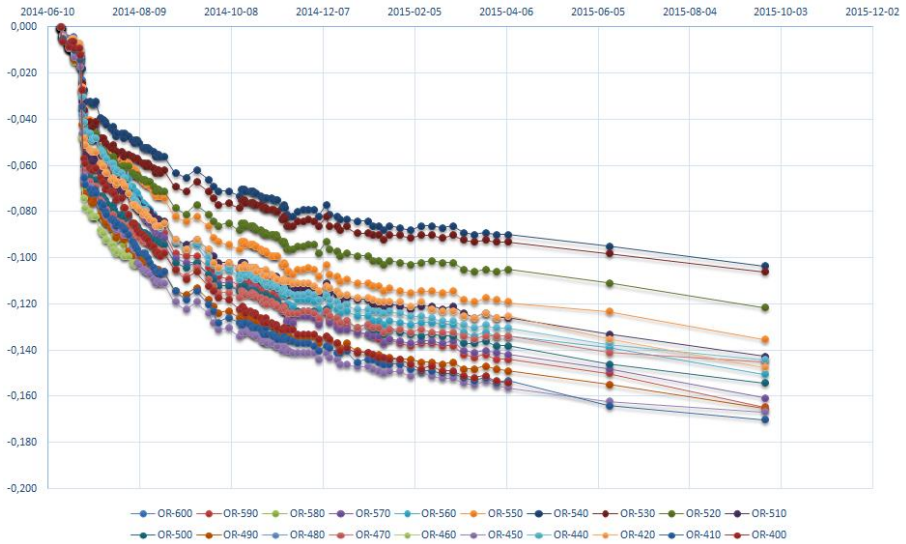


Figure 5 Sättningskurvor Södra banken.

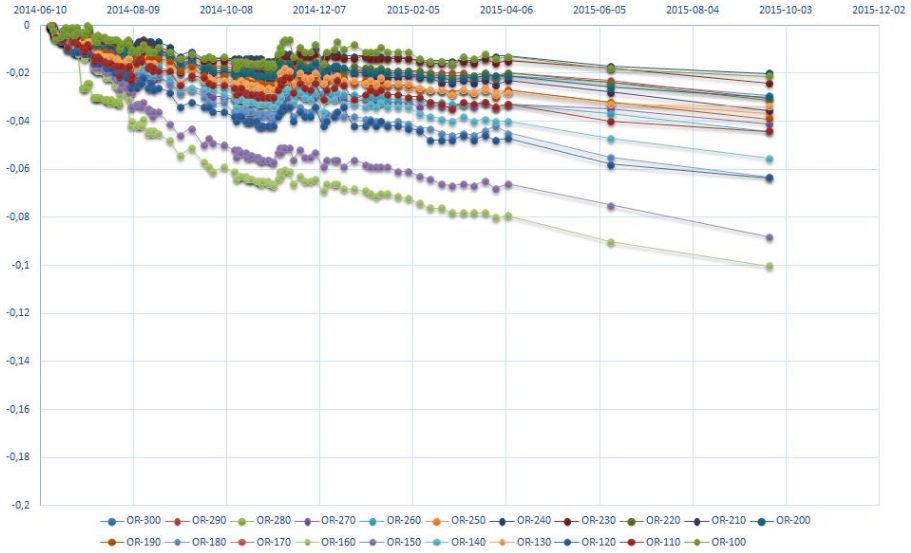


Figure 6 Sättningskurvor Norra banken.

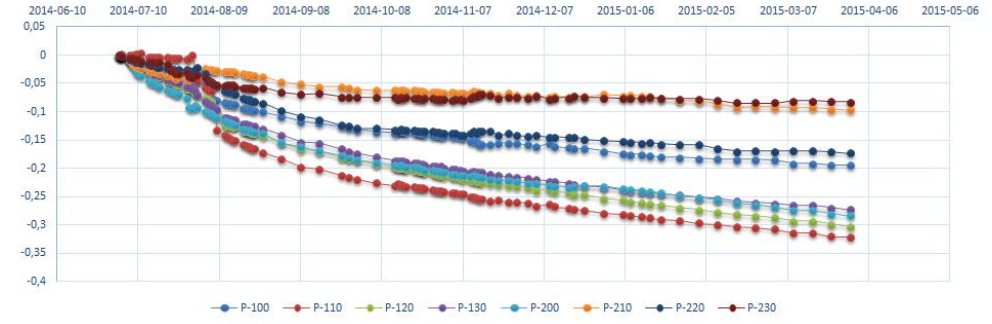


Figure 7 Sättningskurvor tryckbankar.

5 RESULTAT

Beräknad sättning för den norra banken är efter 1 år ca 10 cm, med den största delen av sättningarna utvecklade efter 2 till 3 månader. Uppmätt sättning för samma bank är efter 3 månader ca 2 till 5 cm, samt efter 1 år ca 2 till 9 cm.
Beräknad sättning för den södra banken är efter 1 år ca 16 cm, med den största delen av sättningarna utvecklade efter 2 till 3 månader. Uppmätt sättning för samma bank är efter 3 månader ca 6 till 12 cm, samt efter 1 år ca 10 till 16 cm.
Bedömd slutsättning för tryckbankar på torv uppgår till ca 40 cm, med i princip all sättning utvecklad efter 1 à 2 månader. Efter 2 månader är den uppmätta sättningen ca 5 till 20 cm och efter 1 år ca 8 till 35 cm.

6 SLUTSATS

För de beräknade sättningarna för både norra och södra banken, uppnåddes slutsättning inom ett år.
I sättningskurvorna för krönpeglar på bank har den beräknade slutsättningen ej överskridits efter 1 år av mätningar, men kurvorna visar en variation avseende utplaningen på sättningen.
Att de uppmätta sättningarna även visar en variation avseende storleken på sättningarna bör till viss del bero på att både banktjocklek och jorddjup varierar på sträckan, gentemot vad som antagits i beräkningarna.
Efter 2 månader har ca 60% av den uppmätta 1-årsättningen på tryckbankarna utbildats. Även här visar sättningskurvorna en variation avseende utplaning på sättningen.
Anledningen till den långsammare utbildningen av sättningar kan exempelvis bero på att torvens egenskaper och mäktighet varierar över sträckan.

Forensic engineering of a bored pile wall

Willem Robert de Bruin
Geovita AS, Norway, rdb@geovita.no

Abstract: At present, bored pile walls in Norway are designed and executed in accordance to *regulations of the Norwegian Public Road Administration as described in Handbook R762. During the construction of a 180-meter-long and 18-meter-high bored pile wall for the municipally owned public transporter of Oslo: Sporveien AS, deflections of the wall, the performance of the structural elements and the quality of the welding were monitored on a regular basis. From the evaluation of these data, it was concluded that the geometry of the cross-section did not meet the design requirements. During the construction works, a method was developed to redesign the walls structural characteristics. The performance of materials, products, and structural components used were investigated by forensic engineering. This type of engineering has led to a guideline for future design of bored pile walls. This guideline accounts for:*

- *Design of a bored pile wall with plastic behaviour instead of elastic behaviour;*
- *Calculation of the section modulus in accordance with the achievable structural properties and dimensions;*
- *Design of effective welding with regard to limitations in daily practice;*

It was demonstrated in this case that the bored pile wall still complied with the current design standards and that the guidelines developed may be considered in early design stages with designing and engineering of bored pile walls in future projects.

1 AVLØS STATION

The updating of the Kolsåsbanen includes presence of maintenance and cleaning halls. The intended area however was not big enough and needed to be expanded. In order to widen the area, a large part of an existing slope had to be removed; see the red line in Figure 1 and planned excavation along the retaining wall in Figure 2.

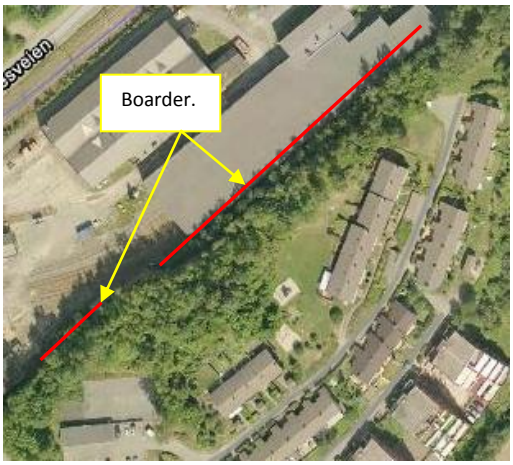


Figure 1 Aerial view of Avløs station,

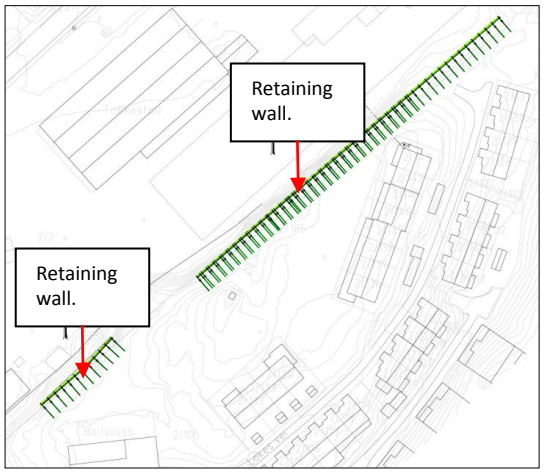


Figure 2 Overview of Avløs station.

1.2 Geological advantages

The geology in the area is a part of the Cambro-Silurian sedimentary rocks of the Oslo region. The sequence consists of limestone, nodular limestone and shale. Figure 3 shows the geological profile.

The stroke direction of the sedimentary rocks is N55^{o} east, which is parallel to the rock slope.

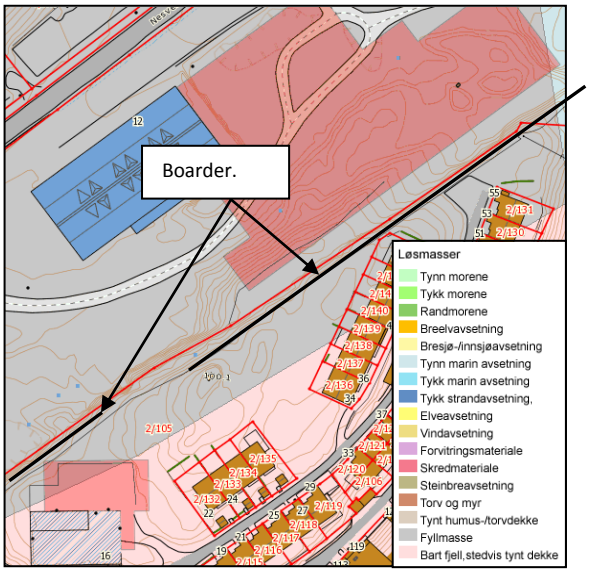


Figure 3 Detail of the geological profile.

The slope angle of the sedimentary rock is 70 to the horizontal, see Figure 4 for a detail. The distance between the fracture planes varies between some centimetres and half a metre.

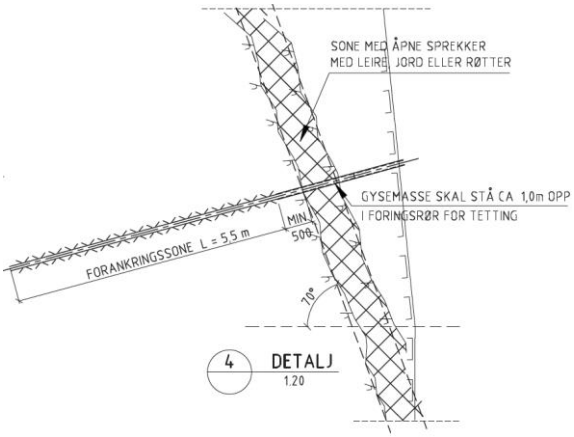


Figure 4 Slope angle of the sedimentary rock.

The only way to remove this type of rock mass was by installing a bored pile wall, to be bored from top in several levels, and removal of stones on the front side afterwards: see Figure 5. The bored piles were installed by a tubular pipe of 273mm in diameter to the required depth, drill out the core and hanging in a steel H-beam. After installing the wall small holes were bored each 0,50 meter small holes, so-called "sømboring". In this way the mass was easier and more gently removable.

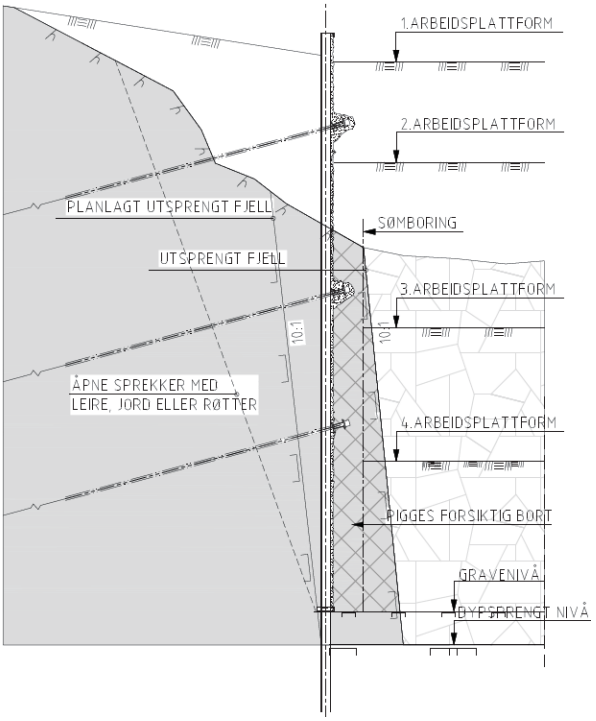


Figure 5 Principal for building of the pile wall.

1.3 Design of the bored pile wall

The design of the bored wall was done by following the next steps:

A. Determining centre distance of the piles and required dimension of the pile.
   The inner pressure arc, or arching effect of the soil mass, plays a decisive factor on the centre distance of the piles. This centre distance is mostly based on experience and engineering judgement because no practical calculation methods for this type of phenomena are available. The centre to centre distance of the piles was set to 600mm which, combined with a tubular pipe of 273mm, created a cap of 327mm. See Figure 6.

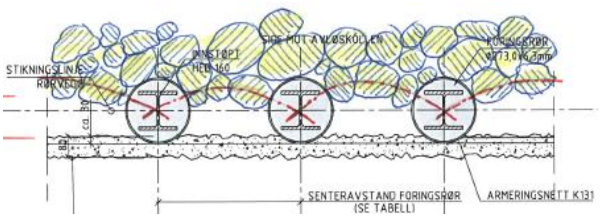


Figure 6 Inner pressure arc or "arching effect".

B. Control of several critical cross sectional areas. The moment of inertia and

sectional modulus of the piled wall as well as required dimensions for the anchors were calculated in both the ultimate limit state and the serviceability limit state.

This process resulted in a bored pile wall according to the following drawings and specifications in Figure 7 and Table 1.

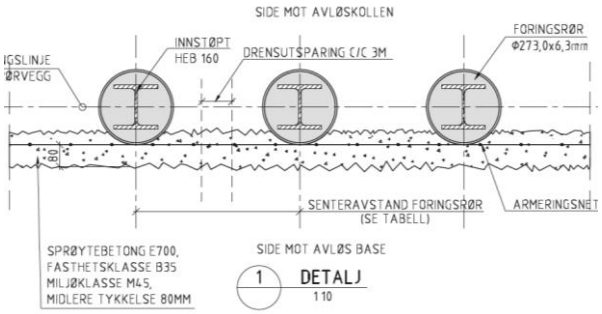


Figure 7 Cross section of the pile wall.

Specifications of bored pile wall at Avløs station		
Total length of bored pile wall	177	m
Maximal height of bored pile wall	18	m
Total number of piles Ø273x6,3	295	pieces
Total length of piles Ø273x6,3	3900	m
Total length of HE160-B piles	3900	m
Total length of braces double UNP350	300	m
Total length of top girdle UNP400	177	m
Total number of anchors	112	pieces
Total length of anchors	735	m
Total cost of materials and installing	16,5 million	NOK

Table 1 Overview of costs and quantities

1.4 Monitoring

In order to achieve the obtained quality, the following steps for monitoring were taken included in the contract:

1. Geometry of the pile wall:
   - Positioning tolerance of the tubular bored pile, +/- 100mm horizontal;
   - Placement tolerance of the installed HE160B: rotation of the axis maximum 1% in relation to theoretical axis;
   - Control of straightness by measurement with electrical inclinometer;
   - Tolerance on HE160B at maximum skewness D = d:1000 with d = core diameter;
   - Tolerance on cutting of the HE160B at +/- 10mm;
   - Tolerance on squareness or perpendicularity of the tubular pipe head: skew D = d:1000 with d = core diameter;
   - Deviation from theoretical designed level pile top of finished mounted pile top: 50mm;
2. Materials of the pile wall:
   - Mortar cement /water factor 0,4 or lower, compressive strength after 28 days: 40 MPa, and further demands from the Norwegian Concrete Association (“Norske Betongforeningen”) publication nr. 14 with necessary tests;
   - Steel grade of the tubular pipes;
   - Material of the HE-B profile;
3. Protocol for each bored pile, including written rapports containing pile number, depth into hard rock, rate of drilling, soil encountered during drilling etc.;
4. Inspection of welding by both visual inspection and inspection with control with x-ray pictures;
5. Inspections of the tightness of the welding by controlling the presence of water in the bored pipe;
6. Inspections of the tightness of the welding by placing water in the pipe, a water lock and to place pressure on the water;

These contractual requirements on quality were carried out in different stages of the process and on a regular basis by control engineers of Sporveien AS with the help of a control plan. The process of installing the bored pile wall had already reached 60% when the control of welding was done by

taking x-ray pictures. The result of these tests showed that up to 60% of all welding work did not meet the requested quality. On top of this, the tests were not sufficient to determine in which degree the welding itself was able to fulfil its duty. The outcome of the test was simply: “approved” of “not-approved”. Besides the fact that the welding was not approved, it showed, during a visit at the building site, that the demand for tolerance on positioning and alignment was exceeded. The image on Figure 8 shows both rotation and translation of the profile beyond accepTable and allowable tolerances. The profiles were displaced with maximum 45 degrees’ rotation in relation to the theoretical axis and in addition against the inner side of the pipe leaving no concrete cover.



Figure 8 Rotated, eccentric and a-symmetric HE-160B profile.

From the evaluation of these data, it was concluded that the quality of the structural cross-section did not meet the design requirements and measures had to be taken.

1.5 Forensic engineering

By contract the tolerance of placement for the HE beams was limited to one-degree rotation. After having spoken with the craftsmen on the job the comment on why the beam had been rotated was: “it will always turn”. There was no further explanation.

The principle is as follows. The straightness of the bored pile depends on the tolerances from both practical side as well as theoretical and contractual side as mentioned before.

Combining these tolerances creates an image as shown in Figure 11 were the bored pile deviates from the theoretical straight line. The different sections, A – D, are sketched in the cross sections below in Figure 9. This Figure shows inconsistency in relation to the theoretical axis.

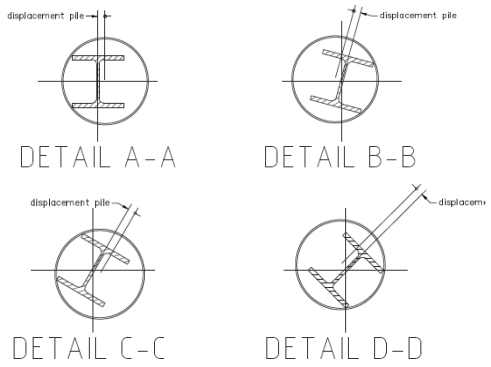


Figure 9 Rotated, eccentric and a-symmetrical profile.

When the HE-B profile is installed, the pile will make contact at one side of the pipe, see Figure 10.

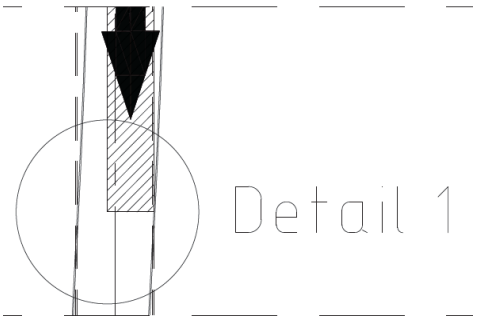


Figure 10 Collison of the profile with the inner side of the pipe.

With this contact the HE-B profile will follow the direction or alignment of the pipe locally which has different directions in cross section A, B, C and D. As a consequence, the HE-B profile will turn and finally rotate.
This process is a direct result of the profiles own weight and therefore the rotational movement goes with great forces which cannot be adjusted during installing neither changed after the profile has reached its final depth.



Figure11: Deviation of practice and theoretical placement.

After having established the very cause of the rotation and displacement of the combined profile, the next step was to check the influence of this changed combined profile.

See Figure 12 for the calculation of the displaced and rotated profile, with corresponding deviation in relation to the obtained capacity. Table 2 shows an overview.

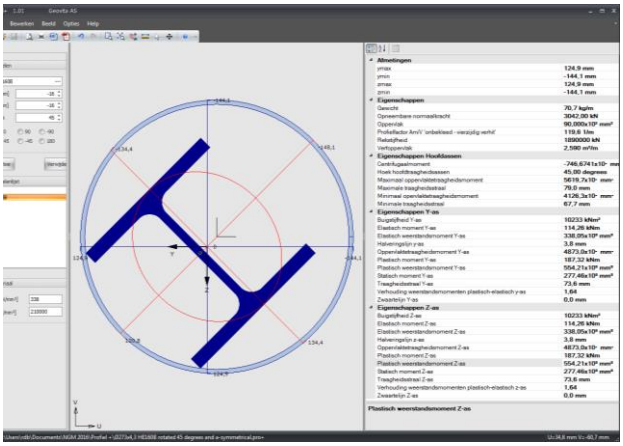


Figure12 Calculation of the rotated, eccentric and a-symmetric composite profile.

Profile: Ø 269,0 x 4,3 + pored HE160-B	Profiel +	Diff. related to centric sym-metric	Profiel+	Diff. related to centric, sym-metric
	$M_{y;el;Rd}$ (kNm)	(%)	$M_{y;pl;Rd}$ (kNm)	(%)
Centric and symmetrical	235,37	100	368,98	57
Rotated 15 gr. + symmetrical	230,87	-2	362,18	54
Rotated 30 gr. + symmetrical	218,58	-7	342,27	45
Rotated 45 gr. + symmetrical	201,78	-14	311,15	32
Rotated 45 gr. + a-symmetrical	190,43	-19	312,20	33
Profile: Ø 273,0 x 6,3 corroded with life span 100 years gives Ø 269,0 x 4,3				

Table 2 Capacity overview of the rotated, eccentric and a-symmetric composite pile profile.

It is not allowed to simply add the moment capacity of the tubular pipe and that of the beam, $M_{pipe}+M_{HEB160}$ = (78,72 + 105) * centre distance (1/0,6) = 306,4 (kNm).

This will give considerable more capacity in relation to the calculated. This is due to the fact that both profiles do not have the same neutral line to be followed with calculating the maximum moment capacity, see Figure 13.

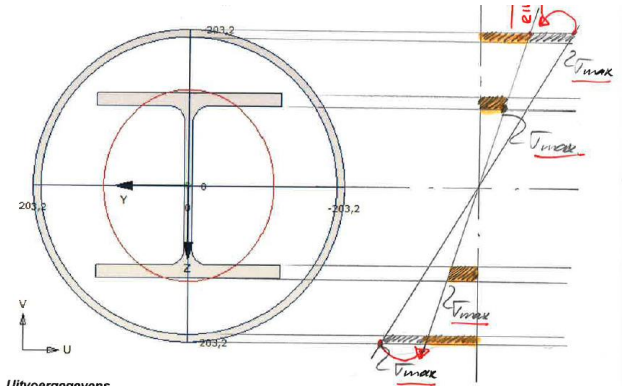


Figure 13 Capacity overview of the rotated, eccentric and a-symmetric composite pile profile.

The capacity of the piles was reduced with 19% in elastic state and approximately 15% for the plastic state. The proper way to calculate the moment of inertia for hybrid profiles with translational and rotational motion is buy using Steiner's theorem.

The challenge with the welding was charted by checking welding protocols on welding positions along the tubular pipe. The charted overview visualized that the first elements which were bored, were 6 meters long, containing no welding.

This led to the conclusion that 100% of the designed capacity was still in place over the first 6 meters, off course with deduction of capacity due to corrosion. Along the remaining part of the wall the capacity was reduced to the sum of the rotated profile and the surrounding concrete. Figure 14 shows that calculated data from Figure 12 and Table 2 still provides enough capacity for the lower 6 meters.

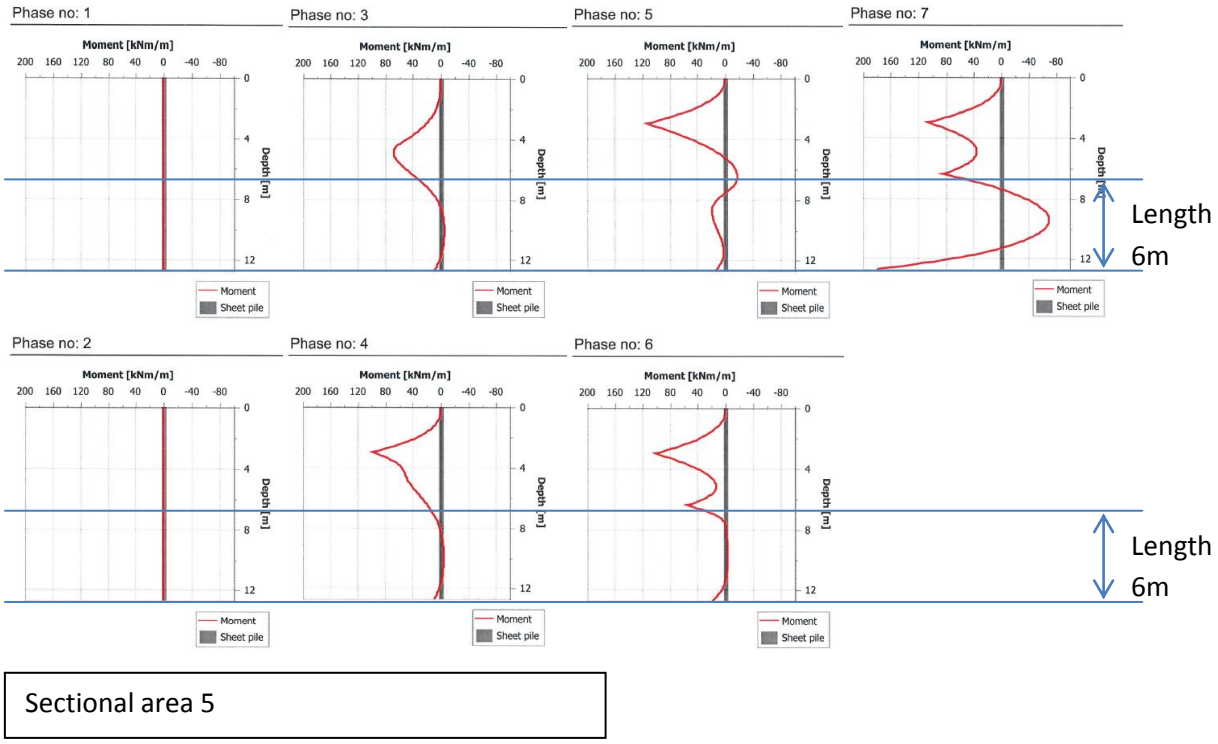


Figure 14 Chartered moment capacities versus placement of welding.

The remaining length was checked by heavily reduced moments of a profile without contribution of the tubular pipe, in addition to capacity calculated as given in the overview of Figure 15 and Table 3. Elastic capacity was reduced with 64% and plastic with 40%.

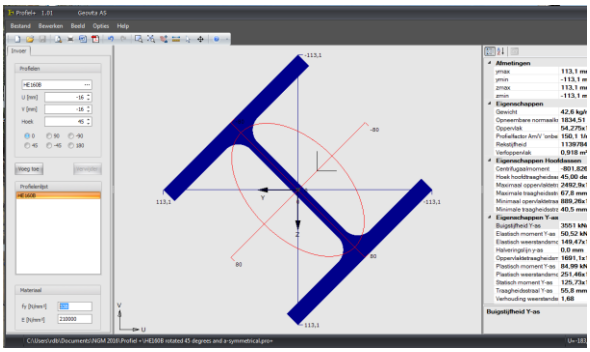
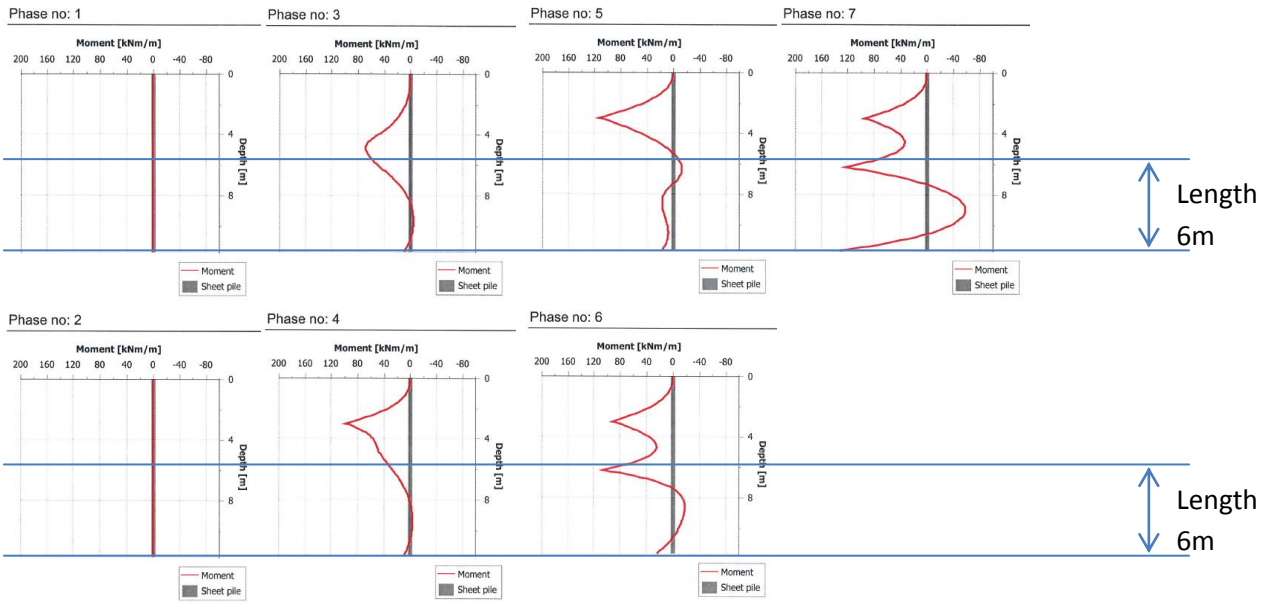


Figure15 Calculation of the rotated, eccentric and a-symmetric non-composite profile.

As shown in Table 3 the capacity of these piles was reduced with 64% in elastic state and approximately 40% for the plastic state in relation to the original capacity.

Profile: Ø 269,0 x 4,3 + pored HE160-B	**Profiel +**	**Diff. related to centric sym-metric**	**Profiel+**	**Diff. related to centric, sym-metric**
	$M_{y;el;Rd}$ (kNm)	(%)	$M_{y;pl;Rd}$ (kNm)	(%)
Centric and symmetrical	175,55	-25	199,48	-15
Rotated 15 gr. + symmetrical	137,15	-42	192,68	-18
Rotated 30 gr. + symmetrical	107,83	-54	172,77	-27
Rotated 45 gr. + symmetrical	84,20	-64	141,65	-40
Rotated 45 gr. + a-symmetrical	84,20	-64	141,65	-40
Profile: HE160-B with ignored poured concrete shell.				

Table 3 Capacity overview of the rotated, eccentric and a-symmetric non-composite pile profile.



Sectional area 5

Figure 16 Chartered moment capacities versus placement of welding.

Other phenomena which need to be checked included:

- Local buckling
- Shear buckling
- Axial – torsional buckling
- Lateral – torsional buckling
- Web crippling and web yielding

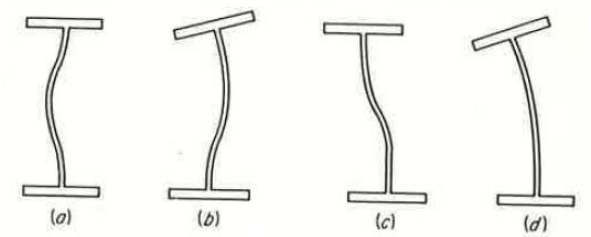


Figure 17 a) Web yielding… d) Web cripling

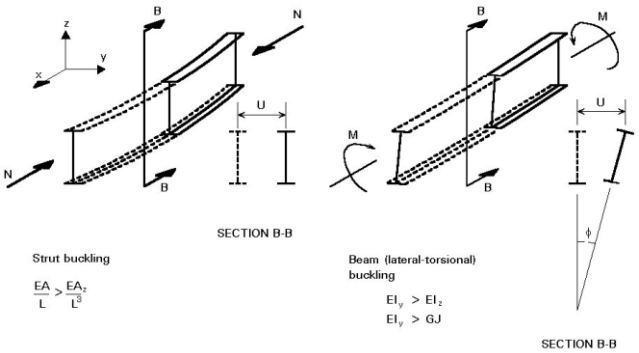


Figure 18 Strut buckling and lateral torsional buckling

The presence of the concrete poured scale surrounding the HE-B profile functioned as plate girder, web stiffener and transverse stiffener which showed to be sufficient after control. The soil anchors with girders functioned as bucking strut, reducing the buckling length considerably.

Controlling capacity after installing showed that in future cases the location of the welding should be done in front. Locations of moment should be linked with necessary welding and described on as-built drawings, preventing welding in the vicinity or directly near locations with large moments in the pile wall. The same is also important for the girders along the pile wall, here it's also possible to end up with welding in the vicinity of or influence zone of large moments. The reduced shear force capacity did not create a problem since this was sufficient from the HE-B profile.

In order to achieve enough covering on the safety a last component was added in the overall control by using the plastic capacity. In order to proceed with this the Eurocode had to be checked whether this way of calculating was permitted.

1.6 CONCLUSION

Monitoring and controlling the bored pile wall showed a considerable amount of inconsistency between design and practice. However solvable the situation turned out, there is a need for improvement of engineering and designing discipline besides the information flow towards contractor in both contract and drawings.
In future projects concerning pile walls it is advisable to take into account the following guidelines:

A. Calculation of the section modulus in accordance with the achievable structural properties and dimensions. Use of reduced moment capacity as a result of rotated HE-profiles, as a preventive tool;

B. Design of effective welding with regard to limitations in daily practice. Homogeneous parts of pipe without welding for the pile wall zones with largest moments. This can also be used as a preventive tool;

C. Design of a bored pile wall with plastic behaviour instead of elastic behaviour, as a corrective tool in case of deviation from the original design.

2 REFERENCES

1. EN 1994-1-1 – Eurocode 4 (2004), "*Design of composite steel and concrete structures, Part 1.1 – General Rules for buildings*", European Committee for Standardizations, Brussels.
2. ENV 1992-1-1 – Eurocode 2 (1994), "*Design of concrete structures, Part 1.1 – General Rules for buildings*", Provisory Version, European Committee for Standardizations, Brussels.
3. EN 1992-1-1 – Eurocode 2 (2004), "*Design of concrete structures, Part 1.1 – General Rules for buildings*", European Committee for Standardizations, Brussels.
4. Gaylord, E.H.jr. & Gaylord C.H. (1975). Design of steelstructures, McGraw-Hill Book company.
5. W.H. Verburg, M.A. Barendsz and C.H. van Eldik (2002). Overspannend staal, deel B. Balkema.



Figure 21 Bored pile wall at Avløs station

Theoretical Analysis of the Relationship between Heave and Net Heat Extraction Rates Based on Freezing Experiments

Deniz Dagli
Luleå University of Technology, Sweden, deniz.dagli@ltu.se

Amin Zeinali
Luleå University of Technology, Sweden

Jan Laue
Luleå University of Technology, Sweden

Tommy Edeskär
Luleå University of Technology, Sweden

ABSTRACT
In order to improve the current design of roads against frost action, the Swedish Transport Administration (Trafikverket) has initiated a research programme. The main goals of the research are to revise the existing frost design models and the frost susceptibility classification system for subgrade soils.

A qualitative theoretical analysis to establish a relationship between frost heave and net heat extraction rates based on experimental data has been done. Experiments were carried on disturbed (hand compacted), saturated samples of same type of soil without any overburden. Several different cold end temperatures were applied to create different boundary conditions to make a more detailed analysis.

Results were analysed and compared to those of other researchers while pointing out the similarities and differences. Potential reasons for these differences have been identified. Based on the findings of the experimental work, suggestions for improvements are given for future testing. Some preliminary results providing hints for the relationship between segregational heave and net heat extraction rates were obtained. At the end it was shown that there exists a significant difference between the findings of the experimental work and the current system being used in Sweden in order to quantify heave.

Keywords: Frost Action in Soils, Laboratory Freezing Tests, Frost Depth, Frost Heave, Heat Flow in Soils

1 INTRODUCTION & BACKGROUND

The relationship between heave and net heat extraction rates at the frost front has been investigated by several researchers at different points during the history of frost action and cold region soil mechanics studies.

Two kinds of conclusions have usually been reached; while the first group of authors (Beskow, 1935; U.S. Army Corps of Engineers, 1958; Loch, 1977; Hermansson, 1999) has claimed that there exists no direct relationship between heave and net heat extraction rates, the second group (Kaplar, 1970; Penner, 1972; Horiguchi, 1978; Loch, 1979; Konrad, 1987) has tried to show the opposite.

The subject has been reviewed once again in Sweden for the research programme BVFF (Bana Väg För Framtiden) sponsored by the Swedish Transport Administration

(Trafikverket) in order to improve the existing methods of heave estimation and frost susceptibility classification. This necessity to improve the current design can be better understood with the help of Figure 1.

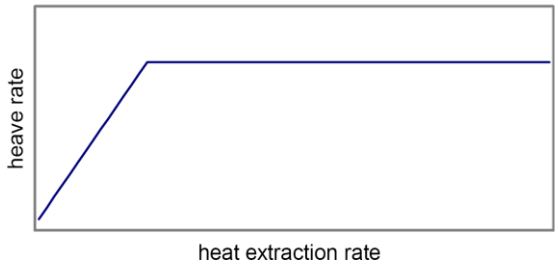


Figure 1 Relationship between heave rate and heat extraction rate at the frost front used in the current Swedish practice (Hermansson, 1999)

Firstly, no attempt is made in the current frost heave model used for pavement design to separate segregational heave from the total heave. In other words, displacements due to heaving are assessed as a whole rather than being treated separately as primary and secondary heave. The importance of secondary heave (also termed as segregational heave) will be explained in the next section. It should be noted that trying to establish a relationship between total heave and net heat extraction rates might result in contradictory results (Konrad, 1987).

Secondly there exists a threshold value of heat extraction rate in Figure 1, which is used in the existing model. Up to this threshold value heave rate is assumed to be proportional with the heat extraction rate. When the threshold is exceeded, heave rate is assumed to be constant and not to be affected by the heat extraction rate. As a result, at relatively higher heat extraction rates the same amount of heave will be estimated which might not necessarily be the case. For such high rates it might also result in overestimation of heave.

To address all these issues a comprehensive experimental study has been undertaken including the development of a freezing test apparatus and laboratory freezing tests.

To this end, laboratory testing of disturbed soil samples under different temperature gradients (i.e. different heat extraction rates) has been conducted. Qualitative assessment of the results has been done. The main focus was on establishing a relationship (by means of plot trends) rather than the numerical accuracy. Details of the experimental work along with the theoretical analyses of results are presented in their respective sections.

2 EXPECTED OUTCOME

Beskow (1935) has demonstrated the importance of secondary (segregational) heave by proving that the volume expansion upon freezing is not the main cause of frost heave by experimenting with benzene (benzene is a liquid that shrinks upon freezing). He showed that samples saturated with benzene can still experience significant heave.

Furthermore, ice lens formations in a frozen soil body also provide hints about the significance of segregational heaving.

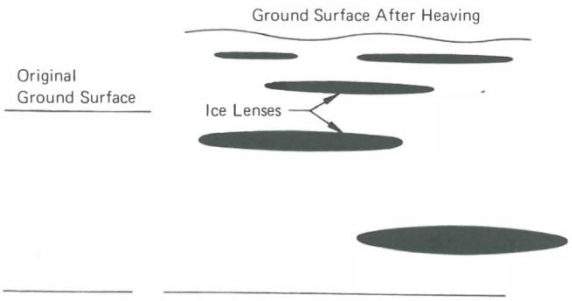


Figure 2 Characteristics of ice lenses and frost heaving (Mitchell, 1976)

Relatively thicker ice lenses observed at the lower depths of a soil body, shown in Figure 2, can be attributed to the segregational heave concept. At the beginning of the winter period where the advancement of the frost line is rapid due to higher heat extraction rates, the thickness of the ice lenses being formed are relatively low. This can be explained due to the lack of time it takes for the surrounding water to reach the frost front due to high frost penetration rates. Towards the end of the winter period, however, frost front almost comes to a halt (i.e. quasi-

stationary) and there usually is enough time for the water to be drawn to the freezing front which causes the formation of thicker ice lenses.

Therefore one might expect that the relationship between segregational heave and heat extraction rates to be of parabolic nature with a peak and approaching to zero for very high and very low heat extraction rates due to the reasons discussed above. This has been verified by the work carried out by Konrad (1987) and can be seen in Figure 3.

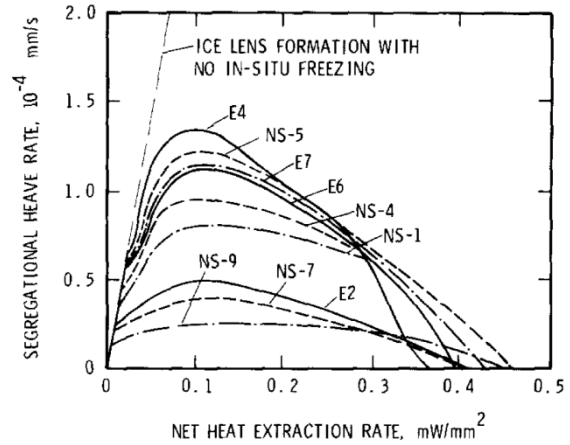


Figure 3 Segregational heave rate versus net heat extraction rate (Konrad, 1987)

Figure 3 shows Konrad's (1987) results in freezing experiments with different temperature boundary conditions conducted on one type of soil (Devon silt). According to this, the samples were found to experience different heave rates for different heat extraction rates with a very clear peak. Interestingly, it has also been found that the same type of soil might undergo different heave rates under a certain value of heat extraction rate. The reason why the same type of soil is experiencing different heave rates for a fixed value of heat extraction is outside the scope of this work but can be attributed to different sample heights and temperature boundary conditions used during experiments.

An in-depth study of segregational heave requires a detailed analysis of water that is being drawn to the frost front during freezing. For this purpose, the movement of water in the surroundings to the frost front has been investigated by different researchers (Loch, 1979; Ito et al., 1998) and their findings are presented in Figure 4 and Figure 5. In these figures the water is shown to be drawn to the frost front at relatively low rates at the beginning phases of the experiment where the heat extraction rate is higher. As the experiment progresses, water is found to be drawn at higher rates, reaching a peak value and decreasing gradually from then on. Importance of this peak and the time it takes to reach it will be discussed in detail in the coming sections.

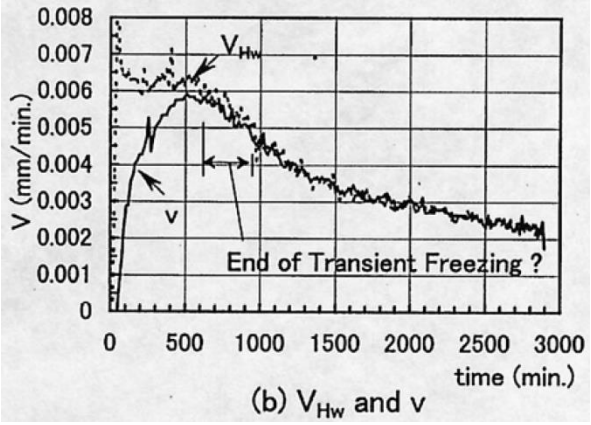


Figure 4 Water intake measurements from a step freezing test (Ito et al., 1998)

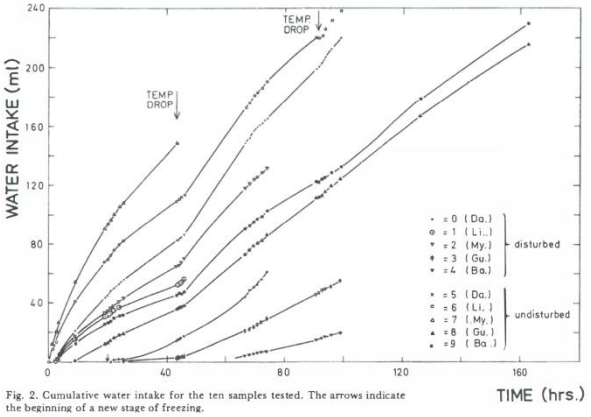


Fig. 2. Cumulative water intake for the ten samples tested. The arrows indicate the beginning of a new stage of freezing.

Figure 5 Water intake measurements during freezing tests (Loch, 1979)

3 EXPERIMENTAL WORK

3.1 Testing Apparatus

In order to further investigate the relationship between heave and net heat extraction rates, a testing equipment has been constructed. Details of the experimental apparatus are explained in the work by Zeinali et al. (2016).

During frost testing, freezing takes place one dimensionally (from sample top to bottom). The sample is insulated from sides in order to minimize heat losses from other dimensions. There are two cooling units supplying cold and warm temperatures to the top and bottom of the sample, respectively. Temperature sensors are placed (penetrating into the specimen) uniformly within the sample in order to keep track of the temperature profile during the test. There is also a supply of water from the sample bottom, so that the water can be drawn from the surroundings to the frost front. Displacements (due to heaving) are recorded by means of a displacement transducer (LVDT) located at the top of the sample. All measurements (temperature data, water intake and displacements) are recorded by means of a data acquisition system during the test which is connected to a computer for further analyses.

3.2 Soil Properties

The same type of soil (sandy silt) has been used under different temperature boundary conditions during freezing tests. The particle size distribution (psd) of the soil is given in Figure 6.

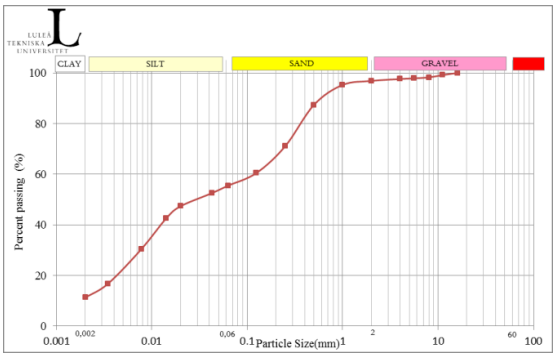


Figure 6 Particle size distribution of the soil tested

The main intention of using the soil which is characterized by the particle size distribution curve in Figure 6 is to conduct freezing tests on a relatively frost susceptible soil. Based on the psd and the silt content it can be concluded that the soil exhibits some degree of frost susceptibility. The specific gravity (G_s) of the soil was 2.68.

3.3 Testing Procedure

All tests have been conducted on disturbed samples. Soil samples were prepared by means of hand compaction in the test cell (cylindrical cell with ϕ=10cm) by compacting five equal layers of soil to a sample height of about 10cm. As a natural outcome of the compaction method, all the samples had porosity values of about n=0.38.

In order to avoid problems of redistribution of water during freezing within the specimen and to make analyses relatively easier all tests have been conducted under saturated conditions. Samples were saturated by allowing water movement from the bottom of the sample to the top; under very low hydraulic gradients in order to prevent particle sorting within the sample.

Once the samples were saturated, they were brought to a steady state thermal equilibrium where the temperatures are constant (within the range of 3-5 ^{0}C) along the specimen. After the steady state phase, cold temperatures were applied on the sample top while keeping the temperature at the sample bottom constant at +3-4 ^{0}C. The freezing phase usually takes 4 days in order to ensure that there is sufficient time for water intake, development of a thermal equilibrium and formation of ice lenses. During the freezing phase there is free access to water (open system).

In addition, another freezing test with varying temperature boundary conditions has been conducted for comparison purposes. For this test different freezing temperatures have been used. Similar to the case described above, the soil was frozen with a fixed temperature on top and enough time was allotted for the

sample to reach steady state conditions and for the water to be drawn to the frost front. At this point the temperature at the top of the specimen was further reduced to an even lower value to create a new freezing condition. Again, enough time was given for the sample to reach steady state and for water to be drawn to the frost front. The aim with this kind of freezing was to make the tests less time consuming as suggested by Penner (1972).

Temperature boundary conditions for different tests are given in Table 1. Typical plots of the temperature data (steady state + transient freezing phases) and displacements from all tests are given in Figure 7 and Figure 8.

Table 1 Summary of the experimental procedure

Test Type		Cold End Temp. (^{0}C)	Warm End Temp. (^{0}C)	Sample Height (cm)
Single Gradient		-3.2	3.5	10
Multiple Gradients	Step #1	-1.4	2.4	10.2
	Step #2	-2.4	2.4	10.2
	Step #3	-3.4	2.4	10.2
	Step #4	-4.4	2.4	10.2

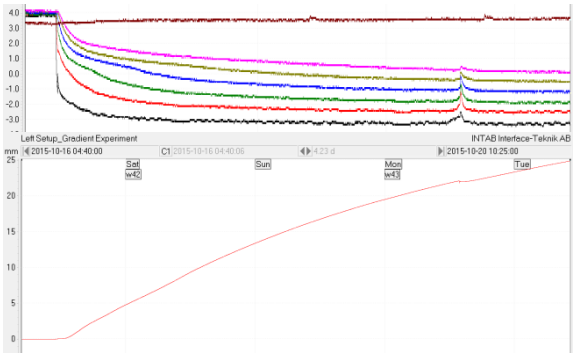
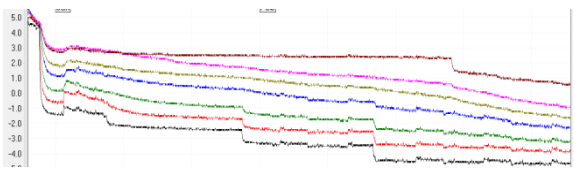


Figure 7 Temperature and displacement data for the single gradient freezing test



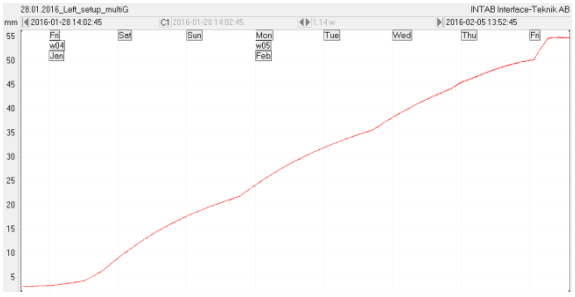


Figure 8 Temperature and displacement data for the multiple gradient freezing tests

4 ANALYSIS RESULTS

In order to establish the relationship between heave and net heat extraction rates for different tests conducted under different temperature gradients, series of theoretical analyses were done. These can be grouped under three categories:

- Calculation of frost depth and frost penetration rate
- Evaluating heave and dividing heave into two parts, namely, "in-situ" heave (due to freezing of pore water) and "segregational" heave (due to water being sucked to the frozen front).
- Calculation of net heat extraction rate at the frost front.

Each of these analyses is treated under its respective section. For the sake of simplicity, the analyses of results for one of the tests have been described in detail. It should be noted that the analyses results given in the forthcoming sections are qualitative, not quantitative. In other words, the accuracy of the numbers is not the primary concern. Therefore, the aim here is to establish a theoretical relationship between heave and net heat extraction rates.

4.1 Calculation of Frost Depth and Frost Penetration Rate

Based on the temperature data given in Figure 7, it is possible to keep track of the frost (0 ^{0}C) line. This is done by comparing temperature readings between two adjacent thermocouples and locating the position of the frost line by means of interpolation (see Figure 9). Figure 9 shows that for results

given in Figure 7 frost line penetrates roughly 8.5 cm into the sample.

The main reason for the downward spike (around *t=75h*) in Figure 9 is the minor disturbance recorded by the thermocouples. This is mainly due to an insulation problem around the sample for a very brief moment and has been fixed immediately during the test. It can be seen in Figure 7 that the readings have returned back to their previous values. Thus, the disturbance is believed to have a negligible effect on the results overall.

By fitting a line into the frost depth vs. time plot and taking the derivative, one can obtain rate of frost penetration. This is done in Figure 9 and Figure 10.

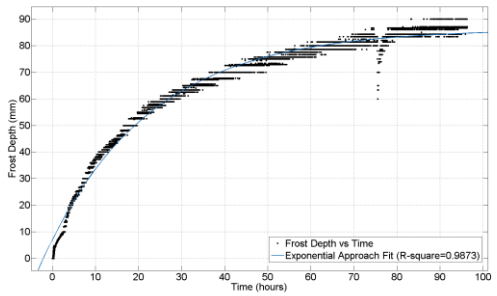


Figure 9 Curve fitting for the frost depth vs. time plot

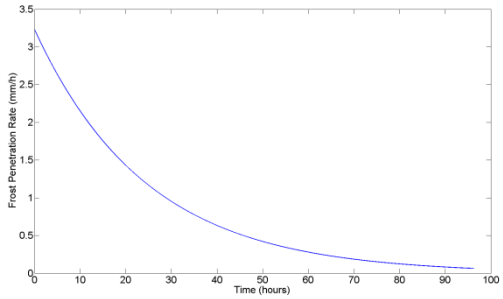


Figure 10 Frost penetration rate vs. time

As expected, the rate of frost penetration is largest at the beginning of the experiment and gradually reduces down to an almost zero value, indicating stationary frost front conditions have been reached towards the end of the experiment.

4.2 Evaluation of Heave

In order to make the analyses as detailed as possible, the total displacement (due to heaving) recorded by LVDT is sub-divided into two components. This can be done in two ways:

- Calculation of "in-situ" heave based on frost penetration rate; which is then subtracted from total heave to obtain "segregational" heave.
- Calculation of "segregational" heave based on water intake measurements; which is then subtracted from total heave to obtain "in-situ" heave.

Due to unexpected problems with the water intake measurement system the first approach was chosen.

For an open system freezing experiment the total heave rate consists of two components and can be calculated as follows:

$$\frac{dh}{dt} = \underbrace{0.09n\frac{dz}{dt}}_{\substack{\text{in-situ} \\ heave\ rate}} + \underbrace{1.09v}_{\substack{segregational \\ heave\ rate}} \quad (1)$$

Where n is porosity, $\frac{dz}{dt}$ is the rate of frost penetration (mm/h) and v (mm/h) is the water intake velocity. Thus, heave rate only due to freezing of pore water can be calculated as:

$$\frac{dh_i}{dt} = 0.09n\frac{dz}{dt} \quad (2)$$

Based on the expression above, the plot of in-situ heave rate vs. time is given in Figure 11.

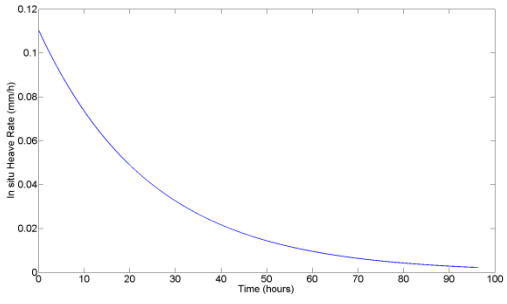


Figure 11 In-situ heave rate vs. time

Integrating the plot given in Figure 11, one can obtain the heave (mm) due to freezing of pore water. If this is then subtracted from the total heave, it is possible to obtain segregational heave, see Figure 12 and Figure 13.

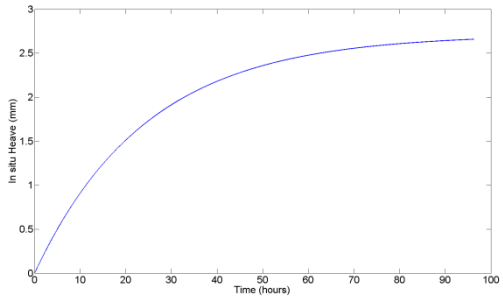


Figure 12 In situ heave vs. time

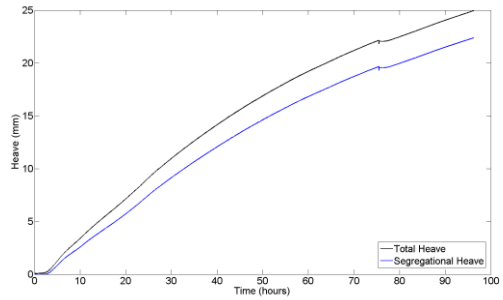


Figure 13 Separation of segregational heave from total heave

Figure 13 is important for two aspects: First, it allows for further treatment of the segregational heave curve to obtain segregational heave rate and water intake velocity. Secondly, it demonstrates the significance of segregational heave. By looking at Figure 13, it is possible to infer that a very large portion of total heave is due to the freezing of water that has been drawn to the freezing front from surroundings.

If a curve is approximated for the segregational heave plot given in Figure 13, it is possible to obtain the segregational heave rate. However, there is one important step that should not be overlooked while doing so. Although it might be tempting to approximate the plot with a single exponential function, doing this will result in a significant flaw for the rest of the analyses. An attempt to clarify this is made in Figure 14 and Figure 15.

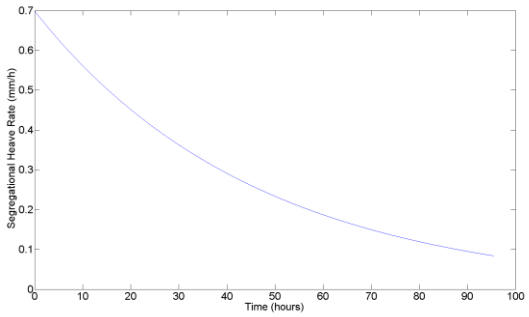


Figure 14 Calculation of segregational heave rate based on a single exponential curve fit

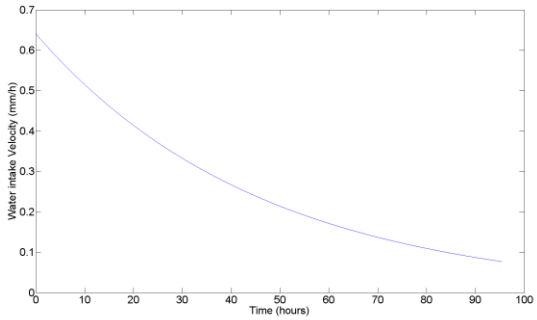


Figure 15 Water intake velocity vs. time plot calculated based on a single exponential curve fit

Figure 14 and Figure 15 would have been obtained if one took the derivative of the exponential function that has been fit to the segregational heave plot in Figure 13. The problem becomes more apparent upon closer inspection of Figure 15. Water intake velocity can be calculated simply dividing segregational heave rate by 1.09 (see Equation 1). However, it does not physically make sense to start with a relatively high value of water intake velocity at the very beginning of the experiment. One would ideally expect the water intake velocity to start from zero at the beginning of an experiment.

The fact that the water intake data should start from zero suggests that the segregation heave curve given in Figure 13 should at least be approximated by two different curves. Thus, in an attempt to estimate the segregational heave rate, segregational heave curve has been approximated by two different fits. The results are given in Figure 16 and Figure 17.

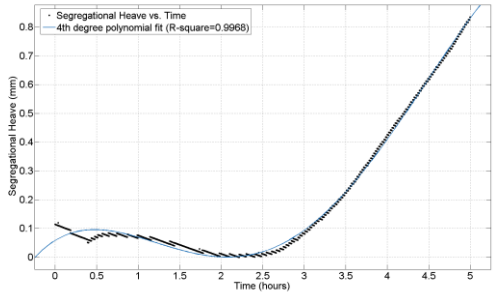


Figure 16 Approximation for the beginning stages of segregational heave curve

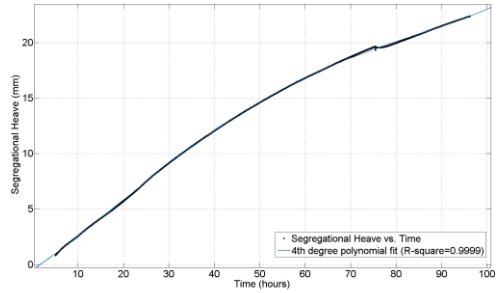


Figure 17 Approximation for the second part of segregational heave curve

Figure 16 demonstrates that the segregational heave rate increases quite rapidly at the very beginning stages of an experiment (during the very first hours of experiment). Later on, the rate of segregational heave reduces gradually. The rate of change in segregational heave can be represented by the plot given in Figure 18.

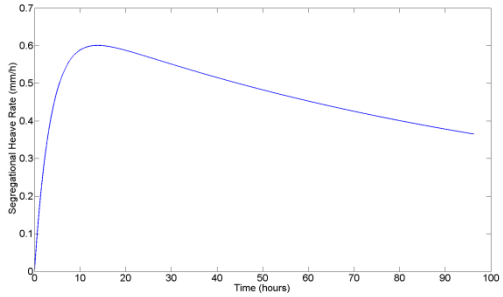


Figure 18 Segregational heave rate vs. time

Figure 18 is generated by taking the derivative of the two curves fit to two parts (Figure 16 and Figure 17) of the segregational heave curve. The derivative functions have then been merged under one plot and approximated by a single curve. There is no doubt that some accuracy has been lost during these approximations, however, the general appearance of the plots (or the trends) still hold true.

Finally, the water intake curve can be obtained dividing segregational heave rate by 1.09. This is given in Figure 19.

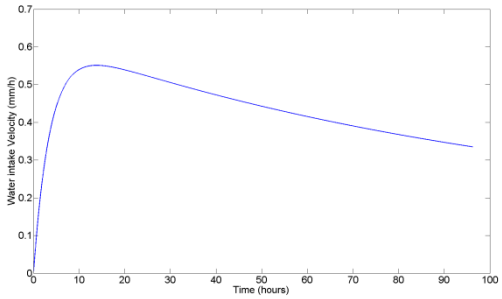


Figure 19 Water intake velocity vs. time

4.3 Calculation of Net Heat Extraction Rate

Having calculated the frost penetration rate and the water intake velocity, one can calculate the net heat extraction rate. The expression to calculate the net heat extraction rate is as follows:

$$q_z = Ln\frac{dz}{dt} + Lv \qquad (3)$$

Where, q_z is the net heat extraction rate (W/m^2) and L is the volumetric latent heat of water (J/m^3). Based on this, variation of net heat flux during the experiment is given in Figure 20.

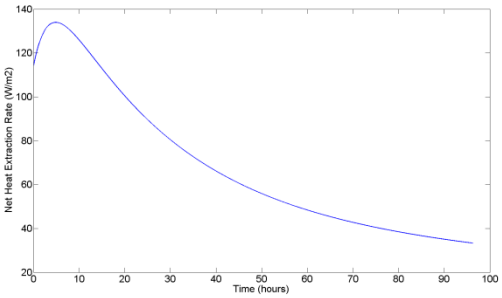


Figure 20 Net heat extraction rate vs. time

With all parameters obtained, the relationship between heave and net heat extraction rates can now be established. This relationship between net heat flux vs. segregational and total heave rates are plotted in Figure 21 and Figure 22, respectively.

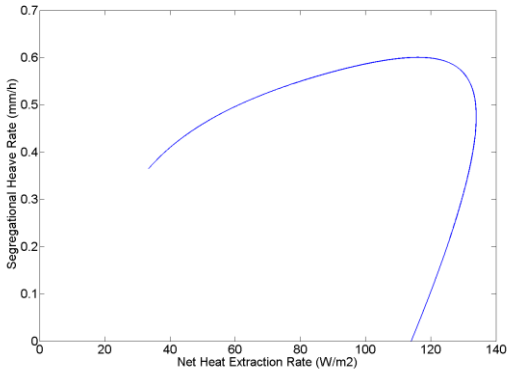


Figure 21 Relationship between segregational heave and net heat extraction rate

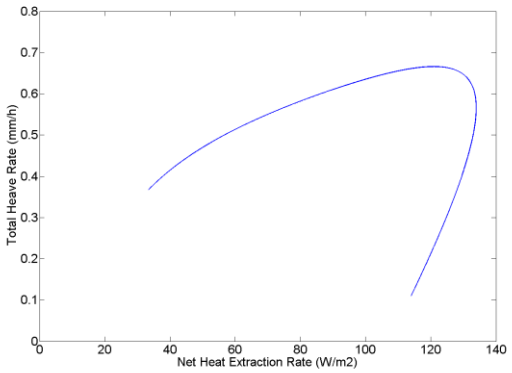


Figure 22 Relationship between total heave and net heat extraction rate

Similarly, the results of the multiple temperature gradient experiments are plotted in Figure 23. Unfortunately, only step numbers 2 and 3 in Table 1 could have been evaluated as the rest of the data were disturbed by outside factors.

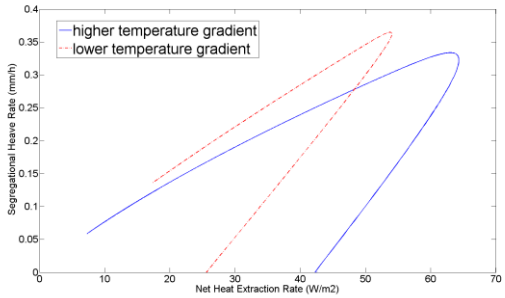


Figure 23 Relationship between segregational heave and net heat extraction rate

5 DISCUSSION

Figure 21, Figure 22 and Figure 23 are somewhat unconventional in the sense that the beginning of the experiment is represented by the data point located at the bottom right of the net heat extraction rate axis. This can be better understood by the help of Figure 20 as the higher rates of heat extraction takes place at the beginning of the experiment and decreases gradually as the test goes on. Keeping this in mind, it can be deduced that higher extraction rates do not always necessarily give the highest heave rates. Furthermore, there seems to be a peak where the highest rate of heave occurs. Increasing the rate of heat removal beyond this point has a negative impact on the heave rate.

The general plot trends obtained in Figures 21, 22 and 23 are also important for discussion. A quick comparison between these figures and Figure 3 (Konrad, 1987) reveals that their shapes are somewhat distorted and gives the impression that the soil might experience different heave rates for a fixed value of heat extraction rate in the early stages of an experiment. It should be pointed out that the shapes of these plots are heavily influenced by their respective water intake vs. time (see Equation 3) curves. For example, in Figure 19 the peak is occurring around the 10 hour mark. If this was happening at a later point (say, 20 hours for instance) the shapes of Figures would have been a lot similar to what one would usually call “normal”. Due to the problems in the water intake measurement system at the time, the authors had no means of accurately determining the location of this peak. Existence of the peak is intuitive, but its location is heavily influenced by the back calculation procedure. As a result, the accuracy of the beginning phases of these plots is affected significantly.

The distinction between the terms *higher* and *lower* thermal gradients that appear in Figure 23 can be better understood with the help of Figure 24. In Figure 24 approximate temperature profiles along the frozen part of the soil body at the end of each testing step is plotted. The initial location of the frost front at the beginning of step #2 experiences a temperature change of ΔT_2 during that step. Similarly, the initial location of the frost front

at the beginning of step #3 experiences a temperature change of ΔT_3 during that step. Since the penetration of the frost line is almost identical between these two steps, it can be concluded that the rate of heat extraction is greater for the second step than that of the third.

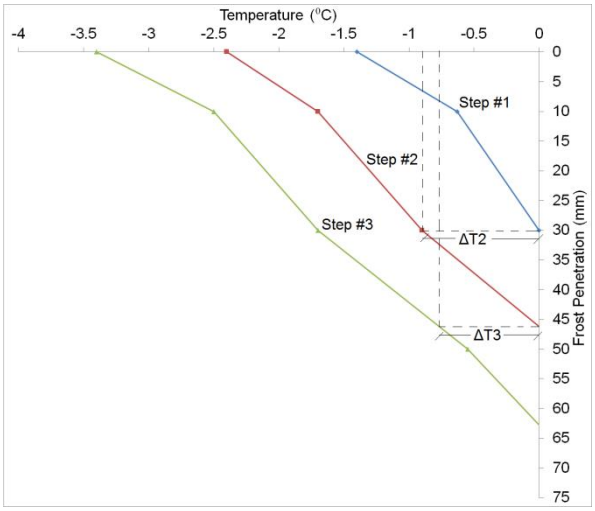


Figure 24 Frost penetration and temperature profiles for multiple gradient tests

Moreover, in Figure 23 there are also some hints that the same type of soil is experiencing similar heave rates for a given rate of heat extraction located at the left side of the peak. The plots get even closer with decreasing heat extraction rates. It is also worth noting that the peaks are located remarkably close to each other. However, more experimental work with a larger variety of thermal gradients needed here to reach more solid conclusions.

Finally, the heat extraction required to freeze a completely unfrozen sample (single gradient experiment) is anticipated to be much higher than the heat extraction required to further freeze down an already partially-frozen sample (multiple gradient experiments) and this is thought to account for the large difference in the range of net heat extraction rate values between Figure 21 and Figure 23.

6 CONCLUSIONS & FUTURE WORK

A theoretical analysis of the relationship between heave and net heat extraction rates has been carried out based on experimental data. It was expected and, to a degree, was shown that segregational heave might come to a halt for relatively high heat extraction rates. For such rates, heave is purely due to freezing of "in-situ" (or pore) water as there is not enough time for the water to be drawn to the freezing front since the frost front is penetrating quite rapidly.

Detailed analyses demonstrated the importance of accurately keeping track of the water intake during experiments. It is essential to be able keep track of the water intake more precisely in order to draw more solid conclusions. Not meeting this criterion was shown to influence the accuracy of the relationship between segregational heave and the net heat extraction rates due to the back-calculation procedure.

Keeping these in mind and considering the similarities between the trends seen in Figure 23, the focus will be on improving the water intake measurement system and continue investigating the relationship between segregational heave and net heat extraction rate as the future work.

7 ACKNOWLEDGEMENT

Authors would like to express their gratitude to Swedish Transport Administration (Trafikverket) for the financial support of the research project within the research programme BVFF. In addition, the invaluable support provided by our colleagues, Prof. K. Kujala, V. Pekkala and T. Pitkänen, at the University of Oulu is greatly acknowledged.

8 REFERENCES

Beskow, G. (1935). Soil freezing and frost heaving with special application to roads and railroads. Swedish Geol. Soc., Series C, No. 375.

Cold Room Studies- Third Interim Report U.S. Army, Corps of Engineers. Tech. Rept. 43. 1958.

Hermansson, Å. (1999). A New Simple Frost Model, Validated and Easy to Use, Proc. Tenth International Conference on Cold Regions engineering, Lincoln New Hampshire USA, August 16 - 19, 1999, (Ed.: Jon E. Zufelt), ASCE, Reston Virginia USA, pp. 199 – 210.

Horiguchi, K. (1978). Effects of the rate of heat removal on the rate of frost heaving. Proceedings of the International Symposium on Ground Freezing, Ruhr-University, Bochum W. Germany, pp. 25 - 30.

Ito, Y., Vinson, T. S., Nixon, J. F. & Stewart, D. (1998). An Improved Step Freezing Test to Determine Segregation Potential. Proceedings of the International Conference on Permafrost. Yellowknife Canada, Collection Nordicana No 55.

Kaplar, C. W. (1970). Phenomenon and Mechanism of Frost Heaving. Highway Research Record 304, pp. 1 - 13.

Konrad, J. M. (1987). The Influence of heat extraction rate in freezing soils. Cold Reg. Science & Technology, 14: 129-137.

Loch, J.P. G. (1977). Frost Heave Mechanism and the Role of the Thermal Regime in Heave Experiments on Norwegian Silty Soils. Norwegian Road Research Laboratory, Meddelelse nr. 50.

Loch, J.P.G. (1979). Influence of the heat extraction rate on the ice segregation rate of soils. Frost i Jord, 20: 19-30.

Mitchell, J. K. (1976). Fundamentals of Soil Behavior. New York: Wiley.

Penner, E. (1972): Influence of Freezing Rate on Frost Heaving. Highway Research Record, No. 393. pp. 56 - 64.

Zeinali, A., Dagli, D. & Edeskär, T. (2016). Freezing-Thawing Laboratory Testing of Frost Susceptible Soils. Proceedings of the 17th Nordic Geotechnical Meeting. Reykjavik Iceland.

Preloaded Road Embankments: monitoring and analysis of results

T. Damtew, M. S. Sani
Norwegian Public Roads Administration, Norway,
tseday.damtew@vegvesen.no, murad.sayd@vegvesen.no

A. K. Anthi, T. H. Johansen
Norwegian Public Roads Administration, Norway,
aina.anthi@vegvesen.no, tor-helge.johansen@vegvesen.no

ABSTRACT
The county road, fv. 115 between Vamma and Ringnesdalen, is a 2,5km road, which was constructed in the period 2011 to 2013. The alignment for the road included large embankment fills at three parts of the road.
The construction manager for this project called for geotechnical solutions that were cost effective. In addition, the project had a flexible time frame for the construction of the road. The roads and geotechnics department at the Norwegian Public Roads Administration (NPRA) performed the geotechnical design for this project. Preloading with surcharge the same as planned embankment and with additional 30% weight of embankments were recommended as a solution for solving settlement issues at four sections of the road. The lengths of these four sections are 75, 40, 80 & 100 m and the heights of planned embankments varied from 5 - 13m.
The preloaded embankments were instrumented with a settlement monitoring system. The project has registered settlement results frequently for the first year of construction of the embankments and supplemented with sporadic measurements for two more years.
Settlement calculations were compared to results from field measurements. Calculated settlements are found to be well comparable to measured settlements. Hence it is concluded that estimation of deformation parameters was relatively accurate for the modelled embankments.
The planned preloading was effective in speeding up the settlement at all modelled sections and served its purpose as expected.

Keywords: Preloading, Settlement, Monitoring, Embankment, Oedometer

1 INTRODUCTION

The county road, fv. 115 between Vamma and Ringnesdalen, is a 2.5 km road, which is part of a road network that connects four towns in the eastern region of Norway.
The road alignment was designed with large embankment fills at four different sections of the road. The construction manager for the project needed to minimize the cost of construction in order to realize the project. Hence, the project opted for low cost geotechnical solutions.

One of the project's geotechnical challenges was to limit settlement with in required limits given on NPRA's standard N200.
The project decided to utilize preloading for mitigation of settlement instead of utilization of lightweight materials in embankments.
Four representative sections were selected and used both for calculation of settlement and monitoring during construction of the road. The sections are named after the road chainage, called 940, 1250, 1800 and 2100.

2 SETTELMENT MONITORING

The profiler of the type Consoil is used to measure settlement during construction of embankments. The profiler consists of a probe and a hydrostatic instrument that measures the depth of its probe.
The probe is pushed through a conduit that is installed just under the terrain along a cross section of the road.
The elevation of the conduit is controlled just after the installation as well as during each and every settlement measurement.
Settlement measurements are made at each meter along the length of the conduit.



Figure 1 Installation of conduit for settlement



Figure 2 Settlement measurement by a profiler

3 DESIGN SECTION - 940

The embankment modelled by the section 940 is 75 m long. The section is chosen because of underlying relatively thick compressible soil and hence expectation of considerable settlement.

The figure below shows the cross section with planned embankment as well as estimated depth to rock.

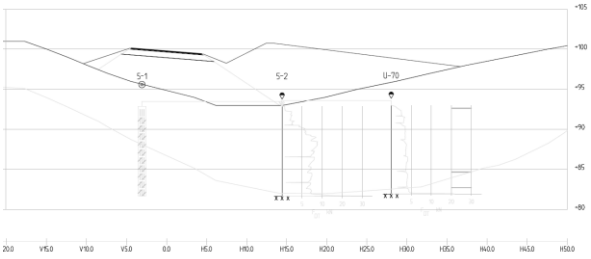


Figure 3 Cross section at chainage 940

3.1 General Soil Properties

The foundation soil consists of thick sea sediments. The soil is classified to be medium sensitive silty clay to clay. The shear strength interpreted to be in the range of 30 – 40 kPa. The shear strength is interpreted from routine laboratory investigation as well as field investigation.

3.2 Deformation Parameters

Oedometer tests of the type CRS (Constant Rate of Strain) were performed on undisturbed samples from Φ 54mm sampler. Two successive sets of specimen were taken at approximately 3.7 and 6.6 m.

A table is given below with our interpretation of deformation parameters from the oedometer test results. The oedometer stiffness (M_{OC}) for both parameter sets is estimated to be 8 Mpa and 5 Mpa for the layers 0-4 m and 4-11 m respectively.

Table 1 Interpreted deformation parameters 940

Parameter set 1					
Depth / Soil layer (m)	σ'_c (kN/m^2)	m (-)	m_{cv} (m2/yrs*kPa)	C_{vOC} (m2/yrs)	C_{vNC} (m2/yrs)
3,7 / (0-4)	140	53	0,08	16	10
6,6 / (4-11)	160	30	0,08	18	12
Parameter set 2					
Depth / Soil layer (m)	σ'_c (kN/m^2)	m (-)	m_{cv} (m2/yrs*kPa)	C_{vOC} (m2/yrs)	C_{vNC} (m2/yrs)
4,0 / (0-4)	140	38	0,05	17	16
6,9 / (4-11)	160	25	0,04	26	25

3.3 Settlement Calculation Results

Settlement was calculated by the software *GeoSuite – Settlement* and by simple Excel based hand calculations.

Calculations were made at section 940 with the deformation parameters presented on Table 1. Results from settlement calculations are presented on figure 4 and 5 below. Calculated settlements are 28cm and 31cm, whereas the time for the preliminary settlement are 4 year and 3.5 year.

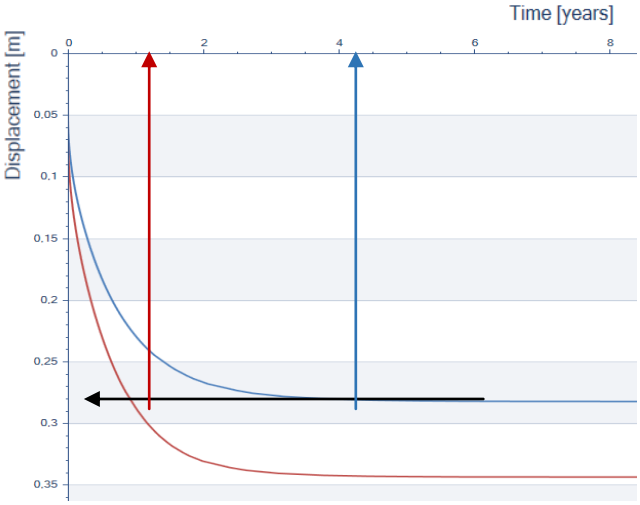


Figure 4 Deformation–time plot_ parameter set 1

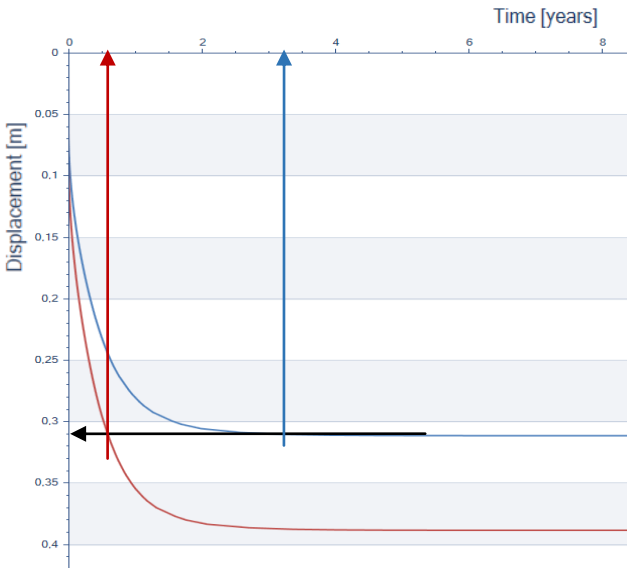


Figure 5 Deformation–time plot_ parameter set 2

The blue curves in *Figure 1* & *Figure 2* indicate settlement for planned embankment. Whereas the red ones show settlement development with a preloading of 30% of the weight of the embankment. As observed on the above two figures the time for settlement is quartered after preloading.

3.4 Field Measurement

The field measurement included monitoring of settlement as well as pore water pressure.

The settlement was measured at section 935 while piezometers were installed at section 920 and 940.
The results from the field measurement are presented in figures 6 - 8.

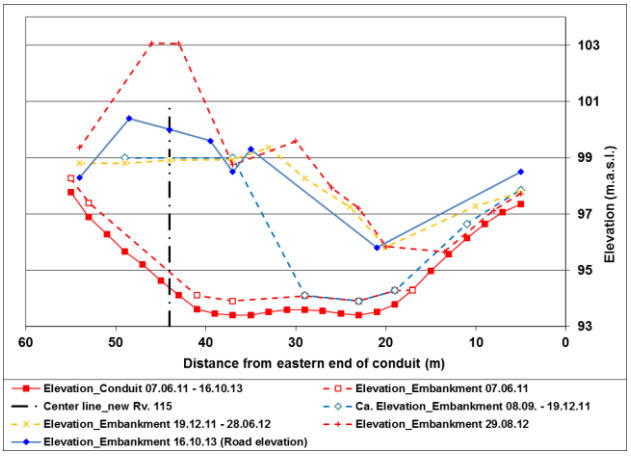


Figure 6 Elevation measurements, section 935

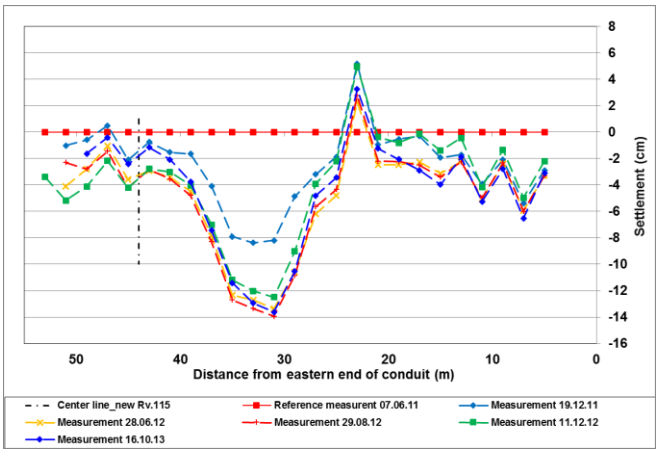


Figure 7 Settlement measurements, section 935

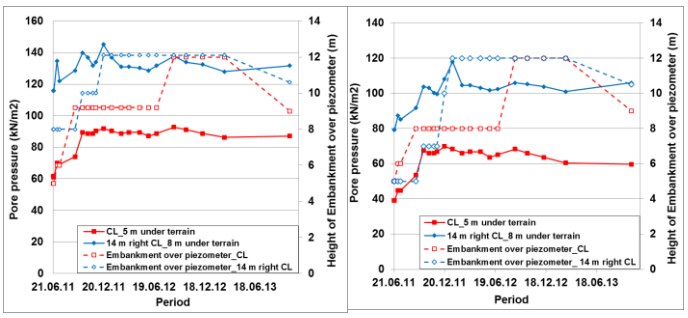


Figure 8 Pore pressure - Section 920 and 940

3.5 Comparison

Calculated settlement values for the two sets of parameters are comparable.
Calculated and measured settlement did not correspond with each other. Therefore, the effect of the preloading was checked by following the pore pressure results.

The reason for lesser settlement values (maximum 14cm) in comparison to the calculated ca. 30 cm settlement could be due to combination of construction of lower embankment as well as the estimation of deformation parameters.
In order to separate these effects further calculation was made with the new geometry for the embankment. The new calculation resulted in a settlement value of 20cm, which is quite comparable to the measured 14 cm value.

4 DESIGN SECTION - 1250

This embankment has a length of 40 m. Design section is chosen at chainage 1250. The figure bellow shows a cross section at 1250.

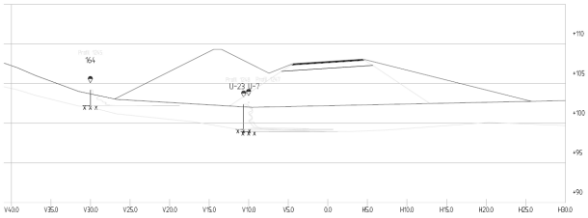


Figure 9 Cross section at chainage 1250

4.1 General soil properties

The soil properties at this cross section are similar to 940.

4.2 Deformation Parameters

CRS oedometer tests were performed on undisturbed sample from Φ 54mm sampler. Two specimen were taken at approximately 1.8 and 2.7 m. The test from 1.8 m was discarded because of poor quality of results. A table is given below with interpreted deformation parameters from the oedometer test result. The oedometer stiffness (M_{OC}) is estimated to be 6 Mpa.

Table 2 Interpreted deformation parameters 1250

Depth / Soil layer (m)	σ'_c (kN/m^2)	m (-)	m_{cv} (m2/yrs*kPa)	C_{vOC} (m2/yrs)	C_{vNC} (m2/yrs)
2.7 / (0-4)	160	20	0,03	20	12

4.3 Settlement Calculation Results

Settlement was calculated by the software *GeoSuite – Settlement* as well as by simple Excel based calculations.

The calculation result is presented on the figure below. Calculated settlement value is ca. 8 cm and the time for preliminary settlement is approximately 7 months.

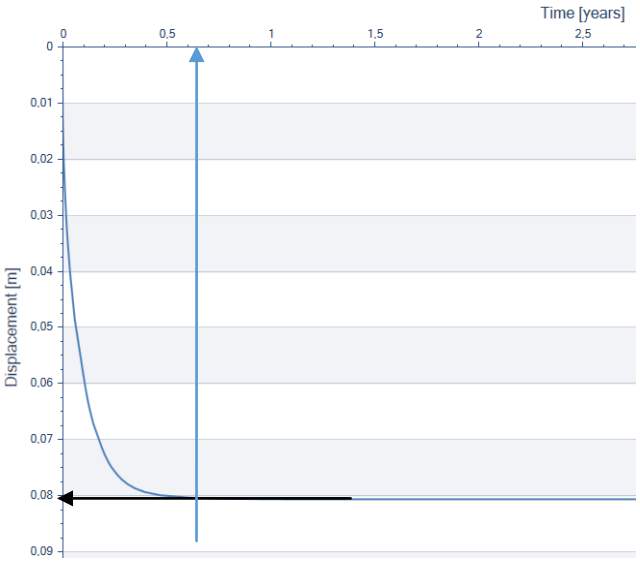


Figure 10 Deformation – time plot, section 1250

4.4 Field Measurement

Settlement and water pressure weremonitored for this section. Both settlement and pore water pressure were measured at 1250. Field measurements are presented below in figure 11 – 13.

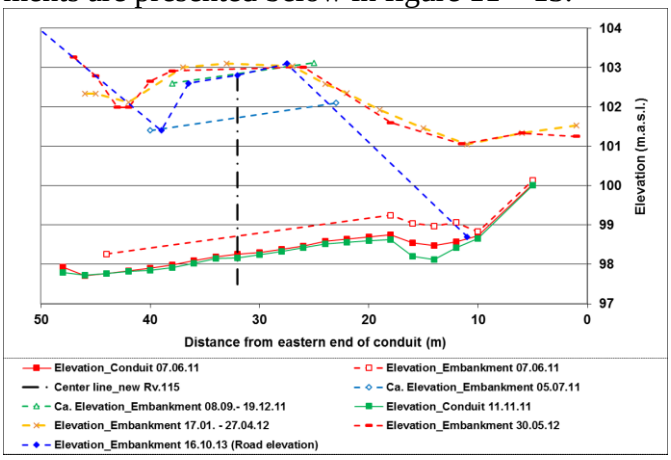


Figure 11 Elevation measurements, section 1250

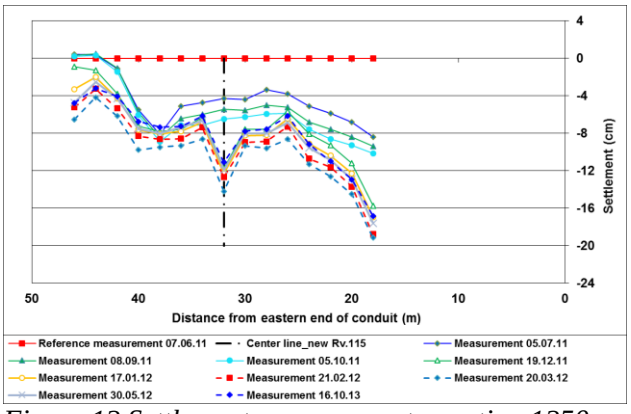


Figure 12 Settlement measurements, section 1250

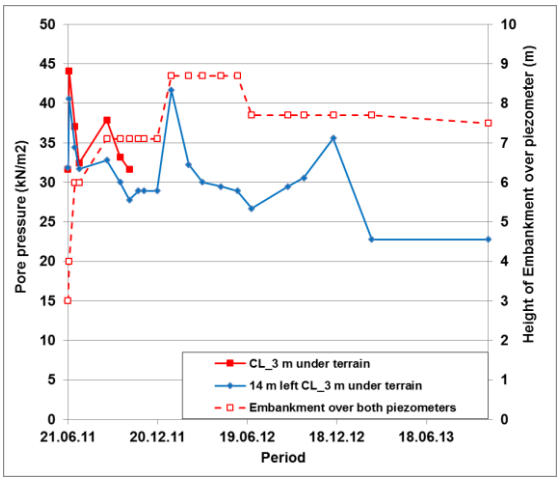


Figure 13 Pore pressure, section 1250

4.5 Comparison

Calculated settlement matched well with the measured settlement. Measured settlement just after the opening of the road is between 8 and 10 cm along the cross section 1250.
Pore water pressure measured at the same time is as expected i.e. a hydrostatic pressure at 3 m depth.

5 DESIGN SECTION - 1810

The embankment modelled by the section 1800 is 80 m in length.

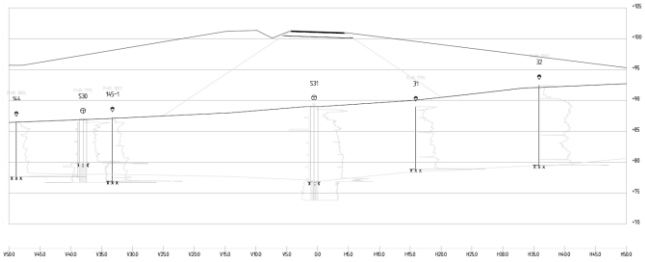


Figure 14 Cross section at chainage 1800

5.1 General Soil Properties

The foundation soil consists of thick sea sediments. The soil is classified as medium sensitive silty clay to clayey silt. The bedrock is 12 m below terrain level.
The undrained shear strength is interpreted to be in the range of 20 – 40 kPa. The shear strength is interpreted from routine laboratory investigation as well as field investigation.

5.2 Deformation Parameters

CRS oedometer tests were performed on undisturbed Φ 54 mm piston samples. Two successive sets of specimen were taken at depth approximately 3.7 and 6.6 m below the terrain level.
A table below is given with interpretation of deformation parameters from the oedometer test results. The oedometer stiffness (M_{OC}) is estimated to be 3 Mpa.

Table 3 Interpreted deformation parameters 1810

Depth / Soil layer (m)	σ'_c (kN/m^2)	m (-)	m_{cv} (m2/yrs*kPa)	C_{vOC} (m2/yrs)	C_{vNC} (m2/yrs)
3,7 / (0-4)	100	31	0,01	2.5	2
6,6 / (4-11)	200	25	0,01	3	2,5

5.3 Settlement Calculation Results

GeoSuite calculations were made at section 1810 with the deformation parameters presented on *Table 3*. The height of the embankment is about 13 m, which corresponds to a surcharge of 260 kPa.
The result from settlement calculation is presented on the figure below. Calculated settlement is about 65 cm, where approximately 13 years is needed for the preliminary settlement.

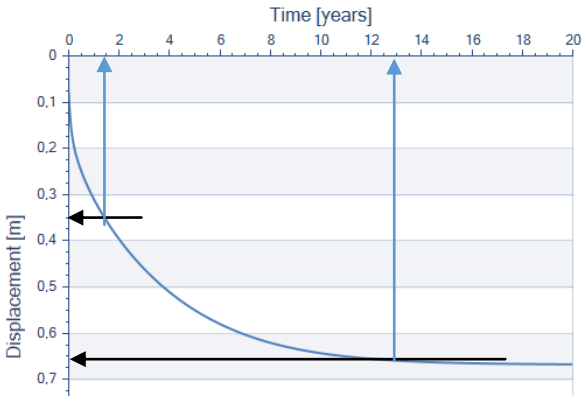


Figure 15 Deformation – time plot, section 1800

Section 1800 was preloaded with the road embankment height. According to NPRA's standard, allowable settlement difference along the road dictates an acceptable maximum settlement of 30cm for the section. Hence as observed on the figure above, it was decided to preload the section for ca. one and a half year.

5.4 Field Measurement

The field measurement included monitoring of settlement as well as pore water pressure.

The settlement was measured at chainage 1810 while piezometers were installed at chainage 1800.
The results from the field measurement are presented in figures 16 - 18.

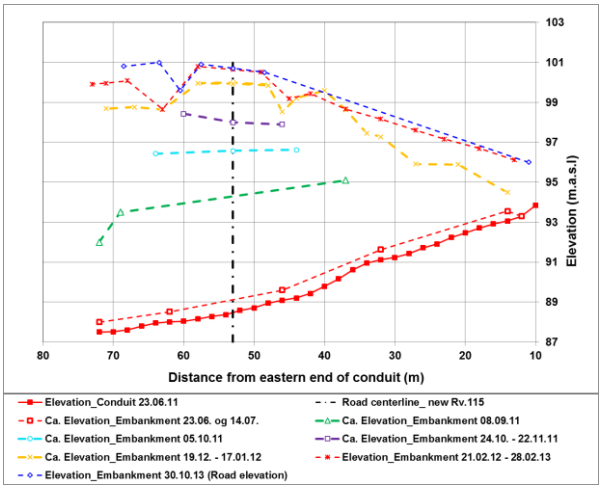


Figure 16 Elevation measurements, section 1800

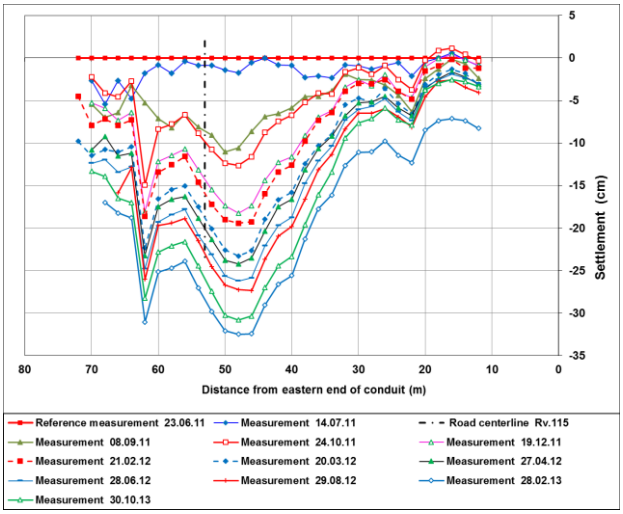


Figure 17 Settlement measurements, section 1810

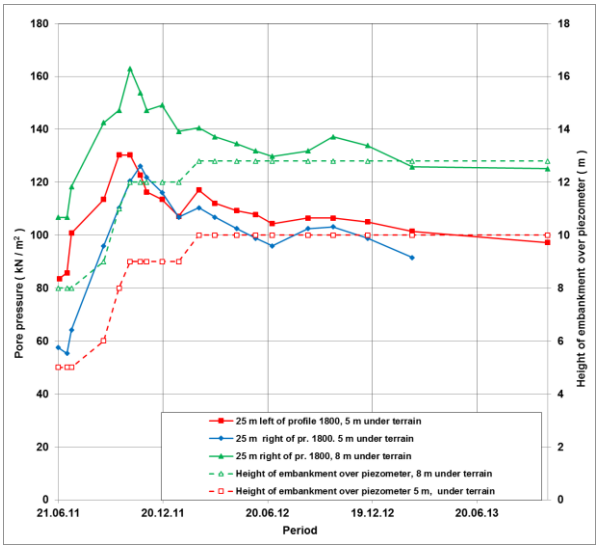


Figure 18 Pore pressure, section 1800

5.5 Comparison

Expected settlement was reached with in the predicted period. Calculation results matched well with measured field results.

6 DESIGN SECTION - 2110

The embankment modelled by the section 2110 is 100 m in length. A representative section is presented on the figure below.

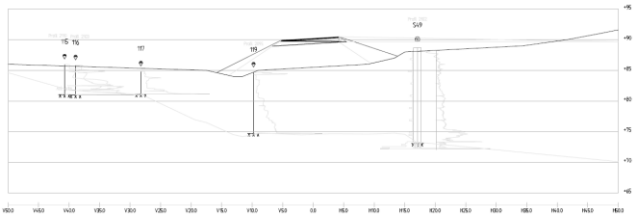


Figure 19 Cross section at chainage 2100

6.1 General Soil Properties

The foundation soil consists of medium sensitive, silty clay and clayey silt. The crust is classified as stiff sandy silt.
The undrained shear strength is interpreted to be in the range of 30 – 50 kPa. The bedrock varies 10-15 m below terrain level. The shear strength is interpreted from routine laboratory investigation as well as field investigation.

6.2 Deformation Parameters

Deformation parameters used for estimation of settlement are interpreted partly from cone penetration tests (CPTU) and partly from assumptions based on earlier experience. Interpreted deformation parameters are presented on the table given below.

Table 4 Interpreted deformation parameters 2100

Depth / Soil layer (m)	σ'_c (kN/m^2)	m (-)	**M** (kN/m^2)	C_v (m^2/yrs)
1-6	$\sigma_o' + 1/2*\Delta\sigma$	20	4000	4
6-12	$\sigma_o' + 1/2*\Delta\sigma$	20	4000	4

6.3 Settlement Calculation Results

Settlement calculation were made with NPRA's Excel based calculation sheet. The height of the embankment is about 4.5m, which corresponds to a surcharge of 90 kPa. Results from settlement calculation is presented on the figure below. Calculated

total settlement is about 37 cm. Time for preliminary settlement is 20 years.

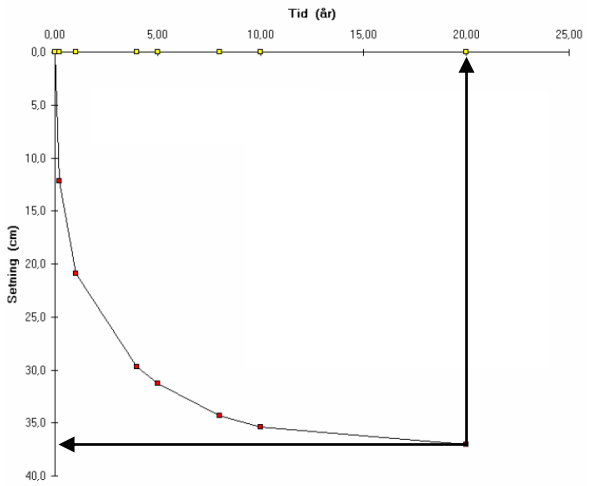


Figure 20 Deformation – time plot, section 2100

NPRA's standard limits acceptable settlement to approximately 8 cm at this road section. The geotechnical design suggested 30% or 50% of embankment height as preloading, which will speed up the time for settlement. In order to fulfil the requirement for acceptable differential settlement the section needed to settle ca. 29 cm. This would take 17 and 11 months respectively for the proposed preloading surcharges.
The magenta and red curves shown on figure 21 represent settlement developments for 30% and 50% preloading. The blue curve is the same as the first part of the settlement curve presented on Figure 20.

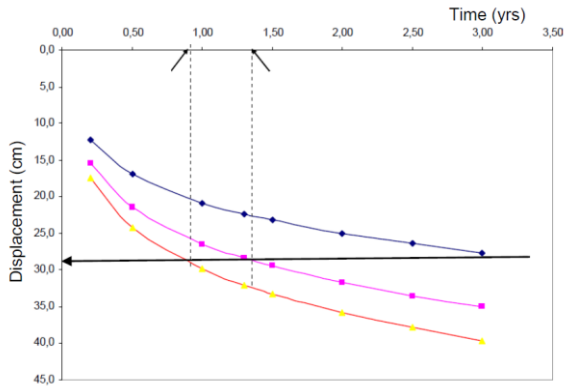


Figure 21 Elevation measurements, section 2110

6.4 Field Measurement

The field measurement monitored both settlement and pore water pressure. Settlement was measured at chainage 2110 while piezometers were installed at chainage 2110 and 2170.

The preloading used along this road section is about 4 m high, which is almost 90 % of the road embankments height. And the duration for the preloading was about 8 months.

The results from the field measurement are presented in Figure 22 – 24.

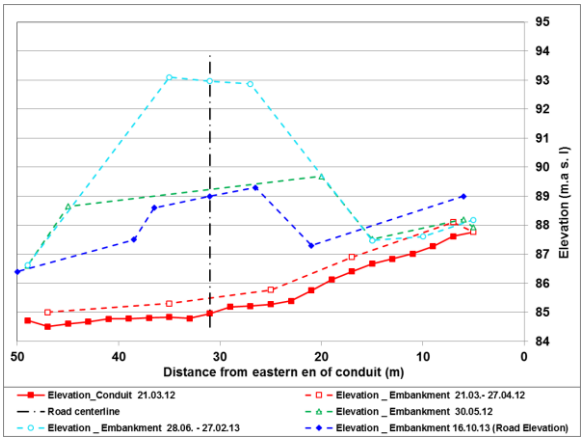


Figure 22 Elevation measurements, section 2110

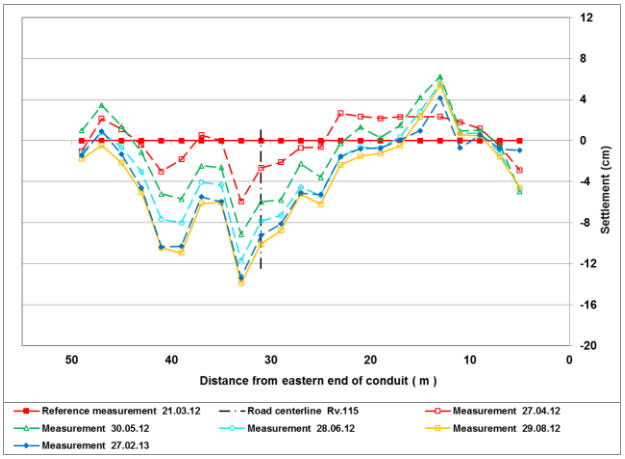


Figure 23 Settlement measurements, section 2110

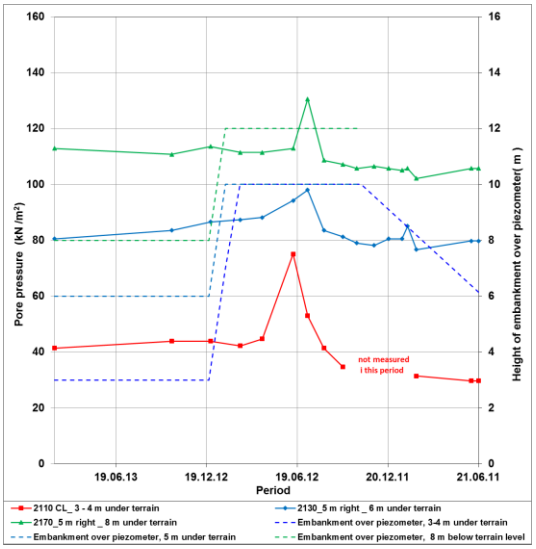


Figure 24 Pore pressure, section 2110 and 2170

6.5 Comparison

Calculated and measured settlement did not correspond with each other. The discrepancy can majorly be accredited to the choice of deformation parameters. In addition the preloading was not constructed as designed. Therefore only pore water pressure measurements were used in deciding when to remove the preloading.

7 CONCLUSION

Measured settlement corresponded well with calculated one for the first three sections where the deformation properties were interpreted from oedometer tests. Deformation parameters interpreted from CPTU and previous experience didn't give comparable results with measured settlement.

Development of pore water pressure was followed and accessed in deciding the removal of preloading in all embankment fills.

8 REFERENCES

Aaboe, R. (1993). Internrapport Nr. 1605: Setningsberegningsprogrammet SETNING. Veglaboratoriet, Vegdirektoratet.
Aaboe, R. (1993). Internrapport Nr. 1609: Setningsprogrammet TID. Program for beregning av setningenes tidsforløp, Veglaboratoriet, Vegdirektoratet.
Kalsrud, K., Lunne, T., Kort, D.A., Strandvik, S. (2005). CPTU Correlations for Clays. Proceedings of the 16th International Conference on Soil Mechanics and Geotechnical Engineering (Osaka, 2005).
Lunne, T., Robertson, P.K., Powell, J.J.M. (1997). Cone Penetration Testing in Geotechnical Practice. Blackie Academic & Professional.
Statens vegvesen (2014), Håndbok V220: Geoteknikk i vegbygging. Veiledning. Vegdirektoratet.
Statens vegvesen (2014), Håndbok V221: Grunnforsterkning, fyllinger og skråninger. Veiledning. Vegdirektoratet.
Statens vegvesen (2014), Håndbok N200: Vegbygging. Normal. Vegdirektoratet.

Undrained shear strength determination and correlations on Søvind Marl

Gitte Lyng Grønbech
Aalborg University, Denmark, glg@civil.aau.dk

Benjaminn Nordahl Nielsen
Aalborg University, Denmark

ABSTRACT
Undrained shear strength on Søvind Marl is found through undrained, volume constant, triaxial testing and is compared to field vane shear strength. Søvind Marl is extremely plastic and highly fissured Eocene clay found throughout Denmark. The fissured structure of Søvind Marl has an influence on both the preconsolidation and the undrained shear strength. Two apparent values of the preconsolidation stresses can be determined due to the fissured structure (Grønbech et al. 2015a) which also considerably decreases the undrained shear strength.
Determination of shear strength of fissured clay is done through field testing or triaxial testing. Christensen and Hansen (1959) tested fissured Danish Oligocene clay and found the undrained shear strength, S_u, be approximately 1/3 of the measured field vane shear strength, c_{fv}. This correlation has since been used in Danish geotechnical practice with little to no further validation through modern triaxial test.
The measured undrained shear strength is normalized using SHANSEP. The strengths are compared to the measured field vane shear strength in order to determine μ ($\mu=S_u/c_{fv}$). The undrained shear strength is found to be increasing with increasing stresses up to a strength of approximately 450 kPa at a stress level corresponding to the lower limit of the preconsolidation stresses. The field vane shear strength is found to reach values of more than 1000 kPa. The ratio between the undrained shear strength and field vane shear strength was confirmed to be approximately 0.3 on Søvind Marl regardless of the stress level.

Keywords: Undrained shear strength, Fissured Clay, SHANSEP, Plastic Clay, Field vane shear strength

1 INTRODUCTION

This article examine the strength parameters, specifically undrained shear strength, S_u (kPa), of a highly fissured overconsolidated Eocene clay called Søvind Marl. Seven samples are tested; with additional data from further four tests. All samples originate from the Søvind Marl formation at Aarhus, Denmark, which in deposit history, structure and characteristic resembles London Clay. The undrained shear strengths are normalised using SHANSEP (Ladd *et al.* 1977) and compared to measured field vane shear strength, c_{fv} (kPa), to determine the influence of the fissured structure.

1.1 Influence of structure on strength

The general presence of a structure in clay, either soft or stiff, has an increasing influence on the strength. Leroueil and Vaughan (1990) and Burland *et al.* (1996) found that a general post sedimentation structure enlarges the boundary surface of a soil in the in situ stress range. The was also found at very high stress levels on stiff clay by Jovičić *et al.* (2006) and on London Clay by Gasparre *et al.* (2008). Both situations result in increasing peak strengths due to the presence of a general post sedimentation structure.
The presence of a fissured structure also has a great influence on the strength of clay. Gasparre *et al.* (2008) and Vitone *et al.*

(2013) found that the peak strength of fissured London Clay and fissured bentonite clay, respectively, were significantly lower than the peak strength of similar, yet unfissured, samples.

Christensen and Hansen (1959) determined that only one third of the field vane shear strength could be used as the undrained shear strength in regards to the bearing capacity of Skive Septarian Clay, a fissured Oligocene clay. The use and determination of the factor between the two strengths, μ (-), is frequently discussed in the Danish geotechnical community. The value if 1/3 by Christensen and Hansen (1959) is widely used in Danish geotechnical practice, even though the used test methods differ from modern triaxial tests. Since then the relation has not been further confirmed using modern undrained triaxial tests on the extremely plastic fissured clays, like Søvind Marl.

2 SØVIND MARL

Søvind Marl is extremely plastic and highly fissured Eocene clay. Søvind Marl and other similar Tertiary clays are found throughout most of Denmark. The tested samples all originate from Aarhus Harbour, Denmark (Figure 1), and are aged between 42 million and 46 million years (Grønbech *et al.* 2015b). At Aarhus Harbour Søvind Marl can be found in great volumes of more than 70 m, starting at a depth of 10 m, situated under a layer of man-made fill (primarily sand) and till. Søvind Marl has a very uniform appearance throughout the depth with only slight changes in colour as the only mesofabric difference. A clear feature throughout the strata is a fine net of fissures running in unstructured directions without any apparent origin. These fissures have a great influence on the stiffness behaviour of the clay (Grønbech *et al.* 2015a) and are expected to also have a great influence on the strength.



Figure 1 Denmark, with Aarhus Harbour marked with ○. Coordinates: 56° 09'N and 10° 13'E.

A distinct characteristic of Søvind Marl is the very high content of clay size particles, with between 60% and 95% below a size of 2 µm, of which 45% to 55% is Smectite. This results in a very high plasticity index of Søvind Marl, with values in the normal range of 100% to 250%, with extreme values above 300%. Søvind Marl also has a high Calcite content, up to 65%, which plays a great part in governing the plastic behaviour of the material. Grønbech *et al.* (2015b) presents a detailed description of Søvind Marl.

*Table 1 Sample classification for tested Søvind Marl samples. * c_{fv} is based on the linear correlation presented in Figure 2 and Grønbech et al. (2015b).*

	Sample						
Test	1	2	3	4	5	6	7
Depth (m)	188	378	280	188	297	421	425
σ'_{v0} (kPa)	300	210	370	525	240	240	240
γ' (kN/m^3)	18.0	18.4	18.5	18.0	18.0	18.2	18.5
W_{nat} (%)	42.7	36.7	37.6	44.0	38.4	38.5	38.7
I_P (%)	143.6	103.2	131.6	188.7	152.9	152.9	152.9
c_{fv} (kPa)*	742	583	818	1053	-	-	-
σ'_1 (kPa)	300	210	370	525	375	750	1125

Table 1 lists significant classification parameters of the presented. Test numbers in correspond to legends in the following figures and tables. σ'_1 (kPa) is the vertical stresses from where the shearing process took place.

2.1 Field Vane Shear Strength

Figure 2 presents the field vane shear strength of 5 boreholes in Søvind Marl at Aarhus Harbour. Samples used in the undrained triaxial tests presented in this study all originate from borehole 10 or 11 (described in Grønbech *et al.* (2015b)). Both the intact field vane shear strength, c_{fv} (kPa), and the remoulded field vane shear strength, c_{rfv} (kPa), show very uniform behaviour independent of the borehole. The strengths increase in a linear behaviour through the strata. The intact field vane shear strength reaches a mean strength of 800 kPa at a depth of 42 m. The high strength is an indication of the extensive geological history of the material. 42 m is the maximum depth in which the field vane shear strength is measured. The mean linear development of the strength is assumed the most accurate description of the strength, and consequently, used as the field vane shear strength of the samples. Due to the uniform behaviour and development of the strength through the strata, the linear development of the strength is assumed continued in lower strata, enabling correlations to be made for samples located at lower depths.

2.2 Preconsolidation

Both the mesofabric and microfabric structures of clay has an influence on the stiffness. Gasparre and Coop (2008) found the determination of the preconsolidation stresses of London Clay was influenced by the fissured structure. Both Gasparre and Coop (2008) and Grønbech *et al.* (2015a) found a lower and upper bound of the preconsolidation stresses of London Clay and Søvind Marl, respectively. Krogsbøl *et al.* (2012) described the loss of stress memory in highly plastic fissured Palaeogene clays and contributed the loss to the high plasticity. These tests were conducted to stress levels up to 4000 kPa and did not reach the upper bounds of the preconsolidation found on similar clays.

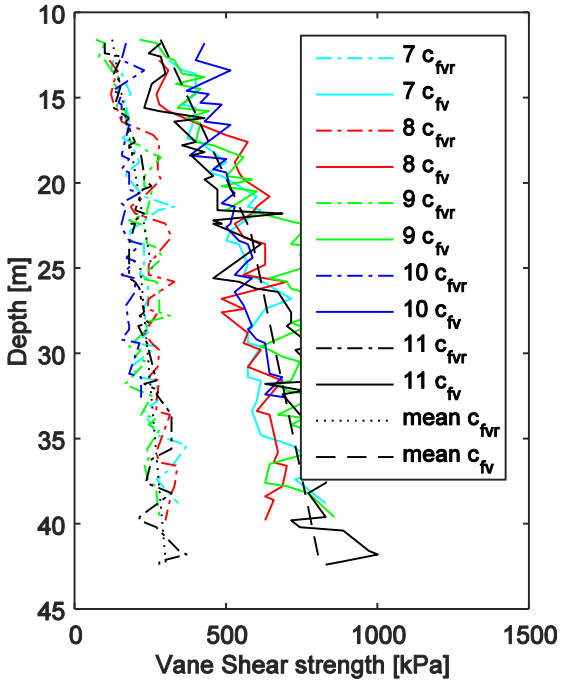


Figure 2 Field vane shear strength of Søvind Marl at Arhus Harbour. After Grønbech et al. (2015b).

Due to the long and extensive geological history of Søvind Marl, high degrees of preconsolidation are to be expected. Grønbech *et al.* (2015a) showed that a lower bound of the preconsolidation stresses can be found between 500 kPa and 800 kPa, which are only two to three times the in situ stresses. By continuing the tests, an upper bound of the preconsolidation stresses were found at approximately 5000 kPa to 9000 kPa (Grønbech *et al.* 2015a). This is more in concordance to the known geological history of the clay. The upper bound of the preconsolidation is related to the geological preconsolidation, while the lower bound is related to the structure. The lower bound is geotechnical speaking to be regarded as the preconsolidation stresses in the tests presented in this study with an approximately value of 750 kPa.

3 TEST METHODS

The undrained shear strength is found using the triaxial apparatus at Aalborg University. Figure 3 shows a sketch of the apparatus. A more detailed description can be found in Grønbech (2015). Samples are 70 mm in initial diameter and height. Stresses in the sample are applied via a load piston (deviatoric forces) and surrounding cell pressure (horizontal stresses). Axial deformation is measured by two displacement transducers, while volumetric deformation is measured by the backpressure system (not illustrated in Figure 3). Samples are saturated with a saline solution resembling the natural pore water in the samples (cl^- of 0.6 and *pH* of 9.2, cf. Grønbech *et al.* (2015b)). Pore pressure in the sample is measured in the centre of the lower pressure head. During testing, a back pressure of 200 kPa is applied to the sample to better enable saturation and drainage of the sample. Four felt drains run across the sample at a 45° angle to ensure even drainage of the entire sample without influencing the measured results.

After initial saturation the samples were re-consolidated to a vertical stress level resembling the lower bound of the preconsolidation stresses (750 kPa). The stress level in the samples is hereafter set at the stresses from which shearing takes place (σ'_1 in Table 1). Tests are all carried out as volume constant undrained triaxial tests. Axial deformation rate is set at 0.5 %/h and adjustable cell pressure is used to ensure a constant volume.

4 STRENGTH PARAMETERS

The tests are performed with the main focus to determine the undrained shear strength.

4.1 Undrained shear strength

The undrained shear strength is the sole strength parameter of an undrained soil, $\tau = S_u$. The undrained shear strength is given by the radius of Mohr's Circle at failure, also expressed as the half of the maximum deviatoric stresses, q_{max} (kPa), Eq.1:

$$S_u = 0.5 \cdot (\sigma'_1 - \sigma'_3) = 0.5 \cdot q_{\max} \quad (1)$$

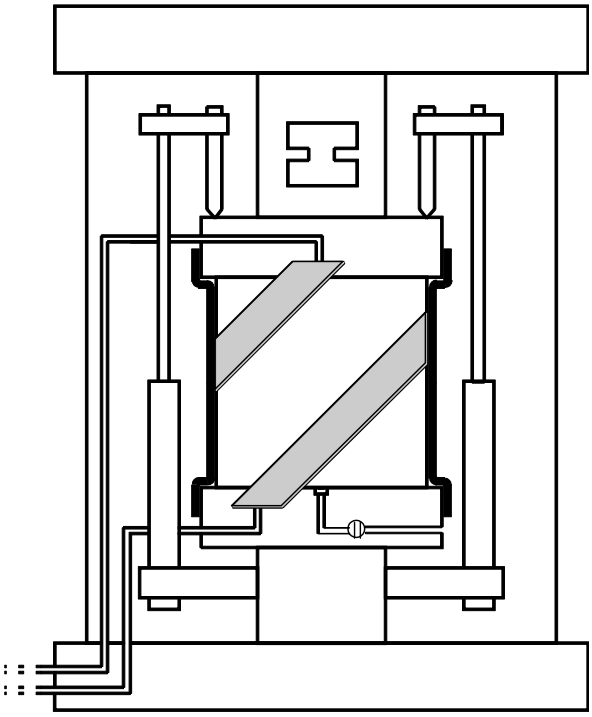


Figure 3 Sketch of the triaxial apparatus at Aalborg University. Figure is not to scale. After Grønbech (2015)

The deviatoric forces are measured directly by the piston in the triaxial setup, and divide on the actual area of the sample. The stress-strain curve for each test presented in Figure 5 is used to determine the maximum deviatoric stresses. The resulting undrained shear stresses using Ep. 1 are listed in Table 2.

All tests depict a "softening" effect just after failure. This is a result of the fissures failing, resulting in a substantial loss of strength as described by Gasparre *et al.* (2008), and not softening in the traditional sense.

Table 2 Undrained shear strength of the tested Søvind Marl samples. Sample data is listed in Table 1.

	Sample						
Test	1	2	3	4	5	6	7
S_u (kPa)	188	378	280	188	297	421	425

*Table 3 Data from additional undrained shear tests on Søvind Marl by Madsen et al. (2008). * c_{fv} is based on the linear correlation presented in Figure 2 and Grønbech et al. (2015b).*

	Sample			
Test	8	9	10	11
Depth (m)	17	31	59	67
σ'_{v0} (kPa)	158	270	494	558
c_{fv} (kPa)*	427	677	1006	1100
S_u (kPa)	105	213	239	413

The undrained shear strength is dependent of the shearing stresses. Figure 6 shows the comparison between these.

The undrained shear strength is seen to increase with increasing vertical effective stresses, as expected. The increase in strength is almost linear until the lower bounds of the preconsolidation stresses. The undrained shear strength seems to reach a maximum strength level at vertical effective stresses equal to the lower bounds of the preconsolidation stresses, at a strength level of approximately 420 kPa. This effect could, however, be accidental due to the limited data above the lower bound of the preconsolidation stresses. More tests are needed to confirm or dismiss this effect.

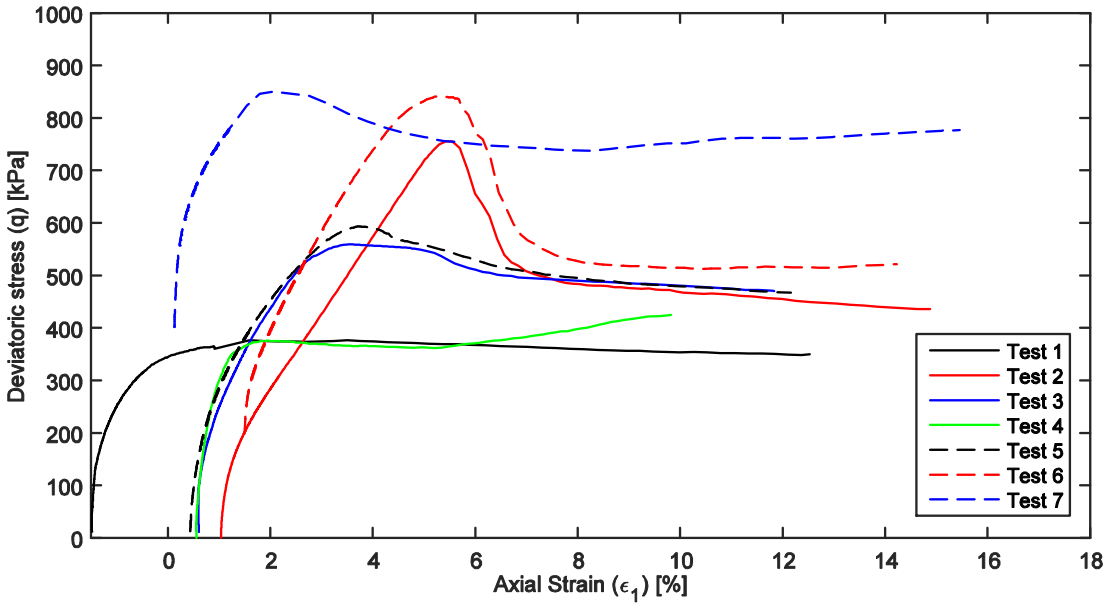


Figure 5 Stress-strain curves for the seven tested Søvind Marl samples. After Grønbech (2015)

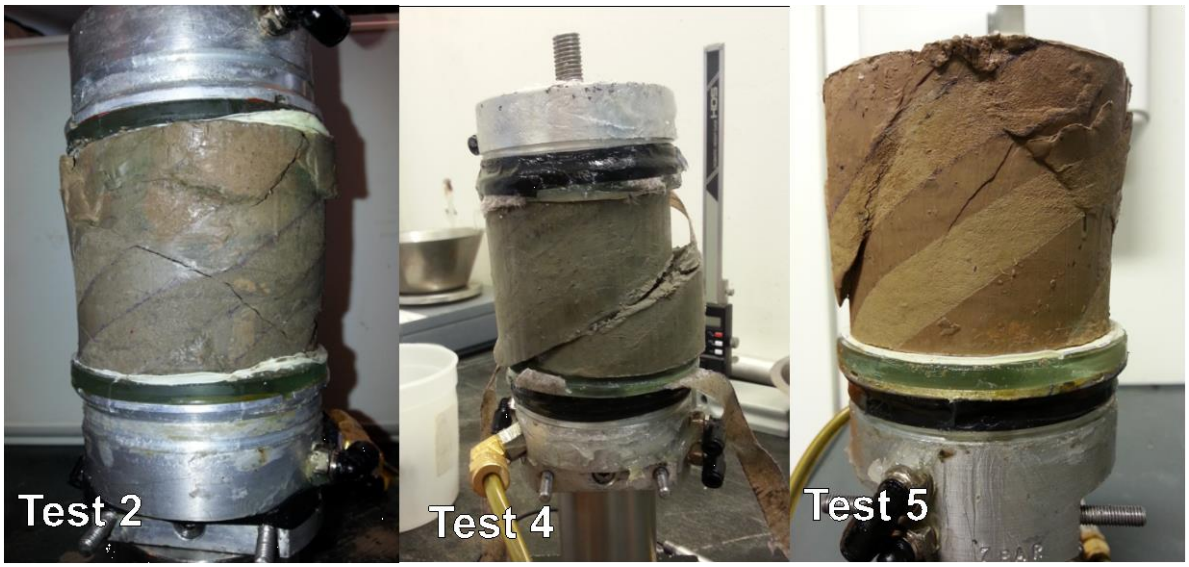


Figure 4 Three of the Søvind Marl samples after testing.

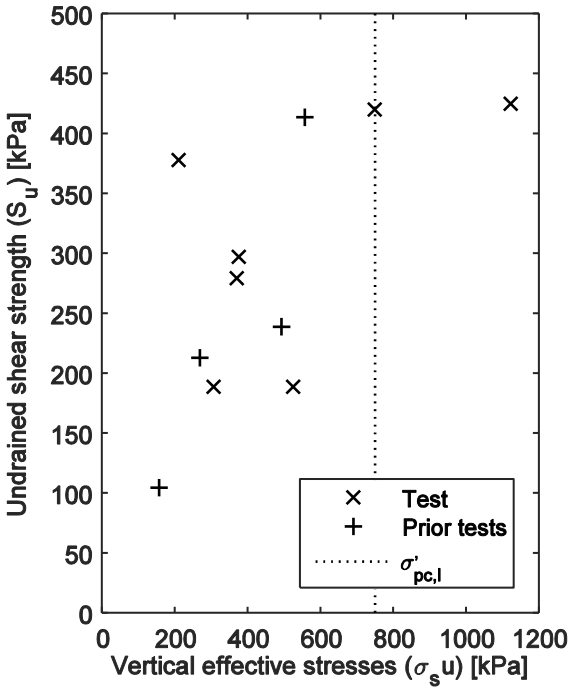


Figure 6 Undrained shear strength compared to the shearing stresses. Prior tests are by Madsen et al. (2008).

Two samples deviate from this, Tests 2 and 4. Figure 4 presents photos of the samples after testing, where Test 5 shows the typical failure pattern for the fissured remaining samples. Test 2 failed in a manner resembling unfissured clay, given a relative high strength. Test 4 seemed to have failed along a pre-existent fissure, yielding a much too low strength, likely a residual strength in the fissures. This is substantiated by the increase in deviatoric stresses at an axial strain of approximately 6% implying additional remaining strength in the sample after initial failure. These tests have been eliminated from further correlations; however, they are marked on following graphs to validate the exclusion of the results.

4.2 SHANSEP

By applying the SHANSEP method (Ladd *et al*. 1977) to the measured undrained shear strength, the undrained shear strengths are normalized to the in situ stresses in relation to the degree of overconsolidation. This enables estimations of the strength parameters using Eq. 2:

$$\frac{S_u}{\sigma'_{v0}} = S \cdot OCR^m \qquad (2)$$

where S (-) and m (-) are SHANSEP parameters and OCR (-) is the degree of overconsolidation.

Figure 7 shows the optimized fit of SHANSEP to the measured undrained shear strengths. The re-consolidation stresses (equals σ'_{pc}) are used in OCR, and the stresses from which the shearing is preformed are used as the in situ stresses ($\sigma'_{v0} = \sigma'_1$). The SHANSEP fit is made both with and without Test 7, which is sheared from stresses above the lower bound of the preconsolidation stresses. This is done based on the almost linear development of the strength and apparent maximum of the strength. Table 4 lists the resulting SHANSEP parameters and the associated coefficient of determination.

Table 4 SHANSEP parameters and the coefficient of determination for the measured strengths.

	W/ 1.5σ'$_{pc}$	**W/O 1.5σ'$_{pc}$**
***S* (-)**	0.51	0.58
***m* (-)**	0.44	0.22
R^2 (-)	0.78	0.82

Ladd *et al.* (1977), Mayne (1988) and Augustesen *et al.* (2005) describe the SHANSEP parameters S and m for less consolidated unfissured clay to be in the following interval:

$$0.25 \leq S \leq 0.55$$
$$0.7 \leq m \leq 0.8$$

However, this interval has not been proven nor evaluated on highly overconsolidated fissured clays, like Søvind Marl.

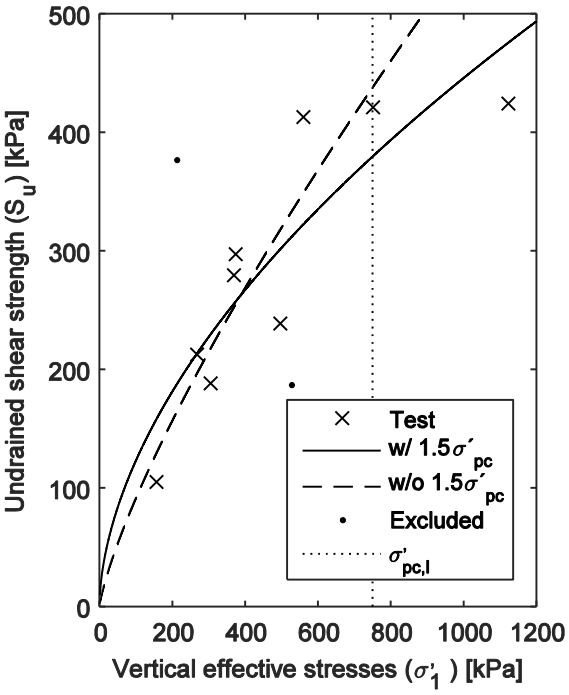


Figure 7 SHANSEP fit the measured undrained shear strength.

The *m*-values listed in Table 4 fall well below the normal interval. This is due to the almost linear development of the undrained shear strength. This indicates the normal development of the strength is influenced by the fissures. This is also shown by the low coefficient of determination (R^2) of SHANSEP to the dataset including Test 7 ($\sigma'_1 = 1.5 \cdot \sigma'_{pc}$). The SHANSEP parameters should, therefore, not be used for stresses above the lower bound of the preconsolidation stresses.

4.3 Effective parameters

The main focus of the tests is to determine the undrained shear strength. However, it is also attempted to determine the effective friction angle, φ' (°), and effective cohesion, c' (kPa), through the stress paths from the tests. Figure 8 shows the measured stress path for each test.

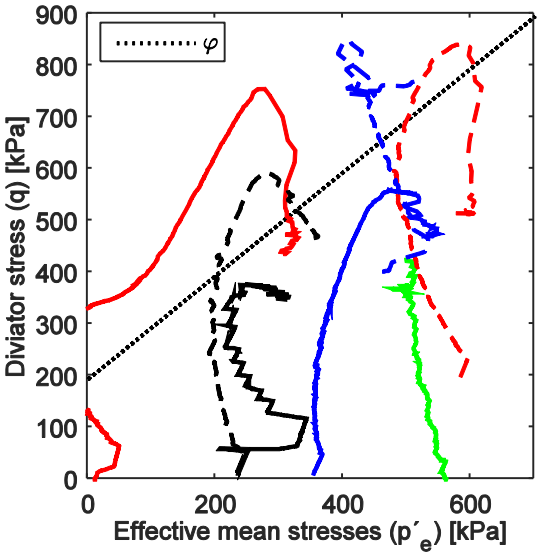


Figure 8 Measured stress path for the seven Søvind Marl samples. See Figure 5 for additional legends.

It is clear that Tests 2 and 4 again, as well Test 7, stand out from the rest. These tests are not included in the estimation of effective parameters. The mean effective stresses, *p'* (kPa), in Test 2 reached a negative state, indicating the pore pressure is larger than the horizontal stresses acting on the sample (cell pressure). This is an indication of the fact that the deformation rate was too high during the shearing process, not allowing the pore water to drain due to the very low permeability of the sample. Thus not allowing the effective parameters to be determined.

A common tangent of the failure stresses for the remaining tests is attempted in Figure 8. The fit of the tangent to the measured stress curves is rather poor, resulting in a poor estimation of the effective parameters. The friction angle can be found using Eq. 3:

$$q = \frac{6 \cdot \sin(\varphi')}{3 - \sin(\varphi')} p' \qquad (3)$$

Table 5 lists the resulting friction angle and effective cohesion.

Table 5 Estimated effective parameters.

	Pore pressure	**Back pressure**
$\boldsymbol{\varphi'}$	25.4	26.0
$\boldsymbol{c'}$	193.5	99.1

The resulting friction angle is very high considering the material. Thøgersen (2001) determined the friction angle of Little Belt Clay (Danish Eocene clay similar to Søvind Marl) to be in the range of 14° to 19°, using a strain rate of 0.1 %/h. Also the effective cohesion is considered to be much too high, as it is almost half of the maximum measured undrained shear strength in any of the tests.
As listed in Table 5, it was also attempted to determine the effective parameters using the back pressure to determine the effective stresses as oppose to the pore pressure. However, this does not improve the accuracy of the effective parameters, as both parameters are considered much too high.
This leaves the effective parameters undeterminable based on the presented tests. In order to estimate the effective parameter, a strain rate much lower than the applied 0.5 %/h should be used, like the 0.1 %/h used by Thøgersen (2001). This will be at the expense of a much longer testing time.

5 CORRELATION TO FIELD VANE SHEAR STRENGTH

The undrained shear strength is often assed using the field vane shear strength, c_{fv} (kPa) using Eq. 4.

$$S_u = \mu \cdot c_{fv} \quad (4)$$

Where μ (-) is the correlation factor between the two shear strengths. μ is considered 1 for unfissured clays. μ is as mentioned earlier dependent of the structure of the cohesion soil, with values as low as one third for fissured clay (Christensen and Hansen 1959).

μ is determined for Søvind Marl comparing both the measured undrained shear strength and the undrained shear strength estimated using SHANSEP to the linear representation of the field vane shear. Only tests where shearing is performed from in situ stresses are included in the correlation (Tests 1, 3, 8 to 11). Figure 9 presents μ through the strata and thereby with increasing stresses.

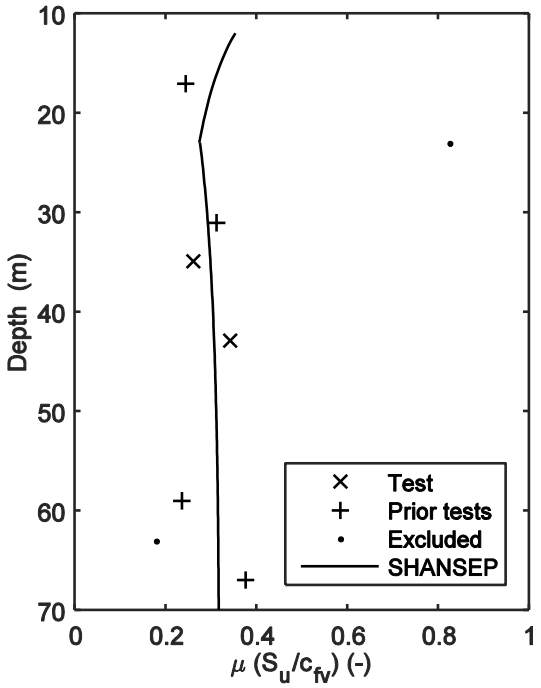


Figure 9 μ found using the measured undrained shear strength and field vane shear strength.

Values for μ fall in the range of 0.25 to 0.38 using the measured undrained shear strength. Using the SHANSEP parameters, μ decreases slightly from 0.35 to 0.28 in the upper part of the Søvind Marl, hereafter μ becomes constant around 0.3 through the remaining of the depth. Based on the tests, a μ-value of 0.3 is recommended for Søvind Marl.

6 CONCLUSION

The undrained shear strength of Søvind Marl was tested. Seven tests were conducted for this study; with additional results from four supplementary tests on Søvind Marl. All tests were conducted at Aalborg University, Denmark. Søvind Marl is highly fissured extremely plastic Danish clay. Søvind Marl is highly overconsolidated, with the appearance of an upper and lower bound of the preconsolidation stresses. The main focuses were to determine the undrained shear strength and its correlation to the field vane shear strength.
The undrained shear strength increases almost linearlyl with increasing stresses. This tendency seems to have an upper cap at stresses equal to the lower bound of the

preconsolidation stresses, with maximum undrained shear strength of approximately 420 kPa. No final conclusion can be made due to very limited data in this stress range. Additional tests are recommended to further investigate this claim.

The stresses are normalised using SHANSEP in order to determine the development of the strength through the depth. The SHANSEP parameters *S* and *m* were 0.58 and 0.22, respectively. Especially the *m*-value is affected by the fissured structure with a very low value, giving the strength found using SHANSEP an almost linear development. The SHANSEP parameters are only valid for stresses below the lower bound of the preconsolidation stresses.

The undrained shear strength was finally compared to previously measured field vane shear strength to evaluate the influence of the fissured structure on the undrained shear strength in regards to the bearing capacity. Both the measured undrained shear strength and the strength estimated using SHANSEP was used. The relation between the shear strengths, μ (-), was between 0.25 and 0.38, with a mean value just above 0.3, confirming the findings of Christensen and Hansen (1959) with μ around 1/3. Based on the presented tests, a recommended value for μ is 0.3 for Søvind Marl.

Figure 10 presents the undrained shear strength throughout the depth using the measured and evaluated strengths with μ=0.3.

There is a good agreement with all the measured and evaluated strengths, validating the findings presented in this paper.

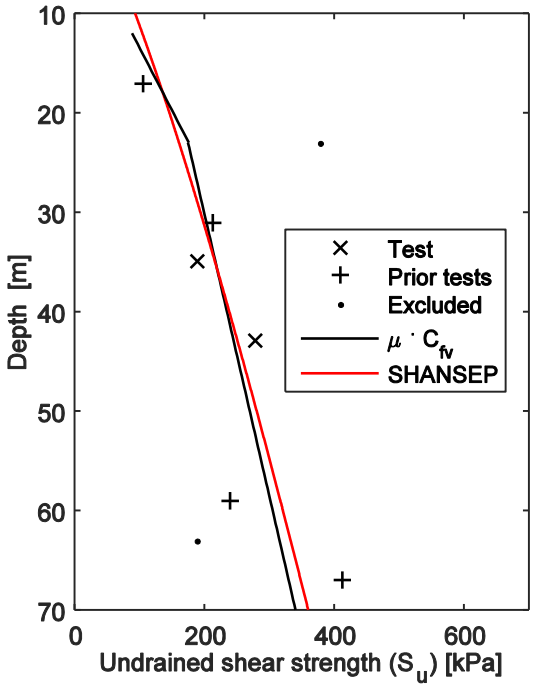


Figure 10 Estimated and measured undrained shear strength through the depth.

7 REFERENCES

Augustesen, A., Andersen, L., and Sørensen, C. S. (2005). Time Function for Driven Piles in Clay. Department of Civil Engineering, Aalborg University. ISBN:1398-6465.

Burland, J.B., Rampello, S., Georgiannou, V.N., and Calabresi, G. (1996). A laboratory study of the strength of four stiff clays. Geótechnique 46(3), 491–514.

Christensen, N.H. and Hansen, B. (1959). Shear strength properties of Skive Septarian clay. Bulletin No. 7. The Danish Geotechnical Institute.

Gasparre, A. and Coop, M.R. (2008). Quantification of the effects of structure on the compression of a stiff clay. Canadian Geotechnical Journal, 45: 1324–1334

Gasparre, A., Nishimura, S., Coop, M.R., and Jardine, R.J. (2008). The influence of structure on the behaviour of London Clay. Geótechnique 57(1), 19–31.

Grønbech, G.L (2015). Søvind Marl – Behaviour of a plastic fissured Eocene Clay. Aalborg University Press. ISBN: 978-87-7112-227-5. PhD-thesis

Grønbech, G.L., Ibsen, L.B. and Nielsen, B.N. (2015a). Preconsolidation of Søvind Marl—A Highly Fissured Eocene Clay. Geotechnical Testing Journal. Vol 38 (4). Pp. 501-510

Grønbech, G.L., Nielsen, B.N., Ibsen, L.B., and Stockmarr, P. (2015b). Geotechnical properties of Søvind Marl - a plastic Eocene clay. Canadian Geotechnical Journal. 52. Pp. 469-478

Jovičić, V., Coop, M., and Simpson, B. (2006). Interpretation and modelling of deformation characteristics of a stiff north sea clay. Canadian Geotechnical Journal 43, 341–354.

Krogsbøl, A., Hededal, O. and Foged, N.. 2012. Deformation properties of highly plastic fissured Palaeogene clay – Lack of stress memory?. In proceedings of NGM 2012, Nordisk Geoteknikermøde Vol. 1/2. 9th-12th of May 2012. Copenhagen, Denmark. 133-140

Ladd, C.C., Foott, R., Ishihara, K., Schlosser, F., and Poulos, H. G. (1977). Stress-deformation and strength characteristics. Proceedings of: International Conference on Soil Mechanics and Foundation Engineering, 9th, 1977, Tokyo, Japan.

Leroueil, S. and Vaughan, P.R. (1990). The general and congruent effects of structure in natural soils and weak rocks. Geótechnique 40(3), 467–488.

Madsen, J.V., Johannesen, C.L., and Vestergaard, K.T. (2008). Geotekniske egenskaber for tertiært ler ved Light*House (In dansih). Department of Civil Engineering, Aalborg University, Denmark. Master Thesis.

Mayne, P.W. (1988). Determining OCR in clays from laboratory strength. J. Geotech. Engng. Div. Am. Soc. Civ. Engrs. 108, GT6, Pp.75–92.

Thøgersen, L. (2001). Effects of experimental techniques and osmotic pressure on the measured behaviour of tertiary expansive clay, Volume 1. Soil Mechanics Laboratory, Aalborg University, Denmark. Ph.D. Thesis, ISSN: 1398-6465 R 2016.

Vitone, C., Cotecchia, F., Viggiani, G., and Hall, S.A. (2013). Strain fields and mechanical response of a highly to medium fissured bentonite clay. International Journal for Numerical and Analytical Methods in Geomechanics 37, 1510–1534.

Analysis of inclined piles in settling soil

F. Resare
ELU Konsult, Sweden, fredrik.resare@elu.se

A.B. Lundberg, G. Axelsson
ELU Konsult, Sweden

ABSTRACT
The use of raked, or batter, piles is an efficient way to handle horizontal forces in constructions. However, if the soil around the pile settles the structural capacity of each pile is reduced because of induced bending moments in the pile. There is currently no validated method in Sweden to analyse horizontal loading from settling soil. In the current paper a non-linear 3D finite element model is validated against a field test from the scientific literature, and the results are compared to three different beam-spring models. These models consist of a state-of-practice model where a subsoil reaction formulation is used, a model where the soil is considered as a distributed load, and a model with a wedge type of failure. Furthermore, a parametric study is conducted for drained soil conditions where the weight and friction angle of the material are varied. The standard soil reaction model yields an induced bending moment almost three times larger than the one obtained from the field test and the two other calculation methods. The latter beam-spring models should therefore be considered in practical design.

Keywords: Raked piles, batter piles, inclined piles, settling soil, soil structure interaction.

1 INTRODUCTION

Simplified beam-spring models are frequently used in design for simulation of axially and laterally loaded piles, (Erbrich et al, 2010). Such models should contain the main mechanisms controlling the soil-structural system, and the validity of the models should be carried out with experimental or numerical methods. Experimental methods include full-scale and field models, which naturally contains empirical evidence of the validity of the model. The latter is the standard method of verification, and should accompanied with a suitable simplified analytical model leads to a robust design methodology, which could however be relatively conservative.

The use of such simplified models outside normal experience, poses the questions about how well the real field case is modelled. Model simplifications comprise material, geometry and boundary conditions. Any of the factors may not be realistically models, which could lead an overtly safe of unsafe design. Some mechanical mechanisms (e.g. changes in pore pressure and creep) occur over longer timescales, which prohibits field verification of the model before the construction is finished. This is a frequent occurring problem in geotechnical design.

This paper discusses numerical simulation of a simplified beam-spring model for a laterally loaded included pile in settling soil for drained soil conditions, which is assumed to be suitable for the long-term conditions of the soil. The structural design, simplified model ground conditions, numerical model and proposed new models of the particular case are discussed.

2 PILE DESIGN CONSIDERATIONS

The Northern Scandinavian ground conditions are characterized by soft soils such as clay and peat, placed on a layer of till deposited on hard rock, (Johannessen & Bjerrum, 1969). A commonly used method to transfer loads for overlying structures to the hard rock is to use relatively slender piles that are installed by driving the pile base into the till layer or drilling the pile base into the rock. These end-bearing piles are in most

cases dynamically tested to control the geotechnical bearing capacity, i.e. the capacity of the end-bearing rock or till beneath the pile.

This particular piling method results in very high utilization of the structural capacity of the pile. In many cases this factor limits the allowable load on the pile. Design calculations for these piles are normally carried out by calculating the buckling load and structural strength, following the procedure described by Bernander & Svensk, 1970. This calculation method has proven to the robust and has resulted in a safe design.

Such end-bearing piles carry a relatively high load: in the case of a concrete-filled 140 mm steel tubular pile with a wall thickness of 8 mm, the allowable load can exceed 1.2 MN, which makes the foundation system very efficient by using a small amount of steel and concrete. But the small diameter of these piles results in a limited lateral pile bearing capacity; especially since the top layer of the soil frequently consist of very soft clay. Inclined piles are instead preferred as a structural solution, where an inclination of 4:1 to the vertical axis is typically used as a maximum inclination. Pile groups subjected to high levels of horizontal load, e.g. a bridge abutment, therefore normally include a large number of inclined piles.

2.1 Alternatives for modelling and design of realistic pile-soil mechanism

Current design methods for the structural strength of piles in settling soil consist of a simplified beam-spring model, outlined in Svan & Alén, 2006 (and Reese et al, 1974, for vertical piles), or a full 3D-FEM-model. The beam-spring model results in limited calculation time and is frequently used in design. 3D-FEM models have not been of extended practical use for the current types of slender piles, although frequently used for lateral loading of larger offshore piles, e.g. Erbrich et al, 2010.

The simplified beam-spring models are obviously a simplification of the soil conditions around the pile, and result from an idealisation in 2D of the soil. The real soil-pile deformation mechanism in 3D can be assessed in laboratory, field and numerical experiments. Because of the relatively complicated processes governing the soil behaviour, including soil settlement, consolidation and creep, field experiments are the most reliable method of assessment. In the scientific literature, field experiments have only been covered in Takahasi (1985). Laboratory models are also discussed in Takahasi (1985) along with both numerical and analytical calculation models. Laboratory experiments are also discussed in Kohno et al, 2010 and Rao et al, 1994. Numerical studies include boundary element models in Poulos, 2006, where the significance of the horizontal load on the piles are discussed in detail, but where a relatively simplified model in adapted to the pile-soil interaction.

The field, laboratory and numerical models mentioned above all detail the resulting bending moments for inclined piles, and a beam-spring model for inclined piles is proposed in Takahasi et al, 1985 and Kohno et al, 2010. No comparison between a full range of soil parameter (friction angle and effective weight) has however been carried out, since this required a large number of simulations, which was outside the scope of these scientific works. In the current paper a numerical model is therefore adapted to an inclined pile, and different beam-spring models are compared to the simulations.

3 CURRENT BEAM-SPRING CALCULATION MODEL

The calculation model used in Sweden today (Svahn and Alén, 2006) is based on the equation for a beam on an elastic foundation. The force distribution in the beam on an elastic foundation can be described as a fourth-order differential equation, Equation 1, by dividing the beam in infinitely small elements.

$$EI\, y^{IV} + N\, y^{II} + D\, k_y\, y = D\, k_y\, y_g - N\, y_i^{II} \quad (1)$$

Where EI is the bending stiffness of the pile, N is the normal force along the pile axis, D is the width of the pile, k_y is the soil reaction transversal to the pile, y_g is the ground settlement, and y^i is the i-th differential of the horizontal position along the pile axis x.

Equation 1 can be simplified to Equation 2 given that the normal force can be assumed to be constant along the pile, which a suitable assumption for an end-bearing piles. The interesting part of the pile is situated at the pile head where the effective stress is relatively low, which makes this assumption relatively correct.

$$EI\ y^{IV} = D\ k_y\ (y_g - y) \qquad (2)$$

In the current calculation model the position of the soil is a function of the depth to replicate the displacement of the soil. The relative movement of the soil is illustrated in Figure 1.

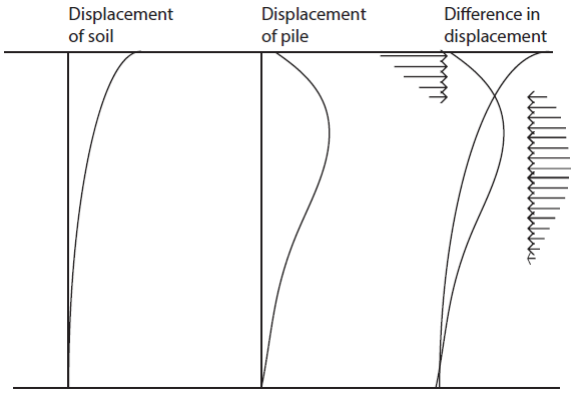


Figure 1 Illustration of the difference in displacement between the settling soil and the pile causing lateral earth pressure.

3.1 Description of the Swedish standard

In the current calculation model the subgrade reaction, k_y, is set according to empirical values recommended by Reese et al. (1974). The settlement is adapted as a relative movement between the soil and the pile. The settlement is divided into a transversal and a longitudinal component, see Figure 2. From this the transversal part is applied as the movement of the soil and the differential equation can be solved.

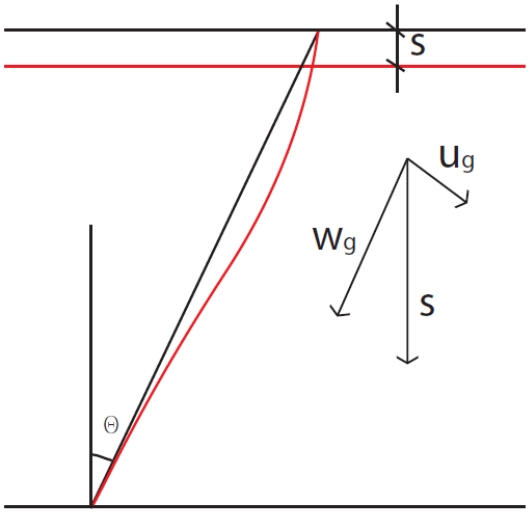


Figure 2 Illustration of the division of the settlement into a transversal and a longitudinal component.

This beam-spring model has been used to calculate the bending moment resulting from the settlement and soil conditions in the field experiments in Takahashi, 1985. The field experiment consisted of soil settlement resulting from deposition of fill on soft clay made for a road structure. Measurements were carried out on instrumented pipe piles driven in inclined pairs along the road. The calculated bending moment, according to Svahn and Alén, 2006, along the pile compared to the measured bending moment can be seen in Figure 3. This Figure also shows that the bending moment is larger close to the top of the pile. In the rest of this article only the maximum value of the bending moment will be referred to, however the distribution of the bending moment is relatively similar for all cases, i.e. at the top part of the pile. It should also be noted that the different between the measured and calculated values of the bending moments seems to be related through a scale factor, signifying the extra moment resulting from the idealization of the 3D pile-soil interaction to a 2D beam-spring model.

There are also some limitations present in the 2D analytical beam-spring model, e.g. only one type of soil can be used for the entire length of the pile. Another limitation is that the settlement profile is fixed and does not always represent the actual settlement, since this has to be simplified to an analytical function, e.g. an exponential function.

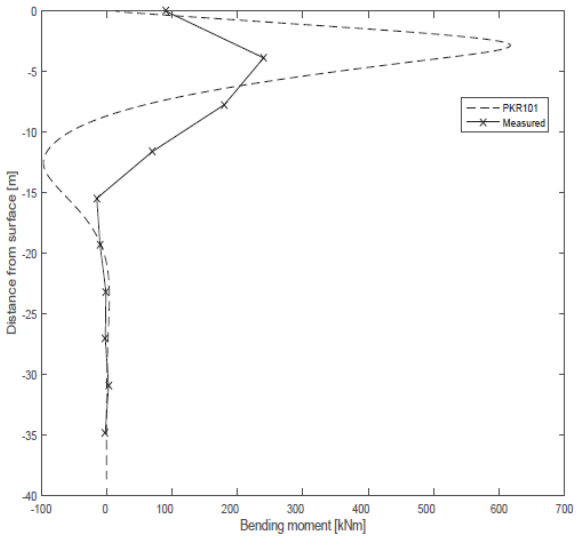


Figure 3 Comparison between the bending moment as calculated with the current method (Svahn and Alén, 2006) and the bending moment as measured in the full scale experiment by Takahasi (1985).

4 ALTERNATIVE BEAM-SPRING MODELS

The comparison between the measured and calculated bending moments in Figure 3 displays that the current model (Svahn and Alén, 2006) clearly overestimates the measured bending moment. This beam-spring model is therefore compared to two different calculation models, described below. The common principle of the two models is that the pressure against the pile is reduced, which means that the force does not exceed the weight of the soil above it. This is a suitable principle to avoid stress distribution resulting which no natural base that result from the simplification of the model.

4.1 Distributed load approach

The distributed load approach is originally discussed in Takahashi, 1985. The model results in a division between the top part of the pile and the following lower part along the principle in Randolph, 2014, to represent the real soil response resulting for the different boundary conditions. The soil is therefore divided into two parts; a distributed load part, and a subgrade reaction. The load is applied as a function of the pile width and is limited to the subgrade reaction of the soil so that no load will be applied if the displacement of the pile is equal or limited to the soil displacement, which is more suitable than a load resulting only from the friction angle and effective stress in the traditional earth pressure approach in the current calculation model. The formulation of this behaviour is summarized in Equation (3). This discretization assumes that the soil goes to failure and therefor becomes a load hanging on the top part of the pile.

$$EI\ y^{IV} = D\ k_y\ (y_g - y) \leq 3\ D\ \gamma\ z\ \sin(\theta) \quad (3)$$

where γ is the weight of the soil and θ is the inclination of the pile relative to the vertical axis.

4.2 Wedge failure approach

Based on a failure mode described by Reese et al. (1974) the top part of the soil is considered to have a cone like plastic failure which is also observed in the 3D finite element model, discussed below. Similar to the distributed load approach the soil is divided into a distributed load along the top of the pile, and a subsequent subsoil reaction along the deeper parts of the pile. The load is suggested to grow with the weight of the cone shown in Figure 4. Furthermore it is assumed that only the transversal part of the weight will act lateral to the pile causing bending moment (and not the load resulting from increased shaft friction), thus only this part of the weight is to be taken into account. The total load acting on the pile can therefore be described as Equation 4.

$$EI\ y^{IV} = D\ k_y\ (y_g - y) \leq \sin(\theta)\ (\gamma\ \alpha\ z^2 \tan(\beta) + \gamma\ z \tan(\beta)\ D) \quad (4)$$

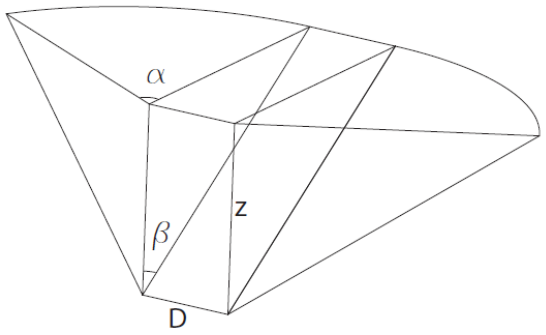


Figure 4 Illustration of the wedge failure and parameters used for Equation 4.

5 3D FEM MODEL

In order to assess the real behaviour of the soil, either laboratory models (Kohno et al, 2010), numerical models (Poulos, 2006), or field models (Takahashi, 1985) are possible approaches. In the current scientific work a 3D finite element model was used to validate the different 2D-models. The advantage of a numerical model is that parameter studies are possible, and the behaviour of the real case can be studies for different configuration without the limitations of a laboratory or field model, (Randolph, 2014). The current analysis was performed in a 3D FEM software (Hibbitt, Karlsson, & Sorensen. (2001)). The computer model was first validated against the field study in Takahashi, 1985. Subsequently a parametric study was carried out to compare the behaviour of the 3D-FEM model to the different and 2D beam-spring formulations.

5.1 Geometry, boundary conditions and FE discretization

Figure 5 represents the geometry of the model, consisting of the pile and the surrounding soil. A symmetry plane along the pile axis has been used to save computational time. The boundary conditions were set so that no displacement perpendicular to the surface will occur except for the top surface which was free to move, and the plane of symmetry where symmetrical conditions were applied.

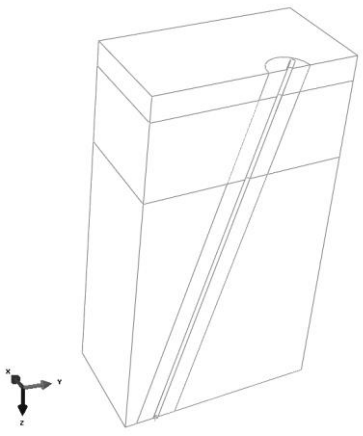


Figure 5 Basic geometry used for the finite element model.

The soil was modelled as 3D solid elements (C3D8 and C3D4 type of elements, (Hibbitt, Karlsson, & Sorensen. (2001)) and the pile was modelled as shell elements (S4 type of elements, Hibbitt, Karlsson, & Sorensen. (2001)) in order to save computational time during the simulation. As settlement per definition is pore water dissipation, drained parameters were used for the clay.

To simulate the settlement a stress-free strain level was induced in the soil body causing the desired settlement profile. The settlement in the soil was modelled using orthotropic temperature dependency hence shrinking the soil in the vertical direction to represent the settlement profile from the experiment. This resulted in a controlled deformation, in which the load against the pile was controlled by the effective stress level in the soil. The excess pore pressure was consequently not included in the model, but since most of the bending moments occur close to the pile head (according to Figure 3), this should have a relatively small influence on the calculation results, possibly resulting in an overestimation of the bending moments in pile compared to the short-term process, in which less settlements occur and the beginning of consolidation. The pile's top was restrained to move in the horizontal direction to represent the pinned condition from the study. Interaction between the pile and the surrounding soil was modelled using penalty type interface. For the normal behaviour a small pretension was applied between the soil and the pile by changing the clearance when contact pressure is zero and for the tangential behaviour a friction coefficient of 0.385 was assumed (Helwany, 2007). This is a suitable estimate following standard values of the interface friction angle, (Randolph, 2014). The behaviour of the steel is assumed to be linear elastic and a Young's modulus of 200 GPa was assumed along with a Poisson's ratio of 0.3.

5.2 Validation of field measurements

The numerical model was calibrated against the field measurements presented in Takahashi, 1985. The field measurements consisted on settlement in a clay soil covered by fill material. The soil was modelled

according to the guidelines presented in Trafikverket (2011a), which are normally used in practical design. The elastic properties of the soil were assumed to be linear and isotropic with a Young's modulus calculated as 250·cu for the clay and 50 MPa for the fill material in the embankment. The plastic behaviour was modelled using Mohr-Coulomb plasticity with a friction angle of 45 degrees for the embankment. As settlement in this case per definition occurs due to the dissipation of water drained parameters were used for the clay body, and an alternating value for the clay to estimate the impact of this value (since no drained parameters were presented in Takahashi, 1985). The friction angle of the clay however had very low effect on the results. Furthermore a Poisson's ratio of 0.3 was assumed for the soil body.

5.3 Parametric study

In order to compare the different 2D beam-spring formulations, (Svahn and Alén, 2006), Reese et al, 1974 and Takahashi, 1985), a parametric study comparing the 3D FEM numerical model to different 2D beam-spring model was conducted. The settlement profile in the 3D-model was predefined, so that the settlement increased linearly over the entire depth. A similar settlement profile was used in the beam-spring model. The density of the soil was set to 0.5, 1.2, and 2 t/m^3 and the friction angle was set to 25, 35, and 45 degrees for a total of 9 combinations, shown in Table 1. The Young's modulus of the soil was set to 50 MPa for the entire depth and a cohesion of 2 kPa was used to prevent numerical problems close to the surface. This results in a simplification of the soil parameters, since the modulus tends to increase with the friction angle, but this was not considered in the model. A total settlement of 25 cm was induced and the maximum bending moments were calculated in the 3D-FEM model and the beam spring models, following the distribution of bending moment shown in Figure 3.The coefficient of subgrade reaction was chosen as 7 MN/m^3 increasing linearly with the depth and limited to 49MN/m^3 for all 2D cases (Trafikverket, 2011b).

Table 1 Studied cases.

weight (kg/m^3) / Friction angle (deg)	500	1200	2000
25	X	X	X
35	X	X	Unable to finish
45	X	X	X

6 RESULTS

6.1 Validation of the numerical model

The numerical model was initially validated against the measurements presented in Takahashi, 1985. The maximum bending moment at each settlement level was calculated, following the distribution shown in Figure 3. The maximum bending moments typically occurred close to the surface at the same vertical level, showing relatively small change during the soil settlement process, (Takahashi, 1985). Figure 6 shows the bending moment against the ground surface settlement in the numerical model and the field measurements. It can be observed that the results are very close to the measured values and it is assumed that the model replicate the field test relatively well. From the results it can also be observed that a wedge like failure mode occurs as shown in Figure 7 indicating that a different failure mechanism occurs in the first few meters than in the rest of the pile.

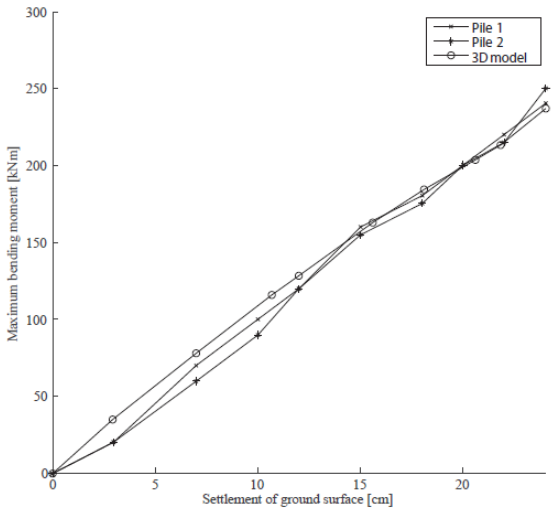


Figure 6 Maximum bending moment plotted against the settlement of ground surface.

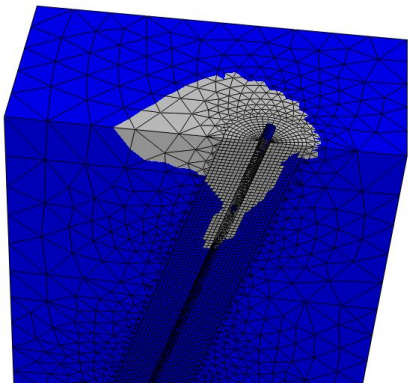


Figure 7 Plastic zones in the completed finite element solution indicating a different failure mode in the top of the pile.

As the 3D finite element model is assumed to replicate the results from the field tests, the validated numerical 3D-FEM model was then adapted for comparison to the different 2D discretization approaches with the field measurements in Takahashi, 1985.

6.2 Beam-spring model according to Svahn & Alén, 2006

Figure 8 shows the bending moment calculated according to Svahn and Alén, 2006, compared to the simulation by the 3D-FEM model. It can be seen that the proposed model gives a maximum bending moment far greater than that obtained in the 3D model.

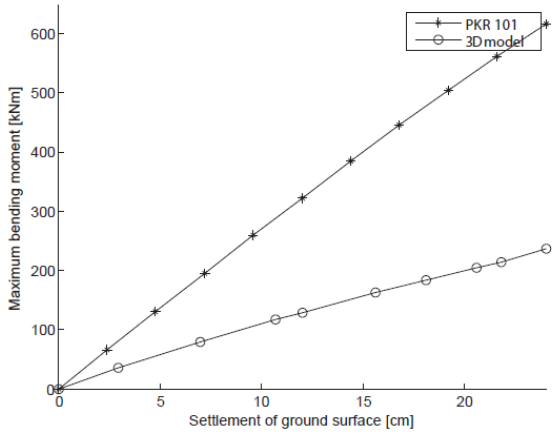


Figure 8 Maximum bending moment plotted against the settlement of ground surface using PKR101.

6.3 Results using the distributed load approach according to Takahashi, 1985

Figure 9 shows the bending moment calculated according to the distributed loading approach, (Takahashi, 1985), compared to the ground surface settlement calculated with the 3D-FEM model. It can be seen that the proposed model gives a maximum bending moment close to the one obtained in the 3D model.

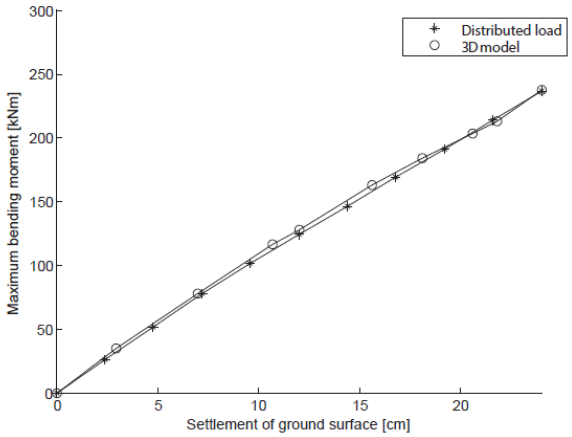


Figure 9 Maximum bending moment plotted against the settlement of ground surface using the distributed load approach.

6.4 Results using the wedge failure approach according to Reese, 1974

Figure 10 shows the bending moment calculated with the wedge approach according to Reese et al, compared to the ground surface settlement calculated with the 3D-FEM model. It can be seen that this model gives a maximum bending moment close to the one obtained in the 3D model.

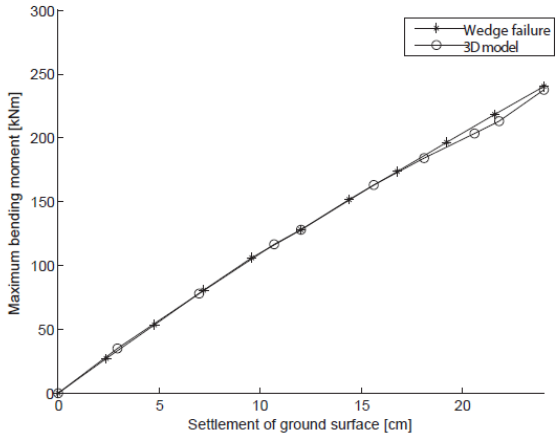


Figure 10 Maximum bending moment plotted against the settlement of ground surface using the wedge failure approach.

6.5 Results from the parametric study

After assessing the different between the beam-spring approaches compared to the field measurement in Takahashi, 1985, a parametric study was carried out. The soil friction angle and the weight of the soil were varied according to Table 1. The results are shown in Figure 11. The abscissa shows the effective weight of the soil and the ordinate the friction angle. It was first be observed that the proposed beam-spring models (Svahn and Alén, 2006, Takahashi, 1985 and Reese et al, 1974) results in different bending moments depending on the friction angle and the weight of the soil. Moreover, it is also noticeable that the distributed load model is independent of the friction angle but gives a maximum bending moment closer to the one obtained in the 3D models in comparison to the wedge failure method. All three ways of calculating the reaction of the pile give results on the safe side, however by using Svahn and Alén, 2006, the calculations results in a bending moment of over 3 times the value obtained from the 3D-FEM simulation.

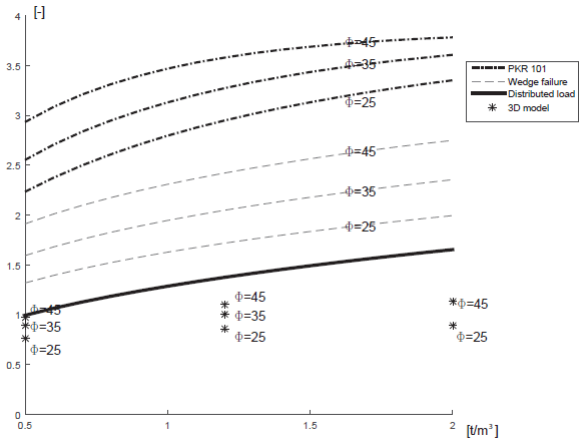


Figure 11 Maximum bending moment in pile divided with the maximum bending moment for a friction angle of 35 degrees and a weight of 1.2 t/m^3 plotted against the weight of the soil.

7 DISCUSSION

Ground settlement, including soil creep, occur over extended time periods, and many factors such as ground water level and presence of organic soil influence the settlement profile and settlement rate. A relatively simplified soil deformation model has been adapted to the inclined pile in settling to simulate the drained soil conditions in the current paper. The vertical strain profile was imposed on the soil according to the field test case, and a Mohr-Coulomb yield model was included in the model to simulate the plastic behaviour during settlement. The results are in line with the wedge yield theory discussed in literature, e.g. Randolph 2014, Reese 1974, Takahashi 1985. It appears from the results that the main response of the soil can be separated into a surface field mechanism, and a deeper earth pressure mechanism, following the standard theory of beam-spring models for horizontal offshore piles, (Randolph, 2014). A numerical parametric study of the variation of the soil weight and friction angle confirms the importance of the geometry of the soil on the inclined pile, in which the bending moments did not change very much when these factors were varied. The mechanism with the least necessary resistance before yield controls the position of transformation between the top and deep yield type through the wedge mechanism in the soil. Because of the relatively large displacement in the top soil layer at yield, more advanced soil models incorporating small-strain behaviour would probably have limited impact on the simulation. However, a soil model including viscoelastic behaviour such as creep would probably improve the numerical model.

8 CONCLUSIONS

Analysis of imposed vertical deformation (simulating ground settlement) shows that a wedge-type yield mechanism occurs in the top part of the soil. This mechanism is not correctly simulated by the current calculation model (Svahn and Alén, 2006), in which an earth-pressure formulation is adapted along the whole pile depth. The alternative beam-

spring models that differentiate between the top layer and bottom layer with either a wedge, e.g. (Reese et al), or with a distributed load depending on the width of the pile, results in a more realistic idealization of the real case. Numerical simulations with a beam-spring model formulation were carried out with the wedge failure (Reese et al, 1974) and the distributed load approach (Takahashi, 1985) and compared with the 3D-FEM model. A subsequent parametric study was also carried out. The simulation results show that the distributed load approach results in calculations which are relatively similar to the 3D-FEM model. The beam-spring distributed load approach (Takahashi, 1985) with a drained earth-pressure formulation is therefore proposed as the preferred design approach for inclined piles in settling soil, both for clay and granular soils. Another conclusion of the numerical simulations is that beam-spring family of models are very simplified design models, consisting of simplifications and idealization of relatively multi-faceted mechanical response of the soil around the pile. Such models should be adapted to design with some care, preferably after a full simulation with a more realistic model. The stress distribution around the pile in the case of settling soil is quite different from that of direct horizontal pile loading, in which case another of the alternative formulations are preferred for granular soil and clay, (Randolph, 2014). The settlement of clay soil is a very slow process that is likely to give a drained soil response, while much faster loading, e.g. traffic load, results in excess pore pressure, and the presented model is not suitable in such a case.

9 REFERENCES

Bernander, S., & Svensk, I. (1970). Pålars bärförmåga i elastiskt Medium under Hänsynstagande till Initialkrökning och Egenspänningar i Pålmaterialet, IVA Pålkommission.

DNV (2010). Offshore standard DNV-OS-J101: Design of offshore wind turbine structures. Technical report DNV-OS-J101, Det Norske Veritas.

Erbrich, C. T., et al. "Axial and lateral pile design in carbonate soils." Proc. 2nd International Symposium on Frontiers in Offshore Geotechnics, Perth, Australia

Fellenius, B. H. (1972). Down-drag on piles in clay due to negative skin friction. Canadian Geotechnical Journal, 9(4), 323-337.

Helwany, S., 2007. Applied soil mechanics with Abaqus application.

Hibbitt, Karlsson, & Sorensen. (2001). ABAQUS/Explicit: User's Manual (Vol. 1). Hibbitt, Karlsson and Sorenson.

Johannessen, I. J., & Bjerrum, L. (1969). Measurement of the compression of a steel pile to rock due to settlement of the surrounding clay. In Soil Mech & Fdn Eng Conf Proc, Mexico 1969

Kohno, T., Tanaka, H., Shirato, M. & Nakatani, S., (2010), Evalutation of bending load in batter piles set in soft clay, US _ Japan bridge engineering workshop, New Orleans, Louisiana

Poulos, H.G., (2006), Raked piles – virtues and drawbacks, Journal of geotechnical and geoenvironmental engineering, 132(6)

Randolph, M. F. McClelland lecture Analytical contributions to offshore geotechnical engineering. ISSMGE, Paris

Rao, S.N., Murthy, T.V.B.S.S. & Veeresh, C., (1994), Induced bending moments in batter piles in settling soil, Soils and foundations, 34(1), 127-133

Reese, L.C., Cox, W.R. & Koop, F.D. (1974). Analysis of Laterally Loaded Piles in Sand. Proceedings of the Sixth Annual Offshore Technology Conference, Houston, Texas, Paper No. 2080. 473-483.

Reese, L.C. og Van Impe, W.F. (2001). Single piles and pile groups under lateral loading. A.A. Balkema.

Reese, L., Cox, W., Ko op, F., 1974. Analysis of laterally loaded piles in sand. In: Offshore Technology Conference.

Svahn, P.-O., Alen, C., 2006. Transversalbelastade pålar statiskt verkningssätt och dimensioneringsanvisningar. rapport 101. Tech. rep., Pålkommissionen.

Sørensen, S.P.H., L.B. Ibsen & Augustesen, A.H. (2010). Effects of diameter on initial stiffness of p-y curves for large diameter piles in sand. Proceedings of the 7th European Conference on Numerical Methods in Geotechnical Engineering (NUMGE 2010) (Benz& Nordal (eds)), Taylor, London, 907-912.

Takahashi, K., 1985. Bending of a batter pile due to ground settlement. Soils and foundations 25, 75-91.

Trafikverket, 2011a. Trafikverkets tekniska krav for geokonstruktioner. Tech. rep., Trafikverket.

Trafikverket, 2011b. Trafikverkets råd bro. Tech. rep., Trafikverket.

Verdue, L., Garnier, J. & Levacher, D. (2003). Lateral cyclic loading of single piles in sand. International Journal of Physical Modelling in Ceotechnics 3 (3), 17-28.

Contributions of Janbu and Lade as applied to Reinforced Soil

Peter Hoffman
Reinforced Soil Research Center, Department of Civil Engineering
University of Colorado Denver, USA, peter.hoffman@ucdenver.edu

ABSTRACT
The expression for Young's Modulus of soil was developed by Janbu [1963] and refined by Lade [1987]. Analogous to reinforced concrete, reinforced soil behavior is characterized by a modular ratio, that is, by the modulus of soil relative to the modulus of reinforcement. With reliance upon these contributions of Janbu and Lade, the capacity and deformation of reinforced soil structures are calculated. These calculations are validated with test data from the U.S. Federal Highway Administration.

Keywords: reinforced soil, elastic, plastic, steel, geosynthetic

1 INTRODUCTION

Without an equation due to Janbu and Lade, deformation of reinforced soil cannot be calculated. This equation is also used in the capacity calculation of steel reinforced soil.

Hooke's law, in Section 2, is fundamental to elastic and plastic calculations. Section 3 explains shear lag in construction materials. Section 4 elaborates on the equations of Janbu and Lade for Young's modulus in soil.

Section 5 shows that geosynthetic reinforced soil exhibits plastic behavior while steel reinforced soil remains elastic. Details of the calculation are relegated to the Appendix, but the "quad chart" is introduced to characterize behavior.

Section 6 validates the calculations and the quad chart.

2 MECHANICS OF REINFORCED SOIL

Poisson's ratio plays a primary role in reinforced soil: vertical compression causes horizontal extension, which mobilizes the reinforcement and increases confining pressure. Elasticity, which always prevails at small loads, determines whether plasticity occurs at large loads in a reinforced soil composite. The compacted engineered fill of a structure is homogeneous, isotropic, and elastic, and it follows from Hooke's law

$$\varepsilon_x = \frac{1}{E}\left[\sigma_x - \nu\left(\sigma_y + \sigma_z\right)\right] \qquad (1)$$

that, for a square or round pier,

$$\frac{K}{K_A} = \frac{K_P}{2 + 2.25W\dfrac{E_S}{E_R}} \qquad (2)$$

where K/K_A is a parameter used by the American Association of State Highway and Transportation Officials (AASHTO); otherwise, K_A and K_P would be eliminated.

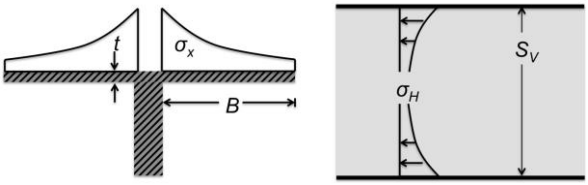
Equation (2) assumes an aggregate that drains well, has negligible cohesion, and has a Poisson's ratio of approximately $\nu = 1/3$. $K = \sigma_H/\sigma_V$ during elastic deformation while $K_A = \sigma_3/\sigma_1$ is the ratio of principal stresses at plastic yield. K_A is the coefficient of active lateral earth pressure, and K/K_A measures the mobilization *(M)* of confining pressure. Elasticity is associated with $K/K_A > 1$, and plasticity with $K/K_A < 1$. $1/K_A = K_P = \tan^2 \alpha_f$, where $\alpha_f = 45° + \phi/2$ is the failure angle and $\phi = \phi'$ is the effective stress friction angle. Analogous to reinforced concrete, the modular ratio E_S/E_R compares soil stiffness and reinforcement stiffness within the

reinforced layer. Shear lag is associated with *W*. Equation (2) also applies to piers when '2.25' is increased to '3', which reduces stiffness.

The parameters *W* and E_S are examined in the next sections.

3 SHEAR LAG AND *W*

Shear lag in reinforced soil is measured by *W*. Shear lag limits the effectiveness of beams with wide flanges. Steel and concrete beams carry less stress at the flange tip than at the web. Similarly, soil contributes less confining pressure at the middle of a soil layer than at the reinforcement.



(a) (b)

Figure 1 Shear lag in (a) beams is analogous to shear lag in (b) reinforced soil.

In a beam, shear lag is determined by the ratio *B*/*t* of flange width and thickness. In sheet reinforced soil, shear lag is determined by the ratio S_V/D_{max} of reinforcement spacing and soil particle diameter (Pham 2009, Adams et al. 2011, Wu and Pham 2013).

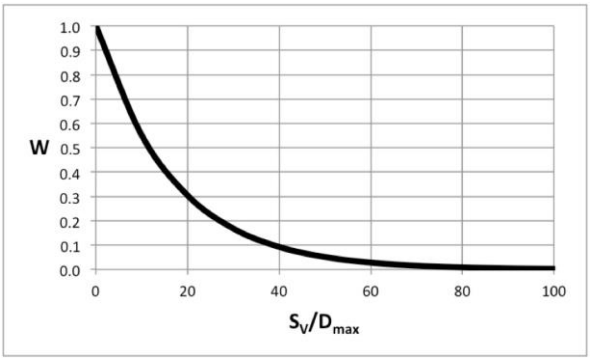


Figure 2 Shear lag is measured by W, a function of sheet spacing and soil particle size.

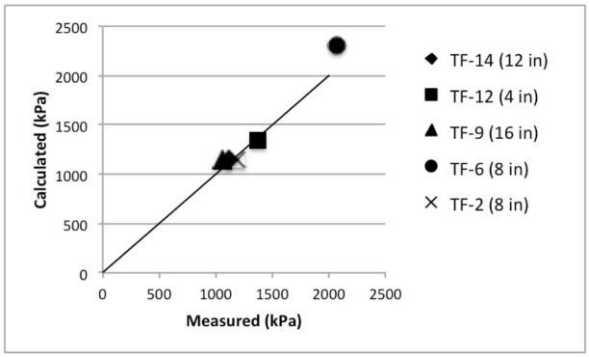
With strip reinforcement rather than sheets, *W* would be much smaller. The US Federal Highway Administration (FHWA) validated the phenomenon of shear lag in geosynthetic reinforced soil. In a series of tests, FHWA loaded faced and unfaced piers to ultimate capacity (Nicks et al. 2013).



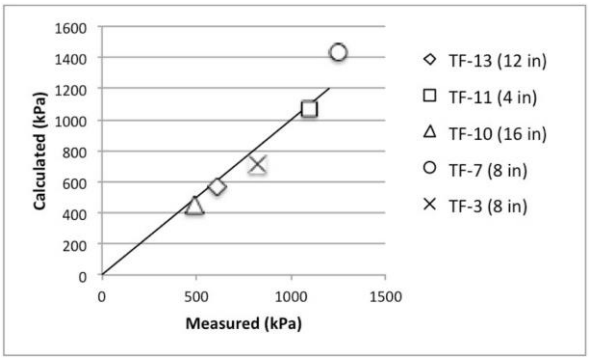
(a) (b)

Figure 3 FHWA tested both (a) faced piers and (b) unfaced piers to ultimate capacity.

Using *W*, capacity is calculated with the Lower Bound Theorem of plasticity theory. Validating *W*, FHWA data show that measured capacities agree with calculated capacities, $Q_{ult} = K_P T_f / S_V$ for faced piers and $q_{ult} = WQ_{ult}$ for unfaced piers. T_f is tensile strength of sheet reinforcement, and S_V is its vertical spacing. Facings withstand lateral pressure of $K_A Q_{ult}$ (Wu and Payeur 2014).



(a)



(b)

Figure 4 Validating W, measurements agree with calculated capacities (a) Q_{ult} for faced piers and (b) $q_{ult} = WQ_{ult}$ for unfaced piers.

4 JANBU, LADE, AND E_S

E_S, the Young's modulus of soil, is required by Equation (2) for calculation of K/K_A. More precisely, E_S is required in order to determine

- capacity of soil reinforced with steel
- deformation of soil reinforced with either steel or geosynthetics

Showing experimental insight, Janbu (1963) provided the well-known expression

$$E_S = Kp_a\left(\frac{\sigma}{p_a}\right)^n \qquad (3)$$

where σ is lateral confining pressure and p_a is atmospheric pressure. Parameters K and n are specific to a soil.

Figures 5 and 6 show Janbu's plots, slightly adapted. Figure 5 shows that $K \approx 500$ for aggregates. Figure 6 indicates that $n = 0$ for solid rock, $n = 1$ for wet clay, and n ≈ 0.5 for aggregates.

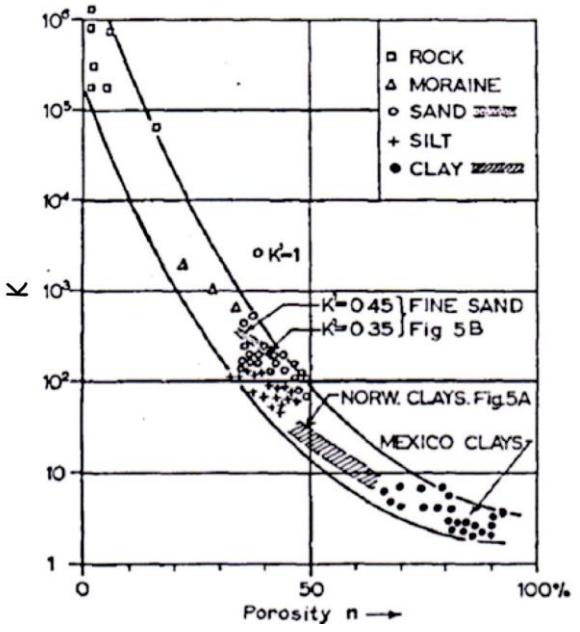


Figure 5 Janbu's data show that K ≈ 500 for aggregates.

Equation (3) poses difficulties. Strain energy is not conserved around load paths that are closed loops involving shear as well as confining pressure.

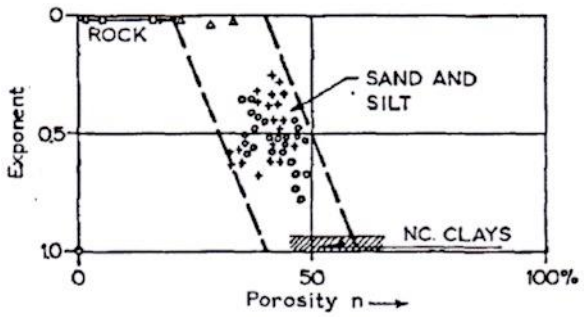


Figure 6 Janbu's data show that n ≈ 0.5 for aggregates.

With analytical elegance, Lade (1987) incorporated shear into the equation

$$E_S = Kp_a\left(\frac{\sqrt{p^2 + rq^2}}{p_a}\right)^n \qquad (4)$$

through the tensor invariants, $p = I_1/3$ for the hydrostatic pressure and $q = \sqrt{J_2}$ and for the deviatoric stress. Then, r is a function of Poisson's ratio only.

While Janbu's approach was entirely experimental, Lade's was totally analytical, using advanced calculus and assuming only the definition of strain energy.

Amazingly, the elastic constant K can be determined from the plastic constant K_P because the elastic zone touches the plastic yield surface in stress space. This enables K to be written as a function of K_P. Observe that $2p = (K_P + 1)\ \sigma_3$ and $2q = (K_P - 1)\ \sigma_3$ in two dimensions. Duncan et alia (1978) published data for 30 aggregates, which are compiled from several laboratories. The best fit is $K = 100\ K_P$, which is consistent with Janbu's $K \approx 500$ for aggregates in Figure 7.

Janbu's data also show that $n \approx 0.5$ for aggregates. This fact is easily shown mathematically for small strains. Because E is presumably a smooth function of strain ε when there is no plasticity (no clay), its Taylor expansion is $E = a_o + a\varepsilon = a\sigma/E$ when cohesion is zero. So, E is proportional to $\sigma^{1/2}$.

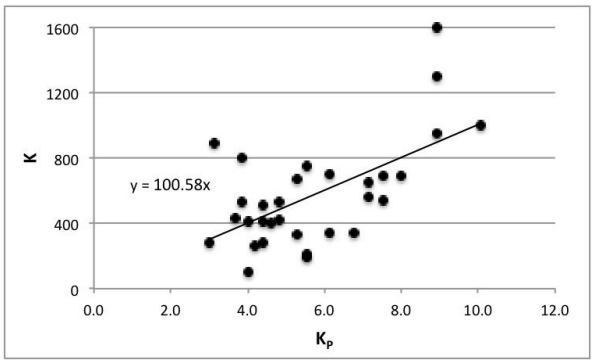


Figure 7 The data show that $K \approx 100\ K_P$ for aggregates.

In summary,

$$E_S = 100 K_P p_a \left(\frac{\sigma_3}{p_a} \right)^{0.5} \qquad (5)$$

is used with Equation (2) and with $\sigma_3 = \sigma_H$ in order to calculate the mobilization $M = K/K_A$.

5 APPLICATION

Consider a square reinforced soil pier with

- 70 kN/m = T_f (sheet tensile strength of reinforcement)
- 0.2 m = S_V (vertical spacing of reinforcement)
- 45° = ϕ (friction angle of soil)
- 0.013 m = D_{max} (diameter of large soil particles)
- 10% & 0.25% = ε_R (extensibility for geosynthetic and steel, respectively)

Extensibility is strain in the reinforcement as T_f is reached. The Appendix provides the detailed calculation. As shown in Figure 8, steel and geosynthetics give reinforced soils that behave quite differently. With ε_R = 3%, fiberglass lies between them and is being installed for reinforced soil foundations beneath commuter rail tracks in the US.

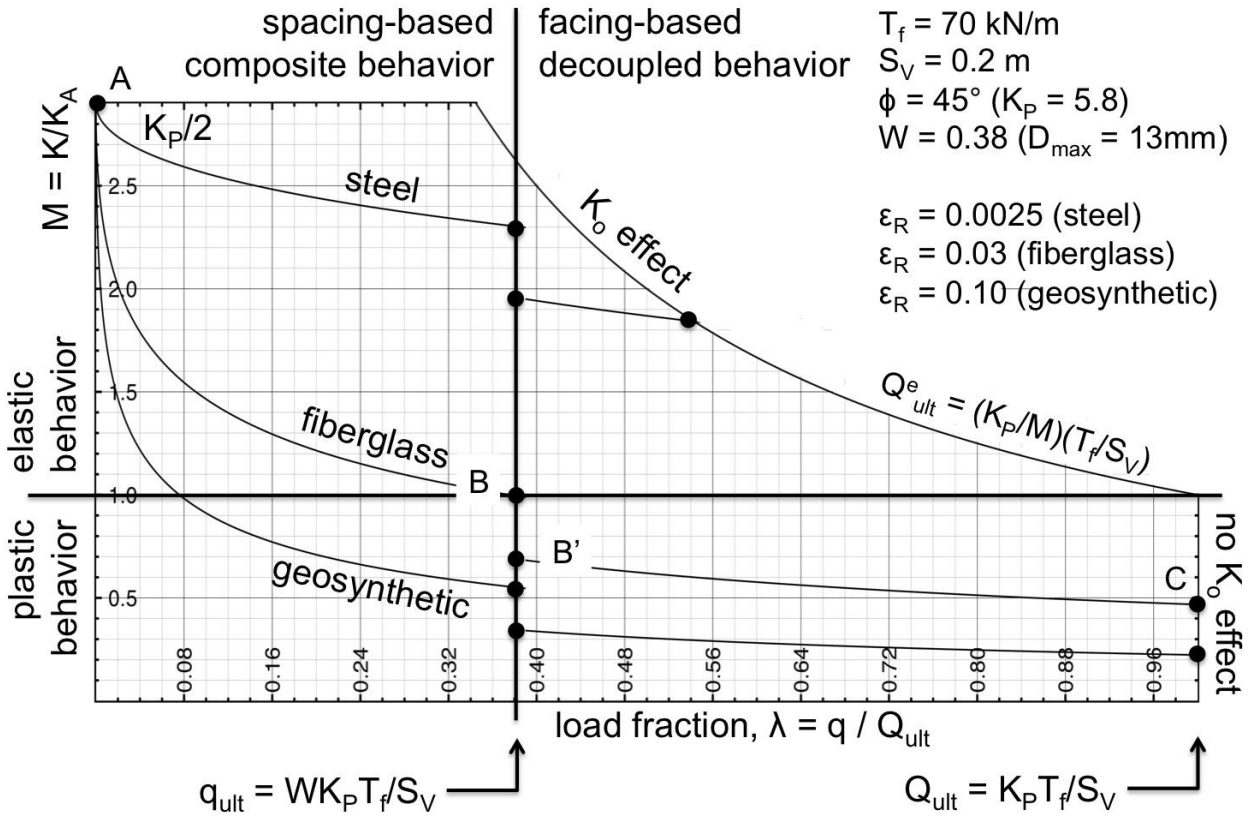


Figure 8 Due to extensibility, geosynthetic reinforced soil behaves quite differently from steel reinforced soil. Between steel and geosynthetic, fiberglass behaves nicely. Lines M =1 and λ = W divide the chart into four quadrants, each with unique attributes. The maximum value is $M = K_P/2$.

At ultimate capacity, both elastic and plastic deformation are present in the geosynthetic reinforced soil. Elastic strain is calculated from E_S. Plastic strain is calculated from the mobilization, $M = K/K_A$, by Figure 9.

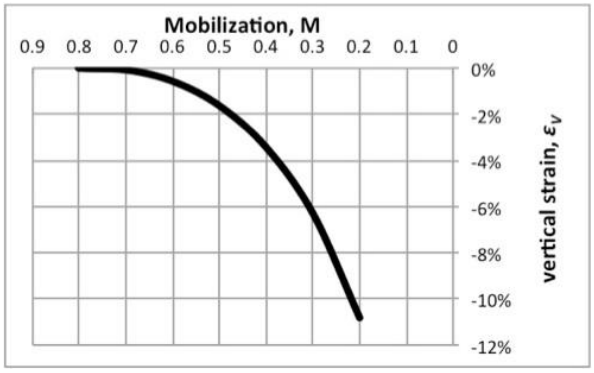
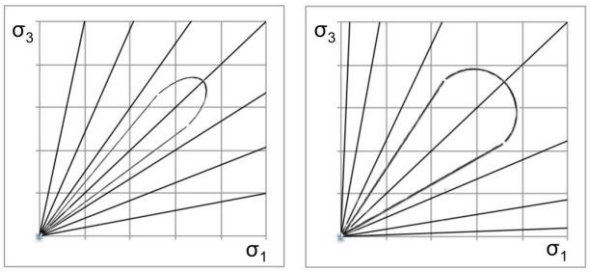


Figure 9 Mobilization, $M = K/K_A$ determines vertical strain due to plasticity.

Figure 9 is derived on the premise that plastic slip accommodates the shortage of mobilized elastic strength when $K < K_A$ (Hoffman and Wu 2015). The derivation uses plasticity theory in the tradition of Prandtl and Sokolovskii before non-associated plastic potentials. The yield surface is drawn in stress space, and in the derivation, the plastic potential is the yield surface drawn in Euclidean space. Stress space distorts geometry, and yield surfaces appear too wide and too strong. For example, lines with slope $\sqrt{K_A}$ or $\sqrt{K_P}$ in Euclidean space have slope K_A or K_P in stress space.



(a) (b)

Figure 10 Compared to (a) Euclidean space, (b) stress space σ_1-σ_3 distorts geometry.

6 VALIDATION

The four quadrants of Figure 8 exhibit individual behaviors. When $K/K_A < 1$, the structure exhibits plastic deformation because soil stiffness exceeds reinforcement stiffness in the sense of Equation 2. When the spacing-based capacity is exceeded, transition occurs as the core of the soil layer decouples from the reinforcement and presses against the facing; therefore, bulging and creep appear.

composite elastic 2	1 decoupled elastic
composite plastic 3	4 decoupled plastic

Figure 11 Attributes of the four quadrants

Examples are now provided for each of the four quadrants.

6.1 First Quadrant

With its curved boundary, the first quadrant appears strange. For steel reinforced soil, capacity involves division by M where $M > 1$, and the curve results from that division.

Poorly-behaved steel reinforced soil lies in the first quadrant. For validation, consider the SS3 steel strip wall constructed at Vicksburg in the USA (Allen et al. 2001). As indicated in Figure 12, failure of SS3 coincides with the quadrant's calculated boundary.

Prior to failure, "significant bulging" was reported for SS3.

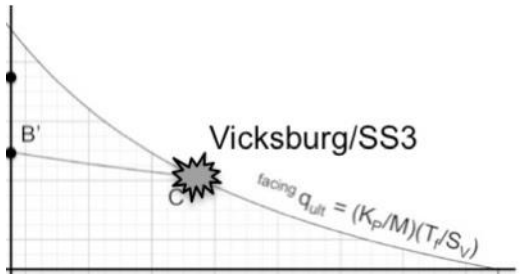


Figure 12 Failure of SS3 lies on the quadrant's calculated boundary. "Significant bulging" preceded failure.

6.2 Second Quadrant

Well-behaved steel reinforced soil structures lie in the second quadrant. As Figure 13 illustrates, their K/K_A curves rise steeply. Consider the welded wire fabric wall, WW1, constructed on I-90 at Rainier Avenue in

Seattle (Bathurst et al. 2009). Figure 13 compares calculations, measurements, and the design curve of the AASHTO Simplified Method (Anderson et al. 2012, Bathurst et al. 2009). The bends in the curves reflect transition between the first and second quadrants.

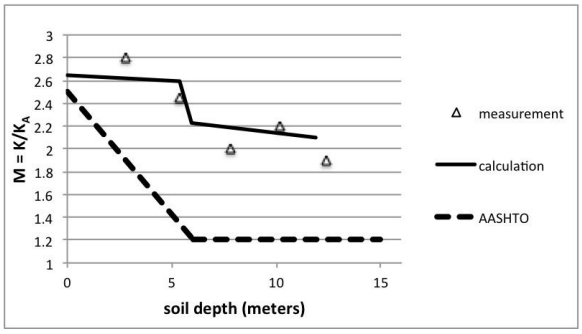


Figure 13 Measurements, calculations, and AASHTO's Simplified Method are compared for welded wire fabric wall WW1.

6.3 Third Quadrant

Well-behaved geosynthetic reinforced soil structures lie in the third quadrant. Consider four early pier tests by Defiance County, Ohio (USA) and FHWA (Adams et al. 2011). Values of K/K_A are calculated, converted to deformations, and compared with test data in Figure 14.

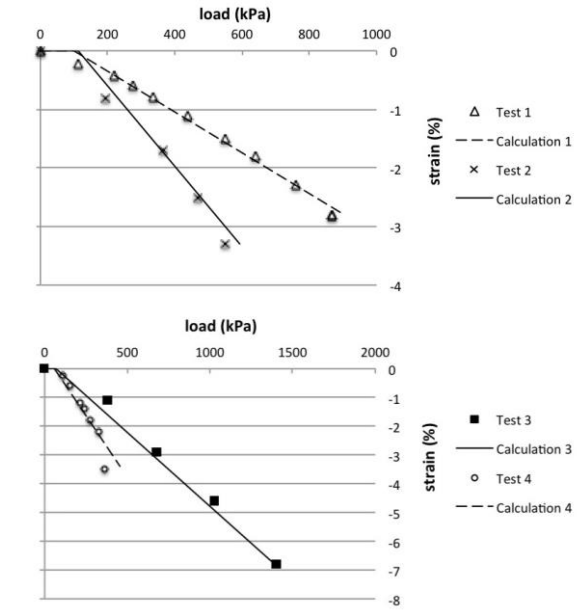


Figure 14 Calculations and measurements for four early pier tests, where load ≤ q_{ult} = WQ

In Figure 14, the final test data point departs from the line in each case. This reflects the onset of transition between the third and fourth quadrants. Increased facing pressure is also associated with transition.

Since 2011, FHWA has upgraded to measure ultimate capacities at very large strains. In Figure 15, transition at $q_{ult} = WQ_{ult}$ (near 500 kPa) is validated by FHWA Tests TF-9 and TF-10 (Nicks et al. 2013). These are faced and unfaced tests with 0.4 m (16 inch) spacing. Large strains are unacceptable in construction, but they reveal behavior and validate the quad chart for reinforced soil.

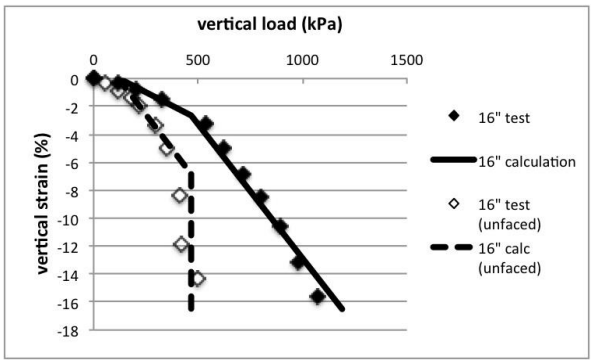


Figure 15 Transition at $q_{ult} = WQ_{ult}$ (near 500 kPa) is validated for faced/unfaced pair of piers.

6.4 Fourth Quadrant

Creep occurs in this quadrant:

- CDOT/aggregate - one of several creep tests conducted by CU Denver and the Colorado DOT (Ketchart and Wu 1996)
- I-90 temp/Seattle - GW16 existed for one year during construction (Allen and Bathurst 2003)
- Japan/GW35 - test wall built by the Public Works Research Institute (Bathurst et al, 2008)
- Yeager Airport - disaster in March 2015 destroyed a 50-home community in West Virginia (Lostumbo 2010). This soil structure predates the publication of shear lag research for reinforced soil.

Figure 16 displays the four creep cases in quad chart format.

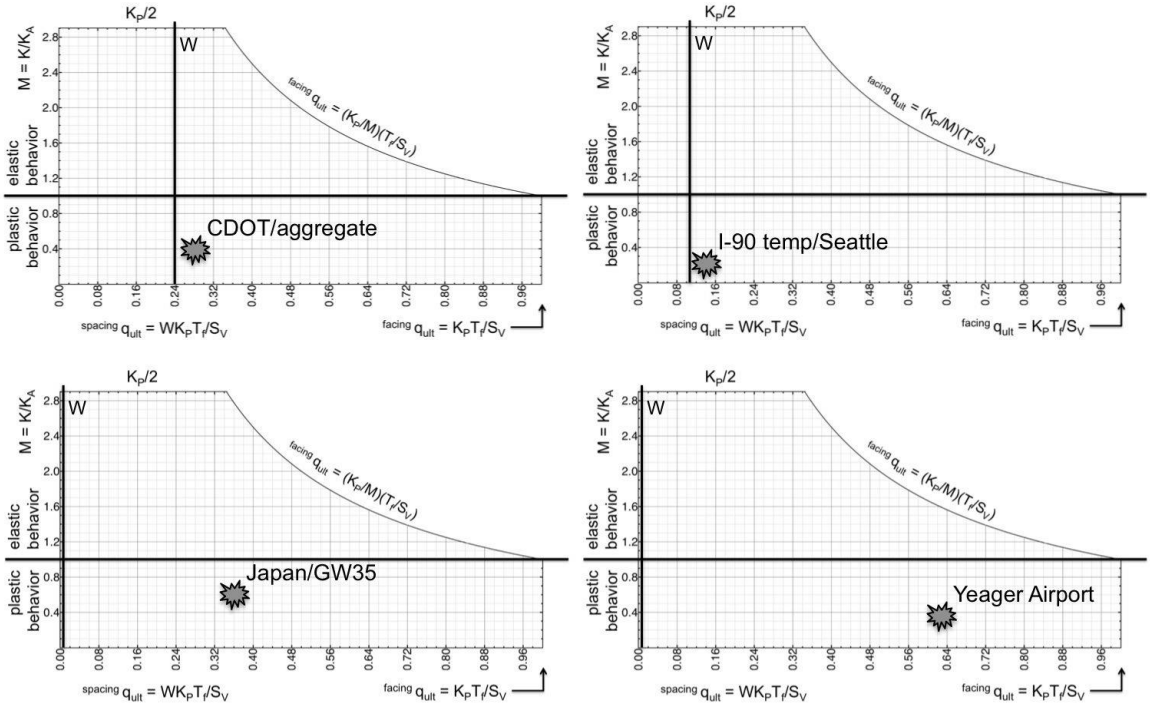


Figure 16 Known cases of creep are right of the transition or W-line.

7 CONCLUSIONS

Increasingly, reinforced soil lurks as a threat within the infrastructure. Collapse of the 75 meter geogrid structure at Yeager Airport (USA) destroyed a 50-home community in 2015. Failures of many small structures are incorrectly attributed to water, which is a secondary cause or accelerant. Bulging and serviceability problems are abundant.

Critical issues are characterized by the quad chart introduced in Section 5. Behavior is determined by shear lag and by the modular ratio between soil stiffness and reinforcement stiffness. Without Janbu and Lade, we would not understand this modular ratio. Their contributions are essential to the quad chart. Their equations reveal that behavior of steel reinforced soil is elastic while behavior with geosynthetics is plastic and quite different.

Safety demands maturity for reinforced soil. Maturity of the industry can be and should be raised toward the level of maturity achieved for reinforced concrete.

8 APPENDIX

The calculation of $M = K/K_A$ uses the method of Hoffman and Wu (2015). Although values can be calculated for any load, they are calculated here for ultimate capacity q_{ult} at its Point B, immediately left of the transition or *W*-line. The calculation is performed here for a geosynthetic wall or abutment.

As in reinforced concrete, Equation 2 reveals the importance of the modular ratio, E_S/E_R. For reinforcement, E_R involves the extensibility ε_R, which is perhaps the most critical parameter in reinforced soil design. For soil, E_S is determined by Equation 5, but confining pressure σ_H must first be estimated.

$$\begin{aligned} \sigma_H^{\max} &= MK_A q_{ult} \\ &= MK_A K_P W T_f / S_V \\ &= MWT_f / S_V \end{aligned} \qquad (6)$$

The average is obtained by evaluating E_S at 0.44 $\sigma_H^{\max}$, not 0.50 $\sigma_H^{\max}$, because of the square root in Equation 5. Thus,

$$\sigma_H = 0.44 M W T_f / S_V \quad (7)$$

$M = K/K_A$ is found by simultaneous solution of Equations 2, 5, and 7.

Parameters for the geosynthetic are T_f = 70 kN/m, S_V = 0.2 m, ϕ = 45°, D_{max} = 13 mm, and ε_R = 10%. At best, they are accurate to two decimal places, and the calculations of this appendix keep two digits of accuracy.

First, the intermediate parameters are

$$K_P = \tan^2\left(45° + \phi/2\right) = 5.8 \quad (8)$$

$$W = 0.7^{S_V / 6D_{\max}} = 0.39 \quad (9)$$

$$E_R = \frac{T_f}{\varepsilon_R S_V} = 3500 \text{ kPa} = 3.5 \text{ MPa} \quad (10)$$

Then, the three equations for $M = K/K_A$ at Point B are

$$\sigma_H = 0.44 M W T_f / S_V = 60M \text{ kPa} \quad (11)$$

$$E_S = 100 K_P \sqrt{p_a}\sqrt{\sigma_H} \text{ kPa} = K_P \sqrt{\sigma_H} \text{ MPa} = 5.8\sqrt{\sigma_H} \text{ MPa} \quad (12)$$

$$M = K_P / \left(2 + 2.25 W \frac{E_S}{E_R}\right) = 5.8/\left(2 + 0.25 E_S\right) \quad (13)$$

The system is solved by iteration in Table 1.

Table 1 Iteration for Point B of geosynthetic

Equation	iter 1	iter 2	iter 3	iter 4
$\sigma_H = 60M$ kPa	60	43	37	34
$E_S = 5.8\sqrt{\sigma_H}$ MPa	45	38	35	**34**
$M = 5.8/\left(2 + 0.25E_S\right)$	.44	.50	.54	.55
(M_{init} = 1.0) $M_{average}$:	.72	.61	.57	**.56**

Two successive values of M are averaged in order to stabilize the iteration. $M = K/K_A$ = 0.56 is plotted in Figure 8.

E_S = 34 MPa is highlighted in Table 1 as it can be used to calculate elastic deformation. With extensibility ε_R = 0.25%, steel gives $M = K/K_A$ = 2.3 at Point B. At 3%, fiberglass is well-behaved with $M = K/K_A$ = 1.0.

9 REFERENCES

Adams, M.T., Nicks, J., Stabile, T., Wu, J.T.H., Schlatter, W. and Hartmann, J. (2011). Geosynthetic Reinforced Soil Integrated Bridge System – Interim Implementation Guide. Report No. FHWA-HRT-11-026, Federal Highway Administration, Washington, DC.

Allen, T.M, Christopher, B., Elias, V., and DiMaggio, J. (2001) Development of the Simplified Method for Internal Stability of Mechanically Stabilized Earth Walls. Report WA-RD 513.1, Washington State Department of Transportation, Olympia.

Allen, T.M., and Bathurst, R.J. (2003). Prediction of Reinforcement Loads in Reinforced Soil Walls. Report WA-522.2, Washington State Department of Transportation, Olympia, WA.

Anderson, P.L., Gladstone, R.A., and Sankey, J.E. (2012). State of the Practice of MSE Wall Design for Highway Structures, Geotechnical Engineering State of the Art and Practice: Keynote Lectures for GeoCongress 2012, Oakland, CA.

Bathurst, R.J., Miyata, Y., Nernheim, A., and Allen, A.M. (2008), Refinement of K-stiffness Method for Geosythetic-reinforced Soil Walls, Report HIIFP-095j , Highway Infrastructure Innovation Funding Program, Ontario Ministry of Transportation.

Bathurst, R.J., Nernheim, A., and Allen, T.M. (2009). Predicted Loads in Steel Reinforced Soil Walls Using the AASHTO Simplified Method, J. Geotech. Geoenviron. Eng. ASCE 135, 177-184.

Duncan, J.M., Byrne, P., Wong, K.S., and Mabry, P. (1978). Strength, Stress-Strain and Bulk Modulus Parameters for Finite Element Analysis of Stresses and Movements in Soil Masses. Report No. UCB/GT/78-02, University of California, Berkeley.

Hoffman, P.F., and Wu, J.T.H. (2015). An Analytical Model for Predicting Load-Deformation Behavior of the FHWA GRS-IBS Performance Test, International Journal of Geotechnical Engineering, Vol 9, Issue 2: 150-162.

Janbu, N. (1963). Soil Compressibility as Determined by Oedometer and Triaxial Tests, European Conference on Soil Mechanics and Foundation Engineering, Wiesbaden, Germany, Vol. 1, pp. 19-25.

Ketchart, K., and Wu, J.T.H. (1996). Long-Term Performance Tests of Soil-Geosynthetic Composites Report No. CDOT-CTI-96-1, Colorado Department of Transportation, Denver.

Lade, P.V., and Nelson, R.B. (1987). Modelling the Elastic Behavior of Granular Materials, International Journal for Numerical and Analytical Methods in Geomechanics, 11, 521-542.

Lostumbo, J.M. (2010). Yeager Airport Runway Extension, Presented at the 2010 Southeastern Transportation Geotechnical Engineering Conference (STGEC), Charleston, WV.

Nicks, J.E., Adams, M.T., and Ooi, P.S.K. (2013). Geosynthetic Reinforced Soil Performance Testing: Axial Load Deformation Relationships, Report No. FHWA-HRT-13-066, Federal Highway Administration, McLean, VA.

Pham, T. Q. (2009). Investigating Composite Behavior of Geosynthetic-Reinforced Soil (GRS) Mass. Ph.D. Dissertation, University of Colorado Denver.

Wu, J.T.H., and Payeur, J-B. (2014). "Connection Stability Analysis of Segmental Geosynthetic Reinforced Soil (GRS) Walls." *Transportation Infrastructure Geotechnology*, 2(1). DOI 10.1007/s40515-014-0013-4.

Wu, J.T.H. and Pham, T.Q (2013). Load Carrying Capacity and Required Reinforcement Strength of Closely Spaced Soil-Geosynthetic Composites, J. Geotech. Geoenviron. Eng. ASCE 139(9), 1468–1476.

Laboratory study on two-dimensional image analysis as a tool to evaluate degradation of granular fill materials

E. Bergliv. Corresponding / primary author
Luleå University of Technology, Sweden, elin.bergliv@ltu.se

T. Edeskär. Co-Author
Luleå University of Technology, Sweden

ABSTRACT
The shape of granular materials is known to affect strength and stiffness properties of soil and fills. Settlements in coarse fills are often explained by rearrangement within the soil skeleton induced by crushing and rounding of the individual aggregates in the intergranular contact points. These processes are not well investigated since it is difficult to measure changes at an aggregate level.

Currently few attempts have been made to effectively measure and classify shape of granular soil and fill materials. One of the more promising methodologies is digital image analysis. Even if there are some studies on both two and three dimensional analyses on shape of aggregates, no study has focused on identifying shape changes as function of degradation effects of the fill materials.

In this study degradation of ballast material has been studied in standardized micro Deval and Los Angeles tests and analysed by two dimensional image analysis and statistical methods. The results showed it was possible to statistically separate the shape and size of the materials before and after the degradation tests. To identify this difference it is essential to use more than one variable each for size and shape.

The conclusion of the study is that two-dimensional image analysis can be used as a tool to measure and quantify shape changes on an aggregate level in order to measure degradation. If further developed, the technique can be useful to study deformation processes, e.g. crushing and rounding of aggregates, in coarse fill materials.

Keywords: Digital image analysis, granular material, degradation, factor analysis.

1 INTRODUCTION

Physical weathering and degradation affects the size and shape of soil and ballast materials. In this study weathering is defined as natural geological processes and degradation the effect of induced loads by use in e.g. roads and railway constructions.

Effects of degradation of the material come with deformations and lower strength, possibly failure. The degradation changes mechanical properties (friction angle, stiffness, strength, and so on) and causes deformations due to wearing, rearranging/sliding, or fragmentation of the individual grains (Alshibli & Alsaleh, 2004; Cho et al, 2006; Cox & Budhu, 2010; Guo & Su, 2007; Hansson & Svensson, 2001; Zeghal, 2009; among others). Currently the standardized methods of measuring (resistance to) degradation are by material quality testing with Los Angeles or micro Deval tests. These tests measure the generated amount of degraded material (smaller than 1.6 mm) after milling. For roads and railways the results from the tests are used as material quality requirements (Trafikverket, 2011; Banverket, 2004).

Image analysis of grains is a new concept to investigate degradation of large grains on particle level, due to the shape and size change that occurs during degradation. If properties of a granular material can be connected to the grain shape, it will be easier to understand how degradation, which causes changed grain shape, affects a material. Granular materials can be evaluated for their performance depending on their grains' shape.

The shape of grains has an effect on properties of granular material (Alshibli & Alsaleh, 2004; Cho et al, 2006; Cox & Budhu, 2010; Guo & Su, 2007; Hansson & Svensson, 2001; Zeghal, 2009; among others). One generally accepted shape division is crushed and natural material; natural material is rounded and smooth and crushed material is angular, rough and has sharp edges. In construction crushed material is often preferred due to interlocking effects of the angular shape and high friction due to the surface friction. In this division between natural and crushed material the shape of the grains are quite different and the materials can be distinguished by ocular inspection.

Another way in which grain shape is taken into consideration for construction purposes is by limiting the amount of flat or elongated grains. Flat and/or elongated grains can bend and therefore give higher deformations (Lambe & Whitman, 1969). This shape factor is measured in two standardized ways; LT-index and flakiness index.

According to Mitchell & Soga (2005) grain shape is described in three different scales, see Figure 1. Morphology is the largest and describes the overall shape of a grain taking the different dimensions into consideration. Examples of descriptive terms are elongated, round, elliptical, cubic, or flat. The intermediate scale is called roundness and takes the level of unevenness and edges into consideration. The edges are described as round or angular. The smallest scale is called roughness, and takes the small edges and the structure into consideration. A grain's roughness is described as smooth/even or rough. There is no distinct line between what characteristics are classified as roundness and roughness, other than that roughness describes shape on a smaller scale than roundness.

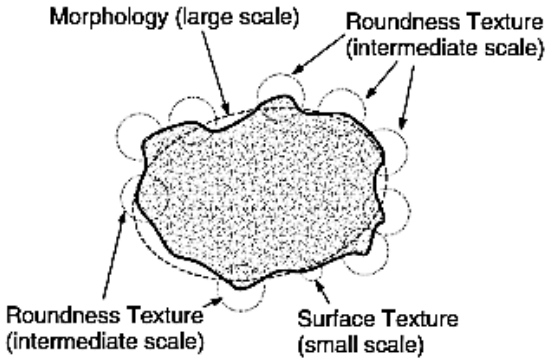


Figure 1. Scale descriptors of a grain (Mitchell & Soga, 2005).

Grain shape can be measured in two or three dimensions. Different measurement methods are hand measurement, photography with image analysis and laser scanning, all with different required equipment, variability and data output (Rodriguez et al, 2013).

Image analysis is a way of performing grain shape measurement. More complex measurements can be taken and more data can be collected faster than by hand. Both 2D and 3D image analysis is possible, where 2D image analysis uses one photograph to identify and analyse grain shape based on one projection. 3D image analysis requires two or more photographs, often orthogonally oriented, to find the shape of a grain. There are different methods of photographing for 3D image analysis, either each grain is mounted in a holder, where one or two cameras capture the shape from two different directions, or an orthogonal camera set up is used to capture the shape of falling grains. Photography for 2D image analysis is faster than for 3D image analysis, but at the cost that only two dimensions are captured.

To be able to use 2D image analysis to investigate degradation it has to be verified that the method can identify shape changes and investigated if, at all, degradation can be identified. In this paper the hypothesis is that 2D image analysis can be used to identify degradation by using shape and size related parameters. This is studied by evaluation of ballast material in standardized micro Deval and Los Angeles tests.

2 MATERIAL & METHODS

The experimental part of the study was conducted according to the schema in Figure 2. The samples for the laboratory testing were prepared to correct size (10-14 mm) by sieving, followed by image acquisition of either the whole sample (mDe) or a representative part of the sample, performing the degradation test and final image acquisition of the sample according to the earlier principle.

The images were analysed with the software ImageJ with respect to the size and shape variables; *area*, *Feret's diameter*, *Feret's minimum diameter*, *aspect ratio*, *circularity*, *roundness*, and *solidity*. The data from the image analysis (seven variables) was processed in MATLAB to find the best matching statistical distribution. These distribution values were plotted and further analysed in Microsoft Excel.

Data from the image analysis (ten variables) was processed in MATLAB by factor analysis. Three size variables were added into the data compared to the distribution analysis; *circumference*, *major* and *minor*.

Two different kinds of degradation tests on ballast materials were performed; standardized Los Angeles (LA) and micro Deval (mDe) tests. The tests were performed by an accredited laboratory and the results from the tests were anonymised.

Los Angeles tests were performed according to Swedish standard SS-EN 1097-2:2010, the micro Deval tests were done according to SS-EN 1097-1:2011. Both the two tests were performed by rotation of granular material and steel balls in a drum, where the steel balls degrade the grains. The milling effect on the ballast materials is different. For Los Angeles tests the degradation mode was fragmentation and for micro Deval it was wearing. The same sized material was used for both tests, 10-14 mm, but more material was used for Los Angeles tests, 5 kg, compared to two subsamples of 500 g each for micro Deval tests. Before the tests started, photographs were taken for the image analysis.

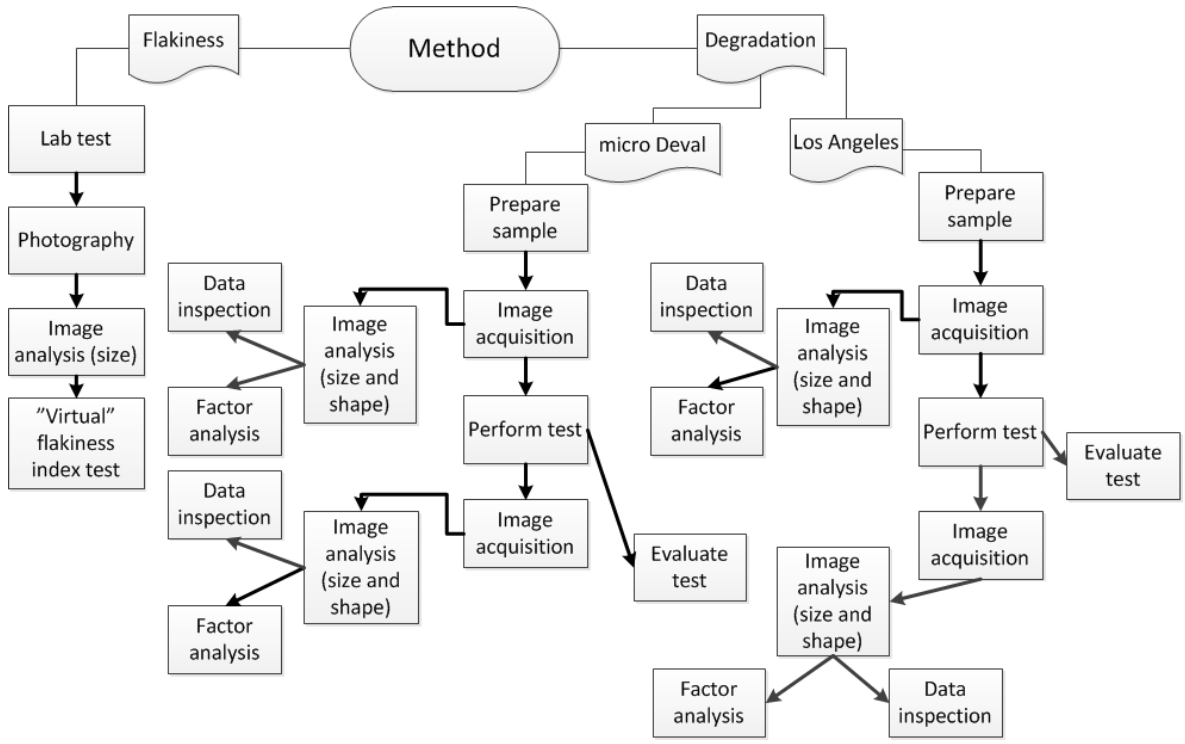


Figure 2. The method description.

The testing procedure and equipment also differs; for Los Angeles tests the drum was bigger and there were fewer but bigger steel balls. The micro Deval testing procedure used many small steel balls and the tests were done in wet condition. The Los Angeles testing is done for 500 revolutions in 31-33 rpm, while 12 000 revolutions were used for micro Deval at around 100 rpm.

After testing the sample was separated from the steel balls and the sample was sieved (the micro Deval samples were dried before sieving). The weight of the material retained on the sieves larger than 1.6 mm is called *m*. The LA and M_{DE} values were calculated with equations 1 and 2.

$$LA = \frac{5000-m}{50} \quad (1)$$

$$M_{DE} = \frac{500-m}{50} \quad (2)$$

For the micro Deval samples the mean value of the two subsamples is used as a representative mean value for the whole sample. The grains that were 4 mm or greater were used for photography, since smaller grains cause dusting and requires higher resolution images to analyse.

The photographs were taken with the camera Nikon D5200 with resolution 24 megapixels. The lens was an AF-S Nikor 18-550 mm f/3.5-5.6G VRII. The camera with lens was mounted on a tripod and angled to take photos from above. Below the camera setup there was a light table, of the size of an A3 paper, covered by 4 mm thick glass. The whole setup can be seen in Figure 3. Two 100 mm scales on a paper below the glass aided in setting up the camera perpendicular to the light table and to identify the size of grains in the image analysis.

The aggregates were randomly dropped to get an arbitrary orientation of the grains and, if it was needed, spread to make sure the whole edge was visible. The grains were also moved from the edge of the light table to cover the entire edge of the grain. Two photos were taken of each grain spread, one that was used for image analysis and one with a note of the unique serial number used for identification and pairing with laboratory results.



Figure 3. Photography setup.

For the Los Angeles tests there was too much material to be able to efficiently photograph all of it. One photograph could contain about 250-300 g of material in the size range 10-14 mm, leading to about 15-20 photographs to document the entire sample (and another 15-20 for identification purposes). To document an entire Los Angeles sample would have been time consuming both in the photography work and in the analysis work. Instead a test was done to see how much material gave a representative sample. The conclusion was that two photographs each containing about 300 g of material gave a representative sample. The whole Los Angeles sample was divided using sample divider three times, leaving about one eighth of the sample (625 g) to be photographed in two photographs. The micro Deval subsamples were of 500 g and using two photographs all the material of the subsample was photographed.

The image analysis was done with the program ImageJ v1.47. After opening an image with the program, the image was inspected for overlapping grains and other faults. Sometimes it was possible to separate the grains (in an image handling program, PaintNet), other times the only option was to delete the overlapping aggregates. When deciding between separating and deleting, the option that would lead to the minimum error was chosen. When the faults have been dealt

with the image analysis could begin. The image was turned into a binary mode (only black and white) and the setting were set to exclude grains on the edge of the light table and to only include grains larger than 20 mm^2 to avoid analysing possible dust (mostly in effect in the post test images). The grain shape parameters used in the image analysis is presented in equations 3-6.

$$Aspect\ ratio = \frac{major}{minor} \quad (3)$$

$$Circularity = \frac{4\pi A}{C^2} \quad (4)$$

$$Solidity = \frac{A}{A_{convex}} \quad (5)$$

$$Roundness = \frac{4A}{\pi \cdot major^2} \quad (6)$$

Where *major* and *minor* (mm) is the greatest and the smallest dimension of the 2D ellipse projection of the grain respectively, *A* is the area (mm^2), *C* is the circumference (mm) and A_{convex} is the area of the grain if all the irregularities would be jointed (mm^2). Despite the name of the last variable, *roundness*, the variables does not measure the intermediate scale (also called roundness) but rather the overall shape of the grain (largest scale).

The output from the analysis was presented in a numbered table containing each grain's data and an outline image with numbered grains. The data was exported to Microsoft Excel where the image analysis result from the scales were identified and removed. Other possible deviant results could also be identified in Excel by sorting from smallest to largest and finding more faults. If faults were discovered, the results were removed or the faults were corrected and the image analysis redone. The data from the two different pictures for each sample were added to the same Excel file.

From Excel the data was imported into MATLAB, where the best statistical distribution for each variable was identified, using the *Distribution fitting tool* and ocular inspection. The best distribution matches of all variables of all samples were documented and the most common distribution for each variable was chosen as the overall best. Using the same distribution for the same variables both before and after and for both kinds of degradation test makes it possible to fully compare the results. The distribution values are imported into Excel where the results are visualized and compared.

To see variations between different shape parameters and how they vary with degradation multivariate data analysis was used. The analysis method factor analysis was used to find fewer independent factors than there are shape and size variables in the image analysis.

The factor analysis was done in MATLAB. There are a number of steps to performing a factor analysis, not covered here, instead a reference handbook in the subject can be used, for example Hair et al, 2010. The most important parts are choosing the number of factors in the analysis and the rotation of the loadings matrix *Λ*. For this analysis the number of factors and the rotation had to be the same for all samples to be able to compare the results.

3 RESULTS

3.1 Lab test

In total twelve micro Deval tests were done, with most values between 10 and 13, but also two values at five and seven each. Seven Los Angeles tests were done with more varied results, from 16 to 32. In Figure 4 and Figure 5 the laboratory results are presented, even though the main purpose of the figures show size parameters from the image analysis.

3.2 Image analysis

The distributions for all variables were found by ocular comparison in MATLAB's *Distribution fitting tool*. For two variables the best distribution was extreme value distribution; *circularity* and *solidity*, for all other variables the best distribution was generalized extreme value distribution.

In the following figures the distribution value (location parameter) for each of the different variables are presented. In Figure 4 the size parameters before and after micro

Deval test are presented. All the parameters show decrease after test. In Figure 5 the same trend can be seen for Los Angeles test, decreasing size after test. The higher the LA value or M_{DE} value, the more the grains are affected by the degradation. Despite this there cannot be found any trend that shows larger size decrease after testing for higher test values.

One can note that before testing *Feret's diameter* is in the range of 15-21 mm, and *Feret's minimum diameter* is in the range of 11-14 mm. Since the samples are sieved to 10-14 mm this result shows that the image analysis does not measure the same dimension as determined by the sieving.

The shape parameters *circularity* and *solidity* from the image analysis is presented in boxplots in Figure 6. The variable *circularity* clearly shows increase after testing for both Los Angeles and micro Deval. This means that the grains become more circular. For Los Angeles tests the *solidity* shows no clear change after testing, but for the micro Deval test the *solidity* show increase, indicating more even grains after testing.

The *aspect ratio* boxplots are seen in Figure 7. For Los Angeles testing the variation decreases after testing and the *aspect ratio* becomes lower after testing, indicating that the grains become more circular. For micro Deval the variation of the *aspect ratio* increases after testing, but the means is approximately the same. This means no clear trend can be seen.

The *roundness* boxplots are seen in Figure 8. The Los Angeles testing results in increased *roundness*, giving more circular grains. The micro Deval *roundness* shows increase variation, but no clear trend caused by testing.

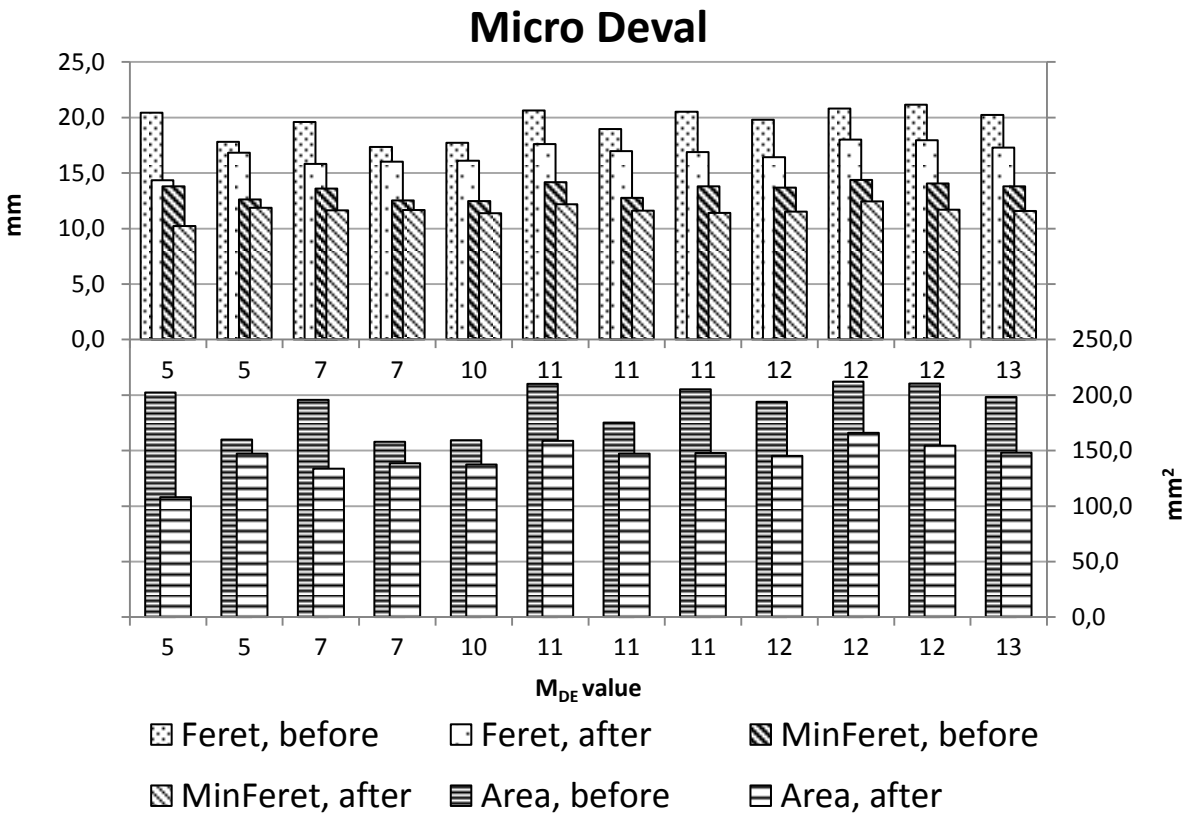


Figure 4. Size parameters for micro Deval samples.

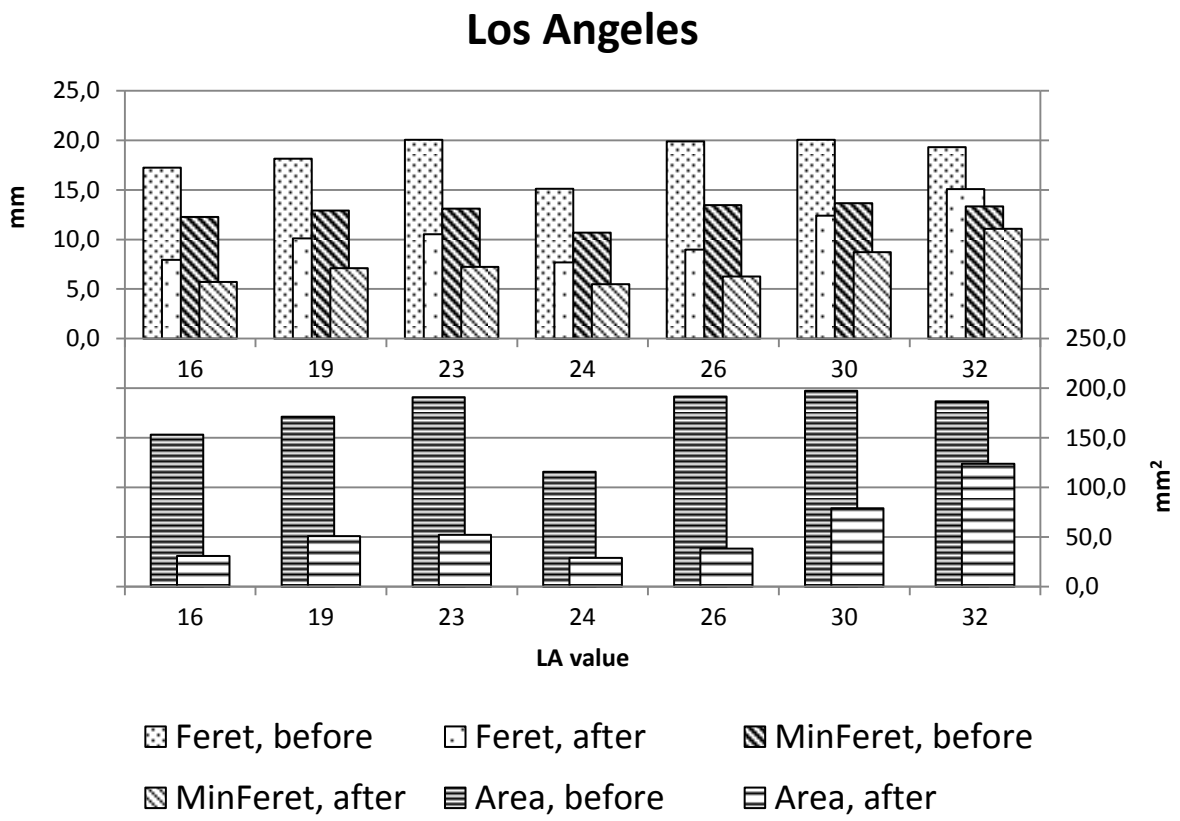


Figure 5. Size parameters before and after Los Angeles test.

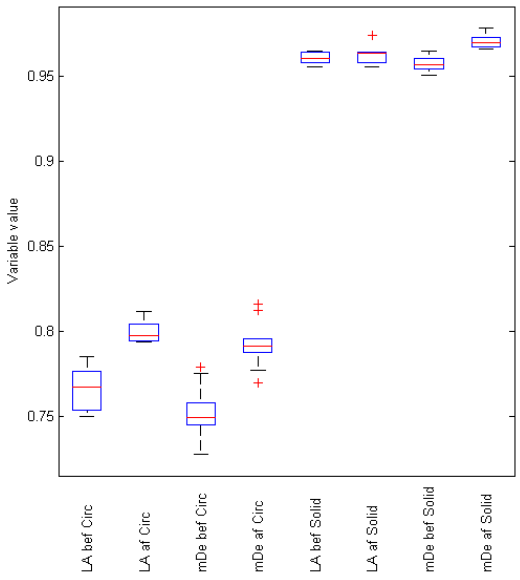


Figure 6. Shape parameters circularity and solidity.

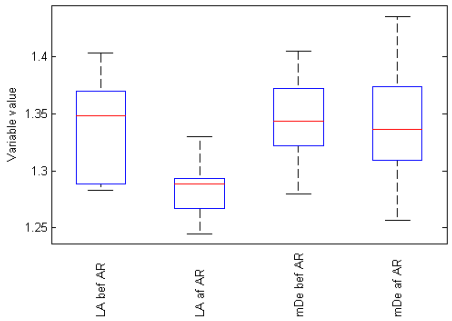


Figure 7. Boxplots for aspect ratio.

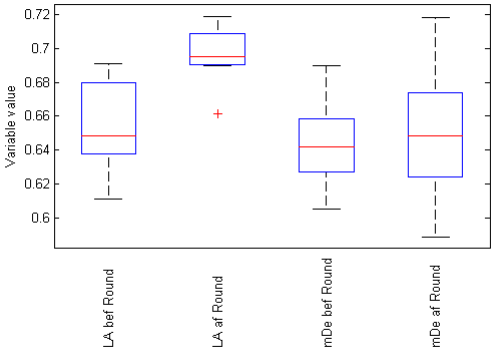


Figure 8. Boxplots for roundness.

3.3 Factor analysis

The factor analysis aims at describing size and shape of the samples with a few factors instead of many variables. Here three factors are used and to have a valuable result the three factors must contain the same variables for different samples, otherwise the factors will not describe the same thing. The rotation that was best in most cases was promax with power 4, and this rotation was used for all samples when comparing the factor analysis results.

Since the samples have different origin the factors do not contain the same variables in the before samples, for neither the micro Deval nor Los Angeles samples. In the Los Angeles after samples factors do contain the same variables, one factor contains *circularity* and *solidity*, and another contains *roundness* and *aspect ratio*. The rest of the variables are grouped in a residue factor describing size, see Figure 9. For the micro Deval after samples there is no clear grouping of the same variables for many samples.

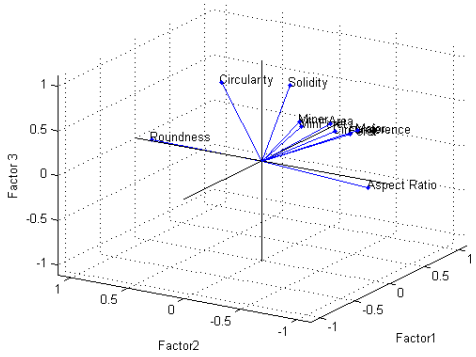


Figure 9. Factor analysis result after Los Angeles test.

4 DISCUSSION

The pre-test samples show a variation in size and shape, indicating that the samples are not homogenous, most likely caused by the different origin. Due to the anonymisation the origin cannot be controlled for the samples.

For both micro Deval and Los Angeles test the grains decrease in size after testing, as expected after a degradation test. The Los Angeles samples decreased in 34-80% in the projected *area* and 17-55% in *diameter*, while the micro Deval samples decreased 8-47% in the projected *area* and 6-30% in *diameter*, showing that the Los Angeles samples decrease more in size than micro Deval samples.

The micro Deval image analysis results show that the grains become more even and more circular (increasing *solidity* and *circularity*) after testing. The Los Angeles results indicate that the grains become more circular (increasing *circularity* and *roundness* and decreasing *aspect ratio*).

In both size and shape parameters there is difference between before and after sample, clearly indicating that degradation can be identified with 2D image analysis, supporting the hypothesis.

The different degradation modes for the tests are fragmentation for Los Angeles test and wearing for micro Deval test. A fragmented material is expected to have smaller grains than a material exposed to wearing. Grains exposed to wearing are also expected to be more even than fragmented grains. The overall shape is predicted to become more circular for the grains after degradation, but it is unclear if anything can be said about which type of degradation give the most circular grains. It is possible to expect more circular grains for wearing than fragmentation since non-circular grains are created when a grain is split (more or less) down the middle. The opposite is also possible, more circular grains can be expected for fragmentation than wearing since this degradation mode affects the grains in greater extent.

The results show that the Los Angeles grains are smaller than the micro Deval grains after testing, supporting that fragmentation occurs for Los Angeles testing. The micro Deval grains become more even after testing, indicating that these grains have been exposed to wearing. These results support that micro Deval tests induce wearing in grains and Los Angeles tests performs fragmentation of grains.

Los Angeles testing shows more circular grains afterwards for all parameters measuring overall shape. The micro Deval

grains show more circular grains for one parameter measuring overall shape (*circularity*) and no clear trends for the other two overall shape parameters (*aspect ratio* and *roundness*).

It is possible to judge if the ballast material has been degraded by micro Deval or Los Angeles test. More studies are needed in order to verify how wearing and fragmentation affect the different geometric measures in the image analysis.

The factor analysis shows the same variables in each factor after Los Angeles test, despite differences in the factors before testing. Having a factor with *roundness* and *aspect ratio* is not strange, since they are the inverse of each other. Another factor uses *solidity* and *circularity* to describe the shape. The "residue" factor, with the remaining variables, describes size. For the micro Deval samples no unified factors could be found, either before or after testing.

Many authors have found relations between shape or roughness parameters of grains and soil properties. Hansson & Svensson (2001) used a shape determining method based on abrasion number from studded tyre tests (surface roughness) and harp sieving (flakiness). In stability testing in a ring chamber, the horizontal stresses were found to be higher for flaky materials than for cubic materials. Alshibli & Alsaleh (2004) measured surface roughness with interferometry. Biaxial tests were performed and the friction and dilatancy angle was found to increase with increasing surface roughness.

Cho et al (2006) determined sphericity and roundness by comparing grains to standard images in a chart by Krumbein & Sloss (1963). Void ratios e_{max} and e_{min} increase for decrease in sphericity and roundness. Guo & Su (2007) determined two different materials to be angular and rounded, respectively, using scanning electron microscope. Triaxial tests were done and higher angularity showed increased shear strength and affected dilatancy characteristics. Cox & Budhu (2010) used digital image analysis and created a weighted shape parameter consisting of data from six different shape parameters. They found that the weighted shape parameter influenced the dilatancy characteristics found in direct shear box testing.

These authors have found good results, but the measuring methods and shape parameters are different and it is difficult to assemble the data to be able to quantify the behaviour of granular materials. Standardized grain shape parameters and measuring methods are needed to be able to quantify the relations between grains shape and soil properties.

Another observation is that this study is unique in targeting degradation and the shape changes that occur for a degradation exposed material. It is now proved that degradation can be identified in the grains' size and shape when the degradation is performed by standardized degradation tests. Continued studies should focus on image analysis of field samples from roads or railways. It would be possible to compare the size and shape of these samples to the after samples from degradation tests.

5 CONCLUSION

The study was conducted to investigate if it is possible to use image analysis to measure degradation in standardized degradation tests.

The results show difference between the results pre and post degradation test, enough to say that degradation can be identified by image analysis. The findings also show difference between the different degradation tests in size and shape change. The Los Angeles grain becomes smaller than the micro Deval grains after testing, and micro Deval grains show more even grains after testing, indicating that Los Angeles tests exposes the grains to fragmentation and micro Deval tests induce wearing the grains.

6 ACKNOWLEDGEMENTS

The laboratory testing was performed at Väglaboratoriet i Norr, an accredited laboratory. Thanks to Jan Hellström, supervisor at Väglaboratoriet, for supporting the study and to Emil Lemon, of Väglaboratoriet, for performing the tests and taking the photographs.

7 REFERENCES

Alshibli, K., & Alsaleh, M. (2004). Characterizing surface roughness and shape of sands using digital microscopy. Journal of Computing in Civil Engineering, 18(1), 36-45. doi:10.1061/(ASCE)0887-3801(2004)18:1(36)

Banverket. (2004). Makadamballast för järnväg. (No. BVS 585.52). Borlänge: Banverket.

Cho, G., Dodds, J., & Santamarina, J. C. (2006). Particle shape effects on packing density, stiffness, and strength: Natural and crushed sands. Journal of Geotechnical and Geoenvironmental Engineering, 132(5), 591-602. doi:http://dx.doi.org/10.1061/(ASCE)1090-0241(2006)132:5(591

Cox, M., & Budhu, M. (2010). Grain shape quantifications and their relationship to dilatancy. (pp. 540-549) American Society of Civil Engineers. doi:10.1061/41095(365)51

Guo, P., & Su, X. (2007). Shear strength, interparticle locking, and dilatancy of granular materials. Canadian Geotechnical Journal, 44(5), 579-591.

Hair, J. F. (2010). Multivariate data analysis: A global perspective Pearson Education.

Hansson, J., & Svensson, P. (2001). Stress distribution in unbound aggregate of road structure: Influence of surface roughness and particle shape. Bulletin of Engineering Geology and the Environment, 60(3), 223-226. doi:10.1007/s100640100103

Krumbein, W. C., & Sloss, L. L. (1963). Stratigraphy and sedimentation (2nd ed.). San Francisco: W.Hh Freeman.

Lambe, T. W., & Whitman, R. V. (1969). Soil mechanics. New York: Wiley.

Mitchell, J. K., & Soga, K. (2005). Fundamentals of soil behavior (3rd ed.) John Wiley & Sons.

Rodriguez, J. M., Edeskär, T., & Knutsson, S. (2013). Particle shape quantities and measurement techniques - A review. Electronic Journal of Geotechnical Engineering, 18(A), 169-198.

Trafikverket. (2011). TRVKB 10 obundna lager. (No. TRV 2011:083). Borlänge: Trafikverket.

Zeghal, M. (2009). The impact of grain crushing on road performance. Geotechnical and Geological Engineering, 27(4), 549-558. doi:10.1007/s10706-009-9256-1

Effect of pile sleeve opening and length below seabed on the bearing capacity of offshore jacket mudmats

Maria Vanberg
Kvaerner Jacket Technology AS, Oslo, Norway, maria.vanberg@kvaerner.com

Tewodros Tefera
Kvaerner Jacket Technology AS, Oslo, Norway.

Annette Jahr
Kvaerner Jacket Technology AS, Oslo, Norway.

ABSTRACT
Extracting hydrocarbons from beneath the seabed requires offshore platforms to be installed at strategic offshore locations. Depending on the water depth, multi-legged steel tubular framed structures called jackets can be used to support the topsides, risers and caissons. In the temporary condition, before piles are installed, horizontal steel plates located at the bottom of each jacket leg are used to support the jacket. The steel plates are called mudmats, and may be large due to the size of the structures they support and the harsh environmental loading conditions. Depending on the seabed soil condition, mudmats are usually designed with vertical skirts placed around the perimeter. During loading the skirts improve both the vertical and horizontal loading capacity. The piles are installed through openings in the mudmats called pile sleeves, and then driven to target penetration. Following this the piles are grouted to the pile sleeves resulting in the permanent foundation system. Extending the pile sleeves below seabed is used as a mitigation measure to avoid soil masses occupying the space in the sleeve, interfering with pile driving or grouting operations. Additionally local soil failure within the pile sleeve openings may occur. One method of evaluating mudmat foundation stability is to calculate the bearing capacity based on the net area of the mudmat. The net area in this case is the gross mudmat area minus the pile sleeve openings. However, by extending the pile sleeves to a sufficient depth below seabed, it is ensured that the gross mudmat area can be mobilized for bearing capacity evaluation. This paper describes a method to find the optimal pile sleeve length below seabed related to the size of pile sleeve opening and mudmat skirt length. Mobilizing the gross mudmat area in the bearing capacity evaluation reduces the required area of the mudmat. This results in smaller mudmat area and thus cost and weight savings for the jacket structure.

Keywords: mudmat, jacket, offshore, bearing capacity.

1 INTRODUCTION

The term mudmat describes the horizontal steel plate foundations used in the temporary phase of jacket installation before piles are driven and grouted to the pile sleeves. After the piles are installed, the environmental loads and the weight of the structure are carried by the piles. One of the main purposes of the mudmat is thus to support the weight of the jacket and additional load from the environment for a short period of time. Additionally it contributes to the stiffness and structural integrity of the pile cluster for the operational phase.

Figure 1 shows a typical pile cluster with pile sleeve openings. The bearing capacity of a mudmat can be calculated based on the net area of the mudmat. The net area in this case is the gross mudmat area minus the pile sleeve openings. The main reason for this is anticipation of local soil failure within the pile sleeve opening. Depending on the number and size of piles in the pile cluster, the reduction in mudmat effective area may be relatively large. However, the pile sleeves can be extended below seabed. This is of special interest, since the pile sleeve length below seabed is directly related to the soil movement within the pile sleeve opening and with that also to the local soil failure.

This paper seeks to understand the impact on the bearing capacity of the mudmat and soil movement within the pile sleeve opening, when the pile sleeves are extended below seabed. The paper further describes a method to find the optimal pile sleeve length below the seabed using an FE method. PLAXIS 2D software is used in the simulation. In the paper two sleeve opening sizes and three different pile sleeve penetration depths below seabed are investigated.

2 MODEL GEOMETRY AND SOIL CONDITIONS

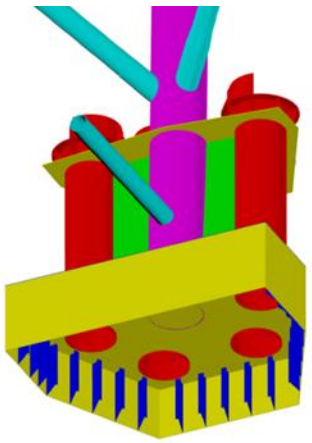


Figure 1: Mudmat with four pile sleeves, skirts and structural stiffeners (Vanberg, 2014).

Skirted mudmats consist of a mudmat plate with thin vertical plates (skirts) connected to the mudmat plate perimeter penetrating the soil. Mudmats for steel jackets are constructed with pile sleeve openings. Piles will be driven through these openings and grouted to the pile sleeve. Figure 1 shows an example of a mudmat with four pile sleeves openings and the mudmat skirt with structural stiffeners. The arrangement and number of pile sleeves and stiffeners varies and are dependent on the specific conditions at the planned location.

The geometry of the mudmat with skirts and sleeves investigated in this study is shown in Figure 2. In the figure, *s* is the depth of the skirt, *d* is the pile sleeve opening and *l* is the penetration depth of the pile sleeve below seabed. *b* is the distance between pile sleeves, and *a* is the distance between the pile sleeve and mudmat skirt. In the study two pile sleeve openings, d = 2.0 m and d = 3.0 m, are considered. The sleeve opening is determined by the pile diameter and required grout thickness. The pile sleeve is usually designed with an extension below seabed to prevent local soil failure within the pile sleeve opening. A mudmat foundation width *w* of 20 m is evaluated in this study, which is found as $w = 2(a) + b + 2(d)$. In the two dimensional space, the mudmat is considered as an infinitely long strip foundation. Three different pile sleeve extension depths below seabed are investigated. The sleeve lengths below the mudmat plate studied are 0.5 m, 1.0 m, and 1.5 m.

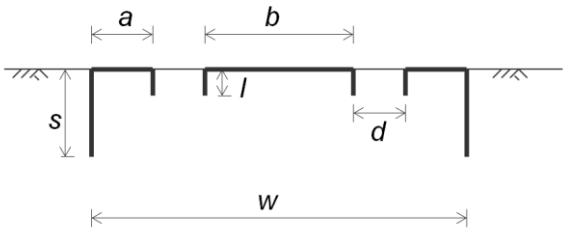


Figure 2: Mudmat model geometry used in the study, with skirt length s = 3 m, pile sleeve distance from the skirt wall a = 2 m, pile sleeve opening d = 2 m and 3 m, pile sleeve length below mudmat l = 0 m, 0.5 m, 1.0 m and 1.5 m.

The soil condition considered in this study is soft clay. Most soft seabed soils show increasing undrained shear strength with depth, and often in a linearly manner.

In this study the undrained shear strength of the soil was assumed to be either constant with depth or to increase linearly with depth according to $s_u = s_{u0} + k \cdot z$, where s_{u0} is the shear strength at the seabed, k is the shear strength gradient with depth as shown in Figure 3 and z is the depth below seabed.

For the mudmat with pile sleeve openings of 2 m and 3 m, the soil deformation within the pile sleeve and the bearing capacity of the mudmat for sleeve extension lengths of 0 m, 0.5 m, 1.0 m, and 1.5 m below the seabed are studied. The base case soil strength below the mudmat is s_{u0} = 5 kPa and k = 2 kPa/m. To investigate the effect of soil strength on the failure mechanism of the soil through the pile sleeve opening, different values of k were used (0, 2 and 5 kPa/m).

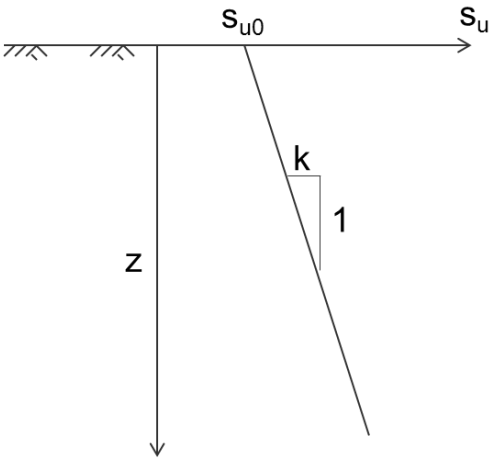


Figure 3: Soil parameters used in the study with linearly increasing undrained shear strength with depth. Base case is s_{u0} = 5 kPa and k = 2 kPa/m.

3 BEARING CAPACITY OF MUDMAT WITH DIFFERENT METHODS

The bearing capacity of a skirted foundation without pile sleeve opening is calculated as a reference case. There is a variety of methods available, and several are based on the proposed equation by Terzaghi (1943), which describes the bearing capacity per unit length, Q, for an infinitely long strip foundation:

$$\frac{Q}{B} = q_f = \frac{1}{2}\bar{\gamma}BN_\gamma + \bar{q}N_q + cN_c \qquad (1)$$

In this formula the parameters are defined as: $\bar{\gamma}$ = effective unit weight of soil, B = width of foundation, N_γ = bearing capacity factor for soil weight. $\bar{q}$ is a unit load acting on the soil surface on the outside of the foundation and N_q is the bearing capacity factor for this unit load. c denotes the cohesion of the soil, and N_c is the factor relating the cohesion to the bearing capacity.

The bearing capacity factors N_q and N_c can be found by the theoretical formulas by Prandtl (1921):

$$N_q = e^{\pi \tan \varphi} tan^2(45° + \frac{\varphi}{2}) \qquad (2)$$

$$N_c = (N_q - 1)\cot\varphi \qquad (3)$$

Where φ = the friction angle of the soil. For the case of pure clay conditions as are evaluated in this paper, the value of the friction angle is zero and the bearing capacity factors above will be N_q = 1 and N_γ = 0.

The above equations are valid for the simple case of a centrically loaded infinitely long strip foundation on a vertical surface with no horizontal load or moments. Meyerhof (1963) and Brinch Hansen (1968) used extended versions of the formula where several factors were included to account for the shape and embedment depth of the foundation, and inclination of the load, base and the ground. Additionally other authors have further developed the above bearing capacity formulations, or developed other formulae, like for example Janbu et. al. (1964).

Equation 1 does not account for any increase in shear strength with depth, and a correction has to be made if the soil is non-homogenous. Davis and Booker (1973) proposed a method for surface strip and circular footings on soil to take into account a linear increase in shear strength with depth. However, the solution by Davis and Booker does not take into account effect of skirt or effect of foundation shape.

4 FAILURE MECHANISM OF SKIRTED FOUNDATION

The failure mechanism of shallow foundations has been widely studied by different researchers. Several parameters influence the failure mechanism of a skirted mudmat with pile sleeve openings. Among others the size and location of pile sleeve openings, the skirt length, the pile sleeve extension below seabed and the soil type under the mudmat. Figure 4 shows a typical general shear failure mechanism of Hill type and Prandtl type (Chen, 1975) for a solid foundation with no pile sleeve openings and skirt. The clear distinction between the Hill and the Prandtl type of failure mechanism is that the downward movement of soil volume just under the foundation is different. Analytical solutions for bearing capacity of rough-based circular surface and shallowly embedded foundations indicate that a Prandtl type mechanism is appropriate for uniform soft soil (Kusakabe et al., 1986; Martin and Randolph, 2001), while a Hill type mechanism is optimal for a soil with increasing profile of undrained shear strength with depth. The width and depth of the plastic failure zone decreases with increasing soil strength with depth.

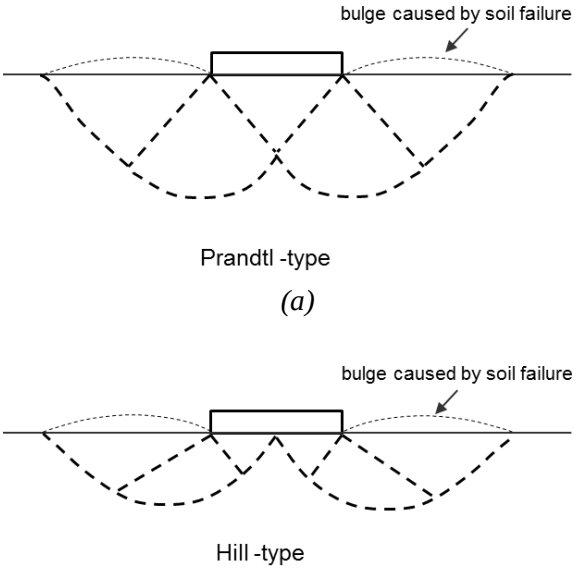


Figure 4: Soil failure mechanisms of shallow foundation (modified from Mana et al., 2012).

5 FEM SIMULATION

2D plane strain FE simulations were carried out using PLAXIS. The main focus of the FE simulation was to study the effect of pile sleeve length below seabed on the failure mechanism of the soil within the pile sleeve opening and the bearing capacity of the mudmat. Figure 5 shows the FE model used in the simulation of the mudmat model shown in Figure 2.

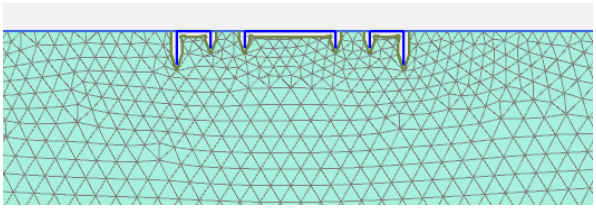


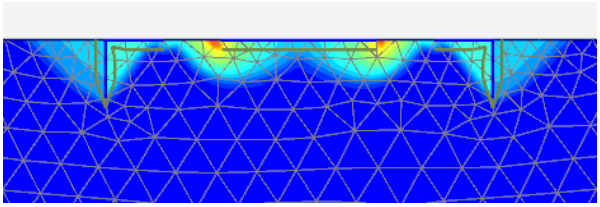
Figure 5: PLAXIS 2D FE model of the soil, mudmat with skirts and pile sleeves extended below seabed, and interface element used in the simulation.

The soil in the model consisted of very soft clay and was modelled as an isotropic elastic perfectly-plastic continuum, with failure described by the Mohr-Coulomb yield criterion. The undrained shear strength increased linearly with depth $s_u = 5 + 2z$ kPa, where z (m) is the depth below seabed. The stiffness modulus at seabed was $E_0 = 3400$ kN/m^2, increasing linearly with depth $E_{inc} = 400$ kN/m^2/m, and the undrained Poisson's ratio $\nu = 0.33$, according to undrained type B model in PLAXIS (2015). The interface roughness of mudmat base, the sides of the skirt and sleeves were taken to be $R = 0.8$.

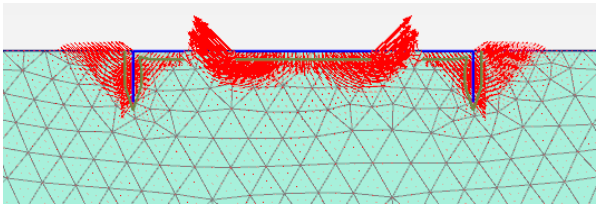
The mesh was composed of triangular elements with a mesh similar to that shown in Figure 5. As finite element analyses are sensitive to number of elements used, the number of elements were increased until the failure loads converged towards the same result.

The failure mechanisms of the soil beneath the mudmat with skirts and pile sleeves were studied by two different approaches, and yet both approaches resulted in similar effect on the soil below the mudmat. The first approach is by applying distributed vertical

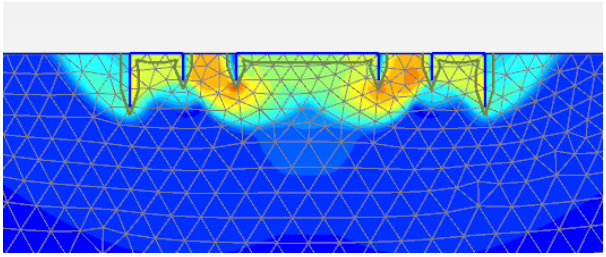
load on the mudmat. The second approach is by applying prescribed vertical displacement of the mudmat. Figure 6 shows the soil deformation pattern under the mudmat and through the pile sleeve openings for both no pile sleeve extension and 1.5 m pile sleeve extension below seabed. The soil deformation pattern based on the above two approaches are similar. Results from both approaches are discussed in the paper.



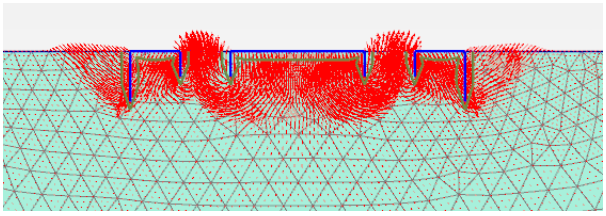
a) No pile sleeve extension



b) No pile sleeve extension



c) *1.5 m pile sleeve extension*



d) 1.5 m pile sleeve extension

Figure 6: Failure mechanism and soil deformation pattern under the mudmat and through the pile sleeve openings, for the case with no pile sleeve extension and 1.5 m pile sleeve extension below seabed for 0.5 m prescribed vertical movement of mudmat.

6 RESULTS AND DISCUSSION

The failure mechanism of skirted foundation with pile sleeve openings is a 3D situation. There are therefore obviously some modelling limitations to simulating the skirted mudmat with pile sleeve openings with a 2D model. However, a simplified 2D model can be used to assess the failure mechanism and to study the effect of pile sleeve length below seabed on the bearing capacity. The simulation results clearly show the effect of pile sleeve length below seabed on both the bearing capacity of the mudmat and the movement of soil mass within pile sleeve opening. Hill-type failure mechanism is observed from the FE simulation for a mudmat with no pile sleeve extension below seabed, Figure 6 (a) and (b). For a mudmat with 1.5 m pile sleeve extension Prandtl-type failure mechanism is observed, Figure 6 (c) and (d).

It can be seen from figure 6 (a) and 6 (c) that the failure mechanism is pushed deeper down in the soil when the pile sleeves are extended to a length of 1.5 m below mudmat. This will have an effect on the bearing capacity, since the undrained shear strength increases with depth, and soil with a higher strength is mobilized. Figure 7 and Figure 8 show the bearing capacity for a mudmat with 2 m and 3 m pile sleeve openings with the three different pile sleeve lengths studied. In the figures base case soil condition are used, and the undrained shear strength is hence increasing with a rate of k = 2 kPa/m.

The curves in Figure 7 and Figure 8 show that as the pile sleeve length below seabed increases the bearing capacity of the mudmat also increases. It can be seen that the capacity is approximately 40 kN/m/m when no pile sleeve extension is included, and 60 kN/m/m when 1.0 m pile sleeve extension is used. Hence, the capacity is increased by about 50 %.

In this case no significant difference in bearing capacity is observed for pile sleeve lengths of 1.0 m and 1.5 m. Pile sleeves longer than 1.0 m may therefore not result in

much gain in the bearing capacity, and 1.0 m pile sleeve length may therefore be considered optimal in this case.

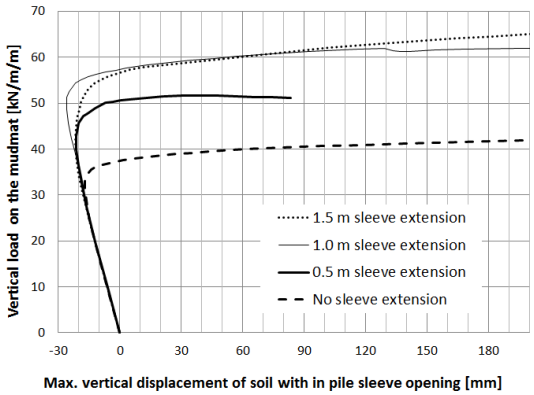


Figure 7: Failure curves for the most critical point within the pile sleeve opening of 2 m diameter.

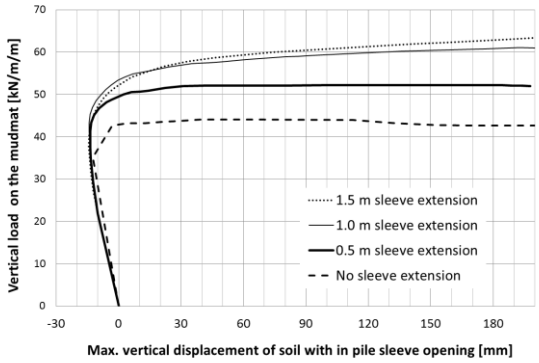


Figure 8: Failure curves for the most critical point within the pile sleeve opening of 3 m diameter.

Figure 6 (b) and 6 (d) shows the pattern of soil movement when the mudmat is pressed downwards with a prescribed displacement of 0.5 m in the simulation. A more detailed study of the soil movement showed that at the beginning of loading, the soil within the pile sleeve follows the vertical elastic downward deformation of the soil. This can also be seen in Figure 7 and Figure 8, since the vertical displacement of the soil is negative relative to the original seabed. As the loading increases, the soil movement within the pile sleeve opening starts to move vertically upward towards failure following the failure mechanism of the soil, as shown in Figure 6 (b) and (d). This point of turn depends on the pile sleeve length below seabed and the size of pile sleeve opening.

The magnitude of the movement within the pile sleeve opening is also depending on the pile sleeve extension below seabed. This can be more clearly seen in Figure 9 and Figure 10 for a prescribed vertical displacement of the mudmat. The figure shows the soil displacement pattern for a point selected at the most critical location (maximum soil movement) within the pile sleeve opening of 2 m and 3 m. In this case the mudmat is given a vertical displacement (vertical axis) and the displacement of the soil (horizontal axis) is relative to the original seabed. Hence, 0 mm vertical displacement of soil means that the selected node in the mesh is at the original seabed.

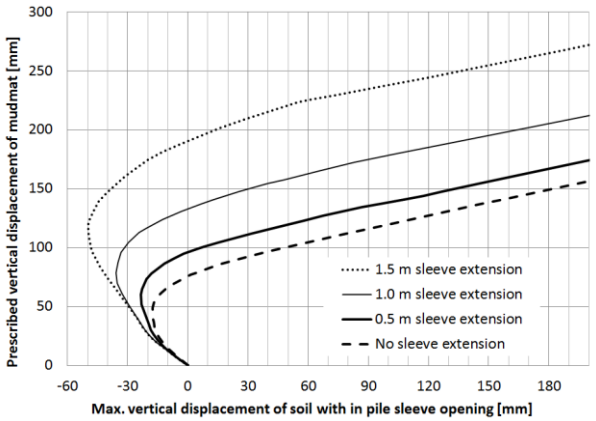


Figure 9: Soil vertical displacement for the most critical point within the pile sleeve opening of 2 m, when the mudmat is pressed vertically.

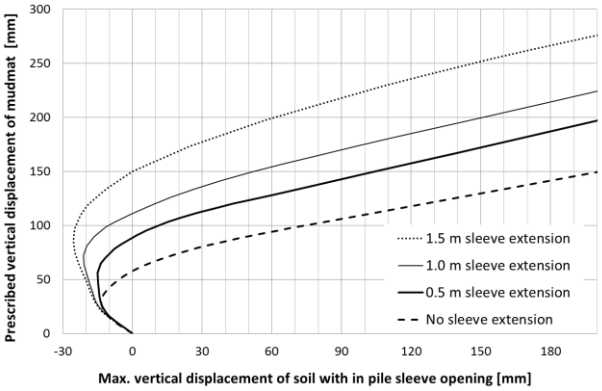


Figure 10: Soil vertical displacement for the most critical point within the pile sleeve opening of 3 m, when the mudmat is pressed vertically.

The vertical upward soil movement within the pile sleeve opening decreases as the pile sleeve extension increases. From Figure 10 at 15 cm prescribed vertical displacement of mudmat, the soil within the pile sleeve opening moves 0 mm, 50 mm, 105 mm, and

200 mm relative to the original seabed for pile sleeve lengths of 1.5 m, 1.0 m, 0.5 m and 0 m respectively.

To investigate further the sensitivity of the results, various analyses were carried out. The increase in soil strength with depth has pronounced effect on the bearing capacity and the deformation pattern of the soil under the mudmat and through the pile sleeve opening. Figure 11 shows the failure curves for a mudmat with 1.0 m long pile sleeve below seabed, when the increase in undrained shear strength with depth is changed.

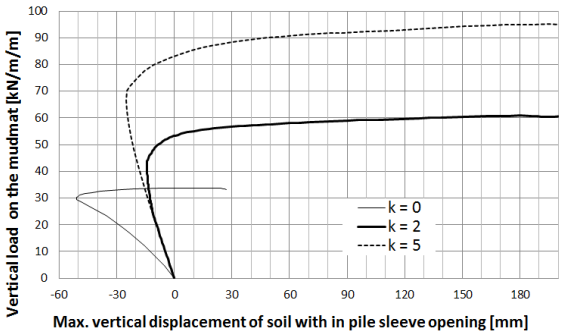


Figure 11: Failure curves for the most critical point within the pile sleeve opening of 3 m, when the pile sleeve length below seabed is 1 m, with different ratios of increasing undrained shear strengths with depth.

The curves show that the increase in undrained shear strength has a significant effect on the bearing capacity. For a soil with constant strength with depth, k = 0 kPa/m, the soil within the pile sleeve actually follows the downward movement of the mudmat, and does not turn to reach its original point at seabed before failure. This can be more clearly seen in Figure 12 where the movement within the pile sleeve opening is plotted against prescribed vertical displacement. The selected critical node in the mesh does not go back to its original point at seabed before the mudmat has moved 45 cm vertically downward. Another consequence of constant strength with depth is that the failure mechanism is pushed deeper down in the soil. However, the undrained shear strength is constant with depth there is not much gain in the bearing capacity.

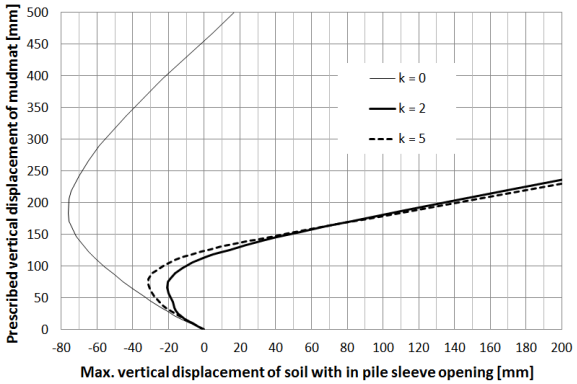


Figure 12: Soil displacements for the most critical point within the pile sleeve opening of 3 m, when the pile sleeve length below seabed is 1 m, with different ratios of increasing undrained shear strengths with depth.

The bearing capacity of the mudmat with pile sleeve extensions are compared with a mudmat with no pile sleeve openings, denoted solid. In the comparison soil displacement outside the mudmat is used as a reference point, i.e. the global failure mechanism determines the bearing capacity. Figure 13 shows the effect of the pile sleeve extension using the base case soil data. The result shows that piles with a sleeve extension of 1.5 m give similar bearing capacity as a solid mudmat.

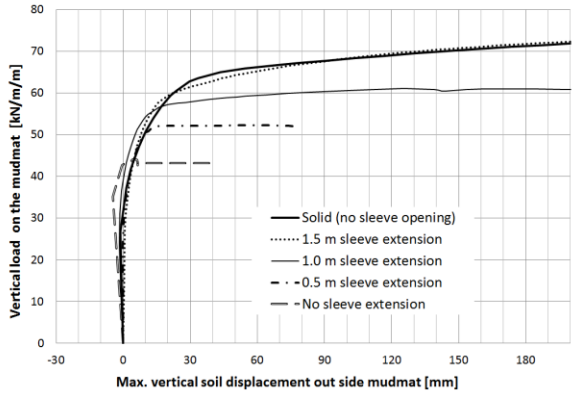


Figure 13: Bearing capacity of the mudmat with different pile sleeve extension below seabed for the pile sleeve opening of 3 m and solid mudmat with no pile sleeve opening.

7 CONCLUSION

In this paper the failure mechanism and the soil movement through the pile sleeve opening of skirted mudmat has been studied. In the study two sleeve opening sizes and

three different pile sleeve penetration depths below the seabed were investigated. Simplified 2D FE method using PLAXIS software was used in the simulation. The results show that the pile sleeve length below seabed has substantial effect on the failure mechanism of the soil and the bearing capacity of the mudmat. For a specific mudmat geometry, pile sleeve opening and soil condition, the analyses show that it is possible to find an optimal pile sleeve length below seabed to control the soil movement within the pile sleeve opening and maximise the bearing capacity. Pile sleeve lengths longer than this optimal length may not result in much gain in the bearing capacity or reduction in soil movement within the pile sleeve opening. By using the optimal pile sleeve extension below the seabed there could be a reduction in gross mudmat area and thus cost and weight savings for the jacket structure.

8 ACKNOWLEDGEMENTS

The authors would like to thank Kvaerner Jacket Technology AS for providing the resources for writing this paper.

9 REFERENCES

Brinch Hansen, J. (1968) A Revised and Extended Formula for Bearing Capacity

Chen W. (1975) Limit Analysis and Soil Plasticity. Elsevier, Amsterdam, the Netherlands.

Davis, E.H. & Booker, J.R (1973) The effect of increasing strength with depthon the bearing capacity of clays. Géotechnique 23(4): 551 – 563

Janbu N., Bjerrum L. and Kjærnsli B. (1964) Soil Mechanics Applied to some Engineering Problems. The Norwegian Geotechnical Institute, Publication N0. 16, Oslo.

Kusakabe O, Suzuke H and Nakase A (1986) An upper bound calculation on bearing capacity of a circular footing on a non-homogeneous clay. Soils and Foundations 26(3): 143–148.

Mana D., Gourvenec S., Randolph M., amd Hossain M. (2012) Failure mechanisms of skirted foundations in uplift and compression. International Journal of Physical Modelling in Geotechnics, 12(2), pp 47-62.

Martin CM and Randolph MF (2001) Applications of the lower and upper bound theorems of plasticity to collapse of circular foundations. Proceedings of the 10th Int. Conf. Int. Assoc. of Computer methods and Advancs in Geomech (IACMAG), Tucson, 2: 1417-1428.

Meyerhof, G. G. (1963) Some recent research on the bearing capacity of foundations

Plaxis 2015. Finite element code for soil and rock analyses, Version 2015.01. Plaxis BV. Delft, Netherlands.

Vanberg M. (2014) Stability Analysis of Mudmat for Steel Jackets. MSc thesis NTNU, Norway.

Terzaghi, K. (1943) Theoretical Soil Mechanics

3D FE tool for time dependent settlement predictions

H. P. Jostad
Norwegian Geotechnical Institute (NGI), Norway, hpj@ngi.no

N. Sivasithamparam
NGI, Norway

B. H. Woldeselassie
NGI, Norway

S. Lacasse
NGI, Norway

ABSTRACT
A newly developed calculation tool for fully coupled general 3D finite element consolidation analyses is presented. The development has been part of an ongoing Research and Development project called GeoFuture and the tool is implemented into the commercial geotechnical software Novapoint GeoSuite. There, the tool is part of an integrated software system for handling geotechnical and geometrical data, with wiki based user assistance for selection of material properties and controlling the simulations, and 3D graphical visualization of input data and results. The paper gives the main background and features of the calculation tool. To demonstrate some of the capabilities of the tool, back-calculations of the measured long-term settlements of a heavy building on a deep soft clay layer in Oslo centrum are presented.

Keywords: FEM, Consolidation, Settlements, Creep, Back-calculation

1 INTRODUCTION

Settlements of foundations and embankments on soft ground are in geotechnical engineering often calculated using idealized 1D methods with simplified assumptions or elastic analytical solutions of load spread distribution with depths, pure vertical pore pressure dissipation and compressibility parameters from oedometer tests. Time dependent creep deformations are in Norway generally added by a simple secondary consolidation phase. However, in some projects more accutate settlement predictions are required or the problem is too complex to be idealizezed by a simplified 1D solution. In these cases, analyses using a fully coupled displacement and pore water flow (consolidation) finite element (FE) program with a proper material model is a good approach. Such a general 3D finite element code is developed as part of the Research and Development (R&D) project GeoFuture (www.geofuture.no) and implemented into the commercial software package Novapoint GeoSuite (www.ViaNovasystems.com). The main differences between this code and other existing Finite Element codes as for instance Plaxis (www.plaxis.nl), is that the tool is an integrated part of a system for seamless handling of project related geotechnical and geometrical data. In geotechnical projects, field and laboratory data is generally already stored in the system, Novapoint GeoSuite Presentation. The main features of this integrated geotechnical calculation tool for settlement analyses are described in the following.

2 FINITE ELEMENT CODE

2.1 FE Formulation

A general finite element code, originally developed at NGI in the nineties, is used to solve the governing equations for consolidation problems. The governing differential equations are the (stress) equilibrium and the mass balance (continuity) equation of water. The equilibrium equation is solved by a clasical small strain displacement based finite element formulation, where the external (nodal point) force vector $\boldsymbol{R}_{ext}$ due to body forces and surface loads should be equal to the internal force vector $\boldsymbol{R}_{int}$ from the total stresses (effective stresses plus pore pressure):

$$\boldsymbol{R}_{ext} = \boldsymbol{R}_{int} \tag{1}$$

Were $\boldsymbol{R}_{ext}$ and $\boldsymbol{R}_{int}$ are calculated according to conventional finite element formulations as for instance described in Zienkiewicz (1977). The relationship between effective stresses and strains are defined by a proper material model. This material model may be rate dependent in order to account for time dependent strains (creep). The strains are derived from the calculated displacement field. For 3D problems the displacement vector $\boldsymbol{r}$ is decomposed into the three global directions, r_x, r_y and r_z.
The pore water flow is solved by a weak form of the water balance equation, where the pore water flow out of the model (nodes) $\boldsymbol{F}_{out}$ must be equal to the global volume change ΔV (given by the displacement field $\boldsymbol{r}$):

$$\boldsymbol{F}_{out} = \boldsymbol{L}^T \boldsymbol{r} \tag{2}$$

Where the vector $\boldsymbol{F}_{out}$ and matrix $\boldsymbol{L}$ are calculated by conventional finite element formulations as for instance described in Potts and Zdravkovic (1999). The water is then assumed to be incompressible.
The relationship between the pore pressure field p and the average (superficial) pore water flow velocity q is given by Darcy's law:

$$q = -\frac{1}{\gamma_w} k \frac{dp_{excess}}{ds} \tag{3}$$

Where k is the permeability coefficient, γ_w is the unit weight of water, dp_{excess}/ds is the spatial gradient of the excess pore pressure (i.e. in excess to the hydrostatic pore pressure). In the code, the flow velocity is decomposed into the 3 global directions (q_x, q_y and q_z) with the corresponding permeability coefficients (k_x, k_y, k_z).
In order to solve the transient problem, where the pore pressure field is changing with time, a weighted average of the pore pressure field within a time increment Δt is used:

$$p_{av} = p(t) + \theta \cdot p(t+\Delta t) \tag{4}$$

where $p(t)$ and $p(t+\Delta t)$ are the pore pressure in the nodes at the beginning and the end of the time increment. θ is a weighting factor, which for classical consolidation problems is recommended to be chosen larger than 0.5. This means that the coupled consolidation problem is solved by a time stepping procedure starting from an initial state. This also open up for that the external loads and boundary conditions (displacements and pore pressure with known/prescribed values at given nodes) may change with time.
In order to solve the non-linear behaviour of the soil, the governing equations within each time step are solved by a Newton Raphson iteration scheme.

2.2 Main feature of the code

The finite element code used in this development has a modular structure, which makes it easy to include new finite element types, material models and solution algorithms. For coupled consolidation analyses the following elements and features are currently included:

- 20-noded isoprametric brick element with pore pressure degree of freedom in the corner nodes and (2x2x2) reduced or (3x3x3) full Gaussian integration
- 10-noded isoparametric tetrahedral element with pore pressure degree of

freedom in the corner nodes and full Gaussian integration
- An automatic time stepping procedure (described in Jostad and Engin, 2013) controlled by the maximum change in the pore pressure within a time step, in addition to a standard procedure with manual input of the time increments for more complex time histories of loads and boundary conditions
- Spatial lateral interpolation of material properties between a number of input profiles
- Spatial lateral interpolation of steady-state pore pressure between a number of input pore pressure profiles. The steady-state pore pressure field may be given as function of time in order to handle specified or known changes in the ground water table
- A library of different material and permeability models. Some of these material models may account for creep (rate effects). A 3D material model developed at NTNU in a PhD study will be implemented in 2016
- Application of a set of time dependent surface loads

2.3 Input of topography and soil layers

For simple geometries (e.g. horizontal soil layers), a cube containing 20-noded brick elements is generated based on input of horizontal and vertical grid lines. In order to generate a 3D finite element model one may simply expand the model/data used in the existing 1D GeoSuite Settlement calculation tool. This means that the graphical user interface (GUI) in this case is the same for 1D and 3D analyses. The 3D finite element model may also be degenerated into a 2D cross-section or a 3D model with only vertical displacement degrees of freedom. For many problems, this will speed up the computation time significantly without significant loss in accuracy.
For more complex geometries, a finite element mesh containing the 10-noded tetrahedral element may be generated by the code Tetgen (2015). An example of a mesh with varying thicknesses of the soil layers and depth to the rock is shown in Figure 1. As bases for generating this model an existing ground observation model (GOM) may be used. The GOM is established based on site specific borehole data and a terrain model. An example of a GOM is shown in Figure 2.

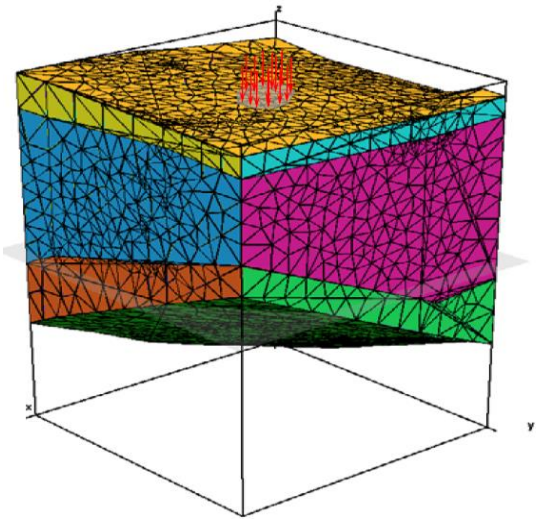


Figure 1 Finite element mesh using 10-noded tetrahedral elements.

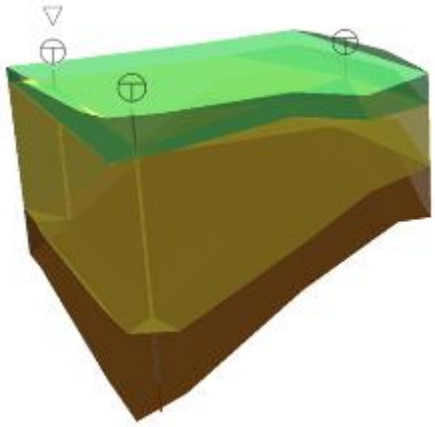


Figure 2 Ground Observation Model (GOM) based on 3 boreholes.

2.4 Wizards assistance to users

Lacasse *et al* (2013) described briefly the Wizard function used in GeoSuite. Wizard is an optional, interactive assistance popping up with information on the selection of soil parameters, the interpretation of *in situ* or laboratory test results, the selection of a type of analysis, the features of the analysis itself or the interpretation of the results of an

analysis. Wizard invites the user to note down its comments within the Web site; Wizard makes topic associations with links; Wizard seeks to involve the user in an on-going process of improvement.
As an example, the scheme of a settlement analysis is shown in Figure 3.

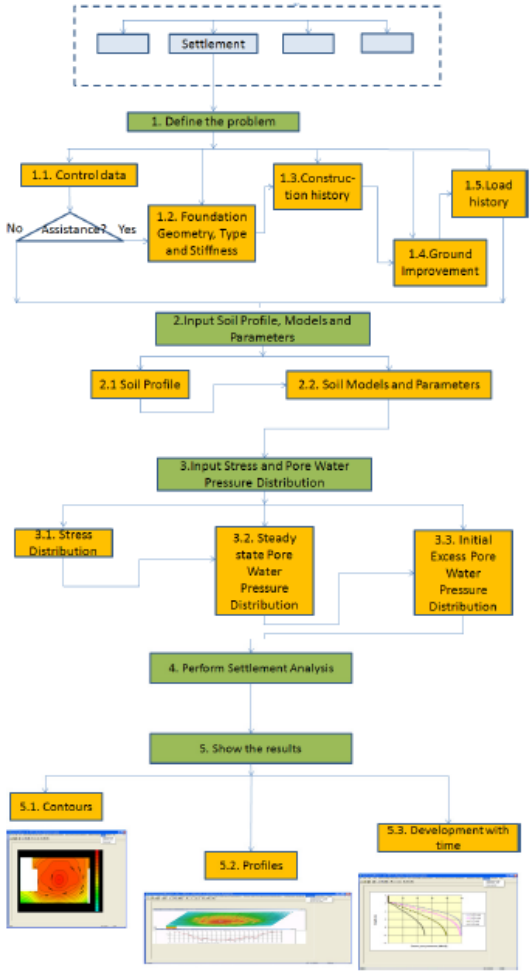


Figure 3 Flow chart for settlement analysis, Step 1 to 5.

3 EXAMPLE

3.1 General background

To demonstrate some of the capabilities of the calculation tool, back-calculations of the measured long-term settlements of a heavy building, Oslo Jernbanetollsted shown in Figure 4, on soft clay in Oslo centrum are presented. Back-calculations of this building have previously been published in Andersen and Clausen (1975) and Svanø et al. (1991). The paper by Andersen and Clausen (1975) gives the details about the soil condition and the construction sequences of the building.

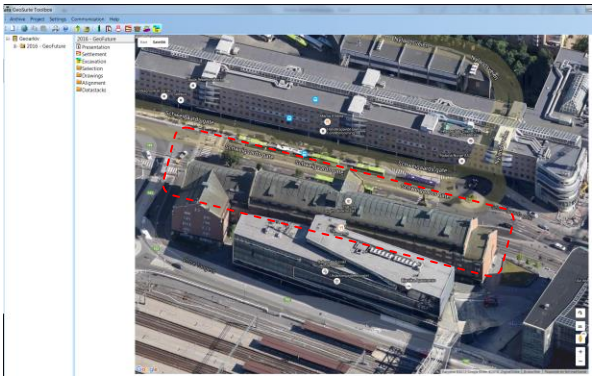


Figure 4 Oslo Jernbanetollsted (second building from the railways). Google picture in the GeoSuite toolbox starting window.

The effects of different available features in the sofware are demonstrated by analyses with increasing degree of complexity.

3.2 Soil condition

The soil consists of a 2.5 m think old fill of gravel and stones, a 7 m thick sandy and silty clay layer with weathering in the upper 2 m, a 1.5 m thick very stiff clay layer, a 22.5 m thick fairly homogenous and nearly normally consolidated marine clay. The depth to the rock is about 80 m. The boring profile is shown in Figure 5. The ground water table is located 0.5 m below the fill.

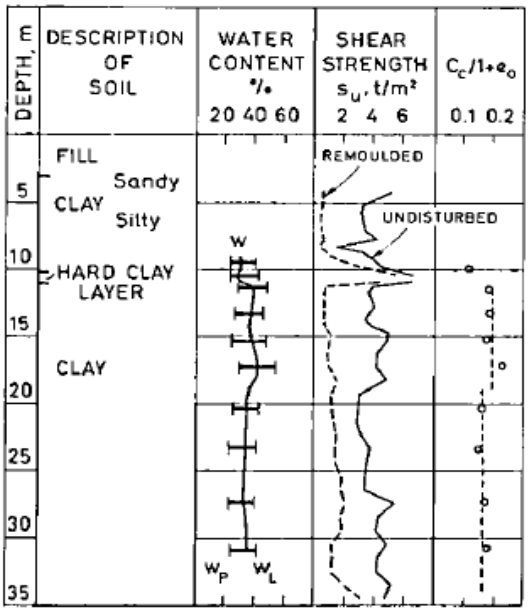


Figure 5 Soil profile close to the building. From Andersen and Clausen (1975).

3.3 Building

The Oslo Jernbanetollsted is a six storeys high building. It covers an area of approximately 140 m times 21 m. The foundation consists of about 5000 wooden piles down to level -9.3 m with a 1-2 m thick reinforced slab at the top, see Figure 6.

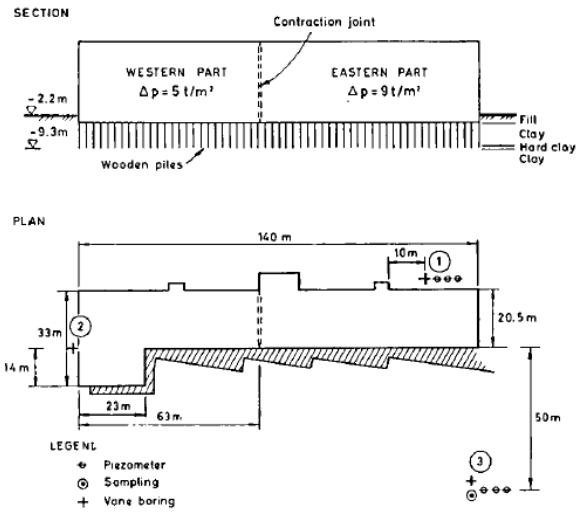


Figure 6 Vertical cross section and plane view of Oslo Jernbanetollsted, From Andersen and Clausen (1975).

The construction of the building started in summer 1920, and finished early in 1924. Two years later the live load had reached the average operational value. The live load was estimated to 50 kPa in the western part and 90 kPa in the eastern part.

3.4 Material model

A material model based on Janbu's resistance concept (Janbu, 1985) is used in the analyses. The material model together with a 1D calculation of the same problem are presented in Svanø et al. 1991.
The constrained (oedometer) vertical strain (rate) $d\varepsilon$ is here given by an effective stress dependent elasto-plastic part $d\varepsilon_{ep}$ and a creep part $d\varepsilon_{creep}$:

$$d\varepsilon = d\varepsilon_{ep} + d\varepsilon_{creep} = d\sigma_v'/M_t + 1/R \qquad (5)$$

The elastic strain for effective vertical stresses σ_v' below the pre-consolidation pressure p_c' is given by an oedometer modulus M_{oc}. For effective stresses in excess of the initial pre-consolidation pressure, the elasto-plastic strain is given by an effective stress dependent tangent oedometer modulus:

$$M_t = m \cdot (\sigma_v' - p_r') \qquad (6)$$

Where m is a dimensionless modulus number and p_r' is a stress intercept that for instance controls the tangential oedometer modulus at p_c'. The time dependent (visco-plastic) creep strain is given by the time resistance:

$$R = R_o + r \cdot (t - t_{ref}) \qquad (7)$$

Where R_o is the time resistance at the reference time t_{ref} (here taken at 24 hours), and r is the dimensionless time resistance number. This means that it is assumed to be zero creep strain at $t = t_{ref}$. However, the creep rate is $1/R_o$ at $t = t_{ref}$. r is varying with the effective vertical stress. It is defined by a value at the in situ condition, at the pre-consolidation pressure p_c' and with a slope after p_c', i.e. the parameters r_o, r_{pc} and $\beta = dr/d\sigma_v'$.

In the present analyses the shear modulus is taken as $G = M_{oc}/3$. For more complex problems (e.g. problems were the soil is loaded to higher shear mobilisation), a more advanced formulation is required for the description of the shear stiffness. Furthermore, no creep is assumed for horizontal and shear strain components.
The soil parameters used in the analyses are presented in Table 1. The parameters are based on Svanø et al. (1991).

Table 1 Soil properties of the clay layers.

Depth (m)	**OCR**	***m***	M_{oc} / $m \cdot p_c'$	R_o (yrs)	r_o	r_{pc}
0–9	1.4	15	5	-		-
9-18	1.4	15	5	0.8	2000	300
18-40	1.4	18	5	0.8	2000	300

The creep parameter β is zero. The (isotropic) permeability k is 0.031 m/years in the top 9 m reducing linearly to 0.022 m/years at 18 m.

3.5 Finite element models

The settlement calculations have been performed with models of increasing complexity:

- 1D models with constant load distribution with depth
- 1D models with load distribution with depth based on Bousinesq (elastic half space solution)
- 2D models of cross sections through the eastern and western part of the building
- 3D model along the centreline of the building (both eastern and western part). This element model is shown in Figure 7

One challenging part here is to calculate the load transfer to the pile tip level. In the finite element analyses a reduced elastic shear stiffness (G = 200 kPa + 100 kPa/m · depth) is used along the periphery of the foundation down to skirt tip level and in the joint between the western and eastern part. The actual stiffness along these soil-soil interfaces affects the loads (pressure) transferred to the skirt tip level. The calculated excess stress distributions versus depth (at maximum load) at the centre of the eastern part are shown in Figure 8.
Drainage is assumed at both the bottom and top of the models. "Roller" boundaries are assumed along the vertical boundaries.

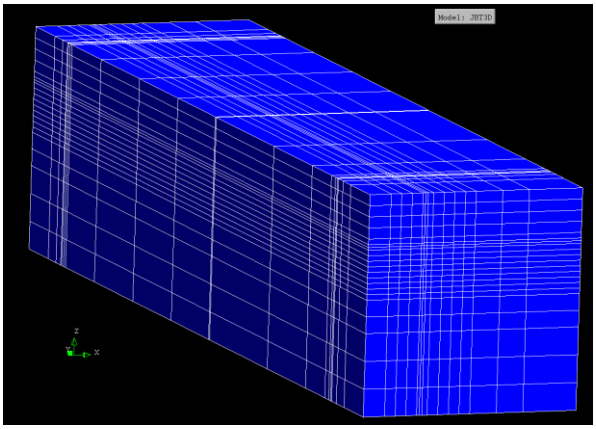


Figure 7 3D FE model of one side of the symmetry plane along the centreline of the foundation.

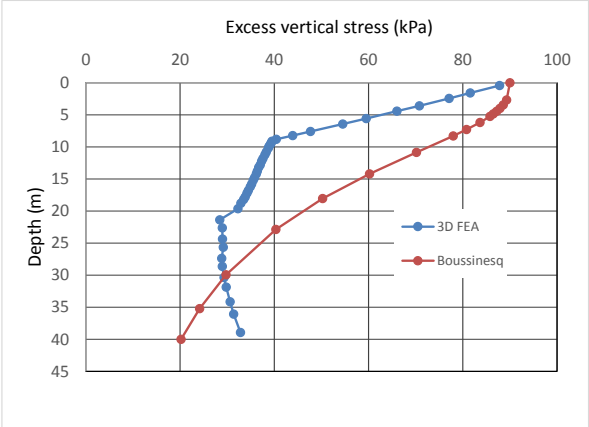


Figure 8 Calculated excess vertical stress versus depth at max loads at the centre of the eastern building.

3.6 Loading history

The actual loading history is sketched in Figure 9. The weight of the old fill (approximately 50 kPa) is in the simulation applied 20 years before construction of the building. This is done in order to account for the increase in pre-consolidation pressure with depth due to creep under this pressure. The maximum foundation loads were reached at the end of 1925.

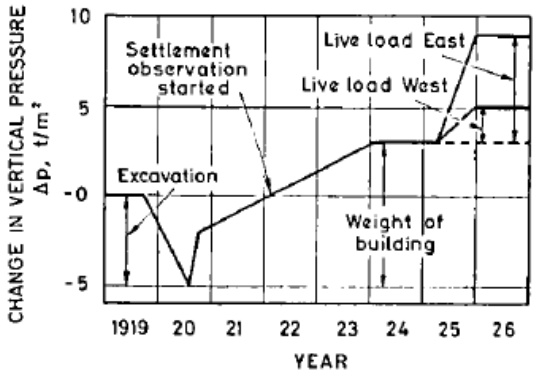


Figure 9 Actual loading history. From Andersen and Clausen (1975).

3.7 Results

The calculated settlements at the centre of western and eastern part of the building are shown in Figure 10.

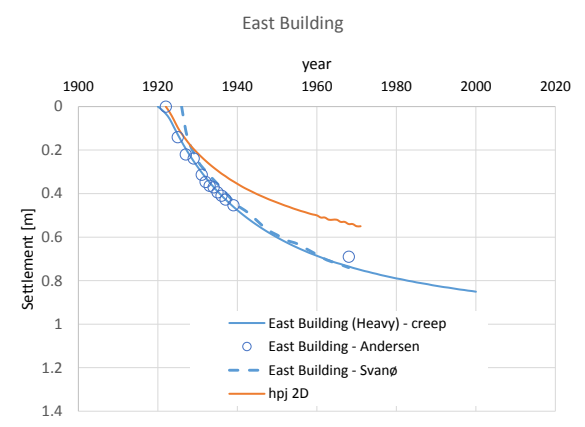


Figure 10 Calculated settlement curves at the centre of the eastern (heaviest) part.

The calculated distribution of the vertical displacements from the 2D cross section trough the eastern part of the building at the end of 1970 is shown in Figure 11.

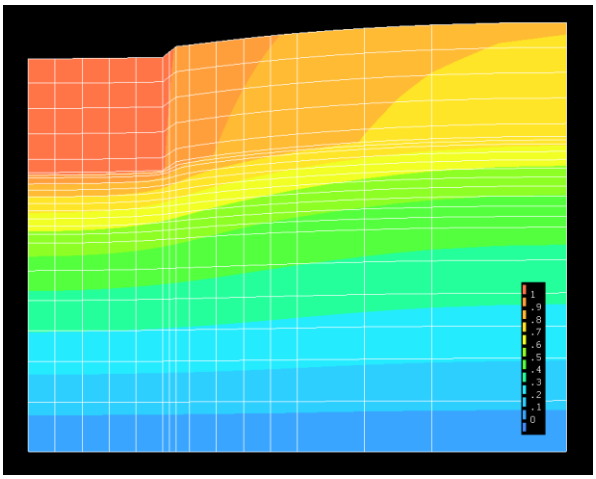


Figure 11 Calculated vertical settlements through the centre of the eastern part at end of 1970, including the settlements due to the old fill. Deformed mesh is magnified by a factor of 10.

The calculated distribution of the vertical displacements from the 3D model at the end of 1970 is shown in Figure 12.
In these calculations the parameters are taken from the paper by Svanø et al. (1991). However, it is clear that by accounting for more advanced calculation of the stress distribution with depth, the parameters used in that idealized 1D calculation should be re-evaluation in order to better fit with the observed settlements.

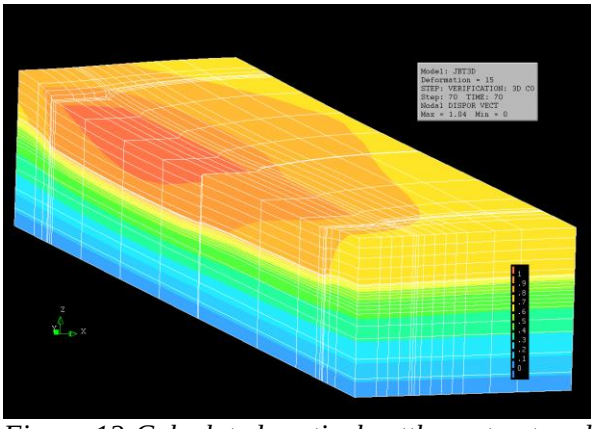


Figure 12 Calculated vertical settlements at end of 1970, including the settlements due to the old fill. Deformed mesh is magnified by a factor of 15. Eastern part toward top left.

4 CONCLUSTIONS

A new calculation tool, based on the finite element method, for time dependent 3D settlement predictions is presented.
The tool may be used to consider the following 3D effects:

- Horizontal pore water flow in two directions
- Stiffness and geometry dependent load (stress) distribution with depth
- Spatial variation in soil properties
- Spatial variation in steady-state pore pressure, which also may vary with time
- More complex soil models accounting for general 3D stress-strain relationships. A 3D material model developed at NTNU will be implemented in 2016

The calculation tool is an integrated part of the Novapoint GeoSuite Toolbox. This means that all relevant project data (e.g. field, laboratory data and soil layering) may be stored in GeoSuite Presentation, imported into BIM (Building Information Modelling) and then used as basis for input to the 3D calculation model.

5 ACKNOWLEDGEMENT

The authors acknowledge the funding of The Research Council of Norway and the technical and financial contributions of the GeoSuite alliance partners: Geovita AS, ViaNova Systems AS, Multiconsult AS, Norconsult AS, ViaNova GeoSuite AB, AG Programutveckling Ekonomisk Förening (AGEF), SINTEF Building and Infrastructure, the Norwegian University of Science and Technology (NTNU), the Norwegian Public Roads Administration (NPRA), the Norwegian Railway Administration (JBV), Skanska AS, Cowi AS, Sweco AS, Rambøll AS and NGI. The contributions A. Rosenquist af Akershult from Vianova GeoSuite AB are gratefully recognized.

6 REFERENCES

Andersen, K.H. & Clausen C.J.F. (1975). A fifty-year settlement record of a heavy building on compressible clay. Settlement of Structures, Conference. Cambridge 1974. Proceedings, pp. 71-78. London, Pentech Press

Janbu, N. (1985). Soil models in offshore engineering. The 25th Rankine lecture. Geotechnique, Vol. 35, No. 3, London, 241-281.

Tetgen (2015). A quality tetrahedral mesh generator and a 3D delaunay triangulator. www.wias-berlin.de/software/tetgen/

Zienkiewicz, O.C. (1977). The finite element method. McGraw-Hill (U.K.)

Potts, D.M. & Zdravlovic, L. (1999). Finite element analysis in geotechnical engineering. Theory. Thomas Telford Ltd (U.K.)

Lacasse, S. Jostad, H.P., Athanasiu C., L'Heureux, J.-S., Sandene. T. and Liu Z.Q. (2013). Assistance for the calculation of settlement. GeoMontréal 2013. Canadian Geotechnical Conference.

Jostad, H.P. & Engin, H.K. (2013). Investigation of different solution strategies for non-linear 3D consolidation problems. Proceedings of the 3rd International Symposium on Computational Geomechanics (COMGEO III), Krakow, Poland, 21-23 August, 2013.

Svanø, G. Christensen, S. & Nordal, S. (1991). A soil model for consolidation and creep. Proc., 10th European Conf. on Soil Mechanics and Foundation Engineering, Vol. 1, Balkema, Rotterdam, Netherlands, 269–272.

Risk analyses in excavation and foundation work

B. Kalsnes
Norwegian Geotechnical Institute, Norway, bgk@ngi.no

B.V. Vangelsten, U. Eidsvig
Norwegian Geotechnical Institute, Norway

ABSTRACT
BegrensSkade was a Norwegian research project finished in 2015 with the aim of developing methods and processes that will help reduce the risk of damages and unexpected settlements as a result of excavation and foundation work. One subproject in BegrensSkade was related to risk assessment and management. The use of risk assessment and management aims at answering some fundamental questions:

- *What can happen?*
- *How likely is it?*
- *If it happens, what are the consequences?*
- *Is the risk level acceptable?*
- *If not, what can be done to reduce the risk?*

A method for assessing and managing the risk in construction acitivities was developed in BegrensSkade, having the above questions in mind. The proposed method is based conceptually on ISO 31000 's Risk Management framework, in that the methodology proposed is divided into five phases; Phase 1: Establish basis; Phase 2: Risk identification; Phase 3: Semi - quantitative risk analysis; Phase 4: Risk Assessment; Phase 5: Risk reduction measures. The method is implemented in a separate spreadsheet.

The risk sub project in BegrensSkade also included a workshop that aimed for constructing a fault tree for a given construction pit. The starting point was an undesirable event, a so-called top event, which in this case was larger settlements than predicted. The event was then decomposed down to a level of detail where the causes of the top event were detected. In the use of fault trees, the probability of the top event can be assessed qualitatively or quantitatively. In this case, a semi-quantitative method was used, as the causes of the undesirable event was ranked according to the expected probability rather than giving exact numbers.

Keywords: Risk, foundation, excavation, settlements, methodologies.

1 INTRODUCTION

1.1 Risk assessment in BegrensSkade

Risk assessment is increasingly used in many different activities over the recent years. For the construction industry, risk can be said to be implicitly included in the dimensioning principles, but risk assessments in the form of a systematic method is only marginally been applied. In the BegrensSkade project, risk was therefore included as a separate subproject (DP5) in order to examine how to incorporate risk assessments in the planning and execution of construction works in general, and for ground and foundation work especially.

The project includes a preparation of a guide for risk assessments for specific building projects. A test example using a fault tree method for risk assessment for a specific construction pit was also a key part of the project.

1.2 What is risk?

From literature we can find countless different definitions of risk. Aven and Renn (2010) divides the definitions into two categories:
(1) risk is expressed by means of probabilities and expected values,
and (2) risk is expressed through events/consequences and uncertainties.
As an expression of these two main categories, definitions of NS5814 and ISO 31000 states: "Risk expresses a combination of the likelihood and consequences of an incident" (NS5814); "Risk is effect of uncertainty on objectives" (ISO 31000).

Risk management is a term for coordinated activities to assess, control and cope with risks a community is exposed to. The risk management objective is therefore to review and possibly reduce the risk if necessary. When the context of risk management is established, the following steps are important in the risk management process in accordance with ISO 31000:
Step 1: Risk Identification: Potential threats and hazards are identified. What can happen?
Step 2: Risk analysis: Probabilities, potential consequences and risks are combined. How likely is it and if an unwanted event happens, what are the consequences?
Step 3: Risk Assessment: The risk is assessed in relation to the criteria for acceptable or tolerable risk. Are the risks acceptable?
Step 4: Risk reduction measures: What can be done to get the risk down to an acceptable level?

2 METHODOLOGY

2.1 General

There are a large amount of tools that can be used in the risk assessment process. The methods can be purely qualitative, a combination of qualitative and quantitative, or purely quantitative. Some methods may be used by personnel without special expertise in risk assessment, whereas such specialization is needed for other methods. The various methods can be effective tools in various stages of a project. When choosing the method to be used, one should also consider various aspects such as data access, available expertise, complexity of the problem, the purpose of the analysis, and who will use the results. The choice of methods should be justified in terms of relevance and applicability. When it is decided to carry out a risk assessment, and the goal and scope is defined, the following should be considered when choosing the methodology:

(1) The purpose of the study. The purpose of the risk assessment will have a direct impact on the methodology to be used. For example, if the purpose of the study is a comparison between different options, it may be appropriate to use less detailed impact models for the parts of the system where there are small differences between the options.
(2) The need for information to decision-makers. In some cases a high level of detail is required to make good decisions, while in other cases a more general understanding is sufficient.
(3) The type and range of risks to be analysed.
(4) The potential magnitude of the consequences. The character of the analysis should reflect the initial perception of the consequences (although this modification may be required beyond the evaluation process).
(5) Availability of resources both related to expertise, time and other required resources. A simple method applied in a good way can give more useful results than a more sophisticated method, as long as the former satisfies the purpose and scope of the assessment.
(6) Availability of data. In the early stages of the project, simple methods can be used, for example based on a qualitative or semi-quantitative approach. Later in the project, when larger amounts of data are available, more sophisticated methods should be

used, probabilistic methods if possible.

(7) Risk acceptance criteria and risk management procedures defined in the project.

2.2 Overview of methods

Quantitative methods aim to estimate both the probability and consequences of adverse events, while semi-quantitative methods aim for ranking of risk by use of relative numbers. Examples of qualitative methods in construction projects are brainstorming among experts, checklists, rough analysis, hazard and operability studies (HAZOP) and "What happens if" analyses (swift). Common quantitative methods are fault tree and event tree analysis, FMEA (Failure Modes and Effect Analysis), MORT (Management Oversight and Risk Tree), SMORT (Safety Management and Organization Review Technique), THERP (Technique for Human Error Rate Prediction), SLIM (Success Likelihood Index Method), Multi Risk, risk matrix and Markov analysis. An overview of the most applied methods and applications is given in Table 1.

3 RISK METHODOLOGY DEVELOPED IN BEGRENSSKADE

3.1 Overview

The BegrensSkade project developed its own method for risk management. The proposed method is based conceptually on ISO 31000's framework, in that the methodology is divided into five phases similar to the ISO 31000 framework; Phase 1: Establish basis. Phase 2: Risk identification; Phase 3: Semi-quantitative risk analysis; Phase 4: Risk Assessment; Phase 5: Risk reduction measures. The method is implemented in the spreadsheet *BegrensSkadeRisikohandtering.xlsm.* The spreadsheet consists of a total of three sheets:

- 01-Basis
- 02-Risk identification
- 03-Risk

, in which all the 5 phases of the risk management process are addressed.

It is recommended that the analysis (using the method and the spreadsheet) is performed by a group of technical experts at various levels and relevant for different phases of the project. As the project progresses and new information becomes available, the spreadsheet should be revised.

3.2 Establish basis

Initially the purpose of the analysis must be clarified, which means that one defines what types of consequence to consider, as well as structuring the project into phases so that one can easily identify sources of uncertainty and potential causes of adverse events. Requested input include the determination of the types of uncertainties and which impact types to be included in the spreadsheet. The example included in the worksheet contains five types of uncertainties and four consequence types, but the user is free to remove and add it's own types. For example, the NS 5815 "Risk assessment of construction work" follows four types of consequence: Life and health, Environment, Economy / tangible assets and Reputation. Consequence types should be of such a nature that they could be subdivided into specific severity classes. Two important criteria for selecting severity classes are (a) that they are the most tangible and (b) that it later in the risk analysis is possible for the user to assess the severity class for the consequence. Specific class boundaries make risk analysis more repeatable and less subjective. Classes must be adapted to the project, i.e. the class limits set are relevant to the project. NS 5815 "Risk assessment of construction work" suggests using the following general classes: K1 = hazardous, K2 = Harmful, K3 = Critical, K4 = Very critical, K5 = Catastrophic. These adjectives can be used as a guideline when more specific class boundaries should be defined.

Probability ranges for the various events also need to be defined. As for consequence classes, the criteria are (a) that they are the most tangible and (b) that it later in the risk analysis is impracticable for the user to assess the probability class an incident ports. The following adjectives may be used as guidance

for the user: S1 = Extremely unlikely, S2 = Very unlikely, S3 = Very unlikely, S4 = Unlikely, S5 = Somewhat likely. This may range from less than 0.1% per annum on Class S1 to more than 10% per annum for Class S5.

In order to make it easier to find sources of uncertainty and potential causes of adverse events, the spreadsheet is built up so that the main processes in the project are identified, numbered and listed. How the project is split up, is defined by the user. The processes can for example be arranged chronologically and/or according to the responsible for the process.

3.3 Risk identification

Risk identification involves going through all the main processes of the project as defined and identify risk sources and causes of adverse events. A semi-quantitative risk analysis starts by entering numerical values for probabilities and consequences for all risk sources. These data are presented as a risk matrix (Figure 1) where probability (on scale 1 to 5) is plotted against impact (on scale 1 to 5) for each of the risk sources. The user also has the opportunity to decide which risk sources should be included in the matrix.

3.4 Risk evaluation

In the risk evaluation, calculated risk is compared with risk criteria to determine if risk reduction measures are necessary. In the spreadsheet, it is built into some simple tools to assist in this process. The risk criteria to be used will be decided by the user.
In a semi-quantitative method risk is not measured explicitly. The resulting risk is subdivided into 5 levels, illustrated with 5 different colors. The colors of the matrix is related to risk by making different assumptions about how the relative scales (1 to 5) for probability and consequences are connected to physical probability and consequence, see Figure 2. The following operating for color coding is implemented in the spreadsheet:
a) Staircase: This method means that the borders between the five different colors in the array looks like a staircase. Using this method corresponds to the color boundaries of constant risk if the relative scales (1 to 5) on the two axes of the matrix corresponds to exponential scale for physical probability and consequence. b) Hyperbola: This method means that the borders between the five different colors of the matrix are hyperbolas. Using this method corresponds to the color boundaries of constant risk if the relative scales (1 to 5) on the two axes of the matrix corresponds to a linear scale for physical probability and consequence.

3.5 Risk mitigation

Risk reduction measures can be structured into two groups; (1) reducing the probability and (2) reducing the impact. For more refined structuring, measures can further be based on uncertainty types and consequence types defined in Phase 1. In the example included in the spreadsheet, the following types are defined:
1. Reduction of probability / uncertainty:
a. Material (M)
b. Design (D)
c. Execution (U)
d. Natural loading (N)
e. External factors (E)
2. Reduction of consequence. Measures to protect the vulnerable elements of injury:
a. Life and health (H)
b. Environment (M)
c. Progress (F)
d. Economy (SE)
In the spreadsheet, the ability to add description of risk reduction measures is included. It is recommended to save the version of the worksheet that contains measures part as a separate file. Various stimulus packages can be analyzed separately and each package of measures can be saved as a separate spreadsheet file. For each package of measures, numerical value of probability and consequence and risk analysis could be revised. The user may then assess whether the measures are sufficient.

4 RISK ASSESSMENT WORKSHOP

4.1 Basis

A workshop within DP5 Risk was held in spring 2015. In all, 10 people involved in the BegrensSkade project participated. The purpose of the workshop was to jointly construct a fault tree diagram for a construction pit in order to explore possible causes for unexpected settlements outside the construction pit.

The work on the preparation of a fault tree diagram was conducted for a construction pit with the following assumptions:
-Area construction pit (45m * 90m).
-Sheet pile walls anchored at 3 levels.
-Base foundation 10 m below ground.
-Foundation: Piles to rock from the molded base plate, lime-cement stabilization along parts of the pit.
- Relief wells in central pit to avoid bottom heave.
-Ground conditions: Varying depth to mountains, fill material, homogeneous clay, groundwater level 1 m below ground level.
- Neighbour building: piled, some piled into mountains, some sole-founded building, large areas of traffic on a page.

4.2 Fault tree analysis

Basically for a fault tree analysis, an undesirable event is called a top event. The incident is then decomposed successively down to the desired level of detail for the events or mistakes that have caused the top event. The method is both qualitative and quantitative in nature.

Fault tree analysis has a relatively wide range of applications and is one of the most widely used methods for risk analysis. It's purpose is to identify the reasons why adverse events occur.

A fault tree analysis consists of three steps: constructing the fault tree, identifying which combinations of events that have caused the top event, and an assessment of probabilities (or relative ranking).

The identified errors and malfunctions are decomposed further down into smaller events. The last step identify the events that started the chain, also called basic events. This is followed by a survey of specific combinations of events. The probability can be assessed qualitatively or quantitatively. For quantitative assessment the probability of the top event is calculated using calculation rules for the logical operators.

The workshop was conducted by first dividing the participants into two groups, where each group had a discussion regarding the possible causes of the top event (settlements in surroundings). The results of these discussions were subsequently codified in plenary by constructing a fault tree diagram under the direction of sub-project leader for DP5.

The result of the exercise in the form of the constructed fault tree diagram is provided in Figure 3. It was indicated three possible independent causal; i) horizontal displacements of sheet piles, ii) pore pressure build-up, and consolidation settlements, iii) mass loss or stirring effect of drilling rods anchoring. These possible causal relations were so decomposed further into two levels.

5 CONCLUSIONS

The studies made in the BegrensSkade project shows that there is a large potential for reducing damages and costs in excavation and foundation works by systematic use of risk assessment methodologies. Risk based decisions can in case be used in every single step in the preparation and construction work. In this work it of special importance to identify potential risk sources, to assess the risk and to mitigate the risk if found required.

6 REFERENCES

Aven and Renn (2010). Risk management and governance. Concepts, guidelines and applications. Springer-Verlag, Berlin Heidelberg, 2010

ISO 31000 (2009). Risk management - Principles and guidelines. International Standard, 2009-11-15

NS5814 (2006). Risikovurdering av anleggsarbeid

Table 1 Overview of risk assessment methodologies

Method (Chapter)	Purpose	Relevant types of projects	Appli-cation	Quali-tative	Semi-quanti-tative	Quanti-tative
Checklists	Hazard identification	All	Conceptual phase	+	-	-
Preliminary hazard analysis	Preliminary hazard identification and risk estimate	All	Conceptual phase	+	+	-
Hazard and operability study (HAZOP)	Hazard and risk identification	Industry/ technical systems	Design phase	+	+	-
What-if analysis (Swift)	Hazard identification and mitigation	Industry/ technical systems	All project	+	-	-
Scenario analysis	Analysis of possible future events	All	Conceptual phase	+	+	-
Observational method	Perform corrective actions based on monitoring		Design and execution phase	+	-	-
Failure Mode and Effect Analysis, FMEA	Identification of failure sources and effects	Technical systems	Design phase	+	+	+
Fault trees	Identification of hazards and events	Technical systems, environ-ment	Design phase	+	+	+
Event trees	Description of events and consequences	Technical systems, accidents	Design phase	+	+	+
Decision tree	Ranking of decision alternatives		Design phase	+	+	+
Risk matrix	Risk evaluation	All	All project	+	+	-
Bayesian	Risk evaluation	All	Design phase	-	+	+
MORT	Barrier analysis	Technical systems, environ-ment	Design phase	+	+	+
Monte Carlo simulation	Calculating expressions including stochastic variables		Design phase	-	-	+
β-method	Calculating expressions including stochastic variables		Design phase	-	-	+

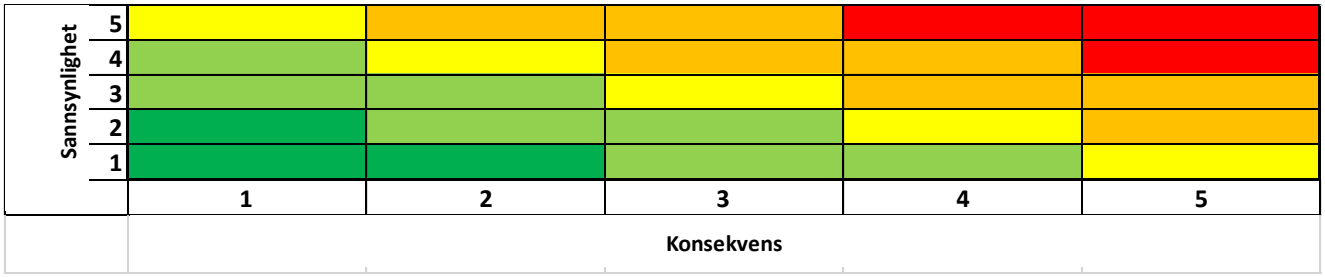


Figure 1 Risk matrix used in the BegrensSkade spreadsheet. Colours define relative risk (from green – very low to red – very high).

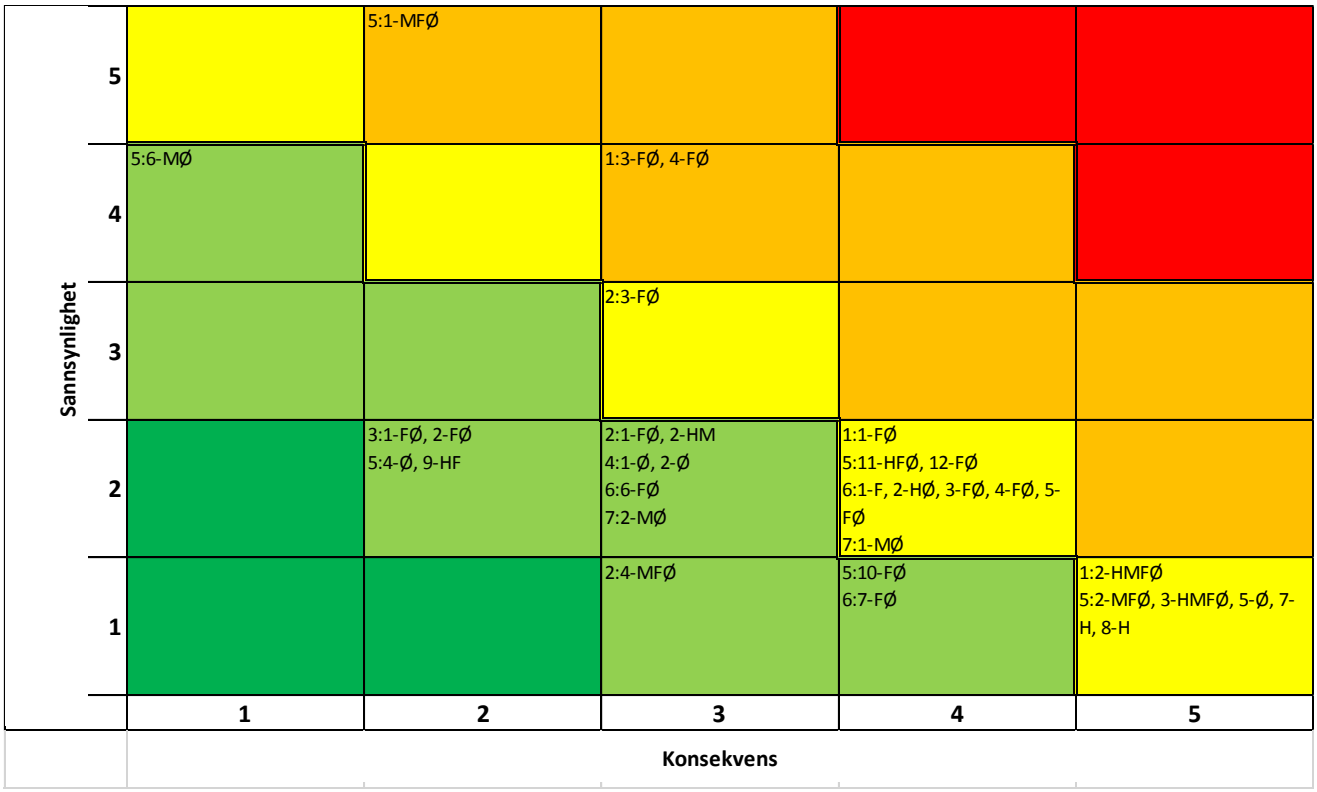


Figure 2 Example of a risk assessment study.

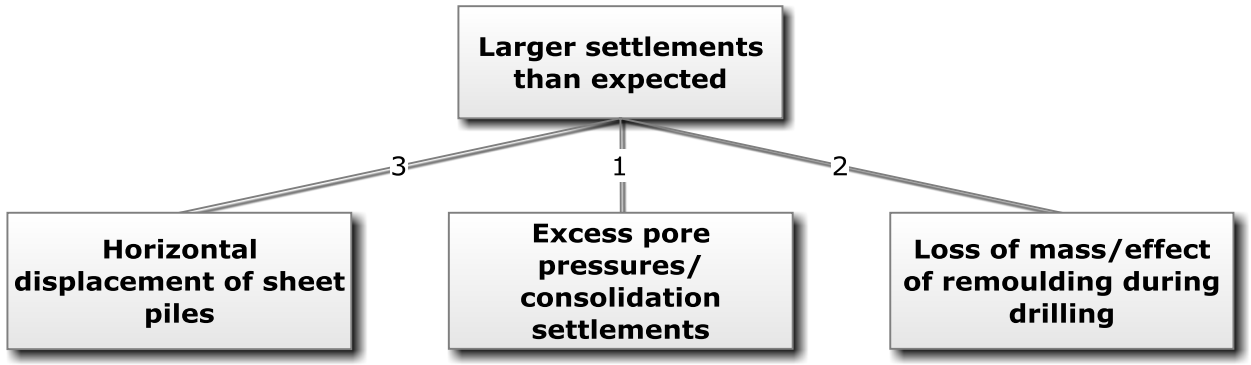


Figure 3 Results of fault tree analysis, level 1

Reliability-based design of a monopile foundation for offshore wind turbines based on CPT data

I. E. V. Overgård, I. Depina & G. Eiksund
Norwegian University of Science and Technology, Trondheim, Norway

ABSTRACT

A reliability-based design optimization (RBDO) of a monopile foundation for offshore wind turbines is conducted to account for the uncertainties in the design process. The RBDO aims at optimizing the cost of construction, installation and failure with respect to the ultimate limit state of a monopile foundation while accounting for the effects of uncertainties in soil parameters and lateral loads. The soil parameters are interpreted via a probabilistic link which is composed of a random field model of CPTU measurements and the transformation uncertainty relating soil parameters to CPTU measurements. The maximum likelihood method is employed to estimate the random field parameters of CPTU measurements. Probabilistic models for soil parameters and lateral loads are coupled with the nonlinear p-y finite element model to predict the response of a monopile foundation. The RBDO problem is solved by coupling the Subset Simulation reliability method with the Simulated Annealing stochastic optimization algorithm.

Keywords: reliability, optimization, RBDO, CPT, random field

1 INTRODUCTION

Geotechnical designs are subjected to uncertainties originating from various sources (e.g., inherent soil variability, measurement errors, transformation uncertainty, modelling assumptions). In geotechnical practice it is common to evaluate the effects of uncertainties on a design with a semi-probabilistic methodology commonly known as the partial factor of safety approach. In the partial factor of safety approach, the uncertainties in the design are quantified implicitly by partial safety factors, as defined in several design codes (e.g., Eurocode). Alternative to the factor of safety approach is the reliability-based design which explicitly accounts for the effects of uncertainties in a design. The application of the reliability-based design is considered as advantageous because it provides an insight in the likelihood of failure as a probabilistic measure (Fenton & Griffiths, 2008). In this study, the application of the reliability-based design is coupled with optimization in a procedure commonly referred to as reliability-based design optimization (RBDO). The goal of the RBDO is to optimize performance criteria of a geotechnical design (e.g., design cost) while explicitly accounting for the effects of uncertainties.

In the context of the offshore wind industry, the application of the RBDO is beneficial due to standardized structural components (e.g., tower, monopile). However, in the majority of studies, deterministic optimization is considered. For example, Uys, Farkas, Jarmai, and Van Tonder (2007) optimized the weight and the cost of an offshore wind turbine tower. Negm and Maalawi (2000) applied the interior penalty algorithm to optimize the natural frequencies of the wind turbine. Fischer et al. (2012) examined the advantages of design optimization design by minimizing the weight of the wind turbine tower and the monopile. Søensen and Tarp-Johansen (2005) conducted an RBDO to minimize the inspection, construction, maintenance, and failure costs of a wind turbine tower with a gravity-based foundation.

This study performs an RBDO of a monopile foundation to minimize the design costs with

respect to a reliability constraint. The design cost is expressed as a function of the monopile diameter, wall thickness, embedded length, and random parameters (i.e., lateral load and soil parameters). Special attention was given to the uncertainties associated with the interpretation of soil parameters relevant for the design of monopile foundations from CPTU measurements. The RBDO is implemented by coupling the Simulated Annealing (SA) optimization method with the Subset Simulation (SS) reliability method.

2 MONOPILE FOUNDATIONS FOR OFFSHORE WIND TURBINES

2.1 Sheringham Shoal Offshore Wind Farm

The RBDO of a monopile foundation from the Sheringham Shoal Offshore Wind Farm (SSOWF) is performed in this study. The SSOWF is an offshore wind farm located in the North Sea, 20 km north of the Norfolk coast, offshore UK. Based on the geotechnical conditions at the site and the conducted site investigations three main soil units are identified at the site, as presented in Figure 1. The Bolders Bank Formation (BDK) is a soil unit found at the seabed. The BDK formation is primarily composed of stiff clay with sand and gravel pockets. The Egmond Ground Formation (EG) is a soil unit found below the BDK formation. The EG formation is a mixture of dense to very dense sands. The Swarte Bank formation (SBK) is a soil unit found below the EG formation. The SBK formation is a mixture of hard silty clay with occasional marine interglacial sediments (Saue & Meyer, 2009).

2.2 Numerical pile-soil model

Given that the monopile foundations for offshore wind turbines are dominantly loaded laterally, the response of a monopile foundation is commonly simulated by the p-y method (e.g.,DNV, 2010). The p-y method models the response of the soil domain to the lateral loading of the pile by a series of nonlinear soil springs. The material behavior of the soil springs is defined by the p-y curves which are developed for different soil types (e.g., clay, sand) and loading conditions (i.e., static, cyclic). In this study, the static p-y curves for stiff clay are implemented to simulate the soil response of the BDK and the SBK soil units. On the other hand, the static p-y curves for sand are implemented to evaluate the response of the EG soil unit.

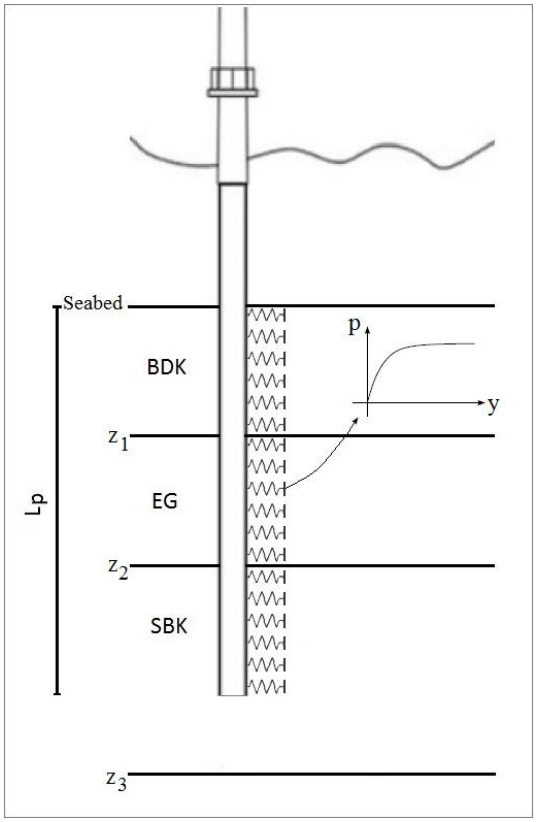


Figure 1: Three main soil units at the SSOWF site.

In addition to several empirical parameters and the soil unit weight, the p-y curves for stiff clay are a function of undrained shear strength, s_u, while the p-y curves for sand are a function of the friction angle φ. Given that soils exhibit spatial variability due to the randomness of geological processes involved in the creation of the soil formations at the SSOWF, the spatial variability of s_u and φ and their effect on the monopile response will be examined. Other parameters of the p-y curves are considered to be deterministic because of a relatively low variability (e.g., unit weight) or due to their empirical and model dependent origins.

The monopile material is steel with density of ρ_s=7800 kN/m^3, and elastic behavior defined by Young's modulus of E_p=2.1 x 10^5 MPa and Poisson's ratio υ_s=0.3.

3 PROBABILISTIC SOIL PARAMETER INTERPRETATION FROM CPT DATA

The derivation of soil parameters for the design of monopile foundations relies primarily on the data obtained from the CPTU profiles at the locations of the planned wind turbines and several boreholes at the site. Soil samples extracted from the boreholes are commonly used to calibrate the relations between the CPTU measurements and soil parameters such that the soil parameters can be estimate at the planned locations of the wind turbines. A probabilistic interpretation of s_u and φ based on CPTU data is examined in this study. The probabilistic interpretation includes the inherent variability of the CPTU measurements and the transformation uncertainty associated with the relations between and s_u and φ and the CPTU measurements.

3.1 s_u interpretation

The relation between the CPTU measurements and s_u can be established as follows (e.g.,Lunne, Robertson, & Powell, 1997):

$$s_u = \frac{q_t - \sigma_{v0}}{N_k} \tag{1}$$

where q_t (MPa) is the corrected cone tip resistance, σ_{v0} (kPa) is the in-situ overburden pressure, while N_k is the empirical cone factor. The parameters of the right site of Eq. 1 are associated with uncertainties. The uncertainties in q_t are a result of both the inherent soil variability and the measurement error. Although σ_{v0} can be influenced by various sources of uncertainty, a deterministic stress state is assumed, dependent on the soil unit weight, soil depth and water level. Given its empirical nature N_k is associated with uncertainties. A study on the values of N_k in Kulhawy, Birgisson, and Grigoriu (1992) reveals that the uncertainty of N_k depends on the soil test used to estimate s_u. Table 1 presents the mean and CoV values of N_k for different soil tests (Kulhawy et al., 1992):

Table 1: Mean and CoV values of N_k for different s_u tests from Kulhawy et al. (1992).

s_u test	**Mean**	**CoV**
CIUC	12.674	35
UU	19.531	29
VST	11.038	40

CIUC, consolidated isotropic undrained triaxial compression test, UU unconsolidated undrained triaxial compression test, VST vane shear test.

The derivation of s_u values from q_t measurements is based on the assumption that q_t measurements are an outcome of a lognormal random field. The corresponding lognormal random field of q_t is defined by a deterministic trend, μ_{qt}, standard deviation, σ_{qt}, and the correlation length, θ_{qt}.

The parameters of the q_t random field are estimated with the maximum likelihood method from the values of the corresponding normal random filed $\ln q_t$ by assuming the exponential correlation model (e.g.,Fenton & Griffiths, 2008). Given the maximum likelihood estimates of the mean, $\mu_{\ln qt}$, standard deviation, $\sigma_{\ln qt}$, and the correlation length, $\theta_{\ln qt}$, the parameters of the lognormal random field can be derived as follows.

$$\mu_{q_t} = \exp\left(\mu_{\ln q_t} + \frac{\sigma^2_{\ln q_t}}{2}\right) \tag{2a}$$

$$\sigma_{q_t} = \mu_{q_t}\sqrt{\exp\left(\sigma^2_{\ln q_t}\right) - 1} \tag{2b}$$

N_k is assumed to be lognormally distributed with a site-specific mean, μ_{Nk}, with the CoV_{Nk} as reported in Table 1. Given that σ_{v0} is deterministic, and both q_t and N_k are lognormally distributed the natural logarithm transformation of Eq. 1 can be utilized to derive the parameters of s_u:

$$\ln s_u = \ln\left(q_t - \sigma_{v0}\right) - \ln N_k \tag{3}$$

Since q_t is lognormally distributed and σ_{v0} is a deterministic value, (q_t-σ_{v0}) is lognormally distributed with the following parameters:

$$\mu_{(q_t-\sigma_{v0})} = \mu_{q_t} - \sigma_{v0};\ \sigma_{(q_t-\sigma_{v0})} = \sigma_{q_t} \quad (4)$$

Since both terms in the right side of Eq. 3 are normally distributed, $\ln s_u$ is normally distributed with the following parameters:

$$\mu_{\ln s_u} = \mu_{\ln(q_t-\sigma_{v0})} - \mu_{\ln N_k} \quad (5a)$$

$$\sigma^2_{\ln s_u} = \sigma^2_{\ln(q_t-\sigma_{v0})} + \sigma^2_{\ln N_k} \quad (5b)$$

where $\mu_{\ln(qt-\sigma v0)}$ and $\sigma_{\ln(qt-\sigma v0)}$ are the parameters of $\ln(q_t-\sigma_{v0})$, while $\mu_{\ln Nk}$ and $\sigma_{\ln Nk}$ are the parameters of $\ln N_k$. The parameters of $\ln(q_t-\sigma_{v0})$ are calculated as follows:

$$\sigma_{\ln(q_t-\sigma_{v0})} = \sqrt{\ln\left(1+\frac{\sigma^2_{(q_t-\sigma_{v0})}}{\mu^2_{(q_t-\sigma_{v0})}}\right)} \quad (6a)$$

$$\mu_{\ln(q_t-\sigma_{v0})} = \ln \mu_{(q_t-\sigma_{v0})} - \frac{1}{2}\sigma^2_{\ln(q_t-\sigma_{v0})} \quad (6b)$$

The parameters of $\ln N_k$ are calculated as follows:

$$\sigma_{\ln N_k} = \sqrt{\ln\left(1+\frac{\sigma^2_{N_k}}{\mu^2_{N_k}}\right)} \quad (7a)$$

$$\mu_{\ln N_k} = \ln \mu_{N_k} - \frac{1}{2}\sigma^2_{\ln N_k} \quad (7b)$$

It is assumed that the transformation does not affect the autocorrelation properties, $\theta_{su}=\theta_{qt}$.
Figure 2 present a realization of an s_u random field based on the following maximum likelihood estimates of a lognormal random field fitted to a CPTU at the SSOWF site; μ_{qt}=1.9 MPa, σ_{qt}=0.6 MPa, and $\theta_{\ln qt}$=1.
For the BDK and SBK soil units the values of μ_{Nk}=15 and CoV_{Nk}=0.35 are selected based on the available laboratory test data from the SSOWF site (Saue & Meyer, 2009).

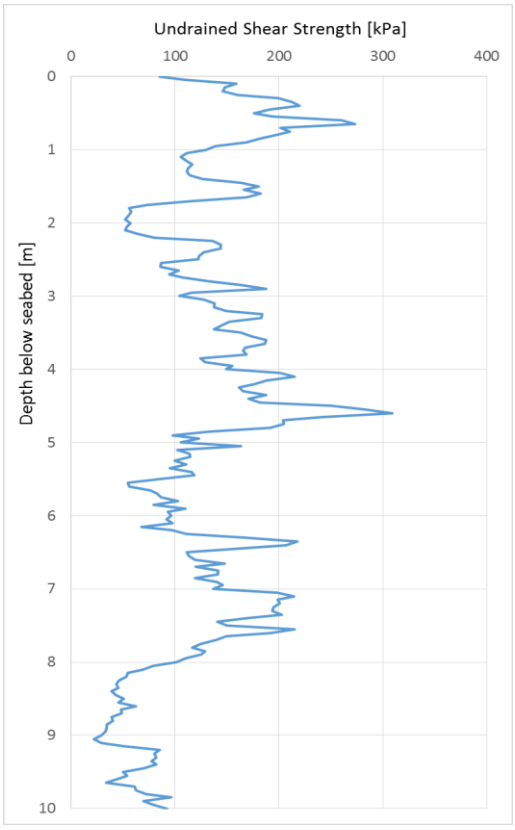


Figure 2: Example s_u profile.

3.2 φ interpretation

The value of φ is interpreted from the CPTU measurements based on the relations proposed by Robertson and Campanella (1983). The value of φ is shown to be dependent on the value of q_t scaled by the effective in-situ stresses, σ'_{vo}.

After examining the established relation between φ and q_t, as presented in Figure 3, it is observed that a relatively simple regression model can be employed to approximate the relation. The regression model has the following formulation:

$$\varphi = 5.03\ln\left(\frac{q_t}{\sigma'_{v0}}\right) + 52.04 + \varepsilon \quad (8)$$

where ε is the transformation uncertainty which accounts for the model error and the regression model error. ε is modeled as a normal random variable with zero-mean and standard deviation σ_ε=2.8°, as reported in Kulhawy and Mayne (1990). It is important to note that the regression model is valid only for the range of φ presented in Figure 3, 30°≤φ≤50°.

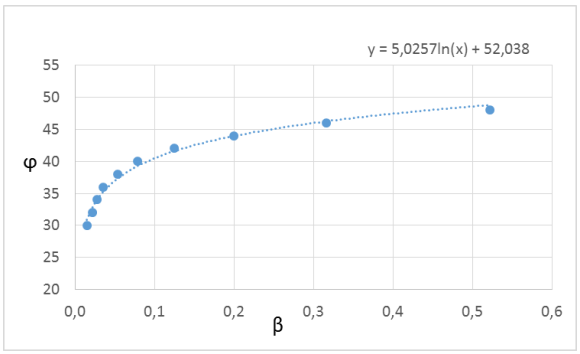


Figure 3: Relation between $\beta=q_t/\sigma'_{v0}$ and φ.

The statistical parameters of φ are derived by assuming a deterministic stress profile σ'_{vo} and that q_t measurements are an outcome of a lognormal random field. As discussed in Section 3.1, the parameters of the lognormal random field can be estimated with the maximum likelihood method.

Given that q_t is lognormally distributed while ε is normally distributed it follows from Eq. 8 that φ is normally distributed with the following parameters:

$$\mu_\varphi = 5.03\left(\mu_{\ln q_t} - \ln \sigma'_{v0}\right) + 52.04 \quad (9a)$$

$$\sigma_\varphi^2 = 5.03^2 \sigma_{\ln q_t}^2 + \sigma_\varepsilon^2 \quad (9b)$$

where $\mu_{\ln qt}$ and $\sigma_{\ln qt}$ are the mean and standard deviation of $\ln q_t$ which are estimated with the maximum likelihood method. It is assumed that the transformation does not affect the autocorrelation properties, $\theta_\varphi=\theta_{qt}$.

An example random field realization of φ is present in Figure 4.

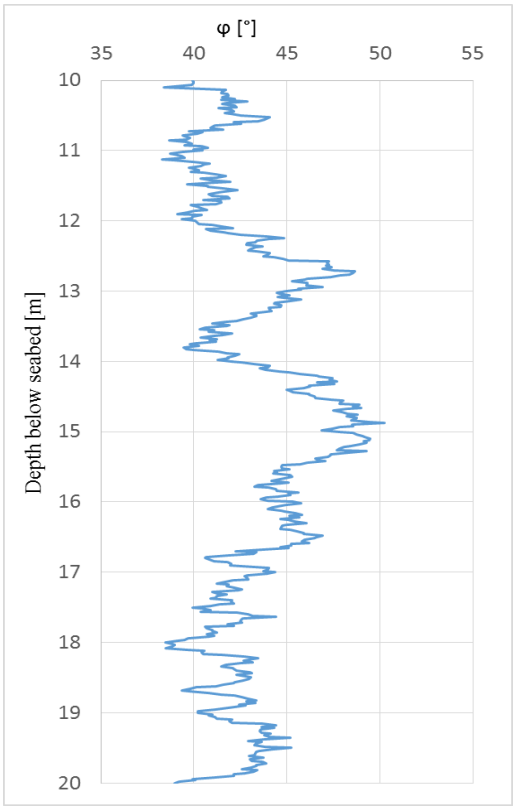


Figure 4: Example φ profile.

4 RANDOM LOAD

The monopile in this study is loaded laterally with a load composed of a horizontal force H and a bending moment $M=H\cdot 30$ m. H is assumed to be random and distributed according to the Gumbel distribution with the mean μ_H=2500 kN and CoV_H=0.2.

5 RBDO OF A MONOPILE FOUNDATION

The RBDO of a monopile foundation is conducted to minimize the total cost with respect to a set of monopile design parameters $\mathbf{t}=[D, w, L_P]$, where D (m) is the monopile diameter, w (m) is the monopile wall thickness, and L_P (m) is the monopile length. The optimization is conducted in the discretized space of random parameters such that $D \in [4, 4.1, ..., 7]$, $w \in [0.03, 0.04, ..., 0.1]$, and $L_P \in [25, 26, ..., 40]$. The design cost of a monopile foundation is approximated by a cost of C_i=2€/kg of the monopile weight, while the expected failure cost is assumed to be $C_F=10^7$€.

The RBDO problem is defined as follows:

$$\text{minimize: } C(\mathbf{x},\mathbf{t}) = C_i L_P \rho_S \pi \left[\left(\frac{D}{2}\right)^2 - \left(\frac{D}{2} - w\right)^2 \right] + C_F P_F(\mathbf{x},\mathbf{t}) \quad (10a)$$

subject to:

$$[4, 0.03, 25] \le \mathbf{t} \le [7, 0.1, 40] \quad (10b)$$

$$P_F(\mathbf{x},\mathbf{t}) \le 10^{-4} \quad (10c)$$

where $\mathbf{x}=[H,\ s_u,\ \varphi]^T$ is a vector of random parameters composed of H, s_u random fields for the BDK and SBK soil units, and φ random field for the EG soil unit, $P_F(\mathbf{x},\mathbf{t})$ is the probability of exceeding the ultimate limit state for a given combination of design parameters.

In this study, the ultimate limit state of a monopile foundation is defined by the yield strength of the monopile steel, σ_{lim}=235 MPa. The ultimate limit state can be defined by the corresponding performance function:

$$g(\mathbf{x}',\mathbf{t}') = \sigma_{\lim} - \sigma(\mathbf{x}',\mathbf{t}') \quad (11)$$

where $\sigma(\mathbf{x}',\mathbf{t}')$ is the maximum stress in the monopile for a given combination of $\mathbf{x}'$ and $\mathbf{t}'$. The probability of exceeding the ultimate limit state, for a given combination of design parameters $\mathbf{t}'$, $P_F=P(g(\mathbf{x},\mathbf{t}')\le 0)$ is calculated with the SS method (Au & Beck, 2001). The SS is an efficient and robust reliability method which expresses the reliability problem by a series of intermediate conditional reliability problems. The conditional reliability problems correspond to, prior to the analysis unknown, series of decreasing intermediate failure limits. The SS method provides efficient performance by specifying the probabilities of the conditional reliability problems sufficiently large (e.g., P=0.1) so that they can be evaluated with a relatively low number of samples of random parameters.

The reliability of a monopile foundation is evaluated with the SS method by defining the probabilities of the intermediate conditional reliability problems to be P=0.1. The conditional probabilities are evaluated with 200 samples of random parameters.

The RBDO of a monopile foundation is conducted by coupling the SA method and the SS method to solve the optimization and reliability problems, respectively. The SA is a stochastic optimization method applied for discrete and continuous optimization problems. The SA method is selected due to its robust algorithm which is capable of avoiding local minima in search of the global minimum (e.g.,Spall, 2005). In order to integrate the reliability constraint in Eq. 10c into the optimization process, the algorithm of the SA method is adapted such that $C(\mathbf{x},\mathbf{t})=\infty$ in case of reliability constraint violation, $P_F(\mathbf{x},\mathbf{t})>10^{-4}$.

6 RESULTS

The SA optimization is initiated with following values of the design parameters: $\mathbf{t}'$= [5.5,0.05,30], with $P_F(\mathbf{x},\mathbf{t}')<10^{-4}$ and $C(\mathbf{x},\mathbf{t}') = 4.03 \times 10^5$€.

The SA algorithm was employed with 1000 iterations to locate the minimum design costs. For each iteration of the algorithm, the probability of exceeding the ultimate limit state of the monopile is evaluated with the SS method. The SS method is implemented with 200 simulations of random parameters per conditional reliability problem. Since the SA method does not provide convergence criteria for the estimate of the minimal design cost, several independent optimizations are conducted to achieve a robust estimate. In total seven optimizations with the SA algorithm are conducted, as presented in Table 2.

Table 2: RBDO results

C [10^5€]	w [m]	L_p [m]	D [m]	P_F [10^{-6}]
2.55	0.04	26	5.0	8.5
2.60	0.04	26	5.1	4.6
2.64	0.04	27	5.0	8.5
2.90	0.04	27	5.7	3.3
2.70	0.04	27	5.1	8.5
2.65	0.04	26	5.2	79
2.75	0.04	26	5.4	39

Figure 5 illustrates the results from three optimizations with the SA method. It is important to note that the estimate of the optimal design cost is the minimal design cost encountered during the optimization process.
As observed from Table 2 the estimate of the minimal design cost is found between 2.55 and 2.90 x 10^5 €. The optimal design costs correspond to the monopile designs with *w* of 0.04 m, L_p 26 or 27 m and *D* between 5 and 5.7 m.

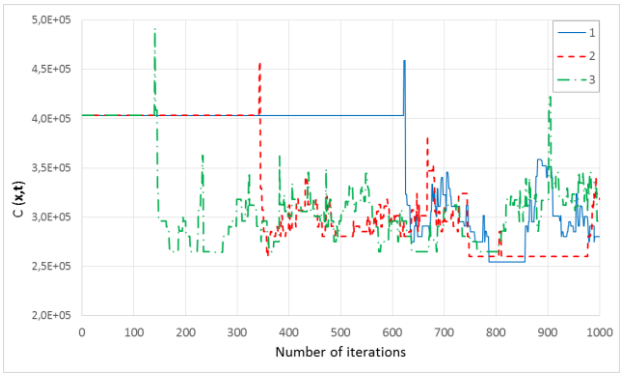


Figure 5: Design cost with the number of iterations of the SA optimization.

The results in Table 2 and Figure 6 demonstrate that the reliability constraint is implemented successfully in the SA algorithm. The reliability constraint is satisfied throughout the optimization process since $P_F \leq 10^{-4}$. The variation in the estimates of P_F in Table 2 can be attributed to the stochastic nature of the SS method.

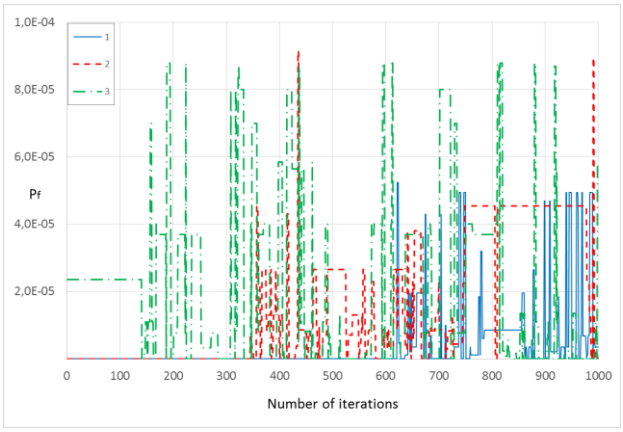


Figure 6: P_F with the number of iterations of the SA optimization.

7 CONCLUSION

This study presented an RBDO of a monopile foundation for offshore wind turbines. The goal was to minimize the design cost which includes the cost of production, installation and failure. The RBDO is conducted with the Simulated Annealing optimization method and the Subset Simulation reliability method.
The Subset Simulation method is implemented to evaluate the probability of exceeding the ultimate limit state of a monopile foundation with respect to the uncertainties in the soil parameters and lateral loads.
Special attention was given to the interpretation of soil parameters relevant for the design of monopile foundations from CPTU measurements. A probabilistic interpretation of undrained shear strength and friction angle based on CPTU measurements is implemented to integrate the inherent soil variability of the cone tip resistance with the transformation uncertainty associated with the corresponding soil parameter.
This study demonstrated that the reliability-based design optimization provides a consistent framework for dealing with uncertainties in the design of monopile foundations.

8 REFRENCES

Au, S.-K., & Beck, J. L. (2001). Estimation of small failure probabilities in high dimensions by subset simulation. *Probabilistic Engineering Mechanics*, *16*(4), 263-277.

DNV. (2010). Offshore standard DNV-OS-J101: Design of offshore wind turbine structures (pp. 142): Det Norske Veritas

Fenton, G., & Griffiths, D. (2008). *Risk Assessment in Geotechnical Engineering*: Wiley.

Fischer, T., Vries, W., Rainey, P., Schmidt, B., Argyriadis, K., & Kühn, M. (2012). Offshore support structure optimization by means of integrated design and controls. *Wind Energy*, *15*(1), 99-117.

Kulhawy, F. H., Birgisson, B., & Grigoriu, M. (1992). Reliability-based foundation design for transmission line structures:

Electric Power Research Inst., Palo Alto, CA (United States); Cornell Univ., Ithaca, NY (United States). Geotechnical Engineering Group.

Kulhawy, F. H., & Mayne, P. W. (1990). Manual on estimating soil properties for foundation design: Electric Power Research Inst., Palo Alto, CA (USA); Cornell Univ., Ithaca, NY (USA). Geotechnical Engineering Group.

Lunne, T., Robertson, P., & Powell, J. (1997). *Cone penetration testing in geotechnical practice*.

Negm, H. M., & Maalawi, K. Y. (2000). Structural design optimization of wind turbine towers. *Computers & Structures*, *74*(6), 649-666.

Robertson, P. K., & Campanella, R. (1983). Interpretation of cone penetration tests. Part I: Sand. *Canadian geotechnical journal*, *20*(4), 718-733.

Saue, M., & Meyer, V. (2009). Geotechnical Report: Sheringham Shoal Wind Farm Soil Investigation (20081313-1). *Oslo, Norway: Norwegian Geotechnical Institute (NGI)*.

Spall, J. C. (2005). *Introduction to stochastic search and optimization: estimation, simulation, and control* (Vol. 65): John Wiley & Sons.

Søensen, J. D., & Tarp-Johansen, N. J. (2005). Reliability-based optimization and optimal reliability level of offshore wind turbines. *International Journal of Offshore and Polar Engineering*, *15*(02).

Uys, P., Farkas, J., Jarmai, K., & Van Tonder, F. (2007). Optimisation of a steel tower for a wind turbine structure. *Engineering structures*, *29*(7), 1337-1342.

Reliability analysis of piles and pile groups based on dynamic load testing

Jimmie Andersson
ELU Konsult, Sweden, Jimmie.Andersson@elu.se

Gary Axelsson
ELU Konsult, Sweden

Anders Beijer-Lundberg,
ELU Konsult, Sweden

ABSTRACT
In Sweden, pile design of end-bearing piles is predominately based on high strain dynamic load testing. The design value is calculated using a partial factor design approach in accordance with the Eurocode. This approach is entirely based on the failure load of single piles. However, a pile group is normally a redundant, statically indeterminate structure, where failure of the geotechnical bearing capacity for one pile does not lead to total failure of the whole pile group. If the pile group carries a stiff structure, the advantage of load redistribution can be utilized to transfer loads between piles.
A comprehensive study was undertaken to examine whether a design in accordance with the Eurocode gives reasonable results for pile groups. This was assessed using a reliability-based design according to the First Order Reliability Method, "FORM". Both individual piles and pile groups were analysed according to the FORM-model and compared to the current design regulations. A case study was conducted based on data from high strain dynamic testing of piles. A comparison of the design was carried out according to the Eurocode and the FORM-analysis. The pile groups were modelled as a parallel system consisting of ductile elements and including the correlation between the piles.
The main results show that the measured variation in bearing capacity greatly affects the safety factor when comparing the FORM-analysis and the Eurocode. Furthermore, the correlation between piles is an important factor that has a major influence on the safety factor. When comparing single piles, the design according to the FORM-analysis yields safety factors of the same magnitude as the Eurocode. However, if the correlation between piles is small to intermediate, the results clearly show that a significant reduction in safety can be utilized for pile groups.
Keywords: Reliability analysis, Pile groups, High strain dynamic testing, β-method, FORM-analysis, Eurocode

1 INTRODUCTION

Major parts of Sweden are covered by glacial soils, frequently consisting of soft clays on top of relatively compact till and hard rock. End-bearing piles are installed by driving or drilling in areas with limited clay coverage. The pile tip of such piles is designed to reach the till or the rock layer. This method provides a stiff resistance, resulting in an end-bearing pile. The bearing capacity of the pile therefore mainly consists of the bearing resistance of the till or rock layer at the pile base. Because of the high strength of the soil or the rock located at the pile base, these piles are subjected to very high loads.

The geotechnical end-bearing capacity is normally very high on either till or crystalline rock. However, the very low shear strength of

the clay means that the structural capacity with regard to buckling, normally calculated according to the method presented in Bernander & Svensk (1970), also has to be checked. The geotechnical bearing capacity is normally determined using high strain dynamic testing with the CASE-method and, in some cases, also CAPWAP-analysis. The end-bearing capacity of these piles typically displays some variation, as a result of the natural variability of the soil or rock beneath the pile toe. Some parts of the total variability may be due to variations in the transferred energy from the hammer during high strain dynamic testing.

When designing in accordance with the Eurocode, these variabilities are accounted for by the use of what is called "correlation coefficients" (ξ_5 or ξ_6). The ξ_5 is used together with the measured mean value and the corresponding partial coefficient. The ξ_6 is used together with the minimum measured value together with the corresponding partial coefficient. The mean value will govern the design value for piles with a calculated coefficient of variation (*COV*) for the measured pile bearing capacity less than 10-12 %. Whereas the minimum measured value will govern the design value for a coefficient of variation above this (Frank et al., 2004). In this way, the Eurocode strives towards handling the variability in the measured pile capacity, preventing either too unsafe or too conservative designs. The reader is referred to EN 1997-1 for more details regarding the design of piles conforming to the Eurocode.

A reliability analysis of singular piles and pile groups has been carried out in the current paper. The method used is a First Order Reliability Method (FORM) and is called the β-method. From the β-method partial safety factors can be calculated and calibrated. The partial safety factors obtained from the β-method have been compared with those obtained using partial coefficients according to the Eurocode. Both the original Eurocode as well as the Swedish national annexes have been compared with the reliability analysis. Furthermore, the effects of piles placed in pile groups have been evaluated using the β-method.

2 THE Β-METHOD FOR PILES

2.1 General formulation of the model

The β-method is a First Order Reliability Method (FORM) that can be used to evaluate the safety and probability of failure for different structures. The method requires knowledge of the probability distribution of the different model parameters, as well as knowledge of the coefficient of variation (*COV*) and the mean value (μ).

The method also includes the safety-index β. The safety-index is directly linked to the probability of failure and by that means a measurement of how safe a structure is. In the current paper, the chosen β-value for the performed analysis as a whole is 4.3, which is the specified value according to the Swedish national annexes (Boverket, 2015; Trafikverket, 2011).

A yield function is needed to perform FORM-analysis. The yield function is an analytical solution for the problem:

$$f = R - S \tag{1}$$

Where f is the yield function, R is the bearing capacity and S is the applied load. Failure will occur for $f \leq 0$.

A transformation is made to the standardized normal distribution according to Hasofer & Lind (1974). The newly-obtained standardized normal distribution can be expressed as:

$$Z_i = \alpha_i \cdot \beta \tag{2}$$

Where Z_i is the standardized normally distributed variable and α_i is the weighting factor for that variable. The weighting factor for each variable in the yield function can be calculated as:

$$\alpha_i = \frac{\frac{\partial f}{\partial Z_i}(\beta\bar{\alpha})}{\sqrt{\sum_{k=1}^{m}\left(\frac{\partial f}{\partial Z_k}(\beta\bar{\alpha})\right)^2}} \tag{3}$$

Where $\bar{\alpha}$ is a unit vector containing all weighting factors. As mentioned earlier, failure occurs when:

$$f(\alpha_1 \cdot \beta, \ldots, \alpha_m \cdot \beta) = 0 \qquad (4)$$

Equation (3) and (4) can then be used to solve α_i and β by iteration. The design value obtained can then be calculated as:

$$x_i^* = \mu_i \cdot e^{-\alpha_i \cdot \beta \cdot COV_i} \qquad (5)$$

Where x_i^* is the design value for variable i and μ_i is the mean value for variable i. The partial safety factor can then be calculated as:

$$\gamma_i = \frac{x_{k,i}}{x_i^*} \qquad (6)$$

Where γ_i is equal to the partial safety factor for variable i and $x_{k,i}$ is the chosen characteristic value (normally μ_i).

2.2 FORM-analysis for piles

A pile group is normally a redundant structural system, e.g. Poulus (2005). The geotechnical bearing capacity for a pile in non-cohesive soil subjected to compression can be simplified as a perfect elastic-plastic behaviour, where increased loading leads to settlements without losing the bearing capacity of the pile (Fleming et al., 2009). This idealization, along with the empirical experience that pile groups normally are redundant structures, make it possible to model a pile group as a parallel system consisting of ductile elements.

In the current paper, a method originally created for lime-cement columns by Bergman (2015) has been adapted to single piles and pile groups. This adapted method takes into account that several uncertainties exist when high strain dynamic testing is used to verify the geotechnical bearing capacity. The uncertainties that the method takes into account are the measured coefficient of variation for the bearing capacity ($COV_{R,m}$), the measurement uncertainty which is always present when measuring (COV_{mf}). The bearing capacity of the pile is measured with a high strain dynamic method, e.g. the CASE-method outlined in Gravare et al., (1980), or the CAPWAP-method, discussed in Rausche et al., (1985). The uncertainty originating from this transformation is called the transformational uncertainty (COV_{tr}). Furthermore, the fact that not all piles are tested introduces another uncertainty, which involves the number of piles tested (N). This uncertainty is considered utilizing the methods described in Ang & Tang (2007). All of the uncertainties are considered log-normally distributed and recommended for material properties as well as model uncertainties in Eurocode 7, Appendix C, (Eurocode 7, 1997).

An interconnected pile group can be modelled as a parallel system consisting of ductile elements; the correlation between the different piles will affect the overall probability of failure for the pile group. This is explained by the fact that the mean value for the group will vary less than that of the different piles, as explained by Lo & Li (2007). Zhang et al., (2001) give the following formula which accounts for the possible variance reduction due to the pile-group:

$$COV_G = \frac{COV_{RS}}{n} \sqrt{n + \sum_i^n \sum_j^n \rho_{ij}} \quad , i \neq j \qquad (7)$$

Where COV_G is the coefficient of variation for the pile group, COV_{RS} is the coefficient of variation for the piles, n is the number of piles in the group and ρ_{ij} is the correlation between pile i and j.

The variance reduction is dependent on the number of piles in the pile group. This, together with the information presented above, can be combined into the following equation in order to describe the total uncertainty in the system:

$$COV_{R,G} = \sqrt{\begin{matrix} (COV_{R,m}^2 - COV_{mf}^2) \cdot \\ \left[\frac{1}{N} + \frac{1}{n^2} \cdot [(n^2 - n) \cdot \rho + n]\right] \\ + \frac{COV_{mf}^2}{N} + COV_{tr}^2 \end{matrix}} \qquad (8)$$

Where ρ is the average correlation between the piles in the group. Equation (8) is based on the principle of how coefficients of variations may be added, as presented by Goodman (1960).

3 COEFFICIENT OF VARIATION FOR DRIVEN CONCRETE PILES

A database containing over 600 high strain dynamic test results from 110 piling projects in Sweden has been analysed. The database was described and partly analysed in Axelsson et al., (2004). The database contains concrete piles driven to refusal in till. The piles were driven until 0-20 mm of sinking per 10 blows was obtained. The fall height and driving equipment may differ between projects. The main dimensions are 235 mm and 270 mm square piles. The number of tested piles in each project ranges from 2 to 12, as can be seen in Figure 1.

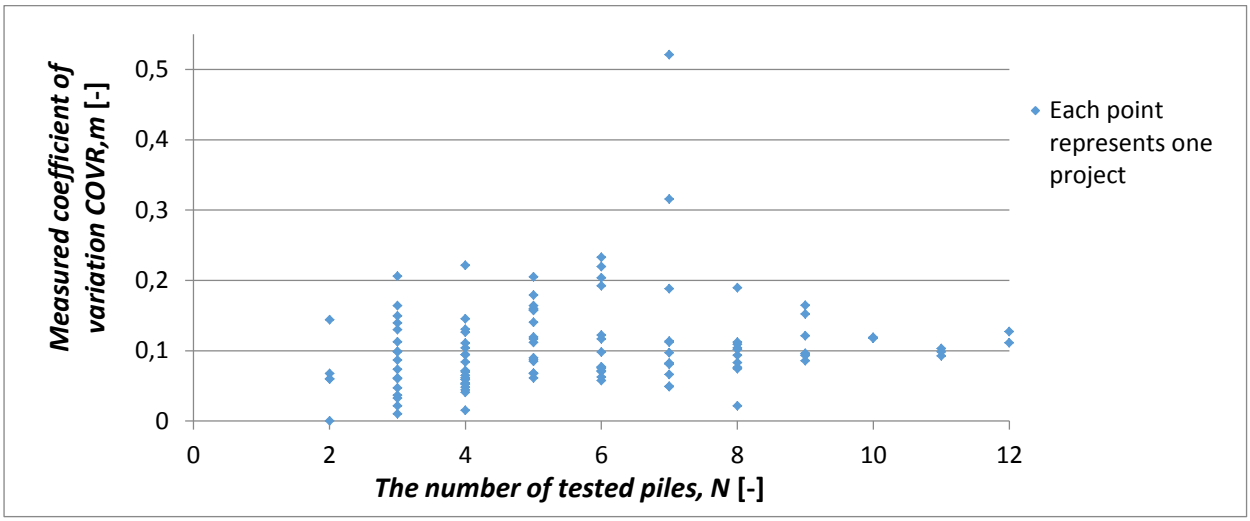


Figure 1: Measured coefficient of variation for concrete piles driven to refusal in till plotted against the number of tested piles. Each point represents one project.

The calculated mean value of the $COV_{R,m}$ for these 110 projects is 10,5 %. As can be seen in Figure 1, most of the piles fall below the $COV_{R,m}$ of 20 %. The percentage of projects with the $COV_{R,m}$ below 10 % is 57 % and the $COV_{R,m}$ below 12 % is almost 73 %. The partial safety factors according to the Eurocode are calibrated to make the mean value control the design value when $COV_{R,m}$ is below 10-12 %. When $COV_{R,m}$ is above 10-12 % the lowest measured value will determine the design value (Frank et al., 2004).

4 ANALYSIS

4.1 General data for analysis

Reliability analysis with the FORM method was carried out with several uncertainties, as presented in Table 1.

Table 1: Coefficient of variation for the uncertainties in eq. (8).

	$COV_{R,m}$	COV_{mf}	COV_{tr}
CAPWAP	10 %	5 %	5 %
CASE	10 %	5 %	7,5 %

The number of tested piles as well as the number of piles in the group may vary between the different analyses and these are clearly specified. The choice of $COV_{R,m}$ in Table 1 is based on the reviewed database, Axelsson et al., (2004), as well as the limit where the Eurocode design values alternates from the mean value to the min value (Frank et al., 2004). COV_{mf} reflects that the ram may be aligned differently during the different blows - thereby reducing or increasing the energy in the blows. This has been estimated to vary between 3-5 %. In this paper 5 % is used. Measurement errors are always present when measuring is carried out. The choice of values for COV_{tr} is based partly on the model uncertainty of CAPWAP compared to static load tests in a study by Likins (1996).

4.2 Comparison between β-method and Eurocode for singular piles

A comparison between the β-method (FORM-analysis) and the Eurocode as well as both Swedish national annexes (Boverket (2015) and Trafikverket (2011)) has been carried out for both CAPWAP- and CASE-methods. Details on performance and evaluation of these methods may be found in Gravare et al., (1980) and Rausche et al., (1985).

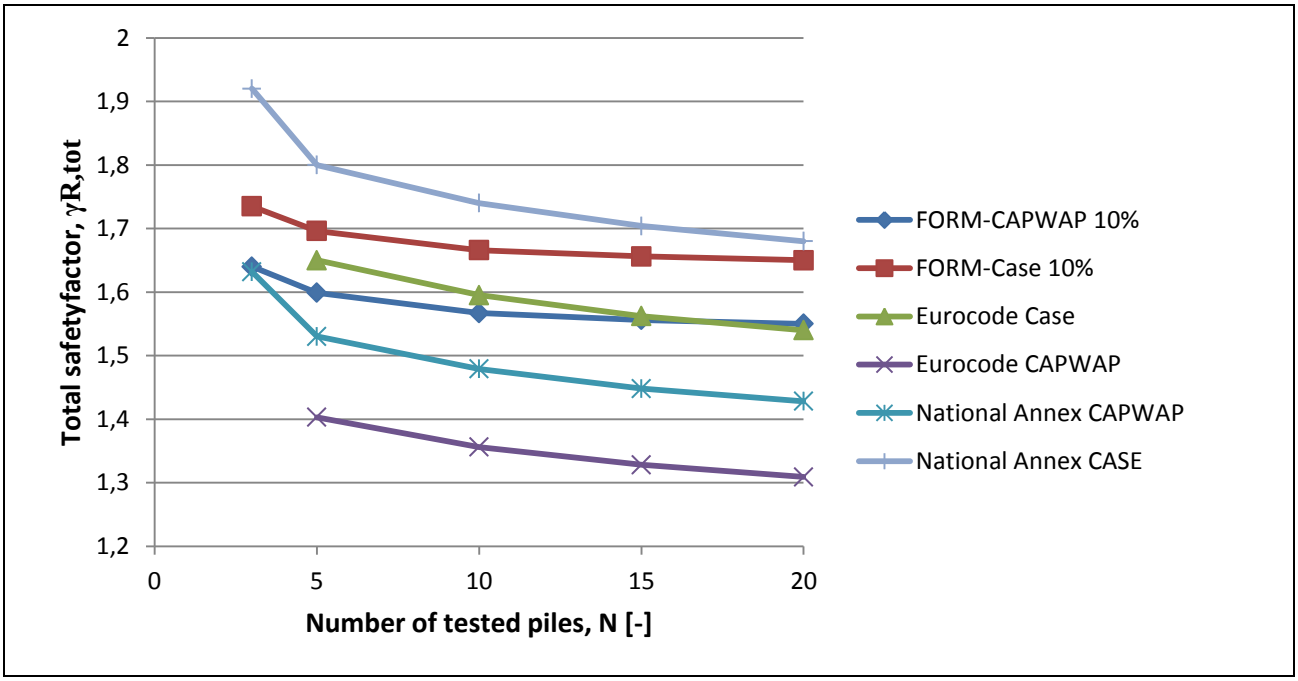


Figure 2: The total safety factor plotted against the number of measured piles.

Figure 2 shows that the required total safety factor according to the Eurocode results in the smallest total safety factor for both CASE and CAPWAP methods. When studying the results from the CASE-method, it is obvious that the β-method is the most favourable design method for this pile type design in Sweden. However, when comparing the CAPWAP-method, the Swedish national annexes are more favourable than the β-method.

In a comparison with the Eurocode, it should however be noted that the loads in Sweden are approximately 10 % lower for safety class 2. By increasing the Eurocode´s partial coefficient with approximately 10 %, comparable total safety factors for the bearing capacity are obtained. The strength of the group effect is related to the correlation between the piles.

A parametric study of how the correlation in the bearing capacity of the piles affects the total safety factor has been conducted. The number of tested piles was 5 and the correlation was varied between 0 and 1. The analysis was based on the CAPWAP-method (Rausche et al., 1985), which was used to evaluate the bearing capacity of the piles. Several different pile group sizes were tested.

As can be seen in Figure 3, the correlation coefficient ρ greatly affects the required total safety factor for the group. The required total safety factor is reduced from approximately 1.6 down to 1.39 or 1.34, depending on the size of the pile group. The ratio between ρ=1.0 and ρ=0 varies between 1.19 and 1.14, depending on the pile group size.

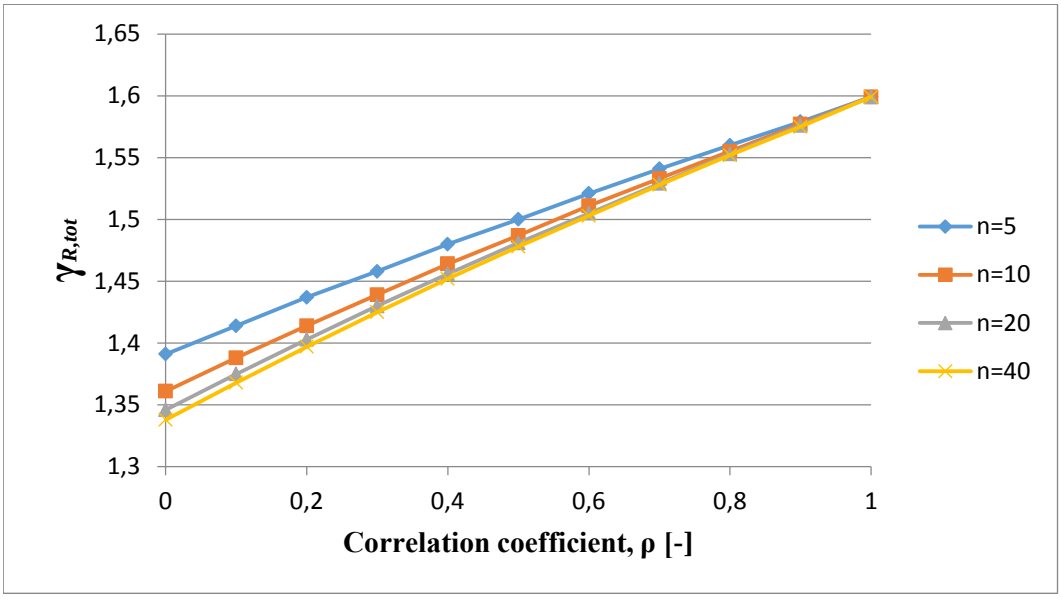


Figure 3: Total safety factor plotted against the correlation coefficient for different pile group sizes

4.3 Selected cases

Two cases have been chosen from the database in order to study how the original Eurocode (EN-1997-1) and the Swedish national annexes (SS-EN 1997-1) compare with the β-method. One case has a low coefficient of variation and the other has a higher coefficient of variation and record both where the mean value and the min value govern the design value. The two cases are named Case 1 and 2 respectively, and the test data is presented in Table 2 and Table 3. Case 1 is titled "Järnvägsbro över Vegeån" and is located close to Landskrona in the southern part of Sweden. The measurements were carried out during June 1996. The pile driving crane was of model "Junttan". The weight of the hammer was 5 tonnes and the fall height was 0.3 m.

Table 2: The measured pile capacity for Case 1

Pile No.	Measured capacity [kN]
1	1980
2	1850
3	1980
4	2060
5	1770
6	1760
7	1770

Table 3: The measured pile capacity for Case 2

Pile No.	Measured capacity [kN]
1	2050
2	2200
3	1840
4	1880
5	1990
6	1830
7	1530
8	1730
9	1770
10	2450
11	2070
12	2190

Case 2 is located at Bro, Gallsäter in the Höga Kusten area in the middle of Sweden. The measurements were carried out during January 1996. The pile crane was again a "Junttan". The hammer weight was 4 tonnes and the fall height was 0.4 m.

In Case 1 the measured coefficient of variation is 0.066. In Case 2 this is 0.127. The measured mean and min values for Case 1 are 1881 kN and 1760 kN respectively. For Case 2 the corresponding values are 1960 kN and 1530 kN respectively. The ratio between the measured min and mean value is 0.78 for Case 2.

4.4 Cases: Singular piles

The calculated total safety factors for the resistance obtained from the FORM-analysis (β-method) for Case 1 and 2 are presented in Table 4 below.

Table 4: The total safety factor for the resistance obtained from the FORM-analysis.

	Case 1	***Case 2***
CAPWAP	1.35	1.76 (1,38)*
CASE	1.47	1.85 (1,45)*

**Recalculated to the total safety factor for the resistance related to the minimum value*

It should be noted that when using the β-method, it is always the mean value and coefficient of variation that will control the design value. When using the Eurocode, the measured minimum value may control the design value. The total safety factors for Case 1 and Case 2 are presented in Table 5 and Table 6 respectively.

Table 5: The total safety factor for Case 1 (resistance), calculated using the Eurocode (EN-1997-1) and the national annexes

Case 1	**National annexes**	**Eurocode**
CAPWAP	1.51	1.38
CASE	1.78	1.63

When the FORM-analysis is compared with the Eurocode and the national annexes, it is clear that in Case 1, the FORM-analysis yields lower total safety factors for the resistance than the Swedish national annexes. The Eurocode's stated values will yield a slightly lower total safety factor for the resistance. When comparing the loads from the Eurocode with the Swedish national annexes, the loads are approximately 10 % smaller for the national annexes compared to EN 1997-1.To get a comparable total safety factor, the load according to the Eurocode would have to be increased with approximately 10 %.

Table 6: The total safety factor for Case 2, calculated using the Eurocode (EN 1997-1) and the national annexes

Case 2	**National Annexes**	**Eurocode**
CAPWAP	1.31*	1.20*
CASE	1.54*	1.43*

**Total safety factor for the resistance related to the minimum value*

Note that for Case 2, the measured minimum value is used to obtain the presented total safety factor. The total safety factors obtained from FORM-analysis can be recalculated to the total safety factor related to the min value by multiplication of the earlier calculated ratio (0.78) between min and mean value to 1.38 for CAPWAP and 1.45 for CASE.

The above presented analysis was performed assuming a deterministic load. If a live load with a *COV* of 30 % and a dead load with a *COV* of 10 % are introduced, the total safety factor obtained from the β-method will change. For this example, a ratio between live load and dead load of 0.2 is used. The obtained total safety factor from the FORM-analysis including variation of the load is presented in Table 7 below. This shows that a load model is required in order to obtain a correct total safety factor for the resistance. However, the results obtained with a deterministic load will be on the safe side.

Table 7: The total safety factor obtained from FORM-analysis (resistance) with variation of the load included in the analysis.

	Case 1	***Case 2***
CAPWAP	1.23	1,62 (1,27)*
CASE	1.34	1,71 (1,34)*

**Recalculated to the total safety factor for the resistance related to the minimum value*

4.5 Cases: Pile group

The positive effect of an interconnected pile group (i.e ξ may be divided by 1,1) is <u>not</u> taken into consideration when the design value is based on high strain dynamic testing according to the Eurocode (Frank et al., 2004). However, the group effect may be taken into consideration when using the calculations based on geotechnical investigation or static load tests (not logical

at all). When using high strain dynamic testing in accordance with the Swedish national annexes it is on the other hand possible to use the positive effect of an interconnected pile group. The results are independent of the numbers of piles in the group. The correlation coefficients (ξ_5 and ξ_6) are divided by 1.1 to account for the group effects. Table 8 and 9 show the total safety factor calculated according to EN 1997-1 and the Swedish national annexes.

Table 8: Calculated total safety factors for Case 1 with regard to group effects.

Case 1	National Annexes	Eurocode
CAPWAP	1.37	1.38
CASE	1.62	1.63

Table 9: Calculated total safety factors for min values - Case 2 with regard to group effects.

Case 2	National Annexes	Eurocode
CAPWAP	1.20*	1.20*
CASE	1.40*	1.41*

**Should be used with the minimum measured value to obtain total safety factors for the resistance*

The pile group under analysis consists of 9 piles. Table 10 shows the results obtained from the FORM-analysis, with regard to group effects and pile group size.

Table 10: Calculated total safety factor from the FORM-analysis with an assumed correlation between the piles.

	Case 1 ρ=0.5	***Case 1 ρ=0***	***Case 2 ρ=0.5***	***Case 2 ρ=0***
CAPW	1.31	1.28	1.23*	1.10*
CASE	1.44	1.41	1.31*	1.18*

**Recalculated to the total safety factor for the resistance related to the minimum value*

As shown, Case 1 is affected less by the group effects than Case 2, simply due to the lower measured $COV_{R,m}$.

5 DISCUSSION

The 110 projects where driven concrete piles driven to refusal in till have been analysed, show that the limits and partial safety factors (partial coefficients, correlation factors and model factors) used by the Eurocode and the Swedish national annexes are reasonable for concrete piles at normal coefficients of variation. It is important to note that this analysis is based on concrete piles driven to refusal in till. However, a more precise installing method, such as drilling into the bedrock would probably yield a significantly lower $COV_{R,m}$ than that of driven piles. Piles drilled to and into the bedrock will most likely show less variability if the bedrock is of good quality – which is generally the case in Sweden. Assuming the same correlation coefficients in the Eurocode (ξ_5 or ξ_6) for piles showing different levels of measured coefficient of variation may result in either an unsafe or a conservative design. This is not reflected in the current design methods, resulting in a considerable variation of reliability depending on the soil conditions.

As shown from the two cases presented above, when considering the correlation coefficient for different piles in a group, the total safety factors for the resistance are reduced to very low levels. With regard to Case 2, the total safety factor for the resistance gets very low when the correlation between the piles is taken into consideration. For Case 2, the ratio between the minimum and the mean measured values are rather low. This greatly affects the converted total safety factor for the resistance. When the coefficient of variation is the same, but the quotient between the minimum and average measured value is higher, the total safety factor in relation to the minimum value will be higher.

The Eurocode is calibrated for a coefficient of variation of 10-12 %, in which the mean value controls the design value. This implies that piles with a lower coefficient of variation will be designed with a conservative approach. The codes need to be designed in this manner to avoid overtly complicated design schemes. However, using FORM-analysis or any other Reliability Based Design method, it is always possible to design for the current situation and soil variability. The model and soil uncertainties are possible to treat in a systematic fashion for both loads and uncertainties in bearing capacity without the risk of over- or underestimating the bearing capacity, provided that the uncertainties are estimated correctly. However, estimating the

transformation error reflected in COV_{tr} is not easy. Even static load testing will contain a transformation error due to the short testing time. The transformation error will affect the calculated total safety factor for the resistance. For normal Swedish conditions, the measured geotechnical bearing capacity of the pile is normally on the safe side due to the small movement (set) of the pile toe during loading. This raises the question whether the transformation error needs to be taken into account since the measured geotechnical bearing capacity of the pile is lower than the actual fully mobilized capacity.

The presented cases show that the group effects resulting from the pile system correlation are less prone to affect the bearing capacity when the coefficient of variation for the bearing capacity is low. The possible reduction of the variance caused by taking the correlation between different piles into account is greater for pile groups with a larger coefficient of variation.

The current FORM-model does not take other significant factors into account. First, the bias is not considered when evaluating the geotechnical bearing capacity through high strain dynamic testing. When the piles are driven to full refusal where the measured set of the pile is none or small, the measured capacity from high strain dynamic testing is typically on the safe side (bias). The model does not take this effect into account. The pile needs to settle around 3-4 mm for its total bearing capacity to be fully activated. Zhang et al., (2001) present bias-factors for high strain dynamic testing. Zhang et al., (2005) have shown how much bias in the failure criterion can affect the calculated probability of failure. High strain dynamic testing is correlated towards Davisson´s failure criterion, which is a conservative failure criterion for piles. This could thereby be handled using bias-factors.

The presented model does not account for the variability of the loading conditions. A fully correct FORM-analysis should include the variability of the load effects, since a deterministic load model results in a conservative estimate of the system reliability. This is explained by the formulation of the weighting factors, α, that is a unit vector. If the load is not included, the weighting factor for the bearing capacity will become 1. Including the load in the yield function of the FORM-model, the resulting total safety factor for the bearing capacity is bound to be lower as is shown in Table 7 above. It can clearly be seen that the obtained total safety factor for the bearing capacity is affected when taking into account the uncertainties in the load.

To promote reliability based design through FORM-analysis or other methods, a load model consisting of mean values as well as the coefficient of variations for different loads need to be specified in the codes. The load model should also state which probabilistic distribution function is to be used and whether the loads should be modelled as normally distributed or log-normally distributed loads.

According to the authors´ knowledge with regard to Nordic conditions, the correlation between different piles has not been evaluated for end-bearing piles. Since the correlation greatly affects the evaluated total safety factor for the resistance, different pile types present an interesting area for further investigation. Chen and Zhang (2013) have analysed the correlation coefficient for piles driven in clay designed from CPT-tests. The correlation coefficient, which varies between 0.27 and 0.41 for the tested piles, is also shown to affect the probability of failure. It should however be noted that piles driven in clay and end-bearing piles may show significantly different correlation coefficients.

In this paper, the uncertainties with regard to the transformation error used were the values used when calibrating the Swedish national annexes. However, these factors influence the calculated total safety factor for the resistance and should therefore be investigated more thoroughly. The same applies to the uncertainty with regard to the measurement error which, in this paper, has been assumed to be 5 % for concrete piles driven to refusal in till.

In order to fully utilize the group effects, the superstructure supported by the pile foundation has to be able to transfer loads

from the weaker piles to the stronger. In addition to this, it has to be investigated how many piles are able to work together. This is of particular importance if inclined piles are used in the designed pile group. In larger pile groups, it may be the case that all the piles are not able work together.

6 CONCLUSION

The reliability-based design method (FORM) has been used to analyze a database of end-bearing piles. The reliability of the piles with the current design method (Eurocode and national annexes) was compared with the β-method, including both model and transformation errors. The analysis shows that there is a difference between the current design method and the presented β-method. The current design method does not take the soil variability into account, resulting either in low or high reliability compared to the reliability-based design methods. When comparing the bearing capacity of piles in groups it is shown that the required safety factor for the resistance of a pile group is reduced with the increasing number of piles in the group. This is highly affected by the correlation between the piles in the group, which for end-bearing piles are relatively unknown. Reduced correlation between the piles reduces the probability of failure for the group, thus reducing the required total safety factor for the resistance. This is accounted for in the Swedish national annexes when using high strain dynamic testing but not in the Eurocode itself. The paper suggests some practical steps to improve the use of reliability-based design in order to control the safety and efficiency of interconnected pile groups in practical design.

7 REFERENCES

Ang, A. H.-S. &Tang, W. H., (2007). Probability Concepts in Engineering. 2nd ed. Hoboken: John Wiley & Sons.

Axelsson, G., Dangré, M., Elvin, L., (2004). Toe resistance of piles driven into dense moraine. In: Seventh International Conference on the Application of Stress-wave Theory to Piles, Malaysia.

Bergman, N., (2015). Aspects of probabilistic serviceability limit state design of dry deep mixing. KTH – The Royal Institute of Technology

Bernander, S., & Svensk, I. (1970). Pålars bärförmåga i elastiskt medium under hänsynstagande till initialkrökning och egenspänningar i pålmaterialet, IVA.

Boverket, (2015). Swedish national annex: Boverkets författningssamling - BFS EKS 10

Cheng, J.-J., Zhang, L., (2013). Effect of spatial correlation of cone tip resistance on the bearing capacity of piles. Journal of Geotechnical and Geoenvironmental Engineering, March 2013.

Eurocode 7, (2004), SS-EN 1997-1

Fleming, K., Weltman, A., Randolph, M. & Elson, K., (2009). Piling Engineering.Third Edition red. Abingdon: Taylor & Francis.

Frank, R., Bauduin, C., Driscoll, R., Kavvadas, M., Krebs Ovensen, N., Orr, T. & Schuppener B., (2004). Designers' guide to EN 1997-1 Eurocode 7: Geotechnical design - General rules. London: Thomas Telford Publishing.

Goodman, L. A., (1960). On the exact variance of products. Journal of the American Statistical Association, 55(292), pp. 708-713.

Gravare, C. J., Goble, G. G., Rausche, F., &Likins, G. E. (1980). Pile driving construction control by the Case method. Ground Engineering: United Kingdom, March issue.

Hasofer, A. M. & Lind, N. C., (1974). Exact and Invariant Second-Moment Code Format. Journal of Engineering Mechanics Division, 100(1), pp. 111-121.

Likins, G., Rausche, F., Thendean, G. & Svinkin, M., (1996). CAPWAP Correlation Studies., Proceedings of the Fifth International Conference on the Application of Stress Wave Theory to Piles. Orlando: Stresswave'96, pp. 447-464.

Lo, S. R. & Li, K. S. V., (2007). Characteristic and design soil parameters: use of statistics. Proceedings of the ICE - Geotechnical Engineering, 160(3), pp. 141-146.

Poulos, H. G., (2005). Pile Behaviour - Consequences of Geological and Construction Imperfections. Journal of Geotechnical and Geoenvironmental Engineering, 131(5), pp. 538-563.

Rausche, F., Goble, G. G., & Likins Jr, G. E. (1985). Dynamic determination of pile capacity. Journal of Geotechnical Engineering, 111(3), 367-383.

Trafikverket, (2011). Swedish national annex: Trafikverkets författningssamling – TRVFS 2011:12, Borlänge: Trafikverket

Zhang, L. M., Li, D. Q. & Tang. W. H. (2001). Reliability of bored pile foundations considering bias in the failure criterion. Can. Geotech. J. 42, pp. 1086-1093.

Zhang, L. M., Tang, W. H. & Ng, C. W. W., (2001). Reliability of axially loaded driven pile groups. Journal of Geotechnical and Geo-environmental Engineering, 127(12), pp. 1051-1060.

A Case Study of the Interaction between a Pile and Soft Soil focusing on Negative Skin Friction using Finite Element Analysis

P. Belinchon
Aarhus University, Department of Engineering, Denmark, pabbeba@gmail.com

K. K. Sørensen
Aarhus University, Department of Engineering, Denmark

R. Christensen
Rambøll and Aarhus University, Aarhus School of Engineering, Denmark

ABSTRACT
This paper presents the findings of an investigation carried out with numerical methods in order to evaluate the interaction between a driven concrete pile and soft organic clay (gyttja) in the case where the soft soil is experiencing settlement relative to the pile. A numerical model was developed based on a full-scale field test that was carried out to investigate the effects of bitumen coating on the development of negative skin friction on driven concrete piles. The bitumen was modelled with interface elements and was controlled by the strength reduction factor R_{inter}. Relevant soil and pile properties were partly obtained from laboratory testing. Numerical and analytical solutions were compared with field test results. Two consecutive scenarios were considered. The first scenario assumed a slightly over consolidated soft soil loaded vertically to around the preconsolidation pressure through the addition of a fill layer at ground level. This scenario reflects the conditions under which the field test was carried out. For the second scenario, additional loading was applied to bring the soft soil into a normally consolidated state. No field results were available for comparison since this scenario will be the next step of the experimental project. Hence, the first part served as a check against the observed field behaviour whilst the second part is used to predict future behaviour.

Keywords: soft soil, finite element modelling, negative skin friction, soil-pile interaction.

1 INTRODUCTION

When loading a single pile driven into soft soil, shaft and base resistance will mobilise to carry the load. Subsequent surface loading of the soft soil is likely to result in settlement of the soil relative to the pile. As a consequence, down drag forces will appear along the pile shaft where the soil settles more than the pile (Fellenius, 1984). This effect is called negative skin friction and can be a problem since it increases the working load of the pile (Tomlinson and Woodward, 2008).

It is common practice in Denmark to apply bitumen coating to the top part of precast concrete piles in order to reduce negative skin friction (Møller et al. 2016). On the basis of the case study presented below, a numerical model is created and presented that investigates the interaction between a pile and soft soil, with emphasis on the development of negative skin friction.

2 CASE STUDY

In 2013, the Research Group of Geotechnical Engineering at Aarhus University in collaboration with Per Aarsleff A/S and Centrum Pæle A/S initiated a project to study the effects of bitumen coating on the development of negative skin friction for driven concrete piles in soft soils.

A full-scale pile test setup was established at Randers Harbour, Denmark. It consisted of four test piles (T) and five reaction piles (R) installed in a row with 3 m centre-centre spacing. A longitudinal section view of the

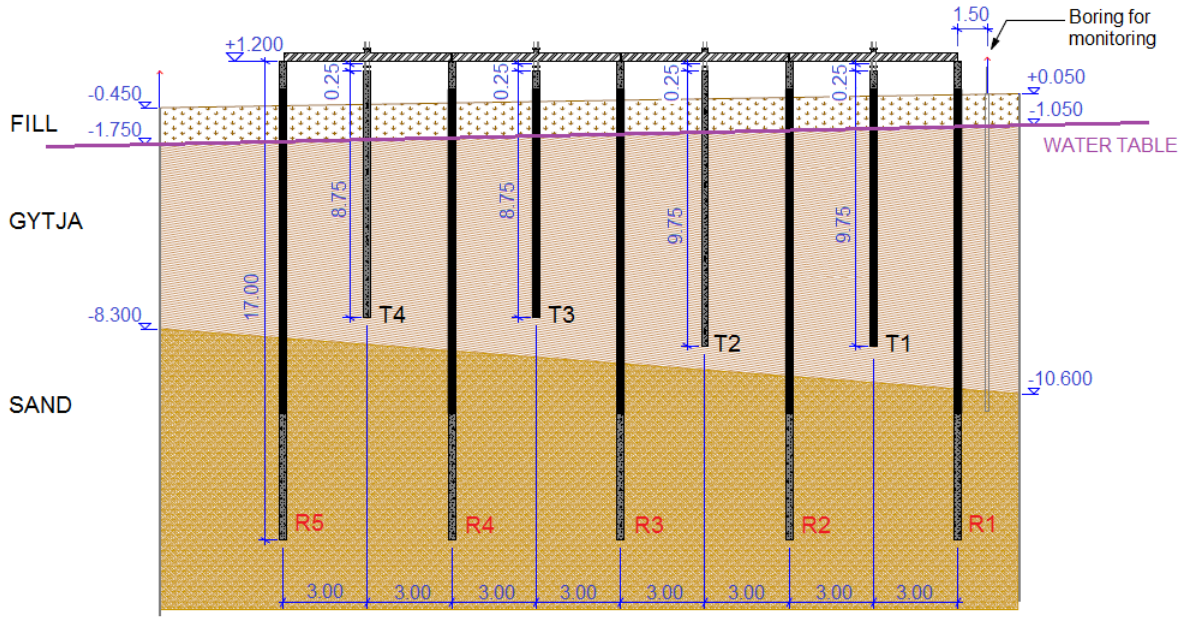


Figure 1 Longitudinal section view of the pile test setup in Randers before terrain loading (after Ventzel and Jensen, 2013). All levels are in meters above mean sea level (DVR90). Distances are in meters.

test setup is illustrated in Figure 1. All piles are precast reinforced concrete piles with a square cross-section (0.25 m width). Bitumen coating was applied to test piles T1 and T3. Piles T2 and T4 are not coated. A HE 280 M beam is directly supported by the reaction piles. The test piles are connected to the beam through an anchor. A load cell is installed between the beam and the anchor, as shown in Figure 2, so the total down drag force on the test pile could be measured.

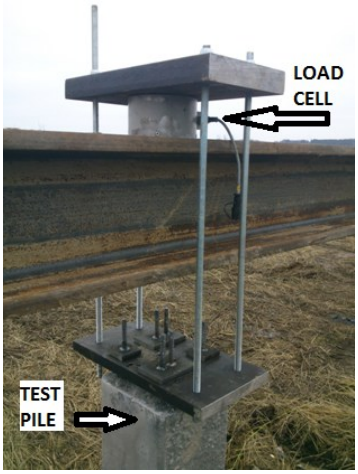


Figure 2 Anchor and load cell at the top of the test pile (after Ventzel and Jensen, 2013).

Other in situ instrumentation comprised four piezometers and four magnetic extensometers located at different depths approx. 1.5 m from R1 (away from the pile row). These have been used to monitor the pore water pressures and the settlements of the soil respectively.

The ground investigation (CPT and boreholes) carried out prior to pile installation showed the soil stratigraphy to consist of: 1.0-1.3 m of fill overlain by 6.5-9.5 m layer of soft organic clay (gyttja) over sand (with gravel). The water table (WT) was at the top of the soft clay (Ventzel and Jensen, 2013).

After pile installation and a period of rest, 0.8 m of fill was placed around the piles to initiate settlement in the soft soil below and hence to generate negative skin friction on the piles. Monitoring of the field test is still on-going, and the results are yet to be published. Preliminary results have been presented by Sorensen (2015).

3 FINITE ELEMENT MODEL

A numerical model has been developed to simulate and further analyse the full-scale field test. The Finite Element software PLAXIS 2D AE is used in the analysis.

A single pile is considered in an axisymmetric model to represent test piles T1 and T2 (pile length of 9.75 m with pile toe at a depth of 8.75 m below original ground level). The original square cross-section is

converted to an equivalent circular cross-section (radius = 16 cm) with the same perimeter (1 m), i.e. the same shaft surface.

The model has a radius of 15 m, large enough to minimise boundary effects. The mesh is formed by 15-noded elements with "fine" global coarseness. WT is assumed at the top of the gyttja. The analysis is carried out as long-term drained. Figure 3 shows the FE model in Plaxis.

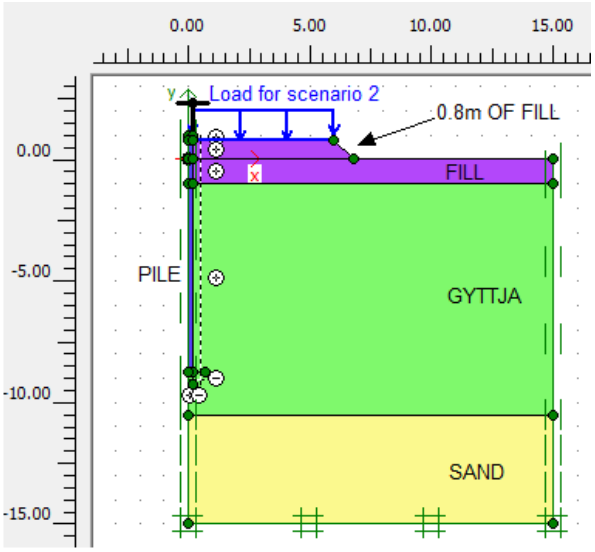


Figure 3 FE model in PLAXIS.

The initial conditions of the soil are obtained by the K_0-procedure followed by a plastic calculation. A subsequent plastic calculation phase is applied to activate the pile, anchor and interface elements. At this stage all displacements are reset to zero.

Two scenarios are considered. In Scenario 1, a surface load is applied by placing an additional 0.8 m of fill at ground level (y = 0 m) with a radius R = 5.8 m. The full-scale field setup reflected this scenario, thus numerical and field results can be compared. In Scenario 2, further loading of the ground level is simulated. The additional applied load ranges from 15 to 50 kPa, and the results are used to predict future behaviour (field test results are presently not available for comparison with the FE model).

The main limitation of the 2D numerical model of a single pile compared to the field setup is that group effects cannot be studied. However, for one row with 3 m centre-centre spacing between the piles (approximately 10 times the diameter) group effects can be neglected according to previous research (Comodromos and Bareka, 2005), (Jeong et al., 1997). Furthermore, as the reaction piles surrounding the test piles have been coated with bitumen in the settling soil layers, this significantly reduces their influence on the settlement of the soil around the test piles.

3.1 Soil models and parameters

The stratification and soil properties assumed in the model are presented in Table 1. Drained (D) parameters are specified in all cases. The properties of the existing and additional fill (soft organic sandy silty clay) and sand layers have been roughly estimated based on the soil description and ground investigation. Simple Mohr-Coulomb (MC) model parameters are used to represent these layers.

Since the settlement and soil-pile interaction is mainly controlled by the properties of the soft organic layer, these properties have in contrast been determined based on laboratory testing (direct shear tests and oedometer tests) carried out by students from Aarhus School of Engineering (Brandt et al., 2015).

3.1.1 Soft organic clay (gyttja)

A soft soil model is chosen to represent the behaviour of the soft organic soil layer, as it is important to reflect accurately the changes in stiffness and strength of the soil with compression. The soft soil model has a logarithmic compression behaviour controlled by the modified compression index λ^* and the modified swelling index κ^* as defined in Figure 4.

The results from oedometer tests have shown the soft organic soil to be slightly overconsolidated. The assumed value of the pre-overburden pressure (POP) is given in Table 1.

In scenario 1, the soft soil experience reloading from a slightly over consolidated state up to around the preconsolidation pressure, i.e. settlement depends primarily on κ^*. While, in scenario 2 where the soil is further loaded, the settlement is primarily governed by the compression of a soil in a normally consolidated state and the parameter λ^*.

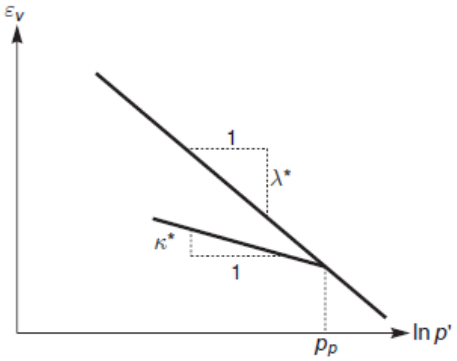


Figure 4 Logarithmic relation between volumetric strain and mean stress (Brinkgreve et al., 2014).

Table 1 Soil parameters and initial stratification.

Parameter	Fill	Gyttja	Sand
Y_{max} [m]	0	-1	-10.5
Y_{min} [m]	-1	-10.5	-15
Material model	MC	Soft soil	MC
Drainage type	D	D	D
Density γ [kN/m³]	18	14	16
Young's modulus E' [kN/m²]	10,000	-	30,000
Poisson ratio ν' [-]	0.25	-	0.3
Eff. cohesion c'_{ref} [kN/m²]	6	2	1
Eff. angle of friction φ' [°]	25	25	35
Angle of dilantancy Ψ [°]	0	0	0
Mod. compr. index λ^* [-]	-	0.1013	-
Mod. swelling index κ^* [-]	-	0.0231	-
Pre-overburden pressure POP [kN/m²]	-	15	-

3.2 *Pile*

A linear elastic model is used for the concrete pile. It is a simple constitutive model but it represents adequately the behaviour of the pile for the stress levels applied. Parameters are given in Table 2.

Table 2 Pile parameters.

Parameter	Pile
Material model	Linear elastic
Drainage type	Non-porous
Density γ [kN/m³]	24
Young's modulus E [GPa]	26
Poisson ratio ν [-]	0.2

3.3 *Interface*

Interface elements are used to model the pile-soil interaction. They are placed along the vertical limit surface between the pile and soil, from the pile top to 0.5 m below the bottom of the pile (see Figure 5). This extra length is very important to avoid non-physical stress oscillations in the corner. Interface elements are also placed at the base of the pile. The roughness between the pile and the soil is defined by a strength reduction factor R_{inter}.

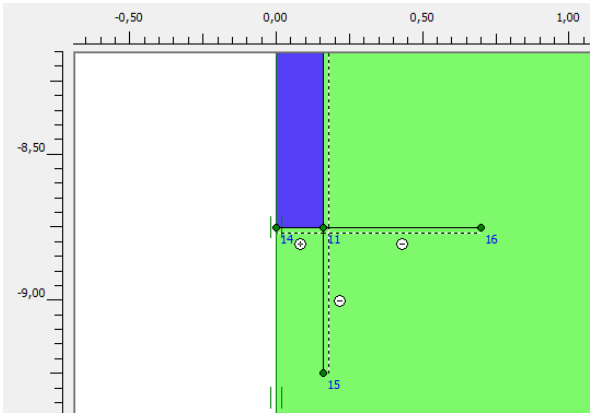


Figure 5 Detail of the interface at the pile toe.

3.4 *Anchor*

The pile is assumed vertically restrained at the top. This is modelled with a fixed-end anchor element. A linear elastic material model is used to define the anchor, where the value of EA = 160,850 kN is determined based on the stiffness of four M16 steel bolts (shown in Figure 2) with a total area A = 256 mm² and a Young's modulus E = 200,000 MPa.

4 ANALYSIS OF SCENARIO 1

4.1 *Settlement of the soil*

During the field test, the settlement of the soil was measured using four extensometers placed at different depths and, approximately, 1.5 m away from reaction pile R1. The measured settlements 315 days after loading (the additional fill layer of 0.8 m) are shown in Figure 6. At this point the pore water pressure and time-settlement curves indicated nearly full consolidation of the soft soil layer (Sorensen, 2015).

Two analytical solutions and the FE PLAXIS solution (at x=1.5 m, using $\lambda^* = 0.1013$ and $\kappa^* = 0.0231$) are also shown in Figure 6 for comparison.

In Analytical Approach A (AA-A), a simple linear relation between settlement (s) and variation of vertical effective stress (σ'_v) is assumed using a constant value of stiffness E_{oed}.

$$s = \frac{1}{E_{oed}} \cdot \sum_i \Delta\sigma'_{v,i} \cdot H_{0,i} \quad (1)$$

An initial thickness of sublayers $H_{0,i} = 0.5$ m is considered. An oedometer modulus $E_{oed} = 4000$ kPa was obtained directly from oedometer tests at an appropriate stress interval.

$$E_{oed} = {}^{\Delta\sigma}/_{\Delta\varepsilon} \quad (2)$$

The linear variation of E_{oed} relative to stress was investigated but over the small stress range, the variation in E_{oed} values obtained from the oedometer testing showed little effect on the results.

In Analytical Approach B (AA-B) settlement of the soft soil is based on the logarithmic relation (in reloading) between volumetric strain (ε_v) and mean stress (p') (Brinkgreve et al., 2014).

$$\varepsilon_v^e - \varepsilon_v^{e0} = -\kappa^* \cdot \ln\frac{p'}{p^0} \quad (3)$$

If the vertical strain is assumed equal to the volumetric strain (no horizontal strain) the settlement can be estimated from Eq. (4).

$$s = \kappa^* \cdot \sum_i \Delta \ln p'_i \cdot H_{0,i} \quad (4)$$

As seen from Figure 6 the measured settlements at levels y = -7.1 m and y = -10.1 m are identical. This suggests that the stiffness of the soil at these depths is very large, something not anticipated for this level of stresses. It is probable that measurements from the extensometer at y = -7.1 m are erroneous due to relative movement between the soil and the extensometer.

Generally, it can be observed that the Plaxis model fairly accurately predicts the measured settlements. AA-A gives results that are fully comparable with the Plaxis results up to a level approximately 4 meters below ground level. Near the ground level, where the stresses are small, AA-A underpredicts the settlement compared to Plaxis. This may be explained by the differences in the logarithmic (PLAXIS) and linear (AA-A) strain-stress relation used.

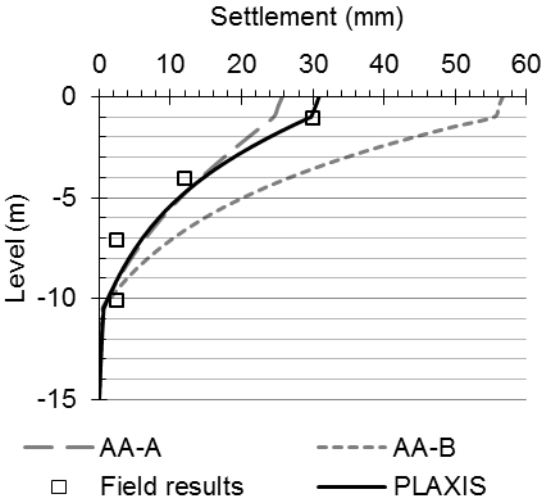


Figure 6 Settlement profile.

AA-B is seen to result in a significant over estimation of the settlements compared to the other solutions and the field results. The main reason for this discrepancy is the assumption of zero horizontal strain, which is not likely to be true. An analytical solution using κ^* (and λ^*) requires further investigation.

4.2 Effect of R_{inter} on the relative settlement between soil and pile

The relative settlement between soil and pile from the PLAXIS model is shown in Figure 7. No neutral point (defined as the point at which the settlement of the pile equals the settlement of the soil) is found since the soil settles more than the pile at all depths. A decrease of the strength reduction factor R_{inter} leads to an increase in relative settlement due to both larger settlement of the soil and smaller settlement of the pile. As discussed in section 4.3, this results in less negative skin friction. Figure 7 also shows that none or very small relative settlement occurs at the pile top. This is due to the low confining

pressure of the fill at the boundary zone. In addition, the cohesion of the fill (6 kPa) results in the soil adhering to the pile top. If c' = 0, the relative settlement would be greater at the top. However, this effect only occurs for a small length (a few centimetres) and it does not affect the results significantly.

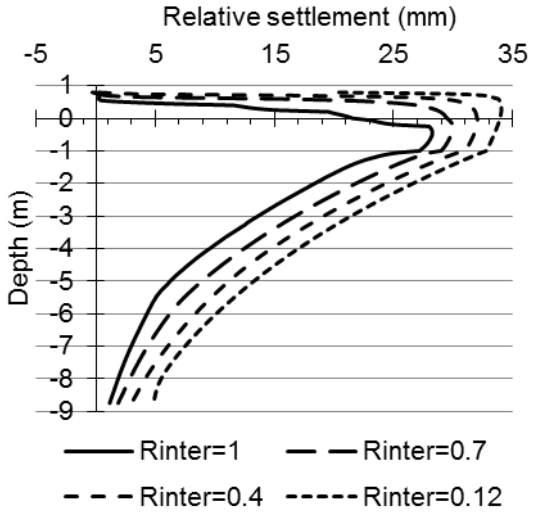


Figure 7 Relative settlement soil-pile.

Figure 8 shows the settlement of the original ground level at distances x from the centre of the pile for different values of R_{inter}. As the movement of the pile is restrained by the anchor it hinders the settlement of the surrounding soil for high values of R_{inter}. For low values of R_{inter} the soil is barely affected by the presence of the pile.

Regarding the previous section, Figure 8 also shows that the settlement of the soil at x = 1.5 m varies a few mm depending on R_{inter}. However, the difference is very small compared to results from AA-B (Fig. 6).

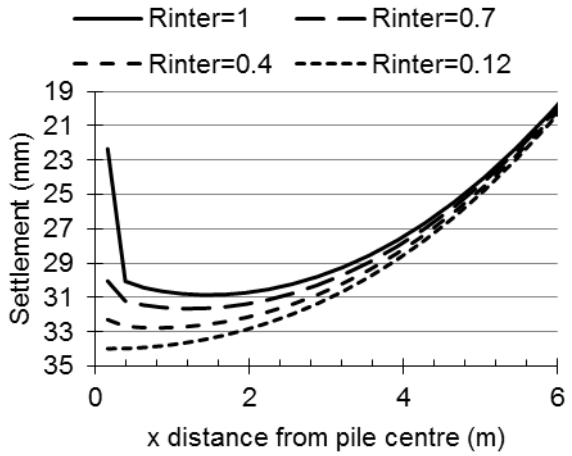


Figure 8 Settlement of the original ground level (y = 0 m) at x distance from pile centre.

4.3 Effect of R_{inter} on shear stresses along the pile shaft

As discussed, the soil settles more than the pile at all depths. Hence, negative skin friction develops along the entire length of the pile. However, the maximum shear stresses are not mobilised over the full length of the pile as seen in Figure 9.

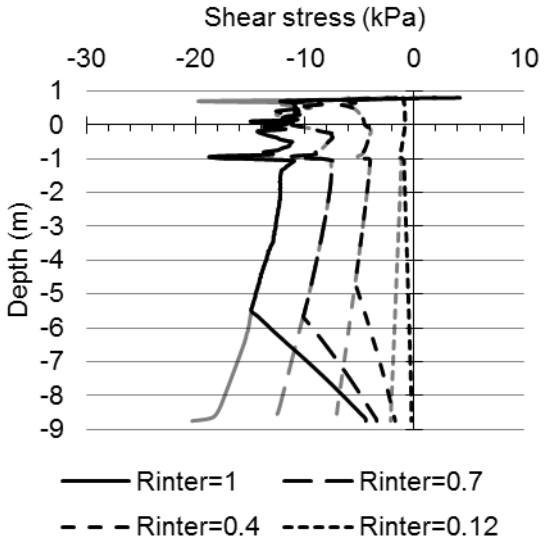


Figure 9 Shear stresses along the pile shaft (black line for mobilised shear stress and grey line for maximum shear stress).

Table 3 shows the total down drag force F_{neg} developed along the pile shaft and the relative settlement s_{rel} required to mobilise full skin friction for the different R_{inter} values.

It shows that a reduction in R_{inter} leads to less F_{neg} and that the relative settlement required for full skin friction to develop increases. Higher settlement normally gives higher mobilised friction, but since R_{inter} is reduced, mobilised friction is less.

Table 3 Total down drag forces and relative settlement to mobilise full skin friction in the FE model.

R_{inter}	1	0.7	0.4	0.12
F_{neg} (kN)	111	77	40	6
s_{rel} (mm)	5	7	12	33

Based on the results of direct shear interface tests $R_{inter} = 1$ is considered for the uncoated piles and $R_{inter} = 0.12$ for the coated piles. $R_{inter} = 1$ might be too high since a rigid interface implies that the soil is able to transfer the full shear stress to the pile which

results in a very large F_{neg} (111 kN). The actual R_{inter} values might be lower since piles are precast and have a fairly smooth concrete surface. For bitumen coated piles $R_{inter} = 0.12$ is considered and numerical results show that $F_{neg} = 6$ kN. This suggests a reduction of 95 % in F_{neg} due to the effect of the bitumen coating. The field test results show that 1 year after surcharging, $F_{neg} = 4$ kN on the coated test pile T1. 41 kN are registered on uncoated test pile T2 with values further increasing.

Greater F_{neg} values are obtained from the numerical FE model compared to the field test results. This may be caused by an over estimation of R_{inter} values, especially in the case of the uncoated piles. The reduction in negative skin friction as a function of R_{inter} is in good agreement with results from similar studies (El-Mossallamy et al., 2012) but using $R_{inter} = 1$ leads to excessively large F_{neg}. Finally, field test results do not assume any resistance force at the pile base whilst in the numerical model this force is approx. 3 kN.

4.4 Effect of anchor stiffness and position

In order to understand better the effect of the anchor the scenario of a floating pile is presented. The same model is used but the anchor is not activated. As the only boundary condition of the pile is the surrounding soil (shaft and base) equilibrium of forces impede negative skin friction to develop along the whole length of the pile.

Figure 10 shows the relative settlement between the soil and the pile for this scenario. The soil settles more than the pile in the upper part (above the neutral point) leading to the development of negative skin friction. Below the neutral point the pile settles more than the soil and positive (upwards) shaft resistance is mobilised. The position of the neutral point is found to be affected by R_{inter}.

If the anchor is activated, then the movement of the pile is restrained and larger negative shear stresses are developed along the pile-soil interface. The movement of the pile depends on the stiffness of the anchor. This has an influence on F_{neg} as shown in Figure 11. Different values of EA are considered. One can identify three trends in the series. For low values of EA, F_{neg} is not affected significantly by the presence of the anchor since the movement restriction is not high enough to allow negative skin friction along the full length of the pile. However, when greater EA is adopted, negative skin friction is mobilised along the full length and F_{neg} increases. For EA > 10^5 kN an increase of stiffness does not significantly affect F_{neg}.

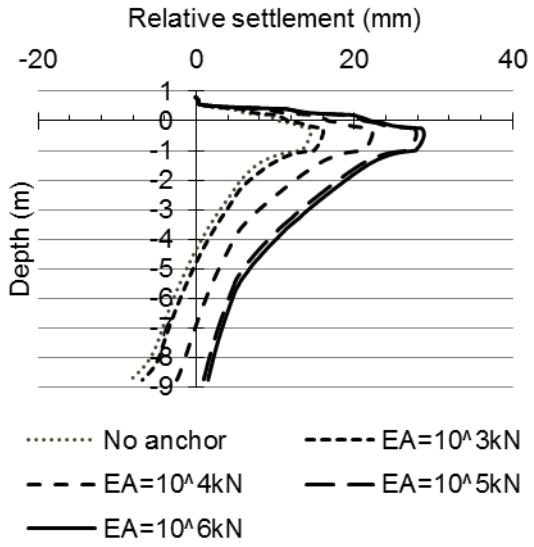


Figure 10 Effect of anchor stiffness on the relative settlement between soil and pile.

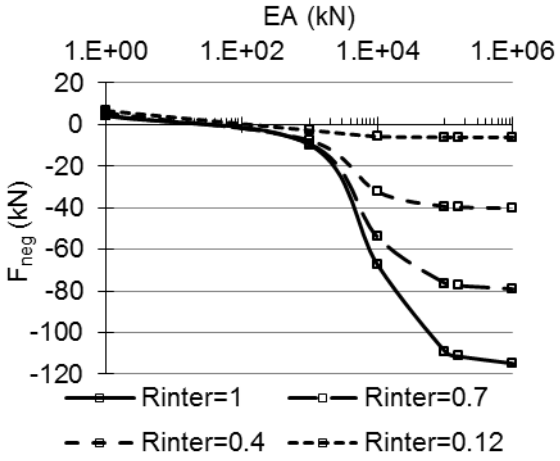


Figure 11 Dependency of total down drag force on anchor stiffness for different values of R_{inter}.

Consider that in the model, EA = 160,850 kN. Therefore, a higher stiffness of the anchor would not increase F_{neg} significantly while a lower stiffness would lead to a lower F_{neg}. In other words, an under estimation of EA is not a problem in this model while an over estimation of EA might lead to excessive F_{neg}. Nevertheless, it is important to say that an equivalent length of 1 m has been used in the model while in the field

setup the anchor length is approximately 70 cm resulting in a greater stiffness (the actual stiffness is EA/L but for practical reasons EA is used in the text as the anchor stiffness, since L = 1 m is considered). Also, the anchor was moved to other positions (0 < x < 0.16 m) but no significant effects were noticed.

4.5 Effect of stiffness parameters of soft soil

The overburden pressure due to the addition of 0.8 m of fill is equal to 14.4 kPa, slightly lower than the pre-overburden pressure (POP = 15 kPa). Settlement of the soil should be only affected by κ^*. Different values from laboratory testing were used (0.0174-0.0285). The best fit between field and numerical settlement results was obtained for κ^* = 0.0231 - the value given in Table 1.

On the contrary, λ^* is not expected to have an influence on the results for scenario 1. Oedometer tests suggest that λ^* values range from 0.1013 to 0.1377 (0.1013 has been assumed in the previous analysis). It has been checked that both values result in the same settlement profile at x = 1.5 m. However, small variations have been found regarding the relative settlement and shear stresses along the pile shaft, which affects F_{neg} as seen in Table 4.

Table 4 Effect of λ^* on down drag forces.

	R_{inter}			
	1	**0.7**	**0.4**	**0.12**
λ^*	**F_{neg} (kN)**			
0.1013	111	77	40	6
0.1377	104	71	35	5

Contrary to the anticipated results, an increase of λ^* (softer soil in the normally consolidated state) leads to a decrease in shear stresses at the lower part of the pile shaft resulting in less F_{neg}. It has been checked that no point of the soil has reached its pre-consolidation pressure, confirming that soil behaviour should not depend on λ^*.

4.6 Effect of strength parameters

The strength of gyttja is stress dependent. Figure 12 and Figure 13 show the total down drag force obtained for different values of φ' (20˚- 35˚) and c' (0 - 4 kPa) respectively.

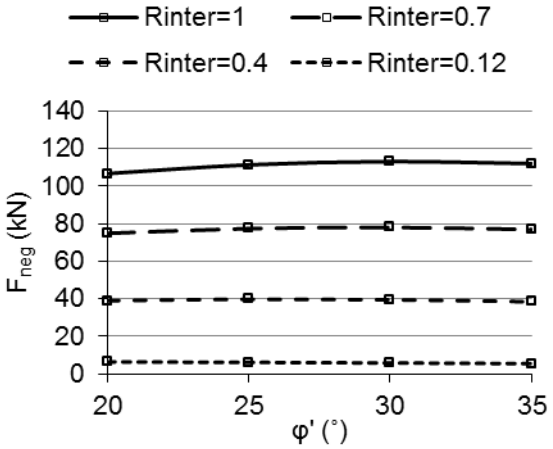


Figure 12 Effect of φ' in the total down drag force.

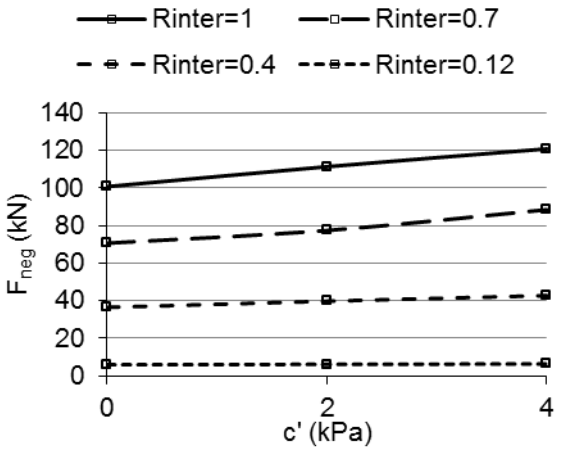


Figure 13 Effect of c' in the total down drag force.

It can be seen that F_{neg} increases with φ' for high values of R_{inter}, especially from 20˚ to 30˚. The shear stress increases with φ' within that range. However, the increase is lower from 30˚ to 35˚ and, for low R_{inter} values F_{neg} decreases relatively little with increasing φ'.

According to the Mohr-Coulomb failure criterion shear stress (τ) can be expressed as:

$$\tau = c' + \sigma'_N \cdot \tan\varphi' \qquad (5)$$

An increase of φ' results in a greater tan φ' but conversely K_0 decreases resulting in a decrease of the normal stress (σ'_N).

On the contrary, an increase of cohesion leads to an increase in negative skin friction independently of the stress level. Figure 13 shows that even for low values of R_{inter} the

total down drag force increases with c'. Hence, the effect of cohesion is greater compared to the effect of friction angle for the investigated range.

5 ANALYSIS OF SCENARIO 2

5.1 Settlement of soil

Figure 14 shows the settlement profile at x = 1.5 m for different load values (q) and range of λ^* obtained from laboratory testing.

If in scenario 1 the maximum settlement was about 30 mm, then in scenario 2 the soil experiences a much greater settlement for a similar increase in the overburden pressure (109 mm of total settlement for q = 15 kPa). This is due to the soil being loaded to a normally consolidated state. For higher q the difference in settlement due to variation of λ^* is higher since more soil is normally consolidated and, hence, settlement is governed by λ^*.

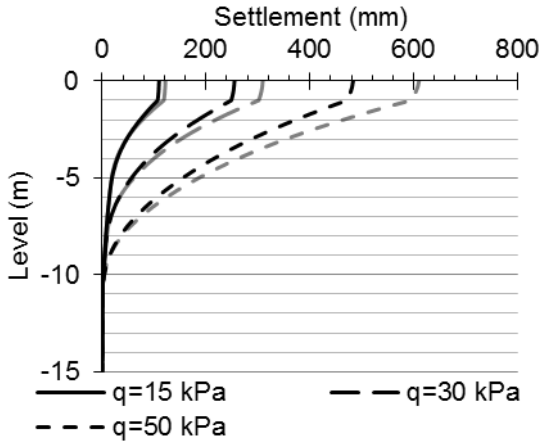


Figure 14 Settlement profile after applying different additional loads (black line for λ^* = 0.1013 and grey line for λ^* = 0.1377).

5.2 Negative skin friction

In Table 5 numerical values for down drag forces are shown. Scenario 1 corresponds to q = 0 kPa so all results can be compared.

It is important to note that, in contradiction to expected results, the low values in the intervals correspond to λ^* = 0.1377 which lead to higher settlements of the soil. It is not quite clear why an increase of λ^* produces a decrease in F_{neg} and, why this effect is greater for q = 0 (when the soil is over consolidated). Hence, this point requires further investigation.

Table 5 Down drag forces.

R_{inter}	1	0.7	0.4	0.12
q (kPa)	F_{neg} (kN)			
0	104-111	71-77	35-40	5-6
15	130-135	92-96	47-50	8-9
30	153-157	113-115	60-61	12-13
50	187-187	138-138	75-75	16-16

Figure 15 shows the results tabulated in Table 5. In agreement with previous studies (Comodromos and Bareka, 2005), (Liu et al., 2012), an increase of the applied loads results in greater down drag forces transmitted to the pile. Also, the effect of soil stiffness on F_{neg} disappears for q = 50 kPa, since full negative skin friction is mobilised along the full length of the pile. Hence, for the same level of stresses, larger settlement does not give higher F_{neg}.

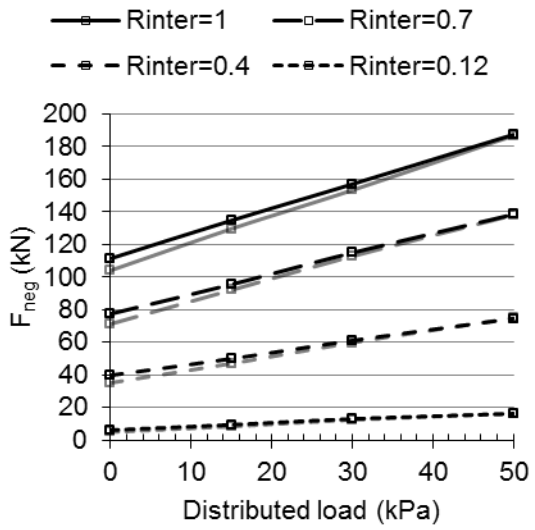


Figure 15 Down drag forces (black line for λ^* = 0.1013 and grey line for λ^* = 0.1377).

6 CONCLUSIONS

Based on a full-scale field test, a numerical model was developed to investigate the soil-structure interaction between a driven concrete pile and soft organic clay (gyttja) with emphasis on the development of negative skin friction due to settlement of the soil relative to the pile.

In scenario 1, relative settlement between the soil and the pile was investigated by

adding 0.8 m of fill at ground level. The calculated total settlement of the soil was similar to field test results (30 mm). A simple analytical solution (AA-A) that considered a constant stiffness gave comparable results to the FE model at a depth greater than 4 m below the ground surface. A more complex analytical analysis (AA-B) that considered similar parameters to those adopted in PLAXIS requires further investigation.

The presence of bitumen was modelled with interface elements and controlled by the interface reduction factor R_{inter}. Based on the results of direct shear interface tests, $R_{inter} = 1$ was considered for the uncoated piles and $R_{inter} = 0.12$ for the coated piles. Numerical results showed that a reduction of R_{inter} leads to greater relative settlement. The presence of a bitumen coating also reduced the length of the pile that experienced full mobilised negative skin friction.

Total down drag forces F_{neg} from the numerical model (104-111 kN) were found greater than the field test results (41 kN) for the uncoated pile. It was assumed that a rigid interface mainly caused this. Group effects were not expected to have a big influence due to the large centre-centre interspacing and since the reaction piles are coated with bitumen within the settling soil layers.

The anchor (stiffness) was found to have an influence on the relative settlement between soil and pile and, hence, on F_{neg}.

Conversely to the anticipated results, the modified compression index λ^* had an effect on numerical results in scenario 1, although the analysis did not indicate any part of the soil matrix to have moved into a normally consolidated state. An increase of λ^* resulted in a reduction of F_{neg}, which could not be explained and requires further investigation.

Numerical results were not significantly sensitive to the effective friction angle φ', but an increase of the effective cohesion c' increased the negative skin friction.

In scenario 2, an additional load q was applied on top of the fill. For a similar overburden pressure applied as in scenario 1, the settlement was approximately three times greater (most of the soil was expected to behave in a normally consolidated state). As expected, the value of λ^* had a greater impact on the settlement with increasing values of q. However, numerical results for q = 50 kPa showed that the stiffness had no influence on F_{neg} (the load was large enough to mobilise full negative skin friction along the full length of the pile).

7 ACKNOWLEDGEMENTS

The authors want to thank Per Aarsleff A/S and Centrum Pæle A/S for their contribution to the project, as well as previous students at Aarhus School of Engineering, who have been involved in the project and contributed with field and lab results.

8 REFERENCES

Brandt, E.S., Haugaard, J.A. and Nielsen, N.B. (2015). Reduktion af negative overflademodstand ved påføring af bitumen. Bachelor project. Aarhus School of Engineering, Aarhus University (In Danish).

Brinkgreve, R. B. J., Engin, E. and Swolfs, W. M. (2014). Plaxis 2D Manual Anniversary Edition.

Comodromos, E.M. and Bareka, S.V. (2005). Evaluation of negative skin friction effects in pile foundations using 3D nonlinear analysis. Computers and Geotechnics 32, 210-221.

El-Mossallamy, Y. M., Hefny, A. M., Demerdash, M. A. and Morsy, M. S. (2012). Numerical analysis of negative skin friction on piles in soft clay. HBRC Journal 9, 68-76.

Fellenius, B. H. (1984). Negative skin friction and settlement of piles. 2nd International Seminar, Pile Foundations, Nanyang Technological Institute, Singapore.

Jeong, S., Kim, S. and Briaud, J. L. (1997). Analysis of Downdrag on Pile Groups by the Finite Element Method. Computers and Geotechnics 21 (2), 143-161.

Liu, J., Gao, H. and Liu, H. (2012). Finite element analyses of negative skin friction on a single pile. Acta Geotechnica 7, 239–252.

Møller, O. et al. (2016). Design of Piles – Danish Practice. ISSMGE - ETC 3 International Symposium on Design of Piles in Europe. Brussels.

Sørensen, K.K. (2015). Fuldskala pæleforsøg på Randers havn/Full-scale pile testing at Randers Habour, presentation, www.danskgeoteknisk-forening.dk, DGF meeting no. 4/2015.

Tomlinson, M. and Woodward, J. (2008). Pile Design and Construction Practice (5th edition). Taylor & Francis, London & New York.

Ventzel, G. K. and Jensen, C. S. (2013). Reduktion af negativ overflademodstand på pæle ved påføring af bitumen. Bachelor project. Aarhus School of Engineering, Aarhus University (In Danish).

Application of Thermal Piles in Thawing a Frozen Ground

G. Sinnathamby*
**Geoengineering, Department of Civil & Environmental Engineering, Aalto University, Finland*
gowthaman.sinnathamby@aalto.fi

H. Gustavsson[&], L. Korkiala-Tanttu[&], C.P. Cervera[$], M.Koskinen[#]
[&]*Department of Civil & Environmental Engineering, Aalto University, Finland*
[$] *Fundación Valenciport, València, Spain*
[#] *City of Helsinki, Finland*

ABSTRACT
The thawing of the frozen ground below an ice rink facility in Myllypuro, eastern Helsinki, Finland was studied in detail through analytical approach and numerical simulations. A malfunction in the floor-heating system caused freezing conditions in the ground underneath. Over the years, frost heave caused significant deformations to the facility and, in 2012 forced an immediate renovation. During the renovation, the existing old foundation was replaced with a new foundation system comprised of a well-insulated concrete floor-slab and a group of around 240 steel thermal piles. Thermal piles were preferred in this case because the frozen ground surrounding individual piles needed to be thawed, hence a direct contact between the soil and the pile shaft can be prevented. This reduces the possible risk of additional load from the frozen ground being applied on the piles.

As part of the ongoing monitoring programme, a thermal modelling of the thawing process was carried out with commercially available SoilVision Heat (version 2.4.10) software programme. The primary objective of this study was to model the thawing process numerically and therefore, the time needed to thaw the frozen ground can be estimated. Upon complete thawing, establishing the required constant temperature that needs to be maintained in the piles in order to prevent the ground from re-freezing was another objective. The ground temperature profiles obtained from the model simulations were compared with in situ temperature measurements as the thawing progresses. The time needed for complete thawing of the frozen ground from the simulations is in good agreement with analytical estimations and in situ observations. The thermal modelling shows that once the frozen ground is completely thawed, a heat injection at around +7°C by the piles is sufficient to prevent the ground from re-freezing.

Keywords: Thermal Modelling; Thaw Settlement; Thermal Piles; Freeze and Thaw; SVHeat.

1 INTRODUCTION

This paper presents the results of a case-study in which steel thermal piles were used to thaw a frozen ground below the Myllypuro ice rink facility (hereinafter referred to as MIR) in eastern Helsinki, Finland. MIR was built in 1976 in order to facilitate winter (ice) sports initially during autumn and spring seasons; however, since 1980's, the facility has been used throughout the year (Vähäaho et al., 2012). Figs. 1a and b show the plan and sectional views of the MIR, respectively. The facility was founded on a clay deposit by incorporating a 100 mm thick expanded polystyrene (EPS) floor-insulation and a heat wire system in order to prevent the ground from freezing and ultimately from frost heave. Over the years, a malfunction in the floor-heating system lead to freezing of the ground below the ice rink as the thin EPS insulation was alone not sufficient to prevent the cold front advancing. Furthermore, since the ice rink was in continuous use after

1980's, it prevented the ground from natural thawing during summer seasons. The ground freezing advanced over the years and uneven ground deformations started to appear, leading to increased maintenance costs.

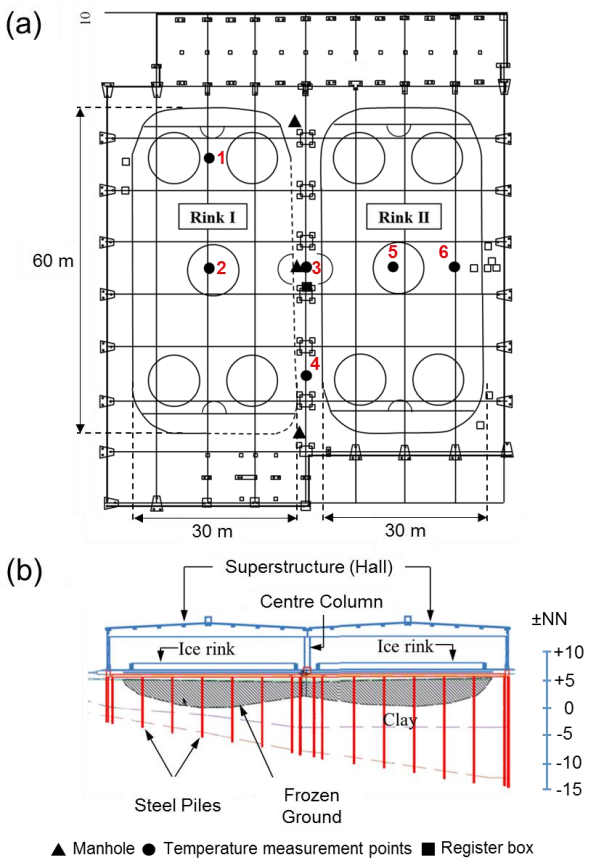


Figure 1. Various observation points at MIR: (a) Plan view and (b) Sectional view (modified from Vähäaho et al., 2012).

In 1996, a monitoring program comprised of several temperature and settlement sensors, and lateral deformation indicators was set up to assess the effects of frost heave. In 2011, the frost heave endangered the structural safety of the MIR by uplifting the centre columns and forced an immediate renovation. In the year 2000, the measured maximum frost depth was around 6.3 m, resembling permafrost conditions (Vähäaho et al., 2012). Deformation measurements taken in 2012 showed that the centre columns in the middle of the hall (Fig. 1b) experienced an uplift of around 88 mm, while a frost heave of around 0.5 m was observed in the centre of the ice rink (e.g. points 2 & 5 in Fig.1a). Furthermore, horizontal movements were also observed. Based on the results from the monitoring program, a renovation of the ice rink was proposed. A new foundation system and a controlled thawing of the contact between the frozen ground and individual piles were incorporated in the renovation. The new foundation system consisted of a well-insulated concrete floor-slab and an array of steel piles (Vähäaho et al., 2012). The piled concrete slab works as a load carrying structure. The concrete slab separates the cooling pipes (the ones used to maintain the icy-surface of the rink) and warming pipes (the ones used to prevent the subsoil from freezing), which are located in the upper and lower parts of the concrete slab, respectively. In addition, a 100mm thick insulation barrier and a drainage system were designed in order to avoid heat transfer between the soil and the cooling system and to keep the structures dry, respectively.

The aim of using thermal piles was to initially thaw the frozen ground only around each piles, hence there would be no contact between the frozen ground and piles. Significant adhesion between the frozen soil and the piles could create excessive negative skin frictions (i.e. additional loading) on the piles. However, the thawing is expected to progress and eventually lead to a complete thawing of the entire frozen ground below the MIR.

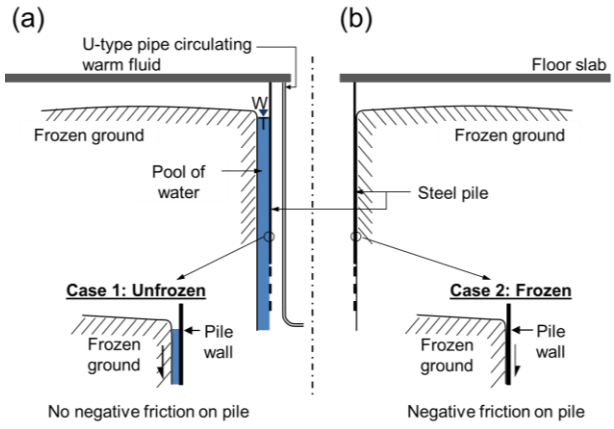


Figure 2. Conceptual figures showing: (a) a thawed frozen ground around a pile that injects heat, and (b) a frozen ground around a pile that does not injects heat and thus, developed negative skin friction along its shaft (not to scale).

Consequently, the number of piles required (and hence renovation costs) would have increased in excess (Fig. 2). The objective of this study was to model the thawing process numerically and to estimate the time needed to thaw the frozen ground around the piles completely. Establishing the required constant temperature that has to be maintained in the piles (of the warming liquid) in order to prevent the ground from re-freezing was another objective.

Several 2D and 3D transient model simulations were run with commercially available SVHeat (version 2.4.10) software programme and the modelling results were compared with analytical estimation of the time required to thaw the ground completely, and also with several in situ temperature measurements.

2 ANALYTICAL APPROACH

The time needed for the complete thawing of the frozen ground was first analytically estimated. The results from the analytical approach are then used to validate the results from numerical simulations. Assuming a 5 m average frozen depth based on the in situ measurements, the total volume of the frozen ground below the ice rink (V_f) is around 23760 m^3 (i.e. *Length* x *Width* x *avg. Depth* = 72 x 66 x 5 m^3). As a first step to the thawing process, the temperature of the frozen ground needs to be raised to 0°C. Considering – 3°C as the average temperature of the frozen ground and the volumetric heat capacity of the frozen ground as 2000 kJ/ m^3K, the total heat energy required to raise the ground temperature from – 3°C to 0°C, q_1, can be calculated from Eq.1.

$$q_1 = V_f \, C_i \, \Delta T \qquad (1)$$

$$q_2 = w_{vol} \, L_f \qquad (2)$$

where V_f is the volume of the frozen ground (in m^3), C_i is the volumetric heat capacity of the frozen soil (in kJ/m^3K), L_f is the volumetric latent heat of fusion of water (in J/m^3) and ΔT is the change in temperature (in K). Therefore, from Eq.1, the total heat energy required for this phase is around 143 GJ (≈ 40 MWh) (i.e. 23760 x 2000 x [0-(-3)] = 143 GJ.

The next step is to calculate the heat energy required for the phase change from ice to water at 0°C, q_2, and can be calculated from Eq.2. Taking the average volumetric water content of the soil as 60 %, w_{vol} is 14256 m^3 (i.e. w_{vol} = 23760 x 0.6 m^3). If L_f is 3.34 x 108 J/m^3, then from Eq.2, q_2 is around 4762 GJ (1323 MWh) (i.e. 14256 x 3.34 x 108 ≈ 4762 GJ). Therefore, the total amount of heat energy required (q_1 + q_2) for the complete thawing of the frozen ground is around 1363 MWh.

The total energy injection can be calculated by measuring the actual inlet and outlet temperatures of the warming fluid, and pressure values (to determine the rate of flow of the warming liquid). The energy that is injected per second (i.e. power) can be calculated from Eq. 3, while the total energy injected can be calculated from Eq. 4.

$$P = Q \times C \times (T_{in} - T_{out}) \qquad (3)$$

$$E = P \times t \qquad (4)$$

where P is the power (in *kW)*, Q is the rate of flow of warming liquid (in *l / sec*), C is the specific heat capacity of the warming fluid (in *kJ/kg-K*), T_{in} is the inlet temperature (in *K*), T_{out} is the outlet temperature (in *K*), E is the energy (in *kW*) and t is the effective operational time of the heat pump (in *sec*).

In situ measurements of the warming liquid showed that the rate of flow was around 4 *l/sec*, and the inlet and outlet temperatures were around +28°C and +20°C, respectively. If a specific heat capacity of 3.5 *kJ/kg-K* is assumed for the warming liquid, the estimated energy injection by the system per second would be around 112kJ (i.e. from Eq.3, P = 4 x 3.5 x [ΔT=8]). Hence, by taking 18 hours of effective daily operation of the heat pump, the total energy injected in one year would be around 735 MWh (Eq. 4), which is less than the total energy required

(1363 MWh). Therefore, more than one year (≈ 680 days) of heat injection is required by the piles in order to thaw the frozen ground completely.

Applying the same calculation for the influence area of one pile (i.e. 5.5 m x 5.5 m) and considering an equal average frozen depth of 5 m, the total number of days required for complete thawing is around 750 days. As the frozen volume of the ground below the MIR is not precisely known, the calculation are done based on realistic assumptions. Hence the results are only approximate; however, the calculations based on the effective area of one pile may better represent the real scenario and is compared with the numerical simulation results later in this paper.

3 THERMAL MODELLING

3.1 Model Geometry, Limitations and Characteristics

The thawing process of MIR was studied numerically with commercially available SoilVision Heat v 2.4.10 software program (herein referred to as SVHeat). SVHeat is capable of modelling various heat transfer mechanisms in soils under saturated and unsaturated conditions. It is also able to model geothermal gradients and the movement of freezing fronts with advanced boundary conditions under steady-state and transient thermal conduction and convection conditions (Thode, 2013).

Two different SVHeat models were created in this study with two distinct objectives: first one was a 2D transient model, simplifying the entire cross section of the ice rink and the other one was a 3D transient model representing the influence area of a single pile. The objective of the 2D model was to study the change in ground temperature profile with time in a bigger scale, while the 3D model investigated the ground temperature profile around a single pile.

The modelled single pile represented the worst-case-pile scenario, i.e. a pile remotely located (at the edge) in the pile-group, where the frozen ground could take longer to thaw because further inside the pile-group, the influence of the heat injection from adjacent piles is significantly higher than that of the remotely located piles, therefore the thawing would be relatively faster. Thus, studying the influence area of a pile located away from the centre of the ice rink (i.e. at the edge of the pile-group) is more appropriate for the monitoring of the worst-case thawing scenario.

The modelling of the entire thawing process was carried out in three phases. At first, initial conditions existed right before the renovation, were established with a steady-state analysis based on the measured in situ temperature data. From this analysis, the ground temperature profile and the frost depth below the ice rink were obtained and validated with the results obtained from the SSR model (Sinnathamby et al., 2015; Sinnathamby et al., 2016). The ground temperature profiles obtained from this phase was used as the initial condition for the subsequent phase of the modelling.

In the second phase, a 1000-day long medium-term transient analysis was carried out, simulating the ground thermal evolution and the thawing process since the facility was reopened after the renovation in December, 2012. During this period, it was assumed that the thermal piles were injecting heat at +20°C (same as the outlet temperature of the warming liquid), resulting in a constant heat injection of 112 kJ per second. In this phase, two different boundary conditions were used for the piles, first one is a constant temperature boundary condition (CTBC) and the second is a constant heat flux boundary condition (CHFBC) (see section 3.3.1).

In the final phase, a 10 year-long transient analysis was carried out with a CTBC on piles. The main objective of the final phase was to determine the required constant temperature that needs to be maintained in the piles in order to prevent the ground from re-freezing. The SVHeat 2D and 3D model geometries are shown in Fig. 3.

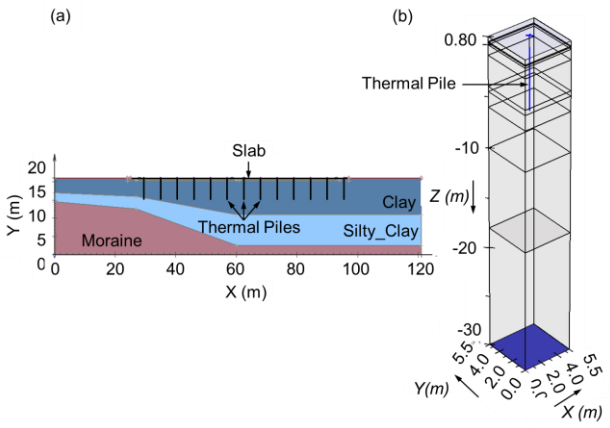


Figure 3. SVHeat model geometries: a) 2D model representing the entire cross section, and b) 3D model representing a single pile and its influence area.

3.2 Materials

The soil profile under the ice rink was divided into three layers, namely clay, silty-clay and moraine (from top to bottom). The average material properties used in the models are shown in Table 1. The thermal properties of the soils were obtained from laboratory tests carried out on in situ soil samples collected from the site (Sinnathamby et al., 2015; Sinnathamby et al., 2016; Cervera, 2013) and also from the literature (Sundberg, 1988; Clauser, 2006; Andersland et al., 1994).

In the 2D models, the thermal conductivity used in the clay layer was calculated as the average of the values obtained in the laboratory test in order to simplify the model and to reduce the simulation time. On the other hand, in the 3D models, the clay layer itself was subdivided into 6 layers with different thermal properties obtained from the laboratory tests in order to get more accurate results. Due to the low-permeable subsoil conditions, no groundwater seepage was considered. The thermal properties of other construction materials such as the concrete slab and the floor-insulation are also presented in Table 1.

Table1. Thermal properties of the materials for the 2D model

		Thermal conductivity, λ (W/m K)	Heat capacity, C_i (KJ/m³K)	Vol. Water content, w_{vol} (m³/m³)
SOIL				
Clay	UF[1]	1.07	2400	0.675
	F[2]	2.46	2000	0.675
Silty-clay	UF	1.75	3000	0.366
	F	3.00	2000	0.366
Moraine	UF	3.01	2700	0.050
	F	3.36	2000	0.050
CONSTRUCTION MATERIALS				
Concrete	UF	1.63	2300	0.1
	F	2.50	2000	0.1
XPS	UF	0.035	52.5	0.01
	F	0.035	52.5	0.01

[1]Unfrozen; [2]Frozen

Freezing and thawing processes and the water phase change (from ice to water) in fine-grained soils are related to the unfrozen water content and to the freezing curve. The freezing curves and realistic residual unfrozen water content in this study were obtained from the existing data in the literature (e.g. Thode & Fredlund, 2012).

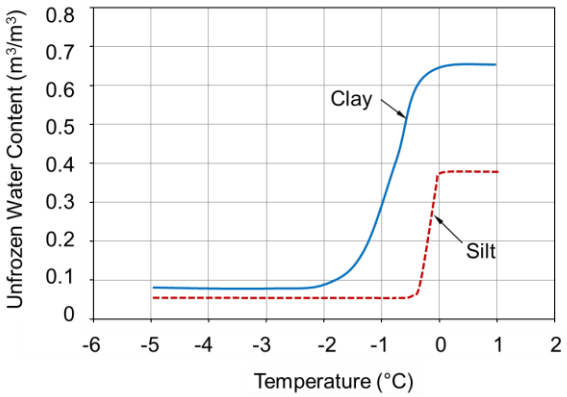


Figure 4. Unfrozen water content curves of clay and silt used in the models (Modified from Thode & Fred, 2012)

It was found that the residual unfrozen water content of the clay and silt varied between 8% - 13% and 5% - 7%, respectively (Thode & Fredlund, 2012; Liu & Li, 2012). The characteristic unfrozen water content curves of different soil layers were calculated as an exponential function according to these unfrozen water content values. Fig. 4 shows the characteristic unfrozen water content

curves and their residual values of clay and silt that are used in the models.

3.3 Boundary Conditions

3.3.1 Constant Boundary Conditions

The following constant boundary conditions were used in the transient models carried out:

Piles (BC4)

The piles were modelled with well boundary condition in which the heat is injected along the perimeter of the pile. Two different models were created with different boundary conditions for comparisons with the in situ conditions. Firstly, a Constant Temperature Boundary Condition (CTBC) was used for the piles in which the temperature along the pile perimeter is constant throughout the simulation.

Secondly, a Constant Heat Flux Boundary Condition (CHFBC) was applied on piles, which means that the pile injects a constant heat flux but the temperature in the pile surface could vary with time as the ground temperature changes. The length of the piles varied between 15 m to 20m, but the depth of the embedment of warming tubes inside the piles was only around 6 m to 7 meters, depending on the frozen depth, and therefore, the piles were modelled up to this depth. Piles in the 2D models were modelled with CHFBC, while the single pile in the 3D model was modelled with both CHFBC and CTBC.

3.3.2 Variable Boundary Conditions

A. Water pool temperature function (BC5)

A pool of water below the ice rinks was noticed during the insitu observations in 2012. The depth of the pool was around 1.3 m from the ground level and presumably resulted from the thawing of the frozen ground. This water was heated due to the energy injection by the piles. Therefore, a boundary condition was used to represent the temperature of this pool of water (Fig. 6a).

The water temperature function was calculated from the averages of in situ temperature measurements taken from three observation manholes below the ice rink. An assumption was made that the last measured in situ temperature of + 5.4°C would remain constant during the transient analysis. This boundary condition was applied between the bottom of the concrete slab and the top of the clay layer in the models.

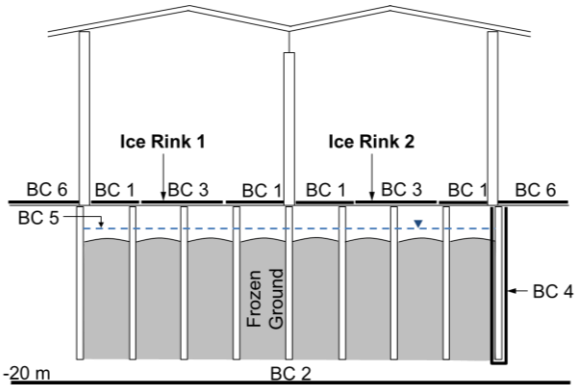


Figure 5. Schematic showing the applied boundary conditions (not to scale)

Table 2. Boundary conditions that are applied in the models

Boundary condition		BC Type	Applied location	
			In 2D models	In 3D models
BC 1	Building	C	+2°C at the floor surface inside the building	-
BC 2	Constant groundwater temperature	C	+7°C at 20m depth below the ground surface (Sinnathamby et al., 2014)	+7°C at 20m depth below the ground surface
BC 3	Ice Rink	C	– 7°C on the ice rink surface	Top layer of the model representing the Ice rink
BC 4	Thermal Piles Heat Flux	C	Border of the pile (Well BC)	Border of the pile (Well BC)
BC 4	Thermal Piles Constant Temperature	C	Border of the pile (Well BC)	Border of the pile (Well BC)
BC 5	Water Pool Temperature Function	V	Between concrete slab and the clay layer	Between concrete slab and the clay layer
BC 6	Climate	V	Ground surface outside the building	-

Note: BC – Boundary condition; C – Constant; V - Variable

B. Climate function (BC6)

A climate function represented the influence of the climate (air temperature) in the thawing process (Fig. 6b). The climate function was estimated based on the mean monthly temperature data of Helsinki, collected over the past 30 years (Pirinen et al., 2012). The climate function was applied as a cyclic function on the ground surface outside the building in the 2D model and repeated annually during the entire transient

analysis. Effect of snow cover and/or solar radiation on the surface temperature was not considered. Table 2 and Fig. 5 summarize the boundary conditions used in 2D and 3D models, and their applied locations in the models.

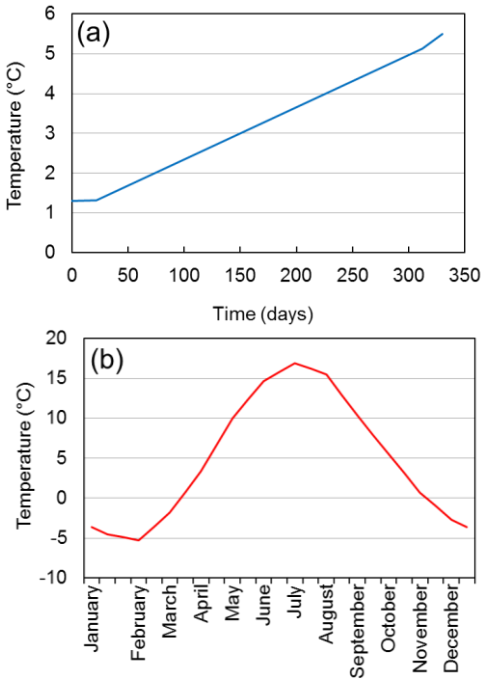


Figure 6. Boundary conditions: (a) Temperature function of the pool of water, and (b) Cyclic climate function of Helsinki (Pirinen et al., 2012).

4 RESULTS AND DISCUSSIONS

4.1 Thawing Process

4.1.1 Initial conditions: Steady-state

The initial steady-state analysis was done in order to establish the existing conditions below the ice rink in Myllypuro right before the renovation. The results from the SVHeat models showed that the maximum depth of the frozen soil varied between 6.5 m and 7 m. The frozen soil depth and the soil temperature profiles obtained from these SVHeat models were similar to the in situ observations made, and thus, validating the model.

4.1.2 Transient Analysis

A. Constant Temperature Boundary Conditions (CTBC): 3D Model

The second phase of the modelling represented the thawing of the frozen ground, starting from the day when the facility was re-opened in December 2012 after the renovation. In this analysis, it was assumed that the piles were injecting heat into the ground at +20°C, at a temperature equivalent to the measured outlet temperature of the warming fluid. Fig. 7 shows the ground temperature evolution at different depths during the transient analysis. From Fig. 7, it can be seen that around 400 – 450 days are needed to thaw the frozen ground across the entire depth. The results obtained with the 3D model are in good agreement with the in situ temperature measurements. The results obtained from the 3D model also validate the preliminary analytical calculations that showed more than one year of heat injection is required in order to thaw the frozen ground completely.

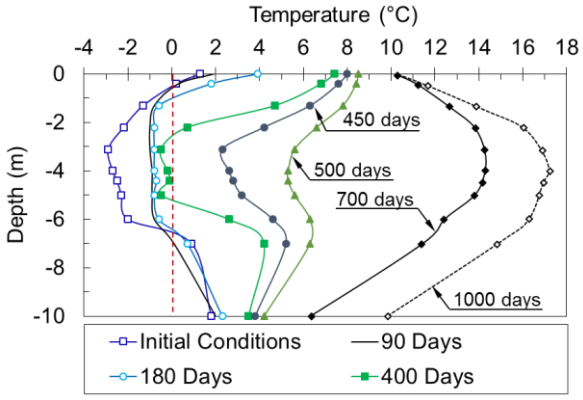


Figure 7. Ground temperature profile from the 3D model under CTBC at different stages of the thawing process in points located in the middle of two piles (d =2.75m).

A ground temperature increase from – 3°C to – 1°C within the frozen depth (0.5 – 6.0 m) can be noticed as soon as the heat injection started (within around 30 days) (Fig. 7). However, it took nearly 400 – 450 days to reach positive temperatures (from – 1°C to – 0°C) within the frozen depth. This was primarily attributable to the phase change of the frozen water and the amount of unfrozen water content presence in the soil. Compared with the preliminary analytical calculations, the results from the 3D model with CTBC showed that around 300-350 less days are required for complete thawing. Fig. 8 shows

the temperature evolution of the ground surrounding the pile at different time steps.

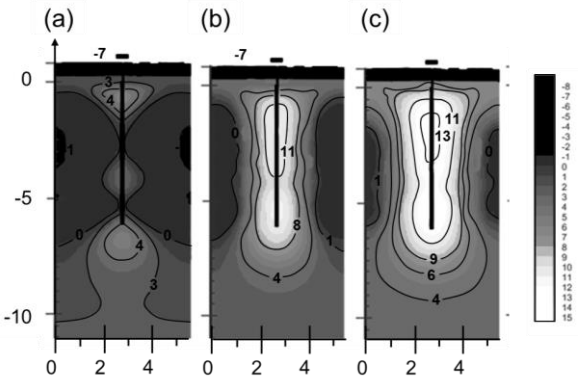


Figure 8. Ground temperature evolution after: (a) 30, (b) 180 and (c) 365 days.

B. Constant Heat Flux Boundary Conditions (CHFBC): 2D and 3D models

Due to the significant discrepancies between the CTBC model results and analytical estimation of the time required to thaw the frozen ground, a new boundary condition was introduced with constant heat flux (CHFBC) of around 112 kW for 240 piles (40320 kJ/day-pile) (Eq.1). Fig. 9c shows the results obtained with the CHFBC boundary conditions and can be noticed that more than 800 days are required for complete thawing of the frozen ground. The results obtained with the CHFBC are in good agreement with the preliminary analytical calculations done based on the influence area of a single pile. The time needed to reach the steady-state in the model and the energy losses through the pile materials (which were not considered in the models) could be the reason for the discrepancies between the model results. Fig. 9b shows the in situ temperature measurements taken from a point near the edge of the ice rink (remote location) and can be compared with the CHFBC results in Fig. 9a.

Similar results in a larger scale was achieved in the 2D model as well. In the 2D model, the total heat flux injected by the piles was divided by the distance between the pile rows (5.5m) in order to get the average energy injected per model-meter.

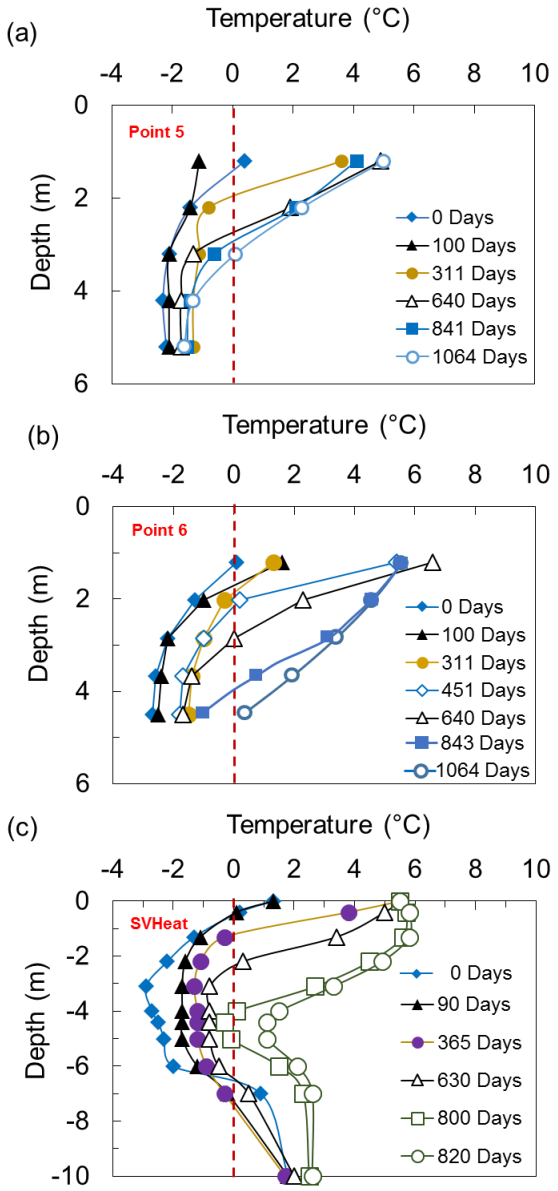


Figure 9. Ground temperature profiles: In situ measurements from (a) point 5 (in the middle of the ice rink; Fig 1a), (b) point 6 (at the edge of the rink: Fig. 1a), and (c) SVHeat (3D model) with CHFBC in points located in the middle of two piles (d=2.75m).

4.2 Modelling the Target Temperature on Pile Surface with CTBC

Final step of the analysis was to establish a constant temperature in the piles that is required to prevent the surrounding thawed soil from re-freezing. This constant temperature has to be as low as possible for efficient energy consumption. Therefore, in order to determine the required target temperature, several models were done with a range of temperatures on the piles at +20°C,

+15°C, +10°C and +7°C. The soil temperature profile obtained in the previous step after 1000 days of heat injection at 112kW (phase 2) was used as the initial condition for these models.

The analysis results showed that once all the ice below the ice rink is melted, heat injection at a minimum temperature of around +7°C is sufficient to prevent the ground from refreezing. It is important to note that in the models, the piles were modelled as a well boundary condition, which means that the piles were modelled as an empty cylinder and their physical and mechanical properties were not considered. Considering this, the target temperature should be at least +7°C at the border of the pile. This means that the temperature of the warming liquid circulating inside the piles should be higher because there would be thermal losses through the pile material.

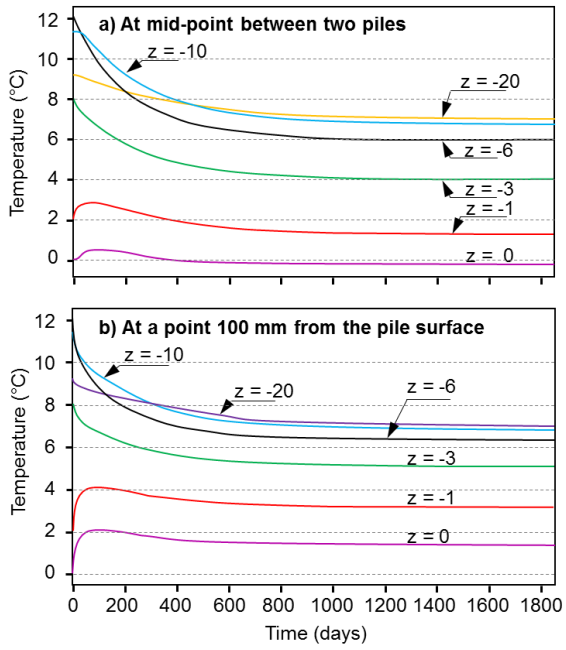


Figure 10. Ground temperature evolution after five years of heat injection at: (a) Mid-point between two piles, and (b) a point 100 mm away from the pile (3D model).

Fig. 10a shows the temperature evolution of the ground between two piles at different depths in the transient analysis when injecting heat at +7°C during a five-year analysis. As it can be seen, the steady state was reached after almost three years.

However, it can be noticed that the ground at shallow depths (within the upper 1 m depth below the ice rink) is still frozen after five years of heat injection at +7°C, mainly due to the circulation of the cooling liquid in the ice rink.

Fig. 10b shows the ground temperature evolution at a point located 100 mm away from the pile border. The temperature of the ground surrounding the piles stayed at above zero temperatures when the heat injected at +7°C. Fig. 11 shows the temperature profile of the ground after one year of heat injection by the piles at +7°C.

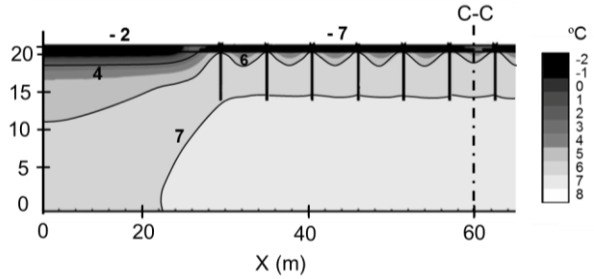


Figure 11. Ground temperature profile after one year of heat injection at +7°C (2D model).

5 CONCLUSIONS

The thawing of the frozen ground below the Myllypuro ice rink facility has been studied in detail through analytical approach and numerical simulations, and compared with in situ conditions. The primary objective of this study was to model the thawing process numerically, so that the time needed for complete thawing of the frozen ground below the ice rink can be estimated and also the ground thermal behaviour can be predicted in advance. Based on the results and insitu observations, the following conclusions can be drawn:

1. Results from the initial steady-state analysis showed that the frost depth below the ice rink was around 6.5 m – 7.0 m, which was in good agreement with the in situ measurements.

2. From the 1000-day long transient analysis that represented the thawing process from

the day when the ice rink was re-opened in December 2012,

a. When a constant temperature boundary condition (CTBC) was applied on the pile border in the 3D model, the simulation results showed that around 400 to 450 days are required to thaw the frozen ground completely. Compared with the analytical estimation based on the influence area of a single pile, this was around 300 to 350 days less. Due to the significant discrepancies in the simulation results and analytical estimation, new simulation with constant heat flux boundary condition was done.

b. Simulation runs with CHFBC showed that around 750 to 800 days are required for complete thawing of the frozen ground and these values were in good agreement with the analytical estimations done earlier.

3. The ground temperature profile obtained from the 2D models under CHFBC showed a good approximation to the measured in situ temperature values.

4. Once the frozen ground below the ice rink is completely thawed, a heat injection at around +7°C by the piles is sufficient to prevent the thawed ground from re-freezing.

6 ACKNOWLEDGEMENTS

This study was funded by the Aalto University. The authors wish to thank Helsinki City Geotechnical Division and Myllypuro Ice Rink operator Nuorisojääkenttä Oy for the cooperation during this study.

7 REFERENCES

Andersland, O.B. & Ladanyi, B. (1994). An introduction to Frozen Ground Engineering. New York, Chapman & Hall.

Cervera, C.P. (2013). Ground thermal modelling and analysis of energy pile foundations. *MSc Thesis*, Aalto University, Espoo, Finland.

Clauser, C. (2006). Geothemal Energy. In: K. Heinloth (ed), Landolt-Börnstein, Group VIII: advanced Materials and Technologies, Vol. 3: Energy Technologies, Subvol. C: Renewable Energies, Springer Verlag, Heidelberg-Berlin, 493-604.

Liu, B. & Li, D. (2012). A simple test method to measure unfrozen water content in clay water systems. Cold Regions Science and Technology, 78 (2012), 97-106.

Pirinen, P., Simola, H., Aalto, J., Kaukoranta, J.-P., Karlsson, P. & Ruuhela, R. (2012). Tilastoja suomen ilmastosta 1981-2010 [Climatological statistics of Finland 1981–2010], Technical report, Finnish Meteorological Institute. ISBN 978-951-697-766-2.

Sinnathamby, G., Gustavsson, H., Korkiala-Tanttu, L., Cervera, C. P. & Koskinen, M. (2016). Case Study: Frost heave and thaw settlement of a frozen ground. XV Panamerican Conference: Selected papers on energy geotechnics, Environmental Geotechnics (ICE), London (accepted for publication).

Sinnathamby, G., Gustavsson, H., Korkiala-Tanttu, L., Cervera, C. P. & Koskinen, M. (2015). Frost heave and thaw settlement estimation of a frozen ground. XV Panamerican Conference, Buenos Aires, Argentina.

Sinnathamby, G., Gustavsson, H., Korkiala-Tanttu, L., & Cervera, C. P. (2014). Numerical Analysis of Seasonal Heat Storage Systems of Alternative Geothermal Energy Pile Foundations. Journal of Energy Engineering (DOI: 10.1061/(ASCE)EY.1943-7897.0000236).

Sundberg, J. (1988). Thermal Properties of Soils and Rocks. Linköping, Swedish Geotechnical Institute, Report No 35.

Thode, R., & Fredlund, M. (2012). SoilVision Verification manual. SoilVision Systems Ltd. Saskatoon, Saskatchewan, Canada.

Thode, R. & Zhang, J. (2012). SVHeat 1D / 2D / 3D Geothermal Modeling Software: Theory Manual, Fredlund, M., Ed., Saskatoon, Canada: SoilVision Systems Ltd., 2012.

Thode, R. (2012). SVHeat 2D / 3D Geothermal Modeling Software: Tutorial Manual, Fredlund, M., Ed., Saskatoon, Canada: SoilVision Systems Ltd., 2012.

Thode, R. (2013). SVHeat Tutorial Manual. SoilVisions Systems Ltd.

Vähäaho, I., Koskinen, M & Uotinen, V. (2012) Suomen paksuin ikirouta. GeoFoor 38, Helsinki, Finland.

A procedure for the assessment of the undrained shear strength profile of soft clays

Vikas Thakur
Norwegian University of Science and Technology, Norway, vikas.thakur@ntnu.no

Odd Arne Fauskerud[1], Vidar Gjelsvik[2], Stein Christensen[3], Frode Oset[4], Steinar Nordal[5], Margareta Viklund[6], Stein-Are Strand[7]
[1]*Multiconsult As, Norway*
[2]*Norwegian Geotechnical Institute, Norway*
[3]*SINTEF Building and Infrastructure, Norway*
[4]*Norwegian Public Roads Administration, Norway*
[5]*Norwegian University of Science and Technology, Norway*
[6]*Norwegian National Rail Administration, Norway*
[7]*Norwegian Water Resources and Energy Directorate, Norway*

ABSTRACT
In the geotechnical research community, there is widespread agreement that the choice of the characteristic undrained shear strength (c_{uA}) is very important and plays an essential role in the design and stability analysis of various geotechnical constructions placed in or on soft clay deposits. Thus, the choice of undrained shear strength, both conservative and non-conservative, could have major economic (and social) consequences in many projects. This paper summarizes the work carried out by engineers and scientists representing various institutions in Norway to provide a sound engineering method to determine characteristic shear strength of soft clays. This paper presents a recommendation on how to determine a characteristic c_{uA} profile based on laboratory and in situ testing methods and discuss the impact of stress history, strain rates, Atterberg's limits, and sample disturbance on the undrained shear strength of soft clays measured at a single borehole location. The discussion is supported by the results obtained from laboratory and field-testing. This paper highlights the key issues related to the extrapolation of undrained shear strength of soft clay from a given borehole location to a large soil volume.

Keywords: Soft clays, undrained shear strength, sample disturbance.

1 INCEPTION

The concept of shear strength goes back to 1773 when Coulomb proposed the following equation:

$$\tau_f = c + \sigma \tan\varphi \quad (1)$$

This was the first time that shear strength (τ_f) was regarded as consisting of two parts, i.e., cohesive resistance (c) and frictional resistance (φ), that increase proportionally with normal pressure (σ). However, the strength parameters c and φ, as introduced by Coulomb, remained difficult to determine, especially when cohesive soils were involved. Based on numerous direct shear tests from 1934 to 1937, Hvorslev reached the two main conclusions that

- cohesion (c) depends merely on water content;
- the angle of internal friction (φ) is a soil characteristic.

Hvorslev replaced the normal pressure in Eq. 1 with effective normal stress or the difference of total stress and pore pressure as

$$\tau_f = c + \sigma' \tan\varphi = c + (\sigma - u) \tan\varphi \quad (2)$$

Here, c is the true cohesion; σ' is the effective normal stress on the failure plane; σ is the total normal stress on the failure plane; φ is the true angle of internal friction.

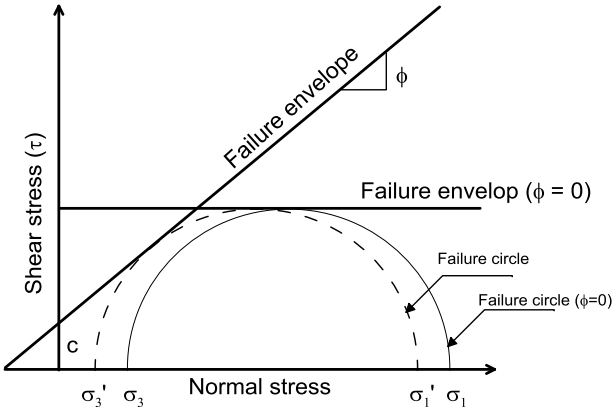


Figure 1. Failure envelopes for geomaterials. Superscript' in the figure refers to effective stresses.

Although this equation has been universally accepted to deduce the drained shear strength of geomaterials, the undrained shear strength of soft clays remains a concern. The nature of shear strength saw considerable discrepancy at the Second International Conference of Soil Mechanics in 1948. At the conference the concept of "$\varphi = 0$ analysis" was raised by Skempton (1948) because saturated cohesive soils exhibit an angle of internal resistance $\varphi = 0$ when brought to failure under undrained shearing. The corresponding strength revealed is the undrained shear strength. Specific to the $\phi = 0$ concept, it was assumed that for a saturated clay specimen under undrained conditions increases in confining stress were carried by the pore water in the sample, with the effective stress in the sample remaining unchanged. This was found consistent with the Terzaghi's effective stress principle; if the effective stress in a sample does not change, the deviatoric stress required to cause failure in the sample does not change. With the development of testing techniques, especially triaxial tests, and the accumulation of data, the fundamental behavior of soft clay was found to follow the effective stress envelope as non-cohesive soils, while the total stress envelope reflects the pore water pressures that develop during undrained shear and the fundamental behavior in terms of effective stresses (e.g. Bell 1915; Fellenius 1922; Terzaghi 1943; Skempton 1948; Lambe 1960; Bjerrum 1961, Aas 1965; Bishop 1966; Janbu 1967; Tavenas and Leroueil. 1987). The undrained shear strength is often determined through field and laboratory tests, such as the triaxial test, simple shear test, direct shear test, cone penetration test with and without pore pressure measurements (CPT /CPTU), field vane test and dilatometer test, fall cone tests, and uniaxial and plane strain test. However, these tests may become expensive if a large number of tests are to be conducted. Therefore, several researchers have developed empirical correlations between undrained shear strength and typical soil properties that can be relatively obtained with index tests. The reader is referred to Lacasse (2016), a paper in this conference, for further details.

2 PROBLEM DEFINITION

In the geotechnical research community, there is widespread agreement that the choice of the characteristic undrained shear strength is very important and plays an essential role in the calculation for the design and stability analysis of various geotechnical constructions placed in or on soft clay deposits. Thus, the choice of undrained shear strength (c_{uA}), both conservative and non-conservative, could have major economic (and social) consequences in many projects.

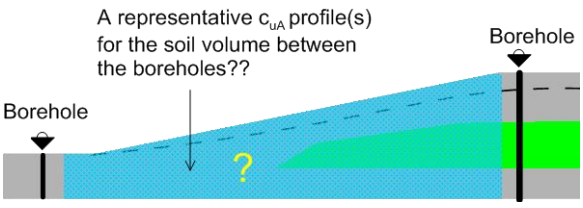


Figure 2 Problem definition.

However, the influence of the stress history, soil fabric, strain rates, Atterberg's limits, sampling technique, and sample disturbance is great on the undrained shear strength of soft clays. Consequently, the assessment of a

representative c_{uA} of soft clays has been challenging since the inception of the concept. A simplified approach is therefore adopted for design purposes. It needs to be emphasized that c_{uA} of the soil is the undrained shear strength that is assumed to be mobilized along the slip surface 45^0 inclined from the major principle stress.

The undrained shear strength c_{uA} profiles with depth are usually established at some selected boreholes where the information is collected. These c_{uA} profiles are later interpolated to the soil volume between the boreholes. Thus, the accuracy of a c_{uA} profile at the boreholes is crucial because the soil volume between the boreholes depends on the representativeness of the c_{uA} profiles at the boreholes. As a first step, this paper presents a procedure for assessing the c_{uA} profile at a borehole. A discussion follows on the important aspects to consider when the c_{uA} profile is estimated for a large soil volume. This paper summarizes the work carried out by engineers and scientists representing various institutions in Norway. The overall aim of the work presented in this paper has been to provide a method to make a sound engineering judgement related to the determination of the characteristic shear strength of soft clays.

3 UNDRAINED SHEAR STRENGTH ESTIMATION

In this paper, a characteristic c_{uA} profile refers to the active undrained shear strength profile most likely to occur, deduced based on available and relevant measurements and experience data. In many cases, this is a mean value or a weighted mean of available data. If measurements (interpreted strength values) show relatively great variation with depth, additional caution must be taken when selecting the c_{uA} profile.

An empirical relationship widely used in Norway is SHANSEP, which stands for stress history and normalized stress engineering parameters (Ladd and Foot 1974). This SHANSEP principle is expressed by the following formula:

$$c_{uA} = \alpha\, OCR^{m}\, p_o' \qquad (3)$$

Where

α = constant
m = constant
OCR = p_c'/p_o' (over consolidation ratio)
p_c' = effective pre-consolidation pressure
p_o' = effective vertical stress.

The SHANSHEP formula suggests that c_{uA} is governed by three parameters—soil density, pore pressure, and stress history—and two empirical constants that have been shown to vary significantly between different clays. For Norwegian sensitive clays, the values of α and m vary between 0.25 and 0.35 and between 0.65–0.75, respectively (see Figure 3).

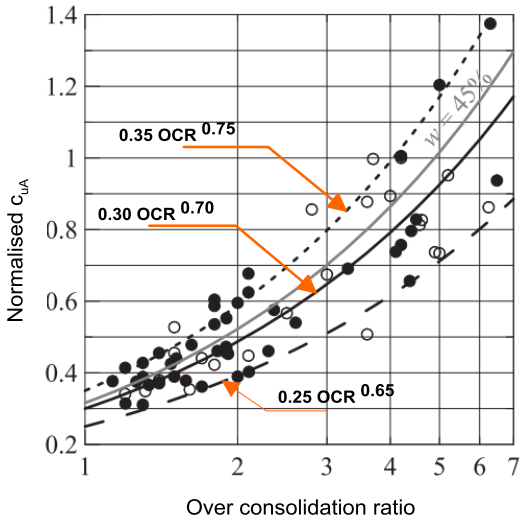


Figure 3 c_{uA} normalized with effective overburden stress versus the soil's stress history for Norwegian clays as suggested by Karlsrud and Hernandez-Martinez (2013). The filled and the open circles in the figure refers to the data for sensitive clays having the sensitivity more than and less than 15, respectively.

4 ASSESSMENT PROCEDURE FOR THE C_{uA} PROFILE AT ONE LOCATION

In this section, a stepwise assessment procedure is provided to establish c_{uA} profiles.

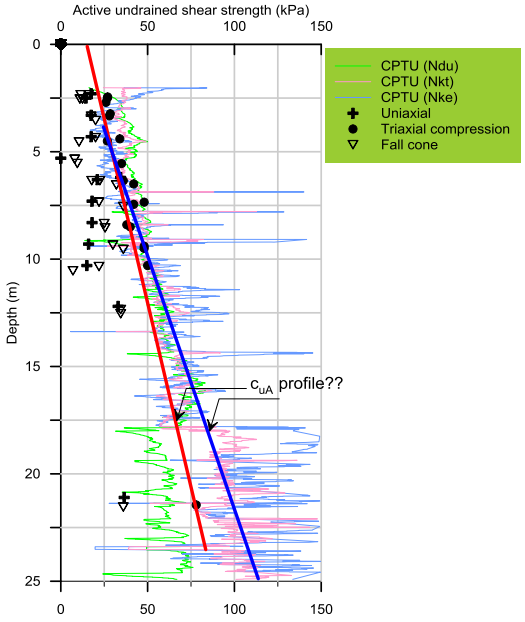


Figure 4 c_{uA} profile at one borehole location.

4.1 Quaternary geologic map

Since there is a close connection between clay strength and pre-consolidation pressure (p_c'), it is important to understand the Quaternary geology of the area of interest. This includes knowledge about the soil depositional history and subsequent natural processes that have shaped the landscape due to, for example, erosion and landslide activity.

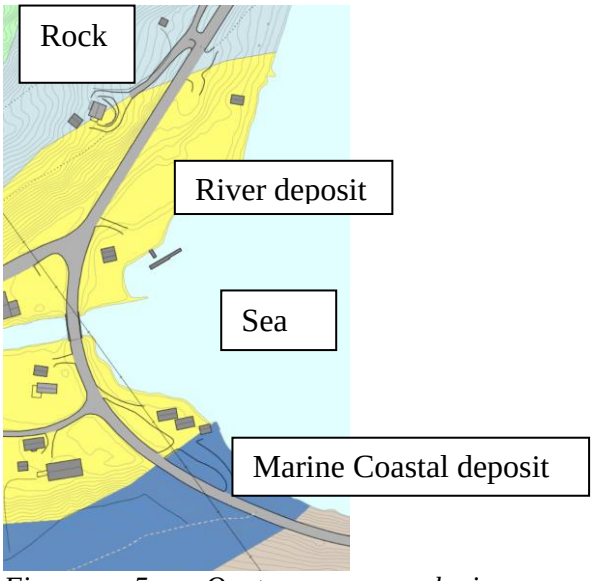


Figure 5. Quaternary geologic map (www.ngu.no).

The assessment of the c_{uA} profile, therefore, often begins with Quaternary and topographic maps. However, the reader must be aware that the quaternary map provides information only on the top layer of sediment deposition. Therefore, it is important to point-out that it often can be marine clay under alluvial deposits and coastal deposits that it is highlighted in Figure 5. In addition, human activity in many places has resulted in significant changes of natural terrain forms. In such cases, useful information may be found in old maps and reports that record what has occurred in an area over the years. In places with clear signs of landslide activity and/or ravines, the landscape often gives certain indications of what can be expected of the OCR and whether masses can be landslide affected. A knowledge about the former seabed level is a useful reference in view of to get an idea about p_c' in soil deposit.

4.2 On-site inspection

An excursion is a prerequisite for planning an effective site investigation. Unfortunately, the geotechnical engineers often undermine this step. It should be realized that excursion could help in updating the information available on maps and aid in making a site investigation plan that is executable.

The soil investigation is a dynamic process in which the measure must be adapted to what is revealed as the planned program is executed. This requires good monitoring and good communication between the field technicians and geotechnical engineers. If a borehole(s) is moved during sampling, this should be justified with proper reasoning. Therefore, the excursion before a site investigation could help avoid such issues. Site investigations should be planned so that a preliminary interpretation of the CPTU results is made before samples are collected.

4.3 Site investigation

A detailed site investigation plan for field and laboratory investigation is prepared based on the additional information gathered through steps 4.1 and 4.2. A strategy should be made

to establish total stations. The total station refers to the reference boreholes where the following information must be collected:

- ✓ Total or rotary sounding
- ✓ Pore pressure measurements (in at least two levels)
- ✓ CPTU, field vane shear tests
- ✓ Soil sampling, using preferably Ø72 mm or Ø54 mm tube sampling of good quality
- ✓ Index parameters, including the Atterberg's limits
- ✓ Odometer test from at least two levels
- ✓ Anisotropically consolidated undrained compression/extension triaxial tests from at least two levels.

For the slope stability calculation, at least two total stations, one at the top and another at the toe of the slope, are recommended. The site investigation should be consistent with the critical sections where stability calculations are to be performed. An assessment is needed of how large the soil volume/area will be because the soil investigation should provide a basis for assessing layering and properties potentially involving soil volume.

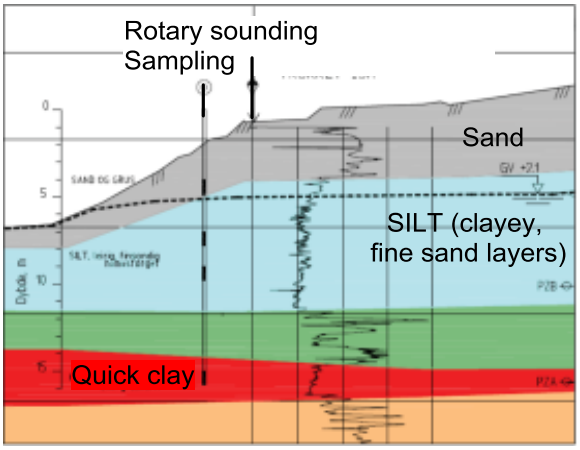


Figure 6 Detection of weak soft clay layers (NIFS report 46/2012).

The detection of weak layers using rotary/total sounding methods can be challenging. Figure 6 shows rotary sounding results taken from an NIFS report (46/2012). These indicate that the tip resistance is decreasing with depth from 5 to 12 m in the layer in light blue; this indicates a layer of sensitive clays. However, the laboratory investigation revealed that this layer consists of silt. On other hand, a similar response was seen between a depth of 15 and 17 m, and this layer was found to be a quick clay layer (highly sensitive soft clay). Therefore, supplementing sounding results with sampling or additional field tests to facilitate and improve the qualitative assessment of the sounding is advisable.

The CPTU is often the first field result relates to the strength profile that goes to geotechnical engineers; it provides a basis for drawing up a characteristic c_{uA} profile. When interpreting the CPTU results, the following questions should be asked: are there indications of weak layers and/or sections of the profile that should be given extra attention? The CPTU also provides a good basis for assessing the soil sampling program. One of the strengths with the CPTU is that the in situ pore pressure (u_0) has little effect on the interpretation. For instance, the interpretation of c_{uA} based on cone resistance does not require information regarding in situ pore pressure. A pore pressure-based assessment of c_{uA} is proportional to Δu (= u_2 – u_0). Since u_2 is usually several times greater than u_0, typically four to five times or more for soft clays, the uncertainty in the estimate of u_0 usually constitutes a small proportion of Δu.

A general difficulty with site investigation methods is the number of result uncertainties, which can be aleatory or epistemic. Aleatory uncertainties are unavoidable, whereas the epistemic uncertainty is related to our lack of knowledge. For example, the resulting c_{uA} profile from the CPTU test can depend on the choice of methods, correlations, and testing procedures. Moreover, not all types of equipment are appropriate for all types of materials, which should be tested with equipment and procedures that satisfy quality class 1 (e.g. Sandven et al. 2012). Based on the preliminary interpretation of the CPTU results from the total stations and at the other boreholes, samples should be taken from the desired depth.

4.4 Soil characterization and sample quality assessment

Literature e.g., Berre et al. (1969), La Rochelle and Lefebvre (1970), Bjerrum (1973), Leroueil et al. (1979), Nagaraj et al. (1990, 2003), Lunne et al. (1997), Ladd and DeGroot (2003), Leroueil and Hight (2003), Karlsrud and Hernandez-Martinez (2013), Amundsen et al. (2015), and Amundsen et al. (2016) suggest that soft clays could be prone to sample disturbance—especially when sampled using tube samplers (54, 76, or 95 mm diameter). On the contrary, block sampling in soft clay is considered to capture a more realistic soil behavior can be captured in the laboratory, as illustrated in Figure 7.

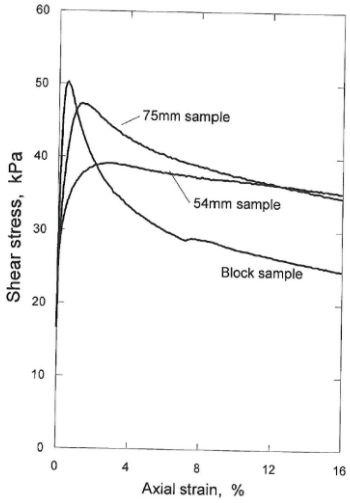


Figure 7 Example of an aniostropically consolidated, undrained, compression, triaxial test carried out by Lunne et al. (2002) on a block sample compared to piston samples from Lierstranda (depth 12.3 m).

Table 1. $\Delta e/e_0$ based sample quality criteria suggested by Lunne et al. (1997) (source: Amundsen et al. 2015)

Class	Description	$\Delta e/e_0$ (OCR 1-2)	$\Delta e/e_0$ for OCR 2-4
1	Very good to excellent	<0.04	<0.03
2	Good to fair	0.04–0.07	0.03–0.05
3	Poor	0.07–0.14	0.05–0.10
4	Very poor	>0.14	>0.10

Given that block sampling is expensive and less suited for sampling at greater depths, effort should be made to take 76-mm diameter samples. Atterberg's limits, odometer tests, and triaxial tests under compression and extension should be performed. Quality assessment of tests should be based on volume change during reconsolidation.

4.5 Assessment of c_{uA} based on laboratory testing

The most reliable laboratory method to assess c_{uA} is triaxial testing. Odometer test(s) should be performed before triaxial testing so that pre-consolidation pressure of the material is known. Pre-consolidation pressure can be measured by different methods, including Casagrande's method (1936), Janbu's method (1963), or Salfors's method (1975). A typical odometer result for a soft clay is shown in Figure 8; this illustrates Casagrande's method to estimate pre-consolidation pressure.

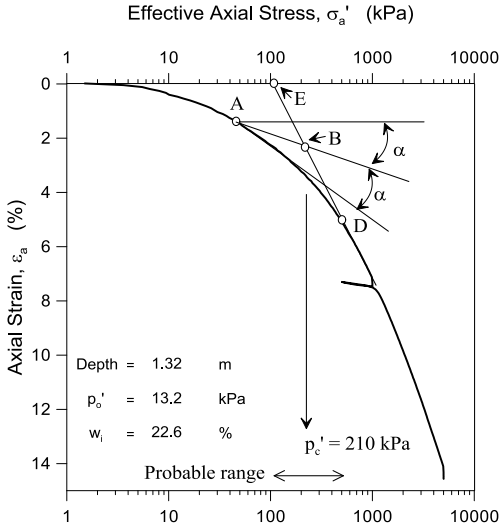


Figure 8 Casagrande's method (Holtz and Kovas, 1981).

In addition, knowledge about the in situ effective stress (pore pressure measurement) at the sample collection depths for the triaxial tests is valuable. In this way, one can estimate an accurate OCR, which can also be used to estimate K_0' for use in triaxial testing. Estimation of the correct K_0' is demanding. However, one can use the approach suggested by Brooker and Ireland (1965) that provides a relatively easy way to estimate K_0' based on soil plasticity (I_p) and the OCR. Caution is needed in using a relatively high K_0' because this will result in a higher average effective stress in the sample, resulting in a high c_{uA}.

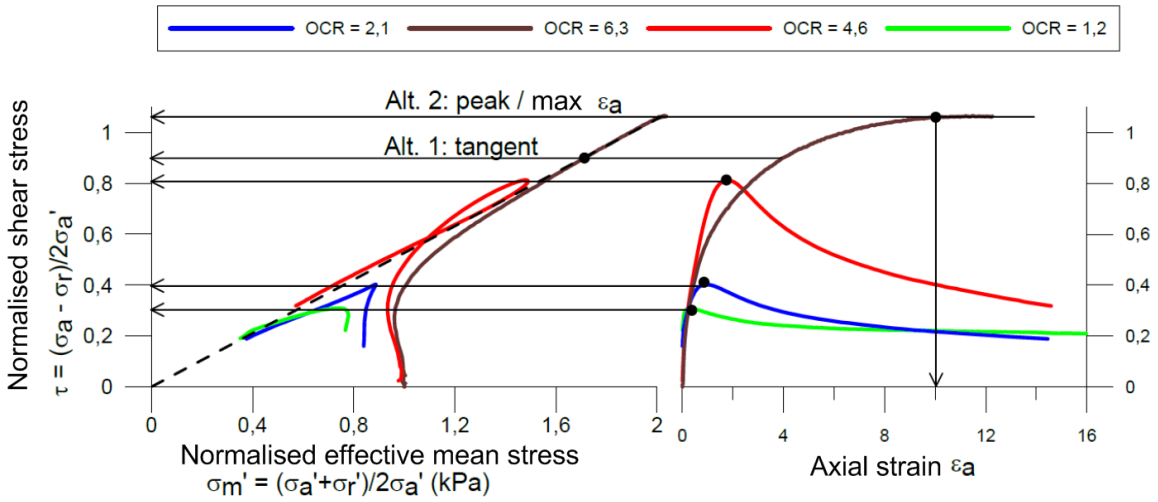


Figure 9 Estimation of c_{uA}.

As in the odometer test, the results of a triaxial test depend on the strain rate (rate dependence). An increase in the strain rate generally results in increased maximum undrained strength and brittle behavior. Lunne and Andresen (2007) showed that there might be a factor of approximately 1.5 in the estimate c_{uA} for very fast rate to a very slow rate. Commonly used strain rates in Norway have been 0.7% to 3.0% per hour. In practice, there is little difference between these experiments, and normally it is not distinguish between these strain rate and strain softening behavior. However, while estimating c_{uA} from triaxial tests, a distinction must be made between dilating and contracting behavior. For the tests exhibiting contracting behavior (positive excess pore pressure build-up during testing), it is recommended to obtain c_{uA} at the maximum measured shear resistance.

A test that first exhibits a contracting behavior but then shows dilation is an indication of sample disturbance. In such cases it is advisable to not go beyond the c_{uA} that shows the point representing the transition between contractancy and dilatancy (see Figure 9). Indeed, dilating materials (highly over-consolidated clays) often attain high strengths; however, this is normally related to high strains. In these cases, it is recommended that the c_{uA} is defined by a given strain, for example 10%.

4.6 Assessment of c_{uA} based on field testing

The most common field test to estimate c_{uA} is the CPT apart from vane shear testing. In Scandinavian countries, the CPT with pore pressure measurements (CPTU) is considered to be the common method for estimating c_{uA} due to its ability to provide information that can help in establishing a continuous c_{uA} measurement along with the depth. The value of c_{uA} is based on three cone factors: N_{kt}, $N_{\Delta u}$, and N_{ke}.

The total tip resistance based c_{uA} is calculated as

$$c_{uA} = \frac{q_T - \sigma_{vo}}{N_{kt}} \quad (4)$$

Here, q_T is tip resistance and σ_{vo} is the total vertical pressure. The pore pressure measurement based c_{uA} is calculated as

$$c_{uA} = \frac{u_2 - u_o}{N_{\Delta u}} \quad (5)$$

Here u_2 is the measured pore pressure and u_o is the in situ pore pressure. The effective tip resistance based c_{uA} is calculated as

$$c_{uA} = \frac{q_T - u_2}{N_{ke}} \quad (6)$$

More information regarding the testing and interpretation of the CPTU can be obtained in the literature (Lune et al. 1997, Karlsrud et al.

2005). It is clear from Eqs. 4–6 that c_{uA} will depend on the cone factors. Several correlations exist for the N_{kt}, N_{ke}, and $N_{\Delta u}$ parameters to calculate c_{uA}. Some of these are discussed below.

The widely accepted method in Norway was proposed by Karlsrud et al. (2005), who compared the CPTU with c_{uA} from block samples and suggested the cone factors N_{kt} and $N_{\Delta u}$ based on the OCR and soil plasticity index (I_p). The N_{ke} parameter was correlated with B_q (pore pressure parameter) and it can be defined as

$$B_q = \frac{u_2 - u_o}{q_T - \sigma_{vo}} \quad (7)$$

Separate suggestions, as listed below, were made for soil having sensitivities less than or more than 15:

For S_t<15

$N_{kt} = 7.8 + 2.5 \cdot \log OCR + 0.082 \cdot I_p$ (8)

$N_{\Delta u} = 6.9 - 4.0 \cdot \log OCR + 0.07 \cdot I_p$ (9)

$N_{ke} = 11.5 - 9.05 \cdot B_q$ (10)

$B_q = 0.88 - 0.51 \cdot \log OCR$ (11)

For S_t>15

$N_{kt} = 8.5 + 2.5 \cdot \log OCR$ (12)

$N_{\Delta u} = 9.8 - 4.5 \cdot \log OCR$ (13)

$N_{ke} = 12.5 - 11.0 \cdot B_q$ (14)

$B_q = [1.15 - 0.67 \cdot \log OCR]$ (15)

Authors are referred to Karlsrud et al. (2005), Sandven et al. (2014) for an elaborated information regarding the CPTU interpretation using Eqns 8-15. Similarly, the Swedish Geotechnical Institute (2007) has suggested the following equation to calculate N_{kt}:

$N_{kt} = 13.4 + 6.65\, w_L$ (16)

Here, w_L is the liquid limit. If w_L is unknown, then one can assume N_{kt} = 16.3 for clays and 9.4 for silty material. In comparing Eqs. 8 and 12 with Eq. 16, a correlation has been established between w_L versus I_p for the Norwegian clays (Figure 10), and c_{uD}/c_{uA} = 0.63 ($I_p \leq 10\%$) and c_{uD}/c_{uA} = 0.63 to 0.80 ($10 < I_p \leq 80\%$) have been assumed on the basis of NIFS (2014). Here c_{uD} refers to direct shear undrained shear strength.

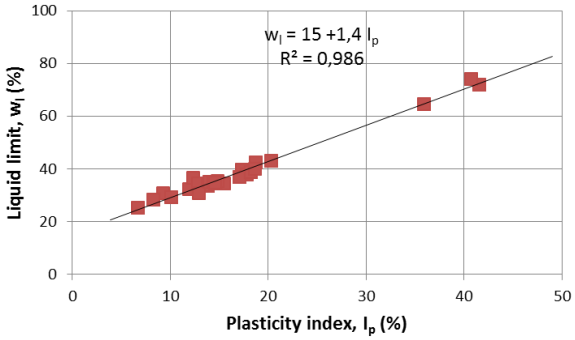


Figure 10 Correlation between w_L and I_p for the Norwegian clays based on the NGI block sample database.

Figures 11 and 12 show that the derived N_{kt} from the SGI is higher than recommended by Karlsrud et al. (2005); thus, the SGI is more conservative in the calculation of c_{uA} in this instance.

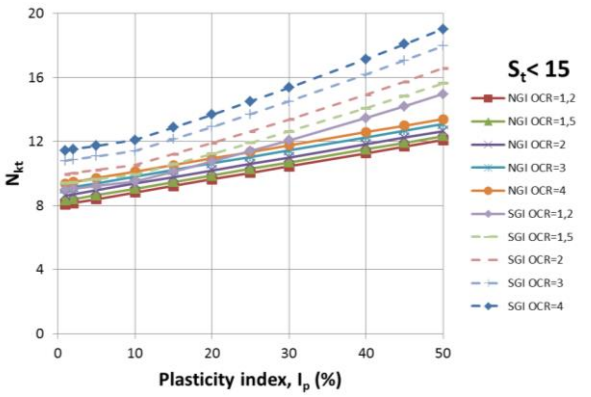


Figure 11 A comparison between the N_{kt} factors suggested by Karlsrud et al. (2005) and SGI (2007) for the clays having S_t <15.

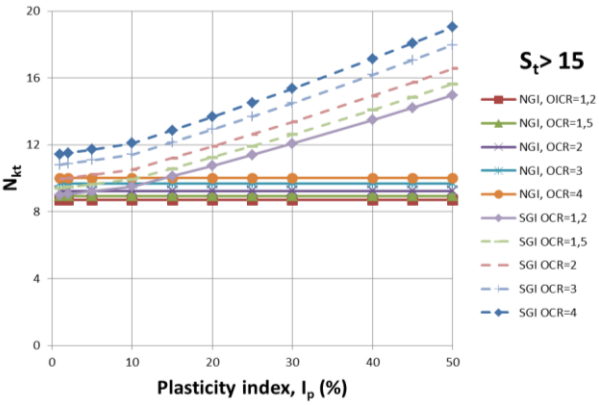


Figure 12 A comparison between the N_{kt} factors suggested by Karlsrud et al. (2005) and SGI (2007) for the clays having S_t >15.

Norwegian geotechnical consultancy firms have also established their own practice to estimate the cone factors. In addition to Karlsrud et al. (2005), Multiconsult and Norconsult use B_q to estimate $N_{\Delta U}$, N_{kt}, and N_{ke} based on Lunne et al. (1997). Tables 2 and 3 present their recommendations, and Figure 13 illustrates these correlations along with the data from Lunne et al. (1997). Some differences are obvious for the N_{ke} and $N_{\Delta u}$ parameters recommended by these two firms.

Table 2. Multiconsult's recommendation (Source: NGF seminar, 2010)

Basis	Factors	Cone factors (based on B_q)
Pore pressure	$N_{\Delta u}$	$N_{\Delta u} = 1.8 + 7.25 \cdot B_q$
Total tip resistance	N_{kt}	$N_{kt} = 18.7 - 12.5 \cdot B_q$
Effective tip resistance	N_{ke}	$N_{ke} = 13.8 - 12.5 \cdot B_q$

Table 3. Norconsults's recommendation (Source: NGF seminar, 2010)

Basis	Factors	Cone factors (based on B_q)
Pore pressure	$N_{\Delta u}$	$N_{\Delta u} = 1.0 + 9.0 \cdot B_q$
Total tip resistance	N_{kt}	$N_{kt} = 19.0 - 12.5 \cdot B_q$
Effective tip resistance	N_{ke}	$N_{ke} = 16.0 - 14.5 \cdot B_q$

Before selecting a value for the cone factors, the basis of selection and the available information in terms of routine investigations, in situ pore pressure, odometer, and triaxial tests are needed, and the choice of the interpretation method needs consideration and justification. Moreover, the validity of the interpretation of factors N_{kt} and $N_{\Delta u}$ and especially for $N_{\Delta u}$ at low B_q must be considered. Vane shear testing is another approach to obtained DSS tests at a desired depth. However, interpretation of undrained shear strength is not very reliable for clays with Ip < 10% as a proper correction factor for low plastic clay has not been established. The reader is referred to Gylland et al. (2016), a paper in this conference, for further details.

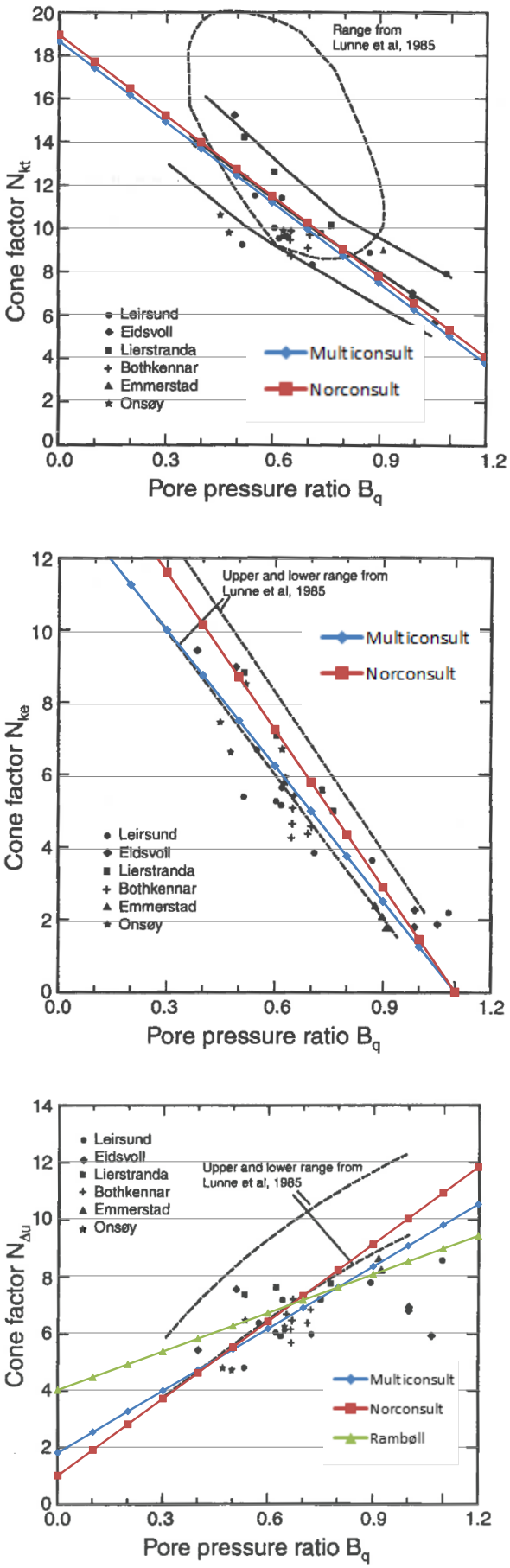


Figure 13 Cone factors versus B_q.

4.7 Presentation and assessment of the c_{uA} *profile*

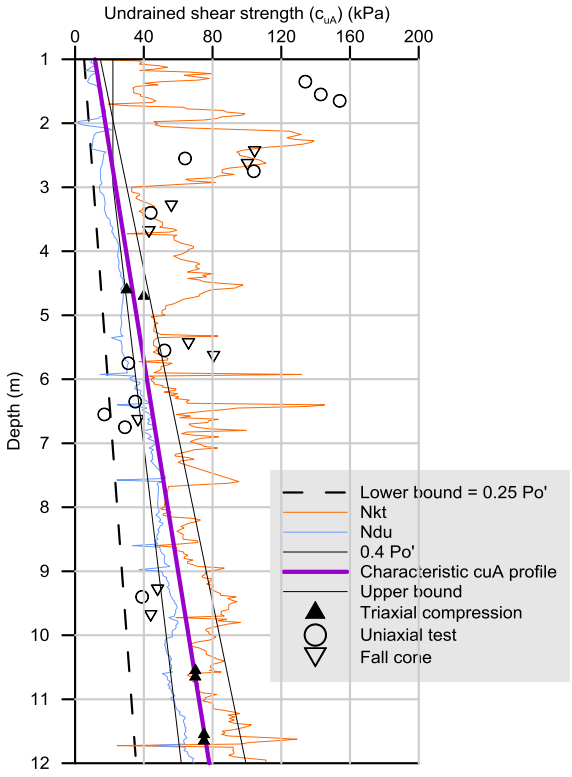


Figure 14 Estimation of a c_{uA} *profile.*

Field and laboratory data used for the interpretation of c_{uA} profiles must be chosen so that the profiles that emerge represent the soil volume to be included in the calculation. It must be substantiated that the data sample is representative of the current profile and soil volume; this includes topography, distance to calculation profile, contour level, previous level of the terrain in the area, effective stress level, pore pressure, variation in soil conditions in the area, soil geological information, and depositional history. Caution should be exercised with the use of index data from routine testing (such as uniaxial tests and the fall cone) to the interpretation of the characteristic c_{uA} profile. The interpretation of the relevant measurements and the experience-based data should be plotted together (as shown in Figure 14). Before selecting the most likely c_{uA} profile based on these data, preference ranking of the measurements and the empirical data should be done in accordance with the following:

1. Triaxial tests (sample quality class 1)
2. CPTU (quality class 1)
3. Experience-based c_{uA}/p_o' or SHANSEP
4. Fall cone/uniaxial test/vane test.

One plot for each borehole is normal, but it could be more appropriate to interpret several boreholes in the same plots. The selected c_{uA} profile should normally lie between the estimated lower and upper bounds of c_{uA} profiles. Experience indicates that the lowest c_{uA} profile for Norwegian clays is $0.25 \cdot p_o'$.

5 ASSESSMENT PROCEDURE FOR C_{uA} FOR A LARGE SOIL VOLUME

Different approaches can be taken to estimate/interpret c_{uA} for a large soil volume. For example, geostatistical approaches allow estimation of soil properties, including c_{uA} using the autocorrelation function and the kriging method (DNV, 2012). For example, if c_{uA} has been measured in a number of positions within the soil volume but is in principle unknown in all other positions, the autocorrelation function for c_{uA} can be established based on the available observations of the c_{uA} profile; using the Kriging technique allows estimating the value of the c_{uA} profile in positions where the c_{uA} profile has not been measured. For each specified position of estimation, the kriging technique provides both an estimate of the c_{uA} profile and a standard error in the estimation, accounting for spatial correlations. This technique is adopted in offshore purposes to estimate various soil properties. However, more research is needed before the method can be practiced as a tool for the engineers working on onshore geotechnics. Moreover, the current state of practice in Norway suggests that one should use engineering judgement when assessing c_{uA} for a large soil volume. In doing so, the followings issues should be considered:

- ✓ Should c_{uA} profiles represent one point or a soil volume?
- ✓ How large a soil volume should firmness profiles represent?

- ✓ Could it be that consistently weak layers will have significance?
- ✓ Are there large variations in the layering and soil conditions detected, or can we interpolate between points where we have data?

Identify how many boreholes must be established and which data need to be included in determining the c_{uA} at each borehole. The number of boreholes for the c_{uA} profile depends on topographic conditions and variations in soil conditions.

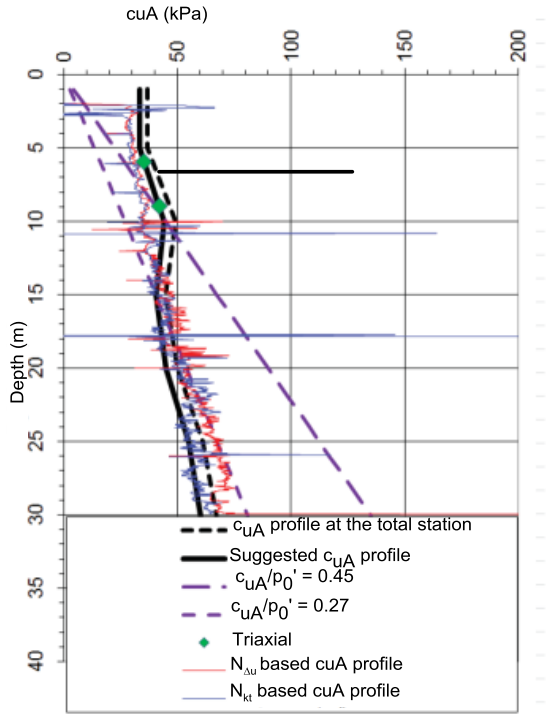


Figure 15 Representative $c_{uA\ profile}$ at a location where insufficient information is available.

For the stability calculation on a hillside, a minimum of two c_{uA} profiles have been established, one representing the shear strength at the top of the slope and one at the bottom of the slope. If there is a large variation in topography and/or soil conditions along the slope, then more strength profiles should be established between the profiles at the top and bottom of the slope. At times, some boreholes between the total stations will have a limited amount of information. In such cases, one needs to be cautious and conservative in establishing the c_{uA} profile. This is exemplified in Figure 15 in which only the CPTU data and two triaxial results are available for a borehole. The level of conservatism is based on the number and quality of the underlying information. In case of doubt, the best solution is to carry out additional field and laboratory testing.

For sensitive clay, the strain-softening behavior needs to be taken into account. If the c_{uA} profile is determined on the basis of laboratory tests on block samples with sample quality "very good to excellent" or data CPTU correlations against such tests, the current practice suggests 15% reduction of c_{uA} to account for the time effect and strain softening. This reduction may be included in the calculation program such as GeoSuite Toolbox by adding a factor of 0.85 at c_{uA} in the calculation.

Eurocode 7, Chapters 2.4.3 and 2.4.5.2 suggest some useful and relevant points to be taken into account in the selection of c_{uA} profiles. These points are summarized here:

- ✓Selection of characteristic c_{uA} should be based on results from the field and the laboratory data, either directly or through correlations/theory/empirical or other well-established and relevant experience.
- ✓The scope of investigations and the type and number of tests/experiments must be taken into account/reflected in the choice of the characteristic c_{uA}.
- ✓The test method for the determination of c_{uA} should be consistent with published and recognized information (practice) for test methods.
- ✓Factors that could cause differences between the measured value in laboratory/field and real behavior in soil shall be taken into account.
- ✓Consideration should be given to geologic information and data from other projects and/or areas with similar soil conditions.
- ✓The order of magnitude of the selected characteristic c_{uA} should be compared with relevant published data and local and general experience. Measured

values should be reconciled with empirical data to verify that the size falls within the expected range of variation.

- ✓The estimated characteristic c_{uA} should be based on a conservative estimate of the values that have the greatest impact on relevant issue/analysis/calculation.
- ✓The magnitude of soil volume included in the calculations/analyses should be reflected in the choice of c_{uA}.
- ✓Because the lab and field tests in most cases will only occupy a very small proportion of the volume of soil that will be involved in an analysis/calculation, so should the characteristic c_{uA} be chosen as a conservative estimate for the mean values of measured/derived values found by experiments in the field.
- ✓It is important to focus on weak areas and/or weak layers that may be significant for the analysis.
- ✓Caution should be exercised in the use of values that require large deformations.

6 CLOSING REMARKS

This paper presents a procedure to assess the undrained shear strength profile of soft clays. In doing so, various aspects relevant for the estimation of the strength profile are discussed in light of existing literature and field and laboratory data. The work here is mainly applicable but not limited to stability problems in Norwegian clays. Finally, this paper suggests that the representativeness of the estimated c_{uA} profile depends on how well the geotechnical information, experience, and engineering judgement are combined.

7 ACKNOWLEDGMENTS

The authors of this paper acknowledge the Natural Hazards–Infrastructure for Floods and Slides Program–NIFS (www.naturfare.no), funded by the Norwegian Public Roads Administration, Norwegian Water Resources and Energy Directorate, and Norwegian National Rail Administration.

8 REFERENCES

Aas, G. (1965) "Study of the Effect of Vane Shape and Rate of Strain on Measured Values of In Situ Shear Strength of Clays," Proc. 6th Int. Conf. on Soil Mech. Found. Engg., Montreal, Vol. I., 141-145.

Amundsen, H. A., A. Emdal, R. Sandven and V. Thakur (2015). On engineering characterization of a low plastic sensitive soft clay. GeoQuebec, Quebec.

Amundsen, H. A., V. Thakur and A. Emdal (2016). Sample disturbance in block samples of low plastic soft clays. 17th Nordic Geotechnical Meeting, Island.

Bell A L (1915). Lateral pressure and resistance of clay and the supporting power of clay foundations. Mi. Proc. Institute for Civil Engineers. Vol 149, 233.

Berre T, T. Lunne, K.H. Andersen, S. Strandvik and M Sjursen (2007). Potential improvements of design parameters by taking block samples of soft marine Norwegian clays. Canadian Geotechnical Journal, Volume 44(6), 698-716.

Berre, T., K. Schjetne and S. Sollie (1969). Sampling disturbance of soft marine clays. Proc. of the 7th ICSMFE, Special Session, Mexico.

Bishop A. W. (1966), The strength of soils as engineering materials. Rankine Lecture, Geotechnique, 16 (2), 91 – 130

Bjerrum, L. (1961). The effective shear strength parameters of sensitive clays. ISSMGE, 5 Paris, 1961, Proceedings Vol. 1, pp 23-28. (NGI pub 45)

Bjerrum, L. (1973). Problems of soil mechanics and construction on soft clays. State-of-the-art report. Proc. of the 8th ICSMFE, Moscow.

Brooker, E.W. and H.O. Ireland (1965). Earth Pressure at Rest Related to Stress History. Canadian Geotechnical Journal, Vol. 2 (1), 1-15

Casagrande, A. (1936). The determination of the pre-consolidation load and its practical significance. In Proceedings of the First International Conference on Soil Mechanics and Foundation Engineering Boston, Vol. III, Discussion D-34, 60.

DeGroot, D. J., S. E. Poirier and M. M. Landon (2005). Sample disturbance-Soft clays. Studia Geotechnica et Mechanica, Vol. 27(3-4), 91-105.

DNV (2012). Recommended Practice DNV-RP-C207- Statistical Representation of Soil Data.

Fellenius W. (1922). Statens Jarnvagars Geoteknisk Kommission, Stockholm

Gylland A, Thakur V, Emdal A (2016), Extended interpretation basis for the vane shear test. 17th Nordic Geotechnical Meeting, Island.

Gylland, A.S, H.P Jostad, S. Nordal,and A Emdal (2013) Micro-level investigation of the in situ shear vane failure geometry in sensitive clay. Geotechnique. 63(14),1264-1270.

Holtz, R.D. and W.D. Kovacs, W.D. (1981). "An Introduction to Geotechnical Engineering," Prentice-Hall, Inc., New Jersey, 733 pp.

Janbu N (1967) Grunnlag i geoteknikk. Tapir

Janbu, N. (1963). Soil compressibility as determined by oedometer and triaxial tests. In Proceedings of the third European Conference Soil Mechanics, Wiesbadem. Vol. 1, pp. 19–25.

Karlsrud K and Hernandez-Martinez F G (2013). Strength and deformation properties of Norwegian clays from laboratory tests on high quality block samples. Canadian Geotechnical Journal, 50(12): 1273-1293.

Karlsrud K., Lunne T., Kort D.A., Strandvik S. (2005). CPTU correlations for clays. In: Proc. of 16th ICSMGE, Osaka. Millpress, Rotterdam: 693-702

La Rochelle, P. and G. Lefebvre (1970). Sampling disturbance in Champlain clays. Proc. of the Symp. on Sampling of soil and rock, ASTM.

Lacasse S (2016). Keynote lecture on undrained shear strength of soils. 17th Nordic Geotechnical Meeting, Island.

Ladd CC, Foot R. (1974). New design procedure for stability of soft clays. Journal of the Geotechnical Engineering Division, ASCE 100(7), 763-786.

Ladd, C.C. and DeGroot, D.J. (2003). "Recommended Practice for Soft Ground Site Characterization." The Arthur Casagrande Lecture, Proceedings of the 12th Panamerican Conference on Soil Mechanics and Geotechnical Engineering, Boston, MA, Vol. 1, pp. 3-57.

Lambe T W (1960). A mechanistic picture of shear strength in clay. ASCE Research conference on shear strength of cohesive soils, 555-580.

Lefebvre, G. and C. Poulin (1979). A new method of sampling in sensitive clay. Can. Geotech. J. 16(1), 226-233.

Leroueil, S. and D. W. Hight (2003). Behaviour and properties of natural soils and soft rocks. Characterisation and Engineering Properties of Natural Soils.

Leroueil, S. and P. R. Vaughan (1990). The general and congruent effects of structure in natural soils and weak rocks. Géotechnique 40(3), 467-488.

Leroueil, S., M. Roy, P. L. Rochelle and F. A. Tavenas (1979). Behavior of Destructured Natural Clays. J. Geotech. Eng. Div. 105(6), 759-778.

Lunne, T. & Andersen, K.H. 2007. Soft clay shear strength parameters for deepwater geotechnical design. Proc., 6th OSIG, SUT, London, UK, 151–176.

Lunne, T., Robertson, P. K. and Powell, J. J. M. (1997): Cone Penetration Testing in Geotechnical Practice. Blackie Academic & Professional.

Lunne, T., Robertson, P.K. & Powell, J.J.M. 2002. Cone penetration testing in geotechnical practice. Spon Press.

Lunne, T., T. Berre and S. Strandvik (1997). Sample disturbance effects in soft low plastic Norwegian clay. Proc. of the Symp. on Recent Develop. in Soil and Pavement Mech., Rio de Janeiro.

Nagaraj, T. S., B. R. S. Murthy, A. Vatsala and R. C. Joshi (1990). Analysis of Compressibility of Sensitive Soils. J. Geotech. Eng. 116(1), 105-118.

Nagaraj, T. S., N. Miura, S. G. Chung and K. N. Prasad (2003). Analysis and assessment of sampling disturbance of soft sensitive clays. Géotechnique 53(7), 679-683.

NIFS (2014). www.naturfare.no

NGF Seminar (2010); NGM seminar NGF seminar om bruk og misbruk av CPTU og vingeboring. CPTU Seminar 24-25.8.2010.

NIFS-rapport 14/2014. En omforent anbefaling for bruk av anisotropifaktorer i prosjektering i norske leirer.

NIFS-rapport 14/2014. En omforent anbefaling for bruk av anisotropifaktorer i prosjektering i norske leirer.

Norsk Standard NS-EN 1997-1:2004+NA: 2008. Eurokode 7: Geoteknisk prosjektering Del 1: Allmenne regler.

Norsk Standard NS-EN 1997-1:2004+NA: 2008. Eurokode 7: Geoteknisk prosjektering Del 1: Allmenne regler.

Rolf Sandven, A. Vik, S. Rønning, E.Tørum (2012). Detektering av kvikkleire fra ulike sonderingsmetoder. NIFS rapport nr. 46-2012. Utgitt av NVE.

Sallfors, G. (1975) Preconsolidation Pressure of Soft High Plastic Clays, Ph.D. thesis, Chalmers University of Technology, Gothenburg, Sweden.

Sandven Rolf, A. Vik, S. Rønning, E.Tørum (2012). Detektering av kvikkleire fra ulike sonderingsmetoder. NIFS rapport nr. 46-2012. Utgitt av NVE.

SGI (2007): Skjuvhållfasthet–utvärdering i kohesionsjord. Information 3.

Skempton, A.W. (1948a). "The ϕ= 0 Analysis of Stability and Its Theoretical Basis", Proc. 2n Intern. Conf. on Soil Mechanics and Foundation Engineering, 1, 72-78.

Tanaka, H. (2000). Sample quality of cohesive soils : Lessons from three sites, Ariake, Bothkennar and Drammen. Soils and foundations 20(4), 57-74

Tavenas, F. and S. Leroueil (1987). State-of-the-art on laboratory and in-situ stress-strain-time behavior of soft clays. Proceedings of the International Symposium on Geotechnical Engineering of Soft Soils, Mexico City, 1–46.

Tavenas, F. and S. Leroueil (1987). State-of-the-art on laboratory and in-situ stress-strain-time behavior of soft clays. Proceedings of the International Symposium on Geotechnical Engineering of Soft Soils, Mexico City, 1–46.

Tergazhi K (1943). Theoritical Soil Mechanics. John Wiley, New York.

Study on the practices for preconsolidation stress evaluation from oedometer tests

P. Paniagua
Norwegian Geotechnical Institute, Norway, priscilla.paniagua.lopez@ngi.no

J.-S. L'Heureux, S.Y. Yang, T.L. Lunne
Norwegian Geotechnical Institute, Norway

ABSTRACT
The preconsolidation stress (p_c') is determined from high-quality oedometer test results by a variety of interpretation methods. Sample quality in the database varies from very excellent to fair (i.e. class 1-2). Results show that the five methods applied give very similar p_c' values when the samples are of good quality, with p_c' varying up to 14% between the five methods.

Keywords: oedometer test, preconsolidation stress, OCR

1 INTRODUCTION

The standard oedometer tests provide the basis for investigating one-dimensional (1D) soil deformation characteristics and soil stress history. During the tests, soft and compressible soil generally exhibit bilinear stress-displacement behavior when the data are plotted on a semi-logarithmic graph. Below a vertical effective yield stress (σ'_{vy}), the displacements are small; and above that threshold value, the soil strains until it reaches a more compressed structured. The σ'_{vy} is known as preconsolidation stress (p_c'). The ratio between p_c' and the *in-situ* vertical effective stress (σ'_v) is known as overconsolidation ratio (OCR).
Most of the clays included in this study are not mechanically over consolidated but have an apparent over consolidation due to aging: an apparent p_c' considered to be created by delayed consolidation (Bjerrum, 1967) and various chemical processes, i.e. not by mechanical unloading. The apparent p_c' is considered as a yield stress that can be estimated from oedometer test results through a variety of methods like those proposed by e.g. Casagrande (1936), Janbu (1969), Pacheco Silva (1970), Butterfield (1979), Becker et al. (1987), Oikawa (1987), Burland (1990), Karlsrud (1991), Jacobsen (1992), Onitsuka et al. (1995) and Boone (2010).

These methods have in common the assumption of a change in soil stiffness from a stiffer to a softer response near p_c'; however, their procedures vary greatly. Ideally, interpretation of p_c' should not depend on the chosen interpretation method nor require subjectivity.
One of the principal objectives of the ongoing internal Strategic Project "SP8- Soil Parameters in Geotechnical Design" (GEODiP) at the Norwegian Geotechnical Institute (NGI) is to help achieving a more consistent interpretation of laboratory and *in-situ* results, and to test/develop procedures for the choice of characteristic design parameters in soft clay. As part of the project SP8-GEODiP, the present work compares the results of applying some of the abovementioned interpretation methods [i.e. Casagrande (1936), Janbu (1969), Pacheco Silva (1970), Becker et al. (1987) and Karlsrud (1991)] for determination of p_c' and OCR on high quality (i.e. fair to excellent) oedometer test results from clay samples collected both on- and off-shore. The purpose is to evaluate the applicability of these methods in a wide range of clays; in order to suggest a more consistent interpretation of p_c'. A short discussion on the evaluation of p_c' on samples of poor quality is presented. Finally, the paper evaluates the interpretation methods in terms of technicalities, source of errors and practical purposes.

2 METHODS FOR EVALUATING P_C'

2.1 Previous works on this topic

After Casagrande (1936) proposed a method for defining the preconsolidation pressure, alternative approaches have been suggested, mostly based on empirical observations regarding the stress and deformations patterns exhibited by the soil during oedometer tests. Grozic et al. (2003, 2005), Clementino (2005) and Boone (2010) present detailed and graphical summaries of these approaches.

In particular, Grozic et al. (2003, 2005) evaluated multiple methods for interpreting p_c' in low plasticity clays and concluded that uncertainties affect all methods, and that some were more difficult and ambiguous than others in application.

As detailed by Boone (2010), scale effects can clearly influence the Casagrande's method. He details also that the conclusion drawn by Grozic et al. (2003) on recommending Becker et al. (1987) and Onitsuka et al. (1995) methods, in addition to Casagrande (1936) and Janbu (1989) methods, may prove difficult and frustrating in practice, and lead to no better results given the level of uncertainty that exist when using these methods.

2.2 Casagrande (1936)

Casagrande (1936) uses an empirical construction from the void ratio, e, and the logarithm of vertical effective stress, σ_v', curve. To determine p_c', a geometrical approach is followed based on Figure 1a: (i) choose by eye the point of minimum radius (or maximum curvature) on the consolidation curve (point A in Fig. 1), (ii) draw a horizontal line from point A, (iii) draw a line tangent to the curve at point A, iv), bisect the angle made by steps (ii) and (iii), (v) extend the straight-line portion of the virgin compression curve up to where it meets the bisector line obtained in step (iv). The point of intersection of these two lines is the most probable preconsolidation stress (point B of Fig. 1). The maximum possible preconsolidation stress is shown as point D while E represents the minimum possible value of the preconsolidation stress.

2.3 Janbu (1969)

Janbu (1969, 1989) suggested to base the determination of p_c' on plots of tangent constrained modulus values versus σ_v'. However, he did not specify in detail how to do the p_c'-determination. The procedure used here is explained in the sketch shown in Figure 1b. Janbu's approach uses the resistance concept. He defined the tangent modulus (or constrained modulus), M, as the ratio of the change in effective stress ($\delta\sigma'$) to the change in strain ($\delta\varepsilon$) for a particular load increment (i.e. $M = \delta\sigma'/\delta\varepsilon$). For a low stress level, around σ'_{v0}, the resistance against deformation (M_0) is large. When σ' increases, this high resistance decreases appreciably owing to partial collapse of the grain skeleton. Resistance reaches a minimum (M_n) around p_c'. Subsequently when σ' is increased beyond p_c', the resistance increases linearly with increasing σ'. In the overconsolidated range M_1 (the average between M_0 and M_n) is often used in design. Behaviour in the normal consolidation stress range can be approximated by a linear oedometer modulus M. Hence, for $\sigma' > p_c'$, $M = m\,(\sigma'-\sigma_r')$ where m is the modulus number and σ_r' is the intercept on the σ' axis and it called the reference stress.

2.4 Pacheco Silva (1970)

The method proposed by Pacheco Silva (1970) to determine p_c' is widely used in Brazil. It uses an empirical construction from the e – log σ'_v curve.

The p_c' is determined graphically as shown in Figure 1c and explained as follows: (i) draw a horizontal line (A–B) passing through the initial void ratio (e_o) of the specimen, i.e., the specimen void ratio before any load has been applied; (ii) extend the straight line portion of the virgin compression curve (C–D) until it intercepts line A–B; (iii) from the point of intersection of lines A–B C–D, draw a vertical line down until it intercepts the e – log p′ curve (Point E); (iv) from Point E draw a horizontal line until it intercepts line C–D (Point F); and then (v) the stress value in the horizontal axis associated with Point F is p_c'. Pacheco Silva (1970) method is independent of the drawing scale (Pinto, 1992).

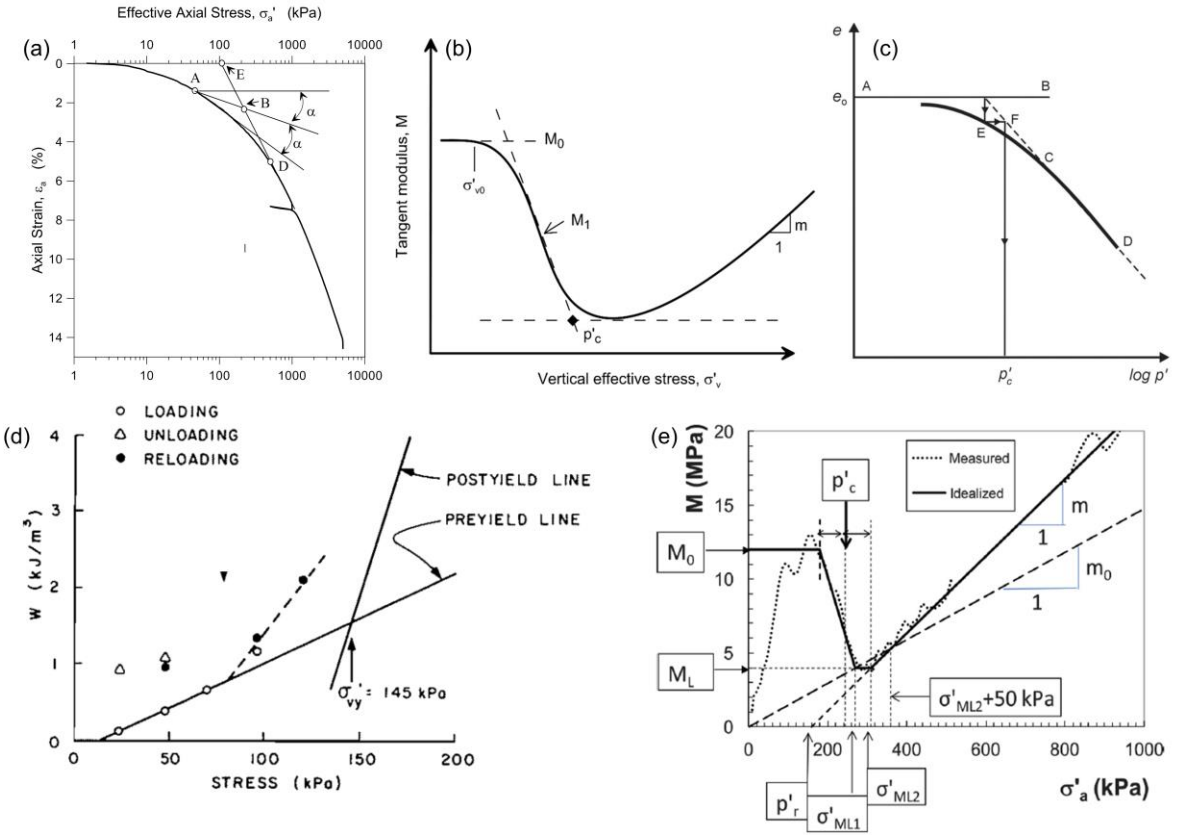


Figure 1. Methods for evaluating p_c': (a) Casagrande (Holtz and Kovacs, 1981), (b) Janbu (Lunne et al. 2008), (c) Pacheco Silva (Grozic et al. 2003), (d) Becker (Becker et al. 1987) and (e) Karlsrud (Karlsrud and Hernandez-Martinez, 2013).

2.5 Becker et al. (1987)

Becker et al. (1987) proposed the work method. They defined the incremental work as:

$$\Delta W_{oed} = \left(\frac{\sigma'_{i+1} + \sigma'_i}{2}\right)(\varepsilon_{i+1} - \varepsilon_i) \quad (1)$$

Where σ'_{i+1} and σ'_i are the effective stresses at the end of i+1 and i loading increments, respectively; and ε_{i+1} and ε_i are the natural strains at the end of i+1 and i loading increments, respectively.

For overconsolidated specimens (Figure 1d), a linear relationship is fitted in the data below *in-situ* stress and the post-yield (i.e. above p_c') data is approximate with a linear relationship. The intersection of those two fitted lines represents p_c'.

2.6 Karlsrud (1991)

Karlsrud (1991) and Karlsrud and Hernandez-Martinez (2013) proposed a slightly modified version of the Janbu (1969, 1989) method.

As detailed in Karlsrud and Hernandez-Martinez (2013), the modulus behaves as follows (see Figure 1e):

a) During loading from zero to the *in-situ* σ_v', the modulus generally increase gradually and then tends to reach a plateau defined as the maximum re-loading modulus, M_0. The modulus then drops off more or less linearly to a minimum level defined as M_L (i.e. M_n), with corresponding stress defined as σ'_{ML1}. After this stress is reached the modulus increases linearly, but for some clays the modulus is constant up to a stress level defined as σ'_{ML2} before it starts to increase linearly. Janbu's modulus number, m, defines the rate of increase beyond this point. This line defines an M = 0 intercept on the stress axis defined as p_r', which is the same definition as used by Janbu (1969). Note that for very stiff as well as disturbed clays, p_r' may be negative.

b) The definition of p_c' is taken as the average stress at which the tangent modulus starts to drop off, until it starts to climb up again along the virgin modulus line.

3 APPLICATION OF METHODS TO INTERPRET P_C'

3.1 Soil index properties

The 169 oedometer tests results (94% as CRSC and 6% as incremental loading - IL) used in the present study come from 18 different sites. The samples were taken with either 72 mm piston sampler, miniblock sampler or block sampler. Table 1 presents a summary of some index properties of the clay materials tested. In particular, water content (w), unit weight (γ_T), plasticity index (IP), clay content (clay) and sensitivity (S_t).

Table 1. Basic properties of the clays studied

Site	w (%)	γ_T (kN/m³)	IP (%)	Clay (%)	St (-)
Eidsvoll	25-35	19-20	13-19	37-48	2-5
Emmerstad	40-48	17-18	3-12	27-40	77-225
Hvalsdalen	31-39	18-20	9-18	40-49	5-20
Kløfta-Nybakk	32-46	18-19	8-19	33-46	7-135
Leirsund	30-39	19	9-18	36-49	5-20
Nybakk-Slomarka	30-45	17-19	7-28	13-67	1-170
Lierstranda	32-42	18-20	13-19	31-36	7-15
Glava	30-35	18-20	15-30	30-60	7-10
Ellingsrud	34-40	18-19	5-8	37	15-61
Klett	25-35	19-20	4-10	30-35	10-240
Kvenild	30-46	17-19	10-14	31-47	22-63
Stjordal	33-43	17-19	7-8	37-38	200
Klett-Bårdshaug	26-35	19-20	6-13	30-33	10-160
Nykirke	25-35	20	4-9	20-55	65-80
Onsøy	60-65	15-16	32-42	20-60	4,5-6
Ghana	90-145	13-15	70-95	45-65	2-6
Johan castberg	22-38	18-20	20-42	30-45	1-3
Bothkennar	66-72	15-16	42-53	17-35	8-13

Table 2. Evaluation of sample quality, after Lunne et al. (1998).

OCR	$\Delta e/e_o$			
1 to 2	< 0,04	0,04-0,070	0,070-0,14	> 0,14
2 to 4	< 0,03	0,03-0,050	0,020-0,10	> 0,10
4 to 6	< 0,02	0,02-0,035	0,035-0,07	> 0,07
Qua-lity	**1: very good to excellent**	**2: good to fair**	**3: poor**	**4: very poor**

3.2 Quality of oedometer tests results

The quality of the samples tested is evaluated based on the initial void ratio and the axial strain at the *in-situ* stress according to the classification proposed by the Norwegian Geotechnical Society (NGF, 2013). This classification is based on Lunne et al. (1998). The quality criteria is presented in Table 2. The data is categorized as high quality (i.e. class 1 and class 2) which varies from good to fair and very good to excellent. Figure 2 shows as an example the variation of sample quality with depth for the data included in the analysis.

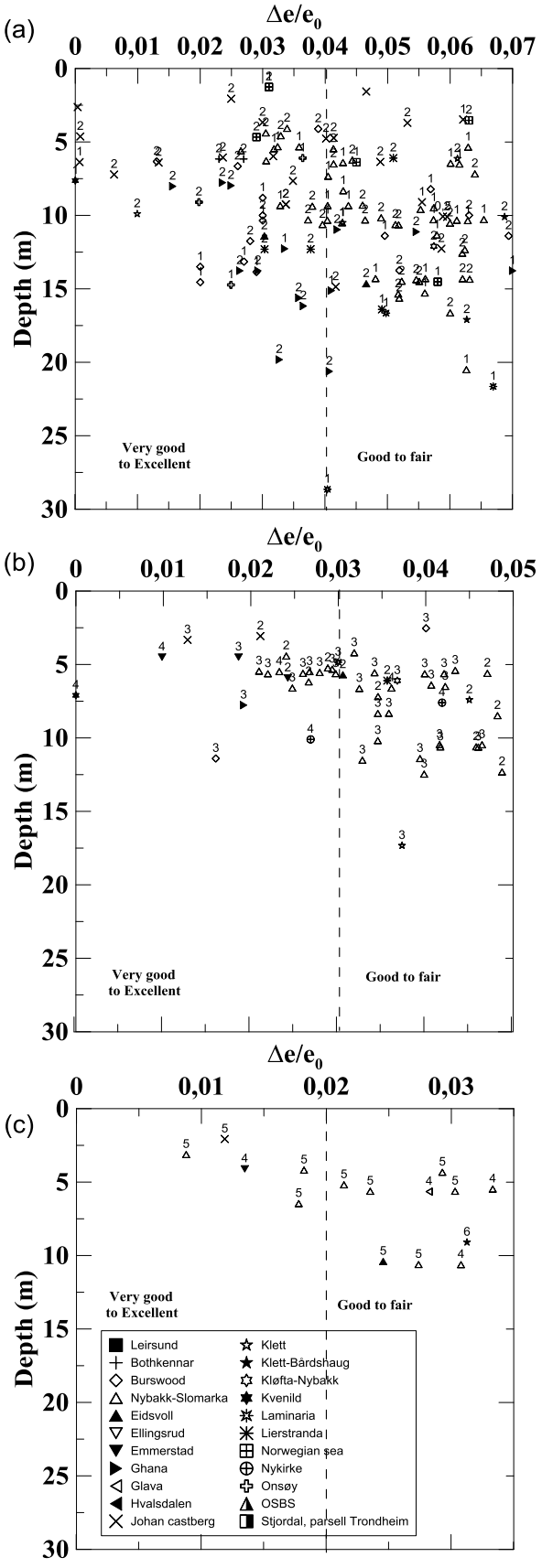


Figure 2. Sample quality for oedometer tests, for OCR between a) 1 and 2, b) 2 and 4 and c) 4 and 6. The OCR is shown over the symbols.

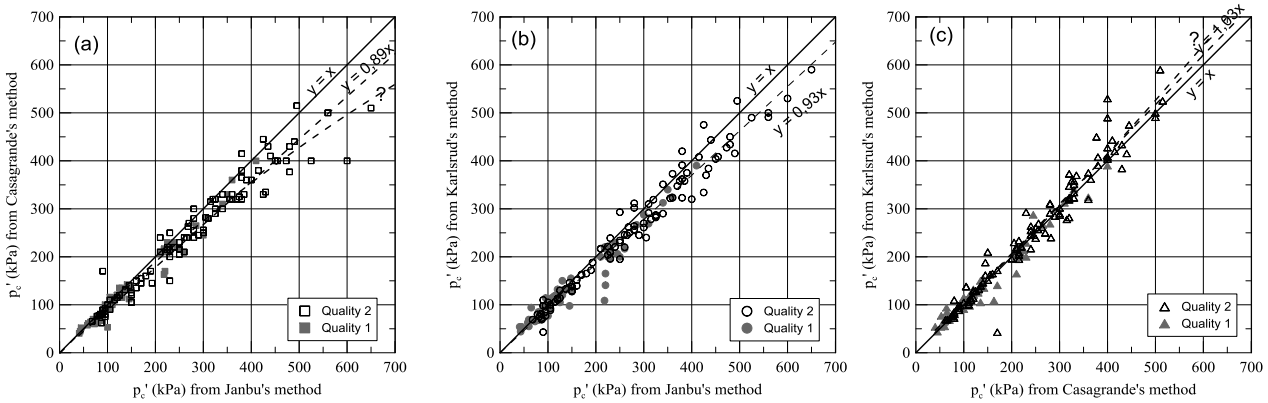


Figure 3. Comparison of p_c' obtained by: a) Janbu's and Casagrande's methods, b) Janbu's and Karlsrud's methods and c) Casagrande's and Karlsrud's methods.

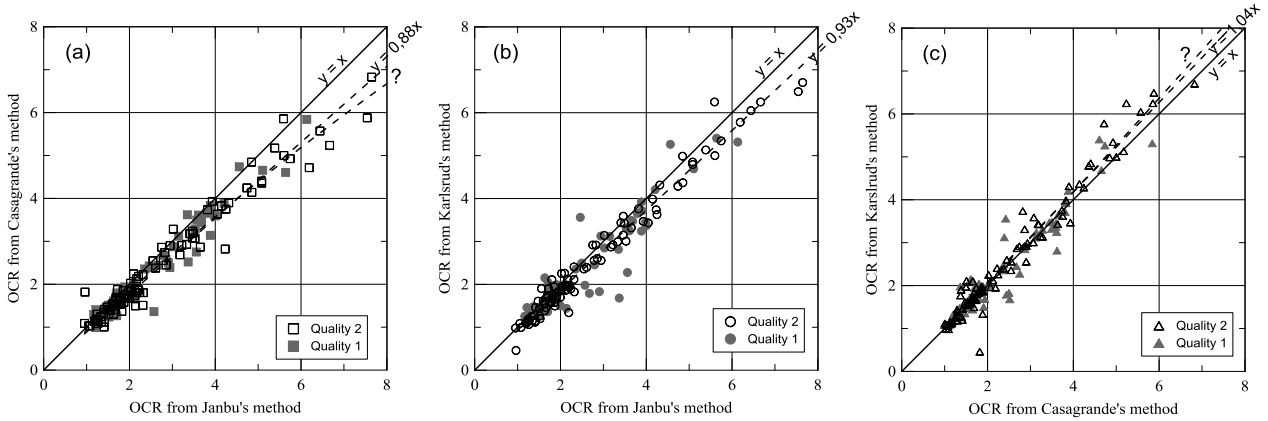


Figure 4. Comparison of OCR' obtained by: a) Janbu's and Casagrande's methods, b) Janbu's and Karlsrud's methods and c) Casagrande's and Karlsrud's methods.

3.3 Results and interpretation

Figure 3 and Figure 4 show the values of p_c' and OCR obtained with Casagrande's, Janbu's and Karlsrud's approaches. These methods give very similar values. Janbu values tend to be slightly higher than Casagrande (as observed by Grozic et al. 2003) and Karlsrud values. Karlsrud's and Casagrande's methods seem to result in similar values.

The values show more scatter for high $p_c'$and higher OCR that adds uncertainties to the data. It seems that the data with quality 2 tend to add more deviation to the expected trend. Some exceptions are observed for data with quality 1, that come from Johan Castberg and Kvenild sites. Data from Johan Castberg site was difficult to interpret regarding the definition of the tangents in the graphical methods. Kvenild data is reported as quality 1 data, however, this couldn't be confirmed by $\Delta e/e_o$ values. The p_c' and OCR values vary between 4-12%. These differences are more visible for high values of p_c' (i.e. p_c' > 400-500 kPa) and OCR (i.e. OCR > 4).

In particular, the differences up to 12% are between Janbu's and Casagrande's methods, and Janbu's and Karlsrud's methods. This result is somehow surprising considering that the Janbu's and Karlsrud's methods are based on the same assumptions. However, in Karlsrud's method, p_c' is calculated as an average from two single values whereas in Janbu's method p_c' is a single point.

Since all of them are graphical methods, the interpreter must have good plot resolution (large enough scale in the range of analysis) in order to clearly define tangents and choose the values with high accuracy.

Karlsrud and Hernandez-Martinez (2013) comment that a comparative study of different other methods for defining p_c' from oedometer tests was applied to 15 of the oedometer tests in the database used by them. Karlsrud's method comes out just about equal to the average of the other methods (0,8% on the high side). Our data shows a higher deviation (i.e. up to 7,5%) when the quality of the sample decreases, and the p_c' and OCR increases.

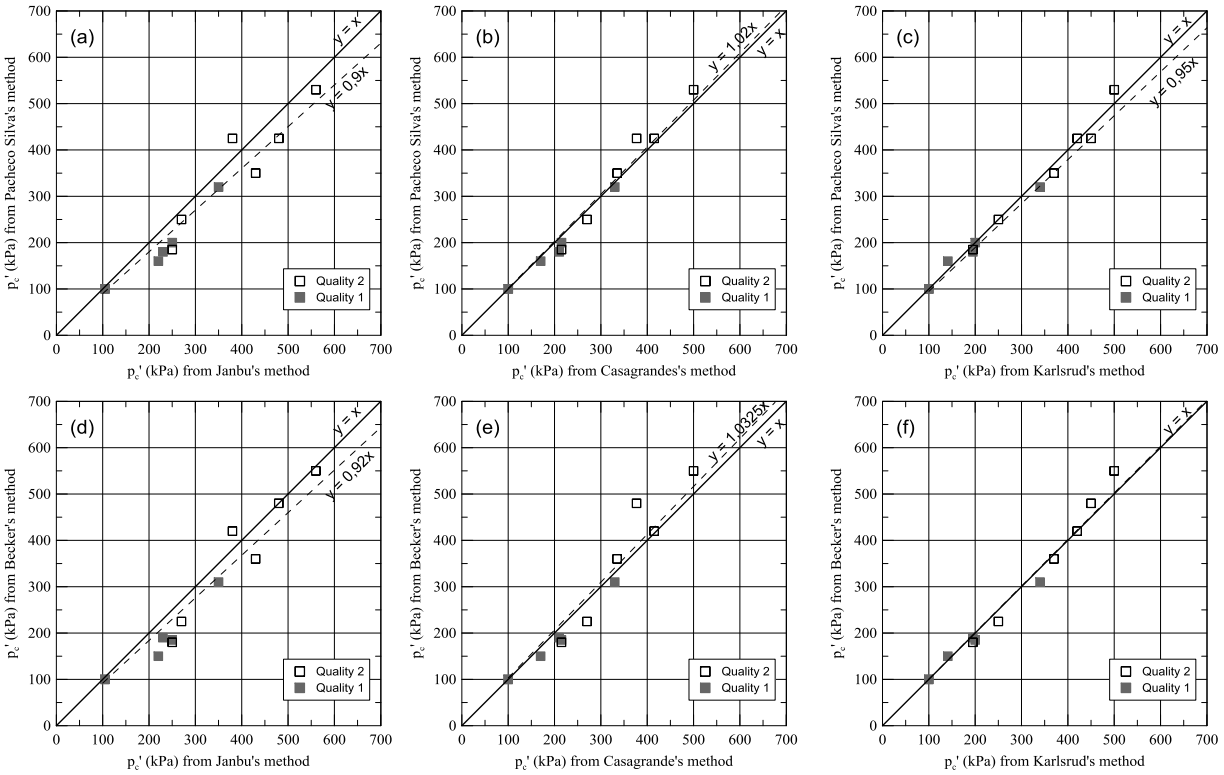


Figure 5. Comparison of p_c' obtained by: a) Pacheco Silva's and Janbu's methods, b) Pacheco Silva's and Casagrande's methods, c) Pacheco Silva's and Karlsrud's methods, d) Becker's and Janbu's methods, e) Becker's and Casagrande's and f) Becker's and Karlsrud's methods.

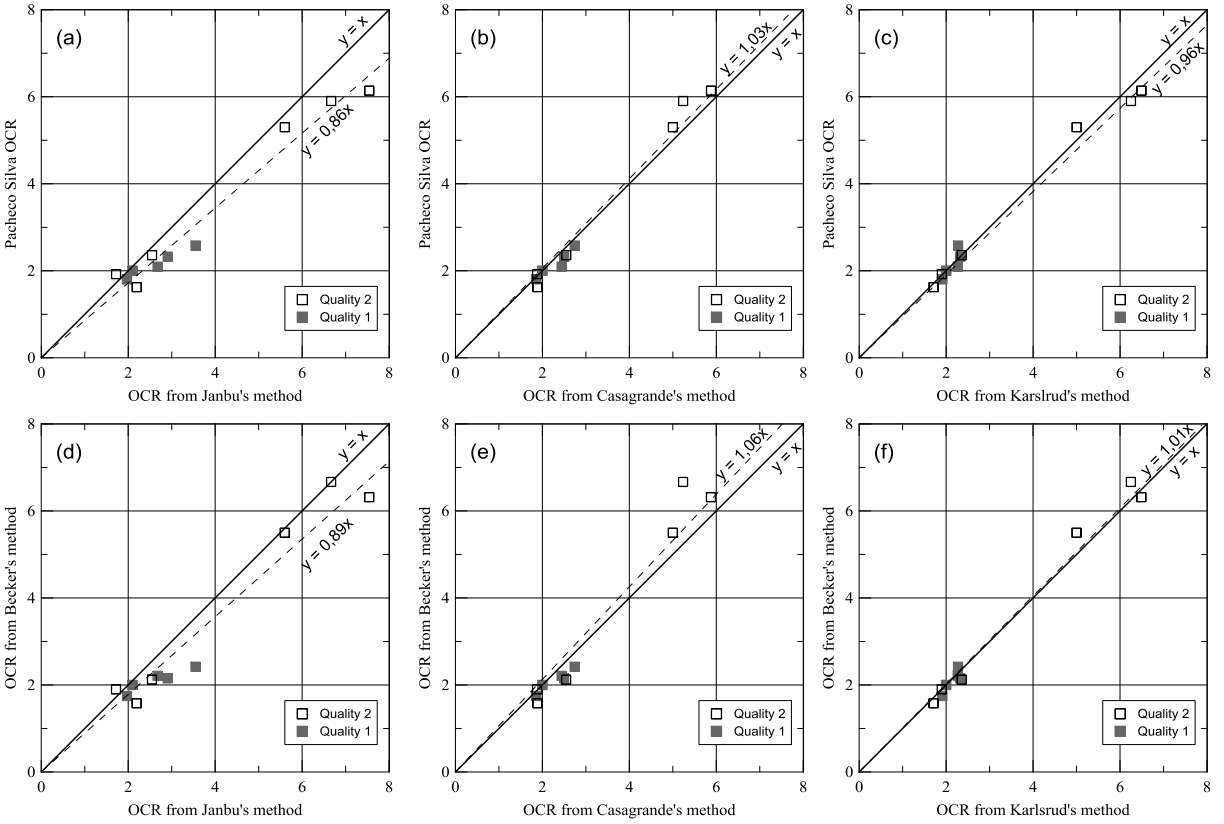


Figure 6. Comparison of OCR obtained by: a) Pacheco Silva's and Janbu's methods, b) Pacheco Silva's and Casagrande's methods, c) Pacheco Silva's and Karlsrud's methods, d) Becker's and Janbu's methods, e) Becker's and Casagrande's and f) Becker's and Karlsrud's methods.

Internationally, most oedometer tests are performed as IL tests (with 24 h load steps). The test in the database used in the present study are mostly CRSC tests. It is generally observed that, p_c' from IL tests will be 15 - 20% lower than CRSC tests.

3.4 Additional methods applied to samples with variable quality

Twelve tests results of the ones studied with Casagrande (1936), Janbu (1969) and Karlsrud (1991) methods (i.e. tests with quality 1 and quality 2, six of each one) were chosen to apply Pacheco Silva (1970) and Becker et al. (1987) methods. In addition, six tests results with quality 3 were included to study the effect of sample quality in the application and determination of p_c'.
Figure 5 and Figure 6 shows the values of p_c' and OCR obtained with these approaches for the different specimens evaluated. As observed before, Janbu's method tends to have higher values of p_c' than the other methods. When compare to Pacheco Silva's method, Janbu's method results up to 14% difference in OCR and 10% difference in p_c'. Pacheco Silva's and Becker's methods fit pretty well with Casagrande's and Karlsrud's methods. Some differences up to 5% are observed between the estimated values of p_c' and OCR. More deviation from the expected trend is observed for high p_c' (i.e. p_c' > 500 kPa) and OCR (i.e. OCR > 4-5) values, and in particular for samples with quality 2 and 3. The difference between Pacheco Silva's and Becker's methods reach 6% for p_c' and OCR.

4 EVALUATION OF METHODS

After these results, no strong p_c' and OCR variations are observed for high quality samples interpreted using Casagrande's, Karlsrud's, Pacheco Silva's and Becker's methods. Janbu's method gives the highest deviations. One reason could give at Janbu's method does not clearly specify the steps to follow for a graphical interpretation, therefore, it depends on the own user experience and judgement. The observation that more scatter is observed for high p_c' and OCR values might be due to the fact that a soil specimen undergoes higher reloading behaviour after sampling and unloading, or recompression, up to the point at which it reaches first the *in-situ* condition and then the apparent p_c' it has experienced in the past, and then the "virgin" compression beyond p_c'. This unloading-reloading process might cause more disturbance in the skeleton and therefore quality reduction.
When comparing all methods, a very significant difference is that Casagrande's method and Pacheco-Silva's method as well as most international methods use double logarithmic scales. Whereas Janbu's method suggests that a linear scale should be used to avoid misinterpretations since double logarithmic scales can hide large scatter in the data.
One of the main difficulties in applying the graphical methods is the definition of the tangents to the data. Usually a stress-deformation curve from a CRSC odometer test has more data points than traditional incremental loading methods and the "best-fit" lines require some judgement and subjectivity.

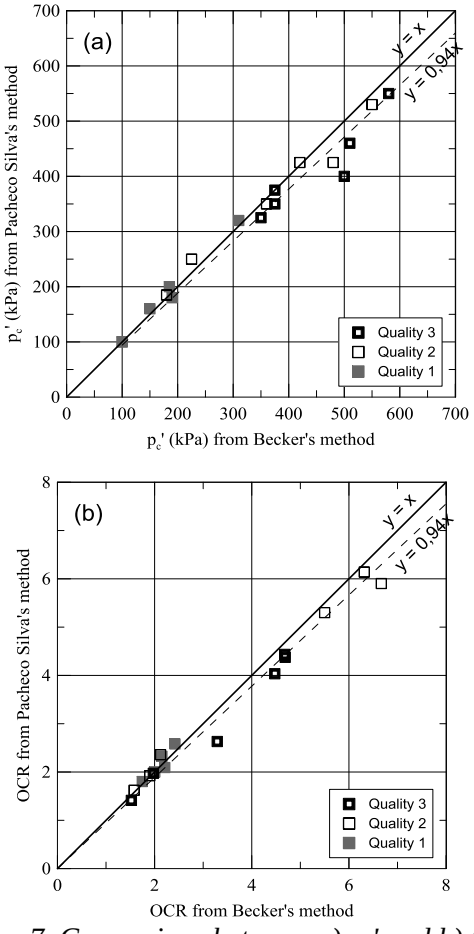


Figure 7. Comparison between a) p_c' and b) OCR from Pacheco Silva's and Becker's methods.

Table 3. Final evaluation of the p_c' interpretation methods applied in the present study

Method	Technicalities	Source of errors	Practicalities	
All the methods	Tangent or "best-fit" lines definition	Subjectivity Scale of the plot (type)	Easy if scale is large	Difficult if scale is small
	Calculation / reading of p_c'	Scale of the plot (size)	Difficult if scale is large	Easy if scale is small
Janbu Becker Karlsrud	Additional calculations (i.e. incremental work or deformation modulus)	Calculation mistakes	Extra time and effort required	
Casagrande	Definition of highest curvature point	Subjectivity	Difficult, it requires judgement	
Janbu	Undefined procedure	Subjectivity	Difficult, it requires judgement and experience	

In particular, it was experienced during the application of the methods, that a small change in the slope of the tangents produced significant changes in p_c'. In addition, the scale type of the plot might increase the difficulties regarding reading the stress values.

Table 3 presents a final evaluation of the methods in terms of technicalities (i.e. small details of the procedure), source of errors and practical purposes (i.e. according to the experience of its application for p_c' determination).

5 CONCLUSIONS

Interpretation of 129 oedometer test results show that, in general, the value of p_c' and OCR does not depend on the interpretation method used when evaluating high quality samples. This is especially true for low values of preconsolidation stress and overconsolidation ratio.

For samples having high values of p_c' and OCR, differences in interpretation methods can lead up to 14% in estimates of p_c' and/or OCR.

In practice, we recommend to employ at least three different methods for evaluating p_c' and OCR. This will guarantee a more consistent choice of parameters for a given user and project. In case of doubts and to reduce uncertainties, evaluation of p_c' and OCR should be performed and/or checked by a colleague.

This work does no pretend to conclude which method is correct. As Becker et al. (1988) mentioned "... the issue is which technique provides the most repeatable result and is least ambiguous."

6 REFERENCES

Becker, D.B., Crooks, J.H.A., Been, K., & Jefferies, M.G. (1988). Work as a criterion for determining *in-situ* and yield stresses in clays: Reply. Can. Geotech. J. 25, 848-850.

Becker, D.R., Crooks, J.H.A, Been, K. & Jefferies, M.G. (1987). Work as criterion for determining *in-situ* & yield stresses clays. Can. Geotech. J. 24: 549-564.

Bjerrum, L. (1967). Engineering Geology of Norwegian Normally-Consolidated Marine Clays as Related to Settlements of Buildings. Géotechnique 17: 83-118.

Boone, S.J. (2010). A critical reappraisal of "preconsolidation pressure" interpretations using the oedometer test. Can. Geotech. J. 47, 281-296.

Burland, J.B. (1990). On the compressibility & shear strength of nat. clays. Géotechnique 40: 329-378.

Butterfield, R. (1979). A natural compression law for soils. Géotechnique 24: 469-479.

Casagrande, A. (1936). The determination of the preconsolidation load and its practical significance. Proc. First Intern. Conf. on Soil Mech. & Found. Eng., Cambridge, 60-64.

Clementino, R.V. (2005). Discussion: An oedometer test study on the preconsolidation stress of glaciomarine clays. Can. Geotech. J. 42, 972-974.

Grozic, J.L.H., Lunne, T. & Pande, S. (2003). An oedometer test study on the preconsolidation stress of glaciomarine clays. Can. Geotech. J 40, 857-872.

Grozic, J.L.H., Lunne, T. & Pande, S. (2005). Reply to the discussion by Clementino on: "An oedometer test study on the preconsolidation stress of glaciomarine clays". Can. Geotech. J 42, 975-976.

Holtz, R.D. & Kovacs, W.D. (1981). An Introduction to Geotechnical Engineering. Prentice-Hall, Inc., New Jersey, 733.

Jacobsen, H.M. (1992). Bestemmelse af forbelastningstryk i laboratoriet. Proceedings of Nordiske Geotechnikermonde NGM-92. Danish Geotechnical Society, Bulletin 9, 455-460.

Janbu, N. (1963). Soil compressibility as determined by oedometer and triaxial tests. Proc. Euro. Conf. on Soil Mech. and Found. Eng. 1, 19-25.

Janbu, N. (1989). Grunnlag i Geoteknikk, Trondheim: Tapir.

Karlsrud, K. & Hernandez-Martinez, F.G. (2013). Strength and deformation properties of Norwegian clays from laboratory tests on high-quality block samples. Can. Geotech. J. 50, 1273-1293.

Karlsrud, K. (1991). Sammenstilling av noen erfaringer med prøvetaking og effekt av prøveforstyrrelse i norske marine leire. NGI report 521500-6.

Lunne, T., Berre, T. & Strandvik, S. (1998). Sample disturbance effects in deepwater soil investigations. Conf. Soil Invest. Found. Behav., London.

Lunne, T., Berre, T., Andersen, K.H., Sjursen, M., & Mortensen, N. (2008). Effects of sample disturbance on consolidation behaviour of soft marine Norwegian clays. Proc. 3rd Int. Conf. on Site Charact. ISC'3, Taipei, 1471-1479.

NGF (2013). Veiledning for prøvetaking, melding nr. 11.

Oikawa, H. (1987). Compression curve of soft soils. Soils and Foundations 27, 99–104.

Onitsuka, K., Z. Hong, Y. Hara, & S. Yoshitake. (1995). Interpretation of oedometer test data for natural clays. Soils and Foundations 35, 61–70.

Pacheco Silva, F. (1970). A new graphical construction for determination of the pre-consolidation stress of a soil sample. Proceedings 4th Brazilian Conference Soil Mechanincs and Foundation Engineering, Rio de Janeiro, 225-232.

Pinto, C.S. (1992). First Pacheco's Silva conference – Part I: Distinguished aspect of Pacheco Silva's activities. Brazilian Geotechnical Journal (Solos e Rochas), ABMS-ABGE. 15 (2), 49–87.

Physical modeling and numerical analyses of vibro-driven piles with evaluation of their applicability for offshore wind turbine support structures

Aligi Foglia
Fraunhofer Institute for Wind Energy and Energy System Technology (IWES), Germany, aligi.foglia@iwes.fraunhofer.de

Martin Kohlmeier and Maik Wefer
Fraunhofer Institute for Wind Energy and Energy System Technology (IWES), Germany

ABSTRACT

Vibro-driven piles can potentially become cost-reducing alternatives to standard impact-driven piles for offshore wind turbine support structures. If these foundations are to be used to support jacket sub-structures, their bearing behaviour in tension has to be explored. In a novel geotechnical testing facility two large-scale vibro-driven piles for jacket sub-structures have been axially tested in tension. In this contribution the experimental tests are thoroughly described and the test results are presented. The applicability of standard CPT methods in predicting the tensile bearing capacity of the piles is evaluated against the experimental results. In addition, a simplified 2D axisymmetric numerical model is adopted to interpret the initial stiffness of the pile-soil interaction. As also pointed out in previous studies the ultimate resistance of the piles turns out to be significantly smaller than the CPT method prediction. Furthermore, as expected, set-up and pre-loading effects are seen to be beneficial to the tensile bearing behaviour of the pile.

Keywords: vibro-driven piles, offshore foundations, large-scale tests.

1 INTRODUCTION

Offshore wind energy is a necessary part of the present and future European energy mix. As reported in Valpy (2014) and Fichtner (2013) the levelised cost of energy (LCOE) decreases for large turbine rated power. Relevant offshore wind potential is still untapped in water depths exceeding 45-50 m. In such water depths, large wind converters will be most likely supported by jacket structures founded on piled foundations. Most offshore piles are installed with impact-driven piles, whose noise must be reduced with expensive techniques in order to limit the damage on sea mammals, as required by the German authority BSH (2013). In sandy soils a viable alternative to impact-driven piles are vibratory-driven piles. Instead of applying a number of strikes on the pile head to penetrate the foundation into the soil, vibratory drivers grip the pile head and apply quick sequences of downward and upward motions to the pile in order to reach the required embedded length. As also presented in Matlok (2015) vibro-driven piles offer, with respect to impact-driven piles, the following advantages:

- No noise mitigation system required when installing
- Faster installation
- No fatigue induced by impact-driving (potential saving in steel for piles)

These advantages might bring savings in the range of 5% to 10% of foundation fabrication and installation costs (Matlok, 2015).

Piles supporting jacket structures (diameter between 1.5 m and 4 m) are mainly subjected to vertical loading in tension and compression. The axial capacity of a piled foundation under compressive loads has two contributions: the base resistance and the shaft resistance. In sandy soils the shaft resistance is assessed based on the CPT cone resistance whereas in clayey soils it is quantified as a function of the undrained shear strength. The ultimate base resistance is defined with an allowable vertical displacement criterion and is calculated by summing the contributions of external pile shaft resistance, base resistance and either soil plug or internal pile shaft resistance. Obviously, in case of tensile loading, the base resistance has no influence on the pile capacity. As emphasized in recent publications (Igoe et al., 2013; Achmus et al., 2015) the tensile loading of piles supporting multipod sub-structures for offshore wind turbines are very important and can in some cases be the design driver.

This paper describes a large-scale experimental campaign investigating vibro-driven piles subjected to tensile loading. The experimental results are then interpreted to estimate the economical viability of this relative novel technology for offshore wind.

1.1 Specific aims of the study

Research on vibro-driven piles has so far focused on installation analysis (Viking, 2002), onshore piles subjected to compressive loading (Lammertz, 2008; Borel, 2006) and offshore piles subjected to overturning moment (LeBlanc et al., 2013). With respect to piles predominantly subjected to axial loads, it is not yet clear whether the economic advantages mentioned above would be able to outweigh a potential increase in pile dimension due to limitations in bearing capacity. In other words, the cost reduction previously outlined can have an impact on the project economics only if vibro-driven piles have similar capacity to the traditionally adopted impact-driven piles. Thus, the first specific aim of this study is to understand whether the ultimate tensile capacity predicted with the standard CPT-methods gives comparable results to the large scale test data presented in this contribution. Another crucial analysis for the complete understanding of the soil–structure interaction concerns the initial axial stiffness of the geotechnical system. The second specific aim of the contribution focuses on this aspect for the axially loaded pile. A 2D axisymmetric finite element model with a simplified pile is validated in terms of initial stiffness against the test results.

The test campaign and the data interpretation was carried out within the European Union-funded project INNWIND.EU which aims at investigating innovative key components of wind turbines with rated capacities between 10 MW and 20 MW.

2 LARGE-SCALE TEST DESCRIPTION

The experimental campaign has been executed by Fraunhofer IWES in the new Test Centre for Support Structures of the Leibniz University in Hannover. Among others, the research facility accommodates a foundation test pit which consists of reinforced concrete walls containing 9 m wide, 14 m long and 10 m deep volume of sand. Abutment walls on one side of the pit and various displaceable steel frames, allow for testing offshore wind foundations subjected to different loading conditions. A picture of the empty sand pit is shown in Figure 1.

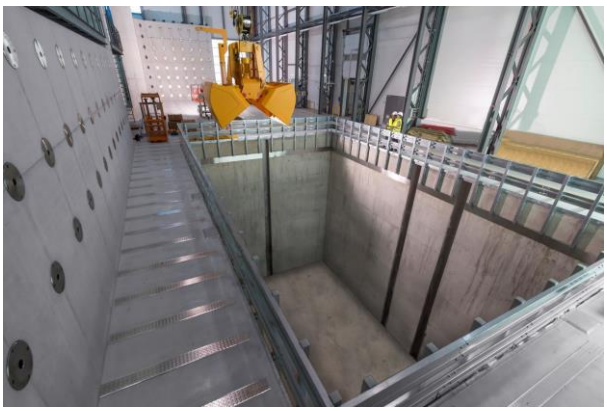


Figure 1 Sand pit of Test Centre before sand filling. Dimensions: 9 m x 14 m x 10 m.

Table 1 Properties of Rohsand 3152.

Property	Symbol	Unit	Value
Maximum void ratio	e_{max}	-	0.83

Minimum void ratio	e_{min}	-	0.44
Specific gravity	G_s	-	2.65
Coefficient of uniformity	C_u	-	1.97
Coefficient of curvature	C_c	-	0.98
Grain diameter to 60% passing material	d_{60}	mm	0.407

The testing material used is uniformly graded siliceous sand called Rohsand 3152, which was provided by the company Schlingmeier Quarzsand GmbH & Co. KG based in Schwülper, Germany. The fundamental properties of the sand are presented Table 1.

2.1 Preparation of the sand sample

High-quality geotechnical experiments require systematic sand preparation procedures to obtain:

- Uniform samples
- Repeatable samples
- A designated degree of compaction

In the present experimental campaign the aim was to create medium dense to dense sand condition (relative density, *Dr* between 55% and 70%), which is representative for sandy deposits of the North Sea. In order to achieve these, the sand was poured into the pit and compacted in subsequent layers. The compaction was performed with direction plate compactors. The sand layers had a thickness of about 30 cm before the compaction which reduced to 25 cm after the compaction. The first three meters from the bottom were prepared with an initial thickness of 50 cm.

2.2 Property of the piles

Two identical piles (Pile 1 and Pile 2), made of steel S355, were installed and subsequently tested. The dimensions of the piles are diameter, D = 0.508 m, length, L = 7,5 m (embedded length L_e = 6 m) and wall thickness, t = 6.3 mm. In order to be able to install and test the pile, a flange to which adaptors for installation and tensile test can be adjusted was appropriately designed. The scale of the model is between 1:4 and 1:8 depending on the prototype considered.

2.3 Assessment of the soil properties

Three soil investigation techniques were adopted to assess the sand status after the soil preparation procedures:

- Soil core samples (CS)
- Dynamic probe light (DPL)
- Cone penetration test (CPT)

The sand pit area was equally divided into six sub-areas. The soil samples were carefully taken with a cylindrical soil sampler (diameter 10 cm, length 12 cm) from every sub-area after each compacted layer. The relative density (*Dr*), averaged over the six sub-areas is plotted against depth in Figure 2. The relative density ranges between 0.55 and 0.72 with an average value of 0.61. It is worth to mention that the relative density calculated with soil core needs neither empirical parameter nor sophisticated empirical equation to be evaluated, and is therefore highly reliable. Thus, the curve referring to soil core samples depicted in Figure 2 is utilized further in this section as mean of comparison to validate the empirical

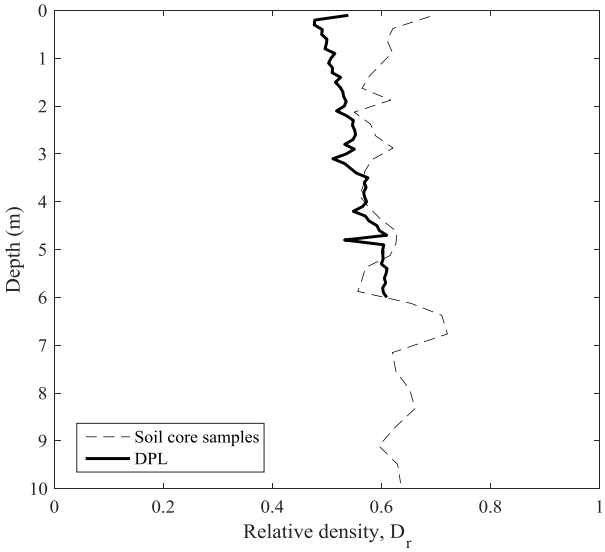


Figure 2 Average relative density calculated over the cross area according to CS and DPL.

methods necessary to evaluate *Dr* with DPL and CPT. Information on the sand pit uniformity can be acquired by calculating the coefficient of variation (COV) of the relative density data of the six samples for each compacted layer.

The COV shows very moderate values (between 0.02 and 0.12), revealing uniform

relative density across the sand pit and small variation with depth.

To gain more insight into uniformity and to predict parameters of the soil, dynamic probing tests (DPLs) and cone penetration tests (CPTs) were performed. More importantly, CPTs were necessary to be able to use CPT-based methods for axially loaded piles (API, 2011). In Figure 3 a plan view of the sand pit with indication of the inspection points (IPs) referring to CPTs and the position of the piles installed, are shown. DPLs and CPTs were performed closed to each other (0.5 m distance) on purpose, to gain a correlation law between the two methods of investigation. DPLs were conducted down until 6 m whereas CPTs down until 9.4 m.

In Figure 2 the average relative density over the cross area on the base of DPLs data, calculated according to EN (1997), is plotted against depth. The soil core samples curve shows good match with the DPLs curve only from a depth of about 3 m. This corroborates the well-known fact that cone resistance is dramatically influenced by the very low confining stresses characteristic of sand at shallow depths.

In Figure 4 the CPT profiles of all the IPs are depicted. The cone tip resistance (*qc*), between 1m and 7m of depth, presents values ranging from 5 to 23 MPa. Approximately the last three meter (roughly between 7m and 9.4m), *qc* decreases. This is most probably due to the different preparation system used in that specific region of the sample. It should be noticed though that this inconsistency will not negatively affect the test results. Indeed, the tensile bearing capacity of piles does not involve soil below the pile but almost exclusively soil adjacent to the pile shaft.

A peek up to 35 MPa in tip resistance can be seen at a depth of 6.2 m. This occurred in position IP3 where most probably the cone came across a stone.

When interpreting CPT data of real sites, it is common to use relationships correlating CPT tip resistance and relative density of the sand (see Baldi et al., 1986; Clausen et al., 200: DIN, 2002; Puech et al., 2002). These approaches are also used here in an attempt to understand which method is the most suitable given the experimental condition described above. The estimation of *Dr* based on the average value of *qc* (across the area of the pit) is plotted against the depth according to four different approaches in Figure 5.

It must be mentioned that these approaches were thought for real scale data and much larger depths. Their applicability in moderate depth (namely 10 m) is not obvious.

By observing Figure 5, it is immediately apparent that the four approaches give very different *Dr* values, particularly within the first two to three meters. This is not surprising, and can be ascribed to the influence of low confining pressure on the cone resistance (see Puech et al., 2002). However, the four approaches seem to be more consistent to each other with increasing depth, as it should be expected. The method Puech et al. (2002) is clearly the most suitable for the sand pit, at least for the first two to three meters. This is a reassuring observation since this particular method was formulated ad hoc for shallow penetration CPTs.

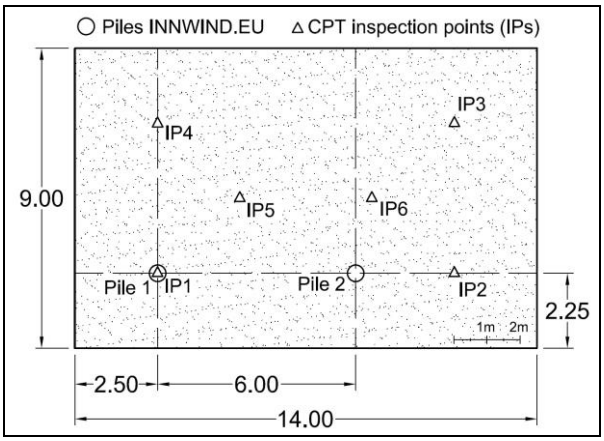


Figure 3 Plan view of the sand pit with indication of the inspection points (IPs) for CPT.

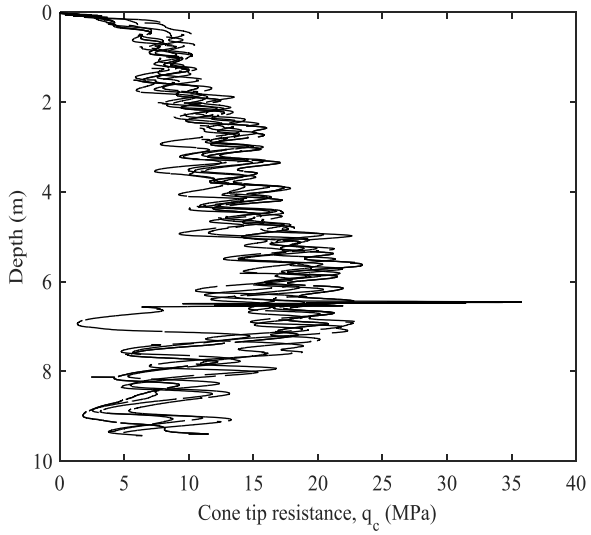


Figure 4 CPT profiles of all the inspection points.

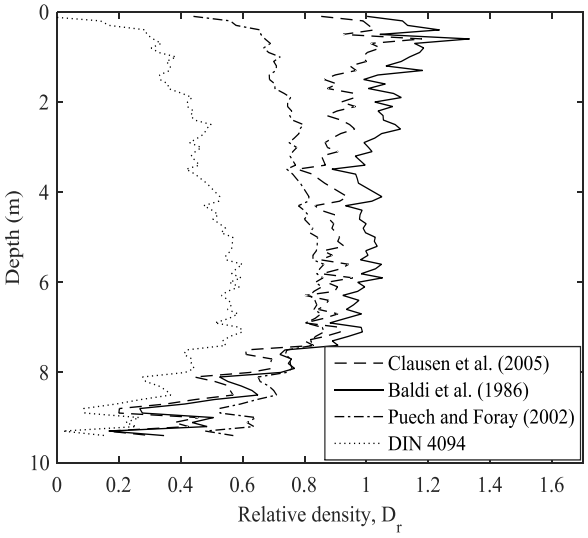


Figure 5 Interpretation of CPT data. Relative density according to four different methods.

From three to seven meter down, the method overestimates *Dr* by 15%. The methods Clausen et al. (2005) and Baldi et al. (1986) overestimate the *Dr* quite remarkably at shallow depth for then being more consistent at six to seven meters depth. The method DIN (2002) underestimates *Dr*, particularly in the first meters. Down at six to seven meters depth DIN (2002) seems to give very appropriate values of *Dr*.

2.4 Test phases

In this section, all the steps overtaken before and during the tensile tests are described. As already mentioned before in the paper, the two piles installed are named Pile 1 and Pile 2. Pile 1 was installed first and was subjected to pre-loading before being tested under tensile loading. Pile 2 was installed thereafter and was only subjected to tensile loading until failure. A picture of the test setup with both piles indicated is shown in Figure 6. During the tensile loading tests the piles were monitored with load cell of the actuator, displacement transducer of the actuator and external displacement transducer. The actuator used for the test has a capacity of 500 kN. The external displacement transducer was installed in order to enable a system-independent measurement of the pile uplift during tensile loading. The external transducer and the internal transducers of the actuator are connected to an analyzer unit which in turn broadcasts the signal to the computer unit where the data are stored with a sampling frequency of 100 Hz.



Figure 6 Picture of the test setup just before the tensile loading test of Pile 2.

The installation of the piles was carried through by an external firm specialized in deep foundations. Pile 1 was installed on February 5th, 2015. Pile 2 was installed on August 6th, 2015. The installation was performed by an excavator. The vibratory hammer was connected to the arm of the excavator which in turn grabbed the adaptor placed at pile head.

The pile penetrated the sand with a velocity of approximately 0.1 m/s. Pile 2 was installed with a vibrator type ICE 8RFB, which has a frequency of 14 Hz. Pile 1 was

installed with a vibrator type Müller MS-5 HFBV, which has a frequency of 45 Hz.

As already mentioned, Pile 1 was subjected to relevant pre-loading before being axially tested in tension. The pre-load applied in this phase consisted of cyclic horizontal quasi-static load with different amplitudes. Additionally, a 0.9 m deep scour was artificially created. In this manner the influence of set-up effect (about 200 days after the installation), scour, installation frequency and pre-loading were to be explored. Given the scale of the system it was not possible to apply the different effects to more than one foundation. As a result of that the implications of these affecting variables could not be possibly decoupled. However, it is well known that the set-up effect is generally beneficial to the bearing behavior of piles as also recently reported by Lehane et al. (2005). Further, scouring phenomena are doubtlessly negative for the bearing behavior. The question arises as whether pre-loading produces beneficial of detrimental effects on the pile shaft capacity. This query could unfortunately not be answered within this experimental campaign.

A very robust steel structure formed by two vertical columns and supporting a horizontal beam was employed to offer the necessary counterweight to the system (see Figure 6). The 500 kN hydraulic cylinder (actuator) was connected to the beam on one side and, by means of a steel adapter plate, to the flange of the pile. A picture of the setup for Pile 2 is illustrated in Figure 7 where displacement transducer, pile and actuator are indicated. The test was performed in a displacement-controlled manner. To make sure that no pore pressure building up could possibly occur during the tensile loading test, a very low displacement rate (0.01 mm/s) designated. This displacement rate was also confirmed by the external displacement transducer.

Before the tensile loading test a difference of 82 cm between soil on the inside and on the outside of the pile was measured (Plug length Ratio of 86%). After the test the difference between soil level in and soil level out the pile was measured again with the same result. This proves that the behavior of the pile was substantially fully plugged during the tensile loading test.

3 PRESENTATION AND INTERPRETATION OF THE EXPERIMENTAL DATA

A magnified view of the curves for the first 10 cm vertical displacement is depicted in Figure 8. The entire load-displacement curve for both tests is shown in Figure 9 together with the CPT methods predictions. In the initial 0.4 mm of vertical displacement the curves appear to be identical. After this similar initial stiffness branch, it is evident that the two piles show essentially different behaviours. Pile 2 keeps hardening for the whole test showing no peak capacity. Pile 1 shows a distinct peak resistance in correspondence to a displacement of about 6 mm (≈1/100 *D*). The ultimate capacity of Pile 1 is 177 kN and was taken as the peak load reached at circa 6 mm of displacement. The ultimate capacity of Pile 2 is 115 kN and was taken according to the well-established 1/10 *D* criterion. Even disregarding the negative presence of the scour and the higher installation frequency, set-up and pre-loading effects seem to benefit the tensile ultimate resistance by 53%.



Figure 7 Pile 2 before the tensile loading test.

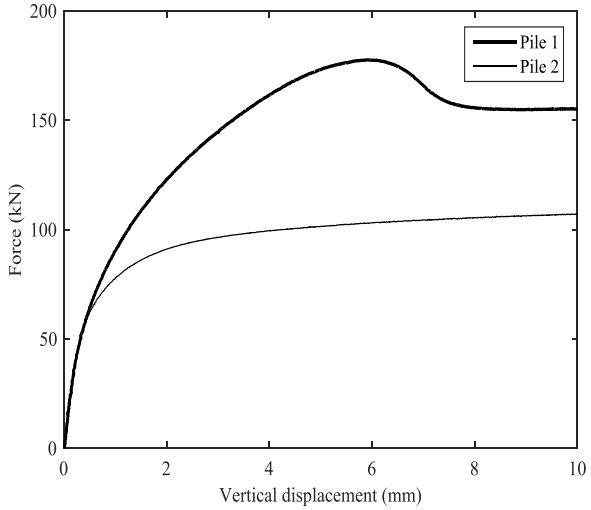


Figure 8 Load-displacement curve of both piles. Initial 10 mm of vertical displacement.

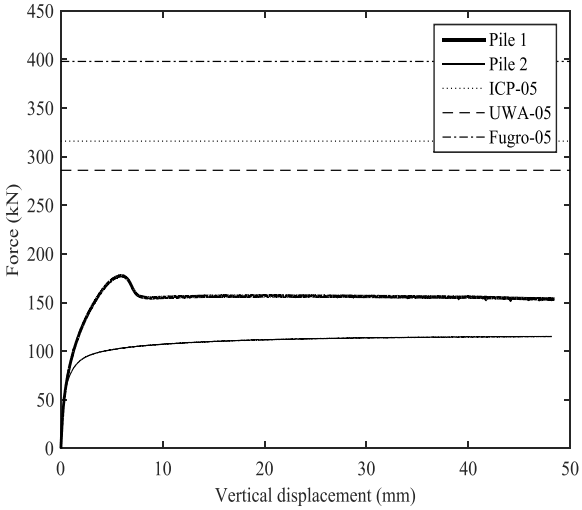


Figure 9 Experimental data in comparison to CPT methods prediction.

3.1 Interpretation of the ultimate resistance by means of the CPT methods

The applied CPT methods for axially loaded piles are the empirical formulas developed by the four different research groups: Imperial College (ICP), University of Western Australia (UWA), Norwegian Geotechnical Institute (NGI) and Fugro. They relate CPT measurements with the axial capacity in tension and in compression of purely axially loaded piles. A comprehensive and comparative review of the methods is given in Lehane et al. (2005). The methods are also included in the offshore foundation standard API (2011) with the names ICP-05, UWA-05, Fugro-05 and NGI-05. This nomenclature will be retained in this paper as well. The calculations concerning CPT-methods presented in this report were performed with the IGtHPile software developed by the Institute of Geotechnical Engineering (IGtH), Leibniz Universität Hannover, Germany.

Usually, the input data for CPT methods are an average of raw CPT data calculated over a specified distance step. The distance step chosen was 0.5 m. Table 2 gives an overview of the CPT based method predictions in comparison with the tensile capacity tests. It is immediately apparent that the experimental tensile capacity is overpredicted by all the CPT methods. The experimental result of Pile 1 is in proportion between 27% and 61% of the CPT methods prediction. The same information is visually presented in Figure 9 where the NGI-05 method is omitted to allow appropriate representation of the experimental data. In accordance to Achmus and Müller (2010) the most suitable approaches for open-ended piles in tension are the ICP-05 and the UWA-05. This seems to be confirmed also by the test data of this study, which show the smaller deviation for the ICP-05 and UWA-05 methods. The quite relevant discrepancy between CPT-based estimation and experimental result is to be ascribed to the installation method used. As already mentioned, CPT-based approaches were calibrated with impact-driven and pressed piles data. A recalibration of CPT-based method on the base of an extensive vibro-driven piles campaign tests is therefore suggested. The tests so far performed, corroborate the previous finding of other researchers (Borel et al., 2006); the shaft resistance of vibro-driven piles is smaller than that of impact-driven piles.

Table 2 Summary of ultimate capacity prediction in comparison to the experimental data.

Method	Ultimate Capacity (kN)	Pile 2/ CPT meth. Prediction	Pile 1/ CPT meth. Prediction
ICP-05	316	0.36	0.56
UWA-05	286	0.40	0.61
Fugro-05	398	0.29	0.44
NGI-05	648	0.18	0.27

3.2 Interpretation of the initial stiffness by means of a numerical model

The numerical model was created with the finite element program ABAQUS (2014). The 2D-axisymmetric model is formed by axisymmetric elements of the type CAX4. The laboratory physical situation is recreated in the model. In the numerical model the distance between the pile axis and the retaining wall (boundary condition) was taken as the minimum distance present in the laboratory (5 pile diameters). The discretization of the model is shown in Figure 10. A very fine mesh was created in the vicinity of the pile. The pile was modelled with a linear-elastic material with Young's Modulus E_{steel} = 2.1·10^5 MPa and Poisson's ratio of ν = 0.3. For the soil the Mohr-Coulomb failure criterion is adopted. The stiffness modulus of the sand, *E*, was derived by means of oedometric tests (11 MPa) and CPTs (17 MPa).

The soil is fully saturated except for the most superficial 20 cm. Despite of that, only one soil strata with effective unit weight, γ' = 10.15 kN/m^3, was considered. A Poisson's ratio of 0.27 was used. The friction angle, ϕ', was chosen as the critical friction angle characteristic for the sand with that particular compaction state. A value of ϕ' = 33º was chosen on the base of direct shear tests previously conducted on the sand.

The hypothesis of pile wished in place was made. The coefficient of lateral earth pressure at rest was calculated as $K_0 = 1 - \phi'$.

The model was constructed so that the pile is a solid section with equivalent weight and stiffness modulus to the real system (pile plus saturated soil inside). As a result of that, only the self-weight of a plugged pile plus the external shaft resistance contribute to the tensile resistance. For modelling the pile-soil contact an elasto-plastic contact interaction was considered. The friction coefficient was calculated with the well-known equation $\mu = \tan(\delta) = \tan(2/3\phi')$. The displacement at which full frictional stress mobilization occurs (elastic slip) was set to 2 mm. The parameters used are listed in Table 3. The model was carefully checked by applying different loads to the pile in tension and compression and by calculating thereafter equilibrium between forces applied and resultant stresses. To enable the achievement of a clear plastic plateau at the end of the curves and also to simulate the physical experiment, the simulations were run displacement-controlled and thus by applying a particular displacement to the pile head. A considerable number of parameter studies was carried out in order to have a clear understanding of the model parameters. The model responded as expected to the parameter change. The displacement-force curves relative to three different *E* moduli are shown in Figure 11. As expected, the three curves present equal ultimate capacity and significantly different initial stiffness. The change in initial stiffness is consistent with the different values of the *E* modulus.

In Figure 12 the model prediction is plotted against the test curves. It can immediately be seen that the load-displacement behaviour of the model calculated with *E* = 17 MPa underestimate considerably the test curve. Indeed, the physical model shows a much higher initial stiffness. In order to have reasonable match with the experimental curve the *E* modulus of the sand has to be increased to 120 MPa. This value of *E* is undoubtedly out of the normally used range.

This indicates that substantial changes in the model are required in order to capture the experimental behaviour with realistic parameters.

Table 3 Parameters used for sand and contact model.

Property	Symbol	Unit	Value
Friction angle	ϕ'	º	33
Soil-pile interface angle	δ	º	22
Effective unit weight	γ'	kN/m^3	10.15
Poisson's ratio	ν	-	0.27
Dilation angle	ψ	º	10
Young's moduli	*E*	MPa	17, 120

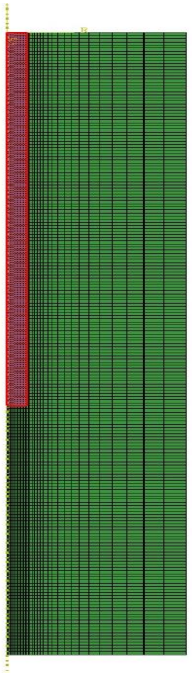


Figure 10 Discretization of the 2D - axisymmetric model. Pile emphasized in red colour.

It is furthermore deemed that by modelling appropriately the soil-steel interface behaviour, the entire response (initial stiffness and ultimate resistance) of a pile under tensile loading can be well simulated.

4 FINAL REMARKS

Two vibro-driven piles have been tested in large-scale to explore their economic feasibility for jacket-supported offshore wind turbines. The following conclusions can be drawn:

- Even disregarding the negative effects of higher installation frequency and scouring, it was found that set-up phenomena and pre-loading are beneficial to the ultimate tensile capacity by 53%. A crucial finding is also that the initial stiffness of the pile was not influenced by them. The number of the large-scale tests was very limited and the specific influence of each and every effect could not yet be decoupled.
- The CPT methods seem to overestimate considerably the experimentally derived ultimate capacity. However, in order to estimate more accurately the discrepancy in ultimate capacity between impact- and vibro-driven piles, the same piles should be installed with impact hammer and tested.
- A simple axisymmetric numerical model could not capture the initial stiffness behaviour with realistic values of *E*. A more sophisticated contact model should be used to gain better simulations with more realistic soil parameters.

ACKNOWLEDGEMENT

The experimental campaign and the data post-processing presented in this contribution have been carried out as part of the INNWIND.EU project (7th Framework

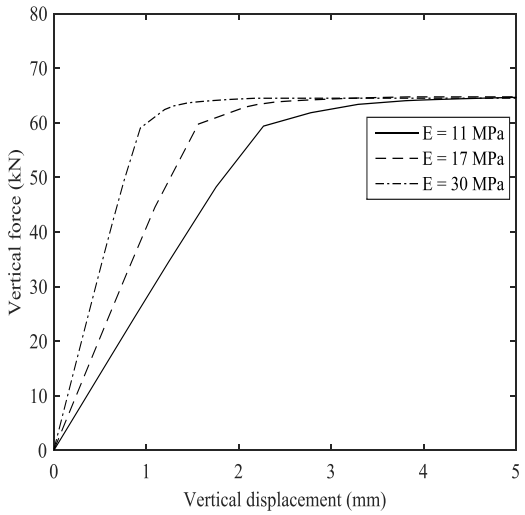


Figure 11 Load-displacement curves of the numerical model with three different E moduli.

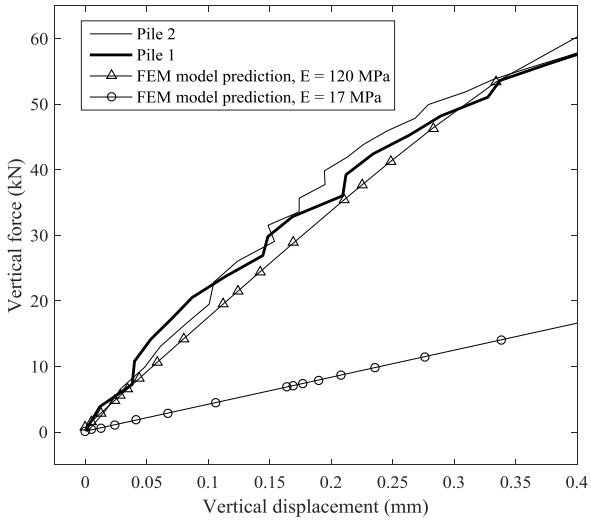


Figure 12 Comparison of load-displacement curves of numerical model and experimental test.

Programme FP7-ENERGY-2012-1-2STAGE under grant agreement No. 308974).

5 REFERENCES

ABAQUS (2014). 6.14 User's Manual. Simulia, Providence, USA.

Achmus, M., Müller, M. (2010). Evaluation of pile capacity approaches with respect to piles for wind energy foundations in the North Sea. 2nd International Symposium on Frontiers in Offshore Geotechnics, 8-10 November 2010, University of Western Australia, Perth.

Achmus, M., Lemke, K., Abdel-Rahman, K., Kuo, Y.-S. (2015). Numerical approach for the derivation of interaction diagrams for piles under cyclic axial loading. Proceedings of the Twenty-fifth International Ocean and Polar Engineering Conference.

API (2011). ISO 19901-4:2003 (Modified), Petroleum and natural gas industries-Specific requirements for offshore structures, Part 4-Geotechnical and Foundation Design Considerations.

Baldi, G., Bellotti, R., Ghionna, V., Jamiolkowski, M., Pasqualini, E. (1986). Interpretation of CPT's and CPTU's. 2nd Part: drained penetration on sands. Proc., 4th Int. Geotech. Seminar: Field Instrumentation and In Situ Measurements, Nanyang Technol. Univ., Singapore, 143–162.

Borel, S., Bustamante, M., Rocher-Lacoste, F. (2006). The comparative bearing capacity of vibratory and impact driven piles. International symposium on vibratory pile driving and deep soil vibratory compaction.

BSH (2013). Offshore Wind Farms Measuring Specification for the Quantitative Determination of the Effectiveness of Noise Control Systems. Bundesamt für Seeschifffahrt und Hydrographie.

Clausen, C. J. F., Aas, P. M., Karlsrud, K. (2005). Bearing capacity of driven piles in sand, the NGI approach. – Proc., 1st Int. Symp. on Frontiers in Offshore Geotechnics, Balkema, Perth, Australia, 677–681.

DNV (2010). Offshore standard DNV-OS-J101: Design of offshore wind turbine structures. Technical report DNV-OS-J101, Det Norske Veritas.

DIN, (2002). Baugrund; Felduntersuchungen. 4094 Teil 1: Drucksondierungen. – Beuth, Berlin.

EN (2007). 1997-2: Eurocode 7: Geotechnical design - Part 2: Ground investigation and testing [Authority: The European Union Per Regulation 305/2011, Directive 98/34/EC,Directive 2004/18/EC].

Fichtner (2013). Cost Reduction Potentials of Offshore Wind Power in Germany.

Igoe, D., Gavin, K., O'Kelly, B. (2013). An investigation into the use of push-in pile foundations by the offshore wind sector. International Journal of Environmental Studies.

Lammertz, P. (2008). Ermittlung der Tragfähigkeit vibrierter Stahlrohrpfähle in nichtbinigem Boden. PhD thesis, Universität Duisburg-Essen.

LeBlanc, C., Liingaard, M.A., Shajarati, A., Kallehave D., Skov Gretlund J. (2013). Vibro-driving of monopiles-experience from Anholt Offshore Wind Farm, Offshore EWEA, Frankfurt.

Lehane, B.M., Schneider, J.A. and Xu, X. (2005). A review of design methods for offshore driven piles in siliceous sand. UWA Report GEO 05358.

Puech, A., Foray, P. (2002). Refined model for interpreting shallow penetration CPTs in sands. – Offshore technology conference (OTC 14275). Houston, Texas.

Valpy, B., English, P., Martínez, A., Simonot, E. (2014). Future renewable energy costs: offshore wind. BVG Associates and KIC InnoEnergy.

Matlock, B.G.W.M. (2015). Comparison of the lateral bearing capacities of hammered and vibrated piles. 5th Internationa Conference Offshore Foundations, Bremen.

Viking, K. (2002). Vibro-driveability – A field study of vibratory driven sheet piles in non-cohesive soils. PhD thesis, Royal Institute of Technology Stockholm.

Influence of deviatoric stress dependent stiffness on settlement trough width in 2D and 3D finite element modelling of tunnelling

Nicolas GILLERON
EGIS / IFSTTAR, France, nicolas.gilleron@egis.fr

Emmanuel BOURGEOIS
IFSTTAR, France, emmanuel.bourgeois@ifsttar.fr
Adrien SAITTA
EGIS, France

ABSTRACT
Finite element simulations of the construction of shallow tunnels tend to provide poor predictions of the settlements induced at the surface. More precisely, the settlement trough width is generally overestimated by numerical simulations. Many parameters have an influence on the numerical results. In this paper, attention is focused on the constitutive law. Two classic methods of settlement predictions are introduced; a plane strain simulation with the load reduction method and a three dimensional model of conventional tunnelling with numerous excavation steps. After showing some particularity of stress state in soil in the case of a shallow tunnel, we develop a dedicated non-linear elastic law concentrating on the decrease of soil stiffness with increase of deviatoric stress. Indeed an increase of this stress invariant during excavation associated with a stability of the mean effective stress have been shown in the vicinity of the tunnel section especially for 3D modelling. The proposed formulation leads to an initial stiffness that does not depend on depth, which allows testing only the influence of the deviatoric stress variations, a feature which is generally renowned to have a significant influence on the settlement trough width. The influence of the differences between stress paths in the two dimensional and three dimensional simulations is precisely discussed as well as the determination of the stress relaxation factor in 2D modelling. Finally, it appears that, despite the differences in the redistribution of stresses, using a model in which stiffness decreases as the deviatoric stress increases does not make it possible to improve the prediction of settlements both in 2D or 3D.

Keywords: Tunnel, Finite Element, Settlement, Non-Linear Elasticity

1 INTRODUCTION

Predicting the surface settlements caused by shallow tunnelling is a fundamental issue for the geotechnical engineer. At the design stage two approaches are currently used (ITA report, 2007). The first one is an empirical method based on the works by Peck (1969). The second approach consists of using numerical models. It is generally admitted that, in spite of numerous refinements, numerical simulations lead to wider settlement trough than empirical modelling (ITA report, 2007). The settlement trough width, defining the deflection ratio, is essential to evaluate impact of settlement on building (Mair & al., 1996). This is why, despite the apparently higher precision offered by numerical modelling, the empirical method is still widely used (Lunardi, 2014; Padrosa, 2014) and can be considered safer (Leca, 2000). Two-dimensional and three-dimensional simulations are currently used. The constitutive model adopted for the ground is considered the key factor which shapes the settlement trough in numerical modelling (Addenbrooke & al., 1997; Hejazi & al., 2006; Do & al., 2013). Many of the advanced models feature a relatively large number of

parameters and mechanisms, and it is generally not possible to identify clearly which one(s) control(s) the settlement trough width, which could be used by tunnel designer as directly as Peck's parameters. In this paper, we investigate the possibility to obtain numerically narrower settlement troughs than those obtained with classical constitutive models, by means of a model in which the shear modulus depends on the deviatoric stress.

After a description of the problem and the parameters under discussion, we propose an original comparison of stress paths in (p',q) plan between 2D and 3D modelling for shallow tunnel design. A simple constitutive model that focuses on the stiffness dependence with deviatoric stress is then justified and clarified. Then, we discuss the settlement troughs obtained in the numerical simulations in 2D and 3D with this new model compared to more simple ones.

All the simulations presented hereafter have been carried out using the finite element package CESAR-LCPCv6, developed by IFSTTAR and ITECH (Humbert & al., 2005).

2 PROBLEM STATEMENT

2.1 Characterization of the settlement trough

The approach proposed by Peck (1969) and developed in ITA/AITES report (2007) is based on numerous field observations, which led to describe the surface settlement $S(x)$ at a given distance x from the tunnel axis by a Gaussian function:

$$S(x) = S_{\max}.\exp(-\frac{x^2}{2i^2}) \qquad (1)$$

The settlement is characterized by only two parameters, S_{max}, the maximal value of the settlement, and i, characterizing the settlement trough width. Given (1), i can be considered as the distance from the axis for which $S(x)$ is approximately equal to 60% of S_{max}. In addition, i is assumed to be the product of the tunnel depth H and a coefficient K which depends on the ground. According to ITA/AITES report (2007) based on Mair & Taylor (1997), typical values of K range from 0.25 for sandy/gravelly soils to 0.5 for clayey soils. These values have been first described by O'Reilly and New (1982).

Apart from the constitutive law, numerical simulations take into account other parameters that have an influence on the width of the settlement trough:

- the depth of the tunnel axis (which is consistent with the observations mentioned above),
- the shape of the tunnel section (Moldovan & al., 2013),
- the initial stress state: for a linear elastic homogeneous ground, lower values of K_0 lead to narrower troughs, as illustrated by Figure 1, in which i has been computed as the distance from the axis where the settlement equals 60% of the maximum value (for simulations carried out under the hypotheses summarized in the next paragraph).

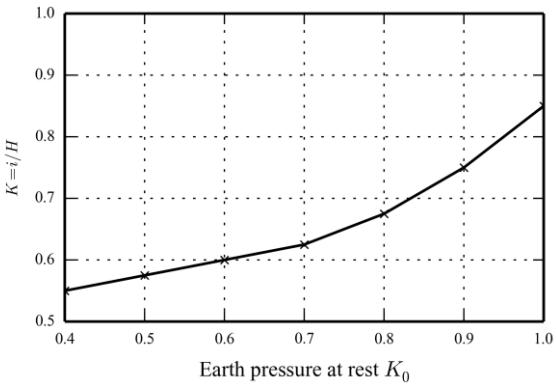


Figure 1. K with K_0 – 2D elastic simulation

2.2 Case studied

We studied a common shallow tunnel in greenfield condition in an homogenous soil. The section has a circular shape with a diameter equal to 10 m, the axis depth is 20 m, thus the tunnel cover is 15 m. The model width is 45 m and its depth is 35 m. For the 3D modelling the model length is 70 m.

Horizontal displacements are restrained for vertical boundaries; horizontal and vertical displacements are restrained at the lower boundary of the domain.

The initial stress state is anisotropic with a coefficient of earth pressure at rest K_0 equal to 0.7, which is representative of many soft

ground layers of the Paris area. The volume weight is equal to 20 kN/m^3.

Although three-dimensional simulations have become common practice in research on tunnels (Eberhardt, 2001; Franzius & Potts, 2005; Do et al., 2013), from an engineering point of view, two dimensional plane strain simulations remain a quick way of estimating the settlements. Both have been here considered.

2.3 Conventional tunnelling modelling

The excavation process is full face excavation with installation of a sprayed concrete lining with steel ribs at 2 m from the excavation face. We voluntarily considered a quite long unsupported span to produce significant settlements and a stiff lining to better show its influence.

For the three dimensional modelling, the lining is activated at each excavation step and is modelled with shell elements (Figure 2), that represent both the sprayed concrete and the steel ribs through a homogenization procedure. Seventeen excavation steps have been considered. The extraction of the settlement trough is made thanks to a differential method inspired from Möller & al. (2003) work.

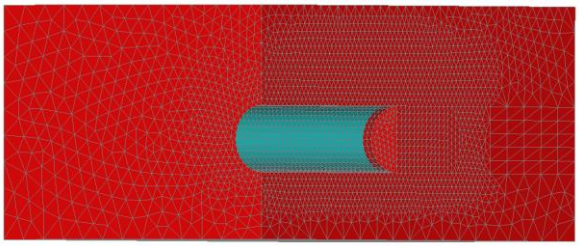


Figure 2. 3D Model of tunnel excavation with lining

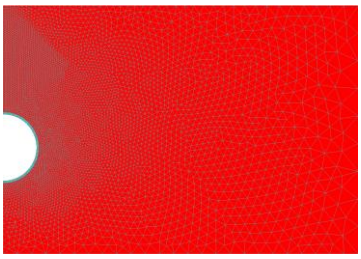


Figure 3. 2D Model of tunnel excavation with lining

For the two dimensional modelling we chose the stress relaxation method to simulate the 3D effect. It is the most used in practice, recommended for design of conventional tunnelling by Plaxis (2015) as well as for back-analysis (Janin & al., 2015). Furthermore this method is the most physically consistent for conventional tunnelling. It respects the forces equilibrium.

It has first been introduced by Panet (1995) for the design of the lining (particularly for deep tunnelling in rock), and then extended to shallow tunnels in soils to predict surface settlements. The main challenge is to determine the stress relaxation factor before the installation of the lining. With this method we consider that a fraction $\lambda<1$ of the initial stress in soil have been relaxed before the lining installation. The remaining stress ($1-\lambda$) is then applied to the successive linings. Several propositions using 3D ground reaction curves (Vlachopoulos et al. 2009), analytical calculations or back-analysis have been developed in the past decades to determine it. It appears that there is no unique solution.

Svoboda & al. (2011) and Janin & al. (2015) have both demonstrated from case studies that the displacement field in 3D and 2D numerical modelling can be well fitted with an appropriate choice of the stress relaxation factor for the 2D modelling. They also both highlight the high dependency of the stress relaxation factor to the soil parameters and constitutive law. The excavation process is not the unique factor. In this study we determine the stress relaxation factor for a considered case by fitting the maximum settlement with the 3D model. We give in the followings sections some limits of the stress relaxation method thanks to the analysis of stress paths.

3 2D AND 3D STRESS PATHS

3.1 Definition of stresses paths

We adopt the usual definitions for the mean effective stress p' and the deviatoric stress q:

$$p' = \frac{\sigma_1' + \sigma_2' + \sigma_3'}{3} \qquad (2)$$

$$q = \sqrt{\frac{1}{2}\left[\left(\sigma_1' - \sigma_2'\right)^2 + \left(\sigma_1' - \sigma_3'\right)^2 + \left(\sigma_2' - \sigma_3'\right)^2\right]} \quad (3)$$

In 3D the stress path is extracted along the longitudinal axis from the non excavated area to the supported area. In 2D the stresses are extracted at each of the 10 considered excavation steps, from 10 % to 100 % of unloading from the initial stress state. We selected 5 points at a distance of one meter from the tunnel section.

3.2 Elastic case without lining

First we consider a non-supported tunnel in a linear elastic soil in 2D (Figure 4).

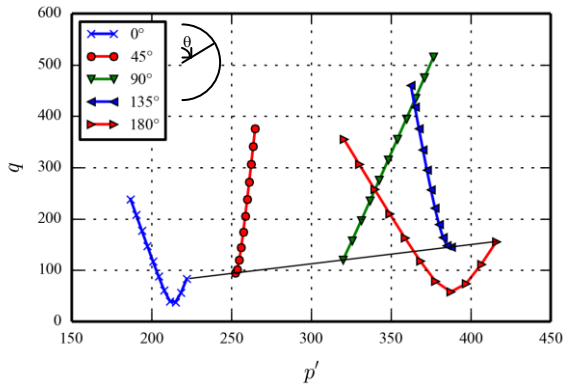


Figure 4. Stress paths around tunnel section – 2D

The mean effective stress variations are relatively small constant during the excavation for all points compared to the evolution of deviatoric stress. The tunnel excavation loading is indeed principally deviatoric. In the extreme case of an isotropic stress state the loading is purely deviatoric (Panet (1995)). The lines would be vertical in (*p',q*) plan.

The mean effective stress decreases on top of the section (θ=0) and in the lower quarter of the section (θ=135 and 180 degrees). It increases on the other two points, where the deviatoric stress increases drastically (+40% of initial at each step). At the crown and at the invert (θ=0 and (θ=180 degrees), due to the inversion of orientation of the principal stress, the deviatoric stress first decreases and then increases, after 50 % of stress relaxation.

Figure 5 compares the stress paths obtained in 3D, where the main changes in stress occur in the vicinity of the excavation face, with the stress paths obtained in 2D.

Two results are significant. First the initial state and final state are very similar for both methods. Secondly the stress path is different

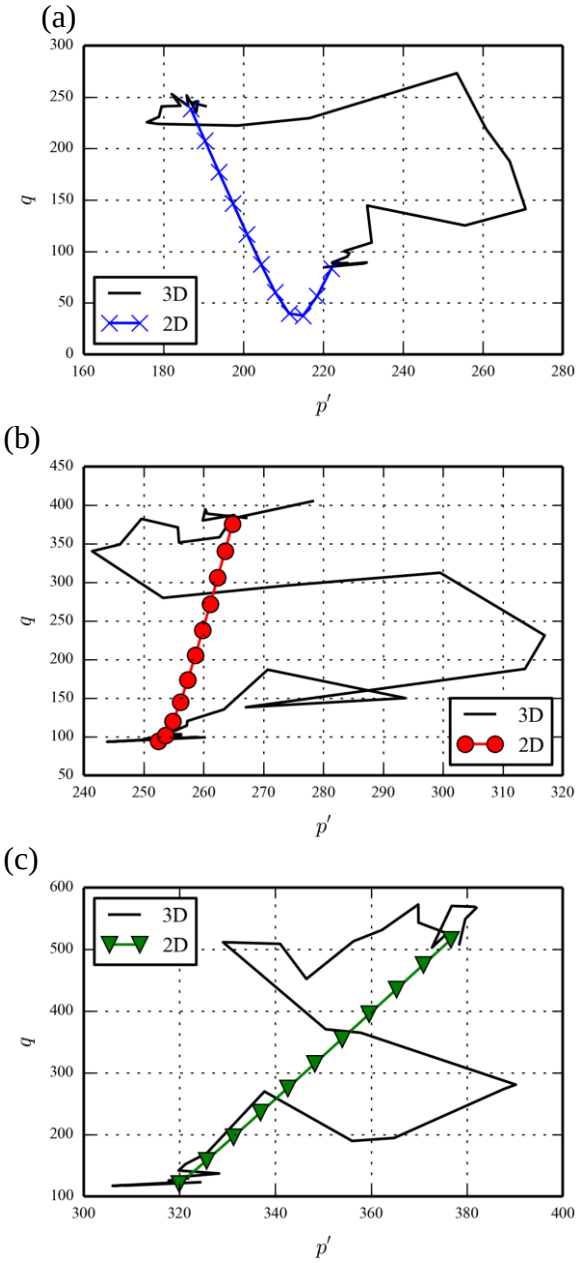


Figure 5. Stress paths in 2D and 3D (a)0°(b)45°(c)90°.

especially in crown. On the 3D model we remark for the three considered points an increase of mean effective stress and deviatoric stress. This is due to the transversal arching effect, as in 2D model, but also to a longitudinal arching effect which is not considered in the 2D modelling. It leads to a significant difference in crown, and in down section, between the 2D and 3D stress paths. Where 2D models lead to an initial decrease of deviatoric stress, the 3D ones show only an increase of deviatoric

stress. As in 2D, the mean effective stress variations are not in the same amplitude than those of the deviatoric stress.

3.3 Lining influence

The former considerations bring to consequences when considering the lining influence.

Figure 6 and Figure 7 repeat Figure 4 and Figure 5 but with the introduction of a lining. We took a stress relaxation factor of 35 % for the 2D modelling to obtain the same maximum settlement in both simulations (see paragraph 4).

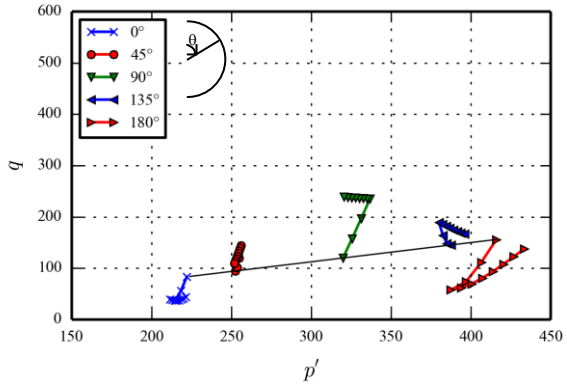


Figure 6. Stress paths around tunnel section – 2D

Due to its high stiffness the lining blocks the 2D stress path as it is installed. We notice especially that the deviatoric stress stay under the initial value at the crown and at the invert of the tunnel section.

Compared with 3D model the initial and final states are different for the two way of modelling contrary to Figure 5. This result does not give confidence on the compatibility of the two way of modelling for lining design. Furthermore the stress path is totally different at the crown between those two models (Figure 7 (a)). These differences might have a significant impact on the calculated settlement, shape of the trough, and state of soil at the end of the calculation between the two ways of modelling, especially if an advanced model is used.

In the following sections we investigate these consequences by using an elastic-perfectly plastic model and a new non-linear elastic model presented just hereafter.

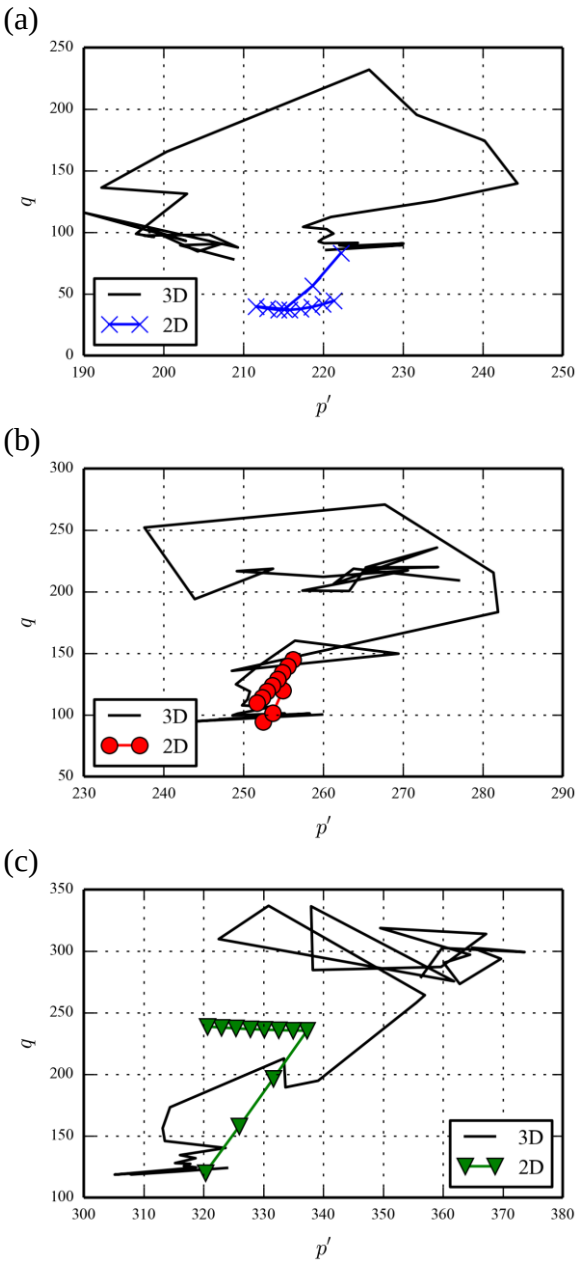


Figure 7. Stress paths in 2D and 3D (a)0°(b)45°(c)90°.

4 MODEL INVOLVING DEVIATORIC STRESS DEPENDENT STIFFNESS

4.1 Opportunity of a deviatoric stress dependent stiffness

As seen previously, the initial stress state has two specificities:

- it is anisotropic: the horizontal stress is lower than the vertical one, the initial deviatoric stress is not equal to zero.

- the initial stresses vary linearly with depth (in contrast with deep tunneling).

The tunnelling process induces an increase in the deviatoric stress near the excavation especially for 3D modelling. It can be expected that the settlement trough shape obtained numerically could be modified if the constitutive model involved a decrease in the elastic moduli when the deviatoric stress increases. Moreover, if the formulation is appropriate, one could get a direct connection between one of the constitutive model parameters and the settlement trough width and highlight a difference in shape between 2D and 3D modelling.

4.2 Non-linear elastic law with shear mechanism

We propose hereafter an isotropic non-linear elastic law adapted from the model proposed for sands by Fahey (1992) and Fahey & Carter (1993). We use an exponential decrease in shear stiffness with increase in stress ratio *q/p'*. Independent parameters permit to pilot the rate of decrease and the initial stress state from where the decrease begins.

The tangent shear modulus is given by:

$$G_t = Min\left[Max(G_{\min}; G_0 \alpha^{(1-\frac{q}{\beta p'})}); G_0 \right] \quad (4)$$

In the proposed model, following Fahey & Carter (1993), Poisson's ratio is chosen so as to maintain the bulk modulus constant:

$$\nu_t = \left[\frac{(1+\nu_0) - \frac{G_t}{G_0}(1-2\nu_0)}{2(1+\nu_0) + \frac{G_t}{G_0}(1-2\nu_0)} \right] \quad (5)$$

Since the initial value of *q/p'* is independent from depth in the initial state, the initial stiffness does not increase with depth (which is known to have an influence on the width of the computed settlement trough). Besides, since (it is expected that) variations of *p* during excavation are small, *q/p'* increases in the vicinity of the tunnel when the excavation forces are applied, which results in the decrease in stiffness sought for.

In the above equations:

- it is assumed that the tangent shear modulus cannot become smaller than a minimum value G_{min},
- it is also assumed that the tangent shear modulus cannot exceed the initial value G_0,
- α is a form coefficient to pilot the rate of stiffness decrease. It is chosen to have a decrease from G_0 to G_{min} in the range of our study stress variations.
- β is defined as the initial value of the *q/p'* factor, which is a function of K_0:

$$\frac{q}{p'} = \frac{3(1-K_0)}{1+2K_0} \quad (6)$$

- ν_0 is the initial Poisson's ratio.

Figure 8 displays the result of a simulation of a triaxial test starting from the initial anisotropic stress state corresponding to a depth of 15 m (crown of the tunnel), for parameters in Table 1. We use a Mohr-Coulomb criterion.

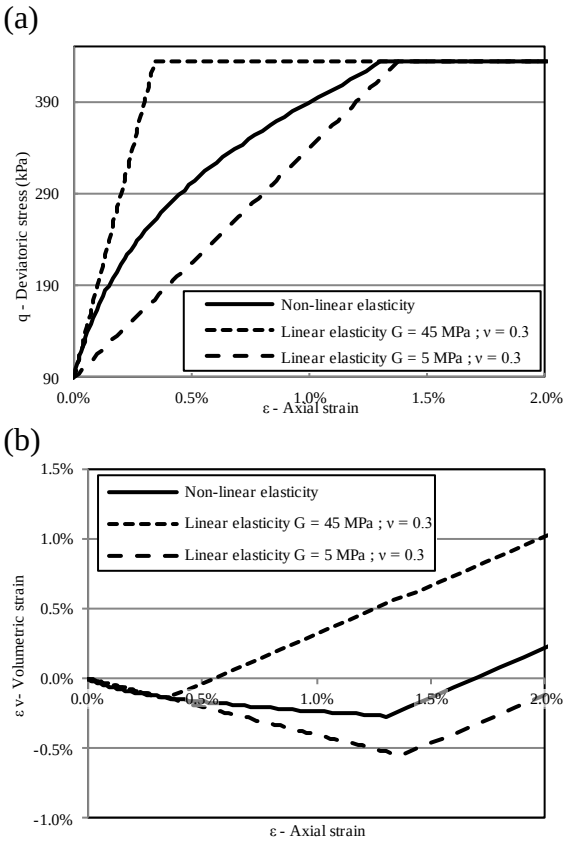


Figure 8. Simulation of triaxial test

Table 1. Non-linear elastic law associated with a Mohr-Coulomb criterion parameters

G_{min} MPa	G_0 MPa	ν_0 -	α -	β -	c kPa	φ *deg*	ψ *deg*
5	45.45	0.1	3	0.375	40	25	15

The parameters have been chosen to have a decrease in the range of excavation stress paths (Figure 5). Figure 9 shows the profile of elastic parameters with progress of excavation which is linked with *q/p'*. The decrease of the shear modulus as *q/p'* increases results in a decrease of the Young's modulus; since the bulk modulus is kept constant, the value of Poisson's ratio increases.

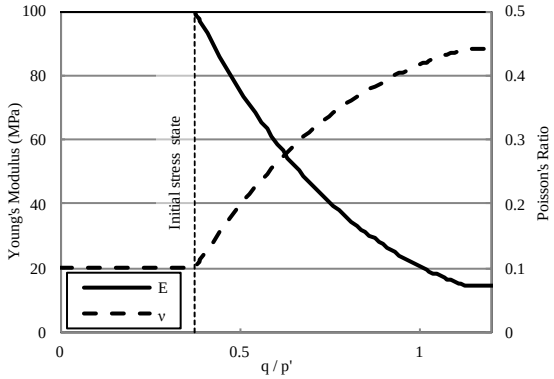


Figure 9. Variation of Young's modulus and Poisson's ratio with stress ratio q/p'

5 CONSTITUTIVE MODEL INFLUENCE

5.1 Linear elastic behaviour

Figure 10 superposes the settlement troughs given by simulations in 2D and 3D without lining, for a linear elastic behaviour, with E=100 MPa and ν = 0.2. The curves are quasi exactly the same, and the computed troughs are wider than that provided by Peck's approach.

In Figure 11, we introduced the lining in the 3D model and set the stress relaxation factor of the 2D model at 35 %, so that the maximum settlements are similar. Shapes are here different, a bit narrower for 3D model and a bit wider for 2D model.

5.2 Linear elastic perfectly plastic behaviour

We performed new simulations with an elastic perfectly plastic model, using the Mohr-Coulomb criterion, and the parameters in Table 2. With these parameters, simulations lead to significant plastic strains in 3D. And then we fitted the maximum settlement with the 2D model with same parameters (Figure 12). In this case the shape of both simulations is the

Table 2. Mohr-Coulomb criterion parameters

c (kPa)	**φ (deg)**	**ψ (deg)**
25	24	15

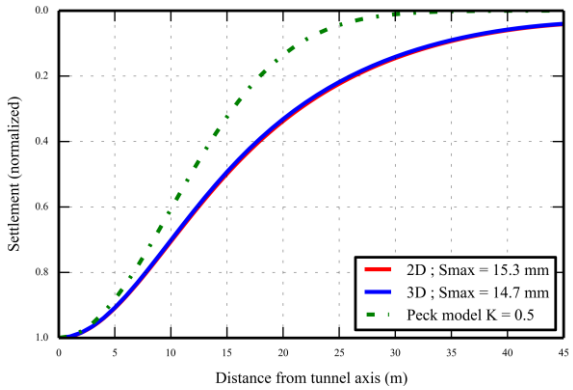


Figure 10. Settlement trough for a linear elastic behaviour without lining

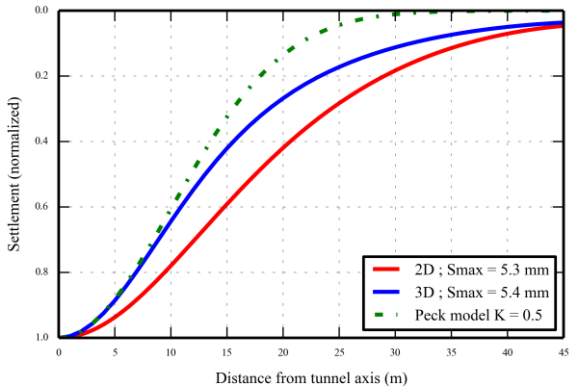


Figure 11. Settlement trough for a linear elastic behaviour with lining. λ= 35 %

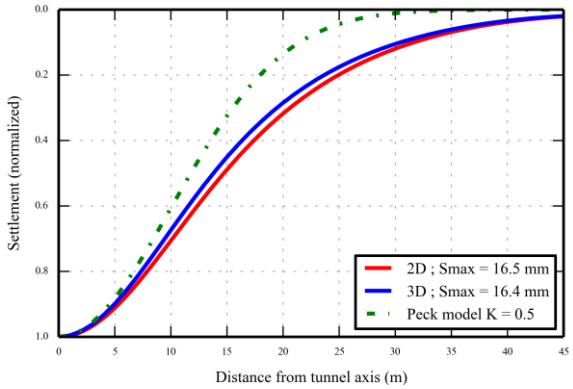


Figure 12. Settlement trough for a linear elastic perfectly plastic behaviour with lining. λ = 65 %

same.The stress relaxation factor obtained is here equal to 65%.

This value is much higher (+86% to elastic case) because of the stress paths differences. It has to be underlined this factor is unique for each cohesion and friction ratio combinations.

Figure 13 compares the areas in which significant plastic strain (larger than 0.5%) occur for both models. In 3D plastic strains occur around the whole section. It is totally different to 2D case where plastic strains occur only at the axis level of the axis.

This shows that, if it is possible to adjust the relaxation factor of the 2D approach to fit the displacement of the 3D model, the plastic strain distribution is significantly different between both cases.

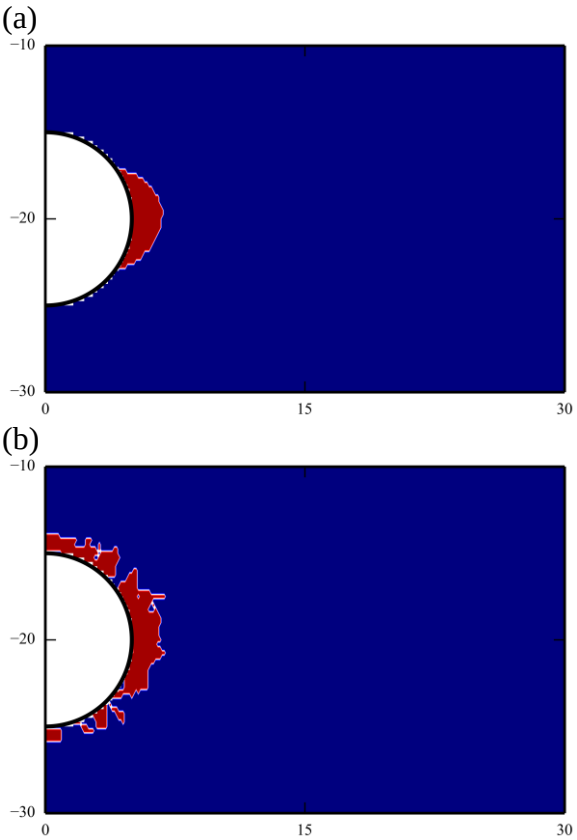


Figure 13. Area where plastic strains exceed 0.5% (a) 2D (b) 3D

5.3 Non-linear elastic behaviour

The excavation load is applied in 10 equal steps where the stiffness is updated for both 2D and 3D simulations.

We consider first the unsupported case in Figure 14. The maximum settlement is increased by a factor 2.22 and 2.65

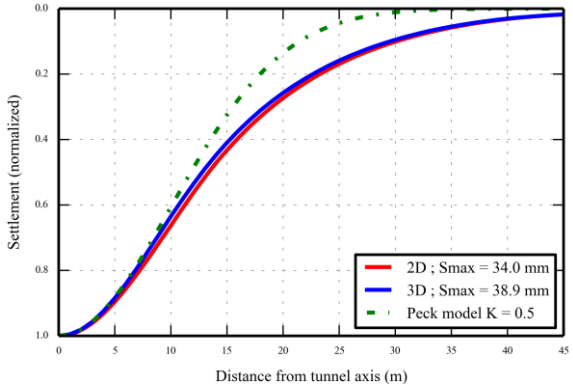


Figure 14. Settlement trough for a non-linear elastic behaviour without lining

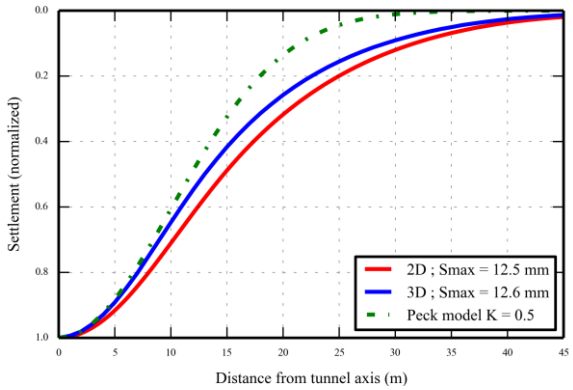


Figure 15. Settlement trough for a non-linear elastic behaviour with lining. λ = 55 %

respectively regarding the linear elastic case, showing the influence of the constitutive law. The maximum settlement between 2D and 3D is here different due to the difference on stress paths. More soil is submitted to deviatoric stress in 3D, leading to lower stiffness, and larger maximum settlement. Regarding the settlement trough width, both simulations have quite the same result, a bit narrower than the linear one but still different from the settlement trough sought for.

The improvement in displacements calculated at a distance axis larger from 20 m is mostly due to the influence of Poisson's ratio.

Considering the lining installation we fitted the maximum settlement with a stress relaxation factor equal to 55 % (Figure 15). This value is higher than the linear elastic case.

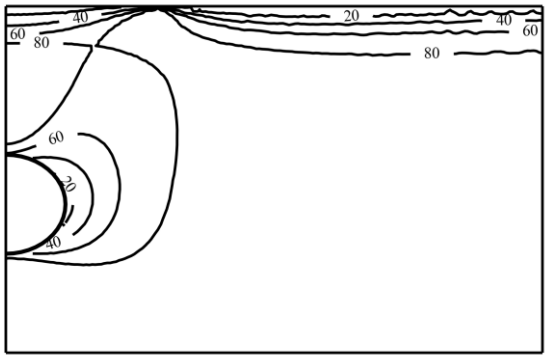
Once again, despite the equivalence in surface displacement, the state of the soil is clearly different before the lining installation

for both methods: this is illustrated in Figure 16, which shows the spatial distribution of the values of the Young's modulus across the mesh: in the 2D case, there is a "stiff" zone above the tunnel crown, i.e. a zone where the modulus takes values larger than 80 MPa, contrary to the 3D case.

It is also remarkable to obtain quasi exactly the same width of settlement trough with such a significant difference between those two way of simulations. In 2D the stiff area above the crown could explain why the non linear model provides no significant improvement in the trough width. But even without this stiff area, the 3D model does not give a narrower trough.

Like in the linear elastic perfectly-plastic case, it is necessary to use a relaxation factor larger than that adopted in the linear elastic case.

(a)



(b)

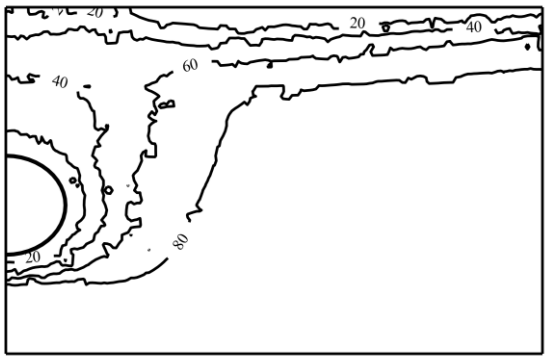


Figure 16. Contour lines of Young's Modulus (a) 2D - (b) 3D

6 CONCLUSIONS

The stress relaxation factor that makes it possible to fit a 2D model with a 3D model is highly dependent from the soil constitutive law, so that the definition of a stress relaxation factor requests a case by case analysis.

In 2D and 3D the shapes of the settlement troughs are globally the same for all cases here studied, once the stress relaxation factor has been chosen to fit the maximum settlement.

Due to differences in stress paths between 2D and 3D modelling the final state of soil, plastic strain or elastic moduli, is different between those two ways of modelling. The 2D modelling cannot reproduce the localization of plastic strains or the localisation of a reduction of moduli with a non-linear law.

The use of a shallow tunnel dedicated non-linear deviatoric stress dependant elastic law has no real impact on the width of settlement trough. This mechanism does not permit to reach and reproduce the narrower empiric settlement trough by 2D or 3D finite element modelling.

7 ACKNOWLEDGEMENTS

This research was supported by the French "Fond Unique Interministériel", CG78 and BpiFrance through the Newtun project.

8 REFERENCES

Addenbrooke, T.L., Potts D.M. & Puzrin A.M. (1997). The influence of pre-failure soul stiffness on the numerical analysis of tunnel construction. *Géotechnique* **47**, No. 3, 693–712.

Do, N.A, Dias, D., Oreste, P. & Djeran-Maigre I. (2013). 3D Modelling for mechanized tunneling in soft ground – Influence of the constitutive model. *American journal of applied sciences* **10**, No. 8, 863-875.

Eberhardt, E. (2001). Numerical modelling of three-dimension stress rotation ahead of an advancing tunnel face. *International journal of Rock Mechanics & Mining Sciences* **38**, 499-518.

Fahey, M. (1992). Shear modulus of cohesionless soil: variation with stress and strain level. *Canadian Geotechnical Journal* **29**, 157-161.

Fahey, M. & Carter, J.P. (1993). A finite element study of the pressuremeter in sand using a nonlinear elastic plastic model. *Canadian Geotechnical Journal* **30**, 348-362.

Franzius, J.N. & Potts, D.M. (2005). Influence of Mesh Geometry on Three-Dimensional Finite-Element Analysis of Tunnel Excavation. *International journal of geomechanics* **5,** 256-266.

Hejazi, Y., Dias, D. & Kastner R. (2008). Impact of constitutive models on the numerical analysis of underground constructions. *Acta Geotechnica*, **3**, 251-258.

Humbert, P., Dubouchet, A., Fezans, G. & Remaud D. (2005). CESAR-LCPC: A computation software package dedicated to civil engineering uses. *Bulletin des Laboratoires des Ponts et Chaussées,* **256-257**.

ITA/AITES Report 2006 on Settlements induced by tunneling in Soft Ground (2007). *Tunnelling and Underground Space Technology*, **22**, 119-149.

Janin, J.P., Dias, D., Emeriault, F., Kastner, R., Le Bissonais, H., Guilloux, A. (2015). Numerical back-analysis of the southern Toulon tunnel measurements : A comparison of 3D and 2D approaches. *Engineering Geology*, **195**, 42-52.

Leca, E. (2000). *Etude du comportement des tunnels creusés en terrain meubles.* Les collections du LCPC, Etudes et Recherches des Laboratoires des Ponts et Chaussées GT66.

Lunardi, P., Carriero, F., Canzoneri, A. & Carini M. (2014). Warsaw Metro's improvements. *Tunnels*, November 2014, 31-37.

Mair, R.J., Taylor, R. & Burland, J. (1996). Prediction of ground movements and assessment of risk of building damage due to bored tunnelling. *Geotechnical Aspects of Underground Construction in Soft Ground* (eds R.J. Mair & R.N. Taylor), Balkema, Rotterdam, 713-718.

Mair, R.J. & Taylor, R. (1997). Bored tunneling in the urban environnement. State-of-the art Report and Theme Lecture. *Proceedings of 14th International Conference on Soil Mechanics and Foundation Engineering*, Hamburg, Balkema, **4**, 2353-2385. *6-12 September.*

Möller, S. C., Vermeer, P. A., & Bonnier, P. G. (2003). A fast 3D tunnel analysis. *Proc., 2nd MIT Conference on Computational Fluid and Solid Mechanics* (ed. K. J. Bathe), Amsterdam, The Netherlands, 486–489.

Moldovan, A.R. & Popa, A. (2013). The influence of different tunnel cross sections on surface settlement. *Acta Technica Napocensis : Civil engineering & Architecture* **56**, No 2.

O'Reilly, M.P. & New, B.M. (1982). Settlements above tunnels in the United Kingdom – their magnitude and Prediction. *Tunnelling* **82**, London, IMM, 173-181.

Panet, M. (1995). *Calcul des tunnels par la méthode convergence-confinement*, Paris : Presses de l'Ecole Nationale des Ponts et Chaussées.

Peck, R.B. (1969). Deep excavations and tunneling in soft ground. In: *7th International Conference on Soil Mechanics and Foundation Engineering, Mexico City State-of-the-Art volume*, 225–290.

Plaxis (2015). Tutorial Manual.

Svoboda, T. & Masin, D. (2011). Comparison of displacement field predicted by 2D and 3D finite element modelling of shallow NATM tunnels in clays. *Geotechnik* **34**, No. 2, 115-126.

Vlachopoulos, NI, Diederichs, M.S. (2009). Improved longitudinal displacement profiles for convergence confinement analysis of deep tunnels. *Roch mechanics and rock engineering* **42**,vol. 1, 131-146.

Bearing Capacity, Comparison of Results from FEM and DS/EN 1997-1 DK NA 2013

Bjørn Staghøj Knudsen
COWI A/S, Denmark, bskn@cowi.dk

Niels Mortensen
nmGeo, Denmark, n@nmgeo.dk

ABSTRACT
The bearing capacity of foundations in Denmark is typically analysed using the closed form equations from DS/EN 1997-1 DK NA:2013, and the present paper compares selected examples with similar results from the finite element method (FEM). The paper includes a discussion of the bearing capacity factors, the shape factors, plane strain considerations, axi-symmetry and three-dimensional analyses.

Keywords: Bearing capacity, Shape factors, DS/EN 1997-1 DK NA:2013, FEM, PLAXIS

1 INTRODUCTION

The present paper compares the bearing capacity estimated using DS/EN 1997-1 DK NA:2013 (EC7-DK NA) with results obtained using the finite element method (FEM). The overall scope is to investigate whether the two approaches will lead to similar bearing capacities. The paper summarises the main aspects covered in the report Banedanmark (2014).

1.1 Main assumptions

The main assumptions used in the investigations are: The base of the footing is placed on a horizontal soil surface comprising either a drained (sand) or undrained (clay) soil; The soil is isotropic and homogeneous; The Mohr-Coulomb failure criterion is applied using associated and non-associated flow; The foundation is loaded vertically with centrically and eccentrically loading included.

2 BEARING CAPACITY FORMULA

The drained bearing capacity formula contains three independent contributions that are calculated separately and added following equation (1). These three contributions are represented through the effective unit weight, γ', the effective surcharge q' and the effective cohesion, c'.
In this study the contributions are first investigated separately to examine the ability to recreate each of these using FEM, after which the combined effect is investigated.

2.1 Drained capacity

The overall drained bearing capacity formula from EC7-DK NA is given in equation (1).

$$\frac{Q_f}{A'} = \frac{1}{2} \cdot \gamma' \cdot B' \cdot N_\gamma \cdot s_\gamma + q' \cdot N_q \cdot s_q \qquad (1)$$

Where Q_f/A' is the vertical bearing capacity, B' is the effective foundation width, N_γ is the bearing capacity factor for the γ'-case with s_γ being the corresponding shape factor, N_q is the bearing capacity factor for the q'-case with and s_q being the corresponding shape factor. The c'-case is a mathematical reflection of the q'-case and is thus left out from this study and of equation (1).
The basis for equation (1) is the two-dimensional case with N_γ from Lundgren & Mortensen (1953), N_q from Prandtl (1920) and with $s_\gamma = s_q = 1.00$. When investigating three-dimensional cases, the empirical factors s_γ and s_q differs from unity. Therefore, the Danish approach with equation (1) is to use the plane strain friction angle, φ'_{pl} for sand in all the analyses; also for a square footing.

Following EC7-DK NA, the plane strain friction angle (secant value) for sand is defined by $\varphi'_{pl} = \varphi'_{tr} \cdot (1.00+0.10 \cdot I_D)$, where I_D is the density index. With $I_D = 1.00$: $\varphi'_{pl} = 1.10 \cdot \varphi'_{tr}$. The effective foundation width *B'* was suggested by Brinch Hansen (1970) to be estimated as B' = B – 2·e, where B is the width of the foundation and e is the eccentricity of the vertical load relative to the vertical centre line. This approach is used and investigated in the study.

2.2 Undrained capacity

In the undrained case, the bearing capacity is calculated as:

$$\frac{Q_f}{A'} = c_u \cdot N_c^0 \cdot s_c^0 + q \qquad (2)$$

Where c_u is the undrained shear strength, N_c^0 is the undrained bearing capacity factor, s_c^0 is the shape factor and *q* represents the total surcharge.

3 METHOD OF INVESTIGATION

Four different aspects are investigated for each of the γ'-case, the q'-case and the undrained case:

- Can 2D FEM be used to validate the bearing capacity factors from EC7-DK NA?
- Can 2D FEM be used to validate the approach with effective foundation width?
- Can axi-symmetrical FEM models be used to validate the shape factor for a square footing from EC7-DK NA?
- Can 3D FEM models be used to validate the shape factor for rectangular footings?

After investigation of each separate case the drained combined capacity is investigated with a case study using EC7-DK NA, plane strain and 3D models.

4 UNDRAINED CASES

The undrained analyses are based on a constant c_u = 10 kPa with Young's modulus, E = 20 MPa. The foundation is assumed weightless with E = 20 GPa. The interface between the soil and the foundation is modelled perfectly rough (10 kPa) or smooth (0.1 kPa).

4.1 Plane strain

A completely rough foundation was loaded vertically by a line load [kN/m] and the effect of different eccentricities was investigated. The load was increased until failure was observed and the bearing capacity factor was then back-calculated from equation (2): $N_c^{BC} = Q_f / (B' \cdot c_u)$. Table 1 summarizes the results from the FEM analyses. The analytical well-determined value of $N_c^0 = \pi + 2 \approx 5.14$.

Table 1: Plane strain Plaxis results for undrained clay. The value of "Acc." represents $N_c^{BC} / (\pi +2)$.

e [m]	B' [m]	e/B [-]	Q_f [kN/m]	N_c^{BC} [-]	Acc.
0.00	4.00	0.000	206.09	5.15	1.002
0.30	3.40	0.075	179.72	5.29	1.028
0.60	2.80	0.150	148.08	5.29	1.029
0.90	2.20	0.225	116.88	5.31	1.033
1.20	1.60	0.300	85.70	5.36	1.042
1.50	1.00	0.375	54.38	5.44	1.058

Table 1 shows that the bearing capacity factor can be accurately calculated using plane strain FEM, and that the effective foundation width concept is accurate within 5 % accuracy if e/B ≤ 0.30. Shear strain contour plots of selected failure mechanism from Table 1 are seen in *Figure 1*.

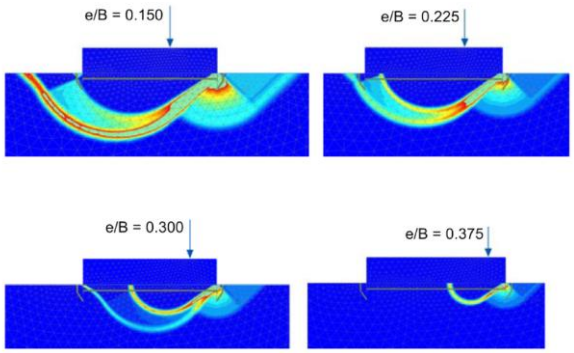


Figure 1 Shear strain contour plots for selected failure mechanisms in Table 1.

The interface strength did not influence the back-calculated bearing capacity factor.

4.2 Axi-symmetry

The axi-symmetric model was initially applied to investigate whether the interface strength would influence the estimated capacity. The back-calculated Plaxis result showed

N_c^{BC} = 6.06 where the theoretical solution implies 6.05, cf. Hansen (1982) and Martin (2004). For the smooth case, the Plaxis model gave 5.71 whereas the theoretical solution implied 5.67. The difference is likely due to the fact that "smooth" in the Plaxis-model was represented through an undrained shear strength of 0.1 kPa. The shear strain contour plots of the failure mechanisms are seen in Figure 2.

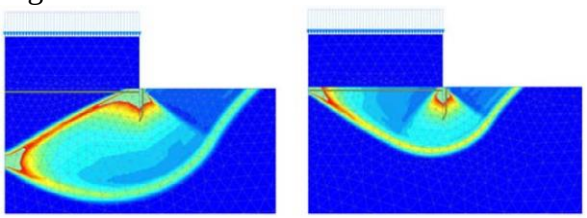


Figure 2: Shear strain contour plots for axi-symmetric failure mechanisms. Left: Completely rough and right: Smooth (0.1 kPa strength).

If the bearing capacity of a square footing equals the capacity of circular footing with the same area, the shape factor is thus s_s^0 = 6.06 / 5.14 = 1.18 for a perfectly rough foundation and 1.10 for a smooth foundation. EC7-DK NA uses s_c^0 = 1.0+0.2·B/L or corresponding to 1.20 for a square footing.

4.3 3D Models

The dependency between s_c^0 and the ratio B/L, where L is the foundation length, is investigated using Plaxis 3D models with a completely rough interface. The mesh of the 3D models include a quarter of the foundation (double symmetry). A vertical load is applied to the foundation, and failure is introduced through φ'-c-reduction. The following analyses are performed:

- A circular foundation in 3D Plaxis representing the axi-symmetrical case available in 2D Plaxis.
- A square footing (B = L).
- Five rectangular foundations (L > B) to investigate s_c^0.

The circular and square footings are compared to the results of the axi-symmetric results in Table 2.
From the results in Table 2 it can be concluded that estimating the bearing capacity of a circular foundation using either axi-symmetry or a 3D analyses leads to very similar results (deviation less than 3%). Furthermore, estimating the capacity of a square or circular footing with equal areas leads to almost identical results.

Table 2: Back-calculated results from Plaxis for circular and square foundations on undrained clay.

Plaxis model	N_c^{BC} [-]
Axi-symmetric (2D Plaxis)	6.06
Circular foundation (3D Plaxis)	6.22
Square foundation (3D Plaxis)	6.16

The results from the five rectangular footings are seen in Figure 3, in which the s_c^0-factor is back-calculated using $s_c^0 = Q_f / (A \cdot c_u \cdot (\pi+2))$.

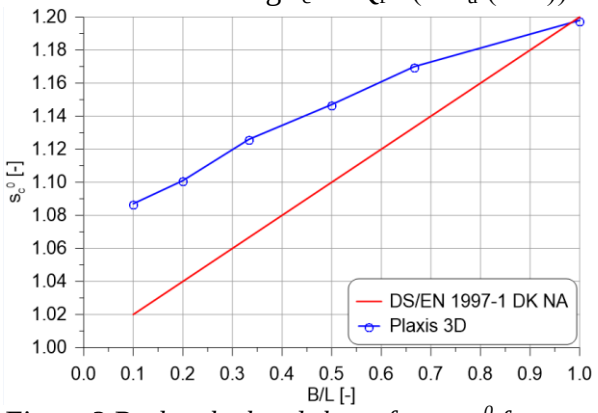


Figure 3 Back-calculated shape factor s_c^0 for undrained clay against the B/L-ratio based on Plaxis 3D results and EC7-DK NA.

Figure 3 shows that as the B/L-ratio decreases the results deviate more and more from EC7-DK NA. However even for B/L = 0.10 the difference is only 6.6 % with EC7-DK-NA being on the safe side, and the results from the two methods may thus be considered almost identical.

4.4 Conclusions

The main conclusions from the undrained analyses are as follows: The N_c^0 value can be estimated correctly using Plaxis 2D and the interface shear strength will not influence the bearing capacity. The adopted principle about the effective foundation width is confirmed up to e/B ≤ 0.30. The theoretical N_c^0 factor for axi-symmetry varies between 5.67 and 6.05 for a smooth and a completely rough interface, respectively. Almost similar results are found using Plaxis 2D models. Compar-

ing plane strain and axi-symmetry reveals a shape factor s_c^0 of 1.10 and 1.18 for smooth and completely rough interface, respectively. EC7-DK NA prescribes 1.20.
Plaxis 3D results indicate that the shape factor s_c^0 from EC7-DK NA is on the safe side.

5 DRAINED ANALYSES q'-CASE

Following equation (1), the drained capacity of a foundation placed on a soil with $\varphi' > 0$, $c' = 0$, $\gamma' = 0$ and a surcharge $q' > 0$ shall be estimated from $Q_f / A' = q' \cdot N_q \cdot s_q$ where the statically admissible solution of N_q is defined by $\tan^2(45°+\varphi'/2) \cdot e^{\tan\varphi'}$ and $s_q = 1.0+0.2 \cdot B/L$ following EC7-DK NA. The formula for N_q is only kinematically admissible for associated flow, i.e. $\varphi = \psi$.

5.1 Plane strain

The plane strain models were based on similar assumptions as for the undrained models except that the undrained shear strength was replaced by φ' and $c' = 0$.
For a vertical and centrally acting foundation load, the 2D Plaxis results were within a 0.5 % accuracy compared to the formula for N_q using φ' in the range of 15° to 45° with associated flow.
The interface shear strength did not influence the 2D Plaxis results.
For $\psi = \varphi' = 30°$, 2D Plaxis revealed $N_q^{BC} = 18.48$ to be compared with $N_q = 18.40$.
Setting $\varphi' = 30°$ and $\psi = 0°$, 2D Plaxis gave $N_q^{BC} = 14.50$ or 22 % reduction compared to associated flow.
Using a partial factor of $\gamma_{\tan\varphi'} = 1.20$ would give a reduction of 38 % for $\varphi' = 30°$. The difference between associated and non-associated flow is thus significant, albeit less significant than the effect of a partial factor of safety.
The influence of the eccentricity of the load was investigated similar to the undrained case, and the result can be seen in Table 3 for associated flow and $\varphi' = 30°$. The load was increased in the calculation until a fully developed failure mechanism occurred.
Table 3 shows that for $e/B < 0.25$ the bearing capacity estimated by Plaxis is up to 8 % higher, while the calculation with $e/B = 0.30$ shows a capacity that is lower than estimated using EC7-DK NA. It was not possible to obtain a failure for $e/B > 0.30$, as this lead to numerical problems.

Table 3: Plane strain Plaxis results for sand. Acc. is calculated as N_q^{BC} / N_q.

e [m]	B' [m]	e/B [-]	Q_f [kN/m]	N_q^{BC} [-]	Acc.
0.30	3.40	0.075	67.45	19.84	1.078
0.60	2.80	0.150	55.41	19.79	1.076
0.90	2.20	0.225	42.37	19.26	1.047
1.20	1.60	0.300	26.81	16.76	0.911

The principle of effective width represents an approximate approach for a drained material, and the accuracy is expected to increase for decreasing friction angles.
Shear strain contour plots of the failure mechanisms from Table 3 are seen in Figure 4.

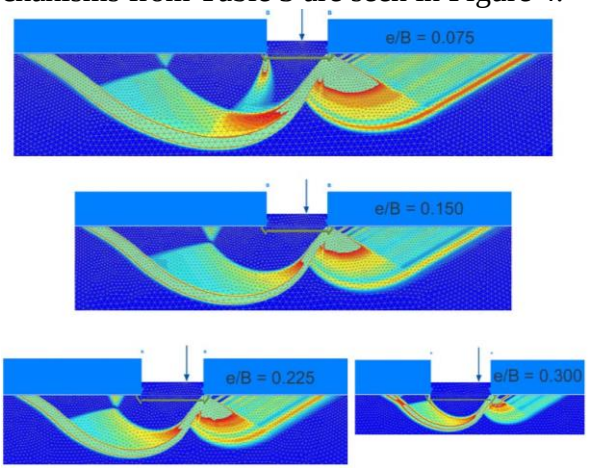


Figure 4 Shear strain contour plots of the failure mechanism investigated in Table 3. The plots are drawn to scale.

5.2 Axi-symmetry

For plane strain the N_q value is unambiguously defined and agreed upon in the literature. This is not the case with the axi-symmetric value of N_q. Albeit not representing a full literature study, some main points are summarized here.
The method of characteristics has been applied by Kumar & Ghosh (2005), Bolton & Lau (1993), Martin (2004) and Hansen (1979). The hoop stress in the model is assumed to be equal to the minor principal effective stress, σ'_3. $N_q = 29.5$ is obtained by Kumar & Ghosh (2005) and by Bolton & Lau (1993) using $\varphi' = \psi = 30°$. Martin (2004) arrives at $N_q = 37.2$ for the same assump-

tions, but he and Hansen (1979) states that the stress characteristics in the Rankine zone (see Figure 5) may cross each other, and the model applied can thus not represent a statically admissible solution.

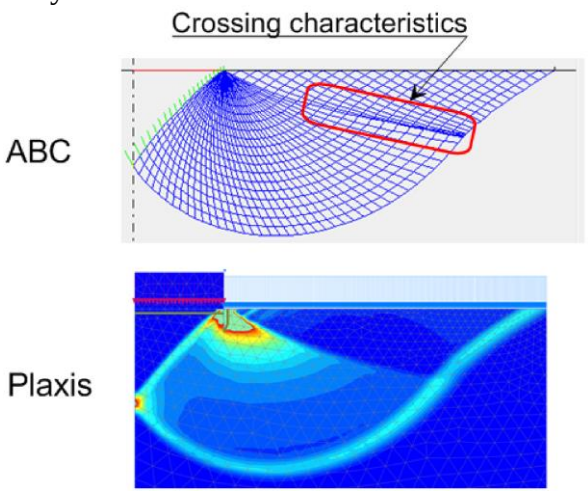


Figure 5 Upper part: Stress characteristics from Martin (2004) using a completely rough foundation base in an axi-symmetric analysis with φ' = ψ = 30°. Lower part: Shear strain contour plot from a similar Plaxis analysis. The plots are drawn to scale.

The observation from Martin (2004) with crossing stress characteristics is not mentioned by Kumar & Ghosh (2005) or by Bolton & Lau (1993), and Martin (2004) writes *"Certainly it appears that many previous researchers, including Cox et al. (1961), Cox (1962), Salençon & Matar (1982a) and Bolton & Lau (1993), have turned a blind eye to the occurrence of crossing characteristics in their meshes, if indeed they were aware of it at all"*.

The results from Martin (2004) do not deviate more than 2 % from similar results using Plaxis for friction angles between 15° and 45°. The approach from Martin (2004) yields almost identical results to those of Lundgren & Mortensen (1953) when calculating drained plane strain problems. In this paper it is therefore assumed that the approach applied by Martin (2004) leads to the "most realistic results".

The approach by Martin (2004) is established as a software code called ABC, which is available online with a documentation manual, enabling the user to calculate failure mechanisms for a wide range of input parameters.

For the q'-case, the shape factor s_q is investigated by the following approach:

- φ'_{tr} is varied from 10° to 45° and φ'_{pl} is estimated from $\varphi'_{pl} = 1.10 \cdot \varphi'_{tr}$.
- ABC is used to estimate the plane strain N_q^{pl} from φ'_{pl}, while N_q^{tr} is estimated from ABC and φ'_{tr}.
- The plane strain and axi-symmetric values are related with: $s_q \cdot N_q^{pl} = N_q^{tr}$.
- N_q^{tr} is estimated using Plaxis to compare.

The results of the investigation are seen in Table 4. N_q^{pl} is derived using φ'_{pl} as the rupture figure for N_q is a plain strain mechanism. A different approach will lead to different values of s_q.

Table 4: Estimated values of N_q using both plane and triaxial friction angles. Comparative axi-symmetrical Plaxis analyses are shown, using φ'_{tr} and associated flow.

φ'_{tr} [°]	φ'_{pl} [°]	N_q^{pl} [-]	N_q^{tr} [-]	N_q^{Plaxis} [-]
10.0	11.0	2.71	2.96	-
15.0	16.5	4.55	5.25	5.28
20.0	22.0	7.82	9.62	-
25.0	27.5	13.94	18.40	-
30.0	33.0	26.09	37.20	37.91
35.0	38.5	52.31	80.81	-
40.0	44.0	115.31	192.73	-
45.0	49.5	290.81	520.62	526.14

Table 4 shows that the values obtained from Plaxis using associated flow resembles those obtained from ABC using the method of stress characteristics. The formula below represents an approximation of the axi-symmetric N_q for a completely rough foundation. The regression coefficient is 0.99:

$$\log_{10}(N_q) = 5.035 \cdot 10^{-4} \cdot \varphi^2 + 3.487 \cdot 10^{-2} \cdot \varphi - 7.776 \cdot 10^{-2} \; [10° \leq \varphi \leq 45°]$$

EC7-DK NA dictates $s_q = 1.20$ for a square footing, independent of φ'. Figure 6 depicts the estimated relationship between s_q and φ' using data from Table 4, Brinch Hansen (1970) and data laboratory tests by de Beer (1970) where $s_q = 1.00 + B \cdot \tan(\varphi')/L$.

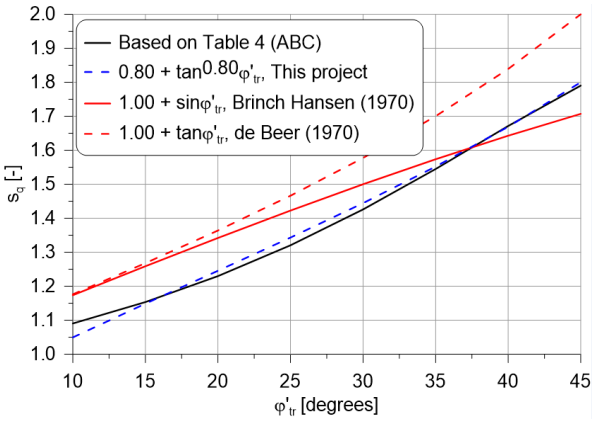


Figure 6: Estimated values of s_q from different approaches.

Using the approach from EC7-DK NA seems to be on the safe side as φ' ≥ ~17°. EC7-DK NA identifies $s_q = s_c$. However, s_c appears to be 10 to 20 % higher than s_q when s_c is evaluated using the procedures applied to estimate s_q.

5.3 3D Models

Modelling in Plaxis 3D were performed to validate the axi-symmetric results and to investigate the s_q factor as the ratio B/L is changed. The investigations were based on completely rough foundations, associated flow with φ' = ψ = 30° and c' = 0.
Failure in the models were found by displacement control. A circular, a square and three rectangular (B < L) foundations were investigated.
Results from the axi-symmetric, circular and square models are shown in Table 5.

Table 5: Back-calculated N_q values from Plaxis models. Martin (2004) estimates N_q = 37.20 for the same case.

Plaxis model	N_q^{BC} [-]
Axi-symmetric, Plaxis 2D	37.91
Circular footing, Plaxis 3D	39.55
Square footing, Plaxis 3D	38.86

Table 5 shows that the results of the axi-symmetric model and the circular foundation in Plaxis 3D leads to very similar values as the difference is less than 4 %. The value of the square footing is almost identical to the circular footing.
Back-calculating results of the Plaxis 3D models leads to an estimate of the s_q factor as seen in Figure 7. The expression from EC7-DK NA and results from de Beer (1970) is shown as well.

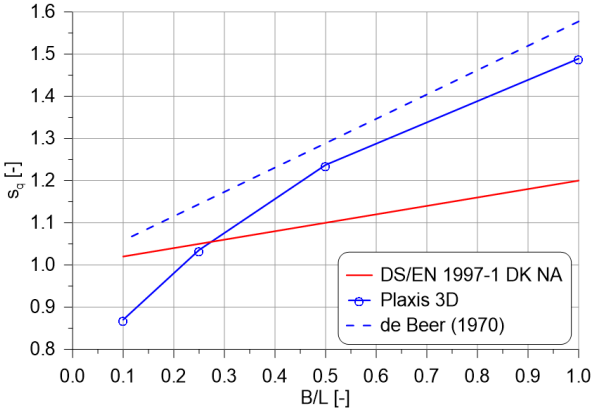


Figure 7: Back-calculated values of s_q for φ = 30° and associated flow.

Figure 7 indicates that the value of s_q from EC7-DK NA is on the safe side for φ' = 30° as the foundation length is below 3-4 times the width. When the length of the foundation exceeds 3-4 times the width the recommendation in EC7-DK NA may be on unsafe side. Results from de Beer (1970) generally show larger values of s_q than the other methods.
The reason for Figure 8 showing $s_q < 1$ for Plaxis 3D results may be due to different failure mechanisms occurring along the foundation. Close to the middle of the foundation the failure will be similar to the plane strain case, while at the ends of the foundation a more complex 3D failure mechanism occurs. This may lead to Plaxis 3D not being able to fully develop failure along the full length of the foundation as the capacity per length of foundation is not equal along the foundation.

5.4 Conclusions

Plane strain analyses with Plaxis leads to similar results as found in Prandtl (1920).
When applying non-associated flow a reduction of the estimated N_q of approximately 20 % is found. For eccentric vertical loads the approach in EC7-DK NA appears on the safe side of e/B < 0.25, for larger values the approach may be unsafe. Comparing plane strain and axi-symmetric models, the s_q value from EC7-DK NA may be unsafe for φ' lower than approximately 20°.
The shape factor from EC7-DK NA for L > B may be on the unsafe side when the founda-

tion length exceeds the width by 3-4 times. However this conclusion might be influenced by numerical issues.
The overall conclusion is that for the drained q'-case results from EC7-DK NA and Plaxis will likely deviate, with Plaxis giving the largest capacities. The size of the overshoot will depend on how the aspects covered in this paper are combined.

6 DRAINED ANALYSES γ-CASE

Following equation (1), the drained capacity for the γ'-case can be estimated from $Q_f / A' = ½ \cdot \gamma' \cdot B' \cdot N_\gamma \cdot s_\gamma$, where B' is the width or diameter of the footing and s_γ is the shape factor, $s_\gamma = 1.0 – 0.4\ B'/L$.
The plane strain value of N_γ was estimated by Lundgren & Mortensen (1953) using a statically admissible solution based on stress characteristics for a Mohr-Coulomb material. Bønding (1970) showed that the solution is kinematically admissible for a wide range of dilation angles ψ. EC7-DK NA includes the following approximation: $N_\gamma = ¼ \cdot ([N_q-1] \cdot \cos \varphi')^{3/2}$, valid for a completely rough interface.
The approach and assumptions described in the q'-case has been reused for the γ'-case, however with the soil weight γ' = 10 kN/m³ and q' = 0 kPa.

6.1 Plane strain

Initially N_γ was investigated using plane strain models. Due to numerical issues a surcharge of q' = 0.1 kPa was added and failure in the model was obtained by either increasing the load (Load) or by adding a prescribed displacement (Disp.). The back-calculated value N_γ^{BC} is found from equation (1) and shown in Table 6. The effect from the surcharge is removed from the Plaxis results.
The results in Table 6 for φ' = ψ = 30° indicate that displacement control may lead to the most accurate results. When using ψ = 0°, the capacity reduces about 20 %, similar to what was found in the q'-case.
The bearing capacity formula is based on superposition of each contribution, and if all the effects from γ', q' and c' are included in one and the same analysis, Lundgren & Mortensen (1953) showed that the estimated bearing capacity would increase by a factor μ being dependent on the ratio $\gamma' \cdot B/(q' + \gamma' \cdot B)$. This effect is not included in the present paper, but the effect can be observed in the results from 2D Plaxis too.

Table 6: Back-calculated plane strain results for sand for a completely rough foundation.

φ' [°]	ψ' [°]	Load-ing	N_γ^{BC} [-]	N_γ [-]	Acc. [-]
15	15	Disp.	1.26	1.18	1.070
30	30	Load	15.96	14.75	1.082
		Disp.	15.49		1.050
35	35	Disp.	36.86	34.48	1.069
30	0	Disp.	12.03	-	-

Table 6 includes analyses covering φ' up to 35° and numerical problems were encountered for higher values of φ'. With φ' = 40° and γ' = 10 kN/m³ the average pressure below a 4 m wide foundation is 1700 kPa, whereas the vertical effective stress on the soil surface next to the footing is 0 kPa. The stress singularity at the edge of the foundation is apparently too strong to allow for a numerical solution with the finite element method.
The effect of eccentric loading was investigated similar to the previous cases and the 2D Plaxis results revealed an overshoot of approximately 5 % for e/B < 0.25. For e/B > 0.25 numerical problems were encountered.

6.2 Axi-symmetry

When the literature is surveyed, the value of the axi-symmetric N_γ–value reveals a significant scatter. Results from Kumar & Ghosh (2005) and from Bolton & Lau (1993) are consistently higher than those values derived from Plaxis and ABC. Bolton & Lau (1993) and Kumar & Ghosh (2005) may not have assumed the critical shape of the failure mechanism.
The Plaxis results from Table 7 are approximately 7 % higher than those obtained from ABC. The lowest row in Table 7 represents a calculation using φ = 30° and ψ = 0°. The estimated capacity is approximately 25 % lower than for associated flow.

*Table 7: Results from ABC and Plaxis used to estimate the axi-symmetric value of Nγ for a completely rough foundation. * ψ = 0°.*

φ' [°]	ABC		Plaxis		Acc. [-]
	Q_f/A [kPa[	N_γ^{BC} [-]	Q_f/A [kPa]	N_γ [-]	
10	6.46	0.32	-	-	-
15	18.7	0.93	20.73	1.01	1.08
20	48.4	2.42	-	-	-
25	121.6	6.08	-	-	-
30	310.8	15.5	335.9	16.61	1.07
35	838.5	41.9	907.0	44.95	1.07
40	2474.5	123.7	-	-	-
45	8356.3	417.8	-	-	-
30*	-	-	249.5	12.29	

Figure 9 shows the shear strain contour plot from Plaxis using φ' = ψ = 35°. Using larger friction angles implied numerical problems.

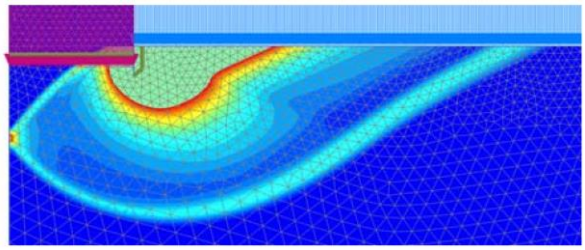


Figure 9: Shear strain contour plot of the axi-symmetric failure mechanism for associated flow, φ' = 30° and a completely rough foundation.

The results from ABC in Table 7 leads to the following approximation of N_γ for a completely rough foundation [10° ≤ φ' ≤ 45°]:

$$\log_{10}(N_\gamma) = 2.576 \cdot 10^{-5} \cdot \varphi^3 - 1.868 \cdot 10^{-3} \cdot \varphi^2 + 1.253 \cdot 10^{-1} \cdot \varphi - 1.581$$

The coefficient of regression is 0.9983.
The shape factor $s_\gamma^{L=B}$ was estimated using the same approach suggested for the q'-case: $s_\gamma^{L=B} = 2N_\gamma^{tr} / (N_\gamma^{pl} \cdot \sqrt{\pi})$, where $D/B = 2 \cdot \sqrt{\pi}$, N_γ^{tr} follows Table 7 and N_γ^{pl} is calculated from Lundgren & Mortensen (1953) with $\varphi'_{pl} = 1.10 \cdot \varphi'_{tr}$. These values are shown together in Figure 10.
In EC7-DK NA $s_\gamma^{L=B}$ is dictated as equal to 0.60 with no dependency on φ', this appears to be on the safe side.

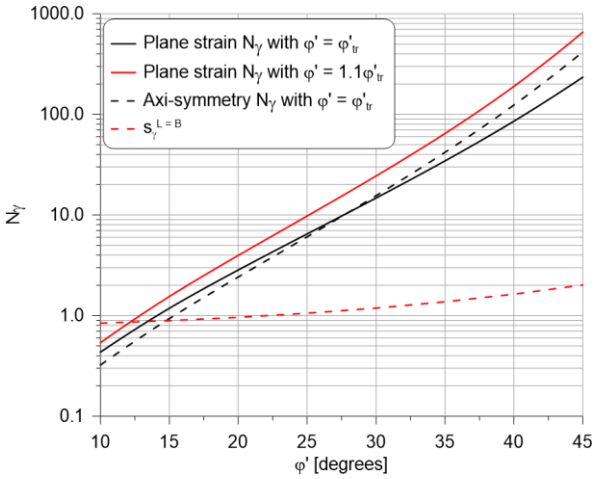


Figure 10: Estimated values of N_γ against the triaxial friction angle. Note that the dashed red curve represents $s_\gamma^{L=B}$ and not N_γ .

6.3 3D Models

The calculations in Plaxis 3D for the pure γ'-case proved to be very challenging to execute to a satisfactory level. As in the Plaxis 2D calculations, a small surcharge was applied to ensure non-zero effective stresses at the soil surface. This was however not enough to ensure stable and reliable calculation results. The results presented in this section are the product of a large number of iterations regarding modelling and numerical parameters, in the attempt to reproduce results similar to the axi-symmetric results and obtain reliable failure mechanism.
It seems that Plaxis 3D calculation for the pure γ'-case is not feasible, as this will lead to numerical issues and results that are not easily reproducible for varying numerical settings. The results of this section should thus be taken as a best estimate based on the work performed within the time frame of this project, and that further work is needed to fully understand the issues involved in executing reliable 3D FEM calculations for a pure γ'-case.
Using q' = 1.0 kPa, γ' = 10 kN/m³ and a diameter of D = 3.54 m, the results shown in Table 8 was obtained.
The failure load is divided by a combination factor μ = 1.18 for φ' = 15° and μ = 1.10 for φ = 30°, before N_γ is back-calculated. This combination factor accounts for the superposition effect of the γ' and q' contribution and is explained in Banedanmark (2014).

*Table 8: Back-calculated values of N_γ for a circular foundation with completely rough interface. * Result from Table 7.*

φ' [°]	Plaxis 3D		Plaxis 2D*	ABC
	Q_f/A [kPa]	N_γ [-]	N_γ [-]	N_γ [-]
15	29.62	1.12	1.01	0.93
30	532.74	25.26	16.61	15.54

Table 8 shows that the 3D models leads to comparable values for φ' = 15°, however for φ' = 30° the values differ by a factor 1.5.
Analyses for rectangular foundations (B<L) were undertaken, and the main results are seen in Table 9. The value of the combination factor μ is calculated based on Banedanmark (2014). The shape factor is calculated as: $s_\gamma = (Q_f/A/\mu - q' \cdot N_q) / (1/2 \cdot \gamma' \cdot B \cdot N_\gamma^{pl})$.
The results for L = B from Table 9 should be directly comparable to Figure 10 as the contribution from q' has been corrected for. For φ' = 15° the values are comparable, however for φ' = 30° they are not.

Table 9: Main results from Plaxis 3D analyses using rectangular foundations with B = 4 m and $\gamma' = 10$ kN/m³.

L [m]	q' [kPa]	φ' [°]	Q_f/A [kPa]	μ [-]	s_γ [-]
4	1.0	15	39.90	1.17	0.973
8	0.1		38.23	1.05	1.162
16			40.01		1.217
40			42.22		1.284
4	1.0	30	387.9	1.09	0.691
8			476.8		0.858
16			489.6		0.882

For the Plaxis 3D analysis with $\gamma' > 0$ and $q' \approx 0$ it has been difficult to identify a clear and consistent final state of failure. Increasing the value of q' will improve converge towards failure.
The singularity at the edge of the foundation is represented by a geometrical point being subjected to a significant foundation pressure at one side and to a stress state of virtually no pressure on the other side, which may cause numerical problems. These problems are present in the 2D and axi-symmetric models as well, however here they only represent a single point in the model, while in the 3D models the singularity is present around the whole circumference of the foundation. The investigation within the time frame available did not allow for a solution of this problem. It might be the case that more elements are needed or that a strength increase in the soil should be present at the points of singularity.

6.4 Conclusions

Plane strain analyses with Plaxis in the γ'-case leads to a bearing capacity factor resembling what can be found from Lundgren & Mortensen (1953) and from EC7-DK NA. The value of N_γ will change as the roughness of the interface is changed. Using non-associated flow will reduce the capacity found by approximately 20 % compared to associated flow for φ' = 30°. For eccentrically acting loads the estimated capacity from Plaxis 2D is approximately 5 % higher for $e/B < 0.25$ using the effective foundation area concept. For larger values of e/B the approach in EC7-DK NA may be unsafe. The theoretical bearing capacity factor N_γ for a circular foundation has been evaluated. It appears that the solution provided by Martin (2004) fits the results of Plaxis 2D. The shape factor s_γ for a square foundation has been found to be larger than given in EC7-DK NA, however the results cannot generally be verified by Plaxis 3D analyses. Plaxis 2D can be used to evaluate the pure γ'-case, however a value of $q' \approx 1.0$ kPa must be used to obtain reliable results. Using q' = 1.0 kPa in Plaxis 3D can be used to evaluate the tendency of s_γ, e.g. it increases with L/B. Back-calculating results from Plaxis 3D with q' = 1.0 kPa has however not turned out to lead to reliable and consistent results. The overall conclusion for the drained γ'-case investigated is that EC7-DK NA and Plaxis will deviate. Mechanisms for plane strain and circular foundations can be studied, but Plaxis 3D results for the pure γ'-case appears to represent a challenge and it is therefore not recommendable to apply Plaxis 3D for capacity calculations in a pure γ'-case. For practical applications however, a pure γ'-case is rarely encountered.

7 COMBINED DRAINED CAPACITY

The combined capacity of the q'- and γ'-case has been investigated in Banedanmark (2014).

The main conclusion are that the results from Plaxis calculations will include the combination factor μ, which is not a part of EC7-DK NA, and a larger capacity will thus be found from Plaxis analyses than using EC7-DK NA. The μ-factor is well-established for the plane strain case, and comparing results from EC7-DK NA and Plaxis 2D including the μ-factor leads to identical results.
The μ-factor is not established for the 3D case, so the influence is not easy to directly isolate. Furthermore the relation between φ'_{tr} and φ'_{pl} is not constant or well determined. Plaxis 3D results will yield a capacity between the values found from EC7-DK NA using respectively φ'_{pl} and φ'_{tr}.

8 CONCLUSIONS

When using Plaxis 2D plane strain to investigate the q'- and γ'-case independently, the bearing capacity factors fit well with EC7-DK NA for vertically acting central loads using associated flow. For eccentrically acting loads, the effective foundation concept is confirmed for a relative eccentricity of up to 0.2 to 0.3 depending on the actual case.
The shape factor s_q as defined in EC7-DK NA may be too high for $\varphi' < 20°$ and too low for $\varphi' > 20°$, using a square footing.
The shape factor s_γ defined in EC7-DK NA is lower than the value found by compared circular and square footings using Plaxis 2D and 3D, however small scale testing from de Beer (1970) supports the approach in EC7-DK NA. Bearing capacity factors for N_q and N_γ are established for circular foundations. Most authors agree in the value for N_q, but N_γ appears to be too high. The results from Martin (2004) fits well with those values established using Plaxis 2D. The results from Plaxis 3D show that the pure γ'-case cannot be analysed and a surcharge must be added. The plane strain effect with $\varphi'_{pl} > \varphi'_{tr}$ cannot be investigated in Plaxis 3D as the material models do not reflect this aspect, so φ'_{tr} must be used in Plaxis 3D. The bearing capacity estimated with φ'_{pl} and EC7-DK NA appears to be higher than found with Plaxis 3D and φ'_{tr}. Shape factors are empirical factors and deriving exact values by the finite element method will be influenced by the choice between φ'_{pl} and φ'_{tr}, the μ-factor and the element net applied.

9 FURTHER WORK

The 3D FEM results reveal a challenge when estimating the capacity for the γ'-case. More work should be undertaken in order to better understand this issue. It might be the case that the mesh used in the calculations is simply not fine enough to reproduce correct results or that other measures should be undertaken in order to handle to singularities at the edge of the foundation.

10 ACKKNOWLEDGEMENTS

The authors are grateful for being allowed to publish the work by Banedanmark.

11 REFERENCES

Bolton, M.D. & C.K. Lau (1993). Vertical Bearing Capacity Factors for Circular and Strip Footings on Mohr-Coulomb Soil, Canadian Geotechnical Journal, Volume 30, pp. 1024-1033.

Hansen, Bent (1982). Geoteknik og Fundering III, 1982, Notat 24, Særlige problemer.

Brinch Hansen (1970). A Revised and Extended Formula for Bearing Capacity, Bulletin 28, The Danish Geotechnical Institute, Copenhagen 1970.

Bønding, N. (1977). Kinematically Admissibility of the Pure N_γ Rupture Figure, Proceedings of the Ninth International Conference on Soil Mechanics and Foundation Engineering, 1977, Tokyo.

de Beer, E.E. (1970), Experimental Determination of Shape Factors and the Bearing Capacity Factors of Sand, Geotechnique 20, Number 4, 387-411.

DS/EN 1997-1, Eurocode 7: Geotechnical Design– Part 1: General Rules, Danish National Annex 2013 included.

Kumar, J. & P. Ghosh (2005). Determination of N_γ for Rough Circular Footings Using the Method of Characteristics, Electronic Journal of Geotechnical Engineering, Paper 2005-0540

Lundgren, H. & K. Mortensen (1953). Determination by the theory of Plasticity of the bearing capacity of Continuous Footings on Sand, Proc. 3rd Int. Conf. Soil Mech., Volume 1, p. 409, Zürich 1953.

Martin, C.M. (2004). User's Guide, ABC - Analysis of Bearing Capacity, Version 1.0, Department of Engineering Science, University of Oxford, OUEL Report No. 2261/03.

Prandtl, L. (1920). Über die Härte plastischer Körper, Nachr. D. Ges. D. Wiss., math-phys. Kl. Göttingen 1920.

Numerical models on anisotropy of rocks

Henok M. Kassa
Statoil ASA, Norway, hmka@statoil.com

Steinar Nordal
Norwegian University of Science and Technology, Norway, steinar.nordal@ntnu.no

ABSTRACT
Most rocks found in nature are inherently anisotropic, which exhibit a variation in mechanical properties in different directions. But due to formation processes rock that we encounter are Transversely Isotropic, which has the same property in one plane and different properties in directions normal to this plane.

To understand and capture the behavior of such rocks, scholars have proposed models (criteria), which are either strength or stiffness dependent. But in this paper among the many criteria proposed so far, only some representatives have been discussed. These criteria are classified in to three groups; mathematically continuous criteria, empirical continuous criteria and weakness plane based criteria. Experimental data have been extracted from literatures; Such as, F. A, Donath 1964, a triaxial data on Martinsburg slate. Strength Anisotropy is used as a main parameter to evaluate the anisotropy of rocks. Then a comparison is performed between the experimental data and the selected failure criteria.

In addition, numerical simulation for layered rock system, which can represent transversal isotropic behavior, has been conducted using a commercially available finite element code PLAXIS. And the result was compared with experimental data for artificially prepared layered rocks, Yi-Shao Lai, 1999.

Keywords: Anisotropy, Bedding plane, Failure criteria, Plaxis.

1 INTRODUCTION

Geo-materials, including rock and soil, are often highly anisotropic, i.e., their properties vary with direction. A material is considered anisotropic if its strength properties are dependent on the direction of the applied stresses. For instance, the elastic stiffness in one direction may be more than double that in another direction. In many engineering application anisotropy is neglected as it is difficult to determine the anisotropy parameters. The structure of a rock is characterized by a number of factors, which may have a particular orientation: bedding, stratification, schistosity planes, foliation, cracking, joints. Anisotropy, which is a characteristic of metamorphic rocks such as schist, slate or gneiss, is due to the existence of mineral foliation. Sedimentary rocks such as sandstone, shale and limestone may be anisotropic, as a result of stratification. On a larger scale, any rock mass may be crosscut by one or more families of discontinuities. In this paper, we focus on a type of rocks with a particular anisotropy which is interesting in that it combines mineral orientation and cracking.

In general the objective of this paper is to evaluate the effect if anisotropy on the strength and deformation characteristic of

transversely isotropic rocks, where linear type of anisotropy is dealt in detail. Furthermore, different proposed anisotropic failure criteria have been discussed and used to estimate the failure strength of transversely isotropic rocks and compare is with experimental results and simulation results from a 2D commercial FEM program, PLAXIS.

1.1 Anisotropy in Rocks

Rock anisotropy is a well-known behavior and is of considerable interest in the field of rock mechanics and engineering. This behavior related to both transport and mechanical properties is highly dependent on the sampling orientation with respect to loading directions.

Natural soils or rocks exhibit two common types of anisotropy in stiffness: *inherent* and *stress induced*

Several types of rocks, such as metamorphic and sedimentary rocks, have inherent or structural anisotropy. Among sedimentary rocks, the most widespread are shale, siltstone and clay stone. These rocks, which are formed by deposits of clay and silt sediment, exhibit strong inherent anisotropy, manifesting itself in a directional dependence of deformation characteristics. The anisotropy is strongly related to the microstructure, in particular the existence of bedding planes which mark the limits of strata and can be easily identified by a visual examination. The study of the mechanical behavior of sedimentary rocks, especially shale and mudstone, is of particular interest to the oil exploration industry as well as to civil and mining engineering.

An induced anisotropy is common in granular soil mass when the materials re-orientation and re-arrangement occurs under stress orientation. Induced anisotropy is directly related to strain-induced particle re-orientation associated with changes in stress (Cassagrande and Carrillo, 1944).

1.2 Representation of Rock Anisotropy

Among different testing techniques and testing methods for determining the anisotropic parameters of rocks, the most classical experiment is the conventional triaxial compression test, with various loading orientations and confining pressures. Results of the investigation are expressed in terms of strength anisotropy which can be represented using plots of stress-strain and compression strength vs. orientation angle of the bedding plane (anisotropy curve). Here the Author prefers to deal with the later type of plots as it is straight forward and can easily explain anisotropy.

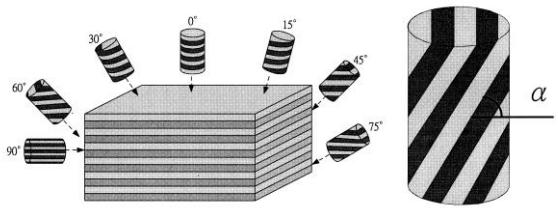


Figure 1 Samples taken at different orientation of bedding or schistocity planes

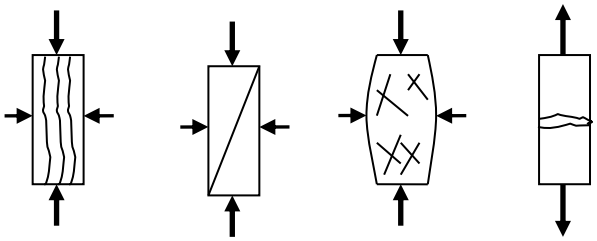
Most anisotropic geo-materials are either orthotropic or transversely isotropic materials. For a general anisotropic material, each stress component is linearly related to every strain component by independent coefficients.

$$\sigma_{ij} = \sum_{k,l} C_{ijkl}\varepsilon_{kl} \tag{1}$$

Failure of transversely isotropic rocks under uniaxial tests have been catagorized in to two types, i.e., failure of the intact rock as a whole (matrix or intact failure) and failure along the weak schistose plane (sliding type failure). Several scholars have developed failure criteria for transversely isotropic and orthotropic rocks that account for strength anisotropy with respect to orientation of bedding angle and confining pressures. Here the author has tried to discuss some of it.

2 FAILURE CRITERIA (MODELS) FOR ANISOTROPIC ROCKS

Analysis of a wide range of problems related to geo-materials requires knowledge of failure processes in the materials. Rock fails when the surrounding stress exceeds the tensile, compressive or the shear strength of the rock formation. There are several types of rock failure depending on rock lithology, rock microstructures and applied confining stresses.



(a) *(b)* *(c)* *(d)*

Figure 2 Rock failure types (a) Splitting, (b) Shear failure, (c) Multiple shear fracture, (d) Tensile Failure

Over the years, a number of failure criteria, which can reasonably estimate the stresses and strength of anisotropic geo-materials have been proposed. The basic frame work of these criteria is derived from isotropic homogeneous bodies.

Failure criteria can be classified as: stress-based and non-stress based types. Stress based failure criteria are mostly for brittle or ductile materials. It is completely dependent on the stresses acting on the material. In order to define such kinds of criteria we need to perform a hand full of tests (such as: uniaxial tension/ compression), whereas, in a Non-stress based criteria, whether a material succeeds or fails may depend on other factors such as stiffness, fatigue resistance, creep resistance, etc.

The various failure criteria for anisotropic materials, based on assumptions and techniques used can also be classified in to three main groups (G. Duveau etal, 1998):

I) Mathematical continuous approach: These criteria consider continuous body with a continuous variation of strength. Mathematical techniques and material symmetries are used to describe anisotropy in strength. W.G. Pariseau, 1972, proposed a model that can be categorized in this approach. The model is basically a modification of Hill Criterion, except that it accounts the strength difference in tensile and compressive loading and the dependency of strength on the mean stress.

II) Empirical continuous criteria: It involves determination of variation laws as a function of the loading orientation for some materials parameters used in an isotropic criterion. The variation laws are fully empirical in nature and are calibrated from experimental investigation. As an example we can have a look at one of the model proposed by J.C. Jaeger, 1971.

III) Discontinuous weakness planes based theories: Criteria (models) under this category include the physical mechanisms in the failure process. Besides, it's assumed that anisotropic bodies fail either due to the fracture of the bedding planes or the fracture of the rock matrix. For instance, E. Hoek, 1983, describes distinctively on the two modes of failure (along bedding plane and rock matrix failure).

2.1 Single plane of weakness theory by Jaeger

It is a discontinuous weakness plane based criteria. In this theory, the anisotropic material is seen as an isotropic body containing one set of weakness planes. The failure in the rock matrix and along weakness

planes is together described by the Mohr-Coulomb type criterion. However, the values of cohesion and friction are different for rock matrix and weakness planes. Thus, the failure criterion is expressed by the following equations:

For rock matrix failure

$$\tau = c + \sigma \tan\phi \qquad (2)$$

For bedding plane (weakness plane) failure

$$\tau_\theta = c' + \sigma_\theta \tan\phi' \qquad (3)$$

Where: ϕ and c are friction angle and cohesion of the intact rock (rock matrix) with τ and σ are the shear and normal stress in the Mohr diagram. But in equation (3), c' and ϕ' are the cohesion and friction angle on the weak (bedding plane) oriented at θ degree from the horizontal plane. In addition, τ_θ and σ_θ are the shear and normal stresses on the weak plane.

This criterion needs four material parameters to define it that are easy to determine from a conventional triaxial test. ϕ and c can be determined from tests conducted on a specimen with bedding plane orientation of θ=0 and θ=90, see *Figure 1*. However, many experimental results show that the strength at θ=0 is different from that of at θ=90. Therefore, it is important to determine cohesion and friction angles for the two cases. Meanwhile, the other two parameters of the model, for failure along the weak plane can be determined from triaxial tests for bedding orientations of $30^\circ \le \theta \le 45^\circ$. This is because failure along weakness plane is usually expected at these values of orientation angles.

Table 1 Martinsburg slate tested by F.A., Donath

	σ_1(Mpa)						
σ_3(Mpa)	θ=0	θ=15	θ=30	θ=45	θ=60	θ=75	θ=90
3.5	128	51	22	43	75	128	194
10	162	82	44	63	102	160	241
35	272	134	87	107	150	216	335
50	355	172	129	150	194	284	410
100	530	286	230	260	315	456	600

This criterion provides a fairly accurate simulation of experimental data for transversely isotropic materials but it requires a wide range of tests and considerable amount of curve fittings. In this paper, for a purpose of comparison, the data from Martinsburg slate tested by Donath F.A., 1964, *Table 1*, has been used.

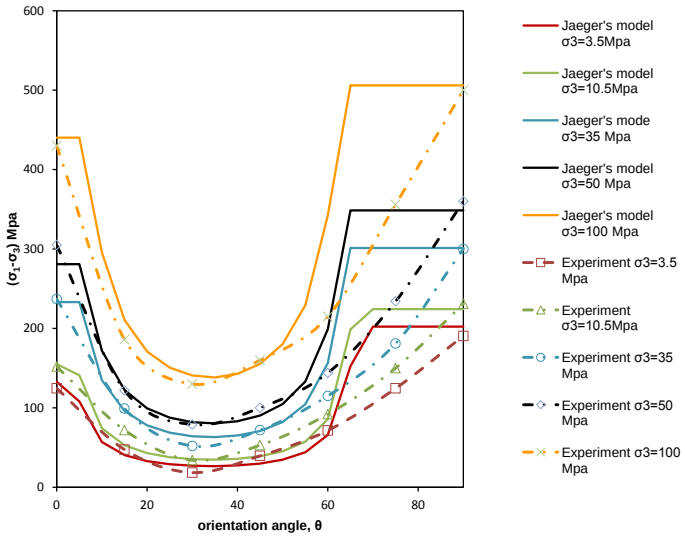


Figure 3 Comparison of Jaeger's single plane of weakness criteria and experimental data

Even if the distinction between the two failure mechanisms may appear too simplistic for such type of discontinuous based failure criterion, we can see good agreement between the numerical and experimental values when the bedding orientation θ<60. But it appears to be a disadvantage of this simple criteria to overestimate the strength when the bedding orientation is 60<θ<90.

2.2 Hoek-Brown Failure Criterion

Based on previous studies by Jaeger, J. C. 1971, Hoek & Brown, 1980 have developed an empirical mathematical model which

adequately predicts fracture propagation in rocks. In developing this empirical relationship between the principal stresses Hoek and Brown have attempted to satisfy the following conditions:

- The failure criterion should give good agreement with experimentally determined rock strength values.
- The failure criterion should be expressed by mathematically simple equations based, to the maximum extent possible, upon dimensionless parameters.
- The failure criterion should offer the possibility of extension to deal with anisotropic failure and the failure of jointed rock masses.

The process used by Hoek & Brown, 1980 in deriving their empirical failure criterion was one of pure trial and error from many experimental data. The proposed criterion is based on major and minor principal stresses.

$$\sigma_1 = \sigma_3 + (m\sigma_c\sigma_3 + s\sigma_c^2)^{0.5} \quad (4)$$

Where, σ_1 and σ_3 are major and minor principal stresses; σ_c is the uniaxial compressive strength of the intact rock matrix. m and s are empirical parameters of this criterion. The constant m has a positive value ranging from 0.001 for highly disturbed rock to 25 for hard intact rocks, while the value of the constant s varies from 0 for jointed rocks to 1 for intact rock mass

The original criteria proposed by Hoek and Brown, 1980 equation (4) was based on isotropic rock mass. But rocks like slates and shales are schistose or layered inherently, which shows different strength on the schistocity plane to that of planes perpendicular to it. In order to determine the strength variations of such rocks in relation to the orientation of the schistocity plane , some modifications on the original theory have been added. Hoek in 1983, proposed a different approach for schistose rocks by making use of the strength variation of a rock mass containing schistosity as described by Jaeger and Cook 1969.

$$\sigma_1 = \sigma_3 + \frac{2(c_i+\sigma_3 tan\phi_i)}{(1-tan\phi_i tan\theta)sin2\theta} \quad (5)$$

Where c_i and ϕ_i are the instantaneous cohesion and friction on the weakness plane. θ is the orientation of bedding plane from the direction of major principal stress. Equation (5) as $\theta \to 0$ and $\theta \to 90$ gives us unrealistic values of strength, which means that the failure criteria in this region is defined by the original criteria as given in equation (4). Hoek and Brown suggested the use of equation (5) when weak plane's orientation is in the range of $\theta = \phi \pm 25$.

Equation (5) is invariably dependent on pre-determined values of the instantaneous cohesion and friction values of the weak plane. In order to determine strength parameters of a rock along its weak plane, various empirical formulations have been suggested. However, in this paper, owing to the fact that several experimental results were found to fit the curves, the relationships detailed in equation (6) – (8) have been selected.

$$\phi_i = A\arctan\left[h\cos^2(30+\frac{1}{3}\arcsin h^{-\frac{3}{2}}) - 1\right]^{-\frac{1}{2}} \quad (6)$$

Where :

$$h = 1 + \frac{16(m\sigma_n + s\sigma_c)}{3m^2\sigma_c} \quad (7a)$$

$$\sigma = \frac{\sigma_1+\sigma_3}{2} - \frac{\sigma_1-\sigma_3}{2} cos2\theta \quad (7b)$$

and the instantaneous cohesion can be calculated from:

$$c_i = \tau - \sigma_n \tan\phi_i \quad (8)$$

Data from the Martinsburg slate, *Table 1*, has once more been used to assess the quality of the Hoek-Brown criterion. And as can be seen from the plots, H-B model vs.

experimental data, prediction of strength variation with schistosity angle is fairly accurate where weakness plane orientation lies within 20<θ<60.

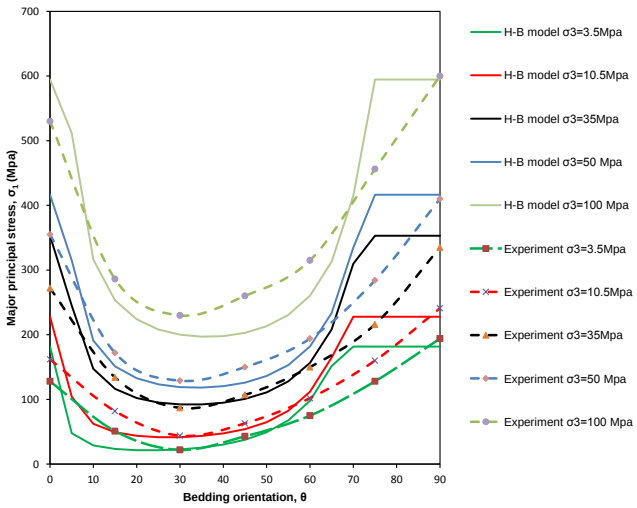


Figure 4 Major principal stress vs bedding oreintation of Martinsberg slate from experimental data as compared to Hoek - Brown Model(H-B)

2.3 Tien and Kuo's criteria for transversely isotropic rocks

Tien and Kuo's failure criterion is one of the criteria that describes the anisotropic response of transversely isotropic rocks such as: schist, slates, genesis, shale, sand stone shale and phylites, where the properties of these rocks are highly dependent on the direction of schistocity.

This model is based on Jaeger's, 1960 criteria and maximum axial strain theory. Unlike Hoek-Brown model, Tien and Kuo, 2001 based their criterion on the deviatoric stress causing the failure of transversely isotropic.

$$S_{1(\theta)} = \sigma_{1(\theta)} - \sigma_3 = \frac{2(c_i+\sigma_3 tan\phi_i)}{(1-tan\phi_i tan\theta)sin2\theta} \quad (9)$$

In addition to the classical modes of failure for transversely isotropic rocks, failure in rock matrix structure and failure along weak plane, Tien and Kuo, 2006 have demonstrated on experimental investigation of simulated transversely isotropic rock that such rocks also may fail due to axial strain accumulation. The axial strains can be calculated from the constitutive equation of transversely isotropic materials, equation (10).

$$\begin{bmatrix}\varepsilon_{11}\\ \varepsilon_{22}\\ \varepsilon_{33}\\ \gamma_{23}\\ \gamma_{31}\\ \gamma_{12}\end{bmatrix} = \begin{bmatrix} \frac{1}{E} & \frac{-\upsilon'}{E} & \frac{-\upsilon}{E'} & 0 & 0 & 0\\ \frac{-\upsilon'}{E} & \frac{1}{E} & \frac{-\upsilon}{E'} & 0 & 0 & 0\\ \frac{-\upsilon}{E'} & \frac{-\upsilon'}{E} & \frac{1}{E} & 0 & 0 & 0\\ 0 & 0 & 0 & \frac{1}{G'} & 0 & 0\\ 0 & 0 & 0 & 0 & \frac{1}{G'} & 0\\ 0 & 0 & 0 & 0 & 0 & \frac{1}{G} \end{bmatrix} \begin{bmatrix}\sigma_{11}\\ \sigma_{22}\\ \sigma_{33}\\ \tau_{23}\\ \tau_{31}\\ \tau_{12}\end{bmatrix} \quad (10)$$

Where E, E', ν, υ', G and G' are elastic constants of a transversely isotropic material on plane of isotropy and on a plane normal to it.

As it is apparetnt, constitutive equation is usually given in local coordinate system but if we have to deal with axial strains we need to transform the elastic parameters of the material in to global system.

$$[K] = [Q]^T[K'][Q] \quad (11)$$

Where $[K]$ and $[K']$ are stress-strain relationship matrices in global and local coordinate axes respectively. $[Q]$ is a suitable 6X6 matrix involving direction cosines of local axes in the global axes.

In this paper a transformation technique introduced especially for transversely isotropic rocks by Amadei, 1996 has been adopted . Amadei's proposal uses the theory of elasticity and considering the above conditions for anisotropic and assuming uniform distribution of stress and strain in the specimen, $\varepsilon_x, \varepsilon_y, \varepsilon_z$ and γ_{xy} can be related to the applied stress σ in uniaxial compression test as follows:

$$\begin{bmatrix}\varepsilon_{xx}\\ \varepsilon_{yy}\\ \varepsilon_{zz}\\ \gamma_{yz}\\ \gamma_{xz}\\ \gamma_{xy}\end{bmatrix}=\begin{bmatrix}a_{11} & a_{12} & a_{13} & 0 & 0 & a_{16}\\ a_{12} & a_{22} & a_{23} & 0 & 0 & a_{26}\\ a_{13} & a_{23} & a_{33} & 0 & 0 & a_{36}\\ 0 & 0 & 0 & a_{44} & a_{45} & 0\\ 0 & 0 & 0 & a_{45} & a_{55} & 0\\ a_{16} & a_{26} & a_{36} & 0 & 0 & a_{66}\end{bmatrix}\begin{bmatrix}0\\ S_1\\ 0\\ 0\\ 0\\ 0\end{bmatrix} \quad (11)$$

Where $a_{11}, a_{22}, \ldots, a_{66}$ are transformation matrix constants and S_1 deviatoric stress$(\sigma_1 - \sigma_3)$.

$$a_{12} = -\frac{\nu'}{E'}\sin^4\theta - \frac{\nu'}{E'}\cos^4\theta + \frac{\sin^2 2\theta}{4}\left(\frac{1}{E'} + \frac{1}{E} - \frac{1}{G'}\right)$$

$$a_{22} = \frac{\sin^4\theta}{E} + \frac{\cos^4\theta}{E'} + \frac{\sin^2 2\theta}{4}\left(\frac{1}{G'} - \frac{2\nu'}{E'}\right)$$

$$a_{23} = -\frac{\nu'}{E'}\cos^2\theta - \frac{\nu}{E}\sin^2\theta$$

$$a_{26} = \sin^2 2\theta\left[\cos^2\theta\left(\frac{1}{E'} + \frac{\nu'}{E'}\right) - \sin^2\theta\left(\frac{1}{E} + \frac{\nu'}{E'}\right)\right] - \frac{\sin 2\theta \cos 2\theta}{2G'}$$

Since the experimental data from Donath F.A., 1964, *Table 1*, is used to verify Tien and Kuo's model, only the stress-strain relationship in the major prinicipal direction, corresponding to a uni-aixl test condition, is considered.

$$\varepsilon_{yy} = a_{22}S_1 \quad (13)$$

$$E_y = \frac{1}{a_{22}} \quad (14)$$

Failure of transversely isotropic rocks may occur due to strain accumulation i.e., when the maximum failure strain reaches prior to rock matrix or weak plane failure. Each bedding plane orientation has its own maximum failure strain which can be expressed in terms of the maximum deviatoric stress.

$$S_{1(\theta)} = \frac{\varepsilon_{yf}}{a_{22}} = E_y\varepsilon_{yf} \quad (15)$$

Where: ε_{yf} is the maximum failure strain that varies with confining pressure independent of bedding plane orientation.

According to Tien and Kuo's model, the strength of a transversely isotropic at bedding orientation angles of θ=0 and θ=90 can be described using Hoek and brown criteria, equation (4). However, several test data is required to calibrate the model parameters where failure along the weak plane (bedding plane) is expected. The experimental data on Martinsburg slate tested by Donath F.A., 1964, has once more been used to check the criterion proposed by Tien and Kuo, 2001.

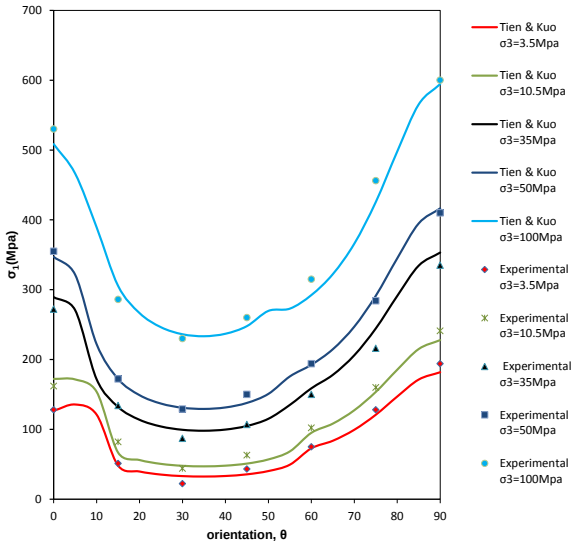


Figure 5 Comparison of experimental data (after Donath F.A., 1964) and Tien and Kuo's 2001 model

The comparison between the experimental work and the prediction from the model shows good agreement for different confinig pressures. In addition, we can observe the sharp change on the curvatures of the model at points where the the assumed failure is changing from non-sliding to a sliding type of failure. This is simply due to change in the mathematical expression used for the criteria at this specific points. Comparing this criteria with the other discontinuous type of criteria discussed above Tien and Kuo's criterion has only seven parameters that can be determined from a few triaxial tests . Moreover, It is versatile and fairly accurate.

3 FEM SIMULATION OF TRANSVERSELY ISOTROPIC ROCK

There have been significant advances in the use of the computational methods in rock mechanics in the last three decades. The complexities associated in the discipline of rock mechanics necessitates the use of modern numerical methods. With the rapid advancements in computer technology, numerical methods provide extremely powerful tools for analysis and design of engineering systems with complex factors that was not possible or very difficult with the use of the conventional methods, often based on closed form analytical solutions.

Rock mass is largely discontinuous and anisotropic by nature, and this makes rock a difficult material to represent it mathematically for numerical modeling. However, several FEM based tools have been developed to capture the essential mechanical behaviour of anisotropic geo-materials. In this paper a 2D FEM program, PLAXIS, is used to simulate the mechanical (stress-strain) relationships of a trasnasversely isotropic material.

3.1 Use of Interface in layered rocks to simulate transversely isotropic rocks

Anisotropic rocks, which have different mechanical properties in different directions, require a lot of experimental samples to determine its properties. Because of high variability of the natural rock due to their formation process, geological environment, weathering and mineral composition, it is difficult to obtain a great number of field specimens with uniform properties. Therefore it is necessary to use artificially created rocks.

Artificially prepared rocks can be used to simulate an interstratified rock blocks that is transversely isotropic rocks. It is enough to use a bilaminated artificial rock in order to simulate variation of strength along with the inclination of the inter bedding planes between the two constituent materials. Here, artificially layered rock triaxial data has been extracted from literature, Yi-shao etal, 1999. Each of the layers are isotropic rocks which can be described with Mohr-Coulomb criterion. For demonstrating purpose artificial rock made of two different cement types is used to represent a layered transversely isotropic rock. The experimental results are shown below:

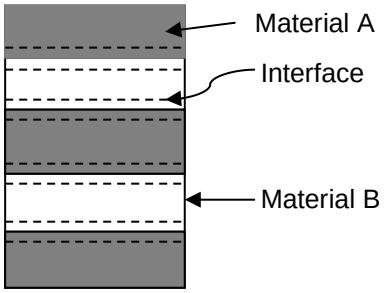


Figure 6 A stack of two different materials representing Bi-layered rock

The objective is to simulate the real situations mentioned above in PLAXIS 2D. The layered rock is modeled as two different isotropic rocks stalking on one another. The contact between the two materials has been simulated using interface elements.

For demonstrating purpose artificial rock made of two different cement types is used to represent a layered transversely isotropic rock. The experimental results are shown below:

Table 2 Maximum principal stress on artificially prepared rock (After Yi-Shao etal, 1999)

σ_3	σ_1 [Mpa]						
[Mpa]	θ=0	θ=15	θ=15	θ=30	θ=45	θ=60	θ=90
0	14.3	12.7	12.6	4.44	3.57	6.72	21.4
2.5	21.3	20.5	17.0	10.77	10.4	13.02	26.5
5	25.4	24.2	22.1	20.5	18.8	20.1	33.1
10	29.3	29.3	27.1	25.0	26.9	30.5	44

From the aforementioned triaxial experiment on the artificially prepared layered material, it was observed that the following kinds of failures were common:

Overall failure mode: this failure mode can be obtained when all the constituent layers

reach their ultimate strength or the critical conditions. It can due to the fact that the constituent layers are ductile and the strength difference between the layers is small.

Mid inclination failure mode: this will happen when only the weakest layer fails, i.e., when $\tau_w = c_w + \sigma_w \tan\phi_w$ is maintained (Where τ_w and σ_w are shear and normal stress in the weak plane; c_w and ϕ_w are the cohesion and friction angle of the weak layer.

Interface failure mode: such a failure happens along the contact (interface) area between the two layers. In this case the failure criteria is dependent on the strength of the interface not on the constituent layers, i.e., $\tau_i = c_i + \sigma_i \tan\phi_i$ (Where τ_i and σ_i are shear and normal stress on the interface; c_i and ϕ_i are the cohesion and friction angle of the weak layer.

Low inclination failure mode: for most artificially prepared layered rocks with bedding angle orientations of $0 \le \theta \le 60$ (low inclination), failures occurs in single consistent layer. In other words low inclination failures are dominated by single layer.

From experimental tests on the two constituent cement like materials of the bi-layered rock used by Yi-shao etal,1999, the following strength and stiffness parameters were found. The interface parameters were obtained by back calculating experimental data for failure along the contact (interface) area. For this case it was observed that failure along the interfaces happens when $\theta = 60$.

Table 3 Stiffness and strength parameters of the constituent materials

	c [Mpa]	**ϕ [°]**	**E [Mpa]**	**ν [-]**
Material A	10.2	25	7000	0.22
Material B	6.34	15	2500	0.13
Interface	0.98	29	-	-

Using the above back calculated parameters, a traixial test was simulated. The geometrical model consists of two different materials, each following Mohr-Coulomb material model. These materials are assumed to be layered on each other and the contact area between the materials is modeled using interface element. For the general geometry of the sample a medium mesh was used but at the interfaces a refined mesh was used.

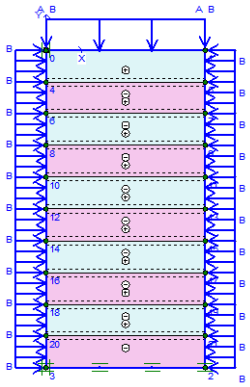


Figure 7 Geometrical model of the layerd material in Plaxis – simulating a triaxial test

The results from the FEM simulations have shown that when the plane containing the interface is oriented in such a way that $45 \le \theta \le 75$ the strength decreases and attains it minimum value at $\theta = 60$. This observation was also manifested from the experimental results. Figure shows the comparison between experimental data and numerical simulation, which are in a very good agreement.

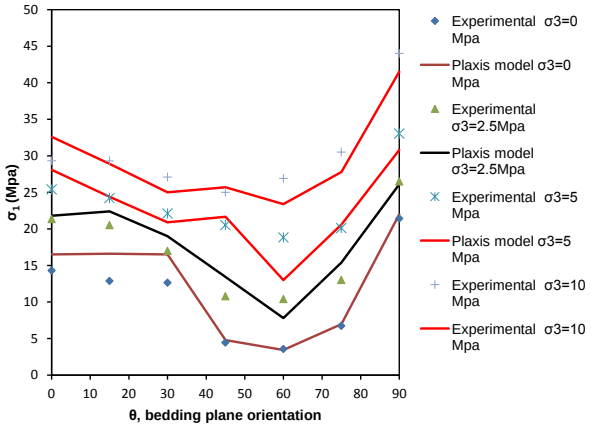


Figure 8 Comparison of results from experiment (Yi-shao etal, 1999) and Plaxis

4 CONCLUSION AND RECOMMENDATION

Summaries of the different failure criteria and numerical simulation using PLAXIS have been discussed in the previous sections. Herein the important findings are presented.

- The compressive strength behavior of anisotropic rocks is a function of both the confining pressure and the orientation of the bedding plane to the applied stress. The minimum compressive strength usually occurs within $30 \le \theta \le 60$, whereas the maximum strength occurs at $\theta = 90$.
- Anisotropic rocks with weak planes of weakness exhibit two kinds of failures which are failure along weak plane and failure in the rock matrix.
- Failure criteria based on weakness plane can describe the strength behavior of anisotropic rocks. However, it is difficult to implement in Finite element programs.
- Layered rock simulation in PLAXIS can give good approximation to transversely isotropic rocks.

From discussions in this paper some questions are answered relative to the strength behavior of anisotropic rocks, but those questions left unanswered will be evident that a great deal more work remains to be done in this field. A better understanding of the mechanics of jointed rock mass behavior is a problem of major significance in geotechnical engineering, and it is an understanding to which both the traditional disciplines of soil mechanics and rock mechanics can and must contribute. The author hopes that the ideas presented will contribute towards this understanding and development.

5 REFERENCES

Amadei B. (1996), Importance of anisotropy when estimating and measuring in situ stresses in rock, International journal of rock mechanics and mining science, Vol. 33, No. 3, pp. 293 – 325.

Casagrande, A. & Carillo, N. (1944), Shear failure of Anisotropic Material, Proceedings of Boston society of civil engineers, Vol. 31, pp. 74 – 87.

Donath F.A. (1964), A strength variation and deformational behaviour of anisotropic rocks, State of stress in Eath's crust, New York, Elsevier, pp. 281-297

Duvea, G. etal (1998), Assessment of failure criteria for strongly anisotropic geomaterials, Mechanics of cohesive frictional materials, Vol. 3, pp. 1-26.

Hoek E. (1983), Strength of jointed rock masses,, Geotechnique, Vol. 33, No. 3, pp. 187 – 223.

Hoek E. & Brown E.T., (1980), Empirical strength criterion for rock masses, Journal of geotechnical engineering division, ASCE, 106, No. GT9, pp. 1013 – 1035.

Jaeger, J.C. (1971), Friction of rocks and stability of rock slope, Geotechnique, Vol. 21, No. 2, pp. 97 – 134.

Jaeger, J.C. & Cook, N.G. (1969), Fundamentals of rock mechanics, Chapman & Hall, London.

Jaeger, J.C. (1960), Shear failure of anisotropic rocks, Geological Magazine, Vol. 97, No. 1, pp. 65 – 72.

Pariseau, W.G. (1972), Plasticity theory for anisotropic rocks and soils, Proceedings of 10th symposium on Rock Mechanics, Vol. 1, AIME, pp. 267-295.

Tien, Y.M. & Kuo, M.C. (2001), A failure criterion for transversely isotropic rocks, International journal of rock mechanics and mining science, Vol. 38, pp. 399 – 412.

Tien, Y.M. etal. (2006), An experimental investigation of the failure mechanism of simulated transverse isotropic rocks, International journal of rock mechanics and mining science, Vol. 43, pp. 1163 – 1181.

Yi-Shao lai, etal. (1999), Modified Mohr-Coulomb type micro mechanical failure criteria for layered rocks, International journal for numerical and analytical methods in geomechnics, Vol. 23, pp. 451 – 460.

Interpretation of Danish Chalk Parameters Applicable to Foundation Design

L. Kellezi
Geo, Denmark, lke@geo.dk

P.B. Hansen & O. Koreta
Geo, Denmark

ABSTRACT
The performance of chalk formations in the installations of different types of structure foundations has been investigated and discussed in different research studies and papers. Several symposiums and publications for many years have helped in increasing the knowledge and the understanding of this rock material. However, while the benefits of using the chalk as a competent foundation stratum are known, the selection of design parameters, due to the difficulties in testing and sampling, remains still a main concern and often associated with many uncertainties. This paper is an attempt in presenting practical guidelines in selecting design parameters of some of Danish chalks and gives guidance in the application of these parameters for foundation design / modelling. Direct interpretations of rock parameters, based on geotechnical boreholes, are carried out and different methods based on international and local recent studies have been used in assessing the rock mass parameters for the design / installation of piles / sheet-piles in chalk. A special attention is given to the conversion of the Hoek-Brown classification parameters into Mohr-Coulomb rock mass parameters. The impact of the used methods in the design bearing capacity of the pile foundations is analysed and discussed. Conventional and Plaxis finite element analyses are utilized applying converted Mohr Coulomb soil parameters and direct Hoek Brown soil model for calculating the pile / sheet pile vertical bearing capacity. Conclusions are drawn by comparing the results from the different methods, emphasizing the importance of site investigation methods, accurate interpretation and classification and full understanding of the soil-foundation interaction.

Keywords: Chalk, Hoek-Brown model, Mohr-Coulomb model, bearing capacity, sheetpile

1 INTRODUCTION

The use of the chalk as an engineering material has been studied and discussed since 1965, when the Institution of Civil Engineers (ICE) organized the symposium Chalk in Earthworks and Foundations. Since then, the performance of chalk formations in the installations of different types of structure foundations has been investigated and discussed in different research studies and papers. Several symposiums and publications for many years have helped in increasing the knowledge and the understanding of this rock material. However, while the benefits of using the chalk as a competent foundation stratum are known, the selection of design parameters, due to the difficulties in testing and sampling, remains still a main concern and often associated with many uncertainties.

The chalk structure geology is composed by a fine grained limestone with low magnesian carbonate and high moisture content. Due to its dual porosity (fine pores in the intact material and larger pores along the fractures) the chalk as an engineering material behaves in different ways.

In this paper, some practical guidelines in selecting design parameters of some Danish chalk and guidance in the application of these parameters for foundation design/ modelling, are presented.

2 SOIL INVESTIGATION / DATA

Typical samples of chalk formation carried out by Geo within the Copenhagen area are given in Fig.1 to 4. The results and samples carried out from this borehole (BH-1) will be used in this paper to interpret the chalk parameters.

The virgin soil conditions within the area consist of a top layer of clay till, with a thickness that varies from (8-12) m, overlaying limestone formation (chalk) to larger depths. Some filling with sand has been found on top of the borehole with a thickness of 1.3 m. This layer it is believed to come due to construction activities within the area.

In Table 1 are shown the depths and descriptions of the layers found in BH-1.

Table 1 BH-1

Depth		Layer Description
From	To	
[m]	[m]	[-]
0.0	1.3	Fill material (Sand)
1.3	12.9	Clay till
12.9	19.5	Chalk (Limestone) Sample no.30 (14.10-15.05) m – Figure 1 Sample no.31 (15.05-16.55) m – Figure 2 Sample no.32 (16.55-18.05) m – Figure 3 Sample no.33 (18.05-19.55) m – Figure 4

In total 4 core samples have been carried out for the chalk formation (limestone). The obtained core recovery varies from (67-77) %. The limestone appears with a high degree of fractures (S4 – S5), which correspond to a strongly fractured limestone with distance between fractures less than 6 cm. The Rock Quality Design (RQD) varies between (0-21) %. The degree of induration varies from (H2-H4) indicating a slightly to strongly indurated limestone. The depth interval of the cores are given in Table 1 and the photos of the core samples with the measured recovery and RQD are given in Figures (1 - 4).



Figure 1 Sample no.30, Chalk, RQD =21, TCR=74 %



Figure 2 Sample no. 31, Chalk, RQD =10, TCR=67 %

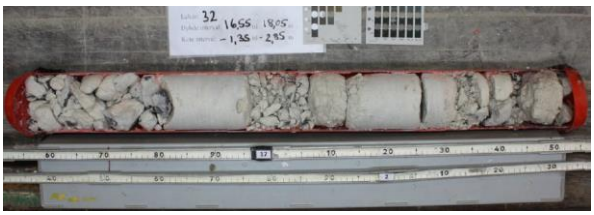


Figure 3 Sample no. 32, Chalk, RQD =20, TCR=67 %

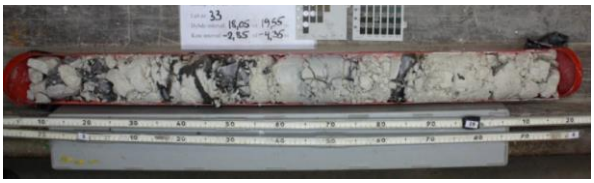


Figure 4 Sample no.33, Chalk, RQD =0, TCR=77 %

3 ESTIMATION OF HOEK-BROWN CLASSIFICATION PARAMETERS

The Hoek-Brown failure criterion was originally developed for estimating the strength of hard rock masses. Because of the lack of suitable alternatives, the criterion has been applied to a variety of rock masses including very poor quality rocks, which could almost be classed as engineering soils. For the derivation of the effective strength parameters from Hoek-Brown rupture criterion, the following classification parameters are calculated (Hoek, 2002).

- Uniaxial compressive strength of the intact mass (q_{uc})
- Geological Strength Index (GSI)
- Material constant for the intact rock (m_i)
- Disturbance factor (D)

3.1 Calculation of the uniaxial compressive strength of the intact mass (q_{uc})

Within the borehole area, no available compressive tests on rock samples were available. However, some Point Load (PL) tests have been carried out in some limestone samples at BH-1. Within the area, Geo has carried out previous geotechnical investigations including UCS and PL tests for the chalk formation. In absence of compressive tests, the point load test index has been used to correlate the UCS. In Fig. 5 and 6, the results of the PL test and UCS have been plotted against the measured bulk density.

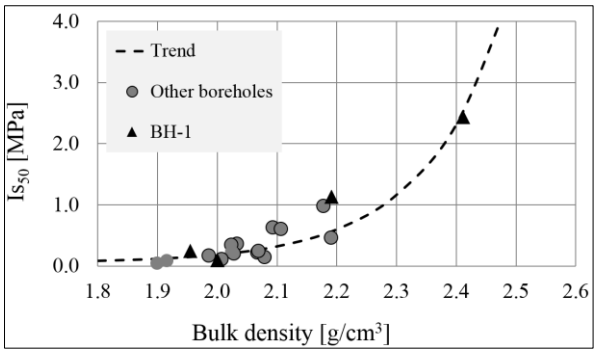


Figure 5 Bulk density vs Is_{50}

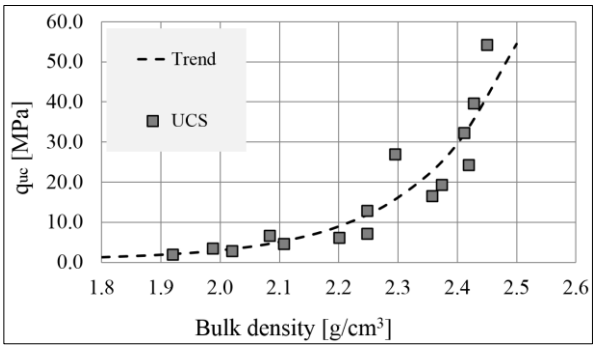


Figure 6 Bulk density vs q_{uc}

From these graphs, the degree of induration was estimated as H=2 for bulk density smaller than 2.1 g/cm^3 and H=3 for bulk density between (2.1 - 2.25) g/cm^3. The correlation between the point load strength index and UCS show a ratio q_{uc}/ Is_{50} between (15 - 20). Taking into account the results of the available data and by considering the previous studies and experience with the Danish chalk in the area, the q_{uc} for the intact rock was estimated as given in Table 2.

Table 2 Estimation of q_{uc}

Degree of Induration	q_{uc} [MPa]	
	Lower bound	Upper Bound
H2	1.0	3.0
H3	5.0	8.0

The values of the q_{uc} given in Table 2 are within the applicable limits for the limestone found in the Copenhagen area (Hansen and Foged, 2002). On the contrary, the strength index (Is_{50}) was found generally lower than the empirical values of the limestone in Copenhagen, which resulted in a higher ratio of q_{uc}/ Is_{50} of about (15 - 20). The averaged uniaxial compressive strength of the formation has been estimated as q_{uc} = 11.3 MPa (lower bound) and q_{uc} = 24.2 MPa (average). The averaged q_{uc} takes also into account the very thin layers with a high degree of induration (H4 and H5). For the top part of the limestone (maximum 2 m of depth), with an estimated degree of induration H2, the q_{uc} was estimated equal to 1 MPa (lower bound) and 3 MPa (average).

3.2 Calculation of the Geological Strength Index (GSI)

The calculation of the GSI has been carried using the correlation with Rock Mass Rating after Bieniawsky (RMR_{89}).

$$GSI = RMR_{89} - 5 \qquad (1)$$

The calculation procedure of the total RMR value by taking into account all the individual contributions of the factors is explained in details by Bieniawski (1989). The following values given in Table 3 have been assigned for the calculation of RMR.

Table 3 RMR and GSI calculation; lower (LB) and upper (UB) bound rating

Factor	Rating	
	LB	UB
q_{uc}	1	1
RQD	3	8
Spacing of discontinuities	5	8
Condition of discontinuities	25	30
Groundwater	7	7
Joint orientation	0	0
RMR total	41	54
GSI	**36**	**49**

The calculated values of GSI are in good agreement with the instructions given by Marinos and Hoek (2004).

3.3 Calculation of the material constant (m_i)

References of the material constant (m_i) are given by Marinos and Hoek (2004). The recommended range given suggests values $m_i=7 \pm 2$. The m_i assigned for this project has been chosen as 6 for the lower bound and 9 as best estimate.

3.4 Calculation of the disturbance factor (D)

Since the limestone structure is not disturbed, a value of D=0 has been assigned.

3.5 Hoek-Brown classification parameters

In Table 4 are summarized the best estimate Hoek-Brown classification parameters.

Table 4 Hoek-Brown Best Estimate Parameters

Hoek-Brown Classification Parameters	Units	Best Estimate Values
q_{uc} (below the sheet pile tip)	[MPa]	11.3
q_{uc} (above the sheet pile tip)	[MPa]	1.5
$\sigma'_{3,max}$	[kPa]	1500
E_m	[MPa]	1418
GSI	[-]	35
m_i	[-]	9
D	[-]	0

The Young's modulus (E) was calculated using the formula given in equation (2) (Hoek, 2002).

$$E_m = \left(1 - \frac{D}{2}\right) * \left(\frac{q_{uc}}{100}\right)^{0.5} * 10^{\left(\frac{GSI-10}{40}\right)} \qquad (2)$$

4 CONVERSION OF HOEK-BROWN CLASSIFICATION PARAMETERS INTO MOHR-COULOMB PARAMETERS

The conventional calculations of the pile/ sheet pile bearing capacity as well as many other geotechnical engineering analyses (conventional and finite element) require Mohr-Coulomb parameters (cohesion and friction angle) as input, even though actual strength envelopes are often non-linear.

4.1 Calculation of equivalent Mohr-Coulomb parameters using RockData 5.003v software

An important feature of RockData software (Rockscience, RockData 5.003v) is the calculation of equivalent Mohr-Coulomb parameters for non-linear failure envelopes. The equivalent Mohr-Coulomb parameters are automatically calculated by determining a linear envelope, which provides a "best-fit" over a given stress range of a non-linear envelope. The results of the Mohr-Coulomb fit (cohesion and friction angle) are displayed in the data legend and on the failure envelope plots. For a given set of input parameters (q_{uc}, GSI, m_i and D), RockData calculates the parameters of the generalized Hoek-Brown

failure criterion (m_b, s and a). The results of the analysis are given in Table 5.

Table 5 RockData results

RockData results	Best Estimate
E_{rm} [MPa]	161
Hoek-Brown parameters	
m_b	0.883
s	0.0007302
a	0.516
Mohr-Coulomb parameters	
φ' [°]	30.1
c' [kPa]	279

Where E_{rm} is the deformation modulus of the rock mass.

4.2 Calculation of equivalent Mohr-Coulomb parameters using the Palmstrøm Jv index and GSI.

The method proposed by Hansen and Foged (2002) and Foged and Stabell (2011) uses the Hoek-Brown failure criterion in combination with the geological strength index (GSI) and with the Palmstrøm Jv index. By using this method, a more realistic rock mass modelling of limestone has been established in Malmö and Copenhagen area. The method used to derive rock mass strength and deformation properties from element tests includes the density, induration, fracturing and weathering, evaluated taking in consideration sample disturbance from face logs and acoustic televiewer logging. In Fig. 7 and 8 are given the derived correlations between GSI - Jv and Jv – (Friction angle and Cohesion) (Foged, 2008). The calculated Mohr-Coulomb parameters are given in Table 6.

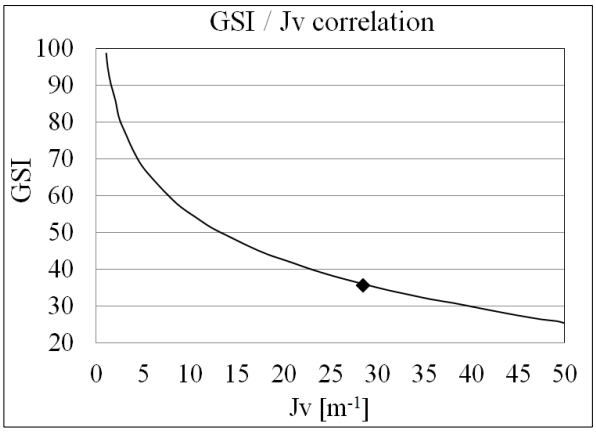


Figure 7 GSI – Jv correlation

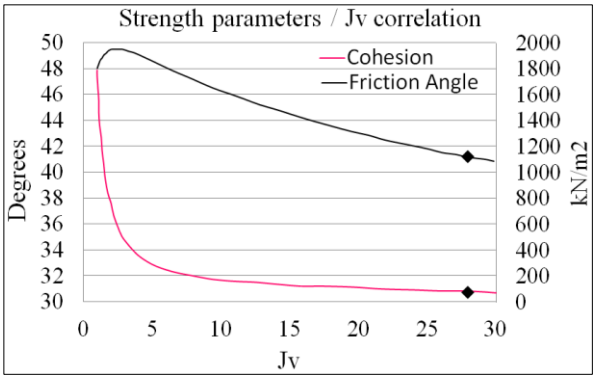


Figure 8 Mohr-Coulomb strength parameters versus Jv

Table 6 Equivalent Mohr-Coulomb parameters using the Palmstrøm Jv index

Hoek-Brown parameters	Best Estimate
GSI	35
Palmstrøm Jv index	
Jv [m^{-1}]	28
Mohr-Coulomb parameters	
φ' [°]	41
c' [kPa]	75

5 DESIGN OF BEARING CAPACITY - STRUCTURES SUPPORTED IN CHALK FORMATION

The derivation and interpretation of the rock mass (chalk) parameters (explained in the previous sections) is one of the most important step in order to design the structures that will be supported on this formation. All the conventional and finite element calculations for design of bearing capacity of piles/ sheet piles, footing or other structures require especially the converted equivalent Mohr-Coulomb parameters. Depending on the project and on the specific situation, the chalk formation may serve as a

good foundation stratum for the installation of steel piles (circular, H-piles or end-bearing piles), sheet piles or shallow footing.

In this paper, an example of the calculation of the axial bearing capacity of sheet piles installed in chalk will be given. The use of sheet piles to support substantial vertical loads is a trend in today's installations and has been mentioned in previous publications since 1991 (McShane, 1991).

5.1 Conventional calculations of axial bearing capacity of sheet piles installed in chalk.

The calculation of the vertical load capacity of the sheet piles will be a combination of the mobilised shaft (side bearing capacity) and end-bearing resistance (tip resistance). In order to assess the contribution of each of the factors, both the side and the cross sectional area of the sheet pile must be assessed. For a chosen sheetpile section AZ 42-700N, the effective width of the sheet pile was estimated as B' =0.07 *h = 0.035 m (Iversen, Augustesen and Nielsen (2010)), where 'h' is the height of the sheet pile section.

The characteristic tip bearing capacity (R_{bk}) of the sheetpile is given from equation (3).

$$R_{bk} = q_k * B' \quad (3)$$

Where:

$$q_k = (c'N_c + p'N_q + 0.5\gamma B N_g s_g)/\xi \quad (4)$$

The term $0.5*\gamma*B*N_g*s_g$ is small compared with c*Nc and is neglected (Tomlinson, 2001). N_c, N_q are the bearing capacity factors according to Tomlinson (2001).

The design tip bearing capacity (R_{bd}) is given from equation (5).

$$R_{bd} = R_{bk}/(\gamma * K_{FI}) = R_{bk}/(1.3 * 1.1) \quad (5)$$

The characteristic shaft side bearing capacity (R_{mk}) is given from equation (6) according to Kulhawy and Phoon (1993).

$$R_{mk} = (\tau * L) * 2 \quad (6)$$

$$\tau = 1 * [0.1 * (q_{uc}/2)]^{0.5} \quad (7)$$

The design shaft side bearing capacity (R_{md}) is given from equation (8).

$$R_{md} = \frac{R_{mk}}{\xi*\gamma*K_{FI}} = \frac{R_{mk}}{1.5*1.3*1.1} \quad (8)$$

where:
L is the embedment of the sheetpile in the chalk layer.

Since the main focus of this paper is the assessment of chalk design parameters applicable to foundation design, the vertical bearing capacity of the sheet piles crossing the clay layer will not be discussed in this paper. The vertical bearing capacity of the sheet piles installed into the top weathered chalk with a considered embedment of about 2 m has been calculated for both derived equivalent Mohr-Coulomb parameters (using RockData software and Palmstrøm Jv index, respectively). The results are given in Table 7.

Table 7 Conventional calculations results – sheet piles installed in chalk

Design Bearing Capacity [kN/m]	RockData parameters (BE)	Palmstrøm Jv index (BE)
R_{bd} (tip)	83	81
R_{md} (shaft)	551	551
Total	634	632

There are no difference between the shaft resistances in the conventional calculations between the two methods. The most important factor affecting the side capacity (equation 7) is the q_{uc}, which is not affected by the Mohr-Coulomb parameters and is the same in both sets of parameters. The tip bearing capacity between the two methods are found to be similar because the terms $c*N_c$ and $p'*N_q$ compensate each other (for RockData parameters Nc=14, Nq=9.5 and for

the parameters derived using Palmstrøm Jv index Nc =26, Nq=24).

5.2 2D Finite Element (FE) Analysis of sheetpiles installed in chalk

In section 5.1, the axial bearing capacity was calculated using conventional analysis and by taking into account both sets of equivalent Mohr-Coulomb parameters. In continuation of this, Plaxis 2D finite element analysis has been performed in order to analyse the vertical bearing capacity by use of numerical modelling. The model used in Plaxis 2D is shown in Fig.9. In order to take into account both tip and shaft resistance, the sheet pile is modelled as solid wall element with a thickness of 35 mm. A plate element with same section properties as the sheet pile has been inserted inside the solid element in order to derive the internal forces. The sheet pile has been considered embedded about 2.1 m into the chalk. Plaxis 2D plain strain analysis has been performed.

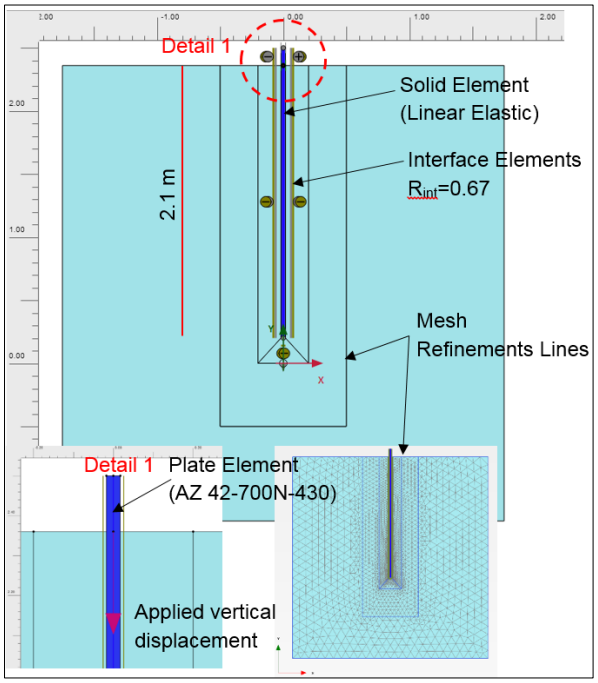


Figure 9 Plaxis 2D FE Model

The size of the model has been chosen in order to avoid any boundary conditions effect. The 15 nodes finite element analysis used in Plaxis 2D are known to give accurate results for the analysis of the foundation vertical capacity. Mesh sensitivity analysis has been performed in order to define the required mesh refinements, especially at the vicinity of the sheet pile. In order to take into account the effect of limestone disturbance during installations, interface elements are used in both sides by reducing the strength by 33% (R_{int}=0.67). The sheet pile is pushed down by applying a vertical force and the measured reaction as function of penetration represents the axial load capacity. By keeping the same model geometry and only changing the soil parameters, the following analyses have been conducted:

- Mohr-Coulomb parameters (φ' and c') determined by Hoek-Brown classification parameters and converted using RockData software (Table 5)
- Mohr-Coulomb parameters (φ' and c') determined using Palmstrøm's Jv index (Table 6)

As an alternative to the above models, another model has been analysed using directly Hoek-Brown parameters (best estimate and upper bound parameters) available in Plaxis 2D. The results from Plaxis 2D are summarized in Table 8.

Table 8 Results from Plaxis 2D FE –Design vertical capacity of sheet piles installed in chalk [kN/m]

MC model (Rock Data parameters)	MC model (Palmstrøm's Jv parameters)	HB model (best estimate/ upper bound parameters)
R_{cd}=807	R_{cd}=412	R_{cd}=(198/410)

In Fig.10 is shown a plot of the total displacements from the Mohr-Coulomb model with Palmstrøm's Jv parameters.

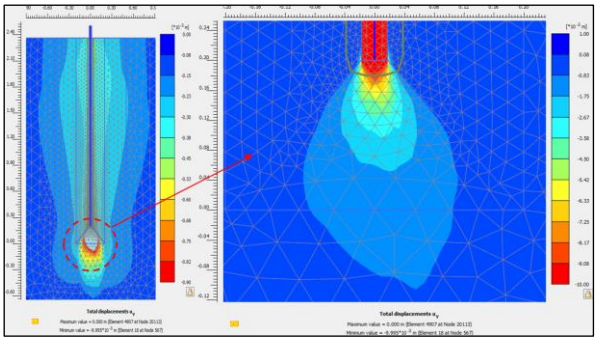


Figure 10 Total displacements u_y (model with Palmstrøm's Jv parameters)

5.3 Conclusions

In this paper, practical guidelines in selecting design parameters of some Danish chalk are given. A direct interpretation of the geotechnical borehole has been carried out. The selection of Hoek-Brown parameters for the available samples as well as calculations of the equivalent Mohr-Coulomb parameters have been explained and analysed in details. Two methods have been presented with regards to the calculation of the Mohr-Coulomb parameters for design purposes. As an example illustration for the application of the derived parameters, the vertical capacity of sheet piles installed in chalk has been analysed conventionally and by use of finite element analysis (Plaxis 2D). The results show that the equivalent Mohr-Coulomb parameters derived using the Palmstrøm's J_v index method look more realistic with regards to assessment of the sheet piles vertical capacity. The results from FE analysis using directly Hoek-Brown parameters show a vertical capacity to the range of the MC model derived by use of Palmstrøm's J_v index method. The equivalent MC parameters derived using RockData (based on Hoek-Brown criterion) are found to overestimate the capacity. The results of this study are in line with the conclusions derived by Foged (2008), with regards to the establishment of a more realistic model of the limestone. However, there are still many uncertainties related with the assessment of the design parameters of the limestone (chalk) and involving engineering subjective estimation of the drilling disturbances, lack of investigations and laboratory tests etc. A more extensive and comprehensive research is needed to reduce the uncertainties of the chalk formations used as foundation stratum.

6 REFERENCES

Bieniawski, Z. T. (1989): Rock Mass Rating System.

Foged, N. (2008): Rock Mass Characterization in Limestone, Ingeniørgeologisk Fjeldklassifikation, Foredrag i Dansk Geoteknisk Forening 2008-04-24.

Foged, N., Stabell, S. & Foged, B. (2011): Rock mass characterization for tunnels in limestone in Copenhagen and Malmö area, Proceedings of the 15th European Conference on Soil mechanics and Geotechnical Engineering.

Hoek, Evert et. Al. (2002), Hoek-Brown Failure Criterion – 2002 Edition.

Kryger Hansen, H. & Foged, N. (2002): Kalkens bjergmekaniske egenskaber, DGF-Bulletin 19.

Kulhawy, F. H. and Phoon, K. K. (1993): Drilled shaft side resistance in clay soil to rock. Proc. Conf. on Design and performance of Found.: Piles and Piers in Soil and Soft Rock. Geotechnical Special Publication No. 38, ASCE, 172-183.

Marinos. P & Hoek. E (2000), GSI: A geologically Friendly Tool for Rock Mass Strength Estimation.

McShane, G (1991), Steel sheet piling used in the combined role of bearing piles and earth retaining members, Proceedings of the 4th International Conference on Piling and Deep Foundations, STRESA, Italy, 7-12 April 1991.

Palmstrøm, A. (2005): Measurements of and correlation between block size and rock quality designation (RQD). Tunnel and Underground Space technology, 20: 363-377, 2005.

Plaxis 2D AE Version 2014.00. Finite Element Code for Soil and Rock Analysis. Delft University of Technology & Plaxis b.v. The Netherlands.

Rock Data 5.003 v (2014), Rockscience software.

Tomlinson, M. J. (2001): Foundation and Construction, 7th edition, Printice Hall.

Zang, L. (2004): Drilled Shafts in Rock, A.A. Balkema Publishers.

GeoBIM for optimal use of geotechnical data

M. Svensson
Tyréns AB, Sweden, mats.svensson@tyrens.se

ABSTRACT
The GeoBIM concept is presented. The GeoBIM concept connects the geotechnical phases data storage, geotechnical modelling, design, visualization and archiving. In order to increase quality assurance, efficiency and optimization of the geotechnical field work, a new database capable of handling all types of geo related data has been developed. With the GeoBIM database being the core of the whole concept, tools for seamless communication with geotechnical 3D modelling tools, design tools, visualisation tools etc have also been developed. The GeoBIM concept have been developed and pilot tested in cooperation with a few large infrastructure projects in Sweden during 2014-2015, i.e. the ESS project in Lund and Varberg railway tunnel. The concept will be implemented in project Ostlänken during 2015-2016. Examples from these projects will be shown. By using the GeoBIM concept a more efficient and quality assured geotechnical model than before have been communicated continuously through the projects. The GEoBIM delivery also gives the opportunity to preserve the data and the geotechnical model for the next phase of the projects and for future in the area in general.

Keywords: GeoBIM, visualization, 3D-modelling, geotechnical, database, TRUST

1 INTRODUCTION

The concept BIM is today more or less used on a regular basis in the building industry above ground, at least to a youngster level. When it comes to underground data and facilities the BIM concept is so far however far from up and running. It is shown in a number of ways, i.e. bad archiving of geotechnical data and lack of tools handling more than a few geotechnical data types. The effect of this is that a lot of investigations are carried out in areas already investigated, it is hard to do an optimized interpretation using results from a number of data sets/methods etc. The central drawback is the lack of a common geotechnical data format, and a general database that can keep good order of all geotechnical data that is produced. Such a database would be the core of a GeoBIM concept. These thoughts were described in an R&D GeoBIM application and resulted in a grant from the Swedish Reseaerch Council (Formas) and Sven Tyréns Stiftelse 2012.

The GeoBIM project was formed and are developing the GeoBIM concept 2013-2016, a cooperation between Tyréns and the department of Soil and Rock Mechanics at Royal Institute of Technology in Stockholm (KTH). The project is run under the TRUST umbrella (www.trust-geoinfra.se)

2 WHAT IS GeoBIM?

The GeoBIM concept consists of the five elements below.

- Data storage (incl input/output)
- Modelling
- Design work
- Visualization
- Uncertainty model

See also Figure 1. If the concept is well developed it is rather a communication tool for explaining geotechnical data and models than a pure engineering tool.

2.1 Data storage (incl input/output)

Proper data handling, including coordinates, and a general enough output data format to be used as input for the geotechnical modelling and design tools is the foundation for the GeoBIM concept. In a large infrastructure project geo related data from approximately 100 different methods has to be handled. Of course the optimal interpretation of the geo model would then be if one could make use of all data in the same tool. This has not been the case in any of the available modelling tools on the market. The reason for that is the lack of a standardized data format, many data formats are instrument/manufacturer specific. Hence, in the GeoBIM project the main focus has been to develop a database capable of importing all geotechnical data formats and transforming them to a standardized/general data format which seamlessly can be used by all the geotechnical modelling and design tools on the market, see Figure 1 and Figure 2.

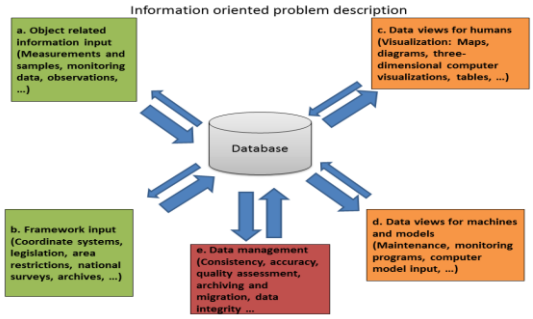


Figure 1 Principle of the GeoBIM database. Import of data from the left (green) and Export of data to the right (orange). The red box illustrates an uncertainty model tool connected to the GeoBIM concept.

The GeoBIM database now developed imports all relevant geotechnical data (approx 100 methods) accompanied by x,y,z coordinates. In case data from a method not available in the database is delivered the method could be conveniently designed for import with a specific tool. The GeoBIM database main window is shown in Figure 2.

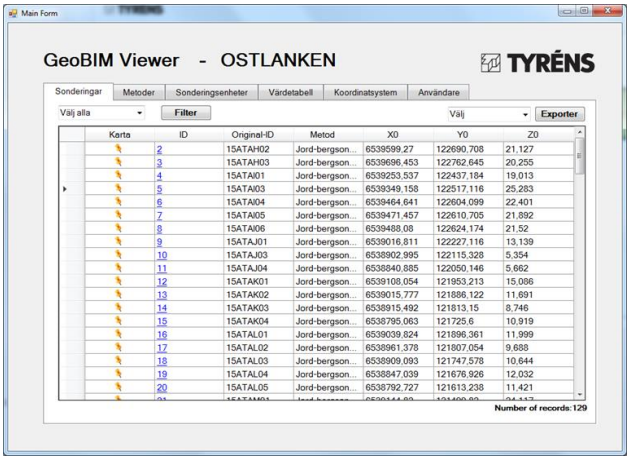


Figure 2 The GeoBIM database main interface with the columns; Map link, ID1, Original ID, Method, Coordinates - X, Y, Z, Value

2.2 Modelling

Following the infrastructure (or any) design process the first geotechnical job after having organized the geotechnical data is to start the geotechnical modelling, to find out the geometry of the soil volume and to characterize the different materials, fracture zones, groundwater chemistry etc. With a proper 3D modelling tool this could be done. On the market there are at least 200 different programs producing some kind of geological or geotechnical model. The GeoBIM concept does not promote any specific programs, but focus on making any of them directly useable from the GeoBiM database. In Figure 3 a 3D geologic model example is shown.

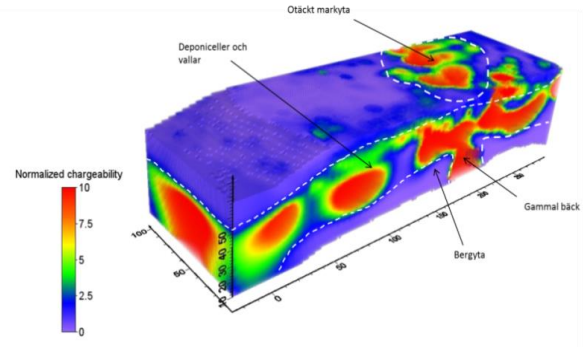


Figure 3 Geometric 3D model showing different properties in a soil volume. Example from Filborna landfill, Helsingborg, Sweden.

2.3 Design work

The geotechnical model defines the physical environment for any project in the building/infrastructure industry. Any building, road, tunnel, railway etc is founded on, or in, the ground, which could be soft soil, hard rock, a combination or anything in between. It is obvious that the most reasonable effort should be spent on finding out the most true geotechnical model. When the imaginary structure is put/placed in its planned environment, which means when you combine the structure design and the geotechnical model, the engineering design work starts. Typical questions raised are; Do we need to pile? Will there be a lot of water in the pit during the construction? Will the clay stand the weight of the building not to get too large settlements? A good geotechnical model and the ability to combine the model with the construction in the design tools (typically Civil 3D) will increase the chance for an optimized design. See Figure 4.

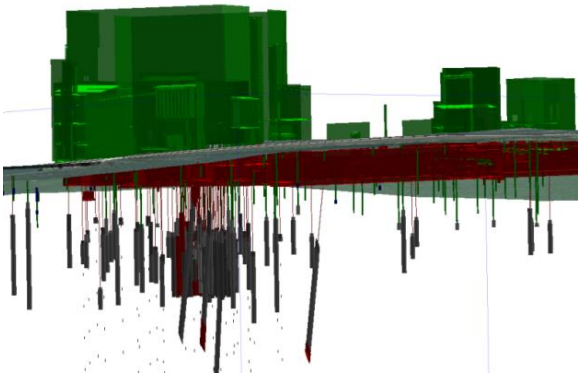


Figure 4 The order of success of the engineering design work is largely increased if the possibility of combining the geotechnical model, as well as the single geotechnical soundings, and the structure in the same design tool is good. Example from ESS, Lund, where the building is combined with the geotechnical model (top of clay till is highlighted) and parts of the sounding results. All information is handled as objects.

2.4 Visualization

Continuously through the design phase there is a need for visualizing geotechnical data and models. Not only for the geotechnical engineers responsible for interpreting the geotechnical data, but also for other engineering disciplines, clients, authorities, politicians etc. A good tool for visualizing the data and the model can't be overrated. See Figure 5.

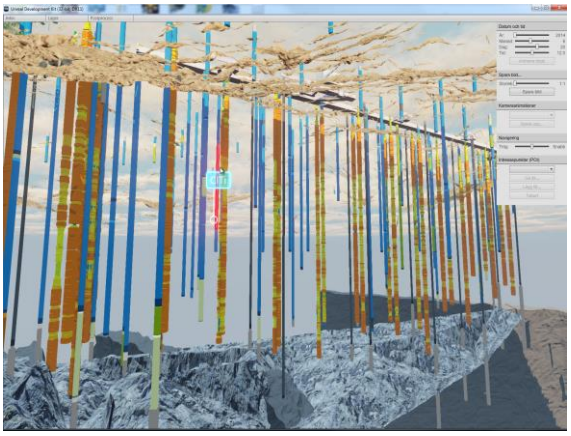


Figure 5 Visualization of geotechnical model and core drillings with the visualization tool TYREngine partly developed within the GeoBIM project. The tool is based on computer game technique, can be run by an X-BOX control unit and also in a VR helmet environment to get the full 3D potential/feeling. ESS, Lund.

2.5 Uncertainty model

The last part of the GeoBIM concept is the uncertainty model. This could be exemplified by the model of the rock overburden. In some areas it is often very well defined by observations of pure rock on the ground surface, whereas in other parts of the area the knowledge of the level is much less due to long distances between the boreholes. A graphical presentation of an uncertainty model is shown in Figure 6.

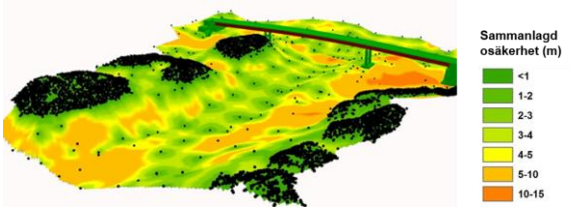


Figure 6 Uncertainty model. Example from Förbifart Stockholm (TRV, Golder)

3 POSSIBILITIES WITH GEOBIM

The GeoBIM concept will close the digital chain in the everyday geotechnical job, overbridge the remaining gaps such as rewriting soil classification between field, lab and geotechnical GIR reporting. The main contribution is however the generalization of the data format giving a number of new opportunities in the fields presented in chapter 2 above, and further explained below.

3.1 Data storage and archiving

With data stored in a general data format all geotechnical data can be stored and organized in the same database. Hence it opens up for better control of whole/complete data sets and long term archiving of data. A complete national geotechnical data archive?

In the projects where the GeoBIM concept have been pilot tested, i.e. Varberg railway tunnel, ESS, the speed with which a geotechnical model can be updated has been at least a magnitude quicker than using former technique, thanks to keeping all data in the same place and data format.

3.2 3D modelling

The possibilities with all data in a common database are many. All the available data can be used in the same 2D/3D modelling software (of your choice). It also opens up the possibility of using a number of modelling software that traditionally not have been used in the geotechnical industry. This will also give a better preciseness of the interpretations and a more precise final geotechnical model. It also gives opportunities for a quicker updating and communication of the models.

3.3 Design process

With the ability of using new geotechnical modelling tools the geotechnical models can be exported as objects to the design tools (ie Civil 3D, Microstation) in he preferred data formats. The other way around, many of these geotechnical modelling tools can also import the designed structure. The software that have been tested during the GeoBIM project have shown to almost seamlessly being capable of moving the models/objects between each other, making the design process (comparing how the current design of the structure fits the geotechnical model) much more convenient than today. An example is shown in Figure 7 (Varberg railway tunnel design). The models/objects that are exported can also keep information, meta data and features between the different software.

3.4 Visualization

Today different data sets are visualized in different format – from paper to 3D models – and it is obvious that the preciseness and full interpretation potential can not be reached. With the ability of visualizing all data sets in the software those parameters will be much improved. The potential of good visualization can hardly be overestimated. And the potential gets larger the less the audience knows about geotechnics. And the partners (more or less) interested in geotechnical data are many:

- Geotechnical engineer
- Other engineering disciplines (bridge, road, railway…)
- Client
- Contractor
- Environmental authorities
- Society/Community
  Stake holders

With a good and custom made visualization of the geotechnical data and the models all these partners can be reached. This has not been the case with 2D profiles on paper.

For non-geotechnical partners the visualization tools developed in the GeoBIM project have evolved to be a proper communication tool of the whole geotechnical work, clarifying a lot and largely impressing and widening the audience caring for what is underground.

One of the key factors for the success is that technique from the computer game

industry have been used. With the two aims of handling really large sets of information and get a more realistic imaging of the underground the core/engine used in computer games is used for processing the geotechnical data sets. The models can also be controlled by an X-Box-unit. To get the final realistic feeling one can also put on a VR-helmet and get a full 3D experience, see Figure 5.

4 EXAMPLES

4.1 ESS – European Spallation Source, Lund

The ESS facility is designed in close cooperation by the partner group researchers-client-consultant-contract under a partnering contract. Since this means designing as you go it requires quick decisions, often redesign and a need for very competent geotechnical modelling and design tools. With using the whole GeoBIM concept those needs have been reached. In Figure 4 parts of the geotechnical model, and parts of the geotechnical soundings are visualized together with the current design of the facility. The design group use this tool on-line on meetings to test how different design aspects are affecting the geotechnical aspects.

4.2 Varberg railway tunnel

A common question in all rock tunnel design projects is: "-What is the rock coverage?" In this project this question was quickly answered in detail by combining the bedrock surface model and the current tunnel design (of that day) exported to the geotechnical modelling software where the calculation of the difference between the bedrock and the tunnel roof was calculated. The result was plotted as iso surfaces on the tunnel roof. This was carried out very quickly.

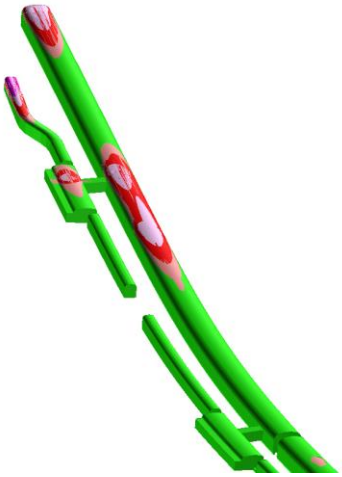


Figure 7 The rock coverage calculated and projected on the tunnel roof for the Varberg railway tunnel.

The bedrock model itself was to a large extent retrieved from seismic measurements, carried out by another TRUST project from Uppsala University, see Mahemir A., 2015. A large number of landstreamer seismic lines were carried out, see Figure 8. After processing and interpretation the seismograms are visualized together with the proposed tunnel line at an early stage, with the purpose of avoiding the most unfavourable rock fractures etc, before the more detailed design is started, see Figure 9.



Figure 8 Landstreamer seismic lines carried out within the Varberg railway tunnel project, primarily to identify the bedrock surface and the rock quality.

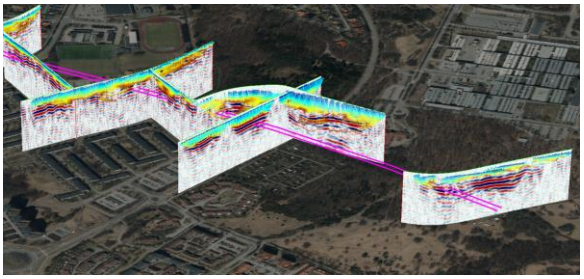


Figure 9 Processed seismic data visualized on top of the aerial photo and combined with the tunnel line in an early stage, to get a first idea of for example any large fracture zones are in an unfavourable position.

4.3 Ostlänken, high speed train – where the first full scale GeiBIM concept is introduced

The design of the next generation of railways in Sweden have started, the eastern part is called Ostlänken, and is split in four design sections. On the section OLP4 the GeoBIM concept will be tested in full scale, resulting in a geotechnical BIM delivery. The field investigations so far have basically included geological outcrop mapping and geophysical (GPR and Resistivity) profiling, and a few soil-rock soundings (Jb). Those three data sets are, in terms of data type, of very different character. With the GeoBIM database all data types are generalized and thereby it has been possible to combine them in a common modelling tool, see Figure 10, and hence produce a comprehensive bedrock model.

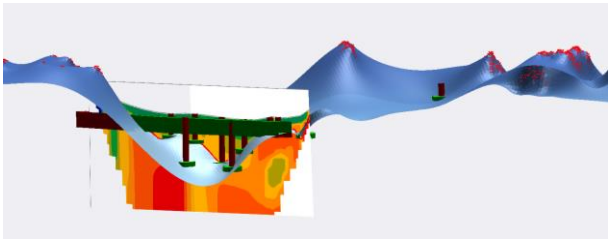


Figure 10 Bedrock model retrieved from three very different data sets – manual geological outcrop mapping, 2D resistivity profiles, soil-rock soundings (Jb) in the Ostlänken (OLP4) high speed train project.

5 UNCERTAINTY MODEL – RISK EVALUATION

Money rules. That is most often the reality. In large infrastructure projects this specifically counts for the unknown risks. The client often knows there is a number of risk, but the usual problem is to put a figure on the risks. Therefore the cost for the unknown risks often makes up a large part of the project budget. The GeoBIM concept has the potential of putting figures on the uncertainties. The potential is large thanks to the good order of the data that can be kept in the GeoBIM database. All data imported to the database can be accompanied with a figure of uncertainty, and further on used different levels of uncertainty estimations or calculations. An example of the concept is shown in Figure 6. The uncertainty module is the final part of the GeoBIM project, and will be the main focus during 2016.

With a well-established uncertainty model of the different geotechnical properties the client can handle the risks, and even use this during the contract process hiring contractors. The risk sharing will then be taken to a new level. Within the GeoBIM project also models for calculating the amount of necessary complementing investigations that are needed to lower the risk to a certain level are developed, Prästings et al, 2014.

6 GeoBIM DELIVERIES

Until today the final delivery of geotechnical data and models to TRV have consisted of:

- Field data as digital data files
- Factual report (GIR / MUR) (pdf)
- Geotechnical PM (pdf)
- Geotechnical 2D models (pdf, digital AutoCAD)

During 2014-2015 also geotechnical information have been required to be delivered as BIM models. However, the definition by TRV is most often vague. However, during the implementation of the GeoBIM concept a definition has evolved

and the following definition of a geotechnical BIM delivery is proposed:

- Field data as digital data files
- The GeoBIM database (-format)
- Digital 3D model (object, incl meta data - properties)
- Digital uncertainty model

The GeoBIM welcomes a discussion on this definition.

7 TRUST

The GeoBIM project is run under the TRUST umbrella, which is a cooperation of nine sub projects, separated in three different types of projects; a) development of preinvestigation methods, b) developing methods and techniques concerning the construction phase, c) development of tools for information handling and visualizing of data and models, see Figure 11. The total budget is 75 million SEK, 2013-2017. Six universities are participating; Lund University, Chalmers, KTH, LTU, Uppsala University and Arhus University. 10 PhD students and approximately 30 senior researchers. Tyréns and NCC are the industry partners. See also www.trust-geoinfra.se and Ask M., 2014; Svensson M., 2015; Hagberg P., 2015; Johansson S. et al, 2015; Malehmir A., 2015; Sparrenbom C., 2015).

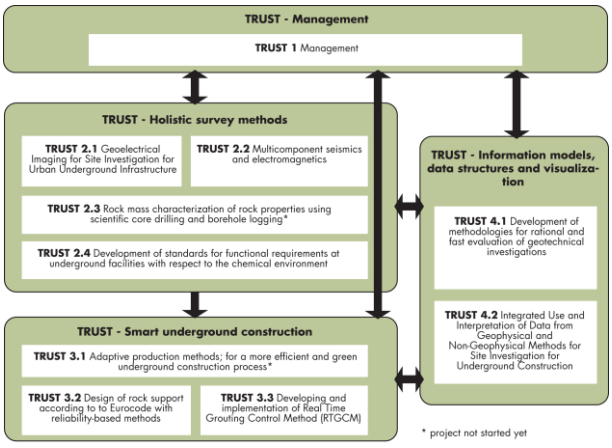


Figure 11 TRUST projects (www.trust-geoinfra.se).

8 SUMMARY

The core of the concept is the GeoBIM database storing data in a more general data format than before – opening up a large number of geotechnical related possibilities. The most important may be a tool for sharing the costs for geotechnical risks in a project and a new way of communicating geotechnical data and models, reaching a much larger community than before.

9 ACKNOWLEDGEMENT

TRUST is financed by a number of partners, the main contributors being Swedish Research Council (Formas), BeFo, SBUF and Sven Tyréns Stiftelse. To those the TRUST group in general is very grateful.

10 REFERENCES

Ask M., Rosqvist. H., Svensson M., TRUST – Sveriges största geoteknik-FoU någonsin?, (2014), SGF Grundläggningsdagen, March

Hagberg P., GeoBIM – en kommunikationsmodell vid undermarksbyggande (2015), SGF Grundläggningsdagen, March

Johansson, S., Fiandaca, G., Dahlin T., Influence of non-aqueous phase liquid configuration on induced polarization parameters: Conceptual models applied to a time-domain field case study (2015), Journal of Applied Geophysics (accepted)

Malehmir, A., Zhang, F., Dehgahnnejad, M., Lundberg, E., Döse, C., Friberg, O., Brodic, B., Place, J., Svensson, M., and Möller, H., (2015). Planning of urban underground infrastructure using a broadband seismic landstreamer – Tomography results and uncertainty quantifications from a case study in southwest of Sweden. GEOPHYSICS, VOL. 80, NO. 6

Sparrenbom. C., Stimulerad reduktiv deklorering identifierad med inducerad polarisation - En möjlighet för övervakning av in-situ sanering av klorerade lösningsmedel? (2015) Renare Mark Vårmöte Stockholm 2015-03-26

Svensson, M. GeoBIM - Optimalt utnyttjande av geotekniken i stora infrastrukturprojekt, (2015) Bygg och Teknik, Nr 1

The role of communication and dissemination during the transition from geotechnical design to construction

Einar Helgason
Veidekke Entreprenør AS, Norway, einar.helgason@veidekke.no

Grete Tvedt
Norwegian Public Roads Administration, Norway, grete.tvedt@vegvesen.no

ABSTRACT
This paper investigates the communication flow between geotechnical design engineers and construction workers. A qualitative interview study was carried out in 2014. The aim of the study was to identify salient features of communication and dissemination of information among participants in construction projects, with a particular focus on ground works.
Dissemination of both general and specific information concerning the execution of special foundation work is an essential factor in successful implementation of construction projects. A problem within the industry is that detailed information is not always communicated from the consulting engineers via the construction client's resident engineers to the construction site. The same applies in reverse, with design engineers tending to receive inadequate feedback on the feasibility of their solutions.
The main findings from the study can be summarized as follows:
The contract between the parties must be financially viable. The success rate is highest in projects where all parties make a profit and the construction client receives an adequate return on investment. Inadequate return on investment leads to conflict, and conflict leads to inadequate return on investment. It is important to realise that the sooner you acquire an overview of risk elements and assess their costs, the greater safety is obtained in the production phase of the project.
Those who perform the job must be actively involved in the project. This applies to both the construction team, construction client team and the designing team. Dedicated project participants are willing to do that little extra. Direct communication between geotechnical design engineers, quality control engineers and the ground contractor is important. An initial meeting with all parties allows everyone to get involved in the terms of the contract, and procedures may be adjusted if necessary. The human factor plays an important role. Are we considered approachable? Do we want to work with people? Can we handle conflicts? In the answer to all of these questions, the level of trust between the parties involved plays a fundamental role.

Keywords: Communication, ground works, dissemination, risk management

1 BACKGROUND

In dense populated and urbanized areas it is vital to utilize areas for property development. As the above ground space is limited, there has been an urge to extend the structure downwards. This often results in deep supported excavation in soft clay deposits. Such excavation has a potential for causing ground settlements and related damage to neighboring buildings and structures.

Based on an initiative by the NGI (Norwegian Geotechnical Institute), the Norwegian Research Council has founded a research project BegrensSkade, i.e. "Damage Limitation". The project has broad support from the Norwegian construction industry with partners representing all major stakeholders (construction clients, contractors, subcontractors, design consultants, real estate and insurance

companies as well as research institutes and universities).
The main goal is to develop new methods for execution and improvement for the whole process, from idea to execution. The improved methods are to limit the risk of damage related to ground and foundation works in the construction industry. BegrensSkade looks at the whole chain of causes and potential remedies within designing, building and monitoring.
"Coming together is the beginning; keeping together is progress; working together is success." Henry Ford's quote summarizes the goal of this subproject within BegrensSkade. This part of BegrensSkade deals with "soft" issues, not the hard-core engineering, excavation or drilling, but the communication between the parties. What are the methods or procedures for communication in Norwegian construction projects? How do we communicate, how do we pass on information from one phase to the next? How do we learn from previous projects? What factors influence our communication pattern and methods?

2 INTERVIEW SURVEY

2.1 Background for study

A qualitative interview survey on the communication and dissemination of information among participants in construction projects was conducted in 2014. Prior to the interview survey, literature study revealed the following topics relevant to address during interviews:

- Laws and construction standards
- Form of contract
- Professional Competence
- Technical aids
- Colocation
- Common understanding of project goals
- Language and challenges with foreign-language employees
- Contract terms must be financially acceptable to all project participants
- Project participants have realistic timeframes for delivery
- Personal relationships and trust

Based on the above, the aim of the study was:

- To identify communication paths
- To identifying the dissemination of information, i.e. drawings, descriptions, 3D models mm.
- To identify the use of information systems, WEB hotels, 3D, etc.

The interview guide was structured to encourage and bring forward a mutual understanding of the problem and the interaction between the actors. The idea of developing new / improved communication and dissemination by strengthening communication in the transition stage from design to construction was a central topic. The focus has also been on communication from the contractor and back to the design engineer. Here the aim was on measures that can reduce or minimize damage risks through the development of a new or improved dialogue process. Further focus has been on trust building through balanced contracts and clarified risk management.

2.2 Execution of the survey

The interview study is based on four reference projects. These include major infrastructure and construction projects. Three of the projects are in the Oslo area, while one is in Trondheim. For each project we interviewed representatives of each party, for example the construction client's resident engineer, consulting geotechnical engineer, main contractor and subcontractor. A total of 12 interviews were conducted.
The informants covered a wide range of knowledge and experience, both high formal education and decades of industry practice. The interviews were based on an interview guide that stipulates 22 items covering general information regarding the project, communication methods and specific conditions. For the most part the informants were allowed to speak freely regarding the project and the conditions.
Minutes from each interview formed the basis for the analysis. The interviewees' responses were categorized and systematized in order to facilitate comparison. The purpose of the analysis was to discover similarities, as well as to bring forward individual comments.

The analysis was, in reality, both subjective and generalized. The analysis focused on factors related to soil conditions and foundation work, but not on the total production in the individual projects. We did not set a benchmark for success of the projects, we focused on the informants' experience of process and project.

3 COMMUNICATION

3.1 Procedures

A major focus of the interview study was to find out how communication takes place between the different participants in construction projects.
This was to see if it is possible to distinguish what makes a successful project and why some projects are not so successful.
As a basis, it is assumed that the main players in a construction project, are the construction client, often represented by the resident engineer (hired or employed by the construction client), the main consultant, sub-consultants, the main contractor and subcontractors.
Communication within the project organizations may be formal or informal. However, to fulfil legal and economic conditions, normally the contract stipulates formal requirements, especially related to modifications, amendments and other binding conditions. Regardless of the form of the contract, most common requirements include formal and clear documentation of contractual conditions.

In the perfect world (the perfect project), we assume that all participants have the information they require at the right time. We assume that communication flows freely and all parties are informed. But this is not always the case, particularly in communication downwards to the lower level of production.

3.2 Contract form

Regarding the contract form our focus has been on typical contracts. There are other contract forms and variations of contract types, but our focus has been on:

- Design-bid-build contract: Client-controlled main contractor (also called unit price contract)
- Design-build contract: Contractor-controlled turnkey
- Divided contracts controlled by a (hired) resident engineer
- Public-private partnership (PPP)

Different forms of contract leads to various communication paths between the parties.
For design-bid-build contracts the construction client is the contracting party for the consultant, while for turnkey contracts the main contractor is the contracting party for the consultant.
Figure 1 shows the principle for the communication path in design-bid-build contracts. For a design-build contract the construction client stands more on the sideline while the other players follow the scheme.

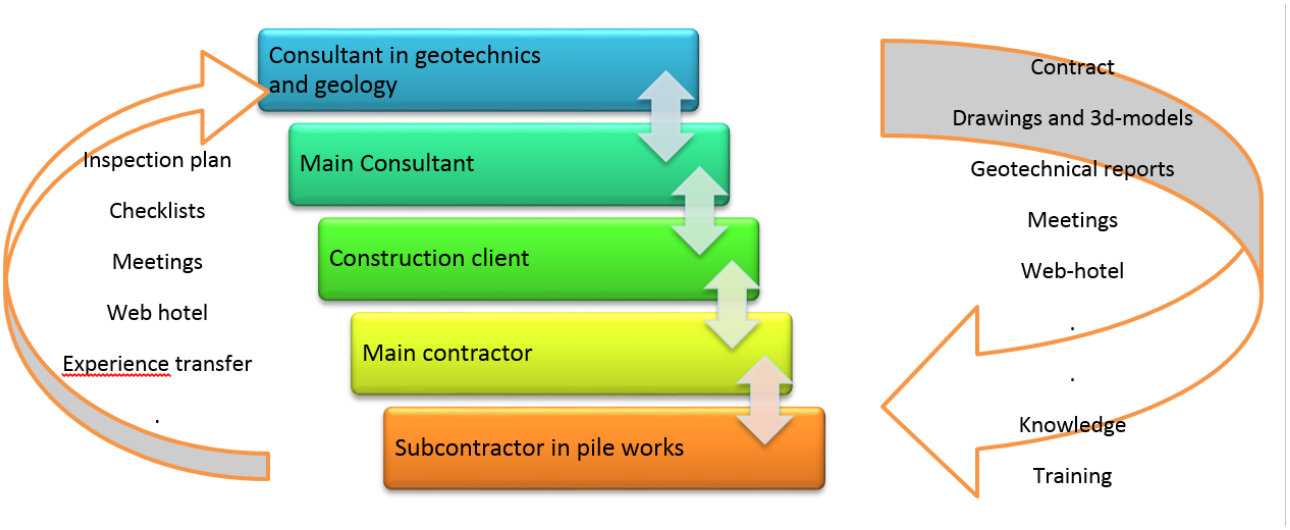


Figure 1 Communication in a design-bid-build contract

Figure 2 illustrates how the construction client transfers the responsibility for management and coordination with different contract forms, where design-build contracts gives the turnkey contractor the most responsibility, and shared construction leaves the construction client with the most responsibility. Independent contract forms will result in shared responsibility between both parties.

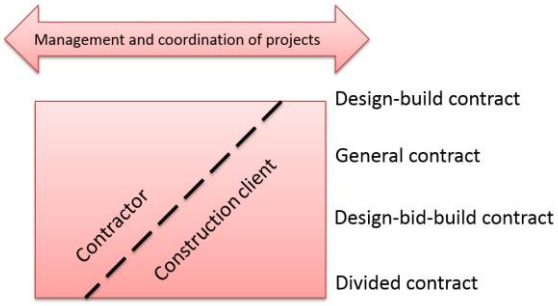


Figure 2 Division of responsibility depending on contract form

The turnkey contract has a clear advantage as there will be a short distance between contractor and consulting engineer. The short communication path will give good practical solutions adapted to the contractor's equipment. The contractor will be involved at an early stage. The drawback is that there can be a long path between the contractor and the future operating organization of maintenance. The operational needs may suffer. There is a risk for sloppy solutions that do not have sufficient quality for prolonged operation time.
In addition, the consultant is often pressed on time, and there is little time and space for innovation when the contractor's wishes are well-known solutions with a low-risk potential.
The design-bid-built contract has its greatest merit in the short distance between the construction client and the consultant, and the construction client and the operational organization. Future management of the facility will be better safeguarded. Furthermore the consultant will, in most cases, be granted sufficient time for the designing process. The downside is that the project will be divided into two phases, where the contractor comes in at a later date in the second phase. The designed solutions can suffer from low practical relevance and will not be designed to fit the contractor's work system. The contract will mainly be awarded after competition on the lowest price. This may make the contract financally unviable for the contractor. Divided contracts have the advantage of the short distance between the construction client's resident engineer and all contractors, suppliers and consultants. The construction client can thus save the contractor's profit on subcontracting. The drawback is the long way between the contractor and the future operating organization of maintenance. When the construction manager as well is recruited outside the main organization, he may not be familiar with the construction client's requirements and culture. There will also be a long way between consultant and contractor. The designed solutions may be poorly adapted to contractors' work systems, and may lead to inefficient progress.
In the interview study the plant manager expressed: "In a unit price contract you can't affect whether something can be done smarter. There is less communication with the construction client. The contractor has really no benefit from having communication with consultant, the soil strata are the construction client's responsibility". Now he is working on a turnkey project where the contractor owns the entire project and will sell the building afterwards: "Here you can customize solutions to fit the subcontractor's equipment. The subcontractor was included in the design process as well as the geotechnical engineer".
The differences between turnkey contracts, unit-price contracts and divided contracts are not that clear in terms of interaction between the geotechnical engineer and geotechnical subcontractor. How they are involved in the interaction and engage indirect dialogue with each other depends on individuals in key positions in between.
Although the contract is financially viable for the contractor, this does not necessarily apply for the subcontractor. It is well known that the subcontractor is often exposed to strong pressure with regard to prices and expected

progress during the negotiations of the contract with the main contractor. According to one informant, the kind of contract is not a determinant for how the communication or communication system works in projects.

3.3 Economic viability

One factor that has a major influence on communication is the economic viability of the contract. It is important that all parties in the project receives a gain for the job being performed. In projects with economically viable contracts, the commitment of the individual players is much higher. Viability means that the focus will be on implementation, optimization and smart solutions rather than economic aspects. In projects where all levels (consultant, main contractor and subcontractors) earn money, and the construction client gains value for the investment, the success rate is highest. Poor return on investment leads to conflicts and conflicts lead to poor return on investment, and this becomes an eternal vicious circle. The parties will focus on personal gain to reduce their loss instead of solving tasks optimally.

Lack of information or lack of understanding of the primary tasks may result in large deviations and major conflicts between the parties. Here, culture and customs play a major role. Subcontractors have often evolved a tradition for specific methods. These may conflict with what is described in tender documents, and deviation ultimately leads to conflict and economic losses. Lack of information and communication between the parties often leads to disputes. One informant from the consultants emphasizes that the contracting of subcontractors must be based on detailed tender documents, drawings and technical descriptions. Information and special restrictions must be communicated down through all levels.

3.4 Involvement in the planning process

In projects where the contractor is involved in the planning and the concept phase or has a direct influence on the engineering, the likelihood of a good execution increases, both in terms of progress and outcome.

An informant from a subcontractor states: "NN (employed by consulting engineering firm of geotechnics and resident quality control engineer) is the main man which one would go to and ask when there are things that pop up. There are issues he cannot take there and then, but then he takes the issue with his boss in the geotechnical firm. NN has tried to look at the most critical problems way before they happen. The consulting engineer has made very good drawings with a good technical specification for the planned work".

Several informants pointed out the importance of communication between the contractor and the consulting design engineer. The importance can be reflected in the fact that the engineer needs to design what the contractor is "willing to" or "able to" to construct, without compromising on quality and/or safety. The contractor’s experience is too often that the designed solutions are not adapted to the equipment or competence available. "We were involved in the process, and took part in the discussion and selection of the technical solution" says an informant from a large contractor. The main conclusion is that it is important to include the contractor in the selection of technical solutions.

In another project there was no form of direct communication between consultant and subcontractor. The representative from the subcontractor did not participate in technical meetings. An informant from the main contractor said: "The construction client decided that the subcontractor should not participate. The subcontractor participated only in some of the economy meetings, so that they would understand that the resident engineer accepted/rejected their claims. "

In that project there were some challenges with subcontractors on piles. The subcontractor did not participate in the meetings. The informant from the consultant stated that "There are both advantages and disadvantages to having the subcontractor participating in the meetings. It is ok to have the subcontractor participating in technical meetings, but in this project the subcontractor got the information they needed through the main contractor."

However, there was direct communication between the construction client and subcontractor on the construction site. An informant from the main contractor stated: "The construction client's quality control engineer was available on the construction site and chatted with the workers. He had a practical eye, understood what was important and what was not so important. "
At a construction site there was an incident with leakage through the sheet pile wall. The construction manager responded, when asked whether the subcontractor contributed to the solution: "They were not at the meetings. It is therefore difficult to say who came up with the solution. I was missing the main contractor's monitoring of the subcontractor. The subcontractor had his own management team, and the main contractor would not take responsibility for the management. The main contractor should take more responsibility for management of the subcontractors. Follow-up between the two could have been better." Later in the interview, he states: "There was a lack of communication between the main contractor and the subcontractor. The subcontractor attended some meetings, not all. The resident engineer's instructions did not always reach down to the subcontractor."
An informant from production informed us about the process by which they were involved in the preparation of solutions. They participated in meetings, where the production resources were utilized positively. The consulting geotechnical engineer could subsequently document the selected solution. The resident engineer approved the financial aspect. An informant from the construction client added that this methodology normally gave a better result with a view to progress and financial outcome.
We also observed a certain difference in how the people involved apprehended the process. For a specific incident an informant, from the ground constructor experienced that they were consulted, while the consulting engineers felt that the solution was developed by themselves. Despite the different involvement, both parties experienced the incident as both constructive and positive. The common view was that this was a good way to solve challenges.

An informant stated that there rarely was direct contact between the geotechnical designing team and the construction team for ground works. Typically, there is a man in between that conveys information in both directions. The man in the middle is normally "construction manager for civil works" or the construction client's resident engineer. Successful implementation can be highly dependent on the personality of this person and on his activity level. "Full overview and control over the site" says an active and diligent construction manager. This attitude can make the difference between success and failure.
An informant from the production side states that in addition they are often held outside the loop, for instance they are not active participants in the planning of the works. The informants are in general agreement that involvement and information flow results in a form of pride or sense of coping. This is especially true for the production people who often lack the theoretical/academic basis. Information and communication about what is to be done, why it should be done and how to do it, gives a sense of appreciation.
An informant from the subcontractors stated that they often did not have access to the total contractual documents. Communication between the main contractor and subcontractor is often in the form of drawings and accompanying Excel lists or technical descriptions. This often leads to unbalanced contracts and unresolved risk management between the parties.

3.5 Risk / risk management

Nowegian construction contracts are based on the principle that each participant basically is affected by the risk of their own work. The participant who has the ability to anticipate and prevent risks should therefore be responsible.
Contract forms will generate different risk distribution between the parties. It is valid for both increased costs (e.g. due to variation in depth to bedrock resulting in longer piles) and for delays in progress.

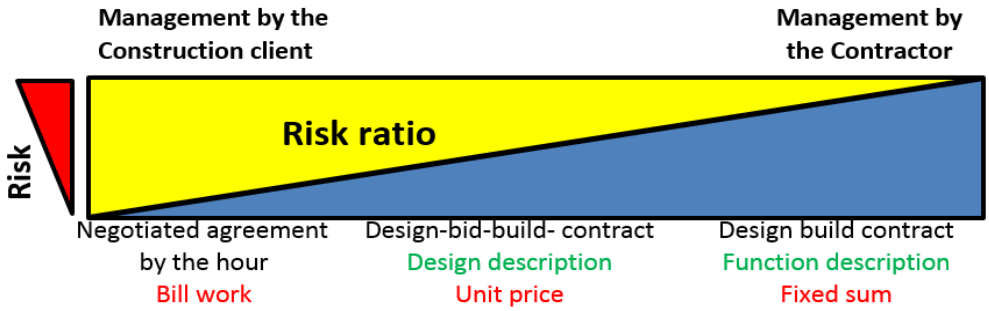


Figure 3 Risk distribution in construction projects. (Øfstedal E.,n.d)

Figure 3 shows how the allocation of risk between contractor and construction client changes with contract form. The construction client holds the largest share of risk if work is performed based on time used and hourly rates. The construction client's risk diminished gradually and is transferred to the contractor as the contract form develops to a turnkey contract. With unit-price contracts the construction client and contractor share the risk. With turnkey contracts the contractor will have the primary responsibility for risk. In a PPP contract the contractor gains even greater risk, including the responsibility for operation and financing as well.

Regardless of the contract form, the construction client will end up paying for risk. The contractor will always add risk expenses to the final bid. For a turnkey project the risk expenses will be higher.

In projects with ground works there is always a certain degree of uncertainty related to the soil conditions. Usually it is "the construction client's ground" and the construction client will be responsible for all extra costs associated with aberrant soil conditions beyond what one might expect from geotechnical or geological reports.

For a unit-price contract the construction client pays for quantity, e.g. meters of pile and is thus responsible for the depth to bedrock. Often the contractor will be responsible for the number of junctions and the cutting of the piles regardless of depth to bedrock.

Risk distribution between parties in different contract forms follows Norwegian standards. Risk displacement can occur if one contractual party includes a clause in the tender documents that distorts the allocation of risk.

In the interview study, risk and risk management was discussed repeatedly as an important factor in a successful project.

A subcontractor said about the planning of the work: "From the start, risk assessment was essential. The construction client was represented by a geotechnical engineer. The subcontractor in this project was well prepared and planned ahead before tasks were to be executed. They had listed up what could happen, and if there was anything unexpected that might emerge. Thus, they had managed to capture the problems before they emerged and developed solutions".

A construction supervisor in another project reported that the project had a risk plan with regard to what should be planned ahead. This was done on paper and showed phases and excavation plans with hand calculations. The contractor felt confident about the method, which also was reflected in the progress.

Another measure to reduce the risk of unforeseen ground conditions was suggested by a consultant: "Execute systematic ground exploration when all traffic is removed, and the area is cleared. The risk will be mitigated with better information. It is often not possible to execute ground exploration on heavily trafficked roads. "

One of the projects included in the interview study had a tender period with competitive dialogue. The dialogue was carried out by generating a risk model. After identification of the main risk elements the contractor worked out solutions and methods to minimize the risk. This process was executed individually with each contractor. When the risk profile for the project was acceptable the contractors calculated their bid individually

without knowledge of the parallel process. This was a successful solution for this particular project and other similar projects where it is difficult to estimate and manage the risk.

3.6 Personal abilities

Trust and personal relations are important cornerstones for good interaction. It takes time to build trust, but it may take less time to tear it down. Trust at the production level is strongly affected by the communication coming from the leaders. Trust at the managerial level in turn depends on confidence at the operational level. Bygg21 (www.bygg21.no) believes there is a lack of procurement expertise in the industry. Their experience is that imbalance in the contractual conditions destroys the interaction between the parties. Balanced and clear contracts create confidence. Contractors wish to compete on other factors than the price in public contracts, but they are often quite skeptical when it comes to using “the construction client’s experience with the contractor from previous projects” as an eligibility criterion. However, in the private market, the parties find each other often based on trust and prior experience. Trust that has been developed in previous project is transferred to the next. This is difficult for construction clients who are subject to public procurement regulations.

The construction client and the contractor share the risks associated with of logistics and progress. Normally the construction client is responsible for the soil conditions, and the contractor for construction. Who is responsible for the foundation engineering depends on contract terms. The sharing of risk has often led to many legal disputes. The aim must be to solve conflicts continuously during the construction period. When working on foundation projects, unforeseen incidents related to the soil conditions will occur. "No one has been there before, other than God" said a site supervisor. Conflicts related to unforeseen soil conditions, are not necessarily black or white. When the construction client and the consultants and/or the contractor normally are disputing both side have partly right and partly wrong. In such conflicts there is a risk of deadlock. To solve a deadlock the usage of a settlement board is a possibility. The settlement board helps the parties to resolve conflicts and economic issues at a new venue without interfering with the daily progress.

3.7 Construction meetings

It emerged during the interviews that construction meetings between geotechnical engineers and contractor are important to enforce a good communication. Furthermore, colocation can be important to enhance the interaction. Successful projects emphasize this as a major factor. It is important that the constructions meetings focus primarily on technique and solutions to challenges faced in the project. Economy and progress should be addressed in separate meetings to prioritize a good technical solution. Here it is also important that the right people are summoned to the meetings. The delegates must have sufficient knowledge to make quick decisions to ensure progress. If the challenge concerns issues involving the subcontractor, a representative from the subcontractor should be present. The construction client and the main contractor have important roles in summoning the right people with the right expertise to the meetings.

3.8 Professional Competence

A knowledge-driven industry creates a basis for trust and mutual respect. Sufficient expertise includes all professions and roles, leadership at all levels, multidisciplinary and comprehensive understanding and good cooperation. In addition to expertise in the technical professions, all parties must have expertise in contract law and progress planning. By creating better conditions for the approval, updating and supplementing of foreign expertise, the industry's major foreign workforce can be utilized in a positive way. It is also important to spread knowledge from the production level to the leader/consulting level, a kind of bottom-up flow of knowledge. The construction workers must also find information on how the task is performed and which restrictions apply.

Technical skills are an important element in the execution of the tasks and in the communication between the parties, "birds of a feather flock together". It can be a major challenge if the parties misunderstand each other due to differences in skills or language. It is important for smooth and seamless communication that the participant speaks the same language, both directly and indirectly. Hence, the transfer of competence and dialogue regarding the task in question is a vital factor.

"It may happen that there is much sloppy execution of geotechnical works. It is difficult to control". This can be interpreted as referring to subcontractors taking shortcuts when the main contractor lacks the expertise to reveal this.

The Norwegian model for management and collaboration characterizes the industry, where involvement and employee participation are central. This develops a sense of responsibility and initiative. Furthermore, it facilitates good utilization of skills, as well as efficient and safe production processes.

The required core competence must be supported through a good education and training system. Learning and knowledge transfer in an industry characterized by project organization can be demanding. There is a huge potential for learning and value creation based on closer cooperation between the players in the construction industry.

Geotechnical training for workers who are not trained in geotechnical engineering from University/College is only offered in a small degree. Geotechnical conferences and seminars are mostly adapted to the University / College group. This may hinder the spreading of expertise among workers in the construction industry. A lack of basic geotechnical competence will affect a worker's insight into the profession and workmanship and will in the long run affect the quality of the work. In a collaboration between the various actors in the industry, it is possible to develop courses on basic geotechnics, which are aimed toward contractors.

The drilling operators expressed in the interviews that they miss the presence of the geotechnical engineer on the construction site. They also believe that project management generally lacks understanding of basic soil mechanics.

In addition, they believe that geotechnical engineers have little practical understanding of the work performed on the site. As a solution, they propose a mandatory practice year as a part of the education program. Senior geotechnical consultants express that the younger engineers should spend more time out on site.

Other measures to spread expertise and disseminate lessons learned can be courses or meetings covering geotechnical issues intended for working geotechnical engineers and skilled workers. This may be achieved by organizing annual events about efficiency in civil works where new projects are presented and experience is shared.

3.9 Communication

In the interview study the question was asked why damage occurs during foundation work. Some of the answers were as follows:

A consulting geotechnical engineer said on the cause of a discrepancy: "Time pressure leads to quick decisions, which are not always good. There may be a lack of understanding of the requirements in the specification. A major factor is the structure of the contract, how it is set up". He also believes that communication back to the design engineer is deficient and can cause deviations: "Lack of feedback to the design engineer: What works in the description? What does not work? It is important to give the designer feedback about incidents: What happened, and how was it solved? "

The same engineer also mentioned: "Excavation depends a lot on how you do it. If the drill procedure is to be gentle, but at the lowest price, these are two factors working against one another. If the contractor is to perform the tasks carefully, it is a must to follow up the work closely. One possible improvement may be to change the terms so that both time and amount of work are taken into account."

An interviewed construction manager believes that the resident engineer should signalize in one of the initial construction meetings if there are specific vulnerable areas. One must go through the procedures that are necessary to ensure a non-leaking construction pit.
The information must be spread to those who will be performing the job. It is not enough to just talk with the management. The workers must know why it should be built in that way, and this must be repeated when new workers are introduced to the site.
The question then becomes how can this be done better with interaction?

4 CONCLUSIONS

The interview study investigated the communication between the various parties involved in construction projects. The interview study showed that the contract terms are not decisive when it comes to communication and interaction between the parties. There is a disadvantage in single procurements as it takes time to build trust between the parties. In general it is possible to achieve confidence with every type of contract.
It emerged during the interviews that the main contractor sometimes lacks knowledge about the subcontractor's skills and ability to perform the works. Therefore, they often are unable to follow up the work. Due to this fact sometimes the subcontractor seems to have a greater opportunity to take shortcuts. The follow-up of subcontractors' work should be prioritized. It is also important to ensure that the special contract provisions are communicated to the subcontractors. In many cases the subcontractor only receives a part of the complete tender documents.
The resident engineer must follow up contract specifications. Deviations from the technical requirements and differences between construction projects lead to unpredictable conditions for the contractor. It is important that the contractors compete on equal terms. Resident engineers must follow up the technical requirements and terms of the contract as closely as they follow up economic terms.
To ensure good cooperation between several parties, it is important that the risk of the contract is reduced during the preparation of tender documents. If all parties profit from the project their desire and readiness for good cooperation increases. Successful development of economic viable contracts requires that the construction client and the consultant are aware that the risk costs regardless of the visibility. Putting it bluntly, if the risk is chased around the project like a short straw, and "all" parties want to push it over to "someone else", this will not benefit the process. It is important to realize that the sooner you acquire an overview of risk elements and their costs, the greater safety is obtained in the production phase of the project. In construction projects, the common goal is to construct a building or facility. Apart from the common goal of contributing to the final product, the participants have various interests in the process itself. For all participants, issues such as finance, production, progress, quality, safety, responsibility and cooperation are included to a lesser or greater extent.
Contract forms where players feel that there is not an equal distribution of risk, responsibility and opportunity for profit, may easily destroy any interest in cooperation. If the construction client has secured the contract so that changes or deviations cause the contractors or consultants to lose money easily, their readiness for cooperation deteriorates.

5 ACKOWLEDGMENTS

The authors would like to thank the Research Council of Norway and all partners in the R&D project "Damage Limitation" for their financial contribution.
Furthermore we would like to thank all participants in the interview study for their contribution.

6 REFRENCES

Øfstedal, E (n.d). http://nvfnorden.org ;taken from the internet on June 15 2014
www.bygg21.no (January 2016)

Load bearing capacity of railway embankments

Torben Thorsen
Geo, Denmark, trt@geo.dk

ABSTRACT
When designing embankments that carry significantly strip load e.g. railway embankments, the Limit Equilibrium Method (LEM) "Method of Slices" with circular slip surfaces has been widely used for decades. With today's software and computationally capabilities more realistic slip surfaces than the circle can easily be analyzed by Method of Slices e.g. through methods where the circle is optimized to a non-circular slip surface or by Finite Element Methods (FEM). In Eurocode 7 it is stated that circular slip surfaces normally are appropriate in homogenous and isotropic soils, but as this article will show, circular slip surfaces might lead to a significant overestimation of the bearing capacity for embankments carrying significant load. The bearing capacity for such embankments will be analyzed and compared using J.Brinch Hansen closed form solution, Limit Equilibrium Method and Finite Element Method. The analyses will be carried out for homogenous and isotropic soils, as well as for multilayered conditions in drained and undrained conditions. A clear recommendation is formulated.

Keywords: Slope stability, Optimized slip surface, LEM, FEM, bearing capacity

1 MOTIVATION

Slope stability has for decades been evaluated using Limit Equilibrium Methods (LEM) and circular formed slip surfaces. Even though thousands of circular slip surfaces today can be calculated within seconds, this does not guarantee that the lowest factor of safety is found for that simple reason, that the most adverse slip surface in most soils is non-circular. This article will demonstrate that using circular slip surfaces in LEM calculations might lead to significant overestimation of the bearing capacity of embankments carrying significant strip load i.e. railway embankments, even in homogeneous and isotropic soils.

2 BACKGROUND

In the Method of Slices, the potential sliding mass is discretized into vertical slices. This was first done in Gothenburg in Sweden in 1916 and presented by Petterson (1955). Fellenius (1936), Janbu (1954) and Bishop (1955) further developed the method during the mid-1950s. During the 1960s the development of computers and the work of Morgenstern and Price (1965) and Spencer (1967) led to more rigorous formulations and effective iterations that took into account the interslice forces (normal and shear) and that would solve for force equilibrium as well as moment equilibrium (Krahn, 2004). Over the last decade or so Finite Element analysis (FEM) in geotechnics has expanded enormously and today - as this method is becoming more and more common – the differences to LEM is truly starting to emerge.

3 FACTOR OF SAFTEY

The Method of Slices' factor of safety FoS is in the more rigorous formulations by e.g. Morgenstern & Prices determined as the ratio between driving and resisting forces summed up over the entire slip surface leading to a global mean FoS. These methods full-fill force as well as moment static equilibrium through an iterative procedure "determining" the necessary interslice forces to comply with just that. This means that the slice forces may not be realistic locally, but the global factor of safety in nonetheless realistic as the

integration procedure involved smoothens out local irregularities (Kahn, 2004). LEM analysis does not full-fill the strain/stress relations ship within the mass as FEM does. In FEM calculations the factor of safety is calculated through a strength reduction method (SRM) or "phi – c reduction" which lowers the strength of the soil (φ' and c') until a clear failure mechanism is formed. Both methods calculates the factor of safety as the ratio between the total available shear strength along the slip surface divided by the summation of the gravitational driving forces (mobilized shear) (Kahn, 2004), and the factor of safety is thereby analogue to the partial safety factors for soil strength used in Eurocode 7.

4 METHODOLOGY

In order to investigate the slope stability for slopes carrying significant strip loads such as railway embankments, the ability for the embankment to carry ultimate limit state load will be investigated as follows. The topic will be divided in three scenarios.

1. Embankment of infinite height
2. Embankment of finite height
3. Embankment on soft soil

The bearing capacity is analysed using design values of soil strength in LEM, thus f = 1.0 gives the design value of the bearing capacity. In FEM characteristic values of soil strength is used, meaning that a factor of safety M_{SF} equal to the desired partial factor of soil strength gives the design value of the bearing capacity (also see paragraph 4.2). The reason for this is, that FEM can have numerical difficulties near failure (M_{SF} =1).

4.1 Geometry

The basic geometry chosen for the local bearing capacity analysis will resemble a typical cross section of a railway embankment use by the Danish Railway authorises (Banedanmark).
The load is evenly distributed to the soil over a width of 2.5m. The distance from the load centre line to the embankment crest is 3.8m and the slope angle is 21.8° (1:2.5 slope). The vertical distance from the slope surface to a virtual line origin at the corner of the load area and running parallel to the slope is 1.02m (this will be used when introducing the overburden in the analytical analysis).

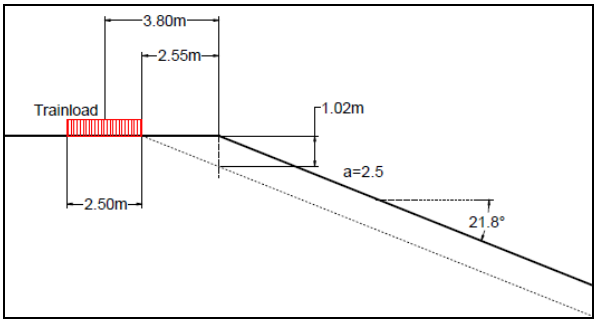


Figure 1a. Typical cross section.

For the embankment of finite height a height of 5 m is chosen, and for the embankment on soft soil a stabilizing berm is included as shown on figure 1b.

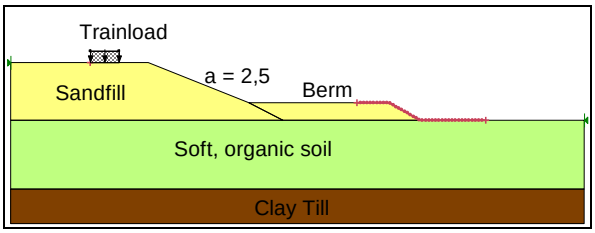


Figure 1b. Model. Embankment on soft soil

4.2 Soil and water conditions

The characteristic soil parameters considered are:

Table 1 Soil parameters. Drained

	γ [kN/m^3]	φ'_k [°]	c'_k [kPa]
Sandfill	20	38	0
Clayfill	20	30	5
Clay	20	30	5

Table 2. Soil parameters. Undrained

	γ [kN/m^3]	$c_{u,k}$ [kPa]
Clayfill	20	80
Soft soil	13	30
Clay	21	100

The stiffness parameters for the FEM modelling are not important for this ULS analysis, and therefore not presented here. The phreatic line is assumed of no influence to the problems analysed.

For the analytical analysis and for the LEM analysis, design values of the above strength parameters are used utilizing partial safety factors on soil strength, γ_M, according to the Danish National Annex to Eurocode 7: DS/EN 1997 – DK NA:2013 which for soil friction angle and effective cohesion is $\gamma_\varphi = \gamma_{c'} = 1.32$ and for undrained cohesion is $\gamma_{cu} = 1.98$ (values given for structures in consequence class 3 e.g. railways). For the FEM analysis the characteristic strength parameters given in table 1 and 2 are used leading to the target factor of safety $M_{sf} = 1.32$ and 1.98 respectively. The FEM bearing capacity is calculated with varying angle of dilatancy equal to $\psi = 0$, $\psi \approx \varphi - 30° = 8°$ and $\psi = \varphi = 30°$ in the sand fill material. For drained analysis in clay fill $\psi = 0$ is adopted. When undrained soil (clay or soft soil) and sand are combined in a FEM model, the joint target factor of safety is $M_{SF} = 1.32$, as the clay undrained strength is given as $c_{u,model} = (c_{u,k} / 1.98) \cdot 1{,}32$.

4.3 Methods

For the analytical bearing capacity the Brinch Hansen solution is adopted (Brinch Hansen, 1970), (reproduced by Hansen, B. (1978)). The LEM analysis is performed using GeoStudio 2007 Slope/w and Morgenstern & Price's Method. For Finite Element analyses Plaxis 2D 2015 is used. In LEM the bearing capacity is found by trial and error using design values of soil strength demanding f = 1.0. In FEM analysis the bearing capacity is found through a "Safety analysis" loading the embankment by trial and error until $M_{SF} = 1.32$ thus giving the desired design strength values and design bearing capacity. 15-node elements and plane strain (2D) conditions are assumed in all FEM analyses.

5 EMBANKMENT OF INIFINTE HEIGTH

5.1 Brinch Hansen solution

The Brinch Hansen (JBH) analytical solution yields the following design bearing capacities for a 2.5 m wide foundation placed at the crest of a 1:2.5 slope with an overburden pressure of $q' = 1.02m \cdot 20kN/m^3 = 20.4kPa$ as indicated on figure 1.

Table 3. Brinch Hansen bearing capacities

	Drained [kPa]	**Undrained [kPa]**
Sand	314	-
Clay	188	177

5.2 Sand embankment

By trial and error in LEM, the load intensity giving FOS = 1.00 is found yielding the load bearing capacity (R_d/A) for the model investigated. For the sand embankment the circular slip surface (CSS) gives $R_d/A = 507$ kPa, cf. figure 2.
For the same model the optimized (non-circular) slip surface (OSS) (using default optimizations settings) gives $R_d/A = 305$kPa, cf. figure 3.
When modelling the exact same geometry in finite element with FEM the geometry of the failure mechanism is shown in figure 4a.
With a load of $R_d/A = 348$ kPa FEM gives af $M_{SF} = 1.32$ ($\psi = 8°$) as required for the fully developed failure mechanism.

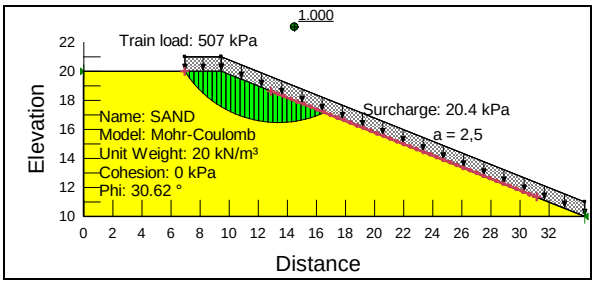


Figure 2. Slope/w. Sandfill. (CSS)

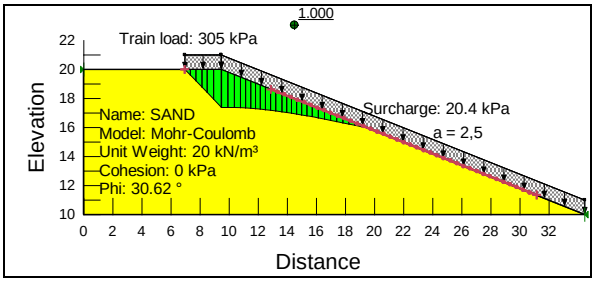


Figure 3. Slope/w. Sandfill (OSS)

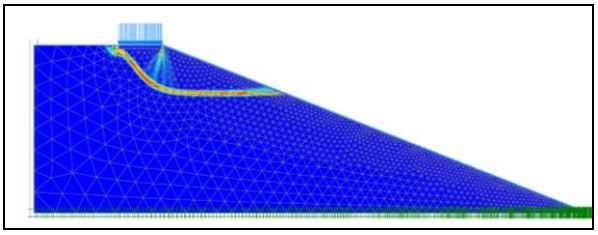


Figure 4a. FEM. Sandfill. Deviatoric strain. ψ = 8°

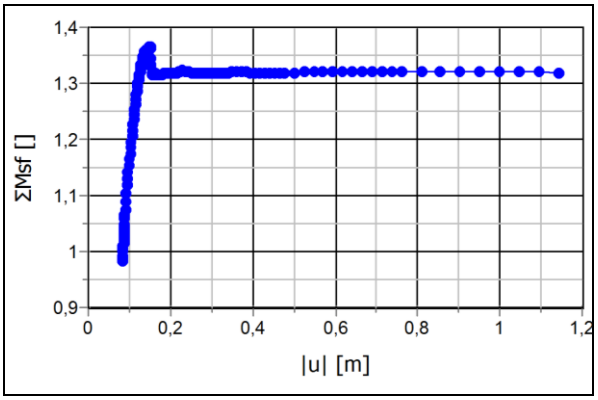


Figure 4b. FEM. Sandfill. M_{SF} vs. deformation

For this purely frictional case the follwing dependenci of the angle of dilatency ψ is found:

Table 4. FEM. Dependenci of ψ

	ψ = 0	ψ = 8°	ψ = 38°
Bearing capacity [kPa]	300	348	425

5.3 Clay embankment – Drained

For the same model using effective strength parameters for clay (drained conditions), LEM gives R_d/A=240 kPa using circular slip surface (CSS):

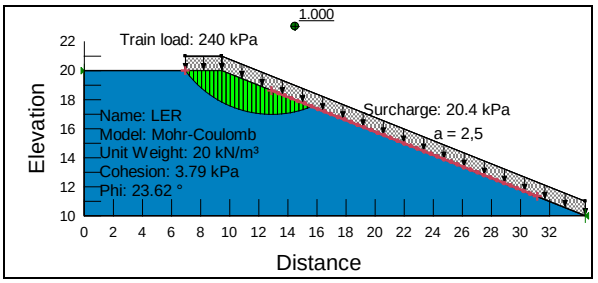


Figure 5. LEM CSS. Clay fill. Drained

The LEM optimized non-circular calculation (OSS) gives R_d/A = 179kPa:

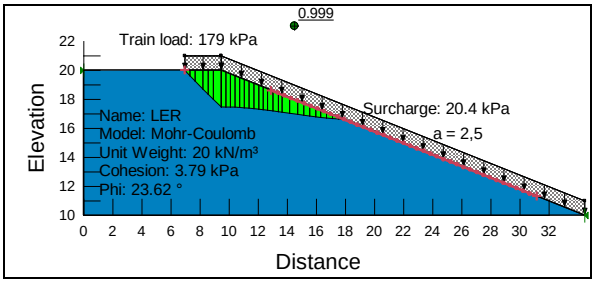


Figure 6. LEM OSS. Clay fill. Drained

For the exact same geometry FEM gives a collapse load of R_d/A = 200 kPa.

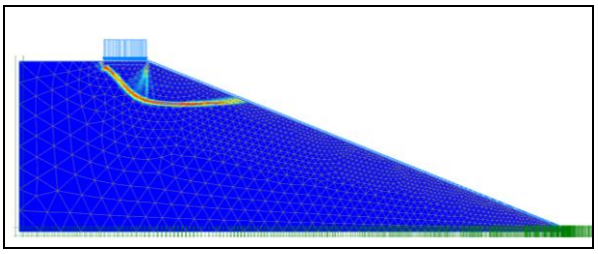


Figure 7a. FEM. Clay fill. Drained. Deviatoric strain

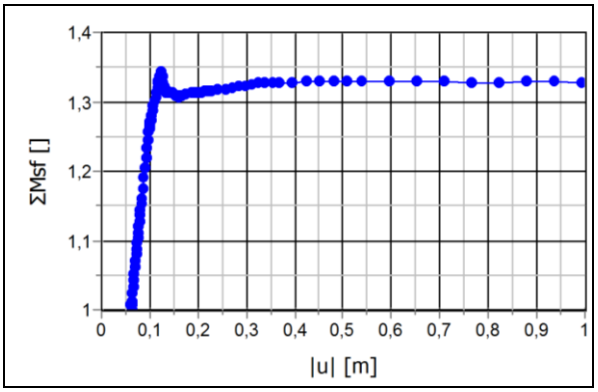


Figure 7b. FEM. Clay fill. Drained

5.4 Clay embankment –Undrained

LEM CSS yields a bearing capacity of R_d/A =182kPa (figure 8), and the LEM OSS R_d/A =168 kPa (figure 9).

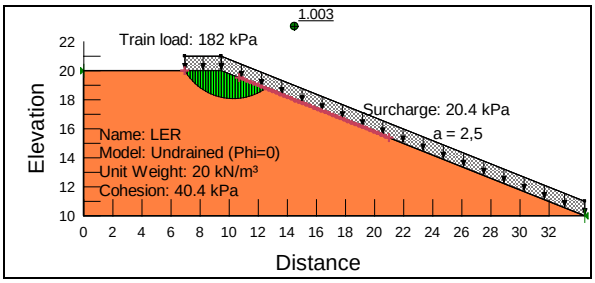


Figure 8. LEM CSS. Clay fill. Undrained

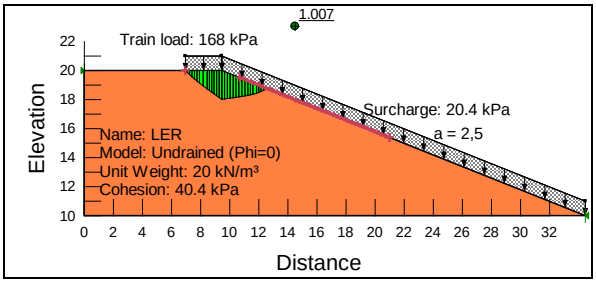


Figure 9. LEM OSS. Clayfill. Undrained

In the undrained FEM analysis a minor adjustment to the strength profile has to be introduced in order analyze the bearing capacity. If constant undrained shear strength is used, the failure mechanism tends to extent to the model boundary leading to total stability failure mechanism instead of a bearing capacity (which is investigated here). Therefore the undrained shear strength profile is modified to c_u = 78kPa at the surface with an increase with depth of Δc_u = 1kPa/m giving an approximate average of c_u = 80 kPa within the depth of interest. The bearing capacity is found to be R_d/A' = 190 kPa (target is M_{SF} = 1.98)

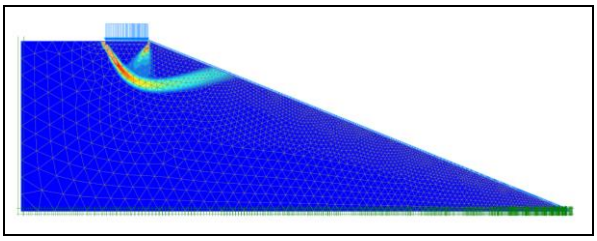


Figure 10a. FEM. Clay fill.Undrained. Deviatoric strain

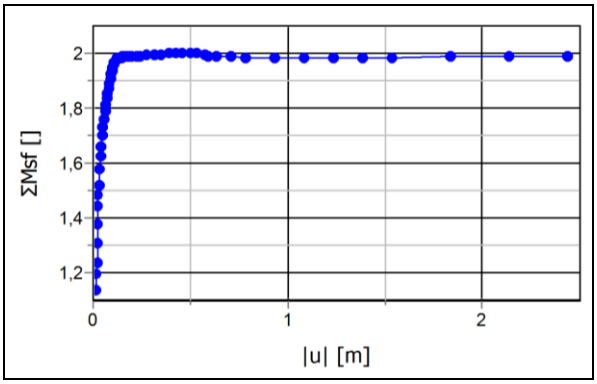


Figure 10b. FEM. Clay fill.Undrained. M_{SF} vs deformation

5.5 Summation

The results above can be summarized as shown in table 5.

Table 5. Results. Embankment of infinite height

Sand fill	JBH	LEM		
		CSS		OSS
	[kPa]	[kPa]		[kPa]
	314	507		305
Deviation	0%	+61%		-3%
		FEM		
		[kPa]		
		ψ = 0	ψ = 8°	ψ = 38°
		300	348	425
Deviation		-4%	+11%	+35%

Clay fill Drained	JBH	LEM	
		CSS	OSS
	[kPa]	[kPa]	[kPa]
	188	240	179
Deviation	0%	+28%	-5%
		FEM	
		[kPa]	
		200	
Deviation		+6%	

Clay fill Undrained	JBH	LEM	
		CSS	OSS
	[kPa]	[kPa]	[kPa]
	177	182	168
Deviation	0%	+3%	-5%
		FEM	
		[kPa]	
		190	
Deviation		+7%	

6 EMBANKMENT OF FINITE HEIGTH

For this situation no analytical solution exists, so this scenario is analysed by LEM and FEM only.

6.1 Sandfill embankment on clay (drained)

For a sandfill embankment placed on clay, the drained bearing capacity is R_d/A = 489 kPa using the circular slip surface (CSS):

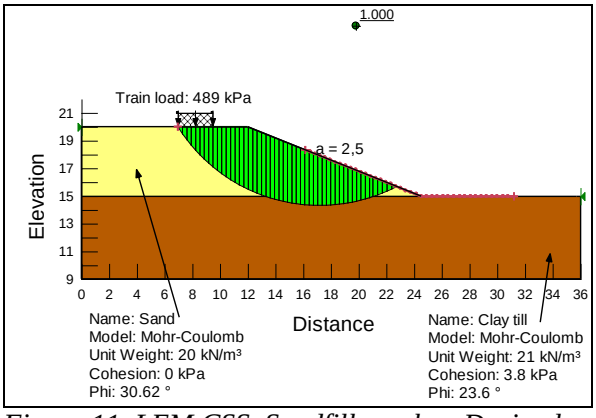


Figure 11. LEM CSS. Sandfill on clay. Drained

The optimized slip surface shows a bearing capacity of R_d/A = 304 kPa as shown on figure 12.

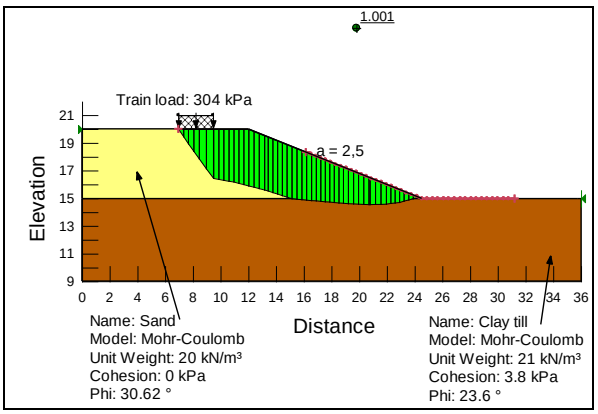


Figure 12. LEM OSS. Sandfill on clay. Drained

FEM gives a bearing capacity R_d/A = 295 / 328 kPa (ψ = 0° / 8° in sand fill).

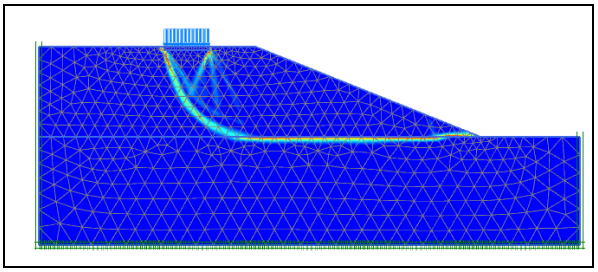


Figure 13. FEM. Sandfill on clay. Drained. Deviatoric strain. ψ = 8° in sand fill

6.2 Sandfill embankment on clay(undrained)

For a sand fill embankment placed on clay the undrained bearing capacity is R_d/A = 514 kPa using the circular slip surface (CSS), cf. figure 14.

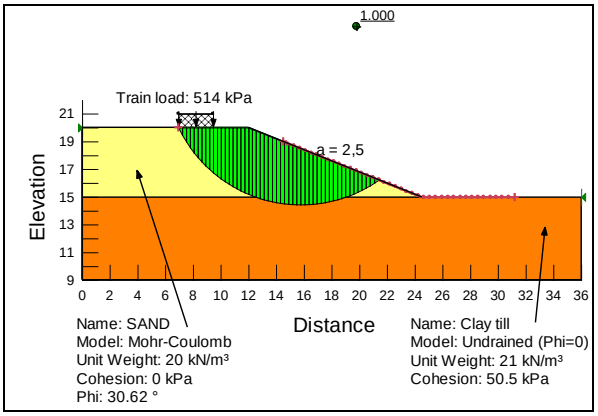


Figure 14. LEM CSS. Sandfill on clay. Undrained

The optimized slip surface shows a bearing capacity R_d/A = 289 kPa, cf. figure 15.

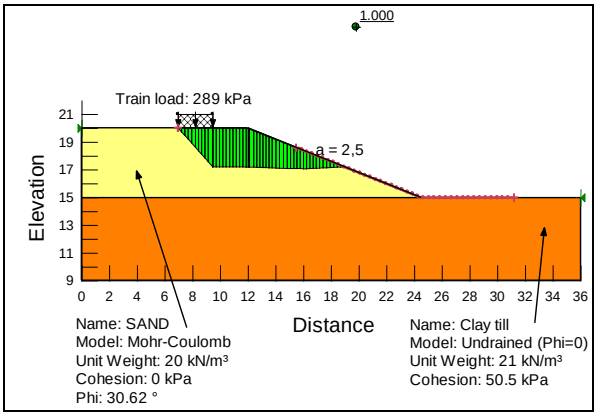


Figure 15. LEM OSS. Sandfill on clay. Undrained

FEM yields a capacity of R_d/A = 290 / 340 kPa (ψ = 0° / 8° in sand fill):

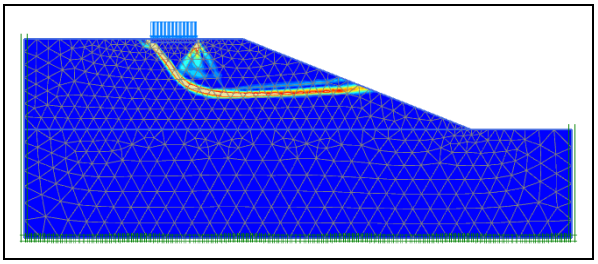


Figure 16. FEM. Sandfill on clay. Undrained. Deviatoric strain. ψ = 8° in sand fill

Below the LEM CSS and LEM OSS capacities are compared to the FEM analysis

Table 6. Results. Embankment of finite heigth

	LEM		FEM[1]
	CSS	OSS	
	[kPa]	[kPa]	[kPa]
Drained	**489**	**304**	**295[1] 328[2]**
Deviation	**+49%**	**+3% -7%**	**-**
Undrained clay	**514**	**289**	**290[1] 340[2]**
	[kPa]	**[kPa]**	**[kPa]**
Deviation	**+51%**	**0%[1] -15%[2]**	**-**

[1] ψ = 0° in sand fill. [2] ψ = 8° in sand fill

Note the similarity between LEM OSS and FEM slip surfaces, and that neither penetrates the clay layer as LEM CSS does.
If the model shown in figure 14 is loaded with the ultimate load from LEM OSS and FEM (with ψ = 0°) i.e. 290 kPa, the slip surface changes radically and a FoS of 1.198 is found, cf. figure 14a:

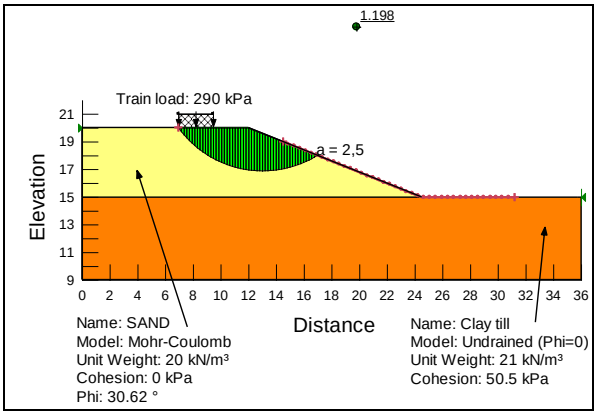


Figure 14a. Model cf. figure 14 loaded with 290 kPa yields FoS = 1.198 with LEM CSS.

On the other hand, if the embankment is loaded with ultimate load from LEM CSS i.e. 514 kPa FoS drops to 0.839 when using LEM OSS, cf. figure 14b:

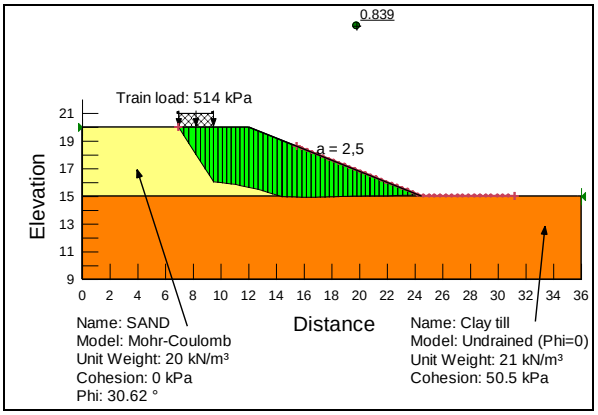


Figure 14b. Model cf. figure 14 loaded with 514 kPa yields FoS = 0.839 with LEM OSS.

7 EMBANKMENT ON SOFT SOIL

When stabilizing an old embankment, a berm could be placed at the embankment foot as countermeasure, as shown on figure 1b. For this situation no analytic solution exists, and therefore the analysis must be conducted by means of LEM or FEM calculations. The LEM CSS yields a bearing capacity of R_d/A = 167 kPa, cf. figure 17, whereas the LEM OSS yields a capacity of R_d/A = 35 kPa, cf. figure 18, with undrained conditions in the soft soil.

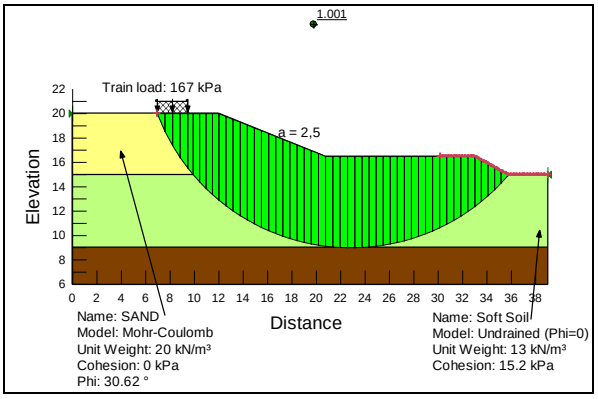


Figure 17. Embankment on soft soil. LEM CSS.

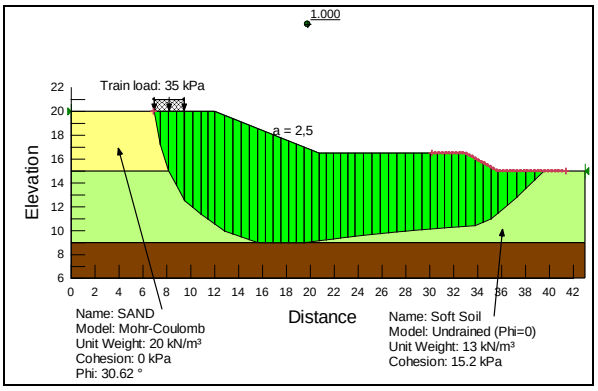


Figure 18. Embankment on soft soil. LEM OSS.

FEM yields the following slip surface and bearing capacities for various ψ of the sand fill material. As in the previous scenarios the bearing capacities are found through a safety analysis in FEM with a target factor of safety M_{SF} = 1.32 giving the desired design values of the soil strength. As the partial factor for undrained strength is 1.98, the soft soil in FEM is modelled with an undrained strength $c_{u,model} = (c_{u,k} / 1.98)\cdot 1{,}32$ so a common target factor of safety M_{SF} = 1.32 can be used.

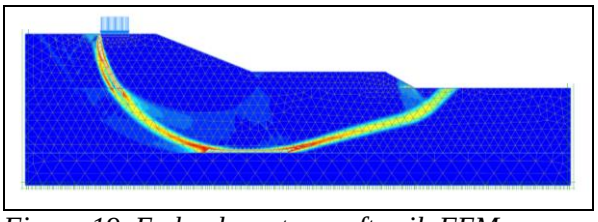


Figure 19. Embankment on soft soil. FEM. Deviatoric strain.

Note the similarity between LEM OSS and FEM slip surfaces.

Table 7. Dependency of ψ

	ψ = 0	**ψ = 8°**	**ψ = 38°**
Bearing capacity [kPa]	55	59	62

No significant dependency of ψ is found in this case.
Below the LEM CSS and LEM OSS capacities are compared to the FEM analysis:

Table 8. Results. Embankment on soft soil

	LEM		FEM
	CSS	OSS	
Soft soil Undrained	167	35	59
Deviation	+183%	-41%	-

8 CONCLUSIONS

For the embankment of infinite height an analytical solution exists and when comparing the results from Limit Equilibrium Methods (LEM) and Finite Element Methods (FEM) with this, it is very clear that LEM with optimized slip surface and FEM both gives results very close to the analytical solution (- 5% to +11%), whereas LEM with circular slip surface over predicts the bearing capacity significantly in the drained calculations for both sand fill and clay fill embankments (+61% and +28%). In the undrained calculations all methods gives results close to the analytical solution (≈+5%).
The over prediction with circular slip surface (LEM CSS) in the sand fill embankment of infinite height is equal to a reduction in the partial factor of safety from $\gamma_\varphi = 1.32$ to $\gamma_\varphi = 1.16$ and in the similar clay fill embankment from $\gamma_\varphi = \gamma_c = 1.32$ to $\gamma_\varphi = \gamma_c = 1.2$. This indicates how much the LEM CSS results are on the unsafe side compared to FEM.
For the 2 layer embankment of finite height an analytical solution does not exist. If the LEM results are compared to FEM, it is again clear that the circular slip surface from LEM significantly over predicts the bearing capacity (+50%). LEM with optimized slip surface yields results very close to FEM in the drained analysis (+3% to -7% depending on ψ used in FEM), and a bit more in the undrained analysis (-18%).
Finally the analyses for the embankment on soft soil with a berm at the embankment foot shows that the circular slip surface very significantly over predicts the capacity compare to FEM (+168%), while the LEM optimized slip surface significantly under estimate the bearing capacity when compared to FEM (-41%).
If the FEM model for the embankment on soft soil with $c_u = 30$ kPa should be able to carry a load of 167 kPa as found in the LEM CSS analysis, the partial factor of safety γ_{cu} =1.98 must be reduced to γ_{cu} =1.27. This indicates how much the LEM CSS result is on the unsafe side. Similar if FEM only should carry the LEM OSS load of 35 kPa, the factor of safety γ_{cu} =1.98 could be raised to γ_{cu} =2.15, which indicates how much LEM OSS is on the safe side compared to FEM for this model.

From the above it seems clear that the LEM with circular slip surface (LEM CSS) in general significantly over predicts the bearing capacity of an embankment. The over prediction found in the examples presented here is so significant, that use of circular slip surfaces should be avoided when evaluating the stability of slopes – at least when a load is present at the embankment top. If used anyway, the safety of the embankment risks being far from what was intended. The optimized slip surface (LEM OSS) in general predicts bearing capacities very comparable to FEM.
Eurocode 7 states as principal text that:

> *2.4.1.6(P): Any calculation model shall be either accurate or err on the side of safety*

Further Eurocode 7 states that:

> *11.5.1(5) Where ground or embankment material is relatively homogeneus and isotropic, circular slip surfaces should normally be assumed.*

It is found from the work presented here, that LEM with circular slip surfaces does not meet 2.4.1.6(P), and that 11.5.1(5) should be seriously questioned - at least when significant loads are present at the embankment top.

9 REFERENCES

Brinch Hansen, J. (1970). A revised and extended formula for bearing capacity. The Danish Geotechnical Institute. Bulletin 28.

DS/EN 1997-1:2007. Eurocode 7: Geotechnical design - Part 1: General rules

DS/EN 1997 – DK NA:2013. Danish National Annex to Eurocode 7:

Fellenius, W. (1936). Calculation of the stability of earth dams. Proceedings of the second congress of large dams, Vol. 4, pp. 445-463

Geo-Studio 2007. SLOPE/w. GEO-SLOPE/W International. Calgary, Alberta, Canada

Hansen, B. (1978). Geoteknik og Fundering – Del II

Janbu, N. (1954). Applications of composite slip surfaces for stability analysis. Proceeding of the European conference on the stability of earth slopes, Stockholm, Vol. 3, pp. 39-43

Krahn, J. (2004). Stability Modeling with SLOPE/W – An engineering Methodolgy

Morgenstern, N.R. and Price, V.E. (1965). The analysis of the stability of general slip surfaces. Geotechnique, Vol. 5 pp. 79-93

PLAXIS 2D - 2015. Plaxis user manual, Delft University of Technology & Plaxis bv. The Netherlands.

Petterson, K.E. (1955). The early history of circular sliding surfaces, Geotechnique, Vol. 5, pp. 275-296.

Spencer, E. (1967). A method of analysis of embankments assuming parallel interslice forces. Geotechnique, Vol. 17 (1), pp. 11-26

Modeling soft Scandinavian clay behavior using the asymptotic state

Jon A. Rønningen
Norwegian University of Science and Technology, NTNU, Norway, jon.a.ronningen@ntnu.no

Gustav Grimstad, Steinar Nordal
Norwegian University of Science and Technology, NTNU, Norway

ABSTRACT

The deformation of soft or sensitive Scandinavian clays can be a complex process in which the structure is continuously changing to accommodate applied loading. This paper presents a pragmatic way of describing this process using differential equations for the Cauchy stress tensor where the normal consolidated state and asymptotic behavior play an important role. An advantage to this approach is that for simple strain paths (e.g. undrained triaxial and oedometer tests) the development of stress can be found analytically. The model provides stress-strain relationships in principle for any strain path, but small strain behavior where isotropic unloading is involved requires further research.

Keywords: soft clays, asymptotic states, barodesy

1 INTRODUCTION

Many of the soft clay models used today have been developed within the theory of plasticity. This framework allows constitutive models to be defined by the elastic stiffness and a minimum of two scalar functions (Hill 1950), the plastic potential and the yield function, where the first will give the orientation of the plastic strain increments and the second will provide the boundary between elastic and elastic-plastic behavior for any stress state.

The well-known Cam-Clay (CC) model (Schofield and Wroth 1968) and subsequent variations have the critical state as a fundamental basis, which is a state observed during large shear deformations when there is no further change in effective stresses or volume (Wood 1990). The CC model was originally developed with reconstituted clays in mind, i.e. rather simple clays without the bonds and fabric (Burland 1990, Länsivaara 1999) found in natural clays. Later much advancement has been made to include the effects of anisotropy, destructuration, rate-dependence and creep (Dafalias 1986, Wheeler, Näätänen et al. 2003, Dafalias, Manzari et al. 2006, Grimstad and Degago 2010, Grimstad, Degago et al. 2010, Olsson 2013).

Although this framework elegantly provides complex stress-strain relationships in a continuum of three spatial dimensions, advanced models may have complicated hardening rules which will simultaneously influence the behavior. This can make model calibration challenging because hardening parameters can influence both isotropic and deviatoric deformation behavior and may or may not have a direct physical meaning. In particular, providing direct input of an undrained ADP shear strength profile (Grimstad, Andresen et al. 2012) in effective stress based models can be a challenge with one set of parameters.

This paper presents a pragmatic model for soft Scandinavian clays formulated as a system of differential equations. It is based on the concept of asymptotic / steady states

(Schofield and Wroth 1968, Poulos 1971) and has three basic underlying hypotheses. Although originally developed separately, the modeling ideas resembles well those of Barodesy (Kolymbas 2012) and have also some similarities to the works of (Joseph 2010) and (Mašín 2012). The model presented here provides stress-strain relationships in principle for any strain path, but with the main focus being on deformation behavior not involving isotropic unloading as it is considered a different process from consolidation. A pragmatic way of modeling isotropic unloading has been described but does require further research for small strain cycles.

Some very useful features from Barodesy are already incorporated and the future objective is to fully formulate the model within this framework.

1.1 Definitions

The formulation presented herein applies to soft or sensitive clays starting from an initial condition towards well defined asymptotic states, which are reached through a continuous deformation process; any reversal is the start of a new process. The strain increment $d\varepsilon_{ij}$ is considered to be acting on the soil while the Cauchy stress tensor σ_{ij} is the reaction or response. Although this is a choice of definition, it is a sensible one considering that shear stress may exhibit post-peak softening making the strain non-unique for a given stress level. On the other hand, strain will always correspond to a unique stress level for the process described here. The isotropic and deviatoric components of the strain increment are defined as:

$$d\varepsilon_p = \frac{d\varepsilon_{kk}}{3} \tag{1}$$

$$d\varepsilon_q = \sqrt{\frac{2}{3}\left(d\varepsilon_{ij} - d\varepsilon_p\delta_{ij}\right)\left(d\varepsilon_{ji} - d\varepsilon_p\delta_{ji}\right)} \tag{2}$$

where $d\varepsilon_p$ is positive in compression and $\delta_{ij} = \delta_{ji}$ is the Kronecker delta. This implies that for triaxial loading with ε_a for axial strain and ε_r for radial strain we have:

$$d\varepsilon_q = \frac{2}{3}\left(d\varepsilon_a - d\varepsilon_r\right) \tag{3}$$

The Cauchy stress tensor is assumed to be composed as follows

$$\sigma_{ij} = p\left(\eta_{ij} + \delta_{ij}\right) \tag{4}$$

All stresses are effective and thus the commonly used ‘-notation has been omitted for convenience. The component p has the unit of stress but is a scalar; η_{ij} is without units but does contain components. In this paper η_{ij} is said to represent the orientation of the stress tensor and p represents the equivalent isotropic magnitude and is the mean effective stress, i.e.

$$p = \frac{\sigma_{kk}}{3} \tag{5}$$

where p is positive in compression. The split of a stress into p and η_{ij} allows the stress measures to be seen as separate: alone their formulation can be quite simple while the combination of the two may provide rather complex soil behavior. For example, the deviatoric stress $s_{ij} = \eta_{ij} p$ may exhibit a peak even though η_{ij} and p does not; if a soft clay reaches its asymptotic orientation before the magnitude of stress a peak will typically develop. The scalar equivalent of η_{ij} is here called the invariant η and is defined as

$$\eta = \sqrt{\frac{3}{2}\eta_{ij}\eta_{ji}} \tag{6}$$

The deviatoric (shear) stress q can then be found as η times p. The more general η_{ij} has been used throughout the derivations so that information about the spatial components of stress is retained.

2 HYPOTHESES

The model has three underlying hypotheses which are stated on the basis of natural soft Scandinavian clay behavior observed mainly in laboratory tests.

The three hypotheses are:

1. Applying strain increments to a clayey soil will asymptotically make it normal consolidated.

2. The stress will eventually reach an asymptotic orientation which is uniquely defined by the orientation of the strain increment responsible for bringing it into this state.

3. The magnitude of the asymptotic stress is uniquely related to the void ratio of the soil.

The three hypotheses above are similar to those which form the basis of Barodesy. In particular, the first two hypotheses are more or less identical to Goldscheider's first and second rule (Goldscheider 1967) but rephrased slightly to accommodate the behavior of clays and the normal-consolidated (NC) state. It follows from the second hypothesis that the asymptotic orientation of stress is independent of initial conditions and the path taken. The third hypothesis is important because it defines the asymptotic value of hydrostatic stress as a state parameter unique to the current void ratio.

From the rules of calculus it follows that contributions from the strain increment components on the stress state can be incrementally superimposed. It is assumed that this is also true in a physical sense.

3 CONSTITUTIVE EQUATIONS

A measure of the process of becoming normal-consolidated has traditionally been given to the over-consolidation ratio, OCR:

$$OCR = \frac{p^m}{p} \tag{7}$$

Where p is the magnitude of current stress and p^m is the stress which retains memory ("m") of prior loading. The incremental form of eq. (7) defines the main differential equation for p and is given by:

$$dp = p\left(\frac{dp^m}{p^m} - \frac{dOCR}{OCR}\right) \tag{8}$$

If the development of the NC state dp^m and the process of becoming normal-consolidated $dOCR$ is given as a function of strain increments, then the development of dp is fully defined. In the derivations below an approach is taken to separate the relative complex stress-strain behaviour into simpler parts: First the process of deformation is seen as an interaction between the normal- and overconsolidated state, then a separation of the magnitude and orientation of stress is made, and finally the contribution from the isotropic and deviatoric strain components are incrementally superimposed. In total this makes the resultant stress behaviour relatively complex while maintaining simplicity in the individual expressions. It is also assumed that memory (OCR) is only related to the magnitude of stress and not the orientation. The change in the stress orientation is thus given as:

$$d\eta_{ij} = \frac{\partial \eta_{ij}}{\partial \varepsilon_p} d\varepsilon_p + \frac{\partial \eta_{ij}}{\partial \varepsilon_q} d\varepsilon_q \tag{9}$$

The following formulations are suggested:

$$\frac{\partial \eta_{ij}}{\partial \varepsilon_q} = \left(\eta_{ij,\infty} - \eta_{ij}\right) \cdot k_{\eta q} \tag{10}$$

$$\frac{\partial \eta_{ij}}{\partial \varepsilon_p} = \frac{\partial \eta_{ij}}{\partial \varepsilon_q} \frac{k_{\eta p}}{k_{\eta q}} \tag{11}$$

where $k_{\eta p}$ and $k_{\eta q}$ are proportionality constants and $\eta_{ij,\infty}$ is the asymptotic value of η_{ij}. The equations (9) to (11) can be integrated analytically for simple strain paths. The ratio κ is introduced:

$$\kappa = \frac{d\varepsilon_q}{d\varepsilon_p} \tag{12}$$

For a constant κ ratio the analytical expression is found as:

$$\frac{\eta_{ij}}{\eta_{ij,\infty}} = 1 - \left(1 - \frac{\eta_{ij,0}}{\eta_{ij,\infty}}\right) e^{-(k_{\eta p} + k_{\eta q}\kappa)\varepsilon_p} \tag{13}$$

where $\eta_{ij,0}$ is the initial orientation and 'ij' denotes each individual component of the tensor. The asymptotic value $\eta_{ij,\infty}$ must be related to the orientation of the strain increment. The framework of Barodesy elegantly provides this relation for the components of the stress tensor through an exponential mapping function (Medicus, Kolymbas et al. 2015) . For the purpose used in this paper it provides the internal friction angle φ and the coefficient at rest K_0^{NC} as possible calibration parameters. For pure deviatoric deformation the steady state strength follows more or less the Matsuoka-Nakai failure criterion (Fellin and Ostermann 2013) while in an oedometer condition it will represent a K_0^{NC} condition. For pure isotropic deformation the asymptotic orientation is zero.

Due to space limitations the presentation here has been made brief, but reference is made to the works of (Kolymbas 2012, Medicus, Fellin et al. 2012) for important derivations and a thorough description.

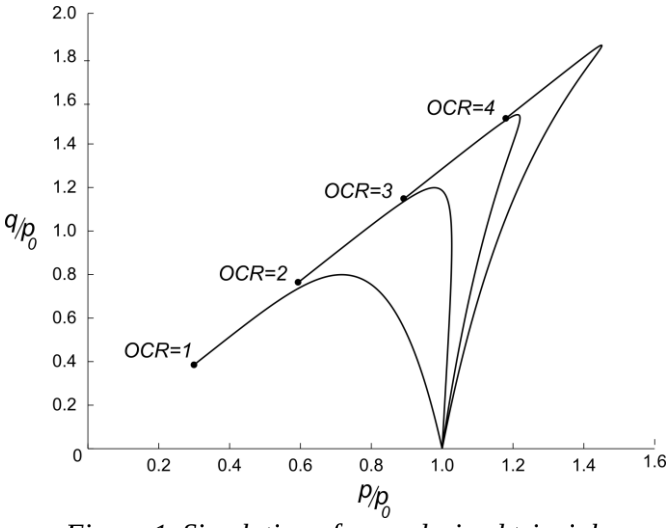


Figure 1. Simulation of an undrained triaxial compression test for various OCRs.

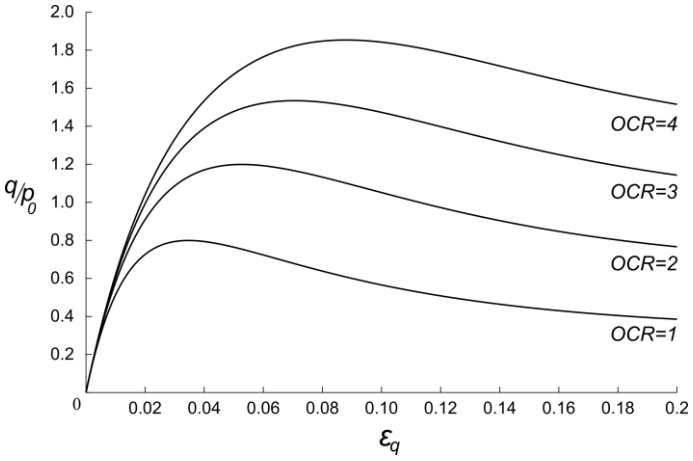


Figure 2. Development of undrained shear strength for various OCRs.

3.1 Normal-consolidated state

Following the simplification in the previous section, i.e. memory only being related to the magnitude of stress, the stress invariant p^m will describe the soil as if it were normal-consolidated and will go towards a steady state value p_∞^m during deviatoric deformation but will grow "exponentially" for isotropic dominated deformation. As such it is a continuously updated target for p .

The change in p^m is given as:

$$dp^m = \frac{\partial p^m}{\partial \varepsilon_p} d\varepsilon_p + \frac{\partial p^m}{\partial \varepsilon_q} d\varepsilon_q \quad (14)$$

The following formulations are suggested:

$$\frac{\partial p^m}{\partial \varepsilon_p} = p^m \cdot k_{mp} \quad (15)$$

$$\frac{\partial p^m}{\partial \varepsilon_q} = \left(p^m_\infty - p^m \right) \cdot k_{mq} \quad (16.a)$$

$$\frac{dp^m_\infty}{d\varepsilon_p} = p^m_\infty \cdot k_{mp,\infty} \quad (16.b)$$

The proportionality constants k_{mp}, k_{mq} and $k_{mp,\infty}$ will later be related to physical quantities and must be non-dimensional. The equations above are written down on the basis of observed behavior: the first equation describes the exponential stress-strain curve seen in isotropic dominant deformation; the second is the steady state stress due to deviatoric (undrained) conditions and the third equation follows from hypothesis number three.

In the derivations to follow the proportionality constant of eq. (16.b) has been set equal to that of eq. (15) but need not be in general; whenever they are equal the "critical state line" (CSL) and the "normal-consolidation line" (NCL) will be parallel with slope k_{mp} in a $\varepsilon_p - \ln p$ diagram.

It should be noted that as long as dp^m divided by p^m is non-dimensional then all stress-strain curves can be normalized by the initial magnitude of stress (fig. 1 and 2) for a given OCR. This can be seen from eq. (8). By considering κ constant for a monotonic strain path, the analytical expressions are obtained as:

$$\frac{p^m}{p^m_{\infty,0}} = e^{k_{mp}\varepsilon_p} \left(1 - \left(1 - \frac{p^m_0}{p^m_{\infty,0}} \right) e^{-\kappa k_{mq}\varepsilon_p} \right) \quad (17)$$

$$\frac{p^m_\infty}{p^m_{\infty,0}} = e^{k_{mp}\varepsilon_p} \quad (18)$$

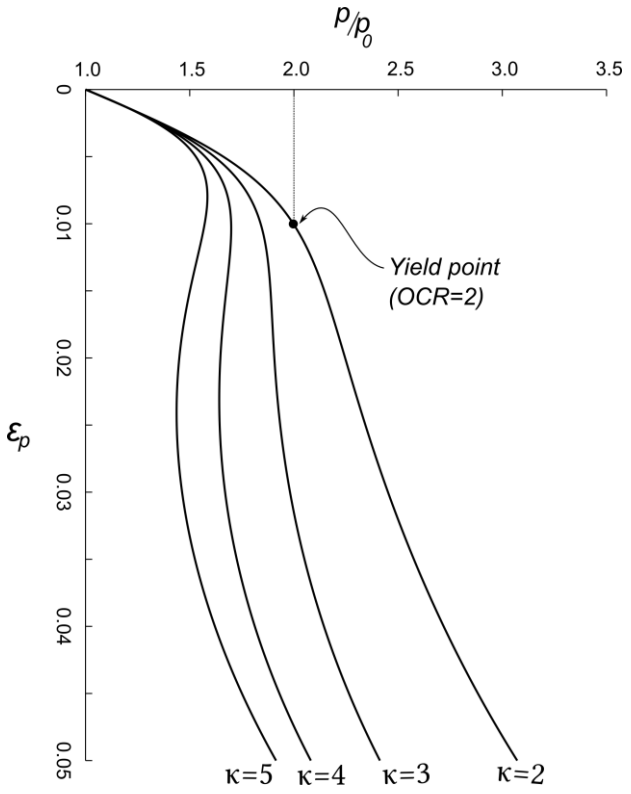


Figure 3. Effect of increasing κ, i.e. introducing more shear deformation relative to $\kappa = 2$ (oedometer condition)

Where p^m_0 and $p^m_{\infty,0}$ are the initial values of p^m and p^m_∞ respectively. The term outside the parenthesis of eq. (17) describes the behavior expected to be seen for pure isotropic strain. The main term inside the parenthesis is due to the deviatoric strain component and will decay and eventually disappear. This is important because as long as there is continuous (positive) isotropic deformation the soil will not fail even though it may temporarily appear to do so, but eventually show an exponentially increasing strength. An illustrative plot of this can be seen in figure 3. Dividing eq. (17) by eq. (18) gives:

$$\frac{p^m}{p^m_\infty} = 1 - \left(1 - \frac{p^m_0}{p^m_{\infty,0}} \right) e^{-\kappa k_{mq}\varepsilon_p} \quad (19)$$

It can be seen that for pure isotropic deformation ($\kappa = 0$) the "contractancy" p^m divided by p^m_∞ remains constant throughout the strain path, but goes towards unity whenever deviatoric deformation is involved.

This is important because it implies a continuous structural degradation with shear strain. First consider a soft clay specimen being consolidated along a K_0- line in a triaxial cell to its in-situ stress. If sheared in an undrained manner the shear strength will typically exhibit a peak due to its relative high contractancy, even if the soil is normal-consolidated. Next compare an "identical" sample consolidated along the same line but far beyond any prior loading so that eq. (19) becomes close to unity. Even though the stress has steadily been increasing due to the isotropic component of deformation the deviatoric strain has been degrading the structure. If sheared undrained the second sample would not exhibit any peak even if the first sample did. This can be seen from the incremental form of the deviatoric stress tensor:

$$ds_{ij} = d\eta_{ij} \cdot p^m + dp^m \cdot \eta_{ij} \tag{20}$$

At this "residual" state, i.e. p^m equal to p_∞^m, only the first term involving the orientation of stress contributes to the development of shear strength since p^m remains constant. Because the orientation of stress does not exhibit a peak in this formulation the shear stress does not either for this case.

3.2 Over-consolidated state

This section describes the continuous process of the soil becoming normal consolidated, with emphasize made on the word continuous because mathematically the process never ends but goes asymptotically towards its steady state value. Any deformation, except where isotropic unloading is involved, will make the soil more normal consolidated and make OCR go towards unity:

$$OCR_\infty = 1 \tag{21}$$

In a most pragmatic form the development of OCR with strain can be formulated as:

$$dOCR = \frac{\partial OCR}{\partial \varepsilon_p} d\varepsilon_p + \frac{\partial OCR}{\partial \varepsilon_q} d\varepsilon_q \tag{22}$$

$$\frac{\partial OCR}{\partial \varepsilon_q} = (1 - OCR) \cdot k_{oq} \tag{23}$$

$$\frac{\partial OCR}{\partial \varepsilon_p} = \frac{\partial OCR}{\partial \varepsilon_q} \cdot \frac{k_{op}}{k_{oq}} \tag{24}$$

Where k_{op} and k_{oq} are proportionality constants. For a constant κ ratio the analytical expression is given as:

$$OCR = 1 - (1 - OCR_0) e^{-(k_{op} + \kappa k_{oq})\varepsilon_p} \tag{25}$$

Where OCR_0 is the initial over-consolidation ratio which can typically be found from an oedometer test using standard determination procedures related to e.g. a measure of curvature. There are some exceptions to this which will be discussed later.

3.3 Isotropic unloading

The only component of deformation that will not make the soil become more normal-consolidated is isotropic unloading and as such is considered a separate process. In this case OCR can be said to be created as the memory of prior loading is being retained. A pragmatic way of incorporating isotropic unloading is to replace eq. (24) with the following expression:

$$\frac{\partial OCR}{\partial \varepsilon_p} = -OCR \cdot k_{op} \tag{26}$$

Since $d\varepsilon_p$ is negative for isotropic unloading the equation above will make OCR go exponentially towards infinity, i.e. making p go towards zero. In addition eq. (11) must change sign. The resulting behavior is realistic for larger isotropic strain cycles but is inaccurate for small cycles such that further research is needed.

3.4 Analytical solution

In the previous section the analytical solutions for a simple κ strain path was presented. The expression for p^m of eq. (17) can be combined with the definition of OCR

eq. (7) to give the following expression for the magnitude of stress:

$$\frac{p\left(\kappa,\varepsilon_p\right)}{p_{\infty,0}^m}=\frac{e^{k_{mp}\varepsilon_p}\left(1-\left(1-\frac{p_0^m}{p_{\infty,0}^m}\right)e^{-\kappa k_{mq}\varepsilon_p}\right)}{1-\left(1-OCR_0\right)e^{-\left(k_{op}+\kappa k_{oq}\right)\varepsilon_p}} \quad (27)$$

The expression for the individual components of stress orientation was found as:

$$\frac{\eta_{ij}\left(\kappa,\varepsilon_p\right)}{\eta_{ij,\infty}}=1-\left(1-\frac{\eta_{ij,0}}{\eta_{ij,\infty}}\right)e^{-\left(k_{\eta p}+k_{\eta q}\kappa\right)\varepsilon_p} \quad (28)$$

Inserting the above equations into eq. (4) will provide the components of the Cauchy stress tensor. In case of a two component $(q-p)$ formulation the deviatoric stress is found as η multiplied by p where η is found from eq. (6). The second argument ε_p could be replaced by the deviatoric strain ε_q divided by κ if desired and then let $\kappa\to\infty$ for undrained conditions. Besides simulating simple monotonic strain paths directly eq. (27) and (28) can be used to calibrate the 5 proportionality constants to quantities found in laboratory tests.

4 PARAMETER DETERMINATION

From the governing equations it seems natural that initial inclinations in stress-stress and stress-strain plots are used to calibrate the proportionality constants. There seems though to be a relative flexibility in choosing the input parameters as long as they come from simple strain-driven laboratory tests. In this paper the following is used:

Stress orientations:

1. The friction angle, φ
2. The earth pressure coefficient, K_0^{NC}

For the NC condition:

3. The oedometer modulus number, m
4. The "contractancy", p_∞^m / p_0^m
5. The undrained shear strength, s_u^{NC} for a triaxial compression test.

For a given OCR:

6. The undrained shear strength, s_u^{OC} for a triaxial compression test.
7. The initial shear stiffness, G_0.
8. The initial oedometer stiffness, M_0.

The proportionality constants can often be obtained directly if related to initial inclinations, but whenever the undrained shear strength is involved a system of non-linear equations must be solved at the initial stage. In the implementation the requirements above are given as 6 equations with expressions obtained from eq. (27) and (28). After these equations have been solved the model is initialized and the proportionality constants are given values. If the initial OCR is different than that calibrated for, the formulation will predict the behavior based on internal relations. All stress-strain curves can be normalized by the initial stress. While the undrained shear strength is considered the most important for typical short term ultimate limit state cases, the same procedure can in principle be done for other responses considered important.

In the next section the conditional equations for the undrained shear strength is provided for the normal-consolidated condition in a two-component ($q-p$) formulation.

4.1 Deviatoric deformation

During undrained shearing the contribution from the isotropic strain increment is considered negligible due to the relative incompressibility of the pore water. Introducing simplifying factors:

$$\alpha=\frac{k_{mq}}{k_{\eta q}},\ \beta_0=\frac{\eta_0}{\eta_\infty}$$
$$\beta=\frac{\eta_p}{\eta_\infty},\ \ \gamma=\frac{p_0^m}{p_\infty^m}-1 \quad (29)$$

where 'subscript p' now denotes peak. Consider a soil specimen that has been pre-consolidated beyond its in-situ stress so that it has become normal-consolidated. For an undrained laboratory test taken to shear failure the deviatoric (peak) strength is found as:

$$\frac{q_p}{q_\infty} = \beta\left\{1+\gamma\cdot\left(\frac{\beta-1}{\beta_0-1}\right)^{\alpha}\right\} \quad (30.a)$$

$$\frac{\alpha}{(1-\beta)} - \frac{1}{\beta}\left(1+\frac{1}{\gamma}\cdot\left(\frac{\beta-1}{\beta_0-1}\right)^{-\alpha}\right) = 0 \quad (30.b)$$

In the case of triaxial tests q_p is equal to $2\cdot s_u$ where s_u is the undrained shear strength. The two equations (30) are non-linear and coupled and can be used to prescribe the undrained shear strength within certain limits, i.e.:

$$\frac{q_p}{p_0} \le \eta_\infty \le \frac{q_p}{p_\infty} \quad (31)$$

If the peak value is larger than the maximum value then the soil must be over-consolidated, while the minimum value will be the steady state value found at large shear strains. As seen from the two equations above (and β) the value of hydrostatic stress at peak p_p will be determined by the model formulation whenever the undrained shear strength is given as input. After the two eq. (30) is solved for α and β, the proportionality constant $k_{\eta q}$ can be obtained as:

$$k_{\eta q} = \frac{1}{\varepsilon_{q,p}}\ln\left(\frac{1-\beta_0}{1-\beta}\right) \quad (32)$$

Where $\varepsilon_{q,p}$ is the deviatoric strain at the peak. It can be seen that the ratio α calibrates the shape in a $q-p$ plot while the value of $k_{\eta q}$ is used to calibrate the stiffness in a $q-\varepsilon_q$ plot. For the OC state a similar procedure can be performed but it is not shown here. As discussed earlier the initialization of proportionality constants are done numerically.

4.2 Yield point

For an oedometer test the ratio κ between deviatoric and isotropic strains is equal to 2 while for a purely isotropic deformation it is zero. Due to the relative high κ value the influence of shear strains on the stress state can become significant at the beginning of an oedometer test, in particular for very sensitive clays. First consider that the model has an initial mean stress of p_0. An oedometer test is simulated and the yield point is defined as the following stress point:

$$p_y = p_0 \cdot OCR_0 \quad (33)$$

where 'y' denotes yield. If p_y is found from an oedometer curve and p_0 is the in-situ stress level, the initial over-consolidation ratio OCR_0 can be obtained from the equation above. The yield point is typically found where it is expected, fig. 4 and 5, but has not been found to be related to a specific measure of curvature. In simulated tests where either the soil is very sensitive or the test boundaries induce much deviatoric deformation, i.e. high κ values, the soil will show heavy stiffness degradation, fig. 3, and standard definitions of the yield point likely no longer applies.

5 IMPLEMENTATION

The governing equations are given in incremental form and will have to be solved for the 9 unknowns:

$$v = \begin{Bmatrix} p \\ \eta_{ij} \\ p^m \\ p_\infty^m \end{Bmatrix} \quad (34)$$

After the vector v has been found at each increment the Cauchy stress tensor can be obtained from eq. (4). The 9 governing equations are assembled in a residual vector:

$$r = \begin{Bmatrix} \Delta p - p\left(\dfrac{\Delta p^m}{p^m} - \dfrac{\Delta OCR}{OCR}\right) \\ \Delta\eta_{ij} - \dfrac{\partial \eta_{ij}}{\partial \varepsilon_p}\Delta\varepsilon_p - \dfrac{\partial \eta_{ij}}{\partial \varepsilon_q}\Delta\varepsilon_q \\ \Delta p^m - \dfrac{\partial p^m}{\partial \varepsilon_p}\Delta\varepsilon_p - \dfrac{\partial p^m}{\partial \varepsilon_q}\Delta\varepsilon_q \\ \Delta p_\infty^m - \dfrac{dp_\infty^m}{d\varepsilon_p}\Delta\varepsilon_p \end{Bmatrix} \qquad (35)$$

Here the operator d has been replaced by Δ to denote that the infinitesimal differentials have been replaced by finite difference approximations. Inserted for the constitutive expressions, the residual vector r is now a set of equations which should become close to zero, a matter which is solved with the Newton-Raphson method.

The implementation is generally stable but does require small steps so that which should have been infinitesimal does not become too finite, in particular since the differential equations are "exponential" in nature and errors could accumulate.

6 RESULTS

Various test cases have been simulated to show the different features described in this paper. The input parameters were given as follows:

Table 1: Example soil properties

Friction angle φ	32°
Coefficient at rest K_0^{NC}	0.55
Oedometer modulus m	25
Contractancy p_∞^m / p_0^m	0.25
Undrained shear strength, s_u^{NC}	$0.4\,p_0$
For an OCR of 2.0:	
Undrained shear strength, s_u^{OC}	$0.6\,p_0$
Shear stiffness, G_0	$75\,p_0$
Oedometer stiffness, M_0	$150\,p_0$

Table 2: Proportionality constants (obtained)

k_{mq}	k_{mp}	$k_{\eta q} = k_{\eta p}$	k_{op}	k_{oq}
13.73	25.00	58.21	240.15	25.52

The figures 1-5 show various responses for this set of input parameters.

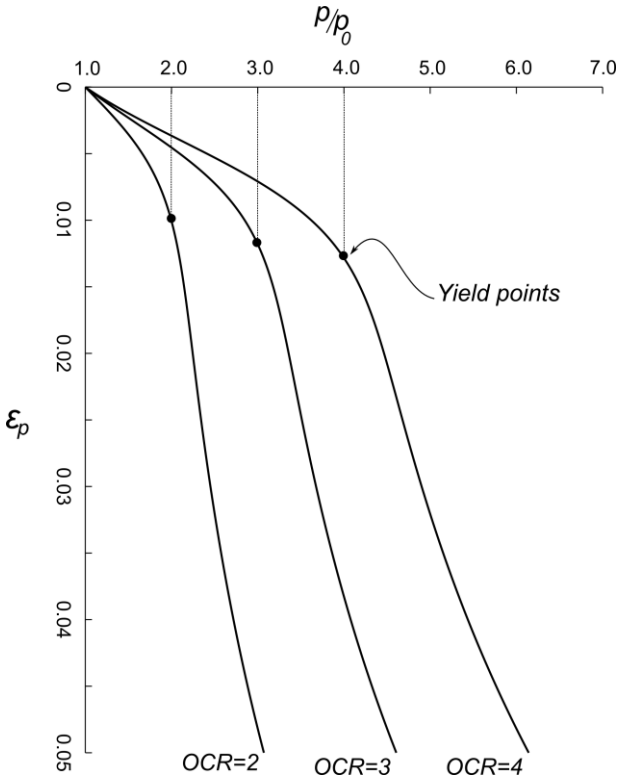


Figure 4. Simulation of an oedometer test for various OCRs.

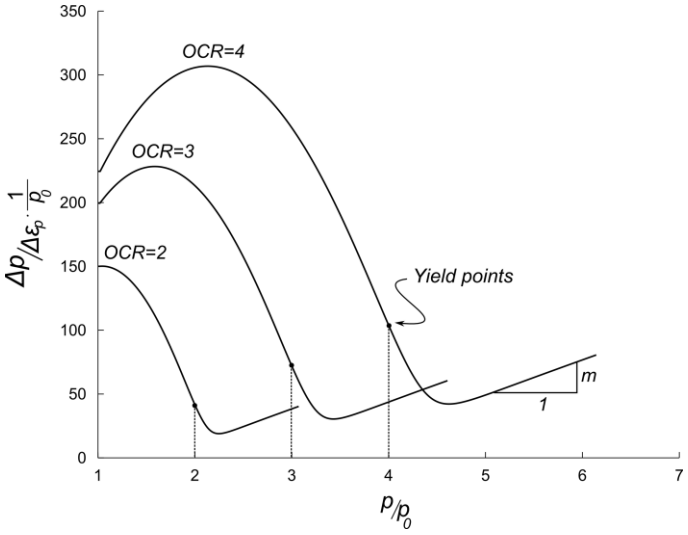


Figure 5. Another representation of the simulated oedometer test.

7 CONCLUSIONS

A constitutive model for soft Scandinavian clays has been formulated as a system of differential equations in a pragmatic way. The model provides stress-strain relationships in principle for any strain path, but deformation where isotropic unloading is involved requires further research for small strain cycles. The formulation is only a minor contribution but does show that it is possible to predict realistic soil behavior from simple assumptions on the process of deformation and the use of calculus. The framework Barodesy takes a similar approach and the future objective is to incorporate the model fully within this framework. Future work will also focus on providing the undrained ADP shear strength ratios as input.

8 ACKNOWLEDGMENTS

The work presented has been carried out under the GeoFuture project, a Norwegian research and development project with major funding from The Norwegian Research Council. In particular Associate Professor Arnfinn Emdal (NTNU) and Adjunct Professor Hans Petter Jostad (NGI/NTNU) are acknowledged.

9 REFERENCES

Burland, J. (1990). "On the compressibility and shear strength of natural clays." Géotechnique **40**(3): 329-378.

Dafalias, Y. F. (1986). "An anisotropic critical state soil plasticity model." Mechanics Research Communications **13**(6): 341-347.

Dafalias, Y. F., M. T. Manzari and A. G. Papadimitriou (2006). "SANICLAY: simple anisotropic clay plasticity model." International Journal for Numerical and Analytical Methods in Geomechanics **30**(12): 1231-1257.

Fellin, W. and A. Ostermann (2013). "The critical state behaviour of barodesy compared with the Matsuoka–Nakai failure criterion." International Journal for Numerical and Analytical Methods in Geomechanics **37**(3): 299-308.

Goldscheider, M. (1967). "Grenzbedingung und Fließregel von Sand." Mechanics Research Communications: 463–468.

Grimstad, G., L. Andresen and H. P. Jostad (2012). "NGI-ADP: Anisotropic shear strength model for clay." International Journal for Numerical and Analytical Methods in Geomechanics **36**(4): 483-497.

Grimstad, G. and S. Degago (2010). "A non-associated creep model for structured anisotropic clay (n-SAC)." Numerical Methods in Geotechnical Engineering:(NUMGE 2010): 3.

Grimstad, G., S. A. Degago, S. Nordal and M. Karstunen (2010). "Modeling creep and rate effects in structured anisotropic soft clays." Acta Geotechnica **5**(1): 69-81.

Hill, R. (1950). The mathematical theory of plasticity, Clarendon Press.

Joseph, P. G. (2010). "A dynamical systems-based approach to soil shear." Geotechnique **60**(10): 807-812.

Kolymbas, D. (2012). "Barodesy: a new hypoplastic approach." International Journal for Numerical and Analytical Methods in Geomechanics **36**(9): 1220-1240.

Länsivaara, T. T. (1999). A study of the mechanical behavior of soft clay, Norwegian University of Science and Technology.

Mašín, D. (2012). "Asymptotic behaviour of granular materials." Granular Matter **14**(6): 759-774.

Medicus, G., W. Fellin and D. Kolymbas (2012). "Barodesy for clay." Géotechnique Letters **2**(October-December): 173-180.

Medicus, G., D. Kolymbas and W. Fellin (2015). "Proportional stress and strain paths in barodesy." International Journal for Numerical and Analytical Methods in Geomechanics.

Olsson, M. (2013). "On Rate-Dependency of Gothenburg Clay." Doktorsavhandling vid Chalmers tekniska högskola.

Poulos, S. J. (1971). "The Stress-Strain Curves of Soils." Geotechnical Engineers, Inc, Winchester.

Schofield, A. and P. Wroth (1968). "Critical state soil mechanics."

Wheeler, S. J., A. Näätänen, M. Karstunen and M. Lojander (2003). "An anisotropic elastoplastic model for soft clays." Canadian Geotechnical Journal **40**(2): 403-418.

Wood, D. M. (1990). Soil behaviour and critical state soil mechanics, Cambridge university press.

A rate-dependent creep model for anisotropic soft soils

J. P. Carter
The University of Newcastle, Australia, John.Carter@newcastle.edu.au

C. Yang
The University of Newcastle, Australia, Chao.Yang@newcastle.edu.au

ABSTRACT
A rate-dependent anisotropic constitutive model for natural soft clays is proposed. The effect of stress-induced plastic anisotropy is investigated assuming kinematic, i.e., rotational, material hardening. The rate-dependent behaviour of soil is incorporated by adopting an elasto-viscoplastic framework. Predictions of the new model are compared with experimental data, obtained from triaxial testing, for a particular clay soil. These predictions are also compared with independent predictions of other soil models appearing in the literature.

Keywords: Creep, viscoplasticity, constitutive modelling.

1 INTRODUCTION

It is well known that many natural soft soils exhibit rate dependence in their response to mechanical loading. This rate dependence may manifest in the short term as soil straining that depends on the rate of application of stress, or in the longer term as continuing creep under constant effective stress. In addition, such soils often also display anisotropic straining and even destructuring in responding to these stress changes. These aspects of soil behaviour are particularly relevant for soft soils initially consolidated in the field under one-dimensional (or K_o) conditions and then subsequently loaded in shear due to the application of construction loads. Predicting such behaviour has been the subject of a number of previous studies, e.g., Kutter and Sathialingham (1992), Rowe and Hirchberger (1998), Kelln et al. (2008), Yin et al. (2010), Sivasithamparam et al. (2015).
In this paper the problem of predicting the rate-dependent response of an anisotropic material is addressed. A new, relatively simple constitutive model for soft soil is proposed based on the well established theory of elasto-viscoplasticity. The validity of the proposed model is demonstrated by presenting model predictions for undrained triaxial compression stress paths and different rates of loading, and then comparing some of these predictions with published experimental data for a particular clay soil and previously published predictions of other soil models.

2 VISCOPLASTIC FORMULATION

2.1 Basic Assumptions

The elasto-viscoplastic soil model described in the following is essentially an extension of the viscoplastic formulation presented by Kelln et al. (2008). Their original model has been augmented here by allowing the possibility of an anisotropic response of the soil.
For this model the following assumptions are adopted:

- Both elastic and time-dependent viscoplastic strains may occur in the soil;
- The elastic strain components are fully recoverable;
- The viscoplastic stain rates and components are given by the so-called “overstress theory” first proposed by Perzyna (1963, 1966) and later adopted for soil by Kutter and Sathialingham (1992), Yin et al. (2010) and others, i.e., they can be defined in terms of gradients of a viscoplastic potential function; and
- The viscoplastic potential has an elliptical shape that may grow in size and also rotate in stress space.

Specific details and the mathematical formulation are provided later in this paper. However, it should be emphasized here that many natural soils initially undergo one-dimensional consolidation under the weight of any overburden. If such consolidation were to occur over the reference time, *T*, then the normal consolidation curve labelled '*Ko*-ncl' in Figure 1 would be followed. In these circumstance the stress state at time *T* would be represented by point A in Figure 1a and the state of the soil by point A´ in Figure 1b. For times larger than the reference time *T*, creep deformations would occur under the constant weight of the overburden (constant effective stress), typically from point A´ to A in Figure 1b. If the initial consolidation had occurred under isotropic stress and strain conditions then the path labelled 'ISO-ncl' in Figure 1b would have been followed.

2.2 Mathematical formulation

For simplicity, the model is presented in terms of the triaxial stress invariants p' and q, defined as:

$$p' = \frac{1}{3}(\sigma'_1 + 2\sigma'_3) \tag{1}$$

$$q = (\sigma'_1 - \sigma'_3) \tag{2}$$

where σ'_1 and σ'_3 are the major and minor principal effective stress components, respectively. In this description, the volumetric and deviatoric strain components are defined respectively as follows:

$$\varepsilon_v = \varepsilon_1 + 2\varepsilon_3 \tag{3}$$

$$\varepsilon_d = \frac{2}{3}(\varepsilon_1 - \varepsilon_3) \tag{4}$$

where ε_1 and ε_3 are the principal strain components.

The total strain rate is separated into elastic (recoverable) and viscoplastic (time-dependent irrecoverable) components, so that the volumentric and deviatoric components of the total strain rate may be written as follows:

$$\dot{\varepsilon}_v = \dot{\varepsilon}_v^e + \dot{\varepsilon}_v^{vp} \tag{5}$$

$$\dot{\varepsilon}_d = \dot{\varepsilon}_d^e + \dot{\varepsilon}_d^{vp} \tag{6}$$

where the subscripts '*v*' and '*d*' refer to volumetric and deviatoric components, respectively, and the superscripts '*e*' and '*vp*' refer to elastic and viscoplastic components of strain and strain rate, respectively.

2.3 Elastic strain rates

It is assumed that the elastic strain increments $d\varepsilon_1$ and $d\varepsilon_3$ instantaneously accompany the changes in effective stress $d\sigma'_1$ and $d\sigma'_3$. The relationships between the time rates of change of the stresses and elastic strains may thus be written as:

$$\dot{\varepsilon}_v^e = \frac{\kappa \dot{p}'}{V p'} \tag{7}$$

$$\dot{\varepsilon}_d^e = \frac{\dot{q}}{3G} \tag{8}$$

where G is the elastic shear modulus of the soil, κ is the slope of the unloading-reloading line in V-lnp' space and V is the specific volume of the soil.

2.4 Viscoplastic strain rates

Following Perzyna (1963), Kelln et al. (2008), Sivasithamparam et al. (2015) and others, the viscoplastic strain rates are written in terms of the gradients of a plastic potential surface in stress space, g, i.e.,

$$\dot{\varepsilon}_v^{vp} = S\frac{\partial g}{\partial p'} \tag{9}$$

$$\dot{\varepsilon}_d^{vp} = S\frac{\partial g}{\partial q} \tag{10}$$

where S is a scalar multiplier and g plots as an ellipse in stress space (Figure 1a), which can be defined as:

$$g = (q - ap')^2 - (M^2 - a^2)(p'_m p' - p'^2) = 0 \tag{11}$$

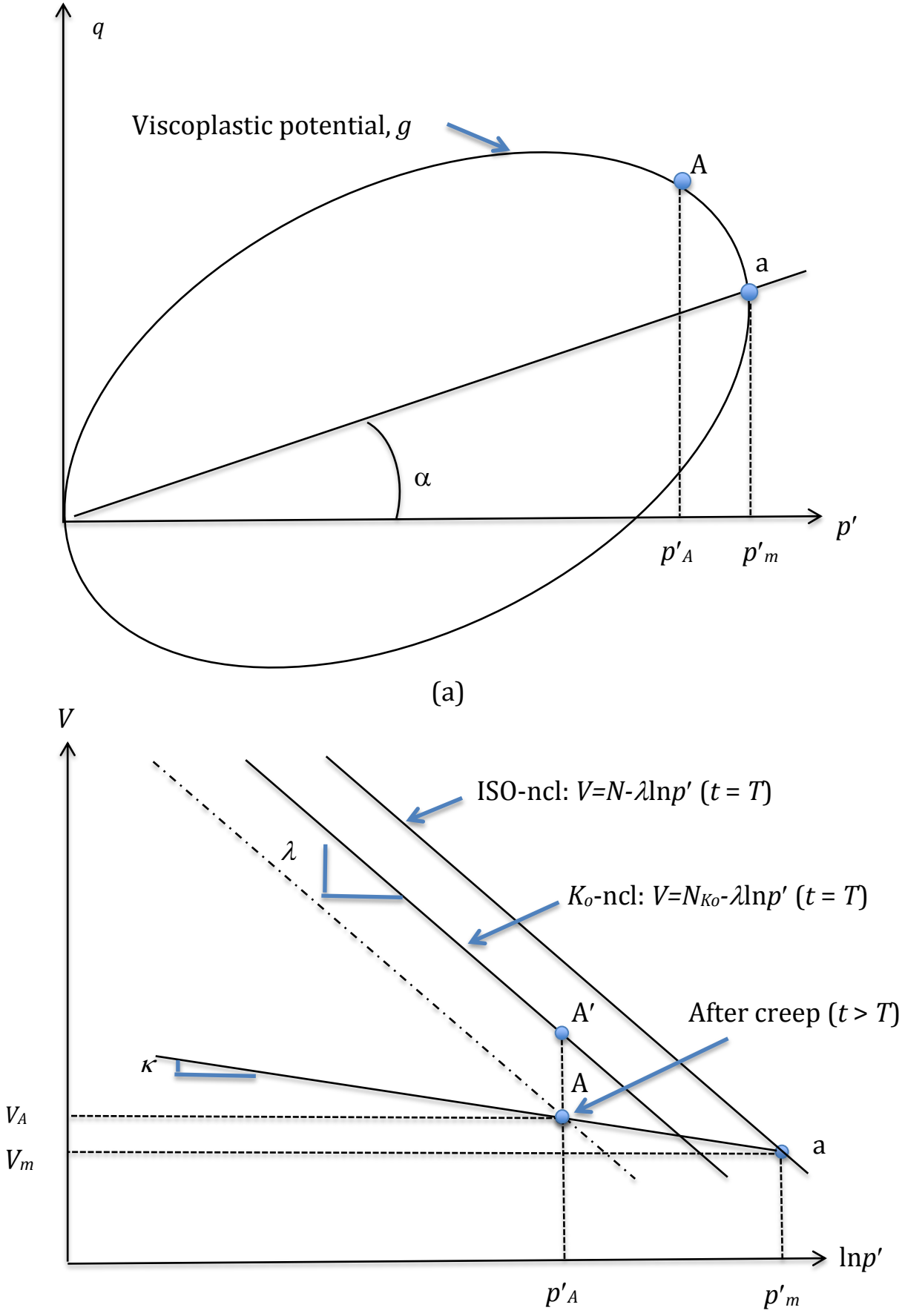


Figure 1 Schematic representation of anisotropic creep model

As indicated by Kelln et al. (2008), a suitable expression for the scalar S is given by:

$$S = \frac{\psi}{V_m T}\exp\left(\frac{V_m - N}{\psi}\right)\left(p'_m\right)^{(1/\psi)}\frac{1}{\left|\partial g/\partial p'\right|} \quad (12)$$

where λ is the slope of the normal compression line in V- lnp' is space, ψ is the slope of the secondary compression line in V-ln$t$ space, and N is the specific volume at unit pressure on the isotropic normal compression line and T is a reference time (usually assumed as 1 day). The specific volume V_m corresponding to p'_m on the particular unloading-reloading line (point a in Figure 1) is given by:

$$V_m = V_A - \kappa \ln\left(\frac{p'_m}{p'_A}\right) \quad (13)$$

where V_A is the actual specific volume of the soil corresponding to the effective stress state p'_A-q_A (point A in Figure 1).
However, unlike Kelln et al. (2008), an anisotropic plastic potential is adopted in stress space in this study, as illustrated in Figure 1, for which it can be shown that the gradients of the plastic potential are equivalent to:

$$\frac{\partial g}{\partial p'} = -2\alpha q + 2\alpha^2 p' + \left(M^2 - \alpha^2\right)\left(p'_m - 2p'\right) \quad (14)$$

$$\frac{\partial g}{\partial q} = 2q - 2\alpha p' \quad (15)$$

2.5 Evolution of anisotropy

The inherent and evolving anisotropy in the response of this ideal soil to changes in stress also has to be defined. In other words, the evolution of the anisotropy parameter α (Figure 1a) must be specified. Following Yang and Carter (2015) and Yang et al. (2015) it is assumed that the parameter α, defining the angle of inclination of the elliptical viscoplastic potential to the hydrostatic stress axis, will change from its initial value, $\alpha_{\square}$, with plastic straining. This variation is defined as:

$$\dot{\alpha} = \omega(\eta)\left(\alpha_E(\eta) - \alpha\right)\dot{\varepsilon}_r^p \quad (16)$$

where ω is a function of the stress ratio $\eta = q/p'$, defined as:

$$w = \exp\left(k_g\left(\frac{\left|\alpha - \alpha_E\right|}{M}\right)^{\frac{|h-\alpha_E|}{M}}\right) \quad (17)$$

where k_g is a model parameter and $\dot{\varepsilon}_r^p$ is the rate of plastic strain defined as:

$$\dot{\varepsilon}_r^p = \sqrt{\frac{\left(\dot{\varepsilon}_v^{vp}\right)^2 + \left(\dot{\varepsilon}_d^{vp}\right)^2}{2}} \quad (18)$$

This formulation assumes that volumetric and deviatoric plastic straining contribute equally to the rate of change of the parameter α. The parameter α_E is the "equilibrium" value of α, which would be achieved after traversing a given stress path at constant stress ratio for sufficient distance. Its value is a function of the stress ratio η and can be calculated from the following equation:

$$\frac{\alpha_E}{M} = \frac{h}{M} + \frac{M}{2\zeta}\left(1 - \left(\frac{h}{M}\right)^2\right)\ln\left(1 - \frac{h}{M}\right) \quad for \frac{h}{M} < 1 \quad (19)$$

where ζ is also a model parameter.

2.6 Strain increments

The elastic and viscoplastic strain increments may now be recovered by integrating equations (7) - (10) over time, after noting the particular expressions in equations (12) – (19).

3 NUMERICAL PREDICTIONS

3.1 Cases Considered

Predictions are provided here for the undrained triaxial compression of Saint

Herblain clay loaded at different rates of axial strain during the same compression test. The experimental data for this material have been extracted from Yin and Hicher (2008), who reported the original source of the data as Rangeard (2002). Some of the same experimental data was also cited in a subsequent paper by Yin et al. (2010).
A single triaxial test is simulated in which the axial strain rate was initially 1%/hour and then reduced to 0.1%/hour, increased to 10%/hour and finally reduced again to 0.1%/hour. The experimental data for this case are plotted in Figures 2 to 4.

3.2 Model Parameters

The values selected for the model parameters in the simulation are listed in Tables 1 and 2. Justification for their choice is provided below.

Table 1 Assumed material properties.

Parameter	Definition	Value
M	Friction constant	1.25
λ	Slope of ncl in V-lnp' space	0.5
κ	Slope of url in V-lnp' space	0.06
ν	Poisson's ratio	0.3
N	Location of Iso-ncl in V-lnp' space	5
ψ	Slope of secondary consolidation line in V- ln$t$ space	0.03
ζ	Anisotropy parameter	1
k_g	Anisotropy rotation parameter	2
T	Reference time (days)	1

Table 2 Assumed initial conditions.

Parameter	Definition	Value
$\alpha_{\square}$	Initial value of α	0.2

The values of the friction parameter for triaxial compression, M □ □□□□, and Poisson's ratio, $\nu = 0.3$, are as suggested by Yin and Hicher (2008), although it is curious that in their later paper, Yin et al. (2010), they adopted slightly different values for these parameters (1.2 and 0.2 respectively). Values of 0.5 and 0.06 have been adopted for the parameters λ and κ respectively. These values have been interpreted independently, from the results of oedometer test reported by Yin et al. (2010), who previously reported a value of 0.48 for λ and 0.022 and 0.038 for κ.

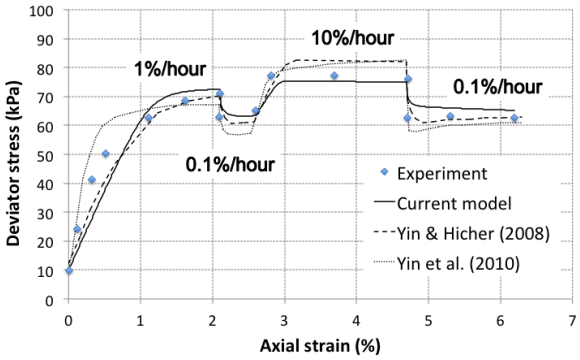


Figure 2 Undrained triaxial test on Saint Herblain clay – Deviator stress versus axial strain.

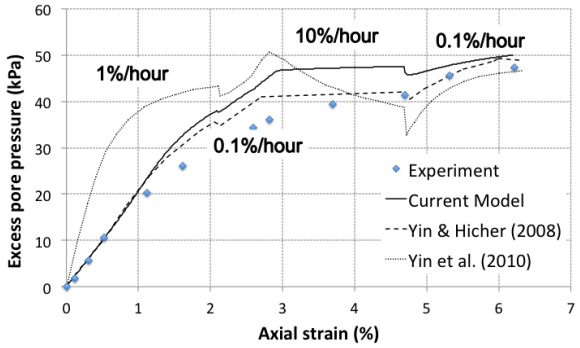


Figure 3 Undrained triaxial test on Saint Herblain clay – Excess pore pressure versus axial strain.

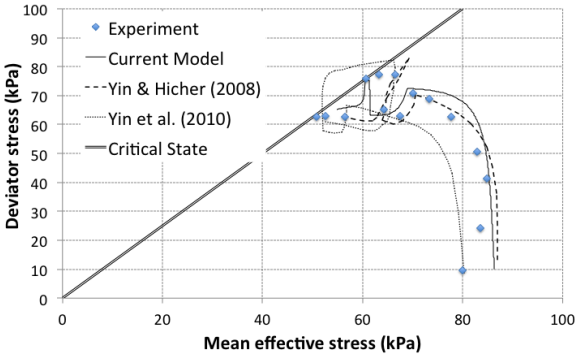


Figure 4 Undrained triaxial test on Saint Herblain clay – Stress paths.

The predictions of the current model are somewhat sensitive to the value of κ □□□□□□□□□□□□□□□□□□□□□

□□□□□□□□□□□□□□□□□□o to some degree the choice here has been influenced by how well the model was able to simulate the experimental results. However, based on the available experimental data, it is noted that the value of κ is open to some interpretation and a value of 0.06 would seem to fit into the range of most likely values, although probably at the high end.
The value of the parameter *N*, determining the position of the isotropic consolidation line in *V*- ln*p*′ space was determined from the available consolidation test data (as published in Yin et al. 2010).
Figure 12 of Yin et al. (2010) provides a plot of voids ratio, *e* (= *V* - 1), versus time plotted on a base 10 logarithmic scale. It also indicates interpreted values of 0.0337 and 0.0341 for the so-called secondary compression index, $C_{\alpha e}$, defined by the following relationship

$$C_{ae} = \frac{\mathrm{D}e}{\mathrm{D}\log_{10}(t)} \tag{20}$$

The parameter ψ is related to $C_{\alpha e}$ as follows:

$$\psi = \frac{C_{ae}}{\ln(10)} = \frac{C_{ae}}{2.303} \tag{21}$$

The value of 0.03 adopted here for the parameter ψ is therefore approximately twice the value that would be interpreted from Figure 12 of Yin et al. (2010) using equation (21). However, it is considered to be of about the correct order and possibly within the range of values that might be interpreted from the available data. Again, it is noted that the choice here has been influenced by how well the model was able to simulate the experimental results for Saint Herblain clay in undrained triaxial compression.
As noted by Yang et al. (2015), virgin consolidation tests at constant stress ratio constitute the cornerstone for describing the effect of plastic anisotropy on the soil fabric. Thus the parameters ζ and k_g are best determined by fitting the model to the behaviour of the soil as measured in such test. However, no such data was readily available for Saint Herblain clay and so the values of these parameters were determined by assessing how well the simulations fitted the data in the undrained triaxial tests.
The value of the initial inclination of the plastic potential surface in stress space, α_i = 0.2, was similarly assessed, due to a lack of appropriate test data.
In summary, where there existed appropriate laboratory test data, these data were used to independently determine the values of the model parameters. Where such data was unavailable, resort was made to curve-fitting the undrained triaxial compression tests. This situation is not entirely satisfactory from the point of view of independently assessing the merits or otherwise of any constitiutive model. Nevertheless, this situation is not uncommon in geotechnics.

4 PREDICTIONS OF OTHER MODELS

Simulations of the undrained triaxial compression response of the Saint Herblain clay, using other published models, are also provided here for comparison purposes. These correspond to the different elasto-viscoplastic stress-strain models proposed by Yin and Hicher (2008) and Yin et al. (2010). The numerical predictions have been extracted from figures in the source references.

4.1 Model of Yin and Hicher

The model proposed by Yin and Hicher (2008) is an elasto-viscoplastic model based on Perzyna's overstress theory and on the elasto-plastic Modified Cam Clay model. This model assumes isotropic behaviour and it would appear from the description provided in the paper by Yin and Hicher (2008) that a constant value of 5,000 kPa may have been assumed for Young's modulus of the clay. If this is correct, then such behaviour would be inconsistent with the usual implementation of Modified Cam Clay, for which it is usually assumed that either the elastic shear modulus or Poisson's ratio is constant but the elastic bulk modulus is pressure (and voids ratio) dependent.
The model of Yin and Hicher differs from the model presented here in at least other two

important ways. First, the model proposed in this paper involves anisotropy in the viscoplastic response, whereas the Yin and Hicher model assumes isotropy. Second, the viscoplastic potential function is different in the two models. The model proposed here adopts the potential defined by equation (11) and the scalar multiplier given by equation (12). However, Yin and Hicher have assumed the Modified Cam Clay ellipse as the potential function and a scalar multiplier, *S*, given by:

$$S = m\left(\exp\left(N\left(\frac{p_c^d}{p_c^s} - 1\right) - 1\right)\right) \quad (22)$$

where μ and N are viscosity parameters assigned values of $\mu = 10^{-9}$/s/kPa and $N = 10$. The parameters p_c^s and p_c^d define the sizes of the so-called static and dynamic loading surfaces.

4.2 Model of Yin et al.

In a later paper, Yin et al. (2010) appear to have extended the model of Yin and Hicher (2008) to include an anisotropic viscoplastic response. This generalisation involves an elliptical viscoplastic potential that can rotate and expand in stress space, much the same as the model presented in this paper but with a differnt law governing that evolution. The latter paper has also adopted a different form for the viscoplastic scalar multiplier, *S*, viz.,

$$S = m\left(\frac{p_c^d}{p_c^s}\right)^N \quad (23)$$

For the predictions made using the model of Yin et al. (2010) the following values were adopted for the new viscosity parameters: $\mu = 7.4\text{x}10^{-8}$/s and $N = 12.9$.
The values of the other parameters assumed in each of these two models are presented and discussed in the source papers and so they are not repeated here.

4.3 Commentary

It is worth noting that the expressions for the scalar multipliers, *S*, adopted in the models of Yin and Hicher (2008) and Yin et al. (2010) (Equations 22 and 23) avoid one of the major difficulties of the model proposed by Kelln et al. (2008) and hence also adopted in the model proposed here (Equation 12). This difficulty arises from the inherent assumption in the model of Kelln et al. that the volumetric component of the viscoplastic strain rate (and therefore also the viscoplastic volumetric strain increment) is constant around the plastic potential surface. As such, the critical state cannot be properly simulated, since no volumetric strain increment should be predicted at critical state. This shortcoming of the model may produce erroneous or inaccurate predictions for stress states at or close to critical state.

5 DISCUSSION

The simulations of all three models considered in this paper are presented in Figures 2 - 4 where they are compared with each other and the experimental data obtained for the Saint Herblain clay sample by Rangeard (2002).
From Figure 2 it can be deduced that all three models provide a reasonable simulation of the stress-strain response of the rate-sensitive clay soil, provided suitable parameter values are adopted in each case. In all cases it is clear that the elasto-viscoplastic model framework is able to capture the rate-sensitivity of the response of this soil during undrained triaxial compression. It is arguable which model provides the most accurate simulation.
Figure 3 reveals that all predictions of excess pore pressure generated by the undrained shearing are perhaps not quite as accurate as the corresponding predictions of the deviator stress.
Figure 4 presents the predicted undrained stress paths. Reasonable, but by no means close agreement, is shown here for all model simultions. It is also notable that the initial curvature of the undrianed stress path displayed in the experiments cannot be explained or predicted by any of these models. As noted by Yin et al. (2010), this is likely to be due to anisotropy in the elastic response of the clay, a feature not captured in any of the models considered here.

6 CONCLUSIONS

A new constitutive model has been presented that can describe the rate-dependent response of soft clay soils. This model builds on the work of previous researchers essentially combining certain aspects of models published previously by Kelln et al. (2008) and Yang et al. (2015).

It has been shown that the model is able to simulate reasonably the rate-dependent response of Saint Herblain clay in undrained triaxial compression. The noticeable changes in the response of the clay as the strain rate was varied during undrained shearing was captured well.

However, it was also noted that other constitutive models can capture this behaviour, arguably, equally as well. Two additional models were considered in this context and all three models were developed within the framework of elasto-viscoplasticty and overstress theory.

Deciding which particular model should be used in engineering predictions of the rate-dependent response of a given soft clay soil is not a straightforward matter, as a number of models possess similar characteristics and capabilities. The choice may ultimately depend on familiarity with the model and the availability of suitable laboratory or field test data from which the values of the model's parameters may be reliably determined.

7 REFERENCES

Kelln, C., Sharma, J., Hughes, D. and Graham, J. (2008). An improved elastic-viscoplastic soil model. Canadian Geotechnical Journal 45 1356-1376.

Kutter, B.L. and Sathialingham, N. (1992). Elastic-viscoplastic modeling of the rate-dependent behavior of clays. Géotechnique 42 (3), 427-441.

Perzyna, P. (1963). The constitutive equations for rate sensitive plastic materials. Quarterly of Applied Mathematics 20, 321-332.

Perzyna, P. (1966) Fundamental problems in viscoplasticity. Advances in Applied Mechanics 9, 243-377.

Rangeard, D. (2002). Identification des charactéristiques hydro-méchaniques d'une argile par analyse des essais pressiométrique. Thèse de l'Ecole Centrale de Namtes et l'Université de Nantes.

Rowe, R.K. and Hirchberger, S.D. (1998). Significance of rate effects in modeling the Sackville test embankment. Canadian Geotechnical Journal 35 (3), 500-516.

Sivasithamparam, N. Karstunen, M. and Bonnier, P. (2015). Modelling creep behaviour of anisotropic soft soils. Computers and Geotechnics 69, 46-57.

Yang, C., Sheng, D-C., Sloan, S.W. and Carter, J.P. (2015). Modelling the plastic anisotropy of Lower Cromer Till. Computers and Geotechnics 69, 22–37.

Yang, C., Liu, X., Liu, X. Yang, C. and Carter, J.P. (2015). Constitutive modelling of Otaniemi soft clay in both natural and reconstituted states. Computers and Geotechnics 70, 83–95.

Yin, Z-Y. and Hicher, P-Y. (2008). Identifying parameters controlling soil delayed behavior from laboratory and in situ pressuremeter testing. International Journal for Numerical and Analytical Methods in Geomechanics 32, 1515-1535.

Yin, Z-Y., Chang, C.S., Karstunen, M. and Hicher, P-Y. (2010). An anisotropic elastic-viscoplastic model for soft clays. International Journal of Solids and Structures 42, 665-677.

Evaluation of soil parameters for creep calculations of field cases

S. A. Degago
Norwegian Public Roads Administration, Norway, samson.degago@vegvesen.no

G. Grimstad
Norwegian University of Science and Technology, Norway

ABSTRACT
Prediction of settlements in-situ are usually establish based on soil data extracted from laboratory tests. Hence it is crucial that the laboratory samples have the desired quality to give acceptable prediction of field cases. It is also vital that soil parameters are interpreted with special emphasis on the numerical model to be used. Hence, one needs to assess the underlying assumptions of a model while interpreting the model parameters. This important consideration should also take into account sample quality. In this study, key parameters governing creep are discussed in light of sample quality and are further illustrated from numerical analyses perspective. An application example is also presented based on a well-documented test fill from Sweden. The test fill, Väsby test fill, was designed and constructed by the Swedish Geotechnical Institute (SGI) in 1947 and is still monitored. Laboratory tests on samples extracted with 50 mm diameter Swedish sampler and 200 mm diameter Laval sampler are used as a basis for the study. These laboratory samples show a distinct difference in sample quality. Based on these samples, effect of sample disturbance on the pre-consolidation stress and soil destructurations are numerically illustrated in light of an isotache based creep model that is available in a finite element code Plaxis. A representative parameter data set is established for the two laboratory tests and then used for analysis of the Väsby test fill. This work shows that sample disturbance play a key role in settlement analysis of clay soils. However, with reasonable simplifications and understanding the implication of key parameters, a relatively simple creep model can capture the overall performance of a field case. The work also gives advice and recommendations as to how one should optimize use of available data along with an available numerical tool.

Keywords: Settlement, consolidation, creep, sample disturbance, parameter interpretation.

1 BACKGROUND AND DEFINITIONS

Consolidation and creep of clayey soils is an extensively studied topic in soil mechanics. Significant advancements have occurred since the formal inception of the classical theory of consolidation for soils (Terzaghi, 1923). The theory disregards time dependent deformations during consolidations. Thus it was already discovered as early as 1936 that the theory cannot capture observed field measurements due to existence of continued deformations after consolidation was finished (Buisman, 1936). The immediate modifications that followed were to divide the total deformations into the primary and secondary consolidation phases where the primary consolidation phase is computed according to the classical consolidation theory and a creep deformation is added afterwards as a secondary consolidation phase. However, shortcoming of such formulation was recognized by earlier researchers that indicated existence of creep during primary consolidation (e.g. e.g. Šuklje 1957; Bjerrum 1967; Janbu 1969). These assertions are substantiated with extensive long-term field measurements that clearly evidenced existence of creep during Primary consolidation (e.g. Larsson, 2003; Leroueil 2006).

In spite of the aforementioned points, the current practice is widely based on calculating settlement by disregarding creep during primary consolidation phase and adding it later if deemed necessary. The reason for still using such approaches could

be the lasting effect of earlier works on consolidation which has an attribute of simplicity for teaching students. This is later carried out for use in the practice. However, it is important to benefit of existing research and level of understanding achieved through extensive works. This also calls for clarifying and re-defining fundamental concepts adhering to common terminologies. Therefore, the deformation of a saturated soil layer under loading can still be considered to consist of two successive phases, namely primary and secondary consolidation. During primary consolidation phase, soil deformation is accompanied by significant excess pore pressure and changes in effective stresses. Whereas during secondary consolidation, the soil continues to deform under approximately constant effective stresses. In a pragmatic sense this can simply be understood as primary consolidation consists of deformations due to effective stress increase and creep while secondary consolidation consists of creep deformation only. This also means that creep starts at the same time with the primary consolidation phase and is thus existent throughout the whole deformation phase. This work builds upon this fundamental understanding and definition of terminologies.

2 ON RATE DEPENDANCY OF NATURAL CLAYS

Soft clay deposits especially soft marine clays are characterized by their strong tendency to undergo significant creep deformation (high rate dependency), distructuration and anisotropy (see e.g. Šuklje 1957; Bjerrum 1967, Burland 1990). For detailed treatment of interplay between these features a reference is made to Grimstad et al. (2010) and Grimstad and Degago (2010). However, within the framework of this work an emphasis is given on elaborating the implication of rate dependency of natural clays in a simplified way and in relation to its practical aspects.

In practice deformations of such soft clay deposits is usually studied based on soil data obtained from laboratory tests. However, the time required to complete primary consolidation is significantly different for a laboratory specimen and an in-situ soil layer. For a laboratory specimen, the primary consolidation could last in the order of minutes; whereas, it could go on for several decades in thick soft clay deposits (Larsson & Mattson, 2003; Leroueil, 2006). The variations in consolidation periods give rise to different strain rates. The dependency of clays on strain rate implies that the resulting effective stress – strain relationship of clays would be a function of strain rate. An important implication of this is that the experienced pre-consolidation stress would be rate dependent. This, referred to as isotache concept (Šuklje 1957), is sketched in Figure 1 by considering two cases with similar incremental loadings up to end of primary (EOP) state. The concept depicted in Figure 1is meant to give a general principle, i.e. fast vs. slow consolidation duration can be understood as either laboratory condition vs. field condition; or a laboratory test conducted at fast rate versus one conducted at a slower test.

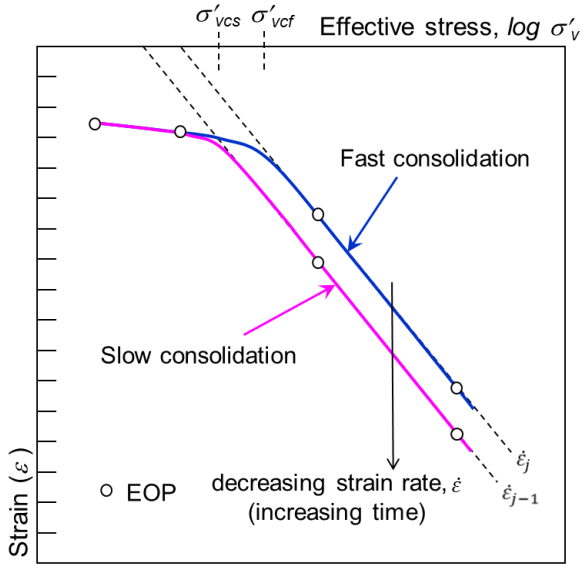


Figure 1. Sketch of effective stress vs. EOP strain relationships under similar load increment but different strain rates

3 ON SIGNIFICANCE OF SAMPLE QUALITY FOR CALCULATIONS

Numerical calculation of settlements of field conditions are normally based on soil parameters interpreted from laboratory tests.

Hence, it is crucial that the laboratory samples have the desired level of quality and be representative to give acceptable prediction of field performances.

In Scandinavia, one typically finds clays in normally consolidated state, with only an apparent over consolidation ratio (OCR) due to aging (Bjerrum 1967). Determination of this OCR is significantly affected by sample disturbance and its correct determination crucially lies on the sample quality (Leroueil & Kabbaj 1987, DeGroot et al. 2005). Different quality of the sample will also give different compressibility with respect to stress and time actions.

Sample disturbance is hardly avoidable in any soil sample extracted from in-situ. However, the degree of disturbance varies and ideally one aims to acquire a sample with highest quality. Still, it is common to encounter situations where field settlement analysis has to be based on samples of low quality. In such instances, it is important to study the implications of using parameters derived from samples of low quality. Hence, in this work such aspects are discussed from the numerical analyses perspective. Laboratory samples depicting effect of sample disturbance are used as a basis for various analyses. In addition, an application example is also presented based on a well-documented test fill from Sweden, i.e. the Väsby test fill (Larsson & Mattsson 2003). This work builds upon an earlier work by Degago & Grimstad (2014) with further extensions and enhancements along with significant elaboration.

4 SOME MODELLING ASPECTS OF NATURAL CLAYS

Constitutive models for clays that are used today are often based on the modified Cam-Clay model (MCCM) (Roscoe & Burland 1968). The MCCM was originally developed to model simple elasto-plastic behaviour of soils under triaxial stress-strain conditions. Various modifications and extensions are applied to the MCCM to account for various features of clays such as anisotropy, destructuration and creep. Typical modifications of the MCCM include:

(1) rotating the yield/reference surface to account for anisotropy (Dafalias 1986),
(2) accounting for an unstable structure by associating the yield/reference surface with a destructuration formulation proposed by Gens & Nova (1993) and
(3) modelling creep and rate dependency by controlling the size of the reference surface using concepts developed by, e.g. Šuklje (1957), Perzyna (1963) or Janbu (1963).

Common for the extensions to the MCCM is the increased complexity that these features bring with them and the need for extra soil parameters, which may require special laboratory tests. Hence, it is essential to consider the benefits of using advanced models compared to simple models. It is also vital to identify cases in which proper use of a simple model could give a better understanding of the problem than using a more advanced model. In this way, one can focus on certain selected aspects of soils and grasp the overall picture of the resulting soil responses. Accordingly, such approach has been used in this study. It is also important to consider that the current practice in the geotechnical consulting industry does not generally use advanced constitutive models that incorporate creep. The state-of-the practice is more inclined towards ignoring creep effect, dividing into primary consolidation settlement (without creep) and secondary consolidation settlements (only creep) or use of a simple isotropic or 1D creep model.

5 PROBLEM IDEALIZATION

Numerical simulation of a real case normally involves certain appropriate idealizations. Accordingly, when reducing a real problem into a numerical idealization that can readily be analysed, it is vital that soil parameters are interpreted with special emphasis on the numerical model and its underlying assumptions as well as the nature of the problem to be dealt with such as the expected stress range and associated time considerations.

This work focuses on settlement analyses of field cases with respect to sample quality.

The subject of the study is essentially on clays with significant potential to undergo creep deformations. In addition, such clays usually exhibit anisotropic behaviour and an unstable structure. For this demonstration, an elasto-viscoplastic soil model available in the FE code Plaxis is selected. This model is referred to as the Soft Soil Creep (SSC) model (Stolle 1999). The SSC is an extension of MCCM, by including the isotache concept (Šuklje 1957). In addition, the model is isotropic and does not take into account the effect of destructuration. However, for the test fill considered in this work, an isotropic formulation is considered sufficient and the effect of destructuration is investigated based on assessing effect of various combination of the input parameters. By keeping anisotropy and destructuration out of the picture, this work focuses on the creep parameters and their implications, based on the isotache formulation as adopted in the SSC model. It is worth mentioning that for problems that are not dominated by volumetric creep, the creep extension adopted in the SSC model is not preferable. Details of a different approach of extending a 1D creep model to 3D creep model is given in e.g. Grimstad et al. (2010).

One other aspect of idealization of settlement calculation is the often used assumption of small deformations. This might, in many cases, be of minor importance. However, when large settlements occur, neglecting the chance in buoyancy will lead to higher value of the calculated settlements as the effective stress change is not reduced in accordance with the increasing settlements. In Degago et al. (2011b) buoyancy and sample disturbance effects are shown to have significant influence on the calculated settlements of the Väsby test fill.

6 KEY PARAMETERS GOVERNING CREEP

To properly calculate the development of settlement and pore pressure histories, a fully coupled analysis with a creep constitutive model for the soil must be used. By observing creep behaviour, in laboratory and field tests, some mathematical equations that fits the observed data can be established. To start with, the isotache concept is quite appealing as it is simple and its parameters are easily determined from standard laboratory tests. Demonstration of how well laboratory tests can be simulated with use of an isotache type of model can be found in e.g. Degago et al. (2011a). Creep stain rate as a function of time, as defined in the isotache concept (Šuklje 1957), is given in Equation 1.

$$\dot{\varepsilon} = \frac{\mu^*}{t} \tag{1}$$

where $\dot{\varepsilon}$ = the strain rate; μ^* = the modified creep parameter; and t = time.

The isotache concept furthermore uniquely relates effective stress state (p^{eq}), reference pre-consolidation stress (p_0^{eq}) and volumetric creep strain rate ($\dot{\varepsilon}_v^{vp}$). This relationship, as used in the SSC model, is given in Equation 2.

$$\dot{\varepsilon}_v^{vp} = \frac{\mu^*}{\tau} \cdot \left(\frac{p^{eq}}{p_0^{eq}} \right)^{\frac{\lambda^* - \kappa^*}{\mu^*}} \tag{2}$$

where λ^* and κ^* = the modified compression indexes for virgin compression and recompression line respectively; τ = a reference time corresponding to the specified OCR or (p_o^{eq}/p^{eq}). Typical value of τ is one day as standard incremental oedometer tests are ran with one day increments.

As can be seen from Equation 2, in addition to μ^*, the ratio $(\lambda^* - \kappa^*)/\mu^*$ and OCR are very important for the calculated strain rate. Combining Equation 1 and Equation 2, one could find an expression for the age of the clay, t_{age}, based on OCR (for the same K_o^{NC}-line, K_o^{NC} is the coefficient of earth pressure under virgin loading) corresponding to a reference time τ, as

$$t_{age} = \tau \cdot OCR^{\frac{\lambda^* - \kappa^*}{\mu^*}} \tag{3}$$

For a certain $(\lambda^* - \kappa^*)/\mu^*$, Equation 3 can be used to estimate either the age of a clay implied when an OCR corresponding to τ is known; or, an OCR corresponding to a certain reference time τ when the age of the clay, t_{age}, is known. This implies that one must assume that the ratio $(\lambda^* - \kappa^*)/\mu^*$ is constant in time.

For example, Waterman & Broere (2005) suggests values of $(\lambda^* - \kappa^*)/\mu^*$ to be in the range 5 ("for soils with considerable amount of creep") to 25 ("for soils with little creep"). This implies that a standard one day incremental oedometer test conducted on a sample taken from a 500 year old clay would give OCR = 1.6 or 11.3 for $(\lambda^* - \kappa^*)/\mu^* = 25$ or 5 respectively. Accordingly, soils with considerable amount of creep are expected to show OCR as high as 11 which seem unlikely. A more practical range for $(\lambda^* - \kappa^*)/\mu^*$ would be 15–50. Furthermore Waterman & Broere (2005) suggest that for $(\lambda^* - \kappa^*)/\mu^* > 25$ that creep could be ignored. This might be correct in some cases where the applied stress increase gives a final stress situation well above the initial pre-consolidation stress. However, in many cases the stress increase is rather moderate and the new situation is around the pre-consolidation stress, making the contribution from creep more significant, regardless of the ratio. For OCR = 1.0 the creep rate becomes independent of the ratio and the actual value for μ^* is more important (see Eq. 2).

In situations where the main interest is the final settlement after a certain period of time, a time independent elasto-plastic model can also be used to calculate long-term settlements. This is done by selecting a single isotache that in average meets the final expected combination of strain and stress. An isotache selected in this way would typically yield a lower OCR and lower λ^*. Equation 4 shows the corrected over consolidation ratio, OCR_{corr}, which should be used in an elasto-plastic analysis when the true undisturbed OCR is known.

$$OCR_{corr} = \left(\frac{\tau}{t_{age}} \right)^{\frac{\mu^*}{\lambda^* - \kappa^*}} \cdot OCR \qquad (4)$$

This principle is sketched in Figure 2 with an attempt to further clarification. The elasto-plastic approach would be the path A-B-D with the elastic part shown by path A-B and the plastic part given by B-C. The path A-C-D gives an elasto-viscoplastic modelling aspect where the elastic part is given by path A-C and the creep part is given by path C-D. The path followed by A-C-D and A-B-D will give similar final settlement.

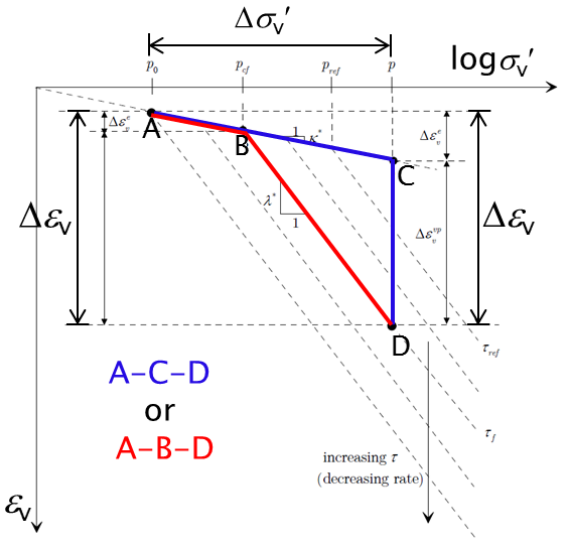


Figure 2. A case of an isotoche formulation and an elastoplastic giving similar final settlements.

The concept sketched in Figure 2 is numerically illustrated for Väsby test fill where exclusion of creep and buoyancy effects gave excellent settlement prediction, as shown in

Figure 3, by adopting models that disregarded creep, i.e. ILLICON and a time independent elasto-plastic model (the Soft Soil model in Plaxis). A detailed treatment of the case of using low OCR (OCR_{corr}) with an elasto-plastic model to counterbalance effect of creep can be found in Degago (2011).

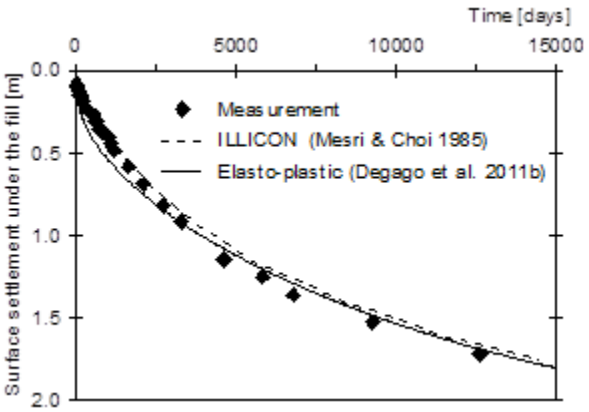


Figure 3. Settlement analyses of the Väsby test fill by ignoring creep and buoyancy effects (after Degago et al. 2011b).

By coincidence such approach, Equation 4 or Figure 2, changes soil parameters in a similar way typical to sample disturbance. This is one of

the main reasons for explaining why some researchers (e.g. Mesri & Choi 1985) have been successful in predicting long-term settlements (

Figure 3) by disregarding creep contribution despite the soil showing a significant effect of creep (Leroueil & Kabbaj 1987, Degago et al. 2011b).

7 THE VÄSBY TEST FILL

The Väsby test fill was designed and constructed by the Swedish Geotechnical Institute (SGI) in 1947. The test fill has been monitored with extensive instrumentations and there exists a detailed documentation of measurements (Larsson & Mattsson 2003). The Väsby test fill consists of a 30 m x 30 m square and 2.5 m high gravel fill constructed within 25 days. The applied total stress due to the fill was 40.6 kPa. The test fill site consists of soft sediments of glacial and post-glacial origin. The soft soil layer under the fill is 14 m thick. The ground water table, which is located at an average depth of 1 m beneath the original terrain, has a hydrostatic pressure distribution. Surface and sub-surface settlements are continuously measured since the construction of the fill.

In order to investigate the effect of sample disturbance, Leroueil & Kabbaj (1987) conducted incremental oedometer tests on the Väsby clay. They took samples with 200 mm Laval sampler and compared it with results from the 50 mm Swedish sampler (conducted in 1967). Even though the samples were extracted from a similar depth of ca. 4.2 m, they show significant effect of sample disturbance. A distinct feature of sample disturbance was that it resulted in lower OCR and λ^*. In Figure 4, the two different laboratory curves are compared. The OCR for the 50 mm is estimated to be 1.1 and for the 200 mm to be 1.6.

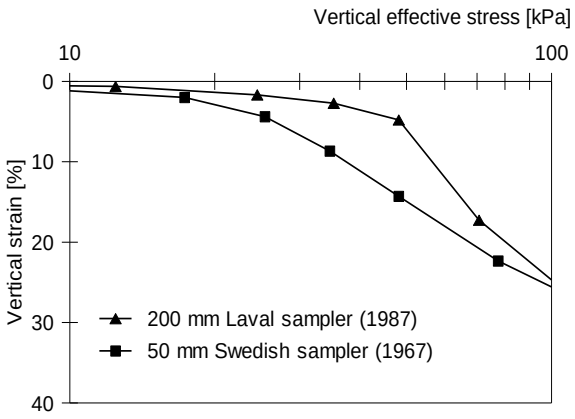


Figure 4. Laboratory incremental oedeometer results on samples taken at 4.2 m depth using two different samplers (after Leroueil & Kabbaj 1987).

8 NUMERICAL ILLUSTRATIONS

Some of the creep aspects highlighted in earlier sections are numerically illustrated based on various parameter sets. These data sets are mainly established as variations of parameters interpreted from oedometer tests of Väsby clay (Figure 4) and are given in Table 1 & 2. One of the soil parameters that can easily be affected by sample disturbance is the OCR. Hence, a distinct variation among the data sets is their OCR and this is used to systematically group the data sets as presented in the two tables. Data set 1, 2 and 3 are characterized by low OCR (= 1.1) as interpreted from the Swedish 50 mm tube sampler, and set 4 and 5 are characterized by high OCR (= 1.6) as interpreted from the Laval 200 mm block sampler. In set 6, an even higher OCR (2.18) is considered based on clay age considerations. A constant average permeability of 4.0e-5 m/day is adopted for all data sets.

Table 1. Data sets with low OCR (OCR = 1.10).

Parameter, Symbol [unit]	**Analysis sets**		
	Set 1	**Set 2**	**Set 3**
κ^* [-]	0.030	0.030	0.030
λ^* [-]	0.191	0.191	0.357
μ^* [-]	0.011	0.021	0.011
OCR [-]	1.10	1.10	1.10
$(\lambda^* - \kappa^*)/\mu^*$[-]	14.6	7.7	29.7
$\dot{\varepsilon}$ [%yr^{-1}]	99.51	369.1	23.62
t_{age} [yr]	0.011	0.006	0.047

where κ^* is the modified swelling index; λ^* is Modified compression index; μ^* is Modified creep index; $\dot{\varepsilon}$ is initial creep rate; t_{age} is the implied " Age of clay"

Table 2. Data sets with high OCR (OCR = 1.60 and 2.18).

Parameter, Symbol [unit]	Analysis sets		
	Set 4	Set 5	Set 6
κ^* [-]	0.030	0.030	0.030
λ^* [-]	0.357	0.571	0.357
μ^* [-]	0.021	0.021	0.021
OCR [-]	1.60	1.60	2.18
$(\lambda^* - \kappa^*)/\mu^*$[-]	15.6	25.8	15.6
$\dot{\varepsilon}$ [%yr^{-1}]	508.2	0.004	0.004
t_{age} [yr]	4.13	497	500

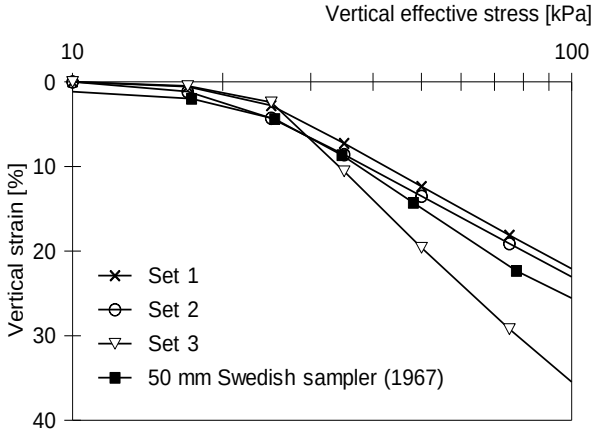


Figure 5. Oedometer simulation using data set 1, 2 and 3 (Table 1) with the test result obtained from 50 mm tube sampler.

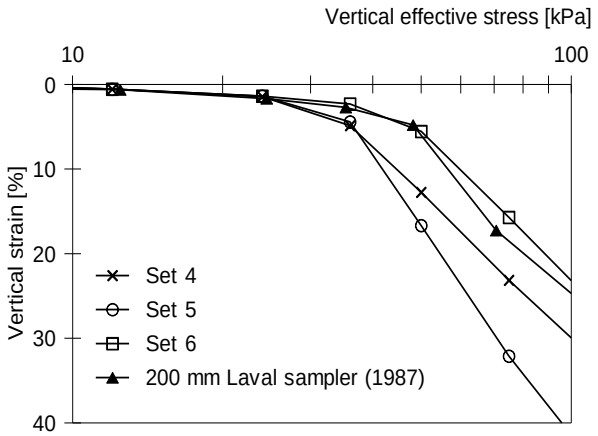


Figure 6. Oedometer simulation using data set 4, 5 and 6 (Table 2) with test result obtained from 200 mm Laval sampler.

8.1 Simulation of laboratory tests

In
Figure *5*, results from laboratory oedometer test simulations corresponding to set 1, 2 and 3, as given in Table 1, are presented along with the experimental results obtained from the 50 mm Swedish sampler. Correspondingly,
Figure *6* gives numerical results of set 4, 5 and 6 (Table 2) along with the test data obtained from the 200 mm Laval sampler. The maximum possible stress increase that can be obtained in the field is about 40 kPa, which means that the results above 70 kPa are of little interest. Furthermore, due to buoyancy and stress distribution with depth, this value will be reduced to less than 50 kPa (Degago et al. 2011b). This must be kept in mind while evaluating laboratory simulation results with respect to laboratory measurements (
Figure *5*-
Figure *6*). Some researchers have reported constant μ^*/λ^* ratios for wide range of soft clays (Mesri & Godlewski 1977). However, for models that assume a linear relationship between strain and log stress (constant λ^*), like SSC model, this will imply a constant μ^*. In reality both λ^* and μ^* are stress dependent (due to destructuration effect) and the ratio must be evaluated over the actual stress range. Hence, a constant value is not expected unless the changes are small. Therefore adjustments to the μ^*/λ^* ratio can be justified.

For set 1, λ^* was interpreted from the 50 mm test data and $\mu^* = 0.06\lambda^*$ was used from literature (Mesri & Choi 1985). Set 2 and set 3 are, respectively, μ^* and λ^* variations of set 1. Accordingly, set 2 fits the 50 mm test data best with set 1 slightly underpredicting and set 3 significantly overpredicting deformations as observed in the test (
Figure *5*). It is worthwhile to notice that set 2 has a higher creep potential (higher μ^*) while set 3 is significantly softer (higher λ^*). However, $(\lambda^* - \kappa^*)/\mu^*$ is higher for set 3 (with a lower μ^*), implying that creep has relatively less importance.

For set 4, λ^* was interpreted from the 200 mm test data and $\mu^* = 0.06$ was adopted. Set 5 and set 6 are variations of set 4. The λ^* value for set 5 is chosen such that for an OCR of 1.6, a clay age of $t_{age} \approx 500$ years is obtained (Eq. 3). In set 6 the OCR is increased such that the age of the clay is $t_{age} = 500$ years. From
Figure *6*, set 6 underpredicts the deformations, while both set 4 and 5 overpredict deformation with set 5 giving the

highest overprediction of the 200 mm test data.

8.2 Simulations of the Väsby fill

The soil parameter data sets given in Table 1 & 2 are adopted in the simulations of the Väsby fill. An axisymmetric model consisting of a very fine mesh was used in the analysis. In addition, an updated-mesh and updated-water pressure procedure were adopted to account for the effect of large deformations and buoyancy effect respectively. The computed vertical deformation patters are shown in Figur xx by selecting results for parameter set 2 and 5. Figure 8 gives 57 years of measured surface settlements, below the centre of the fill, along with the corresponding numerical analysis results.

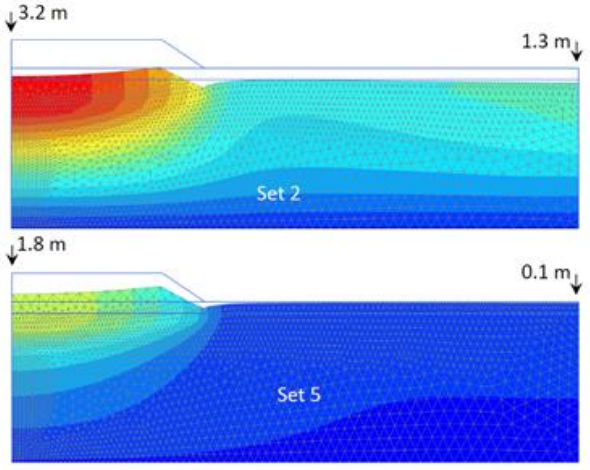


Figure 7. Vertical deformation patterns for two parameter sets inreference to initial geoemtry (arros indicate vertical deformations at 50 m a distance apart)

From data sets with low OCR (Table 1), it is interesting to note that parameter set 1 and 3 only slightly overpredicted the measured settlements despite their low OCR values. Set 2 significantly overpredicted the settlements due to the implied highest initial creep rate of all the other data sets. Set 3 gave the best field prediction even though it gave significantly softer response in the oedometer simulation (
Figure 5). This is because the initial creep rate for set 3 is lower than for set 1 and 2. The ratio $(\lambda^* - \kappa^*)/\mu^*$ is highest for set 3 which means that creep is less important in the far field deformations and for situations where the pre-consolidation stress is exceeded. From data sets with high OCR (Table 2), set 4 also gave excellent prediction while 5 and 6 under predicts the surface settlements. The underprediction by set 6 is small compared to the significantly stiffer response observed in the corresponding oedometer simulations (
Figure 6).

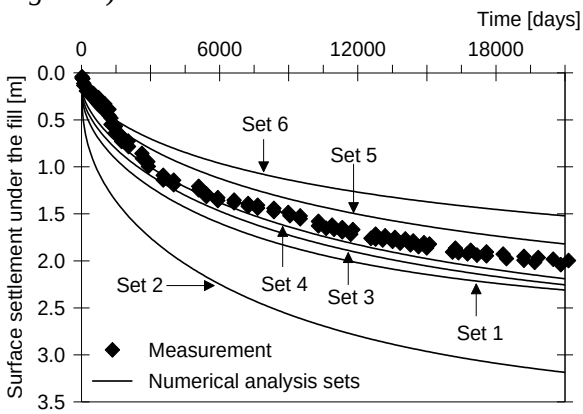


Figure 8. Measured and simulated surface settlement histories below the centre of the fill

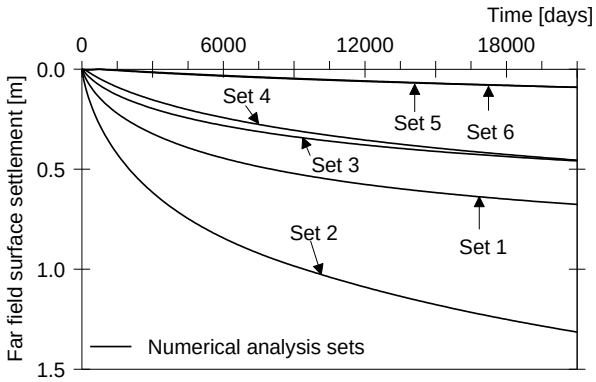


Figure 9. Simulated far field surface settlement histories

It is also important to evaluate far field settlements as it provides a benchmark for controlling analyses results and parameters adopted for the analysis. This would also help to evaluate the contribution of the settlement that is coming from the actual fill load and settlement resulting due to pure creep. Hence, far field settlement, indirectly, reveals how much part of the total settlement under the fill is actually due to the fill. In reality, the far field settlements are relatively insignificant.

Prediction of such far field settlements can only realistically be achieved if age

considerations are taken into account in the selection of the parameters. The far field surface settlements, 50 m from the centreline, as implied by the analyses sets are given in Figure 9. Set 1, 2, 3 and 4 gave significant far field settlements with set 2 giving the highest settlement. This means that a significant part of the settlement obtained using these sets (Figure 8) is actually not related to the fill. Set 5 and 6 gave the lowest and most realistic far field settlements that represent a case of pure creep settlement in a flat natural terrain (Figure 9). This was achieved due to the reasonable age considerations implied by the data sets 5 and 6. Overall, based on Figure 8 & Figure 9, parameter set 5 gave the best surface settlements predictions.

9 FINAL REMARKS AND CONCLUSIONS

Good prediction of long-term settlements of embankments heavily relies on laboratory test results from good sample quality. Hence, it is highly essential that soil parameters for creep analysis are interpreted from samples of high quality. However, in reality, sample disturbance is virtually unavoidable and laboratory samples suffer to a varying degree of sample disturbance.

In this work, the effect of sample quality, by selecting different data sets, for the SSC model, was studied based on laboratory and field measurements. The calculations show that good back calculations of the surface settlement at the centre of the embankment can be made with various sets of parameters. However, the far field settlement can only be realistic when the age of the clay is taken into consideration. A correct combination of the $(\lambda^* - \kappa^*)/\mu^*$ ratio and OCR is important for an overall sound creep settlement analyses. This means that for realistic ratios of $(\lambda^* - \kappa^*)/\mu^*$, valid for the experienced (actual) stress range, satisfactory far field settlement predictions can be justified at the same time as the settlement below a fill is satisfactory predicted.

It is vital to understand the role of parameters using simple models before resorting to advanced models. An example of such advanced model that includes creep, anisotropy and destructuration is the n-SAC model (Grimstad & Degago 2010). Such a model puts even more demand on the sample quality for calibration of input parameters. In fact, with proper use, a simple model like the SSC model can give successful predictions and give the user control on certain key input parameters. However, to further improve predictions additional aspects of natural clays such as anisotropy and destructuration should be accounted for.

10 OUTLOOK

In order to enhance models for settlement analyses, a series of research projects (e.g. the CREEP and Geofuture projects) have recently been initiated in Norway. An EU CREEP project led by the Norwegian University of Science and Technology (NTNU) has been active for the last four years (2011-2015). An RCN GeoFuture project that is led by the Norwegian Geotechnical Institute (NGI) is still active. The GeoFuture project is financed by the Research Council of Norway (RCN) and the industry in Norway. NTNU and the Norwegian Public Roads Administration are working among others work on this task.

11 ACKNOWLEDGMENTS

This work is carried out under the Marie Curie Action, European FP7, CREEP project, Grant number PIAG-GA-2011-286397. Adjunct Professor Hans Petter Jostad, at the Norwegian Geotechnical Institute, is highly acknowledged for his valuable contributions in the work presented in this paper.

12 REFERENCES

Bjerrum, L. (1967). Engineering geology of Norwegian normally consolidated marine clays as related to settlements of buildings. Géotechnique, 17(2): 81-118.

Burland, J.B. (1990). On the compressibility and shear strength of natural clays. Géotechnique, 40(3): 329-378.

Dafalias, Y.F. (1986). An anisotropic critical state soil plasticity model, Mech. Res. Commun. 13(6): 341–347.

Degago S.A. (2011). On creep during primary consolidation of clays. PhD thesis, Norwegian

University of Science and Technology (NTNU), Trondheim, Norway.

Degago, S.A., Grimstad, G., Jostad, H.P., Nordal, S. & Olsson, M., (2011a). Use and misuse of the isotache concept with respect to creep hypotheses A and B. Géotechnique, 61, 897-908.

Degago, S.A., Nordal, S., Grimstad, G. & Jostad, H.P. (2011b). Analyses of Väsby test fill according to creep hypothesis A and B. 13th IACMAG, Melbourne, 1: 307-312.

Degago, S.A. & Grimstad, G., (2012). Significance of sample quality in settlement analysis of field cases. Proc. 8th NUMGE, Delft, The Netherlands,.153-158

DeGroot, D.J., Poirier, S.E. & Landon, M.M. (2005). Sample disturbance - Soft clays. Studia Geotechnica et Mechanica, XXVII (3-4): 107-120.

Gens, A. & Nova, R. (1993). Conceptual bases for a constitutive model for bonded soils and weak rocks, Geotech. Hard Soils–Soft Rocks, Balkema, Rotterdam.

Grimstad, G. & Degago, S.A. (2010). A non-associated creep model for structured anisotropic clay (n-SAC). 7th European Conf. NUMGE, Trondheim, Norway, 3-8.

Grimstad, G., Degago, S.A., Nordal, S. & Karstunen, M., (2010). Modeling creep and rate effects in structured anisotropic soft clays. Acta Geotechnica, 5**,** 69-81.

Larsson, R. & Mattsson, H. (2003). Settlements and shear increase below embankments. SGI, Report 63, 88p.

Leroueil, S. & Kabbaj, M. (1987). Discussion of 'Settlement analysis of embankments on soft clays' by Mesri & Choi. ASCE, 113(9): 1067-1070.

Mesri, G. & Choi, Y.K. (198). Settlement analysis of embankments on soft clays. ASCE, 111(4): 441-464.

Mesri, G. & Godlewski, P.M. (1977). Time and stress-compressibility interrelationship. ASCE, 103(GT5): 417-430.

Perzyna, P. (1963). Constitutive equations for work-hardening and rate sensitive plastic materials. Proc. Vibration Problems, 4(3): 281-290.

Roscoe, K.H. & Burland, J.B. (1968). On the generalized stress–strain behaviour of wet clay. Engineering Plasticity, Cambridge, 535-609.

Stolle, D.F.E., Vermeer, P.A. & Bonnier, P.G. (1999). Consolidation model for a creeping clay. Canadian Geotechnical Journal, 36(4): 754-759.

Šuklje, L. (1957). The analysis of the consolidation process by the Isotaches method. Proc. 4th Int. Conf. Soil Mech. Found. Engng, London, 1: 200-206.

Janbu, N. (1969). The resistance concept applied to deformations of soils. Proc. 7th Int. Conf. Soil Mech. Found. Engng, Mexico City, 1: 191-196.

Waterman, D. & Broere, W. (2005). Practical application of the soft soil creep–Part III. Plaxis Benchmarking, p. 22. http://kb.plaxis.nl/publications

Simulation of the Density-driven Groundwater Flow Using the Meshless Local Petrov-Galerkin Method

Juraj Mužík
University of Zilina, Slovak Republic, muzik@fstav.uniza.sk

ABSTRACT
Density-driven groundwater flow is a complicated nonlinear problem in groundwater hydraulics. The local Petrov-Galerkin method is a promising meshless scheme that is used for solving several difficult problems in different areas. This method applies the weak form of governing equations to the local mesh around every node. The nodes can be randomly distributed in the domain and on the global boundary. Therefore, this method is characterized as meshless. The unknown potentials and concentrations in all of the nodes are approximated by interpolation to obtain a system of linear equations. Solving this system of equations leads to the numerical solution for the main problem. In this paper, a combination of the radial basis function interpolation and the local Petrov-Galerkin method is used to solve groundwater flow problem combined with the transport of pollution, which also influences the density of groundwater..

Keywords: *meshless Local Petrov-Galerkin method, Solute transfer, Density-driven flow, Radial basis functions*

1 INTRODUCTION

Density-driven groundwater flow appears mainly in saltwater intrusion and geothermal processes. Some environmental problems, such as leakage from landfills, can also be influenced by changes in the density and viscosity of groundwater. Modeling density-driven flow problems requires a coupled groundwater flow and transport numerical model. The coupling is realized using the state equations that link density and viscosity variations to pollution concentration or temperature. This coupled problem is nonlinear; therefore, the simulation usually requires large meshes and extensive computational time, even for simulations of testing examples. Because of the high computational costs, most authors have focused on vertical 2D numerical models, although the problems are generally three-dimensional. The typical numerical methods used to solve these problems are based on different formulations of the finite element method (Kolditz et al., 1998; Simpson and Clement, 2003) or the discontinuous Galerkin method (Ackerer and Younes, 2008; Younes et al., 2009). In this paper, we present a meshless numerical method based on the local Petrov-Galerkin method (MLPG) to reduce the large computational requirement. The meshless local Petrov-Galerkin method (MLPG) was introduced by Atluri et al.[5]. This method is characterized as meshless because distributed nodal points that cover the domain are employed. These nodal points can be randomly distributed over the domain. Every node is surrounded by a quadrilateral mesh centered at this point. The unknown variable at this point is then expressed using a weak formulated equations on this local mesh. All of these unknown variables are approximated by interpolation to obtain a system of linear equations. Solving this system of equations leads to the numerical solution. Atluri et al. (2001) used the moving least squares (MLSs) method for the interpolation, but the radial basis functions (RBFs) interpolation has also been used (Sellountos and Sequeira, 2008; Kovarik et al., 2012). Here, the solution of the coupled groundwater flow-mass transfer problem, based on the MLPG is presented.

2 GOVERNING EQUATIONS AND LOCAL WEAK FORMULATION

Density-driven groundwater flow can be written in terms of an equivalent fresh water potential (Ackerer and Younes, 2008)

$$\rho S \frac{\partial h}{\partial t} + \varepsilon \frac{\partial \rho}{\partial x} + \nabla \cdot (\rho \mathbf{q}) = 0 \tag{1}$$

where h is the equivalent fresh water potential, ε is the porosity of the porous medium, and ρ is the density of the solution. $\mathbf{q}$ is the Darcy velocity defined as

$$\mathbf{q} = -\mathbf{K}\left(\nabla h + \frac{\rho - \rho_0}{\rho_0} \nabla \bar{z} \right) \tag{2}$$

where $\mathbf{K}$ is the matrix of hydraulic conductivities and ρ_0 is the initial density of fresh water. To simplify the groundwater flow equation (1), we used the Boussinesq approximation, i.e. density variations are neglected and only the buoyancy term of the Darcy equation depends on the density (Kolditz et al., 1998). The differential equation of 2D groundwater flow with variable density is now expressed as

$$\frac{\partial}{\partial x}\left(K_x \frac{\partial h}{\partial x} \right) + \frac{\partial}{\partial y}\left[K_y \left(\frac{\partial h}{\partial y} + \frac{\rho - \rho_0}{\rho_0} \right) \right] = S \frac{\partial h}{\partial t} \tag{3}$$

where we denote the hydraulic conductivities in x and y directions as K_x and K_y, respectively. The solute mass conservation can be written in terms of the solute concentrations as

$$\varepsilon \frac{\partial C}{\partial t} = \nabla \cdot (\mathbf{D} \cdot \nabla C) - \mathbf{q} \cdot \nabla C \tag{4}$$

where C is the solute concentration and $\mathbf{D}$ is the dispersion tensor. The flow and transport equations are coupled by a state equation linking the density to the solute concentration. For the density, we use a linear model

$$\rho = \rho_0 + (\rho_C - \rho_0)\bar{C} \tag{5}$$

where ρ_c is the density of injected fluid. $\bar{C}$ is the relative concentration defined as

$$\bar{C} = \frac{C}{C_{max}} \tag{6}$$

where C_{max} is the maximum mass concentration. Eq.(3) can be transformed to the following shape

$$\frac{\partial^2 h}{\partial x^2} + \frac{K_y}{K_x}\frac{\partial^2 h}{\partial y^2} = \frac{S}{K_x}\frac{\partial h}{\partial t} - \frac{K_y}{K_x \rho_0}\frac{\partial \rho}{\partial y} \tag{7}$$

To transform (7) to the Poisson equation, we use the following transformation of coordinates

$$\tilde{x} = x \qquad \tilde{y} = y\sqrt{\frac{K_x}{K_y}} \tag{8}$$

and we obtain

$$\frac{\partial^2 h}{\partial \tilde{x}^2} + \frac{\partial^2 h}{\partial \tilde{y}^2} = \frac{S}{K_x}\frac{\partial h}{\partial t} - \frac{1}{\rho_0}\sqrt{\frac{K_y}{K_x}}\frac{\partial \rho}{\partial \tilde{y}} \tag{9}$$

To solve (9) in a two-dimensional domain Ω with a boundary Γ, we apply the weighting residual principle with the Green integration formula (Kovarik, 2000) and we obtain the weak form which will be later discretized using MLPG approach.

3 THE MLPG METHOD AND THE LOCAL WEAK FORMULATION

The meshless Local Petrov-Galerkin method (MLPG) is truly meshless method which requires no elements or global background mesh, for either interpolation or integration purposes. In MLPG the problem domain is represented by a set of arbitrarily distributed nodes (Lin and Atluri, 2001).

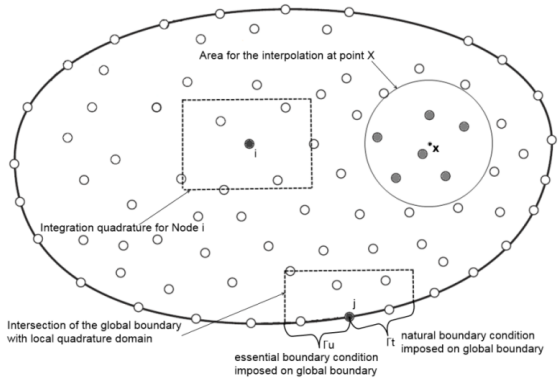


Figure 1 Schematic of local quadrature domain, essential and natural interested boundary.

The weighted residual method is used to create the discrete system equation by integrating the governing equation over local quadrature domains (see. Fig.1). The quadrature domain can be arbitrary in theory, but very simple regularly shaped domain, such as rectangles for 2D problems are often used for ease of implementation.

A generalized local weak form of the Poisson equation (9) defined over local sub-domain Ω_s using backward time difference can be written as

$$\int_{\Omega_s}\left[\frac{\partial^2 h^{n+1}}{\partial\tilde{x}^2}+\frac{\partial^2 h^{n+1}}{\partial\tilde{y}^2}-\frac{S}{K_x}\frac{h^{n+1}}{\Delta t}\right]w d\Omega = \int_{\Omega_s}\left[\frac{h^n}{\Delta t}-\frac{1}{\rho_0}\sqrt{\frac{K_y}{K_x}}\frac{\partial\rho^{n+1}}{\partial\tilde{y}}\right]w d\Omega \quad (10)$$

where index n means time step and w is the test function defined as

$$w(r_i)=\begin{Bmatrix}1-6r_i^2+8r_i^3-3r_i^4;\ r_i\le 1\\ 0\qquad\qquad\qquad ;\ r_i>1\end{Bmatrix}\quad r_i=\frac{\|x-x_i\|}{d_s} \quad (11)$$

where d_s is the size of the local quadrature domain, so it is evident that weighting function value is zero on its boundary. The choice if this test function is motivated by its ability to vanish on the boundary of local quadrature domain. Using the divergence theorem the (10) has changed to

$$\int_{\Omega_s}\frac{\partial h^{n+1}}{\partial\tilde{x}}\frac{\partial w}{\partial\tilde{x}}d\Omega-\int_{\Gamma_{su}}\frac{\partial h^{n+1}}{\partial\tilde{x}}w n_{\tilde{x}}d\Gamma+\int_{\Omega_s}\frac{\partial h^{n+1}}{\partial\tilde{y}}\frac{\partial w}{\partial\tilde{y}}d\Omega- \int_{\Gamma_{su}}\frac{\partial h^{n+1}}{\partial\tilde{y}}w n_{\tilde{y}}d\Gamma+\frac{S}{\Delta t K_x}\int_{\Omega_s}w h^{n+1}d\Omega= \int_{\Gamma_{sq}}\frac{\partial h^{n+1}}{\partial\tilde{x}}w n_{\tilde{x}}d\Gamma+\int_{\Omega_s}h^n w d\Omega-\frac{1}{\rho_0}\sqrt{\frac{K_y}{K_x}}+\int_{\Omega_s}\frac{\partial\rho^{n+1}}{\partial\tilde{y}}d\Omega \quad (12)$$

The values of potential h and density are expressed using the RBF interpolation functions as follow

$$h=\sum_{i=1}^{N}\varphi_i h_i \qquad \rho=\sum_{i=1}^{N}\varphi_i\rho_i \quad (13)$$

where φ is RBF shape function for ith node and N is number of nodes used for interpolation, in this case the Multi-Quadrics Radial Basis function (MQ-RBF), details can be found in (Kovarik et al., 2012).

After substituting (13) into (12) the nodal constants h_i and ρ_i can be moved out of the integral the equation (12) can be expressed as discrete system of linear equations to solve the potential at every node. The mass transfer equations are solved using the same MLPG method and algorithms similar to those used for the potential flow equation. The equations of flow and mass transfer are then coupled by the equation of state, which makes the fluid density a function of the mass solute fraction. The coupling scheme was realized by a sequential-iterative approach using the modified Pickard algorithm according to (Ackerer et al., 2004):

- Step 1: Solve the transfer equations.
- Step 2: Update the fluid density.
- Step 3: Solve the potential flow.
- Step 4: Compute the velocities of flow.
- Step 5: Test the convergence of the process.

This modified scheme converges faster than the classical Pickard algorithm (Ackerer et al., 2004).

4 NUMERICAL EXAMPLE - SIMULATION OF THE HENRY PROBLEM

Unfortunately, we cannot use the usual verification procedure based on exact analytical solutions in this case due to the nonlinear nature of the density-driven problems and we must rely only on comparison with other numerical solutions. Therefore, the MLPG model has been compared with standard Henry saltwater intrusion problem. Numerical example was solved on a workstation equipped with two

Intel I7 4510U CPUs and 16 GB memory. The generalized minimal residual (GMRES) method with simple Jacobi preconditioning was used to solve system of equations (for potentials and concentrations) in every time step and iteration.

Table 1 The parameters of the Henry problem.

S.	Quantity	Value	Unit
ϵ	Porosity	0.35	-
K	Hydraulic conductivity	1.0010×10^{-2}	$m\ s^{-1}$
D_m	Molecular diffusion (Henry solution)	6.6×10^{-6}	$m^2\ s^{-1}$
D_m	Molecular diffusion (Pinder solution)	2.31×10^{-6}	$m^2\ s^{-1}$
q	Discharge of fresh water	6.6×10^{-5}	$m^2\ s^{-1}$
ρ_0	Fresh water density	1000	$kg\ m^{-3}$
ρ_c	Solute density	1025	$kg\ m^{-3}$
S_s	Specific storage	0.0	m^{-1}

The Henry problem is one of the most popular tests used for density driven flow models. This is a 2D problem describing saltwater intrusion into a confined rectangular aquifer that was initially saturated with freshwater. The geometry of the problem is shown in Fig. 2.

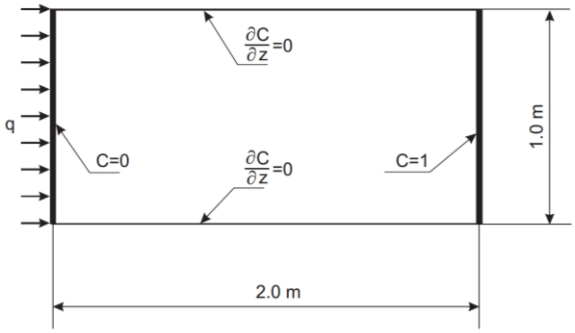


Figure 2 The geometry and boundary conditions of the Henry problem.

The boundary conditions for flow consist of two impermeable parts in the top and bottom of the aquifer. The right vertical part of the boundary is considered the seaside boundary, and a hydrostatic pressure is defined along it. A constant inflow of freshwater into the solved area is assumed along the opposite vertical part of the boundary. Therefore, the boundary conditions for solute transport are quite simple. The maximum concentration $C_{max}=1$ is assigned to the seaside right vertical part of the boundary, and the freshwater condition ($C=0$) is defined along the opposite left vertical part. The zero-flux conditions are used on both horizontal parts of the boundary (Fig. 2). The properties of this problem are listed in Table 1.

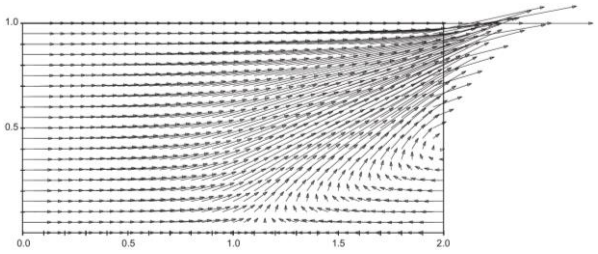


Figure 3 The velocity vectors for the original Henry problem.

In the right bottom part of the rectangular domain (where the density is the highest), the gradient of the hydraulic head is oriented vertically upward, and the gravitational force points vertically downward. These two forces generate a nearly horizontal flow of seawater into the aquifer. The solute density decreases along the bottom part of the boundary as a result of the influence of the freshwater flow from the left-hand side. Finally, the velocity directions are redirected back to the upper right side (Fig. 3). The simulation was performed on 861 regularly distributed nodes (41 horizontally and 21 vertically) (Fig. 4).

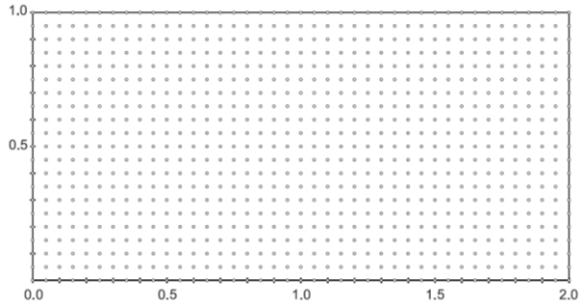


Figure 4 Regular computational network for the solution of the Henry problem.

The initial condition of the problem was an aquifer filled by freshwater. Two different coefficients of molecular diffusion were used for the simulation (Table 1). The first one corresponds to the Henry (1964) solution, and the second one corresponds to the Pinder

solution (1970). The resulting isochlors are presented in Figs. 5 and 6.

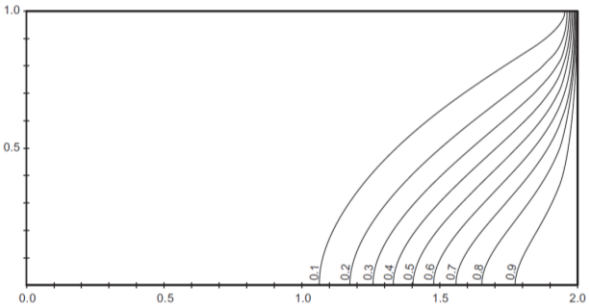


Figure 5 The solute mass concentrations for the original Henry problem.

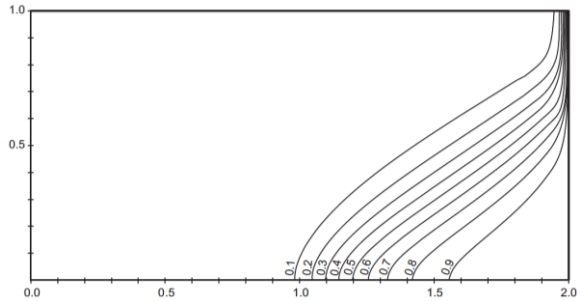


Figure 6 The solute mass concentrations for the Pinder modification of the Henry problem.

The iterative scheme used the modified Pickard algorithm, and the subsequent iterations were employed until the maximum *L2* error in the concentration value for every time step was less than $1x10^{-5}$. For the isochlor *C=0.5*, Fig. 7 compares the simulation results of the original Henry problem with those of other reports (Henry, 1964; Lee and Cheng, 1974; Gotovac et al., 2003; Soto et al., 2007). The results of Voss and Souza's simulation (1987), which used slightly different boundary condition and did not employ the Boussinesq approximation, are also included in this figure. Similarly, Fig.8 compares the isochlor *C=0.5* for the Pinder modification with those of different authors (Pinder and Cooper, 1970; Segol et al., 1975; Gotovac et al., 2003).

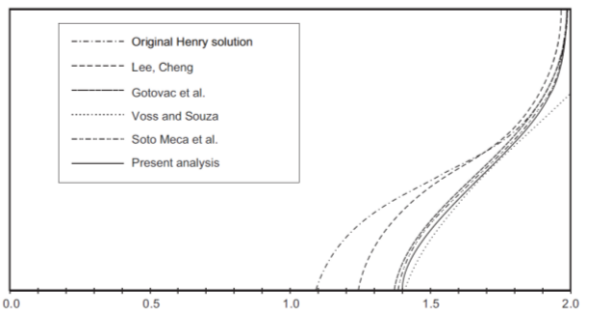


Figure 7 A comparison of the isochlor C=0.5 for the original Henry problem from different authors.

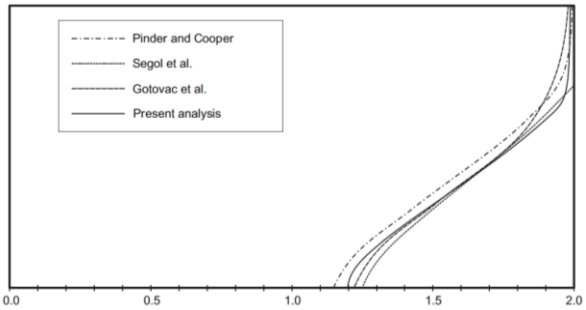


Figure 8 A comparison of the isochlor C=0.5 for the Pinder modification from different authors.

5 CONCLUSIONS

This paper presents a possible use of the MLPG meshless method to model density-driven flow. This method appears to be effective and useful for modeling the density-driven flow. This research is at its initial stages, and a follow-up study should focus on the modification of existing algorithms to enable distributed processing. Choosing suitable tools that allow parallel solving of very large network systems, which usually exist in practical solutions, are needed.

6 REFERENCES

Ackerer P, Younes A, Mancip M (2004). A new coupling algorithm for density-driven flow in porous media. Geophys Res Lett;31:L12506.

Ackerer P, Younes A (2008). Efficient approximations for the simulation of density driven flow in porous media. Adv Water Res;31:15–27.

Divo E, Kassab AJ (2007). An efficient localized radial basis function meshless method for fluid flow and conjugate heat transfer. Trans ASME;129:124–36.

Franke R (1982). Scattered data interpolation: tests of some methods. Math Comput;38:181–99.

Golberg M, Chen C, Bowman H (1999). Some recent results and proposals for the use of radial basis functions in the BEM. Eng Anal Boundary Elem; 23:285–96.

Gotovac H, Andricevic R, Gotovac B, Kozulic V, Vranjes M (2003). An improving collocation method for solving the Henry problem. J Contam Hydrol ;64:129–49.

Hardy RL (1990). Theory and applications of the multiquadrics-biharmonic method (20 years of discovery 1968–1988). Comput Math Appl;19:163–208.

Henry HR (1964). Effects of dispersion on salt encroachment in coastal aquifers, sea water in coastal aquifers. US Geol Surv Supply Pap;1613-C:70–84.

Kansa EJ (1990). Multiquadrics a scattered data approximation scheme with application to computational fluid dynamics. Comput Math Appl;19:127–45.

Kolditz O, Ratke R, Diersch HG, Zielke W (1998). Coupled groundwater flow and transport: 1. Verification of variable density flow and transport models. Adv Water Res;21:27–46.

Kovarik K, Muzik J, Mahmood MS (2012). A meshless solution of two dimensional unsteady flow. Eng Anal Boundary Elem;36:738–43.

Kovarik K (2000). Numerical models of groundwater pollution. Springer-Verlag.

Larsson E, Fornberg B (2003). A numerical study of some radial basis function based solution methods for elliptic PDEs. Comput Math Appl;46:891–902.

Lee CH, Cheng TS (1974). On seawater encroachment in coastal aquifers. Water Resour Res;10:1039–43.

Lin H., Atluri S.N (2001). The Meshless Local Petrov-Galerkin Method for Solving Incompressible Navier-Stokes Equations, Computer Modeling in Engineering & Sciences, pp. 117–142.

Pinder GF, Cooper Jr. HH (1970). A numerical technique for calculating the transient position of the saltwater front. Water Resour Res;6:875–82.

Segol G, Pinder GF, Gray WG (1975). A Galerkin-finite element technique for calculating the transient position of the saltwater front. Water Resour Res;11:343–7.

Sellountos EJ, Sequeira A (2008). An advanced meshless LBIE/RBF method for solving two-dimensional incompressible fluid flows. Comput Mech;41:617–31.

Shu C, Ding H, Yeo KS (2003). Local radial basis function-based differential quadrature method and its application to solve two-dimensional incompressible Navier–Stokes equations. Comput Methods Appl Mech Eng;192:941–54.

Simpson MJ, Clement TP (2003). Theoretical analysis of the worthiness of Henry and Elder problems as benchmarks of density-dependent groundwater flow models. Adv Water Res;26:17–31.

Soto Meca A, Alhama F, Gonzalez Fernandez CF (2007). An efficient model for solving density driven groundwater flow problems based on the network simulation method. J Hydrol;339:39–53.

Voss CI, Souza WR (1987). Variably density flow and solute transport simulation of regional aquifers containing a narrow fresh-water saltwater transition zone. Water Resour Res;23:1851–66.

Younes A, Fahs M, Ahmed S (2009). Solving density driven flow problems with efficient spatial discretizations and higher-order time integration methods.Adv Water Res;32:340–52.

GeoSuite – A Modular System for Geotechnical Design

S. Lacasse
Norwegian Geotechnical Institute (NGI), Norway, suzanne.lacasse@ngi.no

H. P. Jostad, J.-S. L'Heureux and Ø. Torgersrud
NGI, Oslo, Norway
R. Sandven
Multiconsult AS, Norway

ABSTRACT
Remarkable advances in the analysis tools of, for example slopes, embankment stability and settlements have happened since the 90s. Many are due to the information technology revolution in all aspects of geotechnical practice. Although the tools in use today are more sophisticated than earlier, experience, judgment and quality control remain the key to reliable foundation design. Experts agree that one should do calculations with two methods (or two codes) to check "that you have not missed anything of importance". Software is not what differentiates among consultants today. The competence and experience of the personnel and the appropriateness of the parameters and soil models used in the analyses gives the competitive edge. In 2002, the geotechnical profession of Norway and Sweden (consultants, research organizations, universities and government agencies worked) entered an alliance to develop GeoSuite. The development work was funded by the Research Council of Norway in addition to the partners. The first version of GeoSuite was issued in 2006. A new generation was completed in 2015 and a third generation is planned for 2019. The objective of GeoSuite is to make design calculations as simple as possible for the user, and to provide user-assistance along the way. The software provides the practitioner with tools for one-, two- and three-dimensional calculations and visualization, and an integration of geotechnical input data, calculations and results. The paper describes "GeoSuite", a software with modules for the design of geotechnical foundations on land, with stability, settlement, bearing capacity, pile and excavation calculations. Plans are made for add-ons with slope calculations, soil profile decisions and statistical analyses of soil parameters. The paper describes the modules in GeoSuite and gives examples of stability and settlement calculations.

Keywords: Stability, settlement, bearing capacity, software, three dimensions.

1 INTRODUCTION

Civil engineering is moving towards three-dimensional (3D) oriented design for construction and lifelong maintenance. Geotechnical design and calculations need to be compatible with these technologies. GeoFuture has the aim to meet this challenge. As our profession moves forward into the 21st century, Duncan (2013), Wright (2013) and Finn and Wu (2013) recommended to always use more than one computer code when doing geotechnical calculations, to check "that you have not missed anything of importance". It is not the software used that differentiates between two consultants. The knowledge and experience of the personnel and the appropriateness of the specific soil models in the calculations make the difference between two consultants.

GeoFuture is a Norwegian research project funded by the Research Council of Norway, with a budget of 22.4 million NOK (2.5 million EURO, 2016). The project was completed in 2015. Twelve partners from Norway and Sweden, representing industry, research, the university sector and public organisations, formed an alliance to carry out the research. The partners were Skanska AS, Norconsult AS, Multiconsult AS, GeoVita AS, Vianova Systems AS, Vianova GeoSuite AB, AutoGRAF-föreningen AB, the Norwegian Public Roads Administration, the

Norwegian National Rail Administration, NTNU, SINTEF Byggforsk and NGI.

The primary objective of GeoFuture was to supply the building, construction and transport industry with methods and tools for geotechnical calculations for everyday design. The results of the research were implemented in a software package called the GeoSuite Toolbox. At project completion, GeoFuture had developed the prototype of an integrated package for geotechnical calculations, with options for 1D, 2D and 3D calculations and with 3D presentation of geotechnical data together with other infrastructure data (roads, railways, earlier construction).

A series of 1D, 2D and 3D models, finite element formulation and codes were developed for the calculation of stability, settlement and bearing capacity. For each of the calculation modules, GeoFuture developed a knowledge-based system for assisting the practicing engineer to assess and verify geotechnical parameters and calculation results. This "Wizard" is a wiki-based user-assistance available for all steps of the calculation, from the interpretation of laboratory and *in situ* test results, selection of design parameters, the calculation (e.g. choice of method) to the interpretation of the results. The user is enabled, with the option of additional assistance, to do the calculations, integrating either or both classical methods (e.g. limit equilibrium, 1D settlement approximation and closed-form solutions) and advanced finite element formulations with simple or advanced soil models for improved 2D and 3D calculations.

GeoFuture delivered a seamless solution for the life cycle management of 3D data with the development of a new and open 3D soil data model, called the "Ground Observation Model". This model provides geo-solutions that are integrated with the Building Information Models (BIM) and Infrastructure Information Models (IIM) used by other sectors of civil and construction engineering. With the new 3D soil data model in three dimensions, realistic foundation geometry, spatial relationships, interpolation and extrapolation around 3D data volumes are possible. The methods and tools integrate 3D calculations within 3D visualisation, with the option of simple or advanced soil models and simple or advanced calculation methods for the most common foundation problems in the building, construction and transportation industry.

The prototype with a user-friendly and seamless tool for geotechnical design is planned to be commercialized through the company created for the developed software GeoSuite.

The project will continue until 2019 with further enhancements. Some of these are mentioned herein. The paper presents the GeoSuite system, describes the calculations and provides examples of the assistance provided to the user.

2 NEED FOR INTEGRATED SOLUTION

Compared to earlier, solutions are moving towards 3D interactive models and Building Information Modeling (BIM), where different disciplines and work flows interact. The human relationships have also evolved as the engineers and scientists work less in isolation, but increasingly in collaborative, integrated teams.

Contractors, consultants, universities and public infrastructure organizations need a common and integrated 3D engineering model in their work. In a survey, geotechnical engineers also prioritised the need for help with the selection of input parameters and the need for a seamless integration of input data, analysis modules and results. They wished means to model and represent realistic foundation geometries, illustrate and account for spatial extent and variability of geo-data, integrate geo-calculations and enable an "interactive" modelling of foundations. And yes, they felt that there were large uncertainties in even the simpler of analyses.

3 GEOSUITE SOFTWARE

GeoSuite has a series of computer programs especially developed for a designer of geotechnical problems, including stability, settlement, bearing capacity, pile and excavation calculations.

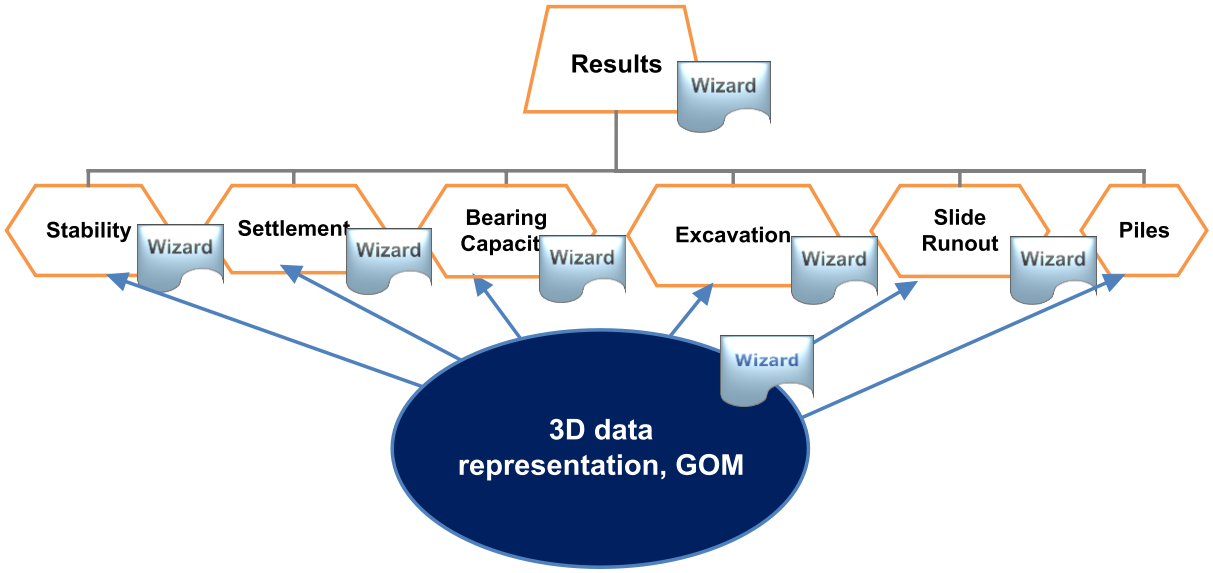


Figure 1. GeoSuite 's six calculation modules and Wizard function.

Figure 1 presents the GeoSuite software package schematically, with each of the calculation modules and the "Wizard" function. In 2015-2016 a module for slide run-out analysis will be included.

The main objective of the software is to address everyday design situations, and to make the calculations efficient for the user[1]. Figure 1 illustrates schematically the geotechnical components of the GeoSuite software. The key development features in recent years have been the integration of a 3D calculation engine, integrated input data and result presentation with possibilities of 1D, 2D and 3D visualization, series of assistance panels for the user for the selection of the soil parameters and the analysis and interpretation of the resultsThe 3D data representation model (the ground observation model, GOM) is the heart of the system and enables the user to build his model accounting for other installations already in the ground and integrating the measurements of soil properties, as available. User assistance (called 'Wizard' in Fig. 1) is provided to help establish the soil profiles for analysis. Each of the calculation modules had an input, calculation and results interpretation part, with a 'Wizard' (user assistance) available when desired by the user.

4 3D DATA REPRESENTATION

4.1 Open data model

The open data model manages the geotechnical data throughout its life cycle, for GeoSuite calculations and for use by other software/systems. The goal of the integrated open data model, is to present in the digital terrain model the input and results in three dimensions.

Geotechnical properties and geological description in the building and construction and infrastructure sectors have gradually become a part of the Building Information Modelling (BIM[2]). The model in GeoSuite meets the requirements in ISO/TC211[3].

The BIM infrastructure requires open standards, integrated and easy import and export of data between the BIM models and

[1] http://www.-vianovasystems.no/Nedlasting/Nova-point-GeoSuite

[2] BIM (Building information modeling) involves the generation and management of digital representations of physical and functional characteristics as a function of location.

[3] ISO/TC 211 is a standard Technical Committee within ISO, covering the areas of digital geographic information, such as used by GIS and geomatics and preparing International Standards and Technical Specifications.

the processes governing several parties collaborating during design.

The open data model provides the geotechnical engineer with not only the data, the subsurface layers and the model used for the analysis, but also provide a visualization of the data and other implementations, such as roads, buildings, excavations and other structures/installations.

4.2 Ground Observation Model (GOM)

One of the key elements of the development was the creation of a ground observation model (GOM) directly from the open data model, and to have it act as an analysis tool for geotechnical design. A 3D part of the open data model can then be selected and analysed.

The 3D data representation module (GOM) integrates seamlessly the information from geological, seismic and geotechnical *in situ* and laboratory investigations and creates a 3D graphical interface. The module creates a subsurface model for input in the geotechnical calculations. GeoSuite also aims at documenting who did what, the parameters used, and the history of the parameters and the analyses. The ground layers, represented in 3D, include all the attributes and parameters relevant for the geotechnical calculations and expertise provided by the Wizard for user assistance (Section 7).

Figures 2 and 3 give two examples of 3D representation: a 3D volume of soil to be analysed (Fig. 2), and the layers in tehclaculation area in 3D (Fig. 3).

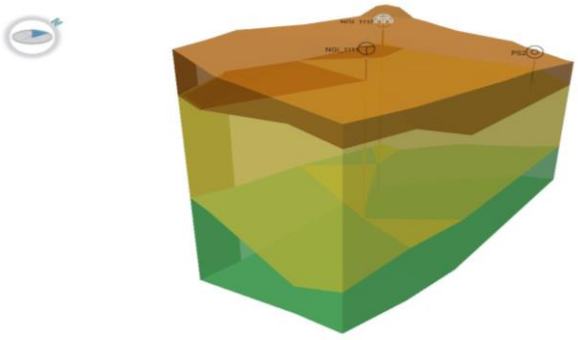


Figure 2. Example of generated 3D soil volume model.

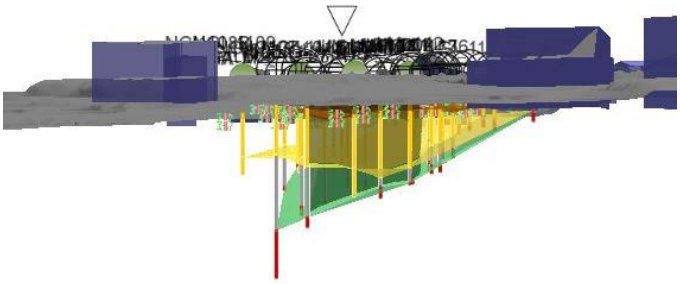


Figure 3. Interpreted layers and calculation area.

5 SETTLEMENT MODULE

The new calculation engine developed at NGI (Jostad and Lacasse 2015) was used to check a simple case of settlement of an OC clay under a uniform load.

Three software were used: Plaxis3D (www.plaxis.nl/plaxis3d), Settle^{3D} (www.rocscience.com/settle3D) and GeoSuite (denoted GS 1D and 3D). Figure 4 compares the results at the centerline and at the corner of the loading. The Boussinesq stress distribution with depth was used in the calculations.

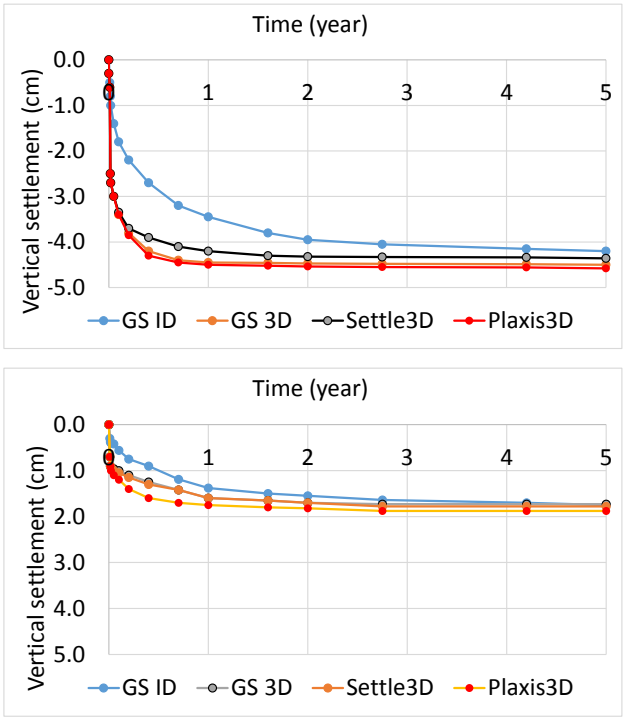


Figure 4. 1D and 3D consolidation settlements, OC clay, at centerline (upper diagram) and under corner (lower diagram) (S. Johanson NTNU, MSc thesis, personal comm. June 2015).

The 3D settlement (initial and consolidation settlements) were significantly larger than the 1D settlements. The GeoSuite3D, Plaxis 3D and Settle^{3D} calculations in 3D agreed well. The GeoSuite and Plaxis results in 1D also agreed well.

Jostad *et al* (2016) and Lacasse et al (2015) present another example of 3D settlement calculations.

6 STABILITY MODULE – 3D EFFECTS

The 3D effects were illustrated for an idealized case (Fig. 5). The effect of slope inclination was checked for inclinations 1:*b* with *b*=1, 2 and 3. The effect of the depth of the slip surface $d = D/H$ (i.e. depth to a strong soil layer or rock) was checked for *d* of 0 and 1, where *D* is the depth from the toe level to the bottom fixed boundary (or to a strong layer/bedrock) and *H* the height of the slope (from toe to crest). The effect of the width of the slide $w = W/H$ was checked for *w* of 1, 2, 4 and infinity.

The NGI-ADP constitutive model, a strain-hardening elasto-plastic total stress model with stress path dependent or anisotropic undrained shear strength was used in the analyses. The input for this constitutive model are the spatial distribution of the undrained active shear strength $s_u^A(x,y,z)$ and the anisotropy strength ratios s_u^{DSS}/s_u^A and s_u^P/s_u^A [4], the corresponding shear strains at failure, γ_f^A, γ_f^{DSS} and γ_f^P, and the initial elastic shear modulus ratio, G_o/s_u^A. The factor of safety FS was calculated from:

$$FS = F_{3D} \cdot N_o \cdot s_u / \gamma H \qquad [1]$$

where F_{3D} is the 3D effect factor, N_o the geometry dependent stability number, s_u the isotropic average undrained shear strength, γ the total unit soil weight and *H* the height of the slope.

Failure was obtained by gradually increasing the total weight γ by a load factor *p*. For a total stress analyses, the *FS* is then equal to *p*. This gives the same result as an analysis with shear strength reduction, where the s_u is gradually reduced by a material factor γ_m until failure. Failure was defined when the tangential stiffness of the system became very small (see also Jostad and Lacasse 2015). At failure, the displacement increased significantly for an infinitesimal increase in the load factor.

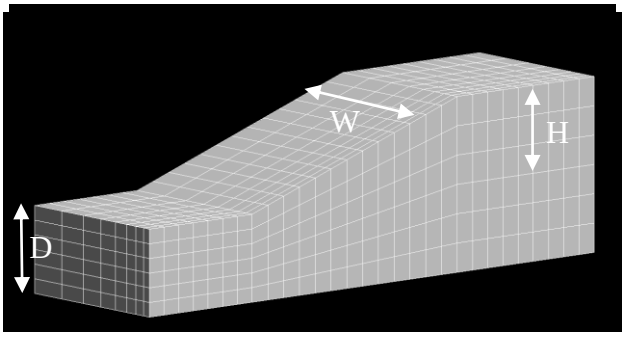


Figure 5. Finite element mesh (1/2 model) for b=3, D=H and w=4 (inclination 1:b; slope height H; slope width W)

The 2D limit equilibrium analyses and 3D finite element analyses gave similar failure mode at the centerline. The 2D and 3D slip surfaces for plane strain conditions differed slightly near the bottom of the slip surface. The factor of safety from limit equilibrium analyses (2D analysis) was 1.26 and the 3D finite element analyses gave a factor do safety of 1.24 for *w* equal to infinity (roller boundary at the side), The two factors of safety were very close.

However, the incremental displacements at failure differed significantly, as illustrated in Figure 6. On the left, the figure shows the incremental displacements. On the right, the contours are show at a vertical cross-section slightly above the toe, in the plane normal to the paper. The figure illustrates that the slip surface in the direction normal to the sliding mass is elliptical.

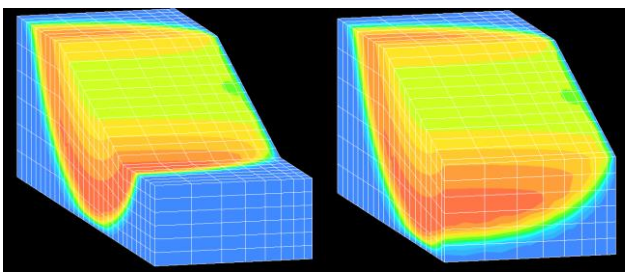


Figure 6. Incremental displacements in entire volume and with a cross-section slightly above

[4] s_u^A, s_u^{DSS}, s_u^P: s_u from triaxial compression, direct simple shear and triaxial extension tests, respectively.

the toe for b=3, D=H and W = 4H (Jostad and Lacasse 2015).

Figure 7 illustrates the importance of the 3D effects as a function of the inverse of the width ratio 1/*w* = *H/W* (plane strain conditions for *H/W* = 0).

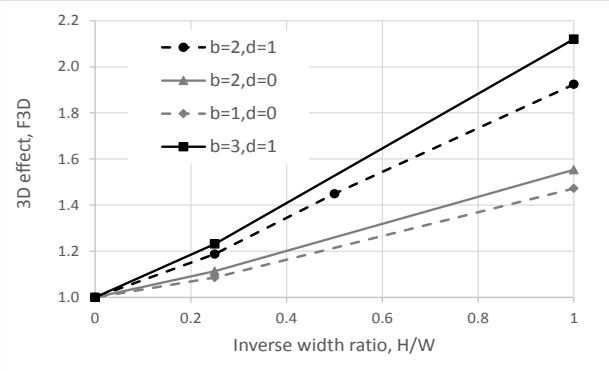


Figure 7. 3D effects vs the inverse of the width ratio H/W for different slope inclinations b and depth ratios d =D/H.

The 3D effect factor F_{3D} represents the increased capacity compared to a 2D plane strain analysis. The factor F_{3D} increases approximately linearly with the *H/W* ratio. It also increases with the depth down to the strong layer (*d=D/H)*, and increases slightly with increasing slope inclination *b*.

7 BEARING CAPACITY MODULE

The bearing capacity module introduces simple calculations, such as Brinch-Hansen's formulas and local guidelines in Norway. In addition, the 3D calculation engine is used for finite element modelling in 2D and 3D loading situations. The FEM modelling is suitable for complex (perhaps more realistic conditions), for example, layered soils, varying strength parameters vertically or horizontally, complex geometries and loadings.

The linear elastic-perfectly plastic Mohr-Coulomb and NGIADP (Grimstad et al. 2012) constitutive laws are implemented in the calculation tool. Figure 8 illustrates an embedded footing analysed in two dimensions, under moment (M), horizontal (H) and vertical (V) loading.

8 WIZARD

Lacasse *et al* (2013; 2016) described briefly the Wizard function used in GeoSuite. Wizard is an optional, interactive assistance popping up with information on how to develop a soil profile, select a parameter, interpret *in situ* or laboratory test results, select a type of analysis, do the analysis or interpret the results of an analysis. Wizard has some but not all of the wiki-characteristics: Wizard invites the user to note down its comments within the Web site; Wizard makes topic associations with links; Wizard seeks to involve the user in an on-going process of improvement.

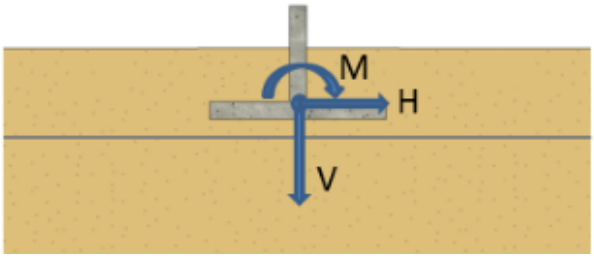


Figure 8. Bearing capacity case analysed

GeoSuite aims at providing efficient calculation tools for day-to-day design, where a balance is held between sophisticated analyses -requiring advanced soil models and parameters and offering answers of higher accuracy-, and less sophisticated and simplified models, leading to less accuracy yet still realistic answers.

For example for settlement analysis, the initial flow diagram presents to the user five steps (see Lacasse *et al* 2013 for diagram): 1) Define problem; 2) Input soil profile, models and parameters; 3) Input stress and pore pressure distributions: 4) Do settlement analysis; 5) Show the results. With the help of the Wizard, the user can initialize the data, the foundation geometry, foundation type and foundation stiffness, the construction history, ground improvement options and the load history. The user can also initializes the stress distribution (e.g. elastic theory, *n*:1 stress distribution with depth or finite element analysis of the stresses), the distribution of the initial steady state pore water (hydrostatic or non-hydrostatic conditions) and any excess pore water distribution.

Wizard also provides assistance on how to obtain soil parameters from cone penetration tests (CPTU) and laboratory tests. For example, the undrained shear strength, s_u, can be derived from the measured cone resistance, the measured excess pore pressure during CPTU testing or the net cone resistance. The preconsolidation stress, as obtained from three methods and the end-of-primary deformation parameters, again by three methods, can be considered in light of earlier experience and in terms of the effects of sample disturbance. The undrained shear strength and overconsolidation ratio can also be obtained from or compared with relationships in the literature. Figure 9 presents an example of a recent correlation for the permeability.

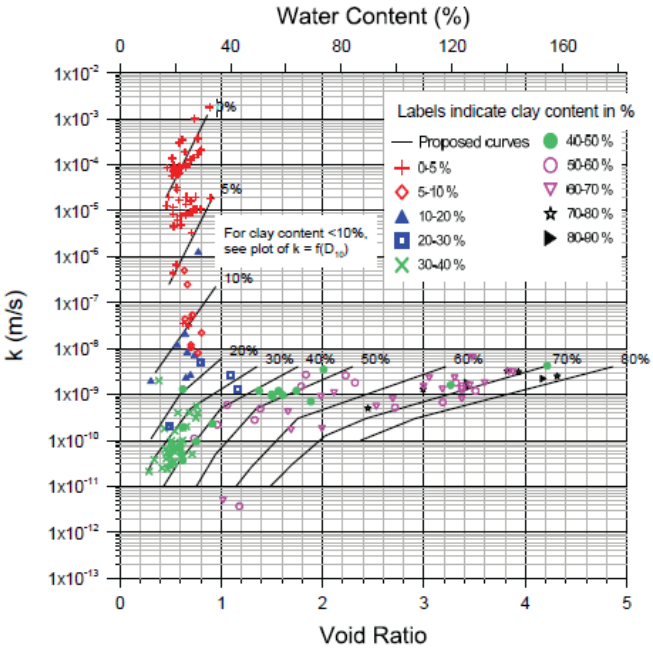


Figure 9. Permeability k vs void ratio, water content and clay content (Andersen and Schjetne 2013).

9 OTHER GEOTECHNICAL MODULES

The other modules (Piles, Excavation and Slide runout) have similar capabilities. In particular, the Piles module looks into both axial pile capacity and soil-pile interaction, and the Excavation module will use the same 3D engine as the other geotechnical modules (3D version to be completed by 2018). The Slide runout module is a recent addition and will present simplified calculation by 2017, with more advanced runout models by 2018. Statistical analyses associated with the selection of parameters will be included in 2016.

10 SUMMARY

The challenge in GeoSuite lies in maintaining a balance between sophisticated analyses, requiring advanced soil models and parameters –and thus offering answers of high accuracy, and less sophisticated and simplified models, leading to less accuracy, often lower design costs –and yet still realistic answers.

The GeoSuite code provides the practitioner the possibility of running one-, two- and three-dimensional calculations and visualization, and helps the user with geotechnical input data, establishing soil profiles, doing the calculations and interpreting the analysis results.

The paper briefly presented the concepts behind the GeoSuite software, and some calculation examples. The system is under continuous development. GeoSuite is a software that can be useful both in design and for checking one's calculation. The authors fully support that one should use more than one computer code when doing geotechnical calculations, to check that one has not missed any significant aspect of the problem.

ACKNOWLEDGEMENT

The authors acknowledge the financial contribution of The Research Council of Norway and the essential technical and financial contributions of the partners in the GeoSuite alliance: Geovita AS, ViaNova Systems AS, Multiconsult AS, Norconsult AS, ViaNova GeoSuite AB, AG Programutveckling Ekonomisk Förening (AGEF), SINTEF Building and Infrastructure, the Norwegian University of Science and Technology (NTNU), the Norwegian Public Roads Administration (NPRA), the Norwegian Railway Administration (JBV), Skanska AS, Cowi AS, Sweco AS, Rambøll AS and NGI. In particular, the contributions of Patrick Mc-Gloin (Vianova AS), Jan Ludvigsson and

Anders Rosenquist af Akershult (Vianova GeoSuite AB) and Torbjørn Johansen (Geovita AS) are recognized.

REFERENCES

Andersen, K.H and Clausen, C.J.F. (1975). "A fifty-year settlement record of a heavy building on compressible clay". Proc. Conference on Settlement of Structures, Cambridge. pp 71-78.

Andersen, K.H. and K. Schjetne (2013). Data base of friction angles of sand and consolidation characteristics of sand, silt and clay. ASCE J. of Geotechnical and Environmental Eng. 139 (7) 1140-1155.

Duncan, J.M. (2013). Slope stability then and now. ASCE GeoCongress. San Diego CA. Keynote. 2191-2210.

Finn, L. and Wu, G. (2013). Dynamic analyses of an earthfill dam on over-consolidated silt with cyclic stran softening. Keynote Lecture. 7th International Conference on Case Histories in Geotechnical engineering. Wheeling (Chicago) IL USA.

Grimstad, G. and Jostad, H.P. 2012. Stability analyses of quick clay using FEM and an anisotropic model. NGM 2012 (16th Nordic Geotechnical Meeting). Copenhagen. 2. 675-680.

Jostad, H.P. and Lacasse, S (2015). 3D effects in undrained slope stability analysis of clays. Proc ECSMGE Edinburgh. Sept. 2015.

Jostad, H.P., Sivasithamparam, N., Woldeselassie, B.H. and Lacasse, S. (2016). 3D FE tool for time dependent settlement predictions. Paper at NGM 2016, Reykjavik. (this conference).

Jostad, H. P. and Engin, H.K. (2013). Investigation of different solution strategies for non-linear 3D consolidation problems. ComGeoIII 3rd Intern. Symp. Computational Geomechanics. Krakow.

Kim, Y. (2015). GeoFuture: Testing of GeoSuite Settlement Module version 2. GeoFuture Report prepared by NGI. 26 October 2015.

Lacasse, S. Jostad, H.P., Athanasiu C., L'Heureux, J.-S., Sandene. T. and Liu Z.Q. (2013). Assistance for the calculation of settlement. GeoMontréal 2013. Canadian Geotechnical Conference.

Lacasse, S., Jostad, H.P., Kim, Y., L'Heureux, J.S, Sandven, R. and jophansen, R. (2015). GeoSuite – an integrated system for geotechnical design. Geoteknikkdagen 2015. Paper 35.

Svanø, G. and Nordal, S. (1991). A soil model for consolidation and creep. Proc. 10th Int. Conf. Soil Mech. Found. Eng, Florence, Italy. I:269-272.

Wright, S.G. (2013). Slope stability. H.B. Seed Lecture. ASCE GeoCongress. San Diego CA USA.

GeoSuite Assistance for the Calculation of Settlement

S. Lacasse
Norwegian Geotechnical Institute (NGI), Norway, suzanne.lacasse@ngi.no

H. P. Jostad, Y. Kim, J.-S. L'Heureux, Z.Q. Liu
NGI, Oslo, Norway
R. Sandven
Multiconsult AS, Norway

ABSTRACT
As part of the development of the Norwegian-Swedish software GeoSuite, a module with geo-assistance was developed and implemented. The paper describes this user-assistance, called "Wizard", helping the user with 1D, 2D and 3D calculations of stability, settlement, piles, excavations, bearing capacity and slope run-out distance. Wizard is an optional, interactive assistance popping up with information on most of the steps of an analysis for design: developing a soil profile, selecting appropriate parameters for an analysis, interpreting *in situ* and laboratory test results, selecting a type of analysis (1D, 2D or 3D), running an analysis and interpreting the results of an analysis. For example in a settlement analysis, the user can, with the help of the Wizard, initialize the data, describe the foundation geometry, foundation type and foundation stiffness, construct the load history and select ground improvement options. The user can also initialize the stress distribution, describe the distribution of the pore water pressure and that of any excess pore water pressure. Wizard has partial wiki-characteristics: Wizard invites the user to note down its comments on a website, it makes topic associations with links and seeks to involve the user in an on-going process of improvement. The module also helps the user do simpler statistical analysis of soil parameters, examine the laboratory test results in terms of sample disturbance and compare soil parameters with published correlations among soil parameters.
.

Keywords: User-assistance, settlement, software, three dimensions.

1 INTRODUCTION

Duncan (2013) described the remarkable changes in geotechnical engineering for the analysis of slopes and embankments since the 70s and 90s. Many changes are due to the revolution in computers and information technology in all aspects of our practice, including possibilities for very thorough and detailed evaluations of slope stability and performance and 3D element analyses of slopes.

As part of the development of the Norwegian-Swedish software GeoSuite, a module with geo-assistance was developed and implemented. The paper describes this user-assistance, called "Wizard", helping the user with 1D, 2D and 3D calculations of stability, settlement, piles, excavations, bearing capacity and slope runout. The paper briefly presents the GeoSuite system, and provides examples of the assistance provided to the user for the selection of the parameters and for settlement analyses.

2 GEOSUITE SYSTEM

Figure 1 illustrates schematically the evolution of civil engineering practice. Compared to earlier, solutions are moving towards 3D interactive models and Building Information Modeling (BIM), where different disciplines and work flows interact. The human relationships have also evolved as the engineers and scientists work less in isolation, but increasingly in collaborative, integrated teams.

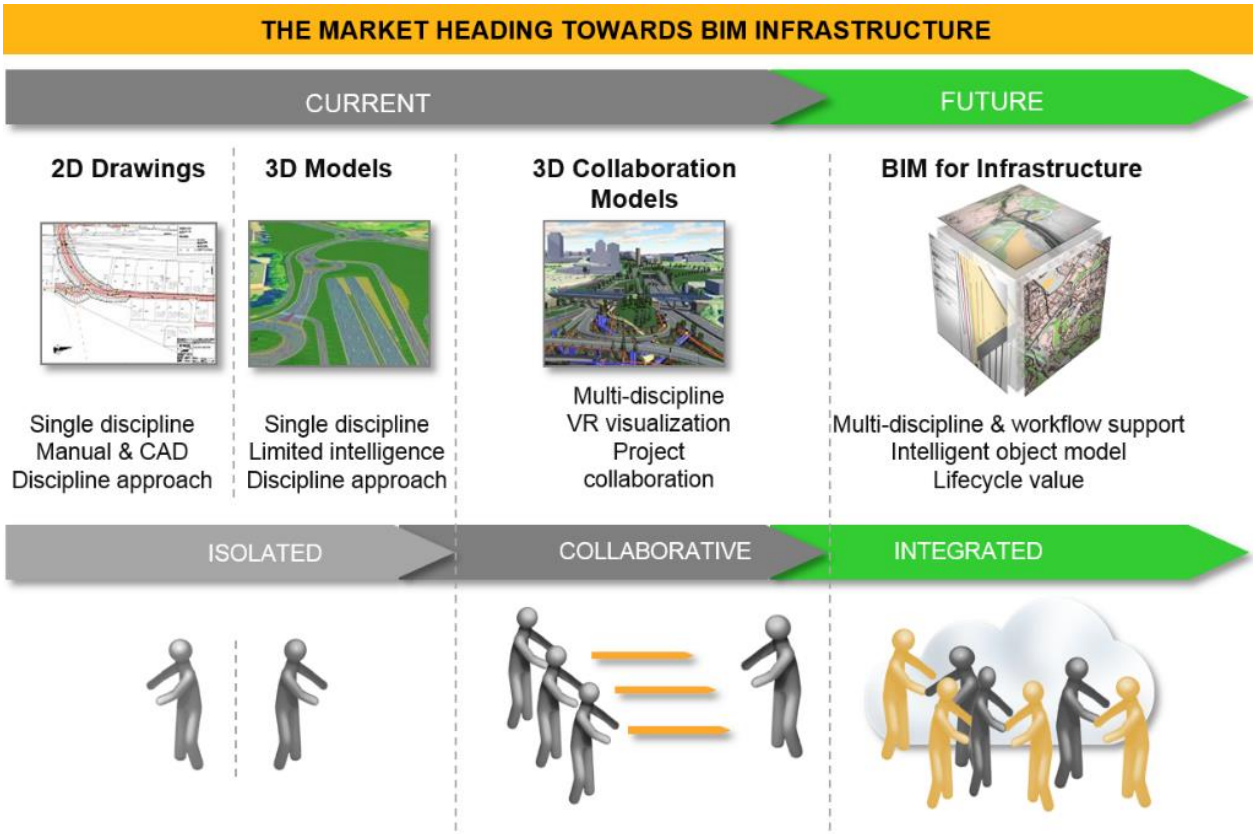


Figure 1. Evolution of civil engineering practice (Vianova AS, P. McGloin, personal communication)

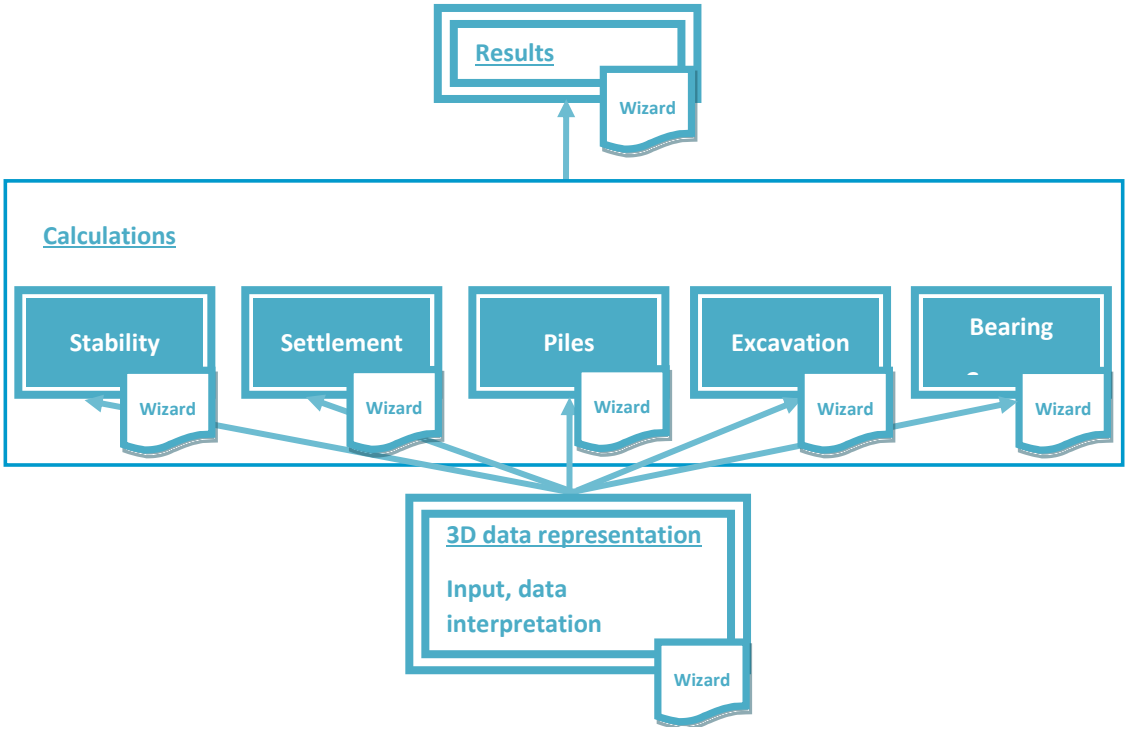


Figure 2. GeoSuite System (2015). New modules for slope runout and soil parameters were added in 2016.

Figure 2 presents schematically the GeoSuite Software. Contractors, consultants, universities and public infrastructure organizations need a common and integrated 3D engineering model in their work. In a survey, geotechnical engineers also prioritized the need for help with the selection of input parameters and the need for a seamless integration of

input data, analysis modules and results. They wished means to model and represent realistic foundation geometries, illustrate and account for spatial extent and variability of geo-data, integrate geo-calculations and enable an "interactive" modelling of foundations, with assistance to the user.

Lacasse *et al* (2016) in a companion paper in this conference describe the GeoSuite system and its different modules for the calculation of stability, settlement, bearing capacity, piles excavation and slope runout.

3 WIZARD FOR USER ASSISTANCE

The user assistance (Fig. 2) is indicated with a symbolic Wizard. The Wizard is an interactive assistance popping up with information on how to interpret and select a parameter, select a type of analysis, do the analysis and interpret the results. The Wizard is organized such that the custodian(s) can add, modify or delete the content via a browser.

The Wiki does the knowledge management and allows note-taking. Editing the user-assistance will be limited to the custodian(s). As described by Ward Cunningham, the developer of the first wiki software, Wizard acts as a "simple online database for multi-users" ('wiki' is Hawaiian for 'fast/quick').

Wizard will act as a database for creating, browsing, and searching through information, and evolving the text. One difference with wiki pages is that the modifications will be reviewed by the custodian before being accepted. Wizard has some, but not all, of the characteristics of the wiki concept: (1) Wizard invites the user to note down its comments within the Web site; (2) Wizard associates topic with links; and (3) Wizard seeks to involve the user in an on-going process of improvement.

4 SOIL PARAMETERS AND SOIL PROFILE

Figure 3 and 4 illustrate the assistance to the user for the establishment of soil profiles. The assistance is at present placed at the before the analyses are done, and enable the user to visualize the background data and to compare with other data available.

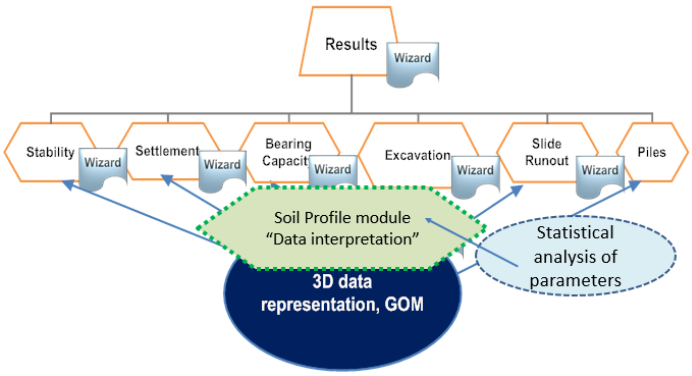


Figure 3. Wizard for soil profiles in GeoSuite

Figure 4 provides the steps in determining the soil properties and soil profiles.

Starting from the left, the user selects the parameters and boring, tests he wishes to see or use for his determination of the soil parameters. Both laboratory and *in situ* data are made available in the Ground Observation Model (GOM, Lacasse *et al* 2016). The data are tabulated and plotted, and will with time have a dynamic link with existing reliable correlations. The data are then assembled onto one or several graphs, spurious points can be eliminated or reinstated and *in situ* tests can be replaced. The data can be exported to different file formats for use in a report.

Throughout the exercise, there is a Wizard function that allows the user to retrieve supplementary or background information, documented experience or publications.

At present, GeoSuite does not have the communication with the central database with the raw laboratory test data (it does with the raw CPT/CPTU data). By the end of the project, this communication will be done.

The user needs to be aware that there is still a need for reflected intervention to select layering, the variations with depth and the parameters. Wizard, however, will:

- Get rid of 5-6 tables or Excel sheets and rather assemble all information together.
- The user select applicable correlations from a set of correlations in the Wizard.
- The user can trace the soil profile and adjust it several times.
- Different files can be saved as appropriate for different calculations.

GeoSuite plans to implement statistical tools in 2016. Figure 6 lists the tools considered.

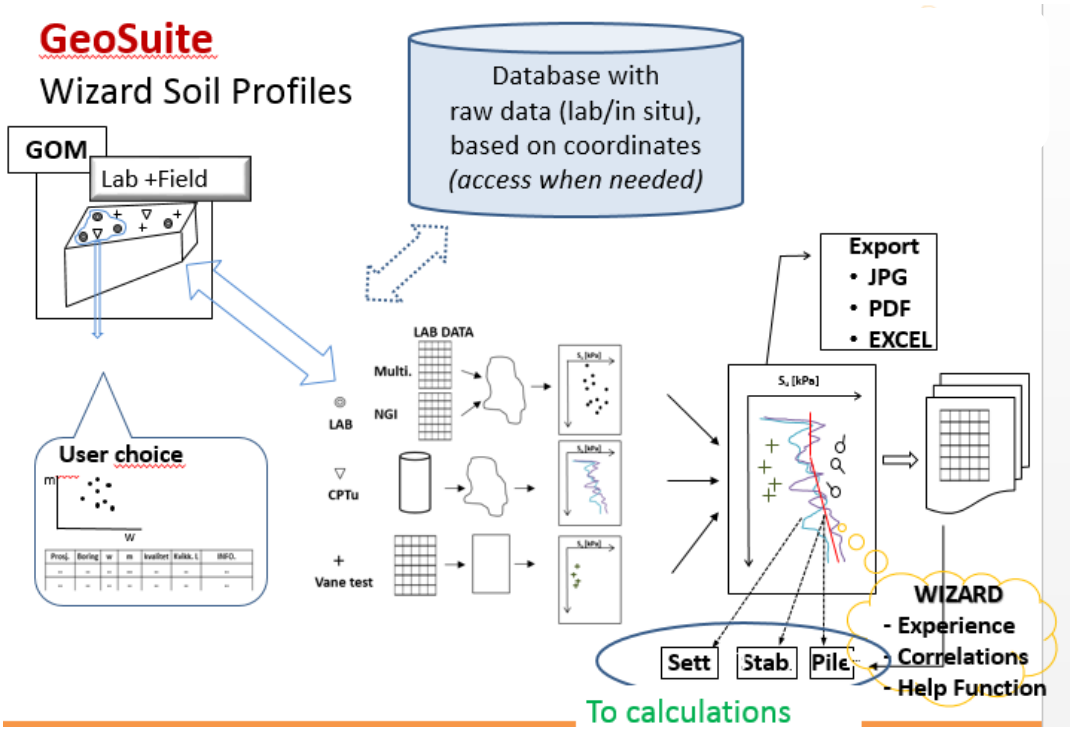


Figure 4. Schematic of Wizard Soil Profiles

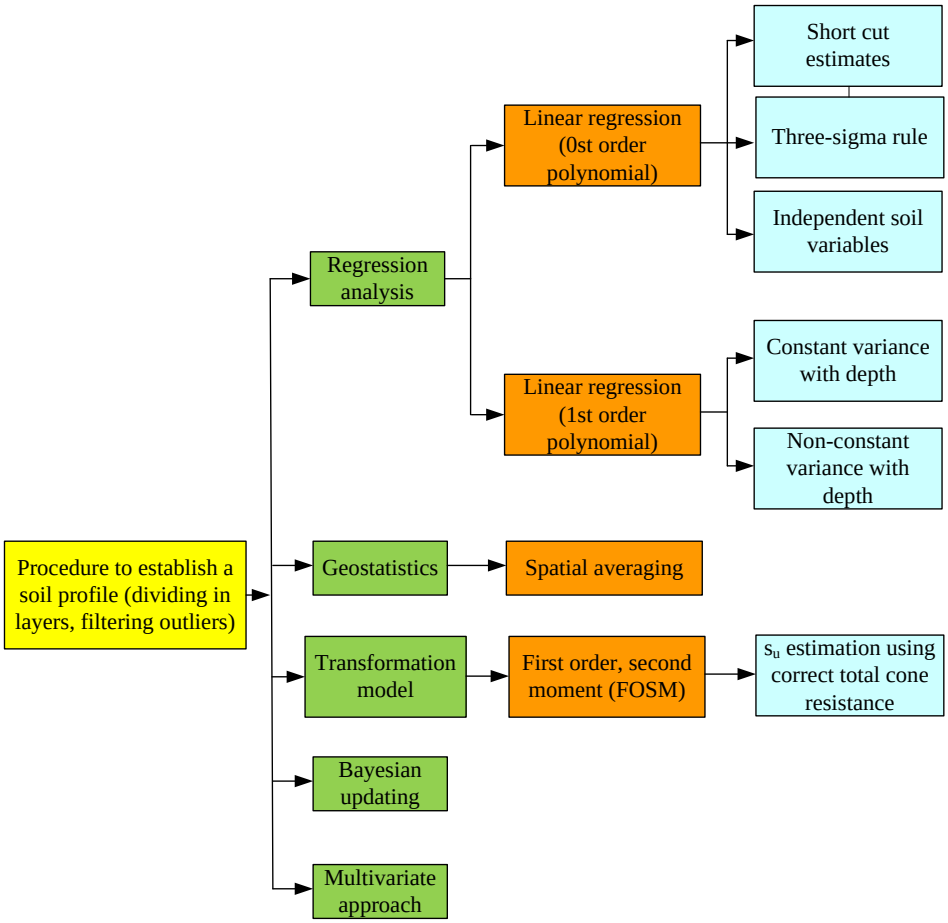


Figure 5. Statistical tools for evaluation of soil parameters

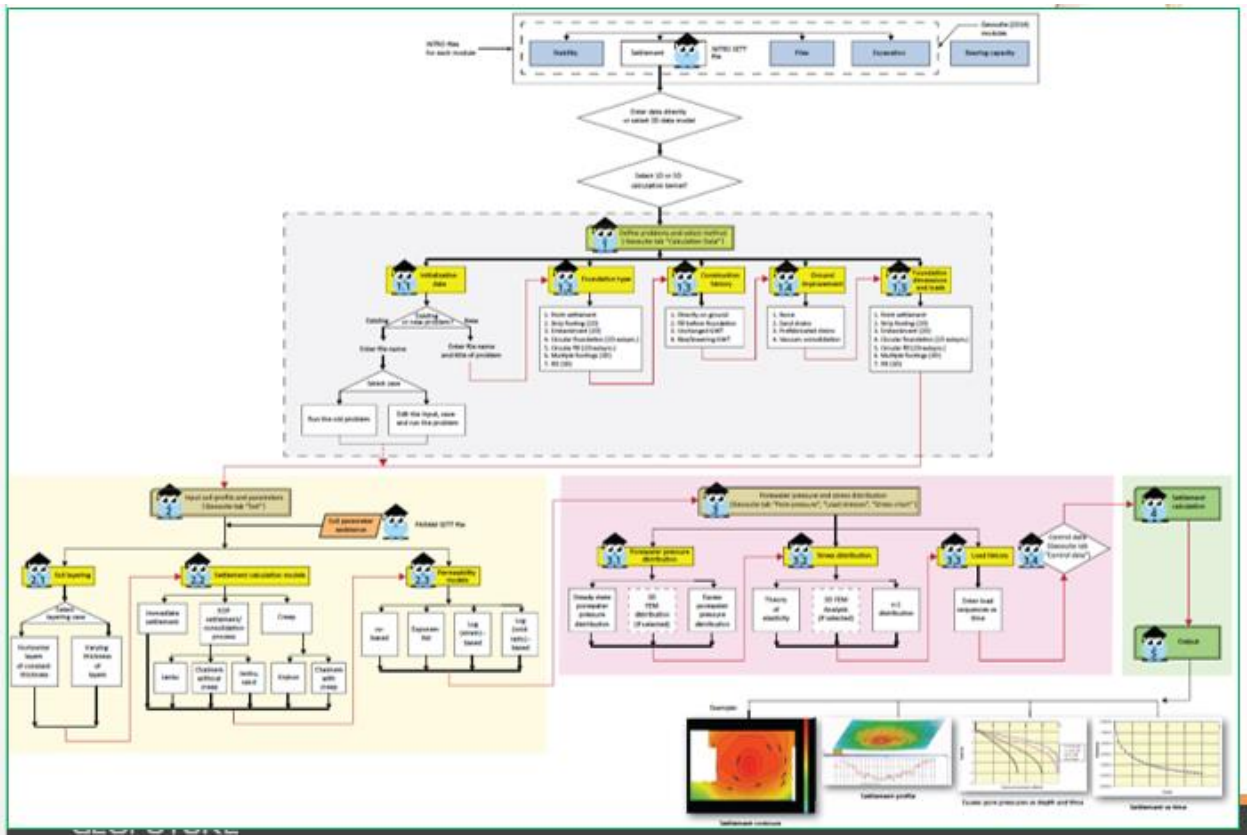


Figure 6. Flow diagram for settlement analysis

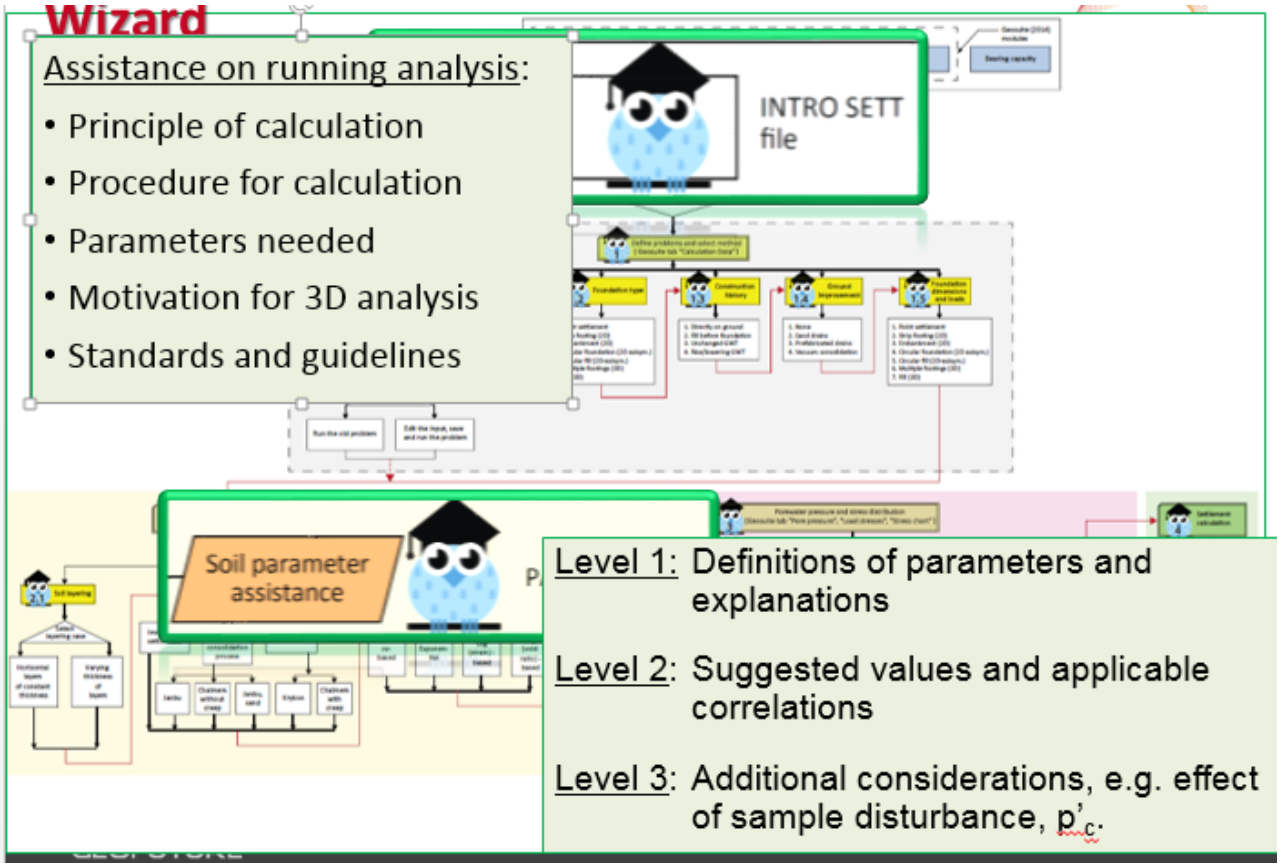


Figure 7. Wizard assistance for settlement analysis (INTROSETT and PARAMSETT file)s

5 SETTLEMENT ANALYSIS

Figure 6 presents the steps for the analysis in the Settlement module. Although nearly unreadable, the flow diagram shows five steps (Fig. 6): 1) Define problem; 2) Input soil profile, models and parameters; 3) Input stress and pore pressure distributions: 4) Do settlement analysis; 5) Show the results.

In step 1 (Fig. 7), the user initializes the data, the foundation geometry, foundation type and foundation stiffness, the construction history, ground improvement options and the load history. In step 3 (Fig. 8), the user initializes the stress distribution (elastic theory, n:1 stress with depth distribution or finite element analysis of the stresses), the steady state pore water distribution (hydrostatic or non-hydrostatic conditions) and the excess pore water distribution.

The Wizard assistance is developed for the ground observation model, the selection of the soil parameters, the selection of the method of analysis and the implications of the different analysis approaches, and for the interpretation of the results of the analyses. The assistance is more detailed on Figure 7. The assistance can be skipped by the user.

At the start of an analysis, the user gets assistance for running the analysis, including:

- Principle of calculation.
- Procedure for calculation.
- Parameters needed.
- Motivation for 3D analysis.
- Standards and guidelines.

For the selection of the parameters, the users get information organized in three levels:

- Level 1: Definitions of parameters and explanations.
- Level 2: Suggested values and applicable correlations (in addition to site-specific data).
- Level 3: Additional information, e.g. effect of sample disturbance, p'_c, effect of interpretation method, newer research etc.

6 ASSISTANCE WITH *IN SITU* TESTS

Figure 8 illustrates the Wizard for obtaining soil parameters from the cone (CPT) and piezocone (CPTU) penetration tests. The flow diagram illustrates the steps in the interpretation and the panels available to the user (orange boxes). For example, the undrained shear strength can be obtained from the cone resistance, the measured excess pore pressure or the net cone resistance. The overconsolidation ratio can be obtained from relationships in the literature.

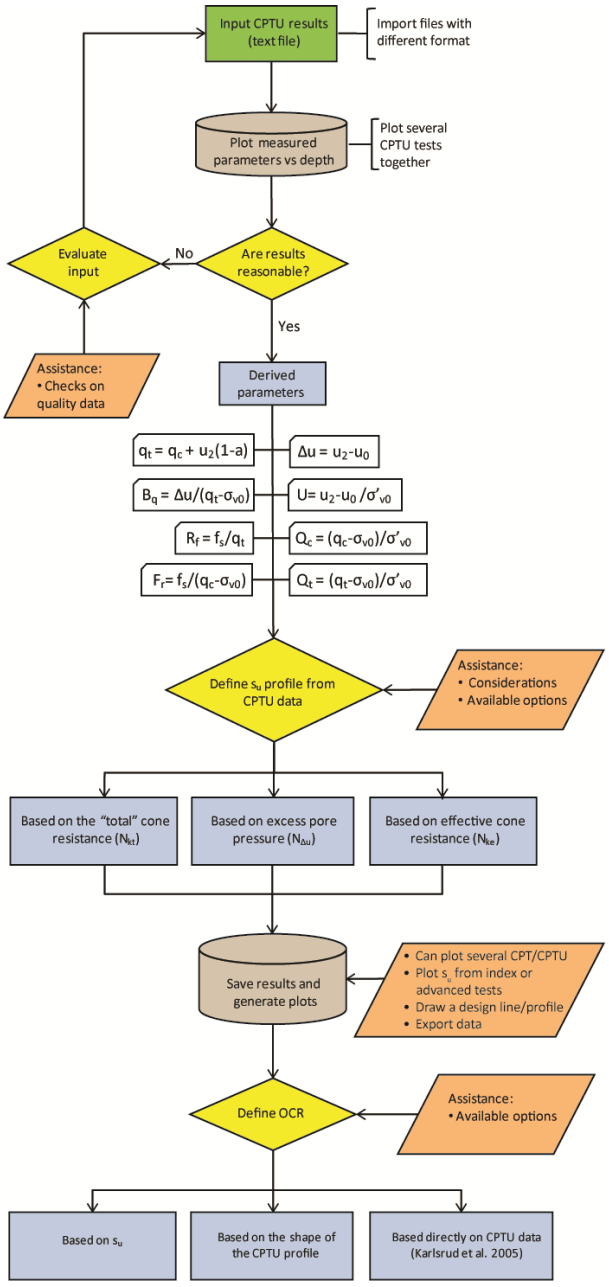


Figure 8. Wizard for CPT/CPTU tests

Figure 10 presents the interpretation of different parameters for the results of laboratory tests, e.g. the preconsolidation stress can be obtained by three methods, so the end-of-primary deformation parameters. Help panels are indicated in orange.

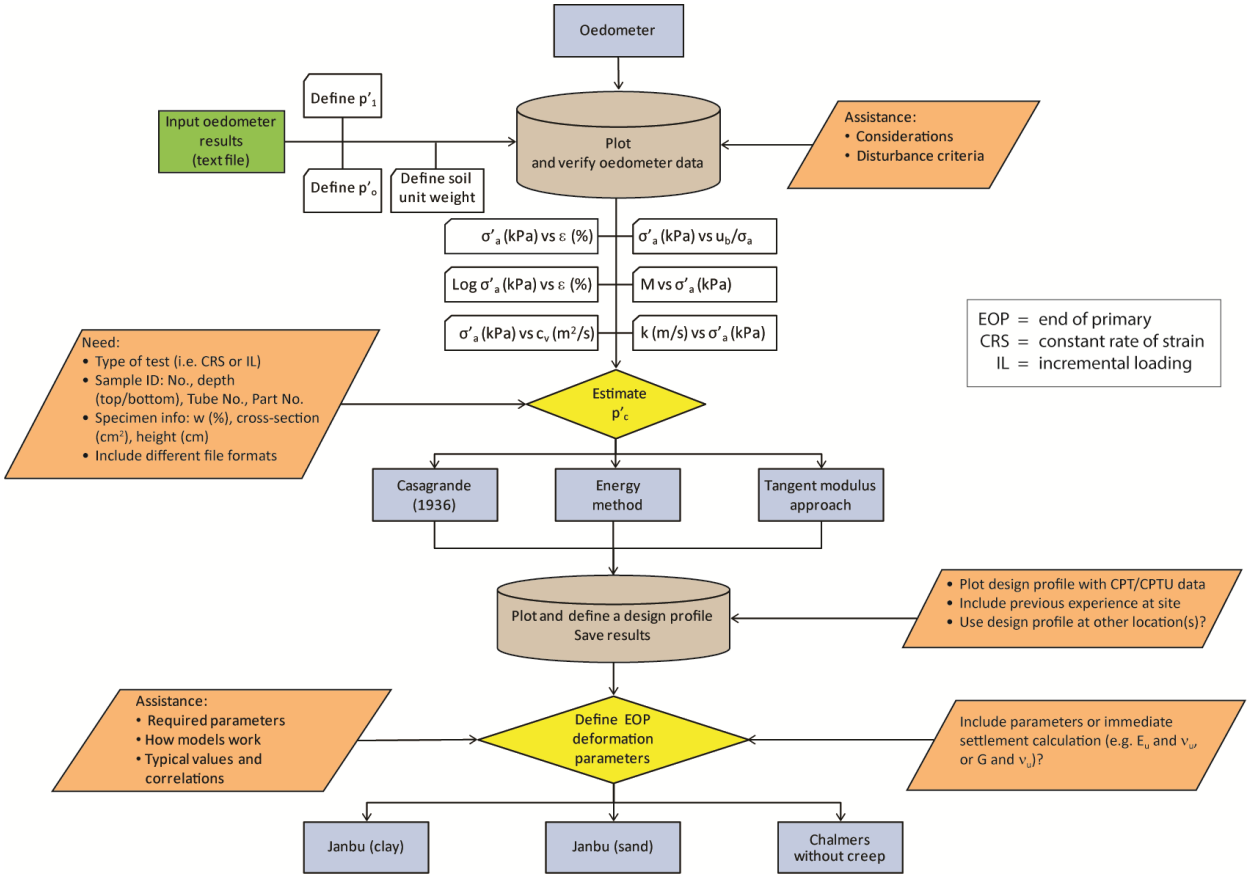


Figure 9. Wizard for oedometer test

Table 1a. Example of user assistance 's_u from CPT or CPTU

Estimation of s_u from "total" q_c and N_k)

The undrained shear strength s_u from CPT using cone resistance is determined from the following equation: $s_u = \frac{(q_c - \sigma_{v0})}{N_k}$

where N_k is an empirical cone factor and σ_{v0} is the total *in situ* vertical stress. For normally consolidated marine clays with field vane as the reference test, the cone factor, N_k, varied between 11 and 19 with an average value of 15 (Lunne and Kleven, 1981).

A modification and improvement of the above approach is to use the cone resistance corrected for pore pressure effects, q_t, instead of measured cone resistance q_c. The cone factor is expressed as:

$$N_{kt} = \frac{(q_t - \sigma_{v0})}{s_u}$$

where σ_{v0} is the total overburden stress. The corrected cone resistance is expressed by $q_t = q_c + u_2(1-a)$,

where a is the area ratio of the cone (area of the central part of the cone divided by the gross area). This ratio is determined by calibration tests in the laboratory as described in Lunne et al. (1997). This area correction reduces or eliminates some of the observed differences in cone resistance obtained by using cones from different manufacturers.

Using the approach presented above, Aas *et al* (1986) and Karlsrud *et al* (2005) presented correlations between cone factor N_{kt} and plasticity index I_p, taking the average laboratory undrained shear strength $s_{u,lab} = (s_u^{\ c} + s_u^{\ DSS} + s_u^{\ E})/3$

where $s_u^{\ c}$, $s_u^{\ DSS}$ and $s_u^{\ E}$ are the undrained shear strength from triaxial compression, direct simple shear and triaxial extension in the laboratory. The results from Karlsrud et al. (2005) are presented in Fig. 1, and suggest that N_{kt} increases with increasing plasticity. Figure 2 presents a similar relationship for the cone factor N_{kt} and the overconsolidation ratio (OCR). On the basis of a detailed study of OCR, I_p and sensitivity S_t, Karlsrud *et al* (2005) proposed the following N_{kt} relationships:

$N_{kt} = 7.8 + 2.5 logOCR + 0.082 - I_p$; for $S_t \leq 15$ and $N_{kt} = 8.5 + 2.5 logOCR$; *for* $S_t > 15$

For the ranges of plasticity and OCR in Figs. 1 and 2, the N_{kt} factor varies between about 6-16. The variation in calculated s_u based on the correlation above typically lies around ±15% for highly sensitive clays and ±30% for the low sensitivity clays. In practice, the method of determining s_u may vary from location to location. It is emphasized that the cone factors are defined for a specific reference value of s_u. The effect of sample disturbance can be important.

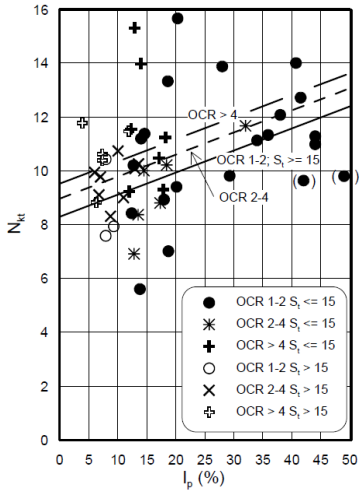


Figure 1: Influence of I_p on N_{kt} (Karlsrud *et al* 2005).

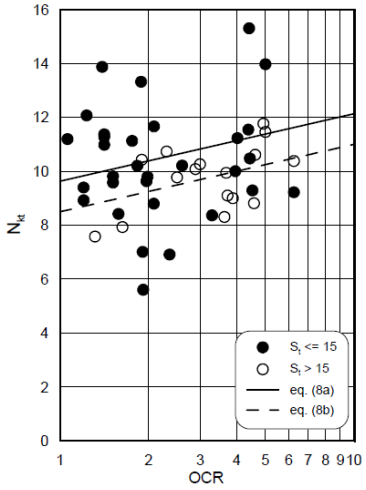


Figure 2: Nkt versus OCR (Karlsrud et al 2005).

References

Karlsrud, K., Lunne, T., Kort, D.A. and Strandvik, S. 2005. CPTU correlations for clays. International Conference on Soil Mechanics and Foundation Engineering, 16. Osaka 2005. Proceedings, 2, 693-702.

Lunne T. and Kleven, A. 1981. Role of CPT in North Sea foundation engineering. Session at the ASCE National Convention: Cone penetration testing and Materials, St-Louis, 76-107.

Lunne, T., Robertson, P.K., and Powell, J.J.M. 1997. Cone Penetration Testing In Geotechnical Practice, Spon Press, Taylor & Francis Group, London and New York, 312 p.

Table 1b. Example of user assistance 'sample quality'

Sample quality

The most common problems associated to sample disturbance when interpreting results from oedometer tests include (Fig. 1):

- Difficulties in estimating p'_c.
- Overestimating the tangent modulus (M) above p'_c.
- The reloading modulus may be underestimated.
- The permeability needs to be corrected for volume changes up to p'_0.The consolidation coefficient (c_v) needs to be corrected for the errors in modulus and permeability.

Sample quality evaluation

The volume change during re-consolidation to the *in situ* effective stresses is an indicator of sample disturbance). Lunne *et al* (1997) proposed a scale for sample quality in terms of the change in void ratio normalized by the initial void ratio (Table 1).

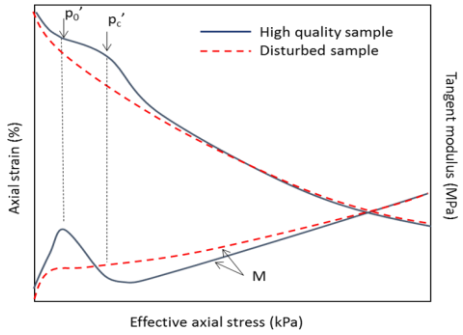


Figure 1: Typical oedometer response

Table 1: Quality index from $\Delta e/e_0$ (Lunne *et al* 1997)

OCR	$\Delta e/e_0$			
	Very good to excellent	Good to fair	Poor	Very poor
1-2	<0.04	0.04-0.07	0.07-0.14	>0.14
2-4	<0.03	0.03-0.05	0.05-0.10	>0.10
4-6	<0.02	0.02-0.035	0.035-0.07	>0.07
Quality	1	2	3	4

In this method, the sample quality is associated to changes in void ratio during the consolidation phase ($\Delta e/e_0$); where Δe denotes the change in void ratio from the start of the consolidation process until the *in situ* stresses are reached (i.e. p'_0), while e_0 is the initial void ratio at the start of the consolidation process.

Volumetric strains are equal to axial strains in the oedometer (i.e. $\varepsilon_{vol} = \varepsilon_a$) and $\Delta e/e_0$ can be found by the following equations for saturated soils: $\Delta e = \epsilon_{vol}(1 + \epsilon_0) = \epsilon_a(1 + \epsilon_0)$ and $\epsilon_0 = \gamma_s \cdot w_i$

where γ_s is the particle density, usually 2.65-2.75, and w_i is the water content at the start of the test.

Reference

Lunne, T., Berre, T., and Strandvik, S. 1997. Sample disturbance effects in soft low plastic Norwegian clay. Proc. Conf. Recent Developments in Soil and Pavement Mechanics, Rio de Janeiro, Brazil, Ed M. Almeida. A.A. Balkema, Rotterdam, NL. 81–102.

Table 1 (parts a, b and c on previous 2 pages) provides examples of the help texts in Wizard, with guidance on the interpretation and methods of calculations.

7 SUMMARY

GeoFuture is based on the concept that it will be used for day-to-day design analyses, where a balance needs to be held between sophisticated analyses, requiring advanced soil models and parameters and offering answers of higher accuracy and less sophisticated and simplified models, leading to less accuracy yet still realistic answers.

Each calculation module in GeoFuture is developed similarly to the settlement module. The Wizard for data representation and selection of parameters are generalized for the Stability, Piles, Excavation, Bearing Capacity and Slope Runout modules. Two features are under development for the Wizard: Interactive correlations for a comparison of the results of *in situ* and laboratory tests and to select the design parameters in each of the analyses, and implementation of statistical approaches.

The introduction of a module for the statistical analysis of the parameters. Soil is a complex material because of the way the deposits are formed and the continuous alteration processes. The uncertainty in soil properties is due to e.g. the natural variability within a volume, insufficient data, imperfect interpretation models, measurement errors and limited knowledge. Statistical estimates should be used as a complement to actual data and engineering judgment when one is selecting parameters for design. The different statistical approaches can be applied to laboratory and in situ testing data, especially when a lot of data are available such as the cone and piezocone penetration tests.

.

ACKNOWLEDGEMENTS

The authors thank the Research Council of Norway for the funding of the R&D. The work is also funded by the industry in Norway and Sweden: *Ge*ovita AS, ViaNova Systems AS, Multiconsult AS, Norconsult AS, ViaNova GeoSuite AB, AG Programutveckling Ekonomisk Förening (AGEF), SINTEF Building and Infrastructure, the Norwegian University of Science and Technology (NTNU), the Norwegian Public Roads Administration (NPRA), the Norwegian Railway Administration (JBV), Skanska AS, Skanska AS, Cowi AS, Sweco AS, Rambøll AS and NGI. The writers acknowledge the contributions of Mr Patrick McGloin from Vianova AS, Mr Jan Ludvigsson from Vianova GeoSuite AB and the initiator of the GeoSuite/GeoFuture idea, Mr Torbjørn Johansen from Geovita AS.

REFERENCES

Andersen, K.H. and K. Schjetne (2013). Data base of friction angles of sand and consolidation characteristics of sand, silt and clay. ASCE J. of Geotechnical and Environmental Eng. 139 (7) 1140-1155.

Duncan, J.M. (2013). Slope stability then and now. *ASCE GeoCongress*. San Diego CA. Keynote. 2191-2210.

Finn, L. and Wu, G. (2013). Dynamic analyses of an earthfill dam on over-consolidated silt with cyclic strain softening. Keynote Lecture. *7th International Conference on Case Histories in Geotechnical engineering*. Wheeling (Chicago) IL USA.

Lacasse, S. Jostad, H.P., Athanasiu C., L'Heureux, J.-S., Sandene. T. and Liu Z.Q. (2013). Assistance for the calculation of settlement. GeoMontréal 2013. Canadian Geotechnical Conference.

Lacasse, S., Jostad, H.P., Kim, Y. L'Heureux, J.S., Sandven, R. and Johansen, T. (2015). Geosuite – integrert geoteknisk dimensjonerings verktøy (Geosuite – an integrated system for geotechnical design). Paper 35. Geoteknikkdagen Oslo. Nov 2015.

Lacasse. S., Jostad, H.P., L'Heureux, J.S., Torgersrud, Ø. and Sandven, R. (2016). GeoSuite – A Modular System for Geotechnical Design. NGM 2016 (this conference)-

Wright, S.G. (2013). Slope stability. H.B. Seed Lecture. *ASCE GeoCongress*. San Diego CA USA.

Modelling of pile groups and implementations of the non-linear effects in structural modelling programs. - The interface between pile group and superstructure.

S. B. Christensen
Ramboll, Denmark, srbc@ramboll.dk

P. H. Sørensen
Ramboll, Denmark

ABSTRACT
As a part of a bypass road project in Denmark, three bridges were designed; the largest with a total length of ~200 m divided over 5 spans. Each of the four middle foundations consisted of 22-25 vertical driven precasted piles whereas the two end foundations consisted of a combination with vertical and inclined driven precasted piles.

The pile groups were modelled implementing the theory of P-Y, T-Z and Q-W curves. The superstructure was modelled in a structural FE program.

In general when modelling pile groups, the interface to the superstructure is often made with an assumption of modelling the foundation as six linear springs placed in the pile groups rotational centre, resulting in a more rigid and conservative design. For the present project an optimization of the interfaces between pile group and superstructure was made by implementing the non-linear effects for the pile-soil interaction into the structural program. Specifically this was done by modelling the piles as "vertical" beam elements with non-linear spring supports i.e. P-Y curves as well as Q-W and T-Z curves. Through an iterative process this resulted in a more soft foundation than in traditional analyses. A softer foundation leads to smaller applied forces for the design of pile groups and by that an optimisation of the pile design with fewer piles.

Keywords: Pile Groups, Pile-Soil Interaction, Optimisation of Pile Design.

1 INTRODUCTION

As a part of a bypass road project in Denmark, three bridges were designed; the largest with a total length of approximately 200 m divided over 5 spans. The project is a "design-and-build project" executed by the company Arkil A/S.

An overview of the bridge is given in Figure 1 and Figure 2. The bridge is to be built over a large water valley which is environmental protected meaning that restraints are put on the design and project when constructing close to the stream.

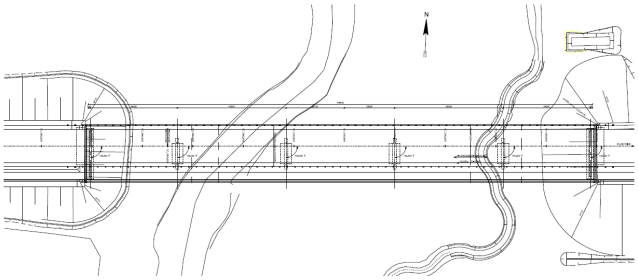


Figure 1: Overview of project - plan drawing

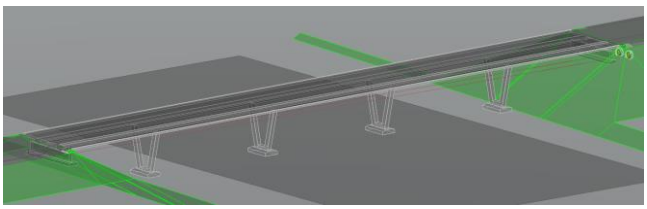


Figure 2: Overview of project - 3D model

Each of the four middle foundations consists of 22-25 vertical driven reinforced precasted piles whereas the two end foundations consists of a combination with vertical and inclined driven reinforced precasted piles. An illustration of the pile configuration for one of the middle foundations is shown in Figure 3.

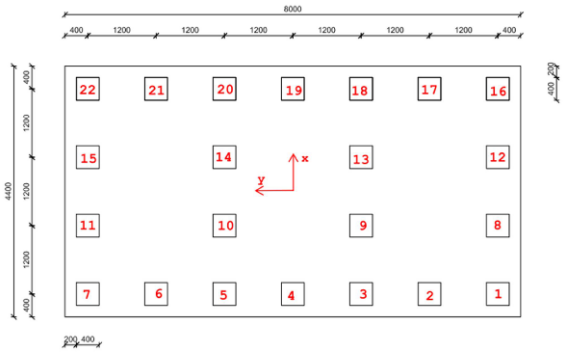


Figure 3: Illustration of pile configuration for one of the middle foundations.

The piles were designed to have a final penetration depth of approximately 15 m. In each pile group the piles have a c-c distance between 3-4 times the widths of the pile, meaning that pile group effects needed to be accounted for when dealing with lateral loading.

In Figure 4 to Figure 8 the construction of the bridge is shown.



Figure 4: Construction of the bridge – excavation for temporary foundations for scaffolding



Figure 5: Construction of the bridge – installation of piles



Figure 6: Construction of the bridge – installation of piles



Figure 7: Construction of the bridge – installation of piles for one of the middle foundation



Figure 8: Construction of the bridge – overview of the site

2 SITE AND GROUND CONDITIONS

The site investigations carried out within the site included both geotechnical borings as well as CPT's.

For each of the foundations a minimum of one boring and a CPT were executed to a depth of 17 to 25 meters below ground surface.

The borings shoved a large variation of soil deposits for the first 0.3-3.5 m with variations between sand/clay and peat. The peat was mostly discovered in the area close to the existing stream. Below the first 3.5 m the majority of the deposits consisted of meltwater sand with embedded layers of meltwater silt and sand till. Secondary deposits consisted of clay till. In Figure 9 a longitudinal soil cross section is seen.

The result from the CPT's shoved similarity with the geological descriptions from the borings.

Only some of the borings was drilled to the limestone reached between 12 m to 18 m depth below ground surface. The limestone is described as a weak material and therefore no refusal when driving into the material was to be expected. In the present analyses the limestone was treated as a frictional material.

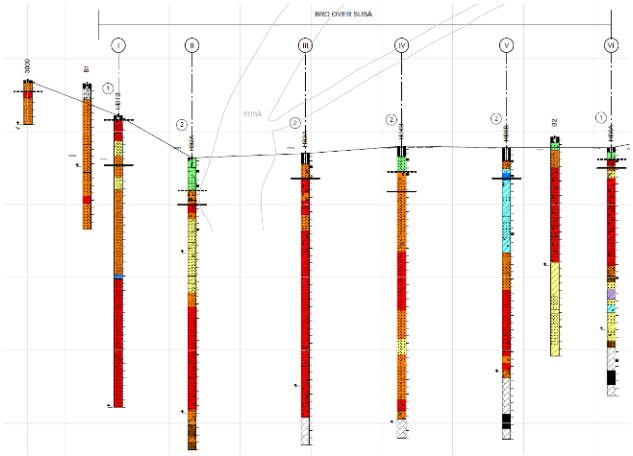


Figure 9: Longitudinal soil profile

For both end foundations and three of the middle foundations the piles were to be driven with pile tip into the meltwater sand while the last middle foundation had pile tip into limestone due to the limestone being reached at a higher level at this position.

Further the two end foundations were to be constructed in a man-made embankment consisting of gravel and sand. The embankments were constructed with a height of up to approximately 15 m.

Because of the specific ground conditions with the pile tip either into sand or into limestone, the bearing capacity for each pile needed to be verified by use of the Danish Pile Driving Formula as well as by use of PDA with CAPWAP for piles with pile tip into limestone.

It was seen that for two of the middle foundations with pile tip into sand, a majority of the piles achieved a much higher bearing capacity than anticipated. This was believed to be a result of compaction around the piles in the areas in which the sand deposits consisted of larger parts of sand till and coarser grains for the meltwater sand deposits.

3 DESIGN METHODS

In general when modelling pile groups, the interface to the superstructure is often made with an assumption of modelling the foundation as six linear springs placed in the pile group's rotational centre, resulting in a more rigid and conservative design in which the full capacity of the pile group is not computed.

For the present project an optimization of the interfaces between pile group and superstructure was made by implementing the non-linear effects for the pile-soil interaction into the structural program used for design of the bridge – in the present case LUSAS.

Through an iterative process it was believed that this would result in a more soft foundation than in a traditional analysis. A softer foundation leads to smaller applied forces for the design of pile groups and by that an optimisation of the pile design with fewer piles.

3.1 Finite Element Programs

Each foundation was calculated in Rambølls own structural FE analysis programme, ROSA. The inputs are the material properties for pile and soil, the geometry and the load cases. In Figure 10 is seen a computer model for one of the end foundations.

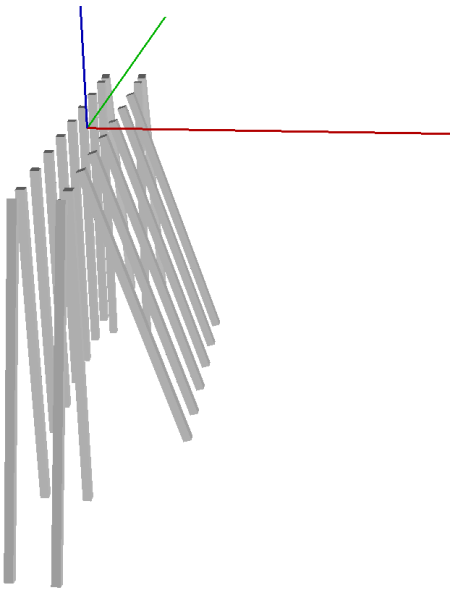


Figure 10: ROSA computer model for end foundation

In the FE-analysis the capacity of the soil and the interaction between soil and pile are determined in form of a set of non-linear soil curves/springs, as illustrated in Figure 11: .

- Lateral interaction. The P-Y curves are modelled by the procedure given in the API Standard.
- Axial Interaction. The T-Z curves for pile soil axial interactions are modelled by smooth curves.
- Tip Load Displacement. The Q-W curves for the tip load displacement relationship are assumed to be tri-linear for compression..

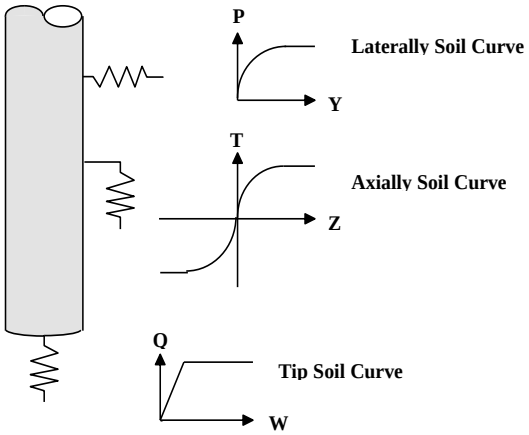


Figure 11Model of non-linear springs used in ROSA

The result is the calculated bearing capacities and the deformations as well as the forces along the pile. The effect from pile forming a group is accounted for according to Mindlin (1936).

To optimize the construction the derived load-displacement curves were implemented into the structural program used for the design of the bridge. Specifically this was done by modelling the piles as "vertical" beam elements with non-linear spring supports as illustrated in Figure 12.

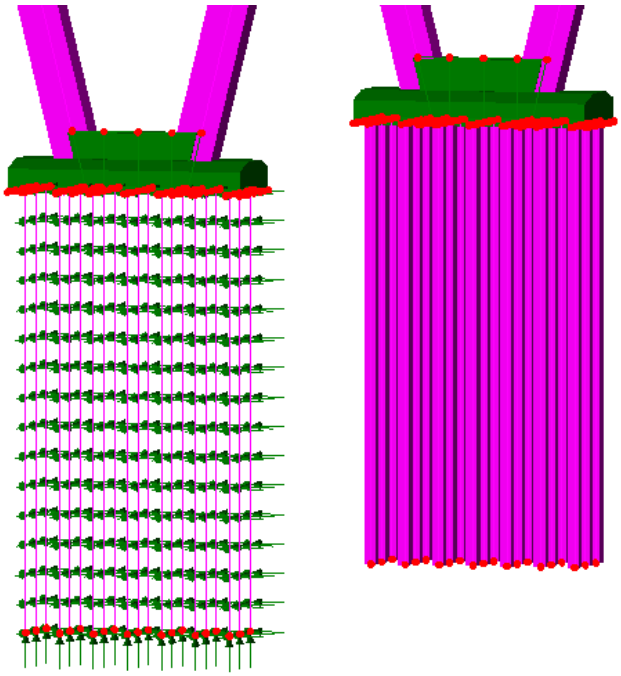


Figure 12Model of pile foundation in the structural FE-program for middle foundation

The process of the calculations was as the following steps:

1. The bridge structure is modelled with external loads and a fixed foundation.
2. Calculations are executed to find the bending moments and forces on the foundations as well as a first estimate of pile configuration.
3. The pile groups are calculated with the above found forces (& moments) as external loads and ends up with pile settlements and internal forces (shear, axial) and bending moments as well as load-displacements curves for each pile.
4. The structure is then recalculated with use of the load-displacements curves as entry data for the model resulting in a new set of forces (& moments).
5. Step 3 and 4 is then repeated

This procedure is an iterative loop, to be repeated until convergence is achieved between settlements (stiffness of bearings/piles) calculated by the structural program and ROSA.

4 RESULTS

Comparison was made for a conventional design without implementations of load-displacements curves in the structural program:

- Conventional design: 32 piles
- Implementation of load-displacements curves: 22 piles

It was found, that by implementation of load-displacement curves, a pile group would consist of approximately 2/3 of the number for the same case using conventional design methods.

5 CONCLUSIONS

It was found, that by implementing load-displacements curves in the structural program and performing an iterative optimization process is cost efficient. It takes that both the structural engineer as well as the geotechnical engineer needs to have an understanding for each other's work.

The process is more time consuming but it is the authors meaning that the extra time used in the design is quickly earned, especially when dealing with larger projects.

Further and important notice is, that because an implementation of p-y curves was introduced in the design, a pile group only consisting of vertical pile could be used as long as the lateral forces was not of a to high magnitude.

The economic potential in using this more advanced approach for optimizing pile foundations is evident especially for pile groups under large lateral loading.

6 ACKNOWLEDGEMENTS

The authors would like to thank Arkil A/S for use of the project material.

7 REFERENCES

API. 2000. Recommended Practice for Planning, Designing and Constructing Fixed Offshore Platforms Working Stress Design. American Petroleum Institute API-RP2A-WSD, Rev. 21st edition

Mindlin, R.D 1936. Force at a point in the interior of a semi-infinite solid. Publishing firm Appel. Phys. Vol. 7.

ROSOIL, RAMBØLL´s Program ROSOIL, Pile soil curves. User's Guide Latest edition.

ROSAP, RAMBØLLs Offshore Structural Analysis Program Package. User's Guide Latest edition.

LUSAS. Engineering analysis software. Finite Element Analysis.

Back-calculation of the Saint-Alban A test embankment with a new modelling approach in LEM

V. Lehtonen
Tampere University of Technology, Finland, ville.lehtonen@tut.fi

T. Länsivaara
Tampere University of Technology, Finland

ABSTRACT
To facilitate the continued use of limit equilibrium method (LEM) in stability design of embankments on soft clays, the new calculation method "Hybrid s_u" (HSU) has been developed. It is used to derive undrained shear strength from effective strength parameters, or to predict the excess pore pressure at failure. The HSU method uses an anisotropic effective stress soil model with volumetric hardening, from which a closed form solution for the effective mean stress at failure p'_f is derived. This in turn is used to derive the anisotropic undrained shear strength (for use in total stress analyses), or excess pore pressure (for use in undrained effective stress analyses). The model accounts for factors such as anisotropy, consolidation state, volumetric hardening and to some extent, rate effects. An advantage of the model over traditional undrained effective stress calculations is that the overestimation of shear strength at $F > 1$ is avoided.

To illustrate the use and results of the model, a back-calculation of the classic Saint-Alban A test embankment failure is presented. In the test, an embankment was built on a soft Champlain clay deposit. The height of the embankment was gradually increased until failure. The HSU model parameters are fitted with data available from literature. The model is then applied to both total stress and undrained effective stress analyses of the case using LEM. It is shown that the relatively simple HSU model gives realistic results with both analysis types, comparable with the results of an advanced FEM analysis and literature data.

Keywords: Slope stability, Modelling, LEM, Undrained shear strength, Pore pressure

1 INTRODUCTION

The stability of existing railway embankments in the Finnish Railway network has been studied extensively in the recent years. In studies commissioned by the Finnish Traffic Agency (FTA), it has been found that the calculated factor of safety (FOS) is very low for many railway embankments on soft subsoils. In some cases the calculated FOS can be as low as $F < 1$, without any partial factors applied. As the embankments are still standing without apparent issues, it seems that there is room for improvement both in the methods used to determine the shear strength of soil, and stability calculation methods.

The traditional stability design method in Finnish engineering practice has been to use a field vane to determine the undrained shear strength of soft soils. The stability calculations are done with the Limit Equilibrium Method (LEM) as total stress ($\varphi = 0$) analyses. In the recent years, better field vane systems and CPTU equipment have been adopted in use, which somewhat improves the situation of strength determination.

An alternative for $\varphi = 0$ analyses is of course the undrained effective stress analysis (φ'-c'). Often such analyses are employed to obtain an alternative result when total stress

analyses are considered unreliable (e.g. due to unreliable strength data) or when data on undrained shear strength is missing altogether. Here, the uncertainty lies in determining the excess pore pressure, which is quite difficult especially in the context of LEM.

While FEM analyses with advanced effective stress models are slowly gaining use in large projects, LEM is still the primary stability calculation tool. One aim of the Finnish Transport Agency has been to improve the accuracy and usability of LEM in undrained *φ'-c'* analyses.

Länsivaara (2010) has proposed the parameter r_u', which is used to model the shear-induced excess pore pressure in normally consolidated clays. With a set of assumptions (triaxial compression, no hardening, normal consolidation), the parameter r_u' is a function of critical state friction angle φ'_c. In conjunction with a separate parameter that models loading-induced excess pore pressure, undrained effective stress analyses are possible.

To further increase the usability of undrained *φ'-c'* stability analyses with LEM, a more complex calculation method Hybrid s_u was developed by Lehtonen (2015). In its current developed form, its main purpose is to predict undrained shear strength based on a derivative of an effective stress soil model.

2 HYBRID SU METHOD

2.1 General

The Hybrid s_u (HSU) method (Lehtonen 2015) can be used for two purposes:

a) Calculation of undrained shear strength (φ = 0 analyses)
b) Calculation of excess pore pressure at failure (undrained *φ'-c'* analyses)

HSU is intended to be used for soft, normally consolidated or lightly overconsolidated inorganic clays. Its main purpose is to provide calculation parameters to LEM stability analyses. HSU takes into account physical factors such as anisotropy, consolidation state and hardening properties.

The anisotropic effective stress soil model S-CLAY1 (Wheeler et al 2003) is used as a starting point. The original S-CLAY1 model is a Modified Cam Clay derivative with an anisotropic initial yield surface, coupled with volumetric and rotational hardening of the yield surface (Figure 1).

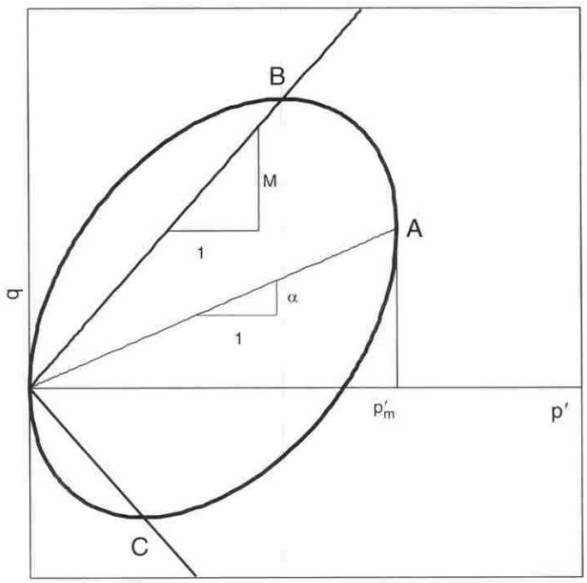


Figure 1 .S-CLAY1 initial yield surface (Wheeler et al 2003)

In HSU, a closed form solution can be derived for effective mean stress at failure p'_f with a set of suitable assumptions. The most notable assumptions are the use of the Drucker-Prager failure surface fitted for triaxial compression, and the omission for rotational hardening from the original S-CLAY1 model. The value of p'_f can then be used to derive either the undrained shear strength s_u or excess pore pressure at failure Δu_f.

The solution for p'_f needs to be omitted here for brevity. For a detailed derivation, see Lehtonen (2015). In essence, p'_f is a function of strength, stress, hardening and anisotropy parameters:

$$p'_f = f(\varphi', c', \sigma'_{v0}, OCR, \lambda/\kappa, C, D, b, \theta) \quad (1)$$

The model parameters of the HSU method are:

φ'	critical state friction angle (°)
c'	effective cohesion at critical state (kPa)
σ'_{vo}	initial vertical effective stress
OCR	overconsolidation ratio
λ/κ	hardening control parameter
C	coefficient for K_{0NC}
D	coefficient for initial K_0 (overconsolidated)
b	intermediate principal stress parameter (assumed b = 0.3)
θ	principal stress rotation angle (°)

Effective cohesion at critical state is included in HSU because some clays do exhibit apparent cohesion at large strains (e.g. Karlsrud & Hernandez-Martinez 2013). While the original S-CLAY1 is a "classical" critical state model with zero cohesion, HSU can model cohesion through a fairly simple coordinate conversion. In the conversion, the "correct" stress state p' is replaced with a calculation value p'_{calc}:

$$p'_{calc} = p' + p'_{att} \qquad (2)$$

where p'_{att} is the value of attraction in the p'-q coordinate system (Figure 2).

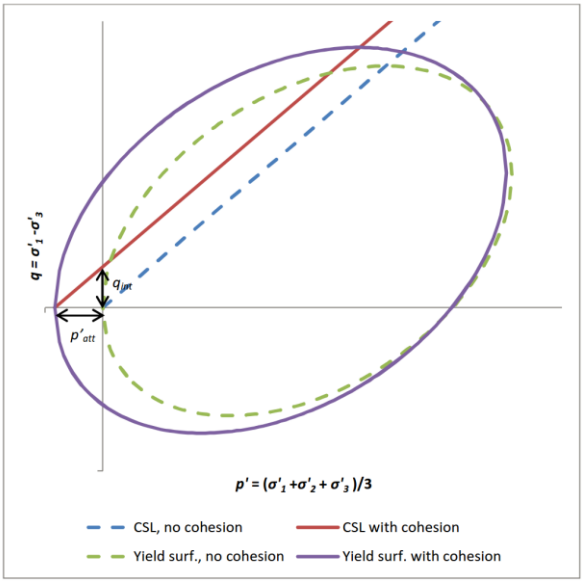


Figure 2. Concept of applying cohesion in HSU via a coordinate shift (Lehtonen 2015)

The hardening control parameter λ/κ is (by its textbook definition) the ratio between the slopes of the normal compression line and unloading-reloading line in the (ln p'-e) coordinate space. Essentially λ/κ is a parameter that controls volumetric hardening, and therefore the direction of the effective stress path (Figure 3).

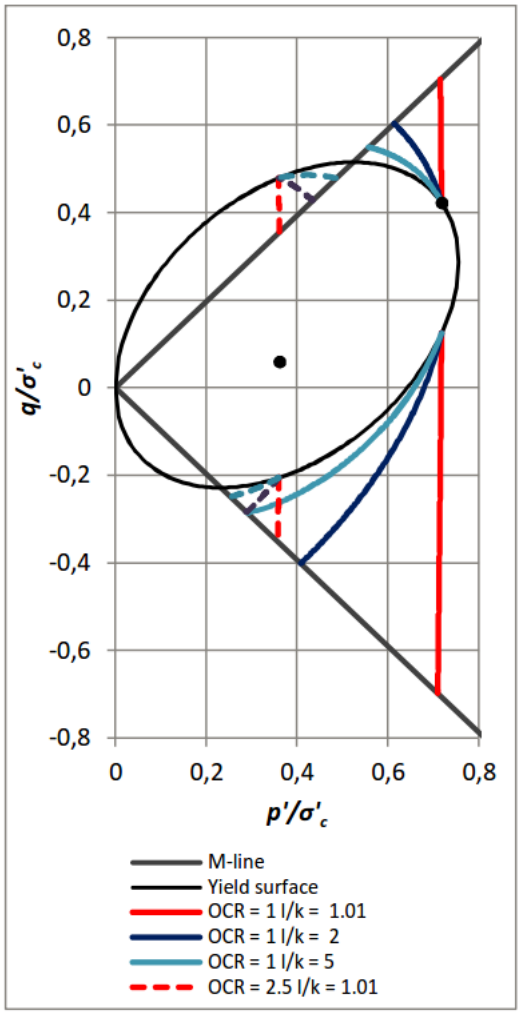


Figure 3. An example of NC and OC effective stress paths predicted by the HSU method. (Lehtonen 2015)

When λ/κ is set to 1, elastoplastic strains are equal to elastic strains, i.e. the behaviour is elastic and the stress path is vertical. When the ratio is increased, plastic strains begin to dominate and the effective stress path becomes more horizontal. This behaviour is completely analogous with any Modified Cam Clay-derivative soil model.

In the intended usage (LEM) strains are not considered, but the predicted strength is important. As such, in HSU the parameter λ/κ

can be decoupled from its physical meaning. It is simply used as a control parameter that allows the user to select a desired effective stress path that is likely for the given type of loading. Even rate dependency of strength and pore pressure response can be modelled with HSU to a certain degree: Faster loading rates result in less excess pore pressure, and consequently higher strength and more vertical effective stress paths - this can be achieved with a low λ/κ value.

Based on model fitting to laboratory data examples and failure back-calculations (Lehtonen 2015), the relevant range of λ/κ would be about $\lambda/\kappa = 2.5\ldots5.0$. As a cautious engineering default value, $\lambda/\kappa = 5$ would be applicable. For very fast loading, λ/κ close to 1 can be possible.

The parameters C and D control the assumed K_0 values as follows:

$$K_{0NC} = C(1-\sin\varphi') \quad (3)$$

$$K_0 = K_{0NC} \cdot OCR^{D\cdot\sin\varphi'} \quad (4)$$

Essentially, C controls the inclination of the initial yield surface through K_0, while D only has a slight effect on the assumed initial stress state. The value of C has a considerable effect on strength anisotropy, especially on extension strength.

The intermediate principal stress parameter b (Habib 1953) controls the relative value of σ'_2.

$$b = \frac{\sigma'_2 - \sigma'_3}{\sigma'_1 - \sigma'_3} \quad (5)$$

For simplicity, it is assumed that b = 0.3. Principal stress rotation θ can be solved for each slice bottom:

$$\theta = 45° + \varphi'/2 - \alpha \quad (6)$$

where α is the inclination angle of the slice bottom.

2.2 Use in φ = 0 analyses

For φ = 0 analyses, HSU is simply used to predict the anisotropic undrained shear strength along the slip surface. The strength is defined (using the Cambridge notation) simply as:

$$s_u = \frac{q_f}{2} = \frac{p'_f \cdot M}{2} \quad (7)$$

As p'_f and s_u are functions of principal stress rotation, the s_u needs to be calculated separately for each slice bottom along each different slip surface. The limit equilibrium analysis for a given slip surface is then conducted as usual, with only the strength input calculated with the HSU method.

2.3 Use in undrained φ'-c' analyses

Lehtonen (2015) presents two different approaches for calculating Δu_f with the HSU method.

The main idea is that in stability calculations, the most important soil variable is the shear strength τ_f that can be attained at failure. In traditional undrained effective stress analyses the calculated shear strength does not correspond to failure, but to the mobilised state. This causes an inherent overestimation of τ_f and F, when $F > 1$, as the pore pressure increase between the mobilised state and failure is disregarded (Figure 4).

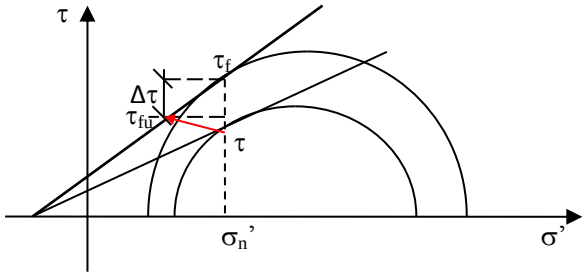


Figure 4. Overestimation of shear strength Δτ in traditional undrained effective stress analyses. τ_f is the assumed shear strength, while τ_{fu} is the actual strength at failure in undrained conditions.

In HSU, priority is given to attaining a "correct" shear strength that corresponds to the failure state. This means that the calculated excess pore pressure does not correspond to the mobilised state, but to failure. The overestimation of shear strength when $F >> 1$ is therefore eliminated.

In the first approach, the excess pore pressure is "forced" so that the resulting shear strength τ_f is equal to the undrained shear strength s_u predicted by HSU:

$$s_u = \tau_f = c' + \sigma'_n \cdot \tan\varphi' = c' + (\sigma_n - u_0 - \Delta u_f) \cdot \tan\varphi' \quad (8)$$

$$\Delta u_f = \sigma_n - u_0 - \frac{s_u - c'}{\tan\varphi_c'} \quad (9)$$

Equation 9 contains the total normal stress acting on the slice bottom. To obtain this, an iteration is necessary. First an assumption of Δu_f is made, the limit equilibrium is calculated and a value for σ_n is obtained from the results. Then Δu_f is calculated again, and the process is repeated until Δu_f converges.

As it is "decided" that $s_u = \tau_f$, the calculated factor of safety of the undrained effective stress analysis is completely identical to the corresponding total stress analysis.

A second, more "traditional" approach with HSU is to calculate Δu_f based on stress changes. From the principle of effective stresses it can be written that:

$$\Delta p' = \Delta p - \Delta u \quad (10)$$

$$\Delta u_f = \Delta p_f - \Delta p_f' \quad (11)$$

The change of effective mean stress $\Delta p'$ can be calculated with the HSU model (the initial stress state is known, and the failure state is calculated). The change in total stresses can be calculated with basic continuum mechanics, based on changes in vertical stresses and an assumption of the pore pressure at failure. Again, a first assumption of Δu_f is made, Δp_f is calculated, a new value for Δu_f is calculated and the iteration is continued until the calculation converges.

Even when Δu_f is calculated based on stress changes, these stress changes correspond to the assumed failure state. Therefore, the pore pressure and the resulting shear strength should also correspond to the actual failure.

3 SAINT-ALBAN TEST FILL A

3.1 Site description

In 1972, a test embankment in Saint-Alban, Quebec, Canada was brought to failure in a testing program by Laval University. The embankment was built on a sensitive Champlain Sea clay deposit. Its height was gradually increased until it failed at a height of 3.9 m. (La Rochelle et al 1974)

The subsoil consisted of a 1.5-2 m thick stiff crust, followed by a slightly overconsolidated clay layer. Figure 5 presents the range of field vane tests and some CIU tests (after Trak et al 1980), as well as model predictions made with the MIT-E3 effective stress soil model.

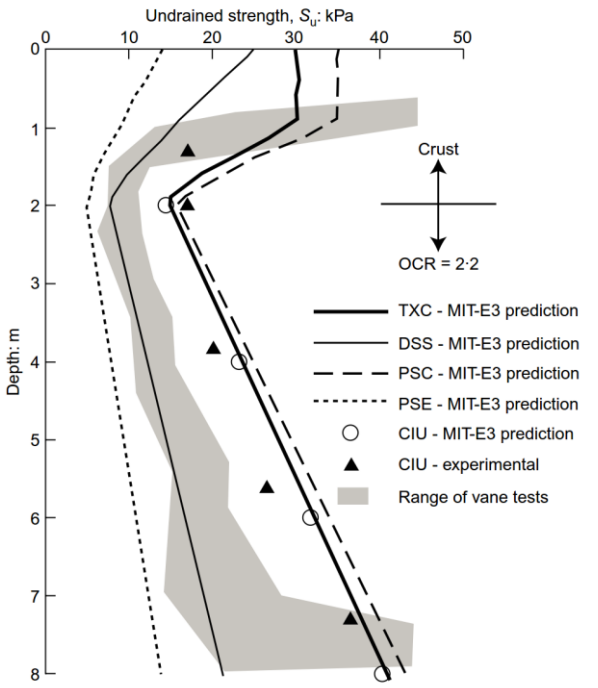


Figure 5. Measured strengths and predicted strength profiles (Zdravkovic et al 2002)

The friction angle in triaxial compression is given as φ' = 27°, and the lateral earth

pressure in triaxial compression is K_{0NC} = 0.49 (Zdravkovic et al 2002).

3.2 HSU parameters and calculation results

To study the validity of the HSU method a back-calculation of the Saint-Alban Test Fill A is conducted. HSU is applied to the soft clay layer below the depth of 2.0 m.

The parameter selection for HSU is fairly straightforward. The given friction angle φ' = 27° is utilized as it is. As the K_{0NC} value is given, the parameter C can be calculated as:

$$C = \frac{K_{0NC}}{1-\sin\varphi'} = \frac{0.49}{1-\sin 27°} \approx 0.90 \qquad (12)$$

The parameter D is left at its default value D = 1, as there is no data available about the in situ lateral stresses. The OCR value for the clay is set to OCR = 2.2 (Zdravkovic et al 2002). Unit weight of γ'_{sat} = 16 kN/m3 is used for the clay (Trak et al 1980).

The embankment and crust properties are given in Table 1. The dry crust is modelled with given s_u values, but different strength profiles are used for the active and passive parts. The values are consistent with data used by Zdravkovic et al (2002).

Table 1. Soil parameters for the embankment and dry crust

	φ' [°]	s_u (kPa)	ds_u (kPa/m)	γ (kN/m^3)
Embankment	44	0	0	19
Crust (z =0-1 m, active side)	0	30	0	19
Crust (z = 1-2 m, active side)	0	30 (top of layer)	-20	19
Crust (z =0-2 m, passive side)	0	13 (top of layer)	-4	19

The only unknown HSU model parameter is λ/κ. Its ”proper” value can be determined by a back-calculation setup where λ/κ is varied.

Figure 6 illustrates the initial yield surface obtained with the given HSU parameters as well as effective stress paths in compression and extension for different λ/κ values. Note that compression and extension stress states are not considered in the stability calculation itself, but the intermediate principal stress parameter is set as b = 0.3, as assumed in the derivation of the HSU method (see Section 2.1).

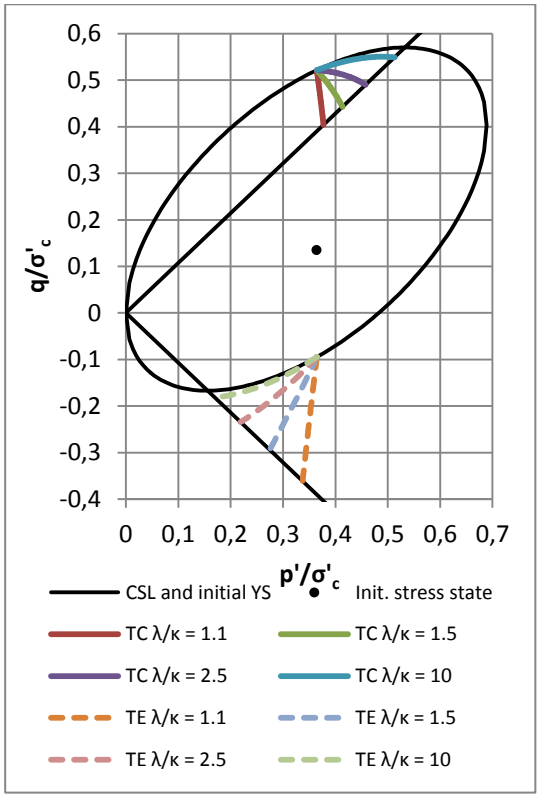


Figure 6. HSU compression and extension stress paths with different λ/κ values. Other parameters are defined in the text.

A circular slip surface with 20 slices, consistent with the observed mechanism (La Rochelle et al 1974), is created (Figure 7). The stress state and other relevant parameters are determined for each slice bottom. It is assumed that the initial state includes only the crust and clay layer. In the failure state the embankment with a height of h = 3.9 m (the stated failure height) is applied.

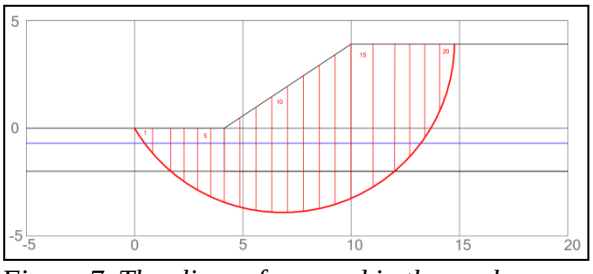


Figure 7. The slip surface used in the analyses

The limit equilibrium calculation was carried out in a spreadsheet using Spencer’s method (Spencer 1967). Practically any other limit equilibrium method could have been used as well, but Spencer’s method can be considered

a good compromise between accuracy and simplicity in spreadsheet applications.

By varying the λ/κ value, the factor of safety can be calculated as a function of λ/κ, with φ = 0 limit equilibrium analyses. The calculated factors of safety versus λ/κ is illustrated in Figure 8.

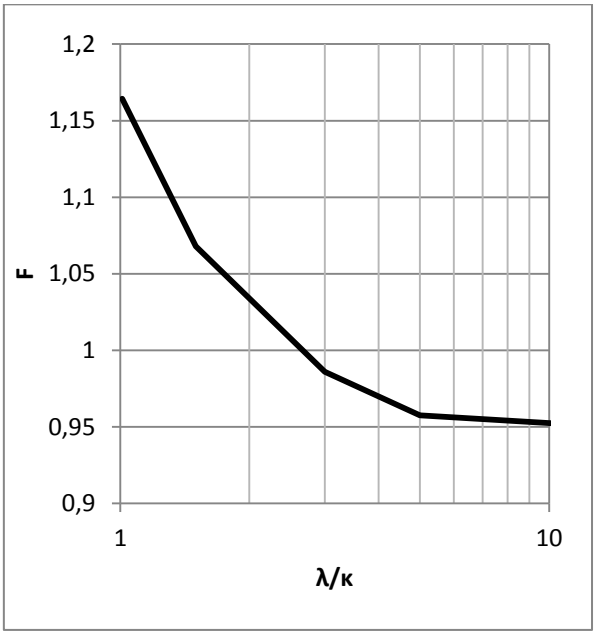


Figure 8. Calculated F versus λ/κ, total stress analyses

From the total stress calculations where HSU is used to calculate s_u in the clay layer, it becomes apparent that F = 1 when λ/κ = 2.53. The resulting strength profile along the slip surface is shown in Figure 9a. For comparison, the strength profile predicted by Zdravkovic et al (2002) with the MIT-E3 soil model is shown in Figure 9b. Note that as the failure surfaces are not exactly the same, the coordinates along the failure surface length differ slightly. Additionally, the HSU strength profile as shown in Figure 9a shows the average strengths calculated for each slice bottom, and includes the embankment in the far right of the graph.

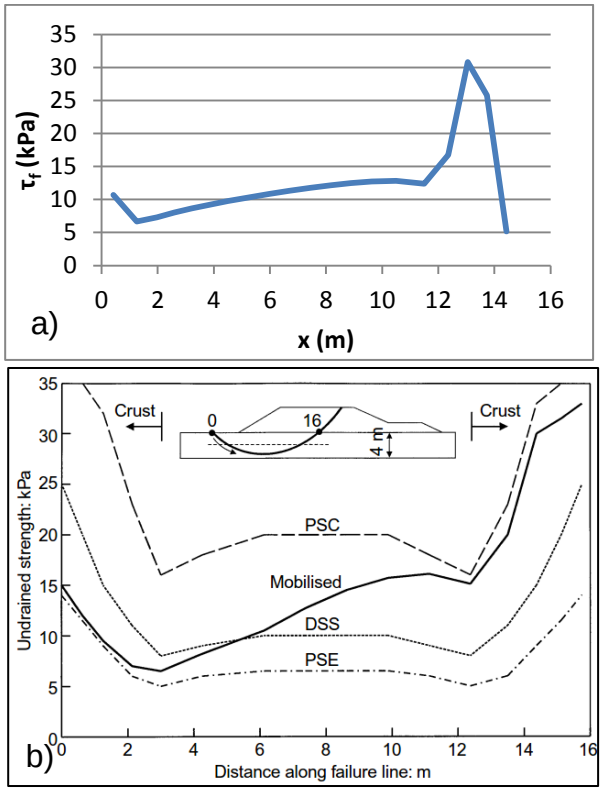


Figure 9. a) Shear strength profile along the slip surface at λ/κ = 2.53, HSU total stress analysis. b) Mobilised shear stress and predicted strength envelope, MIT-E3 (Zdravkovic et al 2002).

The predicted HSU strength profiles (λ/κ = 2.53) against depth are shown in Figure 10. These can be compared to the predicted strength profiles from Zdravkovic et al (2002), see Figure 5.

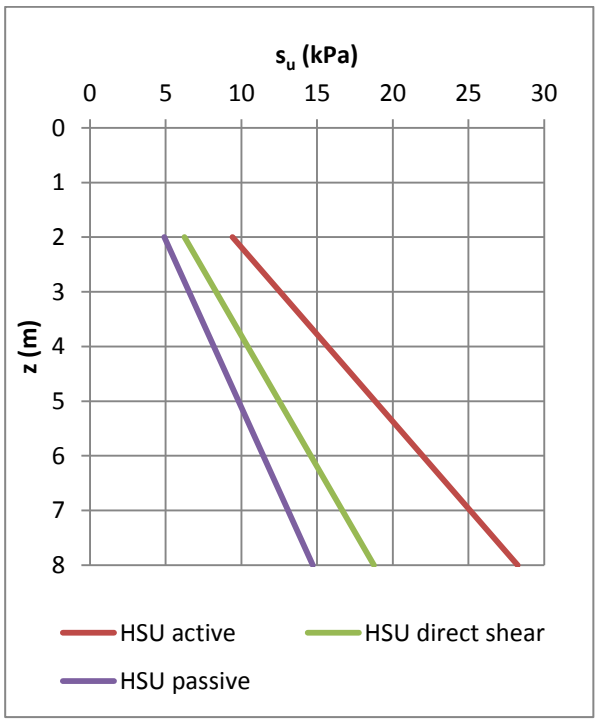


Figure 10. HSU strength profiles at λ/κ = 2.53.

The stability calculation was also conducted as an undrained *φ'-c'* analysis where the HSU method was used to predict the excess pore pressure at failure Δu_f. Figure 11 shows the excess pore pressure distribution at failure (λ/κ = 2.53) for the two different approaches (forcing to a given s_u value, and Δu_f calculation based on stress changes).

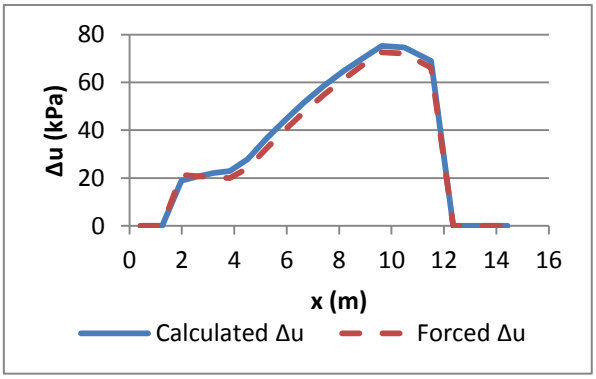


Figure 11. Calculated Δu at failure, HSU undrained effective stress analyses

As the shear strength distribution along the slip surface is exactly the same between the φ = 0 -analysis and the undrained *φ'-c'* analysis with the forced approach, the calculated factor of safety is exactly F = 1 in both cases. The Δu_f distribution based on the calculated stress changes is only slightly larger, and therefore results in a slightly lower shear strength and a factor of safety of F = 0.93.

4 DISCUSSION & CONCLUSIONS

This paper briefly presents the newly developed calculation method "Hybrid s_u" (HSU). The HSU method (Lehtonen 2015) is intended for calculating undrained shear strength or excess pore pressure at failure of clay in LEM stability calculations.

By a process of back-calculation, the HSU method parameters were fitted to the case of the Saint-Alban A test embankment failure (La Rochelle et al 1974). The model fitting is quite straightforward, as the parameters can be chosen directly based on the available basic soil data. The value of the control parameter λ/κ is obtained via back-calculation.

The results of the back-calculation are generally quite plausible. Failure is obtained with λ/κ = 2.53. This represents a typical value in back-calculations and model fits (see Lehtonen 2015), and as such the result is quite plausible. While such a ratio is typical for failure test conditions, natural slope failures might proceed at a much slower rate, which then requires a higher λ/κ ratio to be able to simulate the higher failure induced pore pressure/lower undrained shear strength.

A FEM analysis using the MIT-E3 effective stress soil model (Zdravkovic et al 2002) is used as a benchmark to compare the results.

The mobilized shear strength profile at failure, as predicted by HSU, compares quite favourably to the one predicted by the more advanced soil model. However, when predicted strength profiles against depth are compared, the HSU model underestimates the active (compression) shear strength. This happens because "strength" in the HSU framework is defined as the stress point where the effective stress path reaches the critical state line.

When shearing occurs on the dry side of critical (as it does for active shearing at OCR = 2.2), the model exhibits volumetric softening of the yield surface. This behaviour occurs with all Modified Cam Clay derivatives, such as the S-CLAY1 model from which HSU is developed.

The HSU method is generally intended for use with normally consolidated or lightly overconsolidated clays (e.g. up to OCR ≈ 2). In this case the underestimation of dry side active strength did not affect the end result very much. This is due to the particular slip surface geometry, where only a small portion of the slip surface corresponds to active shearing in the clay layer.

While it is obvious that for OC clays, the HSU method may underestimate active strength compared to measured peak strengths, in design this may actually be beneficial. HSU is not intended for modelling soil, but as a stability calculation tool. As HSU does not include strain softening, it could be dangerous to use it for predicting peak strengths. This is obviously due to the fact that the soil does not achieve peak strengths simultaneously along the slip surface. Instead, the definition of strength in

HSU is a post-peak, or critical state strength for shearing on the dry side of critical.

The method can still be fitted to produce peak strengths, but this requires conscious fitting to peak strength data. In this example, the model fit (namely, the choice of the λ/κ value) was achieved through back-calculation of a failure, which results in an average mobilized shear stress profile at failure.

It may be worthwhile to include the option of changing the definition of strength in subsequent iterations of the HSU. Instead of defining strength as a point on the critical state line, the overconsolidated (dry side of critical) strength could be defined as the peak strength that is obtained when the effective stress path reaches the initial yield surface (Figure 12). This would simplify model fitting to peak strengths to some extent. The choice between the two definitions would then depend on the engineering judgment of the user.

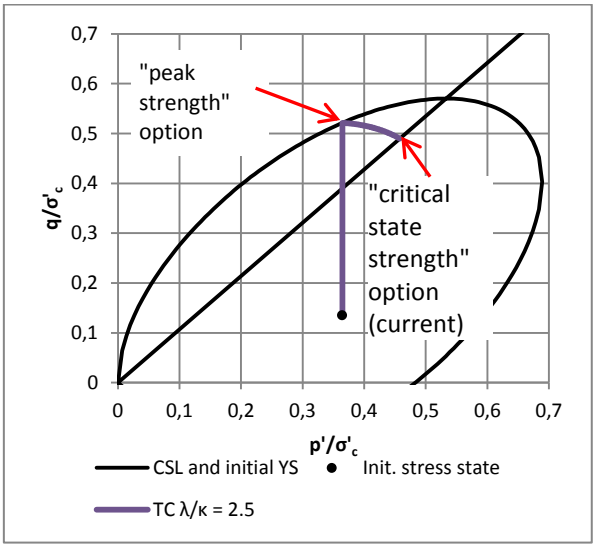


Figure 12. Possible option for the choice of dry side shear strength definition in HSU

The use of the HSU method to calculate Δu_f in undrained effective stress calculations is presented only as a proof of concept. As the goal in the formulation is to obtain results that are similar to corresponding total stress HSU calculations, the use of undrained φ'-c' can be considered redundant. Additionally, the calculations involved in obtaining Δu_f are unnecessarily complicated when compared to the calculation of s_u with the HSU method.

Overall, the HSU method shows promise as a simple yet reasonably accurate design tool in LEM stability calculations. The new method is currently being implemented to a geotechnical design software commonly used in Finland.

5 REFERENCES

Habib, M. P. (1953). Influence of the variation of the intermediate principal stress on the shearing strength of soils. In: Proc. of 3rd Int. Conf. Sial. Mech. Foundation Eng., Vol. 1, pp. 131-136.

Karlsrud, K. & Hernandez-Martinez, F.G. (2013). Strength and deformation properties of Norwegian clays from laboratory tests on high-quality block samples. Canadian Geotechnical Journal, vol. 50, no. 12, pp. 1273-1293

La Rochelle, P., Trak, B., Tavenas, F. & Roy, M. (1974). Failure of a Test Embankment On a Sensitive Champlain Clay Deposit. Canadian Geotechnical Journal, vol 11, no. 1, pp. 142-164

Lehtonen, V. (2015). Modelling undrained shear strength and pore pressure based on an effective stress soil model in Limit Equilibrium Method. Doctoral Thesis, TUT Publication 1337. Tampere University of Technology.

Länsivaara, T. (2010). Failure induced pore pressure by simple procedure in LEM. In: Benz, T. et al.(eds.). Numerical Methods in Geotechnical Engineering. Proceedings of the Seventh European Conference on Numerical Methods in Geotechnical Engineering Numge 2010, Trondheim, Norway, 2-4 June, 2010.

Spencer, E. (1967). A method of analysis of the stability of embankments assuming parallel inter-slice forces. Geotechnique, vol. 17, no. 1, pp. 11-26.

Trak, B., La Rochelle, P., Tavenas, F. & Roy, M. (1980). A new approach to the stability analysis of embankments on sensitive clays. Canadian Geotechnical Journal, vol. 17, no. 4, pp. 526-544.

Wheeler, S.J, Näätänen, A., Karstunen, M. & Lojander, M. (2003). An anisotropic elastoplastic model for soft clays. Canadian Geotechnical Journal, vol. 40, no. 2, pp. 403-418.

Zdravkovic, L., Potts, D. & Hight, D.W. (2002). The effect of strength anisotropy on the behaviour of embankments on soft ground. Geotechnique, vol. 52, no. 6, pp. 447-457

Vacuum preloading for a truck parking area in Luhtaanmäki

M. S. Löfman
Aalto University, Finland, monica.lofman@aalto.fi

L. K. Korkiala-Tanttu
Aalto University, Finland

ABSTRACT
City of Vantaa considers constructing a truck parking area and a filling station on a soft clay deposit in Luhtaanmäki, Vantaa (in Finland). The aim of this study was to evaluate whether vacuum preloading with vertical drains is a feasible ground improvement method for the site. Besides in situ –tests and classification tests, overall 18 oedometer tests were carried out. Preliminary design of vertical drainage was based on Hansbo's solution, and smear effect was taken into account. Time-settlement -calculations were carried out using tangent modulus method and so called equivalent vertical permeability. In calculations, the following loading history is assumed: First, a surcharge fill of 30 kPa is constructed. After that, vacuum of 70 kPa is applied for 8 months. In order to compensate for the settlement caused by vacuum preloading, embankment load of 10 kPa is later applied. Total settlement is 825 mm, and that considered the final embankment height is 1.2 m. After the treatment, the minimum degree of overconsolidation is 220%. According to the results, vacuum preloading suits well for Luhtaanmäki.

Keywords: ground improvement, vacuum consolidation, prefabricated vertical drains, clay, surcharge fill

1 INTRODUCTION

In this paper, soft soil improvement via vertical drains with vacuum preloading is studied. The soft clay deposit in question is located in Vantaa, Finland. City of Vantaa considers constructing a truck parking area and a filling station on this site. Design of vertical drainage and settlement predictions are carried out in order to evaluate whether vacuum preloading is a feasible soil improvement method for the truck parking area. The goal is to acquire a degree of over-consolidation over 120 % after 7-8 months of vacuum preloading. The desirable final embankment height is 1.2 meters.

Vacuum preloading was first proposed by Kjellman (1948) for cardboard wick drains. In this ground improvement method, the site is covered with an air-tight membrane, and suction is created underneath via prefabricated vertical drains (PVDs) by using a vacuum pump. In general, the benefits of vacuum preloading are: (i) faster consolidation (also compared to conventional PVD improvement), (ii) low shear strength of soil will not prevent heavy preloading, (iii) less fill material is needed, (iv) there is no need for heavy machinery, (v) and as heavy preloading is possible, settlements due to creep after construction can be reduced (Brandt et al., 2015; Chaumeny, 2011; Ganesh Kumar et al., 2015; Indraratna et al., 2010; Saowapakpiboon et al., 2010; Voottipruex et al., 2014).

Despite its benefits, vacuum preloading is relatively unknown method in Finland. It was first used in winter 1974–1975 at a soft clay deposit test site Itäkeskus, Helsinki. However, sufficient suction pressure was not reached, and the soil was later improved using traditional preloading (Puumalainen, 1996). Leminen and Rathmayer (1979) presented that the reason for insufficient suction was water flowing out of silt layers or from coarser soil under the soft soil deposit. In vacuum preloading, pumped water should be pore water from clay layers, not freely seeping water. Similarly, Ganesh Kumar et al. (2015) observed that in a vacuum

preloading site in India, the water pumped out was partly from surrounding areas (the sea shore) through thin sand seams. According to Indraratna et al. (2010), cut-off wall is useful at sites that need to be sealed.

In order to avoid these kind of leakage problems, PVDs should not pass sand or silt layers at all. In addition, the distance between PVDs and coarser layers below clay deposit should be at least 1 m. However, the accurate depth and location of coarser soil layers is rarely known. The risk of leakage-related insufficient suction can be decreased by using a membraneless system (Indraratna et al., 2010): The vacuum channel is connected directly to each individual PVD by tubes. As each PVD acts independently, single leak will not affect the whole drainage system. However, according to Seah (2006), the extensive tubing in membraneless system can prolong installation time and add costs.

Despite the fact that the vacuum preloading did not work as expected in Itäkeskus, in another test site in Torpparinmäki, Helsinki it was successful. According to Puumalainen (1996), vacuum preloading is time saving, efficient and economically viable ground improvement method also in Helsinki region.

2 GEOTECHNICAL CONDITIONS OF THE SITE

At the site in Luhtaanmäki, the soft clay deposit has a varying thickness of 5 to 13 meters. In this paper, only one point (point 36) is studied. This point is approximately in the middle of the planned truck parking area. At studied point the clay deposit reaches a depth of 8 meters. Dry crust is 1.5 m thick. Under the clay deposit there is a 4-5 m thick layer of sandy silt, and the deepest soil layer is moraine. The groundwater is pressurized and above the confined aquifer there is perched water table at 1.5 m. Due to pressurized groundwater, conventional PVD improve-ment (without vacuum preloading) would not be efficient.

Both laboratory tests and *in situ* tests were carried out near the studied point. Two kinds of sampling tubes were used: city of Vantaa used tube called ST2 (diameter of 50 mm) and Aalto University used bigger tube TKK-86 (diameter of 86 mm).

Besides several classification tests, overall 18 incremental loading (IL) oedometer tests were carried out. Five of these tests were horizontal IL oedometer tests and one was radial consolidation test. Only samples from TKK-86 tubes were used. As vertical drains reach the clay deposit only, test results below 8 m are not included in the graphs.

Soil layers used in calculations, unit weight γ, water content w and liquid limit w_L are represented in Figure 1. At the studied point, the amount of clay content is mostly 50-80 %. The amount of organic content is less than 2 %.

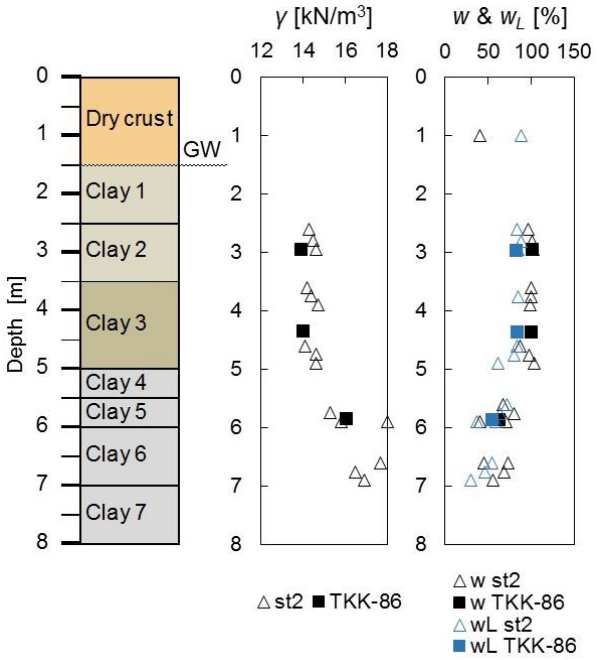


Figure 1 Soil layers, unit weight (γ), water content (w) and liquid limit (wL) from different samplers.

Undrained shear strength c_u was estimated using the results of field vane shear test, CPTU sounding test and fall cone test. Remoulded (=disturbed) undrained shear strength c_{ur} was determined using fall cone test. Soil profile with undrained shear strength determined using different tests can be seen in Figure 2 (right).

Undrained shear strength c_u can be estimated from CPTU results using Equation 1 (Lunne et al., 1997):

$$c_u = \frac{q_c - \sigma_{vo}}{N_k} \quad (1)$$

Where q_c (kPa) is measured cone resistance, σ_{v0} (kPa) is total vertical overburden pressure and N_k is cone factor.

Cone factor N_k is an empirical value, and according to Lunne and Kleven (1981) it usually varies between 10 and 15 for clays when field vane is used as reference test. In present study, fall cone test results were used as reference values, resulting in N_k = 12. This estimated c_u profile is marked as "CPTU" in Figure 2 (right).

Interestingly, fall cone tests carried out on samples from TKK-86 sampling tubes yielded higher values of c_u compared to the ST2 values (Fig. 2). This variation might be due to difference in either sample quality or in test procedure. The determined values of sensitivity were 10-23 for ST2 and 23-37 for TKK-86. Due to scarce amount of TKK-86 results, reference values for CPTU-based estimation were selected from the highest ST2 results instead.

The preconsolidation pressure σ'_p profile was estimated not only using results of oedometer tests but also c_u profile that was estimated using CPTU results. It has been empirically proven, that there is a relation between σ'_p and c_u (Leroueil et al., 1990). Relation between c_u / σ'_p and plasticity index I_p was first proposed by Bjerrum (1972). The ratio c_u / σ'_p has been found to vary between 0.2 and 0.35 (Leroueil et al., 1990). In present study, value of 0.25 was used. The estimated preconsolidation pressure σ'_p profile ("CPTU") is represented in Figure 2 (left). In addition, σ'_p values determined from oedometer test results, selected σ'_p and estimated effective overburden pressure σ'_{v0} profile are represented.

Only the clay layers near the surface are highly overconsolidated; Beneath 3.5 meters overconsolidation ratio (OCR) is between 1.2 and 1.8.

The selected values used in calculations for different soil layers (Fig. 1) are listed in Table 1. Preconsolidation pressure σ'_p profile was defined by giving values at top and bottom borders of each layer. The values of c_u were selected based on ST2 results of fall cone test. For dry crust, c_u of the clay layer underneath was selected.

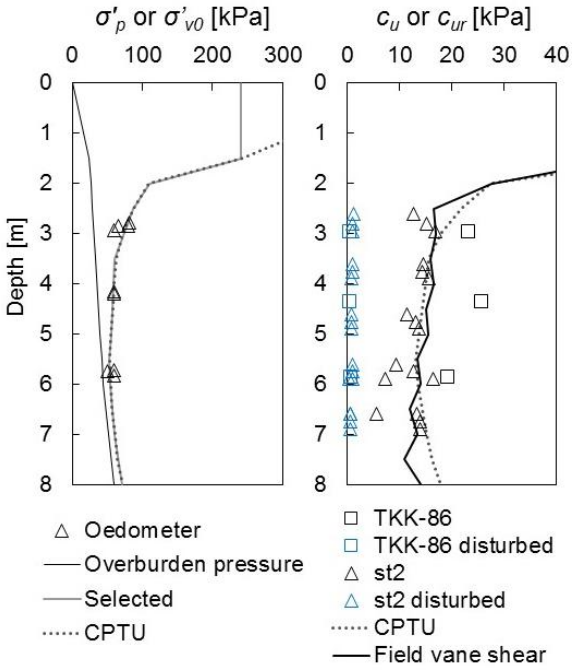


Figure 2 Left: Preconsolidation pressure (σ'_p) and effective overburden pressure (σ'_{v0}) versus depth. Right: Undrained shear strength (c_u) and remoulded undrained shear strength (c_{ur}) versus depth.

Table 1 Values used in calculations.

Layer	γ [kN/m^3]	σ_p' top [kPa]	σ_p' bottom [kPa]	c_u [kPa]
Dry Crust	16	240	240	17
Clay 1	15	240	87	17
Clay 2	14.3	87	60	17
Clay 3	14.3	60	55	15,5
Clay 4	14.5	55	53	14
Clay 5	15.5	53	54	16
Clay 6	17	54	61	14
Clay 7	17.3	61	72	15

3 DESIGN OF VERTICAL DRAINAGE

3.1 Vertical drain theory

In order to evaluate the drain spacing that is needed in order to acquire a certain degree of consolidation at given time, vertical drain theory presented by Hansbo (1981) is often adopted.

According to Technique Systems/Cofra (1995) and Ye at al. (1991), settlement caused by vacuum preloading can be calculated using a vertical load as a substitute for vacuum pressure. Thus, at least in preliminary design, vacuum preloading can

be modelled using methods of conventional PVD improvement.

Hansbo's solution is based on Barron's (1948) "equal strain" solution to the problem of radial (horizontal) consolidation. Hansbo (1981) included smear effect and well resistance into Barron's solution. When vertical drains are installed, the soil near the drain disturbs. This smear effect decreases the horizontal permeability near the drains and thus slows down the consolidation. If PVDs are over 20 meters long, drain resistance must be taken into account (Vepsäläinen and Arkima, 1994). At the studied point the length of PVDs is only 7 m, and thus only smear effect is taken into consideration.

According to Hansbo's solution, the average degree of consolidation for a site with PVDs is (Equations 2–4):

$$U_h = 1 - e^{\frac{-8T_h}{\mu}} \quad (2)$$

$$\mu = \ln\left(\frac{n}{s}\right) + \left(\frac{k_h}{k_s}\right) \cdot \ln(s) - \frac{3}{4} + \pi \frac{2l^2 k_h}{3q_w} \quad (3)$$

$$T_h = \frac{c_h t}{d_e^2} \quad (4)$$

Where U_h is average degree of radial consolidation, T_h is time factor for radial consolidation, c_h is horizontal coefficient of consolidation, t is time, q_w is discharge capacity of PVD, l is drainage length, k_h is average horizontal permeability of the undisturbed zone, $n = d_e/d_w$ where d_e is equivalent diameter of the cylinder of soil around the drain and d_w is equivalent diameter of PVD, $s = d_s/d_w$ where d_s is diameter of the smear zone and k_s is average horizontal permeability in the smear zone.

PVDs are band-shaped, and thus an equivalent circular cross section is needed in order to apply Barron's theory. Originally proposed by Kjellman (1948) and later verified by finite element analysis (Hansbo, 1979), equivalent diameter of PVD can be calculated using Equation 5:

$$d_w = \frac{2(w_{PVD} + t_{PVD})}{\pi} \quad (5)$$

Where w_{PVD} is width of the PVD and t_{PVD} is thickness of the PVD.

Equivalent diameter d_e depends on PVD spacing and pattern. In this paper, triangle pattern is selected, leading to equivalent diameter of $d_e = 1.05a$, where a is drain spacing (Vepsäläinen and Arkima, 1994).

3.2 The determination of horizontal coefficient of consolidation

In Finland, one of the most used method to determine horizontal coefficient of consolidation (and horizontal permeability) is horizontal oedometer test. In this test, the sample is turned 90 degrees, and horizontal parameters are determined as in conventional oedometer test (Puumalainen, 1998; Hassan, 2006). Thus it is assumed, that horizontal water flow is independent of the direction of stress and compression (Leminen and Rathmayer, 1983).

In present study, vertical and horizontal coefficients of consolidation (c_v and c_h) were determined from time–settlement data of oedometer test using both Taylor's and Casagrande's method (Taylor, 1948; Casagrande, 1936). Values determined using Taylor's method at different load increments are represented in Figure 3. In the figure V stands for vertical and H for horizontal.

However, more realistic simulation of drainage and stress conditions of PVD improved subsoil can be obtained using a radial consolidation test. One radial consolidation test was carried out. In the test, a vertical drain made of geotextile with a diameter of 10 mm (=d_w) was installed in the sample. The diameter of the sample was 81 mm (=d_e). Because of the added insulation, only radial drainage occurs during the loading.

The radial coefficient of consolidation c_r is generally determined using methods that are based on Barron's "equal strain" solution. The values of c_r were determined using a method proposed by Sridharan et al. (1996), and these values are represented in Figure 3. For verification, so called inflection point method proposed by Robinson (1997) was adopted as well.

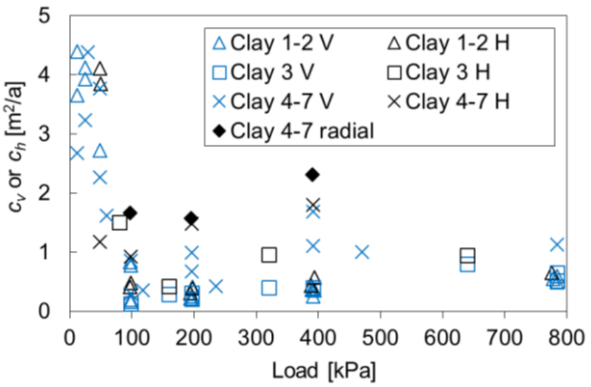


Figure 3 Vertical and horizontal coefficients of consolidation (c_v and c_h) at different load increments and layers.

Radial consolidation test yielded higher values of c_r compared to other values of c_h. In addition, there is no significant difference between c_v and c_h determined from oedometer test results. Puumalainen and Havukainen (1996) observed the same outcome and ended up using estimated value of c_h (= $2c_v$). The assumption made by Leminen and Rathmayer (1983) about insignificance of direction of compression and stress might be incorrect: fine horizontal layers that cause the anisotropic permeability might get distorted due to in-plane compression.

3.3 Smear effect

The intensity of smear effect depends on the diameter of the disturbed zone and the amount of decrease in horizontal permeability in the zone. Due to its impact on the efficiency of the vertical drainage, the smear effect has been studied extensively in both laboratory and on site.

The diameter of the smear zone d_s is often estimated to be $d_s = 2d_m \approx 2d_w$, where d_m is equivalent diameter of the mandrel (Bergado et al., 1991; Hansbo, 1987b; Saowapakpiboon et al., 2010; Voottipruex et al., 2014; Tielaitos, 1994). Indraratna and Redana (1998) investigated the smear diameter in laboratory and observed the ratio d_s/d_w being as high as 4-5. Based on previous studies, Basu et al. (2006) proposed using a ratio of d_s/d_w between 2 and 4.

Similarly, estimates for ratio k_h/k_s vary greatly. Basu et al. (2006) suggest a ratio from 2 to 10. Saowapakpiboon et al. (2010) observed a ratio of 6-7 based on field data back-calculation, and Voottipruex et al. (2014) a ratio from 7 to 10. Based on laboratory tests (large-scale oedometer test), the ratio has been observed to be smaller, only 1-5 (Hansbo, 1987a). According to Bergado et al. (1991), when horizontal coefficient of consolidation is small (less than 2 m^2/a), the ratio stays under 2. Vepsäläinen and Arkima (1994) suggest a ratio of $k_h/k_s = 2$ for preliminary design.

3.4 Design and analysis

The spacing of PVDs was selected based on Hansbo's solution. In design, vacuum of 70 kPa is assumed. Besides vacuum, surcharge fill of 30 kPa is applied. Thus the combined load is 100 kPa, and as such, a representative value of c_h is 1.4 m^2/a. Vacuum is applied for t = 7–8 months. Desirable minimum degree of consolidation at the end of the vacuum consolidation is U_h = 85 %. Needed value of d_e is calculated using Equations 2 and 4.

In design, 100 mm x 6 mm PVD is selected from a type-examined group (Vepsäläinen and Arkima, 1994). Equivalent diameter d_w is calculated using Equation 5, resulting in d_w = 67.48 mm.

In terms of smear effect, three extreme cases were studied. For Case 1, smear effect was considered to be moderate and for Case 2, more realistic values were used (based on laboratory tests and back-calculation conducted by other researches, as discussed in previous section. As for Case 3, worst possible smear conditions were assumed. For Cases 2 and 3, PVD spacing a was adjusted in order to meet desirable values of U and t.

The used parameters in Hansbo's solution (Equations 2–4) and required spacing a in each case are listed in Table 2. For Luhtaanmäki, drain spacing of a = 1 m was chosen.

Table 2 Design of vertical drainage: three cases.

Case	**1**	**2**	**3**
***a* [m]**	1.10	0.75	0.50
***d*$_e$ (triangle) [m]**	1.155	0.788	0.525
n	17.12	11.67	7.780
s	2	3	4
***k*$_h$/*k*$_s$**	2	5	10
μ	2.783	6.101	13.78
***T*$_h$**	0.660	1.447	3.267
***t* [months]**	7.55	7.69	7.72
***t* [a]**	0.63	0.64	0.64

4 SETTLEMENT PREDICTIONS

4.1 Stability analysis

In the case of natural subsoil, a preliminary short term stability analysis (friction angle φ = 0, undrained strength analysis) was carried out. Used parameters (c_u) for clay layers are listed in Table 1. For surcharge fill, suggested values for gravel are used; φ = 36 ° and γ = 20 kN/m^3 (Tielaitos, 1999).

In the safety analysis, the height of the embankment is 1.5 m. This surcharge fill leads to a load of 30 kPa as discussed in previous section. On the embankment, an equally distributed load of 10 kPa is applied.

Safety factor was obtained using method of slices. Several solution methods were applied in order to find the lowest safety factor. Morgenstern-Price method yielded the lowest safety factor F = 1.91. Thus there is no stability issues when the embankment is constructed before the vacuum.

4.2 Settlement without ground improvement

For comparison, total settlement of natural subsoil was estimated using tangent modulus method. The method is based on concepts represented by Ohde (1939) and Janbu (1963).

In present study, the modulus numbers and stress exponents were determined from vertical oedometer test results by curve fitting. In order to avoid possible errors caused by negative stress exponent, a correction method proposed by Länsivaara (2003) was used: stress exponents and modulus numbers were tied to a given preconsolidation pressure σ'_p. This given σ'_p is a product of curve fitting that was used in determination of other parameters of tangent modulus method. The selected sets of parameters are listed in Table 3. The sets are from a single test, and representative sets are selected for each layer. Again, for dry crust, rough estimates are used.

Table 3 Parameters for tangent modulus method.

Layer	σ_p' [kPa]	m_1	β_1	m_2	β_2
Dry Crust	240	100	1	100	1
Clay 1-2	84,4	3,04	-0,89	53,3	0,41
Clay 3	60,3	4,21	-0,72	63,2	0,40
Clay 4-7	46,4	7,24	-0,27	54,6	0,45

As the truck parking area is large and the clay deposit is relatively thin, the embankment can be modelled as an equally distributed extensive load. Therefore, full additive pressure is applied in the deepest layers as well.

Total settlement caused by 2 m high embankment (40 kPa) is 388 mm. Parameters used in the settlement calculation are listed in Tables 1 and 3. The rate of settlement was estimated using the vertical coefficients of consolidation. As expected, without PVDs the time required to reach U = 85 % was significantly longer compared to PVD improved case: With an embankment height of 2 meters, the time required is around 8 years (if U is calculated using total settlements. Using pore pressures, however, the time required is around 4 years).

4.3 Rate of settlement with vacuum preloading

The effect of PVDs and the vacuum to the rate of settlement is taken into account by using an approximate method proposed by Chai et al. (2001). In this method, PVD-improved soil is modelled by using equivalent vertical permeability, which takes into account both vertical and horizontal consolidation. As such, PVD improvement can be modelled under 1D condition. In addition, the effect of the surcharge fill is taken into account as well.

The equivalent vertical permeability k_{ve} according to Chai et. al (2001) is:

$$k_{ve} = (1 + \frac{2.5l^2}{\mu d_e^2}\frac{k_h}{k_v})k_v \qquad (6)$$

Where k_v is vertical permeability, l is drainage length and k_h is horizontal permeability. Other parameters are defined earlier.

The values of vertical and horizontal permeability were determined from oedometer and radial consolidation test results. For all determined coefficients of consolidation, corresponding values of permeability k were calculated using unit weight of water and secant modulus.

Initial permeability k_1 (when vertical strain ε_1 = 0 %) was determined using linear extrapolation in *log k* - ε_1 plot. Values of

initial permeability k_1 are represented in Figure 4. In the graph "direct" means that the permeability was determined using falling-head method integrated with IL oedometer test.

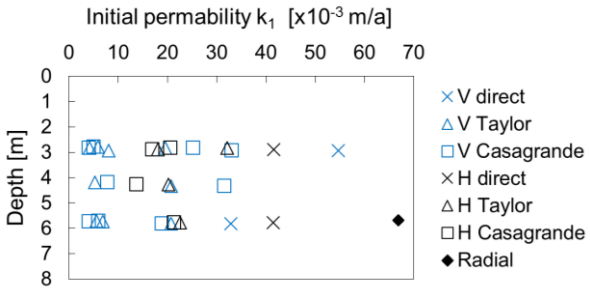


Figure 4 Initial vertical (V), horizontal (H) and radial permeability versus depth.

Direct measurement and radial consolidation test yielded significantly higher values of permeability compared to the ones estimated via coefficient of consolidation. As the amount these values is relatively low, the selected values of permeability are from the group of the highest indirectly determined. Selected values of k_v and k_h are listed in Table 4.

As the PVDs cannot reach the sandy silt layers, drainage length of l = 7.5 m is selected. However, the actual length of PVDs is only 7 m: The suction caused by vacuum affects layers beneath the drains as well. As d_e = 1.155 (Case 1 in Table 2), the affected total depth is approximately 7 m + 0.5$d_e \approx l$ = 7.5 m.

The values of k_{ve} used in calculations are listed in Table 4. Values of k_{ve} are calculated using term μ of Case 1 (Table 2). However, it should be noted that k_{ve} is approximately identical for all three cases if spacing a is adjusted to meet the same requirements for U and t. Decrease in permeability due to compression is not taken into account in the time–settlement analysis.

Table 4 Selected values of permeability.

Layer	k_v [m/a]	k_h [m/a]	k_{ve} [m/a]
Dry Crust	1	1	38.88
Clay 1-2	0.025	0.031	1.199
Clay 3	0.017	0.017	0.661
Clay 4-7	0.021	0.042	1.612

4.4 Loading history and time-settlement for vacuum preloading

Settlement caused by surcharge fill and vacuum is calculated using tangent modulus method. Loads are modelled as vertical equally distributed extensive load Thus compression parameters are the same as for natural subsoil (Table 3).

Applied load history and calculated time–settlement graph are represented in Figure 5. First, an embankment is constructed on the PVDs during one month. Height of the surcharge fill is 1.5 m, resulting in load of 30 kPa. Then, vacuum preloading (suction of 70 kPa) is applied for 8 months. The largest settlement is reached at the end of the vacuum, 890 mm. Soon after the removal of the vacuum, settlement decreases to 823 mm due to heave.

In order to compensate for the settlement caused by surcharge fill and vacuum, height of the embankment is increased by 0.5 m (10 kPa) during 6 moths. The increase in the height of the embankment causes a settlement of 2 mm, resulting in the final value of total settlement of 825 mm. Thus, the final height of the embankment with settlement considered is 1.2 m. The load at the end is 40 kPa.

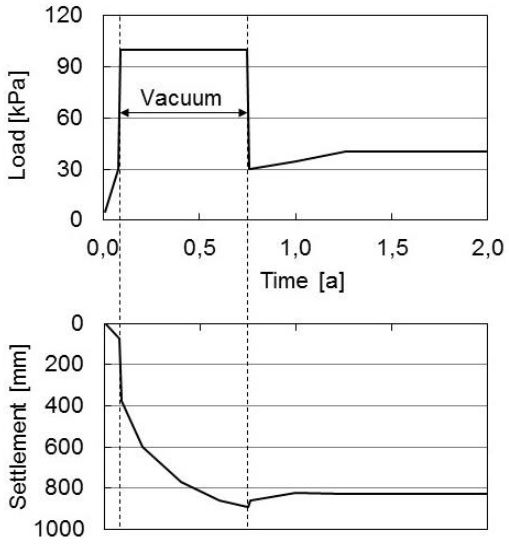


Figure 5 Loading history and time-settlement.

4.5 Discussion

In order to estimate the degree of overconsolidation U_{OC} caused by the vacuum, the values of effective vertical pressure before and after the vacuum were

compared. Preconsolidation pressure, initial effective overburden pressure and effective vertical pressure at different loading conditions (before the vacuum, t = 0.08a, at the end of the vacuum, t = 0.75a and two years after the vacuum, t = 2a) are represented in Figure 6 (left).

At the end of the vacuum (t = 0.75a) some excessive pore pressure is present in the deepest layers ($u \approx 11$ kPa). The degree of consolidation at this point is U = 90…95 %, which is relatively close to the set goal of U = 85 % (Hansbo's solution). Immediately after the removal of the vacuum pore pressures turn to negative. However, using negative values of pore pressure would overestimate the reached value of U_{OC}. Half a year after the removal of the vacuum (t = 1.26a), excessive pore pressure is zero. Thus, U_{OC} is estimated by dividing the maximum "new" preconsolidation pressure at the end of the vacuum by the effective vertical (overburden) pressure half a year after the removal of the vacuum. The effective overburden pressure before any loading is subtracted from these values. The degree of overconsolidation U_{OC} profile and the targeted value are represented in Figure 6 (right).

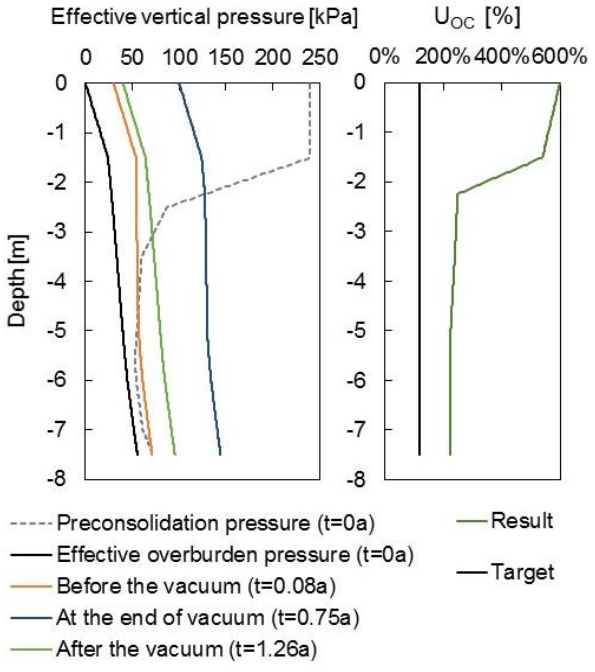


Figure 6 Left: Preconsolidation pressure, effective overburden pressure and; effective vertical pressure before, at the end and after the vacuum. Right: Degree of overconsolidation; target and the result.

In the layers near the surface, the preconsolidation pressure σ'_p does not change as the additive pressure caused by vacuum does not exceed the original values of σ'_p. Thus in these layers, degree of overconsolidation U_{OC} > 250 %. The deepest layers (beneath 2.3 m) are the most critical: The minimum value is only U_{OC} = 222 %. The average value is $U_{OC} \approx$ 229 %. Hence, the average difference between maximum preconsolidation pressure and final effective overburden vertical pressure is 51,5 kPa. At minimum, the difference is 48,9 kPa.

The targeted U_{OC} was far exceeded, and at such high values settlement caused by creep is most certainly at its minimum. Moreover, the design load for the truck parking area will not cause any primary consolidation.

Time-settlement -analysis based on equivalent vertical permeability (Chai et. al., 2001) is simple and fast and seems to agree well with Hansbo's method. However, similarity in estimated degrees of consolidation might be a coincidence, because c_h in normally consolidated state used in Hansbo's method cannot yield similar time-settlement behavior as initial permeability. The reason for apparent similarity is probably in drainage boundary conditions: In settlement calculations, the bottom was assumed impermeable. However, drainage length is already taken into account in the definition of k_{ve}. Nevertheless, for preliminary design this approach seems feasible as set goals for U and t are met.

Treating vacuum preloading as an equally distributed vertical load might lead to errors. Indeed, Indraratna et al. (2012) questioned whether k_{ve} –method can be used to simulate the propagation of vacuum.

The rate of consolidation is probably faster than estimated. Thus here required PVD spacing might be sparser in actual field conditions. There are several reasons for possible error. Firstly, values of permeability in field are probably higher than the ones determined in laboratory. Secondly, the horizontal oedometer test might underestimate the values of horizontal coefficient of consolidation and permeability due to parallel loading conditions. As a matter of fact, in several recent studies radial consolidation test is preferred over horizontal oedometer test in the design of PVD improvement (Bergado et al., 1991; Ganesh

Kumar et al., 2015; Indraratna et al., 2010; Saowapakpiboon et al., 2010). Thirdly, all the methods used in this paper are originally designed for PVD improved subsoil without the effect of vacuum. Compared to conventional PVD improvement, vacuum preloading reduces the time required for consolidation by increasing the back-calculated value of c_h and by decreasing the smear effect (Saowapakpiboon et al., 2010; Voottipruex et al., 2014).

5 CONCLUSION

Clearly, vacuum preloading is a feasible soil improvement method for Luhtaanmäki. With vertical drainage, the rate of primary settlement increases significantly compared to natural state soil.

The targeted degree of overconsolidation (U_{OC} = 120 %) after 7-8 months of vacuum consolidation was easily reached. In the most critical layers the average value is $U_{OC} \approx 229$ %. Vertical drain spacing of 1 m was chosen, but in actual field conditions the needed drain spacing might be sparser.

The final height of the embankment is 1.2 m with total settlement of 825 mm taken into account. Thus the desired height was reached.

In order to increase the accuracy of vacuum preloading design, more reliable values of horizontal coefficients of consolidation and permeability are needed. Either more radial consolidation tests or for example CPTU dissipation tests (t > 24 h) should be conducted. Reliability of time-settlement –analysis could be increased by modelling the decrease in permeability due to compression. Furthermore, the vacuum should be modelled more realistically, for example by setting boundary conditions for pore water pressure. Thus FEM analysis using either axisymmetric unit cell or drain elements in plane strain conditions is needed.

6 NOTATION

a	drain spacing
c_h	horizontal coefficient of consolidation
c_r	radial coefficient of consolidation
c_u	undrained shear strength
c_{ur}	remoulded undrained shear strength
c_v	vertical coefficient of consolidation
d_e	equivalent diameter of PVD-affected soil
d_s	diameter of the smear zone
d_w	equivalent diameter of PVD
k	permeability
k_1	initial permeability
k_h	horizontal permeability
k_s	horizontal permeability in smear zone
k_v	vertical permeability
k_{ve}	equivalent vertical permeability
l	drainage length
n	d_e/d_w
N_k	cone factor
OCR	overconsolidation ratio
q_c	measured cone resistance
q_w	discharge capacity of PVD
s	d_s/d_w
t	time
t_{PVD}	thickness of PVD
T_h	time factor for radial consolidation
U	degree of consolidation
u	pore water pressure
Uh	average degree of radial consolidation
U_{OC}	degree of overconsolidation
w	water content
w_L	liquid limit
w_{PVD}	width of PVD
γ	unit weight
σ_{v0}	total overburden pressure
σ'_{v0}	effective overburden pressure
σ'_p	effective preconsolidation pressure
φ	friction angle

7 REFERENCES

Barron, R.A. (1948). Consolidation of fine grained soils by drainwells. Transactions of ASCE 113, 718-724.

Basu, D., Basu, P. & Prezzi, M. (2006). Analytical solutions for consolidation aided by vertical drains. Geomech. Geoeng. Int. J. 1 (1), 63-71.

Bergado, D.T., Asakami, H., Alfaro, M.C. & Balasubramaniam, A.S. (1991). Smear effects of vertical drains on soft Bangkok clay. Journal of Geotechnical Engineering 117 (10), 1509-1530.

Bjerrum, L. (1972). Embankments on soft ground. Proc., ASCE Specialty Conf. Earth and Earth-Supported Structures, Purdue University. Vol. 2, 1-54.

Brandt, V., Kirstein, J.F., Nörenberg, G. & Wittorf, N. (2015). Winner of German road innovation price: "Peaty soils become suitable foundation ground of a federal highway by implementing the vacuum system. Proceedings of the XVI ECSMGE for Infrastructure and Development, 295-300.

Casagrande, A. (1936). The determination of preconsolidation load and its practical significance. Proceedings of the I ICSMFE, 3. Mass. Cambridge

Chai, J.-C., Shen, S.-L., Miura, N. & Bergado, D.T. (2001). Simple method of modelling PVD-improved subsoil. Journal of Geotechnical and Geoenvironmental Engineering 127 (11), 965-972.

Chaumeny, J.-L. & Kirstein, J. & Reiner, J. (2011). Consolidation of extremely soft mud for the A-380

factory in Hamburg – long time experience. Proc. XV ECSMGE, 2011. IOS Press. 971-976.

Ganesh Kumar, S., Sridhar, G., Radhakrishnan, R, Robinson, R.G. & Rajagopal, K. (2015). A Case Study of Vacuum Consolidation of Soft Clay Deposit. Indian Geotechnical Journal 45 (1), 51-61.

Hansbo, S. (1979). Consolidation of clay by band shaped prefabricated drains. Grnd. Eng. 12 (5), 16-25.

Hansbo, S. (1981). Consolidation of fine-grained soils by prefabricated drains. Proceedings of the X ICSMFE, Stockholm, June 1981. A.A. Balkema, Rotterdam, The Netherlands. Vol. 3, 677-682.

Hansbo, S. (1987a). Design aspects of vertical drains and lime column installations. Proceedings of the 9th Southeast Asian Geotechnical Conference, Bangkok, Thailand. Vol. 2, 1-12.

Hansbo, S. (1987b). Fact and fiction in the field of vertical drainage. Proceedings of the International Symposium on Prediction and Performance in Geotechnical Engineering, Calgary 1987. A.A. Balkema, Rotterdam. 61-72.

Hassan, M. (2006). Deformation behavior and permeability of soft Finnish clay. Master's Thesis. Helsinki University of Technology.

Indraratna, B & Redana, I.W. (1998). Laboratory determination of smear zone due to vertical drain installation. Journal of Geotechnical and Geoenvironmental Engineering 124 (2), 180-184.

Indraratna, B., Rujikiatkamjorn, C. & Sathananthan, I. (2005). Radial consolidation of clay using compressibility indices and varying horizontal permeability. Can. Geotech. J. 42, 1330-1341.

Indraratna, B., Geng, X. & Rujikiatkamjorn, C. (2010). Review of methods of analysis for the use of vacuum preloading and vertical drains for soft clay improvement. Geomechanics and Geoengineering: An International Journal Vol. 5 (4), 223-236.

Indraratna, B., Rujikiatkamjorn, C., Balasubramaniam, A.S and Mcintosh, G. (2012). Soft ground imrpvement via vertical drains and vacuum assisted preloading. Geotextiles and Geomembranes 30, 16-23.

Janbu, N. 1963. Soil compressibility as determined by oedometer and triaxial tests. Europäische Baugrundtagung 1963, Wiesbaden.

Kjellman, W. (1948). Accelerating consolidation of fine grain soils by means of vardboard wicks. Proceedings of the 2nd ICSMFE, Vol. 2, 302-305.

Leminen, K. & Rathmayer, H. (1979). Heikosti kantavan maan hienorakeisen maapohjan parantaminen pystyojituksen ja syvästabiloinnin avulla. Kenttäkokeet Helsingin Itäkeskuksessa. Report 39. VTT Technical Research Centre of Finland Ltd, Geotechnical laboratory, Espoo.

Leminen, K. & Rathmayer, H. (1983). Experience on horizontal oedometer tests to determine the parameter c_h. Improvement of Ground. Proceedings of the XIII ECSMFE, Helsinki 23-15 May 1983. A.A. Balkema, Rotterdam. 647-651.

Leroueil, S., Magnan, J.-P. & Tavenas, F. 1990. Embankments on soft clay. (Translator Wood, D.M.) Ellis Horwood, Chichester.

Lunne, T. & Kleven, A. 1981. Role of CPT in North Sea foundation engineering. Session at the ASCE National Convention: Cone Penetration Testing and Materials, St. Louis. ASCE. 76-107.

Lunne, T., Robertson, P.K. & Powell, J.J.M. (1997). Cone Penetration Testing in Geotechnical Practice. Blackie Academic & Professional, London.

Länsivaara, T. (2003). Problems related to settlement calculations on soft Scandinavian clays. Int. Workshop on Geotechnics of Soft Soils-Theory and Practice. Vermeer, Schweiger, Karstunen & Cudny (eds.). VGE.

Müller, R. & Larsson, S. (2013). Aspects on the modelling of smear zones around vertical drains. Proc., XVIII ICSMGE, Paris 2013, 2965-2968.

Ohde, J. (1939). Zur Theorie der Druckverteilung im Baugrund. Bauingenieur 14, 451-458.

Puumalainen, N. & Havukainen, J. (1996). Vakuumikonsolidointikoe Helsingin Torpparinmäessä. Report 68/1996. Geotechnical Division, Real Estate Department, City of Helsinki.

Puumalainen, N. (1998). Mechanical Modelling of vacuum consolidation (in Finnish). Licentiate's Thesis. Helsinki University of Technology.

Robinson, R.G. (1997). Determination of radial consolidation of consolidation by the inflection point method. Geotechnique 47 (5), 1079-1081.

Saowapakpiboon, J., Bergado, D.T., Youwai, S., Chai, J.C., Wanthong, P. & Voottipruex, P. (2010). Measured and predicted performance of prefabricated vertical drains (PVDs) with and without vacuum preloading. Geotextiles and Geomembranes 28, 1-11.

Seah, T.H. (2006). Design and construction of ground improvement works at Suvarnabhumi Airport. Geotechnical Engineering, Journal of the Southeast Asian Geotechnical Society 37: 171-188.

Sridharan, A., Prakash, K. & Asha, S.R. (1996). Consolidation behaviour of clayey soils under radial drainage. Geotech. Test. J. 19 (4), 421-431.

Taylor, D.W. (1948). Fundamentals of Soil Mechanics. John Wiley & Sons Inc., New York.

Technique Geosystems/ Cofra, J.V. (1995). Design and proposal for the execution of: Vacuum consolidation Shah Alam Expressway Package A, Selangor, Malaysia. Amsterdam.

Tielaitos. (1999). Pohjarakennusohjeet sillan-suunnittelussa. Tiehallinto. Edita Oy, Helsinki.

Vepsäläinen, P. & Arkima, O. (1994). Geotekniikan informaatio-julkaisuja. Nauhapysty-ojitus. Tielaitoksen selvityksiä 42/1994. Helsinki.

Voottipruex, P., Bergado, D.T., Lam, L.G. & Hino, T. (2014). Back-analyses of flow parameters of PVD improved soft Bangkok clay with and without vacuum preloading from settlement data and numerical simulations. Geotextiles and Geomembranes 42, 457-467.

Ye, B.R., Shang, S.Z. & Ding, G.Q. (1991). Consolidation of soft soil by means of combined vacuum surcharge preloading. Proc., Int. Conf. Geotech. Eng. for Coastal Development - Theory and Practice on Soft Ground - Geo-Coast '91 Yokohama 1991, Vol. 2, 277-280.

The influence of the shaft friction and pile shape on the pile tip bearing capacity

Stefan Van Baars
University of Luxembourg, Luxembourg, stefan.vanbaars@uni.lu

ABSTRACT
In 1920 Prandtl published an analytical solution for the bearing capacity of a maximum strip load on an infinite half-space, based on a sliding soil part, with three sliding zones, which is nowadays called the Prandtl-wedge. This solution was extended by Reissner with a surrounding surcharge. Terzaghi wrote the formula with bearing capacity factors and Meyerhof extended this formula with both inclination factors and shape factors.
Because of these developments for shallow foundations, many geotechnical researchers thought that failure of a pile tip in a deep sand layer will also show a Prandtl-wedge type of failure and that the stresses on a pile tip are also constant and do not depend on the shape and size of the pile tip. This would imply that a Cone Penetration Test (CPT) gives the same stress as a real pile tip, and can be used without a reduction for calculating the bearing capacity of a real pile.
Field tests show however that a bearing capacity of a pile tip, based on unreduced CPT data, is too high. Therefore this problem has been modelled and studied, with Finite Element Modelling.
Several remarkable results were found. There is no Prandtl-wedge type of failure at the pile tip, but a general zone of plasticity. Also the stresses below the pile tip are not constant, but higher near the centre of the pile. The difference in bearing capacity between CPT and real pile does not depend on the shape and size of the pile tip, but more on the difference of the definitions of failure between CPT and pile.
Additional calculations show that the pile shaft friction does not influence the stresses at the pile tip, but the normal stresses on the pile tip do influence the shear stresses along the shaft.

Keywords: Bearing capacity, Pile Foundations, Cone Penetration Test.

1 INTRODUCTION

1.1 Prandtl-Reissner

In 1920, Ludwig Prandtl published an analytical solution for the bearing capacity of a soil under a limit pressure, *p*, causing kinematic failure of the weightless infinite half-space underneath. The strength of the half-space is given by the angle of internal friction, ϕ , and the cohesion, *c*. The solution was extended by Reissner in 1924 with a surrounding surcharge, *q*. Prandtl subdivided the sliding soil part into three zones (see Figure 1):

Zone 1: A triangular zone below the strip load. Here the largest principal stress is in the vertical direction.

Zone 2: A wedge with the shape of a logarithmic spiral, in which the principal stresses rotate through $90°$ from Zone 1 to Zone 3. The pitch of the sliding surface equals the angle of internal friction; $\xi = \phi$, creating a smooth transition between Zone 1 and Zone 3.

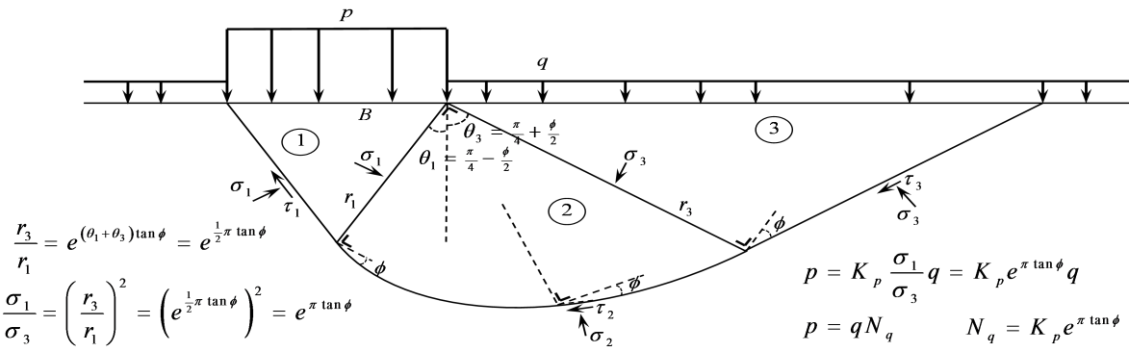


Figure 1 The wedge of Prandtl.

Zone 3: A triangular zone adjacent to the strip load. Here the largest principal stress is in the horizontal direction.

1.2 Meyerhof

Keverling Buisman (1940) and Terzaghi (1943) extended the Prandtl-Reissner formula for the soil weight, γ. And in 1953 Meyerhof was the first to propose equations for inclined loads. He was also the first in 1963 to write the formula for the (vertical) bearing capacity p_v with bearing capacity factors (N), inclination factors (i) and shape factors (s), for the three independent bearing components; cohesion (c), surcharge (q) and soil-weight (γ), in a way it is still used nowadays:

$$p_v = i_c s_c c N_c + i_q s_q q N_q + i_\gamma s_\gamma \tfrac{1}{2}\gamma B N_\gamma . \quad (1)$$

1.3 Pile tip

Because of this analytical solution for shallow foundations, many researchers (for example Meyerhof, 1951) thought that a pile tip in a deep sand layer will also show a Prandtl-wedge type of failure mechanism and equation 1 can be used.

In this article only vertically loaded deep pile tips are considered (so the influence of the soil weight can be neglected), in cohesionless soils, which means that this equation can be reduced to:

$$p = s_q q N_q , \quad (2)$$

in which the surcharge bearing capacity factor is given as (see figure 1):

$$N_q = K_p \cdot \left(\frac{r_3}{r_1}\right)^2 = K_p \cdot e^{\pi\tan\phi} \quad (3)$$

with: $K_p = \dfrac{1+\sin\phi}{1-\sin\phi}$.

This means that the stresses on the pile tip will also be constant and depend only on the friction angle of the soil, the vertical effective stress near the pile tip, and its shape factor and not on the shape and size of the pile tip. This would imply that a Cone Penetration Test will produce the same average stress as a real pile and can in principle be used without a reduction or a scale factor for the calculation of the bearing capacity of a pile, just as Boonstra (1940) showed with his field tests and just as is assumed in many pile bearing capacity predicting models, such as the model of Van Mierlo & Koppejan (1952).

1.4 Validation

The solution of the surcharge bearing capacity factor N_q (equation 3) has been checked by Van Baars (2015) with finite element calculations, and found to be correct. But this does not proof that the Meyerhof equation can also be used for pile tips, because the analytical solution is based on a Prandtl-wedge failure mechanism, while for

circular shallow foundations and pile foundations (see also paragraph "4 Failure mechanism") another failure mechanism is found. Besides, the finite element calculations also show that the solutions of the surcharge shape factor of both Meyerhof (1963) and also De Beer / Brinch Hansen (1970) are not accurate and should be more like (see Tapper et al, 2015):

$$s_q = 1 - 0.55 \cdot \sqrt{B / L}\,, \qquad (4)$$

in which B and L are the width and depth of the pile tip, so for square pile tips: $B / L = 1$.

Another big problem is that many researchers (Jardine et al, 2005, Lehane et al, 2005, Clausen et al, 2005) and recent field tests (Van Tol et al., 1994, 2010, 2012) show that a calculated bearing capacity based on unreduced Cone Penetration Test data, can be more than 30% higher than measured.

2 FINITE ELEMENT MODELLING

In order to find the reason for all this, a pile has been modelled and studied. With the software code Plaxis, displacement controlled, non-updated mesh, 2D axial-symmetric, finite element calculations have been made. In all cases a 10 m deep pile in dry sand has been modelled with a Mohr-Coulomb model, using the soil parameters listed in table 1.

Table 1 Soil parameters.

Parameter	Value
Friction angle	$\phi = 35°$
Dilatancy angle	$\psi = 0°$
Cohesion	$c = 0$
Young's modulus	$E = 50{,}000$ kPa
Poisson's ratio	$\nu = 0.3$
Unit weight	$\gamma = 20$ kN/m^3

Higher-order 15-node elements have been used. The element sizes can be seen in Figure 4.
The idea is to keep the calculation as simple as possible so that differences between two calculations are caused by the change of a pile size, and not due to second order effects of for example a complex soil model. Therefore the pile is a wished-in-place pile; no installation effects are added. For the same reason, no large strain corrections have been made, even though large deformations were applied; First because Plaxis cannot model correctly the flow of a plastic soil, around a pile tip at large displacements. Second because not the exact stresses are sought, but the failure mechanisms and the relative differences between two or three options.

Both the pile tip and the pile shaft have been modelled by a displacement controlled line or soil boundary, without any interface. This represents an infinite stiff and rough pile. For each calculation step an additional pile displacement of 1 mm has been chosen.
The advantage is of this method is that this calculation is very simple and very stable, and the push in force is simply the same as the total reaction force which is standard registered.
The disadvantage is that it is unknown how much of this force comes from the tip resistance and how much from the shaft.

3 SHAPE AND SIZE OF PILE TIP

The first step was to investigate the influence of the shape of the pile tip. First four almost identical calculations have been made: two calculations with normal (flat) pile tips and two with sharp pile tips (pile tip angle $\alpha = 45°$). Two of them were calculations with only the pile tip pushed down and two with both the tip and shaft pushed down (vertical displacement controlled boundary; no horizontal displacements).
Figure 2 shows that the difference in force between a sharp and a normal (flat) pile tip can be neglected. Also three different pile diameters have been tested.
Since the circumference of the shaft is scaled in a different way as the area of the pile tip, only the pushing down of the pile tip has been modelled here (so with free displacements for the shaft).

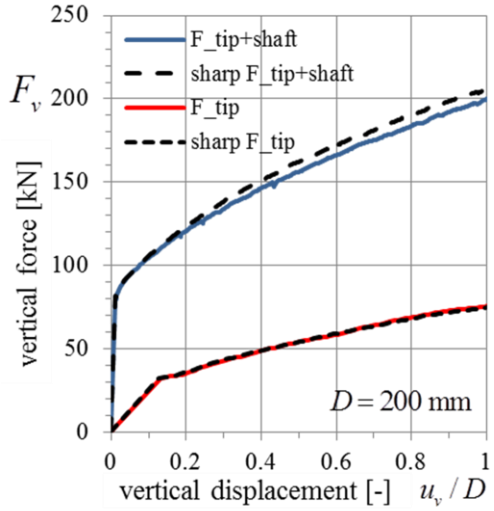


Figure 3 Influence of the shape of the pile tip

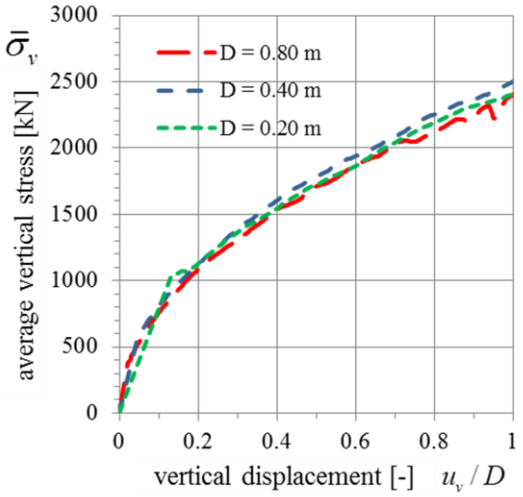


Figure 2 Influence of the pile tip diameter.

Figure 3 shows the average vertical stress below the pile tip $\bar{\sigma}_v$ versus the vertical displacement u_v divided by the pile tip diameter D, proofing that the curves are the same for all three pile diameters, just as the Prandtl solution would predict.

3.1 Continuously growing stresses

The phenomenon of the continuously growing stresses with displacement is very important, since the cone resistance is defined for a (failing) pile tip at an infinite displacement, while the bearing capacity of a real pile is defined for a pile tip at only 10% displacement of (the size of) the pile tip. This difference in definition of failure explains at least a substantial part of the 30% difference of the stresses at the pile tip between the cone (at infinite displacement) and a pile (at only 10% displacement).

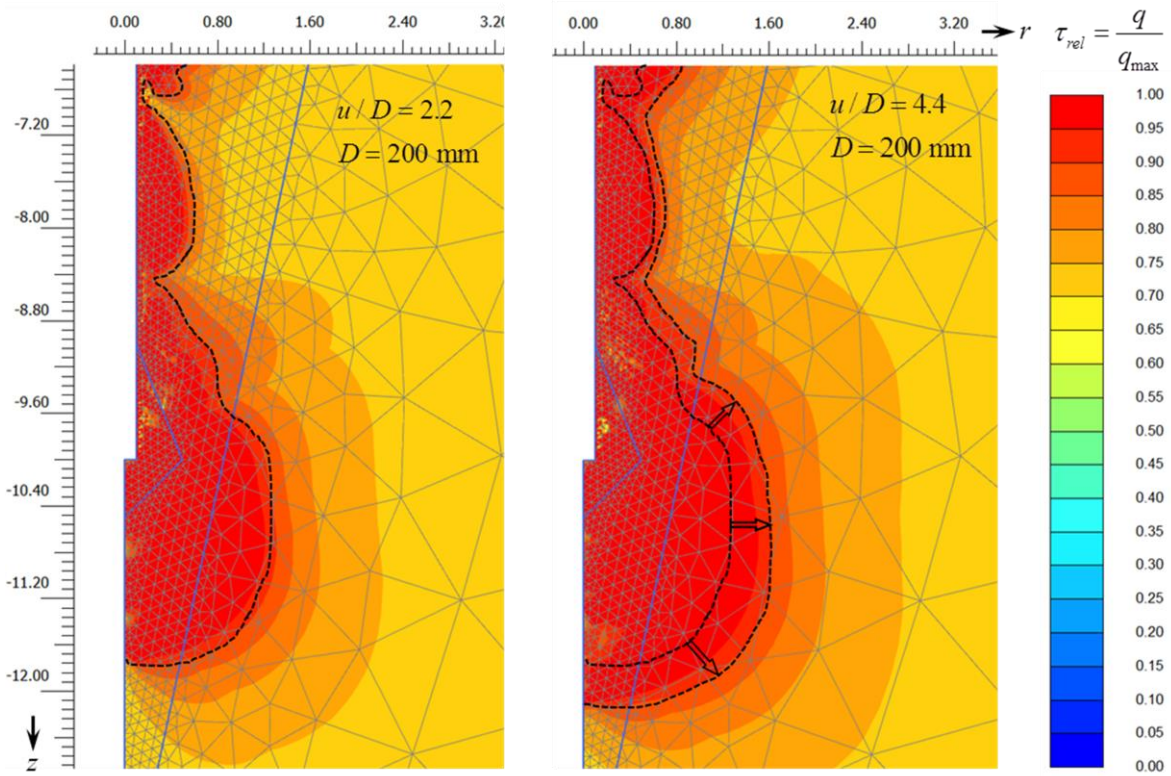


Figure 4 Failing mechanism: growing total plastic zone.

4 FAILURE MECHANISM

Figure 4, on the previous page, shows the relative shear stress τ_{rel} after large pile displacements u_v; 2.2 times (on the left) and 4.4 times (on the right) the pile diameter D. This relative shear stress is defined as the radius of the circle of Mohr divided by the radius of a circle touching the Coulomb line, which means plasticity or failure of the soil, or a relative shear stress of "1".
The failure zone in this figure is not like a Prandtl-wedge. In fact there is an ever growing plastic zone below the pile tip and all along the pile shaft. The fact that the zone is growing, means that the vertical stress (the bearing capacity) is also growing with the displacement. This ever growing bearing capacity was already noticed from figure 2, but follows also from figure 5, which shows the push-in bearing capacity of the shaft and the tip individually (2nd and 3rd line from below), but also together (2nd line from above). Two other lines show the pull-out force of the shaft alone (lowest line) and the summation of the tip push in and the shaft pulled out (3rd line from above).
The highest (dashed) line is found by simply summing up the push-in force of both the pile tip and the pile shaft.
The 3rd line from above is found by summing up the push-in force of the pile tip and the pull-out force of the pile shaft. One could think that for a calculation with both the pile tip and the shaft moving down at the same time, the upper dashed line will be found, but instead the bearing capacity (2nd and straight line) has been found to be clearly lower.
This proofs that the pile shaft and tip influence each other a lot, causing a strong non-linearity or reduction in the bearing capacity.
The question arises if this reduction of the bearing capacity exists because the shaft influences the pile tip or because the tip influences the shaft, or maybe even both. This question will be solved in the next paragraph.

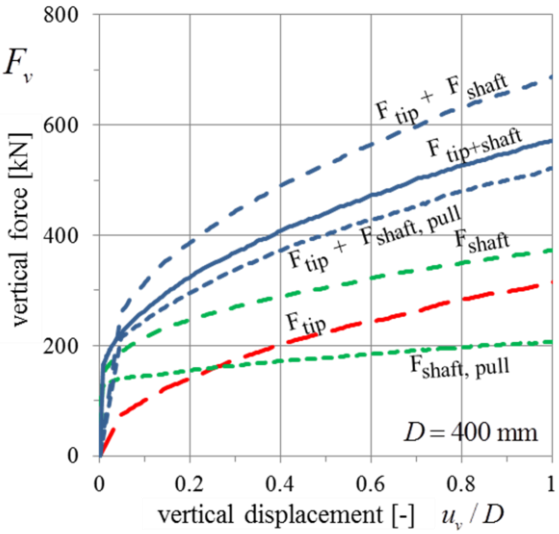


Figure 5 Bearing capacity of the shaft and the tip.

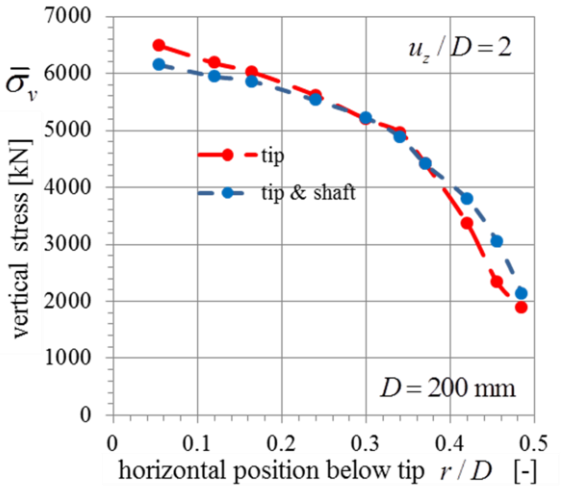


Figure 6 The normal stress below the pile tip.

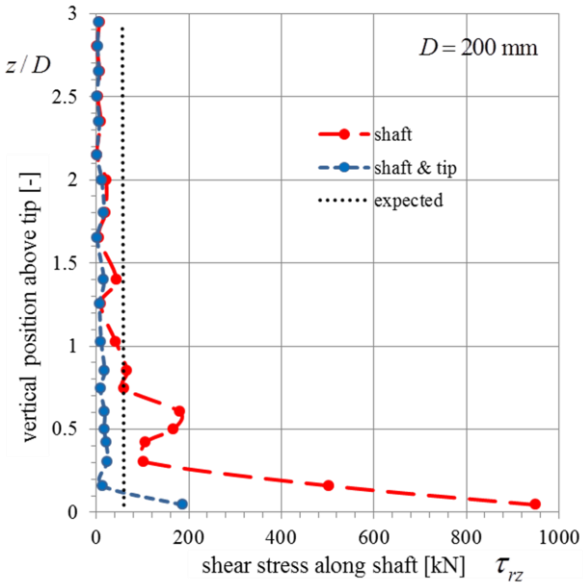


Figure 7 The shear stress along the shaft.

5 STRESSES ALONG THE TIP AND SHAFT

The previous calculations were displacement controlled, which means that only a single total force results from the calculations, and not two independent forces: the force at the tip and the force along the shaft.
Therefore the normal stresses along the (flat) tip have been plotted (Figure 6) and also the shear stresses along the shaft (Figure 7), for both a calculation in which only the tip has been pushed down and also a calculation in which both tip and shaft have been pushed down for a large displacement ($u_z / D = 2$).
These figures show that the normal stresses below the tip are (almost) not influenced by the shaft, but that the shear stresses along the shaft are influenced by the tip.
Figure 6 also shows that the normal stresses below the pile tip are not constant, but higher near the centre of the pile, unlike the Meyerhof equation.
The dotted line in Figure 7 named "expected" is the shear stress related to the vertical effective stress σ'_v and the horizontal earth pressure K_0, according to:

$$\tau_{rz} = \tan\phi \cdot \sigma_v \cdot K_0, \qquad (5)$$

with: $\sigma'_v = \gamma' z$ and: $K_0 = 1 - \sin\phi$.

Figure 7 shows that most of the pile shaft has less shear friction than expected, except near the tip, but also that the pile tip has a big influence on the shaft: the pile tip is pushing down the surrounding soil and reduces in this way the shear stresses along the shaft.

6 CONCLUSIONS

According to field tests, large differences are found between the normal stresses on the cone in a CPT test, and the normal stresses on the tip of a foundation pile, while a good scientific explanation cannot be given. Also the influence of the pile size (scale effect), the influence of the installation (driving or pushing), the influence of the pile tip on the pile shaft and visa-versa and the influence of the horizontal soil stresses are not completely understood. In fact even the type of failure mechanism around the pile tip is still a point of discussion.
A conclusion following from the numerical calculations is that, the shear stresses along the pile shaft do not influence the stresses at the pile tip, but visa-verso the normal stresses at the pile tip do influence the shear stresses along the shaft.
Another conclusion from the numerical calculations, and as expected from the Prandtl theory, is that the shape and size of the pile tip do not matter. But according to this research, there is no Prandtl-wedge type of failure at the pile tip, but a zone of plasticity. And the stresses below the pile tip are not as given by the Prantl theory constant, but higher near the centre of the pile.
The outcome that the shape of the pile has no influence is already what is used in practise; the stresses measured with a sharp cone are assumed to be the same for a flat tip of a foundation pile.
The outcome that the size does not matter might look in contradiction with the field tests, but before concluding this, first future tests should compensate for the difference in failing definition (the 10% displacement rule for a real pile versus the infinite displacement for a Cone Penetration Test).

7 REFERENCES

Bustamente, M. & Gianeslli, L. (1982) Pile bearing capacity prediction by means of static penetrometer CPT. Second European Symposium on Penetration Testing, Amsterdam 24-27 May 1982.

Brinch Hansen, J. A (1970) Revised and extended formula for bearing capacity, Bulletin No 28, Danish Geotechnical Institute Copenhagen, 5-11.

Caquot, A. and Kérisel, J. (1953). Sur le terme de surface dans le calcul des fondations en milieu pulvérulents, Third International conference on Soil Mechanics and Foundation Engineering, Zürich, pp. 336–337.

Chen, W. F. (1975) Limit analysis and soil plasticity, Elsevier.

De Beer, E. E. (1970). "Experimental determination of the shape factors and the bearing capacity factors of sand." Geotechnique, 20, 387– 411.

Eurocode 7, NEN 9997-1 (nl) Geotechnical design of structures - Part 1: General rules, 107-113

Fang, Hsai-Yang (1990) Foundation Engineering Handbook, Kluwer, Norwell-USA / Dordrecht-NL

Hjiaj, M. Lyamin, A.V, Sloan, S.W. (2005) Numerical limit analysis solutions for the bearing

capacity factor N_γ, International Journal of Solids and Structures, No 42, 1681–1704

Keverling Buisman, A. S. (1940). Grondmechanica, Waltman, Delft, the Netherlands, 243

Meyerhof, G. G. (1951) The ultimate bearing capacity of foundations, Géotechnique, 2, 301-332

Meyerhof, G. G. (1953) The bearing capacity of foundations under eccentric and inclined loads, in Proc. III intl. Conf. on Soil Mechanics Found. Eng., Zürich, Switzerland, 1, 440-445

Meyerhof, G. G. (1963) Some recent research on the bearing capacity of foundations, Canadian Geotech. J. , 1(1), 16-26

Meyerhof, G. G. (1965) Shallow foundations, Journal of the Soil Mechanics and Foundations Division ASCE, Vol. 91, No. 2, March/April 1965, 21-32

Michalowski, R. L. (1997) "An estimate of the influence of soil weight on bearing capacity using limit analysis." Soils and Foundations, 37(4), 57–64.

Prandtl, L. (1920) "Über die Härte plastischer Körper." Nachrichten von der Königlichen Gesellschaft der Wissenschaften zu Göttingen, Mathematisch.-physikalische Klasse, 74–85.

Reissner, H. (1924) "Zum Erddruckproblem." Proc., 1st Int. Congress for Applied Mechanics, C. B. Biezeno and J. M. Burgers, eds., Delft, The Netherlands, 295–311.

Tapper, L., Martin, C.M. , Byrne, B.W. Lehane, B.M. (2015) Undrained vertical bearing capacity of perforated shallow foundations, Frontiers in Offshore Geotechnics, Fig. 7, 816

Terzaghi, K. (1943) Theoretical soil mechanics, J. Wiley, New York.

Van Baars, S. (2014) The inclination and shape factors for the bearing capacity of footings, Soils and Foundations, ISSN: 0038-0806, Vol.54, No.5, October 2014

Van Baars, S. (2015) The bearing capacity of footings on cohesionless soils, send for publication to The electronic journal of geotechnical engineering

Van Mierlo, J.C. and Koppejan, A.W. (1952) "Lengte en draagvermogen van heipalen", Bouw 3, 1952

Van Tol, A.F.(1994), Hoe betrouwbaar is de paalfundering, Intreerede 3-6-1994, TU Delft, in Dutch

Van Tol, A. F., Stoevelaar, R., Rietdijk, J. (2010) Draagvermogen van geheide palen in internationale Context, Geotechniek, Dec. 2010

Van Tol, A.F. (2012) Draagkracht funderingspalen, een up-date. Geotechniek Special Dec 2012

Vesic, A. S. (1973) Analysis of ultimate loads of shallow foundations. J. Soil Mech. Found. Div., 99(1), 53.

Vesic, A. S. (1975) Bearing capacity of shallow foundations, H.F. Winterkorn, H.Y. Fang (Eds.), Foundation Engineering Handbook, Van Nostrand Reinhold, New York (1975), pp. 121–147

Yu, H.S., Salgado, R., Sloan, S.W., Kim, J.M. (1998) Limit analysis versus limit equilibrium for slope stability, Journ. Geotechnical and Geoenvironmental Eng., Jan. 1998, Vol 124, No 1, pp 1–11

V-H-M Yield Surface describing Soil Structure Interaction of Sub-sea Structures and Wind Turbines on Caisson Foundations in Soft Clays

C. Athanasiu
Multiconsult ASA, Norway, corneliu.athanasiu@multiconsult.no

M. Brandt
Multiconsult ASA, Norway, madeleine.brandt@multiconsult.no

ABSTRACT
One of the challenges in the design of sub-sea structures and wind turbines on caisson foundations is the realistic representation of foundation-soil stiffness and capacity. Such a representation can be "lumped" as load-displacement relationships at the top of the caisson (sea-bed level).
The paper presents a general V (vertical load) - H (horizontal load) - M (overturning moment) yield surface and back-bone load – displacement (H-δ_h, M-θ and V-δ_v) curves that can be used in geotechnical design of a structure and its caisson foundation. The soil parameters, together with the model formulation and limitations, are presented and discussed in the paper. The last part of the paper illustrates some of the applications of the yield surface in the design.

Keywords: soil-structure interaction, VHM yield surface, back-bone curves.

1 INTRODUCTION

An important tool for the analysis of soil-structure interaction problems, particularly of dynamic soil-structure interaction of sub-sea structures and wind turbines on caisson foundations, are discrete, "force resultant" models. In these models, the details of stresses and deformations in the soil mass and at the interface with the caisson are replaced by the force and moment resultants acting at caisson top centre (seabed level) and the resulting displacements.
The paper presents finite element analyses of caisson foundation in typical North Sea, soft clay. The results confirm the failure envelope proposed by Kay and Palix, 2011 and 2015. The envelope is extended to a yield surface using two kinematic hardening parameters, m_{HM} and m_V, the mobilization degree of lateral and of vertical loading, respectively.
The kinematic hardening rule for lateral loading is based on back-bone curves derived from force-displacement results of finite element analyses.

2 VHM FAILURE ENVELOPE AND YIELD SURFACE

2.1 Failure envelope

Large scale, field tests and small scale, laboratory tests on caisson foundations have shown that a failure envelope can be established as the locus of all load combinations, V-H-M, provided all forces and moment act in the same vertical plane passing through the top centre of the caisson (Houlsby, Ibsen and Byrne, 2005). The shape of the envelope is confirmed by numerical analyses along different load paths.
Kay and Palix, 2011, found that a caisson with diameter D and length L has an elliptical envelope,

Figure 1, expressed as:

$$H^*_{ult}(t)=a_{MH}\cdot\cos(t)\cdot\cos(\varphi_{MH})+ b_{MH}\cdot\sin(t)\cdot\sin(\varphi_{MH}) \quad (1)$$

$$M^*_{ult}(t)= a_{MH}\cdot\cos(t)\cdot\sin(\varphi_{MH})- b_{MH}\cdot\sin(t)\cdot\cos(\varphi_{MH})$$

In Eq.(1) $H^*_{ult}(t)$ and $M^*_{ult}(t)$ are the normalized horizontal ultimate force, H_{ult}/H_o and ultimate moment, M_{ult}/M_o, respectively. $H_o= D\cdot L\cdot s_{u,ave,L}$ and $M_o= D\cdot L^2\cdot s_{u,ave,L}$ are the reference force and moment respectively. $s_{u,ave,L}$ is the average undrained shear strength of soil over the length L of the caisson. The ellipse (the major axis) is rotated from horizontal by an angle of φ_{MH}. The radius connecting the origin with the current point (H^*_{ult}, M^*_{ult}) on the ellipse makes an angle t with the ellipse major axis.

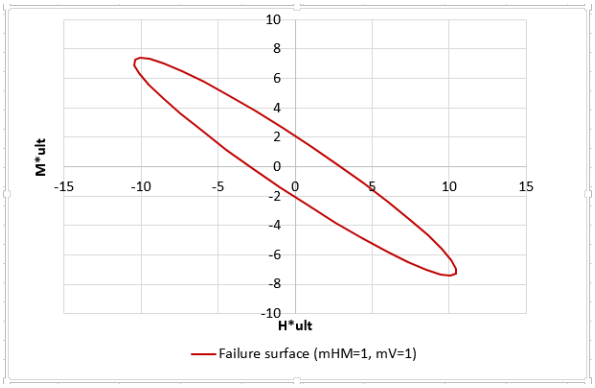


Figure 1. Failure envelope.

The coefficients a_{MH}, b_{MH} and ϕ_{MH} are presented in Kay and Palix, 2011.

2.2 Yield surface

Using the work of Kay and Palix, 2015, a general yield surface can be expressed as:

$$F=H^{*2}\cdot f(h/L)-\xi(m_V)\cdot m_{HM}^2=0 \quad (2)$$

where $m_V=V^*/V^*_{ult}$, $m_{HM}=H^*/H^*_{ult}$ $=M^*/M^*_{ult}$ during loading along M/H=h = constant load path.
The hardening function for vertical load is, according to Kay and Palix, 2015:

$$\xi(m_V) = [1-m_V^{\,bVH}]^{(2/aVH)} \quad (3)$$

with the parameters a_{VH} and b_{VH} linear functions of the ratio L/D.
The function f(h/L) is calculated as:

$$f(h/L) = [(\cos(\phi_{MH})+(h/L)\cdot\sin(\phi_{MH}))/a_{MH}]^2+ [((h/L)\cdot\cos(\phi_{MH})- \sin(\phi_{MH}))/b_{MH}]^2 \quad (4)$$

For any mobilization degree of vertical loading, m_V and of lateral loading, m_{MH}, the normalized lateral loads can be find for any loading path, h/L, as:

$$H^*=m_{MH}\cdot\sqrt{[\xi(m_V)/f(h/L)]} \quad (5)$$

$$M^*=H^*\cdot h/L$$

Finite element analyses of caisson foundation in soft clay from North Sea are performed using PLAXIS 3D to check the applicability of the failure envelope proposed by Kay and Palix. The finite element model is shown in Figure 2. The caisson foundation was modelled as a hollow cylinder using linear elastic plate elements. The cylinder has a length of L = 18.5 m and a diameter of D = 7.5 m.

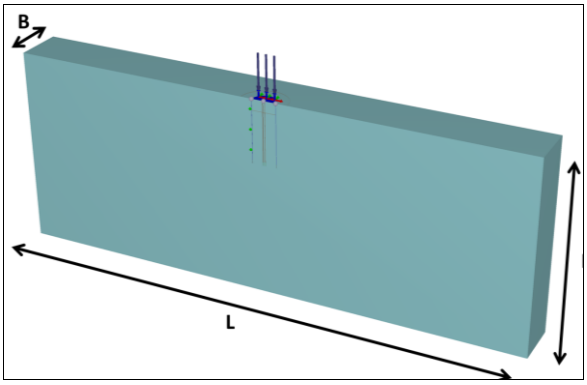


Figure 2. Finite element model.

The vertical (own weight) load, V, is applied as uniformly distributed load over the top plate of the caisson. The horizontal load, H, was applied as a point load at the centre of the caisson lid. To model the moment load, M, two equal vertical loads in opposite direction of each other were applied at the edge of the caisson lid. Both H and M were applied simultaneously in undrained conditions. In each analysis, the ratio, h=M/H, was kept constant (a linear load path in the M-H plot). The combined loading

phase, H and M, was performed by incrementally increasing the loads with a specific maximum load fraction per step until failure occurred.
The soil is modelled using "Undrained B" Mohr-Coulomb model. The soil parameters are described in Table 1. The results of PLAXIS 3D analyses are plotted together with the yield surface, Eq. (2) for m_V=0.5

Table 1. Soil parameters

Parameter	Units	Value
Identification	-	MC clay
Material Model	-	Mohr-Coulomb
Drainage type	-	Undrained (B)
γ	kN/m3	16.4
E	kN/m2	2575
ν	-	0.35
c_{ref}	kN/m2	1.87
E_{incr}	kN/m2/m	2788
z_{ref}	m	0
c_{incr}	kN/m2/m	2.025
z_{ref}	m	0
Tension cut-off	-	Yes
Tensile strength	kN/m2	0
R_{inter}	-	0.5
k_o	-	0.6

and m_{MH}=1 (failure in lateral loading) in Figure 3.a and b.
As can be seen from Figure 3, the yield surface is in good agreement with the results from PLAXIS 3D analyses on soft, North Sea clay.

3 FORCE-DISPLACEMENT BACK-BONE CURVES

The force-displacement and moment-rotation curves from PLAXIS analyses were used to derive expressions for back-bone curves providing the kinematic hardening rule of the yield surface in monotonic loading.
For each loading path with constant load ratio, h=M/H, back-bone curves H-δ and M-θ, are described using the initial stiffness parameters, $K_{\delta max}$ and $K_{\theta max}$, as functions of h/L, and secant stiffness degradation with displacement.

3.1 Initial stiffness

The initial stiffness of back-bone curves vary with the loading path ratio, h/L as shown in Figure 4. The variation of initial stiffness with the loading path ratio h/L is found to be described by:

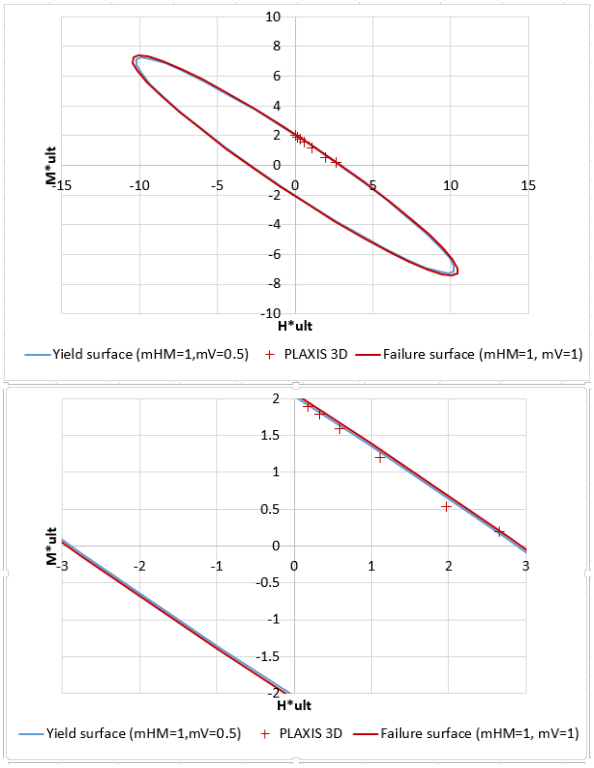


Figure 3 a. Yield surface and PLAXIS 3D results. b. Detail of Figure 3.a.

$$K_{\delta\delta max}=K_{\delta\delta max,max}-k_{1\delta}\cdot x/(1/k_{o\delta}+k_{2\delta}\cdot x/(K_{\delta\delta max,max}-K_{\delta\delta maxo}))$$

$$\text{with } x=\log(h/h_o),\ h_o=0.1\cdot L \qquad (6)$$

Similarly:

$$K_{\theta\theta max}=K_{\theta\theta max,o}+k_{1\theta}\cdot x/(1/k_{o\theta}+k_{2\theta}\cdot x/(K_{\theta\theta max,max}-K_{\theta\theta maxo})) \qquad (7)$$

The coefficients $k_{1\delta}\ldots k_{o\theta}$ are found by curve fitting technique.
The "boundary" stiffness, $K_{\delta\delta max,max}$ is the initial, elastic stiffness for load path ratio h_o/L and $K_{\delta\delta max,o}$ corresponds to load path ratio h_{ult}/L (h_{ult}=1000m). The "boundary" stiffness for rotation, $K_{\theta\theta max,o}$ corresponds to h_o/L and $K_{\theta\theta max,max}$ to h_{ult}/L. The boundary stiffness can be determined by using elastic solutions for caisson stiffness.

For a caisson embedded in elastic soil with soil reaction coefficient varying linearly with depth, k=m·z, the following stiffness relations can be written for soil lateral reactions on the caisson:

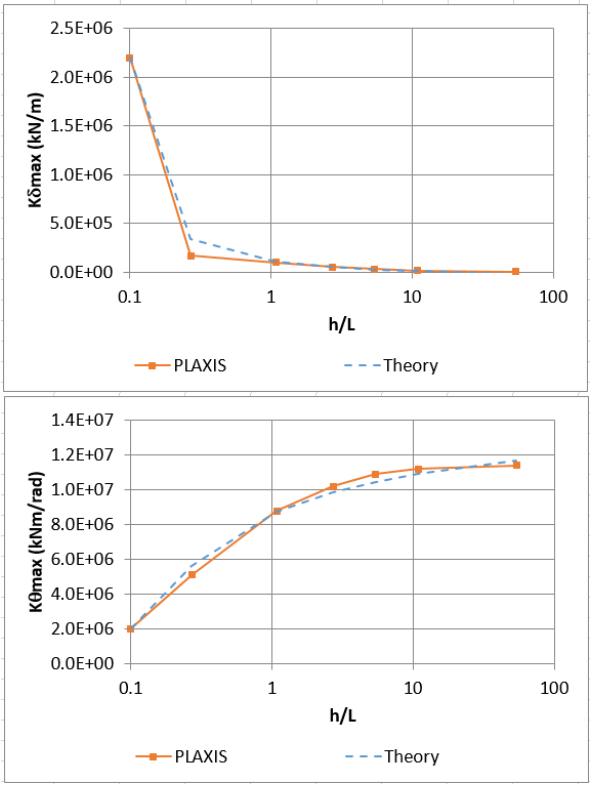


Figure 4 Variation of initial stiffness with h/L

$$H_{lat}=m\cdot D\cdot L^2/2\cdot\delta + m\cdot D\cdot L^3/3\cdot\theta$$
$$M_{lat}= m\cdot D\cdot L^3/3\cdot\delta+ m\cdot D\cdot L^4/4\cdot\theta \quad (8)$$

Using solutions from Gazetas, 2005, the coefficient m can be expressed as a function og G_{max}/s_u as follows:

$$m=2/(1-\nu)\cdot(G_{max}/s_u)\cdot(s_u/p_o')\cdot\gamma'/D \quad (9)$$

Similarly, the stiffness of bottom soil reactions can be expressed using Gazetas equations as:

$$H_{bot}=K_{xb}\cdot\delta+K_{x\theta b}\cdot\theta$$
$$M_{bot}= K_{x\theta b}\cdot\delta+ K_{\theta b}\cdot\theta \quad (10)$$

where:

$$K_{xb}=8\cdot G_b\cdot R/(2-\nu),\ K_{\theta b}=8G_bR^3/3(1-n) \text{ and}$$
$$K_{x\theta b}=(8\cdot G_b\cdot R/(2-\nu)- m\cdot D\cdot L^2/2)\cdot L/3 \quad (11)$$

The total initial stiffness is obtained from the equilibrium of lateral and bottom reaction with the applied force and moment:

$$H=H_{lat}+H_{bot}= K_h\cdot\delta+K_{h\theta}\cdot\theta$$
$$M=M_{lat}+M_{bot}-H_{bot}\cdot L= K_{h\theta}\cdot\delta+ K_\theta\cdot\theta \quad (12)$$

The Eqs.(12) can be written as flexibility equations:

$$\delta=(H\cdot K_\theta-M\cdot K_{h\theta})/\Delta=[(K_\theta-h\cdot K_{h\theta})/\Delta]\cdot H$$
$$\theta=(M\cdot K_h-H\cdot K_{h\theta})/\Delta=[(K_h-(1/h)\cdot K_{h\theta})/\Delta]\cdot M$$
$$\Delta=(K_h\cdot K_\theta-K_{h\theta}^2) \quad (13)$$

The boundary stiffness can now be determined from eq.(13), by selecting h equal to h_o or h_{ult} as explained before.
The boundary stiffness were determined using the ratio su/po'=0.32 as results from PLAXIS input and a ratio G_{max}/s_u=1000, in Eqs.(8)…(13). The values had to be corrected by adjusting coefficients (0.02-0.03 for rotation stiffness and 1.5-1.9 for displacement stiffness) in order to match the PLAXIS results, probably due to the influence roughness used for interface elements and other 3D effects.

Using the corrected values for boundary stiffness and the Eqs.(6) and (7) for initial stiffness a good agreement is shown between PLAXIS and predicted stiffness (Fig.4).

3.2 Kinematic hardening rule for lateral loading

The kinematic hardening rule is described by the back-bone curves force-displacement and moment-rotation using the formulation proposed by Athanasiu et al., 2008:

$$H=(K_\delta/K_{\delta max})\cdot(\delta/\delta_r)\cdot H_{ult}$$
$$M=(K_\theta/K_{\theta max})\cdot(\theta/\theta_r)\cdot M_{ult} \quad (14)$$

with:

$$K_\delta/K_{\delta max}=1-c_{1\delta}\cdot\text{atan}\{\exp[c_{2\delta}\cdot\log(\delta/\delta_i)]\} \quad (15)$$
$$K_\theta/K_{\theta max}=1-c_{1\theta}\cdot\text{atan}\{\exp[c_{2\theta}\cdot\log(\theta/\theta_i)]\}$$

In eqs. (14) and (15), K_δ and K_θ are the secant stiffness corresponding to displacement δ and rotation θ, respectively. $K_{\delta max}$ and $K_{\theta max}$ are initial stiffness parameters. δ_r and δ_i are reference displacement, H_{ult}/ $K_{\delta max}$ and displacement at inflexion point on the curve $K_\delta/K_{\delta max}$ vs. log(δ). The coefficients $c_{1\delta}$ and $c_{2\delta}$ are determined from the ratio $K_{\delta ult}/K_{\delta max}$ and from the slope of the curve $K_\delta/K_{\delta max}$ vs. log(δ) at the inflection point.
Examples of predicted back-bone curves as compared to PLAXIS results are shown in Figure 5.

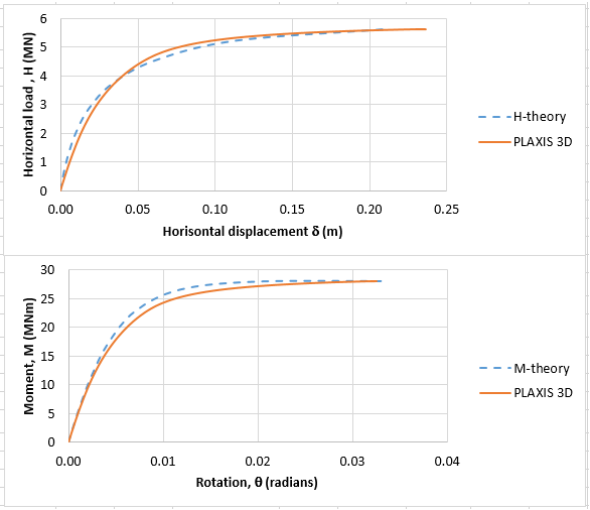


Figure 5. Back-bone curves

The kinematic hardening rule for lateral loading relating the kinematic hardening parameter, $m_{HM=}$ $(K_\delta/K_{\delta max})\cdot(\delta/\delta_r)$ with plastic displacements $\delta_{pl}=H/ K_{\delta max}\cdot[1/(K_\delta/K_{\delta max})-1]$ is determined from back-bone curve (Figure 6).

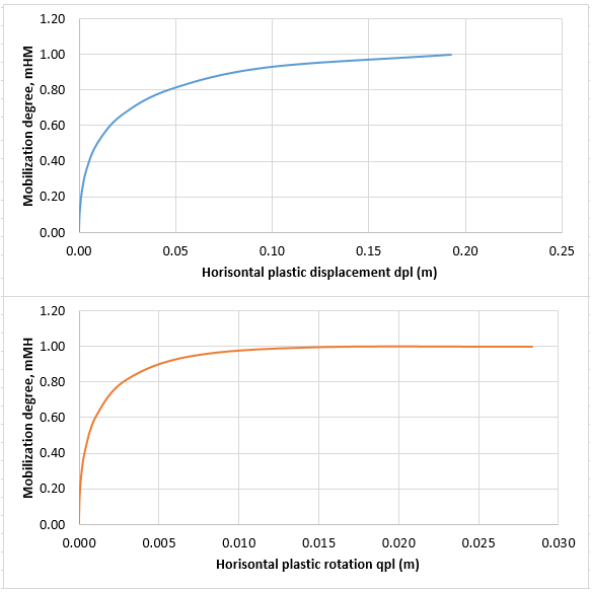


Figure 6. Kinematic hardening rule.

4 APPLICATION OF THE YIELD SURFACE AND BACK-BONE CURVES

4.1 Estimation of safety factor to failure

The key application of the yield surface for mobilization degree $m_{HM}=1$ (failure envelope) is that the envelope allows an explicit consideration of the independent load components and a graphical interpretation of the factor of safety associated with different load paths.
Consider as an example the loading situation in Figure 7. The loading path for permanent load is OA and for environmental loads is represented by the segment AB. Using the definition from ISO 19991-4, the safety factor is SF=AC/AB=1.73. The conventional bearing capacity verification would look at the ratio between vertical bearing capacity including the effect of horizontal load and the total applied vertical load: SF_{conv}= DE/DB=1.56.

4.2 Dynamic soil-structure interaction analyses in frequency domain

The back-bone curves provided by the model are used with a variable secant stiffness procedure in a modal analysis of a sub-sea structure. A loading ratio, h and secant

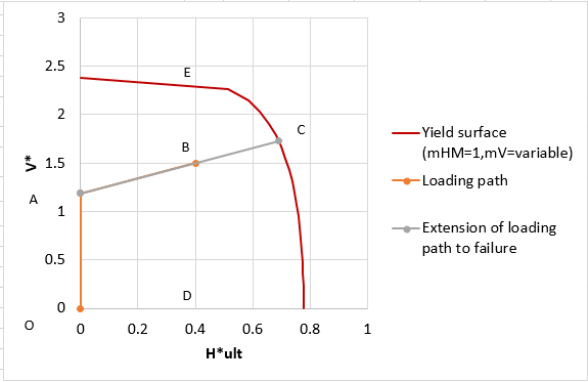
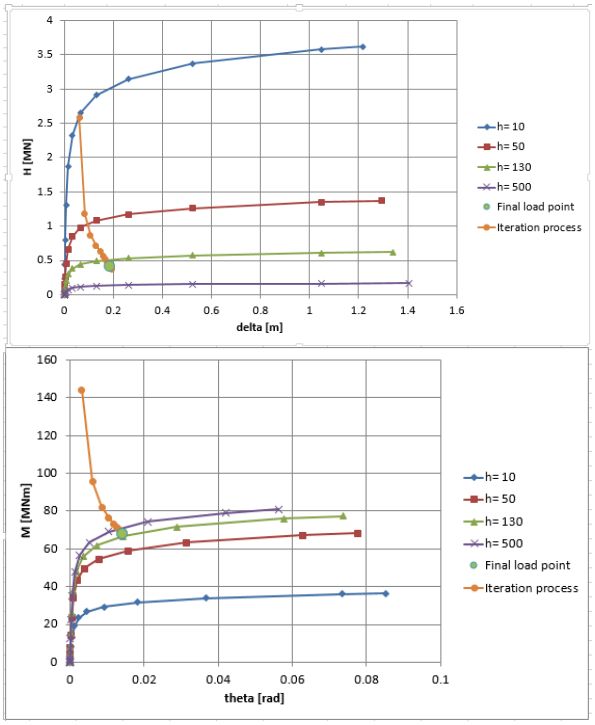


Figure 7. Definition of safety.

stiffness's K_δ and K_θ are initially assumed and a modal analysis is performed. A first estimate of natural frequencies and periods, ω_n and T_n, of dynamic loads, H_{EQ} and M_{EQ} and of displacements, δ_{EQ} and θ_{EQ} as a function of pseudo response acceleration, $PSa(T_n)$, is obtained.
The process converges only if:

- the dynamic stiffness's are compatible to the soil-caisson response stiffness described by back-bone curves;
- The dynamic load ratio $h_{dyn}=M_{EQ}/H_{EQ}$ is the same as the assumed ratio, h;
- The same mobilization degree $m_H=H/H_{ult}=M/M_{ult}$ is obtained for both, dynamic moment and dynamic force;



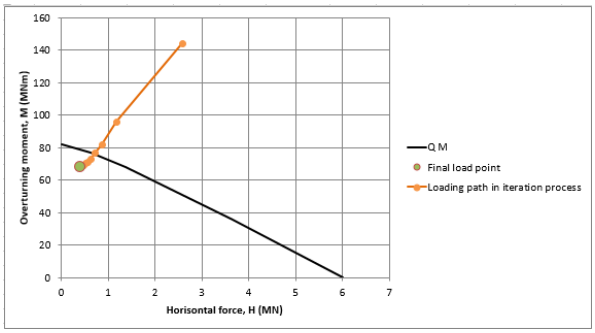


Figure 8. Results from modal analysis

If the convergence is not obtained, a new iteration is performed using the h_{dyn} as the new assumed loading ratio, h and the average mobilization degree of force and moment from the previous iteration to determine the stiffness's. Figure 8 illustrates the results of iteration process.

5 SHORTCOMINGS AND FUTURE DEVELOPMENTS OF THE MODEL

A macro-element model consisting of a yield surface and back-bone curves defining kinematic hardening rule for monotonic loading is presented. It can be used for static and dynamic soil-structure interaction analyses in frequency domain using equivalent, linear secant stiffness.
Adjustments are still required to account for effect of geometry aspect ratio L/D, non co-planar HM loads, gapping, etc. The main shortcoming of the model is that it can not incorporate the effect of load reversal.
The main task for future development of the model is the attempt to describe the elasto-plastic behaviour upon unloading and reloading. This will enable soil-structure interaction analyses of variable, cyclic loading and of dynamic analyses in time domain.

6 ACKNOWLEDGEMENTS

The authors wish to thank their colleagues at Industry Oil and Gas (IOG) Section of Geotechnical Department in Multiconsult for fruitful ideas and discussions during everyday design activity for offshore projects. The assistance from Dr. Steffen Giese, Head of the IOG Section, who encouraged and provided financial support for research work by internal funds, is gratefully acknowledged.

7 REFERENCES

Athanasiu, C., Shahrokhi, F. and Nalbant, R., M. (2008) Geotechnical Challenges of Earthquake Design according to NS3491-12. 15th Nordic Geotechnical Meeting, Sandefjord, Norway.

Gazetas, G. (2005) Foundation Vibrations. Chapter 15 in Foundation Engineering Handbook.

Houlsby, G.T., Ibsen, L.B. and Byrne, B.W. (2005) Keynote Paper: Suction caissons for wind turbines. ISFOG, 2005.

ISO 19901-4: 2003 Requirements for offshore structures. Part 4:Geotechnical and foundation design considerations.

Kay, S., & E. Palix (2011) Caisson capacity in clat: VHM resistance envelope-Part2: VHM envelope equation and design procedures. ISFOG 2011.

Kay, S. (2015) CAISSON_VHM: a program for caisson capacity under VHM load in undrained soils. ISFOG 2015.

Numerical analysis of an upstream tailings dam

L. Hassellund, R. Knutsson, H. Mattsson & S. Knutsson
Luleå University of Technology, Sweden, lovisa.hassellund@ltu.se

ABSTRACT
This paper presents a case study of how the finite element method can be utilized to analyze stability of upstream tailings dams. Upstream tailings dams are usually raised gradually and the increased load normally influences the stability in an unfavorable way; the load generates excess pore water pressures and reduced stability. In this study, an upstream tailings dam in Northern Sweden was numerically simulated with the finite element software PLAXIS 2D in order to assess the stability of the dam. Upstream tailings dams are sensitive to high raising rates since initiated excess pore water pressures might not have time to dissipate. Stability analysis of a tailings dam is an application that is very suitable to carry out using finite element software; once a finite element model of the complex geometry of a dam has been established, it is easy to stepwise add new soil volumes, associated with each new raising, to the model.

In this case study, it was found that strengthening actions were needed in order to maintain a stable structure. Rockfill berms were gradually added on the downstream slope of the model to obtain a factor of safety above a recommended value. The volumes of rockfill needed for the berms were minimized by numerical optimization to reduce costs. The stability between the years 2024 and 2034 was analyzed; with an annual deposition cycle.

The performed numerical study resulted in a future plan for placement of rockfill berms to establish sufficient stability of the tailings dam. It was found that the volume of rockfill in the berms needed, varied during the years studied. Numerical modeling, as presented in this paper, is a useful tool for the dam owner to plan and design for future raisings of a tailings dam.

Keywords: Numerical simulation, tailings dam, stability, excess pore water pressure

1 INTRODUCTION

Waste material from mining facilities has to be taken care of in economic, environmental and safety aspects. This waste material is usually deposited in large impoundments surrounded by embankment dams i.e. tailings dams. The tailings dams have to be raised continuously to maintain storage for new generated tailings material. Tailings dams can be raised mainly by three different methods; upstream construction, downstream construction or centerline construction (Vick, 1990).

The aim of this paper is to show how the finite element method, in this case with the software PLAXIS 2D (Brinkgreve et al., 2014), can be utilized as a tool for dam safety analysis. A tailings dam mainly built by the upstream method is investigated between the years 2024 and 2034 to assess its future stability. The tailings dam is raised annually and its stability is ensured by adding rockfill berms on the downstream slope of the dam. The locations of the berms are optimized with the aim to minimize the total volume of rockfill. If sufficient stability of the studied dam in the existing impoundment can be achieved in the future, the owner does not need to find other deposition options for the generated tailings.

The tailings dam investigated in this paper is located in Aitik in Northern Sweden and has previously been examined by Ormann et al. (2013), Ormann et al. (2011) and Knutsson et al. (2015); where numerical simulations were utilized. Both in Ormann et al. (2013) and Ormann et al. (2011) the time period studied is not the same as in the present study, nor the constitutive model for the tailings material. The study conducted by Knutsson et al. (2015) contains deformation analyses and estimations of excess pore water pressures between the years 2014 and 2024.

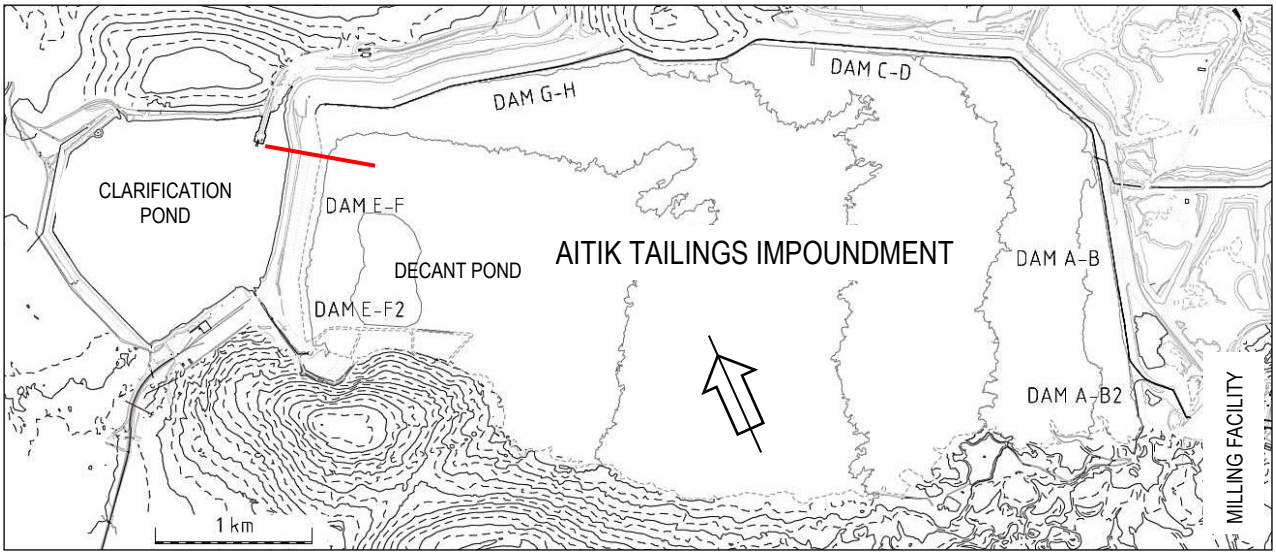


Figure 1 The studied tailings dam E-F is located between the tailings impoundment and the clarification pond. The red line shows the examined cross section of the tailings dam. (Knutsson, 2014)

The results were used to assess the dam stability. By utilizing the factors of safety, *FoS*, alert values were estimated for monitoring programs. Studies regarding tailings material in the Aitik impoundment were carried out by Bjelkevik (2005) and Bhanbhro (2014) where behaviors and material properties of the tailings were investigated.

2 AITIK TAILINGS DAM

The tailings dam studied is located in Aitik, Northern Sweden. The Aitik mine is an open pit copper mine that has been operational since 1968 and is owned by Boliden Mineral AB. The ore contains less than one percent of copper and with an annual production of 39 million tonnes of ore (year 2014) huge amounts of waste material are generated. The impoundment area, where the tailings material is deposited, is approximately 13 km^2 and is surrounded by tailings dams and by natural heights. The tailings dam E-F is chosen for the numerical analysis in this study and is located between the tailings impoundment and the clarification pond, see Figure 1. The most critical failure scenario occurs when a failure of tailings dam E-F results in a failure of the embankment dam surrounding the clarification pond. A failure like this might cause environmental damages downstream of the impoundment facilities. (Sweco Infrastructure AB and TCS AB, 2012)

The tailings material is mixed with water from the processing plant to produce a slurry. Thereafter, the slurry is distributed through pipes and deposited in the impoundment. Between approximately the period 15th of October and 30th of April the tailings material is deposited from a single discharge point from tailings dam A-B, close to the milling facility, see Figure 1 (Sweco Infrastructure AB and TCS AB, 2012). This method is used to prevent freezing in the pipes. Between approximately the period 1st of May and 14th of October the spigot method (Blight, 2010) is used and the tailings are distributed through spigots placed around the impoundment, see Figure 1. The spigot method creates segregation in the tailings material; coarser particles are settled close to the dam structure and finer particles further away. This phenomenon with coarser and finer particles separated, creates good foundation conditions for future dike constructions. The coarser particles contribute to a denser foundation which is required by the upstream method. The dissipation of excess pore water pressures corresponds to the consolidation process where coarser grained soil have higher hydraulic conductivity and allow the phreatic line to disperse faster than finer grained soil. The area between the dam structure and the decant pond is called beach and is required to

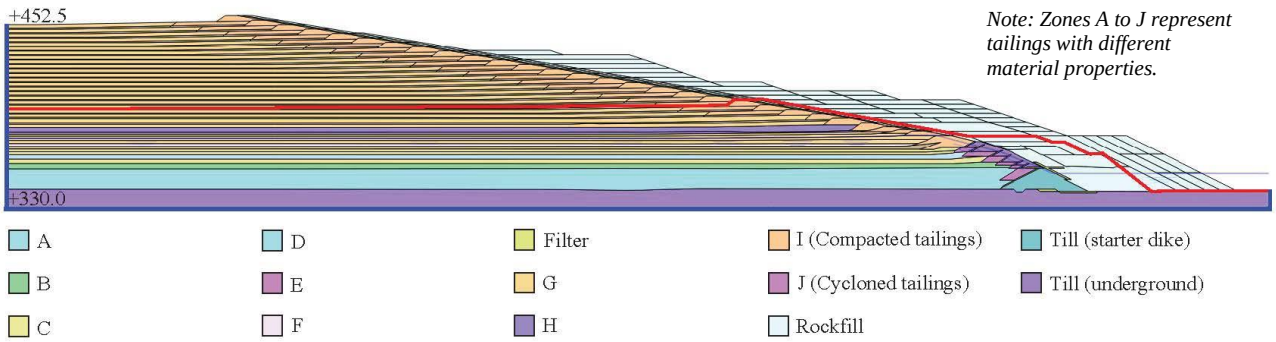


Figure 2 Material zones in the tailings dam. The red lines show the size of the dam year 2015 and the blue lines show the outer boundaries. The whole geometry is presented for year 2034.

make the phreatic level decrease before reaching the downstream slope of the dam. (Lottermoser, 2010) The beach at tailings dam E-F is between 100 and 200 meters wide. (Sweco Infrastructure AB and TCS AB, 2012)

3 FINITE ELEMENT MODEL

To increase impoundment storage for generated tailings, tailings dams have to be raised continuously with sufficient stability. According to Swedish recommendations, the stability of tailings dams has to be sufficient for a very long time; i.e. 1000 years (Bjelkevik, 2005; Svensk Energi AB/SveMin, 2012). Svensk Energi AB/SveMin (2012) recommends factors of safety, *FoS*, for tailings dams to be above 1.5 during normal operation conditions.

Plane strain conditions were applied in the finite element model since the dam was considered to be a long structure i.e. the length of the dam is much larger than the width of the dam; no deformations along the longitudinal direction were expected.

By simulating future raisings at the tailings dam between the years 2024 and 2034 in the finite element software PLAXIS 2D, the dam stability was assessed. If the dam stability in the simulations results in *FoS* values below the recommended value, strengthening actions have to be implemented. In this numerical analysis, rockfill berms were placed on the downstream slope of the dam to increase the dam stability.

Rockfill berms were assumed to be constructed on the downstream slope of the tailings dam between the period 15th of October and 30th of April, to increase the dam stability during the following dike construction. An optimization technique, where the volume of rockfill was minimized to fulfill the recommended stability, was utilized in the simulations. The basic idea with the technique was to place as small volumes of rockfill as possible on the downstream slope of the dam to obtain *FoS* values above the recommended value. The optimization technique used in this study was basically the same technique as used by Knutsson et al. (2015) and Ormann et al. (2013). In this paper and the paper by Knutsson et al. (2015) smaller rockfill berms were placed on several different places on the downstream slope, whilst Ormann et al. (2013) placed the whole volume of rockfill at only one additional suitable position on the downstream slope of the dam. The most suitable positions for the rockfill berms were found by trying various locations and different volumes. The procedure was repeated until a *FoS* above 1.5 was obtained for a reasonable small total volume of rockfill.

3.1 Geometry

The geometry of the dam cross section was provided by the dam owner Boliden Mineral AB. The geometry was extended with future dike raisings with the same layout as the dikes constructed today (year 2015), see Figure 2.

The width of the geometry was chosen sufficiently large to obtain realistic numerical results. The geometry was assumed to be closed for water flow in the left and the right

Table 1 Values of material properties for tailings in the dam structure in Figure 2 (Knutsson, 2014; Pousette, 2007; Bhanbhro, 2014). The material properties are defined in e.g. Brinkgreve et al. (2014).

	Unit	A	B	C	D	E	F	G	H	I	J
E_{50}^{ref}	kPa	7500	7500	4200	4000	3800	3800	2700	3700	3800	3800
E_{oed}^{ref}	kPa	8200	8200	3000	4200	5200	5200	2600	4800	5000	5000
E_{ur}^{ref}	kPa	48000	48000	20000	20000	20000	20000	17000	20000	17000	17000
m	-	0.5	0.5	0.6	0.5	0.7	0.7	0.5	0.9	0.6	0.6
p_{ref}	kPa	250	250	100	100	100	100	100	100	100	100
ν'_{ur}	-	0.3	0.3	0.3	0.3	0.3	0.3	0.3	0.3	0.3	0.3
c'_{ref}	kPa	15	15	13.7	25	14	21	4	15	10	10
ϕ'	°	17.5	17.5	26.7	16.3	17	14	19.4	16.9	26	26
ψ'	°	0	0	0	0	0	0	0	0	0	0
R_f	-	0.48	0.48	0.6	0.58	0.68	0.68	0.8	0.75	0.9	0.9
γ_{unsat}	kN/m³	14.3	14.3	15.45	16.2	15.7	15.7	12.3	14.9	16	16
γ_{sat}	kN/m³	19.3	19.3	20	20.5	20.1	20.1	18	19.5	19	19
e_{init}	-	1.0	1.0	0.83	0.75	0.81	0.81	1.3	0.9	0.5	0.5
k_x	m/days	0.00864	0.04752	0.0864	0.04752	0.04752	0.04752	0.0864	0.04752	0.4752	0.0864
k_y	m/days	8.64E-4	4.752E-3	0.00864	4.752E-3	4.752E-3	4.752E-3	0.00864	4.752E-3	0.04752	0.00864

vertical outer boundaries of the model, see Figure 2. The lower horizontal outer boundary was also assumed to be closed. Both horizontal and vertical deformations were modeled to not occur in the bottom boundary and for the left and right outer boundaries only vertical deformations were allowed.

The foundation for tailings dam E-F as well as the starter dike consist of till, see Figure 2. The first six dike raisings, counted from the starter dike, were also constructed of till. The subsequent dike raisings were constructed of compacted tailings. All dike constructions were equipped with filters and rockfill on the downstream slope to protect the slope from surface erosion. The tailings were disposed and depending on the milling process of the tailings, the material properties vary over the years. The rockfill berms were constructed during the winter, due to less work activity at the impoundment that time compared to summer periods. Furthermore, rockfill materials are less sensitive to freezing and thawing than materials with lower hydraulic conductivity.

3.2 Material properties

The geometry of the tailings dam studied was divided into different subareas to represent different soil layers, see Figure 2. The subareas have various sizes and different material properties. The values of the material parameters in Table 1 and Table 2 correspond to the letters and names shown in Figure 2.

All values of the material properties for the tailings in the impoundment came from laboratory tests presented by Pousette (2007). The constitutive model *Hardening Soil* (Brinkgreve et al., 2014) was chosen for the tailings material, since parameter values were available. Values of material properties for the constitutive model were evaluated by Pousette (2007), Knutsson (2014) and Bhanbhro (2014). The values of material properties for the tailings evaluated for *Hardening Soil* can be seen in Table 1. By using *Hardening Soil*, in the analyses, deformations could be realistically modeled, since *Hardening Soil* is a better constitutive model than the simpler constitutive model

Table 2 Values of material properties for filter, rockfill and till in the dam structure in Figure 2 (Sweco Infrastructure AB and TCS AB, 2012; Jonasson, 2008). The material properties are defined in e.g. Brinkgreve et al. (2014).

	Unit	Filter	Rockfill	Till (starter dike)	Till (underground)
E	kPa	20000	40000	20000	20000
v	-	0.33	0.33	0.33	0.33
$\mathbf{c'_{ref}}$	kPa	1	1	1	1
$\boldsymbol{\varphi'}$	°	32	42	35	37
$\boldsymbol{\psi'}$	°	0	0	0	0
$\boldsymbol{\gamma_{unsat}}$	kN/m^3	18	18	20	20
$\boldsymbol{\gamma_{sat}}$	kN/m^3	20	20	22	22
$\mathbf{e_{init}}$	-	0.5	0.5	0.5	0.5
$\mathbf{k_x}$	m/days	86.4	0.1	0.00864	0.00432
$\mathbf{k_y}$	m/days	86.4	0.1	0.00432	0.000864

Mohr Coulomb when analyzing deformations (Brinkgreve et al., 2014).

The constitutive model *Mohr Coulomb* was chosen for filter, rockfill and till since values of material properties were available, see Table 2. The values of material properties for the *Mohr Coulomb* model were provided from geotechnical investigations reported by Jonasson (2008).

All values used as material properties in the simulations were assumed to be valid also in the future. No studies about future behavior of this tailings material have been composed; for instance, regarding changes of stiffness and strength caused by aging effects.

The increased load from the dike constructions is first carried by the pore water in the form of excess pore water pressures. The excess pore water pressures will then slowly decrease during consolidation and the load transforms gradually over to the soil skeleton. The hydraulic conductivity in the soil material and drainage conditions in the surroundings determines the rate of excess pore water pressure dissipation. This is modeled in PLAXIS 2D for each activity, by first assuming undrained conditions that will change into drained conditions if complete consolidation is achieved.

3.3 Mesh generation

The geometry of the tailings dam was divided into 15-noded triangular finite elements. In order to choose a proper mesh, different element coarseness were tested in the simulations. The most convenient mesh was chosen considering both computation time and accuracy of the results, see Figure 3. Local mesh refinements were performed in the downstream toe of the dam to achieve more accurate results in the computations.

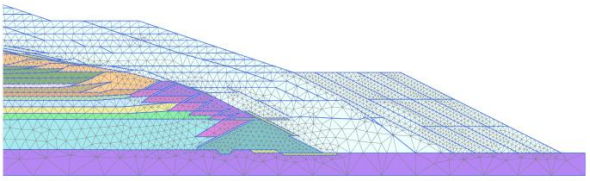


Figure 3 Generated mesh in the model with local mesh refinements at the dam toe.

3.4 Computation phases

All computations in the software PLAXIS 2D were defined with initial conditions, described in an initial phase at a pre-defined time. This initial time point for the studied tailings dam E-F was chosen to be in year 2007, since the raising rate of the dam increased that year. It was assumed, due to the low raising rate earlier, that no excess pore water pressures existed in the dam structure at the defined initial time point. All

deformations were set to zero in the initial phase.

One year was divided into different activities that were inserted in the simulations as computation phases, see Figure 4. Between the period 15th of October and the 30th of April, no discharge of tailings from dam E-F was taking place. This period is called winter in Figure 4. In the vicinity of the analyzed cross section, it was assumed that spigotting of tailings took place between the period 1st of May and 31st of July. Followed by a period of 15 days of rest, 15 days of dike construction and another 15 days of rest. The rests were needed for the working process for dike constructions. After that, spigotting continued 14th of September until 14th of October.

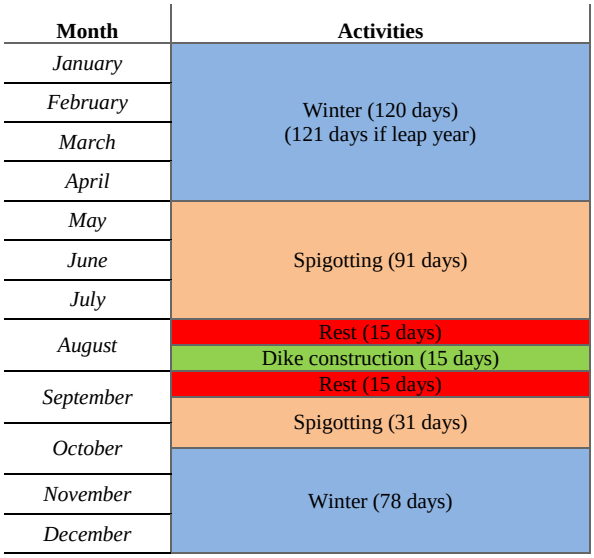


Figure 4 Annual activities at dam E-F used in the computations.

In order to assess the slope stability of tailings dam E-F, consolidation computations were executed. The times defined in Figure 4 correspond to the duration of each activity where consolidation was computed. The worst case was found when the load increased within the dam structure and consolidation was still not completed. This occurred immediately after a new dike was constructed. The increased load gave increased excess pore water pressures and thus decreased *FoS* values.

With the intention of examining the dam stability, safety computations were performed after each consolidation computation. The factor of safety is defined in PLAXIS 2D by

$$FoS = \frac{available\ strength}{strength\ at\ failure} \quad (1)$$

where the *available strength* is the strength from the effective stress state and input strength parameters. The *strength at failure* is obtained by decreasing the input strength parameters in small increments until an unstable structure is obtained. The *FoS* assessed in PLAXIS 2D gives the global *FoS* of the whole dam geometry. (Brinkgreve et al., 2014)

3.5 Water conditions

The phreatic line defined in the simulations was assumed to be at the surface of the tailings material, see a), b) and c) in Figure 5 depending on the activity described in Figure 4. As can be seen, the location of the phreatic line was changing depending on the activity. When the phreatic line reached the point where the beach and the dike construction intersects (dike toe) the groundwater level started to incline as a straight line between fixed measurement points in the dikes, see d) in Figure 5. Thereafter, the phreatic line was assumed to be horizontal. This level represents the highest allowed water level in the clarification pond. The field measurements regarding ground water location were provided by Boliden Mineral AB.

4 RESULTS

Stability analyses were conducted to assess the future stability of the studied tailings dam. The stability of the tailings dam, subjected to raisings, was first analyzed without rockfill berms added on the downstream slope of the dam. The result indicated a trend of decreasing *FoS*. Strengthening actions were therefore required. This was modeled by adding rockfill berms on the downstream slope.

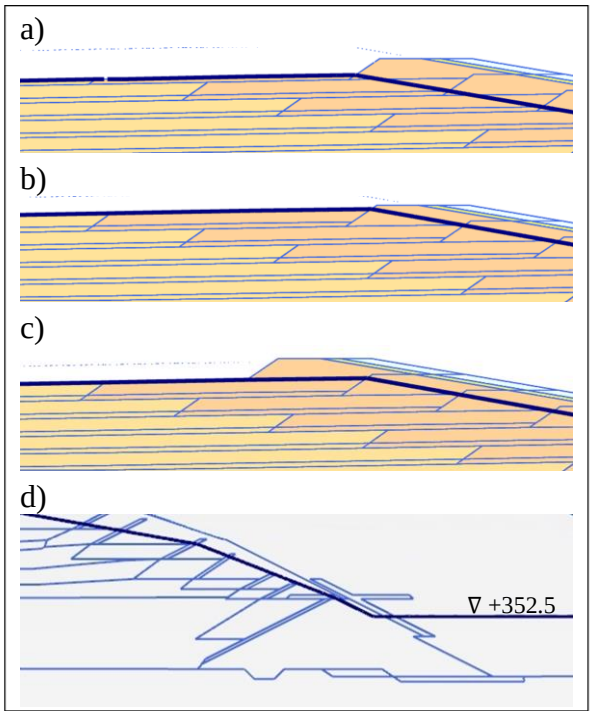


Figure 5 Location of the phreatic line: a) between 14th of September and 30th of April b) between 1st of May and 14th of August c) between 15th of August and 13th of September d) in the dam toe during all activities.

4.1 Stability with no strengthening methods

The studied raisings of the tailings dam were simulated without any strengthening methods on the downstream slope of the dam to investigate if sufficient stability was obtained. It was shown in the simulations that after only three years the *FoS* was decreasing to values continuously below the recommended value of 1.5. Since the *FoS* did not fulfill the recommended value no further analyses without strengthening methods were performed. The result from these simulations gave the *FoS* shown in Figure 6.

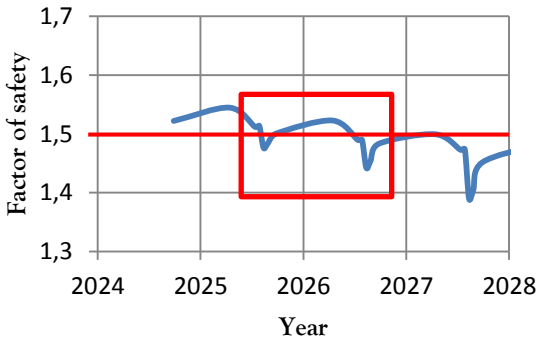


Figure 6 Values of FoS with no rockfill berms added on the downstream slope of the dam.

The highest computed *FoS* value each year occurs when maximum consolidation is achieved, due to decreased excess pore water pressures in the dam structure, see a) in Figure 7. Maximum consolidation is obtained immediately before spigotting in the spring i.e. 30th of April. When the spigotting begins, 1st of May, the *FoS* starts to decrease. This phenomenon occurs because of increased load from newly deposited tailings. The increased load contributes to excess pore water pressures and thereby reduced stability. Later in August when a new dike construction takes place, the *FoS* makes a rapid drop due to increased load which contributes to excess pore water pressures in the dam, see b) in Figure 7. The lowest *FoS* corresponds to the time when maximum excess pore water pressures are obtained, see c) in Figure 7. When consolidation of the tailings material continues after a dike is constructed, the *FoS* starts to increase again.

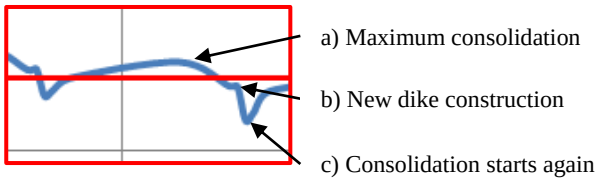


Figure 7 Enlargement of the red rectangle in figure 6. a) maximum consolidation in the soil is obtained, b) load from a new dike construction is applied, c) the soil begins to consolidate, highest values of excess pore water pressure are also find in this phase.

The most critical slip surface in year 2027, associated with the lowest *FoS*, occurred directly after a new dike was constructed, see Figure 8. The slip surface is located in the upper part of the downstream slope of the dam and the shape is almost circular. Since the *FoS* is below the recommended value of 1.5, the dam structure was further investigated by adding rockfill berms on the downstream slope of the dam.

4.2 Stability with strengthening methods

The *FoS* from the simulations with rockfill berms added on the downstream slope of the dam can be seen in Figure 9. The figure shows that the *FoS* for the whole time period studied are above the recommended value of 1.5. It can also be noted in Figure 9 that the

annual distribution of the values of *FoS* is very similar each year. The highest value of the *FoS* occurred when maximum consolidation was achieved and the lowest value of the *FoS* was achieved immediately after a new dike construction, due to increased load giving increased excess pore water pressures. The positions of the added rockfill berms can be seen in Figure 10. The rockfill berms added on the downstream slope of the dam increased the *FoS* so that values above the recommended value were obtained in all computation phases.

The slip surface representing the lowest *FoS* in year 2027 with rockfill berms added on the downstream slope of the dam can be seen in Figure 11. The slip surface is located deep, throughout the whole dam body and embraces a much larger volume of soil than the slip surface in Figure 8. The slip surface obtained in Figure 11 is non-circular.

The volumes of rockfill modeled in the simulations, during winters, on the downstream slope of the dam can be seen in Figure 12. The volumes were calculated with a constant dam length of 1500 meters. Thus, the south end of the dam consists of another dam and the north end of dam E-F consists of a dam corner, see Figure 1. It was noted that different volumes of rockfill were needed different years to obtain values of the *FoS* above the recommended value. Between the years 2030 and 2033, larger amounts of rockfill were needed compared to the other years studied.

5 CONCLUDING REMARKS

It was shown that if no rockfill berms were added on the downstream slope of the dam the slip surfaces were almost circular and located in the upper part of the dam structure. However, the factor of safety, *FoS*, gradually decreased below the recommended value of 1.5 as the dam was raised.

Strengthening actions were required to obtain values of the *FoS* above the recommended value. Rockfill berms were thus added in the simulations on the downstream slope of the dam structure.

It was stated that with enough rockfill berms on the downstream slope of the dam the stability between the years 2024 and 2034 was sufficient according to the recommended value of 1.5. When rockfill berms were added on the downstream slope of the dam the values of the *FoS* increased and the shape of the slip surfaces changed, they started to go deep through the whole dam and embraced larger volumes of soil.

The distribution of the *FoS* has a similar trend during each year in the analyses with rockfill berms. The *FoS* are located above the recommended value in all simulations which

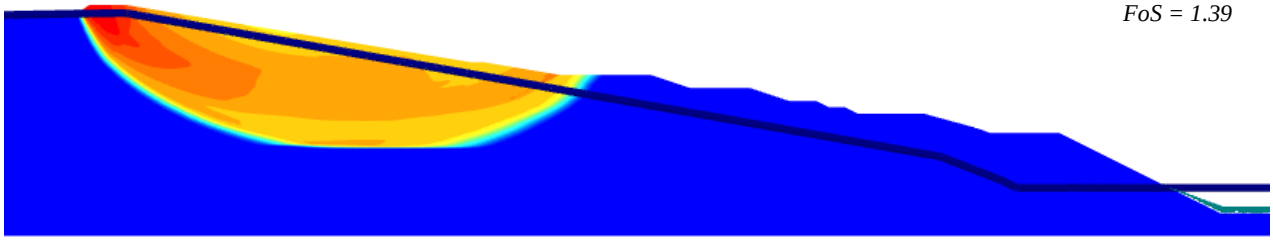


Figure 8 The most critical slip surface after dike construction year 2027; without any rockfill berms added.

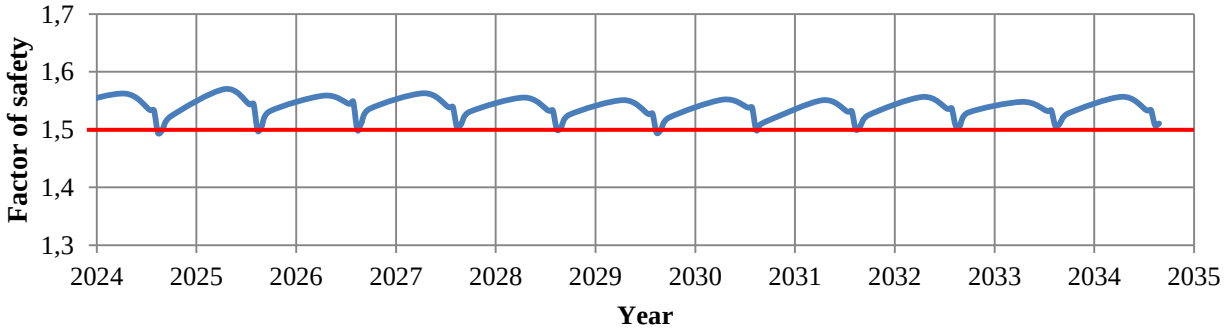


Figure 9 FoS when rockfill berms were added on the downstream slope of the dam.

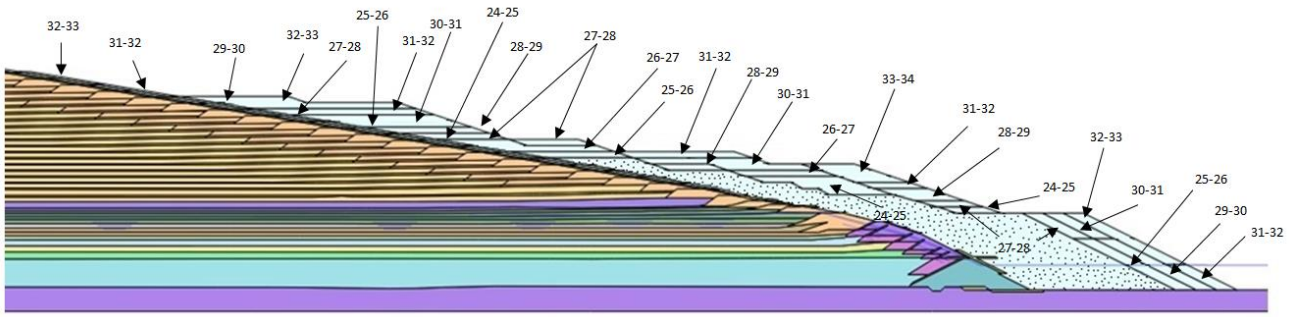


Figure 10 Rockfill plan for future raisings at the studied dam E-F.

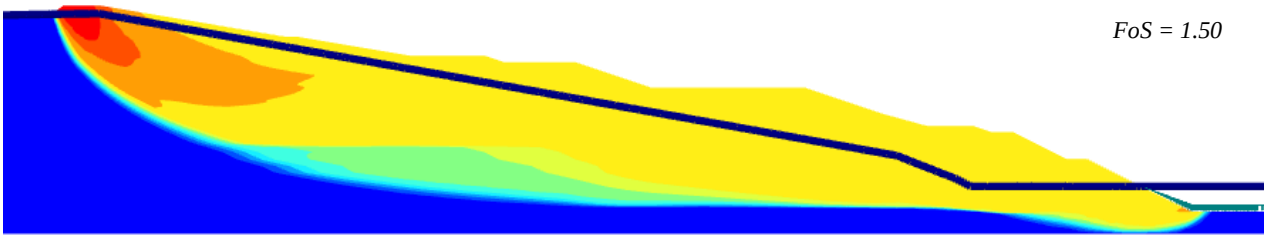


Figure 11 The most critical slip surface after dike construction year 2027; with rockfill berms added.

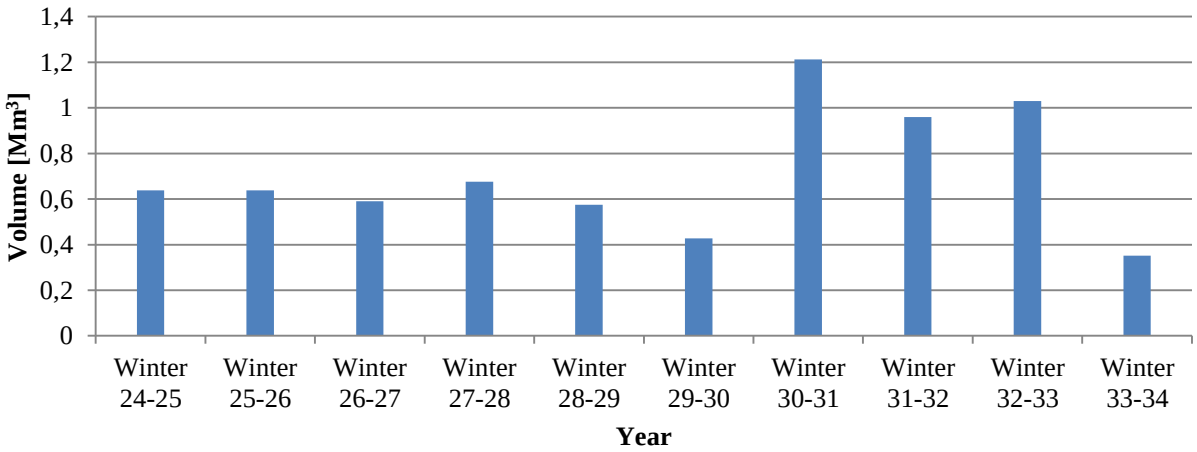


Figure 12 Volume rockfill used on the downstream slope of the dam in the simulations.

indicated that a good optimization of rockfill berms was performed.

Different volumes of rockfill had to be added each year in order to increase the values of *FoS*. The increased dam stability comes from the resisting moment of the added berms and if longer distances, i.e. levers, between the point of rotation and the point of gravity in the berms were utilized, less amount of rockfill had to be used.

Once a geometry of a structure was inserted into a finite element software it is easy to do further investigations and analyses, by stepwise add or remove soil volumes to the structure. Thus, gradual raisings of a tailings dam is a good example of an engineering application that is particularly suitable to analyze in a finite element software.

This study has shown, that the finite element software PLAXIS 2D is a very good tool in finding the most convenient locations as well as volumes for rockfill berms to be added, using stability analysis when raising tailings dams.

6 ACKNOWLEDGEMENTS

The authors would like to express their sincere thanks to Boliden Mineral AB, Sweden for giving us this opportunity to carry out the presented study regarding the tailings dam E-F at the Aitik mine. The authors would also like to express special thanks to Mr. Peter Marthin and Mr. Anders Forsgren, Boliden Mineral AB and Ms. Annika Bjelkevik, TCS AB for encouraging support and site information.

Mr. Riaz Bhanbhro at Luleå University of Technology (LTU), is to be acknowledged for performing laboratory tests and for evaluation of material parameters and Mr. Fredrik Jonasson at SWECO Energuide AB, for providing information from field data.

The research presented was carried out within the environment of "Swedish Hydropower Centre - SVC" at LTU. The support from the SVC environment is highly appreciated and acknowledged for. SVC was established by the Swedish Energy Agency, Elforsk and Svenska Kraftnät together with Luleå University of Technology, The Royal Institute of Technology, Chalmers University of Technology and Uppsala University.

Luleå University of Technology is acknowledged for additional financial support and for providing laboratory resources for the work.

7 REFERENCES

Bhanbhro, R. (2014) Mechanical Properties of Tailings – Basic Description of a Tailings Material from Sweden. Licentiate thesis. Luleå, Sweden: Graphic Production.

Bjelkevik, A. (2005) Water Cover Closure Design for Tailings Dams – State of Art Report. Licentiate thesis. Luleå, Sweden: Universitetstryckeriet.

Blight, G. (2010) Geotechnical Engineering for Mine Waste Storage Facilities. London, U.K.: Taylor & Francis Group.

Brinkgreve, R.B.J., Engin, E. & Swolfs, W.M. (2014) Plaxis 2014. Delft, the Nederlands: Plaxis bv.

Jonasson, F. (2008) PM Förslag på materialparametrar för "Övriga material" vid beräkning i PLAXIS. Project number: 2166133310, Luleå, Sweden: SWECO VBB (In Swedish) (Internal report)

Knutsson, R. (2014) Numerical analyses of Aitik tailings dam. Luleå, Sweden: Luleå University of Technology. (Internal working document)

Knutsson, R., Viklander, P. & Knutsson, S. (2015) The use of numerical modeling in alert level set-up for instrumentation in tailings dams. In Proceedings of 25th Congress and 83rd Annual Meeting of International Commission of Large Dams (ICOLD), Stavanger, Norway, 13 – 20 June 2015. Q.98-R.

Lottermoser, B. (2010) Mine wastes - Characterization, Treatment and Environmental impacts. New York, U.S.: Springer.

Ormann, L., Zardari, M.A. Mattsson, H., Bjelkevik, A. & Knutsson, S. (2011) Numerical Analysis of Curved Embankment of an Upstream Tailings Dam. Electronical Journal of Geotechnical Engineering (EJGE), 16, 931-944.

Ormann, L., Zardari, M.A., Mattsson, H., Bjelkevik, A. & Knutsson, S. (2013) Numerical analysis of strengthening by rockfill embankments on an upstream tailings dam. Canadian Geotechnical Journal, 50, 391-399.

Pousette, K. (2007) Laboratorieförsök på anrikningssand från Aitik. Ödometerförsök, Triaxialförsök. Luleå, Sweden: Luleå University of Technology. (In Swedish) (Internal working document)

Svensk Energi AB/SveMin. (2012) GruvRIDAS - Gruvindustrins riktlinjer för dammsäkerhet. Stockholm, Sweden: Föreningen för gruvor, mineral- och metallproducenter i Sverige. (In Swedish)

Sweco Infrastructure AB, TCS AB. (2012) Bilaga A5 - Teknisk Beskrivning Dammar - Förutsättningar för nuvarande och fortsatt deponering i befintligt sandmagasin vid Aitikgruvan. Stockholm, Sweden: Sweco Infrastructure AB, TCS AB. Project number: 2168053 and 1011202 (In Swedish) (Internal report)

Vick, S.G. (1990) Planning, Design, and Analysis of Tailings Dams. Vancouver, Canada: Bitech Publishers Ltd.

Analysis of settelments in the project The South Marieholm Bridge

A. Kullingsjö
Skanska Sweden AB, Sweden, anders.kullingsjo@skanska.se

C. Edmark, R. Oskarsson
Skanska Sweden AB, Sweden

ABSTRACT
Som en viktig del av Marieholmsförbindelsen byggs Södra Marieholmsbron i direkt anslutning till den befintliga Marieholmsbron och den kommande Marieholmstunneln. Projektet drivs av Skanska MTH som en totalentreprenad och inkluderar totalt 1,5 km järnvägsbro över Säveån, E45:an och Göta älv samt anslutande järnvägsbankar och tre järnvägsbroar med spännvidd mellan 20 och 60 meter.

Projektet innehåller ett flertal geotekniska utmaningar. Djupa schakter för brostöd på land. Stabilitetsförhöjande åtgärder utefter kajerna. Djupgrundläggning av brostöd ute i älven. Breddning av järnvägsbank samtidigt som pågående marksättningar skall brytas.

Samtidigt som dessa utmaningar skall bemästras skall hänsyn tas till befintlig infrastruktur och angränsande verksamheter.

Aktuell artikel behandlar främst hur framtida sättningar vid breddning av järnvägsbanken prognosticerats med beaktande av rådande sättningshastighet på 13 mm/år och angränsande konstruktioner.

As an important part of Marieholm Connection Project the South Marieholm Bridge is constructed directly adjacent to the existing Marieholm Bridge and the upcoming Marieholm Tunnel. The project is run by Skanska MTH as a design and build contract and includes a total of 1.5 km of railway bridge over the Säve river, the E45 and the Göta river together with the adjoining railway embankments and three railway bridges with spans between 20 and 60 metres

The project contains a number of geotechnical challenges. Deep excavation for the bridge foundations. Stability enhancing measures along the quays. Deep Foundations for bridge support, in the river and on land. Widening of existing railway embankments without causing settlement.

While effectively addressing these challenges existing infrastructure and associated activities must be taken into account.

This article deals primarily how settlements from the widening of the embankment were estimated taking into account current settlement rate of 13 mm / year and adjacent structures.

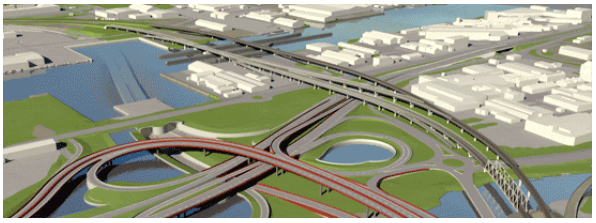
Keywords: Soft clay, settlements, creep, pile foundation, case record

1 INLEDNING

1.1 Bakgrund

Södra Marieholmsbron är en del i Marieholmsförbindelsen som inkluderar vägförbindelse under och ny järnvägsförbindelse över Göta älv i Göteborg. Syftet är att öka kapaciteten av framförallt godstrafik på järnväg samt att minska trafikbelastningen i Tingstadstunneln. Bron finansieras av regionala och nationella intressenter samt genom EU bidrag.

Södra Marieholmsbron är en viktig del i den kommande utbyggnaden av Hamnbanan, järnvägslänken mellan Göteborgs Hamn och övriga Sverige, som idag är enkelspårig. Hamnbanan kommer för att klara det ökade kapacitetsbehovet byggas ut till dubbelspår. (TrV, 2014).



Figur 1. Illustration av Marieholmsförbindelsen, (TrV, 2014).

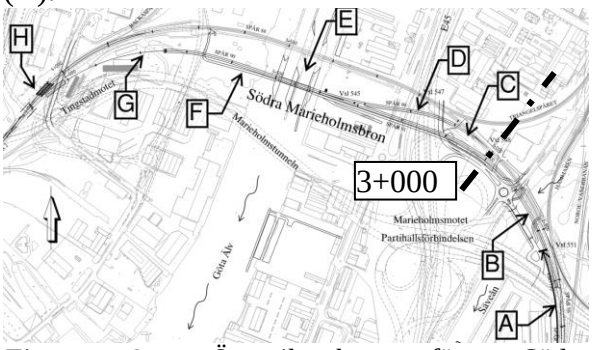
1.2 Entrepenad Södra Marieholmsbron

Södra Marieholmsbron avser bro över Säveån, E45:an samt en lyftsvängbro över Göta älv som byggs strax nedströms den befintliga Marieholmsbron, med en sammanlagd längd på 1,5 km. Projektet genomförs som en totalentreprenad. Utöver den långa bron ingår i projektet tre järnvägsbroar över framtida tunnelramper på Hisingssidan. Förutom projektering av bron och anslutande järnvägsbankar inkluderas projektering och färdigställande av samtliga installationer för lyftsvängbron och BEST arbetena.

I entreprenaden ingår omfattande markarbeten på ömse sidor om älven i form av miljösanering, ledningsomläggningar och grundförstärkningar inför kommande entreprenader i området.

Entreprenaden drivs av ett konsortium mellan Skanska Sverige AB (70%) och MT Højgaard (30%). Projektet bedrivs med utökad samverkan nivå II mellan beställaren trafikverket (TRV) och Skanska MTH.

En översiktsplan för SMB redovisas i Figur 2. Anslutningen mot befintliga spår mot Olskroken, söder om och under Partihallsbron (PHB), utgörs av lättfyllnadsbank (A). Övergångskonstruktionen vid brons landfäste utgörs av bankpålning i kombination med lättfyllning. Passagen över Säveån (B) utgörs av en fackverksbro. Vid (C) skall den befintliga brons element bytas ut för att möjligöra att trafiken leds mellan de bägge broarna. Därefter fortsätter järnvägsbron över väg E45 som trafikeras under hela projektet (D).



Figur 2. Översiktsplan för Södra Marieholmsbron

Passagen över Göta älv (E) utgörs av en lyftsvängbro av stål. På Tingstadsidan fortsätter sedan järnvägsbron ytterligare ca 200 m västerut innan spåret förläggs på bank som förstärkts med bankpålar (G). Marken runt brostöden på Tingstad sidan (F) är grundförstärkt med KC-pelare. Längre västerut mot Backa (H) ingår tre stycken tågbroar som leder trafiken över Salsmästaregatan och kommande tunnelramper.

I projektet kommer projektering och BEST arbeten utföras för drygt 50 Mkr vardera. Några övriga mängder framgår nedan:

- 151 000 m betongpålar
- 210 000 m KC-pelare
- 17 000 m³ betong
- 1 950 ton brostål
- 2 500 m stålpålar (ø406)
- 10 000 m² spont
- 1 800 ton armering

Den nya bron skall tas i drift under våren 2016 och de slutliga arbetena, främst vid Backa färdigställs under vintern 2016-2017.

1.3 Angränsande entrepenader

Marieholmsförbindelsen är uppdelad på olika entreprenader som på olika sätt måste beaktas vid genomförandet av entreprenad SMB, (Kullingsjö, et al., 2015). Främst är det den avslutande entrepenaden för Partihallsbron som har betydelse för de sättningsanalyser som behandlas i denna artikel. Bron färdigställdes 2011, se även (Edstam, et al., 2010)

1.4 Geotekniska utmaningar

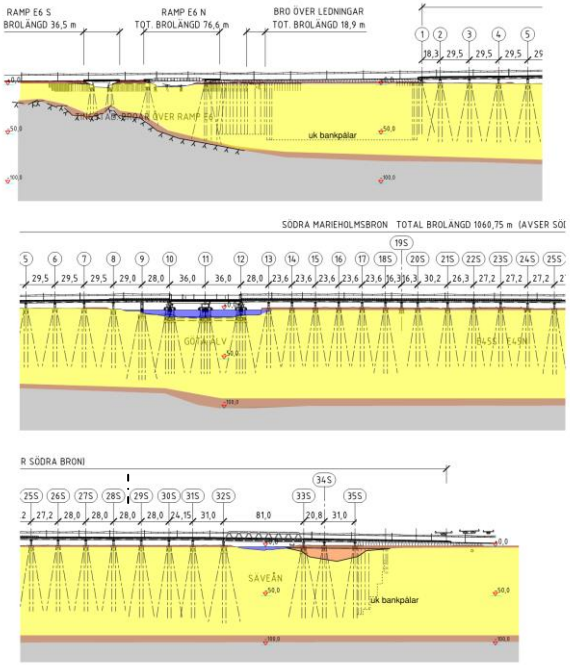
De olika geotekniska utmaningarna I projektet är omgivningspåverkan i såväl utförandeskedet som i driftskedet. Exempelvis bristande totalstabilitet, djupa schakter, massundanträngning till följd av pålning och installation av KC-pelare passage av såväl Säveån som Göta älv. För att få en vidare överblick av projektet hänvisas till (Kullingsjö, et al., 2015).

2 GEOTEKNISKA FÖRUTSÄTTNINGAR

Göta älvs dalgång består i höjd med Marieholm av låglänta områden med tjocka sedimentavlagringar av lera. För det aktuella området, Figur 2, är lerans mäktighet öster om älven mer än 90-100 m. Från älven och västerut är lermäktigheten 60-75 m. Vid passagen av Salsmästaregatan minskar lerans mäktighet till ca 30m vid entreprenadgränsen.

Österifrån mynnar Säveån ut i Göta älv vilket påverkat de geotekniska egenskaperna inom de ostliga delarna, (Hellgren & Svensson, 2005). Dagens flödesriktning på Säveån under PHB är en kvarleva av Göta älv som tidigare flöt runt Marieholm. Två olika områden med helt olika geotekniska egenskaper i leran har konstaterats med en geografisk gräns ungefär mellan stöd 28 och 29 (km 3+000), se Figur 2 och Figur 3.

Det ostliga området präglas av svämsediment bestående omväxlande av gyttjig siltig lera, silt och sand och en större sandlins öster om dagens Säveå. Dessa sediment överlagras idag av fyllning med 1-3 meters mäktighet. Förkonsolideringstrycket är lågt, *OCR*, ca 1,1, genom hela lerprofilen. Sättningar i storleksordningen 6 -13 mm/år har konstaterats.



Figur 3. Längdprofil för (södra) bron.

Det västra området karakteriseras av lera som uppvisar *OCR* i storleksordningen 1,2 – 1,3 vilket stämmer väl med empirin för övrig lera i Göta älvdalen. Observerade sättningar i området är 4 mm/år längst österut respektive 2 mm/år väster om Göta älv.

Vattenkvoten, *w*, är generellt ca 80% på nivå -5,0 avtagande till ca 60% vid ca 50 m djup. Konflytgränsen är i paritet med vattenkvoten eller något högre. Den odränerade hållfastheten, c_u, i västra området är generellt 12-13 kPa ned till 4 meters djup för att sedan öka 1,3 kPa/m.

Sandlinsen verkar haft en dränerande effekt vilket resulterat i högre σ'_{vc} och högre c_u inom sandlinsens närhet. Utanför den direkta påverkan av sandlinsen och svämsedimenten är hållfastheten mellan 13 och 15 kPa ned till 12 meters djup för att därunder öka ca 1,2 kPa/m.

3 PASSAGEN UNDER PARTIHALLSBRON

3.1 Tekniska förutsättningar

Givna dimensioneringsförutsättningar för bropålar öster om Säveån fram till PHB är att marksättningar på 1080 - 1560 mm skall förväntas uppkomma under 120 år, där de största marksättningarna är närmast PHB. Påhängslaster skall beaktas ovan neutrala lagret eller som djupast till nivå -30. Det beskrivs också att dessa marksättningar är krypsättningar

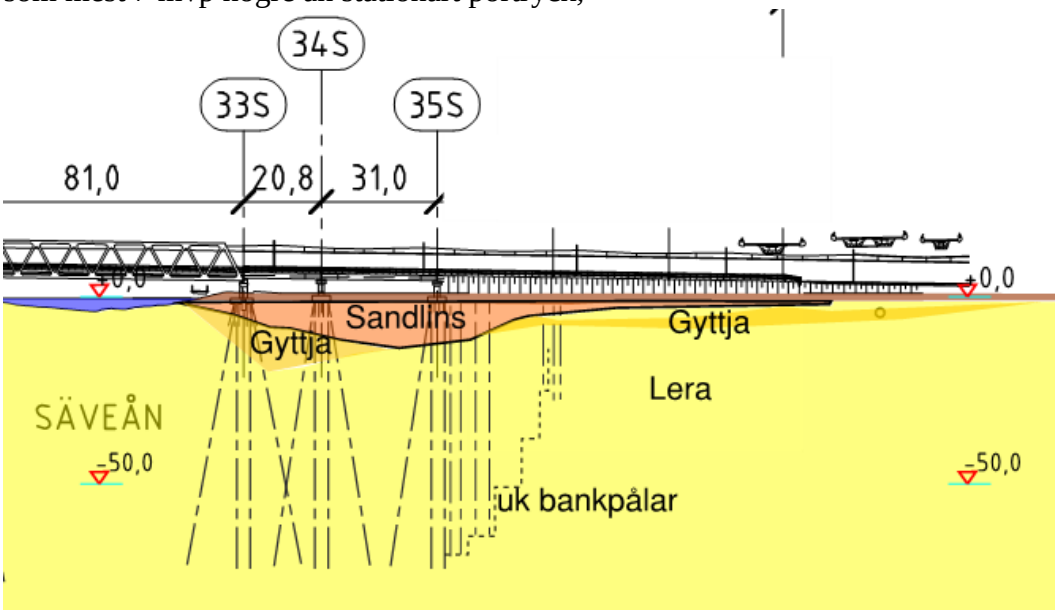
3.2 Geotekniska förutsättningar

Området präglas av sandlinsen och Säveåns utlopp i Göta älv. Sandlinsen underlagras av gyttja, Figur 4.

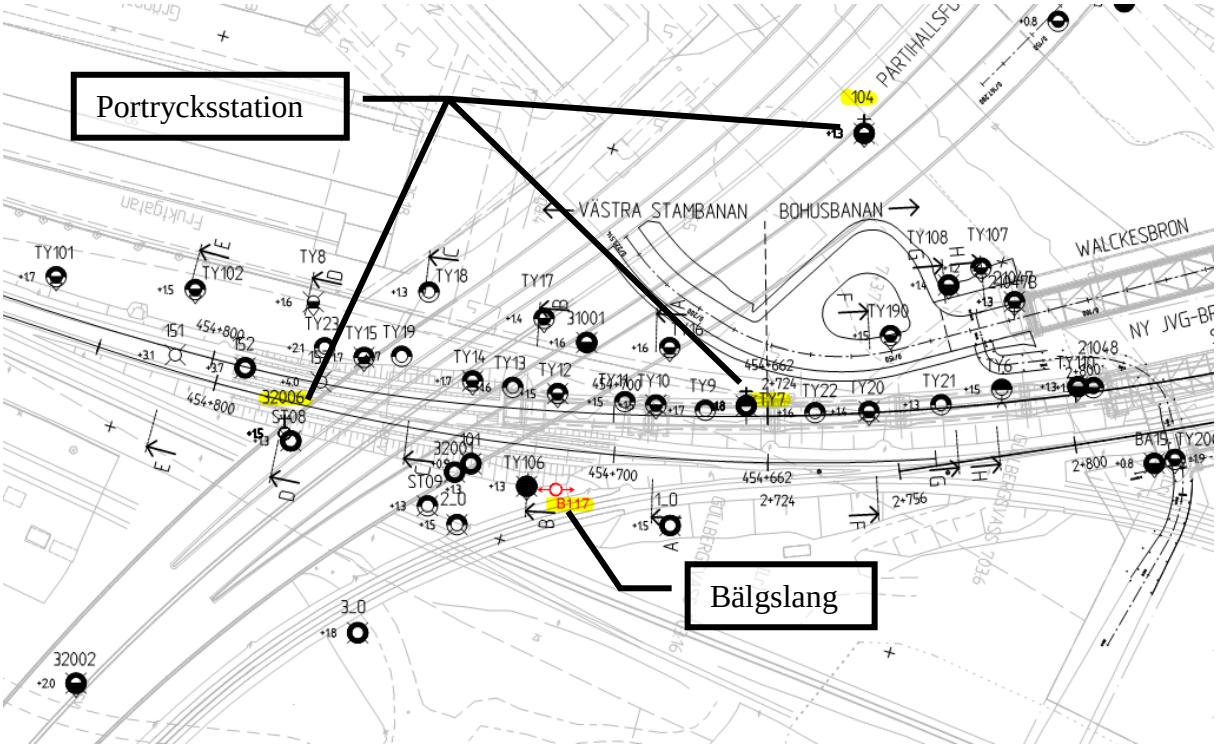
Portrycksmätningar i området indikerar att trycknivån i friktionsjordslagret under leran motsvarar en nivå på 1,2 meter över markytan. I övre magasinet, fyllningen och sandlinsen, ligger grundvattennivån på ca 1,5 meters djup. Utförda portrycksmätningar i leran uppvisar trycknivåer som uppgår till som mest 7 mvp högre än stationärt portryck, Figur 6. Porövertycken i mätstation 104 beror på den generella uppfyllnad som gjorts i området samt av krypinducerat porövertryck. Det förhöjda porövertrycket i mätstation 32006 och TY7 är orsakad av de befintliga järnvägsbankarna.

Sättningarna i området är mätt med bälgslangar installerade ned till 48 meters djup samt med markpeglar. Vid bälgslang B117 i anslutning till befintlig järnvägsbank har 114 mm marksättning konstaterats på 10 år. Den relativa sättning som mäts från underkant bälgslang och till den översta mätpunkten på 5 meters djup är 93 mm. Med antagandet att sättningen i fyllningen är försumbar under mätperioden är det rimligt att anta att sättningarna på 48 meters djup är ca 15 mm under 10-års perioden. De största sättningarna sker dock mellan 5 och 25 meters djup, ca 80 mm under motsvarande period.

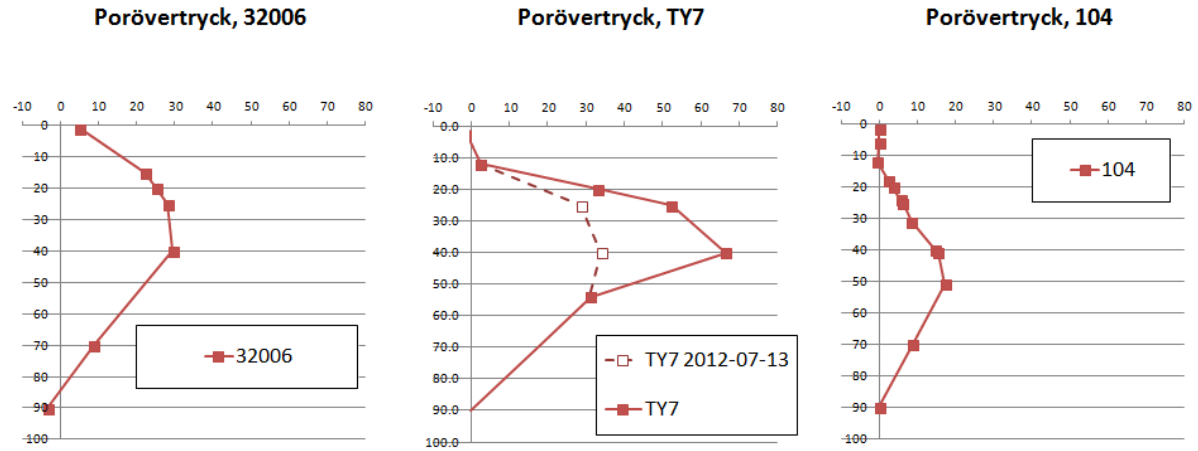
Övriga markpunkter visar sättningar i storleksordningen 6 mm/år och upp till 13 mm/år i anslutning till där järnvägsbankarna är som störst.



Figur 4. Jordprofil vid passagen under PHB



Figur 5. Utförda undersökningar i området



Figur 6. Mätta porövertryck i området.

3.3 Vald lösning

Skanska MTH har förändrat TRV:s förslag baserat på genomförbarhet och för att minimera påverkan på PHB grundläggning.

Enligt förslagsritningen var brons landfäste placerat under PHB med en övergångskonstruktion med 30 m bankpålning och 60 m lättfyllnadsbank. TRV:s förslag innebar att SMB:s landfäste och anslutande bankpålning på en 30 meters sträcka skulle utföras under PHB, vilket bedömdes kostsamt och riskfyllt.

Skanska MTH valde att korta bron 3 fack. Landfästet hamnar därmed 85 m från PHB. I anslutning till landfästet utfördes bankpålning på 30 m sträcka. Resterande bank utgörs av en lättfyllnadsbank, 150 m. För att skona Partihallsbrons grundläggning från tillskottslaster från en breddad bank installerades en mindre bankpålning med injekteringspålar i direkt anslutning till det närmsta brostödet, E4.

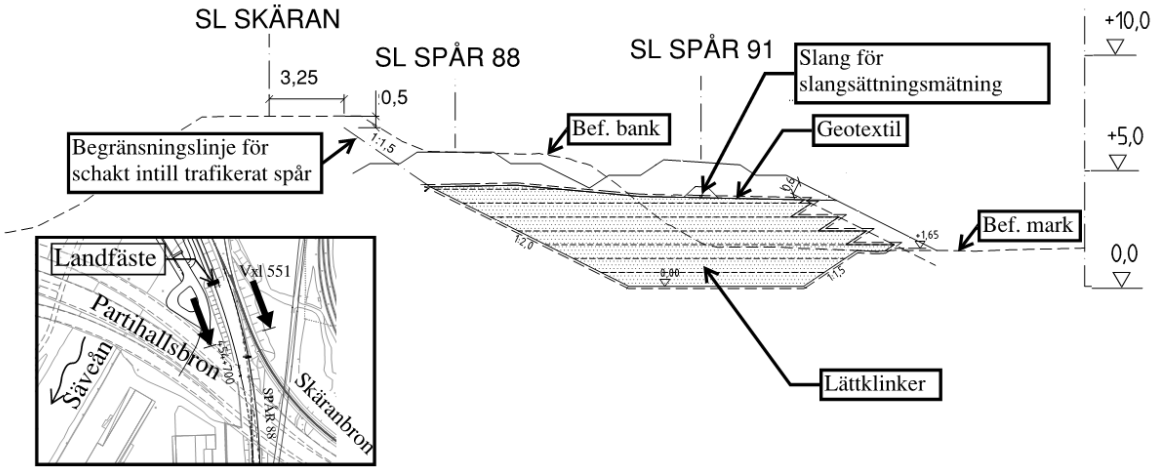
Lättfyllnadsbanken söder om PHB är oförändrad gentemot ursprungsförslaget. Under bron och norrut skiftas så mycket som möjligt, med hänsyn till stabiliteten upp mot

spåret som ansluter mot Skäranbron, ut mot lättklinker.

Baserat på de givna spänningssituationerna i förfrågningsunderlaget skulle utskiftningen innebära en avlastning som medförde *OCR* större än 1,25 ned till 30 m djup vilket var den nivå dit sättningarna skulle beaktas.

I detaljprojekteringsskedet konstaterades dock att de spänningsnivåer som angivits i FU ej var represntativa för det nya spårläget. Detta föranledde mer omfattande analyser än vad som ursprungligen var tänkt.

Under de spårsträckor där lättfyllning nyttjats har rör för framtida uppföljning av sättningarna med slangsättningsmätning installerats.



Figur 7. Tvärsektion i anslutning till PHB.

4 SÄTTNINGSANALYS ÖSTER OM SÄVEÅN

4.1 Konceptuell modell

4.1.1 Allmänt

I den inledande detaljprojekteringen konstaterades att det pågick inte bara sekundär konsosolidering utan även primär konsolidering i området. Vidare konstaterades på grund av de missledande uppgifterna i FU att urskifning ej skulle vara tillräckligt för att med en enkel analys konstatera att OCR större 1,25 skulle åstadkommas.

Den beräkningsmetodik som Skanska MTH tänkt sig använda för att dimensionera pålgrundläggningen baseras på samma metodik som PHB dimensionerats med, (Edstam, et al., 2010). Denna metodik ger spänningar och sättningar efter oändlig tid baserat på att krypdeformationerna avstannar vid ett givet *OCR*, ofta 1,25. Detta angreppssätt är dock EJ tillämpligt då pågående sättningar till stor del består av konsolideringssättningar vilket innebär att tiden måste beaktas.

Ovanstående innebar att en mer detaljerad analys än vad som förutsatts i anbudsskedet krävdes. Modellen för den aktuella frågeställningen att prognostisera framtida marksättningar måste kunna beakta:

- in situ förhållandena med höga porövertryck i leran
- pågående marksättningar
- samverkan med befintliga järnvägsbankar
- samverkan med befintliga pålar
- samverkan med nya grundförstärkningar
- inverkan av existerande sandlins

Inledningsvis nyttjades geosuite för att återskapa dagens portrycksituation och sättningshastighet. Erhållen sättningshastighet var dock allt för liten jämfört med den observerade varför istället valet föll på FE-programmet PLAXIS

4.1.2 Materialegenskaper

En relevant beskrivning av lerans egenskaper är av största vikt för att modellen skall vara trovärdig vid simuleringar av vad som händer under bankens livslängd. Därför används materialmodell ”Soft-Soil-Creep” för att modellera lerans mekaniska egenskaper.. Kalibrering har gjorts gentemot redovisade CRS försök. Kalibreringen har gjorts såväl genom att modellera själva labratorieförsöket men även med hjälp av att studera en 100 m hög jordpelare som fyllts ut på samma sätt som området generellt. Jordpelaren har studerats med avseende på primär och sekundär konsoliering genom jordprofilen och hur stor kryprelaterad överkonsolideringsgrad som erhölls genom profilen. När rimliga förhållanden erhållits nyttjdes först en 2D modell innehållandes såväl de befintliga tågbankarna som sandlinsen. Därigenom konstaterades att det var möjligt att med hjälp av FEA kunna återskapa dagens förhållanden på ett realistiskt sätt.

Därefter nyttjades en 3D modell för att återskapa in situ förhållanden med beaktande av dagens tågbankar och befintliga pålgrundläggningr.

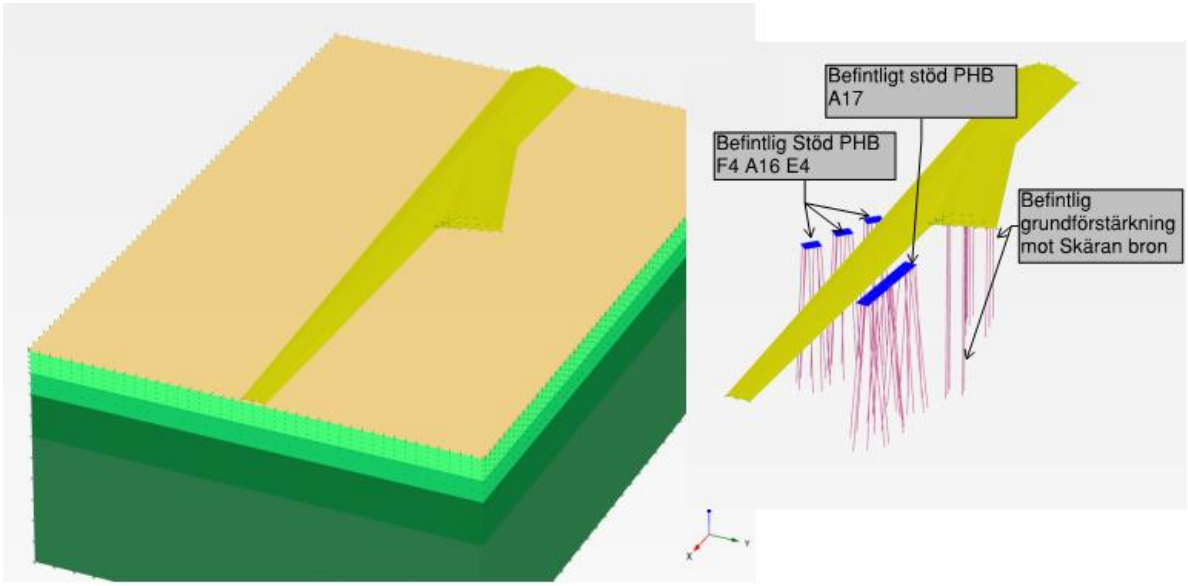
Tanken var att om dagens portryckssituation kunde återskapas i kombination med en sättningshastighet på markytan i samklang med de uppmätta var det trovärdigt att prognosticera effekterna av den nya banken på 40 och 120 år. Vidare var målet att erhålla en liknande överkosolideringsgrad i jordprofilen som de olika labratorieundersökningarna indikerade.

4.1.3 Modellering av pålar

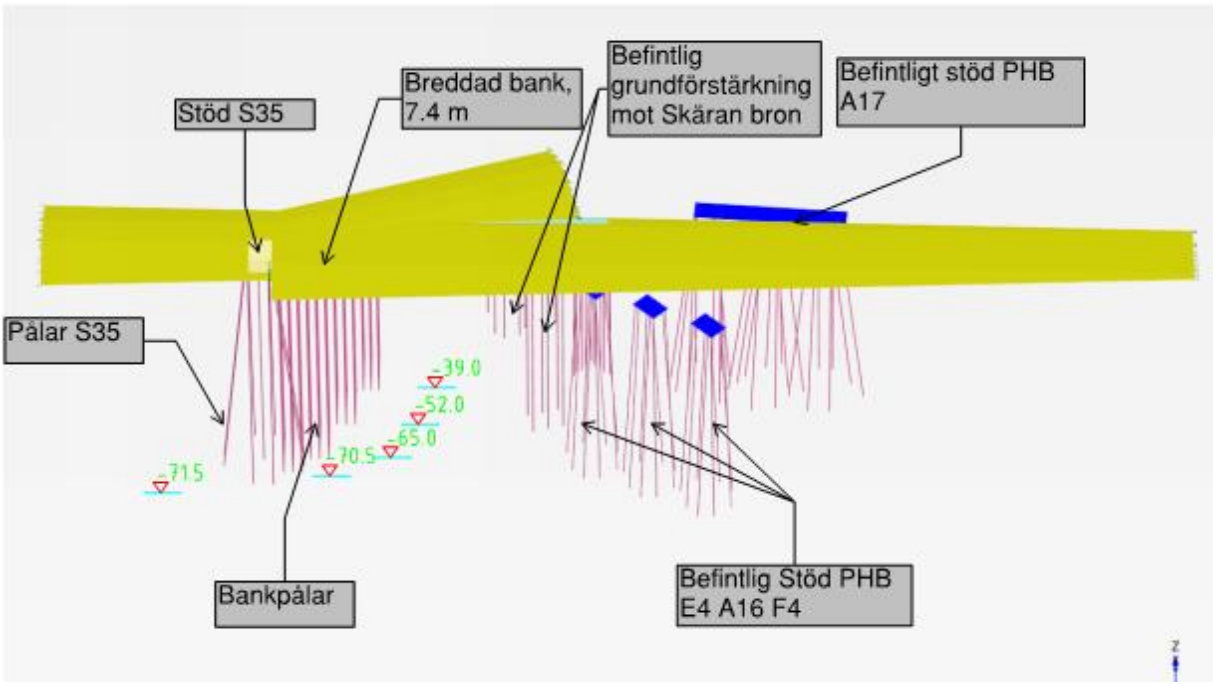
Pålarna beskrivs mha strukturelementen ”embedded piles”, för detaljerad beskrivning hänvisas till PLAXIS manualen. Dessa element har förmågan att överföra longitudinella krafter utefter hela längden. Dessa krafter utvecklas som funktion av relativrörelsen mellan påle och omgivande jord. Mantelkrafterna baseras på okorrigerade hållfastheter från vingborr vilka korrigerats i enlighet med Pålkommissions rapport 100 (Eriksson, et al., 2004).

4.1.4 Geometri

Då lerlagren konstaterats vara mäktigare än 90 m har en förenklad geometri enligt Figur 8 till Figur 8 använts. För att inte skapa en allt för geometrisk komplex modell har bankens krökning mellan sektion 2+820 och 454+866 försummats.



Figur 8. Geometri för befintlig bank och angränsande pålar



Figur 9. Geometri för breddad bank och tillhörande grundförstärkning

4.1.5 Modelleringssekvens

För att återskapa in situ förhållandena påbörjas beräkningen år 1700 med en antagen markyta på ±0.

Steg 1: Fyllning upp till +1.5.
Steg 2 Konsolidering fram till 1900
Steg 3 Uppförande av befintlig bank, inklusive bank mot Skäranbron
Steg 4 Konsolidering fram till 1985
Steg 5 Grundförstärkning anslutningen mot Skäran. *Aktivering av pålar*
Steg 6 Konsolidering fram till byggandet av PHB.
Steg 7 Uppförande av PHB. *Aktivering av pålar samt permanent last*
Steg 8 Konsolidering fram till år 2014

Utvärdering av uppmätta portryck samt pågående marksättningar för a att jämföra med resultat från FE-analysen så att dessa överrensstämmer.

Steg 9 Installation ny bank inklusive grundförstärkning
Steg 10 Konsolidering 2 år (resterande byggtid)
Steg 11 Konsolidering 40 år. Utifrån dessa resultat värderas såväl totalsättning som differenssättning

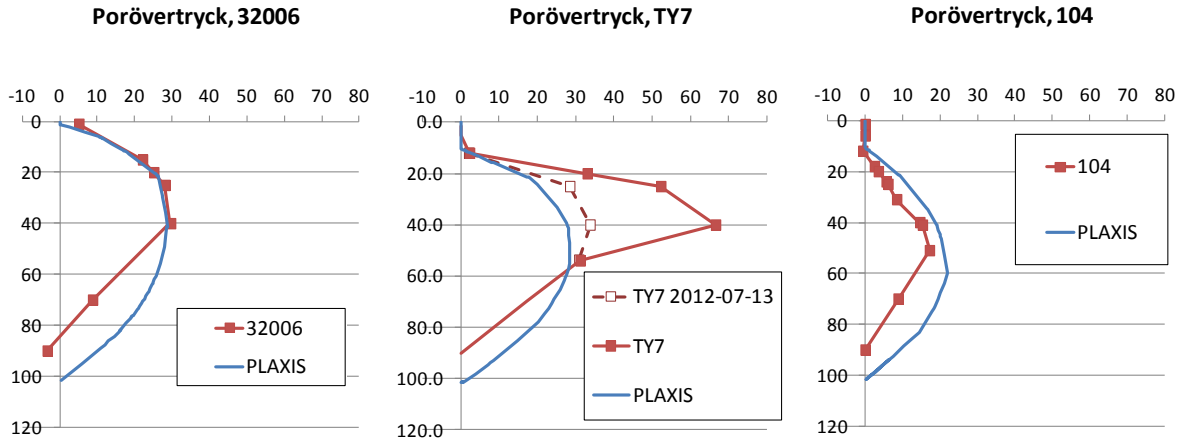
Steg 12 Konsolidering 120 år (ytterligare 80 år). Utifrån dessa resultat värderas sättningen för stöd 35 och påverkan på PHB grundläggning.

Initialtillståndet (år 1700 i beräkningen) definieras av att såväl primär och sekundär konsolidering har avslutats respektive har skett till en överkonsolideringsgrad till 1.25 vilket motsvara den överkonsolideringsgrad som uppträder för naturlig Göteborgslera.
Verifiering av modellen
För att verifiera modellen jämförs resultaten i modellen med uppmätta portryck och aktuell sättningshastighet, efter beräkningssekvens 8.

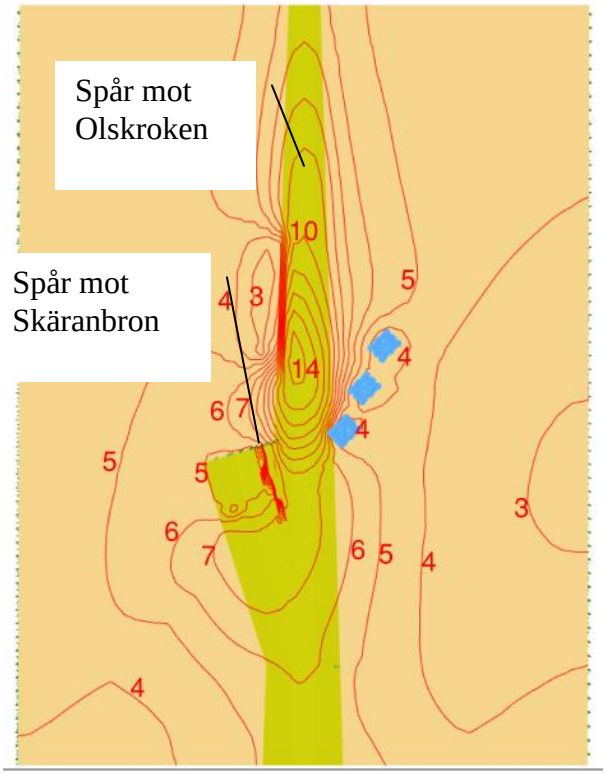
Påförd last i form av fyllning (steg 1) och existerade järnvägsbankar (steg 3) genererar primärt ett porövertryck motsvarande medelspänningsökningen i jorden. Detta porövertryck konsoliderar gradvis bort med tiden med en effektivspänningsökning som följd vilket också kommer att bidra till sekundär konsolidering. Den sekundära konsolideringen kommer fördröja portrycksutjämningen vilket förklarar den relativt stora portrycksbubblan i lerans centrala delar, även efter lång tid.

De portryck som beräknats redovisas tillsammans med mätta i form av porövertryck, Figur 10.

Figur 11 visar den beräknade aktuella sättningshastigheten vilket stämmer väl med de sättningar som mätts i området. Studeras sättningarna på djupet i läge för bälgslang B117 verifierar beräkningen att viss sättning 1 till 2 mm/år sker under 48 meters djup.



Figur 10. Beräknade porövertryck jämfört med mätta

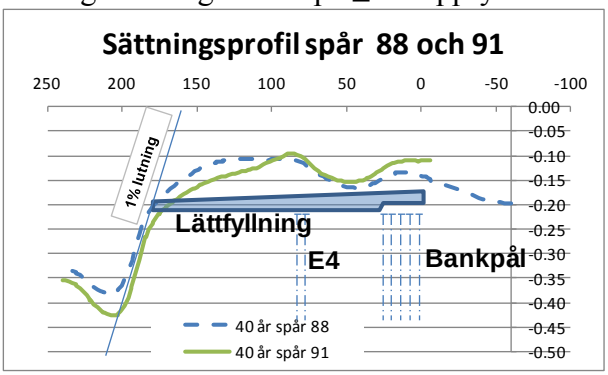


Figur 11. Beräknad sättningshastighet 2014, mm/år.

Såväl sättningshastigheten, porövertryck och spänningssituation stämmer väl med faktiska observationer.

4.2 Sättningsprognos och övriga beräkningsresultat

Baserat på att den valda modellen verkar vara representativ för dagens förhållande har sättningsprognoser upprättats för kommande 40 år, se Figur 12. Aktuella grundförstärkningar har skissats in och prognosen visar att god marginal mot maximal tillåten totalsättning på 30 cm, och att längdsättningskravet på ≤1% uppfylls.



Figur 12. Sättningsprognos för spår 91 (heldragen linje) och spår 88 (streckad linje), 40 år, längdmätningen avser sträcka från landfäste (stöd35) och mot Olskroken.

Studeras kraftspelet i bankpålar är detta det som förväntats. Sättningarna av landfästet visar att neutrala lagret för en 70 m lång påle utbildas på 41 meters djup och att förväntad sättning för landfästet på 120 år är ca 20 cm. Då en skyddspålning utförs runt PHB:s stöd

E4 kommer SMB:s påverkan vara i stort sett försumbar.

4.3 Utförande

Under ett 9 dagar långt tågstopp utfördes merparten av allt arbete med att riva bef bank och bygga ny lättfyllnadsbank på 180 m sträcka.. Arbetena flöt i stort sett utan missöden varför trafiken kunde släppas på 2,5 dygn tidigare än beräknat.

Bankpålarna installerades i förväg men några plattor installerades under tågstoppet då även den befintliga banken för spår 88 schaktades bort och den nya dubbelspårsbanken byggdes upp till stora delar med lättfyllning.



Figur 13. Utläggning av lättklinker för spår 88 och 91 under PHB. T.v. är landfästet upp mot Skäran bron.

Under utförandet uppdagades nya förutsättningar i from av ledningar som inte fick flyttas. Detta medförde att den utförda utskiftningen mellan landfästet och PHB stöd E4 ej kunde genomföras i den utsträckning som projekterats, varför det finns risk att den ”svacka” som kan skönjas ca 50 m från landfästet (stöd 35), se Figur 12 troligen blir större än enligt prognosen.

5 SLUTORD

Oktober 2015, då denna artikel skrevs, är arbetena i full gång på arbetsplatsen. Den breddade banken är på plats och pålarna och grundläggningen för de trebrostöden söder om Säveån är på plats. En nollmätning av slangsättningsmätarna är gjord och under våren kommer vi få en första indikation på hur banken beter sig.

Den geotekniska projekteringen är i stort sett klar och har involverat ett flertal personer på heltid under ett års tid. Fokus har flyttas över till produktionsstöd istället för ren projektering, men det innebär inte att geoteknikerns roll i projektet är över. De stora utmaningarna återstår ju med att följa konstruktionernas beteende i verkligheten.

6 LITTERATURFÖRTECKNING

Edstam, T., Hansson, A., Holmberg, G. & Svahn, P.-O., 2010. *Partihallsbron - ingen koloss på lerfötter.* Stockholm, SGF - Svenska geotekniska föreningen.

Edstam, T. & Kullingsjö, A., 2010. *Ground displacements due to pile driving in Gothenburg clay.* Trondheim, Norway, Taylor & Francis, pp. 625-630.

Eriksson, P., Jendeby, L., Olsson, T. & Svensson, T., 2004. *Kohesionspålar,* Linköping: Pålkommissionen.

Hellgren, L. & Svensson, L., 2005. Partihallslänken - en del i Marieholmsförbindelsen under älven i Göteborg. *Bygg & Teknik*, 1, pp. 29-35.

Kullingsjö, A., Edmark, C. & Oskarsson, R., 2015. *Södra Marieholmsbron.* Stockholm, SGF - Svenska geotekniska föreningen.

TrV, 2014. *http://www.trafikverket.se.* [Online] Available at: http://www.trafikverket.se/Privat/Projekt/Vastra-Gotaland/Marieholmsforbindelsen/ [Använd 30 12 2014].

Effects on an earth- and rockfill dam undergoing dam safety measures

J. Toromanović, H. Mattsson, S. Knutsson
Luleå University of Technology, Sweden, jasmina.toromanovic@ltu.se

J. Sipola
ÅF Hydropower Industry, Sweden

ABSTRACT
Over the lifetime of a dam several measures are usually taken in order to assure the stability and the performance of the dam. In this case a hydropower dam in Northern Sweden is in need of dam safety measures. The question arose, what consequences there might be when such measures are performed. In order to estimate these effects, simulations have been carried out in the finite element programme PLAXIS 2D. Thereby, the deformations and the stability of the dam for the planned work can be evaluated. The performed simulations are based upon previously conducted research at Luleå University of Technology, where soil parameters in the investigated dam were identified by a method of inverse analysis.

Three sections have been analysed: A, B and C. In section A increasing pore water pressure has been observed at the downstream side of the dam. Thereby it has been concluded that a new drainage system is needed; new trenches of large size are to be excavated. In section B new toe berms are planned, due to the requirement that the dam should be able to divert leakage without erosion occurring at the dam toe. This contains soil material that might degrade when stresses are increased, with intensified deformations as a consequence. In section C a new berm is to be constructed, before this can be conducted an excavation is performed at the toe of the dam.

The results have shown deformations of an acceptable magnitude and factors of safety that indicate conditions for the planned dam safety measures. Numerical values of deformations and factors of safety can be utilised as an attempt to establish alarm values for the stability of the dam. The finite element method is a useful tool for this kind of evaluation.

Keywords: dam, numerical modelling, PLAXIS, displacement, factor of safety

1 INTRODUCTION

In Sweden, a number of dams were constructed during the 1960s; some are today in need of measures in order to ensure the dam safety and dam performance. In this paper some dam safety measures are modelled for a hydropower dam by utilising the finite element software, PLAXIS, see Brinkgreve, Engin & Swolfs (2014). The effects of the measures at the dam body are evaluated by analyses of deformations and stability; the usability of the finite element method for this case is studied.

The finite element method (FEM) has been widely utilised for modelling within various disciplines, geotechnical engineering included. Numerical modelling considering geotechnical applications is described in numerous amounts of literature, for instance Potts & Zdravković (1999) and Muir Wood (1990). One of the advantages of performing finite element analyses, is the comprehensive applications when dealing with more complicated geotechnical problems.

By choosing a proper model for representing the soil behaviour during numerical modelling, the reality can be well described. This requires description of the elasto-plastic behaviour of the soil material. Theory of elasticity is often not sufficient, since soil behaves elasto-plastic. Thereby implementation of plasticity is usually required. Information regarding plasticity can be retrieved for example from Yu (2006).

However, no model is perfectly representing the behaviour of the soil material; the choice can be based upon the problem to be solved, the properties of the constitutive model and the available material data.

Problems are often faced when computational modelling is to be conducted for earth and rockfill dams. The reason is usually insufficient amount of reliable data for the material properties. Investigations by field testing are not easily performed, especially in the impervious parts, due to the probable negative effects on the dam performance as well as the dam safety. Therefore other methods, preferably non-destructive, have to be found.

Constitutive behaviour of the soil material within the dam structure can be determined by a method of inverse analysis. This is only possible if the dam is equipped with various instrumentations that are monitoring for instance pore pressures, deformations or seepage. Vahdati (2014) used an error function and a search algorithm combined with the finite element software PLAXIS to identify soil parameters of the dam in the study. Model parameters in the elasto-plastic constitutive models were calibrated until the simulated values for the deformations corresponded to the deformations from the inclinometer data.

2 CASE STUDY

With the aim to improve the dam safety and the performance of a hydropower dam in Northern Sweden, measures have been projected by the consulting company ÅF. The hydropower dam consists of earth- and rockfill, including a central impervious till core. Adjacent to the core, there are fine and coarse filters. As a supporting layer, rockfill is placed at each side of the filters. In some sections there are supporting berms on the downstream side of the dam. The dam body is partially founded on bedrock and partially on glacial till.

Various design solution for the dam safety measures of the dam were suggested by the consulting company ÅF. Thereafter the question arose of what effects these measures would exert on the dam structure. Three cross-sections have been chosen for the analyses; A, B and C in Figures 1-3.

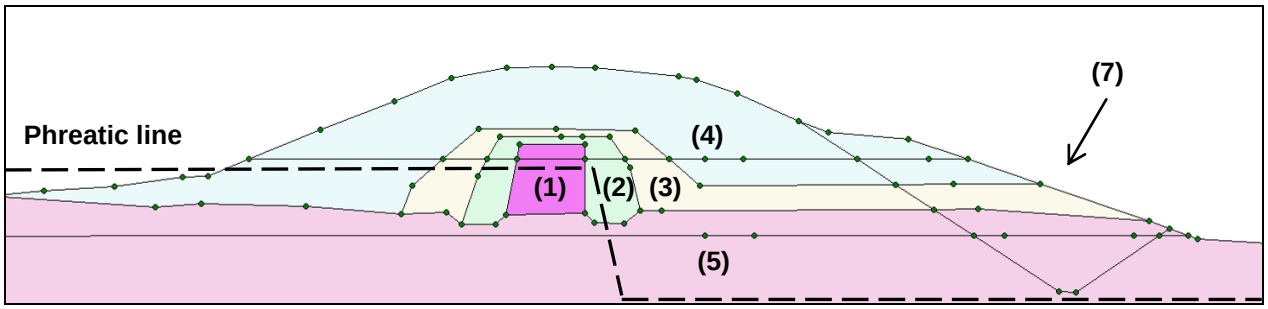


Figure 1 Section A, geometrical model of dam body. The zones are: (1) core, (2) fine filter, (3) coarse filter, (4) rockfill, (5) foundation consisting of till and (7) new trench.

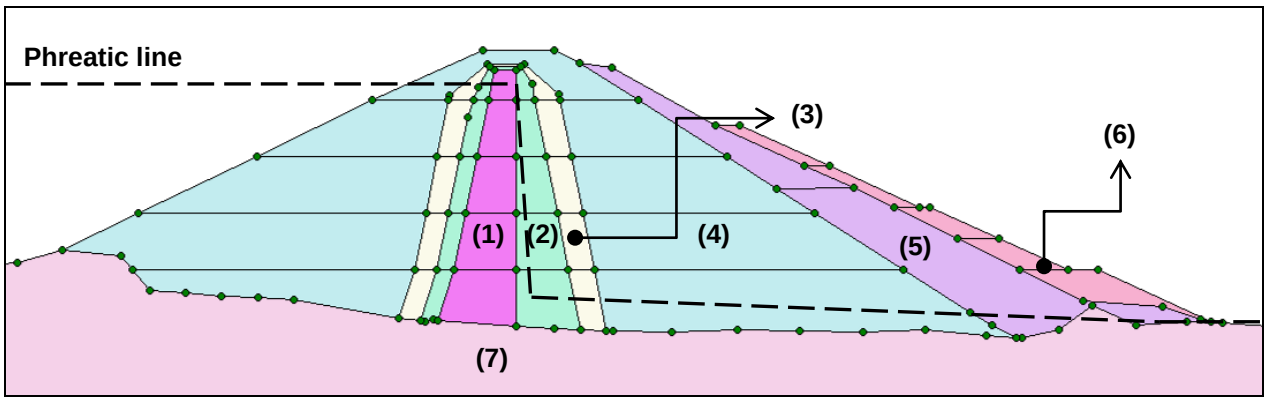


Figure 2 Section B, geometrical model of dam body. The zones are: (1) core, (2) fine filter, (3) coarse filter, (4) rockfill, (5) berm, (6) new berm and (7) foundation consisting of rock.

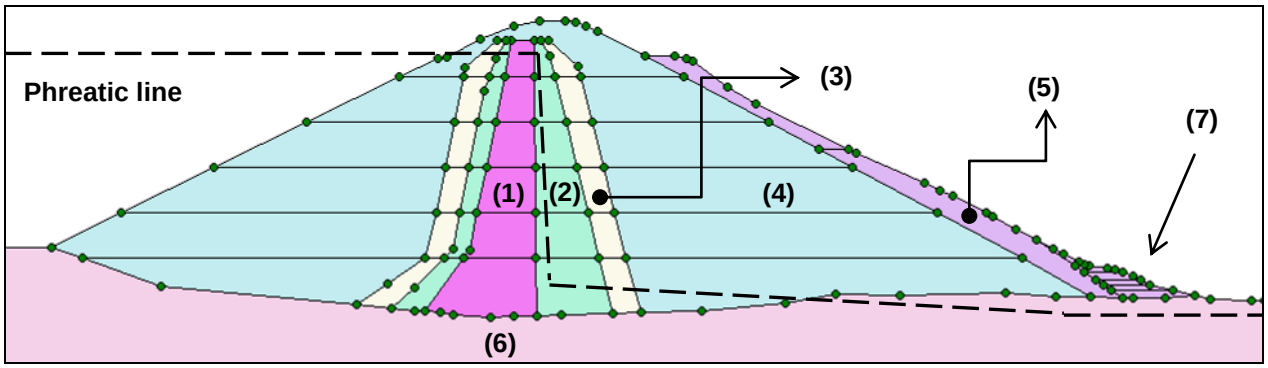


Figure 3 Section C, geometrical model of dam body. The zones are: (1) core, (2) fine filter, (3) coarse filter, (4) rockfill, (5) berm, (6) foundation consisting of rock and (7) planned excavation.

2.1 Section A

In measuring gauges, at the downstream side of the dam, a trend of increasing pore water pressure has been observed. Thereby, the drainage system has been deemed as not properly functioning. A new trench is therefore planned at the dam toe, see Figure 1. In the chosen section the depth of the planned trench is the largest compared to the height of the dam. Thus the most extensive effects of the planned work are expected in this section.

2.2 Section B

According to the Swedish dam safety guidelines, RIDAS by Svensk energi (2002), a dam should be able to divert leakage without erosion occurring at the toe. For the dam studied a new toe berms is required to attain this guideline. The planned berm is shown in Figure 2. The highest section of the dam is chosen for the analysis, due to the largest deformations being expected there.

During the construction of the already existing berm, denoted as (5) in Figure 2, abnormally large deformations occurred at the downstream side of the dam; this was noticed by the dam owner and numerically by Vahdati (2014). A possible explanation of this behaviour is degradation of the rockfill material, due to the added external load. The degradation results in a more fine grained soil mass, which in turn can cause increasing deformations.

Two cases are to be analysed when the new berm is added, one including the degradation of the rockfill material and other without the degradation.

2.3 Section C

In this section, see Figure 3, a new toe berm is needed based upon the same RIDAS requirement as for section B. Due to the insufficient space at the downstream side of the dam, a retaining wall is to be constructed. Before the retaining wall can be constructed, an excavation is performed. The excavation has a limited extent in the transversal direction.

Effects of the excavation are analysed. Influences of the new berm on the dam body are not inspected in this study.

3 CONSTITUTIVE MODELS AND MATERIAL PARAMETERS

The constitutive models Mohr Coulomb and Hardening soil have been utilised during the case study. Both models are regarded as suitable for their respective application area; though the Hardening soil model is in general considered more versatile. The applicability of the models is explained more thoroughly by Brinkgreve et al (2014).

The values for the unit weight, friction angle and permeability have been provided by the dam owner. Values for Poisson's ratio and the cohesion are based on advices from Bowles (1988). The dilatancy angle has been assigned according to an empirical relation from Brinkgreve et al. (2014). The shear moduli and the reference secant stiffness of the core and rockfill was optimised by Vahdati (2014). Material parameter values from the constitutive model Mohr Coulomb are presented in Table 1. For the constitutive model Hardening soil, values are found in Table 2.

Table 1 Material parameter values for the constitutive model Mohr Coulomb, from Vahdati (2014) and ÅF.

Zone	γ_u kN/m³	γ_s kN/m³	E MPa	E_{inc} MPa	v' -	c' kPa	φ °	k_x/k_y m/s
Core	21	23	48.6	1414.8	0.35	20	38	3.0E-7
Fine filter	21	23	106.4	266.0	0.33	0	32	9.0E-5
Coarse filter	21	23	106.4	266.0	0.33	0	34	5.0E-4
Rockfill	19	21	26.6	159.6	0.33	7	30	1.0E-2
Foundation (rock)	21	23	1400	-	0.30	0	45	1.0E-8
Foundation (till)	21	23	20	-	0.30	0	36	1.0E-8

Note: γ_u is the unit weight above the phreatic level, γ_s the unit weight under the phreatic level, E is the Young's modulus, E_{inc} is the Young's modulus increment, v' the effective Poisson's ratio, c' the effective cohesion, φ the friction angle and k_x as well as k_y are the hydraulic conductivity in the horizontal and vertical direction respectively. E and φ for the foundation till are based on field data, provided by ÅF. γ_u, γ_s,v',c' and k_x/ k_y for the foundation till are chosen accordingly with the rock foundation parameter values.

Table 2 Material parameter values for the constitutive model Hardening soil, from Vahdati (2014) and ÅF.

Zone	γ_u kN/m³	γ_s kN/m³	$E_{50}^{ref} = E_{oed}^{ref}$ MPa	E_{ur}^{ref} MPa	m -	c' kPa	φ °	k_x/k_y m/s
Core	21	23	70	210	1	20	38	3.0E-7
Fine filter	21	23	50	150	0.5	0	32	9.0E-5
Coarse filter	21	23	50	150	0.5	0	34	5.0E-4
Rockfill	19	21	10	30	0.5	7	30	1.0E-2
Berm	21	23	10	30	0.5	7	30	5.0E-2
New berm	21	23	25	75	0.5	7	42	1.0E-2
Foundation (rock)	21	23	3000	9000	0.5	0	45	1.0E-8

Note: γ_u, γ_s, c', φ and k_x/ k_y are defined in the note under Table 1. E_{50}^{ref} is the reference secant stiffness for primary loading in a drained triaxial test, E_{oed}^{ref} is the reference tangent stiffness for primary oedometer loading, E_{ur}^{ref} is the reference stiffness for unloading/reloading in a drained triaxial test, m is the power for stress-level dependency of stiffness. The material parameter values for the new berm are based upon values for the previous berm, as well as information from ÅF.

In section B the potential degradation of the rockfill material (4), in Figure 2, can be considered by reducing the moduli with respect to the increased load. The decrease of the values for the moduli values were observed by Vahdati (2014), during the simulation of the construction of the berm (5), in Figure 2. The berm itself (5) is also consisting of the same material. Therefore the moduli values are linearly reduced with respect to increased load for both the rockfill (4) and the berm (5). The values for the reduced moduli are found in Table 3; the original ones are shown in Table 2.

Table 3 Reduced material parameter values due to potential degradation.

Zone	**Reduced** $E_{50}^{ref} = E_{oed}^{ref}$ **MPa**	**Reduced** E_{ur}^{ref} **MPa**
Rockfill	6.9	20.7
Berm	5.9	11.7

4 NUMERICAL MODELLING

The numerical modelling is based upon the research of Vahdati (2014), both considering the values of the material parameters, Table 1 and Table 2, as well as the established finite element model.

Plane strain conditions are assumed, since the dam is a long structure. All cross-sections, A, B and C, have been somewhat modified when importing the data to PLAXIS; some lines have been slightly smoothened out. A number of adjacent geometry points have been removed. However, these modifications have no significant effect on the results.

The size of the geometry model is chosen for all sections in such a way that the extent is sufficient for the accuracy of the computations. Standard fixities in PLAXIS are chosen for generation of boundary

conditions. The outer vertical boundary lines are fixed in the horizontal direction. The horizontal bottom boundary line is fixed in both horizontal and vertical directions. The choice of finite element mesh is an important factor for the numerical solution strategy. A denser mesh usually produces more accurate results, but the computation time increases. A suitable mesh for the computation accuracy was chosen by refinement until the results did not vary significantly. Thereby a sufficient accuracy is obtained, for a minimum computation time.

The dam is built up in several steps, in order to create a proper initial stress field. The horizontal filters are omitted in the geometry models. This modification of the geometry is considered to have no practical influence in this study.

4.1 Section A

The foundation in section A consists of till. No parameter values were available for the till for the Hardening soil model. Therefore, the analyses of section A were conducted with the more simple Mohr Coulomb model for which the parameter values for the till were available.

The modelling of the excavation of the drainage trench is performed in five steps, as shown in Figure 4.

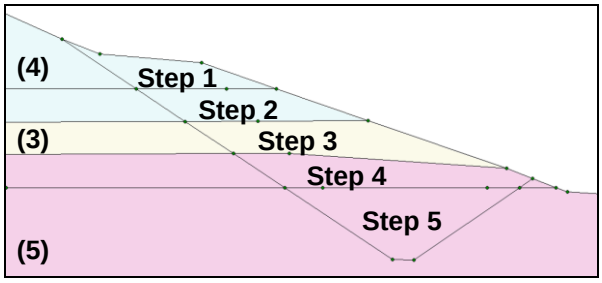


Figure 4 Excavation steps for the new drainage trench, material zones denoted according to Figure 1.

The inclination of the excavation walls is set to 1V:1.5H, based on a design suggestion by ÅF.

The phreatic line, see Figure 1, is assigned upstream to the retention water level, +440.5 metres above sea level (m.a.s.l), since the planned excavation is assumed to be performed under normal conditions. At the downstream side of the dam the water level is assigned to +432.5 m.a.s.l. based upon stand pipe data from the site. The levels of the phreatic line within the dam body have been assumed as in Figure 1. Simulations have shown that it is not necessary with more accurate levels between the known ones at the upstream and downstream side.

Since the dam was constructed during the 1960s, all excess pore pressures are assumed to have dissipated. No excess pore pressures are expected to be built up during the excavation. Therefore no consolidation phases are simulated; the calculation phases are performed as drained phases for the excavation.

4.2 Section B

The advanced constitutive model Hardening soil is chosen for this section, since it is suitable for this application and material parameters are available.

The modelling of the planned berm is performed in five steps, as shown in Figure 5.

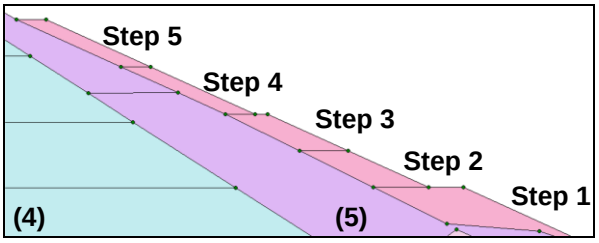


Figure 5 Construction steps for the new toe berm, material zones denoted according to Figure 2.

The level of the phreatic line, illustrated in Figure 2, for this section has been based upon flow computations performed in the programme GeoStudio SEEP/W by the consulting company ÅF. The levels are +440.5 m.a.s.l for the upstream side and approximately +400.0 m.a.s.l for downstream side.

No significant excess pore water pressures are expected to be built up during the berm construction, because of the high permeability of the adjacent material zones. The phases for the construction of the toe berm are modelled as drained phases.

4.3 Section C

The constitutive model Hardening soil is utilised for section C.

The excavation steps of the soil masses at the dam toe are shown in Figure 6.

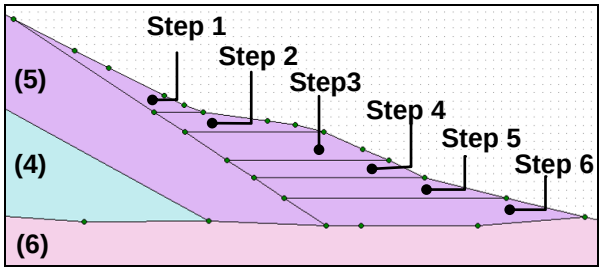


Figure 6 Excavation steps for the removal of the soil at the dam toe, material zones denoted according to Figure 3.

The levels of the phreatic line, seen in Figure 3, is also assigned based upon the results from flow computations in GeoStudio SEEP/W performed by ÅF. The upstream water level is at +440.5 m.a.s.l. and the downstream level is at approximately +400.0 m.a.s.l.

The phases for the excavation at the toe berm are modelled as drained phases.

5 RESULTS

Deformation and stability analyses have been performed in PLAXIS for all sections.

5.1 Section A

Values for the computed factors of safety and accumulated total deformations for each excavation phase are shown in Table 4; the failure surfaces corresponding to the factors of safety, FoS, are shown in Table 8.

Table 4 Section A, factors of safety and accumulated maximum total deformations.

Excavation phase	Factor of safety	Maximum deformation [mm]
Step 1	2.07	9.5
Step 2	1.67	22
Step 3	1.47	36
Step 4	1.37	47.5
Step 5	1.19	60

In Table 4 and Table 8, it is seen that the value of the factor of safety is decreasing for each excavation step. The computed values for the factors of safety gives that the trench slopes are still stable during the excavation phases. The smallest value of the factor of safety is 1.19, which can be considered as relatively low.

For the last excavation phase, step 5, the maximum total deformations in the excavation reached 60 mm. In Figure 7, for the last excavation step 5, the zone affected by the deformations is viewed by colour shadings. The position and direction of the maximum deformations is shown by the arrow. The smaller arrow indicates relative magnitude and direction of the deformation in a point of the right trench wall.

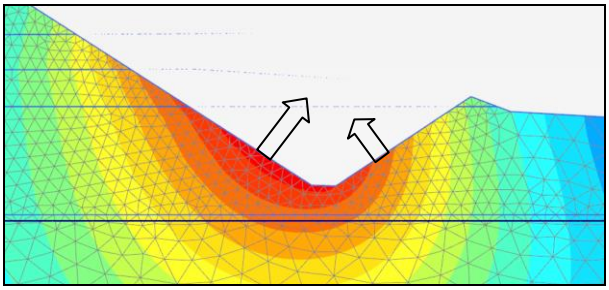


Figure 7 Section A, deformations in excavation step 5.

5.2 Section B

The results are found in Table 5; the failure surfaces are shown in Table 9.

Table 5 Section B, factors of safety and accumulated maximum total deformations.

Toe berm phase	Factor of safety	Maximum deformation [cm]
Step 1	1.36	6.1
Step 2	1.39	6.2
Step 3	1.42	7.9
Step 4	1.45	9.1
Step 5	1.54	10.6

The value of the factor of safety, as seen in Table 5 and Table 9 are increasing with every added step of the berm.

For the final computational phase, step 5, the deformations reached 10.6 cm. The extent of the maximum total deformations is shown by colour shadings in Figure 8; the arrows are indicating the direction of the largest deformations.

When considering the degradation of the rockfill material, the maximum total deformations reached a value of 24 cm in the last phase, step 5. The distribution of the deformations is as shown in Figure 8.

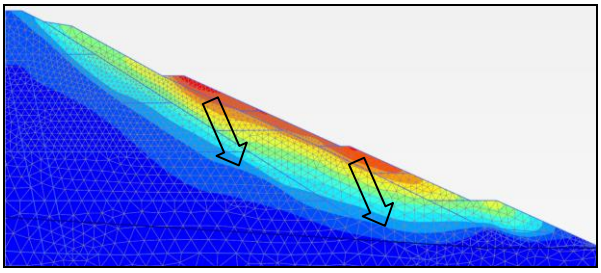


Figure 8 Section B, maximum deformations in part 5.

5.3 Section C

The results from the computations are found in Table 6.

Table 6 Section C, factors of safety and accumulated maximum total deformations.

Excavation phase	Factor of safety	Maximum deformation [mm]
Step 1	1.28	4
Step 2	1.26	5
Step 3	1.25	6
Step 4	1.24	7
Step 5	1.23	10
Step 6	1.20	12

The failure surface for the final excavation phase, step 6, is found in Table 10. This is representable for all excavation phases, step 1-6. The lowest factor of safety is relatively low, with a value of 1.20.

As seen in Table 6, the maximum total deformation reached 12 mm for step 6. The extent of the maximum total deformations at the toe of the dam is shown in Figure 9 by shadings; the main direction is indicated by the arrow.

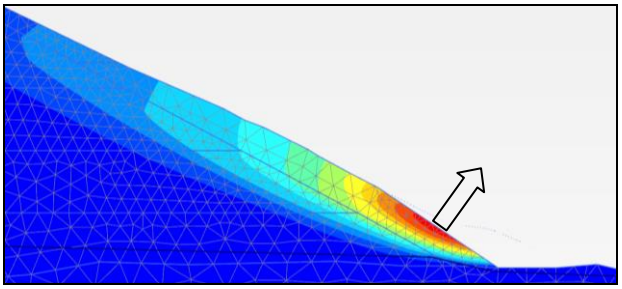


Figure 9 Section C, deformations in excavation step 5.

6 VERIFICATION COMPUTATIONS

In order to determine if the results from the PLAXIS computations are reliable and trustworthy, complementary analyses have been performed with the software GeoStudio SIGMA/W and SLOPE/W, see GeoStudio (2009) and GeoStudio (2008).

6.1 Stability

Verification of the slope stability computations have been performed in GeoStudio SLOPE/W with the limit equilibrium method Morgenstern-Price. The most critical slip surface and associated slip surface is searched for at the downstream side of the dam. For sections A and B, the factors of safety and failure surfaces are shown Tables 8-9.

Due to the fact that all slip surfaces for section C are very similar in location from the finite element analyses, only one limit equilibrium analysis is performed in the verification part for the sixth and final excavation step. Since the slip surface from PLAXIS is not circular, the most critical slip surface in SLOPE/W is specified as in PLAXIS. The factor of safety and corresponding failure surface is presented in Table 10.

6.2 Deformations

In order to verify the computations of deformation from PLAXIS, the programme GeoStudio SIGMA/W is used. The constitutive model Mohr Coulomb has been utilised during the verification computations for section A. For sections B and C, the constitutive model Nonlinear elastic Hyperbolic is chosen in SIGMA/W, since both are based upon the nonlinear formulation by Duncan and Chang (1970). The modelling is performed under the same conditions as in PLAXIS. The maximum deformations are presented in Table 7; the distributions of the deformations are shown in Figures 10-12.

Table 7 Verification of the deformations.

Section	Maximum deformation
A	42 mm
B	13.4 cm
C	15 mm

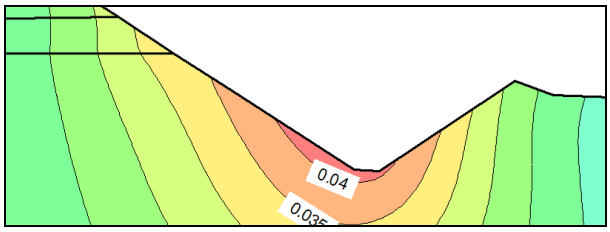


Figure 10 Section A, deformations from SIGMA/W.

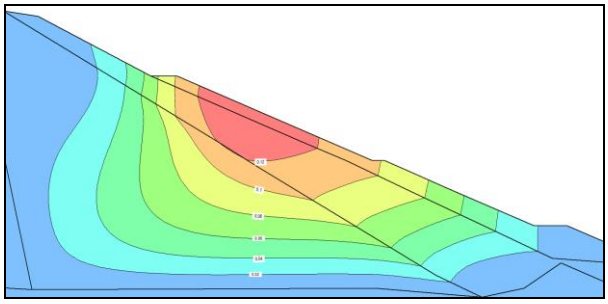


Figure 11 Section B, deformations from SIGMA/W.

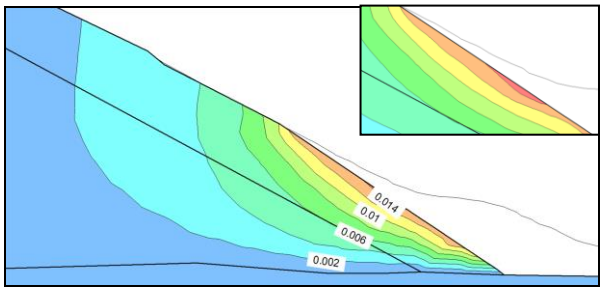


Figure 12 Section C, deformations from SIGMA/W.

The obtained results from the verification computations are well conforming to the results from PLAXIS. Therefore the conclusion is drawn that the results from the numerical analyses in PLAXIS are reliable.

7 DISCUSSION

Even though all the planned measures have indicated stable conditions, meaning a factor of safety above 1.0 during the simulations, it can not be determined if that represents a sufficient stability. This is up to the dam owner to decide. However, in order to assure a safe work environment, deformation monitoring can be conducted during the work in section A, B and C. Alarm values used to determine if the deformations are within reasonable limits, can be chosen prior to the monitoring. This can, for example, be done by inspecting trends of the relationship between computed factors of safety and deformations. This kind of monitoring is intended for the dam in the case study.

Monitoring of the deformations is valuable, since the results have shown relatively low factors of safety for sections A and C. By using the results from the finite element analyses for establishing alarm values, a contribution is made to improve the dam safety. More understanding is gained about the expected dam behaviour. This shows some advantages of using a numerical analysis instead of a more traditional approach as a limit equilibrium method; where only a factor of safety is produced and not deformations.

For section C, the excavation at the toe is limited in the transversal direction. This implies that modelling the problem as a plane strain case in two dimensions is not very appropriate. In a three dimensional case, soil masses at the sides cause resisting forces. Smaller deformations can therefore be expected from such a case compared to a two dimensional case. Since the deformations are already relatively small in plane strain, modelling in three dimensions was not considered as necessary.

8 CONCLUSIONS

Based upon the results, the following conclusions can be drawn:

Section A: The deformations are of largest magnitude in the direct vicinity of the trench. The maximum side of the deformations is 60 mm. The direction of the movements is mostly upward.

Section B: Considering a case where no degradation of the rockfill material is occurring, the deformations will take a maximum size of almost 11 cm in the top of the new berm. The direction of the deformations is mainly awry downwards. For a case including the rockfill degradation, the maximum value of the computed deformations is 24 cm.

Section C: The maximum deformations caused by the excavation at the bottom of the toe berm reaches 12 mm. The directions of the deformations are mostly perpendicularly outwards from the excavation face.

The planned measures can be performed according to the suggestions projected. No deformations of such size that instability is occurring have been shown during the simulations.

The finite element method is a useful tool for this kind of evaluation; considering the physically adequate base of the method, the possibility of determining both deformations and factors of safety as well as the practical application of the results for establishing alarm values.

9 ACKNOWLEDGEMENTS

The author would like to express sincere thanks to Vattenfall vattenkraft AB for giving opportunity to carry out the presented study. Consultancy company ÅF AB, is to be acknowledged for providing the case and all relevant information regarding the dam.

The research presented has been carried out within the environment of "Swedish Hydropower Centre - SVC" at LTU. The support from the SVC environment is highly appreciated and acknowledged for.

10 REFERENCES

Brinkgreve, R.B.J., Engin, E. & Swolfs, W.M. (2014). PLAXIS 2014. Delft, the Netherlands: Plaxis bv.

Bowles, J.E. (1988). Foundation Analysis and Design. Berkshire, England: MacGraw-Hill.

Duncan, J.M. & Chang, C.Y., 1970. Nonlinear analysis of stress and strain in soils. Journal of the Soil Mechanics and Foundations Division, ASCE, vol. 96, no. SM5, pp. 1629-1654.

GeoStudio (2008). Stability Modeling with SLOPE/W 2007 Version. Calgary, Canada: GEO-SLOPE International Ltd.

GeoStudio (2009). Stress-Deformation Modeling with SIGMA/W 2007. Calgary, Canada: GEO-SLOPE International Ltd.

Potts, D.M. & Zdravković, L. (1999). Finite element analysis in geotechnical engineering: theory. London, England: Thomas Telford Books.

Muir-Wood, D. (1990). Soil Behaviour and Critical State Soil Mechanics. New York, USA: Cambridge University Press.

Svensk energi. (2002) RIDAS: kraftföretagens riktlinjer för dammsäkerhet. Stockholm, Sweden: Svensk energi. (In Swedish)

Vahdati, P. (2014). Identification of Soil Parameters in an Embankment Dam by Mathematical Optimization. Licentiate thesis. Luleå, Sweden: Graphic Production.

Yu, H. (2006) Plasticity and Geotechnics. Nottingham, England: Springer.

Table 8 Section A, failure surfaces from PLAXIS and SLOPE/W.

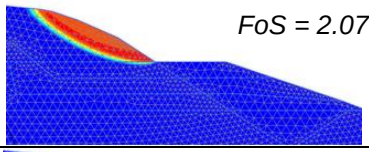
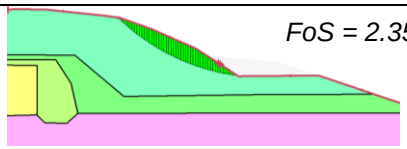
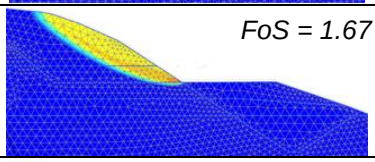
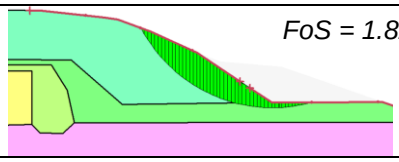
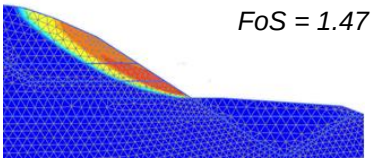
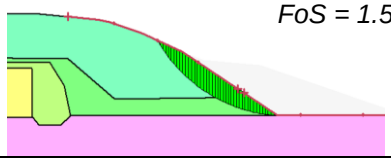
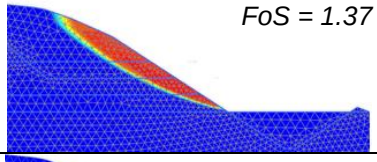
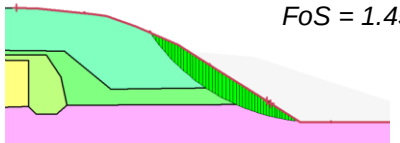
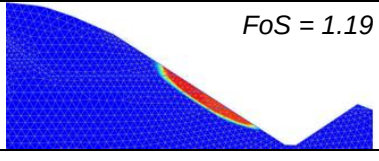
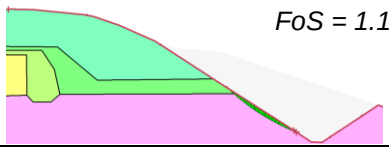
Excavation phase	PLAXIS	SLOPE/W
1	 *FoS = 2.07*	 *FoS = 2.35*
2	 *FoS = 1.67*	 *FoS = 1.82*
3	 *FoS = 1.47*	 *FoS = 1.55*
4	 *FoS = 1.37*	 *FoS = 1.45*
5	 *FoS = 1.19*	 *FoS = 1.15*

Table 9 Section B, failure surfaces from PLAXIS and SLOPE/W.

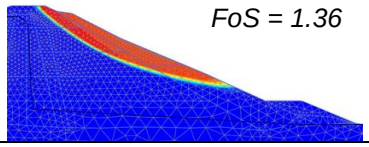
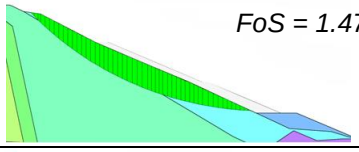
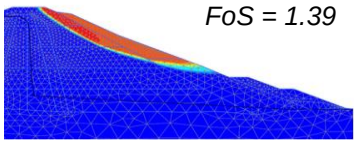
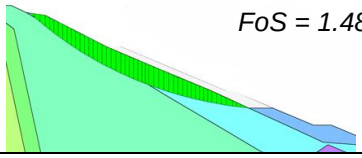
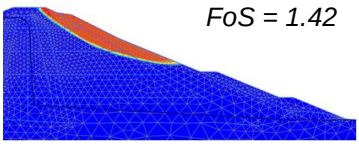
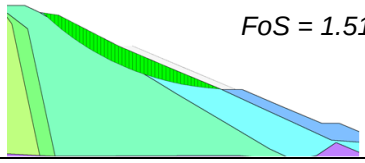
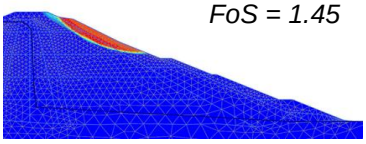
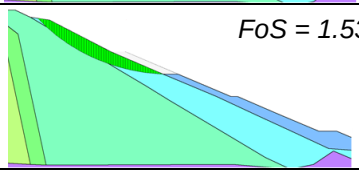
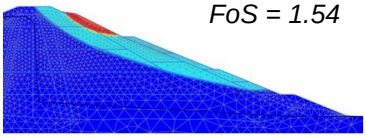
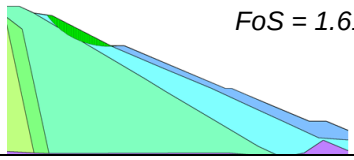
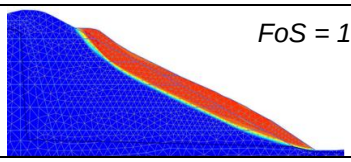
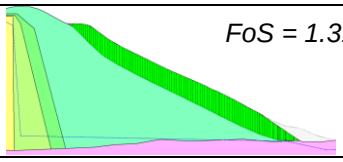
Toe berm phase	PLAXIS	SLOPE/W
1	 *FoS = 1.36*	 *FoS = 1.47*
2	 *FoS = 1.39*	 *FoS = 1.48*
3	 *FoS = 1.42*	 *FoS = 1.51*
4	 *FoS = 1.45*	 *FoS = 1.53*
5	 *FoS = 1.54*	 *FoS = 1.61*

Table 10 Section C, failure surfaces from PLAXIS and SLOPE/W.

Excavation phase	PLAXIS	SLOPE/W
6	 *FoS = 1.20*	 *FoS = 1.31*

Dynamic analysis of Offshore Wind Energy Converters supported on monopiles in the elastic domain

AISSA.M .H / primary author
Departement of Civil Engineering, Faculty of sciences and technology, University of Medea, Algeria, geo.tech468@gmail.com

AMAR BOUZID Dj. Co-Author(s)
Departement of Civil Engineering, Faculty of sciences and technology, University of Blida, Algeria.

ABSTRACT

In the last decades, the Wind Energy field recognised a great challenge in the design and construction of Offshore Wind Turbines structure view that these structures increase in size and capacity which involved manufacturers to project them in considerable depth far from Onshore.

The most commons support structures used are monopiles in the wideworld Offshore Wind Turbines farms. These kinds of foundations have a diameter range between 3 to 7 m, and embedded length between 30 to 40 m. In hence, it makes them behavior rigid against lateral load and overturning moment due to wind and waves. In contrast, the existing design strandards, for exemple the API recommendations based on the p-y method are founded originally for small diameter piles ranging between 0.6 and 2 m used in Oil and Gaz industry which experience all most a vertical loading. This raises questions about the reability of the previous method for large diameter piles.

The aim of this paper is to propose numerical solutions to obtain the stiffness of the foundation assuming the elastic soil behavior, using a semi-analytical approach by finite element analysis validated with different authors. In the other hand, the natural frequency has been determined using a mathematical approach based on an Euler-Bernoulli beam-column with elastic end supports to take into account the effect of the Soil Structure Interaction (SSI). The proposed expressions was used and compared with the commonly used p-y method according to data issues from various offshore wind farm sites in UK.

Keywords: Offshore Wind Turbines; Semi-analytical approach; p-y method; piles foundations; natural frequency.

INTRODUCTION:

Monopiles are the most commonly choice for wind turbines energie. These kinds of foundations are made of steel or concrete, with a diameter (D) ranging between 4m and 7m, and embedded length (L) less than 30m. inhence, they are subjected to lateral loading (H) and overturning moment (M) due to wind and waves (Figure 1). The design is based on the p-y method described by Reese et al (1977) adopted later by the Det Norske Veritas (DNV) Guideline tested originally in full scale piles with small diameter (0.61m), but they are already applied for large piles diameter which is outside the wind applicability domain.

The offshore wind turbines experienced a high dynamic loading. The natural frequency must be designed to avoid resonance between (1P) and (3P) (Figure2). So the soil stiffness must be determined accurately from the soil data for a good estimation of the natural frequency of the system.

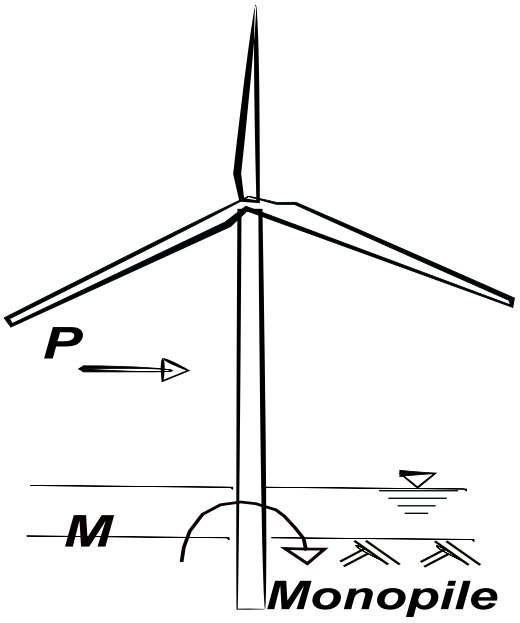


Figure 1 Loads acting on Offshore Wind Turbine Structure.

The aim of this paper is to propose new design formulas of stiffness coefficients by a semi-analytical approach by finit element method (Amar bouzid et al, 2004). many soil profiles are considered and the nature of the interface between the soil and the pile is taken into account (Amar Bouzid et Vermeer, 2007).

In the second part, we check the accuracy of the previous equations using a method based on Euler-Bernoulli Beam-Column with elastic end supports as reported by Adhikari and Bhattacharya (2012) and considering the coupled stiffness term (Laszlo Arany et al, 2014).

Review of semi-analytical approach:

This so called semi analytical approach was proposed in a first time by Wilson (1965) for FE analysis of axisymmetric structures loaded non-axisymmetrically and later by Cook et al (1989). The main idea of this method is to use Fourier Series to resolve three dimensional problems as a two dimensional harmonic model and superposing each term result. We can found many applications of Semi-Analytical Approach in practical cases (For exemple Kim et al, 1994; Zienkiewicz and Taylor, 2000). The present method is very interest because the structure (Pile) is axisymmetric but not the loading.

The six strain components may be related to three displacements components which are the radial displacement μ, the axial displacement υ and the hoop displacement ω. It yields:

$$\varepsilon_r=\frac{\partial_u}{\partial_r},\ \varepsilon_z=\frac{\partial_v}{\partial_z},\ \varepsilon_\theta=\frac{\partial_w}{r\partial\theta}+\frac{u}{r}$$
$$\gamma_{rz}=\frac{\partial_u}{\partial_z}+\frac{\partial_v}{\partial_r},\ \gamma_{z\theta}=\frac{\partial_v}{r\partial\theta}+\frac{\partial_w}{\partial_z},\qquad (1)$$
$$\gamma_{\theta r}=\frac{\partial_u}{r\partial\theta}+\frac{\partial_w}{\partial_r}-\frac{w}{r}$$

The previous displacement can be expressed in the form of Fourier series:

$$\mu=\sum_{n=0}^{L}\bar{u}_n\cos n\theta+\sum_{n=1}^{L}\bar{\bar{u}}_n\sin n\theta$$
$$\upsilon=\sum_{n=0}^{L}\bar{v}_n\cos n\theta+\sum_{n=1}^{L}\bar{\bar{v}}_n\sin n\theta \qquad (2)$$
$$w=\sum_{n=0}^{L}\bar{w}_n\sin n\theta+\sum_{n=1}^{L}\bar{\bar{w}}_n\cos n\theta$$

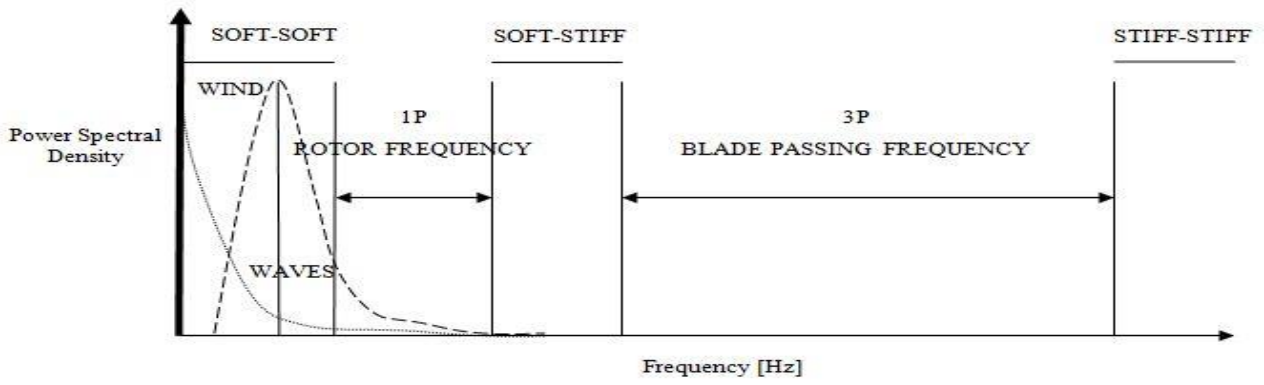


Figure 2 Dyanmic design approach showing the forcing frequency as function of power spectral density.

Where $\bar{u}_n$, $\bar{v}_n$, $\bar{w}_n$ are the amplitudes of displacements that are symmetric with respect to the (θ=0) plane and $\bar{\bar{u}}_n$, $\bar{\bar{v}}_n$, $\bar{\bar{w}}_n$are the amplitudes of displacement that are antisymmetric with respect to the (θ=0) plane, n is harmonic number, and L is the total number of harmonic terms considered in the series.
In most practical problems only the first two terms in the Fourier series are needed. Neglecting the first term, the componenets of loading will be:

$$R=\bar{R}cos\theta.\ Z=\bar{Z}cos\theta.\ T=\bar{T}sin\theta \qquad (3)$$

Where $\bar{R}, \bar{Z}$ and $\bar{T}$are the amplitudes of nodal loading on the first harmonic. For this simple load system displacements of Eq.(2) will reduce to:

$$u=\bar{u}cos\theta,\ v=\bar{v}cos\theta,\ w=\bar{w}sin\theta \qquad (4)$$

Stiffness analysis:

In our analysis we considered a cylindrical pile with D_p is the diameter of the pile, and it's length L_p, Young's Modulus Ep. H_0 is the horizontal load acting on the head of the pile and M_0 is the corresponding overturning moment. The soil is described by its Young's modulus E_s and Poisson's ratio ν_s. In the parametric study we take three types of soil profiles:

- Homogeneous soil with $E_s=E_{sD}$
- Gibson's soil.
- Parabolic soil.

With E_{sD} is the stiffness of the soil at one diameter depth of the pile D_p.
The pile have diameter D_p=3m with variable slenderness ratio L_p/D_p ranging between 1 to 15. The relative rigidity of the pile/soil ratio is taken between 10 and 10^6. The flexural rigidity of the pile $(EI)_p$= 79521564.04kN.m^2 and ν_p=0.25 corresponding to those of concrete material. We choose the poisson's ratio of the soil ν_s=0.499.

The axisymmetric model of the pile is carry out in this paper subject to nonaxisymmetric loads.

We use a Fortran program named Pile-Joint (Figure3). The model consists of 1326 elements of quadratical eight nodes, which 200 elements for pile and 1126 for the surrounding soil. To ensure a good accuracy and because the diameter pile is large we refine the mesh in the pile structure and the interface area. The distance between the horizontale bottom boundary is one length L_p.

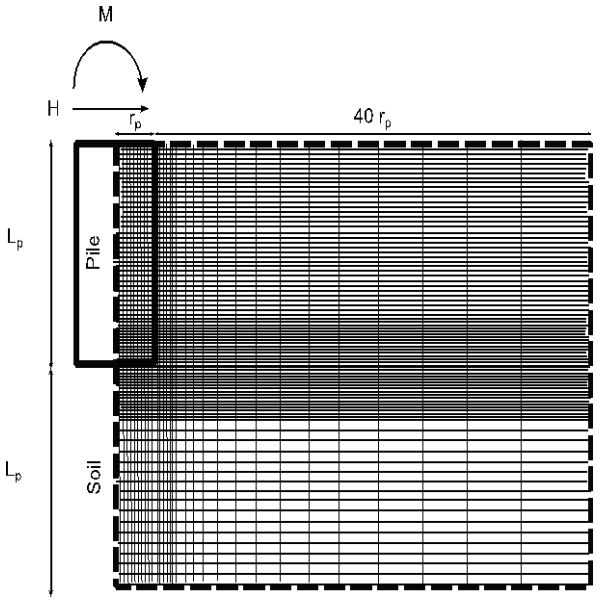


Figure 3 Geometric model taking in this study.

In the horizontal direction, the distance is taken equal to 36 times the radius of the pile. The interface is taken into account for this study. We have to cases: Rough Interface (Normal rigidity $K_n=10^{12}$ and the Shear rigidity $K_s=10^{12}$) and Smooth Interface (Normal rigidity $K_n=10^{12}$ and the Shear rigidity K_s=0).

Results of the stiffness analysis

It have been shown that the slenderness ratio of rigid piles control them behavior and lateral response (Higgins et al, 2013). The results of the stiffness coefficients (K_H, K_M and K_{MH}) have been plotted as function of L_p/D_p and compared with existing solutions proposed by Higgins et al (2013) and those of Carter and Kulhawy (1992). The obtained

results show a good agreement with Higgins et al in both Homogeneous soil and Gibson's soil for rough interface case. However we don't find any equations suggested in the literature for smooth interface case moreover in Parabolic soil profil for validation of the present study results.

The Table 1 shows all the equations obtained from the present analysis.

Therefor, the Table 2 shows the stiffness equations of rigid piles proposed in the literature, and compared with equations of this study:

Table 1 Summary of the stiffness equations obtained in the present analysis

	Rough Interface	**Smooth Interface**
Homogeneous Soil Profil	$\frac{K_H}{E_S D}=2.703\ (\frac{L_P}{D})^{0.6963}$ $\frac{K_{MH}}{E_S D^2}=-1.557\ (\frac{L_P}{D})^{1.6663}$ $\frac{K_M}{E_S D^3}=1.697\ (\frac{L_P}{D})^{2.5198}$	$\frac{K_H}{E_S D}=2.034\ (\frac{L_P}{D})^{0.7523}$ $\frac{K_{MH}}{E_S D^2}=-1.219\ (\frac{L_P}{D})^{1.7063}$ $\frac{K_M}{E_S D^3}=1.211\ (\frac{L_P}{D})^{2.5894}$
Gibson Soil Profil	$\frac{K_H}{E_S D}=1.647\ (\frac{L_P}{D})^{1.6944}$ $\frac{K_{MH}}{E_S D^2}=-1.188\ (\frac{L_P}{D})^{2.6870}$ $\frac{K_M}{E_S D^3}=1.114\ (\frac{L_P}{D}3.6331$	$\frac{K_H}{E_S D}=1.214\ (\frac{L_P}{D})^{1.7482}$ $\frac{K_{MH}}{E_S D^2}=-0.896\ (\frac{L_P}{D})^{2.7316}$ $\frac{K_M}{E_S D^3}=0.815\ (\frac{L_P}{D})^{3.6858}$
Parabolic Soil Profil	$\frac{K_H}{E_S D}=2.830\ (\frac{L_P}{D})^{0.9958}$ $\frac{K_{MH}}{E_S D^2}=-2.942\ (\frac{L_P}{D})^{1.7824}$ $\frac{K_M}{E_S D^3}=3.937\ (\frac{L_P}{D})^{2.5707}$	$\frac{K_H}{E_S D}=2.055\ (\frac{L_P}{D})^{1.0675}$ $\frac{K_{MH}}{E_S D^2}=-2.099\ (\frac{L_P}{D})^{1.8649}$ $\frac{K_M}{E_S D^3}=2.555\ (\frac{L_P}{D})^{2.6863}$

Table 2 Stiffness equations proposed by authors

	Higgins et al (2013)	**Carter and Kulhawy (1992)**
Homogeneous Soil Profil	$\frac{K_H}{E_S D}=2.3952\ (\frac{L_P}{D})^{0.7100}$ $\frac{K_{MH}}{E_S D^2}=-1.4223\ (\frac{L_P}{D})^{1.6698}$ $\frac{K_M}{E_S D^3}=1.7664\ (\frac{L_P}{D})^{2.4594}$	$\frac{K_H}{E_S D}=1.8606\ (\frac{L_P}{D})^{0.6274}$ $\frac{K_{MH}}{E_S D^2}=-1.0345\ (\frac{L_P}{D})^{1.4830}$ $\frac{K_M}{E_S D^3}=1.8854\ (\frac{L_P}{D})^{2.0500}$
Gibson Soil Profil	$\frac{K_H}{E_S D}=0.9161\ (\frac{L_P}{D})^{2.0415}$ $\frac{K_{MH}}{E_S D^2}=-0.6244\ (\frac{L_P}{D})^{3.0618}$ $\frac{K_M}{E_S D^3}=0.6625\ (\frac{L_P}{D})^{3.9417}$	**No equations proposed in the litterature**

Dynamic analysis:

Wind Turbines have increased in size and capacity in the recent few years. In the design approach the support structure are modeled by static springs which lead to an independency of the stiffness coefficients on the natural frequency of the system, that why the Soil Structure Interaction (SSI) is very important in any dynamic analysis of the system. S. Adhikari and S. Bhattacharya (2012) reported the equation of motion of the beam and include with analytical resolution a nondimensional parameters of the foundation stiffness (In this case we find just K_H and K_M term).

Laszlo Arany et al, (2014) give a coupled stiffness term (K_{MH}) and prove by mean of sensitive analysis that the determination of the natural frequency according to two terms is not sufficient.

For our analysis we choose six Offshore Wind Turbines situated in the North Sea and we compare results of the calculated natural frequency determined by two approaches (the approach used in the present study with the equations founded in the DNV/Risø Guideline) with the measured one. Table 3 to Table 8 gives the obtained results from this dynamic analysis.

Table 3 Calculated and measured natural frequency in Walney 1 Wind turbine

Walney 1 Wind turbine			
	Calculated frequency in Rough Interface	**Calculated frequency in Smooth Interface**	**Calculated Frequency with DNV/Risø**
Homogeneous Soil Profil	0.3448	0.3438	0.3359
Gibson Soil Profil	0.3454	0.3446	0.3342
Parabolic Soil Profil	0.3454	0.3445	0.3315
Measured frequency (Hz)	0.35		

Table 4 Calculated and measured natural frequency in Lely A2 Wind turbine

Lely A2 Wind turbine			
	Calculated frequency in Rough Interface	**Calculated frequency in Smooth Interface**	**Calculated Frequency with DNV/Risø**
Homogeneous Soil Profil	0.7602	0.7594	0.7393
Gibson Soil Profil	0.7613	0.7608	0.7358
Parabolic Soil Profil	0.7609	0.7603	0.7302
Measured frequency (Hz)	0.634		

Table 5 Calculated and measured natural frequency in North Hoyle Wind turbine

North Hoyle Wind turbine			
	Calculated frequency in Rough Interface	Calculated frequency in Smooth Interface	Calculated Frequency with DNV/Risø
Homogeneous Soil Profil	0.4479	0.4478	0.4293
Gibson Soil Profil	0.4481	0.4481	0.4258
Parabolic Soil Profil	0.4480	0.4480	0.4212
Measured frequency (Hz)	0.35		

Table 6 Calculated and measured natural frequency in Irene Vorrink Wind turbine

Irene Vorrink Wind turbine			
	Calculated frequency in Rough Interface	**Calculated frequency in Smooth Interface**	**Calculated Frequency with DNV/Risø**
Homogeneous Soil Profil	0.5500	0.5494	0.5326
Gibson Soil Profil	0.5509	0.5505	0.5297
Parabolic Soil Profil	0.5506	0.5501	0.5251
Measured frequency (Hz)	0.546-0.56		

Table 7 Calculated and measured natural frequency in Sheringham Shoal Wind turbine

Sheringham Shoal Wind turbine			
	Calculated frequency in Rough Interface	**Calculated frequency in Smooth Interface**	**Calculated Frequency with DNV/Risø**
Homogeneous Soil Profil	0.4979	0.4967	0.4692
Gibson Soil Profil	0.4996	0.4989	0.4648
Parabolic Soil Profil	0.4990	0.4981	0.4574
Measured frequency (Hz)	0.85-0.96		

Table 8 Calculated and measured natural frequency in Kentish Flats Wind turbine

Kentish Flats Wind turbine			
	Calculated frequency in Rough Interface	Calculated frequency in Smooth Interface	Calculated Frequency with DNV/Risø
Homogeneous Soil Profil	0.6252	0.6234	0.5560
Gibson Soil Profil	0.6282	0.6273	0.5460
Parabolic Soil Profil	0.6272	0.6259	0.5302
Measured frequency (Hz)	0.85-0.96		

The results above reveal two acceptable natural frequency error (Walney and Irene Vorrink) but the error is strongly much higher in the others Offshore sites cases of

the study, for exemple the error in Kentish flats is more than 60%.

Conclusion:

In this study we analysis the stiffness of rigid piles loaded laterally. Equations are founded and proposed in this paper in different soil profils and different interface states validated with existing solutions proposed by authors.

These formulas are of interest if we consider the dynamic behavior of piles. The most piles sensitive to dynamic/cyclique loading are Offshore piles supporting wind turbines which are caracterised by large diameter and deep length.

To check the applicability of the present study equations we use it in the calculation of the natural frequency of Wind Turbines structures and compared with the p-y equations and measured data. The results of the natural frequency of Wind Turbines structures and compared with the p-y equations and measured data.

The results of our study show a well accuracy with the measured natural frequency contrary to the p-y curves results (Walney 1 and Irren Vorrink), this is due to the rigid behavior of these piles, which leads to the useless of the p-y method as sited previously.

In the other hand, the error of the present method is much higher in the others case study (The error in Kentish flats is more than 60% of the measured natural frequency). This is explained by the flexible behavior of the foundations, it means that the length of these piles exceeds the critical length. So this make the applicability of our formulas outside of them range.

REFERENCES:

Amar Bouzid Dj. Analyse semi-analytique par éléments finis des pieux isolés sollicités horizontalement dans un milieu à comportement non-linéaire. Thèse de Magister, Ecole Nationale Polytechnique, Alger, Algérie ; 1997.

Carter J.P; Kulhawy F.H. (1992) Analysis of laterally loaded shafts in rock. Journal of Geotechnical Engineering.118(6), 839-855.

Det Norske Veritas (DNV). (2007). Offshore Standard DNV-OS-J101: Design of Offshore Wind Turbine Structure.

Dj. Amar Bouzid; B.Tiliouine ;P.A. Vermeer. (2004) Exact formulation of interface stiffness matrix for axisymmetric bodies under non-axisymmetric loading. Computers and Geotechnics (31) 75-87.

Djillali Amar Bouzid; Pieter A. Vermeer.(2007) Effect of interface characteristics on the influence coefficients of an embedded circular footing under horizontal and moment loading. Geotech Geol Eng 25:487-497.

Laszlo Arany; Subhamoy Bhattacharya; S.J.Hogan; John Macdonald. (2014). Dynamic soil-structure interaction issues of offshore wind turbines. Proceedings of the 9th International Conference on Structural Dynamics, EURODYN 2014. Porto, Portugal, 30 June-2 July 2014.

Lymon C. Reese. (1977) Laterally Loaded Piles: Program Documentation. *Journal of the Geotechnical Engineering Division*, 287-305.

S. Adhikari and S. Bhattacharya. (2012). Dynamic analysis of wind turbine towers on flexible foundations. Shock and Vibration (19) 37-56.

William Higgins; Celio Vasquez; Dipanjan Basu; D. V. Griffiths. (2013). Elastic Solutions for Laterally Loaded Piles. Journal of Geotechnical and Geoenvironmental Engineering ASCE.

Small-displacement soil-structure interaction for horizontally loaded piles in sand

S. P. H. Sørensen
COWI A/S, Denmark, spso@cowi.dk

A. H. Augustesen
COWI A/S, Denmark

ABSTRACT
Monopile foundations with diameters of 4 to 6 m are often employed for offshore wind turbines. The Winkler model approach, where the soil pressure acting against the pile wall is provided by uncoupled springs with stiffness provided by p-y curves, is traditionally employed in the design. However, the p-y curves currently recommended by Det Norske Veritas and the American Petroleum Institute are developed for slender piles with diameters up to approximately 2 m when considering piles in sand.
In the serviceability limit state, only small rotations of the monopiles are allowed. Hereby, the initial part of the p-y curves, is of high importance in the design of monopile foundations for offshore wind turbines.
The aim of the paper is to investigate the small-displacement stiffness of the soil-pile interaction for large-diameter stiff piles in sand subjected to lateral loading. A modified expression for the static part of the p-y curves is investigated in which the initial slope of the p-y curves depends on the depth below the soil surface, the pile diameter and Young's modulus of elasticity of the soil. Three-dimensional numerical analyses conducted by means of the commercial program FLAC^{3D} incorporating a Mohr-Coulomb failure criterion are the basis for the research.

Keywords: Piles, soil/structure interaction, p-y curve, numerical modelling, sand.

1 INTRODUCTION

The monopile foundation concept is often employed in the design of offshore wind turbines. Monopiles are welded steel pipe piles driven open-ended into the soil. In order to be able to sustain the large forces and moments, the outer pile diameter, D, is typically five to eight meters with an embedded pile length, L_p, in the range of 20 to 35 m. Hence, the slenderness ratio, L_p/D, is around five.

The American Petroleum Institute (ANSI/API, 2011) and Det Norske Veritas (DNV, 2014), recommend to employ the Winkler model approach in the design of monopiles, i.e. the pile is considered as a beam on an elastic foundation. The elastic foundation consists of a discrete number of springs with stiffness determined by means of *p-y* curves. *p-y* curves describe the soil resistance, *p*, acting against the pile wall as a function of the lateral pile deflection, *y*.

For piles in sand, ANSI/API (2011) and DNV (2014) recommend a *p-y* curve formulation, which has been validated for slender piles with diameters up to approximately 2 m, cf. Cox et al. (1974) and Murchison and O'Neill (1984). The formulation has, however, not been validated for piles with diameters of five to eight meter and slenderness ratios around five. Hereby, the influence of pile properties such as the pile diameter and the pile slenderness ratio on the soil response still need to be investigated.

In the serviceability limit state, only small rotations of the monopiles are allowed. Further, strict demands are set to the total stiffness of the foundation in order to avoid resonance with the rotor and blade passing frequencies and with the wind and wave loading. Hereby, the small-displacement stiffness,

e.g. the first part of the *p-y* curves, is of high importance in the design of monopile foundations for offshore wind turbines.

In the present paper, the *p-y* curve formulation recommended by ANSI/API (2011) and DNV (2014) is re-evaluated for static loading conditions. The main focus is on the first part of the *p-y* curves. In the design of offshore wind turbine foundations, the cyclic behaviour is of high interest due to the cyclic behaviour of wind and wave loads. However, the trend of the first part of the *p-y* curves is expected to be similar for static and cyclic loading. According to Kramer (1996) the backbone curve of a soil can be described by two parameters: the initial (low-strain) stiffness and the (high-strain) shear strength. Similarly, it is assumed that the soil-structure interaction similarly can be described by an initial slope, *dp*/*dy*, and an ultimate resistance. An expression of the slope of the *p-y* curves at small displacements, but not the true initial tangent stiffness, is proposed aiming at accurate predictions of the pile behaviour when the pile is exposed to serviceability limit state (SLS) loads and lower bound system frequency analyses. The expression is determined based on a numerical study. The effect on the pile behaviour by incorporating the modified expression for the initial slope of the *p-y* curves in a Winkler model is illustrated for a monopile foundation situated at Horns Rev, Denmark.

2 *p-y* CURVE FORMULATION

ANSI/API (2011) and DNV (2014) recommend the *p-y* curve formulation given in equation (1) for piles located in sand.

$$p(y) = Ap_u \tanh\left(\frac{kx}{Ap_u}y\right) \tag{1}$$

p_u is the ultimate soil resistance, k is the initial modulus of subgrade reaction and x is the depth below the soil surface. A is a dimensionless factor depending on the loading scenario, i.e. static or cyclic:

$$A = \min\begin{Bmatrix} 3.0 - 0.8\frac{x}{D} \geq 0.9 & \text{, Static loading} \\ 0.9 & \text{, Cyclic loading} \end{Bmatrix} \tag{2}$$

The ultimate soil resistance can in accordance with Bogard and Matlock (1980) be estimated as:

$$p_u = \min\begin{Bmatrix} (C_1 x + C_2)\gamma' x \\ C_3 D \gamma' x \end{Bmatrix} \tag{3}$$

C_1, C_2 and C_3 are dimensionless factors varying with the internal friction angle, φ. k depends on the relative density/internal friction angle of the soil. The true initial slope of the *p-y* curves denoted E^*_{py} is thereby:

$$E^*_{py} = \left.\frac{dp}{dy}\right|_{y=0} = kx \tag{4}$$

Hence, E^*_{py} is considered explicitly to be independent of the pile properties, e.g. the pile diameter, D, the slenderness ratio, L_p/D, and the pile bending stiffness, E_pI_p. E^*_{py} varies linearly with depth below the soil surface and the initial modulus of subgrade reaction, k.

Several authors have investigated the influence of the pile diameter on E^*_{py} with contradictory conclusions. Terzaghi (1955), Ashford and Juirnarongrit (2003) and Fan and Long (2005) conclude that the pile diameter has no significant effect on the initial slope of the *p-y* curves. In contrast, Carter (1984) and Ling (1988) propose a linear dependency between pile diameter and initial stiffness.

Based on numerical investigations and a linear variation of E^*_{py} with depth as given in equation (4), Lesny and Wiemann (2006) conclude that the stiffness is overestimated for large depths. Instead, they propose a nonlinear variation of E^*_{py} with depth, i.e. E^*_{py} is proportional with $x^{0.6}$.

Based on theoretical considerations concerning changes in shear modulus as a function of shear strain and a nonlinear increase with depth, Kallehave et al. (2012) suggest a modified expression for the initial slope of the *p-y* curves in sand. They aim at improving the approximation of the natural frequency for offshore wind turbines supported by

monopile foundations. An expression in which the initial slope of the *p-y* curves is proportional to the depth raised to the power of *m* and to the pile diameter raised to the power of *n* is suggested. The values of the dimensionless factors *m* and *n* are site specific. In a benchmark study of full-scale measurements from three wind turbines in the Walney offshore wind farm, values of $m = 0.6$ and $n = 0.5$ are proposed.

Kirsch et al. (2104) has suggested a modification to the initial modulus of subgrade reaction, *k*, in which it is attempted to account for large-diameter effects and the small-strain stiffness.

Based on centrifuge tests on piles with slenderness ratios of 2 to 10, Leth (2013) concludes that the small-displacement stiffness (evaluated at a normalized pile head displacement of 1%) of the *p-y* curves is proportional to the depth below soil surface raised to a power of 0.5 and to the pile diameter raised to the power of 0.6. Hence, while the considerations of Kallehave et al. (2012) aim at predicting the low-strain response, Leth (2013) aims at modelling the pile response corresponding to the serviceability limit state (SLS) loads.

The pile-soil interaction and pile response are affected by the flexibility of the pile. The slenderness ratio for monopiles for modern offshore wind turbines is significantly lower than the slenderness ratio for the piles tested at Mustang Island. Therefore, monopiles used for offshore wind turbine foundations exhibit a rather stiff behaviour in contrast to the rather flexible piles for which the currently recommended *p-y* formulation has been validated.

In conclusion, the *p-y* curve formulation currently recommended by ANSI/API (2011) and DNV (2014) is at first sight not well suited for the design of monopile foundations for offshore wind turbines. Knowledge is especially needed regarding the *p-y* curves at small displacements.

3 NUMERICAL MODELLING

3.1 Establishing the numerical model

A numerical model has been constructed in the commercial program *FLAC*^{3D} (FLAC^{3D} 3.1, 2006), with the objective of determining the behaviour of monopiles exposed to static lateral loading.

Since, the model is symmetric around a vertical plane parallel with the lateral loading direction only half of the pile and surrounding soil is modelled. The pile and the soil are divided into zones consisting of five 4-noded constant strain-rate sub-elements of tetrahedral shape (approximately 20000 zones have been employed). An outer diameter of 40*D* is used whereas the bottom boundary is placed 15 m below the pile toe. This ensures that the model boundaries do not influences the results. Standard boundary conditions have been applied to the model boundary.

For practical reasons the pile is modelled as a solid pile. Therefore, the Young's modulus of elasticity and the density of the solid pile are scaled to ensure that the bending stiffness and the weight including soil are identical to the properties of a tubular pile. The plug ratio is assumed equal to unity. The shear stiffness, A_pG_p, is not scaled correctly, which is of minor importance since bending is governing in the design. Analyses, not presented here, show that the difference in the maximum deflections at the seabed for a pile with $L_p/D = 5$ is less than 2 % when comparing the results based on the solid pile model with the results obtained by means of a tubular pile model.

The Mohr-Coulomb material model is employed for the sand. The reason for using a simple model is that the soil parameters employed in the model can be determined from few experimental tests. Further, it is convenient to have few model parameters in a parametric study. Hence, it seems naturally to incorporate a material model with only one stiffness parameter. The disadvantage with respect to the chosen material model is that the model does not take into account the stress and strain dependency of soil stiffness. However, Achmus et al. (2009), Chik et al. (2009) and Kim and Jeong (2011) have suc-

cessfully modelled horizontally loaded piles by employing the Mohr-Coulomb material model for the soil. The interface between the pile and the soil is modelled by means of a linear Coulomb shear strength criterion allowing gapping and slipping between the pile and the soil.

A displacement-controlled horizontal loading is applied as a velocity to the centre nodes of the pile head. Hereby, a number of steps are prescribed in order to reach the desired pile deflection. To ensure a quasi-static behaviour of the pile-soil system, the velocity of the pile is set to 10^{-6} ms^{-1}.

Damping is introduced since *FLAC*^{3D} is a dynamic, explicit finite difference solver.
The numerical simulations are executed in stages. First, the initial stresses in the soil are generated using a K_0-procedure. Secondly, an equilibrium state is established for the pile and the soil in which the soil properties are employed for the pile material. At this stage, the interface between the soil and the pile is assumed smooth. Thirdly, a new equilibrium state is calculated in which the pile and the interface are given the correct properties. After reaching equilibrium, the horizontal load is applied as described.

3.2 Validation

The numerical model has been validated against 23 laboratory tests conducted in a so-called pressure tank, cf. Sørensen et al. (2015). The laboratory tests were carried out on piles with diameters of 40-100 mm and embedded pile lengths of 200-500 mm embedded in dense to very dense fine sand. The piles were exposed to lateral loading.

Results from one test (L_p/D = 5 and overburden pressure of P_0 = 100 kPa and D = 100 mm) as well as load-settlement curves established by means of the FLAC^{3D} model are shown in Figure 1. A reasonable concordance between the numerical simulations and the test results has been found for y/D less than 0.2.

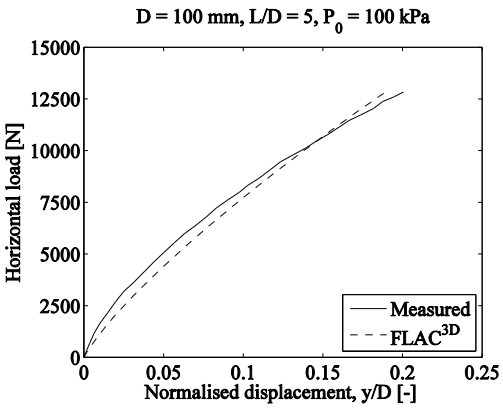


Figure 1 Comparison of numerical simulations and laboratory tests.

3.3 Pile and soil properties

Steel piles with pile diameters of D = 1-7 m and length of L_p = 20 m have been studied. Hence, the slenderness ratio, L_p/D, varies between 3 and 20. For practical purposes the pile wall thickness, *wt*, is assumed constant and equal to 0.05 m. For D = 1 m flexible pile behaviour is expected while a rather rigid pile behaviour is expected for D = 7 m.

According to Klinkvort et al. (2010), the location of the force resultant, *e*, with respect to the embedment length, L_p, influences the shape of the *p-y* curves. Normally, e/L_p is in the interval of 0.5 to 2.0 for the design load of monopiles for offshore wind turbines. In this study, e/L_p = [0.50; 0.75; 1.00; 1.50; 2.00] have been applied.

A Young's modulus of elasticity, E_p, a Poisson's ratio, ν, and a unit weight, γ, of 210 GPa, 0.3 and 77 kNm^{-3}, respectively, have been assumed for the steel material. A homogeneous soil is employed. The internal friction angle, φ, of the sand has been varied between 30-43°. The wall friction angle, δ, between the soil and the pile is as proposed by Brinkgreve and Swolfs (2007) set to:

$$\delta = \text{atan}\left(\frac{2\tan(\varphi)}{3}\right) \quad (5)$$

Hereby, the wall friction angle takes values from 21° to 32°. The dilatancy angle, ψ, of the soil material is given in equation (8) (Brinkgreve and Swolfs, 2007):

$$\psi = \varphi - 30 \quad (6)$$

Young's modulus of elasticity for the soil has been varied in the range 21 to 93 MPa. Generally, the stiffness of sand is stress dependent. However, in order to decouple the influence of soil stiffness and depth below soil surface on E^*_{py}, the Young's modulus of elasticity for the soil, E_s, has been assumed constant with depth in the parametric study of parameters influencing the small-displacement stiffness of the *p-y* curves.

4 RESULTS

4.1 Effects of L_p/D, E_pI_p, e/L_p and soil properties on the pile response

Figure 2 and Figure 3 present pile deflections and bending moment distributions for piles with D = 1-7 m and φ = 37°, respectively. For D = 7 m the pile behaves very stiff. In contrast, the pile with D = 1 m behaves flexible. The depth to the point of zero deflection increases for increasing pile diameter. Furthermore, the depth to the maximum bending moment increases for increasing pile diameter. Since the length has been kept constant at 20 m, the slenderness ratio, L_p/D, varies as the pile diameter is varied. Hereby, it can be concluded that the slenderness ratio has a significant effect on the pile behaviour.

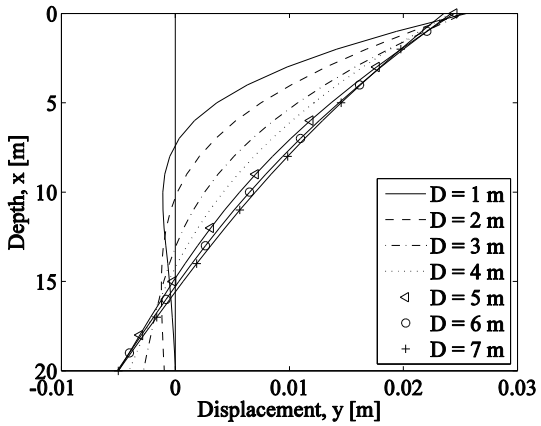


Figure 2 Pile deflection along the pile for φ_{tr} = 37°, E_s = 59 MPa, wt = 0.05 m, L_p = 20 m and e/L_p = 0.75.

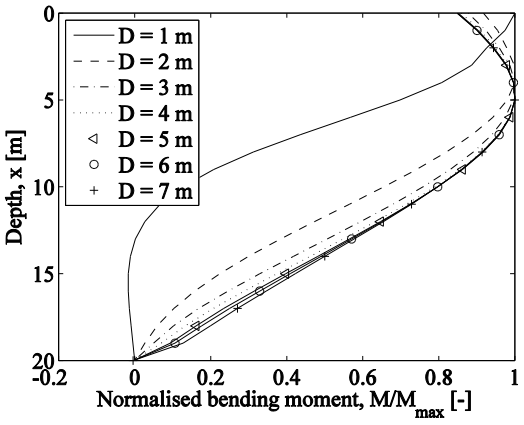


Figure 3 Distribution of bending moment. φ_{tr} = 37°, E_s = 59 MPa, wt = 0.05 m, L_p = 20 m and e/L_p = 0.75.

Figure 4 illustrates the variation of the small-displacement stiffness of the *p-y* curves, E^*_{py} with pile diameter, D, and depth below soil surface. In practice E^*_{py} has been estimated as the secant stiffness for a pile deflection of 1.5 mm. Hence, the small displacement stiffness is investigated and not the true initial stiffness. A non-linear increase of $E_{py}{}^*$ can be observed for increasing depths, which is in contrast to the linear dependency proposed by ANSI/API (2011) and DNV (2014). Further, E^*_{py} is found to increase for increasing pile diameter primarily due to differences in pile deflection behaviour going from flexible for small pile diameters and high slenderness ratios to stiff body rotations for large diameters and low slenderness ratios. In contrast, ANSI/API (2011) and DNV (2014) propose that E^*_{py} is independent of the pile diameter. The rotation of the pile causes discontinuities in the values of E^*_{py} at depths between approximately 8-17 m as the point of rotation changes with the size of loading. Therefore, values of E^*_{py} at these depths are left out in the following figures.

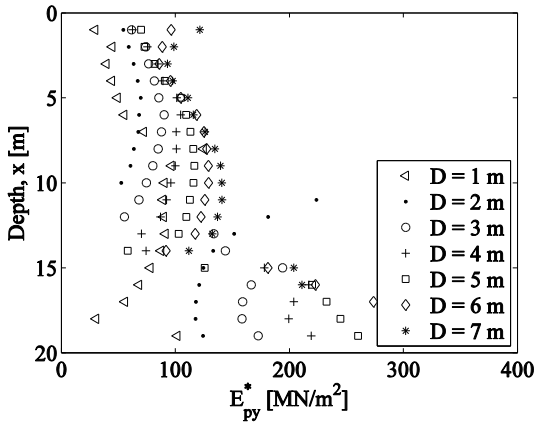


Figure 4 Variation of small-displacement stiffness, E^*_{py}, with depth for φ_{tr} = 37°, E_s = 59 MPa, wt = 0.05 m, L_p = 20 m and e/L_p = 0.75.

Figure 5, Figure 6 and Figure 7 illustrate the variation of the small-displacement stiffness of the *p-y* curves, E^*_{py} with friction angle, φ, Young's modulus of elasticity for the soil, E_s, and loading eccentricity, e/L_p, respectively. According to Figure 5, E^*_{py} is insignificantly influenced by the internal friction angle. Furthermore, Figure 6 indicates that E^*_{py} increases with increasing values of Young's modulus of the soil, E_s. However, ANSI/API (2011) and DNV (2014) suggest that E^*_{py} is independent on the Young's modulus of elasticity of the soil and instead dependent on the internal friction angle. However, it should be noted that Young's modulus of elasticity of the soil and the internal friction angle are interrelated via the relative density of the sand. Figure 7 indicates that E^*_{py} is independent of the loading eccentricity for e/L_p = 0.5-2.0.

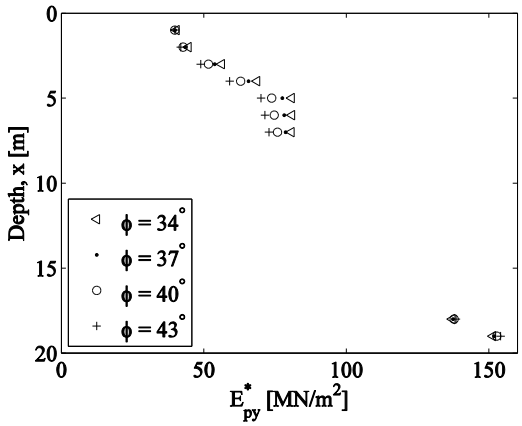


Figure 5 Variation of small-displacement stiffness, E^*_{py}, with depth for varying internal friction angles D = 5 m, E_s = 59 MPa, wt = 0.05 m, L_p = 20 m and e/L_p = 0.75.

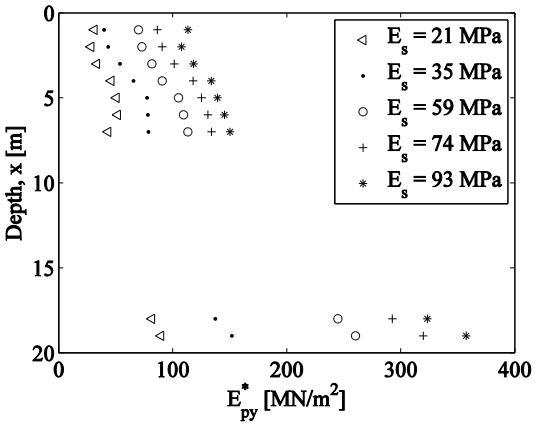


Figure 6 Variation of small, displacement stiffness, E^*_{py}, with depth for varying values of E_s. φ_{tr} = 37°, E_s = 59 MPa, wt = 0.05 m, L_p = 20 m and e/L_p = 0.75.

Figure 8 presents the influence of bending stiffness, E_pI_p, on the *p-y* curves. It can be concluded that E_pI_p does not influence the *p-y* curves. This is in agreement with Fan and Long (2005), but in contrast to Ashour and Norris (2000).

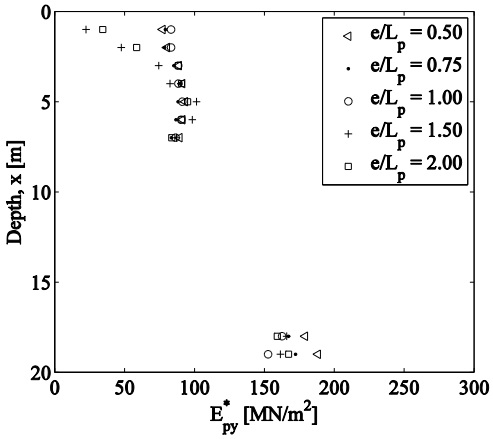


*Figure 7 Variation of small-displacement stiffness, E*py, with depth for varying e/Lp. φ_{tr} = 37°, E_s = 93 MPa, D = 2 m, wt = 0.05 m and L_p = 20 m.*

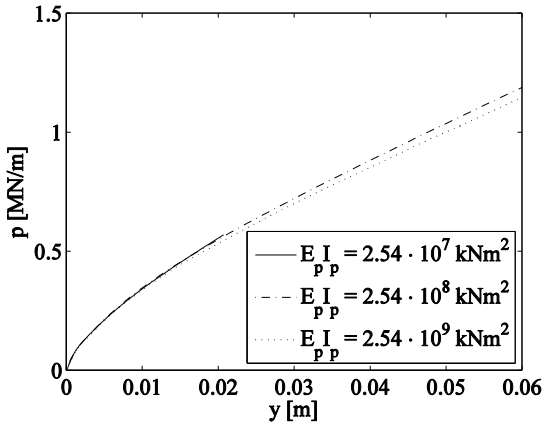


Figure 8 Comparison of p-y curves for varying pile bending stiffness. φ_{tr} = 40°, E_s = 74 MPa, D = 4 m, wt = 0.05 m, L_p = 20 m and e/L_p = 0.75.

4.2 Modified expression for the small-displacement stiffness of the p-y curves

Figure 4 and Figure 6 indicate that the small-displacement stiffness of the *p-y* curves, E^*_{py}, depends on the depth below the soil surface, *x*, Young's modulus of elasticity for the soil, E_s, and the pile diameter, *D*. A modified expression for the small-displacement stiffness is proposed in equation (7).

$$E^*_{py} = a\left(\frac{x}{x_{ref}}\right)^b \cdot \left(\frac{D}{D_{ref}}\right)^c \cdot \left(\frac{E_s}{E_{s,ref}}\right)^d \qquad (7)$$

b, *c*, and *d* are dimensionless constants whereas *a* is a constant specifying the small-displacement stiffness for $D = D_{ref}$ = 1 m, $x = x_{ref}$ = 1 m and $E_s = E_{s,ref}$ = 1 MPa. Further, *x* and *D* should both be inserted in meters and E_s in MPa. Values of *a*, *b*, *c* and *d* have been found to 1000 kPa, 0.3, 0.5 and 0.8, respectively. These compare reasonably well with the values, cf. Section 2, proposed by Kallehave et al. (2012) and Leth (2013).

The constants *a*, *c* and *d* have been determined based on least squares fitting. Due to the discontinuity of the small-displacement stiffness around the point of zero deflection, the constant *b* has been determined by visual fitting of equation (7) with the *FLAC*^{3D} simulations.

Figure 9 shows E^*_{py} normalized with respect to $(E_s/E_{s,ref})^{0.8}$ for varying values of Young's modulus of elasticity for the soil and *D* = 4 m. It can be observed that equation (7) provides a reasonable description of the dependency of the internal friction angle when using *d* = 0.8. Similar results have been obtained for *D* = 1-7. The linear variation of E^*_{py} with depth, *b* = 1, and the non-linear expression proposed be Lesny and Wiemann (2006), *b* = 0.6, overestimates E^*_{py} for large depths.

In Figure 10, a normalised E^*_{py} for an internal friction angle of 40°, E_s = 74 MPa, and varying pile diameters is presented as function of depth. A constant bending stiffness corresponding to a steel pile with a pile diameter of 4 m and a wall thickness of 0.05 m has been employed for all piles in order to isolate the effect of the diameter to equation (7) only. The proposed expression for E^*_{py}, produces a reasonable fit.

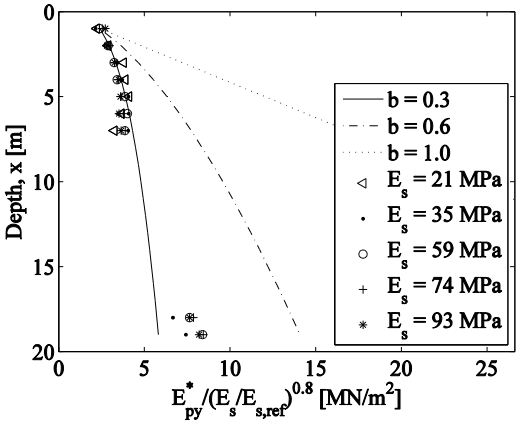


Figure 9 Normalized small displacement stiffness, E^*_{py}, for φ_{tr} = 37°, D = 4 m, wt = 0.05 m, L_p = 20 m and e/L_p = 0.75. The three curves have been forced through the average normalised small-displacement stiffness in a depth of 1 m.

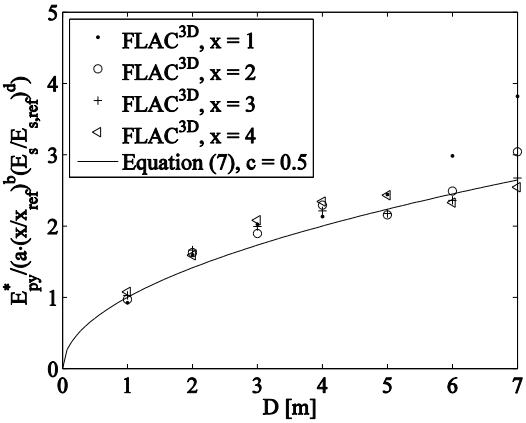


Figure 10 Normalised small-displacement stiffness for varying pile diameter and for φ_{tr} = 37°, E_s = 74 MPa, L_p = 20 m and e/L_p = 0.75. The bending stiffness has been kept constant for all piles.

4.3 Practical implications in relation to the modified expression for the small-displacement stiffness

When using equation (7) for determination of the initial slope of *p-y* curves for investigations of the serviceability limit state, the authors recommend employing an E_s corresponding to $E_{0.1}$, which is the Young's modulus of elasticity for an average axial strain of 0.1%, as monopiles used as foundation for offshore wind turbines are exposed to small deflections/rotations. According to Lunne et al. (1997), this level of strain is reasonably representative for many well-designed foundations.

5 EXAMPLE – HORNS REV 1

5.1 Description of Horns Rev 1 Offshore Wind Farm

The wind turbine considered in this example is a part of Horns Rev 1 Offshore Wind Farm, built during 2003 and located in the North Sea approximately 30 km west of Esbjerg in Denmark. The wind turbines at the site are all of the Vestas V80-2.0 MW type with a total assembly weight of 105.6 Te. The hub height is 70 m above MSL and the site is dominated by westerly winds. The foundations are monopiles having a diameter of 4.0 m. A transition piece with outer diameter of 4.34 m constitutes the transition from the tower to the monopile, cf. Hald et al. (2009).

5.2 Pile and loading conditions

The steel monopile considered is the foundation for wind turbine 14. The length is 31.6 m and the wall thickness, *wt*, and thereby the bending stiffness, E_pI_p, varies along the pile. The monopile has been driven to its final position 31.8 m below the mean sea level leading to an embedded length of 21.9 m.

The pile behaviour is investigated corresponding to the serviceability limit state (SLS): the horizontal load $H = 2.0$ MN and the overturning bending moment $M = 45$ MNm. More information on the pile geometry and the loading conditions can be found in Augustesen et al. (2010).

5.3 Soil conditions

The soil profile consists primarily of dense to very dense sand. The stratigraphy and the soil properties are presented in Augustesen et al. (2010).

For the *FLAC*^{3D} analyses the classical Mohr-Coulomb criterion and a linear elastic material model have been combined to describe the elasto-plastic material behaviour of the soil. Further details on the FLAC3D model of the wind turbine foundation are presented in Augustesen et al. (2010).

5.4 Results and discussion

In Figure 11, the calculated deflections are shown for the case in which the pile is subjected to the static SLS-loads. The pile behaviour has been determined by means of *FLAC*^{3D} and the Winkler model approach employing, respectively, the original API *p-y* curves given by equations (1)-(4) (in the following denoted the API method) and the API *p-y* curves employing the proposed small-strain stiffness given in equation (7) (in the following denoted the modified API method). The deflection patterns predicted by *FLAC*^{3D} and the modified API method have similar shapes. The monopile behaves relatively rigid implying that a "toe kick" occurs; this is especially pronounced when considering the deflection behaviour predicted by means of *FLAC*^{3D} and the modified API method. Below 14 m the deflection pattern estimated by the API method and *FLAC*^{3D} deviate significantly. *FLAC*^{3D} estimates, for example, greater horizontal deflections at the pile toe compared to the API method (Table 1). The deviation in deflection pattern may be due to the fact that the small-displacement stiffness, E^*_{py}, provided by the API method is overestimated at great depths. Since the API method overestimates the stiffness with depth compared to *FLAC*^{3D} and the modified API method, the depth for zero deflection predicted by the API method is located closer to the seabed (Table 1). Furthermore, the maximum horizontal deflection at seabed level determined by means of the API method is much lower compared to the deflections predicted by the other methods (Table 1).

The three approaches predict similar distributions of the moment with depth. Howev-

er, *FLAC*^{3D} estimates slightly lesser and higher moments at moderate and deep depths, respectively, compared to the API method and the modified API method. The maximum moments determined by the three approaches are almost identical (Table 1). The depths to the maximum moment vary between 2.5 m and 3.0 m with *FLAC*^{3D} giving rise to the smallest value.

The *p-y* curves at different depths are shown in Figure 12. Except for the depth $x = 2.1$ m the API method has a tendency to overestimate the soil resistance, *p*, at a given deflection, *y*, compared to the other two approaches. The pressures, estimated by means of *FLAC*^{3D}, mobilised at the depth $x = 7.4$ m are less than the pressures at both $x = 2.1$ m and $x = 3.9$ m for a given deflection *y*. This is due a the lower angle of internal friction and a lower Young's modulus of elasticity at that depth (Figure 12).

Generally, the modified API method predicts the results obtained by *FLAC*^{3D} better than the API method. The deviations, however, in the results determined by means of *FLAC*^{3D} and the modified API method may be caused by: the traditional uncertainties related to numerical modelling; shortcomings in the method proposed by Georgiadis (1983), in which layered soil profiles have been taken into account; shortcomings in the general shape of the *p-y* curves; and shortcomings in the definition of the ultimate soil resistance.

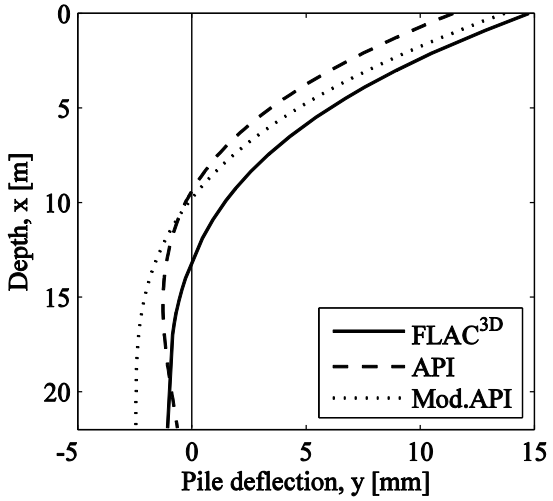


Figure 11 Pile deflection at maximum horizontal load for the monopile foundation of Wind Turbine 14 at Horns Rev 1.

Table 1 Distribution of bending moment, pile deflection and pile rotation.

	***FLAC*^{3D}**	**API**	**Mod. API**
Max moment [MNm]	47.1	48.8	48.3
Depth to max. moment [m]	2.5	3.0	2.8
Pile deflection, seabed [mm]	14.8	11.4	13.7
Pile deflection, toe [mm]	-1.0	-0.6	-2.5
Rotation, seabed [°]	0.12	0.12	0.13
Depth to zero deflection [m]	13.2	9.4	9.8

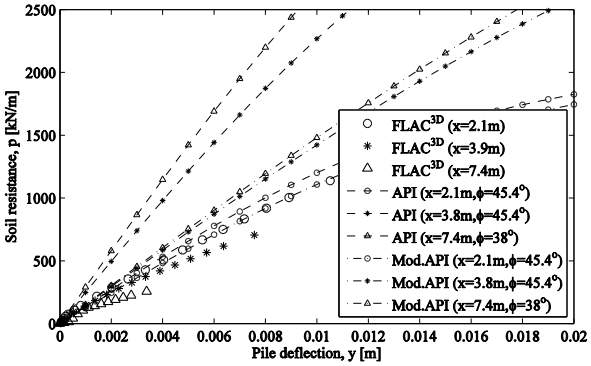


Figure 12 Soil resistance as a function of pile deflection and depth for Wind Turbine 14 at Horns Rev 1.

6 CONCLUSIONS

This paper considers large-diameter stiff monopiles in sand for offshore wind turbines. In design of such piles the first part of the *p-y* curves are especially important. A modified expression for the small-displacement stiffness of the *p-y* curves has been proposed, in which the slope depends on the depth below the soil surface, the pile diameter and Young's modulus of elasticity of the soil. This is in contrast to the method recommended by the American Petroleum Institute (API) in which the initial part of the *p-y* curves is independent of Young's modulus of elasticity and the diameter. The reassessment of the *p-y* curves recommended by the API is based on three-dimensional numerical analyses and the reassessment is aiming for a better prediction of the pile behaviour, especially when exposed to static SLS loads.

The differences in pile behaviour by employing a Winkler model incorporating the current *p-y* curves recommended by API and a modified version in which the expression for the small-displacement stiffness of the *p-y* curves proposed in this paper is employed, respectively, has been evaluated. The assessment is based on a monopile for an offshore wind turbine at Horns Rev, Denmark. A three-dimensional numerical model of the pile at Horns Rev has also been established by means of the commercial software package *FLAC*^{3D}. Generally, the modified API method predicts the results obtained by *FLAC*^{3D} considerably better than the API method.

7 REFERENCES

Achmus, M., Kuo, Y.-S. & Abdel-Rahman, K. (2009). Behavior of monopile foundations under cyclic lateral load. Comput. Geotech., Vol. 36, No. 5, 725-735.

ANSI/API (2011). Recommended Practice for Geotechnical and Foundation Design Considerations, API RP2GEO. American Petroleum Institute, 1. Edition.

Ashford, S.A. & Juirnarongrit, T. (2003). Evaluation of pile diameter effect on initial modulus of subgrade reaction. J. Geotech. Geoenv. Eng., Vol. 129, No. 3, 234-242.

Ashour, M. & Norris, G. (2000). Modeling lateral soil-pile response based on soil-pile interaction. J. Geotech. Geoenv. Eng., Vol. 126, No. 5, 420-428.

Augustesen A.H., Sørensen S. H. S., Ibsen L. B., Andersen L., Møller M. & Brødbæk K. T, 2010. Comparison of calculation approaches for monopiles for offshore wind turbines. In proceedings of Numerical Methods in Geotechnical Engineering 2010, Trondheim, Norway. Benz & Nordal (eds). Taylor & Francis Group. pp. 901-906

Bogard, D. & Matlock, H. (1980). Simplified Calculation of p-y Curves for Laterally Loaded Piles in Sand, Unpublished Report, The Earth Technology Corporation, Inc., Houston, Texas.

Brinkgreve, R.B.J. & Swolfs, W. (2007). PLAXIS 3D FOUNDATION, Material Models manual, Version 2. PLAXIS b.v.

Carter, D.P. (1984). A non-linear soil model for predicting lateral pile response. Civil Engineering Dept., Univ. of Auckland, New Zealand, Rep. No. 359.

Chik, Z.H., Abbas, J.M., Taha, M.R. & Shafiqu Q.S.M. (2009). Lateral behavior of single pile in cohesionless soil subjected to both vertical and horizontal loads. Eur. J. Sci. Res., Vol. 29, No. 2, 194-205.

Cox, W.R., Reese, L.C. & Grubbs B.R. (1974). Field testing of laterally loaded piles in sand. Proceedings of the Sixth Annual Offshore Technology Conference, Houston, Texas, USA, 459-464.

DNV (2014). Design of Offshore Wind Turbine Structures, DNV-OS-J101. Det Norske Veritas, Det Norske Veritas Classification A/S.

Fan, C.C. & Long, J.H. (2005). Assessment of existing methods for predicting soil response of laterally loaded piles in sand. Comput. Geotech., Vol. 32, 274-289.

FLAC^{3D} 3.1 manual (2006). Fast langrangian analysis of continua in 3 dimensions. Itasca Consulting Group Inc., Minneapolis, Minnesota, USA.

Georgiadis, M. (1983). Development of p-y curves for layered soils. In Proc. of the Conference on Geotechnical Practice in Offshore Engineering, 536–545.

Hald, T., Mørch, C., Jensen, L., Bakmar, C.L. & Ahle, K. (2009). Revisiting monopile design using p-y curves – Results from full scale measurements on Horns Rev. European Offshore Wind 2009, Stockholm, Sweden.

Ibsen, L.B., Hanson, M., Hjort, T.H. & Thaarup, M. (2009). MC parameter calibration for Baskarp Sand No. 15. DCE Technical Report No. 62, Department of Civil Engineering, Aalborg University, Denmark.

Kallehave, D., Thilsted, C. L. & Liingaard, M. A. 2012. Modification of the API p-y formulation of Initial Stiffness of Sand. In Proc. of Offshore Site Investigation and Geotechnics: Integrated Techologies – Present and Future, London, UK.

Kim, Y. & Jeong, S. (2011). Analysis of soil resistance on laterally loaded piles based on 3D soil-pile interaction. Comput. Geotech., Vol. 38, 248-257.

Kirsch, F., Richter, T. & Coronel, M. (2014). Geotechnische Aspekte bei der Gründungsbemessung von Offshore-Windenergieanlagen auf Monopfählen mit sehr grossen Durchmessern, Stahlbau.

Klinkvort, R.T., Leth, C.T. & Hededal, O. (2010). Centrifuge modelling of a laterally cyclic loaded pile. Proceedings of International Conference on Physical Modelling in Geotechnics, Zürich, Switzerland, 959-964.

Kramer, S.L. (1996). Geotechnical Earthquake Engineering. Prentice-Hall International Series in Civil Engineering and Engineering Mechanics, William J. Hall (eds.), ISBN0-13-374943-6.

Lengkeek, H.J. (2003). Estimation of sand stiffness parameters from cone resistance. PLAXIS Bulletin No. 13, 15–19.

Lesny, K. & Wiemann, J. (2006). Finite-element-modelling of large diameter monopiles for offshore wind energy converters, Geo Congress 2006, Atlanta, Georgia, USA.

Leth, C.T. (2013). Improved Design Basis for Laterally Loaded Large Diameter Pile: Eperimental Based Approach [Dissertation]. Department of Civil Engineering, The Faculty of Engineering and Science, Aalborg University, Aalborg, Denmark.

Ling, L. F. (1988). Back analysis of lateral load test on piles. Civil Engineering Dept., Univ. of Auckland, New Zealand, Rep. No. 460.

Lunne, T., Robertson, P.K. & Powell J.J.M. (1997). Cone penetration testing in geotechnical practice. Blackie Academic & Professional.

Murchison, J.M. & O'Neill, M.W. (1984). Evaluation of p-y relationships in cohesionless soils. Analysis and design of pile foundations. Proceedings of a Symposium in conjunction with the ASCE National Convention, New York, New York, USA, 174-191.

Sørensen S. P. H., Ibsen L. B. & Foglia A., 2015. Testing of Laterally Loaded Rigid Piles with Applied Overburden pressure. International Journal of Offshore and Polar Engineering, Vol. 25, No. 2, June 2015, pp. 120-126.

Terzaghi, K. (1955). Evaluation of coefficients of subgrade reaction, Geotech., Vol. 5, No. 4, 297-326.

Design of protective dolphins in difficult geotechnical conditions

A. Krivokapic
Ramboll, Denmark, ANDK@Ramboll.dk

H. Sjöstedt
Ramboll, Denmark

ABSTRACT
Many existing bridges are faced with urgency to increase safety due to vessel collision. A number of different approaches are possible depending on the set of constraints which are almost unique for a given project.
This paper describes the design of independent protective dolphins for the Sallingsund Bridge in Denmark. Two concrete structures, supported by tubular steel piles were designed to resist impact of vessels of up to 6000 deadweight tonnage (DWT) and prevent collision with the bridge piers. The design of the dolphins was preceded by risk analysis based on monitoring of the ship traffic through the channel and a concept study which narrowed down the choice of structural system.
The final solution was greatly influenced by the 15m water-depth and presence of a 15m thick layer of gyttja found immediately beneath the seabed, providing very little geotechnical resistance against lateral loads. The solution also had to fit many other constraints such as a limitation of the size of the structures, proximity of existing raked piles below the bridge pier, restrictive budget, etc.
Structural verification was done using state-of-art calculation methods, which took into account time history of the collision event, plastic behaviour of all structural elements (including the vessel), second order effects for piles and pile - group effect. Furthermore, the design was streamlined to maximize the dolphins overall energy dissipation capacity and is optimized with regards to the constructability in the near-shore environment.

Keywords: vessel collision, protection dolphin, gyttja

1 INTRODUCTION

Ship impact to a bridge from a larger vessel is a rare hazard which may have catastrophic consequences. A number of existing bridges do not have sufficient capacity required to resist the collapse of superstructure in the event of critical collision.

For any such bridge, a design of additional protection is required in order to reduce the risk level below the requirements given by the society and applicable codes.
In recent years, Vejdirektoratet (Danish Road Directorate which is the authority and main owner of roads and bridges in Denmark) has initiated assessments of four large marine bridges having unacceptably low safety against ship collision. Ramboll and COWI worked together with Vejdirektoratet on establishing the appropriate acceptance criteria to be met by protective measures following the principles of Eurocode system.

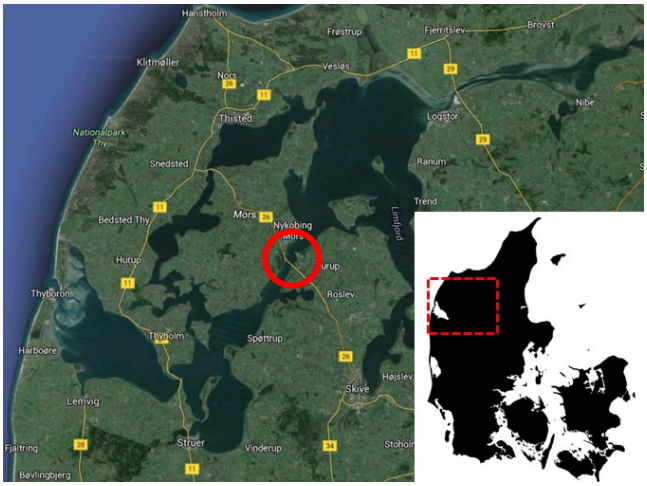


Figure 1 Limfjord (Sallingsund marked with red)

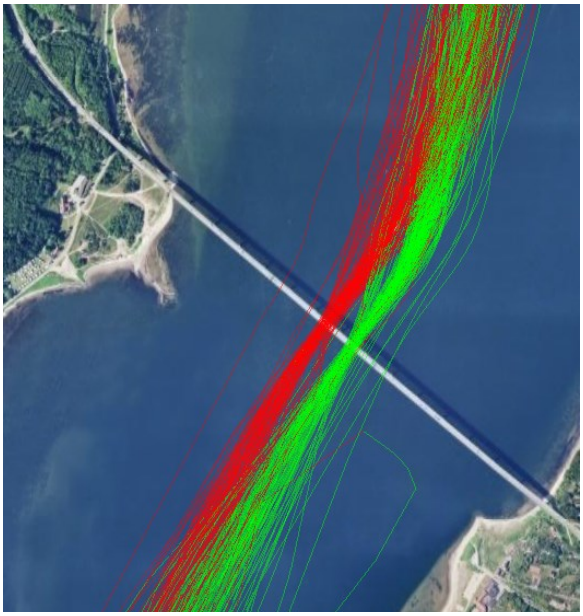
The largest of the analyzed bridges is Sallingsund Bridge, which was opened in 1978 in order to improve the traffic connection between the island of Mors and the Salling peninsula on the Danish mainland (Jutland) – see Figure 1. The total length of the bridge is about 1700 metres, each span between the piers is 93 metres long and the maximum vertical clearance to the sea is 26 metres.

The bridge is constructed of reinforced and pre-stressed concrete. The bridge deck is carried by 18 concrete piers, founded on driven tubular piles.


Figure 2 Sallingsund bridge

1.1 Risk analysis

The design was preceded by a comprehensive risk assessment which included a cost-benefit analysis in order to choose the right solution for the task within a given budget.
The assessment included analysis of vessel traffic through Sallingsund by collecting Automatic Identification System (AIS) data and incorporated mathematical models of vessel deflection upon the impact with a protection structure – see Figure 3.


Figure 3 Overview of AIS data monitoring of the passing ships (red – southbound; green – northbound)

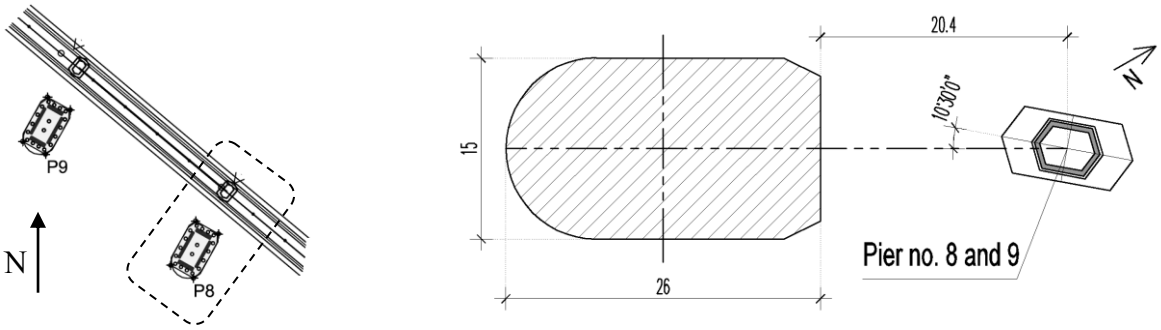


Figure 4 Placement of dolphin in relationship to the pier, overview (left) and detail (right)

The overall findings were that acceptable level of protection would be achieved by placing two independent protection structures south of piers 8 and 9 in order to protect these two piers against ship impact from northbound ships, as shown on Figure 4.
The design vessel was adopted to represent the largest ship that can enter the Limfjord also taking into account planned deepening of the entrance channel from the North Sea. Design vessel properties are shown in Table 2.

The design speed of the ship was determined based on the AIS data and adopted as 4.8 m/s.
The dolphins were designed to fully absorb the kinetic energy from the moving ship and prevent it from hitting the pier.

Table 1 Design vessel characteristics

Vessel type	Ship
Displacement (partly loaded)	6000 t
Width	16 m
Length	97 m
Bow depth	16 m
Draft (partly loaded)	4.7 m
Rake length of bow	4 m

2 SITE CONDITIONS

2.1 - Geotechnical conditions

The water depth at the location of the dolphins is around 15 m. The topsoil consists of a layer of gyttja reaching 15m below the seabed.
The gyttja is followed by a sand layer (17-30m in vicinity of piers 8 and 9) under which there is a layer of mica clay - see Figure 5.

The gyttja layer is very porous and with almost negligible strength and stiffness.
Therefore scour was not considered as an issue that affects the design assumptions. The thickness of the sand layer varies between pier number 8 and pier number 9.
Thicknesses and strength parameters of soil layers are shown in Table 2.
Preliminary design determined that the tip of the piles at the dolphin near pier 8 will end in sand layer with sufficient depth below to insure the full tip bearing capacity. The smaller thickness of the sand layer near pier 9 (in comparison to thickness at pier 8) meant that piles had to be extended into the clay layer making them considerably longer, much resembling those which support the bridge pier.

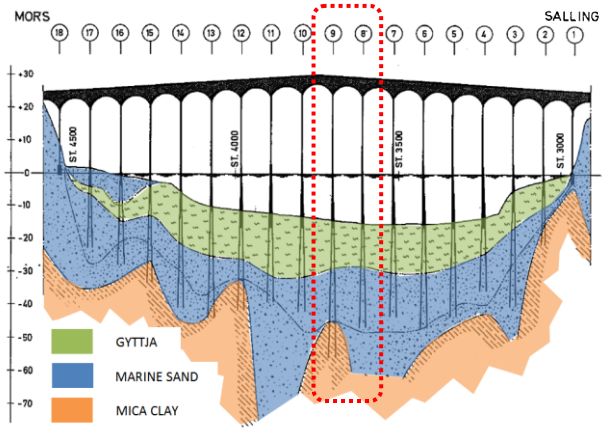


Figure 5 Overview of geotechnical layers which govern the foundation of the bridge

2.2 Existing piers and their piles

The bridge piers are founded on groups of circularly distributed driven piles in two rows, raked with 9% and 32% inclination outwards – see Figure 6. The piles are constructed as driven steel pipes with outer

Table 2 Geotechnical layers and properties

Level [m]		Soil type	c_u [kPa]	φ [°]	N_q [-]	γ' [kN/m³]	r
Dolphin 8s							
-14.7	-28.3	Gyttja	0.0 – 16.3	-	-	1 – 1.5	0.92 – 0.7
-28.3	-39.7	Sand	-	33	26	9.5	
-39.7	-51.7	Sand	-	38	49	9.5	
-51.7	-54.7	Sand	-	39	56	9.5	
Dolphin 9s							
-14.0	-29.0	Gyttja	0.0 – 18.0			2	0.8
-29.0	-46.0	Sand	-	33	26	9.5	
-46.0	-51.0	Clay	80-130/100	-	-	8.0	0.4
-51.0	-65.0	Clay	130/100	-	-	8.0	0.4

diameter of 711.2 mm and maximal bearing capacity of 6000kN in compression.
Tip of the existing piles at pier 8 extends between levels –45.20 and -47.50.
At pier 9, the piles for the foundation of the bridge had to be extended into the clay to achieve required bearing capacity. Tubular piles end in sand (levels -40.0 to -43.0) with steel H pile driven further down into the clay (tip level between -54.13) and -57.80).

3 GEOMETRY AND DESIGN

Preliminary studies eliminated cylindrical sheet pile caissons filled with gravel as unsuitable to the geotechnical conditions. Instead, concrete dolphins on piles were chosen as the concept capable of meeting the capacity required for stopping the design vessel. This solution also provided flexibility regarding the shape in plan and construction methods.

As the dolphins are placed with their "strong" axis at a 10.5° out of the axis perpendicular to the bridge (see Figure 4), their size affects the available width of navigation passages. A requirement from the Søfartsstyrelsen (authority in charge of ship safety) was that a minimal navigable channel width of 60m must be maintained. The width of 16m was chosen for the dolphins to ensure sufficient shading of the piers. The distance between the dolphins and the piers was adopted based on minimal allowable distance between newly installed and existing piles taking into account driving tolerances and mutual interference. Concrete superstructure is identical on both dolphins.
In plan, the dolphin has elongated shape, with their southern edges rounded to increase the deflection capability.
The length of the dolphins was adopted as 24.4m to maximize the lever arm between the opposing rows of vertically loaded piles. The

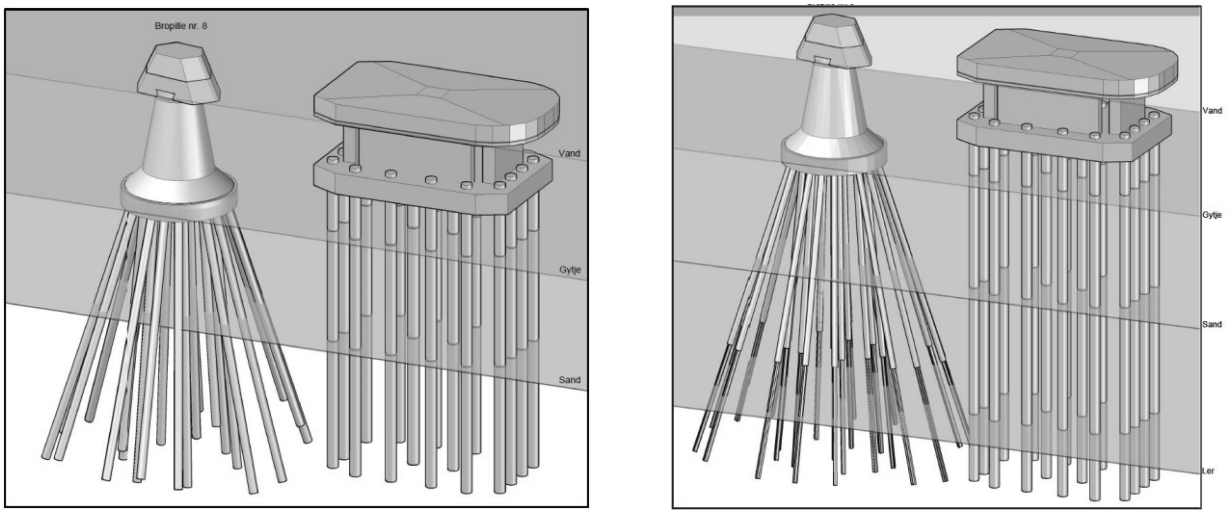


Figure 6 Isometric view of the dolphin and pier 8 (left) and 9(right)

concrete cap is a box-like structure, which consists of a concrete base slab, four walls and a top slab. Each dolphin is founded on 18 steel tubular piles, 1200mm in diameter. Isometric view of the dolphins in relationship to the bridge piers is shown on Figure 6.

The design was partially driven by consideration of the available construction methods. For example, maximal sizes of floating cranes and other construction vessels which can enter the Limfjord were taken into account when the size of prefabricated sections of superstructure was decided.
Driven piles were chosen over the bored shafts. It was considered that for this scope of works, latter choice would be burdened with higher price and lower availability of required construction equipment. The diameter of the piles was chosen as the best compromise between structural requirements, economy and execution concerns.

Driven piles offered the added benefit that the driving log allows for a precise estimate of the bearing capacity without additional testing.
Another important feature of the chosen pile system is that the largest contribution to the pile's vertical/axial capacity comes from the skin friction resistance (both inside and outside), which has a ductile post-yield behaviour. As shown later in this paper, this is an important feature in the system that allows for vertical yielding of piles (plastic segment of the diagram) during the collision. Possible increase of the pile tip area by under-reaming and filling with concrete was excluded as the larger tip resistance obtained in such way is hard to verify and produces brittle failure.

The combined depth from water surface to load bearing soil layers is around 30m (due to the presence of gyttja). With chosen pile diameter, design with a pinned connection between piles and superstructure would require too large deformations in order to stop the colliding vessel.
This challenge was met by designing a cap with extended height in order to shorten the free length of the piles, and by providing a fixed connection between piles and bottom slab.
As the consequence, vertical resistance of the piles was activated through the lever arm between the rows in tension and compression which resulted in the increase of overall structural stiffness.

The ability of the piles to retain maximal moment in the post-yield stage was achieved by maintaining the wall thickness-to-diameter ratio needed to satisfy requirements for compact cross-section class (class 1). As the result, piles were designed with wall thickness of 40mm in expected zones fixation and reduced further down where piles are subjected to normal forces only.

4 MODELLING AND ANALYSIS

The general approach to the design of independent protective structures is to demonstrate that the kinetic energy of the ship can be dissipated through plastic work and acceleration of the mass.
In order to do this, the working curve of the dolphin was obtained by creating a full static model of the structure in the FE software. Model incorporated several non-linear effects such as: horizontal and vertical response of the soil, nonlinear behaviour of the steel in the piles and second order effects (geometric nonlinearities).

4.1 Modelling of geotechnical conditions

The horizontal response of the surrounding soil was modelled using PY-curves which describe the dependency between reaction force, P, in the soil and lateral deformation, Y, of the pile. The PY-curves also vary with type and strength of soil and depth beneath the sea bed as shown on Figure 7.
Group effect was taken into the consideration by reduction of the P-values of the PY-curves for given deformation. Different reduction factors were used depending on the geometric position of the piles with values between 0.6 and 0.95.

The gyttja provides negligible resistance against lateral load compared to the sand layer below where fixation is achieved after

2-3m. The lateral resistance in the clay layer (which is found beneath the sand layer) is irrelevant. Still, it is included in the FE model.

The vertical resistance of the piles is a combination of skin friction and tip resistance. For a plugged pile, the skin friction acts on the outer circumference of the piles, whereas the tip resistance acts on the cross sectional area of the piles and the area of the enveloped soil. For an unplugged pile, the skin friction acts on the inner and outer circumference of the piles and the tip resistance acts on the cross sectional area of the pile's wall. However, to simplify the modelling of the dolphins, the sum of both skin frictional resistance and tip resistance was applied at the tip of the piles, by use of a piecewise linear spring, a TZ curve.

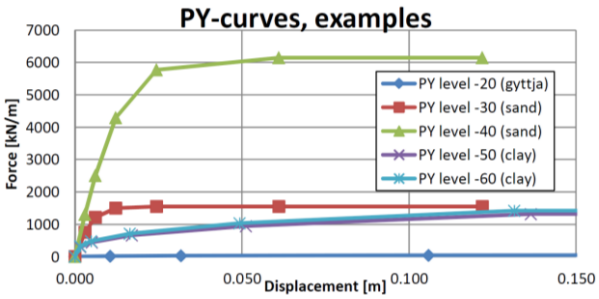


Figure 7 Examples of PY-curves used for piles at pier 9.

Typical examples of such a spring's properties are shown in Figure 8. The group effect was also investigated for vertical loading of the piles and it was found that it had no influence due to sufficient spacing between the piles.

4.2 Modelling of structural elements

The static model of the dolphin corresponds to a sway frame with piles fixed to the concrete super structure and fixation developed in the sand layer – see Figure 9. Yield hinges are expected to develop in the piles at the zones of maximal moments.

The global overturning moment caused by the impact load acting over the vertical distance between the top slab and the level of fixation, augmented by the second order effects, is resisted in two ways: - 1) through compression / tension action of the opposing pile rows and 2) through moment in each individual pile at the fixation level.

The steel piles are modelled as beam elements with perfect elasto-plastic behaviour. This means that bending moment can only increase in the pile until the von Mises yield criterion is reached. Thereafter, the moment is kept constant (or decreases if the normal force increases) with increasing rotation as the yield hinge is formed. Geometric imperfections were taken into acount through applying initial fictive horizontal loading to the beam elements.

All concrete parts were modelled as shell elements with linear material properties. The concrete structural elements were designed to transfer the loads from the ship impact

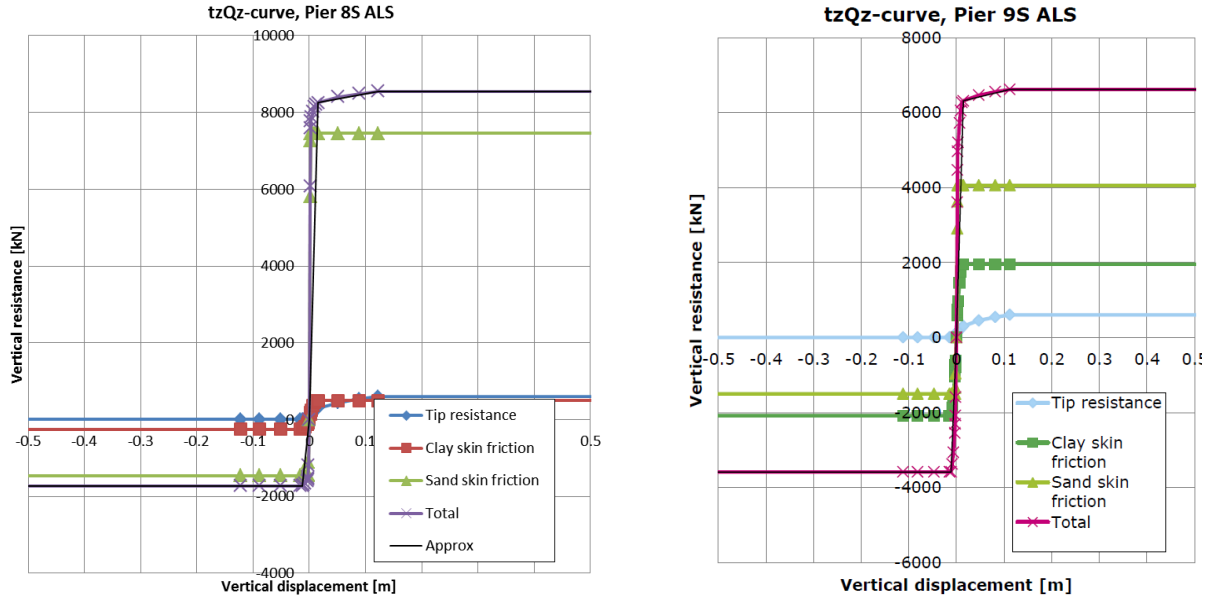


Figure 8 Components of the pile vertical capacity at piers 8 and 9 – TZ curves

without considerable plastic deformations.

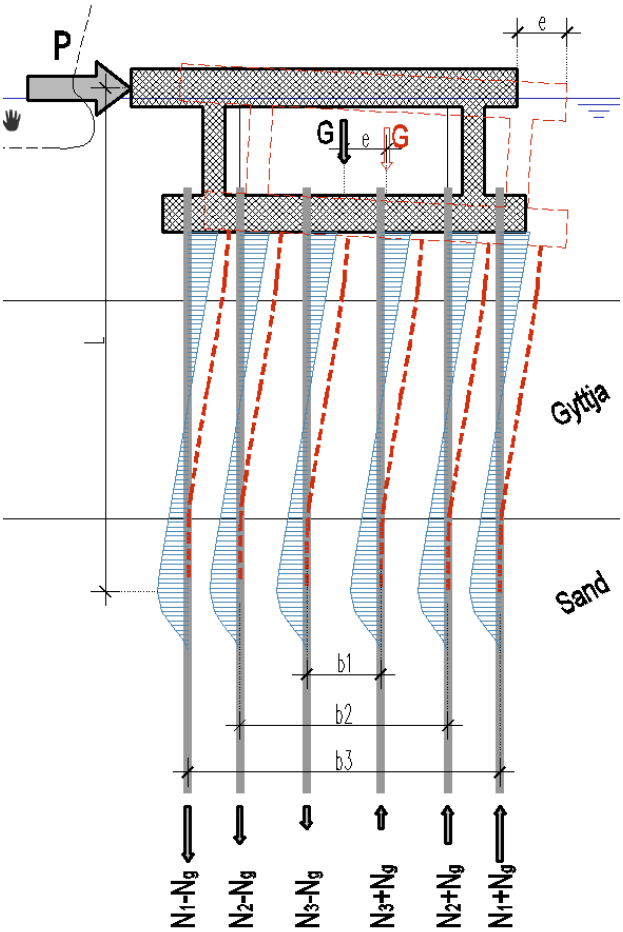


Figure 9 Static system

A horizontal point load of 1000 kN was applied at the top slab (level +1,5), as shown in Figure 9. The load was applied in iterative elasto-plastic analysis, with increasing multiplication factor assigned to each step.

Based on the horizontal deflection of the top slab and the corresponding load factor, a force – deformation diagram or "work curve" was plotted – see Figure 10.

The area beneath the diagram is equal to the dissipated energy of the system through plastic work. Therefore, "work curve" is used to determine the required deflection in order to dissipate the energy from the collision. At the same time, it is used to derive equivalent static impact load to be used for verification of the concrete super structure elements can be found.

The analysis is performed for head-on collision and oblique impact with a deviation angle of 30°. This angle is chosen as maximal proposed by AASHTO without reduction in the collision energy dissipation requirements. This is done in order to insure sufficient lateral stiffness of the dolphin.

5 RESULTS

5.1 Dolphin capacity

Obtained "work curve" of the described iterative elasto-plastic analysis is shown on Figure 10. The corresponding values of the normal forces in piles are shown on Figure 12 and deformed configuration of dolphin 9S is shown on Figure 11.

Only the results of the head on collision are presented here. Results of the oblique impact analysis are the subject of a future publication.

The load-deformation diagram of the structure has a steep linear shape up to the point where two front and rear rows of piles yield in compression / tension and yield hinges have developed in all of the piles. This point marks the peak load factor that the structure is able to resist (denoted by "1" on Figure 10).

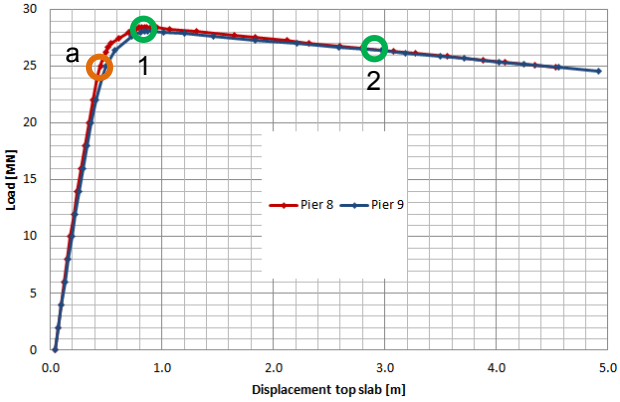


Figure 10 Load-displacement curve of the dolphin 8(red) and 9 (blue)

Prior to reaching the peak value, the curve drops in angle from the previous linear load-deformation response of the dolphin. At this point (marked with "a"), front piles have

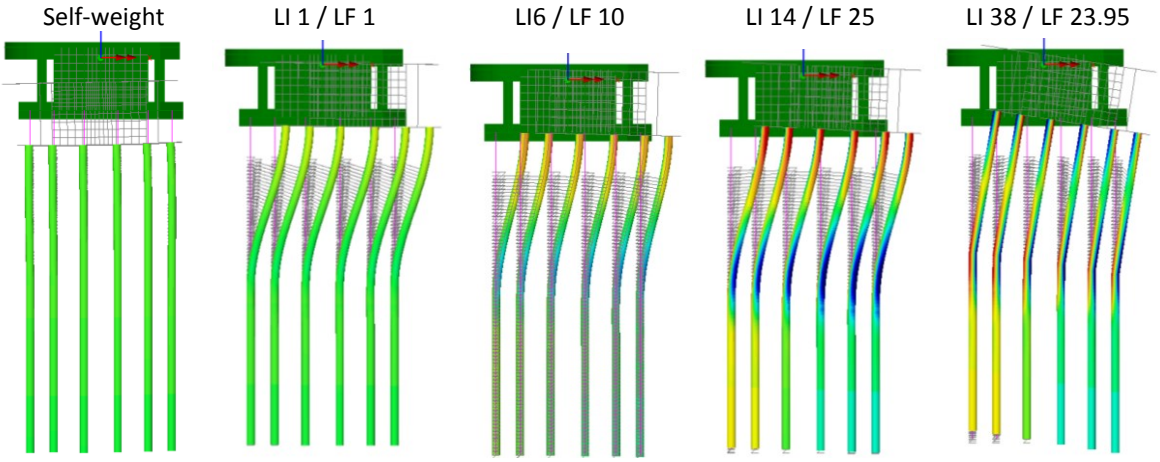
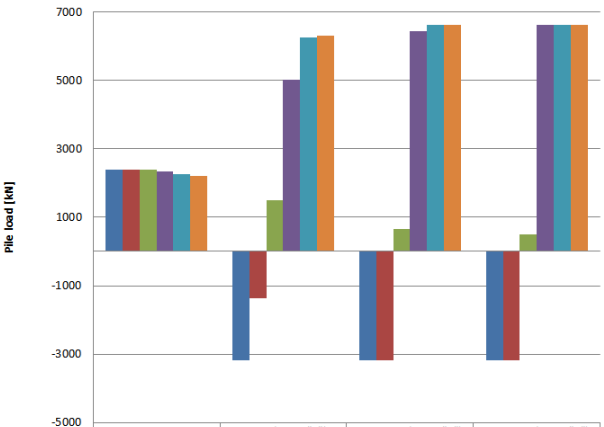


Figure 11 Successive deformed configurations of the dolphin (LI – load increment, LF – load factor)

almost exausted their normal bearing capacity in skin friction which has a steeper TZ curve compared with the tip.

Past the point "1", the deflection continues to increase and the global overturning moment is kept constant. Since the influence of second order effects increases with deflection gain, the load factor will decrease simultaneously.



	LF=0	LF=24 (point "a")	LF=28.06 (point "1")	LF=27.65 (point "2")
Row 1 (back)	2386	-3194	-3194	-3194
Row 2	2383	-1362	-3194	-3194
Row 3	2380	1501	664	491
Row 4	2337	5019	6440	6613
Row 5	2265	6266	6613	6613
Row 6 (front)	2208	6309	6613	6613

Figure 12 Overview of the development of normal forces in the piles compared to the load factor (each coloured bar corresponds to one row of piles and positive values represent compression)

Point "2" indicates the deformation at which the required kinetic energy of the colliding vessel is dissipated by the plastic work of the system. Displacement of the top slab is around 2.9m for both dolphins.

The "work curve" shows that dolphin is capable of deforming further which could indicate that the design is conservative. However, the overall stiff behaviour of the dolphin ensures stopping of the vessel on safe distance from the pier. Also, in the marine environment susceptible to ice loads, stiff structure is less susceptible of inducing unintended damage.

5.2 Energy exchange

Apart from plastic work performed by dolphin structure during the collision, impact energy is absorbed by several other mechanisms. Formost is the crushing of the ship's bow, which is described with non-linear curves in both AASHTO and Eurocode. Curves that describe the dependency between force and deformation are based on the physical experiments (Woisin and Meir-Dornberg).

Simplified curves and maximal values of quasi-static impact forces given in various sources show considerable disparity among each other. This is discussed in AASHTO and there is awareness that this is an area of ongoing research.

In this project, energy exchange between vessel and the dolphin was assessed using time series analysis based on the conservation of momentum at the moment of impact and conservation of energy for motion after the impact. The model is described as two-degrees-of-freedom system connected by

piecewise linear longitudional springs as shown on Figure 13. Spring of the dolphin is modeled after obtained "work curve" and the ship's bow force-deformation curve is addopted from annex C4.4 of EN 1991-1-7.

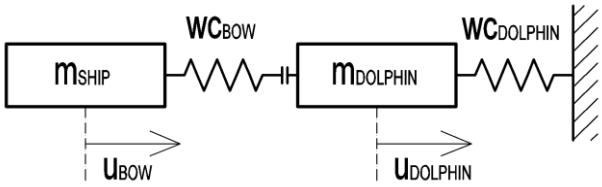


Figure 13 Simplified model for collision analysis

The interaction between the ship and dolphin is simulated using time series analysis peformed with in-house developed program.

Due to relatively large mass of the concrete superstructure compared to the displacement of the vessel, it was assessed that up to 60% of the collision energy could be dissipated by deformation of the bow. However, the assumptions regarding the ship's bow behaviour incorporate substantial uncertainities. Furthermore, recent studies based on detailed FEM models of ship's bow, indicate lower yield load. Collision with deformable structure could limit the deformation of the bow, thereby reducing the amount of energy dissipated in this way.
For this reason, dolphin's pile system, is verified without relying on this mechanism of collision energy dissipation.

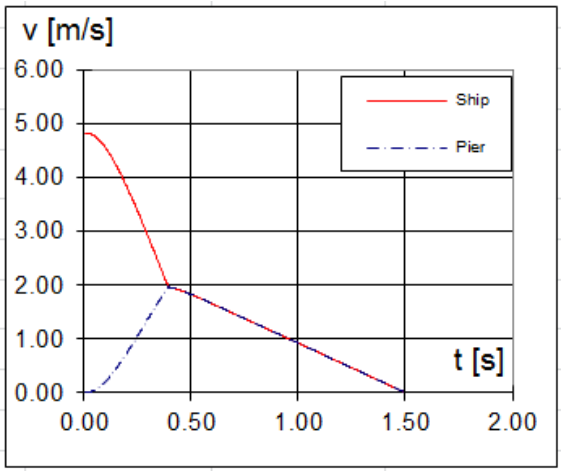


Figure 14 Speed of ship and dolphin over the time

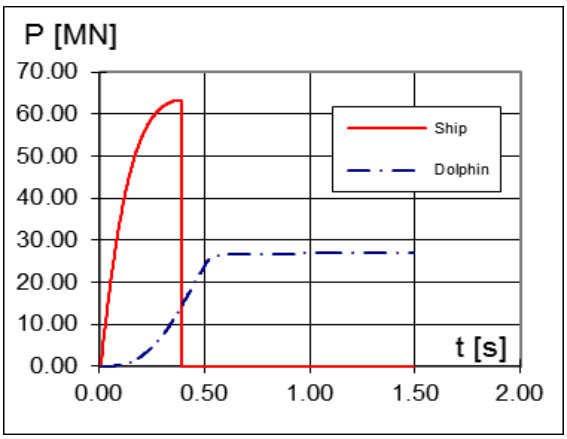


Figure 15 Force in ship's bow and dolphin

5.3 Concrete super structure

Concrete super-structure is dimensioned for the difference between maximal forces in the bow and dolphin shown on Figure 15. The assumption of the peak quasi static force to act on the concrete structure is in this case a conservative assumption. As the peak force is larger than maximal force that can be taken in the pile system, separate model was made where the piles were given unyielding vertical support. In this way, it is ensured that impact load can be transferred by the superstructure and distributed on the pile group as assumed.

6 CONCLUSION

The presented solution successfully meets multiple-constrained design requirements through integration of all available structural and geotechnical energy dissipating components.
The presence of a thick layer of weak organic soil excludes a number of solutions and poses execution and design challenges. With limitation on pile diameter and construction method, the required response of the structure is achieved by an extended concrete superstructure and moment-coupled connection to the piles.
This was facilitated by a concurrent geotechnical and structural design process which verified ductile post-yield behaviour of all elements.
Further possibilities for optimization of future similar structures can be explored

through more advanced modelling of energy transfer between the ship and the dolphin.

7 REFERENCES

AASHTO (2007), Guide Specifications and Commentary for Vessel Collision Design of Highway Bridges, 2nd edition

Eurocode (2007), DS/EN 1991-1-7:2006 General Actions – Accidental Loads (including DK NA:2007), 2nd edition

Bruk av vertikaldren og poretrykkskontroll for bløt leire som er stabilisert med kalk-sementpeler

Dahl,Carl Erik, *Rambøll Norway, carl.erik.dahl@ramboll.no*

Bodholt, Grethe, *Statens vegvesen – Region sør, Norway, grethe.bodholt@vegvesen.no*

Oset, Frode, *Statens vegvesen – Vegdirektoratet, Norway, frode.oset@vegvesen.no*

ABSTRACT

Construction work for the highway E18 between Bommestad and Sky in Vestfold county, Norway, is now under progress. Stabilization of a sloping quick clay area was necessary as preparation before the start of the construction work. The stabilization was designed with 33000 lime- cement columns installed by the dry mixing method. In addition, it was installed a large number of lime-cement columns to be able to handle the soft clay in the construction pit by excavation

Pore pressure build-up has been registered as a consequence of the dry mixing procedure of lime-cement columns in previous projects. In order to avoid triggering of a landslide by the stabilization works for the E18 project, the design included systematic use of vertical drains and piezometers for pore pressure control. The article describes the stabilization works and control measures. The pore pressure measurements will be discussed in relation to the performed work pattern, as a reference basis for the similar situations in comparable projects.

Keywords: soft sensitive clay, lime-cement stabilization, vertical drains, pore pressure control



Bilde 1. Oversikt over parsellen E18 – Sky. Rød ring viser området som er behandlet i denne artikkel

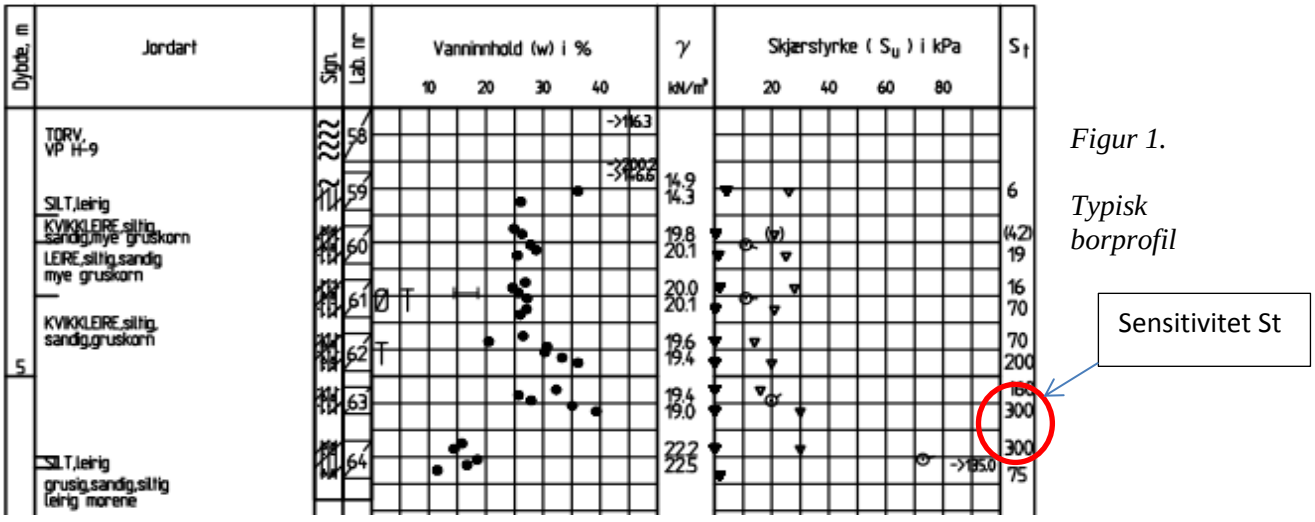


Bilde 2. Området som ble kalk-sementstabilisert. Det ble etablert kjøreveier i området for KC-riggen. Viadukten i bakgrunn er dagens E18

1 INNLEDNING

Det aktuelle området ved Bøkeskogen, som beskrives i denne artikkelen, er en del av veiprosjektet ny 4-felts motorveg E18 Bommestad-Sky. Grunnundersøkelsene er utført av Statens vegvesen og Rambøll Norge. I forbindelse med utførelse av grunnundersøkelsene ved Bøkeskogen ble det avdekket kvikkleire. På bakgrunn av dette utførte Rambøll Norge geotekniske vurderinger med tanke på område-stabilitet, samt de faktiske tiltakene som måtte planlegges.

Motorveien er bygget i to parallelle løsmassetunneler i det aktuelle området. Under byggeperioden ble det etablert en spuntavstivet byggegrop på begge sider langs veglinjen. Det ble forutsatt at dette tiltaket ikke ville ha en negativ innvirkning på områdestabiliteten. Det ble utført stabilitetsberegninger for dagens situasjon samt for endelig situasjon i de snitt der det ble bygget tunneler. I tillegg ble det utført beregninger med stabiliserende tiltak der disse var påkrevet. Det ble utført beregninger for 8 profiler.

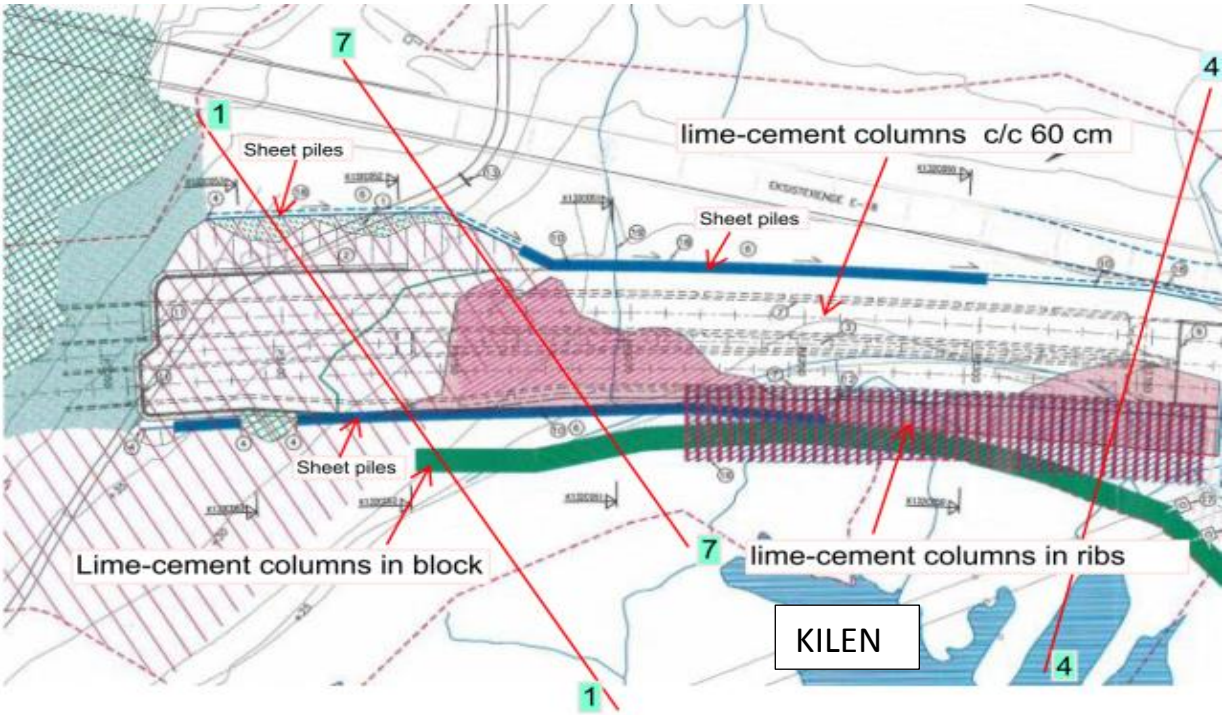


Figur 1. Typisk borprofil

2 GRUNNFORHOLD

Det er avsetninger av til dels meget bløt, siltig leire. De bløte avsetningene ligger som lag under stedvis et noe fastere topplag. Tykkelsen på de bløte avsetningene er økende utover mot Kilen, som er en del av innsjøen Farris. (bilde 1). Den bløte leira inneholder stedvis mye sand, grus og noe stein som er ujevnt fordelt i massene.

Under de bløte avsetningene synes det å være til dels meget faste masser av silt, sand og grus. Det faste laget ligger med noe varierende tykkelse over fjell. Den bløte leira synes å ha en økende sensitivitet ut mot et lavereliggende område som ligger på innsiden av Kilen. Sensitiviteten, St, er målt opp mot 300 (fig 1).



Figur 2. Stabilitetsberegnede profiler

Sensitiviteten synes samtidig å være avtakende inn mot Bøkeskogen. I de utførte stabilitetsberegninger er følgende verdier benyttet for attraksjon og friksjonsvinkel for den bløte avsetningen av leire:

- Kvikk/sensitiv leire a=5,5kPa og φ=20/22/25 grader.
- Ikke sensitiv leire a=4,5kPa og φ=25 grader.

Udrenert skjærstyrke i kvikk /sensitiv leire som er benyttet er valgt på grunnlag av skjærstyrkemålinger utført på 54 mm prøver, med støtte i tolkede CPTU-sonderinger.
For poretrykksforholdene ble det prosjektert med hydrostatisk fordeling, ut fra utførte målinger i 4 punkter sentralt i området. Grunnvannet ble registrert fra terrengnivå til 1.0 meter under terreng.

3 STABILITETSBEREGNINGER

Det ble utført stabilitetsberegninger på total–og efektivspenningsbasis, på eksisterende situasjon, med laveste sikkerhet på 1,26 (profil 1)for en totalspenningsanalyse – ADP og 1,44 (profil 7) for en efektivspenningsanalyse. Profil 1 og 7 ligger utenfor området hvor det ble utført kalk-sementstabilisering i doble ribber (fig 2). Profil 4 som ligger i området for kalk-sementstabiliseringen i ribber, hadde en laveste beregnet sikkerhet på 1,45 for en totalspenningsanalyse – ADP. Krav til sikkerhet for eksisterende situasjon var 1,4 på total og effektivspenningsbasis.
For profil 4 som går gjennom området med doble ribber var det akseptabel sikkerhet for eksisterende situasjon, men med den planlagte overfyllingen over løsmassetunnelen ble det en beregnet sikkerhet på <1,0 på totalspenningsbasis, uten tiltak. For området hvor profil 1 og 7 ligger, så ble det satt krav til rekkefølge av arbeidene for å sikre området. Blant annet så ble terrenget i deler av profil 1 senket, og det ble etablert en vegg av kalk-sement peler langsetter spuntlinjene på hver side før spuntarbeidene ble startet.

4 KALK-SEMENTSTABILISERING

|Begrunnelsen for stabiliseringen var å ha god nok sikkerhet mot brudd i fyllingsfoten for overdekkende sprengsteinsfylling i endelig fase(fig 4). Stabiliseringen ble her utført som doble ribber med diameter 60 cm og overlapping 20 cm. C/C ribber var 3,1 m (fig 3).
I tillegg ville også kalk-sementstabilisering bedre sikkerheten for områdestabiliteten i anleggsfasen og den endelige situasjonen. Ved nedsetting av spunt ble det brukt enkle ribber på hver side av spunten for å begrense omrøringen ved boring og ramming av spunten.

Det ble utført kalk-sementstabilisering i blokk ned til faste masser for en planlagt vannledning og veg på utsiden av spunten mot Kilen og det ble boret enkeltstående kalk-sementpeler inne i selve byggegropen mellom spuntveggene, med diameter 60cm og C/C avstand 90 cm (fig 2). Dette ble utført for å kunne håndtere utgraving av massene i byggegropen. Totalt ble det boret 253 000 m med kalk-sementpeler.

Jfr Håndbok V221 beskriver Statens vegvesen et styrketak på 175 kPa for skjærfasthet for doble ribber etter 28 døgn. Rambøll har vurdert styrke fra enaksiale laboratorieforsøk (utført av NGI). Resultatene er gitt etter 7 og 14 dager med 1% og 2 % tøyning. Forsøkene er utført med innblandingsmengde 100 kg/m3, og forhold mellom kalk og sement på 50/50. Det ble valgt å være konservativ i vurdering av mulig oppnåelse av skjærstyrke i kalk-sementpelene, og det ble brukt 100 kPa som skjærfasthet i kalk-sementpelene. Dette med bakgrunn i usikkerhet mhp innslag av sand, grus og siltlag. Alle kalk-sementpelene ble satt ned til underliggende faste masser.
De første kalk-sement ribbene ble installert med god avstand.
Ved kalk-sementstabilisering i terreng med lav sikkerhet er det fare for at trykkluft kan gi poretrykksøkning, med fare for utløsning av skred, derfor ble det valgt å sette hver 5. ribbe først før det ble fortettet i mellom. Hele ribben ble installert fortløpende med overlapp. Kalk-sementribbene ble utført først før enkeltpelene inne i byggegropen og KC-pelene på hver side av spunten.

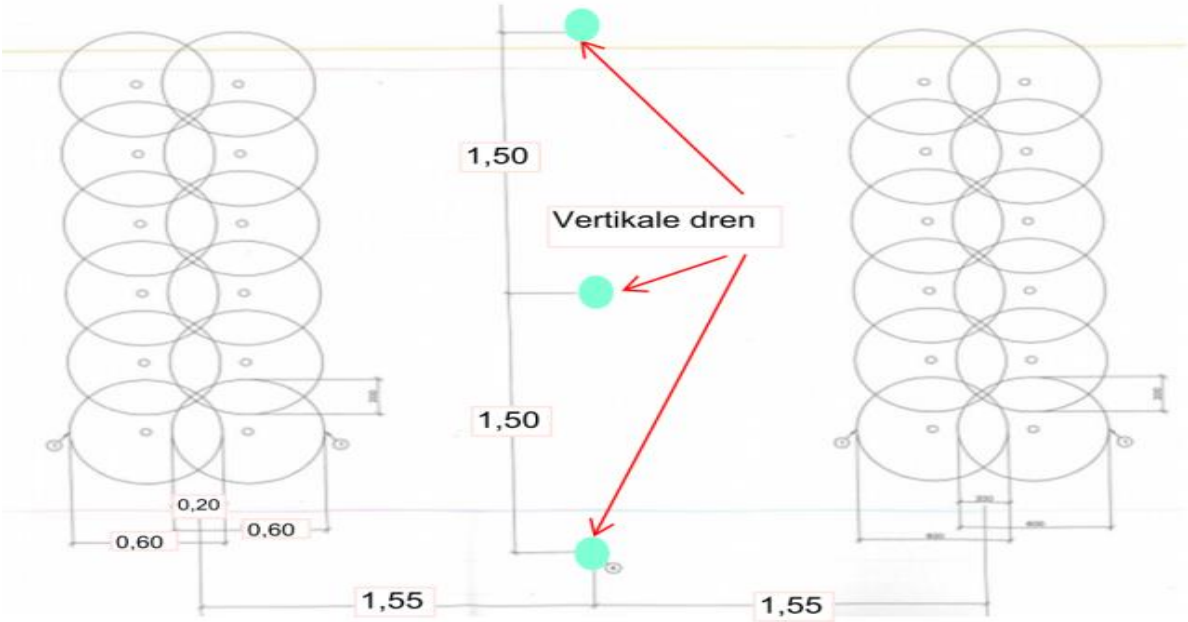
5 VERTIKALDREN

Ved installasjon av kalksementpeler kan innblandingsprosessen føre til økt jordtrykk og poretrykk i omkringliggende masser. Dette gir mulighet for redusert styrke av leire, spesielt kvikkleire, og stabiliteten forverres lokalt. Erfaring har vist at det kan ta fra dager til måneder før poretrykket jevner seg ut. Spesielt ved permeable lag som silt kan de gi poreovertrykk med stor utbredelse.

Erfaring fra tidligere prosjekter har også vist at ved bruk av vertikaldren så var det ikke påvirkning av poretrykk i avstand 10-15m fra kalk-sementpelen. For å ha kontroll med dette så ble det installert vertikaldren mellom kalk-sement ribbene før kalk-sement arbeidet ble igangsatt. Vertikaldrenene ble satt i linje midt mellom ribbene, og hadde en c/c på 1,5 meter. En rad midt mellom hver ribbe. Det vil si 3,1 meter mellom radene med vertikaldren (fig 3). For enkeltpelene inne i byggegropen ble det satt vertikaldren med c/c på 1,5 meter og med en avstand på 7,5 meter mellom radene.



Bilde 3. KC-stabilisering i ribber og vertikaldren mellom ribbene.



Figur 3. KC-peler og vertikale dren

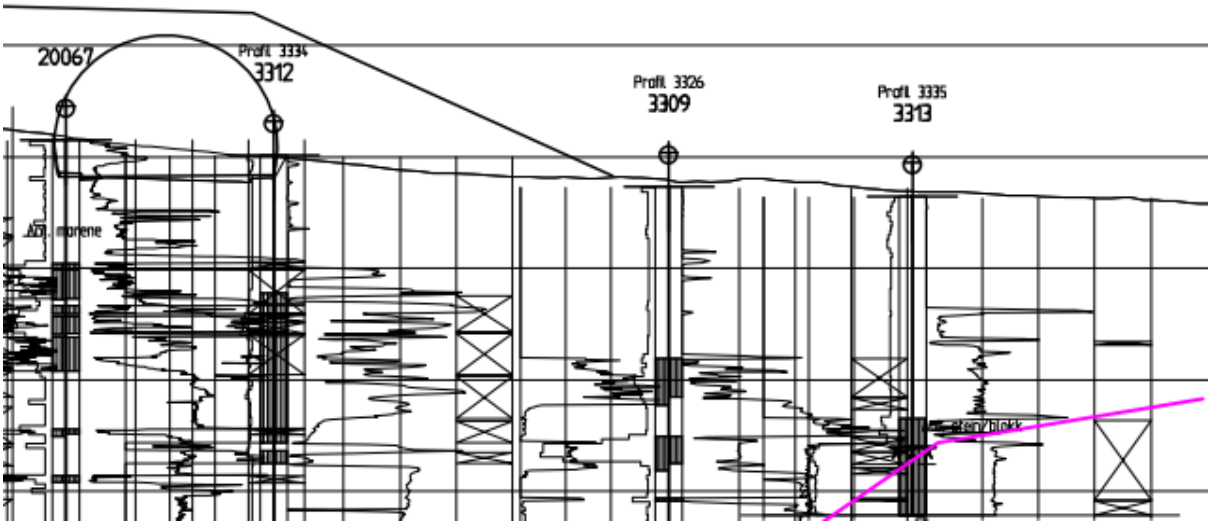


Fig 4. Profilet viser planlagt overfylling over ferdig løsmassetunnel

6 PORETRYKK

For å kontrollere poretrykket, ble det installert elektriske poretrykksmålere fordelt over et stort område i byggegropen (fig 5). Spesielt var det fokus på måling av poretrykket der hvor kalk-sementpelene ble satt som ribber. Det ble i utgangspunktet ikke satt noen alarmgrense for poretrykket. Hensikt med poretrykksmålerne var å få en indikasjon på om det ville bli poretrykksoppbygging ved installasjon, og for å se hvor lang tid ville ta for poreovertrykket å dissipere, og i hvilke utstrekning poretrykks-oppbyggingen ville ha. Dette ville kunne gi informasjon om rekkefølge med hensyn på om arbeidsrekkefølgen av kalksementpelene burde endres under veis. Det ble allikevel etterspurt om en alarmgrense for poretrykksmålere, og at dette måtte settes, samt formidles til utførende entreprenør.
En poretrykksoppbygning pga installasjon av kalksementstabilisering kunne også gripe utenfor kalksementstabiliserings området. Det skulle derfor også overvåkes poretrykk på oversiden av det kalksementstabiliserte området

Kritisk glidesirkel lå om lag 4m under terreng, noe som skulle tilsi en totalspenning på p_0=20*4=80 kPa. I stabilitetsberegningene ble det lagt inn grunnvann tilsvarende ca 0,5m under terreng, noe som tilsa en effektivspenning på ca p_0'=3,5*10+0,5*20=45 kPa ved 4 m dybde. Styrken i jorda er lineært avhengig av effektivspenningen. Det ble da valgt å sette en alarmgrense for poretrykksmålerne med antagelse om 50% reduksjon av styrken som da skal tilsvare en effektivspenning på 22,5 kPa, altså poreovertrykk på 20 kPa (2 m vannsøyle)) forutsatt uendret totalspenning. Ca 50 % reduksjon av styrken i jorda helt lokalt ved installasjonen ble vurdert som akseptabelt i forhold til beregningsmessig sikkerhet i den fasen.

Dette medførte at ved målinger tilsvarende 2 m vann søyle/poreovertrykk på en av målerne installert innenfor kalksementstabilisert område, så skulle arbeidene varsles til geotekniker og vurderes av denne ut fra avstand til de pågående installasjonsarbeidene og verdier for de andre målerne.



Bilde 4. KC-stabilisering med enkeltpeler inne i byggegropen



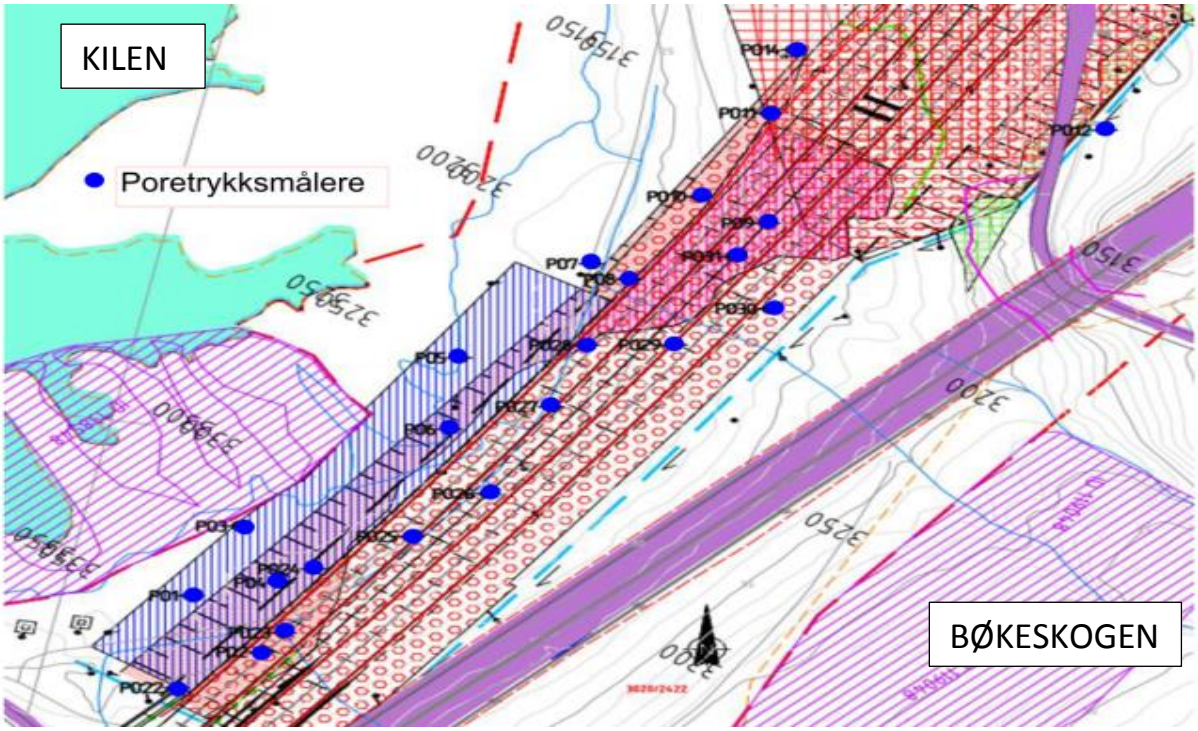
Bilde 6. Ferdig installerte KC - peler i ribber



Bilde 5. Nedsetting av vertikale dren

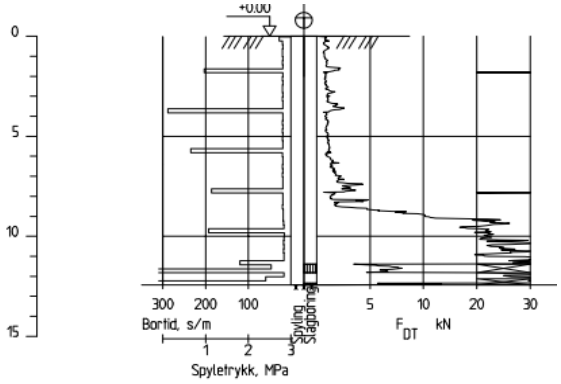
7 RESULTAT

Hyppigheten av poretrykksmålingene varierte. Det ble ikke foretatt målinger så lenge KC-riggen var på 10-15 meter avstand fra de installerte poretrykks-målerne. Det var først når nedboring av KC-peler var 5-6 meter fra måleren at det ble antydning til noe økt poretrykk. Kritisk verdi som var satt for et økt poretrykk var som nevnt 20 kPa, og det var først når boringen av pelene var 1-2 meter fra måleren at det ga et økt poretrykk opp mot og noe over den valgte grenseverdien. Eksempelet (fig 8/ 9) viser hvordan poretrykket økte og hvor raskt det også gikk tilbake. Flere av målerne nært inn mot KC-pelen viste lavere økt poretrykk enn det som er vist her. Som tabellen viser så ble poretrykket redusert etter oppnådd kritisk verdi allerede etter 1 døgn.

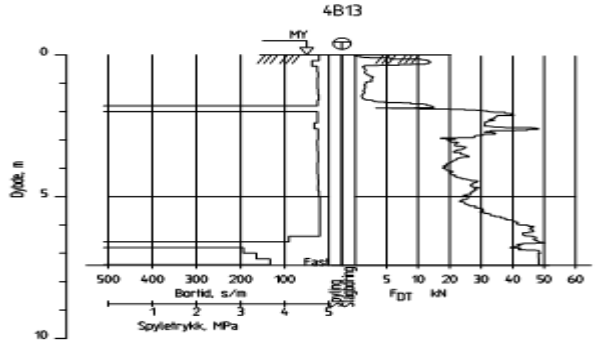


Figur 5. Plassering av poretrykksmålere

Etter 4-5 døgn var poretrykket tilbake til normalt trykk. Som eksempelet viser ble det stedvis også registrert et lavere poretrykk etter KC-stabiliseringen enn det som var registrert før.
Kontroll av kalk-sementpelene ble utført med en enkel løsning. Med bakgrunn i sammensetting av avsetningene som bestod av bløt leire med stedvis stor innblanding av sand og grus, ble det utført kontroll av homogeniteten med 26 stk totalsonderinger gjennom utvalgte peler i etterkant av kalk-sememtstabiliseringen for om mulig kunne vurdere sonderings-resultatene før og etter opp mot hverandre. Eksempel på dette er vist i fig 6/7.
Utgraving av massene inne i byggegropen og fremgraving av de doble ribbene på innsiden av spunten viste at kalk-sementstabiliseringen synes å ha fungert tilfredsstillende (bilde 6). Stedvis, hvor det var mye sand og grus i avsetningene var det vanskelig å se virkningen av innblandingen ved boring med totalsondering i etterkant.



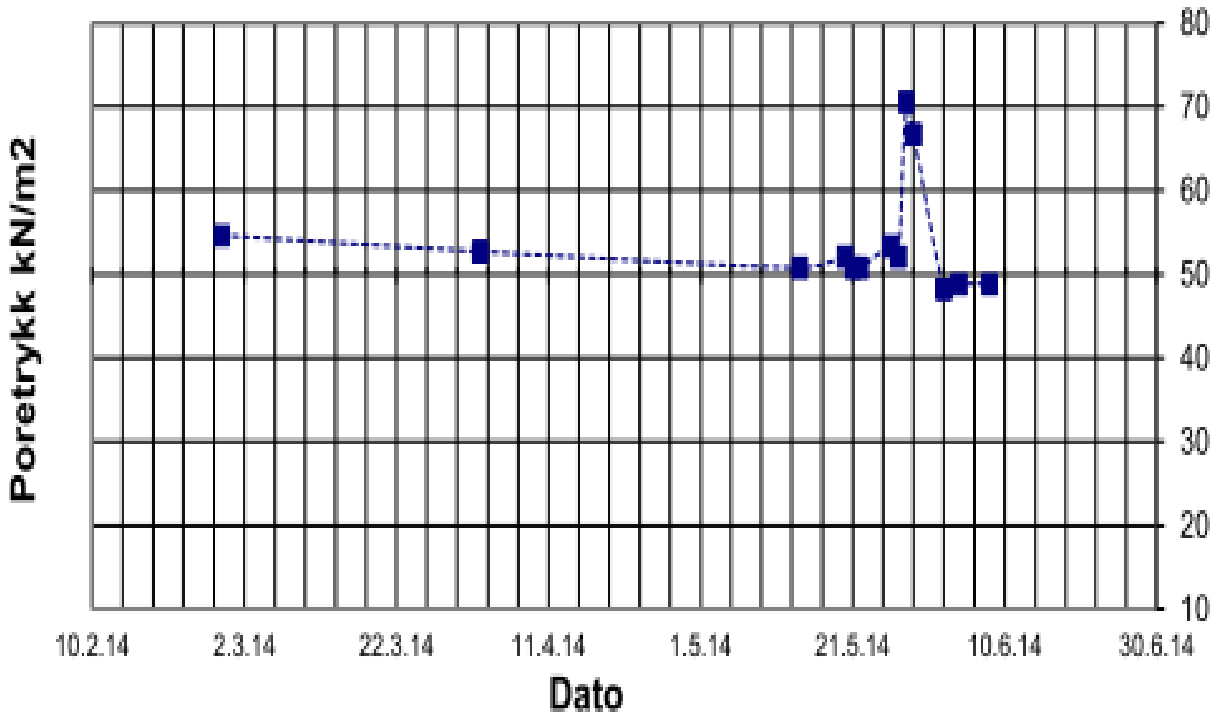
Figur 6. Før KC-stabilisering



Figur 7. Etter KC-stabilisering

27.02.14			1809	54,629	
02.04.14			1812	52,704	
14.05.14			1815	50,776	
20.05.14			1813	52,062	etter vertikaldren
21.05.14			1815	50,776	
22.05.14			1815	50,776	
26.05.14			1811	53,346	etter KC
27.05.14			1813	52,062	etter KC
28.05.14			1784	70,545	etter KC helt inntil
29.05.14			1790	66,745	
02.06.14			1819	48,201	
04.06.14			1818	48,845	
08.06.14			1818	48,845	

Figur 8. Målt poretrykk



Figur 9. Poretrykk / Tid

8 KONKLUSJON

Ved bruk av vertikale dren for å begrense økt poretrykk ved nedboring av kalk-sementpeler, synes effekten av vertikaldrenene å ha stor virkning.

Høyt økt poretrykk ble i dette tilfellet ikke registrert. Maks måling var i størrelse 20-25 kPa. Det ble ikke registrert vesentlig merkbart økt poretrykk i en avstand større enn 5-6 meter fra pågående ks-peling. Samtidig viste også målingene at poretrykket gikk forholdsvis raskt tilbake, da poretrykket var tilbake til tilnærmet hydrostatisk verdi allerede etter 4–5 dager.

Det antas at vertikaldrenene bidrar til effektiv drenering og begrenser poretrykksøkningen. Det var stedvis tydelig en del strømming av vann opp gjennom vertikaldrenene. Det lite merkbare økte poretrykket kan også i dette tilfellet være medvirket av avsetningene i de bløte massene, som stedvis inneholdt en del silt, sand og grus. I mer homogene masser kan det være behov for å sette vertikaldrenene tettere for å oppnå samme effekt.

9 REFERENCES

1. NVE Retningslinjer 2/2011 rev. 15.04.2011: ”Flaum- og skredfare i arealplanar”, med Veileder for: ”Vurdering av områdestabilitet ved utbygging på kvikkleire og andre jordarter med sprøbruddegenskaper”.
2. NS-EN 1997-2:2007 + NA: 2008 Eurocode 7::Geoteknisk prosjektering Del2: Prosjektering basert på grunnundersøkelser og laboratorieprøver
3. Program for økt sikkerhet mot leirskred. Metode for kartlegging og klassifisering av faresoner, kvikkleire. 20001008-2. 31. August 2001, revisjon nr. 3 - 8. Oktober 2008. NGI
4. Statens Vegvesen Håndbok 016. ”Geoteknikk i vegbygging”. Juni 2010.
5. Statens Vegvesen Håndbok V221. «Grunnforsterkning, Fyllinger og Skråninger» 2012.
6. kursmateriell: «Grunnforsterkning» (TEKNA november 2012.)
7. Veiledning for Grunnforsterkning med kalksementpeler (NGF 2012)

Engineering and execution of tight sheet walls

Willem Robert de Bruin
Geovita AS, Norway, rdb@geovita.no

Abstract: *The Eurocode 7 dated 2004, Eurocode 3: Design of steel structures Part 5 and EC NS-EN 12063 dated 1999 contain technical requirements on engineering, contractual description and execution of sealing for steel sheet piles. In 1992 a geotechnical model was developed in the Netherlands in order to enable the designer to make a rational assessment of the rate of seepage for a specific case. In 1998 there was executed research in the Netherlands on oblique bending with steel sheet walls, also with treaded interlocks. Several suppliers of interlock filling materials offer technical information on seepage resistance with the inverse interlock resistance ρ. Comparison of the Eurocode's supplements applying for the Nordic countries reveals that not all the necessary parameters for engineering tight steel sheet walls are available yet. This paper describes a guideline to enable the designer to engineer, contractually formulate, draw and execute sealed steel sheetpiles according to actual requirements, recommendations and guidelines.*

1.1 Engineering tightness of sheet walls

Eurocode NS-EN 12062 supplement E gives an example on how to engineer tightness with the introduction of the new concept of "inverse joint resistance" which was developed as a variation on Darcy's law:

$$q_z = \rho \frac{\Delta p_z}{\gamma_w}$$

with:

q_z = discharge per unit of the joint length at level z, ($m^3/s/m$)
Δp_z = pressuredrop at level z, (kPa)
ρ = inverse joint resistance, (m/s)
γ_w = unit weight of water, (kN/m^3).

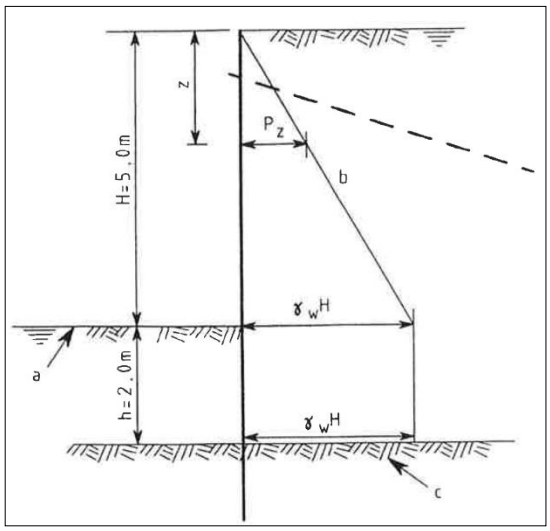


Figure 1: Geometry and units.

Example 1: discharge steel sheet pile wall

Building pit:
Length of perimeter building pit L = 180 m
Steel sheet pile width b = 600mm
Excavation depth H = 5 m
Top excavation – tight layer h = 2 m
Inverse joint resistance $\rho = 5 \times 10^{-10}$ m/s

Total discharge Q:
Number of interlocks:
$n = L/b$
= 180/0,6
= 300 elements.

Discharge per joint:
$Q_1 = \rho \cdot H \cdot (0{,}5H + h)$
$= 5 \cdot 10^{-10} \times 5 \times (0{,}5 \times 5 + 2)$
$= 1{,}125 \times 10^{-8}\ m^3/s$

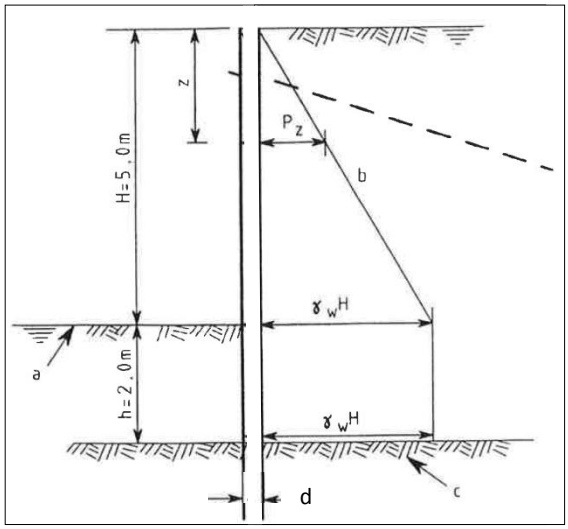
Total discharge into the excavation pit:
$Q = n \cdot Q_1$
$= 300 \times 1{,}125 \times 10^{-8}$
$= 3{,}375 \times 10^{-6}\ m^3/s$
$= 3{,}375 \times 10^{-6} \times 60 \times 60 / (5 \times 180/1000)$
$= 0{,}013\ m^3/hr/1000m^2$

Check with permissible discharge as stated in Eurocode 7 art. 9.4.1 (8). NB: the model can result in a larger amount of discharge than the surrounding area is capable in providing. A check has to be performed with «open» interlocks.

There are no rules to calculate the water seepage for diaphragm walls in Eurocode NS-EN 1538 «Execution of special geotechnical works. Diaphragm walls», and neither for secant-, cut off- or slurry walls. Formulas which apply to this field are according Darcy's law, se reference /1/:

$$Q_{sv} = \frac{K_e(\Delta p/\gamma_w)}{d}$$

with:
Q_{sv} = discharge pr unit of wall, (m^3/s),
K_e = equivalent permeability (m/s),
$\Delta\rho$ = pressure drop on both side of the wall, (kPa)
p_z = inverse joint resistance, (m/s),
γ_w = water density, (kN/m^3)
d = thickness of the wall, (m)



Figur 2: Geometri and units.

Example 2: discharge diaphragm wall

Building pit:
Length of perimeter pit L = 180 m
Steel sheet pile wide b = 600mm
Excavation depth H = 5 m
Top excavation – tight layer h = 2 m
Inverse joint resistance ρ = 5 x 10^{-10} m/s
Total discharge Q = 3,375 x 10^{-6} m^3/s

Calculate equivalent seepage permeability K_e

Specific discharge per unit diaphragm wall:
$Q_{sv} = K_e \cdot (\Delta p/\gamma_w) / d$ *(1)*

Specific discharge per unit steel sheet wall:
$Q_{sp} = (1/b) \cdot \rho \cdot (\Delta p/\gamma_w)$ *(2)*

Comparison of (1) and (2):

$$Q_{sv} = Q_{sp}$$
$$K_e \cdot (\Delta p/\gamma_w) / d = (1/b) \cdot \rho \cdot (\Delta p/\gamma_w)$$

Equivalent K_e-value with estimated diaphragm wall thickness d = 1000 mm:
$K_e = \rho \cdot (1m) / b$
= 5 x 10^{-10} / 0,600
= 8,33 x 10^{-10} (m/s)

1.2 Control groundwater

In both examples 1 and 2 groundwater flow around the pile wall toe has been neglected. This assumption is only correct if the bottom layer is much less pervious than the wall. If this is not the case, then the water flow both trough and around the wall needs to be considered. This is done with the aid of a 2D-seepage calculation program like Slide or Plaxis. Due to the fact that these programs deal with Darcy's flow type only, the behaviour of the steel sheet pile wall has to be treated as a porous media flow, using an equivalent diaphragm wall defined by its thickness $\underline{d}$ and its permeability $\underline{K_e}$.

With $\underline{K_e}$ the designer is then able to:
1. ConFigure groundwater flow and flowrate along the pile foot, see Figure 3;
2. Estimate sinking of the groundwater level, see Figure 3;
3. Predict influence on groundwater level and perimeter or distance, se Figure 4;

Eurocode 7 article 9.4.1 (8), see Figure 13 states "*The resulting equilibrium ground-water flow problem shall be assessed*". The described method enables the designer to control this demand. Further investigation with Eurocode 7 Annex H "*Limiting values of structural deformation and foundation movement*" is also possible now.

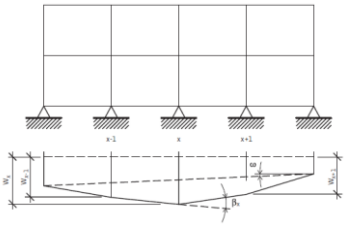


Figure 3: Deformation and movement EC7.

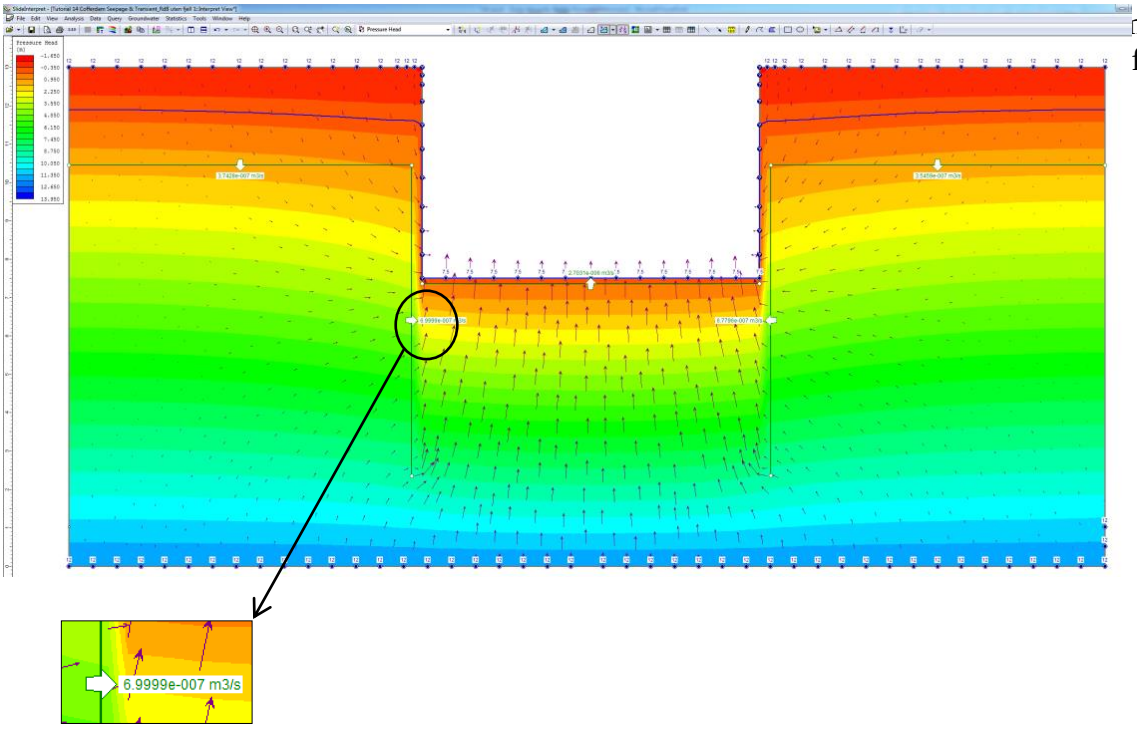


Figure 4: Configuring groundwater flow and estimation of sinking of the groundwater level.

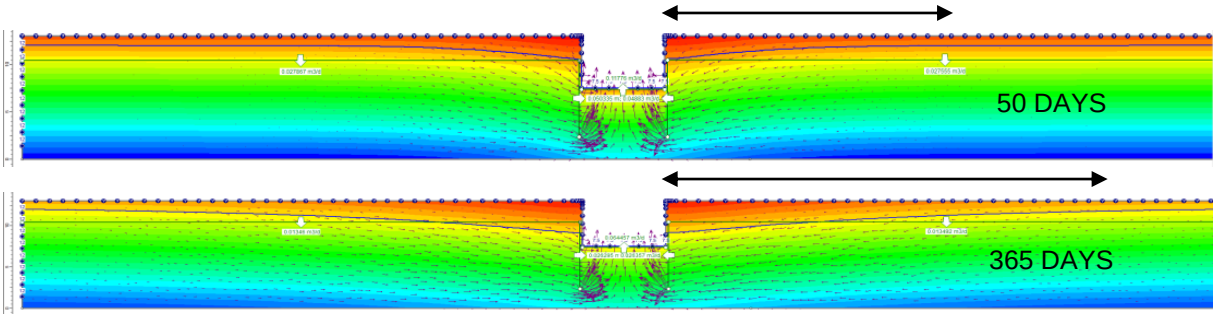


Figure 5: Prediction of influence on the groundwater level and perimeter or distance.

1.3 Reduce strength and stiffness U-piles

U-shaped piles with treaded interlocks contain less sectional modules and stiffness than ordinary piles. This phenomenon has been investigated by the European Coal and Steel Community to provide background for design guidelines to be included in Eurocode. Oblique bending has to be taken into account according Eurocodes:

- NS-EN 12063 art. 7.2.2 and 8.5.2;
- NS-EN 1997-1:2004:2008 art. 9.4.1(8);
- NS-EN 1993-5:2007/NA2010 art. 5.2.2.

Reduction factors which apply to this calculation method can lead up to 70% reduction in section modulus for U-shaped steel sheet pile with treaded interlocks according Tables in the English Eurocode,

Tabel NA.1 fra det tyske nationale anneks DIN EN 1993-5/NA, Dezember 2010.

Tabelle NA.1 — Abminderungsfaktoren β_B (Biegetragfähigkeit) und β_D (Biegesteifigkeit) für U-Bohlen

Bodenart Festigkeit/Konsistenz	Abminderungsfaktoren	
	β_B	β_D
	0,6	0,4
locker bis mitteldicht breiig bis weich[b]	0,7	0,6
dicht bis sehr dicht steif bis fest[c]	0,8	0,7
locker bis mitteldicht breiig bis weich[b]	0,8	0,7
dicht bis sehr dicht steif bis fest[c]	0,9	0,8
locker bis mitteldicht breiig bis weich[b]	0,9	0,8
dicht bis sehr dicht steif bis fest[c]	1,0	0,9

Table 1: Copy of BS NA EN 1993-5: DL National Annex to Eurocode 3.

Factors β_B (for strength) and β_D (stiffness) in the German and the Danish Eurocode include the same factors, see resp. Table 1 and 2.

Jordtype fasthed/konsistens	Reduktionsfaktor	
	β_B	β_D
	0,6	0,4
Løs til middel tæt lejret Meget blød til blød[2)]	0,7	0,6
Tæt til meget tæt lejret Stiv til fast[3)]	0,8	0,7
Løs til middel tæt lejret Meget blød til blød[2)]	0,8	0,7
Tæt til meget tæt lejret Stiv til fast[3)]	0,9	0,8
Løs til middel tæt lejret Meget blød til blød[2)]	0,9	0,8
Tæt til meget tæt lejret Stiv til fast[3)]	1,0	0,9

Table 2: Copy of BS NA EN 1993-5: DK NA to Eurocode 3: Design of steel structures.

Table NA.2 Reduction factors for U shaped sheet piles.

Type of U-pile unit	Number of structural support levels (see Note 1)	Reduction factors β_B and β_D referred to in 5.2.2 (2); (see Notes 2, 3, 4, and 5)			
		Highly unfavourable conditions (see Note 6)		Unfavourable conditions (see Note 7)	
		β_B	β_D	β_B	β_D
Singles or uncrimped doubles	0	0,40	0,30	0,50	0,35
	1	0,55	0,35	0,60	0,40
	>1	0,65	0,45	0,70	0,50
Crimped or welded doubles	0	0,70	0,60	0,75	0,65
	1	0,80	0,70	0,85	0,75
	>1	0,90	0,80	0,95	0,85

Table 3: Copy of BS NA EN 1993-5: UK NA to Eurocode 3: Design of steel structures.

Other Nordic countries like Sweden, Finland and Norway do not offer parameters for β_B and β_D, see Figure 6 for the Norwegian Eurocode. This needs further research and updating.

NS-EN 1993-5:2007/NA:2010
Nasjonalt tillegg NA

NA.5.2.2 Spunt i bøyning og skjær

NA.5.2.2(2) Dette nasjonale tillegget angir ingen verdi for β_B basert på lokal erfaring.

NA.6.4 Konstruksjonsmessige hensyn for stålspunt

NA.6.4(3) Dette nasjonale tillegget angir ingen verdi for β_D.

Figure 6: Copy from NS-EN 19935:2007/NA: 2010. Eurocode 3; Part 5: Piles.

1.4 Reduced overall bending resistance

In the case of differential water pressure exceeding 5 m head for Z-piles and 20 m for U-piles the effects of water pressure on transverse local plate bending should be taken into account to determine the overall bending resistance, see Table 4:

- NS-EN 1993-5:2007/NA2010 art. 5.2.4

Table A-3: Reduction factors ρ_P for plate thickness due to differential water pressure

w	$(b/t_{min})\ \varepsilon = 40{,}0$	$(b/t_{min})\ \varepsilon = 60{,}0$	$(b/t_{min})\ \varepsilon = 80{,}0$	$(b/t_{min})\ \varepsilon = 100{,}0$
1,0	0,99	0,98	0,96	0,94
2,5	0,98	0,94	0,88	0,78
5,0	0,95	0,86	0,67	0,00
7,5	0,92	0,75	0,00	0,00
10,0	0,88	0,58	0,00	0,00

Key:

b is the width of the flange, but b should not be taken as less than $c/\sqrt{2}$, where c is the slant height of the web;

t_{min} is the minimum thickness of flange or web;

w is the head of differential water pressure in m;

$\varepsilon = \sqrt{\frac{235}{f_y}}$, with f_y in N/mm²

Note: These values apply to Z-piles and are conservative for Ω- and U-piles. An increase of ρ_P is possible (for instance if interlocks are welded), but an additional investigation is then necessary.

Table 4: BS NA EN 1993-5- Table A-3.

Transverse bending is a relatively newly recognized mode of failure in sheet piling. Although it interacts with classical bending, it is a separate failure mode of its own.

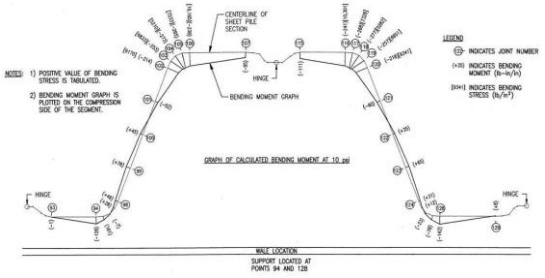


Figure 8: transverse loading on sheet pile.

See Figure 8. In essence, the lateral pressure is flattening the sheet; the plate bending at the corners is the resistance of the sheeting to this flattening.

1.5 Control of driveability

Requirements on driveability are set in Eurocode:

- NS-EN 1997-1:2004-NA:2008, art. 9.4.1
- NS-EN 12063 art. 5.2.1, 5.2.2 and 8.5.

These demands need further investigation in order to reduce the chance of damage and to avoid sheet piles coming out of their locks. The change on declutching is less with U-piles than with Z-shaped steel sheet piles.

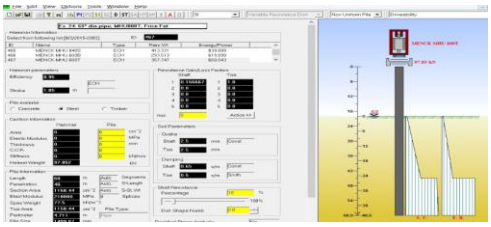


Figure 9: Driveability prediction GRL-Weap

1.6 Proportional contribution leakage

Leakage into building pits often occur as a result of following causes, shown in fig.10:

1) Through the sheet pile wall;
2) Trough and along the anchors;
3) Up along the outside of bored piles;
4) Through cracks and fractures in bedrock.

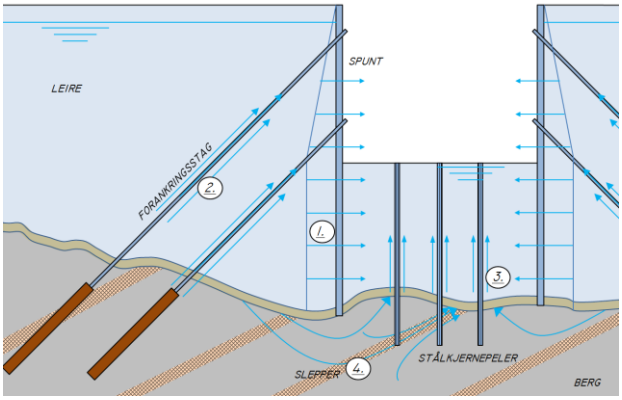


Figure 10: 4 types of leakages.

Modelling these last 3 types of leakage is possible by using Darcy's law, as used for modelling seepage with steel sheet walls. The models are represented in Figure 11 to 13.

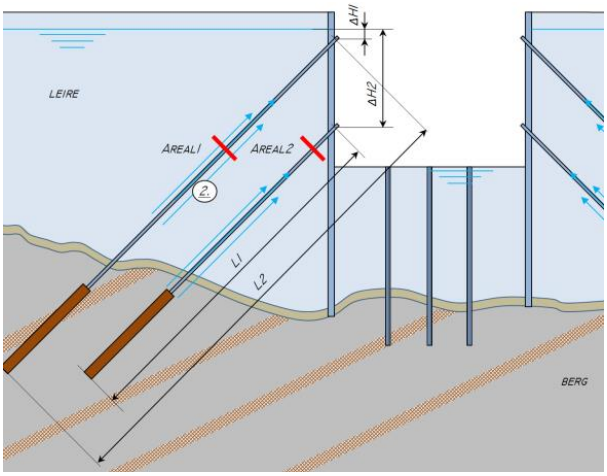


Figure 11: Leakage along / trough anchors.

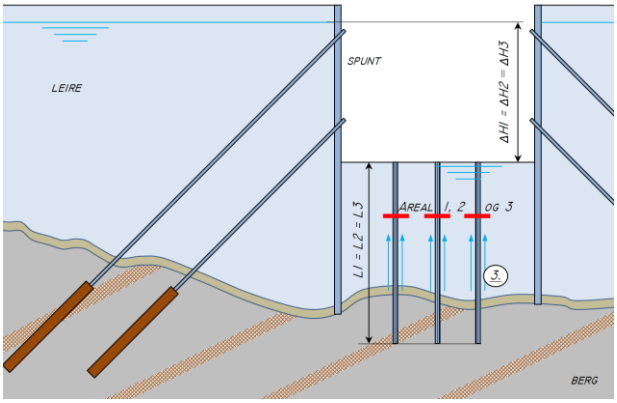


Figure 12: Leakage along bored piles.

Groundwater flow along rammed piles can be calculated using (Darcy's law based) models developed for rammed piles through contaminated landfills, see ref. /8/ and /9/. Leakage trough bedrock can be modelled with (Darcy's law based) models for cracks as plates or channels see ref. /11/.

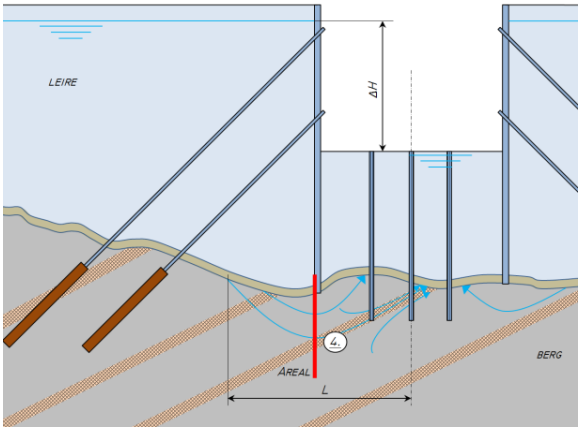


Figure 13: Leakage through cracks and fractures in the bedrock.

Insight into contribution of steel sheet walls compared to other leakage types is shown in Table 5. This approach allows the designer to conFigure the building pit: rammed piles instead of bored piles, struts instead of anchors or extra measures as jet piling.

PERCENTAGES OF DISTIBUTION OF LEACKAGE	4 types of leakage	Rammed piles instead of bored piles	Struts instead of ground anchors
	(%)	(%)	(%)
Trough steel sheet walls	5 – 20	25 – 80	93 – 98
Trough and along ground anchors	5 – 25	15 – 75	0
Trough and along bored piles	65 – 95	0	0
Through cracks / fractures in bedrock	0,1 – 5	2 – 10	2 – 7
Numbers calculated with $K_{cracks\ in\ bedrock}$ =2·10^{-6}(m/s), $K_{along\ bored\ piles}$ = 1·10^{-2}(m/s) og $K_{along\ anchors}$ = 1·10^{-2}(m/s) $Q_{total\ discharge}$ = 3 - 20 (m^3/time/1000m^2), groundwater flow along bored piles presumed coming under pile foot.			

Table 5: Proportional distribution of leakage types.

1.7 Tightening in relation to demands

Eurocode 7 refers to "required degree of water tightness of the finished wall", see Figure 14. There are no defined limits for this degree in Norway.

9.4 Design and construction considerations

9.4.1 General

(8)P The design of retaining structures shall take account of the following items, where appropriate:

— the required degree of water tightness of the finished wall;

— the practicability of constructing the wall to reach a stratum of low permeability, so forming a water cut-off. The resulting equilibrium ground-water flow problem shall be assessed;

Figure 14: Demand on tightness EC 7 art. 9.4.1 (8).

In Germany execution took place of more than a hundred building pits between 1993 and 2000. Authorities responsible for groundwater came to a limit for permissible daily leaking water rates into building pits, see Table 6 ref./6/ and /7/.

Bauwerksart	Leckagerate	
	l/sec je 1.000 m²	m³/h je 1.000 m²
Bauwerke und Baugruben mit normalen Dichtigkeitsanforderungen	1,5	5,4
Bauwerke wie Klasse N, jedoch mit hohen Dichtigkeitsanforderungen	0,05	0,18
Bauwerke wie Klasse N, jedoch mit geringen Dichtigkeitsanforderungen	2,5	9,0

Table 6: Tightnessklasses after Kluckert /6/

These tightness classes were in addition defined as a contractually results obligation: bound to a reference area: 1000m2. This was done to avoid contractual matters with entrepreneurs. The same way as done with tightness classes for tunnels (litre/min/100m). Besides this, the number for permissible daily leaking water rates into building pits is not related to hydraulic head. Tightness classes for building pits in Norway are not yet developed, however tightness classes for tunnels are, see Table 7 from Publication 103 of the Norwegian Public Roads Administration.

3.1 Krav til tetthet og tetthetskriterier

Ekstremt strengt < 1–3 liter pr. minutt pr. 100 m tunnel
Strengt < 3–7 liter pr. minutt pr. 100 m tunnel
Middels strengt < 7–15 liter pr. minutt pr. 100 m tunnel
Moderate krav > 15 liter pr. minutt pr. 100 m tunnel.

Table 7: Permissible leakage water rates in Norwegian tunnelling for diameter 8,5m.

Tightness classes for German tunnels are also defined, see Table 8, ref. /6/.

Tightness Class	Moisture Characteristics	Intended Use	Permissible Daily Leakage Water Quantity (l/sq. m), Given a Reference Length of:	
			10 m	100 m
1	2	3	5	6
1	Completely dry	Storerooms and workrooms, restrooms	0.02	0.01
2	Substantially dry	Frost-endangered sections of traffic tunnels; station tunnels	0.1	0.05
3	Capillary wetting	Route sections of traffic tunnels for which Tightness Class 2 is not required	0.2	0.1
4	Weak trickling water	Utility tunnels	0.5	0.2
5	Trickling water	Sewage tunnels	1.0	0.5

Table 8: Permissible leakage water rates in German tunnelling, use and length related.

Both tunnels and building pits can create groundwater drainage with similar effects on the surrounding area and environment: settlement of buildings due to groundwater level change etc. This makes a comparison possible between the 3 known tightness classes: German and Norwegian tunnels and German building pits, in order to estimate a tightness class for Norwegian building pits. Next to this the following factors were taken into account:

- Measured leakages in Norwegian pits;
- Leakages in building pits abroad;
- Sensitivity analyses on leakage limits;
- Comparison with drainage engineering;
- Compliance on groundwater restrictions;
- Engineering judgement.

A Table with permissible leakage rates and tightness classes for building pits in Norway is defined in Table 10 and was presented on

the "Geoteknikkdag 2015". With these proposed requirements the demand in Eurocode 7 art. 9.4.1 (8), see Figure 14, are fulfilled and it is now possible for the designer to combine the models shown in Figure 11 to 13 with the newly defined limit.

Proposal for permissible leakage for Norwegian building pits		
Class	**Permissible leakage (m^3/time/1000m^2)**	**Functional demands**
Extremely strict	**0,5 – 2**	Sensitive environment
Strict	**2 – 6**	Moderate sensitive
Average	**6 – 12**	Moderate sensitive / Construction dependent
Moderate	**> 12**	Construction dependent

Table 9: Proposal for permissible leakage water rates for Norwegian building pits.

The designer can also estimate the discharge which belongs to a number of bored piles or anchors and hydraulic head towards the limits from Table 6 or Table 9, see Figure 15 and 16.

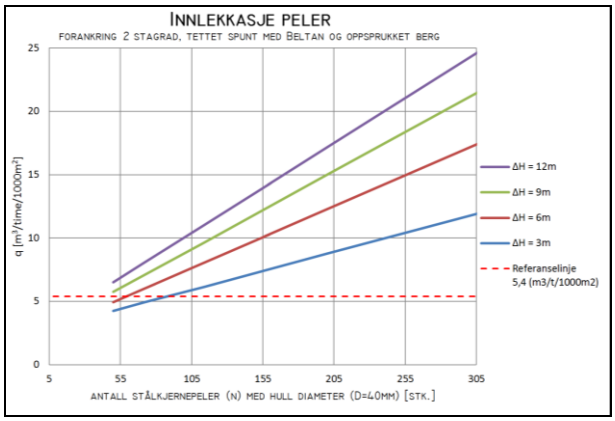


Figure 15: Discharge with bored piles.

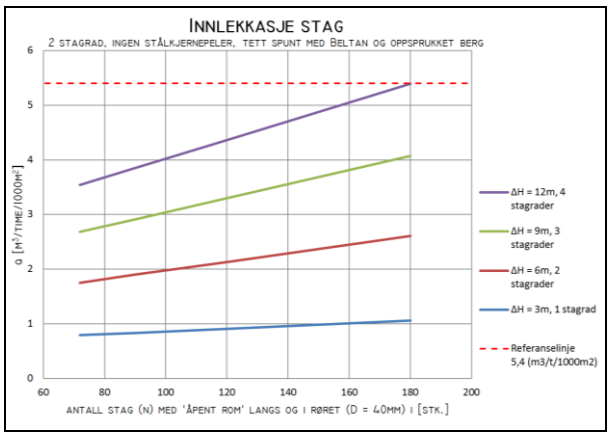


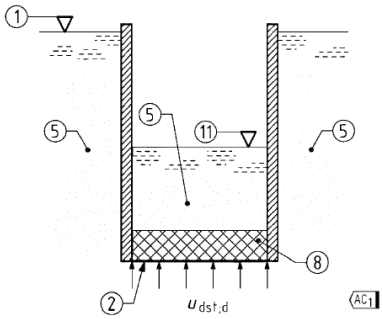
Figure 16: Discharge along anchors.

Figures 15 and 16 are also sensitivity analyses of the defined limit of the permissible leakage: 5,4 m^3/hour/1000m^2.

1.8 Hydraulic failure

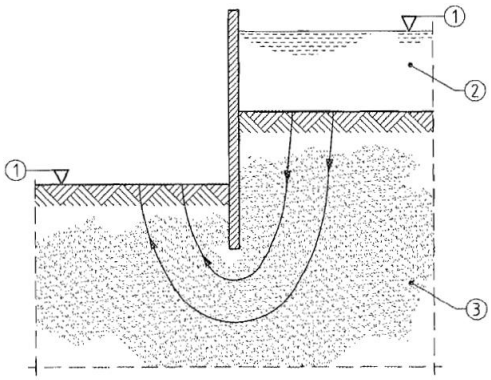
Eurocode 7 applies to four modes of ground failure induced by pore-water pressure or pore-water seepage, which shall be checked:

- failure by uplift: EC 7 -2.4.7.4 / 10.2;
- failure by heave: EC 7 – 2.4.7.5;
- failure by internal erosion: EC 7 – 10.4(1)
- failure by piping: EC 7 – 10.5



d) Execution of a slab below water level

Figure 17: Uplift.



AC1 1 excavation level (left); free-water level (right) AC1
2 water
3 sand

Figure 18: Heave.

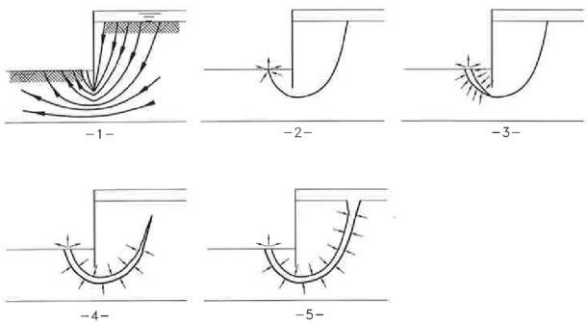
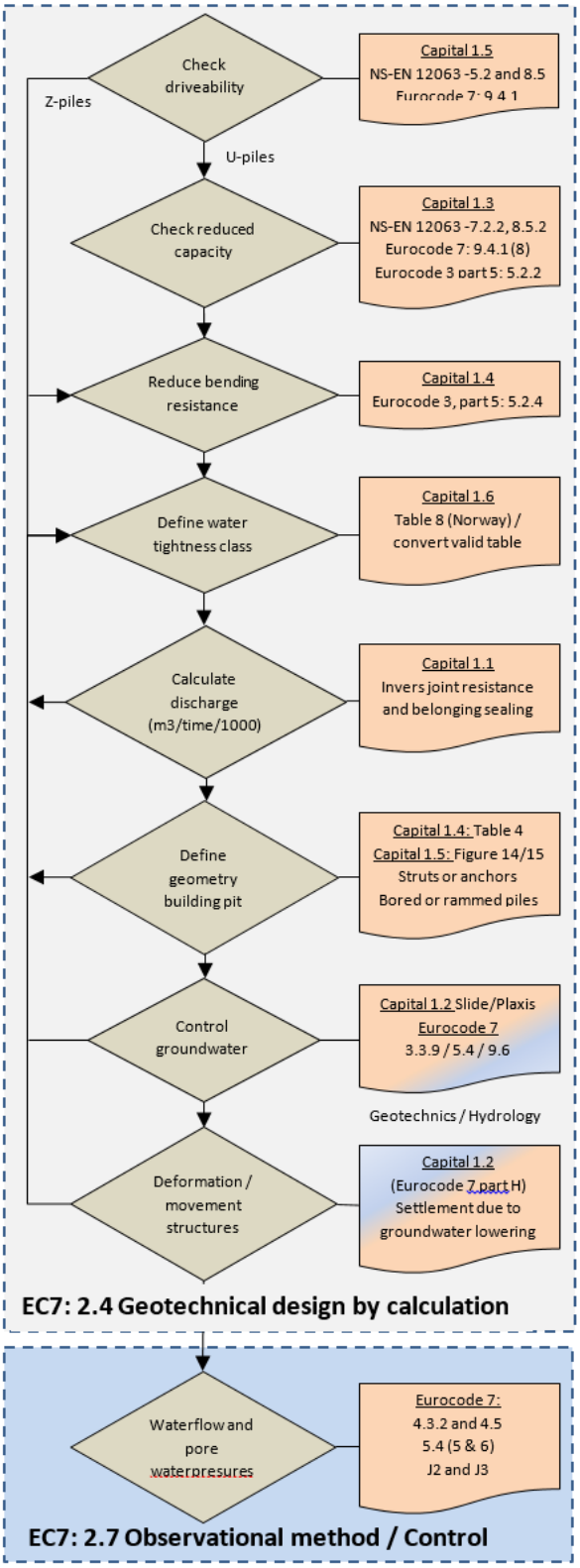


Figure 19: Development of piping.

1.8 Engineering proces for tightness

Engineering a tight building pit is a proces with a number of steps. In order to place the belonging steps in the proper way one can folow the proposed flow chart, after designing length and profile of the sheetpile:



Flow chart 1: engineering tightness in steps.

2.0 Driving with vibrator or drop hammer

In general, both Hoesh and Arcelor Mittal recommend percussively driving.

> It is essential not to overdrive sealed sheet piles with a vibratory hammer as the heat generated by vibro driving may cause the sealant to decompose or burn. If hard driving or refusal is encountered it is recommended that vibro driving ceases at once. The pile should then be driven to level with an impact hammer.

Figure 20: Recommendations on pile driving equipment «Piling handbook» ArcelorMittal.

> **Piledriving instructions**
> Selecting the driving process:
> For preference, piles featuring the HOESCH interlock sealing system should be installed by percussive driving. If circumstances allow, it is also possible to use the vibration driving process.

Figure 21: Recommendations on pile driving equipment: «Piling handbook» Hoesch.

> **Instructions for pile driving**
> Decide on the direction of driving for filled sections at the planning stage. Sheet piling filled with SIRO 88 should be preferably driven with a vibrator, while sheet piling filled with bitumen-based grout should be percussively driven.

Figure 22: Recommendations on pile driving equipment: «Piling handbook» Hoesch.

Control engineers need this information and a way is to take this on working drawings.

2.1 Penetration rate with pile installation

The supplier gives recommendations on minimum penetration rate with vibrodriving. Slow speed gives more energy to the steel sheet wall with viscus sealing as a result that drips out of the interlocks.

> **Piledriving instructions**
> Selecting the driving process:
> For preference, piles featuring the HOESCH interlock sealing system should be installed by percussive driving. If circumstances allow, it is also possible to use the vibration driving process.
> For this, the ground must have good vibrating properties; driving progress must be continuous and no slower than 10 seconds per metre. If it takes longer than this to install the pile, or progress is interrupted, it is better to continue using percussive equipment.

Figur 23: Recommendations on pile driving speed «Piling handbook» Hoesch.

2.2 Puling steel sheet piles

With pile driving it is usual and common to sporadically pull a pile in order to check the condition of the pile foot or to correct the angle of the piles. In this case he sealing should be repaired or the pile should be replaced by a new pile with sealing. See Figure 24.

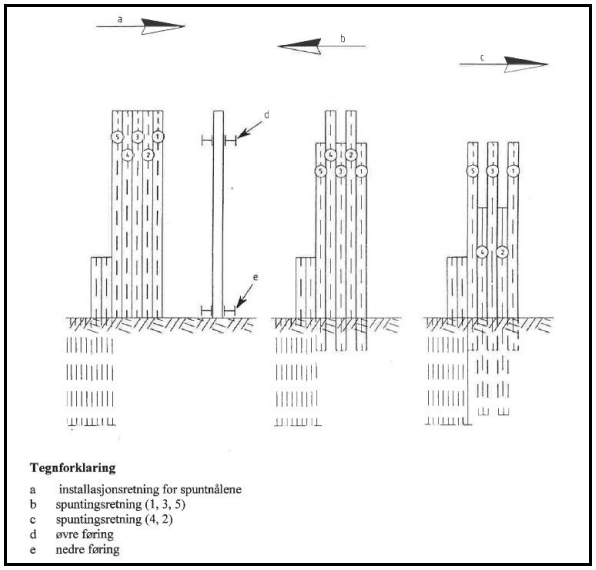
To ensure good joint integrity it is important to control the alignment of the piles in both the horizontal and vertical planes but excessive corrective actions can damage the sealants. If it is necessary to remove a pile then suitable repairs should be carried out to the sealant before reuse. If repair is not practical, withdrawn piles should be replaced by new ones.

Figure 24: Recommendations on pile driving equipment «Piling handbook» ArcelorMittal.

Eurocode NS-EN 12063:1999, article 8.11 handles about puling steel sheet piles

2.3 Ramming method

It is important that steel sheet walls with sealing are installed on a proper way. Eurocode NS-EN 12063 supplement D gives guidelines on ramming methods, see Figure 25.

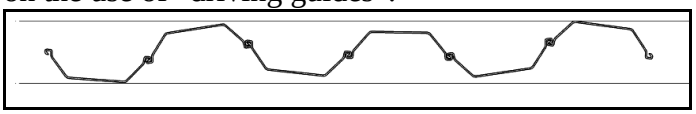


Figur 25: Supplement D Figure D1 from NS-EN 12063:1999.

Different methods for ramming steel sheet piles and guidelines are also available with the supplier: «Panel driving» og «Staggered driving». See also Figure 29. The proper method should be described on the working drawings and in the contract.

2.4 Driving guides

In order to prevent scraping of the sealing while ramming by piles which are twisted, see Figure 27, the supplier gives guidelines on the use of “driving guides”.



Figur 26: Change on scraping of sealing.

Eurocode NS-EN 12063 article 8.5.8 and 8.5.9 also gives instructions and guidelines on use of driving guides for ramming.

8.5.8

Spuntnålene bør ledes på ett eller flere nivåer under spuntingen.

8.5.9

Føringsrammer bør være stabile og robuste og montert på nivåer som sikrer at spuntnålene holdes i riktig horisontal og vertikal stilling under spuntingen. Føringssystemet bør være konstruert for å unngå skade på overflatebelegget på spuntnålene (for eksempel ved å bruke føringsruller).

Figur 27: 8.5.8 and 8.5.9 NS-EN 12063:1999

2.5 Driving direction

Driving direction of steel sheet piles is dependent on type of sealant, type of steel sheet pile: U- or Z-shaped, single or double pile and the phenomenon’s «Piles lagging» or «Piles leading», se Figure 28 and 29.

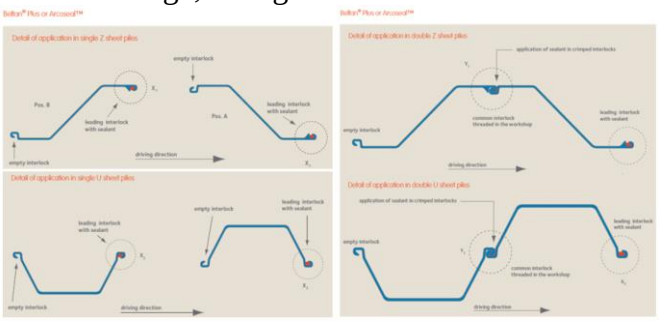
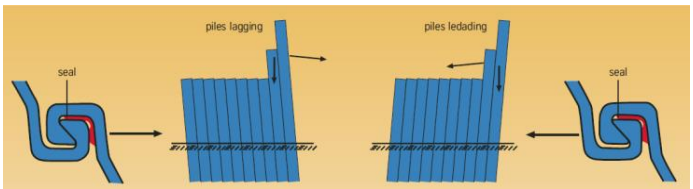


Figure 28: Directions from ArcelorMittal.



Figur 29: Directions «Piles lagging» / «Piles leading» from Hoesch Piling handbook.

2.6 Declutching detector

Declutching detectors can be used in soils that are technically difficult for driving, in order to guarantee a perfect hooking between interlocks. Requirements on monitoring sheet pile driving are given in Eurocode NS-EN 12063 article 9.3.8, see Figure 30. There are several suppliers of different systems for declutching detectors.

9.3 Overvåkning

9.3.8

Ved spunting av kombinert vegg bør det benyttes låssprengningsdetektorer på minst noen av sekundærelementene. Dette bør gjøres i kombinasjon med at inntrengningshastigheten registreres i full dybde slik at rammeprotokollen kan brukes som en kontroll på mulig låssprengning.

MERKNAD Overvåkning av inntrengningshastigheten for spunten under vanskelige forhold gir ofte bare en tilnærmet indikasjon på mulig låssprengning. Detektorer kan være nyttige for å få bekreftet spuntveggens helhet etter ferdigstillelsen.

Figur 30: pkt.9.3.8 NS-EN 12063:1999

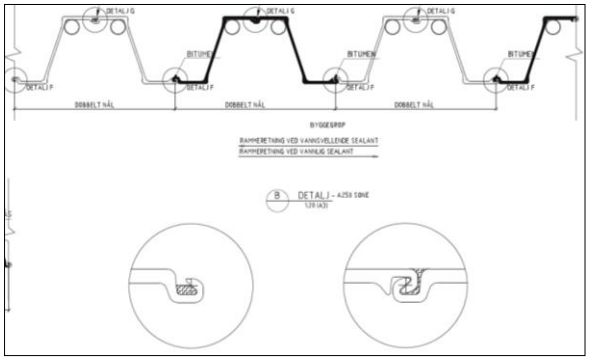
2.7 Working drawing

In Norway steel sheet piles are equipped with steel pipes in order to be able to bore trough these pipes after installation of the piles. This boring is done to install a bolt and therefore secure the foot of the pile. This occurs on the "dry side". However, as Figure 31 shows, the steel sheet pile supplier connects at the factory first the two single piles into one double pile, before the sealing is applied.



Figure 31: Sealing (Arcoseal) project Bjørvikatunnel – Havnelageret.

This implies that the sealing also is placed at the so called "dry side" of the pile, given water the possibility to push the sealing out. Sealing should always be on the "wet side" of the wall. Figure 32 shows proper details on a working drawing.



Figur 32: Details on working drawing.

Conclusion

For the moment there are no tightness classes for building pits in Norway. The suggested method in the different chapters and proposed Table 9 is meant as a tool towards the designer and engineer to come to a tight building pit or retaining wall.

References

1. Arcelor Mittal (2008): "Piling Handbook 8th edition";
2. ThyssenKrupp GfT Bautechnik (2010): "Sheet Piling Handbook 3rd edition";
3. NS-EN 12063: 1999 Utførelse av spesielle geotekniske arbeider.
4. NS-EN 1993-5:2007+ NA:2010 Eurokode 3: Prosjektering av stålkonstruksjoner. Del 5: Peler (spunt)
5. dr.ir. D.A.Kort (oktober 2004): "On the use of Z and U piles", presentation NGF;
6. Kluckert, K.D (Graz 2007).: "Wie dicht ist dicht?, Christian Veder Kollquium;
7. Borchert, K.-M. (1999): "Dichtigkeit von Baugruben bei unterschiedlichen Sohlen-Konstruktionen – Lerhen aus Schadensfällen"
8. T. Katsumi, T.Iniu og M. Kamon (september 8-10, 2009): «In-situ containment for waste landfill and contaminated sites», ISGE 2009;
9. Dr. Gordon P. (Piledriver fall 2004): "Pile foundations – an environmental problem?";
10. Vegdirektoratet Teknologiavdelingen Publikasjon 103 (Oslo, januar 2004): "Berginjeksjon I praksis".
11. Ing. W.R. de Bruin "Prosjektering og utførelse av tett spunt", Geoteknikkdag 2015.

Foundation of a new bridge over the Göta River in Gothenburg

K. Du Thinh
COWI AB, Sweden, kidt@cowi.se

F. Nystrom; L. Johansson
COWI AB, Sweden

ABSTRACT
A new bridge, 1500 m long, is planned to replace the existing bridge, Göta älvbron, in order to secure a good connection between the downtown of Gothenburg and the large industrial Hisingen region to the North in the years to come. The new bridge, named Hisingsbron, is designed with a central section that can be lifted to provide a 28 m high free boat passage. Unlike other bridge spans, this movable part and the sections adjacent to it to the North and the South have to be constructed to high dimensional tolerances, and cannot accommodate any differential settlement. The site consists of a very deep deposit of soft clay, from 40 m to more than 100 m, overlaid by about 3 m fill on either sides of the river. This setting poses a challenge to the foundation work because of creep settlement. This article describes the relevant geotechnical conditions, the foundation for the different supports of the bridge, the calibration of the soft soil creep (SSC) models, and the utilisation of the models to numerically analyse the creep settlement with time as well as its effects on the piles (drag load and downdrag). Suggestions are made to minimize the drag forces by allowing a certain settlement of the piles in the southern and northern bridge sections, eventually in combination with other methods such as protecting the piles, in the part subjected to drag forces, with bitumen or with a sleeve. The protective sleeve will be in contact with the pile at a number of points.

Keywords: Bridge, Pile foundation, soft soil creep, drag

1 THE NEW HISINGSBRO

A new bridge, named Hisingsbron, is planned in downtown Gothenburg. By allowing an efficient connection over the Göta River between the city center and the large island of Hisingen to the North, it will contribute to the development of the city and create a strong region with conditions favorable to the shipping industry.

Figure 1 shows the four present links connecting the northern and southern shores of the Göta Älv River in central Gothenburg.



Fig 1. Present connections between the main land and Hisingen.

In 2013 The Municipality of Gothenburg, owner of the bridge, announced a competition for the design of a new bridge across the Göta River. Five teams were qualified for the final round, and the winner

was the team who presented a design named "Arpeggio" for the specific bridge section across the river. The criteria for the decision were: viability, development and functionality.

In total, the new bridge will be approximately 1500 m long, out of which the Arpeggio part will have a length of 440 m. The movable section is carried by four 50 m high pylons. It will be 12 m above mean water level, but can be lifted up to provide a 28 m high free ship passage.

The existing Göta Älvbron is in bad condition due to ageing brittle steel, which requires a high maintenance cost every year. It is, in fact, necessary to monitor it on a 24 hour basis in order to guarantee traffic safety.

The new bridge must be built and opened for traffic before the existing bridge can be demolished, since this is the only tramway connection between Hisingen and the mainland.

1.1 Layout and location of the bridge

Figure 2 shows an artist rendering of the bridge. The location of the bridge is about 60 m to the east of the aging Göta Älv Bridge that the new bridge will replace.



Figure 2 Hisingsbron looking East (courtesy Trafikkontoret, 2014).

As mentioned above, the bridge will be 12 m high. This is 7 meters lower than the existing bridge. The reason why the bridge will be built lower is that it enables traffic to be rerouted closer to the river and thus release more than 70 000 square meters for housing development. The low height also makes it easier for pedestrians and cyclists to cross the bridge.

Since the bridge in the future will be surrounded by buildings on the southern shore of the Göta River, not much of it will be visible there. However, on the northern shore the bridge will be surrounded by green areas and become a more prominent sight.

The waterway between the two pairs of pylons is about 30 m wide with a depth of about 6.5 m. The bridge central section can be lifted up to 28 m, as shown in Figure 3, to allow tall ships to pass. This operation will be necessary for cargo ships, which can clear the existing 19 meter high bridge. The bridge will not be opened on morning and afternoon at rush hours. This decision has met with opposition from ship owners, as ocean-crossing ships must have a minimum height.



Figure 3 The Bridge in uplift position 28 m above water level (courtesy Trafikkontoret, 2014).

Building of the bridge will start in 2016 and will be completed in 2020, after which the existing bridge can be broken down (an operation that takes about 6 months to complete).

1.2 Historical review

The decision to build a high level bridge was taken in 1933. The bascule bridge, named "Göta Älvbron", started operation in 1939, see Figure 4. It has almost reached its life span and has to be replaced at the latest in 2020, when the new Hisingsbron will be completed.



Figure 4 The Göta Älv Bridge from 1939 onwards (courtesy Trafikkontoret)

1.3 Foundation of the existing Göta Älv Bridge

The bridge is founded on 46 supports, ten of which are over water. Thus the river section has 9 spans, see Figure 5.

The supports are founded on jointed timber piles with a length of 36 meters. The shear strength of the clay at this depth is 4-5 times higher than in the shallow layers. Most of the piles are friction piles except for the ones at the bascule bridge support and the support north of that in the middle of the river section. Since the bedrock rises steeply in this stretch these piles are end bearing. Many of the piles are driven with an inclination of 5:1 and 6:1 (v:h), due to horizontal (mostly dynamical) loads, in addition to gravity loads.

The adjoining fenderings are 110 m and 265 meters long and they are founded on 18 m long timber piles.

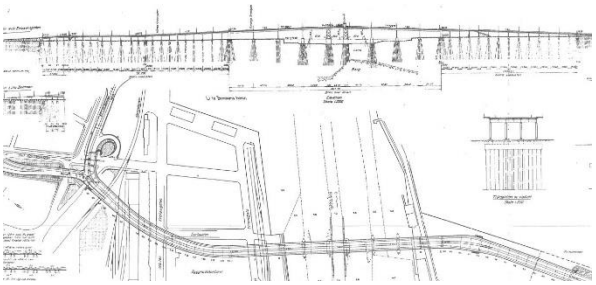


Figure 5 The Göta Älv Bridge. Assembly drawing from 1955 (courtesy Trafikkontoret).

2 THE SITE

The Göta River valley is a low-lying area with a very deep deposit of clayey sediments. The thickness of the clay layers amounts generally to 90 -100 m at the southern shore of the river. In the middle part of the river, the clay deposit is less thick, 30-40 m, because of the presence of a high local bedrock, whose surface is very steep southward. North of this bedrock, the soil depth increases steadily and attains around 70 meters near the northern shore. Further north the clay thickness diminishes again, see Figure 6.

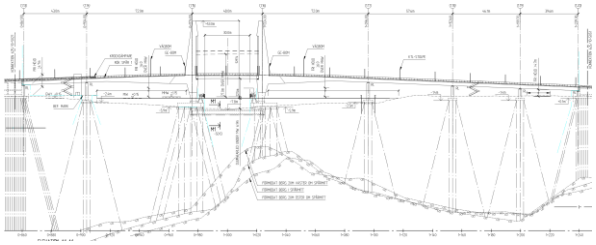


Figure 6 Estimated bedrock surface.

2.1 Geological setting and hydrology

The Southern part of future Hisingsbro will be founded in an area with a very thick clayey deposit, up to about 90 m. The clay there is overlaid by a ca 3 m thick fill and rests on a 3 m thick till layer (sand/gravel) that covers the bedrock. The groundwater level (GWL) is between 0.5 and 1.5 meters below the ground surface (GS).

The undrained shear strength, c_u, is very low to low from GS to 20-25 meter depth. It becomes medium at 40 m depth, and high at greater depths. The clay layers are normally to slightly preconsolidated. The upper part of the clay deposit is post-glacial, whereas the lower part is glacial. Fill materials have been laid out on top of the clays more recently, probably in 1860 and in 1890.

The situation is similar in the North River bank. Here the clay deposit has a thickness of about 50 m, and the fills are laid out probably in 1885 and 1945. In both the northern river and the southern banks the transition zone between glacial and post glacial clay can be found about 5- 10 m above the middle line of the deposit.

2.2 The geotechnical features

The clay at the southern part of the river bank has an undrained shear strength c_u which varies from 15 to 25 kPa at 3 m below GS. From there it increases to 60 ±5 kPa at a depth of about 35 meters and attains 100 kPa at a depth of 60 m, see Figure 7.

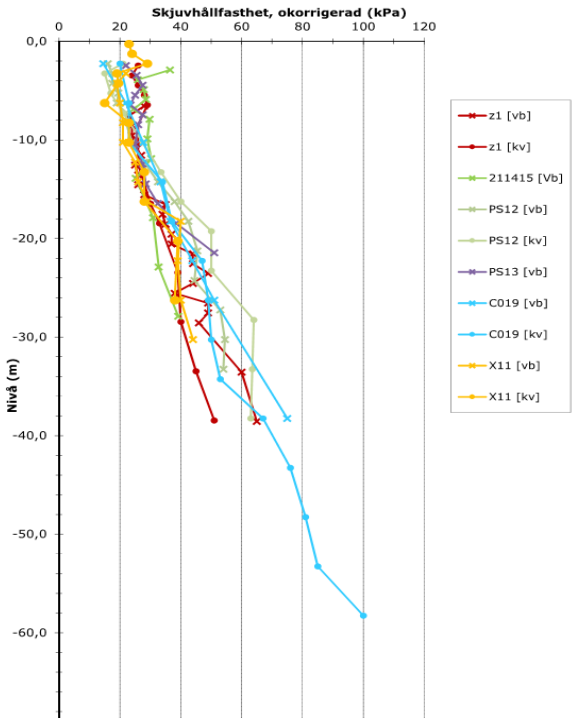


Figure 7 Undrained shear strength at the southern bank.

The bulk density of the clay varies between 1.55 and 1.7 ton/m³; the higher value can be found in the deep soil layers. The water content varies between about 80% and 55%; it decreases generally with depth.

At the Northern Bank, the undrained shear strength c_u increases with the depth, from about 17 to 20 kPa just below the fills to 45 - 55 kPa at about 25 meters below GS, see Figure 8.

The bulk density of the clay varies between 1.5 and 1.7 ton/m³; the higher value belongs to the deep layers. The water content varies between about 90% and 50%; a general decrease with depth has been observed.

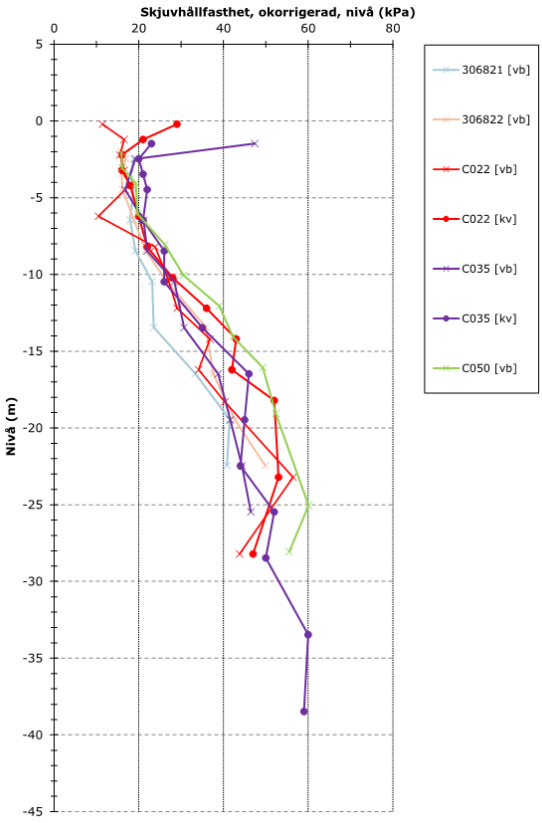


Figure 8 Undrained shear strength at the northern bank.

3 THE FOUNDATION

The pylons of the movable bridge section and the supports of the adjacent bridge spans will be founded on point bearing piles. Most probably circular bored steel piles will be utilized with their toes resting on the bedrock or socketed in the bedrock. The supports of the other spans can be founded on friction piles to allow a certain settlement which reduces the effects of negative skin friction.

3.1 Overview

Topographical survey carried out the last 2-3 decades at different places in the southern river bank reveals a GS settlement of 3-5 mm/year; the higher figure relates to places with 5 m fill. When designing a pile foundation in such a geological setting one must not ignore the drag forces on the piles and the downdrag on the foundation. The negative friction develops with time and must be carefully studied. The situation at hand differs from the usual cases where settlement

of the soil surrounding a pile foundation is essentially caused by fills which are laid out at the construction time. In such a case the settlement and the ensuing negative skin friction can be analysed in a conventional manner using directly the soil parameters at hand. In our case, the surcharge was put on the post glacial clay which rests on the glacial deposit in the 1880s. It induced a new consolidation and creep process, the effects of which are still noticeable today.

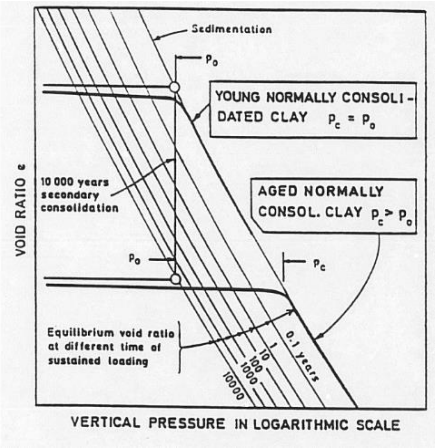


Figure 9 Geological history and compressibility (Bjerrum, 1973).

3.2 Soil models and their calibration

The issue is illustrated in Figure 9 in which Bjerrum (1973) outlined the effect of a recent loading on a clayey deposit that has consolidated and crept for thousands of years. If the loading is large enough, it brings the aged clay to the normally consolidated stage (OCR=1). The quantitative assessment of the process requires the construction of soil models which reflect the geological history and compressibility of the different parts of the construction site and adequately reproduce their behaviour during the last 2-3 decades. Such a soil model will form a basis on which prediction of creep settlement and its effects on the piles can be calculated for the life time (120 y) of the new bridge. The task was done by employing the Soft Soil Creep (SSC) constitutive law which is incorporated in the finite element (FE) program Plaxis 2D-2015. Its application requires input, for each layer, of the strength parameters c', φ', ψ (dilatancy) and the stiffness parameters λ^*, μ^*, and κ^*. The latter are called modified indexes for compressibility, creep, and swelling respectively – modified with respect to similar parameters defined in Critical Soil Mechanics. They are related to the initial void ratio e_i, and the more familiar parameters C_c, C_α, and C_s from incremental oedometer testing.

$$\lambda^* = C_c/2.3(1+e_i) \quad (1)$$

$$\mu^* = C_\alpha/2.3(1+e_i) \quad (2)$$

$$\kappa^* \approx 2C_s/2.3(1+e_i) \quad (3)$$

$$log(k/k_i) = \Delta e/c_k \quad (4)$$

Equation (4) defines the decrease of the coefficient of permeability *k* with the compression ($\Delta e < 0$). Plaxis (2015) recommends setting $c_k \approx C_c$.

In the modelling and calibration work, attention must be given to the geology of the deposits, the loadings in the 1880s, the soil properties, the GS settlement rate during the last 2-3 decades, and the recent observations of settlement pattern and pore water pressures. A major issue remains, however, with the soil properties, because they are derived from field and laboratory investigations conducted in 2014 and do not directly reveal the conditions of the clay layers prior to the loadings in the 1880s. Obviously the void ratio e and the coefficient of permeability k must be higher then. The other parameters were also different since the clays were weaker and more compressible. The work included several series of trial and error FE analyses accompanied by a number of minor hand calculations, always keeping in mind the conditions cited above. Also the empirical values or relationships concerning C_c, C_α, and C_s were utilized. These are reported by P. von Soos and J. Bohác (2002), by K. Terzaghi et al. (1996), and by Trafikverket (2014).

3.2.1 The Northern part

Figure 10 represents the soil model for the Northern part in which a vertical pile row (or

pile wall, PW) is installed 3 m above the bottom till layer. The horizontal lines in the figure delimit the different soil layers whereas the fine red curves represent the magnitude of 120-year settlement within the soil mass. All points on a curve have the same settlement (iso-curves).

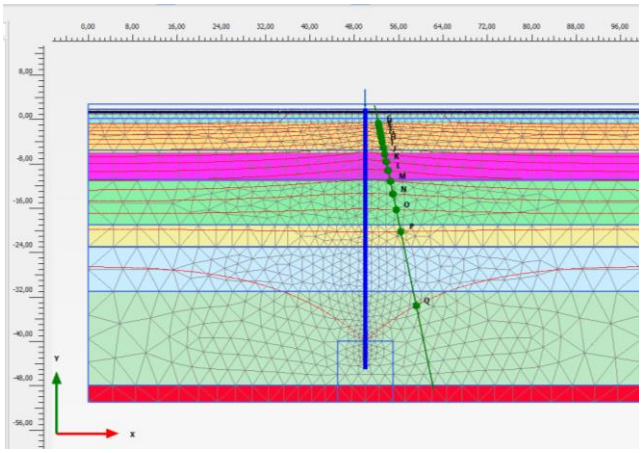


Fig 10 N-soil model for northern river bank.

The model consists of 6 clay layers denoted from top to bottom CL1 to CL6. On top of CL1 are 2 layers of fill, and below CL6 is the bottom till layer. It has been assigned to all clays $c' = 0.1\ c_u$ *(kPa)*, $\varphi' = 30^o$, and $\psi = 0^o$. The other relevant SSC parameters are compiled in Table 1.

Table 1 N-soil model. Relevant SSC parameters

Clay	c'	λ^*	$10^3\ \mu^*$	$10^3\ \kappa^*$	e_i
CL1	1.7	0.1133	0.7931	3.399	2.07
CL2	2.2	0.1226	0.8519	3.672	1.96
CL3	3.8	0.1318	0.5599	4.743	1.64
CL4	5.3	0.1142	1.939	5.255	1.78
CL5	5.9	0.1251	3.128	5.255	1.78
CL6	7.2	0.1210	3.024	6.048	1.66

When calibrating the model, the parameters C_c, C_α, and C_s were taken into consideration, and the ratio $C_s/\ C_c$ was kept within 0.02 ±0.01. As to the fills and the very stiff bottom till layer, their behaviour was simplified to a drained Mohr-Coulomb soil type.

Figure 11 shows the result of the analysis of consolidation-creep in the period from 1885 to 2134. Preceding that calculation phase was a consolidation-creep analysis of the glacial and post glacial deposits without any fill over a period of 10 000 years. It was a preparatory analysis to bring the deposits to the state they were supposed to have in 1885 when the first 1.5 m thick fill was laid out. It was assumed that the second fill (1m) was put on place in 1945.

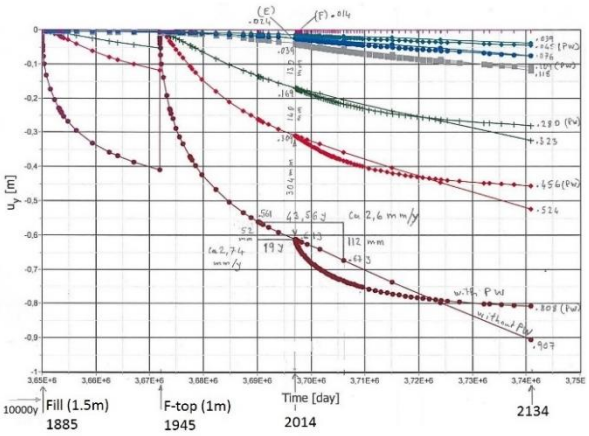


Figure 11 Settlement in period 1885- 2134.

The curves in Figure 11 represent the time settlement of the upper boundary of CL1 to CL6. The lowest curve belongs to CL1, the curve above it to CL2, etc.… The Plaxis technique of resetting displacements to zero while preserving the obtained stress state was utilized in the beginning of the calculation phase 1885-1945 and again in the beginning of the phase 1945-2014 in order to bring the ground surface to the elevation from which it settled down to the 2014 level. It can readily be seen that the GS settlement rate amounts to 2.7 - 2.8 mm/y during the last 2 decades. This result is deemed realistic since the clay deposit here is not as thick as in the south.

Another result worth mentioning is the calculated settlement until year 2014 of the upper boundary of the uppermost clay layer CL1: 613 mm. This means that the GS which was assigned the elevation of +2.7 in the very beginning of the analysis is now lowered to 2.7 – 0.613 ≃ +2.09. If one accounts for some compression of the fills, then the calculated GS elevation is very close to +2.0 which is the result of survey in 2014.

Inspection of figure 11 reveals that 94% of the settlement until 2014 is caused by the compression of the 3 upper clay layers: 304+140+130 = 574 mm. This means that most settlement occurred within the upper 20 m. Also this calculated result correlates well

with field measurements conducted the last few years.

The model was also checked with respect to pore water pressures. These were monitored in 2014 with piezometers installed at elevations -8, -18, and -28. The relative difference between calculated values and field data does not exceed 1.1 %.

Table 2 Pore water pressures (kPa) in 2014

Point (elev.)	Field Data	Calculated value	Relative difference
K (-8)	99.0	99.7	+0.7 %
L (-18)	198.0	200.2	+1.1 %
M (-28)	299.0	297.5	-0.5 %

The results presented in Table 2 are a further validation of the N- soil model.

Figure 10 shows the application of the model for analysing the effects of creep settlement on a pile row over a period of 120 years. The pile row is modelled here as a rough thin concrete pile-wall (PW) loaded on the top with a vertical line load of 600 kN/m. It can readily be seen that the upper soil layers settle down and hangs on the PW (negative skin friction) while the deep seated layers support the PW (positive skin friction). The neutral plane can be found at elevation -20. This result is consistent with the compression pattern described above. The analysis yields also the settlement of PW's toe: 56 mm and PW's head: 70 mm. PW's compression is caused by the load and the drag forces.
The results are deemed realistic. The N-soil model presented here can, therefore, be utilized for investigating the behaviour of a pile group. This task is currently being performed.

3.2.2 The Southern part

The S-soil model for the southern river bank was constructed in the same manner as the N-soil model, but it is less elaborate and has fewer clay layers although the clay deposits are thicker (90m). This simplification diminishes the calibration work load.

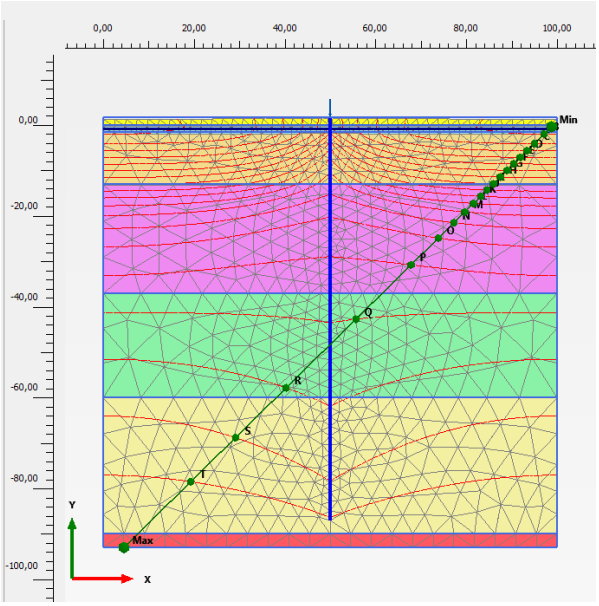


Fig 12 S-soil model for the southern river bank.

The four clay layers in the S-model are denoted from top to bottom CL1 to CL4. Below CL4 is the stiff till layer whose upper boundary is located at elevation -90. On top of CL1 are two fill layers called Fill and F-top. Fill is believed to be deposited in year 1860; it rests now on CL1 at elevation -1.6 and is about 1.6 m thick. F-top was laid upon Fill probably in 1890; it is now about 1.7 m thick. So GS is presently at elevation +1.7. The till and fills are modelled as Mohr-Coulomb materials. Attention on consolidation and creep was given only to the clayey layers; their SSC parameters are collected in Table 3.

Table 3 S-soil model. Relevant SSC parameters

Clay	c'	λ^*	$10^3\,\mu^*$	$10^3\,\kappa^*$	e_i
CL1	2.45	0.1296	4.928	5.188	2.00
CL2	4.50	0.1733	6.242	6.925	1.80
CL3	8.05	0.1854	4.634	7.415	1.58
CL4	11.7	0.1572	3.143	6.286	1.49

The analysis method is the same as for the Northern river bank reported above. It includes several steps: (i) a preparatory consolidation-creep analysis of the glacial and post glacial deposits without any fill over a period of thousands of years to bring them to a state they were supposed to have at the time when the fills were applied; (ii) the application of the first fill in year 1860 followed by a consolidation-creep analysis

until 1890; (iii) the application of the second fill in 1890 followed by a consolidation-creep analysis until 2014 then until 2134; (iv) the installation of a pile row or a pile group in 2014 for studying the effects of creep settlement on it over its life time (120 y).

The results of the steps (i) to (iii) are qualitatively similar to those for the Northern river bank:

- Settlement rate calculated at the upper boundary of the uppermost clay layer CL1: ca 3.2 mm/y during the last 2 decades
- Settlement pattern: about 87% of the settlement until 2014 and beyond 2014 is caused by the compression of the upper 2 clay layers CL1 and CL2 which are post glacial clays (down to elevation -37)
- Calculated pore water pressures: relative difference from the 2014 readings of the piezometers K and L installed at elevation -32 and -48: for K (-32): +3.7%; for L (-48): -0.8%.

The obtained results correlate with field observations. The S-soil model is deemed realistic; it can be utilized for studying the behaviour of structures to be built in the South River bank.

Figure 12 shows the results of such a study with a pile row modelled as a thin concrete pile-wall (PW). PW is loaded on its head with a vertical line load of 600 kN/m; its toe stands 3 m above the stiff till layer. As expected the two upper clay layers settle and drag down PW (negative skin friction) whereas the lower layers support PW (positive skin friction). The neutral plane can be found at about elevation -40. As to the settlement the calculated values are given in Table 4.

Table 4 S-soil model. Settlement after 120 years

PW13	V= 0 kN/m	V= 600 kN/m
Cap	74 mm	102 mm
Toe	58 mm	76 mm

In the case of a non-loaded PW, the toe settlement is less, i.e., in comparison with the loaded pile, the surrounding soil settles more relative to the pile. As a consequence the zone of negative friction becomes longer, and the neutral plane is lowered to elevation ca -45. The same is true in the case where the PW is installed 1 m into the till layer. The toe settlement will be negligible, and the neutral plane will move downwards to elevation -51. These results are logical. They show the applicability of the model in the design of pile foundations.

Figures 13 and 14 exemplify a tentative design of the pile group PG 13 for the pier No. 13 of the future bridge. The pile cap is a 1.5 m thick reinforced concrete plate with the dimension L x W =30 m x 6 m. Parallel to L are four pile rows in equal spacing, and parallel to W seven rows on either side of the middle row which has fewer piles than the other rows. The outer piles are slightly inclined (V: H=7:1), but the inner piles are vertical. The pile rows are modelled as thin vertical concrete plates. The vertical permanent load acting on PG13 amounts to 56 MN.

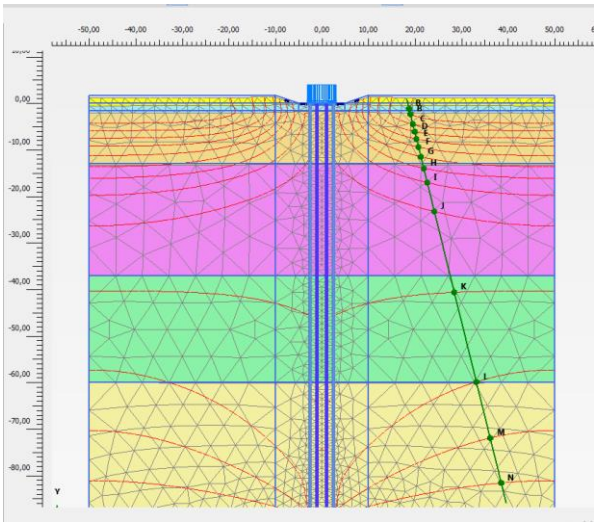


Fig 13 Pile group PG13 in S-soil model.

The pile group PG13 stands 3 m above the bottom till, at elevation -87. It undergoes, over a period of 120 year after installation, a settlement of 156 mm at the toe and 183 mm at the cap. The neutral plane appears approximately at elevation -37 in figure 13.

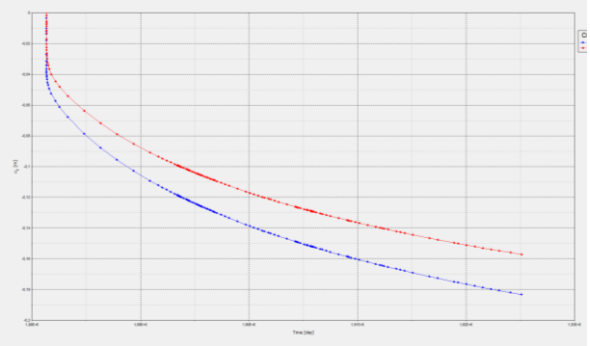


Fig 14 Settlement of PG13 in S-soil model.

It can be seen in figure14 that about 29 % settlement occurs during the first year at the cap: 53 mm. The settlement continues at the rate of about 3.1 mm/y until year 10, then 1.9 mm/y until year 20, and 1.2 mm/y until year 50. With time the settlement rate decreases to less than 1 mm/year.

The above are the results of a 2D analysis of PG13 seen perpendicular to the bridge axis (pile cap cross section 6 m x 1.5 m with 4 pile rows). The real problem is, however, 3D. Another investigation was carried out in the bridge direction with a cap cross section 30 m x 1.5 m. As expected the settlement is more important. The results for both cases are summarized in Table 5.

Table 5 S-soil model. Settlement after 120 years

PW13	**// bridge axis**	**⊥ bridge axis**
Cap	280 mm	183 mm
Toe	259 mm	156 mm
Neutral plane	Elevation -20	Elevation -37

The behaviour in the direction transverse to the bridge axis is believed to better reflect the real situation. This in analogy with the behaviour of a strip footing.

4 DESIGN RECOMMENDATIONS AND CONCLUSIONS

The soil models presented here reflect the site's current behaviour. They can cope with the phenomenon of consolidation and creep settlement as well as their effects on a pile foundation. It was time consuming to construct models, but once done, they constitute a useful tool for studying different pile group designs. Different geometries, loadings, and foundation depths can be readily investigated. The central issue is the settlement including downdrag and the magnitude of drag forces. Parameter studies are being currently conducted to assess the sensitivity of different parameters considering also their uncertainties.

The on-going study focuses on methods to reduce the drag forces by allowing, for example, a certain settlement and/or applying bitumen on the part of the piles which is subjected to negative friction. Also a protective sleeve can be considered. That alternative can, however, cause production problems. Should bitumen be utilized, its effect can be easily simulated using the above soil models by giving the interfaces of the pile portion in question a reduced shear strength.

5 ACKNOWLEDGEMENT

The review of the draft by Dr Dat DuThinh, NIST, Maryland, USA, has helped to improve the article.

6 REFERENCES

Bjerrum, L. (1973). Problems of soil mechanics and construction on soft clays and structurally unstable soils. Proceedings of the 8th ICSM&FE, Moscow, Vol. 3, 111-159.

Plaxis 2D (2015) Reference Manual.

Plaxis (2015) Material Models Manual, 103-115.

Terzaghi, K., Peck, R., Mesri, G. (1996). Soil Mechanics in Engineering Practice. 3rd Edition, 100-121, John Wiley & Sons, Inc.

Trafikkontoret (2014). Förfrågningsunderlag

Trafikverket (2014). Trafikverkets Tekniska Råd för Geokonstruktioner-TR Geo13. Dok ID TDOK 2013:0668, V.1.0, 2014, 18-29.

Von Soos, P., Bohác, J. (2002) Geotechnical Engineering Handbook, Vol. 1, 184-189, Ernst & Sohn.

The traffic junction Lindholmsmotet in Gothenburg: An example of creative geotechnical engineering in the construction phase

T. Edstam
Skanska Sweden AB, Sweden, torbjorn.edstam@skanska.se

A. Kullingsjö
Skanska Sweden AB, Sweden

ABSTRACT
In 2012 Skanska Sweden AB was awarded a contract for expanding the traffic junction "Lindholmsmotet" in Gothenburg. The ground conditions were challenging (very deep deposits of "Gothenburg clay", i.e. a soft, high plastic, slightly over-consolidated marine clay), but the job was mainly a construction-only contract. Therefore, only a minor engagement, handling some temporary works, was expected for the geotechnical engineers at Skanska Technology. However, the engagement successively increased since the design for the operational stage seemed unsafe – at least based on the geotechnical properties prescribed in the contract documents. After several meetings with the Client and the Client´s consultant the geotechnical engineers at Skanska decided to scrutinize the Ground Investigation Report, including e.g. triaxial tests, in detail. Based on this study the Skanska geotechnical engineers concluded that the ground conditions seemed much better - at least partly - than prescribed. Eventually, the Skanska geotechnical engineers redesigned a major part of the geotechnical solutions that were prescribed in the contract documents. The redesign was done in parallel with the ongoing construction works, which made the redesign time schedule somewhat challenging. However, thanks to a very good and close cooperation with the construction units at Skanska and the Client´s representatives, the redesign lead to a cost saving of about 10 % of the contract sum, which was 87 MSEK. A major part of the savings resulted from reducing the prescribed amount of stabilizing lime cement columns by approximately 100,000 linear meters. The redesign also contributed to the construction works being finished about 6 months earlier than originally planned. A comprehensive monitoring program was implemented in order to assure that the construction works did not jeopardize the stability conditions in the surroundings. Especially the displacements of the adjacent existing railway, of major importance for the Port of Gothenburg, was thoroughly monitored.

Keywords: Soft clay, stability, design, monitoring, case record

1 INTRODUCTION

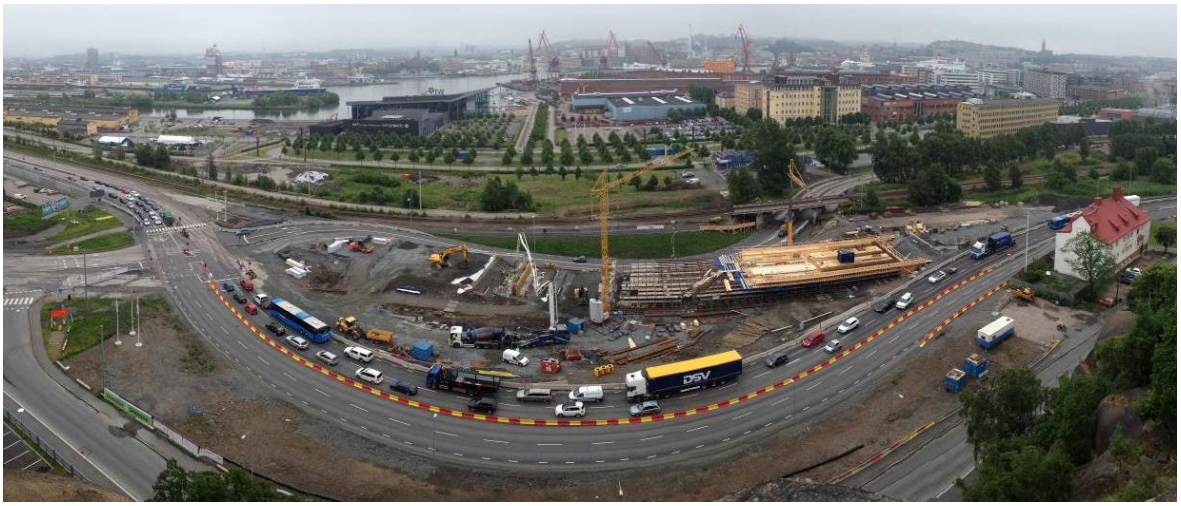
In 2012 Skanska Sweden AB was bidding for a contract for expanding the traffic junction "Lindholmsmotet" in Gothenburg, Sweden. Due to the urban location of the junction there were several geometrical constraints to handle, such as an adjacent railway (of major importance for the Port of Gothenburg) and the existing traffic junction which both should be fully operational during the construction phase, cf. Figures 1-3.
Since the job was a construction-only contract the geotechnical engineers at Skanska were just briefly involved in the tender phase, even though the new junction included up to approximately 6-7 meter deep permanent excavations in challenging ground conditions (very deep deposits of soft clay). As soon as Skanska was awarded the contract the geotechnical department started to examine the site conditions, with focus on the stability conditions in the construction phase. This initial study indicated that the stability stability conditions of the prescribed excavation next to the railway would be far from satisfactory even after the construction works were finished.
Due to this somewhat surprising conclusion Skanska initiated a series of meetings with

the Client (including its in-house geotechnical expert) and its geotechnical consultant. The purpose of these meetings was to get a better understanding of the background to the prescribed geotechnical properties, the prescribed required geotechnical measures and hopefully to figure out a safe and economical solution to this unexpected challenge.

This paper summarizes the outcome of these meetings, the subsequent redesign performed by the geotechnical engineers at Skanska and some experiences from the the actual construction works.



Figure 1. The original traffic junction.



F*igure 2. The new traffic junction during construction.*



Figure 3. The new traffic junction just after completion.

2 THE GEOTECHNICAL PROPERTIES AND THE REQUIRED STABILISING MEASURES ACCORDING TO THE CONTRACT DOCUMENTS

The Contract Documents included a broad description of the ground conditions. Furthermore, the characteristic values of all relevant geotechnical properties, e.g. strength and deformation properties, were prescribed in detail.

In general the ground at the site consists of about 0-4 m of fill on top of "Gothenburg clay" reaching a depth of 50-80 m. The clay is a soft, high plastic, slightly over-consolidated marine clay with a natural water content of 50-100 % and a liquid limit of 40-90 %. The unit weight is about 16 kN/m^3 and the sensitivity is 10-30.

The prescribed undrained shear strength (characteristic value) varied somewhat within the site, but it was in the order of 15-17 kPa in the upper part of the clay layer, while further down increasing by 1.3-1.5 kPa/m with depth. The prescribed preconsolidation pressure (characteristic value) was typically 4.5-5 times larger than the undrained shear strength.

The Contract Documents also included drawings showing the prescribed geotechnical measures that was required in order to fulfil the stability and/or settlement requirements after completion of the new junction. Most of the geotechnical measures consisted of lime cement columns (a total of about 150,000 linear meters), cf. Figure 4. Furthermore, two retaining walls, three sheet pile walls and two regions with embankment piling were prescribed in-depth, even though the contractor should perform the detailed design of these.

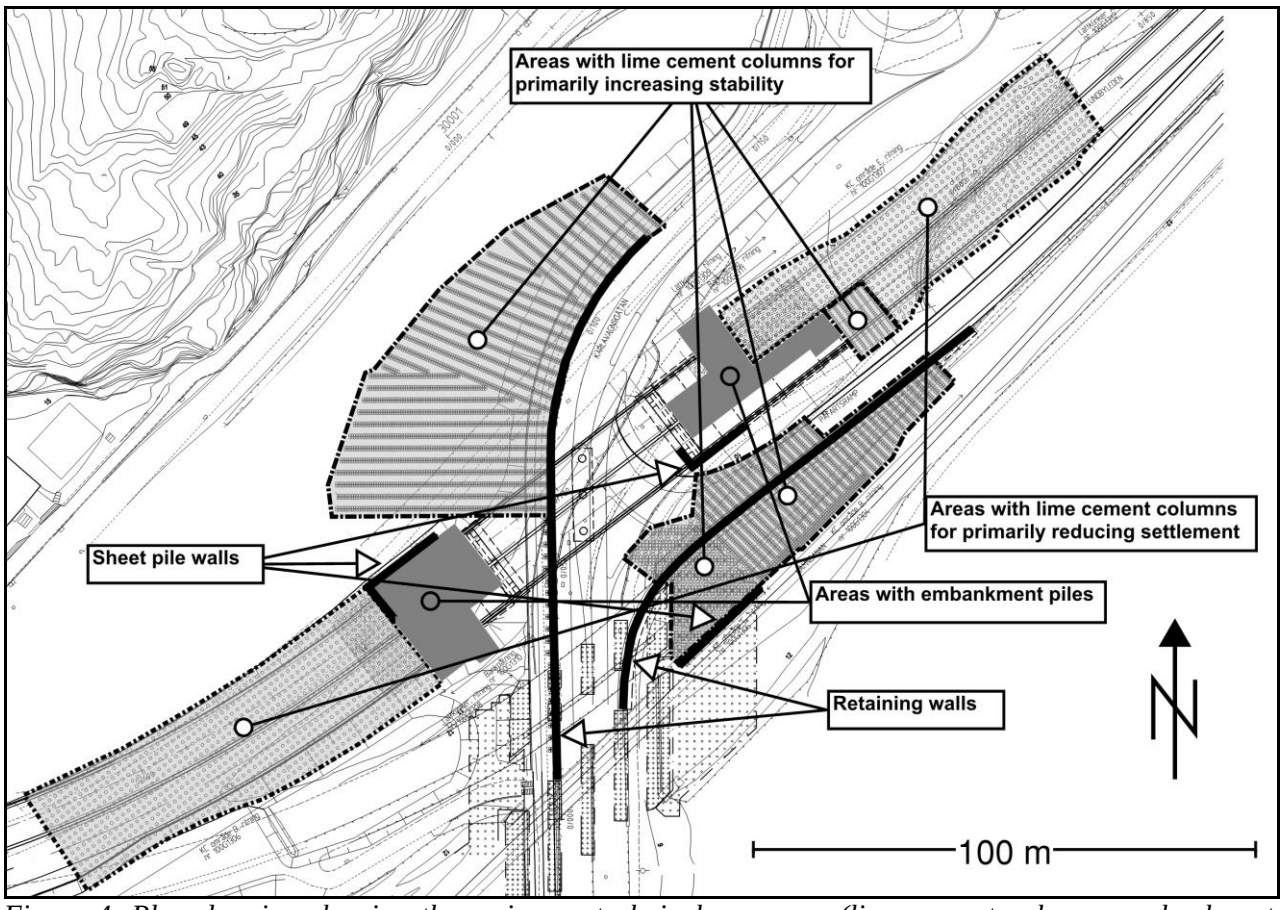


Figure 4. Plan drawing showing the major geotechnical measures (lime cement columns, embankment piles, retaining walls and sheet pile walls) that were required according to the Contract Documents.

3 THE GEOTECHNICAL PROPERTIES AND THE REQUIRED STABILISING MEASURES ACCORDING TO SKANSKA

The required geotechnical measures were prescribed in detail as the job was a construction-only contract. Therefore, in the tender phase the geotechnical engineers at Skanska only glanced through the Contract Documents, concluding that the prescribed geotechnical properties of the clay were within the typical range for "Gothenburg clay". Therefore, at this stage it was believed that only minor modifications (if any) of the prescribed geotechnical measures were possible.

Soon after the contract was awarded some initial stability assessments were made by the geotechnical engineers at Skanska. The focus was on the area next to the railway, since it was believed that the amount of lime cement columns might be reduced compared to what was stipulated in the Contract Documents. However, the results indicated that the stability of the permanent excavation next to the railway would be far from satisfactory even after the construction works were finished. Therefore, more detailed calculations were done, but the result was essentially the same. Skanska immediately informed the Client about this somewhat unexpected conclusion and a series of "emergency meeting" was initiated, since the construction works were imminent. During the first meetings it was successively revealed that the Client´s geotechnical consultant, among other things, had assumed that the strength properties of the clay were more favorable than prescribed in the Contract Documents. Skanska´s geotechnical engineers accepted some of the assumptions, provided that they were supported by the results in the Ground Investigation Report (GIR), but they strongly questioned some other assumptions. Eventually, the geotechnical engineers at Skanska decided to scrutinize the GIR in order to make an independent evaluation of the strength properties of the clay.

The GIR included conventional geotechnical investigations, such as field vane tests, CPT:s and fall-cone tests, but also more advanced tests, such as oedometer tests (CRS), direct shear tests and triaxial tests (both active and passive). The opinion of the geotechnical engineers at Skanska was (and still is) that the results of the more advanced tests are more reliable than the other tests. Furthermore, the geotechnical engineers at Skanska fully appreciate the close connection between the preconsolidation pressure and the undrained shear strength of clay. Therefore, by combining the site-specific results with a substantial in-house experience of the behavior of Gothenburg clay a new strength profile was suggested, cf. Figure 5.

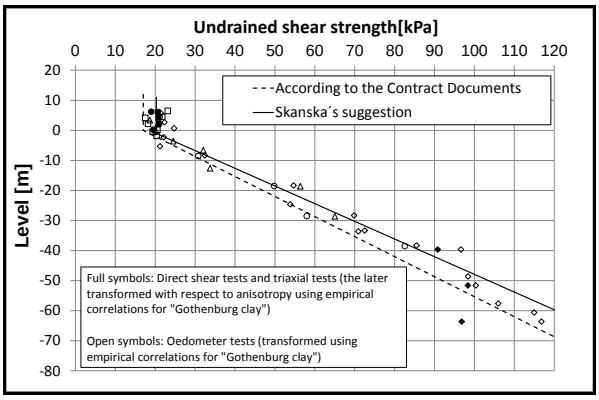


Figure 5. Strength profile of the clay according to the Contract Documents and according to Skanska.

Furthermore, Skanska´s geotechnical engineers concluded that the site specific results made it possible to account for the beneficial effect of stress induced strength anisotropy. During a couple of subsequent "emergency meetings" with the Client and its in-house geotechnical expert the Client accepted Skanska´s suggestions. Then, it was decided that Skanska should redesign all geotechnical measures within the project with focus on both the construction phase and the subsequent operational phase.

Since the construction works were already in full swing the redesign had to be performed in very close cooperation with the construction units at Skanska (especially the production manager) and the Client´s representatives (especially its in-house

geotechnical expert), in order to not delay the construction works.
The geotechnical engineers at Skanska also realized that instead of removing some of the existing timber piles close to the railway (as stipulated in the Contract Documents since the piles were in geometrical conflict with the prescribed lime cement columns) their stabilizing effect could be accounted for. In order to convince the Client on how to quantify this stabilizing effect some 3D finite element analyses were performed, cf. Figure 6, in parallel with more conventional stability analyses. A combination of such analyses and a careful documentation of the actual location of the existing piles made it possible to design a tailor-made installation pattern, in which grids of lime cement columns circumscribed each individual pile.

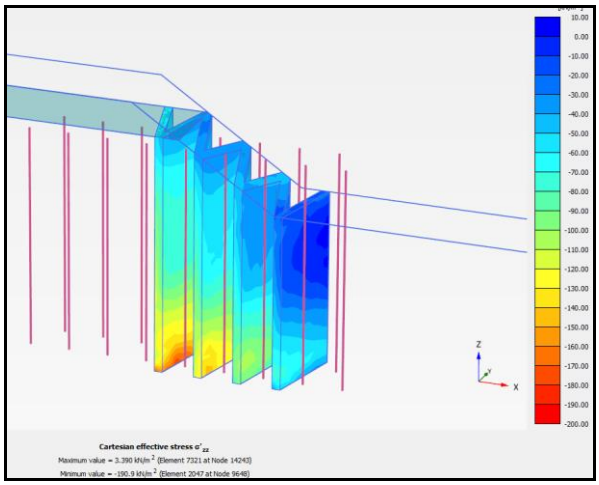


Figure 6. 3D finite element analysis for studying the stabilising effect of timber piles circumscribed by grids of lime cement columns.

Furthermore, together with Skanska´s production manager a working procedure of sequential excavation and refilling was developed.
By accounting for all these beneficial effects the following major changes were achieved due to the redesign:

- The amount of lime cement columns were reduced from about 150,000 to about 50,000 linear meters.
- One of the retaining walls (with a crest length of about 120 m) was not needed.
- No sheet pile walls were needed.
- The amount of embankment piles and pile caps were reduced from about 170 to 120.
- A cost saving of about 10 % of the contract sum, which was about 87 MSEK.
- The the amount of CO2-equivalents was reduced by several thousand tons.

The redesign also contributed to the construction works being finished about 6 months earlier than originally planned.

4 SOME EXPERIENCE FROM THE CONSTRUCTION PHASE

A comprehensive monitoring program was implemented in order to assure that the construction works did not jeopardize the stability conditions or the functionality of the surrounding railways and roads. Especially the displacements of the railway were thoroughly monitored using both automatized inclinometers, installed to a depth of about 20 m as close to the tracks as possible, and manual measurements of the railway tracks. During the installation of the lime cement columns just north of the railway the tracks were expected to displace southwards and upwards, potentially making the tracks untrafficable. The expected final displacement of the tracks and in the underlying ground were assessed in the early stage of the lime cement column installation using a method originally suggested by Sagaseta (1986) and successfully applied for pile installation in Gothenburg clay (Edstam & Kullingsjö, 2010). The assessed displacement of the tracks were larger than considered acceptable according to the Contract Documents, even though the amount of lime cement columns in the area next to the railway had been considerably reduced compared to the original requirements, cf. Figure 7. Therefore, during the installation of the columns a very close

and intense communication between Skanska, the Client and the staff supervising and judging the functionality of the railway was required.

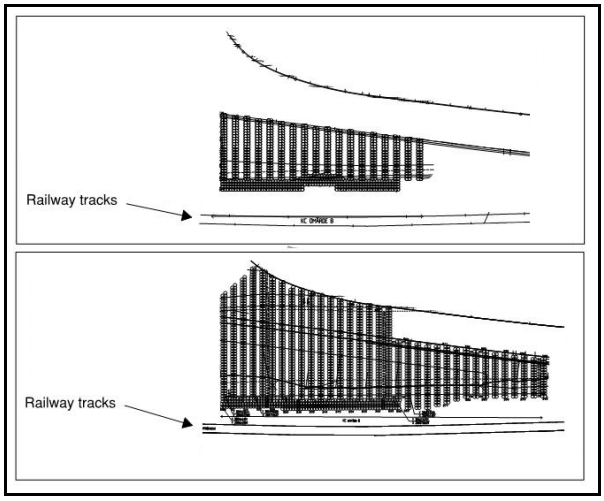


Figure 7. Lime cement columns next to the railway. Lower figure: According to the Contract Documents; Upper figure: After Skanska´s redesign.

As may be seen in Figures 8 and 9 there is a rather good agreement between the assessed and measured horizontal displacements, both at the ground surface (the tracks) and with depth. Even though the measured displacement exceeded the allowable levels the train traffic could proceed without any interruption. Only minor adjustments of the tracks were required and this could be done during time slots where no trains were passing the construction site.

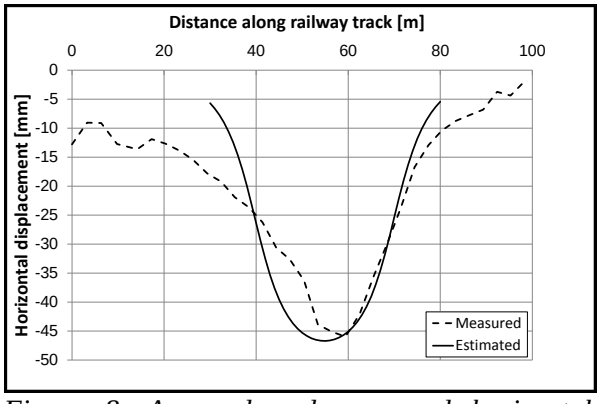


Figure 8. Assessed and measured horizontal displacement of the railway tracks.

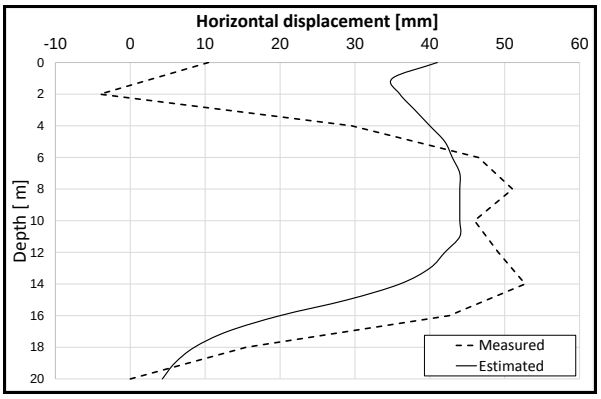


Figure 9. Assessed and measured horizontal displacement in the ground next to the railway.

The lime cement columns were partly installed just behind the crest of an existing slope with a public road next to the toe of the slope. Therefore, Skanska recommended that the stipulated monitoring program should be extended in order to keep track of the displacement of that public road. The displacements were rather modest in the early stage of the column installation. On the contrary, in the later stage the displacement increased very rapidly resulting in considerable concern about the stability conditions. Therefore, it was decided to reduce the installation rate and extend the monitoring program. During the subsequent installation works it was noted that as soon as the installation was interrupted no further ground displacements developed, indicating that the clay was very ductile. Eventually, the road was displaced up to 0,2 m horizontally and 0,45 m vertically, cf. Figure 10.
During the subsequent excavations the rail way tracks were displaced in the opposite direction to that occurring during the column installation. In the final stage, the tracks had returned to almost the same position as before the construction works commenced.

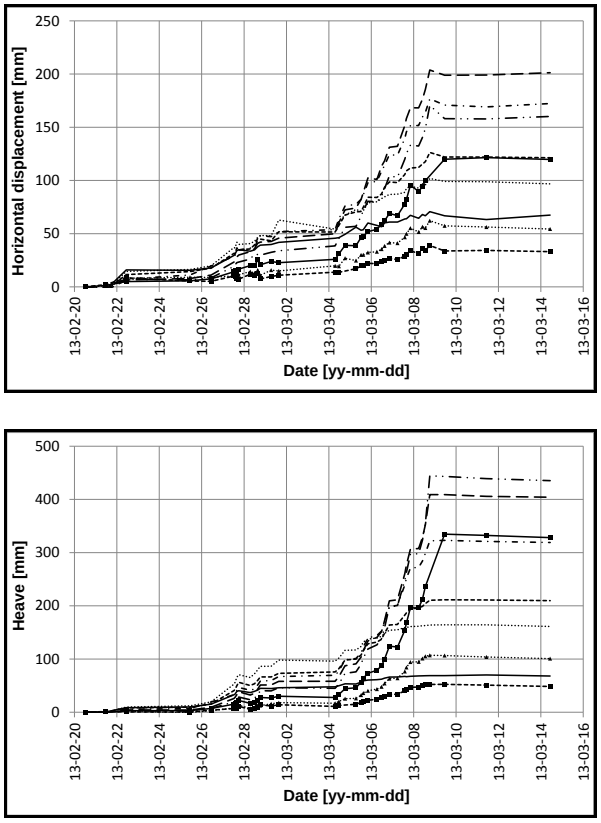


Figure 10. Measured horizontal and vertical displacement at various locations along a road located at the toe of an existing slope.

5 CONCLUSIONS

The construction works for the traffic junction "Lindholmsmotet" in Gothenburg included several geotechnical challenges. In the beginning of the construction phase it seemed as though the stabilising measures prescribed in the Contract Documents were considerably *under*estimated. However, when the geotechnical engineers at Skanska scrutinized the GIR, including fully appreciating the results of the advanced geotechnical laboratory tests, it was realised that the stabilising measures were *over*estimated.
The subsequent redesign by the geotechnical engineers at Skanska resulted in considerable savings in terms of:

- Economy (a cost saving of about 10 % of the contract sum)
- Climate impact (reducing the amount of CO2-equivalents by several thousand tons)
- Construction time (the construction works being finished about 6 months earlier than originally planned)

It is believed that the redesign could only be accomplished, especially in such a short time, due to a very close and fruitful cooperation within Skanska (its skilled and dedicated in-house geotechnical department and its equally skilled and dedicated in-house production managers) and with the Client´s in-house geotechnical expert.

During the construction works a comprehensive monitoring program was implemented, with focus on the adjacent rail way. During installation of the lime cement columns the measured and assessed displacements of the railway track were in rather good agreed agreement (in the order of 4-5 cm). In the final stage, after the construction works were finished, the rail way tracks had returned to almost the same position as before the construction works commenced.

6 REFERENCES

Edstam, T. Kullingsjö, A. (2010). Ground displacements due to pile driving in Gothenburg clay. Proc. 7th European Conference on Numerical Methods in Geotechnical Engineering, Trondheim, Norway

Sagaseta, C. (1987). Analysis of undrained soil deformation due to ground loss. Geotechnique, Vol. 37 No. 3: 301-320.

Frost fracturing of riprap armour stones in Sporðalda Dam, Iceland.

B. J. Björnsson,
Studull Consulting, Iceland, bjb@studull.is

L. Skúlason.
Hnit Engineering, Iceland, leifur@hnit.is

J. S. Úlfarsson
Landsvirkjun Power, Iceland, *Jon.Smari.Ulfarsson@lvp.is*

ABSTRACT
The Sporöldu Dam was constructed in 2011-2013. It is a part of the Búðarháls Hydroelectric Project (95 MW) in Southern Iceland. It is a conventional earth and rockfill dam with a central moraine core. Following the first subzero temperatures in the autumn of 2012 extensive fracturing of recently placed riprap armour stones and coarse grain fill material was noted. Riprap placed during the summer was largely unaffected. Site and laboratory investigation were conducted showing that it is hard to test armour stones for this type of fracturing.

Key words: Earth and rockfill dam, frost fracturing, riprap armour stone.

1 INDRODUCTION

The Sporðalda Dam is located in South Iceland and is a part of the Búðarháls Hydroelectric Project (95 MW) in the Þjórsá-Tungnaá Basin. Figure 1 shows the location of the Búðarháls Project and the Sporðalda Dam. The Dam is 1500 m long conventional earth- and rockfill dam with a maximum height of 26 m and a total volume of 630.000 m^3. Construction took place in 2011-2013. All construction materials were found in the vicinity of the dam. The core is a morainic material borrowed downstream of the Dam. Other construction materials were quarried or borrowed within the reservoir area and are inundated by the reservoir. The Dam is divided up into three sections; the Northwest Dam, the Southeast Dam and a concrete spillway weir. The reservoir formed by the Dam is the intake lake for the Búðarháls Power Station. The lake is 7 km^2 at normal lake levels. The lake is not intended for water storage and variations in the lake level are due to daily fluctuations in the operations of the up- and downstream power plants. The lake level is therefore almost constant. .

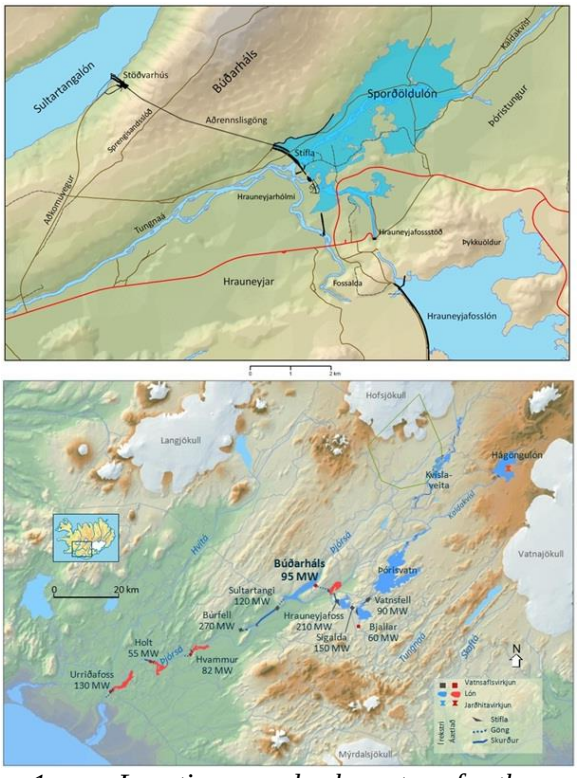


Figure 1. Location and layout of the Búðarháls Hydroelectric Project and the Sporðalda Dam

Figure 2 shows plan view and a longitudinal section of the Dam

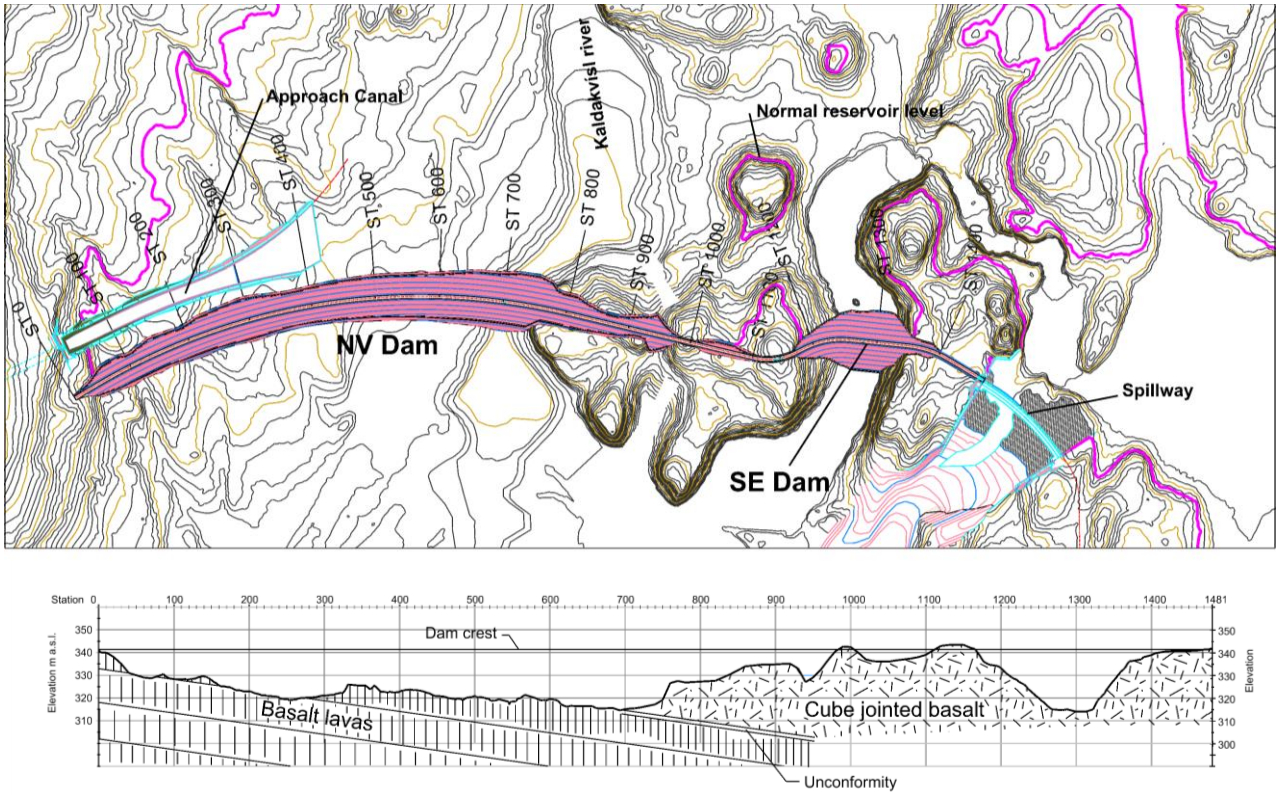


Figure 2. Plan and longitudinal section of the Sporðalda dam

2 GEOLOGY OF THE DAMSITE

The geology of the damsite is simple. Figure 2 shows geology. The northern part the dam foundation is made of gently dipping basaltic lavaflows of quaternary age. The jointing in the basalts lava flows is characterized by unusually large columns. The rock type is unaltered and fresh olivine tholeiite. Figure 3 shows excavation in the Approach Canal. The excavator is loading stones for riprap from the excavation. The columnar jointing is visible in canal wall.

In the southern part of the dam the foundation is made up of basaltic cube jointed formation which lies horizontally on the older basaltic lavaflows. Between these two formations there is an unconformity which is clearly visible at station approximately 750. The structure of the cube jointed basalt is different to that of the lavaflows. The jointing forms irregular cubes that are typically 10 to 30 cm in diameter. The rock is relatively fresh and has a rather porous texture.



Figure 3. Excavation of basaltic lava in the Approach Canal

Figure 4 shows a quarry in the cube jointed basalt and the type of fill material produced from the cube jointed basalt.



Figure 4. Cube jointed basalt quarry

Because of this the Contractor demanded extra payment for quarrying shell material for the NW dam from the cube jointed basalt formation or processing shell material from tunnel spoil. This would have increased the cost of the dam considerably. It was however decided to use the relatively fine grained river gravel for shell material in the NW Dam.

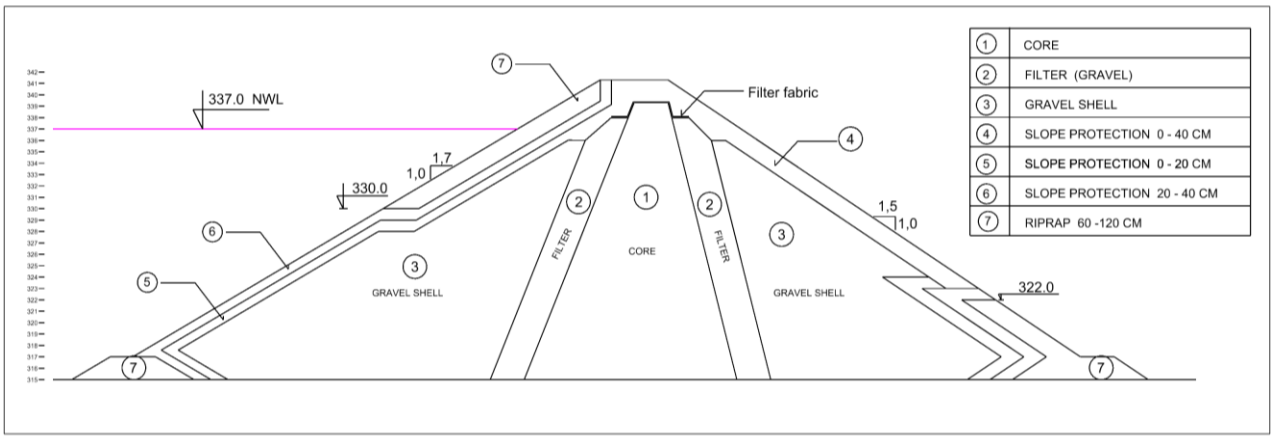


Figure 5. Dam cross section.

3 DAM CROSS SECTION AND CONSTRUCTION MATERIALS

Figure 5 is a cross section of the NW Dam. For core material glacial moraine was used. Filters for the core are sandy gravels or sand taken from an upstream borrow area.

According to the Contract Documents shell materials were to be found as alluvial sandy gravels along the Kaldakvísl river upstream of the Dam and excavated material from the Spillway, the Approach Canal and Headrace Tunnel excavations.

The Contractor chose to use the alluvial sandy gravel for shell material in the NW Dam. The sandy gravel found in the designated borrow area at the Kaldakvísl river was however finer grained than the specified shell material.

Shell materials in the NW Dam are therefore essentially of the same material as the filters adjacent to the core. This placed extra demands on the slope protection material which also acts as a filter between the rip rap and the shell material. Testing a single layer filter that fulfilled the filter criteria, it was found that such filter could not be placed without the risk of segregation.

A solution was found by dividing the filter the other 20-40 cm. This lead to the extra benefit of providing coarser material for the upstream slope protection below and behind the riprap. The 0-20 and 20-40 cm filters were produced from quarries in the cube jointed basalt formation with some extra cost. The SE dam shell material was however produced from the cube jointed basalt.

Most of the riprap material was obtained from the basalt lava flows in the Approach Canal excavation. The rest was obtained from tunnel spoil and a separate quarry in basalt lava formation.

4 FROST FRACTURING OF RIP RAP MATERIAL

Once the filter and shell material problems had been sorted out during the summer of 2012, the dam construction proceeded as foreseen until fall 2012. Considerations of possible floods required that the dam had to filled up to an elevation of 333 m a.s.l. in 2012. On October 22nd 2012 following a weekend break, during which the temperature in the area reached -5 °C for the first time that autumn, it was noted that considerable portion the riprap stones placed during the previous two weeks was fractured. Figure 6 shows an example of this. During that particular weekend the stones in the riprap may have experienced one or two frost/thaw cycles.



Figure 6. Fractured riprap stone.

Examination of the rip rap already placed in the Dam in late October 2012 showed that the riprap that had been placed in the preceding one or two weeks was extensively fractured. This was the case for station 100-350 along the dam axes in the NW dam. Riprap placed during the summer and early autumn at station 400–700 was largely intact. The percentage of fractured stones was determined at six locations. Figure 7 shows the result of this investigation. At each location 60-80 stones were examined. The riprap material in all cases came from the basaltic lava flow formation and appeared to be similar in every respect. The only difference was that the ambient temperature had fallen below 0°C shortly after the rip rap at station 100-350 was placed.

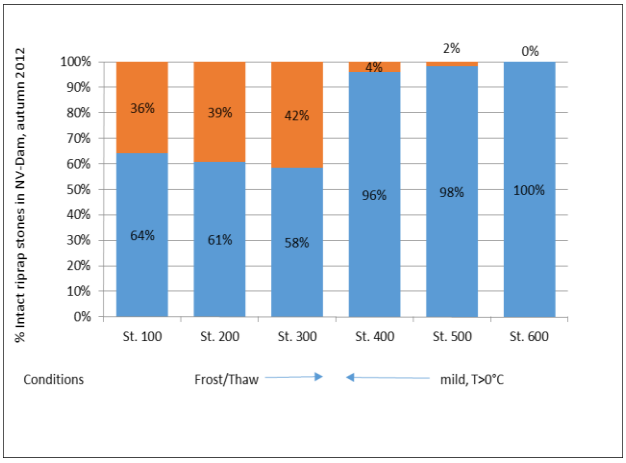


Figure 7. Percentage of intact riprap stones in the NW Dam in autumn 2012

5 SITE TESTING OF RIP RAP STONES

A site test of riprap stones was conducted in November and December 2012. The aim was to observe the progress of fracturing and find if the degree of fracturing was similar in riprap stones from different sources in the basaltic lava formation.

Table 1 shows the quarries, number of stones from each source, date of blasting, date of first exposure to frost, date of transport to test site and first examination of stones. The test site was selected on top of the dam fill so that snow would not cover the stones. Figures 8 to 11 show the test site and stones in the test.

The riprap stones in the test were examined three or four times in the period from November to December 2012 and again in summer 2013. Figure 12 shows the results. It appeared that the stones started cracking following first exposure to mild frost (-5°C). Most of the fracturing took place within the first 10 days. The number of freeze/thaw cycles does not appear to have a significant effect on the progress of fracturing. The degree of fracturing seemed to be independent of stone size.

Table 1. Site test of riprap stones.

Quarry/source	Date of blast	No. of stones	First frost exposure	Transport to test site	First examination
Headrace Tunnel	6.11	28	6.11	6.11	7.11
Approach Canal	31.10	44	31.10	7.11	7.11
New Quarry G1	7.11	25	7.11	7.11	8.11
Approach Canal	8.11	25	8.11	8.11	8.11
Approach Canal	21.11	32	21.11	21.11	22.11



Figure 8. Site test of riprap stones



Figure 9. Fractured riprap stone in the site test

The fracture surfaces are in many cases completely fresh and don't appear to follow pre-existing weaknesses in the rock.



Figure 10. Another fractured riprap stone in the site test



Figure 11. Fractured riprap stone in site test

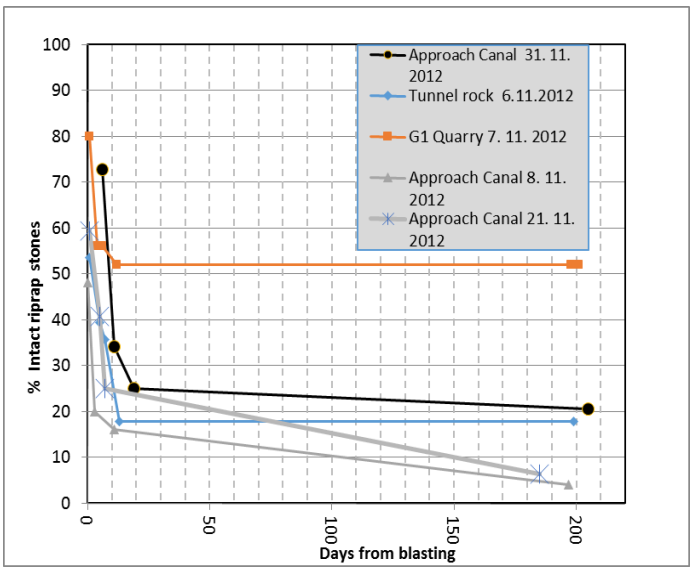


Figure 12. Results of site investigation of riprap stones.

Further surveying of the test stones could have revealed if the fracturing all takes all place within the first month or not. However, the test stones became covered with ice and snow and could not be examined further until next spring. The rock from quarry G-1 appears to have a higher resistance to cracking than rock from other sources in the area. The rock in quarry G1 may not have been saturated at the time of blasting while rock blasted from the Approach Canal and from the Headrace tunnel were probably saturated.

6 RE-EXAMINATION OF DAM RIPRAP.

In June of 2013 when snow had disappeared from the riprap already placed in the Dam the counting of fractured riprap stones was repeated in the same locations as in November 2012, counting essentially the same stones as before. The results are shown in Figure 13.

Comparing the results from 2012 and 2013 reveals that the proportion of fractured rip rap stones that were placed during the summer of 2012 increased to 10 % at station 600 and 500.

For rip rap stones placed at stations 100-300 the fracturing increased considerably. Only 40 % were unfractured in June 2013. The 20 % increase of fractured rip rap stones at stations 100 -300 shows that the initial fracturing was not over by the end of October 2012. At stations 500 to 600 the number of intact stones was about 90 % which is similar to observations from other dams in Iceland. The results at station 400 do not fit into either of the above classes and is unexplained.

7 LABORATORY TESTING OF ARMOUR STONES

To gain a further insight into the behaviour of the riprap stones a laboratory testing program was conducted in a frost-thaw chamber in Reykjavík. Riprap stones cannot be used directly because of size restrictions and the difficulties in handling such large stones. So stones 5-25 kg were used in the experiment, originating from the Headrace Tunnel and the Approach Canal.

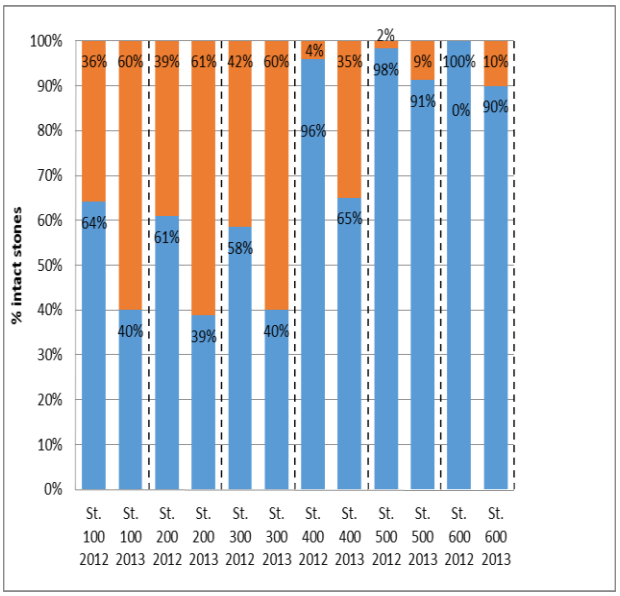


Figure 13. Proportion of fractured rip rap stones along the dam axes in 2012 and 2013.

Most of the stones were submerged in water during the test but a few were tested dry. Air temperature varied from +40°C to -40°C and water temperature varied between +10°C to -10°C. No stones were fractured after 8 cycles. After 25 cycles one stone was found fractured or 4 %. No flacking or weight loss was observed.

8 G_S AND ABSORPTION OF THE RIP RAP STONES.

In table 2 testing of the specific gravity and absorption of the rip rap stones is shown.

Table 2 Specific gravity and absorption of riprap stones from the Búðarháls Project.

Sample	Gs (Mg/m^3)		Absorption
	Apparent	SSD	%
1	2,898	2,810	1,7
2	2,818	2,745	1,5
Notes:	Apparent: Oven dry/(Oven dry in water)		
	SSD: Saturated surface dry/(Saturated, surface dry in water)		
	Absorption: (Saturated surface dry- oven dry)/Oven dry		

9 GUIDELINES FOR SELECTING ARMOUR STONES FOR RIP RAP.

No testing of material for riprap was conducted during the design phase of the dam. This is in accordance with the fact that testing of rip rap materials for dam construction is not usually done in Iceland. By contrast it is rule in the selection of armour stones quarries for breakwaters in the country. An Icelandic classification scheme developed for selecting armour stones for breakwaters (Smarason O.B. et al. 2000) indicates that the riprap rock type in the case of the Sporðalda Dam (olivine tholeiite) is qualified as "good", the specific gravity is also considered "good". The water absorption would be classified as "fair".

Standards and guidelines such as ASTM D4992, Practice for Evaluation of Rock to be used for Erosion Control and Designation USBR 6025-09 Procedure for Sampling and Quality Evaluation Testing of Rock for Riprap Slope Protection give some general guidance as to selection of materials. These documents recommend a petrological examination, frost/thaw, specific gravity and absorption testing, but do not indicate specific requirements.

In CIRIA Rock Manual (CIRIA, CUR, CETMEF 2007) it is assumed that frost resistance in generally sufficient if the water absorption of the rock is < 0,5 %. The quality of armour stones is still considered good if water absorption is 0,5-2,0. Quality is considered excellent if Gs>2,7.

Bulletin 91 from ICOLD (ICOLD 1993) lists similar tests as the above but appears to place more importance on petrological examination of rock. It is also implied that stones for riprap should fulfil the same requirements as aggregates for concrete.

Materials for Embankment Dams (United States Society on Dams 2011) states similar requirements and includes a table over properties such as soundness % loss in magnesium sulphate. The same table shows maximum absorption should be < 2-6 according to the Department of Transportation but < 1 according to the Corps of Engineers.

Norwegian guidelines (NVE 2012) state that certain rocktypes are suitable for slope protection while others are not.

The authors conclusion is that it is unlikely that the frost fracturing of the riprap rock at the Sporðalda Dam would have been strongly indicated by usual laboratory testing.

10 EXPERIENCE FROM OTHER QUARRIES IN ICELAND

Fracturing of newly blasted basaltic rock exposed to freezing temperatures have been observed before in four armour stones quarries in Iceland (Sigurðarson 2015). In all cases the fracturing disappeared when the rock was blasted in temperatures above 0°C. The armour stones from these quarries have performed well after years in a harsh environment, exposed to saltwater and a large number of freeze/thaw fluctuations each year. In one of these quarries, located in Hafnarfjörður Iceland, extensive fracturing took place during quarry operation in sub-zero temperature during construction of a new breakwater in 1999-2001. In this quarry the rock was fresh basaltic rock with large columnar jointing like the rock at the Sporðalda Dam. The armour stones from the same quarry were used for a large breakwater constructed in 1969-1970. Inspection of the rock in that breakwater showed that the armour stones were in excellent condition and fracturing of the stones was minimal.

11 CUBE JOINTED BASALT FILL

As explained earlier the slope protection materials (20-40 cm) and the coarser filter (0-20 cm) were obtained from the cube jointed Sporðalda basalt formation. On that dreadful autumn day in 2012 when the fractured riprap was discovered it was also found that the slope protection material was extensively fractured.

Figures 14 and 15 show this. This was serious not only for the upstream slope protection but also because slope protection material is underlying the riprap wave protection and filter criteria had to be fulfilled. Cube jointed basalt has not commonly been used for damfill materials in Iceland. Parts of many quarries in basaltic material contain some cube jointed basalt. Fracturing due to frost has not been noticed as far as the authors know. Cube jointed basalt with smaller cubes than found at the Sporðalda dam has been used in bearing courses for roads with good results. Therefore, extensive frost fracturing of this material was unexpected.



Figure 14. Frost fractured slope protectionmaterials in autumn 2012.



Figure 15. Frost fractured slope protection materials in autumn 2012.

Figure 16 shows a comparison between fractured and unfractured slope protection material (20-40 cm) from cube jointed basalt. The d_{50} (average grainsize) of the unfractured samples taken during the summer is reduced from approximately 250 mm to 150 mm in a sample taken from the dam in late November. The fractured material still fits the originally specified gradation for slope protection.

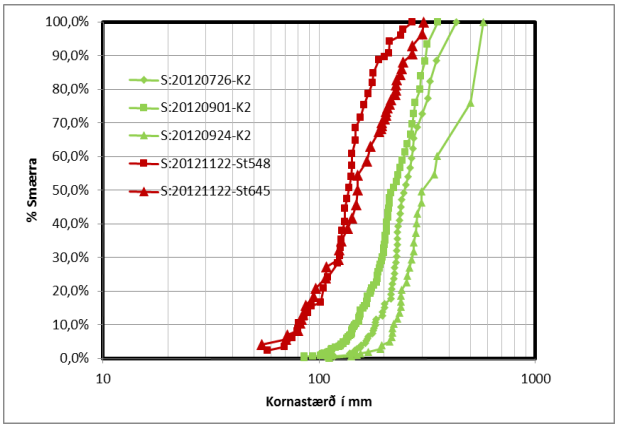


Figure 16. Grain size of frost fractured and unfractured fill from cube jointed basalt. K2:Unfractured fill from K2 quarry, St548 and St645, frost fracutured material from dam.

Figure 17 shows a comparison between the grain size of the fractured slope protection material and measurement of riprap stone sizes from 2012. As can be deduced from Figure 16 classical filter criteria for the rip rap stones is just about fulfilled between the riprap and the slope protection

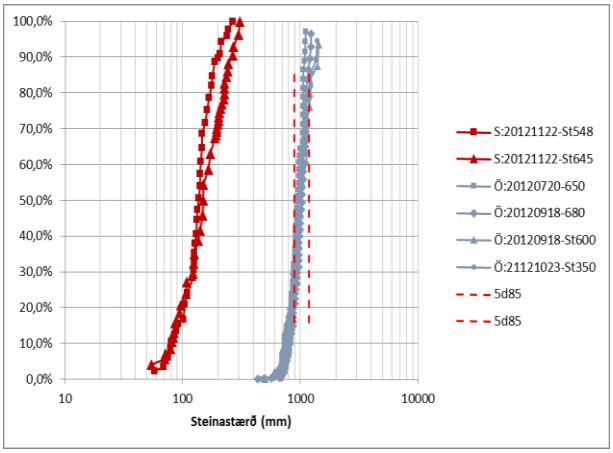


Figure 17. Comparison between the grain size of frost fractured slope protection material and measurement of riprap stone sizes in 2012.

12 TESTING OF THE CUBE JOINTED BASALT FILL

A similar test program as for the riprap was conducted for the cube jointed basalt fill. A site test was made in the source quarry. This revealed that all grains larger than 50 mm fractured due to frost. In one of those field tests the material was kept inside to dry for 3 weeks and then exposed to frost. This had little if any effects on the frost resistance.

A laboratory program using a frost-thaw chamber was conducted both on material directly from the quarry and also on material that had been dried for three weeks in temperatures > 0°C. Table 3 shows the results.

Table 3 Freeze/thaw chamber testing of cube jointed basalt stones.

Preparation of samples	**Test condition**	**Number of stones in test**	**Fractured after 25 freeze/thaw cycles**	
			No.	%
Sample dried for one month before testing	Tested dry	5	4	80
	Tested submerged	12	6	50
Sample tested two days after blasting	Tested dry	4	4	100
	Tested submerged	26	15	58

No flaking or loss of weight was observed. The absorption and specific gravity of samples of the cube jointed basalt were also tested. Table 4 shows the results.

Table 4. Specific gravity and absorption of cube jointed lava.

Sample	**Gs (Mg/m^3)**		**Absorption**
	Apparent	SSD	%
1	2,775	2,726	1,0
2	2,637	2,567	1,7
3	2,590	2,546	1,1
Notes:	Apparent: Oven dry/(Oven dry in water)		
	SSD: Saturated surface dry/(Saturated surface dry in water)		
	Absorption: (Saturated surface dry-oven dry)/Oven dry		

13 REMEDIAL MEASURES.

Riprap was to be placed on the dam from elevation 330 m a.s.l. to the top of the Dam. For flood protection it was necessary to construct the Dam up to elevation 333 m a.s.l. before winter break in 2012. The Dam was finished up to elevation 333 m a.s.l. in the beginning of December 2012 using mainly rock from the G-1 quarry knowing that some of the riprap stones were bound to fracture after placement in the Dam. Next spring the fractured riprap stones were removed but only from the top the rip rap. Replacing of individual stones further down on the upstream slope was not considered feasible, since this would have involved the complete removal of the rip rap from station 0 to station approximately 400. A factor affecting this decision were that the slope protection was well built with tight interlocking between armour stones, filter criteria between the riprap and the underlying slope protection was most likely fulfilled and it was foreseen that the reservoir water level would extremely seldom be lowered below elevation 333 m a.s.l.

Also in 2013 the Contractor was requested to finish blasting of armour stones before the end of September before temperatures dropped to below freezing and stockpile riprap stones for three weeks before placing in the Dam. This however did not quite work out and blasting of riprap stones continued into the winter period. The riprap stones were generally stockpiled for one or two weeks. As a result, some broken riprap stones are to be found in the wave protection.

The use of cube jointed basalt as a slope protection material (20-40 cm) on the upstream slope was discontinued. Instead material processed from tunnel spoil was used. This material had been exposed to several freeze/thaw cycles.

14 SUMMARY AND CONCLUSIONS

Extensive fracturing occurred when armour stones for riprap were exposed to freezing temperatures shortly after blasting. These stones were quarried from a fresh and unaltered columnar jointed basalt. Armour stones from the same quarries that were subjected to the same temperature fluctuations but had been blasted during summer showed only very limited fracturing. Testing for this type of frost fracturing in armour stones is difficult and does not show up clearly in conventional testing program for armour stone quality. To avoid this type of frost fracturing the rock has to be stockpiled for at least 20-30 day or ensure that the wave protection will not be exposed to freezing temperatures for the same length of time. Frost fracturing of cube jointed basalt has not been observed before. Fracturing of this type of rock shows up in freeze/thaw chamber testing. Where this type of rock is to be used as fill material subject to freeze/thaw conditions freeze/thaw testing is mandatory.

15 REFERENCES

ASTM D4992, Practice for Evaluation of Rock to be used for Erosion Control

CIRIA, CUR, CETMEF (2007) The Rock Manual. The use of rock in hydraulic engineering (2nd edition) C683. CIRIA, London

ICOLD (1993) Embankment Dams Upstream Slope Protection, Bulletin 91, CIGB International Commission on Large dams, Paris

NVE Norges vassdrags- og energidirektorat (2012) Vejleder for fyllingsdammer

Sigurðarson, S., (2015). IceBreak Consulting Engineers, Iceland. Personal communication.

Smarason O.B., Sigurdarson S. and Viggoson G., Quarry yield prediction as a tool in breakwater design. Keynote lectures NGM-2000 and 4th GIGS Helsinki 2000. Finnish Geotechnical Society.

United States Society on Dams (2011). Materials for Embankment Dams. Prepared by the USSD Committee on Materials for Embankment Dams.

A geostatistical analysis of variations of permeability within a compacted dam core

HÉBERT, Étienne
Université Laval, Canada, etienne.hebert.3@ulaval.ca

CÔTÉ, Jean
Université Laval, Canada

SMITH, Marc
Hydro-Québec, Canada

ABSTRACT
The spatial variability of the geotechnical properties of compacted till core embankment dams was studied using geostatistical analysis in the past and showed promising results. The main goal of this study is to improve the geostatistical method used to study such parameters. A quasi 3D approach using a 2D interpolation grid representing the entire core and focusing on the assessment of the spatial distribution of permeability within the core of a dam located in north-eastern Québec is presented in this paper. Geostatistics were used as a useful means to enhance the value of construction control data, from which permeabilities were calculated using empirical relationships based on the clay fraction and the fabric of the compacted tills. The study shows that the core's structure is not only stratified according to elevation, but can also vary significantly within a single lift and that this variability is strongly linked to the fabric of the compacted till. The geostatistical method used in this paper shows great potential and versatility as it can be used to model geotechnical properties of an embankment dam even before its impoundment.

Keywords: Embankment dam, Geostatistics, Kriging, Permeability, Construction control data

1 GUIDELINES

The hydraulic barrier performance of compacted till cores of embankment dams is highly dependent on compaction conditions during construction, which alongside basic geotechnical properties may significantly vary spatially. The recent development of new tools and a better understanding of the variability of soil properties enable the integration of such variability in design and behaviour analysis using geostatistics as a good analysis tool.

As geotechnical modelling and analysis projects often proves very costly, a very promising path is to develop new methods to extract a maximum of information from already existing data such as construction control data.

Past studies have shown that geostatistics can be used as a very interesting tool to assess and study the spatial variability of the geotechnical properties of dam materials (Smith and Konrad, 2011; Smith, 2002; Soulié et al. 1983), such as permeability, using georeferenced construction control data. These studies led to advances in the understanding of various issues related to the stratified nature of dams' structures and broadened perspectives for geostatistical analyses in large embankment design.

This study focuses on the assessment of the permeability, based on the analysis of the construction control data of an embankment dam. Permeabilities were estimated based on the aggregated or homogeneous fabric of the compacted till to reflect the significant vulnerability of dams to changes in the compaction conditions during construction. Geostatistics and kriging were used to study

the spatial variability and to detect higher permeability areas that could prove potentially problematic. Kriging is a linear estimation method which, as opposed to other methods like weighted averages and classical regression, takes into account the spatial dependency of the studied parameters. The method was first developed for the estimation of mineral potential in mining engineering (Krige, 1951) and later formalized as a more general statistical method (Matheron, 1963), it is now widely used in various fields as a means to analyze spatially correlated data.

The geostatistical approach presented in this paper is based on the spatial coordinates of the sampling points on a 2D plane representing the entire 3D structure of the dam's core. The whole project will study the impact of performing geostatistical analysis on the estimated values of permeabilities for the various sampling points compared to the parameters that govern permeability. This paper will deal with the analysis of geostatistical results performed on the estimated permeabilities at the various sampling points.

2 TEST SITE

The structure analysed in this project is a compacted till core dam from a hydro-electrical complex in north-eastern Québec. The complete structure of the dam has a maximum height of 171 m, a crest elevation of 410 m, a crest length of 378 m, a crest width of 10 m and a total volume of 6 300 000 m^3. The core itself has a maximum elevation of 169.2 m, a crest elevation of 408.2 m, a crest length of 378 m, a crest width of 4 m and a volume of approximately 905 000 m^3. The structure was built by laying 0.5 m thick lifts following a regular pattern from the right bank to the left bank and back. The important number of construction surveillance data and its regular construction sequence makes this dam the perfect candidate for geostatistical analysis. The layout of the dam's structure is showed on Fig. 1, where the core is highlighted in white color over the grey shaded 3D graph.

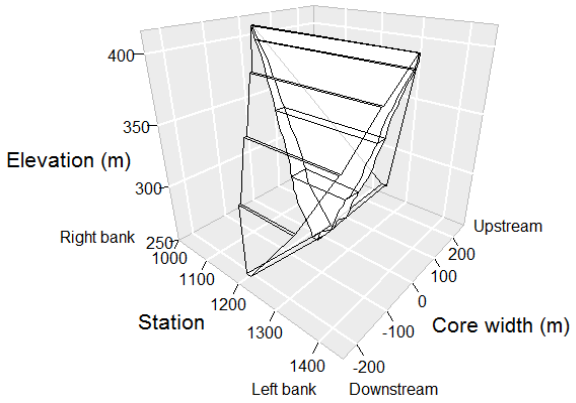


Figure 1 - Geometry and dimensions of the dam

The tills used for the construction of the core come from five borrow pits (DE-9, DE-9A, DE-9B, DE-9Est and DE-12) located around the construction site and presented variable geotechnical properties. Since the focus of this study is to assess the permeability of the core and because this parameter is strongly affected by the distribution of fine content, these properties are presented in Tab. 1 for each borrow pit.

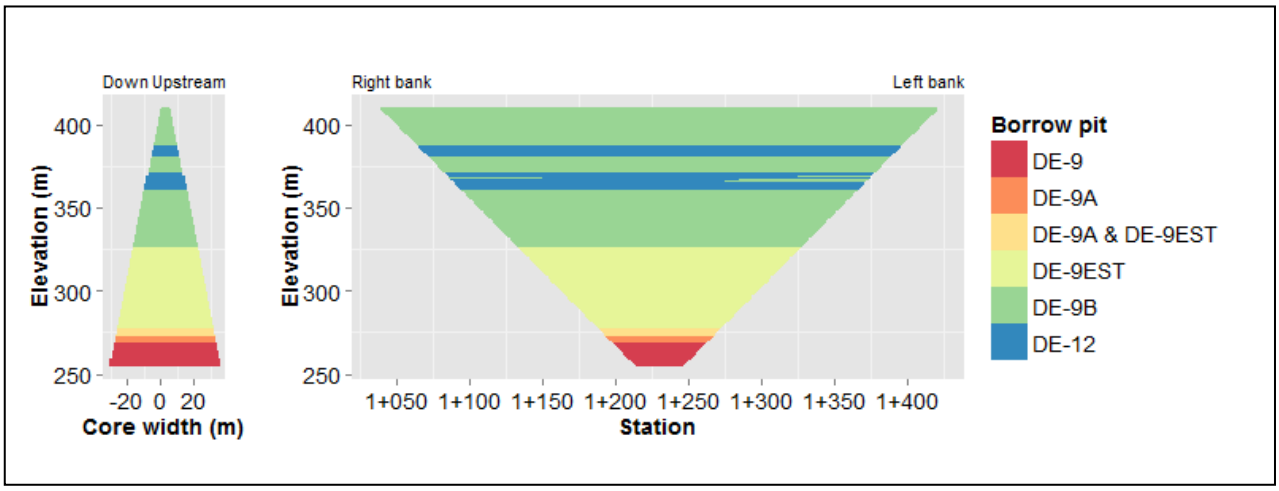


Figure 2 - Core materials distribution

The location of the tills within the core's structure is given in Fig. 2.

Most of the core was built using tills from borrow pit 9, 9A, 9B and 9Est. Those borrow pits are in fact different faces of a same excavation site and show similar grain size distribution. The fines fraction (% passing < 80 µm) varies from 24% to 53% and the clay fraction (% passing < 2 µm) from 1.8% to 8.1%. Tills from borrow pit 12 were used only for a short time and its use was limited to a small part of the core showed in blue around elevations 325 and 360 m in Fig. 2. This borrow pit was exploited because it was closer to the construction site and presented an economic benefit. The use of this till was stoped because of its weak geo-mechanical properties. For example, it had significantly higher fines and clay fractions, 30% to 69% and 2.7% to 11.1% respectively, than the other borrow pits and would lead to weaker strain resistance while resulting in a much lower permeability.

Table 1 – Till fine content distribution

Borrow pit	Fines fraction, % < 80 µm			Clay fraction, % < 2 µm		
	min	max	av.	min	max	av.
DE-9	37	48	43	2.5	5.0	3.1
DE-9A	31	53	37	2.5	8.1	4.5
DE-9B	24	48	34	1.9	6.2	3.0
DE-9E	26	46	37	1.8	5.4	2.8
DE-12	30	69	54	2.7	11.1	7.1

3 GEOSTATISTICS

A simplified flowchart of the geostatistical approach used for this study is presented in Fig. 3 which is detailed in sections 3.1 to 3.4.

The geostatistics analysis computing was realized using the statistically oriented *R* programming language alongside the *gstat* package which includes many useful geostatistics related tools.

3.1 Exploratory statistics

The first step of any geostatistical process should concentrate on the analysis of the available data with simple statistics. This step gives important information about the nature of the data set distribution and about the feasibility of a geostatistical analysis on these data. For example, the study of a data set distribution can highlight the need for a data transformation. Extreme values have an important impact on the variogram and parameters such as permeability, which often shows highly skewed distributions, need to be transformed in a way that allow their use as part of a variographic analysis. In these cases, one of the most commonly used transformations is the logarithm ($\log_{10}$) transform, which transforms the data into a form closer to a gaussian distribution. The next steps of the analysis should be realized on the transformed data.

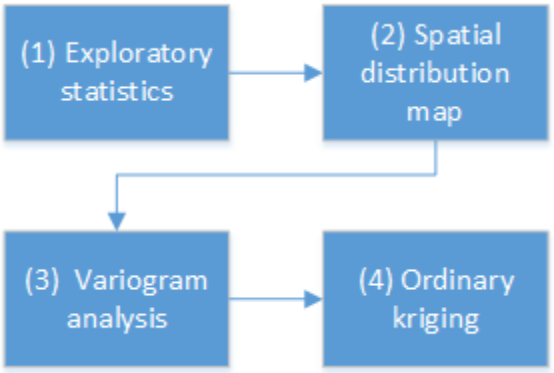


Figure 3 - Geostatistics flowchart

3.2 Spatial distribution map

The goal of this step is to produce a distribution map of the samples to appraise the quality of its spatial distribution and to establish if the available data respects the conditions for kriging. A good spatial distribution should contain enough data points to represent the analysed phenomenon but should also be evenly distributed across the studied area and devoid of data cluster of significant size.

3.3 Variogram analysis

A variogram is a function (Eq. 1) used to assess the spatial correlation of a set of spatial random variables relative to the separation distance between the data points (Cressie, 1993).

$$\gamma(h) = \frac{1}{2n(h)} \sum_{i=1}^{n} [V(x_i) - V(x_i + h)]^2 \quad (1)$$

where $\gamma(h)$ is the spatial variability estimator, V a random variable, h the separation distance between two sampling points x_i and x_i+h and $n(h)$ the number of distinct pairs separated by the lag distance h.

The spatial variability estimation is generally an increasing function which can reach one or more plateau. The first of these plateaus is called the sill and its value is generally very close if not equal to the variance of the studied parameter. The separation distance h at which the sill is reached is called the range and it corresponds to the distance at which the variables are no longer spatially correlated. The value that the estimator $\gamma(h)$ takes when $h=0$, is called the nugget effect, which represent a systematic error caused my micro-scale variations and/or measurement errors.

Following the calculation of the variogram, a variographic model must be fitted to it. The variographic model is an analytic expression which captures the behaviour of the spatial variability observed in the variogram. The most commonly used fitting models are the: a) linear, b) exponential, c) spherical and d) Gaussian models. The adjusted variographic model will then be used in the kriging process to estimate the studied variable at a spatial coordinate as a function of the separation distance between the research point and the sampled data.

It is not recommended to over fit the variographic model as the goal of this step is to capture the major spatial features and general behaviour of the spatial variability. When different models provide similar fits, one should select the simplest one. The more complicated model does not usually lead to more accurate estimates (Goovaerts, 1997).

3.4 Ordinary kriging

Kriging is a method that allows the estimation of a regionalized variable on every coordinates of a research grid by a linear combination of punctual neighbouring data. It is the best linear unbiased estimator (*BLUE*). The method is considered as unbiased because the estimation average error is null and as the best estimator because the estimation error variance is minimized.

To allow ordinary kriging, the analysed data must be stationary, namely that each observations must follow the same probability law, to have the same average and variance and that the auto-covariance between a pair of data be independent from their spatial position.

The kriging equation can be developed as a summation (Eq. 2) or as a matrix (Eq. 3).

$$\hat{\gamma}_{io} = \sum_{j=1}^{n} \omega_j \hat{\gamma}_{ij} - \mu \quad \forall \; i = 1,2,\dots,n \qquad (2)$$

$$\begin{bmatrix} \hat{\gamma}_{11} & \hat{\gamma}_{12} & \cdots & \hat{\gamma}_{1n} & -1 \\ \hat{\gamma}_{21} & \hat{\gamma}_{22} & \cdots & \hat{\gamma}_{2n} & -1 \\ \vdots & \vdots & \ddots & \vdots & \vdots \\ \hat{\gamma}_{n1} & \hat{\gamma}_{n2} & \cdots & \hat{\gamma}_{nn} & -1 \\ 1 & 1 & \cdots & 1 & 0 \end{bmatrix} \begin{bmatrix} \omega_1 \\ \omega_2 \\ \vdots \\ \omega_n \\ \mu \end{bmatrix} = \begin{bmatrix} \hat{\gamma}_{1o} \\ \hat{\gamma}_{2o} \\ \vdots \\ \hat{\gamma}_{no} \\ 1 \end{bmatrix} \qquad (3)$$

where γ is the spatial variability estimator (Eq. 1), ω the weight of the estimation and μ the Lagrange multiplier. Kriging is therefore a system of $n + 1$ equations with $n + 1$ unknowns that can be solved by gaussian elimination. This process is to be applied for each coordinates of the interpolation grid, for which a $n + 1$ by $n + 1$ matrix will have to be solved, where n is the number of sample pairs formed between the grid coordinate and every observations within the correlation range.

The results of kriging are an estimation of the variable at a given point and its estimation error variance σ_R^2 (Eq. 4) which is a very good indicator of the estimation's relative quality.

$$\sigma_R^2 = \sum_{i=1}^{n} \omega_i \hat{\gamma}_{io} - \mu \qquad (4)$$

4 FIELD DATA ANALYSIS

4.1 Nature of the field data

Data used for the analysis of the dam's core are surveillance data collected during the construction of the structure. Materials put in place were regularly sampled after being compacted for laboratory testing of the granulometric curves, water content, saturation degree and density. *In-situ* tests were also realized using a nucleo-densimeter to measure water content, saturation degree, density and compaction degree. Every

sample's spatial coordinates and time stamp are also available.

4.2 Spatial interpolation grid

The spatial and temporal coordinates available for each sampling point allows the reconstitution of the construction sequence and the ordering of the samples into a continuous sequence. For this project, each sample was placed on a 2D continuous plane that represents the core as if each lift was placed next to each other instead of on top of each other. This step is realized to insure the data is ordered in a way that respects its spatial continuity. As Venkovic et al. (2013) demonstrated, because dams are built by stacking lifts on top of each other, spatial variability only exists in the direction of the construction sequence. Even if two lift are on top of each other, it is possible that they were built with significantly different materials and should not be considered continuous and therefore evaluated in the elevation axis.

The interpolation grid used for the analysis of the dam's core is a sequence of rectangles of the same dimensions of each lifts, each of these rectangles are divided in 1m/1m cells and put next to each other following a continuous x axis corresponding to the *station* coordinate. The interpolation grids y axis corresponds to the *core width*. The resulting grid varies from 66 m to 4 m wide (y axis) and is 64 360 m long (x axis). The sample data's *station* coordinates were transformed into a continuous x axis to have the same coordinates than the interpolation grid.

4.3 Empirical permeability calculation

Permeability was not measured during the dam's construction and an empirical model was thus used to estimate this parameter. The model retained in this study was developed by Leroueil et al. (2002) from the analysis of a large number of permeability results of till samples generally used in the construction of compacted till embankment dams, which showed that strong relationships exists between the fines fraction (passing ≤ 80 µm) or clay fraction (passing ≤ 2 µm) of a compacted till. Fig. 4 shows the relationships with clay fraction that had the strongest correlation with permeability. Those relationships are therefore used in this study.

The model in Fig. 4 shows the influence of fabric on the relationship between the permeability and the clay-size fraction of a compacted till. As observed, the influence of the compacted till fabric on permeability is quite important as its impact can make the permeability many orders of magnitude. This difference is caused by the conditions in which a till is compacted.

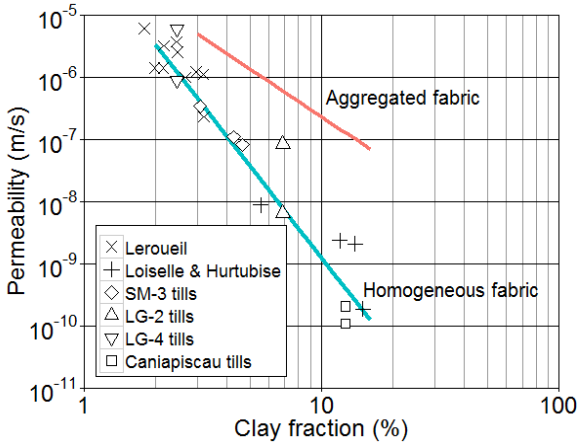


Figure 4 - Relationship between hydraulic conductivity, clay-size fraction and fabric. (Leroueil et al. 2002)

As shown in Fig. 5, if the till is compacted on the wet side of compaction curve ($S_r \geq S_{r\ opt}$), the pores sizes of the compacted till will tend to be homogeneously distributed in the material. On the other hand, if the till is compacted on the dry side of the compaction curve ($S_r < S_{r\ opt}$), the pore size distribution will be evenly distributed and associated to macro pores formed between aggregated clay particles. If the pore structure is heterogeneous, the clay particles are aggregated and the permeability is much higher than for the homogeneous structure because macro pores greatly influences permeability.

The model developed by Leroueil et al. (2002) is best suited for this study because it takes into account the fabric while typical empirical, semi empirical and theoretical models such as Kozeny-Carman are essentially based on homogeneous structure of soils and cannot account for the influence of fabric. The relationships of Fig. 4 were

developed using data from northern Québec dams, including the dam studied in this project. The till properties used for the construction of the core are well within the range of the model, the model is therefore well suited for the estimation of the permeabilities in this study.

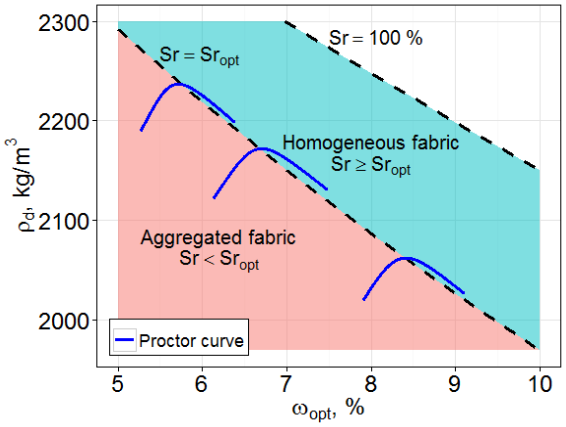


Figure 5 - Proctor compaction curve and fabric

The clay fraction – permeability relationships of Fig. 4 can be mathematically expressed by:

$$k_H = 0.0001 * P^{-4.902} \text{ (homogeneous)} \quad (5)$$

$$k_A = 0.00008 * P^{-2.54} \text{ (heterogeneous)} \quad (6)$$

where k_H and k_A are respectively the homogeneous and aggregated permeabilities (m/s) and P is the clay fraction (% by weight).

5 RESULTS

The geostatistical method was applied on the $\log_{10}$ transformed permeability data, estimated with equations (5) and (6). The statistical properties of the data set are shown in Tab. 2. The presented statistical properties in Tab. 2 focus on describing the data's distribution. As kriging assumes for continuous data, it is an optimal predictor when data follows a normal distribution, skewness, a measure of the asymmetry of the probability distribution of a random variable, is a rather interesting parameter. For the studied data, the skewness values are 1.44 and -1.19 for the untransformed and log-transformed data respectively. The rule of thumb to interpret this parameter is if the skewness is greater than 1 or less than -1, as it is the case here, the asymmetry is considered as substantial (Bulmer, 1979).

Although the transformed data still shows significant skewness, an important improvement is observed from the original data. Doing so allows for a clearer description of the spatial variability and ultimately a better variogram which better represent the spatial behaviour of the studied parameter.

Table 2 - Statistical properties of permeability

Statistical properties	k (m/s)	$\log_{10}$(k)
Number of observation	363	363
Minimum	7.34e-10	-9.13
Maximum	1.64e-5	-4.79
Average	2.65e-6	-6.07
Standard deviation	3.30e-6	0.85
Variance	1.09e-11	0.73
Skewness	1.44	-1.19

The permeability variogram is presented in Fig. 6. The spherical variographic model was used as it shown it was best fitted to model the spatial variability behaviour of the studied parameter. The nugget effect value is 0.445, the sill 0.711 and the range 12200 m.

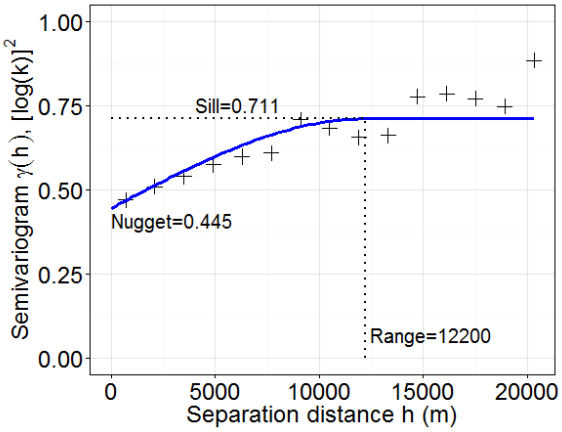


Figure 6 - Variogram, $\log_{10}$(k)

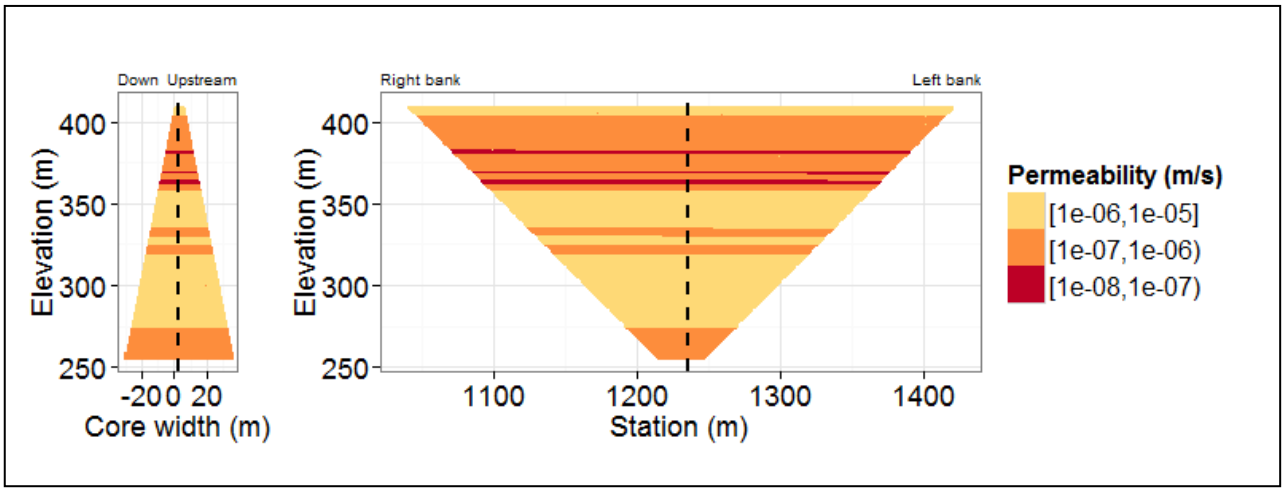


Figure 7 - Permeability ordinary kriging estimation results

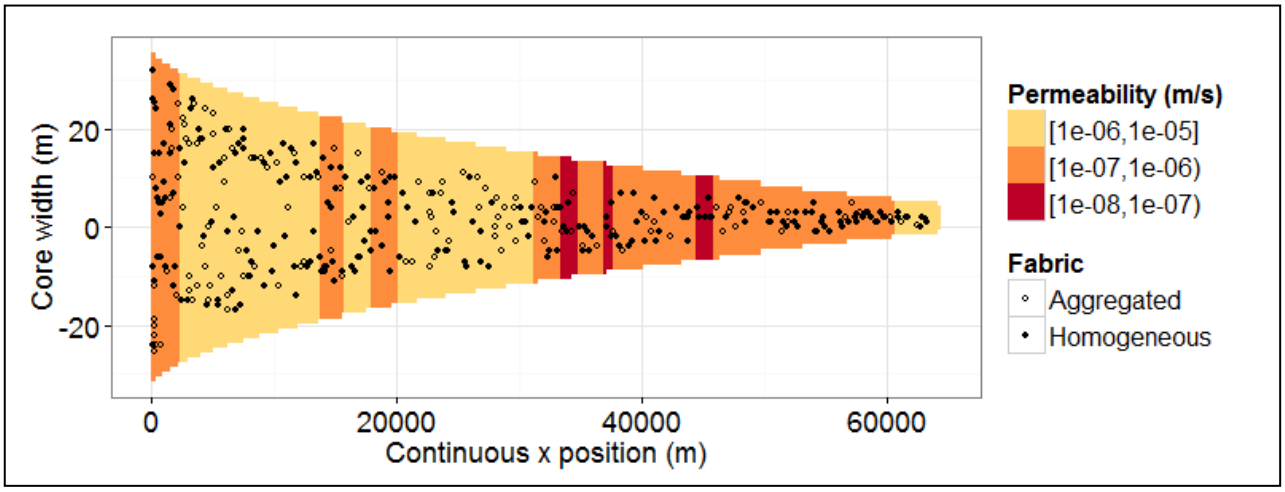


Figure 8 – Permeability ordinary kriging estimation results on unfolded core structure

Finally, Fig. 7 and 8 presents the results of ordinary kriging. Fig. 7 shows the results from two different directions: upstream-downstream and right bank-left bank and Fig. 8 shows the same results placed on the unfolded 2D plane with the fabric of sample data.

6 DISCUSSION

The stratified structure of an embankment dams compacted till core is already well known and the results from this study confirms the results from previous studies. The results shown in Fig. 7 reveal that the geotechnical properties of the core don't solely varies according to elevation, but can also slightly fluctuate within a single lift in every axes, these variations can easily be seen around elevations 330 and 360 m.

Two areas which shows permeabilities of the order of 10^{-6} m/s located in the 360 to 330 m and 320 to 275 m elevation intervals were essentially built using tills from borrow pits 9B and 9Est, which have average clay-fraction values of 3 and 2.8 %. According to Fig. 4, for these clay fractions value, average homogeneous permeabilities should be expected to range from $4.6 \cdot 10^{-7}$ to $6.4 \cdot 10^{-7}$ m/s. Except that based on the optimal and *in-situ* saturation degree fabric criterion, most of the tills from borrow pits 9A and 9Est were compacted on the dry side of the optimal and therefore display an aggregated fabric, which results in higher average permeabilities ($1.7 \cdot 10^{-6}$ and $1.6 \cdot 10^{-6}$ m/s respectively), as observed in Fig. 7 and 8.

Another interesting feature is the bands that shows permeabilities of the order of 10^{-8} m/s around elevations 375 m which corresponds to areas where tills from borrow

pit 12 were used, which showed a significantly higher clay-fraction. It is also observed in Fig. 8 that most samples from this area have a homogeneous fabric. Both the higher clay content and homogeneous fabric explains the lower permeability observed in this area. The areas where permeabilities of the order of 10^{-7} m/s are observed corresponds to homogeneous fabric compacted tills from borrow pits 9, 9A, 9B and 9Est or aggregated tills from borrow pit 12.

According to this ordinary kriging estimation, 57% of the volume of the core is occupied by compacted tills of permeability 10^{-6} m/s or higher, 39% of permeability of the order of 10^{-7} m/s and 4% of permeability 10^{-8} m/s or lower.

The relationship between permeability, clay fraction and fabric used for this study highlights some of the vulnerabilities of compacted till cores. For this case, a low clay fraction materials (9, 9A, 9B, 9Est) and a high clay fraction materials (12) have been used for the construction. The average permeability of a low clay fraction material with a homogeneous fabric is of the order of 10^{-7} m/s, while the same material with an aggregated fabric shows permeabilities of the order of 10^{-6} m/s. The same difference in the variation in the order of magnitude is observed for the high clay fraction material, for which the homogeneous and aggregated permeabilities are of the order of 10^{-8} m/s and 10^{-7} m/s respectively. This relationship shows that the higher the clay fraction is the more important will be the impact of the fabric variations. If a high clay fraction material is put in place with an aggregated fabric, its permeability will be around the same range as a homogeneous low clay fraction material.

The use of geostatistics allowed the assessment of the dam's core geotechnical properties for every 0.5 m^3 of the structure, a feat that couldn't have been possible without the use of powerful mathematical tools. An analysis of those properties on such a high resolution allows a better understanding of the variability and distribution of the materials properties, to target areas which might prove problematic and to better anticipate the problems which might arise during the operational phase of the dam. Coupled with different models, geostatistics could be used to precisely measure seepage rate, predict the behavior of the dam under specific constrains, thus making it a useful tool in the context of climate changes for example, or even to predict the effect of aging on the structure, using time based monitoring data.

However, the precision needed for such modeling is not yet achieved. Different factors could be addressed in order to refine the quality of the estimation. For instance, the trend removal applied in this study could benefit from a finer approach. The use of tills from borrow pit 12 proved problematic for the geostatistical analysis as they introduced two areas which showed very different parameters than the rest of the structure. Such a discrepancy is sure to affect the overall results as kriging is strongly affected by extreme data. Possible solutions to counter that problem could lie in using a) a kriging approach based on different domains, b) universal kriging or c) co-kriging. Another possible avenue to improve the present approach would be to first model each parameter linked to permeability such as clay fraction and fabric separately or as a multi-parameter system and then use the resulting estimations of these parameters in the permeability relationships (Eq. 5 and 6). This last approach sounds very promising as it allows the assessment of the spatial variability behavior of each parameter, which can be very different from each other.

7 CONCLUSION

The stratified structure of dams was already suggested by past use of geostatistics to study the geotechnical properties of compacted till core embankment dams. The use of a 2D plane and spatially correlated data showed the same behaviour and also highlighted that spatial variability occurs not only according to elevation, but in every axes of the core's structure.

Geostatistics and kriging proved a very interesting modelling tool for the assessment of dams' geotechnical properties and in this case permeability. It was shown that the

permeability of the studied dam core can vary from 10^{-6} to 10^{-8} m/s accordingly to the source of the till used in the various area of the structure and construction conditions.

Using an empirical relation including a fabric parameter proved very useful in the analysis of core's permeability, a structure known for its vulnerability to variations of its compaction conditions. The influence of fabric on permeability was indeed very important and the results of ordinary kriging estimation showed the high level of correlation between the two parameters.

The goal of this study was to show that it is possible to use geostatistics and kriging as a reliable tool of modelling dams. Using construction control data with geostatistics is a great way to valorize otherwise less used data and allows the modelling of the dam even before the impoundment, thereby having a very interesting way of predicting the dam's behaviour before it is actually in use.

The approach used in this study can still be greatly improved, especially by refining the kriging strategy of permeability parameters and samples distribution. By improving the approach, the obtained estimations will be more reliable and more precise, which will allow for more diversified uses.

8 ACKNOWLEDGEMENTS

The authors would like to gratefully thank the NSERC-Hydro-Québec Industrial Research Chair for life cycle optimisation of embankment dams (CRIBAR) and its many industrial partners for the provided financial support. The authors also extend their thanks to Hydro-Québec, who allowed for the use of their data banks for this project.

9 REFERENCES

Cressie, N.A.C. 1993. Statistics for Spatial Data. Wiley Series in Probability and Mathematical Statistics: Applied Probability and Statistics. John Wiley & Sons Inc., New York. Revisited reprint of the 1991 edition, A Wiley-Intersience Publication.

Goovaerts, P. 1997. Geostatistics for Natural Ressources Evaluation. Applied Geostatistics Series. Oxford University Press, New York.

Bulmer, M. G. 1979. Principles of Statistics. Dover Publications, NewYork.

Krige, D.G. 1951. A statistical approach to some basic problems on the Witwatersrand. Journal of the Chemical, Metallurgical and Mining Society of South Africa 52, 119-139.

Leroueil, S., Le Bihan, J.-P., Sebaihi, S., Alicescu, V. (2002). Hydraulic conductivity of compacted tills from northern Quebec. Canadian Geotechnical Journal 39, 1039-1049.

Matheron, G. 1963. Principles of geostatistics. Economic Geology 58, 1246-1268.

Smith, M. 2002. Geostatistical analysis of an embankment dam foundation. *In* Proceedings of the 2nd Speciality Conference on Computer Applications in Geotechnics, Winnipeg. Manitoba, 28-30 April 2002. Canadian Geotechnical Society, Winnipeg, Manitoba, 27-32.

Smith, M., Konrad, J.-M. 2008. Assessing hydraulic conductivities of a compacted dam core using geostatistical analysis of construction control data. Canadian Geotechnical Journal 48, 1314-1327.

Soulié, M., Favre, M., Konrad, J.-M. 1983. Analyse géostatistique d'un noyau de barrage tel que construit. Canadian Geotechnical Journal 20, 453-467.

Venkovic, N., Lebeau, M., Konrad, J.-M. 2013. Geostatistical assessment of the hydraulic conductivity of an embankment dam. Proceedings of the 66th Canadian Geotechnical Conference, Montréal, Québec, September 29 to October 3.

Deformation Modelling of Unbound Materials in a Flexible Pavement

Saevarsdottir, Thorbjorg - Corresponding author
EFLA Consulting Engineers, Iceland, thorbjorg.saevarsdottir@efla.is
University of Iceland, Iceland, ths134@hi.is

Erlingsson, Sigurdur
VTI, Sweden
University of Iceland, Iceland

ABSTRACT
A thin flexible test road structure was built and tested in an Accelerated Pavement Test (APT) using a Heavy Vehicle Simulator (HVS) to monitor its performance behaviour. The structure was instrumented to measure stress, strain and deflection responses as a function of load repetitions as well as permanent deformation manifested on the surface as rutting. In the test more than one million load cycles were applied, but mid-way the water table was raised. The raised water level had a significant effect, decreasing the resilient modulus and increasing the rate of accumulation of permanent deformation. The pavement structure has been modelled in an axisymmetric analysis where the responses have been calculated using a 2D multi layer elastic theory (MLET) as well as a 3D finite element method (FEM). The two methods agreed well with the measurements. Further was the observed accumulation of permanent deformation of the unbound layers modelled using two simple work hardening material models; a stress based model and a strain based model. The calculated permanent deformation is compared to the measured one before and after raising the ground water level. The stress based model was found to be sensitive to slight response changes but had a closer fit than the strain dependent model.

Keywords: Unbound granular materials, heavy vehicle simulator, numerical analysis, permanent deformation, rutting.

1 INTRODUCTION

The behaviour of pavement structures is complex and depends on many factors such as the axle/wheel loading configurations, the materials used, the thickness of the layers and the environmental conditions. Today most of pavement structure design is done with empirical methods, but for the development of mechanistic designing methods, the behaviour and properties of pavement materials need to be properly understood. In order to evaluate and calibrate the mechanistic models, it is important to compare the theoretical results with actual measurements in full scale pavement structures.

The many factors that must be considered in flexible pavement design are all easily within the capabilities of three dimensional (3D) finite element (FE) analysis. But FE analyses are computationally expansive and therefore the required computation time can be impractically long for a routine design (Schwartz, 2002; Loulizi et al., 2006). The multi-layer elastic theory (MLET), is commonly used in mechanistic empirical (M-E) pavement design where response calculations are performed several times. MLET is an axisymmetric analysis that can be extended by the superposition principle for multiple wheel loads.

Accelerated pavement tests (APT) of instrumented structures have increased the understanding of pavement behaviour and built a foundation for new, more sophisticated design methods. An APT using a Heavy Vehicle Simulator (HVS) was performed on an instrumented flexible test

road structure (referred to as SE10) at the Swedish National Road and Transport Research Institute (VTI) test facility in 2005. At regular intervals condition surveys and pavement response measurements were performed, providing valuable data. The aim was to get reliable direct measurements of stresses and strains in a flexible pavement structure and to evaluate the structure's performance under "moist" and "wet" conditions, with the water table raised half way through the test (Wiman, 2010).

The response signals gained from the testing were compared with calculated values using MLET and a 3D FE program. The accumulation of permanent deformation and the rutting profile were further modelled using two simple work hardening material models, and the difference evaluated.

2 THE PAVEMENT STRUCTURE AND TESTING PROCEDURE

The HVS machine (HVS Mark IV) is a mobile linear full-scale accelerated road-testing machine with a heating/cooling system to keep a constant pavement temperature. A cross section of the tested structure including the instrumentation embedded within the structure can be seen in Figure 1 and the materials used are listed in Table 1 (Wiman, 2010; Saevarsdottir & Erlingsson, 2013; Saevarsdottir et al., 2014).

In the APT, the structural responses were measured from a single and dual wheel configuration with various tyre pressures and axle loads. Further, a main accelerating loading phase was carried out under constant environmental conditions at 10°C using a lateral distribution of the loading following a normal distribution. A dual wheel configuration was used with tyre type 295/80R22.5 and a centre to centre spacing of 34 cm. The dual wheel load was 60 kN and the tyre pressure 800 kPa. This resulted in a square imprint of contact width 23.5 cm and 16 cm in length corresponding in a circular loading area with a contact radius equal to 10.9 cm. In total 1,136,700 bi-directional load repetitions were applied during the test, but after 486,750 load repetitions water was gently added until it rose to the level of 30 cm below the top of the subgrade (Figure 1). This gave the opportunity to assess the influence moisture had on the response and performance of the structure as no other alternations were made (Wiman, 2010).

The "moist" case simulates a normal field situation with the groundwater table at great depth. The "wet" case simulates a supposedly worst case scenario, with water running in the trenches.

3 RESPONSE MODELLING

The responses were modelled using the computer program ERAPAVE (Erlingsson & Ahmed, 2013) which is MLET based and the 3D finite element (FE) program PLAXIS (3D foundation, version 2) (Brinkgreve, 2007). The bound layers and subgrade were treated as linear elastic materials, where the stiffness of the bound layers was adjusted according to the ambient temperature. The stiffness modulus for the granular materials (base and subbase) was treated as stress dependent.

The responses were calculated using MLET with a circular loading area (Figure 2) and extended by applying the superposition principle for the dual wheel configuration (Huang, 2004; Erlingsson & Ahmed, 2013). To calculate the stress dependent stiffness modulus, E_r, a normalized form of the k - θ expression was used (May & Witczak, 1981; Uzan, 1985; Lekarp et al., 2000a; Erlingsson, 2010):

$$E_r = k_1 p_{ref} \left(\frac{3p}{p_{ref}} \right)^{k_2} \quad (1)$$

where k_1 and k_2 are experimentally determined constants; p is the mean normal stress ($p=⅓(\sigma_1+ \sigma_2+ \sigma_3)$; σ_1, σ_2 and σ_3 are principal stresses) and p_{ref} is a reference pressure (p_{ref} = 100 kPa).

In the FE analysis a hardening soil (HS) model was used to calculate the stress dependency of the soil stiffness (Brinkgreve, 2007). The plastic strains are calculated by introducing a multi-surface yield criterion and the hardening is assumed to be isotropic, dependent on the plastic shear and the volumetric strain (Schanz et al., 1999).

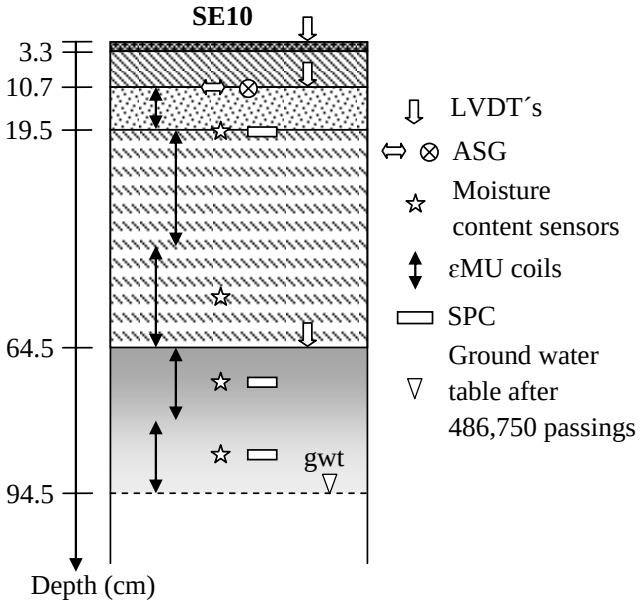


Figure 1 A cross-section of the pavement structure SE10, including the instrumentation embedded within the structure. The structure consisted of asphalt concrete, bituminous base, granular base course, subbase and subgrade.

Table 1 The materials used in the pavement structure SE10

Layer	Thick-ness [cm]	Description	Maximum aggregate size, d_{max} [mm]	Fine content [%]	Optimum gravimetric water content [%]
AC Asphalt concrete wearing course	3.3	AC pen 70/100	16	-	-
BB Bituminous base	7.4	AC pen 160/220	32	-	-
BC Base course	8.8	Unbound crushed rock (granite)	32	~ 6	4-5
Sb Subbase	45	Unbound crushed rock (granite)	90	~ 3	4-5
Sg Subgrade*	~235	Fine graded silty sand	4	25	13

* *over 90% of the grains under 0.5 mm*

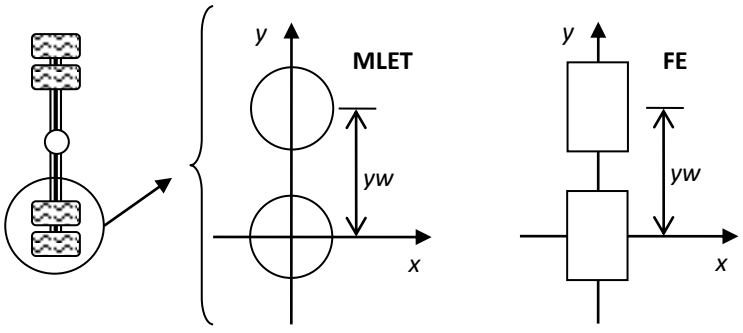


Figure 2 Plan view of the dual wheel setup in MLET (circular loading area) and in FE (square tyre imprint). The size of the imprint of the two setups is the same.

The loading was modelled with constant pressure on a square imprint (Figure 2). The basic parameters for the soil stiffness, *E*, in the hardening soil model are:

Triaxial modulus:

$$E_{50} = E_{50}^{ref} \left(\frac{c \cdot \cos\phi - \sigma_3' \cdot \sin\phi}{c \cdot \cos\phi + p_{ref} \cdot \sin\phi} \right)^m \quad (2)$$

Oedometer modulus:

$$E_{oed} = E_{oed}^{ref}\left(\frac{c\cdot\cos\phi - \sigma_1'\cdot\sin\phi}{c\cdot\cos\phi + p_{ref}\cdot\sin\phi}\right)^m \quad (3)$$

Un-/reloading modulus:

$$E_{ur} = E_{ur}^{ref}\left(\frac{c\cdot\cos\phi - \sigma_3'\cdot\sin\phi}{c\cdot\cos\phi + p_{ref}\cdot\sin\phi}\right)^m \quad (4)$$

where m is the power for stress-level dependency of stiffness; E_{50}^{ref} is the secant stiffness in a standard drained triaxial test; E_{oed}^{ref} is the tangent stiffness for primary oedometer loading; E_{ur}^{ref} is the unloading / reloading stiffness ($E_{ur}^{ref} = 3E_{50}^{ref}$); c is the cohesion and ϕ is the friction angle (Brinkgreve, 2007).

4 THE RESPONSE BEHAVIOUR

Results from indirect tension tests (ITT) of the bituminous layers, repeated load triaxial (RLT) tests of the unbound materials, plate load (PL) tests and falling weight deflectometer (FWD) tests were considered when estimating the material parameters used in the numerical analyses of the pavement responses (Table 2) (Wiman, 2010; Saevarsdottir & Erlingsson, 2013). The material parameters were optimized for a dual wheel configuration, under the centre of one of the tyres, with an 800 kPa tyre pressure and a 60 kN applied dual tyre load. Poisson´s ratio (v) was set as a constant of 0.35 for all the layers. When performing the stress dependent analysis, k_2 and m were set as a constant while k_1, E_{50}^{ref}, E_{oed}^{ref} and E_{ur}^{ref} reduced with increased moisture content (Li & Baus, 2005; Rahman & Erlingsson, 2012). The cohesion, c, was reduced by 10% from "moist" to "wet" state (Theyse, 2002). When comparing the MLET and the FE analysis the ratio between the material parameters in "moist" and "wet" states was similar and between the upper and lower half of the subbase, but between the base and subbase layers some difference was observed. This might be related to the difference in calculation methods as MLET makes some assumptions that the FE method does not make. The FE analysis (square tyre imprint) should capture the behaviour of the asphalt layer better than an MLET analysis (circular loading area), but the difference between FE and MLET becomes insignificant deeper into the structure (Helwany et al., 1998; Huang, 2004; Saevarsdottir & Erlingsson, 2014).

All the figures in this section are from the main accelerated loading phase and the registration taken under the centre of one of the wheels.

In Figure 3, the vertical lines are the average of measured (MM) vertical strains over the depth interval (see Figure 1) whilst the dotted lines represent the calculated strain, using MLET and FE analysis. Some difference was observed between FE and MLET but both methods gave reasonably good agreement between response measurements and calculations. The increased moisture content in the "wet" state caused the stiffness of the unbound layers to decrease and higher strains and lower stresses to be registered (Saevarsdottir & Erlingsson, 2013).

Typical registrations measurements (MM) and calculated (MLET; FE) induced vertical strains and stresses for both "moist" and "wet" states are shown in Figures 4 and 5. The registrations were taken approximately in the middle of the "moist" and "wet" phases respectively. The calculated values were gained by moving the applied static load in short increments. In Figure 4 the vertical strain is displayed over two depth intervals; over the base layer ("moist") and over the top of the subgrade ("wet") (Figure 1). In Figure 5 the vertical stress is shown at two depths; at the bottom of the base ("moist") and in the subgrade ("wet") (Figure 1). No significant difference was observed between the calculated values using MLET and FE and both methods showed reasonable agreement with the measurements. The calculated vertical stress had some tendency to be underestimated in the subgrade.

Table 2 Material parameters used in the response analyses of the HVS tested structure.

Layer	State	MLET & FE			MLET	FE				
		E	γ	k_2 & m [-]	k_1 [-]	E_{50}^{ref}	E_{oed}^{ref}	E_{ur}^{ref}	c [kPa]	Φ [°]
Asphalt concrete	Moist	3500	24	-	-	-	-	-	-	43
	Wet									
Bituminous base	Moist	3500	24	-	-	-	-	-	-	43
	Wet									
Unbound base	Moist	-	20	0.6	500	115	108	345	40	43
	Wet				400	92	86	276	36	
Unbound subbase – upper half	Moist	-	19	0.6	1450	180	168	540	40	43
	Wet				1150	142	133	426	36	
Unbound subbase – lower half	Moist	-	19	0.6	2850	360	336	1080	40	43
	Wet				1550	194	181	582	36	
Subgrade	Moist	50	16	-	-	-	-	-	-	35
	Wet	45								

In table, E – Young modulus of bound materials and resilient stiffness of unbound materials [MPa]; γ – Unit weight [kN/m^3]; E_{50}^{ref}, E_{oed}^{ref} and E_{ur}^{ref} – [MPa].

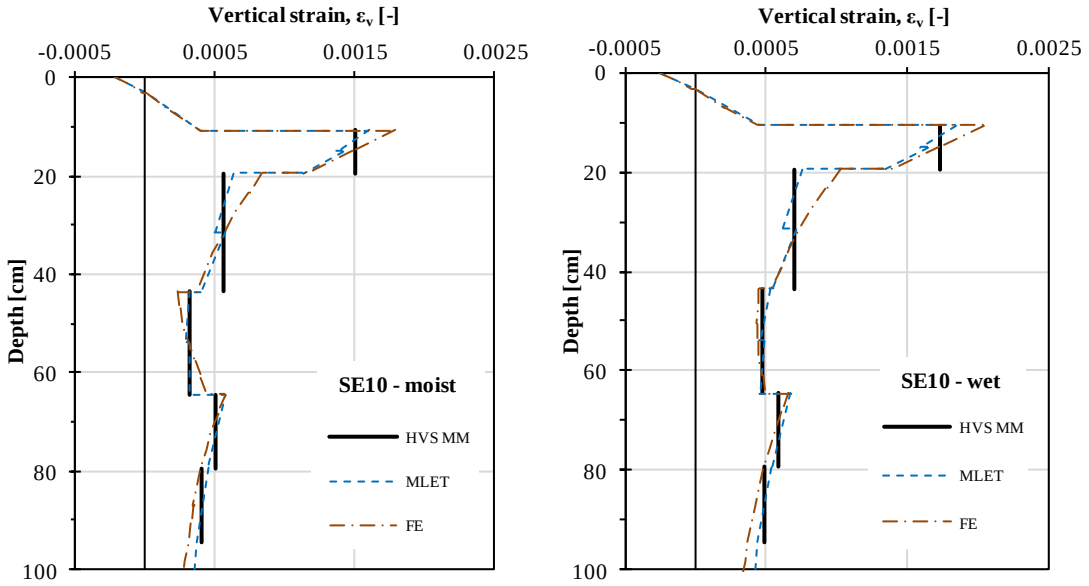


Figure 3 Vertical resilient strain as a function of depth ("moist" state - left; "wet" state – right).

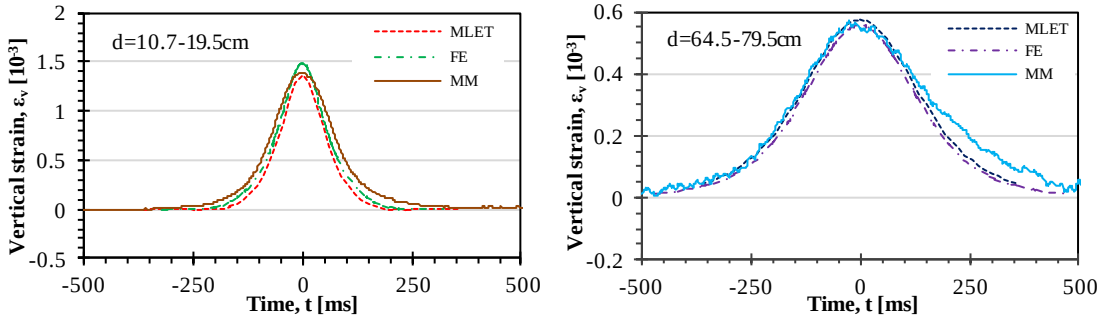


Figure 4 Induced vertical strain registration of εMU sensors and calculations, for depth ranges 10.7-19.5 cm ("moist") and 64.5-79.5 cm ("wet").

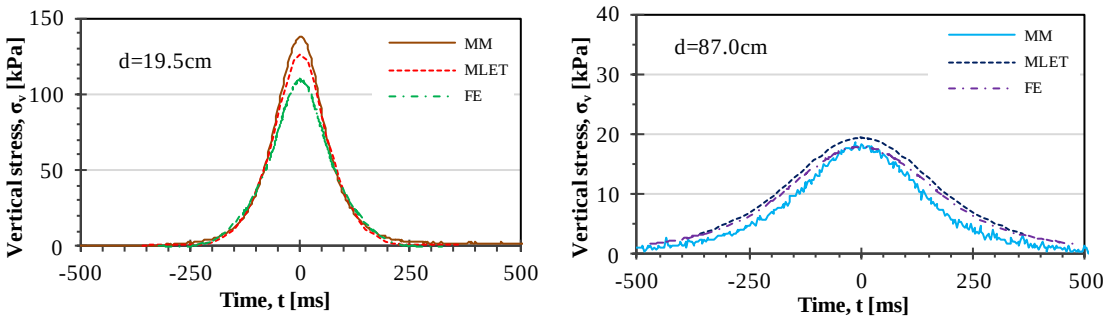


Figure 5 Induced vertical stress registration of SPC sensors and calculations, at depths of 19.5 cm ("moist") and 87 cm ("wet").

5 PERMANENT DEFORMATION PREDICTION MODELLING

Various models exist to evaluate permanent strain/deformation of unbound materials (Lekarp et al, 2000b; ARA, 2004; Korkiala-Tanttu, 2008). Here the accumulation of the vertical strain in the unbound pavement materials was modelled using two models: a procedure developed by Korkiala-Tanttu (KT) (2008, 2009) which is a stress based and by the Mechanistic-Empirical Pavement Design Guide (MEPDG) (ARA, 2004) a strain dependent model. The structure was kept at a constant temperature of 10°C resulting in insignificant permanent deformations within the asphalt layer and therefore not taken into account (Ahmed & Erlingsson, 2014; Hornych et al., 2013; Loulizi et al., 2006).

The KT model (Korkiala-Tanttu, 2008 & 2009) is a simple work hardening material model for unbound materials:

$$\hat{\varepsilon}_p(N) = C \cdot N^b \cdot \frac{R}{A-R} \qquad (5)$$

where $\hat{\varepsilon}_p$ is the accumulated permanent strain; C is a material parameter depending on compaction and saturation degree; N is the number of load repetitions; b is a shear ratio parameter depending on the material and stress state; R is the deviatoric stress ratio:

$$R = \frac{q}{q_f} = \frac{\sigma_1 - \sigma_3}{q_0 + Mp}$$

where

$$M = \frac{6 \cdot \sin\phi}{3 - \sin\phi} \qquad q_0 = \frac{c \cdot 6 \cdot \cos\phi}{3 - \sin\phi}$$

defined by the static Mohr Coulomb failure envelope and A is the maximum value of R, which theoretically is 1 but as R approaches 1 the expression $R/(A-R)$ can increase to indefinite values; A has therefore been taken as 1.05.

The MEPDG model (ARA, 2004) is based on a best fit approach from laboratory testing, where a simple three parameter work hardening model has been used for unbound materials:

$$\hat{\varepsilon}_p(N) = \beta_1 \left(\frac{\varepsilon_0}{\varepsilon_r}\right) e^{-\left(\frac{\rho}{N}\right)^b} \varepsilon_v \qquad (6)$$

where ε_r is resilient strain imposed in a laboratory test to obtain ε_0, ρ and b (ρ, b and $\varepsilon_0/\varepsilon_r$ are obtained by using equations developed by ARA (2004)); ε_v is the average vertical resilient strain in the layer as obtained from the primary response model and β_1 is a calibration factor.

The permanent deformation was gained by multiplying the permanent strain in the middle of each layer with its thickness. The total permanent deformation was gained by dividing each layer into sub-layers and sum up the deformation of the sublayers.

A "time-hardening" procedure was used when taking into account the effects of lateral wander and different water content, on the development of rutting (Lytton et al., 1993; Ahmed & Erlingsson, 2013; Rahman & Erlingsson, 2013).

Table 3 Material parameters of the unbound layers used to predict the permanent deformation with the KT model, calibrations factors are found with best fit approach.

Layer	State	c [kPa]	ϕ [°]	C [10^{-4}] [-]	b [-]
Unbound base (granular)	Moist	40	43	1.1	0.35
	Wet	36		75	0.05
TOP Unbound subbase (granular)	Moist	40	43	0.6	0.33
	Wet	36		40	0.05
BOTTOM Unbound subbase (granular)	Moist	40	43	0.5	0.31
	Wet	36		30	0.05
Subgrade	Moist	14	35	0.05	0.55
	Wet	7		1.5	0.3

Table 4 Material parameters of the unbound layers used to predict the permanent deformation via MEPDG model calibrations factors are found with best fit approach.

Layer	State	W_c [%]	b [-]	ρ [-]	$\varepsilon_0/\varepsilon_r$ [-]	β_1 [-]
Unbound base (granular)	Moist	3.3	0.214	1778	21.2	0.41
	Wet	3.4	0.213	1833	21.2	0.47
TOP Unbound subbase (granular)	Moist	3.0	0.216	1624	21.2	0.70
	Wet	3.2	0.215	1704	21.2	1.02
BOTTOM Unbound subbase (granular)	Moist	3.0	0.216	1624	21.2	0.70
	Wet	3.4	0.214	1789	21.2	1.02
Subgrade 64.5-94.5cm	Moist	7.7	0.179	8036	22.6	1.0
	Wet	16.1	0.127	467485	29.2	8.3
Subgrade 94.5-144.5cm	Moist	7.7	0.179	8036	22.6	0.9
	Wet	18.4	0.116	1996957	32.5	6.0
Subgrade 144.5-194.5cm	Moist	7.7	0.179	8036	22.6	0.8
	Wet	18.4	0.116	1996957	32.5	4.0
Subgrade 194.5-244.5cm	Moist	7.7	0.179	8036	22.6	0.7
	Wet	18.4	0.116	1996957	32.5	2.0

6 PERMANENT DEFORMATION

Listed in Tables 3 (KT model) and 4 (MEPDG model) are the parameters used in the permanent deformation predictions. The material parameters were mainly estimated from RLT tests, PL tests and FWD tests as well as compaction, saturation degree and stress state when appropriate (Wiman, 2010; Saevarsdottir & Erlingsson, 2013). In the KT model the cohesion, c, was reduced by 10% from "moist" to "wet" state in the crushed rock base and subbase layers and by 50% in the fine graded subgrade (Theyse, 2002; Matsushi & Matsukura, 2006). In the MEPDG model the gravimetric water content (W_c) was based on measurements and the calibration factor β_1 was adjusted to get a reasonable resemblance between the measured and calculated values.

When predicting the total deformation, the calibration factor β_1 for the subgrade had to be altered when using the MEPDG model (Table 4). It reduced with depth and the reduction was more in the "wet" state than in the "moist" state. Possible explanations are increased compaction or increased lateral pressure that increases the interlocking between the material particles with depth.

In Figure 6 the rutting profile is displayed after five different load repetitions; two in the "moist" state and three in the "wet" state. As before the calculations were performed by using the KT-model (left) and the MEPDG-model (right), the responses were gained by using both MLET and FE analyses.

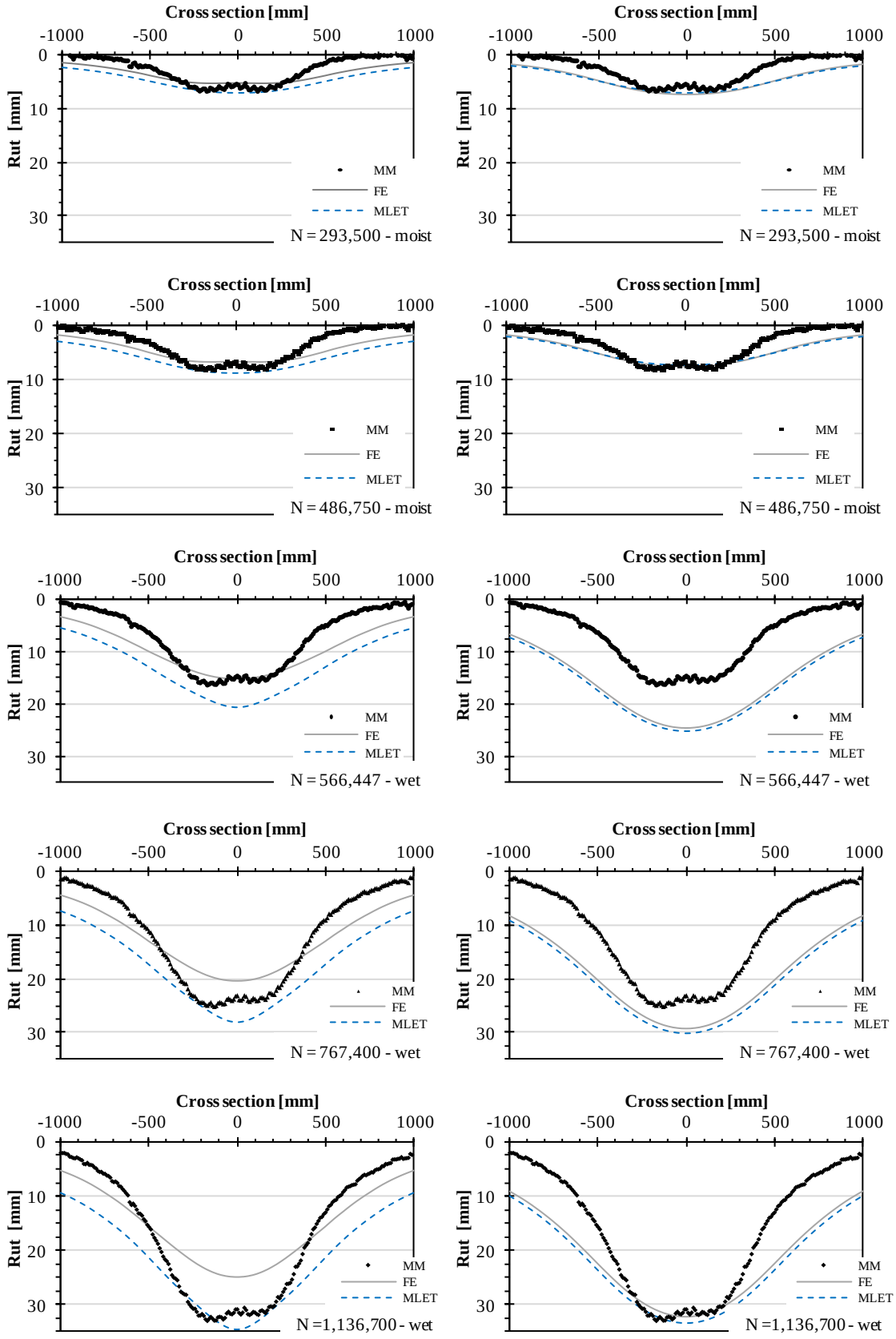


Figure 6 Cross section of the rutting profile after different numbers of load repetitions, two in the "moist" state and three in the "wet" state. The calculated values were obtained by using the KT model (left) and the MEPDG model (right). The response values were obtained from two different analyses, MLET and FE.

For both methods (KT and MEPDG) the rutting profile had reasonable correlation with the measurements in the "moist" state while more variations were observed in the "wet" state. The calculated rutting profile did not have the same shape as the measured one, but the centre values were similar.

The KT model shows a significant difference when using stress values from MLET and FE analyses despite MLET and FE giving similar response results (section 4). The permanent deformation was smaller when using FE stress response compared to the MLET one but the shape of the curves were similar. The change in permanent deformation were bigger than changes in R, q, and q_f indicating some sensitivity in the model.

When using the MEPDG model, similar results were gained when using the vertical strain from MLET and FE analyses as the strain is a linear factor in the model. The method does not resemble well the amount of rutting observed in the middle of the "wet" state but reaches similar values in the end.

7 CONCLUSIONS

In this work, the response and permanent deformation of a flexible pavement tested with an HVS machine was analysed. The structure was studied in "moist" and "wet" states before and after raising the groundwater table. The raised water level had a significant effect on the structural behaviour, increasing the water content in the unbound material layers causing a reduction in the resilient stiffness and increasing the permanent deformation.

The response signals were monitored and compared with calculated values using a 2D axisymmetric MLET method and a 3D FE method. The bitumen bound layers and subgrade were treated as linear elastic materials. Generally good agreements were found between the measured responses and calculated values using both FE and MLET with no significant difference between them.

The accumulation of permanent deformation of the unbound layers was modelled using two simple work hardening material models, one stress dependent, KT, and one strain dependent, MEPDG. The responses used in the permanent deformation prediction were gained from both MLET and FE analyses. When using the MEPDG model similar results were gained when using MLET and FE responses. Despite the MLET and FE analyses providing similar stress responses, the amount of permanent deformation from the KT model varied, indicating some sensitivity in the model.

The calculated rutting profile for KT and MEPDG did not reach the same shape as the measured one, but central values were similar. The MEPDG model does not resemble well the amount of rutting in the initial stages of the "wet" state whilst the KT model had a reasonably good correlation with the measurements after various numbers of load repetitions when using the MLET responses. Both these models are semi-empirical and more analysis and calibration is required to improve their accuracy for various load and environmental situations

8 ACKNOWLEDGEMENTS

The work described in this paper was sponsored by the Icelandic Road Administration (ICERA), The University of Iceland Research Fund, Ludvig Storr's Culture and Development Fund and the Icelandic Research Fund (grant no. 141210-051). Data were used from the Swedish National Road and Transport Research Institute (VTI), and the testing was performed in collaboration with The Swedish Transport Administration (TRV).

9 REFERENCES

Ahmed, A. W. & Erlingsson, S. (2013). Evaluation of permanent deformation models for unbound granular materials using accelerated pavement tests. *Road Materials and Pavement Design*. 14/1, 178-195. doi:10.1080/14680629.2012.755936.

Ahmed, A. W. & Erlingsson, S. (2014). Evaluation of permanent deformation model for asphalt concrete mixtures using wheel tracking and Heavy Vehicle Simulator tests. In *Compendium of Papers of the 93rd Annual Meeting of the Transportation Research Board*, Transportation Research Board of the National Academies, Washington, D.C., January, 2014.

ARA Inc. (2004). "*Guide for the Mechanistic-Empirical Design of New and Rehabilitated Pavement Structures, Final report, NCHRP 1-37A.*" Transportation Research Board of the National Academies, Washington, D.C., USA.

Brinkgreve, R.B.J. (2007). PLAXIS 3D foundation, version 2, manual. PLAXIS, Delft, Netherlands.

Erlingsson, S. (2010). Impact of water on the response and performance of a pavement structure in an accelerated test. *Road Materials and Pavement Design*. 11/4, 863-880.

Erlingsson, S. & Ahmed, A. W. (2013). Fast layered elastic response program for analysis of flexible pavement structures. *Road Materials and Pavement Design*. 14/1, 196-210. doi:10.1080/14680629.2012.757558.

Helwany, S., Dyer, J. & Leidy, J. (1998). Finite-element analyses of flexible pavements. *Journal of Transportation Engineering*. 124, 491-499.

Hornych, P., Balay, J. M., Mauduit, C. & Bodin, D. (2013). Evaluation of the concept of equivalent temperature for pavement design. *Proceedings of the 9th International Conference on the Bearing Capacity of Roads, Railways and Airfields (BCRRA 2013), 25-27 June 2013*. Trondheim, Norway.

Huang, Y. H. (2004). *Pavement Analysis and Design*. 2nd ed. Upper Saddle River, New Jersey, USA: Pearson Education Inc., Prentice Hall and Education Inc.

Korkiala-Tanttu, L. (2008). *Calculation method for permanent deformation of unbound pavement materials.* Espoo, Finland: Ph.D. thesis, VTT Technical Research Centre of Finland.

Korkiala-Tanttu, L. (2009) Verification of rutting calculation for unbound road materials. *Proc. of the Institution of Civil Engineers, Transport 162*. 162/TR2, 107 – 114.

Lekarp, F., Isacsson, U. & Dawson, A. (2000a). State of the art. I: Resilient response of unbound aggregates. *Journal of Transportation Engineering, ASCE*. 126/1, 66-75.

Lekarp, F., Isacsson, U. & Dawson, A. (2000b). State of the art. II: permanent strain response of unbound aggregates. *Journal of Transportation Engineering, ASCE*. 126/1, 76-83.

Li, T. & Baus, R. L. (2005). Nonlinear parameters for granular base materials from plate tests. *Journal of Geotechnical and Geoenvironmental Engineering*. 131/7, 907-913.

Loulizi, A., Al-Qadi, I. L. & Elseifi, M. (2006). Difference between in situ flexible pavement measured and calculated stresses and strains. *Journal of Transportation Engineering*. 132, 574-579.

Lytton, R.L., Uzan J., Fernando, E. G., Roque, R., Hiltumen, D. & Stoffels, S. M. (1993). Development and validation of performance prediction models and specifications for asphalt binders and paving mixes. *The Strategic Highway Research Program Project Rep. No. SHRP-A-357.*

Matsushi, Y. & Matsukura, Y. (2006). Cohesion of unsaturated residual soils as a function of volumetric water content. *Bulletin of Engineering Geology and the Environment.* 65/4, 449-455.

May, R. W. & Witczak, M. W. (1981). Effective granular modulus to model pavement response. *Transportational Research Record 810*. Washington D.C.: National Research Council, 1-9.

Rahman, S. & Erlingsson, S. (2012). Moisture sensitivity of unbound granular materials. *Proceedings of the 4th European pavement and asset management conference (EPAM4), 5-7 September 2012*. Malmö, Sweden, CD-ROM.

Rahman, S. & Erlingsson, S. (2013). Evaluation of permanent deformation characteristics of unbound granular materials from multi-stage repeated load triaxial test. In *Compendium of Papers of the 92nd Annual Meeting of the Transportation Research Board*, Transportation Research Board of the National Academies, Washington, D.C., January, 2014.

Saevarsdottir, Th. & Erlingsson, S. (2014). Modelling of responses and rutting profile of a flexible pavement structure in an HVS test. Road Materials and Pavement Design. doi: 10.1080/14680629.2014.939698

Saevarsdottir, Th., Erlingsson, S. & Carlsson, H. (2014). Instrumentation and performance modelling of Heavy Vehicle Simulator tests. International Journal of Pavement Engineering. doi: 10.1080/10298436.2014.972957

Saevarsdottir, Th. & Erlingsson, S. (2013). Effect of moisture content on pavement behaviour in a heavy vehicle simulator test. *Road Materials and Pavement Design*. doi: 10.1080/14680629.2013.774762.

Schanz, T., Vermeer, P. A. & Bonnier, P. G. (1999). The hardening soil model: Formulation and verification. In Ronald B.J. Brinkgreve (ed.) *Beyond 2000 in Computational Geotechnics- 10 Years of PLAXIS*. A. A. Balkema, Rotterdam, The Netherlands.

Schwartz, C. W. (2002). Effect of stress-dependent base layer on the superposition of flexible pavement solutions. *The International Journal of Geomechanics*. 2/3, 331-352. doi: 10.1061/(ASCE)1532-3641(2002)2:3(331).

Theyse, H. L. (2002). *Stiffness, Strength and Performance of Unbound Aggregate Material: Application of South African HVS and Laboratory Results of California Flexible Pavements*. Report for the California Pavement Research Program, University of California, Pavement Research Center.

Uzan, J. (1985). Characterization of granular materials. *Transportational Research Record 1022, TRB*. Washington, D.C.: National Research Council, 52-59.

Wiman, L. G. (2010). *VTI rapport 628, Accelererad provning av vägkonstruktioner; Referensöverbyggnad enligt ATB Väg*. Linköping, Sweden: Swedish National Road and Transport Research Institute (VTI). (*In Swedish*).

Theoretical and experimental investigation of Continuous Compaction Control (CCC) systems

J. Pistrol
Institute of Geotechnics, Vienna University of Technology, Austria, johannes.pistrol@tuwien.ac.at

M. Hager, D. Adam
Institute of Geotechnics, Vienna University of Technology, Austria

F. Kopf
FCP - Fritsch, Chiari & Partner ZT GmbH, Austria

ABSTRACT
Continuously improved compaction techniques in earthworks and geotechnical engineering require the use of adequate test equipment to assess the achieved compaction success. Conventional and spot like compaction testing methods, especially at large construction sites, are outdated and do not represent the state of the art anymore. Therefore, Continuous Compaction Control (CCC), a roller integrated system, has become the commonly used method for compaction control with vibratory rollers.
In the presented paper the leading CCC systems on the market (Compactometer, Terrameter, ACE) are discussed. Their structure, measurement principle and theoretical background is investigated.
Moreover, large-scale in situ tests were performed with a tandem roller with an oscillating and a vibrating drum. For the first time all three CCC systems and four CCC values are calculated from the accelerations of one single roller. The results of these large-scale tests are compared, dependencies of the CCC values on excitation parameters are investigated and advantages and disadvantages of the CCC systems are outlined.

Keywords: soil dynamics, compaction, roller, vibration, Continuous Compaction Control.

1 INTRODUCTION

Continuous Compaction Control (CCC) is the state of the art method for the assessment of the achieved compaction success with vibratory rollers. CCC is, as the name suggests, a roller integrated compaction measurement method for dynamically excited rollers, that allows to measure the compaction success online and continuously and to document the results during the compaction process. CCC systems measure the accelerations in the bearing of vibratory drums and analyze the motion behavior of the drum to calculate a stiffness proportional CCC value.
There are currently three leading CCC systems on the market, the Compactometer, the Terrameter and the ACE system, which differ in their measurement principle and theoretical background.
These differences are investigated within this paper. Moreover, results of large-scale in situ tests are presented, where all three CCC systems and four CCC values were calculated from the accelerations of one single roller for the first time.

2 VIBRATING ROLLERS

Vibration is the commonly used type of excitation for dynamic drums. The biggest advantage of vibrating rollers in earthworks is their significantly higher vertical loading, which results in larger compaction depths.

2.1 Principle of vibrating rollers

The eccentric masses of a vibrating drum are shafted concentrically to the drum axis, resulting in a mainly vertical loading of the soil. This implies the main characteristics of vibrating drums, the lager compaction depth and higher ambient vibrations compared to oscillating rollers.

2.2 Modes of operation

The vibrating drum and the compacted soil form an interacting system, where the soil starts to vibrate because of the drums excitation, but also influences the drums motion behavior. The soil stiffness, the speed of the roller, the excitation frequency and the ratio between roller and drum mass have a significant impact on the interacting system of drum and soil. Depending on these factors typical modes of operation can be identified (see Figure 1).

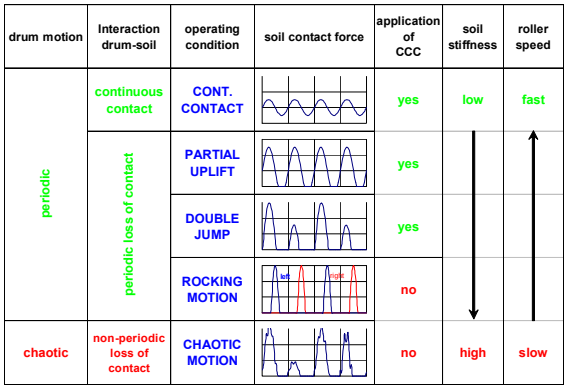


Figure 1 Modes of vibratory roller operation (Adam, 1996).

Continuous Contact
No loss of contact can be observed in the mode of operation “Continuous Contact”. Therefore, the soil must be able to follow the drum motion, which only is the case for very soft soils and loose fillings or small excitation amplitudes.

Partial Uplift
The mode of operation “Partial Uplift” is the typical mode of operation for well designed rollers and also the most efficient mode of operation for vibrating rollers. The increasing vertical force pointing upwards causes a periodic loss of contact between drum and soil in each period of excitation.

Double Jump
If the soil stiffness increases, the drum motion only reproduces with every second period of excitation. The drum is also uplifted during the mode of operation “Double Jump”, but falls back on the soil with one strike of high impact and one strike with lower impact. The high energy transmitted into the soil by the high impacts results in a high compaction. However, it also causes a significant higher wear of the roller, as well as increased ambient vibrations.

Rocking Motion
If the soil stiffness increases further, the longitudinal axis of the drum is alternately tilted to one side and the other and a phase shift in the motion behavior of the drums left and right side can be observed.
The roller can hardly be handled in “Rocking Motion” and controlled compaction work is not possible any longer.

Chaotic Motion
A combination of very high soil stiffness and unfavourable compaction parameters (large amplitude, high frequency, low speed) can cause “Chaotic Motion”. The motion behavior is not periodic any longer and a roller handling is not really possible. Rocking motion and chaotic motion have to be avoided.

3 CCC FOR VIBRATING ROLLERS

3.1 Basic principle, components and existing CCC systems

In contrast to spot like testing methods the CCC is a roller and work integrated method for the assessment of the soil stiffness. The roller is not only used as a compaction device, but also serves as a measuring device at the same time.
The basic principle of a CCC system is to assess the soil stiffness by evaluating the motion behavior of the drum. The parameters that influence the motion behavior of the drum also influence the values of CCC systems. Therefore, the first condition for a CCC system is to keep the rollers properties

of the compaction process like speed, excitation frequency and excitation amplitude constant during the CCC measurements. The second condition for a CCC system is the recording of the motion behavior of the drum. This condition can be fulfilled by recording the accelerations, velocities or displacements of the drum. Usually the accelerations are measured in the bearing of the drum in vertical and sometimes also horizontal direction.
The second part of a CCC system is a processing unit that calculates the corresponding CCC value for the piecewise analyzed acceleration signal (e.g. one CCC value for the time of two excitation periods). The processing unit also saves the CCC values. Moreover, a display unit is used to show the calculated CCC values online.
Early CCC systems used sensors for distance and speed to assign the CCC values to a certain position on the construction site. Modern CCC systems use GPS for an exact assignment of the CCC values.
The first CCC system was built in the late 1970ies. Dr. Heinz Thurner noticed a correlation between the soil stiffness and the motion behavior of a Dynapac vibratory roller during experimental field tests in 1974. He later developed the first CCC system, the Compactometer, together with Dr. Åke Sandström, Dr. Lars Forssblad and Dynapac (Thurner, 1978).
In 1982 the Bomag GmbH presented the Terrameter, an alternative CCC system, which analyzes the accelerations in the time domain to calculate the *OMEGA* value . In the late 1990ies Bomag improved the Terrameter and presented the vibration modulus E_{vib}.
The ACE-System of the swiss Ammann AG Group was introduced in 1999. It calculates the k_B value by analyzing the vertical accelerations in the time domain.

3.2 Compactometer

The processing unit of the Compactometer performs a piecewise fast Fourier transformation (FFT) of the measured vertical acceleration in the bearing of the drum to evaluate the shares of the FFT spectrum at the excitation frequency and its multiples. Thurner and Sandström recognized a correlation between the relation of the shares at the excitation frequency and two times the excitation frequency and the soil stiffness.
Therefore, Thurner and Sandström defined the *CMV* (Compaction Meter Value) of the Compactometer as:

$$CMV = \frac{a(2w)}{a(w)} 300 \tag{1}$$

Where $a(2w)$ is the share at two times the excitation frequency and $a(w)$ is the corresponding share at the excitation frequency.
If the roller operates in the Double Jump mode, a peak at the half of the excitation frequency can be seen in the FFT spectrum. A second value, the *RMV* (Resonance Meter Value), was defined to detect the Double Jump mode:

$$RMV = \frac{a(0.5w)}{a(w)} 100 \tag{2}$$

The Compactometer was the first CCC system and is still used by the roller manufacturers Caterpillar, Dynapac, Hamm and Volvo.

3.3 Terrameter

The Terrameter analyzes the equilibrium of forces on the drum in vertical direction (see Figure 2).

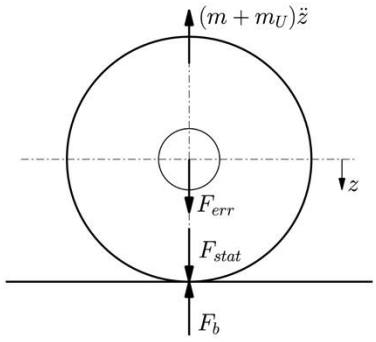


Figure 2 Equilibrium of vertical forces on the drum for the calculation of F_b.

The soil contact force F_b is calculated from the vertical acceleration $\ddot{z}$ under

consideration of the static load F_{stat}, the excitation force F_{err}, the mass of the drum m and the eccentric masses m_U:

$$F_b = -\left(m + m_U\right)\ddot{z} + F_{stat} + F_{err} \tag{3}$$

The displacements z can be obtained from a two times integration of the acceleration signal. The displacements z and the soil contact force F_b can be used to draw a force-displacement diagram for each period of excitation (see Figure 3).

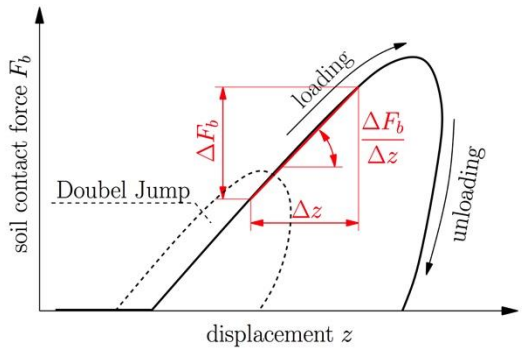


Figure 3 Force-displacement diagram of the vibrating drum for the calculation of OMEGA and E_{vib}.

The force-displacement diagram in Figure 3 is the basis for the CCC values *OMEGA* and E_{vib}.
The *OMEGA* value was the first CCC value of the Terrameter. It is the area under the force-displacement diagram for two consecutive excitation periods T_E:

$$OMEGA = factor \oint_{2T_E} F_b z\, dt \tag{4}$$

OMEGA is proportional to the energy transmitted into the soil.
The newer CCC value of the Terrameter system, the vibration modulus E_{vib} (MN/m^2) describes a soil stiffness by analyzing the inclination of the force-displacement curve between two defined points (40% and 90% of the maximum contact force). The E_{vib} is calculated recursively using a Poisson's ratio of $n = 0.25$:

$$\frac{\Delta F_b}{\Delta z} = \frac{E_{vib}\, 2b_0 p}{2\left(1 - n^2\right)\left\{2.14 + 0.5 \ln C\right\}} \tag{5}$$

with:

$$C = \frac{p\left(2b_0\right)^3 E_{vib}}{16\left(1 - n^2\right)\left(m + m_U + m_R\right) g r} \tag{5}$$

Where r and b_0 are the radius and the half width of the drum respectively.

3.4 Ammann Compaction Expert (ACE)

The ACE system calculates the k_B value (MN/m) by processing the acceleration signals in the time domain. The significant point in the force-displacement diagram for the evaluation is the change from the loading to the unloading phase, where the displacement has its maximum and $\dot{z} = 0$ (see Figure 4).

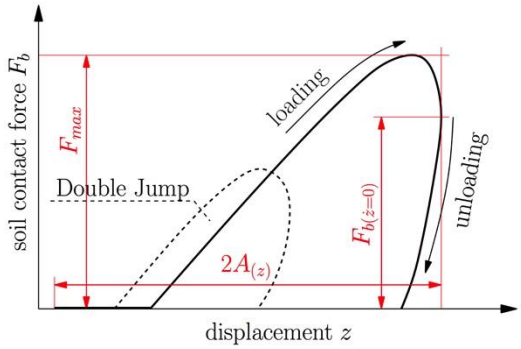


Figure 4 Force-displacement diagram of the vibrating drum for the calculation of k_B.

The ACE system uses two different equations for the calculation of k_B depending on the mode of operation. For continuous contact the k_B value can be calculated as:

$$k_B = w^2 \left[\left(m + m_U\right) + \frac{\left(m_U e_U Vario\right)\cos j}{A_{(z)}}\right] \tag{5}$$

Where $A_{(z)}$ is the amplitude of the displacement and j is the angle of phase shift (see Figure 5).
In case of a periodic loss of contact, the k_B value is calculated using the contact force at the change from the loading to the unloading phase $F_{b(\dot{z}=0)}$:

$$k_B = \frac{F_{b(\dot{z}=0)} - \left(m + m_U + m_R\right) g}{A_{(z)}} \tag{5}$$

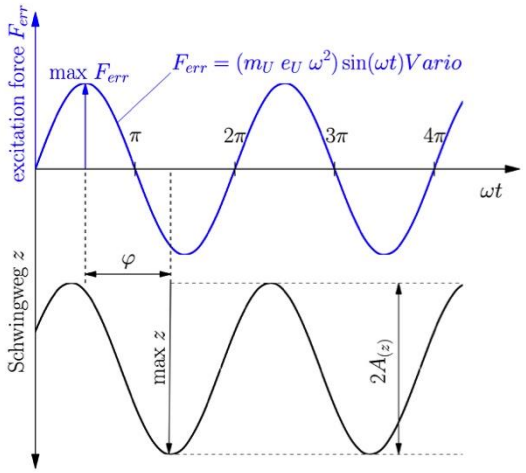


Figure 5 Excitation force F_{err} and displacement z for the calculation of k_B.

4 EXPERIMENTAL FIELD TESTS

4.1 Compaction device

A HAMM HD$^+$ 90 VO tandem roller was used as compaction device. The roller comprises a total mass of 9,830 kg and two drums of about 1,900 kg vibrating mass each. The typical speed during compaction work for this type of roller is 4 km/h and was used throughout the majority of the tests. Depending on the rotational direction of the eccentric masses, the vibratory drum at the front of the roller operates with a vertical amplitude of 0.34 mm or 0.62 mm respectively. For the smaller amplitude a frequency of 50 Hz was used most of the time, while 40 Hz was the standard frequency for vibratory compaction with the large amplitude.
The drum on the rear of the roller is an oscillatory drum that uses a tangential amplitude of 1.44 mm.

4.2 Test layout and measuring equipment

A test area was prepared and equipped in a gravel pit near Vienna for the experimental field tests. The test area comprised four parallel test lanes of loose sandy gravel (to be compacted) with a length of 20 m and a thickness of 0.5 m (see Figure 6). The test field was filled on the highly compacted plane of the gravel pit. The typical layer thickness for compaction with the used roller ranges from about 20 cm to 30 cm. However, the thickness was chosen larger to be able to run more tests without over-compacting the layer. The four test lanes were intended for static, vibratory, oscillatory, and combined vibratory and oscillatory compaction. Two ramps at the beginning and at the end of the test lanes served for roller handling, speeding up and down the roller as well as for lane changes.

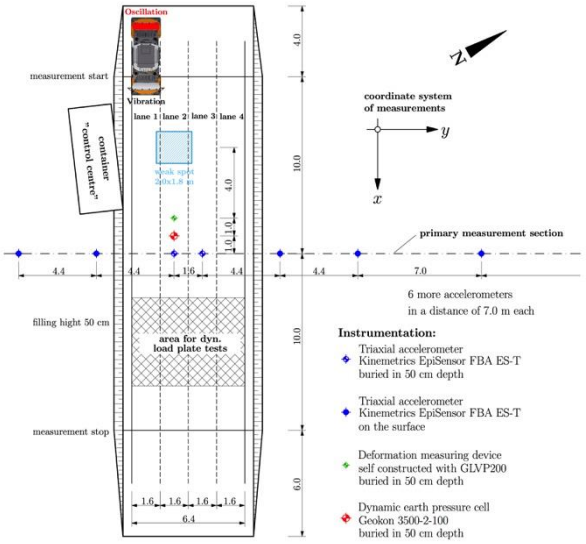


Figure 6 Test layout of the experimental field tests (Pistrol, 2015).

The test field was equipped with tri-axial accelerometers, a deformation-measuring-device and an earth pressure cell to evaluate the impact of the roller on the soil and the surrounding area. The results of these measurements are not discussed within this paper but can be found in Pistrol et al. (2013), Pistrol et al. (2015) and Pistrol (2015).
Two conventional mattresses were buried in a depth of 0.5 m under test lane 2 to simulate a uncompacted, weak spot in the test field and to investigate its influence on the CCC values (see Figure 6).
The vibratory drum of the roller was equipped with 4 accelerometers with a sensitivity of ± 30 g. The accelerometers were mounted on the left and right side bearing of the drum to measure the accelerations in horizontal and vertical direction on the undamped drum. The accelerometer signals were recorded with a sampling rate of 1,000 Hz.

The tandem roller also had a preinstalled Compactometer CCC system which was used as a reference for the calculation of the CCC values.

F

5 RESULTS OF THE EXPERIMENTAL FIELD TESTS

The results of the experimental field tests are discussed in the final paper…

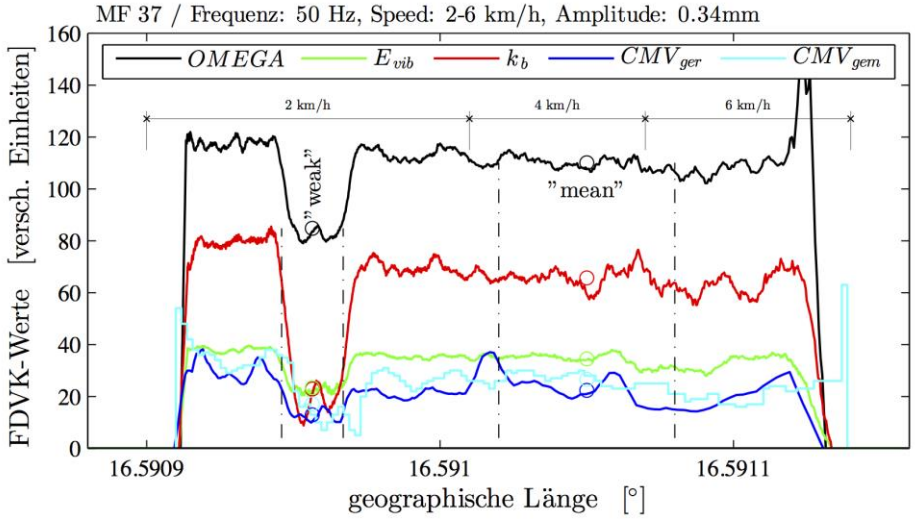


Figure 7 Force - displacement diagram of the vibrating drum for the calculation of k_B.

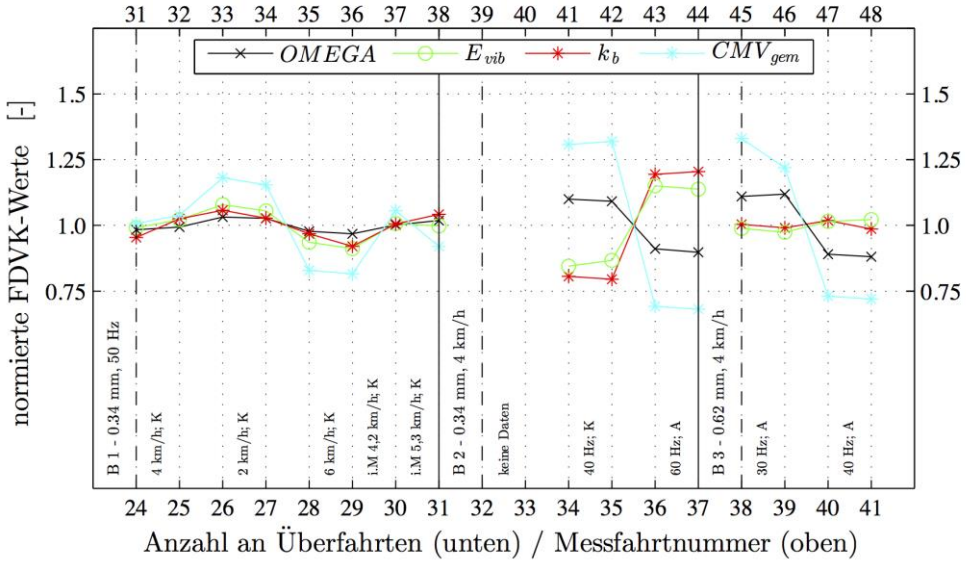


Figure 8 Force - displacement diagram of the vibrating drum for the calculation of k_B.

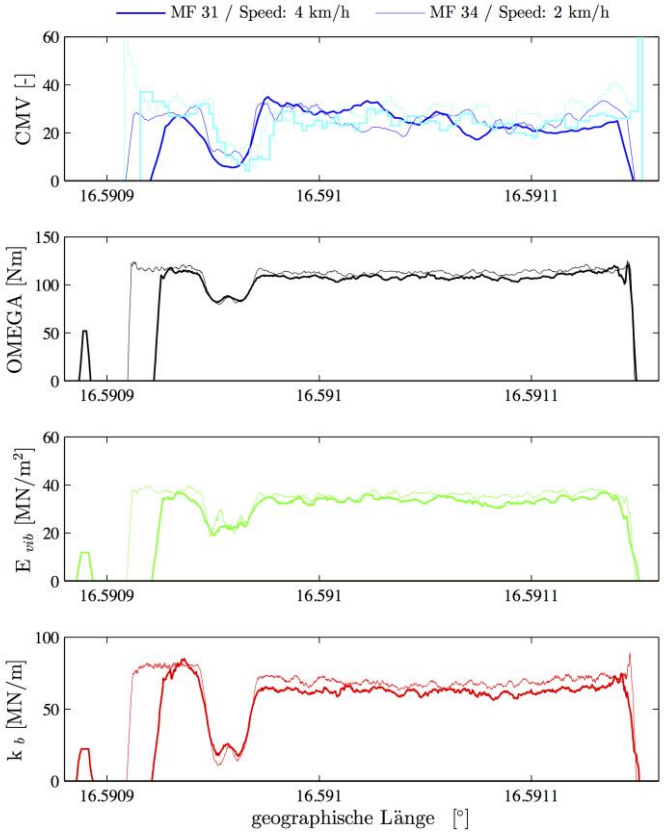


Figure 9 Force - displacement diagram of the vibrating drum for the calculation of k_B.

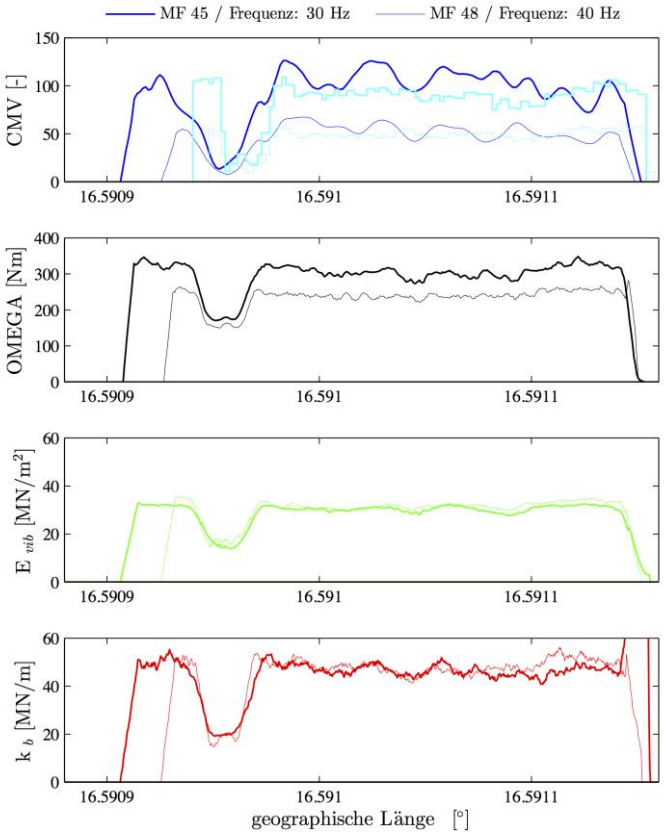


Figure 10 Force - displacement diagram of the vibrating drum for the calculation of k_B.

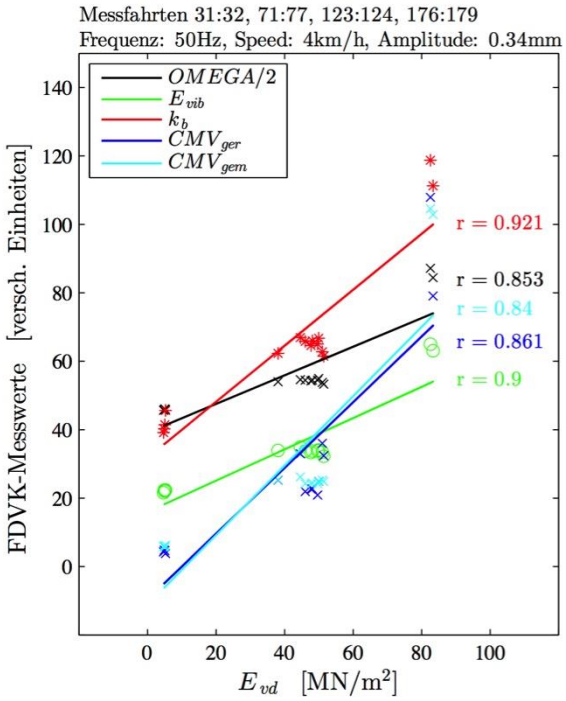


Figure 11 Force - displacement diagram of the vibrating drum for the calculation of k_B.

6 CONCLUSIONS

7 REFERENCES

Adam, D. (1996). Continuous Compaction Control (CCC) with vibrating rollers (Doctoral thesis in German). Vienna University of Technology.

Pistrol, J., Kopf, F., Adam, D., Villwock, S. &. Völkel, W. (2013). Ambient vibration of oscillating and vibrating rollers. Proceedings - Vienna Congress on Recent Advantages in Earthquake Engineering and Structural Dynamics 2013 (VEESD 2013), Vienna, Austria, Paper No. 167.

Pistrol, J., Adam, D., Villwock, S., Völkel, W. & Kopf, F. (2015). Movement of vibrating and oscillating drums and its influence on soil compaction. Proceedings of XVI European Conference on Soil Mechanics and Geotechnical Engineering, Edinburgh, Scotland. 349-354.

Pistrol, J. (2015). Compaction with oscillating rollers (Doctoral thesis in German). Vienna University of Technology.

Thurner, H. (1978). Verfahren und Vorrichtung zur Beurteilung des Verdichtungsgrades beim Verdichten einer Unterlage mit vibrierendem Verdichtungsgerät. Patent: Germany. Offenlegungsschrift 2710811; Aktenzeichen P 27 10 811.8.

The Experimental Pressure and Sealing Plug (EPSP) Experiment as part of the wider European DOPAS project - rock mass improvement and construction

Irena Hanusová
SÚRAO (Radioactive Waste Repository Authority), Dlážděná 6, Prague 1, 110 00 Czech Republic, hanusova@surao.cz

Markéta Dvořáková
SÚRAO, Dlážděná 6, Prague 1, 110 00 Czech Republic, dvorakova@surao.cz

Lucie Bělíčková
SÚRAO, Dlážděná 6, Prague 1, 110 00 Czech Republic, belickova@surao.cz

ABSTRACT
The objective of the DOPAS international project is to design a sealing plug system for deep geological repository (DGR) use, provide detailed plans for the design of such plugs, test both the characteristics of the materials to be used and the construction technology and to install 4 experimental in-situ plugs.
This four-year (2012–2016) project is being funded from European Commission financial resources (7th framework programme, EURATOM) and the project coordinator is Finland-based Posiva. A total of 14 partners from 8 European countries are involved in the project (Posiva, ANDRA, DBE-TEC, GRS, Nagra, NDA, SÚRAO, SKB, ČVUT, NRG, GSL, BTECH, VTT, ÚJV Řež).
The Czech EPSP experiment is being conducted in a rock environment consisting of granitoids at the Josef Regional Underground Research Centre (URC). The concept of the experiment is based primarily on the use of Czech materials and technology available in the Czech Republic and the principal aim is to demonstrate the technical viability and functioning of a pressure-resistant plug located in a future DGR.
The completion of the EPSP experiment will contribute towards both the demonstration of how sealing plug systems behave under real underground conditions and the long-term safety of a future DGR in the Czech Republic.

Keywords: plug and seal, EPSP experiment, grouting.

1 INTRODUCTION

The DOPAS project (the Demonstration of Plugs and Seals), which involves the participation of a total of 14 European organisations, is focused on the structural design of sealing plugs to be used in deep geological radioactive waste repositories and the verification of the functionality of such plugs. The project is being funded by the 7th Framework Programme – EURATOM (grant agreement no. 323273).
The Czech contribution to the DOPAS project (the EPSP experiment) is being conducted at the Josef Regional Underground Research Centre some 50km south of Prague. The aims of the EPSP experiment are to develop, monitor and verify the functionality of such plugs and to determine a detailed characterisation of the Czech materials from which the plug is constructed (low pH concrete, Ca/Mg bentonite etc.).

2 EPSP DESCRIPTION

The EPSP experiment has been divided into 4 stages. The first stage primarily concerned the laboratory verification of the suitability of the materials to be used in the construction of the plug. The second stage consisted of the construction of the in-situ experiment which commenced in 2013 with grouting and drilling work in the SP-59 experimental gallery niche. This was followed by the construction of the plug itself. The third stage consists of pressurisation by means of a number of saturation media (air, water and a bentonite suspension) during which the plug will be exposed to pressure of up to 2MPa (limited by the virgin stress of the surrounding rock mass). The final stage of the experiment will consist of the evaluation of the data obtained employing numerical analysis techniques and modelling.

3 EPSP CONSTRUCTION

3.1 Pressurisation chamber

The chamber (Fig. 1) serves as the principal injection point for the pressurisation media; with this aim in mind, the chamber was equipped with four pressurisation tubes (connected to the technical equipment). Once the shape had been adjusted, the surface of the chamber was treated with a waterproofing layer in order to avoid potential leaks behind the chamber.
The final stage involved the erection of a permeable separation wall between the chamber and the inner plug which served as the formwork for the shotcreting of the inner plug.

3.2 Inner and outer plug

The inner plug was erected over a continuous 23-hour period using shotcrete technology. The concrete was produced at a mixing plant in Prague and subsequently transported by large trucks to the Josef URL (transportation time 1-1½ hours).
The concrete mix was then gradually reloaded onto smaller trucks which transported the wet mix from the tunnel portal to the spraying machine in the experimental niche (distance of 2km).
The plug was erected layer by layer commencing in the rear section (separation wall) so as to gradually fill the plug space with shotcrete. The short time breaks between the separate concreting stages were used for the installation of the instrumentation.
The outer plug was constructed employing the same procedure as that of the inner plug.

3.3 Bentonite emplacement

Bentonite pellets were subsequently emplaced between the inner plug and the filter; the lower parts of the bentonite seal were compacted using the vibration technique.
The upper part of the seal was emplaced using shot clay technology.
The target average dry density following emplacement with respect to both methods was set at a minimum of 1400kg/m^3.

3.4 Filter

The filter serves as a collection point for water which might leak through the EPSP. The filter consists of gravel which is held in place by two permeable separation walls. The filter structure was built gradually in a number of stages as the emplacement of the bentonite progressed – its function is to hold the bentonite in place.
The separation wall of the outer filter has an additional function, i.e. it serves as a hidden formwork for the outer plug.

4 GEOLOGY OF THE EXPERIMENTAL LOCATION

The EPSP experiment is underway in the underground research laboratory (URL) of the Josef facility, a former experimental gold mine which is located near the Slapy dam close to the villages of Čelina and Mokrsko in the Příbram district of Central Bohemia, Czech Republic.
The Josef experimental gallery runs in a NNE direction through the Mokrsko hill rock massif. Geological diversity makes up one of the major advantages of the Josef facility which features two basic geological formations each with very different histories and contact zones (Morávek, 1992).

Moreover, each of the formations exhibits different physical and material properties which change in character towards the contact zone and which feature a variety of local fracture zones and intrusions. This provides a high level of flexibility with regard to choosing the best location for the conducting of experiments depending on the conditions required, for example fracture systems, rock stability, rock strength, mineralogy, etc.
The EPSP experiment itself is located within the M-SCH-Z/SP-59 experimental gallery niche.
The support technology required by the experiment is located in parallel niche M-SCH-Z/SP-55.
The niches are interconnected by means of cased boreholes equipped with tubing for the purpose of the circulation of the pressurisation media (4 leading into the filter and 4 leading into the pressurisation chamber) and for monitoring (5 boreholes equipped with sealed cables).
The experimental gallery niche is traversed by quartz and quartz-carbonate veins with a maximum thickness of 14cm. Information on the dominant joint systems is recorded in historical mining documentation which was subsequently updated according to map source documents owned by Geofond – Dobříš 1-9/34-24, M-SCH-Z/SP-59.
The detailed mineralogical study of the filling of the fissures was conducted in 2013 in niche SP-59 (Dvořáková et al., 2014).

5 ROCK MASS RESHAPING

The EPSP consists of two circular fibre shotcrete plugs (1.8m wide and 3.6m high) emplaced into the rock massif (Fig.1 and Fig. 2). The inner plug is located at a distance of 0.5m from the tunnel face and the outer plug ends at a distance of 7.2m from the tunnel face. The space between the two plugs consists of bentonite pellets with a thickness of 2000mm and a gravel filter positioned between the concrete block structures. The total length of the experimental construction plug is 7.2 metres extending from the excavation tunnel face.

Prior to the commencement of the construction phase of the EPSP experiment, it was necessary to reshape the experimental gallery niche; the main aim of this stage was to prepare the SP-59 niche according to plug requirements.
Work started in October 2013 with initial 3D scanning following which the excavation work necessary for EPSP emplacement began in the SP-59 niche. A Darda EP hydraulic splitting set with a Darda C9N hydraulic wedge was employed for enlargement purposes. The profile of the niche was modified so as to form an approximately circular profile 3.6m in diameter (Záruba, 2015).
Subsequently, 23-meter long connecting boreholes were drilled between the SP-59 experimental niche and the SP-55 technological niche for the purpose of pressurising the experiment and for instrumentation requirements.
Five steel cable heads (Fig. 3) to be used for the passage of cables from the measurement sensors located within the experiment were then installed in the SP-59 niche. In addition, a total of 12 measuring bolts to be used for the measurement of stress were installed in pre-drilled holes around the future plug.

6 ROCK IMPROVEMENT

The surrounding rock mass was injected with polyurethane resin at high pressure so as to improve the quality of the host rock (Fig. 4). The required permeability value of the massif following injection was a minimum of 10^{-8}m/s. The requirement was to improve the quality of the massif surrounding the experiment up to a radius of 5m. The injection mixture, consisting of WEBAC 1401 polyurethane resin, was injected into a total of 72 injection boreholes which were fitted with mechanical packers. The resin was injected into the boreholes by means of a WEBAC IP 2 high-pressure grouting set. Injection was terminated once a pressure level of approximately 35MPa had been attained. A total of 760.45kg of WEBAC 1660, WEBAC 1410, WEBAC 4170T, WEBAC 150 and WEBAC 1403 PU resins

was used so as to achieve the required hydraulic parameters within the rock mass in the required area (Záruba, 2015). Following the construction of both the inner and outer EPSP plugs additional grouting using CarboPurWF and CarboPurWFA resins was performed.

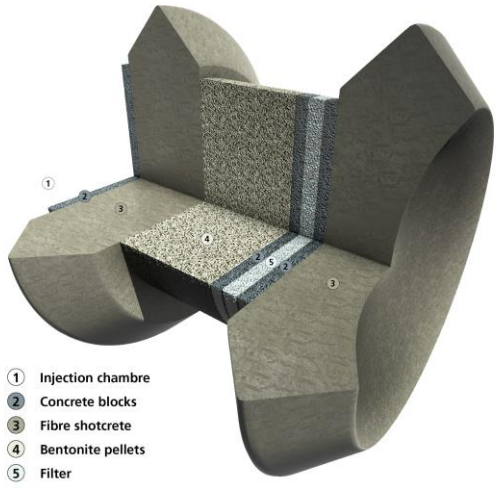


Figure 1 Cross-section through the plug

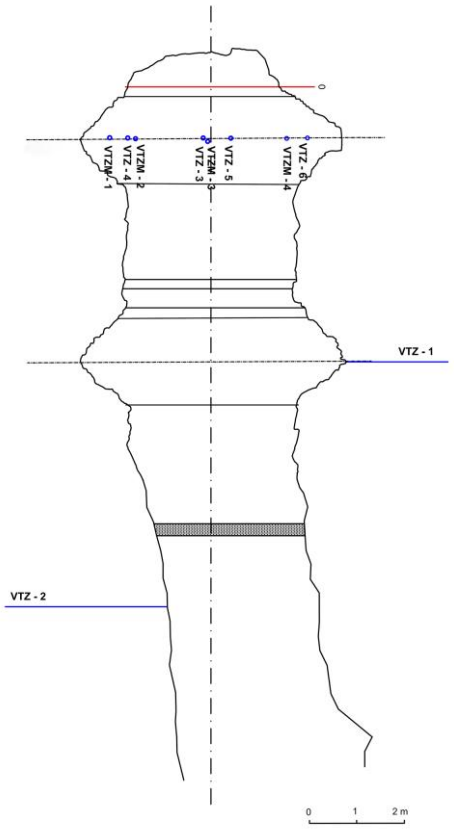


Figure 2 Location of the tested boreholes (WPT in the SP-59 niche)(Záruba, 2015)



Figure 3 Cable head

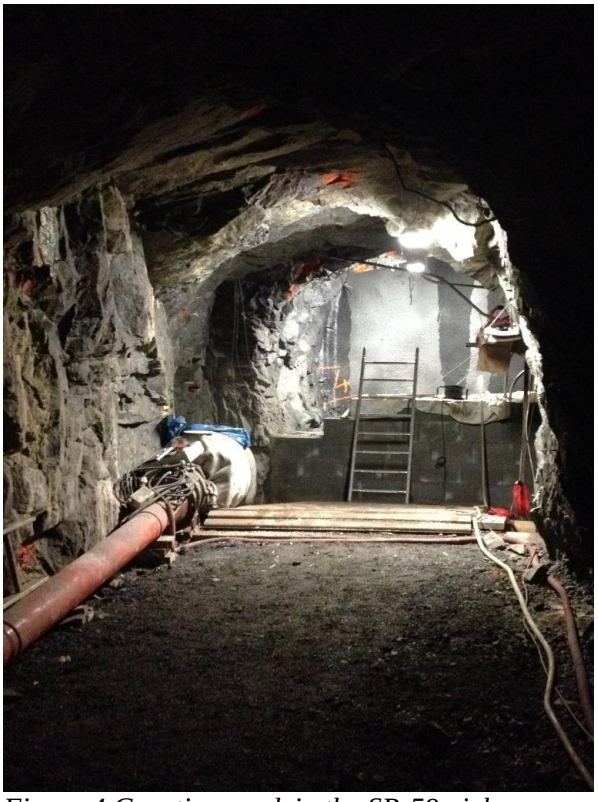


Figure 4 Grouting work in the SP-59 niche

7 RESULTS

7.1 In-situ tests

Water pressure tests (WPT) were conducted for the checking of the grouting of the rock mass in the space intended for the plug. A total of six boreholes 76mm in diameter and 3.1m long (see Fig. 2) were drilled so as to verify the sealing capacity of the rock mass up to a depth of 5m. An additional four boreholes 14mm in diameter and 0.3m long (Fig. 2) were drilled for the verification of the sealing capacity of the near-surface layer of the rock massif in the space intended for the outer plug.

Water pressure testing was conducted both prior to and following the injection of the grouting material.

Once the testing procedure was completed, the boreholes were filled using WEBAC 1660 resin.

Water pressure tests were performed in the VTL-2 horizontal verification borehole. Once a test pressure level of 2MPa had been attained, it was verified that the hydraulic parameters ranged from 3.81E-09 to 7.71E-09m/s. After 2MPa was exceeded, an exponential increase in the consumption of test water was observed (see Tab. 1) and effluents were detected on the surface of the niche (Sosna et al., 2014b).

After attaining a test pressure level of 2MPa in the VTL-3 and VTLM-1 horizontal verification boreholes, it was verified that the hydraulic parameters in the rock massif following injection ranged from 1.24E-10 to 2.49E-10m/s (Tab. 2).

Finally, the VTL-4,5,6 and VTLM-2,3,4 ceiling verification boreholes were also subjected to test pressures up to 2MPa and it was verified that the hydraulic parameters in the rock massif following injection ranged from 1.79E-9 to 2.58E-10m/s (Tab. 3).

Goodman-Jack uniaxial press tests were performed in the VTL-2 borehole with a diameter of 76mm and a length of 4.5m. Tests were conducted at eight incremental depth levels between 0.8 and 4.3m at 0.5m intervals employing alternately the horizontal and vertical rotation of the jaws of the test press.

Table 1 Water pressure test VTL-2 (Sosna et al., 2014b).

WPT VTL-2	**time**	**cm**	**Q(m^3/s)**	**k (m/s)**
Level		**Reading consumption**	**Water consumption**	**Hydraulic conductivity coefficient**
1.25-4.5	11	9.8	1.63E-06	3.81E-09
1.25-4.5	9	32.5	6.62E-06	7.71E-09
1.25-4.5	5	45.5	1.67E-05	1.30E-08
3.0-4.5	10	9.8	1.80E-06	7.59E-09
3.0-4.5	10	13.1	2.40E-06	5.08E-09
3.0-4.5	4	24	1.10E-05	1.55E-08
3.0-4.5	0.5	24.7	9.06E-05	9.57E-08

Table 2 Water pressure test VTL-3 (Sosna et al., 2014b).

WPT VTL-3	**time**	**cm**	**Q (m^3/s)**	**k (m/s)**
Level		**Reading consumption**	**Water consumption**	**Hydraulic conductivity coefficient**
1.13-3.1	4	0.0	0.0	Cannot be evaluated - impermeable
1.13-3.1	30	0.1	1.45E-07	2.49E-10
1.13-3.1	30	0.05	7.23E-08	1.24E-10

Table 3 Water pressure tests in boreholes VTL-4,5,6 and 2,3,4-VTLM (Sosna et al., 2014b).

WPT	**time**	**cm**	**Q (m^3/s)**	**k (m/s)**
Level		**Reading consumption**	**Water consumption**	**Hydraulic conductivity coefficient**
VTL4				
1.24-3.05	14	0.1	3.10E-07	5.57E-10
VTL5				
1.24-3.1	10	0.1	4.34E-07	7.80E-10
VTL6				
1.24-3.12	15	0.05	1.45E-07	2.58E-10
VTLM-2				
0.13-0.31	10	0.05	2.17E-07	1.79E-09
VTLM-3				
0.13-0.29	10	0	N/A	
VTLM-4				
0.13-0.295	10	0	N/A	

The tests were performed using the Goodman-Jack apparatus – Hard Rock type. Stepped load increments were chosen of 5MPa to 20MPa, with strain values at the same step value of 5MPa for all the increments and then the second cycle was

loaded with the same steps until a maximum value of 40MPa was attained (Sosna et al., 2014a).
The results of the constrained modulus (E_p) and elasticity (E_{def}) tests in borehole VTL-2 are presented in Tab. 4:

Table 4 Constrained modulus (E_p) and elasticity (E_{def}) tests in borehole VTL-2 (Sosna et al., 2014b).

Orientation of the jaws	***Depth***	***$E_{def,1}$ GPa***	***$E_{def,2}$ GPa***	***$E_{def,2all}$ GPa***	***$E_{p,1}$ GPa***	***$E_{p,2}$ GPa***	***$E_{p,2all}$ GPa***
	(m)	***5-20 MPa***	***20-40 MPa***	***5-40 MPa***	***20-5 MPa***	***40-20 MPa***	***40-5 MPa***
horizontal	0.8	8.1	10.9	10.0	8.6	13.9	10.4
	1.8	3.8	8.2	6.8	5.3	14.6	7.8
	2.8	10.0	14.3	11.9	10.0	17.8	12.7
	3.8	2.3	5.4	4.5	3.4	16.5	5.0
vertical	1.3	5.1	9.8	8.7	7.1	15.6	9.7
	2.3	5.3	14.2	13.9	11.9	20.0	14.1
	3.3	7.6	9.4	10.0	11.9	15.1	11.0
	4.3	10.8	14.3	13.1	13.1	16.6	13.1

7.2 Laboratory tests

Laboratory tests were conducted for the determination of bulk density, strength in transverse compression, unconfined compression strength and constrained modulus E_{def} (MPa). The tests were carried out on specimens of the rock mass (tonalite in SP-59). Six 50mm-diameter specimens with a slenderness ratio of 1:2 were analysed. The laboratory tests were performed at the ARCADIS CZ a.s. accredited laboratory (Záruba, 2015).

Table 5 Laboratory determination of modulus of elasticity and constrained modulus, unconfined compression strength and strength in transverse compression - average values taken from six analysed samples (Filala et al., 2015).

Unconfined compression strength (MPa)	***Strength in transverse compression (MPa)***	***Modulus of elasticity (GPa)***	***Constrained modulus (GPa)***
121.78	8.4	79.94	79.98
70	6	undefined	undefined

8 CONCLUSIONS

The rock massif around the EPSP experiment was improved by means of grouting using polyurethane resins. Following injection the rock mass demonstrated significantly lower values of permeability. This was later confirmed by the results of water pressure testing (see Tabs. 1,2,3). Other measurements taken of the various geotechnical parameters concerned the overall conditions of the rock mass (see Tabs. 4,5).
As a result of the successful construction of the EPSP experiment, the first objective (the demonstration of the suitability of the technology) of the DOPAS EPSP experiment has been achieved. "Alternative" technologies (such as shotcreting, shotclay application and GBT) and materials (low pH shotcrete, bentonite pellets) have been successfully tested and the experiment is now ready for the commencement of the experimental stage.
Moreover, the successful application of the construction techniques employed in the first stage of the EPSP experiment have helped to prove the safety of a future deep geological repository for radioactive waste in the Czech Republic.

9 ACKNOWLEDGEMENTS

The research is being funded from the European Union European Atomic Energy Community (Euratom) Seventh Framework Programme FP7 (2007-2013) according to grant agreement no. 323273, the DOPAS project.

10 REFERENCES

Dvořáková, M., Hanusová, I., Svoboda, J. & Vencl, M. (2014). EPSP experiment- construction of a plug for a deep geological radioactive waste repository as part of the european DOPAS project. Tunel 23 (2), 4-10.

Filala, Z., Sosna, K., Šebelová, J. & Záruba, J. (2014). Laboratorní stanovení modulů pružnosti a přetvárnosti, pevnosti v prostém tlaku a pevnosti v příčném tahu, Arcadis CZ a.s. Archív SÚRAO (in Czech).

Geofond – Dobříš 1-9/34-24, M-SCH-Z/SP-59.

Morávek, P. (1992). Zlato v Českém masivu. 1. vyd. Praha, Český geologický ústav.

Sosna, K., Černý, D., Kvarda, M., Tocháček, M. & Záruba, J. (2014a). Stanovení deformačních modulů in situ pomocí zkoušky Goodman Jack, Arcadis CZ a.s. Archív SÚRAO (in Czech).

Sosna, K., Vysoká, H. & Záruba, J. (2014b). Výsledky vodních tlakových zkoušek ve vrtu VTL-4,5,6 a VTLM-2,3,4, Arcadis CZ a.s. Archív SÚRAO (in Czech).

Záruba, J. (2015). Experiment EPSP – DOPAS: As-built Documentation – Grouting, drilling and sealing operations for the EPSP experiment conducted under the DOPAS international project, Arcadis CZ a.s. Archív SÚRAO.

Geotechnical Engineering for a new container terminal in Lomé, Togo, West Africa

Morten Anker Jørgensen
NIRAS A/S, Denmark, moj@niras.dk

Arne Hansen
NIRAS A/S, Denmark, aha@niras.dk

ABSTRACT

A completely new large container terminal in Lomé began in 2014 to handle a large number of containers. The container berth is 1.05 km long with water depth of 16.7 meter. The project includes construction of an area of 55 ha for container stacking and building associated works. The purpose of the container terminal is primarily transshipment of containers between large container vessels from Asia /Europe and smaller container feeder vessels serving other ports in West Africa.

In 2011 a geotechnical investigations program with geotechnical boreholes, laboratory testing and CPT (Cone Penetration Tests) was performed. The geotechnical investigations revealed a tricky deep layer of clay under 15 to 20 m of recently deposited sand due to littoral drift along the coast.

The article will focus on a comparison of the assessment in the design phase of the conditions for foundation of the container berth with actual observations during and after construction.

The article is intended to address the following features:

- *Relative density of sand and need for deep compaction*
- *Vertical settlements*
- *Design of diaphragm quay wall*
- *Monitoring of quay wall and track for quay side cranes*

Keywords: Retaining structures, diaphragm quay wall, deep compaction, monitoring of deformations.



Figure 1 Lomé Container terminal in operation. April 2015.

1. INTRODUCTION



Figure 2 Site view. Port of Lomé with terminal site in background. 2011.

The container berth is 1.05 km long with water depth of 16.7 meter. The project included construction of an area of 55 ha for container stacking and associated building works. The purpose of the container terminal is primarily transshipment of containers between large container vessels from Asia /Europe and smaller container feeder vessels serving other ports in West Africa. The port serves also as a gateway to the landlocked countries of Mali, Niger and Burkina Faso and to the northern areas of Nigeria.

The site is almost entirely located in an area which since the construction of Lomé Port in the 1960'es has developed by progression of the shore line due to accumulation of drifting sand. In the quay alignment roughly 13 m of recently deposited sand was recorded with its present ground level at approximately the high water level of the tide.

The employer for the project was Lomé Container Terminal (LCT) with Cyes_Somague JV as the main contractor and responsible for the detailed design. NIRAS prepared tender documents for an EPC-contract and carried out technical supervision of the construction.

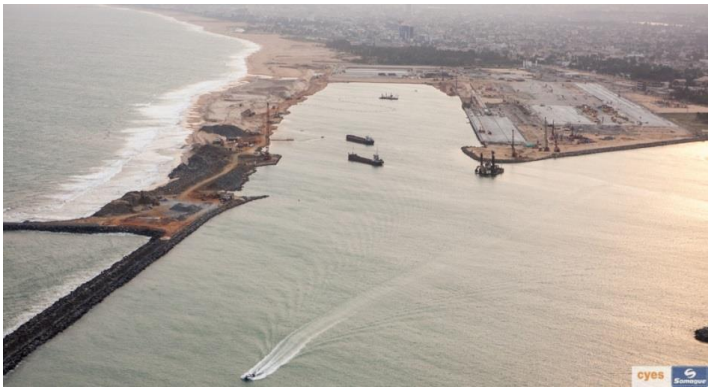


Figure 3 Site with new basin and quay wall (right hand side of basin). Autumn 2013.

2. GEOTECHNICAL INVESTIGATIONS

A preliminary ground investigation program had been undertaken during November 2008 to July 2009 for initial project planning , comprising 7 geotechnical boreholes and 34 dynamic probes.
Before tendering a more extensive investigation was carried out, see Figure 4, including:

- 21 boreholes to depth ranging from 17 m to 51 m.
- 85 CPTU (Cone Penetrations Tests with pore pressure measurements) to depths ranging from 13m to 48 m.
- Laboratory testing for classification and soil strength parameters.

Figure 5 and Figure 6 show the drilling and the CPT rigs that were mobilized for the investigations in 2011. CPT-equipment and counterweight were installed on a sledge towed by a Caterpillar. This vehicle proved convenient for access all over the site.

Later the selected contractor carried out additional investigations as basis for his detailed design.

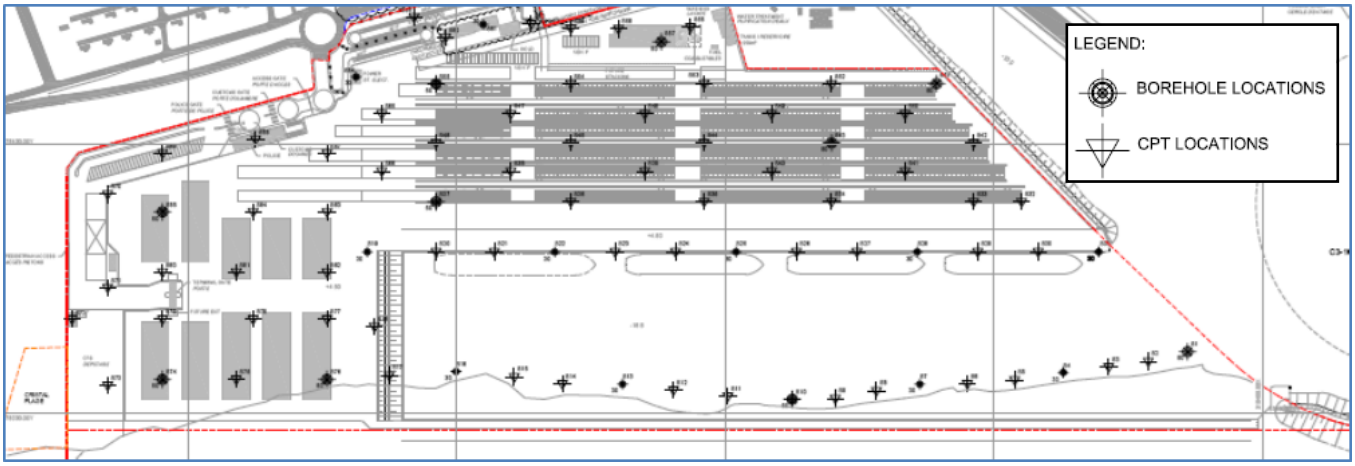


Figure 4 Plan of pre-tender soil investigations 2011.



Figure 5 Geotechnical borehole with an interim dam to the left for protection of sea waves. March 2011.



Figure 6 Cone Penetration Test (CPTU) equipment (20 ton capacity). March 2011

3. SOIL CONDITIONS

A typical cross section in the main quay wall is shown in Figure 7which also includes references to the soil layers A-F. Little variation across the site was detected.

The geotechnical parameters adopted for the layers are summarized in Table 1.

Table 1 Geotechnical parameters.

Layer		γ (kN/m^3)	c' (kPa)	φ' (°)	E (MPa)
B	Sands (SP)	19	0	37	40
C_0	Silt and Silty-Clay (SM to SC)	20.2	0	30	10
C_1		20.1	15	22	8
C_3		20.1	45	23	15
D_1	Silty sands (SM)	21	0	35	40
D_2	Silty Sands (SP)	21	0	35	45
E	Sandy organic clay (CH)	18	12	17	8
F	Silty (SP-SM)	20	0	35	35

The dominating sub-ground is sandy, but the sand is intersected by two cohesive strata C and E throughout the site. The soil investigations and associated laboratory tests resulted in some apparently contradictory properties for the two clay layers which are reflected in design parameters that may be on the conservative side.

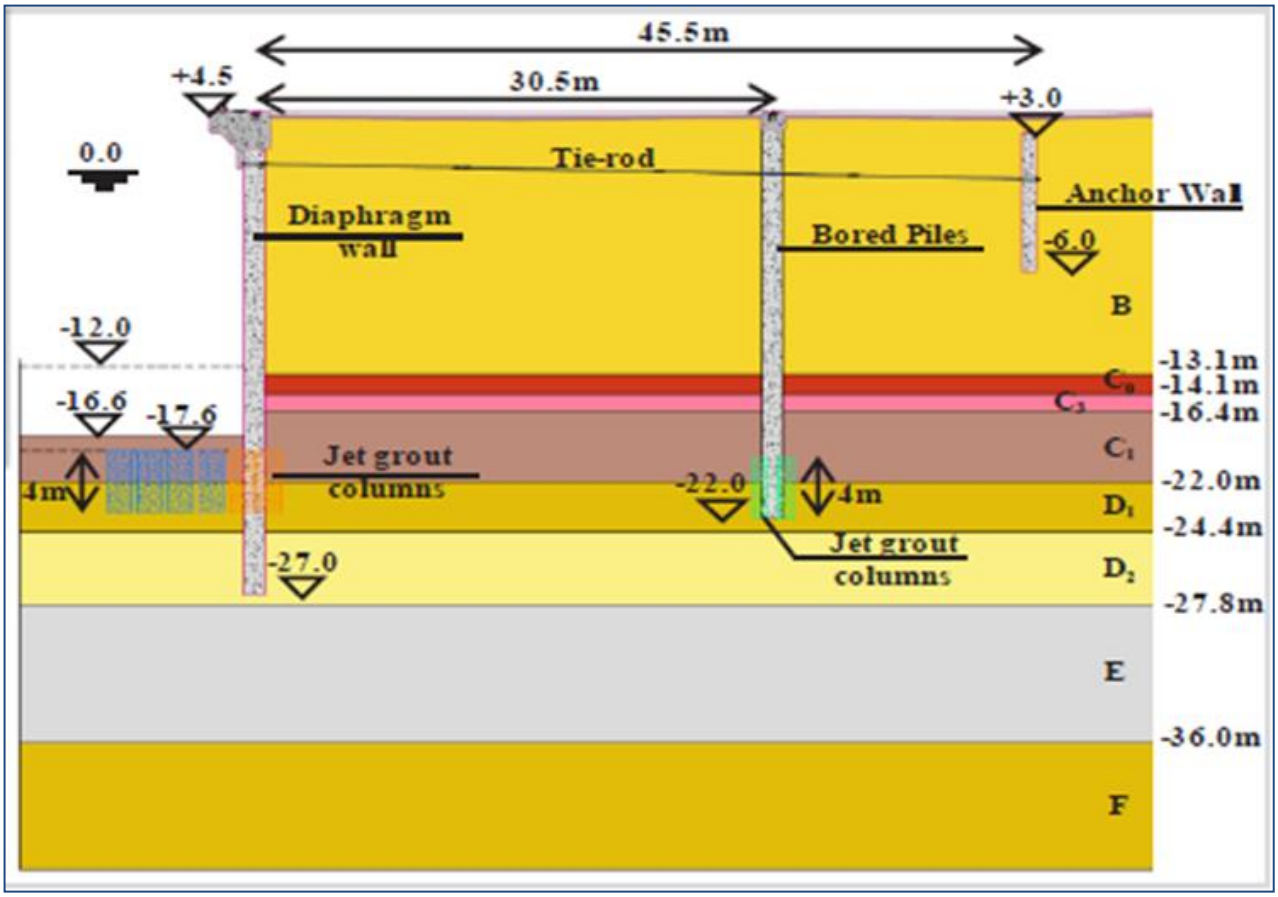


Figure 7 Soil layers and configuration of quay structure.

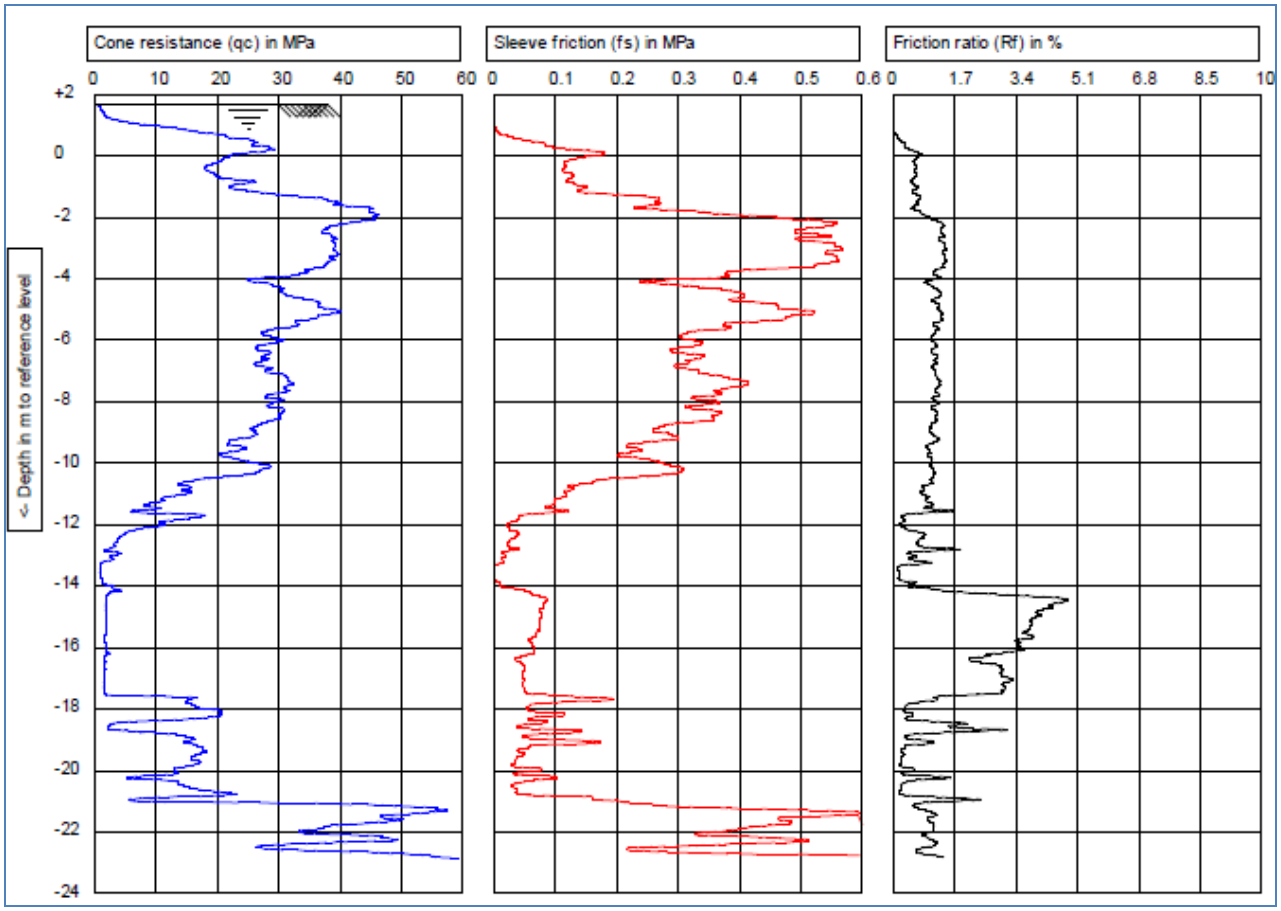


Figure 8 Results from Cone Penetration No. S24 indicating a clay layer at level -14 to -18.

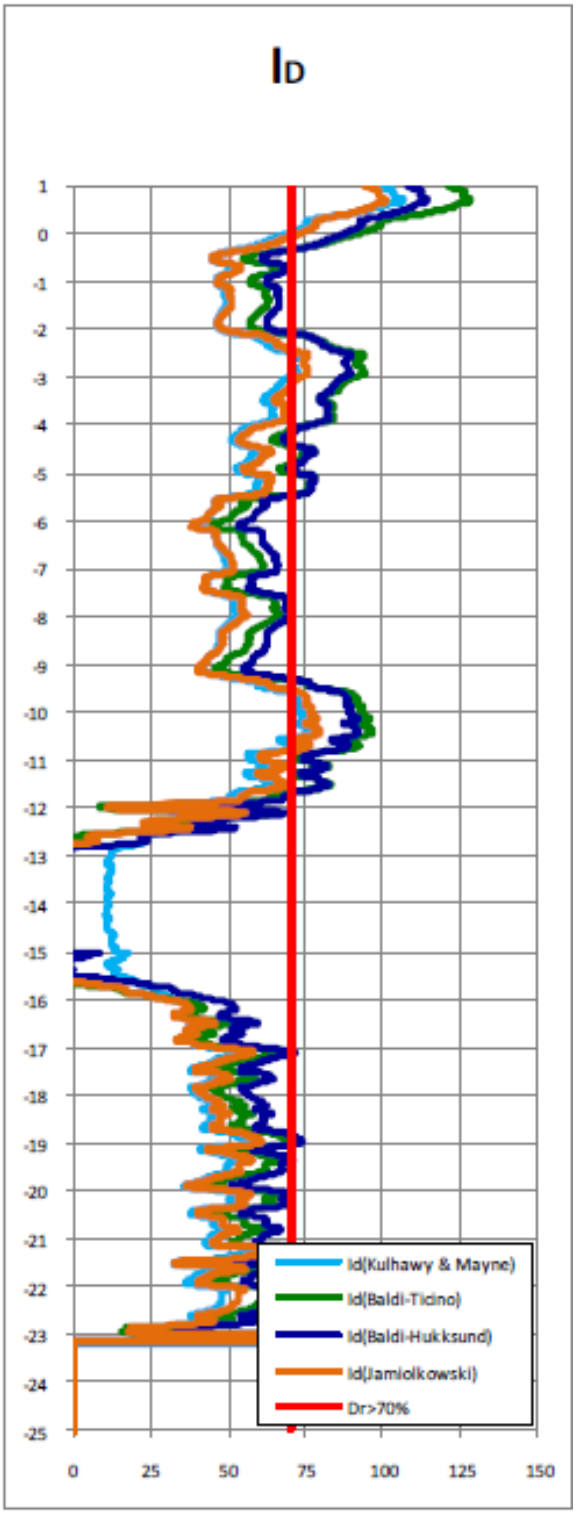


Figure 9 Assessment of relative density I_D, based on CPT-tests.

4. DESIGN AND CONSTRUCTION OF DIAPHRAGM QUAY WALL

The quay structure consists of a 1.2m thick reinforced concrete wall, cast in-situ as a diaphragm wall as shown in Figure 7. The wall is anchored to a separate diaphragm anchor wall by steel tie rods at an average distance of 1.5m between anchors.
A track for quay side container cranes is supported on the quay wall and on separate bored piles on the land side.

The dimensions of the quay structure are constant along the entire length of the main quay. Minor variations in the soil profile are accounted for by local strengthening of critical sections with jet-grouting columns – as shown in Figure 7.

The design of the quay structure was made in accordance with BS6349-2:2010, BS EN 1992-1-1.2004: Euro-code 2 and BS EN 1997-1. 2004: Euro-code 7 and included a large number of load combinations to verify ultimate limit state (ULS) and serviceability limit states (SLS). Several aspects were taken into account, such as water level variation, dredging level variations, STS-crane loads and container live loads on the apron. ULS combinations included limit states GEO and STR.

Typical result schemes are shown in Figures 10 and 11.

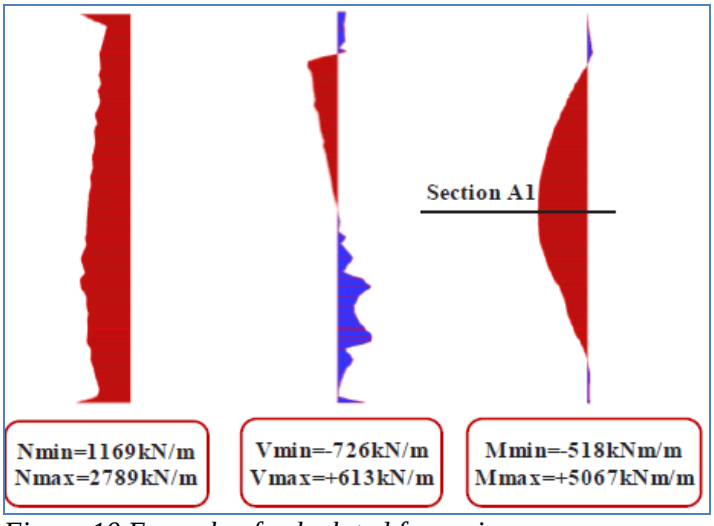


Figure 10 Example of calculated forces in quay wall.

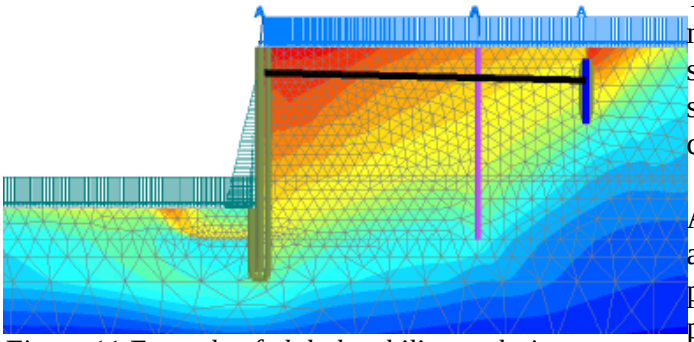


Figure 11 Example of global stability analysis (Plaxis 2D).

The wall was constructed in sections of 3 or 6 m width. Construction included excavation, stabilization of the trench with a bentonite slurry, installation of reinforcement cage and concreting.

All bentonite was recirculated in the works after thorough treatment and testing of properties. Raising the 30 m long, prefabricated reinforcement cages from horizontal to vertical proved difficult and required application of some skill from the contractor's side.

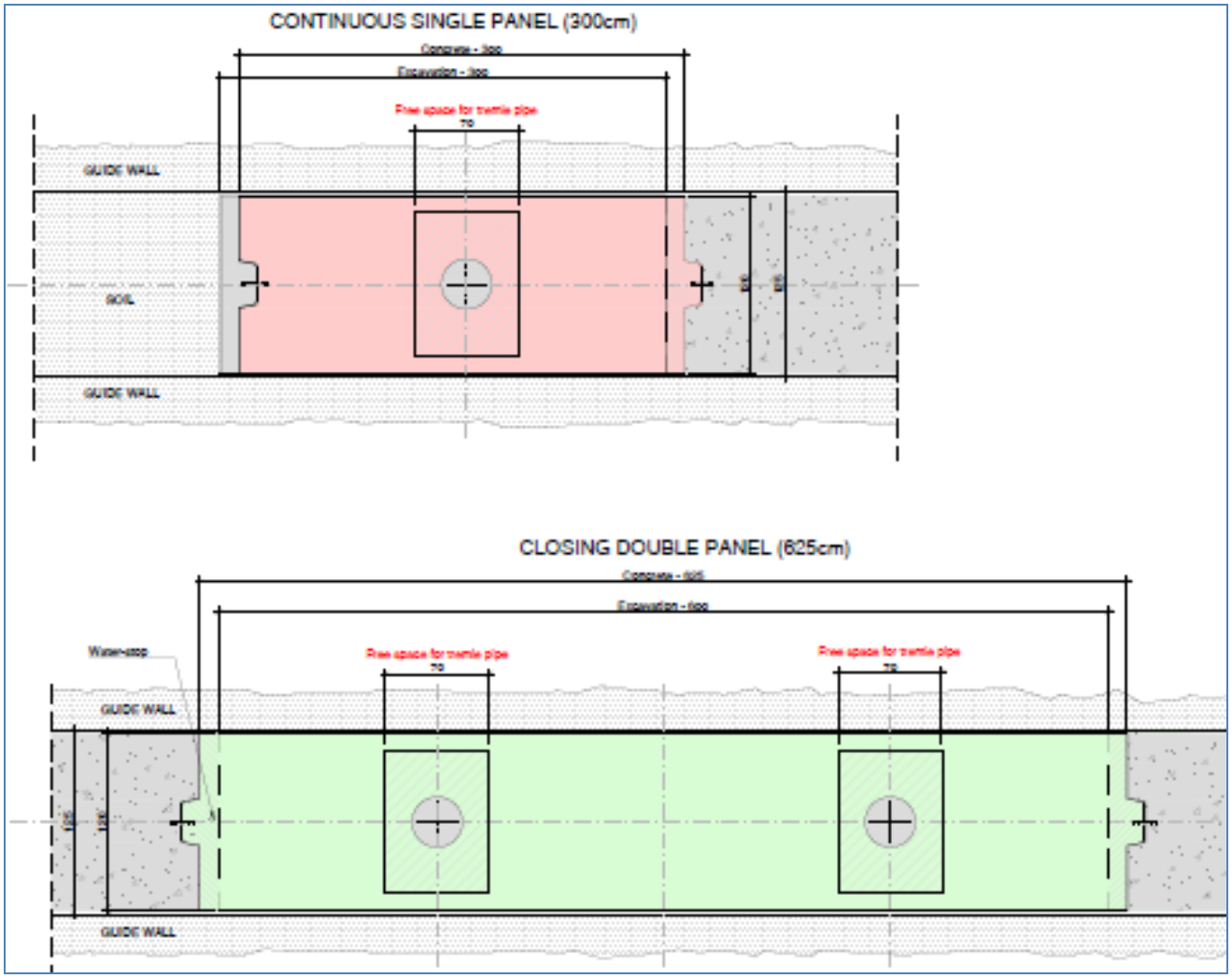


Figure 12 Typical panel sections in diaphragm wall with watertight joints between panels.

Figure 13 to Figure 15 show some views related to the construction of the quay wall.

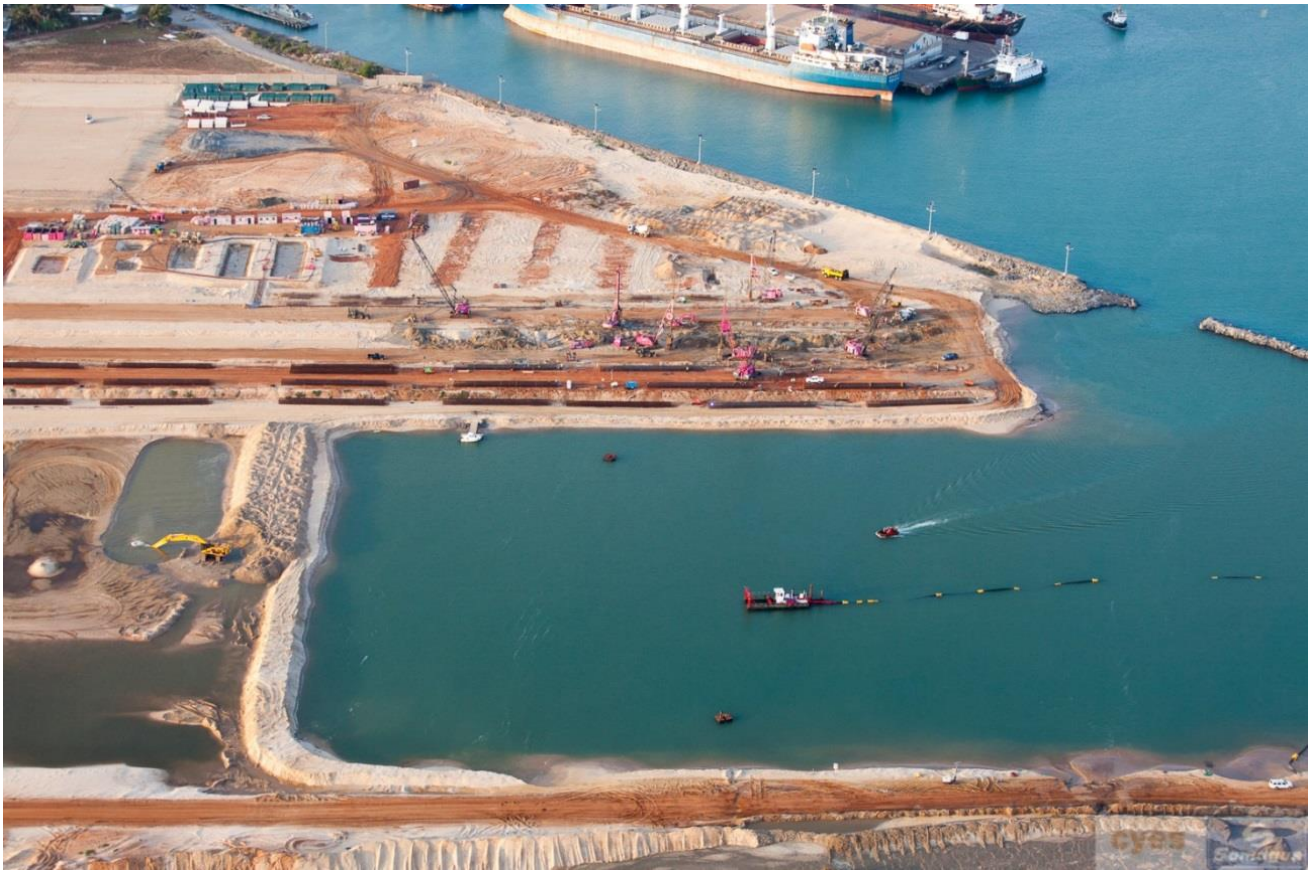


Figure 13 East part of the new basin with reinforcement cages ready to be installed. November 2013.



Figure 14 Machinery for the diaphragm wall and reinforcement cages to be installed. November 2013.



Figure 15 The reinforcement cages (app. 30 m long) for the diaphragm wall were lowered into the trench. November 2013.

The analysis carried out during detailed design included extensive Plaxis-analysis of the performance of the quay structure in terms of displacements of quay wall and rail beams during the different construction phases and after completion when the structure is exposed to traffic loads. According to BS 6349, for quasi-permanent load combinations, the maximum horizontal displacement accepted for a vertical wall is H/300 (where H is the total height of the wall).

Displacements, horizontal and vertical, were calculated for different control points in the quay structure (top of quay wall, crane beams, anchor wall etc.) and for different stages of construction and operation. Typical results from the analysis are shown in Figure 19 where each color represents a defined control point.

A maximum horizontal displacement of 61mm was calculated, meeting the requirement (< H/300 ≈ 100mm). The relative displacements of crane beams were also calculated to be manageable with regard to the selected rail system.



Figure 16 Vibrator for the deep compaction. May 2013



Figure 17 Local recess of the ground surface during the deep compaction. May 2013.

5. RELATIVE DENSITY OF SAND AND NEED FOR DEEP COMPACTION

The work specification included deep vibro-compaction (see Figure 16) of all naturally deposited sand (layer B in Figure 7) to reduce settlements in the future stacking areas.
The contractor's compaction methodology and procedures were initially refined and optimized in a few test sections based on CPT-testing before and after compaction.
From the tests it became clear that in large parts of the construction area the effect of deep compaction would be rather limited. Some densification was achieved in the lower part of the sand layer. But penetration of the upper zone resulted in apparent loosening of naturally dense sand as indicatively shown in Figure 17.
The tests resulted in a significant reduction of deep compaction works.

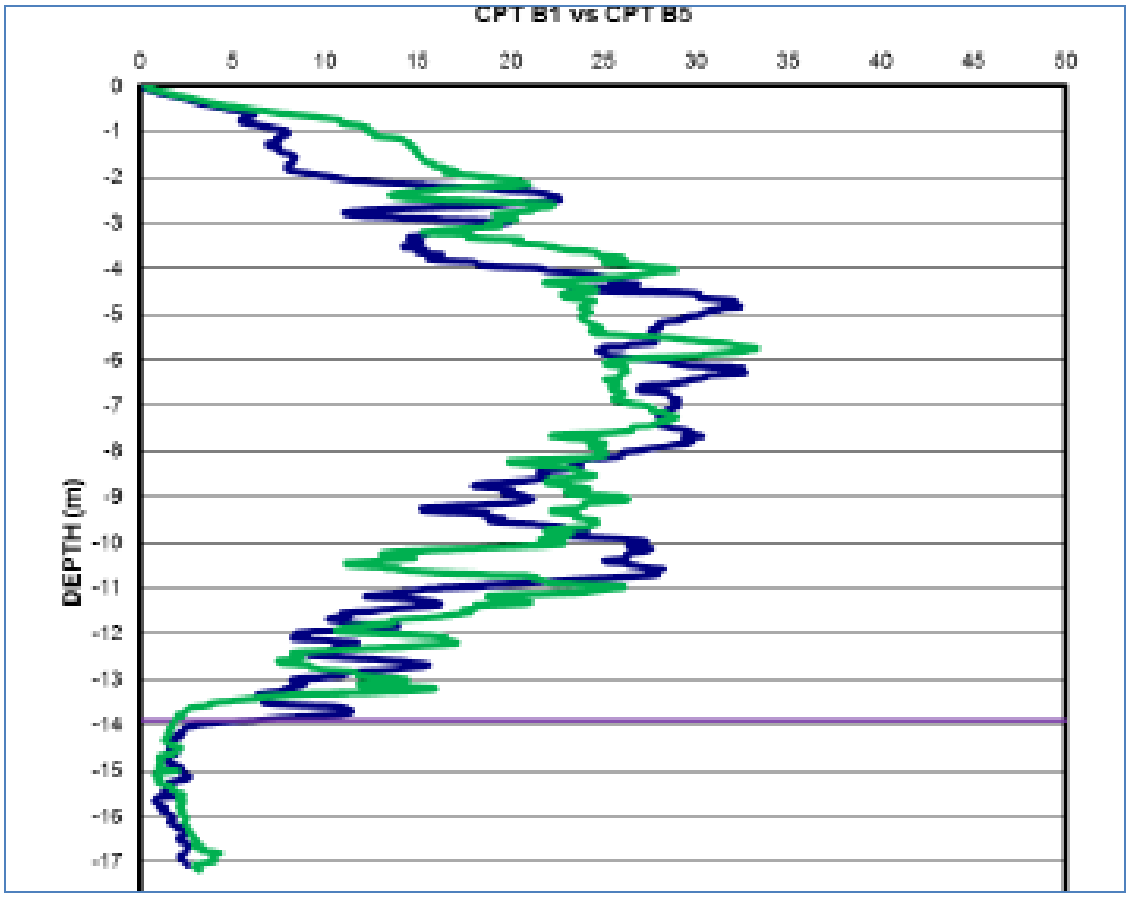


Figure 18 CPT-testing results before and after compaction (Blue color: Before compaction. Green color: After compaction).

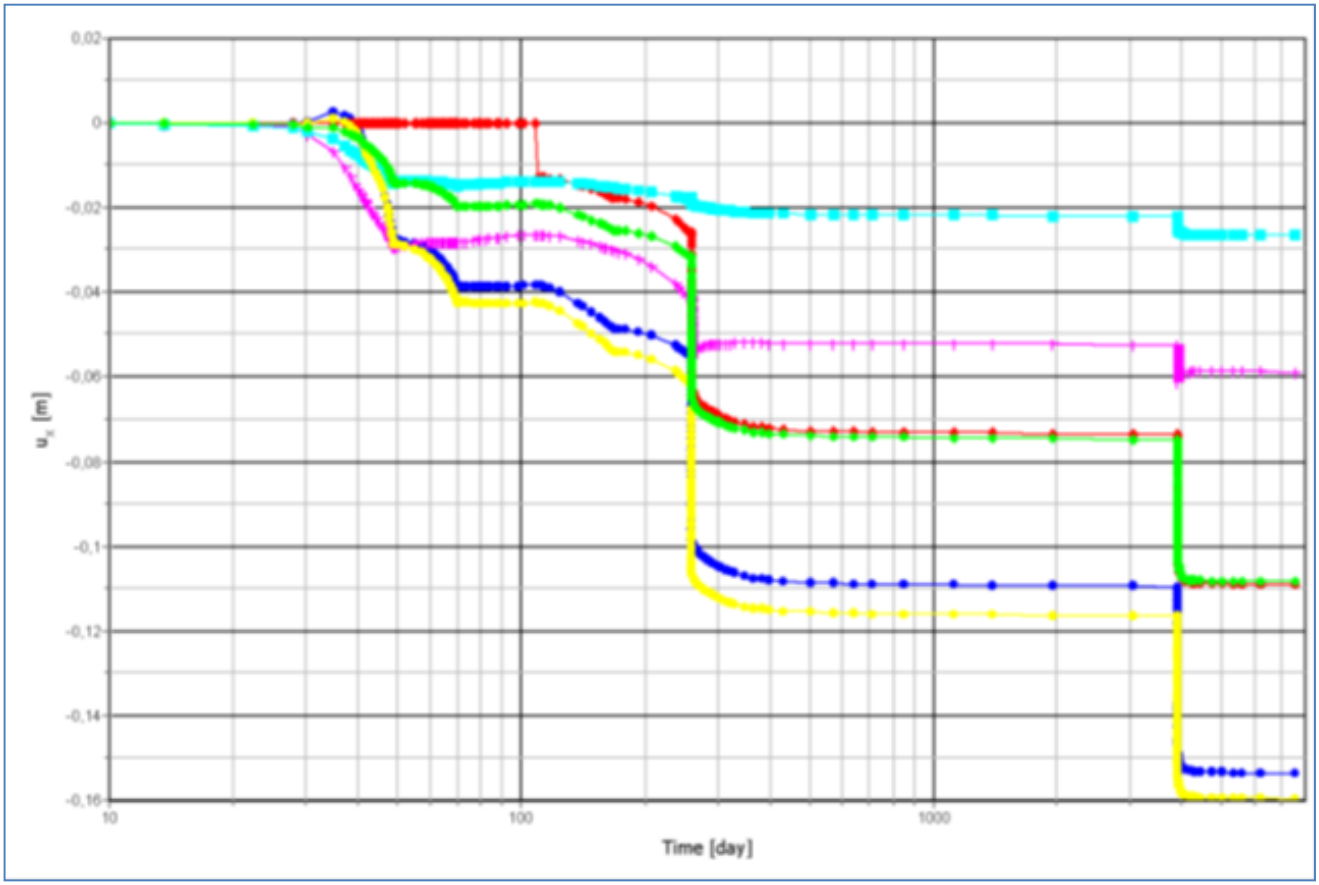


Figure 19 Calculated horizontal displacements with time for different control points.

6. RECORDED VERTICAL SETTLEMENTS

Monitoring included systematic measurement of settlements. The recorded settlements were surprisingly small although the vertical soil stresses increased due to the weight of 2 to 2.5m of sand fill and pavement from raising the general level of the terminal. Settlements of 10 to 15 mm recorded and developed almost instantly.

7. MONITORING OF QUAY WALL AND TRACK FOR QUAY SIDE CRANES

The specified monitoring program also included observation of the movement of quay structures during construction and after exposure to operational loads from quay side container cranes and cargo. The program included horizontal and vertical displacements and inclinometer records.

Until this date the recorded displacements, both vertically and horizontally, have proven significantly smaller than the predicted displacements as described in section 4.

The Plaxis calculations predicted for the front top corner of the quay structure overall horizontal displacements up to 140 mm. The recorded displacements are less than 30 percent of this figure.
The lateral displacements of the seaside crane rail are less than 50 percent of the calculated displacement resulting from crane loads.

8. CONCLUDING REMARKS

One of the major challenges of this type of project is the pre-assessment of the soils to be verified by detailed monitoring of the performance of the structures . The assessment depends on the specification of the geological-geotechnical campaign prior to construction and from the interpretation of the results.

An experience from this project is that in spite of the efforts by several experts in the investigation and design phases, subsequent monitoring of a structure may still show results that deviate quite significantly from the predicted performances.

9. REFERENCES

BS 6349-2 (2010). Maritime works. Code of practice for the design of quay walls, jetties and dolphins.

BS EN 1992-1-1 (2004). Euro-code 2: Design of concrete structures – Part 1-1: General rules and rules for buildings.

BS EN 1997-1 (2004). Euro-code 7: Geotechnical design. Part 1: general rules.

Tomásio, T. et all. (2015). Lomé container terminal. Proceedings of the XVI ECSMGE, 2015

10. ACKNOWLEDGEMENTS

Authors want to thank the owner, Lomé Container Terminal (LCT), for the approval to write and submit this paper.



Figure 20 Machinery for deep vibration compaction. Distance between the points is app. 3 m. July 2013.

The Use of Geosynthetic Reinforced Structures Working as Bridge Abutments in Scandinavia and Europe

M.-T. van Keßel
HUESKER Synthetic GmbH, Germany, vankessel@huesker.de

B. Thesseling
HUESKER Synthetic GmbH, Germany, thesseling@huesker.de

ABSTRACT
The main focus of this paper is directed to the geosynthetic reinforced slopes or walls which have already been built with heights up to 41 m. Typically multiple horizontal layers of geosynthetics, mainly geogrids, are filled with compacted granular material and arranged on top of each other with a vertical spacing of 0.4 m – 0.6 m. In order to prevent slope failure the required design strength and length of the single geogrid layers has to be estimated in a geotechnical design. The paper includes a short overview of European guidelines that regulate the design and the construction of structures using geosynthetics e.g. "Nordic Guidelines for Reinforced Soils and Fills" (2005).
With international case studies and a large scale test the development of geosynthetic reinforced structures specifically for bridge abutment applications is demonstrated. In 1991 for example the construction of geosynthetic reinforced walls working as bridge abutments over the Nyborg-Fredericia main railway line in Ullerslev was instructed by the Danish State Railways (DSB). After an almost 25-year service life the design, the construction and the settlement behaviour are described in this paper.

Keywords: Bridge Abutments, Geosynthetics, Retaining Structures

1 INTRODUCTION

Geosynthetics have been used effectively to overcome many geotechnical, roadway, hydraulic and environmental issues during the last decades. The geotechnical applications mainly include geosynthetics performing the reinforcing, separating and stabilizing functions. Thus they enable the improvement of structures on soft and even organic soils as basal reinforcement elements, they provide reinforcement above concrete piles or as Geosynthetic Encased Columns (GEC, Alexiew et al., 2012). This paper focusses on the introduction and description of geosynthetic reinforced retaining structures (GRS). In general these types of structures are frequently used to construct steep slopes or vertical to sub-vertical retaining walls. Due to the high load carrying capacity, (see Alexiew and Detert, 2008 and section 3.2), of geosynthetic reinforced retaining structures they have also been utilised for bridge abutments all over the world and in the process have become an established construction method.

2 GEOSYNTHTETICS

2.1 Characteristics and Functions

The term 'geosynthetic' includes a wide range of products produced from synthetic raw materials like Polyester (PES), Polypropylene (PP), Polyvinylalcohol (PVA), Polyamid (PA) and Aramid (AR). They are generally used in geotechnical constructions for separating, filtering, draining, reinforcing, protecting and sealing purposes. Best known representatives are perhaps non-woven and woven geotextiles, uni- or bi-axial geogrids and geocomposites. Geogrids can be produced by knitting or weaving of fibers, punching and extrusion of plastic sheets or

the welding of cross-laid synthetic elements. Depending on the raw material and the production process geosynthetics can be divided into several types depending on their inherent mechanical characteristics and consequently appropriate application fields. Their main characteristics are tensile strength, tensile stiffness and their stress-strain-performance with special regard to the long term creep behavior; usually documented in 'Isochrones Curves'. Further general information can be found in SVG (2003) or CUR 234 (2012), EBGEO (2010).

2.2 Guidelines

In Europe all geotechnical structures have to fulfil the requirements and regulations of EN 1997 'Eurocode 7 – Geotechnical Design" (EC 7). Since the EC 7 does not include the normative regulations and recommendations for geotechnical structures using geosynthetics several different guidelines have been published in the European countries like France, Netherlands and United Kingdom. In Scandinavia the Nordic Geotechnical Societies have been developed the 'Nordic Guidelines for Reinforced Soils and Fills' (NG) in 2003. The latest revision has been published in 2005. The previous versions of 'Code of Practice for Strengthened / Reinforced Soils and other Fills' (BS 8006, British Standard Institute 2010) in United Kingdom and 'Recommendation for Design and Analysis of Earth Structures using Geosynthetics' (EBGEO, German Geotechnical Society, 2010) in Germany have been developed in the 80s and 90s of the last century. As can be seen in Table 1 these three guidelines deal in total with nine different geosynthetic applications. The main geotechnical applications being Embankments on Soft Soil, Retaining Structures and Reinforced Earth Structures over Point or Linear Bearing Elements are focussed upon in all of the three referenced guidelines. Only the Nordic guideline deals with information about the design and the use of Soil Nailing. Similarly for the particular applications of Reinforced Foundation Pads, Transport Routes and Geosynthetic Encased Columns these are only described in EBGEO.

Table 1: Applications regulated in the guidelines

	NG	BS		EBGEO
Embankment on Soft Soil	x	x		x
Reinforced Foundation Pads	-	-		x
Transport Routes	-	-		x
Retaining Structures	x	Walls	x	x
		Slopes	x	
Landfill Engineering	-	-		x
Reinfoced Earth Structures over Point or Linear Bearing Elements	x	x		x
Foundation Systems using Geosynthetic Encased Columns	-	-		x
Overbridging Systems in Areas Prone to Subsidence	-	x		x
Soil Nailing	x	-		-

Besides the different applications the guides give information about geosynthetic raw materials and other construction materials as well as their recommended testing procedures.

The design strength estimation of geotextiles is a key issue of guidelines dealing with geosynthetics and is performed differently according to the Scandinavian, British or German guideline and is detailed therein.

Common to all these codes is that the tensile short term strength has to be reduced for the design due to the influence of creep, installation damage, weathering or biological and chemical degradation, for seams and joints and lastly dynamic loads. Depending on the National Annex of each country a partial safety factor has to be considered additionally.

The design strength of a geotextile X_d (kN/m) pursuant the Nordic Guidelines is estimated using equation 1, where X_k (kN/m) is the characteristic short term tensile force in the geogrid. All reduction and the partial safety factors are described in Table 2.

$$X_d = \frac{\eta_1 \cdot \eta_2 \cdot \eta_3 \cdot X_k}{\gamma_M} \quad (1)$$

Table 2: Reduction and Partial Safety Factors

Reduction and Partial Safety Factors	**NG**	**BS**	**EBGEO**
Creep	$\eta_1 = 1/F_{cr}$	RF_{CR}	A_1
Installation Damage	$\eta_2 = 1/F_{id}$	RF_{ID}	A_2
Biological&chemical degradation	$\eta_3 = 1/F_{nv}$	RF_{CH}	A_4
Weathering	-	RF_W	-
Processing (Seams etc.)	-	-	A_3
Dynamic Load	-	-	A_5
Material Safety Factor	γ_M	f_m	γ_M
Partial Safety Factor for Extrapolation		f_s	

According to British Standard the design strength is estimated by using equation 2 and 3. T_{char} (kN/m) is the characteristic short term tensile force in the geogrid.

$$T_d = \frac{\frac{T_{Char}}{RF_{CR}}}{f_m} \quad (2)$$

$$f_m = RF_{ID} \cdot RF_{CH} \cdot RF_W \cdot f_s \quad (3)$$

The design tensile force $R_{b,d}$ (kN/m) in accordance with EBGEO is derived by reducing the characteristic short term strength *Rb,k0* (kN/m) by the partial safety factors described in Table 2.

$$R_{b,d} = \frac{R_{b,k0}}{A_1 \cdot A_2 \cdot A_3 \cdot A_4 \cdot A_5} \cdot \frac{1}{\gamma_M} \quad (4)$$

Detailed explanations of the reduction factors and their derivation based on ISO/TR 20432:2007 'Guidelines for the determination of the long-term strength of geosynthetics for soil reinforcement' can be found in the Dutch report 'Durability of Geosynthetics' (CUR 243, 2012).
More information about the design principles of GRS can be seen in Section 3.2.

2.3 Geosynthetic reinforced retaining structures

One of the most important applications of geosynthetics are geosynthetic reinforced retaining structures (GRS). These structures are used to stabilize slopes, to construct steep slopes as well as vertical walls and are built by vertically stacking single pads consisting of geogrids and compacted granular soil material. Previously heights up to 41 m have been realised. In order to achieve best GRS performance the use of a geogrid is recommended since its open mesh apertures favour a robust interaction between granular soil and geosynthetic reinforcement.
The numerous methods which can be utilised in the construction of such structures results in a wide variety of reinforcement arrangements and associated facing detailing. This latter matter is very important as it has a direct impact on a structures durability against UV radiation, fire and vandalism. For steepened slopes with an inclination up to 45° the face can be covered with 3D synthetic erosion protection matting or biodegradable, pre-seeded vegetation mats to ensure a successful 'greening' of the slope in the form of sown grasses. Another alternative being the direct application of 'hydro seed' mulch. All successful slope surface vegetation depends greatly on the climate and seasonal exposure of the slope and vegetation in question. Besides these so called green facings the GRS face can be constructed with other materials such as; stone or concrete blocks and panels, full or half gabion baskets filled with rocks.
The most common construction method used is the 'Wrap Around' method whereby the soil fill material is placed on top of a horizontal geogrid layer and is compacted in lifts of max. 0.30 m. The geogrid tail which remains protruding from the front edge of the fill material is then wrapped upwards and back on itself over the top of the compacted fill lift and anchored under the next layer of compacted fill to be placed. Typically such wrap around lifts are between 0.3 m to 0.6 m high. A mobile or a lost formwork (e.g. bent steel meshes) assists in forming a regular and tidy lift profile. GRS structures can generally be built without any special construction equipment, and can therefore be considered as suitable low technology systems. Their adaptability during construction and overall flexible nature enables them to be readily suited to a wide variety of applications and geometries. By virtue of their distinct

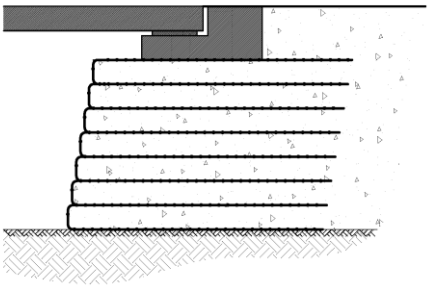


Figure 1 GRS as Bridge Abutment Foundation



Figure 2 Highway A 74 Venlo, Netherland

inherent ductility faced GRS structures performed very favourably during numerous earthquake events in Japan (Tatsuoka et. al., 1998) as well as under seismic load in laboratory tests (see Ling et al., 2013).
Furthermore a GRS is suited to carry high loads (see section 3.2). Especially for this reason the GRS is an attractive alternative to common bridge abutment construction methods.

3 GEOSYNTHETIC REINFORCED BRIDGE ABUTMENTS

3.1 Construction Methods

Geosynthetic reinforced bridge abutments have already become an established construction technique in e.g. Netherlands or Japan that allows a number of construction possibilities, as described.
A bridge superstructure can be founded directly on top of the GRS as performed for the Highway A 74 in the Netherlands (see Figures 1 & 2). The load of the bridge superstructure and traffic is fully carried by the GRS and transferred into the subsoil. The successfully design, construction and long term performance of these types of bridge abutments require a sufficient bearing capacity of the subsoils. Deformation tendencies in the bridge abutment resulting from subsoil settlements can endanger the durability of the rigid elements of the bridge and therefore have to be excluded. The reinforced soil body itself is usually not prone to failure caused by vertical deformations. For the Dutch bridge abutment shown in Figure 1 the potential subsoil settlements caused by loading from the bridge superstructure and live motorway traffic have been additionally allowed for by using a preload performed with concrete blocks placed on top of the GRS structure to simulate the live loadings.
Settlements originating from within the reinforced soil body itself can be minimized by the use of high-quality well graded filling soil with careful compaction in uniform vertical layers. In general the occurrence of these types of settlement is limited largely to the construction phase and can therefore be compensated for easily at this time.
Differential settlements of the bridge abutment and the bridge approach embankments are not expected using this ‘pre-load’ construction method. Any such surface imperfections and cracks due to

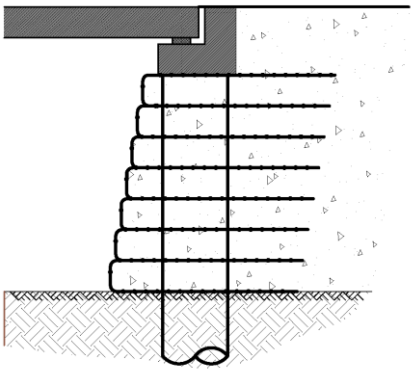


Figure 3 Combination of GRS and deep foundation

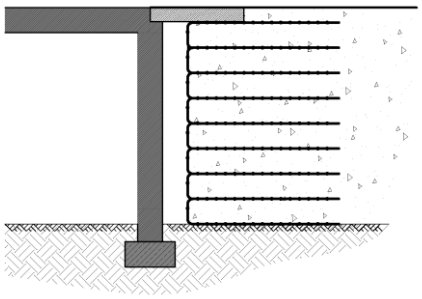


Figure 4 GRS working as Earth Pressure Relief Structure

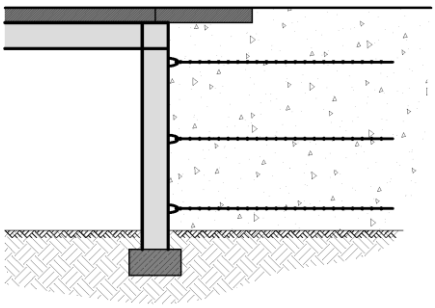


Figure 5 GRS built in soldier beam method



Figure 6, Temporary GRS in Switzerland using locally Fill Material and Soldier Beam Method

differential settlements between the bridge abutment and bridge superstructure may well effect the drive quality and long term durability. For these reasons there always needs to be careful consideration of such serviceability criteria during the design process.

In case of very large bridge spans or very strict settlement requirements a combination of a GRS and deep foundations is an advantageous construction alternative. As can be seen in Figure 3 the loads can be transferred down to a bearing stratum by the use of rigid piles. By using this technique both primary and secondary settlements are almost excluded. In general and especially in this combined bridge abutment construction method the GRS enables the construction of steep side slopes replacing standard reinforced concrete wing walls and thereby also reducing the embankment footprint space requirement.

Figure 4 shows a diagram of a geosynthetic reinforced earth block working as an earth pressure relief wall. The elements of the bridge superstructure and the GRS are not connected but decoupled with a void between them. The bridge structure is therefore not laterally loaded by any earth pressure from the approach embankment fill material. Consequently the dimensions and reinforcement of the (concrete) bridge superstructure and associated foundations can be reduced thereby reducing the overall material costs. Furthermore several special GRS types have been developed, with particular reference to unique individual requirements. Examples of this are shown by in Figures 5 and 6 which illustrate a GRS application in Switzerland where temporary Soldier Beam Walls acting as bridge abutments were constructed and laterally restrained using geosynthetic reinforcement elements. This makeshift bridge enabled the crossing of a railway line and road.

Due to the short installation time of these temporary structures the operation of the railway and road route was ensured. The use of large, locally sourced boulders reduced both the material transport costs and due to their high quality the required tensile strength of the geosynthetic reinforcement.

In summary, depending on the individual project requirements such as load carrying capacity, settlement criteria or even scenic and aesthetic considerations the flexibility and diversity offered by GRS solutions can ensure that a satisfactory solution can almost always be selected.

3.2 Large Scale Test

Many geosynthetic reinforced bridge abutments are already constructed in the Netherlands however prior to this trend full

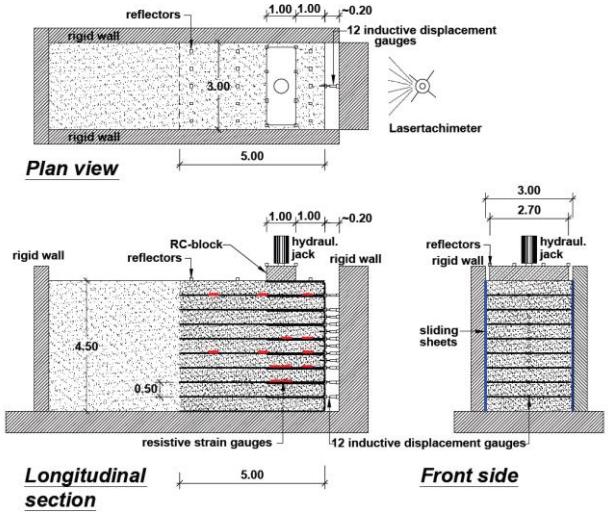


Figure 7 Test wall and measurement equipment, Alexiew and Detert (2008)

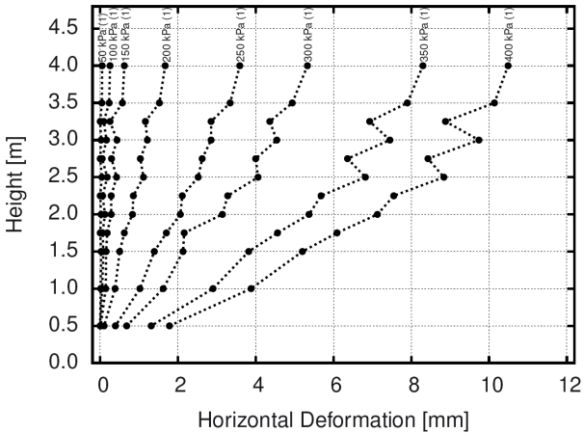


Figure 8 Measured Horizontal Deformation, Test 1

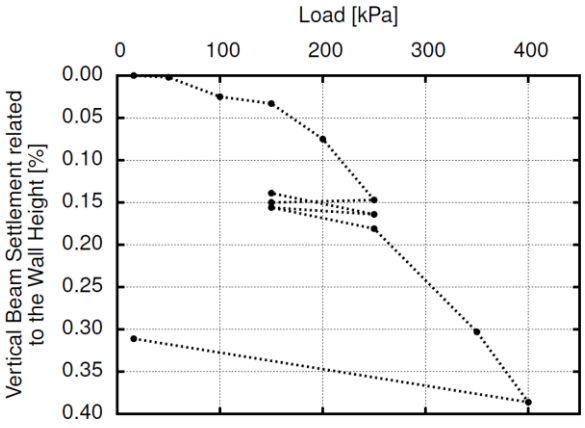


Figure 9 Measured Vertical Beam Settlements, Test 1

scale testing of the concept was carried out to look at the behaviour, stability and deformation of these types of construction (see Alexiew and Detert, 2008).

The experimental concept had been used before for investigations of integral frame bridges and their interaction with GRS abutments (see Plötzl and Naumann, 2005). For the full scale research project referenced *Alexiew and Detert, 2008* a 4.5 m high GRS vertical wall was constructed with nine layers of high strength geogrids made from the raw material PVA. The geogrids had a length of 5.0 m and were installed with a vertical lift height of 0.5 m (see Figure 7), with a 'wrap around' front face detail. The fill material was well graded and was determined to have an angle of friction between 40° and 45° in its compacted, at rest, state.

On top of the GRS structure a RC-block (width 1.0 m, distance form GRS face 1.0 m), served to simulated a typical bridge bank seat foundation beam and was loaded via a hydraulic jack arrangement. The capacity of the hydraulic jack was limited to 600 kPa. However this capacity sufficiently exceeded the typical bridge superstructure bank seat loads of around 200-250 kPa. by a factor of three.

A comprehensive measurement system was installed both within the reinforced soil block and externally to monitor the front face deflections. The use of strain gauges and displacement transducers can be seen in Figure 7.

The test procedure was divided into two parts: firstly load of of 400 kPa was applied to the test structure, then the structure was relieved and afterward a second load of 600 kPa was applied to study the structural deformation as it neared its theoretical failure loading.

As a result the RC-block settlements and the horizontal deformation of the wrapped around facing over the magnitude of the applied loads was visualized in the Figure 8 and Figure 9. The measured settlement under a max. load of 400 kPa was 18 mm which equates to 0.4% related to the GRS height (see Figure 9). It is considered that the initial settlement which occurred in the upper part of the wall during load steps 0 kPa – 200 kPa was most probably caused by additional micro compaction of the fill material, which had been compacted to 95% maximum dry density during construction.

The maximum horizontal deformation measured by the top of 12 deformation gauges was 10 mm (see Figure 9).

During the second part of the test cracks in the RC-block were observed under a load of 500 kPa. Similarly a fissuring in the reinforced earth block was observed to commence around a loading of > 500 kPa. The results of these large scale tests demonstrated the sufficient stability and serviceability of a GRS working as bridge abutment with inherent safety reserves for normal superstructure and traffic loads as well as even higher loads.

3.3 Geotechnical Design

As mentioned previously the guidelines from the United Kingdom, Scandinavia and Germany all include information about the design and construction of GRS.

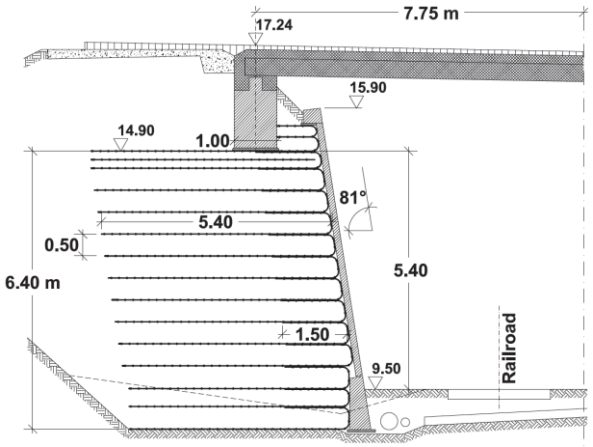


Figure 10 Cross Section, Bridge Abutment Ullerslev

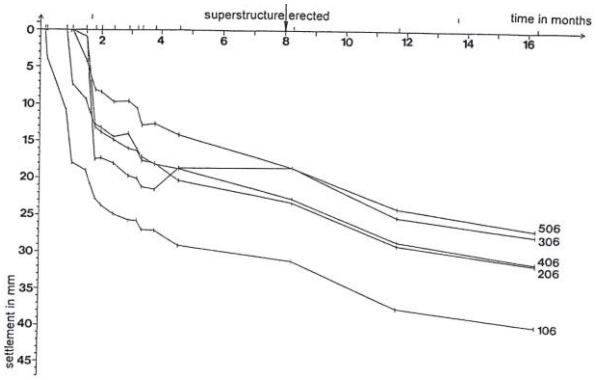


Figure 11 Measured Settlements, Kirschner and Hermansen (1994)

As European geotechnical guidelines they have to fulfil the requirements of the EC 7 and therefore are based on the partial safety factor concepts. Consequently driving forces are increased and resisting forces are decreased by partial safety factors. Those are defined in the National Annexes of each European Country.

Furthermore the guidelines coincide in holding the Ultimate Limit State (ULS, structural and geotechnical failure) and Serviceability Limit State (SLS, intolerable deformations) principles. The therein mentioned typical ULS failure modes for GRS are Pull-out, Rupture of Reinforcement, Internal and Global Slope Stability and Failure of the Facing. Sliding, Bearing Capacity and Settlements have to be considered in the SLS condition.

In conformity with EBGEO the regulations given in DIN 4084 (2009) are also valid for a GRS. Hence slip surfaces cutting the reinforcement layer (internal), not cutting a reinforcement layer at all (global) and slip surfaces cutting at least one reinforcement layer (compound) have to be analysed by using the methods of e.g. Bishop, Janbu or Vertical Slice Method. The same modes have to be analysed in accordance with the Nordic Guidelines. In contrast the British Standard pursues the Coherent Gravity Method and Tie-Back-Wedge method in three different load cases for the internal stability analysis.

Detailed information about the design principles of British Standard, EBGEO and the French Guideline as well as a design comparison of a 7 m high wall can be found in Horgan et al (2014).

3.4 Long Term Behaviour

In 1991 the construction of geosynthetic reinforced walls working as bridge abutments over the Nyborg-Fredericia main railway line in Ullerslev was instructed by the Danish State Railways (DSB) and firstly reported in Kirschner and Hermansen (1994).

Due to the subsoil which was described to be glacial clays DSB was searching for a bridge abutment solution which is not vulnerable to settlements. Nowadays it is usually recommended that a preload equal to or higher than the anticipated total service life load is applied to induce any settlements during the GRS construction as described above (Figure 2) for the Dutch bridge abutment at motorway A 74. However in the 1991 Ullerslev project the settlements were supposed to occur during the service life and therefore a geosynthetic reinforced bridge abutment was preferred due to its ductile and flexible deformation behavior. The aforementioned deformation behavior of the GRS causing uniform settlements of the abutment and the bridge approach (see section 3.1) was exploited in order to increase the durability in terms of ultimate and serviceability limit state of the entire bridge structure.

The Ullerslev bridge abutment (see Figure 10) is built as shown before in Figure 1, viz. the GRS is directly loaded by the load of the bridge superstructure and the traffic load by the use of a concrete block foundation.

The GRS is inclined by an angle of 81° and built using wrapped around geogrids with a

vertical distance of 0.50 m. Below the concrete block the layer distance is decreased in order to optimize the load transfer into the 5.4 m long reinforcing geogrids. Those have an estimated required short term strength of 110 kN/m. In Figure 12 the bridge is displayed shortly after the erection of the GRS and installation of the bridge superstructure.

As described in Kirschner und Hermansen (1994) the northern abutment was equipped with measurement points allowing the determination of vertical and horizontal deformations. The vertical settlements during the time span from December 1991 to April 1993 are shown in Figure 11 in five central and vertical orientated measurement points. Whilst the GRS was being constructed the maximum settlements of 30 mm were recorded at the bottom of the structure mainly caused by subsoil settlements. With the addition of the bridge super structure to the GRS after 8 month measured additional settlements of 10 mm within 16 months were recorded. The internal settlements arising in the reinforced soil body has been measured in a range of 25 mm and 30 mm.

Today the bridge is still in use as can be seen in Figure 13 showing a photograph taken in 2013. Obviously in the meantime the face of the wrap around walls was protected from UV impact, erosion and vandalism by applying a thin shotcrete sheet, although a cover with prefabricated concrete panels was initially designed.

Finally the stability and serviceability of the bridge has been maintained during almost 25 years' service life and the bridge has as resisted well any adverse settlements of the subsoil.



Figure 12 Bridge Abutment Ullerslev in 1991



Figure 13 Bridge Abutment Ullerslev in 2013

4 SUMMARY

The development of geosynthetic reinforced retaining structures (GRS) and their performance for bridge abutments have been introduced. Due to their multifarious construction and design methods GRS are suitable for many construction projects and can be readily adapted to individually unique project requirements.

The geotechnical design for GRS in Europe is based on EC 7 and regulated in National Guidelines dealing with geosynthetics. An overview of the Nordic Guidelines, EBGEO and BS 8006 with regard to the main applications, the design strength estimation and the basis of the geotechnical design of GRS have been presented.

The high vertical load carrying capacity and the deformation behavior under loads up to 650 kPa have been analysed in a large scale test. The vertical and horizontal deformations of the 4.5 m high test wall under typical bridge loads of approx. 250 kPa was measured in a range of millimeters thus substantiating the suitability of GRS for bridge abutments.

After almost 25 years' service life the Danish bridge abutment in Ullerslev was highlighted. With regard to the serviceability and stability these bridge abutments have performed soundly. Due to the ductile deformation behavior of the GRS settlements causing from the clayey subsoil have not restricted the use of the bridge.

5 REFERENCES

Alexiew, D. and Detert, O (2008) Analytical and Numerical Analyses of a Real Scaled Geogrid Reinforced Bridge Abutment Loading Test, EuroGeo4, Edinburgh

Alexiew, D., Raithel, M., Küster, V., Detert, O. (2012), 15 years of experience with geotextile encased granular columns as foundation system. Proceedings of TC 211 Recent Research, Advances & Execution Aspects of Ground Improvement Works, IS-GI Brussels

British Standard Institute (2010), BS 8006-1, Code of Practice for Strengthened / Reinforced Soils and other Fills, London, British Standard Institute

British Standard Institute (2004), BS-EN 1997-1, Geotechnical Design: Part 1, London, British Standard Institute

CUR Building & Infrastructure (2012), Report 243, Durability of Geosynthertics, Gouda, Stichting CURNET

German Geotechnical Society (2010), Recommendation for Design and Analysis of Earth Structures using Geosynthetics, EBGEO, Ernst & Sohn Berlin

Deutsches Insitute für Normung (DIN) (2009), DIN EN 1997, Eurocode 7 Entwurf, Berechnung und Bemessung in der Geotechnik, Berlin, Beuth Verlag

Deutsches Institute für Normung (DIN) (2009), DIN 4084:2009-0, Soil, Calculation of embankment failure and overall stability of retaining structures, Berlin, Beuth Verlag

Horgan G., Hangen. H., Durand, R. and Vanicek, M. (2014), European Reinforced Soil Design – The Codes, 10th International Conference on Geosynthetics, Berlin

International Organization of Standardization, (ISO) (2007), ISO/TR 20432:2007 'Guidelines for the determination of the long-term strength of geosynthetics for soil reinforcement'

Kirschner, R. and Hermansen, E. (1994), Abutments in Reinforcd Soil for a Road Bridge, 5th International Conference on Geotextiles, Geomembranes and Related Products, Singapore, Page 259-260

Ling, Hoe I., Leshchinsky, D., Burke, C., Matsu-shima, K., Liu, H (2003), Behavior of a large-scale modu-lar-block reinforced soil retaining wall subject to earthquake shaking, 16th ASCE Engineering Me-chanics Conference, Seattle

Nordic Geosynthetic Group (NGG) (2005), Nordic Guidelines for Reinforced Soils and Fills, The Nordic Geotechnical Societies

Pötzl, M. and Naumann, F. (2005) Fugenlose Betonbrücken mit flexiblen Widerlagern. Beton- und Stahlbetonbau 100 Heft 8, Berlin, Ernst & Sohn

Schweizerischer Verband für Geokunststoffe (SVG) (2003), Bauen mit Geokunststoffen, Ein Handbuch für den Geokunststoff-Anwender

Tatsuoka, F., Koseki, J., Tateyama, M., Munaf, Y. and Horii, N. (1998), Seismic stability against high seismic loads of geosynthetic-reinforced soil retaining structures" Keynote Lecture, Proc. 6th Int. Conf. on Geosynthetics, Atlanta, Vo.1, pp.103-142

Compressibility and deformation studies of compacted fly ash /GGBS mixtures

Anil Kumar Sharma* / primary author
Amrita University, Coimbatore, India
**Formerly Research Scholar, Indian Institute of Science, Bangalore, India, sharma.kr.anil@gmail.com*

P.V. Sivapullaiah, Co-Author
Indian Institute of Science, Bangalore, India

ABSTRACT
Utilization of industrial wastes that involves the bulk utilization such as embankments, structural fill, construction of roads etc. could not only help in reducing disposal problems but also provides a solution to conserve natural materials like soil. But due to lack of pozzolanic reactivity of certain industrial wastes such as fly ash, these materials remain underutilized. It is advantageous to use a combination of different industrial wastes materials rather than using individually. This paper presents the results of compressibility and deformation characteristics of mixtures of fly ash and ground granulated blast furnace slag (GGBS) mixtures at different proportions. By comparing the compressibility behaviour of fly ash and GGBS between conventional 24 hour and 30 minutes duration of load increment, it was found that 30 minutes was sufficient to assess the compressibility characteristics due to the higher rate of consolidation of such materials. It is observed that the compressibility of the fly ash/GGBS mixtures slightly decreases initially but increase with increase in GGBS content. Addition of lime did not have any significant effect on the compressibility characteristics since the pozzolanic reaction, which is a time dependent process and as such could not influence due to very low duration of loading. The cyclic behaviour holds importance as it will show its potential to perform under traffic loads. Repeated load triaxial test has been carried out on fly ash/GGBS mixture for optimum proportion to study the variation in resilient modulus and accumulation of plastic strain with number of load cycles. The higher resilient modulus values indicated its suitability for use as sub-grade or sub-base materials in pavement construction. Permanent axial strain was found to increase with the number of load cycles. Test results indicate the suitability of fly ash/GGBS mixture for utilization in embankments, structural fills, road construction etc.

Keywords: fly ash, GGBS, pozzolanic materials, compressibility, embankments.

1 INTRODUCTION

A variety of industrial waste materials are produced from many industrial activities in India (Pappu et al., 2007). The excess production of these waste materials due to industrialization and urbanization is the main cause behind environmental pollution. Also, the non-renewable resources are degrading day-by-day because of the increase in demand of raw materials for the industrial activities. Efforts are being made to counter these problems arising out of disposal of the industrial wastes. Recycling these industrial wastes for various beneficial uses would control the environmental problems (Dondi et al., 1997).

The major contributors of industrial solid wastes in India are the thermal power plants producing fly ash and Iron and Steel industries producing blast furnace slag (Singh and Garg, 1999). Fly ash and ground granulated blast furnace slags (GGBS) are well-known pozzolanic industrial by-products that are used in many civil engineering applications such as in blended cements, concretes etc (Puertas et al., 2000). Uses of these materials in manufacture of concrete, brick making, soil-stabilization

treatment covers only a small percentage of the total production. Hence more emphasis is needed in those applications that require bulk utilization such as in embankments, structural earth fills, road sub-grades etc.

Proper assessment and evaluation of industrial waste materials such as fly ash, GGBS etc. should be done for safe and economical utilization. If these materials have to be used as sub-base, sub-grade or as embankment material, one has to check its compressibility characteristics as well as its performance under cyclic load. Estimation of consolidation settlement is important for geotechnical design engineers to ensure no damage or decrease in the serviceability of the structure occurs. Although a lot of compressibility studies have been carried out on fly ash for utilization in embankments, sub-grades etc. (Kaniraj and Gayathri, 2004; Mishra and Das, 2012; Tu et al., 2007), but studies on mixtures of fly ash and GGBS have not been studied so far. This present study shows the investigation on the consolidation and deformation characteristics of fly ash/GGBS mixtures at different proportions to predict its competency in taking the load from any structures to be built on the embankments, pavements or structural fills that are constructed with these materials.

2 MATERIALS AND METHODOLOGY

2.1 Materials

Fly ash was collected from Raichur thermal power plant which is in Raichur district of Karnataka state, India.

Table 1 Physical properties of fly ash and GGBS

Properties	Materials	
	fly ash	GGBS
Specific gravity	2.15	2.84
Sand fraction (%)	24	-
Silt fraction (%)	74	99.7
Clay fraction (%)	2	0.3
Liquid limit (%)	32	40
Plastic limit (%)	Non-Plastic	Non-Plastic
Plasticity index (%)	Non-Plastic	Non-Plastic

GGBS was obtained from Larsen & Toubro ready concrete mix plant in Bangalore where it is used as partial replacement for cement in concrete. The physical properties of fly ash and GGBS are given in Table 1. From the particle size distribution data; it is seen that that GGBS consists of entirely silt-sized particles whereas fly ash has particles in range between sand and silt. SEM images of fly ash and GGBS are shown in Figures 1 and 2 respectively. Fly ash consists of spherical shaped particles as seen from the SEM image. The SEM micrograph of GGBS shows that particles have angular shape and sharp edges.

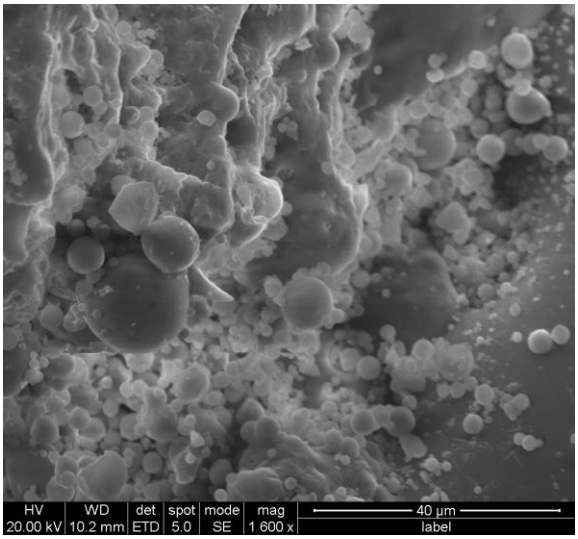


Figure 1 SEM image of fly ash

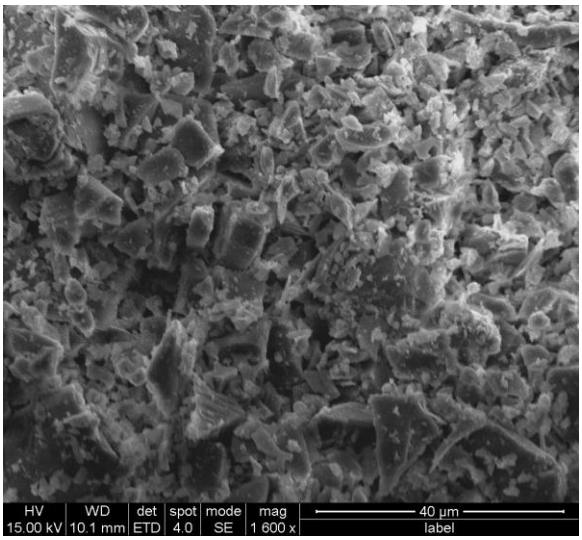


Figure 1 SEM image of GGBS

2.2 Methodology

The compressibility characteristics of the Fly ash-GGBS mixture at different mixing ratios

were determined using oedometer tests as per IS: 2720 (part-15) (1986). The GGBS content varied from 10% to 40% of the dry weight of the mix. The samples were prepared at optimum conditions of the mixture which were obtained from mini compaction test developed by Sridharan and Sivapullaiah (2005).

This section provides the methodology adopted in this present study. The compressibility tests were carried with 30 minutes as duration of load increment since pozzolanic materials like fly ash, GGBS are non-plastic materials and the consolidation process is very fast in these materials. Adopting this methodology could save a lot of time and effort for the experiments. Since fly ash and GGBS are pozzolanic materials and usually require initial chemical activation, hence effect of small amount of lime on the compressibility characteristics is also tried.

The cyclic behaviour of these materials holds importance as it will show its potential to perform under traffic loads. Repeated load triaxial (RLT) test has been carried out on fly ash/GGBS mixture for optimum proportion (70:30) to study the variation in resilient modulus and accumulation of plastic strain with number of load cycles. RLT test is capable of creating dynamic loading conditions similar to pavements. It is currently the most common method to determine the resilient modulus and plastic deformation characteristics of sub-grade soils and unbound aggregates in the laboratory. The repeated load triaxial apparatus for studying the mechanical behaviour has been carried only for the sample containing fly ash and GGBS in the ratio 70:30. The dimensions of the specimen tested were having a diameter of 38 mm and a height of 76 mm. Haversine-shaped load form was applied on the sample at a frequency of 1 Hz upto 1000 cycles. The test was carried out at consolidated-undrained (CU) conditions.

3 RESULTS AND DISCUSSIONS

3.1 Compressibility tests

The stress-strain curves from oedometer test of fly ash-GGBS mixtures are shown in Figure 3. In these figures, symbols FA and GGBS have been used to denote fly ash and ground granulated blast furnace slag respectively. The numbers appearing before each symbol are their respective weight percentages. For example, the sample 80FA20GGBS means fly-GGBS mixture with 80% fly ash and 20% GGBS. It is observed that pure GGBS specimen is more compressible than pure fly ash sample. Since GGBS particles are smaller fly ash, the chances of particle slippage and rearrangement would be more (Rodriguez, 2013). Also the shape of the GGBS particles is angular which makes it more compressible than spherical fly ash particles. However with increase in GGBS content the gradation of the mixture changes from poorly to well-graded and the mixture becomes less compressible. The strain level experienced by the fly ash-GGBS mixtures decreases with increase in GGBS content. It means that the resistance to deformation in the mixtures increases with GGBS content. This may due to the increase in the density of the mixtures with GGBS content. Similar compressibility behaviour is found when 2% lime is added to the fly ash/GGBS mixtures (Figure 4).

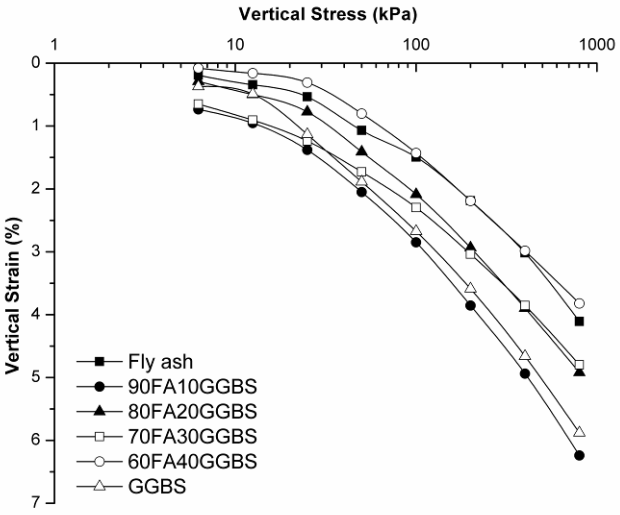


Figure 3 One-dimensional compression curves of fly ash-GGBS mixtures without lime

Since the compressibility tests are completed within a day after the start of the test, the chances of binding of the particles due to pozzolanic reactions are very less. if the test had been conducted at 24 hour load increment duration, addition of lime would have predominant effect on the compressibility characteristics. in this case also, at higher percentage of ggbs, the mixture becomes well packed and shows lower compressibility.

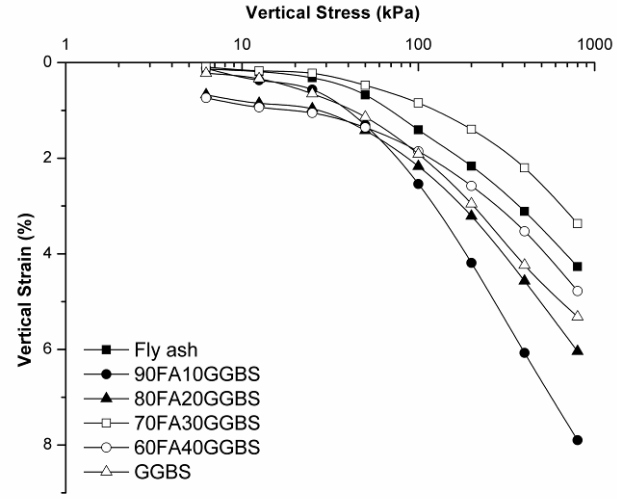


Figure 4 One-dimensional compression curves of fly ash-GGBS mixtures with 2% lime

3.2 Resilient Modulus

The test results show the variation of resilient modulus with number of cycles for 50 kPa confining pressure (Figure 5). The variation in the resilient modulus behaviour with the number of cycles is similar to other studies (Gabr et al., 2013). It is seen that the resilient modulus is more or less constant initially but decreases at higher number of cycles.

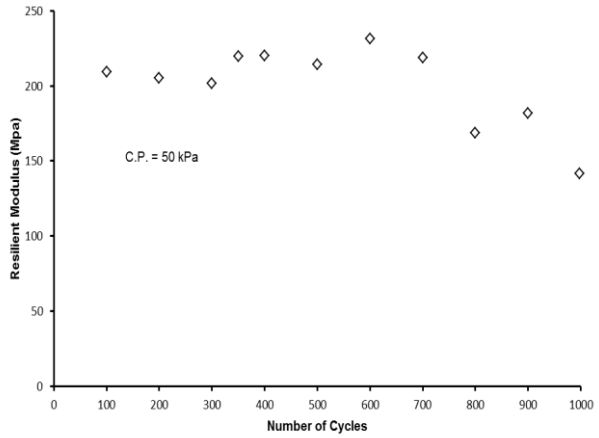


Figure 5 Resilient modulus versus no. of cycles (50 kPa)

At low confining pressure, the failure of the specimen would have resulted in the decrease of the resilient modulus values. The average resilient modulus value was found to be 200 MPa, which is typically good for its utilization in the sub-base and sub-grade materials. At higher confining pressures the variation in the resilient modulus is more or less constant up to 1000 cycles but did not show any sign of failure (Figures 6 and 7). Several studies have shown that morphological properties of the materials like shape, angularity etc. have a significant impact on its performance (Araya, 2011). In general, materials with angular shapes and rough surfaces increase the strength and stiffness of the pavements. Hence addition of GGBS, which are angular particles, may enhance the stiffness properties like resilient modulus when used as sub-grade materials.

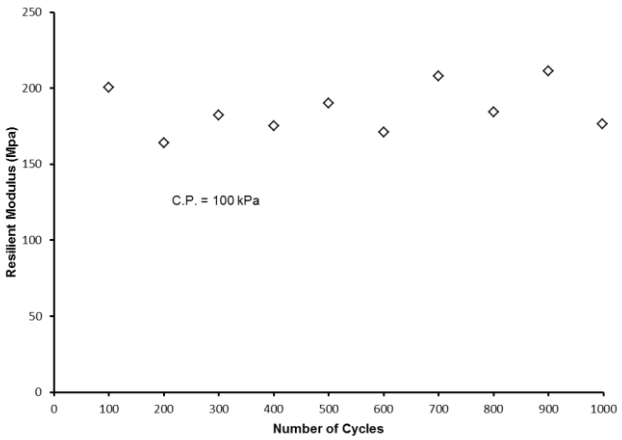


Figure 6 Resilient modulus versus no. of cycles (100 kPa)

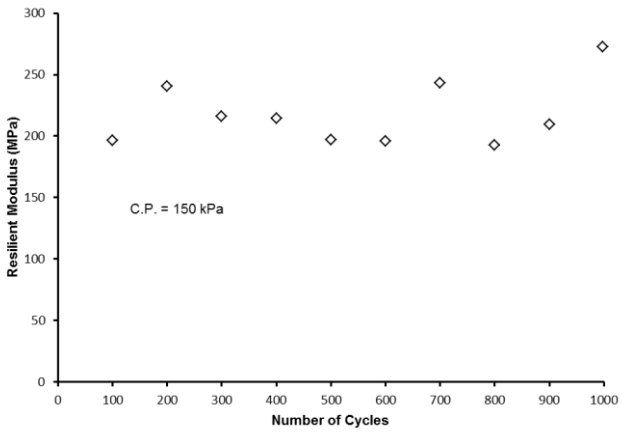


Figure 7 Resilient modulus versus no. of cycles (150 kPa)

3.3 Permanent deformation behaviour

Permanent deformations constitute the non-recoverable part of the deformations and are the mainly responsible for rutting in pavements. One of the key objective of pavement design is that the pavement is able to withstand permanent deformation beyond a certain, tolerable, level while permitting only resilient deformations. Since the deformation of the various layers of the pavement structure leads to irreversible deformations at the pavement surface, a pavement should be designed to such a degree that only small amount of permanent deformation can accumulate in each layer. Figure 8 shows axial permanent strain results at a confining pressure of 50 kPa in relation to the number of loading cycles.

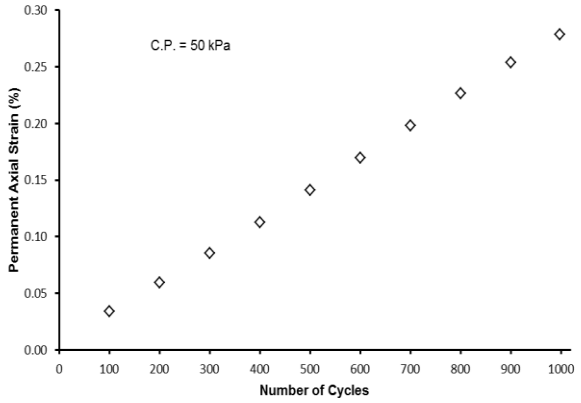


Figure 8 Axial permanent strain versus no. of cycles (50 kPa)

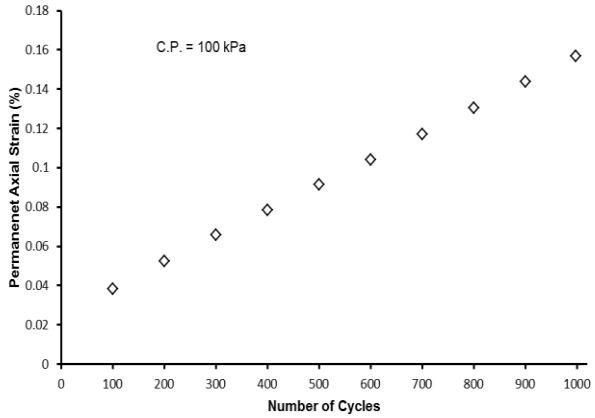


Figure 9 Axial permanent strain versus no. of cycles (100 kPa)

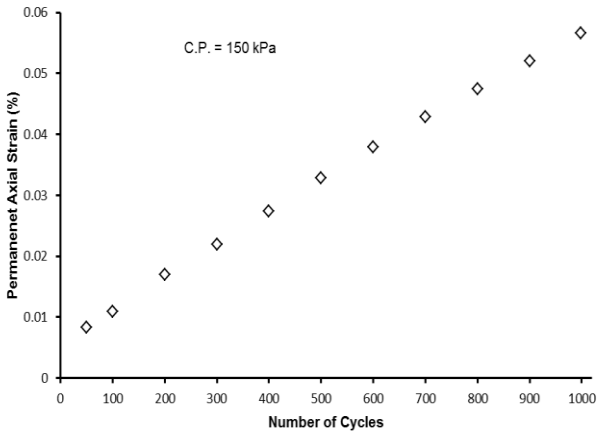


Figure 10 Axial permanent strain versus no. of cycles (150 kPa)

It is clearly seen that the permanent strain follows linear relationship with the number of load cycles. Generally, the permanent deformation rises immediately during the initial first cycles followed by gradual stabilization. But the amount of deformation depends on the material characteristics and applied load. Rounded particles such as fly ash slip over each other very easily and may cause significant permanent deformations. Additions of angular GGBS particles would be beneficial in the reduction of permanent deformation since angular shaped materials have to overcome higher frictional stresses.

It can be clearly seen that with increasing number of load cycles, the magnitude of accumulated permanent strains also increase although stabilization of the strain is not found. Similar linear relationships between permanent axial strain and number of cycles are found with the increase in the confining pressure (Figures 9 and 10). However, the accumulated permanent strain at the end of the load cycles is seen to reduce with the increase in confining pressure with lowest strain at 150 kPa. Table 2 presents the permanent deformations or strains of the sample at various confining pressures at the end of 1,000 cycles. The results clearly illustrate that the increase in the confining pressure reduces the permanent axial strain.

Table 2 Permanent percentage strains at different confining pressures

Confining pressure (kPa)	Plastic Strains, ε_p (%)
50	0.28
100	0.16
150	0.06

3.4 Modeling Permanent Deformation Behaviour

In mechanistic analysis, a number of models provide guidance in terms of resistance of a sub-base or base course layer to plastic damage. Various researchers have investigated the accumulation rate of permanent strain under repeated conditions and found that the rate of permanent strain decreases with the number of load reputations. Various model studies have been carried out by many researchers to predict the permanent strain behaviour from number of load applications. A comprehensive study using cyclic load triaxial test was carried out by Barksdale (1972) on the behaviour of different base course materials. He was the first to establish a well-known relationship between permanent strain (ε_p) and number of load applications (N) using a lognormal method as shown in the following equation.

$$\varepsilon_p = a + b \log N \quad (1)$$

Where *a* and *b* are experimentally derived parameters.

Later, Sweere (1990) modified the lognormal approach and suggested the following equation to relate permanent strain with number of cycles using a log-log relation.

$$\log \varepsilon_p = a + b \log N \quad (2)$$

A large number of models are available to describe the permanent strain behaviour. Because of its simplicity, only the model modified and proposed by Sweere (1990) is applied and validated in this study.

Figure 11 shows the log-log relationship between the permanent strain and number of cycles given by this model at a confining pressure of 50 kPa. It can be clearly noticed that the model fits very well with the experimental results.

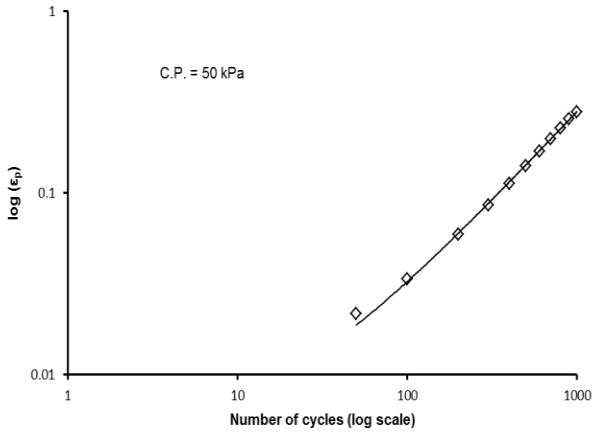


Figure 11 Comparison between the model and the experimental results (50 kPa)

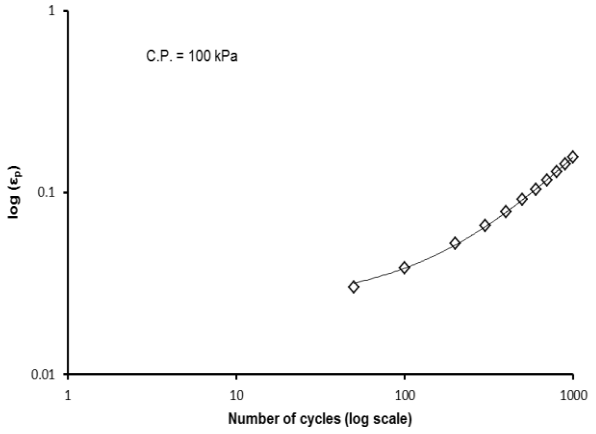


Figure 12 Comparison between the model and the experimental results (50 kPa)

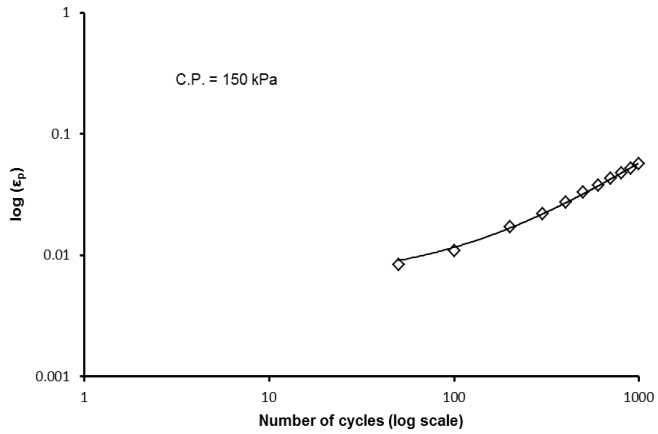


Figure 13 Comparison between the model and the experimental results (50 kPa)

Log-log relation between the permanent strain and number of cycles at higher

confining pressures exhibits similar results and are shown in Figures 12 and 13.

4 CONCLUSIONS

Shape and size of fly ash and GGBS are the main factors controlling the compressibility, resilient and permanent deformation characteristics. The addition of GGBS to fly ash makes the mixture well graded and as a result compressibility is reduced. The higher resilient modulus values indicate that the mixture of fly ash and GGBS can be suitably utilised as sub-grade materials in construction of roads. Permanent axial strain increased with the load cycles. But the accumulation of plastic strain reduced with increase in confining pressure. The compressibility and permanent deformation behaviour test demonstrate that if properly designed, the mixture can be utilised economically for the construction of embankments, road sub-grades etc.

5 REFERENCES

Araya, A.A., 2011, Characterization of unbound granular materials for pavements. Delft University of Tech., Road and Railway Engineering Section, Fac. of Civil Engineering and Geosciences.

Barksdale, R.D., 1972. Laboratory evaluation of rutting in base course materials. In: Presented at the Third International Conference on the Structural Design of Asphalt Pavements, Grosvenor House, Park Lane, London, England, Sept. 11-15, 1972.

Dondi, M., Marsigli, M., Fabbri, B., 1997, Recycling of industrial and urban wastes in brick production: a review (Part 2). Tile & brick international 13, 302-315.

Gabr, A., Mills, K., Cameron, D., 2013, Repeated load triaxial testing of recycled concrete aggregate for pavement base construction. Geotechnical and Geological Engineering 31, 119-132.

Kaniraj, S.R., Gayathri, V., 2004, Permeability and consolidation characteristics of compacted fly ash. Journal of energy engineering 130, 18-43.

Mishra, D.P., Das, S.K., 2012, One-Dimensional Consolidation of Sedimented Stowed Pond Ash. Geotechnical and geological engineering 30, 685-695.

Pappu, A., Saxena, M., Asolekar, S.R., 2007, Solid wastes generation in India and their recycling potential in building materials. Building and Environment 42, 2311-2320.

Puertas, F., Martínez-Ramírez, S., Alonso, S., Vazquez, T., 2000, Alkali-activated fly ash/slag cements: strength behaviour and hydration products. Cement and Concrete Research 30, 1625-1632.

Rodriguez, J.M., 2013, Importance of the Particle Shape on Mechanical Properties of Soil Materials.

Singh, M., Garg, M., 1999, Cementitious binder from fly ash and other industrial wastes. Cement and Concrete Research 29, 309-314.

Sridharan, A., Sivapullaiah, P.V., 2005, Mini compaction test apparatus for fine grained soils. Geotechnical Testing Journal 28, 1-7.

Sweere, G.T., 1990. Unbound granular bases for roads. Technische Universitiet Delft,

Tu, W., Zand, B., Ajlouni, M.A., Butalia, T.S., Wolfe, W.E., 2007, The Consolidation Characteristics of Impounded Class F Fly Ash–A Case History. Proc. World of Coal Ash.

Peaty ground- made for mass stabilization

Madelene Markusson.
WSP Sverige AB, SWEDEN, madelene.markusson@wspgroup.se

ABSTRACT
Roslagsbanan is a narrow gauge railway in the northeast region of Stockholm. The railway was built in the early 1900s. WSP has produced construction documents for the part Rydbo-Åkers Runö and the construction of this part took place in the year 2013 and 2014. The part was divided in three segments. In the second segment there is an area called Täljö station were mass stabilization was used as ground reinforcement. Soil layers at Täljö station generally consist of an upper layer of peat and mud with a thickness of up to 4 m resting on soft clay down to at most 15 meters below the ground surface. The area has previously had problems with settlements and in 2007 tracks adjustment and reinforcement through mass stabilization of peat layer of the existing track was done.
Mass stabilization is a fast and cost effective method for hardening the loose soil layers by adding binding agents. With this method the entrepreneur do not have to transport poor masses to landfill and refill with qualified filling. This saves time, money, and is a gentle metod for reinforcement from an environmental perspective since existing soil layer is used on-site (in-situ) so that transport and thermal ballast are minimized. Another advantage of mass stabilization is that the working area size can often be reduced since the excavation of the slope can be avoided. Based on the good experience from previous stabilization works mass stabilization in combination with lime cement columns in the claylayer were also selected for the new renovation and construction of a new track. Work on Roslagsbanan is a good example of how mass stabilization effectively can be used to reinforce organic soils and cohesive soils under road- and railway embankments.

Keywords: Masstabilisering, kalkcementpelare, torv, peat, järnväg

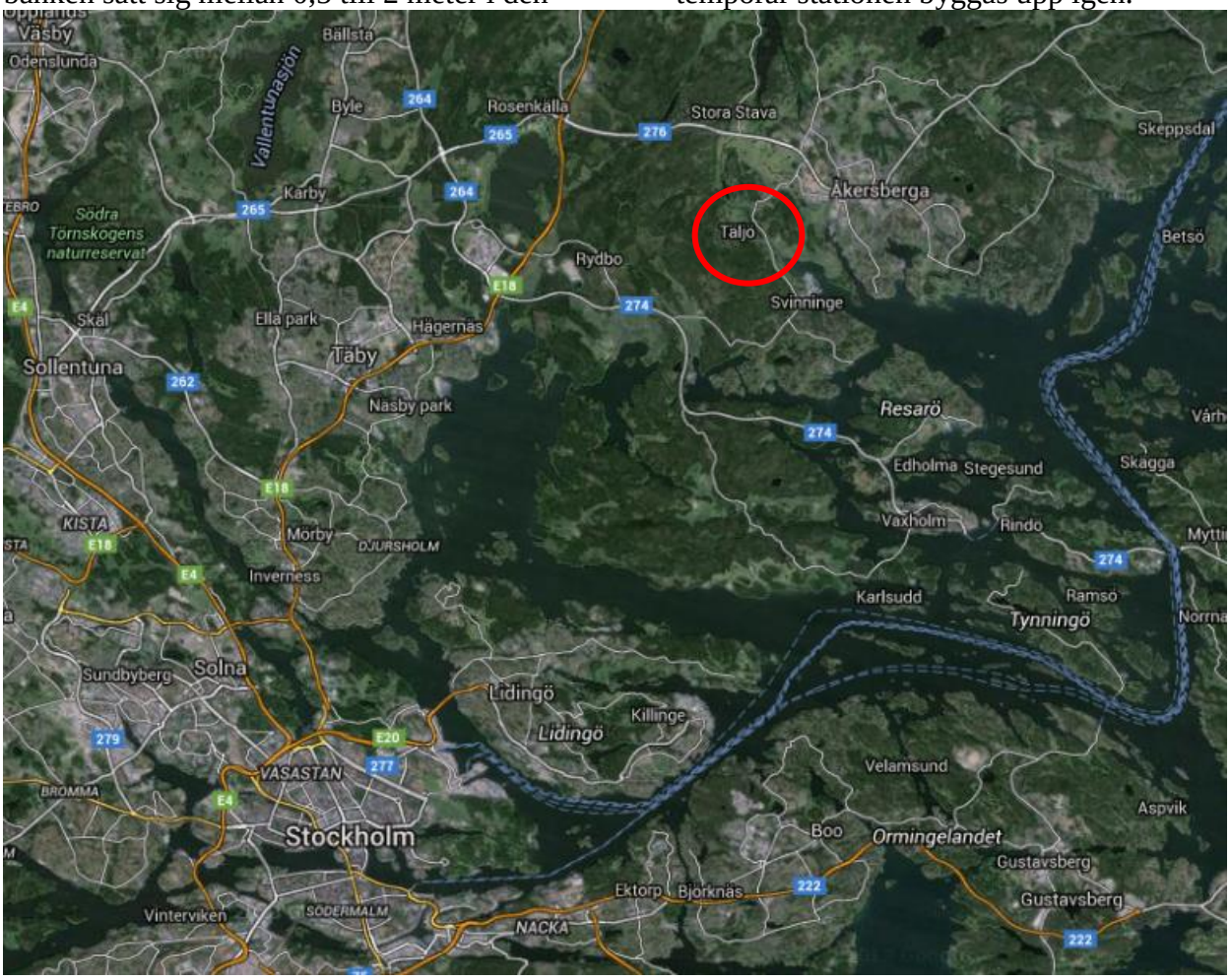
1 BAKGRUND

Roslagsbanan är en smalspårig järnväg från början av 1900-talet. Roslagsbanan trafikerar Stockholms nordöstra förorter och denna artikel behandlar främst Täljö station på sträckan Rydbo-Åkers Runö.
Bansträckningen går genom fastmarkspartier men korsar däremellan gamla havsvikar med organisk jord och sediment av lera.
Banan byggdes genom utläggning av trärustbädd men var i övrigt oförstärkt. När banan skulle färdigställas försenades invigningen på grund av skred i järnvägsbanken, dock ej på aktuell sträcka. Järnvägsbanken har sedan erhållit sättningar som på vissa avsnitt uppgår till ca 1 meter.

2 PROJEKTERING AV UPPRUSTNING STRÄCKAN VIGGBYHOLM-ÖSTERSKÄR

År 2007 projekterade WSP Sverige AB, på uppdrag av Stockholms Lokaltrafik (SL), en upprustning av sträckan mellan Viggbyholm och Österskär. Upprustningen innebar bla att masstabilisering utfördes som förstärkningsåtgärd på en sträcka av ca 500 meter på delsträckan Rydbo- Åkers Runö. En stor del av problemsträckan låg vid Täljö station. Här passerar banan flera områden där jordlagren består av torv och gyttja med underliggande lager av lera vilket med årens lopp inneburit problem med både stabilitet och sättningar vilket resulterat i att regelbundna spårjusteringar erfordrats. Då upprustning av banan beslutades, vilket innebar ökad standard genom att tex betongslipers och helsvetsade räler anlades, fanns mindre tolerans för regelbundna justeringar.

Vid Täljö station förelåg problem med att plattformselementen satt sig och stationen planerades att rivas. Sonderingar genom befintlig bank, utförda år 2007, visade på att banken satt sig mellan 0,5 till 2 meter i den organiska jorden. Upprustningen innebar att den gamla banken ersattes med en ny bank och masstabilisering utfördes under den nya bankens hela bredd. Därefter skulle en temporär stationen byggas upp igen.



Figur 1 Kartbild hämtad från google maps. Aktuellt område är inringat med rött.

3 GEOTEKNISKA FÖRHÅLLANDEN VID TÄLJÖ STATION

3.1 Terräng

Järnvägsträckningen går över kärrmark mellan ca km 23+120 till 23+500. Marknivån över den skogsbevuxna kärrmarken är ca + 24,5 till +25 mellan 23+140 och 23+280 och ca +22 på resterande sträcka, med små variationer.

3.2 Jordlagerbeskrivning

I läget för befintlig järnväg finns överst någon till ett par meter fyllning. Där marken är orörd består jordlagren överst av 1 à 4 meter torv och gyttja. Därunder finns lera som vilar på friktionsjord på berg. Djupet till fasta jordlager eller berg varierar mellan ca 5 till 15 meter. Torven är i allmänhet medel- till högförmultnad. De övre delarna av leran är gyttjig.

Torven och gyttjan har vid sidan av järnvägsbanken en korrigerad odränerad skjuvhållfasthet som är ca 4 kPa ner till 4 meters djup från markytan.

Lerans korrigerade odränerade skjuvhållfasthet bedöms vara 5 kPa på 4 meters djup från markytan, med en ökning av 1,5 kPa/meter mot djupet därunder.

Leran är mellan- till högsensitiv med värden mellan 8 och 63 och under ca 12 meter djup klassificeras leran som kvick. Torvens och gyttjans densitet är ca 1,2 t/m^3. Leran har en densiteten på mellan ca 1,4 och 1,7 t/m^3 där

de lägre densiteten på leran gäller den övre gyttjiga leran.
Den naturliga vattenkvoten (w_N) i torven och gyttjan varierar mellan ca 100 och 550 % och konflytgränsen (w_L) varierar mellan ca 100 till 500 %. Lerans naturliga vattenkvot variera mellan ca 60 till 80 % och konflytgränsen varierar mellan ca 40 och 60 %.
Leran bedöms vara överkonsoliderad med ca 25 – 30 kPa (OCR ca 1,7) under banken. Kompressionsmodulen M_L är låg. I torven och gyttjan bedöms M_L vara ca 130 kPa och i leran ca 150 – 300 kPa.

3.3 Hydrogeologiska förhållanden

Enligt utförda grundvattenmätningar ligger grundvattentrycket i friktionsjorden under leran något över markytenivån.

4 MOTIV TILL VALD FÖRSTÄKNINGSMETOD

Olika åtgärdsmetoder övervägdes såsom förstärkning genom KC-pelare eller påldäck, eller urskiftning av torv- och lerjordar. Valet av masstabilisering motiverades med att metoden bidrar till en miljömässig nytta genom att befintliga massor nyttjas på plats (in-situ) så transporter och tillförd ballast kan minimeras. Masstabilisering bedömdes även vara en snabb och kostnadseffektiv metod att hantera sättningsproblematiken samt att det var ur största vikt för SL att snabbt kunna ta järnvägen i bruk igen.

5 FÖRUNDERSÖKNING OCH GENOMFÖRANDE AV MASSTABILISERADE PROVYTOR

5.1 Provytor

Vald förstärkningsmetod blev masstabilisering genom inblandning av cement och granulerad masugnslagg (Merrit 5000) i den organiska jorden.
För att säkerställa antagandena vid projekteringen och optimera inbladningen av blandningar utfördes provinbladningar på en provyta intill planerad förstärkning.
Det beslutades att ett område närmast Täljö station var bäst lämpad. Provytan var ca 20 x 5 meter och 4 st inblandningar användes vilket innebar att provytan delades in i 5x5 meter stora rutor.

Följande fyra provinbladningar provades

I 200 kg/m^3 och 70/30 (cement/ merit) med extra vatten vid utförandet
II 200 kg/m^3 och 70/30 (cement/ merit) utan extra vatten vid utförandet
III 250 kg/m^3 och 70/30 (cement/ merit) utan extra vatten vid utförandet
IV 250 kg/m^3 och 70/30 (cement/ merit) utan extra vatten vid utförandet, fyllnadshöjd det dubbla strax intill stabilisering.

Provytorna fylldes upp med 0,5 meter fyllning ovan en geotextil strax efter utförd stabilisering utom för provyta nr IV där 1 meter fyllning lades ut ovan geotextilen efter stabilisering. Två peglar installerades mitt på varje provyta. Peglarna installerades på geotextilen innan fyllningen lades ut. Efter 7 dygn lades ytterligare 0,5 meter fyllning upp på ytorna I till III.
Strax innan stabiliseringen genomfördes luckrades jorden upp av en traktorgrävare. Stabiliseringen genomfördes med trumverktyg.

5.2 Provning

Provning genomfördes genom kärnprovtagning med S-Geoborr med en kärndiameter av 102 mm och ytterdiameter av 158 mm. Ett kärnborrhål utfördes på varje yta och 3 till 4 delar av kärnan provtrycktes på SGI´s laboratorium i Linköping.
Ett par KPS- sonderingar med vinge utfördes på alla ytor utom yta IV där endast sondering kunde genomföras pga den stabiliserade ytans höga fasthet. Pelarvingborr gick endast att genomföra i yta I då den stabiliserade jorden i övriga ytor var för fast.
Provning utfördes 1 vecka, 2 veckor samt 5 till 6 veckor efter stabiliseringen.

5.3 Utvärdering av provningen

Den stabiliserade massan var inte homogen och fastheten varierade både mot djupet och i i sidled. Eftersom provningen utförts med olika metoder som provar olika stora volymer samt bedöms ha olika noggrannhet vid utvärdering av den stabiliserade jordens

skjuvhållfasthet gjordes en subjektiv viktning av resultaten med avseende på metodernas noggrannhet och metod vid utvärdering. Kärnprovtagning viktades högst (7/10) och sondering med 50 mm spets respektive CPT-sondering viktades lägst (2/10). Generellt tenderade utvärderingen av skjuvhållfastheten med tryckförsök i laboratorium ge ett lägre värde än vid utvärdering av sonderingar.
Efter 1 till 2 veckor var bindemedlet fortfarande varmt vilket betyder att bindemedlet fortfarande brinner och hållfastheten ökar med tiden. Däremot efter 5 till 6 veckor hade bindemedlet svalnat betydligt. Någon markant förändring av skjuvhållfastheten med tiden noterades dock inte. Slutsatsen var att detta berodde på att provomfattningen var för lite samt att massan var för inhomogen för att kunna göra denna bedömning.
Nedanstående tabell redovisar en subjektiv bedömning av skjuvhållfastheten för respektive delyta med bedömda min- och maxvärden i den stabiliserade volymen.

Tabell 1 Sammanställning utvärderad odränerad skjuvhållfasthet.

Provyta	Min (kPa)	Medel (kPa)	Max (kPa)
I (200 kg/m^3)	80	150	270
II (200 kg/m^3)	110	210	330
III (250 kg/m^3)	200	330	530
IV (250 kg/m^3)	200	390	600

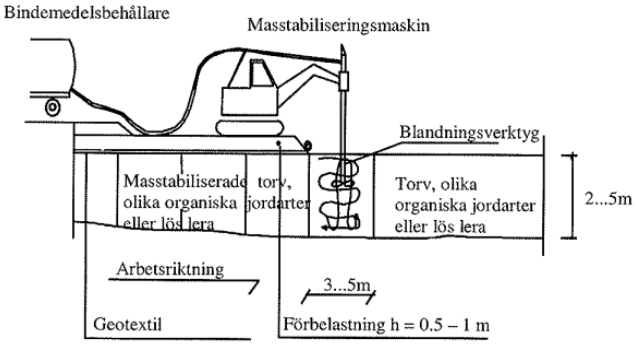
Projekteringen baserades på att skjuvhållfastheten i den masstabiliserade jorden skulle vara minst 50 kPa i hela det stabiliserade blocket och ett snittvärde som borde överstiga 100 kPa vilket samtliga provytor motsvarade.
Någon effekt av tillsatt vatten för provyta I kunde inte skönjas. Det är dock viktigt att torven som har sämst egenskaper vid stabilisering blandas med den underliggande gyttjan och leran.
Med ledning av den utförda provningen valdes mängden 200 kg/m^3 och blandningen 70% cement och 30% Merrit 5000.

5.4 Uppföljning av sättningsmätning I provytorna

Under provningsperioden, dvs ca 6 veckor, har 5 stycken avvägningar av markpeglar utförts. Måttliga rörelser på mellan 0 till 4 cm har uppkommit vid belastning av provytorna. Den provyta som satts sig mest är yta 4 som bedöms ha fått den högsta skjuvhållfastheten och den bästa stabiliserande effekten.

6 GENOMFÖRANDE AV UPPRUSTNINGEN AV BANAN

Åtgärderna för upprustningen utfördes under trafikavstängning varför tillgänglig tid för genomförandet var begränsad.
Vald inblandningsmängd blev mängden 200 kg/m^3 och blandningen 70% cement och 30% Merrit 5000. Förstärkningen genomfördes därefter genom att den befintliga bankroppen samt även överbyggnadsmaterial schaktades bort. Arbetet utfördes succesivt i etapper om ca 5 meter/dag med efterföljande utläggning av underballast efter att den stabiliserade ytan härdat. Arbetena försvårades av att inblandningsverktyget stötte på hinder i form av rustbädd av trästockar. I vissa fall utfördes förschaktning för att rensa bort rustbädden. Efter stabiliseringen påfördes en temporär överlast för att komprimera den stabiliserade jorden. Överlasten lades 1 meter över planerad markyta och med en liggtid av 2 till 4 veckor. Pga den korta tid som överlasten kunde ligga bedömdes att kvarvarande krypdeformationer kan förekomma.



Figur2 Principskiss masstabilisering

7 PROJEKTERING AV SYSTEMHANDLING ÅR 2010 AV STRÄCKAN RYDBO-ÅKERS RUNÖ

År 2010 fick WSP i uppdrag av SL att upprätta en systemhandling för sträckan Rydbo- Åkers Runö där Roslagsbanan föreslog byggas ut till dubbelspår.
Vid Täljö station innebar projekteringen av nytt dubbelspår att nytt spår skulle förläggas på södra sidan utmed befintligt spåret med ett spåravstånd på 9 meter med samma profilnivå. Anläggningen och de åtgärder som planerades skulle också förbereda för en framtida övergång till normal spårvidd med tillhörande ökning av trafiklasten (STAX 22,5 ton).
Befintlig temporär plattform norr om befintligt spår skulle rivas och ny mittplattform skulle anläggas.
I samband med framtagandet av systemhandlingen var det av stort intresse att göra en ny utvärdering av utförda förstärkningar eftersom det planerades att utföra liknande förstärkningar i samband med dubbelspårsutbyggnaden. Därför utfördes ytterligare sättningsuppföljning.
Den tidigare stabiliserade sträckan var ca 10 till 15 meter bred och stabilisering hade utförts till fasta jordlager eller till som mest 4 meters djup. Förstärkningsarbetena hade utförts sommaren 2007 samt sommaren 2008.

7.1 Sättningsuppföljning

Sättningsmätningar hade pågått under perioden 2007-09-10 till 2010-11-26 dvs under drygt 3 år efter att järnvägens överbyggnad var iordningställd. Mätningar hade utförts på slipers i spårmitt med ett c/c avstånd av 20 meter.

7.2 Resultat sättningsuppföljning

Efter analys av sättningsmätningarna syntes det tydligt att de större sättningarna hade utbildats inom områden där det underliggande oförstärkta lerlagrets mäktighet ökade.

Sträckan 23+120 till 23+270
På denna sträcka installerades 7 st mätpunkter. Totalsättningen varierade mellan ca 0,5 till 3 cm. Sättningarna bedömdes ha avklingat.

Sträckan 23+390 till 23+460
På denna sträcka installerades 8 st mätpunkter. Totalsättningen varierade mellan ca 1 till 11,5 cm. Sättningarna hade utbildats relativt jämt över sträckan förutom mellan km 23+360 och 23+380 där en sättningsdifferens på ca 8,5 cm uppmätts vilket därmed ej uppfyllde de krav på differenssättningar i längsled som ställts.
För sträckan 23+390 till 23+360 bedömdes sättningarna ha avklingat. För resterande del mellan km 23+360 och 23+440 bedömdes sättningarna inte ha avklingat. Här uppskattades sättningshastigheten till 3 cm/år. Det gjordes en bedömning att sättningarna skulle fortsätta utbildas i den oförstärkta leran under den masstabiliserade torven.

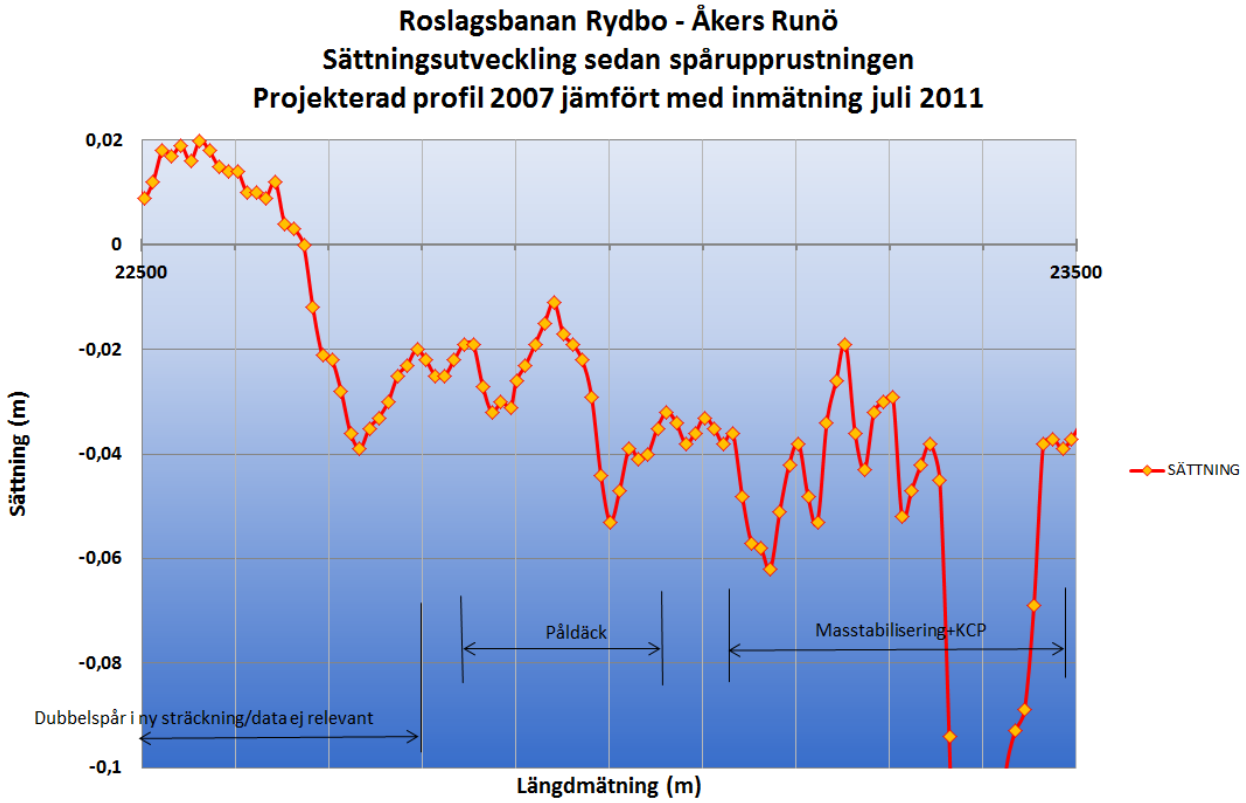
7.3 Konsekvenser för föreslagen utbyggnad till dubbelspår

Nya Täljö station planerades att byggas med spåravstånd 6 meter samt mittplattform på sträckan fram till km 23+360. Detta innebar höga sättningskrav (max 1 cm mellan spår och plattform. Eftersom mätningarna visade på att sättningarna avklingat på denna sträckan bedömdes förutsättningarna som goda för förstärkning av kommande dubbelspår på liknande sätt som utförts för upprustningen.
För sträckan 23+360 till 23+420 visade mätningarna att det fanns risk för att sättningarna under det nya dubbelspåret inte skulle kunna uppfylla ställda krav om förstärkningen utfördes på liknande sätt som för upprustningen. Man rekommenderade därför i systemhandlingskedet att förstärka det nya spåret med KC-pelare alternativt lastkompensation med lättfyllning på hela eller delar av sträckan.

8 PROJEKTERING AV BYGGHANDLING AV STRÄCKAN RYDBO-ÅKERS RUNÖ

8.1 Ytterligare uppföljning av pågående sättningar fram tom juli 2011.

Tidigt i projektering togs beslut om att ytterligare sättningsmätningar skulle utföras mellan december 2010 till juli 2011.

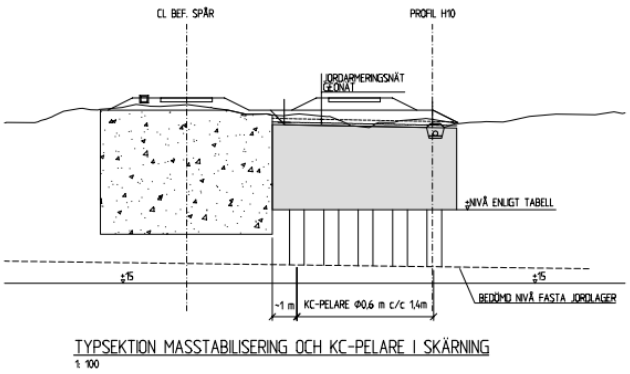


Figur 3 Sättningutveckling på aktuell sträcka sedan spårupprustningen, perioden 2007 tom juli 2011

Sättningsuppföljning för befintlig masstabilisering visar att banken har satt sig mellan 1 och 11,5 cm. Sättningarna under nytt spår bedöms bli större eftersom marken här är obelastad sedan tidigare samt att inom viss del av sträckan så är lerdjupet större än under tidigare utförd masstabilisering.

8.2 Föreslagen förstärkning

Av denna anledning föreslogs masstabilisering i kombination med KC-pelare med en diameter av 60 cm med ett c/c-avstånd på 1,4 m i leran. Utförda beräkningar av framtida sättningar i KC-pelarblocket visar en sättning om ca 0,07 m som till största delen skulle utbildas inom 6 månader.

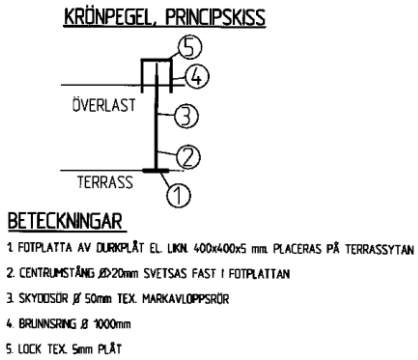


Figur 4 Principsektion masstabilisering med KC-pelare

8.3 Kontrollprogram

För att kontrollera rörelser i samband med entreprenadarbetena samt följa upp

förstärkningsåtgärdernas funktion togs ett kontrollprogram fram. Detta omfattade etablering och mätning av ett antal kontroll sektioner. Dessutom föreskrevs sättningsuppföljning med hjälp av krönpeglar var 20:e meter som installerades höger 5,5 meter och höger 11 meter. Kontroll av krönpeglar skulle utföras vid uppfyllning ca halva bankhöjden samt omedelbart efter avslutad uppfyllning av banken. Därefter 1, 2, 4, 8, 16, 24, 36, 52 veckor efter full uppfyllning av banken.
Enligt kontrollprogrammet skulle även en inklinometer och en slangsättningsmätare installeras i km 23+180.



Figur 5 Principskiss krönpegel

9 UTFÖRANDE

Arbetet pågick fram tom sommaren 2014. Trafiken släpptes på under hösten 2014. Veidekke var huvudentreprenör vid Täljö station och Keller var underentreprenör och ansvarig för masstabiliseringen och KC-pelarförstärkningen.
Första steget i utförandet var att Veidekke demonterade spår och frigjorde ytorna som skulle stabiliseras samt byggde arbetsvägar på ömse sidor om området som skulle stabiliseras. Efter det installerades KC pelare över hela ytan upp till 0,5 meter över den nivå som utförda undersökningar visade på att torvlagret underkant låg på. Detta för att få god kontakt med masstabiliseringen. När KC pelarna installerats kunde masstabiliseringen ta vid. Utrustningen utgörs av en grävmaskin med ett blandningsverktyg se bild nedan, samt bindemedelsvagn med kompressor.

Då bindemedelsvagnen måste fyllas på flera gånger om dagen och uppfyllning tar tid så användes två bindelsvagnar.



Figur 6 Inblandningsverktyg (Foto: Keller Grundläggning)



Figur 7 Masstabilisering med bindemedelsvagn (Foto: Keller Grundläggning)

9.1 Uppföljning i byggskedet

Några mätvärden från slangsättningsmätare har ej erhållits.
Installerad inklinometer vid km 23+180 visar ej på några avvikelser i rörelserna.
Mätvärden från markpeglar har erhållits för perioden 5 maj tom 15 maj 2014 på en del av sträckan mellan km 23+140 till 23+260. Mätresultatet visar på rörelser på upp till 10 mm.
Enligt spårmätning utförd hösten 2014 ligger nedspåret, dvs det nya spåret upp till 4,9 cm lägre i z-led än de projekterade höjderna. Störst avvikelse är det på sträckan där lerdjupet är som störst mellan km 23+350 till 23+420. Enligt samma mätningar ligger uppspår, det befintliga spåret upp till 3,4 cm lägre än projekterade höjder på samma delsträcka.



Figur 8 Masstabilisering (Foto: Keller Grundläggning)

10 SLUTSATSER

Då förstärkning med enbart masstabilisering i torv utfördes, blev resultatet ur sättningssynpunkt ej tillfredställande. Då byggnation av dubbelspår utfördes och metoden med masstabilisering tillsammans med KC-pelare valdes blev resultatet att utbildade sättningarna blev betydligt mindre. En erfarenhet är att det är viktigt att uppföljning utförs enligt föreslaget kontrollprogram och att mätresultaten dokumenteras och sammanställs. Det blir annars svårt att följa upp om sättningarna blev som utförda beräkningar förutspådde. I detta projekt finns brister i uppföljning och dokumentation vilket försvårat analysen av förstärkningens resultat.
Masstabilisering tillsammans med KC-pelare var för detta projekt en snabb och smidig förstärkningsåtgärd då både tidsaspekten och miljöaspekten vägde tungt.

11 REFERENSER

Nilsson Gunnar (2007), Utvärdering av masstabiliserade provytor, upprustning av Roslagsbanan Täljö station 23+100- 23+500, WSP.

Friberg Per (2010), Sätninguppföljning för masstabiliserade ytan mellan 23+120-23+270; 23+320-23+480, WSP

Bygghandling Roslagsbanan, Rybo-Åkers Runö (2013), WSP

Modelling of Earth Pressure from nearby Strip Footings on a Free & Anchored Sheet Pile Wall

H. Denver
Geo, Denmark, hd@geo.dk

L. Kellezi
Geo, Denmark

ABSTRACT
A strip footing from a nearby civil or industrial building or railway track is frequently situated near a sheet pile wall. Assessment of the extra pressure on the wall generated by the footing causes theoretical problems for the designer. The distribution of this pressure depends in fact on many parameters. Besides the location and magnitude of the load, a characterization of the soil and the wall is necessary for a rational design. Furthermore, the movement of the wall has a significant impact on the pressure. In this paper, both a free and an anchored wall are investigated. The problem is solved by means of different analytical methods compared with finite element modelling applied to a number of representative load cases. These comprise different strengths for the cohesionless soil and different load scenarios. After the study of a number of existing methods, simple and robust solutions are proposed for the future design of the sheet pile walls.

Keywords: Sheet pile wall, free wall, anchored wall, strip footing, earth pressure, additional pressure, finite element method, sand, stress distribution

1 INTRODUCTION

Driven sheet pile walls play an important role in many ways, both to overcome topological differences and in connection with excavations often near existing buildings. When the wall is driven in cohesionless soil a robust design is necessary to maintain the integrity. Generally, a substantial resistance against bending is required in the sheet pile wall to resist the pressure on the backside of the wall. This pressure can be a pressure from a water table on the backside, the earth pressure from the self-weight of the soil, and a load on the ground surface behind the wall. The load on the surface may arise from foundations of nearby buildings or from trafficking.

The influence on the wall pressure from especially shallow footings is often difficult to assess in practice and crude estimates are often used in lieu of methods that are more precise.

The paper, which is a continuation of authors work in Denver & Kellezi (2011) & (2013), describes methods to calculate more accurately the additional earth pressure on the wall from a strip or continuous footing behind the wall. Different aspects in connection with loads behind the walls are mentioned and discussed.

A free (unanchored) wall, where the top of the wall moves toward the excavation during rupture, and a wall rotating clockwise about an anchor, (the tip moves against the

excavation wall), are investigated. The results can be used in connection with any method to calculate the ordinary wall pressure. However, an effort has been made to integrate the problem into the Danish method of sheet pile wall design. The method is outlined in the following, illustrating the problem within this frame. The reason for this is that the method is based on actual rupture figures in the soil with respect to the predicted movements of the wall.

2 DANISH EARTH PRESSURE CALCULATION

The Danish earth pressure calculation (EPC) has been introduced by J. B. Hansen (1953) and used in Denmark for half a century. In this method the principle of superposition is used as shown in equation (1) for the normal stress on the wall. Here K is the earth pressure coefficient (different for the three terms). The first term represents the pressure from the selfweight of the soil, γ' is the effective unit weight of the soil and z is the depth along the wall to the point investigated from the soil surface. The second term is the contribution from an infinite surface load (p or q) on the soil surface behind the wall. The third term is the contribution from a cohesion (c). In this paper no cohesion is assumed.

$$e(z) = \gamma' z K_\gamma + pK_p + cK_c \qquad (1)$$

The water pressure (if any) is finally added to find the total pressure.

In the Danish method the wall is considered composed of several rigid parts interconnected by yield hinges. Each part is assumed to rotate about a point and the earth pressure coefficients are functions of the position of this point and the direction of rotation (besides the friction angle of the soil, φ). A few examples of rupture figures used for calculation of K are shown in Fig 1. Examples of walls with yield hinges are shown in Fig. 2.

The result of each calculation, is the total force on the wall and the point of application. The normal component of this force (E) is applied on the wall in a way to obtain a safe design. E.g. when the upper part of a wall, (above an anchor level), moves against the soil in failure, a large part of E is applied near the top, corresponding to a passive Prandtl rupture zone. A pressure jump near the top is thus assumed to ensure that the effect of the distribution, (in terms of total force and moment), is equal with the results from the calculations of the rupture figure.

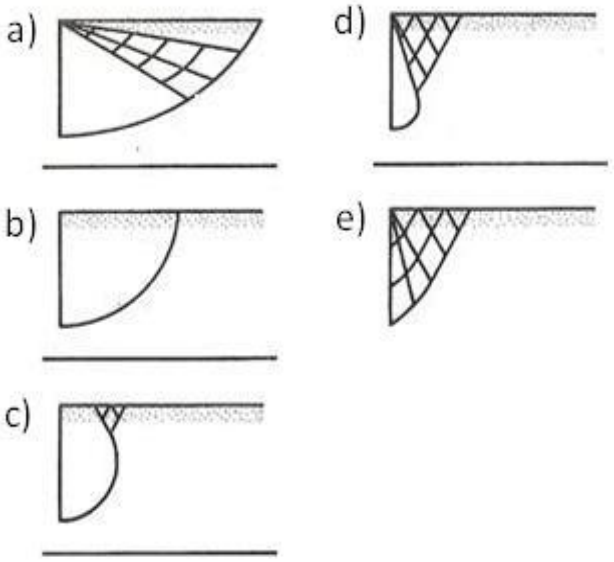


Figure 1 Rupture figures with different rotation points for a stiff wall. Type (e) (with rotation point near the tip) is used for a free wall and type (b) is used for an anchored wall.

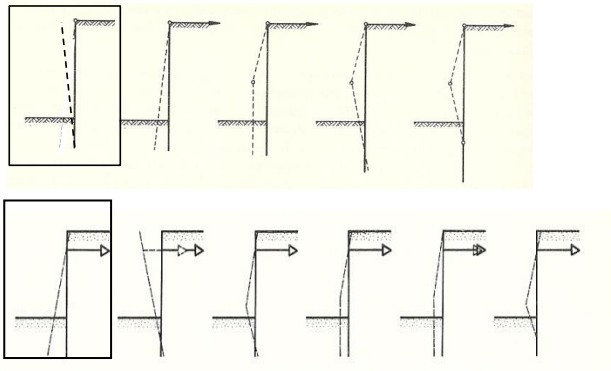


Figure 2 A wall in failure composed of one or more rigid segments connected by yield hinges in failure. This paper deals with the two left hand cases

The method has been described by Mortensen & Steenfelt (2001) and results of different examples calculated, are here compared with finite element (FE) two-dimensional (2D) analyses.

3 DESIGN PROGRAM "SPOOKS"

Although J. B. Hansen (1953) has made a complete set of diagrams to find the values of *K*, the earth pressure calculation for a specific design situation is rather time consuming. To this end Geo, the previous Danish Geotechnical Institute, has made a commercially available computer program called WINSPOOKS to overcome this problem.

Here, apart from the geometry of the excavation, the soil conditions and water tables, only a selection of the total wall movements, as shown in Fig. 2, is necessary as input. The results are a distribution of both, earth and water pressures, diagram of bending moments along the wall, tip level, and anchor force (if any). Altogether, ready for the final selection of the sheet pile profile and anchor.

The scenario when a surface load is present, starting at a certain distance from the top of the wall, can be calculated in WINSPOOKS. This is true if the load is active at an infinite width, which means that *b* in Fig. 3 included in section 5, continuous to infinity. This is incorporated by applying the full surface load at a certain depth below the soil surface. However, if b is finite, the effect of the load on the wall can´t be estimated by WINSPOOKS. In this case, the extra wall pressure must be assessed differently and inserter manually into the program.

4 PARTLY LOADED SURFACE

Applying the principle of superposition, the additional pressure from the strip load can be calculated separately and added to the total pressure on the wall, as a second term. This term is rather complicated to assess. The parameters are *a*, *b* as shown in Fig 3, *γ'*, *p*, and *z*, beside the movements of the wall as referring to Fig 2.

The total number of parameters can be reduced if the problem is treated in a dimensionless form. Still, too many parameters remain to derive a general complete solution applicable to engineering practice. This means that the problem can only be solved by choosing a number of typical cases, calculating them conventionally and numerically. By comparing the results, a simple solution can be derived, to be used as a reasonable approximation in an actual design situation. In the following, different approaches will be discussed.

5 COULOMB'S EXTREME METHOD

An extreme method was early presented by Coulomb (1776). The principle is that straight rupture lines are used to confine a rigid sliding body. This method can be used to calculate the influence of a partial surface loading on a wall. The method will be outlined in the following as it is a serious candidate to a solution of the problem. In Fig. 3 the method is outlined for the present problem.

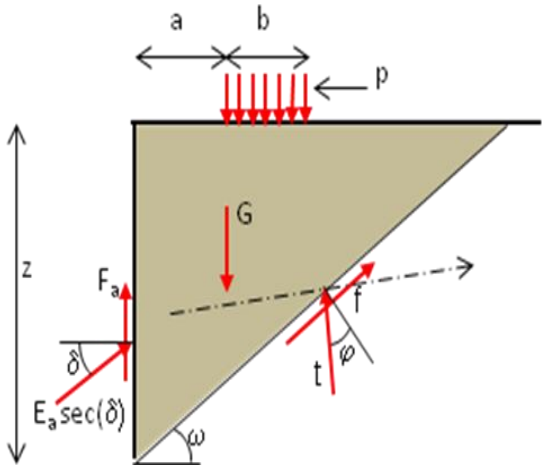


Figure 3 Coulomb's Method

The geometry appears from the figure and *G* is the weight of the shaded body, *t* is the total force from friction on the rupture line, and *f* is the shear force from the cohesion if any. The outer support on the wall consists of a normal force E_a and a shear force F_a. The latter comprises the effect of a wall adhesion (a_h). The frictional roughness is described by a wall friction angle (δ). As the problem is 2D all forces (single arrows in the figure) have units of force / length, whereas the

distributed load p has the dimension force / length^2.

The principle is now that the forces and the load are projected on a line perpendicular to t (the stipulated arrow) and equilibrium is required. This means that the value of the unknown t vanishes. With a given value of ω the force E_a can be determined as $E_a(\omega)$. The value of ω is now varied and $\max E_a(\omega)$ found as the necessary pressure to maintain equilibrium. The figure is made corresponding to a sliding movement to the left. This means that the results correspond to the active pressure. If this procedure is repeated for different values of z, the pressure distribution can be found as $e(z) = dE / dz$ and only applied when e is positive. The rupture line may not meet the soil surface in the so-called correct angle (i.e. it is not possible to construct a Mohr's circle for this point). For this reason, the static conditions are not generally fulfilled for the solution. Furthermore, the straight rupture line is in most cases a crude approximation to the often far more complex boundary rupture line for a more correct rupture figure in Fig. 1.

It is a Danish experience that reasonable solutions are found for wall problems with active ruptures, whereas unusable solutions are found for soil in passive rupture. In this paper, this method has only been applied for walls with soil in active rupture.

6 THEORY OF PLASTICITY

A method to assess the extra soil pressure caused by a partial load on an anchored wall has been introduced by Steenfelt and Hansen (1984). The Danish method to calculate the earth pressure coefficient from a relevant rupture line has been adopted. A circular rupture line is used as an appropriate choice for a rotation about a point at the anchor level. The stresses from the rupture line are determined by the Kötter's differential equation. The total force is found by integration of this equation and presented by Hansen (1953) and shown as the resulting force (F_o) and moment (M_o) about the centre of the circle as shown in Fig. 4.

It should be mentioned that the stress in the starting point of the integration (the top of the rupture line) is assessed empirically as no complete equilibrium can be achieved here.

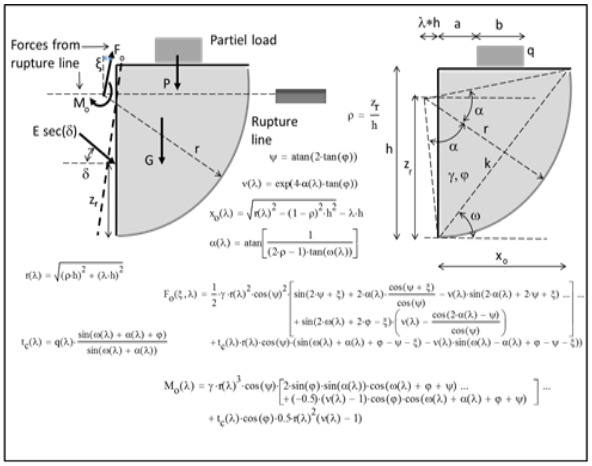


Figure 4 An analytical method where a circular rupture figure is applied. Negative values of φ and δ shall be applied as the rupture is active. The almost eligible formulas are only included to illustrate the complexity of the method.

On the basis of integration of the forces along the rupture line the optimal circle can be determined and the total pressure on the wall calculated. The method is introduced and discussed in details by the authors and the results of a large number of load scenarios are presented in their paper. The authors have made a computer program to solve the problem by the described method. However, some theoretical problems exists when the rupture line starts near or under the loaded area. Furthermore, it can be strongly disputed if the Kötter´s equation in fact can be used when the soil is only partly loaded. Consequently, results from calculations are not included in the final comparison.

7 EMPIRICAL METHOD

It is usual practice to partly apply a soil pressure derived from the distribution of the uniformly loaded surface, where the load itself is multiplied with a factor. A minor part of this distribution load, multiplied with another factor, is applied on the wall in a

depth interval confined by in inclined lines from the loaded area through the soil.

In Fig. 5, a method of this kind, often used in Denmark, is shown.

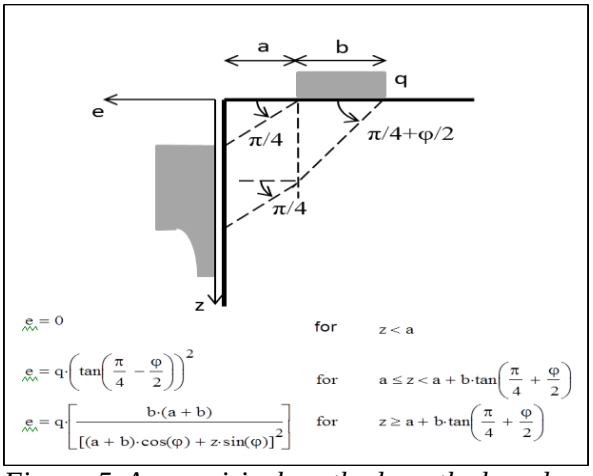


Figure 5 An empirical method partly based on the Coulomb's earth pressure theory

However, a tail below the lower line has been proposed by Mortensen (1976). The author has also pointed out the complexity of the problem and the assumption is a smooth wall that rotates anti-clockwise about a point below the tip of the wall. Consequently, the upper part with the even distribution is given by an active Rankine rupture figure. The tail is probably inspired by calculations by Coulomb's method where the lower part is more dependent of other parameters than *a* and *b*.

This solution has been applied for comparisons regarding the free walls with soil in active rupture for which it is derived.

8 ELASTIC SOLUTION

An elastic solution developed by Boussinesq (1885) as referring to Fig. 6 is also often used because of its simplicity. Besides the theory of elasticity a smooth vertical wall, without any movement, is assumed. This method is often questioned as the resulting distribution is expected to be inaccurate due to the fact that the wall in fact moves during rupture. This is also the authors experience when the movement of the wall is anti-clockwise about a low point in the wall. However, if the movement is a clockwise rotation about the anchor installation point, the assumptions for an elastic solution are more relevant. Consequently, this method has been included in the comparison for anchored walls.

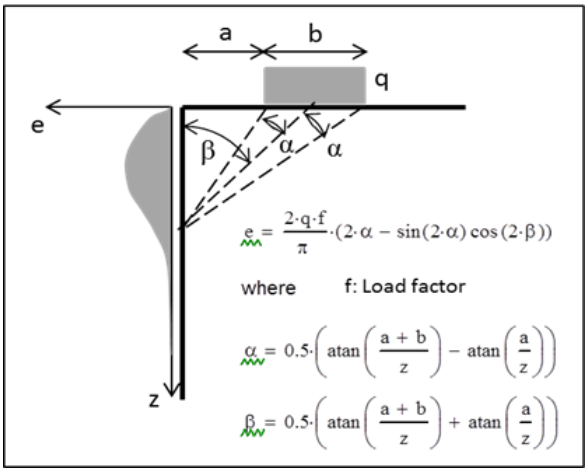


Figure 6 Elastic solution by Boussinesq (1885)

An appropriate triangular distribution as referring to Fig. 7, which approximates the elastic solution, is often used in Denmark because of its simplicity. This approximation has been used in the comparison.

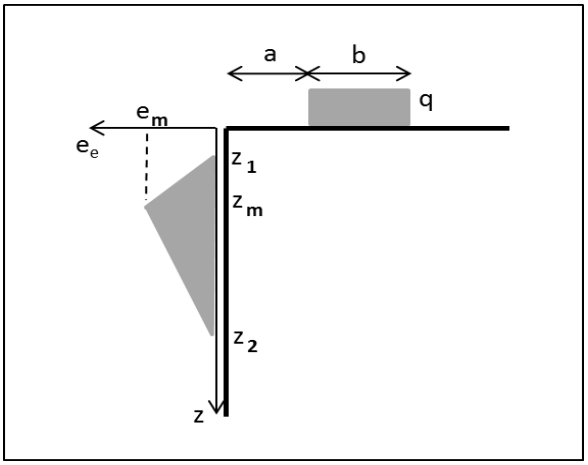


Figure 7 Triangular approximated distribution for the Boussinesq´s solution where the strip footing is assumed as a line load (z_1 = 0; z_m = 0.4(a+0.5b); z_2 = 2.5(a+0.5b); e_m = 0.45qb/(a+0.5b).p.

9 2D FE PLANE STRAIN MODELLING

In order to evaluate and rank the different conventional methods, a number of load scenarios have been calculated and analysed by the FE program Plaxis (2012). A 2D FE mesh has been generated using triangular

finite elements (15-noded). Sand is modelled in drained conditions using Mohr-Coulomb constitutive model. Clay, below the excavation level, is modelled in undrained condition using Tresca constitutive model. This layer has been included to ensure the correct movement of the wall. The wall is modelled as weightless and rigid body. The model is constructed in such a way that the active pressure on the wall does not interact with the passive one. The initial geostatic conditions are calculated first. Mesh sensitivity analyses have been carried out and an optimal mesh pattern with respect to element size and obtained accuracy has been chosen for the final analyses.

For the free wall some results from the calculations are shown in Fig. 8, and for the anchored wall, similar results are shown in Fig. 9.

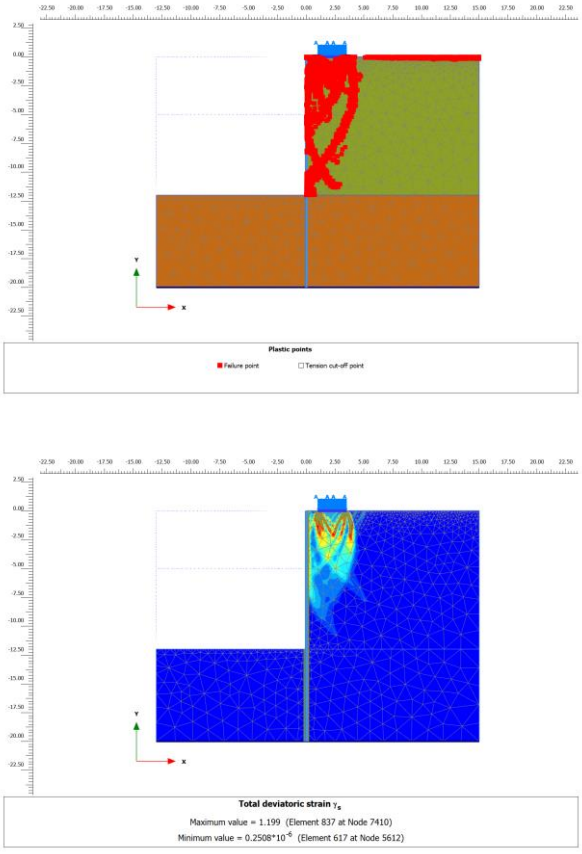


Figure 8 Free Wall, 2D FE plain strain results (plastic points & deviatoric strains), φ=30◦, a=1.0 m, b=2.5 m, or a / b=0.4, p=125 kPa.

Plaxis plastic analyses (small deformation theory) and Updated Mesh (large deformation theory) are both considered in order to see the impact the deformation / movement of the wall has on the results. The calculations are carried out in different ways considering the impact the staged construction (excavating after, before, or at the same time with the load application) has on the results.

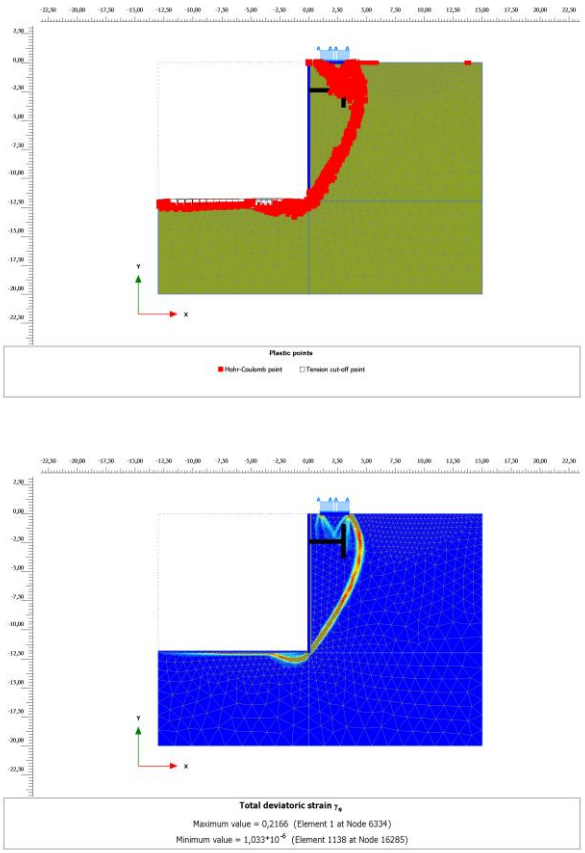


Figure 9 Anchored Wall, 2D FE plain strain results (plastic points & deviatoric strains), φ= 30◦, a=1.0 m, b=2.5 m, or a / b=0.4, p=125 kPa.

The extra pressure on the wall has been calculated as the difference between the pressure from both the soil and the strip footing or partial surface load, and the pressure only from the soil (i.e. two different calculations). From a conceptual point of view, no error is introduced by this procedure. The calculated difference can afterwards be added to the pressure from the soil alone (calculated by other conventional methods) to obtain the combined effect.

Actually, in a FE context, two different rupture patterns are subtracted. And thus, in principle 'two different degrees of total rupture' are subtracted. However, a study of the resulting pressure distribution reveals that the extra pressure is by far and large confined to the upper part of the wall. This means that similar pressure is calculated for the lower part of the wall. This is used as an argument that no substantial error is introduced by this approach.

The failure patterns given in Fig. 8 & 9 in terms of plastic points and total deviatoric strains, indicate the difference in the failure mechanism for the free and the anchored walls, respectively.

10 PROPOSED METHOD

A new method is proposed based on the overall results of the conventional and FE calculations. It is intended to derive a simple and easy to use method, which means that a simple shape of the resulting additional pressure distribution is chosen. This is in line with the recognition of the large inherited uncertainty in the determination of the distribution by simple means. The triangular distribution shown in Fig. 7 fulfils this requirement. The determining values are shown in Table 1.

Table 1 Values of proposed, triangular stress distribution behind the wall referring to Fig. 7, and with ϕ less than $\pi / 4$

Wall	Free	Anchored
z_1	$0.25\ a$	$(9a + 15b)$ $(1\text{-}\tan(\phi))^4$
z_m	$z_1 + 0.5\ a$	$z_1 + 0.5\ (a+b)$
z_2	$z_m + 6.0\ b$	$z_m + 8.0\ b$
e_m	$0.30\ q\ (b/a)^{0.4}$ $(\sin(\phi)+0.5)^{-2.5}$	$0.3\ q\ (b/a)^{0.5}$

The derived procedure of assessing the influence of a strip footing, or a partial loaded surface on a sheet pile wall, should fulfil the condition of converging to the additional load distribution usually applied for a fully loaded surface. In order to achieve that, the following procedure is proposed:

- Calculate the elastic distribution ($e_e(z)$) using the above mentioned guidelines.
- Calculate the distribution usually used for a fully loaded soil surface. Use only the part of this distribution corresponding to the interval of the uniform part of the distribution ($e_p(z)$) shown in Fig. 5.
- The final distribution is: $e(z) = W*e_p + (1-W)*e_e(z)$, where W is a weight function $W = F^3$ and $F = 1.2*b/h$. If $F>1.0$ then $F = 1.0$ is used.

11 COMPARISON OF METHODS

The different methods, conventional and FE, yield significantly different results. In fact, the correct solution depends on many other parameters as earlier mentioned. In order to perform a meaningful analysis of the different methods, the following strategy has been applied without further discussion:

Table 2 Load cases investigated

No	φ	a	b	q	No	φ	a	b	q
	(deg)	(m)	(m)	(kPa)		(deg)	(m)	(m)	(kPa)
1	30	1	2.5	125	5	40	1	2.5	713
2	30	1	1	50	6	40	1	1	285
3	30	2.5	1	50	7	40	2.5	1	285
4	30	5	1	50	8	40	5	1	285
h = 12 m		γ = 14 kN/m^3			c = 0 kPa rough wall				
Height to rotation point for anchored wall:								h_ρ = 9.6 m	

A number of relevant load cases has been selected as referring to Table 2. It should be emphasized that the local bearing capacity of the soil under the partial load or strip footing, is first controlled and ensured. The wall will somehow confine the rupture figure developed under the load as shown in Fig. 8 & 9. The ratio between the applied load and the unit weight has some influence on the solution though. This ratio is defined as $N = 2p / (\gamma\ b)$. With this definition N resembles N_γ from the bearing capacity formula. When choosing the different load scenarios modeled by FE, the N values were pre-calculated ensuring that the load scenarios corresponded to the same N value and bearing capacity of the footing was satisfied.

This was verified by the FE analyses where the loads were applied over a weightless rigid plate modelling the strip footing.

- The results from the 2D plane strain FE calculations are assumed to be superior to other methods. In order to evaluate the different methods, typical values, in connection with the design of a sheet pile wall, have been calculated.
  - For an anchored wall: Moments of the normal stress distribution at depths of 2.4 m (M1: near the anchor) and at the interval (4 - 8) m (M2: near an encastre point) and the shear force in the wall at a depth of 5 m. (T: to simulate the extra anchor force from the surface load).
  - For a free wall: Moment at a depth of 9 m (M2) and the transversal force (T) at the same depth, both near an encastre point.

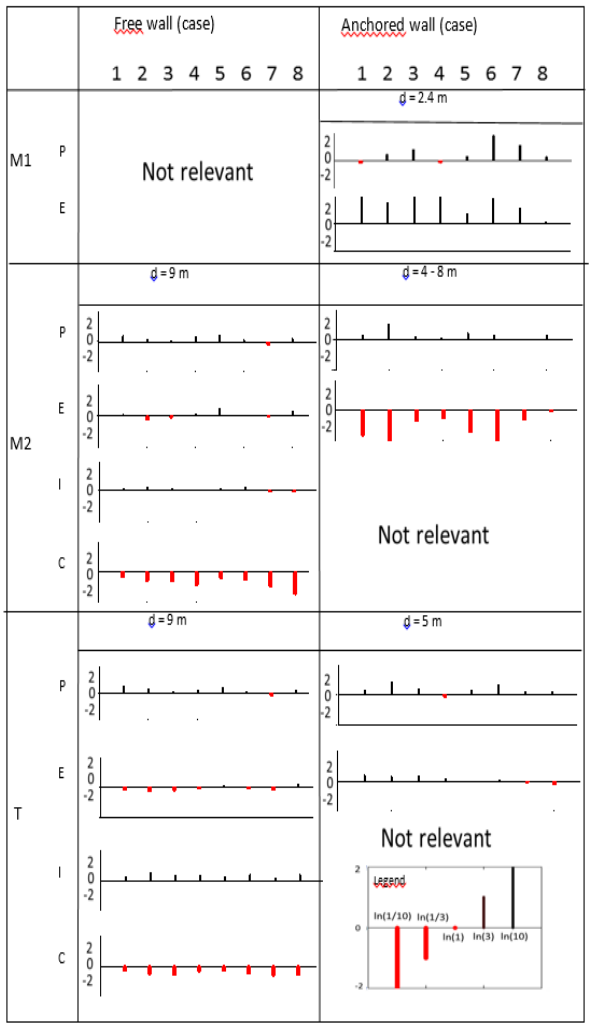


Figure 10

Figure 10 Comparison of different methods. Bars are ln(method / FE) referring to legend. M1, M2, T in the. text. P: Proposed; E: Elastic; I Empirical; C: Coulomb

- For each relevant method and each load case, the value of: ln(result for the method / FE result) has been calculated.
- The results are summarised in Fig 10.

The target values correspond to a value equal to zero (no bar). A black bar equals to +1 means that the method yields an ap. 3 times too safe value compared with the FE result. A black with height +2 (the maximum value shown) means ap.10 times or more too safe values. Values <0 are shown in red colour and mean unsafe values following the same methodology (values 1/3 resp. 1/10).

It is readily observed that:

(i) The proposed method yields superior results,

(ii) The Coulomb´s method is on the unsafe side,

(iii) The theory of elasticity yields unusable results for an anchored wall, and the empirical method yields usable results for a free wall but a calarge underestimate for an anchored wall (not shown, as the method is not intended for anchored walls).

Illustrations of the above comparison of different methods, is given in Fig. 11 & 12.

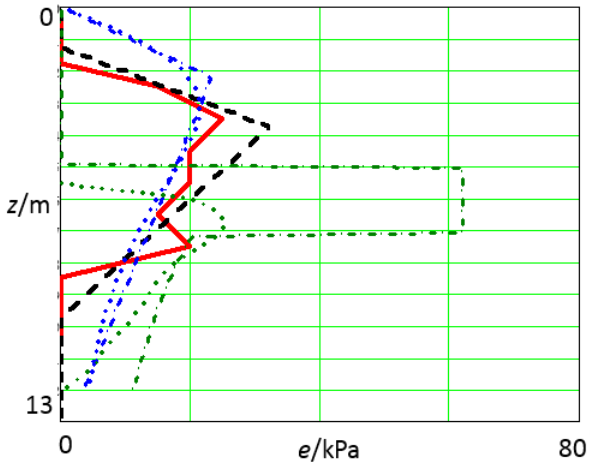


Figure 11: Example of pressure on a free wall Case 8 from Table 2. Traces from top: E (theoretical and approximation), P, FE, I, C (ref. Fig. 10).

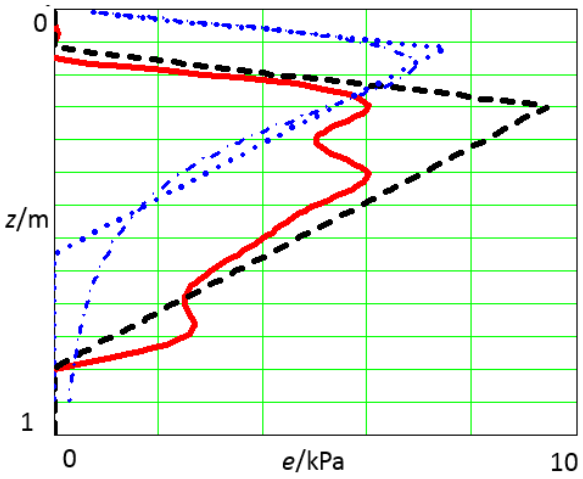


Figure 12: Example of pressure on a free wall Case 8. Traces from top: E (theoretical and approximation), P, FE, I, C (ref. Fig. 10)

The extra pressure on the wall has been calculated as the difference between the pressure from both the soil and the partial surface load and the pressure only from the soil (i.e. two different calculations). From a conceptual point of view no error is introduced by this procedure. The calculated difference can afterwards be added the pressure from the soil alone (calculated by other means) to obtain the combined effect. The only focus on the calculation is the stress distribution on the wall $e = e(z)$. If we denote the result of the FE-calculation, for both, soil and partial load, with $e_{\gamma+p}$ and the FE-calculation for soil alone with e_{γ}, then the extra pressure is calculated by $e_p = e_{\gamma+p} - e_{\gamma}$. We are now satisfied by the accuracy of each of the two terms on the right hand side of this equation, as they emerge from FE calculation, routinely use in the design situations. An extra uncertainty is of course introduced by the subtraction. But this is cancelled out when $e_{\gamma} + e_p$ is used in the design situation. It should be mentioned that the FE calculated e_p is reasonably comparable with the corresponding analytic calculation of this stress distribution used routinely in Denmark.

12 CONCLUSIONS

A new method is proposed to calculate the additional pressure on a free and anchored wall, respectively from strip footing or partial load next to the wall. The comparison study given in Fig. 10 clearly shows that the proposed method is superior to the others and is recommended in a design situation where the load case is reasonably comparable with the cases investigated. It should be added though that, the results depend to a large extent, on the number of other parameters, even including the design practice of the wall itself. The method can be applied, in combination with a conventional sheet pile wall design program like WINSPOOKS, for values of parameters reasonably covered by the current calculations. The method can be applied also for multi-layered soil profiles and multi-strip footings, or multi railway trucks (initial design), to be combined, verified and optimised though, by 2D FE modelling.

13 ACKNOWLEDGEMENTS

The authors acknowledge Geo for the financial support of the project. Furthermore the authors are indebted to Søren Gundorph for a fruitful discussion about the subject.

14 REFERENCES

Boussinesq, J. (1885): Application des potentiels a l'etude de équilibre et du mouvement des solides élastiques. Gauthier-Villars, Paris.

Brinch Hansen J. (1953): Earth Pressure Calculation, Danish Technical Press, Copenhagen.

Coulomb CA. (1776): Essai sur une application des rèles des maximis et minimis a quelques problems de statique. Memoires Acad. Royale des Sciences, Vol. 7. Paris.

Denver H., Kellezi L. (2011): Earth pressure from a nearby building on sheet pile walls. Proc. 17th European Conf. Soil Mechanics and Geotechnical Engineering. Athens.

Denver H., Kellezi L. (2013): Earth pressure from a strip footing on an anchored pile wall. Proc. 18th Int. Conf. Soil Mechanics and Geotechnical Engineering. Paris.

Mortensen, K. (1976): Memo vedr. Aktivt jordtryk fra partial overfladelast. Danish Geotechnical Institute.

Mortensen N.,Steenfelt J.S. (2001): Danish plastic design of sheet pile walls revisited in the light of FEM, Proc. 15th Int. Conf. Soil Mechanics and Geotechnical Engineering. Istanbul.

Plaxis, (2011): FE Code for Soil and Rock Analyses, User's Manual, A.A. Balkema, Rotterdam.

Steenfelt J.S., Hansen B. (1984): Sheet pile design earth pressure for strip load, J. Geotecn. Engrg. ASCE Vol. 110, No. 7.

Geotechnical Infrastructures of New Capital Astana on Problematical Soil Ground

A.Zh. Zhussupbekov
Eurasian National University, Kazakhstan, astana-geostroi@mail.ru

A.R. Omarov
Eurasian National University, Kazakhstan omarov_01@bk.ru
G.A. Zhukenova
Eurasian National University, Kazakhstan, gulnara_home@mail.ru
G.K. Tanyrbergenova
Eurasian National University, Kazakhstan, tanyrbergen_guldy@mail.ru

ABSTRACT
Just as every civilization in the history is originated from the riverside, so the city of Astana - new capital of Kazakhstan has been developed around the Ishim River. As its result,. there are many bridges across the river. Also high rise building such Palace of Peace, Khan Shatur, Abu -Dhabi Plaza, Ministry of Transporation Buildings, International Astana Airport, Mosque Hazret Sultan, New Railway Station, Expo2017 constructions site and other many structures founded in problematical soil ground of Astana. These unigue buildings need performing of deep driving and boring piling foundations. For designing of piling foundations on difficult soils are important investigations of behavior of piles by using of dynamic, static, O-cell, integrity piling tests. This paper includes of fresh results of several piling tests with comparison of numeral analysis by FEM. These investigations of interaction of piles with soil ground of new capital are important for understanding of mechanism of working of different piles on soft and hard soils of Astana. Also this paper introduced of experiences of piling constructions in winter season on freezing ground. The last page of paper includes recommendations and conclusion with proposing of methodic for the obtaining of bearing capacity and settlements of driving and boring piles on problematical soil ground of Astana.

Keywords: Bored piles, dynamic load test, static load test, rapid load test, O-cell testing.

1 INTRODUCTION

Nowadays many megaprojects are emerging in the new capital of Kazakhstan – Astana. The high rates of construction and appearance of high-rise buildings having modern architecture, and engineering megaprojects, led to a wide use of pile foundations.
Modern construction puts modern requirements in front of engineers and designers, and so instead of traditional decisions it came to the use of new economical and ecological efficient technologies such as CFA (continuous flight auger), DDS (drilling displacement system), steel “H” piles, and so on.
It is well known that pile foundation is one of the most widely used types of foundation at the construction sites of Kazakhstan. Application of pile foundation is explained by necessity of ensuring a high bearing capacity for high-rise buildings.
During the last 15 years, many high-rise buildings supported by pile foundation are rising up in Astana, the new capital of Kazakhstan. Following megaprojects are already completed: Ministry of Transportation and Communication, Housing estate – Izumrudny Kvartal (Emerald square),

Cultural and Entertainment Center – Khan Shatyry and so on (Figure 1). Many megaprojects are under construction or in planning. One of the unique projects is the housing estate "Abu-Dabi Plaza" which started on 1 July 2011 in Astana. The project of housing estate was designed by famous architect Norman Foster. By preliminary evaluation, the cost of project exceeds 1.5 billion US dollars. This will be the highest building in Central Asia and ranked 14th in the world. "Abu-Dabi Plaza" - a complex from several towers, united around the main building with a height 382 meters - 88 floors (Figure 1).



Figure 1 Megaprojects of New Capital of Kazakhstan – Astana.

1.1 General aspects of Kazakhstan pile design concept

It has been mentioned previously that existing Kazakhstan standard documentation of pile design is out of date and does not meet the requirements of modern engineering. The standard needs to be revised. Nowadays, conception of pile foundation design is in the process of modernization, as presented in Figure 2.

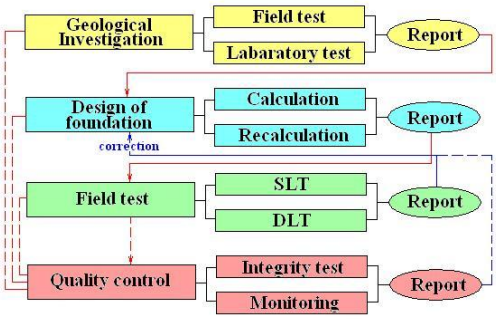


Figure 2 Pile foundation design concept.

Design of pile foundation includes two critical stage of analyses: bearing capacity and settlement analysis. The preliminary design is performed based on the engineering and geological investigation of construction site. Accuracy of pile design generally depends on the accuracy of data presented in geological report. Final pile design project is corrected after approval by field tests.

The preliminary configuration (length and cross section) of pile depends on required bearing capacity of pile and may be determined by following equation, recommended by Kazakhstan Standard:

$$F_d = \gamma_c \left(\gamma_{cR} RA + u \sum \gamma_{cf} f_i h_i \right) \quad (1)$$

Where Y_c – safety factor; Y_{cR} and Y_{cf} – coefficients of soil work condition under the pile tip and surrounding of pile, respectively; R, f_i – soil resistance under the pile tip and shaft resistance respectively, kPa; A – cross section of pile, m^2; h_i – thickness of *i*-layer, m.

In this case, the results obtained by cone or standard penetration tests (CPT or SPT) and plate load test are more valuable, particularly to definition of shaft and tip resistance of soil.

Unfortunately, existing Standards do not take into account soil compaction under the high concrete pressure in case of CFA technology and soil displacement without excavation in case of DDS technology that lead to reduction of settlement and increase in bearing capacities of pile foundation (Sultanov at al, 2010). In connection with aforementioned, it is suggested to use following coefficients of soil working condition as presented in Table 1.

Table 1 Coefficient of soil work condition

Type of pile	Y_{cR}	Y_{cf}
Driving Pile	1,0	1,0
Boring Pile	0,7-1,0	0,7
DDS (FDP) Pile	1,3	1,0
CFA Pile	1,0	1,0

To accurately analyze the bearing capacity of CFA pile, it is necessary to take into account volume change of (∇ r) of borehole, by appearance in borehole additional pressure; with classical solution of Lambe based on theory of elasticity in linear formulation, as defined as (Ashkey, 2008):

$$\nabla r = \frac{(1+\mu)\cdot r \cdot \sigma_h^{concrete}}{E_h} \quad (2)$$

where, μ - Poisson ratio of concrete (μ=0.20); r - normal pile radius; $\sigma_h^{concrete}$ - lateral stress of concrete to soil; E_h - Young modules considering soil layer for horizontal deformation, kPa.

Predictable settlement is performed by «method of layer-wise summation» (word-for-word). The general principle of this method is definition of settlement in limited compaction zone by following equation, recommended by Kazakhstan Standard:

$$S = \frac{\Sigma \sigma_{zp}^{avr} \cdot \beta \cdot h_i}{E_i} \quad (3)$$

where σ_{zp} – stress in soil due to loading, kPa; β – coefficient depending on radial expansion of soil; h_i – height of i- layer of soil, m; E_i – Young modulus of *i*- layer of soil, kPa.

Compaction zone is conditionally equal - when stress from weight of soil quintuple more than stress from pile load. In this case accuracy of Young modulus is very important. Young modulus may be determined by laboratory or field test. It is suggested to use Young modulus with allowance of depth of load application as defined after SLT. The principle of this method is assuming pile as plate (Yenkebayev, 2008). Young modulus may be defined by following equation:

$$\mathbf{E} = \frac{\left(\mathbf{F_d}/\mathbf{A}\right)\cdot \mathbf{d}\cdot \mathbf{K_0}}{\mathbf{S}} \cdot \frac{\omega`_{\mathbf{avr}}}{\omega_{\mathbf{avr}}} \quad (4)$$

where F_d – bearing capacity of pile obtained by SLT of pile, κN; $\mathbf{A}$ – cross section of pile, m2; $\mathbf{S}$ – settlement of single pile by SLT; $\omega_{\mathbf{avr}}$ – parameter depends on relative thickness of compaction layer ($\gamma = \mathbf{H}/\mathbf{b}$) and relationship semi-length of foundation to the semi-width ($\alpha = a/b$). ω'_{avr} - same parameter in case of unlimited thickness of compaction layer.

Generally this method is used for predicting settlement of pile-raft foundation by SLT of single pile. Settlement of piled-raft foundation defined by aforementioned «method of layer-wise summation». Recently forecast by FEM analysis has become more acceptable. FEM allows relatively reliable analysis of pile settlement and bearing capacity in a short time. However, application of FEM analysis is confined by absence of requirements in existing Kazakhstan Standards. Results of FEM analysis depend on calculation model. In case of correct approach FEM analysis gives very satisfied convergence. Example of comparison results of FEM and SLT of CFA pile is presented in Figure 3, using the numerical approach proposed by Prof. Tadatsugu Tanaka. The first diagram shows result of incorrect FEM analysis, second shows FEM analysis taking into account expansion of pile due to of high pressure of concrete. The FEM mesh and average expansion of pile body depending on soil strength is also presented in Figure 3.

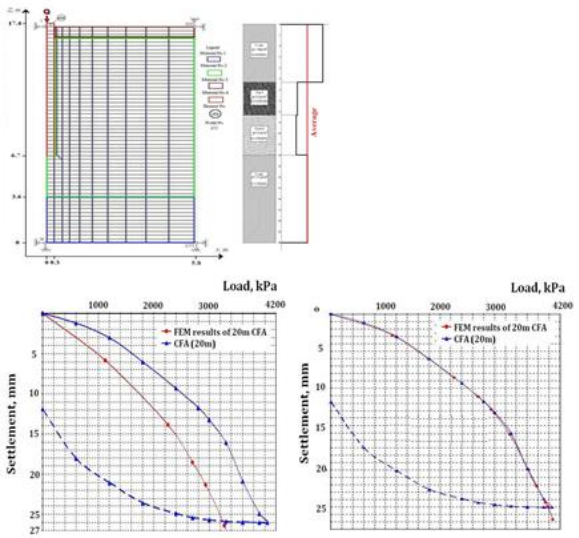


Figure 3 FEM analysis of CFA pile

2 FIELD TEST OF PILE FOUNDATION

2.1 Dynamic load test (DLT)

DLT is a fast bearing capacity analysis field test and give more or less reliable value of pile bearing capacity. For definition of the bearing capacities of piles, it is required to

use average refusal which are obtained during redriving of the piles after their "rest". The rest time depend on soil condition of site: for clayey soil 6 -10 days, for sandy and gravel soils up to 3 days.
Bearing capacity of the piles is defined by following empirical equation:

$$F_u = \frac{\eta AM}{2}\left[\sqrt{1+\frac{4E_d}{\eta AS_a}\cdot\frac{m_1+\varepsilon^2(m_2+m_3)}{m_1+m_2+m_3}}-1\right] \qquad (5)$$

where η=factor, dependent on concrete strength of the piles; A=cross section of tested pile; M=1 – factor, dependent on pile driving hammer's impact; E_d =effective energy of blows of the hammer, kNm.
According to Kazakhstan Standard at least 6 piles must be tested by DLT on each construction site (Fig. 4).



Figure 4 Photo and schema of dynamic load testing in Kazakhstan.

2.2 Static Load Test (SLT)

SLT one of the more reliable field tests in analyzing pile bearing capacity. SLT should be carried out for driving piles after the "rest" and for bored piles after achievements of the concrete strength, by more than 80%.
According to requirements of Kazakhstan Standard - SNiP RK 5.01-03-2002 – ultimate value of settlement of the tested pile is determined as and depending on category of construction is equal to 16 or 24 mm. The last argument shows conditional character of SLT method.
According to Kazakhstan Standard 1% of constructed piles on construction site must be tested by SLT, but at least 2 SLTs in a site must be done (Fig. 5).

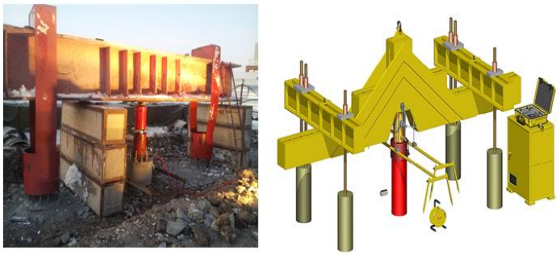


Figure 5 Photo and schema of static load testing in Kazakhstan.

2.3 Comparison of SLT and DLT

SLT and DLT both are practised in Kazakhstan construction. According to experience on construction sites of Astana, some difference exists between SLT and DLT results. Moreover, results of bearing capacity of pile depend on type of hammer. Thus, DLT results obtained by using hydro-hammer are more approximate to the SLT results, namely more reliable than results obtained by using diesel-hammer (Seidmarova, 2008). The safety factor as defined by comparative analysis of many DLT and SLT data is presented in Figure 6.

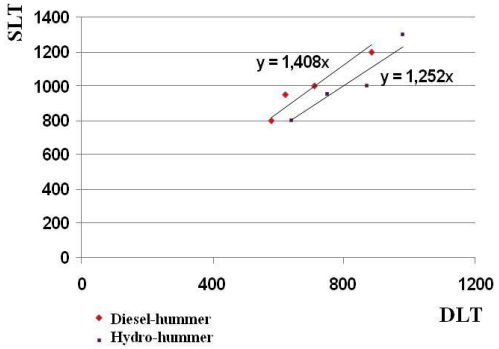


Figure 6 Comparison results of DLT and SLT.

2.4 O-Cell test or static testing of subsoil by the piles with bidirectional load

The target of this tests was obtaining of bearing capacity of piles on problematical soils ground of Expo 2017 (Astana, Kazakhstan).
The method suggested by George Osterberg allows determining the calculated subsoil resistance under the lower end of the pile and on its lateral surface at the same time. The specific thing of the O-Cell test is that the load is applied not on the pile head, but on the pile body where the adjustable jack is set. It works in two directions. Hydraulic

adjustable jack is installed at the depth of 2/3 pile length - 16.8m (Fig. 7).
The test pile was a 1000 mm diameter bored pile. The hydraulic jack assembly comprising of three (3) 500-tonne capacity bi-directional hydraulic jacks, was in-stalled at 16.80m (330.60 m RL) below the Cut off Level (Fig. 7).
The hydraulic jack assembly and steel cages were jointed and lowered into the bored hole. The pile was concreted according to the contractor's method statement (Fig. 8).
There were a pair each of tell-tale rod installed at the top and the bottom of the hydraulic cell assembly. Their movements were measured against a reference frame constructed by the contractor.

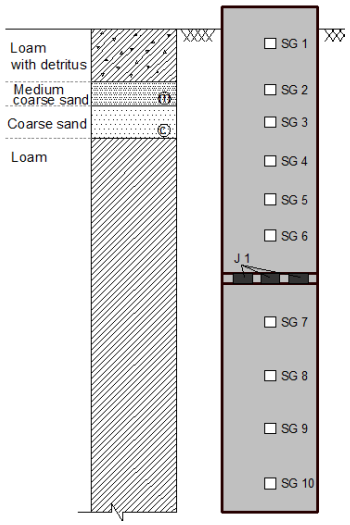


Figure 7 Geotechnical condition and details of piles in construction site of EXPO-2017 (Astana).

Ten levels of vibrating wire-type strain gauges (Geokon- 4911 Sister bar type) comprising four units at each level were installed in the test pile to measure strain at nominated locations. The strain gauges were mounted at designated Level 1 to Level 10 as(SG1 to SG10) shown in the pile layout provided (Fig. 7).



Figure 8 O-cell tests of piles.

Before the tests 10 strain-measuring transducers connected to a data detector (data-logger) were installed in the body of the experimental pile. Unlike a traditional static testing, O-Cell allows to obtain two dependences "load- subsidence": one curve characterizes the resistance of the pile under the bottom end, the second one – on its lateral surface. Therefore, using these two curves we can obtain an equivalent curve "load-subsidence", which is analogous to the curve SLT.
The O-Cell test results are presented in figure 9. At the maximum test load of 100% (14500kN), the maximum displacements of the piles are PTP-1 – 7,30 mm and PTP-2 – 6,50 mm, and at the maximum workload of 200% (29000kN), displacements of the piles are PTP-1 – 18,35 mm, and PTP-2 – 14,40 mm. Figure 9 shows the comparison of the results of piles test by O-Cell method (the equivalent curve).

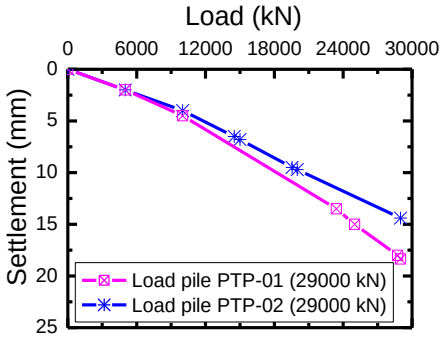


Figure 9 Results of the test O-Cell.

2.5 Alternative Load Test Method

From aforementioned it follows that SLT and DLT both have disadvantages. SLT required a lot of time, works and cost. Prescribed by Standard quantity of required SLT is not enough to adequately realize soil condition of construction site (2 SLT for 200 piles only). DLT is much faster but is not so reliable and is applicable to driving piles only.
Today, in process of adaption into Kazakhstan practice is an alternative load test method which precluded disadvantages of both SLT and DLT – Rapid Load Test (RLT). RLT allow performing up to 10 piles per day and much cost effective than SLT (Zhussupbekov and Matsumoto, 2011). The comparison of SLT and RLT as obtained by Matsumoto are presented in Figure 10 that shows reliability of RLT.

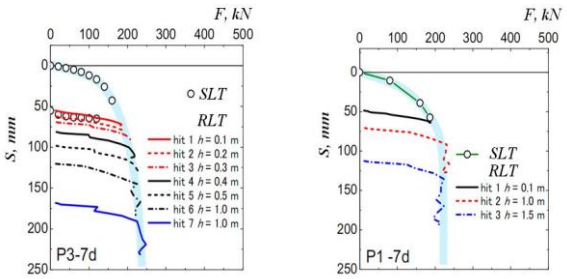


Figure 10 Results SLT and RLT.

3 QUALITY CONTROL OF PILE FOUNDATION

3.1 Pile Integrity Test (PIT)

Pile integrity test is one of the non-destructive methods of pile quality control. This method allows analyzing integrity control for all existing types of piles (boring, injection, driving and so on). PIT is base on wave propagation theory in rigid body and is concerned with one of the modern quality control methods used world-wide. PIT allows detecting pile defects: approximate pile length, expansion and narrowing of pile cross section, modification of soil layers, heterogeneity of pile material, cracks in cross section of pile, extrinsic material in pile body (Fig. 11).



Figure 11 Photo and schema of pile integrity testing in Kazakhstan.

Advantages of PIT are as follows: portable device is easy to carry. One operator will be able to test over 100 piles per day, depends on site condition, pile head preparation and approach to the pile; minimum influence to the construction work on the site; significant defects may be detected in the beginning of the construction. PIT has some limitations: reflection of the bottom of pile sometimes has errors depending on soil condition; little deflection (less than 5 %) of pile cross section cannot be identified.

According to Kazakhstan Standard requirements it is necessary to test 60% of boring piles and 50% of driving piles.

3.2 Geomonitoring

Geomonitoring for foundation settlement is one of the quality control methods that can be carried out during and after construction in exploitation period. Monitoring is indirect control of pile installation evaluation.
The principle of this method is monitoring the settlement of special marks which are installed to interested points of construction. Monitoring starts from the beginning of construction and allows revealing defects of foundation installation.
Result of monitoring for settlement development during construction of «Ministry of Transportation and Communication » building is presents in Figure 12.

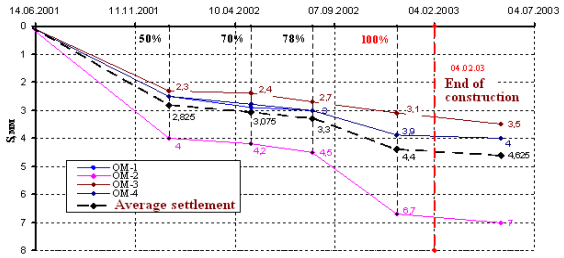


Figure 12 Geomonitoring results.

3.3 Analysis of effect of pile driving on the existing foundation (vibration monitoring)

The article presents the results of the analysis of the effect of vibration exposure pile driving on the existing foundations of a functioning oil and gas complex located in Tengiz city (Fig. 13). The aim of the tests (vibration monitoring) was to determine the smallest allowable distance piling devices excluding the impact of vibration on the foundation and ensuring the safe operation of the plant. The article presents the results of vibration exposure piling at different distances from the base, taking into account the natural oscillations of technological processes, solid foundation and others, as well as the results of excitation of ground

mass at various distances from the source of vibration exposure (pile driving).
The source of the vibration excitation was pile driving (C16-40) through pile-driving equipment Banut 555 with a mass of hydraulic hammer 6,075 tonnes and a maximum drop height 1.0 m. In case of driving of piles was drawn up the statement of pile-driving. Vibromonitoring was carried out by the instrument Profound VIBRA +, with use of the 3D seismic sensors. The interval of measurement of vibration was carried out every 5 seconds. Tests were executed according to requirements of norm of DIN 4150-3 according to which the most allowed level of vibration is equal 5,00mm/sec. (from 0-10 Hz).
The maximum impact on a soil array was recorded at a distance 40m from a source in case of driving of piles No. 3, 5 and 6. In all cases the maximum values of speed of oscillations were recorded when dipping C16-40piles on depth from 5 to 8 m.

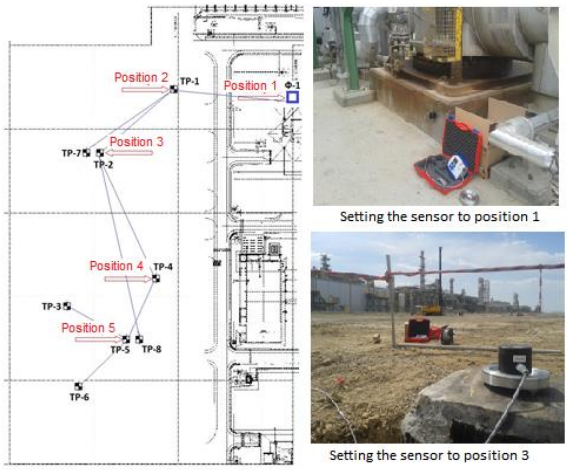


Figure 13 Vibration monitoring at the Tengiz oil and gas facilities

4 CONCLUSIONS

Existing pile foundation Standards practiced in Kazakhstan are out-of-date and are in urgent need for modernization. This paper presented very short descriptions of coming changes to the concept of Kazakhstan pile foundation design.
Presented aspects of modern pile technology design, including FEM analysis, allow making more reliable prediction of bearing capacity and settlement of pile that has become very important for the preliminary design of piling foundation projects. RLT allows performing up to 10 piles per day, much cost effective than SLT, and more authentic than DLT. RLT is a type of DLT and is appropriate for any type of pile, but cannot be used to full extent on construction sites of Kazakhstan due to absence of Standard.
Pile integrity test is in the process of gaining official acceptance in Kazakhstan. PIT is a non-destructive method allowing quality control of pile body whereupon of pile installation and even after many years of building exploitation. Geomonitoring for foundation settlement is indirect control of pile quality evaluation method and has become more relevant, especially for high-rise building construction.
The main advantages of O-Cell method are good applicability for the piles of great length and diameter, especially in cramped conditions; the possibility of pile loading by heavy loads with the increasing the number of adjustable jacks; improving the accuracy of the results due to the absence of pile heave because the anchoring system is not applied; the improvement of safety due to the absence of the reaction system on the ground level and the energy of testing load develops at a sufficient depth.
There is no necessity for engineers to rely on the test piles reduced in scale due to the very high cost of testing of the piles of a large diameter using traditional methods.
The development of bidirectional load on high bearing capacity of the piles gives engineers a new powerful tool for assessing the characteristics of the piles with the subsoil. Along with this we can say that using this method saves funds and time. It is because there is no necessity to use anchoring piles.
Along with the benefits of tests there are some limitations. The applied method is mainly used for bored piles, just as adjustable jack and transducer for measuring displacements have to be pre-installed before testing and after testing they remain in the pile.
Along with the disadvantages, the major advantage of the O-Cell is that it can help to

determine the calculated resistance of subsoil under the lower end of the pile and on its lateral surface, which is of special value for the analysis and evaluation of bearing capacity of piles of a large diameter.

5 REFERENCES

G.A. Sultanov, A. Zh. Zhusupbekov, R.E. Lukpanov, S.B. Enkebaev, Research of Interaction between Displacement Pile and Soil Basement. Proceedings of Kazakhstan-Korean joint geotechnical seminar. 2010, Astana, Kazakhstan, 84-91 pp.

Y. Ashkey. Interaction of CFA bored piles with soil condition in Astana. A dissertation submitted in partial fulfillment of the requirements for the PhD degree. 2008. Astana, Kazakhstan.

S.B. Yenkebayev Interaction between high-rise buildings and soil basement. A dissertation submitted in partial fulfillment of the requirements for the PhD degree, 2008. Astana, Kazakhstan.

SNiP RK 5.01-03-2002 “Pile foundation”.

SNiP RK 5.01-01-2002 “Soil basement and foundations”.

T. Seidmarova. Bearing capacity evaluation by results of static and dynamic load tests. A dissertation submitted in partial fulfillment of the requirements for the degree PhD, 2009. Astana, Kazakhstan

ASTM D1143. "Standard Test Methods for Deep Foundations Under Static Axial Compressive Load".

Guoliang Dai, Weiming Gong. (2012). "Application of bi-directional static loading test to deep foundations". J. of Rock Mechanics and Geotechnical Engineering., 4(3): 269–275.

Osterberg, J.O. (1989). "Breakthrough in Load Testing Methodology" J. Foundation Drilling, Vol. XXVIII, (8), ADSC: 13.

Osterberg, J.O. (1989). "New Load Cell Testing Device". Proceedings of 14th Annual Conference. Deep Foundations Institute: 17-28.

A. Zh. Zhusupbekov , Tatsunori Matsumoto, S.B. Yenkebayev, D.Kemelov, R.E.Lukpanov, Methodology of Spring Hammer Rapid Load Test. Proc. of National Scientific and Practical Conference, ENU, 2011, Astana, 70-75pp.

Report of vibration monitoring. KGS-Astana, from 19 May. Project: PU-341 Sour Gas Dehydration (62-0000-043-10-DH), 2012, p. 32.

DIN 45669. Human exposure to vibration in buildings, Germany,1995-2006: p.8.

C.H. Dowding, Prentice Hall Inc., Englewood Cliffs, NJ, 1996, 620pp

Design and construction of a reinforced soil avalanche barrier at Neskaupstaður

D. J. Halifax
Reinforced Earth Company, United Kingdom, david.halifax@reinforcedearth.co.uk

N. Frietag, J.E. Sankey
Terre Armée International, France

ABSTRACT
Reinforced soil structures offer a number of advantages for the construction of avalanche barriers. This paper describes the design and construction of a 14m high, reinforced soil avalanche barrier constructed at Neskaupstaður in Iceland. It explains the basic design procedure and describes how on-site installation damage testing was employed to assess the effects of using a non-standard fill material on the soil reinforcement.

Keywords: Reinforced soil, avalanche barrier

1 INTRODUCTION

As part of a programme to protect towns and villages in Iceland from the effects of avalanches, a range of protection schemes have been constructed. In certain locations protection is provided by large earth barriers. Two phases of barrier construction have been implemented at Neskaupstaður in north east Iceland. The first phase, completed in 1999, related to the snow path named Drangagil. It consists of a 12m high main catching barrier and smaller breaking barrier protecting the eastern part of the town. The second phase of protection for the western side of the town was constructed in 2012 and related to the avalanche path named Tröllagil. This paper explains the design and construction of the main catching barrier constructed as part of the second phase. The barrier is a Reinforced Earth® structure constructed using the GeoTrel® system supplied by Reinforced Earth Company in the United Kingdom.

The overall scheme is further summarised in Annex D of the European Commision report "The design of avalanche protection dams".

2 STRUCTURE GEOMETRY

The main catching barrier is approximately 650m long and has a facing height of up to 14.2m. The front face has an inclination of 1h:4v. There is a 5m wide horizontal section at the top of the barrier and the rear face of the structure has a slope of 2h:1v. The geometry is shown in Figure 1.

The structure is a reinforced soil steepened slope with structural stability being provided by the interaction between the soil and layers of polymeric strips placed within the compacted soil. The front face is retained with a galvanized steel mesh panel connected to the soil reinforcement by galvanized steel hooks and a curved steel plate.

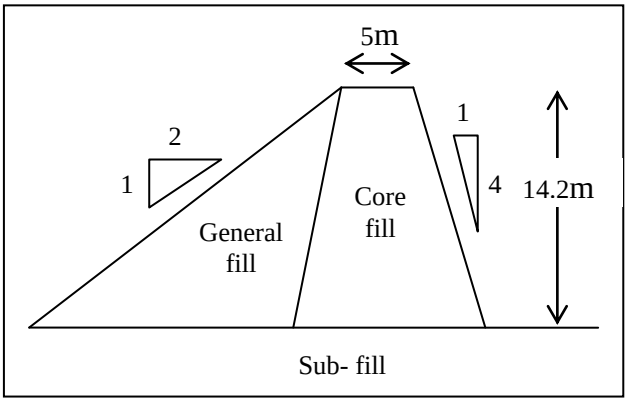


Figure 1 Basic structure geometry.

3 CONSTRUCTION MATERIALS

3.1 Fill materials

The core fill within the reinforced zone is a blasted and crushed igneous rock having a bulk density of 21.5kN/m^3 and a characteristic angle of internal friction of 45°. The general fill forming the rear face has a bulk density of 20kN/m^3 and a characteristic angle of internal friction of 35°. The barrier is constructed above a 3m deep sub-fill layer having the same properties as the core fill within the reinforced zone. All of the fill materials were excavated from local sources.

3.2 Facing panels

The facing panels forming the front of the structure are galvanised carbon steel panels manufactured from 8mm welded steel bars with a 100mm aperture spacing in the horizontal and vertical directions. The bars have a yield strength of 500N/mm^2. The facing panels are hot-dip galvanised with a protection thickness of 140μm. The galvanising provides sacrificial corrosion protection to the facing. The nominal facing panel size is 3.0m x 1.3m with two rows of soil reinforcement connected to each facing, giving a 650mm vertical spacing between layers of soil reinforcement.

3.3 Soil reinforcement

The polymeric soil reinforcement comprises closely packed high tenacity polyethylene terephthalate (PET) fibres encased in a low density polyethylene (LDPE) sheath. A knurled finish is provided to the sheath. The finish helps to provide frictional resistance between the soil and the soil reinforcement, which, in addition to its tensile capacity, enables the structure to resist the applied loads. This type of soil reinforcement has been extensively used for reinforced soil structures since the 1980s; mostly with precast concrete facing panels but more recently also with wire mesh facing panels.

Three different grades of soil reinforcement are used in the construction of the dam. These being 37.5kN, 50kN and 65kN corresponding to the initial strength of the soil reinforcement. Each grade has a width of 50mm. The soil reinforcement is CE marked to demonstrate conformity with the requirements of the harmonised European Standard for soil reinforcement. Representative samples of the soil reinforcement are tested by the manufacturer for tensile strength, elongation, cone puncture resistance, static puncture resistance and durability. The test results allow the manufacturer to provide a Declaration of Performance and a Certificate of Conformity with each batch of materials.

3.4 Connections

Each of the soil reinforcement strips is connected to the facing panel by a galvanised steel hook with a horseshoe shaped steel plate. The hooks and horseshoes are protected against corrosion by hot-dipped galvanisation. The dimensions of the system ensure a non-damaging bending diameter of 60mm for the soil reinforcement as it passes around the connection. It has been demonstrated that diameters smaller than 20mm can have a detrimental effect on the soil reinforcement capacity (Sankey & Lozano 2015).

4 DESIGN

The structure was designed using the principles described in BS8006:2010. This is a limit state procedure considering both ultimate and serviceability limit states. Partial load factors greater than unity are applied to the nominal loads having disturbing effects. Design material properties are calculated by dividing the characteristic properties by the appropriate partial resistance factor.

The ultimate limit state considers the factor of safety against collapse and the serviceability limit state considers the magnitude of deformation that will occur during the service life of the structure. The ultimate limit state assessment considers both the external and internal stability of the structure.

Three load combinations are considered. For Load Combination A, a partial load factor of 1.5 is applied to the permanent and variable loads. This combination usually generates the maxium tension in the soil reinforcement and the maximum foundation bearing pressure.

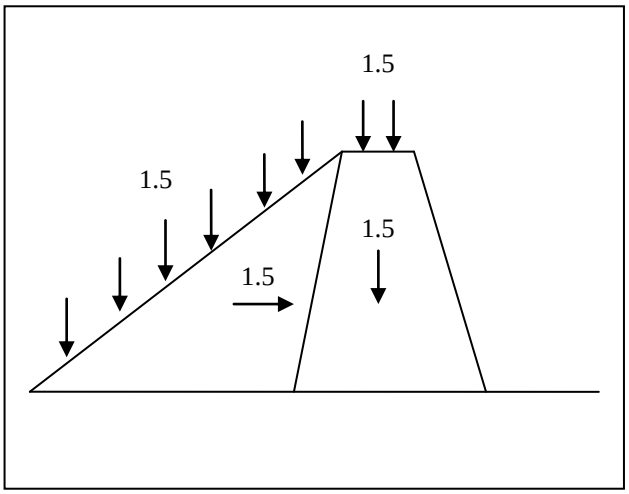


Figure 2 Load Combination A.

For Load Combination B partial load factors of 1.0 are applied to the the mass of the soil within the body of the structure and the variable load behind the structure. No variable load is applied above the reinforced soil mass. This combination usually generates the critical case for overturning and sliding of the structure and normally determines the soil reinforcement requirements for pull-out resistance.

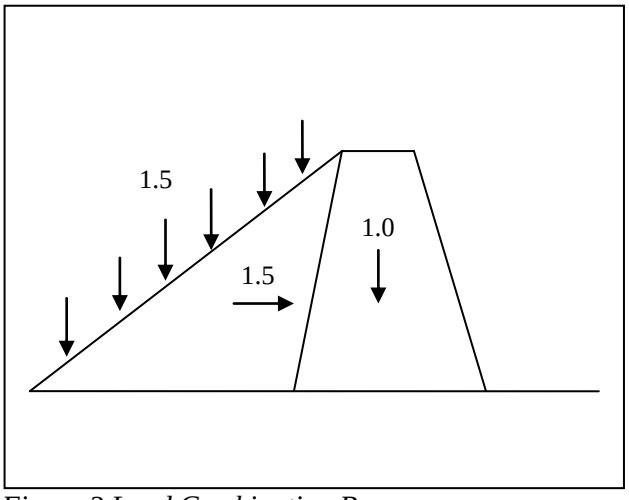


Figure 3 Load Combination B.

For Load Combination C, no variable loading is applied and the load factors for permanent loads are unity. This combination is used to check the serviceability limit state.

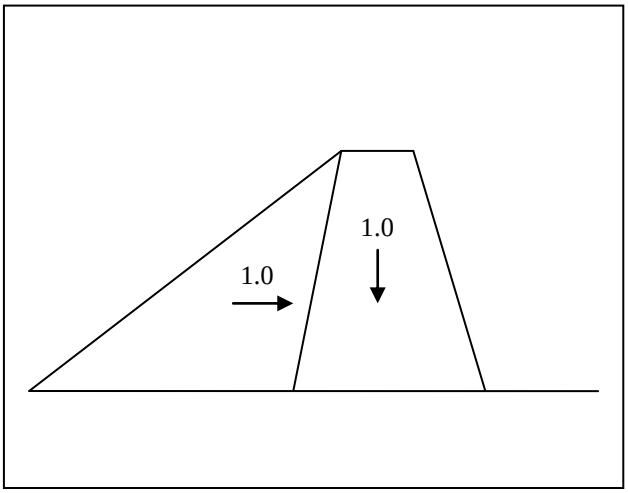


Figure 4 Load Combination C.

4.1 External stability assessment

The external stability assessment considers the possibility of failure by forward sliding, overturning and a bearing capacity or slip circle failure in the supporting soil.

The stability against forward sliding is assessed using the following expression:

$$f_s R_h \leq R_v \frac{tan\phi'_p}{f_{ms}} \qquad (1)$$

Where,
f_s is the partial resistance factor against base sliding;
R_h is the design horizontal disturbing force;
R_v is the design resultant vertical force;
ϕ'_p is the peak angle of shearing resistance under effective stress conditions; and
f_{ms} is the partial material factor applied to tan ϕ'_p

As the materials used in the structure and the foundation have very little fines content, the analysis considers only drained effects and the term relating to effective cohesion is omitted from equation 1.

An assessment of the potential for a global or circular slip failure was undertaken using the procedure described in BS EN 1997-1:2004. The stability was assessed using the Bishop method of slices. Two load combinations were considered with the following partial

factors being applied to the actions and the soil parameters.

Table 1 Partial factors on actions and for soil parameters.

Effects	Comb. 1	Comb. 2
Soil unit weight	1.35	1.0
Variable load	1.5	1.3
Shearing resistance tan ϕ	1.0	1.25
Undrained shear strength Cu	1.0	1.4
Effective cohesion c'	1.0	1.25

The commercially available geotechnical software Talren v5 was used to perform the slip circle analysis. The results for the two load combinations are presented in figures 5 and 6.

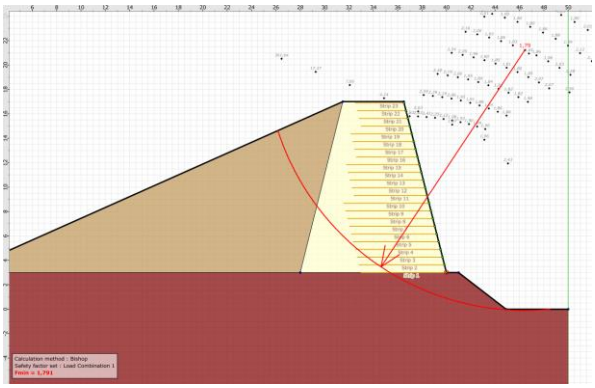


Figure 5 Stability assessment for Load Combination 1.

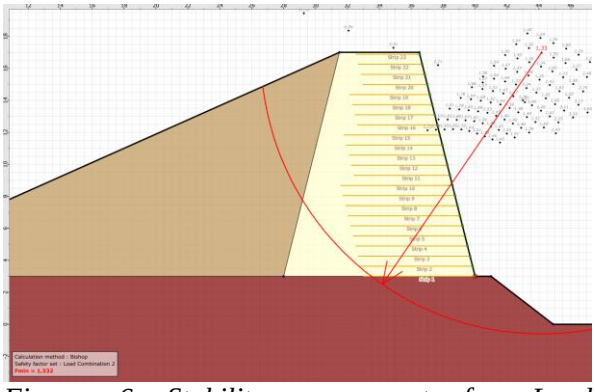


Figure 6 Stability assessment for Load Combination 2.

4.2 Internal stability assessment

The internal stability assessment considers the tensile and adherence capacity of the soil reinforcement, the capacity of the connections and the design of the facing.

4.3 Tensile load in the soil reinforcement

The tension in each layer of reinforcement was determined using the coherent gravity method described in BS8006. The tensile force at each layer is a function of the coefficient of earth pressure (K), the effective vertical stress (σ) and the spacing of the reinforcement (s).

$$T = K\sigma s \qquad (2)$$

The coefficient of earth pressure (K) is considered to vary linearly; from K_o at the surface to K_a at a depth of 6m and beyond.

The effective vertical stress takes into account the eccentricity of the vertical force due to the horizontal earth pressure and variable loading behind the structure. The stress is considered to be uniform at each layer and is determined using a Meyerhoff pressure distribution.

4.4 Tensile capacity of the soil reinforcement

The long-term design strength of the soil reinforcement for the ultimate limit state T_D (kN) is calculated using the following expression from BS8006:

$$T_D = \frac{T_{CR}}{f_m} \qquad (3)$$

Where T_{CR} is the reduction factor for creep and f_m is the material safety factor calculated as shown below.

$$f_m = RF_{ID} \times RF_W \times RF_{CH} \times f_s \qquad (4)$$

Where,

RD_{ID} is the reduction factor for installation damage;
RF_W is the reduction factor for weathering;
RF_{CH} is the reduction factor for chemical / environmental effects; and
f_s is the factor of safety for the extrapolation of data.

The soil reinforcement has been tested for use in a range of different granular fill materials. Installation damage factors have been determined for fill materials with grain sizes of 0 – 5mm, 0 – 32mm, and 0 – 125mm. The fill material used in the construction of the avalanche barrier was a well-graded gravel with sand and cobbles. The material was excavated from a quarry at the Neskaupstaður site and crushed to the required size. The grain size varied from 0.1mm to 200mm. As this was larger than the material used in previous installation damage testing for the soil reinforcement, additional installation damage testing was undertaken to determine the appropriate installation damage factors.

4.5 Adherence capacity of the soil reinforcement

The adherence capacity of the soil reinforcement was determined by the supplier using pull out testing, both extensively in the laboratory and on full-scale structures. The soil reinforcements exhibit an increased friction capacity in granular soil due to the arching effects between adjacent strips from the same layer. This phenomena, though slightly more pronounced, was originally observed in structures using high adherence (i.e. ribbed) steel soil reinforcement.

The tensile capacity of the soil reinforcement is calculated using the following expression.

$$T = \frac{2B\mu}{f_p f_n} \int_{L-Laj}^{L} f_{fs}\sigma_v(x)dx \qquad (5)$$

Where,

- B is the reinforcement width;
- μ is the coefficient of friction between the soil and the soil reinforcement at the appropriate vertical stress level;
- L is the total soil reinforcement length;
- L_{aj} is the length of soil reinforcement beyond the maximum tension line at the appropriate level;
- $\sigma_v(x)$ is the vertical stress along length x of the reinforcement;
- f_n is the partial factor for the economic ramifications of failure;
- f_p is the partial factor for reinforcement pull-out resistance;
- f_{fs} is the partial load factor and
- 2 is for two sides of the soil reinforcement.

4.6 Design of the connections

The capacity of the connections was assessed using full-scale destructive testing. The tests were repeated several times and a statistical approach was used to determine the characteristic strength to be considered, following the requirements of Annex D of Eurocode 0 (EN 1990).

5 INSTALLATION DAMAGE TESTING

The procedure for testing the samples is explained in Appendix D of BS8006:2010. Seven samples of each grade of soil reinforcement (twenty one in total) were placed on a 650mm deep base of fill material that had been previously levelled and compacted. The test area was divided into three zones. In Zone 1, 650mm of crushed rock was placed above seven samples and the material was then compacted using a self-propelled vibratory roller having a mass per metre of 4,690kg. Twenty one samples were placed in Zone 2. This zone was again backfilled with 650mm of crushed rock but was subjected to twice the number of passes with the roller as Zone 1. The same number of samples was placed in Zone 3. This zone had two 650mm layers of crushed rock placed above the samples with compaction taking place after each 650mm layer had been placed. Seven samples of each grade of soil reinforcement were retained as control samples.



Figure 7 Installation damage trial.

After the backfilling and compaction had been completed, the backfill was carefully removed and the samples were visually inspected for damage.

A record of cutting, splitting, bruising and general abrasion was made. On retrieval the samples exhibited very little damage.



Figure 8 Minor damage to reinforcement.

To correctly assess the effects of the installation damage, all samples were subjected to tensile testing to failure. The results of the testing are presented in Tables 2 to 5.

Table 2 Control samples.

Sample	T_D(kN)	T_D(kN)	T_D(kN)
1	41.3	53.8	68.2
2	41.6	53.8	68.8
3	41.6	53.9	69.1
4	41.5	54.0	68.8
5	42.0	53.4	69.2
6	42.1	53.8	69.4
7	40.5	54.4	69.2
Mean	41.5	53.9	69.0

Table 3 Samples subjected to single compaction.

Sample	T_D(kN)	T_D(kN)	T_D(kN)
1	41.1	51.9	64.3
2	41.0	54.3	68.2
3	40.5	50.8	64.0
4	40.0	51.7	64.4
5	41.2	52.6	64.1
6	40.6	46.7	66.1
7	39.4	51.5	63.8
Mean	40.5	51.4	65.0

Table 4 Samples subjected to double compaction.

Sample	T_D(kN)	T_D(kN)	T_D(kN)
1	38.9	48.3	60.7
2	38.2	50.3	65.4
3	38.6	45.1	62.6
4	41.0	51.4	64.6
5	39.3	51.4	64.1
6	38.9	48.9	64.3
7	41.3	51.1	63.6
Mean	39.5	49.5	63.6

Table 5 Samples subjected to double compaction and double backfilling.

Sample	T_D(kN)	T_D(kN)	T_D(kN)
1	40.8	42.8	63.1
2	41.2	52.8	63.5
3	37.3	52.2	63.3
4	39.3	51.3	63.4
5	40.9	52.0	64.4
6	39.2	45.4	63.5
7	40.3	44.6	56.1
Mean	39.9	48.7	62.5

The installation damage factor for each grade of reinforcement was calculated by dividing the lowest mean tensile strength for samples in each test zone by the mean control strength. The limiting case for the 35.5kN grade was from Zone 2 and for grades 50kN and 65kN from Zone 3. In spite of the very coarse nature of the backfill, the reduction factor for installation damage determined through the site specific testing ranged from 1.05 to 1.11 depending on the grade of soil reinforcement.

6 CONSTRUCTION

Construction of the main dam commenced in July 2012. The location of the project site near to a deep water port made delivery of the manufactured materials by sea freight possible.

Following the typical construction procedure, the first row of facing panels were installed directly onto the prepared sub-fill layer. Temporary timber bracing was used to set the first row of panels at the correct inclination. A half-height facing panel was placed at the base of alternative columns of panels to provide a staggered horizontal joint. This technique allowed subsequent rows of facing panels to be connected to the exposed part of the facing panel in the row below. This helped to provide fall protection to the operatives constructing the structure.



Figure 9 Installation of the first row of facing panels.

The first layer of core fill material was placed using a 360° hydraulic excavator and compacted using a self-propelled vibratory roller, as used in the installation damage trials. The first layer of soil reinforcement was then connected to the facing panels and laid on to the compacted fill material. A small mound was constructed approximately half way along the soil reinforcement length to enable a small amount of tension to be applied to the soil reinforcement. This was particularly important to ensure good alignment of the facing panels in the completed structure.



Figure 10 Laying out the soil reinforcement.

The construction sequence was repeated until the maximum structure height was reached.



Figure 11 The completed structure.

7 GENERAL DESIGN CONSIDERATIONS

Avalanche protection dams using reinforced soil techniques exhibit a number of advantages:

7.1 Limited environmental impact

The structures are predominantly made of locally available fill materials. The manufactured materials delivered from remote locations represent a very small proportion of the total weight of the structure. The construction technique offers a number of environmetal benefits. As there are no concrete components in the system and only a small amount of steel components, the CO_2 emissions are small and mostly due to the extraction and placing of the earthworks.

7.2 Limited environmental impact

The technique allows a variety of possible layouts, shapes and face inclinations. This gives designers of avalanche protections structures a high degree of freedom when choosing the layout of their schemes. Smaller breaking mounds and deflecting dams can be constructed using the same technique.

In the event of an avalanche impact, it is possible that some damage may occur as rocks and debris come into contact with the facing. Procedures have been developed to allow localised repair of the facing without the need to dismantle the structure. New facings can be placed in front of the damaged ones and a connection made between the soil reinforcement and the new facing panel.

7.3 A highly resilient structure

Most importantly, reinforced soil structures offer, at low relative cost, an ideal material for sustaining dynamic loads. This is well known for example in Japan, where reinforced soil structures have been widely used based on the outstanding seismic performance, even under the most severe earthquake motions (Otani, 2013). But it is also the case for dynamic impacts, distributed like avalanche or explosion blasts, or localised in the case of rock falls. The last point is also important for avalanche loads since the snow flow is likely to bring other debris which will hit the dam or the braking mounds, like rocks or trees. Recent research on resistance to localised impacts has been initiated in France, in partnership between the Terre Armée group and IFSTTAR (Joffrin, 2016). The test structure was 3.5m high and 3.0m thick. The results are promising and show that the structure could sustain very large impact forces. See Figure 12.

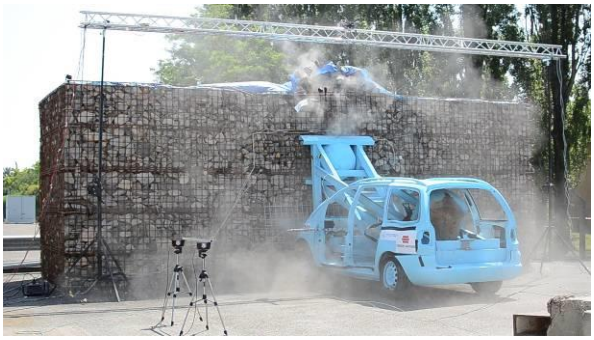


Figure 12 Impact on a reinforced fill protective bund with vertical facing, with an energy of 800 kJ (mass: 2700 kg, impacting speed: 88 km/h).

The localised impacting energy is absorbed by moderate localised internal deformation of the granular fill. Localised damage is likely to be observed in those cases, but procedures have been developed which enable the integrity of the wire mesh facing (and the visual aspect of the structure) to be restored without the need for dismantling part of it. The repair basis consists of simply placing new wire panels in front on the damaged ones and restoring connections between the reinforcing strips and these new panels. The damaged panels are left in place and the volume between both panels is filled with stones.

8 CONCLUSIONS

Reinforced soil structures with steep or vertical faces provide a number of advantages for the construction of avalanche protective barriers of all kinds: braking mounds, deflecting dams and catching dams. The structure at Neskaupstaður, presented in this paper, proved to be a very good example of the versatility of the solution and of its integration within the local environment. A number of other projects are currently under development in Iceland. Involving a reinforced soil specialist designer at the preliminary stage of a project can be beneficial for the optimization of such schemes.

9 REFERENCES

Code of practice for strengthened / reinforced soils and other fills (2010). British Standards Institution. BS8006 Part 1.

Eurocode 7: Geotechnical Design (2013). British Standards Institution. BS EN 1997 Part 1 + A1.

Sankey, J.E., Lozano, R. (2015). Durability of geosyntheric strip at connection in MSE structures. Geosynthetics 2015, Portland, USA. 377-384.

Joffrin, P., Bennani, Y., Rajor, J.-P., Freitag, N.(2016). Real-scale tests on a Reinforced Earth retaining bund by a spehrical projectile at energies up to 800 kJ. Rock and Slope Stability Symposium, Lyon, France.

Jóhannesson, T., Gauer, P., Issler, P. (2009). The design of avalanche protection dams, Recent practical and theoretical developments. European Commission, Directorate-General for Research and Innovation. 2009. Freely downloadable on http://bookshop.europa.eu .

Otani, Y., Takao, K., Sakai, S. Kimura, T., Kuwano, J., Freitag, N., Sankey, J.E.(2013). Investigation of Reinforced Earth structures following the 2011 Tohoku earthquake. International Conference on Soil Mechanics and Geotechnical Enginnering, Paris.

Rafalko, S., Sankey, J.E., Freitag, N. (2011). Sustainability Measures for MSE Walls and Baseline Environmental Impact Evaluations Earth Retention Conference 3, Bellevue, WA, USA. 486-493.

Bearing Capacity, Comparison of Results from FEM and DS/EN 1997-1 DK NA 2013

Bjørn Staghøj Knudsen
COWI A/S, Denmark, bskn@cowi.dk

Niels Mortensen
nmGeo, Denmark, n@nmgeo.dk

ABSTRACT
The bearing capacity of foundations in Denmark is typically analysed using the closed form equations from DS/EN 1997-1 DK NA:2013, and the present paper compares selected examples with similar results from the finite element method (FEM). The paper includes a discussion of the bearing capacity factors, the shape factors, plane strain considerations, axi-symmetry and three-dimensional analyses.

Keywords: Bearing capacity, Shape factors, DS/EN 1997-1 DK NA:2013, FEM, PLAXIS

1 INTRODUCTION

The present paper compares the bearing capacity estimated using DS/EN 1997-1 DK NA:2013 (EC7-DK NA) with results obtained using the finite element method (FEM). The overall scope is to investigate whether the two approaches will lead to similar bearing capacities. The paper summarises the main aspects covered in the report Banedanmark (2014).

1.1 Main assumptions

The main assumptions used in the investigations are: The base of the footing is placed on a horizontal soil surface comprising either a drained (sand) or undrained (clay) soil; The soil is isotropic and homogeneous; The Mohr-Coulomb failure criterion is applied using associated and non-associated flow; The foundation is loaded vertically with centrically and eccentrically loading included.

2 BEARING CAPACITY FORMULA

The drained bearing capacity formula contains three independent contributions that are calculated separately and added following equation (1). These three contributions are represented through the effective unit weight, γ', the effective surcharge q' and the effective cohesion, c'.
In this study the contributions are first investigated separately to examine the ability to recreate each of these using FEM, after which the combined effect is investigated.

2.1 Drained capacity

The overall drained bearing capacity formula from EC7-DK NA is given in equation (1).

$$\frac{Q_f}{A'} = \frac{1}{2} \cdot \gamma' \cdot B' \cdot N_\gamma \cdot s_\gamma + q' \cdot N_q \cdot s_q \qquad (1)$$

Where Q_f/A' is the vertical bearing capacity, B' is the effective foundation width, N_γ is the bearing capacity factor for the γ'-case with s_γ being the corresponding shape factor, N_q is the bearing capacity factor for the q'-case with and s_q being the corresponding shape factor. The c'-case is a mathematical reflection of the q'-case and is thus left out from this study and of equation (1).
The basis for equation (1) is the two-dimensional case with N_γ from Lundgren & Mortensen (1953), N_q from Prandtl (1920) and with $s_\gamma = s_q = 1.00$. When investigating three-dimensional cases, the empirical factors s_γ and s_q differs from unity. Therefore, the Danish approach with equation (1) is to use the plane strain friction angle, φ'_{pl} for sand in all the analyses; also for a square footing.

Following EC7-DK NA, the plane strain friction angle (secant value) for sand is defined by $\varphi'_{pl} = \varphi'_{tr} \cdot (1.00+0.10 \cdot I_D)$, where I_D is the density index. With $I_D = 1.00$: $\varphi'_{pl} = 1.10 \cdot \varphi'_{tr}$. The effective foundation width *B'* was suggested by Brinch Hansen (1970) to be estimated as B' = B – 2·e, where B is the width of the foundation and e is the eccentricity of the vertical load relative to the vertical centre line. This approach is used and investigated in the study.

2.2 Undrained capacity

In the undrained case, the bearing capacity is calculated as:

$$\frac{Q_f}{A'} = c_u \cdot N_c^0 \cdot s_c^0 + q \qquad (2)$$

Where c_u is the undrained shear strength, N_c^0 is the undrained bearing capacity factor, s_c^0 is the shape factor and *q* represents the total surcharge.

3 METHOD OF INVESTIGATION

Four different aspects are investigated for each of the γ'-case, the q'-case and the undrained case:

- Can 2D FEM be used to validate the bearing capacity factors from EC7-DK NA?
- Can 2D FEM be used to validate the approach with effective foundation width?
- Can axi-symmetrical FEM models be used to validate the shape factor for a square footing from EC7-DK NA?
- Can 3D FEM models be used to validate the shape factor for rectangular footings?

After investigation of each separate case the drained combined capacity is investigated with a case study using EC7-DK NA, plane strain and 3D models.

4 UNDRAINED CASES

The undrained analyses are based on a constant c_u = 10 kPa with Young's modulus, E = 20 MPa. The foundation is assumed weightless with E = 20 GPa. The interface between the soil and the foundation is modelled perfectly rough (10 kPa) or smooth (0.1 kPa).

4.1 Plane strain

A completely rough foundation was loaded vertically by a line load [kN/m] and the effect of different eccentricities was investigated. The load was increased until failure was observed and the bearing capacity factor was then back-calculated from equation (2): $N_c^{BC} = Q_f / (B' \cdot c_u)$. Table 1 summarizes the results from the FEM analyses. The analytical well-determined value of $N_c^0 = \pi + 2 \approx 5.14$.

Table 1: Plane strain Plaxis results for undrained clay. The value of "Acc." represents $N_c^{BC} / (\pi +2)$.

e [m]	B' [m]	e/B [-]	Q_f [kN/m]	N_c^{BC} [-]	Acc.
0.00	4.00	0.000	206.09	5.15	1.002
0.30	3.40	0.075	179.72	5.29	1.028
0.60	2.80	0.150	148.08	5.29	1.029
0.90	2.20	0.225	116.88	5.31	1.033
1.20	1.60	0.300	85.70	5.36	1.042
1.50	1.00	0.375	54.38	5.44	1.058

Table 1 shows that the bearing capacity factor can be accurately calculated using plane strain FEM, and that the effective foundation width concept is accurate within 5 % accuracy if e/B ≤ 0.30. Shear strain contour plots of selected failure mechanism from Table 1 are seen in *Figure 1*.

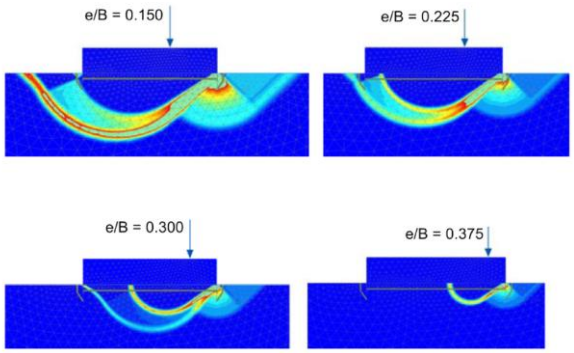


Figure 1 Shear strain contour plots for selected failure mechanisms in Table 1.

The interface strength did not influence the back-calculated bearing capacity factor.

4.2 Axi-symmetry

The axi-symmetric model was initially applied to investigate whether the interface strength would influence the estimated capacity. The back-calculated Plaxis result showed

N_c^{BC} = 6.06 where the theoretical solution implies 6.05, cf. Hansen (1982) and Martin (2004). For the smooth case, the Plaxis model gave 5.71 whereas the theoretical solution implied 5.67. The difference is likely due to the fact that "smooth" in the Plaxis-model was represented through an undrained shear strength of 0.1 kPa. The shear strain contour plots of the failure mechanisms are seen in Figure 2.

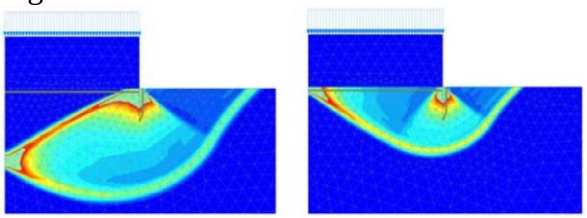


Figure 2: Shear strain contour plots for axi-symmetric failure mechanisms. Left: Completely rough and right: Smooth (0.1 kPa strength).

If the bearing capacity of a square footing equals the capacity of circular footing with the same area, the shape factor is thus s_s^0 = 6.06 / 5.14 = 1.18 for a perfectly rough foundation and 1.10 for a smooth foundation. EC7-DK NA uses s_c^0 = 1.0+0.2·B/L or corresponding to 1.20 for a square footing.

4.3 3D Models

The dependency between s_c^0 and the ratio B/L, where L is the foundation length, is investigated using Plaxis 3D models with a completely rough interface. The mesh of the 3D models include a quarter of the foundation (double symmetry). A vertical load is applied to the foundation, and failure is introduced through φ'-c-reduction. The following analyses are performed:

- A circular foundation in 3D Plaxis representing the axi-symmetrical case available in 2D Plaxis.
- A square footing (B = L).
- Five rectangular foundations (L > B) to investigate s_c^0.

The circular and square footings are compared to the results of the axi-symmetric results in Table 2.
From the results in Table 2 it can be concluded that estimating the bearing capacity of a circular foundation using either axi-symmetry or a 3D analyses leads to very similar results (deviation less than 3%). Furthermore, estimating the capacity of a square or circular footing with equal areas leads to almost identical results.

Table 2: Back-calculated results from Plaxis for circular and square foundations on undrained clay.

Plaxis model	N_c^{BC} [-]
Axi-symmetric (2D Plaxis)	6.06
Circular foundation (3D Plaxis)	6.22
Square foundation (3D Plaxis)	6.16

The results from the five rectangular footings are seen in Figure 3, in which the s_c^0-factor is back-calculated using $s_c^0 = Q_f / (A \cdot c_u \cdot (\pi+2))$.

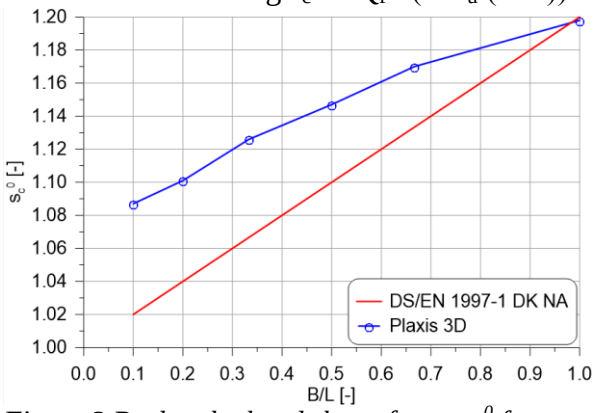


Figure 3 Back-calculated shape factor s_c^0 for undrained clay against the B/L-ratio based on Plaxis 3D results and EC7-DK NA.

Figure 3 shows that as the B/L-ratio decreases the results deviate more and more from EC7-DK NA. However even for B/L = 0.10 the difference is only 6.6 % with EC7-DK-NA being on the safe side, and the results from the two methods may thus be considered almost identical.

4.4 Conclusions

The main conclusions from the undrained analyses are as follows: The N_c^0 value can be estimated correctly using Plaxis 2D and the interface shear strength will not influence the bearing capacity. The adopted principle about the effective foundation width is confirmed up to e/B ≤ 0.30. The theoretical N_c^0 factor for axi-symmetry varies between 5.67 and 6.05 for a smooth and a completely rough interface, respectively. Almost similar results are found using Plaxis 2D models. Compar-

ing plane strain and axi-symmetry reveals a shape factor s_c^0 of 1.10 and 1.18 for smooth and completely rough interface, respectively. EC7-DK NA prescribes 1.20.
Plaxis 3D results indicate that the shape factor s_c^0 from EC7-DK NA is on the safe side.

5 DRAINED ANALYSES q'-CASE

Following equation (1), the drained capacity of a foundation placed on a soil with $\varphi' > 0$, $c' = 0$, $\gamma' = 0$ and a surcharge $q' > 0$ shall be estimated from $Q_f / A' = q' \cdot N_q \cdot s_q$ where the statically admissible solution of N_q is defined by $\tan^2(45°+\varphi'/2) \cdot e^{\tan\varphi'}$ and $s_q = 1.0+0.2 \cdot B/L$ following EC7-DK NA. The formula for N_q is only kinematically admissible for associated flow, i.e. $\varphi = \psi$.

5.1 Plane strain

The plane strain models were based on similar assumptions as for the undrained models except that the undrained shear strength was replaced by φ' and $c' = 0$.
For a vertical and centrally acting foundation load, the 2D Plaxis results were within a 0.5 % accuracy compared to the formula for N_q using φ' in the range of 15° to 45° with associated flow.
The interface shear strength did not influence the 2D Plaxis results.
For $\psi = \varphi' = 30°$, 2D Plaxis revealed $N_q^{BC} = 18.48$ to be compared with $N_q = 18.40$.
Setting $\varphi' = 30°$ and $\psi = 0°$, 2D Plaxis gave $N_q^{BC} = 14.50$ or 22 % reduction compared to associated flow.
Using a partial factor of $\gamma_{\tan\varphi'} = 1.20$ would give a reduction of 38 % for $\varphi' = 30°$. The difference between associated and non-associated flow is thus significant, albeit less significant than the effect of a partial factor of safety.
The influence of the eccentricity of the load was investigated similar to the undrained case, and the result can be seen in Table 3 for associated flow and $\varphi' = 30°$. The load was increased in the calculation until a fully developed failure mechanism occurred.
Table 3 shows that for $e/B < 0.25$ the bearing capacity estimated by Plaxis is up to 8 % higher, while the calculation with $e/B = 0.30$ shows a capacity that is lower than estimated using EC7-DK NA. It was not possible to obtain a failure for $e/B > 0.30$, as this lead to numerical problems.

Table 3: Plane strain Plaxis results for sand. Acc. is calculated as N_q^{BC} / N_q.

e [m]	B' [m]	e/B [-]	Q_f [kN/m]	N_q^{BC} [-]	Acc.
0.30	3.40	0.075	67.45	19.84	1.078
0.60	2.80	0.150	55.41	19.79	1.076
0.90	2.20	0.225	42.37	19.26	1.047
1.20	1.60	0.300	26.81	16.76	0.911

The principle of effective width represents an approximate approach for a drained material, and the accuracy is expected to increase for decreasing friction angles.
Shear strain contour plots of the failure mechanisms from Table 3 are seen in Figure 4.

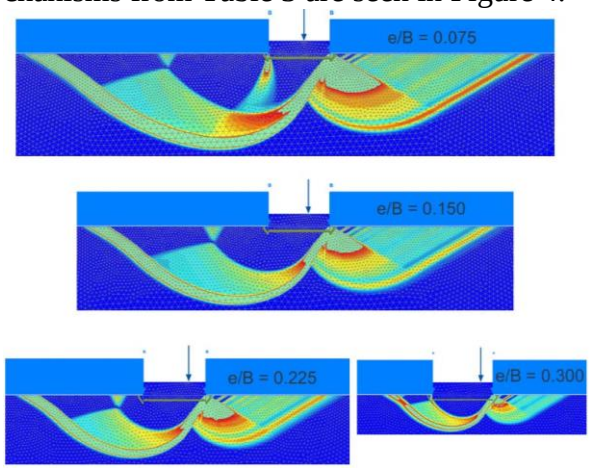


Figure 4 Shear strain contour plots of the failure mechanism investigated in Table 3. The plots are drawn to scale.

5.2 Axi-symmetry

For plane strain the N_q value is unambiguously defined and agreed upon in the literature. This is not the case with the axi-symmetric value of N_q. Albeit not representing a full literature study, some main points are summarized here.
The method of characteristics has been applied by Kumar & Ghosh (2005), Bolton & Lau (1993), Martin (2004) and Hansen (1979). The hoop stress in the model is assumed to be equal to the minor principal effective stress, σ'_3. $N_q = 29.5$ is obtained by Kumar & Ghosh (2005) and by Bolton & Lau (1993) using $\varphi' = \psi = 30°$. Martin (2004) arrives at $N_q = 37.2$ for the same assump-

tions, but he and Hansen (1979) states that the stress characteristics in the Rankine zone (see Figure 5) may cross each other, and the model applied can thus not represent a statically admissible solution.

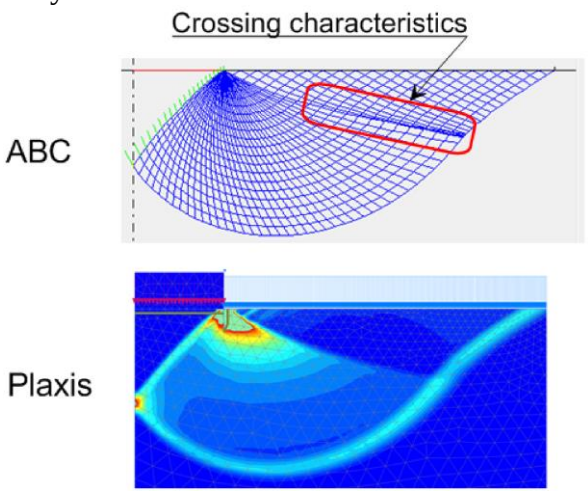


Figure 5 Upper part: Stress characteristics from Martin (2004) using a completely rough foundation base in an axi-symmetric analysis with φ' = ψ = 30°. Lower part: Shear strain contour plot from a similar Plaxis analysis. The plots are drawn to scale.

The observation from Martin (2004) with crossing stress characteristics is not mentioned by Kumar & Ghosh (2005) or by Bolton & Lau (1993), and Martin (2004) writes *"Certainly it appears that many previous researchers, including Cox et al. (1961), Cox (1962), Salençon & Matar (1982a) and Bolton & Lau (1993), have turned a blind eye to the occurrence of crossing characteristics in their meshes, if indeed they were aware of it at all"*.

The results from Martin (2004) do not deviate more than 2 % from similar results using Plaxis for friction angles between 15° and 45°. The approach from Martin (2004) yields almost identical results to those of Lundgren & Mortensen (1953) when calculating drained plane strain problems. In this paper it is therefore assumed that the approach applied by Martin (2004) leads to the "most realistic results".

The approach by Martin (2004) is established as a software code called ABC, which is available online with a documentation manual, enabling the user to calculate failure mechanisms for a wide range of input parameters.

For the q'-case, the shape factor s_q is investigated by the following approach:

- φ'_{tr} is varied from 10° to 45° and φ'_{pl} is estimated from $\varphi'_{pl} = 1.10 \cdot \varphi'_{tr}$.
- ABC is used to estimate the plane strain N_q^{pl} from φ'_{pl}, while N_q^{tr} is estimated from ABC and φ'_{tr}.
- The plane strain and axi-symmetric values are related with: $s_q \cdot N_q^{pl} = N_q^{tr}$.
- N_q^{tr} is estimated using Plaxis to compare.

The results of the investigation are seen in Table 4. N_q^{pl} is derived using φ'_{pl} as the rupture figure for N_q is a plain strain mechanism. A different approach will lead to different values of s_q.

Table 4: Estimated values of N_q using both plane and triaxial friction angles. Comparative axi-symmetrical Plaxis analyses are shown, using φ'_{tr} and associated flow.

φ'_{tr} [°]	φ'_{pl} [°]	N_q^{pl} [-]	N_q^{tr} [-]	N_q^{Plaxis} [-]
10.0	11.0	2.71	2.96	-
15.0	16.5	4.55	5.25	5.28
20.0	22.0	7.82	9.62	-
25.0	27.5	13.94	18.40	-
30.0	33.0	26.09	37.20	37.91
35.0	38.5	52.31	80.81	-
40.0	44.0	115.31	192.73	-
45.0	49.5	290.81	520.62	526.14

Table 4 shows that the values obtained from Plaxis using associated flow resembles those obtained from ABC using the method of stress characteristics. The formula below represents an approximation of the axi-symmetric N_q for a completely rough foundation. The regression coefficient is 0.99:

$$\log_{10}(N_q) = 5.035 \cdot 10^{-4} \cdot \varphi^2 + 3.487 \cdot 10^{-2} \cdot \varphi - 7.776 \cdot 10^{-2} \; [10° \leq \varphi \leq 45°]$$

EC7-DK NA dictates $s_q = 1.20$ for a square footing, independent of φ'. Figure 6 depicts the estimated relationship between s_q and φ' using data from Table 4, Brinch Hansen (1970) and data laboratory tests by de Beer (1970) where $s_q = 1.00 + B \cdot \tan(\varphi')/L$.

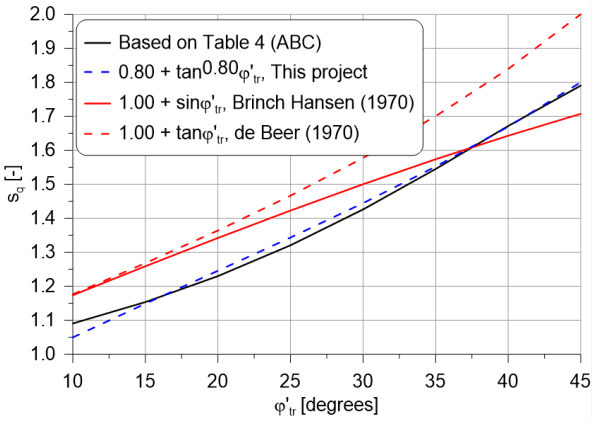


Figure 6: Estimated values of s_q from different approaches.

Using the approach from EC7-DK NA seems to be on the safe side as φ' ≥ ~17°. EC7-DK NA identifies $s_q = s_c$. However, s_c appears to be 10 to 20 % higher than s_q when s_c is evaluated using the procedures applied to estimate s_q.

5.3 3D Models

Modelling in Plaxis 3D were performed to validate the axi-symmetric results and to investigate the s_q factor as the ratio B/L is changed. The investigations were based on completely rough foundations, associated flow with φ' = ψ = 30° and c' = 0.
Failure in the models were found by displacement control. A circular, a square and three rectangular (B < L) foundations were investigated.
Results from the axi-symmetric, circular and square models are shown in Table 5.

Table 5: Back-calculated N_q values from Plaxis models. Martin (2004) estimates N_q = 37.20 for the same case.

Plaxis model	N_q^{BC} [-]
Axi-symmetric, Plaxis 2D	37.91
Circular footing, Plaxis 3D	39.55
Square footing, Plaxis 3D	38.86

Table 5 shows that the results of the axi-symmetric model and the circular foundation in Plaxis 3D leads to very similar values as the difference is less than 4 %. The value of the square footing is almost identical to the circular footing.
Back-calculating results of the Plaxis 3D models leads to an estimate of the s_q factor as seen in Figure 7. The expression from EC7-DK NA and results from de Beer (1970) is shown as well.

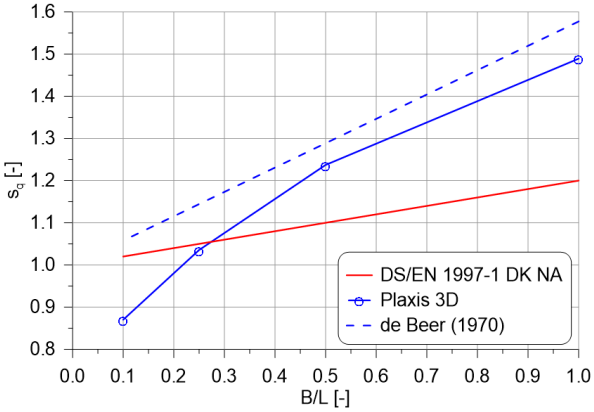


Figure 7: Back-calculated values of s_q for φ = 30° and associated flow.

Figure 7 indicates that the value of s_q from EC7-DK NA is on the safe side for φ' = 30° as the foundation length is below 3-4 times the width. When the length of the foundation exceeds 3-4 times the width the recommendation in EC7-DK NA may be on unsafe side. Results from de Beer (1970) generally show larger values of s_q than the other methods.
The reason for Figure 8 showing $s_q < 1$ for Plaxis 3D results may be due to different failure mechanisms occurring along the foundation. Close to the middle of the foundation the failure will be similar to the plane strain case, while at the ends of the foundation a more complex 3D failure mechanism occurs. This may lead to Plaxis 3D not being able to fully develop failure along the full length of the foundation as the capacity per length of foundation is not equal along the foundation.

5.4 Conclusions

Plane strain analyses with Plaxis leads to similar results as found in Prandtl (1920).
When applying non-associated flow a reduction of the estimated N_q of approximately 20 % is found. For eccentric vertical loads the approach in EC7-DK NA appears on the safe side of e/B < 0.25, for larger values the approach may be unsafe. Comparing plane strain and axi-symmetric models, the s_q value from EC7-DK NA may be unsafe for φ' lower than approximately 20°.
The shape factor from EC7-DK NA for L > B may be on the unsafe side when the founda-

tion length exceeds the width by 3-4 times. However this conclusion might be influenced by numerical issues.
The overall conclusion is that for the drained q'-case results from EC7-DK NA and Plaxis will likely deviate, with Plaxis giving the largest capacities. The size of the overshoot will depend on how the aspects covered in this paper are combined.

6 DRAINED ANALYSES γ-CASE

Following equation (1), the drained capacity for the γ'-case can be estimated from $Q_f / A' = ½ \cdot \gamma' \cdot B' \cdot N_\gamma \cdot s_\gamma$, where B' is the width or diameter of the footing and s_γ is the shape factor, $s_\gamma = 1.0 – 0.4\ B'/L$.
The plane strain value of N_γ was estimated by Lundgren & Mortensen (1953) using a statically admissible solution based on stress characteristics for a Mohr-Coulomb material. Bønding (1970) showed that the solution is kinematically admissible for a wide range of dilation angles ψ. EC7-DK NA includes the following approximation: $N_\gamma = ¼ \cdot ([N_q-1] \cdot \cos \varphi')^{3/2}$, valid for a completely rough interface.
The approach and assumptions described in the q'-case has been reused for the γ'-case, however with the soil weight γ' = 10 kN/m³ and q' = 0 kPa.

6.1 Plane strain

Initially N_γ was investigated using plane strain models. Due to numerical issues a surcharge of q' = 0.1 kPa was added and failure in the model was obtained by either increasing the load (Load) or by adding a prescribed displacement (Disp.). The back-calculated value N_γ^{BC} is found from equation (1) and shown in Table 6. The effect from the surcharge is removed from the Plaxis results.
The results in Table 6 for φ' = ψ = 30° indicate that displacement control may lead to the most accurate results. When using ψ = 0°, the capacity reduces about 20 %, similar to what was found in the q'-case.
The bearing capacity formula is based on superposition of each contribution, and if all the effects from γ', q' and c' are included in one and the same analysis, Lundgren & Mortensen (1953) showed that the estimated bearing capacity would increase by a factor μ being dependent on the ratio $\gamma' \cdot B/(q' + \gamma' \cdot B)$. This effect is not included in the present paper, but the effect can be observed in the results from 2D Plaxis too.

Table 6: Back-calculated plane strain results for sand for a completely rough foundation.

φ' [°]	ψ' [°]	Load-ing	N_γ^{BC} [-]	N_γ [-]	Acc. [-]
15	15	Disp.	1.26	1.18	1.070
30	30	Load	15.96	14.75	1.082
		Disp.	15.49		1.050
35	35	Disp.	36.86	34.48	1.069
30	0	Disp.	12.03	-	-

Table 6 includes analyses covering φ' up to 35° and numerical problems were encountered for higher values of φ'. With φ' = 40° and γ' = 10 kN/m³ the average pressure below a 4 m wide foundation is 1700 kPa, whereas the vertical effective stress on the soil surface next to the footing is 0 kPa. The stress singularity at the edge of the foundation is apparently too strong to allow for a numerical solution with the finite element method.
The effect of eccentric loading was investigated similar to the previous cases and the 2D Plaxis results revealed an overshoot of approximately 5 % for e/B < 0.25. For e/B > 0.25 numerical problems were encountered.

6.2 Axi-symmetry

When the literature is surveyed, the value of the axi-symmetric N_γ–value reveals a significant scatter. Results from Kumar & Ghosh (2005) and from Bolton & Lau (1993) are consistently higher than those values derived from Plaxis and ABC. Bolton & Lau (1993) and Kumar & Ghosh (2005) may not have assumed the critical shape of the failure mechanism.
The Plaxis results from Table 7 are approximately 7 % higher than those obtained from ABC. The lowest row in Table 7 represents a calculation using φ = 30° and ψ = 0°. The estimated capacity is approximately 25 % lower than for associated flow.

*Table 7: Results from ABC and Plaxis used to estimate the axi-symmetric value of Nγ for a completely rough foundation. * ψ = 0°.*

φ' [°]	ABC		Plaxis		Acc. [-]
	Q_f/A [kPa[	N_γ^{BC} [-]	Q_f/A [kPa]	N_γ [-]	
10	6.46	0.32	-	-	-
15	18.7	0.93	20.73	1.01	1.08
20	48.4	2.42	-	-	-
25	121.6	6.08	-	-	-
30	310.8	15.5	335.9	16.61	1.07
35	838.5	41.9	907.0	44.95	1.07
40	2474.5	123.7	-	-	-
45	8356.3	417.8	-	-	-
30*	-	-	249.5	12.29	

Figure 9 shows the shear strain contour plot from Plaxis using φ' = ψ = 35°. Using larger friction angles implied numerical problems.

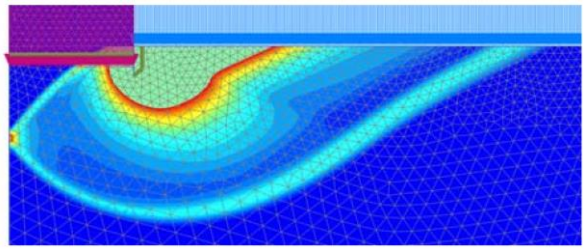


Figure 9: Shear strain contour plot of the axi-symmetric failure mechanism for associated flow, φ' = 30° and a completely rough foundation.

The results from ABC in Table 7 leads to the following approximation of N_γ for a completely rough foundation [10° ≤ φ' ≤ 45°]:

$$\log_{10}(N_\gamma) = 2.576 \cdot 10^{-5} \cdot \varphi^3 - 1.868 \cdot 10^{-3} \cdot \varphi^2 + 1.253 \cdot 10^{-1} \cdot \varphi - 1.581$$

The coefficient of regression is 0.9983.
The shape factor $s_\gamma^{L=B}$ was estimated using the same approach suggested for the q'-case: $s_\gamma^{L=B} = 2N_\gamma^{tr} / (N_\gamma^{pl} \cdot \sqrt{\pi})$, where $D/B = 2 \cdot \sqrt{\pi}$, N_γ^{tr} follows Table 7 and N_γ^{pl} is calculated from Lundgren & Mortensen (1953) with $\varphi'_{pl} = 1.10 \cdot \varphi'_{tr}$. These values are shown together in Figure 10.
In EC7-DK NA $s_\gamma^{L=B}$ is dictated as equal to 0.60 with no dependency on φ', this appears to be on the safe side.

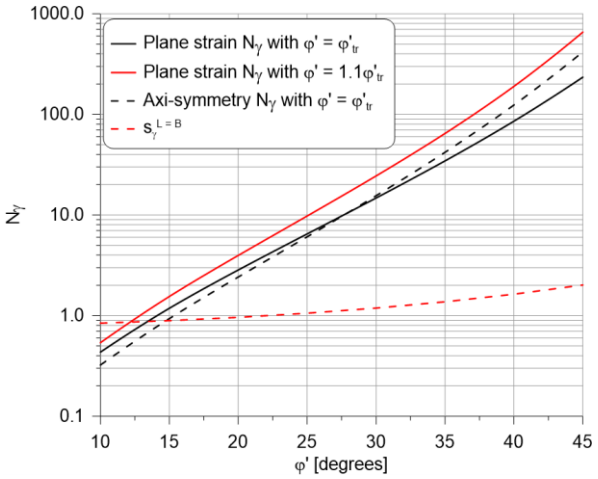


Figure 10: Estimated values of N_γ against the triaxial friction angle. Note that the dashed red curve represents $s_\gamma^{L=B}$ and not N_γ .

6.3 3D Models

The calculations in Plaxis 3D for the pure γ'-case proved to be very challenging to execute to a satisfactory level. As in the Plaxis 2D calculations, a small surcharge was applied to ensure non-zero effective stresses at the soil surface. This was however not enough to ensure stable and reliable calculation results. The results presented in this section are the product of a large number of iterations regarding modelling and numerical parameters, in the attempt to reproduce results similar to the axi-symmetric results and obtain reliable failure mechanism.
It seems that Plaxis 3D calculation for the pure γ'-case is not feasible, as this will lead to numerical issues and results that are not easily reproducible for varying numerical settings. The results of this section should thus be taken as a best estimate based on the work performed within the time frame of this project, and that further work is needed to fully understand the issues involved in executing reliable 3D FEM calculations for a pure γ'-case.
Using q' = 1.0 kPa, γ' = 10 kN/m³ and a diameter of D = 3.54 m, the results shown in Table 8 was obtained.
The failure load is divided by a combination factor μ = 1.18 for φ' = 15° and μ = 1.10 for φ = 30°, before N_γ is back-calculated. This combination factor accounts for the superposition effect of the γ' and q' contribution and is explained in Banedanmark (2014).

*Table 8: Back-calculated values of N_γ for a circular foundation with completely rough interface. * Result from Table 7.*

φ' [°]	Plaxis 3D		Plaxis 2D*	ABC
	Q_f/A [kPa]	N_γ [-]	N_γ [-]	N_γ [-]
15	29.62	1.12	1.01	0.93
30	532.74	25.26	16.61	15.54

Table 8 shows that the 3D models leads to comparable values for φ' = 15°, however for φ' = 30° the values differ by a factor 1.5.
Analyses for rectangular foundations (B<L) were undertaken, and the main results are seen in Table 9. The value of the combination factor μ is calculated based on Banedanmark (2014). The shape factor is calculated as: $s_\gamma = (Q_f/A/\mu - q' \cdot N_q) / (1/2 \cdot \gamma' \cdot B \cdot N_\gamma^{pl})$.
The results for L = B from Table 9 should be directly comparable to Figure 10 as the contribution from q' has been corrected for. For φ' = 15° the values are comparable, however for φ' = 30° they are not.

Table 9: Main results from Plaxis 3D analyses using rectangular foundations with B = 4 m and $\gamma' = 10$ kN/m³.

L [m]	q' [kPa]	φ' [°]	Q_f/A [kPa]	μ [-]	s_γ [-]
4	1.0	15	39.90	1.17	0.973
8	0.1		38.23	1.05	1.162
16			40.01		1.217
40			42.22		1.284
4	1.0	30	387.9	1.09	0.691
8			476.8		0.858
16			489.6		0.882

For the Plaxis 3D analysis with $\gamma' > 0$ and $q' \approx 0$ it has been difficult to identify a clear and consistent final state of failure. Increasing the value of q' will improve converge towards failure.
The singularity at the edge of the foundation is represented by a geometrical point being subjected to a significant foundation pressure at one side and to a stress state of virtually no pressure on the other side, which may cause numerical problems. These problems are present in the 2D and axi-symmetric models as well, however here they only represent a single point in the model, while in the 3D models the singularity is present around the whole circumference of the foundation. The investigation within the time frame available did not allow for a solution of this problem. It might be the case that more elements are needed or that a strength increase in the soil should be present at the points of singularity.

6.4 Conclusions

Plane strain analyses with Plaxis in the γ'-case leads to a bearing capacity factor resembling what can be found from Lundgren & Mortensen (1953) and from EC7-DK NA. The value of N_γ will change as the roughness of the interface is changed. Using non-associated flow will reduce the capacity found by approximately 20 % compared to associated flow for φ' = 30°. For eccentrically acting loads the estimated capacity from Plaxis 2D is approximately 5 % higher for $e/B < 0.25$ using the effective foundation area concept. For larger values of e/B the approach in EC7-DK NA may be unsafe. The theoretical bearing capacity factor N_γ for a circular foundation has been evaluated. It appears that the solution provided by Martin (2004) fits the results of Plaxis 2D. The shape factor s_γ for a square foundation has been found to be larger than given in EC7-DK NA, however the results cannot generally be verified by Plaxis 3D analyses. Plaxis 2D can be used to evaluate the pure γ'-case, however a value of $q' \approx 1.0$ kPa must be used to obtain reliable results. Using q' = 1.0 kPa in Plaxis 3D can be used to evaluate the tendency of s_γ, e.g. it increases with L/B. Back-calculating results from Plaxis 3D with q' = 1.0 kPa has however not turned out to lead to reliable and consistent results. The overall conclusion for the drained γ'-case investigated is that EC7-DK NA and Plaxis will deviate. Mechanisms for plane strain and circular foundations can be studied, but Plaxis 3D results for the pure γ'-case appears to represent a challenge and it is therefore not recommendable to apply Plaxis 3D for capacity calculations in a pure γ'-case. For practical applications however, a pure γ'-case is rarely encountered.

7 COMBINED DRAINED CAPACITY

The combined capacity of the q'- and γ'-case has been investigated in Banedanmark (2014).

The main conclusion are that the results from Plaxis calculations will include the combination factor μ, which is not a part of EC7-DK NA, and a larger capacity will thus be found from Plaxis analyses than using EC7-DK NA. The μ-factor is well-established for the plane strain case, and comparing results from EC7-DK NA and Plaxis 2D including the μ-factor leads to identical results.
The μ-factor is not established for the 3D case, so the influence is not easy to directly isolate. Furthermore the relation between φ'_{tr} and φ'_{pl} is not constant or well determined. Plaxis 3D results will yield a capacity between the values found from EC7-DK NA using respectively φ'_{pl} and φ'_{tr}.

8 CONCLUSIONS

When using Plaxis 2D plane strain to investigate the q'- and γ'-case independently, the bearing capacity factors fit well with EC7-DK NA for vertically acting central loads using associated flow. For eccentrically acting loads, the effective foundation concept is confirmed for a relative eccentricity of up to 0.2 to 0.3 depending on the actual case.
The shape factor s_q as defined in EC7-DK NA may be too high for $\varphi' < 20°$ and too low for $\varphi' > 20°$, using a square footing.
The shape factor s_γ defined in EC7-DK NA is lower than the value found by compared circular and square footings using Plaxis 2D and 3D, however small scale testing from de Beer (1970) supports the approach in EC7-DK NA. Bearing capacity factors for N_q and N_γ are established for circular foundations. Most authors agree in the value for N_q, but N_γ appears to be too high. The results from Martin (2004) fits well with those values established using Plaxis 2D. The results from Plaxis 3D show that the pure γ'-case cannot be analysed and a surcharge must be added. The plane strain effect with $\varphi'_{pl} > \varphi'_{tr}$ cannot be investigated in Plaxis 3D as the material models do not reflect this aspect, so φ'_{tr} must be used in Plaxis 3D. The bearing capacity estimated with φ'_{pl} and EC7-DK NA appears to be higher than found with Plaxis 3D and φ'_{tr}. Shape factors are empirical factors and deriving exact values by the finite element method will be influenced by the choice between φ'_{pl} and φ'_{tr}, the μ-factor and the element net applied.

9 FURTHER WORK

The 3D FEM results reveal a challenge when estimating the capacity for the γ'-case. More work should be undertaken in order to better understand this issue. It might be the case that the mesh used in the calculations is simply not fine enough to reproduce correct results or that other measures should be undertaken in order to handle to singularities at the edge of the foundation.

10 ACKKNOWLEDGEMENTS

The authors are grateful for being allowed to publish the work by Banedanmark.

11 REFERENCES

Bolton, M.D. & C.K. Lau (1993). Vertical Bearing Capacity Factors for Circular and Strip Footings on Mohr-Coulomb Soil, Canadian Geotechnical Journal, Volume 30, pp. 1024-1033.

Hansen, Bent (1982). Geoteknik og Fundering III, 1982, Notat 24, Særlige problemer.

Brinch Hansen (1970). A Revised and Extended Formula for Bearing Capacity, Bulletin 28, The Danish Geotechnical Institute, Copenhagen 1970.

Bønding, N. (1977). Kinematically Admissibility of the Pure N_γ Rupture Figure, Proceedings of the Ninth International Conference on Soil Mechanics and Foundation Engineering, 1977, Tokyo.

de Beer, E.E. (1970), Experimental Determination of Shape Factors and the Bearing Capacity Factors of Sand, Geotechnique 20, Number 4, 387-411.

DS/EN 1997-1, Eurocode 7: Geotechnical Design– Part 1: General Rules, Danish National Annex 2013 included.

Kumar, J. & P. Ghosh (2005). Determination of N_γ for Rough Circular Footings Using the Method of Characteristics, Electronic Journal of Geotechnical Engineering, Paper 2005-0540

Lundgren, H. & K. Mortensen (1953). Determination by the theory of Plasticity of the bearing capacity of Continuous Footings on Sand, Proc. 3rd Int. Conf. Soil Mech., Volume 1, p. 409, Zürich 1953.

Martin, C.M. (2004). User's Guide, ABC - Analysis of Bearing Capacity, Version 1.0, Department of Engineering Science, University of Oxford, OUEL Report No. 2261/03.

Prandtl, L. (1920). Über die Härte plastischer Körper, Nachr. D. Ges. D. Wiss., math-phys. Kl. Göttingen 1920.

A Case Study of Heave of Pile-Supported Structures Due to Pile Driving in Heavily Overconsolidated Very High Plasticity Palaeogene Clay

T. Hørlykke[1,2] and B. Dedenroth[1,3]
[1]*Aarhus University, Aarhus School of Engineering, Denmark*
[2]*Geo, toh@geo.dk* [3]*Rambøll, bdp@ramboll.dk*

K. K. Sørensen
Aarhus University, Department of Engineering, Denmark, kks@eng.au.dk

ABSTRACT
The process of pile driving in high plasticity clays is commonly known to result in full displacement of the soil thereby causing vertical and lateral movements in the ground surrounding the pile. These movements may potentially lead to significant heave and damage of adjacent structures and foundations even when these are supported on piles. This was observed to be an issue during construction of Aarhus Story, an extension to the existing open-air museum Den Gamle By in Aarhus. In this paper the detailed case is presented.

The case involves pile driving for a new 3-story building with a basement structure, which is to be erected in-between and in close proximity to two existing buildings. Pile driving is carried out from the base of a deep basement excavation. Both existing buildings are recent, and both comprise basement structures with pile-supported basement slabs. Hence, all three buildings are supported on piles, and in all cases the piles are driven into heavily overconsolidated very high plasticity clay.

This case study presents a detailed account of the observed gradual heave of the adjacent buildings as pile driving proceeds for the new building. On this basis different parameters are identified which influence the heave of the adjacent buildings. Finally, the results are compared with an analytical model from literature, and it is discussed whether it can be used to predict heave of pile-supported structures.

Keywords: Case study, high plasticity Palaeogene clay, deep excavation, pile driving, heave of pile-supported structures.

1 INTRODUCTION

1.1 Background

The use of driven piles for heavily loaded structures has for long been the favoured foundation solution in many construction projects in Denmark, when permitted by the ground conditions. The speed of construction and hence lower costs as compared to the installation of bored piles is often the main reason for the selection of a driven pile solution.

The process of pile driving in high plasticity clays is commonly known to result in full displacement of the soil. The soil displacement causes vertical and lateral movements in the ground surrounding the pile. These movements may potentially lead to significant heave and damage of adjacent structures and foundations even when these are supported on piles. This was observed to be an issue during construction of Aarhus Story, an extension to the existing open-air museum Den Gamle By in Aarhus. In this paper the detailed case is presented.

The influence of pile driving on existing pile-supported structures is a complex matter, which has only to a limited extend been investigated in past studies. Hence, the presented case study will help to shed light

on the issue and may provide further in-sight into the complex mechanism, which occur in high plasticity clays in connection to pile driving.

1.2 Ground movement in connection to pile driving

When prefabricated reinforced concrete piles or closed ended tubular steel piles are driven into very high plasticity clay the short-term soil displacement will be equal to the volume of the piles, since the clay behaves as incompressible under the fast driving process and due to the very low permeability of the saturated clays.

There are different theories on how the pile driving affects the soil. Early theories derived from field-testing concluded that the displacements where mainly vertical (Hagerty and Peck, 1971). Further analysis has been carried out by Massarsch (1976) using model- and field-tests with pile groups. Wersäll and Massarsch (2013) concluded based on these results and Finite Element Analysis made by Edstam (2011) that pile driving causes mainly lateral movements and that vertical movements can be neglected close to the driven pile. The soil displacement pattern around a driven pile is illustrated in Figure 1.

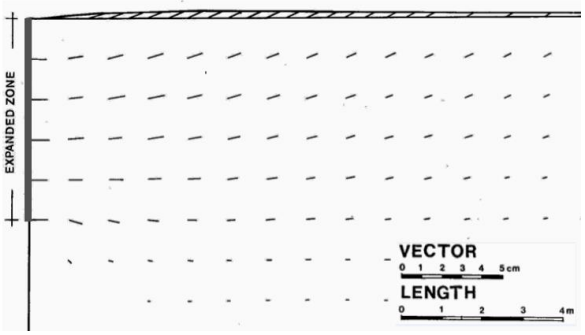


Figure 1 Soil displacement pattern around a driven pile, showing displacement vectors (Wersäll and Massarsch (2013)).

The ground movements in connection to a single pile are equal in all directions assuming uniform ground conditions. When several piles are driven in a pattern (e.g. pile rows or groups), the driving direction has an influence on the heave. Ground heave is greater in front of the pile group in the direction of pile driving, and is reduced adjacent to the location of the piles first driven (Dugan and Freed, 1984 and Wersäll and Massarsch 2013).

Wersäll and Massarsch (2013) have proposed an analytical model to estimate the heave of the ground surface in front of a pile row driven into soft clay. They suggest that the magnitude of heave is controlled by the cross sectional areas of the piles, the pile spacing and the distance from the pile row. These parameters are taken into account by an equivalent soil displacement factor, u_{eq} that corresponds to the cross section area of one-quarter pile divided by the pile spacing.

$$u_{eq} = \frac{\frac{1}{4}a}{c} \quad (1)$$

Where a is the cross section area of one pile and c is the pile spacing.

The pile length on the other hand is suggested to control the zone of influence; defined as the distance beyond which heave is negligible, and also the distance to where maximum heave occurs.

1.3 Heave of pile-supported structures due to pile driving

Existing pile-supported structures located adjacent to an area of pile driving are likely to have a great impact on the vertical movement of the ground, and visa versa the ground movement from pile driving will have an impact on the vertical movement of the pile-supported structure. The heave of pile-supported structures is complex and is expected to be influenced by several factors including the weight of the structure, the length of existing piles and the ground properties. These factors are, in addition to the factors mentioned previously, controlling the ground movement around driven piles. All these factors will influence the impact that pile driving has on existing pile-supported structures.

A series of case studies made by Dugan and Freed (1984) have highlighted the complexity of this problem. Survey points were placed both on the ground and on buildings. The measurements show as

expected that the heave of pile-supported buildings is significantly smaller than the heave of the unrestrained ground surface. The restraining effect of adjacent pile-supported buildings on heave movements is therefore relevant to consider.

At present there exist no models, which can accurately predict the heave of pile-supported structures located adjacent to pile groups driven into clays.

2 CASE STUDY – AARHUS STORY

2.1 Project description

The Aarhus Story project involves pile driving for a new 3-story building with a basement structure, which is to be erected in-between and in close proximity to two existing buildings; Plakatmuseet (Building A) and Den Moderne By (Building B), as shown on the site plan in Figure 2.

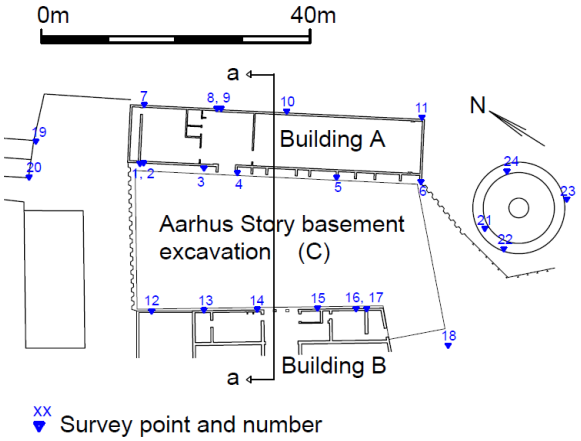


Figure 2 Site plan showing the excavation of Aarhus Story and the location of survey points.

Pile driving is carried out from the base of a deep basement excavation. Both existing buildings are recent, and both comprise basement structures with pile-supported basement slabs. Hence, all three buildings are supported on piles, and in all cases the piles are driven into heavily overconsolidated very high plasticity clay, as illustrated in Figure 3. The figure shows cross section a-a (marked in Figure 2) through the centre of the excavation with average pile lengths of the buildings.

The top of the Palaeogene clay is found at approximately level -10 m in the cross section. All levels given in the paper refer to mean sea level (DVR90).

Building A to the east is supported on a pile-supported concrete slab (steel piles type HE180A) with base level at +5.0 m. The toe level of the steel piles is from level -12 m to -22 m. Building B is also supported on a pile-supported concrete slab but with concrete piles (size 30x30 cm).

The base level of the slab varies since there is not a basement below the entire building. The basement is deepest in the central part, with floor level +1.7 m and base level +0.7 m. The toe level of the concrete piles is approximately -18 m.

The project Aarhus Story includes a basement and lowest excavation level is +3.6 m. The new building is to be pile-supported like the two adjacent buildings. The concrete slap is supported on concrete piles with increasing pile length to the north.

In connection to the excavation a sheet pile wall is established along the north-western side and partially along the southeast side as indicated in Figure 2. All sheet piles were driven before the first survey and therefore do not contribute to the measured soil displacement and where not expected to affect the ground movement during subsequent pile driving. The deepest sheet pile toe is at -8.5 m.

2.2 Site conditions

The ground and water conditions at the site have been obtained from the site investigation carried out by Geo (2013). The ground level before excavation was at level +7.0 m to +9.3 m, rising in the northern direction. Below ground level are found typical glacial deposits consisting of alternating layers of clay till, meltwater sand and embedded glacial floes of high plasticity clays. There is no systematic stratification of these deposits.

Palaeogene clay is found below the glacial layers. In the south-eastern end of the site the top level of the Palaeogene clay is found at -6.0 m to -7.0 m. From here it dives to the northwest, where it is found at level -15.9 m. The Palaeogene clay consists primarily of Søvind Marl and in some areas by thin layers

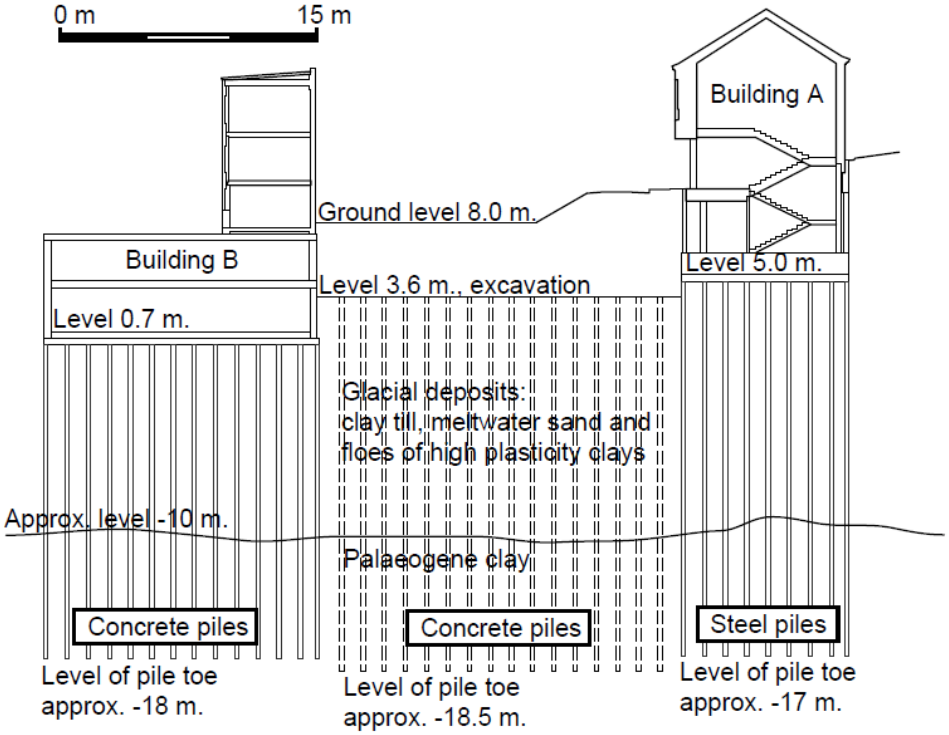


Figure 3 Cross section of the basement excavation for Aarhus Story and the adjacent buildings (Southeast to North-western direction).

of Septarian Clay. Søvind Marl is a marine sedimentary clay. It is heavily overconsolidated and it can be characterized as a extremely high plasticity clay (the liquid limit is typically reported in the range 100-240% (Sorensen and Okkels, 2015)). It is fissured in its natural condition.

The upper part of the formation is very calcareous (25-56%) and Søvind Marl is therefore significantly different from the other high plasticity Palaeogene clays found in Denmark. The plasticity index is between 51-115% and the field vane shear strength, c_{fv} is between 400 kPa – 700 kPa.

The water table in the area varies from level +5.3 m to +8.7 m increasing to the north.

2.3 Monitoring program

A total of 34 survey points were linked to the project. 24 of these were relatively close to the site and the remaining 10 points were located at a distance of up to 100 meters from the site. These 10 points were used as reference points.

All of the survey points were placed on the adjacent buildings from the ground floor to just below the roof structure, between level +7.3 m to +17.5 m. The internal movements in the building are expected to be small with minimal influence on the heave measurements. Figure 2 shows the 24 points located on the adjacent structures. 11 of these points are placed on Building A and 7 points are placed on Building B.

The points were continuously surveyed in 203 days between February 17th and September 8th 2014, corresponding to the beginning of the pile driving until two months after.

Originally, there were only 9 points on the adjacent buildings, but as the foundation project progressed, heave was registered and therefore more points were added. Survey points 1, 3 and 6-11 were added to Building A and 12, 13 and 15 to Building B. Furthermore the frequency of measurements was more concentrated at the second half of the process. Due to the more infrequent measurements at the beginning, the data set was inadequate for analysis in this period.

A surveyor monitored the survey points with a TST (total station theodolite) located

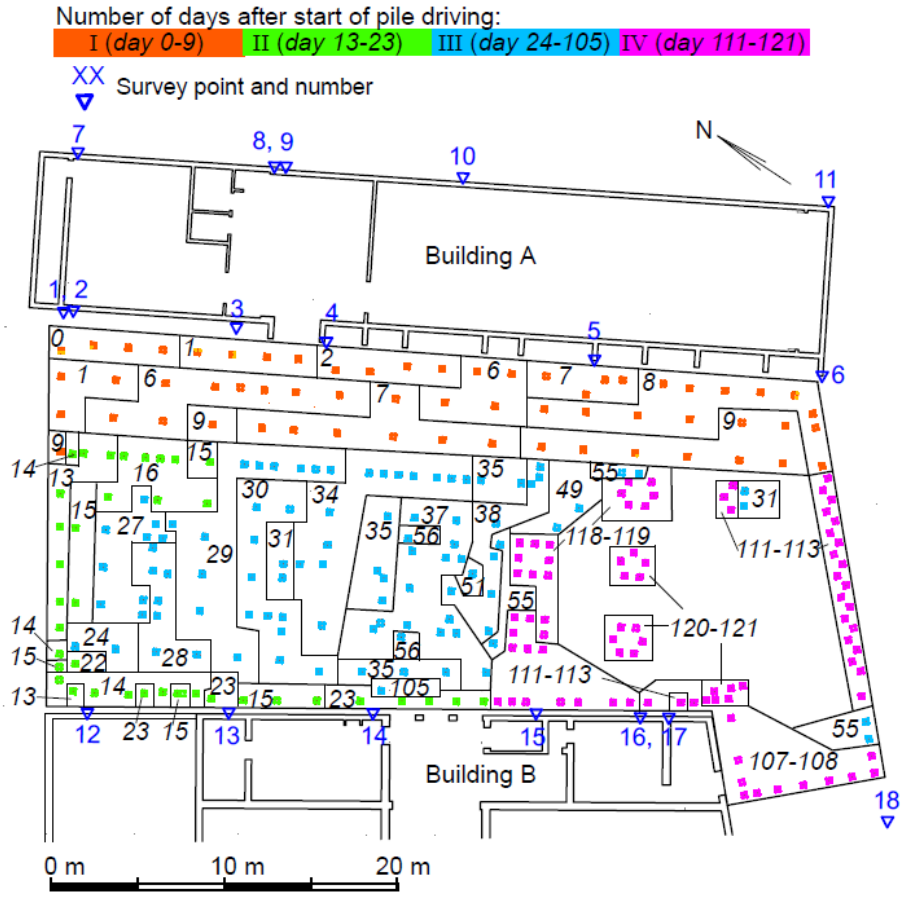


Figure 4 The progress of pile driving at Aarhus Story.

within the construction site. The surveyor reported an uncertainty of measurements of less than 2 mm.

2.4 Pile driving

The project has a total of 280 driven concrete piles and 59 permanent bored in-situ cast micro-piles (GEWI®). The driven concrete piles has square cross section with side length b = 0.25 m, but with different penetration depths from 12 to 25 m. The pile lengths are dependent on the depth of the top of the Palaeogene clay, hence the pile lengths increases from south to north.

The pile spacing varies between c = 0.8 - 2.3 m, which gives a spacing ratio (c/b) of 3-9. Approximately 65% of the piles have a spacing c = 1.5 - 2 m, which gives a narrower spacing ratio of 6-8. Some of the piles have been installed using pre-augering (fully or partial) to minimize further heave. Figure 4 illustrates the location and progress of the driven piles divided into four periods. The bored micropiles are not considered to result in any soil displacement, hence these are not considered in the further analysis and are not shown on the figure. A general specification of the differences in the periods is shown in table 1.

Table 1 A general specification of the driven piles in each period.

Periods	I	II	III	IV
Number of piles	60	39	98	83
Penetration depth [m]	21-25	20-25	19-25	12-17
Pre-augering depth [m]	8-9	9	12	14-16
Displaced soil per pile [m^3]	0,8-1,1	0,8-1,2	0,5-0,8	0,1-0,3

The pile driving took place from March 4th (day 0) to July 3rd (day 121) 2014 and went from north to south, starting closest to the adjacent buildings, as shown in Figure 4.

3 OBSERVED HEAVE OF PILE-SUPPORTED BUILDINGS

In connection to the pile driving, heave of the two adjacent buildings were registered as shown in Figures 5 and 6. The shown heave is the accumulated heave, which is represented by the relative change in vertical movement from the first survey (the reference measurement).

The timeline on the horizontal axis indicate all days on which measurements are made, represented by days after start of pile driving (notice that the timescale is not constant). In the periods between each measurement the numbers of piles driven vary between 1 and 33, however over the full period of driving the number of driven piles was more or less evenly distributed.

The survey points at Building A (point 2, 4 and 5) show a very significant heave of the building in the beginning of the pile driving, followed by a very small increase in the rest of the process (cf. Figure 5). In contrast, the observed heave of Building B shows a gradual heave that develops as the pile driving progresses. As more piles are driven the greater the heave becomes (cf. Figure 6). This is a likely result of the differences in piling driving patterns next to the two buildings, as shown in Figure 4.

It should be noted that not all survey points have the same reference date, due to the fact that some of the points, as mentioned, were added after the start of pile driving.

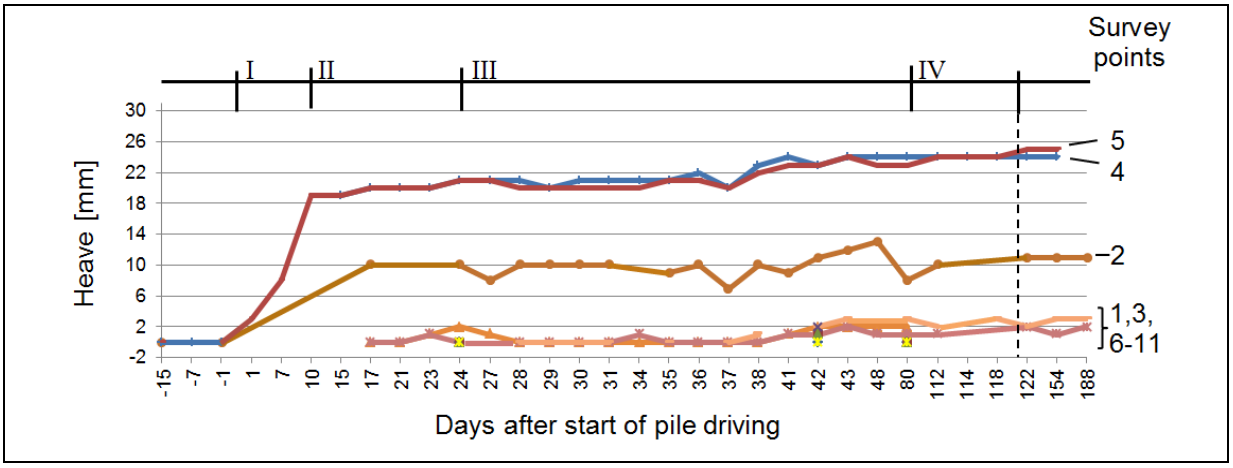


Figure 5 Accumulated relative heave of Building A with an indication of the pile driving periods. The timeline indicates all days on which measurements are made, represented by days after start of pile driving. End of pile driving is on day 121.

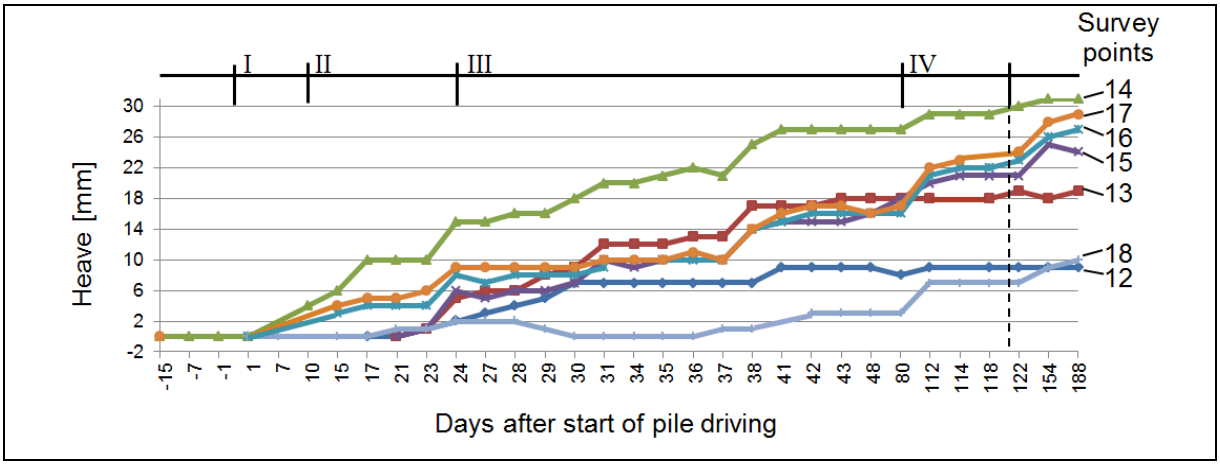


Figure 6 Accumulated relative heave of Building B with an indication of the pile driving periods. The timeline indicates all days on which measurements are made, represented by days after start of pile driving. End of pile driving is on day 121.

As seen in Figure 5 this means that the first survey of several points (1, 3, 6-11) were undertaken after the initial observation of very significant heave for Building A (that occurred in period I, day 0-9). Hence it is likely that the other parts of the facade of Building A facing the area of piling also have experienced similar movement to those shown by survey points 2, 4 and 5, but no data can verify this.

The points 12, 13 and 15 on building B were also added later (day 17-21), which may be the reason why point 13 and 15 have experienced lesser heave compared to point 16 and 14 respectively. The points 13, 16 and 15, 14 are comparable because of their location in relation to the central part of the foundation area.

The maximum accumulated heave of both buildings was observed from survey points facing the central part of the foundation area. Building A experienced 24-25 mm heave observed by survey points 4 and 5, and building B experienced 27-31 mm heave observed by survey points 14, 16 and 17.

Driving of piles in close proximity to the buildings causes significant heave for the survey points closest compared to the points further away. For example measurements on day 23 show that survey points 13-17 experience significant heave (3-5 mm), whereas survey points 12 and 18 on building B and points 1-11 on building A have minimal (-1 to 1 mm) or no displacement.

On day 37, 14 piles were driven in the central part of the foundation area, which resulted in heave (3-4 mm) of survey points 13-17, 4 and 5 that were also facing the central part of the foundation area. An interesting observation is found for the same points on survey day 31-36, where insignificant heave (0-2 mm) is observed although 25 piles were driven in close proximity. This observation is interesting since no larger variation is registered.

The last pile was driven on day 121, yet measurements from day 122-188 show an additional heave of 3-5 mm (points 15-18), which may indicate a delayed response time in the displacements of the clay. These points are located adjacent to the area where the last piles were driven.

3.1 Factors influencing observed heave

The purpose of this analysis is to determine which parameters influence heave of pile-supported structures. The basis of the analysis is formed by data obtained by focusing on significant changes in the vertical movement of the structures (e.g. Figure 6, between day 23 and 24). The increase of heave between two survey days is assumed to be caused only by the displaced volume between these two days. The data listed in Figure 7 and 8 are all obtained by these datasets, which is why the heave is smaller than the accumulated heave in Figure 5 and 6.

In Figure 7 a linear correlation is seen when heave (h_s) is compared with displaced volume (V), which is also suggested in the literature (Dugan and Freed, 1984). The calculation of displaced volume is for all deposits, thus displaced volume in Palaeogene clay only is not investigated. Only heave measurements for distances from 1 to 11 m from the survey point to the centre of the pile group has been included in the figure to minimize the influence of distance. However, some scatter still remains as a result of difference in pile lengths and layout of pile groups.

The data depicted is within the relative distance, s/L = 0.05 - 0.5, where s is the horizontal distance from the centre of the driven pile group to the survey point, and L is the average pile length within the pile group (16.5 m - 23 m).

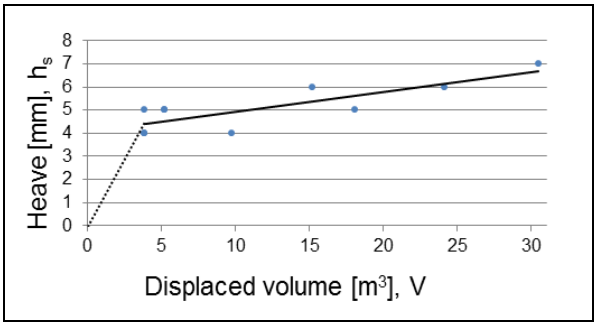


Figure 7 A linear correlation between heave and displaced volume for distances up to 11 m, with a relative distance s/L=0.05-0.5. The trend line is given by h_s=0.085·V+4 for V=4m^3–30m^3.

For this case study the total heave and the inclination of the trend line is relatively small compared to the expected movement of the unrestrained ground surface, since the load from the existing buildings and their pile foundations help to limit the vertical movements.

The trend line from Figure 7 is non-existent for values below $V = 4m^3$ because of limited data. It is assumed that no heave occur with a displaced volume of 0 m^3. The dashed line indicates a greater ratio of heave per displaced volume for $V < 4m^3$, which may be due to tensioning of the piles from compression to tension. This could possibly correspond to the heave of a non-pile-supported structure.

The distance to maximum heave is expected to be related to the pile length. This is also indicated from the observations, as seen in Table 2.

Table 2 The distance to where maximum heave is observed for different pile lengths.

Pile length [m]	Distance to maximum heave [m]
16 – 16.5	5.8 – 7.4
21 – 21.5	8.2 – 13.2
22 – 22.5	9.1 – 15.7

The table shows a correlation between these two parameters. The longer the piles the further away maximum heave will occur.

4 COMPARISON OF OBSERVED HEAVE WITH PREDICTED HEAVE BASED ON ANALYTICAL SOLUTION FROM LITERATURE

In the following the data from this case study is compared to the simplified model proposed by Wersäll and Massarsch (2013) for estimation of ground surface heave in front of a driven pile row. This is done with the aim to evaluate if the model can be used to predict the heave of pile-supported structures in front of a pile group driven into high plasticity stiff clay. Differences between the model and observed behaviour can help to highlight the effects of the existing piles below the pile-supported structures and the spatial difference between pile row and pile groups.

The data from this case study is shown in Figure 8 as heave, h_s normalized by equivalent soil displacement, u_{eq} (1). A value of u_{eq} = 8 - 10 mm was determined.

The red line describes the model by Wersäll and Massarsch (2013), and shows maximum heave of the unrestrained ground surface to be equal to $0.4 \cdot u_{eq}$ in a relative distance 0.3 *s/L* - 1.0 *s/L* from the pile row. According to the model ground heave can be neglected in distances larger than 4 times the pile length. This assumption is based on 2D Finite Element Analysis.

Generally, a large spread is seen in the data in Figure 8, since several factors have not been considered in the plot, amongst others; the effect of pre-augering, the effect of pile-group size and layout and the effect of previously driven piles in front of the pile group.

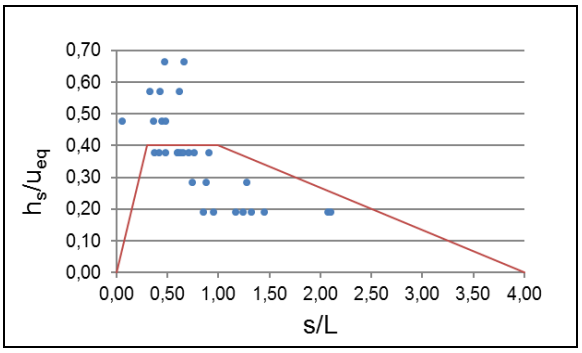


Figure 8 The data from this case study (blue) compared with the model suggested by Wersäll and Massarsch (2013) (red). The data is for displaced volume V=4 m^3–30 m^3.

For a relative distance shorter than 0.7 *s/L* the data shows significantly greater heave than the model, while with increasing distance beyond 0.7 *s/L* a more rapid decay in vertical movement is observed than predicted. The maximum observed heave is nearly 70% greater than predicted by the model.

The greater heave observed at short distances from the driven piles could be expected, as the pile groups are not directly comparable with a pile row, as used in the model. As shown in Figure 4 the groups consist of piles in different patterns (seldom a single row), which is why the influence of

additional "rows" has to be taken into account. The additional "rows" in a pile group can be expected to have greatest effect on the heave at short distances when compared to the single row assumed in the model.

At greater distances from the pile groups the model is found to overpredict the heave. This may be expected due to the spatial differences between the pile groups and the pile row. The limited extend of the pile group compared to the pile row will result in less heave at greater distances.

Furthermore, if no other factors are considered, the model may generally be expected to overpredict the actual heave of a piled structure, since the effect of the resistance of existing piles below the piled structure is not considered.

Additionally, the effect of pre-augering is not included in the model. Hence, if the pile is pre-augered this would lead to lowering of the measured heave compared to the heave predicted by the model.

Generally, the data is connected with large uncertainties due to many variables, which is why the observed dispersion is significant.

5 DISCUSSION

Since the considerations in this article are based only on one case study it is important to consider the results with care.

The survey points are concentrated around the excavation, i.e. placed on the adjacent buildings. Since there are no survey points inside the excavation, and very few outside the construction area, this makes the data very grouped around a limited interval of distances.

Only the heave of structures was registered. If the heave of the ground surface were registered both in and outside the excavation, a more accurate distribution of the heave could be constructed. With such data the displaced volume could be estimated more precisely and more accurate correlations of parameters could be determined.

Generally, the case involves many variables, limited data and uncertainties hence the effect of several important factors is difficult to assess, amongst others; the influences on the results of pre-augering, previously driven piles, pile group layout and driving direction.

It is assessed that the soil's upward movement causes the heave of the pile-supported structures. As the upward moving soil mobilises shaft resistance on the existing piles, the piles will gradually be moving upwards. The combined weight of the building and the mobilised downward shaft friction below the zone of upward movement will help to limit the heave of the piled structure. Hence, if the driven piles are longer than the existing piles and driven close to existing piles, then the driving might result in mobilisation of an upward shaft resistance along most of the pile length of the existing piles, or make the entire soil volume around the existing piles move upward. This could potentially cause significant heave of the structure.

The high plasticity clay has swelling properties, which has not been considered above. With a reduction in stresses, because of the 4-6 meter deep excavation, the long-term heave of the ground might be significant. However, the swelling process is very slow compared to the pile driving period of 4 months. Furthermore it is expected that pile driving to some extend may reduce the negative excess pore pressures caused by excavation and hence lead to a reduction in subsequent swelling (Simonsen and Sørensen, 2016).

6 CONCLUSION

Based on this case study it can be concluded that pile-supported structures are affected by heave when piles are driven into very high plasticity Palaeogene clays. A maximum accumulated heave of 25 and 31 mm was registered for the central parts of Building A and B respectively.

In general it is observed that the survey points near the central part of the foundation area have experienced a greater heave than the survey points at the north-western and south-eastern edge.

After the last pile was driven heave was still observed. From day 122-188 a heave of 3-5 mm was registered, which indicates a delayed response time in the displacements of the clay. Whether the buildings continued to heave or possibly settled in the following months is unfortunately unknown.

The results show that heave depends on the displaced volume and that the distance to where maximum heave occurs depend on the pile length; the longer the pile the further away maximum heave will occur. This confirms previous findings.

In order to make a more thorough analysis of heave of pile-supported structures more studies are needed. But the case study have highlighted the complexity involved if a reliable model is to be developed which can be used to accurately predict the heave of pile-supported structures.

A comparison has been undertaken between data from this case study and the model suggested by Wersäll and Massarsch (2013), which considers the case of vertical ground movement in front of a pile row. Since the actual case in this study is much more complex than considered in the model, the predictions of the model are not directly comparable with the observations. The comparison indicates that the model is likely to overestimate the heave for relative distances larger than approximately 0.7 *s/L* and under predict the heave for relative distances shorter than 0.7 *s/L*. It can be concluded that the model is not applicable in this context.

A further study of the issue has recently been conducted in an experimental project, where soil displacements around a single pile and around pile groups are examined in model tests. The effect of pre-augering is also investigated. The results from the model tests are to be processed and compared with literature as well as the data from this case study. This study will be presented in a future paper.

7 ACKNOWLEDGEMENTS

The authors would like to thank Geo, Viggo Madsen A/S, MT Højgaard, and Aakjaer Landinspektører for providing data for this case study and giving permission to publish the information presented in this paper. The guidance and help by Nik Okkels (Geo) is acknowledged.

8 REFERENCES

Dugan, J. P. and Freed, D. L. (1984). Ground Heave Due to Pile Driving. Proceedings of the International Conference on Case Histories in Geotechnical Engineering.

GEO (2013). Project no. 37094. Rapport 1 – Geotekniske undersøgelser, 14/11/2013, Aarhus, Viborgvej 2, Den Gamle By, Aarhus Story. (in danish)

Hagerty, D. J. and Peck, R. B. (1971). Heave and Lateral Movements Due to Pile Driving. Proceedings of the American Society of Civil Engineers, Journal of the "Soil Mechanics and Foundation Division".

Massarsch, K. R. (1976). "Soil Movements Caused by Pile Driving in Clay". Dept. Soil and Rock Mechanics, Royal Institute of Technology (KTH), Stockholm, Sweden, Thesis in partial fulfillment of the requirements for the Degree Doctor of Engineering, Job-Rapport No 6, 261 p.

Sorensen and Okkels (2015). Correlation between compression index and index parameters for high plasticity Palaeogene clays. 16th European Conference on Soil Mechanics and Geotechnical Engineering, Edinburgh, UK.

Simonsen, T. R. and Sørensen, K. K. (2016). Field measurements of pore water pressure changes in very high plasticity stiff clays adjacent to driven piles. Proceedings of the 17th Nordic Geotechnical Meeting, Reykjavik (same conference as this paper).

Wersäll, Carl and Massarsch, K. R. (2013). Soil Heave Due to Pile Driving in Clay. Sound Geotechnical Research to Practise, Geotechnical Special Publication (GSP 230) Honoring Robert D. Holtz, Edited by Armin W. Stuedlein, Ph.D., P.E., and Barry R. Christopher, Ph.D., P.E., ASCE, pp. 481 – 499.

Erfaringer med boring av stålrørspeler i kvikkleireskråning

S. A. Degago
Norwegian Public Roads Administration, Norway, samson.degago@vegvesen.no

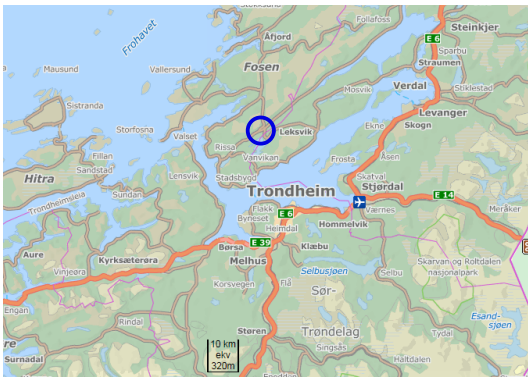
S. Giske, S. Hove, H. S. Tømmervik, Ø. Edvardsen
Norwegian Public Roads Administration, Norway

ABSTRACT
This article presents acquired experiences and measurements made during installation of bored steel pipe piles in a quick clay slope as part of foundation for the Skaudal Bridge in Rissa municipality in Norway. The project area is characterised by a presence of quick clay of large extent. Part of the bridge foundation requires installation of bored steel pipe piles at the top and bottom of the quick clay slope. This is a critical activity as it is very crucial to avoid a possible initial slide that could trigger a much larger slide. Thus, the success of the entire project centrally hinges on avoidance of a possible initial slide during the piling activity. The contractor presented a recently developed down-the-hole (DTH) drilling system. This system is designed to have an enhanced flushing air control such that leakage of compressed air into the surrounding soil body is avoided. The system shall also avoid excess pore pressure development and soil mass displacements. To evaluate the performance of this new method, the client (Norwegian Public Roads Administration (Statens vegvesen)) decided to evaluate the drilling system after a well-documented initial experience. Thus piling for the bridge foundation started where there was no stability problem and the client followed this up with relevant instrumentations. This indicated that the drilling system did not perform as desired as it led to significant excess pore pressure development and mass displacements unacceptable for a quick clay slope. Thus the contractor had to make amendments and confirm their validity with an instrumented pile test. Experiences from the pile test formed a basis to successfully install the piles in the quick clay slope. In this article, the drilling system and the project are briefly highlighted. The pore pressure measurements are also presented and discussed. The main conclusion is that the drilling system itself may be useful in sensitive clays, and that the difficulties in the project mainly is related to lack of knowledge and experience, by the contractor and operator, on use of the drilling system in sensitive clays.

Keywords: ***Highly sensitive (quick) clay, initial stability, DTH drilling method, pore pressure***

1 INNLEDNING OG BAKGRUNN

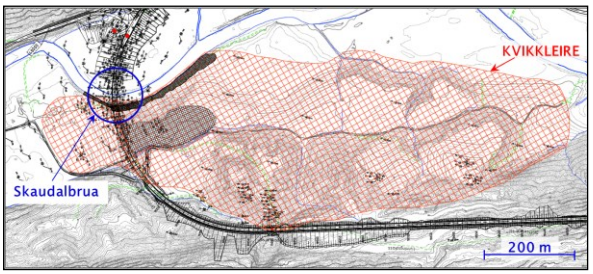
Statens vegvesen bygger utbyggingspakken Fosenvegen i Nord- og Sør-Trøndelag. Dette prosjektet omfatter oppgradering og nybygging av ca. 280 km vei på Fosen. En del av utbyggingspakken er anleggsarbeidet på Fv. 715 mellom Keiserås og Olsøy med totallengde på 17,5 km samt en estimert kostnad på ca. 450 mill. kr. På en del av denne strekningen, Leksvik grense – Olsøy, er det avdekket et stort område med kvikkleire. Se oversiktskart av strekning Leksvik grense – Olsøy i Figur 1.



Figur 1: Oversiktskart (basert på www.finn.no).

Totallengde på Leksvik grense – Olsøy er ca. 3,2 km, og den går i en helt ny trasé. På denne strekningen skjærer vegen på skrå

nedover lia, krysser over dyrka mark og elva Skauga, før den når dagens Fv. 715 med nytt kryss ved Olsøy. Dette innebærer at det bygges ei ny bru over elva Skauga i Skaudalen. Brua har fått navnet Skaudalbrua (se Figur 2). På den ene siden av elva (sørsiden) er brua fundamentert i en skråning med kvikkleire.



Figur 2: Kvikkleiresonen (veglinjen og Skaudalbrua).

2 GRUNN- OG PORETRYKKSFORHOLD

2.1 Grunnforhold på området

Ut fra www.skrednett.no er det påvist kvikkleire i området. På skrednett.no er kvikkleireområder klassifisert med tre faregrader (dvs. høy, middels og lav) og dette kvikkleireområdet er satt til høy faregrad. Med utgangspunkt i skrednett.no er det utført flere omganger med grunnundersøkelser som avdekket en større kvikkleiresone enn det som var påvist på skrednett.no, Figur 2. Opprinnelige ble vegen plassert for å unngå kvikkleiresonen angitt på www.skrednett.no. Likevel krysset den nye veglinjen den utvidede kvikkleiresonen, Figur 2. Dette innebærer også at det på ene siden av elva bygges brufundament i en kvikkleireskråning der kvikkleirelaget ligger høyt. Omfattende grunnundersøkelser er utført i området (SVV rapport (2013a, 2013b og 2014)).

2.2 Grunnforhold rundt Skaudalbrua

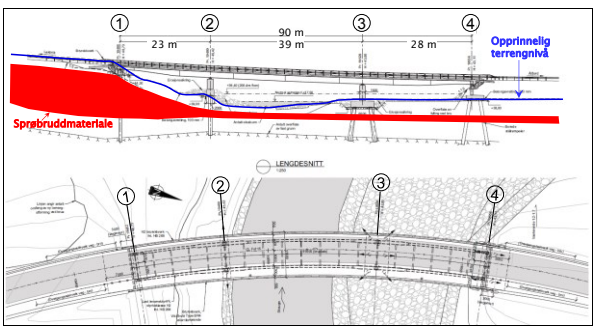
Skaudalbrua er en 90 m lang samvirkende stål/betongbru i tre spenn. Brua har fire fundamenteringsakser. Det ble installert borede stålrørspeler ved toppen (akse 1) og bunnen (akse 2) av kvikkleireskråningen. Grunnforholdene rundt hver akse er oppsummert i Tabell 1.

Grunnundersøkelsene utført i området viser at leiren er preget av generelt høy skjærfasthet og høy overkonsolideringsgrad. Likevel er leiren hovedsakelig meget sensitiv og er klassifisert som sprøbruddmateriale, dvs. omrørt skjærstyrke (c_{ur}) mindre enn 2 kPa. Kvikkleire er definert som en leire med $c_{ur} \leq 0{,}5$ kPa.

Tabell 1: Grunnforhold ved bruaksene

Bru-akse	Løsmasses-mektighet (m) (Fjellkote)	Grunnforhold/lagdeling
1	18,0 (+28,1)	0 – 3 m: Leire (2–3m, meget sensitiv) 3 – 9 m: Kvikkleire 9 – 18 m: Leire (9–12m, meget sensitiv)
2	9,0 (+30,1)	0 – 2 m: Siltig sand/Sandig grusing 2 – 7 m: Leire (2–5 m, meget sensitiv; et tynt kvikkleire lag dvs. 4–4,5 m)) 7 – 9 m: Siltig sandig leire
3	10,1 (+28,4)	0 – 2 m: Grusig sandig silt/Sandig grusing 2 – 6 m: Leire (2–4 m, meget sensitiv) 6 – 10,1 m: Siltig sandig leire
4	10,7 (+27,5)	0 – 2 m: Siltig sand/Sandig grusing 2 – 7 m: Leire (2–5 m, meget sensitiv) 7 – 10,7 m: Siltig sandig leire

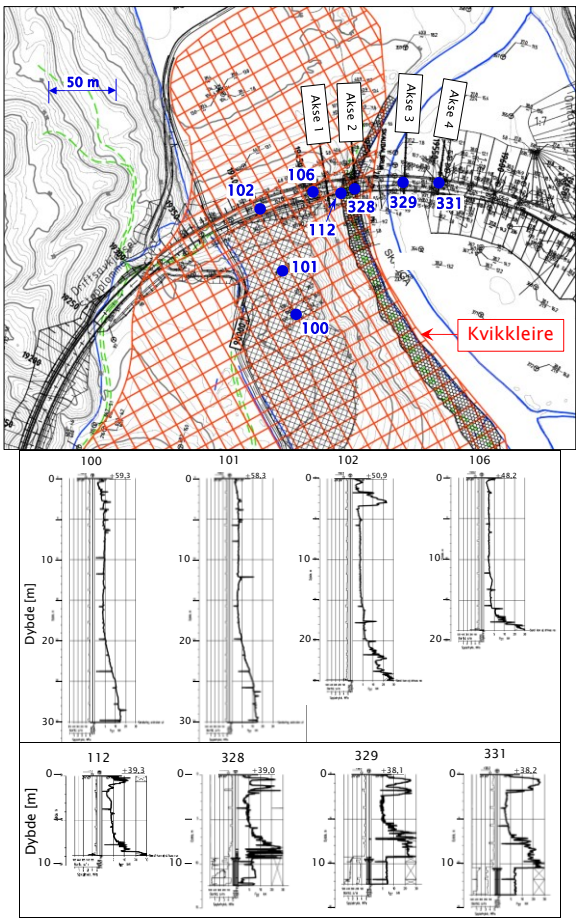
Figur 3 presenterer brua og skisser omfanget av sprøbruddmateriale samt det opprinnelige terrengnivået.



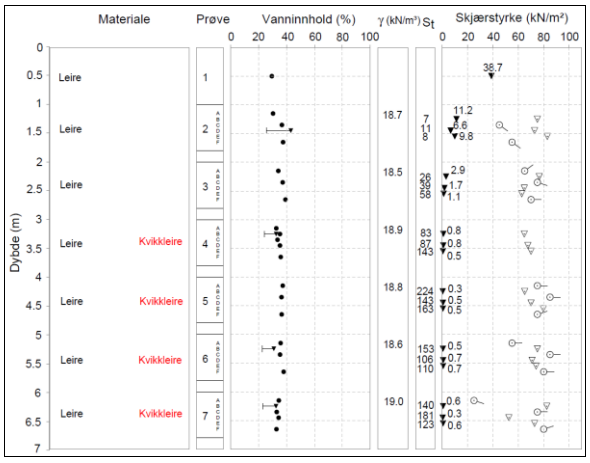
Figur 3: Skisse av omfanget av sprøbruddmaterialet ved brua (øverst-lengdesnitt, nederst-plan).

2.3 Resultater av grunnundersøkelser på utvalgte punkter

Oversikt over plassering av utvalgte borepunkter og utførte totalsonderinger er presentert i Figur 4. Rutineundersøkelse resultater ved bp. 106 framgår av Figur 5.



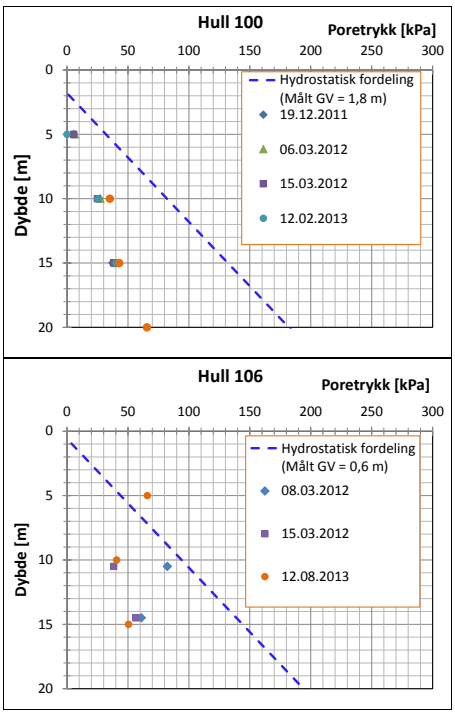
Figur 4: Utvalgte totalsonderingerresultater (se plasseringen på oversiktskartet øverst).



Figur 5: Borprofil, rutine undersøkelsesresultater ved borepunkt 106 (rundt akse 1).

2.4 Grunnvannstand og poretrykksforhold

Kvikkleireskråningen er generelt preget av betydelig underhydrostatiske forhold med et høyt grunnvannstandsnivå som ligger ca. 0,8 m under terrenget. Poretrykksmålinger ved bp. 100 og 106 framgår av Figur 6.



Figur 6: Poretrykksmålinger ved bp. 100 og 106 og en hydrostatisk poretrykksfordeling ut ifra målte grunnvannstandsnivåer.

3 STABILITETSTILSTAND OG VURDERING

Vurdering av skråningens stabilitet er en typisk 3D problemstilling der skråningen faller av i to retninger. Stabilitetstilstanden av skråningen er vurdert med totalspennings- og effektivspenningsanalyser ved å velge kritiske snitt i ulike retninger i henhold til Statens vegvesens (SVV) og Norges vassdrags- og energidirektorat (NVE) sine retningslinjer (SVV Håndbok V220, NVE, 2014, se også Oset mfl. (2014)). Analyser påviste at naturlig skråning har noe lav sikkerhetsfaktor i drenert tilstand og underhydrostatisk poretrykksfordeling. Som en del av følsomhetsanalyse ble det utført en drenert stabilitetsanalyse med hydrostatisk poretrykksforhold. Dette ga en kritisk sikkerhetsfaktor (γ_M) på 1,07. Dette viser at

underhydrostatiske poretrykkforhold i skråningen har bidratt vesentlig til stabilitet av skråningen. Dette viser også viktigheten av å holde poretrykk så lavt som mulig under anleggsfasen. Derfor ble det bestemt å overvåke poretrykk kontinuerlig i anleggsfasen for å ta vare på eventuell poretrykksøkning som kan føre til lavere stabilitet. Grenseverdier for akseptable poretrykkøkninger i anleggsfase ble satt ut ifra drenerte stabilitetsanalyser.

Stabilitetsanalyser er foretatt for å vurdere lokalstabilitet og områdestabilitet i henhold til SVV og NVE sin retningslinjer. For å tilfredsstille kravene i disse retningslinjene ble det nødvendig å utføre tiltak. Disse tiltakene omfatter terrengforbedring med 1,5 m skjæring på toppen av skråningen (terrengsenking), erosjonssikring med sprengstein langs bunnen av skråningen og en midlertidig motfylling (1 m høy) rundt bruakser (i utgravingsfase og under installering av pelene i akse 1 og 2).

En del av stabilitetsvurderingen omfatter vurdering av mulige skredmekanismer. Potensialet for et stort områdeskred er avhengig av blant annet topografiske forhold, jordegenskaper i omrørt tilstand, og muligheten for et initialskred (se f.eks. Bernander (2000), Leroueil (2004), Thakur mfl. (2014)). For at store områdeskred skal oppstå etter et initialskred må imidlertid følgende to kriterier være oppfylt: Sprøbruddmaterialene involvert i bruddet må være fullstendig omrørt, og skredmassene må kunne strømme ut av skredområdet. Derfor er dette prosjekt en «kandidat» for et stort områdeskred. Skråningen er høy (21 m), bratt (en gjennomsnittlig helning på ca. 1:3 mot elva) og består av materialer med omrørt tilstand så lavt som 0,3 kPa. I tillegg ligger skråningen ovenfor ei stor elv som kan «legge til rette» for et eventuelt områdeskred. Derfor er det svært viktig å unngå initialskred som kan føre til fullstendig omrøring av kvikkleire og dermed utløse et områdeskred. I dette prosjektet kan et initialskred mest sannsynlig komme av erosjon eller flom på bunnen av skråningen, eller anleggsaktiviteter. Derfor ble det lagt ut sprengstein langs bunnen av skråninga og ut i elva som sikrings tiltak mot erosjon og flom. Når det gjelder anleggsaktiviteter vil pelearbeidet være mest kritisk siden dette kan potensielt føre til et stort områdeskred. En velkjent hendelse der initiale skred førte til et stort områdeskred er Surte skredet i Sverige (Bernander, 2008). Det finnes også andre områdeskred forårsaket av pelearbeid og store vibrasjoner (Bernander, 2008, Leroueil, 2004). Derfor er det svært viktig å utføre en streng kontroll og oppfølging på pelearbeidet i dette prosjektet.

4 SKAUDALBRUA

4.1 Geotekniske krav og forutsetninger

Brua er prosjektert ut fra noen geotekniske forutsetninger og krav. I prosjekteringsfasen har det vært et tett samarbeid med brukonstruktør slik at brua er dimensjonert med hensyn til aktuelle geotekniske forhold. De viktigste geotekniske begrensningene som måtte tilfredsstilles er oppsummert nedenfor (SVV rapport, 2014).

- Utgraving tilknyttet til brufundamentering må være begrenset til 2,5 m. ved akse 1 for å unngå utgraving i kvikkleire. Det skal heller ikke være utgraving ved akse 2 for ikke å forverre stabiliteten av hele skråningen.
- Fundamentering til brua bør ikke føre til massefortrengning og betydelig poretrykksøkning. Derfor er det valgt å fundamentere brua med borede stålrørspeler og pelene skal etableres ned i berg. Det skal benyttes boresystem som er mest mulig skånsomt for kvikkleire.
- Utførelsen av peler bør ikke kreve, relativt sett, tunge maskiner. Derfor er det valgt pel diameter mindre enn 1 m.

Utformingen av brua og fundamenteringen har hensyntatt de ovennevnte punktene, se Figur 3.

4.2 Fundamentering

Brua fundamenteres på spissbærende borede stålrørspeler. Fundamenteringen omfatter 15 stk. borede stålrørspeler som skal bores minst 1 m i godt berg. Dvs. 2 stk. ∅813×16 mm

peler ved akse 1, 3 stk. ∅914×16 mm peler ved akse 2, 6 stk. ∅813×16 mm peler ved akse 3 og 4 stk. ∅813×16 mm ved akse 4.

5 PLANLEGGING OG UTFØRELSE AV PELEARBEIDET

5.1 Konkurransegrunnlag

I dette prosjektet hadde pelearbeidet ved akse 1 og 2 en svært avgjørende betydning for hele prosjektet. Derfor ble det bestemt å ta med de viktigste geotekniske forhold knyttet til utførelse av pelearbeidet i kontraktsdokumentet. Hensikten var å belyse de aller viktigste punktene slik at det kommer frem tydelig i kontraktsdokumentet for utførende entreprenører. Noen av de viktigste kravene ved utførelse er presentert her.

- Det må benyttes boreutstyr som er mest mulig skånsomt for kvikkleire, dvs. boreutstyr som ikke medfører betydelig poretrykksoppbygging, massefortrenging og omrøring i grunnen. Poretrykksoppbygging skal alltid kontrolleres ved installering av pelene. Ved unormale økninger, utover naturlige svingninger, må arbeidet umiddelbart opphøre, inntil poretrykket har normalisert seg.
- Borearbeidene skal utføres med forsiktighet og tilpasset spyletrykk slik at spylemediene ikke medfører utspyling av masse eller økt poretrykk utenfor peletverrsnittet. Ved boring i bløt- og kvikkleire skal det ikke benyttes luftspyling.
- Under installering av pelene må marktrykk fra boringsutstyr ikke overskride 40 kPa.
- Det kreves utførelse med reversibel boring (RC-metoden).

5.2 Boresystemet

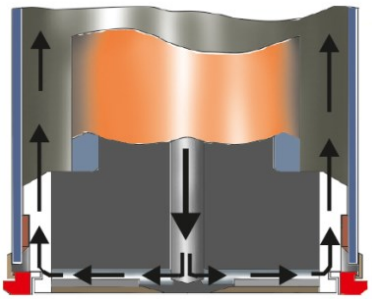
Entreprenøren kom frem med et alternativt og nyutviklet boresystem. Dette ble presentert som et system som tilfredsstiller de geotekniske kravene, dvs. et boresystem som ikke fører til poretrykksoppbygging utover de tillatte verdiene. I tillegg skal boresystemet ikke føre til massefortrengning og fordelt vekt av pelemaskinen overskrider ikke 40 kPa. Prinsippet til boresystemet er beskrevet kort her. Boresystemet hører til rørborings boremetoder, og boreutstyret består av pilotborkrone, ringborkrone og boresko, se Figur 7 og Figur 8.



Figur 7: Pilotkrone.



Figur 8: Pilotkrone med ringborkrone.
(Ringborkrone og boresko er sveiset til stålrøret.)



Figur 9: Skisse over luftkanaler i boresystemet.

Boresko er en forsterkningsring som på den ene enden er sveiset til stålrøret og på den andre enden har ringborkronen festet på. Ringborkronen har litt større diameter enn røret og pilotkronen kobles mekanisk innpå ringborkronen før boring starter.

Ringborkronen og pilotkronen roterer sammen under boring gjennom løsmasser og

inn i berg. Etter at boring er avsluttet blir ringborkronen igjen i grunnen sammen med pelen (derfor er den også kalt for engangskrone). Pilotkronen løses ut og trekkes opp ved venstre rotasjon av borestrengen.

Boresystemet benyttes vanligvis med luft som spylemedium. Det spesielle med dette utstyret er at borekronen er utformet slik at luftstrømmen snus tilbake inn i borestreng og ikke går ut i løsmassen (formasjonen). Lufttrykket for boring kommer gjennom senter på borestrengen og snus 90° radialt i pilotkronen, og returneres sammen med borkaks gjennom åpninger i borkrona ut mot borerøret, se prinsippskisse over luftføringen i Figur 9. Boresystemet tar sikte på en bedre kontroll på retning til lufttrykk under retur.

5.3 Pelearbeid - Plan

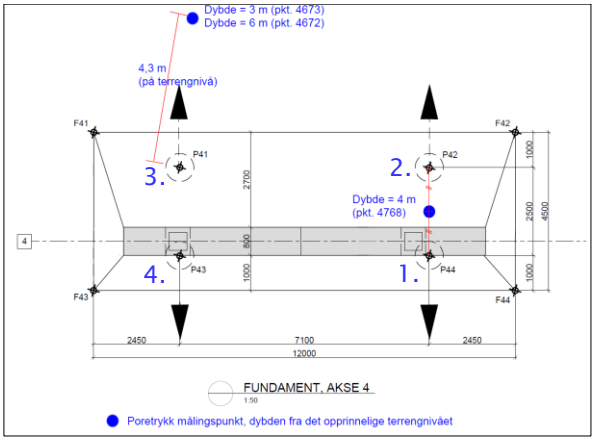
Boresystemet var relativt nytt og uprøvd i kvikkleire. Da er det viktig å kontrollere at systemet fungerer som presentert. For å få erfaring med det nye boresystemet ble det bestemt å starte pelearbeidet i akse 3 og 4, siden det ikke er stabilitetsproblem knyttet til installering av peler ved disse aksene. Akse 3 og 4 ligger på et flatt terreng, mens akse 1 og 2 ligger i en kvikkleireskråning, Figur 3. For å ha god kontroll med konkrete tallverdier ble installering av peler ved akse 3 og 4 kontrollert med rystelsesmålinger og poretrykksmålinger. Disse resultater ble lagt til grunn ved en generell evaluering av boresystemet som var viktig før oppstart boring av peler ved akse 1 og 2.

Ved installering av peler ved akse 3 ble det montert tre rystelsesmåler etter NS 8141-3:2014. Måleren ble plassert med en avstand på ca. 10 m fra senter til pelegruppen ved akse 3. Den maksimale rystelsesmålingen var 27 mm/s, og dette ble målt under boring av steinputen øverst. Hovedkonklusjonen fra dette er at man helst bør unngå boring gjennom steinpute for akse 1 og 2, og at boreutstyret ikke gir betydelige rystelser. Derfor ble det bestemt å fokusere på poretrykksoppbygging som følge av boresystemet. Dette ble gjort i akse 4.

5.4 Plan for poretrykksoppfølging under peling ved akse 4

Ved akse 3 og 4 ligger grunnvannsspeilet 0,5m under terreng, og poretrykksfordelingen er tilnærmet hydrostatisk. Plassering av pelene (P41 til P44) ved akse 4, samt plassering av poretrykksmålere, framgår av Figur 10. Poretrykk ble målt i to punkter og på tre ulike dybder. Poretrykkmåler 4768 ligger midt mellom P44 og P42 som har senter til senter avstand på 3,8 m ved 4 m dybde. Poretrykkmålere 4673 og 4672 ligger 4,3 m fra pelesenter til P41. Avstanden er målt på terrengnivået. Dybdene til målerne er 3 m og 6 m.

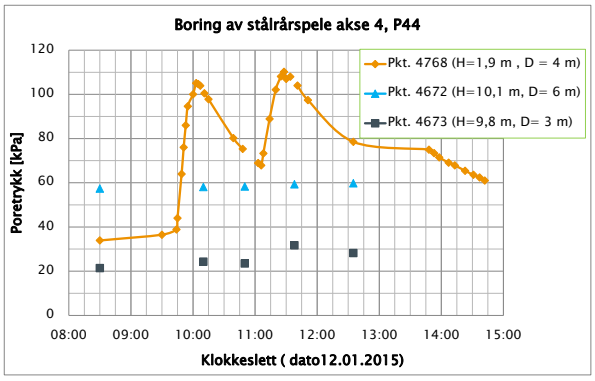
Rekkefølgen for installering av pelene ved akse 4 er P44, P42, P41 og P43. Boringene ble utført den 12.01.15 (P44 og P42) og 13.01.15 (P41 og P43).



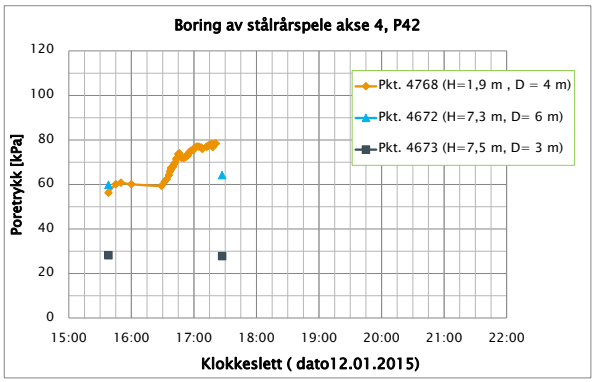
Figur 10: Fundamentering ved akse 4 og plassering av pelene og poretrykksmålerne.

5.5 Poretrykksmålinger under peling ved akse 4

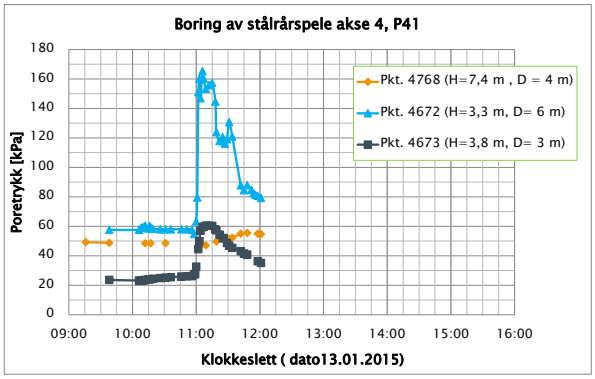
Poretrykk ble målt under installering av tre peler, dvs. P44, P42 og P41 se planen med installeringsrekkefølge (1. til 4. pel) i Figur 10. Disse målingene er gitt i Figur 11 – 13. På figurene er *D* avlesningsdybden fra terrengnivå; og *H* er en horisontal avstand fra pelesenter til måleren målt på et nivå som tilsvarer aktuell målingsdybde. Målingene ble utført av byggherren (Statens vegvesen (SVV)).



Figur 11: Poretrykksmålinger under boring av stålrørspel P44.



Figur 12: Poretrykksmålinger under boring av stålrørspel P42.



Figur 13: Poretrykksmålinger under boring av stålrørspel P41.

5.6 Erfaring og observasjon etter boring ved akse 4

Målingene påviste at boringen med dette systemet ga betydelige poretrykksøkninger. Hovedobservasjoner og erfaringer etter boring ved akse 4 er oppsummert her.

- Maksimale poretrykksøkninger under installering av pel P44, P42 og P41 er henholdsvis 70 kPa (Figur 11), 20 kPa (Figur 12) og 100 kPa (Figur 13). En økning på 70 kPa og 100 kPa er langt over det som kan aksepteres for akse 1 og 2.

- Under boring av P44 og P41 kom ikke mesteparten av tilført luft tilbake innvendig i borerørene og dette førte til en ganske høy poretrykksøkning, dvs. 70 kPa og 100kPa. Under boring P41 (kl. 11:02, Figur 13) kom det luft på utsiden av pelen og nabopelene P44 og P42. Dette skyldes nok blokkering av borekronen.

- Boring av P42 gikk greit i forhold til de andre (det kunne ses at en viss luftmengde kommer opp fortløpende innvendig i røret). Likevel førte dette til poretrykksøkning på 20 kPa. Da er spørsmål hvor mye av luften som egentlig kommer tilbake gjennom røret i forhold til det som brukes.

- Volum jordmasser som kom opp under boring gjennom løsmasser ser betydelige mindre ut enn forventet. Dette indikerte at boringen også fører til massefortrengning. Det så ut til å skyldes at det i borkronen, og langs borstrengen, ble tettet igjen av leire. Dermed kom ikke luften og massene i retur opp pelen, men ut i massene rundt pelen. Om dette skulle forekomme i akse 1 og 2 så ville det være svært kritisk.

Boresystemet ble først og fremst valgt for å unngå betydelige poretrykksoppbygginger og massefortregninger. Erfaring fra akse 4 viste at dette ikke var oppfylt. Det kommer tydelig frem at boringen ikke kan utføres slik som det ble gjort i akse 4 på grunn av at det i akse 1 og 2 er satt strengere krav til tillatte poretrykksoppbygginger. Derfor ble det besluttet at entreprenøren måtte modifisere bruken av systemet for å tilpasse det til kravene ved akse 1 og 2, eller benytte et annet boresystem. Byggherren krevde at det ble benyttet mest mulig vann (spyleboring) og ikke luft i kvikkleiren.

Entreprenøren valgte å gjøre tiltak slik at boresystemet fortsatt kunne benyttes for akse 1 og akse 2. Byggherren krevde et skriftlig tiltak fra entreprenøren. De endelige foreslåtte boretiltakene for boring i akse 1 og 2 var:

- Boringen skjer med kontrollert mating i forhold til løsgjøring av leiren.
- Må påse at det er sirkulasjon gjennom hammeren hele tiden.
- Overvåkning av poretrykk må følges kontinuerlig. Ved stoppordre må det stoppes og stenges omgående.
- Når boringene kommer ned til fastere masser kan lufttrykket og vannet økes igjen. Kompressorskifte.
- Ved innboring i berg må maksimalt trykk og mengder brukes.
- Bore med kortere rørseksjoner på ca. 6 m

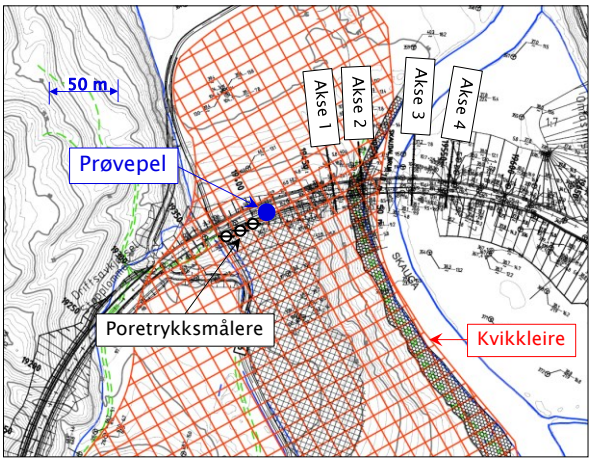
Tilleggsutstyr som entreprenøren skaffet seg var mindre kompressor, regulator for å redusere lufttrykk, vannmåler for å se vannsirkulasjonen, stengekraner for luft og vann, vannpumpe med mer trykk og 2 stk. vanntanker på ca. 2000-3000 liter.

Byggherren krevde at entreprenøren beviste at de foreslåtte tiltakene ga den ønskede effekten ved å utføre en prøvepeling. Byggherren skulle da velge et sted for prøvepelingen (i kvikkleire) og følge opp arbeidet med poretrykksmålinger mens boringen ble gjennomført med de nevnte tiltakene.

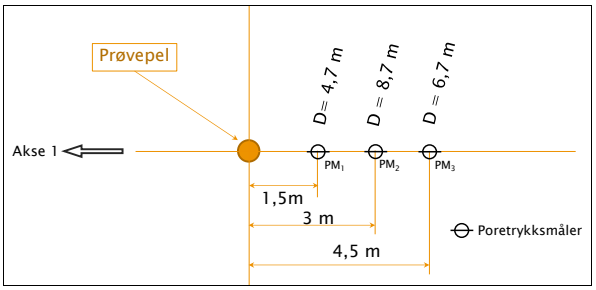
5.7 Prøvepeling

Prøvepelingen (∅813×16 mm pele) ble forsøkt å utføre under forhold tilnærmet forholdene ved akse 1. Derfor ble det valgt å utføre prøvepelingen lengre bak i området der grunnforholdene er sammenlignbare med forholdene i akse 1, og samtidig der det ikke er kritisk i forhold til stabiliteten av skråningen. Med hensyn på disse betraktningene ble det valgt å utføre prøvepelingen ved borepunkt 102 (Figur 4) som ligger 50 m bak akse 1 og der det allerede var god kunnskap om grunn- og poretrykksforhold (Figur 14).

Det ble montert tre poretrykksmålere ved tre ulike dybder og avstander fra pelen. Plasseringen til målerne ble bestemt med tanke på de kritiske punkter som skulle kontrolleres ved akse 1. Etterpå ble det boret en vertikal stålrørspel med de forslåtte tiltakene. Boring startet med et rør på 4 m. lengde og senere ble det sveiset på et 6 m. langt rør. Oversikt over plassering av poretrykksmålerne i forhold til prøvepelen framgår av Figur 15.



Figur 14: Oversikt over plassering av prøvepelen og poretrykksmålere i forhold til brua.



Figur 15: Plassering av poretrykksmålere i forhold til prøvepelen (D er dybden fra det opprinnelige terrengnivået).

Maksimale poretrykksøkninger (Δu_{maks}) som ble målt med poretrykksmålerne PM_1, PM_2 og PM_3 er henholdsvis 9 kPa (fra 17,7 kPa til 26,3 kPa), 1 kPa og 1 kPa. *D* er dybden fra det opprinnelige terrengnivået (kote +50,04 m.o.h.). På måleren som lå 1,5 m fra pelesentret ble det målt en økning på 9 kPa og det var nesten ingen økning på de målerne som lå 3 m og 4,5 m fra pelen.

5.8 Erfaringer fra prøvepelingen

Under prøvepelingen ble det boret et rør på 10 m. lengde (4 m + 6 m). Det ble forsøkt flere tiltak under prøvepelingen for å finne en skånsom måte å bore på. F.eks. bruk av bare vann for boring, bruk av skum som «smøremiddel» under pelingen, å vibrere ned pelen, forsiktig banking fra toppen av røret osv. Det var noen utfordringer slik som at vannet fryser og at øvre leirelag kleber seg på borestrengen. Leiren var så seig at det var vanskelig å fjerne den ved hakking.

Boringen ble startet på terrengnivået etter en lokal utgraving av steinlaget for å unngå boring gjennom steinlaget.

Hovederfaringen fra prøvepelingen var at poretrykksøkningene var innenfor de tillate grenseverdiene for akse 1, og tiltakene så ut til å forbedre boremetoden som helhet. Derfor ble det konkludert at prøvepelingen var vellykket. Fremgangsmåten som fungerte best i forhold til de geotekniske kravene er:

- Start boring på opprinnelig grunn/terreng for å unngå boring gjennom steinlaget (fjerning av steinlaget før oppstart).
- Slag med hammeren skal helst ikke brukes i løsmasser, og må ikke benyttes i det hele tatt ved start av boringen. Dette er viktig siden kvikkleire ligger bare 1 m under terrenget ved akse 1. At slag med hammeren ikke er tilatt kan føre til at det blir en utfordring med styring av røret.
- Boringen skal utføres som en spyleboring med vann samtidig med rotasjon av borkronen. Dette for å løse opp massen.
- Deretter løfte borkronen opp og blåse luft inn i røret. Dette er for å få massene/vannet opp (ut av røret). Dette begrenset lengden på røret. Derfor ble det bestemt å bore med et rør på maks 6 m lengde per omgang og skjøte/sveise etterpå.
- Manuell kontroll på luft- og vanntrykksmengder under boring skal utføres avhengig av fremdriften.

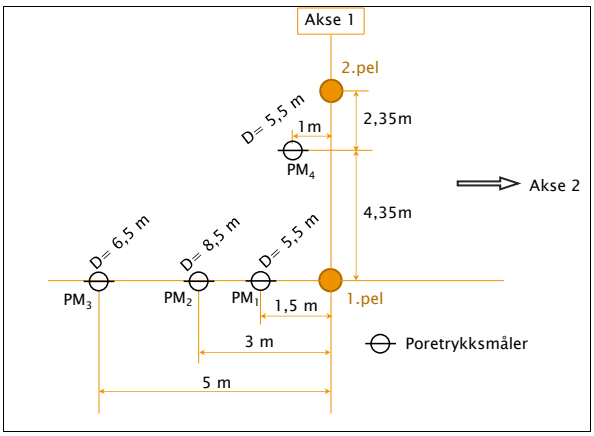
Prøvepelingen påviste tydelig at å utføre boringen i henhold til de geotekniske kravene tar tid. Dette indikerte også at boringene i akse 3 og 4 gikk for fort. Dvs. matehastigheten benyttet under boringen var for stor, og medførte dermed uakseptable poretrykksøkninger og massefortrengning. Generelt er boring en noe tidkrevende prosess. I dette prosjektet ble det enda mer tidkrevende. Bruk av boresystemet som en spyleboring, med fremgangsmåten som beskrevet ovenfor, viste seg å være tungvint og tidkrevende med det utstyret entreprenøren hadde tilgjengelig.

5.9 Peling ved akse 1 og akse 2

5.9.1 Forberedelse og poretrykksoppfølging

Før peling ved akse 1 ble det lagt ut et steinlag på 0,7 m tykkelse (over geotekstil) på oppstillingsplassen, for å etablere et godt fundament til peleriggen. På punkter der pelene skulle bores ble det ikke lagt ut stein. Under pelingen ved akse 1 ble installeringen fulgt opp med poretrykksmålere og plassering av disse målerne i forhold til pelene er gitt i Figur 16. *D* er dybde målt fra det opprinnelige terrenget som var 2,5 m høyere enn hvor boringen startet (dvs. det var 2,5 m avlasting ved akse 1).

Det ble montert fire poretrykksmålere ved akse 1, de første tre målerne (PM_1, PM_2 og PM_3) ble plassert med fokus på å kontrollere installeringen av 1. pel. Disse målerne er plassert for å måle poretrykk på tre ulike dybder fra terreng, og tre ulike horisontale avstander fra pelen. For å ha kontroll på installering av 2. pel ble det montert ytterligere en måler (PM_4) på en kritisk dybde. Dybde til PM_1 og PM_4 representerer midt punktet av den øverste delen av skråningen som ikke får sidestøtte av den midlertidige motfyllingen.



Figur 16: Plassering av poretrykksmålere i forhold til de to pelene ved akse 1.

5.9.2 Peling ved akse 1

Peling ved akse 1 (1. pel) ble utført med røret som ble trukket opp fra prøvepelingen som var 10 m langt. Ved denne installeringen ble det målt Δu_{maks} = 18 kPa ved PM_1 allerede ved liten boringsdybde (ca. 1,5 m). Det så ut som boringen ikke fungerte på grunn av vanskeligheter med å bore ned og få massene opp. Det var også utfordring med styring av røret. Da ble arbeidet avbrutt og røret ble trukket opp for inspeksjon av borkronen. Dette indikerte at åpningene ved pilotkronen var blokkert og vannet i hammeren var frosset. Rommet bak borkronen var fylt opp med ganske faste masser som trengte slag for å løse opp massene. Dette synes å ha ført til massefortrengning og poretrykksøkning.
Etter et kort møte ble det besluttet å redusere lengden på pel til 6 m, og etablere kumringer pga. at det ble en utfordring å holde styringen på røret korrekt med så kort pelelengde.

Boringen startet igjen etter 5 dager (dette på grunn av friperiode hos entreprenørene). Boringen startet med 6 m langt rør gjennom kumringen som ble satt opp for å styre røret. Forsiktig hamring/pressing i toppen av røret ble også benyttet noe i akse 1 slik som det ble gjort ved prøvepelingen. Under installeringen ble det målt Δu_{maks} = 28 kPa (fra 19 kPa til 47 kPa) ved PM_1, 2,5 m fra terrenget (dvs. 2,5 + 0,7 m = 3,2 m fra nivå maskinen sto på). Dette var målt to timer etter at boringen startet, og ved dette tidspunkt ble boringen avbrutt på grunn av poretrykks økningen. Det ble bestemt å stoppe arbeidet midlertidig fram til poretrykket hadde sunket. Røret ble trukket opp og maskinen beltet tilbake til en tryggere plassering bak akse 1. Etter 5 timer gikk poretrykket ned til 35 kPa (fra 47 kPa) og boringen startet igjen, Figur 17. Deretter ble det målt minimale økninger, dvs. Δu_{maks} = 3 kPa, 7 kPa og 5 kPa henholdsvis på PM_1, PM_2 og PM_3. Under installering av 2. pel ble det målt Δu_{maks} = 15 kPa (fra 18 kPa til 33 kPa). Ferdig installert pel var 22 m lang med 1 m boring i godt fjell. Det tok ca. 2 dager per pel. Dette inkluderer blant annet tid for utlegging av stokkmatten, oppstilling av riggen, 3 sveisinger og selve boringen.

5.9.3 Peling ved Akse 2

Før pelingen startet ved akse 2 ble det gjort en del forberedende arbeid. Steinpute brukt for installering av pelene ved akse 1 ble fjernet for å øke stabiliteten av skråningen. Deretter ble den midlertidige motfyllingen justert for å muliggjøre pelingsarbeidene, Figur 18. På boringspunktene ble steinlaget fra den midlertidige motfyllingen og den gamle erosjonssikringen gravd vekk og skiftet ut med leire. Utførelse av boring ble utført hovedsakelig på samme måte som akse 1 og dette gikk greit. Det var ikke poretrykksmåler spesielt montert med tanke på å følge opp peleinstalleringene ved akse 2, men de to poretrykksmålerne som var installert mellom akse 1 og 2 i forbindelse med kontroll av stabiliteten til skråningen ble benyttet. Disse viste svært minimale poretrykksøkninger. Installeringen gikk raskere enn akse 1, og tok gjennomsnittlig ca. 1 dag per pel.



Figur 17: Boring av 1. pel ved akse 1.



Figur 18: Boring ved akse 2 etter installering av to peler ved akse 1.



Figur 19: Ferdig installerte peler ved alle akser (I tillegg viser bilder terrengavlastingen, erosjonssikringen og midlertidig motfylling).

6 KONKLUSJONER/LÆREPUNKTER

Flere forhold ved prosjektet har vært både svært interessante og lærerike. Det skal skrives en erfaringsrapport som tar for seg flere aspekter av prosjektet og med mer detaljer. Hovedkonklusjoner og lærepunkter er oppsummert nedenfor:

- I prinsipp skal borede stålrørspeler være skånsomme i forhold til massefortrengning og poretrykksendringer. Likevel kan dette være annerledes i praksis avhengig av boresystemet/boreutstyret og prosedyrene ved selve utførelsen. Det er viktig å være klar over dette i prosjekteringsfasen og ta høyde for eventuelle avvik fra god praksis. Dersom risikoen i prosjektet vurderes som uakseptabel kan det være aktuelt å vurdere annen peletype.

- I kritiske tilfeller, slik som dette prosjektet der det er viktig å unngå poretrykksendring og massefortrengning, må det benyttes spyleboring med vann og helst ikke luft i løsmassene. Likevel kan man skifte over til boring med luft i berg, og når man er trygg på at det er fast masser. Ved bruk av luft i faste masser må risikoen for at luft går ut i løsmassene vurderes, samt konsekvensene av dette. Spesielt overgangen til faste masser og bruk av luft kan i denne sammenheng være kritisk.

- Det er svært avgjørende at peleentreprenøren har erfaring med boresystem, har erfarne borere og boreledere, samt har god prosedyre for utførelsen.

- Det er meget viktig at man er klar over at boring er en tidkrevende prosess. Matehastigheten under boringen skal primært tilpasses med hensyn på kvalitet (f.eks. geotekniske krav, grunnforhold osv.).

- Hovedkonklusjonen er at boresystemet kan være bra i sensitiv grunn, og at de vansker som oppstod i prosjektet i hovedsak har sammenheng med operatørmessige mangler.

7 REFERANSER

Bernander, S. (2000). Progressive Landslides in Long Natural Slopes. Formation, potential extension and configuration of finished slides in strain-softening soil. Lic. Thesis: Luleå University of Technology.

Bernander, S. (2008). Down-hill Progressive Landslides in Soft Clays. Triggering Disturbance Agents. Slide Propagation over Horizontal or Gently Sloping Ground. Sensitivity Related to Geometry. Luleå: Luleå University of Technology.

Leroueil, S. (2004). Geotechnics of slopes before failure. Landslides: Evaluation and stabilization. Proc. 9th int. symposium on landslides, Rio de Janeiro. Vol 1. Side 863 -884.

NVE (2014): Sikkerhet mot kvikkleireskred. Vurdering av områdestabilitet ved arealplanlegging og utbygging i områder med kvikkleire og andre jordarter med sprøbruddegenskaper. Noregs vassdrags- og energidirektorat. Veileder nr 7-2014. ISSN 1501-0678.

SVV Håndbok (2010): Geoteknikk i vegbygging. Statens vegvesen (SVV)Håndbok V220 (gml. nr. 016).

SVV rapport (2013a): Fv. 715 Keiserås - Olsøy, Parsell: Leksvik grense – Olsøy. Geoteknisk Datarapport (14.05.2013). SVV, Region midt. Sveis Nr. 2012039995-009 /Ud925Ar09.

SVV rapport (2013b): Fv. 715 Keiserås - Olsøy, Parsell: Leksvik grense – Olsøy. Geoteknisk vurderingsrapport (14.08.2013). SVV, Region midt. Sveis Nr. 2012039995-010 /Ud925Ar10.

SVV rapport (2014): Fv. 715 Keiserås - Olsøy, Parsell: Leksvik grense – Olsøy. Geoteknisk vurderingsrapport for Skaudalbrua (30.04.2014). SVV, Region midt. Sveis Nr. 2012039995-013 /Ud925Ar13.

Oset, F., Thakur V., Dolva, B. K., Aunaas K., Sæter, M. B., Robsrud A., Viklund M., Nyheim T., Lyche, E. & Jensen O. A. (2014). Regulatory Framework for Road and Railway Construction on the Sensitive Clays of Norway. Chapter 27, Landslides in Sensitive Clays. Adv. Natural & Techn. Haz. Res., vol. 36, pp. 343-355, Springer.

Thakur, V., Degago, S. A., Oset, F., Aabøe, R., Dolva, B. K., Aunaas, K., Nyheim, T., Lyche, E., Jensen, O.A., Sæter, M.B., Robsrud, A., Viklund, M. & Nigussie, D. (2014): Characterisation of post-failure movements of landslides in soft sensitive clays. Chapter 8, Landslides in Sensitive Clays. Adv. Natural & Techn. Haz. Res., vol. 36, pp. 91-103, Springer.

Dynamic stiffness of horizontally vibrating suction caissons

C. Latini
Civil Engineering Department, Technical University of Denmark, Lyngby, Denmark, chila@byg.dtu.dk

V. Zania
Civil Engineering Department, Technical University of Denmark, Lyngby, Denmark,

M. Cisternino
Civil Engineering Department, Technical University of Denmark, Lyngby, Denmark,

ABSTRACT
The promising potential for offshore wind market is on developing wind farms in deeper waters with bigger turbines. In deeper waters the design foundation configuration may consist of jacket structures supported by floating piles or by suction caissons. Taking the soil-structure interaction effects into consideration requires the prior estimation of the dynamic impedances of the foundation. Even though numerous studies exist for piles, only limited number of publications can be found for suction caissons subjected to dynamic loads. Therefore, the purpose of this study is to examine the dynamic response of this type of foundation using the finite element method (FEM) to account for the interaction with the soil. 3D numerical models for both the soil and the suction caisson are formulated in a frequency domain. The response of the soil surrounding the foundation is considered linear viscoelastic with hysteretic type damping. In addition, non-reflective boundaries are included in the model. Two different soil profiles are presented, one when the rigid bedrock is set close to the seabed and the other one when it is far away.
The dynamic impedances at the top of the foundation are determined and compared to existing analytical solutions suggested for piles. Relatively good agreement has been achieved comparing the numerical results with the analytical solutions. Then, the effect of the soil layer shear wave velocity on the dynamic stiffness coefficients is analysed. The results have indicated that increasing the stiffness of the soil stratum the dynamic impedances grow, while the damping reduces in the frequency range investigated.

Keywords: soil-structure interaction, dynamic stiffness, damping, suction caissons, numerical modelling

1 INTRODUCTION

The offshore wind market is progressing by developing wind turbines with larger rotors and higher capacity generators, in order to deploy deep offshore designs. It is fundamental to assess the resonance frequencies of the wind turbine structure accurately in order to avoid the first resonance frequency of the wind turbines coinciding to the excitation frequencies of the rotor system as delineated in DNV-OS-J101 (2004). In addition, the effect of the soil-foundation-structure interaction should be included in the estimation of the natural vibration characteristics of the OWTs as indicated by several studies (Adhikari and Bhattacharya, 2012; Alexander and Bhattacharya, 2011; Zania, 2014). The majority of installed or operating turbines are supported on fixed foundation system (Bhattacharya, 2014), while deep installations require jackets structures with

floating piles or with suction caissons. In the past, suction caissons have been deployed as anchors or as foundations for offshore platforms. According to Houlsby et al. (2005), suction caissons can be adopted as offshore wind turbine foundations embedded in suitable soil conditions and especially for deeper waters installation, of water depth of approximately up to 40m.

Suction caissons differ from other foundation types such as piles, regarding the installation procedure applied offshore and the geometric properties including the rigid cap and the lateral flexibility (with slenderness ratio lower than 4). Contrary to offshore pile driving, heavy duty equipment is not required in the process of suction caisson installation, which is materialized by using self-weight and suction as the driving forces (Byrne and Houlsby, 2006). This becomes a considerable advantage in the case of deep water installations.

In the literature the problem of the dynamic soil-pile interaction has been extensively investigated. Considering only the studies for linear elastic soil layer, they can be briefly categorized into analytical solutions (Novak and Nogami, 1977; Mylonakis, 2001; Nozoe et al., 1985; Latini et al., 2015) and numerical finite element solutions (Velez et al., 1983; Gazetas, 1984). On the other hand, the dynamic response of suction caissons received less attention (Liingaard, 2006). In the work of Liingaard (2006) the dynamic stiffness coefficients were determined, considering linear viscoelastic soil and modelling the suction caisson using a coupled BE/FE model in homogeneous halfspace comparing the obtained results with analytical solutions for surface foundations.

The purpose of the current study is to investigate the dynamic response of suction caissons for the estimation of the dynamic stiffness and damping coefficients with respect to the frequency. Therefore, 3D FE models were developed and the dynamic impedances to lateral loading were estimated. The results of the numerical models have been compared respectively with the rigorous analytical solution of soil-end bearing pile vibration by Novak et al. (1977) and the analytical solution proposed for floating piles by Latini et al. (2015). The effect of the stiffness of the soil on the soil-caisson system response is further discussed.

2 METHODOLOGY

3D finite element models have been developed to investigate the dynamic impedances of the suction caisson in the commercial software ABAQUS (Simulia, 2013). The numerical models account for the following hypotheses: 1) linear elastic isotropic behaviour of the suction caisson; 2) linear viscoelastic isotropic behaviour of soil with hysteretic type damping and 3) perfect contact between the foundation and the soil during the analysis.

Due to the symmetry of the problem, only half of the foundation and the surrounding soil are taken into account. The suction caisson consists of steel with diameter d=5m, skirt length H=10m, Young's modulus E_p = 210 GPa and Poisson's ratio ν=0.35. The foundation skirt and the cap of the caisson have respectively thickness of t_{skirt}=d/100 and t_{cap}=5t_{skirt}.

Three different suction caisson modelling approaches are presented: 1) shell pile, where the foundation is modelled by shell; 2) caisson with cap; and 3) equivalent solid pile, for which equivalent material properties are applied to match the bending stiffness.

The soil surrounding the foundation has hysteretic type damping of ζ=5.0% and constant profile of shear wave velocity V_s=250-400m/s. Hexahedral elements are used to discretize the soil domain of diameter 24d and height H_s=6d=30m. Infinite elements are placed at the boundaries in order to model the far field soil and avoid spurious reflection. The soil and the foundation skirt and the caisson cap are tied together in order to satisfy the displacement compatibility.

Steady state linearized response of the model subject to harmonic excitation in the frequency domain is performed. The dynamic impedances K_{su}, $K_{s\theta}$, K_{mu} and $K_{m\theta}$ at the level of the pile head are then calculated as shear forces, S, and moments, M, when the head of the suction caisson is subjected to unit displacement, u, and rotation, θ. The mesh size needs to be small enough to capture the

stress wave accurately. A mesh size of at least 10 to 20 elements per wave length is assumed a good approximation for the frequency range of interest, including up to the third eigenfrequency of the soil layer $\alpha_0=5/2\pi$. Note that α_0 is a dimensionless frequency related to the eigenfrequency of the soil layer, since it is given as the product of the wave number and the height of the soil layer:

$$\alpha_0 = \frac{\omega H_s}{V_s} \quad (1)$$

where ω(rad), H_s(m) and V_s(m/s) are respectively the circular frequency, the height and the shear wave velocity of the soil layer.
A view of the model with the mesh refinement is shown in Figure 1.

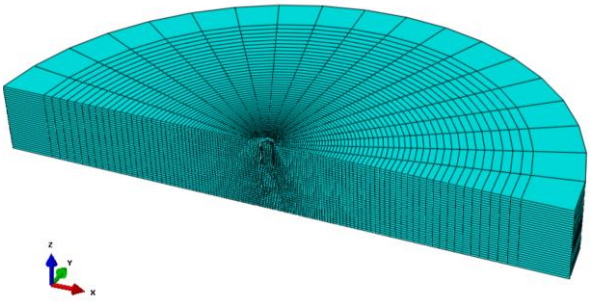


Figure 1 Finite element model of the suction caisson and the surrounding soil.

3 NUMERICAL RESULTS

Two layered soil profile characterized by high stiffness contrast is analyzed. Then, 3D numerical models are developed considering different depths of the surface soil layer with respect to the length of the skirt of the caisson, see Figure 2. In the study the soil profile with height equal to the caisson skirt length is defined as profile 1, while the one with increased height as profile 2.
The results for profile 1 and profile 2 are compared respectively with the rigorous continuum analytical solution formulated for end bearing piles by Novak et al. (1977) and that for floating piles by Latini et al. (2015). The different suction caisson modelling procedures with shell elements and continuum elements are implemented in order to achieve a direct comparison with the analytical solutions. The effect of the stiffness of the soil on the soil-caisson system response is further discussed, by considering stiffer soil formation.

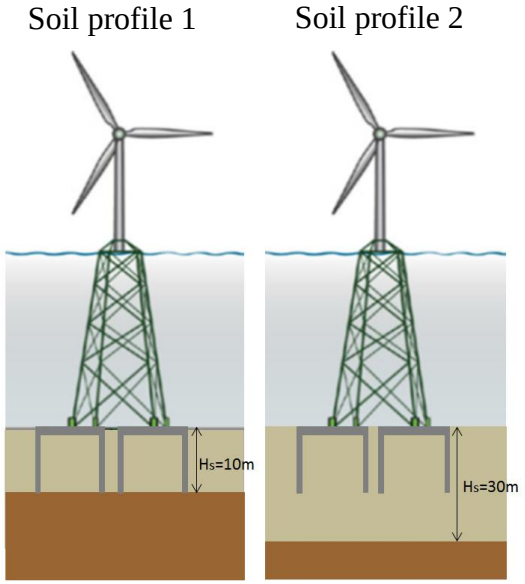


Figure 2 Illustration of the two soil profiles investigated in this study.

The dynamic component (real part of the complex valued stiffness terms divided by the corresponding static component K^0 and imaginary part of the complex valued stiffness terms divided by the corresponding dynamic component K_{xx}) of the three stiffness terms is presented with respect to the non-dimensional frequency α_0.
First the static stiffness coefficients of the different modelling approaches are calculated and presented in Table 1 for the soil profile 1, along with the corresponding ones obtained from the analytical solution.

Table 1 Static suction caisson stiffness obtained from the numerical models and the analytical solution of Novak et al. (1977) for profile 1.

	Ksu [kN]	**Ksθ [kN]**	**Kmθ [kNm]**
Caisson	4.656E+6	-1.223E+7	1.120E+8
Shell pile	5.010E+6	-1.410E+7	1.325E+8
Solid eq. pile	7.109E+6	-2.384E+7	1.731E+8
Novak et al. (1977)	8.845E+6	-3.441E+7	2.148E+8

The stiffness components of the caisson model slightly differ from those of the shell pile, while the difference is more significant with the solid equivalent pile regarding all

the components. In addition, it is observed that the results obtained from the numerical models are overestimated by the analytical solution, particularly regarding the translational and the cross coupling terms.
In Figures 3, 4 and 5, the real (K_{su}, $K_{s\theta}$, and $K_{m\theta}$) and the imaginary ($2\zeta_{su}$, $2\zeta_{s\theta}$, and $2\zeta_{m\theta}$) part of the dynamic impedances are shown. A common trend for all the stiffness components is the observed drop of stiffness at the 1st eigenfrequency of the soil layer ($\alpha_0=1/2\pi$). A change in the pattern slope is attained around the first vertical resonance $\alpha_0=1/2\pi\eta$, where $\eta = \sqrt{\frac{2(1-\nu)}{1-2\nu}}$, which is mainly observed for the translational and rocking component; whereas the cross coupling coefficient is characterized by an increase of stiffness at the same normalized frequency.

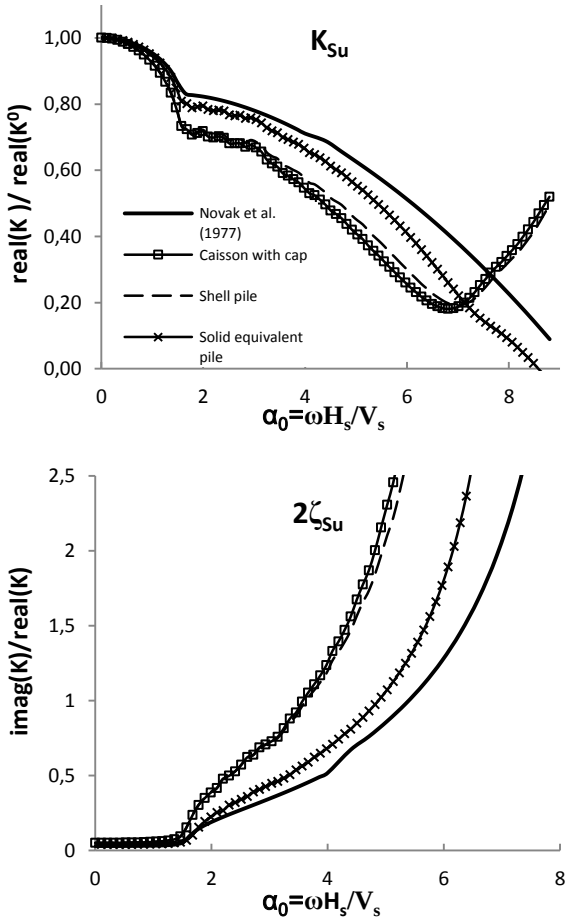


Figure 3 Variation of the translational stiffness and damping coefficients with respect to the dimensionless frequency for profile 1.

The intermediate frequency interval ($\alpha_0=1/2\pi\eta$-6) is characterized by a linearly decrease of the dynamic stiffness consistent for all the components.

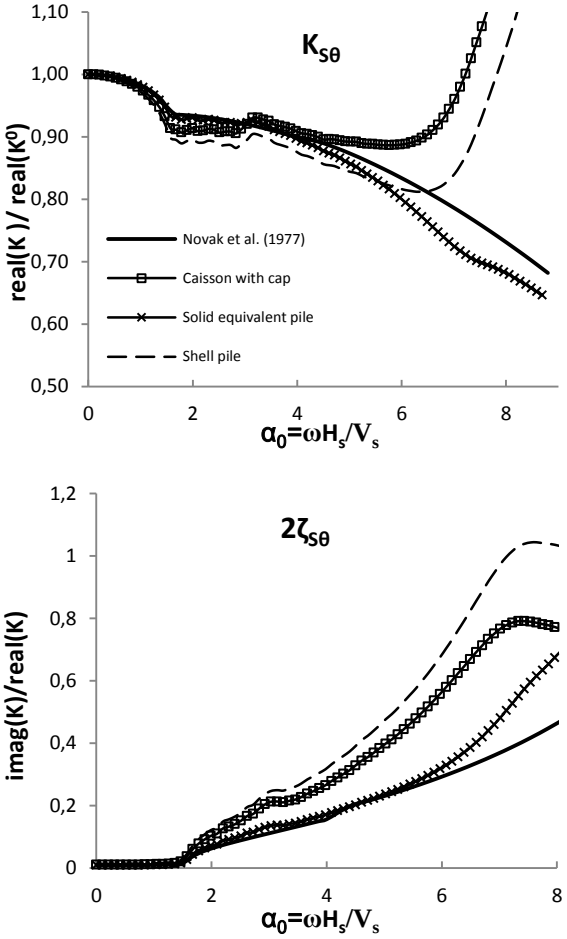


Figure 4 Variation of the coupling stiffness and damping coefficients with respect to the dimensionless frequency for profile 1.

On the contrary, in the high frequency range the solid equivalent pile shows a softer behavior with monotonically decreasing pattern with respect to the other two models for all the components. This trend resembles the one suggested by the analytical solution, although the latter is not able to capture the 1st vertical resonance.

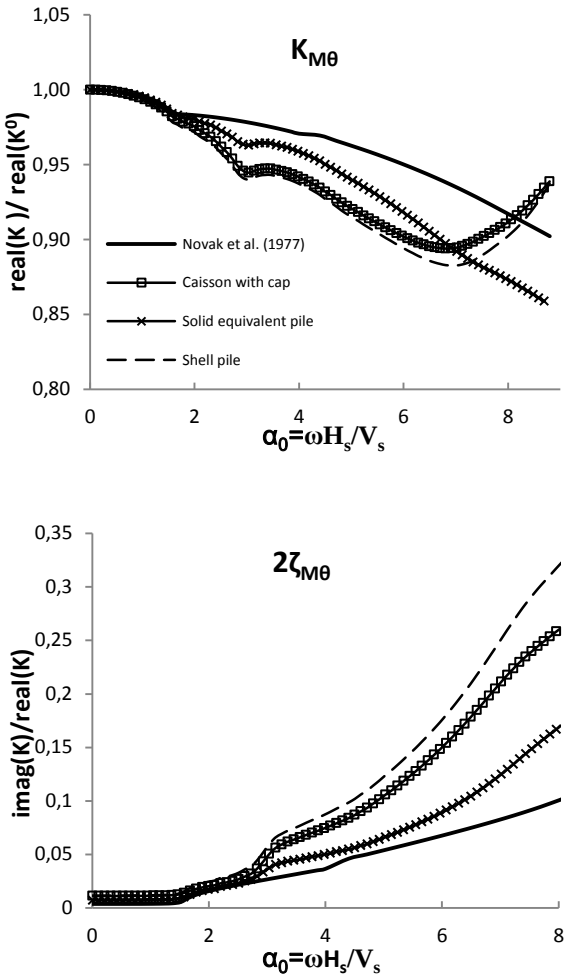


Figure 5 Variation of the rocking stiffness and damping coefficients with respect to the dimensionless frequency for profile 1

On the other hand the caisson and the shell pile model exhibit an exponential increase at the higher frequency range α_0=6.5-7. This is possibly attributed to the presence of a surface wave (Rayleigh wave). Indeed, the displacement contour plot at this frequency (Figure 6) shows that the soil within the foundation and surrounding it experiences a surface wave with wave length almost equal to the diameter of the caisson and displays the occurrence of the Rayleigh wave through the s-pattern on the soil surface propagating radially from the caisson.

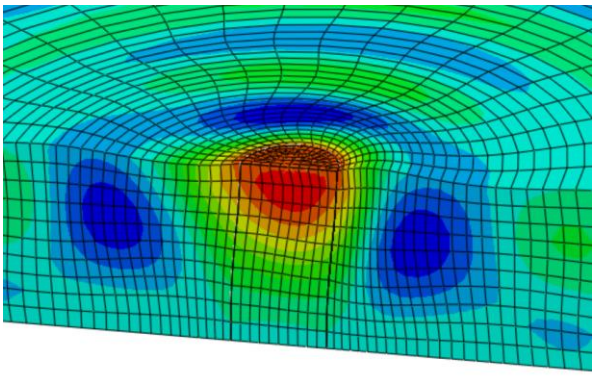


Figure 6 Displacement contour plot illustrating the presence of Rayleigh wave in the soil within the caisson.

The imaginary part of the dynamic component of the dynamic impedances, is associated with the generated damping due to soil-caisson interaction. The radiation damping is generated for frequencies higher than the first eigenfrequency of the soil layer for all the components, and this is demonstrated by the increasing values of the coefficients with frequency (Figure 3,4, and 5). In the case of a linear increase viscous type damping is generated. This type of behavior is observed over the intermediate frequency range (α_0=2-4). A slight change in the slope of the damping is also marked after each eigenfrequency of the soil layer.

Moreover, it might be concluded that the presence of the cap does not affect the dynamic response of the soil-caisson system for the translation and rocking component, since the dynamic response of the shell pile and the caisson match almost perfectly. On the other hand a significant effect is noticed on the coupling stiffness term after the 1st vertical resonance for both stiffness and damping coefficients. The analytical solution is overestimating the dynamic stiffness and underestimating the damping for all the components, however it is in relatively good agreement with the equivalent solid pile. This indicates that the inner soil affects the dynamic response of the caisson, by allowing wave propagation of smaller wave lengths.

The second soil profile describes a deep soil formation. For this case the response of the shell pile is not reported in the graphs, since it matches with the caisson case.

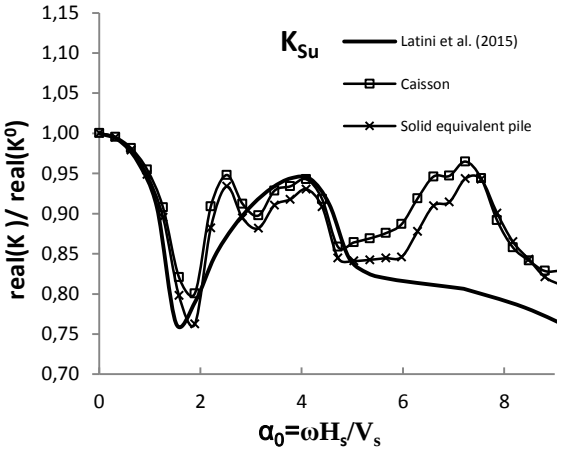
First the static stiffness coefficients were estimated and the results are presented in Table 2.

Table 2 Static suction caisson stiffness obtained from the numerical models and the analytical solution of Latini et al. (2015) for Profile 2.

	Ksu [kN]	Ksθ [kN]	Kmθ [kNm]
Caisson	3.220E+6	-9.237E+6	9.608E+7
Solid eq. pile	3.833E+6	-1.279E+7	1.191E+8
Latini et al. (2015)	4.288E+6	-1.529E+7	1.339E+8

The static stiffness coefficients of the solid equivalent pile are slight higher than those of the caisson model. The analytical solution suggests similar values to those obtained from the numerical models.

In Figures 7, 8 and 9, the real (K_{su}, $K_{s\theta}$, and $K_{m\theta}$) and the imaginary ($2\zeta_{su}$, $2\zeta_{s\theta}$, and $2\zeta_{m\theta}$) parts of the dynamic impedances are presented. A decrease of stiffness is marked after the 1st and 2nd horizontal eigenfrequencies ($\pi/2$ and $3\pi/2$ respectively) and the 1st vertical eigenfrequency of the soil layer for the translational stiffness component.



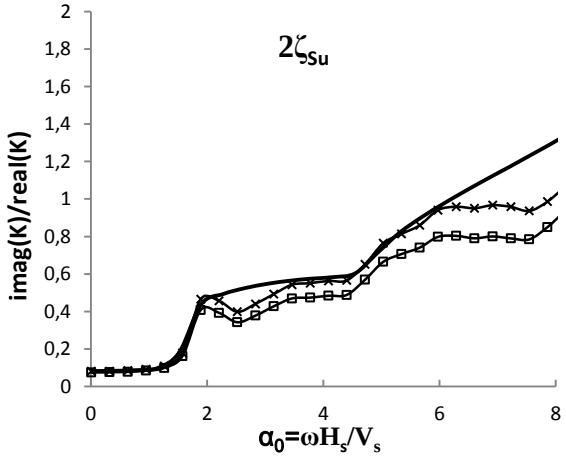
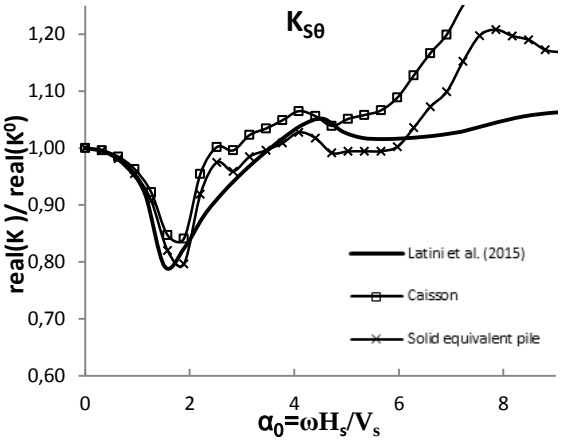


Figure 7 Variation of the translational stiffness and damping coefficients with respect to the dimensionless frequency for profile 2.

While, it seems that the coupling and the rocking stiffness terms are less sensitive to the 1st vertical resonance.



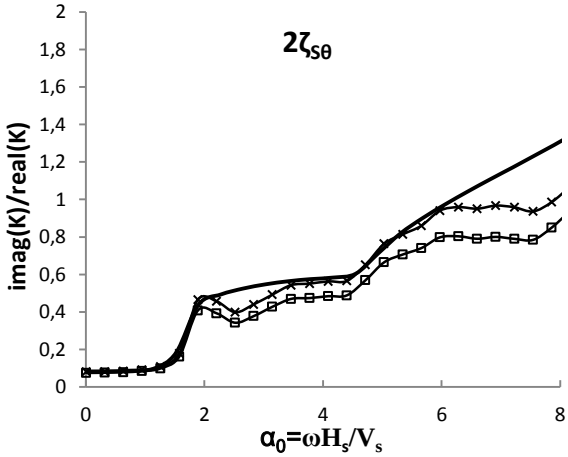


Figure 8 Variation of the coupling stiffness and damping coefficients with respect to the dimensionless frequency for profile 2.

In addition, they are characterized of an increase of stiffness approaching the 3rd eigenfrequency of the soil layer ($\alpha_0=5/2\pi$).

It is evident from the graphs that the dynamic response of the caisson is similar to the one of the solid equivalent pile, clearly for the translational and the rocking stiffness components. Furthermore, the analytical solution shows good agreement with the numerical results up to $\alpha_0 = 5$.

The imaginary part of the dynamic component is also shown in Figures 7, 8 and 9. The radiation damping exhibits a step variation in the frequency range, where the slope changes after each eigenfrequency of

the soil layer. This observation is consistent to previous studies on floating piles (Latini et al., 2015). Furthermore slightly higher damping is associated with the solid pile compared to the caisson.

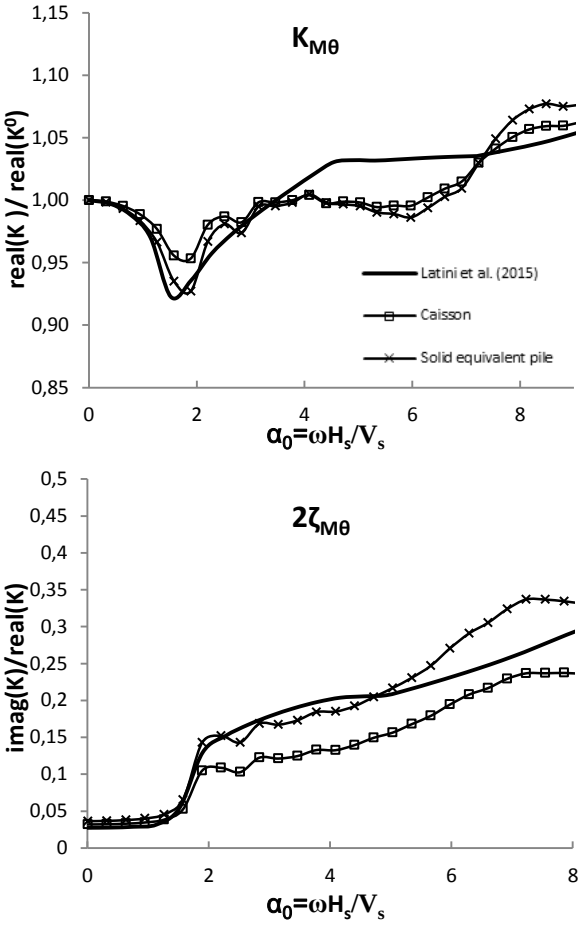


Figure 9 Variation of the rocking stiffness and damping coefficients with respect to the dimensionless frequency for profile 2.

In Figure 10, 11 and 12 the real (K_{su}, $K_{s\theta}$, and $K_{m\theta}$) and the imaginary ($2\zeta_{su}$, $2\zeta_{s\theta}$, and $2\zeta_{m\theta}$) parts of the dynamic impedances are presented for different values of the shear wave velocity of the soil layer (V_s=250-400m/s).

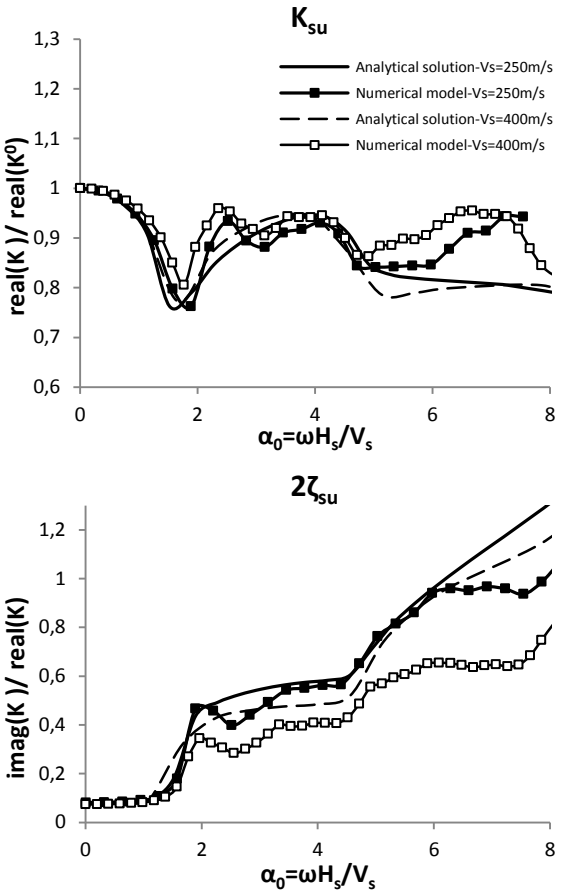


Figure 10 Variation of the translational stiffness and damping coefficients with respect to the dimensionless frequency. Effect of the soil stiffness on the real component and the imaginary component.

The same values as in the reference case are kept for the height of the foundation and the soil layer. Slightly scattered results are obtained by increasing the shear wave velocity of the soil layer. In addition, the drop of stiffness recorded at the first eigenfrequency of the soil layer is slightly more marked for medium soil profiles (V_s=250m/s). Moreover, it is noticed that the cross coupling and rocking stiffness coefficients exhibit higher values than the corresponding static component at higher frequencies.

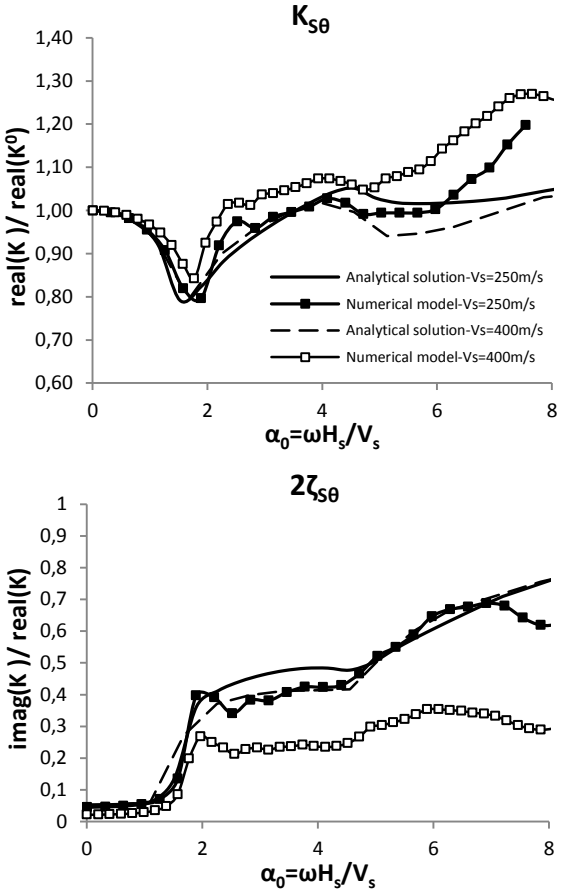
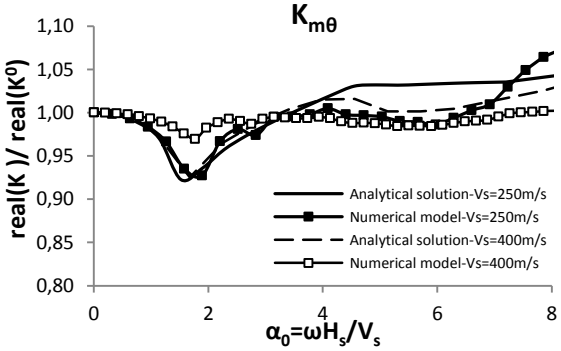


Figure 11 Variation of the coupling stiffness and damping coefficients with respect to the dimensionless frequency. Effect of the soil stiffness on the real component and the imaginary component.

In Figures 10, 11 and 12 the imaginary component is also illustrated for different values of the shear wave velocity of the soil layer. It is observed that increasing the stiffness of the soil or decreasing E_p/E_s the damping decreases. In addition, the radiation damping generated after the 1st eigenfrequency is almost zero for the rocking stiffness component. A significant offset is recorded comparing the numerical models with the analytical solution, when the stiffness of the soil layer is increased.



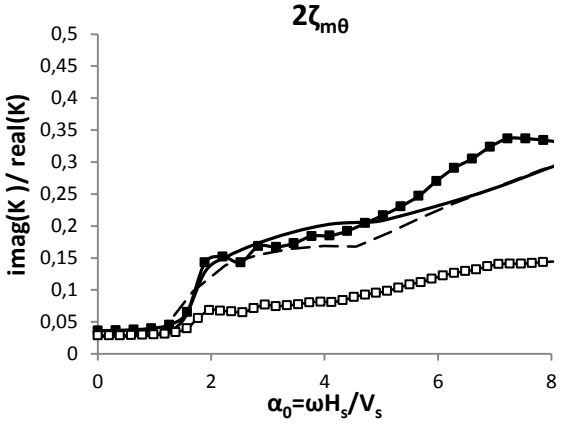


Figure 12 Variation of the rocking stiffness and damping coefficients with respect to the dimensionless frequency. Effect of the soil stiffness on the real component and the imaginary component.

4 CONCLUSIONS

Numerical analysis is undertaken to investigate the dynamic response of suction caissons. The study also provides comprehensive comparison of the numerical models with existing analytical solutions formulated for piles. From the results of this study it seems that the general behavior of the suction caissons follows the trend of the analytical solution suggested by Novak and Nogami (1977) for piles. However for the caisson a Rayleigh wave is experienced in the inner soil with wave-length λ=D in the high frequency range. In addition, the presence of the cap in the caisson design does not affect significantly the dynamic response of the soil-foundation system. The analytical formulation of Latini et al. (1977) provides good agreement with the numerical model of a caisson on a deep soil layer for frequencies up to $\alpha_0 = 5$. Concerning the effect of the soil stiffness on the dynamic impedances, it is noticed that decreasing V_s the damping increases, which it is in agreement with what observed in the analytical formulation. However at larger shear wave velocities a larger discrepancy between the numerical model and the analytical solution was observed. The effect of the inner soil in the dynamic response of the caisson appears more important for shallow soil formations than for deeper ones.

ACKNOWDLEGMENTS

This work has been supported by the Danish Council for Strategic Research through the project "Advancing BeYond Shallow waterS (ABYSS) - Optimal design of offshore wind turbine support structures".

5 REFERENCES

Adhikari, S., & Bhattacharya, S. (2012). Dynamic analysis of wind turbine towers on flexible foundations. Shock and vibration 19, 37-56.

Alexander, N.A. & Bhattacharya, S. (2011). The dynamics of monopole supported wind turbines in nonlinear soil. Proceedings of the 8th International Conference on Structural Dynamics (EURODYN 2011), Leuven, Belgium.

Bhattacharya, S. (2014). Challenges in design of foundations for offshore wind turbines. Institution of Engineering and Technology 10/2014.

Byrne, B.W.& Houlsby, G.T. (2006). Assessing novel foundation options for offshore wind turbines. World Maritime Technology Conference, London, UK.

DNV (2010). Offshore standard DNV-OS-J101: Design of offshore wind turbine structures. Technical report DNV-OS-J101, Det Norske Veritas.

Gazetas, G. (1984). Seismic response of end-bearing single piles. Soil Dynamics and Earthquake Engineering 3(2), 82–93.

Latini, C., Zania, V. & Johannesson, B. (2015) Dynamic stiffness and damping of foundation for jacket structures. Proceedings of 6th International Conference on Earthquake Geotechnical Engineering (6ICEGE 2015), Christchurch, New Zealand.

Liingard, M. (2006). Dynamic behavior of suction caissons. PhD Thesis. Aalborg University.

Mylonakis, G. (2001) Elastodynamic model for large diameter end-bearing shafts. Soils and foundations 41(3), 31-44.

Nogami, T. & Novak, M. (1977). Resistance of soil to a horizontally vibrating pile. Earthquake Engineering and Structural Dynamic 5(3), 249-261.

Novak, M. & Nogami, T. (1977) Soil-pile interaction in horizontal vibration. Earthquake engineering and structural dynamics 5, 263-281.

Nozoe H, Gyōten Y, & Fukusumi T. (1985) Dynamic analysis of a soil-pile system by the finite Fourier-Henkel transformation method – Case of a floating pile in horizontal vibration. Theoretical and applied mechanics 33, 377-392.

Simulia, D. S. (2013) Abaqus 6.13 User's Manual. Dassault Systems, Providence, RI.

Zania, V. (2014). Natural vibration frequency and damping of slender structures founded on monopiles. Soil dynamics and Earthquake engineering, 59, 8-20.

On the design of a deep secant pile wall

Ole Kristian Lied
Geovita as, Norway, okl@geovita.no

Amund Augland
Geovita as, Norway

Josefin Persson
Statens Vegvesen, Norway

ABSTRACT
The Norwegian public road administration is building a new four-lane tunnel between Sandvika and Rud, partly as an open cut & cover tunnel with deep excavation. At Mølla, the new tunnel is located 30 meter below terrain making the retaining wall for the excavation one of Norway's deepest. This area has demanding soil conditions with a 15m layer of soft clay over 15m hard moraine on top of the bedrock, which has large variations in depth over the area. Further, the ground water level is high and a heavy trafficated road is close by.

Because of the difficult ground conditions, secant pile wall with a pile diameter of 1.2 m is chosen for its flexibility and the need of establishing the pile foot into bedrock. Support of the 28 meter high secant pile wall is done by seven levels of tie back anchors. The horizontal load acting on the wall were, during design, predicted to be high and measures for reducing it are taken. In particular, it was predicted that, by lowering the ground water level, the water pressure acting on the wall could be reduced by at least 30%. This is ensured through continuous pumping and the reduction has been verified by measurements.

Due to the some uncertainties in actual horizontal loads acting on the secant pile wall, the complexity of the project as well as the novelty of the design for Norwegian projects, an extended monitoring program has been introduced. The measured pore pressure, wall deformation and anchor loads will be compared to the theoretical predictions in order to validate the design methodology. The excavation has started and will continue until late summer 2016.

Keywords: retaining structures, deep excavations, secant pile wall

1 INTRODUCTION

The Norwegian Public Road Administration is building a new four-lane tunnel between Sandvika and Rud. The tunnel is located outside Oslo and is a part of an upgrade of existing E16 between Sandvika and Wøyen. The tunnel is approximately 2.3 km long and consists in northern part of two cut & cover concrete tunnels, respectively 90 and 500 meters long, with excavation depths of up to 30 meters. The excavation site at Mølla has demanding soil conditions with soft clay over hard moraine on top of the bedrock. The area has large variations in depth which gives challenges related to the design of retaining wall construction. Furthermore, the ground water level is high and a heavy trafficated road is close by.

Due to the large excavation depth and special challenges in the area is this project followed with great interest from the academic community in Norway. This article covers the design of the excavation, with emphasis on engineering assumptions and technical solutions. At the moment, the excavation has started and will continue until late summer 2016.

2 PROJECT DESCRIPTION E16 SANDVIKA – WØYEN

E16 between Sandvika and Hønefoss is the most traffic congested two lane road section in Norway with an YLT of 35,000 vehicles. It has long been in need for an upgrade and the work has been going on since the 1990s. This includes a new four lane road between Wøyen and Bjørum which opened in 2009.

The last part of the E16 towards Sandvika, and connecting to E18, has not have any work done since it was built in the early 1980s, creating major traffic problems. An upgrade of the road has been long awaited, but has been postponed several times due to trace election and political processes.

The Norwegian public road administrations project E16 Sandvika – Wøyen, a 3.5 km new four line main road, consists of 3 major contracts:

- E16 Bjørnegård tunnel from Sandvika to Rud
- E16 Rud - Vøyenenga
- Upgrading the local road system, Sandvika - Emma Hjort

Engineering started with the road planning in 2008 with completed tender documents for the first part of the road, E16 Bjørnegård tunnel, in 2014. The Norwegian public road administration started the construction work for the new tunnel in February 2015 and the expected completion of the road section Sandvika - Wøyen is November 2019. The last part of the project, upgrading the local road system in Sandvika where today's E16 is located, is expected to be completed during 2021. The entire project has a budget of approximately 4 Billion NOK.

The first part of the road will go in two parallel tunnels until the intersection with Bærumsveien, where the road will go in daylight towards Vøyenenga. The northern part of the road tunnel consists of two cut & cover tunnels in deep excavations. At Mølla, where the deepest excavation is located, it will be up to 30 meters from the current ground level down to excavation level for establishment of the two concrete tunnels.

3 PLANNING STAGE – PRELIMINARY INVESTIGATIONS AND ESTIMATES

Due to a fault zone in the bedrock under Statnett's transformation station at Hamang and Franzefoss industrial plant, it was performed a lateral displacement of the tunnel route to the west early in the road planning. Moving the tunnel route, resulted in the need for establish a deep cut & cover concrete tunnel at Mølla, close to existing E16 and high-voltage lines crossing the site 20 meters above terrain. In the next planning stage it was studied various solutions for crossing the local deep area. The options were:

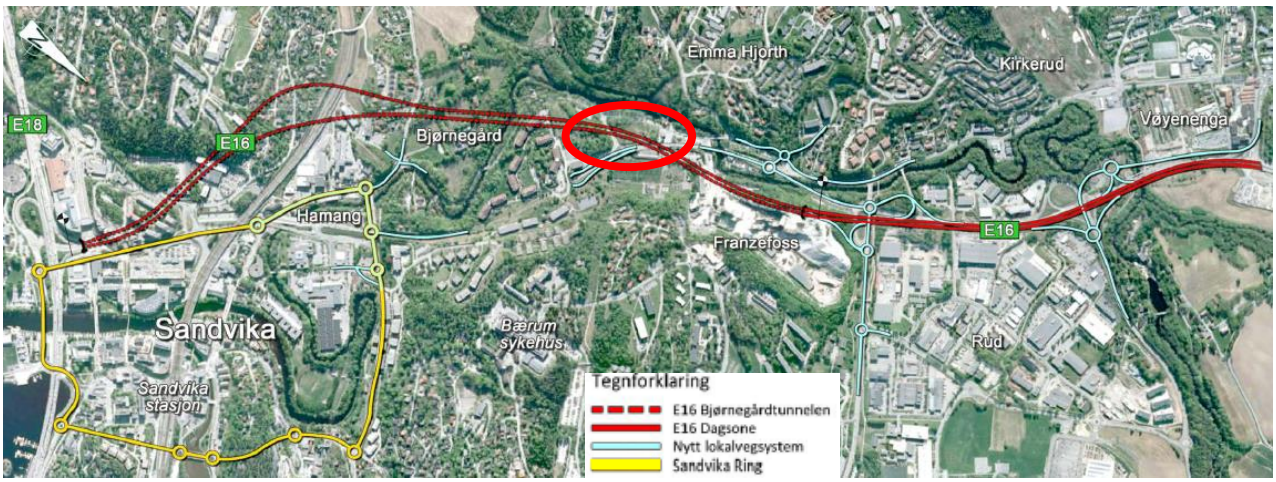


Figure 1 Overview of the project E16 Sandvika - Wøyen

- Open excavation using a supported wall.
- Ground freezing of soils and tunnel driving through frozen material zone
- Tunnel driving securing the tunnel face with a screen

In the process selecting the solution, it was focused on using a robust solution with good feasibility. Use of an open excavation was preferred for its robustness and it has the lowest risk in relation to the technical implementation, although the complexity is uncommon. An important advantage using an open excavation is that the rock tunnels and the concrete tunnel can be built independently. An unforeseen problem on a subset does not give direct consequences for neighboring elements.

3.1 Site investigations

It has been carried out extensive site investigations in connection with the different planning stages, as well as some surveys in previous study phases and building of the existing E16. It is performed total soundings, CPT, piston samples for laboratory testing and piezometeres for water pressure measurements are installed.

The site investigations show layered soil conditions with soft clay and silty clay over hard and stony moraine. It is also registered a sand layer between the clay- and moraine layer in center part of the pit. The thick moraine layer decreases from north to south along the excavation area. Depths to bedrock varies from rock in day to 30 meters depths, and the inclination of the bedrock is steep in each end. The bedrock also falls steeply across the area under existing E16. In the central part of excavation area where the rock level is at its deepest, the ground conditions consisting of 10-15 meters of soft clay over 10-15 meters with hard moraine. A section of the construction pit with stratification and plot of performed soundings is shown in Figure 2.

3.2 Special geotechnical challenges

Establishing an excavation in loose fill of this size has not been performed previously in Norway. Demanding ground conditions with thick layers of soft clay and stone rich moraine, high groundwater level and steep rock stream provides an outer limit of what is technically possible. Also the existing road E16 close by will give strict requirements for deformation of the wall.

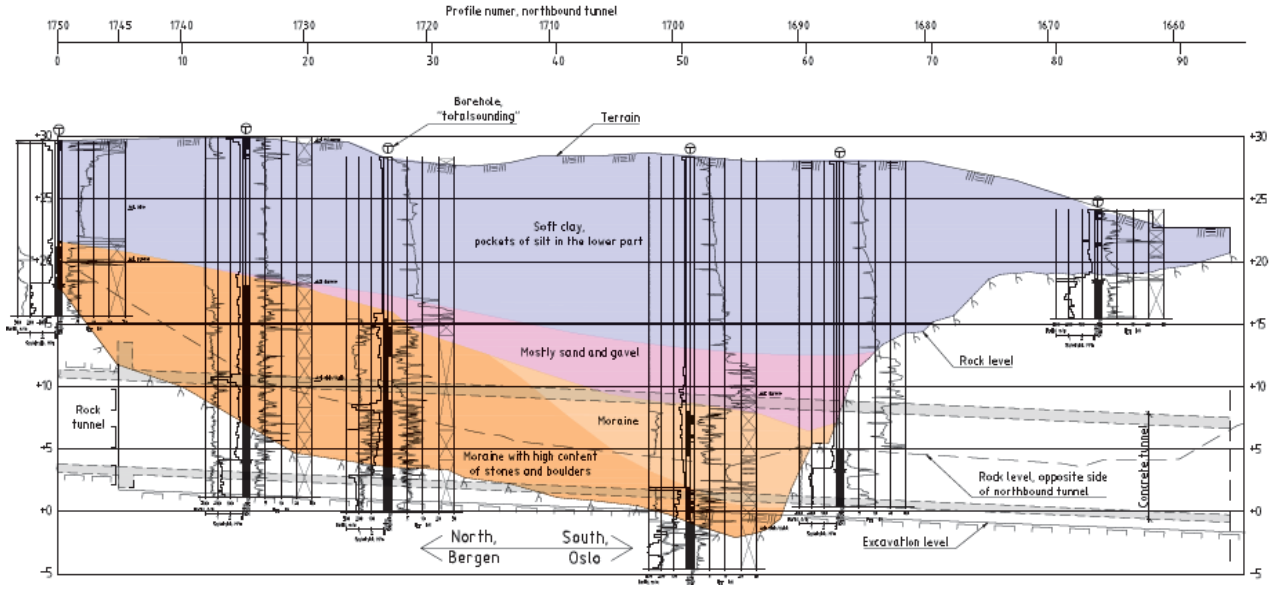


Figure 2 Figure with longitudinal section of the excavation pit showing stratification and plots of performed soundings.

Installed piezometers shows hydrostatic pore pressure with groundwater level at +25 (approximately 3 meters depth), which provides a huge pore pressure on the wall. With a highly permeable moraine layer, there is a desire to establish a dense wall to avoid problems with water intrusion due to excavation as well as limiting deformation at facilities nearby. The great excavation depth gives large horizontal loads acting on the wall with related vertical forces at pile foot in use of back tie anchors. Steep inclination of bedrock, with possible vertical overhang at local parts, bad / fractured rock in the upper part gives the challenges of transferring the forces to bedrock. This is especially a challenge in the area where the bedrock in front of the wall must be removed due to the depth of the tunnel. This gives intersections tightly into the supported wall.

4 DESIGN OF SUPPORTED WALL AT MØLLA

Several types of retaining walls were considered before secant pile wall was selected. Arguments for using secant piles were:

- Rigid and dense wall with large moment-, shear- and axial capacity.
- Possibility of drilling into bedrock that gives great flexibility in the area of steep bedrock surface and gives a secure pile foot.
- Possibility of use of a smaller machine when establishing secant piles under existing high-voltage line.
- Good experiences from other projects in Norway with difficult and varying soil conditions.

The secant pile wall is placed as close to the concrete tunnel as possible to minimize the height of the wall giving substantial cost- and time savings. This because of the drop of bedrock surface across the excavation area, and location far away as possible from the diverted E16 gives the opportunity for lowering the terrain before installation of the wall. The disadvantage would be a short distance between the secant pile wall and blasting contour with up to 10 meters height. Location of the wall and plan for lowering the terrain before installation is shown in Figure 3. The height of the wall is reduced to approximately 28 meters.

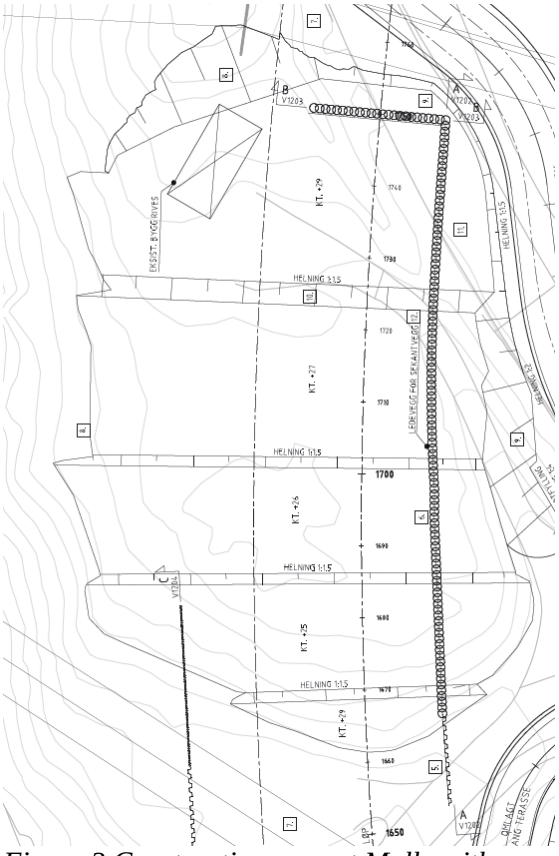


Figure 3 Construction area at Mølla with location of the secant pile wall and excavated terrain level before installation.

With only 1meter distance between the secant pile wall and the blasting contour, while the bedrock surface drops across the excavation area, there will be parts where the secant piles stands on smaller rock surfaces. During excavation the axial force on the rock surface will be large and it was therefore chosen to transferring the axial forces to below bursting level using steel core piles. Figure 4 shows the problem with bursting in front of secant pile wall and the large drop in bedrock level across the excavation area.

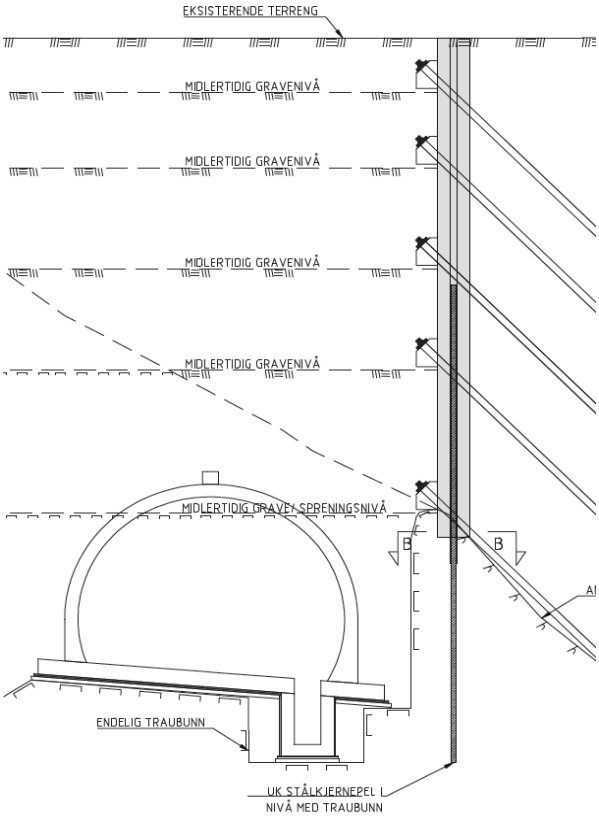


Figure 4 Cross sectional view shows the situation where the axial force at secant pile is transferred to below bursting level with steel core piles.

Other challenges resulting from the presumed steep rock surface and possible vertical overhang was skidding of secant pile and lack of good pile foot in rock at installation. With uncertainties in result of pile foot installation in the steepest area, it was prepared for the use of jet grouting under, in front of and back of the pile foot in addition to insert multiple rows with tie back anchors. Establishing a blasting contour near the secant pile wall also gave uncertainty about the rocks capacity to accommodate the large horizontal forces at the pile foot. The solution here is to pre-stress tie back anchors at pile foot to horizontal equilibrium.

It was in early stage of planning considered to drill the secant pile into rock with stop at bursting level to avoid the above-mentioned issues. But this was considered to be too insecure when there was little experience in Norway with drilling secant piles deep in to bedrock. Since there was uncertainty about the solution and it would increase both the costs and time consumption, a solution that were not dependent on long drilling in bedrock was chosen.

Preliminary calculations showed naturally very large forces on the wall and caused many rows with tie back anchors. Especially when there was a desire to have continuous horizontal pad rows across all computing section and the need for the use of reinforced concrete pads. The starting point was to use 1200 mm secant piles since the piles had great rigidity and capacity for optimization of the support of the wall. Optimizing went on reducing the number of rows with tie back anchors and center distance between the ties. This for taking advantage of the great stiffness and moment capacity of the secant pile wall and reduce construction time, when establishing each back tie level is time consuming due to long anchors and use of reinforced concrete pads. It is considered that only the reinforced secondary piles are taking the forces acting on the wall. The primary piles are filling material to ensure a tight wall.

5 UNDERLYING ASSUMPTIONS FOR DIMENSIONING OF SECANT PILE WALL

In early phase a simpler calculation program was used to get a sense of forces acting on the secant pile wall. Furthermore, it was only the work of FEM simulation program to account for oblique stratifications, slanting rock stream and the impact on the wall from the underlying hillside traffic load from E16. In the drained layers the soil model *"Hardening Soil - Small Strain"* was used with empirical data for input of strength- and deformation parameters. For the soft clay the soil model *"Hardening Soil - Small Strain"* is used in effective stress analysis (long term) and "*NGI-ADP*" in total stress analysis (short term). The soil model "*NGI-ADP*" is developed especially for marine clays.
For a support wall structure of such a dimension that is to be established at construction pit Mølla, there is no possibility of using conservative parameters in the dimensioning. It is dependent on using realistic strength- and stiffness parameters in calculations. Therefore is "soil tests" performed in the FEM program to determine

parameters for the clay which corresponds with the real triaxial tests.

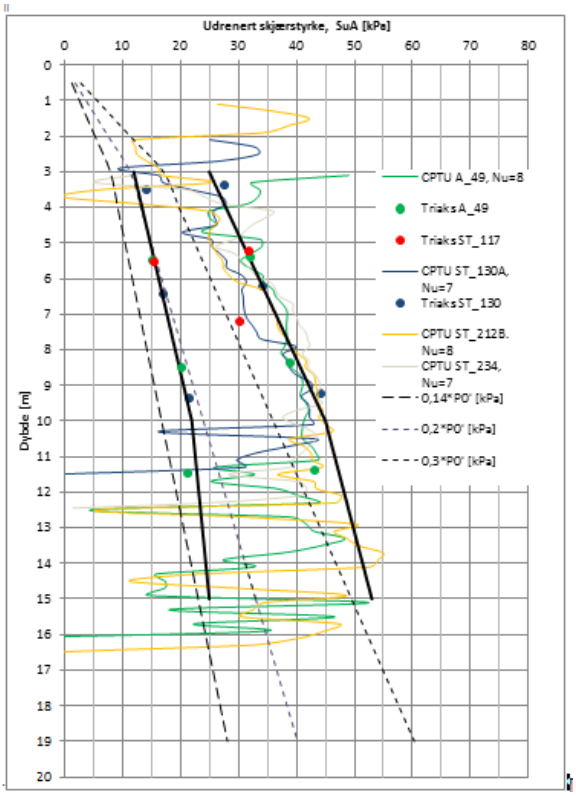


Figure 5 Selected shear strengthening profile for clay layer.

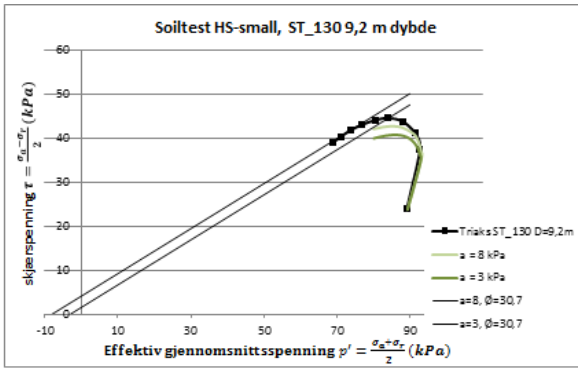


Figure 6 Assembly "soil test" and triaxial testing, ST_130 at D = 9,2m - Small strain.

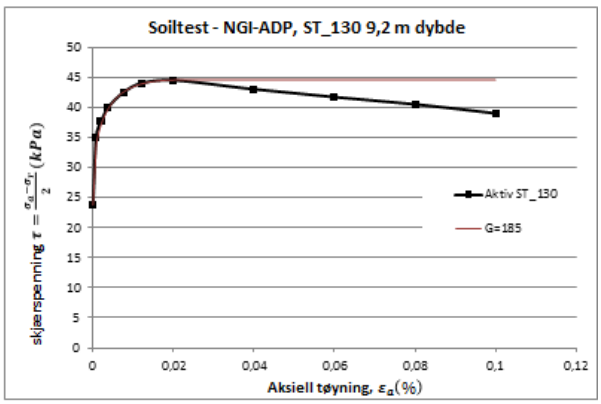


Figure 7 Assembly "soil test" and triaxial testing, ST_130 at D = 9,2m - NGI-ADP.

With high groundwater levels and hydrostatic pore pressure with depth, the large part of the forces acting on secant pile comes from water pressure. Normal practice for design of retaining walls of this type in FEM simulation programs, is to multiply the characteristic forces from the calculation with a load factor, in this case equal to $\gamma_{t=}$ 1.40. This means that the contribution from the water pressure acting on the wall will be multiplied by the load factor, when it is not possible to separate the water pressure as a separate load. Designed forces acting on the secant pile wall will be unnecessarily large as the uncertainty related to the water pressure is minimal. At least in relation to the choice of soil parameters, which the load factor actually is intended for. Calculations are therefore performed with reduced water pressure in the ultimate limit state (ULS). It is additionally performed calculations with full water pressure acting on the wall, but this as an accident limit state (ALS).

With four calculating sections, several soil models, variations in water pressures, testing various number of rows with tie back anchor and center distance of the ties, numerous calculations was performed. With an optimized solution in terms of the number of tie back rows and center distance between the ties, results of the calculations show that the secant pile wall has sufficient capacity in ULS also for full water pressure. The tie back anchors have only sufficient capacity in ALS for full water pressure. When dimensioning the anchors in ULS, the water pressure is reduced to 70% of the original hydrostatic pore pressure.

To reduce the water pressure behind the secant pile wall, several wells will be established to lower the ground water table/water pressure behind the wall during the excavation. Since there was some uncertainty of the permeability of the soil, a full-scale pumping test was performed to verify the effects of groundwater pumping.

6 FULL-SCALE PUMPING TRIALS

The full-scale pumping test was performed with two pumping wells. A total of 6 piezometers, each with indicators at 5 different depths, were installed close to the pumping wells before the beginning of the test. An immediate response was detected by the piezometers when the pumps were started. After only one day of pumping, the desired level of 70 % of the original water pressure level reached. The trial went on for 72 hours and the original water pressure went back quickly after ending the test. The response in the clay layer was slower, as expected, but also here the desired water pressure reached. Figure 9 show the location of wells and piezometers. Figure 8 and Figure 10 results from the pumping test



Figure 9 Location of the pump wells and piezometers in connection with the full scale pumping trials.

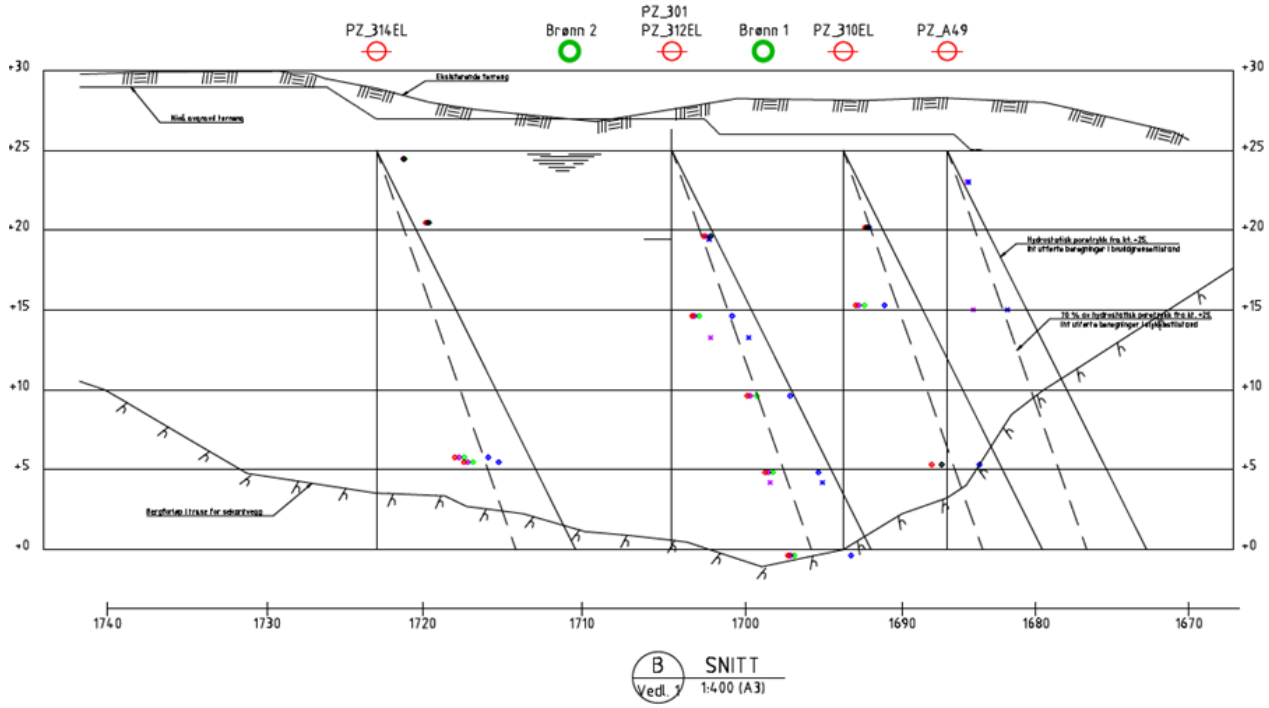


Figure 8 Section along secant pile wall with result from the full-scale pumping test. Blue marker indicates water pressure before pumping, and the other colour shows water pressure after 24, 48 and 72 hours of pumping.

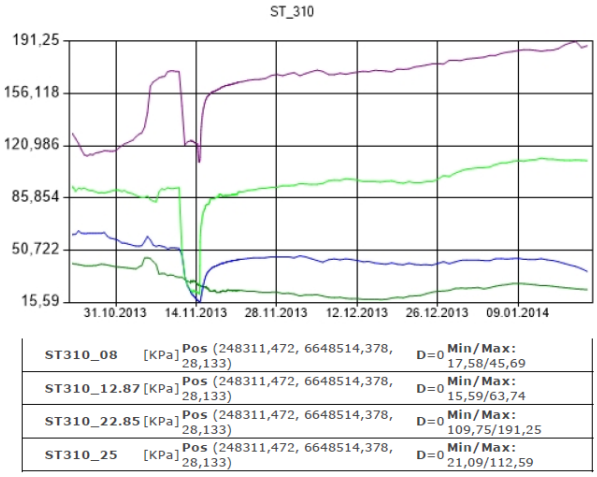


Figure 10 Results from trial pumping at piezometer ST_310. Graphs showing variation in pore pressure at different depts.

The conclusion of the full-scale pumping test is that the soil is permeable and lowering the ground water table to desired level behind the secant pile wall is achievable. Due to the immediate response to original pore pressure level, the construction is dependent on reliable pumps that will continue pumping during the construction phase without interruption. It will therefore be installed two more pumping wells behind the wall for a more robust situation.

The area nearby the excavation site has a thick layer of soft clay over moraine layer and is sensitive for ground deformation due to pore pressure changes. To minimize the effect of the surroundings, and especially the transformation station at Statnett's facility, two or more infiltration wells will be installed. While the ground water table/water pressure is lowered behind the secant pile wall, water will be infiltrated into the ground at the infiltration wells below the transformation station.

7 INSTRUMENTATION OF EXCAVATION PIT MØLLA

The cut and cover excavation at Mølla is unique in Norway and there is little experience in the dimensioning of supporting structures with such large excavation depths. Especially with the challenging soil conditions with soft clay over hard moraine. When it is assumed in the design that the water pressure behind the wall is reduced, close monitoring is important. An extensive instrumentation program of the secant pile wall will be installed. Deformation of the secant pile wall, anchor forces and pore pressure will be followed up close during excavation. All data will be remotely monitored and limits will be set with alarm levels and SMS warning. Considering the surroundings nearby the construction pit, deformation sensors are installed.

For the secant pile wall, deformation monitors will be installed in five sections and load cells mounted on the bars in all levels in three. To verify measured values from remotely monitored load cells, supplementary load cells with manual sensors are used in addition. For control of pore pressure distribution at the wall, already installed piezometers from pumping test will be used. Longitudinal section of secant pile wall with all the remote reading instrumentation installed is shown in Figure 11.

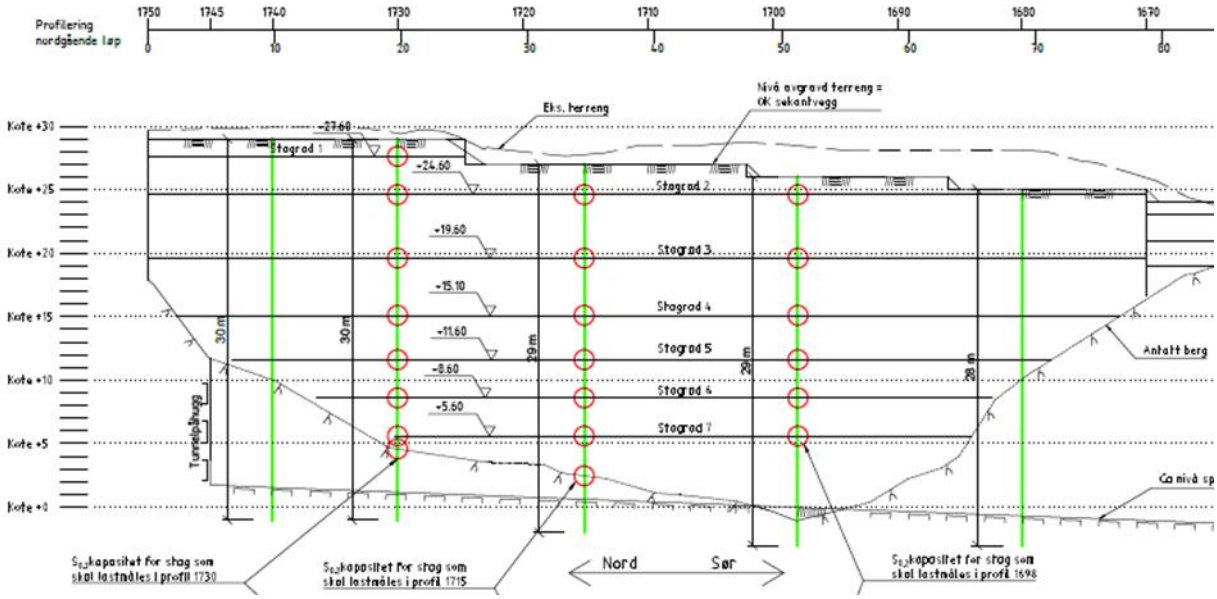


Figure 11 Longitudinal section of the secant pile wall showing remote reading instrumentation. Green lines are location of the displacement monitors and red circles are planned load cells.

Pore pressure reduction and settlements induced by deep supported excavations in soft clay

J. Langford
*NGI, **Norway**, jenny.langford@ngi.no*

G. Baardvik, K. Karlsrud
NGI, Norway

ABSTRACT
As a part of the large research project, "LimitingDamage" (BegrensSkade), common causes of damage or unexpectedly large settlements connected to ground and foundations works have been investigated. It can be seen that drainage is a common cause for settlements when performing deep excavations, causing decrease in pore pressures and consolidation of soft soil.

The article presents monitoring data from numerous building sites, showing that there is often a substantial reduction in pore pressure levels at bedrock. The reduction in pore pressure can be observed hundreds of meters from the excavation. The general effects have been documented before, but the analysis of data in the project "LimitingDamage" shows a clear systematic reduction in pore pressures for the majority of excavation projects. The effects depend on the hydrogeological properties, as well as the extent and duration of the construction work and the mitigation efforts undertaken.

The data and observations from the case studies suggest that the risk of drainage is substantial in the conventional methods and procedures commonly used. Excavating to bedrock level, if under groundwater level, can cause substantial reductions in pore pressure. In addition, it is concluded that drilling for tie-back anchors and bored piles can increase the risk of drainage.

The risk of settlements caused by drainage and pore pressure reduction can be reduced during the early design phase of a project by undertaking the correct type of investigations and understanding the hydrogeology. Furthermore, one may select construction methods, which reduce risk of drainage. Measures may then be designed in order to mitigate the effects, followed by implementation and monitoring during the construction phase.

Keywords: Excavation, drainage, pore pressure, settlement.

1 INTRODUCTION

1.1 LimitingDamage (BegrensSkade)

Ground works such as deep excavations and foundation works performed in soft clay are known to frequently cause damage to neighboring buildings and structures. The costs related to these types of damage can be substantial and there is a large potential for reducing these costs. This is the main topic of a research project funded by the Norwegian Research Council and a wide range of consultants, clients and contractors, as well as the NGI. The project "BegrensSkade" ("LimitingDamage"), is investigating causes of damage.

The main causes of deformation connected to the performance of deep excavations in soft clay are (illustrated in Figure 1):

- Shear-induced ground movements linked to horizontal displacements of the supporting wall

- Leakage causing pore pressure reduction and consolidation settlements, when the effective stress exceeds the preconsolidation pressure
- Installation or "disturbance" effects induced by drilling for tie-back anchors or drilling for piles inside the excavation

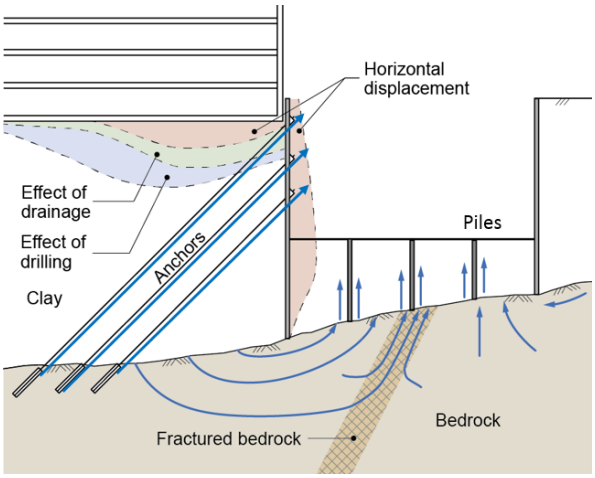


Figure 1 Illustration of the main causes of settlements connected to deep excavations in soft clay.

The settlements due to horizontal displacement of the sheet pile wall can be estimated using numerical tools or data from Peck (1969).
The settlements caused by disturbance of soil during drilling is presented in detail in reports by Lande (2015) and Veslegard et al. (2015).
This article will present results related to potential settlements caused by drainage to deep excavations given in Karlsrud et al. (2015).

1.2 Experience from leakage to tunnels

Experience from tunnels (Karlsrud et. al, 2003) and ground water pumping, shows that small amounts of leakage into a tunnel, can result in substantial decrease in pore pressures at bedrock level (at bottom of clay layer) (Figure 2). The main reason is the very limited recharge that comes through a low-permeable soft clay deposit, which makes the soil or bedrock below act as a confined aquifer. Analysis of data from numerous tunnel projects show that the leakage rate into a tunnel needs to be limited to approximately 3-8 l/m/100 m tunnel to limit pore pressure decrease to 10-30 kPa at the bedrock level (Figure 3). The data also shows that the pore pressure decrease can extend as far out as 200-400 m from the tunnel (Figure 4).

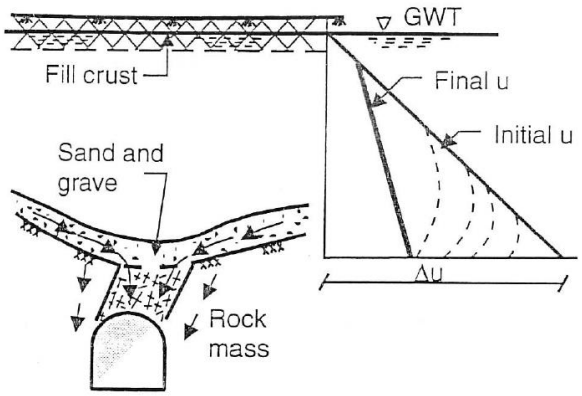


Figure 2 Leakage to bedrock tunnels overlain by clay deposits (from Karlsrud et al., 2003).

Based on the fact that the hydrogeological conditions are the same for excavations, these results implies that for an excavation of dimensions 100 m × 100 m significant pore pressure reduction can occur at the base of the clay outside the excavation, if the leakage exceeds about 5-10 l/min in total. However, the precise magnitude of pore pressure reduction, and the lateral extent of the area subjected to a reduced pressure is difficult to predict and dependant on the local hydrogeological conditions.

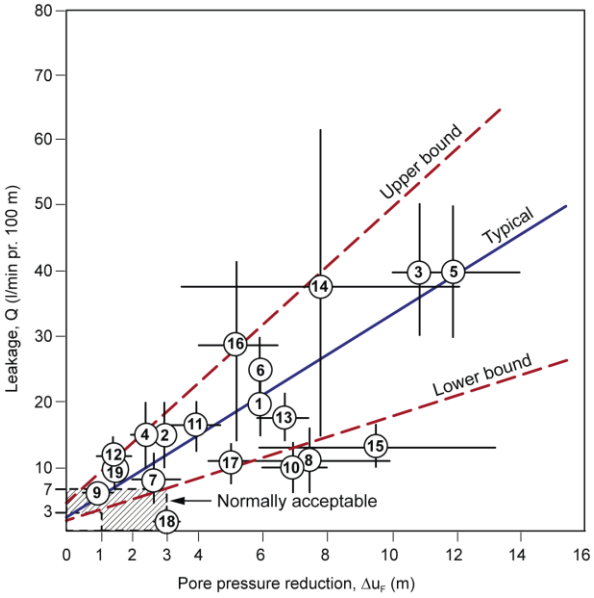


Figure 3 Measured rate of leakage to tunnels plotted against monitored pore pressure reduction at bedrock (from Karlsrud et al., 2003).

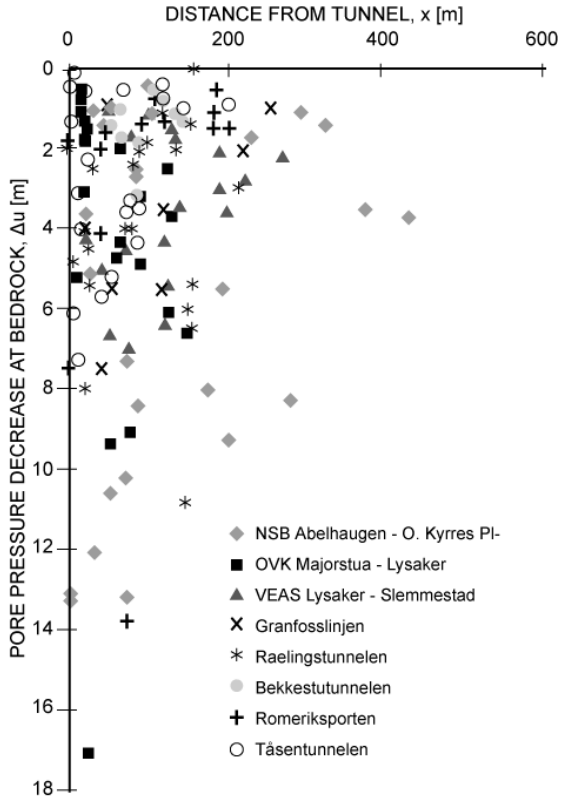


Figure 4 Measured pore pressure decrease at bedrock plotted with distance from excavation (from Karlsrud et al., 2003).

2 DRAINAGE TO EXCAVATIONS

The causes of drainage to an excavation can be many and complex. In addition, varying hydrogeological conditions will govern the effect on the pore pressures. However, the main leakage scenarios for an excavation in soft clay, as illustrated in Figure 5 are:

- Leakage through the sheet pile wall
- Leakage through gaps between the toe of the sheet pile wall and the bedrock
- Leakage through cracked bedrock
- Leakage during drilling for tieback anchors or piles (through the casing or the gap between soil and casing)

Leakage through the sheet pile wall mainly occurs during the cutting of holes for drilling of tie-back anchors. In addition, leakage can occur through unsealed or poorly sealed locks between the individual pile sections.
If the depth of the excavation reaches the bedrock level, resulting in an uncovered bedrock surface, there is a large potential for leakage through fractures. Uncovering the toe of the sheet pile wall also cause a large potential for leakage, especially if the bedrock surface is steep and there is a permeable soil layer on top of the bedrock.
Drilling for installation of piles and tie-back anchors has a potential for leakage when performed from a level below the ground water level or under artesian conditions. The leakage can occur through the gap between the installed steel casing or through the casing itself.

3 MITIGATING MEASURES

The risk of obtaining pore pressure decrease due to leakage into an excavation can be reduced by mitigating measures. The most

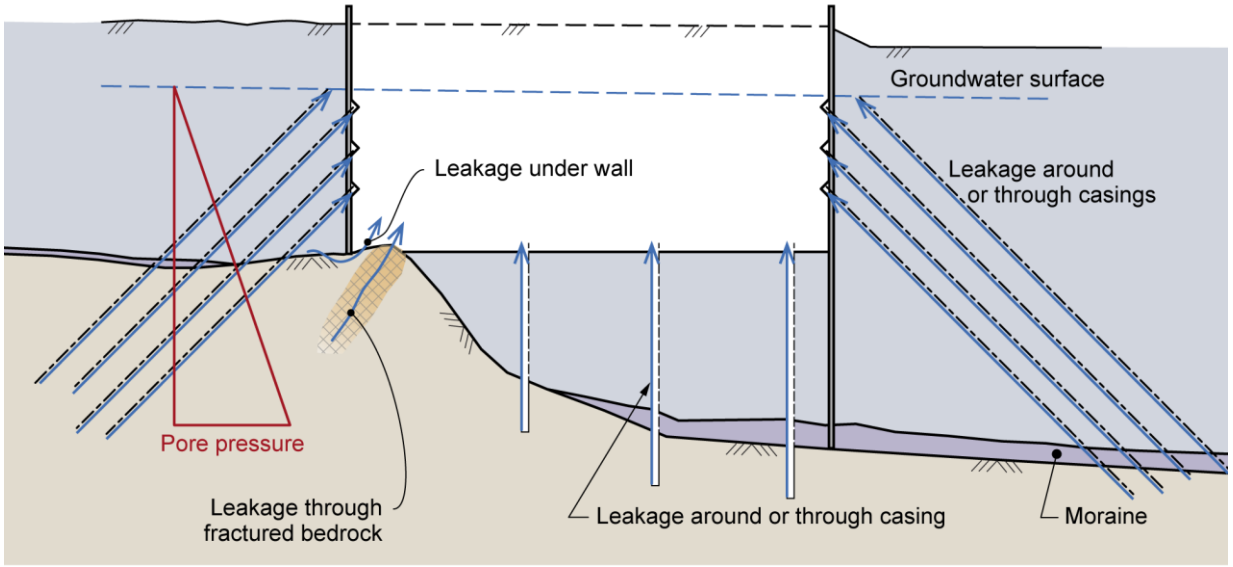


Figure 5 Illustration of possible leakage situations for a deep excavation is soft clay.

common methods for excavations in soft soils over bedrock are:

- sealing the interlocks in the sheet pile wall (with filler materials, polyurethane, polymers, bitumen)
- welding the locks after excavation
- welded double piles, combined with sealing
- mending holes in the wall
- using temporary packers in casings for tie-back anchors or drilled piles
- casting a reinforced concrete beam along the toe of the sheet pile wall cover and seal the gap between the the wall and bedrock surface
- Jet-grouting around and beneath the toe of the sheet pile wall
- rock grouting in the bedrock beneath the sheet pile wall and in the anchor boreholes
- water infiltration into the bedrock

4 CASE STUDIES

As a part of the LimitingDamage-project an extensive number of case studies have been analysed to investigate the most common causes for extensive settlements (Karlsrud et al., 2015). All projects are deep sheet pile wall supported excavations, carried out in normally consolidated soft clays. In this article five case studies are presented, with the aim to illustrate the effects of leakage and pore pressure reduction.

4.1 Case study 1

This case study was the excavation for a new railway tunnel south of Sandvika, Norway. The excavation consisted of a more than 400 m long cut-and-cover tunnel, to a depth of 17 m (15 m below the ground water level). The excavation was supported by up to 4 levels of tie-back anchors installed to bedrock. In total more than 1000 anchors were installed. The soil conditions consisted of soft normally consolidated quick clay, underlain by moraine on top of bedrock. The structure was partly founded on bedrock at the level of the excavation, in addition to drilled steel core piles.

The results from the case study has previously been reported in Braaten et al. (2004). As the excavation proceeded and drilling for anchors was undertaken, considerable pore pressure decrease, amounting to almost 10 m pressure head, at bedrock was observed. Monitored pore pressure levels over time are shown in Figure 6. Infiltration wells were installed, which resulted in stabilisation of the pore pressure levels. However, as the drilling for steel core piles started, the pore pressures decreased further.

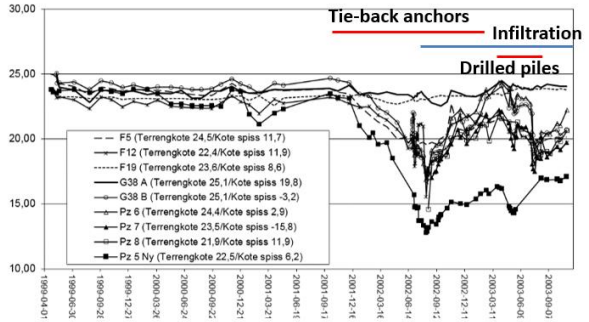


Figure 6 Monitored pore pressure levels and type of construction activities (Braaten et al., 2004).

Significant leakage was observed between the casing for the tie-back anchors and the sheet pile wall, as well as on the outside of the casings for the steel-core piles (Figure 7). The leakage through the casings was stopped by injection of cement in the bedrock. The leakage around the casings were difficult to manage. It increased rapidly and eroded fines material. The leakage decreased after several rounds of grouting with cement suspension and polyurethane grout.

Considerable leakage was also observed at the toe of the sheet pile wall. This was managed by casting a toe beam. Little or no leakage was observed through the bedrock itself.



Figure 7. Observed leakage around drilled casing for steel core piles (Jernbaneverket, Jong-Asker).

4.2 Case study 2

The second case study for a cut and cover road tunnel built in Oslo. The tunnel had a complex geometry due to exit ramps and the excavation was divided in two sections. The main excavation was about 80 m x 80 m and performed to a depth of 16 m, 14 m below the sea level. In the first section, the excavation pit was supported with up to 5 levels of tie-back anchors drilled to bedrock. In the second section, internal struts were used as a support. The main pit was open 2006 until 2010. The second pit endured from 2008 until closing in 2012.
Parts of the tunnel was founded on drilled steel core piles.

The soil conditions consisted of old harbour constructions, rock fill and deposits from excavations during numerous years, over a thin layer of normally consolidated soft clay. A permeable and stiff moraine was underlying the clay, the bedrock was detected assumed at 20-24 m depth.
Due to the moraine and rock fill the depths to bedrock were larger than assumed, and several leakage points were registered beneath the toe of the sheet pile wall. The leakage was stopped by jet-grouting with a centre spacing of 0,8 m. In addition, after the excavation was performed, visible leakage through the interlocks of the sheet pile wall were grouted with a polyurethane mix.

Results of monitored pore pressures at bedrock level in the main section are presented in Figure 8. Pore pressure measurements indicate that pressures at bedrock level corresponded to level 0 to -0,5 before the excavation was started. The pore pressure at bedrock decreased with 1 m during the excavation and the installation of tie-back anchors. It decreased further to a level of -7 m during the period for installation of steel core piles. The work was performed in combination with considerable pumping, to keep the pit dry. The pore pressure increased as the base slab and walls were cast and material was backfilled.

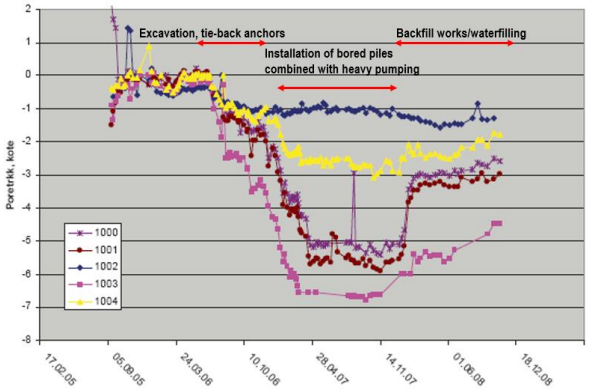


Figure 8 Observed pore pressure levels for first section in case study 2. (Modified after Johansen et. al., 2008 and vegvesen.no).

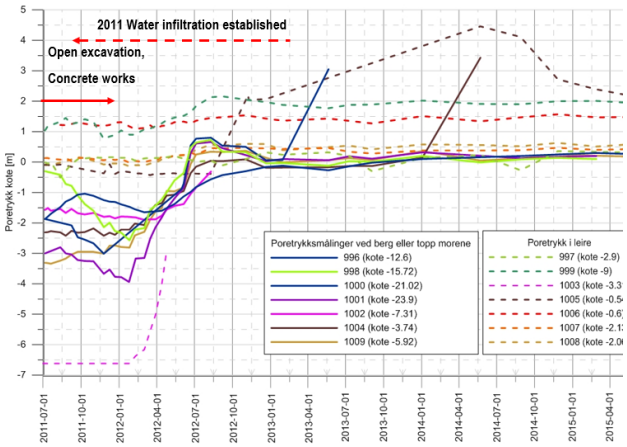


Figure 9 Observed pore pressure levels at the end of phase 2 in case study 2. (Modified after Hauser, 2015 and vegvesen.no). Water infiltration into the bedrock was started in 2011.

The second section of the excavation started in 2008. In 2011 the concrete works were performed and the backfill started, but the pore pressure did not rise to the in-situ level

of 0. Therefore, it was decided to install wells for water infiltration to reduce the risk of settlements on the surrounding areas and buildings. Figure 9 show the pore pressure levels at bedrock at the end of the excavation, as well as the effects of water infiltration into the bedrock. The figure also shows that the pore pressure in the clay is not yet affected by the drainage except for one piezometer.

4.3 Case study 3

This was an extensive excavation in Oslo over an area of about 100 m × 100 m. The excavation was performed to a depth of about 10 m, 8 m below the ground water level. The excavation was supported by a sheet pile wall installed to bedrock, and supported by 1 to 5 levels of tie-back anchors to bedrock. The foundation of the building consists partly of shallow foundations on the bedrock and partly of drilled steel core piles. A typical cross-section of the excavation is shown in Figure 10.

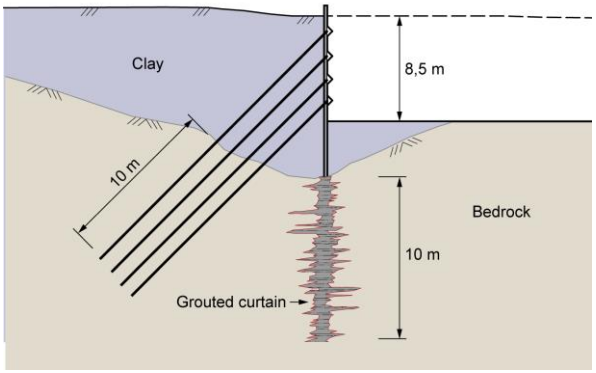


Figure 10 Cross section of case study 3.

The soil conditions consisted of fill over normally consolidated soft clay to bedrock at 2-30 m depth. A permeable layer of silty, sandy material was underlying the clay in one part of the excavation.
Due to the risk of settlements on adjacent buildings and infrastructure, measures were undertaken to reduce the risk of reduction of pore pressures. A cement curtain was grouted in the bedrock, to a depth of 10 m below the toe of the sheet pile wall. In addition, three infiltration wells were installed, tested and running before the excavation started.

Some results of monitored pore pressures at bedrock level and infiltration pressures are shown in Figure 11. Pore pressure measurements indicate pressures at bedrock level corresponding to level +1 to -1 before the excavation was started. The monitoring data shows that the pore pressures at bedrock level started decreasing during drilling of anchor level 3 and 4. During drilling for the anchors leakage was observed, especially between the sheet pile wall and the casing for the anchors, but also through the casing itself. This has been the main cause of pore pressure lowering. An example is shown in Figure 12.

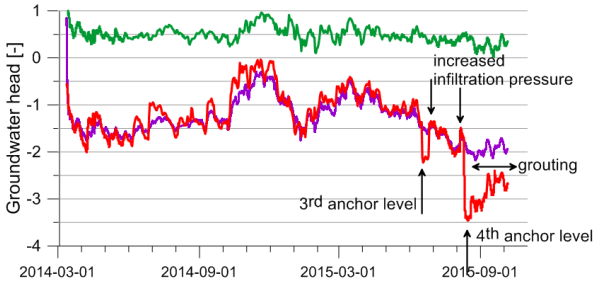


Figure 11. Monitored pore pressure levels and infiltration



Figure 12. Example observed leakage in connection with installing tie-back anchors.

To increase the pore pressure levels at bedrock the infiltration pressure was increased. This had some effect, at the same time efforts were undertaken to stop visual sources of leakage by grouting and welding. The pore pressure decrease was limited to about 1 m.
There was no or little leakage observed through the uncovered bedrock. The grouted curtain underneath the sheet pile wall is assumed to have had the intended effect sealing water bearing fractures.

One of the key factors for limiting the pore pressure reduction is likely the extensive

follow up of the work at the site and reporting sources of leakage and emphasizing the importance of also sealing small sources of leakage. In addition, the combination of grouting and infiltration has been successful.

At the time of writing piles have not yet been installed, at the bottom of the excavation and therefore the effect of drilling for piles cannot be evaluated.

4.4 Case study 4

This excavation in Oslo was performed in close vicinity of several old buildings, some founded on shallow foundations. The excavation for the basement was performed to a depth of 16 m, over an area of about 150 m × 100 m. The excavation was supported by a sheet pile wall installed to bedrock, supported by 5 levels of tie-back anchors drilled to bedrock. The project has also been presented by Eggen (2015)

The soil conditions consisted of fill over 1-2 m dry crust clay over normally consolidated soft clay to bedrock, at 10 to 30 m depth. Beneath 8 m depth, the clay was quick. The foundation consisted partly of drilled steel core piles and partly of shallow foundations on bedrock. In addition, tension anchors were installed into the bedrock to prevent uplift. A typical cross-section of the excavation is shown in Figure 13.

Drainage to existing tunnels in the area had caused decrease of pore pressures at bedrock of 10 - 35 kPa. As a result, ongoing settlement of 20 mm/year were registered at time of construction.

Measures were planned and undertaken to reduce the risk of drainage. The bedrock beneath the sheet pile wall was grouted to a depth of 10 - 15 m below the bedrock surface. The rock grouting was drilled vertical from the terrain level. Six infiltration wells were installed before the excavation started. The pore pressure was monitored at bedrock and in the clay with several piezometers.

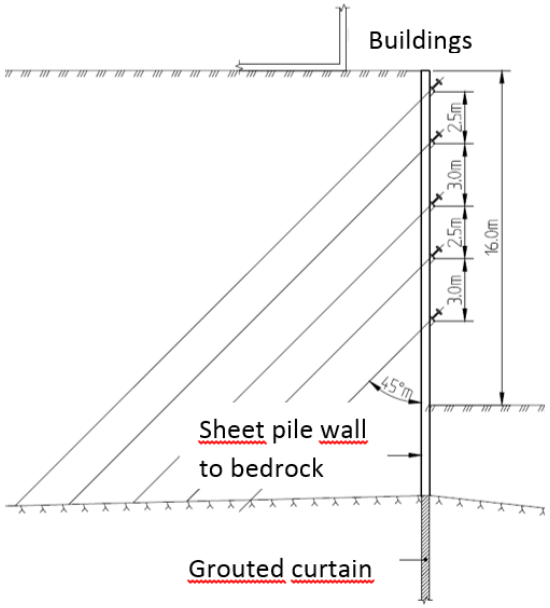


Figure 13 Typical cross section case study 4.

Pore pressure levels decreased as the excavation reached the bedrock. Infiltration wells were then activated, to mitigate the drop in pore pressure. However, the effect of the wells was smaller than expected. Therefore, additional rock grouting of the bedrock was performed, by drilling holes from the excavation pit and normal to the rock foliation resulting in more efficient sealing than the vertical grouting.

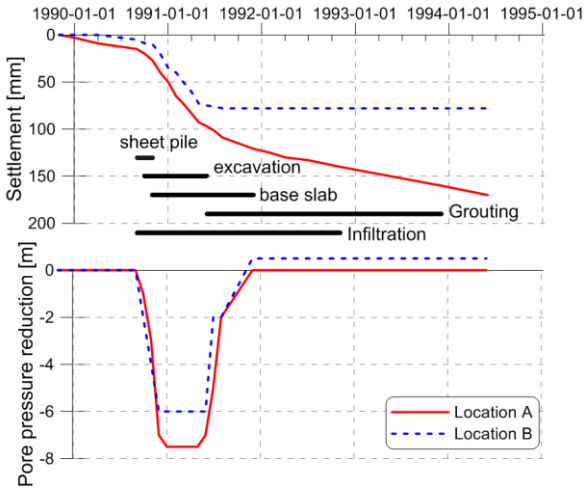


Figure 14 Monitored pore pressures and settlements at two locations.

Some results of monitored pore pressures at bedrock level and settlements are shown in Figure 14. Pore pressure measurements indicate that the grouting and infiltration was effective measurements. The pore pressures

recovered and the settlement rate was decreased to the same levels as before the excavation started. Other important measurements were consistent use of packers in every borehole, where leakage was observed, both for drilled anchors and drilled piles. Furthermore, additional infiltration wells were installed trough the sheet pile wall.

4.5 Case study 5

This excavation in Oslo was an approximately 10 m deep and measuring 90 m × 50 m. The excavation was supported by three levels of tie-back anchors. The sheet pile wall was partly installed to bedrock, partly by installing every third nail to bedrock and using stabilisation with lime-cement columns. The soil conditions consisted of 2 m of fill over normally consolidated clay, with a depth of 15-45 m to bedrock. There were 120 steel core piles installed from the bottom of the excavation.

To ensure safety against bottom heave, it was necessary to lower the water pressure by 6 m inside the excavation using a system of relief wells. The water pressures were monitored outside the excavation and four infiltration wells were installed to mitigate pore pressure decrease.
Before the excavation was started, pore pressure levels in the area had already been lowered by neighbouring excavations. However, the excavation process including the use of relief wells, installation of tie-back anchors, and drilling for steel core piles have resulted in a pore pressure lowering of about 30-40 kPa over a period of about 6 months. The infiltration wells were stopped during a short period to evaluate their effect, showing that their contribution for infiltration corresponded to approximately 20 kPa. After the base slab was casted, the pore pressure levels slowly recovered to the initial levels.

5 ANALYSIS OF DATA

To better understand the effects of drainage to excavations in soft clays, the LimitingDamage-project has collected and interpreted data from 17 case histories, together with previously published data from Braaten et. al (2004), Johansen (1990) and Karlsrud (1990).The results are shown in Figure 15. In the plot, the measured pore pressure reduction at bedrock level, Δu, is normalized with respect to the depth of the excavation below the original ground water surface, H_{max}. The data are plotted against the horizontal distance of the piezometer from the excavation. The data from the five case studies are labelled CS1 to CS5.

The data shows a relatively large scatter, related to varying hydrogeological conditions, amount and duration of the leakage, use of different construction methods and varying mitigating measures. However, some general conclusions can be drawn by organizing the data accoring to the mitigating measures that were undertaken.

Red symbols show cases where no grouting or recharging (infiltration) of water was undertaken, green symbols show cases where some grouting at the toe of the wall and into bedrock was undertaken, and blue symbols represent cases where some grouting as well as infiltration was undertaken.

The figure suggests that even when performing systematic grouting and infiltration, the maximum pore pressure reduction close to the excavation could correspond of 20-50% of the depth of the excavation below the groundwater level. Furthermore, a reduction can be extend as far as 300-400 m laterally from the excavation. It can be concluded that it is challenging to maintain the pore pressure levels, even when mitigating measures are undertaken.

Dashed lines in the figure indicate which range pore pressure drawdown can be expected. It is important to note that the lines are rough estimates. The lower bound could be applied for cases where both infiltration and grouting is performed, and the higher bound can be taken as a worst-case scenario where no mitigating measures are undertaken.

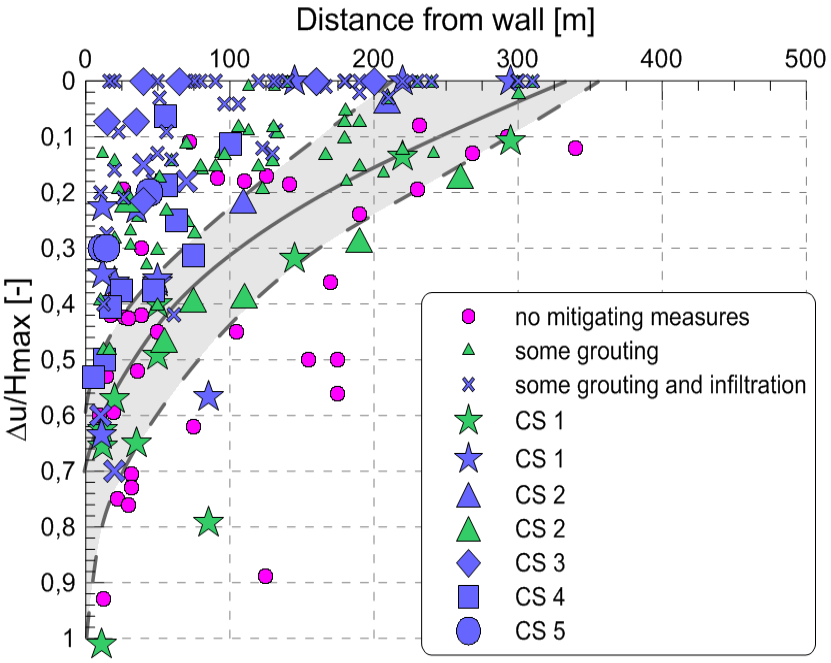


Figure 15 Observed normalized decrease in pore pressure at base of clay layer as function of distance from the excavation based on case records from Norway

However, some projects experience an even larger pressure drawdown, caused by unfavourable conditions at the specific sites.

Analysis of settlement data (Karlsrud et al., 2015) indicate that drilling for piles are associated with a greater risk of leakage than drilling for tie-back anchors. The reason is likely that piles are generally drilled from a deeper level that the anchors. In addition, systematic leakage-testing and grouting for anchors are generally performed to ensure sufficient tension capacity of the grout body. This is generally not undertaken for pile, unless designed as tension pile.

The case records CS1 and CS2 show the largest decrease in pore pressures at bedrock level. For both these projects there was a considerable layer of moraine on top of the bedrock. This is one of the reasons for the relatively large reduction in pressures, due to the fact that there was a large potential for leakage tough the permeable layer at the toe of the wall. In addition, the continuous moraine layer also resulted in a drawdown at a far distance from the wall.

6 CONCLUSIONS

The main conclusion for the analysis of data is that drainage is one of the main causes of settlements that are not accounted for in design. It is seen that measures must be taken from the early planning stage until construction is finished.

6.1 Early design phase

It is important to undertake feasibility studies and assessment of ground conditions including analysis of geotechnical (especially the over-consolidation ratio) and hydrogeological conditions (artesian pressures, sensitivity analysis to drainage), to evaluate the risk of pore pressure decrease with respect to the design depth of the excavation and the distance to the bedrock surface. Time for construction and possible duration for an open excavation pit needs to be evaluated.

At this stage, impact of previous and ongoing construction (ongoing settlements from drainage to tunnels, excavation pits, earthworks and fills, ground water lowering) need to be considered. In addition, alarm limits for pore pressure reduction and requirements for maximum allowable

settlements (including creep) should be evaluated, depending on the sensitivity to damage for buildings, structures and infrastructure surrounding the excavation. The risk for pore pressure decrease due to drilling for tie-back anchors and piles should be evaluated against alternative methods (internal struts and driven piles).

6.2 Detailed design phase

During the design phase, measures to decrease the impact from the excavation and foundation works need to be described:

- Use of temporary packers in casings, and grouting and sealing of boreholes in bedrock
- Assess and choose drilling methods considering risk of erosion, disturbance, drainage
- Request logging of data during drilling

The hydrogeological conditions should be assessed, with respect to permeable layers over bedrock or in the clay, to enable evaluation of the influence of drainage. In addition, hydrogeological tests, geological mapping of cracks and weakness zones can be valuable. Describe measures to prevent drainage into the construction pit, as well as wells for water infiltration.

6.3 Construction phase

A plan for monitoring needs to be established to document the impact of the excavation. Measurements need to start well in advance of construction, to capture seasonal variations in pore pressures, as well as ongoing settlements.

The monitoring of pore pressure should be undertaken in a zone of at least 200 – 300 m, from the excavation to capture the possible effects of drainage. It is crucial to install piezometers in the intersection between clay and bedrock and in permeable layers in the clay, to be able to capture the quick response on pressures caused by drainage.

It is necessary to undertake quality control at the construction site by geotechnical engineers or other qualified staff, including verifying the contractor's procedures and execution for drilling and sealing/waterproofing. Finally, requirements should be made to ensure that the contractors has the requested skills and expertise.

7 ACKNOWLEDGEMENTS

The LimitingDamage-project was financed by the Norwegian Research Council and 22 partner firms, governmental agencies and institutes.

8 REFERENCES

Braaten, A., Baardvik, G., Vik, A. & Brendbekken, G. (2004). Observed effects on the pore pressure caused by extensive foundation work and deep excavations in clay. *Proceedings of the Nordic Geotechnical Conference*, Ystad, Sweden.

Eggen, A. (2015). Erfaringseksempel -bevaring av poretrykk og begrensning av skade. Tekna seminar Grunnvanns senkning og setninger ved dagens urbanisering. 8 oktober 2015.

Johansen, T. (1990). Eksempler fra nyere byggegroper i Oslo (Fjellinjen, Dittenkvartalet). NIF kurs: Tetting av tunneler, bergrom og byggegroper.

Hauser, C (2015). Rapport 20140406-03-R Vurdering av setninger i Oslo S- og Bjørvikaområdet. Statusrapport pr. august 2015.

Karlsrud, K. (1990). Forundersøkelser, funksjonskrav og valg av tettestrategi. NIF kurs: Tetting av tunneler, bergrom og byggegroper.

Karlsrud, K., Erikstad, L. & Snilsberg, P. (2003) Miljø- og samfunnstjenlige tunneler. Undersøkelser og krav til innlekkasje for å ivareta ytre miljø. Statens vegvesen Publikasjon 103.

Karlsrud, K., Langford, J., & Lande E. J., Baardvik G. (2015). Vurderinger av skader og deformasjon knyttet til utførelse av stagforankring og borede peler i byggegroper. BegrensSkade delrapport 1+2.4.

Lande, E. J. (2015). Feltforsøk stagboring. Dokumentasjon av effekter ved boring i leire. BegrensSkade delrapport 4.1.

Johansen, T, Haugen, T. & Brudeseth, Å. Havnelageret – tettbyggegrop i gjenfylt havnebasseng? NFF.Fjellsprengnings-/Bergmekanikk-/Geoteknikkdagen 2008. p 271 – 279.

Peck, P. B. (1969). Deep excavations and tunneling in soft ground. Proc. 7th Int. Conf. on Soil Mech. and Found. Eng. Mexico City. State of the art volume, pp. 225-290.

Statens vegvesen, Vegdirektoratet. Rapport nr. 326. Erfaringsrapport byggegroper. E18 mellom Festningstunnelen og Ekebergtunnelen. Entreprise Havnelageret. Datert 12.06.2014.

Veslegard, G., Lande E. J. & Simonsen A. (2015). Forbedring og videreutvikling borede stag og peler. Metoder, utførelse og dokumentasjon. BegrensSkade delrapport 3.4.

http://www.vegvesen.no/Ferdigprosjekt/Bjorvika/Nyhetsarkiv/

Education of drilling personnel carrying out pile and anchor drilling in Norway – effect on quality and plans for new education in Norway

Ingunn Veimo
Structor Oslo AS, Norway, ingunn.veimo@structor.no

Josefin Persson
Statens vegvesen/Norwegian Public Road Administration, Norway

ABSTRACT
As a part of the research programme "LimitingDamage", it is carried out an interview study on how drilling operators carrying out pile and anchor drilling in Norway are trained.
The background for "LimitingDamage" is that unexpected and undesired damage occur to neighbouring properties and adjacent infrastructure, because of groundwork, and the goal is to find causes and means to limit the damage.

The goal of the interview survey was to identify needs for organized common training. In addition, the desire was to probe the interest of public venues for sharing experiences, and attitudes to certification within the industry.

It was of interest to assess geotechnical understanding among groundwork operators, as this could affect the quality of the work and the possibility to limit damages on neighbouring installations and buildings. It is important to map whether the operators have any chance to learn about geotechnical engineering by training or public venues and if they are interested in such knowledge.

The qualitative interview study consisted of 11 interviews with candidates from seven different foundation companies. The impetus to be interviewed was to have some form of responsibility for training of or be drilling rig operators themselves.

The educational options granted in Sweden and Denmark were also checked out.

It emerges from the interviews that the new drilling rig operators receive in-house training by experienced drillers. The training centres on operating the rig in an efficient manner and maintenance and not on the effects that drilling, e.g. water and air pressure, has on the structures of the soil, i.e understanding of geotechnical effects. The personnel are interested in understanding more of the effects of drilling on the structures of the soils, but have little chance of achieving this kind of knowledge.

Norwegian Association of Heavy Equipment Contractors (MEF) has recently applied to establish a three-year training programme in secondary school level for foundation work

Keywords: Geotechnical drilling works, drilled foundations, micro piles, training of rig operators

1 BACKGROUND

The background for the research project “BegrensSkade”, or translated into English "LimitingDamage", is that ground works such as deep excavations and foundation works performed in soft clay are known to frequently cause damage to neighbouring buildings and structures. The costs related to these types of damage can be substantial and there is probably a large potential for reducing these costs. This is the main topic of the research project funded by the Norwegian Research Council and a wide range of consultants, contractors, clients and institutes.

Improved performance provides savings by reducing the number of damages, facilitating faster implementation, fewer delays and fewer disputes.

"LimitingDamage" aims to develop new methods of execution and improve interaction processes to limit the damage that can be attributed to ground and foundation works in the building, construction and real estate industry. The project has broad support from the Norwegian BAE industry with 23 partners including representatives from all stakeholders (builders, contractors, subcontractors, consultants, real estate and insurance companies as well as research institutes and universities).

The project looks at the whole range of causes and possibilities for improvement from the engineering of ground and foundation work through to the execution and monitoring.

2 TASK DESCRIPTION FOR THE INTERVIEW STUDY

This paper is based on the report from the interview study made by Veimo, I. et al (2015) focusing on the topic "Mapping of Drilling operators’ training in groundwork in Norway".
The main activity for the study was interviews with key people in drilling firms in Norway. Additionally laws and framework governing performance of such work in Norway, as well as the approach to training of personnel in Sweden and Denmark, was reviewed. This paper however, focuses on the training of drilling operators.

A hypothesis is that the industry would benefit from a joint training, which might lead to more equal education and thorough training. This again might lead to better execution of work, and thus as a result less damages caused by foundation work. Said in another way, by better performance through more knowledge, more uniform practices and better reporting, it is likely that the quality of foundation work could be improved.

Possible side effects of common training may be to bring up a discussion on performance between the executing parties as well as to establish contact between personnel that perform the same job in different companies. It is reasonable to expect that arenas for the exchange of experience arise more easily when personnel meet.

As per today, there is little literature on carrying out drilling in Norwegian, anyway which is not related to those supplying equipment. Through systematic training designated training materials would have to be produced.

In the LimitingDamage project, it was also performed comparative experiments in the field of various drilling techniques for drilling rods, and made a report where causes of injuries, phrases and pore pressure variations due to drilling is discussed. Among other things, the use of air pressure and water during drilling are key issues. Knowledge about the mechanisms and causes of reactions in the soil by drilling is very important.

The interview survey focuses on the training of personnel who carry out **drilling** of piles and casings. It may be considered to perform the same kind of research on driven piles,

sheet piling, and installation of rods if "Limit Damage" is expanded later.

3 FRAMEWORK

3.1 Drilling of water wells and drilling for foundations

Drilling of anchors and piles fall under the field of drilling wells and specialty drilling. In industry, it is typical that some firms only are doing well- and specialty drilling and some are working in a wider field within groundwork like sheet piles, driven piles etc. The first group often operates as subcontractors to the latter. This is partly because large projects require larger capacity drilling.
In Norway, there are two associations for well drilling and special drilling. One is Norwegian well driller Association (www.bronnborer.no) and the other is the Department of Low and Special Drilling under Norwegian Association of Heavy Equipment Contractors (www.mef.no). These unions seem to have a good working relationship.
There are no common professional forums for those who carry out practical foundation work where they can discuss their experiences at the operator level. In the interview survey, we ask if there is interest in joint academic arenas.

3.2 Required ssafety and security training

Although there is no requirement for certified training on drilling rigs, the employer is obliged to provide documented safety training (practical and theoretical), if work equipment is considered to require particular care.

3.3 Improved safety and working through drilling

MEF and NAF (regional safety representatives) are working actively to strengthen education within foundation work and safety training for machine operators. This seems to apply both within foundations and rock drilling where there has been many occupational injuries, partly because of dust and noise.

In 2013, the first specialist training for rig operators commenced at the technical college in Stjørdal. However, the number of applications for this study at college level has been low, and MEF has now applied for the establishment of a separate certificate in foundation.

If stricter requirements for training and equipment were to be introduced this would require an amendment of the regulations "Performance of work and use of work equipment". Groups that may have influence on the development of laws and regulations are:
- Regional safety representatives
- Within rock drilling: The reference group for the Labor Inspection’s regulatory forum, and the industry council on tunneling
- The Labor Inspection’s forum for work equipment
- MEF - Norwegian Association of Heavy Equipment Contractors

3.4 The Planning and Building Act, central authentication and search tags

Execution of works involving the drilling rig is regarded as specialist work that should be performed by trained and qualified personnel in order to ensure good quality of execution as well as maintain safety.

Foundation work like piling and sheet piling, including drilling of piles and casings for anchors, fall under the application code “earthworks” in the current Planning and Building Act. Excerpts of the guidance to building regulations (SAK10) which defines the areas for approval with examples show that approval area "earthworks" is a broad. In practice, there are also many machine entrepreneurs / dig firms that use the same authentication area as a special contractor in foundation uses.
This may lead to the requirements of documented knowledge within foundation being too low, or that those with good knowledge of the special work are treated on equal terms as undertakings with lower competence.

In practice foundations, firms sometimes perform work under the main contractor's right to accept responsibility, as the contractor has approval for site preparation, which also includes foundations. A potential separate search code for foundation work may be motivating for specialist companies within foundations. These would require specialist training in this field in order to get approval, which would in turn require the existence of relevant education and courses.

4 INTERVIEW STUDY – IMPLEMENTATION

4.1 Interview Survey

An interview study was chosen as the approach to map current practice of training drill rig operators. Interviews were conducted in the period from February to May, and September 2014. Eleven interviews were conducted.
Choice of interview candidates was random in the sense that the firms contacted picked candidates themselves by the CEO or training / human resources manager. It was requested that the person who was to be interviewed should have primary responsibility for the training of drilling personnel in the current business, but drilling rig operators were also interviewed.

It was decided to interview people in different positions and thus individuals taking part possessed different roles; chairman, mate, construction manager, project manager and experienced drilling operator.
Candidates' age ranged from young people to men with over twenty years of experience.

Information was sent out by e-mail in advance of the interviews. Several of the firms contacted are also partners in "LimitingDamage", and knew the research projects main goals already.

4.2 Main topics

The main goals of the interview survey were:
• To find out how the training of personnel who carry out drilling of piles and struts in Norway is undertaken
• Check the need for/attitude towards joint training, and check what such joint training should encompass
• Identify interest in and possible settings for common arenas for sharing experience
• Map the attitude towards a possible certification for this kind of work

These are further discussed in the next subchapters.

4.3 Mapping of training

Through the interviews, the aim was to answer the following questions:
• Is it true that training varies from company to company?
• Is the training systematically performed?
• Is it easy / hard to conduct training without training material?
• Is joint training desirable?
• Are certification requirements desirable?
• Is it a challenge that there is no official training?

Through the interviews, it was attempted to answer these questions through asking how training was done for the latest new hires at the firm.

4.4 Joint training

The focus of the questions to this topic was to uncover what joint training might encompass. During the interviews both training of personnel already in employment and training of new personnel and recruitment was discussed. The interview subjects were both asked open questions, as well as presented with a list of possible relevant topics in case the interviewee did not have have that many own ideas. Also, the answers from the interviewee was compared to this list. The list comes from the curriculum at the Technical College in Stjørdal.

4.5 Venues for exchange of experience

This point in the interviews was mainly covered through open conversation/ discussion. Initially, some of the candidates believed that they would in any case not have the time or the finances required to allow for such meetings, but after further reflection there were several candidates who expressed

that venues for the exchange of experiences was important. It appeared that the interviews acted to stimulate reflection on this topic for some of the candidates

4.6 Attitudes towards Certification

The topic of certification had in many interviews already entered the discussion previously when you got to this point, e.g. as part of the discussion on the equipment or if the machine operator license came up as part of the discussion on personnel training.
The question was nevertheless brought up at the end again to summarize the attitude towards certification.

4.7 Businesses in the industry

As part of the study, it was attempted to get an overview of the companies in the industry. Below is a list of the companies where interviews were performed, as well as a list of other firms that could have been relevant to talk to.

The capacity to do surveys were limited due to time and resources available, as well as by geography and ability to travel.

Interviews were performed with representatives of the following companies:
- Sør-Norsk Boring
- Brødrene Myhre
- Entreprenørservice
- Fundamentering AS (FAS)
- Nordisk Fundamentering AS, department Smefa and department NSP
- Hallingdal Bergboring
- Seierstad Pelemaskiner

Other potential candidates, not interviewed due to time constraints:
- Holt Risa (now Seabrokers Entrepreneur Service
- HERCULES Fundamentering AS
- Vestnorsk Brunnboring AS
- Båsum Boring
- Norsk Boreteknikk
- Brønn og Spesialboring AS
- KRAFT Energi og Brønnboring

5 SUMMARY OF INTERWIEVS

The outcome of the interviews uncover both similarities and differences between the various drilling contractors and operators. The main results from the interviews can be summarized in five different categories, see below. As can be seen, a new point in addition to those outlined in the interview guide is included, and it is HSE-related issues. This topic often came up in the discussions, and the interviewees asked about their experience with injuries.
The summary is thus divided into the following main categories:

A. In-house training
B. Attitudes towards joint training/courses
C. Common venues for knowledge exchange
D. HSE-related topics
E. Certification

5.1 A. In-house training

Most new employees in drilling firms begin on the floor as mate, in some cases as a welder. They will then usually be appointed an experienced drilling rig operator as mentor/ teacher that demonstrate and instructs them on how to perform the work. They will walk beside the experienced drilling rig operator and get a gradual introduction to the equipment and methods by trial and error with guidance. Many companies have a system for approval of the new drilling rig operator before he can become independent, and often it is an experienced drilling rig operator who gives such approval.

How long it takes a new operator to learn how to maneuver the rig depends on the person. Some learn quickly, while others take longer. It is obvious that people who are used to dealing with machines learn faster and often they can maneuver rig in a week's time. However, it takes longer to become a good drilling rig operator. Candidates reported a span of between 1 and 4 years to become good at drilling and drilling independently.

Once a new employee had begun to drill independently, they could always call for experienced drilling rig operators if there was

a problem. One candidate said that if it were not possible to solve the problem over the phone, the experienced personnel would visit the site to see if it was possible to solve the problem on site. However, one candidate also mentioned that rig operators become independent prematurely because of work pressure and that it would be better if the training period could have lasted longer.

It is considered easier to start with rock drilling compared to soil drilling. This is because it is easier to interpret sound and cuttings from rock drilling. One company reported that they recruit many drilling rig operators from Sweden. This is because they have education in the well drilling and are good at drilling rock. However, they are not as adept at drilling in soils, as this is not included in their education.

One company reported that they have a certificate of drill competence. Other companies viewed this favorably and expressed an interest in similar set-ups. They expressed that there was a competitive advantage when the certificate concerns safety issued and that it is important to establish something similar.

5.2 B. Attitudes towards joint training

The results from questions about training and joint training drilling operators is different. In principle, everyone believes that a common training for drilling operators would be beneficial, but the answers are different when it comes to the time, content and distribution between theory and practice in such training. There are also varying opinions about whether this should be an education at technical college or not.

Many companies wish for a common education in the hope that it will be easier to recruit new people to the firm. All interviewees who participated in the study consider that the training/ course should include both theory and practice. There is a need for courses for both new drill rig operators and those with experience. Such courses could be of varying duration and content depending on the expertise of the participant.

Different proposals came in regarding how long the training should last, ranging from 2 days for experienced drilling rig operator and one month for new employees. Some wanted a longer course up to 2 years, but at the same time, there is a concern that if the training is too long the drill rig operators will not remain within the profession because of high aspirations that drive them to move on with other work. Others believe in an education following high school.

The responses from the interviews are consistent when it comes to that education should include both theory and practice, although in different amounts. Some want a little theory and more practice, while others believe that the practice is taught through at the job training and therefore theory is more important in c course. In general, it may be a challenge that rig operators do not want too much theoretical education, as they have a preference for practical work. As an example, one candidate believed that the Swedish education is too theoretical. There is still a desire by that companies that the drilling rig operators know more about geotechnics.

Several of the candidates believed that the subjects taught in Stjørdal form a good base for training/ courses. What is wanted beyond what exists there is more geotechnics, HSE, and maintenance. The course should also be geared towards geotechnical challenges to capture the interest of drilling rig operators. The theoretical parts of the course should cover geotechnics, geology, drilling techniques and method in order to generate a greater understanding of the craft that a drilling rig operator performs. One candidate expressed that the course should cover new developments, new machines and methods. The practical part should include more on maintenance of machines and hydraulics.

5.3 C. Venues for knowledge exchange

The response to the possibility of creating more common venues for knowledge sharing within the industry was positive. Such venues

might form a good complement to the conferences that exist today, which are often too academic for drill rig operators and foremen. Many said that it might be a good idea to do something in conjunction with fairs where vendors show new equipment. However, if such venues for personnel to meet across corporate boundaries are created they should not be so lengthy that it would negatively influence production. Some thought that it would be difficult to achieve a common day of training and knowledge sharing and suggested instead online training.

The interviews uncovered that there is not much contact between the drilling companies today, and one of the candidates said: "Many entrepreneurs will be reluctant to share information, and therefore it is challenging to exchange experiences."

5.4 D. HSE-related items

Generally, most people were conscious about safety and working environment, and claim that their companies are focused on this too. There are many risky situations occurring during drilling work, and many had also witnessed or heard about accidents. Squeezing injuries and injuries due to falling objects are frequent.

Generally, the candidates were not focused on accidents caused by lack of understanding of soil mechanics, i.e. land and groundwater behavior due to the influence of air and water pressure through drilling.

5.5 E. Certification

There are differing opinions on whether there should be certification required for drilling rigs or not, however, those who do not want such a certificate express that a machine operator license should be required. The interviewees put much emphasis on safety and want a machine operator license/ certification which increases both safety and quality in drilling. Many of the interviewees were generally positive towards a certification.

Several candidates brought up the example that it is not allowed to run a dig at 5 tons without machine operator license, but that there is no requirement to operate a drilling rig at 70 tons. It is a desire that the rules are made stricter in relation to this. As a candidate said: "It is not good that a 16 year old can legally drive such a machine without special training." Otherwise, some thought that it would be difficult to certify the already experienced rig operators. The firms also wanted to know if certification would be a one-time cost or result in a continuous introduction of new requirements.

To summarize, key take-away from the interview study include:
- Beginners learn from experienced drilling rig operators
- It is easier to do rock drilling for starters rather than soil drilling, as drilling in rock provides clearer feedback through to sound etc.
- Machine operator license for drilling rigs should be mandatory.
- There are differing attitudes towards certification by various firm
- Any course should have a large part practical learning. Maintenance of machinery and hydraulics is essential.
- It is interesting to obtain knowledge about the various drilling methods
- Drilling personnel is interested in geotechnics
- Drilling operators are interested in joint training and venues for exchange of experiences
- There is much focus on HSE, and especially safety and working environment. There is less focus and knowledge on risk of damage to the surrounding environment due to land and groundwater behavior through the influence of air and water pressure by drilling

6 TRAINING PROGRAMS NORWAY

This chapter contains an overview of education in Norway on drilling and on general geotechnics for people with practical qualifications. Offerings in high school as part of the programs on building and construction or engineering and manufacturing are not included here.

6.1 Stjørdal Technical College

A training scheme has been developed at Stjørdal Technical College as a one-year program with a scope of 60 credits. The program is organized in modules with both theoretical and practical training.

Candidates would be specialized in one of the following three areas:
1. Foundations
2. Drilling for rock blasting
3. Well drilling

Common topics for all three specializations:
• Machinery and equipment
• Applied geotechnics and geology
• Quality assurance and HSE (laws and regulations, standards and contracts).
• Communication (drilling report, work procedures, checklists)
• Surveying (coordinates and altitudes, launching and surveying points)

6.2 Purposed education program

Heavy Equipment Contractors Federation (MEF) has submitted an application to the Directorate of Education on the establishment of a separate certificate for "Foundation work" in secondary school.

Four different modules are planned:
- Well Drilling
- Rock work (rock blasting, injecting, rock support)
- Foundations (piling, sheet piling and shoring, anchoring)
- Directional drilling

In the draft curriculum received from the MEF in June 2014, it appears that there are also plans for a common part covering the following topics:
• Laws and regulations
• Relevant standards
• Production
• Drilling technique
• Machinery and equipment
• Quaternary Geology
• Hydrogeology
• Safety
• Quality assurance

6.3 Geotechnical subjects in Well Water Project in Buskerud

In connection with the project "Good Water" being implemented in the Drammen region to ensure good water supply in the future (http://www.godtvann.no/), some study programs were created at Buskerud and Vestfold University College.
A course called Geotechnical construction and organization has been taught as part of a bachelor called "Water and Environment". This subject has been taught for personnel with practical competence, and has been possible to take as individual subjects through workshops.

This example is included here to show that there are few opportunities to gain insight into geotechnics without taking engineering education or studying at the university level, but these opportunities are not many in Norway at present.

6.4 Flexible learning, basic geotechnics

A course is under development in flexible learning in basic geotechnics at “Norgesuniversitetet”.

An overarching aim is to increase cooperation between academia and the workplace to raise the geotechnical expertise in the industry. A prerequisite for achieving this is to take advantage of flexible distance learning.

A project consortium has been created with several participants, among them universities, private and public institutions.

The course consist of the following modules:
• Module A: Soil Properties
• Module B: Field and lab
• Module C: Geotechnical structures
• Module D: Calculation
• Module E: Construction geotechnics

6.5 Other courses

Several associations can be/are initiators of courses in geotechnical and drilling technique:
• Tekna

• Norwegian Geotechnical Society (NGF)
• Machine Contractor (MEF) union branch Well and special drilling
• Pile and steel sheet pile contractors association
• Norwegian well drillers association

Tekna and NGF collaborate on courses within geotechnics. In 2014 they had courses in "Stability" and "Peleveiledningen" and "Ground drilling". Courses are generally theoretically based, with the exception of the basic drilling course, and are aimed at engineers who already have basic geotechnical expertise.

MEF has more practically oriented courses for contractors. They provide, for example, courses in piling machines with duration two days. The course gives, together with 40 hours of documented experience, expertise license in piling rigs.

There is as far as we know, little cooperation between the various associations on giving courses. Here the industry has something to gain by better cooperation.

7 7 EDUCATION IN NEIGHBORING COUNTRIES

7.1 Training in Sweden

In Sweden drilling personnel are educated through GEOTEC, which is the well drilling industry's association. They have approximately 80 member companies. GEOTEC offer courses and as a voluntary certification scheme.

SAFE Swedish Grundläggning is a Swedish association for foundations firms. SAFE offers educational programs for operators and functionaries where part of the training is common.

7.2 Training in Denmark

In Denmark, there is training organized by the Association of Danish Well drillers. (www.broendborer.dk)

The following describes the contents of a part of the courses:
• "Removing and description of drill samples" contains a thorough review of Denmark's geological history from the Cretaceous to the present. Moreover, efforts are sampling and description and the legal requirements for reporting to GEUS.
• "Maintenance of equipment and materials" deals including hydraulic systems, pump technology and a statutory welding environment courses.
• "Applied drilling technique» undergo all common drilling methods to onshore drilling compared geology and purpose.
• "Management of drilling tasks" undergoing the relevant legislation and provides an introduction to hydrogeology and water chemistry. Groundwater Lowering be reviewed with calculation examples.

In Denmark, in addition to learning the actual drilling, the courses much focus on the environment and pollution risk. Drilling causing spreading of contamination in groundwater is an important issue in the practice of drilling in Denmark.

8 MAIN CONCLUSIONS, SUGGESTIONS FOR FURTHER WORK

Interviews with eleven candidates from seven different firms have been conducted during winter and spring of 2014 to study the training of personnel who carry out drilling of piles and casings.

In short, the typical findings from the interview study are the following:
- There is a requirement for documented safety work
- Beginners learn from experienced drilling rig operators
- It is easier to do rock drilling than soil drilling for starters, as drilling in rock provides clearer feedback through to sound etc.
- "Heavy Machine driving License" required to drive almost all other equipment like digging machines and groundwork machines should be mandatory also for drilling rigs

- There are differing attitudes towards certification by various firms
- Any course should have a large share of practical learning. Maintenance of machinery and hydraulics is essential
- Insight into the drilling methods and choice of these is interesting to obtain
- Drilling personnel are interested in geotechnics
- Drilling operators are interested in joint training and venues for exchange of experiences
- There is a lot of focus on HSE, and especially safety and working environment. There is less knowledge about risk of damage to the surrounding environment due to land and groundwater behavior through the influence of air and water pressure by drilling

8.1 The way forward

Approval plans in the Planning and Building Act reflects to a small degree foundations and foundation drilling as a specialty. This is another common trait that affects several types of specialty contractors, but should be communicated in the appropriate fora that could cause a small advantage for those who decide to invest in expertise and training. There are several programs in geotechnics and drilling technique under development in Norway now. Among other things, an online course in basic geotechnical, and a certificate in foundation. Within the well and rock drilling there education in both Sweden and Denmark, and one can gain experience there. It is for the group's assessment a minimum to get a claim for machine operator license to carry a drill carriage. Limit Damage to communicate this to the legislators. It should also develop training associated secondary schools that provide some deeper insight and which also ensures recruitment to foundation industry. Limit Damage and MEF should have experience and cooperation on a training plan for drilling operators. Geotechnical Training offered to a small degree for people in the workplace who are not trained in geotechnical engineering from the University / College. Conferences and seminars organized by Tekna and NGF are mostly adapted to this group. It may hinder their expertise spread among more convenient personnel and officials in the construction industry. Missing basic geotechnical competence affecting insights into subjects and workmanship and in turn the quality. In a collaboration between the various associations can develop courses more geared toward entrepreneurs with a practical aspect, and undergo basic geotechnical expertise.
The group proposes that consideration should be given to making the same kind of investigations for example, driven piles, sheet piles, and installation of rods. There has been expressed a desire within the research project "LimitingDamage" to make such investigations in relation to the other disciplines within foundation work as well.

8.2 8.2 Main conclusions regarding courses and exchange of experience

The interviews and the communication environment in general are the following:
• NGF and Tekna organizes today courses in soil mechanics and foundation.
• MEF or similar organizations where contractors and suppliers are more strongly represented should be encouraged to arrange courses in geotechnical and drilling technique.
• Training and exchange of experiences within foundation and geotechnical engineering should be arranged both for the practical construction industry and for the more theoretical advisor industry.
• It is possible to build on the mandatory safety training and the machine-specific training.

9 REFERENCES

Veimo, I., Tvedt, G., Person, J., Johansen, G.M., Lohmann, J. (2015) Kartlegging av maskinoperatørers opplæring innen grunnarbeid

Design of Retaining Walls at Metro Nordhavnen – a Case Story

A. M. Dam
Züblin A/S, Denmark, asbjoern.dam@zueblin.dk

ABSTRACT
Zûblin A/S is a part of the MetNord JV who carries out the construction of the Metro Cityringen – Branch off to Nordhavnen. The project consists of the Nordhavn Station, a Cut and Cover tunnel, a Ramp which takes the trains back to the ground level and a bored TBM tunnel. Züblin A/S has been responsible for the design of the temporary structures which mainly is carried out as multiply supported secant pile walls, supported by ground anchors.

The first design was carried out by modelling the secant pile walls with SPOOKS which uses the theory of Brinch Hansen, and commonly used in Denmark, for the ultimate limit state and the finite element program PLAXIS for the serviceability limit state. Due to the limitation of Brinch Hansen's theory and the discussion about stress-strain compatibility, the Employer had doubt that the deformations necessary for obtaining full active and passive earth pressure were sufficient. Therefore the final design ended up being a combination of SPOOKS for the ultimate limit state and a PLAXIS model for ultimate limit state and serviceability limit state to verify the results of Spooks.

The results of the different design methods are compared together with measured anchor loads from load cell installed on site.

Keywords: Case story, retaining walls, PLAXIS

1 INTRODUCTION

As a part of the Metro Cityringen in Copenhagen the Joint Venture (MetNord JV) consisting of Züblin and Hochtief is building the first part of the branch off to Nordhavnen, consisting of a Station box, Cut & Cover tunnel and a Ramp going towards the surface and an elevated track, see Figure 1.

The retaining walls for the Station Box are made of permanent secant piles supported mainly by 3 layers of temporary pre-stressed ground anchors. The retaining walls for the Cut & Cover tunnel are temporary secant piles supported by 1 and 2 layers of pre-stressed ground anchors. The Ramp area is made with permanent sheet piles and supported by 1 layer of permanent pre-stressed ground anchors.

The deepest excavation, where the TBM drive will start, is around 18 m and decreases along the entire alignment towards the end of the ramp section.

This article will focus on the design of the secant pile walls of the Station Box and the Cut & Cover Tunnel in the temporary situation, where two cross sections will be used as examples. The secant piles have a diameter of 1.2 meter and c/c distance of 0.9 – 1 meter and reinforced by reinforcement cages. The wall is used as cut off wall for the ground water and is therefore drilled and casted until level -20 (DVR90).

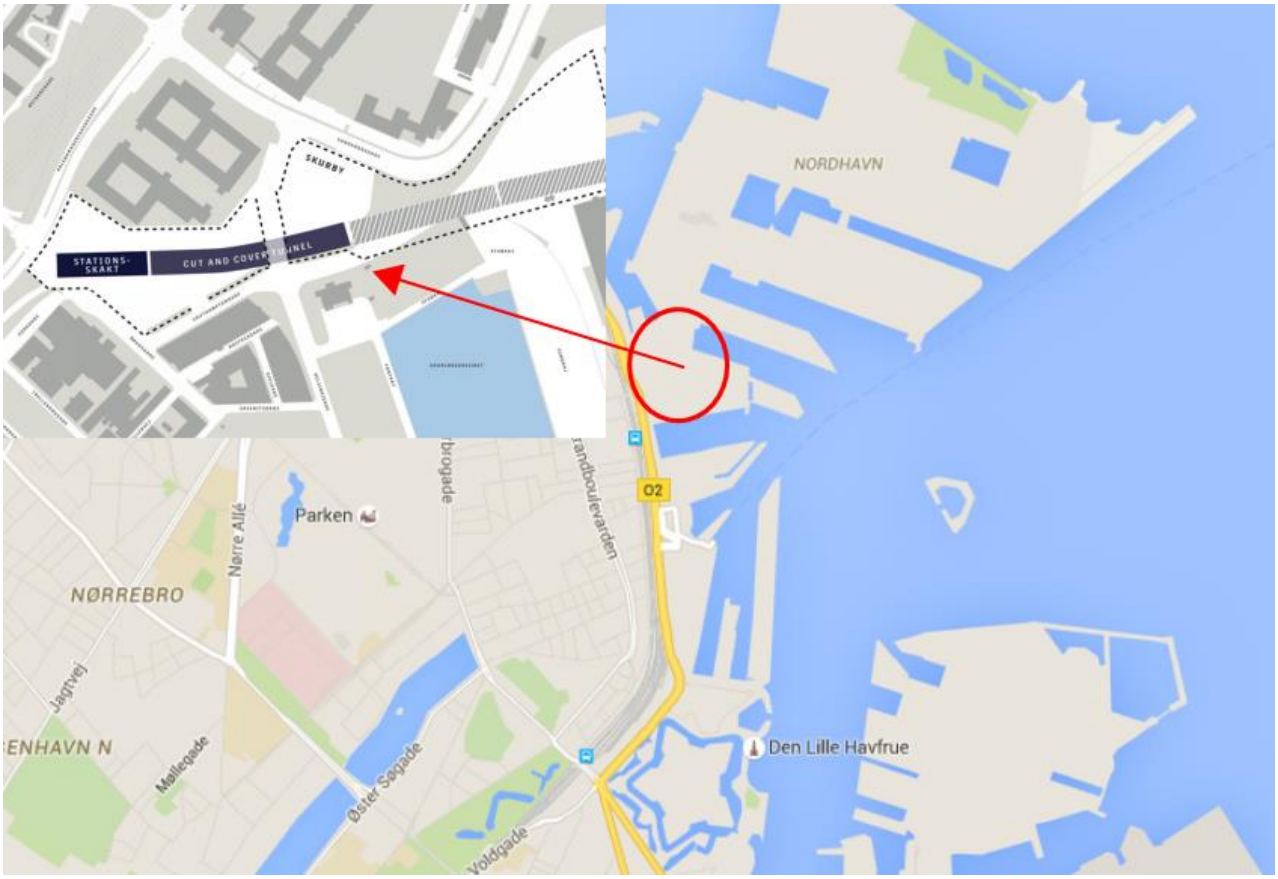


Figure 1: Location of the new Nordhavn Station with Station Box, Cut & Cover tunnel and Ramp (maps.google.dk & m.dk)

2 SOIL AND GROUND WATER CONDITION

2.1 Soil condition

The boreholes made on the location shows fill layers with a thickness variating from 3.5 meter to 11 meter. That matches the fact that it is an old harbour area which is backfilled. Under the fill layer a 2.5 meter to 10 meter thick clay till layer with lenses of sand till and melt water sand is registered. Normally the clay till layer is located on top of the limestone, but in some areas a 6.5 meter thick sand/gravel layer is found. The top level of the limestone is varying throughout the area and has a glacially disturbed zone of around 1 meter. On the safe side a thickness of 2 meter disturbed limestone has been used in the design. The characteristic drained parameters used for the design is shown in Table 2.

2.2 Ground water levels

For the design, a primary and secondary water table is taken into account. The ground water levels used can be seen in Table 1.

Table 1: Ground water level used in the design

Design state	**Primary GWL**	**Secondary GWL**	
		Top level	**Bottom level**
ULS	+1.4	GL	Lower side of fill or clay till layer
SLS	+0.1	GL	

3 DESIGN OF SECANT PILE WALLS

The secant piles are designed in both ultimate limit state (ULS) and serviceability limit state (SLS). The SLS was decisive for amount of reinforcement in the piles as the Employer have strict demands for the crack width at permanent structures. That means that the crack width must not exceed 0.2 mm. In

Table 2: Characteristic strength and stiffness parameters used in the design

Soil layer	Density γ/γ'_m	Plane friction angle φ'	Effective cohesion c'	Oedometer modulus E_{oed}	Poissons ratio ν
	[kN/m3]	[°]	[kN/m2]	[MN/m2]	[-]
Fill	17/19	30	0	3	0.3
Sand	20/20	36	0	15	0.3
Sand till	21/21	40	0	$20+1500\sigma'_{red}$[1]	0.25
Clay till	22/22	34	20	$12+1500\sigma'_{red}$[1]	0.3
Disturbed Limestone	22/22	45	50	750	0.25-0.30
Limestone	22/22	45	100	900	0.25-0.30

[1] *σ'_{red} [MN/m^2] is the vertical stress corresponding to the lowest stress level the soil layer has been subjected to*

many cases the critical part for the crack width was deep under the final excavation level and in that region of the wall which is not necessary for the structural point of view but only as cut off against water.

3.1 SPOOKS

The first design of the secant pile walls was done with the program SPOOKS which uses the earth pressure theory of Brinch Hansen, (Hansen, 1970). The theory is using a combination of zone and line rupture. Furthermore the theory also state, that the necessary displacement to mobilize active and passive earth pressure will be present. From SPOOKS it is possible to get the anchor forces, bending moment and necessary toe level of the retaining wall.

When using SPOOKS it is only possible to add one real anchor layer. When designing multi supported walls, it is necessary to add some of the anchor levels as so called additional pressures. Furthermore it is necessary to check if the anchor force is correct in order to obtain a statically correct solution. The results of the SPOOKS calculations for cross section D and cross section K are shown in Table 3.

Cross section D is a part of the Station box, while Cross section K is a part of the C&C tunnel.

Table 3: Design forces calculated with SPOOKS

	Cross section D	Cross section K
A_1 [kN/m]	230	195
A_2 [kN/m]	636	648
A_3 [kN/m]	388	-
M_{max} [kNm/m]	818	792
Toe level [m]	-16.4	-16.3

The two cross sections are used for comparison as the soil profiles are similar to each other.

3.2 Limitations in SPOOKS

Even though SPOOKS is a well-known program, and has been used in many years, in Denmark, for design of retaining walls, the Employer was concerned about the limitation that it have. The major points for the Employer were:

- Lack of soil-structure interaction, meaning that no stiffness of the system is taken into account.
- Insufficient compatibility between strain and stresses.
- The extra embedment in limestone, which SPOOKS do not take into account.

The Employer was concerned that the deformation necessary to mobilize active earth pressure could not appear as the general system was too stiff. This means that the anchors would be designed for a too low

anchor force. Furthermore the Employer would not accept that the extra embedded part was disregarded even though it does not have any statically importance.

Different approaches were used to convince the Employer about the validity of the design. The first approach was a beam calculation with the earth pressures calculated in SPOOKS together with the effective bending stiffness of the wall, which is determined according to DS/EN 1992-1-1. The deformations were then compared with the deformation requirements in DS/EN 1997-1-1 Appendix C.3. As this was not satisfying for the Employer it was agreed to verify the SPOOKS calculation with an ULS calculation in PLAXIS together with the SLS calculation.

3.3 PLAXIS calculation

The PLAXIS calculation is carried out as a 2D plane strain model with a Mohr-Coulomb soil model with drained parameters. The wall is modelled as a plate element and the ground anchors are modelled as node-to-node anchors with geogrids as the bonded length.

The ULS calculations are carried out with the Design Approach function where the partial safety factors are applied to the soil after the SLS calculation phase. This is done for each excavation sequence where the excavation level is 0.5 meter below the anchor level. An example of the cross section with soil stratigraphy is presented in Figure 2.

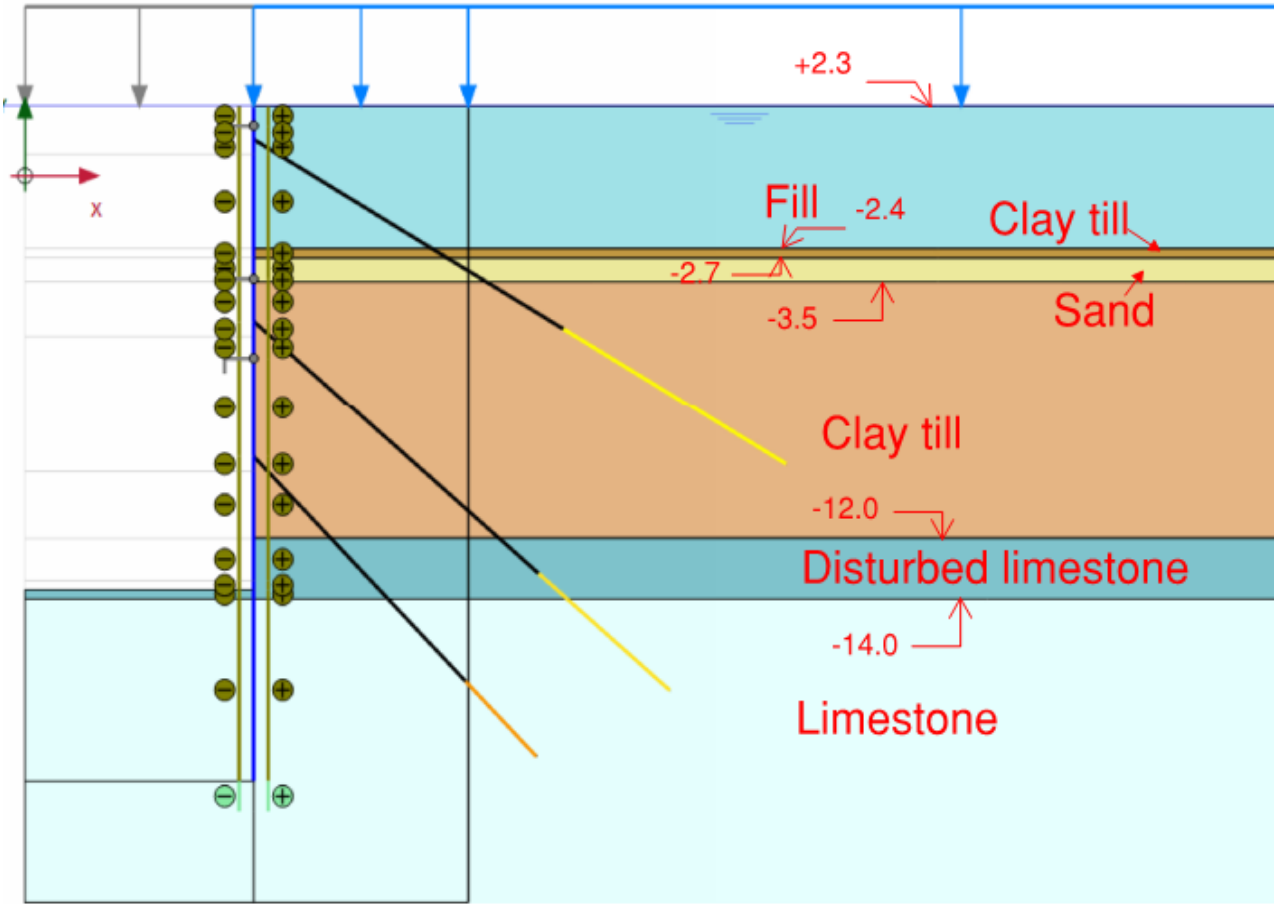


Figure 2: Cross section D with soil layers

The pre-stress load for the anchors is based on the anchor forces found from the SPOOKS calculation. The maximum bending moment and anchor force for the ULS and SLS calculation in PLAXIS are shown in Table 4.

Table 4: Anchor forces and bending moments from PLAXIS calculation

	Cross section D	Cross section K
	ULS / SLS	**ULS / SLS**
A_1 [kN/m]	205 / 180	211 / 186
A_2 [kN/m]	688 / 676	661 / 617
A_3 [kN/m]	384 / 367	-
M_{max} [kNm/m]	709 / 721	926 / 781
Toe level [m]	-20	-20

When comparing the results for Cross section D with the SPOOKS calculation, both the ULS and SLS PLAXIS calculation shows higher anchor force for the second anchor layer, while the other anchor forces are within the same range. The bending moment is around 15% higher in the SPOOKS calculation that in the ULS PLAXIS calculation.

In Cross section K is the anchor forces in both ULS PLAXIS and SPOOKS are within the same range, but the bending moment in the ULS PLAXIS is around 17% higher. This is due to the extra embedment in the limestone which makes it possible to carry more loads in the limestone. This is the SPOOKS calculation not able to take into account. The higher load is present in the part which is not statically needed and it can therefore be discussed if it is relevant for the design.

It is clear that the SLS calculations show values close to the ULS values. This indicates that the active and passive earth pressure in ULS and SLS are similar even though the soil parameters are reduced in the ULS calculations. This could be an indication of missing soil-structure interaction, but that will not be investigated further in this article.

4 COMPARISON WITH MONITORING PROGRAM

During the entire construction period a large monitoring program is in place. The monitoring consists of both inclinometers for deformations and load cells on the anchors to measure anchor forces.

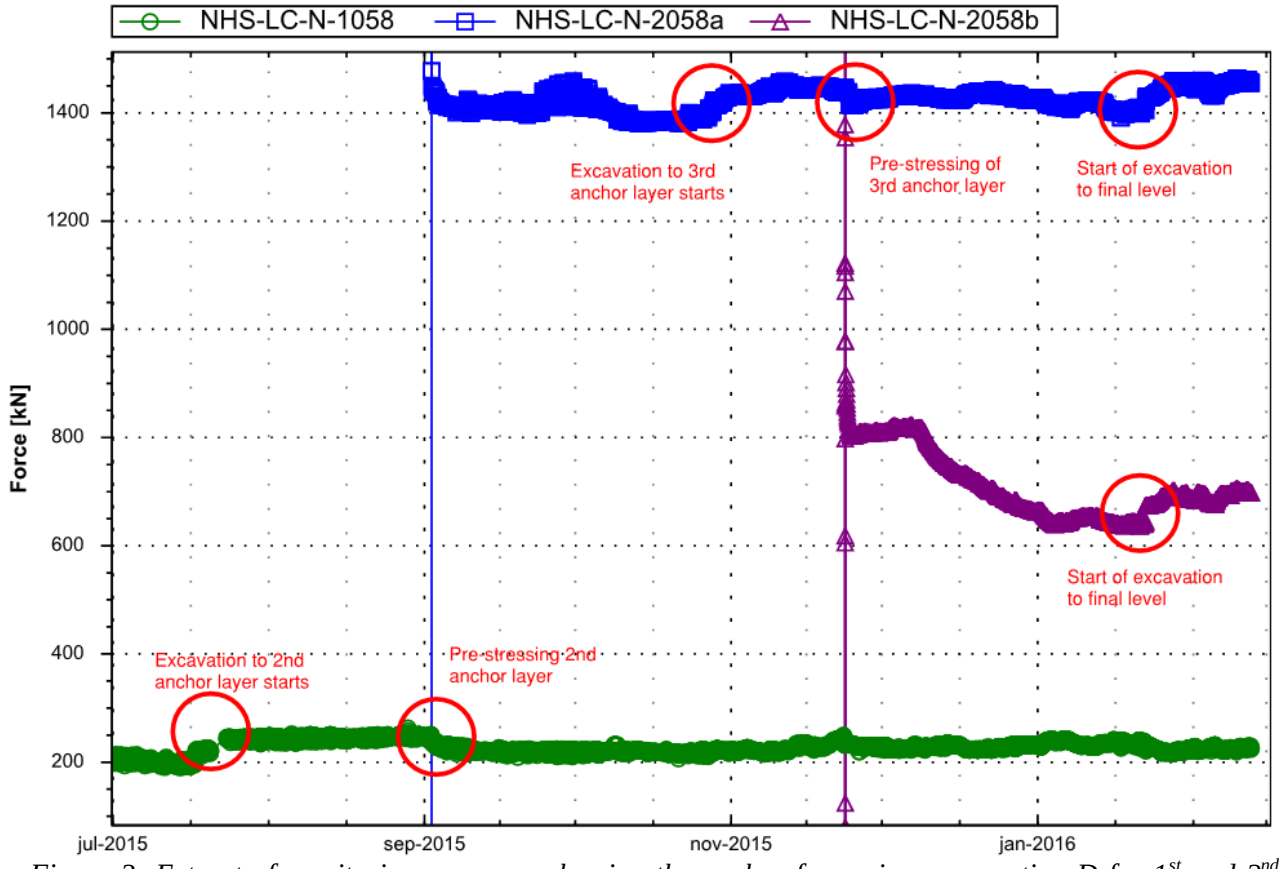


Figure 3: Extract of monitoring program, showing the anchor forces in cross section D for 1st and 2nd anchor layer. The green line is 1st anchor layer, the blue is the 2nd anchor layer and the purple line is 3rd anchor layer.

Looking at the actual anchors forces, see Figure 3, it can be seen that the anchor force in the 1st layer is locked at around 200 kN (87 kN/m). During the excavation to 2nd anchor layer the load increases to around 250 kN, which correspond to 108 kN/m, which is 40% less than calculated in PLAXIS for SLS. When pre-stressing the 2nd anchor the load decreases to around 220 kN (96 kN/m). During the excavation for 3rd anchor layer the load is slightly increased, but decreases again when pre-stressing 3rd anchor layer, meaning the forces is redistributed as expected. For the 2nd anchor layer the pre-stress is around 1400 kN (536 kN/m). As for the 1st layer the anchor load is increasing when the excavation to 3rd anchor layer starts. At the point where the excavation level were reached the anchor force is around 1440 corresponding to 551 kN/m, which is around 18% lower than the calculated SLS value. As the 3rd anchor layer is pre-stressed to around 810 kN (286 kN/m) the anchor force in 2nd anchor layer decreases, as expected, to 1420 kN corresponding to 502 kN/m. During final excavation the load is increasing in both 2nd and 3rd anchor layer and 3rd anchor layer has increases to 700 kN corresponding to 248 kN/m which is 32% lower than estimated in PLAXIS.

It is clear that something is happening in 3rd anchor layer after pre-stressing and it seems that the anchor somehow loses anchor forces even though no activities is going on in the area and therefore no movement of the wall is present. Internally discussions are still ongoing in order to clarify the strange behaviour.

At present there have not been any excavation for Cross section K yet, therefore no measurement can be included in this article.

5 LESSON LEARNED

During the design process of the retaining walls, it has become clear that when designing walls with more than two anchor layers, a kind of Finite Element Method have to be introduced to verify the results founded by the more simple calculation made in SPOOKS. Furthermore the FEM ensure a more correct load distribution to anchors and the wall itself. By introducing FEM in the design it could also reduce the discussion about inadequate compatibility between strains and stresses in the soil as the correct soil-structure interaction is included.
On the other hand one should also keep in mind that the FEM is also just as much a model or method as the SPOOKS calculation and it is therefore difficult to conclude which of the method that is most correct. In the FEM program a lot of different adjustment can be done and it is easy to overlook the consequences when dealing with complex systems. The best way to get an idea of the correct model is to include the monitoring as for example load cells and in that way get an idea of the most correct method and model.

For this project the monitoring shows in general the expected tendencies in respect of increase and decrease of anchor loads during excavation and pre-stressing, but the values of the loads is not in line with the expected values, which could have many explanation, e.g. too conservative soil parameters.

6 REFERENCES

Hansen J.B., “A revised and extended formula for Bearing Capacity”, Bulletin 28, the Danish Geotechnical Institute, 1970.

Suction caissons subjected to monotonic combined loading

B. Penzes
Technical University of Denmark, Kgs Lyngby, Denmark, balint.penzes@gmail.

M. R. Jensen
Technical University of Denmark, Kgs Lyngby, Denmark, mellejensen@hotmail.com

V. Zania
Technical University of Denmark, Kgs Lyngby, Denmark, vaza@byg.dtu.dk

ABSTRACT
Suction caissons are being increasingly used as offshore foundation solutions in shallow and intermediate water depths. The convenient installation method through the application of suction has rendered this type of foundation as an attractive alternative to the more traditional monopile foundation for offshore wind turbines. The combined loading imposed typically to a suction caisson has led to the estimation of their bearing capacity by means of 3D failure envelopes. This study aims to analyse the behaviour of suction caissons for offshore wind turbines subjected to combined loading. Finite element models of the caisson-soil are developed in order to derive the failure envelopes considering both sand and clay profiles. The numerical modelling is being validated by the failure mechanisms reported in the literature for skirted foundations. The sensitivity of the load response curves on the selection of the constitutive soil model is examined. The failure envelopes of a single suction caisson obtained by the numerical models are in good agreement with the corresponding ones suggested by closed-form expressions.

Keywords: suction caisson, failure envelope, numerical modelling, combined loading.

1 INTRODUCTION

In the recent years the energy industry has promoted deeper water installations in seek of increased capacity resources. Thus, floating structures and large wind turbine farms have been increasingly developed and this has favored alternative geotechnical solutions like the suction caisson. The suction caisson foundation system has significant advantage regarding the installation time and cost, and the material requirement compared with the traditional foundation systems, like monopiles. It has been extensively used so far as anchor for mooring systems for buoyant platforms in the offshore oil and gas industry (Andersen et al., 2005). Lately suction caissons have been also suggested as foundation for offshore wind turbines either as monopod or as tripod (Houlsby et al., 2005, Senders 2008). The only known suction bucket foundation which supports an offshore wind turbine is the one installed in 2014 as part of the Borkum Riffgrund Wind Farm. In addition, there have been three successfully installed suction buckets which support met-masts (Horns Rev II, Dogger Bank) and some more intended to support platforms. Furthermore, two prototype projects have been carried out (Wilhelmshaven, Frederikshavn).

The suction caisson is open-ended at the bottom and closed at the top, and installed by applying under-pressure within the caisson after it has penetrated into the seabed by self-weight. The suction caissons are typically made of steel and have a length to diameter ratio (L/D) of 1 to 6. One of the design issues of suction caissons is their capacity when subjected to combined loading. The studies of the bearing capacity of suction caissons in clay for combined V-H loading have concluded in analytical expressions of failure

envelopes, as those proposed by Senders and Kay (2002) and by Supachawarote et al., (2004) after finite element analysis. Extensive experimental investigation of suction caissons in loose and dense sand has resulted in failure envelopes for M-V and H-V load combinations (Byrne, 2000), while recently further experimental results suggest a revised form of the M-V failure for dense sands (Larsen et al., 2013).

The present study aims at analyzing numerically the bearing capacity of suction caissons when subjected to combined V-H loading. Three dimensional (3D) finite element models are developed to study the failure mechanisms of suction caissons in dense sand and in normally consolidated clay. In the case of the sand profile, two different constitutive soil models were examined to analyze the effect on the failure mechanism, while in clay two clay profiles, one with an undrained shear strength profile proportional to depth and one with constant shear strength, were considered. The numerical modelling was validated by the failure mechanisms reported in the literature for skirted foundations. Finally, V-H failure envelopes for the chosen loading conditions were developed for both sand and clay and compared with the ones reported in previous studies.

2 METHODOLOGY

2.1 Numerical modelling

In this study 3D finite element models of monopod caissons were developed in Plaxis 3D AE (Brinkgreve et al., 2015). Due to the symmetry of the geometry and the loading direction only half of the problem was modelled to reduce the simulation time. The suction caissons were wished in place with 6m of diameter, the length to diameter ratio L/D was 1.0, and they were considered as rigid. The boundary conditions were defined as constrained DOF perpendicular to each lateral plane and fully constrained at the bottom of the soil layer. In order to achieve sufficient accuracy and convergence an additional zone with the depth and radius of 2D was defined and a finer mesh close to the caisson was established after convergence analysis, as shown in Figure 1.

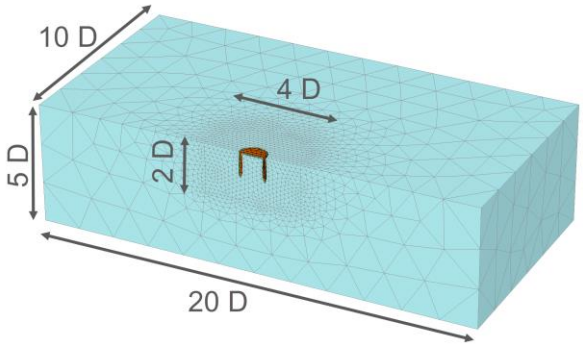


Figure 1 Finite element model of the suction caisson and boundary conditions

2.2 Soil modelling

Two soil profiles were considered representative of normally consolidated clay: (a) undrained shear strength increasing proportionally with depth (z), according to s_u=4.0+5z kPa and (b) constant undrained shear strength of s_u=10.0 kPa. A constant Young modulus ratio was adopted, with E/s_u of 500, and Poisson's ratio was taken as ν = 0.495. The soil parameters for dense sand were the following: the internal angle of friction φ' = 40°, dilation angle ψ = 10° and Poisson's ratio ν = 0.35, cohesion c = 1 kPa. The Young modulus for the Mohr-Coulomb soil model was set to E = 70 MPa. The additional parameters for the HSsmall model (Benz, 2006) are summarized in Table 1. The interface strength properties were assigned to be identical of those of the soil material.

Table 1 Additional soil properties for dense sand

Parameter	Symbol	Value
Elastic modulus	E_{50}	28.5 MPa
Oedometric modulus	E_{oed}	35.2 MPa
Unloading/Rel. modulus	E_{ur}	85.6 MPa
Initial shear modulus	G_0	103.5 MPa
Ref. shear strain	$\gamma_{0.7}$	0.14 mm/ma
Earth pressure coefficient	K_0	0.37

2.3 Modelling approach

The analysis included the following calculation steps: (a) the geostatic phase, when initial stresses were established, (b) the installation of the caisson, by activating the

predefined geometry with the positive and negative interfaces in order to simulate the soil-structure interaction, (c) the loading phase, with vertical, horizontal and inclined applied forces, which were concentrated at the center of the caisson with an angle of 30°, 40°, 50°, and 60° from the horizontal axis. In this study the load, or stress controlled approach was applied for the caissons in clay, while for dense sand, the displacement controlled method was used in order to reduce the convergence issues and to minimize the local stress concentrations at the structural edges during the loading.

Special attention has been drawn to the modelling of the frictional material. The plastic potential in this case can be described based on the application of the associated or the non-associated plasticity theories (Chen & Liu, 1990) in the numerical model. In the case of the simple Mohr- Coulomb failure criterion this is translated as the following two cases: (a) the dilation angle is set equal to the friction angle ψ=ϕ' (associated) and (b) the dilation angle is an initially small value or equal to zero ψ=0° (non-associated) (Vaitkunaite et al., 2012 and Lyamin et al., 2007). However, the true behavior of the dense sand is somewhere between (Potts & Zdravkovic 1999 and Vaitkunaite et al., 2012). Hence as suggested by Bolton (1986) and Houlsby (1991) the dilation angle can be given by:

$$\psi = \varphi' - 30° \quad (1)$$

The available solutions in the literature, which are based on two and three dimensional finite element limit analysis considering associated plasticity theory (Lyamin et al., 2007), can be useful as validation to the adopted numerical modelling approach. Therefore in the present study the axial bearing capacity was investigated on the basis of both plasticity theories. A parametric study was performed to examine the effect of the dilation angle (ψ=ϕ'; ψ=0°; ψ= ϕ'-30°) and the strengthening of the interface element in case of both plasticity theories.

The results of this investigation indicated that a good balance between convergence and accuracy could be obtained for the non-associated model (ψ= ϕ'-30°) which was further applied for the combined loading and the effect of the Mohr-Coulomb and the HSsmall models were studied in case of dense sand.

3 DISCUSSION AND RESULTS

3.1 Axial bearing capacity in dense sand

At first the axial bearing capacity was investigated considering the associated plasticity theory, which meant that the dilation angle was set as ψ=ϕ'=40°. Several convergence issues emerged in this attempt, and a feasible solution was pursued by: (a) changing different numerical control parameters, (the solver, and the arc-length control types as suggested in Brinkgreve et al., 2015), and (b) examining the sensitivity to the strength of the interface and the soil shear strength properties. Nevertheless, none of the above mentioned variations could reach a numerically acceptable outcome. Thereafter the dilation angle was set to zero (ψ=0°) and following Eq (1) as ψ=10° in order to model the non-associated plasticity theory. In this case, convergence issues were met at an early stage of the loading. These issues were attributed to the shear failure along the interfaces, which did not allow the application of higher loading. As a result, the soil bearing capacity was not fully mobilized and the ultimate load could not be assessed. A parametric study was carried out in order to investigate the effect of a strengthened interface on the failure mechanism. As a result of this parametric analysis the cohesion of 70 kPa in the interface was found adequate without any influence on the bearing capacity.

Table 2 The axial bearing capacity of the symmetric caisson foundation in sand

$V^{ult\ (Lyman\ et\ al.)}_{associated}$ $(\psi = 40°)$	$V^{max\ (Plaxis\ 3D)}_{non-associated}$ $(\psi = 0°)$	$V^{ult\ (Plaxis\ 3D)}_{non-associated}$ $(\psi = 10°)$
$661 \cdot 10^3\ kN$	$660 \cdot 10^3\ kN$	$744 \cdot 10^3\ kN$

In Table 2 the ultimate bearing capacity is reported for the various dilation angles considered in this study. The calculated value based on Lyamin et al. (2007) provides an

indication of the load based on the associated plasticity theory. It can be observed that the vertical ultimate load of the non-associated model is significantly larger, which emphasize, that the axial bearing capacity is highly depend on the dilation angle (Houlsby, 1991).

3.2 Combined V-H loading in dense sand

The failure mechanisms for the dense sand profile were analyzed for inclined loads at 30^o, 40^o, 50^o, and 60^o with the horizontal axis. In Figure 2 the incremental deviatoric strains contours depict the failure zones developed for horizontal, vertical and two inclined load cases.

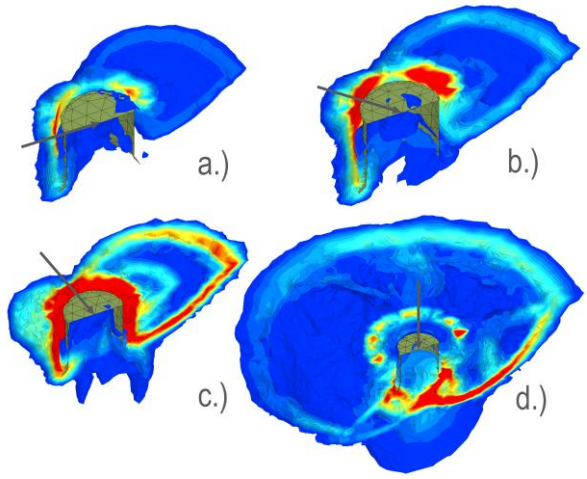


Figure 2 Failure zones in dense sand (M-C soil model) for (a) horizontal, (b) 30^o, (c) 60^o and (d) vertical load.

The failure surface does not extend to the tip of the skirt in the horizontal loading case (Figure 2a.) which is probably related to the absence of passive failure. As the inclination of the load increases, the failure wedge extends to the tip of the skirt and further away laterally as well (Figure 2b and 2c). Because of the vertical load component there is some indication of shaft failure around the caisson which is particularly evident in the case of 60^o load inclination. A fully developed Prandtl-type failure mechanism was observed in case of vertical loading (Figure 2d), which illustrates a wedge at the caisson tip and an extended failure zone propagating to the soil surface.

The effect of the selected constitutive soil model on the failure surface was also investigated and the corresponding results obtained with the HSsmall soil model are shown in Figure 3.

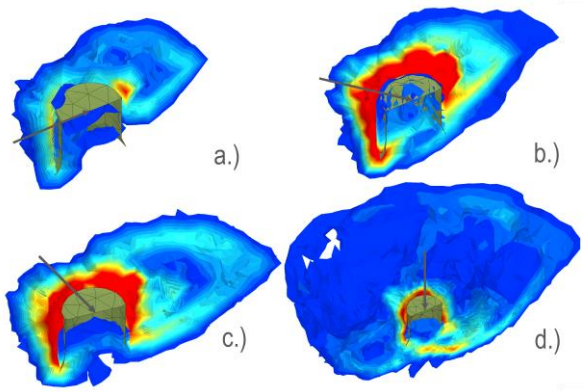


Figure 3 Failure zones in dense sand (HSsmall soil model) for (a) horizontal, (b) 30^o, (c) 60^o and (d) vertical load.

The pattern of the deviatoric strain increments is quite similar comparing Figures 2 and 3. However it is clearly visible, that the strain increments are less localized without clearly defined failure surfaces. Furthermore, the failure along the shaft is quite extensive (Figure 3b and 3c). This is also apparent in case of the pure vertical loading (Figure 3d) while the failure surface around the caisson is not clearly defined.

The load-displacement curves derived for the examined load inclinations and the two constitutive models are shown in Figure 4. It can be observed that smaller displacements are required to reach failure in the case of the HSsmall model compared to the Mohr-Coulomb case. The difference becomes more apparent as the loading inclination increases, thus the largest deviation occurred in case of 60^o load inclination.

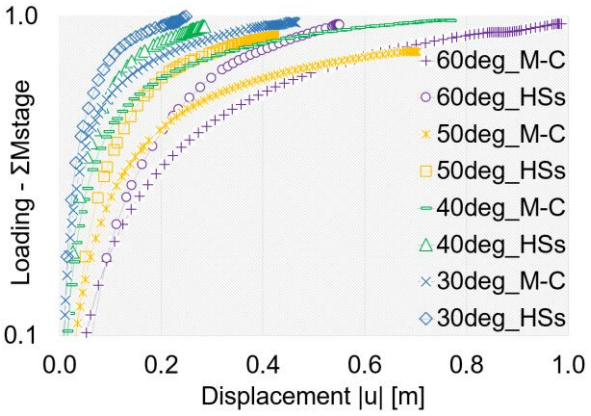


Figure 4 Load-displacement curves for inclined loading in case of dense sand

The ultimate load (resultant) was estimated and the results are summarized in Table 3. The difference in the ultimate load, when comparing the two constitutive models, is within the range of 10%. Considering the fact that the yield criterion for both models is identical, the discrepancy is attributed to the extent of the failure surface within the soil mass, especially in the cases of 30°, 40°, and 50° load.

Table 3 The ultimate bearing capacity in case of M-C and HSsmall soil models

Inclination	V^{ult}_{M-C} ***[kN]***	$V^{ult}_{HSsmall}$ ***[kN]***	**Difference**
90°	$744 \cdot 10^3$	$748 \cdot 10^3$	0.5 %
60°	52250	56400	7.4 %
50°	33600	30450	9.4 %
40°	19400	18600	4.1 %
30°	13152	13150	0.01 %
0°	7546	8550	11.7%

In order to ensure a general comparison of the results the non-dimensional failure envelope (Figure 5) of the vertical and horizontal loads (V-H failure envelope) was developed.

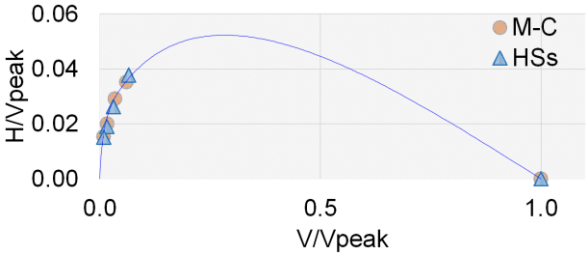


Figure 5 Yield surface for the caisson under inclined loading

The combined failure envelope was established by normalizing the ultimate loads by the vertical ultimate load as suggested by Byrne (2000) in case of suction caissons. The numerical results compare well regarding the shape obtained by experimental results (Byrne, 2000). However, it is recommended in the literature to apply data from field-measurements and swipe experimental tests (Butterfield & Gottardi, 2003) in order to find the appropriate yield curves (Byrne, 2000).

3.3 Axial, lateral and inclined bearing capacity in clay

The axial and lateral capacity of the suction caisson has been estimated considering a linearly increasing and a constant undrained strength profile. The results reported in Table 4 indicate a higher capacity for the linearly increasing soil strength profile. The axial bearing capacity for the constant profile indicate that N_c=9.1, which is consistent with results of plane strain analyses for skirted foundations presented by Yun & Bransby (2007). However the calculated N_c=8.4 for the linear increasing profile is higher than the corresponding value reported in the same study.

Table 4 Axial and lateral bearing capacity for suction caisson in clay

Soil profile	H_0 ***[kN]***	V_0 ***[kN]***
Linear	1599	8101
Constant	988	2564

Inclined loading was applied on the suction caisson for a number of angles with respect to the horizontal axis (10°, 30°, 40°, 50°, 60°, and 80°). The deviatoric strain increment contours indicate the generated failure mechanisms as shown in Figure 6 and Figure 7 for linearly increasing and constant s_u respectively.

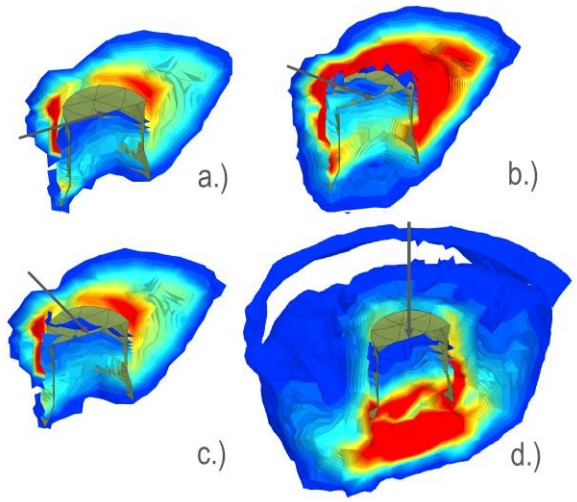


Figure 6 Failure mechanisms in clay with linear increasing undrained shear strength, for (a) horizontal, (b) 30°, (c) 60° and (d) vertical load.

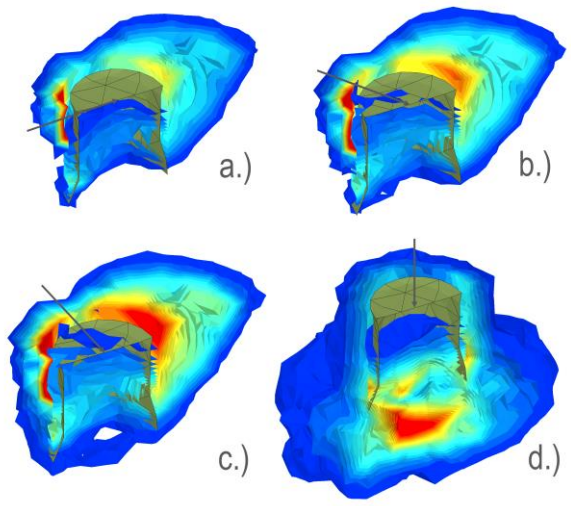


Figure 7 Failure mechanisms in clay with uniform undrained shear strength for (a) horizontal, (b) 30°, (c) 60° and (d) vertical load.

It is observed that the increase of the loading angle causes increased strains below the caisson tip. In the lateral load case the strain increase is localized in the passive side. At the 30° loading angle (Figure 6 b.) the failure surface extended further out on the passive side. The progress in the failure mechanism is almost the same for the clay with uniform undrained shear strength. As the load inclination increases from the horizontal axis the failure surface expands on the passive side and when the load reaches pure vertical the failure surface is concentrated beneath the suction caisson. Comparing the failure mechanisms for the two different normally consolidated clay profiles, the main difference appears when the loading has an inclination angle of 30°.

On the load-displacement curves shown in Figure 8 the loading stages are represented in order to observe the required displacements to fully mobilize the soil capacity. It is observed that displacement required to mobilize the ultimate capacity is independent of the shear strength profile. On the other hand as the load inclination increases the ultimate capacity is reached at higher displacements. At every case the ultimate axial and lateral load were defined and the results are summarized in Table 4.

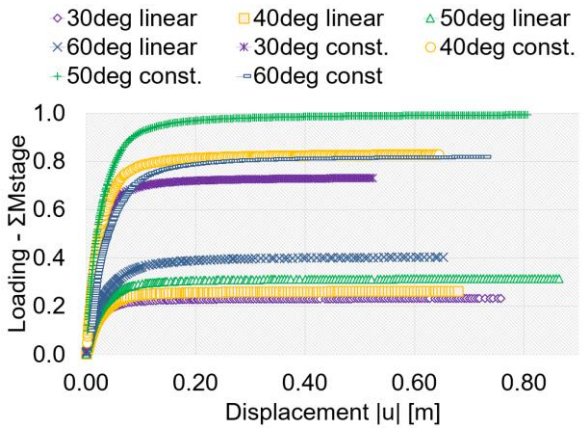


Figure 8 Load-displacement curves for inclined loading in case of clay

Table 4 Bearing capacity for inclined loading of suction caisson in clay with linear increasing shear strength profile

Inclination	$H\ [kN]$	$V\ [kN]$	$V_{lin.}^{ult}\ [kN]$
80°	1209	6857	6963
60°	1634	2829	3267
50°	1638	1952	2549
40°	1630	1368	2128
30°	1628	940	1879
10°	1611	285	1636

Figure 9 shows the comparison of the failure envelope based on the axial, lateral and inclined loading conditions from the present model and an analytical method suggested by Supachawarote, et al. (2004). The analytical solution is the following:

$$\left(\frac{H}{H_0}\right)^a + \left(\frac{V}{V_0}\right)^b = 1 \qquad (2)$$

Where a and b constants are the following:
a = L/D+0.5 and b = L/3D+4.5.

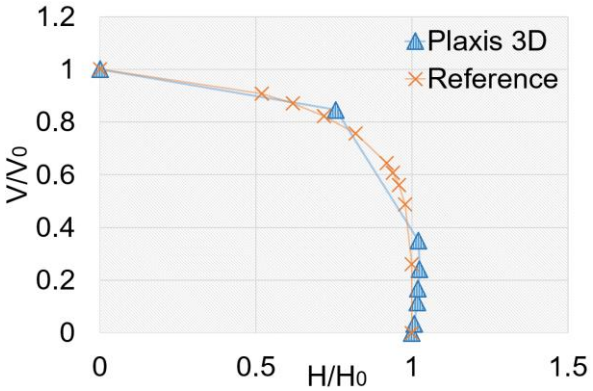


Figure 9 V-H failure envelope for inclined loading in clay with linearly increasing shear strength

As it seems the resulted V-H failure envelope from Plaxis 3D is in very good agreement with the reference line. A better fit could have been obtained with more loading inclinations.

4 CONCLUSIONS

The failure mechanisms of a suction caisson with D/L equal to 1, in dense sand and normally consolidated clay has been investigated by means of numerical modelling in this study. In the case of dense sand the increase of the dilation angle was shown to increase the axial bearing capacity. The different constitutive models employed indicate a different distribution of the deviatoric strains, hence the failure surfaces in HSsmall model are less distinct as there is less strain localization. Shaft failure occurs in case of inclined loading without clearly visible, expanded failure zone. The combined failure envelope is in good agreement with the one suggested by Byrne (2000).

The modelling of the ultimate load in case of normally consolidated clay showed a higher bearing capacity in terms of pure horizontal and vertical loading for clay with an undrained shear strength linearly increasing with depth. The obtained failure envelope was fitted with an ellipsoidal function proposed by Supachawarote et al. (2004), with a good agreement.

5 REFERENCES

Andersen, K. H., Murff, J. D., Randolph, M., Clukey, E. C., Erbrich, C. T., Jostad, H. P., & Supachawarote, C. (2005). Suction anchors for deepwater applications. Proceedings of the International Symposium on Frontiers in Offshore Geotechnics (ISFOG). (M. Cassidy & S. Gourvenec (eds)), CRC Press/Balkema, The Netherlands, 3-30.

Benz, T. (2006). Small-Strain Stiffness of Soils and its Numerical Consequences, Mitteilung des Instituts für Geotechnik der Universität Stuttgart. Germany. Stuttgart.

Bolton, M. D. (1986). The strength and dilatancy of sands. Geotechnique, 36(1), 65-78.

Brinkgreve, R. B. J., Kumarswamy, S. & Swolfs, W. M. (2015). Plaxis 3D Anniversary Edition Manual. Plaxis bv. The Netherlands. Delft.

Butterfield, R. & Gottardi, G. (2003). Determination of yield curves for shallow foundations by "swipe" testing. Magnan et Droniuc ed. Presses de l'ENPC/LCPC. France. Paris.

Byrne, B. W. (2000). Investigation of Suction Caissons in Dense Sand. PhD Dissrtation, Magdalen College. The United Kingdom. Oxford.

Chen, W. F. & Liu, X. L. (1990). Limit analysis in soil mechanics. Elsevier Science Publishers. Development in Geotechnical Engineering. The Netherlands. Amsterdam.

Houlsby, G. T. (1991). How the Dilatancy of Soils Affects Their Behaviour. Soil Mechanics Report (OUEL1888/91) University of Oxford, Department of Engineering Science. The United Kingdom. Oxford.

Houlsby, G. T., Ibsen, L. B. & Byrne, B. W. (2005). Suction caissons for wind turbines. Proceedings of the International Symposium on Frontiers in Offshore Geotechnics (ISFOG). (M. Cassidy & S. Gourvenec (eds)), CRC Press/Balkema, The Netherlands, 75-93.

Larsen, K. A., Ibsen, L. B. & Barari, A. (2013). Modified Expression for the Failure Criterion of Bucket Foundations Subjected to Combined Loading. Canadian Geotechnical Journal, 50(12), 1250–1259.

Lyamin, A. V., Salgado, R., Sloan, S. W. & Prezzi, M. (2007). Two- and three-dimensional bearing capacity of footings in sand. Géotechnique, 57 (8), 647-662.

Potts, D. M. & Zdravkovic, L. (1999). Finite element analysis in geotechnical engineering: theory. Thomas Thelford Publishing. The United Kingdom. London.

Senders, M. & Kay, S. (2002). Geotechnical suction pile anchor design in deep water soft clays. Proceedings of Conference Deepwater Risers Mooring and Anchorings. The United Kingdom. London.

Senders, M. (2008). Suction caissons in sand as tripod foundations for offshore wind turbines. PhD Dissertation, University of Western Australia, Perth, Australia.

Supachawarote, C., Randolph, M. & Gourvenec, S. (2004). Inclined Pull-out Capacity of Suction Caissons. Proceedings of The International Society of Offshore and Polar Engineers. France. Toulun.

Vaitkunaite, E., Molina, S. D. & Ibsen, L. B. (2012). Comparison of Calculation Models for Caisson Foundation in Sand. Department of Civil Engineering, Aalborg University, DCE Technical Memorandum; No. 17. Denmark. Aalborg.

Yun, G. & Bransby, M. F. (2007). The Undrained Vertical Bearing Capacity of Skirted Foundations. Japanese Geotechnical Society. Soils and Foundations, 47(3), 493-505.

Time-related increase in bearing resistance of friction piles

J. Kinnunen
Inspecta Oy, Finland, jussi.kinnunen@inspecta.com

ABSTRACT

The bearing resistance of friction piles usually increases over time after installation. Recently many studies have been made about time-related increase in bearing resistance of friction piles in several countries. Though, in Finnish soil conditions there are little knowledge of time related increase in bearing resistance. The aim of study was to examine the time dependency of friction pile's bearing resistance in Finnish soil conditions. The study consist of experimental and literature parts.

In the experimental part the test results of two test piling sites are introduced and analyzed. Test pilings were conducted at bridge sites which were located in railway from Liminka to Oulu. Soil conditions at the test sites are challenging as the bedrock surface is located in 60–140 m depth based on investigations by Geological Survey of Finland (Breilin & Putkinen 2012). The test piles were close ended steel pipe piles and driven precast concrete piles. The test piles were investigated by dynamic load testing in four phases: the first phase at the end of driving (EOD), the second phase about 24 hours after the EOD, the third phase about 14 days after the EOD and the last phase about 28 days after the EOD. Signal matching for measured signals was also performed.

The study shows that the bearing resistance of friction piles showed significant increase with time. The test results indicate that the major increase happens in two weeks, but also after two weeks the increase is noticeable. According to the literature study the bearing resistance increase will continue over 100 days after EOD.

Keywords: Friction pile, test piling, dynamic load test

1 INTRODUCTION

Railway level crossings are removed and replaced with bridges on railway from Liminka to Oulu. Soil conditions at the bridge sites are challenging as the bedrock surface is located at 60-140 m depth and the layers above the bedrock are loose sands or silts.

Due to the challenging ground condition it is not cost effective to drive piles to the bedrock. Bridge construction piles are designed to work as friction piles and the required pile resistance could not be achieved right after pile driving when major part of the pile resistance comes from the pile toe which is in loose sand or silt layer.

However, piles' bearing resistance usually increases over time. Based on the literature study the time-dependent increase in bearing resistance of frictions piles can be divided into two main causes; stress relaxation (Chow et al., 1996) and soil ageing (Schmertmann, 1991).
In Finnish soil conditions there are little knowledge of time related increase in bearing resistance of friction piles. In Finland end bearing piles are usually used instead of friction piles. The main reason for scarce use of friction piles in Finland is that usually the bearing bottom layer is achieved with relatively short pile length (10–20 m). One reason might also be the lack of knowledge of friction piles and their working principles. In Finland there are also favourable areas for the use of friction piles. Friction piles could be used at the esker margins and regions where thick and loose non-cohesive soil layers exist.
The aim of study was to examine the time dependency of friction pile's bearing resistance in Finnish soil condition. The study consist of experimental and literature parts. In the experimental part the test piles were investigated by dynamic load testing and signal matching.

2 TEST SITES

Test sites are located in Finland, Northern Ostrobothnia. Zatelliitti test site is located in Kempele and Tuuliharju test site is located in Liminka.
Both test sites are at the area of Muhos transition zone which was formed during the last glaciation. At the Muhos transition zone the bedrock surface is located in 60-140 m depth based on investigations by Geological Survey of Finland (Breilin & Putkinen, 2012). Comprehensive geotechnical investigations have been performed at both test sites. Geotechnical investigations included soundings and soil samples.

2.1 Zatelliitti

In Zatelliitti test site the soil surface is at the level of +6,5 and the ground at the test site is flat arable land. Ground water surface is at level +5,5. Working platform is made from 0,5 m thick crushed aggregate.
The soil is sand and sandy silt at the top 2 m. Underneath the top layer is about 6 m thick layer of clay and silt. From the level -1 begins about 30 m thick layer of silt. This layer is partially sandy and partially clayey. Under the silt layer exists about 25 m thick dense layer of sand. The sand layer is uniformly graded.
Underneath the sand layer is extremely dense layer of sandy moraine which alternates to sandy moraine at the level -60. Soil sampling was ended at the level of -60. Sounding diagrams from Zatelliitti test site are presented in figure 1.
At the test site dynamic probing ended at the level -30. The deepest static-dynamic penetration test reached level -56. The static-dynamic penetration test is same as dynamic probing but the sounding rod is rotated during the driving. Rotating the rods during driving ensures that the rod goes straight and same time rod penetrates the soil more easily.

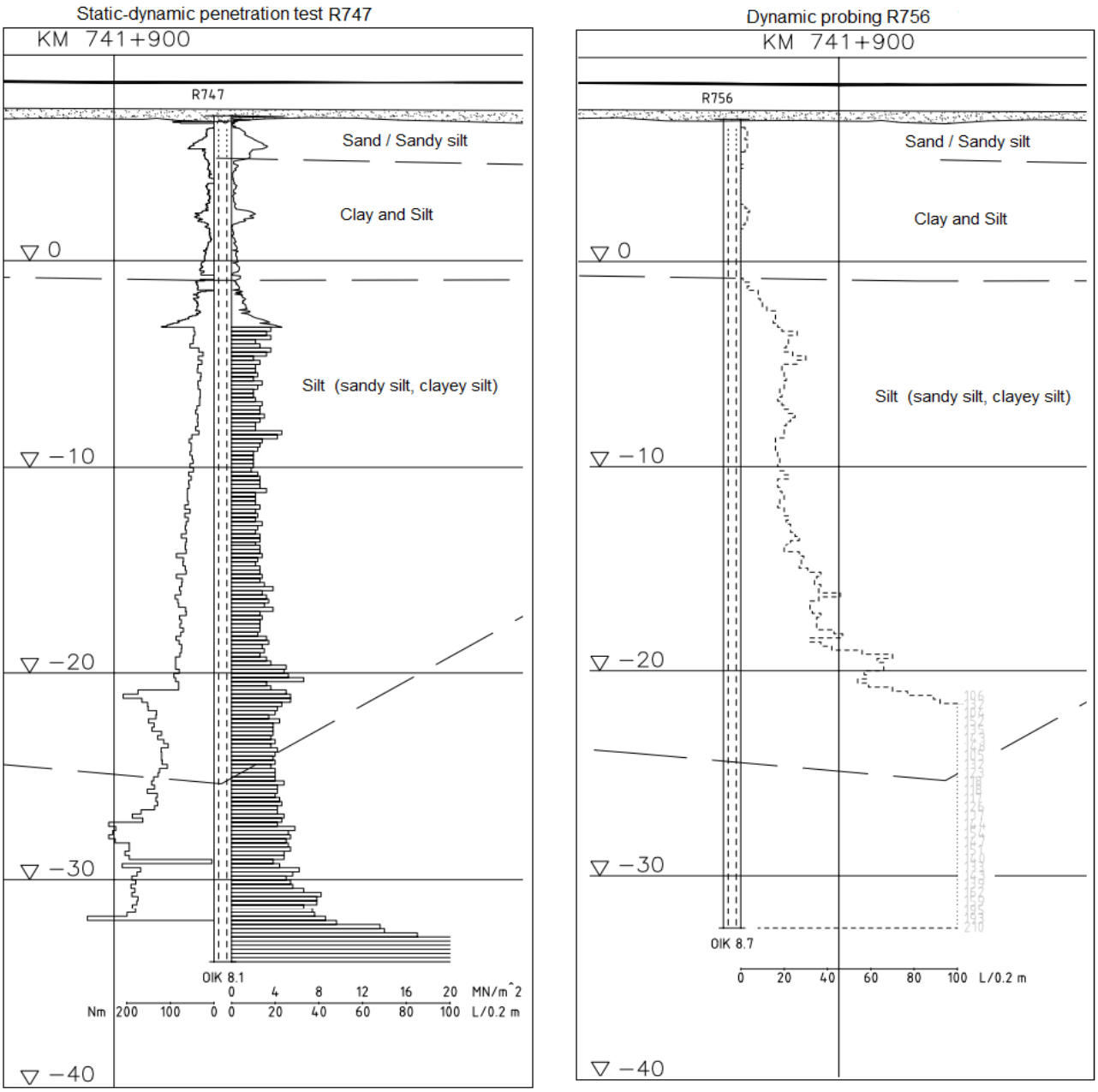


Figure 1 Sounding diagrams from Zatelliitti test site. Distance between investigation points is 10 m.

2.2 Tuuliharju

Soil surface level at Tuuliharju test site is between +4,9–5,6 and ground water level is about 1 m below the soil surface. Working platform is 0,5 m thick. The test site is surrounded by flat arable and forest areas. The soil consists of a thin layer of topsoil at the top. Underneath the topsoil is 1,5 m thick layer of crust. Under the crust is a layer which contains silt, clayey silt and lean clay. This layer grows thinner from the level -20 to level -8 when going towards north parallel to track.

Under the variable thick layer exists layer of sandy silt, silty sand and fine sand. Density of the layer varies from middle dense to extremely dense. Layer from level -25 to level -45 varies from sand moraine to fine sand and fine silt. Sounding resistances from Tuuliharju test site are presented in figure 2. At the test site deepest sounding reached the level -34,5, but typically soundings ended at the level -25.

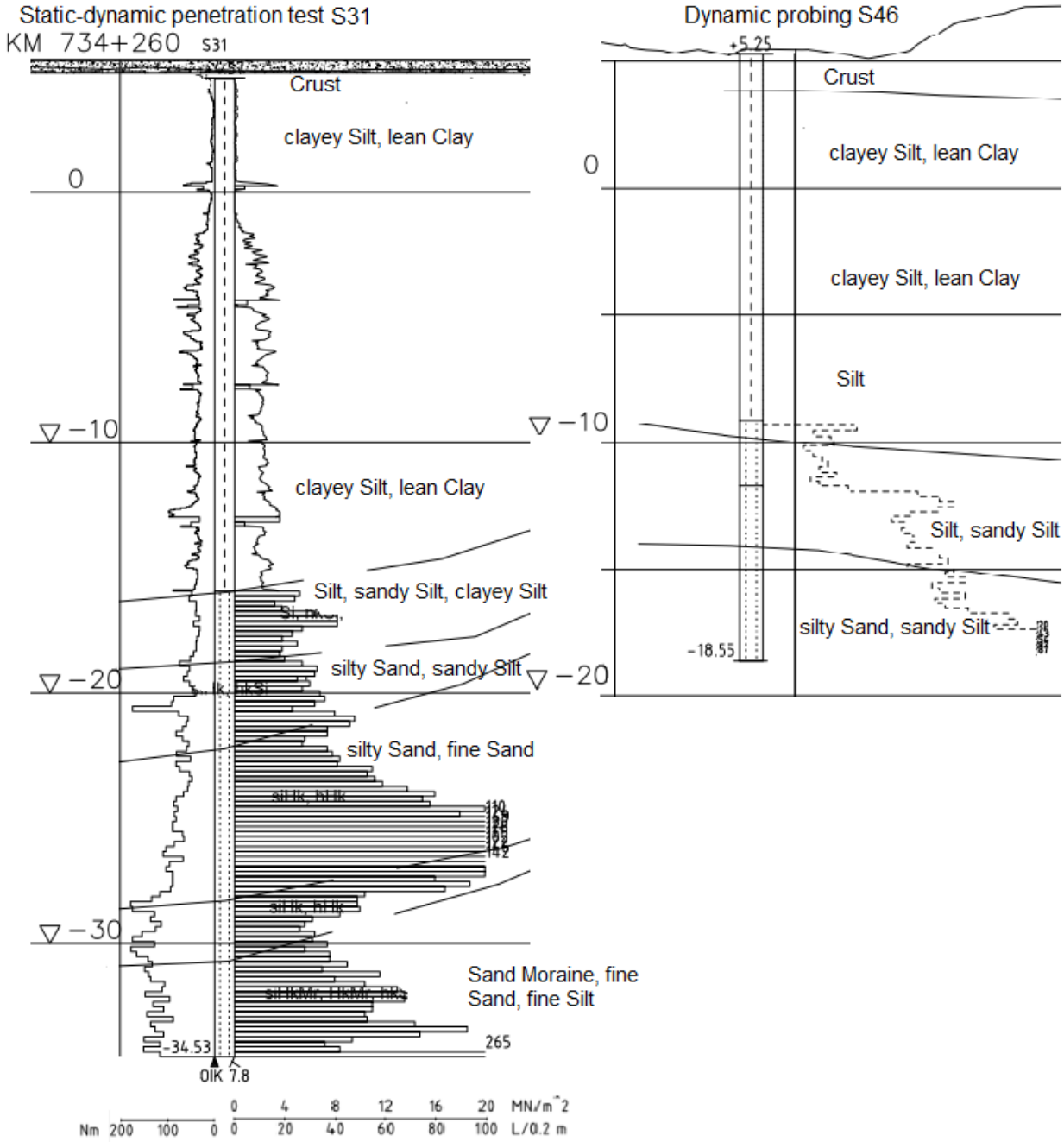


Figure 2 Sounding diagrams from Tuuliharju test site. Distance between investigation points is 32 m.

3 TEST PILING

Test piles were close ended steel pipe piles (diameter 323,9 mm and wall thickness 10 mm, steel grade S440J2H) and driven precast concrete piles (TB300b, 300x300 mm²). There were six steel pipe piles and four precast concrete piles at the Zatelliitti test site and three steel pipe piles and two precast concrete piles at Tuuliharju test site.
At Zatelliitti test site the test piles are divided into north and south groups, both including five piles. Distance between piles inside the group is 5 m and distance between north and south group is 42 meters at shortest. Test piles were driven using Junttan HHK 5A hydraulic hammer (hammer weight 5000 kg, maximum drop height 1,2 m). Information of the test piles is presented in table 1. Pile number starting with letter Z means Zatelliiti test site piles and letter T means Tuuliharju test site pile.

Table 1 Test pile information.

Pile number	Pile type	Element length [m]	Tip level	End of drive criteria s/10 [mm]
ZET1	Steel pipe pile D323,9/10 mm S440J2H	16+16	-23	151
ZET2	Steel pipe pile D323,9/10 mm S440J2H	16+4+16	-27	123
ZET3	Steel pipe pile D323,9/10 mm S440J2H	16+8+16	-30	30
ZPT4	Steel pipe pile D323,9/10 mm S440J2H	16+7+16	-30	184
ZPT5	Steel pipe pile D323,9/10 mm S440J2H	16+3+16	-26	268
ZPT6	Steel pipe pile D323,9/10 mm S440J2H	16+13	-20	254
ZEB1	Precast concrete pile 300x300 mm²	15+3+14	-23	175
ZEB2	Precast concrete pile 300x300 mm²	15+7+15	-28	139
ZPB3	Precast concrete pile 300x300 mm²	15+14	-20	210
ZPB4	Precast concrete pile 300x300 mm²	15+4+15	-25	147
TU-T1	Steel pipe pile D323,9/10 mm S440J2H	16+12	-21	70
TU-T2	Steel pipe pile D323,9/10 mm S440J2H	16+3+9	-20	35
TU-T3	Steel pipe pile D323,9/10 mm S440J2H	16+6+4	-19	26
TU-B1	Precast concrete pile 300x300 mm²	15+12	-20	30
TU-B2	Precast concrete pile 300x300 mm²	15+10	-18	*

*was not measured

At the Zatelliitti test site the pile driving was easy until the level of -27 was reached and the driving resistance increased significantly. At Tuuliharju test site the driving resistance was low until the level -15 was reached. Hammer drop height at the time when end of drive criteria was measured was 30–50 cm for steel pipe piles and 20–30 cm for precast concrete piles. Steel pipe piles were filled with water to 2 m below the surface level to prevent the buoyancy force effect.

4 DYNAMIC LOAD TESTS AND SIGNAL MATCHING

The test piles were investigated by dynamic load testing in four phases: the first phase at the end of driving (EOD), the second phase about 24 hours after the EOD, the third phase about 14 days after the EOD and the last phase about 28 days after the EOD. Signal matching for measured signals was performed for last three phases.
The meaning of second phase was to determine the short-term resistance increase. Meaning of third and fourth phase was to investigate the long-term resistance increase. Long-term resistance increase is expected to happen due to stress relaxation (Chow et al., 1996) and soil ageing (Schmertmann, 1991). Short-term resistance increase is expected to happen mainly due to dissipation of pore water pressure. Stress relaxation and soil ageing also start right after the pile driving. Piles were driven and end of driving dynamic load testing was performed 2.–4.3.2015 for all 15 test piles. Second phase was performed 3.3–5.3. (19–31 hours after EOD). Same accelerated hydraulic hammer Junttan HHK 5A was used in second phase. For all the test piles full geotechnical bearing resistance could not be mobilized in second phase with using the said hydraulic hammer due to insufficient energy.
The third phase was conducted on 18.3. using a heavier Junttan HHK 7A hydraulic hammer (hammer weight 7000kg, maximum drop height 1,2 m). Even with that hammer full geotechnical resistance could not be mobilized for all test piles. Pile TU-T2 was driven 1 m deeper at the time of third load testing phase.
The fourth phase was conducted on 31.3. 10 000 kg drop hammer was used in fourth phase. Precast concrete piles were investigated by dynamic load testing only in first three phases because the structural capacity was achieved at the third phase. The amount of blows per pile during the restrike tests was limited to 2-4 blows so that the dynamic load testing would disturb the set-up as little as possible. Dynamic load testing results as well as signal matchings from all the four phases are presented in table 2.

Table 2 Test piles' geotechnical capacity with Case Method and CAPWAP.

Pile Number	LE [m]	Time after installation	Geotechnical Capacity, Case Method [kN]	Geotechnical Capacity, CAPWAP [kN]			Settlement per blow [mm]	EMX [kNm]
				Total	Shaft	Toe		
ZET1	30,9	EOD	301	301			75	68,9
		29 hours	1148	1075	821	254	25	60,6
		15 days	2551	2619	1977	642	8	68,1
		28 days	3036	2965	2157	808	22	165
ZET2	35	EOD	1363	1363			18	63,7
		31 hours	1917	1882	1196	686	9	54,3
		15 days	2436	2494	1819	675	2	69,9
		28 days	3327	3386	2314	1072	10	151
ZET3	38,8	EOD	1814	1816	863	953	6	59,7
		30 hours	2078	2116	1477	639	4	61,9
		15 days	2549	2614	1947	667	1	70,2
		28 days	3561	3688	2350	1338	3	122,9
ZEB1	31	EOD	864	864			31	35,3
		23 hours	1537	1490	747	743	12	44
		15 days	2463	2528	1628	900	6	59,4
ZEB2	27,5	EOD	977	977			24	33,3
		24 hours	1356	1070	281	790	17	44,6
		15 days	1954	1626	734	891	10	62,8
ZPT4	37,7	EOD	454	572	378	194	45	63,4
		25 hours	1217	1238	1009	229	19	62,2
		16 days	2555	2450	1943	507	6	72,2
		28 days	3533	3489	2716	773	17	159,7
ZPT5	33,6	EOD	480	480			90	74,2
		23 hours	1366	1244	957	287	23	64,4
		16 days	2726	2676	1849	827	7	71,6
		28 days	3450	3441	2492	949	8	137,8
ZPT6	27,6	EOD	303	303			90	75,4
		21 hours	1253	1270	922	347	29	61,7
		16 days	2738	2755	1698	1057	4	71,9
		28 days	3722	3575	2477	1098	12	136,2
ZPB3	27,5	EOD	283	283			39	21,4
		21 hours	1203	1219	970	249	4	37,7
		16 days	2518	2372	1588	784	6	58,1
ZPB4	32,8	EOD	654	654			55	41,7
		22 hours	1629	1590	1020	570	6	39,9
		16 days	2526	2658	1755	903	5	56,2
TU-T1	30,7	EOD	1711	1751	1027	724	17	64,3
		26 hours	2119	2157	1339	818	11	68,2
		14 days	2560	2599	1771	828	7	77,6
		28 days	3085	3053	2140	913	20	145,1
TU-T2	31,6	EOD	1958	1957			10	62,9
		24 hours	2265	2398	1233	1165	8	66,9
		14 days	2774	2792	1617	1175	5	69,5
		28 days	2830	2810	1613	1197	24	152,3
TU-T3	32,7	EOD	1595	1595			16	68,3
		22 hours	1746	1770	487	1283	13	73
		14 days	2314	2273	962	1311	15	69,9
		28 days	2479	2470	1190	1280	25	136,4
TU-B1	25,9	EOD	1530	1530			8	37,7
		20 hours	1635	1662	953	709	8	46,2
		14 days	1966	2100	1308	792	6	60,8
TU-B2	24,2	EOD	847	847			18	25,9
		29 hours	1079	1265	618	647	10	32,4
		14 days	1605	1610	900	710	11	63,6

LE is the pile length below gauges. EMX is maximum energy transferred to pile. Case Method capacity is used in CAPWAP total column if CAPWAP-analysis is not done for that particular load test.
Based on the observations during the dynamic load testing, the required settlement per blow to fully mobilize the geotechnical resistance is assumed to be over 10-15 mm. It can be seen from table 2 that the full geotechnical resistance could not be mobilized for every pile in every phase. Zatelliitti test piles' bearing resistance development is presented in figure 3.

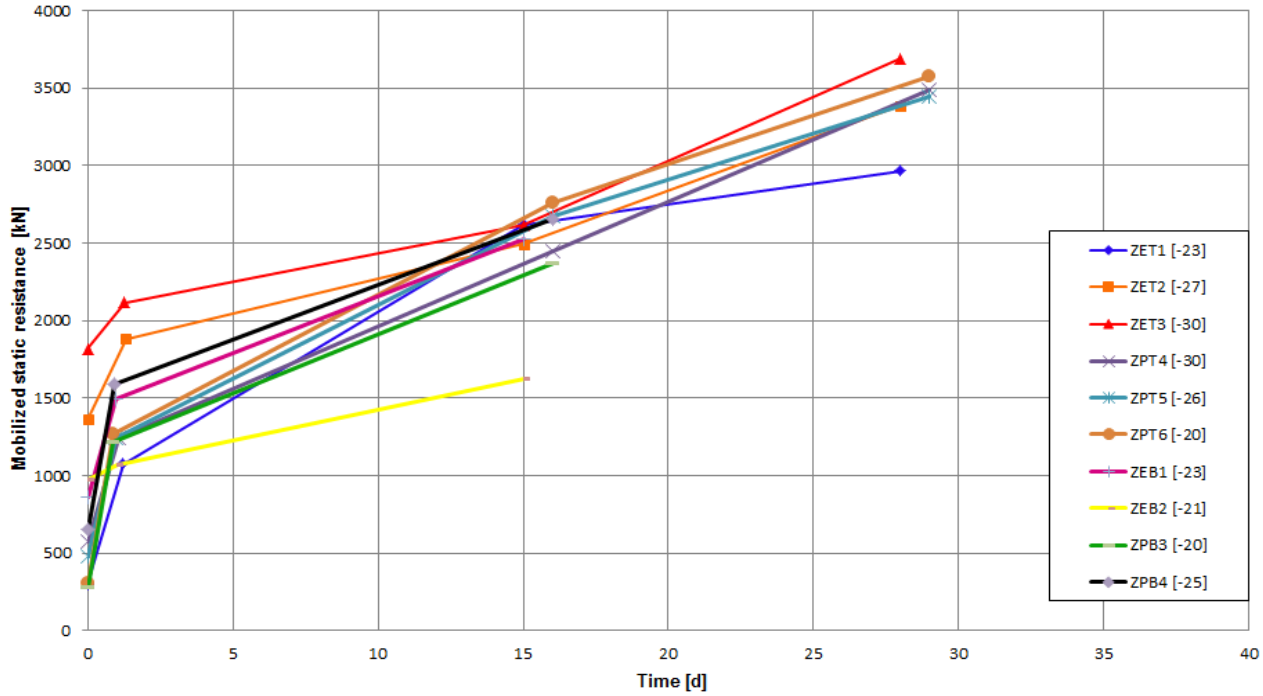


Figure 3 Bearing resistance developments of Zatelliitti test piles.

Shape of the curves for most piles in figure 3 does not truly present the correct time-related bearing capacity behavior because the bearing resistance was not fully mobilized for all of the piles in second and third phase. EOD and most of the 28 d values are correct, but the shapes of the curves between those points are different. At the beginning the increase should be intensive and then equalize as the time goes by.
According to the literature study the bearing resistance increase will continue over 100 days after EOD (Chow et al., 1998; Axelsson, 2000). The main reason for the bearing resistance increase was due to increase in shaft resistance. Shaft resistance development of Zatelliitti steel pipe piles is presented in figure 4. Toe resistance development is not presented because the degree of mobilization for toe resistance varied greatly. Axelsson (2000) showed that the toe resistance was almost constant and did not increase as the shaft resistance did.

One of the precast concrete piles, pile ZEB2, suffered from increasing pile damage during driving. Development of the damage severity was observer from the stress wave graph as the pile driving went on. The pile damage located approximately in the middle of the lowest pile segment which then eventually broke in half. So the pile length shortened and bearing resistance was lower than the bearing resistance of other precast concrete piles, which can be seen in figure 3.

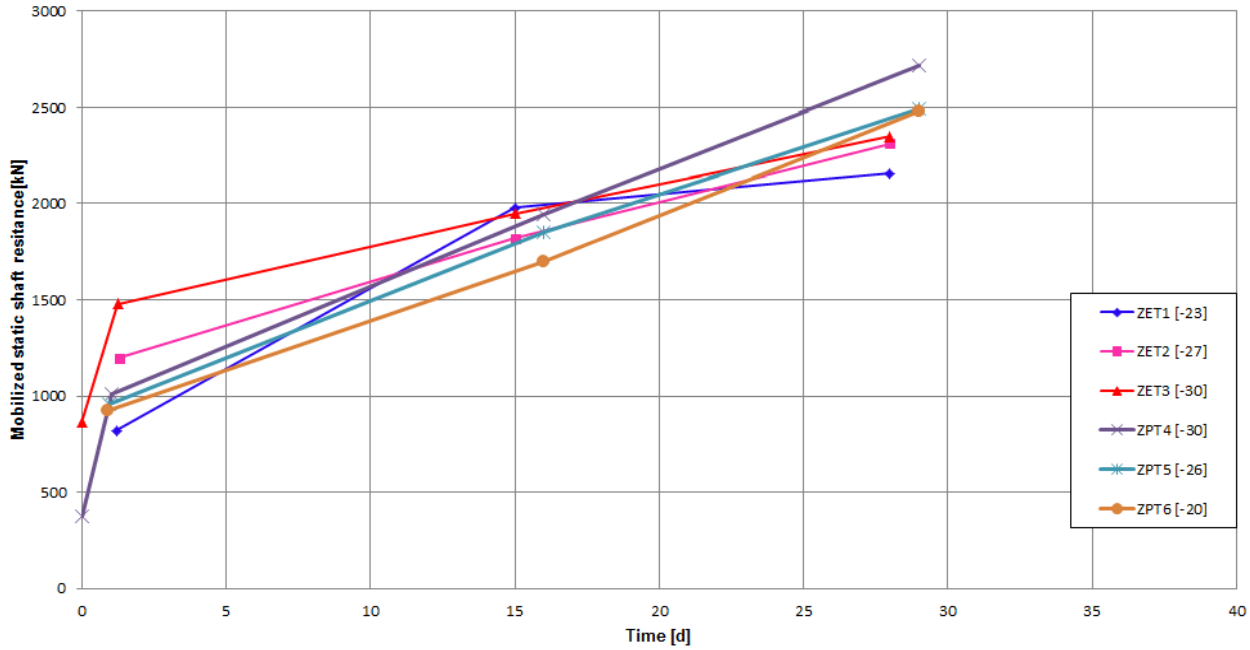


Figure 4 Shaft resistance developments of Zatelliitti steel pipe piles.

It was earlier said that the amount of blows was kept to a minimum so that the set-up would not be disturbed, but in phase 3 piles ZET1 and ZPT5 were disturbed with a great amount of blows. The meaning of the blows was to mobilize the toe resistance, but piles behaved differently to that. It can be clearly seen that the set-up of pile ZET1 was disturbed but the set-up process of pile ZPT5 continued almost normally despite the great amount of blows.

Pile ZPT6 has almost the same shaft resistance as the pile ZPT4 which is 10 meters longer. One explanation to this is that, stiffer soil layers exist on higher level at the location of pile ZPT6.

Pile ZET2 shaft resistance increase as a function of driven pile length is shown in figure 5. Shaft resistance increase curves are based on CAPWAP-analyses. Presented curves are from the last three phases.

It can be seen that the shaft resistance increased below 20 m depth where denser layers exists. Shaft resistance remained almost constant at the upper part of the pile, near the soil surface. Shaft resistance clearly increased as a function of depth in all phases.

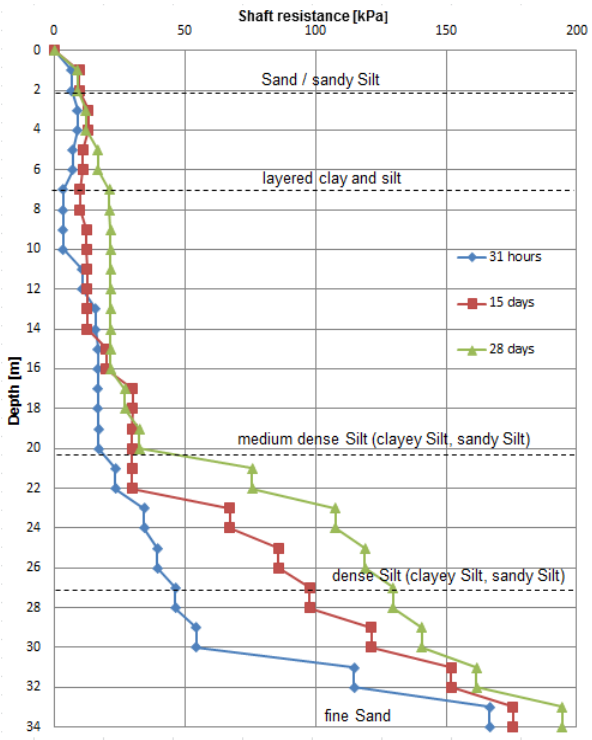


Figure 5 Pile ZET2 shaft resistance increase as a function of driven length.

Tuuliharju test piles' bearing resistance development is presented in figure 6.

Pile TU-T2 was driven 1 m deeper during third phase and that is why the bearing resistance remained constant between third and fourth phase. At Tuuliharju site the increase of bearing resistance was more moderate than at Zatelliitti site. At Tuuliharju site soil layers are mostly fine grained, clay

or clayey layers where as in Zatelliiti site layers are mainly coarser grained. It is possible that the set-up process only takes longer in fine grained soils than in grained soils. Long-term pile set-up results from this study and previous studies are presented in figure 7.

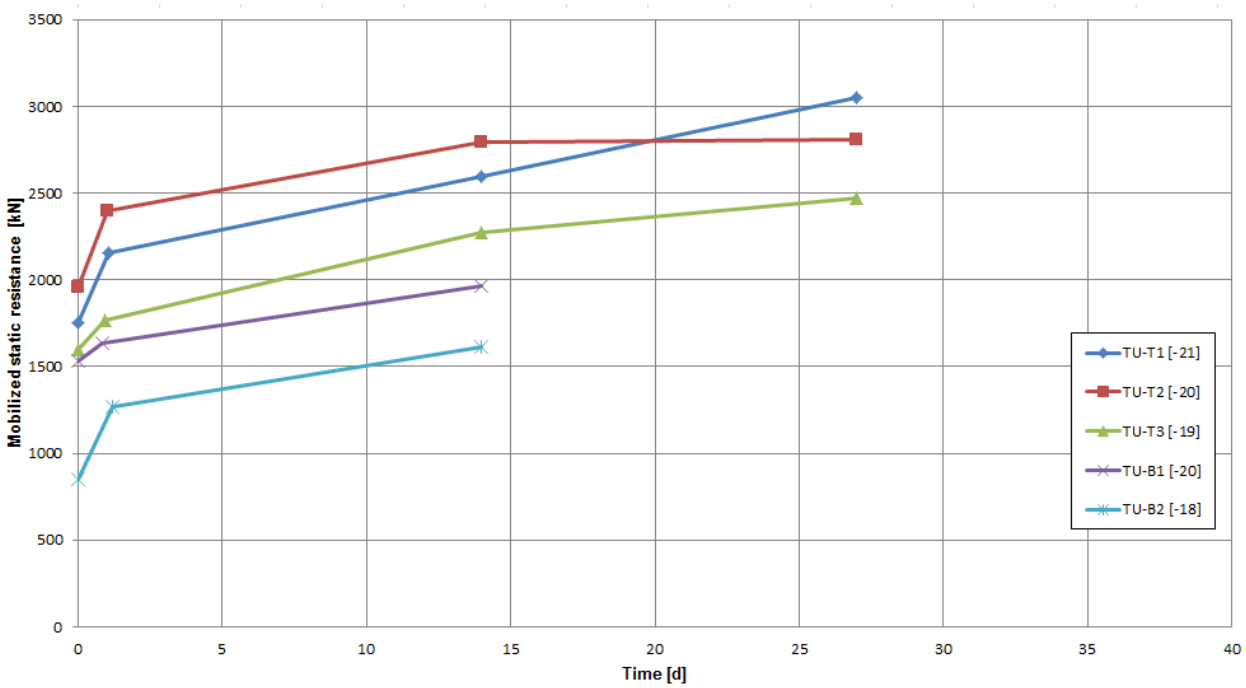


Figure 6 Bearing resistance developments of Tuuliharju test piles.

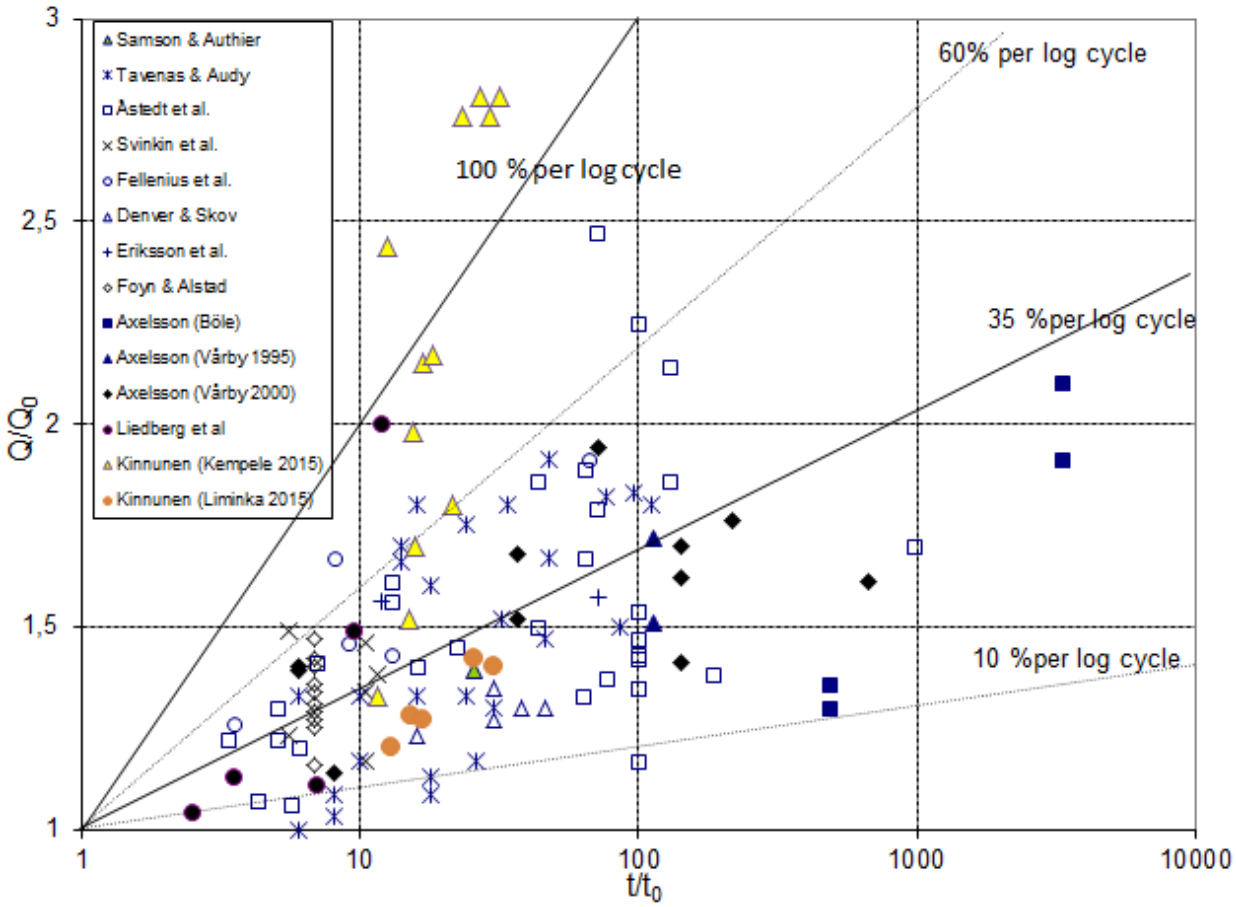


Figure 7 Long-term pile set-ups. Results from Oulu added to original chart presented by Axelsson (2000).

Dynamic load test results where the settlement per blow was less than 10 mm at the second phase are not presented in figure 7. If those results had been presented it would have given incorrect results when the Q-ratio rises. Those pure friction piles from Zatelliitti test site showed over 100 % increase per log cycle. Others Zatelliitti test results are placed on the same area on the chart as the results from the previous studies. Tuuliharju test piles showed fairly moderate increases.

5 CONCLUSION

Based on the experimental and literature studies the magnitude of bearing resistance increase of friction piles' depends on: soil conditions, pile installation method, pile properties and load history of the pile. Study results shows that the pile bearing resistance increased 17–180 % after the dissipation of pore water pressure. At the Tuuliharju test site the increase was more moderate than at the Zatelliitti test site. Although there were more scatter in the increases at Zatelliitti site because some of the piles were end bearing piles with a high bearing resistance at the end of driving and the rest were friction piles with a low end of driving bearing resistance. In Tuuliharju all the test piles worked almost like end bearing piles.

The test results indicate that in cohesionless soils the major increase in bearing resistance happens in two weeks, but also after two weeks the increase is noticeable.

In Finland the use of friction piles is limited due to Finnish geology. In suitable soil condition friction piles are a rational alternative for end bearing piles and remarkable costs in piling projects can be saved if the increase in bearing resistance of friction piles is taken into account. Although, the set-up time and further load tests should be taken into account in friction pile planning and scheduling.

ACKNOWLEDGEMENTS

The paper is based on the Master of Science Thesis of the writer (Kinnunen, 2015).

REFERENCES

Axelsson. G. (2000). Long-term set-up of driven piles in sand. Doctoral Thesis, Royal Institute of Technology. Stockholm.

Breilin, O. & Putkinen, N. (2012). Limingan Vesikari – syvin maaperäkairaus Suomessa. Geologi 64. 100-103.

Chow, F. C., Jardine, R. J., Nauroy, J. F. & Brucy, F. (1998). Effects of time on capacity of pipe piles in dense marine sand. Journal of Geotechnical and Geoenvironmental Engineering. ASCE. Vol. 124(3). 254–264.

Chow, F. C., Jardine, R. J., Brucy, F. & Nauroy, J. F. (1996). The effect of time on the capacity of pipe piles in sand. Proceeding 28th Offshore Technology Conference. Houston.

Kinnunen, J. (2015). Time-related increase in bearing resistance of friction piles (in Finnish: Ajan vaikutus kitkapaalujen geotekniseen kestävyyteen). Master's Thesis, Tampere University of Technology. Tampere.

Schmertmann, J. H. (1991). The mechanical ageing of soils. Journal of Geotechnical Engineering. ASCE. Vol. 117(9). 1288–1330.

Comparison of pile driveability methods based on a case study from an offshore wind farm in North Sea

I. Anusic
Norwegian University of Science and Technology, Trondheim, Norway, ivana.anusic@ntnu.no

G. R. Eiksund
Norwegian University of Science and Technology, Trondheim, Norway

M. A. Liingaard
DONG Energy, Copenhagen, Denmark

ABSTRACT
Significant research effort has been put into pile driveability analyses with the aim of determining a successful, safe and cost-efficient installation. Driveability analysis involves selection of appropriate hammer, determination of pile makeup details and careful review of soil profile to reach desired penetration or capacity with reasonable number of blows without overstressing the pile.
In this paper, pile driving records from the installation of 6.5 m diameter monopiles at a wind farm in southern North Sea are considered. The ground conditions at the site generally consist of between 10-50 m thickness of over consolidated clay with some layers of sand overlying chalk bedrock. The most important of the variables to establish is the Static Resistance to Driving (SRD). There are proposed procedures for evaluating SRD in sands and clays; however, the knowledge about pile driveability in the chalk at the site is very limited. This makes prediction of the soil response after driving the pile into the chalk layers unreliable. The piling records are used to test how well the existing driveability suit the conditions at this site by comparing the predicted blow counts with results from back-analyses of as-measured pile driving records.

Keywords: pile driving, backanalysis, chalk

1 INTRODUCTION

Continuous growth in need of renewable energy demands new economical and technologically feasible innovations. In order to overcome increasing depths, dimensions of the offshore structures as well as foundations become larger.

According to Karimirad (2014), more than 65% of the offshore wind turbines are monopile structures and significant research effort has been put into accurately predicting the pile response to driving.

Pile driveability denotes the ability of a pile to be safely and economically driven to the required depth without causing excessive fatigue damage. The analysis for a particular set of driving equipment, pile material and dimensions, and a specific type of soil at the site involves a detailed static and dynamic soil resistance input parameters to reflect layers that pile penetrates.

Predicting Soil Resistance to Driving (SRD) has been a challenging task and some

of the methods used nowadays include procedures given by Toolan and Fox (1977), Stevens (1982), Alm and Hamre (2001).

The design of monopile foundations for offshore wind turbines relies heavily on experience and approaches used in the oil and gas industry, however these methods were developed when most of piles installed offshore had a diameter of less than 2 m.

This paper aims to evaluate the accuracy of existing methods for 6.5 m diameter monopiles at the Westermost Rough wind farm in southern North Sea where ground conditions generally consist of over consolidated clay with some layers of sand overlying chalk bedrock. Data from pile installations have been gathered and used as input into back-analysis to test how well present driveability models suit the conditions at this particular site.

2 SITE CHARACTERISATION

The Westermost Rough offshore wind farm is located in the North Sea, around 8 km off the Yorkshire Coast north of Hull and covers an area of approximately 35 km^2 (Figure 1).



Figure 1. Location map of the Westermost Rough offshore wind farm

2.1 Seabed and bathymetry

Geophysical survey indicated that within the area water depths range between 11 m LAT (lowest astronomical tide) and 28 m LAT. The seabed generally shoals to the southwest with gradient less than 1 degree, except where current related features, evaluated as possible relict sand waves or eskers, up to 7.0 m high, were present.

2.2 Geological setting

Based on extensive geotechnical, geological and geophysical logging data from ground investigations, it was recognized that the site consists of quaternary soils overlying chalk bedrock.

Holocene Deposits (HLCN)

Holocene Deposits cover seabed across the area of wind farm and are typically comprised of sand, sandy gravels and low to high strength clays between 0.2 m and 3.7 m thick.

Channel Infill Deposits (CHF)

Channel Infill Deposits consist of very low to low strength silty clays and silty sand, with thickness ranging between 3 m and 8 m along the eastern edges of the wind farm site, locally thickened from 16 m to 22 m in the northern corner of the site.

Bolders Bank Formation - Upper (BSBK_U)

The deposits comprise very stiff, high, very high and extremely high strength, slightly sandy to very sandy gravelly clay, reddish brown, becoming brown and greyish brown with depth.

Bolders Bank Formation – Middle (BSBK_M)

The deposits of thickness between 1 m and 10 m comprise gravelly sands, locally encountered as sandy gravel or cohesive soil with a high proportion of granular material.

Bolders Bank Formation – Lower (BSBK_L)

The deposits are between 1 m and 12 m thick and comprise very stiff, high, very high and extremely high strength brown, dark brown to reddish brown, slightly sandy, slightly gravelly clay.

Rough Formation (ROUGH)

Rough Formation deposits are found within local channel features cut into the Chalk, with thickness varying between 1.3 m and 13 m.

The deposit comprises low plasticity, very high to extremely high strength, sandy gravelly clays.

Swarte Bank Formation (SWBK)

Swarte Bank Formation deposits locally underlay the Rough Formation deposits. They comprise a light grey diamict with an almost complete absence of clast lithologies other than chalk and occasional flint. The thickness varies between 1.5 m and 13 m.

Westermost Rough Chalk Formation (WMR)

The top of the chalk surface varies along the site. From the central northern part of the site to its southwestern corner, the top of the chalk surface is from 28 m to 40 m below seabed. On the other positions, though, the top of the chalk surface is observed from 10 m to 19 m below seabed. The chalk comprises generally extremely weak and very weak, low density, creamish white and white chalk. However, this chalk has a general absence of flint bands and marl seams, making it different to chalk of similar age encountered onshore. It is assumed that this particular chalk formation has not been previously logged and therefore it is called the Westermost Rough Chalk Formation.

The relevant chalk characteristics for pile design and installation are the intact strength (directly related to porosity/density) and the fracture condition that is defined by the CIRIA grade (Lord, Clayton, Mortimore, 2002). The chalk at WMR is low to medium density and consists of three geotechnical units: structureless chalk (CIRIA Grade D), structured fractured chalk (CIRIA Grade B and Grade C) and structured assumed intact chalk (CIRIA Grade A).

2.3 Geotechnical profiles at the site

In addition to the identification of soil layers based on the geological description of soil samples recovered from boreholes at selected locations and the interpretation of the geophysical surveys, the formations were recognized by cone penetration tests that were carried out at all wind turbine locations.

The cone penetration test (CPTs) performed at the site were specified as CPTU tests, i.e. including pore pressure readings. The outcome of the CPT classification is a refinement of the complete soil stratigraphy, determination of specific depths of different geological units and identification of layers with different engineering properties being visible from the increase or decrease in the measured cone resistance and skin friction.

CPT data from several observed locations (P01, P02, P03, P04, P05 and P06) are illustrated in Figure 2 and design soil parameters are specified in Table 1, where γ' (kN/m^3) is effective unit weight, D_d (%) is relative density, φ (°) is friction angle and s_u (kPa) is undrained shear strength. Plasticity index PI (%) is 16-17 for ROUGH and BSBK formations and 8-9 for chalk D, CHF and SWBK formations.

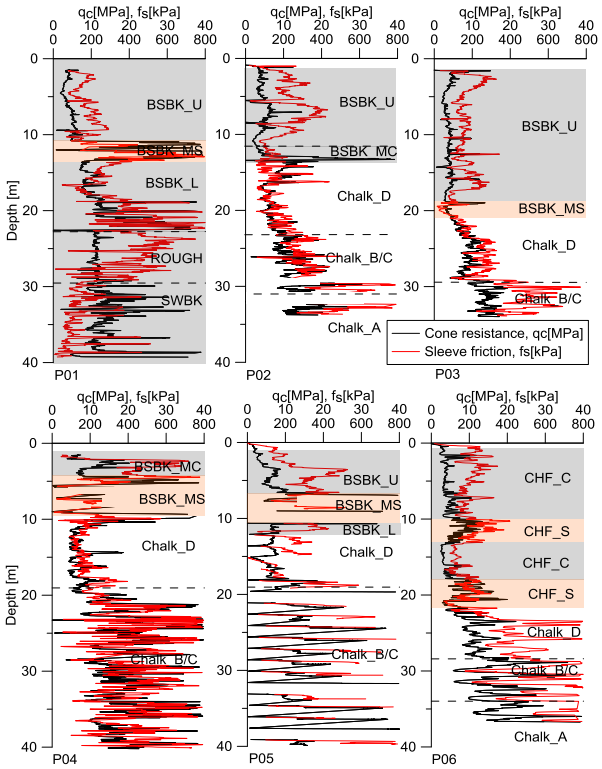


Figure 2. CPT profiles for position P01-P06

Table 1. Soil properties at six positions

	γ' [kN/m^3]	D_r [%]	s_u [kPa] φ [°]
HLCN	7	15[aef], 27[c], 36[b], 46[ad]	35°
CHF_C	11	-	(140-280)[f]
CHF_S	7	(27-40)[f]	(31°-33°)[f]
BSBK_U	11	-	(130-280)[a] (120-330)[b] (130-230)[c] (130-530)[e]
BSBK_L	11	-	(470-1500)[a] 350[e]
BSBK_MC	11	-	(160-240)[b] (240-390)[d]
BSBK_MS	10	15[c] (65-80)[a] (80-100)[de]	(28°)[c] (34°-40°)[ade]
ROUGH	11	-	615[a]
SWBK	10	-	(750-930)[a]
WMR_D	9.3	-	125
WMR_B/C	9.3	-	-
WMR_A	9.3	-	-

* Index a-f corresponds to positions P01-P06, respectively

It should be noted that due to poor CPT readings in sand layers at positions P04 and P05, and in chalk layer of grade B/C at position P05, the values of cone resistance and skin friction at these locations should be taken with caution.

Table 1 also demonstrates how soil parameters can vary significantly from one position to another, even in the same geological unit.

3 DRIVEABILITY ANALYSIS

The total resistance to driving may be divided in a static part, the static resistance to driving (SRD) and a velocity or displacement rate dependent part called the damping. Evaluation and development of correct input of static resistance is of high importance to obtain an accurate model. In order to determine SRD, common practice is to relate it to the Static Soil Resistance; American Petroleum Institute (API) proposes such methods. There are number of methods presented over the years and are still in use in North Sea pile design.

The earliest models like Toolan and Fox (1977) did not include friction fatigue concept, which was presented in 1978 by Heerema who made driveability prediction based on the assumption that skin friction in clay is gradually lost along the pile wall as driving proceeds (Heerema, 1978). Semple and Gemeinhardt's method from 1981 related unit skin friction to clay stress history (Semple and Gemeinhardt, 1981). In 1982, Stevens adopted model by Semple and Gemeinhardt. The methods mentioned above are referred to as traditional methods, while recently developed models are usually based on CPT data (Alm and Hamre, 1998).

Three driveability approaches have been selected for the purpose of this paper, some are slightly modified in order to achieve better estimation of the ground conditions at this particular site and a brief summary of each is described in section below.

3.1 Methodology for estimating SRD

Toolan and Fox (1977)

This SRD model, referred to as Toolan and Fox method in this paper, proposes unit skin friction in clays is equal to remoulded undrained shear strength. However, this parameter is difficult to measure accurately, so a portion of measured undisturbed strength is often assumed, expressed by the factor α. A range of α values were considered in order to determine the most appropriate value for each type of clay at this location and following values were chosen: 0.5 for CHF_C, BSBK_U, BSBK_MC, BSBK_L, and 0.4 for ROUGH and SWBK formations. Unit skin friction is then expressed as

$$f_s = \alpha \cdot s_u \quad (1)$$

The unit end bearing in clay is set equal to the cone tip resistance.

In this study, the unit skin friction for granular soils is not computed according to

original formulation, where it is calculated as fraction of the recorded cone tip resistance (1/300 for dense sand), but according to API (API RP 2A, 1981) as

$$f_s = 0.8 \cdot \sigma'_{v0} \cdot \tan(\varphi - 5°) \quad (2)$$

where σ'_{v0} is the effective vertical stress (kPa) and φ is the angle of internal friction.

Unit end bearing in granular soil is assumed one third of the cone tip resistance. It is generally accepted that the behaviour of large diameter piles is fully coring, implicating that unit skin friction is applied to the external and internal pile wall and unit end bearing to the cross-sectional area of the pile.

The model is also applied for chalk. The grade D chalk is treated as clay. For other grades of chalk, unit end bearing is calculated as 60% of the cone tip resistance, and unit skin friction is set to 20 kPa.

Stevens et al. (1982)

Four cases are normally studied for this method, lower and upper bound coring, and lower and upper bound plugged, but in this analysis, only coring will be considered. In the original paper (Stevens et al., 1982) lower bound assumes that internal skin friction is 50% of the external skin friction, and upper bound assumes they are equal. This analysis considers best estimate case as original upper bound case, where equal skin friction acts on the inside and outside of the pile wall. In granular soils, both unit skin friction and unit end bearing are calculated using static pile capacity procedures.

$$f_s = 0.7 \cdot \sigma'_{v0} \cdot \tan(\varphi - 5) \quad (3)$$

$$q_{tip} = 40 \cdot \sigma'_{v0} \quad (4)$$

For cohesive soils, unit skin friction is computed using stress history approach presented by Semple and Gemeinhardt (1981), and unit end bearing as defined in the API (API RP 2A, 1981).

$$f_s = \alpha \cdot 0.5 \cdot (OCR)^{0.3} \cdot s_u \quad (5)$$

$$q_{tip} = 9 \cdot s_u \quad (6)$$

where *OCR* is overconsolidation ratio and α is parameter calculated using the expression from API (1981).

This model is also applied for chalk and uses the same procedure as Toolan and Fox model. The method is based on best estimate soil parameters, factors are then applied to both calculated skin friction and end bearing according to original paper to obtain different driveability cases. Further on, the method is referred to as Stevens method.

Alm and Hamre (2001)

The model was first introduced in 1998 and updated in 2001 to offer a direct correlation for unit end bearing and skin friction with the CPT. Since major contribution to SRD is due to side friction, this method includes friction fatigue concept, a reduction in unit skin friction with increasing pile penetration. The unit skin friction for cohesive soils is

$$f_s = f_{sres} + (f_{si} - f_{sres}) \cdot e^{k \cdot (d-p)} \quad (7)$$

where f_{si} is the measured cone skin friction and f_{sres} is the residual friction, calculated as

$$f_{sres} = 0.004 \cdot q_c \cdot (1 - 0.0025 \cdot \frac{q_c}{\sigma'_{vo}}) \quad (8)$$

and shape degradation factor is expressed as

$$k = (q_c/\sigma'_{v0})^{0.5}/80 \quad (9)$$

where *d* (m) is depth to the soil layer, *p* (m) is pile tip penetration and q_c (kPa) is cone tip resistance. Unit end bearing is calculated as 60% of the cone tip resistance.

The unit skin friction for granular soils is computed in the same way as for the cohesive soils, however the initial skin friction f_{si} is calculated as

$$f_{si} = K \cdot p'_0 \cdot \tan(\delta) \quad (10)$$

where K is calculated as

$$K = \frac{0.0132 \cdot q_c \cdot (\sigma'_{v0}/p_a)^{0.13}}{\sigma'_{v0}} \quad (11)$$

The residual friction is calculated as 20% of the initial friction, which is equal to measured cone skin friction. The end bearing is computed as

$$q_{tip} = 0.15 \cdot q_c \cdot (q_c/\sigma'_{v0})^{0.2} \quad (12)$$

The chalk is treated as clay for both skin friction and end bearing. The details of this model are given in the original article (Alm and Hamre, 2001). Further on, the method is referred to as Alm and Hamre method.

3.2 Methodology for backanalysis

To simulate the actual driving conditions, the hammer stroke is adjusted according to the driving energy used during installation. Normally a driveability analysis is performed using the full hammer stroke to evaluate if the selected hammer is able to drive the pile to target depth. By adjusting the hammer stroke, the actual hammer energy recorded in the driving log at the time of installation is used to demonstrate how the predicted SRD suits soil conditions. Bearing in mind that the pile experiences both static and dynamic resistance during driving, the method relies on the wave equation analysis program GRLWEAP (Pile Dynamics, 2010), where dynamic forces are represented by damping parameters. Smith (Smith, 1960) gave the total resistance mobilized during dynamic loading as

$$R_d = R_s(1 + J \cdot v) \quad (13)$$

where R_d is dynamic soil resistance, R_s is static soil resistance, J is a damping constant and v is velocity of a pile segment during a given time interval.

The dynamic soil parameters are an integral part of any pile driveability assessment and it is common for an SRD model to have a set of associated quake values and damping factors.

In all cases, the associated side and toe quakes are 2.5 mm and toe damping J_p is 0.5 s/m. The selected parameters are in accordance with the best practice (Pile Dynamics, 2010). The damping parameters used in this analysis are presented in Table 2.

Table 2. Damping parameters

Soil unit	Method	Skin Damping J_s [s/m]
CHF_C BSBK_MC BSBK_U BSBK_L	Toolan&Fox	0.66
	Stevens	0.23
	Alm&Hamre	0.25
HLCN CHF_S BSBK_MS	Toolan&Fox	0.25
	Stevens	0.16
	Alm&Hamre	0.25
ROUGH SWBK	Toolan&Fox	0.23
	Stevens	0.23
	Alm&Hamre	0.25
WMR Chalk	Toolan&Fox	0.65
	Stevens	0.65
	Alm&Hamre	0.25

4 BACKANALYSIS

The main objective of this paper is to show the results of predicting pile driveability based on the methods commonly used in the industry today. Due to the complex local site conditions, the analysis resulted in a significant overestimation of soil resistance to driving in chalk layers and slightly underestimation in clay or sand layers above. The results from only six positions (CPT data illustrated in Figure 2) out of 35 that were analysed, will be discussed below (Figures 4-9).

It is important to outline that the primary concern of analysis done in this paper is prediction in chalk, so only positions that penetrate this formation are referred to as good/poor predictions. Positions located from northwest to northeast generally give poor prediction, especially ones where water depth is larger (indicated with red rectangle in

Figure 3). However, there are exceptions, for example position P06 (discussed later in the paper).

It is stated in the API (API RP 2A-WSD, 2010) that the exact definition of refusal for a particular installation should be defined in the installation contract and should be adopted to the individual soil conditions, hammer and pile dimensions. At this specific location refusal is encountered when one of the following criteria is met: 125 blows per 0.25 m in six intervals of 0.25 m (500 bl/m), 200 blows per 0.25 m in two intervals of 0.25 m (800 bl/m), 325 blows per 0.25 m in one interval of 0.25 m (1300 bl/m) or 325 blows per 0.25 m in two intervals of 0.25 m (1300 bl/m).

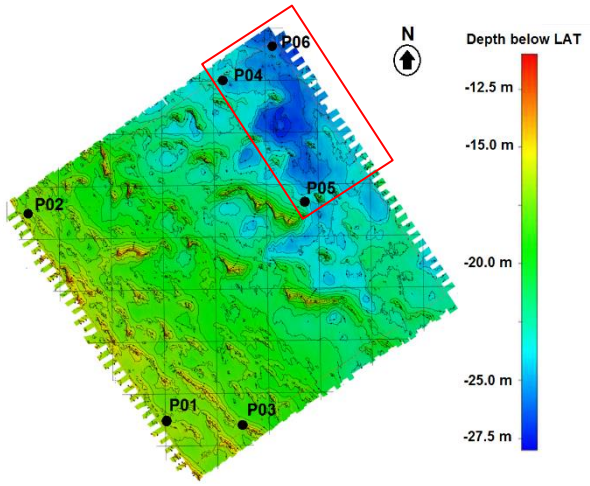


Figure 3. Layout of the windfarm and water depths

Information about pile make up and penetration are given in Table 3. The hammer used in installation process was IHC-S2000, with the rated energy of 2000 kJ and the stroke of 2.02 m.

Position P01 presented in Figure 4 differs from other positions chosen for analysis in this paper because it reaches the target depth without penetrating into the chalk formation.

Table 3. Pile details

	Penetration depth [m]	Penetration into chalk [m]	Wall thickness at tip [mm]
P01	21.66	0.0	73
P02	26.96	13.56	72
P03	31.06	10.26	72
P04	25.96	15.16	72
P05	31.06	20.86	72
P06	28.46	6.76	72

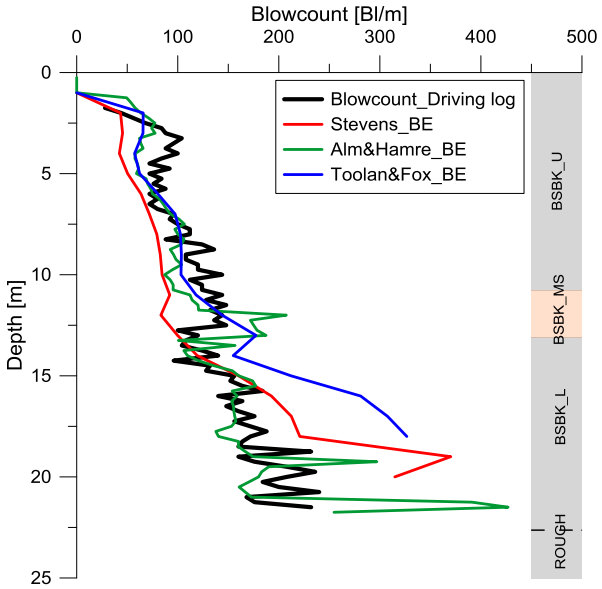


Figure 4. Driveability predictions for P01

As can be observed in Figure 4, both Stevens and Toolan and Fox methods show underestimation in the upper clay layers, but they tend to overestimate number of blows in the lower layers of clay, reaching refusal at 20.9 m and 20.1 m below seabed, respectively. At these depths, the s_u profile, derived from the net cone resistance and a cone factor N_{kt} of 18.5, gives extremely high values of undrained shear strength.

Alm and Hamre method, which relies entirely on CPT data, provided a good best estimate prediction, with a slightly overestimated number of blows in sand layer.

Figures 5-6 show driveability predictions in positions P03 and P06 where chalk formation is found at depth of 20.75 m and 21.7 m below seabed.

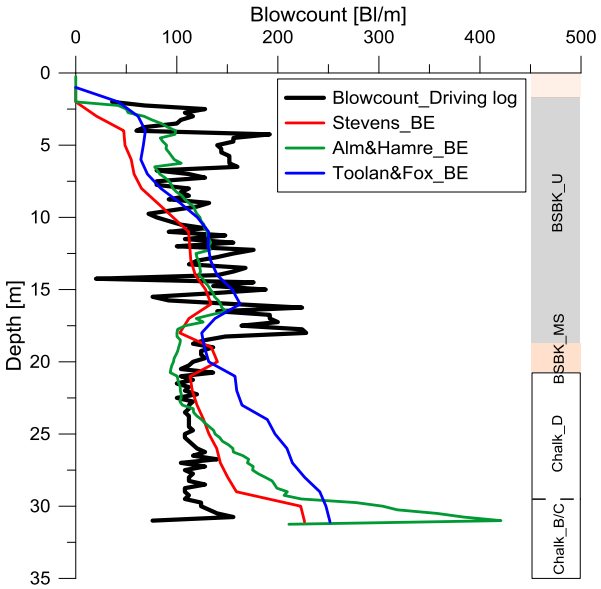


Figure 5. Driveability prediction for P03

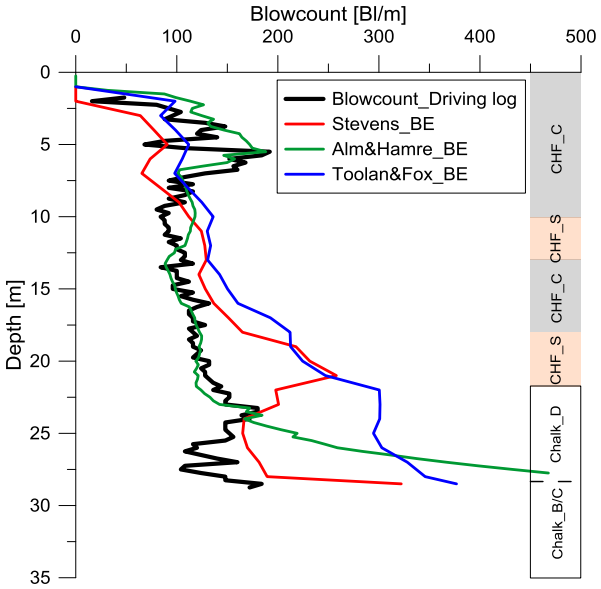


Figure 6. Driveability prediction for P06

These positions are considered to have a reasonable prediction of number of blows in chalk layers by Stevens method. In clay, both Stevens and Toolan and Fox methods underestimate the blowcount, while overpredicting it in sand (from 18.0 to 22.0 m in Figure 6).

The increase in blowcount is visible after depth of 29.5 m (P03) and 28.3 m (P06), which can be related to change in calculation procedure for chalk grade D and B/C.

Alm and Hamre method follows the blowcount trend from driving log but does not predict well number of blows in chalk. It is important to keep in mind that the method was originally developed only for sand and clay, nevertheless in this paper it is also used for chalk under assumption it behaves as clay.

Figures 7-9 show backanalysis results for positions where head of the chalk unit is found at 13.4, 10.0 and 12.1 m below seabed.

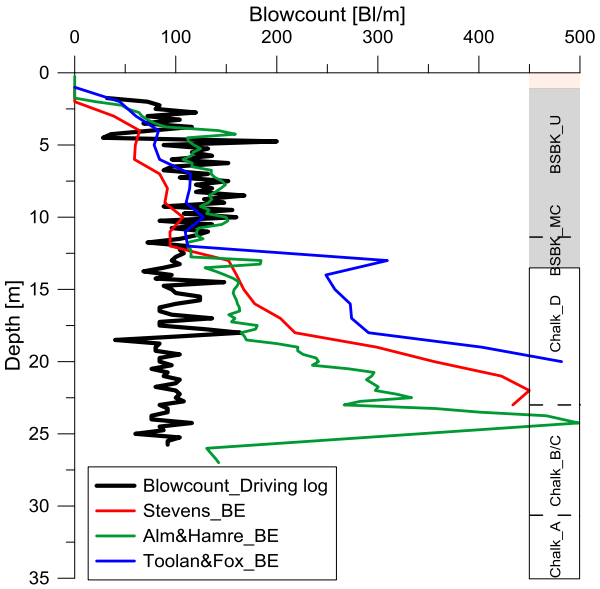


Figure 7. Driveability prediction for P02

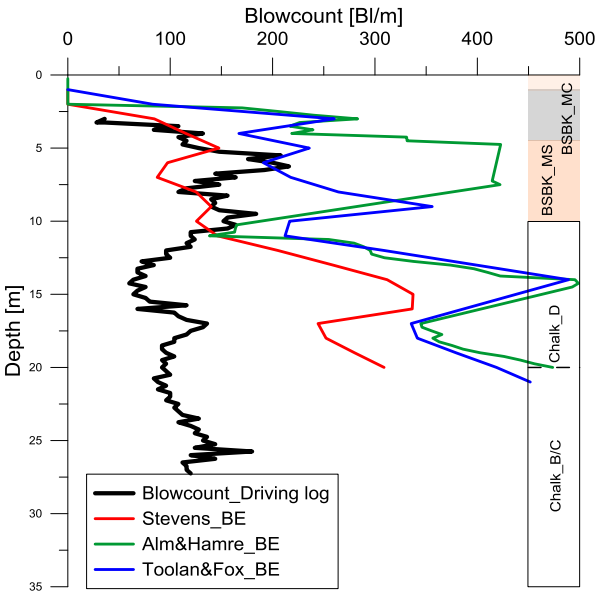


Figure 8. Driveability prediction for P04

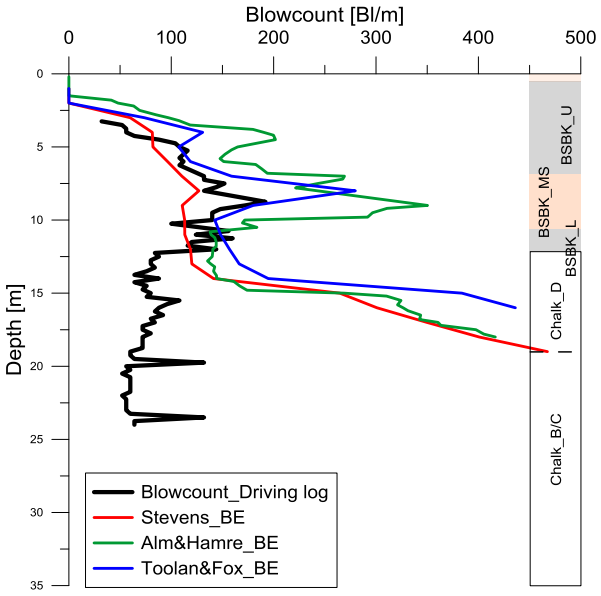


Figure 9. Driveability prediction for P05

Stevens best estimate method gives underestimation of number of blows in clay and sand layers, but then tend to overestimate it greatly in chalk layers below. Refusal is encountered at 24.4 m (P02), 22.1 m (P04) and 19.9 m (P05). Since major part of SRD is due to skin friction, especially for chalk of grade D, the overestimation in results indicates that soil showed much less resistance than expected. Figure 10 representing energy used by the hammer during driving confirms this assumption.

Good prediction of blowcount in clay is found at positions P02 and P05 with Toolan and Fox method, but it tends to overestimate number of blows in sand layer (also seen at P04). Overestimation in chalk at these positions is large, accompanied by reduction of energy used by the hammer.

Alm and Hamre best estimate method captures well blowcount prediction in clay and sand layers at P02, but overestimates it in chalk before meeting refusal at 25.7 m. The same method does not provide good results for sand layers at positions P04 and P05, overestimating the number of blows by up to 100%, what can be explained by poor CPT data found in those layers, since the method relies directly on measured skin friction and cone resistance. The refusal on these locations is met at 5.51 and 8.3 m below seabed. The hammer energy at P04 and P05 was low, around 13 and 18%, meaning that encountered resistance was not high.

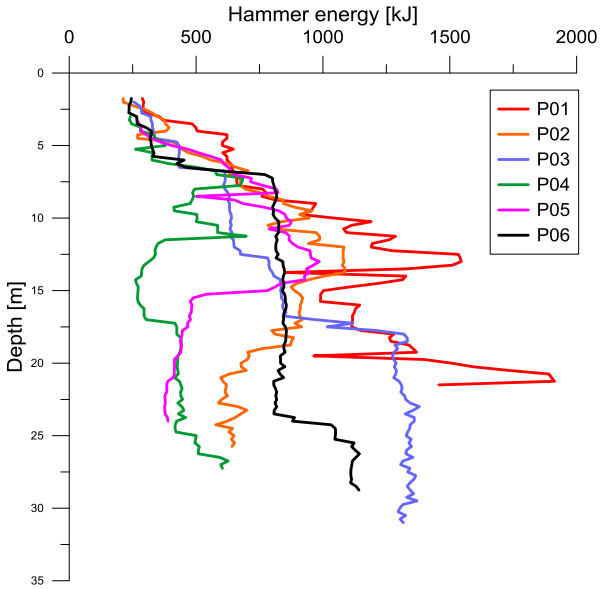


Figure 10. Energy used by the hammer

5 OBSERVATION

One of the possible reasons for deviations in backanalyzed number of blows should be discussed within the energy domain of driveability analysis. Future work will therefore be focused on inspection of static resistance curve that is being used in GRLWEAP model, as the authors' opinion is that analysis with quake and damping settings presented in paragraph 3.2 might work best only for high energy close to rated hammer energy.

6 CONCLUSIONS

Driveability approaches used in industry today were developed for relatively small diameter piles. According to analysis presented in this paper, using these methods to predict behaviour of large offshore monopiles does not provide good estimation, especially when found in complex site conditions. The comparison is done for Toolan and Fox, Stevens and Alm and Hamre

methods, 35 piles were analysed in the original study, but only six of them were discussed in detail.

In general, Stevens best estimate method predicts lower number of blows in the first 10-15 meters, while CPT based Alm and Hamre gives quite a good fit, on condition that CPT profile is reliable.

However, both methods show poor prediction in chalk where it looks as if piles penetrating these layers encountered very low resistance from the surrounding soil.

From the study observed above, it is recommended that correlating soil resistance in chalk directly to CPT measurements should be taken with extreme caution. Further work is required in order to refine calculation procedures to predict the behaviour of piles in chalk layers.

7 REFERENCES

Alm, T. and Hamre, L. (1998). Soil Model for Driveability Predictions. OTC 8835, Offshore Technology Conference, No. OTC 8835, 13.

Alm, T. and Hamre, L. (2001). Soil Model for Pile Driveability Predictions Based on CPT Interpretations. Proceedings of the 15th International Conf. on Soil Mechanics and Foundation Engineering, Istanbul, Vol. 2, pp. 1297–1302.

American Petroleum Institute (API) (1981). RP 2A Planning, Designing and Constructing Offshore Platforms, 12th edition. Washington, DC

American Petroleum Institute (API) (2010). RP 2A-WSD Planning, Designing and Constructing Fixed Offshore Platforms-Working Stress Design, 21st edition. Washington, DC

Lord, J.A., Clayton, C.R.I. and Mortimore, R.N. (2002). Engineering in Chalk CIRIA Report C574. London: CIRIA

Heerema, E.P. (1978). Predicting Pile Driveability: Heather as an Illustration of the "Friction Fatigue" Theory. Proc., European Offshore Petroleum Conference and Exhibition, London, Vol. 1, pp. 413-422.

Karimirad, M. (2014). Offshore Energy Structures. Springer International Publishing, Switzerland.

Pile Dynamics Inc. (2010). GRLWEAP: Wave Equation Analysis of Pile Driving. Procedures and Models Manual, Cleveland.

Semple, R.M. and Gemeinhardt, J.P. (1981). Stress History Approach to Analysis of Soil Resistance to Pile Driving. OTC 3969. Proc. Offshore Tech Conf, Houston, USA.

Smith, E.A.L. (1960). Pile Driving Analyses by the Wave Equation. Journal of the Soil Mechanics and Foundation Division, ASCE, Vol. 86, pp. 35-61.

Stevens, R.S., Wiltsie, E.A. and Turton, T.H. (1982). Evaluating Pile Driveability for Hard Clay, Very Dense Sand and Rock. OTC 4205. Proc Offshore Tech Conf, Houston, USA.

Toolan, F.E. and Fox, D.A. (1977). Geotechnical Planning of Piled Foundations for Offshore Platforms. Proc. Institution of Civil Engineers, London, Part 1, vol. 62.

Large scale driving of concrete piles in stiff to very stiff clay

Thomas Sandene
Norwegian Geotechnical Institute, Norway, thomas.sandene@ngi.no

Ørjan Nerland
Norwegian Geotechnical Institute, Norway

ABSTRACT
BAMA Gruppen AS have constructed a new 44 000 m^2 warehouse, office and distribution centre in Groruddalen in northern parts of Oslo, Norway. Norwegian Geotechnical Institute (NGI) were employed as geotechnical consultants, contributing to evaluation of different foundation methods, design of pile foundations in cooperation with structural engineers and installation of piles in cooperation with the piling contractor. Within the perimeter of the warehouse, the depth to bedrock is between 30 to 50 meters. The typical soil profile is about 2 m of various fill material over 5 to 10 meters of stiff to very stiff clay over a slightly overconsolidated quick clay. Because of the extent of piling, concrete piles were very cost effective for the client. The stiff clay layer however could in theory lead to damaging tension stresses in the concrete piles during driving. For concrete piles up to 50 m length, the total number of blows is also considerable.

NGI performed pile-driving simulations, and the contractor performed test-driving at the site. During test-driving, PDA equipment was mounted, monitoring pile stresses during driving of the whole pile length. Test-driving was successful, and pile stresses observed within acceptable limits. During the early phases of production driving, the number of piles broken during driving was higher than expected. The large number of piles did however give good statistical data to interpret combinations of pile cross section and hammer weight and energy (fall height) which were unfavourable. In cooperation with the piling contractor, NGI continuously evaluated the piling production procedure and stop criteria. The aim was to reduce the number of broken piles, and to establish documentation of the bearing capacity for all piles. In total, the contractor drove about 1600 functional concrete piles, with a combined length of about 71 km.

Keywords: Concrete pile, steel core pile, stiff clay, quick clay

1 INTRODUCTION

Bama Gruppen AS is the largest fruit and vegetable grocer in Norway, distributing domestically produced and imported produce all over the country. In 2012-2013, the company constructed a new main warehouse, distribution centre and main office near Alnabru in the Groruddalen area in the north-eastern part of Oslo. The new warehouse has a base area of about 33 000 m^2 with about 44 000 m^2 of warehouse, distribution centre and office areas. Figure 1 shows the construction site location in Oslo, and *Figure 2* shows an aerial photo of the building more or less finished.

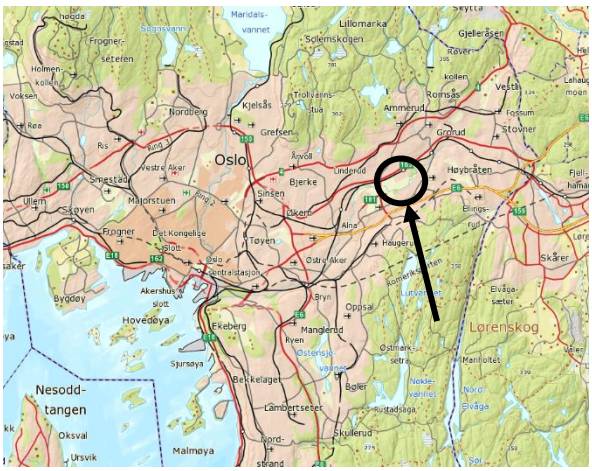


Figure 1: Construction location in Oslo



Figure 2: The finished building (source: bygg.no)

Norwegian Geotechnical Institute (NGI) had a history of studies and investigations on this property, both for the previous owner (ROM Eiendom) and Bama Gruppen. With the background history and knowledge on the site, NGI was hired as geotechnical consultants for foundations of the new building and a new bridge crossing a railway cut, as well as local slope stability improvements where needed.

2 THE CONSTRUCTION SITE

2.1 Brief history

The soil in Groruddalen is mainly composed of thick marine clay deposits. About 8300 years ago, a quick clay slide with a volume of 30 – 40 million m^3 covered the valley bottom (Eggestad, 1978). A moraine formation (the Alfaset morain) obstructed the slide masses from flowing freely further down the valley.

An overview of the slide area and the morain is shown in Figure 3. The slide masses are therefor still covering the "undisturbed" sediments in large areas northeast of the moraine formation, shown in Figure 4.

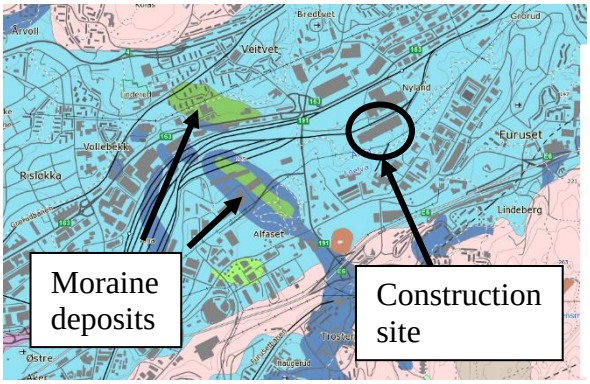


Figure 4: Geological map of the Alnabru area. Green is moraine deposits, blue is marine deposits and dark blue is beach deposits. (source: ngu.no).

In modern times, various landowners have used the construction site property as farming area, landfill, parking and storage area, sports area and most recently a rock crushing plant.

2.2 Topography

The construction site is situated on a plateau at about 118 to 120 masl, and is surrounded by ravines and cuts. To the east, south and southwest, the river Alna flows at the bottom of a ravine about 8 to 12 m deep. To the north, a railway freight line runs past the site. The railway line lies partially at the bottom of an open cut up to 10 m deep, and partially in an open concrete culvert. Figure 5 shows the warehouse location between the river ravine and railway cut.

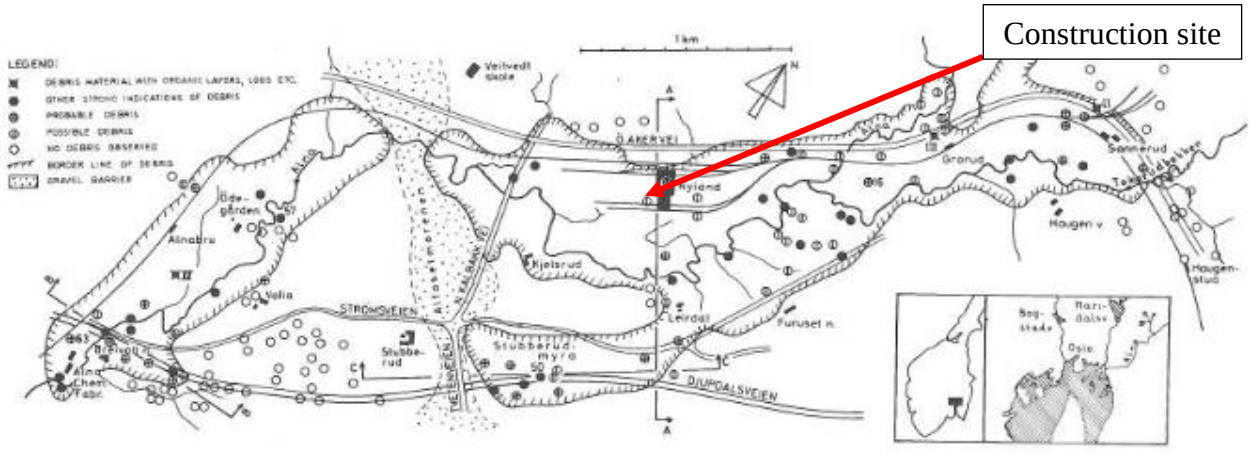


Figure 3: Overview of the Groruddalen quick clay slide (Eggestad, 1978)

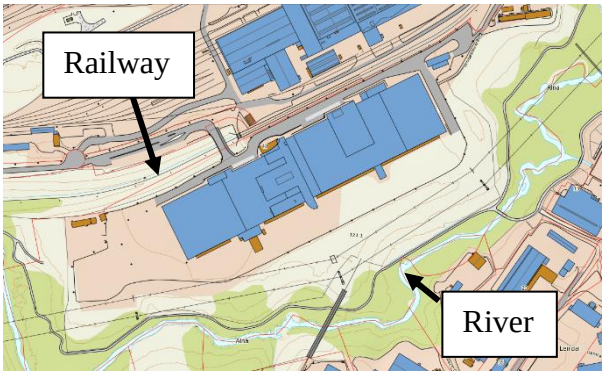


Figure 5: New warehouse in between railway cut and river ravine

2.3 Soil conditions

As previous owners had performed various studies for use of the property, several reports on soil investigations were already available. The evaluation of foundation methods and final design required detailed information, and a supplementary investigation programme was performed by NGI. The supplementary investigation programme included total soundings, rotary soundings, cone penetration testing, soil sampling and measurement of in situ pore pressures by hydraulic piezometers.

Both auger samples of the top fill layer and undisturbed samples of the lower clay layers were analysed in the laboratory for soil classification, routine parameters and oedometer tests.

The general soil profile at the site is about 1-2 m of various fill material over a stiff to very stiff clay layer. The stiff clay layer is the reconsolidated landslide masses from the quick clay slide mentioned earlier, and has a thickness of about 5 to 10 meters at the construction site. Below the landslide masses, the "undisturbed" clay is quick and slightly overconsolidated. Figure 6 shows a general profile of undrained active shear strength based on interpretation of CPTU soundings. The red line is the shear strength of a normally consolidated clay for comparison.

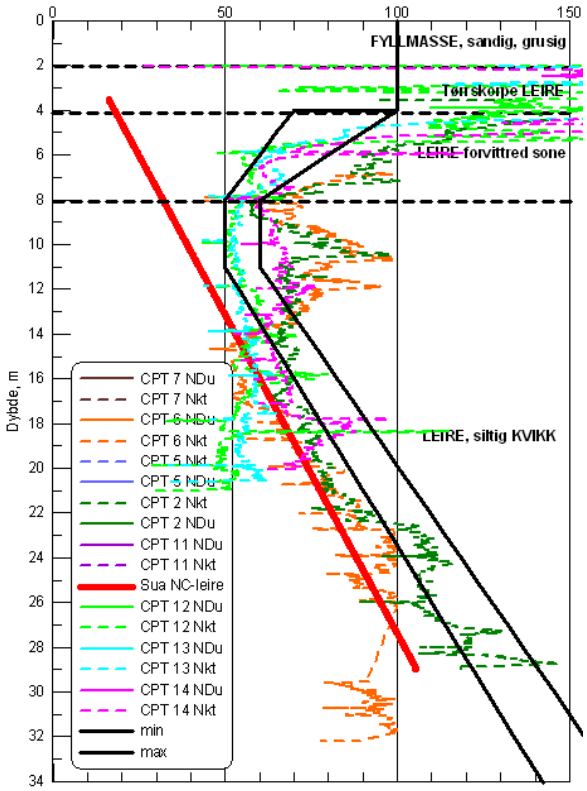


Figure 6: Undrained active shear strength based on CPTU soundings

In southwestern parts of the site the quick clay continues down to bedrock, while in the northeastern parts a moraine layer up to about 15 meters thick covers the bedrock. The depth from terrain to bedrock varies between 30 to 50 meters.

The ground water level was measured to about 3 m below terrain, with a slightly lower than hydrostatic distribution with depth caused by drainage to the ravines.

3 PLANNING

3.1 Evaluation of foundation methods

NGI performed evaluation of various principles for foundations for the new warehouse. Different variations of direct foundations on terrain and pile foundation to bedrock were considered.

The scenarios considered for direct foundations were different levels of adding and/or removing fill material at the site to establish the finished floor at different height levels. Partly removing existing soil top layer and replacing it with lightweight fill material

was also considered. Settlement calculations showed that long term settlements without the use of lightweight fill materials were in the order of 20 – 25 cm. Replacing the top layer with lightweight fill material would give a slight reduction in settlements of about 5 – 10 cm.

Settlements in the order calculated were considered to the acceptable for the warehouse structure, but differential settlements would cause cracking and increased repair and maintenance of the floor. The users of fresh produce warehouse could not accept this uncertainty regarding structural maintenance. Pile foundations were therefor concluded to be the only alternative.

3.2 Pile foundations

Only end-bearing piles to rock or sufficient depth in moraine were considered, as friction-bearing piles would be difficult in the low plastic sensitive clay. The piles types considered were concrete piles, massive steel piles (H-profiles) and bored steel core piles.

The freely supported deck of the warehouse and the structure itself required a certain number of piles almost regardless of the capacity of each pile. Concrete piles would therefore be significantly cost effective compared with the steel piles. The logistics of the large number of piles that were to be installed during a short period also favoured the concrete piles. The planned amount of concrete piles for this project was about equivalent to the total volume of concrete piles casted in Norway in a poor production year.

An applied layer of bitumen coating reduces the effects of negative skin friction on the bearing capacity of all piles.

Pile design in general was done in accordance to the Norwegian pile design handbook Peleveiledningen (The Norwegian Pile Committee, 2005).

4 VERIFICATION OF USABILITY

4.1 Pile stresses during driving

The soil characteristics at the construction site does not favour the concrete pile. The penetration from the stiff to very stiff clay down into the softer quick clay represents a risk of significant tensions stresses in the piles during driving. Most of the piles would also be very long, increasing the risk of breakage as the numberof blows on the piles would be considerable.

A test-driving programme was established at the actual construction site, to test the performance of the piles in the actual soil conditions. NGI performed GRLWEAP analysis of the driving process, concluding that the margin regarding tension stresses should be within acceptable range.

4.2 Test-driving

The test-driving was performed in late June and early July of 2012. A total number of 24 P270NA piles and 2 P230NA were driven using a 60 kN hydraulic hammer. The piles were scattered over the construction site, covering different variations in ground conditions. Out of the 26 test-piles, 2 piles broke during driving. The setup of test-piling at the site is shown in Figure 7.

During test-driving, 7 piles were driven with PDA-sensors mounted. The sensors logged the whole driving process of the piles, from terrain and down to stop criteria when hitting either bedrock or moraine layers. This gave an output of the tension stresses in the piles for all blows during the driving history. Results from PDA measurements confirmed previous analysis results that tension stresses were within acceptable range for the piles, and the project could continue with concrete piles as planned.



Figure 7: Test piling with PDA-testing

5 VERIFICATION OF BEARING CAPACITY

The piles would reach a bearing tip resistance at either rock or in frictional soil material (moraine). Two different procedures stop criteria was developed, and the crane operator would have to use the appropriate procedure based on if he believed the pile had reached rock or moraine.

Stop criteria procedures are normally based on gradually increasing hammer energy, ending up with a number of blows with high energy. Because the piles had already suffered a very high number of blows during driving, the energy during stop driving was reduced to half of what was evaluated to be a normal procedure. Instead, one single control blow with high energy was performed for all piles at the end of the stop criteria driving. Elastic compression and final set was measured for all piles during the control blow, and this information was used to evaluate if the pile had reached the design bearing capacity.

All piles were restruck after a few days, and generally did set a few millimetres during restrike. Another high energy control blow with measurement of elastic compression and set was performed at the end of restrike for all piles.

6 PRODUCTION PILING

6.1 Effect of hammer size

Production piling started in the end of August 2012. The piling contractor mobilized four different piling rigs, with 60 kN, 70 kN, 90 kN and 100 kN hydraulic hammers. The two lighter ones were used for P230NA and P270NA piles, while the two heavier ones were used only for P345MA piles.

The different hammer sizes did, as could be expected, perform differently in terms of percentage of broken piles. Table 1 shows the total number of piles driven with each hammer, including broken piles.

Table 1: Total number of piles driven by hammer size

Hammer	P230NA	P270NA	P345MA
60 kN	398	385	-
70 kN	90	645	-
90 kN	-	-	130
100 kN	-	-	110

Figure 8 shows the distribution of broken piles by cross section and hammer size. The most obvious result is the combination of P230NA piles and 70 kN, which proved to be significantly unfavourable. Driving of the smallest piles with this hammer was therefore stopped completely as soon as the broken piles percentage was identified to be that high compared with other combinations. In general, P230NA and P345MA piles proved to be more difficult with respect to pile breakage compared with P270NA piles.

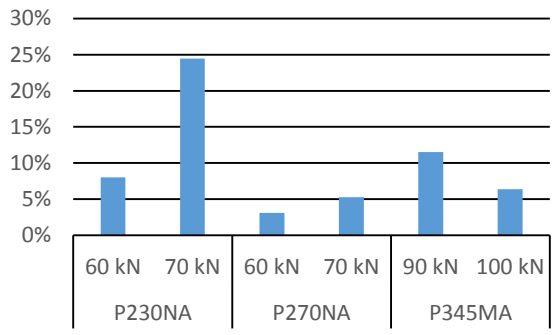


Figure 8: Percentage of broken piles by cross section and hammer size

Another observation from Figure 8 is the fact that the combination of P270NA piles and 60

kN hammer weight was the best combination with respect to number of broken piles. This was the same combination that was used during test-driving, and one could therefor say that the test-driving setup was not able to capture some difficult aspects of the pile-driving job at the site.

6.2 Effect of driving energy

The energy used during pile driving was evaluated from the pile driving analysis and the test-driving. After a large enough number of piles was driven to give statistical indications, driving energy was reduced as much as possible for P230NA and P270NA piles. The contractor still has to have some energy for him to be able to have a reasonable production. For the larger P345MA piles, further energy reduction was ruled out as production speed was already quite low.

Table 2 gives an overview of the total number of driven piles distributed by cross section, hammer size and driving energy. The driving energy is expressed as the free fall height of the hammer.

Table 2: Number of driven piles by cross section, hammer size and driving energy

Energy	P230NA		P270NA	
	60 kN	70 kN	60 kN	70 kN
10 cm	4	1	3	
15 cm	80			
20 cm	285	56	158	532
25 cm			20	
30 cm	28	33	182	104
35 cm				2
40 cm			17	

Energy	P345MA	
	90 kN	100kN
20 cm	11	12
25 cm		
30 cm	13	52
35 cm		43
40 cm	105	3

Figure 9 illustrates the percentage of broken piles by driving energy. Combinations with fewer than 10 piles (ref. Table 2) are left out of the diagram. The hammer-pile-combinations P230NA-70 kN and P345MA-90 kN obviously stand out as generally unfavourable. For other combinations, reducing the energy during driving clearly reduces the number of broken piles. Reducing the energy increases the number of blows required to get the pile down to bearing layers, increasing the sum of dynamic loading on the pile during installation. From reduced energy also follows reduced stresses in the pile during driving, and the reduced stresses means less chance of the pile breaking over time.

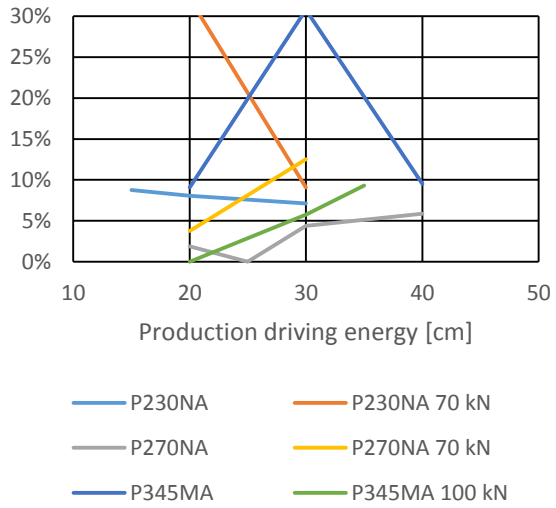


Figure 9: Percentage of broken piles by cross section, hammer size and driving energy

The effect was especially significant when reducing energy from 30 to 20 cm for P270NA piles driven with 70 kN hammer. This combination was used for about 1/3 of the total number of piles in the project (Table 1).

6.3 Effect of pile length

The columns in Figure 10 show an overview of the total number of piles for each cross section and total pile length interval. The graph lines illustrate the percentage of broken piles for the corresponding cross section and total pile length interval.

According to figure 9, the number of broken piles increases significantly when the total pile length increases over about 46-50 m. Almost all P230NA and P345MA piles and about 30 % of P270NA piles longer than 50 m were broken. About 15 to 20 % of P230NA and P345MA piles and 7 % of P270NA piles between 46 to 50 m long were broken.

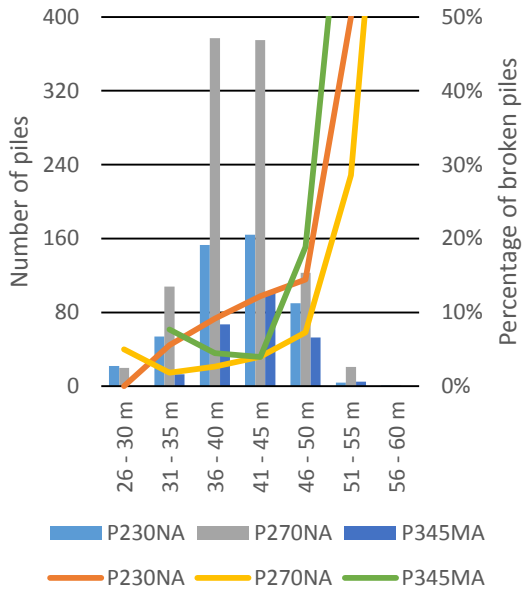


Figure 10: Number of piles and broken piles by pile length

An increasing pile length increases the risk of some kind of unfavourable curvature of the pile, increasing the risk of breakage. The increased length also comes with an increase in total number of blows and cycles of dynamic stresses.

6.4 Steel core piles

Broken concrete piles, or piles which were suspected to be broken, were replaced by drilled steel core piles. Due to earthquake design, some piles for the warehouse structure needed tension capacity, and the steel core piles were therefor always a part of the plan. The logistics and equipment was available at the site, and pile replacement could be designed immediately as the contractor reported broken piles.

The soil conditions at the site also proved difficult during drilling of casings for the steel core piles. During drilling the drill bit would get stuck, sometimes breaking the casing itself causing loss of drilling equipment.

7 OTHER INCIDENTS

7.1 Shallow slope failure

In September 2012, after a heavy rainfall, surface cracks were observed in the slope towards the railway line. The appearance of the crack coincided with pile driving near the top of the slope. Figure 11 shows a picture taken from the other side of the railway cut, with the pile driving cranes working in the background.



Figure 11: Surface crack in slope (marked with yellow dashed line)

Even shallow surface slides could cause concerns regarding operation of the railway line, and driving of concrete piles near the slope was stopped immediately. The slope was instrumented with electronic piezometers and inclinometer casing. The piezometers measured a very high pore pressure, with a magnitude in the order of the same as the vertical overburden (meaning that the effective stresses were very small). Inclinometer measurements were done with short time intervals for the first period of time after installation, but indicated no significant movement in the slope.

For the slope to have a sufficient factor of safety in a permanent situation, the top couple of meters of the slope was planned to be removed and replaced by lightweight fill material. This operation was expedited to increase the safety during the construction phase. Drilled steel core piles replaced the concrete piles within a safety zone from the slope, in order to prevent further build-up of horizontal stresses and pore pressures. The drilled steel core piles was installed as gently as possible (low air pressure and drill speed)

to reduce the risk of further set up of excess pore pressure.

7.2 Thickness of bitumen coating

It was discovered during a late phase of pile installation that the bitumen cover on the piles appeared to the significantly thinner than specified. According to the specifications in NS 3420, the thickness on concrete piles should be at least 2 mm. Measurements later done by both factories which delivered piles to the site confirmed that the layer most probably was generally thinner than specified, often less than 1 mm. The client wondered if the reduced thickness had any implications for the pile capacity, which at this point in the construction process would have been fatal.

According to Claessen & Horvat (1974), shear stress transferred from the soil to the pile through the bitumen layer depends on the shear stiffness (or viscosity) and the thickness of the bitumen layer. The shear stiffness is depended on the temperature of the bitumen layer and the rate of strain. At a high rate of strain, when driving the pile, the layer is stiff and resists wear. At a slow rate of strain, when the soil settles around the pile, the layer is softer and does not transfer much shear stress to the pile. Furthermore, the shear stress transferred through the bitumen is inversely propotional to the thickness of the bitumen layer.

Studies were performed to establish reliable values of the negative skin friction affecting the piles, knowing the actual thickness of the bitumen layer. The increased strength of the piles, taking into account strength development of the concrete after the 28 day design strength, was also evaluated. In total, the structural and geotechnical engineers concluded that there was very little reason to doubt that the piles did have the capacity they were supposed to have, and mainly because the evaluation of negative friction on the piles fortunately had been on the conservative side during the design stage The discovery of the reduced bitumen thickness did raise a few questions in this project. Apparently, the pile factories followed their normal procedures, meaning that there probably are other projects where the bitumen thickness is thinner than specified in the Norwegian standards. Bitumen thickness should be measured after application at the factory and by the contractor at the construction site before the piles are used.

8 SUMMARY AND CONCLUSIONS

Foundations for the warehouse were successfully established with concrete piles supplemented with steel core piles. Despite the difficult ground conditions and the long pile lengths, the solution ended up being effective especially considering costs for the client. The percentage of broken piles was high, but counter-measurements such as close monitoring of unfavourable conditions, dialogue with the contractor and adjustment of the piling procedure when needed was important factors in bringing the number as low as possible. 1758 concrete piles with a combined length of around 71 km were driven. The final ratio of broken piles was about 7 %.

Test-driving was performed with mainly one pile cross section and one hammer size. This combination later proved to be the most favourable one, and other combinations of pile cross section and hammer size were more difficult during the construction phase. Testing all relevant combinations of hammers and cross sections before driving had started could have resulted in better or faster tuning of driving procedures, but the test-driving would also be quite a bit more resource demanding.

Another aspect was the short period of time from test-driving to the start of the actual construction. If the test-driving had ended up proving that the concrete pile would be unsuitable, the whole project would probably have been delayed and costs would have escalated while waiting for new solutions to be implemented.

The effects on slope stability could have been investigated further earlier in the project, but

in the end the solution with drilled piles near the slope would most likely have been used anyway.

Reducing negative skin friction on piles is depended on the thickness of the bitumen layer, not just the application of a layer of random thickness. If important, thicker layers could be specified. Layer thickness should be measured before piles are used.

9 REFERENCES

The Norwegian Pile Committee (2005). Peleveiledningen, revision 2005, The Norwegian Geotechnical Society

Claessen, A.I.M. & Horvat, E. (1974). Reducing Negative Friction with Bitumen Slip Layers, Journal of the Geotechnical Engineering Division, Proceedings of the American Society of Civil Engineers, Vol. 100, No. GT8 August 1974, pp 925-945

Eggestad, Å. (1978) A prehistoric landslide in the Grorud valley near Oslo, Norsk Geografisk Tidsskrift, Det Norske Geografiske Selskab, Vol. 32, pp 153-157, Oslo ISSN 0029-1951

DR Koncerthuset in Copenhagen - a concert hall on three legs

A. B. Christensen
NIRAS, Denmark, abc@niras.dk

N. Bønding
NIRAS, Denmark

ABSTRACT
In 2002 the construction phase of DR-Koncerthuset (the Copenhagen Concert Hall, the Danish Broadcasting Corporation) began. After 7 years of construction the concert hall opened in 2009. The concert hall is a more than 10.000 ton structure resting mainly on three large stair towers like the legs of a three legged chair. With one of the legs leaning outwards the foundation designers was met with severe requirements.
The foundation project was treated as CC3 and geotechnical category 3. As the geotechnical design took place at the same time as the construction work began, a detailed investigation was initiated with a tight time schedule in order to provide sufficient detailed information in due time to cope with the challenging statics of the concert hall and derived foundation requirements.
The Concert hall is designed as direct foundations in glacial deposits of mainly stiff to hard clay till. In order to make use of the high strength of the deposits the geotechnical supervision of the foundation work was integrated with a detailed investigation comprising more than 100 geotechnical boreholes, 24 plate load tests, triaxial tests, and consolidation tests. In addition, the risk of differential settlements caused by variations in the consolidation properties was evaluated by settlement monitoring during construction.
This paper deals with selected geotechnical design considerations, the prediction of the settlement of the main foundations, the interpretation of the results of the settlement monitoring, and how the whole geotechnical design and supervision was integrated.

Keywords: Settlements, Heavy loads, Monitoring.

1 INTRODUCTION

In 1999 the Danish Broadcasting Corporation (DR) commenced the construction of DR-byen. This included The Copenhagen Concert Hall, which is a concert hall with a main auditorium seating 1800 people. The main auditorium is basically a large hollow structure resting on 3 legs of which one of the legs has an outwards inclination thus creating "unstable" statics, illustrated in figure 1.

The three legs are constructed as stair towers. In figure 2 the inclined tower is seen to the right, just next to the stairs leading up to the foyer.

The stair towers are resting on three large footings F09, F10 and F11, where F11 is carrying the inclined stair tower. The foundation layout is shown in in figure 3.

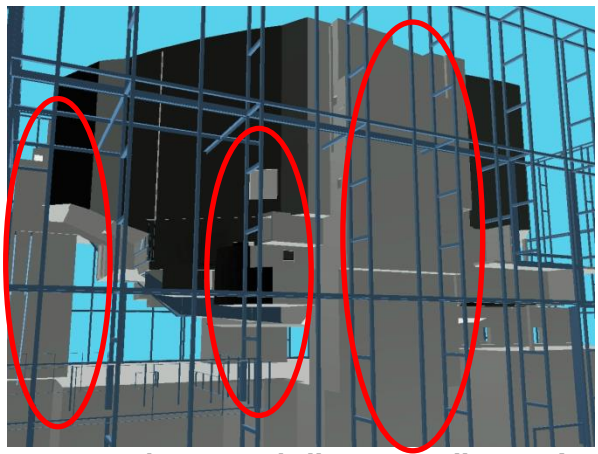


Figure 1: The concert hall structure illustrated in 3D. The red line indicates the location of the three main stair towers (grey) carrying the main auditorium (black). The left most is an inclined stair tower.

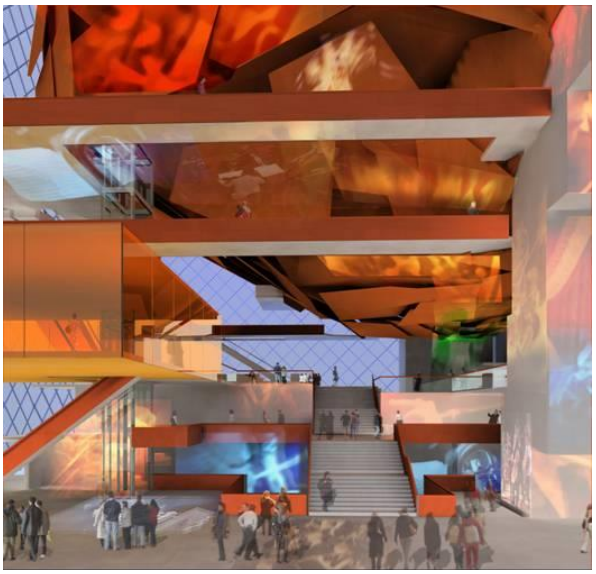


Figure 2: The foyer with the inclined stair tower resting on F11 to the left. The main auditorium is seen over the foyer, and is covered with shells (Illustrations from Ateliers Jean Nouvel).

The foundation was established in approx. level -4, which is about 6 m below ground level in stiff glacial deposits.

One of the issues was settlements caused by the very large foundation loads. Initial settlement calculations indicated a risk of large settlements. For this reason a comprehensive field and laboratory work was introduced along with a revised method for settlement evaluation.

This initial settlement assessment was based on information from a few traditional geotechnical boreholes only. For this reason further analysis and investigations were necessary.

Furthermore the detailed design was taking place as the construction pit was excavated, and the detailed geotechnical investigations adapted to the foundation design was only possible in a short window after the excavation and the general blinding layer was finished – this adding additional challenges to the project.

2 GEOLOGY

The geology on the site is dominated by glacial till deposits, which are heavily overconsolidated. These deposits are mainly clay till but are intercalated by sand till and to a minor degree by melt water sand. The glacial deposits are underlain by limestone in level app. -10.00, which on the upper 1.00 – 2.00 m is hardness H1 – H2 and hereunder hardness H3 or more, but locally the limestone has been encountered from aprox level -9.

The construction site is located on the edge of "Rådhusdalen", a highly permeable erosional valley in to the prequatenary limestone.

3 THE FOUNDATION PROJECT

The three large footings have side lengths in the range 7.80 -23.50 m. More specifically their geometry and loads (SLS) are listed in Table 1.

Table 1: Dimension of SLS loadings on footings

	Dimension	**Load Vertical**	**Moment**	
	(m x m)	(kN)	$M_{S,SLS}$ (kNm)	$M_{L,SLS}$ (kNm)
F09	14.80*23.50	84288	5181	16058
F10	7.80*15.10	49017	3122	53966
F11	8.70*15.15	68134	10142	68143

The footings were concreted directly on the cleaned bottom after removal of some soft spots discovered from plate load tests and vane tests.

The foundation level for the three main footings was generally in approx. -4.00, about 6 m below ground level, and approx. 5 m above top of limestone encountered from approx. level -9.

An overall layout of the foundation geometry is shown in Figure 3. The three main footings are located outside Rådhusdalen, but a very comprehensive groundwater lowering system was established with nearby reinjection. The edge of Rådhusdalen is seen on figure 3 were

the contours indicate a steep surface of the limestone. The groundwater lowering was keep to a minimum and only to a very small depth below foundation level (less than a meter).

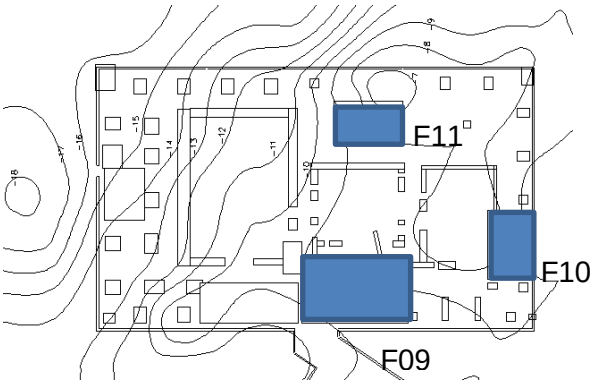


Figure 3: The foundation layout with the three main foundations F09, F10 and F11. The contours shows initially assumed level of limestone. Further boreholes showed limestone from approx. -8,5 to -9 for F10 and F11, and approx. -10 for F09. Rådhusdalen is seen at the left part where the surface of the limestone is steep.

The concreting of the towers and the Concert Hall were done in "lifts" wherefore the load increments were so small, that the load increase may be considered as continuous. The footing were cast ultimo 2003, and the Concert Hall was finished primo 2006, and for this reason the load apply may be considered as very slow.

4 CONSTRUCTION VERSUS DESIGN

The construction of the pit for the basement and foundation work was commenced while the design process was still under way, and only an initial design was present, based on a few boreholes only.

Due to very large foundation stresses and non-conventional structure and statics, the project had to be treated in "Skærpet founderingsklasse" equal to geotechnical category 3.

As a consequence of the very tight project schedule some of the secondary columns and foundations were designed and executed before the detailed design of the concert hall was completed.

Unfortunately a result of the very stiff structure of the concert hall, was that the settlement of the major three footing F09, F10 and F11 would lead to an unaccepted increase of the load on some of these secondary supports. For this reason an assessment of the settlement of the three major footings was of height importance. Particular as the consequence of settlements could be a significant increase of the dimensions of the three major footings.

Detailed investigations were therefore needed, and furthermore the high undrained strength and the large foundation dimensions made traditional foundation inspections hard to carry out using manual methods (hand auger and hand field vane). For this reason all significant footings was both inspected visually and with 1 to 3 geotechnical boreholes, to verify the basis of design. In total more than 100 geotechnical boreholes were executed within the construction area.

This approach provided the basis for detailed investigations, to verify the initial geotechnical design basis.

Caused by a very tight time the installation work for the uplift anchors was commenced right after the pit has been excavated and the blinding layer for the base plate could carry the construction equipment.

The detailed investigations had to be executed in parallel with execution the uplift anchors. This was only possible in close cooperation with the contractor to avoid the geotechnical rigs getting caught in a tight mesh of uplift anchors.

5 THEORY AND COMPUTATIONAL MODEL

The initial evaluation of the predicted settlements was based on the traditional assumption that:

$$K_t = K_{t,0} + \Delta K_t \sigma_{red} \quad (1)$$

where: K_t is the module of consolidation at the stress $\sigma_{red.}$ $K_{t,0}$ is the module of consolidation at the stress 0, ΔK_t is a constant, and σ_{red} is the minimum effective vertical stress since the ice age (occurs immediately prior to concreting).

From experience obtained at nearby sites it was expected that $K_{t,0} \approx$ 20 MPa and $\Delta K_t \approx$ 2500 for clay till and $K_{t,0} \approx$ 50 MPa and $\Delta K_t \approx$ 600 for sand till. The effective weight of the soil was expected to be $\gamma' = 13$ kN/m^3 for clay till and $\gamma' = 11$ kN/m^3 for sand till. σ_{red} is set to $\gamma \cdot z$ where z is the depth under foundation level.

Assuming the footing is modelled by a square footing with side length B yielding the same area as the very footing and assuming a load distribution of 1:2, the consolidation settlement may be determined by:

$$\delta = \int_0^\infty \frac{\sigma(z)}{K_t(z)} dz \quad (2)$$

$$= \int_0^\infty \frac{p_{sls}}{(B+z)^2 (K_{t,0} + \Delta K_{t,0} \gamma z)} dz$$

$$= P_{SLS} \left(\frac{1}{B\left(K_{t,0} - \Delta K_t \gamma B\right)} + \frac{\Delta K_t \gamma \ \ln\left(\frac{\Delta K_t \gamma B}{K_{t,0}}\right)}{\left(K_{t,0} - \Delta K_t \gamma B\right)^2} \right)$$

In the above integration the upper boundary has been set to infinity for the sake of convenience. It shall be emphasized that the ΔK_t term will reduce the settlement contribution rapidly with depth. For this reason the settlement contribution is rather low from top of limestone and below. Integrating to a large depth will tend to give a (slightly) conservative estimate of settlement.

Based on the above information the initial settlement estimate was:

Table 2: Settlement properties from borehole information and calculated settlements

	P_{SLS}	B	$K_{t,0}$	ΔK_t	γ	δ
	(kN)	(m)	(MPa)	(MPa)	(kN/m^3)	(mm)
F09	84288	18.65	20	2500	13	20
F10	49017	10.85	20	2500	13	28
F11	68134	11.48	20	2500	13	35

6 FIELD AND LABORATORY TESTING

As the previous field and laboratory work only comprised a few deep boreholes a more detailed field work was commenced in order to provide sufficient basis for the foundation design.

The main purpose of the field and laboratory testing is of course to obtain more site relevant values of the two parameters $K_{t,0}$ and ΔK_t.

6.1 Field Work

The field testing comprised 17 plate load tests all on Ø30 cm plates. They were carried out in three steps each of 0.5 σ_{SLS}, i.e. to a maximum stress of 1.5 σ_{SLS}.

A plate load test with this small diameter has a rather small influence depth compared to the thickness of the glacial sediments. For this reason the plateload test has been used primary for a local calibration/verification of the stiffness parameters of the till at the actual level, and not as a measure for the total layer of the glacial deposits, which also affects the interpretation as described below.

The evaluation of the tests was based on the middle step to eliminate the bedding effect at the start and to disregard possible curvature above σ_{SLS}. The evaluation was hereafter done by inserting B = 0.266 m (= $(\pi/2)^{0.5} \cdot$ 0,3 m), ΔK_t = 2500 MPa and γ = 13 kN/m^3 in formula (2) and adjust the value of $K_{t,0}$ until the observed settlement is obtained.

The reason for this procedure is that it is impossible to find both $K_{t,0}$ and ΔK_t from just

one set of observations, and since the test mainly involves superficial soil and has a rather limited influence depth, it was decided to lock ΔK_t at its basic value 2500 MPa and determine $K_{t,0}$.

The outcome of this procedure is presented in Table 3: $Kt,_0$ derived from plate load tests. and all derived $K_{t,0}$ values except one are well above the basic value 20 MPa.

Table 3: $K_{t,0}$ derived from plate load tests

Footing	Test No.	Remarks	$K_{t,0}$ (kPa)
F11	P05B		53.610
F11	P06		62.815
F11	P07		36.675
F11	P08B		28.413
F10	P09		52.934
F10	P10		60.180
F10	P11		29.163
F10	P12		55.638
F09	P18		41.439
F09	P19		54.421
F09	P20	Uncertain!	98.907
F09	P21		40.601
F09	P23		43.208
F09	P24	Uncertain!	10.335

6.2 Laboratory testing

The Oedometric tests have been executed by consolidating the samples to their estimated preconsolidation stress $\sigma_{p,c}$ (≈2400 kPa) and hereafter unload/reload to/from 80, 40 and 20 kPa respectively. This stress path has been chosen to enable determination of both $K_{t,0}$ and ΔK_t in one single test, although it must be expected that $K_{t,0}$ will be underestimated due to sample disturbance.i

The preconsolidation stress $\sigma_{p,c}$ is evaluated by the SHANSEP formula with parameters for Danish clay till as presented by Christensen, et al.(1992)

$$0.4\left(\frac{\sigma_{pc}}{\sigma_v}\right)^{0,85} = \frac{c_v}{\sigma_v} \qquad (3)$$

With measured vane strength $c_v \approx 550$ kPa and a overburden pressure $\sigma_v \approx 20$ kPa (3) yields $\sigma_{p,c} \approx 2900$ kPa. On this background it has been chosen (conservatively) to preload all samples to $\sigma_{p,c} = 2400$ kPa.

Initially one Oedometer test was planned per footing, and the main results from these three tests are presented in table 3:

Table 4: Results from initial oedometer tests

Footing	Boring	Sample	Test results	
			$K_{t,0}$ (kPa)	ΔK_t (MPa)
F09	B8	Pose 1	23702	639
F10	B18	38B	30388	4613
F11	B65	5	37337	1651

The combination of $K_{t,0}$ and ΔK_t for footing F09 imply so poor stiffness properties of the soil that a settlement computation based on these, will lead to a settlement of δ≈50 mm. In the light of the general experiences from the area this result looked untrustworthy, and therefore it was decided, to supplement the F09 test with two more oedometer tests.

Table 5: Main results from additional oedometer tests

Footing	Boring	Sample	Test results	
			$K_{t,0}$	ΔK_t
F09	B90	904	10137	2033
F09	B92	916	1109	921

As it is seen, these supplementary tests did not provide results that look realistic, and especially the $K_{t,0}$ values look quite unrealistic. This is no doubt due to sample disturbance.

7 INTERMEDEATE SETTLEMENT EVALUATION

The Oedometer tests gives the best estimate of ΔK_t, and defines this value to 1062, 4613 and 1651 for F09, F10 and F11 respectively (the first figure is the geometric mean of the ΔK_t values from the three F09 tests). Based on these values and based on the same guidelines as described in section 6.1a re-evaluation of $K_{t,0}$ from the plate load tests is done as shown in Table 6 leading to $K_{t,0}$ values of 39392, 40893 and 46717 kPa respectively.

Hereafter the best sediments estimates based all available test are:

Table 6: Intermediate settlement evaluation

	P_{sls} (kN)	B (m)	$K_{t,0}$ (MPa)	ΔK_t (MPa)	γ (KPa)	Δ (mm)
F09	84288	18.65	39.392	1062	13	25
F10	49017	10.85	40.893	4613	13	14
F11	68134	11.48	46.717	1651	13	31

The tables 2 and 6 show in comparison that the field and laboratory testing confirmed the on hand knowledge of settlement conditions of the soil, but did not provide new information.

8 SETTLEMENT MONITORING

When the concreting of the footings was finished, they were all equipped with four levelling bolts (one in each corner), and regular (biweekly) measurements to these bolts started 20th November 2003.

A couple of years later when one third to one half of the SLS loads were applied to the footings it became clear, however, that the settlements were much smaller than expected from the above model. The 20th September 2005 the situation was:

Table 7: Settlement as per 20th September 2005

	P_{SLS}	**Applied Load, Total**		**Settlements**	
Date	Final	2005-09-20		2005-09-20	
	(kN)		% of final load	δ Computed	δ Measured
F09	84288	39304	46.6	12	3
F10	49017	19978	40.8	6	2
F11	68134	22687	33.3	10	3

As it is seen in Table 7 the observed settlements forms only one third to one fourth of the predicted settlements. This calls for a revision of the physical/mathematical model behind the computations.

It shall be noted that the settlements during 2005 were almost constant for the applied load and therefore the small settlement could not be explained as a slow and not completed consolidation.

9 REVISED MODEL

Since the observed settlements are much smaller than the predicted ones, a revised computational model calls for some effect which will lead to increasing soil stiffness with increased load.

The most straightforward way to implement the increase of soil stiffness is to introduce the load itself in the equation governing K_t, implying that the soil has sufficient time to drain of the excess pore pressures due to the increased load and hereby gain additional stiffness, i.e.:

$$K_t = K_{t,0} + \Delta K_t\left(\sigma_{red} + p(z,t)\right) \qquad (4)$$

Where $p(z,t)$ is the stress in the depth z caused by the applied load to the time t.

For convenience and simplification the load is assumed applied linearly with time between $t = 0$ and $t = t_s$, i.e.

$$P(t) = \alpha t \;;\; P_{sls} = \alpha t_s \qquad (5)$$

and we get:

$$P(z,t) = p(t)/(B+Z)^2 \qquad (6)$$

$$= \alpha t/(B+z)^2$$

leading to:

$$K_t = K_{t,0} + \Delta K_t(\gamma z + \alpha t/(B+z)^2) \qquad (7)$$

Hereafter the settlement of a very thin layer, dz, through a very short time, dt, becomes:

$$dd\delta = dp(t,z)/K_t dz \qquad (8)$$

$$= \frac{\alpha dt}{(B+z)^2(K_{t,0} + \Delta K_t(\gamma z + \alpha t/(B+z)^2))dz}$$

$$= \frac{\alpha}{\left(K_{t,0} + \Delta K_t \gamma z\right)(B+z)^2 + \Delta K_t \alpha t}\, dtdz$$

leading to a total settlement of:

$$\delta = \int_0^{\infty} \int_0^{ts} dd\delta \qquad (9)$$

$$= \frac{1}{\Delta K_t} \int_0^{\infty} \ln\left(1 + \frac{\Delta K_t \, \alpha \, \mathrm{t}}{(B+z)^2\left(K_{t,0} + \Delta K_t \gamma z\right)}\right) dz$$

This integration can hardly be carried out analytically, and therefore it has been done numerically.

In Table 8 the results of the revised settlement calculation is shown.

Table 8: Settlements per 20th September 2005. Revised computational method

	P_{SLS}	**Applied Load, Total**		**Settlements**	
Date	Final	2005-09-20		2005-09-20	
	(kN)		% of final load	δ Computed	δ Measured
F09	84288	39304	**4**6.6	4	3
F10	49017	19978	40.8	2	2
F11	68134	22687	33.3	5	3

For this foundation project the settlements calculated with the revised method are more or less equal to the measured settlements, taken the accuracy of the settlement into account.

10 FINAL SETTLEMENT EVALUATION

Based on the revised computational method the final settlement evaluation was made ultimo September 2005. The outcome was:

Figure 4: Settlement for full load.

	P_{sls} (kN)	B (m)	$K_{t,0}$ (MPa)	ΔK_t (MPa)	γ (KPa)	δ (mm)
F09	84288	18.65	39.392	1062	13	10
F10	49017	10.85	40.893	4613	13	5
F11	68134	11.48	46.717	1651	13	13

Additional settlement measurements carried out from the period 2005-09-20 to 2008-09-08 showed additional approx. 2 mm settlement for all three footings - In total 5-6 mm settlement for all three footings at September 2008 were the load on the three main footings were close to full load.

This further settlement development was partly influenced by the end of groundwater lowering (reducing the effective stresses and thereby the settlement increment) and by load redistribution as some large interims support structures was removed.

However, the settlements measured showed that in case of heavy loads and stiff glacial deposits in Copenhagen and similar stiff deposits, settlements may be overestimated using traditional methods without taking stiffness increase into account.

11 CONCLUSION

The settlement assessment has shown that the stiffness increase during the project was an important factor for the settlement developed. Furthermore if the proper stiffness increase is assessed in proper and robust manner, this will provide a basis of a more optimized foundation design.

12 REFERENCES

Christensen J. L., Schjønning E. and Foged N. (1992) Comparison of clay till strength parameters using BS and Danish test procedures. NGM 92. Ålborg Vol 1. pp 75-80

Experimental study on axial and lateral bearing capacities of non-welded composite piles based on pile load test results

J. H. Park.
Korea Institute of Civil Engineering and Building Technology, Republic of Korea,
jaehyeon@kict.re.kr

Y. Shin.
Norwegian Geotechnical Institute, Norway

M. Chung
Korea Institute of Civil Engineering and Building Technology, Republic of Korea

ABSTRACT
In the presented paper, the axial and lateral behaviors of non-welded composite piles were investigated based on pile load test results. Recently, a composite pile composed of steel pipe and PHC pile was introduced into the market in Korea. A steel pile is placed in the upper part to support lateral loads and a PHC pile is placed in the lower part to resist axial load mainly. A mechanical joint is applied at the interface of the two different materials. This could be more favoured to conventional welding method in terms of cost and time in construction. Dynamic load tests and lateral load tests are performed to evaluate the axial and lateral behaviors of composite pile, respectively. The performance of the composite piles were thought to be satisfactory compared to that of steel pipe and PHC piles with a long history of successful applications. Additionally a new design chart was suggested for the design of non-welded composite pile.

Keywords: Composite pile, non-welded, load test, axial behavior, lateral behavior

1 INTRODUCTION

Recently, the number of large-scaled civil engineering works and skyscraper construction sites has escalated and so has demand for piles that can provide high bearing capacity against axial and lateral loads.
Soil conditions and loads applied to superstructures determine the length of piles used in civil and architectural foundation works. The length tends to be shorter in sites where the soil exhibits high strength and the depth of the support layer is relatively shallow. In contrast, the length tends to be longer in marine environments or in reclaimed sites with weaker soil strength and much deeper support layer.
The majority of the commercially manufactured piles in the market are each limited to approximately 15m maximum in length, due to productivity and transportability concerns. For a site deeper than 15m, therefore, piles should be connected for extension, and the most commonly used method is welding. The technique entails procedural requirements regarding weather conditions, wind-speed, and temperature. The workmanship is also one of the main cause to affect the quality of welding, and subsequently that of the entire piling-installation work. Other shortcomings of the welding approach include a rise in costs and a longer construction period because ultrasonic tests are required upon completion of welding as part of quality tests and detecting significant flaws may be identified at the joints.
In recent years, a growing number of local and international construction sites have been looking into the cheaper, faster and safer alternatives to the conventional pile-connecting method, the most prominent of which being non-welded joint, with

aggressive research and development under way (Park et al., 2011; Shin et al., 2014; Shin et al., 2014).
The non-welded pile-connecting method, uses a three-piece side connecting panel and 12 bolts fitting of both the upper pile end and the lower pile top. In such mechanisms, the bending moments and shear stresses from the superstructures are transmitted through the upper pile bottom to the side connecting panel at the joint, which continue to travel down to the lower pile head. However, there are few case histories and research data available for the non-welded pile joint of a composite pile, which necessitates verification through field pile load tests and numerical analysis.
In this study, we analyzed behavior characteristics of non-welding composite piles (NCP) composed of steel pipe piles on top of PHC (pretensioned high spun concrete) piles with applying mechanical joint at the interface of the two different materials of piles. In order to evaluate the axial and lateral behaviors, dynamic load tests and lateral pile load tests are conducted.

2 LOAD TEST DATA

2.1 Site conditions for axial load test

According to the results from our borehole tests and cone penetration tests at the load test site, a silty sand layer was reclaimed on the site up to 1.3~2.3m below the surface, a soft cohesive soil layer (SPT N-value less than 5) existed 18.9~23.5m thick below the landfill layer, and weathered rock layer existed from GL-30.0~31.0m (Figures 1 and 2).

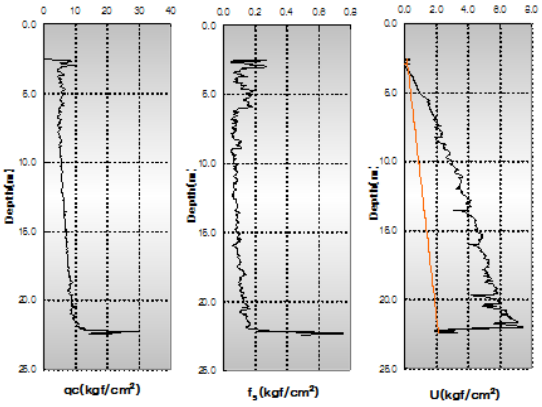


Figure 1 SPT N values of boring holes.

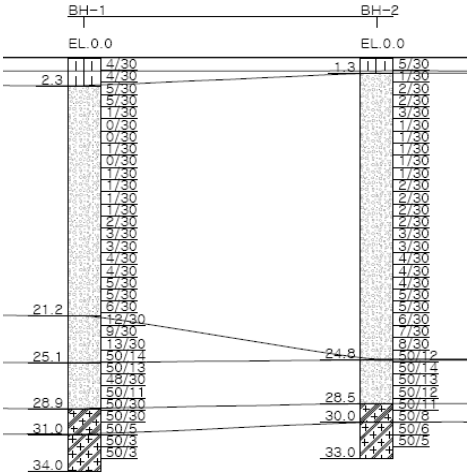


Figure 2 SPT N values of boreholes.

2.2 Site conditions for lateral load test

Field load tests were performed in two sites (Site-A, Site-B) in order to examine the lateral behavior of the NCP and evaluate the stress-transfer effects and structural stability of the joint. For the five composite piles, dynamic load tests were performed by using a PDA (pile driving analyzer). Of the five piles, one was also submitted to axial load tests and three other piles to lateral pile load tests.
The geotechnical investigations were performed in the two pile load testing sites to help examine the soil conditions. Based on the results of the investigations, Table 1 shows the soil profile of each site.

Table 1 Soil conditions at the pile load tests.

Site-A			
Depth(m)	**Soil layer**	**Classification**	**N-value**
0.0~3.9	Fill	Sandy gravel	7~9
3.9~5.1	Residual	Sand	3
5.1~24.8	Residual	Silty clay	2~3
24.8~25.9	WR	Sandy gravel	50/4
25.9~27.0	Soft rock	Rock	RQD:27%

The top-down profile of the soil consisted of the reclaimed layer, the deposits of sand and silty clay, the weathered rock, and the bedrock.

2.3 Load test conditions

We carried out dynamic pile load tests on large-sized (pile diameter =1,000mm) composite piles and PHC piles to analyze (1) drivability of the piles, (2) calculate the axial bearing capacities, and (3) assess the structural safety of mechanical joints.

Each pile had an upper portion made of a steel pipe, 1,000mm in external diameter and 16mm in thickness, and a lower portion comprised of a PHC pile, 1,000mm in external diameter and 140mm in thickness, which were connected by the non-welded pile connecting method.
Dynamic pile load tests used a hydraulic hammer (160kN) and manipulated the stroke between 0.5m and 1.5m.
A total of three medium size (pile diameter = 500mm) non-welded composite piles were used in the lateral pile load tests. Each pile had an upper portion made of a steel pipe, 500mm in external diameter and 12mm in thickness, and a lower portion comprised of a PHC pile, 500mm in external diameter and 80mm in thickness, which were connected by the non-welded pile connecting method.
Table 2 provides the information on the types of the piles used, diameter, and thickness used for axial and lateral load tests.

Table 2 The types and amount of pile load tests.

Pile load Test	Pile No.	Diameter of pile	Thickness of pile
Dynamic	Pile-1	ϕ1000	Steel 16t PHC 140t
	Pile-2		
	Pile-3		
Lateral	Pile-4	ϕ500	Steel 12t PHC 80t
	Pile-5		
	Pile-6		

3 LOAD TEST RESULTS

3.1 Dynamic load test results

Fifteen dynamic pile load tests on large-sized composite piles and PHC piles were performed by using a pile driving analyzer (PDA). For the dynamic pile load tests, we used a 160kN hydraulic hammer and DH 658 pile driver. Bearing capacities and drivabilities of piles and structural safeties of the mechanical joints were assessed and evaluated by dynamic load tests. We implemented the internal excavation construction method (auger device put into pile's inner hole and under-reaming at the bottom of pile) to compare and examine differences between bearing capacities of each construction methods. Dynamic pile load tests were conducted on 3 test piles applying the following conditions summarized in table 2.

3.2 Driveability analysis results

As Pile-1 and Pile-2 were bored piles using the internal excavation construction method, pile driving was carried out at the final process for dynamic load test using PDA. On the other hand, Pile-3 was a driven pile and dynamic load test was performed during pile construction. In order to analyze the difference of bearing capacity according to construction methods, we calculated bearing capacities for the same depth and energy level. Piles built by the internal excavation construction method provided similar values of bearing capacity with driven pile case. The shaft resistance of a pile, therefore, constructed by internal excavation method was seem to be mobilized sufficiently.
Table 3 shows dynamic load test results.

Table 3 Dynamic load test results.

Pile No.	Embedded Depth (GL-m)	Hammer stroke	CSX* (MPa)	CSB* (MPa)	EMX* (kN.m)	RMX* (kN)
Pile-1	32.0	0.7	16.6	6.6	113.3	4,510
	33.0	2.0	33.8	0.0	314.3	4,150
Pile-2	27.5	1.0	1.9	1.1	103.4	4,100
		1.5	2.6	1.4	153.6	4,540
	28.5	0.7	18.9	7.5	98.6	4,130
		1.0	20.0	8.1	117.4	4,520
	29.0	0.5	2.2	1.7	92.7	4,530
		1.0	2.5	2.0	118.6	5,180
		1.5	3.2	2.6	184.2	5,960
Pile-3	32.5	0.5	1.4	1.1	50.4	3,990
		1.0	1.8	1.4	76.5	4,170
		1.5	2.7	1.8	143.0	4,470
	37.5	0.7	2.7	1.7	98.5	9,460
		1.0	3.2	2.5	143.8	10,280
		1.5	3.8	3.6	198.3	11,030

*CSX: Maximum compression stress on gauge
*CSB: Maximum compression stress on bottom
*EMX: Maximum energy
*RMX: Optimal bearing capacity by the case method

3.3 Calculation of allowable bearing capacity from dynamic load test

To calculate allowable bearing capacity through dynamic pile load tests, the Davisson's method (Davisson, 1972) which safety factor of 2.0 is applied to was used to determine yield limit of the total bearing

capacity obtained from CAPWAP analysis (Iskander and Stachula, 2002) and the method that safety factor of 2.5 is applied to total bearing capacity obtained from CAPWAP analysis was used (Korean Geotechnical Society, 2008). Pile-1 and Pile-2 constructed by the internal excavation method were bored into the bottom of weathered soil layer and they have allowable bearing capacity of 1,620~3,061kN. However, Pile-3 was driven and socketed into 6.0m of the weathered rock, and calculated the maximum allowable bearing capacity of it reached to 5,660kN. Since these are the results from the EOID (end of initial driving) tests, we believe that much larger allowable bearing capacity may be calculated if the setup effect is mobilized over time on the soft cohesive soil ground. In order to consider how much bearing capacity would increase due to the setup effect, we conducted a restrike test on Pile-1. However use of a drop hammer in a restrike test led to somewhat deteriorated accuracy in comparison with bearing capacity calculated by using a hydraulic hammer.
Table 4 provides calculation results from dynamic load test.

Table 4 Allowable bearing capacity from dynamic load test.

Pile No.	Skin Friction (kN)	End Bearing Capacity (kN)	Total Bearing Capacity (kN)	Allowable Bearing Capacity	
				CAPWAP (S.F=2.5)	Davisson (S.F=2.0)
Pile-1	1,040	3,410	4,450	1,780	2,225
	2,902	3,220	6,122	2,449	3,061
Pile-2	880	3,170	4,050	1,620	2,025
	900	3,630	4,530	1,812	2,265
	900	3,270	4,170	1,660	2,085
	970	3,560	4,530	1,812	2,265
	910	3,639	4,549	1,820	2,275
	1,010	4,190	5,200	2,080	2,600
	1,120	4,980	6,100	2,440	3,050
Pile-3	670	3,260	3,930	1,572	1,965
	730	3,460	4,190	1,676	2,095
	780	3,700	4,480	1,792	2,240
	4,390	5,270	9,660	3,864	4,830
	4,560	5,960	10,520	4,208	5,260
	4,890	6,430	11,320	4,528	5,660

3.4 Lateral load test results

At the maximum 300kN lateral pile load, the total pile head displacements of all three test piles were 21.82~31.89mm, while the residual displacements were found to be 5.61~9.74mm. Converting the figures to make comparisons with the displacement criterion of 15.0mm, which is known as the serviceability criteria in Korea (MLTM, 2008) led to the load value of 157.6~223.9kN.
And at the maximum 350kN lateral pile load, the total displacement was 54.53mm, while the residual displacement was found to be 25.77mm. Converting the numbers to make comparisons with the dis-placement criterion of 15.0mm led to the load value of 177.3kN. These load value, which is evaluated as the allowable lateral bearing capacities of NCP's, are larger than the design lateral bearing capacity calculated to 120kN of 500mm diameter steel pile.
Results of the LPILE program (Ensoft, 2004) and the field lateral load tests were compared for the three NCP's. In case of the Pile-4, the displacement was found almost identical at the load point for the lateral load of 100kN. Under lateral loading of 200kN, dis-placement of 12.1mm took place during the field pile load tests while the number from the LPILE analysis was 14.1mm at the load point.
For the pile-5, displacement of 21.2mm took place during the field pile load tests against lateral load of 200kN, while the number from the LPILE analysis was 14.4mm at the load point. Comparing the data for Pile-4 and Pile-5, the displacement was presumably due to the differences in pile behavior that are associated with specific location of the non-welded joint. The steel portion of Pile-4 was 12.0m in length whereas that of Pile-5 was 6.0m.
For the pile-6, displacement of 11.6mm took place during the field pile load tests while the number from the LPILE analysis was 14.4mm at the load point under lateral loading of 200kN.
The shear stresses caused by the external lateral load at the depth of non-welded joint are calculated to solve the joint stability problem. The non-welded joints are located

GL-3.9~10.0m for the pile-4, 5, and 6. At the non-welded joint, the shear stresses are calculated to 3.4~214.3kN for the lateral load 100~350kN respectively (Figures 3 and 4).

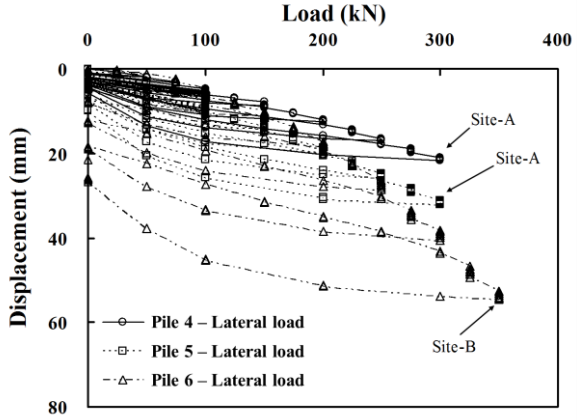


Figure 3 Load-settlement relation of lateral load tests.

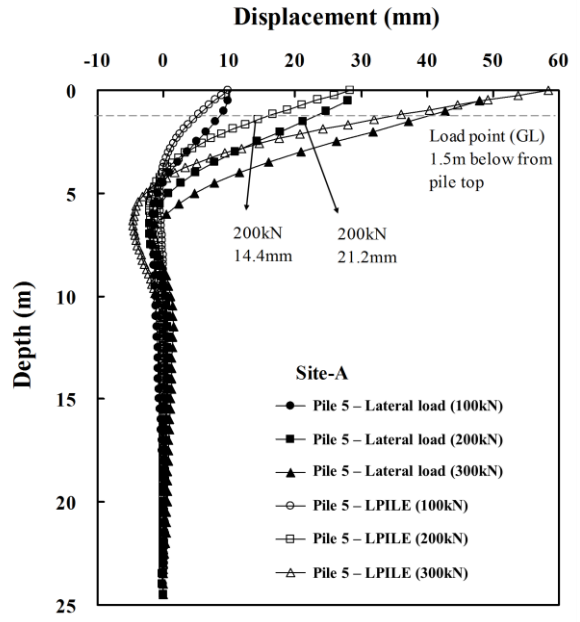


Figure 4 Depth-displacement relation of lateral load tests and comparison with LPILE results at pile-5.

4 CONCLUSION

In this study, we performed the dynamic and lateral pile load tests to evaluate the axial and lateral behaviors of non-welding composite piles composed of steel pipe piles on top of PHC piles.

Based on results from the dynamic pile load tests, drivability was verified as successful without any damage of the piles. From the analysis of differences in bearing capacity by large-sized pile construction method, piles constructed by the internal excavation construction method provided similar values of bearing capacity with driven pile case. Piles located at the lower end of the weathering soil (Pile-1, 2) showed allowable bearing capacity of up to 3,061kN. Piles socketed into 6.0m of the lower part of the weathered rocks (Pile-3) showed the maximum allowable bearing capacity of approximately 5,660kN.

From the lateral pile load tests, NCP (pile diameter=500mm) showed higher lateral bearing capacities (157~224kN) comparing the design value (120kN) of the same diameter steel pile.

Therefore, it is notable that axial and lateral behaviors of non-welding composite pile ensured the stability of connection part.

5 ACKNOWLEDGEMENT

This study was supported by Korea Institute of Energy Technology Evaluation and Planning through the research project "Development of hybrid substructure systems for offshore wind power (No. 20123010020110)".

6 REFERENCES

Davisson, M. (1972). High capacity piles, Proceedings of Soil Mechanics Lecture Series on Innovations in Foundation Construction, ASCE, Illinois Section, Chicago, Illinois, 82-112.

Ensoft, INC (2004). LPILE Plus Version 5.0 Technical Manual.

Iskander, M. G. & Stachula, A. (2002). Wave equation analyses of Fiber-Reinforced Polymer Composite Piling. Journal of Composites for Construction, ASCE, 6 (2), 88-96.

Ministry of Land, Transport and Maritime Affairs (MLTM) (2008). Bridge design specifications (in Korean).

Park, J.H., Kim, S. R., Le, C. H., & Chung, M. (2011). Evaluation of bearing capacities of large size non-welded composite piles by 3-Dimensional numerical analysis. Journal of Ocean Engineering and Technology, 25(6), 35-41 (in Korean).

Shin, Y., Kim, M. M., Ko, J. Y., & Jeong, S. (2014). Proposed design chart of mechanical joints on steel-PHC composite piles. Materials and Structures, 47, 1221-1238.

Shin, Y., Langford, T., Cho, K., Park, J., & Park, J. H. (2014). Design of composite pile foundations for offshore wind turbines, Proceedings of the 24th International Ocean and Polar Engineering Conference, Busan, Korea (CD-ROM).

Deep excavation close to the iconic Havnelageret in Oslo city centre

Torbjørn Johansen
Geovita AS, Norway, torbjorn.johansen@geovita.no

Vegard Woldsengen, Kjetil Fløtre
Geovita AS, Norway, Norwegian Public Roads Administration, Norway

ABSTRACT
Havnelageret is a large former harbour storehouse in Oslo. During the construction of the first part for the Opera tunnel, it was observed that the nearest corner of the building started to settle. New ground investigations and close inspection of the building gave the disturbing fact that the piles on the corner were embedded in a gravel and sand deposit and were not on bedrock.

The excavation second part was 13 meter deep and only 3 meters from Havnelageret. The construction method was steel sheetpiles and a strutted excavation. The excavation was divided in three separate parts to reduce the risk during construction. In addition the corner of the building was strengthen with installation of two supplementary piles bored to bedrock and connected to the existing pillar.

Three sections of the excavation were instrumented with load cells, temperature sensors and inclinometers.

The observed deformations of the sheetpile walls showed good correlation with the design for the HZ wall, but the deformations were larger for the Larssen 430 wall.

The loads in the loadcells showed typically lower value than calculated. The load distribution when removing struts showed the time lag in the redistribution of the earth pressures.

The measured settlements ended up with a total settlement below the estimation prior to the excavation.

Keywords: Deep excavation, sheet pile, deformation, loads.

1 BACKGROUND

1.1 The project

A key element of the Bjørvika project in Oslo is Operatunnelen, a submerged tunnel crossing the harbour. At the western end the tunnel is connected to the existing Festnings-tunnelen under the city centre and it also have ramps up and down to connect to the streets on ground level. One of these ramps is very close to the iconic Havnelageret.

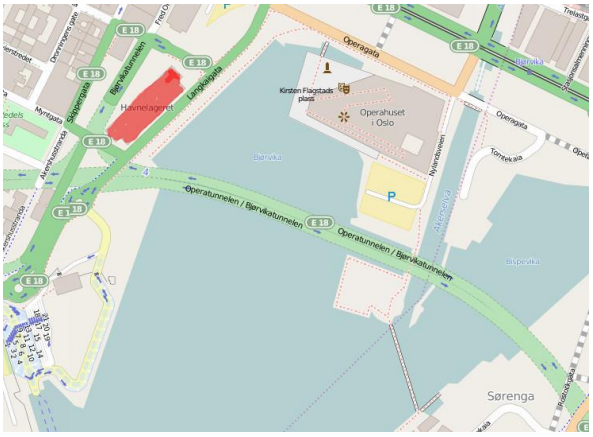


Figure 1 Operatunnelen and Havnelageret.

Havnelageret is originally a large harbour storehouse and was one of the largest concrete buildings in northern Europe when it was completed in in 1920.

Today it is refurbished to a modern office building.



Figure 2 Havnelageret

The original drawings showed that the heavy building is fundamented on large diameter piles to bedrock. When they did the foundation work they had to give up the deep piles due to failures of the base of the piles and they finished the job by extending the large piles with driven concrete piles inside.

1.2 Ground conditions

The ground conditions at site are a top layer of fill material with a thickness of approximately 1 meter. Below is normally consolidated marine clay typically for The Oslo centre.

Over bedrock is a layer of varying thickness of moraine and gravel. This layer is highly permeable.

The bedrock is mainly clay shale with some limestone and menaitt.

2 MAIN EXCAVATION

The main excavation was for the connection of the submerged tunnel and the existing tunnel.

During the main excavation one observed large problems with water leakages both through and under the sheetpile walls resulting in costly and time-consuming jetgrouting and injection works.



Figure 3 Main excavation.

During this excavation it was observed that Havnelageret started to get vertical deformations on the part close to the excavation. It was not expected as the drawings showed piled foundations to bedrock and all existing ground borings to bedrock corresponded in depth with the old foundation drawings.

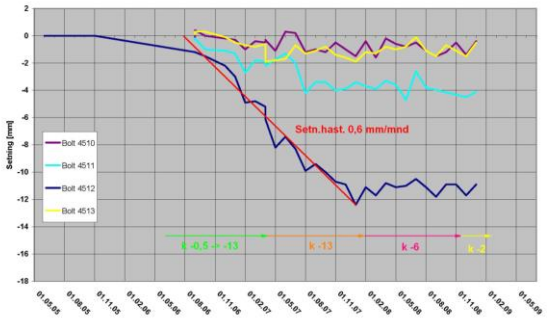


Figure 4 Settlements during main excavation

New borings, and this time closely followed up by the geotechnical engineers, showed that it was a layer of gravel and sand over bedrock that both the piles and the old borings had stopped in.

3 ORIGINAL DESIGN

After the main tunnel was finished (inside the main excavation), ramps to and from the main tunnel up to the city streets were to be constructed.

The original design for this excavation consisted of heavy steel sheet pile walls supported mainly with tie back anchors and some internal bracing.

The construction of the ramps was planned in one large excavation.

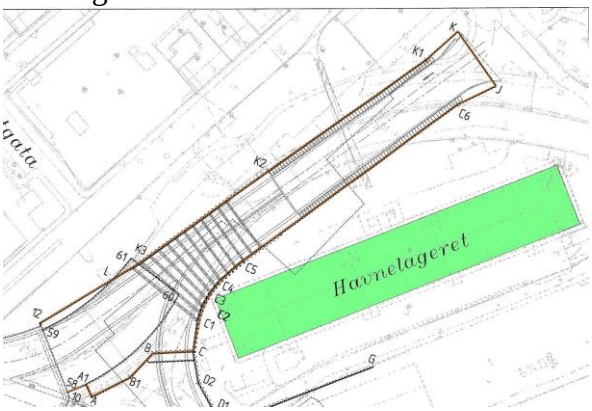


Figure 5 Original plan for excavation for ramps

Parts of the sheet pile were already installed and it was obvious that the sheet piles had not penetrated to bed rock as intended.

The excavation was 13 meter deep and only 3 meters from the nearest corner of Havne-lageret.

4 REVISED DESIGN

4.1 Principle

The main objectives for the revised design were to get a more robust design and reduce the risks during construction.

This included internal bracing which would not give large axial loads in the sheet piles. The sheet piles needed only to penetrate the gravel layer sufficiently to take up the unbalanced earth pressures.



Figure 6 Revised plan for excavation and support.

The excavation was divided in three parts. A potential problem in one part could then be isolated and handled without stopping all construction activity. It did also reduce the size of the excavation close to Havnelageret which should minimize deformations of the support system.

The design ended up with sheet pile walls braced with up to four levels of struts.

The upper strut is placed clear of the concrete tunnel to be constructed later.

When the final excavation level is reached, a preliminary concrete slab is casted to both be uses as a continuous bracing and a working platform for the boring of piles.

After the concrete slab is cured the second and third strut (and fourth) layer is removed.

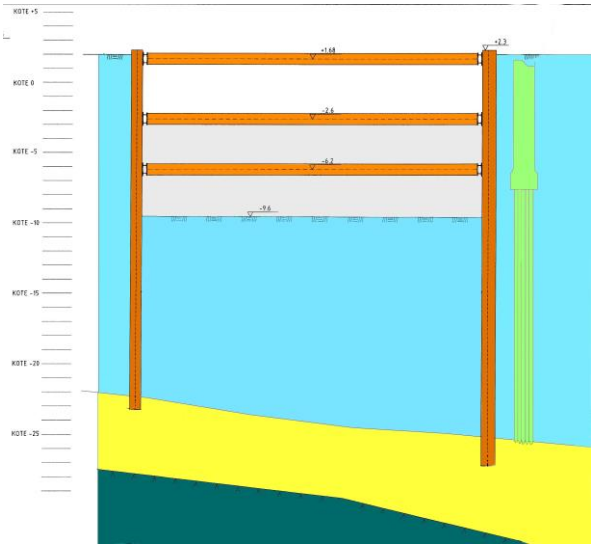


Figure 7 Cross section at the corner

4.2 Sheetpile design

The sheetpile wall was mainly designed using GeoSuite Excavation. In addition some section was designed with Plaxis 2D to document possible influence on the piles for Havnelageret and possible settlements on the basement further from the excavation.

The clay was both modelled with undrained and drained parameters due to relatively high silt content and the long open period of the excavation.

Reliable stiffness and deformation parameters are difficult to obtain from laboratory tests. In this case we used back calculated parameters from inclinometer measurements at the main excavation.

A typical total displacement plot from Plaxis 2D is shown in Figure 8.

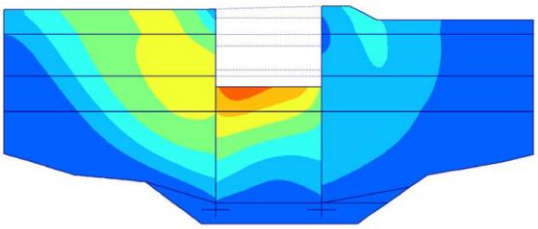


Figure 8 Total displacement.

4.3 Instrumentation

Three sections were instrumented to monitor the perfrmance of the support during excavation.

At each section the instrumentation consisted of:

- Inclinomter channals on both sides
- Load cells at each strut level
- Temerature gauges at upper strut level
- Geodetic measurements point at top sheet piles
- Geodetic measurements point at Havnelageret at each pillar

The instrumantation was provided by the Road Research Laboratory which also performed the readings and reporting of results.

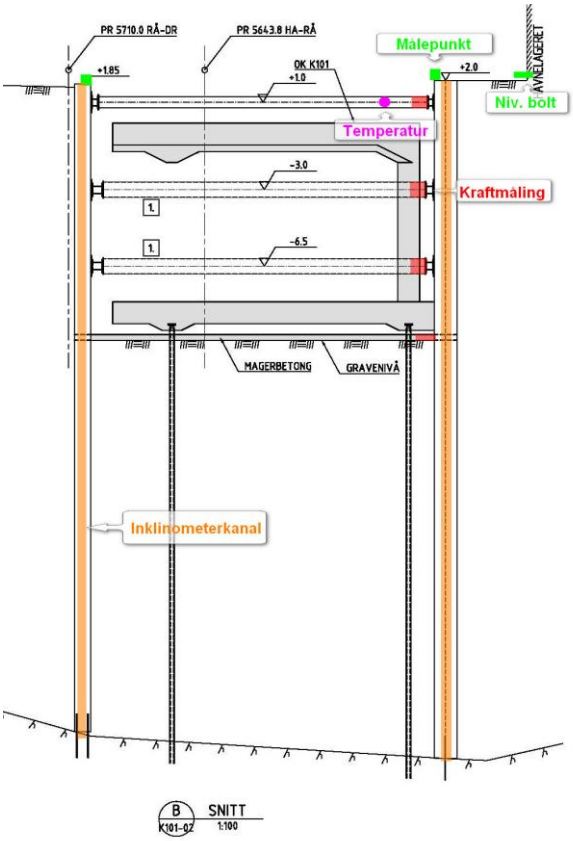


Figure 9 Instrumentation

4.4 Underpinning

In cooperation with the owner of Havne-lageret it was decided to underpin the nearest corner of the building with bored steel piles to bedrock. The purpose was to make sure that eventual deformations of the corner should be directed inwards the building.

The underpinning was done with two Ø180 mm steel core piles bored from terrain, through the basement, and into bedrock. The piles were slightly inclined to avoid the original piles.

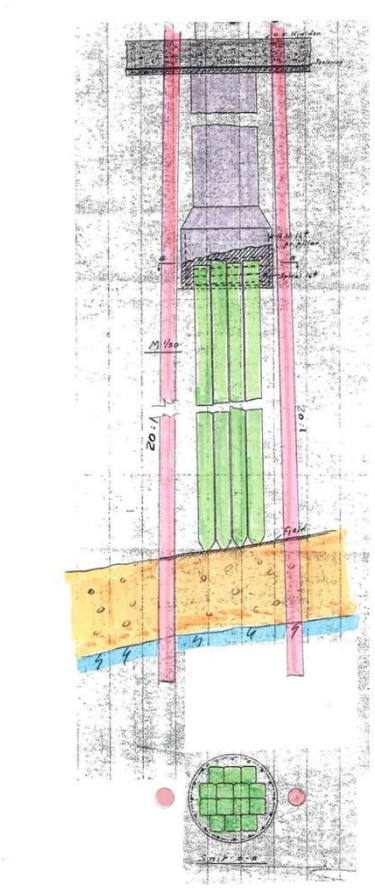


Figure 10 New piles shown on old drawings.

The new piles were connected to the corner pillar in the basement and were design to take the full load of 7000 kN.

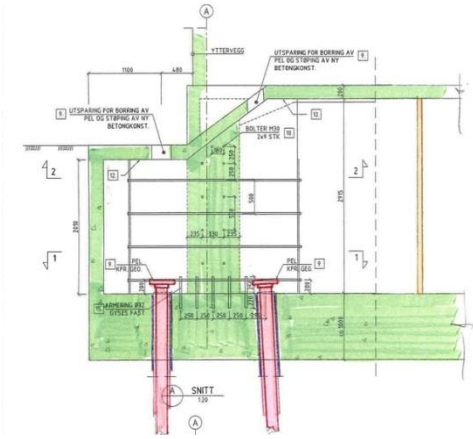


Figure 11 Pile head in the basement.

The new piles were not preloaded. The intention was to allow some settlement and gradually transfer loads to the new piles.

Based on recorded settlements during the main excavation, a prognosis was prepared for the total settlement of the corner of Havnelageret.

The settlement during the main excavation was 12 mm corresponding to 0,8 mm/month. The same settlement rate was assumed for excavation for the ramps and in addition it was assumed some settlements during pile driving.

In total a maximum of 30 mm was the most realistic prognosis. The structural engineers had established maximum criteria for the building of 50 mm.

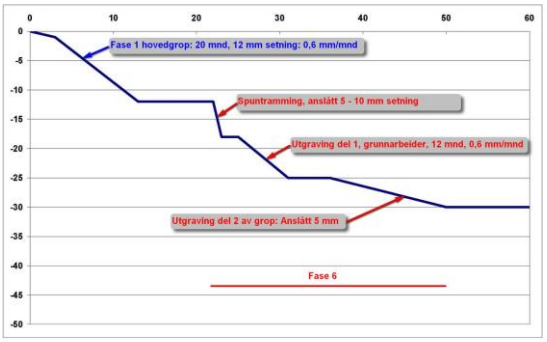


Figure 12 Settlement prognosis

5 OBSERVED BEHAVIOUR

5.1 Horizontal deformations

In general the excavation moved in the direction of Havnelageret.

The left sheet pile wall showed larger deformation than calculated, see Figure 13.

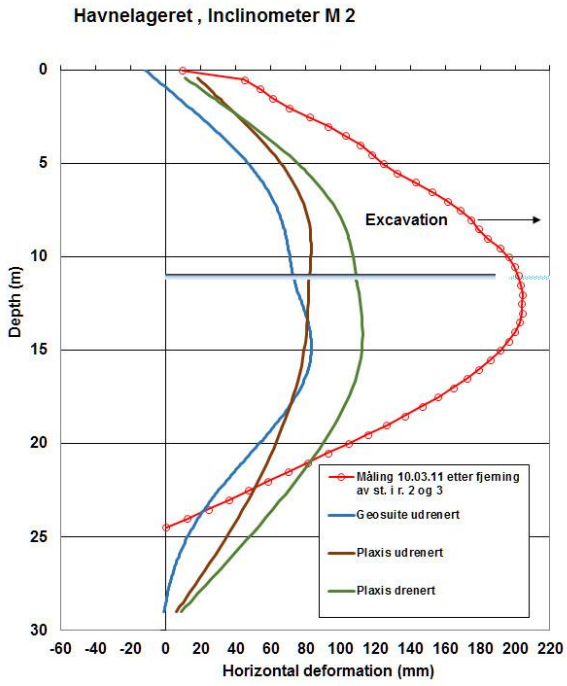


Figure 13 Horizontal deformation, left wall.

Whereas the right wall showed deformation more closely to the calculated values.

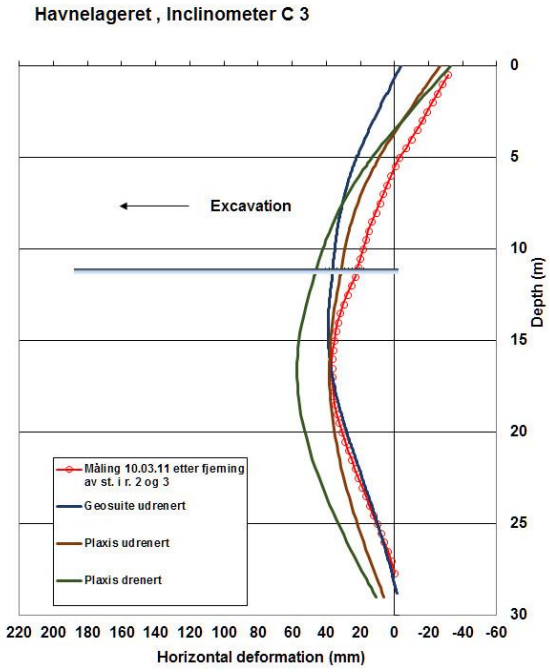


Figure 14 Horizontal deformation, right wall

The right wall is close to Havnelageret. The sheet pile wall consists of a combined wall HZ975 – AZ18. This wall has a high section modulus to minimize deflection. The measured horizontal deformation of 40 mm is close to the calculated values.

The left wall consist of a Larssen 430 section. This section is made of four u-sections which two sections are crimped to form a z-section.

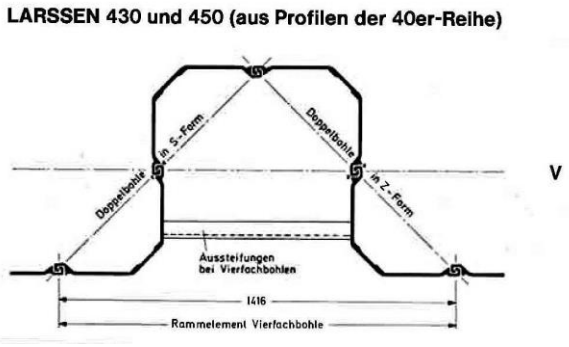


Figure 15 Larssen 430 section

In prior projects in Oslo this section has been installed as a complete section with a stiffener as shown in the figure. At Havnelageret the contractor installed each z-section separately.

The separate z-section proved to be unstable and difficult to tread.

The measured deformation of the Larssen wall is approximately 200 mm which is almost twice the calculated values. We suspects that this could be a results of failures in the crimping of the individual u-sections thus resulting in a much lower stiffness of the wall.

5.2 Loads in the supporting system

The loads in the struts were measured by Glötzl load cells. The load cells were placed in between the whaling and the strut.

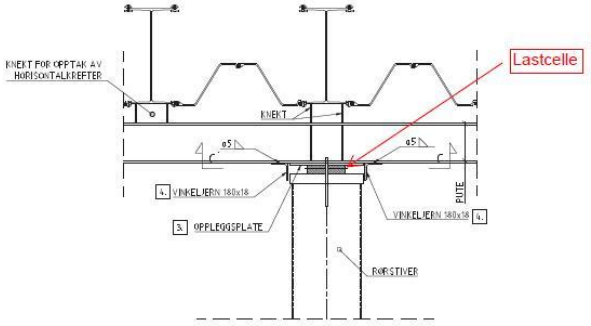


Figure 16 Load cell in strut

In addition to the loadcells it was also installed strain gauges in the concrete slab. The measured strains were calculated to loads using the elastic modulus for the C45 concrete.

A typical load curve is shown in Figure 17 for the struts in section 3.

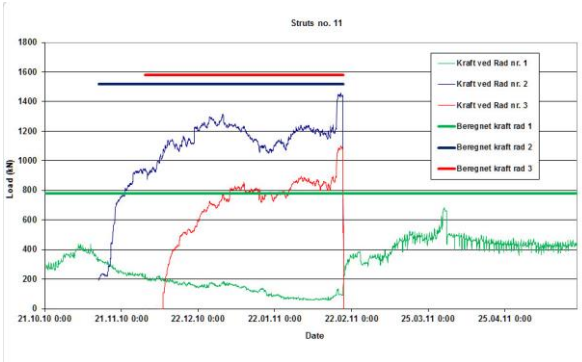


Figure 17 Loads in strut section 3.

The measured loads are shown together with the calculated ones (characteristic loads). The measured loads are all lower than the calculated. In the design it was used upper bound values from the drained and undrained analysis.

The removal of the 2. and 3. strut level resulted in a double of the load in the upper strut level.

When comparing the load in the upper strut level with the load in the concrete slab, it shows that the loads in the 2. and 3. strut level redistributed with approximately 20 percent to the upper strut level and 80 percent to the concrete slab.

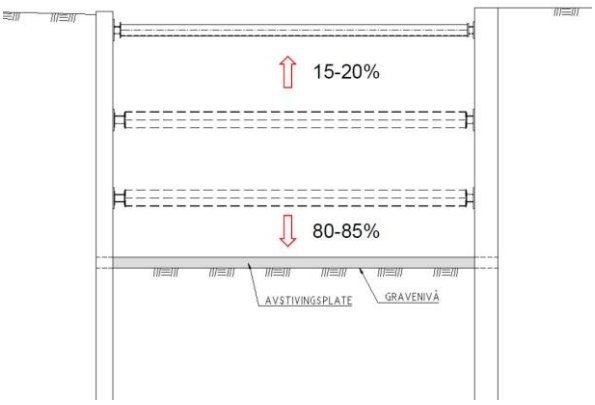


Figure 18 Load distribution when removing struts

5.3 Loads from temperature

In a strutted excavation the increase in loads in the struts can be significantly due to increased temperatures in the steel struts.

During the Easter in 2011 the construction activity was suspended and it was cold nights and sunny days. In the upper strut layer the temperature fluctuation was 25°C resulting in a corresponding fluctuation of the strut force.

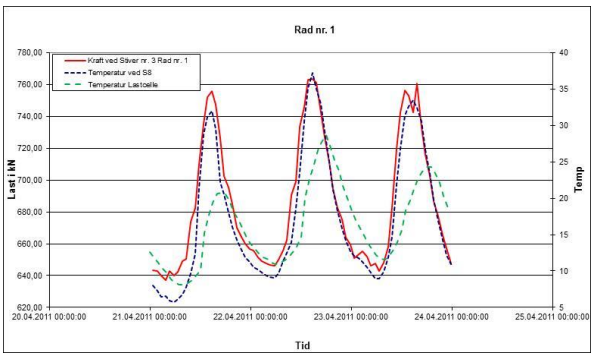


Figure 19 Temperature loads in struts

The increase in loads was 120 kN. If the strut was fully supported the temperature difference should have resulted in an increase of 1000 kN. The degree of support in this case was 12 %.

5.4 Observed settlement of Havnelageret

The total vertical deformation or settlement of the corner of Havnelageret close to the excavation is 22 mm. The prognosis was 30 mm.

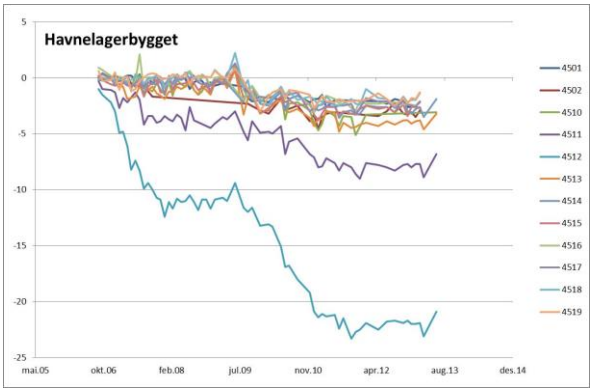


Figure 20 Vertical deformation during the whole construction activity

For the last part the vertical deformation was 8 to 10 mm for the pillars close to the excavation and decreasing away from it.

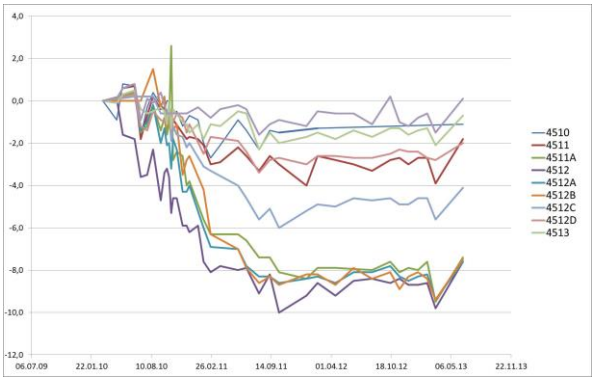


Figure 21 Vertical deformation last phase

Old cracks opened slightly more during the excavation, but as a whole the consequences for Havnelageret was tolerable and within the calculated values.

6 CONCLUSIONS AND RECOMMENDATIONS

The instrumentation worked mostly as planned. A few load cells failed during the excavation and it is recommended to instrument more than one section.

The inclinometer measurements worked well.

The strain gauges in the concrete slab gave better results than anticipated.

The loads in the struts were lower than calculated, but the load in the concrete slab was higher.

The measured horizontal deformation of the HZ-AZ sheetpile wall was close to the calculated values.

The measured horizontal deformation of the Larssen sheetpile wall was almost the double than the calculated values. This is probably due to failures of the crimping of individual sheetpiles.

The vertical deformation of Havnelageret was lower than predicted and it resulted in only minor influence on the building itself.

7 PICTURES



Figure 22 Excavation late January 2011



Figure 23 Upper strut level and concrete support slab May 2011

Decision-making for increased sustainability in underground construction works using Analytical Hierarchy Process

Miriam S. Zetterlund
Swedish Geotechnical Institute (SGI), Sweden, miriam.zetterlund@swedgeo.se

Magnus Eriksson
Swedish Geotechnical Institute (SGI), Sweden

ABSTRACT
Decision-making in infrastructural projects involves technical, economic and environmental aspects in a modern society. The time horizons are long in infrastructural projects and it is difficult to oversee all the costs and effects of each decision. To reach sustainable solutions, decision-making that is both objective and transparent is needed. There can be economical obstacles in form of budget limitations in each phase of the project (design, construction, operation and maintenance) that discourage a long-term and sustainable view of the project solution. Generally, low investment costs are important for the choice of technical solutions to keep the costs within budget limitations. Economically, a life cycle cost perspective is needed since the costs for maintenance can be significant and it is therefore clear that the economical perspective needs to be over a life time perspective.
The aim of this paper is to present how sustainability can be included in decision-making between different technical solutions in tunnelling projects. In the study we refer to, the Analytical Hierarchy Process (AHP) was used as a decision-support tool in the design phase of an infrastructure tunnel. In the tunnel project, there are five potential systems for reinforcement and drainage and these systems were evaluated against three criteria; (I) economy based on life cycle cost, (II) environmental impact and (III) robustness & uncertainty.
The findings indicate that multi-criteria decision methods, such as AHP, are useful for incorporating other criteria than economy into decisions regarding technical solutions in tunnelling projects. The AHP supports the decision-maker as such but also simplify documenting the process and in communication of the final decision.

Keywords: Decision making, LCC, Sustainable solutions, Analytical Hierarchy Process, AHP

1 INTRODUCTION

There are increased demands in society to act in a sustainable way, and most corporations have policies for their sustainability work. However, in daily decision-making, economy tends to be the governing criteria for decisions. To get sustainability more tangible and incorporated into decisions in daily work, the concept needs a clear definition to set the frames for the aim of sustainable development.
The World Commission on Environment and Development (Brundtland Commission) defined sustainable development as "development which meets the needs of current generations without compromising the ability of future generations to meet their own needs" (Bruntland report, 1987). Following the commission, sustainable development has three dimensions:

- Ecologic sustainability
- Sociocultural sustainability
- Economic sustainability

To further define sustainability, Holmberg and Robèrt have developed four non-overlapping principles for a sustainable society (Holmberg et al., 1996; Holmberg, 1998), where they state that "for a society to be sustainable, nature's functions and diversity must not be systematically:

1. Subject to increasing concentrations of substances extracted from the earth's crust.
2. Subject to increasing concentrations of substances produced by society
3. Impoverished by over-harvesting or other forms of ecosystem manipulation.

And

4. Resources must be used fairly and efficiently in order to meet basic human needs worldwide."

The principles give guidance on how to work towards a sustainable society, but in practice there are many decisions where the impact in terms of sustainability between alternatives is not clear. Moreover, it is hard to weigh the three different dimensions on sustainability in relation to each other.

In the tunnelling industry, the concept of sustainability is generally discussed in the top of organisations, but when following the strategy to its end in decisions about technical solutions, there can be conflicts between the traditionally governing economical decision criterion and the other two dimensions. Neither is the evaluation of each dimension straightforward.

In this paper, we present a study where decision theory has been applied to a tunnel project. The aim of the study was to test if we could incorporate other criteria than economy into decisions about technical solutions. The technical solutions concerned what system to choose for drainage and reinforcement of the tunnel. The decision method we applied follows the steps of an Analytical Hierarchy Process (AHP).

The tunnel is a railroad tunnel constructed in crystalline igneous rock. Five different technical systems on drainage and reinforcement were evaluated in an AHP process against the criteria life cycle cost (LCC), environmental impact and robustness & uncertainty.

The decision alternatives, that is, the five different technical systems for drainage and reinforcement are only described as numbers, for technical specifications and differences between the alternatives see Eriksson and Edelman (2014).

2 BACKGROUND ON ANALYTICAL HIERARCHY PROCESS

During decision-making in complex projects decision theory can be used to bring structure and clarity to the process. The purpose of a decision model is to give the decision-maker support to formulate and structure thoughts and opinions. The decisions are often choices between different alternatives where different criteria are considered to be of unequal importance for the decision.

The Analytical Hierarchy Process (AHP) is a method where different alternatives are evaluated against different decision criteria. Thereafter, all different combinations are compared to decide which alternative that best fulfils the stated criteria.

Individual experts representing different expert fields compare each alternative solution par wise to each other in relation to identified criteria. The alternatives can be evaluated equal or one alternative can be evaluated as preferential using a certain scale. Additionally, the different criteria are individually evaluated based on how important they are for the decision-making. Mathematically, the statistically most preferred alternative is calculated using eigenvectors. For more details about calculations, see e.g Saaty (2008, 1980).

3 METHODS AND PROCEDURE

The process of the AHP in this study followed the order shown in Figure 1. Much of the work was done in a project group with experts from the Swedish Transport Administration and the Swedish Geotechnical Institute (SGI). The competences in the project group were rock

mechanics, hydrogeology, geotechnics and maintenance.

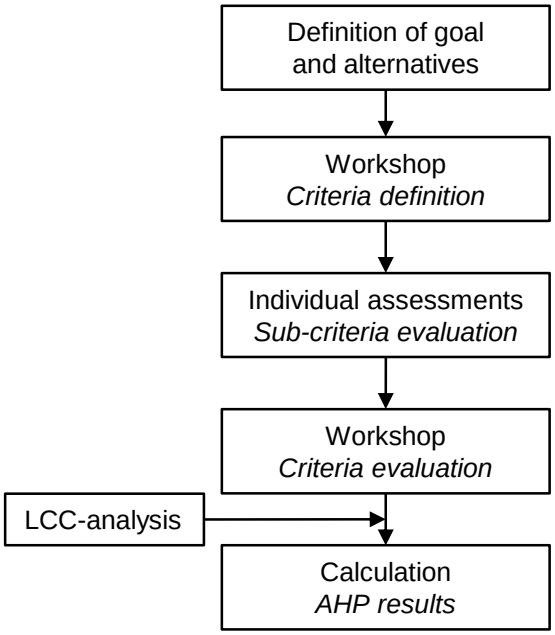


Figure 1. Flowchart of AHP procedure.

3.1 Definition of goal and alternatives

The overall goal of the tunnel project is to build a tunnel that is secure in terms water and rock mechanics. To reach this goal, different systems for drainage and reinforcement are available. The goal of the AHP process was to decide which system to use.

Five systems, based on different technical solutions on drainage and reinforcement were outlined. The systems differ also from an economical point of view, because they have different investment costs and maintenance requirements during the technical life span. The systems are described in detail in Eriksson & Edelman (2014).

3.2 Criteria definition

Important criteria for the choice of system for drainage and reinforcement were discussed in the project group.

Traditionally, an apparent criterion to consider is the investment cost. However, the investment cost does not give the full picture in this study, because the costs for maintenance differ significantly between the systems. Therefore, the life cycle cost (LCC) has been calculated for each system.

The LCC analysis also included the so called "societal costs" which are the indirect costs of disrupting the traffic system during maintenance. Hence, the LCC includes the investment cost and the sum of maintenance and societal costs in net present value.

The different technical systems are also related to different levels of environmental impact, and the Swedish Transport Administration is obliged to reduce the environmental impact of their projects. Another aspect of the decision is whether the systems are reliable or if there are known risks related to any of the systems.

The discussion resulted in three formulated decision criteria:

1. Life Cycle Cost (LCC)
2. Environmental Impact
3. Robustness & Uncertainty

The hierarchy of the decision is illustrated in Figure 2.

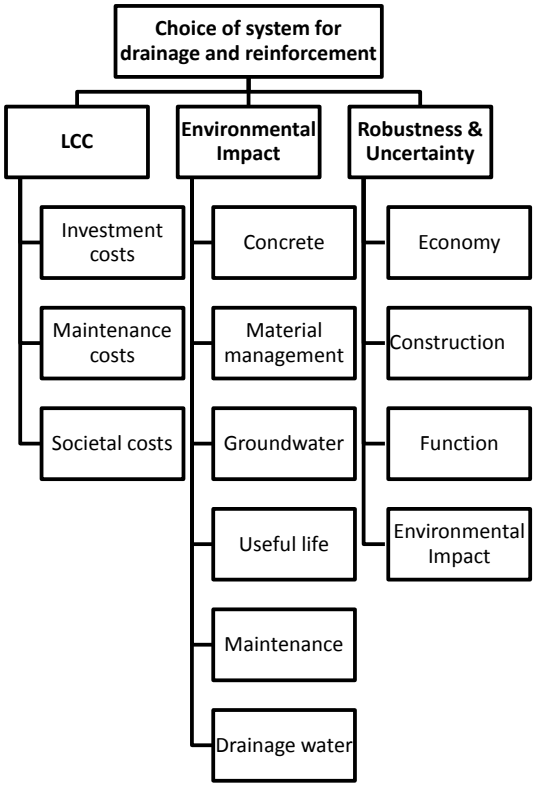


Figure 2. Hierarchy of decision problem. The decision alternatives are excluded from the diagram.

3.3 Criteria LCC– Definition and Input data

LCC is the total cost of investment and future operation and maintenance costs in net present value. A LCC analysis was performed for each technical system separately and the results correspond to the LCC criterion. The results are shown in Table 1.

Table 1. LCC of the five different technical systems.

System	LCC [SEK/m]
1	475 000
2	463 000
3	409 000
4	454 000
5	566 000

3.4 Criterion environmental impact

Environmental impact is a broad criterion that in this limited study only describes the environmental impact of the systems in qualitative terms.

The criterion comprises following parameters that also forms sub-criteria:

- Use of concrete
- Material management
- Groundwater impact
- Useful life
- Maintenance
- Drainage water

3.5 Criterion robustness & uncertainty

The technical systems can be linked to uncertainties and risks not included in the LCC analysis. These are included in the criterion of Robustness & Uncertainty.

One part of this criterion is project risk, which is a possible, but unexpected additional cost that is outside the uncertainty in the budgeted costs (Brinkhoff et al, 2015).

Parameters included in the criterion robustness & uncertainty, that also forms sub-criteria, are:

- Economy
- Construction
- Function
- Environmental and hydrogeological impact
- The system's effect on other technical systems, such as electricity, rails, etc.

A system that is valued high regarding robustness & uncertainty is assumed to result in less unexpected negative events (surprises) during construction and operation. In the early assessments they are considered to suffer from less uncertainty.

3.6 Sub-criteria evaluation

In the first part of the assessment, three experts in hydrogeology, rock mechanics and rock engineering assessed the performance of the five different systems for drainage and reinforcement against the criteria and sub-criteria. The experts made their assessments individually by placing the systems in order of precedence regarding their indirect impact and thereafter order the systems according to a scale between 1 and 5.

The first part of the assessment was formulated as following regarding environmental impact:

1. Place the systems in order of precedence regarding their indirect environmental impact due to use of concrete:
2. Place the systems in order of precedence regarding their indirect environmental impact due to excavation and transport of rock material:
3. Place the systems in order of precedence regarding their indirect environmental and hydrogeological impact during the construction phase:
4. Place the systems in order of precedence regarding their indirect environmental and hydrogeological impact during the operation phase:
5. Place the systems in order of precedence regarding their indirect environmental impact due to handling of drainage water:
6. Place the systems in order of precedence regarding their expected useful life and the environmental impact due to the length of useful life:

7. Place the systems in order of precedence regarding their indirect environmental impact due to maintenance (including transports needed for maintenance):

The scale was from 1 to 5, where 5 means largest environmental impact and 1 means smallest environmental impact.

Regarding robustness & uncertainty, the first part of the assessment was formulated as following:

1. Place the systems in order of precedence regarding their robustness about economy (cost estimations, etc.):
2. Place the systems in order of precedence regarding their robustness about the construction phase:
3. Place the systems in order of precedence regarding their robustness about their function:
4. Place the systems in order of precedence regarding their robustness about environmental and hydrogeological impact:
5. Place the systems in order of precedence regarding their robustness about their impact on other technical systems:

The scale was from 1 to 5, where 5 means high robustness (low uncertainty) and 1 means low robustness (larger uncertainty).

3.7 Criteria evaluation

The second part of the assessment, a mutual assessment of the criteria, took place at a workshop with seven invited experts from the Swedish Transport Administration. Following fields of expertise were represented at the workshop; hydrogeology, rock mechanics, rock engineering, technical maintenance, finance and project management.

Each person was to individually assess the three criteria pairwise against each other by answering a set of questions. A scale was presented as a guide for the evaluation, see Table 2. The questions were:

1a. What is most important - LCC or Environmental impact?
1b. How much more important based on the scale in Table 2?
2a. What is most important - LCC or Robustness & Uncertainty?
2b. How much more important based on the scale below in Table 2?
3a. What is most important - environmental impact or robustness & uncertainty?
3b. How much more important based on the scale in Table 2?

Table 2. Scale for rating of criteria (after Saaty, 1980)

Intensity of importance	Definition	Comment
1	Equal importance	Two factors contribute equally to the objective
3	Moderate importance	Experience and judgement slightly favour one over the other
5	Strong importance	Experience and judgement strongly favour one over the other.
7	Very strong importance	Experience and judgement very strongly favour one over the other. Its importance is demonstrated in practice.
9	Extreme importance	The evidence favouring one over the other is of the highest possible validity.

3.8 Calculation – AHP Results

The points of each system and criterion were summarised and translated into a Saaty scale for comparison, see Table 3.

Table 3. Conversion between points, costs and Saaty scale. The scales of the three criteria were decided within the project group.

Saaty scale	LCC [1000 SEK/ m]	Environmental Impact [points]	Robustness & Uncertainty [points]
1	<40	<30	<21
3	80-120	39-48	29-34
5	160-200	58-66	42-47
7	240-280	77-85	55-60
9	>320	>95	>68

The calculations were made in a spreadsheet template from BPMSG-Business Performance Management (Goepel, 2013).

4 RESULTS

4.1 Criteria evaluation

Based on each workshop participant's pairwise assessment of the decision criteria LCC, environmental impact, and robustness & uncertainty, the individual weighting of the criteria was calculated, see Table 4. It was noted, that the assessments of one person resulted in inconsistent priority of the alternatives, however, the assessments were not excluded from further calculations. For the whole group, a 91% consensus is achieved amongst the individuals, and the prioritisation of criteria is:

1. LCC (48%)
2. Robustness & Uncertainty (41%)
3. Environmental Impact (11%)

Table 4. Individual weights of decision criteria based each participant's assessments.

Criteria	Participants weights (%)						
	1	2	3	4	5	6	7
LCC	33	43	68	30	46	51	62
Robustness & Uncertainty	8	14	6	9	22	10	9
Environmental Impact	59	43	26	62	32	39	30

4.2 Rank of systems according to criteria

Based on the second part of the assessment, i.e. how well the systems fulfil the criteria environmental impact and robustness & uncertainty, an order of precedence of the systems were made for each criterion, see Table 5. The order of precedence for the criterion LCC is based on the calculated costs of the LCC analysis.

Table 5. Order of precedence of the five systems for each criterion.

System	Rank		
	LCC	Environmental Impact	Robustness & Uncertainty
1	4	2	4
2	3	3	3
3	1	1	3
4	2	2	2
5	5	1	1

4.3 Total result AHP

After the final calculations, Systems 3 showed to be the preferred system according to the conditions and decision criteria stated for this study. The total prioritisation is shown in Figure 3.

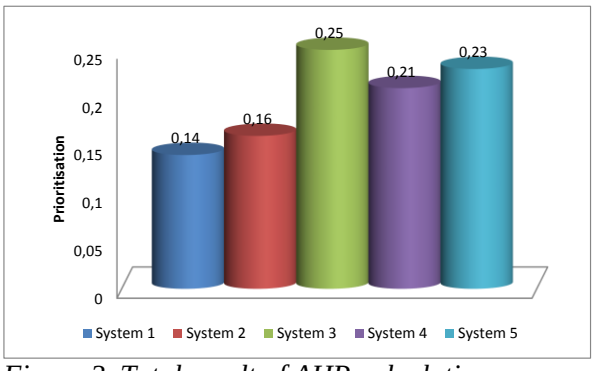


Figure 3. Total result of AHP calculations.

5 DISCUSSION

The aim of this study was test if we could incorporate other criteria than economy into decisions about technical solutions. An initial

hypothesis was that the costs alone are considered as the most important aspect. Hence, it is interesting to notice that the participants in the workshop evaluated robustness nearly as high as the costs. Our interpretation is that certainty in knowing that you get what you have ordered is important.

The criterion environmental impact was not highly prioritised by the group of experts attending the workshop. One reason for this was revealed in the discussion that followed the individual, first part of the assessment. Several of the experts considered that environmental impact of the different systems had a low priority since all alternatives fulfil existing environmental legislations. It should be noted though, that expertise in sustainability or environmental issues were not represented in the group.

No members of the project group had previous experience of working with a decision analyses process, but after an introduction to the AHP method, this was accepted and understood by the project group. The discussion about the decision criteria and their definitions was a learning process itself where different views of the decision were presented by the experts

The choice of decision criteria in an AHP should reflect the decision-maker's preferences. Nevertheless, by choosing and defining criteria it is possible to highlight aspects that easily could be foreseen otherwise. The use of LCC instead of investment costs is a step towards a more holistic view of the costs for an underground project. The criterion environmental impact could be further developed to include a Life Cycle Analysis (LCA). However, both LCC and LCA are time demanding analyses and the assumptions and limitations are often debated.

It is possible to develop the criteria of environmental issues further. It is also possible to include social aspects in the methodology presented here, in order to focus the decision towards sustainability even further.

An underlying question is how to include aspects on sustainability in underground construction works. On one hand, one could argue that the most environmentally sustainable solution should be chosen. However, the economic aspect must be included as well, since gained economic strength for the society can be used to finance other projects. For instance, a cost saving in one project can finance a more sustainable solution in another project. Therefore, decision making that includes several different aspects is necessary for targeting increased sustainability in underground construction works.

6 CONCLUSIONS

The main conclusions from this study are:

- It was possible to apply the AHP method to the decision process in a real case, and it was possible to include environmental impact as one among other aspects considered during the decision making.
- The method was easily accepted by the experts in the project group after a short introduction, indicating that the method is suitable for usage in forums where decision analysis is not commonly adopted.
- The results obtained by using the method are transparent. Moreover, sensitivity studies can easily be performed to demonstrate the robustness of the result in relation to the decision.
- Using decision analyses, in this case AHP, supports including environmental aspects and promotes more sustainable solutions. In the process of doing the decision analysis all questions that should have an impact on the decision will be revealed, hence sustainable solutions will be high lightened.
- The discussions that emerged during the assessment process were valuable, on their own, because they triggered a more creative and interdisciplinary focus in the tunnel project.

7 ACKNOWLEDGEMENTS

The Swedish Transport Administration is greatly acknowledged for financing the study and for good and engaged co-operation.

8 REFERENCES

Brinkhoff, P., Norin, M., Norrman, J., Rosén, L., Ek, L. (2015). Economic project risk assessment in remediation projects prior to construction – Methodology development and case study application. Remediation Journal, vol. 25:2, pp. 117-138.

Bruntland report (1987). Report of the World Commission on Environment and Development: Our Common Future. FN Annex till dokument A/42/427.

Eriksson, M. & Edelman, M. (2014). LCC-analyser för vattenavlednings- och bergförstärkningssystem. BeFo Rapport 131. Stiftelsen Bergteknisk Forskning. Stockholm.

Eriksson, M., Zetterlund, M.S. & Edelman, M. (2015). Inklädnadssystem för järnvägstunnlar (*in press*).

Goepel, K. D., (2013). Implementing the Analytic Hierarchy Process as a Standard Method for Multi-Criteria Decision Making In Corporate Enterprises – A New AHP Excel Template with Multiple Inputs, Proceedings of the International Symposium on the Analytic Hierarchy Process 2013, Kuala Lumpur, Malaysia.

Saaty, T.L. (2008). Decision making with the analytic hierarchy process. *International Journal of Services Sciences*, Vol. 1, No. 1 2008.

Saaty, T.L. (1980). The Analytical Hierarchy Process, MacGraw-Hill, 1980.

Guldborgsund Tunnel. Operation of tunnel and drained ramps

Per B. Laursen
Rambøll, Denmark, pcl@ramboll.dk

Thomas Nicolai Petri
Rambøll, Denmark

Susanne Brix
Rambøll, Danmark

ABSTRACT
The tunnel at Guldborgsund is an immersed tunnel connecting the Danish islands Lolland and Falster. The tunnel is a twin tube road tunnel. The tunnel is approximately 500 m long including portal structures, and has approx. 400 m open ramp on each side of the tunnel. The tunnel is owned and administered by the Danish Road Directorate.
The tunnel was built mid 1980's and opened to traffic in 1988. The tunnel is part of the international European route E47 connecting Copenhagen to Fehmarn. The tunnel was originally built as a 2 lane main road with one carriageway lane and one emergency lane in each tunnel tube, and in 2007 upgraded to a 4 lane highway, where the original emergency lanes were converted to carriageway lanes.
On Falster, the ramp is established in clay till deposits above chalk and on Lolland the ramp is established in sandfill above chalk as this area was used as dry dock to level -10 m during construction works. The dry dock area was refilled with sand after casting and floating the tunnel elements out.
The main water aquifer in the area is the chalk. The original groundwater lowering in the open ramps is described in NGM article 1988 by Claes Thunbo Christensen and consisted originally of approximately 50 relief wells relieving groundwater pressure from the chalk. In the open ramps on both sides of the tunnel the system of relief wells are supplemented with horizontal and deep drains for securing acceptable water levels below the road.
The article focus on the operation and maintenance works done for the last 10-15 years in order to secure the open ramps against hydraulic failure and piping, but do also include work with permissions from Danish authorities. Regeneration with hydrochloric acid and sodium dithionite has been executed, but also additional wells have been supplemented to the system.

Keywords: Immersed tunnel, groundwater lowering, chalk, uplift safety, operation.

1 PROJECT

Structure
The tunnel was designed by CNT CONSULT and built by Christiani & Nielsen in the period from mid-1980's to 1988. The tunnel consists of 2 immersed tunnel elements cast together into one monolithic structure with a total length of 470 m. In both ends dikes are established to shorten the tunnel lengths in the 1200 meter "coast to coast crossing".
The dimensions of the tunnel section is approx. 9 m high and 21 m wide with 0,8 m thick concrete. In both ends portal structures are established connecting the tunnel elements to the open ramps. The portal structures consists of a 12 m high concrete structure with portal reservoir and access tunnel to relief wells in the substructure to level -10 m and with top of structure in + 2.5 m. Road entrance from the open ramp is in level - 6 m. Rambøll has been consultant in O&M activities since start of 00'ies and Per Aarsleff has delivered maintenance services to the system since 2010.



Figure 1.1. Guldborgsundtunnel. Aerial view.

An aerial view is seen in Figure 1.1.


Figure 1.2 Photo from Falster site of tunnel entrance.

Establishment of ramps

The ramps were established dry by use of pumping wells and groundwater lowering in the chalk. The system of pumping wells were in end of the construction period partly converted to relief wells and supplemented by new wells to a relief system to take care of the permanent groundwater lowering system for securing uplift safety in the open ramps.

Open ramp and Relief system

On both sides the ramps are placed in natural soil meaning that on Falster its foundation is in the natural clay till with chalk below in level -10m, and on Lolland the previous dry dock excavated to -10 m is refilled with sand and the ramp is here founded in this fill with the chalk in level -10 m below.

The chalk is the local regional water bearing aquifer with an interpreted permeability of 1 * 10^{-4} m/sec and a water level at rest a little above the water level in Guldborgsund at +0.0 m. The site investigations from GEO (former DGI) at the time of construction emphasizes that permeability might increase by depth estimated by sectional pumping tests.

In the open ramps a relief system is established in order to lower the groundwater level in the chalk and on Lolland also in the sandfill. The system is supplemented by longitudinal drains, but it is only on Lolland in the sandfill this system contributes with relevant drainage. The relief system consisted in 1988 of 7 relief wells on each side of the ramp and 10 relief wells in the bottom of the portal structure for each ramp. The wells on each side of the ramp relieved water to a longitudinal collector pipe and the wells in bottom of the portal structure relieved water directly into the portal reservoir. In total 24 wells in each ramp secured the ramp from piping and hydraulic failure. The relief system was placed in the deep part with surface between -6 and -4 m and was and are still able to secure the entire ramp. The system of wells is shown in Figure 1.3.

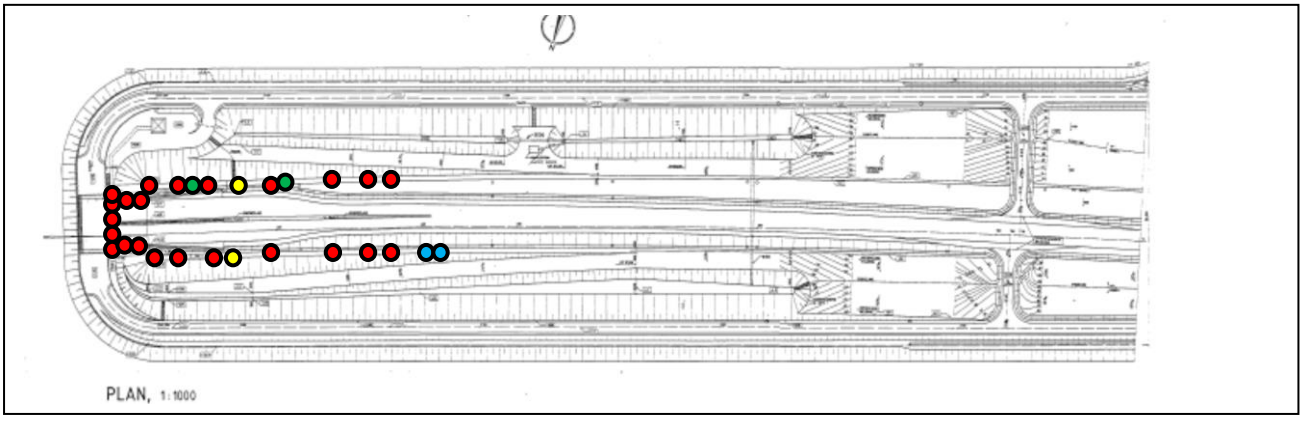


Figure 1.3 System of relief wells. Overview.

2 MAINTENANCE

Maintenance early 90s
The relief system was reconditioned early in the 90s with the conditioner Herli Rapid, but results of this is not well documented. In that process supplementary observation wells were established in order to improve monitoring of water level.

Maintenance early 00s
4 new relief wells (marked with yellow in Figure 1.3) were established in the middle of the ramps on both sides.

Extraordinary maintenance 2009
In 2009 piping was observed in a small local area in the north side of ramp on Lolland and 2 additional relief wells (marked with blue in Figure 1.3) were established.

Maintenance 2009
The monitoring results showed the need for supplementary relief wells as it was agreed with the owner that the project should be treated after EC 7 standards and corresponding partial coefficients and in high consequence class.
From 2009 maintenance also included regular reconditioning of the relief wells, which was executed with hydrochloric acid. The plan was to treat 8-10 relief wells /year in order to treat all wells within 7-10 years. The obvious risk is that wells not handled with regular intervals cannot gain effect by acid treatment.

Maintenance 2010-2014
The relief wells have been under regular treatment as 8-10 wells are being reconditioned each year. The results from capacity tests have shown significant improvements on the majority of the treated wells.
In 2010 reconditioning with sodium dithionite was also implemented as a trial to see if the effect of reconditioning could be extended.

3 RESULTS FROM MONITORING AND MAINTENANCE

Sodium dithionite treatment
Laboratory tests showed a significant improvement of added solubility of ochre in water compared to hydrochloric acid meaning that it might be possible to remove ochre sediments in the filter to a point where repeated sediments in the filters were delayed. The process from free iron Fe^{++} to Fe^{+++} is a process which improves if Fe^{+++} is already present and is delayed if Fe^{+++} is not present. The hope was, that if this treatment was introduced, the time between reconditioning could be increased and thereby keeping the relief system in good operation conditions for longer periods between reconditioning. The focus point was to reduce maintenance costs. 8 treatments were executed but after following the development of these 8 treatments over 3 years it was not possible to see a clear effect allowing for increased periods between reconditioning.

The final solvents from the treatment was sodium and SO_4, which from a discharge point was non problematic after dilution in the portal reservoir in portal structure.

Hydrochloric acid treatment
The treatment was performed and followed normal practice in Denmark after the main part of ochre was removed by capacity pumping followed by adding hydrochloric acid in a dilution of 1:20 with 24 hours of reaction time and ended with a capacity pumping, where the solvents created by the acid treatment was removed.

Very different improvements were identified, but in general improvement above 100-200 % was seen. Improvements in an selected amount of wells are shown in figure 1.4, where “specific capacity” after treatment are shown vs. “specific capacity” before treatment.

Few treatments have shown only little improvements measured in relief yields but the general effect is seen in lowering of water level in the ramp.

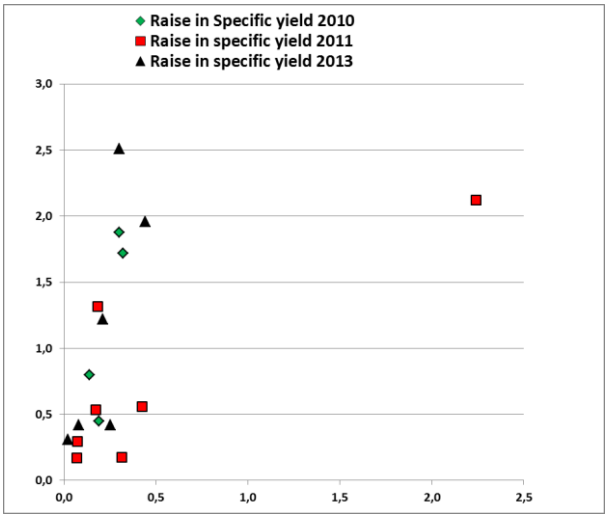


Figure 1.4 Results of acid treatment. Specific capacity after treatment vs. specific capacity before treatment. Units are m^3/hour/m lowering.

Water levels 2001-2015

Water levels in the 12 monitoring wells in the ramps are measured on a monthly basis, giving the water level in top of chalk as well as in a deeper layer of the chalk. The results from the monitoring wells in between the relief wells are used to determine the periods between acid treatments as water level after treatment are lowered around 1 m below target level and in the period up to next treatment water level rises to approximately target level.

On Lolland in the old sand filled dry dock the target level is defined as the bottom of road foundation as water level in the road bearing layer will reduce bearing capacity and reduce the lifetime for road and pavement. On Falster the target level is defined as level with uplift safety approaching 1.0 (incl. γ-values and K_{FI} value) against hydraulic failure and with upwards gradient equal to 0.6.

The spread of monitoring wells are also used to determine, which relief wells are chosen for next treatment in maintenance program.

Typical variations of water level in 2 of these wells are shown for the last 14 years in Figure 1.5. The typical variation is a raise of water level of 3-5 cm per month. Each year 8-10 wells are chosen for acid treatment and bringing the water level down corresponding to the degeneration. Last shown drop on figure 1.4 is related to acid treatment of all 5 wells in the portal reservoir close to L1 and L2 and the drop in water level here is higher than the previous drops in water level.

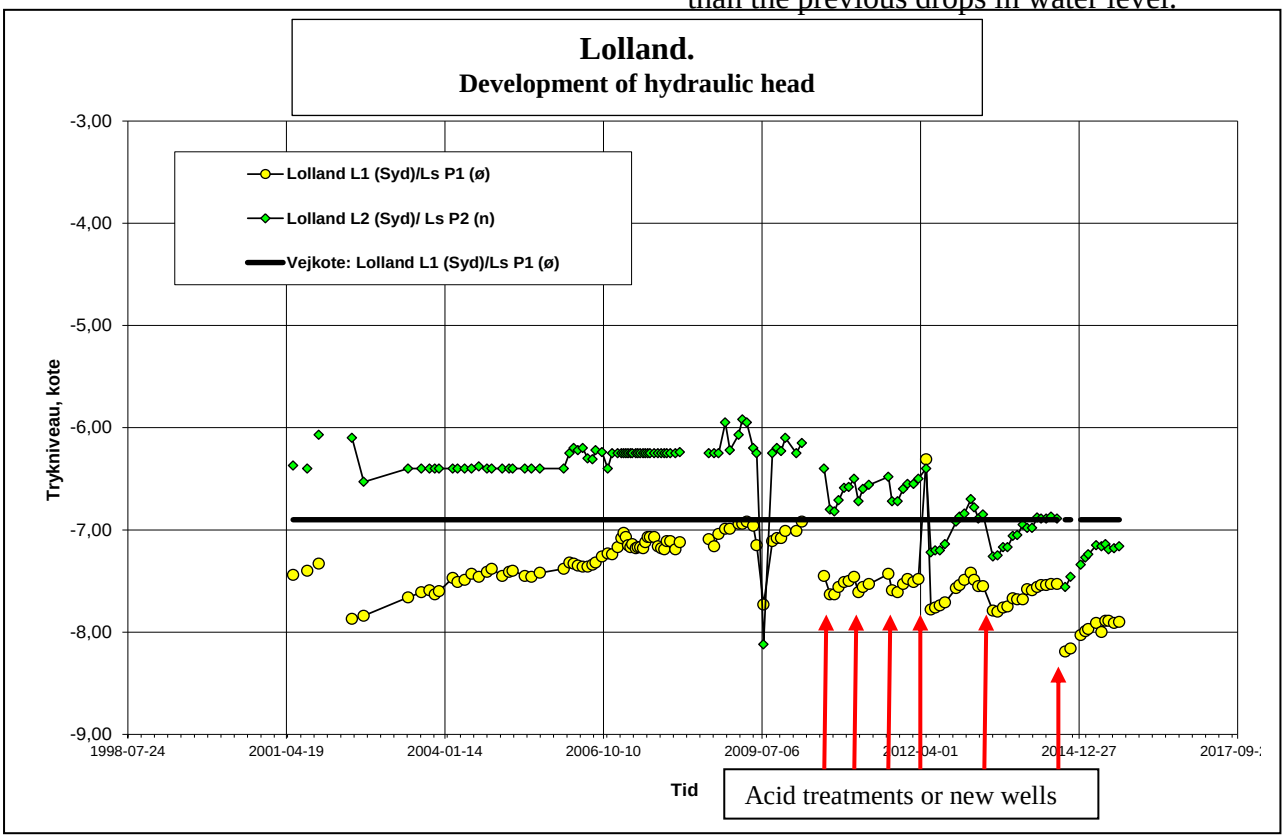


Figure 1.5 Lolland. Overview of water levels in 2 monitoring wells.

Access challenges to these wells gives reasons to take them all in one sequence instead of 1-2 each year. The yellow dots in Figure 1.5 represent water level in upper part of chalk and the green dots represent waterlevels in the chalk 5 m lower. It might not verify the presence of increasing permeability by depth, but it verifies the presents of several flow zones in the chalk. On Falster the clay till layer is present from top chalk to base of road foundation. Here it is accepted that the water level around the deepest part at the entrance to the portal structure is above surface and observation wells here are closed to avoid relief of water. The wells are sealed and are being monitored by manometer. The water level here is monitored and managed in order to have a reasonable uplift safety against uplift, but also to avoid upwards gradients above 0.6.

Relieved water yields

The groundwater relieved from the relief wells are measured manually twice a year, but only measured data on the single wells are available 6-7 years back.

There are only few data available from the initial operation phase and summarized yields from Lolland ramp are shown in Figure 1.6. It is seen that initial relief of groundwater from the wells and drains was approximately 50 m^3/hours and dropped in the period up to 2007 to a little below 15 m^3 /hour. From 2007 a more regular maintenance of the relief wells started.

As seen on Figure 1.6, the initial relief of groundwater from the wells and drains were 50 m^3/hours but are now stabilized on 25 m^3/hours. The initial yield on Falster side is not available but today this yield is also around 20-25 m^3/hour.

This relief yield achieves acceptable relief of upwards groundwater pressure on Falster side. The groundwater level on Lolland side is by the system lowered to below the bearing layers in the highway.

The increase in yields is in general related to the ongoing acid treatment of the wells, but in 2009 it was related to additional 2 wells established to handle the piping area.

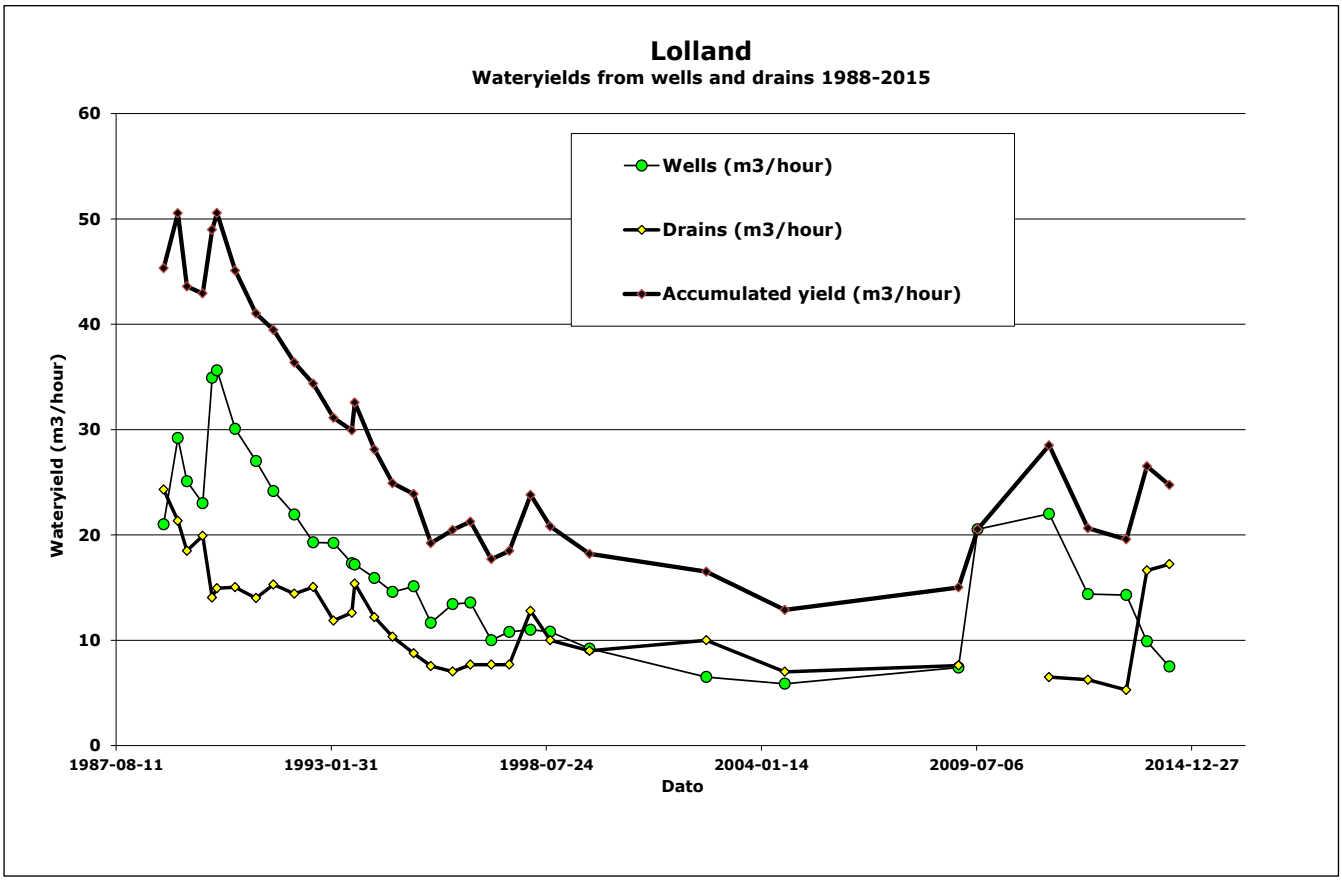


Figure 1.6 Yield measurements1988-2014

Section 4 comprises an explanation to understand, why we in 2016 can maintain acceptable water level for 25 m^3/hours relief, which required 50 m^3/hours in 1988.
Yield monitoring in single wells are ongoing twice a year and used for selecting relevant wells for reconditioning. Measurements for the period 2009 to 2015 are shown in Figure 1.7 for the relief wells on Falster North ramp.

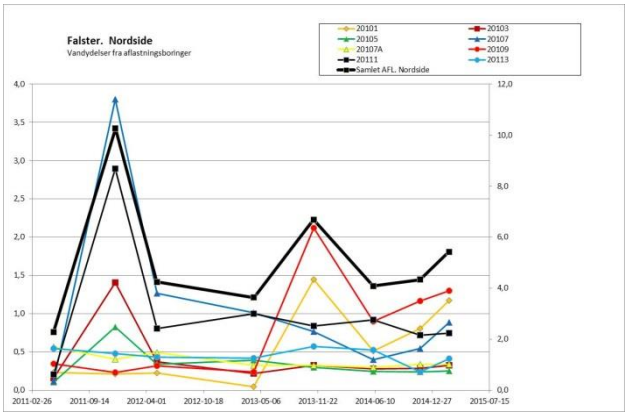


Figure 1.7 Yield measurements Falster North.

Groundwater quality
The groundwater quality at Guldborgsund chalk aquifer differs from Lolland to Falster. On Falster it is a "normal" Danish coast near groundwater quality defined as a groundwater with high salinity and an iron content of 1-2 mg/liter.
On Lolland the groundwater has a significant content of sulfur, which has led to a chemical attack on parts of the concrete structure (portal reservoir) and the relief wells (installations and concrete protective structures). To prevent concrete deteoriation ventilation has been installed in the portal reservoir on Lolland and concrete structures for relief wells have been repaired/ exchanged. On the concrete protection of the relief wells the corrosion is very visible as can be seen on the photo in Figure 1.8.

Permission
A review of all legal basis for the tunnel in 2011 made it clear that this basis had to be updated.



Figure 1.8 Installation of relief well in concrete ring on ramp at Lolland. Photo T.N. Petri.

The process ended with 3 updated permissions adapted to present operation and maintenance including

- Groundwater lowering (500.000 m^3/year)
- Establishment of new wells
- Discharge of relieved groundwater to Guldborgsund.

Well installations
During the maintenance and supervision works on site the following observations have been made related to non-satisfactory construction works.

Damage in filter screen: In one well on Lolland filtersand and blue PVC screen parts with slots were airlifted/pumped up from the well during capacity testing of the well before acid treatment. A following video inspection of the well identified a damaged screen, where a significant "handball size" big hole could be seen in bottom. Se Figure 1.9



Figure 1.9 Still picture from well video.

The well has not been mechanically treated since commissioning and it is likely that the hole has been present since establishment. So far no remedial actions have been taken as the situation seems stable in the chalk.

In one of the wells it was identified that the concrete bottom was not able to resist the pressure from the acid treatment and it was found that only a poor thin blinding layer was present in bottom of the concrete protective structure. In the bottom plate of the concrete structure a recess was made by wood allowing the well to be drilled from surface and the recess could afterwards be sealed. Apparently this was not done. Se photo in Figure 1.10.



Figure 1.10 "Bottom" of well "protection"

4 EVALUATIONS

Relief system
The relief system is well functioning, but requires monitoring as well as maintenance on a regular basis.

Groundwater quality
The presence of sulfur in the groundwater increases maintenance costs as structural parts and installations are worn down faster on Lolland than on Falster.

Monitoring
The level of monitoring seems reliable and adequate in order to plan maintenance activities consisting of acid treatments, new relief wells, monitoring wells and general refurbishment.

Relief yield from the system
The system today can be operated with acceptable water pressure below the ramps for 50% of the initial yield from 1988. It is considered that settlements have caused a reduction in the fractures in the ongoing consolidation process of the chalk.

In Figure 1.11 an overview of the increase in effective stresses are established based on groundwater lowering, dike-establishment and gravity structures. Areas marked with brown indicates stress increases above 100 kN/m2, red is 50-100 kN/m^2, orange is 25-50 kN/m^2 and yellow is below 25 kN/m^2. The figure is not 3-dimensional correct as effective stresses from dike load and gravity structures will decrease by depth due to spreading and increased stresses from the groundwater relief will maintain the full additional effective stress in the whole aquifer to an unknown depth.

Commissioning
Thorough final supervision of all works before commissioning is recommendable as significant deficiencies are registered 28 years after commissioning.

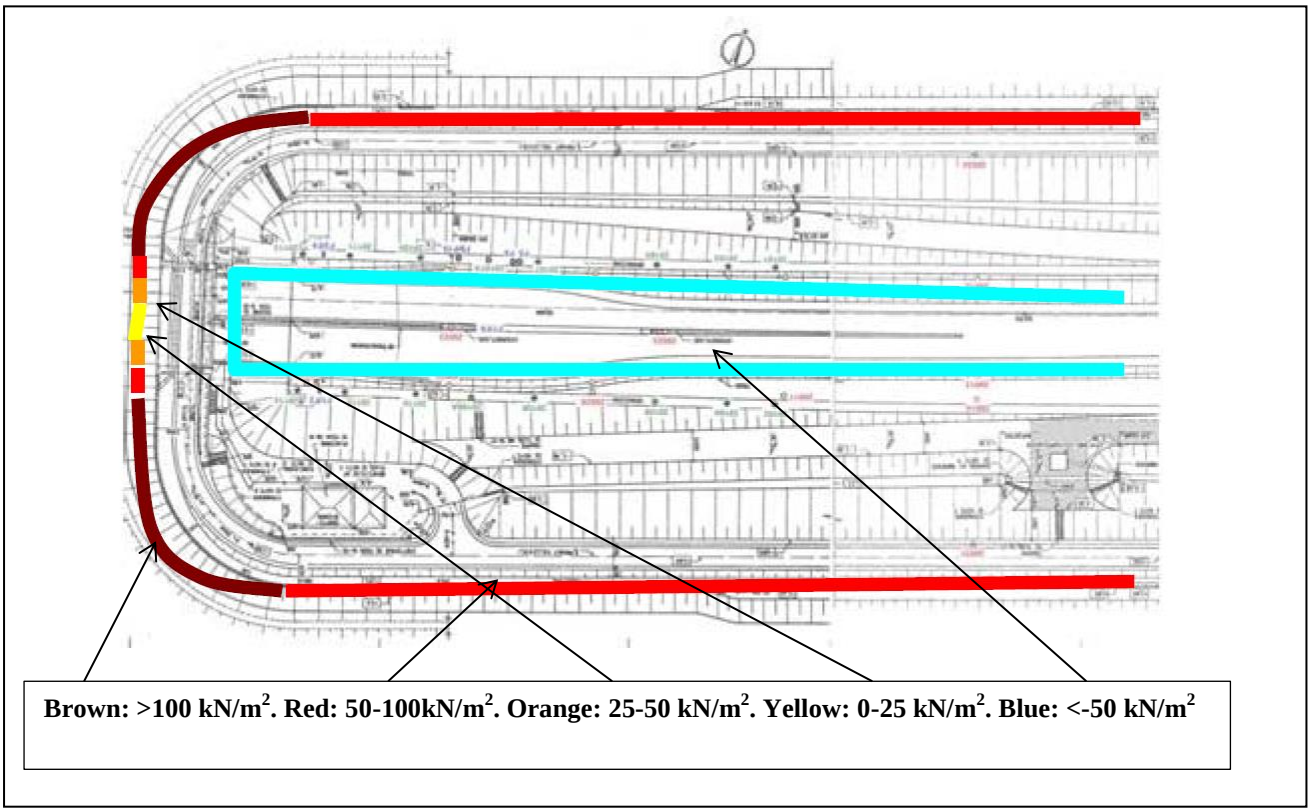


Figure 1.11 Falster overview. Estimated changes in effective stresses.

Freezing techniques made a new tunnel possible

Jens Kofod Nielsen
Züblin A/S, Denmark, jens.nielsen@zueblin.dk

Henning Jensen, Jakob Hausgaard Lyngs and Henrik Henningsen
Züblin A/S, Denmark

ABSTRACT
In the centre of Copenhagen, at Nørreport Station, a new tunnel with 2 escalators has been constructed. The area around Nørreport Station is one of the busiest places in Copenhagen and the construction site was in the middle of it. The construction site was extremely tight, 10x40 m. The execution phase was separated in two main construction stages, a pit and a tunnel. This paper focuses mainly on the tunnel part, which was made underneath an existing bus area and a train tunnel, close to neighbouring buildings and just above two existing metro tunnels. The tunnel part was constructed by using the New Austrian Tunneling Method and freezing techniques.
Züblin A/S was commissioned to plan, design and construct the new tunnel Ny Metrotrappe.

1 GENERAL DESCRIPTION

Frederiksborggade is a busy street with small shops, cafes, restaurants and bank branches. Pedestrians, people with prams and bicycles, etc. come daily in the street as shown in Figure 1.



Figure 1: The construction pit was between the buildings in Frederiksborggade

Frederiksborggade is located in a pedestrian area. Each day 200,000 people pass Nørreport Station and about 40,000 people walk through Frederiksborggade. The construction site was in the middle of one of the busiest parts of Copenhagen.

A new pedestrian tunnel was connected to the existing transfer tunnel at Nørreport Station. At Nørreport Station it is possible to take long distance trains, commuter trains and metro trains.

The proposed tunnel was constructed close to existing buildings, metro tunnels and the Boulevard tunnel (Track No. 1). The Boulevard tunnel is about 100 years old but in good condition. From the construction drawings, it seemed that the base slab as the side walls was slightly reinforced and a membrane had been placed approximately 30 cm above bottom level. The drawings indicated that there were construction joints between the side walls, footings for the columns and the base slab. Furthermore, a retaining wall (soldier pile wall with wooden cladding) had been left in the ground from a previous project. Underneath the new tunnel two metro tunnel tubes were installed. The pedestrian street was in level +9.0m DVR90.

1.1 Soil condition

Fill (FYL): Generally fill was described as sandy, gravelly clay containing organic matter and silty sand. Locally, the fill has been encountered as peat with traces of sand.

The thickness varies from 7m to 10m close to the Boulevard tunnel.

Sand (Gravel): Below the fill layer, fine to medium sand, locally gravelly sand was encountered. This layer was also described in some borehole logs as clayey, gravelly sand till. The thickness has been encountered up to 7m.

Clay Till: The sand layer was underlain by clay till layer with a thickness ranging approximately from 3 to 5m. This soil layer was described as sandy, gravelly clay till, locally with lime grains and flint.

Sand/Gravel: Below the clay till layer, a sand/gravel layer was encountered in general with a thickness of approximately 2m. Locally, this layer is described as gravel till.

Limestone: Below the sand/gravel layer and clay till layer, respectively, limestone was encountered about 18m below the ground surface.

2 Structural form



Figure 2: Construction pit in a late stage

The aim of the brine freezing task was to create a stable body of frozen soil with defined dimensions during excavation.

In general, construction of the tunnel was divided into two different construction methods - a traditional construction pit and a tunnel. The new tunnel connects to the existing metro station, drilled below Nørre Voldgade and up into the street of Frederiksborggade no. 14 (see Figure 2). The width of the tunnel was about 4-5m and the height is about 2.75m. The length of the tunnel is approximately 50m in total.

The execution phase was separated into two main construction stages as follows:

1. pits were constructed from street level with varying excavation depth
2. a tunnel was constructed using the New Austrian Tunnelling Method and freezing techniques to connect to the existing transfer tunnel

It was excavate soil within dry pits formed by secant pile walls. The connection itself was to be constructed by using the New Austrian Tunnelling Method (NATM) and freezing techniques. Freezing pipes were drilled generally from inside of two deep pits (see figure 3 & 4). Prior to excavation under the level of the groundwater the soil was frozen and sealed against the groundwater. The excavation of the tunnel was conducted in steps while the surrounding soil was frozen and a primary lining in the form of shotcrete was installed to create a temporary load-bearing ring. After the connection to the transfer tunnel had been made, concrete works were carried out to construct the permanent tunnel lining. Finally, this was followed by fit-out works.

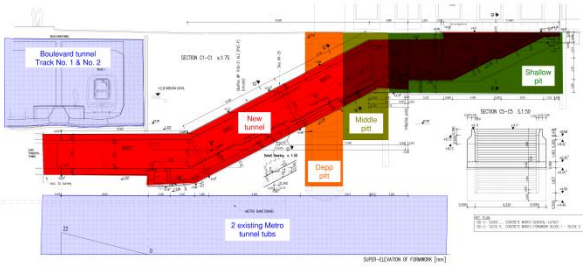


Figure 3: 3 Pits, new tunnel and existing tunnels

In previous freezing projects in Denmark a method with jacks-up had been used. If the freezing was extended too much, then the jacks-ups were prepared to compensate for the vertical deformation. In this project a different method was used. The expected deformation was calculated in the design stage and by monitoring work on site the actual deformation was measured. If the measured deformation values were critical the freezing system was shut down for a

period, while still observing the limits for maximum temperature in the freezing profile.

Due to the narrow location of the new tunnel to the existing metro tunnel the space for placing of freeze pipes was very limited. For that reason the freeze pipes were drilled as steered drilling to achieve a high accuracy of the drilled holes. Furthermore, the location of the holes during drilling was controlled constantly to know the location of the drill head at any time due to the risk of drilling too close to the existing tunnels.

2.1 Construction pits

For the construction of the new pedestrian tunnel, an "entry shaft", in fact pits needed to be constructed. The location of the pits and its geometry was dictated by the new tunnel, the restricted site layout and surrounding buildings and tunnels. These pits vary in excavation depth and were divided into a shallow pit, middle pit and two deep pits (see figure 3 & 4). The pits were excavated in steps and dewatered. The shallow pit, middle pit and deep pits were excavated in different construction sequences. During the excavation, the archaeological excavations were commenced. The archaeological excavations were performed to 6m below ground level, which is above the groundwater level.

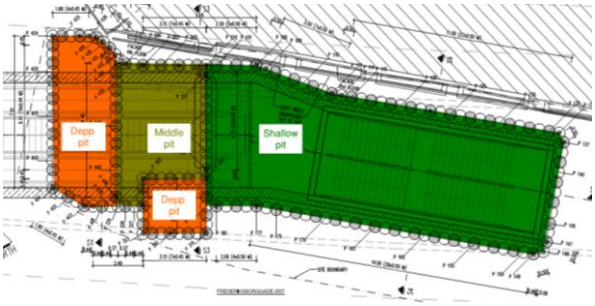


Figure 4: 2 deep, middle and shallow pits

Construction pits were formed by using secant piles. The method of using a secant pile wall minimised noise and vibrations induced in the surrounding buildings and tunnels. This type of construction is very stiff compared to other constructions and only small deflections are anticipated, which could impact the surrounding buildings. The diameter of the piles and reinforcement depends on the geometry, support conditions and static loads from soil, water, neighbouring buildings and surface loads. Furthermore, piles were embedded in clay till, resulting in a groundwater cut-off and it was expected that no groundwater would leak into the pits during construction. The shallow pit is shown in figure 5.



Figure 5: Shallow Pit with freezing system on top

However, jet grouting was planned to be performed to form a deep grouted sealing blanket but it did not work out and instead an ice block was made. After repeated adjustments of the jetgrouting setup it was not possible to get a watertight blanket and furthermore the strength of the blanket was not fulfilled according to the design. No groundwater lowering outside the pits was carried out because of considerations for the surroundings. The pit was secured against uplift of the ground and water ingress. It was intended to the use freezing method for the deep pits after the installation of the secant pile to form a watertight plug close to the level of the pile toe (see figure 6). Freezing pipes were installed from ground surface and only inside the deep pits and the middle pit. The excavation level of the shallow pit was higher than groundwater level in the middle pit.

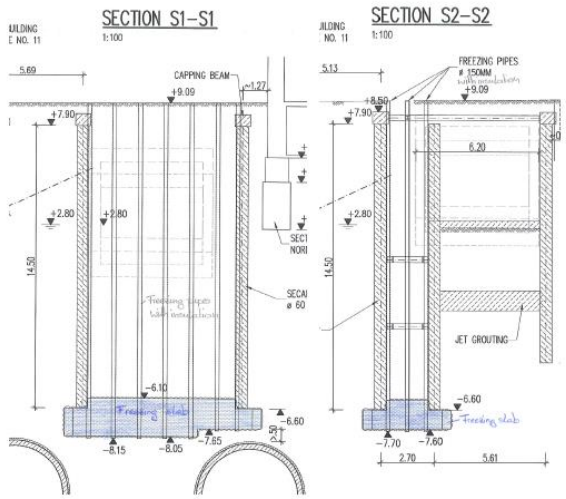


Figure 6: Freezing slab

A capping beam was installed on top of the piles. Depending on the depth of the excavation and loading, the pits were supported by struts and wailings, which were either concrete or steel. Anchors were used too. Ground anchors should maintain a sufficient distance to existing structures to avoid damage.



Figure 7: Temporary bridge on track no. 1

Track no. 1 (see figure 3) in the Boulevard tunnel was temporarily supported before excavation below the track could be commenced. It was intended to install a "rail bridge" inside the Boulevard tunnel and the span of the bridge was the same as the width of the temporary freezing profile. The bridge prevented any trainloads from track no. 1 on the Boulevard bottom slab just above the working area (see figure 7 & 8). The concentrated load was precisely above the centre line of the freezing profile. The design of the track support was done by others.

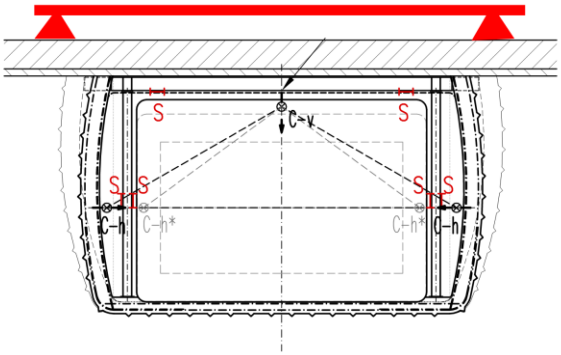


Figure 8: Temporary bridge above working area.

The self-weight of the Boulevard tunnel is mostly carried by the outer wall and the middle pillar between track no. 1 and no. 2.

Main site layout includes grouting plant, agitators, cement silos, disposal collection tanks or basin, workshops, generators, site offices, locker facilities and changing rooms. Mobile equipment consists of a crawler tunnel drilling rig with excavator for handling of the drill rods and the specialized shaft drill rig. For the set-up and dismantling of the site installations a mobile crane or equivalent was needed.

2.2 Freezing system

The following steps had to be executed successfully before switching on the freezing machinery:

1. Drilling of the freezing pipes and the pipes for the temperature monitoring
2. Pressure tests of the freezing pipes
3. Installation of the inner pipe inside the freezing pipes and the pipe heads as well as connection of the pipes with the machinery. The freezing pipes were connected together in groups of approx. 5 pipes.
4. Filling of the brine circuit
5. Start of the temperature monitoring system
6. Start of the freezing process.

Preparations:
First the formation level for the drilling rig was prepared. The starting points of the bore holes and the direction were set out by a surveyor. Secondly the boreholes were

marked out according to the layout specified on the drawings.

Pressure test:
Before starting, the freezing pipes were tested with a pressure test to ensure that no loss of brine would occur. Therefore the pipes were filled completely with water. The pressure for the test was around 10 bar. The system was considered to be pressure-tight, if there were no loss of pressure after 15 min.

Installation:
For the installation of the freeze tubes horizontal boreholes with the length of up to approx. 35m were drilled. The freezing pipes were connected together in groups of approx. 5 pipes. In general, the boreholes were drilled as rotary drilling with casing as drill rod and lost drill bit. The diameter of the casing was outer/inner 114 mm/94 mm. The drill bit was fixed on the casing and was disconnected with the installation of the freeze pipe. Disconnection was initiated by pushing the freeze pipe against a special device, connected with the drill bit. After disconnection of the bit it remained in the bore hole and the casing was pulled back. During the freezing activity the ingoing temperature and the outgoing temperature of every group was metered in the brine itself. In addition the main stream temperatures (ingoing and outgoing), the volume flow rate and the brine pressure were measured and recorded continuously.

Temperature monitoring:
For the temperature monitoring beside the freezing pipes additional pipes were drilled. Inside the pipes temperature sensors in the form of chains were installed. The exact position of the pipes was surveyed to determine the right distance to the freeze body. The sensor chains were connected to the central server. The measurement was continuously and online from the beginning of the freezing activity until the shutdown of the freezing plant. A few days before start-up initial measurements were carried out to verify the initial groundwater temperature.

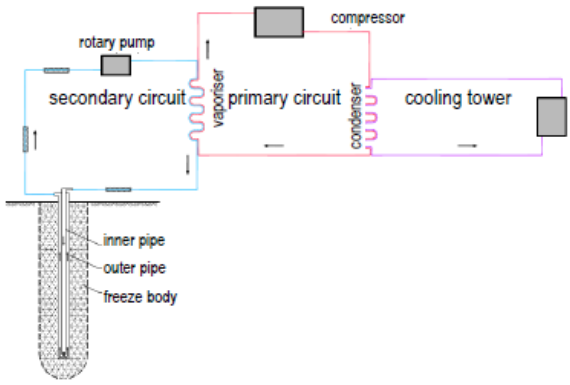


Figure 9: Freezing system

Cool Brine ($CaCl_2$ dissolved in water) was the freezing agent, which extracts the heat of the soil by the freezing pipes which distribute the cooling energy inside it. As a result of this permanent extraction of heat, the groundwater freezes and later on the freeze body is conserved during the works. The brine circulates in a closed system (secondary circuit). In the primary cooling circuit Ammonia (NH_3) is the used inside the mobile freezing plant, see figure 9.

The freezing pipes consist of two pipes laying one inside the other. They are both connected with the freezing plant by isolated flexible pipes. The brine passes through the inner pipe and returns to the plant through the outer pipe.

The drilling was executed in steps together with the excavation of the deep pits. In general drillings were carried out in the shafts with a small specialized drill rig. The upper holes above the groundwater level (from level +5.0m and from level +2.8m) were drilled with the crawler rig Huette 505, wherever possible. Therefore the rig was lifted into the pits and the walls between deep pits and the middle pit were removed.

Most of the grout holes were drilled from excavation level +5.0m. A crawler drill rig carried out the TAM-grouting. The rest of the grout holes could not be reached from level +5.0 m and were drilled after freezing. The work was carried out by a smaller shaft rig.

3 TAM-GROUTING

Grouting was needed because of the insufficient ground water content in the soil and used for pore filling to increase the saturation level of the soil (groundwater accumulation). TAM-Grouting was only needed beyond the upper part of the freezing profile. Tube á manchettes, TAM-grouting, was carried out horizontally from the deep pits and was typically drilled and grouted before drilling of the freeze holes.

For the installation of the TAM-pipes, horizontal or horizontally inclined boreholes with a length between 5.5 m and 22.5m were drilled. In general, the boreholes are drilled with drill tubes of 114.3 mm diameter and lost drill bit.

General procedure for drilling and installation of the TAM-pipes:

1. Setting out the starting points for the bore holes
2. Core drilling through the secant pile wall
3. Establishing the drill rig on the starting point of the bore hole
4. Cased drilling with lost drill bit, casing diameter 114.3 mm
5. Installation of the TAM-pipe
6. Extracting the casing, drill bit remains in the bore hole
7. Closing annulus between bore pile and TAM-pipe with cement
8. Filling the annulus between the bore hole and the TAM-pipe with sleeve grout.

Requirements of the first grouting sleeve were set with W/C value 3.0 pump rate 5-8 l /min. Grouting pressure 3-10 bar. Max 200 l or 10 bar. Requirements of the second grouting were set with W/C value 3.0 pump rate 3-5 l /min. Grouting pressure 3-10 bar. Max 100 l or 10 bar.

3.1 Tunnel work and freezing



Figure 10: 2 deep pits

NATM tunnelling started from the big deep pit (Figure 10 & 11) when the soil freezing had gained enough strength. The frozen soil mass was designed to carry the load from the groundwater pressure and excavation was conducted in steps. A primary lining in form of shotcrete was installed to create a temporary load-bearing ring. After approximately 12m of excavation in a slope of about 28°, the tunnel runs horizontal and after further approximately 15m of tunnelling, the new pedestrian tunnel connects to the existing pedestrian tunnel under the Boulevard tunnel.

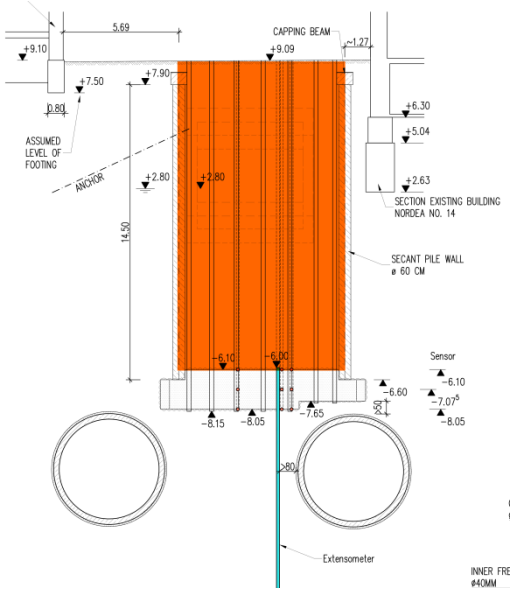


Figure 11: The largest deep pit

The excavation was carried out using a special tunnel excavator (see Figure 12).

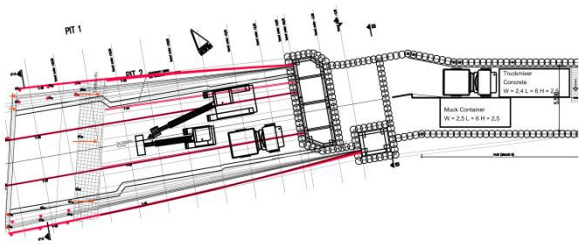


Figure 12: Works in the slope of the tunnel with tunnel excavators



Figure 13: The slope of the new tunnel

The following figure 14 shows possible locations for the sensor chains and the single measurement points. The exact position of the sensor chains and the single measurement points was fixed on site in collaboration with the site management. They were fixed based on the actual position of the freezing pipes and the geometrical situation of the existing structures.

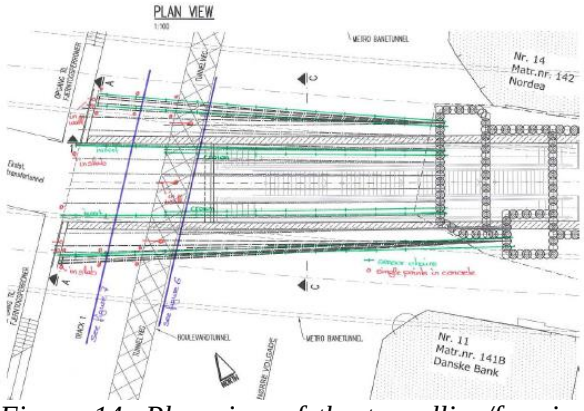


Figure 14: Plan view of the tunnelling/freezing segment with monitoring installations

Beside the freezing pipes additional pipes were drilled for the temperature monitoring. Inside these pipes sensor chains were installed. The sensor pipes were located at the top, the middle and the bottom of the planned freezing slab. The measurements itself were done continuously and online from the beginning of the freezing activity until the shutdown of the freezing plant. The online monitoring system gives several data about the freezing plant (brine temperature, brine pressure, power), the brine in the freezing pipes and the temperatures from the temperature sensors of the chains.
The temperature monitoring gives the real temperatures in the freezing slab, which are decisive for starting the pumping of the water inside the pit and the excavation activity.
The following sketches show the locations for the sensor chains. An example of temperature measuring in the freezing profile is shown on figure 15 and only the measuring point close to the warm transfer tunnel is minimally exceeded compared to the limit.

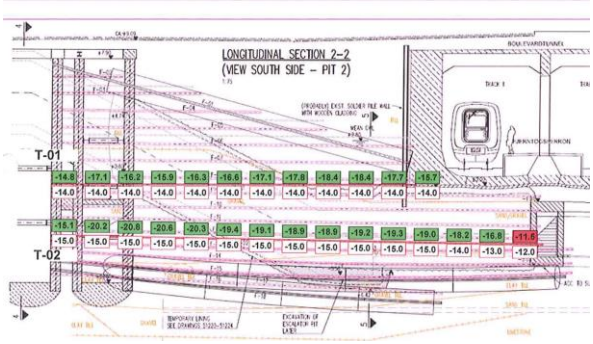


Figure 15: Example of temperature measuring

Figure 16 shows the layout of the freezing pipes and the freezing slab of the deep pit in its vertical expansion.



Figure 16: Layout of vertical freezing pipes in deep pits

In the deep pits vertical freezing was carried out with in situ freezing in the bottom. The freezing slab lies mostly between -6.1m DVR and -7.6m DVR (see Figures 6 & 16). The top of the metro tunnel is at around -8.2m DVR. The normal soil temperature was

assumed to be +12°C. Inside the metro tunnel the temperature is surely higher because of the operating trains. The average temperature inside the freezing slab was -10°C. Based on the short distance between freezing slab and metro tunnel there was interference between them. To ensure the low temperatures inside the freezing slab, the freezing pipe distances above the metro tunnels were decreased.

The design calculations are carried out for single freezing columns. The figures of the slab layout (Figure 17) show various radiuses of the freezing columns. The minimum radius leaves little space in between the columns. The maximum radius results from the maximum pipe distances, but produces overlapping of the single columns. It can be assumed that there is an influence of the neighbouring freezing pipes. The freezing time was calculated to about 3-4 weeks depending on the freezing columns being small or large. But because of the water flow close to the new tunnel, the freezing time was extended.

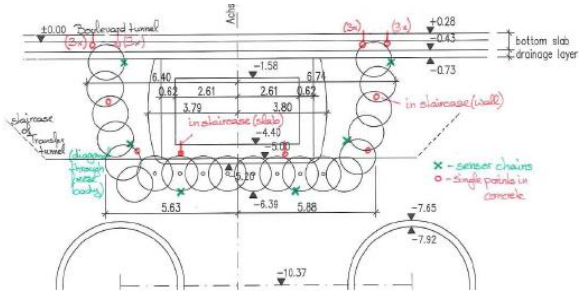


Figure 17: Monitoring installations in section below Boulevard tunnel

4 MONITORING

In addition to the sensor chains, single measuring points were planned to be installed from inside of the Boulevard tunnel to ensure the connection of the freeze body with the existing structure, the measuring points were located inside small boreholes in the base slab and the walls of the Boulevard tunnel and in the staircase conducting to the existing transfer tunnel. Furthermore, measuring points were on buildings, metro tunnel, on the surface of the street etc. The total system included automatic TCA measurements in the metro tunnel, hydrostatic levelling system in the station, vertical inclinometer in the secant piles, piezometer different places, data loggers, noise and vibration measurement system, etc.

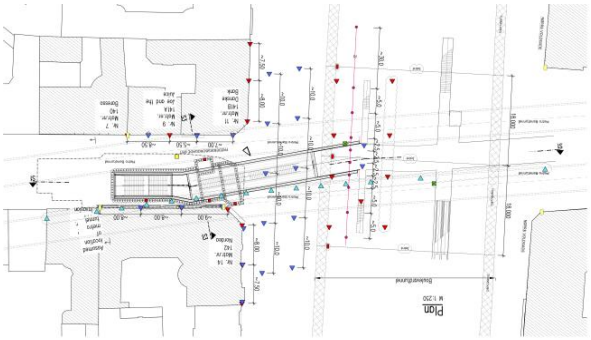


Figure 18: Monitoring plan

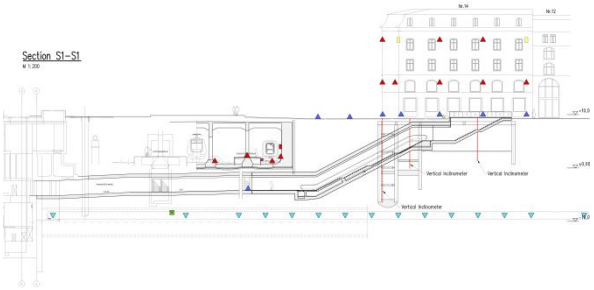


Figure 19: Monitoring

Before any kind of work was carried out reference measurements were made. Furthermore, some limit values for the deformations of the tunnels had been described. Each month a report was made and it described in detail the deformations hour for hour through the whole working period. Figure 18 & 19 show the monitoring set-up.

On the basis of the calculations and the deformations an alarm and emergency procedures were set up.

5 EXPERIENCE FROM SITE

The freezing profile led to vertical deformation in the temporary stages.

- In the paved area on top of the Boulevard tunnel the maximum vertical deformation was almost in line with expectations, but the main part disappeared when the freezing system was shut down (se figure 20)
- The 100 years old Boulevard tunnel had a vertical deformation, which was more than the limit value – this was difficult to

comply with. The freezing system was shut down from time to time to prevent an increasing deformation. Unfortunately, the new tunnel was just underneath an expansion joint in the Boulevard tunnel wall; if this had not been the case the vertical deformation would have been smaller.

- The metro tunnel had a deformation limit at 4 mm and the maximum measured deformation was 3 mm.

In the final design the deformation from the temporary stages was incorporated in the level of the permanent structure. Deformation from the temporary stages should not be a problem in the future for the Boulevard tunnel, metro tunnel, the street level and neighboring buildings.



Figure 20: Pedestrian street just above the tunnel



Figure 21: Freezing pipes at the starting point

The tolerance of freezing work/drilling of the freezing pipes on site was 0.5 m radius. The spacing of two freezing pipes is 0.50 m, at the starting point and it was not possible to reduce the spacing at the starting point in the secant piles (see figure 21). If the spacing between two pipes in the soil was more than 1m the duration of freezing have to be exceeds. To ensure the tolerance every drilling was measured and the result was integrated into an as-built 3D-drawing as shown in figure 22. Every drilling was drilled with high precision.

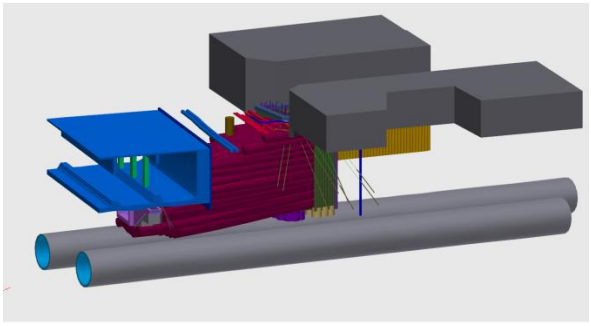


Figure 22: 3D model, as-built of freezing pipes (shown in red)

The vertical freezing pipes had to be very close to the secant pile wall (see figure 23). Therefore, the pit layout including the capping beam had to be designed such that all stages of the construction pit were possible. Furthermore, there had to be enough room for the drilling machine to work, even though the pit was narrow in the deep part. The drilling rig distance to propping systems had to be about 30-40 cm; otherwise it was very difficult to carry out the drilling work.



Figure 23: Vertical freezing pipes close to secant piles

Two dewatering pipes were installed inside the frozen profile. Valves and parker had to be installed at the starting points to avoid inflowing material. In the early stages, the dewatering pipes were a help for indicating watertightness of the frozen profile.

The freezing volume was difficult to control. Some parts of the future tunnel section were frozen and therefore the excavation was difficult to carry out.

Even though the TAM-grouting and the freezing profile combined should be watertight some leakage was observed. The local water flow was beyond the limit (approx. 40 l/hour). The water flow was stopped by local grout drilling as the excavation was carried out.

6 ACKNOWLEDGEMENTS

The Author is grateful for the permission by the Client, Banedanmark, Amerika Plads 15, 2100 Ø. Copenhagen and the Final Owner Metroselskabet, Metrovej 3, 2300 S. Copenhagen, to publish this paper.

Mechanical weathering effect on tailings

Juan M. Rodriguez
Luleå University of Technology, Sweden, juan.rodriguez@ltu.se
University of Sonora, Mexico, juanrguez@dicym.uson.mx

Tommy Edeskär
Luleå University of Technology, Sweden

Sven Knutsson
Luleå University of Technology, Sweden

ABSTRACT
Over the last century the tailing volume generation has grown dramatically due to the mineral demand. Nowadays the mining industry is producing every year millions of tons of tailings. The storage of the tailings has become a challenge due to the increased storage capacity demanded. Physical risk associated to the tailings dams is the stability itself since tailing dams are considered a walk-away solution. Physical changes as breakage and shape occur to the tailing particles affecting the stability of the fills by reduced strength properties. In order to understand the reduction and shape changes of tailing particles degradation test by milling attrition (erosion) and image analysis was conducted. Uniform fractions 1-0.5, 0.5-025, 0.25-0.125 and 0.125-0.063mm were used.
Results have shown that attrition agents e.g. ball attrition can increase the physical erosion but also change the shape of the particles compared with autogenous attrition. However particles shape has become more regular (less elongated) and rounded in coarse fractions 1-0.5 and 0.5-0.25mm while smaller fractions 0.25-0.125 and 0.125-0.063mm seems to have opposite behavior. Comparison with previous milling studies show consistent differences probably due to the breakage of the particles was the objective. In perspective if tailings become more rounded the strength could be compromised. More studies are needed to verify this.

Keywords: Particle shape, particle size, attrition, tailings.

1 INTRODUCTION

Tailings are the mining industry leftovers, for its storage tailing dams are constructed. In the history of the mineral extraction tailings dam incidents has occurred e.g. Val di Stava tailings dam (1985) in Italy and Cananea tailings dam (2014) in Mexico.
As a consequence of the operation and raising procedures of tailings dams, the conditions in the tailings dams could be considered to be dynamic in a longer perspective. Grain size distribution, formation of layers, pore pressures and stress states are continuously changing during the operation (Ormann, et al., 2013).

In general particle degradation occurs due the environmental factors as chemical reactions (Kossoff, et al., 2012) and mechanical factors as stresses generated due the load and creep (Valdes & Koprulu, 2007). Tailings are also affected in the same way.
Mechanical behaviors of granular materials are affected by characteristics as particle size (Islam, et al., 2011), particle shape (Santamarina & Cho, 2004), size distribution (Cabalar, 2011), mineralogy (Clayton, et al., 2004) among others. Erosion changes all physical characteristics thus, its strength and behavior changes through the time.
Tailing dams need to be built with environmental and structural safety. They must stand for long periods in a long time

perspective, even after mining reclamation. To ensure the structural safety not only actual soil characteristics must be taken in consideration but also further changes.

Laboratory mill attrition by uniform sized particles was performed in this study to determine the size and shape changes. Shape according to Cho, et al. (2006) influence the strength of the materials and, from this point of view if particles become more rounded with the pass of time due to mechanical wearing the stability could be compromised.

Results have shown that ball attrition is more effective to erode the tailing particles, ball attrition produce more size reduction (as it was expected) and more shape changes. Results in this study also indicate that coarse fraction 0.5 and 0.25mm become more rounded but smaller sizes are more angular. The effect of the size reduction as the contradictory shape changes effects should be studied in in detail in further research. The statistical methods Mann-Withney test and two sample t-test used to determine shape differences have 96% of agreement, furthermore there is no skew evidence over the results on any of the methods. Thus, it is possible to use two samples t-test for the study of the tailings.

2 THE PARTICLE SHAPE

In this study the word *shape* is used to describe a grain's overall geometry. Furthermore, in order to describe the particle shape in more detail, there are a number of terms, quantities and definitions used in the literature. Some authors (Mitchell and Soga, 2005 and Arasan, et al., 2010) are using three sub-quantities describing the shape but at different scales. The sub-quantities are *morphology/form*, *roundness* and *surface texture*. In Figure 1 it is shown how the scale terms are defined.

At large scale a particle's diameters in different directions are considered. At this scale, describing terms as *spherical*, *circular*, *platy*, *elongated* etc., are used. An often seen quantity for shape description at large scale is *sphericity*. Graphically the considered type of shape is marked with the dashed line in Figure 1. At intermediate scale is focused on description of the presence of irregularities. Depending on at what scale an analysis is done; corners and edges of different sizes are identified. By doing analysis inside circles defined along the particle's boundary, deviations are found and valuated. The mentioned circles are shown in Figure 1**Error! Reference source not found.**; a generally accepted quantity for this scale is *roundness* or the antonym: *angularity*. Regarding the smallest scale, terms like *rough* or *smooth* are used. The descriptor is considering the same kind of analysis as the one described above, but is applied within smaller circles, i.e. at a smaller scale. *Surface texture* is often used to name the actual quantity.

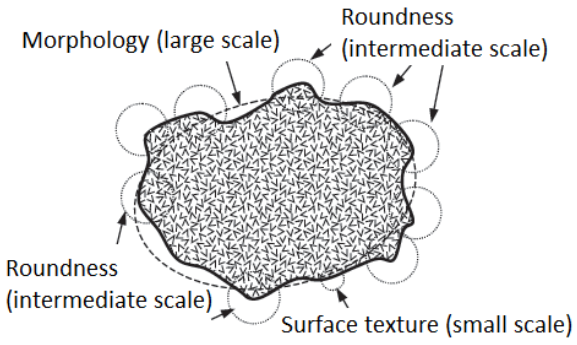


Figure 1 Particle describing the shape scale attributes (Mitchell and Soga, 2005).

3 METHODOLOGY

In this study samples from the Aitik mine has been used. The Aitik tailing dam is located about 100 km North of the Arctic Circle in the boreal parts of Northern Sweden about 15 km from the community of Gällivare. The value mineral is chalcopyrite ($CuFeS^2$). Main sulphides are pyrite, chalcopyrite and sphalerite. Main gangue minerals are quartz, feldspar, plagioclase and mica (Lindvall, M. and Eriksson, N., 2003).

Four range sizes were used in the actual research (see Table 1). Further on the lower size in the range will be used for convenience. Wet sieving was used with Sodium Diphosphate decahydratate ($Na_4P_2O_7 \cdot H_2O$) as a dispersant to enhance the particle separation. After sieving specimens were dried for 24 hours at 105°C.

Smooth steel drum mill with 115mm in diameter and 132mm in length over a rolling

table was used to generate a gentle and a constant flow of tailings material over a constantly rebuilding slope. Speed of 60 rpm (revolutions per minute) was used to ensure a gentle rolling of the particles down the slope and procure the attrition/wearing/abrasion of particles. Speeds close to the terminal velocity were avoided due to it could breakage the particles.

Table 1 Test specimens and particle size ranges

Specimen	Range (mm)
0.5_x	1-0.5
0.25_x	0.5-0.25
0.125_x	0.25-0.125
0.063_x	0.125-0.063

The tests were configured in two different forms the first was using balls to speed up the attrition of the tailing particles and the second was autogenous attrition (no balls). The subscript "*x*" in Table 1 represents the autogenous attrition (absence of balls) for "*a*" and the use of balls for "*b*". A total of 200 gr of tailings were used during each batch with 1000 ml of water. For ball attrition 100 grams of 7 millimeters in diameter steel balls were included.

Degradation was conducted for 2 and/or 3 time periods; for balls attrition time periods was approximately of 2, 6 and 24 hrs., and for autogenous attrition time period consisted of 24, 72 and 120 hrs. Time periods were set after some trial tests to identify the amount of material broken and to avoid running out of material specially when using steel balls. Material broken (in percentage weight) was identified sieving the sample after the test. Total amount of tests and more detailed data can be seen in Table 3.

Particle shape was measured using eleven shape descriptors or quantities (Table 2) through two dimensional image analysis. Graphical description of the quantities can be found in the appendix. Shape change was statistically identified using Mann-Whitney Test (Moses, 2014) and Two-Sample t-test (Snedecor & Cochran, 1989) with 5% significance level. Since the data distribution is not all the time normal it was decided to use the two mentioned statistical tests, the non-parametric test Mann-Whitney test applies for unknown and skew distributions while two samples t-test determine differences when the data is normally distributed.

Sub-quantities were classified according with the authors (Rodriguez, 2012); form is recognized by the "#" and roundness by "+"symbols in Table 2.

Table 2 Quantities use to determine the particle shape

Quantity	Description	Working range	Reference
1	+4πArea/Perimeter^2	0-1	(Cox, 1927)
2	#4Area/¶Major axis^2	0-1	(ImageJ, 2013)
3	+Area/Convex Area	0-1	(Mora & Kwan, 2000)
4	+Fractal dimension	1-2	(Image Pro Plus v. 7.0, 2011)
5	#Square root of Maximum inscribed/Minimum circumscribed, circle diameters	0-1	(Riley, 1941)
6	#Diameter of a circle same area as particle/Minimum circumscribed circle diameter	0-1	(Wadell, 1935)
7	#Perimeter^2/Area *	0-1/4Pi	(Blott & Pye, 2008)
8	#Perimeter of a circle with same area/Perimeter	0-1	(Wadell, 1935)
9	#Area/Area of the minimum circumscribed circle	0-1	(Tickell, 1938)
10	+Perimeter/Convex perimeter *	0-1	(Janoo, 1998))
11	+πAverage Feret/Perimeter	0-1	(Image Pro Plus v. 7.0, 2011)

*Inverse was used to obtain a working range between 0 and 1
Quantity describing the large scale shape descriptor "form"
+Quantity describing the intermediate scale shape descriptor "roundness"

4 RESULTS

Table 3 is showing the result of each individual test arranged by sample, milling time and percentage of fines produced. Fine production percentage was measured in relation to the initial sample weight and the original sieve size. Figure 2 summarizes the results from the tests. Dashed lines are those tests that contains iron balls as degradation agent while continues lines are samples in autogenous attrition. The use of balls as an attrition material speed up the degradation process of the tailings (size change) and it is evident when comparing the general slope of dashed and continues lines (balls and autogenous grinding).

Relative shape change results are shown in Figure 3, gray colored markers and lines shows when most of the shape descriptors or quantities values have changed. Figure 3 left (ball attrition) illustrate that there is a general shape change during all steps for sizes 0.5 and 0.25mm (except last step for 0.25mm).

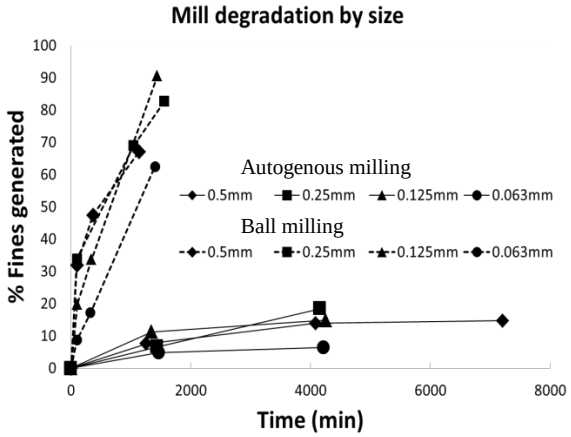


Figure 2 Fines generation in mill test Dashed lines are those tests that contains iron balls as degradation agent while continues lines are samples in autogenous attrition.

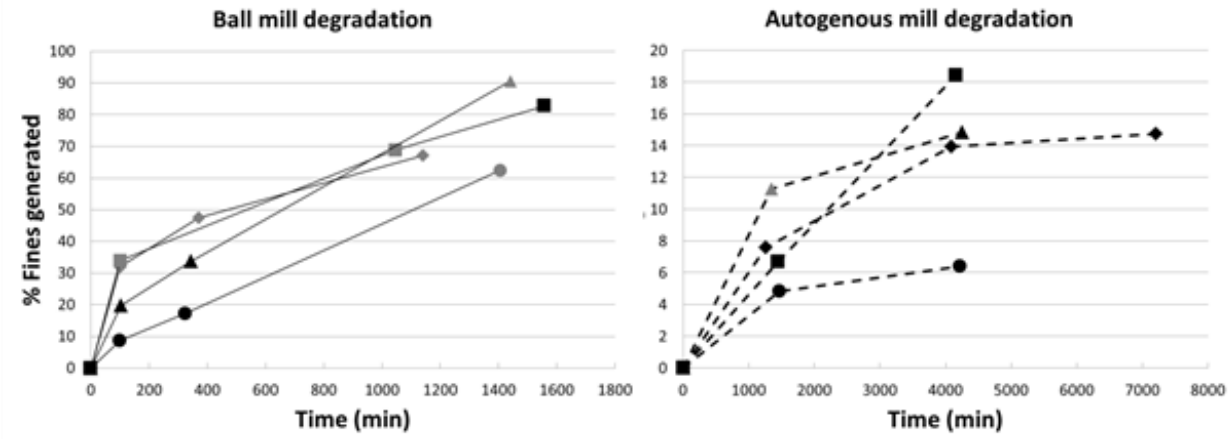


Figure 3 Degradation and shape change by milling agent. Gray leyends indicate shape change. Left ball milling. Right autogenous milling (Fraction sizes are represented by the lower limit)

Table 3 Rolling time periods and percentage of material undergoing the size range (fines generation)

Sample	Time period (min)	% fines generated	Sample	Time period (min)	% fines generated
0.5_a	1260	7.6	0.5_b	100	32.0
	4085	13.9		370	47.5
	7207	14.7		1140	67.2
0.25_a	1442	6.7	0.25_b	100	33.9
	4158	18.4		1046	69.0
				1558	82.8
0.125_a	1344	11.3	0.125_b	103	19.8
	4252	14.8		343	33.7
				1441	90.6
0.063_a	1470	4.8	0.063_b	100	8.7
	4222	6.4		324	17.2
				1406	62.5

Subscripts: *a* for autogenous and *b* for balls attrition

Smaller sizes 0.125 and 0.063mm only show shape change in the last step. From Figure 3 right (autogenous attrition) only 0.125mm size has shown shape change.

In same Figure 3 there is a rapid step increase in the broken percentage in all first step time tests. Particles seem to break more rapidly during the first minutes of the tests (see the initial slope in Figure 3 right and left).

Relative shape changes by time step and quantity are shown in Table 4 represented by a gray shadow. When "↓" appears the particle becomes more elongated or angular otherwise they are more regular in form and rounded. Quantities mean values before and after the time step attrition are presented.

Table 4 Relative shape change time-step, data represent the mean value. Shape change is highligthed by a gray shadow when particles become more regular in form or rounded; the appearace of "↓" means the opposite shape change.

		Balls						Autogenous					
S	**Q**	**2hr**		**6hr**		**24hr**		**24hr**		**72hr**		**120hr**	
A	+1	0.665	0.681	0.681	0.702	0.702	0.732	0.665	0.668	0.668	0.673	0.673	0.672
	#2	0.728	0.742	0.742	0.735	0.735	0.760	0.728	0.743	0.743	0.741	0.741	0.748
	+3	0.924	0.935	0.935	0.943	0.943	0.951	0.924	0.932	0.932	0.932	0.932	0.931
	+4	1.041	1.031	1.031	1.025	1.025	1.022	1.041	1.033	1.033	1.032	1.032	1.031
	#5	0.787	0.802	.0802	0.803	0.803	0.819	0.787	0.796	0.796	0.796	0.796	0.801
	#6	0.786	0.800	0.800	0.799	0.799	0.818	0.786	0.792	0.792	0.792	0.792	0.798
	#7	0.126	0.161	0.161	0.160	0.160	0.160	0.126	0.159	0.159	0.153↓	0.153	0.159
	#8	0.847	0.856	0.856	0.873	0.873	0.887	0.847	0.852	0.852	0.855	0.855	0.851
	#9	0.620	0.642	0.642	0.641	0.641	0.672	0.620	0.631	0.631	0.631	0.631	0.640
	+10	0.929	0.930	0.930	0.946	0.946	0.949	0.929	0.931	0.931	0.933	0.933	0.927↓
	+11	0.296	0.296	0.296	0.301	0.301	0.303	0.296	0.297	0.297	0.297	0.297	0.295↓
B	+1	0.676	0.705	0.705	0.745	0.745	0.746	0.676	0.687	0.687	0.689		
	#2	0.710	0.748	0.748	0.740	0.740	0.771	0.710	0.728	0.728	0.730		
	+3	0.922	0.932	0.932	0.949	0.949	0.948	0.923	0.924	0.924	0.928		
	+4	1.045	1.041	1.041	1.033	1.033	1.033	1.047	1.042	1.042	1.042		
	#5	0.779	0.800	0.800	0.812	0.812	0.822	0.779	0.789	0.789	0.794		
	#6	0.780	0.798	0.798	0.810	0.810	0.823	0.780	0.787	0.787	0.790		
	#7	0.079	0.079	0.079	0.082	0.082	0.082	0.079	0.082	0.082	0.080		
	#8	0.852	0.872	0.872	0.900	0.900	0.902	0.852	0.858	0.858	0.862		
	#9	0.612	0.640	0.640	0.659	0.659	0.680	0.612	0.624	0.624	0.629		
	+10	0.937	0.947	0.947	0.964	0.964	0.963	0.937	0.940	0.940	0.940		
	+11	0.299	0.302	0.302	0.307	0.307	0.307	0.299	0.300	0.300	0.300		
C	+1	0.700	0.703	0.703	0.702	0.702	0.643↓	0.700	0.684↓	0.684	0.696		
	#2	0.706	0.713	0.713	0.710	0.710	0.689	0.706	0.708	0.708	0.719		
	+3	0.936	0.935	0.935	0.939	0.939	0.919↓	0.936	0.926↓	0.926	0.934		
	+4	1.034	1.032	1.032	1.031	1.031	1.038↓	1.034	1.032	1.032	1.032		
	#5	0.784	0.785	0.785	0.787	0.787	0.769↓	0.784	0.778	0.778	0.789		
	#6	0.780	0.784	0.784	0.784	0.784	0.769↓	0.780	0.777	0.777	0.788		
	#7	0.038	0.040	0.040	0.040	0.040	0.039	0.038	0.046	0.046	0.044		
	#8	0.878	0.877	0.877	0.878	0.878	0.843↓	0878	0.865↓	0.865	0.872		

	#9	0.614	0.619	0.619	0.620	0.620	0.597↓	0.614	0.610	0.610	0.625
	+10	0.961	0.960	0.960	0.960	0.960	0.936↓	0.961	0.953↓	0.953	0.953
	+11	0.307	0.306	0.306	0.306	0.306	0.298↓	0.307	0.304↓	0.304	0.304
D	+1	0.700	0.702	0.702	0.713	0.713	0.690↓	0.698	0.713	0.713	0.713
	#2	0.685	0.684	0.684	0.714	0.714	0.688	0.685	0.692	0.692	0.693
	+3	0.931	0.933	0.933	0.937	0.937	0.925↓	0.931	0.939	0.939	0.936
	+4	1.051	1.051	1.051	1.053	1.053	1.061↓	1.051	1.051	1.050	1.050
	#5	0.772	0.773	0.773	0.786	0.786	0.769↓	0.772	0.777	0.777	0.781
	#6	0.768	0.771	0.771	0.782	0.782	0.766↓	0.768	0.772	0.772	0.778
	#7	0.024	0.023	0.023	0.022↓	0.022	0.018↓	0.024	0.023	0.023	0.024
	#8	0.875	0.876	0.876	0.885	0.885	0.869↓	0.875	0.885	0.885	0.883
	#9	0.596	0.600	0.600	0.616	0.616	0.593↓	0.596	0.602	0.602	0.609
	+10	0.964	0.965	0.965	0.967	0.967	0.959↓	0.964	0.971	0.971	0.967↓
	+11	0.308	0.308	0.308	0.309	0.309	0.306↓	0.307	0.310	0.309	0.308↓

S=Sample size,Q=Quantity number, ↓=less regular in form, less rounded

Table 5 Shape change compared with initial state. Mann-Withney and Two-sample t-tests comparison. Shape change is highligthed by a gray shadow when particles become more regular in form or rounded; the appearace of "↓" means the opposite shape change.

		Balls						**Autogenous**					
		2hr		**6hr**		**24hr**		**24hr**		**72hr**		**120hr**	
Size	**Q**	**MW**	**Tt**	**MW**	**Tt**	**MW**	**Tt**	**MW**	**Tt**	**MW**	**Tt**	**MW**	**Tt**
A	+1												
	#2												
	+3												
	+4												
	#5												
	#6												
	#7												
	#8												
	#9												
	+10												
	+11												
B	+1												
	#2												
	+3												
	+4												
	#5												
	#6												
	#7												
	#8												
	#9												
	+10												
	+11												
C	+1						↓		↓				
	#2												
	+3						↓		↓				
	+4						↓						
	#5						↓						
	#6												
	#7												
	#8						↓		↓				
	#9												
	+10						↓		↓		↓		
	+11						↓		↓		↓		
D	+1												
	#2												
	+3						↓						
	+4						↓						
	#5												
	#6												

#7				↓		↓				
#8										
#9										
+10						↓				
+11						↓				

Q=Quantity number; MW=Mann-Withney test, Tt=Two samples t-test

Table 4 shows that tailing particles subject to ball attrition in sizes 0.5 and 0.25 mm in general become more rounded and regular in form as the time-step evolves while for particle sizes 0.125 and 0.063 mm practically no change is seen until last time-step where increase in angularity and irregularity in form is perceived.

For autogenous attrition time-step changes are not recognized in the majority of the quantities (as in ball attrition) for coarse sizes 0.5 and 0.25 mm, however fine fraction 0.125 and 0.063mm present changes in the first time-step with special remark on size 0.125mm that became more angular and irregular in form. Table 5 is showing the shape change with respect to the initial state of the particles. In this table gray cells identify the shape change with respect to the original shape. Mann-Whitney Test (Moses, 2014) and Two-Sample t-Test (Snedecor & Cochran, 1989) are located together to evaluate differences, practically results agree in both tests.

5 DISCUSSION

Mill attrition test were performed for different fraction sizes (Table 1) during different time periods (Table 3). Attrition degradation was identified by sieving (fines generation) and particles shape change by image analysis.

Tailing particles images were also subject to visual inspection and tailings had been classified as very angular to sub angular material base on Powers (1953) comparison chart The results of this classification is in agreement with the conclusion of the general shape of tailings made by e.g. Garga, et al. (1984).Visual inspection of the original material (splitted by size) in the soil containers detects particle breakage; particles are weak enough to be eroded during the handling and sample preparation. This could affect the results since an already broken portion of material could be introduced in the mill. Lade, et al. (1996) suggest that angular particles are very susceptible to break even at low stresses because they concentrate in the angular contact points. Furthermore the particle breakage is also a function of time even under constant stresses (Yamamuro & Lade, 1993). That could explain why sample 0.25mm in figure 3 (left) shows an outstanding breakage at the end point (around 4000 minutes of the running test). It is also shown that particles are broken at higher rate in the initial step.

During this study two statistical methods were used, Mann-Withney test and two sample t-test. Mann-Withney test is applicable to skew distribution where the normality test is not recognized. Two samples t-test is used when the normality distribution of the data is accomplished. Data in the study was detected to be in some cases normal distributed and a comparison of results among these methodologies is of interest (see Table 5). Even if the distribution of the data is not normal results has shown that there is a 96% of coincidence between the two statistical methods. Furthermore the shape change detection is not skew to one of the methods or in a specific quantity. Two samples t-test could be used to determine differences in shape since there is no evidence that the skew distribution of the data affect the results.

Quantities Table 2 are identified as a form or roundness descriptor as Mitchell and Soga (2005) sub-quantities classification (according to authors). The classification is not showing any relation with the attrition results, shape changes are seems not to be related with the shape sub-quantities classification (Figure 1). Choose of the best quantity or shape descriptor is of interest and attempts can be found in literature (Bouwman, et al., 2004) Even if there are some standards e.g. ASTM D3398, D4751 they are only there to avoid unfavorable

shape (e.g. elongated particles) but still there is no general agreement on which shape descriptor, or descriptors, should be considered universally. In the scientific literature some quantities appear more than others e.g. Wadell (1932) comparison chart (recently computerized by Zheng & Hryciw, 2015), aspect ratio (Hawkins, 1993), circularity (Cox, 1927) among others.

Soil strength is shape dependent as Santamarina & Cho (2004) conclude, in perspective the gain in angularity for the smaller fractions (0.125 and 0.063mm) could increase the soil strength but reduce it in the coarser fractions. Any way it is unknown on which size has the major influence thus, more studies should be necessary.

Ulusoy (2008) study shows that ball milling produces more angular and irregular particles opposite of what this study concluded. Furthermore his quantity values were always lower indicating that produced particles are more angular and irregular in form compared with this research. There are two main differences that could affect the results; the mineralogy and the milling process itself. Talk mineral was used by Ulusoy (2008); talk has the lower value in the Mohr hardness scale. The Ulusoy (2008) milling intention was to break the particles while this study the attrition was the objective; it is known that the final shape of the particles is considered to be the result of several factors among them the rigor of the transport (Wentworth, 1922).

6 CONCLUSIONS

Breakage occurs in all states even in sample deposits (bags, trays)

Particles with ball attrition eventually change their initial shape to be more rounded/circular in sizes 0.5 and 0.25mm but fine particles 0.125 and 0.063mm come back to be angular/irregular.

Attrition is more intensive when erosional agents as iron balls are included.

It is possible to use any of the statistical methods Two samples t-test or Man-Withney since there is practically no difference in the results.

There is no skewed shape change difference in between the sub-quantities morphology and roundness.

7 REFERENCES

Arasan, S., Hasiloglu, A. S. & Akbulut, S. (2010). Shape particle of natural and crushed aggregate using image analysis. International Journal of Civil and Structural Engineering, 1(2), pp. 221-233.

Blott, S. & Pye, K. (2008) Particle shape: a review and new methods of characterization and classification. Sedimentology 55, 31-63.

Bouwman, A. M., Bosma, Jaap C.; Vonk, Pieter, Wesselingh, J (Hans) A. & Frijlink, Henderik W. (2004). Which shape factor(s) best describe granules?. Powder Technology, Volume 146, pp. 66-72.

Cabalar, A. F. (2011). The effects of fines on the behaviour of a sand mixture. Geotech. Geolog. Eng. 29, 91-100.

Cho, G., Dodds, J. & Santamarina, J., (2006). Particle shape effects on packing density, stiffness and strength: Natural and crushed sands. Journal of geotechnical and geoenvironmental engineering, 132(5), pp. 591-602.

Clayton, C., Theron, M. & Vermeulen, N. (2004). The effect of particle shape on the bahaviour of gold tailings. London, Advances in Geotechnical Engineering: The Skepton Conference, Thomas Telford.

Cox, E. P. (1927). A method of assigning numerical and percentage values to the degree of roundness of sand grains. 1(3), pp. 179-183.

Garga, V., ASCE, M. & McKay, L. (1984). Cyclic triaxial strength of tailings. Journal of Geotechnical Engineering, 110(8), pp. 1091-1105.

Hawkins, A. (1993). The shape of powder-particle outlines. New York: Wiley.

Image Pro Plus v. 7.0, 2011. http://www.mediacy.com/. [Online].

ImageJ, 1., 2013. version 1.47v. Wayn Rasband, National Institutes of Health, USA.. [Online] Available at: http://imagej.nih.gov/ij/

Islam, M., Hossain, M., Rahman, A. & Asad, M. (2011). Effect of particle size on the shear strength behaviour of sands. Australian Geomechanics, 46(3), pp. 75-85.

Janoo, V. C. (1998). Quantification of shape, angularity, and surface texture of base course materials. Cold Region Research and Engineering Laboratory. US Army Corps of Engineers. Special report 98-1.

Kossoff, D., Hudson-Eduards, K.A.; Dubbin, W.E., Alfredsson, M. & Geraki, T. (2012). Cycling of As, P, Pb and Sb during weathering of mine tailings: implications for fluvial environments. Mineralogical Magazine, 76(5), pp. 1209-1228.

Lade, P.V., Yamamuro, J.A. & Bopp, P.A. (1996). Significance of particle crushing in granular materials. Journal of Geotechnical Engineering, 122(4), pp. 309-316.

Lindvall, M. and Eriksson, N. (2003). Investigation of the weathering properties of tailings sand from Boliden´s Aitik copper mine – a summary of twelve years of investigations. Proceedings 6th International Conference on Acid Rock Drainage.Cairns.

Mitchell and Soga (2005). Fundamentals of soil behavior. 3rd ed. Wiley.

Mora, C.F. & Kwan, A.K.H. (2000). Sphericity, shape factor, and convexity measurement of coarse aggregate for concrete using digital image processing. Cement and Concrete Research, 30(3), pp. 351-358.

Moses, L. E. (2014). Wilcoxon-Mann-Whitney test: Definition and example. John Wiley and Sons.

Ormann, L., Zardari, M., Mattsson, H. & Knutsson, S. (2013). Numerical Analysis of strengthening by rockfill embankments on an upstream tailings dam. Canadian Geotechnical Journal, Volume 50, pp. 391-399.

Powers, M. (1953). A new roundness scale for sedimentary particles. Journal of Sedimentary Petrology, 23(2), pp. 117-119.

Riley, N. A. (1941). Projection Sphericity. Journal of Sedimentary Petrology, 11(2), pp. 94-97.

Rodriguez, J. M. (2012). Particle shape quantities and influence on geotechnical properties: a review, Lulea, Sweden: Lulea University of Technology.

Santamarina, J. & Cho, G. (2004). Soil behaviour: The role of particle shape. London, Skempton Conf. London.

Snedecor, G.W. & Cochran, W.G. (1989). Statistical methods. 8th ed. Iowa: State University Press.

Tickell, F.G. (1938). Effect of the angularity of grain on porosity and permeability. bulletin of the American Association of Petroleum Geologist, Volume 22, pp. 1272-1274.

Ulusoy, U. (2008). Application of ANOVA to image analysis results of talc particles produced by different milling. Powder Technology, 188(2), pp. 133-138.

Valdes, J.R. & Koprulu, E. (2007). Characterization of fines produced by sand crushing. Journal of Geotechnical and Geoenvironmental Engineering, 113(12), 1626-1630.

Wadell, H. (1932). Volume, shape and roundness of rock particles. Journal of Geology, Volume 40, pp. 443-451.

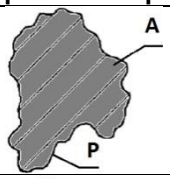
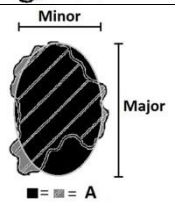
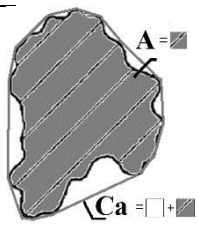
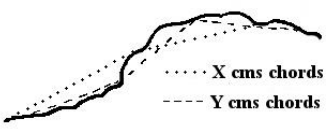
Wadell, H. (1935). Volume, shape, and roundness of quartz particles. Journal of Geology, 43, 250-279.

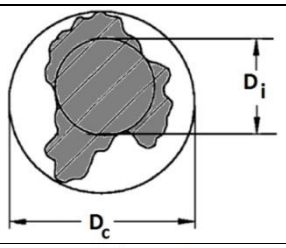
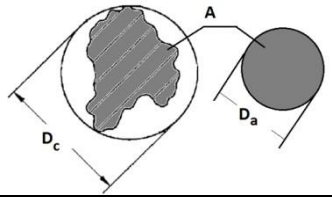
Wentworth, W. (1922). A method of measuring and plotting the shape of pebbles. U.S. Geological Survey Bulletin, Volume 730C, pp. 91-114.

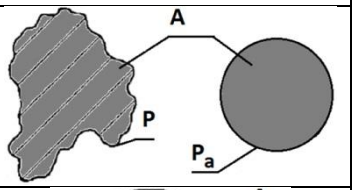
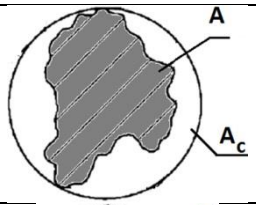
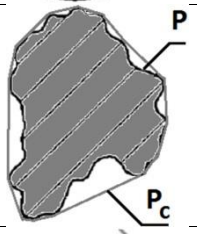
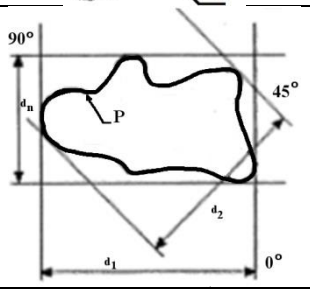
Yamamuro, J. & Lade, P. (1993). Effects of strain rate on instability of granular soils. Geotechnical Testing Journal, 16(3), pp. 304-313.

Zheng, J. & Hryciw, R. (2015). Ttraditional soil particle sphericity, roundness and surface roughness by computational geometry. Geotechnique, 65(6), pp. 494-506.

APENDIX

Q	Description	Graphic description
1*	4¶Area(A)/Perimeter^2(P)	
2*	4Area(A)/¶Major axis^2(Major)	
3*	Area(A)/Convex Area(Ca)	
4	Fractal dimension Fractal dimension use 'strides' (minimum step lengths) of various sizes. The fractal dimension is calculated as 1 minus the slope of the regression line obtained when plotting the log of the perimeter (for various strides) against the log of the stride length. (more info in imageproplus)	

5*	Square root of aximum inscribed (Di)/Minimum circumscribed(Dc), circle diameters	
6*	Diameter of a circle same area as particle(Da)/Minimum circumscribed circle diameter(Dc)	

7	Perimeter^2(P)/Area(A)	See figure in quantity 1 in this table
8*	Perimeter of a circle with same area (Pa)/Perimeter(P)	
9*	Area(A)/Area of the minimum circumscribed circle (Ac)	
10*	Perimeter/Convex perimeter	
11	πAverage Feret/Perimeter(P) Average ferret box is obtained rotating two parallel lines (two degrees each time) and measuring the distance, finally the average ferret is the average distance of all the feret boxes distance measured	
* Figures were taken and modified from Johansson and Vall 2012		

.

Commercialising reclaimed materials in earthworks – guidelines for productization and the process of appending these materials in the Finnish national code of practice

K. Koivisto
Ramboll Finland Oy, Finland
Aalto University, Finland, kirsi.koivisto@aalto.fi

J. Forsman, M. Ronkainen, P. Lahtinen
Ramboll Finland Oy, Finland

P. Kolisoja, P. Kuula
Tampere University of Technology, Finland

ABSTRACT
To decrease the use of non-renewable natural resources as well as environmental effects of earthworks, natural aggregate materials can be replaced with recycled materials acquired from surplus soil, industrial by-products and waste, etc. When wishing to increase the usage of these reclaimed materials (="UUMA"- material), the usage must be straightforward for developers, designers and constructors alike. To make this possible, the materials must have design guidelines for their appropriate applications, they must be productized and CE marked or otherwise authorized, and the construction guidelines for the materials must be included in the Finnish general specifications for infrastructural construction works (InfraRYL). As productization is especially important in increasing the usage of UUMA-materials, guidelines for vendors are being drawn that present information on commercializing reclaimed materials to be used in earthworks. The guidelines for productization are being prepared in the Finnish national UUMA2 program (2013-2017, www.uuma2.fi), which was created to promote the use of recycled materials in earthworks.

Keywords: recycled materials, by-products, waste, productization, earthwork, guidelines.

1 INTRODUCTION

Significant amount of aggregates to be used in earthworks can be replaced with recovered materials acquired from surplus soil, industrial by-products and waste, mildly contaminated soil and reclaimed aggregates from existing earth structures. These materials are called UUMA-materials. The materials can be used either

- in earthworks
- in the raw or
- as components to replace or to improve the properties of non-renewable rock material.

The construction sites can be e.g. roads, streets, ports, industrial sites, parks, sport venues, etc.

Construction consumes over 100 million tons of rock materials in Finland annually. The consumption of aggregates totals on average 70–80 million tons annually.

The promotion of the use of recycled materials is a highly efficient way of improving material efficiency and can lead to a significant decrease in the use of non-renewable natural resources and energy consumption required in their transport. (Finnish Transport Agency 2014)

The use of recovered materials to be utilised in earthworks can be significantly increased by the productization and commercialization of materials and developing construction technology, planning and procurement.

2 UUMA2 PROGRAM

2.1 Goal

The goal of the UUMA2 program is to promote the use of recovered materials in earthworks and thus to decrease the use of untouched natural resources and environmental effects of earthworks (Figure 1). To get to the point where UUMA-materials are treated equally to standard construction materials, it is needed not only that material suppliers push their products to the markets, but also that legislation and public authorities support the use of these materials to create a demand. Both supply and demand are needed for the UUMA-materials to be accepted as standard construction materials. (Koivisto et al. 2015)

The UUMA2 program especially focuses on promoting eco-efficient project-specific material solutions and the productization of earthworks with recovered materials. The main focus of the program is in product development, in the development of planning and acquisitions carried out by clients and the related demonstration projects. UUMA2 program aims to:

- introduce more commercialised UUMA-materials to the markets
- support the development of planning and acquisitions carried out by clients
- decrease the use of rock and gravel materials in earthworks
- produce information for the development of the environmental legislation so that legislation supports eco-efficient new earthworks.

2.2 Development areas

Development is the key focus in UUMA2 program. There are five different development areas that will be advanced during the program:

1. Product development process for materials
   - Technical eligibility
   - Environmental suitability
   - Production process: logistics, storage
   - Applications
2. Development of construction technologies
3. Development of planning and design process
4. Development of acquisition methods
5. Development of environmental legislation.

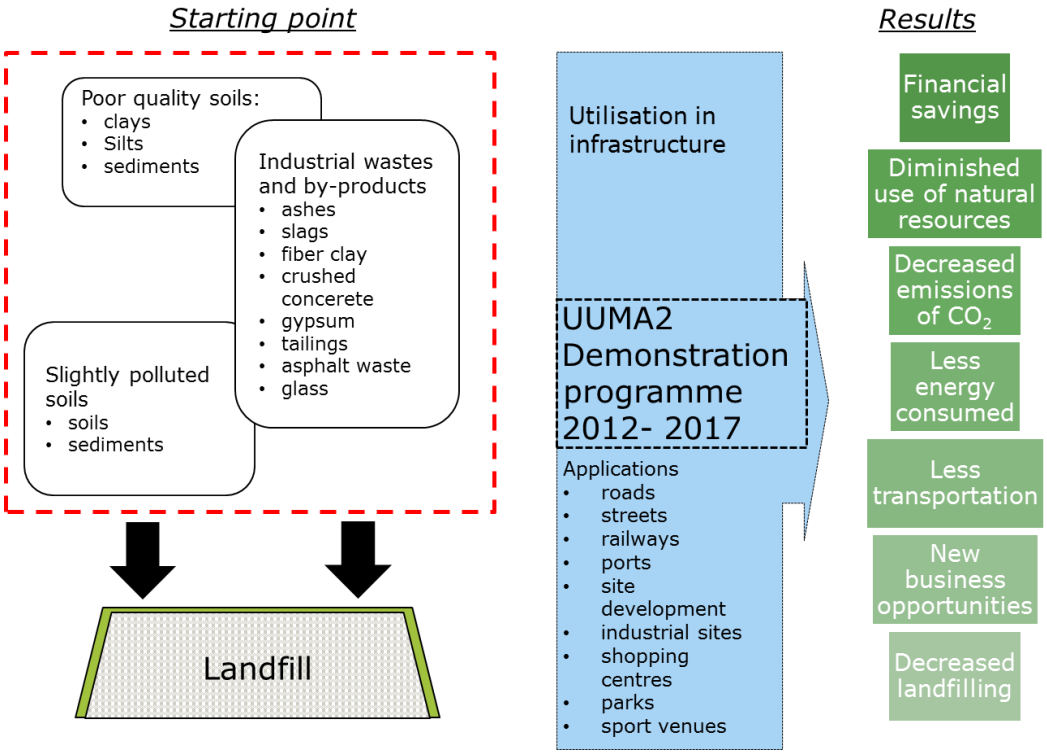


Figure 1. The aim of the UUMA2 program (www.uuma2.fi).

The implementation of the program is divided into different areas: product development, demonstration projects, regional projects, R&D (design processes, acquisition methods, research and development actions stipulated by environmental legislation) and dissemination of information (instructions, web pages, seminars, knowledge transfer to educational institutions).

Demonstration projects are large diverse infrastructure projects that advance the goals of UUMA2 program and serve the productization process of different UUMA-materials. Regional projects aim to increase dialogue and co-operation between different interest groups operating at the same region.

3 PRODUCTIZATION PROCESS FOR UUMA-MATERIALS

To ease the process of introducing new UUMA-materials to the markets, productization guidelines (UUMA2 program 2016a) have been compiled in the UUMA2 program.

The main idea behind productization is to develop a new product and bring them to the market so that the product will be able to compete with traditional materials.

Productization begins when there is a desire to make an actual product of an existing prototype. The basis of the whole process is to create a product that meets the requirements of the client as precisely as possible. Productization process describes the path from innovation of the product to its commercialization.

The first step is to define the requirements and limiting conditions for the product:

- in which structure / structural element does the client use the product
- how does the product fulfil the functional requirements of the structure / structural element
- properties of the product
- quality requirements of the product
- cost of the product
- delivery time and capacity of the product.

To fulfil the defined requirements, the material needs to be tested both in laboratory and in the field. A plan for quality control needs to be prepared to ensure the homogeneity of the material. If not known, the technical properties of the UUMA-material need to be established.

Test structures are used to check how production, delivery and construction can be implemented in practice. After this, pilot and demonstration structures are constructed to present the functionality of the product for developers. Finally, guidelines for design and construction are devised, upon which the production can be launched.

Different phases of productization process have been presented in Figure 2. Each of these phases is broached separately in the following chapters.

As an example of the progression of the productization process, the productization history of crushed concrete in Finland is presented in Figure 3.

4 DEFINING MATERIALS AND REQUIREMENTS FOR APPLICATIONS

4.1 UUMA-materials

The UUMA-materials that are used in Finland have been listed based on the material table presented in appendix A in standard EN 13242 from 2013 (not yet valid). The standard does not include all possible reclaimed materials, so the table has been complemented nationally.

However, the UUMA materials included in the UUMA2 program are defined by the program participants and their interests. At the moment the materials covered in the program are:

- reclaimed asphalt
- crushed concrete
- crushed bricks
- fly ash and bottom ash from municipal solid waste incineration
- fluidized bed combustion bottom ash
- desulphurisation residue from coal power generation industry

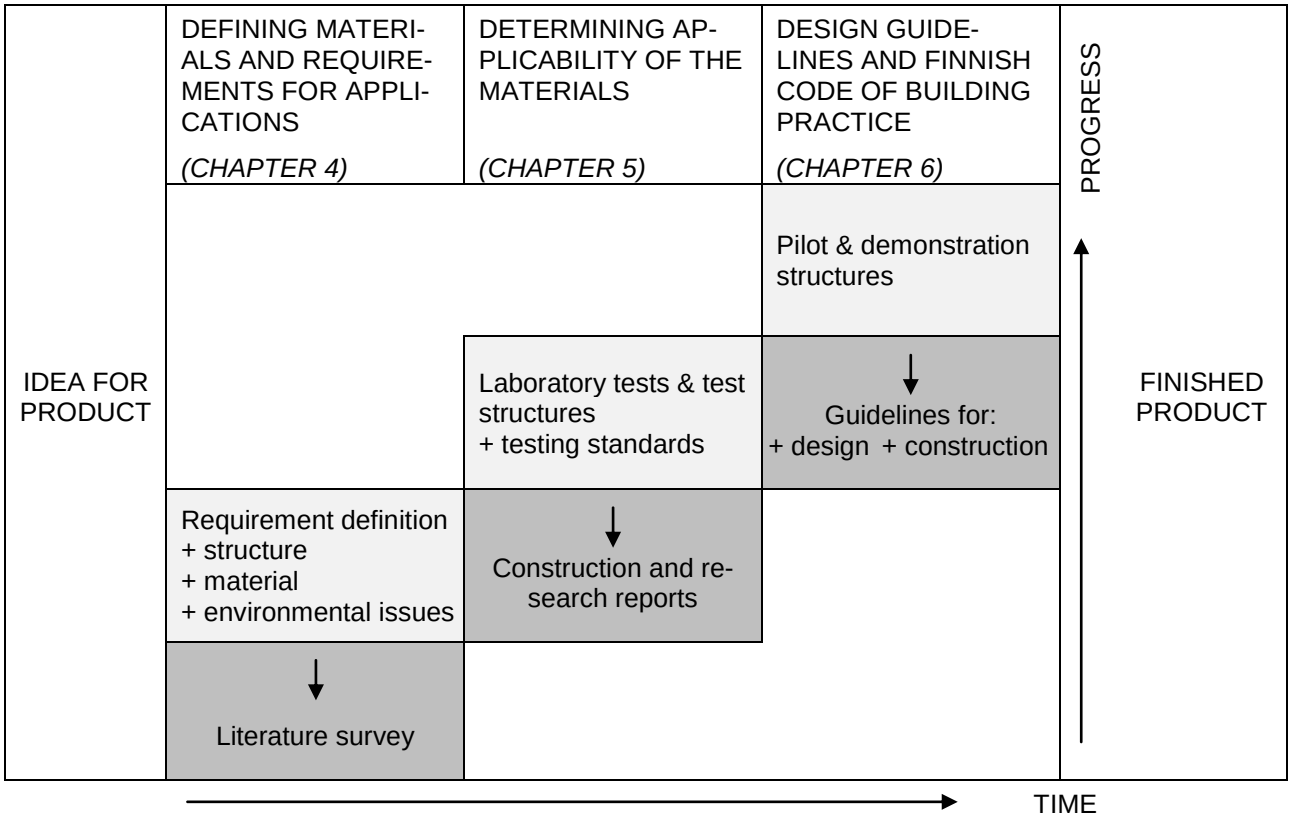


Figure 2 The main phases of the productization of UUMA-materials to earth construction.

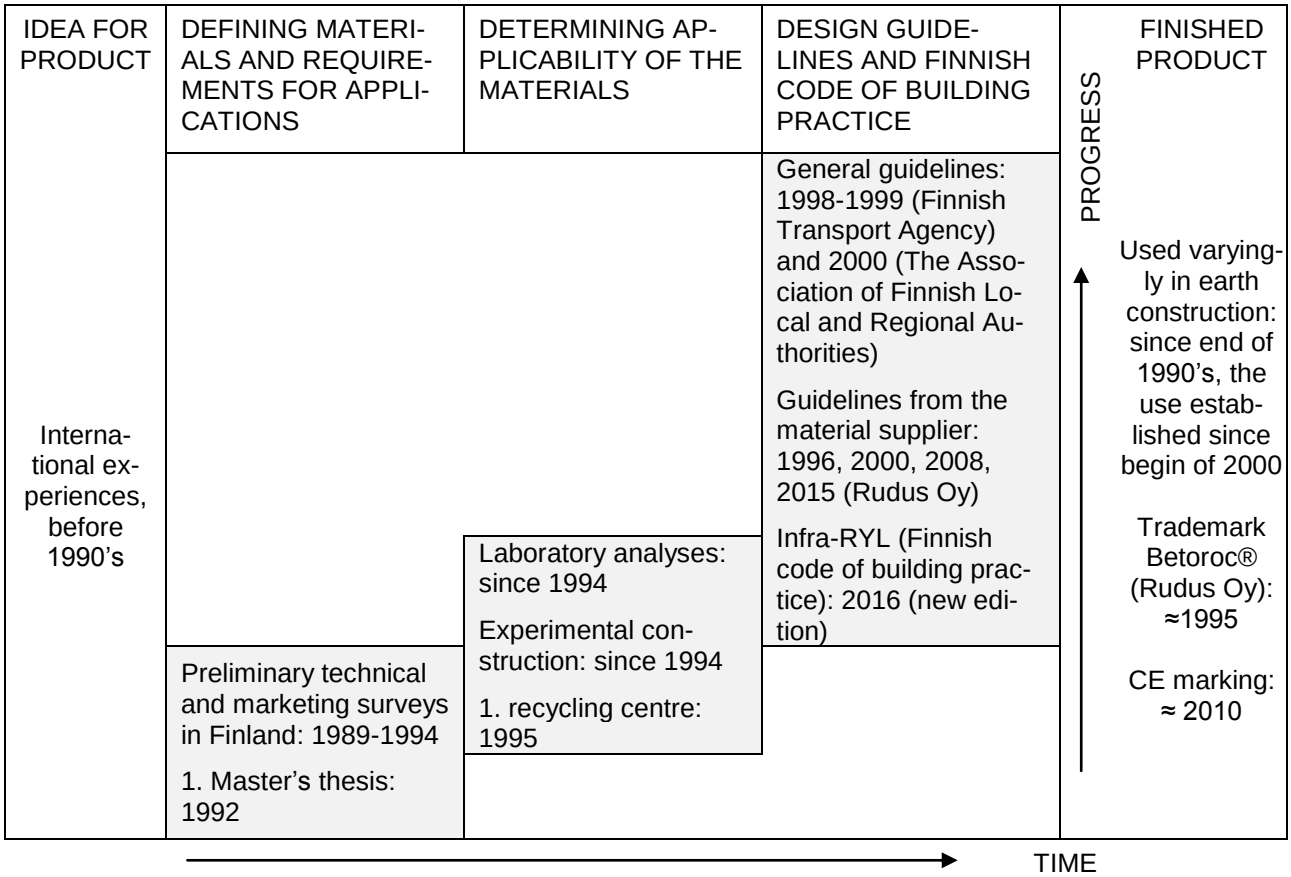


Figure 3 An example of productization of an UUMA-material. Case crushed concrete in Finland.

- coal fly ash and coal bottom ash
- biomass ash
- slags from steel industry
- foundry sand
- tailings sand from calcite mining
- gypsum from phosphoric acid production
- dredge residue and excavated soils
- residue from forest industry.

4.2 Possible applications for the materials

The productization process is based on the technical and functional requirements of the application (structural element). These requirements need to be fulfilled before the product is launched. The requirements are based on Finnish legislation, guidelines given by authorities, European standardization and other design and construction guidelines.

Possible applications for UUMA-materials to be used in covers a wide range of the infrastructural construction sector. Below are given the five main application areas considered in the UUMA2 program:

1. Roads and fields
   - roads, pedestrian and bicycle ways
   - parking areas, industrial areas
   - sports fields
2. Harbours and sea routes
   - used as a component or a binder in stabilisation of contaminated or soft sediments
   - as a massive structure or a mixture component in structural layers of harbour fields
   - in layer stabilisation of the bearing layer of harbour fields
3. Mass stabilisation
   - as binder / binder component in mass stabilisation of soft areas in all infra-construction sites
4. Environmental structures
   - noise barriers
   - flood barriers
   - liner structures in landfills etc.
   - protective barrier structures of tailings
5. Neutralising acidic materials
   - sulphidic clays
   - acidic tailings

Naturally, some UUMA-materials do not have high-enough technical quality for certain applications, whereas to some other applications certain materials have a too high quality.

5 DETERMINING APPLICABILITY OF THE MATERIALS

5.1 *Laboratory tests and test structures*

When material properties are tested, the aim is to find out the properties of a material in optimum conditions, normal working conditions and poor working conditions (e.g. when the compaction of the structure fails). The studies also aim to determine what can be done to eliminate risks and find solutions to circumstances where the risks have realized. (Finnish Transport Agency 2014)

Determining the applicability of an UUMA-material in an application requires laboratory tests. What kinds of tests are required depends on the material and the application where it is to be used. Whether the material is granular or continuum has a remarkable impact on the required test method.

Test construction requires a test site where ground conditions are uniform all over the test area. Test structures are compared to a reference structure or structures constructed on the same area. Design of test structures includes:

- gathering of the initial data and estimating its adequacy,
- finding out prior information and applications of the product,
- documenting of the construction site and materials,
- compiling of a proposition for and designing the test and references structures,
- documenting of the quality control procedures for the material and construction and
- compiling of research and documentation plans for the structures.

5.2 Testing standards

Following a standard ensures that the testing procedure is always the same and the test

results are comparable. This also makes it easier to set down quality requirements. Standards are recommendations by nature until they are made requirements by for example legislation, authorities or customers.

Reclaimed materials are discussed for example in the European standards for aggregates. Several harmonized standards have presented special requirements for certain reclaimed materials that differ from those given to natural aggregates, e.g. loss on ignition for coal fly ash or volume soundness for blast furnace slag. Using certain reclaimed materials as a stabilization binder or as a cement component has also been harmonized.

As part of the productization guidelines, a Standard study for UUMA-materials (UUMA2 program. 2016b) has been compiled, which summarizes the required properties and test methods for materials and applications from different standards and guidelines. To make it easier to consider which materials might be compatible to different test standards, the reclaimed materials have been classified in five different material types (Table 1):

1. granular
2. bound granular
3. massive consolidated, stabilised
4. elastic (under traffic load)
5. liner material

Examples of these material types are shown in Figure 4.

6 DESIGN GUIDELINES AND FINNISH CODE OF BUILDING PRACTICE

The final stage in productization process for UUMA-materials is to compile design and construction guidelines. The aim is to get these different materials included also in the different guidelines from public authorities and the Finnish code of building practice. When the UUMA-materials and their requirements are presented side by side to the natural aggregates in the guidelines, it makes it easier for the developers to accept the use of these less conventional construction materials in their construction projects.

The stage of compiling guidelines for some reclaimed materials included in UUMA2 program and how frequently the materials are used in infra construction is presented in Table 2.

6.1 Code of building practice and InfraRYL

The Finnish code of practice for infrastructures includes the infrastructural nomenclatures, InfraRYL requirements, Infra specifications cards, Regulations cards (laws, decrees, regulations by the authorities) and Product cards.

Table 1 UUMA-materials classified in different material types according to their material properties.

1. Granular		Crushed asphalt, Crushed concrete, Crushed bricks, Bottom ash from municipal solid waste incineration, Bottom ash, Fluidized bed combustion bottom ash, Foundry sand, Stope rejection, Tailings sand from calcite mining
2. Bound granular		Crushed asphalt, Crushed concrete, Granulated blast-furnace slag, Blast-furnace sand, Other slags
3. Massive consolidated, stabilized	***filler***	Fly ash, (coal-, bio-, etc.), Fly ash activated by cement, Ash mixes, Granulated blast-furnace slag, Desulphurisation residue
	+ aggregate	Excavated soils, Heap ash (moist), Dredge residue, Fibre sludge, Existing bearing course - layer stabilization
4. Elastic		Fibre ash (mix of fibre sludge and fly ash), Residues from forest industry, Shredded tires, Fibre sludge
5. Liner material		Excavated soils (fine-grained), Residues from forest industry, Stabilized dredge residue, Fibre sludge

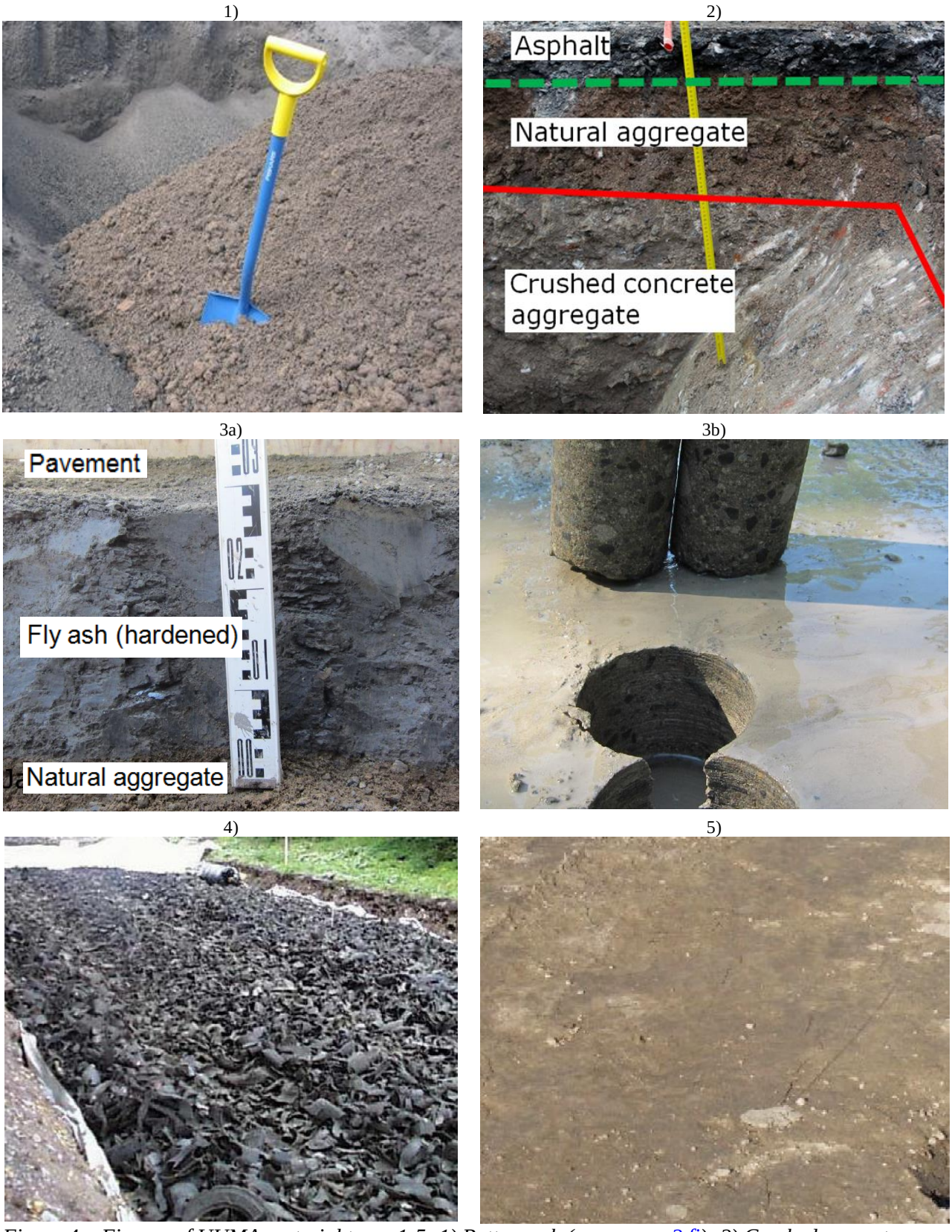


Figure 4 Figures of UUMA-material types 1-5: 1) Bottom ash (www.uuma2.fi); 2) Crushed concrete, re-hardened (Dettenborn et al. 2016); 3a) Cement stabilised fly ash; 3b) Fly ash stabilised crushed aggregate (Tarkkio 2014); 4) Shredded tires as a light weight material of street embankment (Forsman et al. 2002); 5) Stabilised surplus clay as a liner (Forsman & Leivo 2007). The explanations for the material types 1-5 are presented in Table 1.

Table 2 The frequency of use in infra construction and the stage of guidelines for some materials in the UUMA2 program.

Material	Guidelines from material suppliers	General guidelines (e.g. Finnish Transport Agency)	Material commonly used in infra construction*	Included in InfraRYL (2016)
Reclaimed asphalt	-	X	(X)	**-**
Crushed concrete	X	X	X	X
Crushed bricks	-	X	(X)	**-**
Bottom ash from municipal solid waste incineration	-	-	-	-
Coal fly ash	X	X	(X)	- **
Coal bottom ash and fluidized bed combustion bottom ash	X	X	(X)	- **
Desulphurisation residue	-	-	-	- **
Blast-furnace slag	X	X	X	X
Air cooled blast-furnace slag	X	X	X	X
Slags from steel industry	X	X	X	X
Foundry sand	-	-	-	-
Tailings sand from calcite mining	X	-	-	-
Gypsum from phosphoric acid production	-	-	-	-
Dredge residue and excavated soils	-	X	(X)	X
Shredded tires (and whole tires)	X	X	X	X
Fiber sludge, de-inking residue	X	-	(X)	-
Green liquor dreg	-	-	-	-
Lime sludge	-	-	-	-

* "X" = use is common, "(X)" = use is occasional, "-" = not used

** Infra product card under way (estimated to be completed in 2016)

InfraRYL 2010 Code of Building Practice - Infrastructure Handbook is meant for diverse infrastructural construction; -roads, streets, pipelines, bridges, etc. Its technical qualifications cover general quality requirements in construction, and it is continuously updated.

InfraRYL has been outlined into chapters according to the nomenclature. It includes constructional requirements and specifications, but does not contain actual design guidelines.

6.2 Design guidelines

Design guidelines are included in European and Finnish regulations, European standards, client specific design guidelines and design guidelines prepared by associations of the construction sector.

In Finland the most comprehensive ensemble of infrastructure design guidelines has been created by the Finnish Transport Agency, but even those only discuss some recovered materials (Public Roads Authority 2000, Finnish Road Administration 2007, Finnish Transport Agency 2014). Municipalities have collective design guidelines for the design of parks and streets. Also manufacturers of recovered materials have prepared some material specific design guidelines for infrastructures.

UUMA2 program aims to create a reference library of literature and guidelines of recovered materials that will be accessible through the UUMA web pages.

6.3 Bringing UUMA-materials to InfraRYL

So far only a few recovered materials are represented in individual structural elements in InfraRYL. One of the possible methods to include recovered materials in InfraRYL is to create an ensemble of them, where the InfraRYL requirements are discussed by the material. Another method is to produce a set of Infra specification cards of the recovered materials that will be developed into InfraRYL requirements at a later date.

7 SUMMARY

The UUMA2 program aims to have a significant effect on the increased use of recovered materials in infra construction. The result will be more eco-friendly and cost-effective structures and decreased carbon footprint for both the industry and construction sectors.

To ease the process of introducing new UUMA-materials to the markets, productization guidelines have been compiled in the program.

Different phases of productization process define the progress level of the process. In the first phase, requirements for the material and structure are defined as well as the environmental requirements. In the second phase, laboratory tests are done followed by construction of test structures. In the final phase, design and construction guidelines are compiled. The aim there is to get the materials included also in the guidelines by public authorities and the Finnish code of building practice. So far only a few recovered materials are represented in individual structural elements in the code.

8 ACKNOWLEDGEMENTS

The research for this paper was supported by Ram-boll Finland Oy, Aalto University, Tampere University of Technology, City of Helsinki, Ekokem, Finnish Energy Industries, Finnish Forest Industries, The Finnish Transport Agency, Helsinki Region Environmental Services Authority, KFS Finland Oy, Kuusakoski Oy, Lassila & Tikanoja plc, Lemminkäinen Infra Oy, Ministry of Agriculture and Forestry, Ministry of Education and Culture, Ministry of Employment and the Economy, Ministry of the Environment, Morenia Oy, Rudus Oy, Skanska Asfaltti Oy, Skanska Infra Oy, Suomen Erityisjäte Ltd., Suomen maastorakentajat Oy and Valutuoteteollisuusyhdistys ry.

Contact information for UUMA2 program:
Program coordinator Dr Pentti Lahtinen
Ramboll Finland Oy
pentti.lahtinen@ramboll.fi
Tel. +358 20 755 674

Program co-coordinator Marjo Ronkainen
Ramboll Finland Oy
marjo.ronkainen@ramboll.fi
Tel. +358 40 551 1922

9 REFERENCES

Dettenborn, T., Forsman, J., Napari. M., Pekkala, J., Pieksemä, J. & Suominen, M. 2016. Utilization of recycled materials in urban earth construction: crushed concrete, foamed glass and ashes. The 17th Nordic Geotechnical Meeting, Reykjavik Iceland, 25.-28.5.2016.

EN 13242. 2013. Aggregates for unbound and hydraulically bound materials for use in civil engineering work and road construction. 28 October 2013. Withdrawn 10 January 2014.

Finnish Road Administration 2007. Sivutuotteiden käyttö tierakenteissa. [Use of by-products in road structures]. (in Finnish). Helsinki 2007. ISBN 978-951-803-633-6.

Finnish Transport Agency. 2014. Uusiomateriaaliopas [Guide of Reclaimed Materials], draft for test use 28.2.2014. (in Finnish). Helsinki 2014. 78 pages.

Forsman, J., Koivisto, K., Hautalahti, P. & Haatainen, M. 2002. Ekoinfra-projekti: Uusiomateriaalit yhdyskuntien liikenneväylien pehmeikkörakentamisessa, Loppuraportti [Ekoinfra project: Use of reclaimed materials in infra construction over soft soils, Final report],. (in Finnish), 52 p.

Forsman, J. & Leivo, A. 2007. Vuosaaren satama, Melumäki, pystyeristeen, mineraalinen tiivistyskerros, laaduvalvontaraportti 20.2.2008. (in Finnish), [Quality control report of vertical liner constructed with stabilised surplus clay].

InfraRYL 2010 Code of Building Practice - Infrastructure Handbook. (in Finnish)

Koivisto, K., Forsman, J., Ronkainen, M., Lahtinen, P., Mäkelä, H. & Korkiala-Tanttu, L. 2015. Development of design and acquisitions for earthworks with recycled materials - Finnish UUMA2 programme. Edinburgh

Public Roads Authority 2000. Use of reclaimed concrete in pavement structures. [Betonimurskeen

käyttö tien päällysrakennekerroksissa, Mitoitus- ja työohjeet]. Helsinki 2000. TIEL 3200594. 25 pages + app. ISBN 951-726-603-0.

UUMA2 program. 2016a. Productization quide-book for UUMA-materials (in Finnish), draft February 2016.

UUMA2 program. 2016b. Standard study for UUMA-materials (in Finnish), draft January 2016.

Tarkkio, T. 2014. Long term functionality of fly ash in road and field structures (In Finnish). Master's thesis, Tampere University of Technology.

Multi-hazard: Contaminated land vulnerable to natural hazards and effects of climate change

G. Göransson
Swedish Geotechnical Institute, Sweden, gunnel.goransson@swedgeo.se

P. Edebalk, J. Hedfors, M, Carling, K. Odén, H. Branzén, M. Stark
Swedish Geotechnical Institute, Sweden

ABSTRACT
Erosion, slope failure and flooding of contaminated land is a not yet recognized multi-hazard that needs consideration in land use planning. Most cities have developed in the vicinity of surface waters (rivers, lakes, and coastline) and it is also adjacent to these waters most industrial activities have been located and still are. The surface water has been used for transportation as well as recipient for the release of waste waters. Leakage, continuous emissions and accidental spills from hazardous activities have caused the contamination of soils, groundwater, surface waters and sediments. Natural hazards are effective pathways for the release and wide spreading of contaminants from these sites to the ecosystem. Regions experiencing an increased precipitation due to climate change may be exposed to an increased threat from such multi-hazards. Together with Lund University of Technology and Chalmers University of Technology, the Swedish Geotechnical Institute (SGI) conducted research to obtain knowledge on the spreading of pollutants from landslide into rivers and to develop a model framework that can serve as a complement for landslide risk assessments and environmental risk assessments. The results show that there are several contaminated sites that are located on unstable ground and that a landslide induced release of contaminants can cause a clear increase in pollutant concentration in surface water (Göransson, 2013, Göransson et al., 2013). Between year 2014 and 2015, SGI developed and tested a GIS based quick scan method at a river basin scale to identify contaminated sites that may be vulnerable to natural hazards. In addition, a method was developed and tested to assess a specific contaminated site´s vulnerability to natural hazards, including increased precipitation due to climate change (Edebalk et al., in press). The purpose is then to implement these methods as complement to existing methods for risk assessment.

Keywords: Contaminated soil, landslide, erosion, flooding, climate change

1 INTRODUCTION

Contaminated land poses risk for human health and the environment. In Sweden, the national environmental quality standard sets the direction for the environmental work to reduce risks. There are many contaminated sites in Sweden and the investigation and management of contaminated land areas is an important part of the environmental work. A national inventory has been done to identify potentially contaminated sites and until now about 80 000 sites have been identified. Each site has then been risk assessed and classified as posing minor, moderate, high or very high risk, based on type of pollutants and their distribution in the soil.

Although urban areas and industrial sites are commonly located adjacent to surface water, very few studies have paid attention to the risk of mobilization and spreading of pollutants to surface water due to natural hazards like landslides (Göransson et al. 2012). Natural hazards globally strike urban areas yearly but only few studies have looked upon the environmental consequences after

such events (see UNISDR and data statistics at http://www.unisdr.org/we/inform/disaster-statistics).
Methods for the risk assessment of natural hazards include the assessment of the vulnerability to humans, infrastructure, buildings and the environment. Except for flooding, damage to the environment has mostly been about the loss of valuable flora and not damage to hazardous facilities (see for example Bonnard et al., 2004). Likewise, existing methods for environmental risk assessment do not consider natural hazards as potential pathways for catastrophic spreading of contaminants.
Contaminated land is the contamination of soil and (ground) water and is caused by the presence of chemicals or other alteration in the natural soil environment. Soil contamination is usually caused by industrial activities (leakage, spills, and waste disposal), improper waste disposal, agricultural chemicals, urban activities (e.g. waste water) etc. Many of the contaminated sites are located adjacent to surface waters (lakes, rivers, and coasts) for energy production, transportation, receiving waters, and cooling. However, waterfront areas may be exposed to natural hazards.
Landslides, debris flows, erosion and flooding mean that soil is mobilized and transported although in different temporal and spatial scales. Landslides are the rapid movement of soil and rock that occur almost without warning and causes great damage. Erosion is the detachment, transport and deposition of soil particles, usually by running water. Flooding is the overflow of water that submerges land which usually is dry.
A landslide of contaminated soil into surface water will instantaneously release a great amount of contaminants into the water, and over time through erosion and diffusion from contaminated run-out deposits (Göransson, 2013). Continuous bank erosion can cause a diffuse and continuous spread of contaminants to the water (Rhoades et al., 2009; Rowan et al., 1995). The extent of erosion depends on soil type, density, vegetation, flow velocity, and how the water currents affect the slope (Wynn and Mostaghimi, 2006). Erosion can be a trigger for landslide, flooding may enhance erosion, and rainfall can cause flooding but also trigger landslides (Glade, 2003; Pradhan et al., 2012; Van Asch et al., 1999). Flooding of contaminated sites causes leakage of contaminants that are spread further by the water (Dennis et al., 2003). Flooding also can cause increased groundwater level and leakage and spread of contaminants with the groundwater flow. A change (increase) in precipitation (frequency, intensity) affects surface run off and groundwater level. This may in turn change the prerequisites for the spreading of contaminants in the soil to recipients.
The aim of this paper is to highlight the combined risk of natural hazards and contaminated land and to present an approach for identification and vulnerability classification of the hazard at different scales. The overall objective is to develop an approach for the assessment of contaminated site's vulnerability to natural hazards that includes not only landslides but also erosion, flooding and increased precipitation from climate change.

2 METHOD

The papers by Göransson et al. (2009; 2012 and 2013) are the first to highlight the combined risk of contaminated soil at landslide risk. The first paper (Göransson et al., 2009) identified the combination of landslides and contaminated land as a multi-risk and suggested a conceptual model for the governing processes. The second paper (Göransson et al., 2012) applied a non-dimensional advection-dispersion equation for the description of possible sediment and subsequent contaminant transport for the instantaneous release of contaminants from landslides. The third paper (Göransson et al., 2013) suggested a methodology to estimate the environmental risks associated with landslide in contaminated sites adjacent to rivers.
In this paper, an approach is presented that includes three methods based on scale and level of detail in background information. The approach includes methods for quick

scan hazard identification that can either be done at a larger geographical scale (river basin) or at a local scale from a single object. The criterion has been that the approach should be based on existing digital data and that the results could be used as a basis for priority between sites for detailed investigations. Thus, access to data in the GIS format has therefore been governing. The third method for risk estimation is under development and a first conceptualization is presented.

2.1 Quick scan method for hazard identification at a river basin scale

Screening over a larger geographical area for the identification of contaminated sites exposed to natural hazards aims to make a general and rapid assessment of potential risk as a basis for prioritization for detailed investigations and risk assessment.
The method is based on the ability to connect already existing GIS layers with each other, thereby quickly and easy identify where within a larger geographic area (e.g. river basin) the combination of contaminated land areas and areas exposed to natural hazards occur. The consequences of increased precipitation from climate change have not been included at this scale in this study since no spatial GIS layers were available at the time, but can be done.
The GIS method is based on the identification of contaminated sites whose geographical location coincides with the known locations of areas of potential landslide, bank erosion and/or flooding. The method is designed so that the minimum amount of data should provide useful results. Additional data could advantageously be included to increase the reliability of the identification. In Sweden, the basic GIS layers for the method are available through Geodata (www.geodata.se). Additional layers can be search for at different authorities. See Table 1 for specification.
Manual processing is in general required to adapt some of the data before the GIS identification procedure can be run. For example, some of the data is delivered as point information or lines. Such data need to be converted to surfaces.

Table 1. Data base for the GIS identification process.

	Product	Supplier
Basic data	Potentially contaminated sites	The County Administrative boards
	Property map	Lantmäteriet
	National elevation data, GSD	Lantmäteriet
	Flood map	Swedish Civil Contingencies Agency
	Soil map	Swedish Geological Survey
	Map: prerequisites for landslide	Swedish Geological Survey or Swedish Geotechnical Institute
	Map: prerequisites for erosion	Swedish Geotechnical Institute
	Active erosion	Swedish Geotechnical Institute
Additional data	General moraine landslide hazard zonation map	Swedish Geotechnical Institute
	General slope stability hazard zonation map	Swedish Civil Contingencies Agency
	Landslide database	Swedish Geotechnical Institute
	Gully and landslide scar data	Swedish Geological Survey

2.2 Quick scan method for vulnerability assessment of a single object

The method is based on a single object, i.e. a contaminated site that has undergone an environmental risk classification or environmental risk assessment. The aim is here to identify if the site also may be exposed to an increased risk for contaminant transport in the event of natural disaster.
The most likely scenario is that the vulnerability for natural hazards are observed for contaminated sites that have been classified as having high or very high environmental risk, or that are facing measures or land development.
The suggested method aims to gather all existing data on soil movement (slope stability), erosion, flooding and change in precipitation, and to make an overall assessment of whether there is negligible, minor, moderate or major vulnerability for each of the natural hazards to the contaminated site. The method is hence

divided into the following natural hazard categories:

- Soil movement (landslide, debris flow)
- Bank erosion
- Flooding (lakes, rivers, coasts)
- Increased precipitation from climate change

Assessment matrices have been developed for each of the categories. The matrices and the approach how to use these are briefly described below.

The geotechnical data for the assessment of a contaminated site's vulnerability to soil movement may consist of geotechnical investigations (general, detailed, in-depth) or general landslide hazard zonation maps. The available data with maximum degree of detail should be used. Table 2 shows the assessment matrix for geotechnical investigations, based on the national requirements for stability investigations. If a geotechnical survey is available, the lowest value on the slope safety factor should be used in Table 2 to assess vulnerability.

Assessment matrices are also available for data in the form of general landslide hazard zonation maps for fine-grained and coarse-grained soils respectively, and maps showing the prerequisites for landslide in fine-grained soils. Table 3 shows the assessment matrix for the assessment of a contaminated site's vulnerability to soil movement if the site is located on fine-grained soil and if only a general slope stability hazard zonation map is available.

In contrast to the above, there is no national method to map bank erosion. The assessment of vulnerability to riverine, lake or coastal erosion is therefore based on soil type and the contaminated sites distance to beach. The sensitivity to erosion varies with soil type and silt and sand are considered the most erosive soils. Hence, the basic data consists of the soil type map. Table 4 shows the assessment matrix for erosion.

Table 5 shows the assessment matrix for the assessment of a contaminated site's vulnerability to flooding. In Sweden, general flood risk mapping (in fact, flood hazard zonation mapping) are performed by the Swedish Civil and Contingencies Agency. Flood risk maps exist for many of the watercourses in Sweden but not for all. There are updated risk maps of particularly urgent rivers regarding climate change and climate scenarios until year 2098.

The flood risk maps show areas flooded at different return periods of flows, usually 100-year floods. In addition, there are areas marked which can be flooded by a theoretically calculated maximum flow. The updated maps regarding climate change effects also show areas flooded at 50-year return period and climate adapted 100-year floods and 200-year floods. Areas that are flooded already today are considered to have the highest vulnerability.

If there is no flood risk mapping for the case under study such needs to be developed. General flood risk mapping for the coastal areas are only available for Scania and has been developed by the County Administrative Board of Scania. The mapping is based on mean sea water level and high water level for today's situation and future levels with respect to climate scenarios. Also, the Swedish Meteorological and Hydrological Institute (SMHI) has developed a rough map that shows the net effect of sea water level, minus the effect of land upheaval, along the Swedish coast line, and at a global sea water level rise of 1 m until year 2098.

In this study we use climate scenarios for a change in annual mean precipitation as an indicator for the assessment of whether a future change in precipitation may affect the spreading of contaminants.

The level of precipitation increase is arbitrary set to be used together with SMHI's climate scenario maps (available at www.smhi.se). The data is used only as a check that consideration should be taken to changes in precipitation (annual, intensity and frequency). Climate scenarios are displayed as RCPs (Representative Concentration Pathways). RCPs are scenarios of how the greenhouse effect will be enhanced in the future. The RCP scenarios are based on levels of anthropogenic radiative forcing, expressed in watts per square meter. The RCP scenarios are termed with the radiative forcing achieved in year 2100: 2,6, 4,5, 6,0 or 8,5 W/m^2 (https://www.ipcc.ch/report/ar5/).

Table 6 shows the suggested assessment matrix that can be used to assess the vulnerability to increased precipitation. In that matrix, RCP 4,5 has been chosen as the future scenario, but it is possible to use any of the scenarios.

Table 2. Assessment matrix for the assessment of a contaminated site's vulnerability to soil movement when geotechnical stability investigations are available for the contaminated site. The table shows how different values on slope safety factor should be interpreted depending on the investigation's level of detail. F_c = total factor of safety, undrained analysis F_k = total factor of safety, combined analysis, F_φ = total factor of safety, drained analysis, F_{EN} = factor that uses partial coefficients.

Data	Negligible vulnerability	Minor vulnerability	Moderate vulnerability	Major vulnerability
In-depth/additional geotechnical slope stability investigation	$F_c > 1,8$ $F_k > 1,7$ $F_\varphi > 1,5$	$1,5 < F_c \leq 1,8$ $1,4 < F_k \leq 1,7$ $1,3 < F_\varphi \leq 1,5$	$1,25 < F_c \leq 1,5$ $1,2 < F_k \leq 1,4$ $1,15 < F_\varphi \leq 1,3$	$F_c \leq 1,25$ $F_k \leq 1,2$ $F_\varphi \leq 1,15$
Detailed geotechnical slope stability investigation	$F_c > 2,2$ $F_k > 1,8$ $F_\varphi > 1,5$	$1,7 < F_c \leq 2,2$ $1,5 < F_k \leq 1,8$ $1,3 < F_\varphi \leq 1,5$	$1,3 < F_c \leq 1,7$ $1,25 < F_k \leq 1,5$ $1,15 < F_\varphi \leq 1,3$	$F_c \leq 1,3$ $F_k \leq 1,25$ $F_\varphi \leq 1,15$
General geotechnical slope stability investigation	$F_c > 3,0$ $F_k > 2,0$ $F_\varphi > 1,8$	$2,0 < F_c \leq 3,0$ $1,6 < F_k \leq 2,0$ $1,5 < F_\varphi \leq 1,8$	$1,5 < F_c \leq 2$ $1,3 < F_k \leq 1,6$ $1,3< F_\varphi \leq 1,5$	$F_c \leq 1,5$ $F_k \leq 1,3$ $F_\varphi \leq 1,3$
Slope stability investigation based on the method for partial coefficient (F_{EN}) (Eurocode)	The intervals above apply by multiplying F_{EN} for undrained analysis with 1,5 and F_{EN} for drained analysis with 1,3. There is no conversion factor for combined analysis.			

Table 3. Assessment matrix based on general slope stability map for fine-grained soil for the assessment of a contaminated site's vulnerability to landslide.

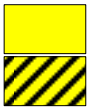
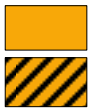
Data	Negligible vulnerability	Minor vulnerability	Moderate vulnerability	Major vulnerability
General slope stability zonation map, fine-grained soils.	 *White zone on stability map.* Areas judged to be satisfactory stable under prevailing conditions.		 *Yellow zone (or yellow with black diagonal lines) on stability map.* Areas previously considered satisfactory stable but that do not follow today's requirements for investigation. Areas in need of review of earlier investigations or measures, especially for areas marked with black lines.	 *Orange zone (or orange with black diagonal lines) on stability map.* Areas judged not to be satisfactory stable. Areas in urgent need of detailed investigations, especially for areas marked with black lines.

Table 4. Assessment matrix for the assessment of a contaminated site's vulnerability to erosion.

Data	Negligible vulnerability	Minor vulnerability	Moderate vulnerability	Major vulnerability
General inventory of the prerequisites for bank erosion	Bedrock/stable ground, erosion protection OR ≥ 200 m to the beach.	Clay OR 100-200 m to the beach.	Sand, silt, flood plain deposits, fill, OR visible erosion in clay AND < 100 m to the beach.	Visible erosion/active erosion in sand, silt, flood plain deposits.

Table 5. Assessment matrix for the assessment of a contaminated site's vulnerability to flooding. CMF = calculated maximum flow, Q_{200} = 200 year flood, Q_{100} = 100 year flood, Q_{50} = 50 year flood, MHWL = mean high water level, MWL = mean water level, GL = ground level, masl = meter above mean sea water level.

Data	Negligible vulnerability	Minor vulnerability	Moderate vulnerability	Major vulnerability
Updated flood risk maps with regard to climate change - rivers	Outside Q_{200} marked area (climate adapted flow)	Within Q_{200} marked area but outside Q_{100} (climate adapted flow)	Within Q_{100} marked area but outside MHWL or Q_{50} (climate adapted flow)	GL < MHWL OR within Q_{50} marked area (climate adapted)
General flood risk maps - rivers	Outside CMF marked area	Within CMF marked area but outside Q_{100}	Within Q_{100} marked area but outside MHWL	GL < MHWL OR within Q_{100} AND GL ≤ 1 MWL
General flood risk mapping - coast	GL ≥ 5 masl	3 masl ≤ GL < 5 masl	1 masl ≤ GL < 3 masl	GL < 1 masl OR prone to flooding today.

Table 6. Assessment matrix for the assessment of a contaminated site's vulnerability to increased precipitation. P_i = increase in mean annual precipitation until 2098 and compared with the reference period 1961-1990.

Data	Negligible vulnerability	Minor vulnerability	Moderate vulnerability	Major vulnerability
Change in precipitation, climate scenario RCP 4,5	P_i < 5%	5% ≤ P_i < 10 %	10% ≤ P_i < 15 %	P_i ≥ 15%

The assessments carried out based on the above mentioned assessment matrices is gathered in an overall assessment matrix for an overview of the natural hazards that have been identified for the contaminated site. A summarized assessment is done to assess the overall need for further investigation/action for each of the identified hazards by filling in the information in a summary matrix (see further the example in 3.2). The need for additional investigation for each of the natural hazard is determined according to:

- Negligible vulnerability: No need for further investigation
- Minor vulnerability: The site cannot be disclaimed from natural hazards, control is needed.
- Moderate vulnerability: A need for in-depth risk assessment regarding identified natural hazard(s), probable need for action.
- Major vulnerability: Urgent need for in-depth risk assessment regarding identified natural hazard(s). A need for action.

2.3 Proposed method for risk estimation of a single object

In Göransson et al. (2013) a probabilistic method was developed to estimate possible environmental risks from landslide of contaminated soil into rivers in order to allow for datasets with large uncertainties and the use of expert judgements. Consequences were divided into impact zones for the estimation of possible consequences in the near-field, along the pathway (river) and in the accumulation area (e.g. estuary, lake). Consequences were assessed in terms of

failure for exceeding certain environmental quality standards since there are no studies on the actual consequences from natural hazards on the spreading of pollutants. It would be possible to use the same approach for other natural hazards than landslides. Such approach could also include all possible natural hazards and the probability that environmental quality standards or other criteria will be exceeded if any of the hazards occurs. This part has not been done yet, thus this paper will only present the suggested approach and a first, very simplified, conceptualization.

3 RESULTS

3.1 Quick scan method for hazard identification at a river basin scale

The identification of contaminated sites vulnerability to natural hazards, and at a river basin scale, is done by superimposing the contaminated land objects with each of the base support mentioned in Table 1. The base support is grouped into four categories: *i)* landslides, *ii)* debris flows, *iii)* bank erosion and, *iv)* flooding.

In our study we chose to display the contaminated sites by a colour-coded star (the colour depends on the environmental risk classification) and a colour-coded square that tells what type of natural hazard the object is vulnerable to. The municipality of Hallstahammar was used as a case study to test the method. Figure 1 displays an example of how the results of the identification can be presented on map. The identified contaminated sites represent concrete and cement industry, dry cleaning, ship yard, saw mill, pulp mill, landfill, etc.

3.2 Quick scan method for vulnerability assessment of a single object

For illustration, we have used the Block Hake in the town Köping, Sweden. The site is located adjacent to Köpingån river and Kölstaån river. Figure 2 shows block Hake marked on an aerial photo. Previous investigations include environmental investigations, a general slope stability

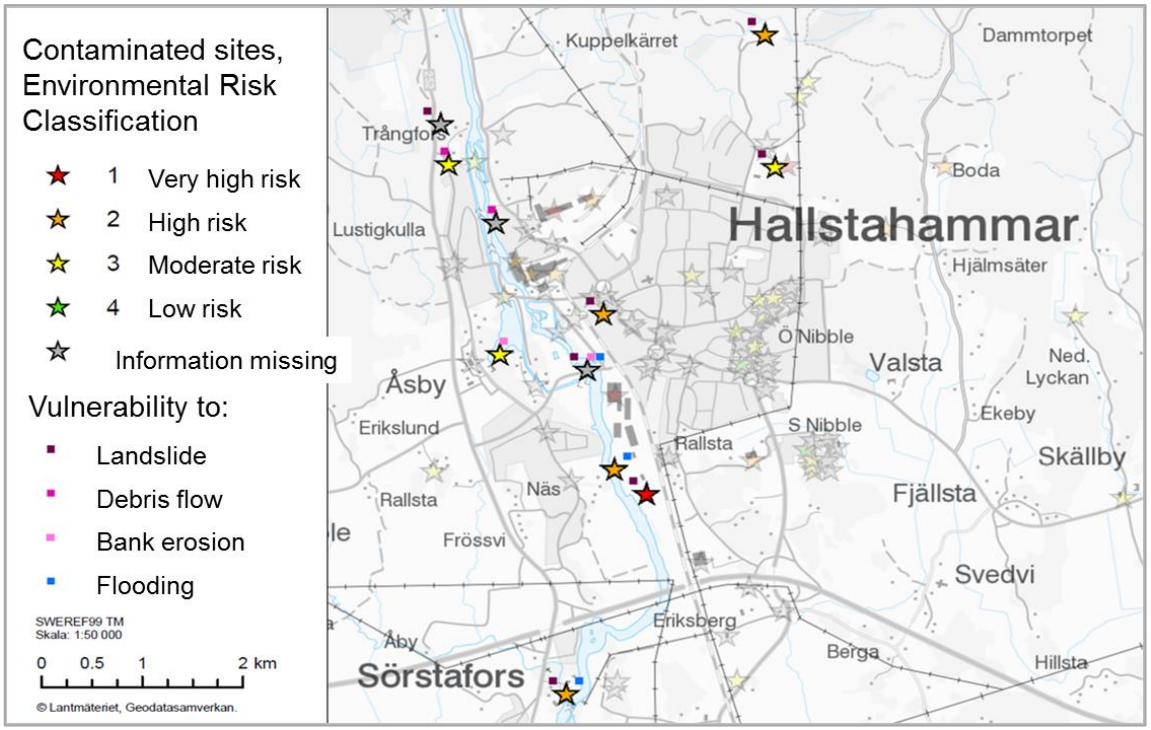


Figure 1. Example of how the results from the hazard identification can be presented on map (here, part of Hallstahammar municipality). All stars are identified as potentially contaminated sites. The highlighted stars are the one with identified vulnerability to landslide, debris flow, bank erosion and/or flooding. © SGI. Lantmäteriet. Geodatasamverkan.

zonation map, a general inventory of erosion conditions, a general flood risk map, and a climate analysis for the County Administrative Board.The site has previously been assessed with a high environmental risk classification (environmental risk class 2). The soil contains both organic and inorganic contaminants. A summary of the results from the existing data on slope stability, erosion, flooding and increased precipitation:

- The general slope stability zonation map shows that the area is situated within a zone that indicates unsatisfactory stability and that detailed investigations are needed.
- The bank material consists of flood plain deposits and there are indications of active erosion.
- According to a flood risk map (not updated for climate change effects), the site is located within an area that will be flooded only during a theoretically calculated maximum flow. However, a thin strip along the shoreline is within the marked area for 100-year flood. The climate analysis for the county shows that future 100-year flood will slightly decline. The climate analysis for the county indicates that annual precipitation will increase by 20% until 2100 with a major increase during winter. The rain intensity will also increase.



Figure 2. Aerial photo that shows case study site Block Hake with the rivers Köpingån and Kölstaån. ©2015 Google Image, ©Lantmäteriet/Metria.

In the summary matrix, a mark (cross) or a text is inserted in relevant box for each identified and vulnerability assessed hazard to aid decisions on further investigations/actions (Table 7).

Table 7. Identification and general assessment of the contaminated site's vulnerability to natural hazards and assessment of the need for additional investigation. The soil is contaminated with high to very high concentrations of PAHs, copper, lead and zinc.

Vulnerability to natural hazards	Negligible vulnerability	Minor vulnerability	Moderate vulnerability	Major vulnerability
Soil movement				Not satisfactory stable according to the general slope stability zonation map
Bank erosion			Flood plain deposits, < 100 m to beach, active erosion, partly covered by erosion protection.	
Flooding		Within CMF marked area, only a limited stretch within Q_{100}, active erosion but partly protected from erosion.		
Change in precipitation				Approx. 20% increase in mean annual precipitation, but also increase of heavy rainfall.
Investigation need	No further investigation is needed.	The area cannot be disclaimed from flooding, monitoring is necessary.	Need for further risk assessment regarding erosion, probable need for action.	Urgent need for in-depth risk assessment regarding landslide risk and precipitation increase, action needed.

With respect to the overall analysis, the preliminary assessment is that the contaminated site has major vulnerability to increased spreading of contaminants from landslide and increased precipitation. Also bank erosion may contribute to the spreading of contaminants. The site is hence in need of more detailed investigations and action with respect to slope stability and climate change effects.

3.3 Proposed method for risk estimation of a single object

The approach to estimate possible environmental consequences from contaminated land exposed to natural hazards include three major parts:

1. To set up a conceptual model that describes governing processes for mobilisation of contaminants from natural hazards and that identifies and characterizes impact zones for possible consequences.
2. To define failure criteria for each of the identified impact zones, decide models to calculate probabilities of failures and to set parameter values and parameter uncertainties into these models.
3. Compute the probability of failure for all identified failures and perform a sensitivity analysis of the results to analyse which probability/-ies that governs failure in order to find cost effective measures.

A first and simplified conceptualization is shown in Fig. 3 and that roughly illustrates a contaminated site and how natural hazards may impact the further spreading of pollutants. In anticipation of more knowledge about real consequences, concentration above Predicted No Effect Concentrations (PNEC) for each contaminant is suggested as criteria for failure. A preliminary and general definition of failure is suggested as the probability that any/all of possible natural hazards may cause an increase of contaminants in, for example, the water body above PNEC. This can be written as:

$$P_f = P_L \times P_E \times P_F \times P_{IP} \times P[C_w > PNEC] \quad (1)$$

Where P is the probability, P_f is the probability for failure, P_L is the probability of landslide, P_E is the probability of erosion, P_F is the probability of flooding, P_{IP} is the probability of increased precipitation, C_w is the concentration in the water body. The probabilities should include climate scenarios for futureThe next step in our study will be to identify possible impact zones in the near field and far field, with respect to ecosystems and humans, and to conceptualize the governing pathways. The general definition of failure must then be refined to describe possible failures in each of the impact zones, and models to calculate probabilities will be developed.

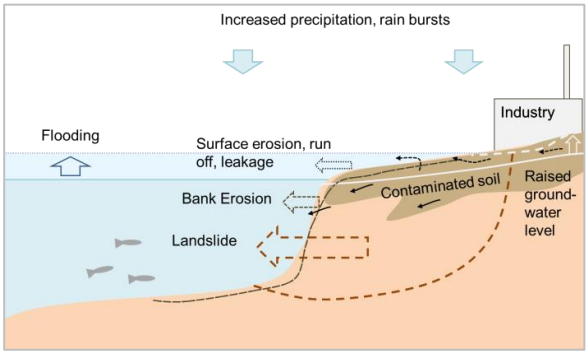


Figure 3. A simplified coneptualization of contaminated land exposed to natural hazards.

4 DISCUSSION

It should be mentioned that the approach presented in this paper is not meant to stand alone for a full risk analysis but is meant to be a complement to existing methods for risk assessments.

The study shows the possibility of using GIS information to identify multi-hazards that otherwise would not have been revealed. By applying one of the quick scan methods an estimation of whether there is vulnerability to natural hazards in contaminated areas can easily be done and decisions on prioritization on detailed investigation and risk assessment can be taken. The quick scan methods will be fully described in a SGI Publication that at the moment is out for review by a number of municipalities, county councils, the Swedish EPA, the Swedish Civil Contingencies Agency, and others. There is a need for instructions for detailed risk assessment and

actions with respect to contaminated sites and natural hazards and how that can be included in already existing methods for risk analysis.

5 ACKNOWLEDGEMENT

The work has been funded by the Swedish Geotechnical Institute.

6 REFERENCES

Bonnard, Ch., Forlati, F., Scavia, C (Eds.) (2004). Idnetification and mitigationof large landslidle risks in Europe. A.A. Balkema Publishers.

Dennis, I., Machklin, M., Coulthard, T., Brewer, P. (2003). The impact of the October-November 2000 floods on contaminant metal dispersal in the River Swale catchemtn, North Yorkshire, UK. Hydrological Processes 17(8), 1641-1657.

Edebalk, P., Carling, M., Göransson, G., Fallsvik, J., Hedfors, J., Odén, K., Branzén, H., Stark, M. (in prep). Bedömning av sårbarhet för naturolyckor vid förorenade områden. SGI Publikation 20.

Glade, Th. (2003). Landslide occurrence as a response to land use change: a review of evidence from New Zealand.

Göransson, G., Bendz, D., Larson, M. (2009). Combining landslide and contaminant risk: a preliminary assessment. J. Soils Sediments 9, 33-45.

Göransson, G., Larson M., Bendz, D., Åkesson, M. (2012). Mass transport of contaminated soil release into surface water by landslides (Göra River, SW Sweden). Hydrol Earth Systm Sci 6, 1879-93.

Göransson, G., Norrman, J. Larson, M., Alén, C., Rosén, L. (2013). A methodology for estimating risks associated with landslides of contaminated soil into rivers. Science of the Total Environment 472, 481-495.

Göransson, G. (2013). Landslide of contaminated soil into rivers – environmental impacts and risks. Dissertation. Lund University, Report No 1059.

Pradhan, B., Chaudhari, A., Adinarayana, J., Buchroithner, M. (2012). Soil erosion assessment and its correlation with landslide events using remote sensing data and GIS: a case study at Penang Island, Malaysia. Environ Monit Asess,

Rhoades, E.L., O'Neal, M.A., Pizzuto, J.E. (2009). Quantifying bank erosion on the South River from 1937 to 2005, and its importance in assessing Hg contamination. Applied Geography 29, 125-134.

Rowan, J.S., Barnes, S.J.A., Hetherington, S.L., Lambers, B., Parsons, F. (1995). Geomorphology and pollution: the environmental impacts of lead mining, Leadhills, Scottland. J of Geochemical Exploration 52, 57-65.

Van Asch, Th., Buma, J., Van Beek, L. (1999). A view on some hydrological triggering systems in landslides. Geomorphology 30, 25-32.

Wynn, T. and Mostaghimi, S. (2006). The effects of vegetation and soil type on stream bank erosion, Southwestern Virginia, USA. J of the American Water Resources Association (JAWRA), 69-82.

Förstärkning av översvämningsdrabbade vägar på torv med lättklinker

Henrik Lundström.
Bohusgeo AB, Sweden, Henrik.lundstrom@bohusgeo.se

Mathias Odén
Leca, Saint-Gobain Byggprodukter, Sweden, mathias.oden@leca.se

ABSTRACT
Roads on peat can be subjected to flooding and settlements causing longer or shorter periods when the roads need to be closed. By elevation of the road profile these problems can be solved. Road renovation and load compensation with lightweight clay aggregate has proven to be a technically as well as financially beneficial methodology to raise the profile for roads on peat.

Keywords: Peat, Leca, Lightweight clay.

1 ALLMÄNT

Under lång tid har det lägre trafikerade vägnätet haft problem med sättningar där undergrunden utgörs av torv. Periodvis har detta vid nederbörd och höga vattenstånd medfört att vägen helt eller delvis legat under vatten. De pågående klimatförändringarna bidrar till att vägarna svämmas över oftare och tillgängligheten minskar, även om sättningarna i torven i det närmaste kan betraktas som färdigutbildade.
Den vanligaste åtgärden har över tid varit att höja vägen med ”tunga” fyllningar vilket gör att sättningarna i torven tar fart igen och många gånger är sättningarna så stora att vägbanan redan efter relativt kort tid ligger på samma nivå som tidigare.

2 VÄG 2029

Nedan redogörs för ett projekt där förstärkning av väg 2029 vid Läresbo utfördes 2004 på en sträcka av ca 150 m. Enligt dåvarande Vägverket utfördes 1999 en höjning av vägen med 0,3 m och efter två år var effekten av höjningen borta då vägen satt sig lika mycket som den höjdes.
Vägsträckan går längs med Öresjö och periodvis svämmades vägen över, se figur 1. Öresjö är en reglerad sjö med en övre dämningsgräns vilket ger högsta högvatten +76,5. Befintlig vägbana är belägen på nivån +76,2 - +76,4



Figur 1. Öresjö finns på höger sida av bilden

2.1 Jordlager

Jordlagren utgörs i princip från vägbanan av:

- 2-3 m tjock vägbank
- 5 m torv
- 1-3 m gyttja
- 13 m lera
- Friktionsjord på berg

Torven har en uppmätt vattenkvot av mellan ca 500 och 1000 % vid sidan av vägbanken. Skjuvhållfastheten är uppmätt till mellan ca 5 och ca 15 kPa vid sidan av vägbanken och mellan ca 20 och ca 25 kPa under vägbanken.

Gyttjan har i regel en uppmätt vattenkvot av mellan ca 200 och ca 250 %. Skjuvhållfastheten är uppmätt till mellan ca 5 och ca 7 kPa vid sidan av vägbanken och mellan ca 15 och ca 20 kPa under vägbanken. **Leran** är i sin övre del gyttjig och vattenkvoten är uppmätt till mellan ca 60 och ca 120 % vid sidan av vägbanken. Skjuvhållfastheten är uppmätt till mellan ca 5 och ca 25 kPa vid sidan av vägbanken.

2.2 Släntstabilitet

Släntstabiliteten för befintlig väg var otillfredsställande och uppfyllde ej gällande krav. Beräkningar med totalsäkerhetsanalys visade på en beräknad säkerhetsfaktor av F=1,0. Föreslagen åtgärd med lättklinker kommer att förbättra släntstabiliteten avsevärt.

2.3 Sättningar

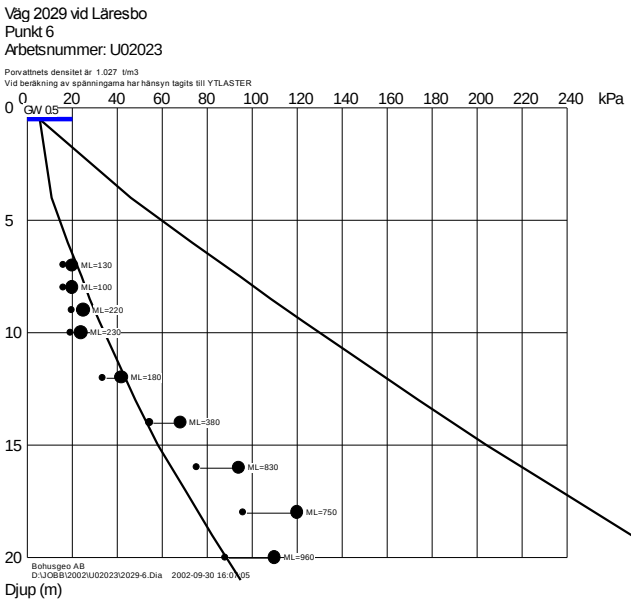
Med ledning av undersökningar genom vägbanken bedödes sättningarna för den befintliga vägen som mest uppgå till ca 2,4 m. Den befintliga vägen är byggd på en stockbädd som ligger på ca 2,4 m djup under vägytan. På delar av sträckan återfanns även en rustbädd ca 1 m under vägytan.

2.4 Grundförstärkning

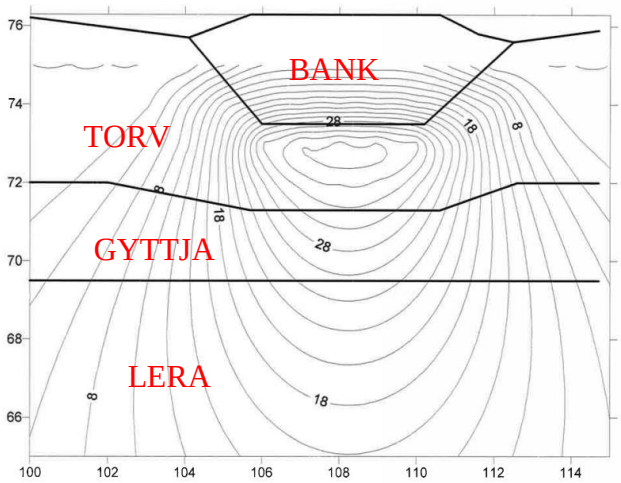
Beräkningsprincipen för grundförstärkningen var enligt följande:

1. Sättningsberäkning för troliga lastfall för befintlig väg där man exempelvis tar hänsyn till den last som fyllning orsakade vid utläggning 1999.
2. Beräkning av sättningar utfördes med beräkningsprogrammet Embankco (beräkningsprogram framtaget av SGI) av troliga kvarstående portryck i underliggande lera för olika lastfall
3. Beräkning av spänningar för hur lastspridningen av ursprunglig vägbank och projekterad lättklinkerfyllningen sprids till underliggande torv, gyttja och lera
4. Beräkningar av kvarstående portryck i leran med hänsyn till avlastningseffekten orsakad av lättklinkerfyllningen.

I figur 2 redovisas lerans konsolideringsförhållanden och i figur 3 redovisas tillskottsspänningen i jorden orsakad av fyllningen för befintlig väg.

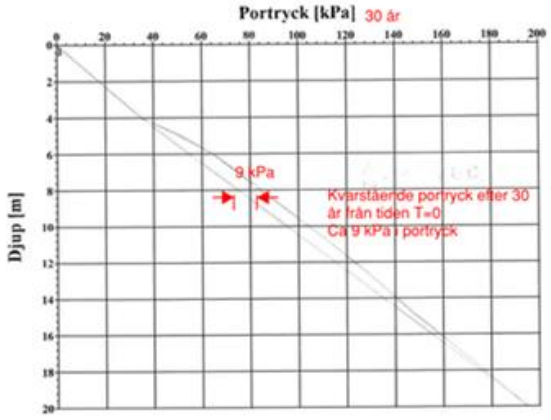


Figur 2. Lerans konsolideringsförhållanden. De stora svarta cirklarna är förkonsolideringstrycket och de små cirklarna är 80 % av förkonsolideringstrycket vilket är den effektivspänning som man i regel antar att krypsättningar börjar utbildas. De heldragna svarta linjerna motsvarartotalspänningen respektive effektivspänningen i jorden.

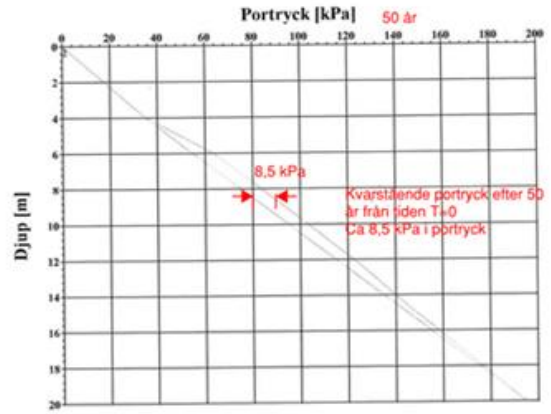


Figur 3. Tillskottsspänningar i kPa orsakad av lasten från vägbanken före lättklinkerfyllningen

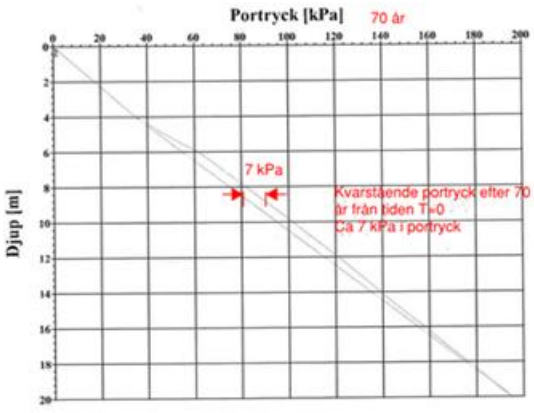
I figur 4 - 6 visas en serie av beräkningar för 30, 50 och 70 år med kvarstående portryck i leran före det att lättklinkern lades ut. Kvarstående portryck i leran beräknas till mellan ca 7 och 9 kPa beroende på hur belastningshistorien över tid har sett ut.



Figur 4. Portryck i leran efter 30 år

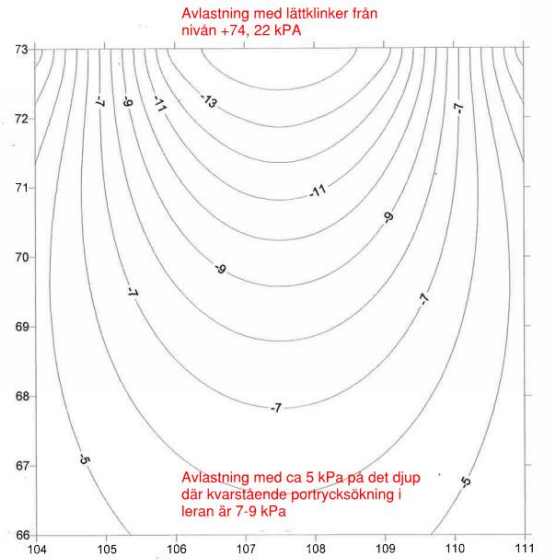


Figur 5. Portryck i leran efter 50 år



Figur 6. Portryck i leran efter 70 år

Hur avlastningen från lättklinkerfyllningen sprider sig mot djupet redovisas i figur 7. Olika alternativ för kvarstående sättningar presenterades för Vägverket och med hänsyn till schaktdjup mm valdes en lättklinkerfyllning som beräkningsmässigt medför att vägbanken kommer att sätta sig upp till ca 0,15 m. Beräkningarna bygger på en kvarstående portrycksökning i leran efter att lättklinkerfyllningen lagts ut på mellan ca 2- 4 kPa.
Kvarstående marginal till HHW blir ca 0,25 m.



Figur 7. Lastspridning för avlastning

3 UTFÖRANDE

För utförande och den slutliga konstruktionen fanns följande frågeställningar som kändes kritiska.

1. Kommer det att gå att hålla läns i schakten ?
2. Är vatteninträngningen hanterbar?
3. Kommer schaktslänterna att vara stabila ?
4. Finns det risk för spårbildning?
5. Hur kommer eventuella sättningar att utvecklas över tid?

Schaktningsarbetet förutsatte att Öresjö inte nådde över befintlig väg för då får man problem med vatten. Under

schaktningsarbetena trängde förvånansvärt lite vatten in i schakten, se bild 8 och 9.



Figur 8. Schakt och återfyllning

Det är dock viktigt att man bevarar en kant och slänt med befintliga schaktmassor så att inte schaktytan kommer i direkt kontakt med torven och att man väljer en torr årstid för arbetena. Vid schaktningsarbetena uppstod en del problem med rustbädden/stockbädden på ca 1 m djup. Uppgrävda stockar ses på vänster sida i figur 8 och 9.
I figur 9 syns även svepningen av lättklinkerfyllningen.



Figur 9. Svepning av lättklinker med nålfiltad geotextil

4 11 ÅR EFTER FÖRSTÄRKNING

Vid platsbesök ca 11 år efter åtgärd syns ingen märkbar spårbildning eller ojämna sättningar på vägbanan, se bild 10. Ett visst ”kanthäng” borde finnas men inte heller det syns. Sannolikt håller geotextilen ihop lättklinkerfyllningen på ett sådant sätt så att konstruktionen blir ganska styv och har då en viss förmåga att jämna ut sättningar. Kontroll av om vägen satt sig har ej utförts.



Figur 10. Väg 2029 ca 11 år efter förstärkning. Öresjö finns till vänster i bilden. Figur 1 visar ungefär samma område som ovan. Kortet är dock taget från andra hållet

5 SLUTSATS

Lättklinker fungerar på ett bra sätt vid förstärkningar av översvämningsdrabbade vägar på torv och det är inget hinder med att vatten kan stå högt vid sidan av vägen om man bara bevarar en slänt och en ”vall” av befintliga massor. För dimensioneringen är det av stor vikt att veta om torven underlagras av gyttja eller lera för att inte komma fel i dimensioneringen. För att veta vad man skall schakta i till exempel eventuella rustbäddar. För att kunna utföra sättningsberäkningar är det nödvändigt att veta tjocklek mm av överbyggnaden vilket kräver undersökningar i och genom vägkroppen.

Landslide hazards in sensitive clays: Recent advances in assessment and mitigation strategies

Vikas Thakur, vikas.thakur@ntnu.no
Norwegian Public Roads Administration, Norwegian University of Science and Technology

ABSTRACT
Sensitive clays, when provoked by artificial or natural causes, have led to several landslide disasters throughout history. Such landslides sometimes involve massive soil movements in the order of millions of cubic meters and represent a major threat to human life, constructed facilities, the infrastructure, and the natural environment. Several efforts are being made in Norway at different levels to ameliorate society's ability to cope with landslides in sensitive clays. In doing so, numerous assessment and mitigation strategies are being developed and implemented. Here, geoscientists (geotechnical engineers and geologists) have a purposeful and systematic role to play by providing reliable tools that can be used for the assessment and mitigation of landslide in sensitive clays. To exemplify this, this paper will present some research results dedicated to sensitive clays from an ongoing intra-governmental research program, Natural Hazard—Infrastructure, Flood and Slides, in Norway. The paper first presents some of the challenges related to the landslides in sensitive clays. Next, it addresses principles regarding requirements with a partial safety factor for local stability as well as a partial safety factor or percentual improvement for large landslides. This paper also points out the manner in which regulations impose increased attention to safety when sensitive clay is encountered. An attempt is made to describe the indicator concerning the prediction of the post-failure movement of landslides. Finally, this paper addresses some ongoing fundamental research being carried-out in Norway to develop new mitigation measures.

Keywords: landslide, sensitive clays, local and overall stability, run-out, natural slopes

1 INTRODUCTION

The work presented in this paper mainly originates from the national research program titled *"Natural Hazards: Infrastructure, Floods, and Slides (NIFS),"* which involves a close collaboration between the Norwegian Water Resources Energy Directorate, the Norwegian National Railways Administration (NNRA), and the Norwegian Public Roads Administration (NPRA). The NIFS project conducted several research activities with the Norwegian Geotechnical Institute (NGI), SINTEF Building and Infrastructure, Multiconsult, Norwegian Geological Survey (NGU), and Norwegian University of Science and Technology (NTNU). In this paper, an effort is made to provide insight into some of the research results related to the assessment and the mitigation of landslide hazards in sensitive clays. The primary aim of this paper is to initiate critical discussions among the relevant scientists, practitioners, and authorities so that well-verified research results can be formulated and implemented into practice.

2 LANDSLIDE CHALLENGES IN SENSITIVE CLAYS

A significant part of the transport infrastructures in Eastern and Central Norway is placed in/on sensitive clays, and a large number of new railways or roads in these regions are being planned on sensitive clay deposits. Sensitive clays constitute a

major threat to nearby infrastructures as they have a tendency to rapidly lose their strength when subjected to excessive shear loading. One must consider the most well-known landslides in Norway: Verdal in 1893 (55 million m³, 116 casualties) and Rissa in 1979 (5 million m³, 1 casualty). It is evident from these that sensitive clays in Norway can cause severe disasters when provoked by artificial or natural causes. Over the last 40 years, there has been approximately 1 or 2 such slides per decade, with a volume exceeding 500,000 m^3 (Oset et al. 2014). Since 1996, no lives have been lost in quick clay landslides, but residential areas and transport infrastructures have been affected to varying degrees of destruction. This is illustrated in Figure 1 (left) using an example of the Mofjellbekken landslides in 2015 that caused the partial collapse of the E 18 Bridge located on the landslide scarp. More than 30 such landslides in Norwegian sensitive clays are reported in the literature listed in Table 1.



Figure 1 Mofjellbekken landslides in 2015 (sources: Orbiton, and Bjorn K Dolva, NPRA).

From these landslides, it is known that a seemingly stable area can be subjected to a major landslide after a small initial slide. Post-failure movement in terms of retrogression distance (L) and the run-out distance (Lu) in these clays is occasionally fast moving, which may involve massive soil volume in the order of millions of cubic meters (See Figure 2).

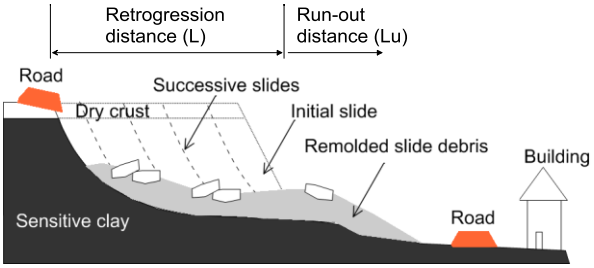


Figure 2 A sketch of retrogressive flow slide in sensitive clays. The retrogression distance (L) and the run-out distance (L_u) are measured from the toe of the slope (Thakur and Degago, 2014).

3 RESEARCH FOCUS

The overall purpose of the work package *sensitive clays* regarding the NIFS project was to obtain a sound basis for the harmonization of the guidelines by the NPRA, NVE, and NNRA. Accordingly, the following research topics were identified:

1. Equity between the local and overall stability of slopes
2. Site investigation database and sensitive clay mapping
3. Sensitive clay landslides along shorelines
4. Detection and characterization of sensitive clays
5. Quantification of the effect of strain softening
6. Post-failure movements
7. Stabilization of critically stable slopes

Research institutions and consultants were engaged to carry out the academic and industrial research as a part of the NIFS project. Some of the key results from the research activities are discussed in this paper.

Table 1 Landslide in sensitive clay (updated after Natterøy (2011), L'Heureux (2012), Thakur et al. (2014a))

Year	Landslide	Type	*L* [m]	L_u [m]	*Volume* [10^5 x m^3]	c_{ur} [kPa]	S_t [-]	I_L [-]	I_P [%]	*References**
1940	Asrumvannet	F				0.1	200	3.1	13	Mayerhof (1957)
1626	Bakklandet	FK	70	50		0.1	30	2	6	Egeland and Flateland (1988)
1988	Balsfjord	F	400		8	1	30	3	6	Rygg and Oset(1996)
1974	Båstad	F	230	700	15	0.53	35	1.8	8	Gregersen and Løken (1979)
1953	Bekkelaget	FK	145	20	1	0.11	150	2.4	11	Eide and Bjerrum (1955)
1953	Borgen	F	165		1.6	0.7	100	1.2	20	Trak and Lacasse (1996)
1928	Brå	FK	197	300	5	0.24	75	2		Holmsen (1929), Reite et al. (1999)
2012	Byneset	F/FK	400	870	3.5	0.12	120	3.9	4.8	Thakur (2012)
1955	Drammen	RS	45		0.04	2.5	4	1.1	11	Eide and Bjerrum (1955)
1625	Duedalen	FK	410		5	0.07	209			Trondheim Municipality reports , Furseth (2006)
1996	Finneidfjord	F	150	850	10	0.4	60			Longva et al. (2003)
1980	Fredrikstad	RS	45	22	1	<0.5	20	1	20	Holmsen and Holmsen (1946), Karlsreud (1983)
1959	Furre	FK/F	300	90	30	0.1	115	2.1	11	Huchinson(1961)
1974	Gullaug	F/FK	150		1.25	2	7.5			Karlsrrud (1979)
1967	Hekseberg	F/FK	700	300	2	0.25	100	2.4	4	Drury (1968)
2014	Hobbel	RS/F	140	200	0.015	<0.2				NGI report nr
2009	Kattmarka	F	300	350	3-5	0.24	63	2.9	8	Nordal et al. (2009)
1994	Kåbbel	F	100	10	1	<0.5	>50	>1.2	20	NVE reports
1944	Lade	F	40	62	0.05	2.12	6.6	1		Reite et al. (1999) Holmsen and Holmsen (1946),
2002	Leistad	FK	250	25		0.15	110	1.5	6	NPRA reports
1989	Lersbakken	RS	65	75	0.75		38-62			NPRA reports
1954	Lodalen	FK	40	10	0.1	17	3	0.8	17	Sevaldsen (1956)
2010	Lyngen	F	153	411	2-3	0.14	51.4	2.1		NVE reports
2015	Motfjellsbakken	FK	80	30	1	0.2	220	2.1	5	NIFS report nr 53/2015
2000	Nedre Kåbbel	RS	120	10	1.8	<0.5	>50	>1.2	20	NVE reports
1978	Rissa	F	1200		50-60	0.25	100	2	5	Gregersen (1981)
1995	Røesgrenda	F	100	50	0.02	0.1	186	>1.2	<10	Larsen (2002)
1974	Sem	FK	100	20	0.68	1.4	8-14			NGI(1974)
1965	Selnes	F	230	>400	1.4	0.35	100	2.3	7	Kenney (1967)
1962	Skjelstadmarka	F	600	2800	20	0.83	80	1.1	10	Janbu (2005)
2014	Statlandet	F	150	1300	3.5	0.2	100	4	3.6	NIFS report nr 93/2014
1816	Tiller	FK			55	0.1	90	2.7	4	Reite et al. (1999)
2012	Torsnes	RS	25		0.063	<0.5			22	NVE reports
1893	Verdal	F	2000	5000	650	0.2	300	2.2	5	Reite et al. (1999)
1959	Vibstad	FK	250	250	10	5	8	0.2	17	Hutchinson JN (1965)

* can be found in the reference list provided by Thakur et al. (2014a)

Landslide types: F = flow slide, FL = flake slide, RS = rotational slide;

Soil poperties: c_{ur} = remolded shear strength, S_t = sensitivity, I_L = liquidity index, Ip = plasticity index

4 RECENT ADVANCES

The NIFS projects and their associated activities have significantly advanced our knowledge related to landslides in sensitive clays. Several research reports are published at www.naturfare.no. In addition, the following articles were released at this conference (Nordic Geotechnical Meeting, 2016):

- *An attempt towards harmonizing the Norwegian guidelines related to construction on sensitive clay*, by Aunaas et al. (2016)
- *In-situ detection of sensitive clays : Part I Selected test methods* by Sandven et al. (2016a)
- *In-situ detection of sensitive clays : Part II Results* by Sandven et al. (2016b)
- *Extended interpretation basis for the vane shear test*, by Gylland et al. (2016)
- *Sample disturbances in the block samples of low plastic soft clays*, by Amundsen et al. (2016)
- *A procedure for the assessment of the undrained shear strength profile of soft clays*, by Thakur et al. (2016)

These papers address sample quality and sample disturbances, regulatory frameworks, the in-situ detection of sensitive clays using e.g., CPTU-R, ERT and AEM, the interpretation of vane shear test results, the effect of strain softening in the stability calculation, strength anisotropy, and the selection of a strength profile. To avoid any repetition and to respect the limited amount of space in this paper, this particular paper is confined to the latest advancements that are not covered by any of the aforementioned papers. At the same time, the authors are referring to these papers to get a complete overview of the contributions made by the NIFS project.

4.1 Local stability, overall stability, and perceptual improvement of material factors

It is a well-known fact that sensitive clays are associated with various risks related to the loss of stability and bearing capacity, as well as substantial ground deformation, which can lead to structural damage and risk regarding the overall stability of an area. The current code of practice (NVE, 2014) suggests that the overall stability of areas that consist of these sensitive clays must be investigated. This overall stability assessment considers areas where there is potential for retrogression and/or the propagation of landslides. It also considers areas that are outside the slide zone but may still be subjected to dangers, such as large movements and structural damages. Therefore, in comparison with local, the overall stability addresses a much wider perspective with respect to the stability of a vast area. Landslide assessments of sensitive clay slopes demand both a local and overall stability calculation (Thakur et al. 2012; Thakur and Degago 2013 &2014; Oset et al. 2014, Aunaas et al. 2016).

However, there has been a challenge in differentiating the extent of local stability from overall stability. In 2014, Frode Oset from the NPRA proposed a pragmatic solution. He suggested that the extent of local stability is the area where the external loading (for example, fill, excavation, etc.) deteriorates the calculated material factor (γ_{mi}) more than 5% in a stability calculation (see Figure 3). This requirement applies for both circular and non-circular slip surfaces.

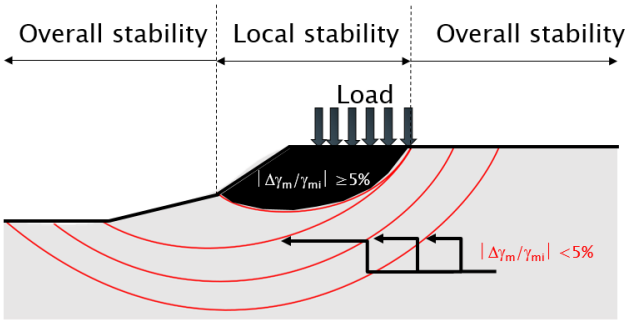


Figure 3 Local and overall stability (Based on NIFS report no. 8/2016).

In 2015, a working group was established by the NIFS project to assess the extent of local

stability according to this suggestion. The working group consisted of

- Kristian Aunaas, Frode Oset, and Hanne Bratlie Ottesen, NPRA
- Stein-Are Strand, Einar Lyche, Trude Nyheim and Ingrid Havnen, NVE
- Margareta Viklund and Mostafa Abokhakil, NNRA
- Odd Arne Fauskerud, Multiconsult AS
- Stein Christensen, SINTEF Building and Infrastructure
- Vidar Gjelsvik, NGI
- Vikas Thakur, NTNU

The NIFS report no. 8/2016, prepared by the working group, validated the proposed solution to determine the extent of local stability using several real cases. The recommended step-wise procedure to calculate the extent of local stability is as follows:

- Select a slope geometry
- Calculate the material factor (γ_{mi}) for sliding surfaces before the external load is placed
- Include the external load in the calculation and find a new material factor (γ_{mo}) for the sliding surfaces from the previous step
- Compare the material factors of the sliding surfaces of the situation before and after the external loading
  - Find $\Delta\gamma_m = \gamma_{mi} - \gamma_{mo}$
  - Calculate $|\Delta\gamma_m / \gamma_{mi}|$
- Identify the part of the slope geometry that is covered by the slip surfaces having $|\Delta\gamma_m / \gamma_{mi}| \geq 5\ \%$ and characterize it as the extent of local stability. This is illustrated in Figure 3.
- If the external loading causes a change in the location of critical sliding surfaces, then the corresponding material factor for this particular slip surface should be calculated for both before and after the loading.
- The safety requirement for the overall stability is based on percentual improvement, as shown in Figure 4.

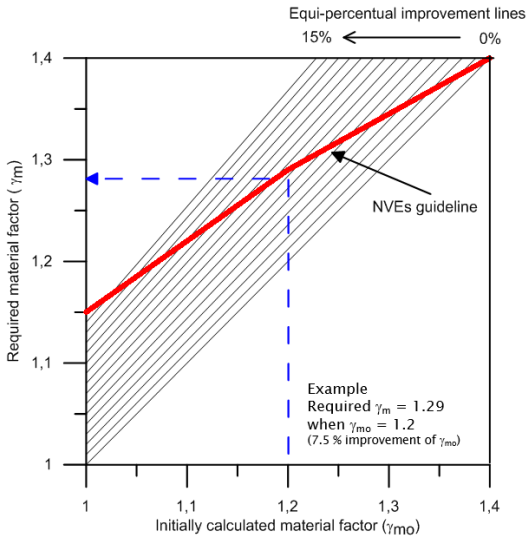


Figure 4 Required material factor (γ_m) for the overall stability of sensitive clay slopes.

- The safety requirement for local stability within the 5% limit deterioration shall be based on the absolute material factor in accordance with the Norwegian Standard or regulations established by the NPRA and NNRA. Safety requirements for impact extend outside the limit based on regulations in TEK 10 and NVEs guideline.

4.2 Total versus effective stress parameters based on stability analysis of natural slopes

The stability of slopes in clays is a geotechnical problem of great social, economic, and technical importance. A good appraisal of slopes' stability is, thus, very important, and it is probably the topic that has received the largest attention in geotechnical engineering. However, there is no unanimity on a specific method to determine strength parameters and analyse the stability of slopes.

In Norway, total stress analysis ($\phi = 0$) is mostly used. The validity of the $\phi = 0$ analysis for calculating the "end of construction" stability of slopes, cuttings, the bearing capacity of footings, and fillings on

clay has been very well adopted in Norway and elsewhere. Leroueil et al. (1983) suggest a pragmatic approach to estimate the factor of safety from total stress based on the over consolidation ratio (OCR) because it seems to be a major factor influencing the factor of safety in total stress analyses. Canadian scientists propose a rough estimation as follows:

Factor of Safety ~ 0.9 OCR

It appears from this equation that, for normally or nearly normally consolidated clays, the factor of safety is not far from 1.0, and it is thought that this is the main reason why total stress analysis has enjoyed certain success in Scandinavia and not in Eastern Canada, where the clays are more heavily overconsolidated. Leroueil et al. (1983) have tested this equation for several landslide cases and found that this simplified approach is rather pragmatic.

However, there has been a longstanding discussion in Norway whether $\phi = 0$ analysis is a rational approach to calculate the stability of natural slopes and if one can use the safety level obtained from using the c-ϕ method (effective stress parameter-based drained analysis) for natural slopes. To achieve a consensus in the geotechnical community in Norway, a working group was established by the NIFS project regarding this definition. The working group consisted of:

- Kristian Aunaas, Frode Oset and Hanne Bratlie Ottesen, NPRA
- Stein-Are Strand, Einar Lyche, Trude Nyheim and Ingrid Havnen, NVE
- Margareta Viklund and Mostafa Abokhalil, NNRA
- Odd Arne Fauskerud and Anders Gylland, Multiconsult AS
- Stein Christensen, SINTEF Building and Infrastructure
- Kjell Karlsrud, Vidar Gjelsvik, NGI
- Steinar Nordal and Arnfinn Emdal, NTNU

Due to the lack of space, only selected recommendations are presented in this paper. Readers are referred to the NIFS report to be published in 2016 to get complete information.

The working group recommends that the drained analysis of slope stability analysis can be allowed for natural slopes in sensitive clays if:

- The slope has a stable and steady stress state situation, that is, the slope is not experiencing stress changes due to, for example, natural erosion
- Natural seasonal variations in ground water conditions are included in the calculation
- The slope is not influenced by extreme precipitation
- The slope has an over consolidation ratio (OCR) greater than 6

Assessing the pore pressure situation is the biggest challenge using the effective stress parameters based analysis. The effect of natural variations in the pore pressure situation due to seasonal variations, extreme precipitation must be accounted in the calculation. Climate-induced changes must be taken into consideration in relation to changes in future ground water levels and the ground water flow regime. The basic premise of adding effective stress parameters based drained analysis as a basis for the stability assessment of a natural slope is that it is not exposed to the geological or human-activities resulting in a deterioration of safety level.

Drained analysis should be considered only if the initial slide (local stability) is not involving the sensitive clay layer in the slope. Stress changes leading to increased shear mobilization in a short duration should be treated as an undrained condition. Both human activities and natural causes such as erosion over a short time can cause an undrained situation in natural slopes. A pore pressure profile should be included in the design basis based on effective stress analysis. Robustness against other natural load variations must be taken into account in the parameter selections. The working group has further advised new criteria for

perceptual improvements of the safety level of natural slopes.

4.3 National database for site investigation results

White paper no. 15 (March 30, 2012) by the Norwegian Parliament emphasizes, among other things, the importance of information being made available from site investigations. The Norwegian Geological Survey (NGU), together with the NIFS project, among others, has developed a national database for site investigation (NADAG), which is a tool for the more effective collection and use of site investigation data. The cost-benefit analysis performed by VISTA assesses the annual economic benefit from such a database as 6 to 7 times higher than the costs for the construction and operation of the database itself (the NIFS project). The NADAG database is now available at http://tempgeo.ngu.no/kart/nadag/.

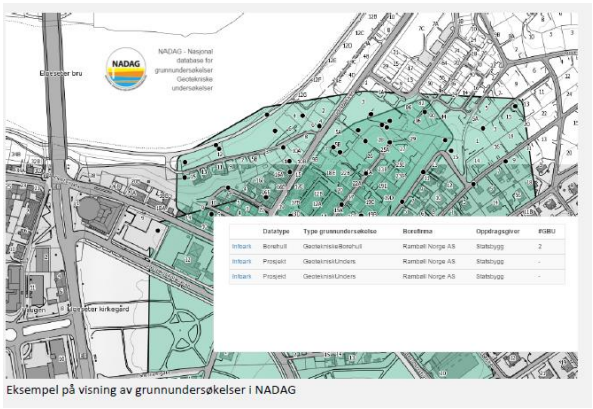


Figure 5 A snapshot from the NADAG database. The dots on the figure refer to the location of boreholes.

4.4 Post-failure movements

Thakur et al. (2014a) present a comprehensive overview of several parameters that may influence the extent of landslides, for example, topography, stability number (*Nc*), remolded shear strength (c_{ur}), liquidity index (I_L), and quickness (Q). The Norwegian landslide data support the fact that large landslides with a retrogression greater than 100 meters are only possible when c_{ur} < 1.0 kPa or I_L >1.2 or Q> 15% and N_c > 4. These criteria are useful and can be utilized as indicators to assess the potential for the occurrence of large landslides (Thakur et al. 2013). However, determining the extent of a landslide with only an individual geotechnical parameter may not be sufficient. A working group was established by the NIFS project to propose an empirical approach to estimate the run-out distance of landslides in sensitive clays. The group consisted of:

- Kristian Aunaas, Frode Oset og Hanne Bratlie Ottesen, NPRA
- Stein-Are Strand, Einar Lyche, NVE
- Odd Arne Fauskerud, Multiconsult AS
- Kjell Karlsrud, Jean-Sebastien L'hueruex, Vidar Gjelsvik, NGI
- Vikas Thakur, NTNU

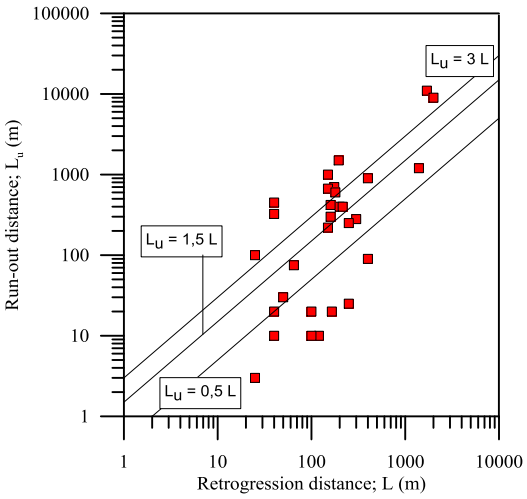


Figure 6 Retrogression distance versus run-out distance (based on Table 1 and Thakur et al. 2014a).

To determine the probable post-failure movements of sensitive clay landslides, it is necessary to identify the landslide type, the the retrogression length (L), and the topography of the downstream region. Accordingly, the following empirical relationships have been proposed by the working group to calculate the run-out distance in sensitive clay landslides (See also Figure 6):

Retrogressive landslide in channelized terrain

$$Lu = 3 * L \qquad (1)$$

Retrogressive landslide in open terrain

$$Lu = 1.5 * L \qquad (2)$$

Flakes or rotational landslide

$$Lu = 0.5 * L \quad (3)$$

A retrogressive landslide occurs when at least 40% of the landslide volume is sensitive clay. Flow slide-type retrogressive slides occur when the remolded shear strength of involved sensitive clays is lower than 1.0 kPa. A flak landslide may occur when the normal thickness of sensitive clay is less than 40% relative to the critical sliding surface, typically in which the sensitive clay is located in layers approximately parallel to the terrain. A flake-type landslide is often registered when the thickness of sensitive clays is relatively low, typically less than 10% to 20%. Rotational landslides, without further retrogressive landslide development, occur when the thickness of sensitive clays is under 40% compared to the critical sliding surface and the location of the slip surface is below terrain level at the toe.

The numerical modeling of the run-out distance of sensitive clay debris has so far received very little focus. Different approaches and methods have been developed in the past for a quantitative risk analysis using dynamic run-out models for debris flows and avalanches. Some of the commonly used models to estimate run-out distances are quasi-two-dimensional numerical models, for example, BING (Imran et al. 2001) and NIS (Norem et al. 1987), and quasi-three-dimensional models, for example, DAN3D (Hungr 1995; McDougall & Hungr 2004), MassMov2D (Beguería et al. 2009), LS-RAIPD (Sassa 1988), and RAMMS (Christen et al. 2002). However, none of these tools is specifically developed for the estimation of the run-out distance of sensitive clay debris. This can be perhaps attributed to, among other factors, an insufficient knowledge about the complex rheological behavior of sensitive clay debris. Accordingly, as a first step, it would be logical to focus on the rheology of sensitive clay debris using existing and available numerical tools before heading for a new numerical tool for modeling the run-out of such types of material. There exist several rheological models, in the numerical tools mentioned above, for run-out modelling (Thakur et al. 2014b). This is illustrated using a very preliminary study presented by Thakur et al. (2014b) to model the run-out of sensitive clay debris using a plastic rheological set-up in DAN3D using a real case, the Byneset flow slide, from Norway. The Byneset flow slide took place on January 1, 2012, in a highly sensitive clay deposit. The slide is located in the central part of Norway. The actual reason for the initiation of the flow slide is unknown, but it is believed that the slide was initiated due to natural erosion at the toe of the slope. The slide area was approximately 150 m in width. The flow slide retrogressed backward to a distance approximately 450 m from the toe of the slope. The slip surface was located between 10-12 m below the terrain. The volume of the slide debris was estimated to be on the order of $3 – 3.5 \times 10^5$ m^3.

Table 2. Soil properties of the sensitive clay involved in the Byneset flow slide.

Unit weight γ kN/m^3	Undrained shear strength c_{ui} kPa	Plasticity index I_p %	Liquidity index I_L	Fall cone yield strength c_{ur} kPa
20	20 – 30	5 –7	5 –7	0.1

The plastic rheology is related to a pseudo-static motion of liquefied debris. The base shear resistance (τ) is assumed to be equivalent to a constant yield strength (c_{ur}) value.

$$\tau = c_{ur} \quad (4)$$

The yield strength (c_{ur}) of sensitive clays in this case is fully remolded shear strength obtained using the fall cone test. The plastic rheology is found to be the simplest among all the rheological models implemented in DAN3D. The rheology required only γ and c_{ur} values, which are easily obtainable (Thakur et al. 2014b). The flow deposit contours obtained from the plastic rheology, with c_{ur} = 0.1 kPa, are shown in Figure 7. The total run-out of the slide debris obtained at the end of the simulation is quite similar to that observed in the field.

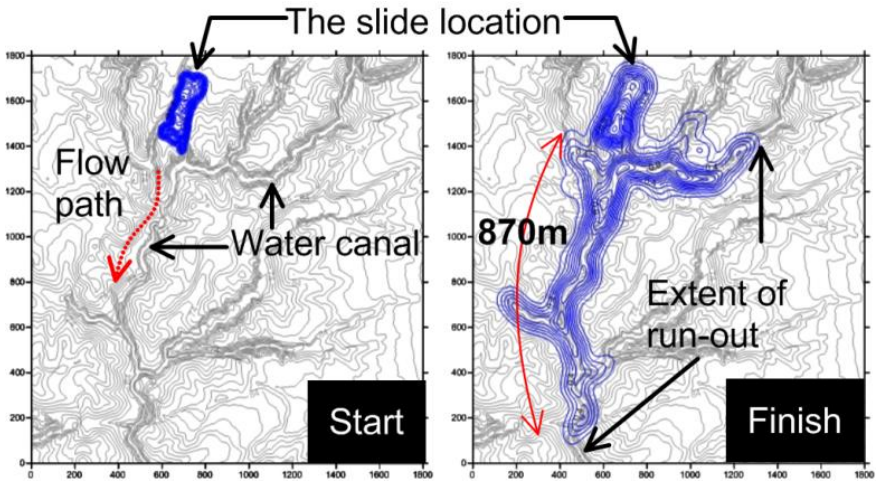


Figure 7 Flow contours obtained from the plastic rheology with c_{ur} = 0.1 kPa (Thakur et al. 2014b).

Thakur et al. (2014) further studied the plastic rheology to see the effect of c_{ur} on the run-out distance for a given geometrical set-up. In Figure 8, the run-out distance was plotted at varying values of c_{ur} to depict the effect of the shear strength on the flow. The result shows that run-out distance logarithmically reduces with increasing c_{ur}. Similarly, the development of run-out with simulation run-out time, plotted in Figure 6, shows that sensitive clays having higher c_{ur} will need less time to reach their final extent of run-out. As an exception, when the basal shear resistance is close to zero, for example, c_{ur}= 0.01 kPa, the extent of run-out and the velocity of debris will primarily be controlled by the topographical aspect.

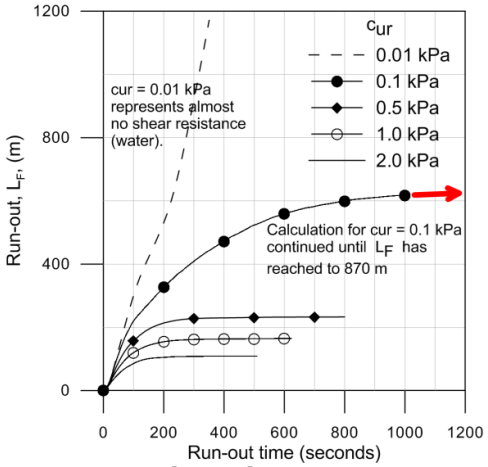


Figure 8 Flow distance at varying shear strengths (Thakur et al. 2014b). L_F in the figure refers to Lu in the context of this paper.

Thakur et al. (2014) use a simplified approach to investigate a very complex problem that has yet to be fully understood. Therefore, several simple approximations were necessary in order to focus on the role of certain parameters governing the basal rheology on the run-out of sensitive clay debris. Thakur et al. (2014) also found that the plastic rheology and the friction rheology seem to predict the run-out distance of the flow slide in Byneset reasonably well. However, the Bingham rheology and the Voellmy rheology, which are sophisticated models, require more parameters that are not readily available for sensitive clays. To advance the knowledge in this area, Issler et al. (2012), NIFS reports no. 38/2013 and 39/2013, Nigussie (2013), Yifru (2014) compared the input parameters of the various models implemented in DAN3D and RAMMS. Similarly, Grue (2015) attempted to measure viscosity on Norwegian sensitive clays. These studies are valuable in developing an advance phehological model that can be used for quick clay slides. Run-out modelling of sensitive clay landslides is an ongoing research activity in Norway as a part of the GeoFuture II project.

5 RESEARCH ON MATERIAL BEHAVIOR

The NIFS project supports two PhD studies at NTNU that deal with the material behavior of sensitive clays. The PhD study by Tonje E. Helle is related to quantifying the improved

geotechnical properties as a result of treating the clay with salt (KCl). The research work includes a large-scale field test related to salt infiltration in sensitive clay layers. Helle et al. (2015a & b) show a significant improvement in the undrained shear strength and the pre-consolidation pressure of a sensitive clay sample after salt treatment. Refer Figure 9 for a typical laboratory test result. The preliminary observations made by this PhD work advocates that due to its beneficial effect on the strength and the deformation properties e.g., intact/remolded shear strength, liquid limit, and plasticity, the salt infiltration technique seems to suit for the stabilization method in sensitive clay slopes.

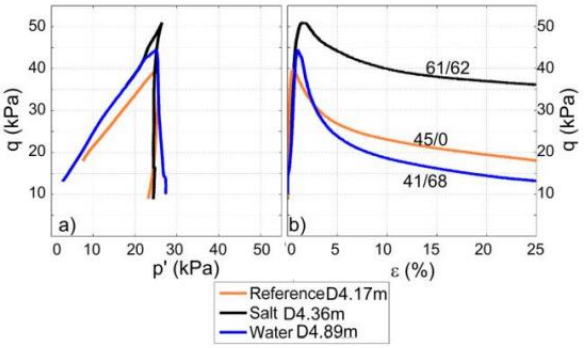


Figure 9 Results from the anisotropically consolidated triaxial test on a block sample and samples stored in de-aired water and KCL. Here, q is the deviatoric stress, p' the mean effective stress, and e the axial strain. Storage time in days is marked in the figure to the right (source: Helle et al. 2015b).

The reliable characterization of fine-grained soil samples requires undisturbed sampling, followed by careful material handling. However, this is not a straightforward task. Moreover, experiences show that, because of the restricted capacity of geotechnical laboratories, fine-grained soil samples are rarely tested immediately after sampling. The storage time of samples may vary from days to weeks and can be as long as several months. A long storage time can significantly alter the behavior of fine-grained soil samples. A PhD study by Helene Alexandra Amundsen is exploring this aspect. Amundsen et al. (2015) show that low plastic sensitive clay samples may behave very differently, even with the matter of a few hours of storage, if the impact of stress relief during the sampling is great (See Figure 10). This PhD work is aiming to find suitable measures to handle this type of challenges in sensitive clay soil samples.

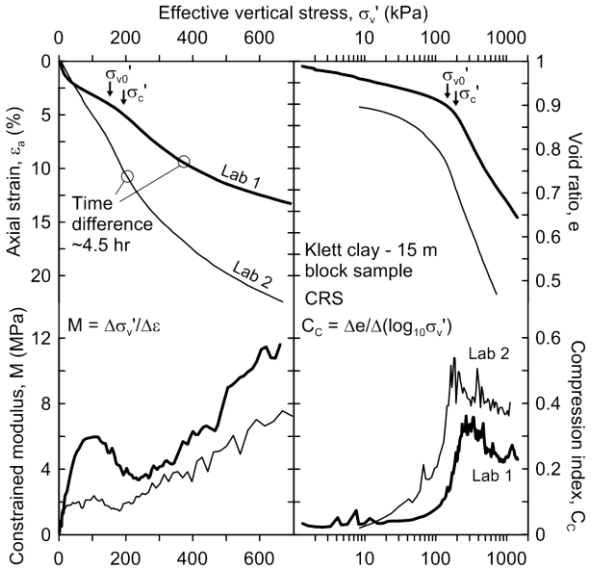


Figure 10 Effect of stress relief and the storage time is illustrated using the non-unique response from a single block sample from Klett tested by two different laboratories (source: Amundsen et al. 2015).

6 CONCLUDING REMARKS

This paper presents some recent advancements made by the NIFS project in relation to the assessment and the mitigation of landslides in sensitive clays. In doing so, a criterion for the estimation of the extent of local stability, the condition for the use of drained stability analysis in natural slopes, and the empirical correlations to estimate run-out distance is addressed in brief. Fundamental research related to salt infiltration in sensitive clays and the effect of storage time in sample quality is discussed. These advancements provides a necessary basis to harmonizing the guidelines by the Norwegian agencies such as NNRA, NVE and NPRA.

7 ACKNOWLEDGEMENT

The author of this paper would like to acknowledge, among others, F. Oset (NPRA), K. Aunaas (NPRA), H. B. Ottesen (NPRA), S. A. Degago (NPRA), B K Dolva (NPRA), S.A. Strand (NVE), E. Lyche (NVE), T. Nyheim (NVE), I. Havnen (NVE), E. E. D. Haugen (NVE), M. Viklund (NNRA), M. Abokhalil (NNRA), V. Gjelsvik (NGI), J.S. L'heuruex (NGI), H. P. Jostad (NGI), K. Karlsrud (NGI), O. A Fauskerud (Multiconsult AS), R. Sandven (Multiconsult AS), A. Gylland (Multiconsult AS), S. O. Christensen (SINTEF), I.L. Solberg (NGU), S. Nordal (NTNU), A. Emdal (NTNU), T.E. Helle (NTNU), H. Amundsen (NTNU) for their valuable contribution to the NIFS project.

8 REFERENCES

Amundsen, H.A. Emdal, A., Sandven, R., Thakur, V. (2015). On engineering characterisation of a low plastic sensitive soft clay. On engineering characterisation of a low plastic sensitive soft clay, GeoQuebec2015 - Challenges from North to South.

Amundsen, H.A. Emdal, A., Thakur, V. (2016) Sample disturbance in block samples of low plastic clays. NGM, Iceland.

Aunaas, K. et al. (2016): An attempt towards harmonizing the Norwegian guidelines related to construction on sensitive clay. NGM, Iceland.

Begueria, S. et al. (2009). A GIS-based numerical model for simulating the kinematics of mud and debris flows over complex terrain. Natural Hazards and Earth System Sciences, 9, 1897–1909.

Christen, M. et al (2002). AVAL-1D: An Avalanche Dynamics Program for the Practice. In: International Congress Interpraevent 2002 in the Pacific Rim - Congress publication, 715-725.

Grue R.H. (2015). Rheological Parameters of Norwegian Sensitive Clays, Focusing on the Herschel-Bulkley Model. Master thesis, NTNU

Gylland et al. (2016). Extended interpretation basis for vane shear test. NGM, Iceland.

Helle, T.E. et al. (2015a) Long-term-effect of potassium chloride treatment on improving the soil behavior of highly sensitive clay – Ulvensplitten, Norway. Canadian geotechnical journal, DOI: 10.1139/cgj-2015-0077.

Helle, T.E. et al. (2015b). Laboratory setup to evaluate the improvement of geotechnical properties from potassium chloride saturation of a quick clay from Dragvoll, Norway. GeoQuebec2015 - Challenges from North to South.

Hungr, O. (2005). Classification and terminology. Debris-flow hazards and related phenomena, 9–24, Springer.

Hungr, O., et al. (2005). Estimating landslide motion mechanism, travel distance and velocity. In: Hungr, O., Fell, R., Couture, R., Eberhardt, E. (Eds.), Landslide Risk Management, 99–128, Taylor & Francis Group.

Imran, J., et al. (2001). 1D numerical model of muddy subaqueous and sub aerial debris flows. Journal of Hydraulic Engineering, 127(11), 959–968.

Issler, D. et al. (2012). Back-analyses of run-out for Norwegian quick-clay landslides. NIFS report available at www.naturfare.no.

L'Heureux, J. S. (2012) A study of the retrogressive behaviour and mobility of Norwegian quick clay landslides. Proc. 11th INASL, 981–988.

Leroueil S., Tavenas F. and Le Bihan, J.P. (1983). Propriétés caracteristiqués des argiles de l'est du Canada. Canadian Geotechnical Journal, 20, 681–705.

McDougall, S. & Hungr, O. (2004). A model for the analysis of rapid landslide motion across three-dimensional terrain. Canadian Geotechnical Journal, 41, 1084–1097.

McDougall, S. (2006). A new continuum dynamic model for the analysis of extremely rapid landslide motion across complex 3D terrain. PhD thesis, University of British Columbia, Vancouver, Canada.

Natterøy, A. (2011). Skredkatalog om kvikkleire. Semester Project, NTNU.

NIFS report nos 38/2013, 39/2013, 93/2014, 53/2015, 8/2016, www.naturfare.no .

Niggusie, D. (2013). Numerical modelling of run-out of sensitive clay slide debris. Master thesis, NTNU.

Norem, H., Irgens, F. and Schieldrop, B. (1987). A continuum model for calculating snow avalanche velocities", In: Avalanche formation, movement and effects, Proceedings of the Davos symposium, IAHS publication no. 162, 363–379.

Norem, H., Locat, J. and Schieldrop B. (1990). An approach to the physics and the modeling of submarine flowslides. Marine Geotechnology, 9, 93–111.

NVE (2014). Construction on brittle clays. Guidelines by NVE, Norway.

Oset, F. et al. (2014). Regulatory framework for road and railway construction on the soft sensitive clays of Norway. Advances in Natural and Technological Hazards Research, 36, 343-354.

Sandven et al. (2016) Detection of sensitive clays: Part I and II. NGM, Iceland.

Sassa, K. (1988). Special lecture: Geotechnical model for the motion of landslides", In: C. Bonnard (ed.), Proc. of 5th Symp. on Landslides, 37–55.

Thakur V. et al. (2012) A critical appraisal of the definition of Brittle clays (Sprøbruddmateriale). Proc. 16th Nordic Geotechnical Meeting Copenhagen, 1, 451– 462.

Thakur, V. et al. (2014a). Characterization of post-failure movements of landslides in soft sensitive clays. Natural Hazards book: Advances in Natural and Technological Hazards Research, 36, 91-103.

Thakur, V., & Degago, S.A. (2012). Quickness of sensitive clays. Géotechnique Letters, 2(3), 87–95.

Thakur, V., & Degago, S.A. (2014b). Quickness approach for assessment of flow slide potential. Inter. Journal SEAGS & AGSSEA, 45(1), 85-94.

Thakur, V., & Degago, S.A. 2013. Disintegration of sensitive clays. Géotechnique Letters, 3(1), 20–25.

Yifru, A. (2014). Assessment of Rheological Models for Run-out Distance Modeling of Sensitive Clay Slides, Focusing on Voellmy Rheology, Master thesis, NTNU.

NIFS project. www.naturfare.no

The Refne landslide, Halden, Norway: case history and use of risk assessment

T. F. Smaavik
NGI, Norway, tone.fallan.smaavik@ngi.no

H. Heyerdahl
NGI, Norway

ABSTRACT
In 2014, a landslide in a steep slope beneath an apartment block in Refne in the city of Halden, Norway led to the evacuation of over 60 residents from their homes.
The landslide is assumed to have been triggered by unusually high levels of rainfall over the preceding months, leading to accumulative long-term rainfall not previously seen in the lifetime of the block. Raised groundwater level and increased pore water in the saturated and unsaturated (vadose) zones are assumed to have contributed to reduced stability of the slope.

An initial risk assessment was performed to aid communication with local authorities and stakeholders and to clarify necessary actions. Following the evaluation of potential scenarios affecting the structural integrity of the pile foundations, the risk to residents was found to be unacceptable, and evacuation was therefore maintained. In particular, the potential development of a quick clay slide would have had catastrophic consequences. In order to improve the basis for further risk analyses and allow the design of stabilising measures, geotechnical site investigations (SI) were undertaken. Following the SI results and the completion of stabilising measures, an updated risk analysis was issued. This concluded a reduced level of risk for all landslide scenarios previously evaluated, and that the risk to residents was adequately reduced.

This paper shows how the visualization of risk using diagrams for risk analysis enabled communication and understanding between the geotechnical and structural engineers, police, local authorities and other stakeholders throughout the project, and formed the basis for decisions regarding evacuations and necessary mitigation measures. Engineering judgment is essential when reviewing risks in any natural hazard situation. Graphical risk analysis tools allow experience to be quantified and communicated to both experts and laymen alike so that operational decisions regarding public safety can be taken.

Keywords: Landslide, risk assessment, risk communication.

1 INTRODUCTION

In 2014, a landslide in a steep slope beneath an apartment block in Refne in the city of Halden, Norway, led to the evacuation of over 60 residents from their homes.

This paper shows how the visualization of risk using diagrams for risk analysis enabled communication and understanding between the geotechnical and structural engineers, police and local authorities throughout the project, and formed the basis for decisions regarding evacuations and mitigation measures.

2 BACKGROUND

NGI was first contacted by local residents regarding cracks and displacements on top of a 16 m high, steep slope beneath the apartment block. An inspection was carried out by NGI and it was discovered that a large slope instability had developed. The slope had deformed visibly and a continuous crack had developed covering the full width of the slope beneath the apartment block. Along the crack, the slope had a vertical deformation of approx. 0,5-1 m. The southern part of the crack followed a ridge leading down to the Refne stream (Figure 2).

The deformations of the slope had uncovered the corner pile foundation, situated at the brink of the slope (Figures 1, 2 and 3).

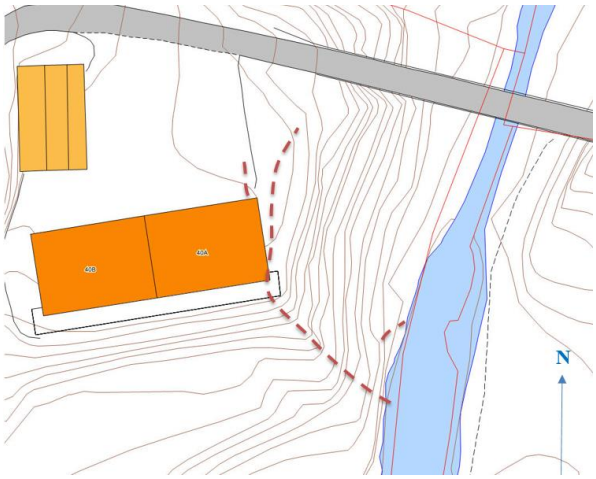


Figure 1 Location of the apartment block and approximate location of cracks in slope. The slope was 16 m high.



Figure 2 The backscarp of the slide. Vertical deformation 0,5-1 m.

Deformations along the side of the block were approx. 1,5-2 m. The backscarp of the slide coincided with the corner pile of the block partially exposed the corner pile foundation (Figure 3). The pile guided the crack in the way that the direction of the backscarp was forced outside the pile.

Following NGI's first inspection, grave concerns for the further development of the landslide and the structural integrity of the pile foundations were communicated to the municipality and the local police authority.

Based on NGI's evaluation of the situation based on available data, the police decided to evacuate all residents from the building.



Figure 3 Backscarp of the landslide restricted by the pile foundation. Concrete pile supporting the corner foundation visible.

3 STAKEHOLDERS

The evacuation of 65 residents involved numerous stakeholders with different requirements and relationships, a few of them mentioned below.

Østfold Police - Although NGI can notify the police of a concerning situation, the local police are ultimately responsible for making a decision regarding the need for evacuation, and when and whether it is safe to return.

Halden Kommune - The municipality is responsible for residents' safety and emergency housing, and have a communications officer for emergency situations.

Insurers and underwriters - Once an evacuation becomes a longer term situation, each resident's insurance policy would come into effect. A separate insurance policy concerned actual damage to the structure itself.

Residents co-ownership committee - The residents had an elected representative who served as NGI's client and who took part in meetings with NGI and other stakeholders.

Print and TV media - Local and national media were involved, most heavily in the early phases when there were more questions than answers.

All stakeholders looked to the engineers for answers on duration of evacuations and cause and effect, as well as future development, of the landslide. Many of the questions lay outside of NGI's mandate and responsibility, and it was therefore essential that communication was as clear as possible.

The day following the evacuation, all stakeholders (except the press) met on site for briefing and later in the town hall to conclude a first statement and suggested process for the further work, need of supplementary information and establishment of responsibilities, tasks and formal roles.

All subsequent results and reports from NGI were issued to the residents' representative who could distribute to other stakeholders.

In later stages the County Governor, the Norwegian Water Resources and Energy Directorate and several contractors were also involved.

4 EMERGENCY PHASE STRUCTURAL AND GEOTECHNICAL ASSESSMENT

4.1 Geology

Geological mapping (NGU, 2014) showed that the area consists of thick deposits of marine sediments, predominantly clay, and that undulating bedrock is locally exposed. Rivers and streams have formed steep ravines, such as the one past the apartment block, seen in Figure 1.

Combinations of slope geometry, river erosion, ground conditions and pore water pressures can reach critical states leading to triggering of small or large landslides. Two known landsides had occurred just upstream of the block in the previous three years. One of these was in a steep silt slope where NGI subsequently designed ground improvement measures.

There were no known quick clay zones in the area, but in areas with marine sediments, it must always be considered a possibility until an SI can document otherwise.

4.2 Foundations and structural sensitivity

The five story block was built in 1974 on driven concrete pile foundations. A sand fill of approx. 2 m was built at the construction site before the piles were driven (Figure 3). Information from construction workers taking part in the construction work in the 1970s indicated that soft, sensitive clay might have been encountered during installation of piles. Assumptions based on typical building methods, construction drawings from local archives and the geological setting formed the basis for the assessment of the block's sensitivity to ground movements and expected behaviour should any of the foundations fail. The early stage evaluation was that failure in any of the piles closest to the landslide could leave the block uninhabitable.

4.3 Geotechnical assumptions and first evaluation

At the initial stage, no ground investigations or detailed knowledge of the local ground conditions were available, however, assumed depth to bedrock under the block was known from construction drawings documenting installation of piles. Decisions in the early phase therefore had to be based on very limited information. Different stakeholders, such as local government employees and politicians, spokespersons for the residents, insurance companies and the police, were all involved in the discussions regarding the need for continued evacuation and required measures, as well as the geotechnical and structural engineers.

Based on results from preliminary geotechnical site investigations (SI) and evaluations, it was concluded that the stability of the slope was not acceptable and that stabilising measures would be required. The question to be answered from day to day was whether the evacuation of inhabitants

from the block would remain, or whether people could move back in to all of, or parts of, the building. From a geotechnical point of view, there was no doubt that the slide would, with time, develop further if measures were not taken. However, with no visible damage on the building and a large number of inhabitants evacuated from the building, the pressure was high to allow people to move back into their homes.

There was an obvious need to aid the communication and enhance the common understanding of the actual risk, taking uncertainties at this early stage and potential consequences of the landslide into account. It was decided to illustrate the situation to the residents and local authorities through a risk assessment for the relevant scenarios.

5 RISK THEORY

Guidelines from the Norwegian Directorate for Civil Protection (DSB, 2011), were used as basis for deciding appropriate probability (return period) boundaries and categorising risk. No current standard or regulation exists for geotechnical stability of existing structures, however the Norwegian project NIFS (Natural hazards, Infrastructure, Flooding, Landslides) have recently suggested risk acceptance criteria (NIFS, 2014).

Table 1 Probability classes for landslide if no stabilising measures are taken

Probability class, P		**Description**
1	Unlikely	1/300 per year Or the scenario cannot occur
2	Less likely	1/50 per year Scenario can happen within 50 years
3	Likely	1/10 per year Scenario can happen within 10 years
4	Very likely	1/1 per year Scenario expected to happen within 1 year

The suggested upper probability before evaluation of measures is needed for existing structures is 1/300 per year (Table 1). In an emergency situation a higher probability could be acceptable for a limited time period but would have to be compensated by increased monitoring of the situation.

Probability classes based on return periods are well known to most people in the context of flooding and are, with some exceptions, translatable and relatable to landslides.

For the case of the apartment block, the consequences in terms of damage to the structure, and whether the block would be considered habitable with a certain level of damage, were considered based on landslide scenarios defining a certain damage to the pile foundations (Table 2).

Table 2 Consequence classes - Damage to structure

Consequence class, C		**Description of damage**	**Block habit-able?**
1	Negligible	Small deformations / lines	Yes
2	Moderate	Deformations / cracks	No
3	Critical	Large structural damage	No
4	Catastrophic	Complete failure	No

Table 3 Evaluating risk from probability and consequence

Risk of damage		Consequence, Table 2			
		1	2	3	4
Probability of scenario which will cause damage, Table 1	1	L	L	L	M
	2	L	L	M	H
	3	L	M	H	H
	4	M	H	H	H

Where risk classes are indicated by colours:
Green: **L**ow. Acceptable risk
Yellow: **M**oderate. Risk needs further assessment
Red: **H**igh. Unacceptable risk

The evaluation of risk is the combination of probability and consequence (Table 3). Thus, an unlikely scenario with catastrophic consequences or a very likely scenario with negligible consequences can still be deemed unresolved and require further assessment.

6 EARLY STAGE EVALUATION AND COMMUNICATION OF RISK

6.1 Probability of given scenarios

Based on available SI results, structural evaluation and the development of the landslide in the early stage, five scenarios were evaluated, each resulting in a specified damage on the pile foundations due to further development of the landslide.

A. Quick clay slide:

If potential quick clay under the block was to slide, all piles would likely follow the slide, break or buckle (Figure 4). Soundings performed in the first phase of the SI did not indicate quick clay underneath the building, but the scenario could not be eliminated before samples were taken and analysed. However, it was deemed unlikely that quick clay could be exposed as a result of further development of the landslide, thereby triggering a major quick clay landslide involving the building, i.e. the lowest probability class P1 was assigned.

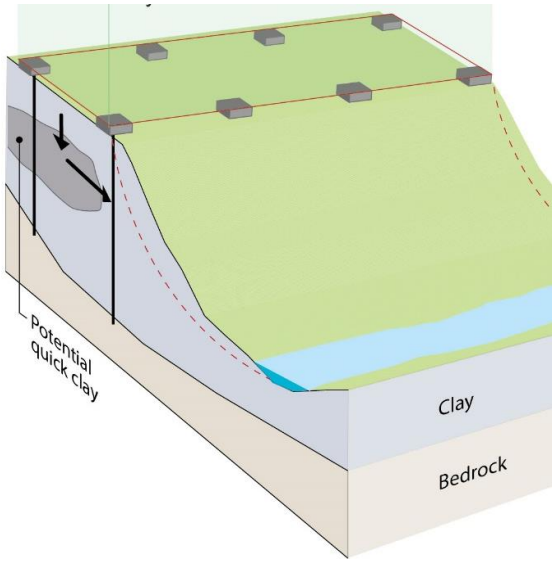


Figure 4 Scenario A - quick clay slide

B. Damage to corner pile:

One of the concrete piles under the block was partly exposed by the landslide (Figure 3). A further development of the landslide would increasingly expose the pile, leaving it vulnerable to excessive lateral loading or horizontal displacement (Figure 5). The probability of damage to the corner pile was evaluated to be in the highest probability class P4, i.e. damage to the pile was expected to occur within 1 year. Further movement of the landslide would certainly be expected in connection with heavy rainfall events.

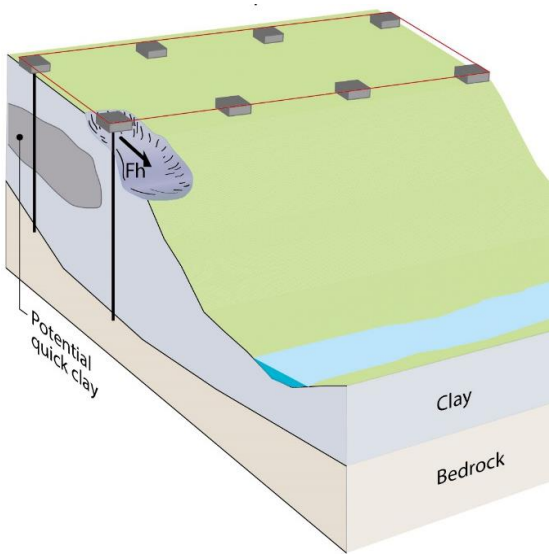


Figure 5 Scenario B - Damage to corner pile

C. Damage to several piles in the pile row closest to the slope:

Should the landslide develop along the length of the slope, more of the piles in the pile row closest to the slope could be exposed or affected (Figure 6).

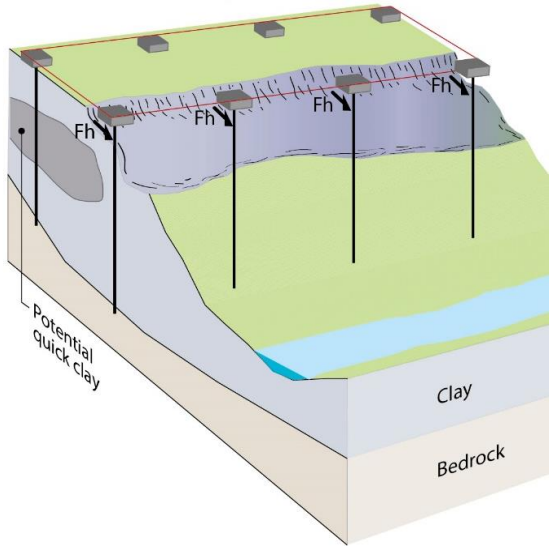


Figure 6 Scenario C - Damage to several piles in 1st row

Due to the orientation of the building not quite parallel to the slope (Figure 1), the distance from the closest piles to the slope edge increases slightly towards the north. This makes a scenario damaging several piles

slightly less probable than damage to the corner pile. For this scenario, the second highest probability class P3 was therefore assigned.

D. Damage to piles in the second pile row from the slope:

The distance between the rows of piles was approx. 6 m. Based on the SI it was considered less likely that the landslide would develop backwards to that extent and cause direct damage on the piles in the second row (Figure 7), i.e. the second lowest probability class P2 was assigned.

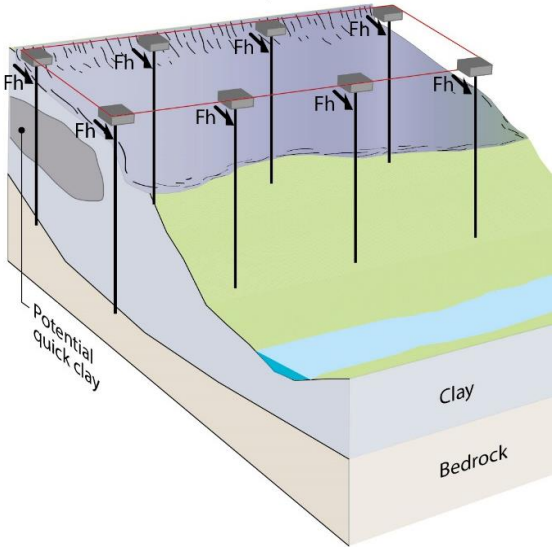


Figure 7 Scenario D - Damage to several piles in 2nd row

E. "Domino effect" – failure of all piles:

A "domino effect" may occur from redistribution of horizontal and vertical loads. It is a relevant scenario if failure of one or several piles leads to deformations that cause additional load on, and potential failure of, the next row of piles (Figure 8). The second highest probability class P3 was assigned for this scenario.

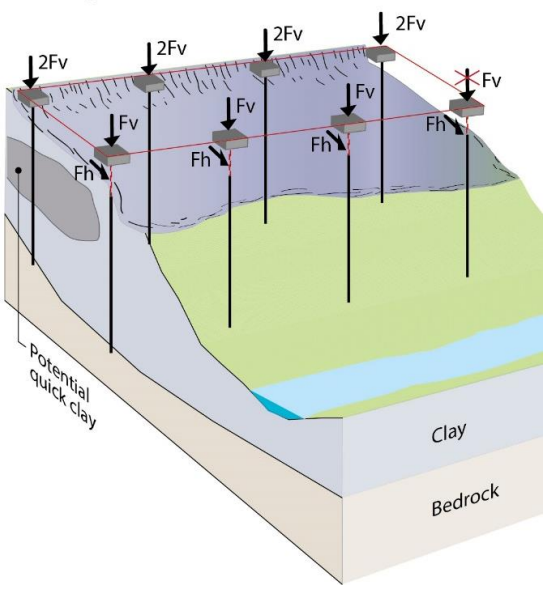


Figure 8 Scenario E - Domino effect - failure of all piles

6.2 Consequences of given scenarios

A structural engineer was engaged to evaluate the structural integrity and sensitivity at this initial stage, coupling landslide scenarios defined by NGI to consequences for the structural integrity of the foundations and the building (COWI, 2014), and a consequence class C1-C4 was assigned to each scenario.

For each of the scenarios, from damage on the corner pile to the quick clay slide, the conclusion from the structural engineer was that the described damage on the foundations would leave the block inhabitable. The expected damage to the building varied from total collapse to cracks or minor displacements, however, even for the smallest damage, moving back into the block under these circumstances was deemed not recommendable.

6.3 Risk

The probability of each identified scenario describing damage to the pile foundation was combined with the subsequent consequence to the block to produce the resulting risk to the block (Table 4). Based on the results in Table 4, all the scenarios were found to give unacceptable levels of risk of damage to the block before stabilising measures were in place.

Table 4 Risk of damage to the block from geotechnical failure scenarios. Green: Acceptable. Yellow: Risk needs further assessment. Red: Unacceptable.

Risk of damage		**Consequence (damage)**			
		1 Negligible	**2 Moderate**	**3 Critical**	**4 Catastrophic**
Probability of landslide (cause of damage)	**1 Unlikely**				Quick clay
	2 Less likely				Damage to piles in 2nd row
	3 Likely			Damage to several piles, 1st row	Domino effect
	4 Very likely			Damage to corner pile	

The risk assessment and its supporting arguements was issued in a report (NGI, 2014a) to the residents' representative and other stakeholders. With the risk assessment as background, the stakeholders understood that the results of the SI alone would not improve the level of risk for all scenarios to an accepbable level, and that the mitigation measures required would take some time.

6.4 Benefits from risk assessment in communication with the media

In NGI's communicatio with the media, it was useful to be able to refer to conclusions from the risk assessment when faced with questions designed to create exciting headlines. For the journalists who are trying to pass on information to the public without having the technical background the nuances in our communication can easily be lost or interpreted the wrong way. The project therefore found it very useful to have graded the levels of probability and consequence so that all outwards communication was kept consistent.

7 GEOTECHNICAL ASSESSMENT POST SITE INVESTIGATIONS

7.1 Topography

Older maps of the area show that the slope beneath the block was as steep and tall before the block was constructed in 1975 as it was before the slide. The topography may have been slightly worsened by fill around the block for parking and walkways at the top of the slope, but the natural slope still had a total height of 16 m and inclinations of up to 40°.

7.2 Precipitation and ground water

A local metrological station in Halden has continuous precipitation data dating back to 1882, which can be accessed on web (MET, 2014). The measured monthly precipitation in February 2014 was almost 300% of the normal. The extreme monthly precipitation values for the months December, January and February from 1970 until 2013 have been collated (Table 5).

Table 5 Extreme values for monthly precipitation, the five highest from 1970 to February 2014 for station 1230, Halden, Norway (MET 2014)

Monthly precipitation (mm)					
	1	**2**	**3**	**4**	**5**
Dec. (Year)	**175 2013**	168 1999	163 2006	145 2011	143 1972
Jan. (Year)	157 2008	136 1999	133 2002	128 1990	124 1988
Feb. (Year)	198 1990	**134 2014**	118 1995	114 1988	104 2002

Table 5 shows that December 2013 had the highest recorded precipitation in December during the lifetime of the block and that February 2014 had the second highest February precipitation. The precipitation for January 2014 was not among the ten highest January recordings, but summing December to February, 2013/2014 gives the highest total precipitation recorded since 1975. In conclusion, the level of precipitation leading up to the landslide was unusually high.

Regional modelling of soil moisture from weather data and simulated water retention shows 80-100% saturation in the days prior to the landslide (NVE, 2014).

7.3 Geotechnical site investigation and laboratory results

The SI, consisting of rotary soundings, CPTUs, extraction of undisturbed samples and pore pressure measurements, was carried out in the week following the evacuation of residents. The interpretations of the SI formed the basis for further assessment of geotechnical stability, the potential for further development of the landslide and design of required stabilising measures.

The SI results show that the block was built on top of a 2-3 m fill layer of sand. The natural ground consists of silt with an increasing clay content with depth. Underneath the silt there is a layer of clay over bedrock. Depths to bedrock from the SI are between 7 m and 16 m, increasing towards the southeast and the base of the slope. The depth to bedrock is assumed to increase further towards the sea shortly south of the area. The thickness of the clay layer above bedrock is assumed to increase with the depth to bedrock.

Electrical piezometers were installed at the top and bottom of the slope for back-calculating the slope stability before the slide, as well as giving data for design and monitoring of stabilising works. At the base of the slope, artesian water pressures equivalent to 3 m above ground level were measured just above bedrock.

An undrained triaxial compression test gave an interpreted effective angle of friction, φ', of approx. 35°, which is less than the natural inclination of parts of the slope.

7.4 Causes of the landslide

Natural silt slopes can be very steep and seemingly stable, even with inclinations higher than the material's effective angle of friction. Stability thus relies on some cohesion. If pore pressure and saturation of such slopes increase due to ground water flow or infiltration, apparent cohesion may be lost and a slide may be triggered. The stability of such slopes is thus very dependent on climatic conditions.

Slopes respond differently to short-term and long-term precipitation, the soil type being significant for the response. Short-term, intense rainfall (from a few hours to a few days), could for silt slopes trigger shallow landslides, typically 1-2 m deep. As a result of more prolonged, less intense rainfall (from a few days to several months), deeper slides can occur, due to an increased ground water level and saturation of the soil above the ground water level to larger depth. Detailed assessment of triggering mechanisms thus requires application of unsaturated soil mechanics.

For the Refne landslide, it is likely that high long-term precipitation (Section 7.2), in combination with the high slope inclination, were the principal causes of the landslide. It is assumed that, in February 2014, critical levels of pore pressures and saturation with respect to slope stability were exceeded for the first time since construction of the block. Stability calculations (NGI, 2014b) show that the slope had a low factor of safety for slope stability even under 'normal' conditions, without extreme precipitation. A moderate change in negative direction would therefore be enough to trigger a slide.

7.5 Slope stability calculations and design of stabilising measures

The stabilising measure aimed at improving slope stability and ease of construction. The slope gradient had to be reduced to very top of the slope and along the full length of the apartment block along the river, to the base of the slope. The stream at the base of the slope needed to be moved a few metres to the east. The embankment was designed to give sufficient improvement to the slope, and at the same time not creating instability of underlying clay when the embankment was put out as undrained loading. The embankment would also serve as erosion protection from the stream.

Table 6 Revised risk assessement after SI and stabilising measures. Arrows indicate changes from the early stage assessment. Green: Acceptable. Yellow: Further assessment needed. Red: Unacceptable.

Risk of damage		**Consequence (damage)**			
		1 Negligible	**2 Moderate**	**3 Critical**	**4 Catastrophic**
Probability of landslide (cause of damage)	**1 Unlikely**			Damage to several piles, 1st row Damage to corner pile	Damage to piles in 2nd row Domino effect
	2 Less likely				
	3 Likely				
	4 Very likely				

Slope stability calculations showed an improved factor of safety of at least 15 % for both drained and undrained analyses. The slope stability was considered satisfactory after the completion of the stabilising embankment. The factor of safety is, however, still lower than the requirement from Eurocode 7 for new builds. When modelling the slope stability prior to the landslide, all calculations resulted in a safety factor FS < 1.0, i.e. the slope should theoretically fail. The slope had, however, remained stable with this topography, through periods with high levels of precipitation for 40 years without failing.

This indicates that the applied model does not capture the slope behaviour. For silty slopes, unsaturated soil mechanics is necessary to include the effect of soil moisture in the vadose zone on soil strength. With a "standard geotechnical approach" we will not know the true improved safety factor of the slope, but an improvement can nevertheless be documented.

8 RE-EVALUATION AND COMMUNICATION OF RISK

The evacuation order remained in place while the geotechnical design and the construction of stabilising measures were completed. In total, the residents remained evacuated from their homes for just over five weeks (which in reality is not long for this kind of operation). In the same way as the risk of a landslide was conveyed to them and other stakeholders, it was important to communicate the improved situation which allowed them to move home again. It was important that they would feel safe and there were also concerns around resale values of the property after the media coverage the landslide.

The improvement to the slope stability documented through calculations was again converted into to classifications of risk. For the scenarios defined, the consequence remains the same. The probability, however, had been adequately reduced for the risk to be considered acceptable.

In the re-evaluation of risk, the first scenario regarding quick clay was discounted, as no quick clay was found in the SI. The four remaining scenarios all showed an improved risk classification as a result of the stabilising measures (Table 6) and were all considered to have a probability of P<1/300 per year, in accordance with guidelines (NIFS, 2014).

The scenarios which remain in the yellow zone are, based on NGI's evaluation, at an acceptable risk level. The probability of these scenarios will be lower as the distance from the top of the slope to the foundations increases away from the corner.

As discussed in section 7.5, the true behaviour of the silt slope and its safety factor against failure, are not easily modelled. The results of the SI, geotechnical calculations and constructed stabilising

embankment therefore give the basis for relative, rather than definitive, answers. This was illustrated in the risk assessment matrix through improved risk classification.

The re-evaluated risk assessment was issued to the residents' representative (NGI, 2014b) as a part of a final report. This gave the right authorities the technical documentation they needed to make decisions regarding the safety of residents and whether they would be allowed to move home.

9 DISCUSSION OF THE USE OF RISK EVALUATION

The initial phase of this project involved many stakeholders with many questions, relying on engineers for immediate answers. This raised the need for a structured analysis of knowns and unknowns, with the gaps filled in by engineering judgement.

Communicating all the aspects taken into consideration in such an analysis to residents, authorities and the media can be a challenge. Through defining scenarios covering both geotechnical and structural failure mechanisms, some of the complexity of the situation could be described. Pairing this with probability in a risk assessment provided a matrix that could be referred to and a guideline terminology for our communication that, hopefully, reduced the potential for misunderstandings. The risk assessment places the results of engineering judgement from geotechnical and structural engineers in a non-technical framework, which allows for a non-technical discussion.

"Do you think the block will end up in the sea?". No, but potentially it could. "Will it collapse in the next week or month?". Probably not. "When can we move back?". We can't say. These are all examples of frustrating communication. Grounded in the risk assessment, these vague answers could be replaced with the explanation that even if something is considered not very likely, the consequence would be so great that the risk is nonetheless unacceptable. Likewise, the probability of any scenario will never be fully eliminated, and thus neither will the risk.

The use of risk assessment aided this project, where all the stakeholders waiting for a geotechnical assessment and report had no background in geotechnical engineering. For the most simplistic of analyses, stakeholders could choose to relate to just three terms; high, moderate or low risk. As engineers working with the public, it is important to strive for this level of communication, and to create a common platform from which operational decisions can be made.

10 REFERENCES

COWI (2014). Landslide by apartment block 2, Refne. (original document title in Norwegian: Ras ved boligblokk 2, Refne), Technical evaluation, dated 2014-02-27

DSB (2011). Guideline. Social security in area planning. The mapping of risk and vulnerability (original document title in Norwegian: Veileder. Samfunnssikkerhet i arealplanlegging – Kartlegging av risiko og sårbarhet). http://www.dsb.no/Global/Publikasjoner/2008/Tema/temasamfunnssikkerhetareal.pdf

NGI (2014a). Landslide Refne, Halden. Evaluation of stabilising measures and risk (original document title in Norwegian: "Jordskred Refneveien 40, Halden. Vurdering av stabiliserende tiltak og risiko"). Document no.: 20140237-01-TN, dated 2015-03-04

NGI (2014b). Landslide, Refneveien 40, Halden. Emergency evaluations, site visits, site investigations and slope stability evaluations (original document title in Norwegian: Jordskred Refneveien 40, Halden. Akuttvurderinger, befaringer, grunnundersøkelser og stabilitetsvurderinger). Document no.: 20140237-01.R, dated 2014-09.01

NGU (2014). Quaternary maps (sediment maps). http://geo.ngu.no/kart/losmasse, Geological Survey of Norway

NIFS (2014). The Natural Hazard Project: Subproject 1 Natural hazard strategy. Risk acceptance criteria for the NIFS programme. Comparison of risk acceptance criteria for landslides and flooding (original document title in Norwegian: Naturfareprosjektet: Delprosjekt 1 Naturfarestrategi. Risikoakseptkriterier for NIFS-programmet. Sammenlikning av risikoakseptkriterier for skred og flom.) Report 26/2014

NVE (2014). http://www.senorge.no, Norwegian Water Resources and Energy Directorate

MET (2014). http://www.eklima.no, Norwegian Meteorological Institute.

Effects of extreme rainfall on geotechnical hazards in the Canadian Rocky Mountains

E. C. Hunter
University of Alberta, Canada, echunter@ualberta.ca

M. T. Hendry, D. M. Cruden
University of Alberta, Canada

ABSTRACT
In June, 2013, southwestern Alberta, Canada experienced an up to 1 in 750 year rainfall. The flooding that resulted led to geotechnical and hydrologic hazards in the Front and Main Ranges of the Canadian Rocky Mountains and on the Bow River watershed. The Main Ranges are folded and faulted limestones, reaching above local tree lines at about 2,000 m. The Foothills to the east are sandstones, shales and coals. Glacial deposits fill the river valleys and have been modified by 10,000 years of stream erosion. Among the hazards observed in 2013 in the mountains were rock falls, earth slides, and debris flows, as well as riverbank erosion, avulsion and overland flow. These posed threats to infrastructure, and in more than 350 cases resulted in damage. This project characterized the damage that occurred to roads and railways, and assessed the qualitative risk of the hazard in each case. Analysis of site reports showed that the greatest concern for highway corridors was debris flows. Of the hazards observed, they were the most numerous and most damaging. We assessed the risks associated by applying a risk template with measures of probability and consequence to each damaged site. The probability measure relates to temporal frequency, and is determined from historic events and data. The consequence measure records the severity of the damage by the hazard. Where available, this information was supplemented with historical records. These ratings can be used to develop a weighted risk map of the area and a prioritized list of sites at risk. This paper provides insights into the geotechnical impacts of a high return period rainfall and flood in similar mountain ranges to the Canadian Rockies.

Keywords: Rainfall, hazard, debris flow, Rocky Mountains, Alberta

1 INTRODUCTION

The western border of the province of Alberta, Canada trends north-westwards from the USA border (49°N latitude), west of the 114° longitude. The border follows the continental divide and the strike of the folded and faulted Palaeozoic sedimentary rocks that form the Canadian Rocky Mountains. The Rockies are a barrier to the eastward flow of moist Pacific air. A low-pressure zone is often trapped east of the mountains by higher pressure air moving up from the south. As the pressure builds, upslope weather develops (Gadd, 1995) and the moist Pacific air, forced to rise against the west side of the mountains, produces intense rainfalls or snowfalls.

1.1 Alberta and the Rocky Mountains

The Rocky Mountains are home to dangerous geotechnical hazards. The Frank Slide, for example, was a landslide that initiated the movement of 30 million cubic metres of limestone on Turtle Mountain and buried the coal mining settlement of Frank (Cruden and Martin, 2007). The 1903 Frank Slide is widely known, but there are other events that have affected the mountains, not least of which is the flood of 2013.

Alberta has experienced several notable floods; in recent years some of the largest on record have been observed. The event in 2013 came on the heels of the floods of 2005 and 2010, which affected the south-west and

south-east of the province, respectively. Until 2013, these were the largest floods in memory.

1.2 The 2013 Flood

In June 2013, southern Alberta experienced a three-day heavy rainfall event. The flood that resulted affected residents, damaged infrastructure and altered the region's landscape. It was the most costly natural disaster in Canadian history (The Canadian Press, 2013), costing the provincial and federal governments more than 5 billion dollars for flood mitigation. In total, 120,000 residents were evacuated from flooded areas, 14,500 homes were damaged, and 4 Albertans were killed (Shaw Media, 2013; the Canadian Press, 2013). Transportation infrastructure was severely damaged, with highways and rail lines being among the most heavily impacted.

The problems began earlier in 2013, with heavy snowfall in the winter and cold temperatures that delayed snow pack melting in the spring. In early June, many areas in the province received rain, which left the ground saturated. These conditions helped to set the stage for the flood that would occur. A low-pressure storm front rolled into Alberta and stalled over the foothills of the Rocky Mountains in the south of the province. When the storm began, the rain-on-snow caused snow melting and excess runoff (Pomeroy, 2014).

Leading up to the 2013 storm, mitigation work and preparations were made for an event similar in scale to the 2005 flood. During that event, there was steady rain with 250 mm falling over the course of a month. In 2013, however, 325 mm of rain fell in just 3 days. Heavy, persistent rain began on June 19th, which in some areas amounted to more than 100 mm per day (Alberta Environment, 2013). By June 21st, flooding was widespread and impacted much of the southern part of the province; several communities declared local states of emergency. In the Rocky Mountains, the damage was particularly severe due to the extremely high incidence of geotechnical hazards (Skirrow, 2015).

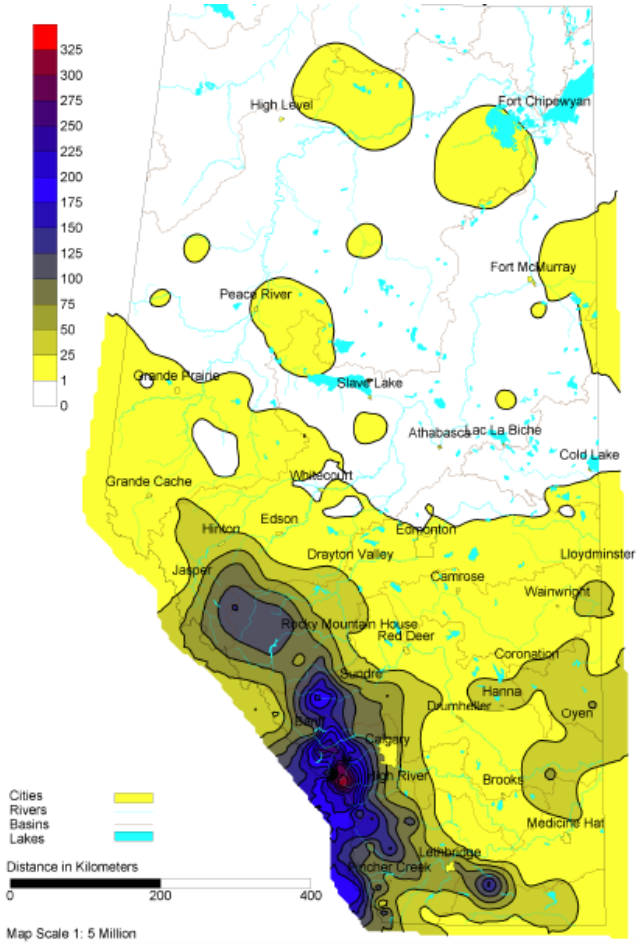


Figure 1 Alberta Precipitation Map for June 19 to 22, 2013 (Adapted from Alberta Environment, 2013)

Flooding was limited, for the most part, to the South Saskatchewan River Basin, which encompasses the Bow, Red Deer and Oldman Rivers, and their tributaries in the southern part of the province (Alberta Environment, 2013). Figure 1 shows the affected area, with the majority of the rain falling south of Red Deer (latitude 52.27°) to Pincher Creek (latitude 49.49°). The rainfall was centered in the mountains, which led to runoff and excess snowmelt into the streams that feed some of Alberta's major rivers. The surge from the mountains then travelled east and through many already waterlogged communities, causing extremely high flows and more damage. Among the most affected were the City of Calgary, and the towns of Canmore and High River.

The Bow River was flowing at 8 times its normal discharge by the time the surge reached the City of Calgary. The flows were approximately 3 times those experienced in 2005 (Government of Canada, 2015). Some areas, such as the community of High River, were particularly hard-hit, and experienced floods double their 100-year return period level (Government of Alberta, 2014). The government of Alberta has defined 100-year return period maps for most major watersheds. They are used for design and development approval purposes.

It is difficult to report on the historical magnitude of the flood. Reliable data extend over only 100 years, from the construction of the Canadian Pacific Railway. Flood frequency analysis and hazard studies have been completed for most watersheds in Alberta. These estimates, however, are based in almost all cases on less than 100 years of data. Many of the studies were completed in the 1980s, and do not include some of the more recent and largest floods on record. The current hazard assessment that defines the 100-year design threshold for the Bow River at the City of Calgary relies on data from 1879 to 1980. This period omits the floods of 2005 and 2013, 2 of the 11 major floods in Calgary's history (Calgary Public Library, 2014; Alberta Transportation, 2001).

It is possible that, due to climate change, the frequency of extreme rain events will increase in the coming years. In Alberta, significant development has taken place in flood-affected areas, and the province is vulnerable to damage from low magnitude floods as well. For this reason, defining design criteria on the basis of historical data may no longer be entirely reliable or practical. It may be necessary to evaluate whether the 100-year flood still provides a valid basis for design, and if so revisit standards to incorporate events as they occur (Skirrow, 2015). Many flood hazard assessments and maps are being revisited for Alberta's major waterways and communities, which will put the flood of 2013 into perspective.

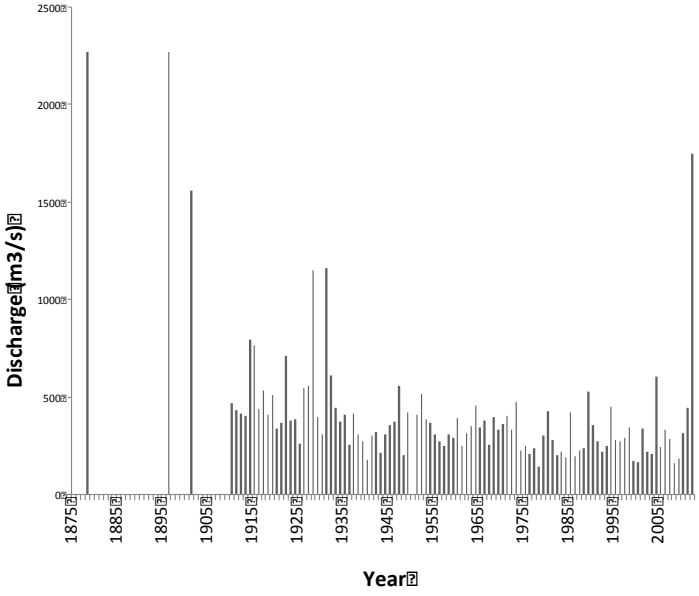


Figure 2 Compilation of historical hydrometric data for the Bow River at Calgary (Government of Canada 2015, Alberta Transportation 2001)

Based on the Calgary study currently in use (Alberta Environment, 1983), the flood was approximately a 70-year return period event. Historic data shows that three events of similar magnitude have been observed in the past 150 years, as can be seen in Figure 2. However, the severity of the event was not consistent throughout the affected area. While communities outside of the mountains may not have exceeded 100-year thresholds, in Canmore, the three-day rainfall had an estimated return period of up to 750 years (BGC, 2013; Alberta Environment, 2015).

2 ANALYSIS

In order to better understand the event, information was synthesized and compiled from available sources on the geotechnical and hydrological impacts to transportation infrastructure in the Rocky Mountains. For the purpose of the study, Alberta highway and rail corridors through the mountains were considered. Linear infrastructure of this type is inherently at risk of being impacted by hazards, and in the case of the 2013 flood both rail and highways suffered significant damage.

2.1 Preliminary Analysis

Information was compiled for rail and highway infrastructure from sources including the Alberta government's transportation department, independent geotechnical consultants, and Canadian Pacific (2015), a major railway operating in Canada and the United States. (Canadian Pacific, 2015; Government of Alberta, 2013; AMEC, 2013; BGC, 2013; Golder, 2013; KCB, 2013; Thurber, 2013).

2.1.1 Alberta Transportation

At the time of the floods in 2013, a large number of geotechnical hazards impacted the highways in the mountains. For disaster relief funding purposes, the Alberta government hired geotechnical consulting firms to document the damage. Five consulting firms were assigned highway corridors through the mountains, and all provided reports detailing the hazards and repairs that had taken place on their length of highway. Because the reports came from several sources, it was necessary to compile and normalize the information to quantify the event. We were interested in determining the types of events that had occurred, how many had taken place, and the damage and risk to each affected site.

Overall, there were 403 sites that had been affected by geotechnical and hydrological hazards on the 11 highway corridors considered. In going through the consultant reports (AMEC, 2013; BGC, 2013; Golder, 2013; KCB, 2013; Thurber, 2013), 8 categories of events were determined to have occurred. All of the affected sites could be assigned to one of the following categories:

- Bank erosion
- Culvert erosion
- Channel aggradation
- Debris flows
- Encroachment and avulsion
- Earth slides
- Overland flow erosion
- Rock falls

In addition to being categorized in this way, each site was rated on a scale from 1 to 4 based on its impact on the highway. Sites with a score of 1 would have eroded the asphalt or made the highway impassable, whereas a site with a score of 4 would not have resulted in damage or traffic disruption.

From this process, it was clear that debris flows were the most frequent hazard; 106 of the 403 reported sites were debris flows. In addition, 32 of 98 sites graded with a severity of 1, and 35 of 100 sites graded with a severity of 2 were debris flows, which indicated that they were also the most impactful hazard. It was decided that the focus of the analysis would be to examine the debris flows that affected highway corridors as a consequence of the 2013 floods.

Debris flows are landslides characterized by high ratios of debris to water. They occur most often in streambeds or channels, and are commonly initiated by shallow landslides in the source material. Debris floods are closely related to debris flows, differing in the water content accompanying the debris. (Jakob and Hungr, 2005). Until the floods of 2013, debris flows had been observed infrequently in the Front Ranges of the Rocky Mountains. Historically, Alberta highways have been affected by an average of one per year (Skirrow, 2015). Debris flows comparable in effects and magnitude to the 2013 hazards have been observed and studied, such as the event at Five Mile Creek in August, 1999 (Cullum-Kenyon et al., 2004). However, they were not common in the Front Ranges, and were not a major concern for the province until over 100 were triggered by this single rain event.

2.1.2 Canadian Pacific

Rail lines were also impacted by geotechnical hazards at the time of the floods. Emergency mitigation was undertaken by CP on their line to repair outages and re-establish service as quickly as possible. Detailed site records were not compiled. Information related to the damage sustained by the railway was gathered by conducting interviews with CP

personnel. The damage was sustained for the most part through the mountains near Canmore, within the City of Calgary, and in the south of the province along the Sheep River (Canadian Pacific, 2015).

Several different hazard types affected the rail lines through Alberta and limited service. However, in contrast to highway infrastructure, it was not clear that one type in particular was the most damaging. One significant observed hazard was overland flow stemming from debris flows, which washed out tracks in several locations. In some cases, action was taken by CP to prevent damage to the track from hazards. Excavators were placed in channels that had become aggraded by debris flows to remove material and prevent the water from overtopping and washing out the tracks. Several bridge piers and abutments were damaged by scouring, and embankment failures left tracks hanging without support in some locations.

2.2 Secondary Analysis

Once the information was compiled from the various sources and evaluated, it was necessary to develop a format to concisely present the information for each site, and a method by which to determine the risk.

2.2.1 Alberta Transportation

A common condensed report format was developed for Alberta Transportation to present basic information about each site. The reports included risk scores by which the sites could be compared. The scores were based on a frequency-severity matrix for debris flows that was developed for the government of Alberta following the floods in 2005 (AMEC, 2006; Bidwell et al. 2010). This risk matrix is complementary to those used by Alberta Transportation to evaluate other types of geohazards. It is shown in Table 1.

Its application involves assigning a score to each site based on the consequence or damage caused by the event, and a score based on the probability of its occurrence. The product of these two factors is a risk score, which in this case can be used as a normalized measure across the reports completed by the consultants.

Table 1 Frequency-severity matrix for debris flows (AMEC 2006).

Probability Factor	
Weight	Description
1	Inactive, debris flow very improbable. No historical or current visual evidence of debris flow activity.
3	Inactive, debris flow improbable.
5	Inactive, remote probability of a debris flow based on channel morphology and presence of debris in the potential source zone.
7	Inactive, occasional debris flow; a debris flow has occurred in the historic past and/or debris buildup in the channel/source area is considered to be ongoing.
9	Debris accumulation normally present in the source area. Fan is considered to be active, with debris flows occurring after the melting of an exceptional snow accumulation or an exceptionally intense rainfall.
11	Active, one or two debris flows per year triggered by annually recurring weather conditions.
13	Active, several debris flows each year.
15	Active, frequent debris flows each year, the area producing debris flows is expanding.
20	Active, a large volume of debris is impounding a large and rising reservoir of water upstream. Overtopping and dam-break is expected.

Consequence Factor	
Weight	Description
1	Debris flow contained by the ditch or able to be conveyed past the road alignment via a sufficiently sized culvert or clear span bridge.
2	Debris flow onto roadway easily removable by maintenance crews. No damage to the road surface. Road closure not required and/or road still passable with reduced speed limit.
4	Partial closure of the road or significant detours would result from a debris flow. Debris flow onto roadway that requires partial closure of the road or significant detours while maintenance crew uses heavy equipment to clear debris and restore road surface. Damage to the road surface possible.
6	Complete closure of the road would result

	from debris flow while maintenance crew uses heavy equipment to clear the roadway and/or remove debris flow deposits lugging culvert or ditch. Geotechnical inspection required to assess post-debris flow stability of road fills. Damage to the road surface likely from debris flows.
8	Same as weighting of 6, along with damage to bridges, bridge accesses or other infrastructure facilities.
10	Sites where the safety of the public is threatened by debris flows, where there will be a loss of infrastructure facilities or privately owned structures if a debris flow occurs.

The risk scores allow the spatial frequency of high-risk sites to be evaluated. From this, highway corridors having overall elevated risk can be identified. The two highest risk sites affect Highway 1 (Trans-Canada Trail) and Highway 1A (Bow Valley Trail) within the Bow Valley corridor. The steep mountain creeks that pass through the communities of Exshaw and Canmore both experienced large and destructive debris flows that affected the nearby communities. This is shown in Figures 3 and 4. The towns are partially developed on alluvial fans, and debris flows and creek avulsion hazards in these locations pose risk to the communities.

The site that saw the most damage was the debris flow fan at Cougar Creek (Figure 4). The channel is active, and has experienced debris flows in the past. The banks of Cougar Creek are lined with homes, many of which were damaged by the flooding in 2013. Figure 5 shows the debris flow passing through Canmore. It blocked and overtopped a large box culvert at Highway 1, and impacted a rail embankment and the overpass at Highway 1A. The debris flow posed a risk to human safety, and damage was done to private homes in addition to other infrastructure. For these reasons, the site was classified as high risk, receiving an overall score of 90. This is the highest score assigned to any site in the 2013 floods. An equivalent score was also assigned to the debris flow at Exshaw Creek, and two instances of bridge collapses on the CP line. In all cases, the risk was classified as elevated because of the risk posed to human safety.

Numerous other potential and active debris flow channels exist through the Bow Valley corridor and adjacent Kananaskis area. The risk scores may provide insight for Alberta Transportation into which sites should be of highest concern. Identifying vulnerable areas that may experience debris flows in the future can guide preparation and mitigation. It may be possible to direct response to areas with sites that have the highest risk, and therefore are most likely to experience damaging hazards. To this end, Alberta Transportation is currently completing an engineering study to identify alluvial fans and river erosion issues along transportation corridors.



Figure 3 Exshaw Creek (Google, DigitalGlobe 2015)



Figure 4 Cougar Creek (Google, DigitalGlobe 2015)



Figure 5 Cougar Creek (Government of Alberta 2015)

2.2.2 Canadian Pacific

From the interviews conducted with CP personnel, information was collected about geohazards of all types that affected the rail lines. The study was not limited to debris flows. A separate reporting format was developed to compile information for the CP sites. It differs from the Alberta Transportation format by using information that is relevant to assess damage to rail. The effect of a hazard on a highway can be gathered by physical damage to the road surface, or presence of materials that make the highway impassable. The important measure for severity of railway impacts, however, is time out-of-service, which indicates the amount of time that trains were unable to move through a section of track due to a hazard.

The frequency-severity matrix was adapted to be applied to rail, taking into consideration the importance of time out-of-service. This matrix is shown in Table 2. It was used to establish consequence, probability, and thereby risk scores for each CP site. The rail risk scores are intended to be equivalent to those applied to highway sites, and should be comparable. However, the matrices rely on different assumptions and measures of what constitutes risk. The scores assigned to the CP sites were included in the reports, along with basic site information and accounts of the events obtained through the interviews.

Table 2 Frequency-severity matrix for geotechnical hazards affecting rail (AMEC 2006).

Probability Factor	
Weight	Description
1	Inactive, occurrence very improbable.
3	Inactive, occurrence or remobilization improbable.
5	Inactive, remote probability of remobilization, uncertainty level moderate, or active but very slow or indeterminate level of activity.
7	Inactive, high probability of remobilization or additional dangers, uncertainty level high, or… Active with perceptible movement rate and defined zones of movement/occurrence.
9	Active with moderate steady, or decreasing, rate of ongoing movement or occurrence.
11	Active with moderate but increasing rate of movement or occurrence.
13	Active with high rate of movement or occurrence, steady or increasing.
15	Active with high rate of movement or occurrence with additional hazards or dangers.
20	Catastrophic situation is occurring.

Consequence Factor	
Weight	Description
1	Hazard does not impact rail, no interruption to service, routine maintenance issue.
2	Hazard impacts rail, resulting in minor disruptions to service. Still able to run trains through at reduced speeds, or by using sidings.
4	Minor damage to rail resulting in disruption to service.
6	Major damage to rail resulting in disruption to service.
8	Major damage to rail and other infrastructure, e.g. bridge structures.
10	Issue presents potential consequences to public safety.

The cumulative time out-of-service for an area is an important consideration for the railway. Over a section of track, several outages may occur that all contribute to the service disruption. The individual effect that each hazard has may be difficult to isolate. A timeline was therefore developed to show when each site was out of service, and determine which hazard ultimately dictated the outage.

In general, hazards affecting track and slope stability were the most damaging. The sites that took the longest to repair and lead to prolonged service issues included washed out culverts, embankment failures, and severely scoured bridges.

All of the information for both rail and highway infrastructure was compiled into a single database, which maps all sites and information together to provide a complete picture of the flood's effects.

3 RECOMMENDATIONS AND FUTURE WORK

The government of Alberta intends to use a 300-year return period for design of debris flow mitigation projects, and 100-year return period for 'clearwater' flood projects. However, as previously mentioned, frequency analysis may be imprecise due to a lack of data, changes in climate, and other factors (Skirrow, 2015). It is possible that we are under-prepared and under-informed about extreme events. It is evident that a better understanding of Alberta's relationship with its changing climate and landscape is necessary in order to better prepare for the future.

To facilitate analysis of future events, a consistent reporting format could be developed for consultants evaluating geotechnical hazards. Including frequency-severity matrices, or a similar agreed upon risk measure, would allow sites to be accurately and consistently rated. In addition, developing agreed upon hazard classifications would make sites easily comparable and allow limited resources to be allocated to high-risk locations.

A challenge facing Alberta, as a relatively new province with little historical information, is that there are many unknowns related to mountain geotechnical hazards. In the interest of being able to prepare and respond to hazards in the future, it will be necessary to look further into the mechanisms, characteristics, and consequences of these events. Heavy rainfall and long, intense storms will likely become more frequent with climate change. Short of being able to predict events, examining the relationship between rainfall and geotechnical hazards can inform mitigation and response, and allow us to better understand the Rocky Mountains.

4 ACKNOWLEDGEMENTS

The authors would like to acknowledge the Alberta Ministry of Transportation and the Canadian Pacific Railway for providing the access and information that made this study possible. This research was made possible by the (Canadian) Railway Ground Hazard Research Program, which is funded by the Natural Sciences and Engineering Research Council of Canada, Canadian Pacific Railway, Canadian National Railway, and Transport Canada.

5 REFERENCES

Alberta Environment (1983). City of Calgary Floodplain Study. Online at http://esrd.alberta.ca/water/programs-and-services/flood-hazard-identification-program/flood-hazard-studies/documents/Calgary-Bow.pdf [accessed January 2015].

Alberta Environment and Sustainable Resource Development (2015). Precipitation data June 19-23, 2013 [retrieved April 10, 2015]

Alberta Environment and Sustainable Ressource Development (2013). Precipitation map June 19-23, 2013 [retrieved January 2015].

Alberta Transportation (2001). Report on Six Case Studies of Flood Frequency Analyses. Online at http://www.transportation.alberta.ca/Content/doctype30/Production/ffasixcase.pdf [retrieved March 2015].

AMEC Earth and Environmental (2006). Geohazards review highway 40/highway 541 corridor southwestern Alberta.

AMEC Environment & Infrastructure (2013). Highway and geohazard assessments of June 2013 flood damage – Highways 940 (Forestry Trunk Road) and 532 (Kananaskis Country).

BGC Engineering (2013). Site inspection forms – Highways 1, 1A and Smith Dorrien/Spray Lakes Trail.

BGC Engineering (2013). Rainfall on June 19-21, 2013. Online at http://www.canmore.ca/About-Canmore/Flood/Mountain-Creek-Hazard-Mitigation.html [accessed January 2015].

Bidwell, A., Cruden, D.M., Skirrow, R., Dickson, R. (2010). Geohazard reviews of highway corridors through Mountainous and Foothills terrain, southwestern Alberta. Proceedings, 63rd Canadian Geotechnical Conference, Calgary, Alberta, 12-16 September 2010, pp. 855-861.

Canadian Pacific (2015). Personal Communication. May and June, 2015.

Calgary Public Library (2014). Calgary Flood Story. Online at http://floodstory.com/ [accessed February 2015].

Cruden, D.M., Martin, C.D. (2007). Before the Frank Slide, Canadian Geotechnical Journal, 44: 765-780

Cullum-Kenyon, S., Heinz, H.K., Sobkowicz, J.C. (2004). Assessment of debris flow hazard at Five Mile Creek. Proceedings, 57th Canadian Geotechnical Conference and 5th Joint CGS/IAH-CNC Conference, Quebec City, Quebec, 24-27 October 2004.

DigitalGlobe (2015). Google Earth captured images.

Gadd, B. (1995). Handbook of the Canadian Rockies, Corax Press, Jasper, Alberta, pp. 205-219, 831.

Golder Associates (2013). Geotechnical flood damage assessment – Highway 66, Highway 68, Powderface Trail and Bragg Creek Alberta.

Government of Alberta (2013). Alberta Transportation photographs of flood damage.

Government of Alberta (2014). Highwood River Basin – Diversion Project. Online at http://www.alberta.ca/highwood-river-basin.cfm [accessed April 2015].

Government of Canada (2015). Water Survey of Canada. Historical Hydrometric Data, City of Calgary [retrieved January 2015].

Klohn Crippen Berger (2013). Flood damage assessment – Highway 541. Summary of flood damage inspection notes.

M. Jakob and O. Hungr (2005). Debris-flow Hazards and Related Phenomena. Praxis. Springer Berlin pp. 9-21.

Pomeroy, J. (2014). Mountain hydrology related to the Alberta flood of 2013. CWRA Alberta Branch Annual Conference, March 2013.

Shaw Media (2013). By the numbers: 2013 Alberta floods. Online at http://globalnews.ca/news/673236/by-the-numbers-2013-alberta-floods/ [accessed January 2015].

Skirrow, R. (2015). Geotechnical considerations from the June 2013 southern Alberta flood. Proceedings, 2015 Conference of the Transportation Association of Canada, Charlottetown, P.E.I., 27-30 September 2015.

The Canadian Press (2013). Alberta floods costliest natural disaster in Canadian history. Online at http://www.cbc.ca/news/canada/calgary/alberta-floods-costliest-natural-disaster-in-canadian-history-1.1864599 [accessed January 2015].

The Canadian Press (2013). Alberta flooding statistics released, demonstrate severity of loss. Online at http://www.huffingtonpost.ca/2013/08/21/alberta-flooding-statistics_n_3787490.html [accessed January 2015].

Thurber Engineering Ltd (2013). Highway and geotechnical assessment of flood damage – highways 40:10/40:12 (Kananaskis Country).

Pore Pressure Response in the Upper Open Aquifer - Field Investigations and Modelling

H. Blomén
Swedish Geotechnical Institute & Chalmers University of Technology, Sweden,
hanna.blomen@swedgeo.se

ABSTRACT
For many slopes in clay where the stability is unsatisfactory, high pore pressures is one of the main potential factors triggering a shallow landslide. During rainfall water infiltrates into the soil, which cause a decrease in soil strength, which can be crucial and decisive for whether the slope fails or not. The pore pressure distribution in the slope is part of the data needed for modelling the stability.
A question of great importance, and where there is a lack of knowledge today, is regarding the variation of the pressure in the upper 10 meters of the soil profile during different rainfall scenarios, in the short as well as during the long term. The pore pressure in this zone is often crucial for the stability, as the pore pressure to a great extent governs the strength of the soil at these shallow depths. The pore pressure must not be underestimated as the prediction then would be on the unsafe side indicating a fictitiously high factor of safety. When a detailed slope stability analysis is made, including expected climate change, reliable pore pressure predictions are important from an economical point of view.
Pore pressure, rainfall and water levels in the nearby rivers have been measured for a long period in two test sites in south-western Sweden. This paper presents an analysis of the measurements and seepage modelling using a commercial seepage modeling software. A better and more reliable prediction of the pore pressure in the entire soil profile, and thereby improving the validity of the stability analysis, can be obtained by using the results presented in this paper together with earlier research.

Keywords: slope stability, pore pressure, clay, modelling.

1 INTRODUCTION

One of the main factors causing a landslide in clay (or silt) slopes is high pore pressures. During rainfall water intrudes into the soil, which can cause a decrease in soil strength, which in turn is crucial and decisive for whether the slope fails or not. When modeling the stability, the pore pressure distribution is part of the data needed for the mathematical modeling. The basis for the conceptual model of the pore pressure regime are pore pressure measurements in a few points at a discrete number of depths. These measurements are often supplemented by measurements of the ground water pressure in the underlying confined aquifer. Based on these measurements a model for the pore pressure regime is made and the stability of the slope can be analyzed.
In moderately to steep slopes slides are, if they occur, often rather shallow. However, if a too high pore pressure is used in the analysis, the risk for a slide might be severely overestimated. Pore pressure variations in the Gothenburg region (southwestern Sweden) was studied by Berntson (1983) where a number of sites seemed to have an upper open aquifer of 4 to 6 meters in which the pore pressure distribution was hydrostatic. These findings has been generalized and is used quite extensively by practicing engineers, in spite of the fact that it is based on a limited number of cases. They also form a hypothesis and background for the geotechnical investigations and measurements presented here. Also Persson (2008) studied pore pressure distributions

along the Swedish west coast. He focused on improvements of a method for estimating the maximum pressure in the confined aquifer and a classification system for groundwater level fluctuations.
The pore pressure must not be underestimated as the prediction then would be on the unsafe side indicating a fictitiously high factor of safety. When a slope stability analysis is made, including expected climate change, reliable pore pressure predictions are important from an economical point of view. This paper presents an analysis of measurements from two test sites in southwestern Sweden; Äsperöd and Linnarhult, see Figure 1, and modelling with a seepage modeling software for one of them. The long term gain with the work are the ability of making better and more reliable predictions of the pore pressure in the entire soil profile and thereby improving the validity of the stability analysis.



Figure 1 Overview Äsperöd and Linnarhult.

2 SITE DESCRIPTION ÄSPERÖD

The test site Äsperöd is situated in southwestern Sweden, 60 km north from Gothenburg, right along the Göta River, see Figure 2. In one slope in the area geotechnical investigations has been done and it has been instrumented with piezometers and a precipitation gauge. The clay slope is, from the river to the outcrop, around 280 meters long. The inclination of the slope is low except from the part next to the river which inclines 1:6. The soil in the area consists mainly of clay.

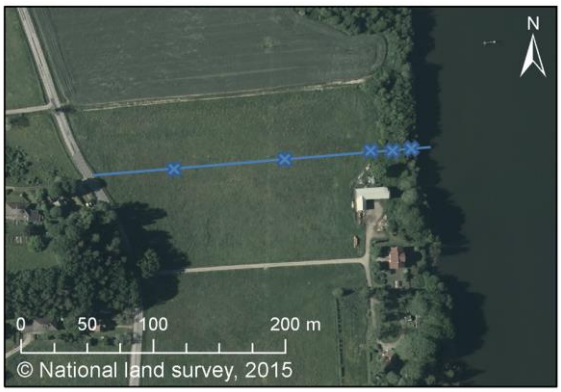


Figure 2 Overview Äsperöd. Blue line represents the instrumented slope.

2.1 Soil properties

At the site, the ground elevation is at +18 meters in the western part (close to the road) and at +14 meters at the crest of the slope. The steepest part of the slope inclines 1:6 from the crest to the toe. In the area the soil consists of 2 meters of dry crust at the top of the soil profile. Below the dry crust there is clay, with a total thickness less than 10 meters in the western part and more than 40 meters close to the river. Some of the clay is silty between 4-10 meters of depth and some contains gyttja. There is also a layer of sand, around 2 meters thick at a depth of around 35 meters close to the river and further back at 16 meter of depth. The clay is underlain by coarse grained soils. Geotechnical properties for the clay are:

- The unit weight of the clay in the area varies between 15-17.2 kN/m^3.
- The natural water content in the clay varies between 53-85%.
- The undrained shear strength in the clay varies between 12-62 kPa.
- In the western part of the section the clay has a high sensitivity and according to Swedish definitions it is quick (sensitivity>50 kPa and

remolded shear strength <0.4 kPa) from 6 meters of depth to firm bottom.
- CRS-tests have been performed in 3 points at 4 levels each. The results show that the clay is overconsolidated with 30-100 kPa, which corresponds to an OCR of 1.2-2.3.
- The permeability in the clay varies according to the CRS-tests between $7 \cdot 10^{-10}$ - $2 \cdot 10^{-9}$ m/s.

2.2 Instrumentation

In the Äsperöd test site 17 piezometers have been installed in 5 different parts of the slope. Eleven of the piezometers where installed in January 2013. The other 6 piezometers where installed in 2007. All the piezometers are constantly logging every 4th hour. The position and installation depths of the piezometers are shown in Table 1 and Figure 3.

Table 1 Position and installation depths of the piezometers in Äsperöd.

Part of slope	Distance from river [meter]	Installation depth [meter]
Back	190	7.1, 18
Plateau	100	0.65, 1.2, 5
Crest	50	0.99, 5, 8.11, 21.3, 34.4, 49
Middle	30	0.8, 1.25, 5
Toe	15	0.69, 1.49, 5

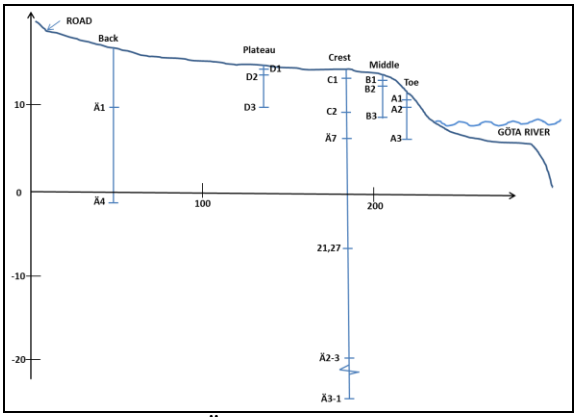


Figure 3 Profile Äsperöd with position and installation depths of piezometers.

A precipitation gauge has also been installed in Äsperöd for collection of rainfall data. For some periods with problems with the gauge, rainfall data from the municipality of Lilla Edet have been used. In Figure 4 the monthly rainfall from January 2013 until August 2015 is shown. It can be seen that the amount of rain in February and March 2013 is very low and that August 2014 was the wettest month, with unusually much rain (300 mm). According to Alexandersson (2001) the normal precipitation (the average of the precipitation values over a 30-year period) for the area are 910 mm/year and the rainiest months are normally October or November with a normal value of 102 mm/month.

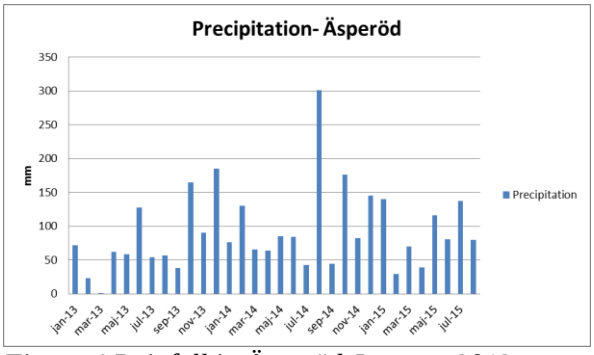


Figure 4 Rainfall in Äsperöd January 2013-August 2015.

All the 17 piezometers and the precipitation gauge have been monitored since January 2013 and are still in use (September 2015). The results from the measurements are analyzed in chapter 5.1.

2.3 Water level in the Göta River

The water level in the Göta River is regulated in favor of power production and the locks, and it is monitored by the power producer Vattenfall. One measuring point is situated in Lilla Edet, 3 km downstream Äsperöd. The water level variations between January 2013 and April 2015 are shown in Table 2.

Table 2 Variation in Göta River, January 2013-April 2015 (Vattenfall, 2015).

	Meters above sea level
Mean	6.9
Max	7.1
Min	6.7

3 SITE DESCRIPTION LINNARHULT

The test site in Linnarhult is situated 15 km northeast of Gothenburg in the Lärje Stream valley, see Figure 1. The valley is a side

valley of the Göta River valley and is known for its many small slides and its meandering stream. The test site is situated at the eastern side of the stream and consists of farmland. At the test site there are 2 instrumented slopes, named Section 1 and Section 2, see overview in Figure 5. The distance between the two sections is around 350 meters. Both sections go perpendicular to the Lärje Stream.

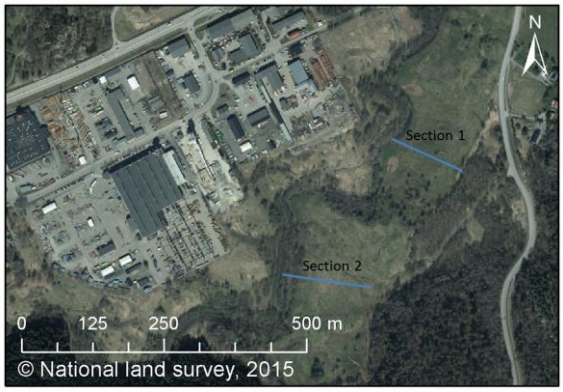


Figure 5 Overview Linnarhult with the 2 sections.

3.1 Soil properties

Site investigations in Linnarhult were performed in December 2014 - January 2015. The ground elevation in section 1 is at +35 meters at the crest of the slope and in section 2 the plateau and crest are situated at +30 meters. In the Lärje Stream the mean value of the water level is at + 20 meters.
The soil in the area consists of 2 meters of dry crust at the top of the soil profile. Below the dry crust there is clay, with a total thickness of 20 meters close to the Lärje Stream and around 30 meters behind the crest of the slope. There is a layer of silt, approximately 2 meters deep, at 6-8 meters of depth below the crest in section 2. The layer is found at a deeper level further back in the section compared to the level below the crest. There is another layer of silt at 20-30 meters below the ground level with a more horizontal inclination. Geotechnical properties for the clay are:

- The unit weight of the clay in the area varies between 16.3-17.8 kN/m^3.
- The natural water content in the clay varies between 65% in the upper part of the clay and 55% in the deeper parts.
- The sensitivity varies between 23-37 kPa and there is no quick clay according to Swedish definitions.
- CRS-tests have been performed in one point at the crest in section 2 at 5 levels. The result shows an OCR of 2.3-3.2.
- The permeability in the clay varies, according to the CRS-tests, between $1.5 \cdot 10^{-10}$ – $7.5 \cdot 10^{-10}$ m/s.

3.2 Instrumentation

In the Linnarhult test site 9 piezometers have been installed in section 1 and 17 piezometers in section 2. All of them where installed between December 2014 and January 2015. The piezometers are constantly logging the pore pressure every 3rd- 4th hour. The position and installation depths of the piezometers are shown in Table 3, Figure 6, Table 4 and Figure 7.

Table 3 Position and installation depths of the piezometers in Linnarhult, section 1.

Part of slope	Distance from river [meter]	Installation depth [meter]
Crest	~ 75	0.5, 1, 5, 10
Middle	~ 33	0.5, 1.4, 6
Toe	~ 6.5	1.3, 5

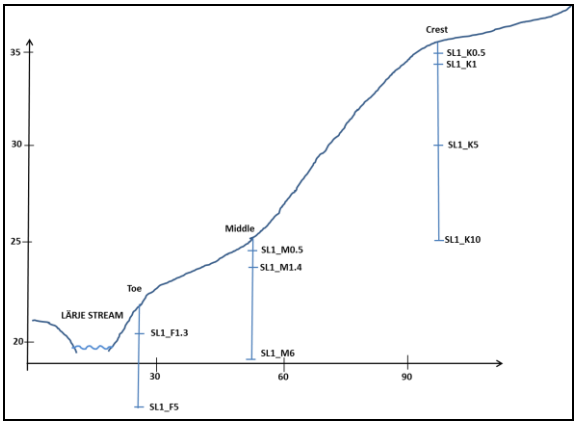


Figure 6 Linnarhult section 1, position and installation depths of the piezometers.

Table 4 Position and installation depths of the piezometers in Linnarhult, section 2.

Part of slope	Distance from river [meter]	Installation depth [meter]
Plateau	~54	0.5, 1.5, 4.5, 7, 15
Crest	~ 40	1, 2, 4, 6.5, 12
Middle	~ 26	2.7, 4, 7
Toe	~ 12	1.75, 4.75, 9.75, 19

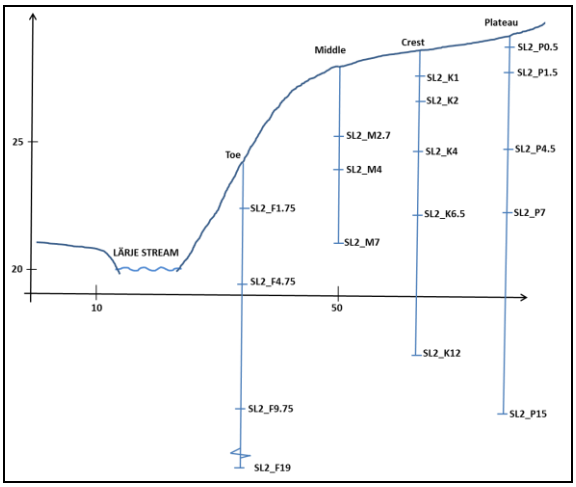


Figure 7 Linnarhult section 2, position and installation depths of the piezometers.

The rainfall measurements used for the Linnarhult area is done by the City of Gothenburg. The precipitation gauge is situated in Komettorget, Bergsjön, 2.5 km from Linnarhult. In Figure 8 the monthly rainfall from January-August 2015 is shown. It can there be seen that the amount of rain is smallest in February (40 mm) and largest in January (193 mm). According to Alexandersson (2001) the normal precipitation for the area are 758 mm/year and the rainiest months are normally October or November with a normal value of 82 mm/month.

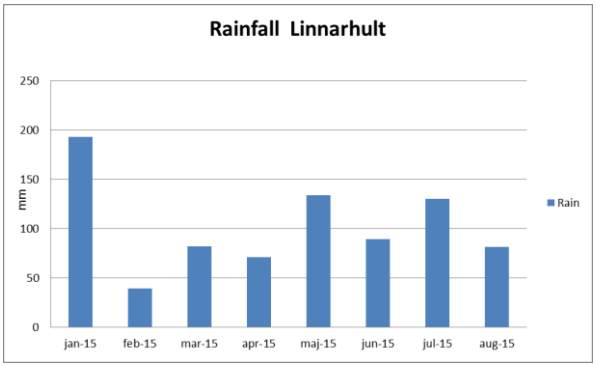


Figure 8 Rainfall in Linnarhult January- August 2015.

The results from the piezometers and rain measurements are analyzed in chapter 5.2.

3.3 Water level in the Lärje Stream

The water level in the Lärje Stream is monitored with a piezometer installed in the stream in section 2. The total head varies between 0.7-2.7 with a mean value of 1.1 for the period January- June 2015.

4 SIMULATION WITH A SEEPAGE MODELING SOFTWARE

In order to simulate different scenarios with various pore pressures and rainfall data, a model of the Äsperöd area has been set up using a commercial seepage modeling software. To validate the model a simulation has been done for a shorter period of time, one month. The selection of time period is based on a combination of pore pressure measurements and rainfall. The simulation started after a period with just a small amount of rain, followed by a large amount of rain in a short period of time. This was done in order to see how the infiltrated rainwater percolates in the soil profile. After data comparison of different periods the start date was chosen to April 1st 2013 and the end date one month later, April 30th 2013.
Before April 1st there was only 4 mm of rain the last month (March 2013). Between April 1st and 30th it rained 62 mm. It is shown in Figure 9 that the piezometers reacted quickly to the rainfall, especially the ones installed at shallow depths (less than 5 meters).

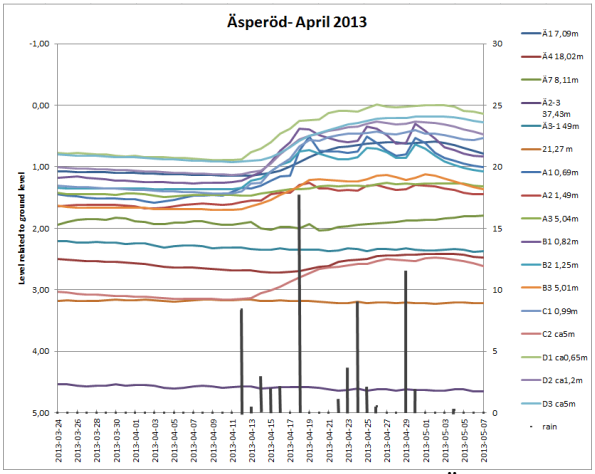


Figure 9 Piezometers and rainfall in Äsperöd April 2013.

The simulations with the seepage modeling software are done in order to simulate the pore pressure situation in the area in April 2013 and to validate the soil properties. The first simulation was a steady state simulation with the values for April 1st 2013. After that a

transient analysis was made for the rest of the month (April 1st -30th 2013). In this analysis the rainfall during the period was included as a hydraulic function with the rainfall for each day added as a constant rain. The sensitivity of the model to changes in the permeability in the clay and in the dry crust has also been studied.

5 RESULTS

The data collected from Äsperöd and Linnarhult has been analyzed and some of the results are presented here. Since there are values for several years from the piezometers in Äsperöd comparisons between the years can be done. Pore pressure profiles with high and low values for the areas are also assembled. Also the results from the simulations with the seepage modeling software are presented and discussed.

5.1 Measurements in Äsperöd

For the piezometers in Äsperöd there are measured values of the pore pressure from the autumn 2007 until September 2015. For the period 2007-2010 there are just values for some periods and not all the piezometers at the same time. In January 2013 another 11 piezometers were installed and since then there are registered values every 4th hour. A fluctuation pattern can be seen for the yearly variations for the piezometers. The difference between the highest and lowest registered values (min- and max-values) in the piezometers varies with installation depth and between different years. The ones that were installed in 2013 at shallow depths (in or close to the dry crust) are the ones with the greatest difference between the extreme values (negative values included). The majority of the piezometers have variations between 10-20 kPa.

When it comes to the response time for the rain in the piezometers it can be seen that the ones at shallow depths have a faster response time and also a more irregular shape, see Figure 10, compared to the ones at larger depths which are slower in their response and the curves have a smother shape, see Figure 11. Persson (2008) describes different types of fluctuation patterns based on observation series such as “quick responding stations”, “medium-slow responding stations with rather pronounced maximum levels” and “slow responding stations”.

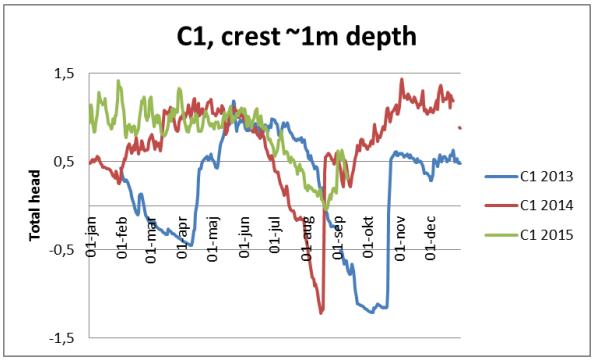


Figure 10 Fluctuation pattern in quick responding station in Äsperöd.

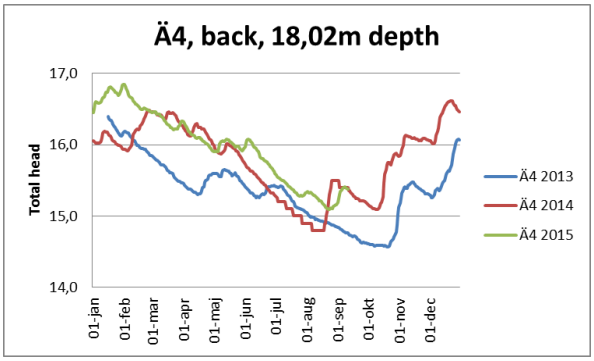


Figure 11 Fluctuation pattern in medium-slow responding station in Äsperöd.

The pore pressure profile for the stations in Äsperöd has been evaluated using measurements representing one period with low values, October 10th 2013, and one representing high values, January 30th 2015. The situation in different parts of the slope is shown in Figure 12- Figure 15. The results show a situation with pore pressures close to hydrostatical values for all stations except for the station at the crest. For the piezometers installed at the crest of the slope (Figure 13) the pore pressure does not follow the same pattern as the other stations. The situation here is diverged from the hydrostatical values and gives instead a lower pressure at 5 meters depth compared to a hydrostatic line starting from the ground surface. One explanation to this may be the distinct crest of the slope that makes the isolines for the pore pressure incline more than the hydrostatical line.

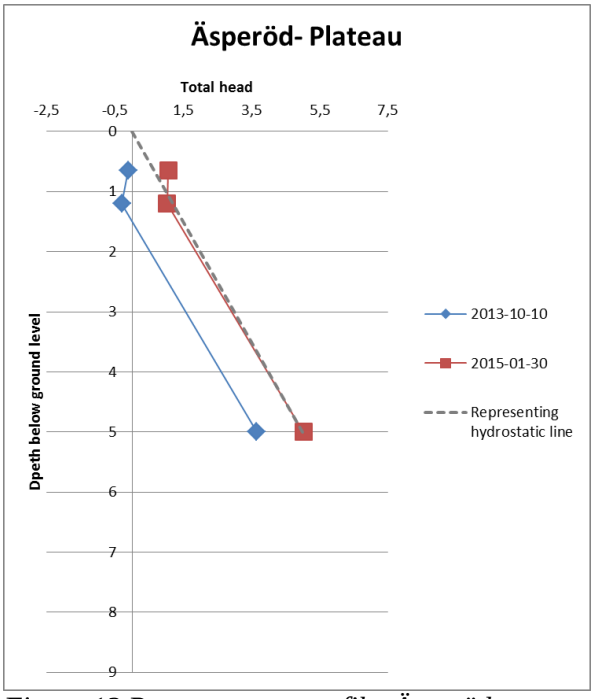


Figure 12 Pore pressure profile, Äsperöd- Plateau.

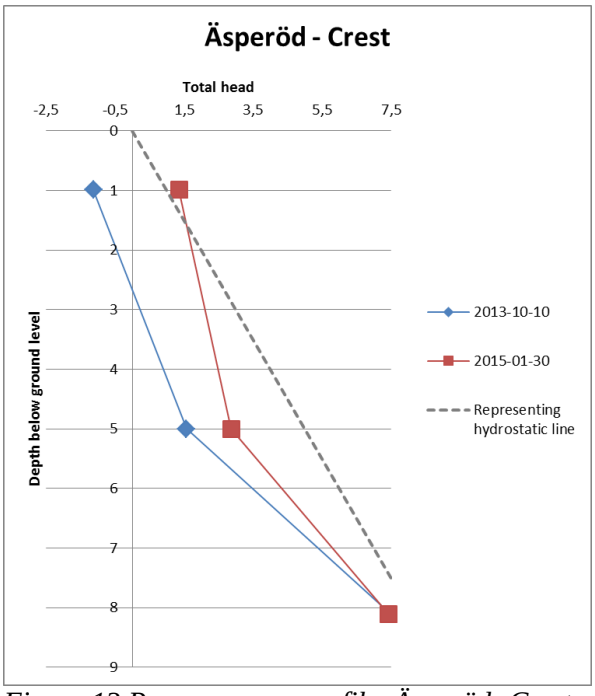


Figure 13 Pore pressure profile, Äsperöd- Crest.

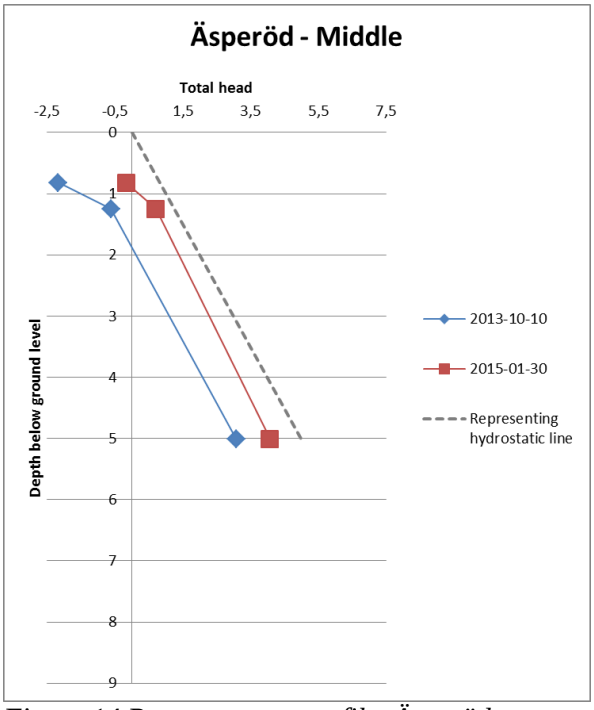


Figure 14 Pore pressure profile, Äsperöd- Middle.

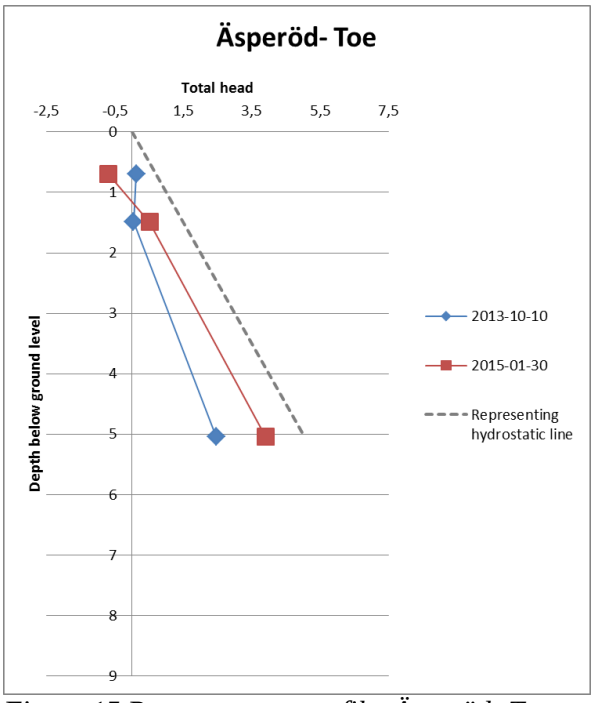


Figure 15 Pore pressure profile, Äsperöd- Toe.

As seen in Table 2 the water level in Göta River varies between 6.7-7.1 meters for the period January 2013- April 2015. Those variations are analyzed together with the rainfall for the period. No correlation is found between the water level in the river and the rainfall for the studied period. Instead it can be concluded that the water level in the river is controlled by the power producer in favor of the power production and locks.

5.2 Measurements in Linnarhult

The pore pressure measurements in Linnarhult have been going on for less than one year, January- September 2015. Most of the piezometers in section 1 have a very coherent pattern over the period with a variation around 10 kPa between the min- and max-values (Figure 16). Also for section 2 the piezometers has a pattern that looks almost the same for most of them with a variation between 5-10 kPa (Figure 17). The piezometers installed at deeper levels vary less than the others.

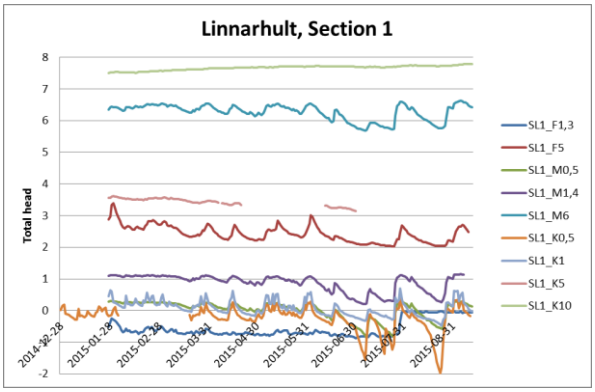


Figure 16 Pore pressure variations in Linnarhult section 1, January- September 2015.

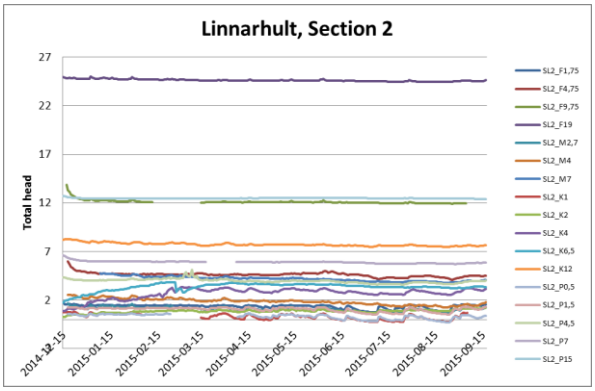


Figure 17 Pore pressure variation in Linnarhult section 2, January- September 2015.

The pore pressure profiles for the piezometers in Linnarhult section 1 has been evaluated the same way as the ones in Äsperöd. Representing a period with low pore pressure values, in this case July 1st 2015 is chosen, and high pore pressure values are from February 2nd 2015. The pore pressures show a situation with almost hydrostatcial values for all stations, see Figure 18- Figure 20.

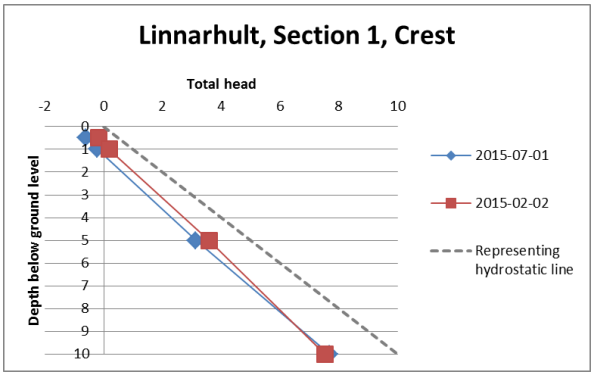


Figure 18 Pore pressure profile, Linnarhult- Crest.

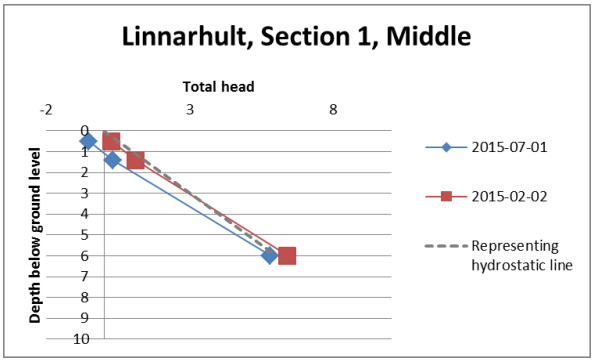


Figure 19 Pore pressure profile, Linnarhult- Middle.

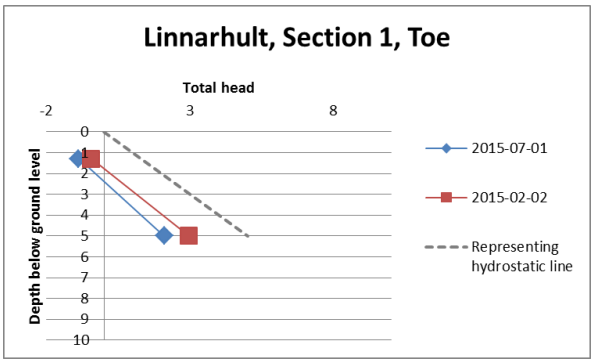


Figure 20 Pore pressure profile, Linnarhult- Toe.

5.3 Results from seepage modeling simulation

The results from the simulation with a commercial seepage modeling software are evaluated and compared for two parts of the slope in Äsperöd, behind the crest of the slope and at the toe of the slope. To visualize the results they have been plotted as time series for points located next to the actual piezometers. Those series have been exported to a spreadsheet and the simulated values are compared with the measured values. In general, the results from the simulation give a larger reaction to the rainfall than the

piezometers do. This might depend on the dry crust being simulated as ”saturated only” which is a simplification of the reality. The agreement between the measured values and the simulated ones is better for the station behind the crest than for the toe of the slope. The results from the simulations with the most aquerate permeability, $k=5\cdot10^{-10}$ m/s in the dry crust, and $k=1\cdot10^{-10}$ m/s in the clay, are shown in Figure 21 and Figure 22. As presented above, the permeability in the clay is $7\cdot10^{-10}$ - $2\cdot10^{-9}$ m/s according to the CRS-tests so it correlates well to the values from the simulations.

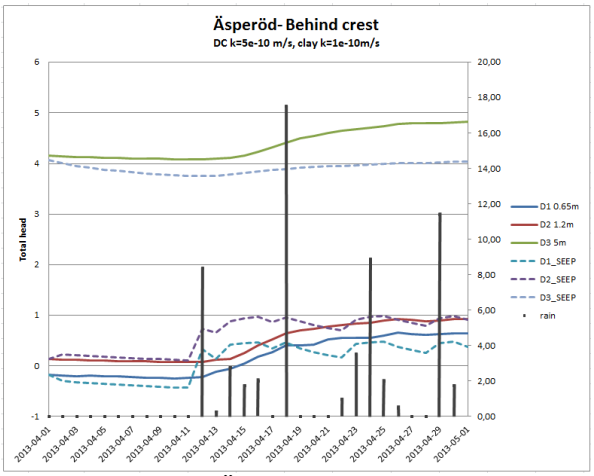


Figure 21 Station Äsperöd- behind crest. Results from simulation compared to piezometer values.

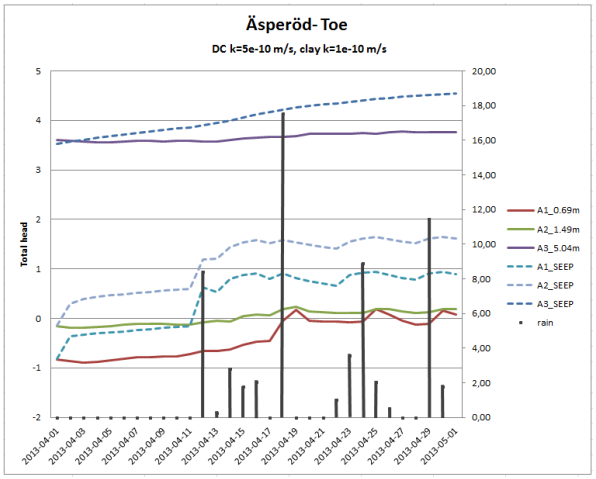


Figure 22 Station Äsperöd- toe. Results from simulation compared to piezometer values.

6 DISCUSSION AND CONCLUSIONS

- According to the presented results it is fair to say that the uppermost 5-10 meters of the soil profile has a hydrostatical pore pressure. This validates one of the assumptions in the hypothesis.
- The conditions in the two sites are rather similar and a clearly distinguished difference cannot be found. However, it shows that at least within the realm of the conditions prevailing at the sites the presented methods may be applied.
- In order to validate the hypothesis, pore pressure profiles for more stations and with other dates needs to be evaluated, especially with focus on the crest of the slope.
- For the section in Äsperöd the station in the crest does not have hydrostatical properties the uppermost 5 meters. Compared to Linnarhult, section 1, the Äsperöd section has a more distinct crest with a steeper inclination towards the river. This makes the pore pressure distribution different and the area around the crest gets lower pressures.
- More simulations with the seepage modeling software will be performed for other dates and other parts of the slope in Äsperöd to validate the results. After that also the sections in Linnarhult will be simulated to validate a wider use of the method.
- Finally this work will lead to recommendations for placement of piezometers, connections to rainfall and how to include pore pressure profiles in slope stability calculations and thereby improving the validity of stability analyses.

7 REFERENCES

Alexandersson H & Eggertsson Karlström C (2001) Temperature and precipitation in Sweden 1961-1990. Second edition. SMHI, Report No 99, Norrköping (In Swedish).

Berntson, J. (1983): Pore pressure variations in clays from the Gothenburg region (in Swedish). Licentiate thesis. Chalmers University of Technology, Göteborg

Persson, H. (2008): Estimation of pore pressure levels in slope stability calculations: Analyses and modelling if groundwater fluctuations in confined

aquifers along the Swedish west coast. Licentiate thesis. Chalmers University of Technology, Göteborg.

SGI (2011) Technical memorandum, geotechnics (Intagan-Ström, Sweden). Swedish Geotechnical Institute, SGI. The Göta River Investigation, GÄU. Dnr 6-1001-0027, Linköping (In Swedish).

Vattenfall (2015). Personal communication regarding water level variations in Göta River.

Climate change induced river erosion as a trigger for landslide

G. Göransson
Swedish Geotechnical Institute, Sweden, gunnel.goransson@swedgeo.se

J. Hedfors, G. Ndayikengurukiye, K. Odén
Swedish Geotechnical Institute, Sweden

ABSTRACT
Most landslides are triggered by precipitation, river erosion, or human impact, or both. Regions experiencing an increase in precipitation from climate change may be at elevated risk for increased landslide frequency. The Swedish Geotechnical Institute is developing a methodology for landslide risk analysis and mapping along Swedish rivers and with the consideration of climate change effects. River geometry is dynamic and is under constant change, however most slope stability analyses are made under the assumption that the condition is static. No consideration is taken to future changes in slope geometry from river erosion. But, is it even possible to assess how river cross sections will change in future along with the effect of increased river flows due to the climate change? There are yet no models that can combine soil mechanics with hydrodynamic processes.
The Swedish Geotechnical Institute is developing a methodology to calculate possible future changes in river cross sections and with respect to climate change effects The approach is based on various measurements and analyses like bathymetric surveys, sediment characterization, hydrodynamic modelling of river flows, analysis of shoreline displacement with time by using aerial photos, and comparison between old and new cross sections. Erosive river flows are assessed and the duration of such flows in future (year 2100) is estimated based on existing climate analyses. Comprehensive calculation of river bed erosion is made in GIS, and is combined with bank erosion calculation in chosen cross sections. Calculation of slope stability and the probability of slope failure are then done for several cross sections, both for today´s geometry and for an expected geometry by year 2100. The approach was first developed in the landslide risk analysis for Göta Älv river, Sweden, and further developed and simplified for Norsälven River, Sweden. Currently, a landslide risk analysis for Säveån river has just been started.

Keywords: Bed erosion, bank erosion, slope failure, climate change

1 INTRODUCTION

When the water current is strong enough, particles will be detached and carried by the flowing water. There will be an exchange of particles on the river bed where some settles and other are detached and erosion occurs when it disappears more particles than what is settled. Sediment transport concerns both fine particles and coarser particles. Simplified, sediment transport is governed by bed slope, flow depth, flow velocities, particle size, and particle fall velocities (see for example Chanson, 2004). The forces that act on the particle are in general lift, drag, buoyancy and gravity. In addition, cohesion, biofilms, consolidation etc. affects. While gravity (and cohesion, biofilm and consolidation) is the stabilizing force, the others (lift, drag, buoyancy) are the destabilizing forces. Mobilization of particles occurs when the destabilizing forces are greater than the stabilizing forces. The threshold for mobilization is very difficult to determine with accuracy but many empirical observations have shown reasonably accurate and consistent responses (Chanson, 2004). Erosion in rivers has been studied by many to understand the processes of bed and bank erosion, sediment transport during peak

flows, sediment fluxes etc. Most studies on fluvial erosion and sediment delivery concern individual flow peaks and are based on historical data (empiric based studies). However, there are yet no reliable models that combine geotechnical properties that act across a watercourse with the hydrodynamic processes that act along a watercourse, and in a long-time perspective. Some attempts have been done (Darby et al., 2007; Midgley et al., 2012; Rinaldi and Darby, 2008) but there is no general approach available. Darby et al. (2007) combined hydraulic erosion and limit equilibrium stability models to simulate mass wasting for cohesive river banks. They simulated erosion for single flow events and only for bank erosion, i.e. bed erosion was not included. Midgley et al. (2012) used a bank stability toe erosion model (USDR-ARS, 2015) to simulate bank erosion for a longer time period. Bed erosion not included. Both Midgley et al. (2012) and Darby et al. (2007) concluded that accurate data on pore water pressure is important and that sediment delivery from undercutting is difficult to manage in the calculations. Lévy et al. (2012) tried to identify the impact of long-term bank erosion for landslide from aerial photographs and laser measurements. They concluded that the method is time and cost effective but depends largely on the quality of available data.

Rinaldi and Darby (2008) concluded that conceptual models might be available but quantitative treatments that include interactions between fluvial erosion and mass failure processes are lacking.

This paper is the first to presents an approach to make prognosis of future river bed and bank erosion with respect to the effects of climate change. The study is part of a landslide risk analysis in a changing climate. The objectives are to *i*) make a prognosis of river bed erosion to year 2100 and with respect to increased river flows from climate change, *ii*) make a prognosis of river bank erosion in representative cross sections and with respect to increased river flows from climate change, and *iii*) to provide basis for forecasting the probability of landslides along the river stretch with respect to both river bed and river bank erosion to the year 2100.

2 METHOD

2.1 Study site description

The study site is the Norsälven River that runs from Lake Lower Fryken and debouches into Lake Vänern, Sweden. The river stretch is 28 km (ca 60 km shoreline) but is separated by two hydropower stations at 5,5 km and 11 km downstream the outflow from Lake Lower Fryken (Fig. 1). The survey area extends 600 m on each side of the river.

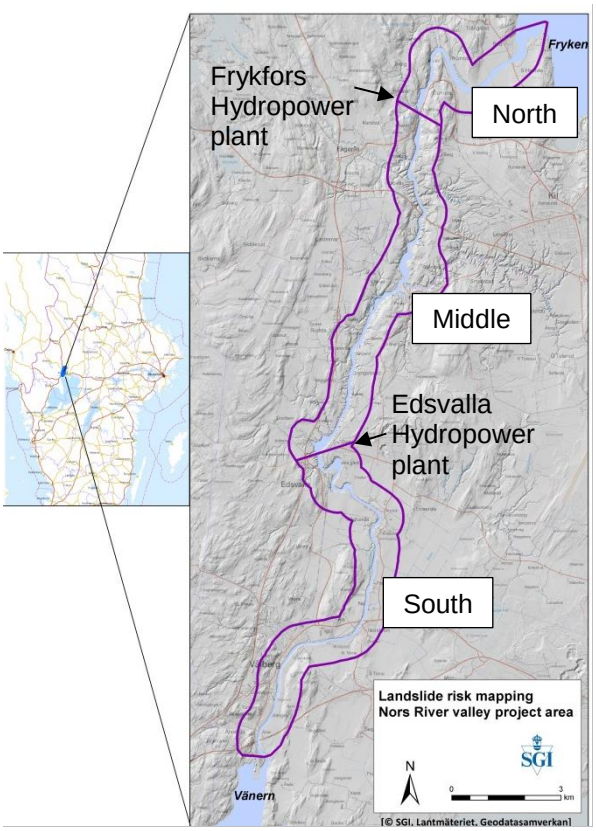


Figure 1. River Norsälven from Lake Lower Fryken to Lake Vänern. The figure displays the area in hill shaded topography and shows the investigated area as part of the Landside risk analysis. The stretch is divided into three parts separated by two hydropower plants. © SGI, Lantmäteriet, Geodatasamverkan.

The river is limited meandering and flows in a glacial sediment-filled valley that is characterized by severe gully formation and landslide scars. The sediment consists mainly of fine sediments that at some parts are underlain by coarser glacio-fluvial deposits. The high silt content in the fine sediment makes the soil vulnerable to erosion.

River mean flow is 51 m^3/s and the mean high water flow is 190 m^3/s. The highest flow

that has been registered between the years 1968-2013 is 393 m^3/s and occurred in May 1997 (open data source: http://vattenwebb.smhi.se/). The 100-year flow (Q_{100}) for today's climate is 276 m^3/s (Persson et al, 2014). According to a climate analysis for the county, precipitation will increase by approximately 20% until year 2100, with the most profound increase during the winter month. As well will the frequency and intensity of rain burst increase (Persson et al, 2014). The climate scenarios do not consider future river flow regulations.
There is no sediment transport data for the river and bathymetric data is limited to a few sounded cross sections for the southern part of the river. Overall, there is very little knowledge of the river characteristics, especially below the water surface.

2.2 Governing equations

The main assumption for the erosion model is that formulas for cohesive sediments should apply for River Norsälven. The general formula for erosion rate in cohesive sediments is written as (Hanson and Cook, 1997; Hanson, 1990; Partheniades, 1965)**:**

$$E = k_d(\tau_0 - \tau_c)^a \quad (1)$$

Where E is erosion rate ($m\ s^{-1}$), k_d is the erodibility coefficient ($m^3N\ s^{-1}$), τ_0 is the average boundary shear stress (Pa), τ_c is the critical shear stress (Pa) and α is generally considered to be 1. The formula may seem simple but the parameters are very difficult to determine without comprehensive in-situ field measurements (= expensive). It requires a large field effort with great resources which have not been possible for the case. Instead, the values of k_d and τ_c must be based on empirical studies reported in the literature.
Hanson and Simon (2001) conducted 83 submerged jet-tests to find an empirical relationship between τ_c and k_d for cohesive silts, silt-clays and clays. They conducted the tests for a wide variety of soils in mid-western United States, with τ_c varying from 0,0 to 400 Pa and k_d varying from 0,001 to 3,75 $m^3N\ s^{-1}$ and developed the following relation:

$$k_d = 2 \cdot 10^{-7}\tau_c^{-0,5} \quad (2)$$

Jet-testing on bank toes suggests that although the exponent is the same, the coefficient is instead 1×10^{-7} (USDR-ARS, 2015):

$$k_d = 1 \cdot 10^{-7}\tau_c^{-0,5} \quad (3)$$

In 2010, Simon et al. refined their analyses (eq. 2) with improved field instrumentation and performed about 1100 jet-tests in fine grained soils from 16 states within the US and compared to earlier results and found the following relation:

$$k_d = 1{,}6 \cdot 10^{-6}\tau_c^{-08264} \quad (4)$$

Karma and Dutta (2011) conducted 58 submerged jet-tests and found that there are a few outlier data points for which it is not possible to fit the data with simple regression. In their case, the robust regression technique they used gives less weights to the outliers and so the results are less sensitive to these outlier, a better fitting is hence given and with higher correlation (p=0,002):

$$k_d = 3{,}16 \cdot 10^{-6}\tau_c^{-0,185} \quad (5)$$

Hanson and Simon (2001) carried out their tests in the river bed, while the study by Karma and Dutta (2011) was carried out for the river banks.
There are other studies (see for example Wynn, 2004) but regardless the method, an estimation of k_d assumes that there is no deposition of the bank material near the bank. In contact with the USDA-ARS (Langendoen, 2014), the equations relating k_d to τ_c are based on data with a lot of scatter. The coefficient and exponent of the relation can vary quite a bit and a re-analysis by Rob Thomas of Andrew Simon's original data (plus many more, Simon et al., 2010) resulted in slightly different values of coefficient and exponent. The range in values reflects the heterogeneity of soils, effects of organics, moisture conditions, etc. According to Langendoen (2014) he typically fit a k_d to τ_c curve through the site-specific, measured

data to remove scatter. These curves can have quite different values than reported in literature. Also, the k_d itself is often slightly modified to obtain better agreement between observed and predicted erosion rates. In summary, there is a lot of uncertainty in the used k_d value but if one get good agreement with eq. 3, it is suggested to use that to evaluate our study objectives (Langendoen, 2014).
Erosion for a given time period is then calculated through the following equation (e.g. Partheniades, 1965; Karmaker and Dutta, 2011; USDA-ARS, 2015):

$$E_t = k_d(\tau_0 - \tau_c)^a \cdot \Delta t \quad (6)$$

Where E_t is erosion (m) for a given time period and Δt is the total time for fluvial erosion (s). This is based on the assumption of constant conditions, i.e. no changes in flow or shear stress etc. It is in general believed that it is the bankfull discharge (i.e. the flow when the river is just about to spill onto its floodplain) that most effectively shape river channels (e.g. Karmaker and Dutta, 2011; Maidment, 1992).
For the case, it is further assumed that if fine sediment is eroded from the river bed, it is not likely that it deposits in the river but is transported to the lake where the river debouches. If one also neglects accumulation, the estimate of erosion in the river is on the safe side.
The average boundary shear stress (τ_0) is an index of the force that the flowing water exerts on the bottom and is therefore closed linked to the flow velocity. Normally, and for turbulent flow, τ_0 is assumed proportional to water velocity squared. Average boundary shear stress for a wide stream (with larger than depth) (e.g. Chanson, 2004):

$$\tau_0 = \rho g d sin\theta \quad (7)$$

Where ρ is the density of the water (kg/m^3), g is the gravity force (m/s^2), d is flow depth (m) and $sin\theta$ is the longitudinal bottom slope (-). Equation 7 can then be rewritten by introducing Manning's formula (Larson, 2014):

$$\tau_0 = \frac{n^2 \rho g v^2}{\sqrt[3]{d}} \quad (8)$$

Where n is Manning's roughness (s/m^3) and v is the water velocity (m/s).
One of the first and most known formulas to estimate critical shear stress is the one based on Shield's parameter and D_{50} (see for example Chanson, 2004). However, none of these are valid for cohesive sediments. Experimental studies that are based on empirical relations between critical shear stress and different sediment characteristics have shown that it is possible to estimate τ_c from the proportion of fine sediments. These studies are presented in Karmaker and Dutta (2011) and have been developed by Dunn (1959), Vanoni (1977) and Julian and Torres (2006):

$$\tau_c = 0{,}1 + 0{,}1179(SC) + 0{,}0028(SC)^2 - 2{,}34E^{-5}(SC)^3 \quad (9)$$

Where SC is the percentage content of silt and clay fraction in the sediment (hence the abbreviation S and C).
In this study, total time for fluvial erosion concerns a prognosis of the re-occurrence of erosive discharges with respect to the effects of climate change in the study area.

2.3 Data

Bathymetric data from different time periods are by far the best data to make prognosis of future changes of river morphology. Also sediment transport data is of good use. However, for the Swedish rivers such data are rarely available, at most you can find information on river flow from the hydropower plants and water levels at some points. Sounding cross sections can be available near settlements and where geotechnical investigations have been made. The collection of existing data covered surface geology, surface topography, sounded cross sections (cross profiles), flow statistics from 1971 until 2013, sections with erosion protection, and climate scenarios until year 2100.
Recent investigations includes *i*) diachronic analysis in GIS of aerial photos from 1965/66

and 2013 to investigate shoreline displacement over time, *ii*) a bathymetric survey (hydro acoustic soundings) with sediment sampling and analyses to yield a bathymetric map and a general marine geological map, *iii*) a 2-dimensional hydrodynamic model to model average shear stresses, depth integrated water velocities, water depths and water levels for different river flows and *iv*) geotechnical surveys in cross sections for the analysis of soil mechanical properties.
The diachronic analysis was done by the Swedish Geotechnical Institute (SGI), the bathymetric survey was done by Marin Miljöanalys AB, sediment analyses was done at the SGI laboratory, the hydrodynamic modelling was done by the Swedish Meteorological and Hydrological Institute (SMHI), and the geotechnical surveys were done by Norconsult (Bergdahl et al, 2015). All data, except for the geotechnical surveys, was delivered as GIS layers.
A marine geological map was constructed based on backscatter data and sediment analyses from the bathymetric survey. Critical shear stresses for these sediments were calculated with eq. 9 to convert the marine geological map into a critical shear stress map.
Average shear stresses was simulated for 11 discharges (20, 70, 150, 200, 250, 300, 350, 400, 450, 500 m^3/s).
Former cross sections were digitalized in CAD and compared with the new bathymetry. Of 21 former cross sections, only four were assessed useful for further analysis (no dredging, no erosion protection, and no accumulation of sediments). These sections had been sounded in 1971. By analyzing the changes (erosion) in these cross sections from year 1971 until 2013, the equation for k_d (eq. 2-5) and the most probably erosive river flows could be chosen. Average shear stresses (τ_0) were obtained from the hydrodynamic model and critical shear stresses were obtained from the converted backscatter data. If calculated erosion according to eq. 6, and by varying flow scenarios and the equations for k_d, did not differ more than ± 0,5-1 m from the measured, it was assumed a good enough agreement.
An estimation of the time for fluvial erosion (Δt) is based on historical data and information on future river flows with respect to the effects of climate change.

2.4 Models

Two models were set up, one GIS model to compute surface covering bed erosion, and one spreadsheet model to compute bank and bank toe erosion in chosen cross sections as the GIS model do not capture the erosive processes that act on the bank and bank toe. The spreadsheet model for bank and toe erosion is only used to simulate changes in bank geometry and not to calculate slope factor of safety, although possible. The reason is that the spreadsheet model uses a slightly different approach compared to the national instructions. To clarify, changes in geometry in chosen cross sections were obtained from the GIS model and the spreadsheet model, and were then inserted into a model for geotechnical solutions to calculate slope factor of safety. Slope factor of safety was hence calculated for today's geometry and for a future forecasted change in geometry, but also for a change in groundwater tables (change in groundwater table from climate change is not included in this paper). The cross sections were chosen to represent different geological and geotechnical units along the river. The GIS model, together with the diachronic analysis, was used for a surface covering prognosis of areas with future erosion and a prognosis of the extent.

3 RESULTS

3.1 Parameter setting for case Norsälven River

Based on the backscatter data the bottom surface sediment was divided into four sediment types and for which critical shear stresses were calculated (Table 1 and figure 2).

Table 1. Classification of backscatter data into sediment type and critical shear stresses.

Backscatter dB-range	Soil classification	Color code in GIS	Critical shear stress (Pa)
0-54	Silty clay	Grey	0,26
54-65	Sandy silt	Yellow	0,21
65-87	Silty sand	Orange	0,14
87-120	Gravel, stone, bedrock	Red	>5

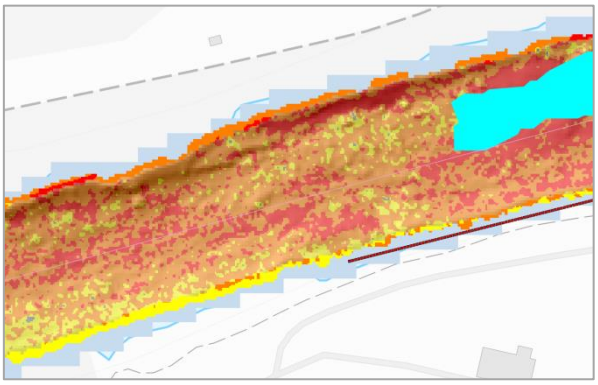


Figure 2. Extracts from GIS showing the interpreted sediment types from backscatter data. The blue areas are presumed bedrock. The red lines are erosion protection. © SGI, Lantmäteriet, Geodatasamverkan.

A new spreadsheet model was set up to carry out the calculation of governing equation for k_d and erosive flow based on the comparison of cross sections from 1971 and the bathymetry from 2013. Equations 4 and 5 could not describe the measured erosion in the analyzed cross sections and the deviation was several meters, sometimes tens of meters. Equation 2 and 3 gave equivalent results and with an accuracy of up to one meter. Both eq. 2 and 3 are used by USDR-ARS (2015) but according to Langendoen (2014), eq. 3 is preferable if it yields good correlation. By using eq. 3, the erosive flow seems to start somewhere below 300 m^3/s, maybe a bit lower but not as low as 250 m^3/s (the hydrodynamic model was not simulated for flows between these levels). Other flows are possible but the variation in results is greater.

Regardless of the equation for k_d and the value of flow that is used, it will not be possible to describe all changes of river geometry but hopefully where a majority of the changes will take place and the approximate size.

It was not possible within the commission's budget limit to conduct a separate climate scenario analysis to answer the project specific issue, meaning that existing information had to be used. For the case, a climate analysis for the County administrative board of Värmland was available (see Persson et al., 2014).

The climate analysis was based on 16 climate scenarios and is made with respect to the reference period 1963-1992, the period 2021-2050 and the period 2069-2098. The results from the analysis shows for instance seasonal water flows, with marks for all scenarios mean flows, the 25 percentile and 75 percentile water flows, and for the three time periods (Persson et al., 2014), see Fig. 3.

The mean flow will never reach as high as the estimated erosive flows, meaning that changes in the mean flow will not be possible to use in order to determine the time for fluvial erosion (Δt). However, it might be possible to use changes of the 75 percentile from the reference period until 2098 and with respect to the erosive water flow, and superimpose that change to the frequency of erosive flows between the years 1971-2013. The most likely erosive flow seems to be slightly below 300 m^3/s. In order to estimate the number of days for critical erosive flow, both 300 and 275 m^3/s has been used. The following equation was set up:

$$\Delta t = T \cdot f_{Qe} \cdot F_{Qe} \qquad (10)$$

Where Δt is the duration of future erosive flows (d), T is the number of days until future (here, the number of days between 2014-2100), f_{Qe} is the percentage of days between 1971 and 2013 with erosive flow, and F_{Qe} is the increase of the percentage of days with erosive flows until 2100 and based on an increase in 75 percentile flow of all the climate scenarios max values and with respect to the reference period (Fig. 3). The number of days between 2014 and 2100 is 31412 days taking into account leap years, f_{Qe} was estimated to 0,35% based on flow statistics from the years 1971-2100 ($Q \geq 300$ m^3/s occurred ca 47d, $Q \geq 275$ m^3/s occurred

ca 61d) and F_{Qe} was estimated to 34% (approximately the mean value of an increase by 10% of Q ≥300 m^3/s and an increase by 58% of Q≥275 m^3/s). With this approach, Δt is estimated to 150 days.

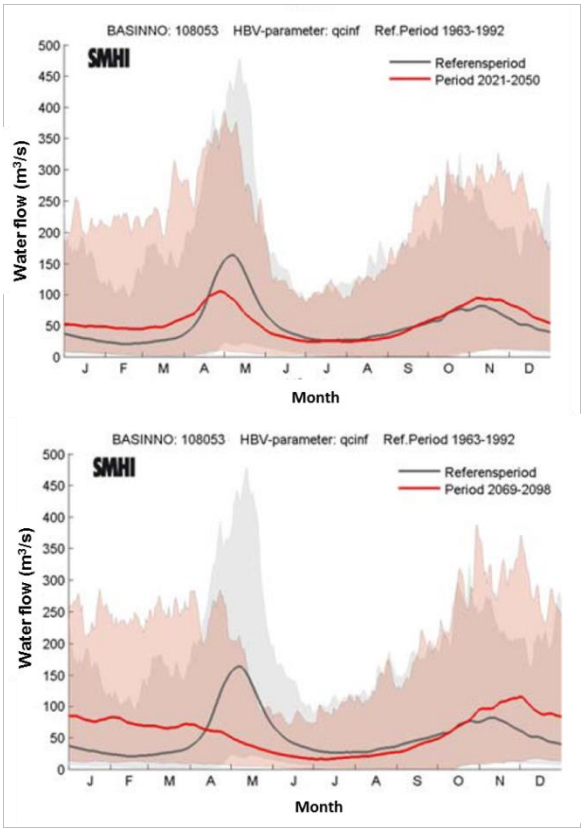


Figure 3. River flows for Norsälven River showing seasonal dynamics for the mean flows for the reference period 1963-1922 (black line) and for the two future time periods (red line). The grey shade shows the variation between the 75 percentiles of all scenarios max values and the variation between the 25 percentiles of all scenarios min values for the reference period. The light red shade shows the same but for the future time periods (2021-2050 and 2069-2098) (in Persson et al., 2014).

3.2 Bed erosion

The GIS layers for parameter setting comprises average shear stresses (5×5 m raster, tif format), critical shear stresses (0,5×0,5 m raster, tif format), a bedrock mesh (vector, shp format) and a watercourse mesh (vector, shp format) for delimitation of output file. The erosion calculation then contains a number of steps to prepare the data, customize the grid and perform the actual calculation according to eq. 6.
Figure 4 displays an example of the output file that shows a prognosis of bed erosion in the river until 2100 considering the effect of climate change with increased river flows.

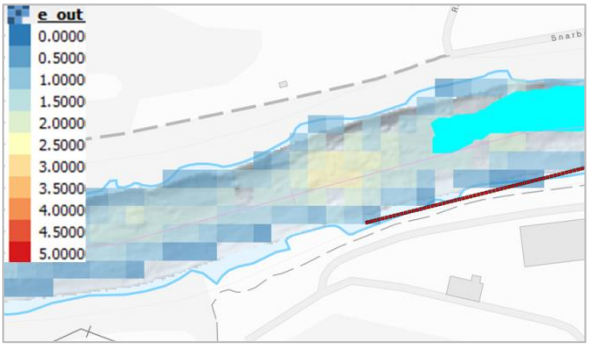


Figure 4. Extracts from GIS output file that shows calculated bed erosion (m) in half meter intervals and for 10×10 meter grids. The figure only displays a minor part of the river stretch. © SGI, Lantmäteriet, Geodatasamverkan.

3.3 Bank erosion

Bank erosion and changes of bank geometry for chosen cross sections were calculated by using the spreadsheet model for bank and toe erosion and combining it with the results from the GIS model to include bed erosion. Input data on geometry and bank material (cohesion, friction angle, saturated unit weight) was obtained from the geotechnical surveys. A limitation in the spreadsheet model for bank and toe erosion is that bank material can only be added as horizontal layers and inclined layers hence had to be modified to horizontal layers.
Data on channel and flow parameters should be added in order to compute average shear stresses but in this case we already have the shear stresses from the hydrodynamic model. Hence, we were sent a version with one of the tabs in the spreadsheet model unlocked (toe model) which made it possible to fit the channel and flow parameters to desired values on τ_0.

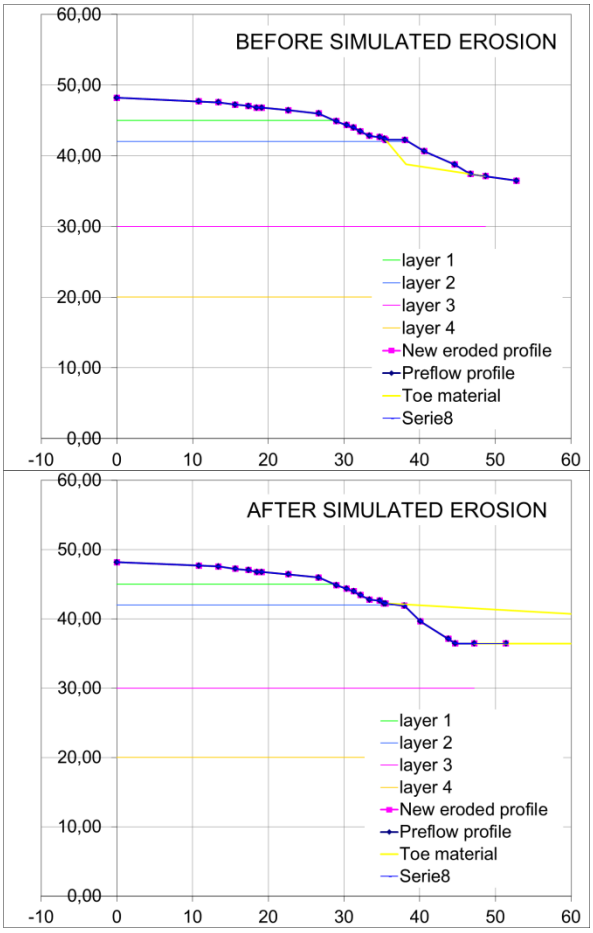


Figure 5. Example of output file from input geometry and simulated bank and toe erosion in the spreadsheet model. The blue line with pink squares represents the original and the eroded profile, respectively. The colour lines represent different sediment characteristics.

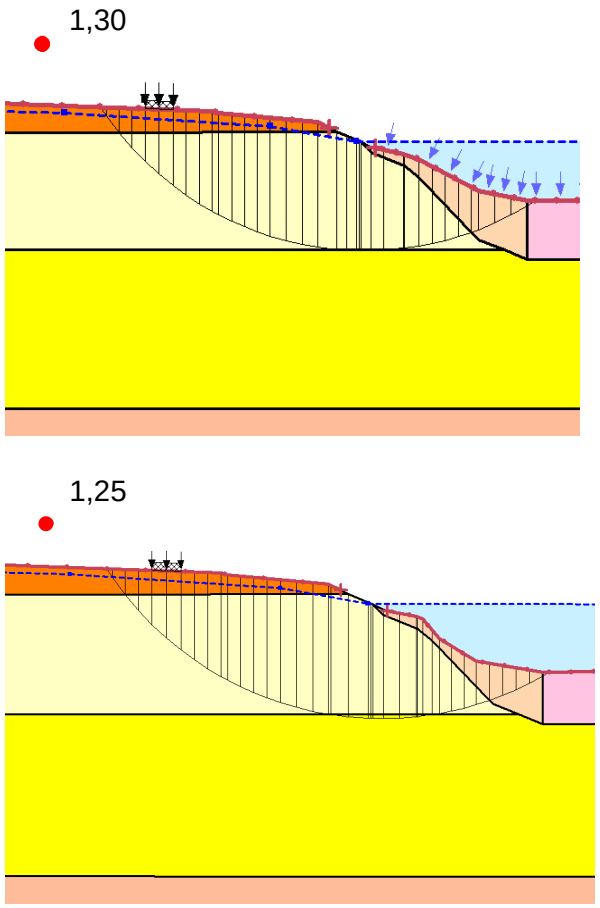


Figure 6. Example of prognosis of future changes in bank and bed geometry for a cross section until year 2100 and considering future erosion from the effects of climate change. The upper figure shows original geometry and factor of safety and the lower shows the factor of safety after simulation of future erosion.

It is possible in BSTEM to simulate erosion in time steps but we had problem to make it work.
Figure 5 displays an example of an output file in BSTEM after simulation, and Fig. 6 displays an example of prognosis of changes in bank and bed geometry for a chosen cross section.

3.4 Assessment of reliability

The reliability of calculated prognosis of bank erosion until year 2100 can only briefly be verified. By comparing the results with the results from the diachronic analysis of shoreline displacement, the reliability of the calculated bank erosion could be assessed. Cross sections that resulted in a clear bank retreat until 2100 had historically (since year 1965) undergone erosion according to the diachronic analysis. And vice versa, cross sections that resulted in no bank retreat showed the same in the diachronic analysis. Calculated bed erosion was compared with historically bed erosion from the comparative study of earlier and recent sounding, however, the same was used to determine parameter values for the calculation which could give circle evidence. There is one exception though, and that is very close to the hydropower plant where a too low value of the critical stress probably was chosen as the bed consists of bedrock. The calculated future erosion indicates almost 9 m erosion until 2100 which is not reasonable.
The yearly land upheaval of ca 3 mm/year (0,26 m until 2100) has not really been taken into account since the resolution in the calculation is within 0,5-1 meter. This could of course be discussed.

The result from the forecasted bed and bank erosion were implemented in the slope stability calculation and the assessment of landslide probability which then resulted in landslide risk maps with different dashed patterns in the river area showing low, moderate or high impact of climate change on landslide probability (not included in this paper).

4 DISCUSSION

This paper describes an approach to make a prognosis of future river bed and bank erosion considering the effect of climate change as a basis for the assessment landslide risk by year 2100. There are no models available for this kind of forecasting that combines soil mechanical forces with hydrodynamic processes. In this study, we therefor used GIS to model future bed erosion and a spreadsheet based model to model future bank erosion in cross sections. The study site is the river Norsälven River in Sweden. Cohesive sediments are dominating the geological feature.

The calculated erosion rate depends partly on the differences between current τ_0 and τ_c, and partly on the duration of this τ_0. High river flows yield larger difference between τ_0 and τ_c but with shorter duration. On the contrary, low flows yield smaller differences between τ_0 and τ_c but longer duration since flows close to the mean occur more frequent than the extremes. Bankfull discharge is often mentioned as the stage with most effective erosion. The bankfull discharge can however be difficult to determine and for the case we used flow scenarios to described measured erosion, i.e. the flows that can explain the measured erosion.

One important uncertainty is that only four former sounded cross sections could be used to measure historical changes in bathymetry and it would have been desirable with more. These four sections were sounded in 1971 and we do not really know which sediment that has eroded away until 2013 when new measurements were made. However, the absence of data is often the case for rivers in Sweden and we have to deal with it.

None of the empirical equations to determine k_d have been able to describe the measured erosion completely accurate. Nevertheless, it has been possible to exclude the equations that were definitely not right. If the chosen equation for k_d and the chosen critical shear stresses could describe the measured erosion by ± 0,5-1 m it was assessed good enough to meet the objectives and considering the many uncertainties, especially with climate scenarios. One possibility could have been to work more with uncertainties and visualize them clearly.

It was not possible to forecast erosion stepwise; consequently, changes in bed condition and sediment characteristics could not be updated. Erosion does not occur at a steady pace, but at single flow peaks. After each erosion event, the geometry is changed and the prerequisite for further erosion is changed especially if erosion causes bank failure.

To conclude, we find the approach useful but cumbersome and there emphasize the need for the development of models and softwares that are able to manage soil mechanics AND hydrodynamics. There are river morphological models available but these models comprise only the river itself and not the adjacent land area with its geological feature and soil properties. We also would like to emphasize the need for repeated bathymetric measurements, not only for the validation of the models but to gain control of erosion and erosion processes. Such data is invaluable.

5 ACKNOWLEDMENT

This study was part of the development of a method for landslide risk analysis along Swedish rivers in a changing climate. The work is funded by the governmental climate funding for the Swedish Geotechnical Institute.

The authors would like to thank Prof. Magnus Larson, Lund University of Technology, Sweden, for reviewing the final result.

6 REFERENCES

Bergdahl, K., Odén, K:, Löfroth, H., Göransson, G., Jönsson, Å., Kiilsgaard, R. (2015). Skredrisker I ett förändrat klimat – Norsälven. Del 2: Metod för kartläggning. Statens geotekniska institut. SGI Publikation 18-2.

Chanson, H. (2004). The hydraulics of open channel flow: an introduction Second edi., Elsevier.

Crosato, A. (2007). Physical explanations of variations in river meander migration rates from model comparison. Earth Surface Processes and Landforms2, 24, pp.1056–1073.

Darby, S.E., Rinaldi, M., Dapporto, S. (2007). Coupled simulations of fluvial erosion and mass wasting for cohesive river banks. Journal of Geophysical Research, 112.

Dunn, I.S. (1959). Tractive resistance of cohesive channels. Journal of the Soil Mechanics and Foundations Division 85(SM3), 1-24.

Fischenich, 2001. Stability thresholds for stream restoration materials. EMRRP Technical Notes Collection (ERDC TN-EMRRP-SR-29), Vicksburg, M.S.

Hanson, G. (1990). Surface erodibility of earthen channels at high stresses: Part I. Open channel testing. Transactions of the ASAE, 33(1), pp.127–131.

Hanson, G. & Cook, K. (1997). Development of excess shear stress parameters for circular jet testing. ASAE, Paper No. 97 - 2227.

Hanson, G. & Simon, A. (2001). Erodibility of cohesive streambeds in the loess area of the Midwestern USA. Hydrological Processes, 15(1), pp.23–38.

Julian, J.P., Torres, R. (2006). Hydraulic erosion of cohesive riverbanks. Geomorphology 76(1-2), 193-206.

Karmaker, T. & Dutta, S. (2011). Erodibility of fine soil from the composie river bank of Brahmaputra in India. Hydrological Processes, 25, pp.104–111.

Langendoen, E. J. (2014). Personal communication with Langendoen at the Research Hydraulic Engineer, Watershed Physical Processes Research Unit, USDA, ARS, Oxford.

Larson, M. (2014). Personal communication with prof. Magnus Larson, department of Water Resources Engineering, Faculty of Engineering, Lund University, Sweden.

Lévy, S., Jaboyedoff, M., Locat, J., Demers, D. (2012). Erosin and channel change as factors of landslides an valley formation in Champlain Sea Clays: The Chacoura River, Quebec, Canada. Geomorphology 145-146, 12-18.

Maidment, D. R. edt in Chief (1992). Handbook of hydrology. McGraw-Hill, Inc. ISBN 0-07-039732-5.

Midgley, T., Garey, A. & Derek, M. (2012). Evaluation of the bank stability and toe erosion model (BSTEM) for predicting lateral retreat on composite streambanks. Geomorphology, 145-146, pp.107–114.

Partheniades, E. (1965). Erosion and deposition of cohesive soils. Journal of the Hydraulics Divison of the American Society of Civil Engineers, 91(HY1), pp.105–139.

Persson, G., Ohlsson, A., Eklund, D., Sjökvist, E., Hallberg, K. (2014). Klimatanalys – Värmlands Län, Publikationsnummer 2014:2, Länsstyrelsen Värmland, Karlstad.

Rinaldi, M., Darby, S.E. (2008). Chapter 9 Modelling river-bank-erosion processes and mass failure mechanisms: progress towards fully coupled simulations. Developments in Earth Surface Processes, Volume 11 Gravel Bed Rivers 6: From Process Understanding to River Restoration, Elsevier.

Simon, A., Thomas, R. E., Klimetz, L. (2010). Comparison and experiences with field techniques to measure critical shear stress and erodibility of cohesive deposits. 2nd Joint Federal Interagency Conference, Las Vegas, NV, June 24-July 1, 2010.

USDA-ARS (2015). http://www.ars.usda.gov/Research/docs.htm?docid=5044, last accessed 2015-09-15. Bank Stability Toe Erosion Model, developed by Simon, A., Thomas, R., Curini, A., Bankhead, N.

Vanoni, V. A. (1977). Sedimentation Engineering, ASCE: New York, NY.

Wood, A. et al. (2001). Bank-toe processes in incised channels: the role of apparent cohesion in the entrainment of failed bank materials. Hydrological Processes2, 15, pp.39–61.

Wynn, T. (2004). The effects of vegetation on streambank erosion. Blacksburg.

Landslide risks in a changing climate, Nors River pilot study area

K. Bergdahl
Swedish Geotechnical Institute, Sweden, karin.bergdahl@swedgeo.se

K. Odén, H. Löfroth, G. Göransson, Å. Jönsson, R. Kiilsgaard.
Swedish Geotechnical Institute, Sweden.

ABSTRACT
The Swedish Geotechnical Institute (SGI) is commissioned by the Swedish government to perform risk assessment for landslides within the national climate change adaptation allowance. Our commission includes mapping the risks in present and future climate conditions.
Making use of material from the previously completed Göta River valley Investigation (GRI), SGI identified and prioritized Swedish watercourses for landslide risk mapping (Bergdahl et al in 2013). The Nors River valley was chosen as a pilot area for the development of a simplified methodology for landslide risk mapping. The investigation along the river is based on the methodology that was developed within the GRI. It aims to provide a sufficient basis for planners in municipalities and county administrative boards in their work with prioritization and preparation of adaptation measures. Methodological development has been carried out in order to reduce the costs of investigation and to simplify the interpretation of the maps, thereby increasing the societal relevance and usability of the results.
The landslide risk analysis along the Nors River valley has resulted in a comprehensive overview of the risk of landslides in the present and future climate, for built-up as well as yet undeveloped land and areas with vital infrastructure. The methodology for risk mapping, that has been developed, is applicable for landslide risk mapping along other streams and river valleys.
The resulting maps are made available in a free GIS Webb application, accustomed to the users of the information.

Keywords: Landslide risk analysis, Climate change, Probability of landslide, Consequenses.

1 INTRODUCTION

Sweden has many areas prone to landslides. Areas along watercourses that flow through loose soil layers are often more vulnerable than others. In such areas the effects of climate change can also become apparent, for example, with increased water flow that causes increased erosion and deterioration of stability in soil layers.
Building further on the Göta River valley Investigation (hereinafter GRI), SGI has developed methods for mapping the risks for landslides. These methods can also be applied for landslide risk mapping in other geographical areas.

The Nors River valley (further referred to by the Swedish name, Norsälven) is the first of a number of subsequent identified river valleys for which the mapping of landslide risk has been planned. Thus Norsälven serves as a pilot area and was presented as a priority in SGI's budget within the national climate change adaptation allowance. There it is described as, "An investigation of a more comprehensive nature that can be used for planning and decision-making by county administrative boards and municipalities in their adaptation work at regional and local level".
With an overall picture of all areas prone to landslides along the current water course it is possible to make a better substantiated

assessment of which areas require more detailed geotechnical investigations and where geotechnical adaptation measures provide the most public benefit and are most cost-effective. In addition, the municipalities concerned receive a more complete basis for the probability and societal consequences of landslides in already built-up areas, and for the landslide probability in areas where new buildings are planned.

The purpose of landslide risk mapping is to produce a comprehensive map of landslide risks along the current river valley. The map presents the distribution of the risk levels of landslide probability and consequences (in pairs), as well as the impact of climate change on landslide probability in a 100-year perspective. The landslide risk map can be used as a basis for planning and prioritization of climate adaptation measures at the municipal level in their comprehensive plans, and for communication with involved stakeholders.

The methods utilized in the Göta River valley Investigation have been applied as far as possible. However, method development has been necessary to reduce the investigative costs and to simplify the interpretation of the maps without leading to a substantial impairment of the usability. Account has been taken of evaluation and comments that arrived after the Göta River valley Investigation. Among other things, this has served to simplify the results and make them more transparent.

Landslide risk mapping contributes to considerable societal benefits by providing material to:

- avoid/mitigate the consequences of landslides,
- reduce the likelihood of landslides,
- support the national environmental quality objectives good built environment (and good non-toxic environment), and
- provide input to planning for adaptation.

1.1 Scope and limitations

The investigation of Norsälven extends from the Lake Lower Fryken outlet in Kil municipality to Norsälven's estuary in Lake Vänern in the Karlstad municipality, see Figure 1. In total, this means a distance of about 30 km, equivalent to 60 km shoreline. The investigated area's width is limited to approximately 600 metres from the shoreline, in some cases a shorter distance when delimitation against solid ground could be made. The area has been divided into sections South, Middle and North, see Figure 1. The sub-division is made primarily on the basis of diverse geological conditions but also for practical reasons, as these sections are divided by two hydropower plants at Frykfors and Edsvalla. Investigation of landslide risks in tributaries or deep valleys that lie within the area of investigation has not been done explicitly, but with assessment based on the results of the calculations along the river.

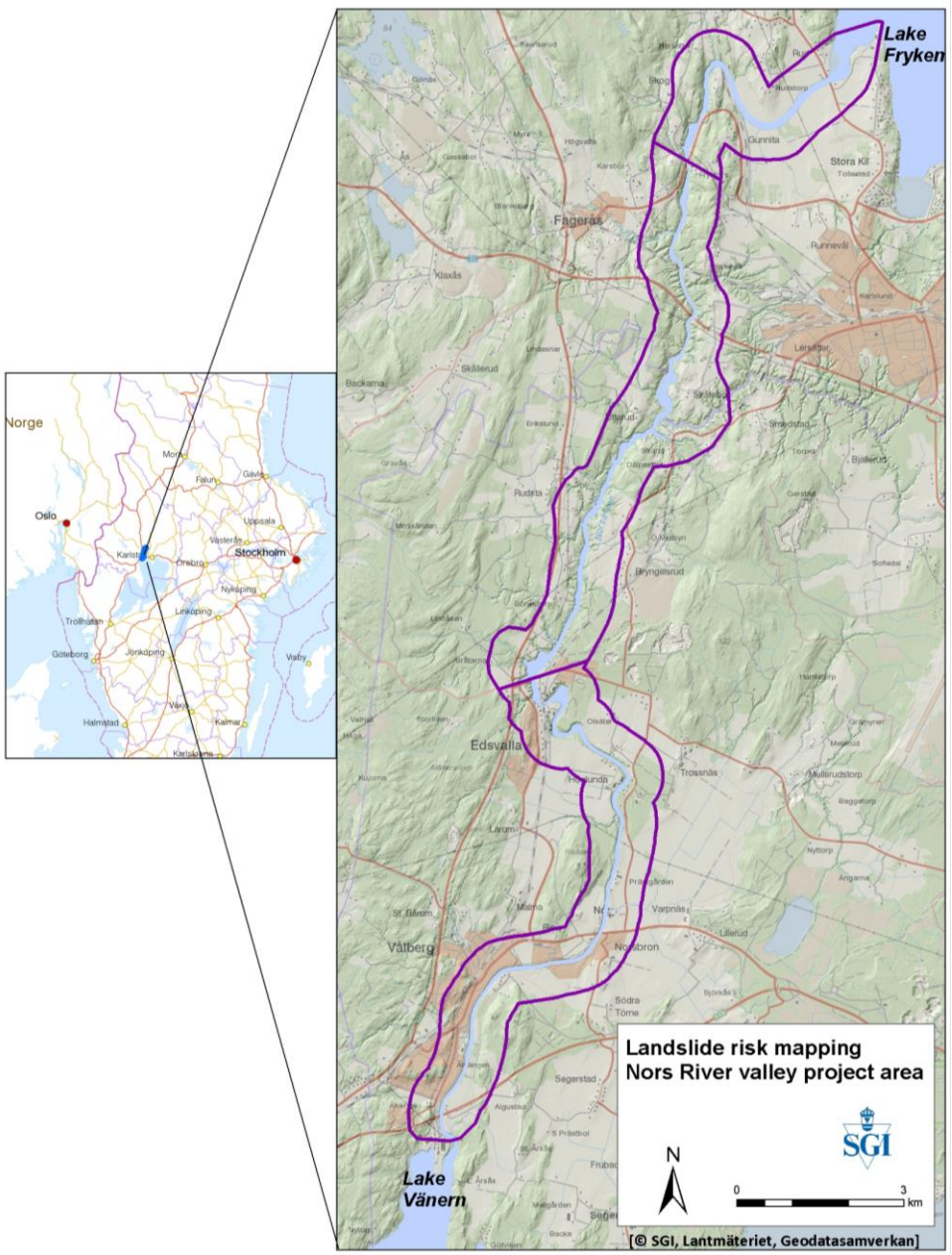


Figure 1 The Nors River pilot study area.

2 PROBABILITY, CONSEQUENCES, AND RISK

2.1 Probability of landslide

In order to obtain as good a description of reality as possible, the traditional calculation of slope safety factors have been complemented by an assessment of the probability of landslides, taking into account the uncertainty that exists in the input parameters. Stability is analysed using parameters which is given a variation that describes their uncertainty. The variation is determined in each case by using experience from similar areas as well as with statistics from surveys and other investigations. Some parameters change over time, and/or as a result of climate change, which means that the calculations must be made both for the current and future situations. The probability has then been calculated using point estimate method, PEM.

The probability of landslides has been divided into five classes, S1-S5, see table 1. The boundaries between the different

probability classes have been based on European and Swedish standards commonly used for design of buildings. Classes have been selected so that probability class S5 means poorer conditions than the worst class that may be accepted for temporary structures, while probability class S1 means better stability than the requirements for common buildings (Berggren et al, 2011, Göta River valley Investigation sub-report 28). The probability in areas between the calculated sections has been estimated based on their geotechnical and geometric conditions in relation to the conditions and results in the calculated sections.
The produced probability map can be used as a guide to show where geotechnical conditions in particular should be taken into account in urban planning.

Table 1 Classification of probability of landslides.

Proba-bility class	Landslide proba-bility	Relative failure probability (Pf)
S1	Negligible	$Pf < 3{\cdot}10^{-6}$
S2	Low	$3{\cdot}10^{-6} \leq P_f < 1{\cdot}10^{-4}$
S3	Some	$1{\cdot}10^{-4} \leq P_f < 3{\cdot}10^{-3}$
S4	Distinct	$3{\cdot}10^{-3} \leq P_f < 1{\cdot}10^{-1}$
S5	Definite	$P_f \geq 1{\cdot}10^{-1}$

2.2 Consequences of landslide

In parallel with the calculation of the probability of landslides, the consequences of landslides along the river have also been assessed. An exhaustive description, and, above all, economic valuation of all possible consequences has not been carried out. The consequences for the buildings and the transport routes in the area have been valued on the basis of four quality criteria; life, environment, economy and social importance. Landslides in the river valley may affect many people and important social functions.
A landslide also means suffering, sorrow or discomfort for many people and thus the overall consequence of a landslide can include various implications for which it is difficult to make a systematic valuation. Possible impact of a changing climate on the consequences has not been assessed since such information so far has been unavailable. However, according to the national comprehensive planning code, planning decisions undertaken by the municipalities are assumed to take into account the existing conditions as well as conditions in a changing climate.
The consequences have been divided into five consequence classes, K1-K5. In the combination of data with various consequences the greatest value within each grid square has determined the consequence class. This ties in with classification from previous landslide risk mapping and corresponds to a gradual increase in the implications of classes, see table 2.

2.3 Classification of landslide risk

The descriptions above imply that all parts in the investigation area are assigned a probability class and a consequence class. The combinations of these two classes make pairs of values that describe a risk class. This classification can also be displayed in a matrix to show how various risk classes relate to one another, see Figure 2.

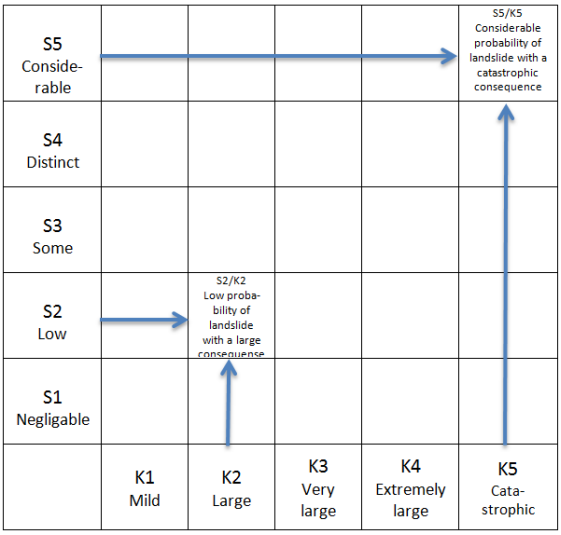


Figure 2 Matrix of risk classes

2.4 Landslide risk levels

In order to simplify the risk assessment the risk categories developed have been grouped into three risk levels consisting of a number of classes that correspond to a similar landslide risk, see Figure 3.

Table 2 Classification of consequences of landslides

Consequence class	Consequences of landslides	Description of Consequences
K1	Mild	No persons are injured or killed. No environmentally hazardous activity/enterprises affected and little environmental risk. Small economic losses. Loss of social function with very little social significance. Other/Minor roads (minor road, tractor road, footpath, running tracks, hiking trail, cable car, ferry route)
K2	Large	A few people are injured or killed. No environmentally hazardous activities/enterprises affected and medium environmental risk. Medium-sized economic losses. Loss of social function with low social significance. Public road class III (width < 5 m); Drive/neighbourhood road.
K3	Very large	Number of wounded or dead persons that corresponds to the number of people in a smaller dwelling with several homes. Environmentally hazardous activities suffer with serious consequences for the environment. Large economic losses. Loss of important social function. Public roads class II (width 5-7 m); Thoroughfare; Road under construction
K4	Extremely large	Number of wounded or dead people that corresponds to the number of people at a larger school, apartment buildings or major railway station. Environmentally hazardous activity involving extremely serious consequences for the environment. Extremely large financial losses. Loss of important social function. Public road separate carriageways; Public road in (width > 7 m)
K5	Catastrophic	Number of wounded or dead people that corresponds to the number of people in an indoor arena (thousands people, high density). Environmentally hazardous activity involving catastrophic consequences for the environment. Catastrophically large economic losses that distinguishes itself from most of the economic losses. Loss of very important social function. All railways; Highways

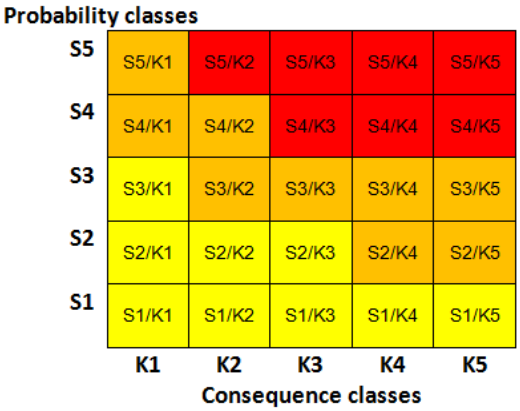


Figure 3 Matrix of risk levels

Risk levels are expressed as low, medium and high risk. See Figure 5 for a more detailed description of the different risk levels.

2.5 Risk of progressive landslides and secondary effects

In areas with highly sensitive clay/quick clay, progressive landslides may occur where large areas may suffer from continuous land sliding. Such an event means that secondary consequences in addition to the losses and damages to the land may occur. Examples of secondary effects that may occur are impoundments of the river (and its tributaries) and tidal waves of different magnitudes depending on the volume of the sliding mass. These secondary consequences may, if the affected area is sufficiently large, exceed the primary consequences in the area. The secondary consequences cannot be predicted with enough certainty, and therefore have not been addressed in the inquiry.

2.6 Climate impact

Anticipated climate change involves increased future flows in the river, implying increased erosion on the river banks and bed, as well as higher groundwater and pore water pressure. This has an impact on the probability of landslides because of slope geometry change within large parts of the area of investigation. This climate impact is expressed in three classes: low, moderate and high impact. Climate impacts are reported on

the landslide risk maps with different dashed patterns in the river area.
Depending on the class of an area, climate change will result in a probability class increase of one to two levels within some sections along the river. In areas with the highest probability class (S5), even a small influence caused by climate change can mean that landslides may occur and thus a high impact level.

2.7 Digital data

In the investigation a large number of external supporting data have been collected and used. Multiple datasets have been acquired via SGI's participation in the Swedish “Geodatasamverkan” or geodata collaboration, for example, concerning different maps, charts and the national elevation database. During the investigation a lot of new data and results have also been produced. When gathering background material, the digital material has been added in databases. The investigation has sought to collect data in a GIS format. The datasets have been managed in a GIS environment where the reference systems, SWEREF99TM in plan, and RH2000 in height has been used. The work has used ESRI ArcGIS, QGIS, and Web-based GIS applications.
Final results in the form of landslide risk classes, probability and consequence classes are made available in a Web-based GIS application that is open to external users. In the map other selected supporting data will also be shown which may be useful when using the survey's results. Supporting external data appears in the so-called WMS version from the data producer.
Figure 4 shows an excerpt from the Web-map application developed for presenting the results from the investigation.

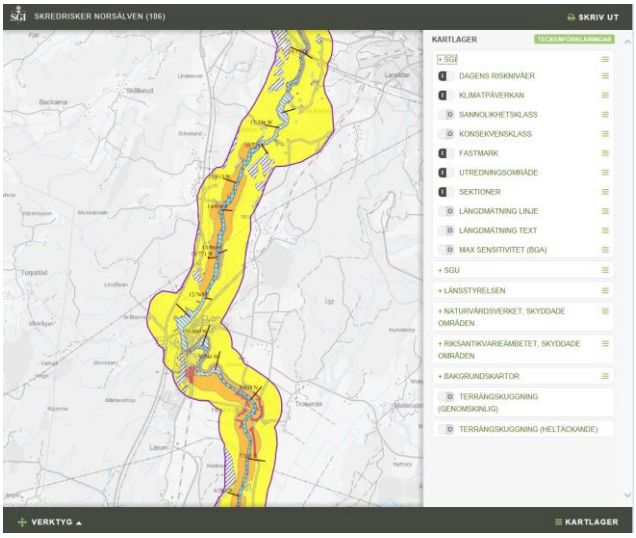


Figure 4 Excerpt from the Web-map application.

3 LANDSLIDE RISK IN NORS RIVER VALLEY

3.1 Summary of the results

In broad terms, the investigation shows that the probability of landslides along Norsälven is definite in much of the South section and parts of the Middle section. In the North section the probability is distinct all along the south western bank of the river, but otherwise mainly low.
The impact is the greatest in the South section where communities of Vålberg and Edsvalla are located, as well as by the major road and rail facilities that exist within the whole area of investigation.
Areas of high landslide risk are relatively limited along the river (2% of the assessed surface). These areas are found primarily closest to the river. Along the greater part of the river valley a medium risk level is assessed and usually closest to the river banks (13% of the assessed surface). The main part of the investigation area has a low level of risk (86% of the assessed surface).
The sensitivity to a future climate change is highest in the South section, the lower part of the Middle section and a limited part of the North section, mainly due to the high probability of landslides already for present conditions.

3.2 Presentation of results in maps

The investigation's results are reported in three different map series at the scale 1:15 000 (A4). The results are separated into probability maps, consequences maps and combined landslide risk maps.
In Figure 5 the different symbols are described as well as designations appearing in the legend on the risk maps. The cumulative risk (of probability and consequence) is reported at three levels: Low, Medium and High risk level.

3.3 Using the maps

The overall consistency of a landslide depends on the size of the landslide. The most common scenario is that a landslide begins at the riverside and evolves backward to different degrees depending on soil mass properties and the topography of the area. Where quick clay is present the landslide could be extensive. The aggregated consequences are not shown in the maps of consequences, but must be assessed in each individual case.

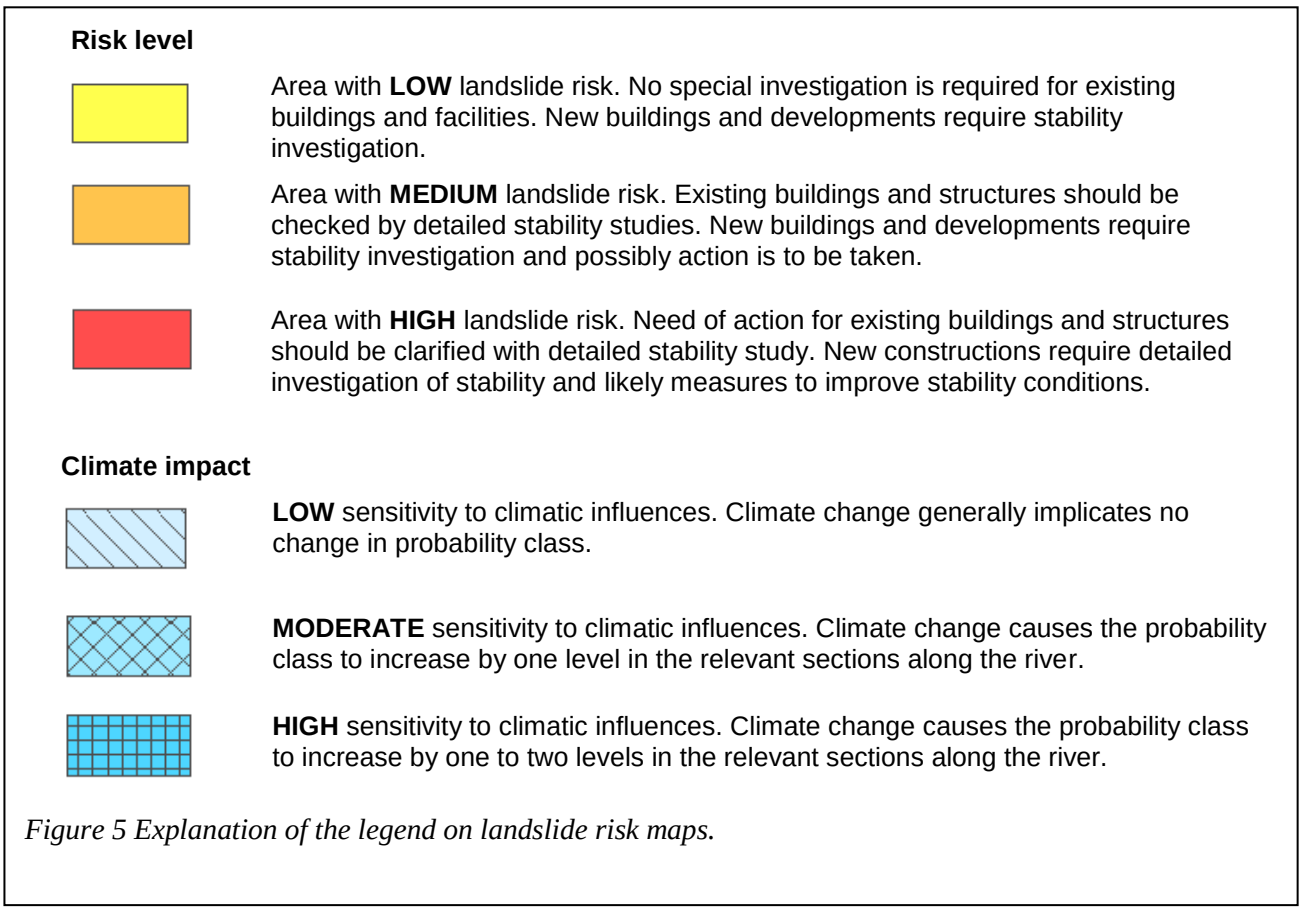


Figure 5 Explanation of the legend on landslide risk maps.

Figure 6 shows mapped historical landslide areas for part of the South section with various map backgrounds. This is given as an example of how to assess probable landslide extent and get a rough idea of the size of the impact.

4 REDUCING LANDSLIDE RISK

Landslide prevention measures are an important part of the work with urban planning, both in view of the current climate and with regard to climate change over the longer term. The landslide risk maps give a

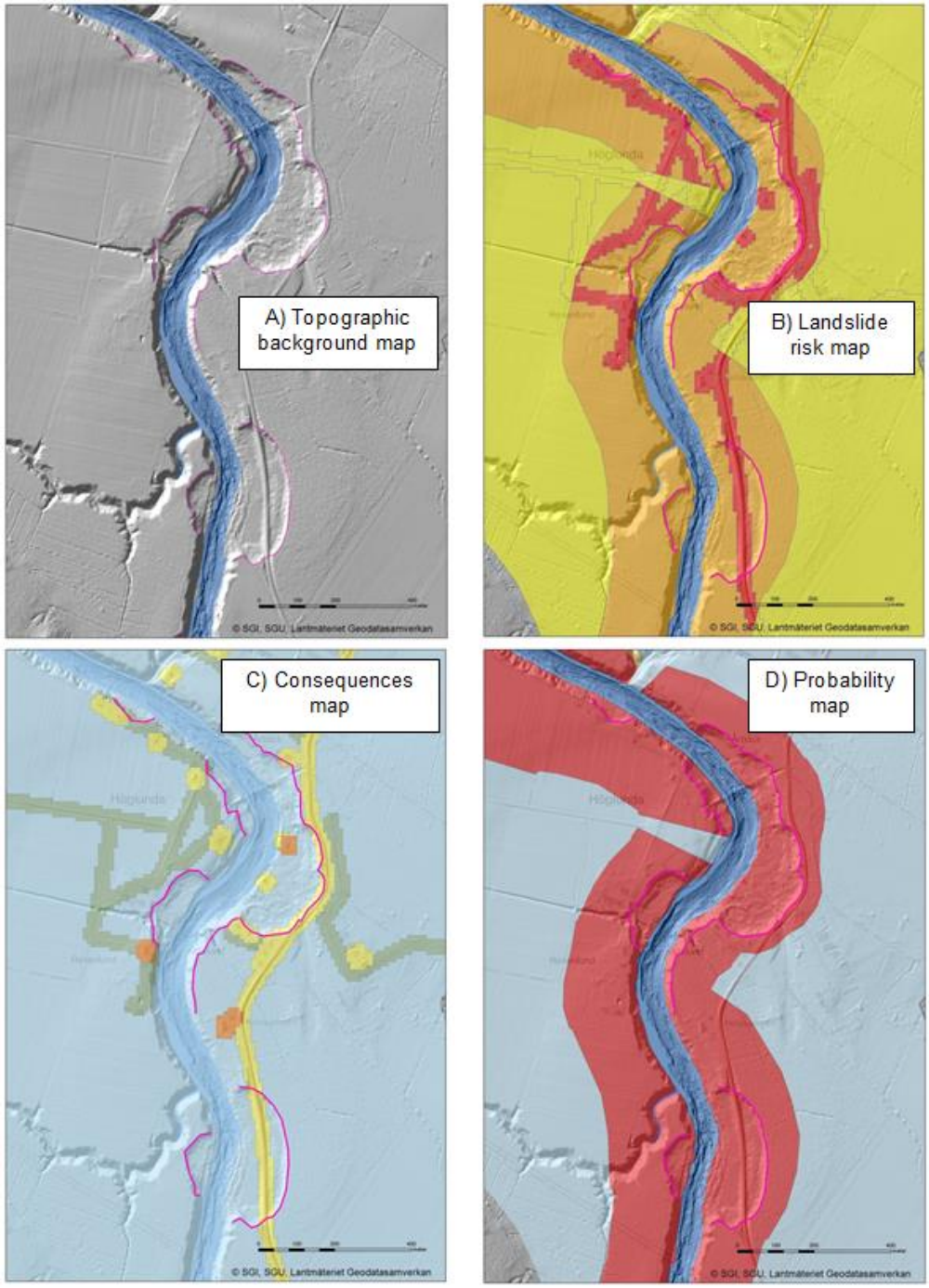


Figure 6 Views of previous landslide expanses (pink line) within the territory of the South section in various maps. The sizes of the landslides are approximately 200 m long and 100 m deep on the western side, and 350 m long and 150 m deep on the eastern side (the southern landslide scar). © SGI, SGU, LM, Geodatasamverkan. A) The topography is from the National elevation-data and bathymetric data, B) Risk levels as Low (yellow), Medium (orange) and High (red), C) Consequence class K2 (green), K3 (yellow), K4 (orange), D) Landslide probability class S5 (red).

picture of where there are sensitive areas to pursue and investigate in more detail by clarifying the geotechnical conditions, as well as the consequences that could arise from a landslide. To do this, one must take account of a "probable" landslide extent because the total consequence of a landslide is the sum of the effects within the probable landslide extent. The maps also provide an indication of the areas likely to be affected most in a changed climate.
The results of this investigation can be used to influence the siting and construction of new buildings and activities so that landslide risks can be prevented. To reduce the risk of landslides along the river, measures to reduce the probability and/or consequences could be taken. Measures to reduce the probability of landslide are usually physical in the form of excavations, supporting fill or erosion control. Measures to reduce consequences can be, for example, moving buildings and facilities. Along Norsälven several examples are found where redemption of property has been used as an action for reducing landslide risks.
Below are summary recommendations for the investigation area along Norsälven:

- Identified areas of high landslide risk levels should be further investigated for possible actions.
- A zone with restrictions, as established by the municipality of Karlstad, may be a good way to verify activities that may affect the stability. It may be relevant to review the extent of the zone.
- When investigating possible actions, it is important to take into account the presence of quick clay, which affects the extension of possible landslides.
- A review of existing erosion control should be carried out within the South sector, with regard to the maintenance and additional measures.

4.1 Urban planning and building

The landslide risk map has a resolution that is suitable for comprehensive planning. It is possible and recommended to consider this in connection with other risk areas for natural disasters, such as flood risks.
For detailed planning and building permits, more detailed geotechnical investigations should be made, taking into account the buildings and the facilities that the planning/building permit will allow. This action should be taken to prevent an increase in the probability of landslides within the current area.
It is also important to consider that the level of risk may be increased as consequences increase, that is to say, if the land is exploited with buildings or facilities. Other changes in land use may also play a role in the landslide risk level. For example, the neglected maintenance of land drainage due to land use change could lead to a build-up of water pressure in the ground that may increase the likelihood of landslides.

4.2 Detailed investigations

Geotechnical stability investigations tend to be made with multi-stage increasing levels of detail. In Swedish documents such as IEG 4:2010 and Skredkommissionen report 3: 95 for planning and IEG 6:2008, rev 1 for design and construction, information is found about regulations and recommendations for geotechnical stability investigations according to Swedish standards.

4.3 Climate adaptation measures

Before making decisions on risk-mitigation measures, a quantitative cost-benefit analysis should be done where the cost of a measure is weighed against the benefits. Then the probability of landslides and the consequences can be studied in more detail for a defined area to decide if the action should aim to reduce the probability of landslide and/or the consequences. Physical measures to reduce the probability of landslide in the form of excavation, supporting fill, erosion control, soil reinforcement, etc. are often costly. Options that reduce the consequences can sometimes be more effective. Such alternatives may include the redemption of property / demolition of building on a property or restrictions in the use of land.

Preventive measures against natural disasters can sometimes counteract each other's' purposes. For example, a flood prevention dike causes a load of soil layers that may impair the stability of the area. It is therefore preferable to coordinate different kind of climate adaptation measures.

5 CONCLUSIONS

In comparison with the GRI the pilot study for Norsälven has resulted in a modified methodology which enables risk analysis at lower cost and yet sufficient accuracy. It gives a comprehensive overview of the risk of landslides in the present and future climate, for built-up as well as yet undeveloped land, and areas with vital infrastructure. The methodology is also applicable for other river valleys, although further adjustments may be needed due to geological and other differences. This will be tested for the next river in line, Säveån in Southwest Sweden, and for the river Ångermanälven representing the Northern parts of Sweden.

6 AKNOWLEDGEMENT

This work would not have been possible without all the other employees at the SGI, to whom we express our deep gratitude.
The study is presented in full in the SGI report "Landslide risks in a changing climate – The Nors river valley, SGI Publication No. 18-1, 18-1E (English version), 18-2, 18-3 and 18-4, 2015.

7 REFERENCES

Bergdahl, K, Cederbom, C, & Göransson, G. (2013), Prioritering av områden för skredriskanalys, Klimatanpassningsanslag 2013, Statens geotekniska institut, SGI Publikation 6, Linköping, Sweden.

Bergdahl, K, & Odén, K. (2015), Skredrisker i ett förändrat klimat - Norsälven, Del 1: Kartredovisning och sammanfattning av resultat, Statens geotekniska institut, SGI Publikation 18-1, Linköping, Sweden. Also available in English version.

Bergdahl, K, Odén, K, Löfroth, H, Göransson, G, Jönsson, Å & Kiilsgaard, R. (2015), Skredrisker i ett förändrat klimat - Norsälven, Del 2: Metod för kartläggning, Statens geotekniska institut, SGI Publikation 18-2, Linköping, Sweden.

Berggren, B, Alén, C, Bengtsson P-E & Falemo, S. (2011), Metodbeskrivning sannolikhet för skred: kvantitativ beräkningsmodell. Statens geotekniska institut, Göta älvutredningen, GÄU Delrapport 28, Linköping, Sweden.

Göransson, G, Hedfors, J, Ndayikengurukiye, G, Blied, L & Odén, K. (2015), Skredrisker i ett förändrat klimat - Norsälven, Framtida erosion i Norsälven med hänsyn till klimatförändring. Del 3: Fördjupningsbilaga, , Statens geotekniska institut, SGI Publikation 18-3, Linköping, Sweden.

Kiilsgaard, R, Bergdahl, K, Öberg, M, Helgesson, H, Enell, A & Ndayikengurukiye, G. (2015), Skredrisker i ett förändrat klimat - Norsälven, Konsekvensanalys Norsälven. Del 3: Fördjupningsbilaga, , Statens geotekniska institut, SGI Publikation 18-4, Linköping, Sweden.

SGI. (2012), Skredrisker i Göta älvdalen i ett förändrat klimat, Statens geotekniska institut, Linköping. Also available in English version.

Structural characterization of hard rock formation using wireline borehole logging techniques in an open pit mine, Norway

Rigler, B.
Ruden AS Geo Solutions, Norway, balazs@rudenas.com

Botsialas, K.
Titania AS, Norway

Cárdenas, M. M.
NTNU, Norway

ABSTRACT
Detailed investigation of hard rock formations is very popular and relevant research area for a successful execution of geotechnical engineering projects such as tunnel and/or bridge construction works, fractured hard rock aquifer projects as well as open pit mines. In conjunction with the analysis of core samples, borehole logging techniques are commonly used for purpose in hammer and even in core drilled boreholes. The primary objectives of such logging works are to reveal structural characteristics of the hard rock formation, to identify fracture zones as well as to verify the level of compactness of rocks including level of weathering. A wide range of logging techniques are generally applied in order to successfully complete the objectives. A logging tool park including acoustic televiewer, optical televiewer, three-arm caliper, full waveform sonic, dual focused resistivity, natural gamma, spectral gamma as well as flowmeter and temperature tools is generally adequate to provide sufficient amount of information for a comprehensive interpretation. The complete logging suite was deployed in an open pit mine in Hauge i Dalane in South-Western Norway. Information obtained from the open pit mine effectively contributed to the completion of rock stability studies. Geophysical borehole logging and core logging results were also compared and revealed sufficient correlation. Even spectral gamma tool was run for checking the behaviour of Potassium, Uranium and Thorium (KUT) concentration variations at fracture zones in order to reveal additional information about presence of clay fillings. Experience shows that even the most conventional logging methods such as resistivity and full waveform sonic can provide sufficient information about the structural characteristics of hard rock formations.

Keywords: geophysical logging, televiewer, sonic, resistivity, spectral gamma

1 INTRODUCTION

The open pit mine is located in Sokndal Municipality in South - Western Norway. It is an open pit mine that produces ilmenite since 1960. The ilmenite ore body is considered as one of the largest in the world. The open pit has a length of about 2.8 km, while the depth today is at 240 meters. The width of the pit varies from 400 to 600 meters. Historically there have been numerous slope instability occurrences, particularly on the hanging wall slopes. In order to cope with these challenges, it was decided that a geotechnical model should be developed. The geotechnical model is the cornerstone of open pit design. It is comprised by four components, the geological, structural, rock mass and hydrogeological models. The development of geotechnical model will allow the definition of the geotechnical domains and the allocation of design sectors. These two steps are

fundamental for the preparation of the final slope designs.

Into this framework the compilation of structural model is of high importance, as it allows describing the geological media that is responsible for the stability conditions and the groundwater flow inside the rock mass. In the case of the open pit mine, the following data sources were used:

1) 3D ortho-rectified pictures were compiled for certain areas of the mine. Mapping of fractures took place, where dip/dip direction, persistence, spacing and aperture (in some cases) were recorded.
2) Aero photos of the mine area were taken during the summer of 2014. These aero photos were inserted into a GIS system, and mapping of all the lineaments inside the pit area was commenced.
3) Structural mapping of the drainage tunnels that are running the perimeter of the mine was made.
4) The structural data and information of geological environment were retrieved from 12 hammer-drilled and from 10 core-drilled boreholes. To cover this objective, a wide range of geophysical logging methods were applied including acoustic (ATV) and optical televiewer (OTV), spectral gamma, dual focused resistivity and full waveform sonic (FWS). In hammer-drilled boreholes, in addition to the sonic formation velocity, FWS data were also used to determine geo-mechanical parameters such as Poisson's Ratio, Shear Modulus, Young Modulus as well as Bulk Modulus with the use of average lithological density data determined in field laboratory. In the 12 hammer-drilled boreholes piezometers were finally installed. The total length of cores that were retrieved is 2285m. Structural data were also retrieved in all boreholes (both hammer- and core-drilled) with the use of optical and/or acoustic televiewer.

By using the data from these four sources, the 3D structural model of the open pit can be compiled. The structural model is part of the geotechnical model, which is a vital part of an effective slope monitoring system. The purpose of this model is to reveal large-scale instabilities as well as local scale movements which are critical components for risk management practices in modern open pits (Panthi and Nilsen, 2006). Open-pit mines are typically enlarged until either the mineral resource is exhausted, or an increasing ratio of overburden to ore makes further mining uneconomic. When pits become larger and as they get deeper, the importance of understanding and controlling slope stability increases. This paper is intended to summarize and highlight the results and necessity of geophysical borehole logging works in an open pit mine by focusing on the acquired geophysical logging data sets regarding rock stability.

2 DRILLING IN TWO PHASES

Hammer drilling of 12 boreholes through the anorthosite – ilmenite-rich norite and diabase formations was completed between the end of April and beginning of June, 2014. Core drilling was completed by January, 2015. The name, length and elevation of each borehole are presented at Table 1 and 2.

Table 1 Hammer drilled boreholes

Drill sequence	Borehole ID	From	To	Length of Borehole (*m*)
1	TEL_F_01	234	-61	295
2	SKOG_F_02	235	105	130
3	SKOG_F_03	230	55	175
4	SKOG_F_04	245	75	170
5	SKOG_E_05	265	-60	325
6	SKOG_H_06	300	-60	360
7	SKOG_H_07	281	-79	360
8	SKOG_H_08	298	-62	360
9	SKOG_H_09	293	-67	360
10	TEL_H_10	206	-44	250
11	TEL_H_11	200	-40	240
12	TEL_H_12	200	-55	255
	TOTAL			3280

Table 2 Core drilled boreholes

Drill sequence	Borehole ID	From	To	Length of Borehole (*m*)
1	TEL_F_01_c	230	-40	270
2	TEL_F_02_c	230	-40	270
3	SKOG_F_03_c	185	-40	228
4	SKOG_F_04_c	200	-40	244
5	SKOG_H_05_c	230	-40	274
6	SKOG_H_06_c	238	-40	282
7	SKOG_H_07_c	185	-40	228
8	TEL_H_08_c	200	-40	244
9	TEL_H_09_c	80	-40	122
10	TEL_H_10_c	80	-40	122
	TOTAL			2285

3 GEOPHYSICAL BOREHOLE LOGGING AS VIRTUAL CORING

The primary objective of the interpretation of the acquired geophysical data was to reveal structural properties (fracture and joint mapping) of the formation as well as to determine geo-mechanical parameters (Poisson`s ratio, Young Modulus, Bulk Modulus, Bulk Compressibility, Shear Modulus) based on sonic P-wave (compressional wave) and S-wave (shear wave) arrivals with the aid of available density data. Fracture and joint mapping was performed by ATV and where it was feasible by OTV as well. The main objective was to combine both the ATV and OTV wherever it could be done to reduce the risk of misinterpretation of televiewer data. Cross plot log evaluation technique was applied in order to present and effectively evaluate the different type of logging data. Resistivity vs. fracture frequency and average aperture, magnetic field vs. resistivity, fracture frequency vs. P-wave velocity, resistivity vs. gamma ray (GR) and fracture statistics (fracture frequency and aperture) vs. geo-mechanical modulus cross plots were made in dedicated intervals for each borehole to reinforce the comprehensive interpretation. A common feature of fracture zone is the inhomogeneity of physical parameters that is sensitive to the variation in the level of compactness of rocks. These indicative physical parameters are

resistivity, acoustic velocity and the calculated geo-mechanical parameters. Total gamma ray (TGR) log, Potassium (K) and Thorium (Th) concentration logs very well indicate the presence or the lack of clay deposits at detected joints or fractures. The main concept of the interpretation was determined and based on the results of the three main logging data sets such as resistivity, full waveform sonic as well as televiewer data in addition to the more conventional log types like three-arm mechanical caliper and gamma ray logs (Rigler, B., 2013; Rigler, B. and Varga, V., 2014); Rigler, B., 2015).

3.1 Full waveform sonic (FWS) logs

FWS data were acquired by a sonic tool, which is equipped with one transmitter and two receivers (3ft and 5ft). The wave trains are recorded by both receivers were processed and finally were cross correlated in order to derive the semblance image to interpret the acoustic formation P- and S-wave velocity. The P-wave and S-wave arrivals and slowness were interactively picked (Figure 1) as well (M. Bala, J. Jarzyna, 1996; R.E. Crowder, J.J. LoCoco and E.N. Yearsley, 1991; Barton, C. et al., 1989; S. Astbury & M.H. Worthington, 1986; N.O. Davis and T.M. Staatz) for the use of calculating the geo-mechanical parameters such as Poisson's Ratio, Shear Modulus, Young Modulus, Bulk Modulus and Bulk Compressibility. In

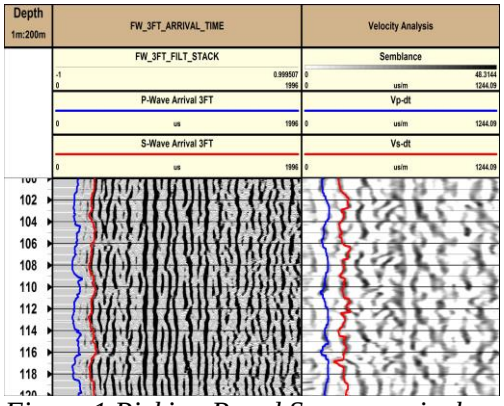


Figure 1 Picking P and S-wave arrivals and slowness values on full wave train and semblance logs

the mine, interpreted formation P-wave velocity values vary between 4000 and 9000 m/s depending on the level of compactness of rock as well as lithology. Acoustic wave propagation is very sensitive to the presence of joints, fractures and/or fissures. The acoustic wave velocity is proportional to the original state of the rock. Therefore, in the zones of weakness or tectonized zones the degree of decrease in velocity can be high. In the strongly fractured sections, the propagation velocity of P-wave (Vp) and S-wave (Vs) decreases (Figure 2) although the ratio Vp/Vs generally increases (Zilahi-Sebess, L., 2003). In high velocity rock formation at small fracture aperture just the opposite might happen, the Vp/Vs decreases with decreasing Vp velocity. All the interpreted fault or fracture zones and larger individual joints were identified on the resistivity log and the acoustic televiewer images as well. From the lithological point of view, acoustic P-wave velocity is generally very high along the entire logging sections, especially in the mother rock anorthosite. Anomalies on the sonic related parameter curves (Vp, Vs,

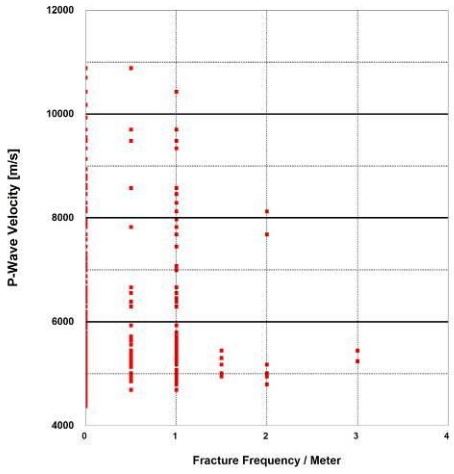


Figure 2 P-wave velocity vs. Fracture frequency / meter (FF/m)- Example from a hammer-drilled borehole

travel time, P-wave and S-wave arrivals as well as Vp/Vs and geo-mechanical modulus) are mainly related to structural variation (Figure 3) as well as level of compactness and weathering of

rock rather than the lithology itself. Geo-mechanical parameters were calculated along the entire borehole sections based on the interactively picked P-wave and S-wave arrivals as well as density values that had been previously determined from lithological

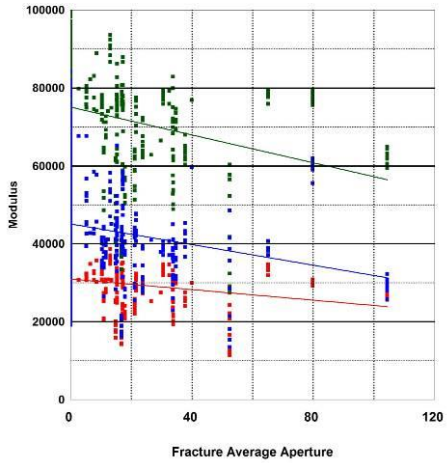


Figure 3 Fracture average aperture vs. Geo-mechanical modulus – Example from a hammer-drilled borehole; Green, blue and red are in respect to Shear modulus, Young`s modulus and Bulk modulus consecutively

samples, which had been taken from several locations in the area of open pit mine (Table 3). Lithological intervals were determined based upon acquired geophysical logs (Figure 4) and preliminary available geological information. Geo-mechanical parameters were calculated as described below (N.O. Davis and T.M. Staatz):

Poisson's Ratio:

$$\sigma = (0.5*(t_s / t_c)^2 - 1) / (t_s / t_c)^2 - 1 \quad (1)$$

Shear Modulus:

$$\mu = \rho_b / t_s^2 \quad (2)$$

Bulk Modulus:

$$k = \rho_b*(1/t_c^2 - 4/3*t_s^2) \quad (3)$$

Young's Modulus:

$$E = 2\mu(1 + \sigma) \quad (4)$$

Where t_s is shear (S) transit time in (μsec), t_c is compressional (P) transit time in (μsec) and ρ_b is bulk density in (g/cm^3)

In most cases, in each borehole, the value of modulus decreases with increasing fracture density and aperture as well as with decreasing degree of compactness of rocks.

Table 3 Density values determined in field laboratory (Rigler, B. and Varga, V., 2014)

Lithology	***Density [g/cm3] (Provided by Titania AS)***
Anorthosite	2.7
Ilmenite	3.3
Diabase	2.92
Ilmenite	3.2
Ilmenite Fresh	3.3

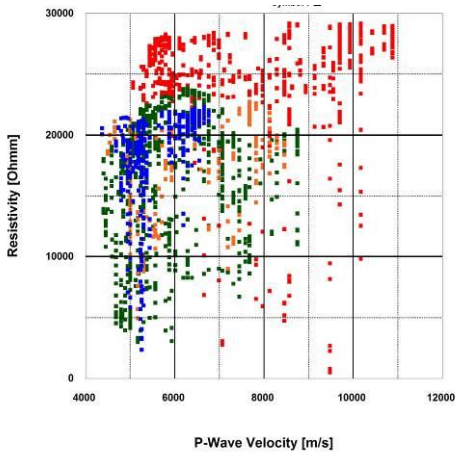


Figure 4 Lithological intervals were determined with the aid of geophysical logging data – Example from hammer-drilled borehole; Red, blue, green and orange are in respect to Norite Zone Nr.1, Anorthosite, Norite Zone Nr.2 and Diabase dyke consecutively

3.2 Dual Focused Resistivity (DLL3) logs

By the fact that dual focused resistivity tool is designed for focusing the injected current towards the formation by guard electrodes, DLL3 is an effective tool for the identification of thin bedding layers, consequently, for

detecting the presence of small scale discontinuities such as fractures and joints. In the open pit mine, resistivity values vary within a wide range between a couple of hundred and maximum detectable 30000 Ωm along the entire logging section. Because the fresh rock itself is a non-conductor, joints or fractures and level of weathering of rock are the reasons for large reduction of resistivity readings. The main reason of this large reduction is the large variation in the degree of weathering of rocks (Danielsen, B.E., Madsen, H.B., 2013), the fracture frequency as well as the size of aperture of fractures or joints (Figure 5). The presence of clay deposits in the joints may also affect the magnitude of subsidence in resistivity. "Fissures representing a porosity of only 0.1% in the measured rock volume reduce the

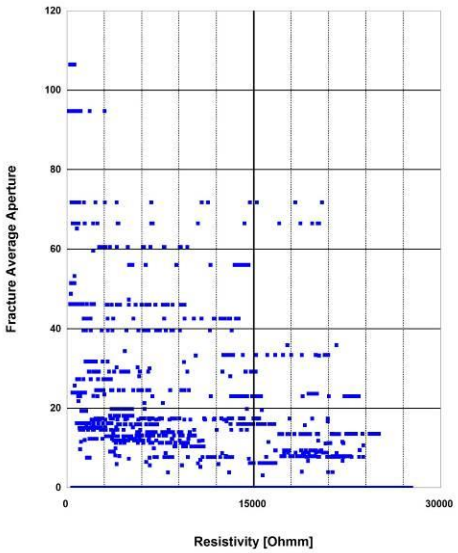


Figure 5 Resistivity vs. Fracture average aperture from a hammer drilled borehole

apparent resistivity of rock to about 1000 Ωm, thus it causes at least one order of magnitude decrease in resistivity compared to fresh rock – while the rock's density are practically unchanged – thus resistivity shows the presence of fractures in a strongly blown up form." (Zilahi-Sebess, L., 2003). Resistivity blown up and its phenomena can be observed at almost each single interpreted joint in each borehole. The highest resistivity and velocity values belong to very compact, fresh rock. Fresh ilmenite is non-conductive (Lohva, J. and Lehtimäki, J., 2005), this is why it has a resistivity range between 20000 and 30000 Ωm (limited by the detectable maximum of DLL3). Diabase has a slightly lower resistivity between 10000 and 25000 Ωm. Resistivity of anorthosite varies within a very similar range compare to the resistivity of diabase.

3.3 Acoustic and Optical televiewer logs

A combination of ATV and OTV logs is always recommended for a reliable fracture mapping. This is due to by the fact that OTV images might easily be misinterpreted in the lack of acoustic caliper and amplitude data. Minor fractures may not be found on an optical image but might be found on an acoustic caliper log and vica versa, bedding planes or foliations might be seen more confidently on an OTV log than on an ATV log. Due to limitations of OTV logging (e.g. opaque borehole fluid), acquisition very often does not even allow us to obtain a good quality optical image (Figure 6).

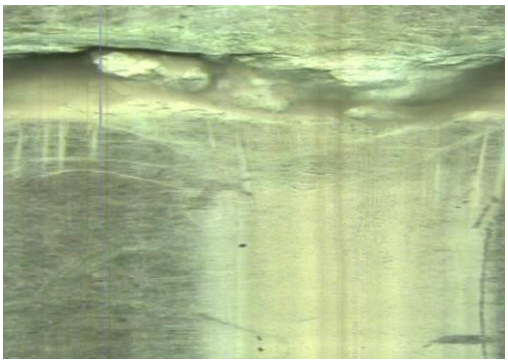


Figure 6 Cascading flow on OTV image – cascading material shades structure details on the image log

On an outstretched cope of borehole image (amplitude, transit time, acoustic caliper or optical) the intersection of a fracture plane generally appears as a sinus wave (Williams, J.H. and Johnson, C.D., 2004). Interpretation of

both the ATV and OTV images were completed by using this concept (Figure 7). The dip and azimuth of fractures were determined and corrected by borehole deviation and are referred to true north after the application of magnetic declination correction. Fracture frequency per meter (FF/m), average aperture and RQD logs were derived from interpreted structural information obtained by televiewer logging.

Table 4 Classification of fractures (Duncan C. Wyllie and Christopher W. Mah, 2010)

Term	Aperture [mm]	Majority
Tight	0	Minor
Very Narrow	0-6	
Narrow	6-20	
Moderately Narrow	20-60	Major
Moderately Wide	60-200	
Wide	200-600	
Very Wide	600-2000	
Cavernous	>2000	

Majority of all individual fractures were also determined by using a classification method (Table 4). Magnetic field data were also acquired and recorded by the three axis magnetometer, which is installed in the televiewer tool body. The magnetic data are mainly used for structure orientation and borehole deviation purpose but it could be used for

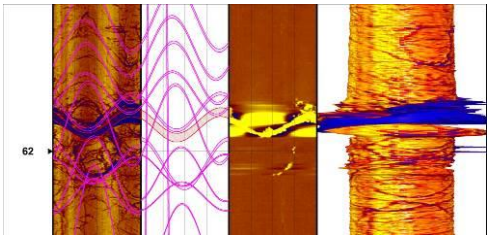


Figure 7 ATV log example from a core drilled borehole

evaluating the lithology (Figure 8), especially to identify Norite (ilmenite-rich rocks). It is important to note that from lithological point of view the recorded magnetic field data can only be evaluated as a relative anomaly in contrast with the magnetizability, which is usually acquired as magnetic susceptibility data. The higher magnitude of magnetic field shows the highest values in norite (ilmenite ore) and relatively high values in diabase dyke. Anorthosite was not observed as a magnetic body due to relatively low magnetic field readings (Rigler, B., 2013).

3.4 Spectral gamma logs

Spectral gamma data was acquired in

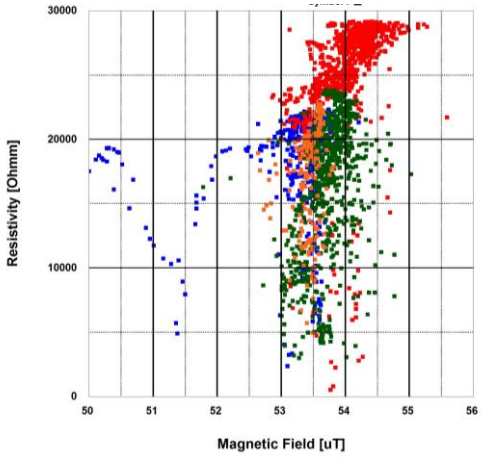


Figure 8 Resistivity vs. Magnetic Field crossplot showing red, green, orange and blu in respect to Ilmenite fresh, Ilmenite poor, Diabase and Anorthosite consecutively

order to calculate the K [%], U [ppm] and Th [ppm] concentrations, which were determined by using the coefficients and formula provided by tool master calibration results. It has been observed that thorium concentration is normally very low along the entire logging sections. The presence of Potassium (K) and the elements of Uranium (U) series dominate. Where potassium is present on the log, thorium concentration decreases but uranium is generally present together with potassium and shows linear relationship with the potassium concentration log. It means that total gamma ray (TGR) as a physical parameter is not suited for making a distinction between norite (ilmenite) and anorthosite. Total gamma as well as KUT concentration

logs were very indicative when it comes to the identification of a large Diabase dyke, which had run through the open pit mine. TGR significantly increases at fractures or joints, where clay deposit to be present. These gamma anomalies are mainly caused by the presence of potassium, which is a very good indicator of clay mineral deposits. At the joints where gamma anomalies are not observed, clay is probably not present.

4 CORE LOGGING

Core logging is one of the fundamental techniques used to obtain geotechnical information and despite the fact that advanced geophysical techniques were used, it was decided that core-logging should still be performed. The actual logging process remains a manual operation that gives a hand-on experience of the geo material, which can be evaluated by the engineering geologists or geo technicians. The main purpose of geotechnical logging of solid core is to divide the core into geotechnical similar intervals (domains), then ascribe geotechnical to each domain (Read, J. and Stacey, P., 2010). The following parameters were collected:

- From, To
- Rock Type/lithology
- Fracture frequency per meter
- Rock quality designation (RQD)
- Total core recovery (TCR), which measures the total length of the core recovered, including broken zones, against the total length of the core drilled, expressed as a percentage (Read, J. and Stacey, P., 2010).
- Solid core recovery (SCR), which measures the total length of solid core, excluding pieces smaller than the core diameter, against the total length of the core drilled.
- Weathering Index, which describes the effect of weathering and/or alteration on the geo material. The ISRM (ISRM, 1978) based method was used in describing the weathering/alteration effect.
- Strength index, which represents the field estimate of the uniaxial compressive strength (UCS) of the intact core.
- The number of joint sets at each meter of core length.
- For each joint the joint alteration number (Ja) was recorded. This number is part of the Q-system (NGI, 2013) and it is used to describe the joint infilling and the roughness.
- Roughness of the discontinuity surfaces, by using the joint roughness coefficient values (ISRM, 1978).

5 COMPARISON OF TELEVIEWER AND CORE LOGGING DATA

A correlation between the results from televiewer and core logging data was attempted. The parameter chosen to evaluate the degree of relationship between the two methods was the fracture frequency per meter (FF/m) as well as RQD. The results from core logging were obtained by visual inspection of every interval in the core box, considering the real length of the run, and not the recovered core. In practice there are some runs that show



Figure 9 Actual core box. It is possible to see that the core stored in a 1m run is not always the full length, as it is clear in the lower three runs

a partial length of the total core only, i.e. 0,95m in a 1 meter run, as shown in Figure 9. All the observed fractures observed were recorded, no matter that they were open or not. Comparison of

core and televiewer logging results was performed in five boreholes. The results normally show a very good correlation, with location of anomalies at same depths and an overall contour that matches correspondingly. Figure 10 represents an example from SKOG_F_03_c borehole in the interval from 38 to 68m. The location of FF/m and RQD anomalies are almost identical on both type of logs. It is also observed that between 49m and 65m, anomalies follow each other with good level of correlation.

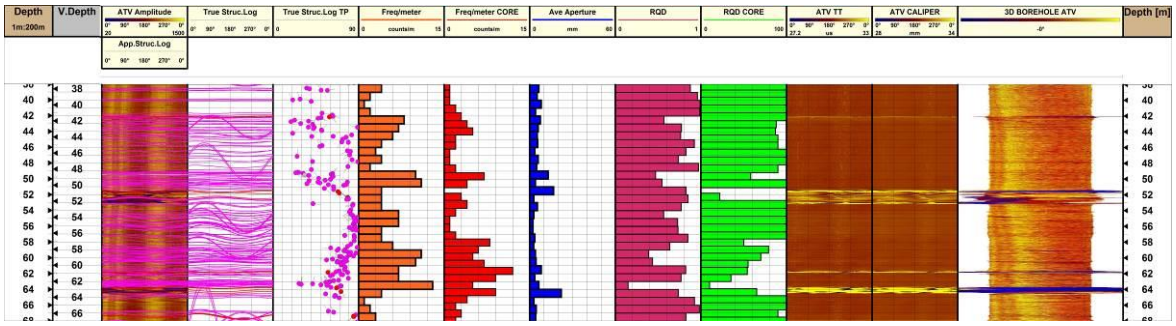


Figure 10 ATV structure logs and statistics including FF/m and RQD logs for comparison of televiewer and core logging data

The reliability of these data sets are just as good as these logs can be used for making decisions on the zones of hydraulic tests or the depths where piezometers could be placed.

6 CONCLUSIONS

Apart from some additional information (TCR, SCR, UCS) given by core sample analysis, the combination of televiewer and other geophysical logging methods on its own provides an overall picture and adequate amount of information about rock quality, structure details, lithological variations as well as geo-mechanics. Televiewer logs supplies with high confidence not only the fracture statistics (e.g. FF/m) but structure orientations as well. Resistivity logs provided very valuable information about level of weathering and compactness of rocks in addition to a valuable support on fracture mapping. In addition to formation velocity, sonic logs provided an overall and reliable picture about the geo-mechanical properties of formation rocks. Apart from Poisson`s ratio, the geo-mechanical modulus parameters are not as accurate as it was determined in laboratories by using core samples. This is mainly because of the restricted availability of formation density information. This might have been improved by running a gamma-density tool as an additional logging service. Due to the method of hammer drilling in very hard formation sections, roughness of borehole walls also made the determination of geo-mechanical parameters little uncertain since sonic data quality is highly affected by the roughness of borehole wall as well. Geo-mechanical parameters were very well estimated anyway and provided a valuable overview about the level of compactness of the rock formation. Gamma logs (both spectral and total gamma) also appeared to be very valuable in terms of identification and determination of lithological intervals, presence of clay at fracture zones as well as depth correlation. Spinner flowmeter logging (R. E. Crowder and K. Mitchell, 2002) was also performed in dynamic and static mode in order to reveal any potential water flow at detected fractures zones or joints. In addition to the geo-technical analysis, geophysical logging results were also

provided valuable inputs for hydraulic (single and double packer testing). The description of these works is outside the scope of this paper.

7 REFERENCES

S. Astbury & M.H. Worthington (1986). The analysis and interpretation of full waveform sonic data. Part I: dominant phases and shear wave velocity. First Break, 1986/7, Vol.4. No.4.

M. Bala, J. Jarzyna (1996). Application of acoustic full wavetrains for the determination of lithology, reservoir and mechanical parameters of formation. Geophysical Prospecting, 1996, 44, 761-787.

Barton, C. et al. (1989). Analysis of full waveform acoustic logging data at ODP Site 642 - Outer Vøring Plateau. Proceedings of the Ocean Drilling Program, Scientific Results, 1989, Vol.104.

R. Carbonell et al. (2010). Geophysical and geological characterization of fractures within a granitic pluton. *Near Surface Geophysics, 2010*, **8,** p.181-193.

R. E. Crowder and K. Mitchell (2002). Spinner Flowmeter Logging, a Combination of Borehole Geophysics and Hydraulics. Well Design and Installation Workshop July 18, 2002, Phoenix, Arizona

R.E. Crowder, J.J. LoCoco and E.N. Yearsley (1991). Application of full waveform borehole sonic logs to environmental and subsurface engineering investigations. Proceedings of the Symposium on the Application of Geophysics to Engineering and Environmental Problems, EEGS, 1991.

Danielsen, B.E., Madsen, H.B. (2013). Resistivity logging as a tool for identifying initial weathering in crystalline rocks. *Near Surface Geophysics, 2013*, **11**.

N.O. Davis and T.M. Staatz: Borehole engineering - A proven cost effective method for determination of engineering parameters. COLOG Division of Layne Christensen Company, Golden, CO

Duncan C. Wyllie and Christopher W. Mah (2010). Rock Slope Engineering Civil and Mining 4th Edition. P. 388.

Glover, P. Spectral Gamma Ray Log. Petrophysics Msc Course Notes, p. 111-120.

ISRM (1978). Suggested methods for the quantitative description of discontinuities in rock masses. International Journal of Rock Mechanics, Mining Sciences and Geomech. Abstr 16(3): 319-368.

NGI (2013). Handbook: Using the Q system. Rock mass classification and support design.

Panthi K. K. and Nilsen B. (2006). Numerical analysis of stresses and displacements for the Tafjord slide, Norway. Bull Eng Geol Env, vol. 65, pp 57–63.

Read, J. and Stacey, P. (2010). Guidelines for open pit slope design. pp 32-33. Csiro Publishing.

Rigler, B. (2013). Structural characterization of crystalline rock formations using wireline borehole logging techniques in Norway. *Meeting of Young Geoscientists in Békéscsaba, Hungary, 2013*

Rigler, B. (2013). Final Report on Borehole Logging in BH5 for Titania AS. Ruden AS Geo Solutions

Rigler, B. and Varga, V. (2014). Final Report on Borehole Geophysical Logging and Hydraulic Testing in 11 boreholes for Titania AS. Ruden AS Geo Solutions

Rigler, B. (2015). Final Report on Structural Logging in 10 boreholes for Titania AS. Ruden AS Geo Solutions

Zilahi-Sebess, L. (2003). Well-Logging methods to investigate a granitic site for radioactive waste deposition. Geophysical Transactions, 2003, Vol.44. No.2. pp. 51-93.

Zilahi-Sebess, L. (2010). The effect of fracturing on results of well logging. *Magyar Geofizika, 2010*, **2.** p.124-142.

Williams, J.H. and Johnson, C.D. (2004). Acoustic and optical borehole-wall imaging for fractured rock aquifer studies. *Journal of Applied Geophysics, 2004*, **55,** p.151-159.

Slope Stability Assessment and Evaluation of Remedial Measures Using Limit Equilibrium and Finite Element Approaches

Manuel Neves
CH2M Hill, UK, manuel.neves@ch2m.com

Victor Cavaleiro and Alexandre Pinto
UBI, Portugal and JetSJ Geotecnia, Portugal

ABSTRACT
Slope stability is a recurrent theme and is of major significance on large scale infrastructure projects such as highways, railways, dams or canals, where having more cost-effective designs becomes a crucial drive on any scheme.

This paper relates to the on-going study of the Covilhã's granitic residual soil, undertaken at UBI, which is commonly used as a construction material in the area, particularly in road schemes.

This paper is primarily focused on the slope stability assessment in granitic residual soils, using different calculation methods and for different soil parameters, geometries, applied loads and groundwater conditions. Additionally, a quantification of the merits of some of the most common remediation techniques are established, drawing a comparison between their effectiveness.

The parametric study makes use of one LE (SLOPE/W) and one FE (PLAXIS 2D) software and has revealed that changes in groundwater level are more detrimental to the stability than increases in the applied surcharge at the crest. Also, reductions in Factor of Safety using LE methods due to rises in groundwater levels appear to be inversely proportional to the cohesion of the intersected materials, i.e., the greater the c' of the soil the lesser are the consequences of groundwater rises.

The comparison between FE and LE methods reveals a significant divergence in the obtained FoS for purely granular materials, with all LE methods overestimating the safety of the slope up to circa 40%. Nevertheless, these differences may have little interest if there is a large uncertainty in the input parameters of the soils.

The remedial options discussed and analysed in this paper should be perceived as concept ideas as their gain in terms of FoS will likely vary from case to case. Furthermore, the benefits of combining the effects of more than one remedial option have been excluded from this study.

Keywords: Slope Stability, Limit Equilibrium, Finite Elements, Remedial Measures

1 INTRODUCTION

Slope stability plays a major role in civil engineering projects, particularly in transportation and infrastructure schemes, and its assessment requires not only an adequate understanding of its triggers but especially a solid understanding and critical analysis of the mechanics behind the software used to arrive at a given conclusion.
This work is part of the on-going study, currently being undertaken at UBI, of one of the region's most abundant resource, its granitic residual soil; which by being a very common construction material in the area, particularly in highway schemes, has raised an interest on its behaviour from a slope stability perspective.
This particular type of soil and its properties, although usually falling within a rather well defined range of values, have been the subject of significant analysis in order to

expedite the design and stability assessment of future and existing earthworks.
An experimental embankment was completed in November 2010 (Figure 1) using the granitic residual soil of the area to help with the study of its geotechnical properties. The embankment shoulders were constructed with varying gradients, from 45º to 80º to the horizontal, having remained stable since its construction. In addition, a surcharge of 10kPa was applied to the crest of the slope, near its steepest section, without any evidence of instability.



Figure 1 View of the experimental embankment.

2 FACTORS INFLUENCING SLOPE STABILITY

Slope movement often is a complex process which involves a continuous series of events from cause to effect, making it rather difficult to pinpoint a single trigger to the movement. It is largely determined by lithology and stratigraphy (influencing strength, deformability and permeability), as well as the hydro-geological conditions, the topography of the terrain and the weather conditions. A combination of these may trigger a failure event along one or more sliding surfaces, which induces the movement of the unstable mass.
Saturation, however, appears to be the primary cause of landslides, especially if resulting from rainfall. Its magnitude depends on both weather conditions (distribution and duration of precipitation and changes in temperatures) and topography. Additionally, human activities can also play a crucial role in slope stability. Disturbing or changing drainage patterns, destabilising slopes and removing vegetation are common human-induced factors that may trigger instability. Other examples include steepening of slopes by undercutting its toe, placing loads on its crest or even the presence of leaking pipes.
At the same time, it is common to witness the development of cracks on the crest of slopes, some of which have been monitored for dozens of years without any noticeable unstable behaviour. According to some researchers (Guidicini and Nieble, 1984) these are often a result of minor shear movements within the slope; which, although individually small, when accumulated may lead to significant slope movement, sufficient to cause a vertical separation on the materials at the top of the slope, thus forming tension cracks.
The fact that these structures are a result of shear movements is extremely relevant, as when a tension crack becomes visible it can be an indicator that a slip surface may have already been formed within the slope and that a shear failure process is underway. Neverthless, it is nearly impossible to quantify just how hazardous this phenomenon is, since it represents the beginning of a complex and progressive failure mechanism. Moreover, there is also the possibility that, in some cases, the appearance of tension cracks is purely associated with a relief in porewater pressure.

3 RESIDUAL SOILS

A residual soil has, by definition, been formed in situ by the decomposition of a parent rock and has not been transported to any significant distance. For this to occur, the decomposition processes tend to typically be quicker than the erosion and transport of the resulting soil grains. However, these soils can also result from erosive processes, as long as they are not transported afterwards, which is often in the genesis of the Portuguese granitic residual soils (Figure 2).



Figure 2 Example of granitic residual soil slopes in the Covilhã region with the parent rock at the bottom.

In fact, and although residual soils cover a very significant extent of the Earth's surface, Soil Mechanics has paid much less attention to them then to sedimentary soils, as its principles were mainly studied and defined in countries where the latter were the most common and problematic. Nevertheless, residual soils can present some particularly complex features, exhibiting a significantly different behaviour from sedimentary soils with similar grading, void ratio and moisture content.
This is thought to be the result of interparticle connections, inherited from the original parent rock, or due to the chemical reactions that occur through the weathering process (Fernandes, 2011). As such, it is questionable just how representative grading curves are for these soils and whether their geotechnical parameters should be extrapolated from them, given that sieving necessarily affects and/or breaks this bond.

3.1 Granitic residual soils of the Covilhã region

Granite rock masses are predominant in the northern part of Portugal and in the surroundings of the Serra da Estrela mountain complex. Here, granitic residual soils are abundant, covering more than 50% of the surface, and can extend to maximum depths of over 18.0m (Cavaleiro, 2001). The typical composition of a granitic residual soil from this region contains kaolinite as the most common clay mineral, which is associated with soils with good engineering properties.
The fine fraction in these soils varies, although predominantly low, and with sand typically being the predominant fraction. Figure 3 below illustrates the grading envelope obtained from circa 15 samples of the soil in analysis, plotted against the historical results obtained from circa 80 different samples of granitic residual soils of the Covilhã region (Cavaleiro, 2001).

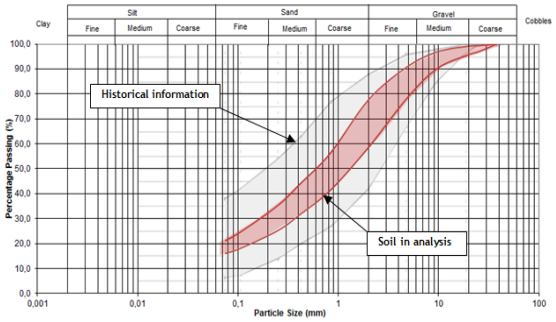


Figure 3 Grading envelopes of historical data and the residual soil in analysis (Neves, 2015).

The grading results are in agreement with the historical information and classify the soil as a well-graded silty very gravelly fine to coarse sand, with a low fines content (less than 20%). Given the low percentage of fines and the fact that its constituent minerals exhibit low plasticity, this residual soil is generally classified as non-plastic. Although the representativity of the grading curves of these materials may be questionable, it is clear that the predominant fraction is typically sand, which is originated from the quartz of the parent rock. Additionally, the clay fraction is often reduced and its minerals present low activity, which explains the non-plasticity of these soils. As a result, their behaviour can be better approximated to a granular than to a cohesive soil.
Most of the geotechnical characterisation of the soil has been undertaken through laboratory testing, in particular drained and undrained consolidated triaxial tests on remoulded samples. These have been used to assess their drained and undrained tangent and secant deformability moduli, as well as

the peak and residual angles of shearing resistance. The results are summarised in Table 1 below, along with the correspondent values for both dry and saturated unit weights. Note the values in brackets correspond to the average results of approximately 15 samples.
The values reported exceed the ones obtained through a wider triaxial test campaign conducted on granitic soils of the region (Cavaleiro, 2001), which reported angles of shearing resistance between 26.9º and 37.7º. However, these were established considering effective cohesion values of up to circa 20kPa, while the values in Table 1 have been derived for null cohesion. When applying the same principle to the historical results, angles of shearing resistances between 31.3º and 42.5º are obtained (Neves, 2015), which in turn agree well with the results of this study.

Table 1 Geotechnical parameters assessed from the triaxial test campaign.

Parameter	Range of values	Average
E_{us} [MPa]	16.6 – 23.3	18.5
E_{ut} [MPa]	25.2 – 37.0	29.4
E_s' [MPa]	12.0 – 34.5	25.8
E_t' [MPa]	21.8 – 46.0	34.3
γ_d [kN/m³]	19.3 – 19.8	19.5
γ_{sat} [kN/m³]	21.0 – 21.9	21.5
φ'_{peak} [°]	37.5 – 43.6	40.6
$\varphi'_{residual}$ [°]	35.3 – 36.9	36.1

Direct shear tests conducted on undisturbed samples of the same materials in Cavaleiro (2001) report effective cohesion values from 4kPa to 42kPa and angles of shearing resistance between 35º and 45º (Figure 4).

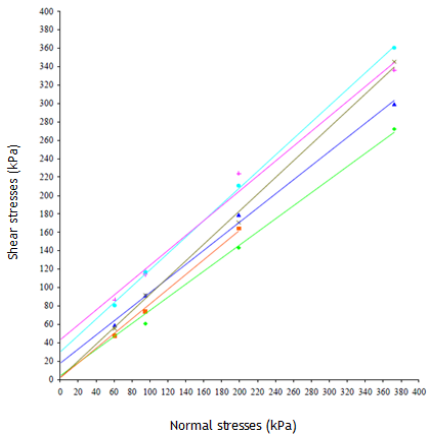


Figure 4 Direct shear test results in samples of Covilhã's granitic residual soils (Neves, 2015).

3.2 Experimental embankment

As mentioned earlier, an experimental embankment was constructed using granitic residual soils from the Covilhã area. The controlled embankment was built with a 16.0m footprint and a 20.0m development (Figure 5) and completed in November 2010.

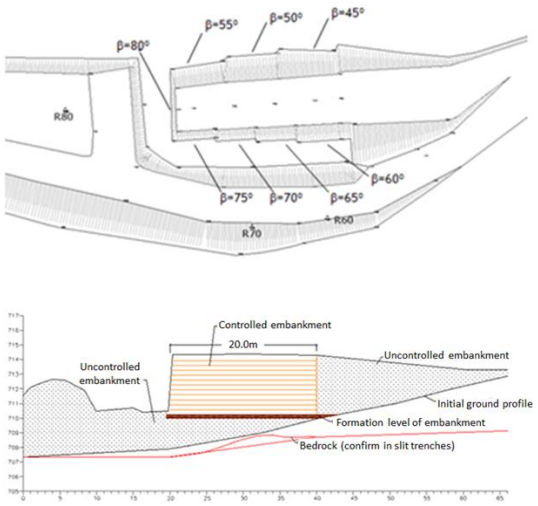


Figure 5 Plan and elevation of the controlled embankment (Neves, 2015).

The embankment height (4.0m) was kept constant across its full extent and its shoulders were built with varying gradients, so as to try to experimentally establish what would be the steepest stable configuration. The side slopes gradients varied between 45º and 80º with the horizontal, in 5º increments (refer to Figure 5 for the location of each of these faces in plan).
Additionally, a surcharge of 10kPa was applied at the top of the embankment, in August 2011, and near its steepest face. Circa 4 years after its application there are still no signs of instability in the slopes. The embankment was initially protected from weathering effects by means of a plastic film, which has deteriorated with time, leaving the embankment unprotected against the erosive effects of rain and wind.

4 METHODOLOGY

There is probably no analysis conducted by geotechnical engineers which has received more programming attention than the limit equilibrium methods of slices. This is due to the fact these methods tend to require

iterative procedures, which are usually numerically undertaken. The available commercial software which assesses slope stability, with both circular and non-circular slip surfaces, has the advantage of enabling a large number of calculations to be carried out in a very short period of time. Additionally, they have the advantage of providing a graphical output, which shows the geometry of all of the analysed slip surfaces and their correspondent MoS.

However, LEM methods consider forces acting on one or several discrete points along the slip plane, whilst assuming that failure occurs instantaneously and that the available shear strength is mobilised along the whole slip plane at the same time. As an alternative, stress-strain methods can be used to overcome these limitations. By considering the stress-strain relationship of the materials during deformation and failure, software can output the type and magnitude of the displacements in the slope which are consistent with its state of equilibrium. They can also provide the slope's MoS, which may be different from the one obtained with limit equilibrium analyses, as no specific failure surface is defined (Matthews et al., 2014).

For the purpose of this work, both LEM and FEM numerical analyses have been undertaken. The commercial software used was SLOPE/W and PLAXIS 2D, respectively for LEM and FEM approaches. Within SLOPE/W the Fellenius', Bishop's simplified and Janbu's simplified methods were used.

For the stability analysis undertaken in this work, the envelope of ground conditions and soil parameters, the latter based on the soil's characterisation and testing, presented in Table 2 was considered.

Table 2 Envelope of parameters and ground conditions.

Parameter	Range of values
Slope angle	1(V):2(H), 1(V):1.5(H), 1(V):1(H) &1(V):2(H)
Slope height	2.0m – 8.0m, with 1.0m intervals
φ'_k	35º, 36º, 37º & 38º
c'_k	0kPa, 5kPa & 10kPa
Groundwater	Dry, Low & High groundwater level
Surcharge	0kPa, 5kPa & 10kPa

Please note that all analysis have been undertaken in compliance with current standards (EC7) and exclusively to Design Approach 1 Combination 2, as this is typically the most critical combination for slope stability. As such, the concept of Margins of Safety (MoS), as opposed to the use of a lump Factor (FoS), has been used.

5 STABILITY ANALYSIS RESULTS AND DISCUSSION

The stability assessments undertaken in this study have selected a few key parameters, internal and external, which have been deemed to most influence the stability of slopes in the granitic residual soil in analysis. With regard to groundwater, and as briefly described in Table 2, three different scenarios have been analysed. Firstly, the different models have been run without the presence of a water table, which then served as baselines to analyse the influence of increasingly higher groundwater levels on the stability of the slope.

A second set of runs has considered the water table to coincide with the toe of the slope, and raising moderately behind the slope's face. A final set of calculations has been considered with the water table passing again through the toe of the slope but rising sharply behind its face, reaching only one metre below ground level at the crest. It should be noted the highest groundwater table is deemed as very conservative and highly unlikely to occur. Therefore, this is considered as an upper limit to the rises in groundwater levels.

As for the surcharges applied on the top of the slope, they have also been factored according to the EC7. As such, surcharges of 0kPa, 6.5kPa and 13kPa have been applied in the models. Also, all analysis have considered a minimum depth of 0.50m for the slip surfaces, as failures shallower than that are not thought of endangering the overall stability of the slope. No consideration has been given to the formation of tension cracks.

To help interpret the results from the numerical trials these have been split to individually cover the effects of an increase

in surcharge on the crest, the consequences of variations in groundwater levels, a direct comparison between the outcomes of all three LEM methods for all sets of conditions and a comparison between the LEM and FEM approaches on all the common sets of conditions.

5.1 Interpretation of the LEM results

Through the application of the three LEM methods the following conclusions have been drawn. It should be noted at this point that although the analyses have been undertaken numerically for the Janbu's method, the correction factor applied to the attained MoS has been assessed manually for each individual case.

5.1.1 Effects of surcharge increases

It has been observed that, in non-cohesive soils, increases in surcharge to 5kPa and 10kPa typically result in maximum reductions in the MoS of circa 5% and 10%, respectively. Also, these changes are quite often negligible. Furthermore, these results are fairly consistent throughout all slope gradients and independent of groundwater conditions. It appears that the critical slip surfaces tend to mostly develop at a shallow depth along the slope's face and therefore are not considerably affected by surcharge variations at the crest.

When an effective cohesion of 5kPa is considered, the repercussions of a surcharge increase are more critical. If groundwater is absent, the reduction in MoS is up to 15%, for a surcharge of 5kPa, and 20% (Bishop) to 25% (Fellenius and Janbu) for a surcharge of 10kPa. However, these extreme values only occur in slopes with heights of 2 to 3m. When ignoring the latter the differences in MoS are reduced to a maximum of circa 5% and 10% for 5kPa and 10kPa surcharges. The conclusions are similar for the remaining groundwater conditions. As opposed to the previous set of conditions (non-cohesive soil) the differences in MoS are noticeable over the full range of heights, whereas before from a height of 5m to 6m the differences were negligible.

If an effective cohesion of 10kPa is considered, and ignoring groundwater, the reduction in MoS is up to 15%, for a surcharge of 5kPa, and 25% for a surcharge of 10kPa. Again, these extreme values occur for small heights (2m to 3m high). When ignoring the latter, the differences in MoS are confined to maximums of circa 10% and 15%, respectively for 5kPa and 10kPa surcharges. The conclusions are similar for the remaining groundwater conditions.

For all LEM methods used in this thesis, increases in surcharge at the crest have been ascertained as more detrimental to the overall stability within cohesive materials, than in purely granular soils. In the latter case, for slopes above 3.0m high the differences are quite often negligible. Lastly, and even though the conclusions are similar regardless of the position of the water table, i.e. reductions in MoS of the same magnitude, having a higher water table leads to a slightly more penalising effect from surcharge increases.

5.1.2 Effect of groundwater level rises

When solely varying groundwater levels in the models, the differences in MoS are far more expressive. For purely granular soils, the consideration of a low groundwater table does not seem to affect the MoS obtained when groundwater is absent. However, rising these levels to what has been defined has a high groundwater table, leads to reductions in the MoS of over 50%.

Nevertheless, and with both high and low water levels, the reductions in MoS appear to be independent from the surcharge applied at the crest, although strongly linked to the slope angle.

For the Bishop's and Janbu's methods, the slopes modelled with the two slacker gradients, 1(V):2(H) and 1(V):1.5(H), have a similar response to groundwater level changes. A greater effect is reported in steeper slopes, particular in a 2(V):1(H) gradient. Sharp drops in the MoS are obtained for slopes over 3m high, when using the Bishop's method, or over 2m to 3m high for the Janbu's method.

A different trend emerges when analysing the results of the Fellenius' method. Here, the reductions in MoS seem to be more expressive for slacker slopes, diminishing as

the slope angle is increased. The maximum reductions are reported under 35%.
Similar conclusions can be drawn from the SLOPE/W runs on slopes in soils with a 5kPa and 10kPa effective cohesion. The only exception to this is that in these cases and when considering slacker slopes, 1(V):2(H) and 1(V):1.5(H), differences of up to 15% are reported between models where groundwater is absent and having a low water table. This is more noticeable as height increases. This might be explained by the fact that as these materials have a certain cohesion value, they drive the critical slip surfaces deeper. As a result, in slacker slopes they will more easily intersect what has been defined as a low groundwater table.
In addition, the reductions in MoS by rising groundwater seem to be inversely proportional to the cohesion of the intersected materials, i.e. greater reductions are reported for lower or null effective cohesion values.

5.1.3 Comparison between LEM methods

The comparison between methods has been undertaken considering the Bishop's method as a reference. As such, all the conclusions below refer to comparisons between the latter and the remaining two methods.
In non-cohesive materials the MoS seems to converge for slacker slopes and for greater heights. Also, and in line with the results of the sensitivity analysis to groundwater changes, results show that for steeper slopes, 1(V):1(H) and 2(V):1(H), the Fellenius' method gives MoS significantly higher than the Bishop's method (up to circa 70%) for high groundwater levels. This is in agreement with the findings of Whitman and Bailey (1967), which reported the Fellenius method to result in errors as much as 60%.
This contrasts with the findings of the Janbu's methods which report a significant reduction in the MoS for the same models by up to 25% when compared to the Bishop's. Again this may be the result of the lesser aptitude/inadequacy of this method to circular slips in non-cohesive soils.
Overall, for slacker slopes, 1(V):2(H) and 1(V):1.5(H), a good correlation is achieved between all methods, with maximum differences of 10% and frequently under 5%.
Different conclusions are drawn for slopes in cohesive materials, with the exception of the Fellenius' method. This still reports significantly higher MoS than the Bishop's method for high groundwater tables within the steepest slopes. On all remaining models the Fellenius's method reveals lesser MoS than the Bishops' but only up to circa 10%.
When comparing the outcome of the Janbu's method, it is clear that overall these results are closer to the Bishop's than those obtained with the Fellenius's method. However, greater divergences are noted for high groundwater levels and in steeper slopes, 1(V):1(H) and 2(V):1(H).
Nevertheless, when groundwater is absent or at a low level, this method generally reports greater MoS than the Bishop's method, albeit marginally.

5.2 Interpretation of the FEM results

By using the HSM available within the PLAXIS 2D software it has been possible to arrive at the following conclusions.

5.2.1 Effects of surcharge increases on the slope's crest

When considering a purely granular soil, significant reductions in the MoS have been obtained by increasing the surcharge to 5kPa and 10kPa, respectively up to circa 20% and 30%. Greater reductions are reported for the 5.0m models than for the 8.0m ones and surcharge increases appear to be less critical for higher water levels.
When an effective cohesion is considered, the repercussions of a surcharge increase are overall less critical (as opposed to the LEM analyses), with reductions generally under 5% and up to a maximum of 6.3%. The effect of the surcharge increase appears to be similar when groundwater is absent and in slopes with a low water table. A lesser effect is noted when groundwater rises to high levels.
These changes report lesser reductions to the MoS as the slope gradient increases, although the pool of results is not sufficiently large to arrive at a definite conclusion.

5.2.2 Effect of groundwater level rises

As opposed to the above, changes in groundwater levels appear to be more critical for cohesive than non-cohesive materials. However, it should be noted that only two non-cohesive models were used and that on these it has not been numerically possible to assess their stability for a high water table.
For cohesive materials no significant differences are reported for effective cohesions of 5kPa or 10kPa. Also, negligible reductions occur for the steepest configuration 1(V):1(H). 1(V):2(H) and 1(V):1.5(H) models show reductions in the MoS of circa 30% and 35% for a high groundwater table, respectively for 5.0m and 8.0m heights.
When considering a low groundwater table reductions are up to 10% and 15%, respectively for 5.0m and 8.0m heights in 1(V):2(H) slope. For a slightly steeper slope, 1(V):1.5(H), these values are reduced to up 5% and 10%, respectively for 5.0m and 8.0m heights.
There is no significant variation with the increase in surcharge, which leads to the conclusion that variations in groundwater levels are substantially more critical than increases in surcharge.

5.2.3 Comparison between LEM and FEM approaches

The comparison between FEM and LEM methods has revealed there is a significant divergence in the obtained MoS for purely granular materials. All LEM methods appear to overestimate the safety of the slope by up to circa 40%. These differences are more expressive as the height and the applied surcharge at the crest increase.
In soils with apparent cohesion the results of the Bishop's simplified method are between circa 5% and 10% higher than the FEM outcomes. The differences appear to increase with the gradient of the slope, with rising groundwater level and the slope's height. No noticeable differences are reported for surcharge increase.
The Fellenius' method presents MoS values both over and under the FEM ones, with differences generally under circa 5% but with values between 5% and 10%. No tendency is apparent for changes in groundwater levels or applied surcharges.
The majority of the MoS values obtained with the Janbu's simplified method present the best correlation with the FEM approach (for soils with apparent cohesion), with differences reported predominantly under 5%. The best correlation occurs for greater applied surcharges and slacker slope gradients.

6 REMEDIAL MEASURES

Remedial measures, as their name suggest, are those carried out after a slope failure event or when excessive deformation is reported which may trigger instability. As such, their design requires an estimate of the relevant soil parameters, a prediction of the geometry of the failure surface and especially an assessment of the factors causing the instability. In general terms, they result from either one or a combination of the following options:

- Modifying slope geometry;
- Installing/improving drainage;
- Installing resisting elements on the slope;
- Setting up retaining walls/elements at the toe.

When a slope becomes unstable, it is very useful to perform a back analysis, to allow an estimation of the "real" geotechnical parameters found on site.
In order to help quantify the benefits of each type of measure, six distinct ground models have been selected (Table 3) to provide a better insight on the most appropriate remedial measure for each set of conditions.

Table 3 Sets of conditions to analyse the benefits of the different remedial measures.

Ground model	**1**	**2**	**3**
Parameter	**Range of values**		
Slope angle	1:1	1:1.5	1:1.5
Slope height	8.0m	5.0m	5.0m
φ'_k	35°		
c'_k	10kPa	5kPa	10kPa
Groundwater	Low	Low	High
Surcharge	0kPa, 5kPa and 10kPa		
Ground model	**4**	**5**	**6**
Parameter	**Range of values**		
Slope angle	1:2	1:2	1:2

Slope height	5.0m	8.0m	8.0m
φ'_k	35°		
c'_k	0kPa	0kPa	10kPa
Groundwater	Dry	Dry	High
Surcharge	0kPa, 5kPa and 10kPa		

For each of the above models the installation of the following structural elements has been analysed on both LEM and FEM approaches: sheet piles, soil nails and the use of gabion wall (Figures 6 to 8).

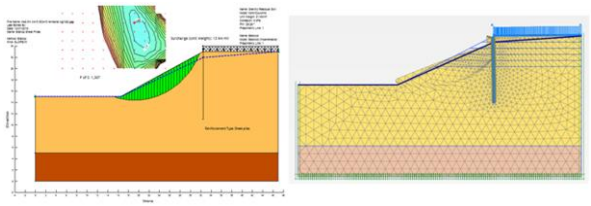


Figure 6 LEM & FEM sheet piles reinforcement and associated failure mechanisms.

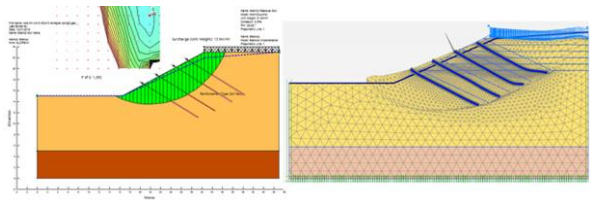


Figure 7 LEM & FEM soil nail reinforcement and associated failure mechanisms.

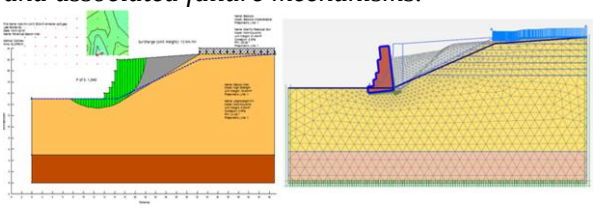


Figure 8 LEM & FEM gabion wall reinforcement and associated failure mechanisms.

6.1 Comparative analysis of remedial solutions

To help in the assessment of the most suited remedial option for each of the scenarios listed above, the gains in MoS for both LEM and FEM approaches are summarised in Table 4 below.

Table 4 Gain in MoS (percentage) of the different remedial measures.

Remedial option	**c'=0kPa**	**c'=5kPa**	**c'=10kPa**
Sheet piles	Minor	5-10% (LEM) <5% (FEM)	10-20% (LEM) 5-10% (FEM)
Soil nails	5-20% (LEM)	20-30% (LEM)	5-30% (LEM)
		25% (FEM)	40-45% (FEM)
Gabion wall	30->50% (LEM) 15-35% (FEM)	30% (LEM) 20% (FEM)	25->40% (LEM) 25-40% (FEM)
GWL lowering*	Not assessed	Not assessed	20->30% (LEM)
Slacking slope	Not assessed	15% (LEM)	15-25% (LEM)

* Only valid when reducing ground water level from high to low. Previous analyses have shown differences in MoS between a low water table and a fully dry slope are insignificant.

By analysing the outcome of the different analyses the following points have been inferred.

Driving sheet piles from the crest of the slope does not appear to result in a significant improvement in the MoS. However, having these elements in place forces the critical slip plane to be shallower and purely along the slope's face. As such, and although the overall safety is not increased substantially, if the priority was to just ensure the safety of the crest of the slope, and accepting that a failure may occur below it, there would be great benefit in this option. FEM modelling also reveals that the overall maximum displacements along the face of the slope are not greatly reduced by adopting this remedial option.

The use of soil nails along the slope appears to be a more effective mean of enhancing its stability, particularly in cohesive soils, than the use of a sheet pile wall. However, the effectiveness of this remedial option is strongly dependent on their length and spacing (both vertical and horizontal).

In terms of displacements this option has proven to reduce the anticipated maximum total displacements along the slope's face between circa 30% and 50%. The FEM approach in these cases has provided a noticeable higher MoS than the LEM approach. This is likely explained by the abrupt change in the failure mechanism, with the resultant critical slip surface being significantly deeper in the PLAXIS 2D models than within the SLOPE/W runs.

The option to construct a retaining wall, for the purpose of this study only a gabion wall has been considered, has proven to have a

similar effect across all options and to result in the greatest increases in terms of MoS. In fact, the failure mechanism after the wall is in place appears to be very much dependent on the properties of the backfill rather than the existing slope's materials.
Further analyses have confirmed that, apart from when lightweight aggregate is used as a backfill to the new wall, the merits of this option are left in between the use of sheet piles and soil nails. However, it should be noted that the above has not taken into account the bearing capacity assessment of the gabion wall foundation.
The benefits of changes in groundwater levels and slope angles have only been assessed through the use of LEM analyses on the six ground models presented above. Changes in the water table are only particular relevant for high water levels and can equate to gains of 20% to 30% in the MoS. As for the slope angle, slacking the slope can result in increases of 15% to 25% in the overall stability of the slope.

7 CONCLUSION AND CRITICS

The majority of slope stability analyses performed in practice still use traditional limit equilibrium (LEM) approaches involving methods of slices that have remained essentially unchanged for decades. Nevertheless, the user-friendliness, simplicity and proven good record of LEM methods are enough to still make them a valuable tool against the use of formulations based on finite element (FEM) principles. The latter however, can help predict stress concentration problems and forecast deformations/displacements within the slope, which have been experienced problematic in LEM analysis and are often crucial in evaluating the performance and acceptability of some slopes which are sensitive to movement.
Also, LEM methods are especially useful when assessing the stability of a slope with a MoS below unity. On such cases, when remedial/strengthening measures are to be installed, it is then possible to quantify their merits in the overall stability of the slope using this approach. FEM methods, on the other hand, can rarely be used to compute a stability problem with a MoS value significantly below unity.
Consequently, it is quite common to undertake LEM back analyses when prescribing remedial measures whilst assessing the factors leading to the instability. These analyses usually try to establish the 'real' strength parameters of the soil (φ' and c') when little information is available and usually by considering the soil as a homogenous material for simplicity.
All stability calculations have been based on the principles of saturated soils. However, for situations where a failure occurs above the groundwater table, thus within the partially saturated zone, slope stability would have been better evaluated using an assumption of an unsaturated soil, which could have been more cost effective, although requiring an advanced understanding of matric suction contribution to slope stability.

8 REFERENCES

Cavaleiro, V.M. (2001). Condicionantes geotécnicas à expansão do núcleo urbano da cidade da Covilhã. UBI, Covilhã.

Fernandes, M.M. (2011). Mecânica dos Solos - Conceitos e Princípios Fundamentais (2ed). FEUP, Porto.

Guidicini, G. & Nieble C. (1984). Estabilidade de Taludes Naturais e de Escavação. Edgard Blucher Ltda, São Paulo.

Matthews, C., Farook, Z. & Helm, P. (2014). Slope stability analysis - limit equilibrium or the finite element method? Ground Engineering (May), 22-28.

Neves, M. 2015. Numerical analysis of slope failure in granitic soil slopes. UBI, Covilhã.

Whitman, R. & Bailey, W.A. (1967). Use of computer for slope stability analysis. ASCE Journal of the Soil Mechanics and Foundation Division 93 (4), 475-498.

Metodik för identifiering av slänter och raviner känsliga för vegetationsförändringar till följd av skogsbruk eller exploatering

K. Lundström

Swedish Geotechnical Institute, Sweden, karin.lundstrom@swedgeo.se

A. Lomander, P. Olsson

Swedish Forest Agency, Sweden

M. Andersson, J. Hedfors

Swedish Geotechnical Institute, Sweden

ABSTRACT

Stability and runoff conditions in coarse grained sediments are depending mainly on topography, soil properties, groundwater conditions and vegetation type and cover. Landslides and debris flow may be triggered by for instance heavy or long duration of precipitation or by changes in the vegetation cover. It has been observed for several years that different forest activities like clear cutting and tracks from forest machines, building of forest roads, soil scarification, ditching and other activities changing run off conditions have caused severe erosion, landslides and debris flows affecting roads and buildings. Erosion due to forest activities may also lead to negative influences on water quality in streams and rivers.

A methodology for general identification of slope areas which have prerequisites for landslides and/or debris flow and thereby are sensitive to changes in vegetation cover has been developed. The basis for the methodology is different layers in a geographical information system, such as slope inclination, length of slope, soil type, gully formations, water courses, type of vegetation cover and consequences (within a given distance). Criteria for these different layers are given and combined into a sensitivity map. The intention is to produce a map easy to understand also by non-scientists.

The methodology has been tested in two areas in Sweden. Changes in vegetation cover have been done in the areas in connection with clear cutting and exploitation for ski resorts. By using the methodology, slopes and gullies have been identified as sensitive to changes in vegetation cover. The methodology and the results from the tests are presented in the paper.

Keywords: slope stability, forest management, GIS, erosion, vegetation cover

1 INLEDNING

Stabilitets- och avrinningsförhållanden för slänter och raviner i friktionsjord påverkas framförallt av topografi, jordens tekniska egenskaper, grundvattennivåer, nederbörd och växlighetens typ och omfattning.

Vegetationsförändringar orsakade av avverkning, markberedning, gallring, dikning, spårbildning från tunga maskiner samt anläggning av vägar, skidpister och bebyggelse påverkar vattenförhållandena såväl på som i marken. Detta leder ofta till att avrinningen på markytan ökar och att vattnet tar nya vägar som i sluttande terräng kan dra med sig stenar, block, träd och orsaka kraftig erosion och ras. Avverkning orsakar en förhöjd grundvattenyta i marken vilket försämrar stabiliteten i slänter. Dessutom leder avverkning, markberedning och spårbildning till att rötterna i marken dör och därmed försvinner den sammanbindning av jorden som rötterna bidrar med, vilket kan utlösa ras. Erosion leder dessutom till

grumling av vatten, vilket påverkar vattenkvalitéten liksom flora och fauna i vattnet negtivt. Klimatförändringen som väntas medföra både torka, häftig nederbörd samt avsaknad av tjäle vintertid, ökar riskerna för ras, skred och erosion ytterligare.

Sverige har en landareal av 407 310 km^2 (SCB, 2015) och av denna är cirka 75 % täckt av morän (SGU, 2015). Ytterligare några procent är täckta med annan grovkornig jord. Av totala landarealen utgörs ca 69 % av skogsmark och 57 % klassas som produktiv skogsmark (Riksskogstaxeringen, 2015). Som produktiv skogsmark räknas, i Sverige, skogsmark med en tillväxt av över 1 m^3sk/ha och år. Inom dessa områden får skogsbruk bedrivas. Överlappet mellan mark där skogsbruk bedrivs eller som utsätts för exploatering och de områden som är täckta av morän är stort. Det föreligger därför ett behov av att översiktligt identifiera vilka områden som kan ha förutsättningar för ras och/eller slamströmmar och som därmed kan vara känsliga för vegetationsförändringar. Detta för att minska risken för negativa konsekvenser på vägnät, bebyggelse och vattenkvalitéten. Framtagen metodik är avsedd att inom Sveriges stora areal lokalisera känsliga områden.

I British Columbia finns en metodik framtagen för identifiering av känsliga områden i en stegvis ökande detaljeringsgrad, se B.C. Ministry of forests (1999). De kriterier som beskrivs där för att avgränsa områden definieras i termer av lutning, jordtyp i markytan, jordlagrens textur, jordmäktighet, morfologi, fuktförhållanden och pågående geomorfologiska processer. Indelning sker i olika stabilitetsklasser där slänter brantare än 32° samt släntområden som lutar mellan 21°-32° och är djupt urskurna av raviner, anges som potentiellt känsliga områden. För raviner finns dessutom kriterier för att bedöma sannolikhet att rasmassor från ovanliggande branta områden når ravinen och där orsakar en slamström.

Høydal et al (2013) beskriver värdering av skogen i Norge som skydd mot ras och slamströmmar. Där anges att det kan finnas förutsättningar för jordskred om släntlutningen är större än 20°. Längs bäckar och i raviner bör geomorfologiska former, avrinningsområdets egenskaper, skogens eventuella skyddande egenskaper och bäckens transportkapacitet analyseras för att värdera förutsättningar för slamströmmar. Man skriver även om behovet att värdera om det finns lösa jordmassor som kan rasa i eller nedanför skogen som ska avverkas.

2 FRAMTAGEN METODIK

Metodiken för identifiering av områden som kan vara känsliga är uppbyggd av ett antal GIS-skikt. Dessa utgörs av jordart, lutningsförhållanden, vattendrag, ravinformationer, slänthöjd, vegetationstyp och konsekvenser. Genom att kombinera kriterier för de olika skikten har en känslighetskarta arbetats fram.

2.1 GIS-skikt

Jordarter har identifierats från digitala jordartskartan framställd av Sveriges geologiska undersökning. Kartorna är framtagna med olika noggrannhet och i olika skalor över Sverige. Kartorna har förenklats genom att slå ihop jordarter med liknande egenskaper, exempelvis har olika grovkorniga sväm- och älvsediment slagits samman och likaså grovkorniga postglaciala och glaciala sediment.

Lutningar, ytformer, slänthöjd och storlek på ytor har identifierats från nationella höjdmodellen framställd av Lantmäteriet. Höjdmodellen har en noggrannhet i medeltal av 0,2 m i höjd och 0,5 m i plan.

För identifiering av olika typer av markanvändning har använts fastighetskartan, framställd av Lantmäteriet, samt karta som visar områden avverkade de senaste 15 åren framställd av Skogsstyrelsen, Kartorna har förenklats genom att slå ihop områden med liknande egenskaper.

Från digitala fastighetskartan, framställd av Lantmäteriet, har konsekvenser i form av bebyggelse, vägar, vattendrag och sjöar identifierats.

2.2 Kriterier

Kriterier för områden känsliga för vegetationsförändringar har arbetats fram för de olika GIS-skikten.

Från jordartskartan har områden med berg i dagen och lera sorterats bort eftersom vegetationen inte anses har någon påverkan på stabiliteten inom dessa områden. Områden med erosionskänslig morän har översiktligt identifierats och kommer utgöra en extra indikator på känslighet.

Slänter med en lutning av mer eller lika med 25° anses ha förutsättningar för ras. Detta bygger på stabilitetsberäkningar för slänter med en grundvattenyta 1 m under markytan, antagande om en glidyta med en tjocklek mellan 1 och 3 m, en slänthöjd mellan 15 och 20 m och med en friktionsvinkel på mellan 30° och 40°. För fall med en friktionsvinkel på 30° ansattes i beräkningarna även ett kohesionsintercept lika med 5 kPa för att återspegla en siltjord. Beräkningar visar på säkerhetsfaktorer kring 1,0 för dessa förhållanden och därför har sådana sluttningar ansetts vara känsliga för vegetationsförändringar. Den valda lutningen motsvarar ungefär ett medelvärde av de lutningar, 21°-32°, som redovisas av B.C. Ministry of forests (1999).

Baserat på stabilitetsberäkningarna sattes även kriteriet att slänter ska ha en höjd av minst 15 m.

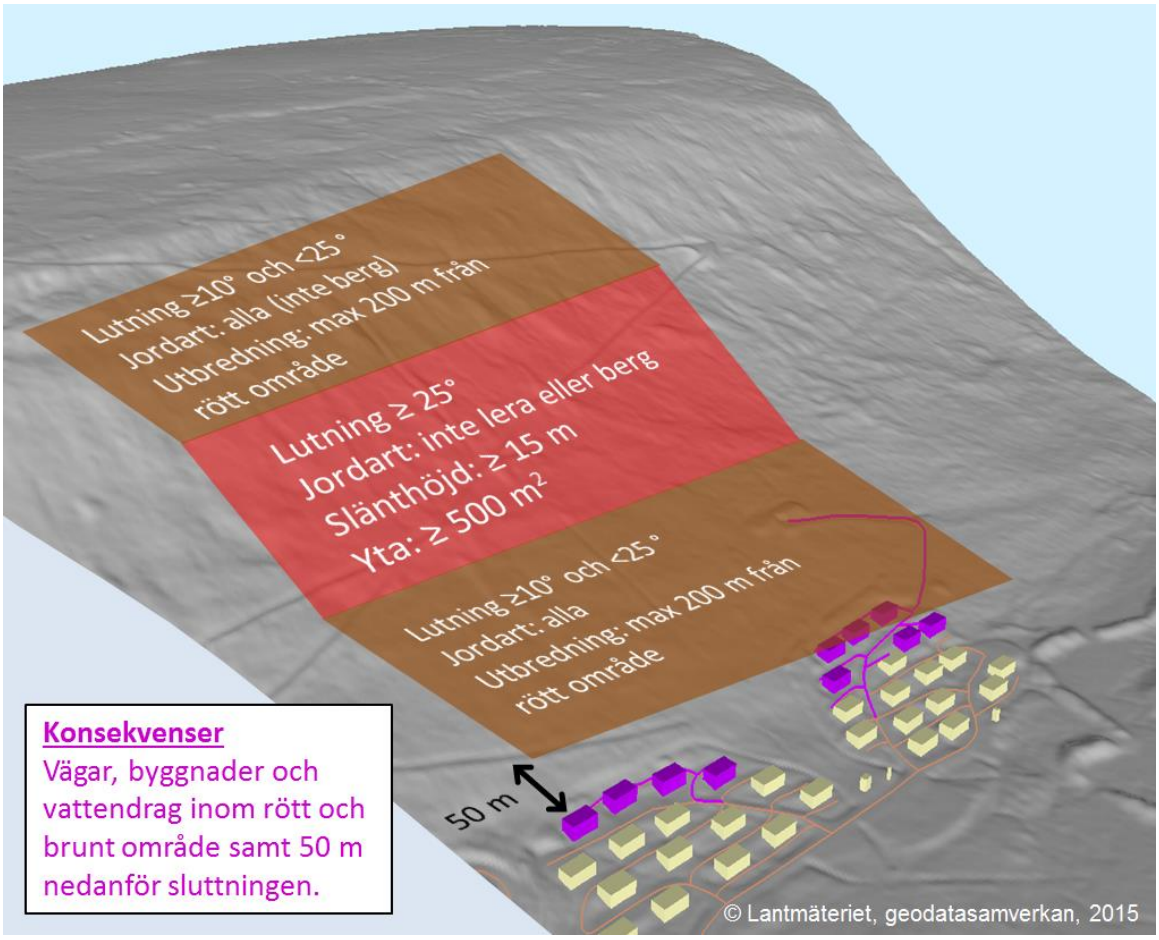
För att slänter med en lutning av minst 25° och med en höjd av 15 meter ska anses som känsliga har även ett kriterium för områdets storlek ansatts. Detta kriterium sattes till 500 m^2.

Bäckar har ansetts ha förutsättningar för slamströmmar om bäcken går i en ravinformation som är högst 50 m bred och med slänter på båda sidor om bäcken som lutar minst 25° och är minst 5 m höga. Dessutom krävs att bäckens botten lutar mer än 2° och att ravinformationen har en yta av minst 50 m^2. Bakgrunden till kriterierna bygger på erfarenheter från inträffade slamströmmar i Sverige. Alla bäckar med dessa kriterier utsätts inte för slamströmmar utan kriterierna är satta med viss säkerhetsmarginal. Förändringar av vegetationsförhållandena inom ett avstånd av 200 m från en utpekad ravin anses kunna påverka avrinningsförhållandena och öka faran för slamströmmar.

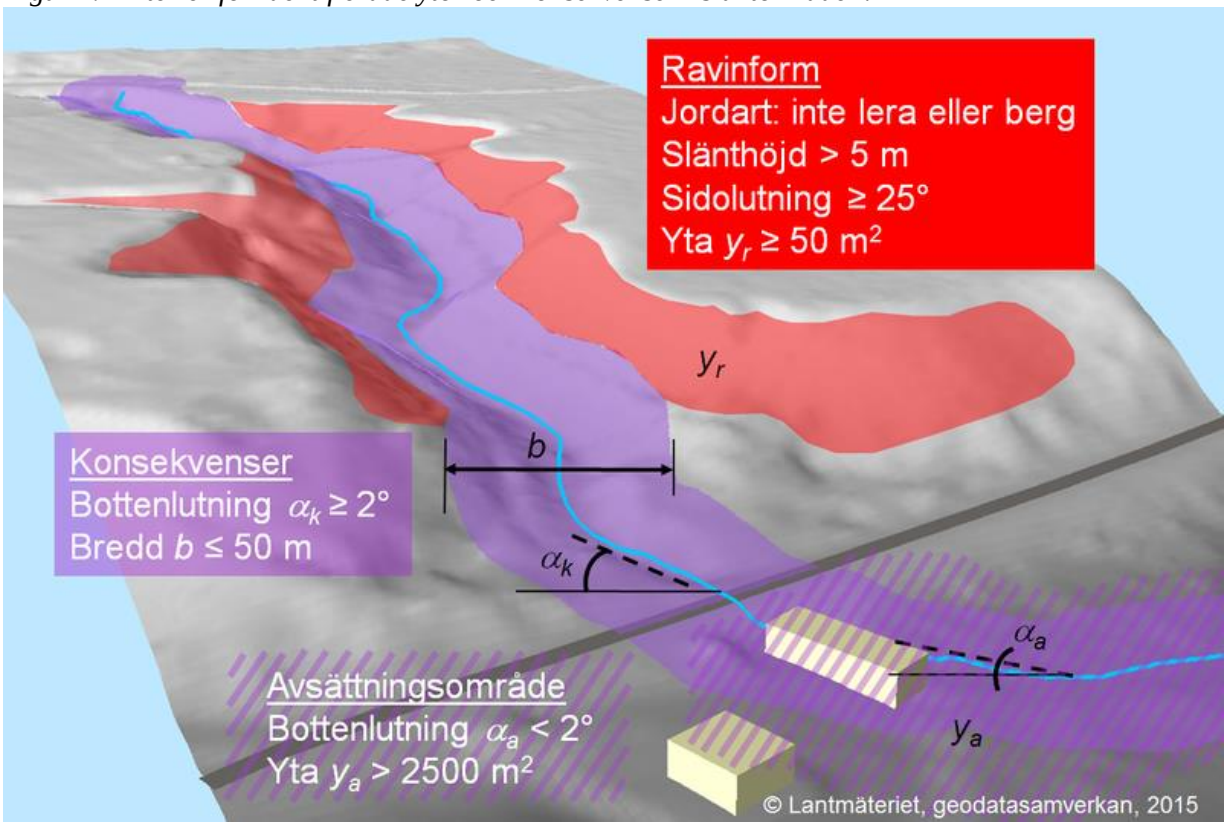
Ytor som saknar vegetationstäckning, områden där tidigare jordrörelser har inträffat eller områden som tidigare utpekats att ha förutsättningar för jordrörelser, kommer utgöra en extra indikator på känslighet.

Konsekvenser i anslutning till slänter som uppfyller ovan givna kriterier, har ansetts vara de som ligger nedanför och ovanför slänten inom ett avstånd av högst 250 m då släntlutningen är mellan 10° och 25°, se Figur 1.**Error! Reference source not found.**Konsekvenser i anslutning till raviner som uppfyller ovan givna kriterier, har ansetts vara de som ligger inom 25 m från bäcken och inom bäckens avsättningsområde. Avsättningsområdet har satts till ett område där bäcken lutar mindre än 2° och har en yta av minst 2 500 m^2, se Figur 2.

De olika skikten kombineras till en känslighetskarta. På känslighetskartan delas områden in i tre klasser; inte känslig, känslig och extra känslig. I denna artikel redovisas resultatet för två testområden för klasserna känslig eller inte känslig för vegetationsförändringar. Känsliga områden är områden markerade med brun, röd och lila färg. Övriga områden anses inte känsliga för vegetationsförändringar. Karta där även den tredje klassen, extra känslig, redovisas är under utarbetning och redovisas inte i denna artikel.



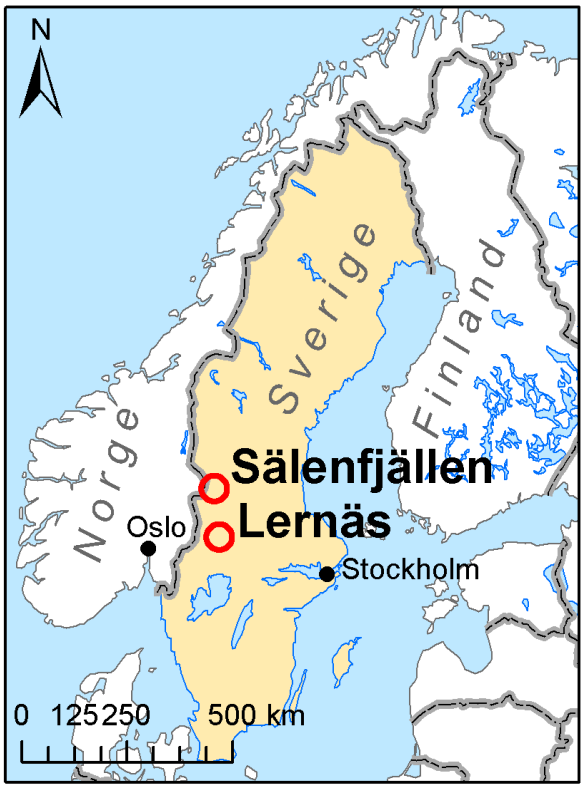
Figur 1. Kriterier för identifierade ytor och konsekvenser i sluttområden.



Figur 2. Kriterier för identifierade ytor och konsekvenser i ravinområden.

3 RESULTAT

Metodiken har hittills använts i två olika områden i Sverige; Sälenfjällen och Lernäs, se Figur 3.



Figur 3. Läget för de två testområdena; Sälenfjällen och Lernäs.

3.1 Testområde Sälenfjällen

Sälenfjällen är Sveriges sydligaste fjällområde, se Figur 3. Området karaktäriseras av runda fjäll som når upp till knappt 1 000 m.ö.h, se Figur 4. Fjällens övre delar, från cirka 800 möh, är kalfjäll. I dalgångarna mellan fjällen rinner bäckar som i vissa områden skurit sig ner i landskapet. Flera ravinformationer och kanjoner förekommer. Sluttningarna har på många ställen lutningar som överstiger 25°.

Sälenfjällen är hårt exploaterade med skidpister, fritidshus, skid- och vandringsleder och infrastruktur.



Figur 4. Vy över del av Sälenfjällen.

Den huvudsakliga jordarten i området är morän som på många ställen är grovkornig. Berg i dagen och tunna jordtäcken förekommer framförallt på fjällens övre delar. I dalgångarna återfinns isälvssediment och torv. För Sälenområdet finns digital jordartskarta i skala 1:100 000.

I bäckar samt i schaktade och på kala släntytor syns spår av erosion och slamströmmar. I sluttningar ner mot raviner och kanjoner inträffar ibland snöskred. I slutet av augusti 2015 kom cirka 90 mm nederbörd på 12 timmar över delar av området, vilket medförde ras, översvämningar, bortspolade trummor och erosion, se Figur 5 till Figur 7.

Hela området där metodiken testats har en yta av 183 000 ha och täcker även områden söder och öster om själva fjällområdet. Vid analys av området enligt framtagen metodik har 991 ha (cirka 0,5 %) kriterier som innebär att de är känsliga för vegetationsförändringar, se Figur 8. Inom identifierade områden återfinns konsekvenser framförallt i form av vägar och bebyggelse men även påverkan på vattendrag nedströms. Resultat från analys av området kring Flatbäcken i norra Sälenfjällen redovisas i Figur 9. Denna bäck identifieras som att ha förutsättningar för slamströmmar. Vid bäcken finns konsekvenser i form av tre vägar där bäcken passerar under i trummor. Vid en eventuell slamström kan trummorna sätta igen och spolas bort.



Figur 5. Ras i slänt söder om Sälenfjällen i samband med regnoväder september 2015. Foto: Jan-Olov Mattsson, Lima besparingsskog.



Figur 6. Högt flöde i Sälen vid regnoväder september 2015. Foto: Erik Stigsmark, Trafikverket.



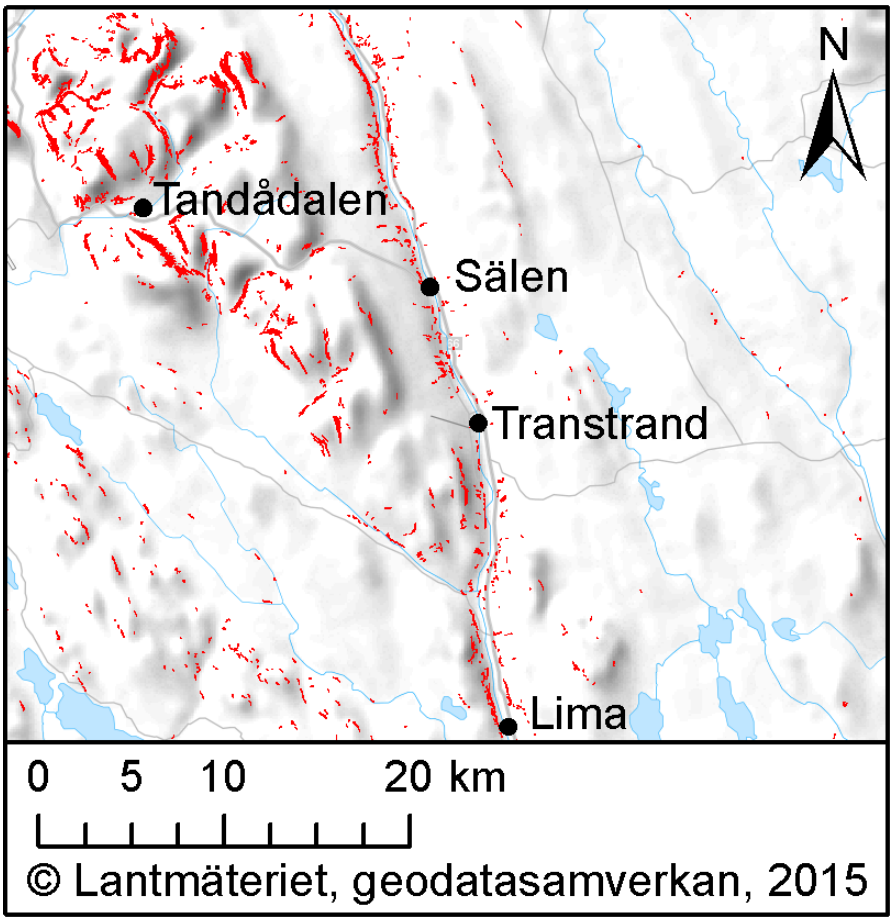
Figur 7. Erosion och bortspolad trumma vid regnoväder september 2015. Foto: Jan-Olov Mattsson, Lima besparingsskog

3.2 Lernäs

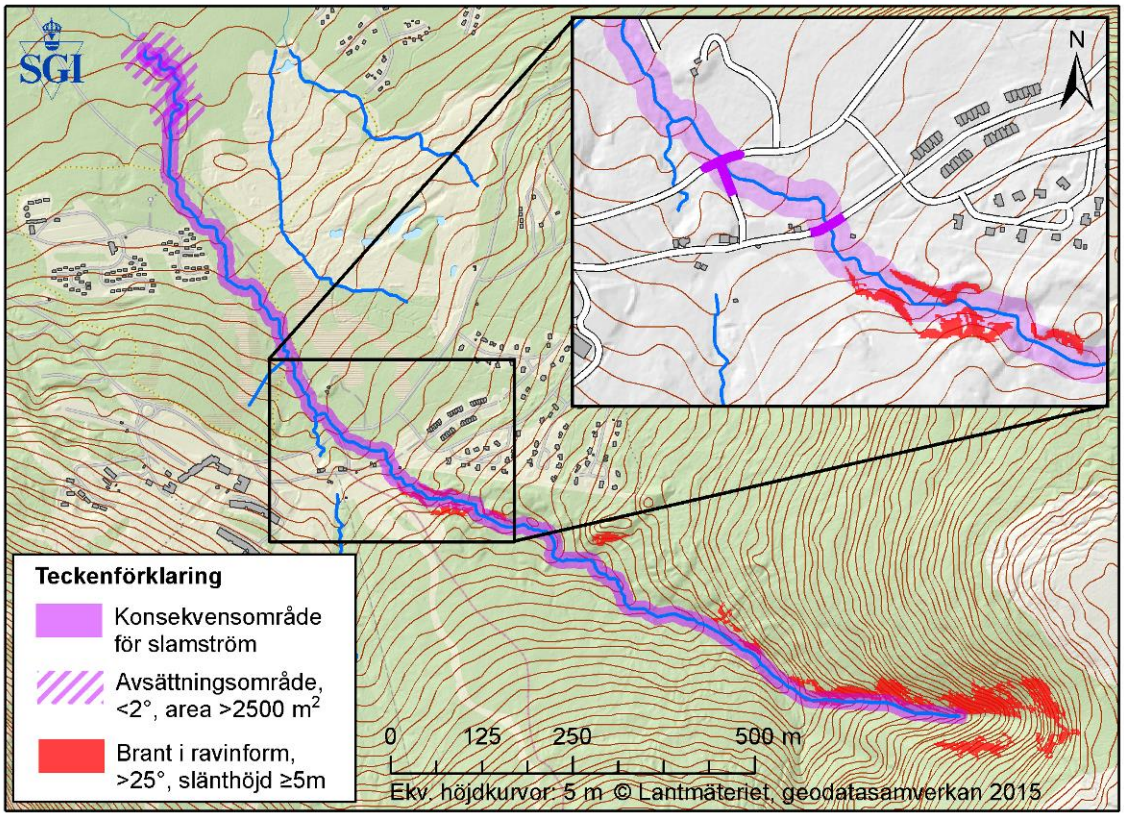
Lernäs ligger på västra sidan om Klarälven. Långa och branta sluttningar sträcker sig upp mot höjderna både på västra och östra sidan om Klarälven, se Figur 10. Höjdskillnaden mellan älven och höjderna i väster är cirka 250 m och lutningen varierar i den brantaste delen ner mot älven med mellan 25° och 38°.

Morän har stor utbredning inom de högre liggande delarna av området. Moränen är i allmänhet sandig-siltig eller sandig. Närmare Klarälven återfinns glacial grovsilt och finsand samt svämsediment. Flera bäckar rinner genom området och i de glaciala avlagringarna har bäckarna skurit ner och bildat ravinformationer. Bebyggelse och infrastruktur är i huvudsak lokaliserad i anslutning till älven.

I sluttningarna längs Klarälvsdalen är ras, erosion och slamströmmar vanligt förekommande. Ett utsnitt ur SGU:s databas över inträffade ras i grovkornig jord och förekomst av ravinformationer visas i Figur 11.



Figur 8. Resultat från analys av testområdet Sälenfjällen. Röda områden i kartan visar översiktligt identifierade områden som kan ha förutsättningar för ras eller slamströmmar.

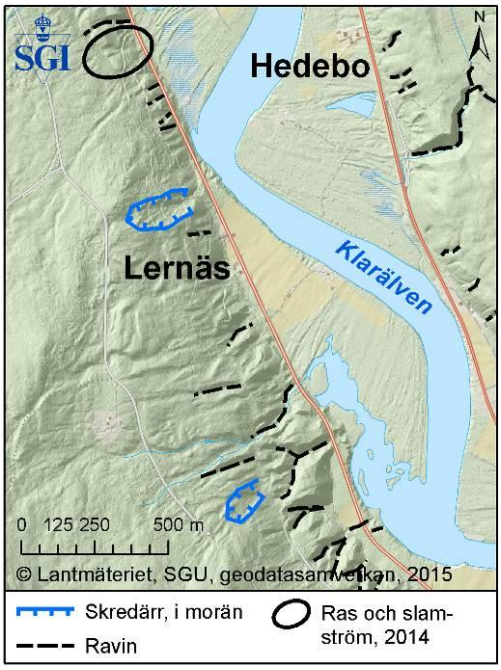


Figur 9. Identifierad bäck, Flatbäcken, med förutsättningar för slamströmmar. Konsekvenser i form av tre vägar.



Figur 10. Vy över Klarälvsdalen.

På våren 2014 inträffade ett ras som utvecklades till en slamström i Lernäs, se Figur 11 och Figur 12. Slamströmmen drog med sig träd och jordmassor ner mot en allmän väg och slänten nedanför vägen rasade ner mot älven. Vid platsen för slamströmmen fanns ingen vägtrumma. I sluttningen, cirka 100 m ovanför vägen, hade ett skogsområde gallrats och en traktorväg anlagts på skrå i sluttningen. Dessa ingrepp kräver inget myndighetstillstånd i Sverige. Gallringen orsakade en ökad avrinning och vattnet infiltrerades i marken i läget för traktorvägen. Det ökade grundvattentrycket orsakade troligen raset och efterföljande slamström. Händelsen har utretts av Trafikverket och den finns presenterad av Hellstrand (2014).



Figur 11. Ras och ravinformationer i Lernäs från SGU:s databas samt ras och slamström 2014.



Figur 12. Slamström i Lernäs 2004.

I området kring Lernäs där metodiken testats har en yta av 760 ha. Vid analys av området enligt framtagen metodik har 42 ha (drygt 5 %) kriterier som innebär att de är känsliga för vegetationsförändringar, se Figur 13. I området finns även bäckraviner med förutsättningar för slamströmmar. Inom identifierade områden återfinns konsekvenser i form av en väg och påverkan på Klarälvens vattenkvalité.

Skogsstyrelsen har inom identifierade känsliga områden i Lernäs skattat virkesvolymer. För analysen användes en rasterprodukt som grundar sig på laserskanningen från nationella höjddatan, NH, och provytor från riksskogstaxeringen. Totalt finns inom områdena (totalt 42 ha) en virkesvolym av 10 600 m^3.

4 DISKUSSION

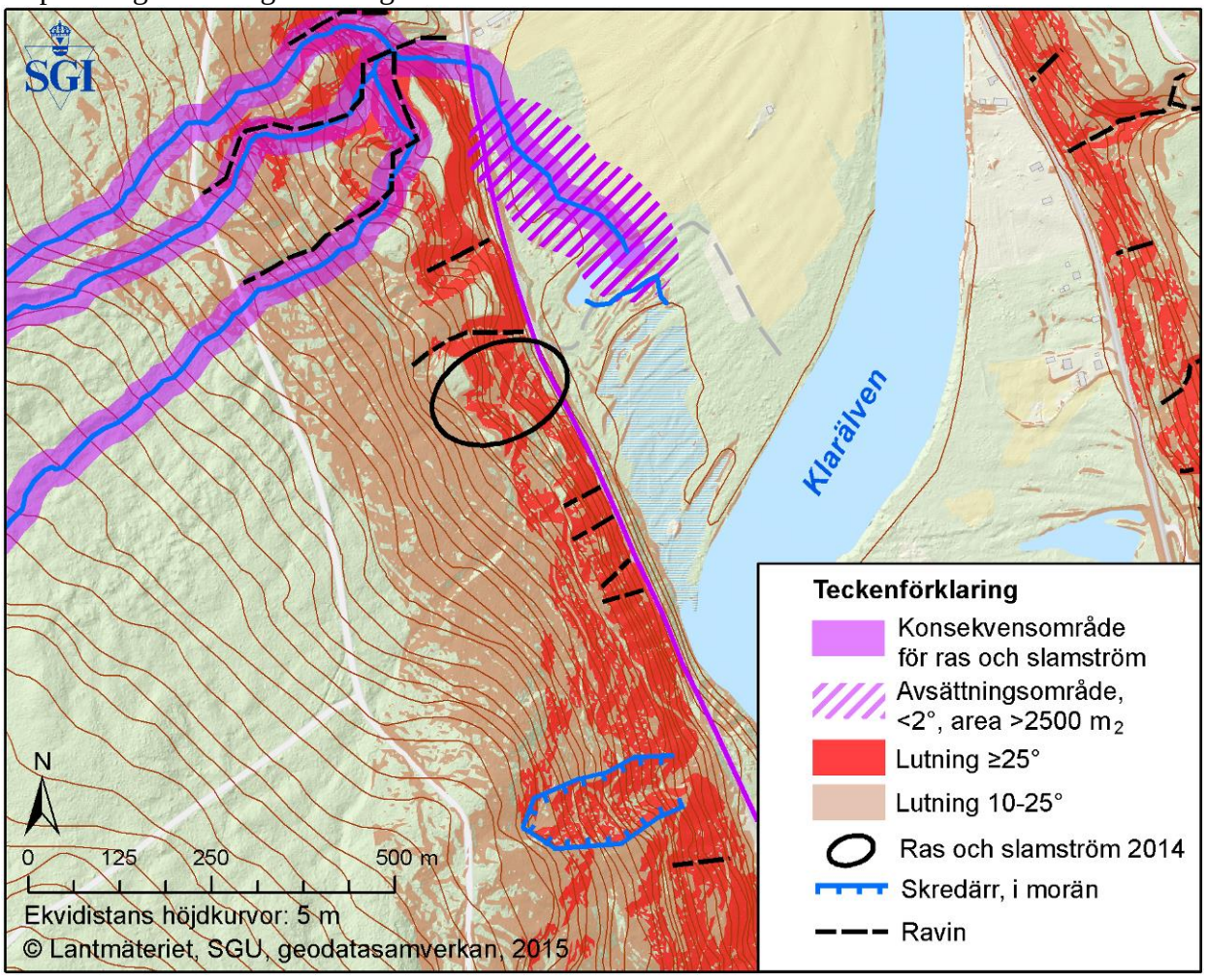
Framtagen metodik är tänkt att användas för att översiktligt identifiera områden som kan ha förutsättningar för ras och/eller slamströmmar och därmed vara känsliga för vegetationsförändringar. Dessutom ska metodiken ge indikationer på vilka områden som är extra känsliga beroende på jordens sammansättning och tidigare inträffade händelser. Resultatet ska framförallt användas av myndigheter (exempelvis

Länsstyrelser, kommuner, Trafikverket, Skogsstyrelsen). Delar av resultaten kommer även göras tillgängligt och förståligt för markägare, maskinförare, skogsentreprenörer, skogsförvaltare och andra myndigheter.

Till kartan kommer det att kopplas råd och anvisningar för hur arbeten i områden klassade som känsliga eller extra känsliga kan utföras. Det kan exempelvis handla om att inte avverka hela sluttningen vid samma tillfälle, att undvika underröjning, att leda vatten till ett icke känsligt område, att dämpa vattenhastigheten eller undvika körskador.

Inom svenskt skogsbruk råder kunskapsbrist och ovana att hantera instabila marker. Utbildning liksom diskussion och medvetandegörande av hela problematiken krävs därför. Som framgår av presenterade resultat över testområdena påverkas produktiv skogsmark av problematiken. Anpassningar av skogsbruksåtgärder inom dessa områden i syfte att bibehålla ett vegetationstäcke kan snabbt leda till minskad produktion och därmed inkomstbortfall för den drabbade markägaren, varför alternativa skötselformer, som inte medför betydande ökande kostnader, är viktiga att arbeta fram.

Kartan visar vilka sluttningar som kan ha låg säkerhet mot stabilitetsbrott och i vilka bäckar som slamströmmar kan uppkomma. Dock visar den inte att stabiliteten är låg eller att slamströmmar kommer inträffa. Det bör även noteras att det kan finnas områden utanför de av metodiken identifierade områdena som har förutsättningar för ras; exempelvis slänter påverkade av yttre laster eller erosion från is, vind eller fartygstrafik. Resultaten ska därför endast användas som en indikation på att det, vid förändringar av vegetationstäcket eller annan markpåverkan inom dessa områden, bör vidtas försiktighetsåtgärder.



Figur 13. Resultat från analys av områden i Lernäs som kan vara känsliga för vegetationsförändringar.

Det geologiska underlaget som används i metodiken är av varierande noggrannhet och digitala jordartskartor finns inte över hela landet, vilket är en brist. Moränens sammansättning finns endast för vissa områden angiven på SGU:s kartmaterial och utbredningen av erosionskänslig morän har i de flesta områden därför endast kunnat tas fram översiktligt.

Vid utarbetning av GIS-beräkningarna har svårigheter uppstått bland annat med kriteriet för slänthöjd. Med slänthöjd avses höjdskillnad mellan högsta och lägsta punkten i sluttningens fallriktning. För raviner avses höjdskillnaden i riktning vinkelrätt mot bäcken. Kring raviner har slänthöjden ett lägsta värde om fem meter använts, medan lägsta värdet för slänthöjden för långa, branta sluttningar har satts till 15 meter. Beräkningen av slänthöjden för sluttningarna har gjorts genom att med stöd från den nationella höjdmodellen (NH) beräkna lägsta respektive högsta punkt inom varje sluttning respektive ravinsläntt. Differensen mellan dessa värden ger ett teoretisk värde på slänthöjden. Förutsättningarna för att detta värde för slänthöjden ska vara korrekt är att det lutar huvudsakligen i en riktning. När det gäller slänthöjder för ravinformationer kring vattendrag, blir det beräknade värdet nära det tänkta om vattendraget ligger i relativt plan terräng. När det gäller raviner som ligger längsmed en sluttning, blir det beräknade värdet på slänthöjden inte alltid det som avsetts, då slänthöjden beräknas som skillanden mellan lägsta och högsta punkten inom området. Detta är viktigt att ha i åtanke för resultatets noggrannhet och kan innebära att ravinformationer med lägre slänthöjd än de 5 meter faller ut vid användning av metodiken . Ett annat problem som varit svårt att lösa har varit att lutningen för bruna områden uppströms röda områden inte kunnat styras. Således kan vissa av dessa luta i motsatt riktning jämfört med sluttningen inom det röda området.

Stabiliteten för sluttningar i grovkornig jord påverkas i hög grad av grundvattennivån. Det finns idag ingen möjlighet att bestämma aktuell grundvattennivå i ett visst område annat än genom mätningar av i jorden installerade grundvattenrör. Kunskapen i Sverige om vanligt förekommande nivåer i sluttningar saknas och inga mätningar utförs kontinuerligt. Detta är en brist och mer kunskap skulle kunna tillföra viktiga data för metodiken.

Metodiken är under framtagande. I slutet av nästa år (2016) kommer den finnas tillgänglig för några myndigheter och ska testköras under några år. Därefter kommer en utvärdering och eventuell anpassning att krävas. Det kan exempelvis visa sig att orimligt stora områden klassas som känsliga eller att konsekvenser inte faller ut som tänkt.

5 SLUTSATS

Med framtagen metodik kan områden som skulle kunna vara känsliga för vegetationsförändringar identifieras. Vid förändringar inom dessa områden, exempelvis avverkning, gallring, dikning, spårbildning från tunga maskiner samt anläggning av vägar och bebyggelse, bör faran för ras och slamströmmar beaktas. Även om nuvarande metod troligen ger en bra indikation över var det finns riskområden så måste metodiken användas skarp under ett antal år, för att sedan utvärderas och justeras. Det finns ett behov av att förbättra GIS-beräkningarna, förbättra kartunderlag samt att mäta och analysera grundvattennivåer i branta slänter.

6 REFERENSER

British Columbia Ministry of Forests & British Columbia Ministry of Environment (1999). Mapping and assessing terrain stability guidebook, 2 nd edition, Forest Practices Code of British Columbia, Victoria, B.C.

Hellstrand, S. (2014). Stöllet väg 957, skred. Utredningsrapport. Trafikverket, Borlänge

Høydal Ø, Breien H, Sandersen F (2013). Forslag til kriterier for vernskog mot skred NGI Rapport 20120078-01-R. Oslo

Riksskogstaxeringen (2015). Statistik om skog från Riksskogstaxeringen http://www.slu.se/riksskogstaxeringen

SCB (2015). Statistiska centralbyrån http://www.statistikdatabasen.scb.se

SGU (2015). Sveriges geologiska undersökning www.sgu.se

Effects of soil-structure interaction on the excitation and response of RC buildings subjected to strong-motion

J.Th. Snæbjörnsson
School of science and engineering, Reykjavik University, Iceland, e-mail: jonasthor@ru.is

S. Rahpeyma, B. Halldórsson
Earthquake Engineering Research Centre, University of Iceland, Iceland

F.G. Sigtryggsdóttir
Department of Hydraulic and Environmental Engineering, NTNU, Norway

ABSTRACT
The objective of the paper is to investigate if and how site effects caused by a complex combination of rock and sediment layers affect the response characteristics of reinforced concrete buildings. The study focuses around two buildings in the town of Selfoss in South Iceland. The buildings were monitored during and/or after major earthquake events. In an effort to recreate the observed variation in the structural behaviour, a finite element model has been constructed of the structures including the foundation effects through simple spring elements. The models have been applied to match the numerical response to the recorded response. Analyses of recorded seismic response indicates considerable influence from the foundation on the structural behaviour and the dynamic response of the reinforced concrete structures. It is also deduced, that when subjected to an earthquake, the dynamic properties of the soil/rock foundation will change in terms of shear strength and damping as a function of the intensity of the excitation. This is probably especially true for the underlying sedimentary layer as the amount of strains in the sedimentary layer to a large degree controls the frequency response. The response spectra obtained indicate that the large damping and the excitation frequency shift created by the soil layers in the foundation generally reduces the higher frequency amplitudes of the accelerations at basement level within the buildings but increases the lower frequency acceleration amplitudes. For tall and medium-rise buildings this may increase the overall acceleration levels of the building compared to a rock based foundation, whereas for low-rise buildings this may reduce the story drift and thereby the overall structural strains.

Keywords: Earthquake, Site effect, Acceleration, Building, Response.

1 INTRODUCTION

Earthquake induced strong-ground-motion in Iceland has been monitored over the last three decades (Sigbjörnsson et al., 2014). In earthquake engineering practice in Iceland, site effects are generally not considered in earthquake resistant design, mainly because before construction starts, the relatively thin topsoil is in most cases removed from the uppermost competent rock (e.g., lava rock, hyaloclastite, dolerite, etc.). However, for lava rock the presence of pronounced site effects was reported after the earthquake in June 21, 2000 (Bessason and Kaynia, 2002). The study presented herein, revolves around two specific buildings located in Selfoss, a rural town in south-Iceland, which is located within the South-Iceland-Seismic-Zone (SISZ). Earthquake induced acceleration and ambient seismometer data is available for both buildings, in addition to structural analysis and finite element modelling.

Recorded data and observations made during three strong earthquakes within the South-Icelandic seismic zone, two in June 2000 and one in May 2008, with magnitudes of 6.5, 6.4 and 6.3 respectively (Sigbjörnsson et al, 2007 and 2009), revealed an interesting and somewhat unexpected phenomenon influencing structural response. The paper will discuss some of the key findings regarding the response characteristics observed and the relevance of the geological settings for earthquake resistance of similar buildings.

2 SURFACE GEOLOGY

The surface geology in South Iceland was mostly formed during and after the last ice age. The costal topography is of low elevation, approximately flat and largely covered with postglacial basaltic lavas, as well as tuff layers, intercalated with Quaternary sediments of mainly fluvial, glacial and glaciofluvial origin (Atakan et al., 1997).
The youngest lavas are from the Holocene (not more than 200 years old), while the oldest formations are up to 3.3 Myr old.

During glacial periods, Iceland was covered with a plateau glacier. During warmer interglacial periods, the ice melted and the glaciers retreated, which resulted in sea level changes of up to 200 m. The South Iceland Lowland was then, a seabed, accumulating marine sediments. During warm periods and towards the end of the Pleistocene, when the glaciers were retreating and the land was undergoing isostatic rebound, glacial streams formed thick sediment layers, composed chiefly of sand and fine-grained gravel.
In the postglacial period, some of these sediments were covered by lava, which adds to the complexity of the geological structure of the surface. The lava layers may be as thick as 10 m while the sediment layers can be up to 20 m thick or even more.
This has resulted in geological profiles consisting of recurring layers of basaltic lavas, as well as tuff layers, often with intermediate layers of sediments or alluvium. It will be demonstrated herein, that this geological structure has an effect on overall structural excitation and behaviour in earthquakes.

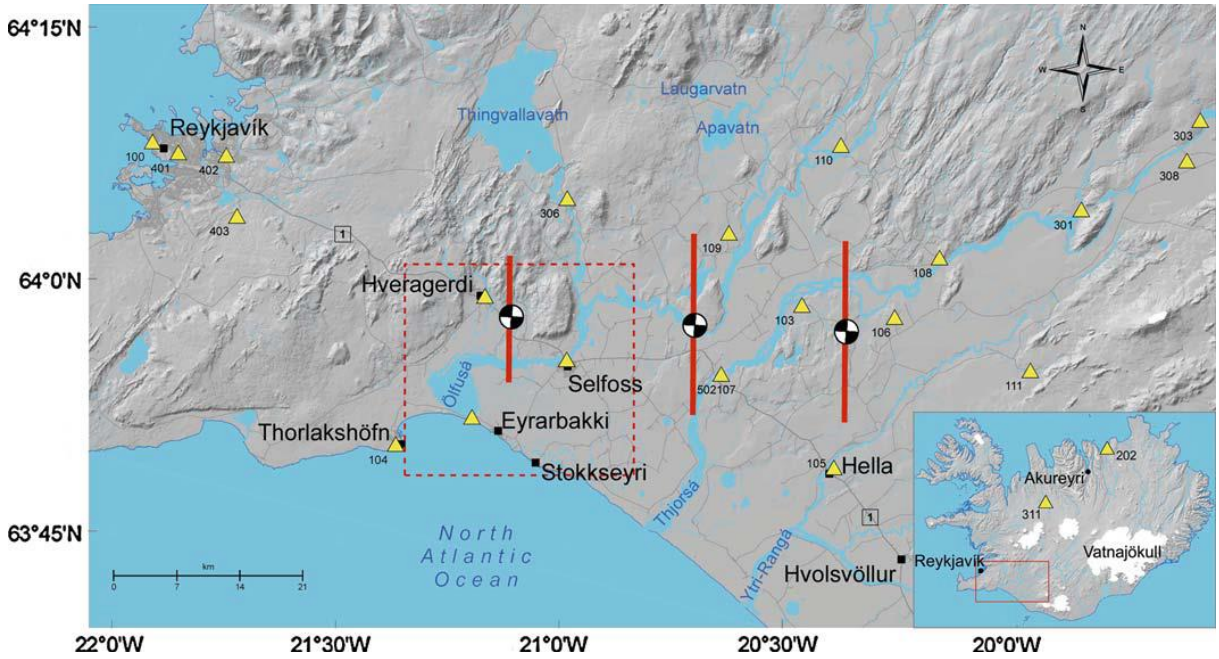


Figure 1 A map, showing the South-Iceland-Seismic-Zone, the epicentres of the Earthquakes in 2000 and 2008 and the location of the town of Selfoss (Sigbjornsson et al. 2009). The triangles show the locations of the recording stations of the Icelandic Strong-motion Network.

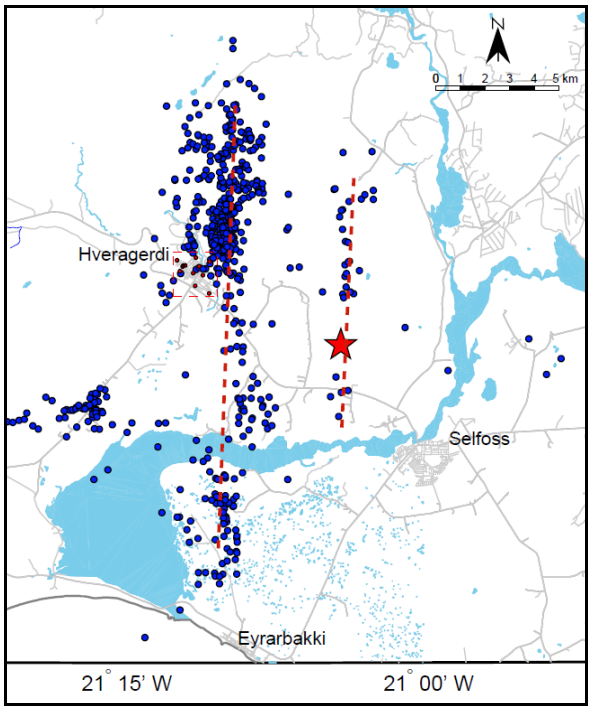


Figure 2 The N-S trending alignments of the seismicity distribution of aftershocks for the 15:45 UTC 29 May 2008 Ölfus earthquake (blue circles) indicate the location of the causative faults (dashed lines). The red pentagram shows the epicenter of main-shock.

3 THE EARTHQUAKE EVENTS

A damaging South Iceland earthquake sequence began on 17 June 2000 at 15:41, with an earthquake that had an epicentre just north of the rural village of Hella (see Figure 1). The earthquake had a surface wave magnitude of 6.6 and a moment magnitude of 6.5. It was followed by major seismic activity throughout the entire South Iceland Seismic Zone.

The second earthquake in the sequence occurred on 21 June 2000 at 00:52. It had a surface wave magnitude of 6.6 and a moment magnitude of 6.4. The epicentre was approximately 17km west of the epicentre of the first event (see Figure 1) (Sigbjörnsson et al. 2007).

A Third damaging earthquake occurred in South Iceland on Thursday 29 May 2008 at 15:45 UTC. The epicentre was in the Olfus District about 8 km north-west of the town of Selfoss (see Figure 2). The magnitude of the earthquake was 6.

The earthquake can be characterized as a shallow crustal earthquake. It occurred on two parallel, near vertical north-south trending right-lateral strike slip faults approximately 4.5 km apart. While the epicenter was located on the eastern fault, around 5 km N-W of Selfoss, the majority of the aftershocks occurred on the western fault that ruptured ~2 seconds after the eastern fault. The basic properties of this event are found to be similar to the characteristics of the South Iceland earthquakes in June 2000 (Sigbjornsson et al. 2009).

4 THE BUILDINGS

Both buildings studied herein, are located in the town Selfoss (see Figure 1 and 2). The riverbed of Ölfusá (e. Ölfus river) runs through the centre of Selfoss. On the west bank there is relatively solid bedrock from the last ice age both lava and tuff, ca 1.500.000 years old. On the east bank, on the other hand, there is the large post glacial Thjórsárhraun lava field ca 7.800 years old. The Thjórsárhraun lava is the biggest scoria lava field in Iceland exceeding 900 km^2 and may have flowed over distances of 120 km. The lava thickness may be up to twenty or thirty meters. The river has been running in its current riverbed from the time of Þjórsárhraun. As the old bedrock on the west side of the river is much more solid than the Þjórsárhraun lava the river has mainly been eroding the softer bedrock of the east bank.

4.1 The Town Hall

The Town Hall at Selfoss (see Fig. 3) is a cast-in-place reinforced concrete building with 3 stories and a basement. It is about 11 m high from ground level to the rooftop, and about the same distance from the basement floor to the top floor, with the basement reaching 4 meters below ground level. It is rectangular in plan, about 41 m long (east-west direction) and 13 meters wide (north-south direction). The structural system is composed of outer shear walls a shear core and two rows of interior concrete columns and interconnecting floor beams that carry the slabs. The orientation of the building is such that the length of the building approximately aligns along an ESE-WNW axis. The building was renovated and retrofitted in the period of 1997 to 2001.



Figure 3 The Town Hall at Selfoss, view from NE.

The building was instrumented in 1999 and earthquake induced acceleration data has been systematically collected there since. The instrumentation is located at two levels, the basement and the top storey (the 3rd floor if the ground floor is no. 1). A tri-axial accelerometer is located in the elevator shaft in the basement, measuring the three components of base (ground) acceleration. On the top floor three uni-axial accelerometers are located, one measuring motion in the E-W direction and two measuring in opposite corners (i.e. N-W and S-E) measuring motion in the N-S direction. This makes it possible to detect torsional effects in the building response. The sampling rate is 200 Hz.

The accelerations induced by the earthquakes of June 2000 and May 29, 2008 were recorded in the building, both at the basement level and on the third floor. The events in June 2000 had an epicentral distance of 32 km and 15 km from the building and the ground acceleration at the building site was less than 15% g (see Table 1). The structural capacity of the building was therefore not severely tested at that time.
The epicentre of event in May 2008, was less than 8 km away, and the peak ground acceleration (PGA) at the building site was 54% g. It is therefore not surprising that the Town Hall suffered some minor structural damage in this event such as visible cracks in the concrete walls. The damage was however not sufficient to change the structural characteristics of the building which continued to serve its function.
Unexplained dissimilarities are observed in the structural response characteristics for these two events. It is suspected that site effects and/or soil-structure-interaction effects are causing the differences observed. The peak accelerations recorded during these three main events are listed in Table 1.

Table 1 Peak accelerations recorded at the Town Hall in 2000 and 2008.

Date of event	Magnitude	Distance from site (km)	Peak ground acceleration (%g)			Peak response acceleration (%g)		
			Vert	N-S	E-W	W: N-S	C: W-E	E: S-N
June 17, 2000	6.5	32	2.9	7.6	5.5	14.6	12.1	15.8
June 21, 2000	6.5	15	6.8	12.7	11.2	30.2	21.4	29.2
May 29, 2008	6.3	8	26.6	53.8	33.4	74.6	47.3	68.2

4.2 The Bell Tower

The bell tower of the Church of Selfoss is a square 4 m by 4 m cross section, see figure cast-in-place, reinforced concrete shear wall building (see Figure 4). It is approximately 23 m high, making it one of the tallest building in Selfoss. The tower is connected to two small adjacent buildings, of an approximately 7 m in hight on the North and the East side.
The roof is made of timber girders and stiffeners of timber and a cooper cladding.

Three church-bells, 75 cm, 67 cm and 56 cm in diameter and weighing 240 kg, 170 kg and 100 kg, respectively, are at the top of the concrete structure. Each level of the tower is approximately 3 m in height having concrete staircase in between each level.
During the earthquake a fracture opened through the entire perimeter of the tower, see Figure 5. The fracture opened both on the outside of the tower as well as on the inside. The location of the crack is at the height of the adjacent buildings, i.e. at about 7 m from the ground. This location is vulnerable due to abrupt changes in the stiffness of the tower at

this height, but also there was also a construction joint at this level.



Figure 4 The bell tower of Selfoss church.



Figure 5 The crack in the Bell tower.

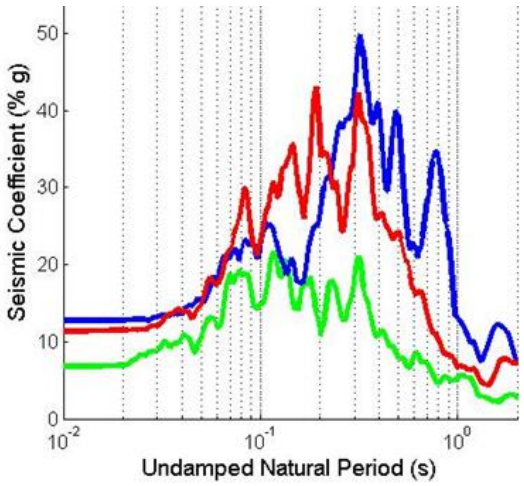
No instrumentation was in the bell tower when the three largest earthquakes occurred. The nearest instrument was located in the Town Hall of Selfoss about 350 m east of the tower.
After the earthquake on May 29, 2008, and the consequential damage to the tower, two strong-motion accelerograph units were installed on the top-floor of the tower in the south-east and north-west corner of the tower. The locations were selected to obtain the torsional motion of the structure. These two units monitored response to aftershocks and ambient vibration of the tower.

5 STRUCTURAL ANALYSIS

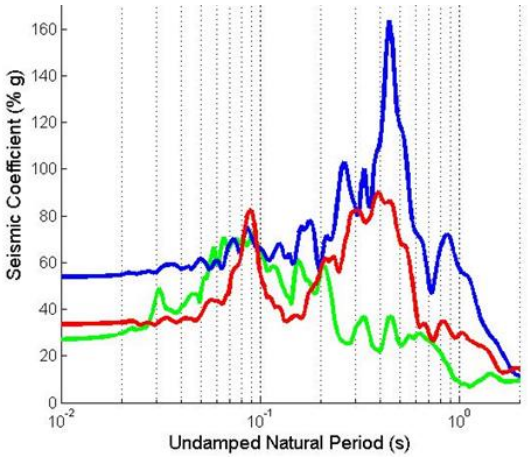
The behaviour and response of both buildings have been analysed on the bases of FE-modelling and recorded acceleration. In both instances it is observed that the recorded response cannot be described by a structural model of the buildings alone. This will be demonstrated further in the following.

5.1 The Town Hall

The instrumentation system in the Town hall recorded all three main events as well as many smaller earthquake events over the last 17 years. Herein the focus will be on two earthquakes, i.e. the M6.4 on June 21, 2000 and the M6.3 on May 29, 2008,
When comparing the recorded surface and response accelerations from these two events a clear difference in the frequency content and thereby the characteristics of the response is noticed. The response spectra are computed from the recorded accelerations in the basement and shown in Figure 6. The horizontal components show a significant response from about 0.1 s up to 0.8 s, for both events. However, for the 2008 event a strong response peak is observed at 0.4-0.5 s. This response peak is likely caused by local site effects that control the frequency content of the surface motion. The vertical acceleration response seems less affected by possible site-effects but the response spectra for the May 2008 event is slightly shifted towards the low-period range. This is most likely caused by the near-field characteristics of the motion, enhancing the contribution of the low period pressure wave.
Figures 7 and 8 reveal the frequency content of the relative accelerations at the third floor during these two main events. Comparing the E-W components (see Figure 7), shows more or less the same spectral peaks but they are shifted about 1 Hz towards lower frequency values for the 2008 event.



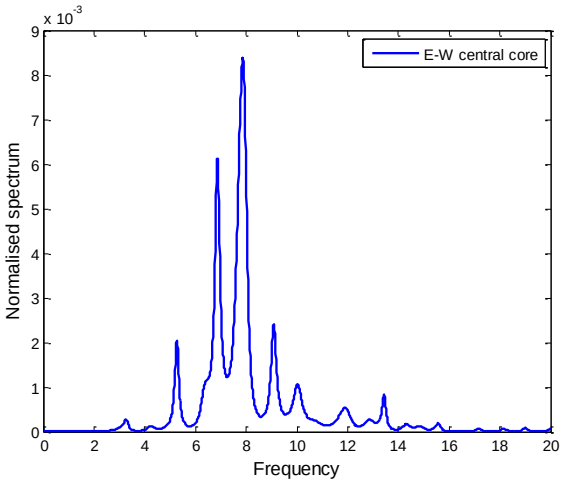
(a)



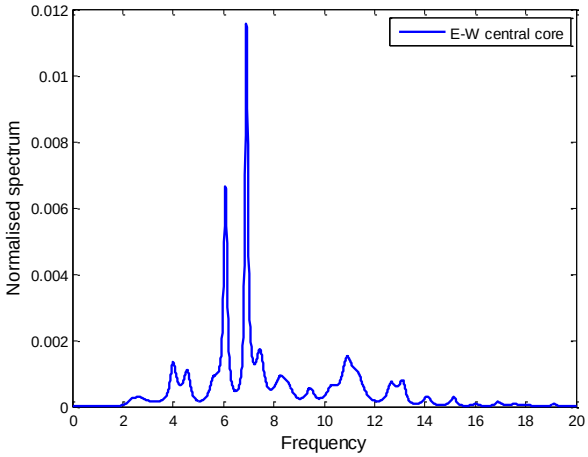
(b)

Figure 6 Response spectra evaluated from the basement records. (a) The event on June 21. 2000. (b) The event on May 29. 2008. The blue line is the N-S component, red line is the E-W component and the green line is the vertical direction. The damping is 5% of critical damping.

Comparing the N-S components (see Figure 8), a much more dramatic difference is observed. Again the frequency peaks are shifted about 1 Hz towards lower frequency values for the 2008 event, but it is also seen that the energy is distributed between 2 and 5 Hz in the 2008 event whereas it was mainly distributed between 5 and 10 Hz in the 2000 event. This dramatic shift in frequency content may indicate that the site-effects dominate the response from the earthquake in 2008. The difference in the response between the east and west gable demonstrates that the east side of the building has considerably more stiffness in the N-S direction than the west side of the building.



(a)

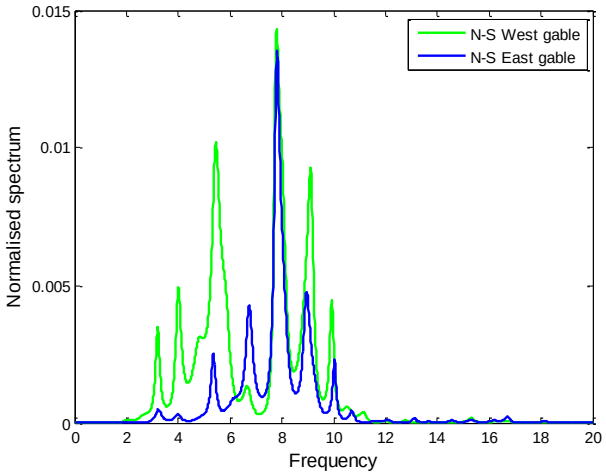


(b)

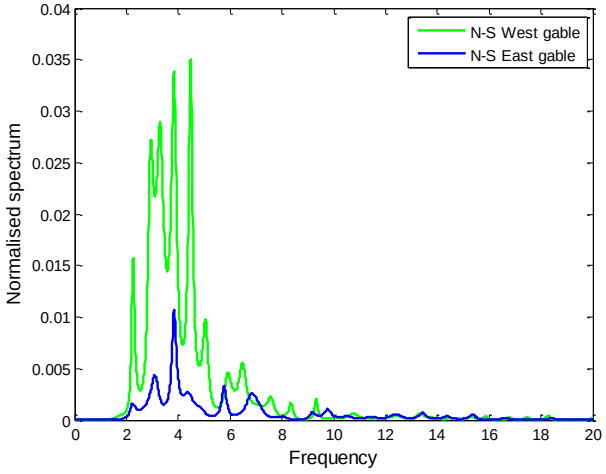
Figure 7 Power spectral densities of relative acceleration response on the third floor. (a) The E-W comp. from the event on June 21. 2000; (b) The E-W comp. from the event on May 29. 2008.

A system identification was done using a combined subspace algorithm provided by the MACEC toolbox (Reynders et al. 2011). The basement records were used as an input in an MIMO analysis. The shift in frequency for comparable mode shapes was confirmed and several modes are found in the 2008 event that are not seen in the 2000 event. Figure 8 shows the H/V-ratio (Nakamura 2008) evaluated based on the recorded basement motion in June 2000 and May 2008. As can be seen the H/V-ratio further establishes the difference in the soil-rock response between the two events studied. In 2000 the main soil-response is seen to be at 8 and 15 Hz, whereas in 2008 the main soil-response is seen at 2 and 4 Hz. This indicates that the shear wave velocities in the rock-soil

layers underneath the building were considerably lower in 2008 than in 2000.



(a)



(b)

Figure 7 Power spectral densities of relative acceleration response on the third floor. (a) The N-S components from the event on June 21, 2000; (b) The N-S components from the event on May 29, 2008.

Two different finite element models have been made of the Town Hall, using Ruaumoko-3D (Stray, 2010) and SAP2000. Both models verify, along with system identification of data, that the fixed-base building has natural frequencies above 6 Hz, as seen in figure 7(a) and 8(a).

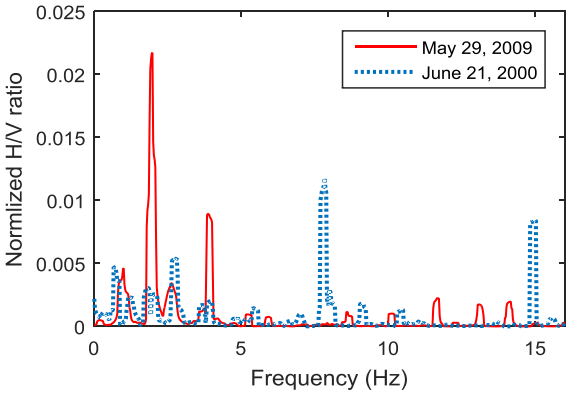
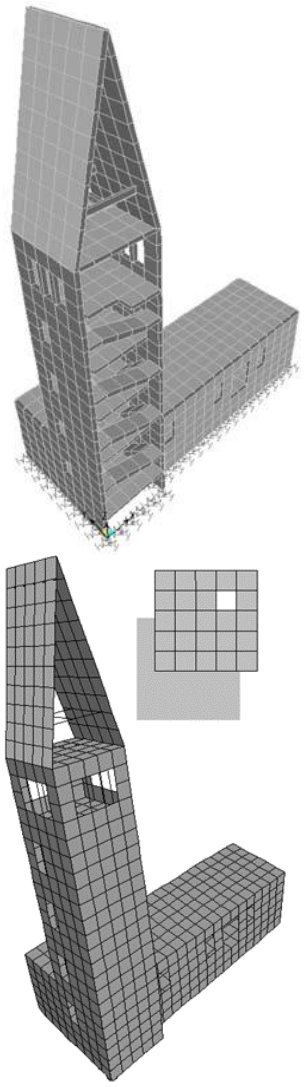


Figure 8 Normalised H/V-ratio as a function of frequency for the earthquakes in 2000 and 2008.

5.2 The Bell Tower

A three-dimensional linear finite element model of the tower was created using the finite element computer programs SAP2000 and ETABS (Bardarson, 2009). The model was based on the design drawings of the tower as well as an on-site survey and measurement of the dynamic modulus of elasticity. The tower was modelled using shell and frame elements. The FE model (see Figure 9) was designed to represent the structural geometry as accurately as possible and the weight of the roof structure and the church bells was included to insure a correct mass distribution.



(a) *(b)*

Figure 9 The Finite element model with spring supports (a) and its first mode of vibration (b). The first mode has a frequency of 5 Hz.

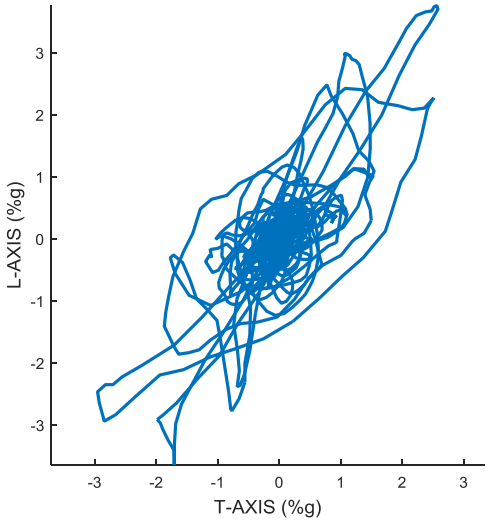


Figure 10 A plot of the two horizontal acceleration components recorded in an aftershock.

During test runs the model was not found to represent the dynamic behaviour observed in the aftershock and ambient excitation data recorded in the tower. The model was considerably stiffer, with a first natural frequency of 7.5 Hz, whereas the recorded data showed response at 5 Hz (0.2 s). After some consideration, it was determined necessary to consider foundation-structure interaction in the modelling to reproduce the observed behaviour. The foundation-structure interaction was modelled by placing springs at each foundation joint of the structure. According to Wilson (2000), the use of appropriate site-dependent free-field earthquake motions and selection of realistic massless springs at the base of the structure is the only modelling assumptions required to include site and foundation properties in earthquake analysis of most structural systems.

Ambient vibrations have been successfully applied to calibrate computational models in dynamic analysis of civil engineering structures (Jaishi and Ren, 2005). After the introduction of properly tuned springs, the model was found to correspond well with the recorded data. Figure 10, shows a plot of the two horizontal acceleration components for an aftershock record. The main vibrations follow a diagonal pattern, consistent with the first mode of the structure as calculated by the FE-model (see Figure 9b).

In 2002 test holes were drilled at four locations, along the Ölfusá river. One of them at the riverbank close to the church. Based that hole the geological profile shown in Figure 11 was put forward for the church site by Imsland (2002).

The tower and the layered soil profile characterized by velocity reversals was modelled as a classically damped 5 degree-of-freedom linear oscillator. Where each model component, i.e. the tower, the lava, scoria and sediment layers, have a mass and stiffness. The mass and stiffness of the tower is taken from the FE-model whereas the mass and stiffness of the soil layers are based on reasonable estimates of density (2200, 2000 and 1800 kg/m^3) and shear velocity (1800, 1200 and 200 m/s). The effective area of the tower foundation is used to define the

masses. Eigen frequency analysis gave the results shown in Figure 12. It can be noticed that the first mode has a frequency of 5.2 Hz, which corresponds well with the acceleration recordings and the updated FE-model. Excluding the tower from the model and considering only a soil-rock column of unit area gave the same frequency for the first mode, i.e. 5.2 Hz. It should be noted that modes 2 and 3 have a much higher natural frequency of 40 and 72 Hz.

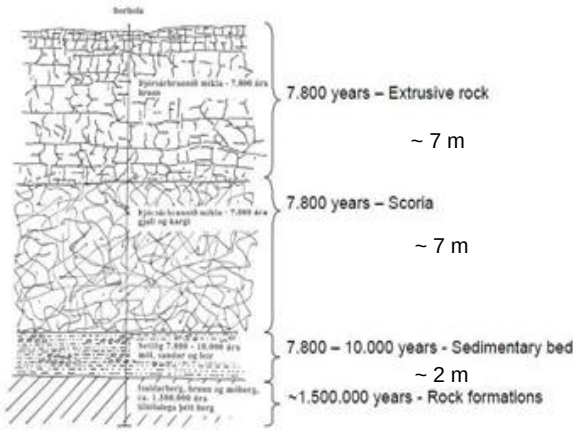


Figure 11 A hypothetical rock-soil profile

5.3 Evaluation of HSVR

Spectral analysis of microseismic (ambient) vibrations via the HVSR method are used to estimate the site response in urban environment (D'Amico, 2008). Microseismic data is easily obtained and can provide additional constraints on site characterization using the HVSR method.

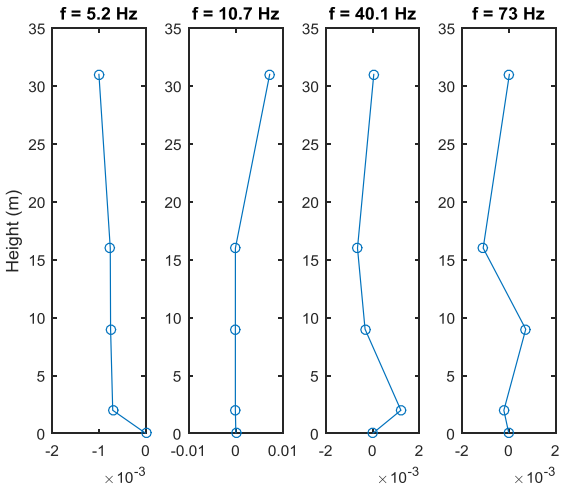
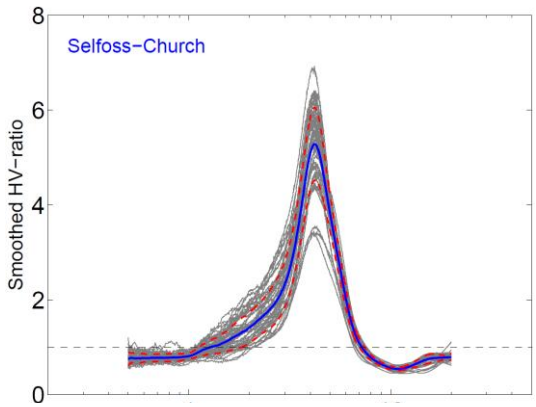


Figure 12 The modes of vibration of a simple soil-structure model.

Continuous ambient noise recordings of minimum one-hour duration were performed at ISMN sites in Selfoss, as well as in the church, using REF TEK 130-01 Broadband Seismic Recorders and Lennartz LE-3D/5s Seismometers. Raw data from these sites have been analysed using Nakamura's method, Horizontal to Vertical Spectral Ratio (HVSR) (see Nakamura, 2012). The HVSR method uses three-component single station ambient noise records, and involves the ratio of the combined horizontal frequency spectrum, H, to vertical, V, frequency spectrum at the studied site. The final mean HVSR for each site was determined by calculating the geometric mean of the HVSRs from all the individual time windows analysed. The results are shown in Figure 13. The HVSRs figures show magnification at frequency between 4 and 5 Hz, which is observed very strongly at the church site, but less so at the Town-Hall. Then there is some response at 7 Hz in the plot for the Town-Hall.

It is well know that the shear stiffness of the soil layers is very dependent on the state of shear stress in the soil, decreasing rapidly with increased strain levels (Kramer, 1996). Therefore, ambient measurements of this type are not conclusive regarding site effects in strong near-fault earthquakes, but it is interesting to see that the frequency of the HSVR response at the church sites more or less coincides with previous evaluation based on monitoring and structural modelling.



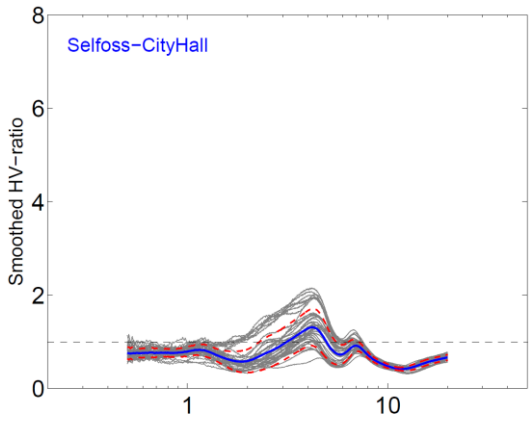


FIGURE 13 Mean HVSR +/- one standard deviation from ambient noise measurements. The grey lines show 20-min ambient noise windows used to derive the mean HVSR (blue line) and standard deviation (red dashed line).

6 DISCUSSION AND FINAL REMARKS

The analysis confirm the influence of the soil-rock layers beneath the buildings on the building response. It seems clear that the behaviour of the different soil-rock layers underneath the building should be recognized and included in the structural modelling. Especially, the soft sedimentary layer that exists underneath the younger lava layers. When subjected to earthquake motion of different intensity, the material properties will change in a non-linear fashion in terms of shear strength and damping. The amount of strains in the sedimentary layer will, to a large degree control the frequencies of response. There are also indications that the damping effects created by the soft layer could reduce the amplitude of the ground accelerations, as well as lowering the frequency content of the excitation.
The site effects/soil-structure interaction observed in the earthquake in May 29, 2008, has most likely been beneficial for the earthquake response of the buildings.
In the wake of the latest South-Iceland earthquake sequence that started in 2000, the importance of the foundation on the overall earthquake behaviour of buildings has become clear. A good understanding and modelling methods that include soil-structure interaction and or site-effects are therefore essential, both to insure a reliable design of new structures as well as for estimating the risk of damage for existing buildings. The case studied herein, is intended to serve as a contribution to increased awareness of the importance of site-effects and soil-structure interaction.

7 REFERENCES

Atakan K, Brandsdóttir B, Halldórsson P, Friðleifsson G. (1997). Site Response as a Function of Near-Surface Geology in the South Iceland Seismic Zone. Nat Hazards, 15:139–64.

Bárðarsson, H. (2010). Assessment of earthquake-induced structural behaviour and damage, MSc thesis, University of Iceland.

Bessason, B. and Kaynia, A.M. (2002). Site amplification in lava rock on soft sediments, Soil Dynamics and Earthquake Engineering, 22(7), pp.525-540.

D'Amico V, Picozzi M, Baliva F, Albarello D. (2008) Ambient noise measurements for preliminary site-effects characterization in the urban area of Florence, Italy. Bull Seismol Soc Am; 98:1373–88.

Imsland, P. (2002) Borun í bakka Ölfusár í janúar 2002 – stutt greinargerð (in Icelandic).

Kramer, S. L. (1996). Geotechnical earthquake engineering. Prentice Hall.

Nakamura Y. (2008). On the H/V spectrum, The 14th World Conference on Earthquake Engineering, Beijing, China. Y.

Reynders, E., Schevenels, M. and De Roeck, G. (2011). MACEC 3.2: A MATLAB toolbox for experimental and operational modal analysis- Users Manual, Report BWM-2011-01, Katholieke Universiteit Leuven.

Sigbjörnsson, R., Ólafsson, S. and Snæbjörnsson, J.Th (2007). Macroseismic effects related to strong ground motion: a study of the South Iceland earthquakes in June 2000. Bull Earthquake Eng., 5(4):591-608.

Sigbjörnsson, R. Ólafsson, S. Rupakhety, R. Halldórsson, B. Acharya P. Snæbjörnsson, J. (2014) Strong-motion monitoring and accelerometric recordings in Iceland, 2nd European Conf. on Earthquake Eng. & Seismol. (2ECEES), Istanbul, Turkey, paper no. 2034.

Sigbjörnsson, R., Snæbjörnsson, J.Th., Higgins, S.M., Halldórsson, B. and Ólafsson, S. (2009). A note on the Mw 6.3 earthquake in Iceland on 29 May 2008 at 15:45 UTC. Bull Earthquake Eng., 7(1), DOI:10.1007/ s10518-008-9087-0.

Stray O. (2010). Earthquake induced response and soil-structure interaction effects. MSc thesis, University of Stavanger.

Jaishi, B., Ren, W.-X., 2005. Structural Finite Element Model Updating Using Ambient Vibration Test Results. Journal of Structural Engineering 131, 617–628.

Wilson, E.L., 2002. Three-Dimensonal Static and Dynamic Analysis of Structures: A physical approach with emphasis on earthquake engineering, 3. ed. Computers and Structures, Berkeley, California USA.

On the HVSR estimation at Icelandic strong-motion stations

B. Halldorsson
Earthquake Engineering Research Centre, University of Iceland, Selfoss, Iceland (skykkur@hi.is)
Faculty of Civil and Environmental Engineering, School of Engineering and Natural Sciences, University of Iceland, Reykjavík, Iceland. (EERC & FCEE, SENS, University of Iceland)

C. I. Olivera
ECS Mid-Atlantic, LLC, 6710 Oxon Hill Road, National Harbor, Maryland 20745, USA.

S. Rahpeyma, S. Ólafsson
EERC & FCEE, SENS, University of Iceland

R. A. Green
Department of Civil & Environmental Engineering, Virginia Tech, Blacksburg, VA, USA.

J.Th. Snæbjörnsson
School of science and engineering, Reykjavik University, Iceland

ABSTRACT
In this study Nakamura's H/V Spectral Ratio (HVSR) method was applied to ambient noise data and earthquake recordings collected at selected stations of the Icelandic Strong-motion Network (ISMN). In particular, continuous measurements of ambient noise, with minimum one-hour recordings, were performed while the strong-motion data set consisted of earthquake events recorded by the ISMN. The ambient noise data was analysed using various parameters such as time window duration, smoothing factor, different methods of averaging the two horizontal components and mean HVSR, respectively. For 20 minute recording window of ambient noise, applying the Konno and Ohmachi smoothing function with B = 20, combining the horizontal components and averaging the individual HVSR curves using the geometric mean, a stable HVSR amplification curve was obtained for a given site. The earthquake recordings were analysed using this common procedure by analysing the S phase instead of the entire time history. This unified procedure is applied in the HVSR method for characterization of the contribution of localized site effects at strong-motion stations in Iceland so that any similarities or differences observed can be attributed to factors other than data processing itself. The study serves as the first look at HVSRs at selected ISMN recording sites in Iceland using earthquake data. The results are expected to provide better insight into the localized site effects in view of the lack of geotechnical information which hampers the understanding of the relationship between Iceland's characteristic sub-surface materials and their dynamic response.

Keywords: HVSR, site effects, ISMN, lava, rock, soil.

1 INTRODUCTION

Iceland is located on the Mid-Atlantic Ridge, the diverging plate boundary of the North American and Eurasian plates in the North Atlantic Ocean. Crossing the island from southwest to north, the onshore part of the plate boundary shifts eastward, resulting in two transform zones: the South Iceland Seismic Zone, SISZ, which is completely onshore and the Tjörnes Fracture Zone, TFZ which is largely offshore. Destructive earthquakes in these regions have been well documented in historical annals of the last 1000 years. In the SISZ strong earthquakes up to magnitude 7 have repeatedly taken place in the past, generally as single events or sequences of magnitude 6-7 earthquakes every 100-120 years or so (Einarsson et al. 1981; Stefánsson and Halldórsson 1988; Einarsson 1991; Bjarnason et al. 1993; Stefánsson et al. 1993; Ambraseys and

Sigbjörnsson 2000; Pagli et al. 2003; Bellou et al. 2005). Consequently, the SISZ and TFZ are the regions in Iceland that have the greatest potential for the occurrence of large earthquakes, and thus, have the highest earthquake hazard (Sólnes et al. 2004). In fact, the most expensive natural disaster in Iceland was the 29 May 2008 M_w6.3 Ölfus earthquake in South Iceland which caused widespread damage. Site effects, or the amplification (or deamplification) of earthquake ground motion amplitudes, have long been known to be a major factor influencing the distribution of earthquake damage. In the official standard for earthquake resistant design in Iceland (Eurocode 8) the site effects are specified in terms of the average shear wave velocity in the uppermost 30 meters ($V_{S,30}$). The majority of the free-field stations of the Icelandic Strong-motion Network (ISMN) have thus been estimated to fall into the rock class ($V_{S,30} > 750$ m/s). However, this site classification has been based on surface geology because quantitative information on physical parameters of the geologic profile beneath the recording sites of the ISMN is virtually nonexistant.

Earthquake ground motions at a given site are often amplified over a narrow frequency range due to the dynamic response of local soil layers below the site. For particularly intense strong-motions, deamplification of high-frequency waves due to nonlinear soil behaviour may be observed. The large impedance contrast between the few tens of meters of soil and underlying bedrock has been shown to affect the amplification of seismic waves, somewhat disproportionally compared to the overall length of the propagation path from the source to site (Anderson et al. 1996; Boore and Joyner 1997). Where enough borehole and strong-motion data exists, e.g., in California, surface geology, which at least to the first approximation can be assumed to be representative of the of the uppermost few tens of meters of the geologic profile , has been found to correlate with $V_{S,30}$ (Wills et al. 2000). Surface geological mapping however cannot be expected to apply between regions with different geological evolutionary history and tectonic environment.

The surface geology of Iceland was formed during and after the last Ice Age. During the glacial period, Iceland was covered with a plateau glacier. It was not until the warmer interglacial periods and towards the end of the Pleistocene did sediment layers begin to form. As the glacier was retreating and the land rising, glacial streams formed thick sediment layers, composed primarily of sand and fine-grain gravel. In the postglacial period, some of those sediments were covered by lava, which added to the complexity of the geological structure of the surface in Iceland. Hence, in general, the surface geology of Iceland is described as a pile of basaltic lavas, as well as tuff layers, often with intermediate layers of sediments or alluvium (Einarsson and Douglas 1994). In addition, the surface geology is further complicated by fractures, fissures and faults of tectonic origin (Clifton and Einarsson 2005; Angelier et al. 2008). For practical purposes, the topsoil is easily removed resulting in most sites being considered as rock. However, a comprehensive study on site characterization at Icelandic strong-motion stations has not yet been carried out.

One of the most common procedures for estimating site effects, the horizontal-to-vertical spectral ratio (HVSR) method is based on recordings of ground shaking as a function of time in the horizontal, H, and vertical, V, directions, respectively, and calculating their amplitude as a function of frequency (Nakamura 1989). Analyzing the HVSR as a function of frequency allows one to capture the characteristics of the site conditions that may amplify earthquake shaking. Although the method's physical basis and theoretical background have been questioned (Lachetl and Bard 1994; Mucciarelli 1998), the advantages of the approach are several fold, foremost being that it is a relatively inexpensive and easy to implement for obtaining information needed in seismic hazard and risk analysis (Atakan et al. 1997; Bessason and Kaynia 2002).

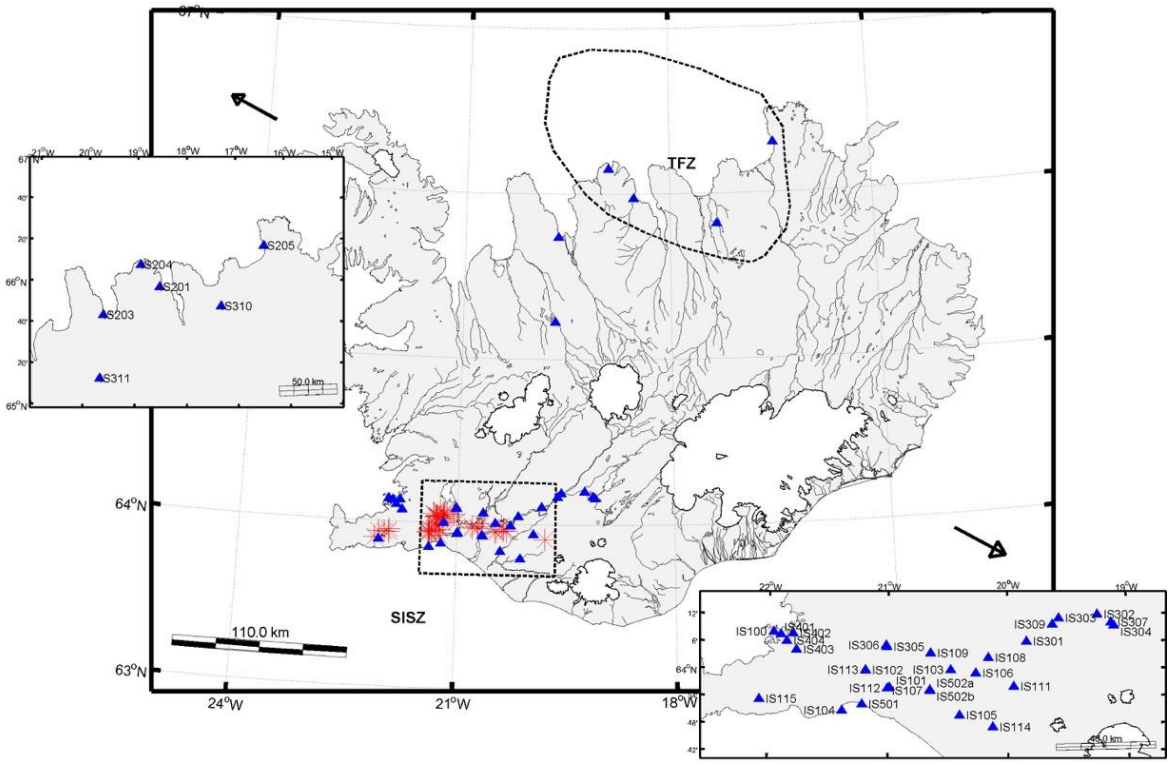


Figure 1. Stations of the Icelandic Strong-motion Network (represented by blue triangle symbols) and earthquake events (represented by red stars) recorded since its deployment (up to 2010). The inset picture at the bottom right shows the ISMN strong-motion stations along with station ID-codes with respect to the South Iceland Seismic Zone, SISZ, in the lowlands of south Iceland. The inset picture at the top left shows the ISMN strong-motion stations in the Tjörnes Fracture Zone, TFZ, in north Iceland.

The current study aims at investigating the characteristics of site response at selected strong-motion stations in Iceland shown in Figure 1. This study uses the HVSR method on earthquake data and can be considered as complementary to a study using microseismic data (Olivera et al. 2014). This study also augments the previous one by presenting results from a sensitivity analysis in determining the optimal parameters used in generating reliable HVSR from microseismic data, which were also used for estimating HVSR from earthquake data. As in the previous study, the aim is to estimate local site effects and relate to site characterization in terms of HVSR amplitudes and the corresponding predominant frequencies.

2 MICROSEISMIC DATA AND HVSR PARAMETER ESTIMATION

The guidelines published by SESAME for HVSR analysis (Bard and SESAME-Team 2005) were considered in this study in an attempt to test the procedure for processing both ambient noise and earthquake data sets for HVSR analysis at Icelandic sites. For ambient noise data and earthquake recordings, the procedure would include all steps for HVSR analysis, from selecting a window length for analysis, merging the two horizontal components of the Fourier Amplitude Spectra, FAS, smoothing the combined horizontal, H, and vertical, V, components of the FAS, and calculating the mean HVSR for each site. The tests were carried out on the microseismic data recordings at four different stations exhibiting different HVSR signatures. Only the results for one station are shown herein, the Selfoss church station (IS117) which is located on lava rock but exhibits a clear HVSR predominant frequency corresponding to a relatively high amplification. For this purpose, continuous measurements of ambient noise with minimum one-hour recordings, were performed using a REF TEK 130-01 Broadband Seismic Recorder

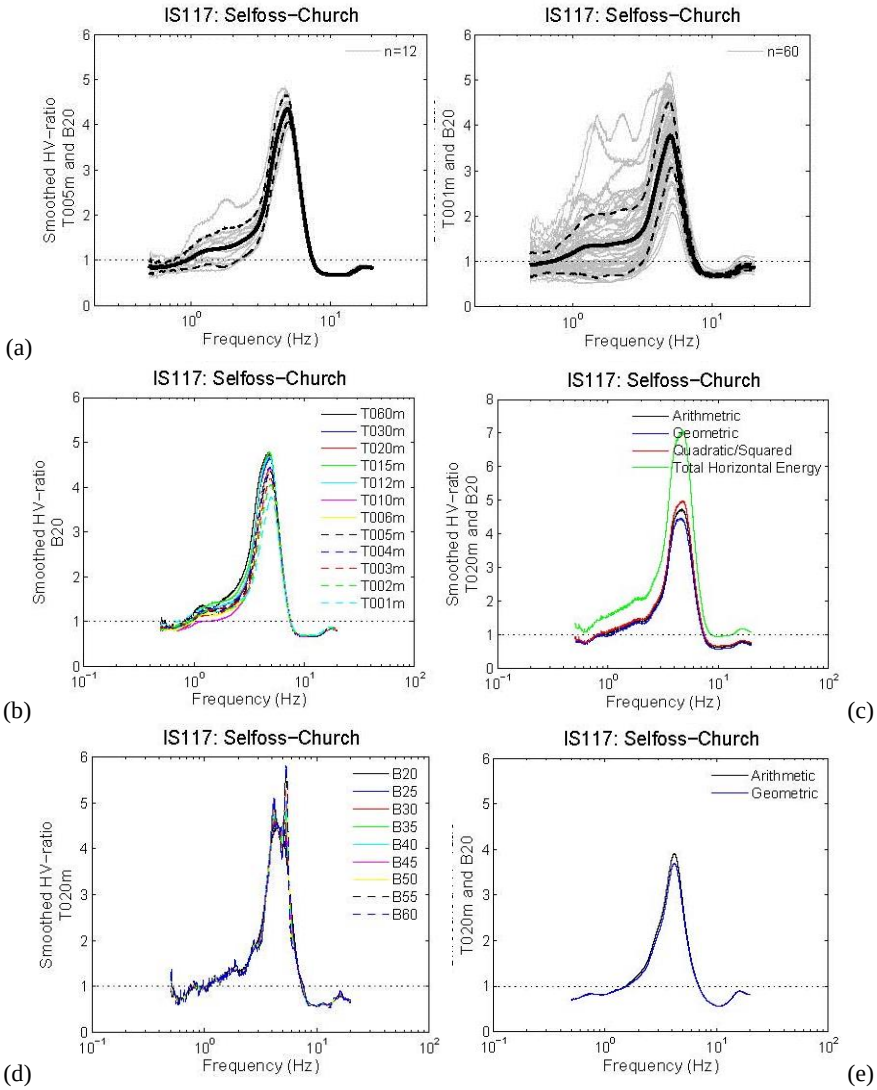


Figure 2. The HVSRs from test site IS117 used to investigate the effects of (a) different window lengths of 5 minutes (left) and 1 minute (right) for the same 60 minute microseismic recording, (b) (c), different methods for merging the horizontal components (d), different values for the Konno and Ohmachi smoothing coefficient, B (e), arithmetic and geometric mean on determining the mean HVSR, using twelve 20 minute time windows of ambient noise data.

and Lennartz LE-3D/5s Seismometer from the Icelandic instrument bank, Loki, which is operated through the Icelandic Meteorological Office, IMO.

One 60-minute recording of ambient noise was selected and divided into time windows of varying lengths (1, 2, 3, 4, 5, 6, 10, 12, 15, 20, 30, and 60 minutes) on which HVSR analyses were performed to determine the effects of various window lengths on the mean HVSR of a site. The variations of HVSRs of the different window lengths are shown for IS117 in Figure 2a. In an attempt to further investigate the influence of window lengths on the mean HVSR of a site, Figure 2b compares the mean HVSRs for all the window lengths considered. Despite the inconsistencies observed in Figure 2a, Figure 2b shows that the influence of the window length on the mean HVSR of this site is insignificant. These findings allowed the optimal window length of 20 minutes to be determined and used for HVSR analysis of ambient noise recordings. There is an increased inconsistency among individual HVSRs are found for window lengths shorter than 20 minutes.

For ambient noise data and earthquake recordings, the horizontal component of motion used in the HVSR method is obtained by combining the FAS of the two orthogonal horizontal components. The most commonly

used methods for combining both horizontal components in HVSR analysis are the following:

Arithmetic mean

$$H(f) = \frac{N(f) + E(f)}{2} \quad (1)$$

Geometric mean

$$H(f) = \sqrt{N^2(f) * E^2(f)} \quad (2)$$

Quadratic/Squared mean

$$H(f) = \sqrt{\frac{N^2(f) + E^2(f)}{2}} \quad (3)$$

Total horizontal energy

$$H(f) = \sqrt{N^2(f) + E^2(f)} \quad (4)$$

where $H(f)$ is the combined horizontal component FAS and $N(f)$ and $E(f)$ are the (two orthogonal) horizontal components of the FAS as a function of frequency, respectively.

In an effort to compare the above methods, a test was conducted at IS117 where one 20 minute time window of ambient noise was selected and HVSR analysis conducted using the four methods given by Equations (1) to (4). As observed in Figure 2c, HVSR results are consistent in overall general shape, predominant frequency, and amplification, except for the total horizontal energy method. Therefore, the geometric mean was selected to merge the horizontal components.

Prior to computing the HVSR the horizontal and vertical components can be smoothed (which in fact, is highly recommended and done in nearly all HVSR studies). The Konno and Ohmachi smoothing function is the most used and recommended for HVSR analysis (Konno and Ohmachi 1998):

$$S(f) = \left[\frac{\sin\left(B \cdot \log\left(\frac{f}{f_c}\right)\right)}{B \cdot \log\left(\frac{f}{f_c}\right)}\right]^4 \quad (5)$$

where f is the frequency, f_c is the central frequency, and B is the bandwidth (or smoothing) coefficient. The smoothing coefficient may vary between 0 and 100, where a coefficient 0 gives a very strong smoothing and a coefficient of 100 provides a very soft smoothing. To further investigate the effects of smoothing coefficients on HVSR analysis, one 20-minute time window of ambient noise was selected and smoothed using coefficients ranging from 20 to 60. The HVSR results from the test are presented in Figure 2d. The general overall shape, predominant frequency, and amplification are consistent irrespective of the smoothing coefficient applied in HVSR analysis. A smoothing coefficient of 20 was selected to smooth the combined horizontal component of the FAS for both ambient noise and earthquake recordings in HVSR analysis.

The final step in HVSR analysis is determining the mean HVSR for each measurement site. For both ambient noise and earthquake recordings, the mean HVSR for a site is determined by calculating the average of all the HVSRs computed for each selected time window. Although the geometric mean is the most commonly used, the arithmetic mean has also been used in HVSR studies. They are defined as follows:

Arithmetic mean

$$A(f) = \frac{\sum_{i=1}^{n} a_i(f)}{n} \quad (6)$$

Geometric mean

$$A(f) = \sqrt[n]{\prod_{i=1}^{n} a_i(f)} \quad (7)$$

where $A(f)$ is the mean HVSR of a site as a function of frequency, $a_i(f)$ is the HVSR for one time window, and n is the total number of available time windows used to derive the mean HVSR for each site. For station IS117 the results are shown in Figure 2e; the mean HVSRs are identical irrespective of the method used to complete the task. Therefore, the final mean HVSR for ambient noise and earthquake recordings for each site was determined by calculating the geometric mean of the HVSRs from all the available time windows at a measurement site.

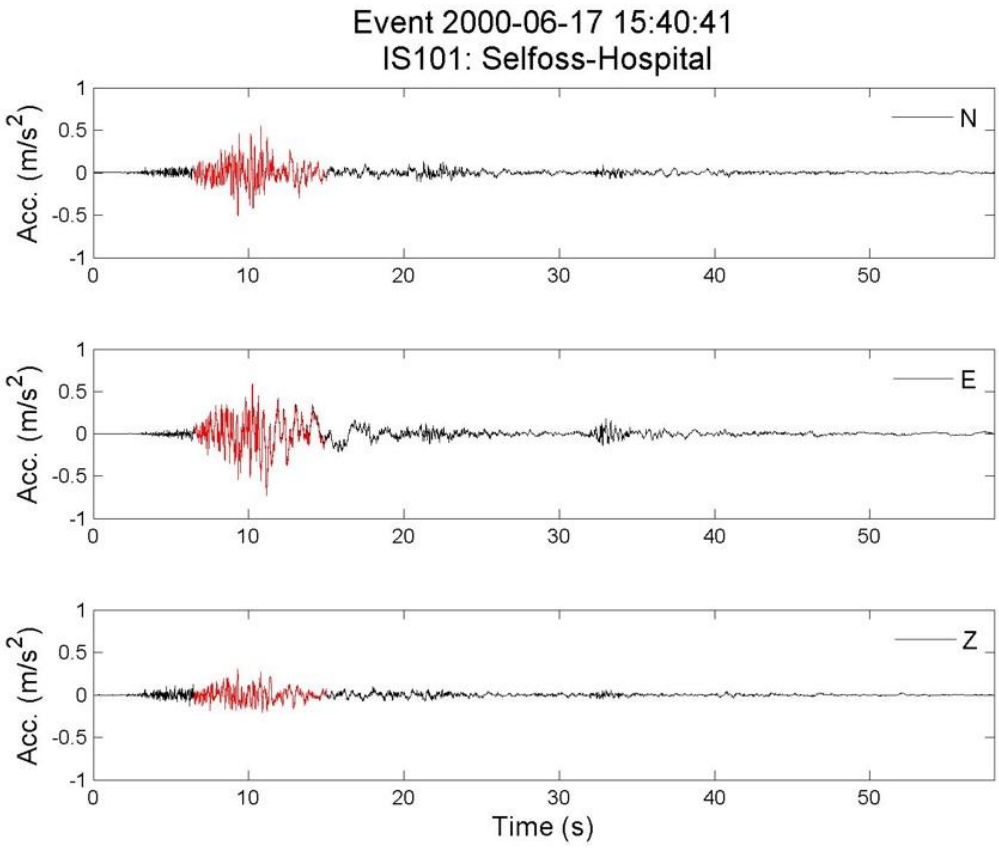


Figure 3. Recorded acceleration at ISMN station IS101 for the earthquake event of 17 June 2000 at 15:40 (M_w6.50, epicentral distance 30 km). The highlighted area indicates the S-phase of the recorded earthquake event on which HVSR analysis was conducted.

In this way a unified procedure was implemented to consistently process ambient noise data and earthquake recordings: (a) calculating the Fourier Amplitude Spectra for the selected time window and combining both horizontal components using a geometric mean, (b) applying the Konno and Ohmachi smoothing function with a smoothing coefficient of $B = 20$, and (c) creating a horizontal, H, to vertical, V, spectral ratio for the selected time window. The final mean HVSR for each site was determined by calculating the geometric mean of the HVSRs from all the individual time windows, from step (c) above. In this way, any similarities or differences observed can be attributed to factors other than data processing itself. For ambient noise data, 20 minute time windows were selected for HVSR analysis (Olivera et al. 2014), whereas for strong-motion data, the S phase of the earthquake recordings was selected as the time window for HVSR analysis.

3 STRONG-MOTION DATA

Over the past three decades the ISMN has collected hundreds of ground response time series (e.g., earthquake event recording shown in Figure 3) (see e.g., Table 2 in Sigbjörnsson et al. 2014). The recordings by the ISMN are accessible within the framework of the ISESD-project (Internet-Site for European Strong-Motion Data) (Ambraseys et al. 2004). Station locations (see Table 1 in Sigbjörnsson et al. 2014) were selected on the basis of the geographic distribution of the population and locations of industrial power plants, and main lifeline systems (Sigbjörnsson et al. 2004). The network consists of 40 permanent stations, approximately half of which are free-field (Sigbjörnsson et al. 2004; Sigbjörnsson and Ólafsson 2004). The instruments are located inside buildings for two reasons: (1) the severe climate conditions in Iceland make it difficult and expensive to operate sensitive

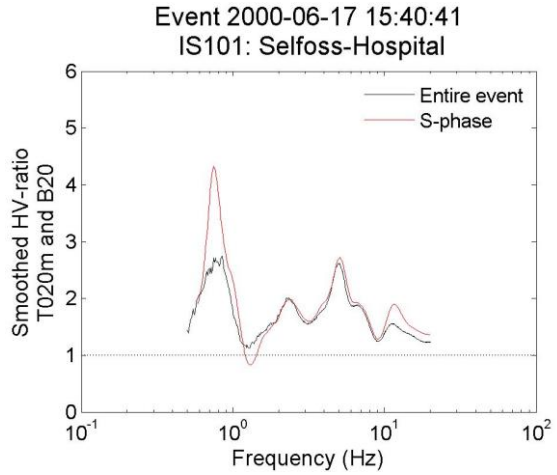


Figure 4. Comparison of the HVSRs computed over the entire earthquake event (black) and the S-phase only (red) of the acceleration time history shown in Figure 3.

equipment outdoors and (2) to ensure that the data obtained represent the direct seismic effects on the structural foundations. The instruments act in triggered mode detecting events when the ground acceleration exceeds a prescribed threshold (Sigbjörnsson et al. 2014).

In regards to earthquake recordings, the selection of the time window for HVSR analysis of strong-motion data required an investigation of the influence of different phases of an earthquake event on HVSR analysis, particularly the S phase. Previous studies using the HVSR method with strong-motion data have interchangeably used different parts of an earthquake recording. While some studies have used the entire earthquake recording (Mucciarelli et al. 2003; Triantafyllidis et al. 2006), most have concentrated on the S phase (Lermo and Chávez-García 1993) for HVSR analysis of strong-motion data because the S phase offers estimates of local amplifications in addition to predominant frequencies (Lermo and Chávez-García 1993). In the case of short source-to-site distances where it is difficult to separate the P and S arrivals, and thus difficult to isolate the S phase, studies have resorted to using the entire earthquake recording for HVSR analysis. In this study an investigation on the use of an entire recording versus the S phase for HVSR analysis was conducted. In general, minimal differences were observed when the time history used contained the P, S, and coda waves versus only using the S waves and first part of coda. However, in some cases discrepancies were observed at low-frequencies, an example of which is shown in Figure 4 for the recording shown in Figure 3. Nevertheless, in this study the S phase of earthquake recordings is used in HVSR analysis.

4 RESULTS AND DISCUSSION

The results of the HVSR analysis on earthquake data at selected ISMN strong-motion stations are shown in Figure 5. The stations, numbered IS101 through IS112 are the oldest stations of the network and are all located in the SISZ, and station IS100 is located in Reykjavík. In general, the HVSRs appear to be quite variable. Nevertheless, and unlike the HVSR derived from microseismic recordings (Olivera et al. 2014), the reliability of the HVSRs derived from earthquake data appear to depend to some extent on the number of records used at each station. With the exception of stations IS100 and IS111 for which only one recording was used, IS107 for which only three were used, and for station IS112 where the individual HVSRs diverge at low frequencies, most stations appear to have relatively stable, near constant and low amplitude HVSR. Such characteristics were to be expected for rock sites. Notable exceptions however are seen at stations IS104, IS105, IS107, and IS109. Station IS104 is located on a relatively young (<10 th.y) and thin (a few tens of meters or less) lava rock which has been shown to produce a characteristic HVSR (Bessason and Kaynia 2002; Rahpeyma et al. 2016). Station IS105 is located on ancient seabed and river deposits of unknown thickness, and is classified as “stiff soil.” Finally, station IS109 which also has been classified as “stiff soil” has a relatively flat near constant HVSR, characteristic of a “rock” site, apart from it exhibiting a curious peak above 10 Hz. However, the peak and the associated predominant frequency cannot be considered reliable due to the few observations used.

At some stations, especially Selfoss, Hveragerði, Thorlakshofn, Hella, and Tjorsartun there are multiple low-frequency

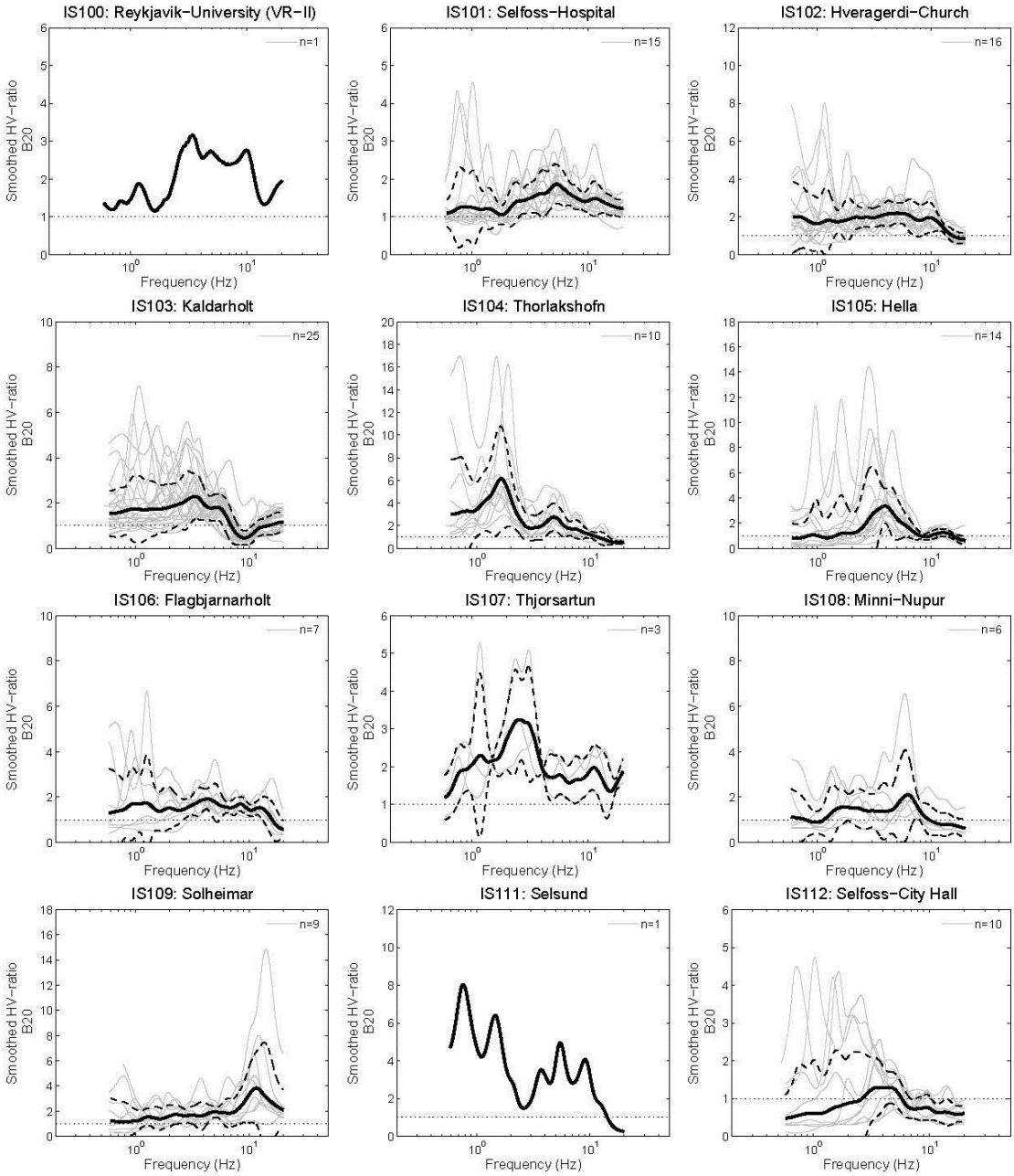


Figure 5. Mean HVSR +/- one standard deviation from earthquake recordings with a Konno and Ohmachi smoothing coefficient, B=20 where n is the number of available earthquake events used to derive the mean HVSR for the ISMN strong-motion stations.

HVSR peaks. The lack of a corresponding consistent predominant frequency at each site indicates that it is not a site characteristic. Rather, the low-frequency peaks are most likely due to intense low-frequency and large amplitude near-fault horizontal ground motions due to directivity effects and/or permanent tectonic displacements associated with the three strong earthquakes in 2000 and 2008. These results indicate that additional constraints are needed to validate the results, in particular accounting for obvious wave effects from earthquake recordings (near-fault pulses, surface waves, etc.) and comparing with results from microseismic studies (Olivera et al. 2014).

5 CONCLUSIONS

Site effects are known to significantly affect outcrop earthquake strong-motions. The HVSR method has been shown to be a useful method for identifying dominant frequencies with respect to localized site

amplification and for classifying measurement sites. In the absence of HVSR analysis and geophysical data about the geologic profiles in Iceland at ISMN recording sites, most sites are classified as "rock" on the basis of surface geology.

This study is a part of a comprehensive effort of estimating HVSR at Icelandic strong-motion stations from microseismic data (Olivera et al. 2014) and from both earthquake and microseismic array data at recording sites of the Icelandic strong-motion arrays (Halldorsson et al. 2009; Halldorsson et al. 2012; Rahpeyma et al. 2016). It aims at establishing a clearer understanding of the site response by estimating reliable HVSRs for Icelandic strong-motion recording sites. Towards this end, we focus on establishing a consistent procedure for collecting and analyzing microseismic data and calculating the HVSRs. Using this procedure, we analyze earthquake recordings at selected stations of the ISMN and calculate their corresponding HVSRs. As expected for rock sites, most stations exhibit relatively constant HVSR (over the frequency range considered) of low amplitude. However, there appear to be significant exceptions to this trend, even for sites classified as rock. The results warrant a further study and comparison of HVSR from microseismic and earthquake data for all ISMN strong motion stations.

An example of such comparison is shown in Figure 6 for station IS104 in Thorlakshofn where the earthquake HVSR appears to have two predominant frequencies, one of about 2 Hz and another at 5-6 Hz, while the microseismic data only reproduces the peak at the lower predominant frequency. Such results need to be interpreted on the basis of as much geological and geotechnical information as possible. From shallow boreholes in the area the top layer is a relatively young lava rock with a softer sedimentary layer below (introducing a shear wave velocity reversal), and possibly repeating such "soil structure" at greater depths. The predominant frequencies of oscillation of such soil structure (considering a unit-area vertical column) with velocity reversals acting as flexible structural elements, can be efficiently modelled using

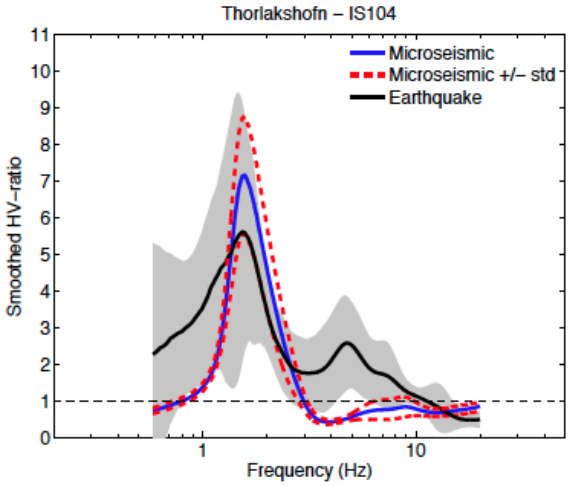


Figure 6. Mean HVSR and its 68-percentile limits from earthquake data (black solid line and shaded area) and microseismic data (blue solid line and red dashed lines) using smoothing coeff. B=20 at station IS104 in Thorlakshöfn, South Iceland.

dynamic response theory of a linear oscillator subjected to a base excitation (Rahpeyma et al. 2016).

6 ACKNOWLEDGEMENTS

This work was carried out at the Earthquake Engineering Research Centre (EERC) of the University of Iceland in Selfoss, South Iceland. The work was supported by the Icelandic Centre for Research (Grants of Excellence no. 141261-051 and 052), the Icelandic Catastrophe Insurance (Grant no. S112-2013) and the University of Iceland Research Fund. Christian I. Olivera was supported by the Leifur Eiriksson Foundation, Virginia Tech and the EERC. The seismographs used in this study were rented from the LOKI instrument bank at the Icelandic Meteorological Office.

7 REFERENCES

Ambraseys NN, Douglas J, Sigbjörnsson R, et al (2004) Dissemination of european strong-motion data, volume 2. In: Proceedings of the13th World Conference on Earthquake Engineering. p 13

Ambraseys NN, Sigbjörnsson R (2000) Re-appraisal of the seismicity of Iceland. Acta Polytechnica Scandinavica 2000-003:1–184.

Anderson JG, Lee Y, Zeng Y, Day S (1996) Control of strong motion by the upper 30 meters.

Bulletin of the Seismological Society of America 86:1749–1759.

Angelier J, Bergerat F, Stefansson R, Bellou M (2008) Seismotectonics of a newly formed transform zone near a hotspot: Earthquake mechanisms and regional stress in the South Iceland Seismic Zone. Tectonophysics 447:95–116.

Atakan K, Brandsdottir B, Halldórsson P, Fridleifsson GO (1997) Site response as a function of near-surface geology in the South Iceland Seismic Zone. Natural Hazards 15:139–164.

Bard PY, SESAME-Team (2005) Guidelines for the implementation of the H/V spectral ratio technique on ambient vibrations: measurements, processing, and interpretations. SESAME European research project.

Bellou M, Bergerat F, Angelier J, Homberg C (2005) Geometry and segmentation mechanisms of the surface traces associated with the 1912 Selsund Earthquake, Southern Iceland. Tectonophysics 404:133–149.

Bessason B, Kaynia AM (2002) Site amplification in lava rock on soft sediments. Soil dynamics and Earthquake engineering 22:525–540.

Bjarnason IT, Cowie P, Anders MH, et al (1993) The 1912 Iceland Earthquake Rupture: Growth and Development of a Nascent Transform System. Bulletin of the Seismological Society of America 83:416–435.

Boore DM, Joyner WB (1997) Site amplifications for generic rock sites. Bulletin of the Seismological Society of America 87:327–341.

Clifton A, Einarsson P (2005) Styles of surface rupture accompanying the June 17 and 21, 2000 earthquakes in the South Iceland Seismic Zone. Tectonophysics 396:141–159.

Einarsson P (1991) Earthquakes and present-day tectonism in Iceland. Tectonophysics 189:261–279.

Einarsson P, Björnsson S, Foulger G, et al (1981) Seismicity pattern in the South Iceland seismic zone. Earthquake Prediction 141–151.

Einarsson Þ, Douglas G (1994) Geology of Iceland: rocks and landscape.

Konno K, Ohmachi T (1998) Ground-motion characteristics estimated from spectral ratio between horizontal and vertical components of microtremor. Bulletin of the Seismological Society of America 88:228–241.

Lachetl C, Bard P-Y (1994) Numerical and Theoretical Investigations on the Possibilities and Limitations of Nakamura's Technique. Journal of Physics of the Earth 42:377–397.

Lermo J, Chávez-García FJ (1993) Site effect evaluation using spectral ratios with only one station. Bulletin of the Seismological Society of America 83:1574–1594.

Mucciarelli M (1998) Reliability and applicability of Nakamura's technique using microtremors: an experimental approach. Journal of earthquake engineering 2:625–638.

Mucciarelli M, Gallipoli MR, Arcieri M (2003) The Stability of the Horizontal-to-Vertical Spectral Ratio of Triggered Noise and Earthquake Recordings. Bulletin of the Seismological Society of America 93:1407–1412.

Nakamura Y (1989) A method for dynamic characteristics estimation of subsurface using microtremor on the ground surface. Quarterly Report of Railway Technical Research Institute 30:25–33.

Olivera CI, Halldorsson B, Ólafsson S, et al (2014) A first look at site effects at Icelandic strong-motion stations using microseismic data. In: Proceedings of the 2nd European Conference on Earthquake and Engineering Seismology (2ECEES). Istanbul, Turkey,

Pagli C, Pedersen R, Sigmundsson F, Feigl KL (2003) Triggered fault slip on June 17, 2000 on the Reykjanes Peninsula, SWIceland captured by radar interferometry. Geophysical Research Letters 30:1273.

Rahpeyma S, Halldorsson B, Olivera CI, et al (2016) Site effect characterization of the Icelandic small-aperture strong-motion array (ICEARRAY I) in the presence of strong velocity reversals. Soil Dynamics and Earthquake Engineering (in review).

Sigbjörnsson R, Ólafsson S (2004) On the South Iceland earthquakes in June 2000: Strong-motion effects and damage. Bollettino di Geofisica teorica ed applicata 45:131–152.

Sigbjörnsson R, Ólafsson S, Rupakhety R, et al (2014) Strong-motion Monitoring and Accelerometric Recordings in Iceland. In: Proceedings of the 2nd European Conference on Earthquake and Engineering Seismology (2ECEES). Istanbul, Turkey,

Sigbjörnsson R, Ólafsson S, Thórarinsson Ó (2004) Strong-motion recordings in Iceland. In: Proceedings of the 13th World Conference on Earthquake Engineering. Mira, Vancouver, BC, Canada, p Paper no. 2370

Sólnes J, Sigbjörnsson R, Elíasson J (2004) Probabilistic seismic hazard mapping of Iceland: Proposed seismic zoning and de-aggregation mapping for EUROCODE 8. In: Proceedings of the 13th World Conference on Earthquake on Earthquake Engineering. p 14

Stefánsson R, Böðvarsson R, Slunga R, et al (1993) Earthquake prediction research in the South Iceland Seismic Zone and the SIL project. Bulletin of the Seismological Society of America 83:696–716.

Stefánsson R, Halldórsson P (1988) Strain release and strain build-up in the South Iceland seismic zone. Tectonophysics 152:267–276.

Triantafyllidis P, Theodulidis N, Savvaidis A, et al (2006) Site effects estimation using earthquake and ambient noise data: The case of Lefkas town (W. Greece). In: Procceedings of the 1st European Conference on Earthquake and Engineering Seismology (1ECEES), Geneva, Switzerland. pp 3–8

Wills CJ, Petersen M, Bryant WA, et al (2000) A site-conditions map for California based on geology and shear-wave velocity. Bulletin of the Seismological Society of America 90:S187–S208.

Seismic Response of Squat Walls Founded on Gravel Cushions

Sara Rose Nodroff
University of Iceland, Iceland, sara.nodroff@gmail.com

Bjarni Bessason
Sigurður Erlingsson
Rajesh Rupakhety
University of Iceland, Iceland

ABSTRACT
In the South Iceland Seismic Zone (SISZ) earthquakes of magnitude up to seven can be expected. Recent well-recorded earthquakes in this region have caused significant damage to buildings. Many buildings in SISZ are 1-3 story reinforced concrete buildings founded on shallow foundations laid on gravel cushion. Interaction of shear walls with the relatively flexible foundation are believed to result in partial isolation of the superstructure from the effects of ground shaking. The beneficial effect of such interaction seems evident from field observations. For example, buildings in the village Hveragerði, located only 3-5 km from the fault rupture, have experienced peak ground acceleration close to 90% of gravitational acceleration and performed very well during the May 2008 Ölfus Earthquake with a recorded moment magnitude of 6.3. Even at a peak horizontal ground acceleration level more than twice the current design specification, a majority of the residential buildings escaped collapse. Structural yielding was not significant, possibly due to reduced base shear demand and energy dissipation at the foundation. This contribution presents the preliminary results of an ongoing study on the effects of flexible foundation on seismic response of squat shear walls.

Keywords: Soil Foundation Structure Interaction (SFSI), Near-fault ground motions, Squat Wall

1 INTRODUCTION

Soil-Foundation-Structure-Interaction (SFSI) plays an important role with the study of structures supported on flexible soils. The dynamic interaction between the soil, foundation, and structure during an earthquake can significantly impact the response of the system by altering the natural period and damping of the fundamental mode. Dynamic SFSI problems merit a direct time domain approach, in which non-linear effects are considered. In the case of strong earthquakes, the conventional linear elastic soil structure interaction (SSI) process lacks consideration of the nonlinear geometrical and deformation effects present at the soil-foundation interface. Structural assessments following the Ölfus Earthquake in 2008 concluded that, given the intensity of the earthquake, some of the buildings performed better than would have been expected. Dissipation of seismic energy in the form of foundation uplift and plastic soil deformation likely served to reduce the forces transmitted to the structures.

Ground motion characteristics in Iceland are relatively well understood through monitoring and modelling activities (Halldórsson and Sigbjörnsson 2009). Construction methods in the region including foundation materials are also well documented. With the availability of high-quality data from a realistic practical setting, the Icelandic landscape provides a natural laboratory for the study of Soil Foundation Structure Interaction (SFSI) systems.

1.1 Seismotectonics of Iceland

The North-American tectonic plate and the Eurasian tectonic plate meet at the diverging Mid-Atlantic Ridge which is currently expanding the Atlantic Ocean in the northern hemisphere at an average rate of 2 centimeters per year as shown in Figure 1.

The plate boundary and relative plate motion can be determined by the observed focal mechanisms of earthquakes in seismic zones and from GPS measurements. One segment of the Mid-Atlantic Ridge called the Reykjanes Ridge traverses Iceland where it extends above sea level. The onshore part of the plate boundary crosses the island from southwest to north, and contains two transform zones, the South Iceland Seismic Zone, SISZ, and the Tjörnes Fracture Zone, TFZ. Seismic activity occurs everywhere on the plate boundary but these two main seismic zones are regions where the earthquake hazard is the highest and large earthquakes have the greatest potential for occurrence (Fig. 1).

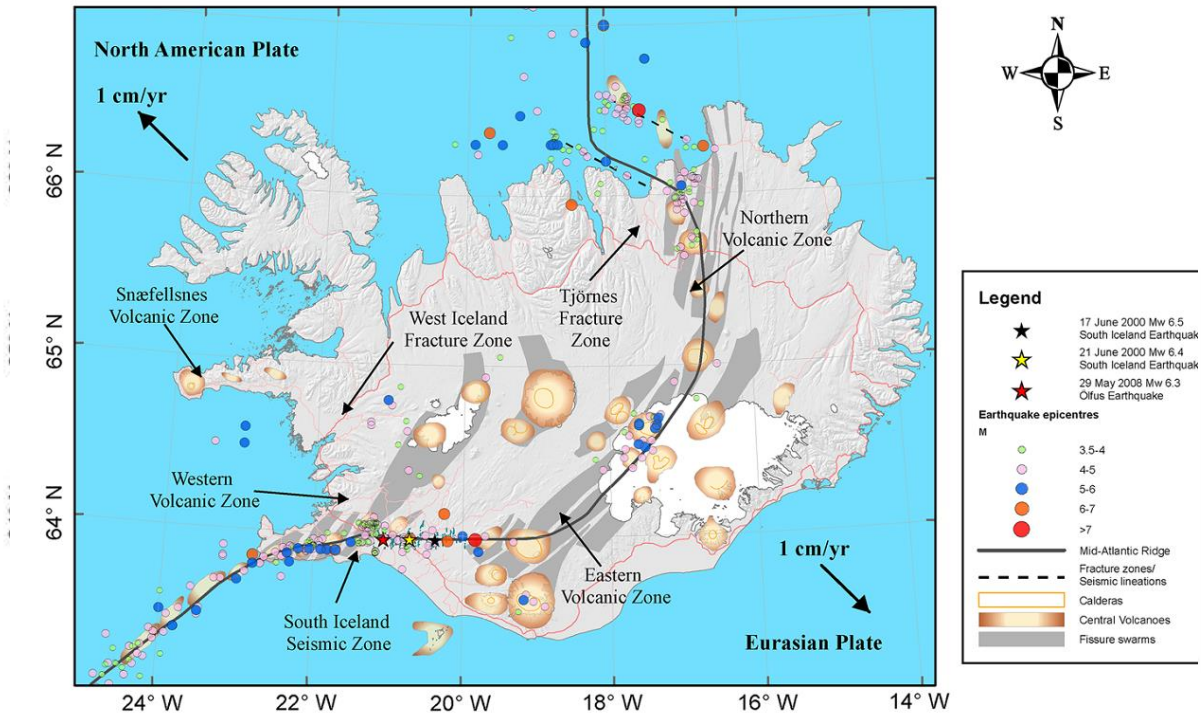


Figure 1: Seismotectonics of Iceland showing the Mid-Atlantic Ridge, the major rifts and fracture zones (D'Amico 2015)

1.2 SISZ

Since 1896, the most destructive earthquakes have occurred in the SISZ, a region with a high population density relative to the rest of the country and several critical infrastructures including hydropower plants, geothermal power plants, and transportation networks. In 1896, six earthquakes larger than Magnitude (M) 6.0 occurred over a two-week period within 50 km (Einarsson et al. 1981; Stefánsson and Halldórsson 1988). Since then an M7.0 occurred in the easternmost part of the SISZ in 1912, a M6.0 occurred in Vatnafjoll in 1987, two Mw6.5 occurred in south Iceland in 2000, and an Mw6.3 occurred in the Ölfusá district in 2008 (Einarsson 1991; Halldórsson and Sigbjörnsson 2009; Halldórsson et al. 2007; Pagli et al. 2003; Sigbjörnsson et al. 2009; Vogfjord 2003). Earthquakes up to magnitude 7 can be expected in SISZ (Halldórsson 1992).

The SISZ spans E-W roughly 80 km in length and about 25 km wide. A maximum fault length of up to 18 km has been observed with horizontal and vertical offsets up to 2 m and 0.5 m respectively. During the 17 June and 21 June 2000 earthquakes, source faults were distanced at approximately 15 km (Khodayar et. al 2010).

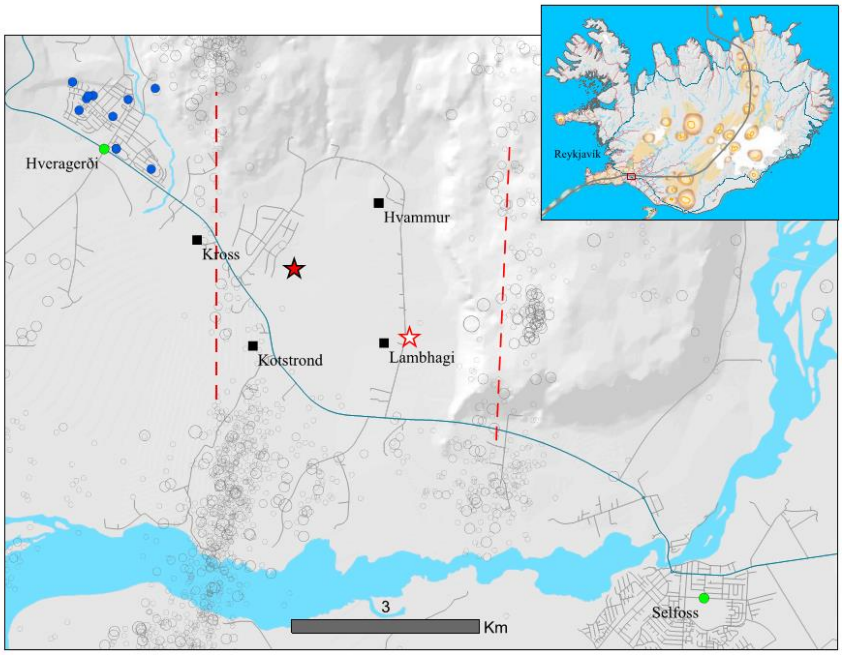


Figure 2. A map of South Iceland showing the epicentral area of the 15:45 UTC 29 May 2008 Ölfus Earthquake, the approximate locations of the two causative faults are delineated by the red dashed lines, the Ingólfsfjall fault to the east and the Kross Fault to the west. The solid red star marks the macroseismic epicenter and the hollow star marks the epicenter estimated from strong ground motion data (Sigbjörnsson et al. 2009). The blue circles in Hveragerði are locations of ICEARRAY recording stations. The grey open circles are epicenters of earthquakes recorded from 23 May to 31 June 2008. The top right inset picture shows Iceland with the mid-Atlantic ridge (grey curve) and the study area is marked by a red rectangle (Rupakhety 2015).

The Ölfus Earthquake, a seismic event of recorded moment magnitude 6.3, occurred on the 29th of May 2008 at 15:45 UTC. The macroseismic epicenter originated beneath Ingólfsfjall roughly 6-7 km east of the town Hveragerði between the towns of Selfoss and Hveragerði. The earthquake occurred almost simultaneously on two parallel, nearly vertical, north–south oriented faults with right-lateral strike-slip mechanism. The faults and the macroseismic epicenters are shown on Figure 2. The earthquake motions were recorded by the Icelandic Strong-motion Network and ICEARRAY network, a dense array in the village of Hveragerði (Halldórsson and Sigbjörnsson, 2009). The Ölfus Earthquake ground motion can be characterized by short duration, high intensity movements.

The Earthquake Engineering Research Centre (EERC) of University of Iceland carried out a detailed survey of damage to the buildings in Hveragerði. A majority of the buildings were built before earthquake design codes were established and enforced. Many of the buildings were damaged in the earthquake but there were almost no reports of collapse. The average damage on residential buildings was about 5% of their insured value, remarkably small given the intensity of the ground motion (Rupakhety and Sigbjörnsson, 2014). This is in agreement with other studies of damage of low-rise buildings in the area after the 2008 Ölfus Earthquake (Bessason et al. 2012) Unreinforced masonry buildings suffered the most damage. Damage to concrete as well as timber buildings was mostly limited to non-structural elements such as wall and floor tiles, paints, ceilings, doors and windows, etc. The earthquake excitations on the buildings far exceeded the codified design loading but a majority of buildings performed well and withstood the high accelerations. Most buildings in Hveragerði are one to two stories, include shear wall lateral load resisting systems, made of concrete, symmetric, and regular in both plan and

elevation (Rupakhety et al. 2015; Bessason et al. 2014).

Several houses had noticeable foundation deformation where permanent tilt, extensive damage to floors, and cracking in foundation walls. In Iceland, structures are often founded on gravel fill atop shallow bedrock. The gravel cushion deforms and serves as a damping mechanism for the dissipation of seismic energy. These type of foundations can reduce the base shear loads or inertial forces transmitted to the structure. This effect may have helped the buildings to withstand the event practically unscathed. For a gravel cushion, the dynamic behavior will have strong non-linear characteristics and is more likely to interact with the structure. The dynamic response of the structure as a whole depends on the dynamic characteristics of the foundation and thus the interaction of the system must be accounted for. An example time series from an accelerometer installed at the Hveragerði Retirement House is provided in Figure 3:

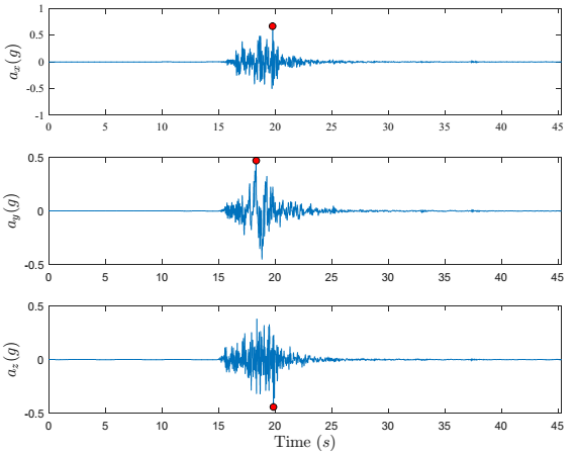


Figure 3: Corrected accelerometer readings from the Ölfus Earthquake that occurred on 29 May 2008. Maximum ground accelerations recorded at the site in the East-West, North-South, and vertical directions were 0.66g, 0.47g, and 0.44g, respectively. These readings were taken from the Hveragerði Retirement House station at an epicentral distance of 9 kilometres (Fig. 2).

2 SOIL-FOUNDATION-STRUCTURE INTERACTION

2.1 Introduction

In most practical engineering applications, depending on the soil conditions and the structural type, the foundations are partially or totally embedded in the ground and the effects of the surrounding soil greatly alter their static and dynamic response. Many buildings in SISZ are 1-3 story reinforced concrete buildings founded on shallow foundations wherein the shear walls are classified as squat walls and energy dissipation is dominated by structural yielding, sliding, and bearing capacity mechanisms.

As opposed to a fixed base structure subjected to free-field ground motion, the presence of a structure founded on compliant substrate will modify the free-field motion and the interaction between subsystems will modify the expected response.

Studies have shown that allowing significant sliding, uplifting, and even mobilization of bearing capacity failure mechanisms can result in a more distributed inelastic phenomenon through the structure and foundation, and yet acceptable permanent translational and rotational deformations. However, when unintended and uncontrolled, these mechanisms can produce adverse effects, such as, excessive permanent deformation resulting in excessive damage to the foundation, excessive cracking on the shear walls, non-structural damage, etc. Thus there is a need to understand the energy dissipation contributions of the different mechanisms in squat walls founded on soft/medium soil, and to quantify how yielding can be apportioned to the different mechanisms in the structure and the foundation to obtain a good design solution.

2.2 Squat Walls

For structural walls, the behavior of the lateral force resisting system during a seismic event will vary with the aspect ratio and wall layout. Walls with low aspect ratios (≤2.0) are known as squat walls. Squat walls typically have a height to length ratio smaller than 0.5 and have a very high stiffness and strength capacity. Lateral forces are resisted through a combination of the strength of the concrete and distributed horizontal and vertical reinforcement, forming a diagonal strut mechanism. The three major failure modes of squat walls are diagonal tension, diagonal compression, and sliding shear

(Gulec 2005). Squat walls can experience a complex interaction of flexure, shear, and sliding shear failure modes.

For squat walls with very small aspect ratios (aspect ratios ≤2.0), they tend to have a high inherent shear strength and low ductility demands. The ductile mechanism of flexural yielding is limited by the geometry of squat walls; thus they tend to fail in either flexure shear or shear sliding.

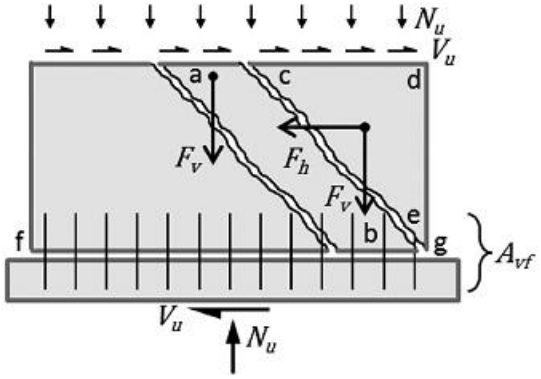


Figure 4: Shear yielding and sliding in a squat wall (Moehle 2011).

Shear yielding occurs when the wall develops inclined cracks, as shown in Figure 4. Shear sliding typically occurs at the structure-foundation interface. Shear failure modes are regarded as undesirable brittle failure modes since rapid loss of strength and stiffness occurs after very little deformation (Whyte 2013). With such quasi-brittle responses as the main indication of deformation, they occur suddenly, and are not preceded by significant yielding, either in flexure or in tension induced by shear.



Figure 5: Typical squat wall structure in the SISZ.

Squat walls are relatively rigid structures, their natural frequency of vibration are in the sensitive range to peak value ground motions, most of which tend to fall in the 0.2 to 0.5 second range. A typical 1 story reinforced concrete structure has a natural period below 0.2 seconds if assumed to be founded on rock. Squat walls have an insufficient amount of ductility to dissipate seismic energy. When founded on soft foundation, the vibration frequency of the structure is reduced. Given the rigidity of the structure and the flexibility of the foundation, the foundation is expected to deform while the squat wall remains elastic. If damage occurs in the structure, it will likely be either flexural or shear cracks in the plane of the wall.



Figure 6: Damaged squat wall in Hveragerði after the 2000 earthquake with visible shear crack.

Stiff structures tend to develop large deformation ductility demands if loaded beyond the elastic range. In order to reduce the demand on the shear walls, allowance of inelastic deformation of the foundation seems to be favorable. Such deformation needs however to be limited so as to avoid excessive damage to the foundation permanent displacement and tilting of buildings.

2.3 Soil Profile and Foundation

At many sites in Hveragerði, there is a thin organic soil layer up to 3 meters in depth. During construction, it is common procedure to excavate and remove this soil and to either build directly on rock or to put the foundation on a 1–2 m thick compacted gravel refill, drained conditions can be assumed with no volumetric changes under shear. At some other locations in South Iceland there are thick sediments of stiff sand and gravel sites where some soil interaction can be expected (Bessason and Erlingsson 2011). With the squat walls embedded below grade, the lateral earth pressure from the surrounding soil prevents sliding of the wall relative to the foundation.

2.4 Preliminary Modelling

An equivalent linear system model of the shear walls, foundation, and soil can be established for numerical simulation of seismic response. A number of assumptions were made to formulate a discrete model representative of a simple 1 story structure, typical of those found in the SISZ. To investigate the potential impact of SFSI in the response of a typical construct, a crude model will be introduced.

The first mechanism of focus is the uplifting of the foundation, which causes a shift in the natural period of the system and results in additional energy dissipation due to the rocking of the foundation.

The conventional soil-structure interaction methodology replaces the actual structure by an equivalent simple oscillator supported on a set of frequency-dependent springs and dashpots which represent the stiffness and damping of the underlying medium.

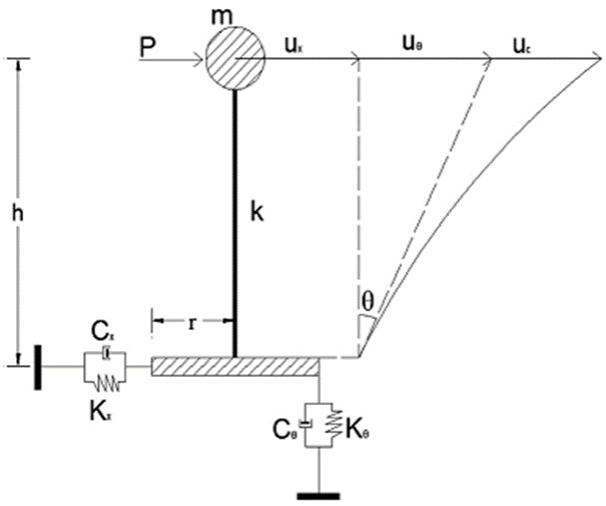


Figure 7: Maravas (2008) soil-structure system deflection diagram.

The structure shall be represented as an SDOF system, which can be an idealization of a one story structure, height h, with a lumped mass, m, concentrated at the story level, damping ratio ζ, which may be viscous (linearly proportional to frequency) or linearly hysteretic (independent of frequency), and stiffness, k. The stiffness of the structure can be represented by a massless column or frame which has an effective height h derived from the fixed-base natural period of the structure. The foundation is assumed to be a circular shallow raft foundation of radius r. The shear wall structure is assumed to have a gravel foundation substrate immediately beneath the foundation. The compliance of the substrate beneath the mat foundation is included at the supports with two frequency-dependent springs, K_x and K_θ, representing stiffness in two degrees of freedom for translational (swaying) and rocking oscillations, respectively. Damping is represented by C_x and C_θ, a pair of dashpots representing energy dissipation due to hysteresis and unbounded wave radiation (Veletsos & Nair 1974). By representing the structure, foundation, and underlying soil in this manner, equivalent natural properties, such as $\tilde{K}, \tilde{T},$ and $\tilde{\zeta}$ of the linear Soil-Foundation-Structure (SFS) system, can be determined.

During a seismic excitation, the SFS model depicted in Figure 7 will undergo three different modes of vibration: translation motion of the lumped-structure mass, translational motion of the lumped-foundation mass, and rotational motion of the system about the foundation. The total horizontal deflection of the system can be decomposed into a summation of independent deflections:

$$u_{total} = u_x + u_\theta h + u_c \qquad (1)$$

Where u_{total} is the total displacement of the lumped structural mass relative to the ground, $u_x(\omega)$ is the horizontal displacement of the foundation, $u_\theta(\omega)$ is the foundation rotation, $u_c(\omega)$ is the flexural deformation of the column supporting the structural mass, and $\omega\left(^{rad}/_{s}\right)$ is the cyclic excitation frequency. Generally, the impedance functions are dependent on the geometry of the foundation, the frequency of excitation, and the characteristics of the underlying soil. Maravas (2006), Luco and Westman (1971), and Veletsos and Wei (1971) suggest the dynamic impedance of the system is complex valued and frequency dependent. The dynamic impedance for the jth degree of

freedom of the SFS system, can be expressed as follows:

$$K_j^*(\omega) \equiv \mathrm{k}_j\left(1 + 2\mathrm{i}\zeta_j\right) \quad (2)$$

Where k_j is the static stiffness and real component of the impedance and ζ_j is the energy loss coefficient.

From equation (1), the impedances associated with each degree of freedom are assumed to act in parallel and can be expressed through a summation rule yielding the following expression for the total dynamic impedance of the SFS system:

$$\frac{1}{\widetilde{K}^*} = \frac{1}{K_x{}^*} + \frac{1}{K_\theta{}^*}\left(\frac{h}{r}\right)^2 + \frac{1}{K_s{}^*} \quad (3)$$

Where $\widetilde{K}^*$ is the overall dynamic impedance of the SFS system, $K_x{}^*$ is the complex stiffness associated with the translational oscillations, $K_\theta{}^*$ is associated with the rocking oscillations, $K_s{}^*$ is associated with the structure, and h/r is the slenderness ratio.

Veletsos et al (1977) presented a series of dimensionless parameters to relate the properties of the structure-soil system to an equivalent fixed base structure. Maravas (2006) expanded upon the procedure and established analytical expressions for the linear damping and fundamental natural period of the SFS as an iterative method involving the aforementioned frequency-dependent impedances and system geometry. Simplified approaches such as the one briefly mentioned in this section could be utilized to simulate the mechanisms of the SFS system.

2.5 Near Fault Effects

Since the village of Hveragerði is located only 3-5 km from the fault rupture, the behavior indicative of the peculiar characteristics of near fault ground motions is observed. In the small area covered by the array (spatial dimensions are only ~2 km), there was a large variability as indicated by the range of PGA as well as the frequency-content of ground-motion (Halldórsson and Sigbjörnsson 2009).

The records also showed forward-directivity effects, i.e. a near fault focusing of seismic energy in the fault-normal direction, evidenced by the dominant long-period pulses in the velocity time series (see Rupakhety et al. 2011).

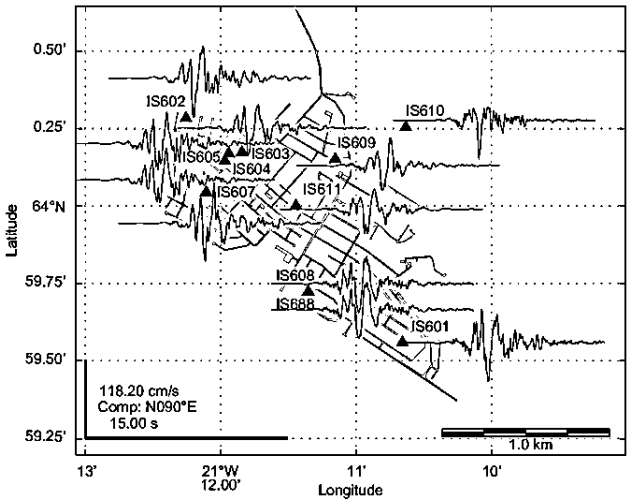


Figure 8: East-west components of the strong-motion velocity time series recorded by the ICEARRAY during the Ölfus Earthquake on 29 May 2008(Halldórsson and Sigbjörnsson 2009).

Near-fault ground motions, specifically the ground velocity and displacement, have a pulse-like nature which seems to reduce the beneficial effects of soil-structure interaction. The ground motions are characterized by a few cycles of intense shaking, and therefore energy dissipation due to hysteresis at the foundation is not as efficient as in the case of ground motion with many cycles of shaking. The response seems to be controlled by the dominant velocity pulses contained in the ground motion (a strong pulse in the long period range). Base-isolated buildings could experience severe displacement demands due to displacement pulses within the near-fault ground motion if designed according to standard provisions (Hall et al. 1995).

This was the case for the base isolated Óseyrarbrú bridge during the May 2008 Ölfus Earthquake (Jónsson, Bessason and Haflidason, 2010). Rupakhety et al. (2010) conducted a study of near-fault ground motions in detail and the possible impact on engineering structures. If the near-fault pulse is resonated with the structure, this may result in a permanent tilt since excessive demand is experienced by the foundation. If the ground motion was composed of more cycles, then there is potential for more dissipation of seismic energy and recentering mechanisms to restore the system. A time

history analysis using a large set of near-fault ground motions needs to be performed to investigate the effects of foundation flexibility.

2.6 Attenuation and Amplification Effects Due to Soil Profile

Geologically, Iceland is characterized by basaltic lavas, as well as tuff layers, often with intermediate layers of sediments or alluvium. The soil composition could potentially impact the ground motion as in the case of the Ölfus Earthquake, where the causative faults were located at a relatively shallow depth but were not visible on the surface (Sigbjörnsson et al. 2009). The characteristics of the soil can greatly influence the nature of shaking at the ground surface during an earthquake. The sediment layers overlaying the bedrock, can act as "filters" to seismic waves travelling to the surface by attenuating motions at certain frequencies and amplifying them at others. The geological profile in the town of Hveragerði is fairly uniform (see geological map of the area in Sæmundsson and Kristinsson 2005) but this would be an important consideration for sites outside of Hveragerði.

3 CONCLUSION

From field observations, the beneficial effects of considering flexible foundations on seismic performance of buildings seems evident—for example, buildings in Hveragerði during the May 2008 Ölfus Earthquake performed very well The flexible foundation acts like a 'fuse', a 'natural isolation mechanism', wherein yielding of foundation limits the seismic forces transmitted to the superstructure.

Building design codes are overly simplified in that the assumptions cannot capture the non-linear dynamic interaction between the structure-foundation-soil system during seismic events. A full-scale validation of structural response through recorded earthquake excitations is important. Eurocode 8 allows full scale earthquake testing using a computational or scaled test model in addition to the prescribed methods provided that the design fulfils the code requirements.

3.1 Next Steps

- Efficient and reliable mechanical modelling of SFSI systems that are suitable for the Icelandic environment will be investigated, presented, and verified with experimental data.
- Through case studies the 'natural isolation mechanism' which can act like a 'fuse' and under what circumstances the deformation of the foundation becomes excessive and uncontrolled will be determined.
- The objective is to propose potential simplifications in modelling for everyday design office use while still capturing the dynamic characteristics of the system.
- Numerical simulations using the mechanical model will be critically analyzed to identify trends, to understand the most important effects, and to suggest possible mitigation strategies.
- The results will shed light on factors such as relative distribution of yielding mechanisms in the structure and the soil, and the scenarios that result in favorable and unfavorable failure mechanisms.
- This study will also seek to quantify the effects of different parameters of the soil, the structure, and ground motion, on the overall response of the structure.

4 REFERENCES

Bessason, B., Bjarnason, J.Ö., Guðmundsson, A., Sólnes, J., Steedman, S., (2014). Analysis of damage data of low-rise buildings subjected to a shallow Mw6.3 earthquake. Soil Dynamics and Earthquake Engineering, 66, 89-101

Bessason, B., Bjarnason, J.Ö., Guðmundsson, A., Sólnes, J., Steedman, S., (2012). Probabilistic damage curves for low-rise buildings based on field data. Earthquake Spectra, 28:4,1353-1378.

Bessason, B., Erlingsson, S., (2011). Shear wave velocity in surface sediments, Jökull, 61,51–64.

Chopra, A. K. (2006). Dynamics of Structures (3rd ed.). New Jersey: Prentice Hall.

D'Amico, V., Albarello D., Sigbjörnsson, R., and Rupakhety R. (2015) Seismic hazard assessment for Iceland in terms of macroseismic intensity using a site approach. Bulletin of Earthquake Engineering.

Decriem J, Anadóttir T, Hooper A, Geirsson H, Sigmundsson F, Keidling M, Hreinsdóttir S, Einarsson

P, LaFemina P, Bennett RA (2010) The 2008 May 29 earthquake doublet in SW Iceland. Geophys J Int 181:1128–1146

Einarsson, P. (1991). Earthquakes and present-day tectonism in Iceland. Tectonophysics, 189, 261–279.

Einarsson, P., Björnsson, S., Foulger, G. R., Stefánsson, R. and Skaftadóttir, Th. (1981). Seismicity Pattern in the South-Iceland Seismic Zone. Earthquake Prediction - An International Review. American Geophysical Union, Maurice Ewing Series, 4, 141–151.

Gulec C.K. (2005). Ultimate Shear Strength of Squat Rectangular Reinforced Concrete Walls, MS Thesis, Department of Civil, Structural and Environmental Engineering, State University of New York at Buffalo, Buffalo, NY.

Halldorsson P (1992) Seismic hazard assessment based on historical data and seismic measurements. International conference on preparedness and mitigation for natural disaster, Iceland.

Halldorsson, B. and Sigbjörnsson, R. (2009). The 6.3 Ölfus Earthquake at 15:45 UTC on May 29 2008 in South Iceland: ICEARRAY strong-motion recordings. Soil Dynamics and Earthquake Engineering. 29:6, 1073-1083.

Jónsson, M. H., Bessason, B. and Hafliðason E. (2010). Earthquake response of a base-isolated bridge subjected to strong near-fault ground motion, Soil Dynamics and Earthquake Engineering 30:6, 447-455

Khodayar, M., Bjornsson, S. (2010), Surface Deformation of May 29, 2008 earthquake near Hveragerði , South Iceland Seismic Zone and Hengill geothermal area, Iceland Geosurvey, ISOR - 2010/033.

Kramer, S. L. (1996). Geotechnical earthquake engineering. Upper Saddle River, N.J.: Prentice Hall.

Luco J.E., and Westman R.A., (1971). Dynamic response of circular footings. Journal of the Engineering Mechanics Division,97, 1381–1395.

Maravas, A. (2006). “Discrete model for dynamic soil-structure interaction of structures on rigid surface or pile foundations”, MS. Thesis, University of Patras.

Moehle, J., Ghodsi, T., Hooper, J., Fields, D., Rajnikanth, G., (2011). Seismic Design of Cast-in-Place Concrete Special Structural Walls and Coupling Beams. Nation Earthquake Hazards Reduction Program (NEHRP). National Institute of Standards and Technology. United States Department of Commerce.

Rupakhety, R. (2011). Contemporary issues in earthquake engineering research: processing of accelerometric data, modelling of inelastic structural response, and quantification of near-fault effects. University of Iceland.

Rupakhety, R., Sigbjörnsson R, Ólafsson S (2015) Damage to residential buildings in Hveragerði during the 2008 Ölfus Earthquake: simulated and surveyed results. Bulletin of Earthquake Engineering.

Rupakhety R, Sigbjörnsson R (2014b) The 2008 Ölfus Earthquake: damage to residential buildings in Hveragerði. In: Proceedings of second European conference on earthquake engineering and seismology, Istanbul 25–29 August 2014.

Sæmundsson, K. and Kristinsson, S. G. (2005). Hveragerði: Hitamælingar í jarðvegi og sprungur. Report, Íslenskar orkurannsóknir, ÍSOR-2005/041. 16 p. + 2 maps.

Sigbjörnsson R, Snæbjörnsson JTh, Higgins SM, Halldórsson B, Ólafsson S (2009) A note on the Mw 6.3 earthquake in Iceland on 29 May 2008 at 15:45 UTC. Bulletin of Earthquake Engineering 7:113–126.

Veletsos, A. S. (1977) “Dynamics of Structure-Foundation Systems”, in: Hall, W. J.(ed.), Structural & Geotechnical Mech., Prentice-Hall.

Veletsos, A.S. & Meek, J.W. (1974). “Dynamic behavior of building-foundation systems”,Earthq, Engng & Struct, Dyn,, 3(2), 121-138.

Veletsos, A.S. & Nair, V.V. (1975) “Seismic interaction of structures on hysteretic foundations”, Journal of Structural Engineering, ASCE, 101(1), 109-129.

Vetetsos A.S., and Wei Y.T. 1971. Lateral and rocking vibration of footings. Journal of the Soil Mechanics and Foundation Division 97, 1227–1248.

Whyte Catherine.A., Bozidar Stojadinovic (2013). Hybrid Simulation of the Seismic Response of Squat Reinforced Concrete Shear Walls. PEER Report 2013/02, Pacific Earthquake Engineering Research Center, University of California, Berkeley, CA.

An attempt towards harmonizing the Norwegian guidelines related to construction on sensitive clay

Aunaas, K.
Norwegian Public Roads Administration (NPRA), Norway, kristian.aunaas@vegvesen.no

Thakur, V[1], Oset, F.[2], Ottesen, H. B.[2], Strand, S.A.[3], Nyheim, T.[3], Havnen, I.[3], Lyche, E.[3], Viklund, M.[4], Abokhalil, M.[4]

[1]*Norwegian University of Science and Technology (NTNU), Norway*
[2]*Norwegian Public Roads Administration (NPRA), Norway*
[3]*Norwegian Water Resources and Energy Directorate (NVE), Norway*
[4]*Norwegian National Rail Administration (NNRA), Norway*

ABSTRACT

Parts of the Norwegian road and railway network have been constructed on sensitive clays. Several new projects are facing challenges in areas with deposits of sensitive clay. The design codes and guidelines of the Norwegian Public Roads Administration (NPRA) and the Norwegian National Rail Administration (NNRA) have been developed over many years with respect to ground investigations and safety requirements. These regulations are specific for road and railway construction. In addition, there are general design codes such as Norwegian Standards and the regulations established by the Norwegian Water Resources and Energy Directorate (NVE) concerning the safety of larger areas adjacent to e.g. roads and railways. The differences in these regulations can lead to challenges during the planning of new projects, as well as in maintenance of existing roads and railways. The multi-disciplinary research project entitled "Natural Hazards" (NIFS) is a joint enterprise involving the NNRA, NPRA and NVE. This project attempts to harmonize the regulations of those three government bodies. Some specific topics were selected: definition and safety factor of local and overall stability, detection of sensitive clays using various sounding techniques, run-out distance and anisotropy. This paper addresses these topics in light of field results and numerical calculations.

Keywords: Sensitive clays, regulations, local and overall stability, landslide.

1 INTRODUCTION

In recent years, several quick clay landslides have occurred in Norway. Both natural events, like erosion, and human activity have been the causal factors, but it appears that the latter has been more frequent, at least in recent years. As discussed in the work of Oset et al. (2013), the most well known are the landslides in Verdal in 1893 (Janbu et al. 1993) and Rissa in 1979. Another well known, and more recent quick clay slide, the Skjeggestad slide, occurred on European route E18 near Mofjellbekken bridge in February 2015. Fortunately, no lives have been lost since 1996, but the socioeconomic consequences have been significant.

The three government agencies, the Norwegian Public Roads Administration (NPRA), the Norwegian National Rail Administration (NNRA) and the Norwegian Water Resources and Energy Directorate (NVE), each maintain their own regulatory

framework, in which the appropriate design criteria for construction on sensitive clay deposits are addressed. These frameworks all meet the requirements set forth in national standards and Eurocode 7, but they differ in respect to i.e. the level of partial factors required for local stability and percentual improvement. Percentual improvement is allowed because the natural slope, in its current location, has a safety factor of at least 1.0. Any improvement of the safety factor is an actual improvement, and not encumbered with uncertainty in the chosen strength parameters, which would be the case when using an absolute material factor (NVE, 2014).

The NPRA, NNRA and NVE have initiated a national R&D project called "Natural Hazards", abbreviated NIFS (NIFS, 2012). Challenges associated with sensitive clays is one of the main topics for one of the NIFS subprojects (Subproject 6: Quick clay (SP6)). One of the main objectives for SP6 is to facilitate the development of regulatory frameworks (guidelines) suggested by the NIFS partners. This includes, but is not limited to, assessment of Norwegian landslide hazard mapping plans, definition and safety factors of local and overall stability, detection of sensitive clays using various sounding techniques, post-failure movements of landslides in terms of the retrogression and run-out distance, and anisotropy. By harmonizing the guidelines, regardless of who or where we build, will help achieve an equal practice in areas with sensitive clays. In the following, this paper will give a brief overview of the existing regulatory framework before presenting proposed changes in the guidelines of the NPRA, NNRA and NVE. The first part of this paper is taken directly from Oset et al. (2013) to provide the reader with an overview of the regulatory development in Norway.

2 HISTORICAL DEVELOPMENT OF REGULATIONS IN NORWAY

In the 1970s, limit state design was introduced in the Norwegian construction standards. There was a need for a corresponding set of design regulations for geotechnical aspects. A committee established by the Norwegian Geotechnical Society provided a guideline that was published by the Norwegian Standardisation authorities in 1979 (NS, 1979). In addition to earth pressure, bearing capacity, etc., this guideline also gave the first national set of regulations for the evaluation of stability of slopes and fills. The guideline established two principles regarding the partial safety related to soil strength. First, the partial safety related to effective stress analyses was differentiated with respect to damage consequence and failure mechanism, as shown in Table 1. The effective stress analyses are performed using the effective stress parameters; cohesion (c') and the frictional angle (ϕ'). Such analyses are performed to study the long-term (or drained) stability of slopes. In 1973, Janbu proposed to use the effective stress analyses along with an appropriate pore pressure profile to compute the short-term stability of natural slopes. However, during the years, total stress based undrained analyses to calculate short-term stability has been the most applied method. The undrained shear strength (c_u) is usually derived from confined triaxial tests. The principles in Table 1 have been adapted also for design based on undrained analyses.

Table 1 Partial safety factors for effective stress and total stress analyses according to Norwegian construction standards (Oset et al. (2013)).

Damage consequences	Failure mechanism		
	Dilatant	Perfectly plastic	Brittle and contractant*
Less serious	1.2	1.3	1.4
Serious	1.3	1.4	1.5
Very serious	1.4	1.5	1.6

**Sensitive clays exhibit brittle behaviour, i.e. strain softening behaviour.*

Secondly, the guideline stated that the established practice in some cases had been to take precautions that reduced the calculated mobilised shear stress along potential slip surfaces with 10–20%. This procedure for undrained total stress analyses was mainly handled as a contingency

procedure for roads, railways and construction works until the introduction of the NVE regulations in 2008.

2.1 Regulatory framework by the Norwegian Public Roads Administration (NPRA)

The NPRA guidelines for geotechnical design in road construction was published in 1990, and they have been developed to the present sixth edition (NPRA, 2010). The principles in Table 2 have been maintained and adapted both for effective and total stress analyses. From the beginning, the main focus of the NPRA guidelines was safety requirements regarding local stability of construction works and slopes directly affecting the road. The stability of adjacent terrain was addressed when the stability was obviously poor, but there was no systematic requirement for the slopes not directly affected by the road construction works.

Table 2 Partial safety factors for effective stress and total stress analyses according to the NPRA guidelines (Oset et al. (2013)).

Damage consequences	Failure mechanism		
	Dilatant	Perfectly plastic	Brittle and contractant
Less serious	1.2/1.4*	1.3/1.4*	1.4
Serious	1.3/1.4*	1.4	1.5
Very serious	1.4	1.5	1.6

**The Norwegian national application of Eurocode 7 from 2008 requires γ_M > 1.4 for total stress analyses.*

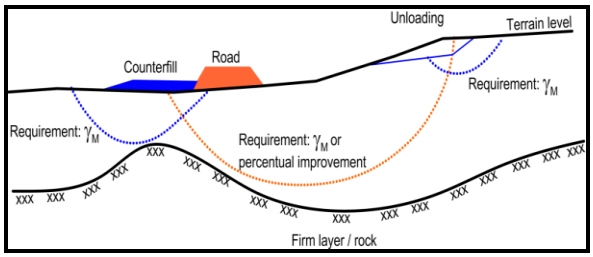


Figure 1 Principle regarding requirements with partial safety factor for local stability and partial safety factor or percentual improvement regarding larger progressive slides. Adopted from NPRA (2010).

In 2006, the possibility of percentual improvement was implemented in the NPRA regulations as a contingency procedure. The illustration in Fig. 1 was introduced in 2010 to clarify the use regarding the overall stability of larger areas. However, the local stability related to construction elements still needs to satisfy a partial safety factor as shown in Fig. 1.

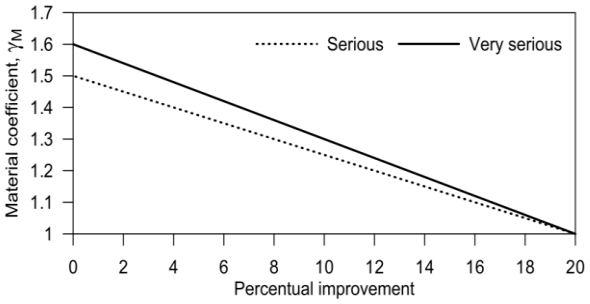


Figure 2 NPRA's recommendations concerning the percentual improvement of material coefficients regarding the overall stability of larger areas based on the consequence categories "serious" and "very serious". (Oset et al. (2013)).

2.2 Regulatory framework by the Norwegian National Rail Administration (NNRA)

The NNRA regulations (2013) for the design of railway structures are in a wiki-based framework, which is revised on a yearly basis. Safety requirements for railway construction activities are described with an absolute safety factor. For the railway embankments, the requirement in safety factor depends on the method of analysis used (drained or undrained), anisotropy, the consequence of failure and the failure mechanism. The required safety factor for railway embankments varies between 1.2 to 2.0 according to Table 3 and 4.

Table 3 Safety requirements for railway embankments analysed using drained parameters (c' and φ') and undrained (cu) parameters including anisotropic behaviour of soil (Oset et. al (2013)).

Damage consequences	Failure mechanism		
	Dilatant	Perfectly plastic	Brittle and contractant
Less serious	1.20	1.30	1.40
Serious	1.30	1.40	1.50
Very serious	1.40	1.50	1.60

Safety requirements for railway cuttings are normally met by using the framework restrictions for slope inclination for the

different type of soils presented in Table 5. In the case of poor ground conditions, high cuttings or the possibility of erosion, a thorough study of slope stability has to be carried out. In that case, the safety factors according to Table 3 and 4 are required.

Table 4 Safety requirements for railway embankments analysed using undrained (cu) parameters without anisotropy factors (Oset et al. (2013)).

Damage consequences	Failure mechanism		
	Dilatant	Perfectly plastic	Brittle and contractant
Less serious	1.40	1.55	1.70
Serious	1.55	1.70	1.85
Very serious	1.70	1.85	2.00

Table 5 Maximum slope inclination for railway construction (Oset et al. (2013)).

Ground conditions	Stone rock	Gravel coarse sand	Fine sand/silt		Clay
			Dry	Layered, water dense	
Maxi inclina-tion	1:1.25	1:1.5	1:2	Special invest-igation	1:2

The presence of sensitive clay will lead to a stricter requirement for the safety factor according to Table 3. If the possibility of a progressive slide is present, safety for corresponding areas has to be investigated according to the NVE guidelines, as described in the following chapter.

2.3 Norwegian Water Resources and Energy Directorate (NVE) 2014

In 2008, the NVE published guidelines on how to assess landslide hazards in land use planning, with an emphasis on the level of zoning plans. From 2011, the guidelines were adopted as official guidelines for Norwegian regulations (NVE, 2008). The NVE revised the guidelines in 2014. The revision included a differentiation of the complexities of the planned projects and the inherent need to identify, limit and evaluate areas with quick clay. The guidelines enforce that the overall stability has to be taken into consideration in all projects in order to meet the requirements stated in section 28-1 in the Norwegian Planning and Building Act, defined in chapter 7 in the Technical Regulations (TEK10) (DiBK, 2011).

Before the guidelines were approved, geotechnical consultants and local authorities dealt with this issue at the construction stage, after the stage of zoning plans. This usually meant that overall stability was ignored in both the planning and construction stages.

The method for assessing overall stability for zoning plans can be described as a step-by-step procedure. This procedure has to be carried out by a professional geotechnical consultant, specialized in evaluating these kinds of overall stability problems.

The natural prerequisite is that the project is located under the marine limit. If this prerequisite is fulfilled, then the following steps must be carried out:

Step 1: Assessing the possibility of marine clay

This step includes a geotechnical evaluation of the terrain by using existing maps showing quaternary deposits. If these maps indicate that marine clay might be present within or adjacent to the area of the zoning plan, then the next step must be carried out.

Step 2: Evaluating the terrain

The geotechnical consultant has to evaluate if the terrain shows slopes or ravines with inclination or height differences sufficient to lead to progressive failures. If these criteria are considered to be present, then the next step must be carried out.

Step 3: Finding and evaluating existing ground investigations

This step could also be carried out together with Step 1, but it is here described as a separate exercise. The step implies that the geotechnical consultant gathers further knowledge about the presence of sensitive clay within and adjacent to the area of the actual zoning plan, gathers information about existing ground investigations, executed in accordance with other projects. Field and laboratory testing shall be performed if

ground conditions are not known a-priori. Placement of boreholes must be adjusted to the actual topography. Execution of boring and laboratory testing must fulfil the requirements given in the guidelines and adjoining Norwegian standards for boring procedures (NGF, 2011). After analysing the existing ground conditions, the geotechnical consultant should evaluate if the distribution of marine clay found in Step 2 should be limited or extended, and in which levels below the ground surface marine clay could be found. The investigations might indicate whether the marine clay found can be characterized as brittle clay (defined as remoulded shear strength $\leq$ 2.0 kPa and Sensitivity $\geq$ 15 in the NVE presently valid guidelines).

Step 4: Limiting and classifying the area with potential danger

The natural boundaries for where initial slides can occur, and the area that may be affected by the development of the slide, have to be mapped. At present time, the run-out area has to be assessed by examining existing literature and/or using simple empirical values from Karlsrud et al. (1985). Together with NGI, NTNU and Multiconsult, the NIFS project is conducting a research activity on how the release area and run-out distance should be assessed. The recommendations from this activity will be incorporated in the next revision of the guidelines.

Step 5: Analysing stability and suggesting necessary preventive measures

This step includes calculations of overall and local stability, together with suggestions for preventive measures where deemed necessary to obtain a satisfactory level of safety. The NVE guidelines suggest a partial safety factor of minimum 1.4, or using percentual improvement of the initially calculated partial safety factor. The latter method implies that instead of reaching a partial safety factor of minimum 1.4, it is possible to improve the initial safety factor for every potentially critical slip surface through the zone up to a certain level. The percentual improvement required depends on the initially calculated safety factor, and the consequence category.

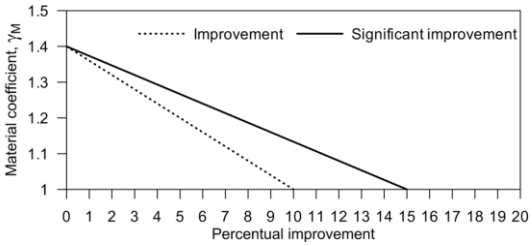


Figure 3 NVE's recommendations regarding the percentual improvement of material coefficients. "Improvement" or "significant improvement" is dependent on under which consequences category the project falls ((Oset et al. (2013)) and NVE (2014)).

It is important to state that percentual improvement can only be used by making geometrical changes (loading or unloading) in the surrounding area, or by using lightweight materials (Fig. 4). The stability calculations have to be performed as both drained and undrained analyses. The use of conventional calculation programs using limit equilibrium methods or finite element methods is allowed. The use of percentual method when calculating progressive landslides leads to the realization of more plans and projects, as it might reduce the cost of necessary preventive measures.

2.4 Eurocodes

The European Committee for Standardization (CEN) consists of members of the European countries. The committee has developed a set of design rules, which are to be used for the construction phase. These rules are to be unison for all countries participating in the committee. In 2008, the rules were officially adopted by the Norwegian authorities. Before the Eurocode came into use, Norway had its own set of national design rules for the construction phase. The Eurocode gives only a brief description of the fact that progressive failures have to be taken into account in the design. Table NA.A.4. in the Eurocode, presented in this paper as Table 6, indicates the use of an "absolute material factor" γ_M of minimum 1.25 on the friction angle and 1.4 for undrained shear strength. At the same

time, the Norwegian National Annex allows for the use of percentual improvement, without any distinct requirements. Table NA.A.4. in Eurocode 7 suggests, *"material factor is increased beyond the values shown in the table at risk for progressive fracture development in brittle materials considered to be present and when it is required to bring it in line with recognized practice for the stability calculation and the present issue"*. The table further mentions "*by analysis of overall stability as conditions appear without measures one may find a lower initial material factor than mentioned in table NA.A.4 shall be assessed in relation to the landslide hazard and stability. It is usually assumed that the constructive measures are implemented in a manner that provides unchanged or increased material factor, and so that the factors which may trigger a failure or a landslide are avoided."* This corresponds with the principles of percentual improvement in the NVE regulations, but Eurocode 7 does not indicate how much increase in the material factor must be considered to account for the progressive failure mechanism.

Table 6 Partial factor for soil parameters

Soil parameters	Symbol	Values
Friction angle	$\gamma_{\varphi'}$	1.25
Effective cohesion	$\gamma_{c'}$	1.25
Undrained shear strength	γ_{cu}	1.4
Unconfined undrained strength	γ_{qu}	1.4
Unit weight	γ_{γ}	1.0

3 HARMONIZATION OF REGULATIONS

Research institutions and consultants, such as SINTEF, Multiconsult AS, the Norwegian Geotechnical Institute (NGI) and the Norwegian University of Science and Technology (NTNU), have been engaged to assist the SP6 with academic and industrial research. An important challenge for the NIFS project is to provide the basis for a harmonization of the safety regulations for the three governmental authorities. Some of the topics addressed are mentioned below:

3.1 Equality between partial safety factors and percentual improvement

This is a central issue in the harmonization of regulations, and it has been addressed in a report from SINTEF/Multiconsult (Tørum et al., 2012). Based on this report, a concept will be further investigated, in which local stability requirements are based on a partial safety factor, and the larger progressive slides may be prevented by either percentual improvement or partial safety factor requirements. The use of percentual improvement will probably be provided with a set of precautions, including requirements for the on-site control.

3.2 Definition of local and overall stability

Subproject Quick clay has proposed the following definitions and boundaries between local and overall stability. These definitions have been included in the NVE guidelines (NVE, 2014).

Local stability refers to a locally defined stability condition with the possibility of ground failure (slide). For development projects, triggering factors may be excavation/filling, base loading, piling, etc. In natural slopes, the triggering factors may be erosion or natural changes in pore pressure. The failure (slide) is limited to the area of influence of the stress changes, which are caused by the triggering factor, or that have risen in the slope due to natural changes. Typical examples are: local failure during filling or construction of a foundation (bearing capacity failure), local slide as a result of an excavation in a construction pit or in conjunction with road/railway construction (stability failure), or a local slide as a result of changes in pore pressure or erosion. Measures taken to safeguard against local stability failures must meet the requirements regarding absolute material factors, as described in the Norwegian national design rules (NS-EN 1997-1:2004+NA:2008). Any gradation of material factor beyond the specified minimum level is

done in accordance with the client's guidelines.

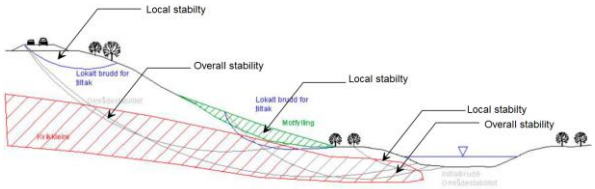


Figure 4 Local and overall stability (NIFS report 72-2012; www.naturfare.no).

Overall stability refers to a condition in which a local failure (see above) can initiate a comprehensive progressive forward or backward retrogressive slide in brittle materials, typically sensitive clay. The local failure can be initiated in both dilatant and brittle materials. In both cases, the local failure will influence and initiate a progressive failure of the brittle adjacent materials. If the brittle material has a greater extent and thickness outside the local influence area, larger areas can be affected and develop into slides. These slides can become quite extensive in areas where the remoulded brittle material has a free outlet in sloping terrain. The run-out distance of the slide will depend on downstream terrain gradient and local topography, the remoulded shear strength of the brittle material, and its thickness and volume above the release area. The level of safety for overall stability must be assessed in adjacent areas containing sensitive clays (Danger zones). The safety requirements are defined in TEK10, and specified in the NVE guidelines R2/2011.

3.3 Anisotropy

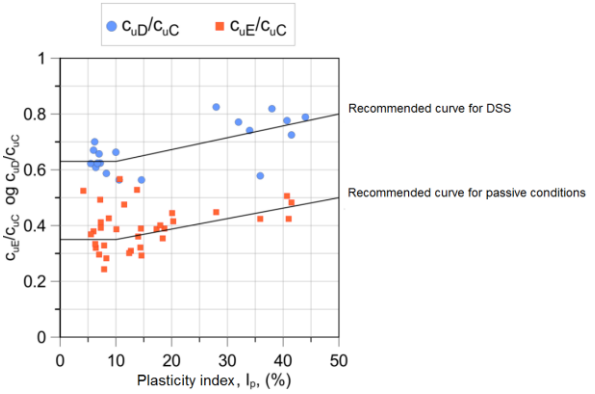


Figure 5 Recommended curves for anisotropy factors for design in Norwegian clays, correlated with plasticity index, Ip. (NIFS report 77-2014; www.naturfare.no).

The NIFS project is aiming for a standard in which the anisotropy conditions are evaluated from local conditions, and in which the use of empirical values is an exception. However, for less complex projects, empirical values can be considered adequate. As a result, during 2014, a working group comprising representatives from NGI, Multiconsult AS, SINTEF Byggforsk, NNRA, NPRA and NVE, drafted a report with a joint recommendation for the use of anisotropy factors for design in Norwegian clays (Thakur et al. 2014). The database for anisotropy related to plasticity index and other index parameters should be extended to provide a better base for the empirical relations. The report is freely available at www.naturfare.no.

3.4 Effect of strain softening

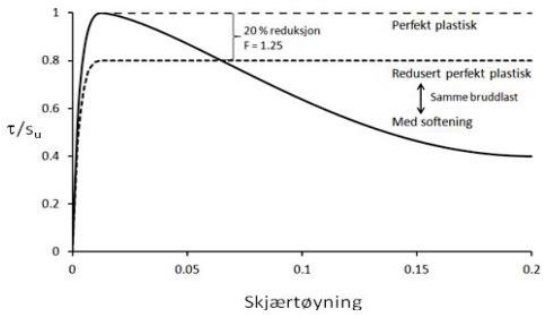


Figure 6 Effect of softening (Fornes et al. 2014).

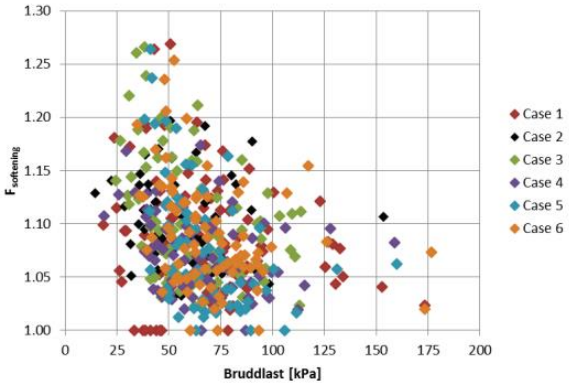


Figure 7 Correlation between softening factor and failure load for six cases with different combinations of parameters (Fornes et al. 2014).

Capacity or stability analyses performed using classical limit equilibrium theory-based calculation methods like the "method of slices" (Bishop and Morgenstern (1960) and Janbu (1973)), are based on the assumption that soil behaviour is "perfectly-plastic". However, for soft sensitive clays these classical theories have limited validity, because capacity or safety factors are overestimated if the effect of strain-softening is not accounted for in the analyses. The Norwegian code of practice suggests different material coefficients for construction activities on soft sensitive clay deposits. The guidelines by the NPRA suggest an increase in the required material coefficient from 1.4 to 1.5 or to 1.6 (about 7-14% increase) depending on the consequence category, to account for the effect of strain softening. The NVE guidelines for evaluating overall stability in areas with quick and sensitive clays suggest a material coefficient ≥1.4. The Norwegian National Annex to Eurocode 7 suggests an unspecific increase in the material coefficient from 1.4 to account for the effect of strain softening. Neither the NVE nor the Eurocode 7 guidelines are specific about an increase in the material coefficient to account for the strain softening. Using finite element calculations, Jostad et al. (2013) and Fornes et al. (2014) suggest that the capacity of Norwegian soft sensitive clays may be overestimated by an average of 6% if the effect of strain softening is neglected. From this study, it can be noted that the recommendation in the NPRA guidelines is suitable. However, further deliberations are necessary in order to find out how these results should be implemented.

3.5 Safety principles for assessing existing/natural slopes

The NIFS project initiated a workshop with participants from NTNU, NGI, Multiconsult, SINTEF and NIFS. The objective of the workshop was to establish criteria for when effective stress analyses can be used as a design basis for assessing the safety levels of natural/existing slopes. The main conclusions were that the effective stress analysis gives an accurate assessment of natural slopes, given the following circumstances: 1) The slope is in a stable and virtually stationary state, besides seasonal pore pressure variation and the impact of prolonged (extreme) precipitation. 2) The pore pressure distribution in the slope is examined thoroughly, and extreme values of pore pressure that may be critical for the slope are accounted for. Further, the effects of water-filled cracks is taken into account. 3) The effects of erosion, which could potentially lead to undrained stress changes, are attended to. 4) The robustness of the slope is satisfactory – in principle, this means that the factor of safety from an undrained analysis is above 1.2.

3.6 Post-failure movement of landslide and landslide potential in sensitive clays

According to the current practice in Norway, brittle clay is defined by a $S_t \geq 15$ and a $c_{ur} \leq$ 2.0 kPa. Thakur et al. (2012) initiated a discussion on the definition of brittle clay. This study shows that we need to understand the mechanical properties of sensitive clay better, not only numerically but also physically. Thakur et al. (2013) present a comprehensive overview of several parameters that may influence the extent of landslides, e.g. topography, stability number (Nc), remoulded shear strength (c_{ur}), liquidity index (I_L) and quickness (Q). The Norwegian landslide data as presented by Thakur and Degago (2012) and Thakur et al. (2013) support the fact that large landslides with retrogression greater than 100 metres are only possible when $c_{ur} < 1{,}0$ kPa or $I_L > 1{,}2$ or $Q > 15\%$ and $N_c > 4$. These criteria are useful and can be used as indicators to assess the potential for occurrence of large landslides. However, determining the extent of a landslide with only an individual geotechnical parameter may not be sufficient.

A complete stress-strain behaviour of soft sensitive clays must be accounted for in the calculation of the post-failure movement of landslides. Thakur and Degago (2013) and Thakur et al. (2013 and 2015) suggest a concept of defining remoulding energy for Norwegian sensitive clays; see Figure 8.

Their work proposes determination of remoulding energy based on stress-strain relationship of sensitive clays obtained using field vane shear tests. Their work shows that a representative stress-strain behaviour of soft sensitive clays can be established using electric field vane shear method. They suggest that required remoulding energy provides a better basis for understanding the post-failure movements in terms of the retrogression and the run-out distance of landslides in sensitive clays. The finding is supported by the Canadian data.

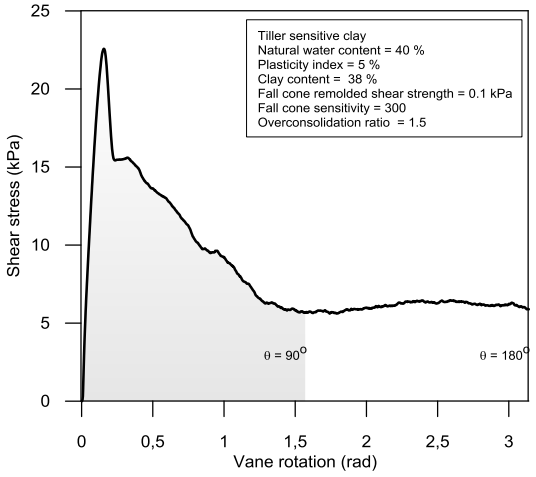


Figure 8. Shear stress vane rotation curve for the tested Tiller sensitive clay at 8.5 m depth (Thakur et al. 2015). The area covered by the stress-strain curve refers to the remoulding energy.

4 CLOSING REMARKS

By taking steps to harmonize the guidelines related to construction on sensitive clays, the NIFS project and its partners have initiated a process that will yield socioeconomic positive results. In addition, a harmonized regulatory framework will enable both private and public builders to realize both more complex and less complex projects that would previously have been rejected because of regulatory contradictions, without compromising on safety. The NIFS project represents a broad collaboration between universities and private and public sectors. This collaboration has ensured a consensual understanding and interpretation of both the safety philosophy regarding sensitive clays in Norway, as well as the physical and theoretical behaviour of brittle materials. This knowledge, and common understanding, is paramount when it comes to developing new regulatory frameworks that will ensure the safety of everyone building or living on brittle or quick clay.

5 ACKNOWLEDGEMENTS

The authors wish to acknowledge the National research program *"Natural Hazards: Infrastructure, Floods and Slides (NIFS)"* for supporting this initiative. The authors greatly acknowledge the contributions of NTNU, NGI, SINTEF and Multiconsult to Subproject (SP6) - Quick clay.

6 REFERENCES

Bishop AW, Morgenstern N R (1960) Stabilitycoefficients for earth slopes. Geotechnique 10(4), 129-50

DiBK: Direktoratet for Byggkvalitet (2011), Veiledning om tekniske krav til byggverk, 24-38

Fauskerud OA, Athanasiu C, Havnegjerde CR et al (2012). Use of anisotropy factors in stability calculations for brittle clay slopes. NIFS report nr 75. ISBN 978-82-410-0863-4

Fornes, P., Jostad HP, Karlsrud, K. and Lacasse, S. (2014). NIFS N-6.5.2 Sikkerhet ifm utbygging i Kvikkleireområder – oppsummeringsrapport. NIFS report nr. 88. ISBN 978-82-410-1037-8

Janbu N, Nestvold J, Røe Ø et al (1993) Leirras – årsaksforhold og rasutvikling. Særtrykk fra Verdalsboka Ras i Verdal, bind B (Clay slides, causes and development. Offprint from the book "Verdalsboka Ras i Verdal, bind B"). Verdal kommune. ISBN:8-9909500-8-5 (in Norwegian)

Janbu N (1973) Slope stability computations. The embankment Dam engineering, Casagrande Volume. Editors Hirschfeld and Poulos. John Wiley &Sons, p 47-86

Janbu N, Nestvold J, Røe Ø et al (1993) Leirras – årsaksforhold og rasutvikling. Særtrykk fra Verdalsboka Ras i Verdal, bind B. (Clay slides, causes and development. Offprint from the book "Verdalsboka Ras i Verdal, bind B.) (In Norwegian.) ISBN 8-9909500-8-5

Jostad HP, Fornes P, Thakur V (2013) Effect of strain-softening in design of fills in gently inclined areas with soft sensitive clays. First international

workshop on landslide in sensitive clays. Quebec, Cananda.

Karlsrud K, Aas G Gregersen O (1985) Can we predict landslide hazards in soft sensitive clays? Summary of Norwegian practice and experiences. NGI publication no 158. ISBN 82-546-0119-4

Lulseged A (2014) Masteroppgave "utbredelse av kvikkleireskred", NTNU.

Mitchell RJ, Markell AR (1974) Flow slides in sensitive soils. Canad. Geotech. J., 11(1):11–31

NGF: Norsk geoteknisk forening (2011). Veiledning for symboler og definisjoner i geoteknikk identifisering og klassifisering av jord.

NIFS: Natural Hazards – Infrastructure for flood and slides (2012) Programplan 2012-2015 for etatsprogrammet, (In Norwegian) ISSN: 1501-2832

NIFS-rapport 21-2013. Utstrekning og utløpsdistanse for kvikkleireskred basert på katalog over skredhendelser i Norge. Datert 21.11.2012. Utarbeidet av NGU – Jean-Sébastien L'Heureux, Inger Lise Solberg. Utgitt av NVE.

NIFS-rapporter 38-2013og 46-2013. Q-BING – Utløpsmodell for kvikkleireskred. Utarbeidet av NGI - Dieter Issler, José Mauricio Cepeda, Byron Quan Luna, Vittoria Venditti , Jean-Sébastien L'Heureux, Utgitt av NVE.

NIFS-rapport 77-2014. Valg av karakteristisk c_{uA} – profil basert på felt – og laboratorieundersøkelser. Datert 19.05.2015, utarbeidet av Frode Oset, Margareta Viklund, Odd Arne Fauskerud, Stein Christensen, Steinar Nordal, Stein-Are Strand, Vidar Gjelsvik, Vikas Thakur. Utgitt av NVE.

Nigussie D (2013) Masteroppgave på "utbredelse av kvikkleireskred", NTNU.

NNRA: Norwegian National Rail Administration (2013) Regulations for design of railway construction. (In Norwegian), https://trv.jbv.no

NPRA: Norwegian Public Roads Administration (2010) Håndbok V220 Geoteknikk i Vegbygging. http://www.vegvesen.no/Fag/Publikasjoner/Handboker

NS: Norges Byggstandardiseringsråd (1979) Sikkerhetsprinsipper i geoteknikk. Veiledning for bruk av grensetilstandsmetoden (In Norwegian)

NVE: Norwegian Water Resources and Energy Directorate (2011) Flaum- og skredfare i arealplanar. Regulation no. 2/2011. (in Norwegian), ISSN: 1501-9810

NVE: Norwegian Water Resources and Energy Directorate (2014) Sikkerhet mot kvikkleireskred. Regulation no. 7/2014. (in Norwegian), ISSN: 1501-0678

Oset F., Thakur, V., Dolva B. K., Aunaas K., Sæter M. B., Robsrud A., Viklund M., Nyheim T., Lyche E., and Jensen O. A. (2013). Regulatory Framework for Road and Railway Construction on the Sensitive Clays of Norway.

Thakur V, Degago SA (2012) Quickness of sensitive clays. Géotechnique Letters 2(3):87-95

Thakur V, Degago SA (2013) Disintegration energy of sensitive clays. Géotechnique Letters 3 DOI 10.1680/geolett.12.00062

Thakur V, Degago SA, Oset F et al (2013) Characterisation of post-failure movements of landslides in soft sensitive clays. First international workshop on landslide in sensitive clays. Quebec, Cananda

Thakur V, Gylland S A, Sandven R, Degago S A Oset F (2015) In-situ determination of disintegration energy of sensitive clay. 68th Canadian Geotechnical Conference, Quebec, Canada. Sept. 2015.

Thakur, V., Degago, S. A., Oset, F., Aabøe, R., Dolva, B.K., Aunaas, K., Nyheim, T., Lyche, E., Jensen, O. A., Sæter, M. B., Robsrud, A., Viklund, M. & Nigussie, D. (2014): Characterisation of post-failure movements of landslides in soft sensitive clays. Chapter 8 in book Landslides in Sensitive Clays. Advances in Natural and Technological Hazards Research, volume 36, 2014, pp 91-103, Springer.

Thakur V., Degago S.A., Oset, F., Dolva, B. K. & Aabøe, R. (2013) A new approach to assess the potential for flow slide in sensitive clays. Une nouvelle approche pour évaluer le potentiel de Coulée dans les argiles sensibles. International conference on soil mechanics and geotechnical engineering, ISSMGE, Paris, France, pp 2265-2268.

Thakur V and Degago S (2013) "Disintegration Energy of sensitive clays" Geotechnique Letters. Vol. 3, pp 20-25.

Thakur V, Oset F, Degago S A, Berg P O, Aabøe R, Wiig T, Elisabeth E D, Lyche E, Sæter M B, Robsrud A (2011) "A critical appraisal on the definition of Brittle clays". Nordic Geotechnical Meeting. Copenhagen, May 2012, pp 451-462.

Thakur V and Degago S (2012) "Quickness of sensitive clays" Geotechnique Letters. Vol. 2, pp 87-95.

Thakur V, F. Oset, S.A. Degago & R. Aabøe, A. Watn (2013) Transportation infrastructure on soft sensitive clays: Some essential aspects and examples. Second international conference on transport geotechnics. Advances in Transportation Geotechnics II – Miura et al. (eds) 2012 Taylor & Francis Group, London, ISBN 978-0-415-62135-9, pp 836-842.

Tørum E, Christensen S, Narjord H et al (2012) Likestilling mellom bruk av absolutt materialfaktor og prosentvis forbedring? SINTEF/Multiconsult report SBF2012A0309. ISBN 978-82-410-0860-3

Experiences of integrated GPR and Laser Scanner analysis – We should not only look down but also around

Timo Saarenketo, PhD, adj.prof., CEO
Roadscanners, Finland, timo.saarenketo@roadscanners.com

ABSTRACT

The underlying causes of geotechnical problems on roads have traditionally been tackled by drilling and/or taking samples through and under the road structure. These types of investigation are however both expensive and traffic intrusive and, as the latest tests with new non-destructive road survey techniques have shown, can often lead to false diagnostics and rehabilitation solutions that do not work in the long term.

This paper will demonstrate the benefits of the integrated analysis of ground penetrating radar (GPR) and laser scanner (lidar) data in road structural condition surveys. This will include the analysis of drainage condition, the use of GPR in detecting anomalous moisture in road structures and subgrade soils, and how laser scanner data can provide information regarding drainage structures and drainage related deformations on the road surface. Cases will be provided on how GPR can be used to detect ice lenses and unfrozen water in the frozen ground as well as examples of the use of GPR and laser scanner analysis in road embankment stability problem diagnostics. Finally, examples of the integrated analysis of GPR, Laser Scanner and Traffic Speed Deflectometer data, collected in Finland, will be summarised.

Keywords: ground penetrating radar, laser scanner, diagnostics, drainage, permanent deformations

1 INTRODUCTION

The main traditional procedure for engineers working in road problem diagnostics and rehabilitation design has been to look directly under the pavement. This assumes that all of the sources of problems are related to pavement structure thickness and material properties, and the moisture content of road structures and subgrade soil beneath the pavement. This strategy has however often led to imprecise conclusions as to where the root causes of the underlying problems really are. A good example is that of capillary action which is described in almost all figures in civil engineering text books as a vertical force adsorbing moisture from the subgrade under the road.

Such traditional strategies have now started to be challenged thanks to the results obtained by modern road survey techniques and their integrated analysis. When considered together good visualisations can be produced of the relationship between road structures, road geometry and the condition of the road surroundings over different seasons. As an example, the results of these new methods of evaluation have given new valuable information concerning the importance of well functioning road drainage. A good drainage system is not just an issue for summertime, it should be also be maintained during the wintertime.
This paper will present experiences and latest findings of road problem diagnostics made based on the results of GPR, Laser Scanner and Traffic Speed Deflectometer surveys carried out by Roadscanners.

2 SURVEY METHODS

2.1 Ground Penetrating Radar

Ground Penetrating Radar systems use discrete pulses of radar energy with a central frequency varying from 10 MHz up to 2.5GHz to resolve the locations and dimensions of electrically distinctive layers and objects in materials. Pulse radar systems transmit short electromagnetic pulses into a medium and when the pulse reaches an electric interface in the medium, some of the energy will reflected back while the rest will proceed forwards. The reflected energy is collected and displayed as a waveform showing amplitudes and time elapsed between wave transmission and reflection. When the measurements are repeated at herz frequencies (currently up to 1000 scans/second) and the antenna is moving, a continuous profile is obtained across the target (Saarenketo 2006). In addition to pulse radar GPR systems (Figure 1) stepped frequency radar systems are also entering the road survey markets.

The propagation and reflection of the radar pulses is controlled by the electrical properties of the materials, which comprise 1) magnetic susceptibility, i.e. magnetism of the material, 2) relative dielectric permittivity and 3) electrical conductivity. The magnetic susceptibility of a soil or road material is regarded as equal to the value of the vacuum, and thus does not normally affect the GPR pulse propagation. The most important electrical property affecting GPR survey results is dielectric permittivity and its effect on the GPR signal velocity in the material and, as such, it is very important to know precisely how to calculate the correct depth of the target (Hamrouche and Saarenketo 2012).

In road surveys the GPR method has been traditionally used to measure the thickness of the pavement structure layers. Recently however GPR systems have been improved and their data analysis has also enabled material properties such as moisture content and susceptibility to permanent deformations to be calculated (Saarenketo 2006, www.roadex.org).



Figure 1. Road survey system equipped with ground penetrating radar system (in front) and a 2D laser scanner (at the back).

2.2 Laser scanner

Laser scanning is a technique where distance measurement is derived from the travel time of a laser beam from the laser scanner to the target and back. When the laser beam angle is known, and beams are sent to a range of directions from a moving vehicle with a known position, it is possible to make a 3D surface image, or 'point cloud', of a road and its surroundings. The point cloud can have millions of points, with every point having x, y & z coordinates and additional reflection or emission characteristics. The accuracy of a laser scanner survey can be affected by factors that reduce visibility, such as dust, rain, fog or snow. High roadside vegetation can also prevent the capture of information from the hidden ground surface.

A laser scanner is composed of three parts: a laser canon, a scanner and a detector. The laser canon produces the laser beam, the scanner circulates the beam and the detector measures the reflected signal and defines the distance to the target. The distance measurement is based on the travel time of light, or phase shift, or a combination of both. Laser scanner systems can be classified into two types of system: 3D laser scanners that can be used for mobile mapping, and 2D laser that is designed to be used in basic pavement engineering projects (Figure 1) (Saarenketo et al. 2012).

The great advantage of laser scanner data compared to, for instance, profilometer data is that data can be collected outside the pavement area. This allows the connections between drainage defects and pavement failures to be shown visually. The greatest benefits of 2D and 3D laser scanning systems are gained when they are used together with other NDT pavement systems.

2.3 Traffic Speed Deflectometer

Deflection measurements have a key role in evaluating the structural condition of a pavement structure and the fatigue level of the asphalt. With the help of deflection surveys, it is possible to locate road sections that are still visually in good condition but which will become distressed very soon if appropriate measures are not taken. Traditionally deflection surveys have been carried out with falling weight deflectometer systems but their limitation is that they are point measurement and are traffic intrusive. The new solution for this problem is the traffic speed deflectometer (TSD) (Figure 2) that measures continuous deflections of a pavement under a moving 10 tonne axle load using Doppler sensors. The normal survey speed with this truck is 80 km/h so it does not require any protection during the survey. Deflection bowls similar to FWD can be calculated from the TSD measurements.



Figure 2. TSD truck used deflection surveys in Finland.

3 INTEGRATED DIAGNOSTICS USING GPR, LASER SCANNER AND TSD DATA – SELECTED CASES

3.1 Damages related to private access road culverts

ROADEX research using modern survey methods has revealed new findings regarding the factors that affect the condition of low volume roads in Northern Europe (www.roadex.org). One of these is the significant amount of road damages that are related to poorly performing private access road culverts. Figure 3 presents examples from Rd 934 in Finland where more than 50% of high frost heaves were located close to private access roads. The culverts at these points were clogged in the early spring when the snow started to melt and the road was still frozen. This caused water to infiltrate into the frozen road structures causing frost heaves. Figure 4 shows the consequence of this infiltration, which can be normally seen as permanent deformations in the road shoulder.

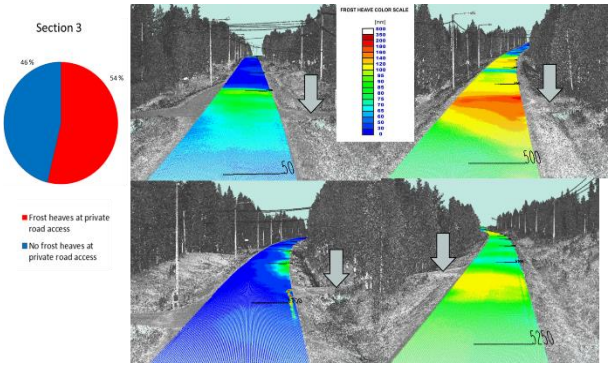


Figure 3. Examples of 3D laser scanner frost heave survey data. Frost heaves are clearly related private access roads and their clogged culverts. Statistics on the left show that more than 50% of the frost damages are linked to private road access.

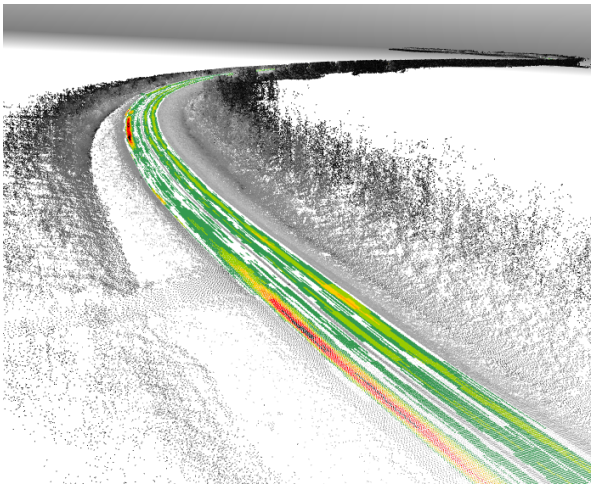


Figure 4. Rutting analysis, based on 2D laser scanner data, shows that shoulder deformation can be related to private access road.

3.2 Main road culverts and slope stability

A new development in GPR analysis is the analysis of the saturation level in the road structure. This is based on the fact that at high saturation levels (>80%) the material attenuates the high frequency components of the signal and thus the relative amount of low frequencies is increased. This can be presented on GPR profiles as Figure 5 from Rd A83 in Scotland shows. In this case a main road culvert was clogged under a road located on sloping ground. Due to this the embankment around the culvert was saturated with water, and this had already caused a shear failure close to road shoulder at the time of the survey.

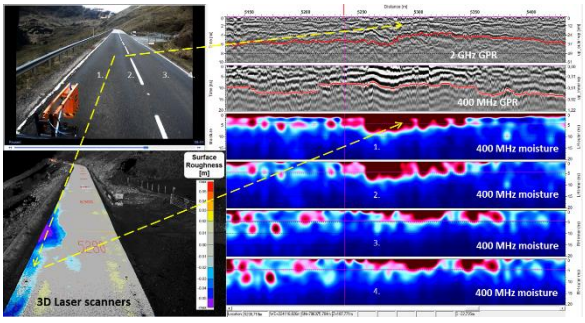


Figure 5. GPR data and moisture analysis and laser scanner profile from Rd A83 in Scotland

3.3 Frozen main road ditches

Frost heave analyses based on laser scanner surveys have shown that the depth of the ditch is not the only critical factor in road drainage management. Figure 6 presents a case from HW4 in Finland where ice has formed in the bottom of a ditch during the winter and has eventually filled it. In springtime the water melting from the snow infiltrates into the frozen road structure causing formation of ice lenses and differential frost heaves. This problem could be detected in 2011 and 2013 as figure 6 shows.

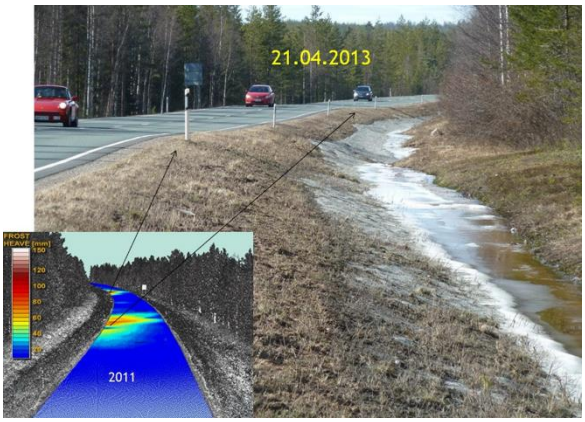


Figure 6. Laser scanner data based frost heave analysis from HW4 in Finland. The ditch is filled with ice and in the summer the bottom of the ditch is 60 cm deeper than the ice surface.

3.4 Detecting unfrozen water in frozen pavement structures

The GPR moisture analysis technique is also sensitive in detecting unfrozen water in frozen material, i.e. the presence of segregation ice. This information, together with laser scanner data analysis, has brought valuable new information regarding the importance of early snow removal from road shoulders. Figure 7 from Rd 3662 in Finland shows that water melting from the road shoulder is infiltrating into the frozen pavement and base course forming ice lenses. Permanent deformations can be seen to take place exactly on these locations later as a result of the excess amounts of water melting from the ice lenses. Rutting analyses reveal 1.5-2 times higher rut depths at these locations.

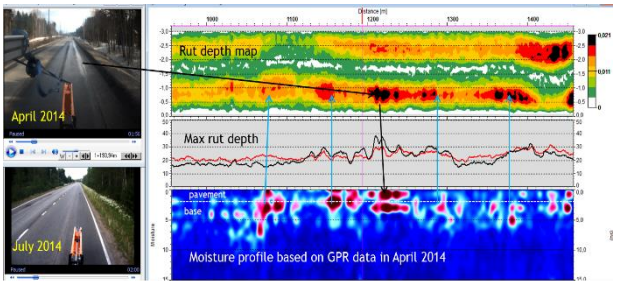


Figure 7. Rut depth maps from right line (top), maximum rutp depths (middle) and GPR moisture analysis (bottom) from 2 GHz data measured in April 2014 (photo left above).

3.5 TSD and laser scanner data analysis and Mode 2 rutting

Traffic Speed Deflectometer data and its integrated analysis can also provide new information on the failure mechanism of both highways and low volume roads. A good finding has been the close relationship between the Base Curvature Index (BCI), calculated from the TSD data, and Mode 2 rutting that can be seen as shoulder deformations in laser scanner data. Figure 8 provides a good example from Rd 3662 in Finland where severe road shoulder deformations were found on sections with BCI values higher than 80. Very often these sections with high BCI values also had problems with poor drainage.

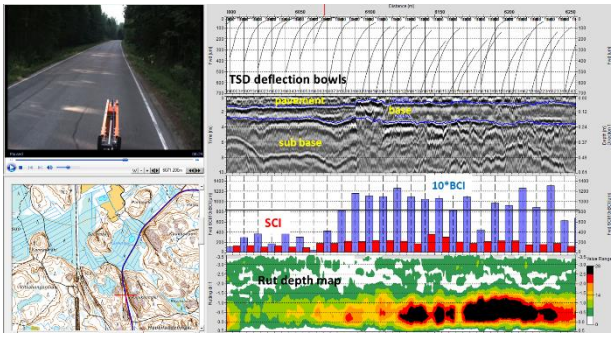


*Figure 8. TSD deflection bowls (top field), 2 GHz GPR data (2nd field), SCI and 10*BCI values (third field) and laser scanner rut depth map from Rd 3662 in Finland.*

4 CONCLUSIONS

The experiences of integrated analysis of GPR, Laser Scanner and TSD data over the last few years have provided greater understanding of the root causes of road problems in cold climate areas. Poor winter maintenance and delayed removal of snow walls, for example, seem to have a great effect on the formation of permanent deformations on road shoulders. This is especially the case on narrow low volume roads. Clogged access road and main road culverts are also often the main reason for early phase pavement damages on roads.

These types of problems can however be easily treated through better maintenance policies and standards. The new technologies presented in the paper will also be a great help in moving towards more proactive maintenance strategies in the future. This will lead to substantially longer pavement lifetimes with the consequential potential for major savings in annual road paving costs.

REFERENCES

Hamrouche, R. and Saarenketo, T. (2012). Improvement of coreless method to calculate the average dielectric value of the whole asphalt layer of a road layer. Proceedings of 15th International Conference on Ground Penetrating Radar, Brussels, Belgium.

Saarenketo, T. (2006). Electrical properties of road materials and subgrade soils and the use of ground penetrating radar in traffic infrastructure surveys. Acta Univ.Oul. A471, 2006. 125 p.

Saarenketo, T., Matintupa, a. and Varin, P. (2012). The use of ground penetrating radar, thermal camera and laser scanner technology in asphalt crack detection abd diagnostics. 7th RILEM International Conference on Cracking in Pavements. A.Scarpas et al. (Eds.) pp.137-145.

Full scale reinforced road embankment test sections over soft peat layer, Võõbu, Estonia

J. Forsman
Ramboll Finland Oy, Finland, juha.forsman@ramboll.fi

T. Dettenborn
Aalto University, Finland

P. Skepast
Skepast&Puhkim AS, Estonia

M. Mets and M. Olep
AS Geotehnika Inseneribüroo G.I.B, Estonia

A. Ellmann
Tallinn University of Technology, Department of Road Engineering, Estonia

I. Vallas, T. Tõnts and Kontson, K.
Maanteeamet, Estonia

ABSTRACT
Various road embankment reinforcements on over of a 2 to 4 meter thick peat deposit have been constructed in 2015 in the area of Kose-Võõbu in the northern part of Estonia. The test sections consist of five different reinforced road embankments: one layer of georeinforcement, two layers of georeinforcements, geocell mattress, light weight aggregate (LWA) and expanded polystyrene (EPS) light-weight embankment structures with georeinforcement. An additional test section is a traditional mass replacement. To accelerate the consolidation of the peat, reinforced test sections are loaded with surcharge. This paper presents information about peat laboratory tests, construction and field monitoring. The settlements of each test section are precisely measured with settlement plates installed over the peat layer, over e.g. EPS and LWA layers and surface dressing (bituminous layer). In addition, the surface treatment layer has been mapped by high-resolution laser scanning, also after surcharge removal the scanning will be conducted to obtain settlement profile due the surcharge. The intent of the research is to validate technical and economic feasibility of different reinforcement methods over designed road alignment (road E263).

Keywords: test embankment, reinforcement, peat, instrumentation, light weight material

1 INTRODUCTION

Various road embankment reinforcements on top of a 2 to 4 meter thick peat deposit have been constructed in summer and autumn 2015 in the area of Kose-Võõbu in Estonia (Fig. 1). The test sections consist of six different road embankments. Test sections are numbered as follows (Fig. 2):

0. mass replacement
1. one layer of georeinforcement
2. two layers of georeinforcements
3. geocell mattress
4. light weight aggregate and
5. EPS light-weight embankment.



Figure 1. Location of the Võõbu test area.

Some details of the project:

- total length of test sections: ≈200 m
- number of test sections: 6 (sections 0 - 5)
- length of each section: 30 m
- width of embankment: 23 m (from toe to toe) and
- 98 measurement points for determining settlements.

To accelerate the consolidation of the peat layer the test sections were loaded with surcharge (pre- and over-loading embankments).

2 SITE DESCRIPTION

2.1 Geology

The test site is located in Järvamaa, Paide Region alongside the Tallinn–Tartu–Võru–Luhamaa road at km posts 67.076–67.256. The test area is a part of Kõrvemaa swamp area. Based on the soundings and ground penetrating radar (GPR) results the thickness of the peat layer appeared to be 1.8-3.4 m at the test area. The ground surface level varies from +74.2 to +74.3. Between the section 5 and 0 there is a shallow ditch where the ground level is lower. Underlying the peat layer is clayey silt, fine sand and sand with gravel (moraine).

2.2 Soundings and laboratory tests

The test area layout and the location of sounding points are presented in Fig. 4. Most of the soundings and samples were taken in June 2015 but some soundings are older. In total 13 boreholes and 6 vane shear test were carried out and ≈130 disturbed and some undisturbed samples were collected.

The thickness of the peat layer is approx. 1.8-3.4 m. According to soundings and samplings there are three different layers of peat (Fig 2). The presented shear strength are unreduced and from initial conditions.

- z=0-0.5 m: low degree of decomposition, contains roots, branches and stumps
- z=0.5-1.5 m: medium to high degree of decomposition, w≈400-600 %, τ≈9 kPa
- z=1.5-3.5 m: medium degree of decomposition, w≈700-900 % τ≈4 kPa

Comprehensive oedometer compression tests were conducted on samples from borehole no. 13. Tests were carried out according to standard CEN ISO/TS 17892-5.

The ground investigation results from borehole no. 13 are presented in Fig. 2 and results of oedometer tests in Table 1.

Table 1. Oedometer compression test results for the peat samples from borehole no. 13. Used loading steps were σ=10 (1 h); 25 (22 h); 50(24 h); 75 (24 h); 100 kPa (24 h).

Depth	σ	w	ρ_d	C_C	C_α	c_v *	k *	m_v *	e
[m]	[MPa]	[%]	[t/m^3]	[-]	[-]	[m^2/a]	[m^{-10}/s]	[MPa^{-1}]	[-]
0.85 - 0.95	0	910	0.10	6.65	-	-	-	-	15.2
	0.05				0.31	26.2	250	3.0	8.6
	0.075				0.47	10.64	56	1.6	7.1
	0.1				0.16	-	-	-	6.7
1.35 - 1.45	0	1043	0.09	7.50	-	-	-	-	17.2
	0.05				0.39	25.4	92	1.1	8.8
	0.075				0.38	9.4	137	4.6	7.5
	0.1				0.11	-	-	-	6.8
2.15 – 2.25	0	800	0.11	5.70	-	-	-	-	12.8
	0.05				0.32	6.0	54	2.8	7.4
	0.075				0.38	11.0	30	0.9	6.4
	0.1				0.12	-	-	-	5.7
2.75 – 2.85	0	630	0.14	4.57	-	-	-	-	10.2
	0.05				0.32	28.6	136	1.5	6.6
	0.075				0.31	2.6	6.9	0.8	5.9
	0.1				0.37	-	-	-	5.2

* Calculated σ = 0.25-0.05 Mpa; σ = 0.05-0.075 MPa

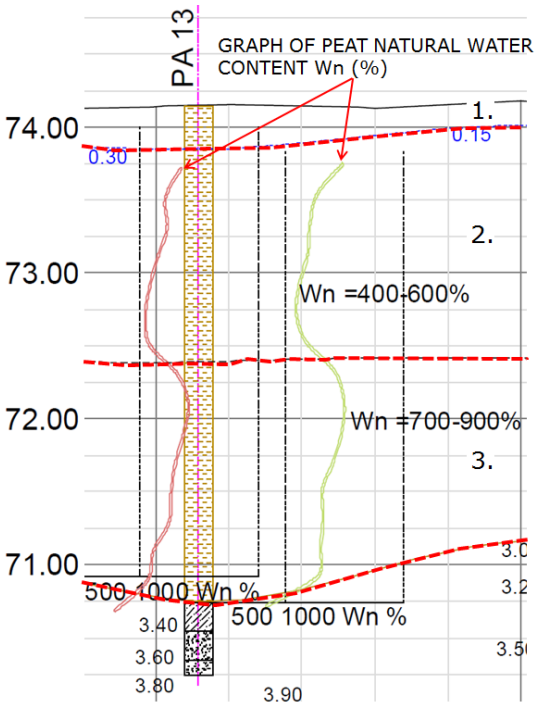


Figure 2. Bore hole 13. Three peat layers and natural water content of peat in two points.

2.3 Ground penetrating radar (GPR)

Before construction works the thickness of peat layer in test area was measured (June 2015) with ground penetrating radar (GPR).

The used GPR antennas were: 400 MHz and 100 MHz GSSI antennas and also 500 Hz MALA antenna. The GPR-measurement results were calibrated with borehole data. The average measured dielectric constant was E_r=44 which indicates that peat has a high water content. Because of the high water content only 100 MHz antenna data was used for the thickness analysis.

3 CONSTRUCTION OF TEST SECTIONS

Construction of the test structures took place from June to October 2015 starting from the section 1 and ending with the construction of the surcharge (surcharge is estimated to remain in place until autumn 2016).

The contractor was Lemminkäinen Eesti AS. The construction is presented in the time lapse construction video, presented in the following link: https://onedrive.live.com/redir?resid=30E9DBABB750EB6F!183&authkey=!AJ7ke3VSUyp9s58&ithint=folder%2cdocx.

The longitudinal profile of test sections and peat layer thickness is presented in Fig. 5. The realized construction timetable for embankment height and loading on the peat layer is presented in Table 2.

This paper presents the designed heights of the constructed embankments. The effect of the settlements during construction and its affect to embankment height and load magnitude of the peat layer will be analysed with settlement follow-up measurements and reported in later reports and articles during 2016-2017.



Figure 3. Test sections. 0. mass replacement, 1. one layer and 2. two layers of georeinforcements, 3. geocell mattress, 4.light weight aggregate and 5. EPS light weight embankment structure. Tallinn is on the left.

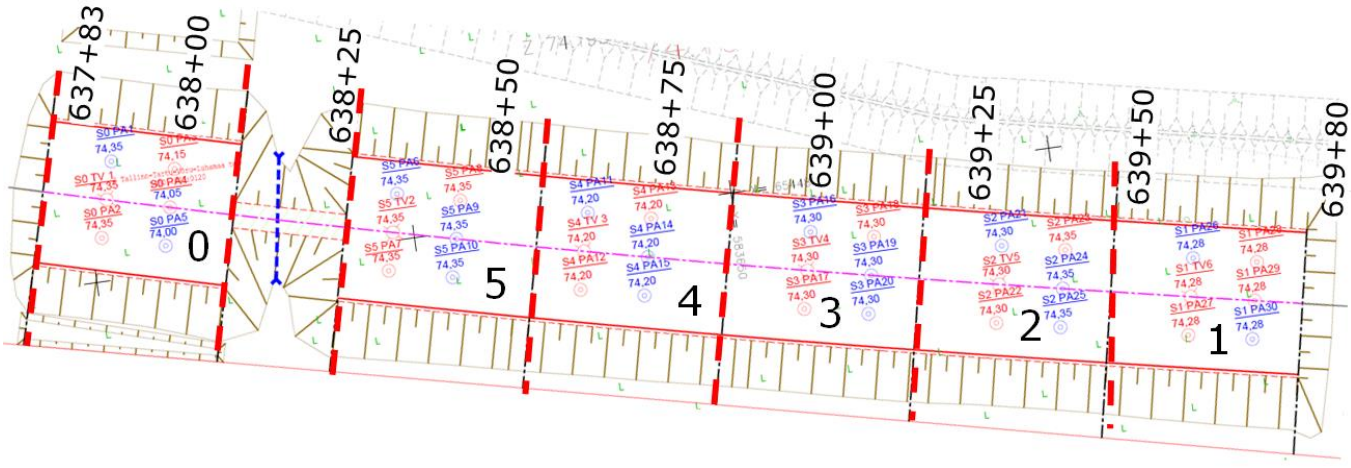
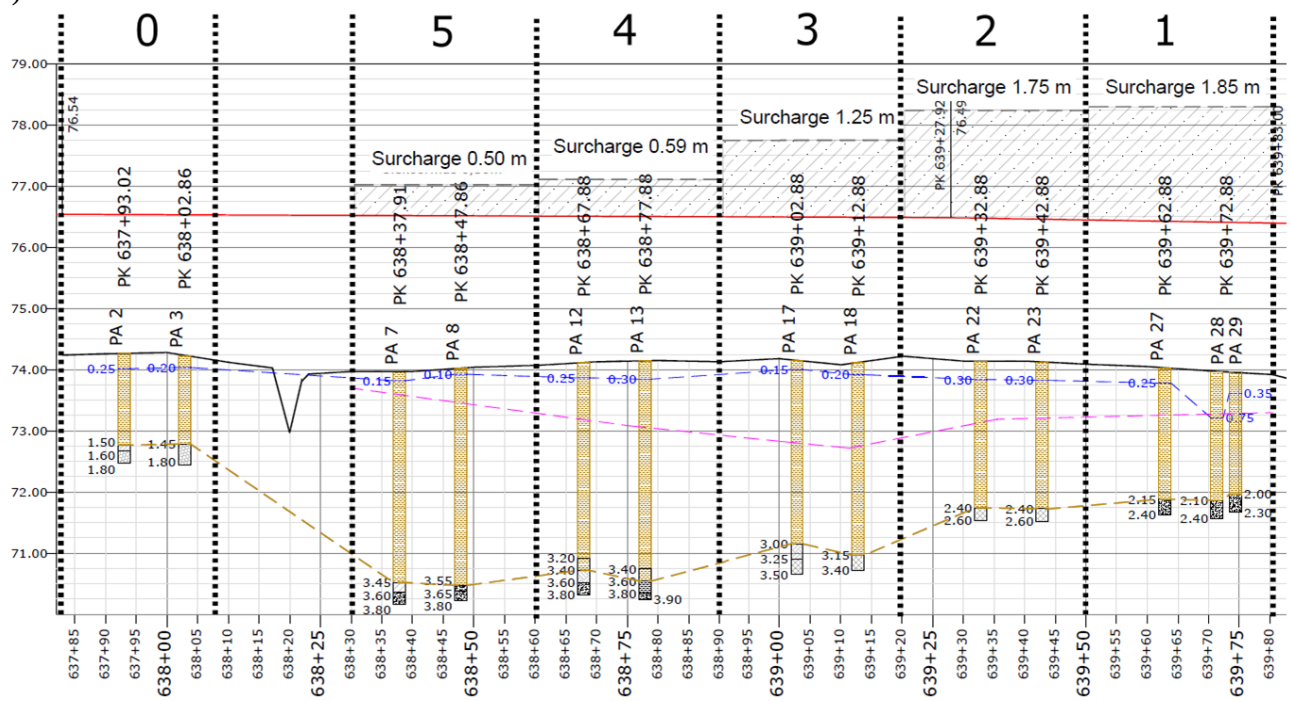


Figure 4. Location of ground investigations points. Distance between posts 639+80 -637+83 is ≈200 m.

a)



b)

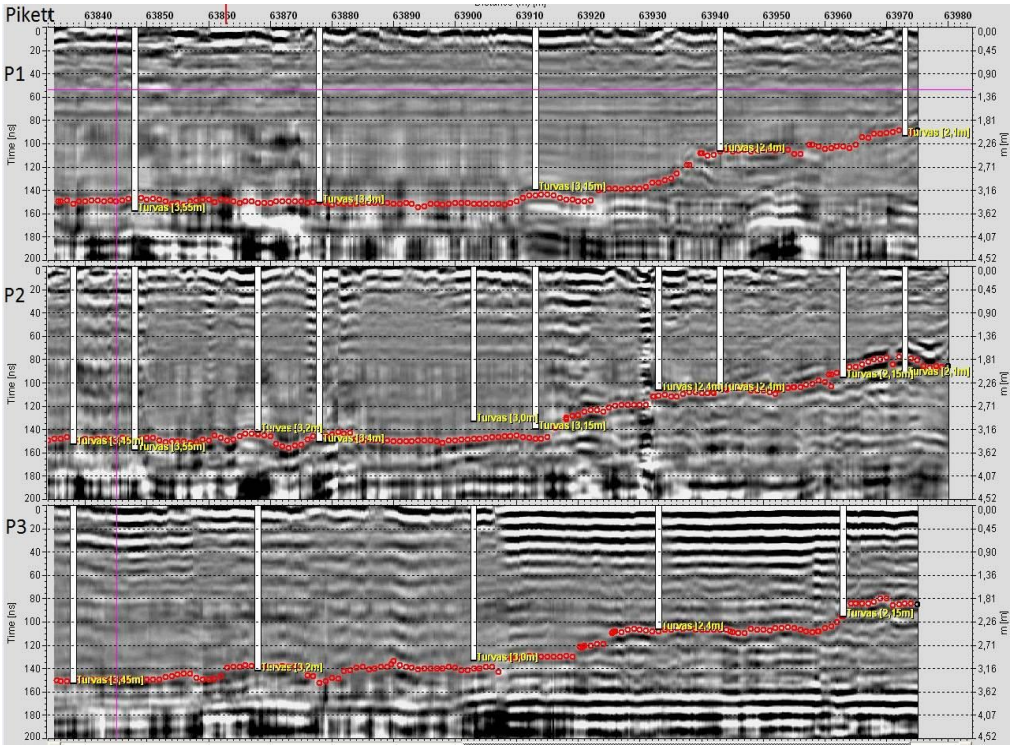


Figure 5. a) Longitudinal profile of test area. The red line is the designed level of the road surface. b) soundings and georadar results from 3 lines (red dotted line is the interpreted bottom of the peat layer).

3.1 Preparation works

The preparation works in the test area including cutting the trees and milling the stumps, sticks, small branches, grass etc. on top of peat layer (Fig. 6). By milling, a uniform and load-bearing working platform was created.

Typically, topsoil is removed before construction. In this case, removal of the topsoil would have exposed a very soft peat, which would have been easily disturbed and the construction site would had been hard or impossible to operate as a result.



Figure 6. Milling the topsoil (stumps, roots, small sticks, grass etc.) for working platform.

3.2 Test section 0

Section 0 consisted of mass replacement. The excavated peat was replaced with a sand and gravel embankment. The top of embankment (0.15 m) was constructed with crushed limestone #2/64 mm and after that surfaced with a layer of crushed limestone # 8/12 mm.

3.3 Test section 1 (Fig. 7, and 12)

The section 1 consisted of 1-layer reinforcement (woven polyester strength 600/50 - warp/weft) on top of peat. In the edges of the embankment reinforcement was wrapped around at least 5.7 m towards the centre line. The designed height of final designed road embankment was ≈2.5 m (from red line to initial peat surface). On top of the road embankment the surcharge layer with thickness of ≈1.85 m was loaded. In total the designed embankment height (including surcharge) over the peat is ≈4.35 m. However, due to the settlements during construction works the height of the constructed embankment is in reality greater (≈5 m).

3.4 Test section 2 (Fig. 12)

The Section 2 consisted of 2-layer reinforcements -bottom geotextile on top of the peat was 400/50 and the upper geotextile inside the embankment was 200/50. Vertical distance between the reinforcements was 0.5-0.8 m. In the edges of the embankment reinforcements were wrapped around at least 5.0 m towards centre line. The height of the final designed road embankment was ≈2.5 m. In total the designed embankment height (including surcharge) over the peat is ≈4.25 m and in reality ≈5 m.

3.5 Test section 3 (Fig. 7 and 12)

Section 3 consisted of geocell mattress. Before installing the geocell mattress a nonwoven geotextile and geogrid (40/40) were placed on top of the topsoil. The height of the geocell was 1 m and it was filled with # 0/64 mm limestone aggregates. The filling was not compacted inside the geocells. The height of the final designed road embankment was ≈2.5 m. On the top of the road embankment was installed surcharge of ≈1.25 m. In total the designed embankment height (including surcharge) over the peat is ≈3.75 m and in reality ≈5 m.

Table 2. Table presents time after beginning of construction the section, loading magnitude of the peat layer and designed heights of embankment in each stage.

Section	Load [kN/m]	Height [m]	Construction duration [d]	Type
1	48	2.40	0-4	Embankment
1	51	2.55	11-13	Surface dres.
1	88	4.40	81-89	Surcharge
2	48	2.40	0-17	Embankment
2	51	2.55	26-28	Surface dres.
2	86	4.30	76-84	Surcharge
3	20	1.00	0-3	Geocell
3	51	2.55	15-16	Embankment
3	76	3.80	63-71	Surcharge
4	6	1.50	0-3	LWA
4	24	2.40	4-5	Embankment
4	36	2.99	52-60	Surcharge
5	10	0.50	0-2	Preload
5	16	1.95	17-30	EPS
5	34	2.85	37-42	Embankment
5	44	3.35	42-50	Surcharge

3.6 Test section 4 (Fig. 8 and 12)

Section 4 consisted of light weight aggregate (LWA #10/20 mm = "leca") layer. Before installing the LWA a geotextile reinforcement 400/50 was installed on top of topsoil. At the edges of the embankment a 1 m thick aggregate barrier (Fig 12f) was built, and the LWA layer 1 to 1.5 m was installed between the barriers. At the edges the minimum thickness of the LWA was 1.0 m. The final height of the designed road embankment was ≈2.5 m. On top of the embankment is the surcharge of ≈0.6 m. In total the designed embankment height (including surcharge) over the peat is ≈3.1 m.

3.7 Test section 5 (Fig. 9 and 12)

The section 5 consisted of EPS-block layer. The EPS-blocks were connected to each other with PVC-pipes (≈25 mm) and plastic connectors at the surface of the EPS-layer. The EPS-blocks were protected with 0.5 mm thick linear low-density polyethylene-plastic membrane (LLDPE). The EPS-layer was covered with 0.9 m thick aggregate layer. To obatin better bearing capacity for the final road structure a geogrid (40/40) was installed to the aggregate layer.

Section was constructed in following phases:

1. installation of georeinforcement (400/50) on top of peat layer,
2. preloading of the peat with 0.5 m thick sand embankment for ≈2 weeks,
3. levelling of the preloading embankment and installation of the EPS-blocks,
4. installation of the membrane,
5. installation of the aggregate layers and geogrid (40/40) and
6. paving of the embankment at the level of red line (the thin paving was made for the measuring of the surface of the embankment before and after the overloading).

The total height of the embankment over peat in section 5 is ≈2.5 m.

3.8 Geotechnical dimensioning calculations

Geotechnical calculations for sections 1 to 4 (stability and settlement) were made by Olep (2015) and for Section 5 by Korkiala-Tanttu et al. (2015). Stability calculations have been completed with Novapoint GeoCalc 3.1-geotechnical dimensioning program developed by ViaSys VDC Oy (http://www.viasys.fi/).

Any back calculations have not been conducted but they will be made later during 2016-2017.

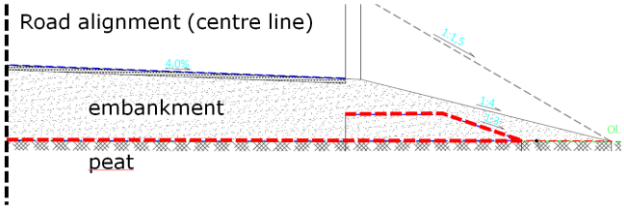


Figure 7. Cross-section of test section 1. 1-layer georeinforcement.

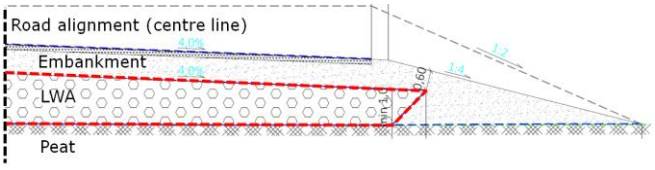


Figure 9. Cross-section of test section 4. Light weight aggregate (LWA) layer.

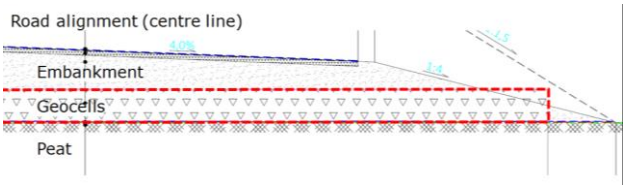


Figure 8. Cross-section of test section 3. Geocell mattress.

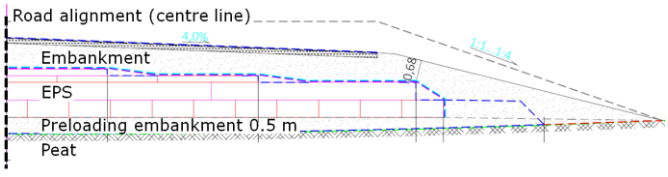


Figure 10. Cross-section of test section 8. EPS-block layer.

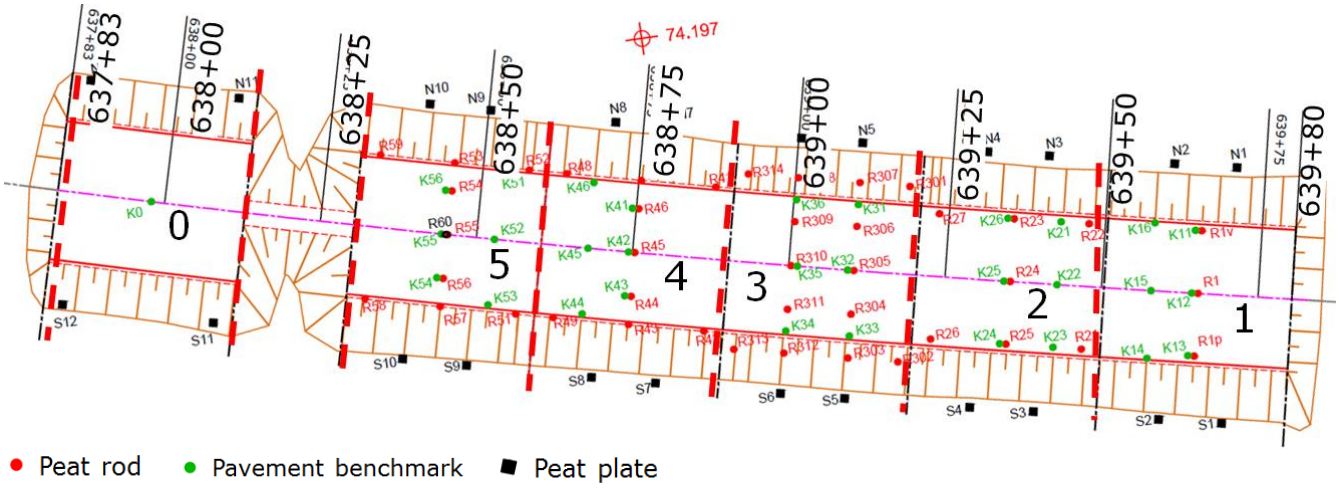


Figure 11. Locations of the leveling benchmarks (red –peat rods, green –pavement benchmarks, black – peat plates, and also the Section 0 slope plates) (Ellmann 2015)



a) Start of construction of sec. 1 (20.7.2015)



b) Construction of embankment sec. 1 (20.7.2015)



c) Installed upper reinforcement, sec. 2 (21.7.2015)



d) Construction of Geocell structure (31.7.2015)



e) Construction of Geocell structure at sec 3. (31.7.2015)



f) Construction of edge barrier at sec. 4. Peat rod in bottom right corner. (12.8.2015)



g) Compaction of the embankement. sec.1 (24.8.2015)



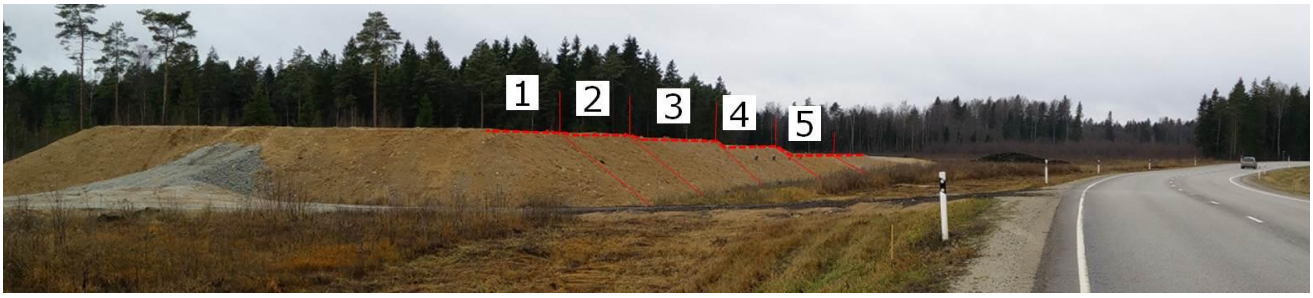
h) Construction of LWA layer at sec 4. (25.8.2015)



i) Installation of EPS-blocks at sec. 5 (16.9.2015)



j) Surface of the EPS-layer at sec. 5. Plastic connectors on between EPS-blocks (24.9.2015)



k) Test sections 1-5 after surcharge loading (11.11.2015)

Figure 12. Photos from the construction of the test embankment.



Figure 13. 3D surface model created from the RPAS photos combined with aerial photos (Julge 2015). Surface after construction of surcharge loading 5.11.2015 (RPAS=Remotely Piloted Aircraft System).

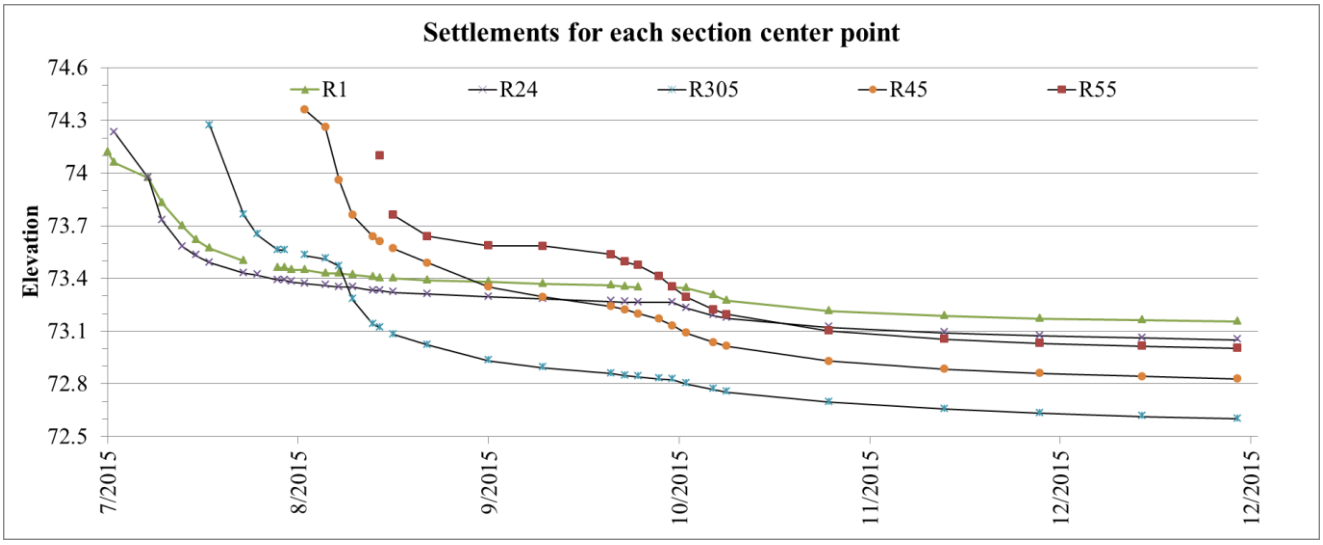


Figure 14. Test sections 1-5 settlement results for the test section center aligment peat rod.

4 INSTRUMENTATION OF THE TEST EMBANKMENTS

4.1 Settlement plates

Altogether 98 measurement points were mounted at the test site. Of this figure:

- 36 settlement plates were placed on top of the geotextile-covered peat layer (Fig. 15)
- 6 settlement plates on top of the upper layer of geotextile in Section 2 (≈1 m above peat layer)
- 1 settlement plate on top of the EPS layers, in the centre of Section 5
- 30+1 settlement plates on top of the uppermost (paved) road layer
- 20 ceramic plates on top of the peat layer (1 m off from the lower edge of the road slope)
- 4 wooden plates on the Section 0 slopes.

Locations of the instrumentations are presented in Fig. 11. The first installed settlement plates were observed (within the time period of 17.07.2015 until 15.10.2015) 30 times, the minimum amount (for the last installed peat sett. plates, 26.08.2015) of measurements was 14, in average each peat rod was levelled for 20 times. (Ellmann 2015).

4.2 Measured settlements

In test section 1 and 2 the thickness of the peat layer is approximately 2.0-2.15 m and in test sections 3, 4 and 5 from 3.0 to 3.5 m. The test sections 1, 2 and 3 were constructed with natural aggregates and in test section 4 and 5 was used lightening of the embankment.

The settlement results for each test sections centre line are presented in Fig. 14. During first month after construction in test sections 1 and 2 roughly of 90 % of settlements had occurred before installing surcharge loading. Surcharge load to test section 1 and 2 was installed approximately 3 months after starting construction. The settlements 5-6 months after construction were 880-930 mm.

In test section 3 the peat layer is thicker and due to that settlements higher. In test section 3 settlements after 5 months were 1670 mm. However, in test section 1, 2 and 3 the relative compression of the peat layer after 5 to 6 months is between 43-55 %.



Figure 15. Peat roads placed in pre-designed locations on top of the geotextile-covered peat layer. (Ellmann 2015)

The surface of the embankment has been measured by RPAS in several phases. An example of the result of the RPAS measurement is presented in Fig. 13 where is combined 3D surface model created from the RPAS (Remotely Piloted Aircraft System) photos and aerial photos by Julge (2015).

5 CONCLUSIONS

The test sections construction and field-monitoring has provided valuable information of construction at peat areas. The construction and field-monitoring of the test sections are well-documented and will aid further analysis of the test section in future. All of the methods have some technical benefits and some (geo) technical or economic limitations. Which method is most suitable in different construction cases and places, must be considered case by case.

Below are preliminary geotechnical conclusions on the basis of experiments of test section construction in Võõbu:

- All the methods described can be applied to constructing roads on layers of peat.
- Test sections were constructed with sufficient global stability (no failures).
- The milling of stumps, sticks, etc. and leaving them to remain in place was a success. Excavating and clearing the surface layer would have otherwise disturbed the soft peat layer and the construction site would have almost impossible to operate.
- Installation of one reinforcement layer instead of two is easier to construct. Possible technical advances of two reinforcement layers for the behaviour of the structure have not been identified yet.
- Installation of geocell mattress is very labour intensive and it's not yet clear if it is technically better than section with one or two reinforcements (more measuring time and analysing is needed).
- With a 2 m thick layer of peat, it seems the best approach is the removal of the peat layer altogether. When the layer is thicker other solutions are recommended.
- The consolidation of the peat increases the strength of peat significantly – even over two or three times the strength – this phenomenon should be studied and utilized in design and construction.
- In addition, construction of mass stabilization is a considered to be a viable option for ground improvement method for Võõbu area (Forsman et al. 2009).

Analysis of measuring results and other observations will provide valuable results which can be used in the design of the road E263 (from Tallinn to Tartu) on its new alignment at peat area. Those analysed results are also a valuable basis for the development of national (Estonian Road Administration) guidelines.

Further analysis of the settlements and comparison of the different test sections performance is planned to be published during 2016–2017.

6 ACKNOWLEDGEMENTS

Authors would like to thank Maanteeamet (Estonian Road Administration) for constructing the full-scale test section and for comprehensive field and laboratory survey from the test area.

7 REFERENCES

Forsman, J, Dettenborn, T & Skepast, P. 2015. Kose-Võõbu test embankment construction report 11/2015. Ramboll Finland Oy. 36p + 276 app.

Forsman, J., Hakari, M., Jyrävä, H., Ritsberg, K. & Skepast, P. 2009. Mass stabilisation of E263 highway section Kose–Mäo in Estonia. XXVII International Baltic Road Conference Riga, Latvia, 24-26.9.2009.

Ellmann, A. 2015. Mounting and monitoring of levelling benchmarks in the Võõbu road construction test site. Tallinn University of Technology, Tallinn.

Julge, K. 2015. 3D-model from aerial photos. https://sketchfab.com/models/43081376e08f45c89eb5736ec9a4a975

Korkiala-Tanttu, L., Gustavsson, H. & Lojander, M. 2015. Mnt2 nr 2 Tallinn-Tartu-Voru-Luhamaa-Kose-Voobu Sektsioon 5 Pk 638+30,50 – 638+60,50, EPS-structure, calculation report. Aalto University, Geoengineering Group. 12 p.

Olep, M. 2015. T2 Võõbu test embankment section, geotechnical calculations (during June and July 2015).

Refraction seismic for mapping of limestone surface in a tunnel project in Copenhagen

L. C. Bagger
Rambøll Danmark, Danmark, lc@ramboll.dk

R. Wisén
Rambøll Danmark, Danmark, rgw@ramboll.dk
M. Jørgensen
Niras, Danmark, mjo@niras.dk
M. Jensen
HOFOR, Danmark, meje@hofor.dk

ABSTRACT
The Damhusledningen (Damhus pipeline) project in Copenhagen will improve water quality in and around the Damhus river and secure the area from flooding at downpour. The tunnel is constructed with "Pipe Jacking" in the top of the limestone. In the summer of 2014 the tunnel front reached an area where it unexpectedly broke through the top of the limestone into a permeable gravel layer. This led to loss of air pressure and inability to keep stability in the tunnel front. Drillings in the area indicated the possibility of a dramatic topography of the limestone surface, but none had indicated depressions into the tunnel alignment. To map the extent of the depression with sufficient lateral resolution it was decided to use refraction seismic tomography in combination with drillings. The seismic results showed very good correlation with available drillings and with the level of the limestone surface as found in the tunnel front. After grouting of the permeable layer the construction could continue successfully. Based on these encouraging results it was decided to use refraction seismic also at a crossing of a large railway embankment where it had been difficult to place enough drillings. The Danish Railway Administration's strict requirements on vertical displacement of the tracks required further knowledge on whether there exist any depressions in the limestone surface under the embankment. The embankment and the railway constituted a serious challenge to the refraction seismic method and great care was taken to ensure good results. It was finally concluded that the limestone surface under the embankment did not show any dramatic drops. With this information the project could go on with acquiring permission for the construction from the Danish Railway Administration.

Keywords: Site investigation; Refraction seismic; Pipe jacking; Limestone; Risk management

1 INTRODUCTION

HOFOR is establishing a new sewer pipe in Copenhagen (Damhusledningen København) with Niras as consulting engineers. The pipe has a diameter of three meters and was to begin with installed using pipe jacking, but is now driven with an EPB micro-tunnelling machine. In the Copenhagen area tunnelling has historically been preferred at some depth into the limestone. This is due to the characteristics of the limestone, which normally gives a safe and stable tunnelling process with little risk for settlements. The Damhusledningen has been placed in the very top of the limestone to minimize the depth of the shafts and pipe connections. However, in the top of the limestone there is a risk that the tunnel at some point come out

of the limestone, due to the considerable variations in the limestone topography that can occur. When the tunnel comes out of the limestone and enters soil materials the risk for settlements becomes much higher. In an urban environment this can be a problem in many places, even if the tunnel, as in this case, is placed mainly along a recreational area as the Vigerslev Park that run along the Damhus River. This paper will demonstrate the use of the refraction seismic method as a tool, together with drilling, in mapping the top of the Copenhagen limestone. Two cases are presented, one where a breakout of the tunnel into the soil caused washout of sediments and settlements, and one where the tunnel is to cross a railway embankment and where settlements cannot be allowed.

1.1 Geology

The geological sequence in the study area comprises the following main layers, from the surface and downwards:

1. Fill layers mainly composed of sand, peat, mull, clay and gravel with various artefacts;
2. Postglacial freshwater deposits, mainly peat, sand and gravel;
3. Late glacial and glacial deposits, generally composed of meltwater deposits (mainly sand and gravel, occasionally with large boulders), but occasionally with sections of glacial till;
4. Glacially disturbed limestone, soft, with clayey zones. This zone may be up to around 2 m thick; and
5. Undisturbed and generally hardened limestone of Danien age.

Depth to the top of the undisturbed limestone is 4 – 14.5 m in the study area, and it varies considerably, sometimes within short distances.

In the Copenhagen area, the morphology of the limestone surface is to a large extent controlled by structures in the limestone, i.e. faults, fractures and folds. The two main orientations of these structures are NW/SE and NNW/SSE (Jakobsen et al., 2002). The orientation of the valley with the Damhus River more or less follows these orientations, a fact which may indicate that the valley is structurally controlled. This would be a plausible explanation of the observed strong gradients of the limestone surface.

1.2 Case One

In the summer 2014, the tunnel front unexpectedly broke through the top of the limestone into a permeable gravel layer. This led to loss of air pressure and inability to keep stability in the tunnel front. A refraction seismic survey was done by Rambøll in order to get a better understanding of the local geology through mapping of the limestone surface. This helped delineate the volume of gravel that the tunnelling machine needed to pass before entering into limestone again. It was decided to use grouting to increase stability and decrease permeability. After grouting, the drilling could continue without further stability problems. The survey is described as Case One below.

1.3 Case Two

At a later stage of the works, the sewer pipe is planned to cross under a large and old railway embankment, which holds six tracks. If a similar depression in the limestone surface is encountered here unexpectedly, it can have a large negative effect on both the project economy and time schedule. Furthermore, the Danish Railway Administration allows only very small displacements of the railway tracks during the tunnel construction. The embankment holds the main tracks into Copenhagen and a settlement of the tracks would have large consequences, not only for the local, but also for the national traffic.

Drilling a set of boreholes across the embankment to get the geological profile is very costly due to the need for rail safety measures and short time windows at night, in which the work must be done. An alternative could be a horizontal drilling under the embankment, but also this is very costly. Refraction seismic is a comparably cheaper solution and with the good results from Case One in mind, it was decided to use refraction seismic to map the top of the limestone. This is described as Case Two in this paper.

2 SEISMIC REFRACTION METHOD

Sound travels at different speeds depending on the stiffness of the material it travels through. Following Snell's law on reflection, there will be a refracted wave travelling along the interface between a low-velocity and high-velocity layer (Figure 1).

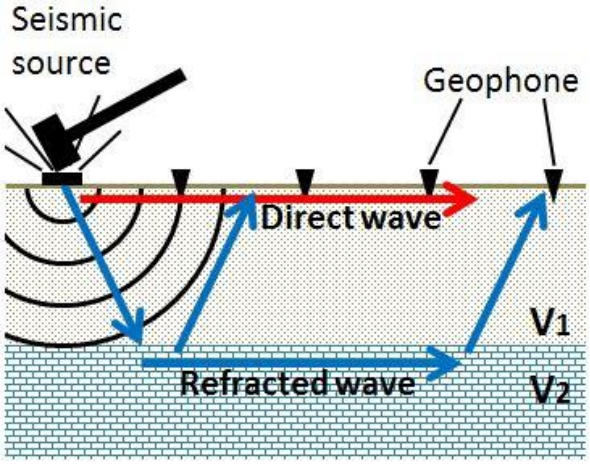


Figure 1 Physical principle in seismic refraction surveys. The top layer has a lower velocity than the bottom layer ($V_1<V_2$).

In simple terms, measuring the travel times of the direct and the refracted wave along a line, where the sensors (called geophones) are kept at constant locations and the seismic source (e.g. a sledgehammer) is moved along the line, you can calculate the sound velocity in the two layers and the depth to the layer interface (see e.g. Keary et al., 2002). The result is a velocity model for the subsurface. There are various methods for this calculation. Traditional methods like the plus-minus method (Hagedoorn, 1959) or the generalized reciprocal method (Palmer, 1981) are computationally simple, but do not handle topography well and only provide a crude one-dimensional model of the subsurface. Here we have used tomographic inversion, which handles topography variations better and provide a two-dimensional model of the subsurface. The processing was done in the software Rayfract, from Intelligent Resources Inc., that utilizes a wavepath eikonal traveltime tomography (Schuster and Quintus-Bosz, 1993).

3 CASE ONE – ENCOUNTERED LIMESTONE DEPRESSION

As described earlier the seismic data for Case One was collected after the tunnelling had to be temporarily stopped when a gravel layer in an unexpected limestone depression had been encountered.

3.1 Survey setup

The survey area was in the Vigerslev Park in the southeast part of Copenhagen. To map the top of the limestone, seven seismic profiles where recorded (see **Error! Reference source not found.**). The geophone distance was 2-2.5 meters. Often refraction seismic surveys use a geophone distance of five meters, but here a higher resolution was desired. The source was a 40 kg accelerated weight drop. A test was made with a seven kg sledgehammer that showed data that was possible to interpret, however the signal to noise ratio was on the border to what can be allowed and so it was decided to use a slightly more powerful source. The data was collected in day-time and in a city like Copenhagen there will always be a significant amount of seismic background noise during the day.

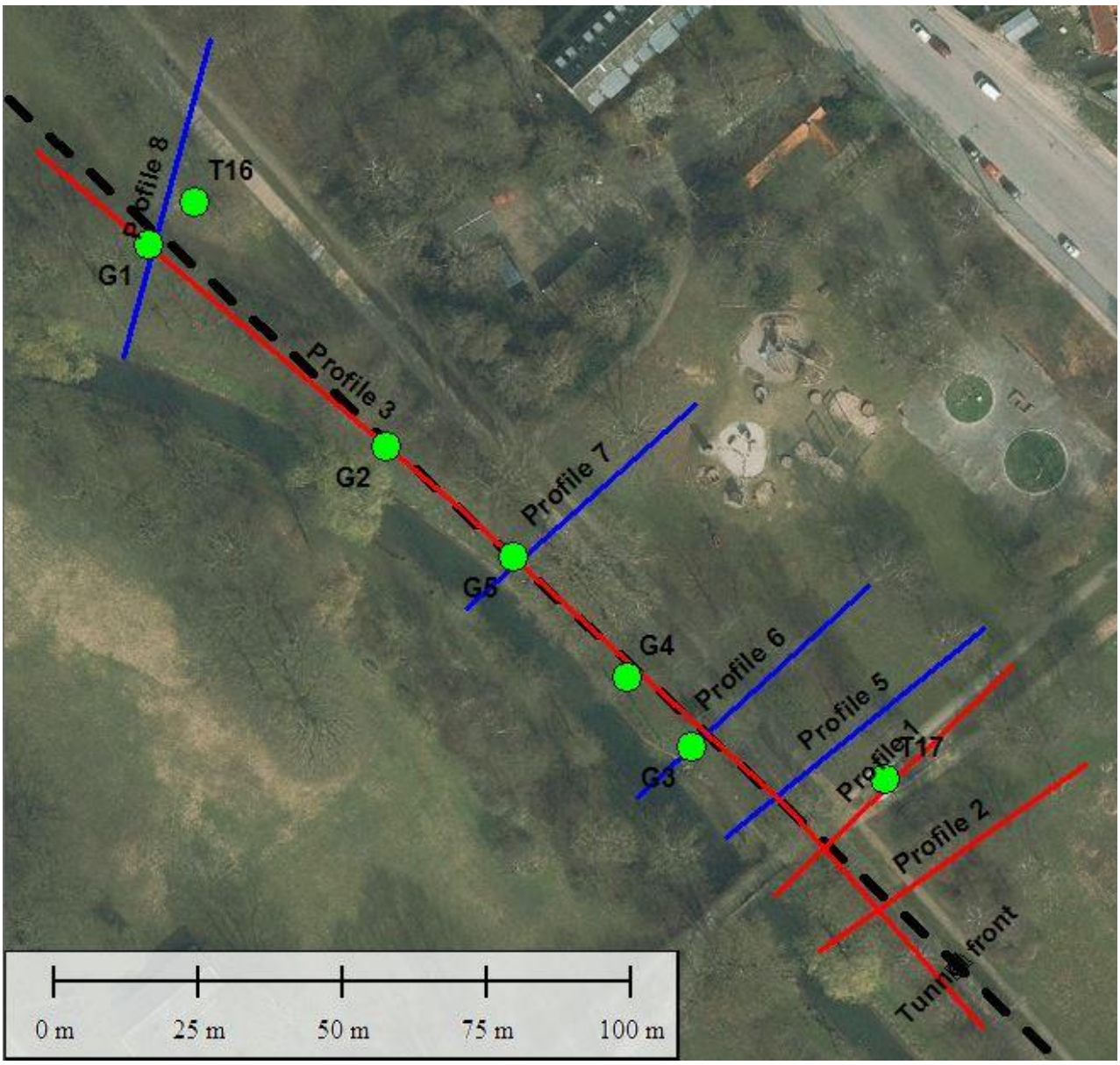


Figure 2 Line placements. Dashed black line is the projected tunnel path. Red lines show profiles part of this paper, blue lines profiles not treated here. Green dots are drillings.

3.2 Results for Case One

The first two profiles that were collected, Profile 1 (Figure 4) and Profile 2 (Figure 5), showed good correlation with the available reference data from boreholes. The level of the limestone surface in drilling T17 was used to verify and calibrate the interpretation of the limestone surface, and the level of the limestone surface as seen in the tunnel front fit very well with what was seen in the refraction seismic in Profile 2. Even though it was known that the level of the limestone surface could vary considerably, it was surprising that it was encountered at tunnel level so close to a geotechnical boring that had indicated that it should be placed several meters higher. The seismic results showed that there clearly is a local depression of the limestone here, and it is the eastern flank of this that can be seen in Profile 1 and 2.

The available drilling information, some of it available from the original site investigation and some acquired as new drillings in the same time as the seismic survey, showed very good correlation with the seismic results. The top of the limestone as interpreted in the drillings correlates with a velocity of 1500 m/s in the refraction seismic. This velocity is slightly lower than you would expect from a hard limestone and this indicates that the top of the limestone is fissured and fractured. As described in the geology section it is expected to find up to

two meters of disturbed limestone. A few drillings, such as G4 on Profile 3 (Figure 3), which does not correlate, is explained by the fact that they are placed at some distance from the line. Another reason for not having perfect correlation is that the interpretation of top of limestone in drillings is made by a geologist based on the materials present in the drilling, while the seismic method do not see different geological materials but rather the stiffness of the ground. Due to this it is often necessary to take the condition of the top of the limestone into account when comparing it to the seismic result. However, this was not a big problem for Case One.

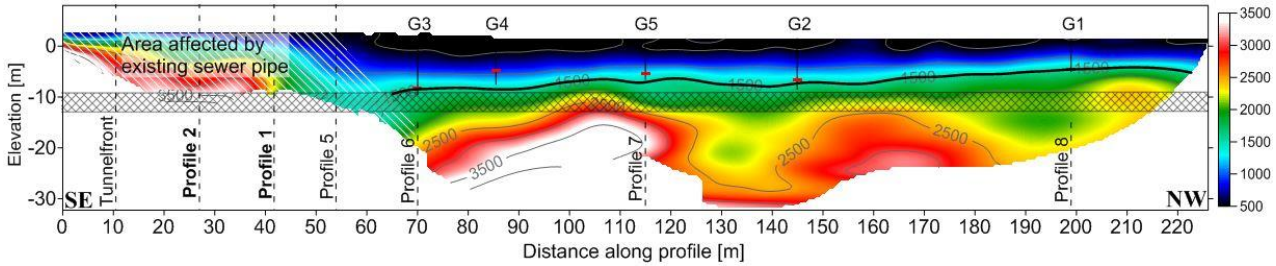


Figure 3 Profile 3. Cross-lines are shown as dashed lines. Bold names indicate the two other profiles shown in this paper, Profile 1 and 2. The tunnel is drilled from SE to NW with the projected position shown as a crosshatched area. Letter G indicates position of borehole and red marking the top of the limestone from the borehole log. Black line along the 1500 m/s isoline shows the top of limestone as interpreted from the seismic profile.

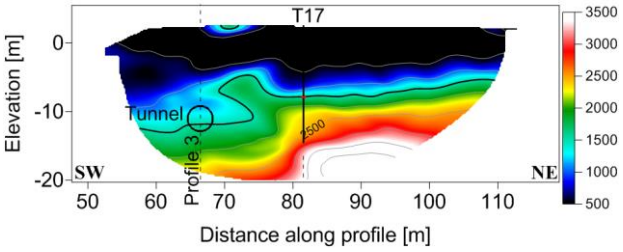


Figure 4 Profile 1. Cross-line is shown as a dashed line. Projected tunnel is shown as a circle. The strange extreme shape of the limestone, as interpreted along the 1500 m/s isoline, is probably an artefact of the inverse modelling. However, it can be expected that there is a very sudden drop in the limestone level towards SW.

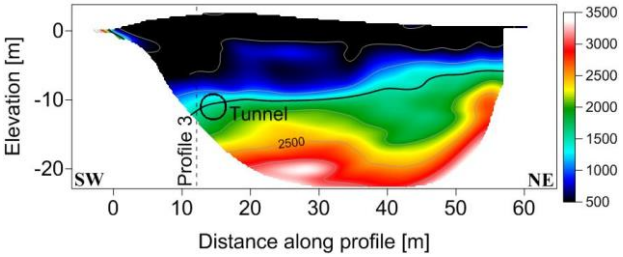


Figure 5 Profile 2. Cross-line is shown as a dashed line. Projected tunnel is shown as a circle. Black line along the 1500 m/s isoline shows the top of limestone as interpreted from the seismic profile.

4 CASE TWO – RAILWAY EMBANKMENT

At one location it is planned that the tunnel cross under a 6 track wide and 10 meter high railway embankment that was constructed over several stages during the past more than 100 years. Due to the age of the embankment there is not sufficient documentation on how it is constructed and therefore it must be treated with care. As described before the allowed settlements for the railway tracks are very small and therefore it becomes important to map the limestone under the embankment to reduce the risk of unexpected geological conditions. Two drillings where made as close to the embankment as possible on each side, still leaving an un-investigated stretch of 95 m under the embankment. After the successful survey described in Case One it was decided to perform a refraction seismic survey over the embankment. Even if a seismic survey in a place like this is complicated and costly compared to the survey in Case One, the alternatives would be to perform complicated and very expensive drilling on the embankment or horizontally under the embankment with budgets far exceeding the one for seismic.

4.1 Survey setup

To map the top of the limestone, three seismic profiles where recorded (see Figure 6). The geophone distance was 2.5 meters. The measurements where conducted at night to avoid train traffic. As a consequence the seismic background noise was very low. The source was a seven kg sledgehammer since this was the only source that was possible to bring on to the embankment without special arrangements.

For practical reasons the measurements where divided into stages. The first stage was to instrument the area outside of the tracks with geophones. A full dataset was collected along the instrumented line, and in addition a few source points where placed on the tracks. These points made it possible to test the signal to noise ratio of the source without time consuming instrumentation on the tracks. For this first stage all measurements on the Profile 10 (purple line in Figure 6), except the part over the tracks, where performed. A preliminary processing of stage one was made that showed encouraging results and so the second stage with geophones on the tracks was performed. This required three nights of work where the first night was used to get the cables in place under the rails and to mount geophones. The second night was used to shoot the line, and the last night used to remove the instrumentation on the tracks. In a third stage a Profile 10 parallel to the tracks was performed (yellow line in Figure 6). Furthermore, a profile was made north of the embankment (blue line in Figure 6) to get results closer to the planned tunnel alinement. Results from that profile were poor due to effects two from major sewer pipes crossing the line at an acute angle and are not treated here.

For this survey there were several things to take into account when planning, performing and interpreting the survey. The most obvious problem was the logistical needs to perform a survey over a busy six-track railway in a large city as Copenhagen. In addition it was essential to control the data quality and to make sure that the strong surface topography did not cause negative effects during modelling. As a further complication there are concrete structures in the embankment close to the planned tunnel. The positions of these are presented in Figure 8. The seismic lines had to be placed at sufficient distance away from these to make sure that these structures did not prevent mapping of the limestone. This is why the profiles where placed at a little distance from the planned tunnel, as can be seen in Figure 7. The structures where a combined bicycle/sewage water tunnel running parallel to the planned tunnel about 12 m to the side, and another sewage tunnel only 2 m to the side of the planned tunnel. From this there is also a shaft going to the surface of the embankment to a railway platform.

There were also technical matters with the instrumentation to consider, like how data is affected when railway sleepers have to be used as source points, when geophones are placed in materials that are far from natural, like macadam, or how other types of fill that creates a very heterogeneous structure effect the modelling of the data. In addition the railway use high power electricity to drive the majority of their trains and high enough currents will be picked up by the analog seismic cables through induction.

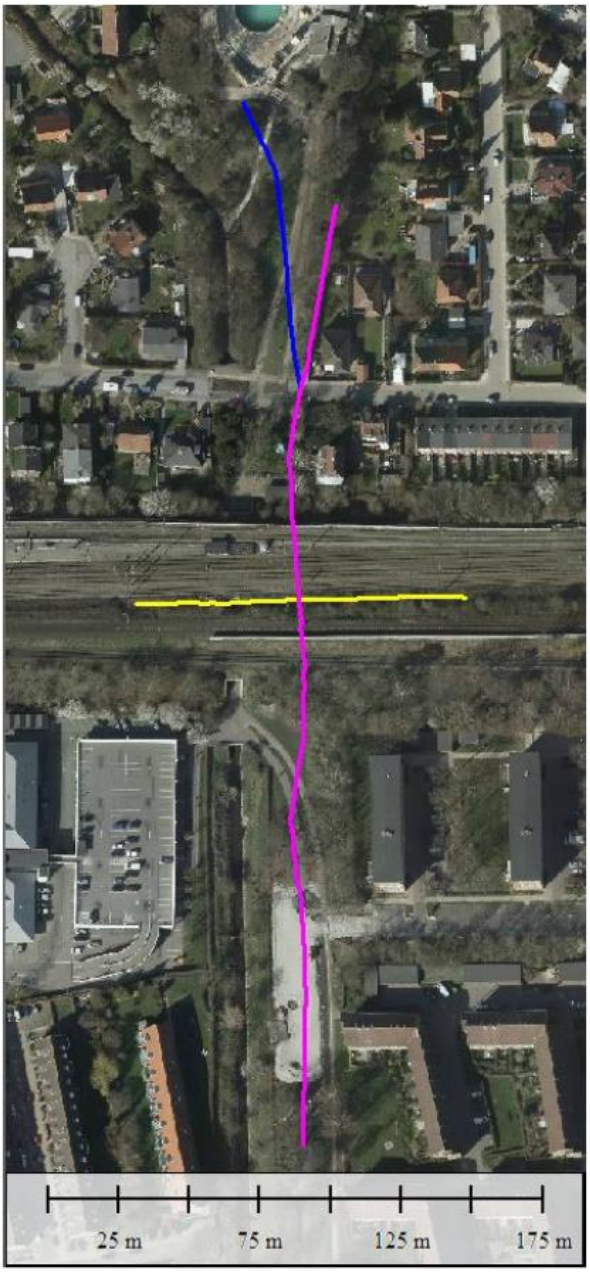


Figure 6 Profile 9 (Pink) and profile 10 (yellow). Profile 11 (blue) is not treated in this paper.

4.2 Results for Case Two

When all of these matters had been dealt with we could conclude that we had collected a high quality dataset on which it was possible to do a qualified interpretation of the limestone surface (Figure 7 and Figure 8). In the raw data there was clear evidence of the existing concrete structures, especially when crossing water culverts north of the embankment, but with good control of where the existing structures are placed the effect from this could be almost completely removed in processing. In the velocity profiles there is almost no evidence of these structures, as can be seen for example between 30-50 m in Figure 8.

The correlation with drillings on the north side of the embankment is very good (T57 and T02 in Figure 7), while on the south side it seems that the seismic find the limestone slightly lower than the drillings (S1 and T03 in Figure 7). To some extent this might be due to the distance between drillings and the seismic line but another reason might be that the limestone surface in the drillings are interpreted based on the geological material while the seismic method measures the stiffness of the ground. Drillings to the north show a sharp transition from the softer top-soil to a stiff limestone. To the south the drilling records show a gradual transition from top-soil over a very soft limestone to a stiff limestone.

After verification and calibration with drilling data it can be concluded that the interpretation of the limestone surface lies at safe distance above the planned tunnel, and does not show any irregular behaviour under the railway embankment. This can be clearly seen at 160-220 in Profile 9 (Figure 7) and at 40-60 in Profile 10 (Figure 8).

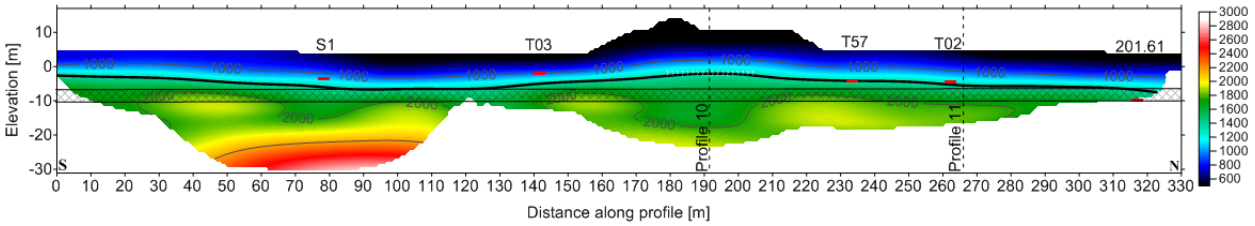


Figure 7 Profile 9 from Hvidovre Station. Cross-lines are shown as dashed lines. The tunnel is drilled from SE to NW with the projected position shown as a crosshatched area. S1, T03, etc. indicates position of borehole and red marking the top of the limestone from the borehole log. Black line along 1500 m/s isoline shows top of limestone as interpreted from seismic profile. Drilling 201.61 is more than 100 years old and the location is highly uncertain.

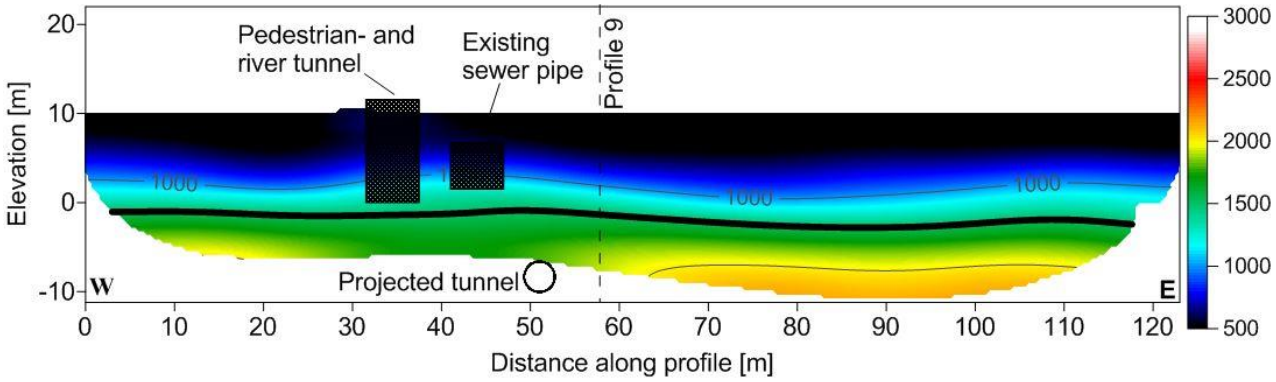


Figure 8 Profile 10 from Hvidovre Station. Cross-line is shown as a dashed line. Approximate dimensions of concrete constructions in the embankment are shown.

5 DISCUSSION AND CONCLUSION

In Case One, refraction seismic in combination with drilling proved to be a robust method to map the limestone surface. Through this an unexpected situation that had temporarily stopped tunnelling was cleared out. A gravel layer in a limestone depression could be assessed and grouted, where after tunnelling commenced.

In Case Two, the refractions seismic was used together with drilling in a technically very challenging environment. Despite this, the refraction seismic method provided good and useful results. They are used to document the geology and lower the expected risk when drilling under the embankment. This is crucial in the documentation towards the Danish Railway Administration prior to obtaining permission for the construction work.

Even though the seismic method has larger local uncertainty than drilling it has to be considered that drilling can't be used to achieve continuous information along a tunnel alignment, the effect of this being clearly seen in Case One. Based on the two cases presented here we conclude that the combination of refraction seismic and drilling is a powerful tool, even in a challenging urban environment.

6 REFERENCES

Hagedoorn, J.G. (1959). The plus-minus method of interpreting seismic refraction section sections: Geophysical Prospecting, 2, 85-127.

Jakobsen, P.R., Fallesen, J. and Knudsen, C. (2002). Strukturer I den Københavnske undergrund – folder forkastninger og sprækker. Dansk Geologisk Forening Bulletin 19, 19 – 29.

Keary, P., Brooks, M., Hill, I. (2002), An introduction to geophysical exploration (3rd). Blackwell Publishing. ISBN-10:0-632-04929-4.

Palmer, D. (1981). An introduction to the generalized reciprocal method of seismic refraction interpretation. Geophysics, 46(11), 1508-1518.

Schuster ,G.T. and Quintus-Bosz, A. (1993). Wavepath eikonal traveltime inversion: Theory. Geophysics, 58(9), 1314-1323. doi: 10.1190/1.1443514

Impact of data acquisition parameters and processing techniques on S-wave velocity profiles from MASW – Examples from Trondheim, Norway

G. Sauvin, M. Vanneste, J.S. L'Heureux
Norwegian Geotechnical Institute (NGI), Norway, guillaume.sauvin@ngi.no

P. O'Connor, S. O'Rourke, Y. O'Connell, T. Lombard
Apex Geoservices, Ireland

M. Long
University College Dublin, Ireland

ABSTRACT
The shear modulus is one of the most important engineering parameters, and it relates directly to the soil's shear-wave velocity. Shear-wave velocities can be derived from both laboratory measurements (e.g., bender elements) and various field methods (seismic CPT, surface wave analysis, and shear-wave reflection/refraction surveys). The major advantage of field measurements is that the soil is tested in its natural state, thus mitigating the effects of sample disturbance caused by e.g. drilling, tube insertion, extraction, transportation, storage, trimming, and reconsolidation.
In recent years, Multi-channel Analysis of Surface Waves (MASW) has become a powerful and common method for obtaining in situ shear-wave velocity data that can subsequently be used for geotechnical site characterization. Whereas this method is proven, it is important to be aware of its potential pitfalls and limitations from survey design to final interpretation of the results. Indeed, the receiver and source geometry, the time sampling, the processing methods as well as the inversion method and parameters used may influence the resulting shear-wave velocity profile. All survey design, processing and analysis parameters should be thoughtfully chosen taking into account the given site as well as the target. In addition, lateral variations (inhomogeneity, dipping layers) disturb the 1D assumption typically adopted in surface waves inversion. Therefore, it is important in engineering geophysics to investigate the reliability, potential and limitation of this prospecting method, properly take into account uncertainties and show that differences in sampling techniques and inversion may lead to differences in shear-wave velocity profiles and thus influence the site characterization.
In this study, we present data from one MASW experiment nearby Trondheim. The receiver and shot-geometrical effects are revealed and the necessity for careful survey design as well as the need for systematic data evaluation is highlighted. Shear-wave velocity profiles were inverted using two different algorithms revealing discrepancies, hence the need for appropriate inversion parameter selection.

Keywords: Surface wave analysis, *in situ* shear wave velocity, acquisition parameters, inversion parameters, soft clay

1 INTRODUCTION

Because of its direct correlation to the shear modulus and the possibility to obtain in situ measurements, the shear-wave velocity (*Vs*) is widely used in geotechnical engineering.

One of the methods used to extract in situ *Vs* is based on the characteristics of surface wave propagation and velocity dispersion. The common approach these days is the Multi-channel Analysis of Surface Waves (MASW) method (Stokoe et al., 1994).

For onshore applications, the analysis typically exploits the dispersive nature of Rayleigh waves in vertically heterogeneous media (Nazarian, 1984; Stokoe, 1988; Stokoe et al., 1994). The phase velocity dispersion results primarily from the variation of shear wave velocities with depth. An active MASW experiment includes (Socco et al., 2004):

1. Data acquisition during which the wave field related to the propagation of a perturbation generated by a controlled dynamic source is recorded by geophones or accelerometers on the ground surface (without clipping);
2. Extracting the dispersion curves from the seismic data; and
3. The inversion process, based on wave propagation in layered media, which allows establishing the S-wave profile as well as an uncertainty or error margin.

Each of these steps requires careful parametrisation.

Here, the need for adapted survey designs, objective dispersion curve extraction and careful inversion parameter selection will be discussed. Then, the latter is exemplified using data from various MASW surveys around Trondheim, Norway. Note that Rayleigh waves are only one of several surface waves that can be generated. Others are Love waves, generalized Rayleigh waves or Scholte waves. The study solely focuses on Rayleigh waves.

The wave equations have multiple solutions at given frequencies or wavenumbers, which explains the multi-modal character of surface wave dispersion.

2 THE FIELD PROCEDURE

For an MASW experiment, one typically uses a set of vertical receivers, usually geophones. These are spread (often in a linear array) on the ground surface to record the ground motion induced by the propagation of seismic waves generated by a source (see Figure 1). When using a vertical source (e.g., sledgehammer, weight drop), more than two thirds of the total generated seismic energy is emitted as surface waves, which stand out on the seismic gathers as high-amplitude events with variable waveform that propagate with low velocity. Therefore, the surface waves are the easiest seismic wave to generate onshore. Despite this, efficiently recording surface waves requires appropriate field configurations and acquisition parameters in order to reliably record the planar Rayleigh waves.

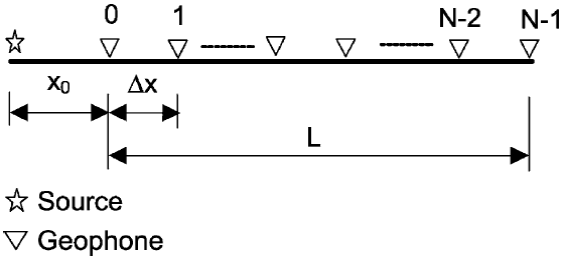


Figure 1 A scheme of MASW field setup, where x_0 is the source to 1st geophone offset, so-called near-offset, Δx is the geophone spacing, and L is the length of the receiver spread.

2.1 Importance of the near-offset

As the surface wave method requires the analysis of horizontally-travelling Rayleigh waves, it is important to avoid recording non-planar components. Surface waves only become planar after travelling a certain distance from the source. This distance is a function of wavelength (longer wavelengths require larger offsets), and thus it is site-specific (Stokoe et al., 1994; Park et al., 1999). Although the half-wavelength criterion ($x_0 > \lambda_{max}$, Stokoe et al., 1994) has been adopted as a rule of thumb in this rule can be relaxed significantly (Zhang et al., 2004) and the proper near-offset distance is highly sensitive to the wavelength itself. One also has to keep in mind that a larger value of the near-offset (x_0) and a longer receiver spread (L) will increase the likelihood of recording higher-mode surface waves.

2.2 Importance of the length of the receiver spread

The maximum investigation depth (Z_{max}) depends on the longest wavelength (λ_{max}) of the surface waves and is often used as $Z_{max}=0.5\lambda_{max}$. Also, λ_{max} is governed by the energy and area of impact of the seismic source, which may be active (e.g. sledge hammer or accelerated weight drop). The longer λ_{max}, (deeper the Z_{max}) can be achieved

with greater source power and lower frequencies in the source signal. For unusually shallow investigation, a relatively light source with higher frequency content (>50 Hz) should be used. When conducting active measurements, ambient noise can be significantly reduced by vertical stacking of multiple impacts.
Typically, vertical low-frequency geophones (e.g., 4.5 Hz) are recommended and although planted geophones give the highest sensitivity, the coupling provided by a land streamer can be equally efficient. The high end of geophone frequency is not critical.
The length of the receiver spread (L) is directly related to the longest wavelength (λ_{max}) that can be analysed, which in turn determines the maximum depth of investigation (Z_{max}). Therefore, L usually has to be equal to or greater than Z_{max}.
The maximum extent of the receiver spread is also limited by body waves and higher mode surface waves which tend to dominate over the fundamental mode at far offsets and at higher frequencies (Park et al., 1998; 1999). Due to its relatively lower attenuation, the body waves (including refracted, and often guided waves) tends to dominate with offset. Because of its inherent complexity, it is difficult to assess the maximum offset simply based upon one single parameter, such as wavelength. Nonetheless, the resolution/sharpness of the dispersion curve image increases rapidly with the length of receiver spread and the number of active geophones (Park et al., 1998; 2001). When higher modes tend to take most of the energy and need to be separated from the fundamental mode, the resolution issue becomes critical. A longer receiver spread is therefore recommended, and also needed for the lower frequencies.

2.3 Importance of the geophone spacing

The receiver spacing (Δx) is related to the shortest wavelength (λ_{min}) and therefore determines the shallowest resolvable depth of investigation (Z_{min}). If the frequency content generated from the source is high enough, a short Δx is required to capture small Vs variation at shallow depth. Moreover, as the number of active channels increases, the ability to acquire data along a profile without roll-along is increased.

2.4 Importance of time

Finally, time sampling should be small enough to avoid aliasing, and a one-millisecond of sampling interval is commonly used with a 1 second recording time. However, a smaller time sampling would be necessary for processing of body waves, and a longer recording time mandatory in case of extremely low velocities or if a long receiver spread is used.

3 DISPERSION ANALYSIS

Extracting dispersion curves is critical in surface wave analysis, as the results are directly used in the data inversion.

3.1 Dispersion curve extraction principles

The dispersion curves are typically extracted after remapping the data into a different domain where the surface waves stand out as high-energy branches (e.g., frequency as a function of wavenumber, wavelength, slowness or phase velocity) that can be easily picked. To this end, the phase-shift method is one option, in addition to the more traditional methods like tau-P or the f-k method because it achieves higher resolution.
The standard data processing scheme is as follows. A multi-channel field record is first decomposed via FFT into individual frequency components, and then amplitude normalization is applied to each component. Then, for a given testing phase velocity in a certain range, necessary amount of phase shifts are calculated to compensate for the time delay corresponding to a specific offset, applied to individual component, and all of them are summed to make a total energy. This is then repeated for the different frequency components. When all the energy is summed in frequency-phase velocity space, it will show a pattern of energy accumulation that represents the dispersion curves. In case of multi-modal dispersion, the behaviour of energy will appear as multiple branches in the remapped domain. Other methods have also been suggested in the literature to achieve higher resolution such as

the high-resolution radon transform method (Luo et al., 2009).

3.2 Considerations on the dispersion analysis

Several aspect of the dispersion curve extraction should be addressed carefully. When applying normalization to the frequency phase velocity spectrum, the direction of normalization will introduce artefacts which can be misleading for dispersion curve picking. It is therefore necessary to keep in mind this normalization aspect when conducting the dispersion analysis, and to exclude frequencies that are not contained in the original recordings.
The maximum energy associated with the surface waves in the phase velocity or FK diagram, is not necessarily associated to the propagation of the fundamental mode. Higher modes do not only appear at high frequencies, they can also exist at low frequencies and mode jumps may take place. Also, whenever trying to extract information from deep subsurface, one has to remember the limitation introduce by the field acquisition itself, i.e., the source weight and geophone natural frequency as well as the length of the array. Additionally, the energy accumulation at low frequency is usually poor, leading to smeared maximum and ambiguities. Recording passive seismic is a one way to enhance the lower frequency content and increase the confidence in the picking.
When not only the fundamental but also higher modes are present, one may wish to increase the resolution of the frequency-phase velocity diagram to help discriminate them. Long array length is then recommended; otherwise, trace padding would be advantageous.

4 DISPERSION CURVE INVERSION

Extracting dispersion curves is critical in surface wave analysis, as the results are directly used in the data inversion

4.1 Inversion principle

Inversion or inversion modelling, in general, attempts to seek the cause to a result when the result is known, whereas predicting the result from the given cause is referred to as forward modelling. An inversion is typically non-unique, thus multiple solutions exist. Rayleigh inverse problems are ill-posed implying that a given experimental dispersion curve may correspond to more than one soil profile. From a mathematical point of view, non-uniqueness in the solution of an inverse problem is either caused by a lack of information to constrain its solution or, alternatively, because the available information content is not independent. In light of this, including a priori information is often a good strategy to enforce uniqueness in the solution of an inverse problem.

4.2 Kinematic mode inversion

Whereas the goal of a field survey and data processing in MASW is to establish the mode dispersion curves accurately, theoretical kinematic dispersion curves can be determined for a given earth model using a proper forward modelling scheme (e.g., Schwab and Knopoff, 1972). The most important issue with the inversion process is to determine the best-fit earth model among many different models as efficiently as possible. The root-mean-square (RMS) error is usually used as an indicator of the fit between the measured and theoretical dispersion curves. The final solution is taken as the 1D Vs profile with a small value of RMS error. For the optimization, one can either use a deterministic method (e.g., least-squares method; Menke, 1989; Xia et al., 1999) or a random approach (e.g., Socco and Boiero, 2008). The former type is typically the faster at the expense of the increased potential of finding a local, instead of global, minimum. Another pitfall common to both types is the risk of numerical artefacts. For example, although a solution with a smaller RMS error is numerically acceptable, it may not necessarily represent a more realistic one. The multi-modal inversion technique utilizes both the fundamental and higher-mode curves for the inversion. This is done in order to increase the accuracy of the final 1-D Vs profile by narrowing the range of solutions with 1-D Vs profiles otherwise equally well suited if only the fundamental curve was

used. This method can also be used to alleviate the inherent problem with the inversion method of non-uniqueness in general.

4.3 Dispersion Image Inversion

The method of inversion includes the use of dispersion image data (the frequency-phase velocity diagram) instead of discrete dispersion curves, and does not involve the extraction of modal curves (Ryden et al., 2004; Forbriger, 2003a; 2003b). This approach eliminates the drawbacks of the modal-curve based inversion such as mode-misidentification and mode-mix problems (misidentifying higher mode curve as a fundamental curve) if data acquisition and subsequent processing are not properly performed. Dispersion curves, when misidentified, may lead to erroneous Vs profiles because of the lack of compatibility in the inversion process trying to match measured and theoretical curves.

4.4 Full-waveform Inversion

This type of inversion utilizes the raw multichannel record instead of the one processed for dispersion imaging (Forbriger, 2003b). In the process, the scheme attempts to compare the whole seismic waveforms observed with synthetic waveforms generated from a forward modelling scheme. This type of approach may be advantageous over others for the fact that it is not biased by any other kind of data processing or remapping. However, it has to take into account the attenuation and interference issues, as well as layer parametrisation, since all of these can contribute to the shaping of a seismic waveform.

4.5 2D Vs Inversion

This approach uses the final outputs of 1D Vs profile from current typical inversion approach as input to the second phase of the inversion based on a different forward modelling scheme. The main objective is to consider the smearing effect caused by the lateral variations during dispersion analysis as much as possible by adopting another scheme accounting for the local variation of Vs. For this purpose, the Vs structure is provided by the co-location of the previous 1D Vs output as an initial starting model to account for the local variations observed within an individual field record to update the 2D Vs model.

4.6 Considerations on the inversion parameters

Before proceeding with the inversion, one should be confident with the field data as well as with the use and evaluation of dispersion curves or wavefield transformations, considering that inversion is not objective but rather a numerical data interpretation approach.
The result of the classical fundamental mode inversion approach, is entirely subject to the correctness of the picking. Using an erroneous modal dispersion curve, the optimization adopted within the inversion will not overcome this problem.
Moreover, one has to keep in mind that the forward modelling for surface wave analysis is typically 1D. Therefore, one should be careful when applying MASW in laterally heterogeneous media.
For any type of inversion process, an initial earth model is specified to initiate the iterative inversion process. For MASW, the earth model usually consists of velocity (Vp and Vs), density, and thickness parameters. Among these four parameters, Vs has the most significant effect on the convergence of the algorithm, followed by the layer thickness. The choice of the initial model is important. If the initial model is significantly different from "true model", the inversion method used should still converge to a reliable result. An initial Vs profile could be defined by making the simple assumption that Vs at a depth z is a factor of the measured phase velocity (Stokoe et al., 1994; Park et al., 1999).
The number of individuals/models and generations to adopt has to be proportional to the algorithm effort to achieve a good solution. Parameters then have to balance the number of layers, i.e. more layers means more freedom for the system and higher computing effort, and the width of the “parameters space”. The search space can be defined according to prior geological and

stratigraphic information, and to the known Vs of the most common lithological types. If a site stratigraphy is known, the layer thickness and number can be set in order to give Vs a wider range. As such, one also reduces the freedom of the system and the numbers of individuals and generations to consider.
Finally, before interpreting the velocity spectrum, one should keep in mind the original data (traces) quality: the quality of the results depends on the quality of the input and on the parameters adopted for the inversion process, which must be clearly understood in its basic founding and driving principles. Surface wave analysis is not a trick giving a solution even if data quality is low. Other signals, particularly the guided waves, can result in dispersive signals that could wrongly be read as surface waves. Besides, the different modes can interfere with each other and give misleading or wrong results.
The user should be suspicious of any unexpectedly high propagation velocity (a value about the double what one would expect) that needs to be related to guided waves whose propagation depends on the Vp but not on Vs (e.g. Robertsson et al., 1995; Roth and Holliger, 1999).

5 SELECTED EXAMPLES FROM TRONDHEIM, NORWAY

Seismic data presented in this section were acquired close by Byneset, approximately 18 km west of Trondheim, Norway. The study area is composed of thick marine clays overlaying mica-gneiss bedrock. Here, a large quick clay landslide occurred in 2012.Three MASW profiles were recorded in the vicinity of this landslide (Figure 2). All profiles were acquired using 24 10 Hz vertical geophones. Profile Sh1098 and Sh1152 were acquired at the same location with two different setups: 1 and 3 m geophone spacing, a record length of 1 and 2 s, a 5 and 10 kg sledge hammer and 1 m and 8 m near-offset respectively for Sh1098 and Sh1152. Profile Sh1094 has the same setup as for Sh1098 with 12 m near-offset.

Using the commercial WinMASW software (Dal Moro et al., 2015), the seismic traces are time windowed to remove unwanted signals, e.g., the high frequency refracted waves (first arrival), before extracting both the phase velocity and FK spectra.
The fundamental mode is then picked in phase-velocity domain (with quality control. in FK domain), and subsequently stored for inversion. The dispersion curves are then used for inversion using WinMASW and NGI in-house inversion routine based on LAYSAC forward modelling (Kaynia, 1996).

5.1 Raw data analysis

The field setup was defined according to the a priori information and limited by the available equipment. Therefore only the Rayleigh wave fundamental mode is considered here. First, the geometry setting is controlled and data quality is assessed both in time and frequency domain (Figures 3 to 11). The data quality is good with high signal-to-noise ratio and no pre-processing is required prior to surface wave analysis With the short receiver spread, the recording time of 1 s is sufficient.



Figure 2 MASW profile location map. The blue star indicates the location of the seismic-CPTu. One can notice the remoulded surface where the quick clay landslide took place.

Looking at both data sets, one can notice that for Sh1098, the channel closest to the source (22-24. 3-1 m offset) is contaminated by near-source effects as well as direct and

refracted waves. On the other hand, Sh1094 with 12 m near offset and Sh1152 with 8 m near offset, are free from near source interference and the planar assumption is met from trace 1. Due to the short spread length, the far offset are not contaminated with body wave energy, but higher modes already start to show up.

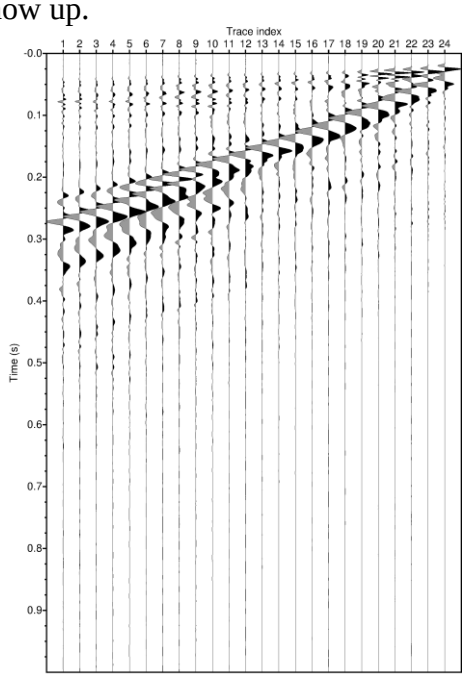


Figure 3 Sh1098, source at 1 m and 1 m geophone spacing.

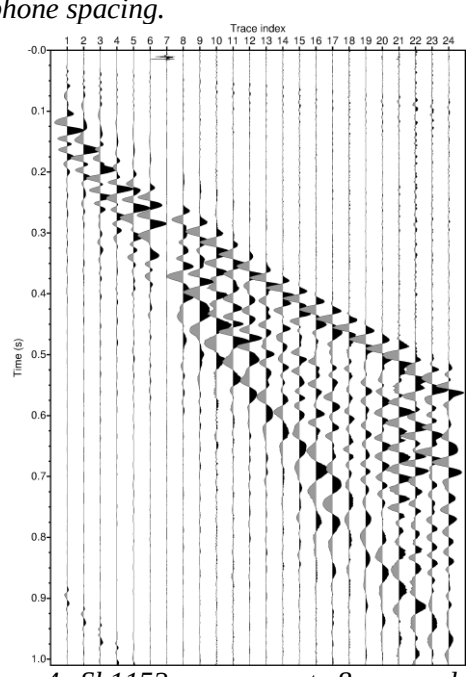


Figure 4 Sh1152, source at 8 m and 3 m geophone spacing.

5.2 Dispersion analysis

Frequency-phase velocity and frequency-wave number are computed from raw data and displayed without normalization. Guided by direct modelling and the a priori geological knowledge, the fundamental mode dispersion curve alone is picked in the frequency-phase velocity domain. The picks are then controlled in the frequency-wave number diagrams. Picking is achieved down to approximately 5 Hz in both cases, which is questionable considering the field setup. Picking is limited to around 32 Hz for Sh1098 and 25 Hz for Sh1098 and Sh1152 respectively, mainly because of the mode-mixing at higher frequencies.
Comparing the frequency-phase velocity diagrams of Sh1098 and Sh1152, one can already notice large discrepancies. Indeed, the fundamental mode energy is more widely spread for Sh1098 than for Sh1152, therefore reducing the uncertainty on the picks at low frequency. On the contrary, due to higher mode being more energetic, the fundamental mode frequency content is higher for Sh1098 than for Sh1152, but mode separation is easier for Sh1152.

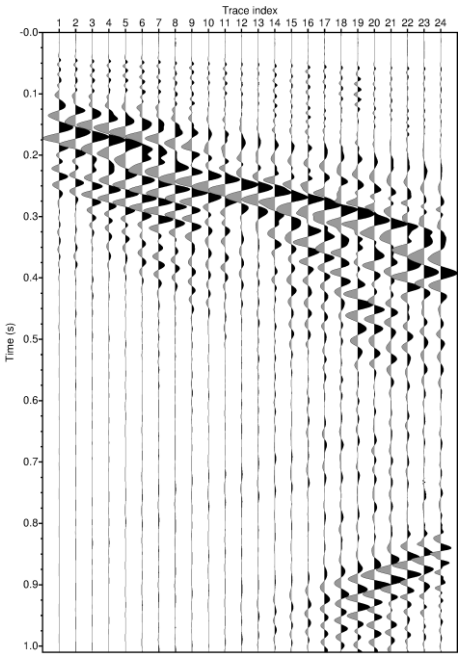


Figure 5 Sh1094, source at 12m.

5.3 Fundamental mode dispersion inversion and results

An initial model must first be defined. A 6 layer (including half space) model is chosen and the velocity and thickness constraints for the search space are defined according to the dispersion curve. The winMASW inversion is then run with 80 generations for the optimization procedure and 80 models of the

population. The best model (the one with the smallest misfit) and the mean one (in this case defined according to a Marginal Posterior Probability Density computation, see Dal Moro et al., 2007) result in almost similar *Vs* model for both sites (Figures 12 and 13). If a discrepancy occurs between the two models, it would suggest that the inversion parametrisation was inappropriate. Inversion is also run using NGI in-house routines using the same initial models. The *Vs* models obtained are similar to the one obtained using winMASW inversion algorithm. Nevertheless, the retrieved depths of investigation differ significantly.

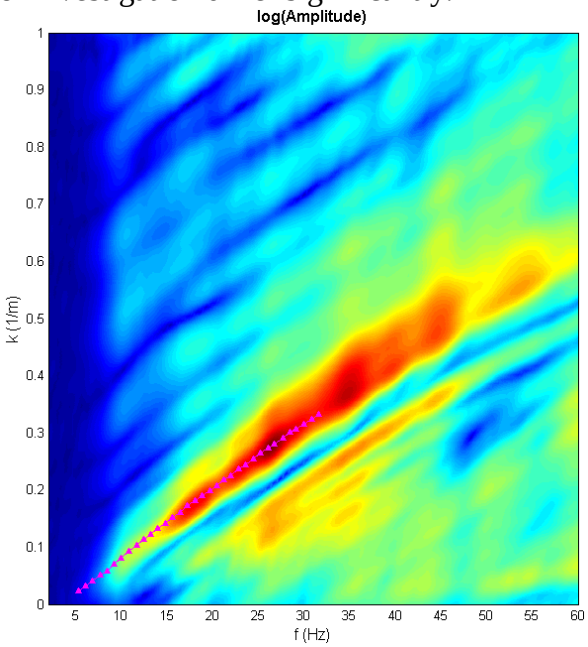


Figure 6 Sh1098, corresponding FK diagram with fundamental dispersion curve picks superimposed.

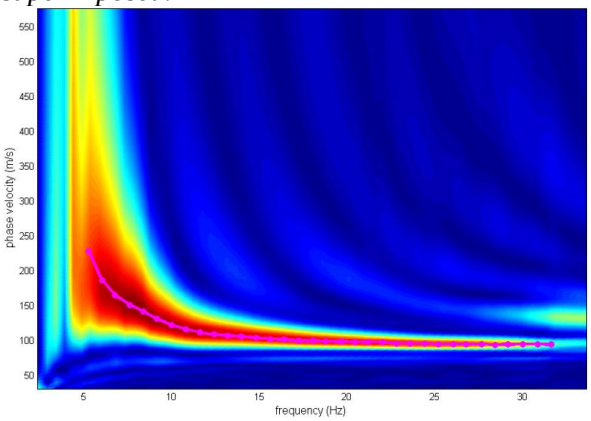


Figure 7 Sh1098, corresponding frequency - phase velocity spectrum with superimposed fundamental dispersion curve picks.

However, additional layers would have permitted the NGI inversion routine to reach equivalent depth.

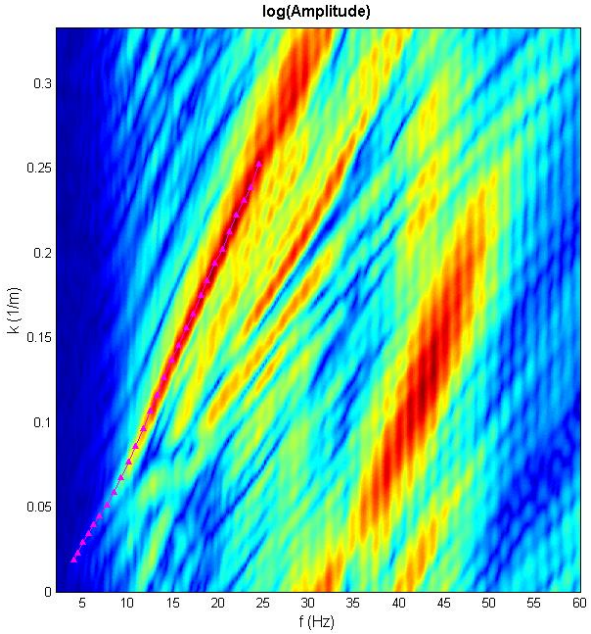


Figure 8 Sh1152, corresponding FK diagram with fundamental dispersion curve picks superimposed.

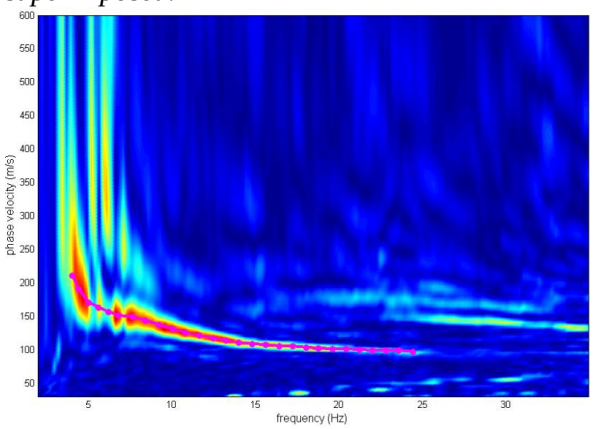


Figure 9 Sh1152, corresponding frequency - phase velocity spectrum with superimposed fundamental dispersion curve picks.

Comparison with the seismic cone penetration testing (SCPT) and a crosshole test (Eide 2015) is also available at Sh1094 (Figure 13). Even if the SCPT lack in coherence with depth, the comparison with the *Vs* derived from the MASW process shows good agreement, validating the inversion results.

Boreholes in the vicinity of the MASW profiles indicate that the bedrock should be deeper than 40 m, therefore, the high *Vs* found at depth in the winMASW results might be erroneous.

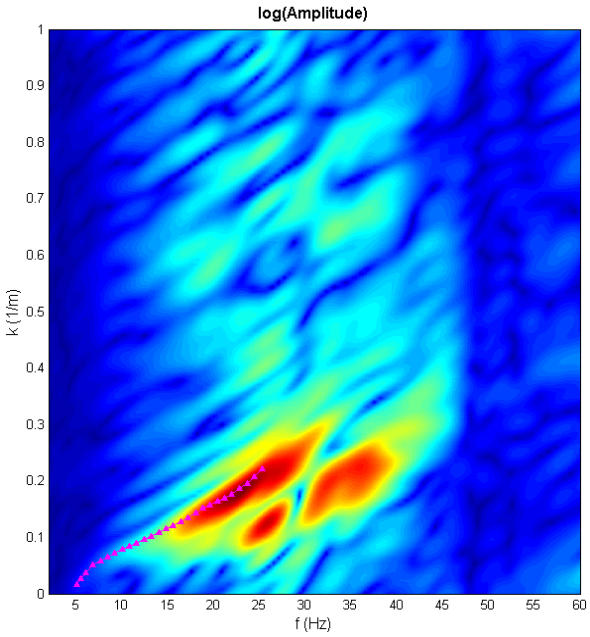


Figure 10 Sh1094, corresponding FK diagram with fundamental dispersion curve picks superimposed.

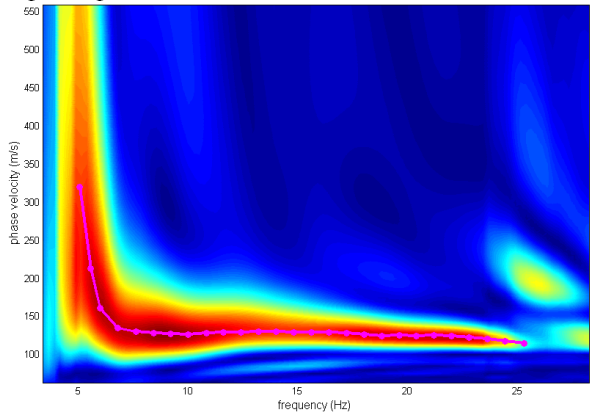


Figure 11 Sh1094, corresponding frequency - phase velocity spectrum with superimposed fundamental dispersion curve picks.

6 CONCLUSIONS

The shear wave velocity of soils is an important parameter in geotechnical design. It is, for example, widely used for seismic design criteria in the Eurocode 8. Uncertainties in the choice of Vs can have large consequences on project economy and design methods in practice. One of the main method used nowadays to gather Vs data is the MASW technique. It is of upper most importance that geophysicists and geotechnical engineers be aware that even this method can lead in uncertainties in the choice of Vs. Care is necessary when planning field surveys and when analysing

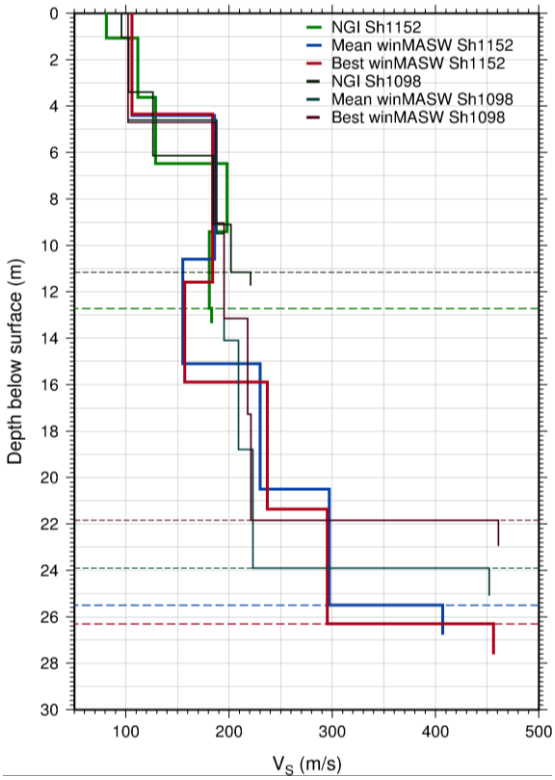


Figure 12 Sh1098 and Sh1152 inversion results.

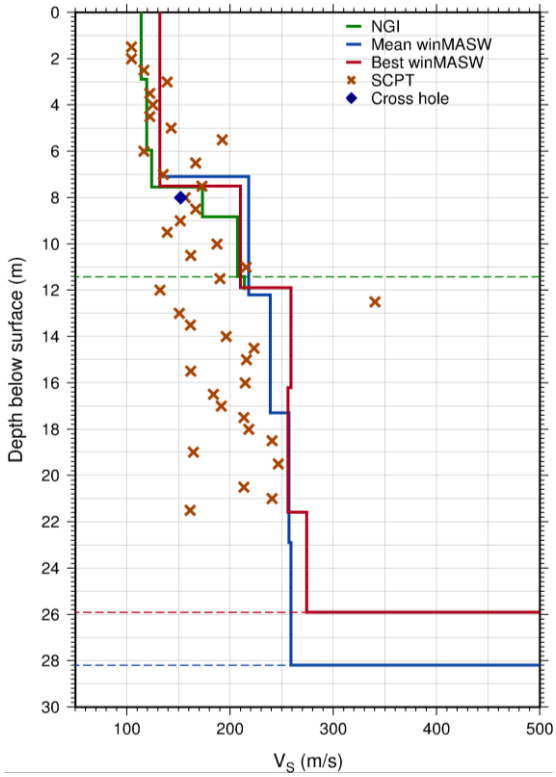


Figure 13 Sh1094 inversion results and comparison with seismic-CPTu and cross-hole.

such data. The present study showed that MASW field acquisition setup directly impact the dispersion analysis results. The near-offset distance, the geophone spacing, the array length, and the source frequency content directly affect the dispersion

diagram. Stable dispersion spectra with good resolution can be obtained when the optimal acquisition parameters are employed. A target oriented field setup is therefore mandatory for proper dispersion analysis, and, to estimate the optimum acquisition parameters, it is necessary to obtain information on the approximate velocity range.

Once a good dispersion results has been achieved, dispersion analysis of fundamental and higher modes should be conducted with good care, keeping in mind the field setup and limitations. In order to avoid introducing subjectivity through dispersion curve picking, velocity spectrum or raw data inversion should be preferred. Then, cautious inversion parametrisation is crucial to avoid falling in local minima. Finally critical interpretation of the resulting *Vs* model will make a successful MASW analysis.

7 ACKNOWLEDGEMENTS

Thanks to NGI's internal funding within the SP8 Geodip project. The authors are also grateful to the APEX Geoservices team who collected the data.

8 REFERENCES

Dal Moro G., Pipan, M. & Gabrielli, P. (2007). Rayleigh Wave Dispersion Curve Inversion via Genetic Algorithms and Posterior Probability Density Evaluation, J. Appl. Geophysics, 61, 39-55.

Eide H.T. (2015). On shear wave velocity testing in clay. Master Thesis at the Norwegian Universtity of Science and Technology.

Kaynia, A.M. (1996). Green's Functions in Layered Media under Fluid, in: NGI (Ed.). NGI, Oslo.

Forbriger,T. (2003a). Inversion of shallow-seismic wavefields:I. Wavefieldtransformation: Geophysical Journal International, 153, 719-734.

Forbriger,T. (2003b). Inversion of shallow-seismic wavefields:II. Inferring subsurfaceproperties from wavefield transforms: Geophysical Journal International, 153, 735–752.

Luo, Y., Xia, J., Miller, R.D., Xu, Y., Liu, J. & Liu, Q. (2009). Rayleigh-wave mode separation by high resolution linear Radon transform. Geophys. J. Int. 179, 254–264.

Menke, W. (1989). Geophysical Data Analysis: Discrete Inverse Theory, Revised Edition, Academic Press, Inc., New York.

Nazarian, S & Stokoe, K.H. (1984). In situ shear wave velocities from spectral analysis of surface waves. Proceedings of Eighth Conference on Earthquake Engineering, San Francisco, 3, 38–45.

Park, C.B., Miller, R.D., Ryden, N., Xia, J. & Ivanov, J. (2005): Combined use of active and passive surface waves: Journal of Environmental & Engineering Geophysics, 10 (3), 323 334.

Park, C.B., Miller, R.D. & Xia, J. (2001). Offset and resolution of dispersion curve in multichannel analysis of surface waves (MSW): Proceedings of the SAGEEP 2001, Denver, Colorado, SSM-4.

Park, C.B., Miller, R.D., & Xia, J. (1999). Multi-channel analysis of surface waves (MASW): Geophysics, 64 (3), 800-808.

Park, C.B., Miller, R.D. & Xia, J., (1998). Imaging dispersion curves of surface waves on multi-channel record: Expanded Abstract: Society of Exploration Geophysics, 1377-1380.

Richart, F.E., Hall, J.R. & Woods, R.D. (1970). Vibrations of soils and foundations, Prentice-Hall, Inc., New Jersey, 414.

Robertsson, J.O.A., Pugin, A., Holliger, K. & Green, A.G. (1995). Effects of near-surface waveguides on shallow seismic data. 65th SEG, Meeting, Houston, USA, Expanded Abstracts, 1329–1332.

Roth, M. & Holliger, K. (1999). Inversion of source-generated noise in high-resolution seismic data. The Leading Edge 18, 1402–1406.

Ryden, N., Park, C.B., Ulriksen, P. & Miller, R.D. (2004). Multimodal approach to seismic pavement testing: Journal of Geotechnical and Geoenvironmental Engineering, 130, 636-645.

Schwab, F.A. & Knopoff, L. (1972). Fast surface wave and free mode computations, in Bolt,B. A., Ed., Methods in computational physics: Academic Press, 87–180.

Socco, L.V. & Boiero, D. (2008). Improved Monte Carlo inversion of surface wave data: Geophysical Prospecting, 56, 357-371.

Socco, L.V & Strobbia, C. (2004). Surface wave methods for near-surface characterisation: A tutorial: Near Surface Geophysics, 2, 165-185.

Stokoe, K.H., Wright, G.W., Bay, J.A. & Roesset, J.M. (1994). Characterization of geotechnical sites by SASW method. In: Woods ED, editor. Geophysical characterization of sites. Rotterdam: A.A. Balkema. 15–25.

Stokoe, K.H., Nazarian, S, Rix, G.J., Sanchez-Salinero, I., Sheu, J. & Mok, Y. (1988). In situ seismic testing of hard-to-sample soils by surface wave method. Earthquake engineering and soil dynamics II—recent advances in ground motion evaluation. Geotechnical Special Publication No. 20, 264–277.

Xia, J., Miller, R. D. & Park, C.B. (1999). Estimation of near-surface Shear-wave velocity by inversion of Rayleigh waves. Geophysics 64, 691–700.

Zhang, S.X., Chan, L.S. & Xia, J. (2004). The selection of field acquisition parameters for dispersion images from multichannel surface wave data. Pure and applied Geophysics, 161, 185-201.

Underwater ERT Surveys for Urban Underground Infrastructure Site Investigation in Central Stockholm

T. Dahlin
Engineering Geology, Lund University, Sweden, torleif.dahlin@tg.lth.se

R. Wisén
Engineering Geology, Lund University, Sweden & Rambøll A/S, Denmark

ABSTRACT
Several underwater ERT surveys have been carried out in central Stockholm as part of pre-investigations for tunnels planned to pass under water, in the sea and in Lake Mälaren. The water passages are associated with major tectonic zones that can potentially be very difficult from a tunnel construction point of view.

The aim was to identify variations in depth of the bottom sediments as well as variations in rock quality including possible presence of weak zones in the rock. As a complement to refraction seismic that focuses on the mechanical properties ERT gives valuable information related to hydrogeological and petrophysical properties in the rock. Survey conditions are complicated by boat traffic, and electrical disturbances from the power grid and train traffic.

The ERT surveys were performed with different electrode cables placed on the sea bottom. The different cables used had either 64 electrodes at 7 meter intervals, 64 electrodes with 5 meter intervals or 128 electrodes with 5 meter intervals. Generally a multiple gradient array was used, but pole-dipole configuration was also employed in some cases in order reach deeper. The water depth was mapped using sonar combined with recording pressure transducers, and water resistivity as function of water depth was recorded using geophysical borehole logging equipment. Water resistivity as function of depth was integrated in the inversion model.

The results show that the rather difficult survey conditions could be handled in a satisfactory way thanks to adequate equipment, careful planning and attention to details. The measured data contains information that is relevant for creating coherent models of the variation in depth to rock, which corresponds well with data from drilling. The results also indicate that information in variation in rock quality that can be of critical importance for planning of underground construction can be derived from the data. Further comparisons against reference data are required for a full evaluation of the results.

Keywords: ERT, resistivity, underwater, tunnel, pre-investigation.

1 INTRODUCTION

Underwater Electrical Resistivity Tomography (ERT) surveys were carried out in a part of the sea called Saltsjön (Salt Lake) and Lake Mälaren in downtown Stockholm as part of pre-investigations for new tunnels. In one case for a new line for the Stockholm metro (T-bana) and in the other case for a road tunnel at Stockholm Förbifart. Measurements have also been performed for the Swedish Road Administration for road tunnels. The aim in all surveys was to identify variations in the depth of the bottom sediments, as well as variations in rock quality and the possible presence of weak zones in the rock.

The bedrock on the islands surrounding the investigated areas consists of granite, granodiorite and metagreywacke with mica schist. Several tectonic zones with different directions are expected, and tectonic breccia and myolinite have been mapped nearby. (Persson et

al. 2001; Stockholm Municipality 1997) The soil layers covering the bedrock are expected to include till and various recent sediments.

The sites are rather difficult from a survey point of view. Seismic investigations nearby have not been successful due to gas in the bottom sediments. Electromagnetic methods were ruled out because of electric cables lying on the sea bottom. The variation in water depth, and vertical and lateral variation in salinity, requires attention. Furthermore the rather intense boat traffic in the Saltsjön area puts demands and restrictions on survey logistics.

2 METHOD DESCRIPTION

2.1 ERT

The ERT surveys, also known as CVES or 2D electrical imaging (e.g. Dahlin 1996), were performed using an electrode cable that was placed on the seabed. For the measurements in Saltsjön an electrode cable with 64 electrodes and a take-out spacing of 7 meters was used, giving a total layout of 441 meters. For the measurements in Mälaren the cable had 128 electrodes and 5 m spacing, giving a total length of 635m. In Mälaren the measurements were extended onto land using 21 extra land electrodes, resulting in a line of 735 m.

In Saltsjön five lines were measured using pole-dipole configuration in order to maximize depth penetration, where a 3500 metre cable was used for the remote electrode that was placed in the water east of the study area. The field survey was completed in 3 days, where one line was measured during the first day when time was also spent on installing the remote electrode apart from deploying the electrode cable etc. A measurement protocol with 3256 data points per measurement line was used to provide good resolution and depth penetration.

In Mälaren only one line was measured. The more resistive lake water allowed for a gradient configuration to be used. This saves a lot of work since it does not require the use of a remote electrode. The amount of data is similar to that of Saltsjön and the measurements were performed during one night. It should be noted that two full datasets were collected for the purpose of analysing effects of urban noise.

An ABEM Terrameter LS with 12 measurement channels was used for the measurements, where multi-channel measurement provided a quick measurement process despite the large number of data points. Interpreted sections of the resistivity distribution in the bottom sediments and bedrock were created using the inversion software Res2dinvx64. L1 norm (robust) inversion with water overlying the electrodes was used (Loke et al. 2003; Loke and Lane 2004). The inversion software was adapted to meet the requirements of this project by allowing several water layers with different resistivity.

2.2 Water Depth and Resistivity

In order to be able to get useful estimates of resistivity in soil and rock, it is necessary to integrate the water depth and the resistivity of the water in the interpretation model. Errors in water depth or resistivity leads to artefacts in the model as the inversion program compensates for surplus or deficit in conductance in the water model by corresponding increase or decrease in the resistivity. In this case the bottom topography varies greatly and the resistivity varies with depth in the sea, hence it is of utmost importance to measure both bottom topography and resistivity depth distribution in the water for each survey line to avoid misleading results.

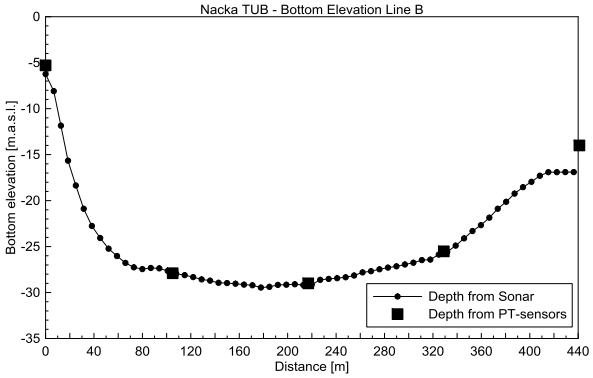


Figure 1 Example of depth profile determined with sonar and pressure sensors.

3 RESULTS AND INTERPRETATION

3.1 Saltsjön

The water depth in the study area was mapped using multi-beam sonar. The location of the survey lines were measured using side scan sonar where the measuring cable was identified in the measurement results. Depth profiles of the survey lines were then calculated by extracting information from the deep water model of the area along these lines. For quality assurance the electrode cable were fitted with 5 automatically recording pressure transducers of type Diver that

were used to calculate the depth in a number of reference points.

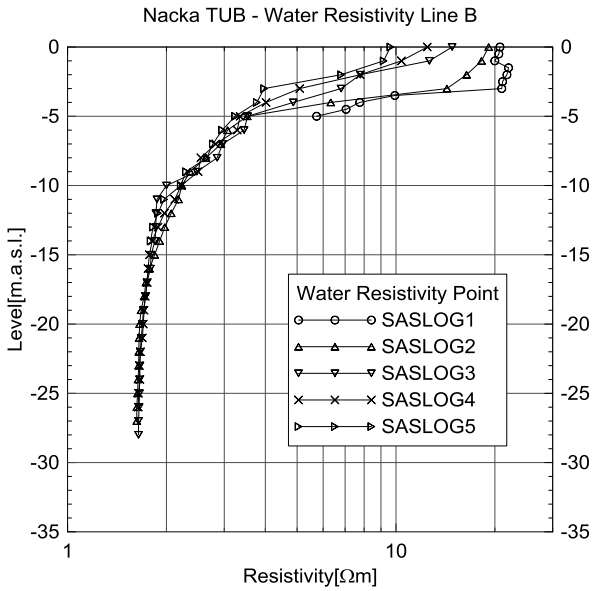


Figure 2 Example of water resistivity variation.

The water resistivity as a function of depth was measured with different geophysical borehole logging equipment for the two surveys. An ABEM Terrameter SAS4000 together with a SASLOG borehole log was used for measuring resistivity in both surveys.

Inspection of full waveform recordings done throughout the measurements reveal that there are high noise levels including 50 Hz, 16⅔ Hz and strong variation in background levels within the measurement cycles. The 16⅔ Hz noise is most likely caused by train traffic as it is the operating frequency of the Swedish rail system. The variation in background level may be caused by e.g. the underground train system (T-bana) which operates with DC power supply, or variation in the load in the commuter and national rail systems. Despite the noise resistivity data are of sufficiently good quality so that no culling of data points was needed before further processing, showing that the digital filtering of the instrument functions well. The bottom topography based on a combination of sonar surveying and pressure sensors was included as part of the models. The water resistivity distribution was simplified to a model of 5 layers with different resistivity. Each layer is assumed to be homogeneous in the horizontal direction; the variation in resistivity close to the surface was considered to be of limited importance. The inversion resulted in models showing vertical sections of resistivity variation (see example in Figure 3). The models have acceptable residuals (about 6-7%), which shows that there is relatively good agreement between model and data.

The resistivity sections show fluctuations which can be interpreted as a superficial layer with lower resistivity, which probably can be associated with soil layers of varying thickness and composition. Below are generally higher but varying resistivities that can be interpreted as bedrock zones of weakness and possibly varying composition. The top of the inverted sections are characterized by resistivities substantially lower than 12 Ωm with maximum thicknesses of up to about 20 m in the central parts of the lines. This

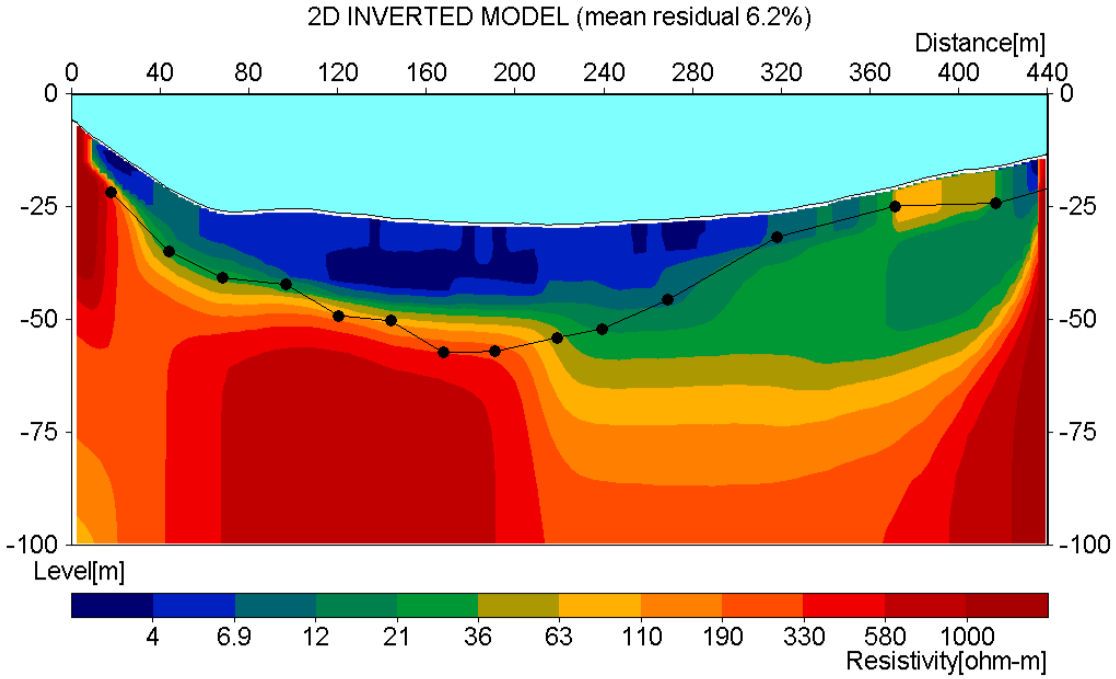


Figure 3. Resistivity model for Line A in Saltsjön, with water levels and interpreted depth to the bedrock from the geotechnical drilling indicated.

can be interpreted as unconsolidated sediments.

In the distance range of 220 to 440 m on Line A there is a zone with resistivities in the range of 12 to 36 Ωm in the upper low-resistivity zone down to several tens of meters. A corresponding zone appears on the other nearby lines, and without access to other data from the region, this could have been interpreted as a zone of anomalous composition of the rock or fractured and weathered rock. Alternatively, it could be interpreted as a sharp increase depth to bedrock, where the rock is overlain by sediments with different composition or salinity than in the upper parts of the sediments. At the beginning of each line low resistivities indicate that there may be a zone of weakness in the rock. Since the zone is located at the edge of the lines, the resolution is however poor. The low resistivity at the edge might also be caused by structural elements in quay construction, but because the survey lines are oriented perpendicular to the layout direction impact should be relatively limited. There are more or less vertical structures in the deeper parts of the sections that can be interpreted as tectonic zones, and separating more highly resistive zones (> 1000 Ωm) from zones with intermediate resistivities (a few hundred Ωm). The high-resistivity zones can be interpreted as crystalline rock with low degree of fracturing, while the zones of lower resistivity can be interpreted as rock with differing quality that is probably fractured and weathered rock.

Interpreted depths to bedrock from geotechnical drilling have been superimposed in the resistivity section of Line A (Figure 3). Interpreted depth to rock is generally well consistent between methods. Local variations in the depths may be due for example to the rock surface topography varying in three dimensions while the ERT survey is based on a two-dimensional approximation of reality. Rock levels show that the zone of relatively low resistivity in the range 220 to 440 m on line A consists of low-resistivity rock, which may be the uppermost part of a larger zone of differing properties of the rock.

3.2 Mälaren

As for the first case from Saltsjön most of the background noise is expected to come from the underground train system (T-bana) which operates with DC power supply. While most noise from AC sources can be filtered out the DC noise can only be avoided by measuring when the trains do not run, i.e. at night. In this survey measurements were taken on two occasions to be able to study the effect of DC noise. These results show a variance of 0-4% on the data measured at night and 0-20% on the data measured during the rush hours in the morning. The data measured during rush hours are still possible to process and interpret, but the higher noise rate during the day indicates that it might be a good idea to perform sensitive measurements or measurements close to infrastructure during the night.

The resistivity data are of good quality. The bottom topography based on a combination of sonar surveying and pressure sensors was included as part of the models. There was no variation of resistivity in the water so the water resistivity distribution was simplified to a single layer model of 62.5 Ωm. The inversion resulted in a model showing vertical sections of resistivity variation (Figure 4). The models have a low mean residual (about 3%), which shows that there is good agreement between model and data.

The resistivity section shows a superficial layer characterized by resistivities lower than 10 Ωm, in the distance interval 150 – 550 m, with maximum thicknesses of up to about 20 m. This can be interpreted as unconsolidated and/or clayey sediments. Below are generally higher but varying resistivities that can be interpreted as bedrock zones of harder rock in each end of the profile and a broad weaker zone in the centre.

In the distance range of 315 to 385 m there is a vertical zone with resistivities in the range of 23 to 44 Ωm in the deeper parts of the profile. This can be interpreted as a tectonic zone. On each side of this there are zones of around 100 m width with intermediate resistivity (a few hundred Ωm) and outside of these there are zones of high resistivity (> 1000 Ωm). The high-resistivity zones can be interpreted as crystalline rock with low degree of fracturing, while the zones of lower resistivity can be interpreted as rock with differing quality that is probably fractured and weathered rock.

Interpreted depths to bedrock from seismic measurements and geotechnical drilling have been superimposed in the resistivity section (Figure 4). Interpreted depth to rock is generally well consistent between methods. The interpreted weak zone in the centre of the profile is found both in drillings and in seismic. The weak zone in seismic at 550-600 m cannot be seen in the resistivity results, but it should be noted that the

seismic line is placed about 20 m offline in the North end of the profile. The seismic data was collected in 2008 and raw data has not been available for analysis here.

4 CONCLUSIONS

The results show that the rather difficult survey conditions could be handled in a satisfactory way thanks to adequate equipment, careful planning and attention to details. The measured data contains information that is relevant for creating coherent models of the variation in depth to rock together with data from drilling. The results also indicate that information in variation in rock quality that can be of critical importance for planning of underground construction can be derived from the data. Further comparisons against reference data are required for a full evaluation of the results. It would have been helpful if geophysical borehole logging was conducted as a supplement in some drill holes along the lines. Such data could provide an interpretative key of the connection between rock resistivity and rock quality.

With about 20 m of water, as we have in these cases, a significant part of the current is transferred in the water instead of in the ground. The resistivity of about 1.5 Ωm, as in Saltsjön, means that more current is transmitted in the water than in the ground. This puts strict requirements on correct input of geometry of the seabed and resistivity of the water in order to get a good result. The surveying conditions are more favourable in Lake Mälaren thanks to the much higher water resistivity.

With the results presented here we conclude that resistivity measurement is an important contribution in urban investigations over water passages.

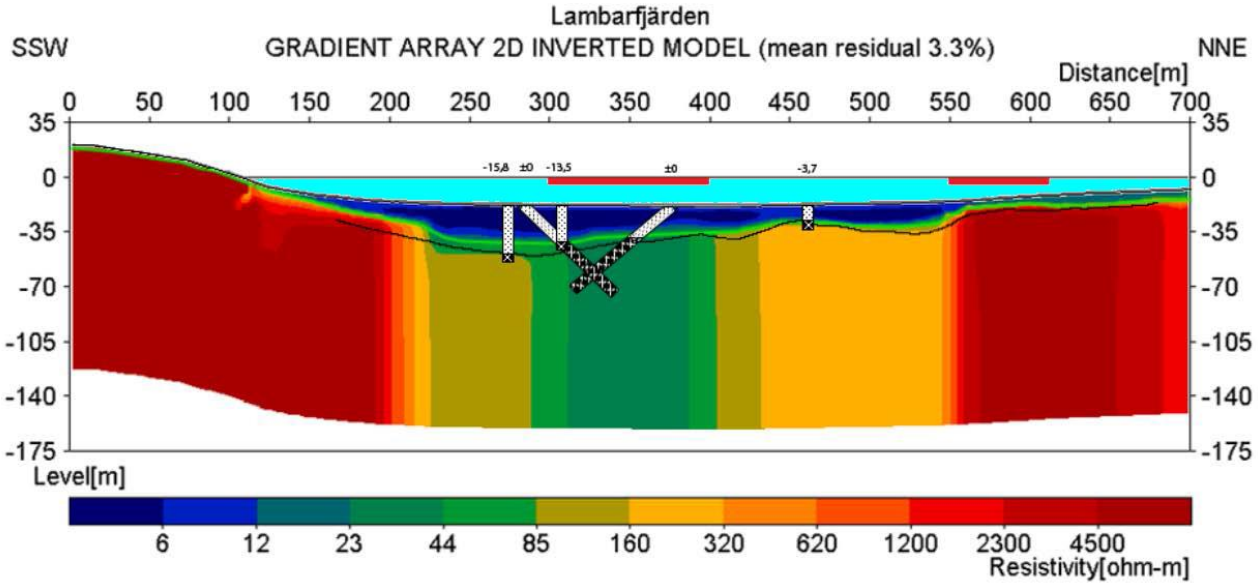


Figure 4. Resistivity model for Line in Mälaren, with water levels, drillings with noted weak rock (black fill in drillings), interpreted bedrock from drilling and seismic (black line) and interpreted weak zones in seismic (red lines in top of profile).

5 ACKNOWLEDGEMENTS

We thank Stockholms Läns Landsting (SSL) who financed the T-bana Nacka survey for permission to publish the results. We also wish to thank Jonas Siikanen, Marcus Höök, Roberth Colliander and Thomas Sträng for the good cooperation throughout the project. We wish to thank Elisabeth Lindvall, Erik Warberg and Matteo Rossi for their excellent contributions during the field campaign in Lake Mälaren.

Funding which made this work possible was provided by BeFo, Swedish Rock Engineering Research Foundation, (ref. 314 and 331) and SBUF, The Development Fund of the Swedish Construction Industry, (ref.12718 and 12719) and Formas, The Swedish Research Council for Environment, Agricultural Sciences and Spatial Planning, provided funding for this presentation of the results (ref. 2012-1931) as part of the Geoinfra-TRUST framework (http://www.trust-geoinfra.se/).

6 REFERENCES

Dahlin, T. (1996) 2D resistivity surveying for environmental and engineering applications, *First Break*, 14(7), 275-283.

Loke M.H., Acworth I. and Dahlin, T. (2003) A comparison of smooth and blocky inversion methods in 2D electrical imaging surveys. *Exploration Geophysics*, 34, 182-187.

Loke M.H. and Lane J.W. (2004) Inversion of data from electrical resistivity imaging surveys in water-covered areas. *Exploration Geophysics*, 35, 266-271.

Persson L., Sträng M. & Antal I. (2001) *Berggrundskartan 10I Stockholm* (Bedrock Map 101 Stockholm), Scale 1:100 000, Series Ba, No 60, Swedish Geological Survey, Uppsala.

Stockholm Municipality (1997) *Byggnads-geologisk karta* (Engineering Geological Map), https://iservice.stockholm.se/open/GeoArchive/Pages/Search.aspx (accessed 2014-04-15).

An integrated approach to Geotechnics and Geophysics on the Electrification Programme in Denmark

David Ross Alvin
COWI A/S, Denmark, dra@cowi.dk

Ole Frits Nielsen, Carsten Steen Sørensen
COWI A/S, Denmark, COWI A/S, Denmark

ABSTRACT
The Electrification Programme is a design and construct project involving the electrification of approximately 1500 km of railway line in Denmark. As a part of the geotechnical basis for the project, an integrated approach to geotechnics and geophysics was adopted, in order to provide the tenderers with sufficient information regarding the expected ground conditions and with due consideration to the time schedule for the project. A combination of traditional geotechnical site investigation including on track Cone Penetration Testing and geophysics using Electrical Resistivity Tomography was performed. The results of the fieldwork were combined with existing geotechnical data along the railway alignment in order to prepare tables presenting geotechnical parameters and design soil profiles. Furthermore, all existing and new geotechnical data - such as borehole profiles and geotechnical reports - were made easily accessible through a homepage containing a GIS platform with online access for the Tenderers. This approach enabled the vast amounts of geotechnical and geophysical data to be presented in an easily accessible and usable format. The integrated approach to the geotechnical and geophysical investigations proved to be an ideal solution for a project of this size and complexity.

Keywords: Site investigation, Cone Penetration Testing, Electrical Resistivity Tomography, GIS Platform.

1 INTRODUCTION

The Electrification Programme (EP) consists of electrifying existing and new railway lines for Banedanmark (Rail Net Denmark). It is one of the largest infrastructure projects, ever undertaken in Denmark. The project consists of electrifying approximately 1500 km of railway line on 15 separate sections (including 5 new railway lines) in the majority of the country.

As shown in Figure 1, only the green sections of the railway network in Denmark are electrified today. The red and yellow sections of the network are scheduled for electrification in the period 2015 – 2029. The total budget for the Electrification Programme is 12 billion Danish kroner (approximately 1.6 billion Euros).

Given the tight time schedule for preparation of the tender documents for the project, the challenge for the geotechnical team was to provide a sufficiently robust geotechnical and hydrogeological basis for tendering purposes. A strategy was developed by COWI-SYSTRA involving a combination of existing available data with new data from supplementary geotechnical investigations and geophysical surveys. In all 270 geotechnical boreholes and 140 km of ERT (Electrical Resistivity Tomography) were undertaken for the project. All the existing and new data was collated and presented in a single, easily accessible GIS database for all project users.

The database, known as EacoWeb, is accessible on-line through a homepage that was set up specifically for this purpose. As part of the data package in the tender documents a desktop version was provided making it possible to access the data also when off-line.



Figure 1, A map of Denmark showing the extent of the planned works with red and yellow lines. Green lines represent already electrified railway sections.

2 STRATEGY FOR INTEGRATING GEOTECHNICS AND GEOPHYSICS

As the project involves electrification of vast lengths of track, a methodology for covering these very large distances was thus required.

The strategy for geotechnics was based on a cost benefit principle, in which the greater the degree of geotechnical knowledge made available at tender stage, the greater the risk reduction in unforeseen ground conditions is achieved. However, at a given point in time, the incremental reduction in risk becomes minimal in relation to the time restraints and cost of performing the investigations. Thus a certain minimum of data had to be provided – a minimum that would still be enough to reduce the risk of unforeseen ground conditions significantly.

This could be achieved if enough data was available to form the basis for a rough model of the ground conditions. The model provides information on the geotechnical strength parameters along the railway lines. To reduce the risk for the client and the tenderers it should be provided in the tender documents and serve as the basis for the tenderers' design calculations. It was therefore decided to aim at a level of information high enough to set up a rough, but still realistic model for the geotechnical strength parameters in the uppermost 8 m below ground level along the ca. 1400 km of railway track.

This challenge was overcome by combining existing data from Banedanmark, GEUS (Geological Survey of Denmark and Greenland) via the Jupiter Database and COWI's own geotechnical database with a series of new geotechnical boreholes including CPT tests at selected locations as well as a series of geophysical surveys performed parallel to the track at selected locations.

The focus of the new supplementary data was to gain more information on the fill and intact geological deposits along the railway lines. This information was obtained by conducting geophysical surveys parallel to the railway combined with geotechnical boreholes off-track. Compared to conducting boreholes on-track at night during the limited available track possessions the off-track geotechnical investigations proved to be both faster, more flexible and significantly cheaper. Having the vast majority of supplementary geotechnical boreholes drilled off-track reduced the cost of the supplementary geotechnical investigations significantly.

The geophysical ERT surveys could further reduce the number of geotechnical boreholes needed and at the same time give continuous

information along the survey lines parallel to the railway lines. As the geotechnical and geophysical methods are highly complementary, the combined use provided detailed information on the ground conditions along the alignment.

3 PLANNING OF SUPPLEMENTARY GEOTECHNICAL AND GEOPHYSICAL DATA

On the basis of 1:25.000 and 1:200.000 surface geological maps prepared by GEUS, existing boreholes from JUPITER, existing geophysical data from GERDA (Geophysical Relational Database), geomorphological maps, historical maps and existing data from Banedanmark consisting of existing geotechnical boreholes and reports, the supplementary geotechnical and geophysical investigations were planned.

The planning of supplementary investigations was based on existing data. The focus was primarily on the type and density of existing data as well as on the expected geological complexity at a specific location. However, also more practical considerations were taken into account, such as available railway possessions, time constraints and access conditions along the railway track.

Initially, a desk study of possible access roads to the railway or in the proximity of the railway was carried out. A combination of orto photos and topographical background maps was utilized to identify possible access points to the railway where off-track geotechnical investigations could be carried out. The result of the desk study was used in the planning of the supplementary geotechnical investigations and furthermore, provided for the tenderers as part of the tender material.

The supplementary geotechnical boreholes were drilled at carefully assessed locations, in order to provide supplementary geological and geotechnical information, including geotechnical properties of the soils and rocks encountered. In addition, standpipes were installed in all off track boreholes in order to provide information on groundwater levels.

The geophysical investigations were planned along selected sub-sections of the railway in order to supplement the geotechnical investigations. The ERT survey lines were planned in order to give 2D continuous information on the soil layers along the track. This was utilized directly in the geotechnical model for the soil layers. In addition it gave information on the geological complexity in a specific area and provided additional focus on prospective locations for boreholes. In some areas it even reduced the number of boreholes and thereby reduced the cost of the geotechnical investigations further.

4 FIELDWORK

4.1 Geotechnical Investigations

The geotechnical investigations for the project consisted of both on-track and off-track boreholes, supplemented with insitu testing consisting of CPTu (Cone Penetration Testing with pore pressure measurement) and SPT (Standard Penetration Test). Planning of the geotechnical investigations (i.e. type of investigation and location) was undertaken using the GIS software Mapinfo in order to collate all the existing information along the track regarding geology, geotechnical and geophysical investigations and reports, information on utilities, access and terrain conditions, property owners, etc.



Figure 2, Drilling rig mounted on wagon ready for on-track work

The on-track boreholes were performed by a drilling rig mounted on a wagon with a hole in the floor. The rig was transported to the

drilling location by shunter. The drilling work was undertaken during track possessions at night. The boreholes were located between the sleepers and centrally between the rails. The challenge for the drilling teams was to perform the works within the tight duration (3 – 6 hours) of the track possessions, including transport to and from the drilling location. Depending on the duration of the track possession and distance to the drilling location from the siding, a borehole with a drilling depth up to 8 m below track level including recovery of disturbed and undisturbed soil samples, performing field vane shear tests in cohesive soils and undertaking 1 – 2 nos. CPTu to 8 m below track level could be performed in a single track possession. Due to time restraints and long term railway safety considerations, standpipes were not installed in on-track boreholes.

Concurrent to the on-track fieldwork, off-track geotechnical investigations were undertaken at selected locations where access was possible. Due to railway safety restrictions, the locations of these investigations were limited to a minimum safety distance of 8 m to the nearest rail. The off-track geotechnical investigations consisted primarily of geotechnical boreholes including recovery of disturbed and undisturbed samples, performing field vane shear tests in cohesive soils and undertaking SPT and CPTu in situ testing.

Figure 3 below shows a typical borehole log with in situ testing.

Standpipes were installed in all off-track geotechnical boreholes in order to monitor the groundwater levels along the railway.

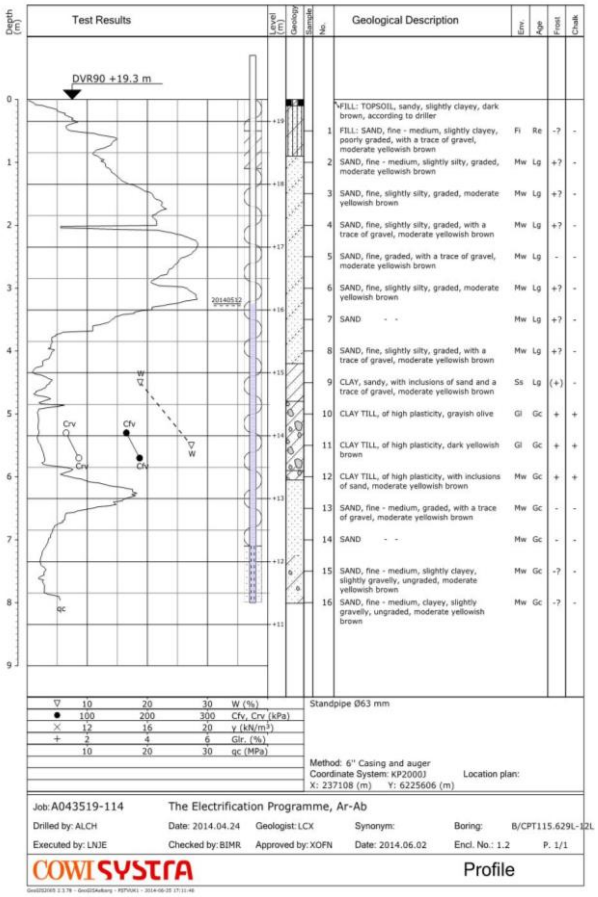


Figure 3, Off-track borehole log with CPTu and field shear vane testing

4.2 Geophysical Investigations

The geophysical investigations were conducted as ERT (Electrical Resistivity Tomography) using a minimum electrode distance of 5 m. An ABEM SAS4000 Terrameter was utilized transmitting a minimum current of 20 mA. The Gradient Array geometry was applied in a setup with 41 electrodes giving a maximum penetration depth of up to 60 meters.

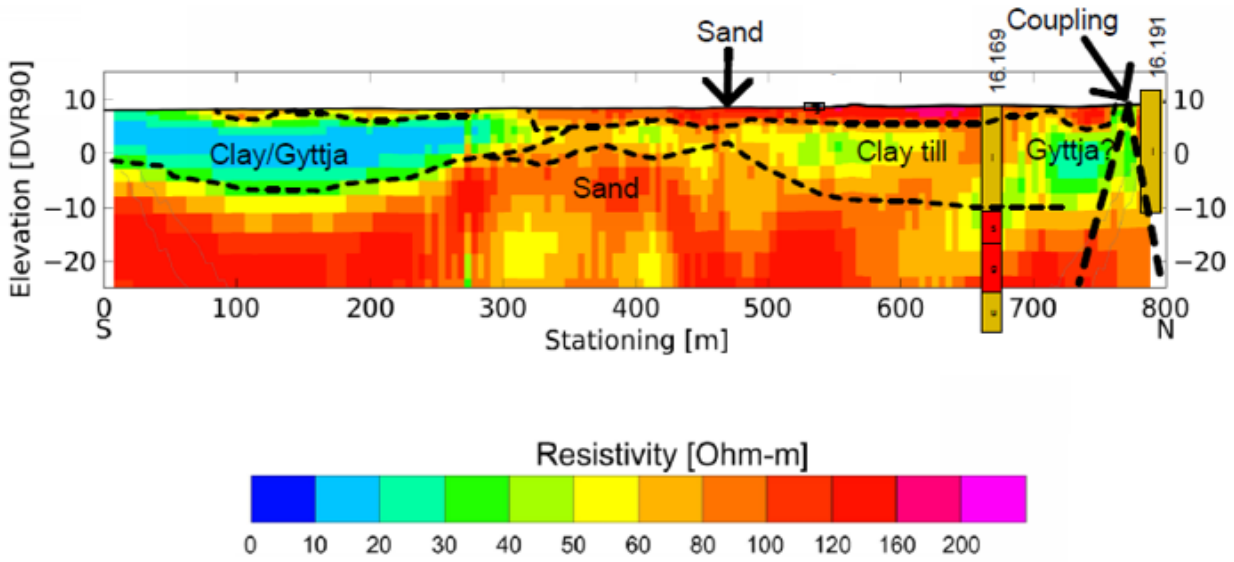


Figure 4, Example of interpreted model section of an 800 m long ERT profile along the railway line. Two existing boreholes have been projected onto the profile (at 670 m and 790 m).

The ERT survey lines were placed 50-75 m from the railway line in order to avoid electrical coupling to the railway tracks or underground utilities along the track. At some locations a short survey line was placed perpendicular to the line parallel to the railway in order to provide detailed spacial information on the soil layers.

The fieldwork was carried out by two operators. An ATV (All-Terrain Vehicle) was used to carry the equipment between the subsections.

5 GIS-PLATFORM AND EACOWEB

All geotechnical and geophysical data was collated together with relevant hydrogeological data gathered in a central database. The data was geocoded and made accessible through a GIS-platform displaying boreholes, geotechnical reports and relevant geophysical data along the railway lines. The geotechnical reports can be opened directly via a hyperlink to a pdf-version of the report. On the EacoWeb homepage borehole logs can be directly generated from the database from a selected borehole. Cross sections along a self-defined (crooked) line can be generated showing topography and boreholes within a selected distance from the profile alignment. This feature makes it possible to visualize and better understand the geological setting in a specific area.

The purpose of delivering the geo-data in a GIS-platform was to provide a clear overview and easy access to all geo-data, which in time will save time and money. Furthermore, the GIS-platform will also help to ensure that all available data are utilized in the project. The amount of existing data along the railway lines is extensive and represents a very high value for the client. Banedanmark's geotechnical archive was established at the beginning of the 19th century, however the geological and geotechnical data are still applicable regardless of age as this type of information remains almost unchanged over time.

The GIS-platform with all the geo-data was part of the data package in the tender documents. It was delivered both as a stand-alone desktop version to be used when off-line and as an on-line version. The latter is accessible through Banedanmark's EacoWeb homepage and, in contrast to the desktop version, interlinked with the national borehole database and EP's borehole database. This means, that Eacoweb is continuously updated with new boreholes. All boreholes drilled by the contractor will thus become available on EP's EacoWeb homepage throughout the project.

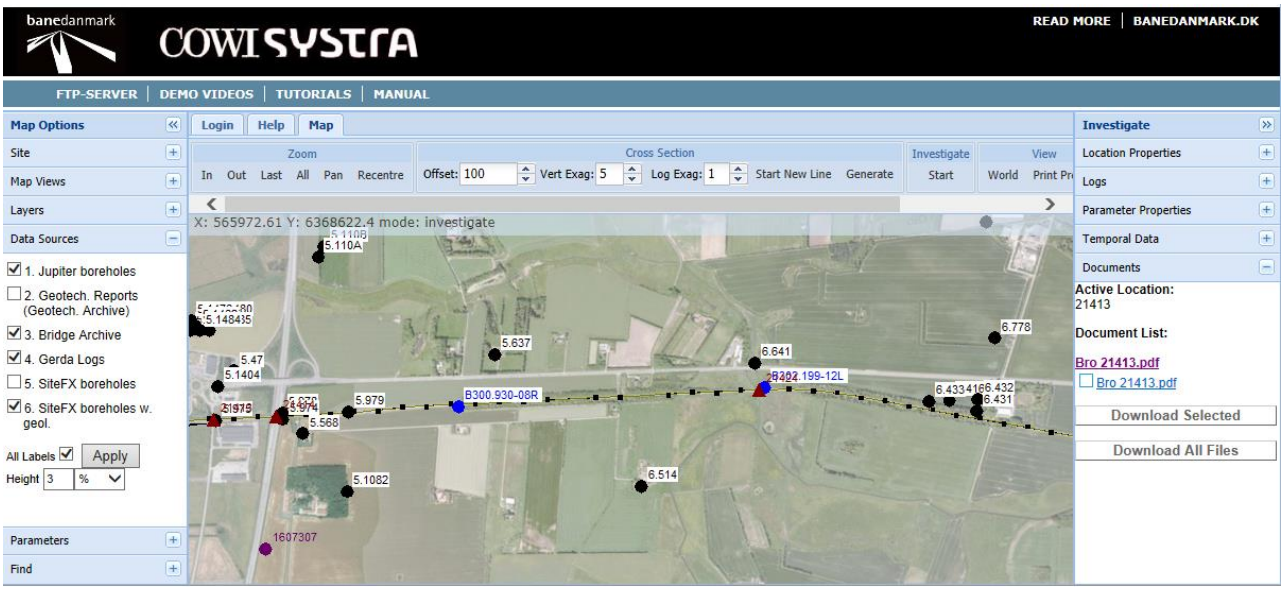


Figure 5, Example from Banedanmark's EacoWeb homepage for the Electrification Programme showing a close-up of the railway section Aalborg-Frederikshavn. Accessible data seen here are boreholes, borehole logs and geotechnical reports. Click on the link (purple text) in the right column to open the selected report as a pdf-file. Borehole logs can be generated directly from the database under the menu Logs and under the menu Cross Section you can generate cross sections with topography and boreholes projected from a selected offset distance.

6 ASSESSMENT OF SOIL AND ROCK PARAMETERS

In order to provide a uniform basis for tendering the project, a set of characteristic geotechnical parameters for the soils and rocks encountered down to 8 m below terrain and geotechnical profiles for all sections of track were provided for the tenderers. This required collation of all available data from existing sources (geological maps, historical maps, borehole logs, geophysical surveys, reports, memos, etc.) as well as the geotechnical and geophysical investigations performed for the project by COWI-SYSTRA for the client.

7 ADVANTAGES & RESERVATIONS

The combined approach in undertaking geotechnical and geophysical supplementary investigations in order to provide a sufficiently detailed and robust basis for the preparation of tenders has proven to be ideal for a project of this size. The methods are highly complementary and the integrated interpretation increases the achievable level of information.

On-track geotechnical boreholes can provide data very close to the location of a future mast foundation – but at a significant cost, whereas off-track boreholes are positioned at locations, where off-track access is available, and thus costs are less, however the off-track location may not correspond to the location of a proposed mast foundation. Due to the considerable extra costs involved in planning and drilling on-track geotechnical boreholes, as compared to off-track geotechnical boreholes, a well-considered balance between the numbers of these alternative types of boreholes in the drilling programme is required.

The interpreted model section from the geophysical ERT surveys have shown to be directly applicable to the model of the characteristic geotechnical parameters of the soil layers.

Where possible, the results of the geophysical ERT surveys have further been incorporated into the planning of the supplementary geotechnical investigations in order to optimize their location. In some instances, the geophysical information was not available in time for planning of the geotechnical investigations, typically due to weather or access issues. However, the geophysical ERT surveys give a solid geological basis in which the contractor can use in eventual planning of additional geotechnical investigations.

Similarly, the results of the geophysical surveys can also be used to assess the sections of railway in which the distance between the geotechnical investigations can be increased without compromising the overall quality of the basis geotechnical information for the project.

The geophysical surveys cannot be used directly to assess the characteristic geotechnical parameters for the soils and rocks encountered and as such, they cannot be used as a standalone investigation method for the purposes of this project. However, the ERT profiles provide continuous data which combined with boreholes can extrapolate the information from the borehole(s) along the ERT profile. This greatly enhances the value of nearby boreholes.

Due to electrical disturbances from the signaling cables that can affect the ERT data, the geophysical surveys were typically located 50 – 75 m from the railway. As such, the results of the geophysics need to be considered in this light when interpreting the geological longitudinal sections along the track.

In built up areas such as towns, in forests or in periods of frost or snow it was not always possible to perform the geophysical surveys.

The use of one single and easily accessible GIS platform to store and access all geotechnical, hydrogeological and geophysical project data is an enormous advantage compared to paper format, and not just with regards to presenting the information in the tender documents, but just as importantly, during the design and construction phases of such a large project. The fact that all users can access the same data simultaneously is an important factor in reducing the number of misunderstandings between the different parties working on the project.

The quality of the overall database is only as good as the quality of the individual input data. As such, stringent controls need to be in place in order to ensure that the quality of the input data is assured.

The use of the GIS tools Mapinfo and EacoWeb was a major factor in collating the vast amounts of data. Furthermore, these GIS tools were very efficient in facilitating the

tasks of planning the supplementary geotechnical and geophysical investigations as well as assessing the characteristic values of the geotechnical parameters for soils and rocks encountered.

8 FUTURE APPLICATIONS

On major infrastructure projects such as roads, motorways, railways, as well as large utility projects, for example laying gas lines or electricity cables, the combination of geotechnical investigations and geophysical surveys can be used to optimize the number and location of investigation points, particularly over large distances, where scarce placement of geotechnical investigations is a necessity.

The complementarity of the two investigation methods raises the achievable level of information. This is possible when an integrated interpretation of the two data sets is made. Thus, it is strongly recommended that a geotechnical borehole is drilled along a geophysical survey line and vice versa.

The use of a single, easily accessible internet based GIS platform such as EacoWeb is a very efficient way of storing, maintaining, sharing and updating data for all project users.

Statistical analysis of thaw index for thaw weakening design purposes

Tommy Edeskär. Corresponding / primary author
Luleå University of Technology, Sweden, tommy.edeskar@ltu.se

Adam Fredriksson. Co-Author
Luleå University of Technology, Sweden

ABSTRACT
In frost action research and design most focus has been put on frost heave. There are several models available to predict frost heave and the concept of statistical re-occurrence times of frost index is commonly used in design. Less effort has been put on thaw weakening modeling and design even though thaw weakening causes a lot of damage on infrastructure such as road and railways. In e.g. Sweden the Transport Administration collects temperature data during the freezing season for frost heave design purposes on project levels but thawing effects are conventionalized by reference tables on a regional level.

The aim of this study is to define and quantify the thawing event in such way that it could be applied on a project level in a similar way as temperature measurements are used for frost design. In this study thaw index has been analysed statistically based on air temperature data from 50 stations, collected from year 1951 and onwards by the Swedish Meteorological and Hydrological Institute (SMHI), in Sweden. The temperature thaw seasons have been correlated to the Swedish Transport Administrations frost depth measurement stations.

A reference table has been developed based on reoccurrence times of thawing seasons based on the magnitude of thawing index. Based on the statistical distribution of thawing indexes Sweden was divided into three regions in this study. It seems, by statistical means, to be fully possible to develop reference values for thawing periods where thawing index is the working unit. In order to implement the results in e.g. pavement design thawing temperature measurements on a local or semi-regional level are required.

Keywords: Thaw weakening, pavements, temperature analysis

1 INTRODUCTION

In seasonal frost regions frost action has major effect on pavement lifetime. Frost heave causes cracking of the pavement surface and unevenness on the road surface and thaw weakening decreases the bearing capacity. Both of these phenomena decrease the pavement life time, Berglund (2009).
In frost action design often the concept of an estimation of the frost heave based on a design winter temperature, commonly expressed as frost index (*FI*), from a nearby located metrological station. Thaw weakening design is in general more based on best practice. In e.g. the Swedish framework the thaw weakening is encountered for by seasonal adjustments of the stiffness modulus in the pavement design procedures on a regional level, Trafikverket, (2011).

Thaw weakening on roads is effected by a range of varaibles, e.g. temperature at freezing and thawing, soil type, the access to water in the freezing and hawing season, the local draining conditions and the traffic, Phukan, (1985). The variation of the degree of thaw weakening is in high degree related to the temperature gradient in spring time. High temperature gradients results in severe thaw weakening and at low temperature gradients the thaw weakening is less severe, Berglund (2009).
Design charts for frost depth and design frost index has been used in pavement and foundation design for decades, e.g. Stål and Vedel, (1984). Similar charts or analysis has so far not been adapted for thaw weakening. In this study temperature from Sweden has been analysed statistically during thaw events for over 50 years in order to propose design criteria for thawing periods. Variation and re-occurrence of temperature scenarios has been studied. A concept of forecasting thaw weakening based on temperature readings and historical temperature data is proposed based on a model suggested by Hicks et al. (1985). Thaw weakening may be divided into surface weakening, affecting the uppermost layers in the superstructure, and deap weakening, affecting the subgrade, Gandahl, (1987). Hicks et al. (1985) and this study focuses on the deap weakening in the subgrade only.

2 METHODOLOGY

2.1 Outline of study

In this study long time series of air temperature data has been used for statistical analyses of the variation thawing events in spring time and its spatial distribution in Sweden. To model the thawing event an air temperature based model proposed by Hicks et al. (1985) has been used. The results have been validated by monitoring data from frost depth measurements. Since the analysis not is site specific a range of simplifications has been used; the thaw weakening is only regarded in the subgrade, thermal properties are considered to be constant etc.

2.2 Air temperature data

The air temperatures used in this study are open climate data provided by the Swedish Metrological and Hydrological Institute (SMHI, 2015). Data from 50 temperature stations in Sweden from 1951-2014 has been analysed. The locations range from Malmö in the south to Luleå in the north of Sweden. The location of the stations is shown to the left in figure 1.

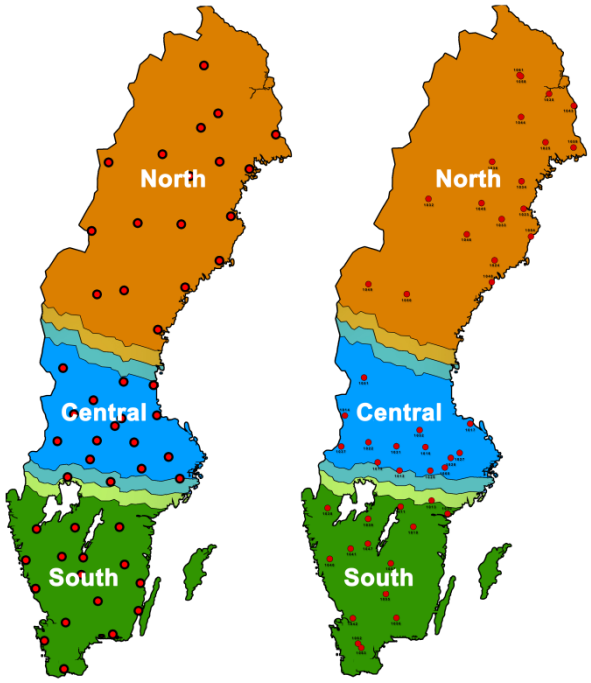


Figure 1 To the left: Location of the SMHI air temperature monitoring stations used in this study. To the right: Location of the Swedish Transport Administrations thaw depth monitoring stations used in this study.

2.3 Frost depth monitoring data

Monitoring data from the Swedish Transport Administrations thaw depth measurement stations has been used to study spatial variations in thaw weakening over the country and to validate the results from the statistical analysis of the air temperatures. There is totally 54 thaw depth stations, of 48 are in operating status, monitoring thaw depth since 2006, Trafikverket, (2015). The operating stations are displayed on the map to the right in figure 1. The stations monitors thaw depth 12-24 times a day at an intermediate distance of 5 cm between the sensors, down to 2 m depth below the surface. In this study monitoring data has

been aggregated to daily average values. The monitoring stations of frost depth lack air temperature monitoring. In order to correlate the frost depth readings by air temperatures has air temperature data from adjacent weather stations for road maintenance been use (VViS-stations).

2.4 Analysis of frost depth and thawing seasons

The monitoring data from the frost depth analysis has been used to quantify the length of the thawing season. The length of the thawing season is defined between the starting date when the upper temperature reading > 0˚C until the whole soil profile is > 0˚C. The thawing period for each station is compiled by an average time length *t* based on the all the recorded seasons.
The average length of the thawing season of each station has been correlated to the geographical position (here in SWEREF) by linear regression in the program MINITAB 17, Minitab, (2015) in order to explore the variation in thawing season from the south to the north of Sweden. Based on the results the monitoring stations are grouped into regions for further analysis. The average regional thawing period is calculated and further on referred to as t_{max}. The time is used for computation of TI_{acc} for each region, i.e. the thawing index needed to thaw the subgrade in the region.

2.5 Thaw model

Hicks et al. (1985) proposes a thaw model based on thawing index. The thawing index *TI* is the accumulated air temperature above the freezing relative a reference thawing temperature. The procedure for calculating the thawing index *TI* follows the procedure presented in Berglund et al. (2011).

$$\mathrm{TI} = \left(T_m - T_{ref}\right) \cdot \Delta \mathrm{t} \qquad (1)$$

Where; T_m is the average daily temperature, T_{ref} is the temperature at thawing starts (here 0 ˚C), and Δt time step (here 1 d) in the thawing period. The thawing index is accumulated over time in the thawing period, TI_{acc}. To account for intermediate freezing events the accumulated thawing index decreases by half of the freezing index *FI* (Hicks et al. 1985), equation 2.

$$TI_{acc} = \sum(TI - 0.5 \cdot FI) \qquad (2)$$

When $T_m \leq 0$˚C the freezing index *FI* is calculated according to equation 3.

$$\mathrm{FI} = \sum(0 - T_m) \qquad (3)$$

The start of the thaw period id defined when a limit value of the accumulated thaw index ($TI_{acc,lim}$) has been exceeded. In this study has the proposed thawing index limit by Hicks et al. (1985) been used. For thicker pavements, comparable to engineered roads, the proposed limit is $TI_{acc,lim} \approx 14$ ˚d (approximation from Fahrenheit). An additional condition for defining the start of a thaw period in this study to have subsequent positive daily average air temperatures after $TI_{acc,lim}$ has been reached.
To determine if frost action may be present Stefan's formula has been used. Based on a thickness of 0.5 m superstructure at least a frost index $FI \geq 50$˚d is needed.

2.6 Data analysis

Thaw index is calculated for all the SMHI climate stations there complete data series are present. The starting date for the individual season is defined as when $TI_{acc,\,lim}$ for the station. T_{acc} are the calculated up to t_{max}, the defined end of the thawing season. For stations where several thawing seasons has been observed in the frost depth measurements more than one thawing season are modelled if the temperature data implies so.
Statistical data analysis has been applied in the progress of the thawing index. The analysis has been performed on the individual analysis of thaw index from t=3 days to t_{max}. The choice to start the analyses at day t=3 are based on to have a continuous thawing event in progress and to avoid effects of extreme temperatures during a very small time interval.
In the statistical analysis the computed T_{acc} for each station, season and day t=3 to t_{max} are used as data series [x_1: x_n]. A continuous statistical distribution fitting the data set is

needed in order to be able to compute reoccurrence, Benjamin & Cornell, (1970). The reoccurring thaw index TI_{acc} is denoted x_t where the index t denotes the time unit. In this study the time unit is number of thawing seasons per year. If the dataset belongs to the continuous statistical distribution *F(x)* (Castillio, 1988):

$$\mathrm{F(x)} = \mathrm{P(X} \leq x_t) = \frac{1}{t} = p \qquad (4)$$

The statistical distribution gives the probability of the stochastic variable *X* to have a value less than x_t. In this case is the complementary outcome of interest.

$$P(X \geq x_t) = 1 - F(x) = F_c(X) \qquad (5)$$

or

$$\mathrm{t} = \frac{1}{F_{c(X)}} \qquad (6)$$

Based on the statistical distribution *F(X)*, or in this case the complementary distribution function, x_t, can be computed from equation 6.
The distribution *F(X)* has been analysed, based on the TI_{acc}-values by the software EasyFit, Mathwave, (2015). Three possible distributions were identified as possible: Burr type XII, Johnson S_b, Johnson S_u, All of these distributions requires four input parameters, Johnson & Kotz, (1970). To determine the best fit of distribution the Anderson-Darling test was used.
Based on the chosen distribution the re-occurrence of x_t for $t \in$[2, 5, 10, 15, 20, 25, 30, 50, 75, 100, 150].

2.7 Evaluation of thaw events

In this study the thaw events have been classified the number of thawing periods per season.

3 RESULTS

3.1 Thaw periods

The average thawing period (t_{max}) for all individual stations are plotted vs. the latitude coordinate in figure 2. The inserted trend line shows a high correlation between the length of the thawing season and the latitude, R^2=0.82. As seen in the figure the variation increases in the north for the length of the thawing period.

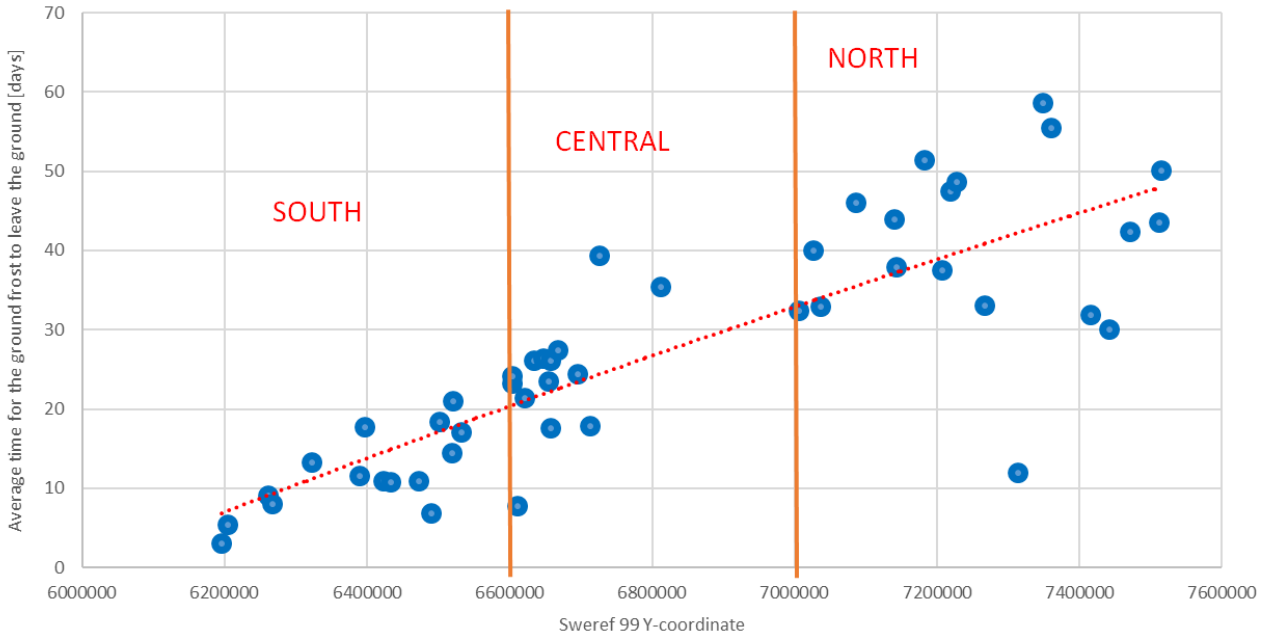


Figure 2 Average time t_{max} in days for the thawing period vs. the Y-coordinate in the SWEREF-coordinate system (from south to north).

Based on the results in figure 2 the stations were divided into three different regions; north, central and south, indicated in figure 1 and 2. In table 1 is the average thawing periods t_{max} presented for the three regions.

Table 1 The average thawing periods t_{max} for the three different regions.

Region	t_{max} [d]
North	41
Central	24
South	12

The number of years included in the analysis and the average number of thawing periods for the three regions are summarised in table 2.

Table 2 The average thawing periods t_{max} for the three different regions.

Region	No. years of data	No. of thawing periods
North	822	1.23
Central	831	1.11
South	831	1.04

EVALUATION OF THAWING
Reference values ∑(TI-0.5FI)
Thawing index evaluation

Region (as per map)

North	1-F(X)⁻¹ [år] \ Δt [d]	3	4	5	6	7	8	9	10	11	12	13	14	15	16	17	18	19	20	21	22	23	24	25
	T2	9,6	12,1	14,6	17,1	19,6	22,1	24,6	27,2	29,8	32,7	35,9	39,2	42,7	46,8	50,1	54,2	58,6	64,5	68,5	73,6	78,8	84,2	89,8
	T5	14,6	19	23,4	27,6	32,1	36,6	40,9	45,2	49,7	54,4	59,5	64,9	70,6	75,9	82,4	88,8	95,6	103,8	110,2	117,8	125,4	133,3	141,2
	T10	17,3	22,8	28,3	33,7	39,2	45	50,6	56	61,5	67,3	73,4	79,9	86,7	92,5	100,7	108,2	115,9	125,1	132,6	141,2	150	159	168
	T15	18,6	24,7	30,9	36,8	43	49,5	55,7	61,7	67,8	74,1	80,8	87,9	95,1	101,4	110,1	118,1	126,4	135,9	143,9	152,9	162,1	171,6	181,2
	T20	19,5	25,9	32,5	38,8	45,5	52,5	59,2	65,7	72,1	78,8	85,8	93,3	100,8	107,5	116,4	124,8	133,3	143,1	151,3	160,5	170	179,8	189,8
	T25	20,1	26,8	33,7	40,4	47,3	54,8	61,8	68,6	75,4	82,3	89,6	97,4	105	112,1	121,1	129,7	138,4	148,3	156,7	166,1	175,8	185,8	196
	T30	20,6	27,5	34,7	41,6	48,8	56,6	64	71	78	85,2	92,7	100,7	108,4	115,9	124,9	133,6	142,4	152,5	161	170,5	180,3	190,4	200,9
1.05 Seasons	T50	21,9	29,4	37,2	44,8	52,8	61,5	69,7	77,5	85,2	92,9	101	109,6	117,7	126,2	135	144,1	153,2	163,5	172,3	182	192,1	202,6	213,5
	T75	22,9	30,8	39,1	47,8	55,8	65,3	74,2	82,6	90,7	98,9	107	116,4	124,7	134,3	142,6	151,9	161,3	171,6	180,6	190,4	200,7	211,4	222,7
	T100	23,5	31,8	40,3	48,9	57,8	67,9	77,3	86,1	94,6	103,1	112	121,1	129,5	140	147,8	157,3	166,7	177,2	186,2	196	206,4	217,2	228,7
	T150	24,3	33	42	51,1	60,6	71,5	81,6	91	100	108,9	118	127,7	136,2	148,1	154,9	164,6	174,2	184,6	193,7	203,5	214	225	236,8

Central	1-F(X)⁻¹ [s.] \ Δt [d]	3	4	5	6	7	8	9	10	11	12	13	14	15	16	17	18	19	20	21	22	23	24	Degree of s
	T2	9,5	12,1	14,7	17,2	19,6	22,1	24,6	27,1	29,7	32,4	35,2	38,1	41	44	47,1	50,5	54,1	57,9	61,9	66,1	70,4	74,9	1
	T5	14,3	18,4	22,7	27,2	31,5	35,9	40,1	44,2	48,5	52,8	57	61,6	66,4	71,4	76,4	81,8	87,4	93,4	99,8	106,5	113,4	120,6	2
	T10	17	22	27,2	32,8	38,2	43,7	49	54,2	59,6	65,1	70,4	76	82	88,2	94,4	100,1	107,8	115	122,8	130,8	139,1	147,7	3
	T15	18,4	23,9	29,6	35,7	41,6	47,7	53,6	59,5	65,7	71,8	77,7	84	90,7	97,6	104,4	111,6	119,1	126,9	135,3	144	153,1	162,4	4
	T20	19,4	25,2	31,2	37,6	43,9	50,4	56,8	63,1	69,8	76,4	82,8	89,6	96,8	104,2	111,4	119,1	127	135,2	144	153,2	162,7	172,4	5
	T25	20,1	26,1	32,4	39	45,6	52,5	59,1	65,9	73	80	86,8	93,9	101,5	109,2	116,8	124,8	133,1	141,5	150,7	160,2	170	180,1	6
	T30	20,6	26,9	33,4	40,2	47	54,1	61	68,1	75,5	82,9	90	97,4	105,3	113,3	121,2	129,5	138	146,7	156,1	165,8	176	186,3	7
1.11 Seasons	T50	22,1	29	36,1	43,2	50,6	58,4	66,2	74,2	82,6	91	98,9	107,2	116	124,9	133,6	142,5	151,8	161,1	171,2	181,5	192,4	203,5	8
	T75	23,2	30,6	38,2	45,5	53,3	61,7	70,1	78,9	88,2	97,3	106	115	124,5	134,1	143,4	153	162,7	172,5	183,1	193,8	205,4	216,9	9
	T100	23,9	31,6	39,7	47	55,2	64	72,9	82,2	92,1	101,3	111	120,6	130,6	140,7	150,5	160,4	170,6	180,7	191,5	202,6	214,5	226,4	10
	T150	24,9	33,2	41,7	49	57,8	67,1	76,7	86,9	97,6	108,2	118	128,6	139,3	150,1	160,5	171	181,7	192,2	203,4	214,9	227,4	239	11

South	1-F(X)⁻¹ [s.] \ Δt [d]	3	4	5	6	7	8	9	10	11	12	Degree of severity
	T2	9,5	12,1	14,7	17,4	20	22,5	24,8	27	29,4	31,9	1
	T5	14,4	18,4	22,5	26,8	31,1	35,4	39,5	43,5	47,6	51,8	2
	T10	17,3	22,2	27,1	32,3	37,7	43	48,3	53,4	58,5	63,6	3
	T15	18,8	24,3	29,6	35,3	41,2	47,2	53	58,8	64,4	70	4
	T20	19,9	25,7	31,4	37,4	43,5	50	56,3	62,5	68,4	74,3	5
	T25	20,7	26,8	32,7	38,9	45,4	52,1	58,8	65,3	71,5	77,6	6
	T30	21,3	27,7	33,7	40,2	46,8	53,8	60,8	67,5	74	80,2	7
1.23 Seasons	T50	23,1	30,1	36,6	43,6	50,8	58,6	66,3	73,7	80,8	87,4	8
	T75	24,4	32	38,9	46,3	53,9	62,3	70,6	78,6	86	93,1	9
	T100	25,4	33,4	40,5	48,1	56,1	64,8	73,6	82	89,8	97	10
	T150	26,7	35,3	42,8	50,8	59,2	68,5	77,8	86,7	95	102,5	11

Figure 3 Excerpt from the reoccurrence table. The table contains the TI_{acc}-values at the past number of days in the thawing periods for different reoccurrence periods. The table contains values up to t_{max}=41 for the north region.

3.2 Statistical distribution

In general the Johnson S_b-distribution had the best fit on the data with a few exceptions. The station in Kalmar in region south followed a Johnson S_u-distribution instead.

4 DISCUSSION

4.1 Regional effects on thawing

As expected the thawing season is longer in the north compared to the south. But the intensity in the thawing is similar independent on the latitude location. The low variation support the simplification used in this study of dividing a large are into a few regional areas as also done in e.g. the Swedish Transportation Administrations frost design guidelines. In this study the effect of location in longitude position has not been investigated since the it in the south part of Sweden is a very high correlation between the latitude position and the variation in the north is hard to explain by statistical means due to lack of monitoring stations. It is reasonable to assume that in the north part of Sweden it would be relevant to divide the thaw weakening into at least two groups

based on the longitude locations (coast land and in-land).
It is interesting that the TI_{acc} is in the similar range for all stations during t<12 d.

4.2 The thaw-index model

The thaw-index model, based on Hicks et al. (1985) is based on several simplifications. In this study these simplification has been implemented fully since the aim has been to study the regional effects on thawing events. To be able to fully use this methodology the value of T_{ref} will need to be adjusted for both the pavement construction thickness and material thermal properties and the subgrade properties. This step needs calibration studies to verify. The error induced in this assumption will be systematic but not affect the overall conclusions.

4.3 Thaw weakening reference table

The reference table provides a guidance if the current season or location is representative for the given latitude position. By monitoring local temperature data the point when TI_{acc} has been reached it can be judged if the thaw weakening is moderate, normal or severe. If TI_{acc} normally is reached early, a consequence of high air temperatures, the site based on is local climate conditions are more subjected to severe thaw weakening than expected at its location.
The first 12 days in the reference table are similar in between the three different regions. After 12 days the variation increases between region central and north. It is possible to merge region south and central's tables to one.

4.4 Statistical distribution of thawing events

In this study the statistical distribution of thawing events has been studied. In Sweden most of the data follows the normal distribution transformation Johnson distributions. Thus it is easy to statistically handle thawing events if a design tool incorporating thawing will be developed.

4.5 Comparison to the Swedish guidelines for pavement frost design

In the Swedish guidelines, Trafikverket, (2011), regarding frost design of pavements thaw weakening is incorporated by assigning reduced stiffness modulus in the superstructure layers and the subgrade during a time period defined by the location in climate zone 1-5 of the road according to the map in figure 4.



Figure 4 The five climate zones in Sweden used for frost design of pavements. Trafikverket, (2011).

In table 3 the length of the deep thawing season and a rough mapping between the climate zones in figure 4 and the regions in figure 1 are showed. The current guidelines assign longer periods of thawing compared to the results in this study. The longer periods for the thaw weakening season in the guidelines is expected since it also includes the recovery of the stiffness modulus after the thawing has stopped.

Table 3 Comparison between the length of the deep thawing season in Trafikverket, (2011) and the average thawing season found in this study. The table also roughly maps the climate zones in Trafikverket, (2011) to the regions in this study.

Current guidelines					
Climate zone	1	2	3	4	5
t_{max} [d]	15	31	45	61	91
This study					
Region	South		Central	North	
tmax [d]	12		34	41	

If the deep thaw weakening should be included in the design based on the local climate conditions there is a need to separate the deep thawing season and the recovery time since the length of the thawing time is strongly correlated to the latitude, as shown

in this study, and the recovery time probably are more effected of the material properties, e.g. Phukan, (1985), Andersland and Anderson, (1978) among others.

5 CONCLUSION

Based on historical air temperature data and frost depth measurements the following conclusions can be drawn in this study about thawing in Swedish roads:

- There is a strong correlation in latitude position and the thawing period length.
- The intensity in thawing is similar independent on the latitude positions
- Thawing follows normal statistical distribution transformations

6 ACKNOWLEDGEMENTS

This study is a part of the research project frost action within the Swedish Transportation Administration research program BVFF (Bana Väg För Framtid). The authors want to thank Jonas Hallenberg at the Swedish Transportation Administration for providing the data from the frost depth monitoring stations.

7 REFERENCES

Andersland, O. and Anderson, D. (1994). An introduction to Frozen Ground Engineering. McGraw-Hill Inc. ISBN 0-412-98201-3

Berglund, A. (2009). Tjäle- en litteraturstudie med särskilt fokus på tjällossning. Forskningsrapport, LTU, Luleå. ISSN 1402-1528. (In Swedish)

Berglund, A., Edeskär, T. and Knutsson, S. (2011). Comparison between thaw weakening prediction model and field observations. Proceedings of the 21th International Conference on Port and Ocean Engineering under Arctic Conditions, Montreal. Paper 11-087.

Benjamin, J.R., and Cornell, C.A. (1970). Probability, Statistics and Decision for Civil Engineers, McGraw-Hill Company, New York. ISBN 07-004549-6

Gandahl, R. (1987). Tjäle och tjälskydd: Erfarenhet från FoU-verksamhet vid SVI och VTI. VTI meddelande. Linköping. ISSN 0347-6049

Hicks, R.G., Mahoney, J.P. and Rutherford, M.S. (1985). Guidelines for spring highway heave restrictions. WA-RD-80.01. Washington State Department of Transportation, Washington.

Mathwave. (2015). EasyFit. URL: www.mathwave.com. Accessed 23-10-2015.

Minitab. (2015). MINITAB 17. URL: www.minitab.com. Accessed 23-10-2015.

Phukan, A. (1985). Frozen Ground Engineering. Prentice Hall, New Jersey. ISBN: 0-13-330705-0

SMHI (2015). Climate data from 1951-2014. Open for research and education purposes. www.smhi.se. Accessed the 24-04-2015. (In Swedish)

Stål, T. and Wedel, P. (1984). Handboken Bygg. Geoteknik. Liber förlag, Stockholm. ISBN 91-38-06077-9. (In Swedish)

Trafikverket. (2011). TRVK VÄG. TRV DOK 2011:072. Borlänge. ISBN 978-91-7467-137-7. (In Swedish)

Trafikverket. (2015). Thaw depth measurement stations. URL: www3.vv.se/tjaldjup/. Accessed 23-10-2015. (In Swedish)

Johnson, N.L., and Kotz, S. (1970). Continous Univariate Distributions – I: Distributions in statistics. Vol. 1. Wiley & Sons. ISBN 0-471- 44626-2

Resistivity measurements as a tool for optimizing groundwater protection at a highway construction in Sweden

Roger Wisén Corresponding / primary author
Rambøll Danmark A/S, Denmark; Lund University, Sweden, rgw@ramboll.dk

Elisabet Hammarlund
Ramböll Sverige A/S, Sweden

Torleif Dahlin
Lund University

ABSTRACT
The Swedish road administration is planning to increase the capacity on highway E22 to a 4 field motorway outside the city of Kristianstad in southern Sweden. The sedimentary bedrock of the Kristianstad plains compose a large and very important groundwater aquifer. The government of Sweden have approved the construction of the road on the condition that necessary protective action is taken so to assure that the aquifer is not polluted. There are means to design the road with groundwater protection but this is costly and as an alternative it has been suggested to allow the clayey soils in the area to act as groundwater protection. Site investigations with a range of geotechnical, hydrogeological and geophysical methods have been performed to determine the protective properties of the natural soils in order to ensure that they constitute a sufficient protection of the aquifer. It is well known that electrical resistivity is strongly connected to the hydrogeological conditions of geological materials and it was therefore suggested that Continuous Vertical Electrical Sounding (CVES) should be used for continuous mapping along the planned road. The CVES results constitute the basis for determining if the upper soil layer is a natural barrier for surficial pollution or if there is need for active protection design of the road. There is a clear relationship between the content of fine grained material in the soils (clay and silt) and the resistivity. Since the fine grain content is also strongly connected to the hydraulic properties a resistivity section gives a continuous image that reflects the hydraulic properties of the ground along a road stretch. For the majority of the road it was concluded that the geological materials act as a sufficient protective barrier while a small part of the area requires design with a protective barrier to protect either surface water or groundwater.

Keywords: Groundwater protection, site investigation, hydrogeology, geophysics, resistivity measurements.

1 INTRODUCTION

The Swedish road administration is planning to increase the capacity on highway E22 to a 4 field motorway outside the city Kristianstad in southern Sweden. The 14 km stretch to be constructed starts at the northern slope of the Linderöd horst structure, and then crosses a part of the Kristianstad plains and thereafter the glaciofluvial deposits of Helgeåsen. The sedimentary bedrock of the Kristianstad plains composes a large and very important groundwater aquifer. Figure 1 shows a schematic map of the new road stretch.

1.1 The environmental and road planning process and their influence on the road design

The government of Sweden have approved the construction of the road on the condition that necessary protective action is taken so to

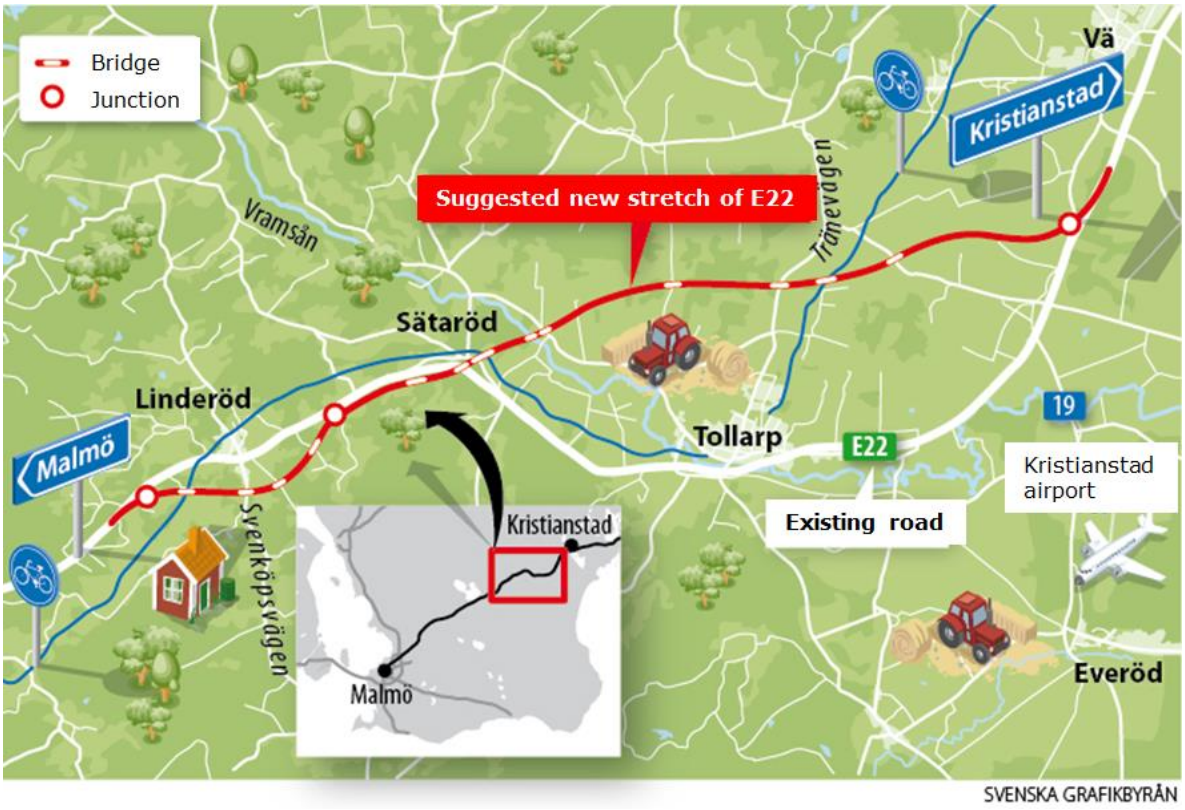


Figure 1 Schematic map of the new E22 stretch south of Kristianstad in southern Sweden (http://www.trafikverket.se/contentassets/ebc058a233d54ad5b9d3b0de6f0eaa97/nyvaglinje_ver6.jpg ***Trafikverket/Svenska grafikbyrån)***

.

assure that the aquifere is not polluted. There are means to design the road with groundwater protection but this is costly and as an alternative it has been suggested to allow the clayey soils in the area to act as groundwater protection.

2 THE CONCEPTUAL HYDROGEOLOGICAL MODEL

Information from the Swedish Geological Survey (SGU) was used to create an initial conceptual geological and hydrogeological model to be used as a base for interpretation. Specifically the geological maps for soil and rock as well as SGU's borehole database.

The thick layer of clay till that is present in the majority of the area acts as a long term protection of the groundwater aquifere. The layer of interest here is however the overlaying clayey sand till. If the permeability of this till is sufficiently low it will act as a shallow barrier that will allow immediate remediation of pollutants that accidently is spilled on or next to the road.

3 HYDROGEOPHYSICAL SITE INVESTIGATION

Site investigations with a range of geotechnical, hydrogeological and geophysical methods have been performed to determine the protective properties of the natural soils in order to ensure that they constitute a sufficient protection of the aquifer. There is a clear relationship between the content of fine grained material in the soils (clay and silt) and the resistivity (Archie, 1942). Since the fine grain content is also strongly connected to the hydraulic properties a resistivity section gives a continuous image that reflects the hydraulic properties of the ground along a road stretch. It was therefore suggested that Continuos Vertical Electrical Sounding (CVES) should be used for continuous mapping along the planned road. The CVES results constitute the basis for determining if the upper soil layer is a natural barrier for surficial pollution or if there is need for active protection design of the road. For verification and calibration

of the CVES results a combination of geotechnical and hydrogeological tests where performed.

3.1 Resistivity measurements

The CVES method has been used for a long time and is well established for groundwater and geotechnical investigations (e.g. Dahlin, 1996; Wisén et. al. 2008). The measurements were performed with a Lund System setup with 5 m electrode spacing utilizing an ABEM Terrameter LS. Four cables of 100m length make up a 400m long layout that is sucessively moved 100 m at a time in a roll-along manner. A multiple gradient configuration (Dahlin and Zhou, 2006) was used and in this specific case gave a depth penetration of about 70 m.

Data were processed as 2D resistivity tomography using the software Res2Dinv from Geotomo software SDN BHD. Also a layerbased pseudo 2D interpretation was done as a complement and for verification. This was done using the Laterally Constrained Inversion (LCI) (Auken and Christiansen, 2006) in the software Aarhus workbench from Aarhus Geophysics Aps.

3.2 Hydrogeological and geotechnical tests

Drilling and installation of standpipes was performed in positions that were selected based on the resistivity results. Slug tests were made in the standpipes of some drillings to get an estimate of the hydraulic conductivity in the different soil materials. Also other geotechnical investigations were performed. The most important information for verification and calibration of the resistivity data was depth to bedrock from drilling, hydraulic conductivity from slug tests and soil grain size distribution from geotechnical analysis.

4 RESULTS, GEOLOGICAL AND HYDROGEOLOGICAL INTERPRETATION

The resistivity in the area varies from 20 to 1000 Ωm. Lowest resistivity, around 20-100 Ωm, corresponds to clay or alternatively clay till. Sandy till is found in the interval 100-300 Ωm. Unsaturated sand near the ground surface gives around 300-1000 Ωm. The bedrock in the area has a resistivity in the interval 300-1000 Ωm and the chalk gives around 120-500 Ωm. Results from the two resistivity profiles that follow the planned new stretch of the highway are presented in figure 2.

Close to the Linderöd horst the soil depth is relatively small, but at the foot of the horst there is a fault zone where soil depths suddenly increase to more than 70 m. The fault zone is noted as zone A in figure 2.

The soil depth in the Kristianstad plain is around 50 m in most of the area and decreases as expected towards northeast. There are 20-30 m thick deposits of clay or clay till that fills out a valley structure in the bedrock. These layers are clearly visible in the results over a stretch of about 8 km. On top of this layer there are clayey to sandy tills. In parts of the area the resistivity result shows two or more tills on top of each other, visible with different resistivity for the different tills. In figure 2 this zone is noted as zone B where two layers of clay till is clearly visible in the results, and as zone C where only one layer of clay till is visible.

In the northern part of the area there are thicker layers of chalk rock. The interpretation of the resistivity results is more difficult in this part of the area since the contrast in resistivity is smaller between the till and the chalk and also between the chalk and the bedrock. This zone is characterized as a zone with more heterogeneoys soil layers and it is noted as zone D in figure 2, the Helgeåsens border zone. Geotechnical sounding have verified areas with sedimentary clay in this zone. However, these clays does not have enough coverage to act as a barrier.

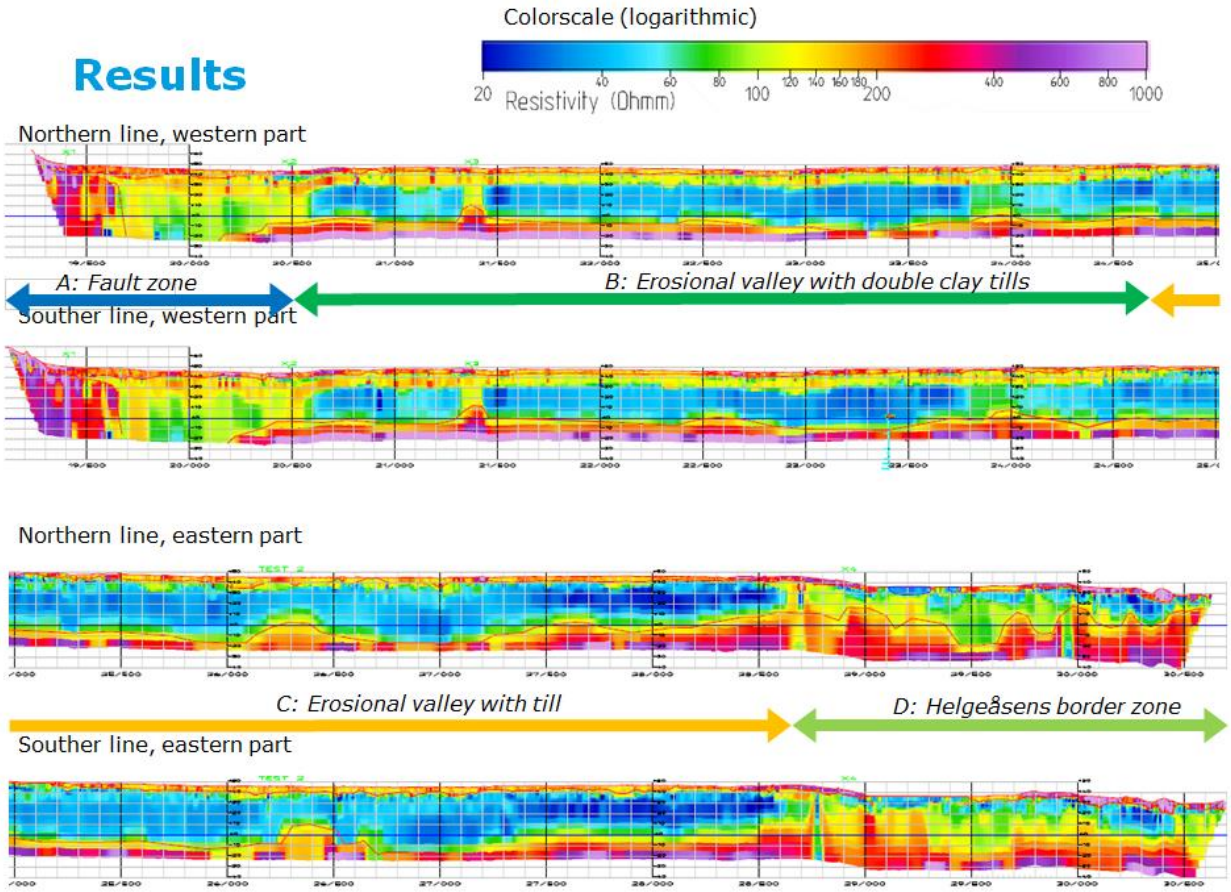


Figure 2 Results from the two parallel resistivity lines. The lines are approximately 11 km long and spaced 25 m apart. The interpretation of the geology is divided into three main zones as shown in the figure: A. The fault zone of the Linderöd horst, B. Erosional valley of the Kristianstad plains with double clay tills, C. Erosional valley with one clay till and D. The Helgeåsen border zone.

There is a clear relationship between the content of fine grained material in the soils (clay and silt) and the resistivity (Figure 3). Since the fine grain content is also strongly connected to the hydraulic properties a calibration of the resistivity results can be made where a certain resistivity range in the soils can define low permeable materials that gives sufficient groundwater protection. In this case it was found that even sandy silty till with a resistivity just above 100 Ωm, that is present in the shallow soil layer in the majority of the area, acts as a protective layer. This allows for example for emergency clean up of pollutants e.g. after an accident. The thick low resistive clay till layer that is also present in almost the entire area acts as an efficient long term protection of the aquifere that is present in the chalk rock below.

On the slope of the Linderöd horst there is bare rock or very thin soil cover that will not provide sufficient protection. In this area it is required to design the road with measures to protect groundwater. At and around Helgeåsen the soil is permeable with a thick unsaturated zone and also in this area it is required to construct the road so that the ground water is protected.

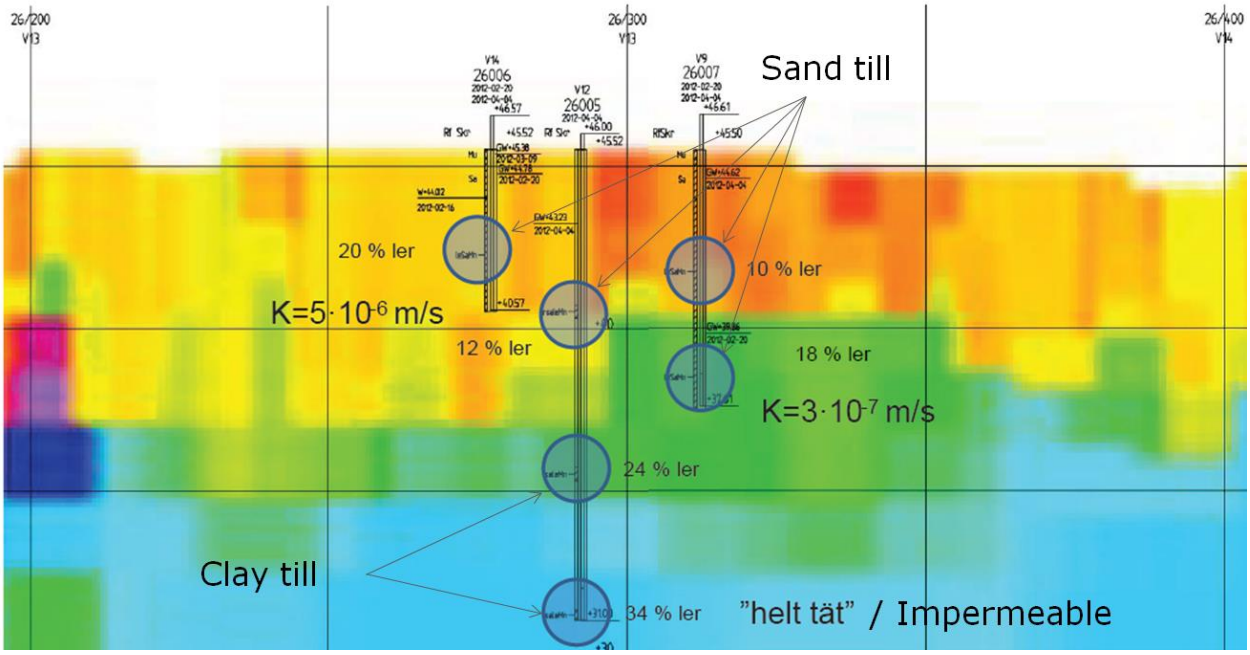


Figure 3 Detail from geotechnical and hydrogeological tests on top of the resistivity model. The amount of clay (ler) is given for 6 samples from geotechnical testing. Four samples from sand till show clay conten from 10-20% and two samples from clay till show clay content of 24 and 34%.

Figure 4 presents a schematic drawing of the result from this investigation. For the majority of the road it is concluded that the geological materials in the area act as a sufficient protective barrier, for some areas it is concluded that there is a need for designing the road with a protective barrier to protect either surface water or groundwater and for about 10% of the area further investigations are needed.

4.1 Reccomendations for groundwater protective measures

For the majority of the road it was concluded that the upper clayey sand till act as a sufficient protective barrier while a small part of the area requires design with a protective barrier to protect either surface water or groundwater. In two areas around the Helgeåsen border zone there is a need for further investigations.

5 CONCLUSIONS

CVES resistivity has been used together with geotechnical and hydrogeological methods to achieve a continuous image that reflects the hydraulic properties of the ground along a road stretch. The purpose was to map the vulnerability for pollutants to penetrate into the precious groundwater magazine under the Kristianstad plains. The investigation shows that a large part of the area is covered by impermeable layers in the form of a thick clay till. Large parts of the area is covered with sandy till over clay till, and this sequence has been determined to have a permeability that gives sufficient protection of the aquifer below. In parts of the area, close to the Linderöd horst where soil cover is thin or non-existent and at the glaciofluvial deposits at and around Helgeåsen it is motivated to construct the road so that the ground water is protected. In about 10 % of the investigated area it will be necessary to perform further investigations to define the need of groundwater protection as part of the road design.



Figure 4 For the majority of the road it is concluded that the geological materials in the area act as a sufficient protective barrier (white lines), for some areas it is concluded that there is a need for designing the road with a protective barrier to protect either surface water (orange lines) or groundwater (blue lines) and for a small part of the area further investigations are needed (purple lines).

6 ACKNOWLEDGEMENTS

We acknowledge: Trafikverket, the Swedish road administration, for letting us present this material; and Björn Holmqvist for his valuable work with the geological interpretation.

7 REFERENCES

Archie, G.E. (1942) The Electrical Resistivity Log as an Aid in Determining Some Reservoir Characteristics, *Petroleum Transactions of the AIME (146)*, 54-62.

Auken, E. and Christiansen, A.V.,2004, Layered and laterally constrained 2D inversion of resistivity data, *Geophysics* (69), 752-761.

Dahlin, T. (1996) 2D resistivity surveying for environmental and engineering applications, *First Break 14(7)*, 275-283.

Dahlin, T. and Zhou, B. (2006) Gradient array measurements for multi-channel 2D resistivity imaging, *Near Surface Geophysics (4)*, 113-123.

Hammarlund, E. (2013) PM Tolkning av resistivitetsundersökning, E22 Sätaröd-Vä. Trafikverket 2013

Wisén R. (2013) Resistivitetsmätning 2012 Datarapport, E22 Sätaröd-Vä. Trafikverket 2013

Wisén, R., Christiansen, A.V., Dahlin, T., and Auken, E., (2008) Experience from Two Resistivity Inversion Techniques Applied in Three Cases of Geotechnical Site Investigation, *Journal of geotechnical and geoenvironmental engineering, (134)*, 1730-1742.

Automated co-interpretation of geophysical data for site investigation

Kristofer Hellman
Lund University, Sweden, kristofer.hellman@tg.lth.se

Roger Wisén, Torleif Dahlin
Lund University, Sweden

ABSTRACT
A methodology for automated co-interpretation of ERT (electrical resistivity tomography) and seismic refraction data is applied to a combined dataset collected in the S-E part of Norway. Seismic methods and seismic refraction in particular is a standardized tool for tunneling site investigations in Norway, while ERT is gaining increasing acceptance as a tool in this application. There is an underlying issue in using the two results and creating a manual joint interpretation. Therefore, we suggest a different approach. By using an algorithm that can do the interpretation without any bias, a further level of repeatability will be attained. Furthermore, the use of joint inversion could assist in the improvement of the overall resolution. The Norwegian road administration is planning a new 8.5 km long stretch of four lane highway from Bjørum to Skaret. The project is complex from the point that 4.2 km of the total stretch is planned to be tunneled. The results from the survey are presented in three steps. Firstly, the ERT section, secondly, the seismic refraction profile and lastly the automatically co-interpreted profile. There is no indication of changes in velocity below approximately 30 meters depth, although the ERT results indicate that there are zones delineated by lower resistivities. The automatically co-interpreted profile result is easier to interpret and helps the interpreter to find the common patterns that are more subtle in the separate profiles. The method cannot, however, create perfectly unambiguous interpretations of the geophysical data as there are different setup parameters that affect the results, but it is a tool to aid in the interpretation of the geophysics.

Keywords: Inverse modelling, ERT, refraction seismics, joint inversion

1 INTRODUCTION

1.1 Seismic refraction and geoelectrics as tools for site investigations in Norway

Seismic methods and seismic refraction in particular is a standardized tool for tunneling site investigations in Norway (Rønning et al. 2009). Seismic refraction has the ability to detect fracture zones, aid in the assessment of thickness of these zones and yield a specific seismic velocity for the investigated bedrock. The seismic velocity can then be used to qualitatively evaluate the bedrock.

There are basically two main approaches to the evaluation of seismic refraction data. Either using layer models and trying to fit the data to these models or using a tomographical approach. The advantage of using the tomographical approach is the possibility of detecting fracture zones with a limited extent in relation to the survey profile. A difficulty that appears in regions where glaciation has effectively scrapped the weathering zone clean is that there is a difficulty in transferring energy into the bedrock; this problem is often pronounced in most parts of Norway. This implies that it will be most difficult to attain information from within the bedrock, meaning that the dip and depth of fractured zones will be unknown.

ERT (electrical resistivity tomography) can be used to locate fracture zones within the bedrock, yielding further information such as zone thickness and dip (Rønning et al. 2009; Reiser et al. 2009)

1.2 Joint interpretation and joint inversion

Joint interpretation and joint inversion may yield similar results. Often they do not, joint interpretation of seismics and resistivity can be achieved by simply looking at the results from the two methods and create a joint interpretation. A further step would be to let the data from both methods assist each other while inverting the data.

There is an underlying issue in using the two results and creating a manual joint interpretation. The issue is the fact that two different interpreters will attain two different interpretations of the profiles.

By using an algorithm that can do the interpretation without any bias, a further level of repeatability will be attained. Furthermore, the use of joint inversion could assist in the improvement of the overall resolution and possibility to describe the lithology (Infante et al. 2010).

The approach that we use was first demonstrated by (Günther et al. 2006). This approach is extended by using a clustering algorithm and hereby automatically organizing the resistivities and velocities in groups with spatial coincidence. This approach takes the process one step further and into a fully automated co-interpretation of the data.

1.3 E16 Bjørum – Skaret

The Norwegian road administration is planning a new 8.5 km long stretch of four lane highway from Bjørum to Skaret. The project is complex from the point that 4.2 km of the total stretch is planned to be tunneled. The selected piece for this particular analysis is only about 700 meters long in order to reduce the amount of data for analysis.

The new E16 highway between Bjørum and Skaret is a difficult project from several perspectives. As almost half of the stretch will be tunnel, the need for deep bedrock quality assessment is pressing.
The site is located in the S-E part of Norway, as described in Figure 1. Rambøll conducted the field survey and wrote a report (Rambøll 2012) for the Norwegian geological survey and GeoVita AS. The results from the survey were interpreted and used to update an expected geological section that was first created by using the geological maps and surface mapping by an experienced local geologist.

1.4 Geology

The field site is situated in within the Oslo Rift. The rift can be subdivided into three major graben structures from the north, the Askershus Graben (AG), the Vestfold Graben (VG) and the Skagerrak Graben (SG). During Perm, the rift was experiencing volcanic activity that peaked 295-285 million years ago. Volcanic deposits of porphyry and basalt are predominant and there are volcanic rock dikes over 40 meters wide. The volcanic layers in the area are surrounded by faults and syenite dikes. Glacial events has removed large amounts of heavily weathered bedrock and replaced it with thin till layers.

2 RESULTS

2.1 ERT and seismic refraction from December 2011

The results from the survey are presented in three steps. The ERT results are presented in Figure 2. A high (1250-3980 Ωm) resistivity strip can be seen close to the surface. The underlying layer shows two vertical anomalies at 300 and 450 meters respectively. The apparent horizontal stratification pattern suggests horizontal geological structures. These patterns coincide with expected volcanic structures. The vertical high (1250-3980 Ωm) resistivity band at 300 meters coincides with dolerite findings at the surface, indicating a vertical dyke.

The inverted velocity section in Figure 3 shows one or two low (1000-3500 m/s) velocity layers. These layers are on top of a high (3501-5200 m/s) velocity layer, divided into three separate parts at 100 and 450 meters. The outer part of this layer contains ever higher velocities (4500-5200 m/s). The

possible dolerite indicated in the resistivity profile could be present at 300 meters, indicated by a high (4500-5200 m/s) velocity zone. There is a low (3500-4000 m/s) velocity part just left of this, possibly indicating some weathering adjacent to the dyke.

The co-interpreted section in Figure 4 is based on joint inversion of the two data sets followed by cluster analysis. At 300 meters, there is visible diabase at the surface; this diabase zone could be in coherence with the blue zone. The dominating turquoise zone is more difficult to interpret, it probably consists of less weathered bedrock. The green and yellow near surface outcrop zones are probably diabase and volcanic rocks in different stages of weathering.

3. CONCLUSIONS AND OUTLOOK

The ERT results exhibit a model section with structural information throughout the depth of the sections, with zones of lower resistivities indicated to large depths. For the seismic refraction, on the other hand, there is no indication of changes in velocity below approximately 30 meters depth.

The automatically interpreted section can be easier to interpret and helps the interpreter to find the common patterns that are more subtle in the separate profiles. The evidence of a vertical volcanic dike becomes very clear in this profile.

It should be noted that the method cannot, however, create perfectly unambiguous interpretations of the geophysical data as there are for example different setup parameters that affect the results. It is a tool to aid in the interpretation of the geophysics.

Following up the geophysics with a drilling campaign is a natural step. The drilling campaign may be designed by using the results from the geophysical and thereby making the most of the drillings. A future outlook is to include drill-data and revise model using drill-data. This facilitates a very detailed assessment of rock quality and fracture zone extension.

4. REFERENCES

Günther, T., Bentley, L. & Hirsch, M., 2006. A new joint inversion algorithm applied to the interpretation of dc resistivity and refraction data. In *Proceedings of XVI International Conference on Computational Methods in Water Resources*.

Infante, V. et al., 2010. Lithological classification assisted by the joint inversion of electrical and seismic data at a control site in northeast Mexico. *Journal of Applied Geophysics*, 70(2), pp.93–102. Available at: http://www.sciencedirect.com/science/article/pii/S0926985109001499.

Rambøll, 2012. *Grundundersøgelser for ny e16 mellem bjørum og skaret*,

Reiser, F. et al., 2009. Resistivity Modelling of Fracture Zones and Horizontal Layers in Bedrock. NGU rapport 2009.070. , p.120 sider.

Rønning, J.S. et al., 2009. *NGU Rapport 2009.064 Resistivitetsmålinger og retolking av seismikk langs E6 og Dovrebanen ved Mjøsa.*,

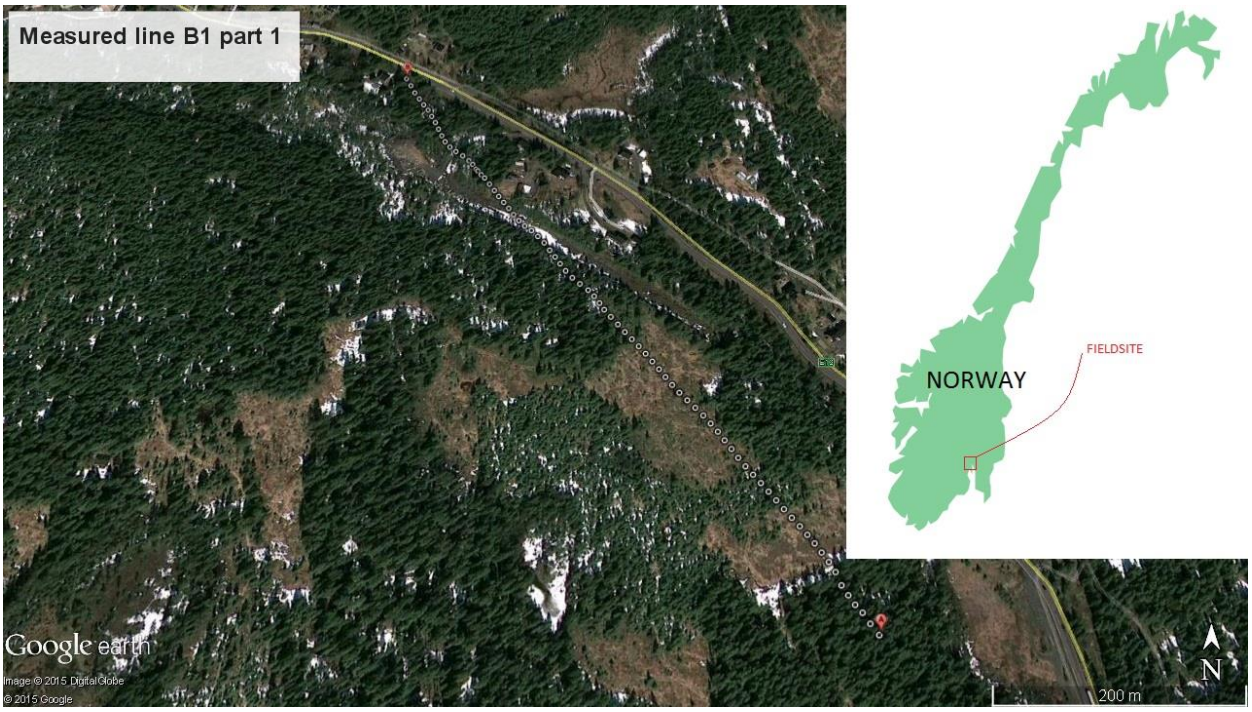


Figure 1, The B1 line positions

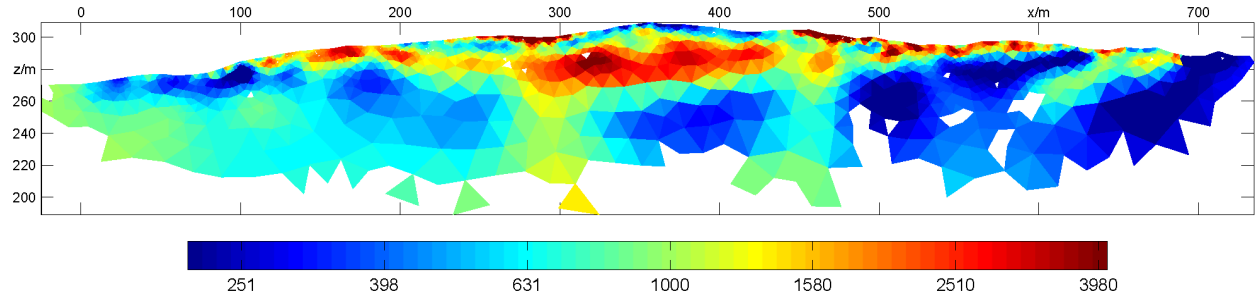


Figure 2, resistivity profile [Ohm-m]

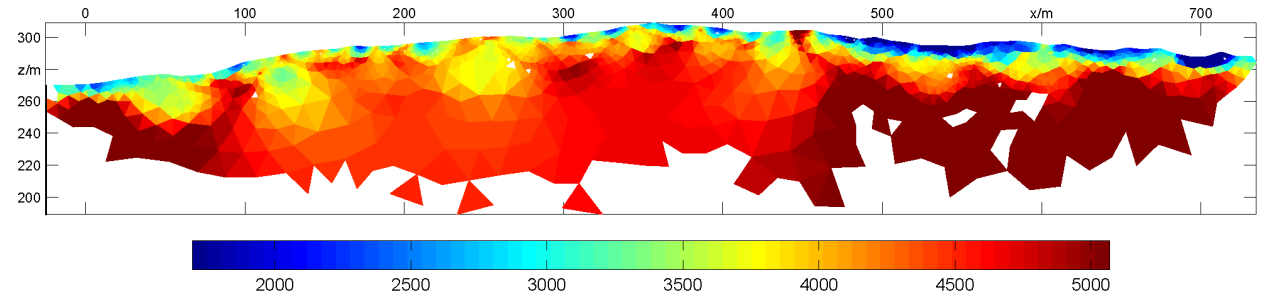


Figure 3, refraction profile [m/s]

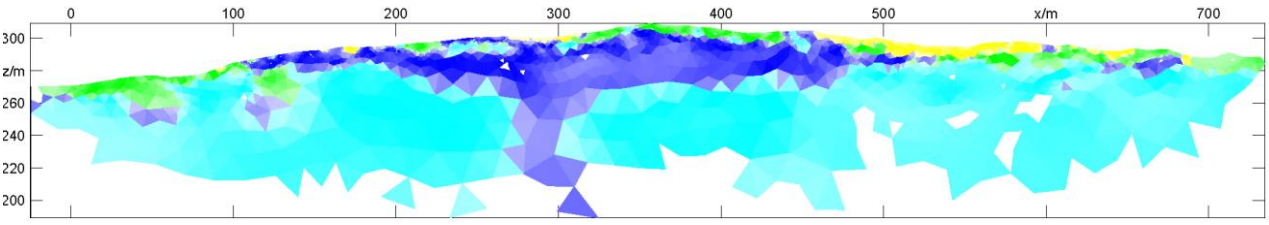


Figure 4, co-interpreted results, 4 clusters

Authors Index

Abokhalil, Mostafa, D2-2
Adam, Dietmar, C4-4
Alvin, David Ross, C4-1
Amundsen, Helene Alexandra, B1-6
Andersen, Jan Dannemand, B4-2
Andersson, Jimmie, A4-3
Andreassen, Katrine Alling, C4-5
Anthi, Aina K., P3-7
Anusic, Ivana, P1-4
Athanasiu, Corneliu, P4-6
Augland, Amund, C2-2
Augustesen, Anders Hust, A1-2, B5-4
Aunaas, Kristian, D2-2
Auvinen, Turo, P3-2
Axelsson, Gary, A4-3
Baardvik, Gunvor, C2-4
Barral, Camille, B2-5
Beijer Lundberg, Anders, A1-6
Belickova, Lucie, P2-1
Belinchón, Pablo, P4-14
Bellis, Angela, B4-5
Bergdahl, Karin, C5-2
Bergliv, Elin, A2-3
Bessason, Bjarni, C1-5
Biryaltseva, Taisiya, P3-3
Björnsson, Björn Jóhann, C3-3
Blomén, Hanna, A3-5
Bodholt, Grethe, A5-2
Botsialas, Konstantinos, P7-1
Bourgeois, Emmanuel, D1-2
Brandt, Madeleine, P4-6
Branzén, Helena, P7-2
Brix, Susanne, C2-3
Bruin, Robert, A5-3
Carling, Maria, P7-2
Carter, John Phillip, P4-11
Cervera, C.P., A4-4
Chalmas, Rémi, B2-1
Christensen, Helle Foged,
B2-1 Christensen, Stein, B1-5
Christensen, Rune, P4-14
Christensen, Søren Bjerregaard, P4-2
Christiansen Bagger, Lars, C1-3
Chung, M, P1-6
Côté, Jean, C3-4
d'Ignazio, Marco, B2-3, C5-3
Dagli, Deniz, B4-4, P3-6
Dahl, Allan, B2-5
Dahl, Carl Erik, A5-2
Dahlin, Torleif, C1-2, C2-5, P5-1, P5-2
Dam, Asbjørn Mathias, P1-1
Damtew, Tseday, P3-7
Davidovic, Nenad, A5-1
de Bruin, Willem Robert, P3-5
Degago, Samson, A3-1, A4-1, B2-2, P4-12
Delmas, Philippe, B2-5
Denver, Hans, D1-6, D1-5
Dettenborn, Taavi, B3-3, P3-2
di Buò, Bruno, B2-3
Dolva, Bjorn Kristoffer, D2-2
Du-Thinh, Kien, C3-1
Dvorakova, Marketa, P2-1
Edelback, Paul, P7-2
Edeskar, Tommy, A2-3, B4-4, C4-3, C5-4, P3-6
Edmark, Cecilia, P4-8
Edstam, Torbjörn, C3-2
Eidsvig, U., A3-2
Eiksund, Gudmund Reidar, P1-4
Emdal, Arnfinn, B1-6, B3-5
Eriksson, Magnus, A5-4
Erlingsson, Sigurður, C1-5, C4-2
Fallsvik, Jan, P7-2
Fauskerud, Odd Arne, B1-5
Foged, Niels Nielsen, C4-5
Foglia, Aligi, D1-1, P3-3
Foldager, Rasmus, B2-1
Forsman, Juha, B3-3, D2-3, P3-2
Fredriksson, Adam, C4-3
Freitag, N., P2-7
Gilleron, Nicolas, D1-2
Giske, Steinar, A4-1
Gjesvik, Vidar, B1-5
Gorniak, Joanna, B2-5
Goth, J.N., B5-4
Green, Russel A., C1-4
Grimstad, Gustav, P4-10, P4-12
Gustavsson, H., A4-4
Gylland, Anders Samstad, B1-1 B-2, B3-5
Göransson, Gunnel, C5-1, C5-2, P7-2
Hager, Mario, C4-4

Halifax, David J., P2-7
Halldórsson, Benedikt, C1-1, C1-4
Hammarstrom, Elisabet, P5-1
Hamza, Omar, B4-5
Hansen, Arne, P2-2
Hanusova, Irena, P2-1
Hassellund, Lovisa, P4-7
Haugen, Eigil, B2-2
Havnen, Ingrid, D2-2
Hedfors, Jim, P7-2, C5-1
Helgason, Einar, D2-5
Hellman, Kristofer, P5-2
Hébert, Étienne, C3-4
Hoffman, Peter, A2-1
Horlykke, Tobias, A1-5
Hove, Svein E., A4-1
Hunter, Emily Catherine, A3-4
Hyrve, Oddvar, B2-5
Hørlykke, Tobias, P4-14
Isacsson, Ulrika, P3-4
Jahr, Annette, A2-4
Jensen, Henning, P6-3
Jensen, Morten Elton, C1-3
Johannesson, Björn, C2-1
Johansson, Lennart P. A., C3-1
Jorgensen, Mikael, C1-3
Jorild, Sara, P3-4
Jostad, Hans Petter, A2-5, P4-15, P4-16
Juncher, Rasmus, B4-1
Jönsson, Åsa, C5-2
Jørgensen, Morten Anker, P2-2
Kahlstrom, Mats, P6-1
Kalsnes, B., A3-2
Kardan, Caesar, B1-4
Kåsin, Kristoffer, B1-1, B-2, B3-4
Kassa, Henok Mekonnen, D1-4
Katic, Natasa, B2-1
Kellezi, Lindita, D1-6, D1-5
Kiilsgaard, Ramona, C5-2
Kim, Yunhee, A2-5, P4-16
Kinnunen, Jussi, P1-3
Kirkevollen, Ole Vidar, B2-2
Klinkby, Lone, B4-1
Knudsen, Bjørn Staghøj, D1-3
Knudsen, Jannie, A1-3
Knutsson, Roger, P4-7
Knutsson, Sven, C5-4, P4-9, P4-7
Kohlmeier, Martin, D1-1
Koivisto, Kirsi, D2-3
Kolisoja, Pauli, D2-3
Kopf, Fritz, C4-4
Koreta, Olsi, D1-5, ,
Korkiala-Tanttu, Leena Katariina, A1-4, A4-4, P4-4
Koskinen, M., A4-4
Kreiter, Stefan, P3-3
Krivokapic, Andrija, A5-1
Kullingsjö, Anders, C3-2, P4-8
Kuula, Pirjo, D2-3
l'Heureux, Jean-Sebastien, B5-2, B5-3, C1-6, P4-15, P4-16
Lacasse, Suzanne, A2-5, P4-15, P4-16
Lahtinen, Pentti, D2-3
Laier, Martin, B4-1
Langford, Jenny, C2-4
Länsivaara, Tim, B2-3, C5-3, P4-3
Larsen, Kim André, B4-2
Larson, Magnus, P7-2
Larsson, Stefan, B1-4
Latini, Chiara, C2-1
Laursen, Per Beck, C2-3
Lehtonen, Ville Jussi, P4-3
Leth, Caspar Thrane, B4-2
Lied, Ole Kristian, C2-2
Liingaard, Morten Albjerg, P1-4
Liu, Z.Q P4-16
Lodahl, Michael Rosenlund, B5-1
Lombard, Tony, C1-6
Long, Mike, B1-1, B-2, B3-2, B5-3, C1-6
Lopez-Soto, Jamie Fitzgerald, B2-4
Lundström, Henrik, P7-3
Lunne, Tom, B5-2
Lyche, Einar, D2-2
Lyngs, Jakob Hausgaard, P6-3
Löfman, Monica Susanne, P4-4
Löfroth, Hjördis, C5-2
Madsen, Thomas, B4-2
Markusson, Madelene, P2-5
Mattsson, Hans, P4-7, P4-9
Medhus, Anna Bondo, B4-1
Mets, Mait, B3-3
Michaelsen, Jes, C3-5
Moerz, Tobias, P3-3
Montafia, Alberto, B1-1 B-2
Montalvo-Bartolomei, Axel Manuel, B2-4
Morales Cárdenas, Mario, P7-1

Mortensen, Niels, B5-1, D1-3
Muzik, Juraj, P4-13
Nerland, Ørjan, P1-5
Nielsen, Jens Kofod, P6-3
Nielsen, Ole Frits, C4-1
Nigussie, Daniel, B2-2
Nik, Leyla, B1-4
Nodroff, Sara Rose, P6-2
Nordal, Steinar, B1-5, D1-4, P4-10
Norrman, Jenny, P7-2
Nyheim, Trude, D2-2
Nystrom, Fredrik, C3-1
O'Connell, Yvonne, C1-6
O'Connor, Peter, C1-6
O'Rourke, Shane, C1-6
Odén, Karin, P7-2, C5-1, C5-2
Odén, Mathias, P7-3
Okkels, Nik, P3-1
Olep, Mattias, B3-3
Olivera, Cristian, C1-4
Olsen, Christian, P6-1
Oset, Frode, A5-2, B1-5, D2-2
Oskarsson, Robert, P4-8
Ottesen, Hanne, D2-2
Overgård, Ida Elise Vikestad, A4-2
Ólafsdóttir, Elín Ásta, C1-5
Ólafsson, Símon, C1-4
Paniagua, Priscilla, B5-2
Park, Jae Hyun, P1-6
Pedersen, Belinda Dedenroth, A1-5
Pedersen, Karsten, B4-1
Pekkala, Jarmo, P3-2
Penzes, Balint, P1-2
Persson, Josefin, C2-2, D2-4, D2-5
Petri, Thomas, C2-3
Pfaffhuber, Andi, B1-1 B-2
Pieksemä, Jani, P3-2
Pistrol, Johannes, C4-4
Powell, Toby, P6-1
Rahpeyma, S., C1-4
Rasmussen, Morten Schousboe, A1-1
Resare, Fredrik, A1-6
Rigler, Balazs Bela, P7-1
Robbins, Bryant Andrew, B2-4
Rodriguez, Juan, C5-4
Ronczka, Mathias, C1-2
Ronkainen, Marjo, D2-3
Rosborg, Anne, B4-1
Rosenquist af Åkershult, Anders, A2-5
Rudkjaer Jensen, Mette, P1-2
Rønningen, Jon Abusland, P4-10
Saarenketo, Timo, B3-1
Saitta, Adrien, D1-2
Sandene, Thomas, P1-5
Sandven, Rolf, B1-1, B-2, P4-15, P4-16
Sankey, J.E., P2-7
Sauvin, Guillaume, C1-6
Sayd, Murad Sani, P3-7
Sejbæk, Johan Sandal, P6-3
Selänpää, Juha, B2-3
Sharma, Anil, P2-4
Shin, Y., P1-6
Sigtryggsdóttir, Fjóla Guðrún, C1-1
Simmonds, Tony, A2-2
Simonsen, Thomas Rye, B4-3
Sinnathamby, Gowthaman, A4-4
Sipola, Johanna, P4-9
Siren, Rosa Marja Margareet, A1-4
Sivapullaiah, Puvvadi Venkata, P2-4
Sivasithamparam, Nallathamby, A2-5
Sjöstedt, Hanna, A5-1
Skepast, Peeter, B3-3
Skúlason, Leifur, C3-3
Smaavik, Tone Fallan, A3-3
Snæbjörnsson, Jónas Þór, C1-1, C1-4
Sorensen, Kenny Kataoka, A1-5
Steenfelt, J.S., B5-4
Stenfeldt, Fredrik, P5-3
Stephens, Isaac Jed, B2-4
Strand, Stein-Are, B1-5, D2-2
Suominen, Mikko, P3-2
Svedholm, Christoffer, A1-6
Svensson, Mats, D2-1
Sævarsdóttir, Þorbjörg, C4-2
Sørensen, Carsten Steen, C4-1
Sørensen, Kenny Kataoka, B5-1, P4-14
Sørensen, Pia Hald, P4-2
Sørensen, Søren Peder Hyldal, A1-2, P6-1
Tankéré, Marie, B2-5
Tefera, Tewodros, A2-4
Thakur, Vikas, B1-5, A3-1, B3-5, A4-1, B1-6, D2-2
Theßeling, Bernd, P2-3
Thorarinsson, Andres, A2-2
Thorsen, Torben, P4-1
Torgersrud, Ø P4-15

Toromanovic, Jasmina, P4-9
Trafford, Andy, B3-2
Trankjær, Helle, B5-1
Tvedt, Grete, D2-5
Tönts, Taavi, B3-3
Úlfarsson, Jón Smári, C3-3
Vallas, Ivo, B3-3
Valsson, Sigurður Már, B1-3
van Baars, Stefan, P4-5
van Keßel, Marie-Therese, P2-3
Vanberg, Maria, A2-4
Vangelsten, B.V., A3-2
Vanneste, Maarten, C1-6
Veimo, Ingunn, D2-4
Viking, Kenneth, B1-4
Viklund, Margareta, B1-5, D2-2
Watn, Arnstein, B2-5
Wefer, Maik, D1-1
Wennermark, Marcus, C1-2, P5-2
Wisén, Roger, C1-2, C1-3, C2-5, P5-1, P5-2
Wood, Judith, C3-5
Xiang, Yu, B2-2
Yang, Shaoli, B5-2
Zania, Varvara, C2-1, P1-2
Zeinali, Amin, B4-4, P3-6
Zetterlund, Miriam S., A5-4
Zhussupbekov, Askar, P2-8

Conferens Sessions

A1-1 Test of bored piles and the outcome of the Danish standard for designing bored piles
Morten Schousboe Rasmussen
Züblin A/S, Trige, Denmark

A1-2 Small-displacement soil-structure interaction for horizontally loaded piles in sand
Søren Peder Hyldal Sørensen, Anders Hust Augustesen
COWI A/S, Aalborg, Denmark

A1-3 Is it reasonable to reduce the shaft resistance for bored piles?
Jannie Knudsen
COWI A/S, Vejle, Denmark

A1-4 Tensile capacity of steel pipe piles drilled in the bedrock
Rosa Marja Margareet Siren, Leena Katariina Korkiala-Tanttu
Aalto University, Espoo, Finland

A1-5 A Case Study of heave of pile-supported structures due to pile driving in heavily over consolidated very high plasticity palaeogene clay
Kenny Kataoka Sorensen, Tobias Horlykke, Belinda Dedenroth Pedersen
Aarhus University, Aarhus C, Denmark

A1-6 Analysis of inclined piles in settling soil
Fredrik Resare1, Anders Beijer Lundberg2, Christoffer Svedholm1
1Royal Institute of technology, Stockholm, Sweden
2ELU Konsult AB, Stockholm, Sweden

B1-1 In situ detection of sensitive clays – Part I: Selected test methods
Rolf Sandven1, Alberto Montafia1, Anders Samstad Gylland1, Kristoffer Kåsin2, Andi Pfaffhuber2, Mike Long3
1Multiconsult, Trondheim, Norway
2Norwegian Geotechnical Institute, Oslo, Norway
3University College Dublin (UCD), Dublin, Ireland

B1-2 In situ detection of sensitive clays – Part II: Results
Rolf Sandven1, Alberto Montafia1, Anders Samstad Gylland1, Kristoffer Kåsin2, Andi Pfaffhuber2, Mike Long3
1Multiconsult, Trondheim, Norway
2Norwegian Geotechnical Institute, Oslo, Norway
3University College Dublin (UCD), Dublin, Ireland

B1-3 Detecting quick clay with CPTu
Sigurður Már Valsson
Molde, Norway

B1-4 Influence of Operator Procedures on Obtained Accuracy in CPTu Testing
Kenneth Viking1, Caesar Kardan2, Leyla Nik3, Stefan Larsson4
1NCC Teknik, Solna, Sweden
2Grontmij, Sweden
3Geosigma, Sweden
4KTH, Sweden

B1-5 A procedure for the assessment of undrained shear strength profile of soft clays
Vikas Thakur1, Odd Arne Fauskerud2, Vidar Gjesvik3, Stein Christensen4,
Frode Oset5, Steinar Nordal1, Margareta Viklund6, Stein-Are Strand7
1NTNU, Trondheim, Norway
2Multiconsult, Norway
3NGI, Norway
4SINTEF, Norway
5Norwegian Public Roads Administration, Norway
6Norwegain National Rail Administration, Norway
7Norwegian Water Resources and Energy Directorate, Norway

B1-6 Sample disturbances in block samples on low plastic soft clays
Helene Alexandra Amundsen, Vikas Thakur, Arnfinn Emdal
NTNU, Trondheim, Norway

C1-1 Effects of soil-structure interaction on the excitation and response of RC buildings subjected to strong-motion
Jónas Þór Snæbjörnsson1, Fjóla Guðrún Sigtryggsdóttir2,
Benedikt Halldórsson2
1Reykjavik University, Reykjavík, Iceland
2University of Iceland, Reykjavík, Iceland

C1-2 ERT and seismic refraction tomography test at Äspö Hard Rock Laboratory
Marcus Wennermark, Torleif Dahlin, Roger Wisén, Mathias Ronczka
Lund University, Lund, Sweden

C1-3 Refraction seismic for mapping of limestone surface in a tunnel project in Copenhagen
Roger Wisén1, Lars Christiansen Bagger2, Mikael Jorgensen3,
Morten Elton Jensen4
1Rambøll/Lund University, Copenhagen, Denmark
2Rambøll, Denmark
3Niras, Denmark

4Hofor, Denmark

C1-4 On the HVSR characteristics at Icelandic strong-motion stations

Benedikt Halldórsson1, Jónas Þór Snæbjörnsson2, Cristian Olivera1,
S. Rahpeyma1, Símon Ólafsson1, Russel A. Green3
1University of Iceland, Reykjavík, Iceland
2Reykjavik University, Reykjavík, Iceland
3Virginia Polytechnic Insititute and State University, Blacksburg, USA

C1-5 Effects of measurement profile configuration on estimation of stiffness profiles of loose post glacial sites using MASW

Elín Ásta Ólafsdóttir, Bjarni Bessason, Sigurður Erlingsson
University of Iceland, Reykjavík, Iceland

C1-6 Impact of data acquisition parameters and processing techniques on S-wave velocity profiles from MASW - Examples from Trondheim, Norway

Guillaume Sauvin1, Peter O'Connor2, Shane O'Rourke2,
Maarten Vanneste1, Mike Long3, Jean-Sebastien l'Heureux1,
Yvonne O'Connell2, Tony Lombard2
1Norwegian Geotechnical Institute, Oslo, Norway
2Apex Geoservices, Wexford, Ireland
3University College Dublin, Dublin, Ireland

D1-1 Physical modeling and numerical analyses of vibro-driven piles with evaluation of their applicability for offshore wind turbine support structures

Aligi Foglia, Martin Kohlmeier, Maik Wefer
Fraunhofer Institute for Wind Energy and Energy System Technology (IWES), Hannover, Germany

D1-2 Influence of deviatoric stress dependent stiffness on settlement trough width in 2D and 3D finite element modelling of tunnelling

Nicolas Gilleron1, Emmanuel Bourgeois1, Adrien Saitta2
1Université Paris Est, Marne La Vallée, France
2EGIS, Paris, France

D1-3 Bearing Capacity, Comparison of Results from FEM and DS/EN 1997-1 DK NA 2013

Bjørn Staghøj Knudsen1, Niels Mortensen2
1COWI A/S, Aarhus C, Denmark
2nmGeo, Allerød, Denmark

D1-4 On numerical models for anisotropy of rocks
Henok Mekonnen Kassa1, Steinar Nordal2
1Statoil ASA, Oslo, Norway
2Norwegian University of Science and Technology, Trondheim, Norway

D1-5 Interpretation of Danish Chalk Design Parameters Applicable to Foundation Design
Lindita Kellezi, Hans Denver, Olsi Koreta
Geo, Kgs. Lyngby, Denmark

D1-6 Modelling of Earth Pressure from nearby Strip Footings on a Free & Anchored Sheet Pile Wall
Hans Denver, Lindita KelleziGeo,
Kgs. Lyngby, Denmark

A2-1 Contributions of Janbu and Lade as applied to Reinforced Soil
Peter Hoffman
University of Colorado Denver, Denver, Colorado, USA
A2-2 New Developments in On-line Monitoring of Geotechnical Data
Andres Thorarinsson1, Tony Simmonds2
1Vista Data Vision / Vista Engineering, Reykjavik, Iceland
2Geokon, Inc., Lebanon, USA

A2-3 Laboratory study on two-dimensional image analysis as a tool to evaluate degradation of granular fill materials
Elin Bergliv, Tommy Edeskar
Luleå technical university, Luleå, Sweden

A2-4 Effect of pile sleeve opening and length below seabed on the bearing capacity of offshore jacket mudmats
Maria Vanberg1, Tewodros Tefera2, Annette Jahr2
1Kværner Jacket Technology, Oslo, Norway
2Kvaerner Jacket Technology AS, Oslo, Norway

A2-5 3D FE tool for time dependent settlement predictions
Hans Petter Jostad1, Nallathamby Sivasithamparam1, Anders Rosenquist af Åkershult2, Yunhee Kim1, Suzanne Lacasse1
1NGI, Oslo, Norway
2Vianova GeoSuite AB, Stockholm, Sweden

B2-1 OATV for strength estimations in Copenhagen Limestone
Natasa Katic1, Rasmus Foldager2, Rémi Chalmas2, Helle Foged Christensen2
1Geo, Kgs., Lyngby, Denmark
2Geo, Kgs. Lyngby, Denmark

B2-2 A preliminary attempt towards soil classification chart from total sounding
Eigil Haugen1, Samson Abate Degago2, Ole Vidar Kirkevollen2, Daniel Nigussie2, Yu Xiang1
1Norwegian Public Road Administration, DRAMMEN, Norway
2Norwegian Public Roads Administration, Trondheim, Norway

B2-3 Preliminary results from a study aiming to improve ground investigations data
Bruno di Buò, Marco d'Ignazio, Juha Selänpää, Tim Länsivaara
Tampere University of Technology, Tampere, Finland

B2-4 Solutions for Various Obstacles Encountered with Laboratory Piping Tests
Axel Manuel Montalvo-Bartolomei, Jamie Fitzgerald Lopez-Soto, Isaac Jed Stephens, Bryant Andrew Robbins
Engineer Research and Development Center - US Army Corps of Engineers, Vicksburg, MS, United States of America

B2-5 Determination of pull-out strength and interface friction coefficient of geosynthetic reinforcement embedded in expanded clay LWA
Joanna Gorniak1, Marie Tankéré1, Camille Barral2, Philippe Delmas2, Arnstein Watn3, Oddvar Hyrve4, Allan Dahl4
1Texinov, La Tour du Pin, France
2Cnam, Ecole SITI, Paris, France
3Sintef Building and Infrastructure, Trondheim, Norway
4Saint-Gobain Weber, Oslo, Norway

C2-1 Dynamic stiffness of horizontally vibrating suction caissons
Chiara Latini, Varvara Zania, Björn Johannesson
Technical University of Denmark, Kgs. Lyngby, Denmark

C2-2 On the design of a deep secant pile wall
Ole Kristian Lied1, Josefin Persson2, Amund Augland1
1Geovita as, Oslo, Norway
2Statens Vegevesen, Oslo, Norway

C2-3 Guldborgsund Tunnel. Operation of tunnel and drained ramps
Per Beck Laursen, Thomas Petri, Susanne Brix
Rambøll, København, Denmark

C2-4 Pore pressure reduction and settlements induced by deep supported excavations in soft clay
Jenny Langford, Gunvor Baardvik
NGI, Oslo, Norway

C2-5 Underwater ERT Surveys for Urban Underground Infrastructure Site Investigation in Central Stockholm
Torleif Dahlin, Roger Wisén
Lund University, Lund, Sweden

D2-1 GeoBIM for optimal use of geotechnical data
Mats Svensson
Tyréns AB, Helsingborg, Sweden

D2-2 An attempt towards harmonizing the Norwegian guidelines related to construction on sensitive clay
Kristian Aunaas1, Vikas Thakur2, Frode Oset1, Hanne Ottesen1, Stein-Are Strand3, Ingrid Havnen3, Trude Nyheim3, Einar Lyche3, Margareta Viklund4, Mostafa Abokhalil4, Bjorn Kristoffer Dolva1
1Norwegian Public Roads Administration, Oslo, Norway
2Norwegian University of Science and Technology, Trondheim, Norway
3Norwegian Water Resources and Energy Directorate, Norway
4Norwegian National Railways Administration, Norway

D2-3 Commercialising reclaimed materials in earthworks - guidelines for productization and the process of appending these materials in the Finnish national code of practice
Kirsi Koivisto1, Juha Forsman1, Marjo Ronkainen1, Pentti Lahtinen1, Pauli Kolisoja2, Pirjo Kuula2
1Ramboll Finland Oy, Espoo, Finland
2Tampere University of Technology, Finland

D2-4 Education of drilling personnel carrying out pile and anchor drilling in Norway - effect on work quality and new plans for education in Norway. Ingunn Veimo Structor Oslo AS, Norge
Ingunn Veimo1, Josefin Persson2
1Structor Oslo AS, OSLO, Norway
2Statens vegvesen, Oslo, Norway

D2-5 The role of communication and dissemination during the transition from geotechnical design to construction
Einar Helgason1, Grete Tvedt2, Josefin Persson2
1Veidekke Entreprenør AS, Oslo, Norway
2Statens vegvesen, Region Øst, Norway

Plenum 4 – Antonio Gens
Vice-President of the ISSMGE for Europe 2013-2017
The current status and ongoing work at ISSMGE with a special focus on the activities of the TCs

Plenum 5 – Fjóla Guðrún Sigtryggsdóttir,
NTNU, Department of Hydraulic and Environmental Engineering, Trondheim, Norway
The Icelandic National Lecture - Hydropower dams in the Land of Ice and Fire

A3-1 Landslide hazards in sensitive clays: Recent advances in assessment and mitigation strategies
Vikas Thakur1, Samson Degago2
1NTNU, Trondheim, Norway
2Norwegian Public Roads Administration, Trondheim, Norway

A3-2 Risk analyses in excavation and foundation work
B. Kalsnes, B.V. Vangelsten, U. Eidsvig
Norwegian Geotechnical Institute, Oslo, Norway

A3-3 The Refne landslide, Halden, Norway: case history and use of risk assessment
Tone Fallan Smaavik
NGI, Oslo, Norway

A3-4 Effects of extreme rainfall on geotechnical hazards in the Canadian Rocky Mountains
Emily Catherine Hunter
University of Alberta, Edmonton, Alberta, Canada

A3-5 Pore pressure response in the upper open aquifer- field investigations and modelling
Hanna Blomén
Swedish Geotechnical Institute, Gothenburg, Sweden

B3-1 Integrated analysis of ground penetrating radar and laser scanner
Timo Saarenketo
Roadscanners group, Rovaniemi, Finland

B3-2 Some recent developments on geophysical testing of peat
Mike Long1, Andy Trafford2
1University College Dublin (UCD), Dublin, Ireland
2APEX Geoservices, Ireland

B3-3 Full scale reinforced road embankment test sections over soft peat layer, Estonia
Juha Forsman1, Taavi Dettenborn1, Peeter Skepast2, Mait Mets3,
Mattias Olep3, Ivo Vallas4, Taavi Tönts4
1Ramboll Finland Oy, Espoo, Finland
2Skepast&Puhkim AS, Estonia
3AS Geotehnika Inseneribüroo G.I.B., Estonia
4Maanteeamet, Estonia

B3-4 Installation of fully grouted piezometers
Kristoffer Kåsin
NGI, Oslo, Norway

B3-5 Extended interpretation basis for the vane shear test
Anders Samstad Gylland1, Vikas Thakur2, Arnfinn Emdal2
1Multiconsult, Trondheim, Norway
2The Norwegian University of Science and Technology, Trondheim, Norway

C3-1 Foundation of a new bridge over the Göta River in Gothenburg
Kien Du-Thinh, Lennart P. A. Johansson, Fredrik Nystrom
Cowi AB, Göteborg, Sweden

C3-2 The traffic junction Lindholmsmotet in Gothenburg: An example of creative geotechnical engineering in the construction phase
Torbjörn Edstam, Anders Kullingsjö
Skanska Sverige AB, Gothenburg, Sweden

C3-3 Construction of the Sporðöldu Dam, Iceland
Björn Jóhann Björnsson1, Leifur Skúlason2, Jón Smári Úlfarsson3
1Stuðull, consulting engineers, Hafnarfjörður, Iceland
2Hnit Consulting Engineers, Reykjavik, Iceland
3Landsvirkjun, the National Power Company, Reykjavik, Iceland

C3-4 A geostatistical analysis of variations of permeability within a compacted dam core
Étienne Hébert, Jean Côté
Université Laval, Québec, Canada

C3-5 Temporary Groundwater Control for Construction of Railway Tunnels in Copenhagen
Jes Michaelsen, Judith Wood
Ramboll, Copenhagen, Denmark

A4-1 Experience and challenges in using a new pile drilling method in highly sensitive clays
Samson Abate Degago1, Steinar Giske1, Svein E. Hove1, Vikas Thakur2
1Norwegian Public Roads Administration, Trondheim, Norway
2Norwegian University of Science and Technology, Trondheim, Norway

A4-2 Reliability-based design of a monopile foundation for offshore wind turbines based on CPT data
Ida Elise Vikestad Overgård
NTNU, Trondheim, Norway

A4-3 Reliability analysis of piles and pile groups based on dynamic load testing
Jimmie Andersson, Gary Axelsson
ELU Konsult, Stockholm, Sweden

A4-4 Application of Thermal Piles in Thawing a Frozen Ground
Gowthaman Sinnathamby1, H. Gustavsson1, L. Korkiala-Tanttu1,
C.P. Cervera2, M. Koskinen3
1Geoengineering, Aalto, Finland
2Fundación Valenciaport, València, Spain
3City of Helsinki, Helsinki, Finland

B4-1 COBRA Cable Site Investigations in the Wadden Sea, Denmark
Lone Klinkby1, Rasmus Juncher2, Martin Laier1, Anne Rosborg1,
Anna Bondo Medhus1, Karsten Pedersen1
1COWI, Vejle, Denmark
2Energinet.dk, Fredericia, Denmark

B4-2 Founding on (un)known chalk in Aalborg
Caspar Thrane Leth1, Kim André Larsen1, Thomas Madsen1,
Jan Dannemand Andersen2
1COWI A/S, Aalborg, Denmark
2GEO, Brabrand, Denmark

B4-3 Field measurements of pore water pressure changes in very high plasticity stiff clays adjacent to driven piles
Thomas Rye Simonsen
Geo and Department of engineering, Aarhus University, Aarhus, Denmark

B4-4 Freezing-Thawing Laboratory Testing of Frost Susceptible Soils
Amin Zeinali1, Deniz Dagli1, Tommy Edeskar1
Lulea University of Technology, Lulea, Sweden

B4-5 Investigation into the effect of uncertainty of CPT-based soil type estimation on the accuracy of CPT-based pile bearing capacity analysis
Omar Hamza1, Angela Bellis2
1University of Derby, Derby, United Kingdom
2Atkins ltd, United Kingdom

C4-1 An integrated approach to Geotechnics and Geophysics on the Electrification Programme in Denmark
David Ross Alvin, Ole Frits Nielsen, Carsten Steen Sørensen
COWI A/S, Århus, Denmark

C4-2 Deformation Modelling of Unbound Materials in a Flexible Pavement
Þorbjörg Sævarsdóttir1, Sigurður Erlingsson2
1EFLA consulting engineers, Reykjavík, Iceland
2University of Iceland, Reykjavík, Iceland

C4-3 , Statistical analysis of thaw index for thaw weakening design purposes
Tommy Edeskar1, Adam Fredriksson1
Luleå University of Technology, Luleå, Sweden

C4-4 , Theoretical and experimental investigations of Continuous Compaction Control (CCC) systems
Johannes Pistrol1, Mario Hager1, Dietmar Adam1, Fritz Kopf2
1Vienna University of Technology, Vienna, Austria
2Fritsch, Chiari & Partner ZT GmbH, Vienna, Austria

C4-5 Strength and deformation properties of volcanic rocks in Iceland
Niels Nielsen Foged, Katrine Alling Andreassen
Technical University of Denmark, Kgs. Lyngby, Denmark

A5-1 Design of protective dolphins in demanding geotechnical conditions
Andrija Krivokapic, Hanna Sjöstedt, Nenad Davidovic
Ramboll, København S, Denmark

A5-2 On the use of vertical drains and pore pressure control for soft soil stabilization with lime/cement columns
Frode Oset1, Carl Erik Dahl2, Grethe Bodholt1
1Norwegian Public Roads Administration, Oslo, Norway
2Rambøll, Norway

A5-3 Engineering and execution of tight sheet walls
Robert Bruin
Geovita as, Oslo, Norway

A5-4 Decision-making for increased sustainability in underground construction works by use of Analytical Decision-making for increased sustainability in underground construction works using Analytical Hierarchy Process
Miriam S. Zetterlund, Magnus Eriksson
Swedish Geotechnical Institute, Gothenburg, Sweden

B5-1 Oedometer tests with measurement of internal Friction between Oedometer ring and reconstituted clay specimen
Michael Rosenlund Lodahl1, Kenny Kataoka Sørensen2, Niels Mortensen3, Helle Trankjær4
1COWI A/S and Aarhus University, Aalborg, Denmark
2Aarhus University, Department of Engineering, Aarhus, Denmark
3nmGeo, Denmark
4COWI, Aarhus, Denmark

B5-2 Study on the practices for interpretation of preconsolidation stress from oedometer tests
Priscilla Paniagua, Jean-Sebastien l'Heureux, Shaoli Yang, Tom Lunne
NGI, Trondheim, Norway

B5-3 Correlations between shear wave velocities and geotechnical parameters in Norwegian clays
Jean-Sebastien l'Heureux1, Mike Long2
1Norwegian Geotechnical Institute (NGI), Trondheim, Norway
2University College Dublin, Dublin, Ireland

B5-4 Triaxial testing of overconsolidated, low plasticity Clay Till
A. H. Augustesen, J.N. Goth, J.S. Steenfelt
COWI A/S, Kongens Lyngby, Denmark

C5-1 Climate change induced river erosion as a trigger for landslide
Gunnel Göransson1, Jim Hedfors2, Karin Odén2
1The Swedish Geotechnical Institute, Gothenburg, Sweden
2Swedish Geotechnical Institute, Gothenburg, Sweden

C5-2 Landslide risks in a changing climate, Nors River pilot study area
Karin Bergdahl, Karin Odén, Hjördis Löfroth, Gunnel Göransson, Åsa Jönsson, Ramona Kiilsgaard
The Swedish Geotechnical Institute, Gothenburg, Sweden

C5-3 Strength increase below an old test embankment in Finland
Marco d'Ignazio, Tim Länsivaara
Tampere University of Technology, Tampere, Finland

C5-4 Mechanical weathering effect on tailings
Juan Rodriguez, Tommy Edeskär, Sven Knutsson
Luleå University of Technology, Luleå, Sweden


SIMSG
ISSMGE
JTFÍ
IGS